MMM 2026

71st ANNUAL CONFERENCE ON
Magnetism and Magnetic Materials

ABSTRACT BOOK



November 2 – 6, 2026
Honolulu, Hawaii

Hilton Hawaiian Village Waikiki Beach Resort

as of October 27, 2026

www.magnetism.org

Jointly sponsored by AIP Publishing LLC
and the IEEE Magnetics Society

IEEE MAGNETICS

AIP Publishing

TU: TUTORIAL: APPLICATIONS OF MAGNETIC MICRO/NANO ROBOTS

Chair(s): C. Dennis, *National Institute of Standards and Technology, Gaithersburg, Maryland, United States*
Monday, November 2, 2026
02:30 PM-05:00 PM
Coral 3

TU-01. Electromagnetically Controllable Micro/Nanorobots for Precise Robotic Interventions and Cell Therapies

H. Choi
Department of Biomedical Engineering, University of Massachusetts Amherst, Amherst, Massachusetts, United States

Medical micro/nanorobots, often smaller than a millimeter, are designed to perform specific tasks within the human body. Integrating electromagnetic actuation systems with these robots offers unprecedented precision and innovative control methods for next-generation healthcare. This presentation introduces both tethered and untethered micro/nanorobots for precise vascular interventions and targeted cell delivery. First, I will present a microrobotic guidewire equipped with a soft magnetic steerable robot (MSR) at its tip for active neuro- and cardiovascular intervention. Supported by a human-scale electromagnetic actuation system, biplane X-ray imaging, and remote-control capabilities, this approach enables active, teleoperated guidewire and catheter navigation, thereby improving intervention precision. Second, I will discuss magnetically actuated untethered micro/nanorobots, highlighting their ability to achieve selective neurite alignment, establish neuronal connections, and perform in vitro, ex vivo, and in vivo cell delivery. For example, magnetic neurospheroid microrobots (Mag-Neurobots), which integrate primary neuronal cells with superparamagnetic iron oxide nanoparticles (SPIONs), demonstrate both morphological and functional neural connections, paving the way for the reconstruction of artificial neural networks. These advancements toward a future where electromagnetically controlled micro/nanorobots become integral clinical tools, enabling minimally invasive vascular interventions, enhanced cell therapies, and next-generation cancer treatments that bring unprecedented precision to patient care.

TU-02. Design Principles for Untethered Magnetic Microrobots in Bounded Fluid Environments

E. Evans
Elon University, Elon, North Carolina, United States

Magnetic microrobots enable the directed manipulation of micromaterials in a non-contact, tetherless manner, offering a powerful platform for remote operation within biological systems. Such devices support a range of biomedical applications, including selective capture and transport in vivo, fluid manipulation, targeted drug delivery, and the assembly or disruption of biological structures. In this tutorial, we will explore foundational principles of untethered microrobots driven by external magnetic fields in fluid environments, with particular emphasis on how magnetic torque and environmental boundary conditions combine to produce predictable motion.
We begin by distinguishing two broad modes of magnetic actuation: translation by magnetic field gradients and rotation by magnetic torque. While gradient-based pulling can transport magnetic objects, torque-driven systems provide a richer design space in which microrobot shape, magnetic anisotropy, and local boundary conditions determine function. The central challenge then is twofold: to develop microrobot geometries with high magnetic anisotropy that experience large magnetic torques, and to convert the controlled rotation that results into translation, pumping, drilling, or payload delivery in a viscous, low-Reynolds-number fluid environment.
These principles will be explored through a series of case studies. Rotating nickel microrods demonstrate how high-aspect-ratio structures can swim along a boundary through hydrodynamic symmetry breaking, enabling steerable motion as well as capture and manipulation of microbeads and cells. Soft alginate capsules containing magnetically aligned nanorods extend this surface-tumbling strategy to larger, biocompatible, deformable robots capable of navigating tissue surfaces, climbing inclines, and manipulating objects. These millirobots function as magnetically guided vessels for region-specific drug delivery on tissue surfaces, including the brain and spinal cord. Finally, magnetic microdrills show how combining magnetic force and magnetic torque can enhance transport through dense biological matrices and disrupt bacterial biofilms.
Together these devices show how careful microrobot design transforms externally applied magnetic fields into diverse, programmable behaviors for manipulating materials and delivering therapies in complex biological environments.

TU-03. Magnetic Small Scale Wireless Robots for Noninvasive Medical Applications

V. Magdanz
University of Waterloo, Waterloo, Ontario, Canada

Wireless small scale robots are promising to revolutionize conventional medical procedures such as drug delivery and surgery by providing non-invasive, highly localized action. Magnetically controlled robots are especially intriguing thanks to the ability of magnetic fields to penetrate the human body safely and easily, the response of the robots to these external rotating magnetic fields, and imaging contrast in ultrasound or X-ray. The here presented work highlights the development and in vitro and ex vivo validation of small scale magnetic robots for medical interventions such as local kidney stone dissolution, drug delivery and blood clot removal.

SESSION AA: BEYOND THE LIMITS: NEXT-GENERATION INNOVATIONS IN HARD DISK DRIVE TECHNOLOGY

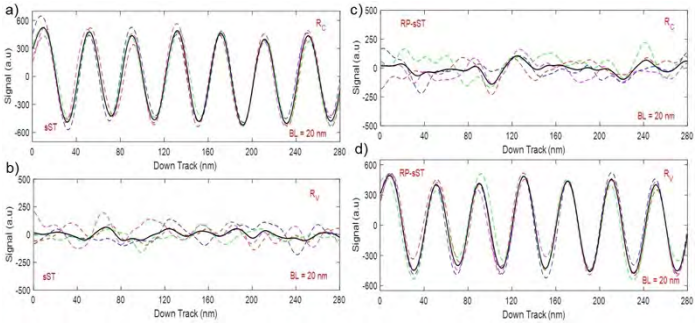
Co-Chair(s): S. Hernandez, *Seagate Technology, Bloomington, Minnesota, United States* and A. Venugopal, *Seagate Research, Seagate Technology, Edina, Minnesota, United States*
Tuesday, November 3, 2026
08:30 AM-12:00 PM
Coral 3

AA-01. Performance Limits and Design Optimization of Vector Recording

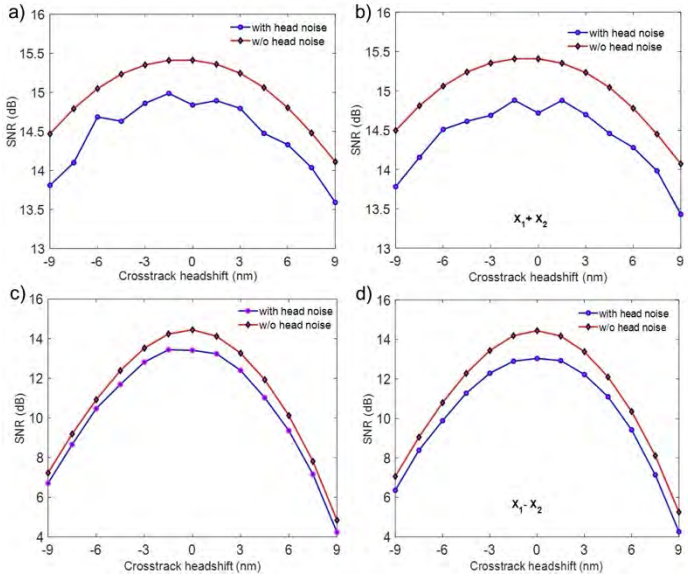
R. H. Victora, K. Hosen
ECE, University of Minnesota, Minneapolis, Minnesota, United States

The hard disk drive industry continues to demand higher data storage capacity, motivating the development of advanced technologies such as heat-assisted magnetic recording (HAMR). However, achieving areal densities beyond 4 Tb/in^2 will require improved reader resolution [1], [2]. In this presentation, vector recording is investigated as a promising solution to this challenge. A dual-reader architecture is proposed that senses both perpendicular and in-plane magnetic field components, enabling the detection of four distinct magnetization states (++, --, +-, -+) [3], [4]. Micromagnetic simulations demonstrate that the proposed vector reader achieves resolution comparable to conventional readers, with similar signal-to-noise ratio (SNR), PW50, and frequency response. Crosstalk between the orthogonal sensing components is shown to be minimal, ensuring independent signal detection as shown in Fig. 1 [4]. To assess practical feasibility, alternative reader configurations with 45° and 135° biasing are introduced, addressing biasing challenges associated with 0° and 90° designs, and are shown to produce equivalent performance. In addition, the fundamental limits of vector recording are systematically analyzed by incorporating key system-level effects, including reader magnetic noise, inter-track interference, write synchronization, and transition-induced crosstalk. Results indicate that thermally induced magnetization fluctuations in the reader introduce a consistent SNR degradation of approximately 1–1.5 dB as shown in Fig. 2, which still provide an inherent SNR advantage of about 3 dB compared to conventional TDMR. Overall, this work demonstrates that vector recording offers a scalable and robust pathway toward achieving ultra-high areal density in next-generation HAMR systems.

[1] R. H. Victora and P. Huang, “Simulation of heat-assisted magnetic recording using renormalized media cells,” IEEE Trans. Magn., vol. 49, no. 2, pp. 751–757, Feb. 2013.
[2] M. T. Kief and R. H. Victora, “Materials for heat-assisted magnetic recording,” MRS Bull., vol. 43, no. 2, pp. 87–92, 2018.
[3] M. F. Erden, W. Eppler, S. Granz, and S. Hernandez, “Vector recording: A new read process at ultra-high tpis,” presented at the IEEE TMRC Conference, 2023.
[4] K. Hosen, M. F. Erden, and R. H. Victora, “Vector recording: Advancing areal density in hamr with innovative read head design,” *IEEE Transactions on Magnetics*, vol. 62, no. 3, pp. 1–8, 2026



Readback signals of conventional (Rc) and vector (Rv) reader for different single tone writing patterns; a) and b) same single tone on both tracks, c) and d) opposite polarity on each track



SNR characteristics: (a) R_c with same single tone on both tracks (sST), (b) 45° and 135° readers with sST, (c) R_v with reverse polarity (RP-sST), and (d) 45° and 135° readers with RP-sST

AA-02. Developments in Three-Dimensional Magnetic Recording

S. Greaves[1], H. Suto[2], Y. Nakamura[3], Y. Kanai[4]
[1]Tohoku University, Sendai, Japan, [2]NIMS, Tsukuba, Japan, [3]Ehime University, Matsuyama, Japan, [4]Niigata Institute of Technology, Kashiwazaki, Japan

In this talk we will report on the progress of our JST-CREST project to develop a three-dimensional magnetic recording system. The aim of the project is to develop dual structure magnetic recording media that can support areal densities exceeding 4 Tbit/in^2.

The basic structure of the recording media is: SUL / Seed layer(s) / RL1 / IL / RL2, where RL1 and RL2 are the storage structures and are based on FePt [1]. In the initial media both RL1 and RL2 were 6 nm thick and the IL was 3 nm thick.

Media parameters obtained from experiments were used to create a medium model for use in micromagnetic simulations of recording. The most influential parameters were: the average grain size $\langle D \rangle$, the Curie temperature distribution among grains σT_c, and the difference in Curie temperature between RL1 and RL2.

A grain switching probability (GSP) model was trained using the results of micromagnetic simulations and used to study the effect of σT_c and $\langle D \rangle$ on the user areal density (UAD). Fig. 1 shows an example for RL2, where the areal density of recorded bits was 2.07 Tbit/in^2 (12 nm bit length, 26 nm track width) [2]. In the absence of readback errors the UAD would also be 2.07 Tbit/in^2, but as the number of readback errors increases the UAD decreases. Fig. 1 shows that the UAD only exceeded 2 Tbit/in^2 when the average grain size was below 5.3 nm and σT_c was less than 24 K (T_c was 620 K).

The situation for RL1 was much worse, given the increased distance between RL1 and the read head, and the maximum UAD for RL1 was 1.6 Tbit/in^2, assuming perfect deconvolution of the waveforms from RL1 and RL2.

A further problem was that at high linear densities the signal from RL1 became less than the noise from RL2. To solve this problem the medium was redesigned with a focus on boosting the signal from RL1. First, the thickness of RL1 was increased to 8 nm and a high M_s capping layer added to the upper 4 nm of RL1. At the same time the thickness of RL2 was decreased to 4 nm and the interlayer thickness decreased to 1 nm.

The noise (and signal) from RL2 could also be reduced by increasing the non-magnetic grain boundary thickness in RL2, or by heating the medium during readback to temporarily lower M_s of RL2 relative to that of RL1. Taking account of Curie temperature distributions, the required difference in T_c between RL1 and RL2 was estimated to be at least 140 K in order to prevent data in RL1 being erased when recording on RL1. This assumes that RL2 has the lower Curie temperature, which is consistent with experiments.

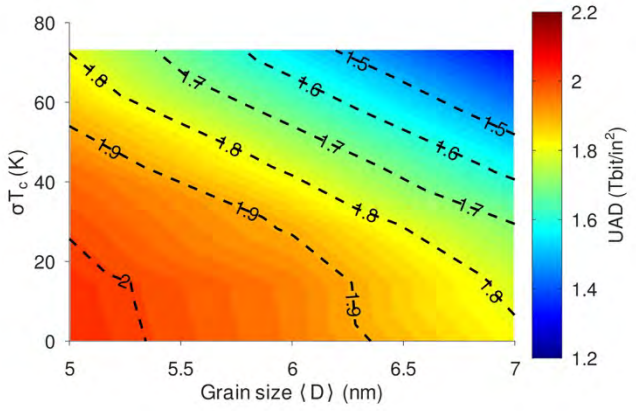
Next, the bit aspect ratio (BAR) was optimised. For a given areal density there should be a BAR at which the SNR is maximised. The readback signal decreases as the linear density increases (bit length decreases), but shorter bits can be wider, which may allow the use of a wider reader. At a target areal density of 2 Tbit/in^2 the optimum BAR for RL1 was found to be 1.9, whereas it was 2.7 for RL2.

The GSP model was retrained using data from tracks written on the new media design and the UAD calculated. Fig. 2 shows the results for the old (6 nm / 3 nm / 6 nm) and the new (8 nm / 1 nm /4 nm) media. The average grain size was

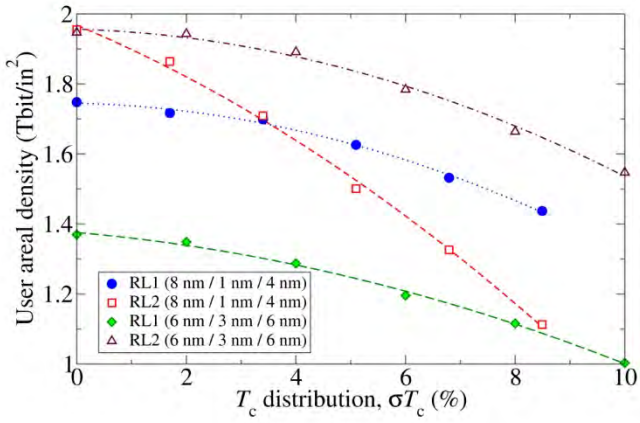
6 nm and the bit length was 12 nm for the old media and 13 nm for the new media. The UAD of RL1 was about 0.4 Tbit/in^2 higher when using the new media. In the absence of Curie temperature distributions the UAD of RL2 was about the same for both media, but the new media was more susceptible to σT_c. This is likely a result of the decreased thickness and lower energy barrier of RL2 in the new media. Nevertheless, a total UAD of 3.4 Tbit/in^2 should be possible with the new media with σT_c of 3.4%.

Signal processing techniques have also been developed to deal with the convoluted signals from RL1 and RL2 [3].

[1] P. Tozman, S. Isogami, I. Suzuki et al., Acta Materialia 271, 119869, (2024).
[2] S. J. Greaves, H. Suto, Y, Nakamura and Y. Kanai, IEEE Trans. Magn. 60(9), 3200605-1-5, (2024).
[3] Y. Nakamura, M. Nishikawa, S. J. Greaves, Y. Kanai and Y. Okamoto, Jpn. J. Appl. Phys. 63, 08SP11-1-3, (2024).



User areal density (UAD) of RL2 as a function of average grain size and Curie temperature distribution among grains.



User areal density vs. Curie temperature distribution for two different media structures with $\langle D \rangle$ = 6 nm.

AA-03. Advances in Heat-Assisted Magnetic Recording (HAMR) for High-Capacity Data Storage and Beyond HAMR Technologies

Y. Quessab
Recording Media Operations, Seagate Technology, Fremont, California, United States

The recent widespread adoption of artificial intelligence applications, and the increased use of cloud computing and video streaming have accelerated global data generation beyond the capacity of traditional data storage technologies. Heat-assisted magnetic recording (HAMR), a next-generation of magnetic data storage technology has allowed Seagate to deliver mass-capacity data storage solutions to address today's challenges. In 2020, Seagate demonstrated 20 TB hard disk drives followed by the first shipments of 30 TB+ HAMR drives in 2023. Recently, Seagate announced the delivery to hyperscale cloud providers of HAMR drives with a capacity of up to 44 TB. HAMR lies at the intersection of integrated photonics, plasmonics and high-anisotropy FePt granular media. The increase in the reported data storage capacities has been driven by improvements in each of these areas. In this presentation, we will focus on the enhancement of the magnetic and thermal properties of HAMR media that enabled the increase of areal density capacity. We will also discuss the remaining challenges of HAMR and the next generation of recording technologies beyond HAMR, such as all-optical magnetic recording, aimed at achieving capacities of 10 TB per disk.

AA-04. Thermal spin-torque heat-assisted magnetic recording for large data storage in HDDs

S. Isogami[1], Y. Sasaki[1], Y. Fan[2], Y. Kubota[3], J. Gadbois[2], K. Hono[1], Y. K. Takahashi[1, 4]
[1]NIMS, Tsukuba, Japan, [2]Advanced Technology Development, Seagate Technology, Bloomington, Minnesota, United States, [3]Recording Media Organization, Seagate Technology, Fremont, California, United States, [4]RIEC, Tohoku University, Sendai, Japan

The hard-disk-drives (HDDs) community has made tremendous efforts to develop revolutionary recording technologies to break recording density, providing cost efficient solutions to large volume data storage. Many research and developments have been extensively performed to reduce the grain diameter and its distribution. Furthermore, heat-assisted magnetic recording (HAMR) has been developed as a breakthrough technology to achieve

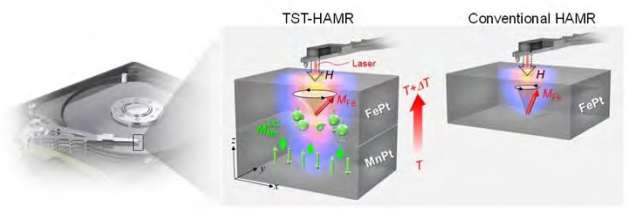
both high thermal stability and writability in the FePt granular media. The multi-level recording in HAMR has been proposed recently [1], as one of the approaches to achieve the loadmap of data capacity that is forcasted by ASRC[2].

To enhance recording reliability, it is desirable to reduce the laser heating temperature in FePt grains of the media. Here, we focus on utilizing the temperature gradient (ΔT) to exert the spin-transfer torques (STT) on the magnetization of FePt, that is inevitably formed in the HAMR media by the heating of laser pulses. The ΔT works as a driving force of the magnetiztion switching, in addition to the conventional thermally activated (TA) switching. This is the magnetic recording based on the hybrid effect of STT and TA, leading to an advanced thermal spin-torque (TST)-HAMR media in the future [3].

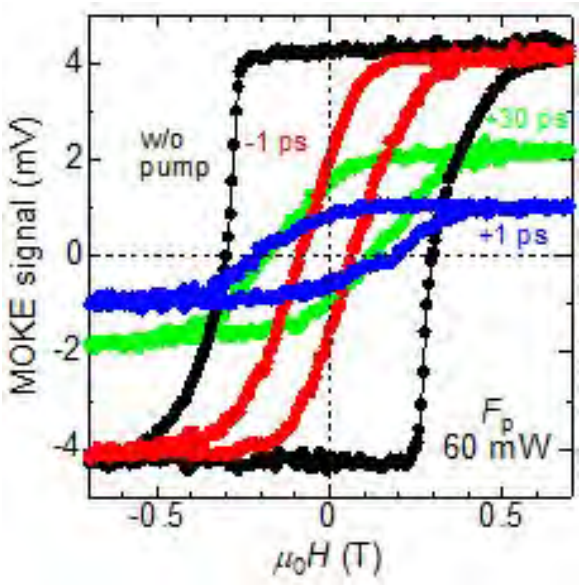
Figure 1 illustrates the principles of TST-HAMR, as compared to the conventional HAMR. Laser irradiation induces ΔT along out-of-plane direction in the antiferromagnetic MnPt layer, which generates the spin current, resulting in more efficient magnetization switching owing to the STT. The spin current injection from MnPt to FePt layers is attributed to the spin-Seebeck effect (SSE)[4-8]. That is, the spin momentum (σ) with z-orientation originating from the possible uncompensated magnetic moment at the MnPt/FePt interface, represented by the green allows with balls in Fig. 1, could be transferred by ΔT. Therefore, the efficient magnetization switching is not expected for the conventional system without MnPt layer.

Figure 2 shows the representative results of pump-probe MOKE hysteresis loops with various delay time (Δt) and pump power of 60mW. We verify that the MOKE hysteresis loop without pump pulse (black symbols) agrees with the magnetic hysteresis behavior measured using magnetic properties measurement system. In contrast, the loops are dramatically impacted by pump pulses, showing dependence on the Δt: similar signal with remarkably small H_c at Δt = -1 ps (red symbols), and remarkably small MOKE signal with large H_c at Δt = +1 ps (blue symbols), followed by the increase of MOKE signal with the decrease of H_c obtained at Δt = 30 ps (green symbols). Magnetization value of FePt, i.e., MOKE signals in Fig. 2, is governed by the temperature in general. Therefore, magnetization decreases by ~75 % of initial value at Δt = +1 ps, suggesting the highest temperature in the FePt layer induced by the pump laser heating. Then the magnetization starts recovery to the initial magnitude, suggesting heat dissipation from the FePt layer. It is inferred from the measurement that the magnetization is fully recovered before the irradiation of next pump pulse. On the other hand, H_c of the FePt layer adjacent to the MnPt spin source layer is governed by hybrid phenomena with STT and TA, which is the specific characteristic in TST-HAMR media. Although the details are discussed in the talk, the additional STT component was estimated to be approximately 36% of the entire driving force of magnetization switching. These results show the promising technology to reduce the laser heating temperature, but maintaining the recording efficiency of the conventional HAMR.

[1] Tozman *et al*., Acta Mater. 271 (2024) 119869.
[2] Roddick et al., 2022 IEEE 33rd Magnetic Recording Conference.
[3] Isogami *et al*., Acta Mater. 286 (2025) 120743.
[4] Uchida *et al*., Nature 455 (2008) 9.
[5] Seki *et al*., Phys. Rev. Lett. 115 (2015) 266601.
[6] Wu *et al*., Phys. Rev. Lett. 116 (2016) 097204.
[7] Gray *et al*., Phys. Rev. X 9 (2019) 041016.
[8] Rezende *et al*., Phys. Rev. B 93 (2016) 014425.



Concept of the thermal spin-torque heat-assisted magnetic recording (TST-MAHR) with the $L1_0$-MnPt / $L1_0$-FePt bilayer system, together with the conventional HAMR.



Magnetic hysteresis loops measured via pump-probe MOKE with various delay time (*Dt*) and pump power of 60 mW. The loop without pump laser is shown by black symbols.

AA-05. Atomistic Modeling of Picosecond All-Optical Magnetization Switching

R. Hao, R. H. Victora
University of Minnesota, Minneapolis, Minnesota, United States

Recently, ultrafast magnetization switching driven by an ultrashort laser pulse has attracted much attention [1]-[4], partly owing to its potential application to massive data storage. Here using an atomistic spin model, we studied the magnetization dynamics in a 3-layer structure by engineering the temperature pulses applied to the free and reference layers. Like some previous work, our free layer is switched to parallel (antiparallel) direction by the spin-polarized electrons from the demagnetization (remagnetization) process of the reference layer [4]. Currently most experimental and theoretical studies are based on continuous films [2]-[3], which can be easily designed to be thermally stable, as their Curie and blocking temperatures are similar. However, data storage applications would require discrete nanoscale grains, which have very different Curie and blocking temperatures, creating difficulties for all-optical switching. Here we examined free and reference layers with a 6 nm x 6 nm cross-section.

The simulation results show that, for P-to-AP switching (Fig. 1), we first heat and nearly demagnetize both layers; then as the reference layer starts to remagnetize, it applies downward STT to free layer, leading to an AP state. Stability is reached at ~20 ps. For AP-to-P switching, we utilize the reference layer's demagnetization to apply a strong upward STT pulling $M_{z,free}$ from ~0 to a large positive value, as shown in Fig. 2(a). This is critical because $M_{z,free}$ needs to be large enough to remain positive against downward STT and additional thermal noise from the reference layer's remagnetization. Fig. 2(b) shows it takes ~70 ps for free layer to stabilize against the adverse STT.

Technologically relevant materials are employed that have no rare earths and are thermally stable. The interactions considered are exchange coupling, anisotropy, thermal magnetic noise, and STT with field-like ratio 0.3.

[1] I. Radu, K. Vahaplar, C. Stamm *et al. Nature* 472, 205–208 (2011)
[2] J. Igarashi, W. Zhang, Q. Remy *et al. Nat. Mater.* 22, 725–730 (2023)
[3] Q. Remy *Phys. Rev. B* 107, 174431 (2023)
[4] H. Singh, A. Anadón, J. Igarashi *et al. Phys. Rev. Lett.* 136, 056701 (2026)

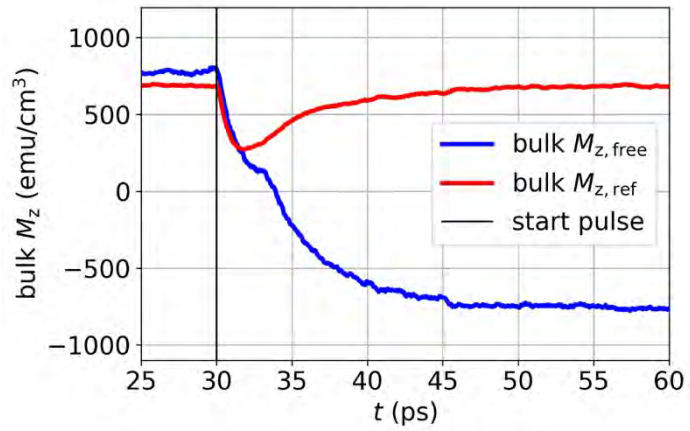


Fig. 1 Simulated P-to-AP switching dynamics under specified temperature pulses. The laser pulse is assumed to be applied from free layer side.

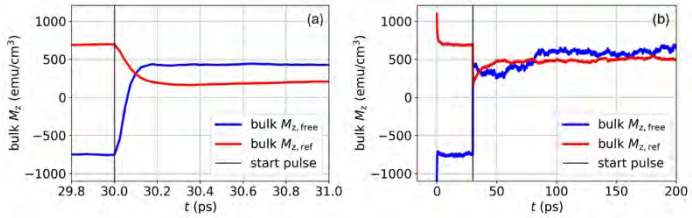


Fig. 2 Simulated AP-to-P switching dynamics. (a) is zoom-in of (b).

AA-06. Thermal stability in dual-layer granular FePt media for heat assisted magnetic recording

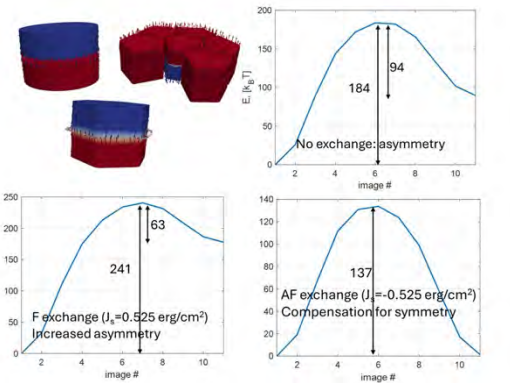
A. Bolyachkin[2], J. Duan[1], H. Sepehri-Amin[2], V. Lomakin[1]
[1]ECE, University of California, San Diego, La Jolla, California, United States, [2]National Institute of Material Science, Tsukuba, Japan

Multi-layer recording using dual-layer granular FePt media has been proposed for extending areal density of heat assisted magnetic recording. In such media, the two magnetic layers are intended to be written and read independently. However, interlayer interactions arising from magnetostatic and exchange coupling as well as grain composition can significantly influence the long-term thermal stability. A quantitative understanding of these effects is essential for reliable multi-layer operation.

In this work, we analyze thermal stability of dual-layer granular FePt media by explicitly accounting for interlayer magnetostatic and exchange coupling between separated

recording layers. Thermal stability is evaluated through micromagnetic calculations of energy barriers and attempt frequencies. We examine how layer separation, grain-to-grain coupling, anisotropy, and microstructural variability modify the effective energy landscape and dynamical prefactors governing long-term stability. The results reveal that even weak interlayer coupling can lead to non-negligible modifications of both energy barriers, thereby altering retention times relative to isolated-layer predictions. Additionally, lateral interactions between surrounding grains can significantly affect the energy barriers, combined with the vertical interactions betweens the dual-layer media. These findings show the necessity of incorporating interlayer interactions and grain composition in the design and modeling of dual-layer granular FePt media and provide guidance for optimizing thermal stability in potential multi-layer magnetic recording systems.

Figure 1 shows the types of dual-layer grain structures considered in the characterization of the thermal stability. The figure also shows energy barriers and minimal energy paths for various cases of ferromagnetic (F) and anti-ferromagnetic (AF) coupling between the layers of dual-layer FePt media. The AF coupling allows balancing the barriers between different recorded states thus increasing the overall thermal stability.



Dual-layer FePt granular media considered as well as minimal energy paths and energy barriers for ferromagnetic (F) and anti-ferromagnetic (AF) coupling between the layers.

AA-07. The effect of reader undershoot on HAMR pre-channel and ADC performance

N. A. Natekar, T. Olson, G. Baiao De Albuquerque, V. Le, K. Tanahashi
Western Digital, San Jose, California, United States

HAMR is accelerating towards achieving areal density capacity (ADC) beyond 4 Tbpsi [1] thanks to efforts related to writer design improvement [2], change in Near Field Transducer (NFT) designs for increase in reliability and thermal gradients [3, 4], media designs for lower noise [5, 6], and improvements in reader design [7, 8]. The reader's shield structures, however, lead to undershoots within the vertical response function (Fig. 1) and undershoot impacts performance negatively. Our modeling study utilizes an ideal writing process, where all grains in a bit's low-frequency region point in the same direction; this removes any noise due to misaligned grains. We note that this amplifies the effects of undershoot; as writing becomes less ideal, the impact of undershoot lessens. We then isolate undershoot's effect by artificially, selectively eliminating it from the sensitivity function. Two different, independent recording models are used to study the effect of reader undershoot on pre-channel parameters (like DCSNR) and ADC. Fig. 2 shows the SNR analysis with different readers with vertical undershoot eliminated in the crosstrack (CT) and /or downtrack (DT) directions. A Gaussian reader is taken as the reference, which is similar to the realistic reader design, with all undershoot removed. When undershoot is present in both the DT and CT directions, DCSNR falls by ~ 2dB as indicated by both models. This loss arises from a decrease in signal power (SP) and an increase in noise power (NP). A 2 dB loss in DCSNR can translate to ~ 12% loss in ADC despite a perfect writing process, which clarifies the potential impact of undershoot as writing becomes more ideal. Eliminating undershoot only for |DT| > 20nm primarily increases signal, whereas eliminating undershoot only for |CT| > 20nm primarily decreases noise. This behavior, and impacts on other pre-channel parameters and ADC will be covered at the conference

[1] L. Xu, R. M. Brockie, N. A. Natekar and E. Roddick, doi: 10.1109/TMAG.2022.3221782
[2] Y. Wang, Y. Xu, Y. Chen, et.al., doi: 10.1109/TMAG.2021.3112495
[3] A. Datta and X. Xu, doi: 10.1109/TMAG.2016.2595496
[4] S. Bhargava and E. Yablonovitch, doi: 10.1109/TMAG.2014.2355215
[5] N. A. Natekar, P. -O. Jubert, T. Olson, et.al., doi: 10.1109/TMAG.2025.3597238
[6] N. A. Natekar, W. Tipcharoen, and R. H. Victora, doi: 10.1016/j.jmmm.2019.165253
[7] X. Liu et al., doi: 10.1109/TMRC56419.2022.9918608
[8] K. Hosen, M. F. Erden and R. H. Victora, doi: 10.1109/TMAG.2025.3612279

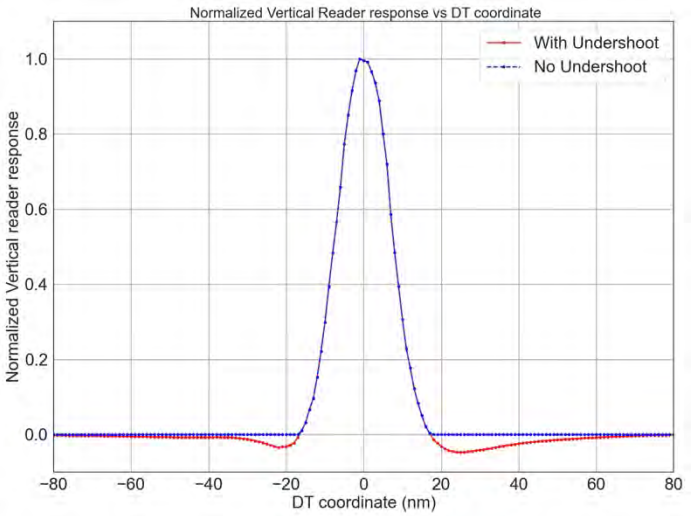


Fig. 1 Normalized Vertical reader sensitivity functions with and without undershoot vs DT coordinate

Physics-Agnostic Model

Reader	Gaussian	Reader with Und	Reader with No Und	Reader with No Und |CT| > 20nm	Reader with No Und |DT| > 20nm
DCSNR	21.7 dB (Ref)	-2.3 dB	-0.33 dB	-1.2 dB	-1.3 dB
DCSP	67.47	-0.53 dB	-0.01 dB	-0.53 dB	+0.23 dB
DCNP	0.452	+1.7 dB	+0.32 dB	+0.69 dB	+1.5 dB

Reader	Gaussian	Reader with Und	Reader with No Und	Reader with No Und |CT| > 20nm	Reader with No Und |DT| > 20nm
DCSNR	26.0 (Ref)	24.2 (-1.8dB)	26.0 (0dB)	25.3 (-0.66dB)	24.8 (-1.1dB)
DCSP	2.9	2.6 (-0.47dB)	2.8 (-0.16dB)	2.6 (-0.48dB)	2.7 (-0.31dB)
DCNP	0.007	0.01 (+1.31dB)	0.007 (-0.16dB)	0.008 (+0.18dB)	0.009 (+0.79dB)

Fig. 2 DCSNR, DC Signal Power (DCSP) and DC Noise Power (DCNP) variation in absolute terms and dB, based only on vertical reader response and variation in reader undershoot

SESSION AB: MAGNETIC MATERIALS DESIGN AND DISCOVERY

Chair(s): H. Zeng, *Physics, University of Buffalo, Buffalo, New York, United States*

Tuesday, November 3, 2026

08:30 AM-12:00 PM

Coral 5

AB-01. Rare-Earth-Free Permanent Magnet Discovery through Quantum Simulations and Machine Learning

J. Chelikowsky[1, 2]

[1]*Physics, University of Texas at Austin, Austin, Texas, United States,* [2]*Oden Institute, University of Texas at Austin, Austin, Texas, United States*

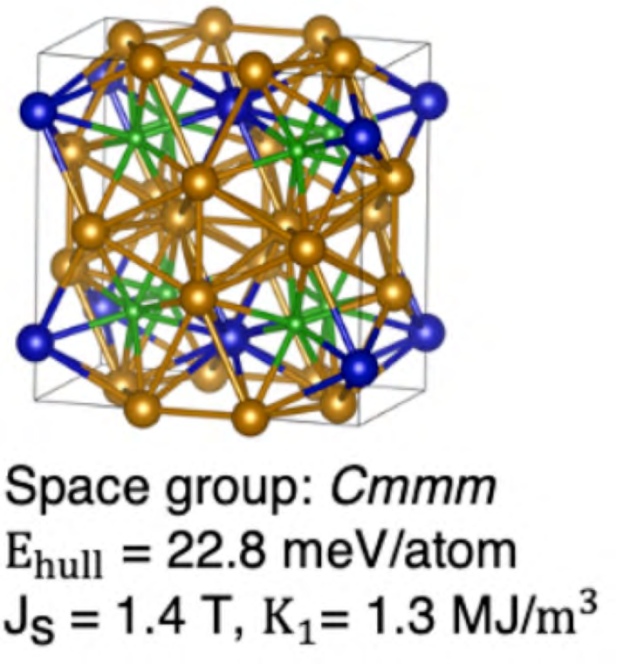
Rare-earth permanent magnets, such as $Nd_2Fe_{14}B$ and $SmCo_5$, underpin technologies that convert mechanical and electrical energy, owing to their exceptional combination of high saturation magnetization, large magnetocrystalline anisotropy, and high Curie temperature. However, their reliance on scarce rare-earth elements raises concerns regarding cost, supply security, and long-term sustainability. A central challenge in permanent magnet research is therefore to identify rare-earth-free materials with magnetic performance comparable to $Nd_2Fe_{14}B$ and $SmCo_5$.

In this work, we explore ternary Fe-Co-X compounds (X = B, C, Si, P, S), guided by structure–property relationships that seek to combine the high saturation magnetization of Fe-Co alloys with the strong magnetocrystalline anisotropy enabled by low-symmetry crystal structures. Although Fe-Co alloys possess large magnetic moments, their commonly observed cubic phases exhibit insufficient anisotropy for hard-magnet applications. We show that incorporation of light main-group elements can stabilize new non-cubic Fe-Co-X phases-such as orthorhombic or tetragonal structures that substantially enhance magnetic anisotropy without sacrificing magnetization.

A central result of this study is the prediction and experimental realization of the previously unknown compound Fe_3CoB_2. Synthesized via rapid non-equilibrium processing (rapid quenching), Fe_3CoB_2 crystallizes in an orthorhombic structure and exhibits a large uniaxial magnetocrystalline anisotropy (~1.2 MJ m^{-3} at 300 K), together with a high saturation magnetization (~1.4 T) and a Curie temperature near 750 K—values approaching the magnetic performance of $Nd_2Fe_{14}B$ Structural and magnetic measurements, including X-ray diffraction and magnetometry, are in close agreement with first-principles predictions.

More broadly, our computational screening indicates that related Fe-Co-X systems, including Fe-Co-C, Fe-Co-Si, Fe-Co-P, and Fe-Co-S, can also crystallize in low-symmetry structures and show promise as rare-earth-free, high-anisotropy, high-magnetization magnets without reliance on critical elements. Overall, this work demonstrates how ML-guided exploration combined with density functional theory based validation can accelerate the discovery of sustainable permanent magnets and help close the performance gap with state-of-the-art rare-earth systems.

1. W. Xia, M. Sakurai, B. Balasubramanian, T. Liao, R. Wang, C. Zhang, H. Sun, K.-M. Ho, J. R. Chelikowsky, D. J. Sellmyer, and C.-Z. Wang, *Proc. Natl. Acad. Sci.* 119, e2204485119 (2022).
2. T. Liao, W. Xia, M. Sakurai, R. Wang, C. Zhang, H. Sun, K.-M. Ho, C.-Z. Wang, and J. R. Chelikowsky, *Phys. Rev. Materials* 7, 034410 (2023).
3. W. Xia, M. Sakurai, T. Liao, R. Wang, C. Zhang, H. Sun, K.-M. Ho, J. R. Chelikowsky, and C.-Z. Wang, *APL Machine Learning* 2, 046103 (2024).
4. J. R. Chelikowsky, C.-Z. Wang, T. Liao, Z. Tang, Q. Zhang, and W. Xia, *J. Magn. Magn. Mater.* 646, 173978 (2026).



Ball-and-stick model of orthorhombic Fe_3CoB_2. A low-symmetry crystal structure stabilized by boron that exhibits strong uniaxial magnetocrystalline anisotropy.

AB-02. Large language models for magnetic materials prediction

J. Zang
University of New Hampshire, Durham, New Hampshire, United States

The discovery of magnetic materials with high operating temperature ranges and optimized performance is essential for advanced applications. Current data-driven approaches are limited by the lack of accurate, comprehensive, and feature-rich databases. In this talk, I will present how to address this challenge by using Large Language Models (LLMs) to create a comprehensive, experiment-based, magnetic materials database named the Northeast Materials Database (NEMAD), which consists of 67,573 magnetic materials entries (www.nemad.org). The database incorporates chemical composition, magnetic phase transition temperatures, structural details, and magnetic properties. Enabled by NEMAD, we trained machine learning models to classify materials and predict transition temperatures. Our classification model achieved an accuracy of 90% in categorizing materials as ferromagnetic (FM), antiferromagnetic (AFM), and non-magnetic (NM). The regression models predict Curie (Néel) temperature with a coefficient of determination (R2) of 0.87 (0.83) and a mean absolute error (MAE) of 56K (38K). These models identified 25 (13) FM (AFM) candidates with a predicted Curie (Néel) temperature above 500K (100K) from the Materials Project. This work shows the feasibility of combining LLMs for automated data extraction and machine learning models to accelerate the discovery of magnetic materials. This method can be generalized to build database on thermoelectric and superconducting materials.

This work was supported by the Office of Basic Energy Sciences, Division of Materials Sciences and Engineering, U.S. Department of Energy, under Award No. DE-SC0020221.

1. Y. Zhang, S. Itani, K. Khanal, E. Okyere, G. Smith, K. Takahashi, J. Zang, J. Magn. Magn. Mater. 597, 172001 (2024).
2. S. Itani, Y. Zhang, J. Zang, Nature Communications 16, 9415 (2025)
3. S. Itani, Y. Zhang, J. Zang, Computational Materials Science 253, 113855 (2025)
4. S. Itani, Y. Zhang, R. Itani, J. Zang, arXiv:2512.10847

AB-03. A Framework for Altermagnet Discovery Unifying Experimental Databases, Graph Neural Networks, and Symmetry Screening

B. Schoener[1], Y. Liu[1], P. Zhang[1], J. Xiong[2, 3], I. Zutic[1], H. Zeng[1]
[1]Physics, University at Buffalo, Buffalo, New York, United States, [2]Institute for Artificial Intelligence and Data Science, University at Buffalo, Buffalo, New York, United States, [3]Computer Science and Engineering, University at Buffalo, Buffalo, New York, United States

Incorporating Machine Learning (ML) into material property prediction has become a crucial step in accelerating materials discovery but is often hindered by the lack of reliable training data. One plausible solution is to build large scale experimental databases using data extracted automatically from literature using large language models, though such databases lack complete structure information and thus cannot be directly utilized for training advanced ML models such as Graph Neural Networks (GNNs). In our recent work, we developed an approach to train GNNs from experimental databases through an alignment process with the Inorganic Crystal Structure Database (ICSD). Here we apply these models as part of a workflow for the discovery of new Altermagnets (ALMs), a class of antiferromagnetic materials with symmetry-enforced spin polarization. We train two models, one for classifying ferromagnets (FMs) and antiferromagnets (AFMs), and the other for classifying AFMs and ALMs. From here are three stages: ML powered screening for ALMs, automated symmetry analysis for potential spin configurations, and validation of ALM candidates via Density Functional Theory (DFT). Material candidates from the Materials Project (MP) and ICSD are screened by first identifying AFMs and subsequently narrowing the set to ALMs. During the symmetry analysis stage, possible spin configurations of each candidate ALM are automatically generated and tested for broken symmetries indicative of ALMs. Finally, the spin configurations that can host altermagnetism are tested for stability and spin splitting through DFT. Stage one reduced our ALM candidates from ~100,000 to ~100 and stage two identified altermagnetic spin configurations in 75% of these, providing a list of likely ALMs that will be validated in stage three. We further utilize our Neel temperature predictive model to assess the suitability of these candidate materials for practical applications. Our work opens the door towards the use of advanced ML techniques in ALM discovery, addressing the bottleneck of lacking spin configurations.

This work was supported by The University at Buffalo Institute for Artificial Intelligence and Data Science, NSF DMR-2242796 and Fulbright Fellowship.

Schoener, B., Hu, Y., Wanlapha, P., Rengarajan, A., Moog, I., Wang, M., ... & Zeng, H. (2026). A New Workflow for Materials Discovery Bridging the Gap Between Experimental Databases and Graph Neural Networks. *arXiv preprint arXiv:2602.00756*

Gao, Z. F., Qu, S., Zeng, B., Liu, Y., Wen, J. R., Sun, H., ... & Lu, Z. Y. (2025). AI-accelerated discovery of altermagnetic materials. *National Science Review*, *12*(4), nwaf066.

Jain, A., Ong, S. P., Hautier, G., Chen, W., Richards, W. D., Dacek, S., ... & Persson, K. A. (2013). Commentary: The Materials Project: A materials genome approach to accelerating materials innovation. APL materials, 1(1)

Bergerhoff, G., Hundt, R., Sievers, R., & Brown, I. D. (1983). The inorganic crystal structure data base. Journal of chemical information and computer sciences, 23(2), 66-69.

Gallego, S. V., Perez-Mato, J. M., Elcoro, L., Tasci, E. S., Hanson, R. M., Momma, K., ... & Madariaga, G. (2016). MAGNDATA: towards a database of magnetic structures. I. The commensurate case. Applied Crystallography, 49(5), 1750-1776.

Xiao, Z., Zhao, J., Li, Y., Shindou, R., & Song, Z. D. (2024). Spin space groups: Full classification and applications. Physical Review X, 14(3), 031037.

Jain, A., Ong, S. P., Hautier, G., Chen, W., Richards, W. D., Dacek, S., ... & Persson, K. A. (2013). Commentary: The Materials Project: A materials genome approach to accelerating materials innovation. APL materials, 1(1)

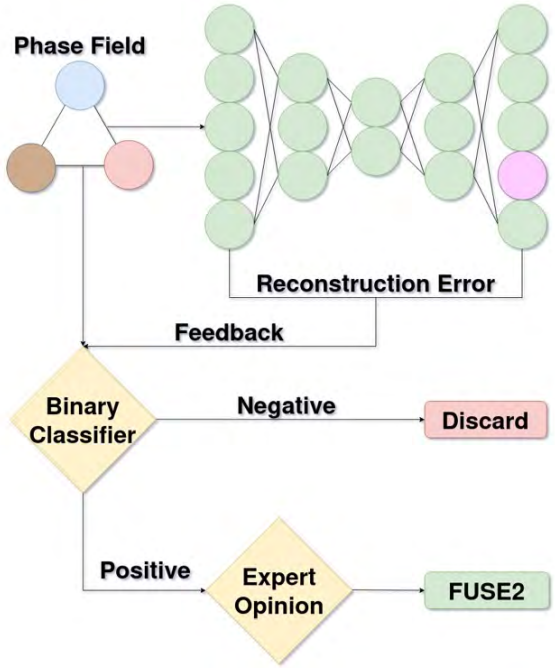
AB-04. Incorporating Magnetism into High-Throughput Crystal Structure Prediction Procedures

J. E. Griffiths[1], M. Dyer[1, 2], G. Darling[1], M. Rosseinsky[1, 2]
[1]Chemistry, The University of Liverpool, Liverpool, Merseyside, United Kingdom, [2]Leverhulme Research Centre for Functional Material Design, Liverpool, Merseyside, United Kingdom

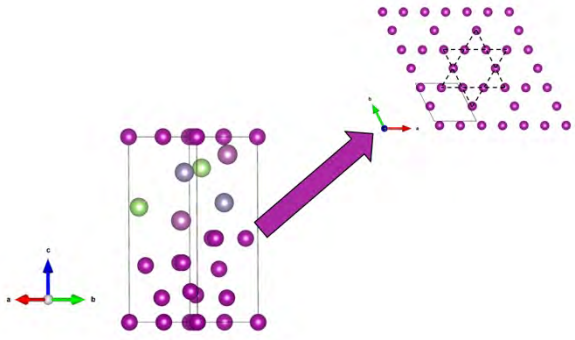
The exploration of material space is hindered by its combinatorial size; there are infinite compositions and structures within a single combination of elements, or phase field.[1] Computational methods of exploration often focus on structural stability, relying on the generation,

modification, and geometry optimisation of several thousand structures to provide confidence that a space has been sufficiently searched.[2] Geometry optimisation is the bottleneck of the process due to the cost of density functional theory (DFT) calculations. To combat this, high-throughput routines typically exclude one important aspect from their energy calculations - magnetism. Given the already vast and complicated nature of material space, the inclusion of magnetism poses too large of a combinatorial challenge. Even in the simplest collinear DFT calculation, introducing N magnetic atoms gives 2^N possible magnetic configurations if symmetry reduction is ignored. Nonetheless, the discovery of novel magnetic materials is more crucial than ever, such as for superconductors,[3] spintronics,[4] and data storage.[5] In this work, phase fields were identified through machine learning models trained on curated intermetallic datasets, which were subsequently explored by computational methods. A two-step approach, employing binary classifiers and autoencoders, ranked phase fields on their probability of containing structures displaying magnetically interesting motifs (e.g. kagome nets) and their chemical synthesisability.[6] The crystal structure prediction (CSP) software, FUSE2,[7] was then used to relax over 1500 structures across more than 20 compositions within several phase fields. Introducing magnetism at the end of the CSP routine resulted in dramatic shifts in the energy landscape, with some being stabilised by over 300 meV/atom. Importantly, this raises the question of if and how magnetism should be incorporated earlier in CSP workflows.

[1] A. Vasylenko, D. Antypov, V. V. Gusev et al., npj Computational Materials, Vol. 9, p.164 (2023)
[2] V. V. Gusev, D. Adamson, A. Deligkas et al., Nature, Vol. 619, p.68-72 (2023)
[3] R. M. Scanlan, A. P. Malozemoff and D. C. Larbalestier, Proceedings of the IEEE, Vol. 92, p.1639-1654 (2004)
[4] E. C. Ahn, npj 2D Materials and Applications, Vol. 4, p.17 (2020)
[5] R. L. Comstock, Journal of Materials Science: Materials in Electronics, Vol. 13, p.509-523 (2002)
[6] N. L. Gulay, D. Wen, J. E. Griffiths et al., Advanced Science, 12, p.35 (2025)
[7] C. C. Collins, H. M . Sayeed, G. R. Darling et al., Farraday Discussions, Vol. 256, p.85-103 (2025)



Flowchart pictorialising the computational work flow to identify chemically feasible phase fields that are predicted as likely to host magnetically interesting structures.



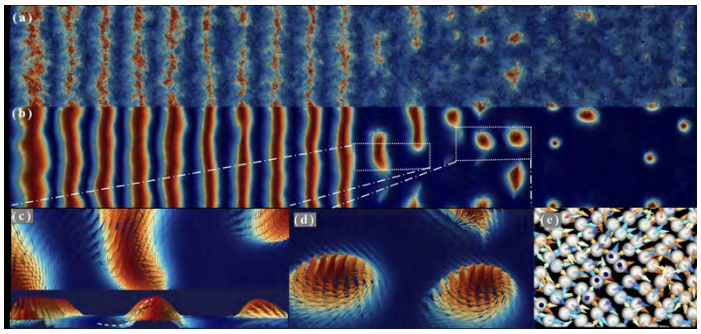
Exemplar low energy structure evolved through the computational workflow, with one of the hosted kagome nets shown as an inset.

AB-05. Magnetic Molecular Dynamics and Foundation Models for Metalic Magnetic Materials

B. Xu
Tsinghua University, Beijing, China

Designing magnetic materials with controllable properties requires a predictive description of the coupled evolution of atomic structure and magnetic order. This is especially important for noncollinear and topological spin textures, where lattice distortion, chemical disorder, thermal fluctuation and spin reorientation are strongly intertwined. Here we present a unified framework that integrates magnetic molecular dynamics with a magnetic materials foundation model for atomistic materials design.
Our approach establishes a data-to-dynamics pipeline based on three developments. DeltaSpin [1] provides self-adaptive spin-constrained first-principles calculations for generating accurate noncollinear magnetic excited-state data. DeepSPIN [2] learns the coupled spin-lattice energy landscape and predicts energies, interatomic forces and magnetic torques for large-scale magnetic systems. TSPIN [3] introduces a symplectic spin-lattice dynamics algorithm, enabling stable long-time evolution under different thermodynamic conditions. Together, these methods allow atomic rearrangement and magnetic-moment rotation to be simulated within the same trajectory.
As a representative application, we study FeGe, a prototypical chiral magnet hosting skyrmions. The simulations capture the pathway from thermally fluctuating local moments to helical and conical modulations, and further to skyrmion textures under magnetic field, temperature and lattice perturbations. By resolving atomic motion, local magnetic torques and spin-texture evolution simultaneously, the framework provides atomistic insight into skyrmion nucleation, stabilization and annihilation.
We further extend this capability through a transferable magnetic foundation model covering 47 alloying elements, more than 6,000 magnetic alloy systems and over 700,000 nonequilibrium noncollinear magnetic configurations. This work provides a practical computational foundation for understanding magneto-structural coupling and accelerating next-generation magnetic materials design.

[1] Z. Cai, K. Wang, Y. Xu, S.-H. Wei, and B. Xu, *A self-adaptive first-principles approach for magnetic excited states*, Quantum Frontiers 2, 21 (2023).
[2] T. Yang, Z. Cai, Z. Huang, W. Tang, R. Shi, A. Godfrey, H. Liu, Y. Lin, C.-W. Nan, M. Ye, L. Zhang, H. Wang, and B. Xu, "Deep learning illuminates spin and lattice interaction in magnetic materials," Physical Review B 110, 064427 (2024).
D. Zheng, X. Peng, Y. Huang, *et al.*, *Integrating deep-learning-based magnetic model and non-collinear spin-constrained method: methodology, implementation and application*, npj Computational Materials 12, 52 (2026).
[3] Z. Huang, H. Wang, and B. Xu, *Symplectic Spin-Lattice Dynamics with Machine-Learning Potentials*, arXiv:2506.12877 (2025)



Representative subregion extracted from the full-machine extreme-scale spin–lattice simulation, illustrating the spatial evolution from helical order to skyrmionic textures in a magnetic stripe.

AB-07. Computational electronic structure-based search for stable magnetic systems: failures and successes

V. Antropov
Ames National Laboratory, Ames, Iowa, United States

I will discuss the status of computational electronic-structure-based searches for new stable systems, with a focus on magnetic compounds. The current successes and failures of artificial intelligence, machine learning, and high-throughput methods for theoretical predictions of solid-state magnetic materials will be presented for different types of systems. More details will be provided for HTP screening of magnetic materials and their properties. Specific property-dependent peculiarities of such screenings will be discussed for magnetic structure determination, the critical temperature of the magnetic phase transition, magnetic anisotropy in rare-earth magnets, and altermagnetism. Numerous examples of experimentally verified predictions for stable systems with different magnetic orders will be shown, and possible applications will be discussed.

AB-08. Digital twin of permanent magnet for simulation-guided microstructure optimization

N. Kulesh, A. Bolyachkin, T. Ohkubo, H. Sepehri-Amin
National Institute for Materials Science, Tsukuba, Japan

Digital twins in materials science enable virtual experiments and provide an effective link between microstructure and functional properties, incorporating experimental complexity into physics-based simulations [1]. Such models reveal features critical for magnet performance, including nucleation and pinning sites and the 3D arrangement of secondary phases. We develop a digital twin for a Ga-doped, heavy-rare-earth-free sintered Nd–Fe–B magnet [2] based on FIB–SEM tomography and use it for statistical and micromagnetic analysis.

A volume of ~13 × 29 × 33 μm^3 was reconstructed with ~30 nm slice spacing and ~20 nm lateral resolution. The dataset was preprocessed for drift correction, contrast equalization, and noise reduction. Several deep-learning models were tested for segmentation, and a phase-field postprocessing step was introduced to remove residual artifacts (Fig. 1). Statistical analysis yielded grain sizes, phase composition, and spatial arrangement. TEM confirmed that thick (>50 nm) intergranular phases are resolved, while grains that appear connected in SEM are separated by thin (~3 nm) Fe-rich ferromagnetic phases. Unresolved grain boundaries were treated as ferromagnetic phases providing exchange coupling. This allowed us to construct a grain-connectivity map and quantify the exchange-coupled contact area (~9%), which was incorporated into the model.

Coercivity and magnetization reversal were analyzed using a micromagnetic model built from the digital twin. Due to computational restrictions, the model was divided into representative patches and scaled down. We varied the magnetic properties of the thin intergranular phase and texture, and analyzed coercivity in different patches, including the role of large Nd oxide inclusions in reducing local switching fields. The digital twin proves useful for parametric analysis, helping identify weak links and explain extrinsic magnetic properties [3]. This talk will summarize current progress and limitations and discuss future directions.

[1] A. Bolyachkin, E. Dengina, N. Kulesh et al., npj Comput Mater., Vol. 10, 34 (2024)
[2] T. Sasaki, T. Ohkubo, Y. Takada et al., Scripta Mater., Vol. 113, 218 (2016)
[3] N. Kulesh, A. Bolyachkin, H. Nakamura, et al., Adv. Intel. Disc. e202500200 (2026)

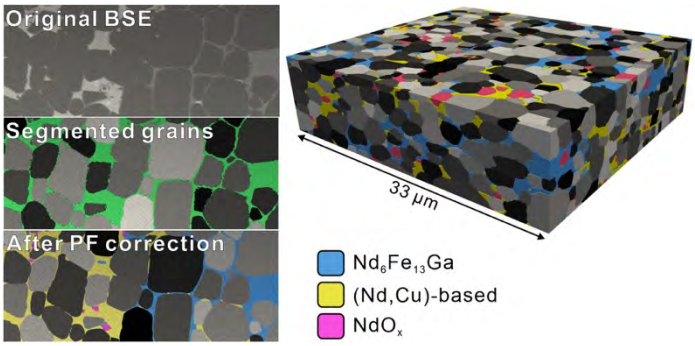


Fig. 1. 2D slice at an arbitrary angle from the BSE volume, the as-segmented volume, and the volume after phase-field (PF) postprocessing. The multiphase volume is shown on the right, with the secondary phases listed below.

AB-09. Automated design exploration of two-dimensional magnonic crystals using a combinatorial optimization approach

R. Nagaoka[1], T. Yamazaki[2], C. Mitsumata[3], Y. Iwasaki[4], M. Kotsugi[1]
[1]Tokyo University of Science, Tokyo, Japan, [2]Yokohama National University, Yokohama, Japan, [3]University of Tsukuba, Tsukuba, Japan, [4]National Institute of Materials Science, Tsukuba, Japan

Magnonic crystals (MCs) are periodic magnetic microstructures that manipulate spin-wave propagation through engineered magnonic band dispersions, making them promising platforms for next-generation spintronic information processing. However, design guidelines for optimizing target properties (e.g. magnonic bandgaps) remain unclear because of the complex relationship between lattice geometry and band dispersions. Recently, inverse-design approaches based on mathematical optimization and machine learning have enabled the non-empirical discovery of functional structures in metamaterials, nanophotonics, and magnonic systems [1-3]. Here, we demonstrate an inverse-design framework for discovering unconventional MC geometries with enhanced magnonic bandgaps.

Frequency-domain micromagnetic simulations were integrated with a metaheuristic genetic algorithm (GA) to automate the design optimization process [4]. The spin-wave dispersion of a bicomponent Fe/EuO MC was calculated using frequency-domain Landau-Lifshitz-Gilbert (FD-LLG) simulations [5], formulated as an eigenvalue problem with Bloch-Floquet boundary conditions (Fig. 1). The optimization problem was defined to maximize the

relative width of complete magnonic bandgaps by searching the binary material distribution of Fe and EuO in a unit cell. This formulation yields a combinatorial design space of $2^{36} \approx 10^{10}$ possible configurations, which was efficiently explored using the GA.

Fig. 2a shows the structural evolution of MCs during optimization for the bandgap between the 2nd and 3rd modes. As optimization progressed, the bandgap increased, and the calculated band dispersion clearly showed the opening of a complete bandgap with a relative width of 0.598 (Fig. 2b, 2c). The proposed framework successfully identified several previously unreported MC designs with nontrivial topologies. These results demonstrate the effectiveness of proposed framework for fast, automated spin-wave device design beyond human intuition.

[1] L. Norder et al., *Nature Communications*, 16, 2753 (2025)
[2] Q. Wang et al., *Nat. Commun*., 12, 2636 (2021)
[3] A. Voronov et al., *npj Spintronics*, 3, 19 (2025)
[4] R. Nagaoka et al., arXiv:2603.05132v1 (2026)
[5] Z. Lin et al., *AIP Advances*, 13, 015216 (2023)

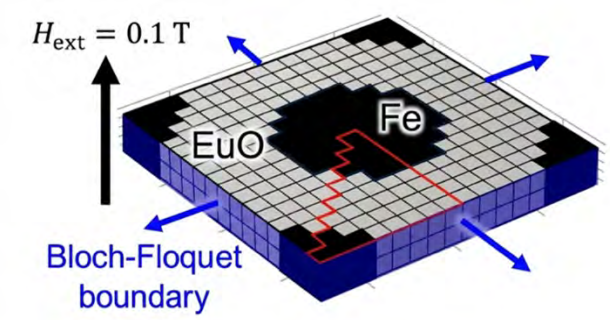


Fig.1: Model geometry for calculating magnonic band dispersions.

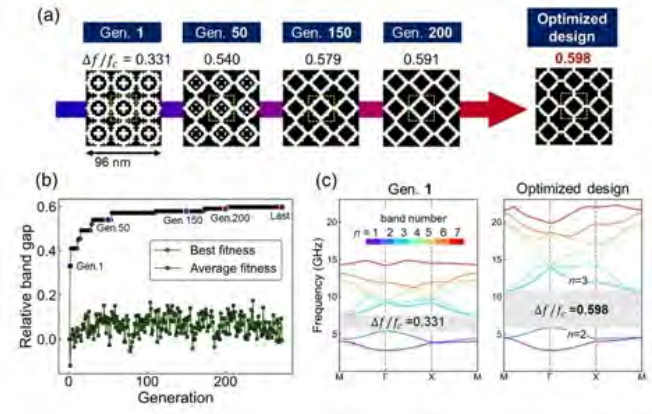


Fig.2: (a) Topological evolution of the MC during the optimization process. (b) Optimization history of the bandgap width. (c) Magnonic band dispersions before and after the optimization.

SESSION AC: TWO-DIMENSIONAL MAGNETISM
Chair(s): C. Gong, *University of Maryland, College Park, Maryland, United States*
Tuesday, November 3, 2026
08:30 AM-12:00 PM
Coral 1

AC-01. Raman Spectroscopy of Moiré Magnetism in Twisted Double Bilayer CrI_3 and Spin-Induced Nematicity in XY-Type Magnet $NiPS_3$

R. He
Texas Tech University, Lubbock, Texas, United States

Van der Waals (2D) materials with intrinsic magnetism have attracted massive interest because of their potential applications in data storage and spintronics devices. Atomic layers of chromium triiodide (CrI_3) are one of such 2D ferromagnetic (FM) materials that have been demonstrated to realize long range FM order in its monolayer limit. Raman spectroscopy is a noninvasive and powerful technique to probe the lattice, electronic, and magnetic excitations in 2D magnets. Using low-temperature magneto-Raman spectroscopy, we have revealed the emergence of finite net magnetization that originates from spin frustrations and noncollinear spin texture introduced by moiré superstructures in rhombohedral-stacked twisted double bilayer CrI_3.[1,2] Recently, we have also demonstrated a clear symmetry evolution in hexagonal-stacked twisted double bilayer CrI_3.[3] In XY-type magnet $NiPS_3$, we have tracked characteristic Raman peaks as the $NiPS_3$ thickness decreases. We have shown that the static, long-range antiferromagnetic order in bulk $NiPS_3$ evolves into a spin-induced nematic state in few-layer.[4] Our Raman spectroscopy studies offer an unprecedented venue for probing novel magnetic states and phases in diverse 2D magnets.

[1] H. Xie, X. Luo, G. Ye, et al., *Nature Physics* 18, 30–36 (2022).
[2] H. Xie, X. Luo, Z. Ye, et al., *Nature Physics* 19, 1150–1155 (2023).
[3] Z. Sun, G. Ye, X. Wan, et al., *Nature Physics* https://doi.org/10.1038/s41567-026-03275-7 (2026).
[4] Z. Sun, G. Ye, C. Zhou, et al., *Nature Physics* 20, 1764–1771 (2024).

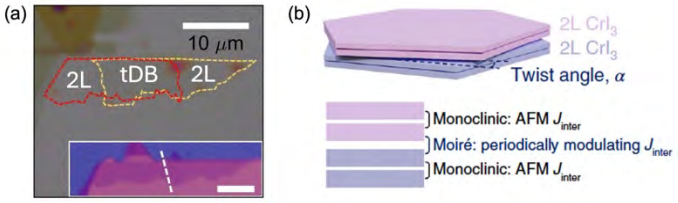


Fig. 1 Optical image (a) and schematic drawing (b) of twisted double bilayer CrI_3.

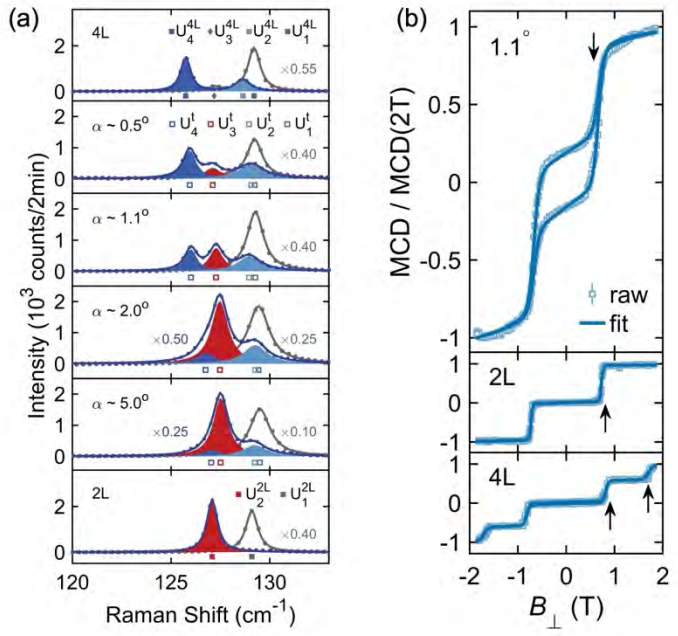


Fig. 2 Raman spectra (a) and MCD spectra (b) of twisted double bilayer CrI_3. Spectra from natural bilayer and four-layer CrI_3 are included for comparison.

AC-02. Magnetoelectric Effect in van der Waals Ferromagnetic/Ferroelectric Heterostructures

J. Eom[1], J. Lee[1], S. Park[2], J. Choi[1]
[1]Center for Spintronics, Korea Institute of Science and Technology, Seoul, Korea (the Republic of), [2]Department of Physics, Soonsil University, Seoul, Korea (the Republic of)

Van der Waals (vdW) materials provide a versatile platform for engineering atomically clean, well-defined interfaces between distinct material families. Such heterostructures enable unprecedented tuning of two-dimensional (2D) material properties through strain, electrostatic gating, proximity effects, twist-angle control, and optical excitation, allowing direct manipulation of the fundamental parameters governing key model Hamiltonians.

Here, we fabricate heterostructure devices combining two distinct vdW material families and investigate their interfacial coupling. Specifically, we demonstrate a strain-mediated magnetoelectric effect in vdW ferromagnet (FM) / ferroelectric (FE) heterostructures composed of exfoliated Fe_3GeTe_2 and α-In_2Se_3 flakes [1]. Magneto-optical Kerr effect (MOKE) measurements reveal that the Fe_3GeTe_2 magnetic coercivity decreases under both positive and negative gate voltages. Complementary Raman micro-spectroscopy shows homopolar, voltage-induced red-shifts in both the α-In_2Se_3 and Fe_3GeTe_2 Raman modes, indicating the emergence of tensile strain in both layers. The strong correlation between the MOKE and Raman voltage responses indicates that the observed modulation of Fe_3GeTe_2 coercivity and magnetic anisotropy originates from voltage-induced strain generated in α-In_2Se_3 and transferred across the vdW interface. Density functional theory calculations corroborate this picture, showing that strain substantially modifies the magnetic anisotropy of Fe_3GeTe_2. These results establish voltage gating as an effective route to control interfacial magnetism via coupling between vdW FM and FE layers, and point toward a viable strategy for low-power, voltage-controlled vdW spintronic devices based on the magnetoelectric effect.

[1] J. Eom et al., Nature Communications, Vol. 14, p. 5605 (2023)

AC-03. Kondo Effect and Magnetic Properties of CVD-Grown Polycrystalline 1T-$V_{1-x}Fe_xSe_2$ Thin Films

V. Samanta, S. Chandran
Physics, Indian Institute of Technology Madras, Chennai, Tamil Nadu, India

Vanadium diselenide (VSe_2), a van der Waals (vdW) layered material, has potential applications across diverse fields, including electronics, spintronics, memory devices, and energy applications due to its unique physical and chemical properties, such as high electrical conductivity [1], charge density wave (CDW) [1], and intrinsic ferromagnetism in mono to few-layers [2]. However, synthesizing high-quality contiguous VSe_2 thin film for potential applications remains a significant challenge.

Here, we examine large area (~ 1 cm × 1 cm) CVD-grown contiguous 1T-$V_{1-x}Fe_xSe_2$ (x = 0, 0.08, 0.13, 0.17, 0.25) thin films on Si/SiO_2 substrate to study tunable electrical, magneto-transport, and magnetic properties of VSe_2 with Fe doping. Electron microscopy studies show that highly compacted growth of VSe_2 and Fe-doped VSe_2 nanocrystals

on the substrate. Electrical-transport measurements indicate that CDW ordering in VSe_2 is gradually suppressed with increasing Fe doping concentration, with the appearance of a new metal-to-insulator transition at ~170 K [3]. The presence of weak Kondo effect in VSe_2 and Fe-doped VSe_2 thin films (Fig. 1a) is signified from low-temperature magneto-transport studies with the appearance of negative magnetoresistance (MR) at low magnetic field (< 4T) region, regardless of the magnetic field's orientation relative to the electric current [4]. Furthermore, pristine VSe_2 thin film exhibits weak ferromagnetism with a ~ 3 to 4 times enhancement for Fe-doped VSe_2 (~ 25 *at.* %) thin film (Fig. 1b). The defects and magnetic dopant induced weak ferromagnetism in $V_{1-x}Fe_xSe_2$ thin films, partially suppresses the Kondo effect by lowering the probability of spin flip scattering of localized moments of interlayer V ions. The large area contiguous $V_{1-x}Fe_xSe_2$ thin films hold promise for next-generation electronics and spintronics applications.

[1] Y. Xue *et al.*, *Nanotechnology*, vol. 31, no. 14, (2020).
[2] M. Bonilla *et al.*, *Nat. Nanotechnol.*, vol. 13, no. 4, pp. 289–293, (2018).
[3] C. S. Yadav and A. K. Rastogi, *J. Phys. Condens. Matter*, vol. 20, no. 46, (2008).
[4] S. Barua, M. C. Hatnean, M. R. Lees, and G. Balakrishnan, *Sci. Rep.*, vol. 7, no. 1, (2017).

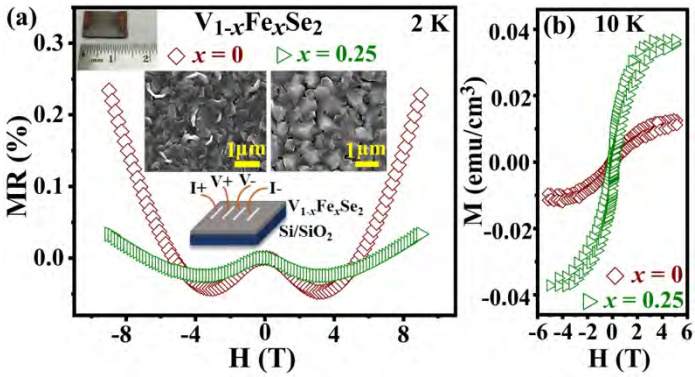


Fig. 1. (a) Comparative MR (%) at 2 K and (b) linear background subtracted magnetic signal at 10 K of $V_{1-x}Fe_xSe_2$ (x = 0 and 0.25) thin films. Insets in (a) show a large area (~ 1 cm × 1 cm) CVD-grown sample on Si/SiO_2 substrate and comparative morphology of $V_{1-x}Fe_xSe_2$ (x = 0 and 0.25) samples.

AC-04. Space-Confined CVD Growth of Fe_3GeTe_2:Structural, Vibrational, and Magnetic Properties

B. P. Jena, S. Chandran
Department of Physics, IIT Madras, Chennai, Tamilnadu, India

Fe_3GeTe_2 is a layered van der Waals material widely studied for two-dimensional magnetism and spintronic applications [1], [2], [3]. However, its controlled growth via chemical vapor deposition (CVD) remains challenging due to competing Fe-Te phase formation in the Fe-Ge-Te system. In this work, we examine the role of growth environment on the phase formation during CVD synthesis. A conventional substrate arrangement predominantly yields $FeTe_2$, whereas a confined (sandwich-type) configuration facilitates the formation of Fe_3GeTe_2 along with the secondary phase formation. The underlying growth mechanism is attributed to the suppression of vapor diffusion in the confined geometry, which increases local precursor concentration and interaction time, enabling balanced incorporation of Fe, Ge, and Te, thus stabilizing the ternary phase (Fe_3GeTe_2). The formation of hexagonal phase is confirmed through structural characterization of the synthesized sample. Scanning electron microscopy (SEM) image shows the layered structure with hexagonal shaped flakes (Fig. 1a), with the nominal composition of Fe:Ge:Te ~ 3:1:2. Flake thicknesses down to ~ 10 nm are achieved. Further, Raman spectra of Fe_3GeTe_2 flakes exhibit characteristic vibrational modes at 123 cm^{-1} and 152 cm^{-1}, consistent with the literature. Temperature dependent and polarised Raman studies are performed to explore phonon anharmonicity and crystal symmetry, respectively. Magnetic characterization as a function of temperature (Fig. 1b) reveal the presence of ferromagnetic behavior in the synthesized samples. These results show that growth conditions strongly influence phase selectivity in the Fe-Ge-Te system, and facilitates the formation of Fe_3GeTe_2, with implications for tuning magnetic behaviour in layered tellurides for spintronics applications.

[1] H. Ren and M. Lan, "Progress and Prospects in Metallic Fe_xGeTe_2 ($3 \leqslant x \leqslant 7$) Ferromagnets," *Molecules*, vol. 28, no. 21, 2023, doi: 10.3390/molecules28217244.
[2] H. J. Deiseroth, K. Aleksandrov, C. Reiner, L. Kienle, and R. K. Kremer, "Fe_3GeTe_2 and Ni_3GeTe_2 - Two new layered transition metal compounds: Crystal structures, HRTEM investigations, and magnetic and electrical properties," *Eur. J. Inorg. Chem.*, no. 8, pp. 1561–1567, 2006, doi: 10.1002/ejic.200501020.
[3] B. Chen *et al.*, "Magnetic properties of layered itinerant

electron ferromagnet Fe_3GeTe_2," *J. Phys. Soc. Japan*, vol. 82, no. 12, pp. 1–7, 2013, doi: 10.7566/JPSJ.82.124711.

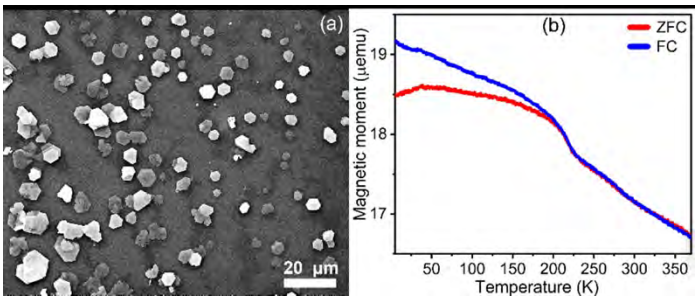


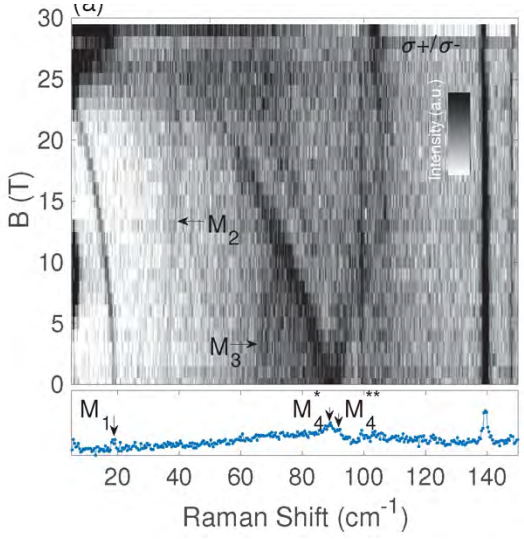
Fig.1. (a) SEM image showing the morphology of the CVD grown Fe_3GeTe_2 sample. (b) Temperature dependence of the dc magnetization measured under an applied field of 1000 Oe in zero-field-cooled (ZFC) and field-cooled (FC) conditions.

AC-05. Orbital moment and spin dynamics in vanadium trihalides

J. Pospíšil[1], D. Hovančík[1], O. Michal[2], T. Haidamak[1], D. Repcek[2], F. Borodavka[2], P. Dolezal[1], M. Veis[1], S. Kamba[2], M. Orlita[3], V. Sechovsky[1]
[1]Charles University, Prague, Czechia, [2]Czech Academy of Sciences, Prague, Czechia, [3]Laboratoire National des Champs Magnétiques Intenses, Grenoble, France

Vanadium VX_3 trihalides (X = Cl, Br, I) are vdW magnetics in which the necessary magnetocrystalline anisotropy cannot be explained by a simple spin-orbit coupling model. In most 3*d* vdW magnets, the orbital moment (OM) is quenched due to the octahedral crystal field (OCF) of ligands. We have proven by XMCD that the magnetic ground state of VI_3 is associated with the V^{3+} ion ($3d^2$ configuration), bearing an unquenched OM due to the electronic correlation mixed with the trigonally distorted OCF[1, 2]. We will demonstrate that the intrinsic OM in VX_3 trihalides plays a key role in their magnetism, magnetic excitations, spin dynamics, and magnetoelastic coupling (MEC) with implications for the design of next-generation spintronic and quantum devices. We employed pulsed-field magnetization measurements and a combination of IR, THz, and Raman spectroscopies under steady magnetic fields.
The OM atiparallel to spin moment reduces the saturation magnetization relative to the S=1 spin-state-only value. Moreover, OM accompanied by in-plane AFM interaction shifts the metamagnetic transitions of VBr_3 and VCl_3 to a tens-of-T range. In the ferromagnet VI_3, a unique high-energy FM resonance associated with OM-violating Fleury-London theory appears in the THz range. This magnon is the first demonstration of ultrafast spin dynamics in a 2D van der Waals ferromagnet, highlighting the potential of VI3 for THz spintronics [3]. Both AFMs, VBr_3 and VCl_3, exhibit Raman spectra of gapped AFM magnons, indicating biaxial magnetic anisotropy. The effect of the metamagnetic transition on the Raman spectra of VBr_3 in an out-of-plane magnetic field demonstrates strong MEC, as evidenced by pronounced phonon shifts. The complex magnetic structures with tilted magnetic moments driven by the orbital component lead to clear magnon-phonon and magnon–magnon coupling (Fig. 1) for in-plane orientation of the magnetic fields in both AFMs. All these findings establish VX_3 compounds as a promising playground for studying fundamental magnon physics.

[1] D. Hovančík, et al., Nano Letters 23 (2023), 1175–1180.
[2] D. Hovančík, et al., Physical Review B 108 (2023), 104416.
[3] D. Hovančík, et al., The Journal of Physical Chemistry Letters 13 (2022), 11095.
[4] D. Hovančík, Charles University, doctoral thesis, 2026.



Magnetic field dependence of Raman spectra of VCl_3 [4].

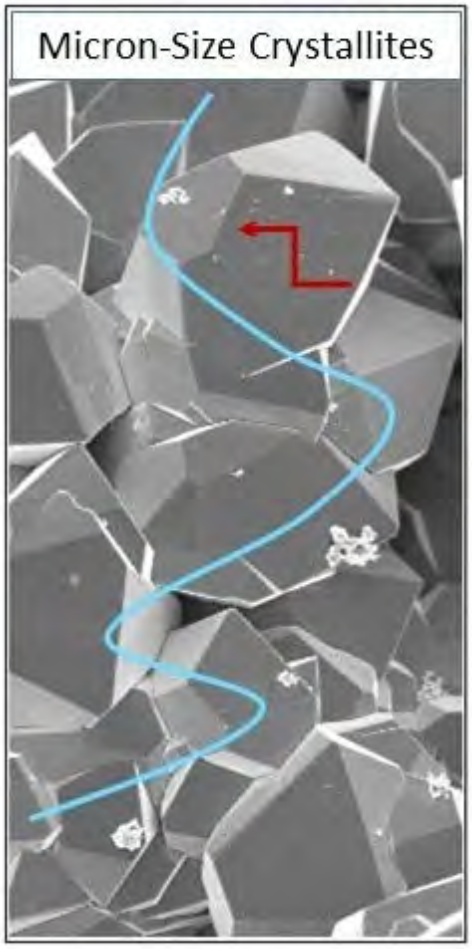
AC-06. Nature of Electrical Transport in Quasi Two-Dimensional antiferromagnet SrRu2O6

A. Kumar, S. Nair, A. Bajpai
Physics, Indian Institute of Science Education and Research, Pune, Maharashtra, India

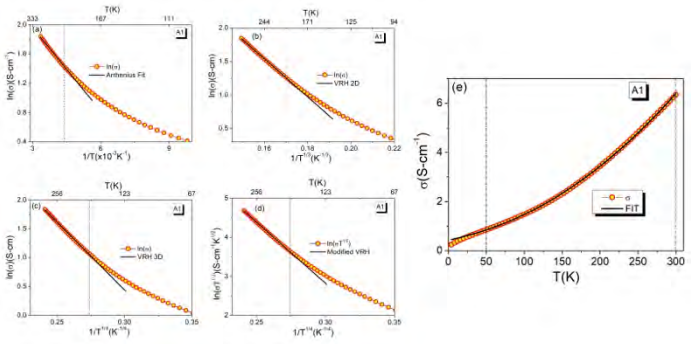
SrRu2O6 is one of the rare 4d based antiferromagnets (AFM) with exceptionally high Neel temperature, TN of 563K. It possesses an inherently layered crystal structure in which

Ru-O-Ru bonds form a honeycomb lattice, separated by Sr layers on either side. Here the honeycomb is that of antiferromagnetically coupled Ru atoms with high spin-orbit coupling [1,2]. This not only provides opportunity for exploring unconventional excitations but also offers immense potential for applications owing to its high TN. SrRu2O6, first synthesized by Hiley et.al [1] using hydrothermal technique, forms in regular shaped micronsize crystalites. These crystallites can also be exfoliated in the form of ultra -thin sheets [2]. Electronic structure calculations indicate that this compound is a p -type semiconductor. However, the band gap estimated from fitting of the Arrhenius model to the high temperature region (300K-200K) of the electrical- transport data in SrRu2O6 pellets is typically found to be significantly smaller than the theoretically predicted value. Here we show that in high temperature region, the Arrhenius, the Variable Range Hopping (VRH) as well as modified VRH exhibit similar goodness of fit, when fitted to transport data in the pressed pellets of SrRu2O6,(consisting of regular shaped crystallites (Figure 1) . Interestingly, the Fluctuation-Induced Tunneling (FIT) model is observed to exhibit an excellent fit in a much wider temperature range from 300-50K (Figure 2). For SrRu2O6, which inherently possesses a quasi two-dimensional crystal structure, the FIT model point towards the intriguing possibility of thermal fluctuations induced tunneling of charge carriers across the conducting and insulating layers. Data on multiple samples brings out the profound role of intrinsic defects and associated strain in the nature of electrical conduction, especially at lower temperatures. We also present magneto transport data on SrRu2O6, elucidating the role of anitiferromagnetically coupled magnetic hexagons comprising of heavy Ru -atoms.

1. Hiley C I, Scanlon D, Sokol A, Woodley S, et al. Physical Review B 92 104413 ,2015.
2. TianW, Svoboda C, Ochi M, Phys Rev B, B 92(10) 100404, 2015
3. Homkar S, Chand B, Rajput S S, et.al, ACS Applied Nano Materials 4 9313–9321, 2021.



SEM image SrRu2O6 crystallites. The blue line depicts the intergranular and inter-layer transport paths.

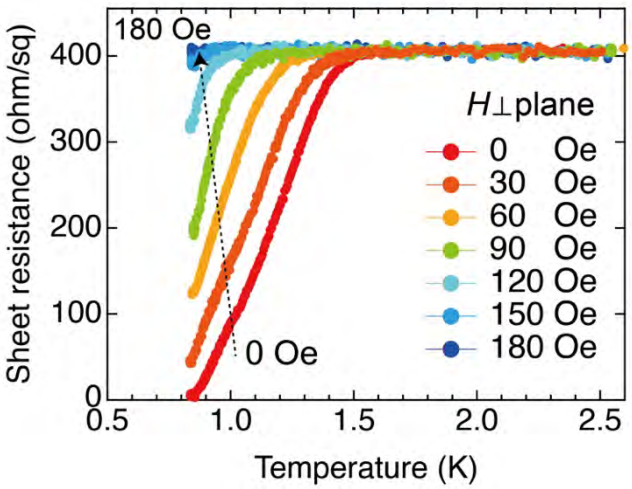


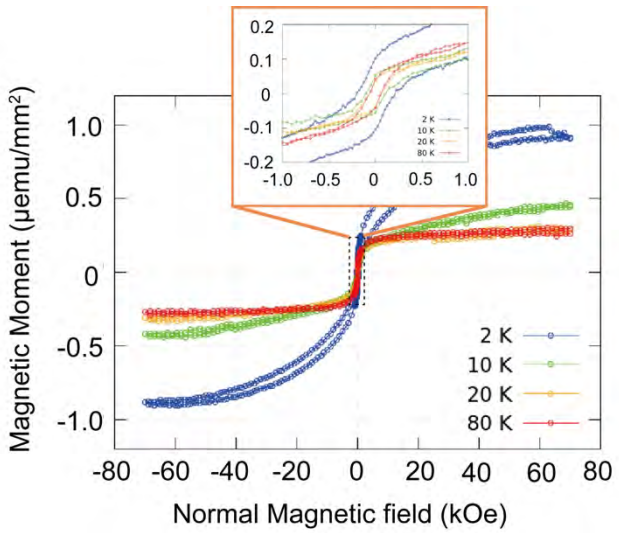
Temperature variation of conductivity data fitted to various conductiivity models

AC-07. Superconductivity and Emergent Magnetism in Yb-Intercalated Graphene with Site-Selective Valence States

R. Akiyama[4, 1], S. Sato[1], Y. Miyai[2], Y. Hashimoto[3], J. Jung[1], R. Hobara[1], Y. Kumar[2], A. Kumar[2], S. Shimizu[1], R. Minakawa[1], Y. Yamamoto[3], H. Tomita[3], T. Tadamura[3], T. Moriki[3], Y. Yamada[3], S. Ideta[2], K. Shimada[2], T. Matsushita[3], S. Hasegawa[1]
[1]The University of Tokyo, Tokyo, Japan, [2]Hiroshima University, Higashi Hiroshima, Japan, [3]Nara Institute of Science and Technology, Ikoma, Japan, [4]Kyoto University, Kyoto, Japan

Atomic intercalation is a promising route to induce superconductivity in graphene. While superconductivity induced by alkali and alkaline-earth intercalation has been widely studied, superconductivity in Yb-intercalated graphene had not been realized for nearly two decades since the report of superconductivity in Yb-intercalated graphite in 2005 [1]. In this talk, we present the first observation of superconductivity in Yb-intercalated graphene and discuss its origin focusing on atomic configuration and valence states [2].
In Fig. 1, the temperature dependence of the sheet resistance, measured by in situ 4-probe electrical transport, is shown, and the superconductivity transition temperature is 1.2 K.
In addition, angle-resolved photoemission spectroscopy reveals that Yb intercalation leads to strong hybridization between Yb 4f states and graphene π bands. Photoelectron holography and X-ray photoelectron spectroscopy further determine the real-space positions and valence states of Yb atoms. Yb^{2+} ions are located between graphene layers and are primarily responsible for superconductivity, while Yb^{3+} ions reside at the graphene/SiC interface, resulting in intrinsic mixed valence.
Notably, the presence of Yb^{3+} ions with localized spins suggests that ferromagnetism seems to be induced in the system as shown in Fig. 2, and we are beginning to explore such signatures. These results reflect the sensitivity of superconductivity to dimensionality, atomic configuration, and valence. I will conclude by outlining future perspectives toward correlated electronic states in two-dimensional intercalated graphene systems.
[1] T. E. Weller et al., Nature Phys. 1, 39 (2005)., [2] R. Akiyama et al., JCS-Japan 133, 508 (2025).





AC-08. Magneto-Electronically Coupled Quasiparticle States in Monolayered MoS_2 Driven by Proximity Effect of Ultrathin $SmFeO_3$

H. Chen, C. Hsieh, C. Yang
Material Science and Engineering, National Yang Ming Chiao Tung University, Hsinchu, Taiwan

Magnetic proximity effect (MPE) of magnetic substrate provides an effective route to manipulate spin/valley-dependent quasiparticles in two-dimensional transition-metal dichalcogenides (TMDs) without requiring large external magnetic fields. Herein, we demonstrate a magneto-electronically coupled transition between spin-polarized exciton and trion states in monolayered MoS_2 (ML-MoS_2) interfaced with an ultrathin $SmFeO_3$(111)

antiferromagnetic (AFM) film. Owing to the uncompensated spin configuration at the (111) surface of $SmFeO_3$, a pronounced magnetic circular dichroism (MCD) of ML-MoS_2 appears in spin-resolved photoluminescence (SR-PL), in contrast to the magnetically compensated $SmFeO_3$(001) counterpart. Through applying field-cooling (FC) treatment under opposite field polarities, the interfacial exchange is reversibly facilitated, leading to a simultaneous reversal of spin-polarization and a distinct energy shift corresponding to exciton–trion transition. Temperature-dependent SR-PL reveal a critical temperature of ≈20 K, below which the magneto-electronic coupling becomes prominent, accompanied by an unconventional enhancement of magnetization in ultrathin $SmFeO_3$(111) film. Control experiments under zero-field cooling (ZFC) confirm that the phenomenon originates from a field-trained magnetic state of $SmFeO_3$(111) film rather than direct field effects. We propose that the coupled magnetic and potential ferroelectric order in $SmFeO_3$ modulates the interfacial charge distribution, enabling tunable carrier doping and quasiparticle repopulation in ML-MoS_2. These results establish a platform for magnetically programmable exciton–trion states and highlight the potential of AFM oxide heterostructures for low-field valleytronic and multifunctional spintronic applications.

AC-09. Studying the evolution of spin-polarized trion in monolayered MoS_2 via magnetic proximity effect of YIG
C. Hsieh, F. Chan, C. Yang
Material Science and Engineering, National Yang Ming Chiao Tung University, Hsinchu, Taiwan

This study investigates the mechanisms governing valley spin polarization in monolayer MoS_2 interfaced with a sputtered yttrium iron garnet (YIG) film. Structural and spectroscopic characterizations confirm successful transfer of high-quality MoS_2 with minimal strain, while revealing significant electron doping that modifies the exciton–trion population. Temperature-dependent spin-resolved photoluminescence (SR-PL) measurements show that both Zeeman splitting and spin accumulation contribute to valley spin polarization at low temperatures, manifested by energy splitting and intensity asymmetry in the spectra. As temperature increases, the energy splitting diminishes and vanishes above ~40–50 K, whereas the polarization asymmetry persists up to ~200 K. This behavior indicates a crossover from a Zeeman-dominated regime at low temperature to a spin-accumulation-driven mechanism at elevated temperatures. The results suggest that magnetic proximity effect (MPE)-induced spin accumulation, particularly associated with trion states, governs valley polarization at higher temperatures. These findings reveal a nontrivial interplay between quasiparticle population, spin accumulation, and symmetry breaking, and provide insight into magnetically controlled valley physics in two-dimensional heterostructures.
[1] Fang-Mei Chan et al., *Nanotechnology* 36, 335701 (2025).

AC-10. Magnetic Emergence in Van der Waals Materials
S. Gilbert Corder
Advanced Light Source, Lawrence Berkeley National Laboratory, Berkeley, California, United States

The study of emergent magnetic phenomena in two-dimensional (2D) van der Waals (vdW) materials is fundamental for the development of next-generation spintronics. These systems provide a unique platform where intrinsic magnetic, electronic, and optical properties can be precisely controlled through lattice strain, defects, and layer stacking. Our research focuses on uncovering the novel magnetic insights revealed when these control mechanisms are probed at the nanoscale.

To isolate the origins of this magnetic emergence, we employ a sophisticated multi-probe approach that integrates Synchrotron Infrared Nanospectroscopy (SINS) with Magnetic Force Microscopy (MFM). By combining the high brightness of synchrotron radiation with nanoscale spatial resolution, SINS allows us to map chemical and structural heterogeneities. When coupled with MFM, this approach provides a direct correlation between elementary excitations, such as lattice vibrations, and the resulting local magnetic ordering. By further incorporating Kelvin Probe Force Microscopy (KPFM) and Conductive Atomic Force Microscopy (c-AFM), our methodology offers an unprecedented view of the coupled vibrational, electronic, and magnetic anisotropy. This multi-probe synergy is essential for identifying the precise nanoscale drivers of magnetic behavior in complex vdW heterostructures.

Ultimately, these findings highlight how the SINS-MFM methodology advances our fundamental understanding of 2D magnetic systems. By uncovering the complex interplay between magnetic, vibrational, and electronic properties at the 20 nm scale, this research provides the scientific insights necessary to observe and manipulate magnetic emergence.

AC-11. Novel characterization of spin waves in twisted CrSBr/CrSBr homostructures via DFT/QFT modeling and experiments

A. J. Winchell[1], P. Aislinn[1], E. Lambertson[2], T. Zuehlsdorff[2], A. Saenz Rodriguez[3], Z. Sofer[4], P. Dhagat[5], O. Ostroverkhova[1]
[1]Physics, Oregon State University, Corvallis, Oregon, United States, [2]Chemistry, Oregon State University, Corvallis, Oregon, United States, [3]Mathematics, Oregon State University, Corvallis, Oregon, United States, [4]Inorganic Chemistry, University of Chemistry and Technology Prague, Prague, Czechia, [5]Electrical Engineering and Computer Science, Oregon State University, Corvallis, Oregon, United States

We present a combined experimental, density functional theory (DFT), and quantum field theory (QFT) approach to understanding spin waves in twisted 2D magnetic heterojunctions. In particular, we investigate twisted CrSBr/CrSBr bilayers to reveal how interlayer twist angles and structural variations affect spin wave generation, propagation, and coherence. Experimentally, we fabricate twisted CrSBr homostructures with controlled rotation angles and probe their exciton and magnon properties as functions of twist angle, magnetic field, and temperature (Figs. 1-2). Complementary DFT calculations provide the local atomic geometry and exchange coupling parameters, which are incorporated into a QFT framework to model spin wave dispersion relations (Fig. 1D) in twisted and defect-engineered structures. By correlating theoretical dispersion features with experimentally mapped spin-wave dynamics, this integrated methodology reveals how interlayer twist and nanoscale morphology affect magnon behavior in van der Waals magnets.

[1] K. Momma and F. Izumi. *J. Appl. Crystallogr.* Vol. 44, pp. 1272-1276 (2011).
[2] M. Horton, P. Huck, R.X. Yang, *et al. Nat. Mater.* Vol. 24, pp. 1522-1532 (2025).
[3] A. Jain, S.P. Ong, G. Hautier, *et al. APL Mater.* Vol. 1, p. 011002 (2013).
[4] Y.J. Bae, J. Wang, A. Scheie, *et al. Nature.* Vol. 609, pp. 282-286 (2022).
[5] G.M. Diederich, J. Cenker, Y. Ren, *et al. Nat. Nanotechnol.* Vol. 18, pp. 23-28 (2023).
[6] Y. Sun, F. Meng, C. Lee, *et al. Nat. Phys.* Vol. 20, pp. 794-800 (2024).
[7] P. Aislinn, A. Winchell, E. Lambertson, *et al. MRS Advances*. Vol. 10, pp. 1985-1992 (2025).

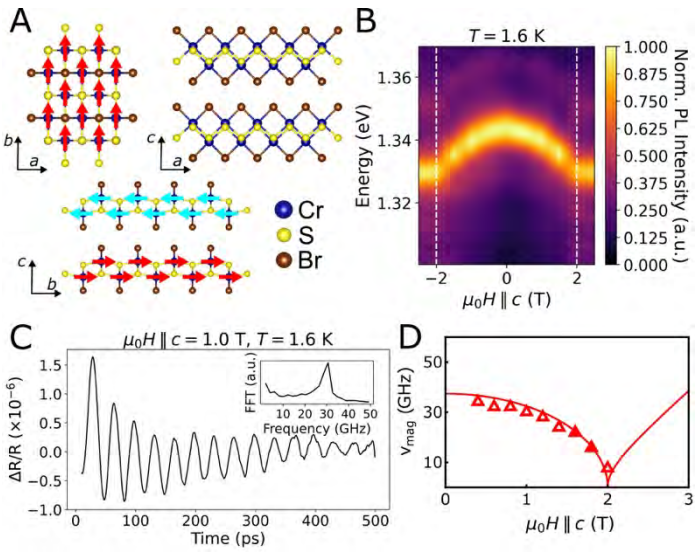


Fig. 1: Magneto-optical coupling and magnon-excitons in pristine CrSBr. *A.* Crystal structure of CrSBr, generated using VESTA[1] and data from Materials Project[2,3]. *B.* Photoluminescence (PL) vs. out-of-plane magnetic field for a bulk CrSBr flake. Exciton energy shifts with field until saturation at ±2 T (vertical lines). *C.* Time-resolved reflectance for a bulk CrSBr flake. Oscillations are attributed to magnon-excitons[4-7]. *Inset*: Fast Fourier transform (FFT) of time-resolved signal, with a peak FFT amplitude (magnon frequency) at 30.6 GHz. *D.* (Triangles) Experimental magnon frequency vs. magnetic field. (Curve) Fit generated from QFT derived spin wave dispersion and the solid triangles.

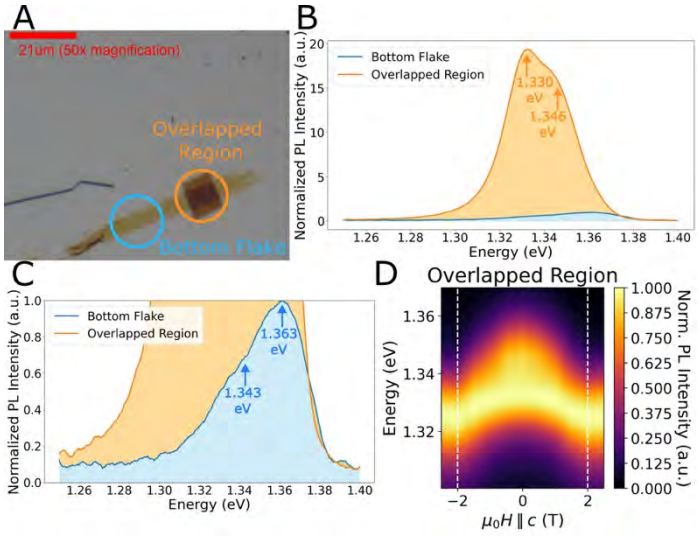


Fig. 2: Steady-state optical properties of 90° twisted CrSBr/CrSBr homostructure. *A.* Microscope image of sample.

B, *C*. Photoluminescence (PL) of the bottom flake and overlapped region of the 90° sample, normalized with respect to the bottom flake, at 0 T and 1.6 K. Lorentzian fits reveal exciton peaks of 1.343 eV and 1.363 eV for the bottom flake and 1.330 eV and 1.346 eV for the overlapped region. *D*. PL vs. out-of-plane magnetic field in the overlapped region. Saturation is observed at ±2 T (vertical lines).

AC-12. Quantum simulation of the Hubbard model on a graphene hexagon: strengths of IQPE and noise constraints

M. Mirzakhani, K. Moon
Dept. of Physics, Yonsei university, Seoul, Korea (the Republic of)

Quantum computing offers transformative potential for simulating real-world materials, providing a powerful platform to investigate complex quantum systems across quantum chemistry and condensed matter physics. In this work, we leverage this capability to simulate the Hubbard model on a six-site graphene hexagon using Qiskit, employing the Iterative Quantum Phase Estimation (IQPE) and adiabatic evolution algorithms to determine its magnetic properties. In noiseless simulations, IQPE converges within a few iterations to exact GSEs, while adiabatic simulations yield charge and spin densities and correlation functions in excellent agreement with exact diagonalization. However, deploying IQPE and adiabatic evolution on today's noisy quantum hardware remains highly challenging. To investigate these limitations in IQPE, we use the Qiskit Aer simulator with a custom noise model tailored to the characteristics of IBM's real hardware. Further, we implement the IQPE algorithm on IBM's ibm_strasbourg and ibm_fez devices, enabling direct comparison between simulated and real hardware noise. While ibm_fez runs closely match exact results, discrepancies highlight the gap between modeled and physical noise. Extending the study to systems up to N = 6 sites,we benchmark IQPE's scalability, demonstrating its potential and current limitations for simulating strongly correlated materials under realistic conditions.

M. Mirzakhani and K. Moon, EPJ Quantum Technology, 12:134 (2025)

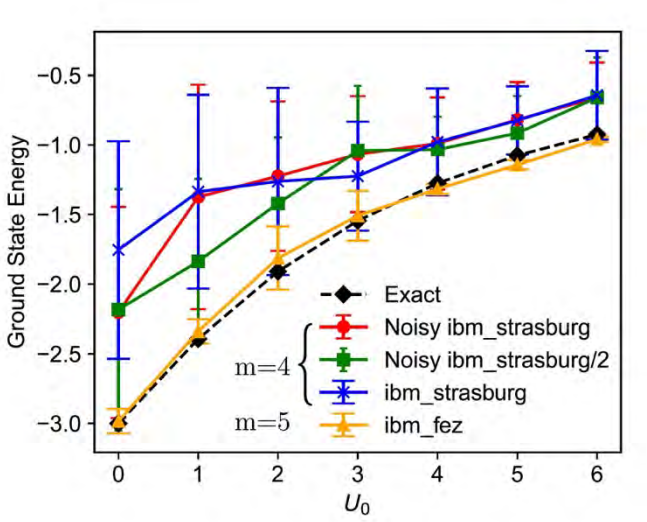


Fig. 1 Ground state energy as a function of on-site interaction strength U_0

AC-13. Formation of Order in the Two-Dimensional DMI-Antiferromagnet $Ba_2CuGe_2O_7$

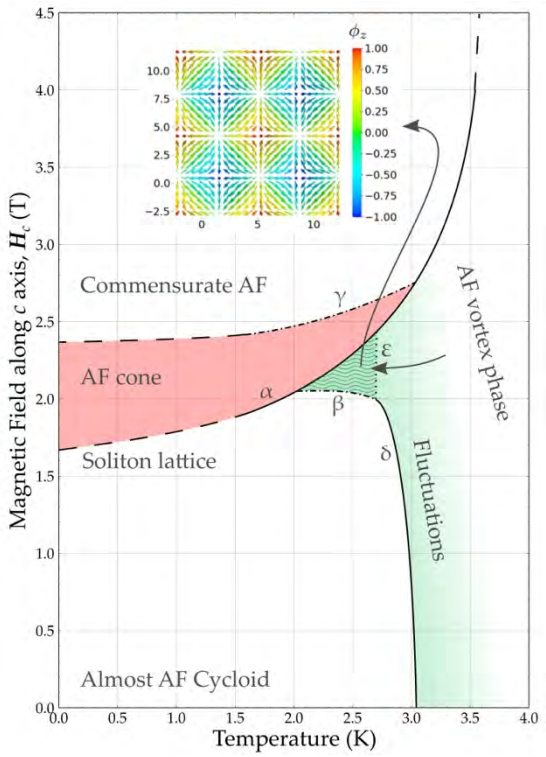
P. Wild[1], M. Dembski-Villalta[1], K. Fellner[1], M. Garst[2], S. Mühlbauer[1]
[1]TUM / MLZ, Munich, Germany, [2]KIT, Karlsruhe, Germany

Antiferromagnetic $Ba_2CuGe_2O_7$, characterized by a quasi-2D structure with Dzyaloshinskii-Moriya interactions (DMI), exhibits spiral spin structures with potential non-trivial topology and combines them with a variety of unconventional magnetic phase transitions. $Ba_2CuGe_2O_7$ is an insulator characterized by a tetragonal, non-centrosymmetric space group P-42_1m. The main features of the magnetic structure are due to the Cu^{2+} ions in a square arrangement. Below the Néel temperature T_N = 3.05K, the DMI term leads to a long-range incommensurate, almost AF cycloidal spin spiral in the ground state.

Using neutron diffraction, the magnetic fluctuations are investigated near the phase transition to a long-range ordered incommensurate cycloid spin spiral in the antiferromagnetic insulator $Ba_2CuGe_2O_7$. We find that these fluctuations possess a two-dimensional character and, as a consequence, cover an extended cylindrical manifold in reciprocal space. Their distribution can be explained with a ratio of in- and out-of-plane stiffness of 0.027, in agreement with previous reports. The temperature dependence of the correlation length is consistent with a crossover from 2D antiferromagnetic Heisenberg fluctuations to

incommensurate fluctuations with decreasing temperature, highlighting the plethora of phase transitions associated with spiral magnetic textures. Recently, a new phase with a vortex-antivortex magnetic structure has been theoretically described. It has been experimentally confirmed in a pocket in the phase diagram at around 2.4K and an external field along the crystalline c-axis of around 2.2T. A lack of evidence for a thermodynamic phase transition towards the paramagnet in high resolution specific heat measurements and a finite linewidth in energy and momentum of the incommensurate peaks in neutron scattering, as opposed to the cycloidal ground state, seem to mark the vortex phase as a slowly fluctuating structure at the verge of ordering. Polarization measurements and neutron experiments including E-field in order to investigate its interplay with an external magnetic field are already planned and will allow for further pinning down multiferroic properties of $Ba_2CuGe_2O_7$.

[1] S. Mühlbauer et al, Rev. Mod. Phys, 91, 015004, 2019
[2] S. Mühlbauer et al. Phys. Rev. B, 96(13):1–9, 2017
[3] A. Zheludev et al. Phys. Rev. B, 54 (21):15163- 15170, 1996
[4] B. Wolba. PhD thesis, KIT, 2021
[5] H. Murakawa et al. Phys. Rev. Lett., 103(14):2–5,2009



Magnetic phase diagram of $Ba_2CuGe_2O_7$

SESSION AD: 3D, PATTERNED AND LAYERED MAGNETISM
Chair(s): Z. Chen, *Physics, Georgetown University, Washington, District of Columbia, United States*
Tuesday, November 3, 2026
08:30 AM-12:00 PM
Coral 2

AD-01. Magneto-thermoelectric effects in three-dimensional interconnected networks of ferromagnetic nanowires and nanotubes

T. da Câmara Santa Clara Gomes[1, 2], N. Marchal[2], F. Abreu Araujo[2], J. de la Torre Medina[3], L. Piraux[2]
[1]Instituto de Engenharia de Sistemas E Computadores – Microsistemas e Nanotecnologias (INESC MN), Lisbon, Portugal, [2]Institute of Condensed Matter and Nanosciences, Université catholique de Louvain, Louvain-la-Neuve, Belgium, [3]Instituto de Investigaciones en Materiales/Unidad Morelia, Universidad Nacional Autónoma de México, Morelia, Mexico

Three-dimensional (3D) networks of interconnected magnetic nanowires (NWs), nanotubes (NTs), and multilayers (Fig. 1) are fabricated by direct electrodeposition into track-etched polymer templates with crossed nanochannels [1,2]. This approach yields flexible polymer–magnetic nanofiber composite films with exceptionally high interconnectivity [3], enabling in-plane measurements of magneto-thermoelectric properties while confining thermal and electrical currents along the nanofiber axes.
We demonstrate that 3D NW and NT networks made of ferromagnetic metals retain the intrinsic bulk thermopower down to diameters d of ~23 nm (Fig. 2) [4]. We report the first magneto-thermoelectric measurements of 3D interconnected nickel NT networks (Fig. 2b), revealing distinct behavior compared to NWs [4]. In ferromagnet/Cu multilayer architectures (Fig. 2c–d), only minor reductions in thermopower relative to bulk are observed [1]. These multilayered 3D networks enable in-plane measurements with negligible contact resistance while enforcing current-perpendicular-to-plane transport, leading to large magnetothermopower effects analogous to giant magnetoresistance (Fig. 2c).
These systems constitute high-performance spin-caloritronic platforms, combining power factors comparable to state-of-the-art thermoelectrics with room-temperature magneto-thermoelectric modulations up to 34% (~5.5 μV/K), while enabling direct extraction of spin-dependent Seebeck coefficients [1]. Integration into 3D NW-based thermocouples further enables magnetically activated thermoelectric switches with effectively infinite magneto-

thermopower ratios for thermally powered logic operations [5]. These macroscopic nanostructured materials bridge nanoscale functionalities and bulk performance, offering scalable, flexible platforms for thermoelectric and spin-caloritronic applications.
[1] T. da Câmara Santa Clara Gomes, F. Abreu Araujo and L. Piraux, Science Advances., Vol. 5, p. eaav2782 (2019)
[2] T. da Câmara Santa Clara Gomes et al., Chap. 23 in Magnetic Nano- and Microwires: Design, Synthesis, Properties and Applications, 3rd ed., edited by M. Vázquez (Woodhead Publishing, 2026).
[3] T. da Câmara Santa Clara Gomes et al., Physical Review Research., Vol. 6, p. 023211 (2024)
[4] T. da Câmara Santa Clara Gomes et al., Applied Physics Letters., Vol. 124, p. 092406 (2024)
[5] T. da Câmara Santa Clara Gomes et al., Advanced Materials Technologies., Vol. 7, p. 2101043 (2021)

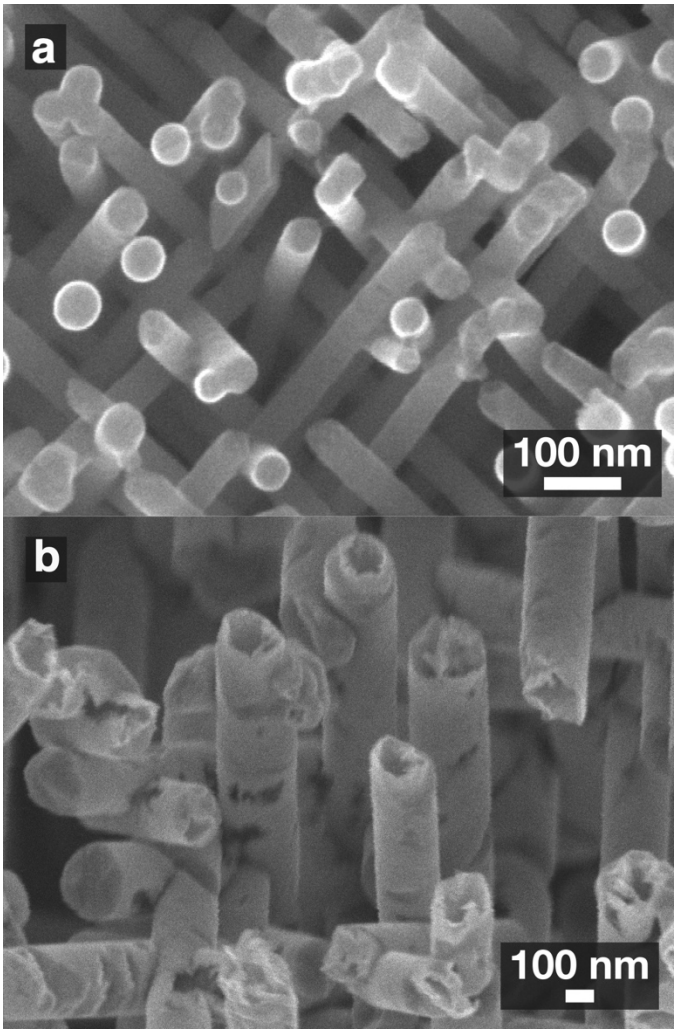


Fig. 1 Scanning electron microscope (SEM) images of self-supported networks of interconnected Ni NWs (a) and NTs (b).

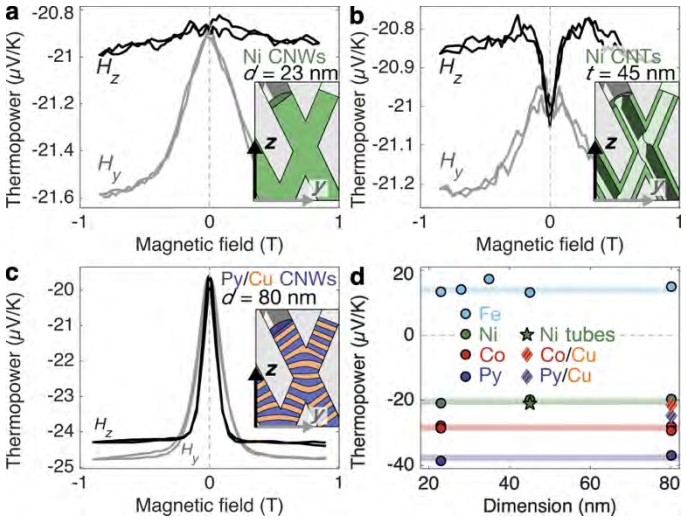


Fig. 2 (a–c) Magnetothermopower of crossed Ni NWs (d = 23 nm), Ni NTs (d = 230 nm, thickness t ~45 nm), and Py/Cu multilayer NWs (d = 80 nm) under in-plane and out-of-plane magnetic fields. (d) Room-temperature thermopower as a function of NW diameter and NT thickness.

AD-02. 3D magnetic nanostructures and effects of curvature

D. Bhattacharya[1, 2], C. Langton[1], B. J. Fugetta[1], D. W. Raftrey[3, 4], C. Fernandez-Gonzalez[5], S. Satapathy[3], O. Bezsmertna[6], A. Sorrentino[5], D. Makarov[6], G. Yin[1], P. Fischer[3, 4], K. Liu[1]
[1]Physics Department, Georgetown University, Washington, District of Columbia, United States, [2]Rowan University, Glassboro, New Jersey, United States, [3]Materials Science Division, Lawrence Berkeley National Laboratory, Berkeley, California, United States, [4]University of California, Santa Cruz, Santa Cruz, California, United States, [5]ALBA Light Source, Barcelona, Spain, [6]Helmholtz-Zentrum Dresden-Rossendorf, Dresden, Germany

Three-dimensional (3D) nanomagnetic structures provide a fertile ground for stabilizing unconventional spin configurations. In particular, curvature can intricately modify the energy landscape and govern magnetic characteristics, including topology and chirality. Recently, we have demonstrated curvature-induced modification of magnetic configuration in a Co/Pd multilayer thin film deposited over Cu nanowires (NWs) [1]. The overall domain orientation was influenced by the underlying NW-defined curvature. Domain wall (DW) chirality was also strongly affected by curvature. In particular, Néel DWs were promoted, and the effective

DMI contribution was found to be ~1/3 of the intrinsic DMI of the Co/Pd film.

In another study, we have realized a prototypical 3D topological nanostructure, magnetic Möbius bands and demonstrated that their magnetic behaviors are governed by the geometric constraints of the structure [2]. Magnetometry and First Order Reversal Curve (FORC) measurements reveal a geometry-driven rotation of the spin configurations that is opposite to the geometric chirality of the bands. Furthermore, this unique geometry also promotes the fragmentation of larger domains into complex nontrivial arrangements in regions of maximal curvature. These findings are corroborated by micromagnetic simulations, and soft X-ray magnetic imaging. The resulting spin textures can then be preferentially driven along the structure by applied magnetic fields.

Our results demonstrate the potentials of using 3D nanomagnetic systems to explore how geometry influences domain structures and spin configurations across distinct material systems. This work is supported in part by the NSF (DMR-2005108, DMR-2320636 and ECCS-2429995) and DOE BES (DE-AC02-05-CH11231, NEMM program MSMAG).
[1] D. Raftrey, et al, ACS Nano, 19, 31609 (2025).
[2] C. Langton et al, submitted.

AD-03. Influence of Mean and Gaussian Curvature on Magnetic Textures in 3D Nanowire Arrays

C. Langton[1], B. J. Fugetta[1], C. Fernandez-Gonzalez[2], A. Sorrentino[2], D. Bhattacharya[3], P. Fischer[4, 5], G. Yin[1], K. Liu[1]
[1]Department of Physics, Georgetown University, Washington, District of Columbia, United States, [2]MISTRAL Beamline, ALBA Light Source, Cerdanyola del Vallès, Spain, [3]Department of Electrical & Computer Engineering, Rowan University, Glassboro, New Jersey, United States, [4]Materials Science Division, Lawrence Berkeley National Laboratory, Berkeley, California, United States, [5]Department of Physics, University of California Santa Cruz, Santa Cruz, California, United States

The ability to precisely control the local energy landscape makes 3D nanomagnetic structures a versatile platform for engineering magnetic configurations. Previous studies have demonstrated that local curvature plays a critical role in modifying this landscape[1-3]. Here we report a systematic study of the effects of controlled mean and Gaussian curvatures on magnetic configurations in thin films deposited over intersecting nanowires.
The nanowire scaffolds are fabricated using two-photon lithography with diameters ranging from 200 nm to 500 nm (Fig. 1b). Thin films of Co/Pd/Ta with were deposited over the nanowire arrays by magnetron sputtering, whose compositions were carefully tuned to balance the Dzyaloshinskii-Moriya interaction (DMI) to near zero. Thus, the specific impact of 3D curvature on the resulting magnetic textures can be highlighted. Soft X-ray nanotomography (Fig. 1a) at the ALBA Synchrotron MISTRAL beamline[4] was used to fully reconstruct the 3D nanoscale textures. Our imaging reveals a complex landscape of nominally in-plane magnetic domains that are strongly modulated by the underlying 3D geometry. Two key properties are observed. First, out-of-plane (OOP) domains are more prominent on wires with larger diameters (Fig. 1c). In contrast, regions with smaller diameter wires contain domains that remain continuous with the in-plane orientation of the flat film. Second, in the intersecting areas where OOP domains are most prevalent, they are pinned at the inner intersections where the mean and Gaussian curvatures are negative (Fig 1c). These findings highlight an intricate relationship between curvature and the magnetic energy landscape, opening new avenues for future 3D spintronic applications.

This work has been supported by the NSF (ECCS-2429995 and DMR-2320636) and DOE BES MSE under Contract # DE-AC02-05-CH11231, NEMM program (MSMAG)

[1] G. Gubbiotti *et al.*, *J. Phys. Condens. Matter.* 37, 143502 (2025)
[2] P. Fischer et al., *APL Mater.* 8, 010701 (2020)
[3] D. Raftrey *et al.*, *ACS Nano* 19, 31609 (2025)
[4] A. Sorrentino *et al.*, *J. Synchrotron Radiat.* 22, 1112 (2015)

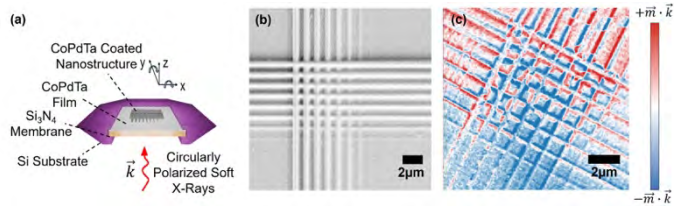


Fig. 1: (a) Magnetic imaging setup. (b) SEM image of nanowire array. (c) Magnetic projection at normal incidence showing domains parallel to the beam path.

AD-04. Ferromagnetic resonance in a strongly coupled 3D-stacked square artificial spin ice

A. Walters, E. Iacocca
University of Colorado Colorado Springs, Colorado Springs, Colorado, United States

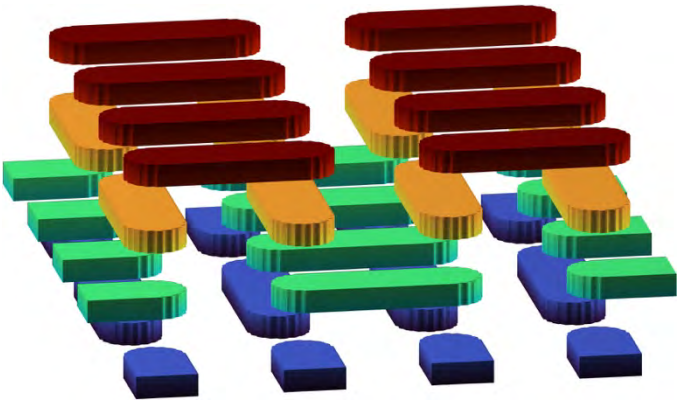
Artificial spin ices are geometric arrangements of single-domain nanomagnets where geometric frustration is present [1]. Growing interest in three-dimensional (3D) structures and artificial spin ices [2] have predominantly focused on the magnetization configurations stabilized by geometry. 3D structures offer additional dynamic coupling that enriches their FMR response [3]. Here, we investigate a 3D stacked square artificial spin ice (3D-ASI) where the vertical and horizontal sublattices are staggered to maximize edge coupling. The lattice is composed of orthogonally oriented nanomagnetic layers vertically spaced by 5 nm, forming a square geometry in z-projection, schematically shown in Figure 1.

Using micromagnetic simulations with Mumax3 [4], we computed the ferromagnetic resonance (FMR) by exciting the system with a 10 ps out-of-plane field pulse with a 10 mT magnitude. Analysis of the magnetization dynamics at zero applied field reveals traditional bulk and edge modes with lifted degeneracies stemming from the additional degrees of freedom. For example, we found that the spatial distribution of the modes depends on the relative permutations of the 3D-ASI layers. The field-dependent FMR is shown in Figure 2, where a dense mode spectrum is apparent. In addition, there is a field-independent edge mode at 3.61 GHz that demonstrates the strong dynamic coupling between nanomagnets. The bulk modes follow the traditional Kittel dependence, indicating weaker bulk interaction.

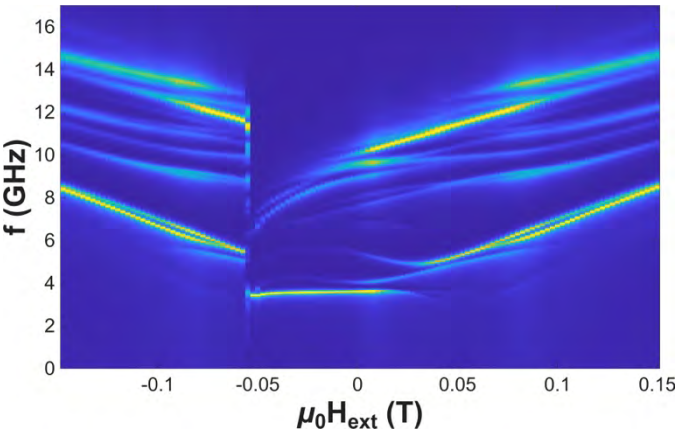
The presence of dominant edge modes demonstrates that strong dynamic coupling can be achieved in three-dimensions by vertically aligning the caps of the nanomagnets, while the tightly packed and staggered structure further enhances intra- and interlayer coupling. The existence of a reproducible remanent state and several modes suggests that the 3D-ASI could be useful for reservoir computing applications. It would also be interesting to investigate the waveguide characteristics of the 3D-ASI.

This material is based upon work supported by the National Science Foundation under Grant No. 2532497.

[1] R. Sultana et al., J. Appl. Phys. 138, 061101 (2025)
[2] G. Gubbiotti, et al., J. Phys. Cond. Matt. 37, 143502 (2025)
[3] T. Dion, et al., Nature Comm. 15, 4077 (2024)
[4] A. Vansteenkiste, et al., AIP Advances 4, 107133 (2014)



3D-ASI composed of color-coded, orthogonal layers of aligned nanomagnets.



Field-dependent FMR with color corresponding to normalized magnetization amplitude.

AD-05. Reconfigurable 3D magnetic nanostructures and their prospective for magnonic networks

S. Wintz
Helmholtz-Zentrum Berlin, Berlin, Germany

Three-dimensional nanomagnetism has become a rapidly growing research field, where extending magnetic functionality into the third spatial dimension enables new physical phenomena and application concepts, including sensing, data storage, and unconventional computing [1,2]. This invited talk proposal highlights recent advances in reconfigurable 3D magnetic nanostructures enabled by focused electron beam–induced deposition (FEBID), a

fabrication technique offering genuine three-dimensional design freedom with sub-100 nm resolution.

A key challenge in 3D nanomagnetism is the controlled manipulation of complex magnetic states in non-planar geometries. Using a Co_3Fe tetrapod as a model system, the proposed talk will show how magnetization reversal processes in individual branches can be directly resolved by scanning transmission X-ray microscopy and quantitatively reproduced by finite-element micromagnetic simulations [3]. The results demonstrate that different components of a single 3D nanostructure can be switched individually and sequentially by selecting the direction of the applied magnetic field, enabling full reconfigurability of the three-dimensional magnetic configuration. These results establish reconfigurable 3D nanomagnets as a promising platform for future magnonic networks with programmable, non-reciprocal spin-wave functionality [4] in three dimensions.

[1] A. Fernández-Pacheco, R. Streubel, O. Fruchart, R. Hertel, P. Fischer, R. P. Cowburn, *Nat. Commun.* 8, 15756 (2017).
[2] C. Donnelly, S. Finizio, S. Gliga, M. Holler, A. Hrabec, M. Odstrčil, S. Mayr, V. Scagnoli, L. J. Heyderman, M. Guizar-Sicairos, J. Raabe, *Nat. Nanotechnol.* 15, 356 (2020).
[3] S. Koraltan, F. Porrati, R. Kraft, S. Barth, M. Weigand, C. Abert, D. Suess, M. Hutz, S. Wintz, *Adv. Funct. Mater.* 35, e15338 (2025).
[4] R. A. Gallardo, M. Weigand, K. Schultheiss, A. Kakay, R. Mattheis, J. Raabe, G. Schütz, A. Deac, J. Lindner, S. Wintz, *ACS Nano* 18, 5249 (2024).

AD-06. Thin-Film Micrometer Scale Circular Halbach Patterns for Localized Field Generation

S. Kulakarni, A. El-Ghazaly
Electrical and Computer Engineering, Cornell University, Ithaca, New York, United States

Halbach arrays, known for concentrating magnetic flux on one side, have been widely implemented using discrete permanent magnets [1]. Thin-film linear Halbach structures produce sinusoidal near-field profiles that are unsuitable where uniform localized fields are needed [2]. Circular Halbach geometries offer an alternative, but to the best of our knowledge, have not yet been realized in thin-film form [3]. Here, we present the simulation and ongoing fabrication of thin-film, micrometer-scale circular Halbach rings capable of generating localized, non-volatile magnetic fields.

Each ring was divided into 8 $Fe_{65}Co_{35}$ [4] segments with prescribed in-plane magnetizations and simulated in Ansys Maxwell. An ON state (sequential magnetization rotation) and an OFF state (circumferential magnetization) were defined for localized generation or suppression of the center field (CF), respectively. In the ON state, the ratio of CF (~2-6 mT) compared to the stray field 5 µm outside the ring was used as the primary figure of merit (FOM). The 8-segment configuration was selected as the optimal design, balancing strong ON/OFF suppression and ease of fabrication. Parametric studies revealed that ring thickness variations had a negligible effect due to the strong shape anisotropy in thin-film patterns, while increasing ring width at fixed inner radius (5 µm) and thickness (200 nm) yielded a proportional increase in CF.

The fabrication of thin-film arrays involves sputtering $Fe_{65}Co_{35}$ onto lithographically patterned Si wafers, two opposite segments at a time. During each deposition, an applied field is used to define the magnetization along the chosen anisotropy axis for both segments. Geometry-matched rectangular test structures are patterned on Si wafers for VSM. The hysteresis data from the resulting BH curves are incorporated into the simulations to validate and refine the modeled field distribution. These results establish a scalable platform for spatially patterned thin-film Halbach arrays at the microscale.

[1] K. Halbach, *Nuclear Instruments and Methods*, vol. 169, no. 1, pp. 1–10, Feb. 1980.
[2] F. Dumas-Bouchiat *et al.*, *Applied Physics Letters*, vol. 96, no. 10, Mar. 2010.
[3] P. Blümler and Helmut Soltner, *Applied Magnetic Resonance*, vol. 54, no. 11–12, pp. 1701–1739, Oct. 2023.
[4] T. Hasegawa *et al.*, *Scientific Reports*, vol. 7, no. 1, Oct. 2017.

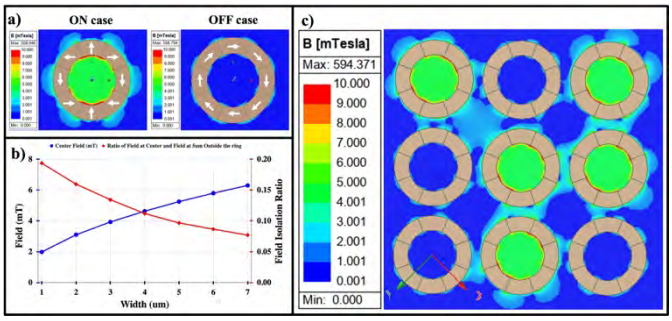


Fig.1: a) ON/OFF states with segment magnetizations, b) CF & Field isolation ratio vs ring width, c) 3×3 array of ON/OFF Halbach rings.

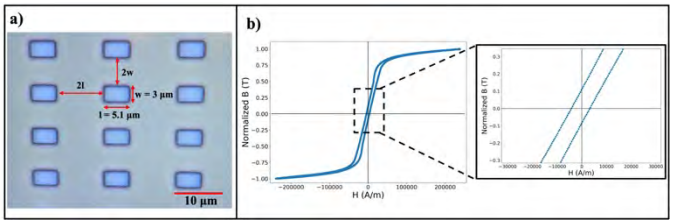


Fig.2: a) Geometry-matched rectangular units, b) BH curve showing a coercivity of 3618 A/m.

AD-07. Nonlinear Minimizer for Artificial Spin Ice Using a Minimal Semi-Analytical Model

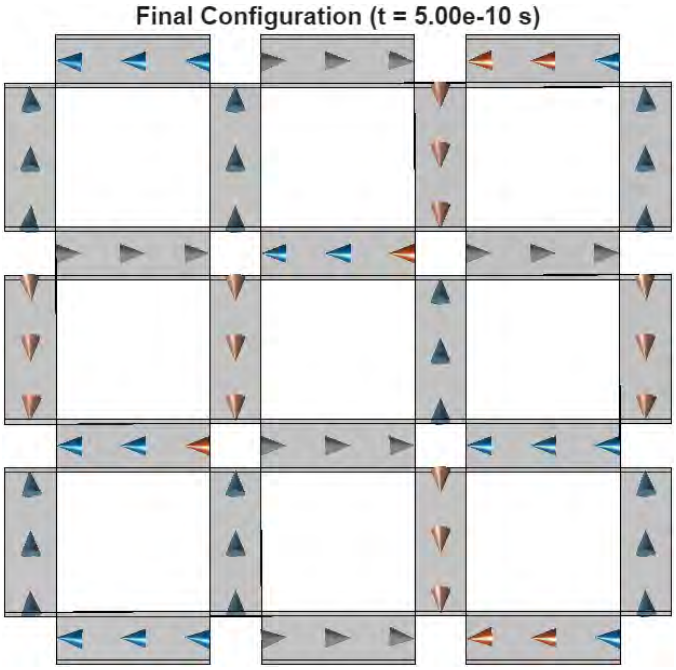
H. Braun, E. Iacocca
Physics, University of Colorado Colorado Springs, Colorado Springs, Colorado, United States

Artificial spin ices (ASIs) are metamaterials composed of geometric arrangements of nanomagnets that exhibit frustration [1]. There has been an interest in using ASIs as magnonic crystals with spin-dependent ferromagnetic resonance and band structures [2]. The computation of band structures can be time-consuming when performed with micromagnetic simulations. As a consequence, a minimal model called Gænice was introduced [3], leading to a dramatic speed-up in the computation. However, the band structures depend on the magnetization state introduced, leading to quantitative discrepancies with micromagnetic simulations and experiments.

Here, we introduce GæniceN, a nonlinear solver within the Gænice framework for computing equilibrium magnetization configurations in ASIs. In essence, the program computes the stationary solutions of the damped Landau–Lifshitz equation. The approach supports both periodic boundary conditions, used to approximate infinite lattices, and finite boundary conditions, which capture edge effects and confinement-induced states.

The implementation accommodates arbitrary two-dimensional lattice geometries and incorporates the main field contributions for ASIs: external field, shape anisotropy, exchange interaction, dipole field, and perpendicular magnetic anisotropy. Our preliminary results qualitatively indicate that the Gænice minimal framework is sufficient to capture the relevant physics. The nonlinear solver will be interfaced with the Gænice eigenvalue solver to compute ferromagnetic resonance and band structures. We expect these combined tools to aid in the modeling of ASIs for magnonic applications.

This material is based upon work supported by the National Science Foundation under Grant No. 2532497.
References:
[1] R. Sultana, et al., J. Appl. Phys. 138, 061101 (2025)
[2] S. Gliga, E. Iacocca, and O. G. Heinonen, APL Materials 8, 040911 (2020)
[3] G. Alatteili, et al., J. Magn. Magn. Mater. 589, 171603 (2023)



A vortex state is stabilized in a 3x3 square lattice.

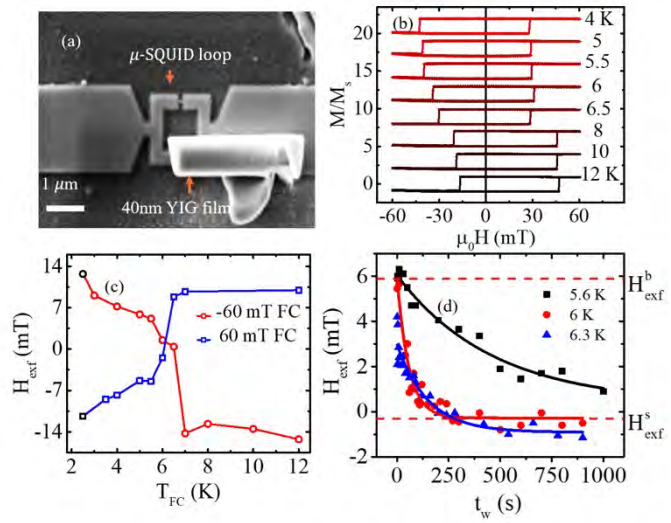
AD-08. Tunable Exchange Bias from Interfacial Spin Frustration in YIG/GGG

U. C. Thuwal[1], S. Maity[1], R. Pervin[1], R. Medwal[1], J. Vas[6], Y. Fukuma[2, 3], H. Courtois[5], C. B. Winkelmann[4], A. K. Gupta[1]
[1]Department of Physics, Indian Institute of Technology, Kanpur, Uttar Pradesh, India, [2]Kyushu Institute of Technology, Iizuka, Japan, [3]Center for Neuromorphic AI Hardware, Kitakyushu, Japan, [4]Univ. Grenoble Alpes, CNRS, Grenoble INP, IRIG-PHELIQS, Grenoble, France, [5]Univ. Grenoble Alpes, CNRS, Grenoble INP, Institut Neel, Grenoble, France, [6]The Ernst Ruska-Centre for Microscopy and Spectroscopy, Forschungszentrum Julich, Germany

Ferrimagnetic $Y_3Fe_5O_{12}$ (YIG) thin films grown on the (001) surface of paramagnetic $Gd_3Ga_5O_{12}$ (GGG) exhibit exchange bias attributed to magnetism originating from an interfacial layer between the two materials [1-3]. We show that YIG

films grown by sputtering and subjected to lower post-annealing temperatures than in previous studies [3] display a significantly reduced blocking temperature of the interfacial magnetic layer, reaching approximately 7 K in micron-sized films while preserving a strong exchange bias. A micron-sized rectangular YIG/GGG sample was placed close to a Nb μ-SQUID, shown in a scanning electron micrograph [Fig. 1(a)]. The magnitude and sign of the exchange bias are tunable via the magnetic field-cooling (FC) protocol, as evidenced by M–H loops measured after different field-cooling temperatures T_{FC} [Fig. 1(b)]. The exchange field H_{exf} as a function of T_{FC} for opposite cooling-field directions is shown in Fig. 1(c), demonstrating tunable exchange bias and reflecting slow, frustrated spin dynamics within the interfacial layer near the blocking temperature. Furthermore, the waiting-time dependence of the exchange field follows an exponential relaxation [Fig. 1(d)]. Angle-resolved μ-SQUID measurements are interpreted considering magneto-crystalline anisotropy and the coupling of the sample's vector magnetic moment to the μ-SQUID. In YIG (100), additional rotational hysteresis is observed, consistent with irreversible magnetization dynamics influenced by interfacial exchange bias.

[1] A. Mitra, O. Cespedes, Q. Ramasse, *et. al.*, "Interfacial origin of the magnetisation suppression of thin film yttrium iron garnet", Sci. Rep. vol. 7, p. 11774 (2017).
[2] M. J. Roos, P. Quarterman, J. Ding, M. Wu *et. al.*, "Magnetisation and antiferromagnetic coupling of the interface between a 20 nm $Y_3Fe_5O_{12}$ film and $Gd_3Ga_5O_{12}$ substrate," *Physical Review Materials*, vol. 6, no. 3, p. 034401, (2022).
[3] J. M. Gomez-Perez, S. Velez, L. McKenzie-Sell *et. al.*, "Synthetic antiferromagnetic coupling between ultrathin insulating garnets," *Physical Review Applied*, vol. 10, no. 4, p. 044046, (2018).



(a) SEM image of the micron-sized YIG/GGG sample positioned on a Nb *μ*-SQUID. (b) M–H loops measured after different field-cooling temperatures T_{FC}. (c) Exchange field H_{exf} as a function of T_{FC} for opposite cooling-field directions, showing tunable exchange bias. (d) Variation of the exchange field H_{exf} with waiting time t_w for representative FC temperatures T_{FC}. Solid lines are an exponential fit illustrating the slow relaxation of the exchange field.

AD-10. Modification of Interfacial Exchange Coupling and Magnetic Training in FeCo/CoO Heterostructures

R. Gupta[1], K. Sangeeth[1], A. Gupta[2]
[1]School of Instrumentation, Devi Ahilya University, Indore, Madhya Pradesh, India, [2]Department of Physics, University of Petroleum and Energy Studies, Dehradun, Uttarakhand, India

From an application perspective, thin films featuring ferromagnetic (FM) layers coupled with antiferromagnetic (AFM) layers are highly significant. For example, the exchange-bias (EB) thin film, which is a critical component in spin-valve devices utilizing the giant magnetoresistance (GMR) effect. [1, 2]. EB systems are essential for locking FM layer magnetization in spin-valve structures. Because of this, characterizing exchange bias is a necessary step [2]. A common challenge is the training effect, where the exchange bias value diminishes during field cycling; however, for practical applications, maintaining a consistent exchange bias field (H_{EB}) throughout repeated cycles is highly desirable.
In this work, we describe the FeCo/CoO film's magnetization reversal behavior following ion irradiation and thermal annealing. Kerr microscopy is being used to assess magnetization in the temperature range of 80 K-270 K after

field-cooling from the Neel temperature. There is no asymmetry in the hysteresis curve at 80 K for the first and second magnetization reversals, and the exchange bias value of the as-deposited film does not vary with the number of loops as shown in fig. 1. Similarly, there is no significant change in the case of an ion fluence of $3X10^{13}$ ions/cm^2 shown in fig. 1.The training behavior of the FeCo/CoO system is unaffected, although the value of H_{EB} drops at an ion fluence of $1X10^{14}$ Au ions/cm^2. After thermal annealing at 673 K, the value of H_{EB} has been increased. In contrast to ion-beam-implanted films and as-deposited films, the training effect in thermal annealing is entirely different. In terms of technology, the FeCo/CoO combination creates a stable magnetic state configuration that would work well for spin valves that are completely insensitive to infinite field sweeping. In more accessible terms, the FeCo/CoO pairing acts like a "magnetic anchor." Technically speaking, it creates a highly stable magnetic setup that is ideal for spin valves. The standout feature here is that this configuration remains completely unaffected by external magnetic forces, no matter how strong or frequent those magnetic "sweeps" are.

[1] J. Nogués and I. K. Schuller, Exchange Bias, J. Magn. Magn. Mater. 192, 203 (1999).
[2] V. Skumryev, S. Stoyanov, Y.Zhang, G. Hadjipanayis, D. Givord and J. Nogues, Beating the superparamagnetic limit with exchange bias, Nature 423, 850 (2003).

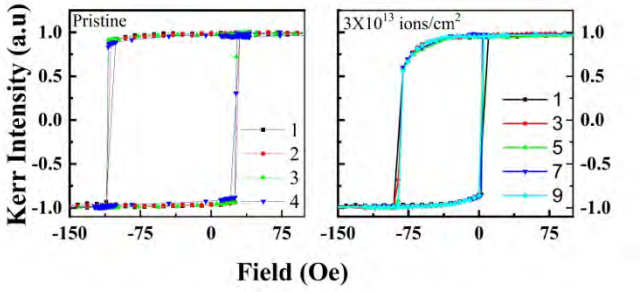


Fig. 1 Hysteresis behavior of pristine and after $3X10^{13}$ Au-ions/cm^2.

AD-11. Magnetic Vortex Microdots for Multistate Memory Enabled by NanoSQUID Readout

A. V. Pan, C. Eker
ISEM/Physics, University of Wollongong, Wollongong, New South Wales, Australia

Magnetic vortex states arise as a distinctive form of magnetic domain configuration when ferromagnetic materials are confined to the nanoscale, where they minimize magnetostatic energy. A particularly compelling aspect of vortex physics is the controlled manipulation of vortex polarity via external field pulses. The ability to reversibly switch vortex polarity using magnetic or electric stimuli holds significant promise for next-generation magnetic memory and logic devices. In this work, we employ a nanoSQUID-based readout to realize multi-bit (degenerate) memory cells in Permalloy microdots and directly visualize the read/write functionality of magnetic vortex states driven by external magnetic pulses, enabling prospects for high-density data storage. The behavior of the memory cell is investigated using a time-dependent Ginzburg–Landau framework in conjunction with micromagnetic simulations, providing detailed insight into vortex dynamics and enabling visualization and characterization of vortex-state evolution in ferromagnetic microdots. Our results reveal three distinct and addressable memory states, corresponding to positive, negative, and neutral vortex polarities, that can be reliably manipulated using experimentally feasible parameters, underscoring the viability of vortex-based memory architectures. Furthermore, we demonstrate that the performance and functionality of the memory access device depend sensitively on the superconducting material employed in the nanoSQUID, highlighting an additional degree of freedom for device optimization.

AD-12. Opto-mechanical control over the properties of magnetostrictive thin film via liquid crystalline networks

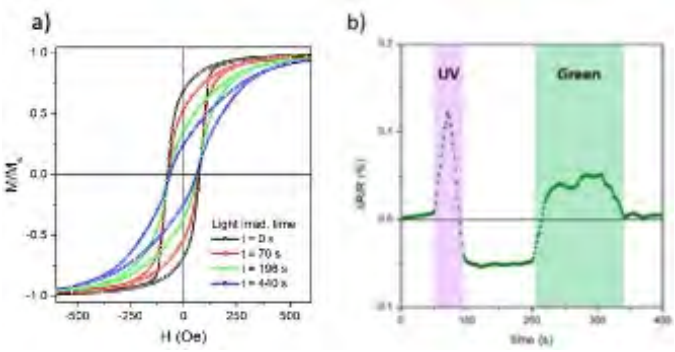
G. Barrera[1], D. Martella[2, 4], F. Celegato[1], A. Magni[1], M. Coisson[1], C. Parmeggiani[2, 4], D. Wiersma[3, 4], P. Tiberto[1]
[1]Advance Materials and Life Sciences, INRIM, Torino, Italy, [2]Department of Chemistry "Ugo Schiff", Università di Firenze, Firenze, Italy, [3]Physics, Università di Firenza, Firenze, Italy, [4]European Laboratory for Non Linear Spectroscopy (LENS), Firenze, Italy

Composite magnetic materials with multiple responses to environmental stimuli, such as light, are expected to have a significant impact on various applications, particularly in sensing and actuation devices.

This work explores the combination of magnetostrictive thin films (FeGa and Ni) with soft photo-responsive polymers, specifically liquid crystalline network (LCN). The proposed composite material allows to finely tune the magnetic properties of the thin film without the need for a magnetic field, but only through light irradiation, leading to an advantage in terms of energy consumption compared to the use of conventional magnetic field applicators [1]. Specifically, UV light irradiation leads to polymer contraction along the *x*-axis and expansion along the *y*-axis, exploiting the isomerisation of the dye in the LCN. This photo-actuation transfers a mechanical stress to the magnetostrictive thin film, whose magnetic domains rearrange under the effect of uniaxial stress anisotropy with respect to the sign of the magnetostrictive coefficient. Irradiation with green light (l = 505 nm) can be used to restore the original molecular order in the polymer, inducing a gradual release of the stress in the magnetic thin film and, consequently, to recover its pristine magnetic properties.

Hysteresis loops of the composite were measured by applying a magnetic field *H* in the film plane along both *x* and *y*-directions after irradiation with UV (see Figure 1a for FeGa/LCN sample) for a selected time. In addition, anisotropic magnetoresistance measurements were performed under opto-mechanical control of the magnetization. Specifically, the $\Delta R/R$ value is recorded for an interval of time during which UV light and green light are properly switched on and off, revealing a magnetic memory effect (see Figure 1b). This study analyses the coupling between the opto-mechanical properties of the substrate and the magnetostrictive behavior of the magnetic layer.

[1] G.Barrera, D. Martella, F. Celegato, N. Fuochi, M. Coïsson, C. Parmeggiani, D. S. Wiersma, P. Tiberto, *Advanced Science*, 11 2408273 (2024).



a) hysteresis loop of the FeGa/LCN sample in as-deposited state and after UV light irradiation time; b) evolution of the $\Delta R/R$ curve triggered by UV irradiation and green light.

SESSION AE: MEASUREMENTS TECHNIQUES

Chair(s): S. Gliga, *Center for Photon Science, Paul Scherrer Institut, Villigen, Switzerland*
Tuesday, November 3, 2026
08:30 AM-12:00 PM
South Pacific 1/2

AE-01. A New Approach to Radio-Frequency Susceptibility of Superparamagnetic Nanoparticles Breaks the Old Rules

R. Goldfarb
National Institute of Standards and Technology, Boulder, Colorado, United States

A challenge for the measurement of magnetic susceptibility of nanoparticles is accounting for the effect of magnetostatic interactions. Traditional models assume a value for the intrinsic susceptibility and deduce what would be the measured susceptibility as a function of particle concentration and interaction fields. For quality assessment, the inverse approach yields the intrinsic susceptibility from actual measurements. The measured susceptibility of particles in toroidal holders requires no correction for demagnetizing factors.

The traditional dogma of superparamagnetism, the absence of hysteresis, can be extended to frequencies where magnetization is hysteretic. At radio frequencies, the magnetic susceptibility of single-domain nanoparticles is often a complex quantity, indicative of losses. Thus, the equations for derived intrinsic susceptibility can be expanded into real and imaginary parts. Traditionally, small, single-domain particles are either superparamagnetic or

blocked. However, the intermediate, magnetically viscous state actually covers many orders of magnitude in frequency.

The concept of blocking temperature is usually applied to zero-field-cooled, quasi-static measurements. However, blocking frequency is important in radio-frequency measurements. Hard blocking requires either anisotropy energy to be much larger than the thermal energy or measurement frequency to be very much larger than the Néel relaxation frequency.

R. B. Goldfarb, "Radio-Frequency Toroid Susceptometry of Magnetic Nanoparticles: What Goes Around Comes Around," *IEEE Access*, vol. 14, pp. 22335-22355, Jan. 2026, doi: 10.1109/ACCESS.2026.3657951.

AE-02. Temperature-dependent Pauli susceptibility of an altermagnet candidate RuO_2

S. Paul[1, 2, 3], G. Mattoni[2], H. Matsuki[4], A. Ikeda[3], T. Johnson[2], J. Schmalian[5], C. Sow[1], S. Yonezawa[3], Y. Maeno[2]
[1]Department of Physics, Indian Institute of Technology Kanpur, Kanpur, Uttar Pradesh, India, [2]Toyota Riken–Kyoto University Research Center (TRiKUC), Kyoto, Kyoto, Japan, [3]Department of Electronic Science and Engineering, Graduate School of Engineering, Kyoto University, Kyoto, Kyoto, Japan, [4]Institute for Chemical Research, Kyoto University, Uji, Kyoto, Japan, [5]Institute for Theory of Condensed Matter and Institute for Quantum Materials and Technologies, Karlsruhe Institute of Technology, Karlsruhe, Karlsruhe, Germany

Altermagnets are a newly recognized class of symmetry-driven antiferromagnets. Following pioneering work in 2019 and the review by Libor Šmejkal [1], RuO_2 has emerged as a key candidate, driving extensive studies since 2020 to clarify its magnetic nature. Over the past several years (2020–2025) have relied on crystals with residual resistivity ratios (RRR) between about 12 and 160. Because extrinsic disorder can strongly influence magnetic signatures, the growth of exceptionally clean RuO_2 crystals is essential for determining the intrinsic ground state.

We present the growth of ultra-high-purity RuO2 single crystals with residual resistivity ratios (RRR) exceeding 1200 [2]. Depending on the growth parameters, the crystals show either bulk-like or needle-like morphologies [2]. We observe a low-temperature upturn in the DC magnetic susceptibility that can be attributed to dilute paramagnetic impurities at the level of only a few tens of ppm [2-3]. Curie–Weiss analysis yields Curie constants of 1.8×10^{-5} (RRR = 400) and 7.7×10^{-6} emu K/mol (RRR = 1200), corresponding to impurity concentrations of approximately 36 ppm and 15 ppm, respectively. The extremely large RRR of these ultra-clean samples enables us to conclude that bulk RuO2 is intrinsically paramagnetic. The temperature-dependent susceptibility is well described with the inclusion of a nonanalytic T^2 ln T contribution [3]. Consistently, the field-dependent spin susceptibility follows an H^2 ln H scaling, as expected for a Fermi liquid [3]. Furthermore, the electronic specific heat, magnetic susceptibility, and T^2 resistivity collectively indicate that RuO_2 behaves as a weakly correlated three-dimensional Fermi liquid, in agreement with the Wilson and Kadowaki–Woods ratios [3].

[1] L. Šmejkal et. al., Physical Review X 12, 040501 (2022)
[2] S. Paul et. al., Journal of Crystal Growth 673, 128405 (2025).
[3] S.Paul et. al., arXiv:2512.03108 (2025)
[4] Z. Wu, S.Paul et. al., Physical Review X 15, 031044 (2025)
[5] T. Osumi, S.Paul et. al., Physical Review B 113 (8), 085116 (2026)

AE-03. Comparison of device-level determination of Heisenberg exchange in STT-MTJ devices with film-level measurement by Brillouin light scattering

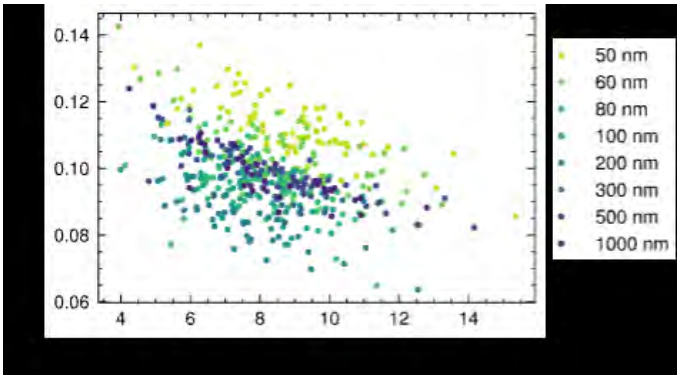
S. Liu[2, 1], C. Swindells[1], T. Santos[3], G. Mihajlović[3], H. T. Nembach[1], M. Pufall[1]
[1]National Institute of Standards and Technology, Boulder, Colorado, United States, [2]University of Colorado Boulder, Boulder, Colorado, United States, [3]Western Digital, San Jose, California, United States

A key parameter in determination of spin dynamics in magnetic thin films is Heisenberg exchange. For thin films on the order of ~1 nm relevant to magnetic tunnel junction (MTJ) devices, there are primarily two techniques for measuring exchange. The first method is by measuring field switching distributions (FSDs) of MTJ devices and fitting the domain wall magnetization reversal droplet model to the experimental data [1]. The second is Brillouin light scattering (BLS) measurement of spin wave dispersion in blanket films in the Damon-Eshbach and backward volume geometry [2]. In this work, we perform FSD measurements on sets of MTJ devices ranging from 50 nm to 1000 nm nominal diameter and repeat these measurements for five different material stacks. We use the droplet model to fit the FSD distributions and extract the exchange and the effective anisotropy energy (Fig. 1) and analyze the parameter space of the model to quantify uncertainties and correlations in determining these parameters. The results

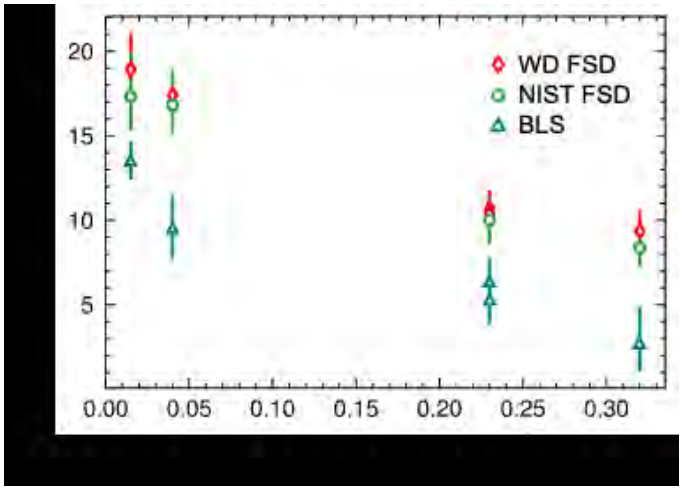
are compared with the exchange determined from film-level BLS measurements of the same five material stacks. A consistently lower exchange stiffness is obtained from BLS than for FSD (Fig. 2), though the same general trend with tungsten insertion layer thickness is observed. The free layer thickness and saturation magnetization are required to extract the exchange stiffness from the BLS measurements and are also important parameters for the FSD fits. The impact of these parameters, measurement approaches, and fitting methods are analyzed to better understand the differences in exchange stiffness measurement.

[1] Mihajlović, G., Smith, N., Santos, T., Li, J., Terris, B. D., & Katine, J. A. (2020). Thermal stability for domain wall mediated magnetization reversal in perpendicular STT MRAM cells with W insertion layers. Applied Physics Letters, 117(24).

[2] Xu, J.-W., Riley, G. A., Shaw, J. M., Nembach, H. T., & Kent, A. D. (2023). Brillouin light scattering from quantized spin waves in nanowires with antisymmetric exchange interactions. Physical Review B, 107(5), 054402.



Scatter plot of fitted Heisenberg exchange A_{ex} and effective anisotropy K_{eff}. for a sample of 407 devices on the same wafer across different patterned diameters. $A_{ex}=e_{dw}w_{dw}/(8ln2)$ and $K_{eff}=ln(2)e_{dw}/(2w_{dw})$, where domain wall width $w_{dw}=d\delta$, d is the diameter of the MTJ. Normalized domain wall width δ and domain wall energy e_{dw} are fitting parameters extracted from the FSD.



Comparison of median exchange A_{ex} fittings for devices under 150 nm in diameter performed independently by WD (red diamonds) and NIST (green circles) and A_{ex} values obtained through BLS on blanket films by NIST (teal triangles).

AE-04. Single-Cell Magnetometry Reveals State-Dependent Magnetic Heterogeneity in Sickle Cell Disease

L. Nguyen T. Tran[1], S. Rodriguez Caballero[1], P. Iyer[2], K. Paz Gonzalez[1], K. Rova[1], M. Zborowski[3], P. C. Desai[4], L. Tijani[5], J. Chalmers[2], J. Gomez-Pastora[1]

[1]Chemical Engineering, Texas Tech University, Lubbock, Texas, United States, [2]William G. Lowrie Department of Chemical and Biomolecular Engineering, The Ohio State University, Columbus, Ohio, United States, [3]Department of Biomedical Engineering, Cleveland Clinic, Cleveland, Ohio, United States, [4]Wake Forest School of Medicine, Levine Cancer Institute, Advocate Health, Charlotte, North Carolina, United States, [5]Department of Medical Oncology, Division of Hematology and Medical Oncology, Texas Tech University Health Sciences Center, Lubbock, Texas, United States

ickle cell disease (SCD) arises from hemoglobin S polymerization, producing oxygen-dependent changes in red blood cell (RBC) deformability and magnetic susceptibility [1]. While vaso-occlusive crisis (VOC), the acute symptomatic phase of SCD, drives morbidity, current diagnostic approaches do not resolve disease state based on intrinsic single-cell biophysical properties. Endogenous hemoglobin magnetism therefore remains underexplored as a quantitative marker of cellular heterogeneity and disease progression.

Here, we present cell tracking velocimetry (CTV) as a high-gradient platform for intrinsic single-cell magnetometry,

enabling direct measurement of magnetophoretic and hydrodynamic behavior of individual blood cells. By applying a constant magnetic energy gradient orthogonal to gravity, the system simultaneously resolves magnetically induced motion and settling dynamics, providing a label-free, physics-based characterization of cell-to-cell variability.

We show that RBC populations exhibit broad, asymmetric distributions of magnetophoretic mobility, reflecting intrinsic magnetic heterogeneity. In SCD samples, these distributions are significantly altered relative to healthy controls, with the emergence of distinct high-response subpopulations. Critically, a systematic redistribution toward higher-mobility cells is observed under crisis conditions, indicating that disease state is encoded in the evolution of the distribution tail rather than average properties. Beyond erythrocytes, this framework reveals altered magnetic response in circulating monocytes, consistent with uptake of hemoglobin-derived material and associated increases in intracellular iron content. This highlights the broader applicability of intrinsic magnetic phenotyping across multiple blood cell types.

This work establishes single-cell magnetic phenotyping as a quantitative, label-free framework for resolving disease-associated heterogeneity in blood and provides a direct foundation for selective magnetophoretic manipulation of pathological cell populations. More broadly, it highlights the potential of leveraging intrinsic magnetic contrast to enable next-generation diagnostic and blood processing technologies.

[1] L. R. Wallace and S. R. Thibodeaux, “Transfusion support for patients with sickle cell disease,” Transfus. Apher. Sci., vol. 61, no. 5, p. 103556, Oct. 2022, doi: 10.1016/j.transci.2022.103556.

AE-05. Towards Nanoscale Sensing of Spin Precession with a Free-Space Electron Probe

A. Jaros, J. Antl, I. C. Bicket, M. Seifner, P. Haslinger
Physics, Atominstitut, Vienna, Austria

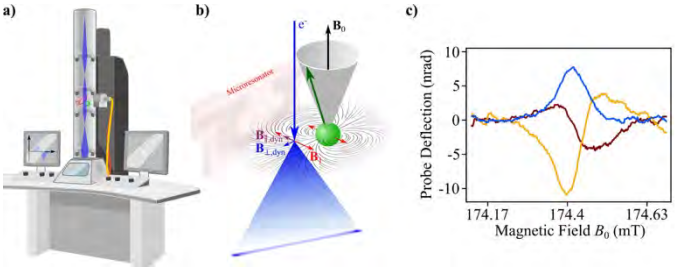
Spin precession describes how magnetic systems dynamically evolve over time, and it underlies a wide range of phenomena, from collective spin motion to spin waves. Conventional techniques (electron spin resonance - ESR; ferromagnetic resonance - FMR) detect spin precession but spatially average over micrometer-scale volumes, leaving the local nanoscale dynamics inaccessible. Complementary methods extend this picture to smaller length scales: Brillouin light scattering [1] is non-contact, though diffraction-limited to ~250 nm, X-ray techniques [2] provide element-specific imaging down to ~25 nm but require access to large-scale synchrotron facilities, and scanning-probe methods achieve atomic-scale resolution while being largely restricted to surfaces. Resolving spin precession with both high sensitivity and nanoscale spatial resolution in a broadly applicable experimental platform remains a major experimental challenge [3].

We present a fundamentally different approach [4]: using the free-space electron probe of a transmission electron microscope (TEM) as a highly local detector for the precessing spins (Fig. 1a). A custom impedance-matched microresonator integrated into a dedicated sample holder [5] drives spin precession at GHz frequencies and the resulting transverse field B_{dyn} imparts a Lorentz deflection on the transmitted electrons (Fig. 1b).

We have recorded both ESR spectra [4, Fig. 1c] and FMR spectra via the electron probe. Crucially, the spatial resolution is defined by the probe size, which in a scanning TEM can be focused down to the nanometer scale, potentially exceeding the capabilities of even X-ray methods. This opens a realistic pathway toward nanometre-scale mapping of spin precession [6], with theoretical analysis [7] suggesting that single-spin sensitivity may become achievable. Recent advances in this framework will be discussed at the conference.

[1] Heussner, F., Talmelli, G., Geilen, M., Heinz, B., Brächer, T., Meyer, T., ... & Pirro, P. (2020). Experimental realization of a passive gigahertz frequency-division demultiplexer for magnonic logic networks. *physica status solidi (RRL)–Rapid Research Letters*, *14*(4), 1900695.
[2] Sluka, V., Schneider, T., Gallardo, R. A., Kákay, A., Weigand, M., Warnatz, T., ... & Wintz, S. (2019). Emission and propagation of 1D and 2D spin waves with nanoscale wavelengths in anisotropic spin textures. *Nature nanotechnology*, *14*(4), 328-333.
[3] Liu, C., Ai, F., Reisbick, S., Zong, A., Pofelski, A., Han, M. G., ... & Zhu, Y. (2025). Correlated spin-wave generation and domain-wall oscillation in a topologically textured magnetic film. *Nature Materials*, *24*(3), 406-413.
[4] Jaros, A., Seifner, M. S., Toyfl, J., Czasch, B., Beltrán-Romero, S., Bicket, I. C., & Haslinger, P. (2026). Sensing Spin Precession with Free Electrons. *ACS nano*.
[5] Jaroš, A., Toyfl, J., Pupić, A., Czasch, B., Boero, G., Bicket, I. C., & Haslinger, P. (2025). Electron spin resonance spectroscopy in a transmission electron microscope. *Ultramicroscopy*, 114224.

[6] Haslinger, P., Nimmrichter, S., & Rätzel, D. (2024). Spin resonance spectroscopy with an electron microscope. *Quantum Science and Technology*, *9*(3), 035051.
[7] Beltrán-Romero, S., Gaida, M., Haslinger, P., Rätzel, D., & Nimmrichter, S. (2025). Quantum Metrology of Spin Sensing with Free Space Electrons. arXiv preprint arXiv:2509.14982.



(a) Schematic of the TEM with a custom sample holder for sensing spin precession. (b) Sample-holder region: spins are aligned by the B_0 field while a microresonator provides microwave excitation. The electrons are deflected by B_1 and B_{dyn}, enabling phase-locked detection over billions of cycles. (c) Spatially resolved ESR spectra via electron probe.

AE-06. Effective control and probe of Néel order in polycrystalline NiO films: a combined approach to study antiferromagnets

P. Wu, S. Wang, C. Yang
Materials Science and Engineering, National Yang Ming Chiao Tung University, Hsinchu, Taiwan, Taiwan

Antiferromagnetic (AFM) materials are promising for next-generation spintronic applications, however, practical implementation remains challenging due to difficulties in controlling the Néel order and the lack of sensitive, device-compatible readout techniques. In this work, we demonstrate spin Hall magnetoresistance (SHMR) as an effective and versatile approach for probing Néel order, even in polycrystalline AFM films. Using NiO/Pt and $LaNiO_3$/Pt bilayers as model systems, we show that SHMR measurements can detect the Néel temperature (T_N), monitor spin-flop transition, and reveal field-induced orientation of the Néel order [1]. Crucially, we establish that the control of Néel order with non-volatility is effective when initiated from the "soft" AFM phase at elevated temperature (380 K) via field-cooling (FC), enabling robust alignment of Néel order without the need for adjacent heavy metals as spin current sources. This spin-current-free control greatly expands the flexibility and scalability of AFM device design, especially in the form of polycrystalline microstructure. The results highlight the combined FC and SHMR technique as a powerful and flexible platform for both manipulation and sensitive readout of AFM states, providing a reliable basis for the design and characterization of a broad class of AFM materials and devices [1].

[1] Chun-Chieh Hsu et al., *Sci. Rep.* 16, 6079 (2026).

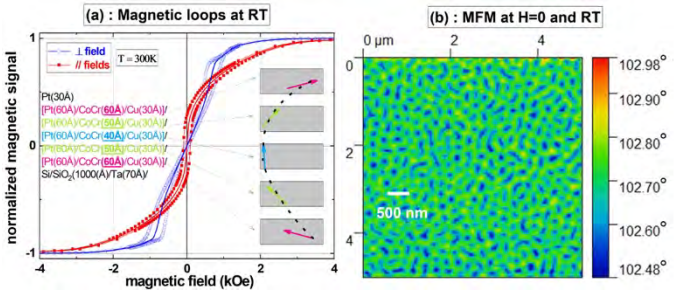
AE-07. Magnetic metamaterials with anisotropy gradients around a spin reorientation

F. Fettar[1], L. Abbassi[1], E. Mossang[1], N. Rougemaille[1], B. Borgnic[1], F. Gay[1], P. David[1], D. Barral[1], J. Tonnerre[1], L. Ortega[2], G. Beutier[3], D. Lacour[4], M. Hehn[4], E. C. Passamani[5], V. P. Nascimento[5]
[1]Neel Institute, CNRS, Grenoble, France, [2]LPS, CNRS, Orsay, France, [3]SIMaP, UGA, Saint Martin d'Hères, France, [4]Institut Jean Lamour, CNRS, Nancy, France, [5]Physics, Universidade Federal do Espirito santo, Vitoria, Brazil

The existence of solitonic magnetic textures such as skyrmions requires a fine balance between Dzyaloshinskii-Moriya Interaction (DMI) and other magnetic energies. To date, it is still difficult to generate 3D magnetic textures with a high homogeneity, large density and moderate size, without complex and ad hoc magnetic fields protocols. Such procedures remain important even in multilayer systems which exploit spin reorientation transitions (between in-plane and out-of-plane orientations) to promote skyrmion stability [1-6]. In these references, the thickness of the magnetic layer is fixed. Interestingly, reduced effective anisotropy constants K_{eff} have been measured, like K_{eff}≈-10^5J/m^3 [2]. More recently, by inserting a $[Pt/Co(14Å)/Al]_{15}$ multilayer with robust perpendicular magnetic anisotropy between 2 gradient structures containing planar anisotropies, Grelier *et al* [7] have observed a toron magnetic texture where K_{eff}≈-0.52 10^5 J/m^3. *We propose a new way to generate 3D magnetic textures from metamaterials behaving anisotropies gradient around the spin reorientation*. Sputtered $[Pt/Co_{80}Cr_{20}(t_{CoCr})/Cu]_{x5}$ multilayers are used with different CoCr thickness (t_{CoCr}) in the stack. Here, an SRT takes place at t^*_{CoCr}=50Å. Then, we choose t_{CoCr}=(60-50-40-50-60)Å from the bottom to the top of the stack as drawn in Fig.1(a). In Fig.1, are plotted the magnetic hysteresis at RT [Fig1(a)] and a magnetic force microscopy image [Fig1(b)] at 0T after applying $H_\perp$=150 mT. K_{eff}≈0.2 10^5 J/m^3 is measured, this value being lower in absolute values than ones in [1-7]. In Fig.1(b), the magnetic textures are somewhat oblong, with a density reaching≈15 µm^{-2}. Here, the magnetic entities persist in the (-100/100) mT field range, meaning the field is not necessary for the appearance of magnetic objects. The

gradually reorientation of the magnetization from the bottom to the top of the sample might be an interesting way for generating 3d magnetic textures.

[1] R. Tolley *et al*, Physical Review Materials 2, 044404 (2018).
[2] L. Wang *et al*, ACS Appl. Mater. Interfaces 11, 12, 12098–12104 (2019).
[3] S. Cheng *et al*, Physical Review B 108, 174433 (2023).
[4], S. Zhang *et al*, Commun Phys 1, 36 (2018).
[5] S. Saha *et al*, Physical Review B 100, 144435 (2019).
[6] M. He *et al*, Physical Review B 97, 174419 (2019).
[7] M. Grelier *et al*, Nature communications 13 6843 (2022).



Magnetic loops at RT [(a)] for ⊥ and // magnetic fields (see the winding of the magnetization in the right-part) and the magnetic force magnetic image at RT [(b)] after applying $H_{\perp}$=150mT, for a $[Pt/Co/Cu]_{x5}$ metamaterial containing an anisotropies gradient around SRT (t^*_{CoCr}=50 Å).

AE-08. Demagnetizing Factor Corrections for Assemblies of Single-Domain Magnetic Nanoparticles

S. Oberdick[1, 2]
[1]Physics, University of Colorado, Boulder, Boulder, Colorado, United States, [2]Applied Physics, NIST, Boulder, Boulder, Colorado, United States

Single-domain magnetic nanoparticles are regularly characterized by magnetometry. To prepare samples for measurement, nanoparticles in liquid solution are often dried into a packed powder. The internal magnetic field of the sample, which is the field felt by the nanoparticles, changes as a function of the geometry and structure of the powder assembly. Demagnetizing field corrections can be used to estimate the internal field, perform quantitative data analysis, and calculate the intrinsic properties of the nanoparticles.

For certain types of materials and sample geometries, such as continuous magnetic materials and ellipsoidal sample shapes, demagnetizing correction factors are well known and regularly used. For more complex systems, like assemblies of magnetic particles, demagnetizing corrections are used less frequently. To complicate things further, the proper demagnetizing corrections for particle-based samples are not well agreed upon—the literature contains several conflicting suggestions.

I present magnetic measurements from packed assemblies of iron oxide nanoparticles and use a recently developed, single-domain magnetic nanoparticle demagnetizing correction to analyze the data [1]. The correction gives consistent nanoparticle properties for several sample geometries and measurement orientations. For example, Figure 1 shows magnetization versus applied magnetic field for two different measurement orientations at 2 K before and after correction. The uncorrected data have qualitative differences between orientations, resulting in different measured remanent magnetizations. After correction, however, the data show consistent trends and similar remanent magnetizations. I also present analyses of low-field nanoparticle susceptibility and the Curie-Weiss interaction temperature. I discuss how the single-domain demagnetizing correction differs from other types of demagnetizing corrections that are sometimes misused for powder samples.

[1] M. Zambach et al., arXiv:2502.03394 (2026)

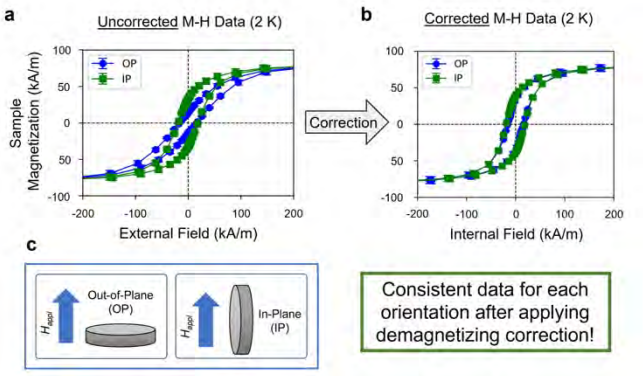


Figure 1. (a) Uncorrected sample magnetization (measured magnetic moment divided by total sample volume) for disk-shaped sample at 2 K as a function of external field for two measurement orientations, in-plane (IP) and out-of-plane (OP). (b) Sample magnetization at 2 K as a function of internal field, which was calculated using the single-domain magnetic nanoparticle demagnetizing correction. (c) Schematic displaying IP and OP measurement orientations.

AE-09. Machine-Learning-Based Evaluation of Material Properties from Metallurgical Microstructures

I. Hiraoka, S. Sharmin, C. Mitsumata
Univ. Tsukuba, Tsukuba, Japan

In this study, we apply Principal Component Analysis (PCA), a multivariate analysis technique, to perform machine learning (ML) on microstructural images of metallic materials. Machine learning of spectral data using PCA enables the construction of mathematical models that link film properties with the deposition process during plasma analysis in sputtering. In the present study, we extend this technique to image analysis[1]. We then analyze how the features extracted from these images influence the resulting material properties.

In this method, microscopic images of metallic microstructures are first acquired as the input data. After applying noise reduction, edge detection is performed to enhance the morphological features of the crystal microstructure. The resulting microstructural data are then subjected to Fourier transformation to quantify shape related characteristics. To facilitate the extraction of structural information contained in the Fourier domain, the transformed images are further converted into power spectra.

Since the power spectrum data are multidimensional vectors indexed by wavenumber, the vectors obtained from multiple samples are integrated and subjected to dimensionality reduction using PCA. As a result, the PCA processed data form a data space structured according to the characteristic features of the metallic microstructures. By representing the premeasured material properties as mathematical functions within this PCA derived data space, it becomes possible to identify the microstructural features required to achieve the desired material properties.

[1] R. Minami, et.al., “Estimation of valence state and growth rate using principal component analysis of plasma emission in reactive sputtering deposition”. Science and Technology of Advanced Materials: Methods, 5(1), 2544523 (2025).

AE-10. Interface-resolved magnetism of metal-organic (Fe^{57}/ $C_{42}H_{28}$) Thin films; Studies under X-ray standing waves

M. Priyadarsini[1], S. Singh[1], I. Sergeev[2], D. Kumar[1]
[1]Physics, UGC DAE Consortium for Scientific Research, Indore, Madhya Pradesh, India, [2]Physics, Deutsches Elektronen-Synchrotron, Notkestraße, Hamburg, Germany

Ferromagnetic/Organic semiconductor (FM/OSC) interfaces, referred as the spinterface (spin-interface), play a crucial role in achieving high spin polarization, long spin relaxation, and low impedance mismatch in organic spin-valve devices [1]. In recent years, probing magnetic spinterface has gained significant interest due to some peculiar properties such as local hybridization-induced interfacial magnetic anisotropy and organic overlayer-induced perpendicular magnetic anisotropy [2]. Thus, it necessitates a detailed study of FM/OSC interfaces. In this study, the depth-resolved magnetism at the Fe^{57}/Rubrene ($C_{42}H_{28}$) interfaces has been investigated in the presence of X-ray standing wave (XSW) using the synchrotron-based grazing incidence nuclear resonant scattering (GI-NRS) technique. Based on theoretical simulations utilizing the sample structure, we show that the antinode positions of XSW in waveguide structures allow to probe ^{57}Fe-diffused and ^{57}Fe-bulk components independently in the same sample just by changing the incident angle [3]. Time spectra were acquired at these two resonance conditions and analyzed using REFTIM. The best fit to the data is obtained by considering three magnetic hyperfine fields (Bhf), 32.5 T, 28.5 T and 25 T. The 32.5 T component dominates in the bulk ferromagnetic layer, whereas the reduced Bhfs (28.5 T and 25 T) originate from the interfacial diffused ^{57}Fe region. This decrease in Bhf at the interface as relative to the bulk is attributed to the formation of Fe nanoparticles embedded within the Rubrene matrix. Temperature-dependent measurements were further performed to examine the evolution of structural and magnetic properties. These results highlight the strength of the GI-NRS technique for depth-resolved magnetic characterization, which is challenging to achieve using conventional laboratory-based methods.

[1] Ilaria Bergenti et. al, Nano Mat. Sci. 1, (2019).
[2] K. Bairagi et. al, Phys. Rev. Lett. 114, 247203 (2015).
[3] S. Kaushik et. al , Hyperfine Interact. 242, 1 (2021).

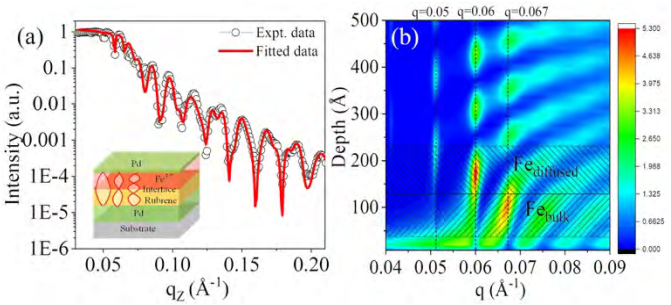


Figure.1 Shows X-ray reflectivity (a), simulated X-ray standing wave structure for the pristine sample (b). The inset shows the sample strcuture.

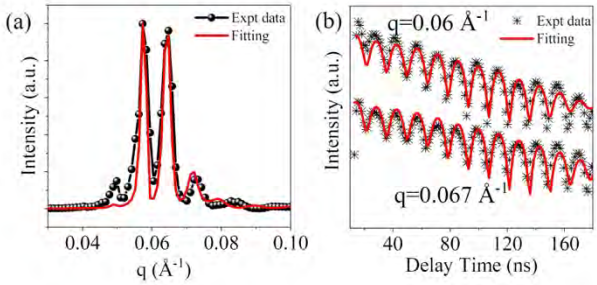


Figure 2. Nuclear Resonance Reflectivity (a), and time spectra (b), along with their corresponding fitting for the pristine sample at two different incident angles.

AE-11. The ESTIA beamline – a new paradigm for polarized neutron reflectometry

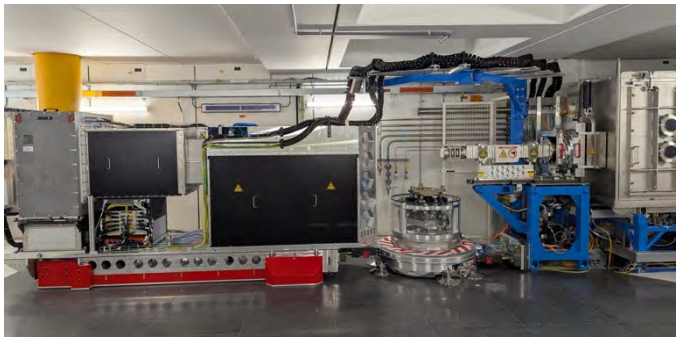
J. Cooper[1], G. Causer[1], A. Glavic[2]
[1]Large Scale Structures Division, European Spallation Source, Lund, Sweden, [2]LIN, Paul Scherrer Institute, Villigen, Switzerland

Polarized neutron reflectometry is a powerful tool for investigating magnetic thin films and interfaces, acting as a depth dependent absolute magnetometer. Dozens of reflectometers exist around the world, enabling scientific breakthroughs across many fields, including multilayer exchange coupling, skyrmion and helical systems, exchange bias, topological insulators and more.

In this talk I showcase the power of polarized neutron reflectometry and introduce the newly constructed ESTIA instrument at the European Spallation Source [1] - the worlds first fully focusing neutron reflectometer.

This groundbreaking instrument will have exceptionally high neutron intensity, and will uniquely be able to probe samples below the millimeter length-scale enabling some real devices to be measured during in-operando conditions. Experiments which previously took hours or days will instead take minutes. As a result, ESTIA will enable a new generation of neutron reflectometry experiments, bringing nanoscale magnetic characterization closer than ever to real-world devices.

[1] Nuc. Instr. Meth. Phys. A v.957 2020, 163402



SESSION AF: TERAHERTZ, ALTERMAGNETIC AND ANTIFERROMAGNETIC SPINTRONICS

Chair(s): A. Laraoui, *Mechanical and Materials Engineering , University of Nebraska-Lincoln, Lincoln, Nebraska, United States*

Tuesday, November 3, 2026
08:30 AM-12:00 PM
South Pacific 3/4

AF-01. Magnon chirality in altermagnetic FeF_2

J. Sears[1], V. Garlea[2], D. Lederman[3], J. Tranquada[1], I. Zaliznyak[1]
[1]Brookhaven National Laboratory, Upton, New York, United States, [2]Oak Ridge National Laboratory, Oak Ridge, Tennessee, United States, [3]UC Santa Cruz, Santa Cruz, California, United States

The classical antiferromagnet FeF_2 and its analog MnF_2 have long been considered well-characterized model antiferromagnetic systems [1,2]. Surprisingly, it appears that these materials need to be re-examined in light of new work identifying a previously unrecognized class of magnetic materials, now known as altermagnets, which feature spin-split electronic bands [3]. While FeF_2 is highly insulating and not amenable to electronic band structure measurements, altermagnetism can also manifest as a characteristic chiral splitting in the magnon bands [4]. We present very high-resolution inelastic magnetic neutron scattering measurements characterizing the magnetic

excitations and quantifying the chiral splitting in this material [5]. We also show that FeF_2 is in a regime where dipolar coupling dominates over altermagnetic interactions, resulting in mixing of the chiral modes. These results highlight the importance of dipolar interactions on magnon chirality in insulating materials where longer-range altermagnetic interactions are weak.

[1] B.D. Rainford et al., 5th IAEA Symp. on Neutron Inelastic Scattering, p 655 (1972)
[2] S. M. Rezende, A. Azevedo, R. L. Rodríguez-Suárez, J. Appl. Phys. 126, 151101 (2019)
[3] L. Smejkal et al., Phys. Rev. X 12, 040501 (2022)
[4] L. Smejkal et al., Phys. Rev. Lett. 131, 256703 (2023)
[5] J. Sears et al. https://arxiv.org/html/2601.04303v1 (2026)

AF-02. Electrical Readout of Sub-THz Spin Dynamics in Ferrimagnetic Thin Films

A. Regmi[1, 2], J. Hanson-Flores[2], R. Gupta[4, 3], L. Ramos[3], D. A. Arena[3], E. del Barco[1, 2]
[1]Department of Material Science and Engineering, University of Central Florida, Orlando, Florida, United States, [2]Department of Physics, University of Central Florida, Orlando, Florida, United States, [3]Department of Physics, University of South Florida, Tampa, Florida, United States, [4]Department of Physics, University of Gothenburg, Gothenburg, Sweden

Antiferromagnets (AFs) have attracted significant interest for enabling ultrafast spintronic functionality due to their exchange-enhanced collective modes that extend into the sub-terahertz and terahertz (THz) regimes [1]. However, utilizing the THz spin dynamics in AFs remains challenging as (a) AF materials lack a net magnetic moment that facilitates control and modulation of THz emission; (b) AF domains are small and challenging, with difficulties in maintaining pure AF dynamical modes, and (c) in thin films, high-frequency excitation modes in AFs can couple to scattering centers and decay quickly [2]. Ferrimagnets provide a complementary platform; they exhibit antiferromagnet-like eigenmodes and inertia-driven dynamics while retaining ferromagnet-like actuation and detection capabilities [3]. Despite these advantages, experimental investigations of THz spin dynamics in ferrimagnetic materials remain limited. Here, we investigate the effect of temperature and alloy composition of rare-earth-based ferrimagnets to elucidate the spin dynamics in the vicinity of magnetic and angular momentum compensation points. Specifically, we report results on conventional in-plane and out-of-plane ferromagnetic resonance (FMR) using the spin pumping technique in thin-film heterostructures of FeCoGd/Ta. The results reveal high-frequency ferrimagnetic dynamics and spin-to-charge conversion across a bandwidth extending to 250 GHz. Our study provides polarization-dependent spin pumping mapping with strong Inverse Spin Hall Effect signals in correspondence to the large spin-orbit coupling of the α-phase Ta capping layer used for spin-charge interconversion.

[1] P. Vaidya et al., Science, vol. 368, no. 6487, pp. 160-165, 2020.
[2] G. Fritjofson *et al.*, *Physical Review Letters,* vol. 135, no. 21, p. 216704, 2025.
[3] Y. Zhang et al., Applied Physics Reviews, vol. 10, no. 1, 2023.

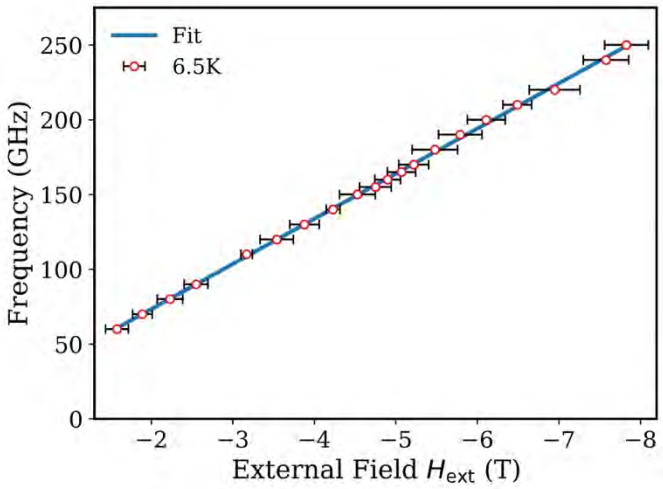


Fig. 1: Illustration of the resonance positions for an easy-plane FeCoGd(15 nm)/Ta(4 nm) heterostructure, alongside the computed resonance (solid line) for in-plane mode. The position corresponds to the Inverse spin Hall effect signal at the resonance for the sample. Measurements were conducted with the microwave field oriented perpendicular to the in-plane DC magnetic field.

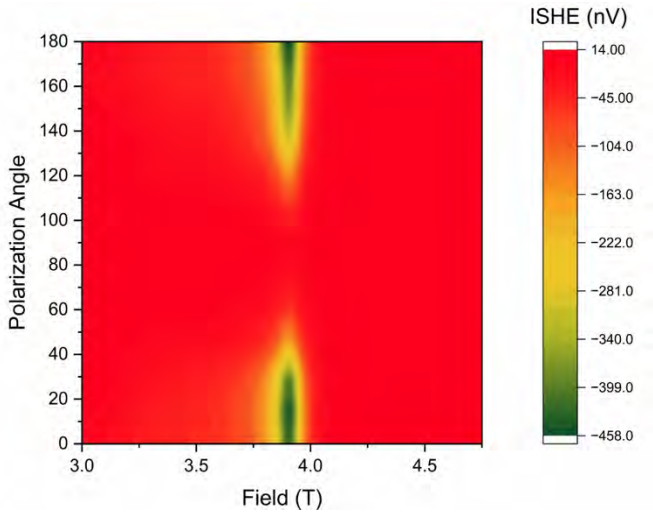


Fig. 2: Contour map for Inverse spin hall effect (ISHE) measurement as a function of the microwave polarization angle.

AF-03. Conductivity Mismatch in Topological-Insulator-Based Spintronic Terahertz Emitters

O. M. van 't Erve[1], N. S. Sirica[1], J. K. Gustafson[2], N. Combs[1], E. Cobas[1], M. Noyan[1], C. Li[1]

[1]Naval Research Laboratory, Washington, District of Columbia, United States, [2]Army Research Laboratory, Adelphi, Maryland, United States

Terahertz emission from magnetic heterostructures comprised of surface engineered 3D topological insulators, are compared. Despite an enhancement in spin-orbit torque efficiency, a ~ 5-fold reduction in the terahertz emission amplitude is observed. Such discrepancy between reciprocal measurements on identical samples of spin-charge conversion is understood to result from a conductivity mismatch across the interface.

Terahertz (THz) emission has emerged as a powerful spectroscopic technique to sensitively probe the electronic symmetry and conversion efficiency in spin-orbit torque devices, through measuring the inverse, spin-to-charge conversion process in magnetic heterostructures.

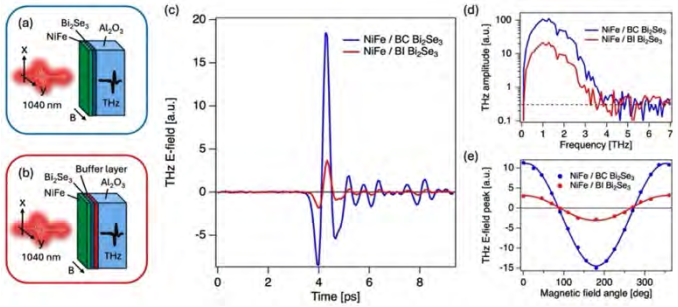
Here, we report THz emission from magnetic heterostructures comprised of surface engineered Bi_3Se_3 to assess how the position of the chemical potential affects the resultant emission properties. [1] The emission spectra of bare topological insulator (TI) films reflect the *3m* point group symmetry of Bi_2Se_3, while that from magnetic heterostructures follows from the magnetic dipole symmetry of ultrafast demagnetization. Bulk-insulating Bi_2Se_3 heterostructures show a ~ 5-fold reduction in the terahertz emission amplitude as compared to their bulk-conducting counterparts.

Using Kerr rotation and second harmonic Hall measurements on identical samples we find a 4-fold reduction in critical current density to switch an adjacent NiFe layer and a 5–10-fold enhancement in SOT efficiency for bulk-insulating Bi_2Se_3 heterostructures. [2]

This discrepancy is attributed to the direction of the flow of spin and the conductivity mismatch across the $Ni_{80}Fe_{20}/Bi_2Se_3$ interface brought on by the low carrier density and high sheet resistance of the bulk-insulating film.

1. J. Gustafson,N. Sirica and N. Combs, Physical Review B, Vol. 113, p. 014302 (2026)

2. M. Noyan, X. Zhang and J. Moon, Nanoletters. Vol. 25 p. 6357 (2025)



(a) NiFe / Bulk-conducting Bi2Se3 and (b) NiFe / Bulk insulating Bi2Se3 (c) THz traces (d) power spectra (e) THz peak amplitude a a function of in-plane field angle.

AF-04. Terahertz Emission Across Magnetic Compensation for GdCo and GdFe Ferrimagnetic Systems Showing Single-Pulse All-Optical Switching

J. Compton-Stewart[1], G. Nava Antonio[2], P. Chailloleau[1], Y. L. Guen[1], J. Hohlfeld[1], T. Hauet[1], M. Hehn[1], C. Ciccarelli[2], S. Mangin[1]

[1]Institut Jean Lamour, Université de Lorraine, Nancy, Meurthe et Moselle, France, [2]Unviersity of Cambridge, Cambridge, United Kingdom

All-optical helicity-independent switching in rare-earth–transition-metal ferrimagnets offers a route toward ultrafast and energy-efficient magnetic control [1]. To clarify the spin-current dynamics accompanying this process, we investigate cryogenic terahertz emission from various GdCo and GdFe based heterostructures as the temperature is swept across the magnetic compensation point. In GdCo

under an applied field, the terahertz signal is strongly suppressed before reversing sign on crossing compensation, whereas a clear emission persists in zero field [2]. Figure 1 shows a similar evolution observed for GdFe.
These results, and their evolution under different magnetic fields, show that the extinction of terahertz emission at compensation is governed by the equilibrium magnetic configuration and domain formation, rather than by a complete cancellation of rare-earth and transition-metal spin currents one might expect from a compensated ferrimagnet. For GdCo, the room-temperature response is dominated by the transition-metal sublattice, while slower rare-earth dynamics only become significant at low temperatures.
Extending the same approach to GdFe reveals the same dominant sublattice and signal destruction around compensation, while highlighting material-dependent spectral fingerprints and temperature trends. Our results connect terahertz emission, ultrafast demagnetisation, and all-optical switching, and establish terahertz spectroscopy as a powerful probe of sub-picosecond spin transport in ferrimagnets relevant for ultrafast spintronic devices.
[1] Hadri *et al. Journal of Physics D: Applied Physics* 50, 133002 (2017)
[2] Nava Antonio et al., Advanced Optical Materials 13, 2500056 (2025)

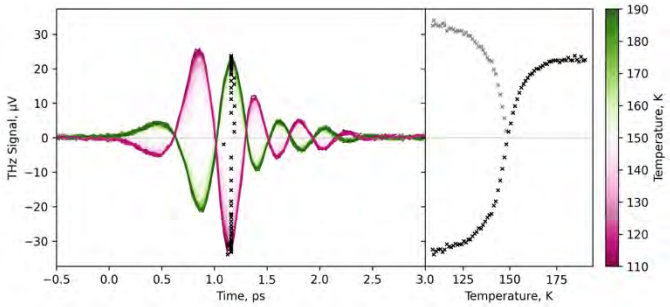
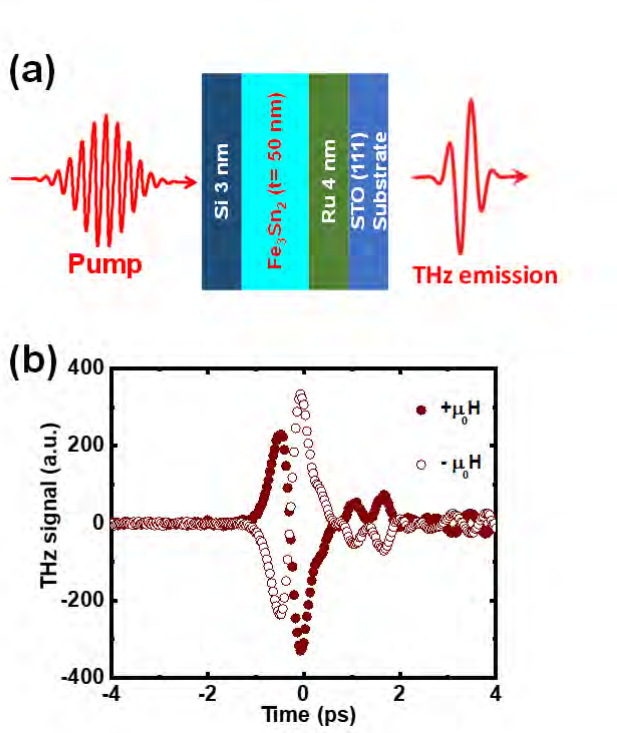


Fig. 1: (Left) The THz emission from a $Gd_{33}Fe_{67}$(5nm)\Pt(3nm) sample across a temperature range of 110-190 K under a constant magnetic field of 200 mT. The peak values of each trace are highlighted and plotted (right), showing the destruction of the THz signal around compensation, here 150K. The absolute values are plotted in grey.

AF-05. Terahertz Emission in Thin Film Kagome Ferromagnet Fe_3Sn_2

A. De[1], Z. Jin[1, 2], E. Lesne[3], K. Nukui[1, 2], S. Miki[1], C. Felser[3], A. Hirohata[4, 3], S. Mizukami[1, 4]
[1]Advanced Institute for Materials Research, Tohoku University, Sendai, Japan, [2]Graduate School of Engineering, Tohoku University, Sendai, Japan, [3]Max Planck Institute for Chemical Physics of Solids, Dresden, Germany, [4]Center for Science and Innovation in Spintronics, Tohoku University, Sendai, Japan

Terahertz (THz) emission from magnetic materials has recently emerged as a powerful means of probing ultrafast spin and charge dynamics, which is highly relevant for next-generation spintronic devices. In this context, topological kagome magnets are promising due to their non-trivial electronic structure featuring Dirac fermions, flat bands and large Berry curvature. These characteristics can lead to large anomalous Hall effects, strong spin–orbit coupling and efficient spin–charge conversion, which are expected to play a key role in THz generation following femtosecond laser excitation. While the transport properties [1–3] and spin excitations [4,5] of Fe_3Sn_2 have been studied, THz emission from this material has not yet been reported. Fe_3Sn_2 hosts a bilayer kagome lattice of Fe atoms separated by Sn layers. We observe a strong and efficient THz emission from epitaxial Fe_3Sn_2 thin films grown on $SrTiO_3$ (111) substrates with a Ru seed layer. Measurements are performed using a home-built THz emission spectroscopy setup [6,7] driven by a Ti:sapphire amplified laser. We observe a reversal in THz signal polarity depending on the direction of pump excitation (capping side vs. substrate side) and the polarity of the magnetic field which suggest that the mechanism behind THz emission is consistent with the spin-to-charge conversion. Our results establish kagome magnets as promising platforms for spintronic THz emitters and highlight the influence of topological electronic structure in governing ultrafast spin–charge conversion.
This work is partially supported by JSPS KAKENHI (24K21234, 26H02126), MEXT X-NICS (JPJ011438), and JST ASPIRE (JPMJAP2409). ZJ. thanks to JST SPRING and GP-Spin at Tohoku Univ.
(1) L. Ye. et al., Nature 555, 638 (2018)
(2) H. Zhang et al., Phys. Rev. B 103, L201101 (2021)
(3) T. Chen et al, Sci. Adv. 8, eabk1480 (2022)
(4) I. Lyalin et al., Nano Lett. 21, 6975 (2021)
(5) C. Lee et al., PNAS, 120, e2220589120 (2023)
(6) Y. Sasaki et. al., Appl. Phys. Lett. 111, 102401 (2017)
(7) R. Mandal et al. NPG Asia Mater. 16, 30 (2024)



(a) Schematic of the sample and laser induced THz emission (b) THz emission for positive and negative directions of the magnetic field.

AF-06. Terahertz Emission Spectroscopy of Fe/Pt Multilayers

T. Nakazono[1], S. Isogami[2], Y. Sasaki[2], Y. K. Takahashi[2, 3], T. Satoh[1], K. T. Yamada[1]

[1]Department of Physics, Institute of Science Tokyo, Tokyo, Japan, [2]National Institute for Materials Science (NIMS), Tsukuba, Japan, [3]Research Institute of Electrical Communication, Sendai, Japan

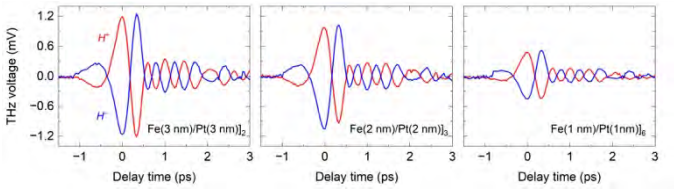
The dissipation of spin angular momentum during ultrafast demagnetization generates picosecond spin-current pulses [1]. The spin currents flow into an adjacent non-magnetic layer and are converted into transient electric currents via the inverse spin Hall effect, leading to the emission of terahertz (THz) electromagnetic waves through the electric dipole radiation process. By engineering the multilayered structure, The THz emission efficiency can become comparable to those of nonlinear THz crystals [2]. The strategy of increasing the number of layers works for enhancing the total spin-current conversion but complicates the emission process for the additional interfacial scattering and optical absorption losses. In this study, we performed THz emission spectroscopy on Fe/Pt multilayers to elucidate ultrafast spin-current generation and conversion processes in such multilayer structures.

Fe/Pt multilayers with a fixed total thickness were fabricated by dc sputtering on glass substrates: [Fe(3 nm)/Pt(3 nm)]$_2$, [Fe(2 nm)/Pt(2 nm)]$_3$, and [Fe(1 nm)/Pt(1 nm)]$_6$. The multilayers were excited by 100-fs optical pulses at a repetition rate of 80 MHz using a Ti:sapphire oscillator with a central wavelength of 780 nm. The emitted THz waves were measured using a standard electro-optic sampling technique [3]. Fig. 1 shows the THz waveforms of the multilayers at a pump fluence of 3.68 μJ/cm^2. The polarities of the emitted THz waveform reverse upon inversion of the spin polarization direction of the Fe layer. The peak amplitudes decrease with increasing the number of layers. In addition, we also observed a non-monotonical dependence of the peak amplitude on the pump fluence in the low-fluence regime, which becomes more pronounced with increasing stacking repetition. These results suggest that the spin-current generation via ultrafast demagnetization across the hetero-interfaces is susceptible to the excitation fluence. In the presentation, we will discuss these findings in detail and focus on the origin of the observed nonmonotonic tendency.

[1]M. Battiato, K. Carva, and P. M. Oppeneer, Physical Review Letters, Vol. 105, p.027203 (2010)

[2]T. S. Seifert et al., Nature Photonics, Vol. 10, p.483-488 (2010)

[3]P. U. Jepsen, D. G. Cooke, and M. Koch, Laser & Photonics Reviews, Vol. 5, p.124-166 (2011)



THz waveforms from Fe/Pt multilayers under positive and negative magnetic fields for multilayers consisting of [Fe(3 nm)/Pt(3 nm)]$_2$, [Fe(2 nm)/Pt(2 nm)]$_3$, and [Fe(1 nm)/Pt(1 nm)]$_6$

AF-07. Ultrafast Opto-Magnetism: Unlocking the Unconventional Inverse Faraday Effect

C. Hareau[1], B. Pauriche[2], S. Boujday[2], B. Vodungbo[2], M. Mivelle[1]
[1]CNRS/ Sorbonne University, Paris, France, [2]Sorbonne University, Paris, France

The Inverse Faraday Effect (IFE) provides a powerful mechanism for the all-optical generation of magnetism through the transfer of angular momentum from photons to matter [1]. While recent theoretical models and simulations demonstrate that plasmonic nanoantennas can confine and enhance these interactions far below the diffraction limit—generating stationary magnetic fields in the Tesla range [2] and subverting standard IFE symmetry rules [3,4,5,6]—direct experimental evidence remains scarce. To bridge the gap between advanced theoretical predictions and practical applications, we experimentally probe the ultrafast dynamics of the nanoscale IFE. We employ time-resolved pump-probe Magneto-Optical Kerr Effect (MOKE), enabling us to decouple the IFE from competing magneto-optical phenomena and reconstruct its sub-picosecond dynamics [7,8].

Our investigation focuses on a new generation of non-trivial plasmonic architectures designed to demonstrate unconventional magneto-optical responses. Specifically, we provide experimental validation of magnetization optically induced by linearly polarized light in plasmonic nanorods, as well as chiral nano-antennas that generate magnetization exclusively under specific circular polarizations. By directly capturing these theoretically predicted responses, this work bridges the gap between numerical models and experimental reality, paving the way for the development of novel all-optical, ultrafast spintronic devices and next-generation high-density data storage.

[1] X. Yang et al., "Tesla-Range Femtosecond Pulses of Stationary Magnetic Field, Optically Generated at the Nanoscale in a Plasmonic Antenna", ACS Nano 16 (1), 386-393 (2022)
[2] X. Yang et al., "An inverse Faraday effect generated by linearly polarized light through a plasmonic nano-antenna", Nanophotonics 12 (4), 687-694 (2023)
[3] X. Yang et al., "From dark modes to topology: light-induced skyrmion generation in a plasmonic nanostructure through the inverse Faraday effect", Nanophotonics, 14 (14), 2453-2462 (2025)
[4] X. Yang et al., "Twisting Light, Steering Spins: Gold Nanoparticle Magnetization via Inverse Faraday Effect and Orbital Angular Momentum", Nano Lett. 25 (30), 11549–11553 (2025)
[5] C. Hareau et al., "Engineering Magnetization with Photons: Nanoscale Advances in the Inverse Faraday Effect for Metallic and Plasmonic Architectures", ACS Photonics 12 (12), 6535–6547 (2025)
[6] O. H-C. Cheng et al., "Light-induced magnetism in plasmonic gold nanoparticles", Nano Lett. 22 (13), 365-368 (2022)
[7] A. K. Gonzáles-Alcalde et al., "Enhanced inverse Faraday effect and time-dependent thermo-transmission in gold nanodisks", Nanophotonics 13 (11), 1993-2002 (2024)
[8]V. V. Kruglyak et al., "Ultrafast third-order optical nonlinearity of noble and transition metal thin films", J. Opt. A: Pure Appl. Opt. 7, S235–S240 (2005)

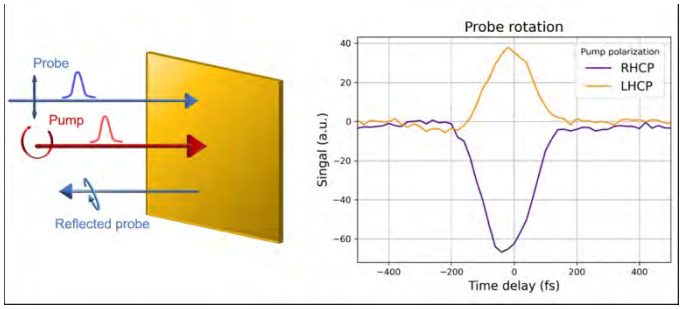


Fig. 1. Time-resolved MOKE measurements of a Gold thin film. (Left panel) Experimental setup: an intense pump beam (red) excites the sample out of equilibrium, while a delayed, linearly polarized probe (blue) monitors transient changes. (Right panel) Recorded probe polarization rotation upon reflection, directly measuring induced magnetization dynamics via MOKE. Under circularly polarized excitation (RHCP/LHCP), the signal characterizes the Inverse Faraday Effect (IFE), driven by spin angular momentum transfer to conduction electrons.

AF-09.* Electric Field-induced Antiferromagnetic Resonance in $MnPS_3$

J. Hanson-Flores*[1], A. Regmi[1], J. Keum[6], J. Tang[3], J. Park[6], R. Cheng[2], S. Singh[4], A. D. Kent[7], D. A. Arena[5], E. del Barco[1]
[1]Physics, University of Central Florida, Orlando, Florida, United States, [2]Electrical and Computer Engineering, University of California, Riverside, Riverside, California, United States, [3]Physics and Astronomy, University of California, Riverside, Riverside, California, United States, [4]Physics, Carnegie Mellon University, Pittsburgh, Pennsylvania, United States, [5]Physics, University of South Florida, Tampa, Florida, United States, [6]Physics and Astronomy, Seoul National University, Seoul, Korea (the Republic of), [7]Physics, New York University, New York, New York, United States

The control of antiferromagnetic order via electrical means has been a longstanding challenge due to the vanishing net magnetization and the high charge current densities required to generate conventional spin–orbit torque (SOT). Recent theoretical work predicts that the topological properties of electronic bands in intrinsic magnetic topological insulators can give rise to staggered adiabatic torques on the Néel vector, commensurate with the alternating spin structure between sublattices (1). These torques can be generated by an externally applied electric field, without the need for a spin injector (monostructural actuation) and without dissipative current flow. Here, we report the first experimental verification of the proposed effect in the magnetic insulator $MnPS_3$. Specifically, we demonstrate that electrically induced adiabatic SOT enables sub-THz resonant excitation of the primary antiferromagnetic modes of $MnPS_3$ via direct coupling to the rf electric field of the microwave stimulus. The measured electric-field-induced adiabatic SOT is stronger (by a factor of five) than the antiferromagnetic resonance excited by the rf magnetic field of the microwaves, which is consistent with the theoretical prediction. These results demonstrate a fundamentally new mechanism for antiferromagnetic state control and open pathways toward dissipationless adiabatic spintronics.

J. Tang, H. Zhang, R. Cheng, *Nat Commun.,* 16, 7790 (2025).

AF-11. Altermagnetic non-reciprocal magnon transport in insulating d-wave orthoferrites

E. Galíndez-Ruales[1], W. Yang[3], T. Dannegger[2], M. Kundu[2], J. Köhler[1], C. Schmitt[1], F. Fuhrmann[1], A. Akashdeep[1], D. Tran[1], X. Ma[3], G. Jakob[1], S. Cao[3], U. Nowak[2], M. Kläui[1]
[1]Institute of Physics, Johannes Gutenberg University, Mainz, Germany, [2]Fachbereich Physik, Universität Konstanz, Konstanz, Germany, [3]Materials Genome Institute, Institute of Quantum Science and Technology, International Center for Quantum and Molecular Structures, Shanghai University, Shanghai, China

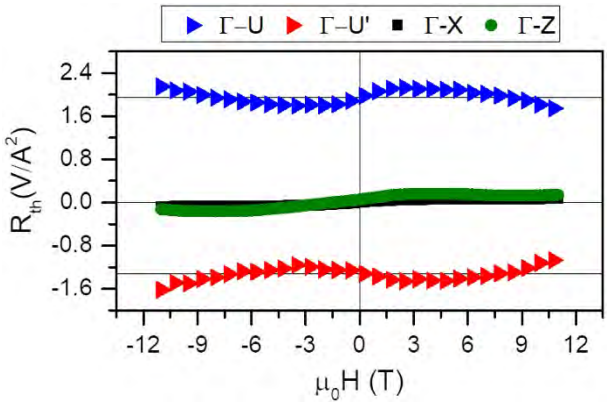
Altermagnetic materials have recently been predicted to host unconventional magnonic phenomena despite their vanishing net magnetization. These include chiral magnon modes, anisotropic magnon lifetimes, and momentum-dependent magnon band splitting, which can enable anisotropic spin transport without external symmetry breaking [1].

Here, we demonstrate non-local magnon transport in the insulating rare-earth d-wave orthoferrite altermagnets $LuFeO_3$ and $YFeO_3$ [2] using Pt devices on orthoferrite single crystals. For spin-Hall-driven magnon injection, we observe a finite non-local spin-transport signal at zero magnetic field, indicating field-free spin-bias magnon transport. This could stem from intrinsic magnon spin splitting of altermagnets.

To unambiguously demonstrate the spin splitting, we use thermal excitations that lead to the spin Seebeck effect. By measuring the thermal non-local transport, we observe a zero field signal, which is not possible in non-altermagnetic antiferromagnets. In particular, a pronounced directional dependence of the thermal non-local signal is found. Transport along the crystallographic Γ–U direction exhibits the opposite sign compared with transport along Γ–U′ and is dominated by a field-independent contribution, while the external magnetic field only modulates the signal, as shown in Fig. 1. In contrast, the signal vanishes when transport is aligned along or perpendicular to the easy axis, consistent with symmetry-imposed suppression along these crystallographic directions and ruling out a significant contribution from the small canted moment of the orthoferrites or antiferromagnetic transport.

These observations are reproduced by atomistic spin-dynamics simulations and support the interpretation of non-local transport mediated by altermagnetically spin-split magnons. Our results provide experimental evidence for key theoretical predictions and establish insulating altermagnets as promising platforms for low-power, field-free magnonic spintronic devices.

[1] L. Šmejkal, A. Marmodoro, K. Ahn *et al.*, *Phys. Rev. Lett.*, vol. 131, no. 25, p. 256703 (2023)
[2] E. Galindez-Ruales, , W. Yang, T. Dannegger, *et al.*, *arXiv*: arXiv:2508.14569.



Non-local spin transport along different crystallographic directions as a function of applied magnetic field, showing sign-inversion with respect to the crystallographic direction.

AF-12. Below-Gap Second-Harmonic Generation as a Geometric Probe of Néel Order in PT-Symmetric Antiferromagnetic Insulators

F. Xue, S. Ahmad
Physics, University of Alabama at Birmingham, Birmingham, Alabama, United States

Detecting Néel order in antiferromagnets remains a central challenge because many conventional linear-response probes are forbidden or strongly suppressed by symmetry. This is especially important in PT-symmetric antiferromagnets, where linear optical and transport responses such as the anomalous Hall effect are constrained to vanish even though the magnetic order can strongly reshape the electronic wave functions. Here, we show that intrinsic second-order responses provide a symmetry-allowed and highly sensitive route to detecting Néel order in such systems.

We develop a gauge-consistent theory of nonlinear conductivity that unifies the length- and velocity-gauge formulations. In the adiabatic dc limit, we show that the apparent discrepancy between these approaches is resolved once all Fermi sea and Fermi surface contributions are retained, eliminating spurious clean-limit terms and establishing a consistent foundation for nonlinear magnetic response. Building on this result, we focus on below-gap second-harmonic generation (SHG) in antiferromagnetic insulators, where real absorption is absent but virtual interband processes generate a finite intrinsic response. We show that this response is controlled by Hermitian-connection and generalized-derivative matrix elements, including geometric structures such as r^a r^{b;c}, which directly encode the quantum geometry of the occupied and unoccupied bands.

Importantly, the below-gap SHG response is symmetry-sensitive to the Néel order parameter and can remain finite in PT-symmetric antiferromagnets even when linear probes are forbidden. We further show that the effect can be strongly enhanced in topological insulating phases, where band inversion and small interband gaps amplify the relevant geometric matrix elements. These results establish below-gap SHG as a nonabsorptive, geometry-driven probe of hidden magnetic order and provide a unified theoretical framework for nonlinear optical detection of antiferromagnetic and topological magnetic materials.

SESSION AG: SPIN-CHARGE INTERCONVERSION

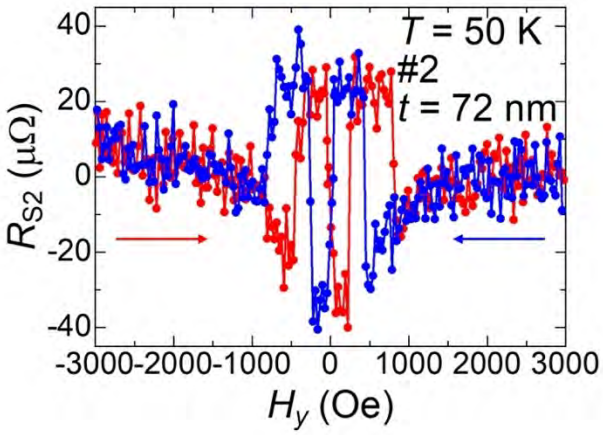
Chair(s): C. Rinaldi, *Physics, Politecnico di Milano, Milano, Italy*
Tuesday, November 3, 2026
08:30 AM-12:00 PM
Sea Pearl

AG-01. Spin-phase detection by spin current in a chiral helimagnet

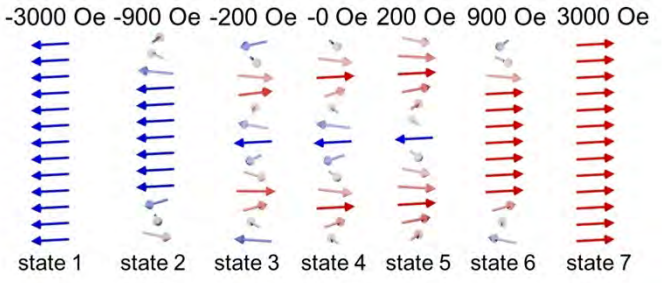
N. Jiang[1, 2, 3], S. Suzuki[1], I. Sasaki[1], K. Yamada[1], R. Kawahara[1], S. Takada[1, 3, 4], Y. Shimamoto[5], H. Shoji[5], Y. Kousaka[5], J. Ohe[6], Y. Togawa[5], Y. Niimi[1, 2, 3]
[1]Department of Physics, The University of Osaka, Toyonaka, Osaka, Japan, [2]Center for Spintronics Research Network, The University of Osaka, Toyonaka, Osaka, Japan, [3]Institute for Open and Transdisciplinary Research Initiatives, The University of Osaka, Suita, Osaka, Japan, [4]Center for Quantum Information ad Quantum Biology, The University of Osaka, Toyonaka, Osaka, Japan, [5]Department of Physics and Electronics, Osaka Metropolitan University, Sakai, Osaka, Japan, [6]Department of Physics, Toho University, Funabashi, Japan

Helical magnets host an internal phase degree of freedom of the helical spin texture. In a finite-size crystal, the spin-phase is encoded in the direction of the surface magnetic moment, which is difficult to access with conventional charge-transport probes that average over the bulk. Surface-sensitive techniques such as x-ray magnetic circular dichroism and spin-polarized scanning tunneling microscopy can reveal the surface magnetization, but they often require specialized environments. Here we demonstrate an all-electrical readout of the spin-phase in the van der Waals chiral helimagnet $CrNb_3S_6$ [1] using a nonlocal spin-valve geometry, where a $CrNb_3S_6$ flake is integrated as the spin-sensitive element and the nonlocal voltage is monitored as a function of magnetic field [2]. We first determine a spin diffusion length of about 5 nm in $CrNb_3S_6$, which is nearly an order of magnitude shorter than the helical pitch of about 48 nm, so that the injected spin accumulation primarily probes the near-surface region. Consistent with this surface sensitivity, the nonlocal signal (Fig. 1) exhibits a characteristic field dependence that follows the evolution of the surface magnetic moment associated with the spin-phase (Fig. 2). Micromagnetic simulations reproduce the measured nonlocal response and confirm that the detected signal is governed by the field-driven reconfiguration of the helical texture at the surface. Our results establish spin currents as a practical probe of the spin-phase in helimagnets and provide a route toward phase-domain control and phase dynamics in nanoscale

spintronic devices.
[1] Y. Togawa *et al*., Phys. Rev. Lett. 108, 107202 (2012).
[2] N. Jiang *et al*., Phys. Rev. B 112, L180402 (2025).



Nonlocal spin-valve signals measured for samples with a thickness of approximately 1.5 helical periods.



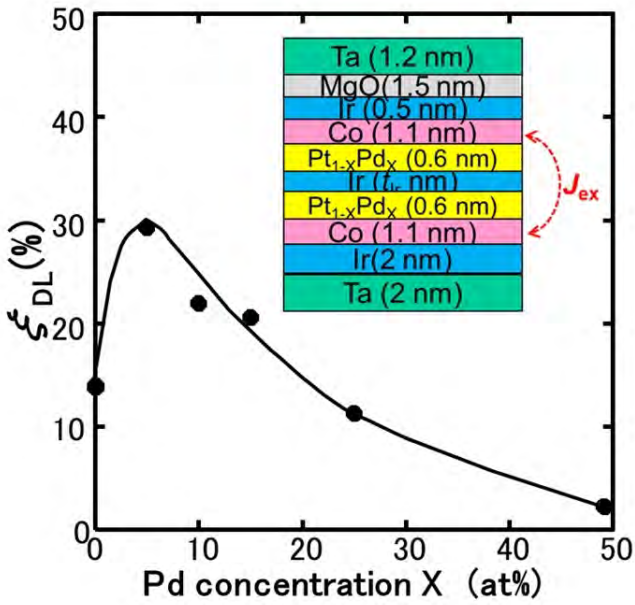
The corresponding magnetic configurations at each magnetic field for samples with a thickness of approximately 1.5 helical periods.

AG-02. Large Damping-Like Spin-Orbit Torque Efficiency in Synthetic Antiferromagnetic System with Pt-Pd/Ir/Pt-Pd Spacer

Y. Saito[1], T. Nguen[1], S. Ikeda[1, 2, 4], T. Endoh[1, 3, 4]
[1]Center for Innovative Integrated Electronic Systems, Tohoku University, Sendai, Miyagi, Japan, [2]Center for Science and Innovation in Spintronics, Tohoku University, Sendai, Miyagi, Japan, [3]Department of Electrical Engineering, Graduate School of Engineering, Tohoku University, Sendai, Miyagi, Japan, [4]Research Institute of Electrical Communication, Tohoku University, Sendai, Miyagi, Japan

Current-induced spin-orbit torque (SOT) has been intensively researched since it can switch magnetization electrically, which is crucial for developing the next generation magnetic memories such as SOT-MRAM. For realizing these memories, metallic electrode with both high damping-like SOT efficiency (ξ_{DL}) and low resistivity (ρ_{xx}) is necessary. We reported that the magnitude of ξ_{DL} increases linearly with increasing the magnitude of interlayer exchange coupling (J_{ex}) in the perpendicular magnetized synthetic antiferromagnetic (AF) system with Pt/Ir/Pt spacer and showed the enhancement of ξ_{DL} with low ρ_{xx} [1-3]. However, the power consumption of SOT-MRAM using this material is still larger than that during the writing of SRAM [2]. Therefore, we need to make more effort to realize SOT-MRAM.
In this work, we study ξ_{DL} in synthetic AF systems using Pt-Pd alloy/Ir/Pt-Pd alloy spacer layers. There is a report in which the $Pt_{75}Pd_{25}$ alloy results in much improved SOT efficiency (ξ_{DL} =26%) [4] compared to Pt. Because the Pt-Pd alloy has a fcc structure, the same structure of Ir and Pt alloys suggests that the topological characteristic of the Fermi surface of Ir and Pt alloys is nearly the same [5]. Therefore, the structure combined with our proposed synthetic AF system [1-3] and Pt-Pd alloy might be an excellent candidate simultaneously exhibiting large J_{ex} and large ξ_{DL} .
As a result, nearly the same magnitude of J_{ex} through Pt-Pd alloy/Ir spacer as that of Pt/Ir spacer was observed. We also found that the magnitude of ξ_{DL} for synthetic AF system using Pt-Pd alloy/Ir/Pt-Pd alloy spacer with Pd concentration of 5 at% is larger than those for the $Pt_{75}Pd_{25}$ alloy system [4] and the synthetic AF system using Pt/Ir/Pt spacer (Fig. 1). The observed maximum magnitude of ξ_{DL} is 29.3% for the synthetic AF system using $Pt_{95}Pd_5$ alloy/Ir/ $Pt_{95}Pd_5$ alloy. The synthetic AF system with Pt-Pd alloy will be a promising building block for future nonvolatile high-speed memories and logic circuits using the spin Hall effect.

This work was supported by the CIES Consortium, X-NICS (JPJ011438), and JSPS KAKENHI (JP24H00030).
[1] Y. Saito et al., Phys. Rev. B 105, 054421, (2022).
[2] Y. Saito et al., Appl. Phys. Exp. 16, 013002 (2023).
[3] Y. Saito et al., Phys. Rev. B 108, 024419 (2023).
[4] L. Zhu et al., Adv. Funct. Mater. 29, 1805822 (2019).
[5] P. Bruno and C. Chappert, Phys. Rev. Lett. 67, 1602 (1991).



Pd concentration dependence of ξ_{DL} in the syntetic AF system with PtPd/Ir/PtPd spacer.

AG-03. Crossover between spin orbit torque dominated and thermally assisted magnetisation switching regimes in CoFeTaB/Pt

K. Dhaliwal[1], R. Fan[1], D. M. Burn[1], O. Inyang[2], A. Hindmarch[2], P. Steadman[1]
[1]Physical Science Division, Diamond Light Source, Didcot, Oxfordshire, United Kingdom, [2]Department of Physics, Durham University, Durham, United Kingdom

Previous studies on current driven magnetisation reversal in CoFeTaB/Pt bilayers have shown that the applied current reorients the magnetisation orthogonal to its flow direction, and the reversal is not uniform across the whole CoFeTaB layer [1,2]. Here we utilise X-ray magnetic reflectivity (XRMR) to investigate the temperature evolution of current induced magnetisation reversal over 100-290K temperature region. The XRMR measurements are performed at the Fe L_3 resonance while applying a cyclic current in a direction orthogonal to the scattering plane so that magnetisation reversal is in the scattering plane to which circular dichroism is most sensitive [3]. The magnetic signal is extracted using XRMR asymmetry ratio defined as the difference divided by the sum of reflectivities measured using opposite helicities of circular polarisation. The XRMR asymmetry shows hysteretic behaviour under current cycling with relatively sharp transitions between two magnetic states at low temperatures. With increasing temperatures, the hysteresis curves evolve into slanted loops. The vertical extent of hysteresis curves h (refer to fig.1), serving as a proxy for net magnetisation participating in the reversal process, is calculated and compared with saturation magnetisation M_s of the film obtained independently from magnetometry measurements (fig. 1). Above ~200K, h and M_s show similar temperature dependence (fig. 1), however the ratio $M_s(T)/h(T)$ varies with temperature suggesting h(T) decreases more rapidly than $M_s(T)$ with increase in temperature (fig. 2). The observations suggest that at low temperatures, current induced spin orbit effects dominate the reversal process, whereas at higher temperatures, thermally assisted pathways become increasingly important. Even though thermal activation assists the reversal process, the fraction of magnetisation participating in reversal is reduced relative to the available moment, indicating a crossover from torque limited to thermally assisted but less efficient magnetisation reversal with increasing temperature.

[1] D. M. Burn, R. Fan, O. Inyang, Phys Rev B, Vol. 106, p. 094429 (2022).
[2] Kiranjot, R. Fan, R. O. M. Aboljadayel, Jpn. J. Appl. Phys., Vol. 63, p. 098004 (2024).
[3] R Fan, Kiranjot, R. O. M. Aboljadayel, J. Synchrotron Rad., Vol 31, p. 493-507 (2024).

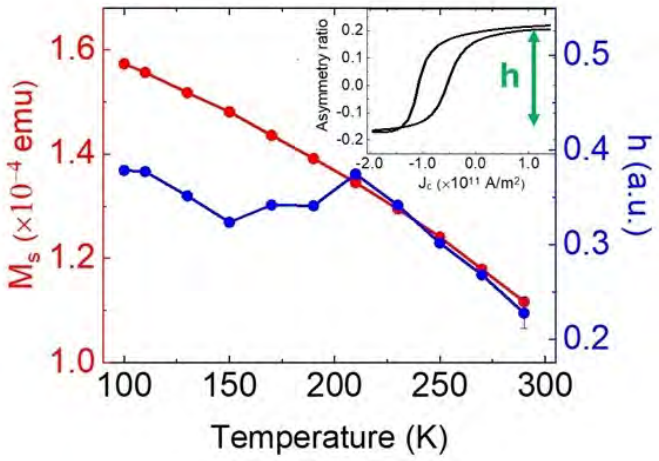


Fig.1: Comparison of h(T) and M_s(T), h: vertical extent of hysteresis curves (defined in the inset for a representative current-driven hysteresis loop)

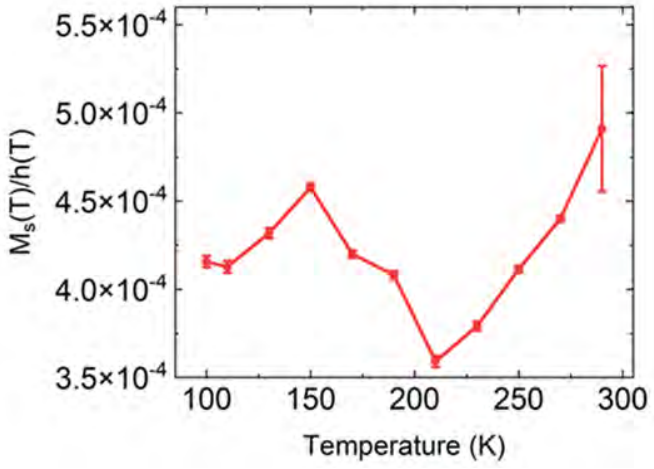


Fig.2: M_s/h vs temperature

AG-04. Observation of *canted*-spin Hall effect in low-symmetry bulk crystal α -$PdBi_2$

Y. Samukawa[1], K. Nakashima[1], N. Jiang[1, 2, 3], K. Kudo[1, 3], Y. Niimi[1, 2, 3], K. Kondou[2, 3]

[1]Department of Physics, The University of Osaka, Toyonaka, Osaka, Japan, [2]Center for Spintronics Research Network, The University of Osaka, Toyonaka, Osaka, Japan, [3]Institute for Open and Transdisciplinary Research Initiatives, The University of Osaka, Suita, Osaka, Japan

Unlike the typical spin Hall effect (SHE) in transition metal, low-symmetry crystals exhibit *canted*-SHE, in which the spin polarization has both components of perpendicular and parallel to the spin-current propagation direction [1]. Interestingly, it has been reported that these materials may exhibit not only the *canted*-SHE but also spin diffusion lengths that are significantly longer than those of conventional transition metals [2,3]. Although the *canted*-SHE has been studied in many two-dimensional materials such as Td-WTe_2 and 1T'-$MoTe_2$[4,5], most cases originate from interface- or layer-number-dependent symmetries. Thus, it can be strongly suppressed by interface roughness. Here, we focus on a low-symmetry bulk crystal, α-$PdBi_2$ [6], to observe the *canted*-SHE and robust spin-orbit torques. Figure 1(a) shows the crystal structure of α-$PdBi_2$ with the space group *C2/m*. Using the mechanical exfoliation technique, we exfoliated α-$PdBi_2$ single-crystal flakes and evaluated the SHE at room temperature by means of spin-torque ferromagnetic resonance (ST-FMR) [7], as illustrated in Fig. 1(b).

Figure 1(c) shows results of ST-FMR measured with an α-$PdBi_2$ (185 nm) / Py (15 nm) bilayer at magnetic-field angles of 45° and 135°. Unlike the case of conventional transition metals such as Pt, there is an obvious difference between 45° and 135° due to the out-of-plane spin polarization from α-$PdBi_2$, suggesting an unconventional SHE arising from the low crystal symmetry. In addition, Fig. 2 shows that the charge-to-spin conversion efficiency of the in-plane spin component (*y*-spin) increases even in a thick regime far beyond spin diffusion lengths of several nm in typical transition metals. It may indicate the long spin diffusion length exceeding 100 nm in our α-$PdBi_2$. These results highlight low-symmetry bulk crystals such as α-$PdBi_2$ as promising platforms for realizing robust *canted*-SHE and long-range spin transport.

[1] A. Roy *et al*., Phys. Rev. Mater. 6, 045004 (2022).
[2] P. Song *et al*., Nat. Mater. 19, 292 (2021).
[3] M. Vila *et al*., Phys. Rev. Res. 3, 043230 (2021).
[4] D. MacNeill *et al*., Nat. Phys. 13, 300 (2016).
[5] G. M. Stiehl *et al*., Phys. Rev. B 100, 184402 (2019).
[6] K. Dimitri *et al*., Phys. Rev. B 97, 144514 (2018).
[7] L. Liu *et al*., Phys. Rev. Lett. 106, 036601 (2011).

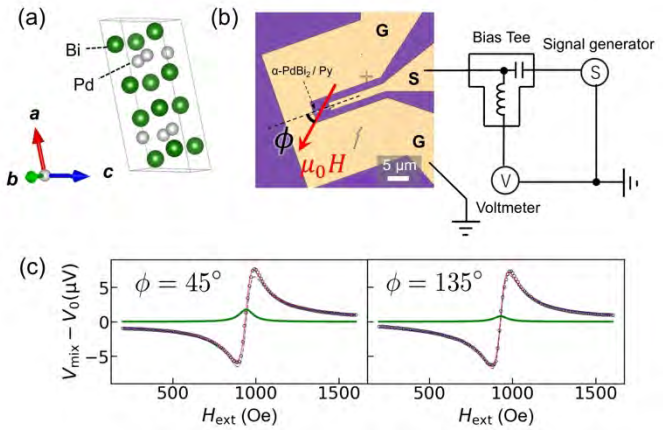


Fig.1. (a) Crystal structure of α-$PdBi_2$. (b) Device structure and measurement set up. (c) Observed ST-FMR signals.

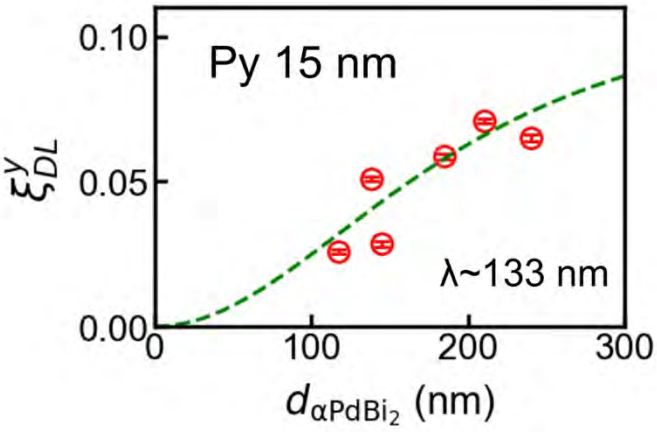


Fig.2. Thickness dependence of the charge-to-spin conversion efficiency for the *y*-spin component.

AG-05. Influence of Giant Spin Hall-Induced Hall Effect on Spin-Orbit Torque in Metallic Magnetic Bilayers

D. Nam[1], S. Ko[1], G. Baek[1], B. Park[2], A. M. Park[1], K. Kim[1]
[1]Physics, KAIST, Daejeon, Korea (the Republic of), [2]Materials Science and Engineering, KAIST, Daejeon, Korea (the Republic of)

The spin Hall effect (SHE) generates transverse spin currents from a longitudinal charge current, enabling spin–charge interconversion. These spin currents give rise to Hall responses such as the spin Hall–induced anomalous Hall effect (SH-AHE) and planar Hall effect (SH-PHE), studied in heavy metal/magnetic insulator (HM/MI) heterostructures [1]. In such systems, the spin current is reflected at the HM/MI interface, undergoes spin precession governed by the spin mixing conductance, and is converted into a transverse charge current via the inverse SHE.

In this study, we report a giant SH-AHE in metallic heavy metal/ferromagnet (HM/FM) bilayers. As shown in Fig. 1, the SH-AHE in HM/FM exhibits a positive and significantly larger magnitude than in HM/MI systems, indicating a distinct mechanism.

Within the SHE framework, both the damping-like torque (DLT) and SH-PHE originate from the same spin current [2] and are expected to show similar material dependence. However, our results reveal a clear deviation. As summarized in Table 1, SH-PHE is larger in Pt-based systems, whereas DLT is larger in Ta-based systems, demonstrating inconsistent scaling.

This discrepancy suggests additional contributions beyond the spin Hall mechanism. In particular, the anomalous behavior in Ta-based structures, where SH-PHE deviates significantly from DLT trends, points to possible orbital-related contributions. Previous reports of unusually large and positive DLT in Ta/Ni systems [3] further support that orbital-mediated torque may influence overall efficiency.

Our findings establish that SH-AHE in metallic HM/FM bilayers can become a dominant and unconventional Hall contribution, with magnitude and sign distinct from HM/MI systems. These results highlight the need to revisit the microscopic origin of Hall responses in metallic spintronic systems and suggest a role of orbital effects beyond the SHE framework.

[1] S. Husain *et al.* Appl. Phys. Lett. 122, 062403 (2023)
[2] Y. -T. Chen *et al.* Phys. Rev. B 87, 144411 (2013)
[3] D. Lee *et al.* Nat. Commun. 12, 6710 (2021)

This work was supported by the National Research Foundation of Korea (NRF) grant funded by the Korean government (MSIP) (Grant No. RS-2023-00275259).

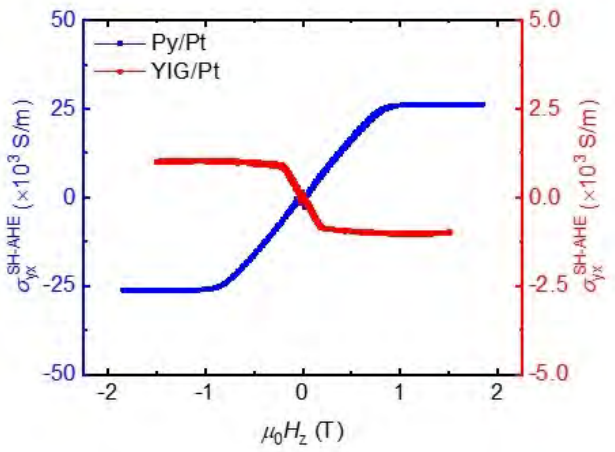


Figure 1 Hall resistivity of Pt/Py and YIG/Pt systems

Sample set	B_{DLT} (mT)	$\Delta\sigma_{yx}^{SH-PHE}$ ($\times 10^3$ S/m)	$\Delta\sigma_{yx}^{SH-AHE}$ ($\times 10^3$ S/m)
|| Py(4)/MgO(2)/Ta(2)	~ 0	0	0
|| Pt(4)/Py(4)/MgO(2)/Ta(2)	1.29	28.87	30.05
|| Pt(4)/Cu(3)/Py(4)/MgO(2)/Ta(2)	1.80	14.13	14.71
|| Ta(4)/Py(4)/MgO(2)/Ta(2)	6.00	6.66	2.99
|| Ta(4)/Cu(3)/Py(4)/MgO(2)/Ta(2)	3.45	8.21	1.33

Table 1 A summary of damping-like torque, Hall conductivity difference with ||Py(4)/MgO(2)/Ta(2) sample in terms of SH-PHE and SH-AHE for different series of samples. || means Si/SiO_2 substrates. The number represents the thickness of layer in nm scale.

AG-06. Role of impedance in spin-torque ferromagnetic resonance

F. Wang, W. Lin
School of Physics, Southeast University, Nanjing, Jiangsu, China

Spin-torque ferromagnetic resonance (ST-FMR) has been widely used to quantify spin-charge conversion efficiency of various materials such as heavy metals, topological insulators, van de Waals materials, and antiferromagnets. However, ST-FMR signals may include other contributions such as eddy current and dielectric substrate, leading to over-estimation of spin Hall angle. We show impedance dependent phase in spin rectification plays a crucial role in line-shape of dc voltages in ST-FMR measurements.By tuning impedance via wiring of waveguide, ratio of symmetric dc voltage peak to antisymmetric one is larger than 10 in $Al/Ni_{81}Fe_{19}/Al$ trilayer, which would deduce an unphysical large spin (orbital) Hall angle. Current modification of linewidth can be explained by quadratic rectification due to magnetoresistance, rather than spin-orbit torques. Our results indicate ST-FMR is unreliable to quantify spin (orbital)-charge conversion efficiency.

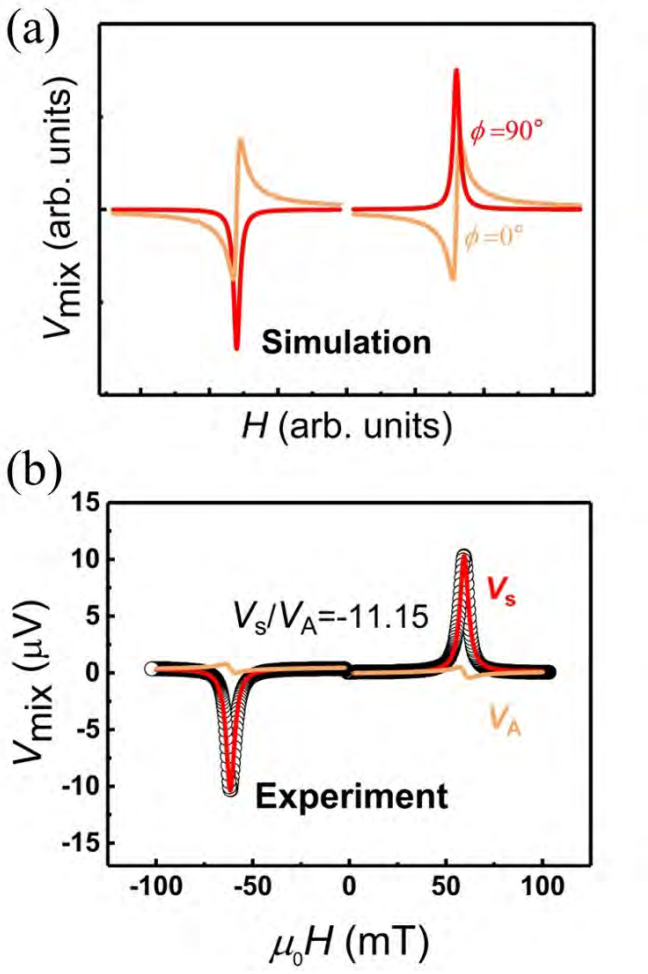


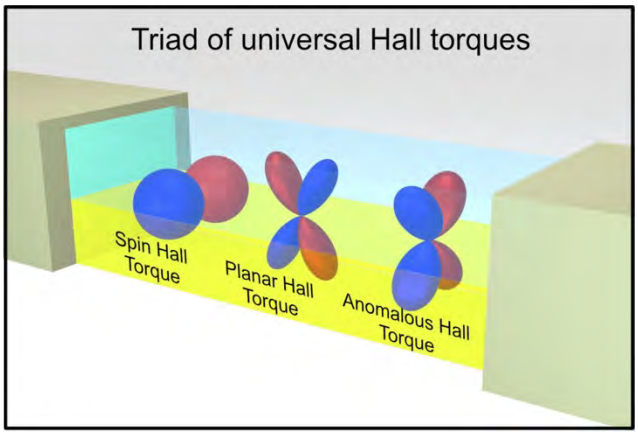
Fig. 1 (a) Simulated ferromagnetic resonance voltage as a function of magnetic field for impedance phases of 0° and 90°, respectively. (b) Field dependence of voltage in $Si/SiO_x/Al$(2 nm)/Py(3 nm)/Al(2 nm)/Al_2O_3(3nm). The symmetric and antisymmetric voltages are indicated by lines.

AG-07. Universal Hall Torques

E. A. Montoya
Physics and Astronomy, University of Utah, Salt Lake City, Utah, United States

Spin–orbit torques provide a powerful route for electrically manipulating magnetization and are central to emerging energy-efficient information technologies. Traditionally, giant spin–orbit torques have been realized in ferromagnet/non-magnet bilayers, where broken inversion symmetry produces Rashba and spin Hall torques [1,2]. More recently, it has become clear that ferromagnetic conductors can themselves generate large torques through their intrinsic Hall transport. The planar Hall torque and the newly identified anomalous Hall torque are examples of self-generated torques, acting back on the spin order within the same magnetic layer in which the current originates [3–5]. These torques exhibit unusual symmetries that distinguish them from conventional spin–orbit torques and open additional routes for controlling magnetic dynamics. Together with the spin Hall torque, they form a universal triad of Hall torques expected to arise broadly in magnetic conductors. In this talk, I will introduce the framework of Universal Hall Torques, discuss their underlying mechanisms, and discuss their implications for future spintronic devices.

1. I. M. Miron et al. Nature Materials 9, 230–234 (2010).
2. L. Liu, et al. Science 336, 555–558 (2012).
3. C. Safranski, E. A. Montoya, and I. N. Krivorotov, Nature Nanotechnology 14, 27–30 (2019).
4. Safranski, C. et al. Physical Review Letter. 124, 197204 (2020).
4. E. A. Montoya, X. Pei, and I. N. Krivorotov, Nature Nanotechnology 20, 353–359 (2025)



The Spin Hall Torque, Planar Hall Torque, and Anomalous Hall Torque form a triad of Universal Hall Torques.

AG-09. Modulation of Damping in the Magnetic Weyl Semimetal Co_2MnGa by Intrinsic Spin-Orbit Torques

F. Weidenhiller[1, 2], L. Chen[1, 2], C. H. Back[1, 2]
[1]*School of Natural Sciences, Technical University of Munich, Garching, Germany,* [2]*TUM Center for Quantum Engineering, Garching, Germany*

Conventional spintronic devices rely on heterostructures of magnetic and non-magnetic materials. Magnetic Weyl semimetals (MWS), on the other hand, generate spin currents intrinsically via spin-momentum locking at the Weyl nodes, removing the need for a separate non-magnetic spin source. The magnetic Heusler compound Co_2MnGa is established as a high Curie temperature MWS (T_C > 600 K) [1], making it a compelling candidate for room temperature spintronic devices.

To quantify the intrinsic MWS-induced spin-orbit torque (SOT) in Co_2MnGa, we employ the modulation-of-damping method [2], in which the FMR linewidth is tracked as a function of an applied DC charge current to extract the damping-like SOT. We apply this technique to a 5 nm epitaxial Co_2MnGa film grown on GaAs and capped with aluminum oxide. Experimentally, we observe a pronounced and systematic change in the damping of the system as the DC charge current is varied. Quantitatively, we observe ferromagnetic resonance linewidth changes of about 20% at room temperature, linear in the DC charge current and reversing sign under current reversal, ruling out thermal contributions. We corroborate these findings with a magneto-optical Kerr effect (MOKE) based spin-orbit torque magnetometry technique first introduced by Xin Fan et al. [3]. Here, we also observe sizeable SOTs, comparable in magnitude to those found in heavy-metal/ferromagnet heterostructures. Together, these measurements support the interpretation of an MWS-induced torque acting on the magnetization from within the Co_2MnGa layer itself, highlighting the potential of Co_2MnGa as a platform for heterostructure-free spin-orbit torque devices.

[1] I. Belopolski et al. 'Discovery of topological Weyl fermion lines and drumhead surface states in a room temperature magnet', Science 365, 1278–1281 (2019)
[2] L. Chen *et al.* 'Signatures of magnetism control by flow of angular momentum', Nature 633, 548-553 (2024)
[3] X. Fan *et al.* 'Quantifying interface and bulk contributions to spin–orbit torque in magnetic bilayers', Nature Communications 5, 3042 (2014)

AG-10. Channel–Less SOT–MRAM Integration with Embedded Spin–Orbit–Torque Track for Reduced Switching Current

J. Urrestarazu Larranaga, V. Kateel, A. Palomino Lopez, A. Das, N. Paul, G. Talmelli, V. Nguyen, R. Carpenter, S. Rao
imec, Leuven, Belgium

Spin-orbit torque magneto–resistive random–access memory (SOT–MRAM) is one of the most promising alternatives to the charge–based static random–access memory (SRAM) [1]. The limitations related to the high switching current values for the write operation are being addressed with new device concepts such as the channel–less SOT–MRAM [2]. Conventional SOT–MRAM integration decouples write and read current paths through the SOT channel (Fig.1a), offering a solution to the challenges present in spin–transfer torque (STT)–MRAM [3]. The channel–less SOT–MRAM aims to reduce the switching current (Isw) by minimizing the lateral SOT channel (Fig.1b). This direction is driven by scaling trends [4] which collectively push the device towards lower operational current. In this work, we integrate the channel-less SOT-MRAM devices in 300 mm platforms (Fig.1c) and further explore the electrical and magnetic properties dependency on the overlap between the BE and MTJ.

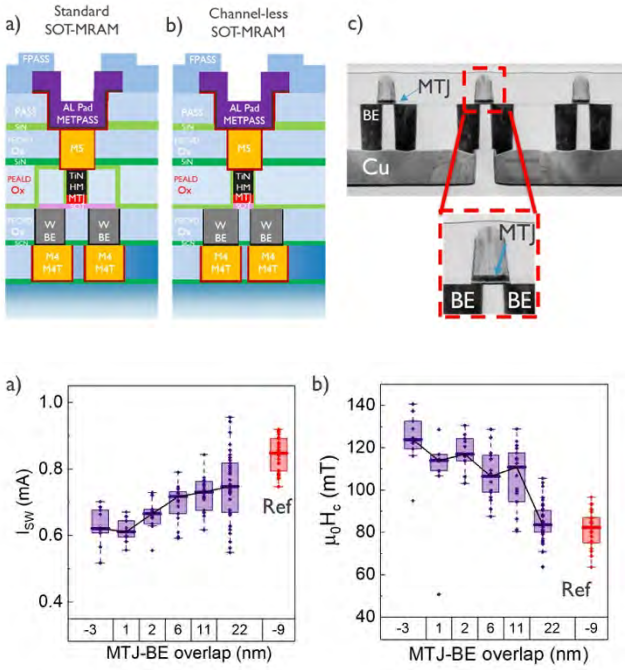
Fig.1: (a) Schematic of the process flows that compares (a) the conventional and (b) the channel–less integration scheme. (c) TEM images where the MTJ overlaps with the electrodes.

A transmission electron microscope (TEM) image of the channel-less device sitting on top of the BEs is illustrated in Fig.1c. Here, the SOT track was etched altogether with the MTJ pillar, removing the complexities related to the MTJ etch that require a controlled landing on the SOT channel. Fig.2 shows how the channel–less SOT–MRAM devices with CoFeB/MgO/CoFeB and β–tungsten (W) provide 25% lower switching current values compared to the equivalent reference device. Interestingly, the coercive field is increased for devices with little overlap compared to reference data.

Fig.2: (a) Switching current and (b) coercive field for channel-less devices depending on the overlap between the MTJ and the BEs.

The channel–less integration scheme increases the overall learning cycle speed while also introducing certain integration challenges. In this work, we discuss the consequencesc due to this channel–less approach and propose certain methods to overcome them. We will also show sub–ns switching experiments, back–hopping phenomena correlation with overlap and field-free options.

[1] V. Krizakova et al., *J. Magn. Magn. Mater.*, Vol. 562, p. 169692 (2022).
[2] E. Liu et al., *IEEE Int. Electron Devices Meet. (IEDM) Tech. Dig.*, pp. 1–4 (2024).
[3] V. D. Nguyen, S. Rao, K. Wostyn et al., *npj Spintronics*, Vol. 2, p. 48 (2024).
[4] S. Van Beek et al., *IEEE Int. Electron Devices Meet. (IEDM) Tech. Dig.*, pp. 1–4 (2023).



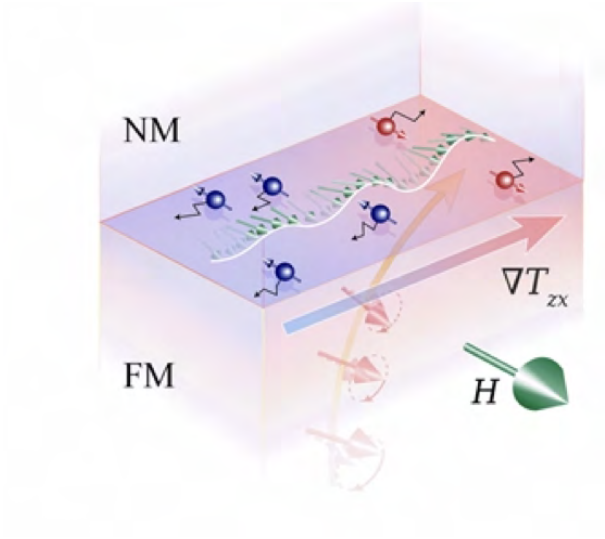
AG-11. When magnons drag electrons: the phenomena of interfacial magnon drag

A. De[1, 2], D. Prabhakaran[3], S. Nair[1]
[1]Physics, IISER Pune, Pune, Maharashtra, India, [2]Weizmann Institute of Science, Rehovot, Israel, [3]University of Oxford, Oxford, United Kingdom

The thermal Hall effect owing to magnons - the quanta of collective spin wave excitations- offers an indirect probe of the magnonic band structure. We demonstrate that a measurement geometry comprising of a heavy non-magnetic metal deposited on top of a ferromagnet could be used to measure the magnon Hall effect. Using a measurement geometry typically used in the past for spin-

caloritronic measurements, we identify a voltage that arises as a consequence of the dragging force which surface magnons of a pyrochlore ferromagnet impart on the conduction electrons of the adjacent metal layer. Besides offering a new means of measuring the magnon Hall effect, this also suggests that surface magnons could potentially be interrogated using electrical means

A. De, D. Prabhakaran, and Sunil Nair, Phys. Rev. B 111, 054435 (2025)



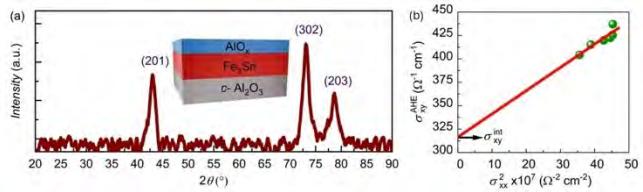
AG-12. Large Self-Induced Inverse Spin Hall Effect and Damping-Like Torque in Single-layer Kagome Magnet Fe_3Sn

N. Kandwal[1], H. Bangar[2], A. Saxena[1], V. Yadav[1], R. S. Yadav[1], A. Sahoo[1], S. P. Dash[2], P. K. Muduli[1]

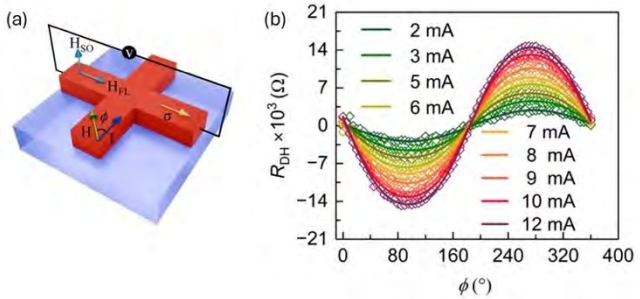
[1]Physics, Indian Institute of Technology Delhi, South Delhi, Delhi, India, [2]Microtechnology and Nanoscience, Chalmers University of Technology, Gothenburg, Sweden

Fe_3Sn, a kagome ferromagnet within the Fe-Sn family, hosts a wide variety of topological features [1], including Weyl points and flat bands [2], that facilitate large anomalous Hall conductivity (σ_{xy}^{AHE}). In this work, we investigate the potential of Fe_3Sn thin films for spintronic applications. The GI-XRD data in Fig. 1(a) confirms the growth of polycrystalline films via co-sputtering, yielding a σ_{xy}^{AHE} of 404 ± 2 $\Omega^{-1}cm^{-1}$, at 300 K. Figure1 (b) displays σ_{xy}^{AHE} plotted as a function of the square of the longitudinal conductivity (σ_{xx}^2). The significant non-zero y-intercept indicates that a substantial portion of σ_{xy}^{AHE} originates from the intrinsic anomalous Hall conductivity (σ_{xy}^{int}). The inverse spin Hall effect (ISHE) measurements on the single-layer Fe_3Sn reveal a significant self-induced voltage that is absent in other Fe-Sn compositions, confirming that the spin-to-charge conversion is intrinsic to the Fe_3Sn phase. From the thickness dependence of the ISHE voltage, we extract a spin diffusion length of λ_d = 2.72 ± 0.18 nm. By evaluating the damping-like torque via the d.c. planar Hall effect (PHE) (Fig. 2(b)), we highlight the limitations of the ISHE technique for single-layer systems. A large damping-like torque conductivity of σ_{DL} = 3.74 ± 0.18 (×10^5 h-cut/2*e*) $\Omega^{-1}cm^{-1}$, provides a first direct demonstration of self-induced spin-orbit torque in kagome materials. The value of σ_{DL} for Fe_3Sn exceeds the conventional 3d transition metals like Co, Ni, and NiFe [3] [4], and is also highly competitive with complex Heusler alloys, such as Co_2MnGa [5]. These results establish single-layer Fe_3Sn as a highly efficient spin current source, offering a promising platform for advanced spintronics without the need for heavy-metal interfaces.

[1] K Fujiwara, Y Kato, T Seki, et al. *Commun. Mater.*, *2.1*, 113 (2021).
[2] Z. Liu, M. Li, Q. Wang, et al. *Nat. Commun.*, *11*(1), 4002 (2020).
[3] T. Seki, Y.C. Lau, S. Iihama, et al. *Phys. Rev. B*, *104*(9), 094430 (2021).
[4] Q. fu, L. Liang, W. Wang, et al. *Phys. Rev. B*, *105*(22), 224417 (2022).
[5] L. Bainsla, Y. Sakuraba, A. Kumar, et al. *ACS nano*, 19.19, 18534-18544 (2025).



(a) Grazing-incidence x-ray diffraction (GIXRD) pattern of Fe_3Sn thin film grown on the Al_2O_3 substrate with a 3 nm Al capping. (b) Anomalous Hall conductivity (σ_{xy}^{AHE}) plotted against the square of the longitudinal conductivity (σ_{xx}^2).

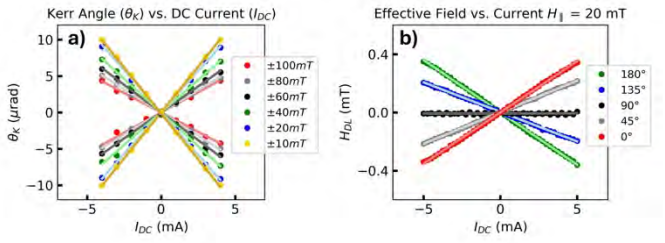


(a) Schematic of the Hall bar device used for PHE measurements. H_{SO} and H_{FL} denote the spin-orbit and field-like effective field, respectively. (b) Difference between the opposite current polarity of PHE curves (R_{DH}) for various d.c. current levels.

AG-13. Magneto-Optic Studies of Spin Orbit Torques in Synthetic Ferrimagnets

A. K. Aykin[1], A. K[2], S. Petit-Watelot[2], M. S. Yactayo[2], L. Badie[2], S. Mangin[2], M. Hehn[2], C. Rojas-Sanchez[2], A. D. Kent[1]
[1]Center for Quantum Phenomena, Department of Physics, New York University, New York, New York, United States, [2]Institut Jean Lamour, Université de Lorraine, CNRS, Nancy, France

Rare-earth/transition-metal synthetic ferrimagnetic structures have been used to enable current-driven operations while exhibiting exciting phenomena, including, but not limited to, self-torques and efficient charge-to-spin conversion. By engineering the thickness of the layers that make up the ferrimagnetic system, magnetic properties can be easily tuned. Current-induced torques in synthetic ferrimagnets have been extensively studied in the past using electrical transport measurements, such as 2nd harmonic Hall and spin-torque FMR measurements. Here, we report on high-sensitivity magneto-optical measurements of the current-induced torques in these synthetic ferrimagnetic systems using a Zero-Area Loop Sagnac Interferometer (ZALSI) based on Magneto-Optic Kerr Effect (MOKE). We have achieved a Kerr sensitivity of ~50 nrad, enabling us to probe very small magnetization deflections induced by spin-orbit torques while avoiding effects such as current-mediated rectification and other unidentified artifacts in the estimation of current-induced torques by electrical methods. We optically probe spin-orbit-torques in bilayers of Co/Gd on SiO2 substrates with different capping layers, such as Al, Pt, and Ta, along with reversal of the bilayer stacking to understand the effect of Gd on efficiency and the role the interfaces play. We verify our results and quantify the current induced artifacts by comparing ZALSI-MOKE measurements with the results of second-harmonic Hall studies on the same samples.



a) Kerr angle as a function of I_{DC} for different in-plane field magnitudes. The sample has the structure, Gd(2)/Pt(2)/Co(2)/Pt(2). The magnetization lies in the plane, and it is aligned with the current. b) Corresponding damping-like effective field as a function of I_{DC} for different orientations of magnetization with respect to current. 0° corresponds to when current and magnetization is aligned.

SESSION AP: RARE-EARTH PERMANENT MAGNETIC MATERIALS (POSTER SESSION)

Chair(s): Y. Tatetsu, *University Center for Liberal Arts Education, Meio University, Nago, Okinawa, Japan*
Tuesday, November 3, 2026
09:30 AM-12:30 PM
Coral 4

AP-01. Industrial Perspectives on Nd–Fe–B Strip Casting with Rare-Earth Alloying

G. Kumari
Eutectix, LLC, Tolleson, Arizona, United States

Strip casting remains the industrially dominant route for producing precursor alloys for sintered Nd–Fe–B magnets, yet the translation of laboratory-scale understanding to full-scale manufacturing continues to present challenges in process stability, microstructural control, and reproducibility. This work focuses specifically on the formation of strip-cast flakes at industrial scale with a capacity of 650 MT, emphasizing the critical links between melt processing, solidification conditions, and the resulting microstructure.
Using production-scale casting conditions, a representative melt was processed (approximately 130 kg) with rare-earth as Nd/Pr and characterized in terms of chemical composition and microstructural features, as shown in Figure 1. The results reveal the persistence of characteristic heterogeneous solidification features, including variations in grain morphology and Nd-rich phase distribution, which are strongly influenced by thermal gradients and interfacial heat extraction. Particular attention is given to the formation and uniformity of the flake structure, as this stage governs downstream hydrogen decrepitation and jet milling behavior.
While specific process parameters cannot be disclosed, this study highlights key considerations necessary for robust industrial operation, including control of heat transfer at the wheel interface, mitigation of melt fluctuations, and maintaining compositional homogeneity during casting. The observations demonstrate that even under constrained processing windows, microstructural consistency can be achieved through careful management of these factors.
The findings provide practical insight into bridging lab-scale optimization strategies with industrial-scale execution,

offering guidance for improving flake quality and ensuring reliable feedstock for high-performance Nd–Fe–B magnet production.

1) L. Q. Yu, et. al., "On the cooling rate of strip cast ingots for sintered NdFeB magnets", Physica B, 393 (2007), 1-3.
2) J. Bernardi, et. al.,"Microstructural analysis of strip cast Nd–Fe–B alloys for high BHmax magnets" J. Appl. Phys. 83 (1998), 6396.

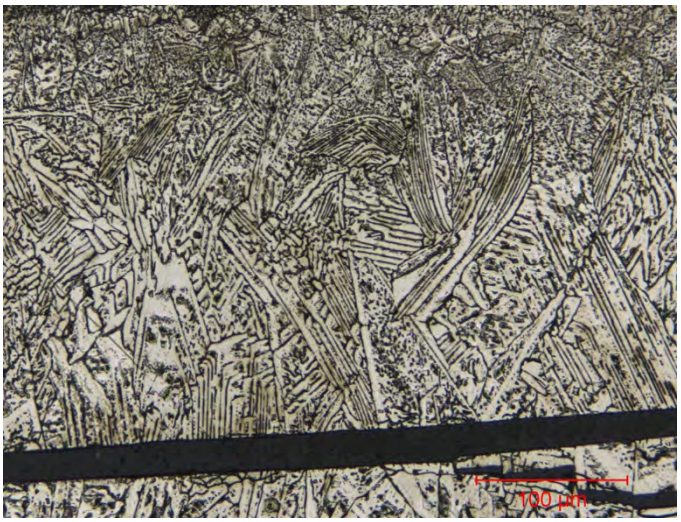


Figure 1a: OM micrograph for strip casted NdFeB flake at 200X



Figure 1b: OM micrograph for strip casted NdFeB flake at 500X

AP-02. Mechanically Robust Nd–Fe–B Sintered Magnets with High Magnetic Performance

B. Cui, X. Liu, W. Tang, I. C. Nlebedim, J. Cui
Division of Critical Materials, Ames National Laboratory, Ames, Iowa, United States

Rare-earth permanent magnets (REPMs), especially Nd–Fe–B and Sm–Co sintered magnets, are essential to technologies ranging from electric vehicles and wind turbines to electronics and medical devices due to their exceptional magnetic performance. However, sintered REPMs are inherently brittle, owing to limited slip systems for plastic deformation. This brittleness leads to high failure rates and material waste during manufacturing, particularly for thin or complex components, and necessitates added precautions in high-stress or vibration-prone applications. Developing mechanically robust REPMs without sacrificing magnetic performance is therefore of critical importance.

Here, we report a “tough Neo,” a class of Nd–Fe–B sintered magnets with enhanced mechanical robustness, improved manufacturability, and greater recyclability. We explore microstructural engineering strategies to improve flexural strength while preserving magnetic properties. These include grain size and grain boundary engineering, such as a novel clustered bimodal coarse/fine-grained microstructure, along with the introduction of ductile metallic grain boundary phases (GBPs) and reinforcing additives. Because fracture in Nd–Fe–B magnets is primarily intergranular and governed by crack initiation at GBPs, strengthening these regions is key.

Our micromechanical modeling and experiments reveal that fracture strength depends on matrix grain size, interfacial energy release rate, crystal structure, composition, and the elastic properties, distribution, and volume fraction of GBPs and additives. Increasing grain size and enhancing the toughness, content, and dispersion of ductile GBPs significantly improve mechanical strength by suppressing crack initiation and propagation. As a result, substantial gains in flexural strength are achieved alongside improved intrinsic coercivity H_{ci}. For example, flexural strength increases from 333 MPa to 480 MPa and H_{ci} from 14.4 kOe to 16.6 kOe, while maintaining 90% of the maximum energy product $(BH)_{max}$. These results demonstrate a viable pathway toward mechanically robust, high-performance Nd–Fe–B sintered magnets. The toughened magnets can improve efficiency in the use of critical materials and reduce part costs.

AP-03. Selective Boundary Fracture Milling (SBFM) for High-Performance Nd-Fe-B Magnets

H. Parmar, X. Liu, B. Cui, I. C. Nlebedim
Division of Critical Materials, Ames National Laboratory, Ames, Iowa, United States

This work establishes a drop-in alternative to jet milling, addressing a key bottleneck in sintered Nd-Fe-B magnet manufacturing. Milling is a critical step in Nd-Fe-B processing because it defines powder characteristics that impact alignment, densification, and magnetic performance. Following hydrogen decrepitation, milling produces fine (~3-5 μm) particles required for magnetic alignment during pressing. Beyond size reduction, it controls particle size distribution, surface chemistry, and grain-boundary exposure, which influences density, sintering, and magnetic hardness.

While technically mature, jet milling is capital-intensive and supply-constrained, limiting rapid scale-up as demand for Nd-Fe-B grows. There is therefore a need for process innovations that decouple magnet milling from high-cost, specialized jet milling operations to enable more distributed and scalable production. Alternative approaches [1-3]: including ball, impact, vibratory, knife, and burr milling methods typically yield inferior demagnetization behavior relative to jet-milled powders.

Here, we report a novel Selective Boundary Fracture Milling (SBFM) technology for Nd-Fe-B applicable to both virgin production and end-of-life (EOL) magnet recycling. Unlike jet milling, which relies on high-velocity gas streams and often requires size classification, SBFM promotes controlled intergranular fracture, enabling preferential separation along existing microstructural boundaries. It minimizes crystal damage and reduces contamination risk, hence preserves powder properties for high-performance sintered magnets.

Fig. 1a shows the microstructure of SBFM-milled EOL Nd-Fe-B magnet, highlighting selective boundary liberation. The SBFM-milled EOL magnet was used to produce sintered magnets with demagnetization curves and the milling times (1–5 min) in Fig. 1b. Fig. 1c shows the demagnetization curve for SBFM-processed virgin feedstock, confirming applicability to both recycling and virgin production pathways.

1. E. Herraiz Lalana, *Production of Sintered NdFeB Magnets from Scrap Alloy Powders*, Ph.D. dissertation, University of Birmingham, 2017
2. Zakotnik, M., Devlin, E., Harris, I.R., Williams, A.J., 2006. Proceedings of the 19th Workshop on Rare Earth Permanent Magnets and Their Applications, 289-295.
3. Zakotnik, M., Harris, I.R., Williams, A.J., 2009. Multiple recycling of Nd-Fe-B-type sintered magnets. Journal of Alloys and Compounds, 469, 314-321.

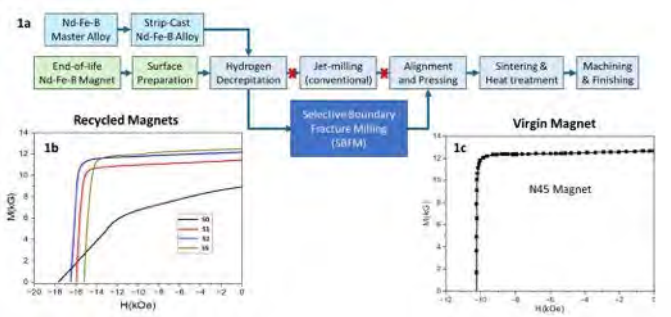


Fig. 1: (a) Microstructure of SBFM-processed end-of-life Nd-Fe-B. (b) Magnetic hysteresis loops of SBFM processed recycled magnet, as a function of milling time (1-3 min), (c) Magnetic hysteresis loop of virgin feedstock processed via SBFM method.

AP-04. A guide to design the composition of Nd-Fe-B sintered magnets for achieving high-coercivity *via* Pr-based grain boundary diffusion process

S. Lee[1], S. Kim[1], H. Cha[1], T. Kim[1], K. Bae[2], D. Kim[2], J. Lee[1]
[1]Korea Institute of Materials Science, Changwon, Korea (the Republic of), [2]Star Group Ind. CO., Ltd., Daegu, Korea (the Republic of)

The grain boundary diffusion process (GBDP) using heavy rare-earth elements (HRE = Dy, Tb) has been widely employed to resolve thermal demagnetization of Nd-Fe-B magnets by forming high-anisotropy HRE-rich shells around $Nd_2Fe_{14}B$ grains[1)]. However, the use of HRE has been limited by high cost and scarcity of HRE[2)]. As an alternative, GBDP using light rare-earth Pr enhances the coercivity ($\mu_0 H_c$) without HRE. Pr-GBDP forms high-anisotropy Pr-rich shells that suppress reverse domain nucleation and Pr-dissolved grain boundary phases (GBPs) that weaken exchange coupling between $Nd_2Fe_{14}B$[3)]. However, the $\mu_0 H_c$ of Pr-GBDP magnets is not yet large enough to replace HRE-GBDP magnets. This indicates that the microstructure of Pr-GBDP magnets should be further improved; however, a key microstructure for achieving high $\mu_0 H_c$ in Pr-GBDP magnets

is still veiled, thus a clear guide for microstructure design is required. Herein, based on detailed microstructure analysis, a key microstructure for μ_0H_c in Pr-GBDP magnets was elucidated and a guide for designing the composition of magnets and Pr-based GBDP source was provided. For this work, two base magnets with identical elements but different compositions were used: compared to sample 1, sample 2 has lower total rare-earth (TRE) and higher Cu, Ga, and Fe concentrations. The same amount of Pr-Cu-Al-Ga GBDP alloy was diffused into the samples. As shown in Fig.1, μ_0H_c of sample 2 significantly increases after Pr-GBDP and post-annealing, with a greater effect of post-annealing on the μ_0H_c improvement than in sample 1. Due to this, record-breaking μ_0H_c of 2.6 T was realized in the magnets by HRE-free Pr-GBDP. The TEM analysis revealed that high-μ_0H_c realized in Pr-GBDP sample2 is attributed to increased $RE_6Fe_{13}Ga$ GBP formation, and to obtain such microstructures, $RE_5(Cu,Ga)_3$ should be formed before annealing. Based on these findings, we establish μ_0H_c-composition maps as a function of Ga/TRE and Fe/Ga, closely related to $RE_6Fe_{13}Ga$ formation, thereby providing guidelines for designing both base compositions and diffusion sources. Furthermore, the validity of the proposed maps will be proved by optimizing GBD source composition, leading to further enhanced μ_0H_c of Pr-GBDP sample 1.

1) H. Sepehri-Amin *et al*., Acta Mater., Vol. 61, p.1982 (2013)
2) H. X. Zeng *et al*., J. Mater. Sci. Technol., Vol. 36, p.50 (2020)
3) M. Tang *et al*., Scr. Mater., Vol. 117, p.60 (2016)

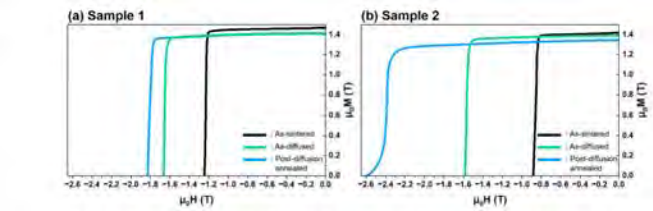


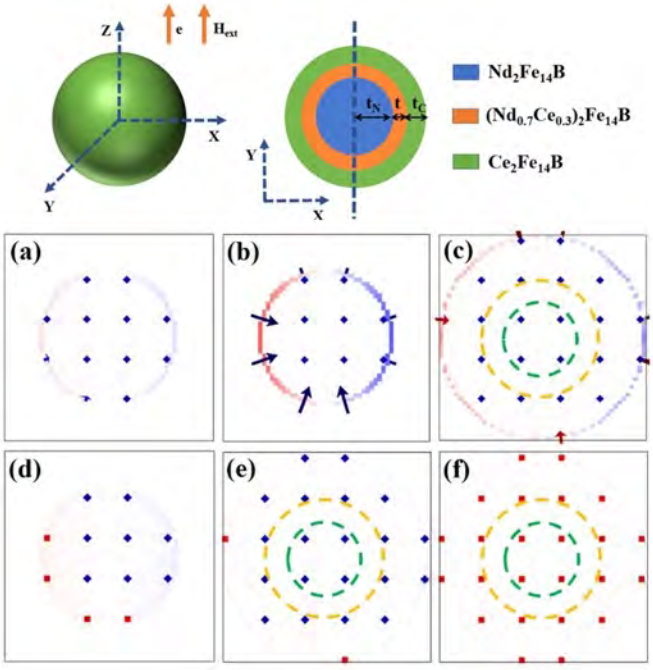
Fig.1

AP-05. Micromagnetic Simulation of Nd-Ce-Fe-B core-shell magnets using Mumax3

J. Zuo, J. Qi, C. Li, F. Pan, M. Zhang
School of Science, Inner Mongolia University of Science and Technology, Baotou, China

In this study, grain models of RE-Ce-Fe-B core-shell structures with transition layers in nanoscale were established by using the micromagnetic simulation software Mumax3. the effects of core-shell thickness and transition layer composition on the magnetic properties were investigated, and the demagnetization energy and magnetic moment distribution were studied, thereby providing a theoretical basis for improving the magnetic properties of RE-Ce-Fe-B magnets. For core ($Ce_2Fe_{14}B$)-transition layer $(Nd_{0.7}Ce_{0.3})_2Fe_{14}B$-shell ($Nd_2Fe_{14}B$) grain model, as $Ce_2Fe_{14}B$ thickness increases, the Ce content in the grain increases and the Nd content decreases, and the anisotropy field of the grains gradually decreases; meanwhile the remanence and maximum energy product decreases, the coercivity of $Ce_2Fe_{14}B$ with a thickness of 3nm is slightly higher than that of 2nm. Demagnetization energy is also an important factor affecting coercivity, the demagnetization energy of the entire grain decreases progressively when $Ce_2Fe_{14}B$ thickness increases. A decrease in demagnetization energy is conducive to an increase in coercivity. Nevertheless, the coercivity decreases gradually on the whole. Therefore, it can be concluded that the reduction in the average magnetocrystalline anisotropy field has a greater influence on the coercivity than the demagnetization energy.
The changes in in-plane magnetic moment under different external fields were also studied. At an external field of 30 kOe, the magnetic moments in the outer region of the $Nd_2Fe_{14}B$ layer start to rotate first. When the external field increases to 67.5 kOe, the surface magnetic moments of the $Nd_2Fe_{14}B$ layer reach maximum deflection. With a further increase in the reverse field to −68 kOe, irreversible flipping occurs inside the magnet, and all magnetic moments form an angle of 180° with the external field. It can thus be inferred that the surface magnetic moments of the $Nd_2Fe_{14}B$ layer are the first to deflect during the demagnetization process, whereas the magnetic moments in the transition layer and the $Ce_2Fe_{14}B$ layer remain undeflected under external fields up to H = −68 kOe.

[1] Yang C, Li W, Zhu Q, Hou Y, Xu Z, Ni F, Zhou Q, Liu X, Xu Y, Yang H, Wang D, Huang Y 2025 *Applied Physics Letters* 126 111908
[2] Liu X B, Nlebedim I C, Altounian Z 2021 *IEEE Transactions on Magnetics* 57 1
[3] Oikawa T, Yokota H, Ohkubo T, Hono K 2016 *AIP Advances* 6 056006

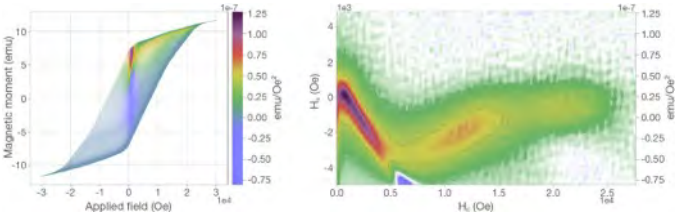


AP-06. First Order Reversal Curve Study of 3D Printed NdFeB

C. Radu[1], B. Dodrill[1], D. Daughton[1], S. Krishnan[2], J. Shield[2]
[1]Lake Shore Cryotronics Inc, Westerville, Ohio, United States, [2]University of Nebraska – Lincoln, Lincoln, Nebraska, United States

Recent advances in additive manufacturing have enabled new pathways for the fabrication of permanent magnets with complex three-dimensional geometries, tailored internal features, and compositionally graded structures. Such design freedom provides opportunities to optimize magnetic performance while reducing manufacturing constraints. However, systematic characterization is required to assess the microstructural and magnetic consequences of these processing routes. Here we present FORC based magnetic analysis and VSM measurements comparing sintered and 3D printed NdFeB magnets, highlighting the magnetic signatures associated with additively manufactured architecture. The additively manufactured sample exhibits a broad coercivity range reflecting microstructural heterogeneity. Two distinct switching regions associated with magnetically soft and hard phases are observed, connected by a moderate ridge indicative of interphase interactions dominated by magnetostatic coupling. The presence of a negative region in the FORC diagram further suggests irreversible and non-uniform magnetization reversal processes. This study demonstrates the effectiveness of FORC analysis in resolving complex magnetic behavior in additively manufactured systems and provides insight into structure–property relationships critical for performance optimization.

S. Krishnan, A. Natarajan, Q. Guo, and J. Shield, Altering the Solidification Kinetics of NdFeB Alloys Through Alloying Additions for 3D Printed Magnets, Magnetism and Magnetic Materials (MMM) 2025 Conference Poster, 2025.
A. Stancu, Characterization of Magnetic Nanostructures with the First-Order Reversal Curves (FORC) Diagram Technique, Magnetic Measurement Techniques for Materials Characterization, edited by V. Franco and B. Dodrill, 455 – 453, Springer, 2021.



Measured FORC and FORC diagram for 3D printed NdFeB

AP-07. Synthesis and Magnetic Properties of Exchange-coupled $SmCo_5$/Fe-Co Composite using Ultrasound-assisted Electroless Plating

K. Lee[1, 2], G. Lee[3], H. Lee[1], J. Ahn[1], J. Kim[1]
[1]Materials Science and Chemical Engineering, Hanyang University, Ansan, Korea (the Republic of), [2]Convergence Institute of ERICA, Hanyang University, Ansan, Korea (the Republic of), [3]M4ALL Inc., Ansan, Korea (the Republic of)

To miniaturize and improve the energy efficiency of next-generation electric motors, it is essential to improve the (BH)max value, which represents the magnetic flux density per unit volume. Nd-Fe-B magnets have been the industrial standard due to their high (BH)max (~50 MGOe). However, they face critical challenges: a vulnerable supply chain of rare-earth elements and poor thermal stability caused by a low curie temperature (~ 300 °C).
To overcome these limitations, exchange-coupled hard/soft magnetic composites have emerged as a breakthrough. By coupling a hard magnetic phase with a soft magnetic phase at the nanoscale, these composites can theoretically achieve an energy product far exceeding that of conventional Nd-Fe-B magnets. Despite their theoretical potential, experimental realization remains challenging. Achieving effective exchange coupling requires precise microstructural control within a critical dimension (typically below twice

the domain wall thickness).
In this paper, a unique strategy to prepare exchange-coupled hard/soft nanocomposites with anisotropic properties was proposed. First, High-performance $SmCo_5$ particles were synthesized using a modified chemical approach based on our previous work [1]. Using these $SmCo_5$ particles as a core material, exchange-coupled $SmCo_5$/Fe-Co composites were synthesized via an ultrasonic-assisted electroless plating method with controlled ultrasonic on/off cycles. In general, electroless plating methods, an Fe-Co layer is formed locally on the surface of the aggregate. In this structure, magnetic properties are degraded by dipole interactions between the $SmCo_5$ and Fe-Co phases. In contrast, it was found that conformal deposition of the Fe-Co layer occurred on the $SmCo_5$ particles dispersed by ultrasound treatment during the plating process. Consequently, the exchange coupling effect led to a 32% increase in (BH)max without compromising the magnetic squareness of the pure $SmCo_5$.
[1] Lee, K., Lee, G., Ahn, J., Lee, H., Cho, E., & Kim, J, *Journal of Magnetism and Magnetic Materials*., 173393 (2025)

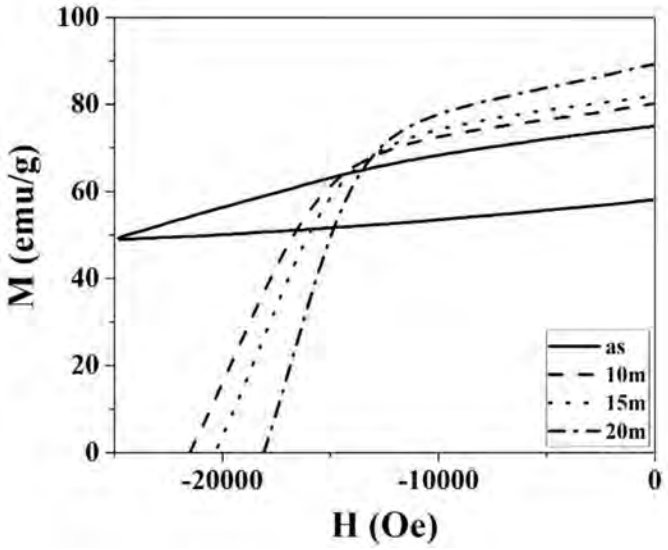


Fig. 1. Hysteresis loops of $SmCo_5$/Fe-Co composites electroless-plated for various times with an ultrasound cycle of 10s/20s

	Measured values			Calculated values			
Plating time [min]	Ms [emu/g]	Mr [emu/g]	Mr/Ms	D_{mix} [g/cm^3]	t_{Fe-Co} [nm]	V_{Fe-Co} [vol%]	$(BH)_{max}$ [MGOe]
as	77.3	75.1	0.97	8.831	0	0	16.25
10	82.4	80.2	0.97	8.805	1.65	3.23	18.13
15	83.8	82.0	0.98	8.797	2.15	4.18	19.13
20	92.1	89.3	0.97	8.754	5.05	9.46	21.48

Table 1. Measured magnetic properties and calculated values of $SmCo_5$/Fe-Co composites electroless-plated for various times with ultrasound cycle of 10s/20s

AP-08. High-performance Sm-Fe-N magnets produced by adding Cu powder

T. Saito
Chiba Institute of Technology, Narashino, Japan

The $Sm_2Fe_{17}N_3$ phase has been produced by nitrogenation of Sm-Fe alloy powder. The resulting $Sm_2Fe_{17}N_3$ phase is in powder form. However, conventional powder metallurgy processes are unsuitable for producing $Sm_2Fe_{17}N_3$ bulk magnets because this phase is unstable at high temperatures, decomposing into α-Fe and SmN above 873 K. A recently developed consolidation technique, known as the spark plasma sintering (SPS) method, allows for the consolidation of powders into bulk forms in a relatively short time and at lower temperatures. It has been shown that Sm-Fe-N magnets can be produced using the SPS method. However, the magnetic properties of the Sm-Fe-N magnets reported so far have not matched those of the original $Sm_2Fe_{17}N_3$ powder. In this study, we blended $Sm_2Fe_{17}N_3$ powder with a newly developed fine Cu powder, which exhibited excellent low-temperature sintering at approximately 473 K. We examined the structures and magnetic properties of the Sm-Fe-N magnets produced by adding Cu. Although Sm-Fe-N magnets were not obtained at temperatures below 673 K using the SPS method, we successfully produced magnets containing 5% and 10% Cu at temperatures below this threshold. The addition of Cu powder effectively lowered the sintering temperature of $Sm_2Fe_{17}N_3$ powder. The Sm-Fe-N magnets prepared at these low temperatures exhibited high coercivity. Figure 1 illustrates the hysteresis loop of the Sm-Fe-N magnet containing 5% Cu, which was prepared at 473 K using the SPS method. This magnet had a high density of 7.2 g/cm^3 and exhibited a coercivity of 11.4 kOe. Thus, a high-performance Sm-Fe-N magnet was successfully produced via the SPS method by adding Cu powder.
[1] J. M. D. Coey and H. Sun, J. Magn. Magn. Mater. 87, L251 (1990).
[2] M. Tokita, J. Soc. Powder Technol. Jpn, 30, 790 (1993).
[3] T. Saito, J. Magn. Magn. Mater. 320, 1893 (2008).

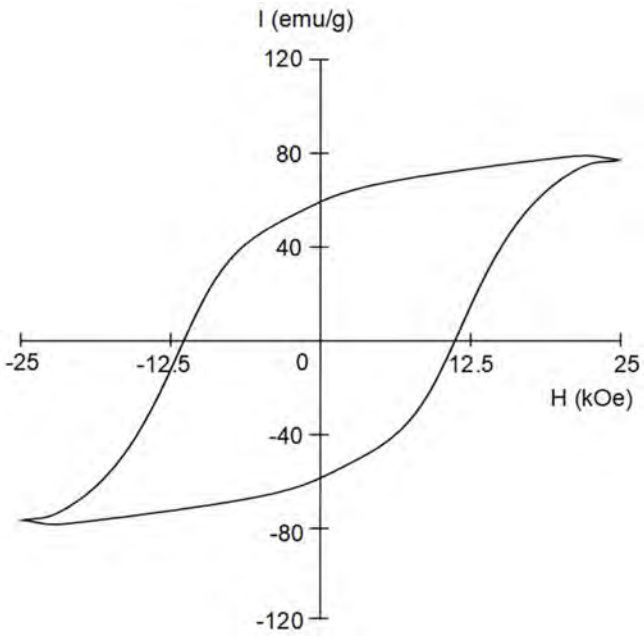
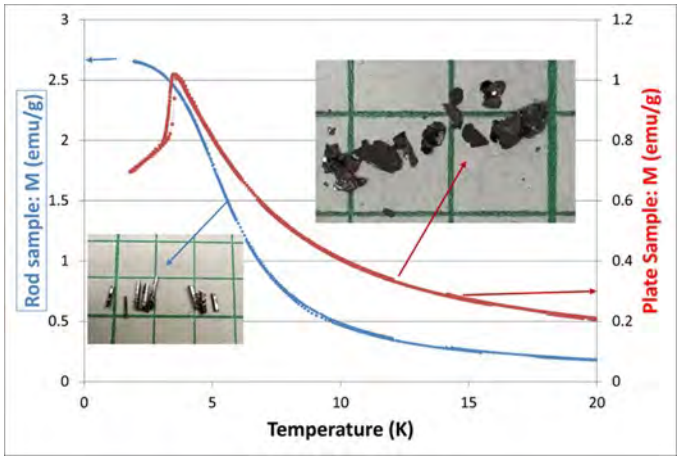


Figure 1 Hysteresis loopsof the Sm-Fe-N magnet containing 5% Cu prepared at 473 K using the SPS method.

AP-09. Low-Temperature Magnetic Transitions in Anisotropic Ce-Based Intermetallic Single Crystals

M. Goodman, A. S. Poulo, T. Lamichhane
School of Engineering, University of Central Oklahoma, Edmond, Oklahoma, United States

We report distinct low-temperature magnetic behavior observed in two morphologically different single-crystalline samples of a newly synthesized Ce-based intermetallic compound. Magnetization measurements (M–T) between 2 and 20 K reveal a pronounced anisotropy between rod-like and plate-like crystals, with the rod samples showing a sharp upturn near 5 K, suggesting a ferromagnetic transition. In contrast, the plate samples exhibit a gradual magnetic response with reduced saturation magnetization, indicative of antiferromagnetic or competing exchange interactions or crystallographic orientation effects. These variations highlight the sensitivity of the magnetic ground state to growth conditions and sample geometry, pointing to possible coexistence of local-moment and itinerant-electron magnetism in these compounds. Ongoing work aims to correlate morphology-dependent magnetic anisotropy with structural and electronic characterization to elucidate the role of Ce 4f–ligand hybridization in the emergence of magnetic order.



AP-10. Analysis of angular dependences of the coercivity of permanent magnets on the basis of magnetic domain wall motion model

T. Kawai[1], H. Yamamoto[2], M. Ohtake[1]
[1]*Yokohama National University, Yokohama, Kanagawa, Japan,*
[2]*Neojiconsul, Kyoto, Japan*

The measured angular dependence of coercivity at high angles in permanent magnets is not as large as Kondorsky's law [(1)]. In this report, the measured demagnetization curves are analyzed by using a domain wall motion model. The magnetic field at which the magnetic polarization becomes zero due to demagnetization of irreversible magnetization reversal is newly defined as the domain wall coercivity (H_w), and the angular dependence of H_w is analyzed by using Kondorsky's law. Fig. 1 shows the magnetization curve tilted 75° from the aligned axis for a Nd-Fe-B magnet. The figure also shows a method for estimating H_w after subtracting demagnetization due to reversible magnetization rotation. Next, the demagnetization curves due to irreversible magnetization reversal are calculated by using the domain wall motion model where the alignment of magnet is approximated by Gauss distribution. When half of the particles have reversed, the maximum angle (ϑ_c) at which their easy magnetization axis is tilted from the direction of the magnetic field corresponds to H_w. Fig. 2 shows the results of plotting H_w against $1/\cos\vartheta_c$ when the demagnetization curves are measured with magnetic field tilted from the aligned axis. A linear relationship holds, and it can be seen that Kondorsky's law holds. The only deviation from the simple Kondorsky's law is the presence of a vertical intercept. However, when plotting the angular dependence of coercivity of Barium ferrite particles obtained by breaking a large single-crystal, which satisfies Kondorsky's law [(2)], it has also a vertical intercept. The only difference from permanent magnets is the magnitude of their absolute values. In conclusion, these considerations suggest that the angular dependence of coercivity of permanent magnets can be explained by adding a constant term to Kondorsky's law.

(1) Y.Matsuura, IEEJ Trans 2025, DOI:10.1002/tee.24264.
(2) D. V. Ratnum and W. R. Buessem, J. Apply. Phys., 43. pp. 1291 (1972).

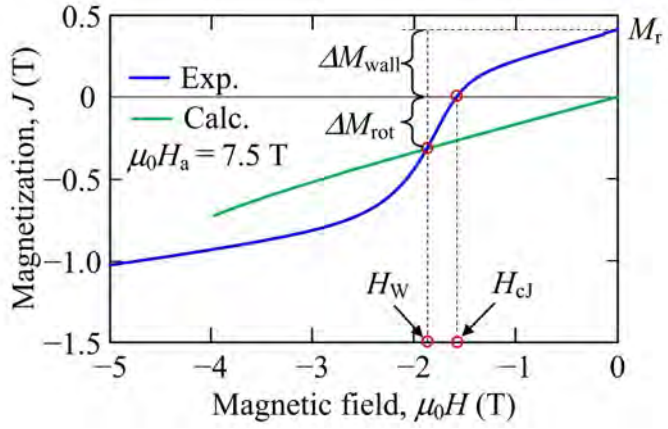


Fig. 1 Measured demagnetization curve (blue) and the estimated demagnetization curve (green) due to magnetization rotation, which is calculated as the half value of the sum of 2nd and 3rd quadrant. The crossing point gives the H_w.

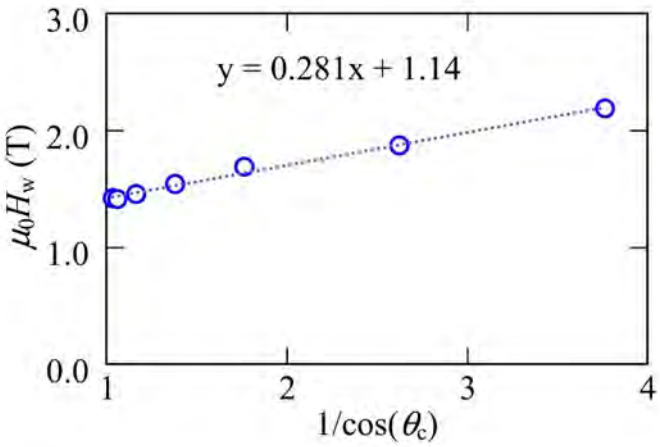


Fig. 2 Angular variation of coercive force for the Nd-Fe-B magnet plotted as $\mu_0 H_w$ vs. $1/\cos\vartheta_c$. The linear approximation formula is also shown in the figure.

AP-11. Magnetic alignment α_m by the magnetic measurement and crystallographic alignment α_c by EBSD analysis of sintered NdFeB, Sr ferrite and anisotropic injection molded (IM) bonded SmFeN magnets

H. Yamamoto[1], H. Fukunaga[2]
[1]President, Neoji-consul, Kyoto, Kyoto, Japan, [2]Electric Dept., Nagasaki University, Nagasaki, Nagasaki, Japan

The magnetic alignment of permanent magnets is a very important parameter of the anisotropic permanent magnets. The remanence B_r directly affects the maximum value of the motor torque. The magnetic alignment of permanent magnets is reported previously, (1) by evaluating the criteria parameter B_r/J_s, where B_r is remanence and Js is saturation polarization. This criteria of B_r/J_s are sometimes inappropriate especially for bonded SmFeN magnets with high H_A=200kOe (2) because of the non-linearity of $1/H^2$ extrapolation curve (3) to determine J_s. The authors therefore propose alternatively a new criteria of magnetic alignment α_m defined by J_{ra}/J_{rc}, where the J_{ra} and J_{rc} are the remanence in the hard and easy axis respectively. The crystallographic alignment is already reported, but the relationship between magnetic alignment and crystallographic alignment is not examined in detail. This paper investigates the numerical relationship of the magnetic alignment α_m and crystallographic alignment α_c of NdFeB, Sr ferrite and anisotropic bonded SmFeN magnets. The *J-H* curves in easy and hard axis were measured with 7T by pulsed field BH tracer. The authors also defined the crystallographic alignment α_c by the standard deviationσ_c of the Gaussian distribution by analyzing EBSD. Assuming that the grain alignment is Gaussian and the hysteresis is determined by Stoner-Whalfarth model, the magnetic alignment α_m defined by J_{ra}/J_{rc} can be calculated as a standard deviation σ_m in Gauss distribution. Therefore, the magnetic alignment α_m can be directly compared with α_c in the same unit of degree. The result of EBSD of NdFeB in Fig.1 clarified that the grain distribution is Gaussian with standard deviation σ_c=10.3 degrees and the coefficient of determination of R2=0.996. Table 1 summarizes the values of α_m, σ_m, and σ_c for each magnet. The values of σ_m determined from α_m are in approximate agreement with σ_c determined from EBSD. This indicates that α_m is an effective alignment index that accurately reflects the crystallographic alignment α_c.

References

(1) Y. Matsuura, IEEE Trans. Magn, 54(11), p.2101405(2018)
(2) D. H. Kim et al, J. Magn. Magn. Mater, 163, p.373-377 (1996)
(3) Kuno et al, J. Jpn. Soc. Powder Powder Metallurgy, vol.63, No,13, p.1053-1059 (2016)

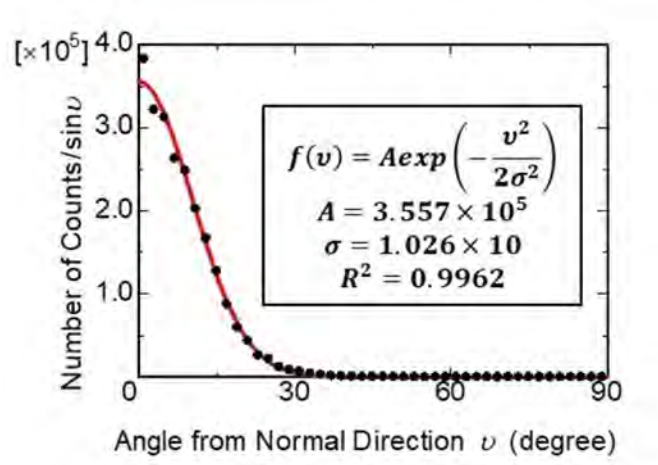


Fig.1 Crystallographic alignment σ_c of NdFeB magnet by Gaussian analysis.

	Jra (T)	*Jrc* (T)	α_m (=*Jra*/*Jrc*)	σ_m	α_c (=σ_c)
Sr ferrite	0.086	0.38	0.22	15°	18.7°
NdFeB	0.166	1.31	0.13	9°	10.3°
SmFeN	0.06	0.61	0.1	7°	5.6°

Table 1 The αm, σm and αc of Sr ferrite, NdFeB and SmFeN.

AP-12LB. Controlling and Understanding Grain Boundary Diffusion in Sintered Commercial Grade NdFeB Magnets

H. Baldino[1], C. Chinnasamy[2], J. A. Haynes[3], P. Kulik[4]
[1]Material Science and Engineering, University of Central Florida, Orlando, Florida, United States, [2]Manufacturing Science Division, Oak Ridge National Laboratory, Oak Ridge, Tennessee, United States, [3]Materials Science and Technology Division, Oak Ridge National Laboratory, Oak Ridge, Tennessee, United States, [4]Electrical and Computer Engineering, Unversity of Central Florida, Orlando, Florida, United States

Magnets today have hit a limit on their magnetic properties that can be created during the sintering process. To alleviate this “Grain boundary diffusion” (GBD) has been explored as an avenue to improve NdFeB magnets post sintering. One advantage of GBD has been its ability to reduce the heavy rare earth elements, Dy and Tb, in the sintering process and diffuse a small amount of these elements in post sintering processing [1-4]. However, very little about the depth of diffusion and its interaction with

the intergranular phase is unknown during the process. Here we show through the use of the low melting temperature eutectic alloy of PrCu, melting temperature 470 °C, how the diffusion mechanism switches between long low temperature annealing, <600 °C, and shorter higher temperature annealing, >600 °C, providing insight into how to maximize coercivity without disruption of grain size in the bulk. This was done on commercial grade N42 garde magnets to better reflect the impact on a standard magnetic grade rather than lab scale variation in properties. In low temperature annealing we note that the diffusion is driven by large vacancy mobility in the intergranular phase whose melting temperature is around 600 °C and reduces with diffusion. At 700 °C, above the intergranular phase melting temperature, the system is primarily moving through a liquid-liquid mixing, with prolonged annealing times, >24hrs, showing some $Nd_2Fe_{14}B_1$ grain growth. At 900 °C, the system is at 83% the melting temperature of the $Nd_2Fe_{14}B$ phase which under prolonged annealing times leads to phase change from the diffusion of Pr and Cu through the grains along with large grain growth. These results allow for the creation of a novel time, temperature, magnetism (TTM) picture providing insight into how to better develop alloys that may be used for GBD modification of NdFeB magnets.

1. Bae K. et al., *IEEE transactions on magnetics* 49.7 (2013): 3251-3254
2. Liu L. et al., *Scripta Materialia* 129 (2017): 44-47
3. Kim T. et al., *Scripta Materialia* 178 (2020): 433-437
4. Want Z. et al., *Acta Materialia* 248 (2023): 118774

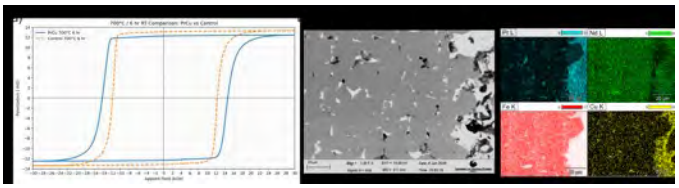


Figure 1. Comparison of the B(H) curve of the 700 °C 6hr annealed sample with the control showing a 20% increase in H_C(a). The EDS profile of the same magnet showing the diffusion of Pr and Cu into the N42.

SESSION AQ: EMERGING MAGNETIC SENSORS AND FUNCTIONAL ELECTROMAGNETIC SYSTEMS (POSTER SESSION)

Chair(s): C. Zhang, *Hebei University of Technology, Tianjin, China*

Tuesday, November 3, 2026
09:30 AM-12:30 PM
Coral 4

AQ-01. Phase-Sensitive Detection of Magnetic Nanoparticles Using an Optically Pumped Magnetometer

S. Sato[1], S. Taue[1], T. Sasayama[2]
[1]Kochi University of Technology, Kami, Japan, [2]Kyushu University, Fukuoka, Japan

Magnetic particle imaging has attracted considerable attention for medical applications, particularly for minimally invasive tumor localization using magnetic nanoparticles (MNPs) [1,2]. In this study, we investigate the detection of MNPs using an optically pumped magnetometer (OPM).

The phase delay of the MNP signal arising from the relaxation process of the magnetic nanoparticles is detected. An excitation magnetic field at 200 kHz with an amplitude of approximately 2 μT or less is applied along the z-axis. The magnetization of the MNPs follows the excitation field with a phase delay governed by relaxation mechanisms, including. Néel relaxation, associated with internal magnetization dynamics, and Brownian relaxation, arising from the physical rotation of the particles [3]. The response characteristics depend on particle size and the viscosity of the surrounding medium.

Because the OPM detects both the excitation field and the MNP signal, phase-sensitive detection using a lock-in amplifier is employed to separate these components. By using the excitation field as a reference and adjusting the phase offset, the phase-delayed MNP response is extracted as a quadrature component.

Furthermore, measurements were performed in the presence and absence of MNPs, and the difference between the two measurements was used to isolate the MNP signal. This approach enables imaging of both the signal intensity and the spatial distribution of the phase. Scanning imaging was conducted over a 10 mm × 10 mm area with 16 × 16 pixels. The MNPs were positioned in the upper region of the

imaging area, and a clear signal attributed to the MNPs was confirmed in the corresponding region of the reconstructed image.

These results demonstrate that phase-sensitive detection of MNPs using an OPM is feasible. This method enables MNP detection under magnetic field conditions safe for the human body, offering potential for future tumor location estimation.

[1] B. Gleich and J. Weizenecker, Nature., 435, pp.1214-1227 (2005)
[2] S. Bai, A. Hirokawa and K.Tanabe, J. Magn. Soc. Jpn., No.39, pp.216-219 (2015)
[3] T. Knopp and T. M. Buzug, Magnetic Particle Imaging., pp.22-25 (2012)

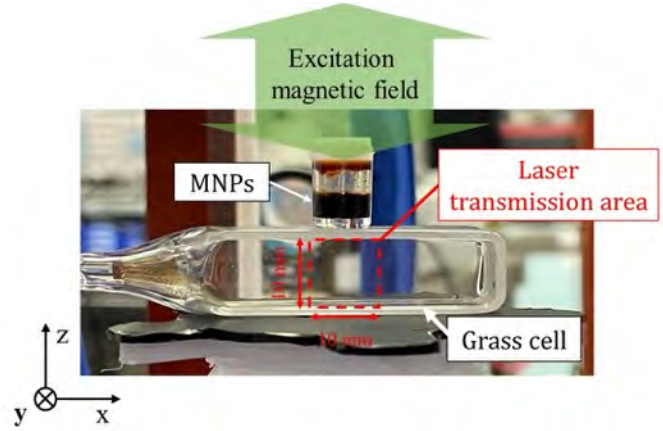


Fig. 1 Picture of the glass cell and the MNPs in the plastic pod

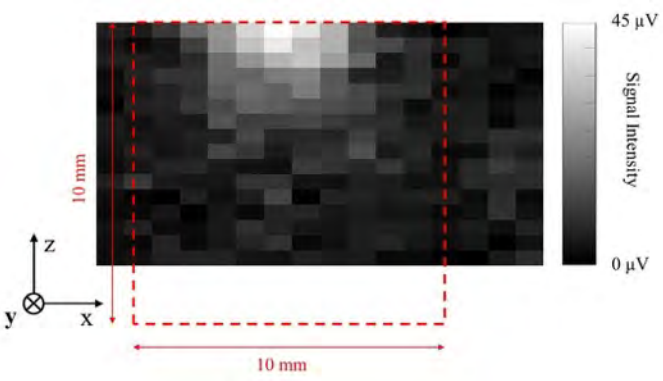


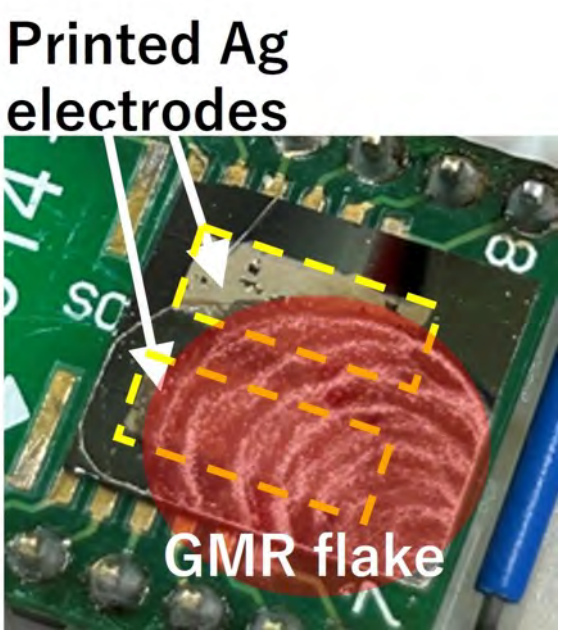
Fig. 2 MNPs signal intensity distribution

AQ-02. All solution patterning for fabrication of spin valve giant magnetoresistive sensing device

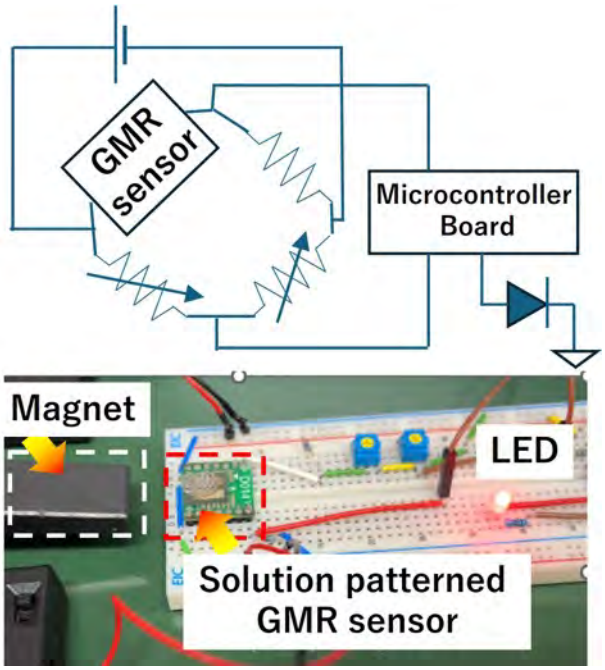
Y. Kurokawa, M. Taguchi, S. Miura, H. Yuasa
Graduate School and Faculty of Information Science and Electrical Engineering, Kyushu University, Fukuoka, Japan

Printable devices are attractively studied because its fabrication process is sustainable technology due to minimize raw materials. In the spintronics research field, the printed giant magnetoresistive (GMR) sensor using $[Py/Cu]_{30}$ multilayer flakes has been reported [1]. Furthermore, we previously successfully fabricated a spin Seebeck device on plastic film using a printing technique, that simultaneously exhibits electromotive force equivalent to that of a uniform film and sufficient flexibility [2]. In this study, we fabricate spin-valve (SV) type giant magnetoresistance (GMR) device using solution patterning technology including printing method to realize a higher sensitivity than the multilayer GMR sensors. The structure of the SV-GMR film is Au(5)/Ta(3)/Ru(2)/IrMn(7)/CoFe(2)/Cu(3)/CoFe(1)/NiFe(3)/Cu(1)/Ta(3)/Au(5) (unit: nm), where the lower and upper Au layers have the function of electrically connecting the flakes to each other. This film was deposited on a Si substrate coated with a photoresist as a sacrificial layer, using magnetron sputtering. The photoresist dissolves through ultrasonic treatment, and at the same time, the SV-GMR film dissolves in acetone, becoming flake-like, which is then used as GMR ink. On the other hand, the Ag electrodes were printed on Si substrate using an inkjet printer (PIO-1515, SIJ Technology Inc.) and commercially available Ag ink. Then, the GMR ink was dropped onto the Ag electrodes by a pipette. After that, the sample was annealed at 543 K under magnetic field of 0.4 T. Fig.1 shows a photograph of all solution patterned GMR device composing GMR flakes and Ag electrodes. We successfully realized the all solution patterning process providing the GMR sensor with the high sensitivity. Finnaly, we show a magnetic field sensing device using Microcontroller Board. Fig 2 shows the circuit diagram and photograph of magnetic field detection. The LED was successfully turned on by detecting magnetic field using all solution patterned GMR device.

[1] M. Ha, G. S. Cañón Bermúdez, T. Kosub, et al., Adv. Mater. 33, 2005521 (2021).
[2] Y. Kurokawa, K. Yamada, and H. Yuasa, Adv. Eng. Mater., 26, 2301069 (2024).



Photograph of solution patterned GMR device



Circuit diagram and photograph of GMR sensing device

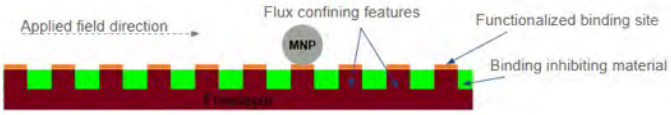
AQ-03. Improvement of Sensitivity for Large Area Low Aspect Ratio Giant Magnetoresistance (GMR) Based Biosensors Using Flux Confiners

R. A. Mendonsa[1], S. Liang[2], J. Wang[1, 2]
[1]Electrical and Computer Engineering, University of Minnesota, Minneapolis, Minnesota, United States, [2]Chemical Engineering and Materials Science, University of Minnesota, Minneapolis, Minnesota, United States

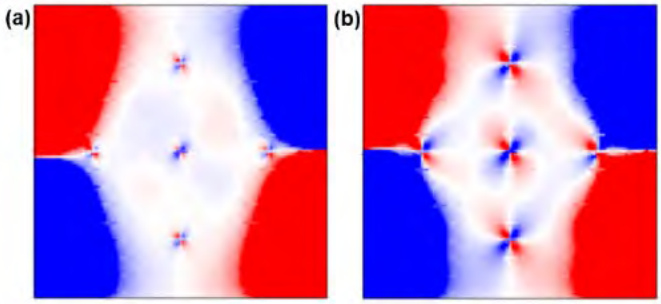
After the discovery of GMR [1], biosensors using magnetic nanoparticles (MNPs) and GMR sensors are being developed that promise zeptomole concentration detection capabilities [2].Most works focused on stripe sensors, but large area low aspect sensors, have shown to have linear response capabilities [3] and use the phenomenon of reverse nucleation sites [4]. Previous works in this area [5] have shown that the capability of GMR large area low aspect ratio sensors saturate over a couple orders of magnitude, and modelling using OOMMF [6] has shown this to be due to the size of the reverse nucleation sites as detected by the GMR sensor [7]. With this knowledge of reverse nucleation site size being a limiting factor to scaling the range of sensitivity, we explore methods of confinement for the reverse nucleation site and explore the gains in linear sensitivity range for GMR based biosensors. An example of such a reverse nucleation site confinement technique is shown in Fig. 1 with simulation results comparing reverse nucleation site size with and without confiners is shown in Fig. 2.

1) Baselt, David R., et al. "A biosensor based on magnetoresistance technology." Biosensors and Bioelectronics 13.7-8 (1998): 731-739.
2) Srinivasan, B. et al. A detection system based on giant magnetoresistive sensors and high-moment magnetic nanoparticles demonstrates zeptomole sensitivity: potential for personalized medicine. Angew. Chem. Int. Ed. 48, 2764–2767 (2009).
3) Su, Diqing, Kai Wu, and Jian-Ping Wang. "Large-area GMR bio-sensors based on reverse nucleation switching mechanism." Journal of Magnetism and Magnetic Materials 473 (2019): 484-489.
4) Feng, Yinglong, et al. "Localized detection of reversal nucleation generated by high moment magnetic nanoparticles using a large-area magnetic sensor." Journal of Applied Physics 122.12 (2017).
5) Mendonsa, Riyan, et al. "Micromagnetic Simulations of Concentration Detection Capability of Large-Area and Low-Aspect-Ratio GMR Sensors in Biomedical Diagnostics." IEEE

Transactions on Magnetics (2025).
6) M. J. Donahue, OOMMF Users Guide, Version 1.0 (1999)
7) Mendonsa, Riyan, et al. "Variable exploration of micromagnetic simulations of concentration detection range of large area low aspect ratio GMR sensors in biomedical diagnostics." AIP Advances 16.2 (2026).



Side view depiction of flux confiner features in a GMR based biosensor freelayer.



OOMMF simulations showing reverse nucleation sites with confiner (a) and without confiners (b)

AQ-04. Vortex-type TMR sensor arrays for compact NMR system

A. Sakamoto[1], S. Takano[1], T. Nakano[1], M. Oogane[1, 2]
[1]Graduate School of Engineering, Department of Applied Physics, Tohoku University, Sendai, Miyagi, Japan, [2]Center for Spintronics Integrated Systems (CSIS), Tohoku University, Sendai, Miyagi, Japan

Nuclear magnetic resonance (NMR) is a powerful tool for chemical and structural analysis, but its miniaturization remains challenging because conventional systems rely on inductive coil detection and large magnetic fields. Although microcoils improve mass sensitivity for small-volume samples, concentration sensitivity remains limited, requiring alternative approaches for high-sensitivity NMR detection [1, 2].
In this study, we propose vortex-type tunneling magnetoresistance (TMR) sensor arrays for compact NMR systems. The vortex magnetic structure forms a closed flux configuration, suppressing stray magnetic fields while maintaining a linear response in low magnetic fields through vortex core displacement [3, 4]. This enables sensor placement close to the sample with reduced magnetic disturbance, advantageous for miniaturization and near-field detection of weak signals.
The sensors were fabricated by magnetron sputtering and microfabrication using Ar ion milling and photolithography. The TMR stack consists of Ta(5)/Ru(40)/Ta(5)/CoFeSiB(70)/Ta(0.2)/CoFeB(3)/MgO/CoFeB(3)/TaB(0.1)/CoFe(0.8)/Ru(0.8)/CoFe(3)/IrMn(10)/Ta(5)/Ru(7) (thicknesses in nm), forming a magnetic tunnel junction. The devices consist of circular free layers with diameters of 10–70 μm and pinned layers of 5-10 μm, integrated into 8-series and 40-parallel arrays.
The sensors exhibit a nearly hysteresis-free and linear magnetoresistance response in low magnetic fields (Fig. 1), suitable for weak-field sensing. The sensors show a minimum magnetic field detectivity of 22 pT/√Hz above 15 kHz, where 1/f noise is negligible, indicating operation in the white noise regime (Fig. 2). This frequency range improves the signal-to-noise ratio in NMR detection. A detectivity of 42 pT/√Hz was obtained at 2.1 kHz, corresponding to the proton Larmor frequency under the geomagnetic field (~50 μT), demonstrating applicability to ultra-low-field proton NMR.
These results demonstrate the potential of vortex-type TMR sensor arrays for compact NMR systems. This work was supported by the SIP Project, BRIDGE project, X-nics project, KAKENHI, the GP-spin program, CSIS and CIES, Tohoku University.
[1] M. Mompeán, R. M. Sánchez-Donoso and A. de la Hoz, Nat. Commun., Vol. 9, 108 (2018) , [2] J. Smits, J. T. Damron and P. Kehayias, Sci. Adv., Vol. 5, eaaw7895 (2019), [3] M. Endo *et al.*, Journal of Physics D, 55 195001 (2022), [4] Behncke C *et al.*, Magnetic vortices Topology in Magnetism (Springer Series in Solid-State Sciences) (2018).

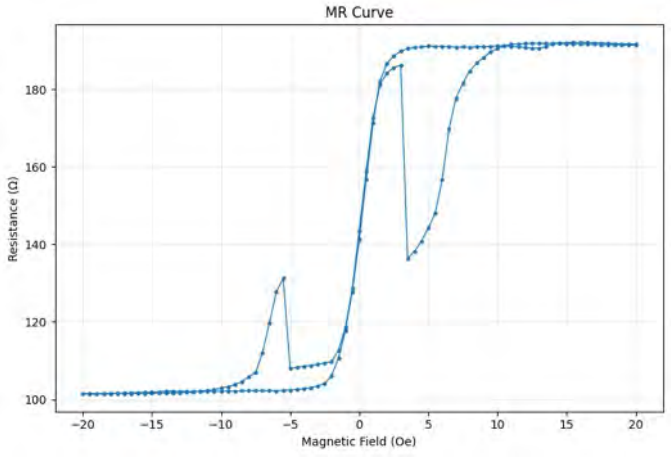


Fig. 1 Magnetoresistance curve.

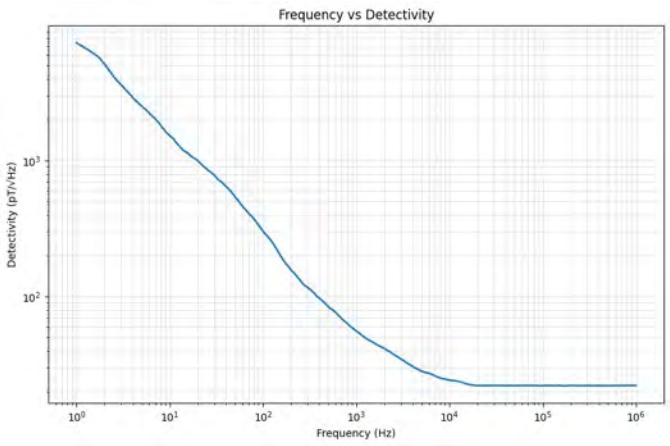


Fig. 2 Magnetic field detectivity.

AQ-05LB. Magnetoresistive Sensor With 90 Degree Optically Reprogrammable Sensing Axis

F. van Riel, B. Koopmans, D. Leitao
Applied Physics, Eindhoven University of Technology, Eindhoven, Noord-Brabant, Netherlands

Magnetoresistive sensors with multiaxial sensitivity are interesting for field mapping applications where local measurement of multiple magnetic field components is needed[1]. Existing device designs are often bulky or require many electrical contacts. We propose to reprogram the sensing axis of individual sensing elements on-demand using light and optically active materials[2]. In this work, we demonstrate an anisotropic magnetoresistive sensor with 90° togglable sensitivity[3]. Our device consists of an optically active Co/Gd thin-film bilayer grown on top of permalloy. When illuminated with a femtosecond laser pulse, Co/Gd undergoes all-optical switching whereby the magnetization is reversed by 180°. To turn this into a 90° rotation, the film is patterned into a crossed ellipse shape (Fig. 1) that stabilizes two orthogonal in-plane magnetization directions[4]. A single laser pulse toggle switches the magnetization direction in the center of the cross back and forth by 90°, as illustrated in Fig. 2. The state of the device is electrically read out using anisotropic magnetoresistance and planar Hall effect. From the field-dependence in Fig. 2 we deduct that the center of the device has indeed rotated by 90°. Our results mark the initial step towards optically reprogrammable integrated magnetic vector sensors.

[1] Leitao et al., npj Spintronics 2 (2024)
[2] van Riel et al., Communications Materials 6 (2025)
[3] van Riel et al., IEEE International Magnetic Conference-Short Papers (2026)
[4] Das et al., Applied Physics Letters 117 (2020)

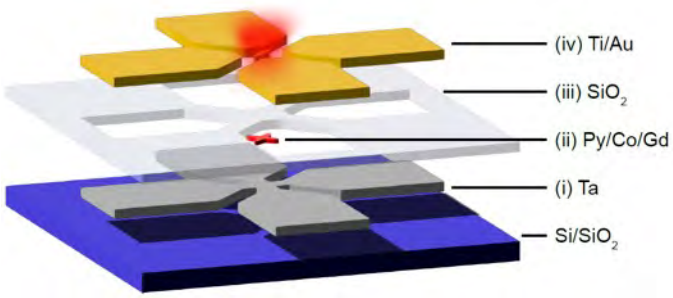


Figure 1: Schematic overview of the structure of our device, consisting of a tantalum bottom electrode (i), crossed ellipse of permalloy, cobalt and gadolinium (ii), a passivation layer (iii) and gold contacts (iv). Each ellipse in the cross measures 8 µm × 0.5 µm. A gold shield (iv) is deposited on top of one ellipse to shield it from the laser.

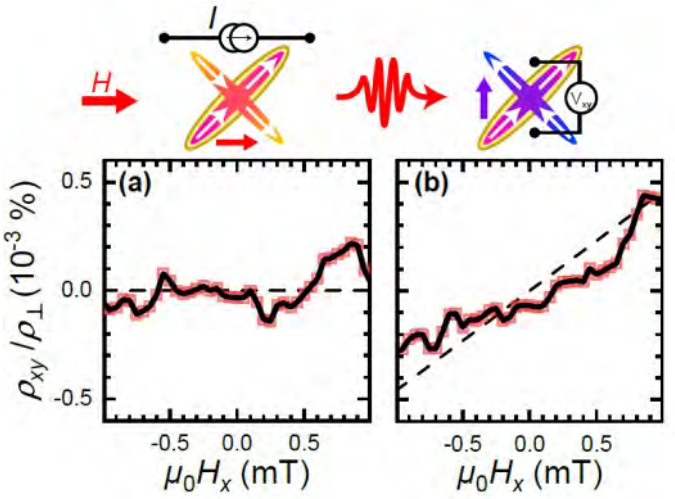


Figure 2: Planar Hall effect measurement as a function of field with current and field applied in the x-direction. The slope before (a) and after (b) the laser pulse arrives is changing, suggesting a 90° rotation in the center. The squares are measured data, the dashed lines are the expected slopes.

AQ-06. Development of an MTJ-Based Calibration Mechanism for Analog Integrated Circuits

T. Mizoguchi[1], M. Islam[2], M. Goto[3], Y. Ando[1]
[1]Department of Electronics and Physical Engineering, Osaka Metropolitan University, Sakai, Osaka, Japan, [2]Department of Information and Communications Engineering, Institute of Science Tokyo, Meguro, Tokyo, Japan, [3]Department of Physical Engineering, Tokyo University of Science, Shinjyuku, Tokyo, Japan

With the rapid advancement of wireless communication and the Internet of Things (IoT), the importance of analog integrated circuits (ICs) continues to grow. Compared with digital ICs, analog circuits are more susceptible to performance variations arising from device mismatches, which pose a fundamental challenge to further transistor scaling. Such variations are typically compensated after fabrication through trimming or circuit modification. However, these approaches require individual adjustment, leading to increased cost. Moreover, once calibrated, the circuits cannot be readily readjusted, making it difficult to accommodate device degradation and environmental changes.
As illustrated in Fig. 1, we propose a technology that enables repeated and dynamic calibration of analog circuits by incorporating spintronic devices. The key requirements for such devices are continuous analog tunability of resistance and long-term retention of the programmed state. To meet these requirements, we develop magnetic tunnel junction (MTJ) devices optimized for analog circuit applications. Continuous resistance modulation is achieved by controlling either the relative magnetization angle between the two ferromagnetic layers or the area ratio of parallel and antiparallel magnetic configurations. In addition to their intrinsic nonvolatile resistance, MTJs offer high-speed control of magnetic configurations via spin torque, enabling dynamic calibration functionality.
Figure 2(a) shows an operational amplifier waveform intentionally distorted by an offset voltage. By applying MTJ-based calibration using an external magnetic field, the waveform is successfully restored, as shown in Fig. 2(b).
In this presentation, we report the development of MTJ devices satisfying the required performance criteria, strategies for stabilizing analog resistance states, and experimental demonstrations of dynamic calibration in practical analog circuits.

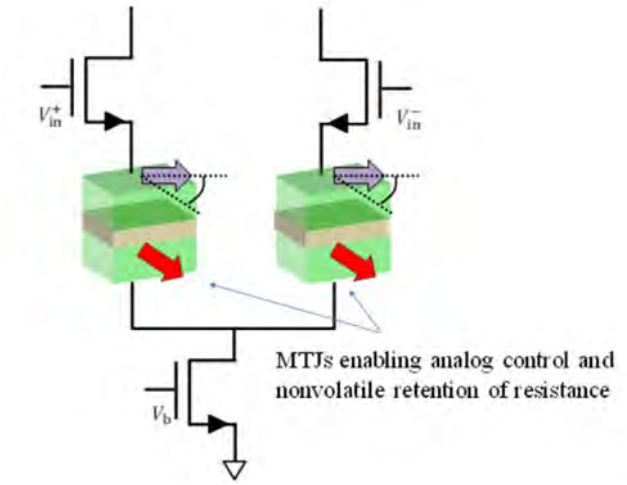


Figure 1 Schematic of an analog IC with analog-tunable MTJ devices.

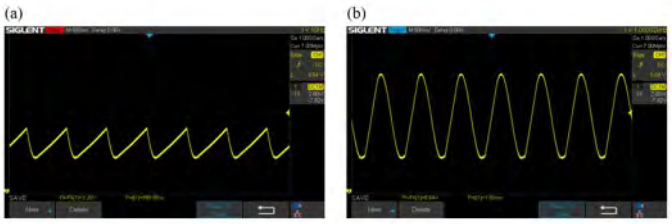


Figure 2 (a) Output waveform when intentionally distorted by applying an offset voltage and (b) Waveform corrected by controlling the MTJ device with an external magnetic field.

AQ-07. Design of Robust and Easily Installable Coreless Current Sensor with Parallel Magnetic Sensor Arrays

S. Mizuta, J. Inoue, Y. Okada
Mitsubishi Electric Corporation, Amgasaki, Japan

We developed a robust and easily installable coreless current sensor with parallel magnetic sensor arrays to realize an energy-efficient factory.
Achieving the factory requires overcoming challenges in visibility, decision-making, and operational tradeoffs among energy, productivity, and quality. As a first step to monitor energy consumption of an individual load, installing a number of current sensors is needed. Current transformers with magnetic cores make installation laborious. Coreless current sensors with simple structures allow easy installation. However, they are easily affected by conductor position and external magnetic fields. In the design of coreless current sensors, the sensor arrangement and signal

processing algorithm are crucial for suppressing these effects [1—3].

In this study, we propose a design method of a robust and easily installable coreless current sensor with parallel magnetic sensor arrays. As shown in Fig. 1, 10 magnetic sensors are symmetrically arranged with their sensitivity axes characterized by angle parameters ϑ_α and ϑ_β. A current I flowing in a conductor is measured based on a weighted sum of the magnetic sensor output signals V, where w_α and w_β are weighting factors. For the inner 6-sensor array and outer 4-sensor array, we calculated the error caused by the off-center position of the conductor as a function of design parameters. The results show that proper sets of parameter values make outputs of both arrays robust to the conductor position simultaneously (see Fig. 2). Although outputs of the inner and outer arrays alone are easily affected by external magnetic fields, combining the inner and outer arrays allows cancelling the effect of external magnetic fields that they suffer from. An effective cancelling is realized by a suitable combination of the inner and outer arrays, and by adjusting the value of w_β. Our proposed method showed a feasible robust performance against conductor position and external magnetic fields.

[1] L. D. Rienzo, R. Bazzocchi and A. Manara, IEEE Trans. Instrum. Meas., Vol. 50, p.1093 (2001).
[2] Q. Guo, P. Fu, G. Gao, L. Jiang, L. S. Wang and Y. R. Bai, IEEE Trans. Plasma Sci., Vol. 46, p.1227 (2018).
[3] W. Peng, S. Li, C. Guo and H. Zhang, 2021 4th International Conference on Electron Device and Mechanical Engineering (ICEDME), p.101 (2021).

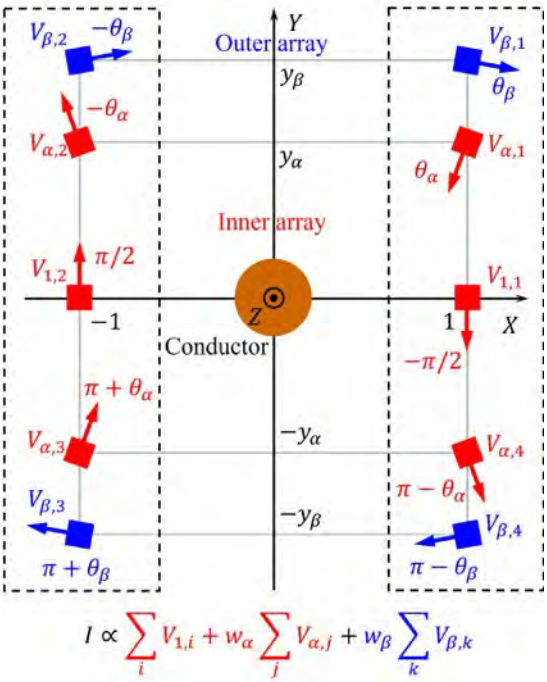


Fig. 1 Coreless current sensor made of 10 magnetic sensors with their sensitivity axes.

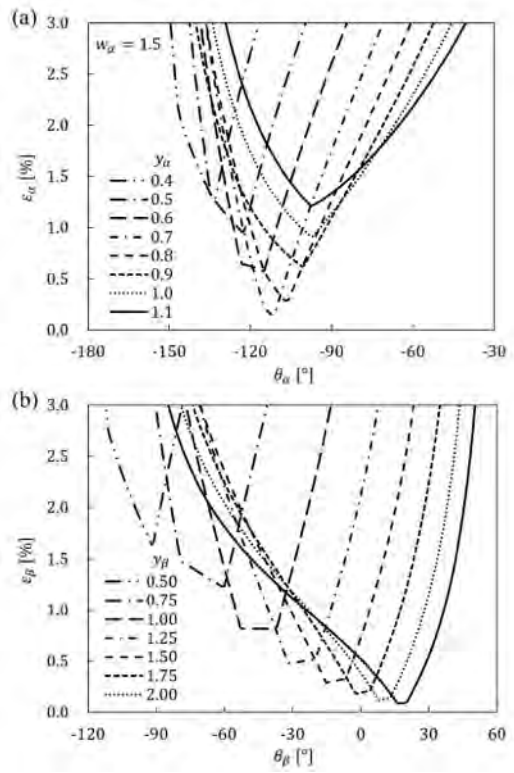


Fig. 2 Maximum relative error ε caused by the off-center position of the conductor within 0.6×0.6 square region: (a) for inner array with w_α = 1.5 and (b) for outer array.

AQ-09. Low-Loss Wideband Magnetoacoustic RF Isolators Enabled by Highly Non-Collinear Dipolar-Coupled FeGaB/SiO_2/FeGaB Heterostructures

B. Luo[1], A. Winkler[2], H. Schmidt[2], V. Sharma[3], S. Wohlrab[2], M. Wu[3, 1], N. X. Sun[1]

[1]Department of Electrical and Computer Engineering, Northeastern University, Boston, Massachusetts, United States, [2]SAW Lab Saxony Leibniz IFW, Leibniz Institute for Solid State and Materials Research, Dresden, Germany, [3]Department of Physics, Northeastern University, Boston, Massachusetts, United States

Nonreciprocal RF isolators and circulators are essential for full-duplex wireless systems and RF power amplifier protection [1]. Non-reciprocal magnetoacoustic devices offer a compact, CMOS-compatible alternative to bulky ferrite-based isolators, yet prior demonstrations often suffer from high insertion loss (>40 dB) due to the inefficiency of higher-order SAW harmonics [2–5]. Additionally, devices with giant nonreciprocity often exhibit narrow bandwidths, and vice versa [2–5].

Here we demonstrate a low-loss, wideband nonreciprocal magnetoacoustic RF isolator based on a non-collinear dipolar-coupled FeGaB (20 nm)/SiO_2 (5 nm)/FeGaB (20 nm) heterostructure driven by SAW fundamental mode at 2.87 GHz on a piezoelectric 128° Y-X cut $LiNbO_3$ substrate. By intentionally misaligning the uniaxial anisotropies of the two FeGaB layers (10° and 70° relative to surface acoustic wave vector k_{SAW}) via varying in-situ growth field angles, we realized an insertion loss of only ~13 dB at fundamental SAW mode frequency 2.87 GHz, over 27 dB lower than prior reports [2, 3]. At bias field angle ϕ_{DC} = 114°, we realized wide nonreciprocal bandwidth spaning 2.4–3.3 GHz (900 MHz) (Fig. 1), which is 18 times broader than a slightly non-collinear stack (50 MHz). Peak magnitude nonreciprocity reaches ~50 dB (~167 dB/mm) and phase nonreciprocity ~220° (~733°/mm) is nearly 10× higher than prior reports [2, 3] (Fig. 2). Tuning H_{DC} from 0–80 Oe yields wide alternating positive and negative nonreciprocity branches, enabling field-reconfigurable isolation. The ultra-compact, low-loss, wide-band non-reciprocal, integrated magnetoacoustic isolator simultaneously sets three performance records of bandwidth (900 MHz), insertion loss (~13 dB), and nonreciprocity (~50 dB, 167 dB/mm) and shows great potential for full-duplex radio/radar commmunication systems [1], NV-center control [6], and quantum transduction [7].

[1] A. Nagulu and H. Krishnaswamy, IEEE J. Microwaves, Vol. 1, p. 447 (2021)
[2] P. J. Shah, D. A. Bas and I. Lisenkov, Science Advances, Vol. 6, p. eabe5024 (2020)
[3] D. A. Bas, P. J. Shah and M. R. Page, Phys. Rev. Appl., Vol. 18, p. 044003 (2022)
[4] M. Küß, S. Glamsch and M. Albrecht, ACS Appl. Electron. Mater., Vol. 6, p. 1790 (2024)
[5] M. Küß, S. Glamsch and M. Weiler, ACS Appl. Electron. Mater., Vol. 5, p. 5103 (2023)
[6] D. Labanowski et al., Science Advances, Vol. 4, p. eaat6574 (2018)
[7] D. D. Awschalom et al., IEEE Trans. Quantum Eng., Vol. 2, p. 1 (2021)

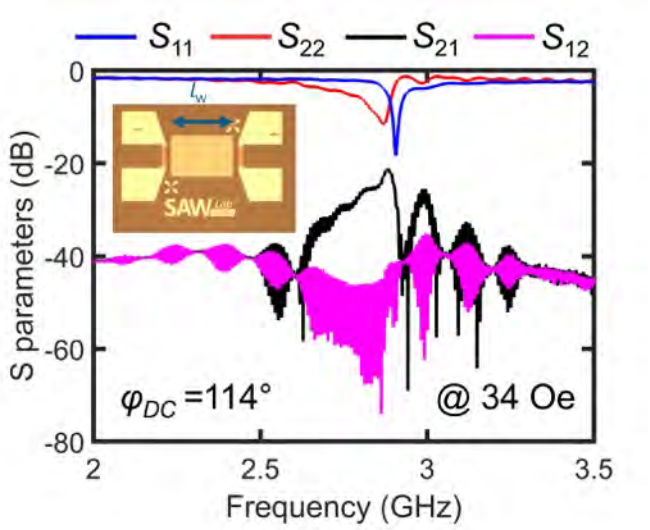


Fig1. Device schematic and S-parameters of non-collinear FeGaB/SiO_2/FeGaB magnetoacoustic isolator (l_w = 300 μm).

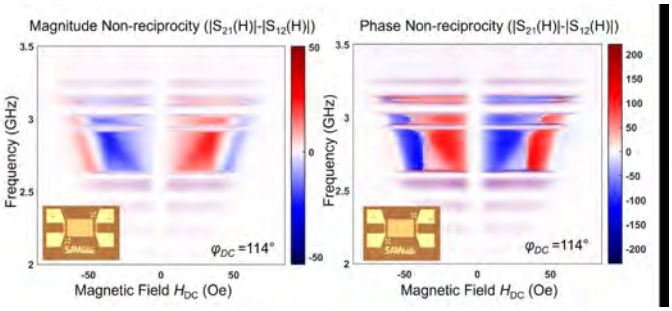


Fig2. Magnitude (left) and phase (right) nonreciprocity colormaps versus frequency and DC bias field applied at ϕ_{DC} = 114°, showing 900 MHz nonreciprocal bandwidth, ~50 dB magnitude nonreciprocity, and ~220° phase nonreciprocity.

AQ-10. A New TDR-Based High-Speed Non-Destructive Testing Method for Magnetic Sheets

S. Yabukami[1, 2], Y. Okuyama[2], T. Endo[2], Y. Imai[1], K. Okita[2], M. Yamaguchi[1]
[1]Tohoku University, Sendai, Japan, [2]Tohoku-TMIT, Sendai, Japan

This study presents a high-speed non-destructive testing (NDT) method for magnetic sheets using time-domain reflectometry (TDR). Defects in magnetic materials cause local changes in permeability, which manifest as impedance variations in TDR signals, allowing defect positions to be accurately identified. A simple model is introduced to explain the relationship between permeability and impedance, and parallel line TDR probes are fabricated. Fig. 1 illustrates the experimental setup, comprising the network analyzer, coaxial cables, the parallel two-wire probe, and the sample. First, the Noise suppression sheet(NSS , Tokin, EFS-01, 0.1 mm thick) was placed in close proximity to the probe, and a reference measurement was performed in a state free of debris or scratches. Subsequently, the sample was translated along the probe, and the characteristic impedance was measured via TDR. Finally, the deviation from the reference state was calculated. Experiments demonstrate that adhered debris as small as 1 × 1 × 0.1 mm^3 on a NSS can be detected and located, proving the effectiveness of TDR for rapid inspection. In the case of small debris, the characteristic impedance change of around 0.5 Ω was successfuly detected as shown in Fig. 2. Furthermore, our TDR-based non-destructive testing successfully detected a defect with dimensions of 3 mm × 5 mm and a depth of 0.1 mm, demonstrating the high sensitivity of this approach.

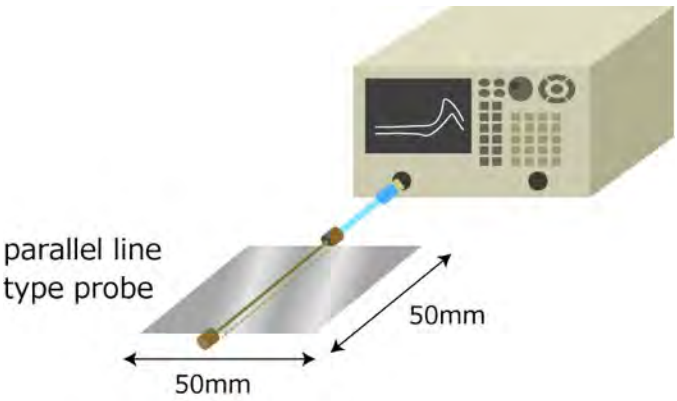


Fig. 1 Schematic view of the system setup.

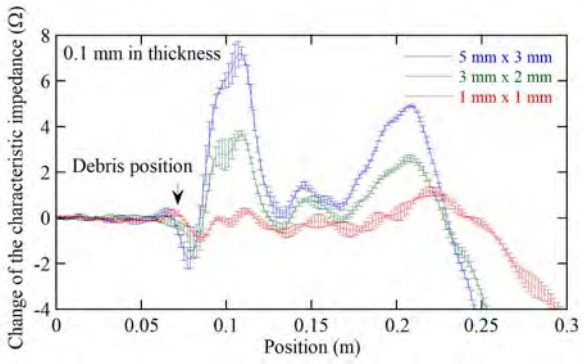


Fig. 2 The characteristic impedance change of 0.1 mm-thick NSS in 5 mm x 3 mm, 3 mm x 2 mm, and 1 mm x 1 mm when NSS was sandwiched by wires.

AQ-11. Magneto-mechano-electric energy harvesting performance depending on magnet mass and position on the piezoelectric plate

S. Yoon[1, 2]
[1]Korea Institute of Industrial Technology, Gwagnju, Korea (the Republic of), [2]University of Science and Technology, Daejeon, Korea (the Republic of)

Harvesting stray magnetic fields for power generation offers a compelling pathway for developing self-powered devices. In particular, alternating current (AC) magnetic fields with a fixed frequency are typically found near power cables. Among the harvesting strategies, magneto-mechanical conversion is particularly effective for transforming magnetic field into electrical power [1-3].
In this study, we experimentally characterize the magneto-mechanical response of a piezoelectric plate with magnetic mass under ambient AC magnetic fields. To optimize bending deformation of the piezo plate, the magnetic poles at the edges were arranged in an anti-symmetric configuration. The oscillation of the piezo plate under AC magnetic field were captured via ultra slow-motion camera and synchronized with real-time piezoelectric voltages. The 3D simulations were employed to optimize the magnet mass with spatial positioning on electromechanical performance. A comprehensive discussion of the experimental methodologies and results will be provided.

[1] N. Godard, L. Allirol, A. Latour, S. Glinsek, M. Gérard, J. Polesel, F. Domingues Dos Santos, and E. Defay, Cell Rep. Phys. Sci. Vol 1, 100068 (2020)
[2] Q. Wang, K.-B. Kim, S.-B. Woo, Y. Song, and T.-H. Sung, Energies Vol 14, 2387 (2021)
[3] H. Lee, R. Sriramdas, P. Kumar, M. Sanghadasa, M. G. Kang, and S. Priya, Energy Environ. Sci. Vol 13, 1462 (2020)

AQ-12. Noncontact Magnetic Sensing of Rear-Side Induction-Hardened Depth Using Electromagnetic Force-Induced Vibration

Y. Hosono[1], A. Kano[1], Y. Gotoh[2]
[1]Graduate School of Science and Engineering, Oita University, Oita, Japan, [2]Faculty of Science and Engineering, Oita University, Oita, Japan

Induction-hardening is widely used to improve the wear resistance and surface hardness of heavily loaded steel components. In some components, the hardened layer is formed on rear surface that are difficult to access directly, creating a need for evaluation of the rear-side hardened depth. Electromagnetic testing methods have been proposed to measure the hardened depth by the differences in electromagnetic properties between hardened and unhardened regions [1-5]. However, these methods are limited by the skin effect, making rear-side evaluation challenging.

This research proposes an electromagnetic force-induced vibration sensor for evaluating rear-side hardened depth in a 20-mm-thick induction-hardened steel plate. Figure 1 shows the sensor configuration and sensing principle. A neodymium magnet and AC excitation coils were placed 5 mm above the accessible unhardened surface. Because the unhardened region has higher magnetic permeability than the hardened region [1-3, 6], the static magnetic flux density B is distributed mainly in the unhardened layer. As the rear-side hardened depth increases, the remain unhardened layer becomes thinner, thereby the static magnetic flux density B increasing on the accessible surface. In contrast, eddy current J_e are distributed only to the accessible surface due to the skin effect and are therefore unaffected by the rear-side hardened depth. The vibration intensity generated by the interaction between B and J_e varies, detected by a microphone as the airborne sound pressure [7-8].

Figure 2 shows the sound pressure measured by the microphone as the rear-side hardening depth ranges from 1 mm to 5 mm. The sound pressure increased from 16.76 Pa to 26.40 Pa. The maximum relative deviation from the mean was 8.2% for 10 measurements. Coupled three-dimensional finite-element (3D FEM) analysis [7, 8] of the magnetic field, electromagnetic force, and vibration displacement supported the experimentally observed increase in the sensing signal with rear-side hardened depth.

[1] Y. Gotoh and H. Tanaka, IEEE Trans. Magn., Vol. 50, Art. no. 7001204 (2014)
[2] Y. Gotoh, S. Onita and T. Horino, IEEE Trans. Magn., Vol. 54, Art. no. 6202404 (2018)
[3] Y. Gotoh, N. Sasaguri and N. Takahashi, IEEE Trans. Magn., Vol. 46, p.3137 (2010)
[4] T. Goda, Y. Haga and T. Tomioka, Electromagn. Non-Destruct. Eval. (XXI), p.130 (2018)
[5] J. Cuffe, H. Sun and Y. Plotnikov, 17th World Conf. Nondestruct. Testing, p.25 (2008)
[6] Y. Kai, Y. Tsuchida and M. Enokizono, J. Optoelectron. Adv. Mater., Vol. 10, p.1078 (2008)
[7] S. Niwa, A. Hagisaka and I. Yamada, Mater. Trans., Vol. 64, p.596 (2023)
[8] S. Niwa, I. Yamada and Y. Gotoh, IEEE Trans. Magn., Vol. 58, Art. no. 6201306 (2022)

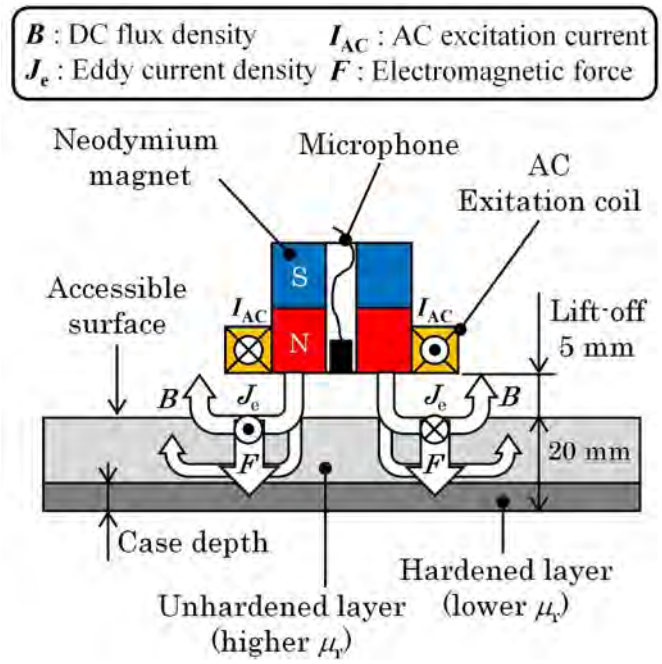


Fig. 1 sensor configuration and sensing principle for noncontact backside case depth evaluation in induction hardened steel

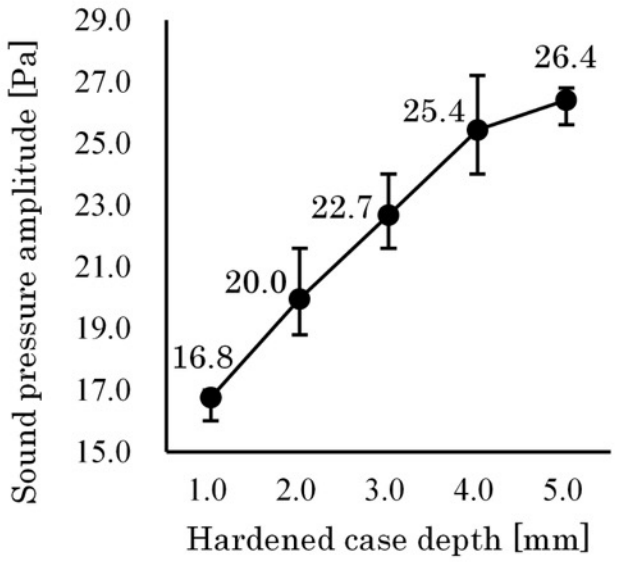


Fig. 2 Mean sound pressure for 10 measurements (error bars indicate the minimum and maximum values)

AQ-13. Wave-Driven Electromagnetic Energy Harvesters: Developing and Testing a Triple-Harvester System with Integrated Water-Based Evaluation

E. E. Ivanova, J. Park, N. M. Wereley, A. Flatau
Aerospace Engineering, University of Maryland, College Park, Maryland, United States

As ocean utilization has expanded, there is a growing demand for continuous energy supply to support ocean monitoring and equipment. Consequently, wave energy harvesting has become an active area of research [1]. The research focuses on developing a wave-driven electromagnetic energy harvester capable of capturing energy from low-frequency ocean waves (<0.3 Hz). The system utilizes levitating magnet motion within the harvester to convert slow oscillatory wave motion (0.2 Hz) into electrical power for marine and environmental monitoring applications. The integration of a guiding rod with linear bearings reduced friction in the levitating magnet motion and increased power output by 5.5%, resulting in an average power of 248 mW. This performance exceeds that of the configuration without the guiding rod and bearings, where friction between the levitating magnet and the harvester sidewall limited the power output [2].
A triple-harvester configuration was implemented to scale power output by operating three units simultaneously [Fig.1]. Initial testing showed reduced generation of 115–150 mW per harvester due to magnetic interference caused by close spacing. Increasing the separation between harvesters by 20 mm improved performance, yielding a 38.7% increase in power generation to 165–190 mW per unit [Fig.2]. Despite this improvement, the power output remained lower than that of a single harvester and constrained magnet motion compared to the single-unit design.
A vertical linear harvester was developed to extract energy from large-scale vertical wave oscillations through electromagnetic induction. Experimental results demonstrate that stacking these modules in a series configuration facilitates further voltage gains by maximizing the frequency of magnetic interactions. This series orientation enables the achievement of higher voltage outputs while minimizing the device footprint, thereby enhancing performance within a compact spatial area.
[1] Zhao et al, "Recent progress in blue energy harvesting for powering distributed sensors in ocean", Nano Energy, 88, 106199 (2021)
[2] Park et al, "Wave-driven electromagnetic energy harvesters: Analysis of different magnetic configurations" AIP Advances, 15, 035016 (2025)

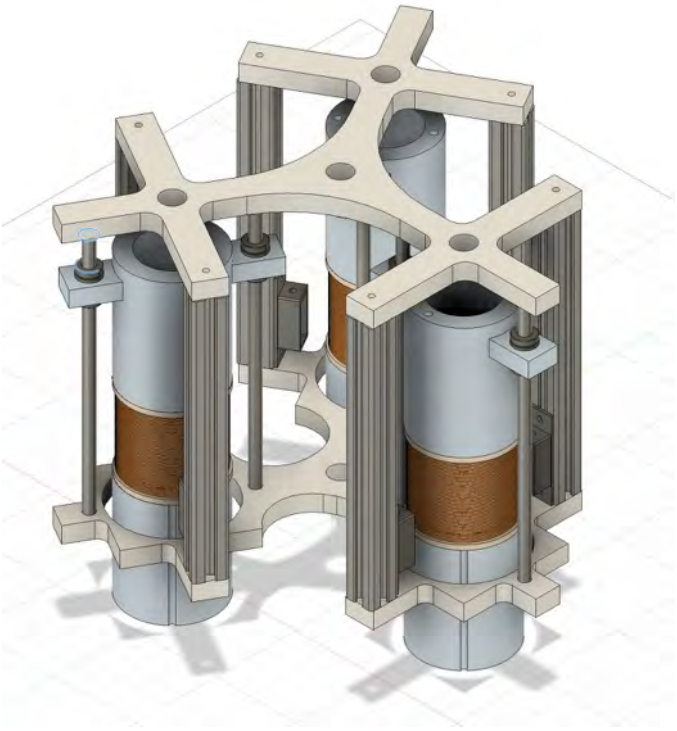


Fig.1 Fusion 360 3D CAD model of the triple harvester system with increased separation between harvesters.

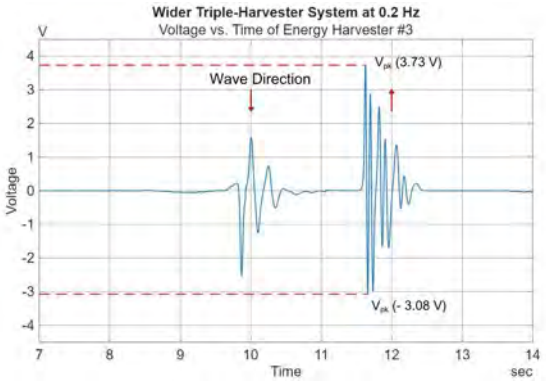


Fig.2 Voltage readings from a single cycle at 0.2 Hz of the triple harvester design with wider spacing between harvesters.

AQ-14. Investigation of a method for measuring steel plate thickness by applying steady-state AC vibration using Electromagnetic-Force-Induced Vibration

A. Kano[2], K. Sakamoto[1], Y. Hosono[1], Y. Gotoh[2]
[1]Oita University, Oita, Japan, [2]Faculty of Science and Engineering, Oita University, Oita, Japan

Petroleum storage tanks at thermal power plants require periodic internal inspections of bottom plates to prevent leakage from degradation. Common non-destructive testing methods include Magnetic Flux Leakage (MFL), DC-magnetized Eddy Current Testing (ECT), and Ultrasonic Testing (UT)[1][2]. However, MFL and DC-ECT require magnetizing plates near saturation, generating powerful attractive forces that necessitate high-torque motors. UT requires couplants, increasing operational man-hours. To address these issues, this study proposes a thickness measurement method using Electromagnetic-Force-Induced Vibration, eliminating the need for couplants and excessive magnetization.

Fig. 1 illustrates the configuration and vibration principle of the proposed sensor. It consists of two neodymium magnets and an AC excitation coil, with a condenser microphone at the center. The magnets supply magnetic flux *B*, and the AC coils induce eddy currents J_e in the plate surface. Their interaction generates a Lorentz force *F* in the z-axis direction, inducing vibration in the steel plate. As plate thickness increases, *B* distributes over a wider area, decreasing the flux density at the surface. Meanwhile, Je remains confined to the surface due to the skin effect, independent of thickness. Thus, the Lorentz force decreases with increasing thickness. Increased rigidity in thicker plates further reduces vibration. Thickness is estimated from the resulting acoustic pressure.

The method was validated through experiments and 3D-FEM analysis. Five JIS SS400 steel plates (equivalent to ASTM A36 and EN S235JR) with thicknesses of 5–9 mm were tested. The numerical analysis coupled electromagnetic and vibration fields with nonlinear magnetic properties. Fig. 2 shows the results: the plates vibrated in the z-axis direction, and acoustic pressure decreased with increasing thickness, correlating well with experimental data and demonstrating the potential of the proposed method. Future work will focus on improving reliability by calibrating absolute values and proposing noise-reduction techniques.

[1] D. Wu, Y. Hong and J. Wang, *IEEE Access*, Vol. 13, p. 9089 (2025)
[2] Z. Ji, D. Wang and H. Chen, *Sensors*, Vol. 25, p. 6923 (2025)

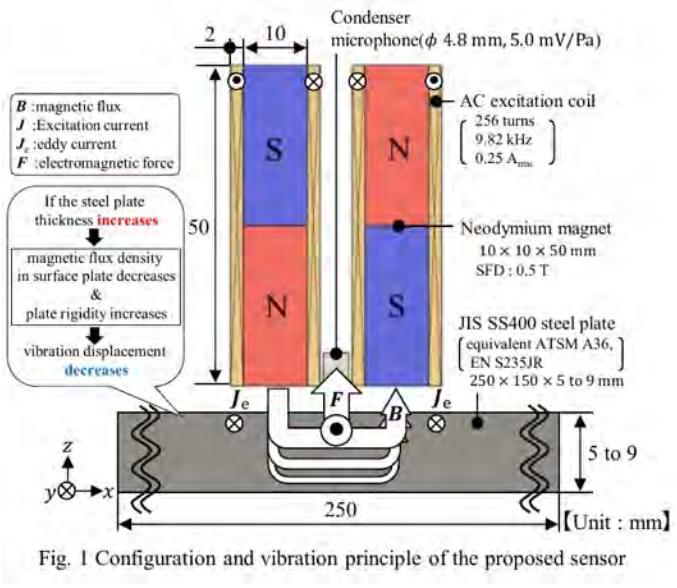


Fig. 1 Configuration and vibration principle of the proposed sensor

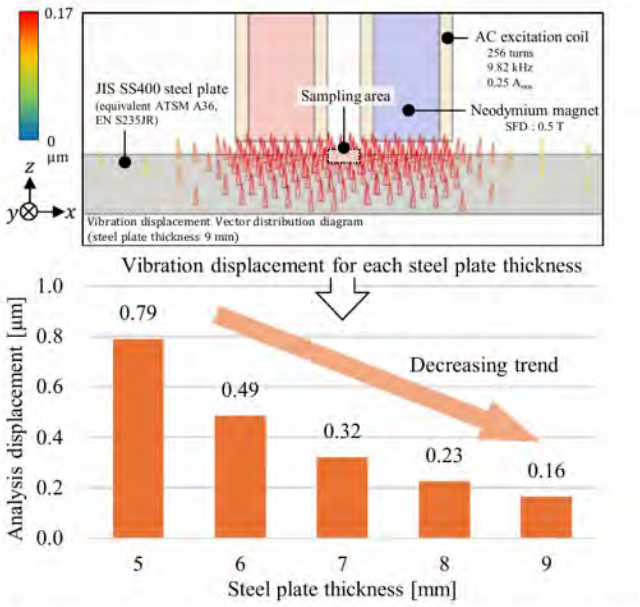


Fig. 2 Numerical analysis results for vibration response of the steel plate

Numerical analysis results for vibration response of the steel plate

AQ-15. Measurement of Hot Spring Scale Thickness Inside Steel Pipes in Geothermal Power Plants Using Electromagnetically Induced Vibrational Intensity

Y. Nagahara[1], K. Yamada[1], Y. Gotoh[2], T. Sasayama[3], T. Taguchi[4]

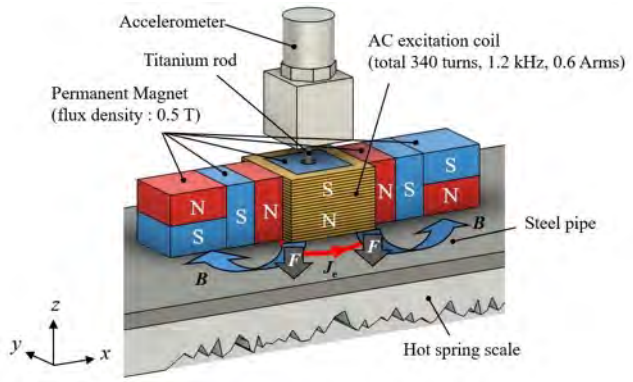
[1]Graduate School of Science and Technology, Oita University, Oita, Japan, [2]Oita University, Oita, Japan, [3]Kyushu University, Fukuoka, Japan, [4]Fukuoka Industrial Technology Center, Fukuoka, Japan

Hot spring scale predominantly accumulates on the inner surfaces of reinjection well steel pipes in geothermal power plants, leading to a reduction in power generation efficiency. Traditionally, the thickness of this scale has been measured using radiographic techniques [1,2]. However, this radiographic method has several drawbacks, such as the requirement for large equipment and high cost. This study proposes a non-destructive testing method for estimating the thickness of hot spring scale inside reinjection well steel pipes from the outside the pipe based on electromagnetically induced vibration intensity measurements.

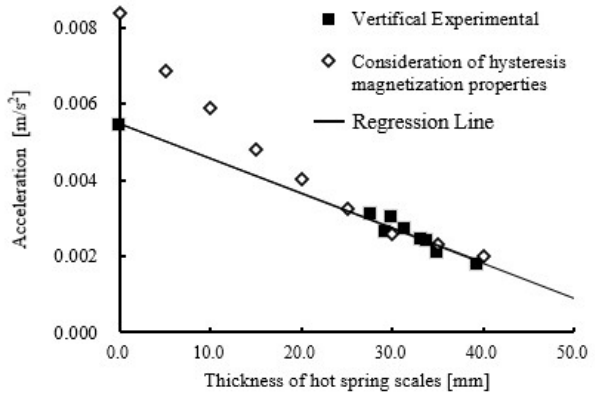
Figure 1 shows the proposed measurement sensor and inspection model. The proposed sensor consists of a permanent magnet, an AC excitation coil, and an accelerometer. Electromagnetic vibrations are generated on the surface of steel pipe by the magnetic flux density from permanent magnets and the eddy currents induced by AC excitation coil. Vibration on the outer surface of the steel pipe is measured using an accelerometer to estimate internal scale thickness. For steel pipes under inspection, the maximum thickness of the scale reaches 40 mm, requiring high-intensity vibrations. Therefore, a Halbach array was adopted, providing a stronger and more uniform magnetic field than a conventional NS array [3]. To elucidate the vibration generation mechanism, a combined DC–AC magnetic field analysis using the play model and a structural displacement analysis were conducted based on three-dimensional finite element theory [4–7].

The analysis showed that steel pipe displacement decreases with increasing scale thickness. This is because the local rigidity of the steel pipe increases with scale thickness. Verification experiments were conducted on steel pipes with known scale thicknesses. Figure 2 shows measured vibration acceleration and numerical results versus scale thickness, indicating that vibration acceleration decreases with increasing scale thickness. This relationship allows us to estimate the thickness of hot spring scale that adheres to the inside of the steel pipes in the reinjection wells of a geothermal power plant.

[1] S.Gholizadeh, Portugal, Procedia Structural Integrity 1, pp.050–057. (2016)
[2] A. Hagisaka, S. Niwa, S. Shiota, Y. Gao, Y. Gotoh, Int. J. Appl. Electromagnet. Mech., vol. 71, no. S1, pp. S483–S491, (2023)
[3] Jae Seok Choi, Jeonghoon Yoo, *IEEE Trans. Magn.*, 555 Vol. 44, No. 10, (2008)
[4] T. Matsuo, Y. Osaka, and M. Shimasaki, 559 IEEE Trans. Magn., vol. 36, no. 4, pp. 1172–1177,(2000)
[5] S. Bobbio, G. Milano, C. Serpico, and C. Visone, IEEE Trans. 561 Magn., vol. 33, no. 6, pp. 4417–4426, (1997)
[6] T. Matsuo, D. Shimode, Y. Terada, and M. Shimasaki, IEEE Trans. Magn., vol. 39, no. 3, pp. 1361–1364,(2003)
[7] T. Matsuo and M. Shimasaki, IEEE Trans. 565 Magn., vol. 41, no. 10, pp. 3112–3114, (2005)



Configuration of the measurement system



Experimental and analysis results

AQ-16. Research on Multilayer Transmission Lines using High-Frequency Magnetic Materials with Negative Permeability

H. Nakayama, S. Inomata, Y. Kobayashi, Y. Kobayashi, T. Miyata, H. Tanaka, K. Amiya
Mechanics and Robotics Course. Department of Engineering, National Institute of Technology (KOSEN), Nagano College, Nagano, Japan

In high-frequency transmission lines, reducing dielectric loss and conductor loss are problems for loss reduction. While the development of low-loss materials for dielectrics is progressing, the influence of the skin effect on conductors is unavoidable, and no materials more effective than copper have been found. In this research, we are proposing a method using a multilayered structure of positive and negative permeability materials for the purpose of suppressing skin effect loss[1]-[3]. For the multilayer structure of positive/negative permeability materials, the planar multilayer structure in Fig. 1 (a) is being investigated; however, in this case, since the effect is only in the thickness direction, it is necessary to consider a multilayer structure in the width direction as well. In this research, considering the plating process for printed transmission lines, we verified that a three-directional asymmetrical multilayer structure, as shown in Fig. 1 (b), is effective, and we report the results of verification by electromagnetic field simulation using HFSS. We assumed the FR4 for the dielectric material, copper for the positive permeability material and permalloy for the negative permeability material, and applied the frequency characteristics of permeability of permalloy based on the LLG equations. The structures of transmission line was microstrip line structures. In the three-layer model with three-directional asymmetrical multilayer, by varying the thicknesses of copper layer and permalloy layer, we obtained conditions that allow for lower loss than a single copper layer at specific frequencies and thickness conditions. An example of the results is shown in Fig. 2. The vertical axis represents the difference ΔS21 between the single copper layer and the multilayer structure; positive values indicate loss reduction effect. Due to the frequency characteristics of negative permeability material, a loss reduction effect was obtained at 15 GHz above, and it was confirmed that the appropriate combination of lamination thicknesses differs depending on the magnitude of permeability.

[1] M. Yamaguchi et al., "Skin effect suppressed Ni–Fe/Cu electroplated multilayer wiring for high data-rate and low delaytime I/O interface board", IEEE Trans. Magn., 54, 1–5 (2018).
[2] Y. Aizawa et al., "Theoretical study on lowering loss of skin effect suppressed multi-layer transmission line with positive/negative (Cu/NiFe) permeability materials for high data-rate and low delay-time I/O interface board", AIP Advances, 10, 015124 (2020).
[3] Kim H. et al., "Cu/Co meta-interconnects for 112 Gbps high speed applications", Front. Electron. Volume 6 (2025). 6:1493911. doi: 10.3389/felec.2025.1493911.

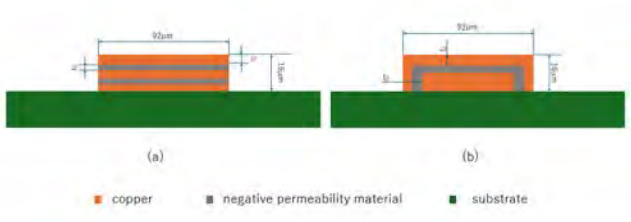


Fig. 1 Model of considered multi-layered structures.

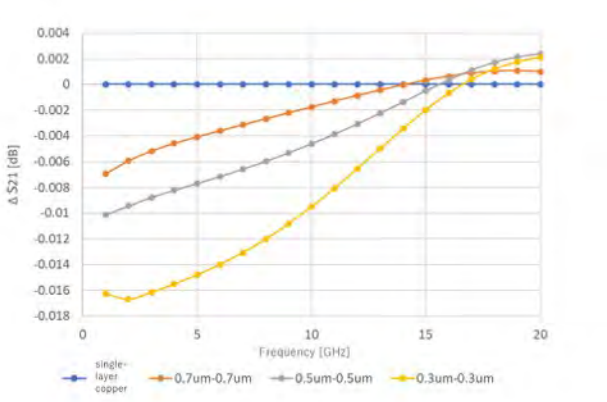


Fig. 2 Result of transmission coefficient of multi-layered transmission-line.

SESSION AR: ULTRAFAST MAGNETISM, MAGNONICS AND SPIN DYNAMICS I (POSTER SESSION)

Chair(s): Y. Sasaki, *International Center for Young Scientists, National Institute for Materials Science (NIMS), Tsukuba, Japan*

Tuesday, November 3, 2026

09:30 AM-12:30 PM

Coral 4

AR-01. Spin-current-induced modulation of magnon-phonon cooperativity

A. Nagao[1], K. Yamanoi[1], Y. Nozaki[1, 2]

[1]Department of Physics, Keio University, Yokohama, Japan, [2]Center for Spintronics Research Network, Keio University, Yokohama, Japan

Spin waves have attracted significant interest for their potential in information and signal processing applications; however, their short decay length remains a key limitation. To overcome this issue, coupling spin waves with surface acoustic waves (SAWs), which exhibit long propagation lengths, has been actively explored [1]. The interaction between magnons and phonons is characterized by the cooperativity *C*, which quantifies the ratio between coupling strength and dissipation. Achieving electrical control of *C* would provide a pathway toward functional magnonic devices.

In this study, we investigate modulation of *C* via spin current from the spin Hall effect, which exerts spin torque on magnetization and modifies damping. To enhance coupling, we used a Fabry–Pérot-type SAW resonator and high-overtone SAWs. A Ta(20 nm)/Ni(60 nm)/Pt(20 nm) trilayer was deposited on a 128° Y-cut $LiNbO_3$ substrate with interdigital transducers to excite high-overtone SAWs. Transmission spectra of the 9th overtone SAW were measured under an external magnetic field with and without DC current.

Spectral peaks in Figs. 1(a) and (b) were fitted using Lorentzian function to extract the half-width at half maximum (HWHM), from which the cooperativity *C* was estimated. The value of *C* increases from 0.008 at 0 mA to 0.067 at 20 mA, indicating a significant enhancement under current injection with a current density of 2×10^9 A/m^2. In addition, spin-torque ferromagnetic resonance (ST-FMR) measurements (Fig. 2) shows that the HWHM increased with positive current and decreased with negative current, confirming current-induced modulation of magnetic damping. This behavior is consistent with a reduction of magnon losses, leading to an increase in *C*. These results demonstrate electrical control of magnon–phonon hybridization via spin torque, providing a promising approach for tunable magnonic systems.

[1] D. Hatanaka, M. Asano and H.yamaguchi, Phys. Rev. Appl. 17, 034024 (2022)

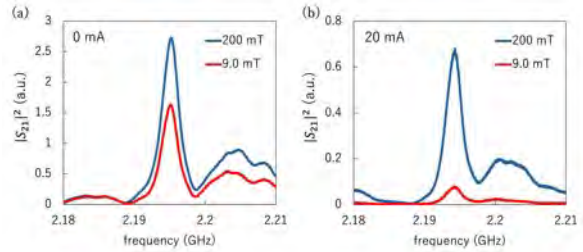


Fig. 1 $|S_{21}|^2$ spectrum as a function of frequency measured under external magnetic fields of 200 mT (blue) and 9.0 mT (red): (a) without DC current and (b) with a DC current of 20 mA.

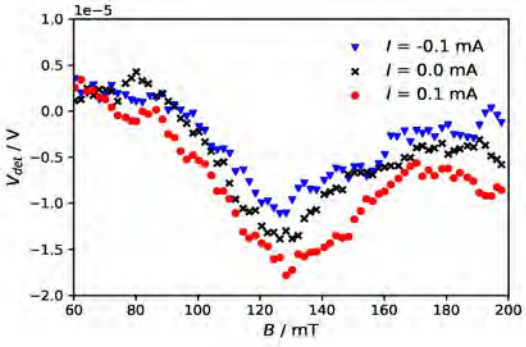


Fig. 2 ST-FMR spectra measured as a function of external magnetic field. The HWHMs values are 23.5 mT at -0.1 mA (blue), 24.7 mT at 0 mA (black), and 30.0 mT at +0.1 mA (red).

AR-02. Quantum to classical crossover and magnetization curves of few-atom nanomagnets

H. Lichtl[1, 2], L. Veldman[1, 2], N. Betz[1, 2], J. Schust[1], L. Farinacci[3], S. Baumann[1], S. Loth[1, 2]

[1]Institute for Functional Matter and Quantum Technologies, University of Stuttgart, Stuttgart, Germany, [2]Center for Integrated Quantum Science and Technology, Stuttgart, Germany, [3]University of Würzburg, Würzburg, Germany

As the size of a magnetic structure increases it undergoes a transition from a quantum system to a classical magnet, yet the evolution of the magnetization behavior at this crossover is only partially explored. In antiferromagnetic Fe spin chains on Cu2N (1), shown in fig.1, this transition can be directly accessed via their magnetization reversal dynamics. We use a low temperature scanning tunneling microscope (STM), to record high-speed magnetization curves of these nanomagnets. By using the local magnetic field of the STM tip (2) we can reach ramp rates of the magnetic field of up to 40kT/s. This enables real-time access to the switching between the two Néel like states.

For short chains the magnetization curves exhibit sharp features at 0T local field corresponding to avoided level crossings, where superposition states facilitate quantum spin tunneling. With increasing chain length, these features diminish, tunneling is suppressed and the magnetization curves evolve, classical behavior. Fig. 2, shows the magnetization curve of the five atom chain at different ramp speeds of the magnetic field, where we see quantum spin tunneling at the avoided level crossing and classical thermal relaxation outside the crossing.

We can also use the real-time access to the state behavior to demonstrate that the switching probability at the avoided level crossing follows the Landau-Zener dependence on ramp speed. Our results highlight that magnetic state transitions can be induced via fast modulation of the STM tip, opening new possibilities for rapid control of spins at the nanoscale.

[1] S. Loth, S. Baumann, et al. Science 335, 196-199 (2012)
[2] S. Yan, DJ Choi, et al. Nature Nanotech 10, 40-45 (2015)

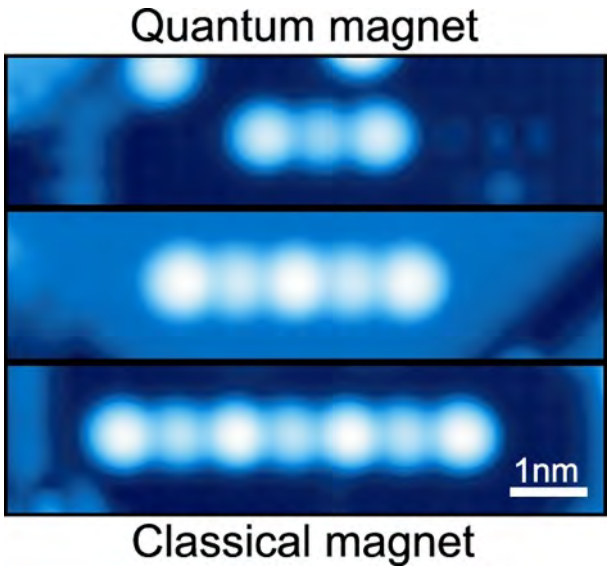


Fig. 1: Spin polarized topographies of Fe nanomagnets containing three to seven atoms on a Cu_2N surface.

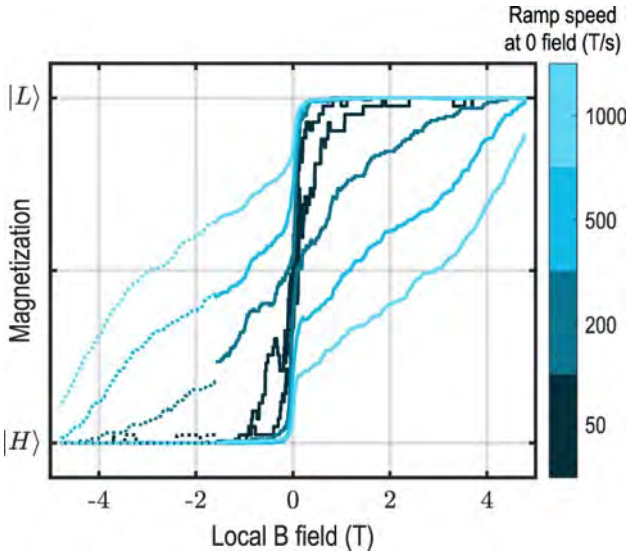


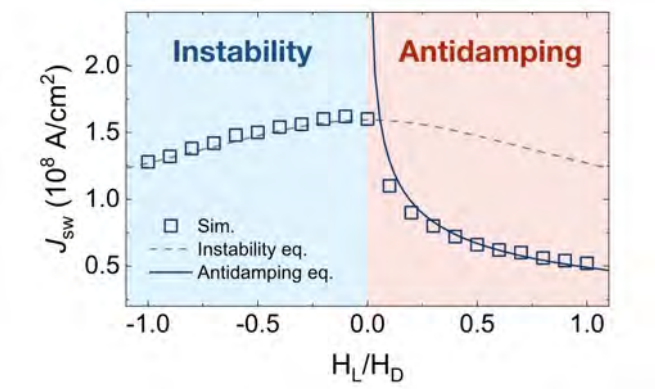
Fig. 2: Magnetization curves of five atom spin chain at different ramping speed of the local magnetic field.

AR-04LB. Reduction of spin-orbit-torque switching current via current-induced anisotropy torque

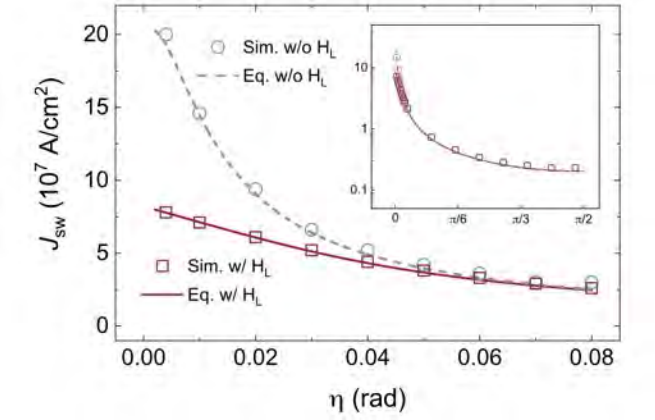
Y. Park[1], G. Lee[2], K. Lee[2]
[1]Department of Materials Science and Engineering, Korea Advanced Institute of Science and Technology, Daejeon, Korea (the Republic of), [2]Department of Physics, Korea Advanced Institute of Science and Technology, Daejeon, Korea (the Republic of)

A recent study has shown that current-induced orbital densities modify magnetic anisotropy via orbital exchange interactions, giving rise to a current-induced anisotropy torque [1]. However, its effect on magnetization dynamics, particularly on magnetization switching, remains largely unexplored. Here, we theoretically and numerically show that the anisotropy torque induced by the orbital quadrupole l_{xy}, characterized by an anisotropy field {\mathbf H}$_L$=H_L(m_y{\hat x}+m_x{\hat y}), significantly reduces the spin-orbit-torque (SOT) switching current. The x and z axes correspond to the charge-current and film-normal directions, respectively. The switching mechanism depends on the sign of H_L/H_D, where H_D is the damping-like SOT effective field: for $H_L/H_D>0$, switching is governed by the antidamping condition, leading to a substantial reduction in the switching current. In contrast, for $H_L/H_D<0$, switching is determined by the instability condition, as in conventional SOT switching [2]. This difference originates from the relative alignment between the y-polarized spin (σ_y) and the anisotropy-torque-induced magnetization component m_y. Furthermore, we investigate the effect of anisotropy torque on SOT switching driven by a tilted spin polarization σ=(0, cosη, sinη). For small η, the anisotropy torque further reduces the switching current beyond the reduction enabled by the z-polarized spin component (σ_z) [3, 4]. Our results suggest that the current-induced anisotropy torque can modify magnetization dynamics substantially, offering a route toward energy-efficient SOT switching.

[1] G.-H. Lee, K.-W. Kim, and K.-J. Lee, Nat. Commun. 17, 2236 (2026).
[2] K.-S. Lee, S.-W. Lee, B.-C. Min, and K.-J. Lee, Appl. Phys. Lett. 102, 112410 (2013).
[3] T. Taniguchi, J. Grollier, and M. D. Stiles, Phys. Rev. Appl. 3, 044001 (2015).
[4] D.-K. Lee and K.-J. Lee, Sci. Rep. 10, 1772 (2020).



Switching current density as a function of the relative anisotropy-torque strength H_L/H_D.



Switching current density as a function of the tilt angle η of the spin polarization σ=(0, cosη, sinη). The inset shows the switching current density over a wider range of η.

AR-05. Antimagnon-to-Magnon Conversion via a Localized Boundary Mode

J. Kwon, J. Do, C. You
DGIST, Daegu, Korea (the Republic of)

Antimagnons are negative-energy spin-wave excitations defined on a dynamically stabilized reversed magnetization background [1]. Since magnon and antimagnon dispersions typically occupy distinct frequency regimes, directly connecting antimagnon modes to propagating magnon modes remains challenging. Consequently, previous studies have relied on antiferromagnetically exchange-coupled regions together with spatially varying magnetic fields to enable coupling between these modes [2,3].
In this work, we use micromagnetic simulations to investigate a route for converting antimagnon modes into propagating magnon modes. We focus on the boundary

between a stable and a dynamically stabilized magnetization region, where a localized boundary mode mediates this conversion. We consider a nanowire with a local constriction, where the spin dynamics inside and outside the constriction are distinctly different. Within the constriction, the high current density generates a spin-orbit torque that overcomes damping and sustains a dynamically stabilized magnetization background [4]. This region therefore supports magnon and antimagnon branches, whereas the surrounding region remains in the conventional magnon state. As a result, a boundary mode forms at the interface between the two regions, exhibiting localized precession. Above a threshold current density, the system is driven into the exceptional point regime, where the magnon and antimagnon branches coalesce and the localized response is strongly enhanced [1]. We find that this enhanced internal mode couples to the boundary mode and is converted into coherent propagating magnon modes outside the constriction.

These results demonstrate that the boundary mode acts as a bridge between the internal antimagnon dynamics and the external magnon channel, mediating the conversion across the frequency mismatch between the two regimes. This provides a new route to extract antimagnon dynamics without multilayer coupling or spatially varying magnetic fields.

[1] J. S. Harms, H. Y. Yuan and R. A. Duine, AIP Adv., 14, 025303 (2024)
[2] J. S. Harms, H. Y. Yuan and R. A. Duine, Phys. Rev. Appl., 18, 064026 (2022)
[3] A. L. Bassant, M. E. Y. Regout and J. S. Harms, Phys. Rev. B, 110, 094441 (2024)
[4] H. Kurebayashi, J. Barker and T. Yamazaki, Nat. Mater., 25 (2026)

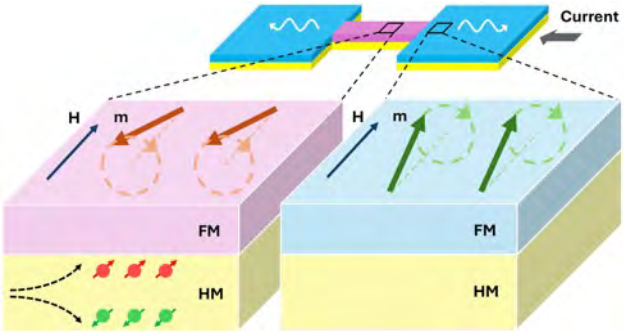


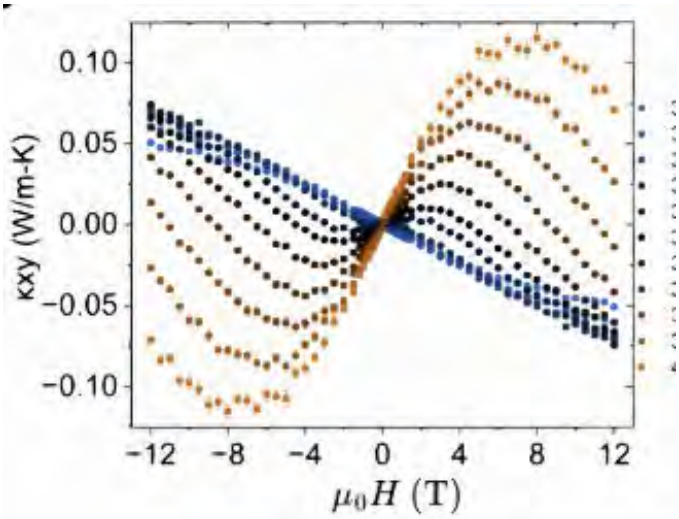
Fig. 1 Schematic of a constricted ferromagnet/heavy metal nanowire. Spin-orbit torque stabilizes a reversed region in the constriction, and a localized boundary mode converts internal antimagnon dynamics into propagating magnon modes.

AR-06. Wiedemann–Franz law violation and topological magnons in a Kagome metal

A. Banerjee, J. Choi, L. Leao, M. Neupane, B. Belbase, A. Unnikrishnan, N. Zaidi, J. Vayrynen
Department of Physics and Astronomy, Purdue University, West Lafayette, Indiana, United States

We investigate the relationship between heat and charge transport in the ferrimagnetic Kagome metal TbCr6Ge6. Below 5 K, the Lorenz ratios are strongly suppressed and the transverse Lorenz ratio undergoes a sign change, revealing a clear decoupling between heat and charge transport dominated by magnetic excitations in a metallic kagome system. In this temperature range, the thermal Hall response is well described by a minimal multiband magnon model, where multiple avoided magnon band crossings produce a topological heat current associated with magnon Berry curvature. Remarkably, at the ferrimagnetic critical point Tc ~ 8 K, we discover a pronounced violation of the Wiedemann–Franz (WF) law, despite a robust metallic charge response, providing clear evidence of dense charge-neutral chiral magnetic quasiparticles. The results place 1-6-6 Kagome metals as prime candidates for investigating chiral-spintronics. [1]

[1] https://arxiv.org/abs/2512.16868



The evidence of topological bosons and two-band crossing with alternating Chern numbers.

AR-07. Anisotropy-driven detour of spin rotation in the ferrimagnetic Weyl semimetal NdAlSi

H. Kim, S. Lim, J. Seo, K. Jeong, J. Hong, N. Lee, Y. Choi
Department of physics, Yonsei University, Seoul, Korea (the Republic of)

As a representative Weyl RKKY magnet, NdAlSi provides a unique platform where magnetic order is mediated by Weyl fermions, leading to a complex interplay between topology and magnetism. While previous studies have established field-driven spin-flip transitions along the *c*-axis into collinear UUD and DDU states, the in-plane anisotropic response and the underlying spin-reorientation dynamics remains elusive. Here, we establish the in-plane magnetic energy landscape of NdAlSi by focusing on its commensurate phase at 2 K ($T < T_{N1}$ =3.6 K), integrating torque magnetometry and magnetization measurements with an anisotropic spin Hamiltonian. Our magnetization data at 2 K reveal a pronounced directional anisotropy within the basal plane, identifying [110] as a significantly harder axis than the *a*-axis ([100]). By probing the angular torque response in the (111) and (101) planes, we resolve characteristic anomalies that are reproducible only when in-plane MCA is explicitly incorporated into the Hamiltonian. Notably, we identify a non-trivial spin-reorientation process at this temperature characterized by a "detour" trajectory; the spins bypass the high-energy barrier of the [110] axis through an angular deviation rather than following a direct rotation path. These results demonstrate that basal-plane MCA is a decisive factor in selecting field-induced rotation pathways, providing a quantitative framework for how anisotropy-controlled magnetism interfaces with Weyl-mediated interactions in the ground state of topological materials

AR-08. VCMA-driven Magnetization Switching in Thick Magnetic Bilayers at Finite Temperature for Spatial Light Modulators

M. Kawana, K. AOSHIMA, K. MACHIDA, Y. Miyamoto, N. Funabashi
Science & Technology Research Labs., NHK (Japan Broadcasting Corp.), Tokyo, Japan

Voltage–controlled magnetic anisotropy (VCMA)–driven magnetization switching is a promising approach for ultra–low–power MRAM [1-3]. Because VCMA is an interfacial effect, it has been mostly used for switching ultrathin magnetic films (~1 nm), while switching in thick magnetic films has been little studied. Switching thick films could broaden applications such as spatial light modulators (SLMs) [4, 5]. Previous simulations have demonstrated successful VCMA-driven switching in a thick magnetic bilayer at 0 K [6]. However, the switching instability became more noticeable with an increase in temperature, suggesting the need for additional calculations to identify magnetic characteristics for stable switching at 300 K. In this study, we investigated the parameters affecting VCMA switching using Landau–Lifshitz–Gilbert simulations that include the thermal fluctuation field H_{th}.
Figure 1 shows the bilayer model, which consists of VC and light-modulation (LM) layers. Previous results [6] suggest that thermally induced magnetic disorder in the LM layer contributes to instability; therefore, this study focused on the exchange stiffness that governs magnetic coherence. The simulation parameters were as follows: the exchange stiffness constant in the LM layer (A_{LM}) varied from 1–10 pJ/m, and the interlayer exchange stiffness constant between the VC and LM layers ($A_{VC\text{-}LM}$) varied from 0.1–1.0 erg/cm^2. Initially, the layers were magnetized along the +z direction. Figure 2 shows the normalized magnetization dynamics in the LM layer for various $A_{VC\text{-}LM}$ and A_{LM} under five H_{th} cases. Unstable precession was observed at $A_{VC\text{-}LM}$ = 0.1 (Fig. 2(a–c)), with greater instability and switching failures observed as A_{LM} increased. Conversely, stable switching occurred at $A_{VC\text{-}LM}$ = 1 (Fig. 2(d–f)), although the precession-period variation increased with A_{LM}. Stable magnetization precession was obtained at $A_{VC\text{-}LM}$ = 1 erg/cm^2 and A_{LM} = 3 pJ/m. These results indicate that $A_{VC\text{-}LM}$ and A_{LM} are critical parameters governing VCMA switching in thick magnetic layers at finite temperature, thus providing key design guidelines for VCMA-driven SLM devices.

[1] T. Nozaki, T. Ichinose, T. Yamamoto, et al., APL Mater., Vol. 12, p. 091109 (2024). [2] T. Yamamoto, T. Nozaki, H. Imamura, et al., Nano Lett., Vol. 20, p. 6012 (2020). [3] T. Nozaki, M. Endo, M. Tsujikawa, et al., APL Mater., Vol. 8, p. 011108 (2020). [4] K. Aoshima, N. Funabashi, R. Higashida, et al., Opt. Express, Vol. 31, p. 21330 (2023). [5] H. Takagi, K. Nakamura, T. Goto, et al., Opt. Lett., Vol. 39, p. 3344 (2014). [6] M. Kawana, N. Funabashi, K. Aoshima, et al., J. Magn. Soc. Jpn., Vol. 49, p. 76 (2025)

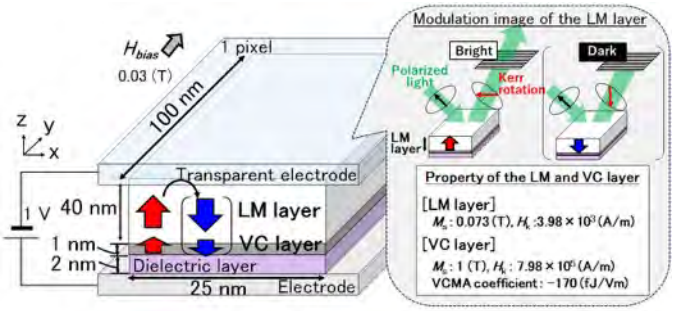


Fig. 1 Model with thick LM layer

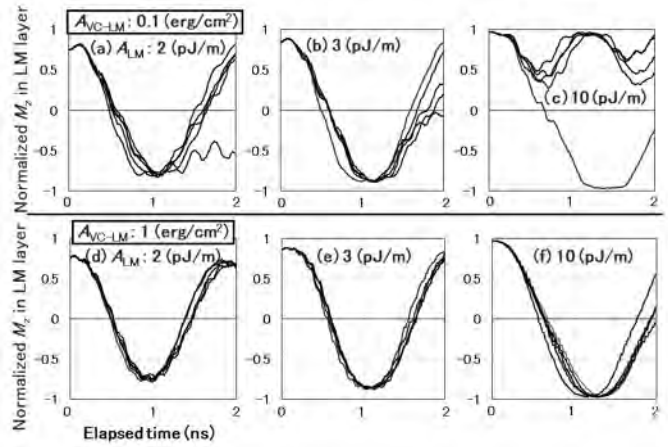


Fig. 2 M_z in LM layer under VCMA for various A_{VC-LM} and A_{LM}

AR-09. Geometry-Dependent Transition from Thermal-Assisted to SOT-Driven Non-Thermal Switching in Mn3Sn

E. Jun[1], S. Lee[1], E. Im[1], G. Baek[2], S. Yang[3], K. Kim[2], S. Kim[1]
[1]Department of Physics and Energy Harvest Storage Research Centre, University of Ulsan, Ulsan, Korea (the Republic of), [2]KAIST, Daejeon, Korea (the Republic of), [3]Quantum Magnetic Sensing Group, Quantum Technology Institute Korea Research Institute of Standards and Science, KRISS, Daejeon, Korea (the Republic of)

Antiferromagnetic materials are promising for next-generation spintronic devices due to their negligible stray fields and fast dynamics. In the non-collinear antiferromagnet Mn3Sn, current-induced magnetic octupole switching has been widely studied for high-speed and energy-efficient memory applications.
Although spin–orbit-torque (SOT)-driven switching has been demonstrated, the relative contributions of thermal-assisted switching induced by Joule heating and non-thermal SOT-driven switching remain unclear, particularly regarding the boundary between these regimes.
In this work, Mn3Sn thin films with thicknesses of 15, 20, 25, and 30 nm were fabricated, and device geometries were systematically varied by fixing the channel width at 5 μm and changing the channel length from 30 to 100 μm in 10 μm steps. This approach enables direct control of the current path aspect ratio and associated Joule heating conditions.
Current-pulse-induced switching measurements reveal a clear dependence of switching behavior on device geometry. In particular, devices with larger aspect ratios exhibit enhanced thermal-assisted switching, while reduced aspect ratios suppress thermal contributions and favor SOT-driven non-thermal switching.
These results indicate the presence of a geometry-dependent transition between thermal-assisted and non-thermal switching regimes. The observed transition behavior provides insight into the role of Joule heating in Mn3Sn switching and suggests a practical route to achieving non-thermal switching through device geometry design.

[1] *ACS Nano* 2025, 19, 39747–39756.
[2] *Phys. Rev. B* 2017, 95, 094406.
[3] *Nature* 2022, 607, 474.
[4] *Nat. Mater.* 2023, 22, 1106–1113.

AR-10. Single-shot magnetization switching in [Co/Pt] spin valves via heat control

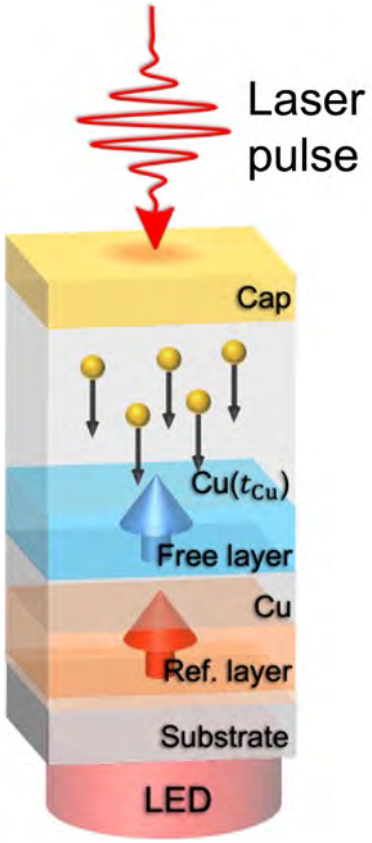
K. Ishibashi[1, 2, 3], J. Igarashi[4, 5], A. Anadón[4], M. Hehn[4, 7], Y. L. Guen[4], S. Iihama[6], J. Hohlfeld[4], J. Gorchon[4], S. Mangin[4, 7], G. Malinowski[4]
[1]Department of Materials Engineering Science, the University of Osaka, Toyonaka, Osaka, Japan, [2]Department of Applied Physics, Tohoku University, Sendai, Miyagi, Japan, [3]Advanced Institute for Materials Research (AIMR), Tohoku University, Sendai, Miyagi, Japan, [4]Université de Lorraine, Nancy, France, [5]National institute of Advanced Industrial Science and Technology, Tsukuba, Japan, [6]Department of Materials Physics, Nagoya University, Nagoya, Japan, [7]Center for Science and Innovation in Spintronics (CSIS), Core Research Cluster (CRC), Tohoku University, Sendai, Japan

The ultrafast manipulation of magnetization using ultrashort laser pulses, typically lasting a few tens of femtoseconds, has been intensively studied over the past decades. Single-shot magnetization reversal has been demonstrated in ferrimagnetic materials containing rare-earth elements such as Gd [1,2]. Recently, single-pulse-induced ultrafast magnetization reversal was demonstrated

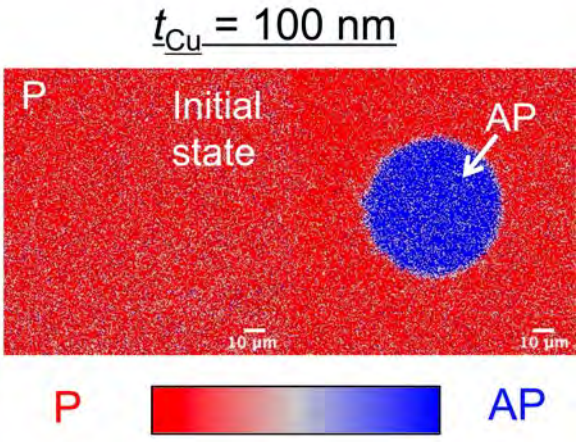
in rare-earth-free [Co/Pt]/Cu/[Co/Pt] ferromagnetic spin valves [3]. However, many open questions concerning the mechanisms still remain without answer. A fundamental question is whether light itself is necessary for the reversal, or whether other heat-inducing stimuli can produce similar switching. This question is motivated by previous studies showing that hot-electron pulses can efficiently carry heat and induce ultrafast demagnetization in ferromagnetic layers [4,5].

In this study, we address this question by comparing direct laser excitation and indirect excitation via hot-electron pulses in Co/Pt-based ferromagnetic spin valves. A wedged Cu layer was deposited on top of the spin valve to tune the energy transmission to the magnetic stack [Fig. 1]. For a 100-nm-thick Cu layer, the laser pulse cannot directly reach the spin valve. Nevertheless, clear single-shot magnetization switching from the parallel (P) to antiparallel (AP) state is observed, as shown in Fig. 2, demonstrating that hot-electron pulses generated in the capping layer are sufficient to trigger magnetization reversal of the free layer. We systematically investigate the influence of laser fluence, Cu thickness, laser pulse duration, laser incidence direction, and MgO insertion. Our results indicate that full demagnetization of the free layer, driven by a rapid rise in its electronic temperature, is the key factor enabling magnetization reversal via either direct laser excitation or hot-electron excitation [6]. In the presentation, we will discuss the experimental results in detail, focusing on the role of electronic temperature in the switching process.

1) I. Radu *et al.*, Nature 472, 205 (2011).
2) T. A. Ostler, *et al.* Nat. Commun. 3, 666 (2012).
3) J. Igarashi *et al.*, Nat. Mater. 22, 725(2023).
4) N. Bergeard, *et al.*, Phys. Rev. Lett. 117, 147203(2016).
5) N. Bergeard, *et al.*, Appl. Phys. Lett. 117, 222408 (2020).
6) K. Ishibashi *et al.*, Phys. Rev. Lett. 135, 116702(2025).



Schematic image of sample stack and experimental configuration



MOKE images of intial state and after irradiation of a laser pulse on Parallel (P) initial state. Red and blue represent P and Anti-parallel (AP) states.

AR-11. Predictive Indicator of Critical Point in Equilibrium and Nonequilibrium Magnetic Systems

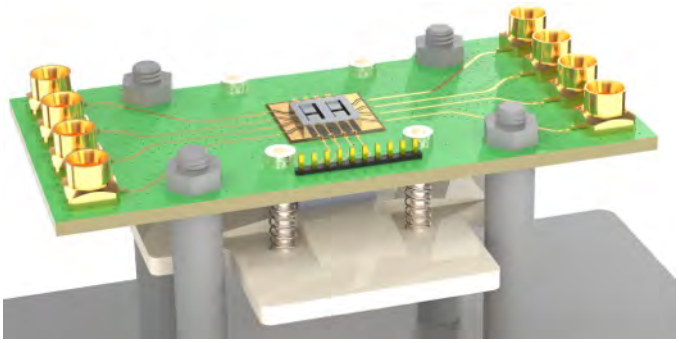
T. Zhang, X. Han, C. Wan
Beijing National Laboratory for Condensed Matter Physics, Beijing, China

Determining critical points of phase transitions from partial data is essential to avoid abrupt system collapses and to reduce experimental or computational costs. However, the complex physical systems and phase transition phenomena have long hindered the development of unified approaches applicable to both equilibrium and nonequilibrium phase transitions. In this Letter, we propose predictive indicators to determine critical points in equilibrium and nonequilibrium magnetic systems based on the frequency-dependent response function. For equilibrium phase transitions, such as magnetization switching under a magnetic field, the static magnetization response function to a perturbing magnetic field diverges at the critical field, serving as a noise-resilient predictive indicator that also reflects the transition order and critical exponents. In contrast, for nonequilibrium phase transitions such as magnetization switching driven by transfer torque, static response fails to signal criticality. Instead, the dynamic response at ferromagnetic resonance frequency diverges at the critical point, which is also robust against thermal noise. We further demonstrate that these static and dynamic indicators can be unified in the frame of first-order linear differential systems, offering a generalizable strategy for predicting criticality in both equilibrium and nonequilibrium transitions.

AR-12. A Standalone Multi-Channel Magnonic Phase Shifter Bank for Phased-Array Systems

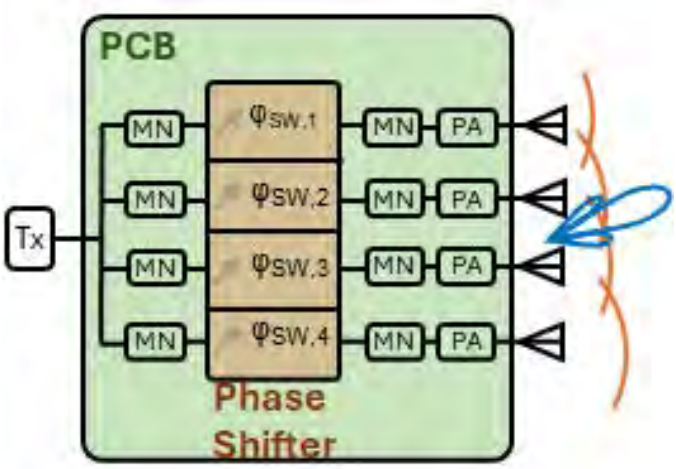
J. Greil[1], A. Angotti[2], F. Kohl[3], A. Papp[4], M. Wagner[3], M. Cocconcelli[2], A. Del Giacco[2], F. Maspero[2], B. Heinz[3], G. Csaba[4], R. Bertacco[2], M. Becherer[1], P. Pirro[3]
[1]School of Computation, Information and Technology, Technical University of Munich, Garching bei Muenchen, Bavaria, Germany, [2]Department of Physics and Polifab, Politecnico di Milano, Milano, Italy, [3]Fachbereich Physik and Landesforschungszentrum OPTIMAS, Rheinland-Pfälzische Technische Universität Kaiserslautern-Landau, Kaiserslautern, Germany, [4]Faculty of Information Technology and Bionics, Pázmány Péter Catholic University, Budapest, Hungary

Highly integrated and energy-efficient beamforming front ends are central to next-generation communication and sensing systems [1]. Here, we extend the functionality of a hybrid magnonic phase shifter from single-channel operation to a parallel four-channel phase-shifter bank, enabling phase control for phased-array applications. The presented platform combines four spin-wave (SW) transmission channels on a Yttrium-Iron-Garnet (YIG) magnonic chip with a flip-chip microelectromechanical (MEMS) actuation scheme [2], allowing local tuning of the effective magnetic field in the channels via micron-sized soft magnets. The hybrid chip is embedded in a printed circuit board (PCB).
The input signal is distributed to the four channels via an RF power splitter on the PCB, while dedicated input and output matching networks ensure efficient impedance matching towards the wire-bonded hybrid chip [2,3]. Additionally, a 20 dB low-noise amplifier with bypass capability is integrated per channel.
The complete system is realized as a compact, standalone RF module equipped with surface-mount SMP connectors for direct integration into existing RF environments. The full system functionality is demonstrated without electromagnets, using a permanent magnet mounted on a spring-loaded platform to provide the global bias field. This approach reduces the power consumption of the system to the voltage supply of the MEMS structures and lies in the sub-mW range.
This work represents a key step toward practical magnonic RF systems by combining multi-channel parallelization, microwave-spin-wave co-design, and system-level integration.
[1] K. Levchenko, K. Davidkova, et al. IEEE Transactions on Magnetics 1-1 (2026)
[2] A. Ghisi, N. Boni, et al. Eng. Proc. 2021, 4(1), 17
[3] F. Kohl, B. Heinz, et al. preprint, arXiv:2050.08656
[4] R. Erdelyi, G. Csaba, et al. Sci Rep 15, 9806 (2025)



Visualization of the standalone multi-channel phase shifter bank. In a basic configuration, 4 input/output channels are realized without matching networks or amplifiers. The PCB

layout is optimized for the hybrid phase shifter chip, as shown in Fig. 2. The static bias field is provided by a permanent magnet mounted on a spring-loaded platform under the PCB.



Sketch of the standalone multi-channel magnonic phase-shifter bank with one input distributed to the four independent SW transmission channels. Matching networks (MN) and power amplifiers (PA) enable seamless integration into phased-array systems.

AR-13LB. Ballistic propagation of ultrashort coherent spin-wave pulses in antiferromagnets

P. K. Kim[1], J. Groefsema[1], B. Ivanov[1], V. Radovskaia[1], M. Na[1], M. Strugatsky[2], A. V. Kimel[1], D. Afanasiev[1]
[1]Radboud University, Nijmegen, Netherlands, [2]V.I. Vernadsky Crimean Federal University, Simferopol, Ukraine

Antiferromagnets support collective spin dynamics at high frequencies and with high propagation velocities, making them promising platforms for ultrafast spin-wave transport [1]. Near the Brillouin-zone center, antiferromagnets host approximately linear spin-wave dispersions, enabling broadband wave packets to propagate with minimal dispersive broadening and providing a platform for high-speed, ultrashort spin-wave pulses analogous to femtosecond optical pulses [2]. Here, we demonstrate the optical generation, propagation, and coherent control of spin-wave pulses in the prototypical easy-plane canted antiferromagnet, $FeBO_3$. A single femtosecond UV pulse launches a broadband coherent spin excitation that propagates through the bulk of the crystal, with its evolution tracked using time-resolved magneto-optical measurements in complementary front-side and back-side probe geometries. We observe a ballistic, pulse-like wavefront with a group velocity of v_g=13.7 km/s, a temporal width of approximately 12 ps, and a propagation distance exceeding 16 μm. The ballistic wavefront is followed by a dispersive tail arising from the wave-vector-dependent group velocity induced by the small spin-wave gap. By inverting the magneto-optical sensitivity function, we reconstruct the spin-wave packet in reciprocal space, directly resolving its broadband wavevector distribution across the linear and nonlinear regions of the dispersion. Finally, using a double-pump excitation, we coherently interfere two spin-wave packets to selectively suppress a substantial portion of the low-frequency dispersive tail, providing a route toward coherent pulse shaping and isolation of the ballistic pulse front. Together, these results demonstrate the optical generation and coherent control of broadband spin-wave pulses, establishing a platform for manipulating propagating magnonic excitations on ultrafast timescales.

1. Němec, P., Fiebig, M., Kampfrath, T., Kimel, A.V. *Nat. Phys.* 14, 229–241 (2018)
2. Kimel, A. V., Ivanov, B. A., & Afanasiev, D. *Newton* (2026)

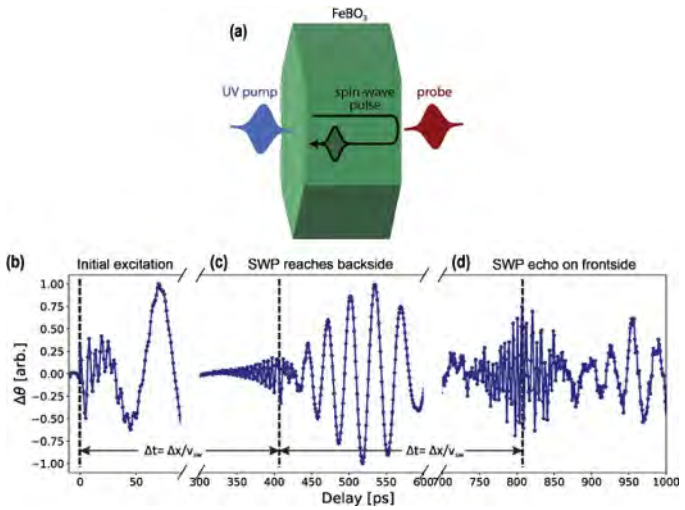


Figure 1. (a) Schematic of optical excitation and detection of spin-wave pulse. (b-d) Detection of spin-wave pulse showing (b) the initial excitation on the front surface, (c) the reflection of the spin-wave pulse at the back surface, and (d) the spin-wave pulse echo returning to the front surface.

AR-14. Anomalous FMR linewidth broadening in Fe thin films coupled with [Ta/Co/Pt] multilayers exhibiting perpendicular magnetic anisotropy

S. Baek[1], M. Okawa[1], S. Komori[2], T. Taniyama[1]
[1]Nagoya University, Nagoya, Japan, [2]Osaka Metropolitan University, Osaka, Japan

1. Introduction

The magnetization dynamics of a ferromagnetic (FM) layer coupled with an adjacent FM layer with perpendicular magnetic anisotropy (PMA) are of both fundamental and technological importance[1]. Ferromagnetic resonance (FMR) is a widely used technique for characterizing such magnetization dynamics, particularly magnetic damping, via the microwave absorption linewidth ΔH. However, the effect and role of the PMA layer on the ΔH of the adjacent FM layer remains unclear. In this study, we investigate the relationship between ΔH and the resonance frequency f_{res} in Ta/[Ta/Co/Pt]$_{15}$/Ta(t_{Ta})/Fe/STO(111) structures (Fig. 1), in which the PMA component of the [Ta/Co/Pt]$_{15}$ multilayer modifies this relationship. Notably, we observe anomalous broadening of the ΔH by stacking the [Ta/Co/Pt]$_{15}$ multilayer, attributed to two-magnon scattering (TMS) and the magnetic drag effect in the Fe layer.

2. Experimental details and results

A 30-nm-thick Fe film was grown on a $SrTiO_3$(111) substrate at 150 °C, followed by the deposition of Ta(2.8 nm)/[Ta(0.2 nm)/Co(1.2 nm)/Pt(2.0 nm)]$_{15}$/Ta(t_{Ta}) at room temperature. Initially, the sample was magnetized in the out-of-plane direction. FMR measurements were then performed by sweeping the frequency and magnetic field from low to high (up sweep). Measurements for a reverse sweep from high to low (down sweep) were also carried out. Figure 2 shows ΔH versus f_{res} for both the up and down sweeps. During the down sweep, a peak feature is seen in ΔH at 10 GHz, which is likely due to TMS. During the up sweep, however, ΔH continuously increases as f_{res} decreases. We attribute this distinct behavior to the different stray fields from the multilayer during the up- and down-sweeps, which are caused by the different magnetization configurations of the multilayer inducing different non-uniform fields within the Fe layer. This results in the distinct ΔH versus f_{res} behaviors.

This work was supported in part by JSPS KAKENHI Grant Nos. JP24H00380, JP24K21732, JP23KK0086, JSPS International Joint Research Program with the UK (JRP-LEAD with UKRI) JPJSJRP20241705, JST FOREST JPMJFR212V, JST SPRING, Japan Grant Number JPMJSP2125.

1) Y. Wei et al., J. Appl. Phys. 126, 053901 (2019).

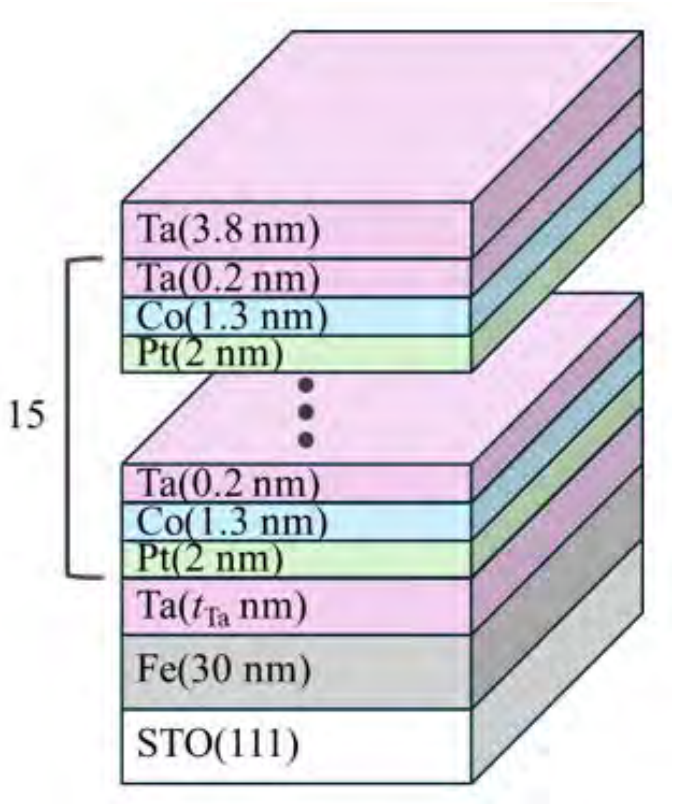


Fig. 1. Sample structure

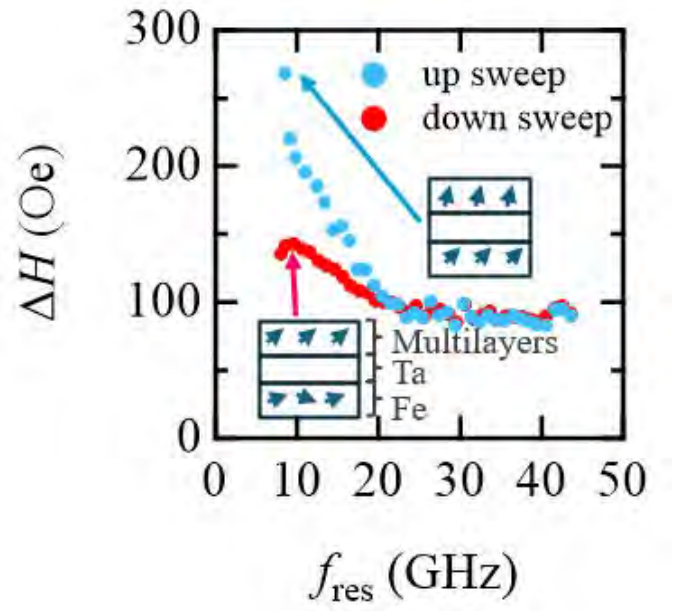


Fig. 2. ΔH vs f_{res} measured during up and down sweeps.

AR-15. Stress-controlled spin-wave dynamics in superellipse-shaped FeGa nanostructures

E. A. Saavedra Díaz[1], H. Vigo[2], C. Saji[1], D. Laroze[3], M. Al Bahri[4], J. Escrig[1, 5]
[1]Universidad de Santiago de Chile, Santiago, Chile, [2]Universidad Privada del Norte, Trujillo, Peru, [3]Universidad de Tarapacá, Arica, Chile, [4]A'Sharqiyah University, Ibra, Oman, [5]Center for Nanoscience and Nanotechnology (CEDENNA), Santiago, Chile

Controlling spin-wave dynamics using low-power external stimuli is a central challenge for next-generation magnonic and spintronic devices. Magnetostrictive nanostructures provide a promising pathway toward strain-mediated control of magnetization dynamics without the need for large magnetic fields or electrical currents.

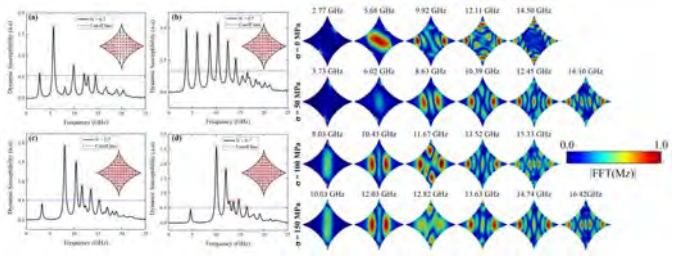
Here we investigate the ferromagnetic resonance and spin-wave spectra of FeGa nanostructures with superellipse geometries using micromagnetic simulations. Superellipses provide a versatile geometry in which a single parameter continuously transforms the nanostructure shape, enabling systematic control of the internal magnetic field distribution and the resulting magnetic states.

Our results reveal that the interplay between geometry and stress-induced anisotropy stabilizes different magnetic textures, including vortex, quasi-single-domain, and metastable antivortex configurations. The spin-wave spectra are strongly governed by these equilibrium states. In vortex configurations, several radial and edge modes are identified whose frequencies depend on the superellipse shape parameter. In contrast, antivortex states exhibit distinct resonance spectra with pronounced mode splitting and asymmetric responses when mechanical stress is applied.

Both tensile and compressive stresses significantly modify the dynamic susceptibility, inducing additional resonances, hybridization between spin-wave modes, and stress-driven transitions between magnetic configurations. These effects arise from the competition between exchange, dipolar, and stress-induced anisotropy energies, which reshape the internal field landscape and the stability of topological spin textures.

These findings demonstrate that the combined engineering of geometry and magnetoelastic coupling provides an efficient strategy to actively tune spin-wave spectra in magnetostrictive nanostructures. Superellipse-shaped FeGa nanostructures therefore constitute a promising platform for stress-controlled magnonic devices, reconfigurable microwave components, and flexible spintronic technologies.

[1] E. Saavedra, H. Vigo-Cotrina, C. Saji, D. Laroze and J. Escrig, Appl. Phys. Lett., Vol. 127, p. 032402 (2025).
[2] E. Saavedra, H. Vigo-Cotrina, M. Al Bahri, C. Saji and J. Escrig, J. Appl. Phys., Vol. 139, p. 064305 (2026).



AR-16. Magnetization Dynamics of Exchange Coupled CoFeB/NiO/CoFeB Trilayers

R. Mehta[1], T. Sharma[1], I. Pershad[1], P. K. Pal[2], A. Barman[2], D. A. Arena[3], S. Saha[1]
[1]Physics, Ashoka University, Rai, Haryana, India, [2]Physics, S. N. Bose National Center for Basic Sciences, Kolkata, West Bengal, India, [3]Physics, University of South Florida, Florida, Florida, United States

Ferromagnet/Antiferromagnet (FM/AFM) heterostructures are particularly intriguing, as interfacial exchange coupling leads to phenomena such as exchange bias, providing a powerful route to tailor magnetic properties and device performance [3,4]. In this work, we have studied the magnetization dynamics in CoFeB (5 nm)/NiO (t nm)/CoFeB (5 nm) trilayers by varying the NiO spacer thickness to understand various magnetic properties such as magnetic damping,
The CoFeB (5 nm)/NiO (t nm)/CoFeB (5 nm) trilayers were deposited at room temperature on self-oxidized silicon wafers using DC/RF magnetron sputtering. The NiO spacer thickness was varied as t = 2, 5, 20, and 50 nm, and all samples were capped with a 2 nm Ta layer to prevent oxidation. Initial structural and magnetic characterization was carried out using XRD, AFM, VSM, and PPMS techniques. An exchange bias is observed at low temperatures for all films, while it is absent at room temperature. However, room-temperature hysteresis loops clearly indicate that for t = 2 nm the two FM layers are strongly coupled, whereas for t = 50 nm they are completely decoupled [see Fig. 1(a)]. Room-temperature magnetization dynamics of the trilayers with varying NiO thickness were studied using FMR. A single resonance peak is observed for t = 2 nm, indicating strong

coupling between the two CoFeB layers. As t increases, a second resonance peak emerges, and for t = 50 nm two distinct resonance peaks are clearly observed, as highlighted in Fig. 1(b). The linewidth (ΔH) extracted from the absorption spectra shows a systematic increase with both microwave frequency and NiO thickness. The broadening of the FMR linewidth in thicker NiO samples indicates enhanced magnetic damping as shown in Fig. 1(c). Additionally, the resonance peaks exhibit a twofold anisotropy when the sample is rotated from 0° to 360° [See Fig. 1(d)]. These results offered promising pathways for tunable spin transport in AFM-based spintronic devices.

Acknowledgement :
RM acknowledge Ashoka University for AXIS bank PhD fellowship. SS and RM gratefully acknowledge the financial support of SERB, File No. SRG/2022/000191, and the financial aid provided by the Axis Bank to support this research work at Ashoka University. RM and SS acknowledge CRF, IITD for PPMS measurement.

[1] J. Zhou, et.al. Phys. Rev. B, 101, 214434 (2020)
[2] V. Baltz, et. al. *Rev. Mod. Phys.*, 90, 015005, (2018).
[3] S. M. Rezende, et. al *J. Appl. Phys.*, 93, 7717, (2023).

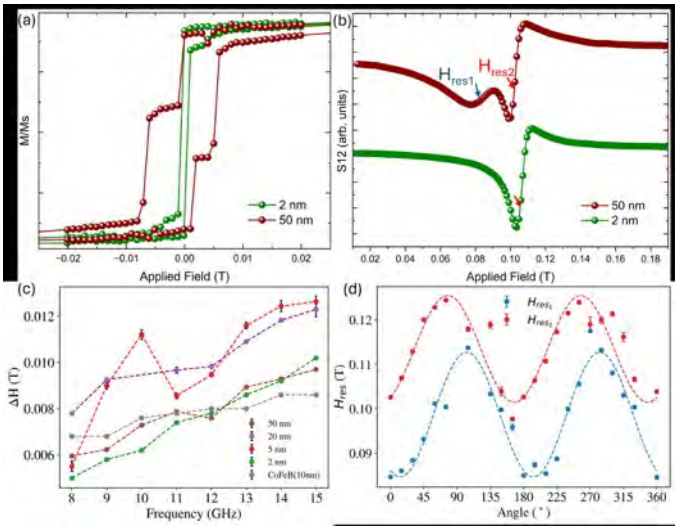


Fig.(a) The M–H loops of trilayers for t = 2 and 50 nm. (b) FMR spectra measured at 12 GHz . (c) Linewidth vs frequency (d) In-plane angular dependence of resonance field for t = 50 nm measured at 12 GHz.

XA: SPECIAL SESSION: MAGNETISM IN NUCLEAR FUSION

Co-Chair(s): C. Dennis, *National Institute of Standards and Technology, Gaithersburg, Maryland, United States* and R. Goldfarb, *National Institute of Standards and Technology, Boulder, Colorado, United States*

Tuesday, November 3, 2026
12:30 PM-01:30 PM
Coral 5

XA-01. Influence of Ferromagnetism and Diamagnetism on the Magnetic Field Configuration of the Helical Fusion Reactor

N. Yanagi[1, 2], M. Lindero-Hernández[3], F. Trillaud[4], L. Montoya-Santiyanes[5], G. dos Santos[6], D. Garfias-Dávalos[7], Y. Narushima[1, 2], Y. Raiymbekov[2], S. Miura[1, 2], X. Li[1, 8]
[1]National Institute for Fusion Science, Gifu, Japan, [2]SOKENDAI (The Graduate University for Advanced Studies), Gifu, Japan, [3]Instituto de Ingeniería, Universidad Nacional Autónoma de México, Mexico City, Mexico, [4]Université de Lorraine, GREEN Lab, Vandoeuvre-lès-Nancy, France, [5]Unidad de Alta Tecnología, Facultad de Ingeniería, Universidad National Autónoma de México, Querétaro, Mexico, [6]Universidade Federal do Rio de Janeiro, Rio de Janeiro, Brazil, [7]Karlsruhe Institute of Technology, Karlsruhe, Germany, [8]Technische Universität München, München, Germany

Magnetic confinement fusion reactors require highly accurate magnetic field configurations to efficiently confine high-temperature, high-density plasmas using superconducting magnets. For example, the Large Helical Device (LHD), which operated for 28 years at National Institute for Fusion Science (NIFS), was constructed in the 1990s to achieve a tolerance of ±1 mm in the major diameter of 7.8 m. In the future, a helical fusion reactor capable of producing 100 MW of electricity can be realized by enlarging LHD to two times or more. For a fusion reactor, blankets will be installed between the plasma and superconducting magnets to convert the kinetic energy of neutrons into thermal energy, breed tritium from lithium, and provide radiation shielding for the magnets. A feasible candidate material for the walls of a box-like structure of blankets is Reduced Activation Ferritic/Martensitic (RAFM) steel, which is effective in reducing the amount of long-lived radiation produced by bombardment with high-energy neutrons. Since RAFM is a ferromagnetic material, the distortion of the confining magnetic configuration is a concern. To understand its impact, a full 3D model has been built in the commercial finite element solver COMSOL Multiphysics®, including the coils and blankets. The magnetic field over the plasma confining region is computed with a precisely modeled blanket on the basis of a non-linear B-H curve. The results show limited distortion due to the toroidal symmetry.

Another concern regarding magnetic distortion in a fusion reactor is the diamagnetic effect in superconductors. Recently, High-Temperature Superconductors (HTS) have emerged as a viable candidate for fusion reactor magnet designs, particularly among startup companies. The Rare-Earth Barium Copper Oxide (REBCO) HTS tapes have broad surface areas, which may induce large shielding currents. For the helical fusion reactor, the STARS (Stacked Tapes Assembled in Rigid Structure) conductor is a candidate for the magnet. The STARS conductor features REBCO tapes simply stacked without twisting or transposition. The shielding currents induced in the stack of REBCO tapes are analyzed, also using COMSOL. The current distribution is incorporated into the magnetic field calculation of the helical fusion reactor with simplified modeling. The results will be reported in the presentation.

XA-02. Predictive modeling of cryogenic magnetization in austenitic stainless steels for the SPARC tokamak

P. Ermoshkina, C. Snyder, T. Clark, C. Dennett
Commonwealth Fusion Systems, Cambridge, Massachusetts, United States

Commonwealth Fusion Systems (CFS) is developing a high-field, compact tokamak, SPARC, enabled by REBCO-based high temperature superconducting (HTS) magnets. Austenitic stainless steels are the primary structural materials chosen for their high strength and low magnetization in SPARC operating conditions (<25 K, >10 T). However, manufacturing process differences and cryogenic exposure can induce phase transformation to ferromagnetic phases (ferrite and martensite) in these steels. These magnetic heterogeneities create deleterious error fields that interfere with plasma control and sensor accuracy.

Validation of magnetizable material design targets in SPARC relies on room temperature, flux distortion method magnetic permeability testing (μ_r). However, these measurements do not linearly extrapolate to the operating conditions of SPARC. In this work, we present a volumetric phase fraction modeling approach for estimating full magnetization (M - H) behavior of austenitic stainless steel 316L (UNS S31603) across the entire operational range. Our

model correlates room temperature magnetic permeability data with cryogenic vibrating sample magnetometry (VSM) and microstructural phase quantification. We validate the approach through computational simulations of the magnetic permeability probes and VSM measurements with known magnetic phase fractions. This study also establishes a framework for setting standardized design values for magnetic permeability in high-precision high-field superconductor electromagnet applications, balancing the trade-offs between custom material chemistries and the logistical demands of mass manufacturing.

SESSION BA: MAGNETISM FOR BIOMEDICINE: FROM BIOLOGICAL SYSTEMS AND FUNCTIONAL MATERIALS TO THERAPY

Chair(s): P. Tiberto, *INRIM, Torino, Italy*
Tuesday, November 3, 2026
02:00 PM-05:30 PM
Coral 3

BA-01. Magnetotactic Bacteria, Living Biorobot for Biomedical Application

D. Villanueva[1], A. G. Gubieda[2], L. Gandarias[3], D. de Cos Elices[4], A. Abad[2], A. García-Prieto[5], M. Fernandez Gubieda[1]
[1]Electricidad y Electrónica, Universidad del Pais Vasco (UPV/EHU), Leioa, Spain, [2]Inmunologia, Microbiologia y Parasitologia, Universidad del País Vasco (UPV/EHU), Leioa, Spain, [3]Institute of Biosciences and Biotechnologies of Aix-Marseille (BIAM), Saint-Paul-lez-Durance, France, [4]Fisica, Universidad del País Vasco (UPV/EHU), Leioa, Spain, [5]Física Aplicada, Universidad del País Vasco (UPV/EHU), Bilbao, Spain

Magnetotactic bacteria (MTB) are a group of motile aquatic microorganisms capable of aligning and orienting themselves along the Earth's magnetic field, a phenomenon known as magnetotaxis. This behavior is enabled by magnetosomes, intracellular magnetic nanoparticles synthesized and organized by the bacteria into chains along the longitudinal axis of the cell. MTB exert strict genetic control over the composition, morphology, and size of these magnetosomes, as well as over their chain organization, resulting in diverse magnetic responses depending on the species. In addition to magnetotaxis, MTB possess an oxygen-sensing mechanism called aerotaxis, which allows them to navigate toward regions with optimal oxygen concentrations. The combination of magnetotaxis, aerotaxis, and self-propulsion via flagella has led to the concept of using MTB as biorobots for therapeutic and diagnostic applications. In particular, MTB can be guided by external magnetic fields and are naturally drawn to hypoxic regions, such as those found in tumors, motivating their exploration in applications including magnetic resonance imaging (MRI), targeted drug delivery, and magnetic hyperthermia.

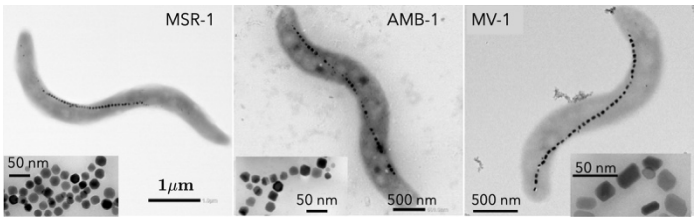
In this work, we present recent research on the collective control of bacterial navigation under rotating magnetic fields (RMF) and periodic magnetic field reversal (PMFR), with field strengths ranging from 0 to 1000 μT and frequencies between 0.1 and 0.5 Hz [1]. We demonstrate how field strength and frequency influence both individual and collective motility characteristics, including motion patterns, population alignment, angular dispersion, and swimming velocities.

We also present a comparative analysis of the heating capacity, or specific absorption rate (SAR), across different MTB species [2]. Although all species synthesize magnetite, the size and morphology of their magnetosomes are species-specific (see Fig. 1), which strongly influences their magnetic anisotropy and, consequently, their heating efficiency. As magnetic anisotropy increases, higher saturated SAR values can be achieved; however, this also raises the threshold magnetic field required to obtain a SAR response. This is a crucial factor in determining the most suitable bacterial species for hyperthermia applications.

In addition, we investigate the cytotoxic effects of magnetosome-mediated magnetic hyperthermia in lung carcinoma cells using in vitro assays, demonstrating the therapeutic potential of these biogenic magnetic nanoparticles. We also analyze the kinetics of intracellular degradation of magnetosomes in the cellular environment [3]. We observe two distinct processes: the degradation of magnetite in magnetosomes, which oxidizes to maghemite, and the biosynthesis of small magnetite and ferrihydrite nanoparticles, allowing us to better understand their stability and biocompatibility.

Finally, we show that incorporating dopant elements such as gadolinium (Gd) and terbium (Tb) into the magnetosome crystal lattice produces multifunctional magnetic nanomaterials with enhanced biomedical potential [4]. Specifically, Tb incorporation imparts luminescent properties, enabling potential use as biomarkers, while Gd incorporation enables dual-contrast capability for MRI by introducing T_1 contrast in addition to the inherent T_2 contrast of unmodified bacteria.

[1] D. Villanueva et al, Small, 21, e09375 (2025)
[2] D. Villanueva et al, ACS Applied Materials & Interfaces, *16* (49), 67216-67224 (2024)
[3] A. G. Gubieda et al, Journal of Nanobiotechnology, 22, 529 (2024)
[4] L. Gandarias et al, Materials Today Bio, 20, 100680 (2023)



TEM images of *Magnetospirillum gryphiswaldense* (MSR-1); *Magnetospirillum magneticum* (AMB-1) and *Magnetovibrio blakemorei* (MV-1).

BA-02. Iron Metabolism and Magnetic Characterization of Breast Cancer Stem Cells: Could Iron Be A Universal Marker for Label-Free Sorting?

K. Paz Gonzalez[1], R. Farrell[2], L. Nguyen T. Tran[1], X. Wu[3], E. Rodriguez[1], M. Venere[4], J. Chalmers[5], K. Chen[2], J. Gomez-Pastora[1]
[1]Chemical Engineering, Texas Tech University, Lubbock, Texas, United States, [2]Biological Sciences, Texas Tech University, Lubbock, Texas, United States, [3]Boston Institute of Biotechnology, Southborough, Massachusetts, United States, [4]Radiation Oncology, The Ohio State University College of Medicine, Columbus, Ohio, United States, [5]Chemical and Biomolecular Engineering, The Ohio State University, Columbus, Ohio, United States

Isolating breast cancer stem cells (CSCs) is crucial for understanding tumor development, metastasis and therapeutic resistance [1-3]. However, current isolation approaches remain technically challenging as they rely on antibody labeling, which introduces variability, cost, and potential perturbation of cell biology [4-6]. Here, we explore label-free magnetophoresis to sort CSCs exploiting their unique magnetic properties, arising from altered cellular iron metabolism. Using single-cell magnetometry (Fig.1-A), we found that CSCs show increased magnetic response compared to non-stem tumor cells, indicating a distinct magnetic susceptibility (Fig.1-B). These observations are consistent with altered iron metabolism in CSCs, as confirmed by our molecular data indicating differential expression of genes involved in iron import, and export processes.

Expanding on our magnetic characterization, we utilized numerical models to predict the behavior of CSCs in a quadrupole magnetophoretic sorter (Fig.2-A). The results show that adjusting the flow rate balances the competing effects of magnetic and hydrodynamic forces, therefore controlling the trade-off between CSCs recovery and sample purity (Fig. 2-B). Preliminary experimental results further indicate that these magnetic susceptibility differences, driven by iron metabolic pathways, can reliably distinguish CSCs from other tumor cell types without external markers. This methodology offers a scalable, low-complexity solution for isolating rare cell populations in oncological research and clinical contexts.

1 Torti, S. V. & Torti, F. M. *Nature Reviews Cancer* . V 13, P: 342-355 (2013).
2 Manz, D. H., Blanchette, N. L., Paul, B. T., Torti, F. M. & Torti, S. V. *Ann N Y Acad Sci.* V: 1368, P: 149-161 (2016)
3 El Hout, M., Dos Santos, L., Hamaï, A. & Mehrpour, M. *Seminars in Cancer Biology*. V: 53, P: 125-138 (2018).
4 Sun, H. *et al. Clin Transl Oncol* V: 15, P: 46-54 (2013)
5 Meyer, M. J., Fleming, J. M., Ali, M. A., Pesesky, M. W., Ginsburg, E. & Vonderhaar, B. K. *Breast Cancer Res* V: 11, P: R82 (2009)
6 Kim, W. T. & Ryu, C. J. *BMB Rep* V: 50, P: 285-298 (2017).

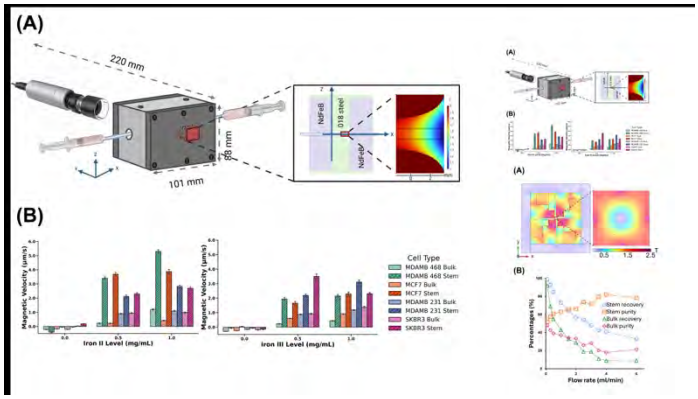


Figure 1. (A) Device for single-cell magnetometry analysis. (B) Single-cell magnetometry results with bar plots of the average magnetic velocity, error bars represent 95% confidence intervals.

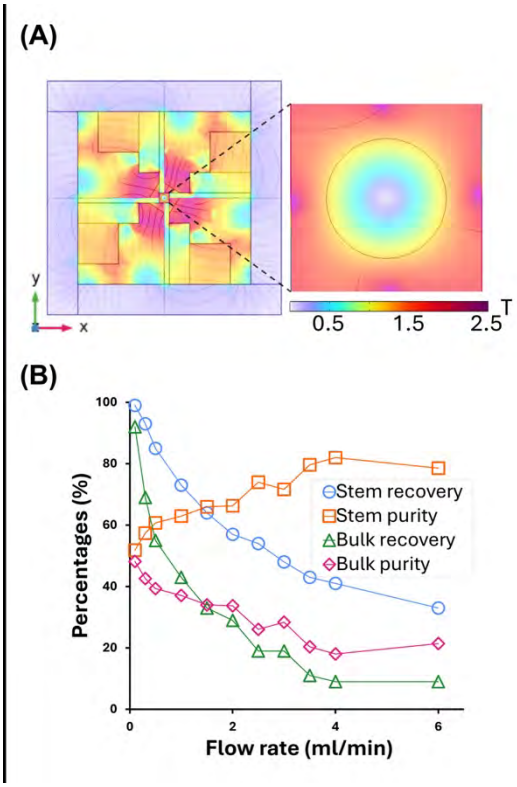


Figure 2. (A) Magnetic flux density generated by the sorter. (B) Simulation results of the flow rate dependent recovery and purity of MDAMB 468 stem and non-stem cells supplemented with 0.5 mg/mL of ferrous iron.

BA-03. From functional materials to biomedicine: exploiting the electronic and microstructural versatility of magnetic shape memory Heuslers

F. Albertini, M. Takhsha, R. Cabassi, F. Casoli, S. Fabbrici
IMEM-CNR, Parma, Parma, Italy

Magnetic shape memory (MSM) Heusler alloys represent one of the most promising classes of materials for multicaloric effects and multi-stimuli actuation. Beyond these functionalities, they possess attractive properties for applications in energy harvesting and spintronics. Their multifunctional behavior is mainly governed by a reversible martensitic phase transformation, which enables a wide range of responses to external stimuli. Although MSM Heuslers have been extensively investigated for technological applications, their potential in biomedical contexts remains largely unexplored, unlike conventional shape memory alloys such as Nitinol, which are already widely employed in medical devices.

In recent years, we have carried out extensive studies on the structural, microstructural, and magnetic properties of Ni–Mn–Ga epitaxial thin films and micro- and nanoparticles. These investigations also addressed size-scaling effects and the impact of different external stimuli on the martensitic transformation in this class of materials [1 and references therein].

The development of MSM Heusler-based thin films, coating layers, and micro-/nanostructures opens new opportunities for innovative biomedical applications, taking advantage of their electronic adaptability and tunable microstructural characteristics.

A key step toward the use of MSM Heuslers in biomedical applications is the evaluation of their cytotoxicity. To this end, we have performed in vitro biological tests to assess cytocompatibility and cell morphology of human fibroblast cells cultured on Ni–Mn–Ga epitaxial thin films [2]. These results provide a robust starting point for exploring the biomedical potential of MSM Heuslers and for identifying their most promising functionalities for future medical devices and therapeutic strategies.

In this talk, several potential applications will be discussed [3]. In particular, we will present the use of MSM Heusler particles as self-regulating agents for magnetic hyperthermia. Experimental results have been analyzed through numerical simulations to identify the dominant heat dissipation mechanisms. Our findings emphasize the crucial role of the sharpness of the martensite–austenite transformation in achieving efficient self-regulation. Additionally, we will report results on fluids containing MSM microdisks, highlighting their potential for the magneto-mechanical destruction of cancer cells.

[1] M. Takhsha Ghahfarokhi et al., Acta Materialia, Vol. 284, p. 101058 (2025)
[2] M. Takhsha Ghahfarokhi et al., ACS Appl. Bio Mat. Vol. 6, p. 5009 (2023)
[3] M. Takhsha Ghahfarokhi et al., Materials Today Chemistry, Vol. 48, p. 103006 (2025)

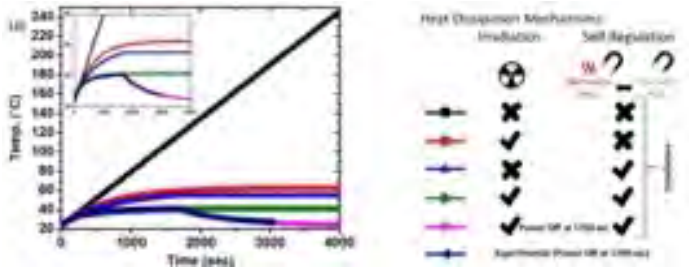


Figure 1. Experimental curve measured for the Ni-Mn-Cu-Ga powder sample up to 4000 sec (with power OFF at 1700 sec) and the simulated temperature curves for the dispersant in different conditions, where the irradiation and self-regulation mechanisms are considered.

BA-04. MagSense: Bringing Magnetic Detection of Molecules to the Nanoscale

P. M. Braganca[2], H. J. Richter[2], C. Dai[2], L. Wang[2], Y. Fan[2], J. Gibbons[2], J. Katine[2], K. Honer[1]
[1]Roche Sequencing Solutions, Santa Clara, California, United States, [2]Research, Western Digital, San Jose, California, United States

Most medical diagnostic technologies rely on optical labels, so their spatial resolution is limited by the wavelength of light. Magnetic sensors have no such limitations as the fields from label particles decrease rapidly with distance from a sensor, allowing for sensor densities 10-100X larger than optical systems allow. Here, we describe a platform utilizing superparamagnetic tags that, compared to optical labels, offers single-molecule resolution, higher detection density, and increased multiplexing.
Previous magnetic biosensor studies [1]-[3] demonstrated detection of a single particle, however these were with sensors > 400 nm and particles > 200 nm. In this study, we fabricated 40-100 nm diameter magnetic tunnel junction (MTJ) sensors, achieving length scales suitable for ensuring that only one molecule binds per sensor. To identify the ultimate achievable spatial resolution, 60 nm diameter sensors were characterized using an Atomic Force Microscope (AFM) with magnetic nanoparticles functionalized on a probe tip as shown in Fig. 1(a), precisely mapping the sensor's electrical response as single particles were scanned across as shown in Fig. 1(c) and confirming nanoparticles down to 20 nm diameter can be detected. Following this single-particle detection demonstration, massively parallel arrays of 8 million MTJs were fabricated directly onto CMOS detection circuitry as shown in Fig. 2(a). The system's background sensor noise limit was characterized at less than 1000 counts per sample run. This work supports magnetic sensors as a highly scalable and ultra-sensitive platform for next-generation multiplexed diagnostics.

[1] G. Li, V. Joshi, R. L. White, S. X. Wang, J. T. Kemp, C. Webb, , R. W. Davis, and S. Sun, "Detection of single micron-sized magnetic bead and magnetic nanoparticles using spin valve sensors for biological applications," *Journal of applied physics*, vol 93, pp.7557-7559, 2003.
[2] P. Manandhar, K. S. Chen, K. Aledealat, G. Mihajlović, C. S. Yun, M. Field, G. J. Sullivan, G. F. Strouse, P. B. Chase, S. von Molnár, and P. Xiong, "Detection of specific biomolecular interactions with micro-Hall magnetic sensors," *Nanotechnology*, vol 20, p.355501, 2009.
[3] Y. C. Liang, L. Chang, W. Qiu, A. G. Kolhatkar, B. Vu, K. Kourentzi, T. R. Lee, Y. Zu, R. Willson, and D. Litvinov, "Ultrasensitive magnetic nanoparticle detector for biosensor applications," *Sensors*, vol 17, p.1296, 2017.

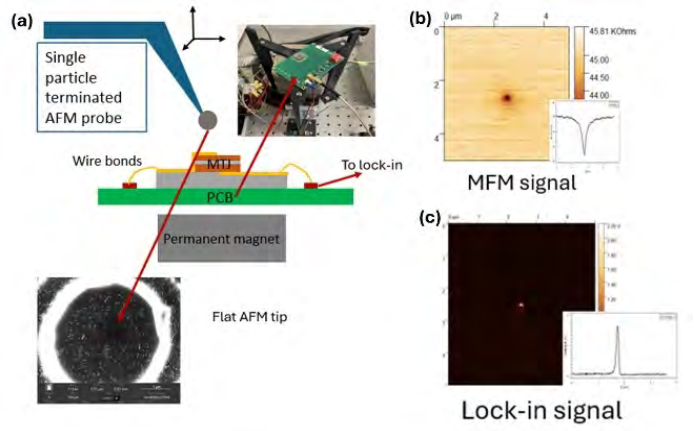


Fig. 1. (a) schematic of AFM test system with SEM micrograph of flat tip with particles. (b) MFM signal around sensor and (c) lock-in signal from sensor indicating localized response to a single particle

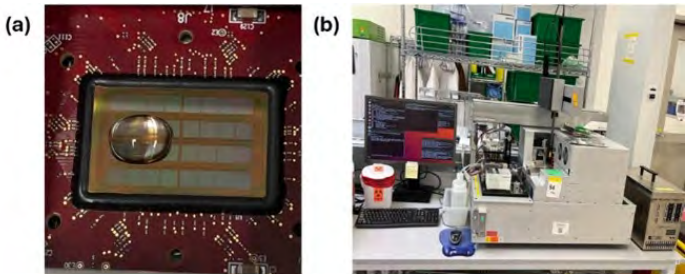


Fig. 2. (a) optical image of MagSense chip. (b) MagSense tester with liquid handling and microfluidic chip socket for CMOS chip

BA-05. Magnetic Relaxation Phenomena and Apoptotic Cell Death by Hyperthermia Treatment in PEGylated $NiFe_2O_4$ Magnetic Nanoparticles

K. Ohara[2], K. Nakazawa[2], N. Kataoka[2], Y. Ichiyanagi[1, 2]
[1]Graduate School of Engineering Science, The University of Osaka, Toyonaka, Japan, [2]Physics, Yokohama National University, Yokohama, Japan

Research on the medical applications of magnetic nanoparticles has advanced rapidly in recent years. We have previously demonstrated their potential for cancer hyperthermia and as magnetic resonance (MR) contrast agents [1], and have clarified the relationship between AC

magnetic susceptibility and heat dissipation [2].

In this study, nickel ferrite nanoparticles encapsulated with biocompatible polyethylene glycol (PEG) were synthesized. Their structural and magnetic properties were systematically characterized, and their heating performance under an alternating magnetic field was evaluated. Furthermore, the mechanism of hyperthermia-induced cell death was investigated. The particle size was controlled in the range of 3–17 nm by varying the water content during synthesis.
DC magnetic susceptibility measurements indicated superparamagnetic behavior, characterized by low coercivity and rapid magnetization saturation in low magnetic fields. The AC magnetic susceptibility indicated a single Debye-type relaxation process. The optimal particle size for maximizing the specific absorption rate (SAR) at the experimental frequency was determined to be 15–17 nm, indicating that Néel relaxation is the dominant mechanism

Temperature measurements under an alternating magnetic field (H = 150 Oe, f = 15 kHz) showed that the 17 nm particles exhibited the highest temperature increase, consistent with the relaxation analysis. The temperature rise was sufficient to induce cytotoxic effects in cancer cells. In vitro experiments using human breast cancer cells (MDA-MB-231) confirmed a significant anticancer effect. Furthermore, analysis of the cell death mechanism revealed that apoptosis was the predominant pathway. This result suggests a favorable therapeutic profile with important pharmacological implications.
1. H. Katayanagi, Y. Ichiyanagi et al., *ChemNanoMat.*, (2022) e202200014.
2. K. Ohara, Y. Ichiyanagi et al., *AIP Advances*, 13 (2023) 0252386.

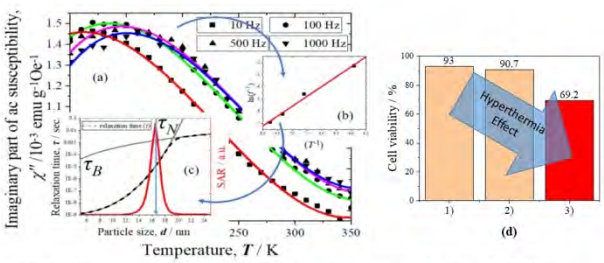


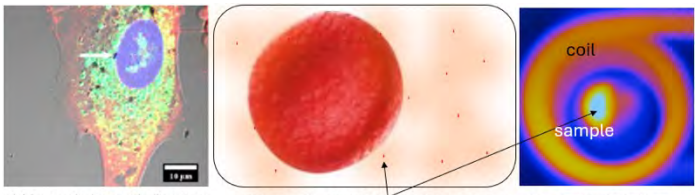
Fig. 1. (a):Temperature dependence of AC magnetic susceptibility at various frequencies for the 14 nm Ni-ferrite sample. (b): Arrhenius plot from result (a). (c): Relaxation time and SAR calculated from (b). (d): Cell viability of human breast cancer cell for 1) control, 2) field only and 3) hyperthermia.

BA-06. Magnetic nanobars from self-dispersing cellular labels up to organ nanowarming agents

B. Stadler
Electrical and Computer Engineering, University of Minnesota, Minneapolis, Minnesota, United States

Electroplating into nanoporous templates, such as track etched polycarbonate (TEPC) and anodic aluminum oxide (AAO), can yield magnetic nanoparticles (MNP) with diameters of 10nm to 200nm and lengths of 1nm to 100μm. The aspect ratios are easily controlled to enable nanodisks (eg: 1nm x 200nm), nanoparticles (eg: 10nm x 10nm), magnetic nanobars (MNB, eg: 10nm x 100nm), and magnetic nanowires (MNW, eg: 10nm x 10μm). Interactions with living organisms range in scale from single cells to whole organs, where labels can be used to either encourage or discourage cellular uptake. Importantly, the dimensions and materials (eg: Fe, Ni, Co, alloys) can be engineered to provide selective motion, sorting, heating, and barcoding signatures in magnetization and/or high frequency absorption.
Cellular attachment and uptake of MNWs can be encouraged by coatings, such as peptides to link to integrin which is over-expressed by cancer cells. This configuration presents cells with a pseudo extracellular matrix to which the cells attach and, upon division and motility, the cells self-disperse the MNWs throughout the population [1]. Subsequent sorting of cells is also possible, if the bonding is strong [2]. Nanowarming is a rapidly developing bio-application in which cryopreserved organs are warmed rapidly and uniformly to avoid cracking and crystallization, respectively [3]. In nanowarming, MNBs are: 1-DISCOURAGED from cellular uptake as they are perfused into an organ's vasculature during freezing, 2-warmed in an alternating magnetic field, 3- removed from the vasculature immediately upon thawing. MNBs promise to provide three orders of magnitude faster heating than SPIONs. Finally, barcoding can be utilized either in bulk samples, or by again linking MNBs and MNWs to cells/tissues of interest. In barcoding, controlled magnetization has been shown to enable both contrast in magnetic resonance imaging [4] and labelling with readout methods such as projection of first order reversal curves (FORC) [5]. At high frequencies, ferromagnetic resonance (FMR) provides an RFID like signature for bio-labels of cells and tissues [6].
1. Inducing cells to disperse nickel nanowires via integrin-mediated responses. Nanotechnology (2018)
2. Enrichment and quantification of epitope-specific CD4+ T lymphocytes using ferromagnetic iron-gold and nickel nanowires. *Scientific reports (2018).*

3. Nanowarming using Au-tipped Co35Fe65 ferromagnetic nanowires. Nanoscale (2019)
4. Electrodeposited Fe and Fe–Au nanowires as MRI contrast agents. Chemical communications (2016)
5. Facile decoding of quantitative signatures from magnetic nanowire arrays. Scientific reports (2020).
6.Magnetic nanowire biolabels using ferromagnetic resonance identification. ACS Applied Nano Materials (2021)



a) Magnetic barcode/heaters *inside* cancer cell

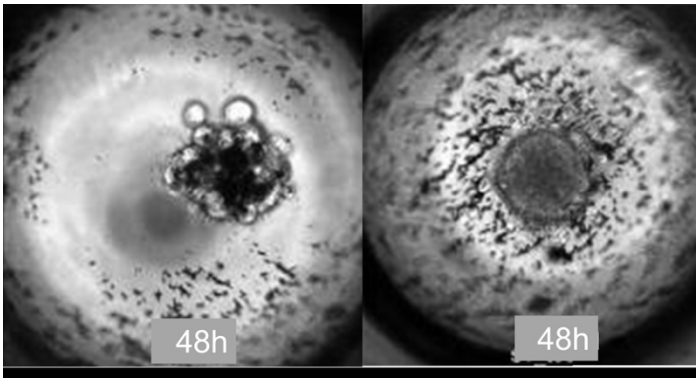
b) Magnetic NanoBars *outside* cells- heated to 400°C in 2 sec.

BA-07. Towards physiologically relevant in-vitro models for magneto-mechanical stimulation of cancer cells

A. Visona[1, 2], R. Morel[1], H. Joisten[1], C. Naud[1], A. Nicolas[2], P. Obeid[3], A. Millet[3], F. Berger[4], B. Dieny[1]
[1]SPINTEC, Univ. Grenoble Aples, CEA, CNRS, Grenoble, France, [2]LTM, Univ. Grenoble Alpes, CNRS, Grenoble, France, [3]BIOMICS, Univ. Grenoble Alpes, CEA, INSERM, Grenoble, France, [4]Braintech, Univ. Grenoble Alpes, INSERM, Grenoble, France

Magneto-mechanical stimulation of cancer cells involves dispersing anisotropic magnetic particles among cells and actuating them at low frequencies (typically 1–5 Hz) to generate mechanical forces and torques. The resulting local mechanical stress can be tuned through the magnetic field parameters (amplitude, direction, and frequency) as well as through the intrinsic properties of the particles, including their shape, volume, magnetic anisotropy, and concentration. In this study, Au-coated NiFe vortex microdiscs were employed.
This approach has been shown to efficiently induce cancer cell death in several cell lines under in vitro conditions, particularly in conventional two-dimensional (2D) cultures[1]. However, it is well established that both cellular metabolism and the ability of magnetic particles to vibrate and transmit mechanical stress strongly depend on the cellular microenvironment, especially its visco-elastic properties[2]. Consequently, the development of in vitro models that more faithfully reproduce in vivo conditions is essential.
A first step toward such biomimetic environments consisted in culturing cancer cells on soft polyacrylamide substrates with tissue-like mechanical properties. These compliant substrates are known to promote cellular states closer to those found in vivo. Experiments performed on U87 glioblastoma cells revealed that substrate stiffness significantly modulates the cytotoxicity of magnetic particles. In particular, softer environments amplify particle-induced toxicity in a cell-type-dependent manner[3]. Furthermore, we demonstrated that the mechanical properties of the surrounding matrix critically influence the cellular response to magneto-mechanical stimulation. Notably, microdisc actuation induces more pronounced effects in cells grown on soft substrates—whose stiffness better matches that of human tissues—than on rigid plastic surfaces. This behavior can be attributed to stiffness-dependent variations in cytoskeletal organization and cell rheology, as well as to enhanced microdisc motion in more compliant environments.
A second class of biomimetic models was developed using three-dimensional (3D) multicellular spheroids[4]. When cultured in ELPLASIA plates, cells spontaneously aggregate into 3D structures whose organization and architecture closely resemble those of native tissues, making them more physiologically relevant than traditional 2D systems. We investigated magneto-mechanical stimulation in organoids derived from healthy pancreatic cells (H6c7) and tumoroids derived from pancreatic cancer cells (PANC-1). Following particle spreading among the cells, cancer cells exhibited a significantly higher uptake than healthy cells, likely due to the more heterogeneous and porous structure of tumoroids[4]. Upon mechanical stimulation for 30 minutes at frequencies between 2 and 5 Hz, a marked increase in cancer cell death was observed, while healthy cells remained largely unaffected. This selective cytotoxicity can be attributed to differential particle uptake. However, it is also interesting to note that lot of cancer cell lines overexpress mechanosensitive ion channels such as PIEZO1[5]. These channels open in response to mechanical stress, leading to calcium influx, which can trigger cell death when intracellular Ca^{2+} levels become excessive. This mechanism can make magneto-mechanical stimulation relevant for many cancer types.
Overall, the use of advanced in vitro models enables systematic exploration of stimulation parameters and facilitates the optimization of magneto-mechanical strategies for future clinical applications, while reducing reliance on animal experimentation.

1. S.Leulmi et al, Nanoscale, 7, 15904 (2015)
2. A. Visona et al, Nanoscale Adv. 8, 1570–1584 (2026)
3. A.Visona et al, Nanoscale Advances, 7, 219-230 (2025)
4. B.Dieny et al, Phys.Rev.Appl.23, 010501 (2025)
5. X.Chen et al, Neuron 100, 799–815 (2018)



After 48h of incubation, differential uptake of magnetic particles by PANC1 tumoroids (left) and H6C7 healthy organoids (right)

SESSION BB: ORBITRONICS MEETS SPINTRONICS: INTERPLAY BETWEEN ORBITAL AND SPIN ANGULAR MOMENTA

Co-Chair(s): K. Lee, *Korea Advanced Institute of Science and Technology (KAIST), Daejeon, Korea (the Republic of)* and T. G. Rappoport, *INL Braga, Rio de Janeiro, Brazil*
Tuesday, November 3, 2026
02:00 PM-05:30 PM
Coral 5

BB-01. Orbitronic Route to Electric Control of Magnetism

D. Go
Department of Physics, Korea University, Seoul, Korea (the Republic of)

The discovery of spin–orbit torques a decade ago revolutionized spintronics by enabling electric control of magnetization. To enhance efficiency, mechanisms such as the spin Hall effect, Rashba spin–momentum locking, and topological surface states have been explored. However, these approaches rely on strong spin–orbit coupling, restricting usable materials to heavy elements that are scarce and often unsuitable for large-scale applications.

We recently proposed a fundamentally new route based on orbital angular momentum (OAM) and its current for electric manipulation of magnetism [1,2]. Although orbital moments are quenched in equilibrium, we showed that OAM and orbital currents can be efficiently generated in nonequilibrium by an external electric field [3,4]. Crucially, orbital current generation is an order of magnitude more efficient than spin current generation and is largely independent of spin–orbit coupling strength. This opens a promising pathway toward energy-efficient and environmentally friendly spintronic devices. In this talk, I will present the theoretical framework underlying orbital-current-induced torque, discuss material insights from first-principles calculations, and highlight recent experimental demonstrations [5,6].

[1] Go et al. Phys. Rev. Res. 2, 013177 (2020)
[2] Go et al. Phys. Rev. Research 2, 033401 (2020)
[3] Go et al. Phys. Rev. Lett. 121, 086602 (2018)
[4] Choi et al. Nature 619, 52 (2023)
[5] Hayashi et al. Nature Electronics 7, 646 (2024)
[6] Gao et al. Nature Physics 20, 1896 (2024)

BB-03. Time-resolved measurement of long-range orbital diffusion driven by ultrafast demagnetization

S. Kim, G. Choi
Department of Energy Science, Sungkyunkwan University, Suwon, Korea (the Republic of)

The utilization of orbital angular momentum has emerged as a new frontier in spintronics, yet experimental investigation of orbital dynamics remains challenging. Conventional electrical measurements are limited to steady-state properties, whereas recent terahertz (THz) emission studies are constrained by indirect detection and ballistic transport in ultrathin films. Here, we report the direct measurement of long-range, diffusive orbital transport in Cu driven by ultrafast demagnetization using time-resolved magneto-optical Kerr effect (TR-MOKE). To isolate the orbital contribution, we employed a Co/Insertion Layer/Cu architecture, comparing 5d transition metals (Pt, W) with 4f rare-earth metals (Tb, Gd). We identified that the Tb layer acts as a highly efficient spin-to-orbital converter, exhibiting orbital signal intensity significantly higher than that of 5d metals. Notably, by interpreting the Kerr ellipticity as the orbital signal, we identified a distinct temporal delay relative to the Kerr rotation (spin signal), enabling decoupling of spin and orbital dynamics. Our thickness-dependent analysis further revealed that orbital generation originates from both the Co/Tb interface and the Tb bulk, with the interfacial contribution dominating. By extending the Cu thickness to 100–200 nm, we observed distinct transport velocities for spin (v_s = 120 nm/ps) and orbital (v_o = 82 nm/ps) currents. This velocity retardation, combined with a one-dimensional diffusion model, yields an orbital diffusivity of D_o = 4030 nm^2/ps and a relaxation length of l_o = 280 nm. These results provide direct evidence of an orbital diffusive mechanism, fundamentally

distinguishing it from ballistic transport reported in prior THz studies. Our findings establish Cu as a promising medium for orbital transport and demonstrate TR-MOKE as a probe of ultrafast orbital diffusion dynamics.

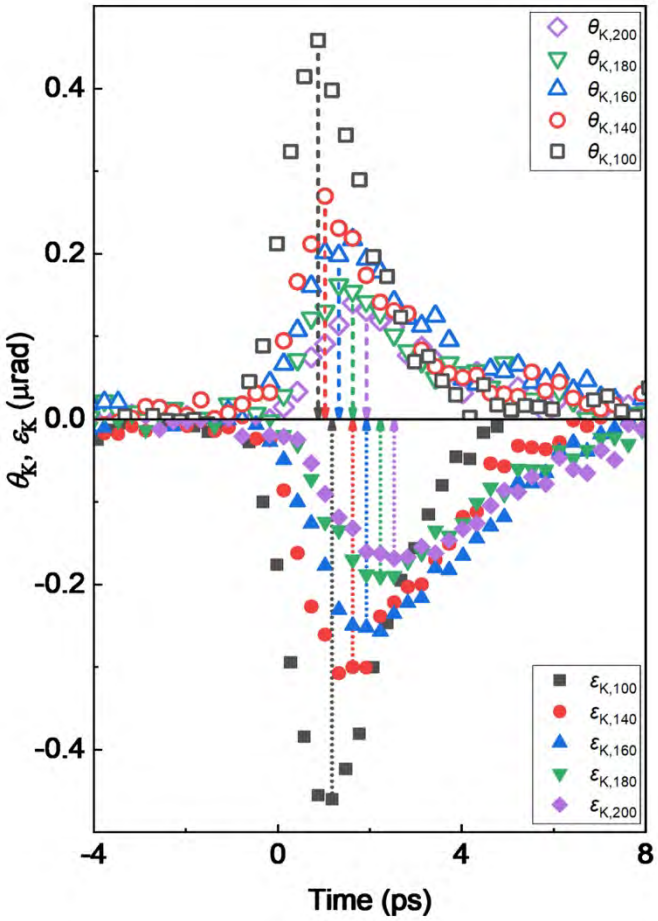


Fig. 1. Long-range orbital transport through Cu thickness (d_{Cu}) of 100 ~ 200 nm. The real (θ_K, top) and imaginary (ε_K, bottom) parts of the Kerr rotation.

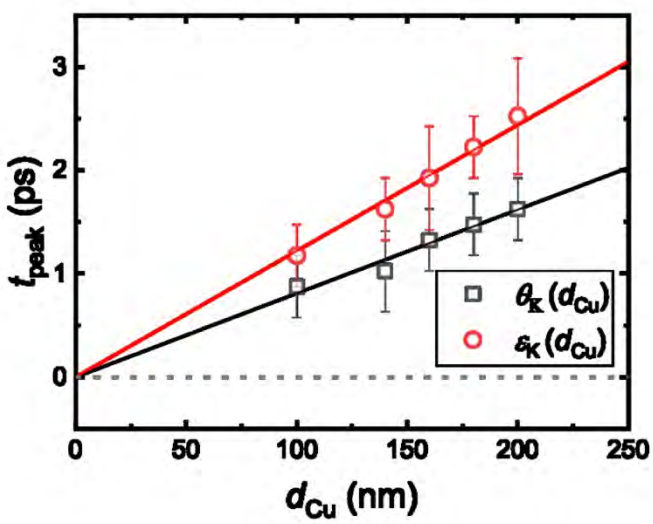


Fig. 2. The peak position (t_{peak}) of θ_K and ε_K versus d_{Cu}. From the linear fit, the spin and orbital propagation speeds are determined to be 123 nm ps^{-1} and 82 nm ps^{-1}, respectively.

BB-04. Experimental Evidence for Dominant Orbital Transport

E. Santos[1], J. L. Costa[1], J. E. Abrão[1], J. B. Mendes[2], A. Azevedo[1]
[1]Physics, Federal University of Pernambuco, Recife, Pernambuco, Brazil, [2]Department of Physics, Federal University of Viçosa, Vicosa, Minas Gerais, Brazil

The transport of orbital angular momentum is emerging as a new paradigm in magnetism, extending conventional spintronics toward orbitronics. Here, we present a systematic experimental investigation of orbital current generation, propagation, and charge conversion in magnetic heterostructures using spin pumping under ferromagnetic resonance excitation and spin Seebeck under temperature gradient excitation [1]. We demonstrate that orbital-to-charge conversion via the inverse orbital Hall effect (IOHE) and inverse orbital Rashba effect (IORE) can substantially exceed conventional spin Hall signals, even in materials with weak spin–orbit coupling. Strong orbital conversion is observed across a broad class of transition metals, including light elements and semiconducting systems, revealing that orbital transport is more universal than previously anticipated [2]. We further show that interfaces play a decisive role in orbitronic conversion, where orbital Rashba-like states at naturally oxidized metallic surfaces produce pronounced signal enhancement. In antiferromagnetic heterostructures, we observe anomalous inverse orbital Hall responses that depend on magnetic order and symmetry,

suggesting that orbital Hall conversion must be described by a higher-rank tensor formalism analogous to recent extensions of anomalous spin Hall theory [3]. These results establish magnetic heterostructures as efficient generators and detectors of orbital currents, clarify the interplay between spin and orbital angular momentum transport, and open pathways toward orbital torque devices, orbitronic memories, and low-power magnetic functionalities beyond conventional spintronics.

[1] E. Santos, et al., Probing orbital currents through inverse orbital Hall and Rashba effects, Commun Phys 9, 98 (2026)
[2] J. L. Costa, et al., Dominance of the orbital Hall effect over spin in transition metal heterostructures, Phys. Rev. B 112 (5), 054443 (2025)
[3] J. E. Abrão, et al., Anomalous spin and orbital Hall phenomena in antiferromagnetic systems, Phys. Rev. Lett. 134, 026702 (2025)

BB-05. Total angular momentum generation in semiconducting and metallic chiral crystals

J. Slawinska
Zernike Institute for Advanced Materials, University of Groningen, Groningen, Netherlands

Chiral crystals, materials that lack inversion and mirror symmetries, offer a unique platform for efficient control of electron's angular momentum using purely electrical means. Our recent studies have shown that in semiconducting tellurium, chirality gives rise to remarkably efficient charge-to-spin and -orbital conversion, accompanied by long-range spin transport. These two properties, traditionally viewed as mutually exclusive, are reconciled through the emergence of slow collective relaxation modes, or *slow relaxons*, which suppress spin dephasing despite strong spin-orbit coupling.

In this talk, I will present recent progress in understanding how crystal chirality impact spin and orbital accumulation and spin relaxation in quantum materials. Building on our work on elemental tellurium, we now explore how these mechanisms extend to metallic chiral systems such as $TaSi_2$, OsSi, $NiTa_3S_6$ and $CrNb_3S_6$ where symmetry-enforced spin texture is persistent over large regions of the Brillouin zone. Our results highlight chirality as a powerful design principle for efficient total angular momentum generation, robust spin transport, and ultimately, spintronic devices.

Acknowledgment
J.S. acknowledges the Rosalind Franklin Fellowship from the University of Groningen, the Dutch Research Council (NWO) - grants NWA.1418.22.014 and OCENW.M.22.063, and the research program 'Materials for the Quantum Age' (QuMat, registration number 024.005.006) for financial support. Part of the research was funded by the European Research Council - ERC Consolidator Grant FERRERO. The calculations were carried out on the Dutch national e-infrastructure with the support of SURF Cooperative and on the Habrok high-performance computing cluster of the University of Groningen.

1. B. Kilic, S. Alvarruiz, E. Barts, B. van Dijk, P. Barone, J. Slawinska, *Universal symmetry-protected persistent spin textures in nonmagnetic solids*, Nature Communications 16, 7999 (2025)
2. E. Barts, K. Tenzin, J. Slawinska, *Efficient spin accumulation carried by slow relaxons in chiral tellurium*, Nature Communications 16, 4056 (2025)
3. K. Tenzin, B. Kilic, R. Sattigeri, Z. He, C. Chen Ye, M. Costa, M. Buongiorno Nardelli, C. Autieri, J. Slawinska, *Persistent spin textures, altermagnetism, and charge-to-spin conversion in metallic chiral crystals* TM_3X_6, npj Spintronics 3, 46
4. J. Slawinska, *Spin selectivity in elemental tellurium and other chiral materials,* Applied Physics Letters 123, 240504 (2023)
5. K. Tenzin, A. Roy, F.T. Cerasoli, A. Jayaraj, K. Tenzin, M. Buongiorno Nardelli, J. Slawinska, *Collinear Rashba-Edelstein effect in nonmagnetic chiral materials*, Physical Review B 108, 245203 (2023)
6. A. Roy, F.T. Cerasoli, A. Jayaraj, K. Tenzin, M. Buongiorno Nardelli, J. Slawinska, *Long-range current-induced spin accumulation in chiral crystals,* npj Computational Materials 8, 243 (2022)

BB-06. Crystal symmetry dependent Orbital Rashba Edelstein effect in epitaxial CuO thin film

R. Xiao[1], T. Zhao[1], I. Baek[2], H. Lee[2], Z. Zheng[1], S. Shi[1], Z. Xie[3], Q. Zhang[1], L. Jia[1], P. Yang[4], X. Yu[4], D. Song[3], H. Lee[2], J. Chen[1]
[1]Department of Materials Science and Engineering Material Science and Engineering, National University of Singapore, Singapore, Singapore, [2]Department of Physics, Pohang University of Science and Technology, Pohang, Korea (the Republic of), [3]Institutes of Physical Science and Information Technology, Anhui University, Hefei, China, [4]Singapore Synchrotron Light Source, Singapore, Singapore

Orbital angular momentum (OAM) [1,2] generated by orbital Hall effect (OHE)[3] or orbital Rashba-Edelstein effect (OREE)[4] has recently been demonstrated as a promising approach to manipulate magnetic order in spintronic devices[5,6].Although the generation of OAM has mainly

been attributed to the electron hopping behavior[7,8], which in principle should be strongly related to the solid's crystal property, the current investigations usually treated the generation of OAM as isotropic. Clear evidence supporting the impact of the crystal symmetry on OAM remains absent. In this work, we reported a crystal-symmetry-dependent OREE in a distinct epitaxially grown CuO thin film with four-fold crystal symmetry. A crystal-symmetry-dependent sign change of spin torque efficiency is observed in the CuO/ferromagnetic heterostructures, verified by second harmonic Hall measurement and current-induced perpendicular magnetization switching. The experimental results, together with the first-principles calculation, indicate the existence of a strong four-fold anisotropy of OREE in crystalline CuO, which is a direct manifestation of the crystal symmetry's impact on OAM. Our findings highlight the necessity of incorporating crystal symmetry into orbitronic research and facilitating the application of OAM in advanced spintronic devices.

1. Go D, Jo D, Kim C, Lee H-W. *Physical Review Letters* 121, 086602 (2018).
2. Jo D, Go D, Lee H-W. *Physical Review B* 98, 214405 (2018).
3. Choi Y-G, *et al. Nature* 619, 52-56 (2023).
4. Ding S, *et al. Physical Review Letters* 125, 177201 (2020).
5. Zheng Z, *et al. Nature Communications* 15, 745 (2024).
6. Gupta R, *et al. Nature Communications* 16, 130 (2025).
7. Oh S, Choi HJ. *Scientific Reports* 7, 2024 (2017).
8. Lyalin I, Alikhah S, Berritta M, Oppeneer PM, Kawakami RK. *Physical Review Letters* 131, 156702 (2023).

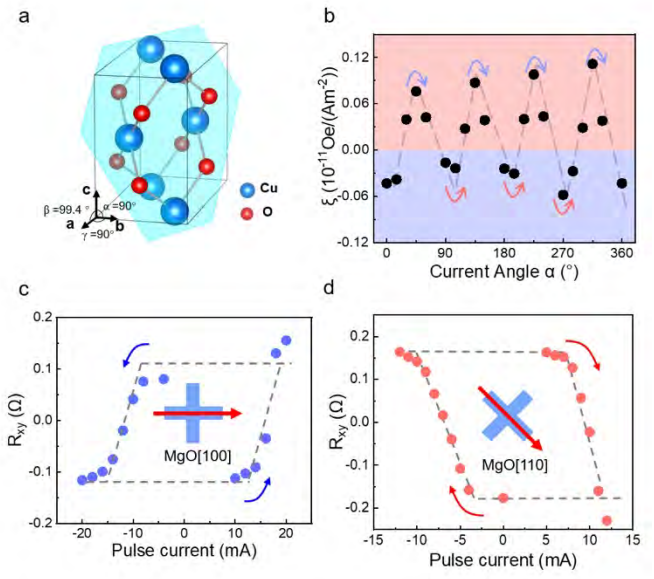


Figure1 a, Schematic of a monoclinic CuO structure. The cyan plane indicates the (111) plane of CuO. b, Damping-like torque efficiency ξ as a function of current angle α. The grey dashed line is for guidance. c and d, Current-induced switching curves in two devices where α = 0° b and 45° c, respectively.

BB-07. All orbitronics concepts with orbital magnets

A. Du[1], C. Schmitt[1], S. Krishnia[1], M. Zeer[2], E. Galíndez-Ruales[1], M. Loyal[1], J. Köhler[1], L. Micus[1], T. Kikkawa[3], H. Arisawa[3], T. Denneulin[4], A. Kovács[4], D. Tran[1], F. Kronast[5], D. Go[1, 2], L. Pourovskii[6], R. E. Dunin-Borkowski[4], T. Kuschel[1], M. Leaic[1], J. Sinova[1], E. Saitoh[3], G. Jakob[1], O. Gomonay[1], Y. Mokrousov[1, 2], M. Kläui[1, 7]

[1]Institute of Physics, Johannes Gutenberg University Mainz, Mainz, Germany, [2]Peter Grünberg Institut and Institute for Advanced Simulation, Forschungszentrum Jülich and JARA, Jülich, Germany, [3]Department of Applied Physics, The University of Tokyo, Tokyo, Japan, [4]Ernst Ruska-Centre for Microscopy and Spectroscopy with Electrons, Forschungszentrum Jülich, Jülich, Germany, [5]Helmholtz-Zentrum Berlin für Materialien und Energie, Berlin, Germany, [6]CPHT, CNRS, École Polytechnique, Institut Polytechnique de Paris, Palaiseau, France, [7]Center for Quantum Spintronics and Department of Physics, NTNU, Trondheim, Norway

Generation and transport of large orbital angular momentum (OAM) currents in solids have recently emerged as a key research area in the field of orbitronics (1-2). In contrast to spin currents, whose generation depends on weak spin-orbit coupling mechanisms, OAM current can be directly generated from charge current because the crystal momentum of charge carriers (i.e., electrons) couples directly to their orbital angular momentum. This leads to a more robust and orders-of-magnitude larger current-induced OAM generation, even in light, abundant, inexpensive, and environmentally friendly materials (Cu, Al, Cr and Ti) (3-4). These advantages position new emerging field of orbitronics as a promising platform for future energy-efficient information processing, storage, and neuromorphic technologies (5).

A major challenge has been to exploit these giant orbital currents in magnetic systems, where static magnetization is dominated by spin. We show that this limitation can be overcome by employing magnetic materials in which OAM contributes significantly to the static magnetization. Using these orbital magnets, we demonstrate two orders of enhancement of orbital Hall magnetoresistance (in CoO/Cu*), compared to the spin counterpart (CoO/Pt) (Fig 1).

This enhancement originates from the interaction of the dynamic OAM generated in light metals with the static orbital moments of the orbital magnet. Our results establish a pathway to harness giant OAM currents for device functionalities that cannot be achieved with conventional spin-dominated magnets [6].

(1) D. Go et al., Phys. Rev. Lett., 121, 086602 (2018).
(2) S. Ding et al., Phys. Rev. Lett., 125, 177201 (2020).
(3) D. Go et al., EPL, 135, 37001 (2021).
(4) L. Salemi et al., Phys. Rev. Mater., 6, 095001 (2022).
(5) S. Fukami et al., Nat. Phys. 2025.
(6) C. Schmitt et al. arXiv 2603.06425 (2026) (in press Science, 2026).

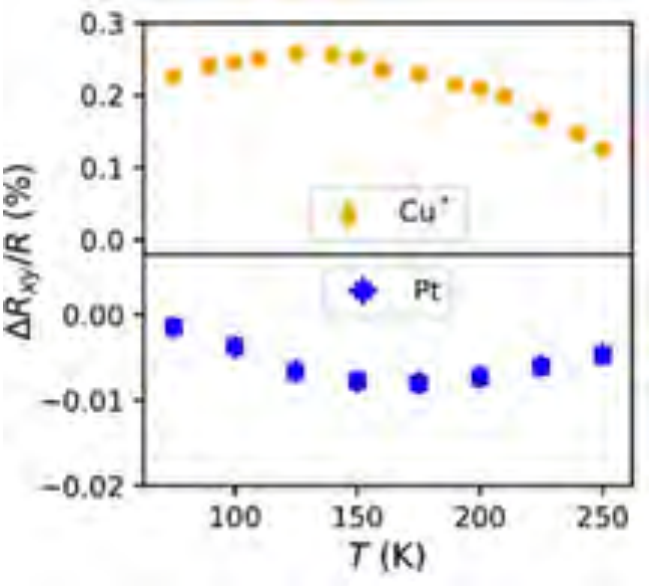
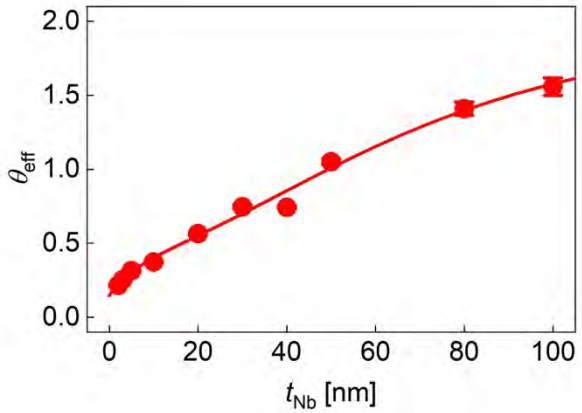


Figure 1 Orbital Hall magnetoresistance as a function of temperature in orbital antiferromagnet CoO interfaced with Cu* and Pt. The top panel presents the results for orbital current from Cu* (in yellow), while the bottom panel shows the results for spin current from Pt (in blue).

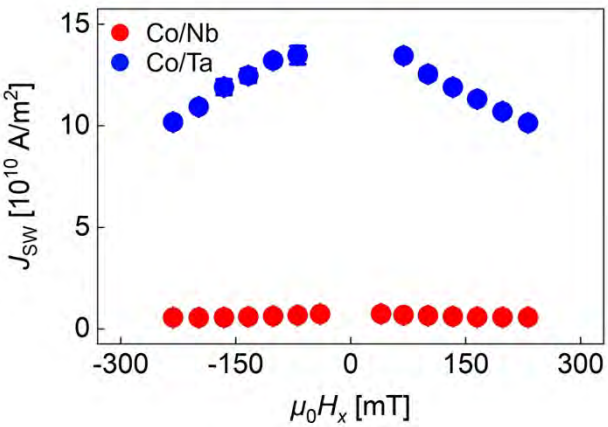
BB-08.* Giant orbital torque without orbital-to-spin conversion layer

M. Kim*[1, 2], S. Choe[2], D. Kim[1]
[1]Korea Institute of Science and Technology (KIST), Seoul, Korea (the Republic of), [2]Seoul National University, Seoul, Korea (the Republic of)

The recently-discovered orbital Hall effect holds great promise owing to its inherently high orbital conductivity, which far surpasses that of spin-based phenomena. However, this advantage is limited by significant inefficiencies associated with the conversion of orbital currents into spin currents during the generation of orbital torque. This issue poses a fundamental challenge to fully exploiting orbital torque for practical applications.
Here, we experimentally demonstrate the direct generation of orbital Hall torque without orbital-to-spin current conversion layer. By achieving an exceptionally large orbital Hall angle of 140% for Nb (Fig. 1), we demonstrate current-induced magnetization switching at significantly lower current densities compared to conventional spin Hall-driven devices (Fig. 2). These results represent a significant advance in the fundamental understanding of orbital torque and offer a promising route toward highly efficient, low-power magnetic switching.



The effective Hall angle ϑ_{eff} as a function of Nb thickness t_{Nb} in Co/Nb(t_{Nb}) samples.



The current-induced switching current density J_{SW} as a function of in-plane magnetic field $\mu_0 H_x$ of Co/Nb and Co/Ta samples.

SESSION BC: EMERGING MAGNETIC PHENOMENA IN LOW-DIMENSIONAL SYSTEMS

Chair(s): S. Itani, *Physics and Astronomy, University of New Hampshire, Durham, New Hampshire, United States*
Tuesday, November 3, 2026
02:00 PM-05:30 PM
Coral 1

BC-01. The Critical Role of Interface Quality in van der Waals Heterostructures for Exchange Bias

A. Puthirath Balan[1, 2], A. Kumar[2], S. Hameed[2], P. Reiser[3], T. Scholz[4], T. Denneulin[5], J. Vas[5], Z. Lin[6], S. Fu[7], A. Shahee[2], M. Tschudin[3], C. Pellet-Mary[3], D. Dutta[3], C. Schrader[3], J. Geuchies[2], K. Leutner[2], X. Wang[2], L. Gao[7], A. Kovács[5], H. Wang[7], G. Jakob[2], A. Bonanni[8], J. Yang[6], O. Gomonay[2], U. Nowak[9], J. Sinova[2], B. Lotsch[4], R. E. Dunin-Borkowski[5], P. Maletinsky[3], M. Kläui[2, 10]
[1]Rice University, Houston, Texas, United States, [2]Johannes Gutenberg University, Mainz, Germany, [3]University of Basel, Basel, Switzerland, [4]Max Planck Institute for Solid State Research, Stuttgart, Germany, [5]Forschungszentrum Jülich, Jülich, Germany, [6]Peking University, Beijing, China, [7]Max Planck Institute for Polymer Research, Mainz, Germany, [8]Johannes Kepler University, Linz, Austria, [9]University of Konstanz, Konstanz, Germany, [10]Norwegian University of Science and Technology NTNU, Trondheim, Norway

Exchange bias (EB) [1]—the unidirectional magnetic anisotropy arising from interfacial coupling between ferromagnetic (FM) and antiferromagnetic (AFM) layers—has long been central to spintronic technologies. The emergence of two-dimensional (2D) van der Waals (vdW) magnets has revived this concept at the atomic scale, where stacked heterostructures provide atomically sharp, strain-free interfaces and tunable magnetic interactions. These features have led to the assumption that vdW interfaces approach the ideal limit of magnetic coupling.
However, our recent work demonstrates that vdW interfaces can be significantly more complex, particularly in air-sensitive magnets. Thermal cycling [2] and ambient exposure can induce interdiffusion, amorphization, and oxidation [3], thereby modifying interfacial magnetic coupling. While typically considered detrimental, these "non-idealities," when understood and controlled, can be exploited to tune exchange bias and related spin phenomena.
Furthermore, we investigate a vdW heterostructure in which the interfacial magnetic moments are orthogonally oriented. Upon exchange coupling, this configuration leads to asymmetric switching behavior in the ferromagnet, resulting in exchange bias. This unconventional mechanism—arising from antiferromagnetic proximity-induced domain nucleation within the ferromagnet—differs from the conventional picture of pinned uncompensated spins and is unique to vdW systems.
Overall, our results highlight the critical role of interfacial quality and structure in determining the strength and nature of exchange bias in vdW heterostructures. This presentation will discuss anomalous exchange bias in orthogonally oriented pristine interfaces [4], and demonstrate how deliberate interface and defect engineering can serve as effective design strategies for vdW-based spintronic devices, in light of recent advances in exchange bias in vdW heterostructures [5].
[1] Meiklejohn, W. H., & Bean, C. P., *Physical Review* 105, 904 (1957).
[2] Puthirath Balan, A. *et al*., *Advanced Materials* 36, 2403685 (2024).
[3] Puthirath Balan, A. *et al., ACS Nano* 18, 8383–8391 (2024).
[4] Kumar, Aditya *et al*., *Small* 21, e06284 (2025).
[5] Kumar, Aditya *et al*., *Newton*, 100469 (2026).

BC-02. Exploring the Magnetic Quantum Phases in $MnSb_2Te_4$ by First-Principles Calculations

M. Tardieux[1], A. Isaeva[1, 2, 3], I. Aguilera[1]
[1]Institute of Physics, University of Amsterdam, Amsterdam, Netherlands, [2]Faculty of Physics, Technical University of Dortmund, Dortmund, Germany, [3]Research Center Future Energy Materials and Systems, Dortmund, Germany

Magnetic topological insulators (MTIs) are a class of quantum materials in which non-trivial band topology and magnetic order give rise to exotic quantum states [1]. By breaking time-reversal symmetry, MTIs can host dissipationless chiral edge transport in the absence of an external magnetic field (presently up to 7 K [2] in $MnBi_2Te_4$), coined the quantum anomalous Hall effect (QAHE). This makes them highly attractive for spintronics and quantum-information technologies [3].
In this work, we use first-principles methods to identify promising routes toward the QAHE in $MnSb_2Te_4$ (MST). The three fundamental criteria for the observation of the QAHE are: (1) a topologically non-trivial electronic structure, (2) a ferromagnetic order, and (3) a global electronic band gap. While theory predicts stoichiometric MST in its ferromagnetic state to be a Weyl semimetal and its antiferromagnetic counterpart to be topologically trivial,

experiments have shown that MST with Mn–Sb site intermixing is a ferrimagnet [4,5]. The central challenge is therefore to optimize this material toward higher magnetic ordering temperatures and a gapped topological electronic structure.

As a first step, we construct supercells that reflect the Mn-Sb intermixing observed experimentally and use DFT+*U* to study how site mixing and Mn excess modify the magnetic ground state and band topology of the material [6]. Our calculations predict that Mn excess stabilizes three antiferromagnetically coupled Mn sublattices, consistent with experiments that show a T_c increase to about 70 K [6]. We further investigate how uniaxial strain and hydrostatic pressure tune topological phases in ferromagnetic MST [7]. By using Monte-Carlo simulations, we then estimate magnetic exchange constants and Curie temperatures as a function of external parameters, getting a deeper understanding of how lattice changes impact the magnetic order. By varying composition, strain, and pressure, we map the phase diagram and identify regimes in which a full band gap opens while the non-trivial topology is retained. Overall, our results show that lattice-driven band inversion provides a powerful route for engineering topological phases in magnetic van der Waals materials.

[1] C.-Z. Chang, J. Zhang and Q.-K. Xue, Science, Vol. 340, p. 167–170 (2013)
[2] Y. Deng, Y. Yu and Y. Zhang, Science, Vol. 367, p. 895–900 (2020)
[3] Y. Tokura, K. Yasuda and A. Tsukazaki, Nat. Rev. Phys., Vol. 1, p. 126–143 (2019)
[4] Y. Liu, L.-L. Wang and J. Yan, Phys. Rev. X, Vol. 11, p. 021033 (2021)
[5] T. Murakami, Y. Nambu and H. Kageyama, Phys. Rev. B 100, p. 195103 (2019)
[6] E. Kochetkova, M. Tardieux and A. Isaeva, Chem. Mater., Vol. 37, p. 1446–1456 (2025)
[7] M. Tardieux, M. F. Tanzim and I. Aguilera, accepted in Mater. Today Quantum (2026)

BC-03. Magnetic Properties in Non-Centrosymmetric Kondo Lattice Heavy Fermion CeFeGe3

T. Park, S. Yousuf, H. Lee, J. Sung, T. Lee
Physics, Sungkyunkwan University, Suwon, Gyeonggi-do, Korea (the Republic of)

Kondo lattice compounds with f-electron local moment provide model platforms to explore the competition between two fundamental energy scales: Kondo and Ruderman-Kittel-Kasuya-Yosida (RKKY) interaction [1][2]. Despite substantial progress, a comprehensive understanding of these systems remains challenging owing to the intricate interplay between these interactions [3]. CeFeGe3 with stable Ce^{3+} configuration is characterized by a large Sommerfeld coefficient (γ ≈150mJ/mol-K^2) and a high Kondo temperature (T_K ≈ 100K) [4], making it an ideal platform for probing magnetic and Kondo lattice behavior. Here, we report the successful growth of high-quality single crystals of CeFeGe3, a non-centrosymmetric heavy-fermion compound, and reveal an unexpected sensitivity of its ground state to synthesis conditions. While previous studies on polycrystalline samples have suggested a single nonmagnetic ground state, our single-crystal investigations demonstrate that CeFeGe3 can host either an antiferromagnetic (AFM) or a paramagnetic heavy-fermion ground state without any apparent change in its crystal structure. Comprehensive measurements of magnetic susceptibility, electrical resistivity, and heat capacity establish a clear AFM transition at approximately 5.5 K in one type of crystal, while others remain in a paramagnetic heavy-fermion state. This coexistence of distinct ground states within the same structural phase highlights the delicate balance of competing interactions in CeFeGe3. We propose that the system is situated near the phase boundary in the Doniach phase diagram, where subtle variations in hybridization strength and Fe-site occupancy can tip the balance between magnetic order and Kondo screening.

[1] G.R. Stewart, *et al*., Heavy-fermion systems, *Reviews of Modern Physics, 56 (1984)*.
[2] P. Coleman, Heavy Fermions: Electrons at the Edge of Magnetism, Handbook of Magnetism and Advanced Magnetic Materials, (2007)
[3] S. Nakatsuji, *et al*., Intersite Coupling Effects in a Kondo Lattice, *Physical Review Letters, 89 (2002)*.
[4] H. Yamamoto, *et al*., A concentrated Kondo compound with a stable valency and high Kondo temperature, *Physical Review B, 52 (1995)*.

BC-04. Quantum simulation of geometrically constrained spin reorientation in a spin–orbit-entangled iridate

S. Lim, K. Jeong, J. Seo, J. Hong, J. Byeon, H. Ryu, K. Moon, N. Lee, Y. Choi
Department of Physics, Yonsei University, Seoul, Korea (the Republic of)

Quantum simulation of real magnetic materials requires capturing not only exchange interactions but also the interplay between lattice symmetry, spin–orbit coupling, and anisotropic interactions. Here, we demonstrate a hardware-based quantum simulation of field-driven magnetism in the spin–orbit-entangled iridate Sr_2IrO_4. The J_{eff}=1/2 isospin manifold enables a direct mapping onto qubits, while the Dzyaloshinskii-Moriya (DM) interaction introduces symmetry-governed geometric constrains on spin configurations. Using an effective J_{eff}=1/2 Hamiltonian within a variational quantum eigensolver on both a noiseless simulator and a 127-qubit superconducting processor (*ibm_yonsei*), we observe domain-selective magnetic reorientation arising from weak in-plane anisotropy, reproducing anisotropic magnetization. In the ultra-high-field regime, a distinct anisotropic response emerges: fields parallel to the DM vector yield full alignment, whereas transverse fields remain geometrically constrained and do not reach complete saturation. These results demonstrate that DM interactions govern magnetism through symmetry-imposed geometric constraints that unify low-field domain selection and high-field spin response. More broadly, they establish quantum simulation as a viable framework for probing symmetry-driven magnetic phenomena beyond experimentally accessible regimes and highlight the capability of current quantum hardware to address complex correlated magnetic systems.

Peruzzo, A. et al., Nat. Commun., Vol. 5, p.4213 (2014)
Kim, B. et al., Phys. Rev. Lett., Vol. 101, p.076402 (2008)
Wu, L. et al., Phys. Rev. B, Vol. 108, p.L020403 (2023)
Liu, H. and Khaliullin, G., Phys. Rev. Lett., Vol. 122, p.057203 (2019)

BC-05. Theoretical Studies and Ground State Configuration of an Artificial Spin Ice on the Ammann-Beenker Tiling

E. Weightman, S. Coates, L. O'Brien
University of Liverpool, Liverpool, United Kingdom

Artificial spin ices (ASIs) consist of nanomagnets decorated on geometric lattices. They possess a high degree of frustration and, as such, often display exotic and emergent behaviour, as well as highly degenerate and complex ground states [1]. So far, studies of ASI have focused primarily on periodic geometries, such as square or Kagome lattices. There have been limited studies of ASI on aperiodic lattices, which are defined as having no unit cell or translational symmetry but still possess long range order, with work focusing mainly on the Penrose P3 tiling [2,3]. We expand the study of aperiodic ASIs using a lattice of the aperiodic Ammann-Beenker tiling and propose a ground state for this ASI system.

We employ micromagnetic simulations to identify the energy states of each of the 6 vertex types in the tiling, and Monte Carlo simulations to perform a simulated cool of the system. The energy of spin interactions is calculated with a coupling between all spins and an enhanced coupling for nearest neighbours. Analysis of this energy and charge landscape is then used to inform our proposed ground state configuration.

Using our proposed solution, we highlight the competition of magnetic domains in the simulated spin states, as well as the spin behaviour along domain walls and the high degeneracy of the ground state system.

[1] Skjærvø SH et al. Nature Reviews Physics. 2020 Jan 15;2(1):13-28.
[2] Shi D et al. Nature Physics. 2018 Mar;14(3):309-14.
[3] Kwon HY et al . Scientific Reports. 2022 Sep 2;12(1):15026.

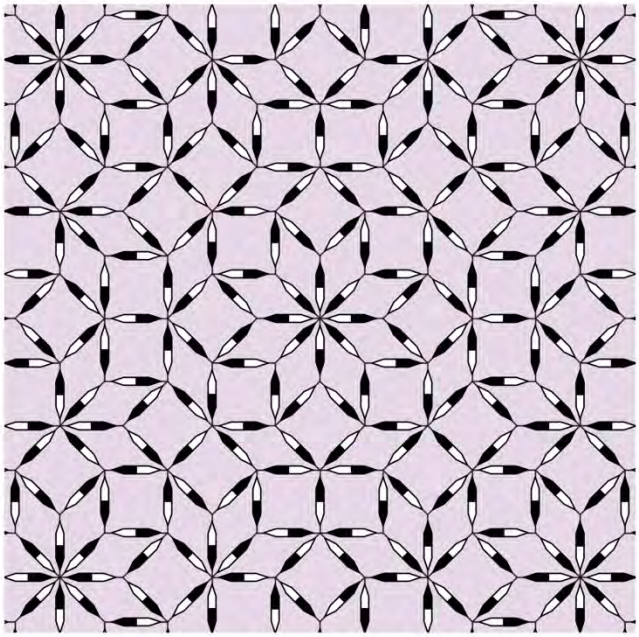


Fig 1: Ammann-Beenker tiling decorated with macrospins on the midpoints of tile edges, as indicated by ellipsoids with black and white poles.

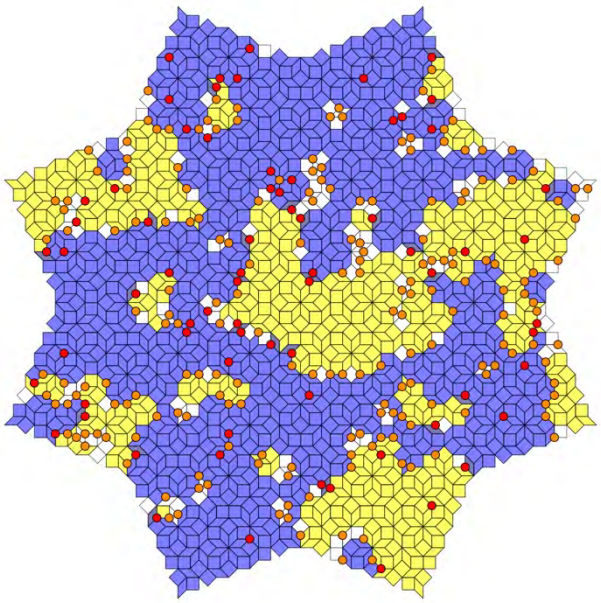


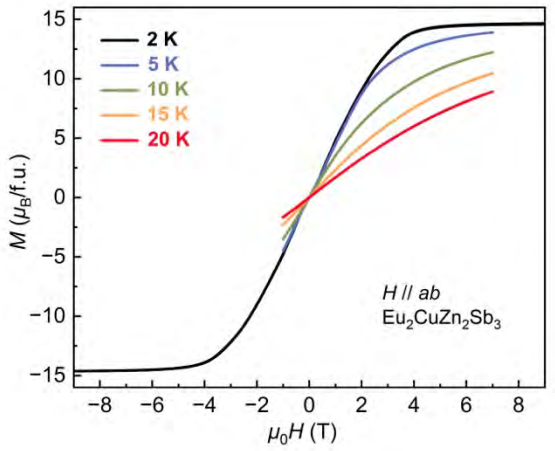
Fig 2: A final simulated spin state. Tiles are coloured by the ground-state domain they match, shown only where they form clusters of three or more. Vertex excitations are indicated in orange and red for first- and second-level excitations respectively.

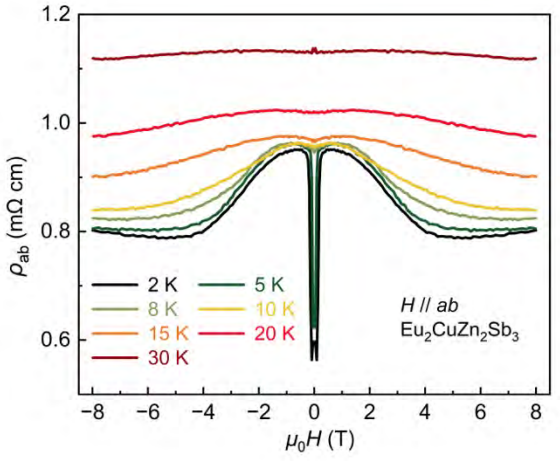
BC-06. Structural design and magneto-transport properties of intergrowth compound $Eu_2CuZn_2Sb_3$

Y. Duan, X. Chen, Z. Wang
Department of Physics, Southeast University, Nanjing, Jiangsu, China

The magnetic topological materials have the potential to serve as next-generation information carriers, enabling high-density and low-power memory. A promising strategy for designing such materials is to integrate structural units with strongly correlated magnetic orders and topological properties. By stacking units derived from helical magnet EuCuSb (hexagonal) and the magnetic topological material $EuZn_2Sb_2$ (trigonal), we synthesized a new layered quaternary compound $Eu_2CuZn_2Sb_3$. $Eu_2CuZn_2Sb_3$ shows dominant in-plane magnetic correlations at 10 K, mainly originating from the $EuZn_2Sb_2$ structural units, while long-range antiferromagnetic order develops at 5 K. The compound exhibits first-order-like metamagnetic response under magnetic fields, associated with the EuCuSb structural units. The electronic transport reveals typical metallic behavior, with a pronounced peak anomaly in resistivity near 10 K that is strongly suppressed by magnetic fields. Furthermore, Hall effect measurements confirm the dominance of the ordinary Hall effect contribution. This work reports on the novel layered antimonide $Eu_2CuZn_2Sb_3$, providing initial insights into its magnetism and magneto-transport properties. These results demonstrate that the modular block-layer design offers a versatile and effective route for exploring magnetic topological materials.

1.XY, Chen, ZW, Wang and WZ, Yang, PHYSICAL REVIEW B., Vol. 111, p.184441 (2025)
2.XY, Chen, ZW, Wang and WZ, Yang, PHYSICAL REVIEW B., Vol. 112, p.134419 (2025)
3.J, Wang, YB, Wang and ZY, Wang, PHYSICAL REVIEW B., Vol. 111, p.054428 (2025)





BC-07. The first-principles investigations of electronic structures and magnetism on K intercalated and substituted for H in *p*-terphenyl

R. Chen[1], Z. Guo-Hua[2], H. Lin[1]
[1]Institute for Advanced Studies in Physics and School of Physics, Zhejiang University, Hangzhou, Zhejiang, China, [2]Shenzhen Institutes of Advanced Technology, Chinese Academy of Sciences, Shenzhen, Guangdong, China

Ambient-pressure and high-temperature superconductivity has recently attracted great attention, especially for high-temperature superconductors dominated by light-weight elements. Aromatic hydrocarbons are a type of ambient-pressure and high-temperature superconductors. For example, Chen et al. first reported that potassium (K) doped *p*-terphenyl ($C_{18}H_{14}$) exhibited a superconducting signal of 123 Kelvin [1]. Subsequently, some experimental observations also implied the possibility of synthesis and superconductivity [2-5]. Most recently, Chomas et al. synthesized K-doped *p*-terphenyl using another method and observed superconductivity at 120 Kelvin [6]. However, possible magnetism in these compounds is still unknown. In addition, what would happen to the electronic structures and its magnetic properties if one replaces H atoms by K atoms on organic molecules? These studies are helpful for understanding the superconductivity of this system, but they are still lacking.

In this work, we have systematically studied the electronic structures and magnetic changes when inserting different amounts of K atoms into *p*-terphenyl and replacing H atoms with different amounts of K atoms, based on the first principles calculations. For the six K concentration intercalation cases considered, only $K_1C_{18}H_{14}$ and $K_{1.5}C_{18}H_{14}$ exhibit antiferromagnetic (AFM) metal properties, while the rest cases exhibit non-magnetic (NM) metal states. We systematically observed the changes in electronic structures caused by K intercalation. For K substituted for H atoms, the results show that no the transition from insulator to metal occurs. Although there is charge transfer, the transferred charge is localized on the adjacent benzene ring, unlike the formation of charge channels on organic molecules during doping. This suggests that superconductivity does not arise from K atoms replacing H atoms, but may be due to K intercalation.*Corresponding authors: gh.zhong@siat.ac.cn (G.-H. Zhong); hqlin@zju.edu.cn (H.-Q. Lin)

[1] R.-S. Wang, et al., Superconductivity above 120 kelvin in a chain link Molecule, arXiv:1703.06641.
[2] P. Neha, et al., Physica C 554, 1, (2018).
[3] H. Li, et al., Phys. Rev. B 100, 064511 (2019).
[4] M. Carrera et al., J. Phys. Chem. C 123, 5264 (2019).
[5] Q. He, et al., Phys. Rev. Res. 8, 013238 (2026).
[6] A. J. Chomas, et al., Synthesis and Characterization of K_x:*p*-Terphenyl Materials for Superconductivity (unpublished).

BC-08. Exotic magnetic phases of Tsai-type approximant crystals: From 1/1 to 5/3 approximant structures

T. Sugimoto[1], T. Yamada[2]
[1]Electrical, Electronic, and Information Engineering, Kansai University, Suita, Osaka, Japan, [2]Institute of Materials Structure Science, High Energy Accelerator Research Organization (KEK), Naka-gun, Ibaraki, Japan

Tsai-type approximant crystals (TACs) bridge the gap between quasicrystalline and periodic systems, sharing the local atomic structure of quasicrystals while maintaining translational symmetry. Experiments have revealed various low-temperature magnetic phases in TACs, including spin-glass, ferromagnetic, and antiferromagnetic states [1]. Magnetism originates from localized rare-earth moments at icosahedral vertices within nested polyhedral clusters (Fig. 1(a)). These moments interact via the Ruderman-Kittel-Kasuya-Yosida (RKKY) mechanism and single-ion anisotropy specific to rare-earth ion. We previously developed a phenomenological spin model to evaluate these roles, finding that single-ion anisotropy dominates for several rare-earth elements [2].

Gd-based TACs, however, exhibit negligible anisotropy as the trivalent Gd ion lacks orbital angular momentum. Despite this, compositional tuning experimentally reveals various magnetic orders [1]. We investigated this using an RKKY-only model, assuming compositional changes shift the Fermi wavevector k_F via electronic density variations. Using simulated annealing, we reproduced multiple magnetic phases (Fig. 1(b)) consistent with observations [3]. Comparison with experimental Weiss temperatures θ_W further validated our approach. Analysis of icosahedral clusters in the 1/1 approximant showed that local magnetic configurations (Fig. 1(c)) are crucial for understanding global magnetic order [4].

We now extend this investigation to 2/1, 3/2, and 5/3 approximants, which structurally resemble infinite quasicrystals more closely. We present ground-state phase diagrams for these higher-order approximants and discuss their magnetic behavior relative to the 1/1 approximant.

[1] A. Ishikawa, et al., Phys. Rev. B 93, 024416 (2016); ibid. 98, 220403(R) (2018); S. Yoshida, et al., ibid. 100, 180409(R) (2019); K. Inagaki, et al., ibid. 101, 180405(R) (2020).

[2] T. Sugimoto, T. Tohyama, T. Hiroto, R. Tamura, J. Phys. Soc. Jpn. 85, 053701 (2016).
[3] H. Miyazaki, T. Sugimoto, K. Morita, T. Tohyama, Phys. Rev. Mater. 4, 024417 (2020); F. Labib, T. Sugimoto, H. Takakura, A. Ishikawa, R. Tamura, Phys. Rev. B 111, 174409 (2025).
[5] S. Suzuki, R. Tamura, T. Sugimoto, Mater. Trans. 64, 367 (2021); T. Sugimoto, S. Suzuki, R. Tamura, T. Tohyama, J. Phys. Soc. Jpn. 93, 045001 (2024).

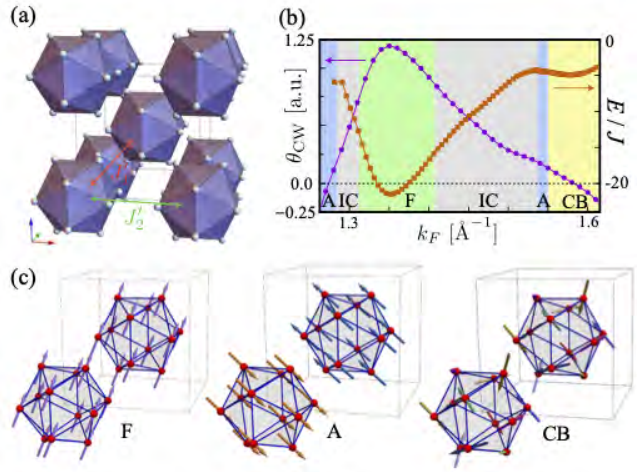


Fig. 1: (a) Crystal structure of rare-earth ions on icosahedral vertices in the 1/1 TAC. (b) Magnetic phase diagram and Wiess temperature with respect to Fermi wavenumber. (c) Magnetic configuration of each order.

BC-09. Quantum computation of ultra-weak magnetic anisotropy in a frustrated spin-1/2 antiferromagnet

K. Jeong, J. Seo, S. Lim, J. Hong, H. Ryu, J. Byeon, K. Moon, N. Lee, Y. Choi
Department of Physics, Yonsei University, Seoul, Korea (the Republic of)

The intrinsic equivalence between electron spin and qubit offers a natural foundation for quantum simulations of magnetic materials. However, incorporating magnetocrystalline anisotropy (MCA), a key ingredient governing real magnetic behavior, remains a major challenge. Here, we develop a quantum simulation framework for MCA in $CuSb_2O_6$, a spin-1/2 antiferromagnet with frustrated, anisotropic exchange interactions in a nearly square lattice. The Cu^{2+} spin network is modeled as a four-qubit square lattice, with four paired ancilla qubits introduced to encode angle-dependent MCA, thereby overcoming the limitation that squared Pauli operators yield only the identity. Using the variational quantum eigensolver, we determine an exceptionally weak easy-axis MCA constant, only 0.00022% of the nearest-neighbor exchange interaction, yet sufficient to drive a 90° spin-flop reorientation accompanied by a pronounced angular torque response. By integrating quantum amplitude estimation, statistical uncertainty is significantly reduced compared with conventional shot-based VQE, enabling reliable resolution of ultra-weak energy scales under finite sampling. Extending the same framework to ultra-high fields further reveals a half-saturated magnetic phase stabilized by anisotropic next-nearest-neighbor interactions. These results demonstrate the feasibility of resource-efficient quantum simulations for resolving complex and subtle magnetic phenomena in real materials.

BC-10. Magnetic properties of quasiperiodic tilings: a case study on the hexagonal golden-mean tiling

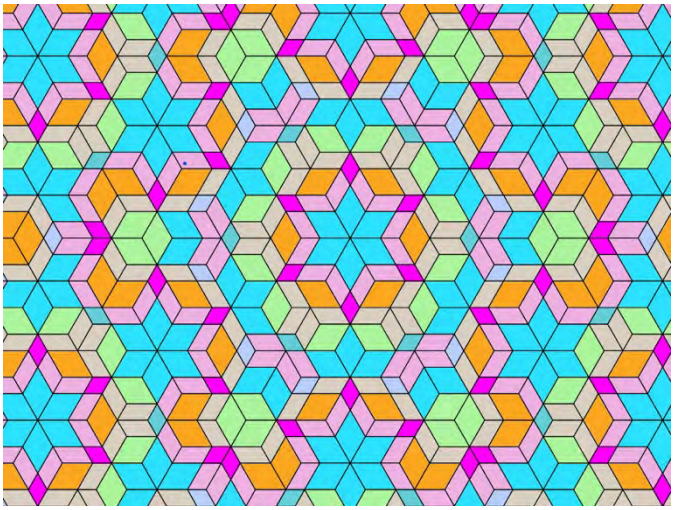
S. Coates
University of Liverpool, Liverpool, United Kingdom

Structural order exists on a spectrum — from amorphous disorder to perfect periodicity. The magnetic properties at both extremes are well understood, but between them lies quasiperiodicity: long-range order without a repeating unit. Quasiperiodic phases appear naturally in many materials, particularly intermetallic alloys, and the recent discovery of long-range magnetic order in ternary alloy quasicrystals [1,2] has sharpened a fundamental question: what does magnetic order look like in a quasiperiodic material?

Two-dimensional tilings offer the most tractable entry point — the Penrose and 'Hat' monotile tilings being the most familiar. I will present the magnetic properties of the half-filled Hubbard model on the 2D hexagonal golden-mean tiling, a member of a broader family of hexagonal tilings, uniquely distinguished by its ferrimagnetic order. The tiling's vertex model is bipartite, with a sublattice imbalance of $5/(6\tau^3)$, where τ is the golden mean, which produces macroscopically degenerate states at E=0 in the noninteracting tight-binding limit.

Introducing the Coulomb interaction lifts this degeneracy, inducing finite staggered and uniform magnetization whose spatial distribution evolves continuously with interaction strength. Time permitting, I will discuss how arbitrary or deliberately designed tilings can be used to tune magnetic behaviour more broadly.

Tamura, Ryuji, et al. "Experimental observation of long-range magnetic order in icosahedral quasicrystals." *Journal of the American Chemical Society* 143.47 (2021): 19938-19944.
Tamura, R., et al. "Observation of antiferromagnetic order in a quasicrystal." *Nature Physics* 21.6 (2025): 974-979.



A patch of the golden-mean hexagonal tiling

BC-12. Theory of 2D Ferromagnetism and Anisotropy-driven Topological Spin Textures in Fe_3Sn

T. Bayaraa, S. M. Griffin
Lawrence Berkeley National Laboratory, Berkeley, California, United States

The search for two-dimensional (2D) ferromagnetism is driven by its fundamental significance and its potential impact on technologies such as low-power electronics and quantum computing. Despite its significance, there have been few reports of 2D ferromagnetism. In a recent collaborative effort with experimental teams, we identified 2D magnetism in the bulk 3D Fe_3Sn [1]. Here, we look at the emergence of 2D ferromagnetism and topological spin textures in Fe_3Sn by means of first-principles calculations and ab-initio Monte-Carlo simulations. We investigate the origins of the reported 2D vortex-type spin structures and appearance of an XXZ ferromagnetism proposed due to the degeneracy in the in-plane spin easy axis, and present a microscopic understanding behind them.
[1] Large ordered moment with strong easy-plane anisotropy and vortex-domain pattern in the kagome ferromagnet Fe3Sn. Lilian Prodan, Donald M. Evans, Sinéad M. Griffin, Andreas Östlin, Markus Altthaler, Erik Lysne, Irina G. Filippova, Sergiu Shova, Liviu Chioncel, Vladimir Tsurkan, István Kézsmárki; Appl. Phys. Lett. 10 July 2023; 123 (2): 021901. https://doi.org/10.1063/5.0155295

BC-13. Investigating Thermal Phase Transitions in a Spin-1/2 Heisenberg Antiferromagnet on a Lieb-lattice of Orthogonal Dimers

J. Strecka, K. Karlova, A. Zoshki
Pavol Jozef Safarik University, Kosice, Slovakia

We investigate magnetic properties and finite-temperature phase transitions of the antiferromagnetic spin-1/2 Heisenberg model on a Lieb lattice of orthogonal dimers in a presence of the external magnetic field . Thiis frustrated two-dimensional quantum spin system hosts four flat-band modes, three of which correspond to a dimer singlet formed either on a nodal or a decorating dimer. The three localized flat bands enable to establish a quantum-to-classical mapping onto an effective Ising model on a square lattice elucidating low-temperature features of the original quantum spin system. This mapping consquently allows to predict in a highly frustrated parameter regime a surface of discontinuous thermal phase transitions, which is bounded at high temperatures by a line of continuous phase transitions from the standard Ising universality class. Using quantum Monte Carlo simulations of the original spin-1/2 Heisenberg antiferromagnet on the Lieb lattice of orthogonal dimers developed specifically in a dimer basis to avoid the sign problem, we unambiguously confirm discontinuous and continuous themal phase transitions as predicted by the effective description. Classical Monte Carlo simulations of the effective Ising model indeed quantitatively capture the corrresponding results of quantum Monte Carlo simulations and thus provide a unified and consistent description of the magnetic behavior including the discontinuous and continuous thermal phase transitions.

This work was supported by the grant of the Slovak Research and Development Agency under the contract No. APVV-24-0091 and by the grant of The Ministry of Education, Research, Development and Youth of the Slovak Republic under the contract No. VEGA 1/0298/25.

SESSION BD: HEAT ASSISTED MAGNETIC RECORDING

Co-Chair(s): V. Lomakin, *ECE, University of California, San Diego, La Jolla, CA, California, United States* and S. Hernandez, *Seagate Technology, Bloomington, Minnesota, United States*

Tuesday, November 3, 2026

02:00 PM-05:30 PM

Coral 2

BD-01. Analytical Approach to Predict Performance of Heat-Assisted Magnetic Recording

P. Jubert, T. Tang, R. Brockie

Western Digital Corporation, San Jose, California, United States

Heat-assisted Magnetic Recording (HAMR) has been introduced in recent hard-disk drives (HDDs) and advances in HAMR head and media components are expected to deliver additional areal density capability and larger capacity HDDs in the coming years. In HAMR, the write process is performed while locally heating the FePt-based granular recording medium to near its Curie temperature, Tc, using a near-field transducer excited by an embedded laser in the write head. The improved areal density capability results from high down-track and cross-track temperature gradients combined with narrow switching temperature distributions of the FePt recording medium. The HAMR media switching distributions can be determined under recording conditions (times, fields, switching dynamics) using temperature and field mapping (THMap) measurements [1]. The method is based on band DC-noise measurements with varying applied temperatures (laser current) and applied fields (writer current). Conventional THMap measurements start from band DC erased magnetization state and evaluate the proportion of magnetic clusters that switch as the peak temperature increases, while a field of opposite polarity to the preparation state is applied. Additional THMap measurements with the applied field of same polarity to the preparation state, or with thermally erased initial state are also reported in this work. Fig. 1 shows representative THMap curves for both initial states and different write field polarities. Analytical expressions of the integrated noise power have been developed to fit all these measurements simultaneously and derive the HAMR media distributions [2]. The fits yield detailed HAMR media properties: at large field, the probability of switching as a function of temperature is very well reproduced with a skew-normal distribution that captures the low temperature tail of the switching distribution. To match the noise power curves at low applied field the model needs to include a reduction of the cluster size for applied temperatures larger than Tc, or, alternatively, the possibility to form multi-domain grains at low field and high temperatures. The excellent agreement between the THMap measurements and the analytical noise model allows to extract the FePt grains' switching distributions under recording conditions and to reveal details of the HAMR media switching processes at high temperatures.

The noise analytical expressions discussed above were initially derived assuming infinitely wide tracks [2]. Using a micro-track approach, these expressions have been extended to analytically predict the signal and noise of isolated written tracks recorded at increasing laser power. The inputs to the model are the HAMR media switching distributions measured by THMap, the measured cross-track temperature profile and the read head sensitivity profile. With additional considerations of the grains' temperature and field history, the signal and DC-noise resulting from consecutive write processes can also be calculated. This yields analytical predictions of signal, DC-noise and DC-SNR for overlapping written tracks corresponding to conventional-magnetic recording (CMR) or shingled-magnetic recording (SMR). Fig. 2 illustrates model predictions of DC-SNR as a function of the laser power or peak temperature for CMR at selected squeeze track pitches. Comparison to experimental measurements show very good agreement. The proposed analytical model enables fast predictions of the SNR performance of the HAMR system across variations in media properties and head designs.

[1] P.-O. Jubert *et al.*, *IEEE Transactions on Magnetics*, vol. 59, no. 3, Art no. 3200405, (2023)

[2] P.-O. Jubert, *IEEE Transactions on Magnetics*, vol. 61, no. 11, Art no. 3000613, (2025)

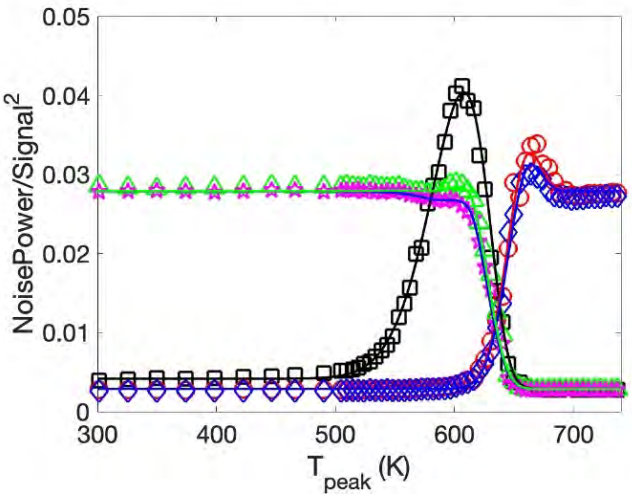


Fig. 1: THMap data (symbols) and results of analytical fitting (lines). The initial state is -DC saturated (black, blue, red) or thermally erased (green, magenta). The writer current varies from +/-2mA (blue/red) and +/-65mA (black, green/magenta).

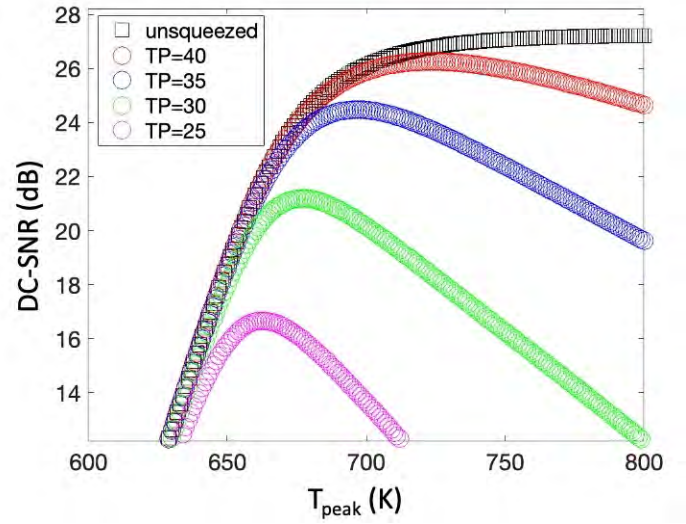


Fig. 2: Analytical model prediction of DC-SNR as a function of T_{peak} (laser power) for an isolated track (black) and double-sided squeezed tracks with varying track picthes.

BD-02. FePt-BN granular media for the thermal spin-torque heat assisted magnetic recording

S. Ratha[1], M. Ullerithodi[1], Y. Sasaki[1], H. Sibi[1], G. K. Shukla[1], D. Angayarkanni Ramamurthy[1], S. Isogami[1], Y. Fan[2], Y. Kubota[3], J. Gadbois[2], Y. K. Takahashi[1, 4]

[1]Research Centre for Magnetism and Spintronic Materials, National Institute for Materials Science, Tsukuba, Ibaraki, Japan, [2]Advanced Technology Development, Seagate Technology, Bloomington, Minnesota, United States, [3]Recording Media Organization, Seagate Technology, Fremont, California, United States, [4]Research Institute of Electrical Communication, Tohoku University, Sendai, Tohoku, Japan

Heat-assisted magnetic recording (HAMR) enables high-density storage recording media [1]. We experimentally demonstrated enhanced switching efficiency in thermal spin torque (TST) - HAMR through coercivity modulation from spin current injection [2]. To achieve the manufacturing of hard-disk drives with TST-HAMR system, we have studied the formation of granular media on the spin source material. VN(10)/{MgTiO (MTO) or TiO}(2)/FePt-BN(6)/C(3)(in nm) films were deposited on the (001)MgO substrate by DC magnetron sputtering. It is reported that the $L1_0$-FePt granular microstructure is formed on the MTO underlayer [3,4]. Deposition temperatures were 400 °C (VN), 500 °C (MTO/TiO), and 700 °C (FePt-BN). Structure and composition were analyzed by XRD, TEM, and EDS; TEM samples were prepared by FIB lift-out (cross-section) and chemical etching (in-plane).

Figure 1 presents the out-of-plane XRD profile and magnetic hysteresis loops of (001)MgO //VN(10)/MTO(2)/FePt-BN(6)/C(3) thin film. A strong peak at $2\theta/\omega \approx 43°$ appears near the MgO (002) diffraction and is attributed to the VN (002) underlayer. Additional peaks at ~ 23° and ~ 48° correspond to the (001) superlattice and (002) fundamental diffraction of $L1_0$-FePt, confirming atomic ordering with an order parameter of 76%. From the out-of-plane and in-plane hysteresis loops, perpendicular magnetic easy axis was confirmed. The film exhibits $\mu_0 H_c \approx 1.6$ T, $\mu_0 M_s \approx 1$ T, $\mu_0 H_k \approx 7.5$ T, and an estimated uniaxial anisotropy energy density $K_u \approx 3$ MJ/m^3. Figure 2 shows cross-sectional HAADF-STEM and in-plane bright-field TEM images of the sample with a 2 nm MTO insertion layer. Despite its 2 nm thickness, the MTO layer showed crystallization on the VN layer, which plays a crucial role in forming the FePt–BN granular microstructure. A similar granular structure and magnetic properties were obtained for the TiO insertion layer. The switching efficiency of FePt-BN layer owing to the MTO/TiO insertion will be shown at the conference.

1. D. Weller et. al., *J. Vac. Sci. Technol.B*, 34, 060801-1-10 (2016).
2. S. Isogami et. al., *Acta Materialia*, 286, 120743 (2025).
3. A. Dilipan et. al., *Scripta Materialia* 268, 116885 (2025).
4. B. Varaprasad et. al., *J. Appl. Phys*. 113, 203907 (2013).

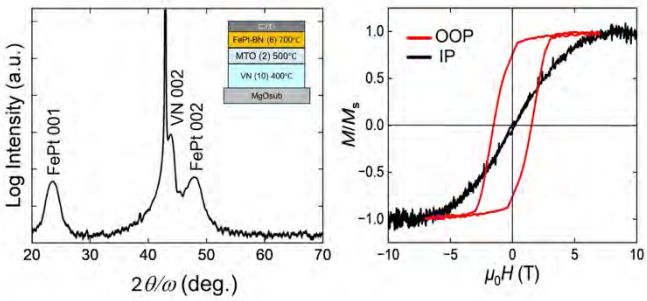


Fig. 1. Out-of-plane XRD profile and in-plane (IP) and out-of-plane (OOP) magentic hysteresis loops of (001)MgO//VN(10)/MTO(2)/FePt–BN(6)/C(3) (nm).

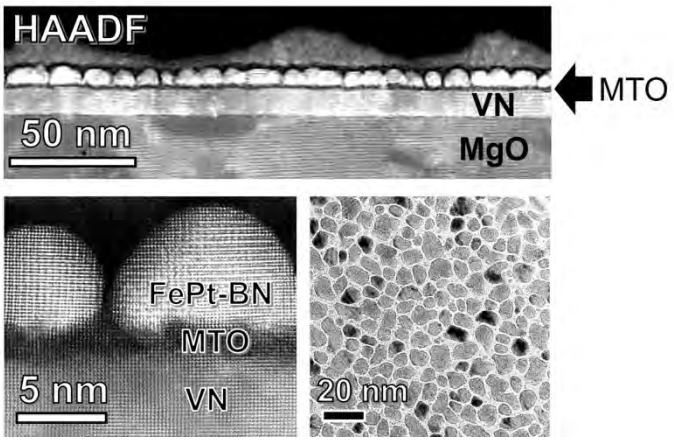


Fig. 2 Cross-sectional and in-plane HAADF-STEM images for the (001)MgO//VN(10)/MTO(2)/FePt-BN(6)/C(3) (nm)

BD-03. Microstructural and Magnetic Property Engineering of FePt-X/Mo-X/FePt-X (X=C, *h*-BN) Granular Films for High-Density Data Storage

H. Sibi[3, 2], D. Angayarkanni Ramamurthy[1], A. Bolyachkin[1], D. Ogawa[1], Y. Sasaki[1], S. Kasai[1], Y. K. Takahashi[1, 2, 4]
[1]RCMSM, NIMS, Tsukuba, Ibaraki, Japan, [2]Materials Innovation, University of Tsukuba, Tsukuba, Ibaraki, Japan, [3]RCMSM, NIMS, Tsukuba, Ibaraki, Japan, [4]RIEC, Tohoku University, Sendai, Miyagi, Japan

The rapid expansion of digital information requires storage technologies that remain reliable and economically sustainable. Increasing the areal density of hard-disk drives (HDDs) is therefore critical. Multi-level heat-assisted magnetic recording (HAMR) provides a pathway toward ~10 Tbit in^{-2}. The first multi-level HAMR based on FePt/Ru/FePt trilayer, exhibited in-plane variants, weak $L1_0$ ordering in the initially deposited (~1 nm) top FePt layer, and a disturbed [001] texture due to insufficient lattice-misfit strain between Ru and $L1_0$-FePt. Larger lattice mismatch and the associated interfacial strain are known to suppress in-plane variant formation and stabilize strong [001] texture.

To address this limitation, Mo was explored as a spacer layer, offering a 15.3% lattice misfit to $L1_0$-FePt and low solubility into FePt grains according to Fe–Mo and Pt–Mo phase diagrams. Emphasis was placed on achieving a smooth FePt/Mo interface to enhance structural coherence and top-layer growth. FePt-C (3.5 nm)/Mo-C (2 nm)/FePt-C (3.5 nm) trilayers were deposited at 600°C by ultra-high-vacuum magnetron sputtering on MgO (001) substrates (base pressure 7 × 10^{-6} Pa). XRD and MPMS measurements (up to 7 T) confirmed strong perpendicular anisotropy with a total coercivity of 2.05 T. TEM revealed well-isolated grains (grain size~8.6 nm), while magnetic loop displayed two-step behavior indicating independent switching of the two FePt layers with H_{c1} ≈ 0.92T for top FePt and H_{c2} ≈ 3.04T for botton FePt layer. HAADF-STEM image in fig.1 showed a smooth FePt/Mo interface promoting ordered growth of top layer, although EDS detected ~0.5 nm Mo interdiffusion (fig. 2). Deposition parameters were refined to maximize coercivity while preserving $L1_0$ ordering, and BN was also tried as a segregant material, aiming toward scalable and industrially compatible multi-level HAMR media for next-generation high-density HDD applications.

[1] Hono, K., et al. "Heat-assisted magnetic recording media materials." *MRS Bulletin* 43.2 (2018): 93-99.]1
[2] Tozman, P., et al. "Dual-layer FePt-C granular media for multi-level heat- assisted magnetic recording." *Acta*

Materialia 271 (2024): 119869.
[3] Wang, J., et al. "Effect of MgO underlayer misorientation on the texture and magnetic property of FePt–C granular film." *Acta Materialia* 91 (2015): 41-49.
[4] Hsiao, S. N., et al. "Effect of FePt/Mo interface on ordering transformation." *Journal of Magnetism and Magnetic Materials* 310.2 (2007): e775-e776.

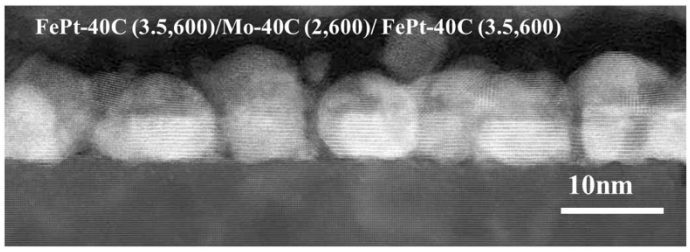


Fig. 1. Cross-sectional HAADF image of FePt-40vol%C (3.5nm,600°C)/ Mo-40vol%C (2nm, 600°C)/ FePt-40vol%C(3.5nm,600°C)

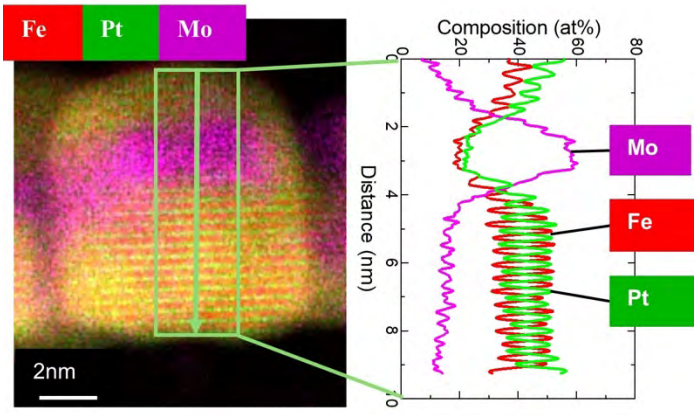


Fig. 2. EDS map with line scan of FePt-40vol%C (3.5nm,600°C)/ Mo-40vol%C (2nm, 600°C)/ FePt-40vol%C(3.5nm,600°C)

BD-04. A Study of 3B–2T Code and Its Recording Schemes for Dual-Layer HAMR

Y. Nakamura[1], S. Greaves[2], Y. Kanai[3], Y. Okamoto[1]
[1]Ehime University, Matsuyama, Japan, [2]Tohoku University, Sendai, Japan, [3]Niigata Institute of Technology, Kashiwazaki, Japan

To significantly increase the areal recording density of hard disk drives (HDDs), a recording scheme that combines heat-assisted magnetic recording (HAMR) with dual-layer recording medium (DL-HAMR), in which two recording layers are formed on one side of the medium, has been proposed [1]. In dual-layer magnetic recording, the readback signal from the second recording layer, which is farther from the read head, is more strongly affected by spacing loss than that from the first recording layer. To mitigate this influence, we apply the 3B-2T code [2], which converts a 3-bit information sequence into a 2-symbol ternary sequence.

In this study, we apply the proposed 3B-2T code to the DL-HAMR read/write channel and evaluate the symbol error rate (SER) performance using the partial response maximum likelihood (PRML) detection for dual-layer recording [3].

Table 1 shows the proposed 3B-2T coding and its recording scheme. The 3B-2T coding reduces patterns in which different information is recorded in the top (first) and bottom (second) recording layers, as well as hard-to-discriminate patterns. As shown in the table, a 3-bit information sequence (a_k, a_{k+1}, a_{k+2}) is first converted into a two-symbol ternary code sequence (b_k, b_{k+1}). Then, for the first and second recording layers, respective 2-bit information sequences $\{(c^1_k, c^1_{k+1}), (c^2_k, c^2_{k+1})\}$ are recorded to express the ternary symbols. The superscripts indicate the first and second recording layers. In the proposed coding scheme, discrimination of the "0" level is improved by prohibiting state transitions that remain at the "0" level every two time intervals.

Using the reproducing waveforms from dual-layer granular medium with an areal recording density of 2 Tbit/in^2 per layer [4], the SER was calculated by using the two-dimensional PRML detection [3]. As a result, the SER of the proposed scheme was 8.2×10^{-3}, which is approximately one-quarter of that of no-coding system, 3.5×10^{-2}, indicating a significant reduction in the number of error symbols.
[1] T. Y. Chang, et al., IEEE Trans. Magn., vol.59, no.3, 3200107, Mar. 2023.
[2] H. Kasai, et al., IEEE Trans. Commun., vol.31, no.2, pp.302

—306, Feb. 1983.
[3] Y. Nakamura, et al., Proceedings of Intermag 2021, 21414406, Nov. 2021.
[4] Y. Nakamura, et al., Digest of TMRC 2025, P1-6, July 2025.

3-bit information (a_k, a_{k+1}, a_{k+2})	2-symbol ternary $(b_{k'}, b_{k'+1})$	Respective 2-bit information $\{(c^1_{k'}, c^1_{k'+1}), (c^2_{k'}, c^2_{k'+1})\}$
(0, 0, 0)	(−, −)	{ (0, 0), (0, 0) }
(0, 0, 1)	(−, 0)	{ (0, 0), (0, 1) }
(0, 1, 0)	(−, +)	{ (0, 1), (0, 1) }
(0, 1, 1)	(0, +)	{ (1, 1), (0, 1) }
(1, 0, 0)	(0, −)	{ (0, 0), (1, 0) }
(1, 0, 1)	(+, −)	{ (1, 0), (1, 0) }
(1, 1, 0)	(+, 0)	{ (1, 1), (1, 0) }
(1, 1, 1)	(+, +)	{ (1, 1), (1, 1) }

Table 1. 3B-2T coding and its recording scheme.

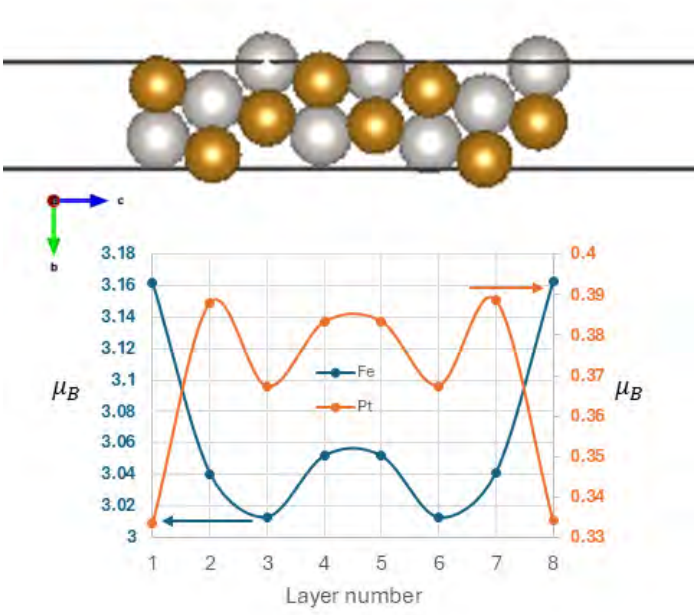
BD-05. Magnetic properties of $L1_0$ FePt at different surface terminations

A. Venugopal[1], I. Chatratin[1], X. He[2], V. Blum[2, 3], T. Klemmer[4], O. Heinonen[5]
[1]Seagate Research, Seagate Technology, Bloomington, Minnesota, United States, [2]Thomas Lord Department of Mechanical Engineering and Materials Science, Duke University, Durham, North Carolina, United States, [3]Department of Chemistry, Duke University, Durham, North Carolina, United States, [4]Recording Media Organization, Seagate Technology, Fremont, California, United States, [5]Recording Head Organization, Seagate Technology, Bloomington, Minnesota, United States

FePt is the key storage material enabling state-of-the-art heat-assisted magnetic recording (HAMR) disk drive technology [1, 2]. The rapidly growing demand for data storage—further intensified by AI-driven workloads—necessitates ever higher areal densities in FePt-based magnetic media. Achieving this goal requires a deeper understanding of the fundamental properties of the material. In this work, we carry out first-principles investigations of FePt thin films with (111), (010), and (001) surface terminations, using the all-electron FHI-aims code [3].

The relatively high saturation magnetization and very high magnetocrystalline anisotropy (MAE) of the $L1_0$-phase of FePt are some of the important properties that have enabled HAMR. In this work, magnetic moment variation with thickness is calculated; contributions from Fe and Pt are extracted along the thickness of the film for the thicknesses considered. We also evaluate contributions from both spin- and orbital-moments as well as the MAE of the samples. Finally, we also investigate the impact to the MAE when cobalt is deposited on the 001-terminated film.

[1] T. Y. Chang, P. Steiner, A. Venugopal, J. Jury, P-W. Huang, A. Ghoreyshi, S. Hernandez, "Zero-State Insert Dual-Layer HAMR Media Recording," IEEE Transactions on Magnetics, vol. 59, no. 3, pp. 1-7 (2023).
[2] W-H Hsu, R.H. Victora, "Heat-assisted magnetic recording — Micromagnetic modeling of recording media and areal density: A review,", Journal of Magnetism and Magnetic Materials, vol. 563, 169973 (2022).
[3] V. Blum, R. Gehrke, F. Hanke, P. Havu, V. Havu, X. Ren, K. Reuter, and M. Scheffler, "*Ab initio* molecular simulations with numeric atom-centered orbitals," Computer Physics Communications 180, 2175-2196 (2009).



Spin-moment for Fe and Pt plotted separately for an 8 monolayer FePt film with (111) surface termination.

BD-06. Intrinsic Optical and Thermal Properties of Segregant Materials for HAMR Applications

E. Yitamben, P. Jubert, A. Bourez, G. Bertero, R. Brockie, I. Okamoto
Western Digital, San Jose, California, United States

In heat assisted magnetic recording (HAMR) media, segregants define nanoscale grain boundaries and control lateral exchange coupling. Beyond these structural roles, they govern optical field penetration, local absorption, and lateral thermal spreading, directly determining achievable temperature gradients and required laser power. Their intrinsic optical and thermal properties are therefore critical design parameters for HAMR efficiency.
Here, we systematically investigate the optical and thermal properties of common HAMR segregant materials and their impact on media level optical and thermal performance. Several widely used segregants, including C, BN, SiO2, TiO2, and TiN, are studied as standalone thin films to isolate intrinsic behavior.
Films are deposited by physical vapor deposition and structurally characterized by xray diffraction and transmission electron microscopy. Wavelength dependent optical constants (n, k) are extracted using spectroscopic ellipsometry, revealing differences in refractive index and extinction coefficient across segregant classes (Fig. 1). Time domain thermoreflectance is used to quantify thermal conductivity and interfacial heat transport. Bulk thermal conductivity is evaluated using single layer films of varying thickness, while interfacial transport is assessed using multilayer stacks consisting of 10 to 20 alternating layers of the segregant and FePt. The measured thermal conductivities span a wide range among segregants (Fig. 2), leading to distinct optical thermal trade offs independent of magnetic integration. Optical and thermal modeling based on these measurements show that reducing the effective refractive index of the composite layer by 0.5 decreases optical efficiency by ~20%, whereas reducing in plane thermal conductivity by a factor of two improves thermal efficiency by ~15%. These results demonstrate that segregants act as functional layers whose properties must be co optimized alongside magnetic and structural design.

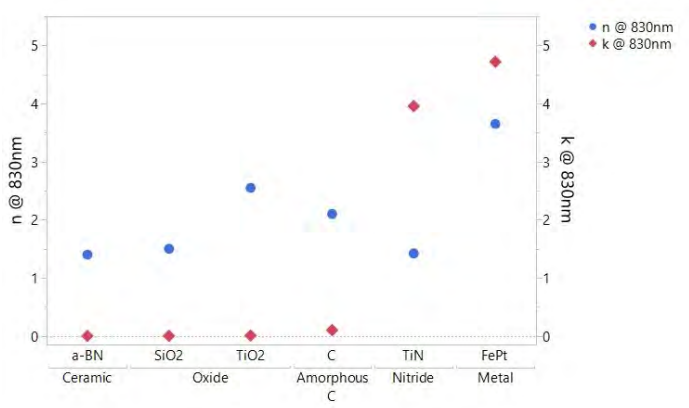


Fig.1: Refractive index (n) and extinction coefficient (k) of segregant materials measured by spectroscopic ellipsometry

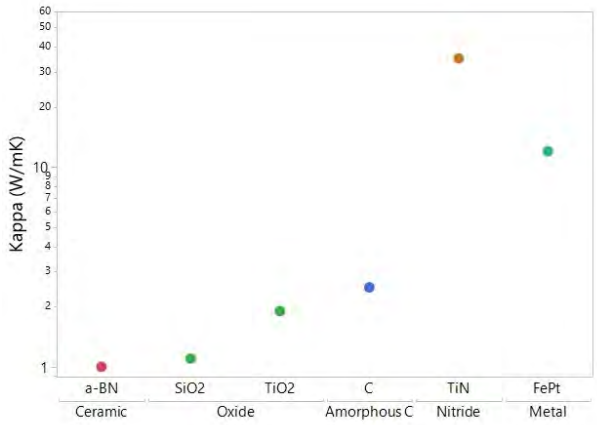


Fig.2: Measured thermal conductivity of segregant materials, highlighting material dependent differences relevant to heat localization

BD-07. FePt/Ir/FePt Dual-Layer HAMR Media for Multi-Level Magnetic Recording

J. Chang[1, 2], B. L. Reese[1, 2], D. E. Laughlin[1, 2, 3], J. Zhu[1, 2, 3]
[1]Data Storage Systems Center, Carnegie Mellon University, Pittsburgh, Pennsylvania, United States, [2]Materials Science and Engineering, Carnegie Mellon University, Pittsburgh, Pennsylvania, United States, [3]Electrical and Computer Engineering, Carnegie Mellon University, Pittsburgh, Pennsylvania, United States

Dual-layer granular $L1_0$-FePt media with a non-magnetic spacer layer could enable three-level recording for heat-assisted magnetic recording (HAMR) [1]. The ability to tune the Curie temperature and other magnetic properties of the

FePt layers separately may also support independent recording of each layer [2]. However, a critical challenge is that the exchange-breaking layer needs to facilitate the correct texture and chemical ordering of the upper $L1_0$-FePt layer [3]. In this study, we investigated iridium as a potential breaking layer due to its small lattice mismatch with $L1_0$-FePt (~0.8%), high thermal stability, and immiscibility with Pt. Dual-layer magnetic recording media with the general structure, FePt-*h*BN (4.5 nm) / Ir-*h*BN (2 nm) / FePt-*h*BN (4.5 nm), were prepared by magnetron sputtering. The dual-layer media exhibited an average grain diameter of 7.2 nm and an average pitch distance of 9.3 nm. Cross-sectional STEM imaging confirmed Ir immiscibility with the grain boundary material (*h*BN) while also enabling the growth of well-isolated, columnar grains. We observed that the Ir breaking layer flattens the bottom layer and produces a smooth FePt/Ir interface; this promotes good $L1_0$ ordering and (001) texture in the top FePt layer (Fig. 1(a)). The room temperature magnetic hysteresis loop of the dual-layer media exhibited a small step near M/M_s ~0.5 (Fig. 2). The minimal step height, less than half the total magnetization reversal, suggests that coercivity in both layers is dominated by well-ordered L10-FePt rather than a disordered soft phase. In summary, we demonstrated that Ir is a viable breaking layer that grows epitaxially on $L1_0$-FePt and retains chemical ordering in dual-layer HAMR media.

[1] J.-G. Zhu, IEEE Transactions on Magnetics, Vol. 271, (2026)
[2] S. Greaves, Journal of Magnetism and Magnetic Materials, Vol. 588, (2023)
[3] P. Tozman, S. Isogami, I. Suzuki et al., Acta Materialia, Vol. 271, (2024)

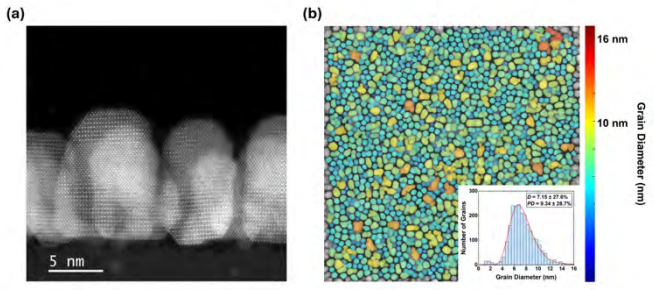


Fig. 1 (a) Cross-sectional and (b) plane-view HAADF-STEM micrographs of dual-layer media with a 2 nm Ir spacer layer.

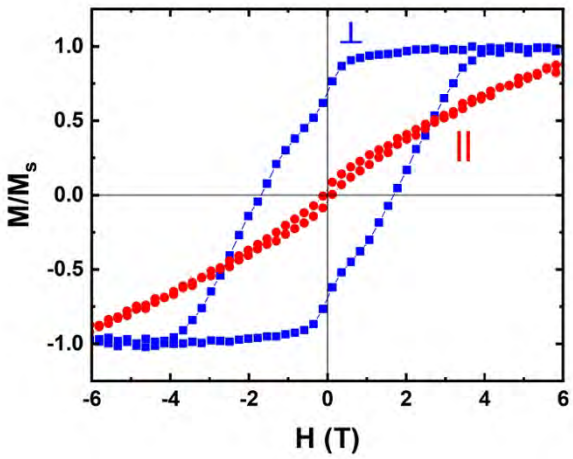


Fig. 2 In-plane (||) and out-of-plane (⊥) magnetization curves of dual-layer media with a 2 nm Ir spacer layer.

BD-08. Read Head Design for Vector Recording in HAMR

J. Zhu
DSSC, Electrical and Computer Engineering, Carnegie Mellon University, Pittsburgh, Pennsylvania, United States

Extremely high anisotropy field gradient facilitated by the FePt-L10 media characteristics enables very narrow written tracks. Such capability could support recently proposed vector recording scheme [1]. In this work, we present a read head design for vector recording scheme that senses the signal from the split half-tracks. Fig. 1(a) shows an illustration of the design. The read head sensor is a magnetic tunnel junction (MTJ) with both its electrodes working as free layers. As shown in the figure, the magnetizations of the two free layers are scissored in the cross-track direction, biased by a flux matched synthetic antiferromagnet abutted at the top (or back) of the free layer stripes (Fig.1(b)). A pair of horizontal permanent magnet are abutted at the side edges of the read sensor to provide horizontal bias. As shown in Fig. 1(c) and Fig. 1(d), the split half-track will produce a horizontal signal flux in the cross track direction that will either making the magnetization scissoring angle greater , as shown in Fig.1(c), or smaller, as shown in Fig. 1(d). Using a full micromagnetic model and both down track and cross-track performance are studied. Fig. 2 shows a normalized on-track read back signal (red) along with its spatial derivative (blue) for reading a transition from a (+,-) split half-track pattern to a (-,+) pattern. In the talk, read back signal for the transitions from to or to will be analyzed and discussed. The effect of reader physical track width as well as the effect of

the written track width will also be discussed in great detail.
[1] R. H. Victora, K. Hosen, and M.F. Erden, "Vector Recording: Advancing Areal Density in HAMR with Innovative Read Head Design", TMRC 2026, Sendai, Japan

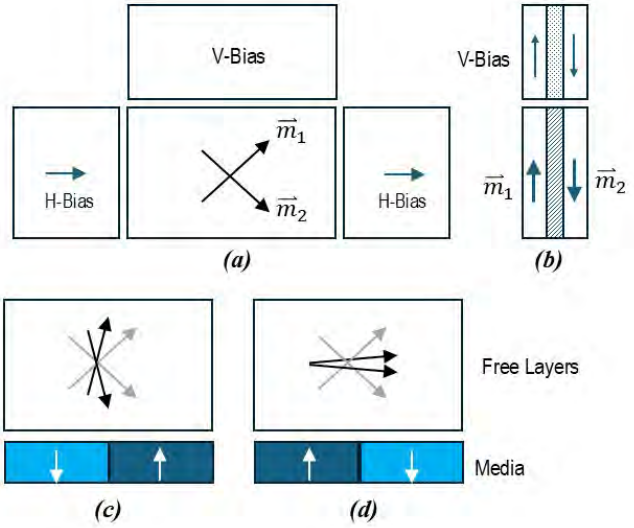


Fig 1 (a) Illustration of the reader design. The free layers are stabilized by common horizontal bias field provided by abutted horizontal magnets and are vertically biased by an exchange pinned synthetic antiferromagnet abutted at the top of the stripe. (b) Side view of the MTJ sensor and the vertical bias structure. (c) Illustration of free layer magnetization rotations while reading a (+,-) split half-track pattern. (d) free layer magnetization rotations while reading a (-,+) pattern.

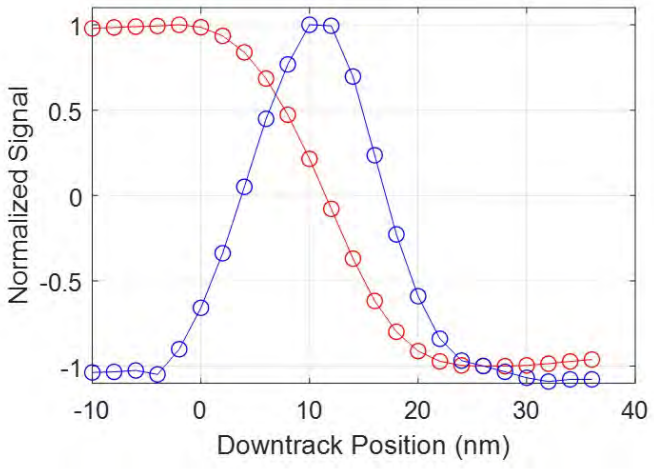


Fig 2 Dow-track readback signal for a transition across from (+,-) to (-,+) split half-track patterns. The shield-to-shield physical spacing is 16nm and head-medium spacing 5nm.

BD-09. HAMR Areal Density Scaling Beyond 5Tb/in^2
A. Ghoreyshi, A. Venugopal, P. Czoschke, S. Hernandez
Seagate Technology, Bloomington, Minnesota, United States

Heat-assisted magnetic recording (HAMR) is the most promising technology to sustain hard-disk areal-density growth in the AI era. HAMR showed that scaling areal density is the most viable path to address the data storage demand. To show HAMR scalability beyond 5 Tb/in^2, a multidimensional geometric scaling is required to coordinated advances across the writer, reader, and media to minimize the recording footprint on the magnetic media [1]. In this study, we present a system-level analysis that maps target areal density to quantitative design constraints on the thermal profile, writer magnetic field, media microstructure and magnetic properties, reader resolution and signal-to-noise (SNR). Using a switching probability model, we perform cross-component co-optimization to outline a realistic roadmap for HAMR areal density. We show that areal density ~ 4.5Tb/in2 is achievable using advanced scaling: thermal gradient ~ 17 K/nm; write-plus-erase (WPE) width ~ 11 nm; reader MT10 ~ 25 nm and PW50 ~ 19 nm; and media with ~ 6.5 nm grain size and ~ 14% grain-size distribution. Furthermore, by employing shingled magnetic recording (SMR) and two-dimensional magnetic recording (TDMR), we show that the areal density can be extended beyond 5 Tb/in^2.
1. Ghoreyshi, Ali, et al. "HAMR Areal Density Optimization Using Deep Neural Networks." *2023 IEEE 34th Magnetic Recording Conference (TMRC)*. IEEE, 2023.

BD-10. Multilayered Magnetic Recording Media Stabilized by Ta Doped $Pt_{1-x}Ta_x$ Interlayers
B. L. Reese[2, 1], J. Chang[2, 1], D. E. Laughlin[2, 1], J. Zhu[2, 1, 3]
[1]Materials Science and Engineering, Carnegie Mellon University, Pittsburgh, Pennsylvania, United States, [2]Data Storage Systems Center, Carnegie Mellon University, Pittsburgh, Pennsylvania, United States, [3]Electrical and Computer Engineering, Carnegie Mellon University, Pittsburgh, Pennsylvania, United States

Multilevel magnetic recording is a promising method that can achieve significantly improved data storage capabilities over conventional binary technologies. In particular, for heat assisted magnetic recording, a zero magnetization level state can be added by writing in zero recording field. Although it has been shown that a third zero polarization state can improve linear storage densities by nearly 60%, development of a suitable multilayered magnetic recording media has remained difficult [1, 2]. In general, multilayered

media consists of two magnetic recording layers (MRL), typically $L1_0$-FePt, separated by a non-magnetic spacer layer. Currently, there exists few suitable spacer layer materials that integrate well with the surrounding FePt. As design requirements, the spacer layer should support good (001) texture of the second FePt layer while maintaining immiscibility with FePt and common grain boundary materials like *a*-C and *h*-BN at temperatures near 650°C. Platinum is one spacer layer material that has received interest due to its small lattice mismatch of ~1.3% with $L1_0$-FePt. However, Pt tends to intermix with the surrounding FePt modifying the stoichiometry of the adjacent FePt phase or forming an ordered $FePt_3$ phase. In general, the FePt / Pt / FePt system equilibrates toward single phase FePt. The phase equilibria of this system makes it especially interesting to study regarding spacer layer interdiffusion. Here we provide an experimental survey evaluating the role of Ta addition to a Pt spacer layer as a means to inhibit interdiffusion. X-ray diffraction shows that the formation of $FePt_3$ can be suppressed within FePt / $Pt_{1-x}Ta_x$ / FePt multilayers by adding roughly 16 at% Ta to the Pt spacer layer. We show that Ta addition helps stabilize the multilayers at high temperatures by acting as a natural diffusion barrier within the Pt spacer layer. This is further confirmed by high resolution STEM imaging; Fig. 2 shows a clear and sharp interface between either FePt layer and the $Pt_{1-x}Ta_x$ spacer layer. Relevant structural, magnetic, and compositional data will be presented.

[1] J.-G. Zhu, "Single-Pass Three-Level Recording with Granular FePt-L10 Medium," *IEEE Trans. Magn.*, pp. 1–1, 2025, doi: 10.1109/TMAG.2025.3634394.

[2] P. Tozman *et al.*, "Dual-layer FePt-C granular media for multi-level heat-assisted magnetic recording," *Acta Mater.*, vol. 271, p. 119869, Jun. 2024, doi: 10.1016/j.actamat.2024.119869.

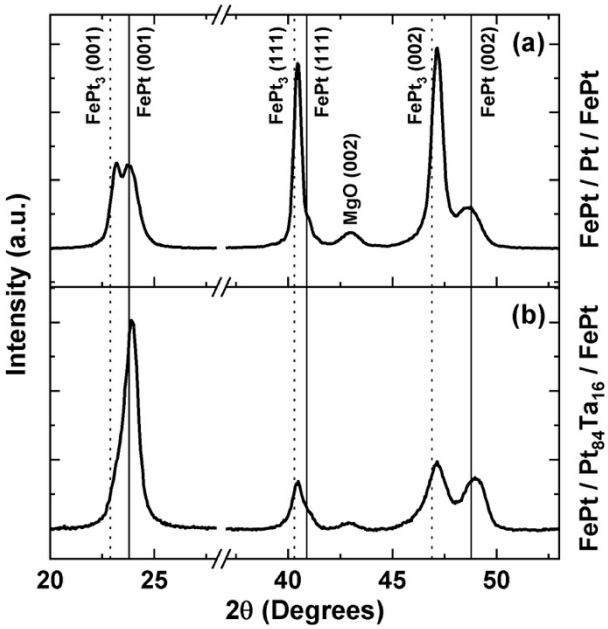


Fig. 1: XRD for FePt / Pt / FePt (a) and FePt / $Pt_{84}Ta_{16}$ / FePt (b).

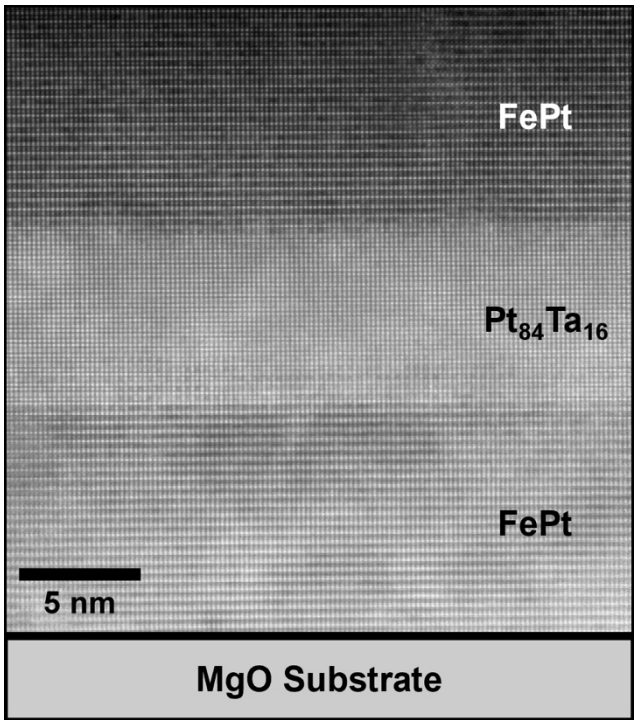


Fig. 2: STEM-HAADF of FePt / $Pt_{84}Ta_{16}$ / FePt interface.

BD-11. Femtosecond laser induced birefringence in NiO/Pt thin films

F. Ikeda[1], S. Iihama[1], B. Kunyangyuen[2], J. Lin[2], A. Yoshida[1], Y. Suzuki[1], K. Hayashi[1], G. Malinowski[2], M. Hehn[2], S. Mangin[2], T. Moriyama[1]
[1]Department of Materials Physics, Nagoya University, Nagoya, Aichi, Japan, [2]CNRS, Institut Jean Lamour, Université de Lorraine, Nancy, Meurthe-et-Moselle, France

Antiferromagnets (AFMs) have emerged as promising candidates for next-generation memory devices owing to their lack of stray fields and robustness against external magnetic fields [1-2]. In recent years, extensive research has been conducted to demonstrate the control of AFM domain structures. The electrical control of magnetic domain structure of NiO, a prototypical collinear AFM, has been intensively studied recently[3,4]. Despite the maturity of all-optical switching (AOS) in ferromagnetic and ferrimagnetic materials [5-7], the optical control of AFM domain structures remains under way[8]. In this work, we study how AFM domain structures in NiO/Pt thin films are controlled by femtosecond (fs) laser irradiation.

A 20 nm thick NiO thin film was deposited on an MgO(100) substrate capped with a 3 nm thick Pt layer. Ti:sapphire fs-laser with a wavelength of 800 nm and a pulse duration of 35 fs was used in the experiment. Linearly polarized fs laser was irradiated onto the thin-film sample with various laser parameters including laser fluence, number of pulses, and polarization directions. Figure 1(a) shows schematic illustration of fs-laser-induced control of the magnetic structure in NiO. The domain structures were detected using polarizing microscopy. Figure 1(b) shows a domain image taken by the polarizing microscopy after irradiation with 10 shots of fs-laser pulses. The contrast variations with changing in-plane sample rotation [Fig. 1(b)] indicates that change in contrast is induced by the birefringence. A large birefringence induced in NiO/Pt thin film may originate from changes in the magnetic and/or strain states of NiO caused by the fs-laser irradiation. In the presentation, we will discuss the laser parameter dependences of the images and the mechanism behind the emergence of the birefringence.

[1] V. Baltz, T. Moriyama *et al., Rev. Mod. Phys.* 90, 015005 (2018).
[2] T. Jungwirth *et al., Nat. Nanotechnol.* 11, 231 (2016).
[3] T. Moriyama *et al. Sci. Rep.* 8, 14167 (2018).
[4] H. Meer *et al. Nano Lett.* 21, 114 (2021).
[5] C. D. Stanciu *et al. Phys. Rev. Lett.* 99, 047601 (2007).
[6] C. -H. Lambert *et al. Science* 345, 1337 (2014).
[7] S. Mangin *et al. Nat. Mater.* 13, 286 (2014).
[8] H. Meer et al., Adv. Funct. Mater. 33, 2213536 (2023).

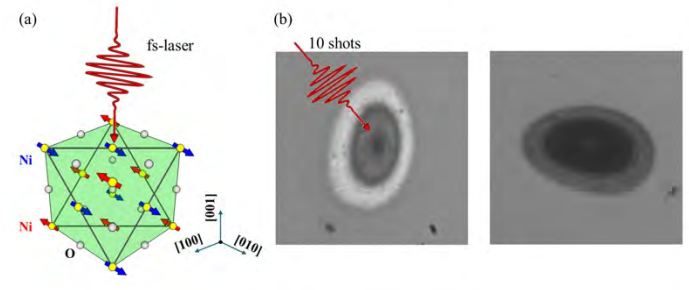


Figure 1(a) Schematic illustration of fs-laser-induced control of magnetic structure. (b) Images of polarizing microscopy after irradiation of fs-laser with different sample angle 0 deg. (left) and 90 deg. (right) with respect to the polarization of microscopy.

BD-12. Demonstrating magnetic memory in iron-rhodium thin film structures using a wide-field quantum diamond microscope

K. V. Ung[2, 1, 3], G. M. Stephen[4], N. Blumenschein[4], A. Edwards[4], S. LaGasse[4], S. P. Bennett[5], A. T. Hanbicki[4], R. Walsworth[2, 1, 3], A. Friedman[4], P. Petruzzi[4]
[1]Joint Quantum Institute, College Park, Maryland, United States, [2]Physics, University of Maryland, College Park, Maryland, United States, [3]Quantum Technology Center, College Park, Maryland, United States, [4]Laboratory for Physical Sciences, College Park, Maryland, United States, [5]Naval Research Laboratory, Washington, District of Columbia, United States

Iron-rhodium (FeRh) has a first order phase transition near room temperature between antiferromagnetic (AFM) and ferromagnetic (FM) phases, making it a promising candidate for heat assisted magnetic recording (HAMR) hard drives with a relatively modest temperature differential compared to current technology. Despite great effort, however, AFM-based magnetic memory using FeRh or other materials has not yet been realized. We employ both wide-field and scanning nanoscale quantum diamond microscopes (QDMs) to directly image the magnetic field of a patterned FeRh thin film structure under ambient conditions, demonstrating a direct relationship between the Néel and FM vector directions that can be reliably read out in the AFM phase, even after repeated cycling past the phase transition temperature. We experimentally show that the magnetic orientation of the FM phase uniquely determines the Néel

vector in the AFM phase, due to pinned uncompensated magnetic moments (UMMs) in the FeRh structure; and thus, the magnetic orientation is maintained when the system is cycled to the AFM phase, providing the foundation for a practical, AFM-based magnetic memory. Using an AFM material is functionally similar to the current high-coercivity HAMR media, but with the bit writing temperature reduced to the phase transition temperature rather than the Curie temperature, a reduction of at least 250 K. FeRh is thus a potentially better material in terms of engineering complexity, latency, lifetime, magnetization stability, and reliability for HAMR drives than currently used materials.

SESSION BE: IMAGING, SENSING AND ELECTROMAGNETIC DEVICES

Chair(s): R. Goldfarb, *National Institute of Standards and Technology, Boulder, Colorado, United States*
Tuesday, November 3, 2026
02:00 PM-05:30 PM
South Pacific 1/2

BE-01. Play it again – Recovering historic audio from degraded magnetic tapes using X-ray magnetic dichroism

S. Gliga
Paul Scherrer Institute, Villigen PSI, Switzerland

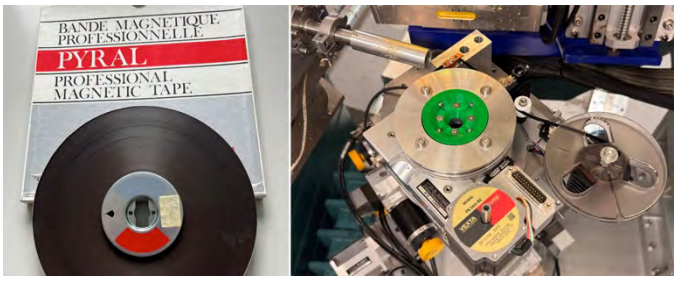
A significant fraction of twentieth-century audiovisual heritage is stored on magnetic tape. Between the 1930s and the late 2000s, professional audio and video recordings were predominantly made on tape. However, magnetic tapes deteriorate over time through wear and chemical degradation [1], which can prevent playback in conventional tape players, where the playback head is in physical contact with the tensioned tape. Despite major digitization efforts over the past decades, millions of unique recordings could not be digitized because of chemical decay and are becoming irrecoverable [2]. In addition, original playback machines and spare parts are becoming significantly harder to obtain, further limiting access to many recordings.

In the Play It Again project, we are developing a contactless, non-destructive technique using synchrotron X-rays to recover information from such heavily damaged magnetic media, while minimizing the risk of further damage. We performed initial proof-of-concept measurements on ferric oxide tape at the Swiss Light Source using circularly polarized hard X-rays to probe the recorded magnetization by exploiting the X-ray magnetic circular dichroism (XMCD) effect. We initially measured the tape in transmission, but the magnetic contrast was only ca. 0.3%. We therefore switched to resonant inelastic X-ray scattering (RIXS-MCD) [3,4]. Although the photon yield is lower, the magnetic contrast increased to as much as 6% at the Fe K pre-edge owing to the enhancement provided by Fe 1s2p RIXS-MCD. Measurements at the GALAXIES beamline (SOLEIL) [5] and the ID20 beamline (ESRF) [6] allowed us to read the analogue magnetic waveform recorded on reel-to-reel audio tapes, including severely degraded samples. As examples, we successfully measured audio frequency sweeps and test tones from physically damaged tapes with folds and cracks. Whereas conventional playback introduced distortions, RIXS-MCD recovered the original signal without such artefacts.

An important limitation on readout speed is the time required to switch the beam polarization to measure the dichroic signal. This makes the recovery of long audio segments impractical. We will therefore present our solutions to further increase readout speed and alleviate this limitation. These solutions, combined with dedicated data processing, have resulted in an increase in readout speed of about two orders of magnitude, allowing us to digitize segments of recordings, such as B.B. King's 1980 concert at the Montreux Jazz Festival and Beethoven's Symphony No. 5 performed at the Verbier Festival, both in Switzerland.

These results are very promising for the development of a contactless recovery method. So far, alternative approaches for retrieving data from damaged magnetic media have relied on measuring the stray fields generated by the recorded domain patterns. These include, for example, magnetoresistive sensors [7], scanning SQUID microscopy [8], and magneto-optic films [9]. In contrast, RIXS-MCD probes the magnetic state throughout the tape thickness rather than only the stray fields, which can be complex and difficult to interpret in damaged tapes. We therefore believe that RIXS-MCD could enable the recovery of tapes degraded beyond the reach of conventional digitization technologies, helping to preserve endangered magnetic-tape recordings.

[1] B. M. Cassidy, *et al*., Anal. Chem. 87, 9265-9272 (2015)
[2] The Magnetic Tape Alert Project by UNESCO and IASA. https://www.iasa-web.org/magnetic-tape-alert-project (2023)
[3] A. Juhin, *et al*., J. Phys.: Condens. Matter 28 505202 (2016)
[4] M. Sikora, *et al*., Phys. Rev. Lett. 105, 037202 (2010)
[5] J.M. Ablett, *et al*., Rev. Sci. Instrum. 96, 053104 (2025)
[6] M. Moretti Sala, *et al*., J. Synchrotron Rad. 25, 580–591 (2018)
[7] D. P. Pappas, *et al*., J. of Electronic Imaging, 14, 013015 (2005)
[8] M. Read, *et al*. SPIE-Int. Soc. Opt. Eng. Proceedings of SPIE – the International Society for Optical Engineering 2941, 13-18 (1997)
[9] J. Blondeau, U. Franke, PhotonicsViews 16, 46-49 (2019)



Left: Master recording on magnetic tape from 1980. © EPFL/Alain Dufaux. Right: Setup for X-ray readout.

BE-02. Physics-Informed Tomographic Reconstruction of Chiral Magnetic Textures

A. J. Setescak[1], P. Mitchell[2], A. Chavan[1], C. Donnelly[2], C. Abert[1]
[1]University of Vienna, Vienna, Austria, [2]Max Planck Institute for the Chemical Physics of Solids, Dresden, Germany

Three-dimensional chiral magnetic textures hold significant promise for next-generation spintronic and information processing devices. While X-ray Magnetic Circular Dichroism (XMCD) tomography provides a powerful probe of these internal structures [1, 2], the reconstruction from experimental data presents substantial challenges, particularly when faced with limited angular ranges, sparse sampling, or significant noise. To enhance the reliability of these reconstructions, we propose a physics-informed framework implemented within a differentiable programming environment using Python and the JAX library for high-performance numerical computing [3]. This approach formulates the reconstruction as a joint minimization problem that balances experimental data fidelity with micromagnetic energy regularization, with the optimal tradeoff selected via the L-curve criterion [4]. Specifically, we employ a differentiable forward model to map the three-dimensional magnetization field to two-dimensional XMCD projections. This model is integrated with the NeuralMag library [5, 6] to ensure physical validity by penalizing the total micromagnetic energy of the system [7], accounting for critical interactions such as exchange, Dzyaloshinskii-Moriya, and demagnetizing fields. This approach effectively bridges the gap between experimental tomography and computational micromagnetics, providing a robust tool for physics-consistent tomographic reconstruction of 3D topological magnetic materials.

[1] C. Donnelly, M. Guizar-Sicairos and V. Scagnoli, Nature., Vol. 547, p.328 (2017)
[2] C. Donnelly, S. Gliga and V. Scagnoli, New Journal of Physics., Vol. 20, p.083009 (2018)
[3] J. Bradbury, R. Frostig and P. Hawkins, Astrophysics Source Code Library., p.2111.002 (2021)
[4] D. Calvetti, S. Morigi, L. Reichel and F. Sgallari, Journal of Computational and Applied Mathematics., Vol. 123, p.423 (2000)
[5] C. Abert, F. Bruckner and A. Voronov, npj Computational Materials., Vol. 11 (2025)
[6] A. Setescak, F. Bruckner and D. Suess, arXiv., p.2602.17180 (2026)
[7] C. Abert, The European Physical Journal B., Vol. 92 (2019)

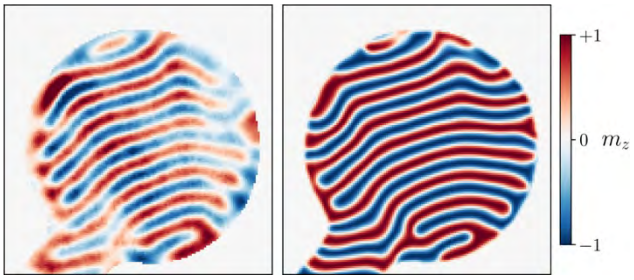


Fig. 1. Central cross-section of the out-of-plane magnetization component m_z for a 300 nm thick, 1100 nm wide $Co_8Zn_9Mn_3$ cylinder, reconstructed from experimental XMCD tomography data. Left: unregularized data-only inversion. Right: physics-informed reconstruction with micromagnetic regularization.

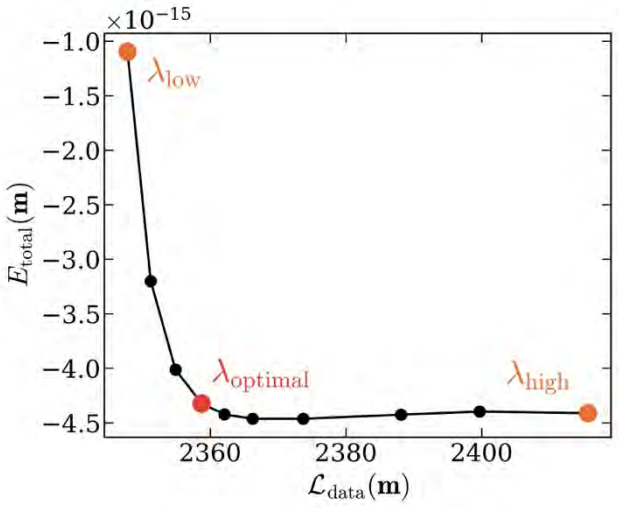


Fig. 2. L-curve analysis for the $Co_8Zn_9Mn_3$ cylinder. Data misfit L_{data} is plotted against total micromagnetic energy E_{total} as the regularization parameter λ is swept. The corner of maximum curvature selects $\lambda_{optimal}$, the value that best balances data fidelity against micromagnetic energy.

BE-03. Light-induced control of spin state and anisotropy in out-of-plane ferromagnets.

S. Bodnar[1], I. Soldatov[1], V. Neu[1], Y. Vaynzof[1, 2]
[1]Institute for Emerging Electronic Technologies, IFW Dresden, Dresden, Germany, [2]TU Dresden, Dresden, Germany

Control of magnetic anisotropy in ferromagnetic materials is one of the most actual scientific and technological challenges, which is required for many device applications associated with data storage. Among different methods of control of magnetic anisotropies, such as ion bombardment, thermal annealing, and composition control [1–3], laser-included control of magnetic anisotropy shows a number of advantages, such as precise positioning of the anisotropy modifications, which opens the way towards laser-induced patterning of magnetic thin films without actual lithography.
In this work, we show anisotropy control in a CoPt multilayered system with strong out-of-plane anisotropy, as well as helicity-dependent optical control in such a system. Using MOKE microscopy, we have determined that the part of the sample that was exposed to laser pulses of high fluence (1.4 mJ/cm^2) shows an increase in the critical field from 20 mT up to 60–80 mT, as well as an increase in the domain size from approximately 10 microns up to approximately 100 microns. This increase in the domain size can be explained by lower pinning sites and an increase in the anisotropy strength.
In the low fluence (0.14 mJ/cm^2) regime, we identified that magnetization can be controlled with circularly polarized light in a helicity-dependent fashion. The modification of the domain pattern in such a case can be completely erased using an external magnetic field, with no traces of optical switching left. At the intermediate fluence (0.7 mJ/cm^2) regime, we observe simultaneous observation of domain pattern changes due to the modification of the anisotropy, as well as helicity-dependent switching. Particularly at higher fluence regimes, we can create magnetic domains that are increased in size by a factor of 10 (from a few microns up to 50 microns) with high asymmetry in the domain distribution (up to 80%) of one type of domains, with the magnetization that is co-aligned with the angular momentum transferred by circularly polarized light.
[1] M. Jaafar et al., "Pattern-induced magnetic anisotropy in FePt thin films by ion irradiation," Phys. Rev. B 83, 094422 (2011).
[2] B. Rodmacq et al., "Influence of thermal annealing on the perpendicular magnetic anisotropy of Pt/Co/AlOx trilayers," Phys. Rev. B 79, 024423 (2009).
[3] M.Dreyer et al., "Composition-driven change of the magnetic anisotropy of ultrathin Co/Au(111) films," *Physical Review B* 59, 4273–4281 (1999).

BE-04. MOKE-Based Analysis of Commercial Grade NdFeB Magnets Using Automated Domain Characterization

S. E. Rego[1], H. Baldino[2], J. Williams[1], P. Kulik[1, 2]
[1]Electrical & Computer Engineering, University of Central Florida, Orlando, Florida, United States, [2]Material Science & Engineering, University of Central Florida, Orlando, Florida, United States

Magnetic characterization remains a high-cost and time-consuming endeavor, creating a barrier to high-throughput characterization. Despite being a low-overhead technique for magnetic characterization, Magneto-Optical Kerr effect (MOKE) imaging has mostly been used as method for making magnetic hysteresis loops [1,2]. Very little work has been done regarding the quantitative relations between magnetic properties and magnetic domain width. Despite this, prior work has shown MOKE microscopy can extract magnetic saturation and magnetocrystalline anisotropy from NdFeB magnets through their relationship with magnetic domain width [3]. Merging prior MOKE-domain analysis methods with machine learning would allow for large-scale

magnetic characterization. Presented here, is an automated method to analyze NdFeB magnet surface images to infer the magnet grade. An optimized form of the Segment Anything Model [4] was created to provide object segmentation of the magnet's surface. Standard commercial NdFeB magnets from Arnold Magnetic Technologies with grades between N35 and N52 as well as high temperature AH and SH grades were studied. Using the manufacturer specifications for magnetic saturation of each grade, the magnetocrystalline anisotropy was extracted (figure 1). NdFeB crystal orientations were probed using MOKE imaging, while the microstructural properties including grain density, crystal size, and Nd-rich phase wetting were evaluated with traditional optical microscopy (figure 1). Electron backscatter diffraction data was collected to confirm the model's accuracy in determining crystal alignment and the composition of each grade was evaluated through energy-dispersive X-ray spectroscopy. These results demonstrate how the use of MOKE imaging can help differentiate magnet grades at a high-throughput pace but also understand how the magnetic properties are formed from the composition and microstructural features.

[1] N. A. Morley, M. R. J. Gibbs and E. Ahmad, *Journal of Magnetism and Magnetic Materials*., Vol 300, p. 436-444 (2005)
[2] A. Stupakiewicz, A. Chizhik and M. Tekielak, *Rev. Sci. Instrum*., Vol 8, p 103702 (2014)
[3] D Goll, R Loeffler and J Herbst, *J. Phys.: Condens. Matter*., Vol 26, p 064208 (2014)
[4] A. Kirillov, E. Mintun and N. Ravi, *arXiv*., arXiv:2304.02643 (2023)

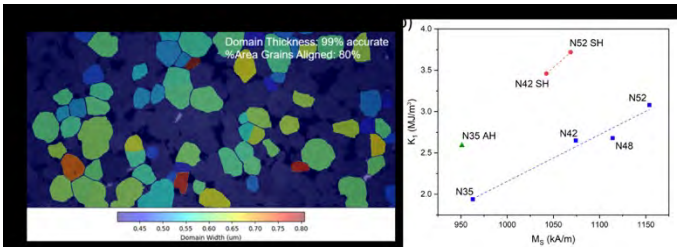


Fig. 1 Analysis of an N48 grade magnet. Crystal domain width and overall area alignment determined from a MOKE image (a). The extrapolated association between the magnetocrystalline anisotropy, K_1, and the saturation magnetization, M_S, of each magnetic grades explored (b).

BE-05. Chirality-Selective Imaging of Spin Wave via Nitrogen-Vacancy Circular Dichroism

E. Im[1], H. Kim[1], E. Jun[1], B. Hayden[2], T. Ono[4], U. Vool[2], S. Kim[1, 3], Y. Choi[1, 2]
[1]Physics, University of Ulsan, Ulsan, Korea (the Republic of), [2]Max Planck Institute for Chemical Physics of Solids, Dresden, Germany, [3]Center for Quantum Dynamics of Angular Momentum, Pohang University of Science and Technology, Pohang, Korea (the Republic of), [4]Institute for Chemical Research, Kyoto, Japan

Nitrogen-vacancy (NV) centers in diamond provide a versatile platform for nanoscale magnetic sensing under ambient conditions. Here, we use a scanning single-NV probe positioned ~50 nm above a magnetic surface to image nanoscale magnetic textures via optically detected magnetic resonance (ODMR), achieving sub-100-nm spatial resolution while preserving spin coherence.
Beyond static stray-field imaging, we use ODMR to detect propagating spin-wave dynamics through their oscillating RF magnetic fields, enabling real-space mapping of dynamic modes. We further implement NV circular dichroism (NVCD), exploiting the circularly selective transitions of the NV spin triplet to distinguish the local left- and right-handed components of the RF field, thereby achieving chirality-resolved imaging of spin waves.
We apply this method to a magnetic thin film Py and image spin-wave excitations with chirality-dependent contrast. Utilizing the circularly selective microwave transitions of the NV spin triplet, we resolve the spatial distribution of left- and right-handed RF magnetic field components associated with the spin-wave dynamics. This enables real-space mapping of spin-wave polarization symmetry under ambient conditions. Our results demonstrate chirality-resolved imaging of spin waves, providing direct access to the handedness of magnetic excitations at the nanoscale. These results establish scanning NV magnetometry as a powerful platform for imaging anisotropy- and magnetization-dependent spin-wave dynamics under ambient conditions.

1. J. M. Taylor, et al. High-sensitivity diamond magnetometer with nanoscale resolution. Nat. Phys. 4, 810 (2008).
2. G. Balasubramanian, et al., Nanoscale imaging magnetometry with diamond spins under ambient conditions. Nature 455, 648 (2008). 3. P. Maletinsky, et al. A robust scanning diamond sensor for nanoscale imaging magnetometry. Nat. Nanotechnol. 7, 320 (2012).

BE-06. Nanoscale Imaging of Antiferromagnetic Domains in Epitaxial Mn_3GaN Thin Films

D. R. Lawati[1], Y. Yao[2], P. Pal[2], M. A. Elekhtiar[3], R. Timalsina[1], J. Kumar[1], M. Rzchowski[4], E. Y. Tsymbal[3, 5], C. Eom[2], A. Laraoui[1, 3, 5]

[1]Mechanical & Materials Engineering, University of Nebraska-Lincoln, Lincoln, Nebraska, United States, [2]Materials Science and Engineering, University of Wisconsin-Madison, Madison, Wisconsin, United States, [3]Department of Physics and Astronomy, University of Nebraska-Lincoln, Lincoln, Nebraska, United States, [4]Department of Physics, University of Wisconsin-Madison, Madison, Wisconsin, United States, [5]Nebraska Center for Materials and Nanoscience, University of Nebraska-Lincoln, Lincoln, Nebraska, United States

Nitride-based antiperovskites are interesting due to their tunable spin characteristics arising from the strong spin-lattice coupling that is sensitive to external perturbations such as magnetic fields, strain, and temperature. Of particular interest is Mn_3GaN, a metallic antiperovskite exhibiting AFM order with a Néel temperature (T_N) exceeding 300 K [1,2], which is predicted to host a momentum-dependent spin polarization and support extraordinary tunneling magnetoresistance [3,4]. Despite these promising properties, the nucleation and dynamics of magnetic domains in Mn_3GaN remain largely unexplored but are expected to control its functionalities. Here, we perform nanoscale magnetic stray-field imaging of AFM domains in Mn_3GaN films using nitrogen-vacancy (NV)-based scanning probe microscopy [6]. Mn_3GaN films are grown epitaxially on (001)-oriented LSAT substrates using reactive magnetron sputtering [1]. We study the effect of film thickness (15-60 nm), temperature (290-350 K), and magnetic field cooling on Mn_3GaN spins configurations. The magnetization profiles of AFM domains are reconstructed using reverse propagation techniques [5], enabling vector components of the magnetic texture. Temperature dependence derived from NV measurements yields $T_N \approx 340$K, in good agreement with neutron diffraction [2]. Complementary DFT and atomistic simulations are employed to elucidate the magnetic properties. The calculations yield a magnetic anisotropy of 0.22 meV/atom favoring the AFM Γ_{5g} phase of Mn_3GaN. Based on the DFT-derived exchange parameters, atomistic simulations reproduce the transition temperature of $T_N \approx 340$K. Theoretical modeling of domain-wall dynamics shows that domain morphology is strongly influenced by magnetic field orientation, providing a framework for understanding the observed stray-field patterns. Our results establish a route for imaging and controlling of AFM domains in epitaxial Mn_3GaN films, relevant to AFM spintronics and ultrafast spintronic devices.

We acknowledge the support of NSF (2044049, 2328822, 2316665, 2522667, 2522669); the Vannevar Bush Faculty Fellowship (N00014-20-1-2844); the Gordon and Betty Moore Foundation's EPiQS Initiative (GBMF9065); and DOE (DE-FG02-06ER46327 (C.B.E.)).

[1] T. Nan *et al.*, Nat. Commun. 11, 4671 (2020).
[2] C. Quintela *et al.*, Sci. Adv. 6, eaba4017 (2020).
[3] G. Gurung *et al.*, Phys. Rev. Materials 5, 124411 (2021).
[4] G. Gurung *et al.*, Nat. Commun. 15, 10242 (2024).
[5] A. Erickson *et al.*, Adv. Funct. Mater. 34 (48), 2408542 (2024).

BE-07. Imaging 3D Magnetic Domains with Electron Interferometry and Polarimetry

B. McMorran

Department of Physics, University of Oregon, Eugene, Oregon, United States

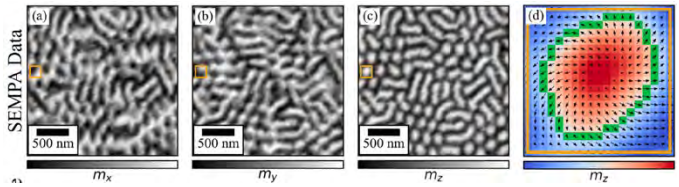
The nontrivial 3D topology of chiral spin textures such as magnetic skyrmions affects their robustness and evolution under applied currents and fields, providing new degrees of freedom for logical bits in future spintronics devices and next-generation magnetic memories. Here we discuss the combined use of specialized electron microscopies, Lorentz TEM, STEM holography, and scanning electron microscopy with polarization analysis (SEMPA) to characterize the 3D structure of magnetic skyrmions [1].

Lorentz TEM projects images of the average projected magnetic field inside a specimen. We use this technique to image the evolution of skyrmions and other chiral domains while varying an external field or temperature [2,3]. Lorentz TEM works by recording phase gradients imparted to electrons by nanomagnetic fields, so it is insensitive to the field component along the beam path (the z-direction), yet the 3D chirality of spin textures can still be determined by tracking the evolution of domains over a field sweep [4].

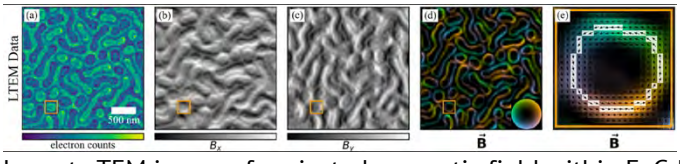
SEM with polarization analysis (SEMPA) [5] is a surface-sensitive technique that can image all three vector components of the surface magnetization. Special detectors measure the average spin polarization of secondary electrons, providing complete, quantitative imaging of the in-plane and out-of-plane magnetic nanostructure as well as normal SE contrast.

Combining these techniques to image skyrmions in multilayer compounds, we find that skyrmions have a more complex 3D structure [1]. TEM techniques indicate skyrmions have a Bloch-like structure within the bulk of the material, yet SEMPA indicates that the skyrmion is Néel like at the surface [6]. We find that this can be theoretically described as a Hopfion structure with half-integer topological charge [7]. This work illustrates how multimodal magnetic electron microscopy can be used to provide 3D information about nanomagnetic structures.

1. Parker, W. S. *et al.* Real space imaging of dipole-stabilized hybrid skyrmions in magnetic multilayer thin films. *Phys. Rev. B* 112, 094415 (2025).
2. Montoya, S. A. *et al.* Tailoring magnetic energies to form dipole skyrmions and skyrmion lattices. *Physical Review B* 95, 024415 (2017).
3. Chess, J. J. *et al.* Streamlined approach to mapping the magnetic induction of skyrmionic materials. *Ultramicroscopy* 177, 78–83 (2017).
4. Chess, J. J., Montoya, S. A., Fullerton, E. E. & McMorran, B. J. Determination of domain wall chirality using in situ Lorentz transmission electron microscopy. *AIP Advances* 7, 056807 (2017).
5. Scheinfein, M. R., Unguris, J., Kelley, M. H., Pierce, D. T. & Celotta, R. J. Scanning electron microscopy with polarization analysis (SEMPA). *Rev. Sci. Instrum.* 61, 2501 (1990).
6. Moraski, R., Gilbert, I., Montoya, S. A., Fullerton, E. E. & McMorran, B. J. Electron Microscopy Spin Analysis of Topological Magnetic Domains in Amorphous Fe/Gd Thin Films. *Microscopy and Microanalysis* 28, 1688–1689 (2022).
7. Parker, W. S., Reddinger, J. A. & McMorran, B. J. Hybrid skyrmions in magnetic multilayer thin films are half-integer hopfions. *Phys. Rev. B* 110, 224420 (2024).



SEMPA image of surface magnetization on FeGd compound.



Lorentz TEM image of projected magnetic field within FeGd compound.

BE-08. Magnetic decoupling of a PMSM machine for flywheel energy storage systems

A. Bellini[1], C. Bianchini[2], G. Petrelli[3]
[1]*Alma Mater Studiorum, University of Bologna, Bologna, Italy,*
[2]*University of Modena and Reggio Emilia, Modena, Italy,*
[3]*University of Nottingham, Nottingham, United Kingdom*

Energy storage systems (ESSs) are a key enabling technology for the transition to renewable and sustainable power systems. Electrochemical batteries are the current standard due to their high energy density and maturity, but they are limited by slow dynamic response, reduced efficiency under transients, and degradation over time. Hybrid energy storage systems (HESSs) address these issues by combining batteries with power-oriented technologies such as flywheel energy storage systems (FESSs), where the flywheel manages fast power fluctuations and transients, reducing battery stress and extending its lifetime.

A further enhancement of system performance can be achieved through the introduction of a magnetic joint between the motor/generator and the flywheel rotor. This element operates as a non-contact magnetic coupling, enabling torque transmission while simultaneously providing mechanical decoupling and vibration damping. In particular, the magnetic coupling acts as an effective filter for torsional oscillations and high-frequency mechanical disturbances, reducing shaft misalignment effects, friction losses, and wear of rotating components. This results in improved rotational stability, longer discharge duration, higher overall efficiency, and increased system lifetime. The effectiveness of the magnetic coupling strongly depends on its electromagnetic and mechanical design parameters, including air-gap geometry, magnetic stiffness, damping characteristics, and torque transfer capability. Therefore, this paper focuses on the optimal design and parameterization of the magnetic coupling, with the aim of maximizing dynamic performance, reducing mechanical stresses, and improving the overall reliability of the hybrid storage system.
A prototype of FESS with magnetic joint was realized, fig. 1, with the following features: NdFeB 35SH magnets, internal diameter: 75mm, external diameter: 100 mm, axial length: 60 mm, 10 poles.

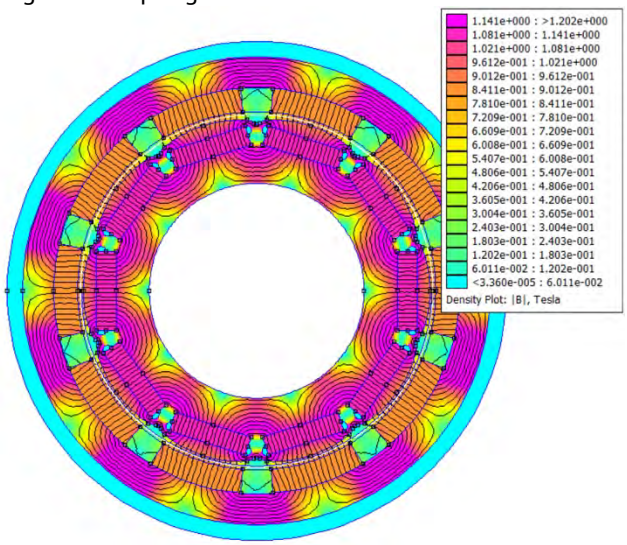
[1] T. S. Babu, K. R. Vasudevan, V. K. Ramachandaramurthy, et al, "A Comprehensive Review of Hybrid Energy Storage Systems: Converter Topologies, Control Strategies and Future Prospects," in *IEEE Access*, vol. 8, pp. 148702-148721, 2020.

[2] A. Alzhrani and K. Atallah, "Electrodynamic Magnetic Bearings for Flywheel Energy Storage System," *2024 Conference on Renewable Energy Technologies and Modern Communications Systems: Future and Challenges*, Shaqra, Saudi Arabia, 2024, pp. 1-6.

[3] K. Atallah and D. Howe, "A novel high-performance magnetic gear," in *IEEE Transactions on Magnetics*, vol. 37, no. 4, pp. 2844-2846, July 2001.



Prototype of the FESS system with close-up view of the magnetic coupling interface.



Finite element analysis (FEA) of the magnetic coupling showing the magnetic flux density distribution.

BE-09. Performance Improvement of a Rare-Earth-Lean Electro-Thermal Multi-Energy Motor with a Heterogeneous Halbach Array Based on Ferrite-Assisted Excitation

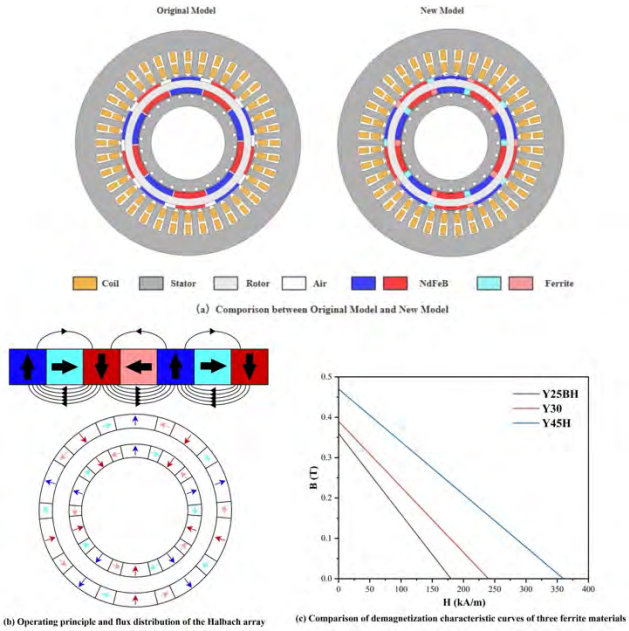
J. Yuan[1, 2], M. Zhang[1, 2], F. Xiao[1, 2], H. Wang[1, 2], Z. Cai[4], D. Dong[3]
[1]School of Electrical Engineering and Automation, Wuhan University, Wuhan, Hubei, China, [2]State Key Laboratory of Power Grid Environmental Protection, School of Electrical Engineering and Automation, Wuhan University, Wuhan, Hubei, China, [3]Xiangtan Electric Manufacturing Co., Ltd, Xiangtan, Hunan, China, [4]School of Electrical Engineering and Automation, College of Chemistry and Molecular Sciences, Wuhan University, Wuhan, Hubei, China

The permanent magnet electro-thermal multi-energy motor is a novel device capable of directly converting wind energy into both electrical and thermal energy. To ensure efficiency, high-performance rare-earth permanent magnets are typically used for excitation; however, they face supply chain concentration and significant price fluctuations. Replacing expensive NdFeB with low-cost ferrite is a viable path to reduce the dependence and cost of wind motors. Nevertheless, due to the low remanence of ferrite, direct replacement leads to a decrease in air-gap flux density and significant performance degradation.
To address this contradiction, this paper proposes an electro-thermal multi-energy motor with a novel rare-earth-lean flux-focusing structure. The device employs a heterogeneous Halbach array assisted by high-coercivity ferrite. By leveraging the one-sided magnetic field enhancement and self-shielding characteristics of the Halbach array, it ensures high-performance output while maximizing magnetic material utilization. The topology of the novel device is shown in Fig.1(a),where the excitation pole consists of a ferrite-NdFeB hybrid, and the magnetization pattern is illustrated in Fig.1(b).
Initially, ferrite material selection was investigated at a 0.82 ：0.18 pole ratio among Y25BH,Y30,and Y45H as shown in Figure 1(c).Simulation results demonstrate that high-coercivity Y45H yielded the best matching results. Compared to the baseline model, this heterogeneous auxiliary excitation structure boosted the electrical and total power by 14.59% and 2.76% respectively, as illustrated in Figure 2(a) and Figure 2(b).Subsequently, inner and outer main pole ratios were optimized to 0.8 and 0.79 by treating performance non-degradation as a rigid constraint and minimized rare-earth usage as the objective. Compared to the pure rare-earth model, this optimized design increased the power per unit cost to 33.72 kW/$ with a 7.86% improvement, achieving significant cost benefits while

ensuring electromagnetic performance as presented in Figure 2(c).

[1]Peng B, Yuan J, Wang H, et al. Electromagnetic Parameter Design and Finite Element Analysis of a Novel Dual-Stator Electric-Thermal Output Machine[C]//2024 IEEE 21st Biennial Conference on Electromagnetic Field Computation (CEFC).IEEE,2024:01-02.

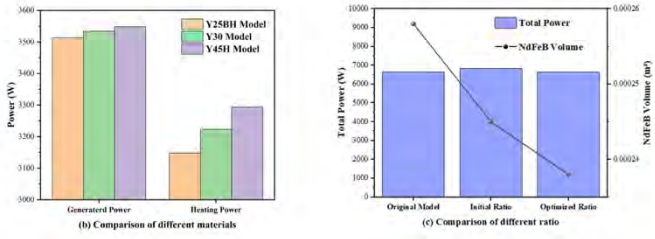
[2]Jiaxin Yuan, Hao Wang, Bin Peng, Hang Zhou, Qiong Wang, Xiaoguo Chen; Composite dissimilar material based heating power optimization method for electro-thermal multi-energy flexible generator. *AIP Advances* 1 February 2026; 16 (2): 025101.



Topological structure and comparison of auxiliary material characteristics

(a) Comparison of power outputs between different materials

	Original Model	Y25BH Model	Y30 Model	Y45H Model
Tatal Power	6.6575kW	6.6614kW	6.7564kW	6.8413kW



Comparison of optimization

BE-10. FEA Modeling of Rare Earth Permanent Magnets with Grain Boundary Diffusion Used in Large Size Electrical Machines

J. Shen, J. Lu
Zhejiang University, Hangzhou, China

NdFeB permanent magnets (PMs) added with light rare earth Ce are used in large size electrical machines so as to reduce the consumption of Nd and Pr. Such PMs need to be processed with grain boundary diffusion (GBD) of Dy or Tb to enrich the coercivity. Thus, the unevenness of the PMs must be considered during the finite element analysis (FEA) [1], where the PM is traditionally divided into some pseudo even layers.

When the machine has a large size at the scale of meters, the PMs are usually at the scale of centimeters, whilst the layer thickness of the GBD PM is only of millimeters or even less. For example, in a 280 kW, 60 r/min prototype with stator core OD of 1.61 m and PM size of 4*2*5 cm, the unit motor being shown in Fig.1, each PM has 6 layers, 1.25 mm thick for layers 1~5. The demagnetization curves of the GBD PM at different layers can be measured directly. Meshing must be carefully tuned, otherwise the FEA cannot work due to the very wide dimensional range, or the computing resources are extremely required.

A homogeneous equivalent model of the GBD PM is then proposed in this paper. Refer to Fig.2, the MMF and reluctance outside the PM are F_o and R_o. In the layered PM model, each layer has its own MMF F and reluctance R, all layers are in series. Whilst, in the proposed model, the PM is an even material, its reluctance is the sum of all layers, while its MMF is decided in such a way that the produced flux Φ_o is identical to that in the layered model. Hence, the equivalent demagnetization curve can be identified. Clearly, the overall excitation of the PM is unchanged, but the FEA meshes can be made at a larger dimensional scale, avoiding meshing the thin layers directly.

The conventional layered model and homogenized model are compared in FEA for the prototype machine. In aspects of back EMF, electromagnetic torque, core loss and eddy current loss, the calculation result difference is always around 0.1%. However, by using the homogenized model, meshing does not need to be tuned manually, and the computing time becomes 39% less. It is particularly efficient when FEA for large size machine is iteratively performed during design optimization.

[1] F. Chen, T. Zhang, W. Zhang, L. Zhang, and Y. Jin, "Dependence of the demagnetization behavior on the direction of grain boundary diffu-sion in sintered Nd-Fe-B magnets," Journal of Magnetism and Magnet-ic Materials, vol. 465, pp. 392–398, Nov. 2018

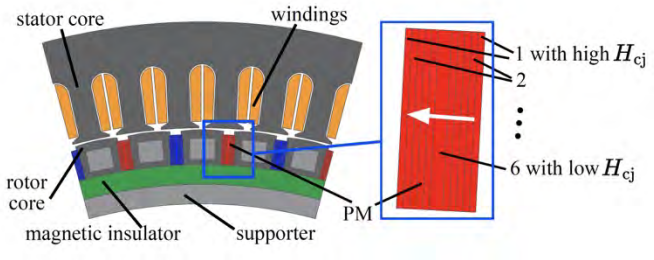


Fig.1 Unit motor

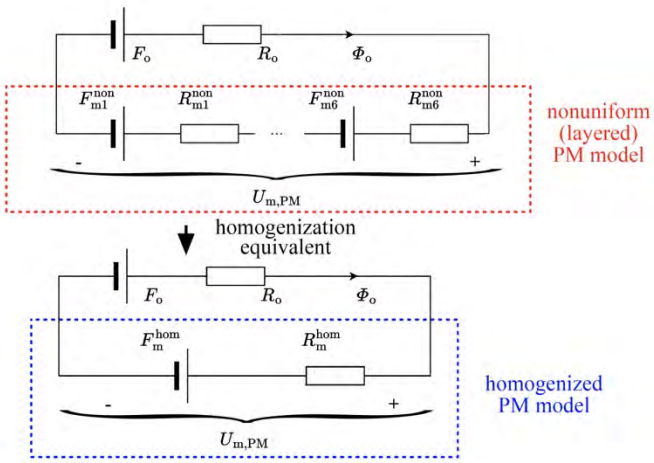


Fig.2 PM Modeling

BE-11. Vibration Characteristic Analysis for Large Transformer Core

R. Takeda[1], M. Namikawa[2], H. Inoue[1], T. Omura[1], T. Overboom[3], M. Schmid[4], S. Mokkapaty[5], M. Milone[5]
[1]Steel Research Laboratory, JFE Steel Corporation, Kurashiki, Japan, [2]Steel Research Laboratory, JFE Steel Corporation, Kawasaki, Japan, [3]Royal Smit Transformers, SGB-SMIT Group, Nijmegen, Netherlands, [4]SGB Transformers, SGB-SMIT Group, Regensburg, Germany, [5]SGB-SMIT Group, Regensburg, Germany

Understanding transformer no-load noise under three-phase excitation requires accurate characterization of the vibration response of the transformer core[1,2]. Among the mechanical properties of the laminated cores composed of electrical steel sheets, the out-of-plane shear modulus is regarded as a key factor which influences vibration characteristics[3–5]. In this study, a 40 MVA transformer was analyzed by modeling its laminated core as an equivalent orthotropic body and calculating its vibration response by finite element analysis (FEM). The no-load noise spectrum was predicted by combining the measured magnetostrictive characteristics and calculated vibration response, and was compared with the results of actual measurements. The out-of-plane shear modulus of the core was identified by using a genetic algorithm based on the similarity between the predicted and measured no-load noise spectra. The identified shear modulus was approximately 1/500 of the bulk property of the electrical steel, indicating a significant reduction due to lamination. Fig. 1 compares the measured and calculated no-load noise spectra of a 40 MVA transformer at the identified shear modulus, showing good agreement between calculation and measurement. The quantitative effect of increasing the leg shear modulus on no-load noise reduction was also demonstrated.

[1] M. Ishida, S. Okabe, and K. Sato, Kawasaki Steel Tech. Rep. 39, 29–35 (1988).
[2] A. Moses, P. Anderson, and T. Phophongviwat, *IEEE Trans. Mag.*, 52(10), 7100615 (2016).
[3] S. Takajo, T. Ito, T. Omura, and S. Okabe, *IEEE Trans. Mag.*, 53(9), 201606 (2017).
[4] T. Omura, H. Yamaguchi, Y. Ishigaki, S. Okabe, and H. Toda, *IEEJ Trans. Fundam. Mater.*, 135, 414 (2015).
[5] S. Okabe, Y. Ishigaki, and T. Omura, *AIP Adv.*, 8, 047902 (2018).

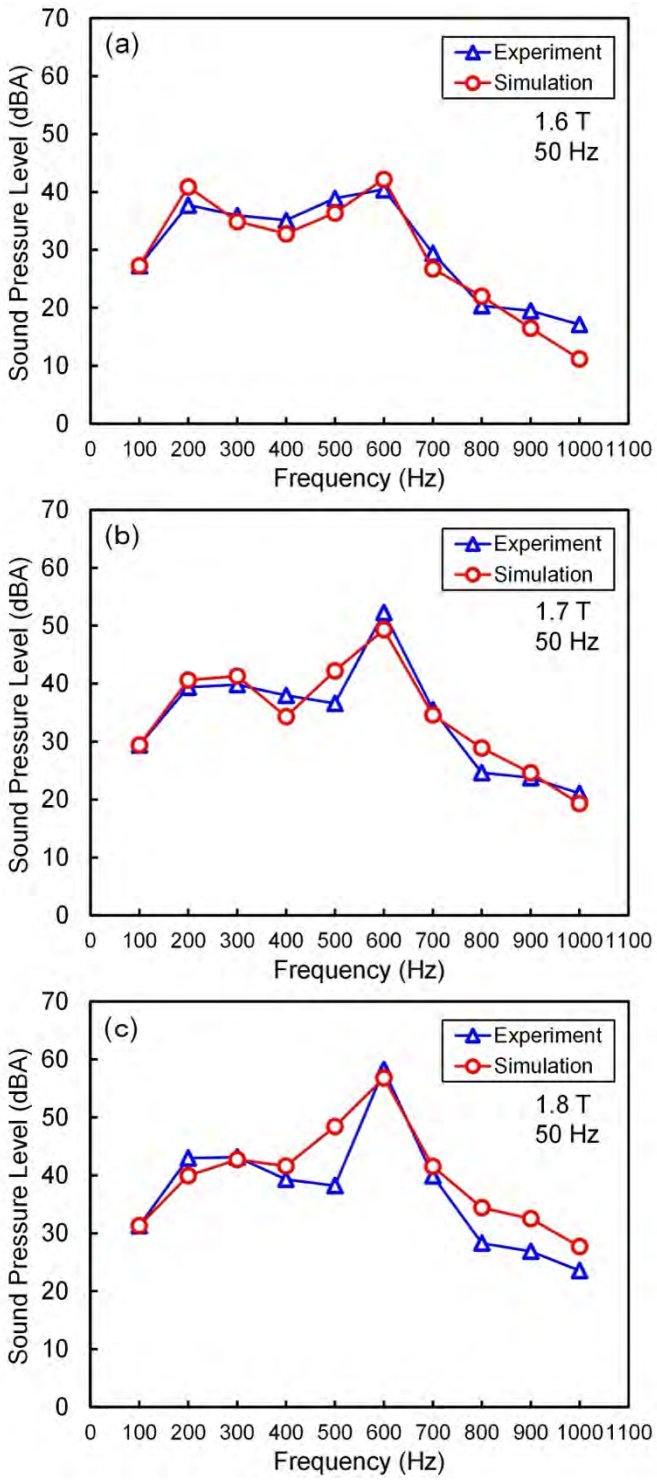


Fig. 1. Measured and calculated no-load noise spectra of the 40 MVA transformer at identified shear modulus: (a) 1.6 T, (b) 1.7 T and (c) 1.8 T.

BE-12. CNN-Based Recognition of Underwater Magnetic Tags

S. Ben Mbarek, S. Rana Muhammad, I. Nasri, S. Amara, H. Bagci, G. Setti
CEMSE, KAUST, Thuwal, Saudi Arabia

Magnetic tags offer a compelling alternative to existing identification methods owing to their durability, compatibility with underwater environments, and non-line-of-sight detection capability [1] [2]. Our previous work established the theoretical feasibility of magnetic tag recognition using far-field measurements [3] [4]. In this work, we present a real-world implementation extending that foundation to real-time measurement and CNN-based recognition of underwater magnetic tags across varying axial distances. The sensing system consists of four SparkFun Magnetic Imaging Tiles arranged in a 2x2 configuration, forming 16x16 Hall-effect sensor array that captures spatially resolved magnetic field patterns [5]. The array is encapsulated in urethane resin for underwater protection (Fig. 1-a). The magnetic tags consist of permanent magnets arranged in distinct polarity configurations, yielding 81 unique tag classes, each recognizable by its magnetic field signature. Data are collected by fixing the magnetic tag (Fig. 1-a, d) and scanning the sensor array along the z-axis from z = 15 mm to z = 45 mm using a translation stage. The resulting dataset comprises 81 tag configuration classes, corresponding to all unique polarity arrangements of the magnet array, with 450 images per class, captured at multiple axial distances and processed using a Python-based acquisition pipeline (Fig. 1-c, d, e). Tag recognition was performed using a convolutional neural network trained on the 16x16 magnetic field images, evaluated through a leave-one-distance-out validation strategy to assess generalization across axial distances. Figure 2 presents the normalized confusion matrices showing a near-perfect diagonal structure for different distances changing from z=15 mm to 45 mm for all the tag configurations. This indicates a strong discriminative capability and reduced inter-class confusion. These results confirm that CNN-based classification of magnetic-field signatures provides robust underwater tag identification.

References

[1] Liu, T., Rong, L., Dai, H., Zhang, J., Zheng, S., Qiu, L., Yu, S., Wu, J. and Zhang, G., 2025. Advancements in magnetic dipole detection: Direct magnetic gradient tensor data versus total magnetic intensity derived calculations. *Measurement*, *253*, p.117386.

[2] Kohls, N.D., Zheng, A.X., Kim, J., Mohler, G. and Mazumdar, Y.C., 2021. Magnetic tags with unique self-assembly patterns for tracking applications. *Journal of Magnetism and Magnetic Materials*, *535*, p.168045.
[3] S. B. Mbarek, S. Amara and G. Setti, 2026 "Magnetic Dipole-Based Tag Recognition from Far-Field Measurements via Euler Deconvolution," in *IEEE Transactions on Magnetics*, vol. 62, no. 1, pp. 1-6.
[4] Ben Mbarek, S., Amara, S. and Setti, G., 2026. Magnetic tag recognition via high-order projection of far-field measurements. *AIP Advances*, *16*(2).
[5] sparkfun," 21 4 2026. [Online]. Available: https://www.sparkfun.com/sparkfun-magnetic-imaging-tile-8x8.htFig.

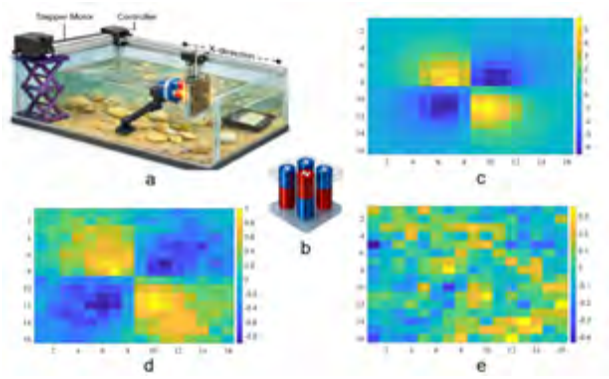


Fig. 1: Experimental setup: a-underwater measurement setup, b-magnetic tag, c, d, e-Magnetic pattern for configuration NSSN for z=15 mm, 25 mm,and 45 mm.

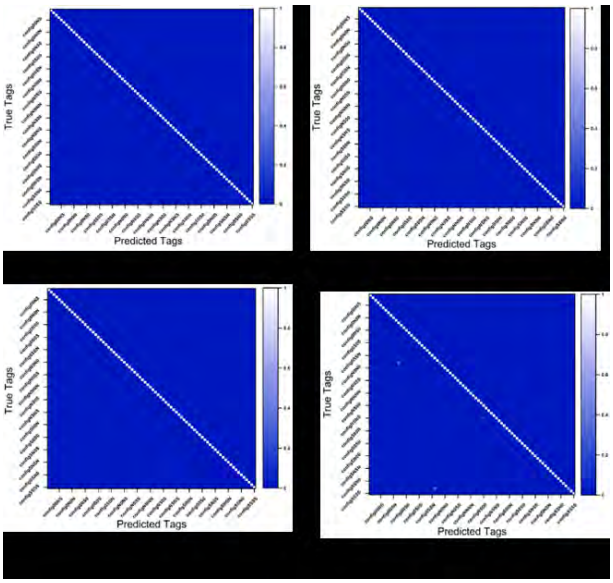


Fig2: Recognition results: a-z=15mm, b- z=25mm, c-z=35mm, and d-z=45mm.

BE-13. Transient Magnetic Edge Intelligence for Adaptive Sensing

A. Upadhyay
Electrical and Computer Engineering, University of Texas at Austin, Austin, Texas, United States

Magnetically instrumented sensing systems are increasingly used in environmental and agricultural monitoring but are typically designed for persistent operation, leading to unnecessary energy use and long-term material accumulation. This work introduces a transient edge intelligence framework for magnetic sensing nodes operating within task-relevant windows.
We develop a resource-adaptive inference system on microcontroller hardware that selects models from a pre-trained bank with varying quantization levels. A lightweight controller optimizes selection under memory, latency, and energy constraints, enabling efficient operation in constrained environments.
The sensing platform integrates magnetic field-responsive elements for detecting subsurface variations relevant to soil composition and microplastic presence. To support environmental deployment, the system is co-designed with biodegradable polymer-based substrates, enabling controlled degradation or deactivation after task completion.
Results show reduced memory and energy use while maintaining accuracy versus static models. Magnetic sensing signals are processed under constrained conditions, demonstrating the feasibility of combining low-power inference with distributed magnetic sensing.
This work establishes a pathway toward sustainable intelligent sensing by integrating adaptive edge inference with transient system design, with applications in environmental monitoring, precision agriculture, and distributed sensor networks.

S. Tumanski, Meas. Sci. Technol., Vol. 18, p. R31 (2007)
P. Ripka and M. Janosek, IEEE Sens. J., Vol. 10, p. 1108 (2010)
J. G. Webster, Wiley Encyclopedia of Electrical and Electronics Engineering (2015)
V. Sze, Y. Chen and T. Yang, Proc. IEEE, Vol. 105, p. 2295 (2017)
S. Han, H. Mao and W. Dally, NIPS, p. 1135 (2015)
Y. LeCun, Y. Bengio and G. Hinton, Nature, Vol. 521, p. 436 (2015)
S. Hwang, H. Tao and D. H. Kim, Adv. Funct. Mater., Vol. 30, p. 1904523 (2020)
J. A. Rogers, T. Someya and Y. Huang, Science, Vol. 327, p. 1603 (2010)

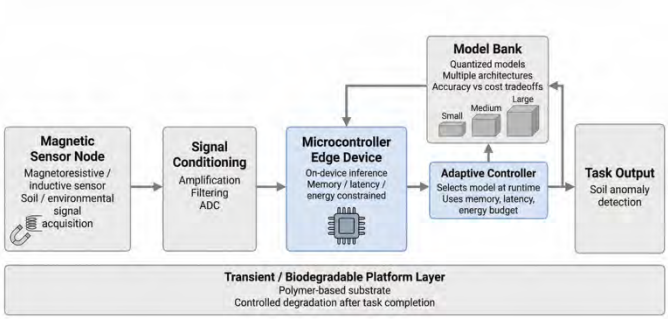


Figure 1: System architecture of the transient magnetically enabled edge intelligence platform, showing magnetic sensing, signal conditioning, adaptive model selection, and microcontroller-based inference on a biodegradable substrate.

SESSION BF: ALTERMAGNETIC AND ANTIFERROMAGNETIC SPINTRONICS I

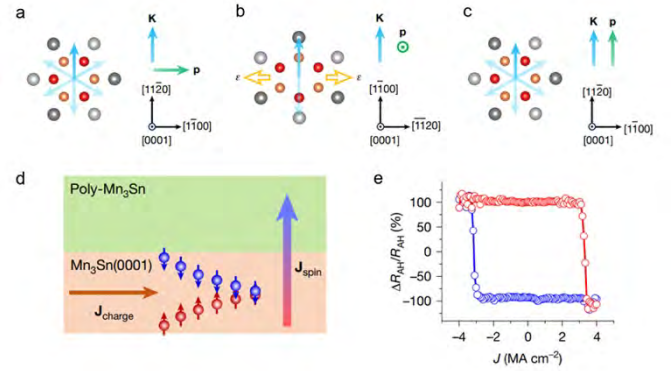
Chair(s): J. Kang, *Electrical and Computer Engineering, Northwestern University, Evanston, Illinois, United States*
Tuesday, November 3, 2026
02:00 PM-05:30 PM
South Pacific 3/4

BF-01. Highly-efficient field-free full switching of chiral antiferromagnets

C. Song, Z. Zhou
Tsinghua University, Beijing, China

Chiral antiferromagnets host octupole order and combine the advantages of antiferromagnets and ferromagnets. Despite the development of numerous switching strategies [1,2], the field-free full switching remains elusive, posing a critical obstacle to their practical application in memory technology. Here we prepared a homo-junction constituted of Mn_3Sn(0001) bottom layer and polycrystalline Mn_3Sn top layer. The tilted Kagomé geometry in polycrystalline Mn_3Sn divides the out-of-plane spin polarization from Mn_3Sn(0001) layer into the out-of-Kagomé-plane and in-Kagomé-plane component, generating the symmetric (antiferromagnet-type) and asymmetric (ferromagnet-type) driving force, respectively. The former accelerates octupole rotation while the latter determines switching chirality. Field-free full switching is realized in the unconventional protocol that integrates the advantages of both antiferromagnetic and ferromagnetic switching. It goes beyond conventional full switching framework requiring perpendicular uniaxial anisotropy. An unprecedented switching efficiency is achieved, with both current density and power consumption an order of magnitude lower than in previous configurations, by virtue of the highly-efficient driving forces due to spin-torque characteristics of octupole order and the ultra-low energy barrier arising from easy-plane anisotropy, overcoming their trade-off in conventional protocols. The zero-field switching has octupole-programmable chirality [3]. Our work opens up new avenue for all-chiral-antiferromagnetic memories with ultra-dense integration, ultra-high efficiency, ultra-fast speed and flexible controllability.

[1] H. Tsai, *et al.* Nature 580, 608 (2020).
[2] T. Higo, *et al.* Nature 607, 474 (2022).
[3] Z. Zhou, *et al.* Nature 651, 341 (2026).



Configuration innovation and the field-free full switching of chiral antiferromagnetic order by homo-junction design. p and K represent the current-induced spin polarization and chiral antiferromagnetic order, respectively. Poly-Mn_3Sn is the abbreviation of the polycrystalline Mn_3Sn. J_{charge} and J_{spin} represent the charge current and spin current, respectively. J denotes the current density. $\Delta R_{AH}/R_{AH}$ represents the switching ratio.

BF-02. Multistate probabilistic computing in the chiral kagome antiferromagnet Mn_3Sn

P. Madhusudan Rao[1], J. Jeon[1], K. Callahan-Coray[2], K. Camsari[2], S. Parkin[1]
[1]Nanosystems for Ions, Spins and Electrons, Max-Planck Institute of Microstructure Physics, Halle(Saale), Germany, [2]Department of Electrical and Computer Engineering, University of California, Santa Barbara, Santa Barbara, California, United States

Chiral kagome antiferromagnets such as Mn_3Sn are promising candidates for spintronic applications, owing to their large anomalous Hall effect driven by non-vanishing Berry curvature [1]. Unlike collinear antiferromagnets, Mn_3Sn hosts a non-collinear 120° spin structure. Its magnetic ground state exhibits a six-fold degeneracy [2], naturally supporting multistate information processing, beyond the binary paradigm of conventional spintronic devices. While previous studies have demonstrated spin-orbit torque (SOT) control of the magnetic states in Mn_3Sn [3], they have been limited to binary states. Here, in W/Mn_3Sn bilayers, we electrically resolve the six degenerate ground states through their domain-dependent anomalous Hall conductivities and demonstrate electrical switching between them. Above a critical current density, thermally assisted SOT drives stochastic fluctuations of the anomalous Hall resistance, whose probability distribution is continuously tunable with nanosecond electrical pulses. We thus realize antiferromagnetic probabilistic bits (p-bits) with multiple accessible states, characterized by a sigmoidal current response. Leveraging these multistate p-bits, we solve an NP-hard graph-coloring problem with a 1000-fold reduction in the computational state space over a binary implementation – drastically reducing the required number of p-bits. Our work establishes the first multistate antiferromagnetic p-bit and opens a new direction for beyond-binary spintronic hardware for probabilistic computing.

1. Nakatsuji, S., N. Kiyohara, and T. Higo, Large anomalous Hall effect in a non-collinear antiferromagnet at room temperature. Nature, 2015. 527(7577).
2. Liu, J. and L. Balents, Anomalous Hall Effect and Topological Defects in Antiferromagnetic Weyl Semimetals: Mn3Sn/Ge. Phys. Rev. Lett., 2017. 119(8).
3. Higo, T., et al., Perpendicular full switching of chiral antiferromagnetic order by current. Nature, 2022. 607(7919).

BF-03. Write error rate in Mn_3Sn nanodots driven by chiral spin rotation using sub-ns pulses

Y. Fushimi[1, 2], Y. Sato[1, 2], H. Iwai[1, 2], Y. Yamane[1, 3], S. Kanai[1, 2, 4], S. Fukami[1, 2, 4]
[1]Laboratory for Nanoelectronics and Spintronics, Research Institute of Electrical Communication, Tohoku University, Sendai, Japan, [2]Department of Electronic Engineering, Tohoku University, Sendai, Japan, [3]Frontier Research Institute for Interdisciplinary Sciences, Tohoku University, Sendai, Japan, [4]Center for Science and Innovation in Spintronics, Tohoku University, Sendai, Japan

Antiferromagnets (AFMs) are promising for high-speed and external field-robust spintronic devices [1,2]. Among them, a noncollinear AFM Mn_3Sn provides an excellent platform for electrical detection and manipulation of AFM order, including readout via the anomalous Hall [3] and tunnel magnetoresistance effects [4], as well as writing through current-induced switching [5] and chiral spin rotation [6,7]. For practical applications, it is essential to understand the stochastic contributions to switching. Here, we investigate the dependence of the write error rate (WER) on current pulse width t_{pulse} and current density J_{HM} in Mn_3Sn nanodots, and clarify switching characteristic associated with the chiral spin rotation.

We fabricate an epitaxial Mn_3Sn (20 nm) nanodot [8] with a diameter of 150 nm on a Ta (3 nm)/W (2 nm) channel deposited on a MgO (110) substrate [Fig. 1 (a)]. Clear binary switching is observed by both out-of-plane magnetic-field and applied current, displayed in Figs. 1(b), (c). We measure WER as functions of t_{pulse} and J_{HM}, under various in-plane magnetic field H. The measured WER exhibits oscillatory behavior at H = 0 [Fig. 2], consistent with coherent chiral-spin rotation. A minimum WER of less than is obtained at t_{pulse} = 0.1 ns and J_{HM} = 60 MA/cm^2. Interestingly, minimum value of WER decreases as t_{pulse} decreases, which we attribute to the suppression of thermal fluctuations under shorter pulses, leading to reliable coherent control. These results provide useful insight into high-speed and reliable operation in antiferromagnetic devices.

This work was partly supported by JSPS Kakenhi, JST-PRESTO, MEXT X-NICS, and RIEC Cooperative Research Projects.

[1] T. Jungwirth, X. Marti and P. Wadley, Nat. Nanotechnol., Vol. 11, p.231 (2016)
[2] V. Baltz, A. Manchon and M. Tsoi, Rev. Mod. Phys., Vol. 90, p.015005 (2018)
[3] S. Nakatsuji, N. Kiyohara and T. Higo, Nature., Vol. 527, p.212 (2015)

[4] X. Chen, T. Higo and K. Tanaka, Nature., Vol. 613, p.492 (2023)
[5] H. Tsai, T. Higo and T. Nomoto, Nature., Vol. 580, p.608 (2020)
[6] Y. Takeuchi, Y. Yamane and J.-Y. Yoon, Nat. Mater., Vol. 20, p.1364 (2021)
[7] Y. Takeuchi, Y. Sato and Y. Yamane, Science., Vol. 389, p.830 (2025)
[8] Y. Sato, Y. Takeuchi and Y. Yamane, Appl. Phys. Lett. Vol. 122, p.122404 (2023)

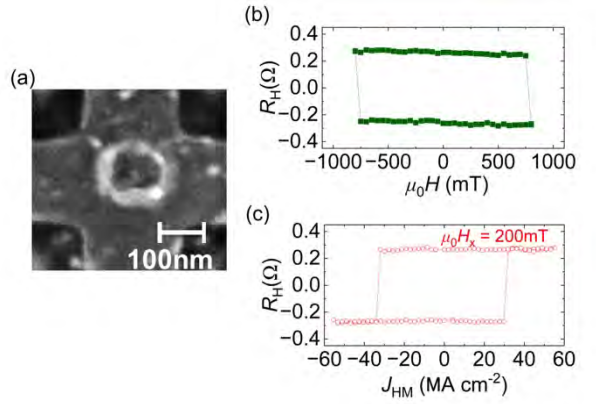


Fig. 1. (a) SEM image, (b) R_H-H, and (c) R_H-J_{HM} curves of Mn_3Sn nanodot devices.

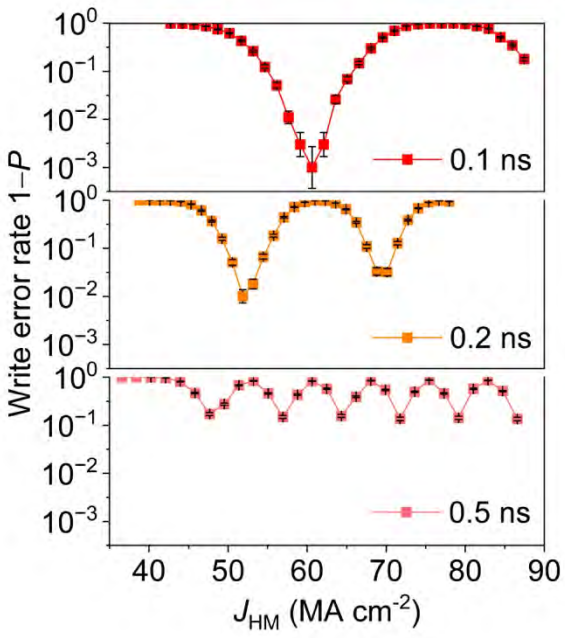


Fig. 2. Pulse width t_{pulse} dependence of WER under zero magnetic field in nanodot device (Fig.1).

BF-04. Fast Spin-Orbit and Octupole-Driven Spin-Transfer Torque Switching of Non-Collinear Antiferromagnetic Tunnel Junctions

N. Zogbi[1, 2], V. C. Rogers[1, 2], S. B. Hamid[1, 2], M. Hamdi[3], J. Kang[3], S. Arpaci[4], E. Matt[4], S. Cheung[3], P. Khalili Amiri[3, 4], J. Incorvia[1, 2]
[1]Chandra Dept. of Electrical and Computer Engineering, University of Texas at Austin, Austin, Texas, United States, [2]Microelectronics Research Center, University of Texas at Austin, Austin, Texas, United States, [3]Department of Electrical and Computer Engineering, Northwestern University, Evanston, Illinois, United States, [4]Applied Physics Program, Northwestern University, Evanston, Illinois, United States

Antiferromagnetic tunnel junctions (ATJs) have emerged as a platform for ultrafast, energy-efficient memory technologies due to the intrinsically rapid dynamics of non-collinear antiferromagnets. ATJs leverage exchange-dominated dynamics of the antiferromagnetic order parameter that can operate in the picosecond regime. Recent demonstrations of both spin-orbit torque (SOT) and octupole-driven spin-transfer torque (OTT) switching in ATJs involving $PtMn_3$ electrodes have established that these devices can be electrically written and read using mechanisms analogous to ferromagnetic MTJs [1, 2]. These advances position ATJs as a candidate for next-generation non-volatile memory with substantially higher intrinsic speed potential.
In this work, we demonstrate current-induced switching in 300 nm diameter ATJs using both SOT and OTT, achieving switching with 30 ns write pulses and exhibiting device TMR values up to 300% [3]. With the structure of the devices shown in Fig. 1, SOT and OTT induced switching loops confirm electrical control of the antiferromagnet (AFM) order in a $PtMn_3$-based ATJ stack. Beyond deterministic switching, we observe that metastable magnetic configurations in the collector and emitter electrode allow 200 nm devices to express at least 4 bits with nearly perfect retention for 2 minutes, shown in Fig. 2. We experimentally characterize the stability of the intermediate states over time, quantify their evolution, and employ a channel capacity analysis to estimate the information capacity of the ATJs over a range of write-read delays. Collectively, the demonstration of both SOT and STT switching pathways, combined with the presence of well-defined intermediate states, establishes ATJs as a scalable and ultrafast multi-level memory-cell technology well suited for future high-speed, low-energy computing architectures.
[1] Shi, J. et al. Electrically Controlled All-Antiferromagnetic

Tunnel Junctions on Silicon with Large Room-Temperature Magnetoresistance. *Advanced Materials* 36, 2312008 (2024).
[2] Kang, J. et al. Octuple-driven spin-transfer torque switching of all-antiferromagnetic tunnel junctions. *Arxiv. 2509.03026* (2025).
[3] Zogbi, N. et al. Fast Current Induced Spin-Orbit and Octupole-Driven Spin-Transfer Torque Switching of multi-bit Antiferromagnetic Tunnel Junctions. *Under Review.*

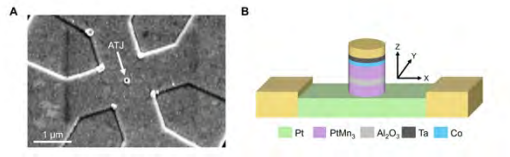


Fig. 1: (A) SEM image of a representative device with a 100 nm diameter ATJ. (B) Schematic of the ATJ memory cell.

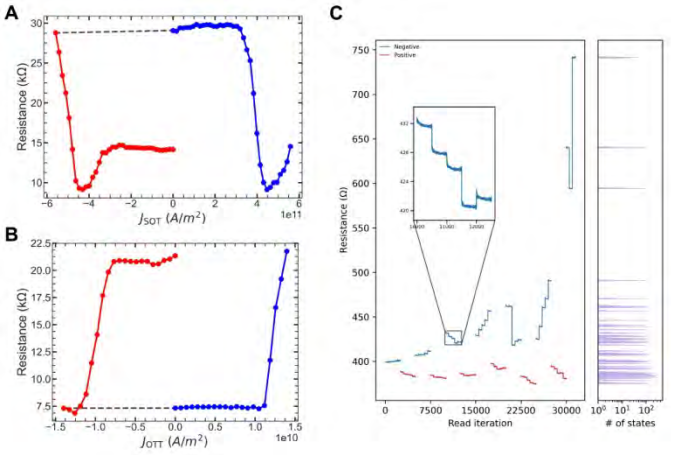


Fig. 2: (A) SOT switching loop of a 300 nm ATJ using a 30 ns write pulse. (B) OTT switching loop of a 300 nm ATJ using a 30 ns write pulse. (C) Retention measurement of the 200 nm ATJ showing multi-bit write and a histogram of at least 25 unique resistance states.

BF-05. Thickness-Dependent Spin–Orbit Torque and Spin Diffusion in Epitaxial Mn_3Sn Thin Films

P. Zhang[1], J. Lu[1], V. Lomakin[2], J. Hong[3]
[1]HBUT, Wuhan, China, [2]UCSD, La Jolla, California, United States, [3]UC Berkeley, Berkeley, California, United States

Efficient spin-current generation and control are central to next-generation spintronic technologies. The noncollinear antiferromagnet Mn_3Sn, characterized by a kagome lattice and strong Berry curvature near the Fermi level, exhibits pronounced anomalous Hall and spin Hall effects that establish it as an intrinsic spin-current source [1]. Its nearly compensated magnetic structure suppresses stray fields while preserving topological spin transport. Spin–orbit torque (SOT) generation has been demonstrated in Mn_3Sn-based heterostructures [2–4]; however, systematic investigations of thickness-dependent torque efficiency and intrinsic spin diffusion in epitaxial films remain limited. Here, we study SOT generation in epitaxial Mn_3Sn/Py bilayers with Mn_3Sn thickness varied from 5 to 40 nm. Using spin-torque ferromagnetic resonance and x-ray magnetic dichroism, we extract the damping-like torque efficiency as a function of thickness. We observe a clear and reproducible evolution of torque amplitude, reflecting a competition between bulk Berry-curvature-driven spin Hall contributions and interfacial spin transmission, from which the effective spin diffusion length is determined. The combination of sizable torque efficiency and antiferromagnetic order suggests compatibility with exchange-enhanced spin dynamics characteristic of antiferromagnets, offering prospects for high-speed topological spintronic platforms.

[1] S. Nakatsuji, N. Kiyohara, and T. Higo, Nature 527, 212 (2015).
[2] S. Hu et al., Nat. Commun. 13, 4447 (2022).
[3] S. Lu et al., Chin. Phys. B 33, 107501 (2024).
[4] S. Lu et al., Nano Lett. 26, 4, 1220–1227, (2026).

BF-06. Low frequency noise in W/Mn_3Sn spin-orbit torque devices

W. Liang[1], S. Sakamoto[1], J. Chen[1], X. Piao[1], H. Kosaki[1], T. Higo[2], M. Asakura[2], S. Nakatsuji[1, 2, 3], S. Miwa[1]
[1]The Institute for Solid State Physics, The University of Tokyo, Kashiwa, Japan, [2]Department of Physics, The University of Tokyo, Tokyo, Japan, [3]Institute for Quantum Matter and Department of Physics and Astronomy, Johns Hopkins University, Baltimore, Maryland, United States

In ferromagnetic systems, low frequency noise (LFN) measurements have been used to study spin dynamics, such

as the thermally excited hopping of domain walls in magnetic tunnel junctions [1]. Recently, antiferromagnetic spintronics has attracted significant attention due to the ability to control the antiferromagnetic spin structure using spin-orbit torque. While the non-collinear spin structure of Mn_3Sn has been controlled by spin-orbit torque [2-4], spin dynamics of the auto-oscillation, known as chiral spin rotation [3], has not been fully understood. In this study, we investigated the dynamics of the chiral spin rotation of Mn_3Sn in detail by LFN measurements.

We fabricated epitaxial W (6 nm) / Mn_3Sn (5 nm) multilayers on the MgO (110) substrate by molecular beam epitaxy, as shown in Fig. 1. The Hall bar devices were fabricated using standard photolithography, Ar-ion milling, and lift-off techniques. Noise behavior in the Mn_3Sn Hall-bar devices was investigated using the LFN measurement setup illustrated in Fig. 1. To suppress preamplifier noise, we employed a cross-correlation technique. As shown in Fig. 2, we find that an increase in the applied current enhances the low-frequency power spectrum density (PSD) and changes its spectral profile. This variation in the 1/f- and Lorentzian-like PSD features indicates the presence of additional noise induced by spin-orbit torques, which we attribute to chiral spin rotations [3] of the non-collinear spin structure in Mn_3Sn.

We thank K. Kobayashi. for the discussion. This work was partially supported by JST-Mirai program, JST-ASPIRE, JST-SPRING, JSPS-KAKENHI, Spin-RNJ, and X-nics.

[1] S. Ingvarsson *et al.*, Phys. Rev. Lett., Vol. 85, p.3289 (2000)
[2] T. Higo *et al.*, Nature, Vol. 607, p.474 (2022)
[3] Y. Takeuchi *et al.*, Nat. Mater., Vol. 20, p.1364 (2021)
[4] S. Sakamoto *et al.*, Nat. Nanotech., Vol. 20, p.216 (2025)

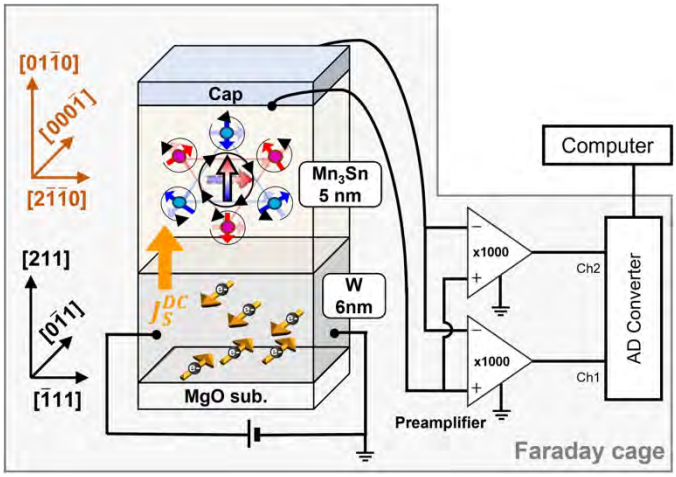


Fig.1 Experimental setup for low frequency noise measurement

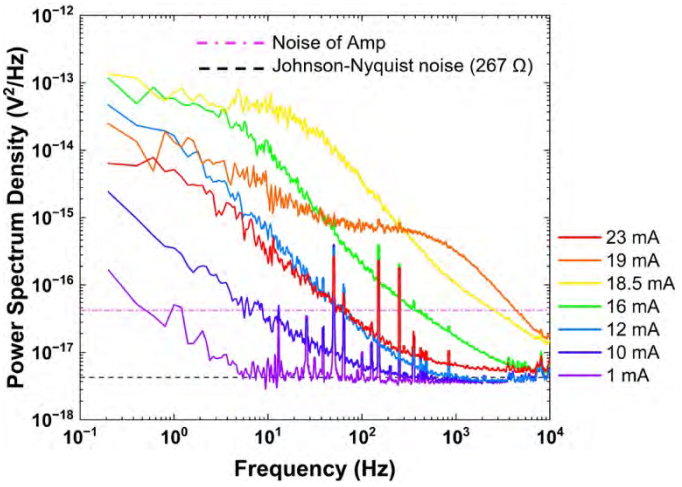


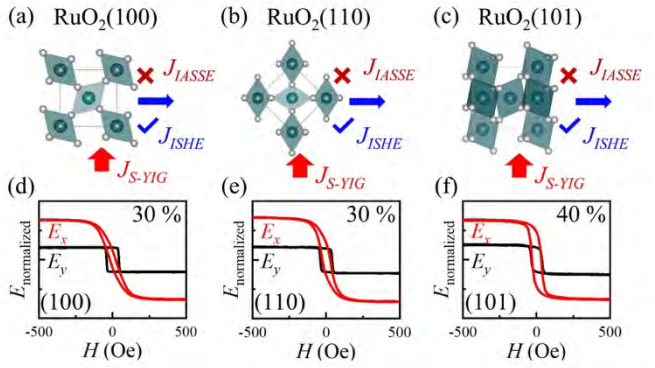
Fig.2 Current dependence of power spectrum density

BF-07.* Absence of Transport Altermagnetic Spin-Splitting Effect in RuO_2

Y. Wang*[1, 2], Z. Shen[1], C. Lin[1], W. Hsu[1], Y. Chen[2], Y. Chin[3], A. Singh[4], W. Lee[4], C. Chen[5], S. Huang[1, 6], D. Qu[2, 6]
[1]Department of Physics, National Taiwan University, Taipei, Taiwan, [2]Center for Condensed Matter Sciences, National Taiwan University, Taipei, Taiwan, [3]Department of Physics, National Chung Cheng University, Chia-Yi, Taiwan, [4]Institute of Physics, Academia Sinica, Taipei, Taiwan, [5]National Synchrotron Radiation Research Center, Taipei, Taiwan, [6]Center of Atomic Initiatives for New Materials, National Taiwan University, Taipei, Taiwan

Altermagnetism has recently emerged as a distinct magnetism that combines the advantages of both ferromagnetism and antiferromagnetism. Characterized by non-relativistic spin-splitting bands and vanishing net magnetization, altermagnets serve as a platform for next-generation spintronic applications. Among various candidates, the rutile structured ruthenium dioxide (RuO_2) has attracted significant attention due to its metallic state, high Néel temperature, and predicted d-wave spin splitting. Numerous spin-dependent transport studies have reported fingerprints of altermagnetism in RuO_2 thin films, citing anisotropic or unconventional spin-dependent phenomena as evidence of its spin-splitting effect [1]. However, recent spectroscopic measurements have challenged this consensus, suggesting an absence of the magnetic moment. If RuO_2 is not a true altermagnet, the origin of the previously observed transport signatures remains an open

and pressing question. Resolving this controversy is essential for establishing whether RuO_2 represents an altermagnetic ground state.
In this work [2], we investigate spin-to-charge conversion in epitaxial RuO_2 films using thermal spin injection from the ferrimagnetic insulator yttrium iron garnet (YIG). As shown in Fig. 1, by comparing (100)-, (110)-, and (101)-oriented RuO_2, we demonstrate that the spin-splitting effect is absent, and that the anisotropic spin Hall effect dominates spin-dependent transport. These phenomena are fully explained by the three independent spin Hall conductivity tensors allowed by the low crystal symmetry of the rutile structure. Therefore, our work not only resolves the transport controversy in RuO_2, but also highlights that anisotropic spin Hall effect can mix with the altermagnetic spin-splitting effect in all altermagnetic materials with low crystal symmetry.
[1] C.-T. Liao, Y.-C. Wang, Y.-C. Tien *et al.*, Separation of Inverse Altermagnetic Spin-Splitting Effect from Inverse Spin Hall Effect in RuO_2, *Phys. Rev. Lett.* 133, 056701 (2024).
[2] Y.-C. Wang, Z.-Y. Shen, C.-H. Lin *et al.*, Absence of Transport Altermagnetic Spin-Splitting Effect in RuO_2, *Nano Letters* 26, 2548 (2026).



Schematic illustrations of the spin current injected into (a) (100)-, (b) (110)-, (c) (101)- oriented RuO_2, converting to a transverse charge current originating from inverse spin Hall, not inverse altermagnetic spin splitting. The normalized spin Seebeck voltage is measured for the (d) (100)-, (e) (110)-, (e) (110)- oriented RuO_2 samples.

BF-08. Magnetotransport in Altermagnets: Spin-Splitter Torque and Anisotropic Phenomena

S. Karube
Kyoto University, Uji, Japan

Altermagnetism [1] is a recently proposed magnetic phase that forms a third class of magnetism alongside ferromagnetism and antiferromagnetism, and it has been experimentally confirmed in recent years. Although antiferromagnetic, altermagnets break time-reversal symmetry via crystal-symmetry-dependent magnetic order, resulting in spin-split bands. These bands give rise to unusual magnetotransport phenomena.
A representative example is the anomalous Hall effect (AHE), which occurs when symmetries such as PT or mirror symmetry are broken by specific crystal planes or magnetic easy axes. This generates a finite Berry curvature integrated over the Brillouin zone, producing a measurable Hall response. Accordingly, AHE has been observed in several altermagnets, including RuO_2 [2].
Another key Hall-related phenomenon is the spin-splitter effect, a mechanism for generating spin current from spin-split bands. Since its theoretical proposal [3], it has been experimentally demonstrated in altermagnetic RuO_2 by multiple groups [4]. In our work, we epitaxially grew RuO_2 thin films and confirmed spin current generation across different crystal orientations, verifying the spin-splitter effect. Moreover, the unconventional out-of-plane spin polarization enables field-free switching of perpendicular magnetization in adjacent magnetic layers, highlighting its potential for spintronic applications [4].
To date, this effect has mainly been observed in altermagnets with d-wave spin symmetry, such as RuO_2, while reports in other materials remain limited. CrSb, another metallic altermagnet, is a promising candidate; however, its intrinsic g-wave spin symmetry is not expected to support the effect. Here, we focus on strain effects in the epitaxial thin films. By employing strain-induced d-wave-like spin symmetry [5], we examine whether the spin-splitter effect can emerge in CrSb [6]. This presentation overviews altermagnetism and discusses spin current generation in RuO_2 and CrSb.

[1] Phys. Rev. X 12, 031042 (2022), Phys. Rev. X 12, 040501 (2022).
[2] Nat. Electron. 5, 735 (2022).
[3] Phys. Rev. Lett. 126, 127701 (2021).
[4] Phys. Rev. Lett. 129, 137201 (2022).

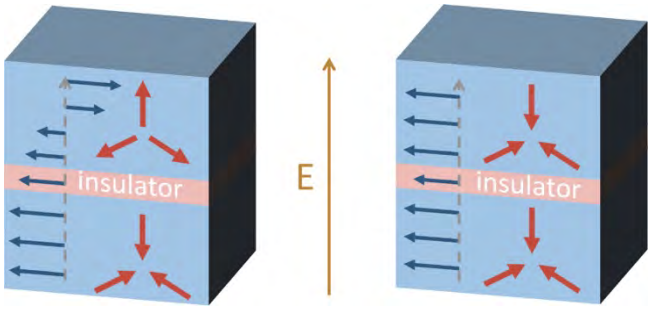
[5] Phys. Rev. Lett. 134, 086701 (2025).
[6] Under review.

BF-09. Non-Relativistic spintronics phenomena in Antiferromagnets

J. Zelezny
Institute of Physics, Czech Academy of Sciences, Prague, Czechia

Contrary to the early view of antiferromagnets as more limited than ferromagnets, a rich landscape of phenomena has been demonstrated in antiferromagnets that can be utilized for various spintronics functionalities. These effects rely primarily on relativistic spin–orbit coupling. While spin–orbit coupling reduces symmetry and thus enables many phenomena, it is, in most systems, only a small perturbation. In contrast, applications of ferromagnetic spintronics rely primarily on non-relativistic effects. Here, we discuss recent advances demonstrating a wide range of non-relativistic phenomena in antiferromagnets. These include effects analogous to those found in ferromagnets, such as spin-polarized currents [1,2] and the resulting spin-transfer torque [3], which can be utilized in an antiferromagnetic tunnel junction (see Fig. 1). In addition, we demonstrate novel effects that do not commonly appear in ferromagnetic materials, such as non-relativistic analogs of spin–orbit torque [4] and anisotropic magnetoresistance [5]. We also present a code for the symmetry analysis of response phenomena, applicable to both relativistic and non-relativistic effects [6].

[1] J. Zelezny, Y. Zhang, C. Felser et al., Phys. Rev. Lett. 119, 187204 (2017)
[2] R. González-Hernández, Libor Šmejkal, Karel Výborný et al., Phys. Rev. Lett. 126, 127701 (2021)
[3] S. Ghosh, A. Manchon, and J. Zelezny, Phys. Rev. Lett. 128, 097702 (2022)
[4] R. González-Hernández, P. Ritzinger, K. Výborný et al., Nature Commun. 15, 7663 (2024)
[5] P. Ritzinger, O. Sedláček, J. Zelezny, arXiv:2506.22115 (2025)
[6] J. Zelezny, arXiv:2602.21034 (2026)



Two states of an antiferromagnetic tunneling junction.

BF-10. Electrical and Thermal Transport in Altermagnetic CrSb

D. Kriegner
Institute of Physics of the Czech Academy of Sciences, Prague, Czechia

Altermagnets are compensated collinear magnets in which opposite sublattices are related by crystal symmetries that permit momentum-dependent spin splitting despite vanishing net magnetization [1]. Among the experimentally established examples, CrSb is a particularly attractive platform because of its simple binary composition, high Néel temperature, and semimetallic electronic structure [2,3]. Recent progress in thin-film growth further extends its potential as a materials platform for altermagnetic electronics [4].
In this talk I will discuss recent progress in understanding altermagnetism in CrSb from complementary transport studies. First, I will present Shubnikov-de Haas measurements in microstructured single crystals in magnetic fields up to 68 T, combined with first-principles calculations. The observed oscillation spectrum, its temperature dependence, and its angular evolution consistently track calculated extremal orbits and confirm the predicted spin-split multiband Fermi surface of altermagnetic CrSb [5]. Second, I will show how extended-field electrical and thermal magnetotransport establish CrSb as a benchmark altermagnetic semimetal. We observe large nonsaturating magnetoresistance, a pronounced nonlinear Hall response, and high-mobility transport channels, while thermal measurements reveal a nonlinear thermal Hall effect and deviations from a simple Wiedemann-Franz description [6]. Together, these results show how altermagnetic symmetry shapes both the Fermi-surface topology and the coupled electrical and thermal response of CrSb.

[1] L. Smejkal, J. Sinova and T. Jungwirth, Phys. Rev. X, Vol.

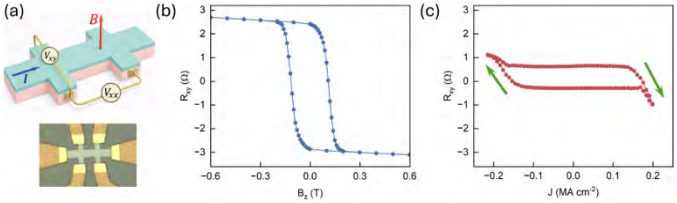
12, p.031042 (2022); Phys. Rev. X, Vol. 12, p.040501 (2022)
[2] J. Krempaský, L. Smejkal and S. W. D'Souza, Nature, Vol. 626, p.517 (2024)
[3] S. Reimers, L. Odenbreit and L. Smejkal, Nat. Commun., Vol. 15, p.2116 (2024)
[4] S. P. Bommanaboyena, C. Müller and M. Jarošová, Phys. Rev. Materials, Vol. 9, p.064402 (2025)
[5] S. Naduvile Thadathil, B. V. Schwarze and J. Ansari, arXiv:2602.24033 (2026)
[6] S. Naduvile Thadathil, C. Müller and R. Firouzmandi, arXiv:2603.25820 (2026)

BF-11. Current-induced magnetization switching in altermagnet/van der Waals magnet heterostructures

H. Bangar[1], P. Tsipas[2], L. Pandey[1], A. Dimoulas[2], S. P. Dash[1]
[1]Chalmers University of Technology, Göteborg, Sweden, [2]National Center for Scientific Research, Athens, Greece

Magnetization switching driven by spin–orbit torques can enable low-power memory and neuromorphic technologies [1]. One main challenge is the realization of efficient and intrinsic spin-current sources that drive deterministic control of magnetic states [2]. Recently, a new class of materials called altermagnets has been discovered [3]. They combine vanishing net magnetization with momentum-dependent spin splitting, offering symmetry-driven pathways for charge-to-spin conversion [4]. When integrated with van der Waals (vdW) magnetic systems, they open a versatile platform for engineering spin transport and interfacial phenomena [5]. Here, we report current-induced magnetization switching in epitaxial MnTe/Cr_xTe_y heterostructure grown by molecular beam epitaxy on InP(111) substrate. Hall bar devices (Fig. 1a) fabricated from MnTe (40 nm)/ Cr_xTe_y (16 nm)/AlO_x (2 nm) stacks exhibit clear anomalous Hall effect (AHE) [Fig. 1b] and reproducible current-driven switching over a temperature range of 60–175 K. Deterministic switching is achieved with a modest in-plane assisting field of 30 mT [Fig. 1c], with critical current densities as low as 0.12 $MAcm^{-2}$. This is among the lowest reported values in comparison to other systems. Systematic measurements of pulse width and assisting field dependence confirm robust switching behavior. Temperature-dependent studies reveal correlated trends in AHE resistance and coercive field, indicating strong coupling between magnetic order and transport. A parallel conduction analysis shows that ~93.6% of the current flows through the Cr_xTe_y layer, indicating dominant spin current generation from the interface . Additionally, long-term potentiation and depression measurements suggest potential for neuromorphic applications. Overall, this work shows altermagnet/magnet heterostructures as a conceptually new platform where altermagnet interfaces act as intrinsic spin-current sources, enabling energy-efficient spintronic and neuromorphic devices.

[1] I. M. Miron, et al., *Nature* 476, 189 (2011); A. Manchon, et al., Rev. Mod. Phys., 91, 035004 (2019).
[2] L. Liu et al., Science 336, 555 (2012); J. Sinova et al., Rev. Mod. Phys. 87, 1213 (2015).
[3] L. Šmejkal, J. Sinova, and T. Jungwirth Phys. Rev. X, 12, 031042 (2022); Bangar et al., arXiv:2505.14589.
[4] L. Šmejkal, J. Sinova, and T. Jungwirth Phys. Rev. X, 12, 040501 (2022).
[5] Zhao et. al., arXiv:2602.24046; Bangar et al., arXiv:2505.14589.



(a) Schematic of the Hall bar device and optical image of the measured device. (b) Anomalous Hall effect (AHE) and (c) its corresponding magnetization switching loop for the MnTe/ Cr_xTe_y heterostructure at 150 K.

SESSION BG: MAGNETO-OPTICAL COUPLING IN FUNCTIONAL MAGNETIC MATERIALS AND DEVICES AND HARD MAGNETIC MATERIALS IV: NANOPARTICLES AND RARE-EARTH-FREE MAGNET DESIGN

Co-Chair(s): W. Geerts, *Physics, Texas State University, San Marcos, Texas, United States* and K. Park, *National Institute of Advanced Industrial Science and Technology, Nagoya, Aichi, Japan*

Tuesday, November 3, 2026
02:00 PM-05:30 PM
Sea Pearl

BG-01. High-Speed Active Lens Based on a Magnetic Domain Hologram in a Magnetic Garnet Film

T. Goto[1], H. Miyashita[1], T. Watanabe[2], E. Negishi[2], K. Ishiyama[1]
[1]RIEC, Tohoku University, Sendai, Japan, [2]Shin-Etsu Chemical Co., Ltd., Annaka, Japan

Dynamically controlling focal length via external signals is a key capability for active lenses used in augmented reality displays, high-speed imaging, and object tracking systems.

Conventional approaches relying on liquid crystals [1] or piezoelectric drivers generally exhibit switching times in the millisecond-to-microsecond regime, which falls short of the demands of ultrafast imaging. Magnetic garnet films present an attractive alternative through their magneto-optical (MO) effect, whose intrinsic response reaches the nanosecond regime [2]. Although various MO-based active lens concepts have been put forward theoretically, experimental realization has remained elusive.

Here, we report the first experimental demonstration of an MO active lens that can be driven by an externally applied magnetic field. A magnetic domain hologram patterned after a Fresnel Zone Plate was written into a magnetic garnet film to produce focusing, as shown in Fig. 1. The pattern comprises a central disk surrounded by five concentric rings composed of 0.8-mm-diameter sub-disks. For fabrication, 175 samarium-cobalt permanent magnets were arranged within a brass jig, and a cerium-substituted yttrium iron garnet film was placed above this assembly to imprint the magnetic pattern.

Illuminating the device with a 633 nm He-Ne laser at a beam diameter of 12.5 mm produced a focused spot of 0.7 mm diameter at a 3.1 m focal distance (Fig. 2), with the power density at the focal point enhanced by a factor of approximately 3.0 - on par with or marginally exceeding theoretical estimates. Pulsed magnetic fields enabled repeatable ON/OFF toggling of the focusing action. After optimizing the magnetic-field driving circuit, we obtained a switching time of 10.8 microseconds, faster than what is typically reported for ferroelectric-liquid-crystal-based active lenses.

Although the focusing performance itself leaves room for improvement, substantial gains are anticipated from incorporating micron-scale magnetic hologram recording and ultrashort pulse excitation. These results provide the first experimental proof-of-concept for MO-effect-driven active lenses and pave the way toward intrinsically fast optical components.

Acknowledgements: The authors gratefully acknowledge support from JSPS KAKENHI (Grant Nos. 23H01439 and 23K17758), the JSPS Bilateral Joint Research Program (No. JPJSBP120249401), NEDO (No. 23200047), the Amada Foundation and the Inamori Foundation.

[1] T. Goto, R. Morimoto and J. W. Pritchard, Opt. Express, Vol. 24, p.17635 (2016).

[2] S. Mukherjee et al., Opt. Express, Vol. 29, p.8258 (2021).



FIgure 1. Conceptual view of beam convergence produced by the reflective MO hologram lens.

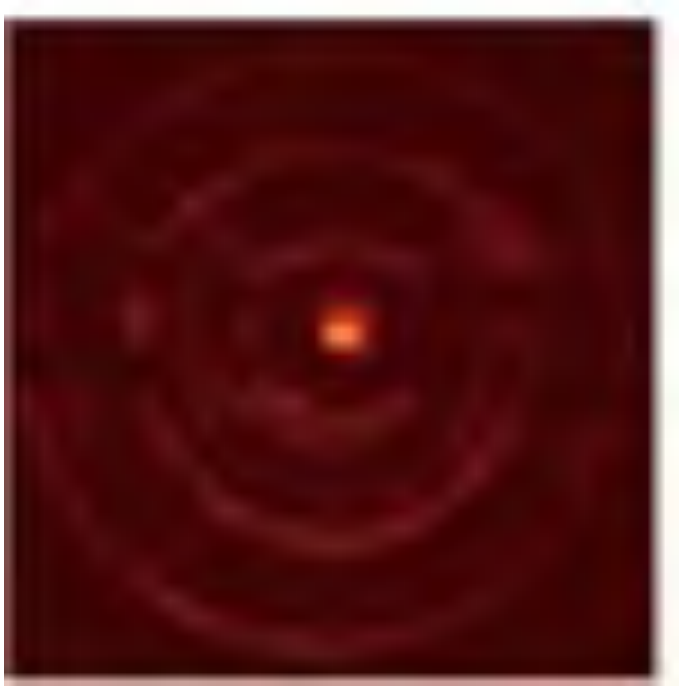


Figure 2. Measured intensity profile of the focused beam at the focal plane.

BG-02. Strain-induced changes in perpendicular magnetic anisotropy probed by operando X-ray magnetic spectroscopies in GdFeCo films on flexible polyimide sheet

J. Okabayashi[1], Y. Fujii[2], H. Yoshikawa[2], A. Tsukamoto[2]

[1]UTokyo, Tokyo, Japan, [2]Nihon Univ., Funabashi, Japan

Amorphous magnetic alloys composed of heavy rare earth (RE) and transition metal (TM) elements exhibit antiparallel coupling between RE and TM, as well as perpendicular magnetic anisotropy (PMA). Ferrimagnetic GdFeCo alloys have been extensively studied, particularly for magneto-optical recording and ultrafast magnetization dynamics, leading to research on all-optical magnetization reversal [1,2]. To investigate the origin of PMA from an electronic

structure, it is necessary to examine the changes in the element-specific electronic state due to strain, which is expected to have applications in sensing technology. Therefore, in this study, we aim to investigate the origin of PMA in GdFeCo alloys using X-ray magnetic circular dichroism (XMCD) with applying external strain into a flexible polyimide substrate.
$Gd_{0.28}Fe_{0.63}Co_{0.09}$ thin film was deposited by magnetron sputtering on a 125-μm-thick polyimide sheet coated by a 5-nm-thick SiN layer. The film composition was deliberately chosen so that the effective PMA vanishes within the range of strain investigated in this study. The sample was fixed to a jig with a cambered shape of varying curvature to allow for the application of bending strain. XMCD was conducted at the KEK Photon Factory BL-7A. The sample was designed to allow for the application of a reversible lattice strain.
We confirmed that the XMCD signals of Fe and Co have the same sign, while that of Gd has the opposite sign, indicating an antiparallel spin arrangement. Element-selective magnetization curves based on the magnetic field dependence of XMCD at each absorption edge confirmed the presence of PMA. Furthermore, in XMCD under applied strain, the XMCD magnetization curve began to exhibit an in-plane magnetic easy axis through the tensile strain of several percentage. We found that, to exhibit PMA, the Gd site deviates from an isotropic charge distribution in the half-filled shell $4f^7$ configuration and becomes anisotropic [3] with the spin arrangement of Fe and Co in the opposite direction. These results indicate that the change in magnetic anisotropy is accompanied by a modulation of the charge distribution within the Gd atom due to external strain.
[1] I. Radu et al., Nature 472, 205 (2011). [2] M. Hennecke et al., Phys. Rev. Lett. 122, 157202 (2019).
[3] Y. Miura and J. Okabayashi, J. Phys.: Cond. Mat. 34, 473001 (2022).

BG-04. Cubic magneto-optic Kerr effect in (111)- and (001)-oriented magnetic thin films

M. Gaerner[1], R. Silber[2], J. Hamrle[3], T. Kuschel[4]
[1]Bielefeld University, Bielefeld, Germany, [2]VSB - Technical University of Ostrava, Ostrava, Czechia, [3]Charles University Prague, Prague, Czechia, [4]Johannes Gutenberg University Mainz, Mainz, Germany

The magneto-optic Kerr effect (MOKE) describes the change of polarization state apon reflection of polarized light from a magnetized sample [1]. Initially, this effect has been assumed to be proportional to the magnetization *M* of the investigated sample and, thus, became a standard tool to study magnetic thin-film systems, e.g. via Kerr spectroscopy, time-resolved MOKE, or Kerr imaging [2]. In addition, in the last two decades contributions of second order in *M* have been explored [3]. The so-called quadratic MOKE (QMOKE) is proportional to M^2 and can be utilized, e.g., to study antiferromagnetics since the MOKE linear in *M* vanishes here.
We have investigated QMOKE in Fe [4] and Heusler compound thin films [5] linearly depending on the structural order of the Heusler compound in a wide spectral range. We identified the angular dependence of QMOKE with respect to the crystal orientation of the thin films via the eight-directional method. Here, we apply a magnetic field in eight in-plane directions and add up / subtract the respective magneto-optic responses (Fig. 1). Recently, we have identified MOKE contributions of third order in magnetization (cubic MOKE, CMOKE) being proportional to M^3 and studied its dependence on the structural domain twinning of Ni(111) thin films (Fig. 1) [6].
In this contribution, we will briefly introduce CMOKE and how it can be identified using the eight-directional method. While it is quite simple to find CMOKE in (111)-oriented films, it is not straightforward to identify it in (001)-oriented samples [7]. We will discuss the reasons. Finally, we will show that the CMOKE in Co(111) thin films can reach up to 30% of the linear MOKE [8] which is promissing for future research applications such as CMOKE microscopy, spectroscopy and pump probe experiments.
[1] J. Kerr, Lond. Edinb. Dublin philos. mag. j. sci. 3, 321 (1877)
[2] A. Hubert, R. Schäfer, Magnetic Domains, Springer (1998)
[3] J. Hamrle et. al., J. Phys. D: Appl. Phys. 40, 1563 (2007)
[4] R. Silber, TK et al., Phys. Rev. B 100, 064403 (2019)
[5] R. Silber, TK et al., Appl. Phys. Lett. 116, 262401 (2020)
[6] M. Gaerner, TK et al., Phys. Rev. Applied 22, 024066 (2024)

[7] R. Silber, TK et al., arxiv: 2603.03477
[8] M. Gaerner, TK et al., arxiv: 2603.05348

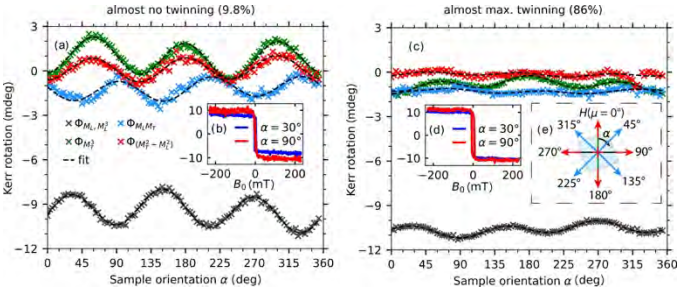


Fig. 1: QMOKE (M_T^2-M_L^2 and M_LM_T contributions) and CMOKE (M_L^3 and M_T^3 contributions) data of Ni(111) thin films with (a) almost no twinning and (c) almost maximum twinning. The three-fold angular dependence is revealed by the eight-directional method (see (e)) with a magnetic field of 230 mT and a photon wavelength of 635 nm. (b),(d) MOKE curves (magnetic field loops) for exemplary sample orientations. The figure is taken from Ref. [6].

BG-05. Environmental Degradation and Nanoparticle-Augmented Protective Coatings for NdFeB and SmCo Permanent Magnets: A Comparative Review and Perspectives

S. Hughes, T. Lamichhane
Engineering, University of Central Oklahoma, Edmond, Oklahoma, United States

Rare-earth permanent magnets, mainly NdFeB and SmCo, sit behind most modern electric motors, wind generators, and high-performance actuators. What limits their service life is rarely the material itself. It is how they degrade in real environments. The published literature on that degradation is broad but oddly disconnected. Most papers cover one magnet type, one exposure (chloride, acidic, humid, hydrogen, or thermal), and one method, and few link the corrosion mechanism to actual magnetic-property loss. Coating studies have the same problem. A typical paper tests one chemistry in one electrolyte, with little data on cross-environment behavior, adhesion, or thermal cycling.

We will present a comparative review of the NdFeB and SmCo degradation literature using a single mechanistic frame that connects environment chemistry, microstructural attack sites, surface and coating response, and where measured, magnetic performance. In both magnet families, attack appears to localize at minor secondary features: the Nd-rich grain-boundary network in sintered NdFeB and the Cu/Fe-partitioned cell boundary in 2:17 SmCo [1]. The environment then shapes severity, morphology, and sometimes the dominant pathway itself, particularly with hydrogen [2], humid, and acidic exposure. Coating performance follows the same pattern: layered systems usually beat single films in their tested environments, though cross-environment data are scarce. Some of the strongest reported gains come from nanoparticle-modified coatings, including iron-titanium nanopastes in epoxy [3] and pulse-electrodeposited MXene-Ni composites [4], which appear to slow chloride ingress better than conventional barrier layers.

We will present perspectives on an experimental program that incorporates nanoparticles into existing coating chemistries, including epoxy and electrodeposited metallic systems, and tests these nanoparticle-augmented coatings across chloride, acidic, humid, and elevated-temperature exposures, rather than treating any one formulation as a single-condition solution. Corrosion testing is paired with magnetic-property measurement so surface protection can be evaluated against magnet service life rather than corrosion rate alone.

[1] H. Sepehri-Amin, J. Thielsch and J. Fischbacher, Acta Mater., Vol. 126, p.1 (2017).
[2] J. Tejada, J.M. Hernandez and M.C. Duran, J. Magn. Magn. Mater., Vol. 195, p.476 (1999).
[3] J. Liu, L. Jiang and Z. Yang, Coatings, Vol. 13, Art. 1897 (2023).
[4] J. Xu and others, Appl. Surf. Sci., Vol. 694, Art.162813 (2025).

BG-06. High-Performance Ultra-Pure $Nd_2Fe_{14}B$ Powders through A One-step Calciothermic Reduction-Diffusion

R. Kuchi, A. Palasyuk, I. Z. Hlova, Y. Mudryk
Ames national laboratory, Ames, Iowa, United States

Synthesis of high-purity $Nd_2Fe_{14}B$ powders remains a bottleneck for next-generation rare earth permanent magnets. Here we report a single step calciothermic reduction diffusion (CRD) route that directly converts Nd_2O_3 to $Nd_2Fe_{14}B$ by heating at 1050 °C for 3 h. We systematically examine the effect of Fe precursor particle size (10, 20, 45 μm) and excess Ca reducing-agent (5–30 wt.%) on phase evolution, microstructure, chemical purity, and room-temperature magnetic properties. A gentle ball-mill-assisted washing protocol is demonstrated to be essential for complete removal of Ca/CaO and for producing de-agglomerated, phase-pure powders with particle sizes <5

μm. Powders synthesized from 20 μm Fe precursors display the most uniform morphology, the lowest residual Ca, and a favorable balance of fine-particle fraction and oxygen uptake. Optimization of Ca content identifies ~20 wt.% excess Ca as the optimum, yielding single-phase $Nd_2Fe_{14}B$ (Rietveld confirmed) with saturation magnetization exceeding 95% of the theoretical value and enhanced coercivity. These findings establish practical processing windows control of precursor particle size, minimization of ultrafine fractions, and precise reducing agent stoichiometry that enable production of high-quality $Nd_2Fe_{14}B$ powders suitable for downstream densification into magnets for high-performance applications

BG-07. Role of Size, Shape, and Higher-Order Anisotropy in Coercivity of $Nd_2Fe_{14}B$ Nanoparticles

J. Lisik[1], A. Terko[1], T. Schrefl[2], E. Girt[1]
[1]Department of Physics, Simon Fraser University, Burnaby, British Columbia, Canada, [2]Center for Modelling and Simulation, University for Continuing Education Krems, Wiener Neustadt, Austria

Understanding single-particle reversal is essential for advancing nanoparticle technologies from biomedicine to permanent magnets. We present a comprehensive micromagnetic study of the coercivity, H_c, of single $Nd_2Fe_{14}B$ (K_1=4.9 MJ/m^3) particles across 13 shapes from 5 nm to 1 μm (Fig. 1).

Below the coherent rotation size, H_c achieves the Stoner-Wohlfarth switching field, H_{SW}. Above this size, ellipsoids reverse via curling (H_c reaches an asymptote), while non-ellipsoids undergo nucleation-and-expansion (H_c decreases logarithmically). The dodecahedron transitions between these modes at ~50 nm.

While aspect ratio dominates H_c at small sizes, roundness dominates at large sizes (Fig. 1). Spheroids maintain the highest H_c, followed by rounded prisms, then prisms & cylinders. This is governed by the transverse demagnetizing field, $H_d^{\perp}$, at the nucleation site. $H_d^{\perp}$ tilts the local effective field (sum of demagnetizing, exchange, and applied fields) away from the easy axis, creating a torque. Nucleation occurs when this effective field reaches the local H_{SW}. Sharp features amplify $H_d^{\perp}$, reducing the applied field required for nucleation (H_c).

Rounding corners & edges of rectangular prisms reduces $H_d^{\perp}$, yielding a ~13% H_c boost for 0.5–1 μm prisms (Fig. 1) with minimal packing fraction loss (1 to 0.97). This suggests that grain rounding could significantly improve the maximum energy product of coercivity-limited magnets.

However, higher-order anisotropy alters this. We extend the Stoner-Wohlfarth model to include the second anisotropy constant, K_2, which raises H_{SW} for tilted fields. Thus, when $H_d^{\perp}$ tilts the effective field, a larger H_c is required for nucleation than when K_2=0. K_2 (=0.13K_1 for $Nd_2Fe_{14}B$) boosts $\mu_0 H_c$ by 0.2–0.5 T in non-ellipsoids ⩾50 nm (Fig. 2). Because sharper features generate a larger tilt, they receive a greater H_c boost from K_2: largest for prisms & cylinders, smaller for rounded prisms, and zero for spheroids. Consequently, the ~13% H_c improvement from rounding the 0.5 μm prisms drops to ~8% when K_2 is included, highlighting a critical design tradeoff.

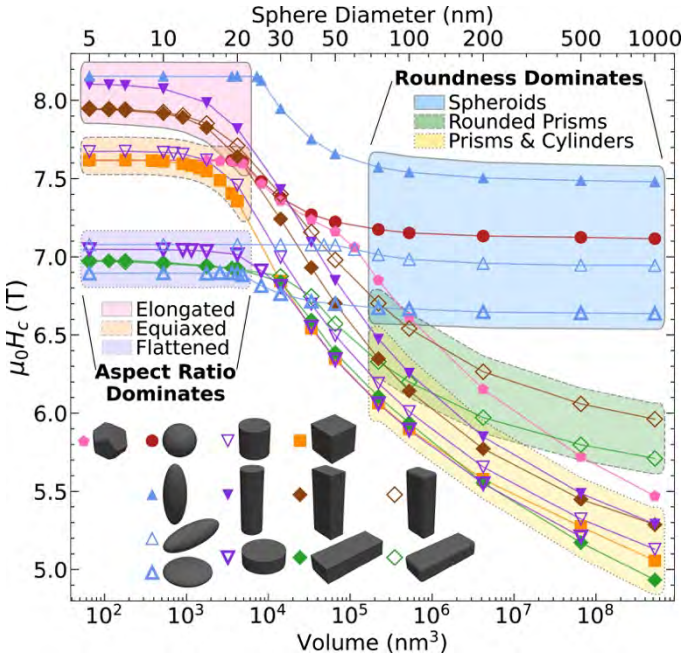


Fig. 1: Coercivity vs. volume (bottom) and sphere diameter (top) for 13 shapes.

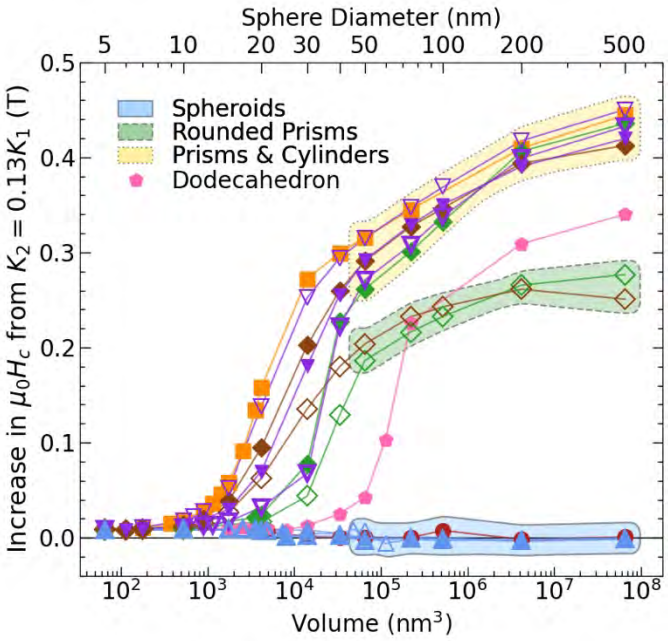


Fig. 2: Increase in coercivity due to K2 (shape legend shared with Fig. 1).

BG-08. Enhanced coercivity in Rare-earth-free Fe-Co-B nanoparticles via atmosphere-controlled wet-chemical synthesis

T. Parida, A. Karati, X. Liu, I. C. Nlebedim
Division of Critical Materials, Ames National Laboratory, Ames, Iowa, United States

Rare-earth-free permanent magnets are gaining renewed attention due to supply-chain risks and cost volatility associated with critical elements such as Nd and Dy. Among emerging candidates, Fe-Co-B has been identified through experimental and theoretical studies as a promising system, exhibiting high saturation magnetization, elevated Curie temperature, and moderate magnetocrystalline anisotropy suitable for intermediate-performance applications [1,2]. However, achieving high coercivity essential for permanent magnet performance remains a major challenge, with reported values typically limited to ~900 Oe [3], largely due to insufficient control over phase formation and microstructure.

In this work, we develop a wet-chemical synthesis route for Fe-Co-B nanoparticles under controlled atmospheres (air, argon, and nitrogen) to address this limitation. The synthesis environment is shown to strongly influence phase evolution: samples produced under inert conditions (argon and nitrogen) exhibit the desired tetragonal phase associated with enhanced anisotropy, while those synthesized in air predominantly form a cubic phase. Correspondingly, the as-synthesized nanoparticles exhibit coercivities of 1037 Oe (argon) and 1061 Oe (nitrogen), exceeding previously reported values.

Post-synthesis heat treatment further enhances magnetic performance, yielding coercivities above 1500 Oe while maintaining high saturation magnetization (140-160 emu/g). These improvements are attributed to increased crystallinity and stabilization of the anisotropic phase. This work demonstrates a scalable pathway to overcoming coercivity limitations in Fe-Co-B and advances its potential as a rare-earth-free permanent magnet.

Acknowledgement
This work is supported by the Critical Materials Innovation Hub, an Energy Innovation Hub funded by the U.S. Department of Energy, Office of Critical Minerals and Energy Innovation (CMEI), Advanced Materials and Manufacturing Technologies Office (AMMTO).

1. T.N. Lamichhane, O. Palasyuk, V.P. Antropov, I.A. Zhuravlev, K.D. Belashchenko, I. C. Nlebedim, K.W. Dennis, A. Jesche, M.J. Kramer, S.L. Bud'ko, R.W. McCallum, P. C. Canfield, V. Taufour, , J. Magn. Magn Mater. 513 (2020) 167214.

2. A. Musial, W. Marciniak, Z. Sniadecki, M. Werwinski, P. Kuswik, B. Idzikowski, M. Kolodziej, A. Grabias, M. Kopcewicz, J. Marcin, and J. Kovac, J. Alloys Compd. 921, (2022) 166047.

3. K.M. Kim, H.W. Kwon, J.G. Lee, and J.H. Yu, IEEE Trans. Magn. 54(2018) 1.

BG-09. High Coercivity Ce-Nd-Fe-B Nanoparticle

H. Parmar, C. I. Nlebedim, X. Liu
Critical Materials Innovation Hub, Division of Critical Materials, Ames National Laboratory, Ames, Iowa, United States

NdFeB permanent magnets are the strongest magnets and are widely used in many applications. Nevertheless, their growing demands lead to strain on the supply of rare earth elements, including Nd, Pr, Dy and Tb. Hence, Ce can be applied to produce magnetic materials. Also, it is much less utilized coproduct of Pr/Nd mining [1]. However, Ce-Fe-B has far inferior intrinsic magnetic properties than Nd-Fe-B.

It was shown theoretically that Ce-Fe-B magnetic property can be improved by partial replacement of Ce by Nd or Pr. Additionally, the calculation reveals that the magnetic property is enhanced in nanoscale particles [2]. Conventional sintering techniques are unable to achieve the nanostructure in Ce-Fe-B. In this work, we have reported the magnetic properties of Ce-Nd-Fe-B nanoparticles prepared using a reduction diffusion approach. We have successfully prepared a series of Ce-Nd-Fe-B nanoparticles at various reduction-diffusion temperatures. Maximum coercivity 14kOe was achieved for 10 wt.% added Ce-Fe-B sample, while Ce-Fe-B sample has achieved 8.8kOe maximum coercivity.

A. K. Pathak et al., "Cerium: An unlikely replacement of dysprosium in high performance Nd-Fe-B permanent magnets," Adv. Mater., vol. 27, no. 16, pp. 2663–2667, Apr. 2015.

X. B. Liu et al., "Theoretical Correlation of Elemental Distribution of Nd and Pr in Ce-Fe-B Microstructure with Hard Magnetic Properties, IEEE Transactions on Magnetics, vol. 57, no. 2, Feb. 2021

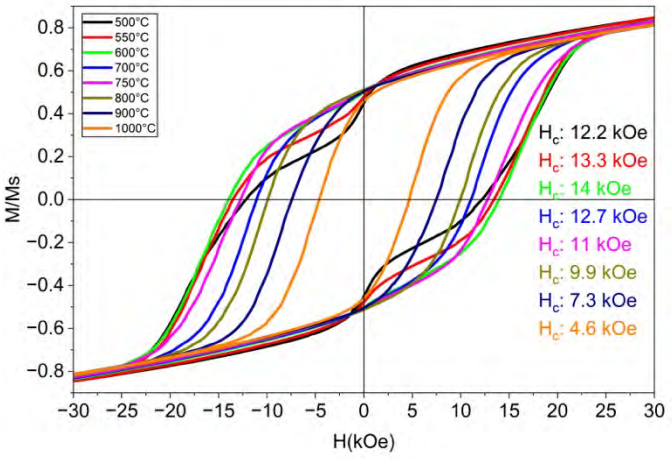


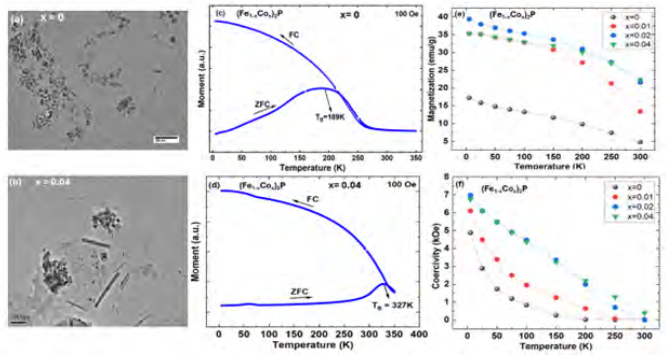
Fig. 1 Hysteresis loop of particles synthesized with 10 wt.% Nd at different reductio-diffusion temperature

BG-10. Effect of Cobalt Substitution on Magnetic Properties of Fe_2P Nanoparticles

T. Karki, H. Abbas, P. Joshi, J. Mohapatra, P. Liu
Physics, The University of Texas at Arlington, Arlington, Texas, United States

The hexagonal Fe_2P phase has recently attracted attention as a promising rare-earth-free magnetic material due to its large magnetocrystalline anisotropy (K_1 ~ 2.68 MJ/m^3). However, its practical applicability is constrained by a relatively low Curie temperature (T_c ~ 214 K) [1]. Here, we report a chemical synthesis of $(Fe_{1-x}Co_x)_2P$ (x = 0, 0.01, 0.02 and 0.04) nanocrystals and investigate the impact of Co substitution on their structural and magnetic properties. X-ray diffraction confirms that all compositions retain the hexagonal Fe_2P crystal structure without detectable secondary phases. Notably, transmission electron microscopy (TEM) reveals a pronounced morphology evolution upon Co incorporation, with particles transforming from quasi-spherical to rod-like nanostructures (Figure 1 (a, b)). Magnetic measurements (Figure 1 (c, d)) indicate that cobalt substitution markedly increases the blocking temperature from 189 K to 327 K and the Curie temperature from 244 K to 330 K as x rises from 0 to 0.04. Concurrently, the saturation magnetization rises from ~18 emu/g to ~40 emu/g, while the coercivity increases from 4.9 kOe to 6.9 kOe at 5 K when x increases from 0 to 0.02 (Figure 1 (e, f)). The increase in coercivity is ascribed to synergistic effects of shape and magnetocrystalline anisotropy. These results demonstrate that Co substitution provides an effective route to simultaneously tune morphology and substantially improve the magnetic properties of Fe_2P nanocrystals, advancing their potential for rare-earth-free magnetic applications.

1. He, Y., et al., Intrinsic magnetic properties of a highly anisotropic rare earth free Fe_2P based magnet, Advanced Functional Materials, 2022. 32(4): p. 2107513.



SESSION BP: MAGNETORESISTANCE AND SPIN INJECTION (POSTER SESSION)

Chair(s): E. Iacocca, *Physics, University of Colorado Colorado Springs, Colorado Springs, Colorado, United States*

Tuesday, November 3, 2026

03:00 PM-06:00 PM

Coral 4

BP-01. Spin-Orbit Torque Generation in In-Plane Magnetized Co Films on c-Sapphire Substrate

S. Mochizuki[1], S. Hirata[2], T. Ono[2, 3], T. Satoh[1], K. T. Yamada[1]

[1]Department of Physics, Institute of Science Tokyo, Meguro-ku, Tokyo, Japan, [2]Institute for Chemical Research, Kyoto University, Uji, Kyoto, Japan, [3]Center for Spintronics Research Network, Kyoto University, Uji, Kyoto, Japan

Spin–orbit torques (SOTs) enable control of magnetization by in-plane currents and are applied to high-speed magnetic memory devices. Improving SOT efficiency has been intensively pursued through optimization of crystallinity and composition of heavy metals as well as engineering the symmetry and topological properties [1, 2]. Here, we report efficient SOT generation in in-plane magnetized Co films grown on c-sapphire substrates. Pt(5 nm)/Co(5 nm) bilayers were deposited on a c-sapphire substrate by dc sputtering at room temperature. For comparison, we prepared reference trilayers of Pt(5 nm)/Co(5 nm)/Ta(5 nm) and Ta(5 nm)/Co(5 nm)/Pt(5 nm), where the injection of spin currents from both interfaces leads to substantial SOTs. All the films were processed into Hall devices using photolithography and ion milling. The SOT efficiencies were evaluated using the second harmonic Hall measurement technique [3]. Fig. 1 shows the second-harmonic Hall resistance ($R_{2\omega}$) as a function of in-plane magnetic field angle (φ), defined as the angle between the current and magnetic field directions.The φ and 3φ components reflect the damping-like (DL) and field-like (FL) torques, respectively. The φ and 3φ components per current density for the Pt/Co bilayer on c-sapphire substrate reach values comparable to those of the Pt/Co/Ta and Ta/Co/Pt trilayers. For the Pt/Co bilayer, the calculated effective fields for DL and FL torques are 2.4 and 0.16 mT per 1 × 10^{11} A/m^2, which are comparable to those of the trilayers. These results indicate that the Co/c-sapphire interface plays a significant role in generating SOTs. In the presentation, we show the measurement configuration and analysis in detail and discuss the possible origins of the efficient generation of SOTs at the Co/c-sapphire interface.

[1] M.-G. Kang, S. Lee, and B.-G. Prak, npj Spintronics, Vol. 3, p.8 (2025).
[2] Z. Han, Y. Huo, and Y. Yu, Appl. Phys. Rev., Vol. 13, p.011305 (2026).
[3] C. O. Avci, K. Garello, and M. Gabureac, Phys. Rev. B, Vol. 90, p.224427 (2014).

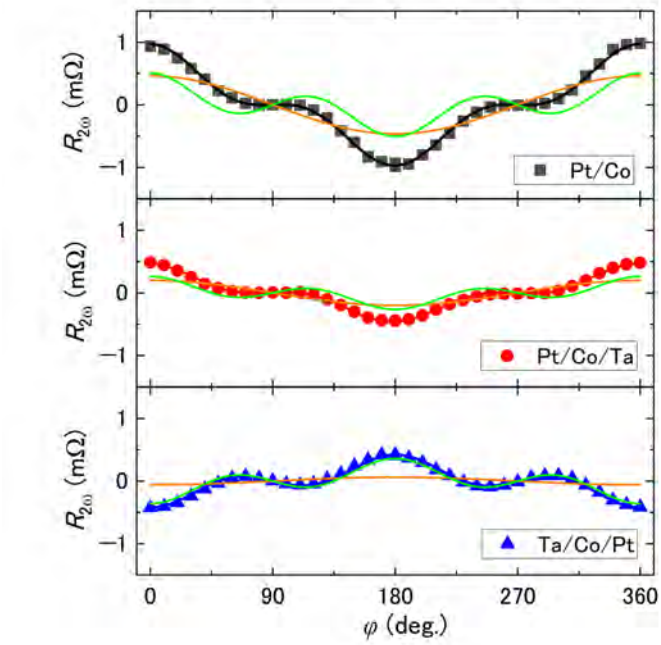


Fig.1 Second harmonic Hall resistance $R_{2\omega}$ for each sample, normalized by the electric density of 1×10^{11} A/m^2, as a function of the external magnetic-field angle φ. The magnitude of the external magnetic field is set to 34.5 mT. The orange and green curves represent the φ and 3φ-dependent components, respectively.

BP-02. Gaussian Superparamagnetic Tunnel Junction

T. Kinoshita, N. Caçoilo, M. Ohtani, H. Kaneko, S. Kanai, S. Fukami

Tohoku University, Sendai, Japan

Probabilistic computers (p-computers) based on superparamagnetic tunnel junctions have emerged as a promising low-power hardware platform which exploits stochasticity for computation [1][2]. While most existing implementations rely on binary outputs, extending them to continuous or multi-state variables is desirable for improved data representation and flexibility [3]. In this study, we propose a Gaussian superparamagnetic tunnel junction (G-sMTJ) that generates continuous Gaussian random numbers. The stack structure, shown in Fig. 1(a), is deposited on a Si/SiO_2 substrate by dc and rf magnetron sputtering,

patterned into elliptic MTJ devices, and annealed at 300°C for 2 h. The thickness of CoFeB free layer above MgO is varied in a wedge shape, to continuously change the effective anisotropy field , a key parameter for realizing the G-sMTJ. The device employs an orthogonal magnetic configuration, in which thermally induced fluctuations of the free-layer magnetization follow an approximately Gaussian distribution under a small-angle approximation. These magnetization fluctuations are converted into resistance fluctuations via the tunnel magnetoresistance effect, allowing direct electrical readout of Gaussian-distributed signals.

Time-domain measurements confirm Gaussian outputs with good agreement to Gaussian fitting ($R^2 > 0.99$) (Fig.1(b)). Furthermore, we demonstrate the controllability of mean μ and variance σ^2 of the generated distribution, which is essential for p-computing [3]. Specifically, μ is modulated by applied current I (Fig. 2(a)), whereas σ^2 is controlled by the out-of-plane magnetic field H_z (Fig. 2(b)).

The proposed G-sMTJ provides a scalable hardware platform for p-computing with continuous variables and may enable efficient implementations of computational tasks beyond conventional binary p-bit approaches.

[1] K. Y. Camsari *et al.*, Phys. Rev. X 7, 031014 (2017).
[2] W. A. Borders *et al.*, Nature 573, 390 (2019).
[3] N.S. Singh *et al.*, IEEE Int. Electron Devices Meet. IEDM, https://doi.org/10.1109/IEDM50854.2024.10873478 (2024).

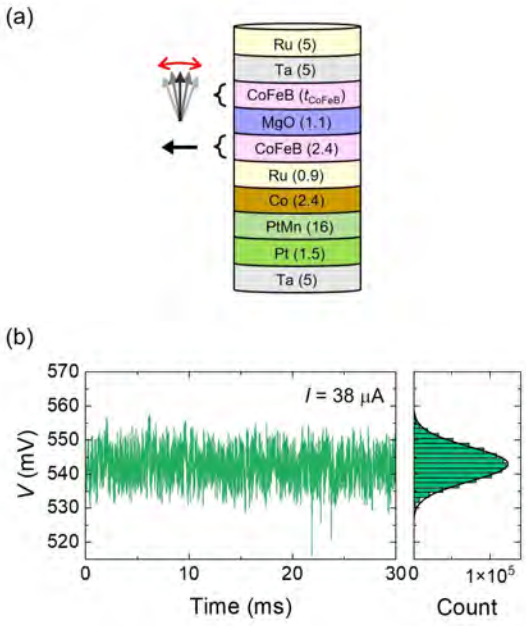


Fig.1 (a) Stack structure of the G-sMTJ. (b) An example of time-domain behavior of the G-sMTJ along with a histogram showing the distribution N of voltage levels V.

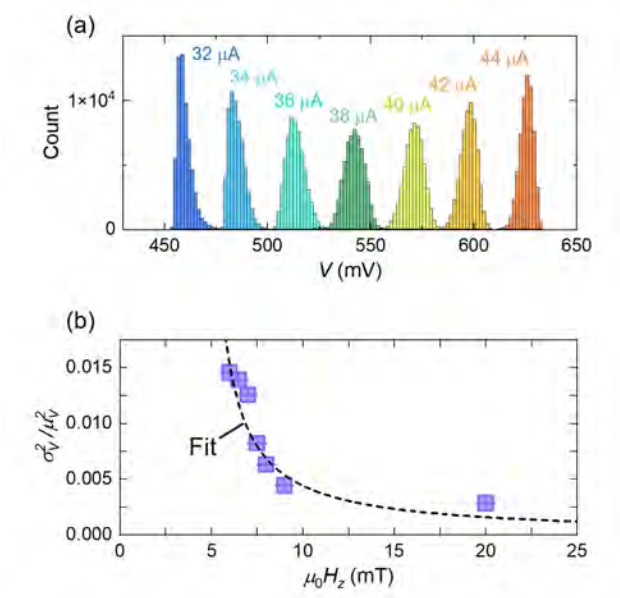


Fig.2 (c) Histograms of the distributions of V as a function of I. (d) Voltage variance normalized by mean as a function of H_Z.

BP-03. Voltage Generation by Ferromagnetic Resonance in Magnetic Bilayers with Perpendicular Magnetic Anisotropy

A. K. Dhiman, M. Matczak, P. Kuswik, P. Graczyk
Institute of Molecular Physics, Polish Academy of Sciences, Poznan, Wielkopolskie, Poland

Magnetoelectric effects, such as the induction of currents or voltages by magnetization dynamics, are key to enabling efficient interconversion between magnetic and electric signals [1]. These mechanisms play an important role in the development of low-power spintronic devices and novel sensing platforms for advancing next-generation functional materials and nanoscale technologies.

In this work, we have performed detailed numerical simulations of the ac and dc voltages generated in an MgO/Fe/Al/Co/Au structure due to spin pumping and spin-dependent conductivity in ferromagnets. The study considered the effects of external magnetic fields, the thickness of the Al spacer and Fe layer to determine the generated voltage signal. We also studied the direction, frequency, and amplitude of microwave excitation in presence of other dielectric spacer layer in the stack. Our calculations indicate that replacing the aluminum spacer with a low-electronic-conductivity material, such as semiconducting silicon, leads to a significant enhancement of the voltages generated by magnetization precession.

To experimentally observe the voltage signal as Shukla et

al. [2], we have deposited the stacks of MgO/Py/Al(d_{Al})/Co/Au with varying Al layer thickness, using magnetron sputtering. The deposited stack is patterned by using, electron beam lithography to perform charge-mediated magnetoelectric measurements. The schematic design of our patterned device is demonstrated in Fig. 1, which will be experimentally measured by VNA-FMR to study the voltage generation.

[1] S. Kopyl, R. Surmenev, M. Surmeneva et al., Materials Today Bio 12, 100149 (2021)
[2] A. S. Shukla, A. Chouhan, R. Pandey et al., Sci. Adv. 6 : eabc2618 (2020)

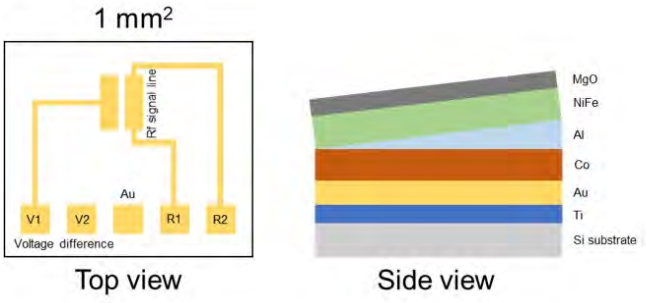


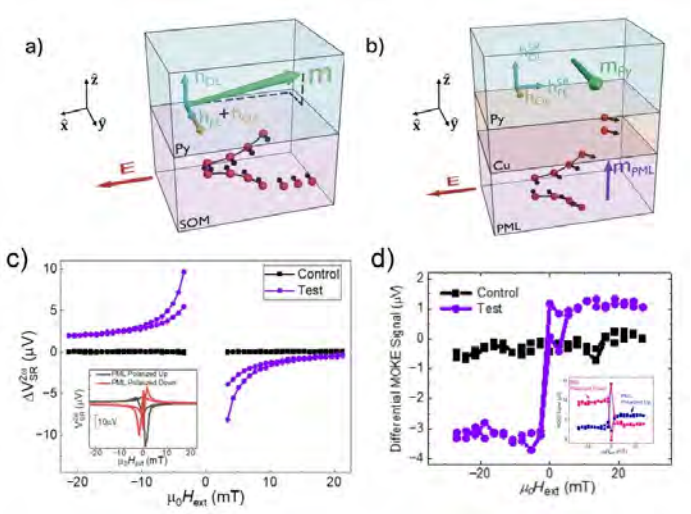
Fig. 1: Patterned device system. Left) Top view of the schematic of electron beam lithography patterned device to measure magneto-electric effect. Using the device, voltage difference is measured (between V_1 and V_2) from the RF signal-induced (through R_1 and R_2) field generation. Right) Side view of the sample structure prepared from Co (out-of-plane magnetic anisotropy) and NiFe (Py – in-plane anisotropy) layer separated by a wedge shaped non-magnetic spacer layer. The rf field drives magnetization precession, which pumps a spin current into the spacer. Spin-dependent conductivity in the ferromagnetic layers converts this spin current into a measurable voltage at the electrodes.

BP-05LB. Quantitative Understanding of Field-like Spin-orbit Torque Using Spin Rotation

K. J. Peterson, E. D. DeVisscher, E. R. Morris, N. Boyd, R. W. Greening, B. L. Zink, X. Fan
Physics and Astronomy, University of Denver, Denver, Colorado, United States

Field-like spin-orbit torque plays an important role in many spintronics applications. However, its microscopic origin remains unsettled, mainly because of the difficulty to experimentally disentangle it from the Oersted field. Here we use a perpendicular magnetized film as a spin source to generate field-like spin-orbit torque with spin rotation, which is isolated from the Oersted field. We show that the extracted field-like spin-orbit torque is inversely proportional to the thickness of the ferromagnetic spin absorbing layer, similar to the damping-like spin-orbit torque. We further show that the ratio between the field-like and damping-like spin-orbit torque remains a constant even when the spin source is changed. These results suggest that the field-like and damping-like spin-orbit torque may both arise from the same spin current generated by the spin source.

[1] Humphries, A.M., Wang, T., Edwards, E.R.J. *et al.* Observation of spin-orbit effects with spin rotation symmetry. *Nat Commun* 8, 911 (2017). https://doi.org/10.1038/s41467-017-00967-w
[2] Amin, V. P., Baez Flores, G. G., Kovalev, A. A. & Belashchenko, K. D. Direct and indirect spin current generation and spin-orbit torques in ferromagnet/nonmagnet/ferromagnet trilayers. *Phys. Rev. B* 110, 214427 (2024).



a) Equivalent fields due to damping-like, field-like spin-orbit torques and Oersted field generated in a bilayer film consisting of Py and a nonmagnetic spin-orbit material. b) Equivalent fields due to DL and FL SOT with spin rotation generated in a trilayer film consisting of Py and a perpendicular magnetized layer (PML) separated by Cu.Here, y-component of spin polarizations (parallel to Py magnetization) due to conventional spin Hall effect does not generate SOT. c) 2nd harmonic Hall measurement in the spin rotation configuration. The purple data is for the test sample PML/Cu(3)/Py(3)/AlOx(3). The black data is the control sample PML/Cu(3)/Ta(3)/Py(3)/AlOx(3). The inset shows raw data for the test sample with PML magnetization polarized up and down. d) differential MOKE signal between PML magnetization polarized up and down is presented for the test and control samples. The inset shows raw data for the test sample with PML magnetization polarized up and down.

BP-06. Fabrication of giant magnetoresistance ink with high sensitivity at a low field

S. Miura, M. Taguchi, Y. Kurokawa, H. Yuasa
Kyushu Univ, Fukuoka, Japan

Printing technology is a promising alternative, and previous studies have demonstrated inkjet-printed device patterning for enhanced spin Seebeck output, as well as the fabrication of printable multilayered-GMR ink [1] [2]. However, when using multilayered-GMR ink, the magnetization switching field is too large for the sensor. Therefore, we focus on the fabrication of spin-valve GMR ink. Unlike the multilayered-GMR ink, an annealing process is required to obtain the exchange bias from an antiferromagnet layer. In addition, we tried to further restrain the switching field of the free layer by decreasing the interlayer coupling field (H_{in}). Since H_{in} is inversely proportional to the free layer thickness, this study investigates the effect of free layer thickness on H_{in}. First, GMR multilayer films with the structure Au (5)/Ta (3)/Ru (2)/IrMn (7)/CoFe (2)/ Cu (3)/CoFe (1)/NiFe (3 or 10)/Cu (1)/Ta (3)/Au (5) (unit: nm) were deposited on thermally oxidized Si substrates with or without photoresist as a sacrifice layer by sputtering. Second, the photoresist was dissolved by ultrasonic treatment in acetone and simultaneously the GMR film became flakes with a size of several micrometers. As they were dissolved in acetone, resulting in GMR ink. Then, the GMR ink was dropped on thermally oxidized Si substrates with Pt electrodes. Finally, by annealing them at 543 K in an in-plane magnetic field of 0.42 T, the ink with spin-valve GMR flakes was fabricated. Fig.1 shows the MR curves at a low field for uniform films and the GMR ink with thicknesses of NiFe, t = 3 nm and 10 nm. First, note that after optimizing the amount of GMR ink dispensed, sufficient electrical contact was achieved even with the GMR ink. It was confirmed by microscopy that the flakes partially contact and the flake size is almost the same regardless of the free layer thickness. As designed, a reduction in H_{in} was successfully observed in both the uniform films and the GMR inks by using the thick free layer. This demonstrates the potential to achieve high sensitivity at a low magnetic field in printable GMR sensors through film thickness design.

[1] Y. Kurokawa, et al., Adv. Eng. Mater. 26, 2301069 (2024).
[2] M. Ha, et al., Adv. Mater. 33, 2005521 (2021).

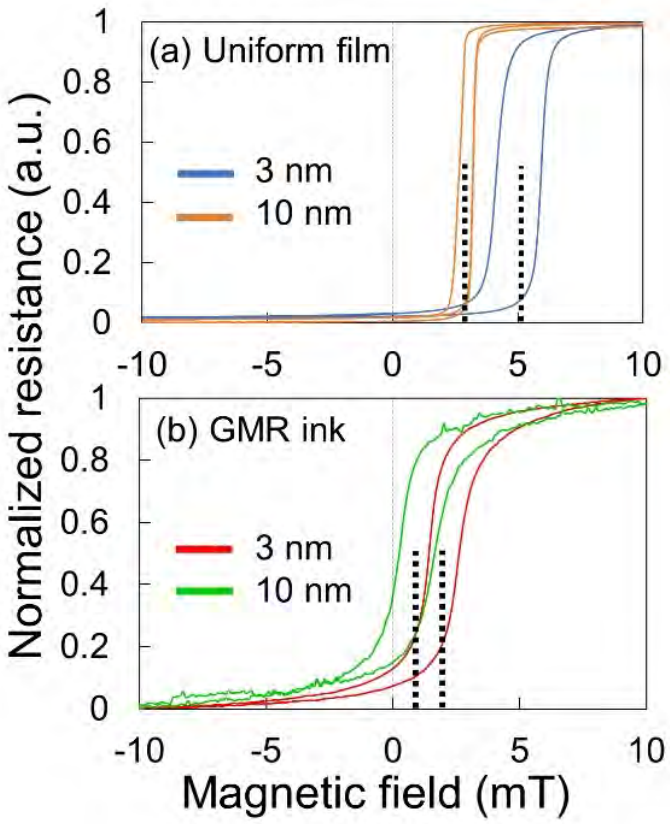


Fig.1 MR curves for uniform film (a) and GMR ink (b) in a smaller magnetic field than ±10 mT.

BP-07. Transport Signature for Orbital Magnetic Moment Texture in Chiral Semiconductor Tellurium

S. Okumura, R. Tanaka, D. Hirobe
Shizuoka University, Shizuoka, Japan

Chirality, defined by non-superimposability onto a mirror image, offers a symmetry-adapted route for coupling structural handedness to electronic magnetism. This connection has been reshaped partly by chiral-induced spin selectivity, whereby chiral systems generate spin-polarized transport without magnetic order [1]. Extending this concept to condensed matter is a key trend in spintronics, including chiral organic conductors based on molecular chirality [2] and crystallographic chirality [3] as emerging platforms. Elemental Te, a chiral semiconductor with helical atomic chains, is appealing because its handedness, carrier density, and nonreciprocal charge transport are accessible in field-effect devices [4,5]. Here we report a transport signature of chiral orbital magnetic-moment texture in Te [6]. We measure nonlinear electrical conduction (NEC), bilinear magnetoresistance producing a voltage proportional to I^2B, in Te field-effect transistors with current I and magnetic field B along the helical c axis. The angular dependence follows the predicted selection rule, enabling isolation of a specific component, G_{zzzz}, of the nonlinear conductance tensor. The sign of G_{zzzz} reverses between right- and left-handed Te, showing the chirality origin of the response (Fig. 1). Gate-dependent Hall and harmonic-voltage measurements reveal a nonmonotonic carrier-density dependence: G_{zzzz} shows a broad low-density peak at a low temperature (Fig. 2). We rationalize these observations using semiclassical Boltzmann kinetic theory including Zeeman coupling to spin and orbital textures. The orbital part is larger than, and opposite in sign to, the spin part near the valence-band top. Thus, the orbital contribution determines the observed enantiospecific sign and accounts for the low-density anomaly. Our results suggest that NEC serves as a sensitive electrical probe of orbital texture, accelerating exploration of chirality-induced orbital physics beyond conventional spin-texture descriptions.

[1] B. P. Bloom, Y. Paltiel, R. Naaman, et al., Chem. Rev. 124, 1950 (2024)
[2] F. Pop, N. Mroweh, P. Auban-Senzier, D. Hirobe (5th, co-corresponding), et al., J. Am. Chem. Soc. 147, 27749 (2025).
[3] R. Nakajima, D. Hirobe (co-corresponding), G. Kawaguchi, et al., Nature 613, 479 (2023).
[4] F. Calavalle, M. Suárez-Rodríguez, B. Martín-García, et al., Nat. Mater. 21, 526 (2022).
[5] D. Hirobe, Y. Nabei and H. M. Yamamoto, Phys. Rev. B 106, L220403 (2022).
[6] S. Okumura, R. Tanaka and D. Hirobe, Phys. Rev. B 110, L020407 (2024).

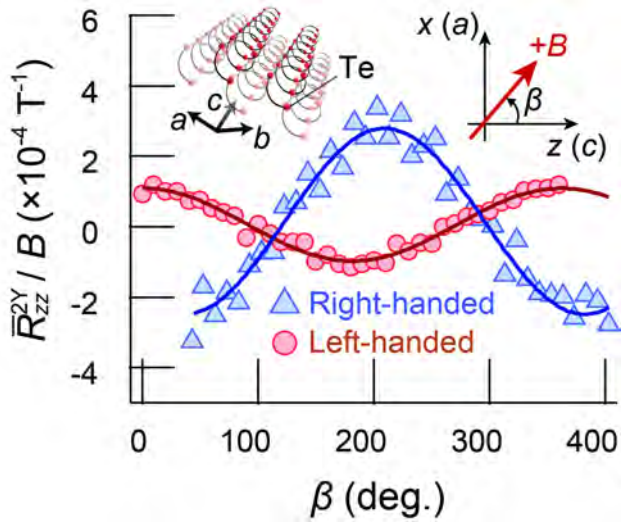


Fig.1. Angular dependence of the bilinear magnetoresistance, measured at 50 K. Root mean square current was set to 10 and 18 μA for right- and left-handed devices.

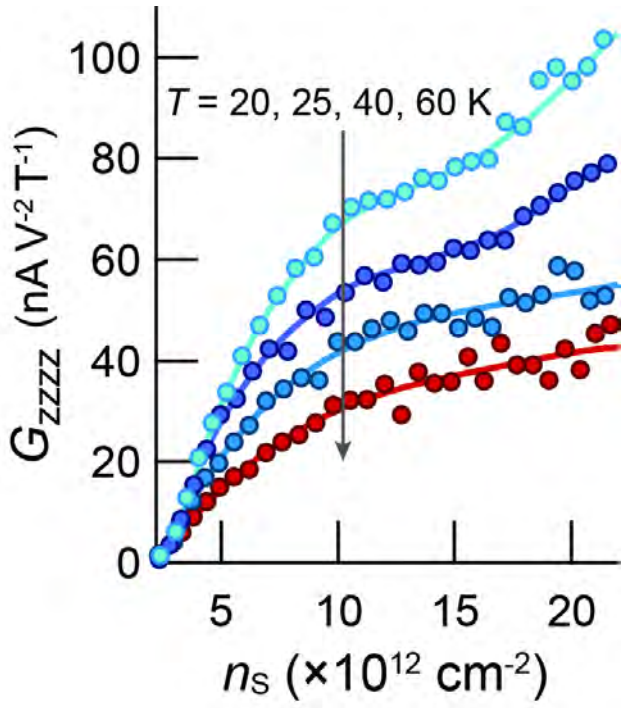


Fig. 2. Sheet carrier density dependence of the nonlinear conductance.

BP-08. Ferromagnet-DNA-Ferromagnet Junction Built-in Nanowire Spintronic Device Fabrication and Characterization

R. Kizil[3], A. Moreira[1], A. Heltman[2]
[1]Departamento de Física e Astronomia, Faculdade de Ciências da Universidade do Porto, Porto, Portugal, [2]Department of Physics, Penn State University, University Park, Pennsylvania, United States, [3]Department of Chemical Engineering, Istanbul Technical University, Istanbul, Turkey

A nanoscale polymeric junction comprising a 12-base-pair-long (12dGC) double-stranded oligonucleotide was grown between two ferromagnetic segments within a single nanowire for the fabrication of on-chip spintronic devices. Template-assisted metal electrodeposition was combined with the chemical self-assembly of dithiolated DNA on nickel surfaces, enabling, for the first time, the incorporation of a Ni–DNA–Ni junction within nanowires (Figure 1). The oligonucleotide layer confined between two Ni-segments was characterized by FESEM and micro-Raman spectroscopy to confirm its growth and elucidate the chemical composition of the molecular barrier. The DNA layer exhibited an average length of nearly 10 nm and showed a high degree of uniformity across nanowires. Growth is attributed to polymerization on electrochemically roughened metal deposits, driven by mobile Ni adatoms on nickel surfaces under ambient conditions, which act as catalytic sites. SEM analysis indicates that chemisorption of oligonucleotides via nickel thiolate (Ni–S) bonding produces a smoother nickel–molecule interface compared to the metal–metal (Au–Ni) interface.

Nanowire-based spintronic devices were fabricated through electric-field-assisted assembly of DNA-integrated nanowires using an AC field (30 V, 10 kHz). Dielectrophoretic forces arising from the non-uniform electric field enabled the alignment of individual nanowires between lithographically predefined Au microelectrodes on a Si-wafer within a minute. Electrical characterization was performed via two-terminal DC I–V measurements, revealing semiconducting behavior of the DNA barrier without additional wiring. Magnetoelectronic measurements were conducted using a He closed-cycle cryostat with appropriate device wiring. I–V characteristics measured at 2 K under varying in-plane magnetic fields exhibited pronounced magnetoconductance above 4 V (Figure 2), consistent with prior predictions [4]. Spin selectivity of the DNA layer was further evaluated by modulating the magnetization direction and recording corresponding I–V responses. The talk covers the synthesis of DNA-integrated ferromagnetic nanowires, device fabrication, and their electronic and magnetoresistive properties.

1.H. X. Wong, F. R. Fischer. Electric-Field-Driven Localization of Molecular Nanowires in Wafer-Scale Nanogap Electrodes. Nano Letters 2024, *24*, 10155-10160
2.S. J. Boehm, L. Lin, N. Brljak, N. R. Famularo, T. S. Mayer, and C. D. Keating . Reconfigurable Positioning of Vertically-Oriented Nanowires Around Topographical Features in an AC Electric Field. Langmuir 2017, *33*, 10898-10906.
3.Z. Xie, T. Z. Markus, S. R. Cohen, R. Naaman. Correction to Spin Specific Electron Conduction through DNA Oligomers. Nano Lett. 2011, 11, 4652–4655
4.E. Yudiarsah, T. Adiansyah. he electrical properties of poly(dA)-poly(dT) DNA molecule: electrical current influenced by magnetic field and electric field.Journal of Physics Conference Series 2021. 1816(1):012055

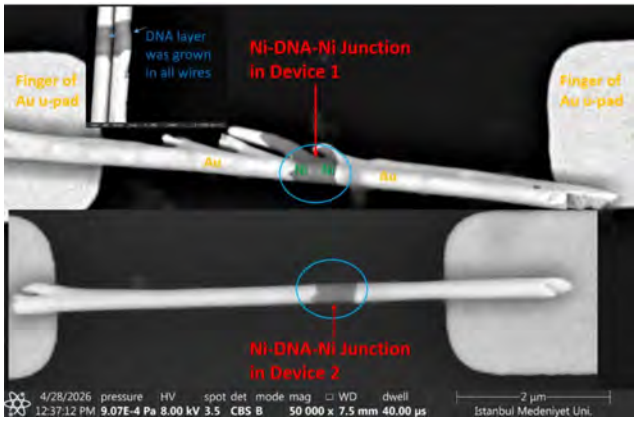


Figure1

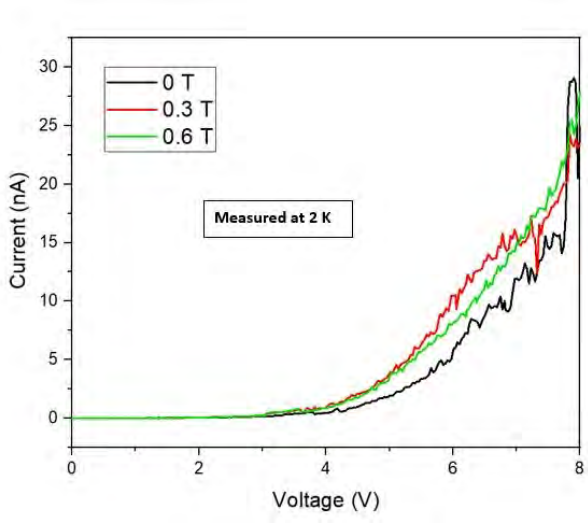


Figure2

BP-09. Co Thickness Dependent Unidirectional Magnetoresistance in Pt/Co/Ru/Co Synthetic Antiferromagnet

H. Oh, J. Do, C. You
DGIST, Daegu, Korea (the Republic of)

Synthetic antiferromagnet (SAF) is a magnetic multilayer structure where two ferromagnet (FM) layers are antiferromagnetically coupled with an interlayer exchange coupling (IEC). The magnetization dynamics of SAF are more complex compared to FM, as the two FM layers are coupled through IEC.
The spin Hall effect (SHE) induce spin accumulation at the heavy metal (HM) / ferromagnet (FM) interface, which drives magnon creation and annihilation in the FM layer, modulating the magnetization and giving rise to magnon creation-annihilation magnetoresistance (m†mMR) [1]. Simultaneously, the spin accumulation generates a field-like torque (FLT) on the FM layer, which makes an in-plane rotation of the magnetization [2].
We fabricated Pt(6)/Co(5, 7.5)/Ru(1.4, 0.8)/Co(5, 7.5)/Ru(3) (thickness in nm) stacks using DC magnetron sputtering. The Ru spacer thickness was tuned to 1.4 nm, and 0.8 nm to ensure that the exchange field remains within a measurable range. The hysteresis loop shows a clear difference between the FM thickness, which is related to exchange length of FM layer. In thin FM sample, magnetic behavior is well described by the macro-spin model, however in thick FM sample, it is not well described due to the twisted magnetization configuration in each FM layer. Using harmonic measurement, we observed different origins of unidirectional magnetoresistance (UMR) signals in SAF structure. For both samples, the UMR signals are attributed to two distinct origins: m†mMR, and FLT. Our observations provide a deeper understanding of magnetotransport within SAF structures.
[1] P. Noël, R. Schlitz, E. Karadza, C.-H. Lambert, L. Nessi, F. Binda, and P. Gambardella, Nonlinear longitudinal and transverse magnetoresistances due to current-induced magnon creation-annihilation processes, Phys. Rev. Lett. 134, 146701 (2025).
[2] A. Manchon, J. Železný, I. M. Miron, T. Jungwirth, J. Sinova, A. Thiaville, K. Garello, and P. Gambardella, Current-induced spin-orbit torques in ferromagnetic and antiferromagnetic systems, Rev. Mod. Phys. 91, 035004 (2019).

BP-10. Strain-enhanced magnetoresistance under invariant magnetic phase boundaries in a room temperature van der Waals antiferromagnet

J. Seo, H. Shin, S. Lim, K. Jeong, J. Hong, H. Ryu, J. Byeon, K. Moon, N. Lee, Y. Choi
Physics, Yonsei university, Seoul, Korea (the Republic of)

Strain engineering offers a versatile route to manipulate magnetic properties in van der Waals (vdW) materials, yet its role in room-temperature antiferromagnets remains largely unexplored.[1-3] Here we demonstrate strain-enhanced magnetotransport in the itinerant vdW antiferromagnet $(Fe_{0.54}Co_{0.46})_5GeTe_2$. Reversible in-plane tensile strain up to 0.043% at room temperature enhances the negative magnetoresistance by nearly a factor of two, while the spin-flop and high-field crossover transitions remain nearly invariant. This unusual coexistence of strong transport tunability and robust magnetic phase boundaries enables dynamic strain control of resistance under a fixed magnetic field. Calculations based on an anisotropic spin model reveal a compensating renormalization mechanism: tensile strain suppresses the interlayer antiferromagnetic exchange while enhancing magnetocrystalline anisotropy, thereby stabilizing the spin-flop field and amplifying the magnetotransport response. As a result, strain selectively reshapes the spin configuration within each phase without altering the phase diagram itself. This decoupling of magnetic phase stability and transport tunability establishes a distinct strain-control regime in vdW antiferromagnets and provides a pathway toward fixed-field antiferromagnetic spintronic functionality at room temperature.
[1] E. Henríque, A. M. Ruiz and M. Galbiati, Advanced Materials, Vol.37, p.2506695 (2025)
[2] W.-Q. Xie, C.-C. and He, X.-B. Yang, The Journal of Physical Chemistry C, Vol.127, p.17194 (2023).
[3] K. S. Burch, D. Mandrus, J.-G. Park, Nature, Vol.563, p.47, (2018)

BP-11. Observation of the Spin Seebeck Effect (SSE) in FM/NM Heterostructures

M. Maryam, P. Wongjom
Division of Physics, Thammasat University, Rangsit, Pathum Thani, Thailand

The spin Seebeck effect (SSE) and the anomalous Nernst effect (ANE) are the two fundamental mechanisms of spintronics. The normal metal (NM) and the ferromagnetic metal (FM) behave as a detector and an injector, respectively. Here, we reported the detection of the SSE in high entropy alloy (HEA). In recent years, HEAs have gained considerable attention due to their distinct magnetic and thermal properties. Cobalt-Chromium-Nickel-Iron (CCNF) is a HEA suitable for spintronic applications, as it exhibits good ductility, thermal stability, high strength, and toughness. CCNF thin films have been prepared via physical vapor deposition (PVD) with a thickness of 3nm. The NM consists of Pt, Pd, Al, Cu and Au, have a thickness of 10 nm. The thin CCNF film of 3 nm only shows ANE signal, while the coefficient of ANE (N_{ANE}) is ~0.0265 μV/K. While CCNF/Au gives a weak SSE signal with spin voltage (V_{ISHE}) ~ 0.0012 μV/K, CCNF/Pd has 0.00260 μV/K and CCNF/Pt shows combined ANE (N_{ANE}) and inverse spin hall effect (V_{ISHE}) of ~0.0192 μV/K. Although in the CCNF/Al the coefficient of ANE (N_{ANE}) is 0.009 μV/K. The magnetic properties of FM/NM thin films were analyzed by VSM, revealing M_s for CCNF ~1000 emu/cm^3 while CCNF/Al, CCNF/Au and CCNF/Pt have M_s ~445 emu/cm^3, 778.3 emu/cm^3 and 589.5 emu/cm^3, respectively, indicating strong interface effects in ultrathin films. As Al is very reactive and forms Al_2O_3 magnetic dead layer, reducing the M_s. The surface roughness of bare CCNF, CCNF/Al, CCNF/Au and CCNF/Pt is 58.19 pm, 939.5 pm, 28.46 pm and 28.21 pm, respectively and was measured by AFM. Overall, these findings contribute to understanding ferromagnetic bilayer systems, providing strategies for enhancing their performance in future spintronic technologies.

K.Uchida et al., et al., Observation of the spin Seebeck effect, Nature 455, 778–781 (2008).
Naoto Nagaosa et al., Anomalous Hall effect, Reviews of Modern Physics 82, 1539 (2010).
Gerrit E. W. Bauer et al., "Spin caloritronics," Nature Materials 11, 391–399 (2012).
Eiji Saitoh et al., "Conversion of spin current into charge current at room temperature: Inverse spin-Hall effect," Applied Physics Letters 88, 182509 (2006).

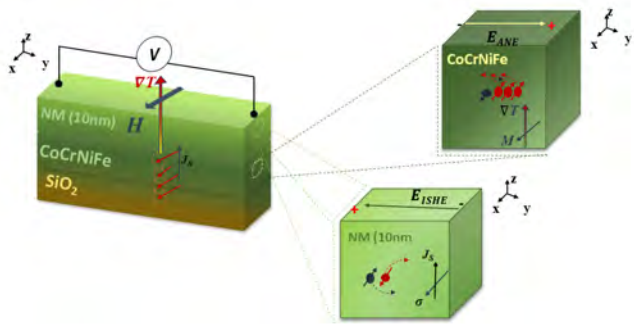


Fig. 1. Schematic illustration of the longitudinal spin Seebeck effect (LSSE) and anomalous Nernst effect (ANE) measurement geometry. A temperature gradient is applied along the out-of-plane direction (z-axis), generating a spin current in the CCNF layer. An anomalous transverse voltage is simultaneously produced in CCNF due to ANE. The injected spin current is converted into a transverse electric field via the inverse spin Hall effect (ISHE) in the NM.

BP-12. Conductance Study of an Octametallic Molecular Complex Via Conductive Probe Atomic Force Microscopy and Magnetic Tunnel Junction Testbed

P. Tyagi, M. Savadkoohi
University of the District of Columbia, Washington, District of Columbia, United States

Transport through a single octametallic molecular complex, comprising a metal cluster core functionalized with alkane tethers terminated in thiol groups, was investigated using two complementary device architectures. In the first configuration, molecules self assembled on a NiFe permalloy substrate were contacted using a gold coated conductive probe AFM tip. The resulting IV characteristics consistently exhibited a conductance gap followed by a sharp current onset near 2 V, suggesting transport dominated by the molecular core behaving as a quantum dot. The observed gap implies a HOMO LUMO separation of approximately 4 V (Fig. 1). In contrast, when ensembles of the same molecules were integrated laterally between the exposed edges of a NiFe (10 nm) AlOx (2 nm) NiFe (10 nm) tunnel junction, the IV response transitioned from the native nonlinear tunneling behavior to a nearly linear, resistor like profile. This dramatic change indicates that covalent bonding through thiol terminated tethers enables strong electronic coupling to both electrodes, fundamentally altering the transport mechanism relative to the AFM tip configuration, where only physical contact to the core is

established. This comparative study highlights how electrode molecule bonding geometry governs charge transport pathways and reveals the stark contrast between weakly coupled, quantum dot like behavior and strongly coupled, near ohmic conduction in octametallic molecular systems.

BP-13. Current-induced drastic change in resistivity–temperature characteristics: Mechanism of spin-related transport in a polycrystalline $NiCo_2O_4$ film

S. Sugiyama[1], M. Tanaka[1, 2, 3], R. Nakane[1, 2, 4]
[1]Deptartment of Electrical Engineering and Information Systems, The University of Tokyo, Bunkyo-ku, Tokyo, Japan, [2]Center for Spintronics Research Network (CSRN), The University of Tokyo, Bunkyo-ku, Tokyo, Japan, [3]Institute for Nano Quantum Information Electronics, The University of Tokyo, Bunkyo-ku, Tokyo, Japan, [4]Systems Design Lab (d.lab), The University of Tokyo, Bunkyo-ku, Tokyo, Japan

$NiCo_2O_4$ (NCO) is theoretically a half-metallic ferrimagnet and a promising source of spin-polarized electrons for spintronic devices. In experiments, polycrystalline NCO exhibits degraded magnetic order and semiconducting temperature-dependent resistivity (ρ-T) owing to weakened double-exchange interactions[1,2], where ideally only down-spin electrons hop between Ni cations. Nevertheless, its detailed properties remain unclear. In double-exchange systems, current is known as a powerful probe of the spin alignment and electron transport mechanism[3], since their electrical and magnetic properties are strongly correlated. Here, we leverage this approach to polycrystalline NCO, and find that a current-induced drastic change in ρ-T, which uncovers the electron transport mechanism related to spin alignment.

In an ultra-high vacuum electron-beam evaporation chamber, a 1-nm-thick $MgAl_2O_4$ buffer layer was deposited on a Si(001) substrate at a substrate temperature T_{sub} of 650°C. Then, a 36-nm-thick NCO layer was deposited at T_{sub} = 315°C using RF oxygen plasma (2×10^{-3} Pa, 200 W), and RHEED confirmed its polycrystalline structure. The sample was annealed at 400°C for 30 min in 1 atm O_2. Then, ρ was measured by a four-terminal method under a constant current I.

Figure 1 shows the ρ-T curves at 35–290 K with I = 100 nA–1 mA. As I is increased, the ρ-T feature changes from semiconducting-like to unimodal, accompanied by a peak shift toward higher T and lower ρ. Since the peak T value corresponds to the Curie temperature T_C of regions with degraded magnetic order[3,4], this peak shift reveals the T_C enhancement of the defective regions near grain boundaries. All the observations are well explained by the mechanism proposed in Fig. 2. The degree of spin alignment is weak near grain boundaries and has high activation energies of hopping between sites initially. When I is applied, spin-polarized electrons from less-defective inner-grain regions flow toward grain boundaries, enhancing spin alignment, and thereby increasing T_C and reducing ρ.

[1]C. Jia, F. Yang, L. Zhao, et al., Nanoscale Research Letters, Vol. 14, p.10 (2019).
[2]Y. Fujishiro, K. Hamamoto, O. Shiono, et al., Journal of Materials Science: Materials in Electronics, Vol. 15, p.769 (2004).
[3]T. Ono, A. Kogusu, S. Morimoto, et al., Applied Physics Letters, Vol. 84, p.2370 (2004).
[4]N. Zhang, W. Ding, W. Zhong, et al., Physical Review B, Vol. 56, p.8138 (1997).

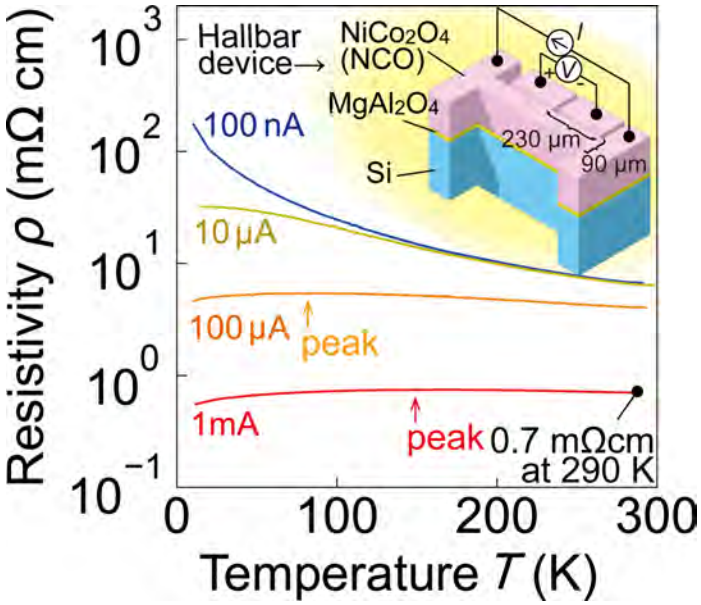


Fig.1 Temperature-dependent resistivity (ρ-T) measured at various current I.

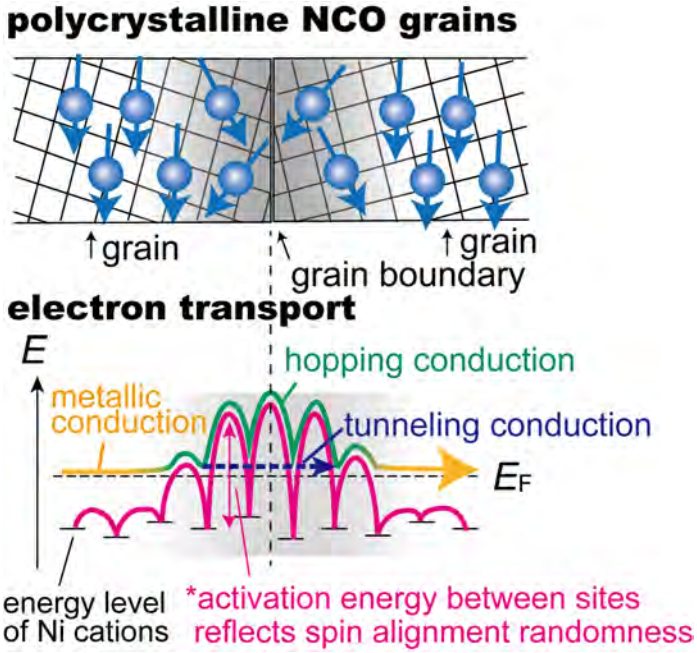


Fig.2 Schematic illustration of the electron transport mechanism across inner-grain and near-grain-boundary regions.

BP-14. Exploration of Spin-Dependent Tunneling for Electrical Detection of Spin States in Diamond NV Centers

K. Higashikawa[1], S. Nakamura[3, 4], M. Kawashima[5], H. Morishita[2, 4], S. Onoda[6], Y. Ando[1]

[1]Department of Physics and Electronics, Osaka Metropolitan University, Sakai, Osaka, Japan, [2]Center for Science and Innovation in Spintronics, Tohoku University, Sendai, Miyagi, Japan, [3]Center for Science and Innovation in Spintronics, Tohoku University, Sendai, Miyagi, Japan, [4]WPI Advanced Institute for Materials Research, Tohoku University, Sendai, Miyagi, Japan, [5]Department of Applied Physics, Tohoku University, Sendai, Miyagi, Japan, [6]National Institutes for Quantum Science and Technology, Takasaki, Gunma, Japan

A nitrogen-vacancy (NV) center in diamond has attracted significant interest as a candidate for solid-state qubits because of good spin coherence. For scalable quantum computing, it is essential to reduce the distance between neighboring qubits. However, the required spatial resolution falls below the optical diffraction limit. If the spin state of an NV center could be electrically detected using ferromagnetic electrodes, individual qubit control would become feasible. In this study, we aim to realize electrical detection of the NV spin state by exploiting spin-dependent tunneling.

Diamond substrates were prepared by nitrogen ion implantation (1 keV, Dose; 1×10^{14} cm^{-2}). TRIM simulations indicate that NV centers are formed at a depth of approximately 2 nm from the surface, enabling electron exchange with adjacent metal electrodes. A Co thin film was then deposited. Figure 1(a) shows photoluminescence (PL) mapping of the NV centers, where clear emission attributed to NV is observed. We further investigated changes in the PL intensity under applied bias to the Co film. When a positive voltage is applied, a decrease in PL intensity is observed, suggesting a transition from NV^- to NV^0 due to electron extraction (Figs. 1(b) and 2). Notably, the NV^0 state remains stable even after the voltage is removed, and the NV^- state is restored upon application of a negative voltage. These results indicate that, if spin-dependent tunneling is realized, the spin state could be detected electrically via charge-state modulation. In the presentation, we will also report ongoing efforts toward the realization of spin-dependent tunneling.

Acknowledgments:S.N. and H.M. thank CSRN of CSIS at Tohoku Univ. and Spin-RNJ.

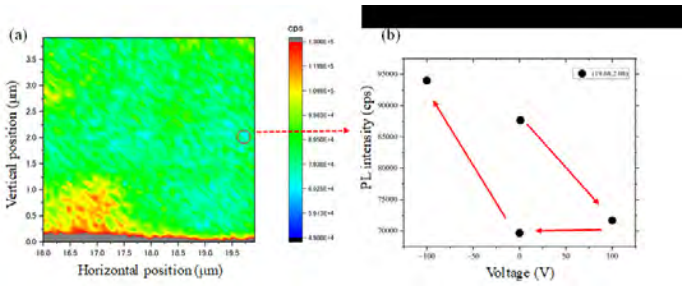


Fig. 1: (a) PL mapping of diamond NV centers. The emission wavelength is 637 nm. NV centers are observed over the entire field of view. (b) Variation in the PL intensity of a selected NV center under voltage application to the Co thin film.

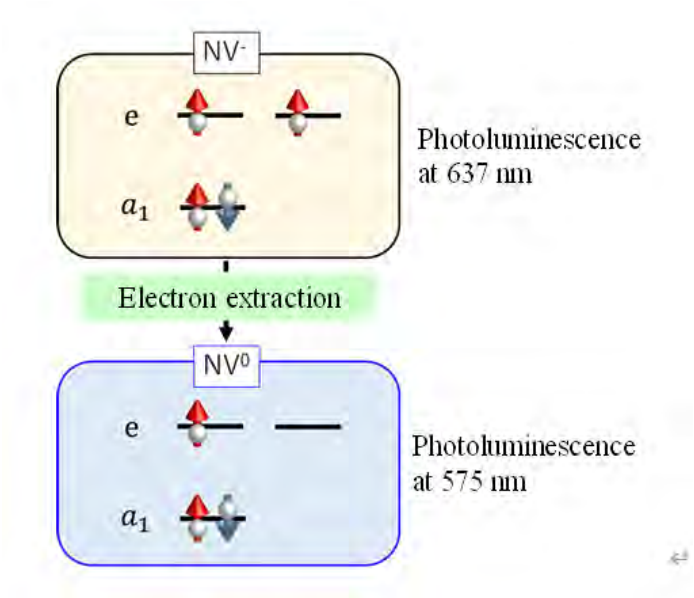


Fig. 2: Spin states of NV centers used for verification of spin-dependent tunneling. Although electrical detection is the ultimate goal, PL is used for state readout in this study, as the primary focus is on realizing spin-dependent tunneling.

BP-15. Spin Orbit Torque in Synthetic Antiferromagnetic Structure Using Rh and IrMn Capping Layer

D. Tanaka, Y. Chen, Y. Kurokawa, H. Yuasa
Kyushu University, Fukuoka, Japan

Magnetization switching by spin orbit torque (SOT) under zero-field is required for realization of a sustainable MRAM. Synthetic antiferromagnetic (SyAF) structure has been proposed as a candidate and zero-field switching was demonstrated. [1,2]. When utilizing this structure, it is important to design the strength of SyAF coupling, perpendicular magnetization anisotropy (PMA), and Dzyaloshinskii-Moriya interaction (DMI) originated from the special asymmetry. In this study, we introduce a Rh layer as a spacer providing a stronger SyAF coupling than Ru or Ir, and an IrMn capping layer to break the spatial symmetry, and then quantified the magnitude of SOT efficiency. A film of Ta (3)/Pt (4)/Co (1.3)/Pt (0.2)/Rh (1.6)/Pt (0.2)/Co (1.3)/$Ir_{22}Mn_{78}$ (1.1)/SiN (3) (unit: nm) was deposited by magnetron sputtering, where Rh thickness was optimized to have an appropriate SyAF coupling for SOT measurements. It was patterned into Hall bar structures using photolithography and SOT efficiency was obtained using the evaluation technique widely used [3]. As shown in Fig. 1, SOT efficiency showed broad peaks, which is a unique characteristic observed in SyAF structure [2]. Since SyAF coupling is broken at about ±50 mT, SOT efficiency showed the maximum value. Therefore, careful consideration is necessary when determining the damping-like torque, which is the intrinsic SOT efficiency. More important for practical applications is the fact that the SOT efficiency was obtained as 5 x 10^{-12} (mT/(Am^{-2})) at zero magnetic field. The field at which the STO efficiency is zero is a positive value between 20 mT and 50 mT, which is consistent with the field at which magnetization did not switch in previous report [2]. Thus, the quantitative evidence for magnetization switching under zero-field by SOT was obtained.

[1] L. Zhu et al., Appl. Phys. Lett. 117, 112401 (2020).
[2] Y. Saito et al., Phys. Phys. B. 108, 024419 (2023).
[3] C. Pai et al., Phys. Phys. B. 93, 144409 (2016).

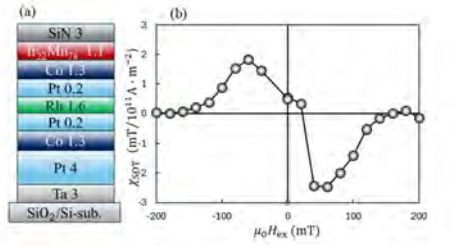


Fig. 1 (a) Sample structure. (b) Spin–orbit torque efficiency as a function of applied in-plane field.

BP-16LB. Magnon-phonon coupling using multiple-overtone surface acoustic waves

K. Yamanoi, Y. Nozaki
Keio University, Yokohama, Japan

Surface acoustic waves (SAWs) offer a platform for exciting magnons with well-defined frequencies and wave vectors. We demonstrate broadband probing of magnon–phonon resonances using a multiovertone SAW device incorporating an epitaxial Co_2FeSi film on $LiNbO_3$ [1-2]. A low fundamental frequency of 193 MHz provides densely spaced overtones at approximately 400 MHz intervals. Figure 1 (left) shows SAW excitation up to the 29th harmonic (5.6 GHz). Magnetic-field-dependent SAW attenuation reveals spin-wave resonances across multiple harmonics. As shown in Fig. 1 (right), the experimental resonance conditions agree well with those predicted by spin-wave dispersion calculations at the corresponding SAW wave vectors in both monostable and bistable magnetization regimes. This agreement supports resonant magnon excitation with

frequencies and wavelengths matched to those of the SAWs. These results establish a broadband approach to probing wave-vector-matched magnon–phonon interactions within a single device.

[1] S. Yamada et al. Adv. Sci. 12, e11250 (2025).
[2] K. Yamanoi et al. Phys. Rev. Applied 26, L031002 (2026).

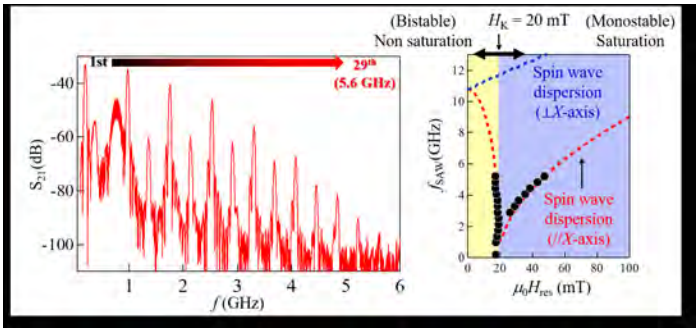


Fig. 1 (left) Frequency dependence of S_{21} parameter for multiple overtones SAW device, and (right) SAW frequencies as function of resonant fields. Red (blue) curve represents the calculation for the SW dispersions.

SESSION BQ: ADVANCED PERMANENT MAGNET AND INDUCTION MACHINE TECHNOLOGIES (POSTER SESSION)

Chair(s): J. Xiao, *Hinetics Inc., Champaign, Illinois, United States*

Tuesday, November 3, 2026
03:00 PM-06:00 PM
Coral 4

BQ-01. Torque and Rotor Current Prediction of Induction Motors Using Per Unit Slip Frequency and Current Based on Equivalent Circuit Correction

T. Kim[1], J. Kim[1], E. Kim[1], M. Lim[1], H. Ban[2], J. Choi[2], K. Shin[3]
[1]Department of Smart Manufacturing Engineering, Changwon National University, Changwon, Korea (the Republic of), [2]Department of Electrical Engineering, Chungnam National University, Chungnam, Korea (the Republic of), [3]Department of AI Electrical Engineering, Changwon National University, Changwon, Korea (the Republic of)

In conventional equivalent circuit analysis, fixed parameters are generally used, although magnetizing inductance and leakage related parameters vary with current level and slip frequency owing to magnetic saturation [1]. This limitation can cause prediction errors, especially under high current and high slip conditions. [2]. Therefore, this paper proposes a correction method for an equivalent circuit that can accurately analyze the torque and rotor current of an induction motor in the operating region according to slip frequency and current conditions.

Fig. 1 shows the motor configuration, including the stator, rotor, windings, and rotor bars, together with the experimental setup and equivalent circuit model used in this study. The rotor current and torque were calculated using the equivalent circuit model. In the proposed method, the operating region was segmented based on the per-unit slip frequency and current, and the magnetization inductance was corrected according to each operating condition.

Fig. 2 presents electromagnetic characteristics and the validation results. The flux density distributions show that the magnetic field varies significantly with slip frequency and current level. The comparison of sensitivity indicates that magnetizing inductance variation has a stronger effect on torque prediction than leakage inductance variation. The rotor current and torque under low and high current conditions with correction were compared with the finite element analysis results. The corrected analysis technique agrees well with the finite element analysis results. From these results, it is indicated that correcting the magnetization inductance according to the operating point is effective in improving the performance prediction of induction motors using equivalent circuits

[1] Du-Ha Park., *IEEE Trans.Magn.* 60 (9), 1–5 (2024).
[2] L. Monjo, F. Córcoles, and J. Pedra, *IEEE Trans. Energy Convers.* 28(1), 243–254 (2013).

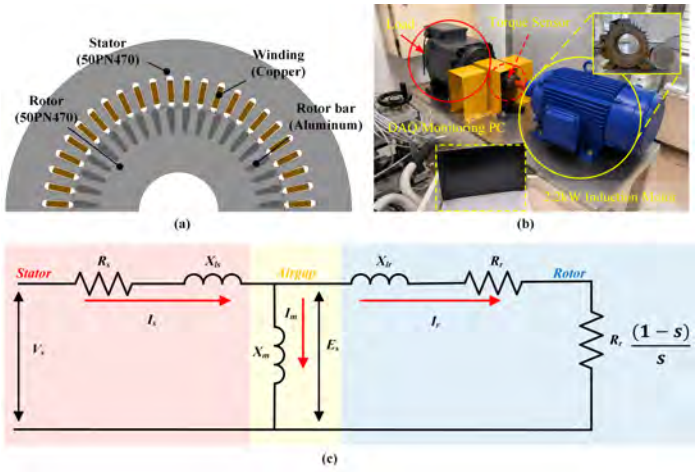


Fig. 1. Industrial induction motor model and equivalent circuit: (a) motor cross section, (b) experimental setup, and (c) per phase equivalent circuit.

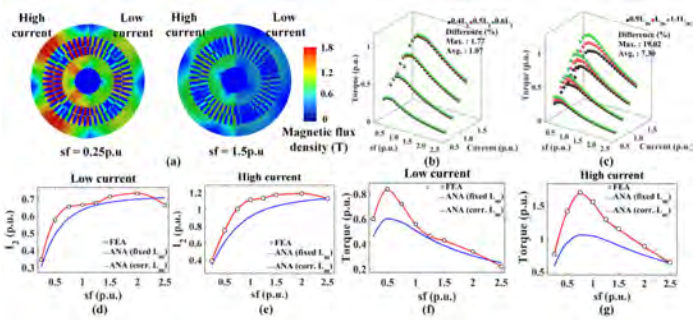


Fig. 2. Electromagnetic characteristics and analysis results: (a) flux density, (b) leakage reactance ratio effect on torque, (c) magnetizing reactance ratio effect on torque, and (d)–(g) rotor current and torque at low and high currents.

BQ-02. Multiphysics Analysis and Experimental Verification of Electromagnetic Vibration and Noise in an Interior Permanent Magnet Synchronous Motor Considering SVPWM Inverter Excitation

G. Lee[1], G. Shin[1], M. Kim[1], S. Kim[2], J. Choi[2], K. Shin[1]
[1]Changwon National University, Changwon, Korea (the Republic of), [2]Chungnam National University, Daejeon, Korea (the Republic of)

Interior permanent magnet synchronous motors (IPMSMs) driven by space vector pulse width modulation (SVPWM) inverters are widely used in traction and compressor drive systems [1]. However, inverter switching harmonics distort the air gap magnetic field and generates additional electromagnetic force components, which can intensify electromagnetic vibration and noise (e-NVH) [2]. This paper presents a multiphysics analysis and experimental verification of inverter-induced e-NVH in a 6-pole, 27-slot V-type IPMSM [3].

Fig. 1 shows the analysis procedure proposed in this paper. First, an evaluation system is constructed, motor geometry modeled, and electromagnetic, spatio-temporal 2D-FFT, and modulation analyses performed, mapping extracted magnetic forces to the stator to predict vibration and noise via modal and harmonic response analysis. Fig. 2 compares the characteristics under ideal sinusoidal and SVPWM excitation conditions. The SVPWM current harmonics amplify the magnetic pressure force components, distort the unbalanced magnetic force trajectories, and excite structural resonances, thereby increasing the equivalent radiated power in the high-frequency region.

Results indicate that carrier sideband harmonics from the SVPWM inverter interact with stator vibration modes and spatial force orders, producing strong resonances that are absent under ideal sinusoidal excitation. Experimental measurements from the motor drive test-bed strongly align with these predicted acoustic and vibration characteristics. Therefore, the proposed method provides a practical tool for identifying inverter related excitation sources before manufacturing and for reducing high-frequency noise in the IPMSM system.

[1] S. Zhu, W. Zhao, J. Ji, G. Liu and C. H. T. Lee, IEEE Trans. Transp. Electrific., Vol. 10, pp. 9513–9528, (2024).
[2] R. Yan, D. Wang, C. Wang, W. Miao, and X. Wang, IEEE Trans. Magn., Vol. 61, Art. no. 8200206, (2025).
[3] F. Soresini, D. Barri, F. Ballo, M. Gobbi and G. Mastinu, IEEE Trans. Transp. Electrific., Vol. 10, pp. 8728–8745, (2024).

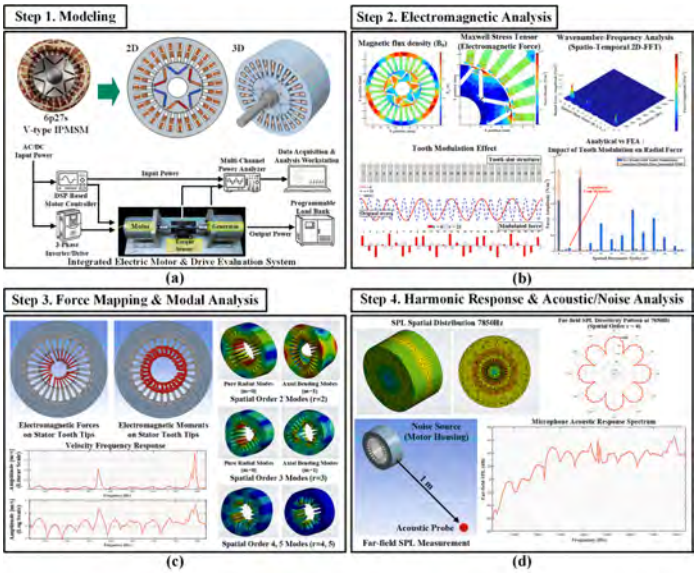


Fig. 1. Proposed multiphysics procedure for electromagnetic vibration and noise prediction: (a) IPMSM modeling and test system, (b) electromagnetic analysis, (c) force mapping and modal analysis, and (d) harmonic response and acoustic analysis.

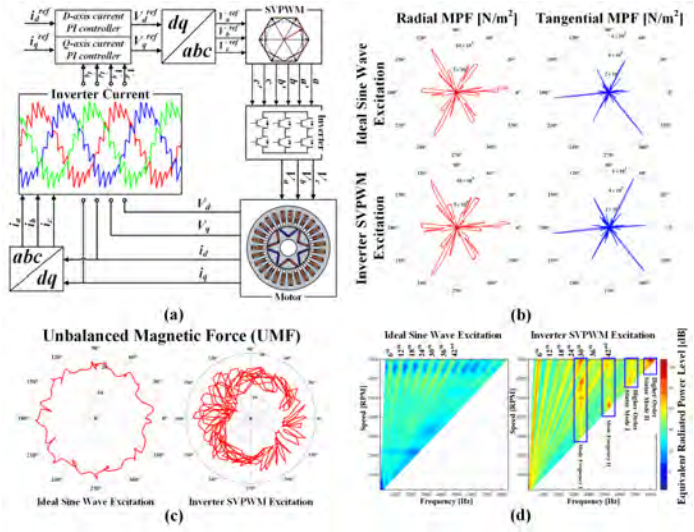


Fig. 2. Comparison of electromagnetic force and vibration characteristics under ideal sinewave and SVPWM excitation: (a) inverter control system, (b) radial and tangential magnetic pressure forces, (c) unbalanced magnetic force trajectories, and (d) equivalent radiated power spectrograms.

BQ-03. Comparative Study on Design and Analysis of Interior Permanent Magnet Synchronous Motors with Different Rotor Structures based on Magnetic Equivalent Circuit and Finite Element Method

H. Lee[1], M. Kim[1], M. Seo[1], W. Lee[1], K. Yu[2], J. Choi[2], K. Shin[3]
[1]Smart Manufacturing Engineering, Changwon National University, Changwon, Korea (the Republic of), [2]Electrical Engineering, Chungnam National University, Daejeon, Korea (the Republic of), [3]Electrical Engineering, Changwon National University, Changwon, Korea (the Republic of)

The interior permanent magnet synchronous motor (IPMSM) offers several advantages such as high-power density, high torque capability, and improved efficiency, making it an ideal choice for traction applications [1]. The rotor structure of an IPMSM significantly influences its electromagnetic performance, efficiency, and torque characteristics [2]. Therefore, understanding and optimizing the rotor structure is crucial to further improve the efficiency and power density of IPMSMs.

In this study, the initial design of bar-type and V-type IPMSMs using the magnetic equivalent circuit (MEC) method and detailed analysis and comparison by finite element analysis (FEA) and experimental study are carried out. First, the design and analysis of the flux linkage and inductance of the IPMSM according to the rotor structure are carried out using MEC. The derived models are analyzed in detail for electromagnetic characteristics such as electromagnetic losses and torque by FEA. Finally, experimental studies are conducted to compare the driving characteristics and performance evaluation results. Based on the requirements and constraints of the system, the structures of the bar-type and V-type IPMSMs are shown in Fig. 1(a). As shown in Figs. 1(b) and 1(c), design models satisfying the requirements can be derived from MEC for calculating the magnetic flux linkage and d-q axis inductance according to the design flow and rotor structure. The composition of the prototypes and the experiment set is shown in Fig. 2(a). Fig. 2(b) shows the performance characteristics of each model and compares the results at the rated operating point. Figs. 2(c) and (d) show the efficiency maps with the main, rated, and maximum speed operating points for each model.

The detailed design, analysis results, discussions, and measurements of the IPMSMs will be presented in the full paper.

[1] Y. Hu, S. Zhu, C. Liu, and K. Wang, IEEE Trans. Energy Convers., Vol. 33, pp. 199-208, (2017).
[2] A. Wang, Y. Jia, and W. Soong, IEEE Trans. Magn., Vol. 47, pp. 3606-3609, (2011).

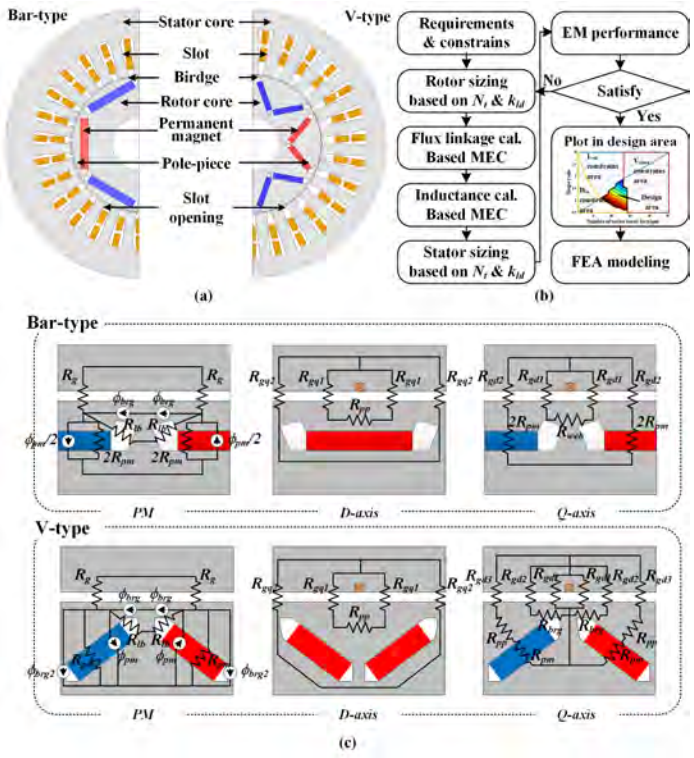


Fig. 1. (a) Analysis models of IPMSM, (b) flow chart of initial design with MEC, (c) MEC model with bar-type and V-type IPMSM.

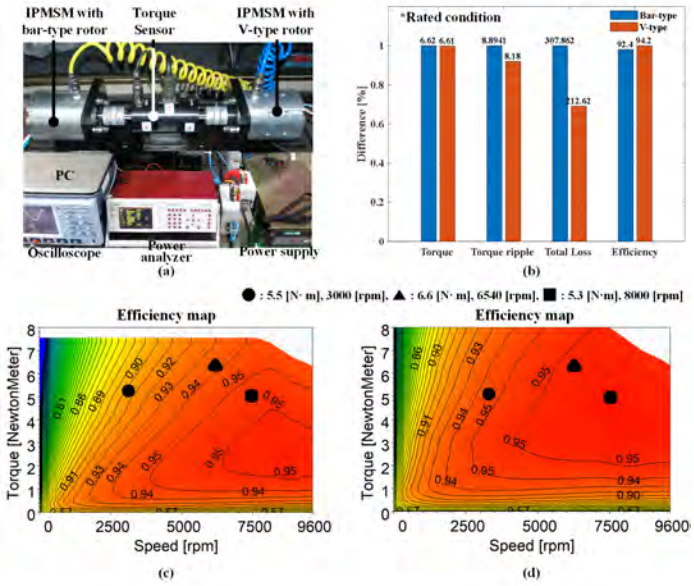


Fig. 2. (a) Experimental setup (b) electromagnetic analysis under rated conditions, efficiency map from (c) bar-type IPMSM and (d) V-type IPMSM.

BQ-04. Magnetic coupling control between permanent magnet flux and induced rotor currents in line-start permanent magnet machines

J. Lee[1], M. Park[1], Y. Noh[1], K. Lee[1], J. Lee[2]
[1]Korea Electronics Technology Institute, Bucheon, Korea (the Republic of), [2]Hanyang University, Seoul, Korea (the Republic of)

Line-start permanent magnet synchronous motors (LSPMs) exhibit complex electromagnetic coupling between permanent magnet flux and induced rotor currents, resulting in magnetic braking and degraded starting performance. Although this phenomenon has been widely reported, the magnetic mechanisms associated with rotor flux distribution and saturation remain insufficiently clarified. This study investigates the role of permanent magnet placement in controlling flux–current interaction in LSPMs and proposes a magnetically driven rotor design strategy to mitigate magnetic braking while preserving high synchronous efficiency.
A distributed V-type permanent magnet configuration is introduced to spatially modulate rotor flux distribution. Magnet-free squirrel-cage regions are intentionally formed to enhance induced current density during startup, while magnet-assisted regions maintain strong magnetic torque at rated operation. Flux saturation and magnetic flux line analyses show that the proposed design suppresses excessive flux concentration near embedded magnets and redistributes air-gap flux to favor induced current generation in non-magnetized regions, thereby weakening magnetic braking effects.
The proposed rotor was evaluated through electromagnetic simulations and experimentally validated using a 5.5 kW prototype motor. Measured back-electromotive-force waveforms agreed with analytical predictions within 1% error, confirming the effectiveness of the flux modulation concept. Experimental results demonstrated an efficiency improvement exceeding 3% compared to a conventional induction motor under rated conditions.
These results clarify how permanent magnet distribution and rotor flux modulation govern electromagnetic coupling in LSPMs. The proposed approach establishes a magnetism-oriented rotor flux engineering framework for mitigating magnetic braking while preserving synchronous performance.

Acknowledgement
This work was supported by the Korea Insitute of Energy Technology Evaluation and Planning(KETEP) grant funded by the Korea government(MOTIE) (RS-2024-00419152)
Y. Ould Lahoucine, R. Raute and C. Caruana, Energies, Vol. 18, p. 4545 (2025).
L. Yin, J. Yan, B. C. Sales and D. S. Parker, Physical Review Applied, Vol. 17, p. 064020 (2022).
H. J. Park, H. B. Hong and K. D. Lee, *Energies*, Vol. 15, p. 9644 (2022).
K. Srinivasan, F. P. Delgado, H. Hofmann and J. Sun, IEEE Trans. Energy Convers., Early Access , p. 1-14 (2025) DOI: 10.1109/TEC.2025.3599748

BQ-05. Two-Step Split Magnetization Strategy for Post-Assembly Magnetization of Axial Flux Permanent Magnet Rotor

J. Lee, J. Moon, Y. Lim, C. Lee, W. Kim
Gachon University, Seongnam, Korea (the Republic of)

Axial flux permanent magnet (AFPM) motors have attracted significant attention due to their high torque density and compact axial structure. However, the conventional magnetization-before-assembly method degrades assembly workability and limits automation in mass production. Post-assembly magnetization has therefore been considered as an alternative approach, but achieving a high magnetization ratio in AFPM rotors remains challenging due to their structural characteristics.

In AFPM magnetizers, the narrow pole spacing and nearly constant teeth cross-section lead to early magnetic saturation and difficulty in forming an effective magnetizing flux path. As a result, the effective magnetic flux delivered to the magnets is reduced, making single-step magnetization insufficient.

To overcome these limitations, this paper proposes a two-step split magnetization strategy. In this method, magnets are divided into target and non-target groups, allowing the magnetic flux to be concentrated on the target magnets during each step. This improves magnetization performance under the same power supply conditions. However, the reverse magnetic field applied to non-target magnets can cause irreversible demagnetization.

To mitigate this issue, a sub-teeth structure is introduced to control the magnetic flux path and suppress demagnetization. The thicknesses of the teeth and sub-teeth are selected as key design parameters and optimized through three-dimensional finite element analysis.

A prototype two-step AFPM magnetizer is fabricated and experimentally validated. The results show that the air-gap flux density decreases by 7.25%, while the no-load back-EMF decreases by only 0.92%, indicating negligible performance degradation. These results demonstrate that the proposed method enables effective post-assembly magnetization of AFPM rotors with high magnetization performance and reduced demagnetization.

R. Shao, R. Navaratne, M. Popescu, and G. Liu, "Design and construction of axial-flux permanent magnet motors for electric propulsion applications—A review," IEEE Access, vol. 9, pp. 158998–159017, 2021.

R. Shao, R. Navaratne, M. Popescu, and G. Liu, "Design and construction of axial-flux permanent magnet motors for electric propulsion applications—A review," IEEE Access, vol. 9, pp. 158998–159017, 2021.

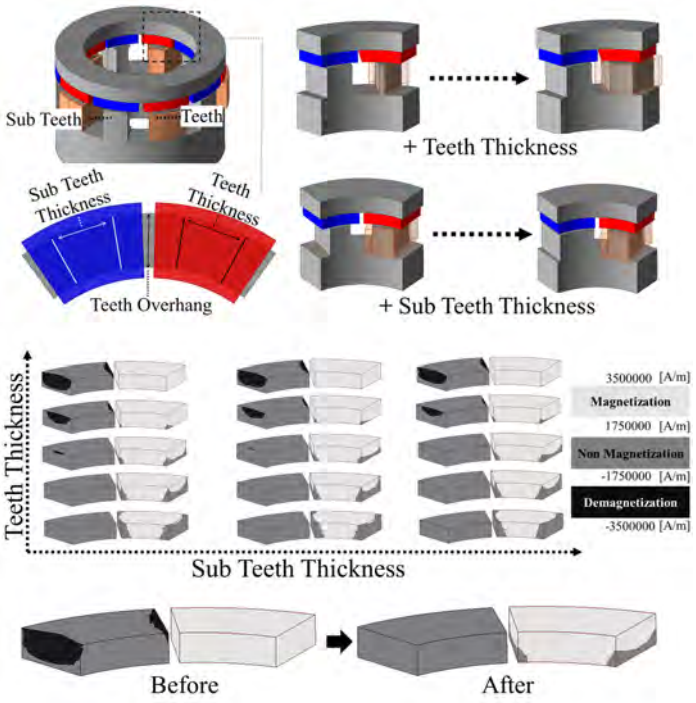


Figure 1.Design parameters of teeth and sub-teeth and comparison of target and non-target magnetization with varying thickness in the AFPM magnetizer

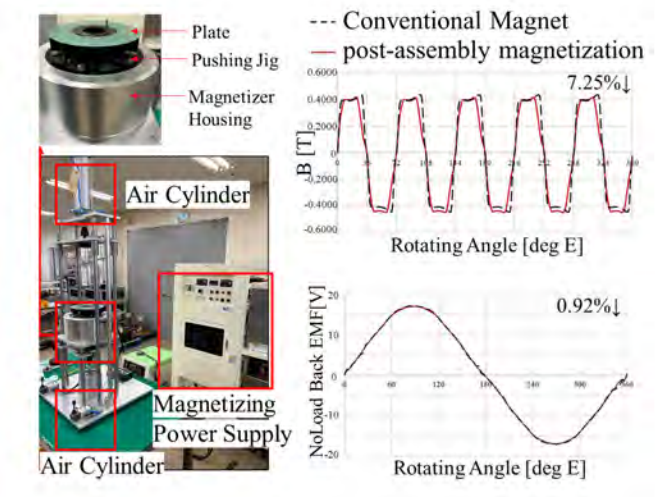


Figure 2. Experimental setup, fabricated two-step AFPM magnetizer optimized by FEA, and corresponding experimental results.

BQ-06. Multi-Objective and Multi-Fidelity Automatic Design Framework for Squirrel Cage Induction Motors Using Tree Search Based Reinforcement Learning

M. Lim[2], T. Kim[2], E. Kim[2], J. Kim[2], H. Ban[1], J. Choi[1], K. Shin[3]
[1]Electrical Engineering, Chungnam National University, Daejeon, Korea (the Republic of), [2]Smart Manufacturing Engineering, Changwon National University, Changwon, Korea (the Republic of), [3]AI Electrical Engineering, Changwon National University, Changwon, Korea (the Republic of)

Optimizing induction motors requires balancing inherent trade-offs between efficiency and material consumption. Automatic design methods using tree search and reinforcement learning can efficiently search for candidate models. However, it is difficult to apply automatic design techniques to induction motors because there is a large error between the equivalent circuit model, finite element analysis (FEA), and experimental results [1], [2]. Nonlinear FEA provides high accuracy but has the disadvantage of requiring high computational cost for design exploration [3].

This paper proposes a multi-objective and multi- fidelity automated design framework for squirrel-cage induction motors using tree search-based reinforcement learning and a Gaussian process regression metamodel. Fig. 1 shows the structure of the induction motor, including stator, rotor, bar, and coil variables. The design search tree explores discrete and continuous variables, and the evaluation flow combines a surrogate model, a low-precision equivalent circuit model, and a multi-fidelity meta-model to update correction factors. Sequential data generation improves consistency between predictions and high fidelity results.

Fig. 2 shows the optimized motor and verification results. The Pareto front is refined from the first to third data generation, and the error rate is reduced by the sequential correction process. For the selected optimal design, the torque curve obtained from equivalent circuit analysis is good agreement with the results of FEA and measurements across the operating range. This framework provides an efficient and reliable design path for high-efficiency induction motors under multi-objectives. Detailed implementation and further experimental verification will be presented in the full paper.

[1] S. Ahn and S. Min, Multi-Fidelity Model-Based Size Optimization of Electric Machines., IEEE Access, vol. 10, pp. 75898–75908, (2022)
[2] T. Sato and K. Watanabe, A data-driven automatic design of induction motors based on tree search and reinforcement learning considering multiple objectives., IEEE Trans. Magn., vol. 60, pp. 1–4, (2024)
[3] H. Sato and H. Igarashi, Automatic Design of PM Motor Using Monte Carlo Tree Search in Conjunction With Topology Optimization., IEEE Trans. Magn., vol. 58, Art. no. 7200504, (2022)

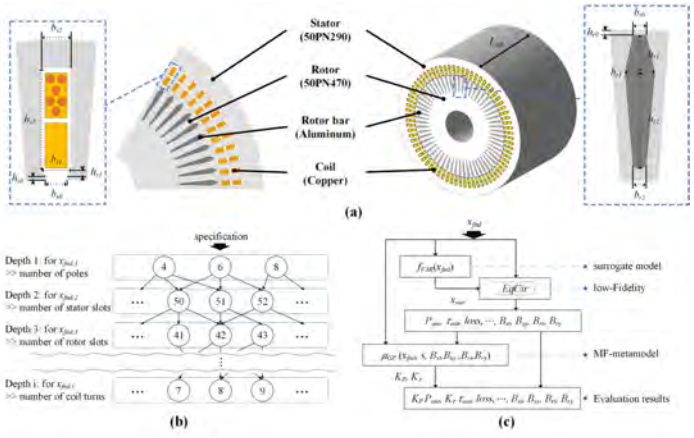


Fig. 1 Proposed automatic design framework: (a) 75 kW squirrel cage induction motor model and design variables, (b) tree search structure, and (c) multi-fidelity evaluation flow.

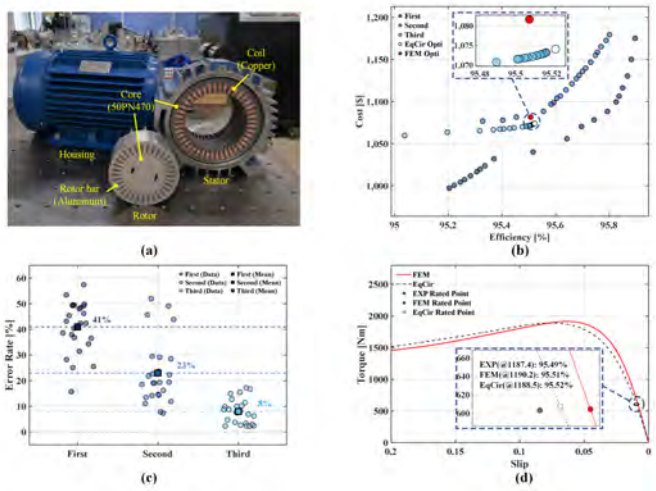


Fig. 2. Optimization and validation results: (a) optimized induction motor, (b) Pareto fronts by data generation, (c) error rate comparison, and (d) torque curve comparison among FEM, EqCir, and experiment.

BQ-07. AFPM Design Process Integrating Electromagnetic Design and Formula-Based Stiffness Analysis

Y. Lim[1], H. Kim[1], C. Lee[1], S. Park[1], W. Kim[2]
[1]Department of Next Generation Smart Energy System Convergence, Gachon University, Seongnam-si, Gyeonggi-do, Korea (the Republic of), [2]Department of Electrical Engineering, Gachon University, Seongnam-si, Gyeonggi-do, Korea (the Republic of)

This paper proposes a design process integrating the electromagnetic design and structural stability verification of an axial flux permanent magnet motor (AFPM) satisfying high torque density within a limited volume.
As industrial development and system integration demands increase, AFPM has attracted attention as an alternative motor for achieving high torque in limited space. AFPM is advantageous for achieving high power density with a thin structure, however, rotor deformation may occur due to the axial electromagnetic force and centrifugal force during rotation, which may alter the air-gap distribution and degrade performance and operational stability [1].
Therefore, structural stability evaluation is essential in AFPM design. However, conventional electromagnetic FEA-based stiffness analysis requires three-dimensional modeling and analysis of actual geometry, imposing significant time and computational burdens during iterative design [2]. Accordingly, in this study, a Formula-based Stiffness Analysis method based on the elastic solution of a rotating annular disk and the von Mises equivalent stress equation was established and integrated into the AFPM design process.
The proposed process derives the final model through one-turn-model-based electromagnetic design after selecting the pole-slot combination, and verifies structural stability using Formula-based Stiffness Analysis. Using this process, a 200W AFPM was designed, and Formula-based Stiffness Analysis of the final model yielded an equivalent stress of 0.802 MPa at the evaluation point. In addition, comparison with electromagnetic FEA-based stiffness analysis showed an equivalent stress error of approximately 1.3%, confirming the high accuracy of the proposed method. Finally, a prototype motor was manufactured and tested, and the validity of the proposed design process was verified through comparison with finite element analysis results.
Therefore, this study presents a practical design process for efficiently integrating high-torque AFPM electromagnetic design and structural stability evaluation, and provides meaningful design implications for improving iterative design efficiency and ensuring structural stability in high-torque AFPM design.

[1] H. Ouldhamrane, B. Bechki and A. Houari, "Optimal Design of Axial Flux Permanent Magnet Motors for Ship RIM-Driven Thruster," Machines, vol. 10, no. 10, Art. no. 932, Oct. 2022.
[2] A. Lehikoinen, A. Arkkio and A. Belahcen, "Reduced Basis Finite Element Modeling of Electrical Machines with Multi-Conductor Windings," IEEE Trans. Ind. Appl., vol. 53, no. 5, pp. 4252–4259, Sep./Oct. 2017.

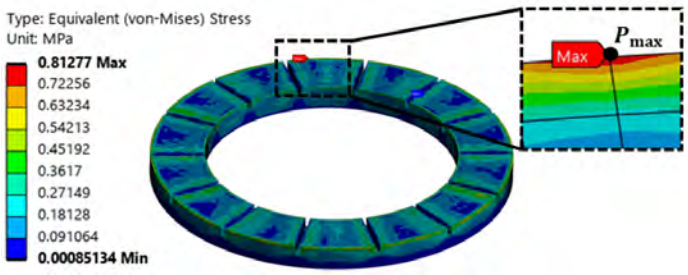
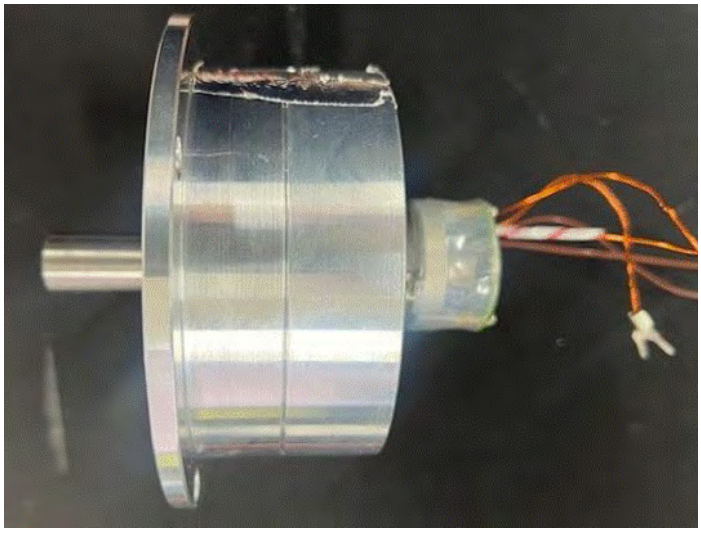


Fig.1


Fig.2

BQ-08. Hybrid Permanent Magnet Structure Design for Improving Torque Density in Axial Flux Permanent Magnet Motors

Y. Lim[1], H. Kim[1], J. Moon[1], C. Kim[2], W. Kim[3]
[1]Department of Next Generation Smart Energy System Convergence, Gachon University, Seongnam-si, Gyeonggi-do, Korea (the Republic of), [2]Department of Electrical Engineering, Wonkwang University, Iksan-si, Jeonbuk-do, Korea (the Republic of), [3]Department of Electrical Engineering, Gachon University, Seongnam-si, Gyeonggi-do, Korea (the Republic of)

This paper presents an effective magnet-structure design for a double stator-single rotor (DSSR) axial flux permanent magnet motor (AFPM) by comparing surface-mounted permanent magnet (SPM) and interior permanent magnet (IPM) configurations to reduce permanent-magnet usage while improving torque density [1].
Recently, AFPM has attracted attention as an alternative in next-generation electric drive systems that simultaneously require stable high-torque operation in the low-speed region and a thin profile, because it can achieve both high torque density and thinness. In particular, the DSSR AFPM is advantageous for realizing high torque density and a thin structure because the two stators create a symmetric flux distribution [2]. Conventional SPM-type AFPMs have a simple structure and stable electromagnetic performance, but require more permanent magnets under the same output condition because of the limitation in air-gap flux utilization efficiency. In contrast, IPM-type AFPMs can improve torque performance per permanent-magnet usage by exploiting reluctance torque and flux-concentration effects resulting from the rotor-embedded magnet arrangement, but they are limited by flux leakage, local saturation, and manufacturing complexity.
Accordingly, this study proposes an IPM-based hybrid permanent-magnet structure employing bar-shaped and *I*-shaped magnets. The proposed structure was designed to maximize flux concentration through the rotor core while securing an effective magnet area toward the air gap, and to improve magnet retention, thereby also providing an advantage in structural rigidity. Under identical physical dimensions and electrical loading conditions, comparison between the conventional SPM structure and the proposed structure confirmed that the proposed structure exhibits superior torque characteristics per permanent-magnet volume and can effectively suppress leakage flux.
Therefore, this study presents a DSSR AFPM design approach that can efficiently realize low-speed high-torque characteristics through changes in permanent-magnet structure and shape, and provides meaningful design implications for simultaneously improving torque density, permanent-magnet utilization, and structural stability.
[1] G. Zhang, Q. Tong, T. Zhang, J. Tao and A. Qiu, "Design of a High Torque Density Robot Joint and Analysis of Force Control Method Applied for a Light Exoskeleton," Electronics, vol. 12, no. 2, Art. no. 397, Jan. 2023.
[2] H. Wang *et al*., "A Novel Double-Sided Offset Stator Axial-Flux Permanent-Magnet Motor Topology," *Machines*, vol. 13, no. 3, Art. no. 52, 2022.

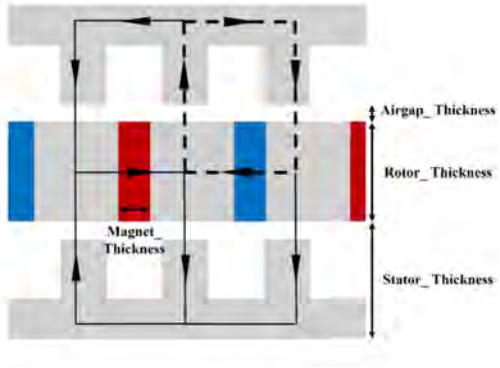


Fig.1

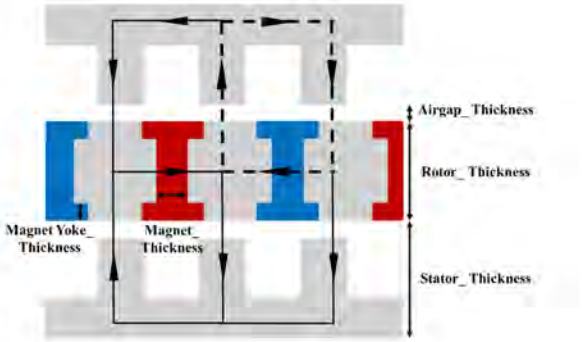


Fig.2

BQ-09. Analysis of Local Loss Density and Thermal Hotspots Driven by 3D Spatial Flux Harmonics in Axial Flux Permanent Magnet Motors

S. Oh, D. Kim, H. Kim, H. Lee
Dankook University, Yongin, Korea (the Republic of)

In recent years, the demand for Axial Flux Permanent Magnet (AFPM) motors has significantly increased in the fields of electric mobility and high-power industrial drives due to their superior power density and high torque performance within limited spaces. However, the spatial flux non-uniformity caused by the unique three-dimensional (3D) magnetic structure of AFPM motors remains a critical challenge for electromagnetic loss prediction and thermal management. This study performs a Multiphysics analysis and experimental validation to clarify the correlation between non-uniform flux density distribution, harmonic components, and the formation of thermal hotspots within AFPM motors. First, flux density data were extracted at key spatial positions along the radial and circumferential

directions using 3D transient electromagnetic Finite Element Analysis (FEA). These data were subsequently converted via Fast Fourier Transform (FFT) to quantitatively quantify the spectral distribution of spatial flux harmonics and their contribution to local iron losses. The analysis results confirmed that amplified harmonic components at specific spatial locations cause a non-uniform distribution of local losses. These findings were utilized as input conditions for a thermal analysis model to precisely predict the internal thermal behavior of the motor. Finally, by comparing the interpreted results with temperature data obtained through thermocouples and infrared thermography during operational experiments, it was verified that the spatiotemporal correlation between harmonic-induced losses and experimental thermal mapping. The results of this study provide precise electromagnetic-thermal combined design guidelines to pre-emptively predict local heating issues caused by 3D flux distortion and to maximize the reliability and lifespan of AFPM motors during the design stage.

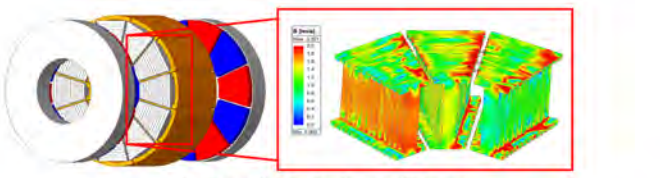


Fig 1. Non-uniform flux distribution in AFPM motor

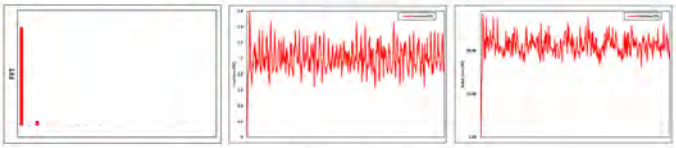


Fig 2. Harmonic and loss data of an AFPM motor

BQ-10. Performance Improvement of Permanent Magnet Machines With an ICP Rotor Through Optimal Stator Design

S. Song

Department of Electrical Energy Engineering, School of Electrical and Advanced Materials Engineering, Kyungguk National University, Andong, Korea (the Republic of)

As demand for high-performance and high-power-density permanent magnet machines increases, innovative rotor structures have been studied to improve electromagnetic characteristics. Among them, the inter-pole compartment (ICP) rotor has attracted attention because it can enhance flux utilization and torque performance compared with conventional rotor topologies. However, unlike conventional permanent magnet machines, the application of an ICP rotor introduces axial leakage flux, which disturbs internal flux distribution and degrades machine performance. This axial leakage flux affects not only the rotor but also the stator core, teeth, and yoke, resulting in reduced effective air-gap flux, local magnetic saturation, torque reduction, increased torque ripple, and additional iron loss.

In conventional permanent magnet machines, stator axial leakage flux has rarely been considered a major issue because the dominant flux path is radial. In contrast, in ICP rotor-based machines, the stator becomes an additional path for axial leakage flux due to the increased axial component of the magnetic field. This means that conventional stator design is insufficient for ICP-based machines and that stator optimization specialized for the ICP rotor is required.

This study investigates the generation mechanism of stator axial leakage flux caused by the ICP rotor and proposes an optimal stator design to reduce its effects. Three-dimensional finite element analysis was performed to evaluate the influence of axial leakage flux on stator magnetic behavior and machine performance. Key stator design parameters, including tooth shape, yoke thickness, slot opening, and stack length, were analyzed.

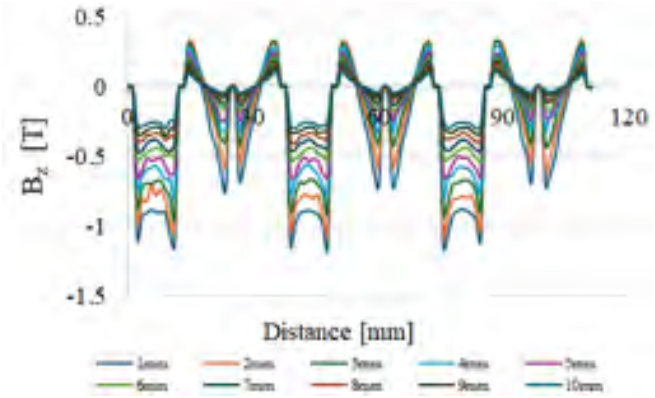
The results show that the proposed stator design effectively suppresses axial leakage flux, alleviates magnetic saturation in the stator, stabilizes air-gap flux density, and improves overall machine performance. In addition, torque ripple and iron loss are reduced. These findings demonstrate that stator optimization is essential for fully exploiting the advantages of the ICP rotor and provide a design guideline for next-generation permanent magnet machines with axial leakage flux.

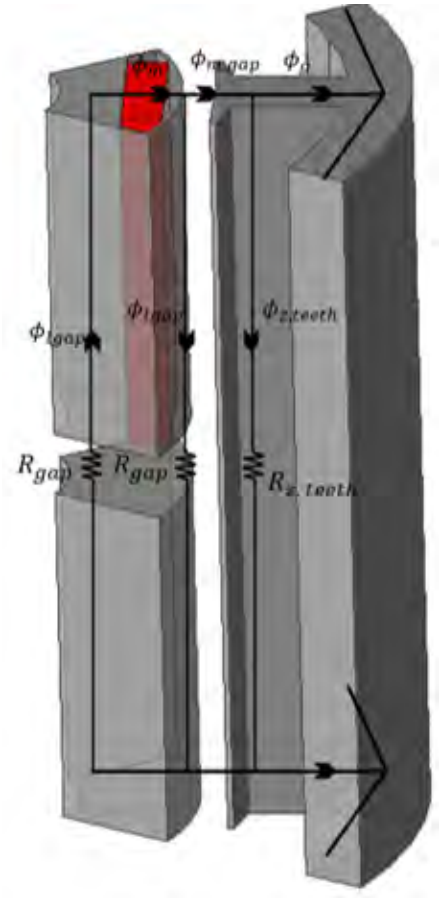
[1]R. I. Rivera, E. C. Quispe and J. R. Gómez, "Efficiency determination of converter-fed AC induction motors according to method A of IEC 60034 2-3 standard," 2019 IEEE Workshop on Power Electronics and Power Quality Applications (PEPQA), 2019, pp. 1-5, doi: 10.1109/PEPQA.2019.8851552.

[2]G. Bucci, F. Ciancetta, E. Fiorucci and A. Ometto, "Uncertainty Issues in Direct and Indirect Efficiency Determination for Three-Phase Induction Motors: Remarks About the IEC 60034-2-1 Standard," in IEEE Transactions on Instrumentation and Measurement, vol. 65, no. 12, pp. 2701-2716, Dec. 2016, doi: 10.1109/TIM.2016.2599459.

[3]F. J. T. E. Ferreira, G. Baoming and A. T. de Almeida, "Reliability and Operation of High-Efficiency Induction Motors," in IEEE Transactions on Industry Applications, vol. 52, no. 6, pp. 4628-4637, Nov.-Dec. 2016, doi: 10.1109/TIA.2016.2600677.

D. -H. Jung, Y. Kwak, J. Lee and C. -S. Jin, "Study on the Optimal Design of PMa-SynRM Loading Ratio for Achievement of Ultrapremium Efficiency," in IEEE Transactions on Magnetics, vol. 53, no. 6, pp. 1-4, June 2017, Art no. 8001904, doi: 10.1109/TMAG.2017.2662943.





BQ-11. Comparative Analysis of Electromagnetic Characteristics in Hollow Shaft Slotless Surface-mounted Permanent Magnet Synchronous Machines Using Analytical Method Considering Halbach Array

S. Yoon[1], J. Yang[1], S. Kim[1], H. Yu[1], C. W. Choi[1], Y. Yoon[1], K. Shin[2], J. Choi[1]

[1]Chungnam National University, Daejeon, Korea (the Republic of), [2]Changwon National University, Changwon, Korea (the Republic of)

Surface-mounted permanent magnet synchronous machines (SPMSM) require rare earth magnets with high flux density to achieve the high power density essential for advanced industries such as robotics, aerospace, and defense [1]. To meet the demands for improved electromagnetic performance and a lightweight rotor in such applications, this paper was applied a slotless Halbach array motor [2]. Without stator teeth in slotless motor, have linear current characteristics for electromagnetic performance, but the magnetic flux density is low due to the large effective air gap. To mitigate this, high grade magnets and Halbach array are applied [3]. Especially, Halbach array improve rotor core flux saturation and low flux density hollow shaft type slotless motor [4]-[6]. Therefore, this paper proposes the improvement in electromagnetic performance achieved using Halbach array and presents a discussion on the mitigation of rotor core flux saturation.

Finite element analysis (FEA) is accurate, it is time consuming and lack flexibility in the initial design phase, making analytical methods efficient. Figure 1(a) shows the basic structure of a rare earth hollow shaft slotless SPMSM. Figure 1(b) shows the simplified analytical model. The accuracy of the analytical method was verified by comparing the analytically calculated air gap flux density and no load back-electro motive force (back EMF) with the FEA results in Fig. 1(c), (d). Figure 2(a) shows the flux line and magnetization models of the Halbach array classified by the number of segments. Finally, the changes in air gap flux density and no load back EMF performance according to number of segments are analyzed in Fig. 2(b), (c).

In this paper, the electromagnetic characteristics of a hollow shaft slotless SPMSM with a Halbach array applied were analyzed using the analytical method. Detailed process of the analytical method will be explained in the full paper [7].

1. A. M. El-Refaie, IEEE Trans.Magn. 57 (1), 107–121 (2009)
2. C.-P. Yu, C.-H. Huang and C.-C. Lan, IEEE Access 11, 114378-114389 (2023)
3. P. R. Upadhyay, K. Rajagopal and B. Singh, IEEE Trans.

Magn. 40 (4), 2023-2025 (2004)
4. Z. Zhu, D. Howe, E. Bolte and B. Ackermann, IEEE Trans.Magn. 29 (1), 124–135 (2002)
5. Z. Zhu and D. Howe, IEE Proc.-Electr. Power Appl. 148 (4), 299–308 (2001)
6. T. Okita and H. Harada, IEEE Access 11, 2078-2091 (2023)
7. K. Atallah and D. Howe, IEEE Trans.Magn. 34 (4), 2060–2062 (1998)

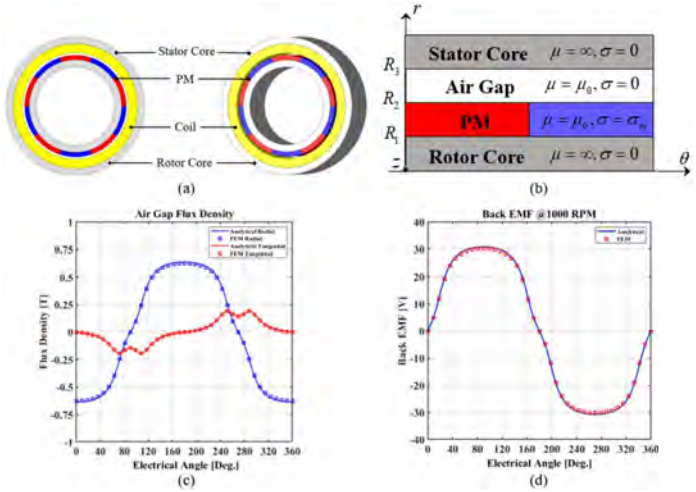


Fig.1 Hollow shaft slotless SPMSM (a) base model, (b) simplified analytical model, comparison analytical and FEA (c) air gap flux density, (d) back EMF

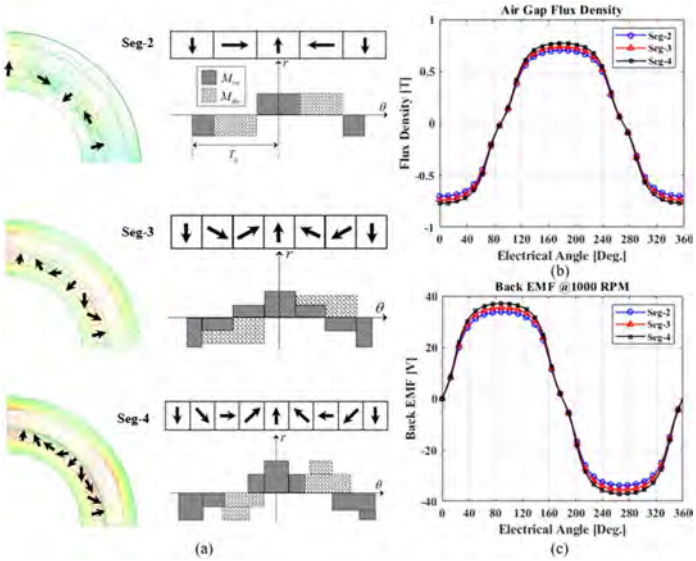


Fig.2 Number of segments (a) Halbach array magnetization model, (b) air gap flux density, (c) back EMF

BQ-12. Harmonic Modeling of PMa-SynRM under PWM Excitation Considering Nonlinear Inductance

H. Yu[1], S. Kim[1], Y. Yoon[1], C. W. Choi[1], S. Yoon[1], K. Shin[2], J. Choi[1]
[1]Electrical Engineering, Chungnam National University, Daejeon, Korea (the Republic of), [2]AI Electrical Engineering, Changwon National University, Changwon, Korea (the Republic of)

Permanent Magnet-assisted Synchronous Reluctance Motors(PMa-SynRMs) employ multi-layer rotor topologies to maximize reluctance torque. However, these complex geometries induce unbalanced magnetic saturation and spatial harmonics. Existing studies rely on assumptions of ideal sinusoidal excitation or constant circuit parameters[1]-[4]. Such simplifications fail to characterize the dynamic intermodulations between high-frequency pulse-width modulation(PWM) transients and the motor's inherent spatial harmonics in actual inverter-driven environments. These high-order intermodulations distort the harmonic spectra and torque characteristics, making high-fidelity performance predictions challenging for conventional linear models.

This paper proposes a systematic framework, as shown in Fig. 1, which integrates carrier-based PWM principles with the motor's nonlinear characteristics. First, the nonlinear *d-q* axis parameters are identified using 2-D finite element analysis(FEA) to account for magnetic saturation and spatial harmonics in (a). Simultaneously, the inverter output voltage is numerically modeled to decompose switching harmonics in (b). By formulating these components within a frequency-domain harmonic impedance matrix in (c), a high-fidelity electromagnetic analysis model is established. This approach is compared with FEA co-simulation results in (d). Figure 2 shows the experimental environment for validating the proposed model, where (a) is the analysis model, (b) is the control process block diagram considering space vector PWM, (c) is the experimental setup, and (d) provides a comparison of current harmonic spectra. These experimental results validate the high predictive accuracy of the model. Detailed analysis results are provided in the full paper.

1. M. Fasil, C. Antaloae, and N. Mijatovic, Appl. Supercond., Vol. 26 , p.1 (2016)
2. S. Dai, J. Wang, Z. Sun and E. Chong, IEEE Trans. Ind. Electron., Vol. 69, p.9817 (2022)
3. W. Liang, J. Wang and P. C.-K. Luk, IEEE Trans. Energy Convers., Vol. 29, p.673 (2014)
4. Z. Wu, Z. Yang and K. Ding, IEEE Trans. Power Electron.,

Vol. 37, p.820 (2021)
5. A. M. Hava, R. J. Kerkman and T. A. Lipo, IEEE Trans. Ind. Appl., Vol. 34, p.1059 (2002)
6. P. Yi, X. Wang and D. Chen, IEEE Trans. Transp. Electrif., Vol. 8, p.1794 (2021)
7. J. Jacob, O. Bottesi, and S. Calligaro, IEEE Trans. Ind. Appl., Vol. 57, p.4884 (2021)
8. D. Chen and L. Xiao, IEEE Access, Vol. 8, p.170002 (2020)

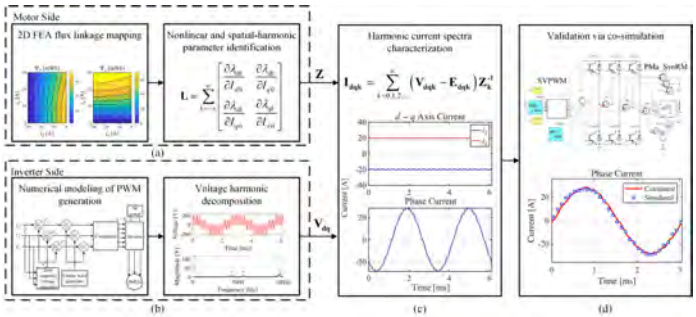


Fig. 1. Systematic framework for electromagnetic analysis of PMa-SynRM: (a) nonlinear parameter identification, (b) PWM harmonic decomposition, (c) frequency-domain harmonic matrix formulation, and (d) comparison of FEA co-simulation results.

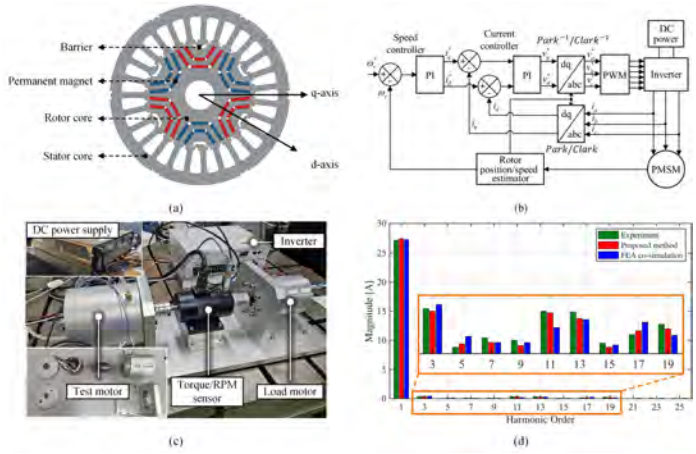


Fig. 2. Experimental environment for validating the proposed model: (a) 2-D PMa-SynRM geometry, (b) control block diagram considering space vector PWM, (c) experimental setup, and (d) comparison of current harmonic spectra.

BQ-13. Robust Model-Free Predictive Current Control for PMSM via Pole-Zero Cancellation

J. Liu, Y. Luo, K. Yang
School of Electrical and Electronic Engineering, Huazhong University of Science and Technology, Wuhan, Hubei, China

To address the trade-off among transient overshoot, phase lag, and high-frequency noise inherent in traditional nonlinear term observers for the model-free predictive control (MFPC) of permanent magnet synchronous motor (PMSM), this paper proposes a direct algebraic model-free predictive current control strategy based on a pole-zero cancellation (PZC) method. This strategy artificially configures the parameters of the observer's error transfer function to achieve precise PZC. Consequently, the second-order asymptotic observation dynamics are strictly reduced into a first-order convergence process without overshoot. Furthermore, the system's differential signal is directly extracted using the constructed observer equation. The lumped disturbance in the ultra-local model is then directly solved via an algebraic subtraction law, eliminating the inherent lag defects of traditional integral-type observers. Comparative simulation results verify that the proposed method effectively enhances the robustness of the system against disturbances.

Y. Luo, K. Yang and Y. Zheng, IEEE Transactions on Industrial Electronics, Vol. 70, p.10800-10810 (2023)
F. Wang, Y. Wei, J. Rodriguez and C. Garcia, IEEE Transactions on Power Electronics, Vol. 40, p.10846-10864 (2025)
Y. Zhang, J. Jin and L. Huang, IEEE Transactions on Industrial Electronics, Vol. 68, p.993-1003 (2021)
Y. Wei, Y. Chen, C. Garcia, Z. Yin, F. Wang and J. Rodríguez, IEEE Transactions on Industrial Electronics, Vol. 73, p.1620-1631 (2026)
X. Zhang, Q. Xu, Y. Miao, Y. Wang, X. Wang and S. Liu, IEEE Transactions on Industry Applications, Vol. 61, p.9425-9438 (2025)

BQ-14. Multi-Objective Design Optimization of Squirrel-Cage Induction Motor Using MOBO and Sensitivity Analysis

T. Kim[1], H. Ban[1], S. Eom[1], K. Shin[2], J. Choi[1]
[1]Department of Electrical Engineering, Chungnam National University, Daejeon, Korea (the Republic of), [2]Department of AI Electrical Engineering, Changwon National University, Changwon, Gyeongsangnam-do, Korea (the Republic of)

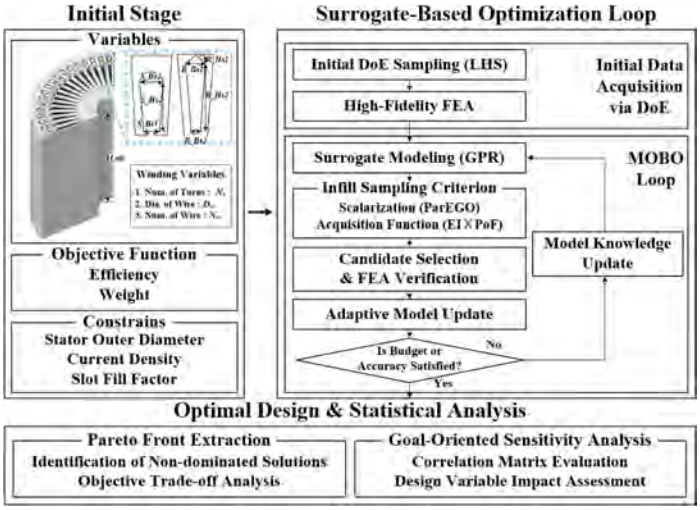
Squirrel-cage induction motors are widely used in industrial applications due to their robustness and reliability [1]. However, electromagnetic performance evaluation of induction motors typically relies on high-fidelity finite element analysis (FEA), which requires substantial computational time and cost, especially when multiple design variables are involved. Therefore, efficient optimization strategies that can reduce computational burden while maintaining optimization accuracy are required. To address this issue, this paper proposes a surrogate-assisted multi-objective Bayesian optimization (MOBO) framework for efficient exploration of computationally expensive design spaces [2].

Fig. 1 illustrates the overall optimization framework. Design variables including stator, rotor, and winding parameters are defined, and efficiency and weight are selected as objectives. Initial samples are generated using Latin hypercube sampling and evaluated by FEA, followed by surrogate model construction and iterative candidate selection. After convergence, Pareto-optimal solutions and sensitivity analysis are obtained.

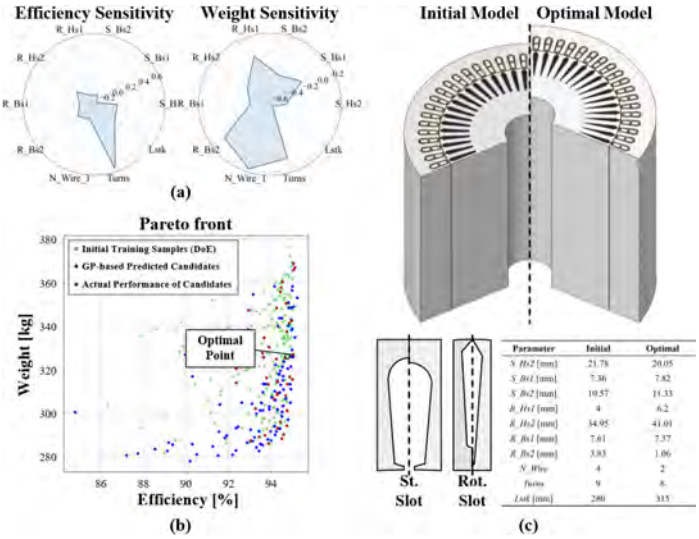
Fig. 2 summarizes the optimization results and design insights. Fig. 2(a) presents the sensitivity analysis of design variables for efficiency and weight, identifying dominant parameters affecting each objective. Fig. 2(b) shows the Pareto front obtained from the multi-objective optimization, demonstrating the trade-off relationship between efficiency and weight. Fig. 2(c) compares the initial and optimized motor geometries, highlighting design changes achieved through optimization.

The proposed MOBO-based optimization framework effectively identifies optimal design solutions with reduced computational cost. The optimized motor achieves improved efficiency, confirming the effectiveness of the proposed approach for practical induction motor design. Further details will be provided in the full paper.

[1] A. T. de Almeida, F. J. T. E. Ferreira, and J. A. C. Fong, "Standards for efficiency of electric motors,"*IEEE Industry Applications Magazine*, vol. 17, no. 1, pp. 12–19, 2011.
[2] J. Rossmann, M. J. Kamper, and C. M. Hackl, "A Global Multi-Objective Bayesian Optimization Framework for Generic Machine Design Using Gaussian Process Regression," IEEE Transactions on Energy Conversion, vol. 23, no. 4, pp. 997–1004, Dec. 2008.



Multi-objective optimization process for squirrel-cage induction motor design.



Optimization results showing: (a) sensitivity of design variables, (b) Pareto front, and (c) initial and optimized motor geometries.

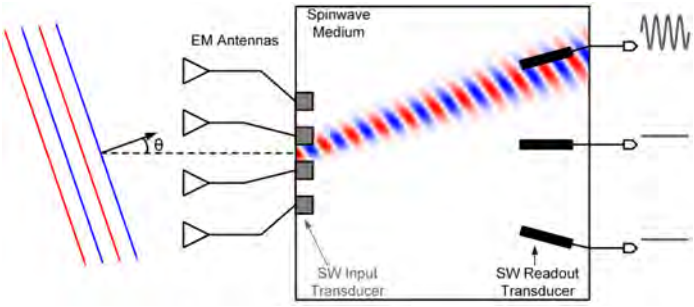
SESSION BR: ULTRAFAST MAGNETISM, MAGNONICS AND SPIN DYNAMICS II (POSTER SESSION)
Chair(s): T. Hioki, *The University of Tokyo, Tokyo, Japan*
Tuesday, November 3, 2026
03:00 PM-06:00 PM
Coral 4

BR-01. Spin Wave Based Phased Array Beamforming
J. Fletcher, A. Jander, P. Dhagat
Electrical Engineering and Computer Science, Oregon State University, Corvallis, Oregon, United States

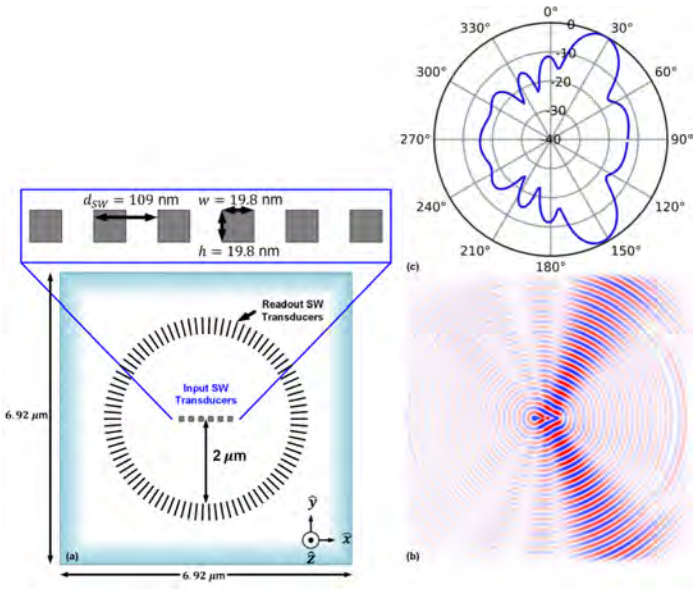
Spin waves hold promise for low-power analog processing of RF signals in modern communication systems [1]. We present a device concept for steering and filtering radio waves incident to an array antenna in a compact form factor by using spin waves to implement phased array beamforming. As shown in Fig. 1, the electromagnetic (EM) signal received by an antenna is converted into a spin wave (SW) by a SW transducer. The relative phase delay between the spin wave excited at each transducer is set by the direction of arrival (θ) of the EM wave. The interference between the excited spin waves results in a SW beam whose radiation pattern is a function of θ. The beam then propagates to a set of "readout" transducers which convert the spin wave back into an electromagnetic wave. Due to the spin wave beam being spatially confined, each readout transducer will only see a signal if the spin wave beam points in the direction of that readout transducer. This enables spatial filtering of the EM waves incident to the antenna without the need for power hungry active phase shifters. Further, due to their short wavelengths, spin waves offer a path to for chip-scale beamforming at sub-10 GHz frequencies, where EM implementations would be prohibitively large [2].

We simulated the interference of spin waves, via micromagnetic modeling, in a 100 nm thick yttrium-iron-garnet (YIG) film with the input SW transducers positioned as shown in Fig. 2a. The relative phase between the excited spin waves was varied and the radiation pattern of the resulting beam “readout” by the SW transducers placed in an arc at a distance from the input transducers. Shown in Figs. 2b and 2c respectively are example plots of a SW beam and its radiation pattern. The presentation will further discuss the results to highlight research and development opportunities for passive, and there by low-power, beamforming with spin waves in small form factors.

[1] K. O. Levchenko, K. Davídková, J. Mikkelsen, arXiv:2411.19212 (2025)
[2] A. Azari, A. Skrivervik, & H. Aliakbarian, *Sci Rep* 14, 1245 (2024).



Schematic diagram of the proposed spin wave beamformer.



(a) Device model used for micromagnetic simulation of spin wave interference (b) Example plot of in-plane magnetization component in the YIG film, showing a spin wave beam being generated (c) Corresponding radiation pattern of the spin wave input transducer array.

BR-02. Spin-Orbit Torque Lubrication at Pt/Co interface for Tunable Deterministic Switching with Stochasticity

M. Yang, C. Yang
Materials Science and Engineering, National Yang Ming Chiao Tung University, Hsinchu, Taiwan

Deterministic switching in spin–orbit torque magnetoresistive random access memory (SOT-MRAM) has long been a central goal in SOT research. Meanwhile, the stochastic switching behavior of SOT-MRAM has recently attracted growing interest as an on-chip entropy source for true random number generators (TRNGs). In this work, a moderate Cu dusting at the interface of Pt/Co bilayer of perpendicular anisotropy enables to tune the stochasticity of intermediate states under the deterministic SOT switching framework. With increasing Cu dusting content at the Pt/Co interface, the switching behavior transits from gradual (analog) to deterministic (digital) switching while accompanying with the increasing randomness at the intermediate states. Besides, the introduction of Cu at the Pt/Co interface enables to reduce the critical current density for the deterministic SOT switching together with the tunable stochasiticity for the TRNG application. The results demonstrate that Cu dusting offers a simple interfacial-engineering route to flexibly control switching randomness, enabling energy-efficient initialization and a tunable stochastic window in the Pt/Co system. The tunable randomness can serve as an ideal entropy source for CMOS-compatible TRNGs, probabilistic computing, and machine-learning applications.

BR-03. Simulation Analysis of Anisotropy-Gradient-Assisted SOT Magnetization Switching

K. Harada[1], K. Yamada[2], Y. Nakatani[1]
[1]Graduate School of Informatics and Engineering, University of Electro-Communications, Chofu, Tokyo, Japan, [2]Faculty of Engineering, Gifu University, Gifu, Japan

Spin–orbit torque MRAM (SOT-MRAM) with perpendicular magnetization is promising for high-speed, durable memory [1]. However, deterministic switching without external fields or assist mechanisms remains challenging. Symmetry-breaking approaches such as tilted anisotropy [2], in-plane exchange coupling [3], and DMI [4] have been proposed. Here, we focus on an anisotropy gradient, where perpendicular magnetic anisotropy varies spatially, and evaluate its assist effect using micromagnetic simulations. Two gradient types were considered: a linear gradient, where the anisotropy constant K_u varies along the x-axis, and a step-like gradient with discrete changes [Fig. 1(a,b)]. Simulations were performed for a circular thin film at room temperature (300 K). Switching probability was evaluated versus current density and pulse width through multiple runs. Effects of field-like (FL) torque and gradient strength were also examined. To study pulse-shape effects, rectangular and triangular current pulses were applied. As shown in Fig. 2, a linear gradient combined with a triangular pulse yields high switching probability over a wide range [Fig. 2(b)]. For the step-like gradient, triangular pulses are also effective, achieving 100% switching depending on the gradient profile [Fig. 2(c)]. Furthermore, under linear-gradient and triangular-pulse conditions, complete switching is obtained with large negative FL torque and strong gradient, highlighting their key roles [Fig. 2(d)].

These results provide design guidelines for reliable SOT devices operating without external magnetic fields.

[1] F. Oboril, *et al*., *IEEE TCAD*, 34, 3, 367 (2015).
[2] L. You, *et al*., *Proc. Nat. Acad. Sci. USA*, 11, 2, 10310 (2015).
[3] Lau, YC., *et al*., *Nature Nanotech*., 11, 758 (2016).
[4] Dai, M., Hu, JM., *npj Comput. Mater*., 6, 78 (2020).

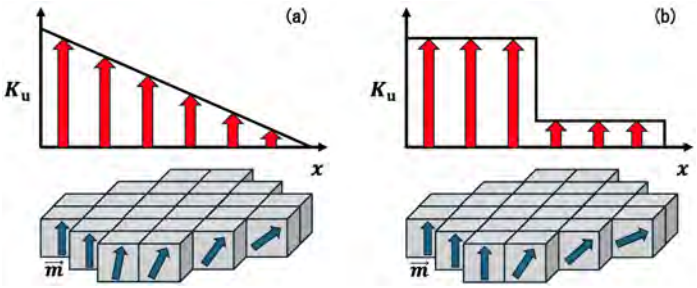


Fig. 1 Conceptual diagram of a circular magnetic thin film with an anisotropy gradient (a) Linear anisotropy gradient (b) Step anisotropy gradient.

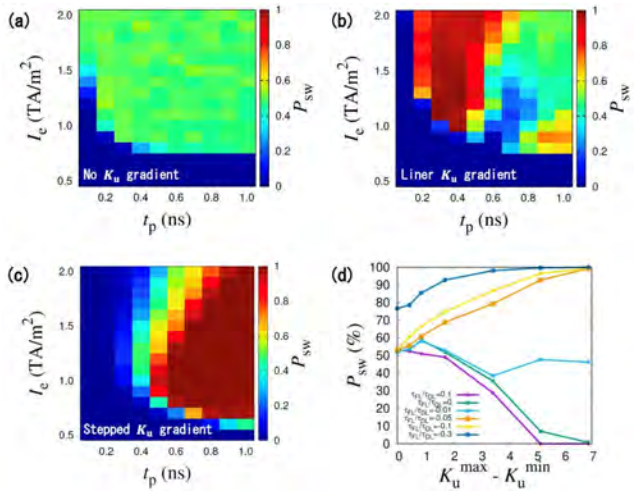


Fig. 2 (a-c) Changes in magnetization swithing probability due to current pulse width and current density (triangular pulse drive). (d) Changes in swithing probability due to the strength of the linear anisotropy gradient.

BR-04. Revealing origin of two-magnon scattering in YIG

J. Marquez Chavez, O. Wojewoda, C. A. Ross
MIT, Cambridge, Massachusetts, United States

Magnonics is developing rapidly as a platform for low-power microwave technologies and emerging computing concepts, including inverse-designed devices. Among the most promising material systems is yttrium iron garnet (YIG) [1], a ferrimagnetic garnet with exceptionally low magnetic damping [2] whose properties can be widely tuned by chemical substitution. Realizing the full potential of YIG, however, requires a detailed understanding of extrinsic dissipation channels beyond intrinsic Gilbert damping. Here, we investigate the origin and anisotropy of two-magnon scattering in thin YIG films [3]. Because two-magnon scattering is constrained by the spin-wave isofrequency contour, its efficiency is strongly affected by the anisotropic spin-wave dispersion of the film and scattering center distribution in space. In YIG grown on GGG(110), we observe a pronounced angular dependence of the ferromagnetic-resonance linewidth, which we attribute to elongated, highly directional defects that selectively enable scattering only for a limited range of in-plane propagation angles. In contrast, nearly defect-free YIG grown on GGG(111) exhibits virtually no measurable two-magnon contribution.

We describe these results using the Lippmann–Schwinger scattering formalism within the Born approximation, which links the scattering intensity to the product of the defect Fourier spectrum and the anisotropic density of accessible spin-wave states. Experimentally, the extracted angular dependence of the two-magnon scattering strength is compared with reciprocal-space analysis of atomic-force-microscopy topography, revealing a direct correspondence between defect orientation and linewidth anisotropy.

Our results provide a microscopic picture of anisotropic two-magnon scattering in YIG and establish defect morphology as a key handle for engineering dissipation in future magnonic devices.

[1] A. A. Serga, A. V. Chumak and B. Hillebrands, J. Phys. D: Appl. Phys., Vol. 43, p.264002 (2010)
[2] C. Dubs, O. Surzhenko and R. Thomas, Phys. Rev. Mater., Vol. 4, p.024416 (2020)
[3] J. Lindner, I. Barsukov and C. Raeder, Phys. Rev. B, Vol. 80, p.224421 (2009)

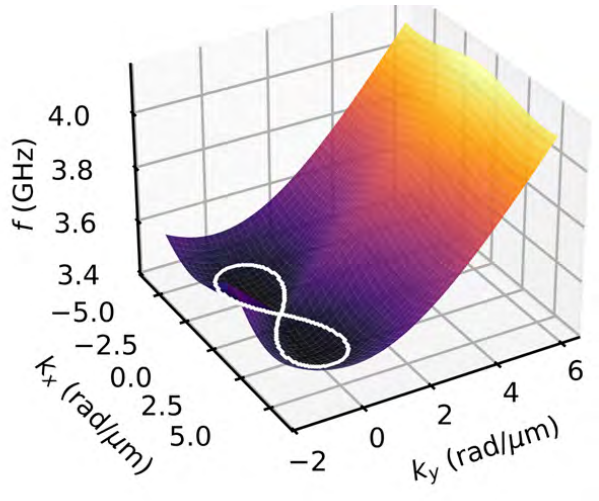


Fig. 1 Anisotropic dispersion relation of the thin YIG layer. The isofrequency line for ferromagnetic resonance frequency is highlighted.

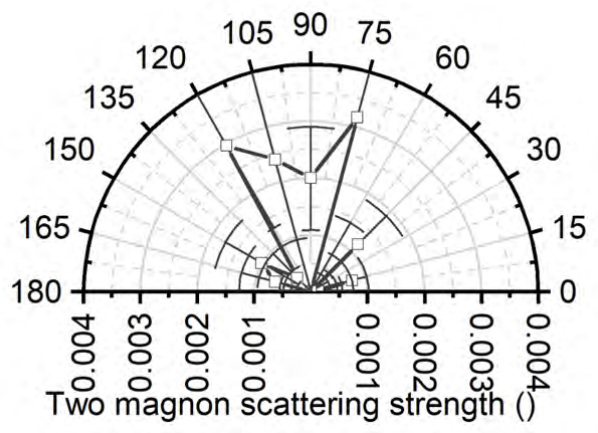


Fig. 2. Strength of the two magnon scattering measured for YIG grown on GGG (110). The highly anisotropic scattering intensity is visible.

BR-05. Wavevector-dependent Regeneration of Propagaing Magnons via Substrate Phonons in YIG/GGG

Y. Soon[1], M. Song[1], P. Cao Van[2], J. Baek[1], B. Park[3], J. Jeong[2], A. M. Park[1], K. Kim[1]

[1]Physics, Korea Advanced Institute of Science and Technology, Daejeon, Korea (the Republic of), [2]Materials Science and Engineering, Chungnam National University, Daejeon, Korea (the Republic of), [3]Materials Science and Engineering, Korea Advanced Institute of Science and Technology, Daejeon, Korea (the Republic of)

Magnons, quanta of spin waves, have attracted much attention as information carriers for efficient quantum transducer, owing to their frequency tunability, rich nonlinear behavior, and intrinsic nonreciprocity [1-3]. Coupling magnons with phonons provides a promising approach, as it enables integration with established phononic architectures while leveraging the low dissipation of acoustic excitations [4, 5]. Despite these advantages, most previous studies have focused on magnon-phonon interactions involving the uniform ferromagnetic resonance mode with zero wavevector (k = 0) [6, 7]. Extending such studies to propagating spin waves at finite k is important for wave-based signal transport and hybrid functionalities such as logic devices [8].

Here, we study the interaction between propagating magnetostatic surface spin waves (MSSWs) and acoustic waves in a YIG/GGG heterostructure. Epitaxial yttrium iron garnet (YIG) on gadolinium gallium garnet (GGG) provides a favorable platform to study magnetoelastic interaction owing to the ultralow damping of YIG and the small lattice mismatch at the interface. Using two spatially separated antennas on a 200 nm-thick YIG film, we measure transmission using a vector network analyzer (VNA). The transmission spectra exhibit periodic modulations with a characteristic spacing of ~3.5 MHz, arising from magnetoelastic coupling to substrate standing acoustic waves [6]. As the magnon wavevector k is increased by reducing the antenna width, these phonon-related features are progressively suppressed and eventually vanish. This trend reflects the k-dependent magnetoelastic coupling, likely linked to a k-dependent intensity profile across the film thickness. Time-gated analysis further shows that the phonon-induced contribution appears at lower frequencies than the directly excited MSSW modes, indicating that phonons predominantly regenerate low-k propagating magnons. Moreover, the phonon-induced modes exhibit markedly longer propagation lengths, providing an effective pathway for long-distance spin wave transmission. These results demonstrate the k-sensitive magnon-phonon hybrid dynamics and the emergence of low-damping propagating magnons enabled by phonon-induced regeneration.

[1] D. Lachance-Quirion, et al., Science Vol. 367, p. 6476, 425-428 (2020).
[2] M. You, et al., Nature Communications (2026)
[3] M. Jamali, et al., Scientific Reports Vol. 3, p. 3160 (2013).
[4] X. Zhang, et al., Science advances Vol. 2(3), p. e1501286 (2016).
[5] Y. Hwang, et al., Physical Review Letters Vol. 132, p. 056704 (2024).
[6] R. Schlitz, et al., Physical Review B Vol. 106, p. 014407 (2022).
[7] P. Sgarro, et al., Physical Review Applied Vol. 23, p. 064049 (2025).
[8] L. Zheng, et al., Journal of Physics D: Applied Physics Vol. 55, p. 263002 (2022).

This work was supported by the National Research Foundation of Korea (NRF) grant funded by the Korean government (MSIP) (Grant No. RS-2023-00275259).

BR-06. Probing dynamics of magnetic interactions of rare-earth orthoferrites with double pulse THz emission spectroscopy

P. van Kuppevelt, A. V. Kimel
Ultrafast Spectroscopy of Correlated Materials, Radboud University, Nijmegen, Gelderland, Netherlands

Antiferromagnets are promising for next-generation technologies due to their ultrafast spin dynamics and robustness against external perturbations. Due to the interplay of several magnetic interactions, rare-earth orthoferrites represent one of the most appealing classes of antiferromagnets that inspired fundamental studies of antiferromagnetism for more than six decades [1]. Here we report on optical control and ultrafast dynamics of magnetic interactions in rare-earth orthoferrites using the technique of double pulse THz emission spectroscopy.

In particular, using such a technique we can probe the frequency of the antiferromagnetic resonance after the first and after the second pulse respectively (see Fig.1) [2]. In this way, we demonstrate a transient, laser-induced modification of the magnon spectrum on sub-picosecond timescales. Studying ultrafast dynamics of this effect, we argue that light predominantly modifies the antisymmetric exchange interaction (Dzyaloshinskii–Moriya interaction). Since the effect is present at least 55 ps after the ultrafast laser pulse, we suggest that the effect is due to real electronic excitations with sufficiently longer lifetimes. We believe that our results provide new insights on materials with tuneable magnetic interactions on demand.

[1] A. V. Kimel and A. K. Zvezdin, Photonics Insights 1, C03 (2023).
[2] P.M.P. van Kuppevelt and A.V. Kimel (submitted)

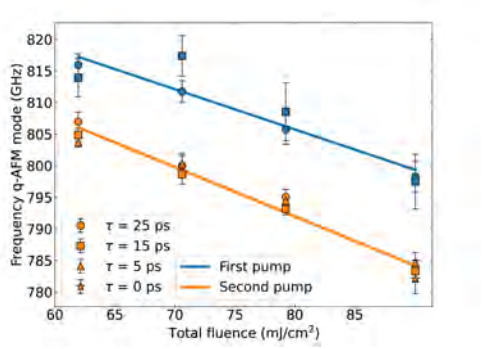


Fig. 2: The frequency after the first (blue) and second (orange) pump pulse at different inter-pulse time delays τ and pump fluences. The data is fitted using a linear regression.

BR-08. Plateau Dynamics and Optimal Pulse width in Sub-Nanosecond Spin-Orbit Torque Switching

J. Shin, S. Choe
Department of Physics and Astronomy, Seoul National University, Seoul, Korea (the Republic of)

Spin-orbit torque (SOT) enables ultrafast magnetization switching and is widely regarded as a key mechanism for next-generation spintronics devices [1-2]. However, in the sub-nanosecond time regime, SOT-driven switching can be delayed by its intrinsic dynamics [3].
In this work, we identify a bottleneck in SOT switching: a transient plateau state of the magnetization near the equator of the magnetization [4]. Using time-resolved magneto-optical Kerr effect (TR-MOKE) measurements with sub-nanosecond current pulses, we directly observe that the magnetization rapidly approaches the in-plane region but remains temporarily trapped in a plateau before completing switching.
We show that this plateau originates from a dynamic balance between the damping-like torque induced by SOT and the precessional torque induced by the in-plane magnetic field. When the current pulse is turned off, this balance is broken, and the remaining precessional torque drives the magnetization toward complete switching. Consequently, the time to reach the plateau, t_{reach}, defines a lower bound for the pulse width required for deterministic switching.
We develop an analytical model for t_{reach} based on the Landau-Lifshitz-Gilbert (LLG) equation. The validity of this model is confirmed by quantitative agreement with both micromagnetic simulations (MuMax3) and experimental data, particularly in the fast-switching regime below ~100 ps [5]. This model provides a practical design rule for optimizing pulse conditions in ultrafast SOT devices.

[1] S. Fukami and H. Ohno, Jpn. J. Appl. Phys. 56, 0802A1 (2017).
[2] A. Kent and D. Worledge, Nat. Nanotechnol. 10, 187 (2015).
[3] G. Finocchio, M. Carpentieri, E. Martinez, and B. Azzerboni, Appl. Phys. Lett. 102, 212410 (2013).
[4] J.H. Shin and S.-B. Choe, Appl. Phys. Lett. 128, 132404 (2026)
[5] A. Vansteenkiste, J. Leliaert, and M. Dvornik, *et al.*, AIP Adv. 4, 107133 (2014).

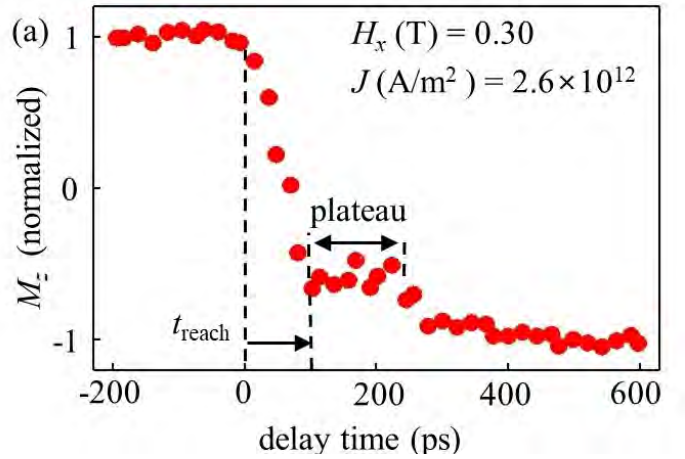


Fig. 1. Time-resolved measurement results of as a function of the delay time under different values of J and H_x. The horizontal arrow indicates t_{reach} and the duration of the plateau.

BR-09. Spin Wave Dynamics in 2D Connected Kagome Artificial Spin Ice

N. ., R. Mehta, S. Saha
Physics, Ashoka University, Rai, Haryana, India

Artificial spin ices were originally developed to mimic the behaviour of spin ice, such as the rare-earth titanate pyrochlores [1]. The smallest building blocks in artificial spin ices are single- domain nanomagnets arranged in such a way that their moments are frustrated [2]. In this study, we explore the spin wave dynamics in distinct magnetic phases of Kagome Artificial spin ice
[3]: Long-range order, Kagome Ice II, and Kagome Ice I by solving the Landau-Lifshitz-Gilbert equation using micromagnetic simulations. The magnetization dynamics changes significantly as the system goes from an ordered state to a disordered state and an asymmetric spin wave propagation is also observed in such system. The asymmetry in magnetic materials is realized through the Dzyaloshinskii–Moriya interaction, as shown in Fig 1. whereas in Kagome artificial spin ice phases, it arises from the internal magnetic configuration in the absence of DMI. These findings imply the potential to utilize Kagome artificial spin ice structures as reconfigurable, direction-sensitive magnonic platforms for signal routing and logic operations based on internal magnetic states rather than structural changes.

Acknowledgement
All the authors gratefully acknowledge the financial support of SERB with file Number SRG/2022/000191 and the Axis Bank Grant at Ashoka University for the funding. Naintara acknowledges SERB with file Number SRG/2022/000191 for the fellowship.

References

S. T. Bramwell et al., Science, vol. 294, no. 5546, pp. 1495–1501, 2001.
S. H. Skjærvø et al., Nature Reviews Physics, vol. 2, no. 1, pp. 13–28, 2020.
L. Anghinolfi et al., Nature Communications, vol. 6, p. 8278, 2015.

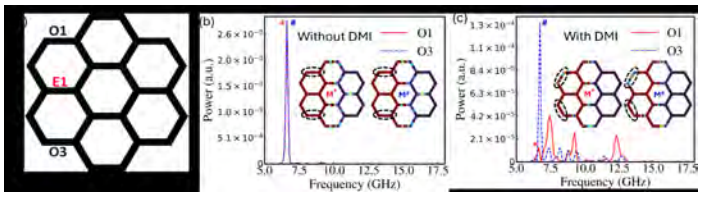


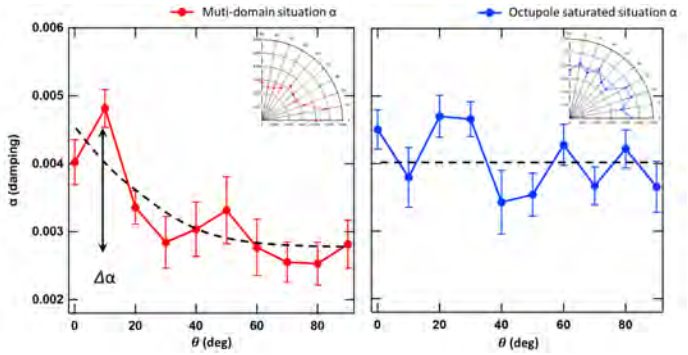
Figure 1: (a) Schematic of the simulated Kagome lattice having uniform magnetization with excitation antenna E1 and observation points O1 and O3. Simulated FFT spectra at geometrically symmetric points O1, O3 with the inset showing spatial profile obtained for (b) the absence of DMI and (c) the presence of DMI.

BR-10. Cluster Octupole Contribution to Spin Dissipation in Mn_3Sn/Co Bilayer Systems

J. Pi[1], S. Lee[1], E. Im[1], H. Kim[1], T. T. Nguyen[1], J. Park[2], S. Kim[1]
[1]University of Ulsan, Ulsan, Korea (the Republic of), [2]Daejeon University, Daejeon, Korea (the Republic of)

Spintronics based on non-collinear antiferromagnets (NC-AFMs) is garnering significant attention as a candidate for next-generation spin devices due to the absence of stray fields and the potential for magnetization control via ultrafast spin dynamics and spin torque. A representative non-collinear antiferromagnet, Mn_3Sn, possesses a structure where Mn atomic spins are arranged at 120° on a Kagome lattice, forming a cluster octupole magnetic order. Consequently, while Mn_3Sn exhibits an extremely small net magnetization (~6 mμ_B per Mn atom), it breaks time-reversal symmetry and induces Berry curvature, resulting in a large anomalous Hall effect (AHE).[1] Such Kagome-based electronic structures and non-collinear spin arrangements play a crucial role in the generation and transport of spin currents, enabling anomalous spin transport phenomena such as the magnetic spin Hall effect (MSHE). These characteristics position Mn_3Sn as a unique spin source

material capable of simultaneously controlling the generation, transmission, and dissipation of spin angular momentum, thereby enabling the transfer of spin information, including angular momentum and spin currents, to an adjacent ferromagnetic (FM) layer. Conversely, spin angular momentum generated by the magnetization dynamics of the FM layer can be pumped into and dissipated within the Mn_3Sn layer, implying that spin torque can be transferred back to the Mn_3Sn. Understanding the magnetic damping induced by this spin dissipation is essential for elucidating the dynamics driven by spin angular momentum transfer.
In this study, we investigate the spin dissipation at a Mn3Sn/FM interface through conducting ferromagnetic resonance (FMR) measurement, inverse spin Hall effect (ISHE) and spin-orbit torque (SOT) switching. Various spin octupole configurations and SOT efficiency will be discussed to understand the spin dissipation phenomena at the Mn_3Sn/FM interface.
1. S. Nakatsuji, N. Kiyohara and T. Higo, Nature, Vol. 527, p.212–215 (2015)



Angle Dependence of the Damping Constant in Mn_3Sn for Octupole Saturated and Multi-Domain States

BR-11. Characteristics of multi-mode magnon hybrid interaction

A. M. Park[1], Y. Soon[1], S. Yang[1], J. Lee[1], P. Cao Van[2], J. Jeong[2], K. Kim[1]
[1]Korea Advanced Institute of Science and Technology, Daejeon, Korea (the Republic of), [2]Chungnam National University, Daejeon, Korea (the Republic of)

Hybrid magnonic systems, which couple collective spin excitations in magnetically ordered materials to other physical degrees of freedom, provide a versatile platform for studying coherent dynamics and enabling new functionalities across classical and quantum regimes. While quantum sensitivity of hybrid quantum magnonic systems, capable of single-magnon level detection has drawn initial attention to the field [1], recent developments in classical regime shows the extensibility of hybrid magnonic system. Structured photonic environments such as flat-band lattices have been shown to enhance magnon–photon interactions via collective effects analogous to superradiance, enabling robust and scalable strong-coupling regimes [2]. In parallel, nonlinear and driven magnonic systems have revealed new avenues for band engineering and dynamical control, including Floquet magnon states arising from intrinsic interactions [3,4]. Building on these advances, exploring interference-driven control of magnon–photon interactions provides a complementary route to manipulating their spectral response.
Here, we investigate a hybrid magnon–photon system composed of multiple coupled split-ring resonators (SRRs) interacting with a collective spin excitation. By engineering both resonator coupling and magnon-mediated pathways, we demonstrate that the transmission spectrum exhibits antiresonant features arising from destructive interference between multiple excitation channels. By changing the position of thin film yttrium iron garnet (YIG) element on the coupled resonator structure, we achieve a selective coupling at both resonant and antiresonant frequencies. Moreover, we show that changing the direction of an external field, enables continuous control of the absorption spectrum through modulation of the interference condition. Our results establish coupled SRR–magnon platforms as a versatile testbed for exploring interference-based magnon–photon interactions and antiresonance physics, with potential applications in absorption-based signal processing

This research was supported by Basic Science Research Program through the National Research Foundation of Korea (NRF) funded by the Ministry of Education(2019R1A6A1A10073887)
[1] D. Lachance-Quirion, et al., *Science* 367, 425 (2020).
[2] Q. Hong, et al., *Nature Communications* 17, 2438 (2026)
[3] J. Xu, et al., *Phys. Rev. Lett.* 125, 237201 (2020).
[4] C. Heins, et al., *Science* 391, 190 (2026).

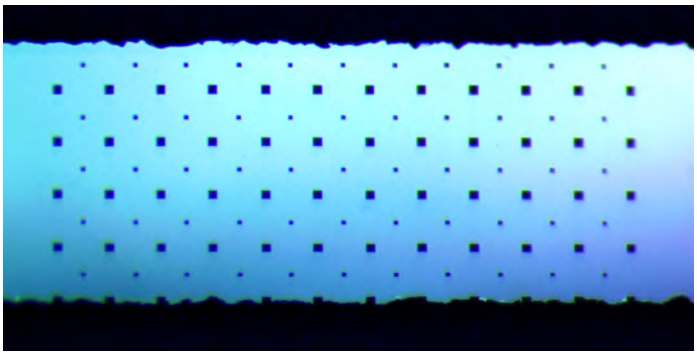
BR-12. Spin wave propagation in magnonic crystals implemented by laser ablation.

C. L. Ordonez Romero[1], G. Pirruccio[1], Z. Lazcano[2], N. Qureshi[3]
[1]Instituto de Fisica, Ciudad de Mexico, Mexico, [2]Instituto de Fisica, BUAP, Puebla, Mexico, [3]ICAT, Ciudad de Mexico, Mexico

The use of patterned surfaces to tailor the frequency response of magnetic materials is of utmost importance in the field of magnon-spintronics and microwave photonics due to their potential to allow the design and development of exciting technological applications such as microwave delay lines, high frequency and bandwidth CHIRP signal sources and microwave sensors, among others. Here, we demonstrate a method to fabricate one- and two-dimensional magnonic crystals with arbitrary symmetry and use it to engineer the amplitude-frequency characteristic of magnetostatic surface spin waves excited in a magnetic material. The technique is based on the gentle microablation of the sample surface by focused femtosecond laser pulses. Constrain the illumination in a tiny spot consents the use of modest energy levels and enhance the achievement of micrometre precision. The induced changes in the measured transmission characteristics reveal the strong and complex symmetry-dependent interaction of the spin waves with Bravais and non-Bravais lattices. The microfabrication method described here facilitates and speeds up the realization of complex magnonic and photonic components and provides an efficient tool to explore complex microwave and magnetic dynamics in scattering lattices.

This work was supported by UNAM DGAPA PAPIIT Grant IG100521 and IG101424).

Y. Garcia, B. Vargas, D. Ley, F. Peña, E. Mendoza, A. Reyes, N. Qureshi, C. Ordóñez, G. Pirruccio, *J. Appl. Phys.* 133, 063903 (2023).



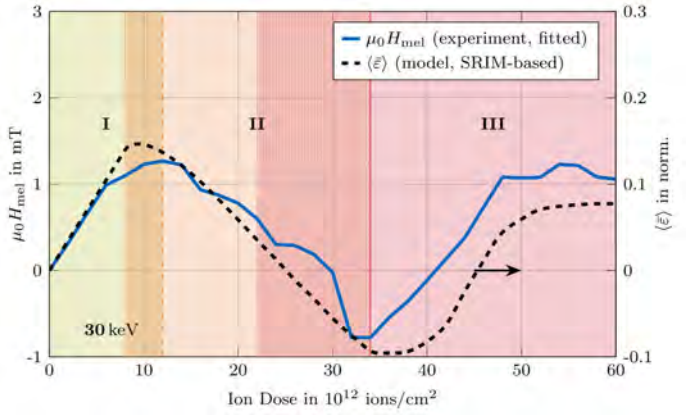
BR-13. The Driving Mechanism of FIB-Induced Spin-Wave Routing: A Magnetoelastic Origin

F. Naunheimer[1], J. Greil[1], V. Ahrens[1], M. Hofschen[1], D. Albano[1], L. Maucha[2], A. Papp[2], G. Csaba[2], M. Becherer[1]
[1]Technical University of Munich, Munich, Germany, [2]Pázmány Péter Catholic University, Budapest, Hungary

Spin-wave optics is an emerging field enabling highly integrable, non-Boolean hardware, where controlled spin-wave routing facilitates analog computing schemes [1]. A key approach to such quasi-optical manipulation is the realization of graded refractive-index (GRIN) profiles via spatial variation of magnetic parameters [2]. Using direct focused ion beam (FIB) writing, our group has demonstrated precise tuning of the effective magnetization M_{eff} in yttrium iron garnet (YIG), enabling GRIN-based lensing for spin-wave focusing and defocusing [3]. Ion irradiation is generally assumed to modify M_{eff} through strain-induced anisotropy, with increasing dose ultimately leading to partial amorphization of the crystal structure [4]. However, the observed nonmonotonic dependence of M_{eff} on ion dose reported in [3] remains insufficiently understood, indicating a more complex ion-induced strain mechanism [5].
In this work, we identify the key mechanism underlying ion-induced spin-wave routing in YIG thin films as the magnetoelastic effect arising from stress–strain deformation. We introduce a qualitative model describing the evolution of strain during ion irradiation, with ion dose–dependent damage estimated via Monte Carlo simulations (SRIM) [6] and mapped onto a mean relative strain $\langle \varepsilon \rangle$. To validate the model, we quantify the magnetoelastic contribution H_{mel} to the spin-wave dispersion across regions exposed to varying Ga^+ doses. Spatially resolved dispersion measurements are obtained using time-resolved magneto-optical Kerr effect (trMOKE) microscopy at multiple frequencies and analyzed with the Kalinikos–Slavin formalism to extract H_{mel}. The resulting dose dependence at 30 keV ion acceleration (Fig. 1) is well reproduced by the model, revealing three distinct deformation regimes and confirming magnetoelasticity as the dominant mechanism. Consistent results are obtained at 16 keV and 8 keV.

[1] G. Casba et al., Journal of Applied Physics 115, 17 (2014): 17C741.
[2] Davies, Carl S., Low Temperature Physics 41.10 (2015): 760-766.
[3] M. Kiechle et al., Small 19, 21 (2023): 2207293.
[4] I. Fodchuk et al., Crystals 12, 10 (2022): 1485.
[5] Was, Gary S., Heidelberg: Springer Berlin Heidelberg, 2007.

[6] Ziegler, James F. et al., Nuclear Instruments and Methods in Physics Research Section B: Beam Interactions with Materials and Atoms 268.11-12 (2010): 1818-1823.



Magnetoelastic field contribution H_{mel} (blue solid line), extracted from Kalinikos–Slavin dispersion fits to trMOKE measurements of spin waves in regions exposed to varying ion doses at 30 keV. The modeled mean relative strain $\langle\varepsilon\rangle$ (black dashed line) reveals three distinct deformation regimes (I–III) in the YIG film.

BR-14. Fabrication and Characterization of VCMA-Based Artificial Spin Ice Toward Electrical Control of Magnon Mode

O. Nakatani[1], S. Yoshii[2, 1], Y. Ando[1]
[1]Department of Physics and Electronics, Osaka Metropolitan University, Sakai, Osaka, Japan, [2]Department of Physics, Imperial College London, South Kensington, United Kingdom

The quantized spin waves, magnons, have been attractive for the novel inforamation carrier, which can be used for carrier transport with low-heat consumption and quantum information process. Artificial spin ice (ASI) has been proposed as a platform for controlling magnon mode[1]. ASI consists of arrays of closely spaced ferromagnetic nanostructures, in which magnetic interactions give rise to frustrated magnetic states. In previous studies, magnon modes in ASI have been controlled by tuning the magnetization configuration using external magnetic fields. However, this approach does not allow for individual control of each nanostructure [1, 2].

In this study, we focus on voltage-controlled magnetic anisotropy (VCMA) as an alternative approach[3]. VCMA enables the possibility of individually controlling the magnetization state of ferromagnetic nanostructures via an applied gate electric field. The ultimate goal of this work is to achieve control of magnon states by manipulating the magnetic configurations of ASI using VCMA. To this end, while previous studies have employed lift-off processes to fabricate ASI structures, our approach requires fabrication using etching processes such as ion milling.

In the experiment, we firstly investigated microfabrication processes suitable for VCMA-controlled ASI. Co (20 nm) were deposited by sputtering and ASI patterns were defined using electron beam lithography. After development, the ASI patterns were fabricated by Ar ion milling. An optical microscope image of the fabricated device is shown in Fig. 1(a), demonstrating well-defined ASI structures with minimal defects.

Magnetic force microscopy (MFM) measurements were performed to observe the magnetic configurations of the fabricated ASI. In the absence of an external magnetic field, complex domain structures such as vortices were observed as shown in Fig. 1(b). In the presentation, we will also report on ferromagnetic resonance measurements and the results of VCMA-based control in the fabricated ASI structures.

[1] J. C. Gartside *et al.*, Nat. Nanotech. 17, 460(2022).
[2] S. Yoshii *et al.*, arXiv:2507.06065.
[3] T. Maruyama *et al.*, Nat. Nanotech. 4,158(2009).

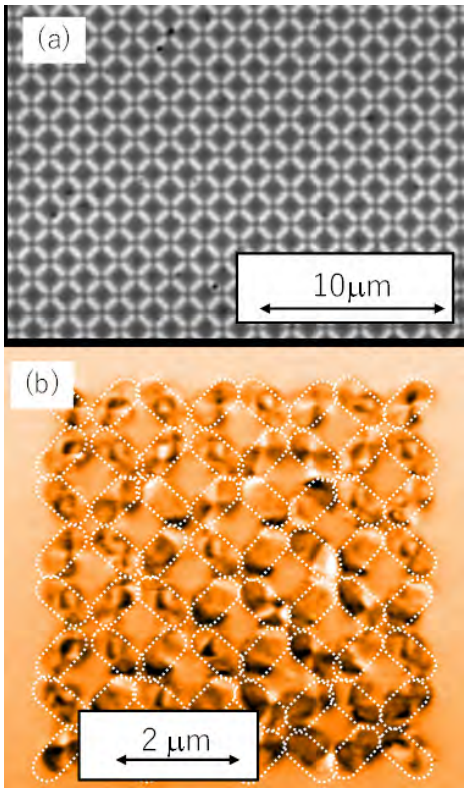


Fig. 1: (a) Optical microscope image of the ASI structure fabricated by a milling process and (b) magnetic force microscopy (MFM) image.

BR-15. Floquet Magnons in Placoid-like Magnetic Lattices
J. Lima de Medeiros, F. H. SIlva Sales, M. da SIlva Tavares
Department of Physics, Federal Institute of Education, Science and Technology of Maranhão, São Luís, Maranhão, Brazil

Spintronics emerged in the 1980s and, in less than five decades, has revolutionized the
fundamental concepts of electronic circuits, which were traditionally governed by the
presence and transport of charge. Its central premise is the expansion of the electronic
paradigm by enabling information to be carried through an additional degree of freedom, the spin. One of the key perspectives in spintronics lies in the dynamics of spin waves, which offer advantages such as reduced energy dissipation, increased information capacity per carrier, enhanced non-volatility in memory devices, and improved optimization of the storage–processing relationship, thereby mitigating the von Neumann bottleneck. Numerous studies have explored these excitations in lattices with diverse topologies, aiming to exhaust their potential technological applications. These platforms provide a fertile ground for the development of fundamental components such as magnetic transistors, magnetic diodes, and logic gates, which are essential for modern computational architectures. Within this context, novel lattice geometries have attracted significant attention, including kagome and Lieb lattices. In particular, we highlight the placoid lattice, originally inspired by the geometry of fish scales found in predatory fish such as sharks and rays. This structure is known to enhance hydrodynamic performance and may offer analogous advantages for information transport in magnonic circuits. The present work aims to analyze a dynamic modulation of inter-site distances along the q_y direction, in the Brillouin Zone, following a periodic pattern. This induces an effective time-periodic Hamiltonian, creating favorable conditions for the emergence of exotic excitations known as Floquet magnons. These quasiparticles arise in out-of-equilibrium regimes, exhibiting nontrivial behaviors such as energy gap opening and the potential induction of topological phases. The study is based on the Heisenberg Hamiltonian, from which we derive the dispersion relation and evaluate key physical properties, including the energy spectrum,band structure, group velocity, presence of van Hove singularities, density of states, and density of states.
[1] M. S. Tavares, R. C. F. Pinto, E. V. Silva and A. V. N. Monroe, Solid State Communications, Vol. 372, p. 115286 (2023).
[2] S. A. Owerre, Journal of Physics Communications, Vol. 1, p. 021002 (2017).
[3] F. Bloch, Zeitschrift für Physik, Vol. 61, p. 206 (1930).
[4] T. Holstein and H. Primakoff, Physical Review, Vol. 58, p. 1098 (1940).

BR-16LB. Magnetic-Field-Assisted Thermal Evolution from Stripe to Bubble Domains in Fe_3GaTe_2
C. Hsu[2], H. Shiu[1], W. Chen[1], P. Chang[3], Y. Su[4]
[1]National Synchrotron Radiation Research Center, Hsinchu, Taiwan, [2]Department of Physics, Chung Yuan Christian University, Taoyuan, Taiwan, [3]Department of Physics, Tamkang University, Taipei, Taiwan, [4]Jülich Centre for Neutron Science (JCNS) at Heinz Maier-Leibnitz Zentrum (MLZ), Forschungszentrum Jülich GmbH, Garching, Germany

Fe_3GaTe_2 (FGaT) is a van der Waals ferromagnet with strong perpendicular magnetic anisotropy (PMA) and a Curie temperature above room temperature, making it promising for spintronic applications [1]. Room-temperature magnetic skyrmions and Dzyaloshinskii–Moriya interaction (DMI)-related stabilization have also been reported in FGaT systems [2,3], while external magnetic fields provide an effective means of modulating stripe and bubble domains [4].
Here, we investigate the thermal and magnetic-field-assisted evolution of magnetic domains in FGaT using scanning transmission X-ray microscopy (STXM). Temperature-dependent measurements reveal a pronounced reduction in stripe-domain width near 55 °C, together with a clear dependence on the local FGaT thickness (Fig. 1). After annealing at 165 °C, the zero-field condition predominantly preserves stripe-like domains, whereas annealing under an applied magnetic field of 550 Oe markedly promotes the formation of bubble-like and mixed stripe–bubble configurations (Fig. 2). Energy-dependent STXM measurements across the Fe L_3 absorption edge further support the Fe-specific magnetic origin of the observed domain contrast. The stripe-to-bubble evolution reflects the competition among PMA, dipolar interactions, domain-wall energy, and magnetic-field effects, and is compatible with DMI-assisted stabilization [3]. These results demonstrate effective thermal and magnetic-field control of magnetic textures in FGaT, highlighting its potential for tunable van der Waals spintronic applications.
[1] G. Zhang *et al*., "Above-room-temperature strong intrinsic ferromagnetism in 2D van der Waals Fe_3GaTe_2 with large perpendicular magnetic anisotropy," Nature

Communications 13, 5067 (2022).
[2] C. Liu *et al*., "Magnetic Skyrmions above Room Temperature in a van der Waals Ferromagnet Fe_3GaTe_2," Advanced Materials 36, 2311022 (2024).
[3] Z. Li *et al*., "Room-temperature sub-100 nm Néel-type skyrmions in non-stoichiometric van der Waals ferromagnet $Fe_{3-x}GaTe_2$ with ultrafast laser writability," Nature Communications 15, 1017 (2024).
[4] M.-H. Hsu *et al*., "Magnetic domain modulation in van der Waals material Fe_3GaTe_2 via external magnetic field," Journal of Alloys and Compounds 1071, 188703 (2026).

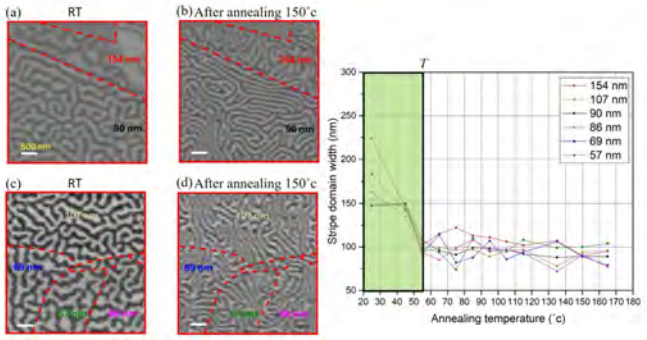


Figure1.The characteristic stripe-domain width exhibits a pronounced temperature dependence, including a substantial reduction near 55 °C

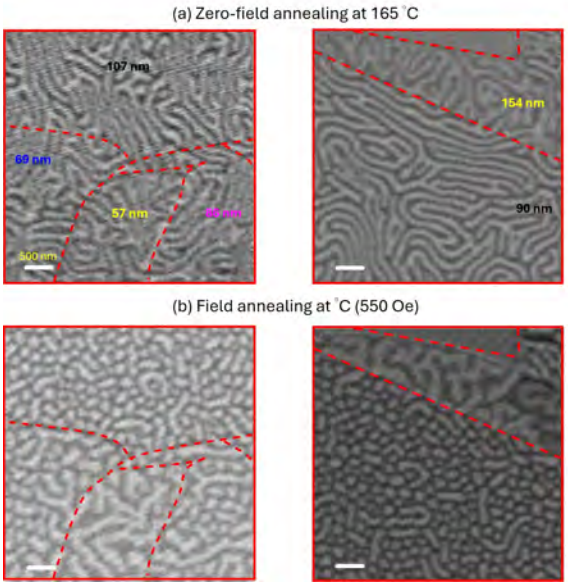


Figure 2. STXM magnetic-domain images of Fe_3GaTe_2 after annealing at 165 °C (a) without and (b) with an applied magnetic field of 550 Oe. Red dashed lines indicate regions of different thicknesses. Field annealing promotes stripe-to-bubble domain evolution.

BR-17LB. Symmetry-Preserving Graph Neural Networks for Large-Scale Spin Dynamics in Metallic Magnets

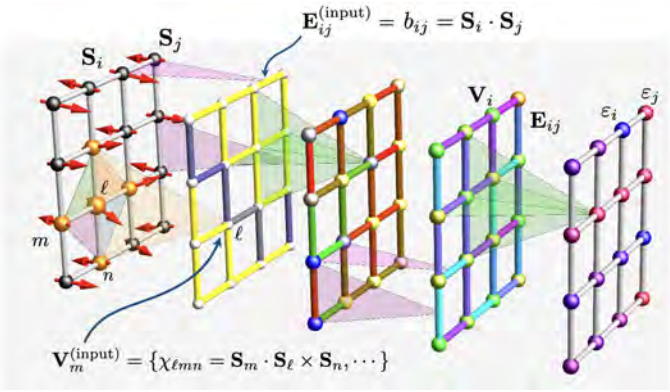
A. Rayat, Y. Fan, G. Chern
University of Virginia, Charlottesville, Virginia, United States

Metallic magnets host noncollinear and topological spin textures relevant to spintronics, but simulating their dynamics requires costly, repeated electronic calculations. Their electron-mediated interactions depend collectively on the spin configuration and generally cannot be captured by fixed pairwise exchange alone. Machine-learning force fields offer a route around this bottleneck, yet our previous approach relied on explicitly constructed symmetry-preserving local descriptors [1,2]. Message-passing neural networks provide a general framework for molecular property prediction [3] and atomistic force fields [4]. Here we represent the magnetic lattice directly as a graph and introduce a symmetry-preserving message-passing neural network (Fig. 1). Spin-rotation invariance is encoded in the initial features, while the graph construction and aggregation respect lattice symmetries. The network predicts site energies, and effective magnetic fields follow by differentiating their sum with respect to the spins.

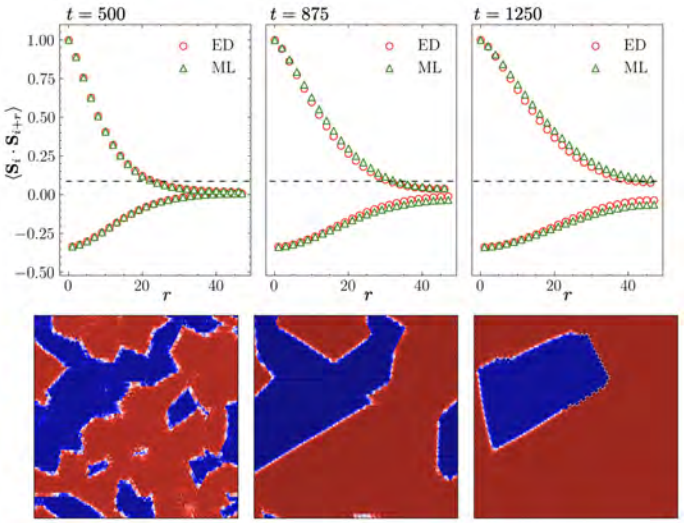
For the s-d exchange model of localized moments coupled to itinerant electrons, we benchmark the learned spin dynamics against simulations using exact diagonalization and find quantitative agreement in equal-time spin-correlation functions over extended dynamical evolution (Fig. 2, top). By replacing repeated electronic calculations, the learned model enables simulations on much larger lattices and longer time scales. As an application, we resolve the growth and competition of chiral domains in a noncoplanar spin texture on scales beyond the practical reach of simulations using exact diagonalization (Fig. 2, bottom). This architecture provides a physically motivated hierarchy for learning electron-mediated interactions: successive message-passing layers build symmetry-preserving many-spin representations over progressively larger magnetic environments without requiring an exhaustive enumeration of invariant descriptors.

[1] G.-W. Chern, Y. Fan, S. Zhang, and P. Zhang, "Machine-learning force-field models for dynamical simulations of metallic magnets," AIP Adv. 16, 025031 (2026).
[2] G.-W. Chern, Y. Fan, S. Zhang, and P. Zhang, "Machine-learning modeling of magnetization dynamics in quasi-equilibrium and driven metallic spin systems," J. Magn. Magn. Mater. 642, 173898 (2026).
[3] J. Gilmer, S. S. Schoenholz, P. F. Riley, O. Vinyals, and G. E.

Dahl, “Neural Message Passing for Quantum Chemistry,” Proc. Mach. Learn. Res. 70, 1263–1272 (2017).
[4] K. T. Schütt, H. E. Sauceda, P.-J. Kindermans, A. Tkatchenko, and K.-R. Müller, “SchNet—A deep learning architecture for molecules and materials,” J. Chem. Phys. 148, 241722 (2018).



Equivariant graph network: symmetry-preserving initialization from the spin configuration, followed by message passing and site-energy prediction.



Top: equal-time spin correlations from learned spin dynamics and exact-diagonalization-based simulations. Bottom: large-scale coarsening of chiral domains in a noncoplanar spin texture.

SESSION CA: MAGNETIC RANDOM-ACCESS MEMORIES: WHAT'S COMING NEXT?

Chair(s): J. Nozieres, *CNRS, Grenoble, France*
Wednesday, November 4, 2026
08:30 AM-12:00 PM
Coral 3

CA-01. Spintronic Memory Evolution: STT-MRAM, SOT-MRAM, and Voltage-Controlled Switching Technologies

H. Yoda
YODA-S, Inc., Tsukuba, Japan

Advances in spintronics—most notably room-temperature tunneling magnetoresistance (TMR) and spin-torque switching—have enabled the commercialization of both field-writing MRAM and spin-transfer-torque (STT) MRAM. To date, however, their use has been largely limited to relatively low-density storage-memory applications. As a result, the overall market size of MRAM technologies remains modest compared with that of the broader semiconductor industry.

The next major target for MRAM may be working-memory applications, where virtually unlimited endurance and low write energy are essential. However, entering this domain is challenging for conventional MRAM, as its limited endurance and relatively high write energy continue to pose significant obstacles.

Building on the potential of spintronics, several additional switching mechanisms—such as spin-orbit-torque (SOT) magnetic switching and voltage-controlled magnetic switching—have recently been demonstrated as MRAM storage cells[1]-[4]. Among these, SOT-MRAM is considered a particularly promising candidate for future working-memory applications because it offers intrinsically lower write energy than conventional MRAM while maintaining virtually unlimited endurance.

In this talk, we first review the critical switching current (I_{csw}) and retention energy (ΔE_r) of MTJs with lateral dimensions between 50 nm and 230 nm for SOT-MRAM. We then present empirical equations that describe the dependence of I_{csw} and ΔE_r on lateral device size between 50nm and 100nm. Using these equations, we evaluate smaller MTJs with dimensions in the 20-40 nm range to assess whether their performance can surpass that of conventional MRAM technologies. Finally, based on the derived equations, we estimate the operating window of voltage-controlled spintronic memory and discuss whether it is sufficiently wide for practical implementation.

[1] H.Yoda, Y.Ohsawa, T.Kishi, *et al. AIP Advances* (Vol.14, Issue 2) 025327 (2024).
[2] Huang, YL., Song, M., Lee, CM. *et al. Nat Electron* 8, 794–802 (2025).
[3] T. Nozaki, Y. Shiota, S. Miwa, *et al. Nature Physics*, volume 8, pages491–496 (2012).
[4] H. Yoda, N. Shimomura, Y. Ohsawa, *et. al. 2016 IEEE International Electron Devices Meeting*, pp. 27.6.1-27.6.4.

CA-02. Novel Type-C SOT-MRAM: Achieving Minimum Cell Size with Field-Free Switching

M. Song
tsmc, Hsinchu, Taiwan

The rapid development of artificial intelligence in recent decades has been continuously driving new software and hardware advancements. A novel type-C SOT-MRAM exhibits field-free operation while maintaining strong data retention and excellent performance. The high-speed write capabilities with pulse durations as short as 1 ns are demonstrated, along with excellent thermal stability (Δ=70k_BT), validated across multiple devices and an 8kb memory array. SOT-MRAM device structure with >100x scalable resistance and read current are demonstrated to address the persistent problems of the traditional 2D crossbar array, leveraging its read-write path separation nature.

CA-03. Exploring synthetic anti-ferromagnet magnetic tunnel junctions for low power, high-speed magnetic memories

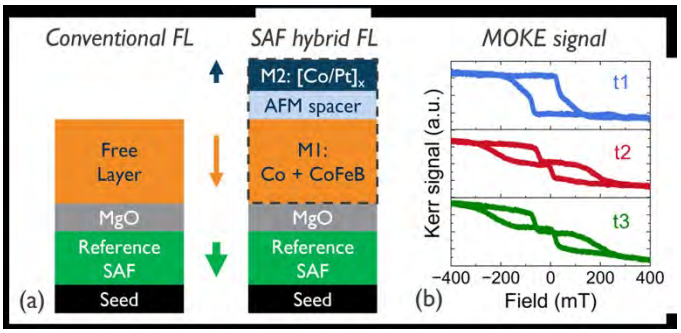
D. Narducci[1], F. Garcia Redondo[2], L. Verschueren[1], R. Carpenter[1], X. Piao[1, 3], J. Chatterjee[1], M. Gama Monteiro[1], A. Palomino[1], N. Jossart[1], K. Wostyn[1, 4], S. Couet[1, 4], M. Bardon[1], G. Hellings[1], G. Sankar Kar[1], S. Rao[1]
[1]imec, Leuven, Belgium, [2]imec UK, Cambridge, United Kingdom, [3]University of Tokyo, Tokyo, Japan, [4]Vertical Compute SRL, Leuven, Belgium

AI-based compute platforms have demonstrated fantastic progress owing to advances in compute architectures and learning models [1]. This, in turn, has resulted in increased memory capacity and bandwidth needs [2]. Emerging memories, such as MRAM, are well-positioned to serve these needs owing to their low leakage, operating power and compatibility with standard backend-of-line (BEOL) and complex heterogeneous integration processes [3, 4].

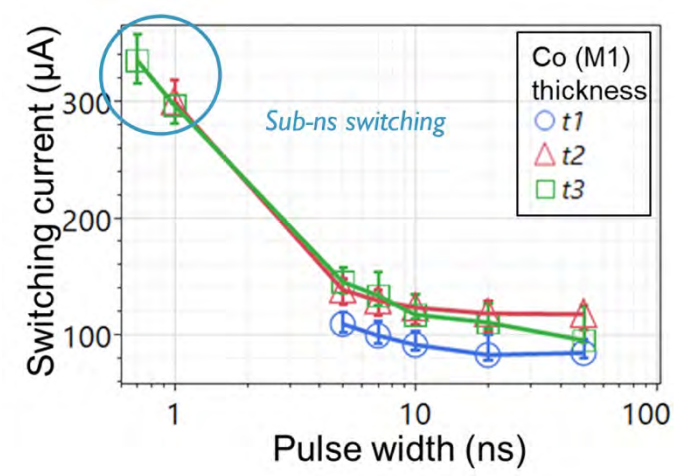
However, MRAM devices consume higher write power than other emerging memories. In conventional MTJs, the free layer design imposes a linear relationship between switching current and thermal stability, thereby limiting the margins. Synthetic anti-ferromagnets (SAF)-based free layers offer a promising alternative as they can decouple the switching-thermal stability tradeoff, while offering ultra-fast switching dynamics and enhanced magnetic tolerance [5]. In this work, we present a novel SAF-based hybrid free layer (HFL) design that overcomes this tradeoff.

Figure 1(a) depicts the conventional FL and the SAF-HFL MTJ stacks. In SAF-HFL, the M1 magnet is designed for high TMR and STT absorption, while the M2 magnet is designed to enhance thermal stability. Optimization of the HFL enhances the AFM coupling, as shown in Figure 1(b). We confirm ultra-fast switching dynamics in SAF-HFL, as evidenced by sub-ns switching shown in Figure 2. In this talk, we will describe the design guidelines to enable low STT switching current while simultaneously enhancing thermal stability. Furthermore, we will show that the SAF-HFL concept is scalable down to 30nm-sized devices. These design explorations enabled us to achieve 1ppm error-free write for 5ns pulses, $\Delta > 40\ k_BT$ at I_{write} = 150 uA. We also extend the ppm-level error-free operation down to 1ns pulses. Finally, we will discuss the correlation between electrical performance and stable magnetic configurations in the SAF-HFL, highlighting the existence of rich and diverse magnetization dynamics and opportunities for further research into SAF-based MTJs.

[1] A. Smith et al., *IEEE ISSCC*, 11.1, pp 208-210 (2024)
[2] A. Gholami et al., arXiv:2403.14123 (2024)
[3] E. Beyne et al., *IEEE IEDM* 3.6, pp. 71-74 (2021)
[4] S. Rao et al., *IEEE IMW*, pp. 1-4 (2021)
[5] S. Couet et al., *IEEE VLSI.*, pp. 1-2 (2021)



(a) FL stack schematics. (b) Optimizing M1 thickness activates the AFM coupling, as shown in MOKE reversal curves.



STT switching current trends with pulse-width for three SAF-HFL stacks

CA-04. Measuring retention of perpendicular STT-MRAM cells with diameter around 20 nm

G. Mihajlović, W. Jung, N. Davila, H. J. Richter, M. Tran, T. Santos, J. Katine, M. Grobis
Western Digital, San Jose, California, United States

Retention is a key performance metric for a memory technology. For spin-transfer torque magnetic random access memory (STT-MRAM) cells with perpendicular magnetization, retention is the amount of time the free layer can retain its written state, up or down, until a thermally activated reversal. The retention bake method is the gold standard for determining retention, whereby an ensemble of STT-MRAM cells is exposed to a certain temperature (by baking in an oven) for a certain time, and then the number of cells that flipped their magnetization is determined by comparing the resistance state before and after the bake [1].

The thermal stability factor Δ, which is the main parameter for characterizing retention, can also be determined by an alternative, faster method that utilizes magnetic field switching probability measurements that are fit with a domain wall reversal model. For cell diameters > 55 nm, this method has been shown to agree well with the retention bake method [2-4]. For cell diameters < 25 nm, free layer switching by coherent reversal is expected, and therefore the field switching probability data should be fit using a macrospin model. As STT-MRAM technology progresses and

cell size continues to scale down to the macrospin regime, it is important to verify if this accelerated method of evaluating Δ is in agreement with the more time-consuming retention bake method, and we have not seen such a comparative study reported.

With STT-MRAM cells having diameter near 20 nm, we report here [5] our experiments to determine Δ using both field switching probability measurements and the retention bake method, and we find excellent agreement of mean Δ and sigma from the two methods. Thus, the field switching method can be reliably used to accelerate determination of cell retention. In addition, we compare these results with a third method [5], whereby Δ is found by fitting the pulse-width dependence of the STT switching voltage in the thermally-activated regime, and we will describe how this method either under- or over-estimates Δ.

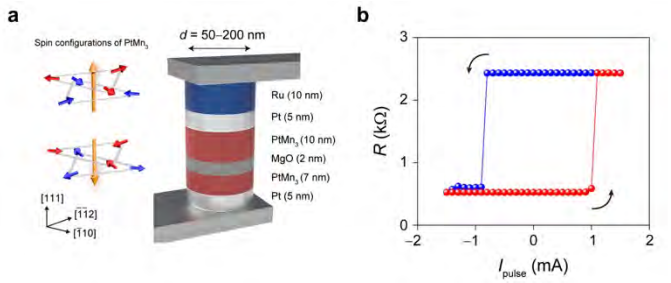
[1] L. Thomas, G. Jan, S. Le *et al*, *Appl. Phys. Lett.* 106 162402 (2015)
[2] L. Thomas *et al, 2025 IEEE Int. Electron Devices Meeting (IEDM)* p 26.4.1
[3] L. Tillie *et al, 2016 IEEE Int. Electron Devices Meeting (IEDM)* p 27.3.1
[4] G. Mihajlović, N. Smith, T.S. Santos, *et al*, *Appl. Phys. Lett.* 117 242404 (2020)
[5] G. Mihajlović, W. Jung, T.S. Santos *et al*, *J. Phys. D: Appl. Phys.* 59 025002 (2026)

CA-07. Octupole-driven spin-transfer torque switching of all-antiferromagnetic tunnel junctions

J. Kang[1], M. Hamdi[1], S. Cheung[1], L. Yuan[1], M. A. Elekhtiar[2], E. Matt[1], N. Zogbi[8], W. Rogers[1], A. Meo[3], P. G. Lim[1], M. N. Tey[1], A. D'Addario[4], S. Konakanchi[5], J. G. Athas[1], S. Arpaci[1], A. Devincenti[1], S. Mehta[6], V. K. Sangwan[1], J. Fowlie[1], P. Upadhyaya[5], M. Carpentieri[3], V. P. Dravid[1], M. C. Hersam[1], J. C. Incorvia[8], J. Katine[6], G. Fuchs[4], G. Finocchio[7], E. Y. Tsymbal[2], J. M. Rondinelli[1], P. Khalili Amiri[1]
[1]Northwestern University, Evanston, Illinois, United States, [2]University of Nebraska-Lincoln, Lincoln, Nebraska, United States, [3]Politecnico di Bari, Bari, Italy, [4]Cornell University, Ithaca, New York, United States, [5]Purdue University, West Lafayette, Indiana, United States, [6]Western Digital Corporation, San Jose, California, United States, [7]University of Messina, Messina, Italy, [8]University of Texas at Austin, Austin, Texas, United States

Magnetic tunnel junctions (MTJs) based on ferromagnets are canonical devices in spintronics, with wide-ranging applications in data storage, computing, and sensing. They simultaneously exhibit mechanisms for electrical detection of magnetic order through the tunneling magnetoresistance (TMR) effect, and reciprocally, for controlling magnetic order by electric currents through spin-transfer torque (STT). It was long assumed that neither of these effects could be sizeable in tunnel junctions made from antiferromagnetic materials, since they exhibit no net magnetization. Recently, however, it was shown that all-antiferromagnetic tunnel junctions (AATJs) based on chiral antiferromagnets do exhibit TMR due to their non-relativistic momentum-dependent spin polarization and cluster magnetic octupole moment, which are manifestations of their spin-split band structure [1,2]. However, the reciprocal effect, i.e., the antiferromagnetic counterpart of STT driven by currents through the AATJ, has been assumed non-existent due to the total electric current being spin-neutral. Here, in contrast to this common expectation, we report nanoscale AATJs exhibiting this reciprocal effect, which we term octupole-driven spin-transfer torque (OTT). We demonstrate current-induced OTT switching of $PtMn_3$|MgO|$PtMn_3$ AATJs, fabricated on a thermally oxidized silicon substrate, exhibiting a record-high TMR value of 363% at room temperature and switching current densities of the order of 10 MA/cm^2 [3]. Our theoretical modeling explains the origin of OTT in terms of the imbalance between intra- and inter-sublattice spin currents across the AATJ, and equivalently, in terms of the non-zero net cluster octupole polarization of each $PtMn_3$ layer. This work establishes a new materials platform for antiferromagnetic spintronics and provides a pathway towards deeply scaled magnetic memory and room-temperature terahertz technologies.

[1] P. Qin et al. Room-temperature magnetoresistance in an all-antiferromagnetic tunnel junction, Nature 613, 485 (2023)
[2] J. Shi et al. Electrically controlled all-antiferromagnetic tunnel junctions on silicon with large room-temperature magnetoresistance, Adv. Mater. 36, 2312008 (2024)
[3] J. Kang and M. Hamdi et al. Octupole-driven spin-transfer torque switching of all-antiferromagnetic tunnel junctions, arXiv:2509.03026



a, Spin configurations (red and blue) and associated cluster magnetic octupole (orange) in $PtMn_3$ (left). Material stack of AATJs used in the experiment (right) b, Current-induced switching measurements on a 100 nm-diameter AATJ device.

CA-05. Deterministic Field–Free SOT–induced Magnetization Switching of Perpendicularly Magnetized CoFeB Dots via Stacked Ferromagnetic and Nonmagnetic SOT Channels

M. Yoshikawa, R. Kawashige, T. Li, N. Umetsu, M. Quinsat
Frontier Technology R&D Institute, KIOXIA Corporation, Yokohama, Japan

Spin–orbit–torque MRAM offers intrinsically fast switching and high endurance through its three–terminal structure that decouples read and write paths, while perpendicular MTJs ensure strong data retention. However, the spin Hall effect generates only in–plane–polarized spins, making deterministic field–free SOT–induced switching of perpendicular magnetization fundamentally difficult, as previously reported [1].

In this work, we investigate the SOT–induced magnetization switching behavior and switching probability of perpendicularly magnetized CoFeB dots, employing an orthogonal magnetization configuration approach [2] to generate spin currents polarized along the out–of–plane direction. Stacked SOT channels, composed of a W spacer and an in–plane magnetic anisotropy (IMA) ferromagnetic layer, are evaluated and compared with conventional W–based SOT channels. To characterize the SOT switching behavior, Hall–bar devices integrating perpendicularly magnetized CoFeB dots with diameters of approximately 500 nm are fabricated. Our results demonstrate successful field–free SOT–induced magnetization switching, with the switching behaviors depending on the bias magnetic field applied along the x direction (H_x) in the stacked W/IMA ferromagnet SOT channels, as shown in Fig.1. Furthermore, we observe a higher switching probability than that of conventional W–based SOT channels, as illustrated in Fig. 2. Although the stacked SOT channel operates as intended in concept, the observed switching probability remains approximately 70 % and does not reach 100% in this system. This limitation is likely attributed to fluctuations and instability in the IMA ferromagnetic layer, which may be intrinsic to Hall–bar devices. Improving the SOT switching probability will require stabilizing the magnetization in the IMA ferromagnetic SOT channel.

[1] M.G.Monteiro *et al.*, IEDM Tech. Dig. 15–1, 2025.
[2] A. Davidson *et al.*, Physics Letters A 384, 126228 (2020).

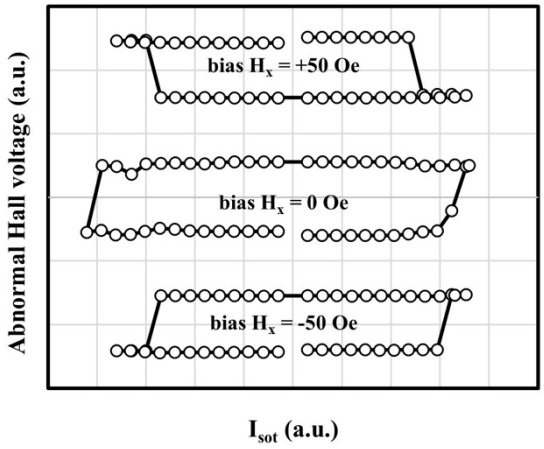


Fig. 1 SOT induced magnetization switching curves dependent on the bias magnetic fields.

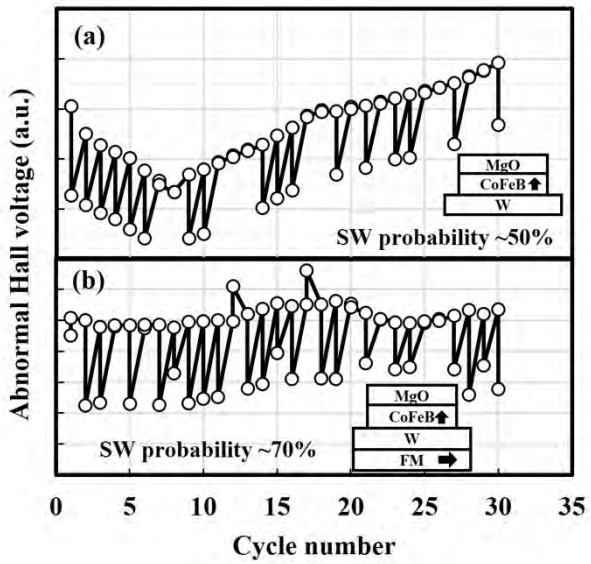


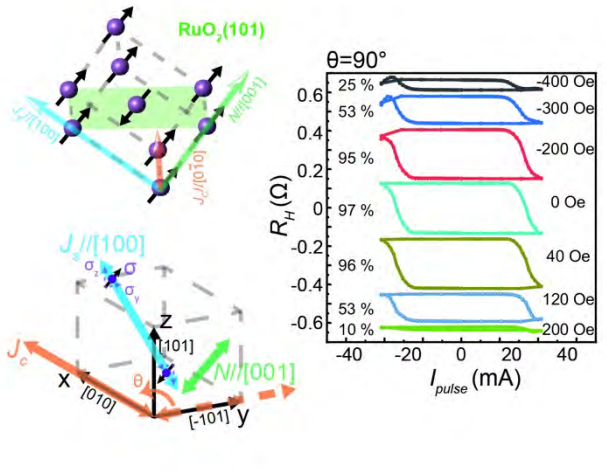
Fig. 2 Cyclic SOT switching behaviors for perpendicularly magnetized CoFeB dots. Film stacks are illustrated in the inset.

CA-08. Field-Free Magnetization Switching Enabled by Intrinsic Out-of-Plane Spin Polarization in Altermagnetic RuO2

Z. Li[3, 2, 1], Z. Zhang[3, 2, 1], X. Lu[3, 2], Y. Xu[3, 2, 1]
[1]School of Electronic Science and Engineering, Nanjing University, Nanjing, China, [2]School of Integrated Circuits, Nanjing University, Suzhou, China, [3]State Key Laboratory of Spintronics, Nanjing University, Suzhou, China

Altermagnetism, an emerging magnetic phase with intertwined ferromagnetic and antiferromagnetic characteristics, offers new opportunities for spintronics. Here, we report the deterministic, field-free spin-orbit torque (SOT) switching of a perpendicular [Co/Pt] multilayer, driven by the altermagnetic spin-splitting effect (ASSE) in a RuO2(101) epitaxial layer. The ASSE generates an out-of-plane spin-polarized current, which exerts an anti-damping torque to achieve complete magnetization reversal without an external magnetic field. This spin current exhibits a strong anisotropic character, maximized when the charge current flows along the RuO2 [010] direction, confirming the alignment between spin polarization and the Néel vector. Magneto-optical Kerr effect microscopy directly visualizes the domain-wall propagation that mediates the reversible switching. Compared to conventional spin Hall materials, RuO2 produces a significantly larger effective field and superior switching stability, sustaining performance under external magnetic fields exceeding 400 Oe. This robustness stems from the high-quality epitaxial films that suppress antiferromagnetic domain formation, ensuring efficient spin transmission. This work provides compelling evidence for the altermagnetism in RuO2 and establishes it as a superior spin source, paving the way for energy-efficient, field-free SOT-MRAM and other spin-torque devices.

[1] Šmejkal L., Sinova J., Jungwirth T., Phys. Rev. X 2022, 12, 040501.
[2] Bai H. et al., Phys. Rev. Lett. 2022, 128, 197202.
[3] Bose A. et al., Nat. Electron. 2022, 5, 267.
[4] Guo Y. et al., Adv. Sci. 2024, 11, 2400967.
[5] Li Z. et al., Adv. Mater. 2024, 36, 2406924.



CA-09. Voltage-assisted Single Laser Pulse in Magnetization Switching of Tb/Co-Based Magnetic Tunnel Junctions

Q. Trinh[1], J. Lin[2], B. Kunyangyuen[2], D. Salomoni[1], S. Auffret[1], G. Malinowski[2], E. Pargon[3], I. Prejbeanu[1], M. Hehn[2], S. Mangin[2, 4], L. D. Buda-Prejbeanu[1], R. Sousa[1]
[1]Université Grenoble Alpes, CEA, CNRS, Grenoble INP, SPINTEC, Grenoble, France, [2]Université de Lorraine, CNRS, Institut Jean Lamour, Nancy, France, [3]Université Grenoble Alpes, CNRS, CEA/LETI-Minatec, Grenoble INP, LTM, Grenoble, France, [4]Center for Science and Innovation in Spintronics, Tohoku University, Sendai, Japan

All-optical switching (AOS) in Tb/Co multilayer–based magnetic tunnel junctions (MTJs) is a promising approach for next-generation Magnetic Random Access Memory (MRAM), demonstrating ultrafast switching[1,2] and reliable resistive switching under single-pulse excitation[3,4]. However, in densely integrated arrays, the laser spot size greatly exceeds individual nanopillar dimensions, leading to the simultaneous switching of multiple devices and limiting selective write functionality. In this work, we demonstrate voltage-controlled tuning of the switching probability in Tb/Co-based AOS-MTJ devices. The experiments were performed on an 80-nm-diameter pillar using single laser pulses (25 fs, 800 nm) at a repetition rate of one pulse per second. The switching performance increases at high DC bias voltage, and reaches a maximum switching probability at -200 mV and -400 mV for a laser fluence of 3.5 mJ/cm^2 (Fig. 1). Analysis of the switching field (H_{sw}) extracted from magnetoresistance hysteresis loops indicates a significant contribution from Joule heating under applied voltage bias. This thermal-assisted process reduces the effective

magnetic anisotropy of the pillar, which favors in-plane magnetization precession, lowers the switching threshold, and broadens the switching range. Macrospin simulations further support these findings, showing that a lower quality factor (weaker anisotropy) tilts the anisotropy axis away from the out-of-plane direction, reducing the threshold fluence (TF) and expanding the switching fluence range (Fig. 2). These results demonstrate the voltage-selective control of multiple AOS devices on a single chip, enabling the development of CMOS-compatible magneto-photonic memories.

1. Peng, Y., et al. "In-plane reorientation induced single laser pulse magnetization reversal." *Nature Communications* 14.1 (2023).
2. Mishra, Kshiti, et al. "Dynamics of all-optical single-shot switching of magnetization in Tb/Co multilayers." *Physical Review Research* 5.2 (2023).
3. Mondal, Sucheta, et al. "Single-shot switching in Tb/Co-multilayer based nanoscale magnetic tunnel junctions." *Journal of Magnetism and Magnetic Materials* 581 (2023).
4. Salomoni, D., et al. "Field-free all-optical switching and electrical readout of Tb/Co-based magnetic tunnel junctions." *Physical Review Applied* 20.3 (2023).

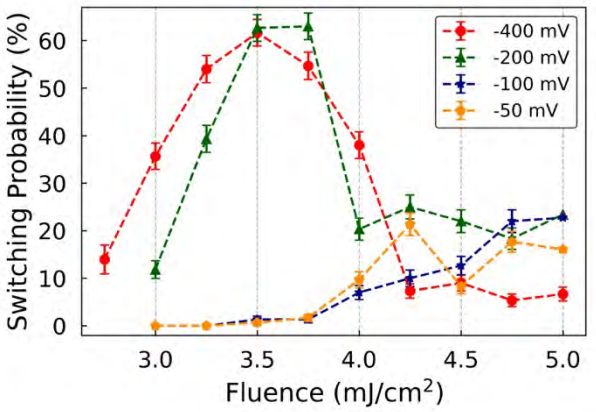


Fig. 1. Switching probability versus laser fluence and DC bias voltage at negative polarity.

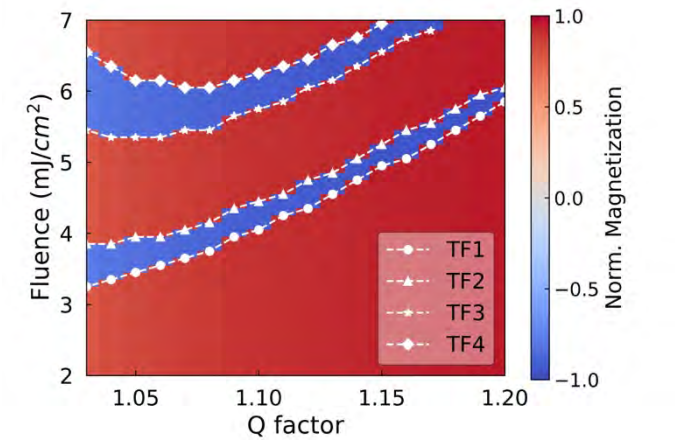


Fig. 2. AOS threshold fluence (TF) dependence on the magnetic anisotropy of the system. The quality factor Q = K_u/K_d quantifies the competition between magneto-crystalline anisotropy (K_u) and shape anisotropy (K_d). Initial state of the MTJ has the magnetization pointing “up”.

SESSION CB: SEEING MAGNETISM DIFFERENTLY: EMERGING PHASES REVEALED BY ADVANCED X-RAY IMAGING

Co-Chair(s): L. Kern, *Massachusetts Institute of Technology, Cambridge, Massachusetts, United States* and K. Litzius, *Institute of Physics, University of Augsburg, Augsburg, Germany*

Wednesday, November 4, 2026
08:30 AM-12:00 PM
Coral 5

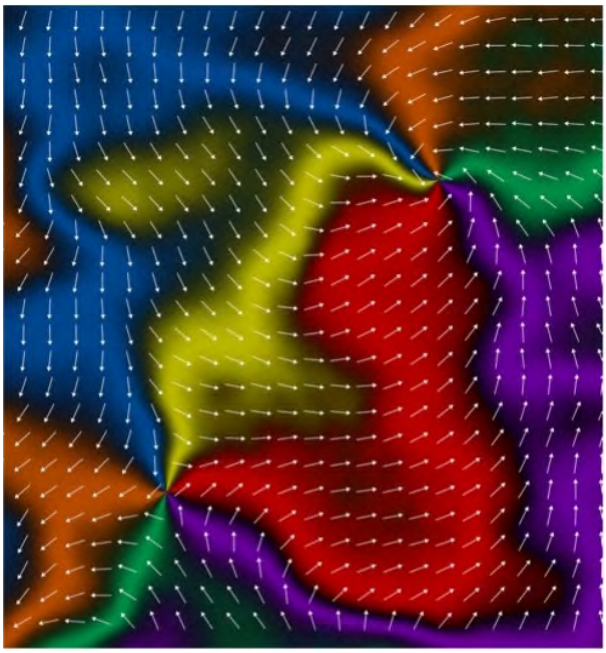
CB-01. Utilising altermagnetic properties for unique imaging and spectroscopy in MnTe

P. Wadley, A. Dal Din, O. Amin
School of Physics and Astronomy, University of Nottingham, Nottingham, County, United Kingdom

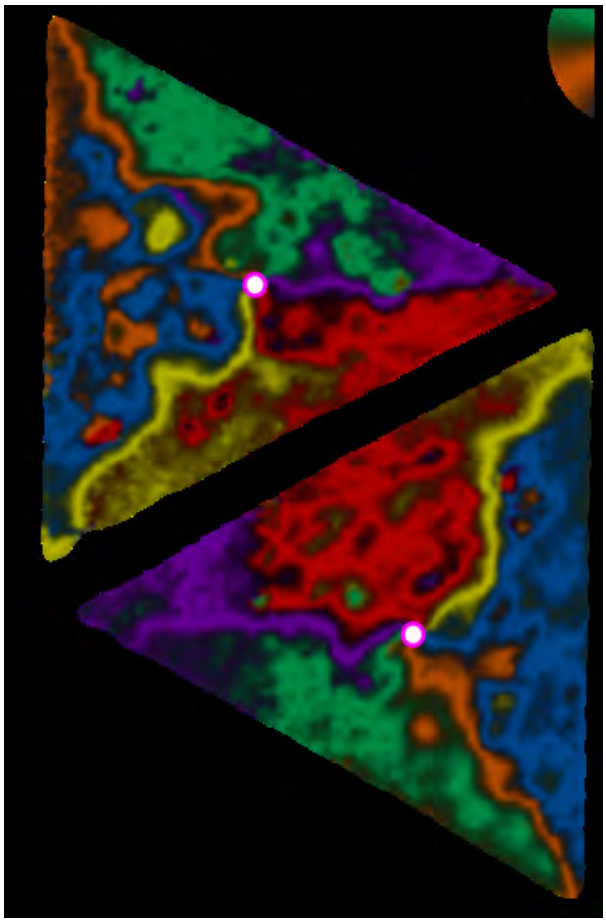
Altermagnetism is a newly identified class of magnetism which combines properties from both ferromagnets and antiferromagnets, making them highly promising candidates for spintronic applications[1,2]. We recently demonstrated the spin split nature of the altermagnetic electronic band structure in MnTe[3]. In this talk, I will describe how the unique resultant properties of altermagnets can be used to image them in unprecedented detail, and to control them in different ways[4,5].
Utilising a combination of spin resolved, angle resolved photoemission microscopy (SARPES), x-ray and optical

spectroscopy and microscopy, we show unique symmetries in the electronic band structure and new ways of imaging the real space magnetic order. This allows for imaging of all 6 domain types in a single instrument ,revealing not only merons but also their vorticity(Fig. 1). In addition, we utilise a combination of patterning and field cooling to nucleate single, stable domains of our choosing from the micron to nanoscale. We also show generation and control of the position and vorticity of single vortices(Fig. 2).

1. Smejkal, L., Sinova, J. & Jungwirth, T. *Beyond Conventional Ferromagnetism and Antiferromagnetism*: A Phase with Nonrelativistic Spin and Crystal Rotation Symmetry. Physical Review X 12, 031042 (2022).
2. Smejkal, L., Sinova, J. & Jungwirth, T. *Emerging Research Landscape of Altermagnetism. Physical Review* X 12, 040501 (2022).
3. Altermagnetic lifting of Kramers spin degeneracy
J. Krempaský, P. Wadley et al Nature 626, 517–522 (2024) https://doi.org/10.1038/s41586-023-06907-7*A*
4. *Nanoscale imaging and control of altermagnetism in MnTe*
O. J. Amin, A. Dal Din, P. Wadley et al Nature 636, pages348–353 (2024)
5. Unconventional relativistic spin polarization of electronic bands in an altermagnet
A. Dal Din,D.A. Usanov, Wadley et al
http://arxiv.org/html/2511.01690v1



XPEEM images showing all six domains type and a vortex anti-vortex pair



XPEEM imaging showing a single vortex in each equilateral triangle. For a given field cool direction the vorticity is opposite in each triangle. Reversing the field cool reverses both vorticities.

CB-02. X-ray Photoelectron Emission Microscopy of Crystallographic and Magnetic Domains in Non-Collinear Antiferromagnet Mn_3Sn Thin Films

S. Sakamoto[1, 2, 3], T. Higo[4], Y. Fukui[5, 3], Y. Sumida[5, 3], H. Kosaki[2], K. Amemiya[6], S. Nakatsuji[4, 2, 7], T. Ohkochi[5, 8, 3], S. Miwa[2, 3]
[1]Institute for Materials Research, Tohoku University, Sendai, Miyagi, Japan, [2]The Institute for Solid State Physics, The University of Tokyo, Kashiwa, Chiba, Japan, [3]SPRing-8 Center, RIKEN, Sayo, Hyogo, Japan, [4]Department of Physics, The University of Tokyo, Bunkyo, Tokyo, Japan, [5]Laboratory of Advanced Science and Technology for Industry, University of Hyogo, Sayo, Hyogo, Japan, [6]Institute of Materials Structure Science, KEK, Tsukuba, Ibaraki, Japan, [7]Institute for Quantum Matter and Department of Physics and Astronomy, Johns

Hopkins University, Baltimore, Maryland, United States, [8]Japan Synchrotron Radiation Research Institute, Sayo, Hyogo, Japan

The kagome antiferromagnet Mn_3Sn is a focal point in antiferromagnetic spintronics, as its cluster magnetic octupole induces a large anomalous Hall effect despite its negligible net magnetization [1]. The development of epitaxial thin films has enabled various spintronic functionalities, including electrical switching of the octupole order [2] and the spin-torque diode effect [3]. To accelerate device development, it is essential to resolve the microscopic crystallographic grain structures and their relationship to magnetic domain configurations.

X-ray techniques offer unique advantages for this purpose due to their sensitivity to magnetic order and chemical environments at nanoscale spatial resolutions. While previous studies demonstrated that octupole order can be probed by X-ray magnetic circular dichroism (XMCD) [4,5], we show in this work that orbital anisotropy, intrinsically linked to the crystal structure, can be detected via X-ray linear dichroism (XLD) in Mn_3Sn (Fig. 1). Leveraging the established X-ray absorption (XAS), XMCD, and XLD spectra, we performed photoelectron emission microscopy (PEEM) on Mn_3Sn epitaxial thin films with thicknesses of 10, 15, and 20 nm. We observe clear XMCD contrast arising from the cluster magnetic octupole order, alongside XAS and XLD contrast reflecting the crystallographic grains (Fig. 2). Crucially, we find that octupole domains extend across multiple crystallographic grains, suggesting significant intergranular exchange coupling. This indicates that magnetic domain walls are not strongly pinned at grain boundaries, potentially facilitating fast domain wall motion. The demonstrated simultaneous mapping of the octupole polarization and the underlying grain structure provides a comprehensive framework for advancing the fundamental understanding and control of antiferromagnetic spintronic materials.

This work was supported by JSPS-KAKENHI, JST-Mirai Program, JST-ASPIRE, X-nics, Spin-RNJ, and Murata Science Foundation.

[1] S. Nakatsuji *et al.*, Nature 527, 212 (2015)
[2] T. Higo *et al.*, Nature 607, 474 (2022)
[3] S. Sakamoto *et al.*, Nat. Nanotech. 20, 216 (2025)
[4] S. Sakamoto *et al.*, Phys. Rev. B 104, 134431 (2021)
[5] M. Kimata *et al.*, Nat. Commun. 12, 5582 (2021)

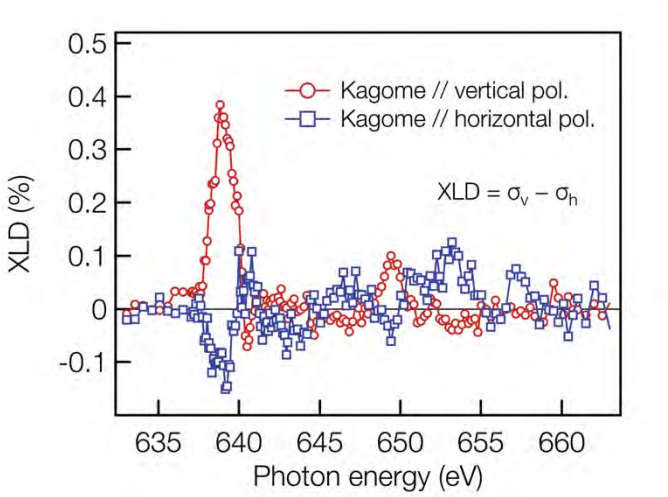


Fig. 1. XLD spectra. The kagome planes were oriented parallel to either the horizontal or vertical x-ray polarization.

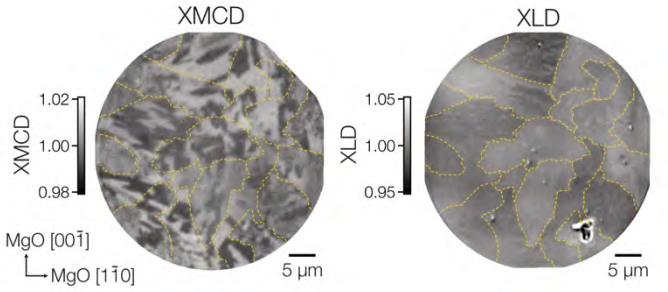


Fig. 2. XMCD and XLD contrast maps. Dashed curves denote grain boundaries determined via XAS mapping.

CB-03. Imaging the Magnetic-Field-Induced Reorientation of the NiO Néel Vector using XMLD-PEEM

D. Backes[1], E. Heppell[1, 2, 3], S. Langridge[3], G. van der Laan[1], T. Hesjedal[1, 2]
[1]Diamond Light Source, Didcot, United Kingdom, [2]Department of Physics, University of Oxford, Oxford, United Kingdom, [3]ISIS Neutron and Muon Source, STFC Rutherford Appleton Laboratory, Didcot, United Kingdom

Antiferromagnets, which were previously overshadowed by ferro- and ferrimagnets, have recently become central to condensed matter physics thanks to breakthroughs like spin-orbit torques and antiferromagnetic magnetoresistance. These developments allow for direct manipulation of antiferromagnetic spin structures [1], paving the way for durable and high-speed spintronic devices based on antiferromagnets [2]. Unlike ferromagnets,

antiferromagnets have nearly zero overall magnetization and their domain structures are mainly determined by exchange interactions, making them difficult to study with traditional characterization techniques.
Nickel oxide (NiO) serves as a prototypical antiferromagnet, with its spin structure examined either directly through XMLD-based PEEM [3,4] or indirectly by observing effects on adjoining ferromagnets via XMCD [5]. XMLD-PEEM imaging has demonstrated the influence of electrical currents on NiO's spin configuration, thereby providing valuable insight alongside transport measurements. Although current-induced switching represents a prevalent method for manipulating antiferromagnetic spin structures, alternative approaches not requiring patterning are sought after.
We found that NiO/Co bilayers exhibit an inverse coupling effect, allowing the NiO spin structure to be reoriented by a magnetic field when paired with a thin Co layer [6]. XMLD imaging revealed two regimes based on Co thickness: thin Co layers cause NiO to follow the Co magnetization, while thicker Co layers result in conventional exchange bias with NiO pinning. The transition occurs at about 3nm of Co. This method enables large-area control of antiferromagnetic order using moderate magnetic fields, ideal for applications needing uniform switching without current injection or microstructuring.
[1] X. Marti et al., Nature Mater. 13, 367 (2014).
[2] T. Jungwirth et al., Nature Nanotechnol. 11, 231 (2016).
[3] J. Stöhr et al., Phys. Rev. Lett. 83, 1862 (1999).
[4] E. Arenholz et al., Appl. Phys. Lett. 93, 162506 (2006).
[5] G. van der Laan et al., Phys. Rev. B 83, 064409 (2011).
[6] E. Heppell et al., Phys. Rev. Mater. 9, 014408 (2025).

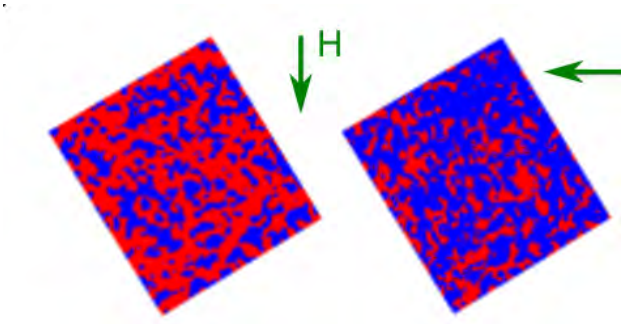


Fig. 1. Antiferromagnetic domain maps of NiO(001) with 3nm Co deposited on top, reconstructed from XMLD-PEEM images at the Ni L_2-edge. Two types of antiferromagnetic domains are observed, with the Néel vector either vertically (blue color) or horizontally (red color) aligned in the in-plane direction. They show the domain structures after applying magnetic fields of 0.3T in perpendicular directions. The field-of-view was 12x12 μm^2.

CB-04. What do linear and circular X-rays probe in altermagnets?

H. Jani
Physics, University of Oxford, Oxford, United Kingdom

The discovery of altermagnets has intensified interest in using advanced X-ray techniques to probe unconventional magnetism [1]. Traditionally, circularly polarised X-rays probe magnetic moments in ferromagnets, whereas linearly polarised X-rays detect the symmetry and orientation of compensated spins in antiferromagnets. Altermagnets present an intriguing new situation: despite having no net magnetisation, they possess spin-polarised electronic bands protected by crystal symmetry. Naïvely, one might therefore expect altermagnets to exhibit both circular and linear X-ray dichroism. This naturally raises the question: what do circularly and linearly polarised X-rays actually measure in altermagnets?

In this talk, I will begin by discussing the microscopic origins of X-ray absorption and scattering, showing how they give rise to circular and linear dichroism in altermagnets. I will then show how these concepts underpin recent advances in vectorial X-ray imaging, in which the relative orientations between the magnetic order, X-ray polarisation and crystallographic axes are exploited to quantitatively map compensated magnetic order [2-5]. By combining this approach with state-of-the-art X-ray imaging modalities, including X-ray photoemission microscopy [4], transmission microscopy [6,7], holography [8] and ptychography, we have visualised nanoscale antiferromagnetic states under distinct *in-situ* stimuli, including temperature, strain and field. I will demonstrate how these capabilities enabled the discovery and reproducible control of a broad family of topological spin textures, including antiferromagnetic half-skyrmions, bimerons and domain walls [4-9], and discuss how the same X-ray contrast mechanisms provide new insight into the emerging physics of altermagnetic solitons [9]. I will conclude by highlighting how these techniques will enable new studies of ultrafast spin physics in antiferromagnets and altermagnets for next-generation spintronic technologies [10].
[1] L Šmejkal et al. *Physics Review X* **12**, 040501 (2022).
[2] N W Price, et al. *Physical Review Letters* **117**, 177601 (2016).
[3] FP Chmiel, et al. *Nature Materials* **17**, 581 (2018).
[4] H Jani, et al. *Nature* **590**, 74 (2021).
[5] OJ Amin, et al. *Nature* **636**, 348 (2024).

[6] H Jani, et al. *Nature Materials* **23**, 205 (2024).
[7] J Harrison, et al. *ACS Nano* **19**, 42118 (2025).
[8] J Harrison, et al. *Optics Express* **32**, 5885 (2024).
[9] D Mallon, et al. *Arxiv*:2605.00815 (2026).
[10] ZS Lim, et al. *MRS Bulletin* **46**, 1053 (2021).

Team Acknowledgement: This work is a culmination of research performed with the P.G. Radaelli group (Oxford), Ariando group and T. Venkatesan group (Singapore), M. Atatüre group (Cambridge), C.B. Eom group (Wisconsin-Madison). Team includes J.-C. Lin, J. Harrison, J. Chen, C. Godfrey, Z. Zheng, S. Prakash, S. Hooda, G.J. Omar, J. Hu, P. Nandi, M. Lal, F. Maccherozzi, S. Finizio, J. Raabe, T.A. Butcher, N. Jaouen, P. Bencok, M Valvidares, P. Gargiani, M. Forester, M. Nino Orti, F. Kronast, S. Valencia, A. Tan, M. Hogen, H Knowles, C. Castelnovo et al.

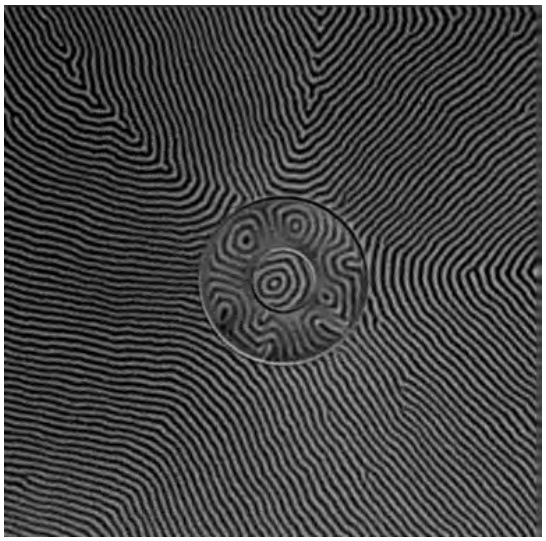
CB-05. Curvature engineered unconventional 3D spin textures in amorphous $Fe_{0.58}Ge_{0.42}$ thin films

J. Sands[1, 2], S. Satapathy[1], O. Bezsmertna[3], S. Virasawmy[1], A. Gashi[1], S. Dhuey[1], A. T. Hammack[1], C. Fernandez-Gonzalez[4], A. Sorrentino[4], T. Bayaraa[1], D. Makarov[3], S. M. Griffin[1], F. Hellman[1, 5], P. Fischer[1, 2]
[1]Lawrence Berkeley National Laboratory, Berkeley, California, United States, [2]UC Santa Cruz, Santa Cruz, California, United States, [3]Helmholtz Center Dresden-Rossendorf, Dresden, Germany, [4]ALBA, Cerdanyola del Vallès, Spain, [5]UC Berkeley, Berkeley, California, United States

The scientific and technological exploration of three-dimensional magnetic nanoscale systems is a rapidly emerging research field that opens the path to exciting novel physical phenomena, originating from the increased complexity in spin textures, topology, and frustration in three dimensions [1-3]. An alternate approach to explore and harness the full three-dimensional space is to use curvature as a design parameter, where the local curvature impacts physical properties across multiple length scales, ranging from the macroscopic to the nanoscale at interfaces and inhomogeneities in materials with structural, chemical, electronic, and magnetic short-range order [4,5]. Curvature-induced Dzyaloshinskii–Moriya interaction (DMI) provides a powerful means to create chiral spin textures, enabling studies of topology in nanomagnets and the design of skyrmion-based devices on flexible or patterned materials. We report the first observation of curvature-induced, localized skyrmionic textures in amorphous $Fe_{0.58}Ge_{0.42}$ (a-FeGe) thin films, deposited by DC magnetron co-sputtering onto toroidally curved (aka "*Mexican hat*") Si_3N_4 membranes patterned by e-beam lithography. Using magnetic soft X-ray nanotomography at MISTRAL/ALBA with XMCD contrast (~30 nm resolution) at RT, we found that flat substrates host conventional stripe domains, while curved regions with nonzero Gaussian curvature nucleate skyrmions coexisting with stripes elsewhere. Target skyrmions — precursors to hopfions — were observed. Micromagnetic simulations confirm curvature–magnetization coupling even in disordered materials, revealing geometry as a tool to engineer nanoscale magnetic landscapes and potentially generate higher-order topological spin states via tailored curvature.

Supported by U.S. DOE-BES (contract DE-AC02-05-CH11231 (NEMM FWP)), NSF (DMR- 2005108, DMR2320636 and ECCS-2429995), and Ministry of Research&Innovation Spain, Generalitat de Catalunya and EUFEDER funds.

[1] A. Fernández-Pacheco, R. Streubel, O. Fruchart, R. Hertel, P. Fischer and R. P. Cowburn, *"Three-dimensional nanomagnetism"*, Nature Communications 8, 15756 (2017)
[2] S. Ladak, A. Fernandez-Pacheco, P. Fischer, Science and Technology of 3D Magnetic Nanostructures (Editorial), APL Materials 10 120401 (2022)
[3] 2025 Roadmap on 3D Nano-magnetism, Gianluca Gubbiotti et al 2025 J. Phys.: Condens. Matter 37 143502
[4] D. Makarov and D. D. Sheka, *Curvilinear Micromagnetism*. (Springer Cham, 2022)
[5] R. Streubel, E. Tsymbal, P. Fischer, Perspective: Magnetism in Curved Geometries, JAP 129 210902 (2021)



Magnetic Soft X-ray Microscopy image obtained at the Fe L3 edge of an a-Fe0.58Ge0.42 layer deposited on a curved substrate oriented at normal incidence of the X-ray beam onto the sample's surface.

CB-07. Nanoscale mapping of unconfined magnetic systems using pre-edge phase 3D magnetic vector imaging

J. Neethirajan[1], B. Daurer[2], M. Di Pietro Martínez[1], A. Hrabec[3,4], L. Turnbull[1,2], R. Yamamoto[1,5], M. Raboni Ferreira[1,6,7], A. Stefancic[8], D. Mayoh[8], G. Balakrishnan[8], P. Vir[1], C. Shekhar[1], C. Felser[1], M. Kazemian[2], B. Kaulich[2], C. Donnelly[1,5]
[1]Max Planck Institute for Chemical Physics of Solids, Dresden, Germany, [2]Diamond Light Source, Harwell Science and Innovation Campus, Didcot, United Kingdom, [3]Laboratory for Mesoscopic Systems, Department of Materials, ETH Zurich, Zurich, Switzerland, [4]Laboratory for Multiscale Materials Experiments, Paul Scherrer Institute, Villigen PSI, Switzerland, [5]International Institute for Sustainability with Knotted Chiral Meta Matter (WPI-SKCM2), Hiroshima University, Hiroshima, Japan, [6]Brazilian Synchrotron Light Laboratory, Brazilian Center for Research in Energy and Materials, Campinas, Brazil, [7]Gleb Wataghin Institute of Physics, University of Campinas, Campinas, Brazil, [8]Department of Physics, University of Warwick, Coventry, United Kingdom

The stability and tunability of topological magnetization configurations under external stimuli, such as currents and magnetic fields, have made them a rapidly growing field of research. With recent advances in 3D magnetic vector imaging techniques, there has been a growing interest in 3D magnetization configurations such as Bloch points, vortex rings [1] and hopfions [2]. The emergence of these configurations in unconfined magnetic systems is intriguing, with the added spatial dimension allowing for the formation of complex 3D magnetization configurations.

In order to probe the magnetization in a magnetic system, we use the X-ray Magnetic Circular Dichroism (XMCD) effect, which is strong at on-resonance energies of the magnetic element. Although conventional absorption-based soft X-ray microscopy has been successful in characterizing thin films, systems exceeding a few hundred nanometers in thickness are challenging to image. So far, nanoscale transmission imaging has been limited to rare-earth-containing systems with hard X-rays [3]. This limitation has rendered the study of extended micrometer-thick magnetic systems, especially transition-metal-based magnets, particularly difficult. This challenge is schematically shown in Fig. 1, where we identify a distinct thickness gap in which certain compositions of magnetic systems in an extended geometry remain difficult to image.

Here, we overcome this challenge by establishing pre-edge phase XMCD (Φ_{XMCD}) magnetic imaging of micrometer-thick extended systems using soft X-ray ptychography, enabling nanoscale imaging of magnetic systems of arbitrary composition. By gaining access to the complex transmission function of the sample using soft X-ray ptychography, we use the prominent pre-edge Φ_{XMCD} signal to demonstrate the imaging of the magnetization configuration of samples up to 1.7 μm in thickness, an order of magnitude larger than typically measured with absorption-based soft X-ray microscopy techniques [4]. This new capability thus opens the door to nanoscale imaging of a wide variety of samples, including naturally-occurring magnetite micro-magnets that until now, have not been possible to experimentally measure [5].

Furthermore, combining pre-edge Φ_{XMCD} imaging with 3D magnetic vector imaging techniques [1] opens a direct route to mapping the magnetization vector field in a variety of extended samples. Chiral magnets are especially fascinating in this context, as the Dzyaloshinskii-Moriya interaction, competing with the exchange interaction, facilitates the formation of topologically non-trivial chiral magnetization configurations in 3D [6,7]. Here, by performing pre-edge Φ_{XMCD} 3D magnetic vector imaging, we map the 3D magnetization configuration of a wedge-shaped lamella (thickness varying from 170 nm to 500 nm) of an anisotropic chiral magnet $Mn_{1.4}PtSn$, with nanoscale spatial resolution. The thickness gradient gives rise to a significant variation in domain size and the emergence of distinct domain defect types. Intriguingly, the 3D vector imaging reveals the presence of a 3D network of Bloch points, topological singularities in the magnetization vector field, which so far have only been investigated as isolated structures. This insight paves the way for the investigation of the interaction between Bloch point singularities and provides a platform to investigate their dynamics with an external stimuli, important both for technological applications as well fundamental physics.

1. C. Donnelly, *et al*, Nature Physics 17, 316-321 (2021).
2. F. Rybakov, *et al*, APL Mater 10, (2022)
3. C. Donnelly, *et al*, Phys. Rev. B. 94, 064421 (2016).
4. J. Neethirajan, *et al,* Phys. Rev. X 14, 031028 (2024).
5. R. J. Harrison, J. Neethirajan, *et al,* Comm. Earth and Environment 6, 810 (2025).
6. F. Zheng, *et al,* Nature Comm. 12, 5316 (2021).
7. F. Zheng, *et al,* Nature 623, 718-723 (2023).

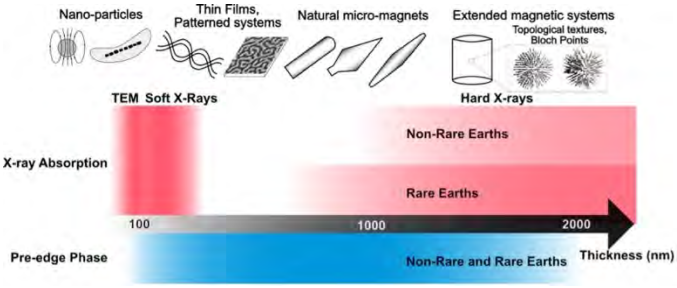


Fig. 1: Schematic illustration of the comparison between established magnetic imaging capabilities for magnetic samples of varying thicknesses. Figure adapted from [4].

CB-08. Seeing Through Magnets: Full 3D Imaging of a Hybrid Skyrmion Lattice via Soft X-Ray Vector Ptycho-Tomography

H. Fang[1], I. Binnie[1], B. Shearer[1], S. Yazdi[2], S. Montoya[3], E. Fullerton[3], T. Feggeler[4], J. Zou[5], C. Liao[6], E. Cating-Subramanian[1], D. Shapiro[7], J. Miao[8], H. C. Kapteyn[1], M. M. Murnane[1]

[1]JILA, Department of Physics, University of Colorado Boulder, Boulder, Colorado, United States, [2]Renewable And Sustainable Energy Institute, University of Colorado Boulder, Boulder, Colorado, United States, [3]University of California, San Diego, La Jolla, California, United States, [4]Brookhaven National Laboratory, Upton, New York, United States, [5]King Fahd University of Petroleum and Minerals, Dhahran, Saudi Arabia, [6]Indiana University Bloomington, Bloomington, Indiana, United States, [7]Lawrence Berkeley National Laboratory, Berkeley, California, United States, [8]University of California, Los Angeles, Los Angeles, California, United States

Nanoscale topological defects in spin texture called magnetic skyrmions have recently attracted great interest for next-generation energy-efficient data storage and computing due to their topological protection with associated high energy barriers for decay [1-6].

While traditionally studied as 2D structures, skyrmions in materials with non-negligible thickness also show variation along the 3rd dimension [7-9]. However, direct visualization of 3D spin textures such as skyrmion lattices is very challenging due to their few-nanometer exchange length, limited magnetic contrast, extensive vector field information to be reconstructed, and extended textures beyond the field of view.

Here we represent a 3D imaging procedure based on soft X-ray vector ptycho-tomography [10] that can successfully image 3D skyrmion lattice structures in an extended thin film material with unprecedented spatial resolution (8 nm voxel size) and field of view (7 sq. μm x 88 nm, 24+ distinct magnetic features). We observe the formation of hybrid skyrmion tubes with rotating helicities throughout the depth of the multilayer, which confirms the predictions of micromagnetic simulations. This enables us to directly observe how these nanoscale hybrid lattices are structured in 3D, as well as paving the way for the discovery and characterization of various intrinsically 3D magnetic textures.

1. Y. Zhou et al., Adv. Mater. 2025, 37, 2312935.
2. A. Fert et al., Nature Nanotech 8, 152–156 (2013).
3. J. Grollier, et al., Proceedings of the IEEE, vol. 104, no. 10, pp. 2024-2039, Oct. 2016.
4. A. Kurenkov, et al., Appl. Phys. Lett. 27 February 2017; 110 (9): 092410.
5. S. Luo, et al., Nano Letters 2018 18 (2), 1180-1184.
6. J. Grollier et al., Nat Electron 3, 360–370 (2020).
7. S. Zhang et al., Proceedings of the National Academy of Sciences 115, no. 25 (2018): 6386–91.
8. H. Zhang et al., Nature Communications 15, no. 1 (2024): 3828.
9. W. S. Parker et al., Phys. Rev. B 112, 094415 (2025).
10. A. Rana, et al., Nature Nanotechnology 18, no. 3 (2023): 227–32.

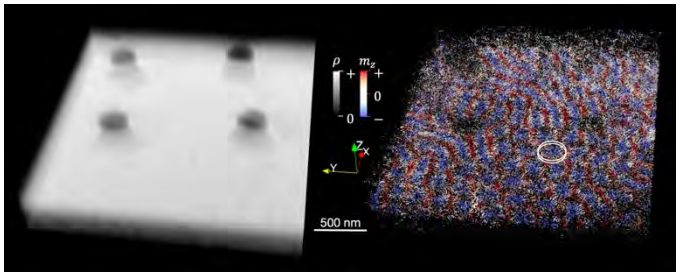


Fig. 1: Side-by-side overview of structural and magnetic tomography reconstructions.

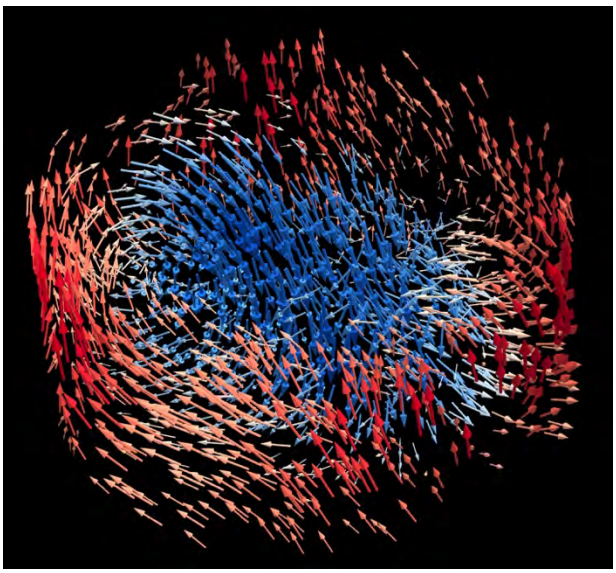


Fig. 2: A single skyrmion from the circled region in magnetic reconstruction.

CB-09. 3D magnetic imaging of magnetic texture with X-ray Holography at SOLEIL SEXTANTS beamline: status and perspectives with SOLEIL II

J. J. Chiliquinga-Jacome[2], H. Popescu[1], M. Grelier[3], M. Di Pietro Martínez[4], A. Wartelle[5], G. Beutier[5], V. Cros[2], N. Reyren[2], N. Jaouen[1]
[1]Synchrotron SOLEIL, St Aubin, France, [2]Laboratoire Albert Fert, Palaiseau, France, [3]Spin-Ion Technologies, Palaiseau, France, [4]LCPMR, Paris, France, [5]Inst. Néel, Grenoble, France

Non-collinear spin textures in ferromagnetic ultrathin films have attracted renewed interest, driven by the possibility of finely engineering magnetic interactions—most notably the interfacial Dzyaloshinskii–Moriya interaction (i-DMI) in multilayer systems. This enables the stabilization of complex chiral spin textures such as chiral magnetic domain walls, spin spirals, and magnetic skyrmions. We have recently demonstrated that circular dichroism in resonant x-ray scattering (REXS) is a powerful approach to determine domain wall characteristics, namely their type (Néel or Bloch) and sense of rotation (chirality) in ferromagnetic and antiferromagnetic multilayers [1–3]. We will show how angular-dependent circular dichroism measurements in REXS allow us to retrieve three-dimensional information on chiral magnetic textures [4], supported by quantitative REXS simulations [5].
In the second part, we will focus on recent results obtained using x-ray Fourier transform holography (FTH). Several experiments performed at the SEXTANTS beamline illustrate its capability to image magnetic materials with element selectivity and spatial resolution down to a few tens of nanometers in two dimensions [6]. The current status of the sample environment (magnetic field, electric field, femtosecond laser excitation, temperature control) as well as developments in 2D detector systems will be presented. We will also describe recent advances enabling three-dimensional reconstruction of magnetic textures using tomographic FTH [7].
Finally, we will discuss the respective limitations and complementarity of REXS and FTH approaches. In particular, we address the intrinsic limitations of REXS in scattering geometry for magnetic imaging at the current SOLEIL storage ring, and outline the perspectives opened by SOLEIL II, especially in view of the expected increase in coherent flux at the SEXTANTS beamline for 3D magnetic imaging.
This work is supported by EU project SkyANN (reference no. 101135729), by ANR-DFG number BU 3297/4-1 (Topo3D) and by ANR-22- EXSP-0002 PEPR SPIN CHIREX and grant no. ANR- 22-EXSP-0008 PEPR SPIN SPINCHARAC).
[1] J.-Y. Chauleau, et al, Phys. Rev. Lett 120, 037202 (2018)
[2] W. Legrand, et al, Science Adv. 4, eaat0415 (2018).
[3] C. Léveillé, et al, Phys. Rev. B., 104(6), L060402 (2021).
[4] E. Burgos-Parra, et al. Scientific Reports 13, 11711 (2023).
[5] S. Flewett, et al., Phys. Rev. B 103 (18), 184401 (2021).
[6] H. Popescu et al., J. Synchr. Radiation, 26(1) 280 (2019).
[7] Di Pietro Martinez et al, Phys. Rev. B 107(9), 094425 (2023).
[8] J. J. Chiliquinga-Jacome et al., accepted in Phys. Rev. B and arXiv:2601.14889

SESSION CC: VAN DER WAALS MAGNETS AND MATERIALS

Chair(s): H. Yuasa, *Graduate School and Faculty of Information Science and Electrical Engineering, Kyushu University, Fukuoka, Japan*

Wednesday, November 4, 2026
08:30 AM-12:00 PM
Coral 1

CC-01. All-Electrical Manipulation of Néel Vector in Van der Waals Antiferromagnet

H. Guo[1], Z. Lin[1], C. Yu[2], Y. Hou[2], J. Yang[1], Z. Luo[1]
[1]School of Physics, Peking University, Beijing, China, [2]School of Materials, Sun Yat-Sen University, Shenzhen, China

Two-dimensional antiferromagnets that combine the dual advantages of van der Waals (vdW) and antiferromagnetic materials, provide an unprecedented platform to explore

emergent spin-related phenomena[1]. However, electrical manipulation of Néel vectors in vdW antiferromagnets —the cornerstone of antiferromagnetic spintronics—remains challenging. Here, we report layer-dependent electrical switching of the Néel vector in an A-type vdW antiferromagnet $(Fe,Co)_3GaTe_2$ (FCGT) with perpendicular magnetic anisotropy. The Néel vector of FCGT with odd-number vdW layers can be 180° reversed via spin-orbit torques. Furthermore, we achieve field-free switching in an all-vdW, all-antiferromagnet heterostructure of FCGT/CrSBr in which the noncollinear interfacial spin texture breaks the mirror symmetry[2]. Based on these findings, we are now extending this route toward, all-electrical antiferromagnetic memory devices at room temperature. Our results establish layer-controlled spin symmetries and interfacial spin engineering as universal paradigms for manipulating antiferromagnetic order, paving the way for realizing reliable and efficient antiferromagnetic memory devices[2,3].

[1] Z. Lin, Z. Luo* and J. Yang*, Chinese Physics B., 31, 087506 (2022)
[2] H. Guo†, Z. Lin† and Z. Luo*, Nature Communications., 16, 8911 (2025)
[3] C. Yun†, H. Guo† and Z. Luo*, Science Advances., 9, eadj3955 (2023)

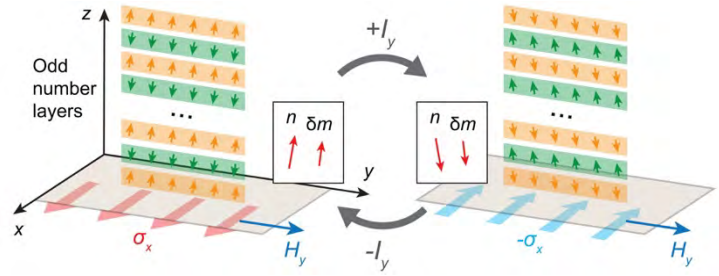


Fig.1 Schematics illustrating spin-orbit torque 180° switching of the Néel vector in Pt/FCGT with odd-number vdW layers.

CC-02. Covalent 2D Magnets: Expanding the Landscape of Layered Magnetism

H. Zeng[1], C. Huai[1], G. V. Silva[2], G. Miao[2], R. Sabirianov[3]
[1]Department of Physics, University at Buffalo, SUNY, Buffalo, New York, United States, [2]University of Waterloo, Waterloo, Ontario, Canada, [3]University of Nebraska-Omaha, Omaha, Nebraska, United States

The emergence of atomically thin magnets has transformed the study of low-dimensional magnetism, driven largely by exfoliated van der Waals (vdW) systems. While these materials have enabled breakthroughs in spintronics, their reliance on weak interlayer bonding limits chemical diversity and tunability. This invited talk will introduce a new class of covalent 2D magnets formed through self-intercalation of native 3d transition metal cations within transition metal dichalcogenides, producing layered magnets with formula $M_{1+\delta}X_2$. Unlike vdW magnets, these covalently bonded structures offer robust control over exchange coupling, magnetic order, and spin textures via self-intercalation. The presentation will cover synthesis strategies, including Cr_2Te_3 and heterostructures grown by "dative epitaxy," a novel technique we developed for integrating 2D magnets with semiconductors. It will then reveal a new mechanism behind unconventional anomalous Hall effect, driven by the nodal structures in the electronic bands modulated by the noncolinear spin texture. Leveraging such a mechanism, we demonstrate reversible anomalous Hall polarity switching via solid-state ionic gating, opening new pathways for spintronics and unconventional computing beyond conventional vdW frameworks.

1. Advanced Science 12, 2407625 (2025)
2. Adv. Mater. 34, 2200117 (2022)
3. Adv. Mater. 33, 2105079 (2021)
4. Mater. Res. Lett. 9, 205–212 (2021)
5. Chem. Mater. 23, 3769–3774 (2011)

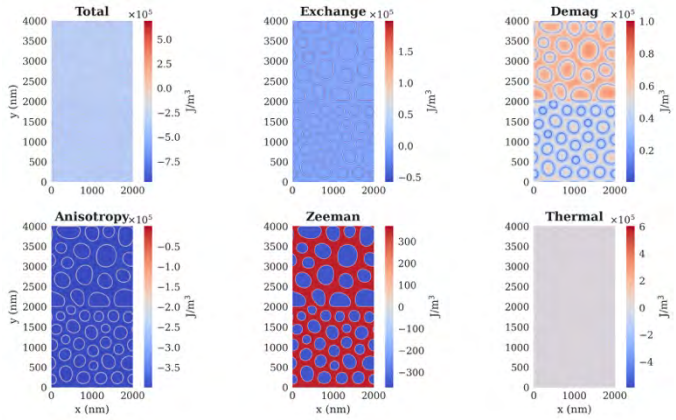
CC-03. Topological Spin Textures in 2D Ferromagnets: From Fundamental Stabilization to Dynamic Phase Transformations

P. Cai[1], J. Garland[17, 18], J. Fullerton[18], J. Huang[2], T. Zhu[2], X. Ma[3], Z. Wang[4], R. Basnet[19], S. Chhetri[19], J. Hu[19], R. Zhang[6], Y. Hao[2], J. Lu[5], L. He[2], J. Xu[2], Y. Zhang[7, 8], W. Jiang[9, 10], J. Tao[4], S. Lei[11], P. Parchinskiy[12], Y. Li[18], A. Petford-Long[18, 20], L. Wang[5], W. Niu[13], X. Zhang[16], P. Li[2], C. Phatak[18, 20], E. Santos[1, 14, 15]
[1]School of Physics and Astronomy, The University of Edinburgh, Edinburgh, United Kingdom, [2]School of Microelectronics, University of Science and Technology of China, Hefei, Anhui, China, [3]College of Integrated Circuits and Optoelectronic Chips, Shenzhen Technology University, Shenzhen, Guangdong, China, [4]Department of Physics, University of Science and Technology of China, Hefei, Anhui, China, [5]Hefei National Research Center for Physical Sciences at Microscale, University of Science and Technology of China, Hefei, Anhui, China, [6]School of Integrated Circuits, Huazhong University of Science and Technology, Wuhan, Hubei, China, [7]State Key Laboratory of High-end Heavy-load Robots Corporate Research Center, Midea Group, Foshan, China, [8]Corporate Research Center, Midea Group, Foshan, China, [9]State Key Laboratory of Low-Dimensional Quantum Physics

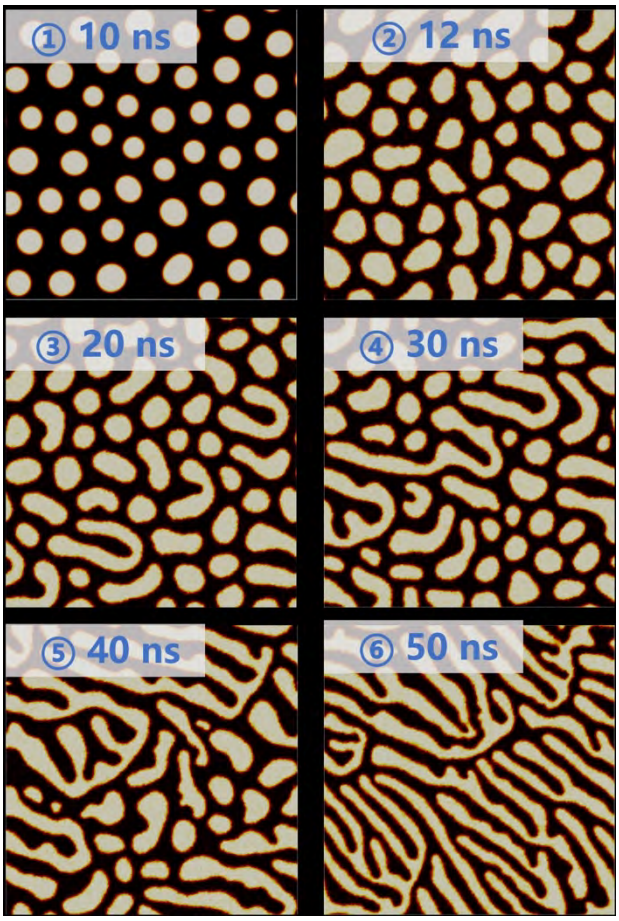
and Department of Physics, Tsinghua University, Beijing, China, [10]Frontier Science Center for Quantum Information, Tsinghua University, Beijing, China, [11]Hong Kong University of Science and Technology, Hong Kong, Hong Kong, [12]Department of Semiconductor and Polymer Physics, National University of Uzbekistan, Tashkent, Uzbekistan, [13]New Energy Technology Engineering Laboratory of Jiangsu Province, Nanjing University of Posts and Telecommunications, Nanjing, Jiangsu, China, [14]Higgs Centre for Theoretical Physics, The University of Edinburgh, Edinburgh, United Kingdom, [15]Donostia International Physics Center, Donostia-San Sebastián, Spain, [16]School of Physics, Southeast University, Nanjing, Jiangsu, China, [17]Applied Physics Program, Northwestern University, Evanston, Illinois, United States, [18]Materials Science Division, Argonne National Laboratory, Lemont, Illinois, United States, [19]Department of Physics, University of Arkansas, Fayetteville, Arizona, United States, [20]Materials Science and Engineering Department, Northwestern University, Evanston, Illinois, United States

Magnetic skyrmions in two dimensional van der Waals ferromagnets offer a highly tunable platform for next-generation spintronic and neuromorphic computing systems. Realizing these applications requires a comprehensive understanding of both the static stabilization of topological textures and their dynamic manipulation. In this work, we present a unified micromagnetic investigation into the evolution and active transformation of topological spin textures in Fe_3GeTe_2 (FGT) and Fe_3GaTe_2 (FGaT) systems. We first elucidate the fundamental stabilization mechanisms by detailing the thickness-dependent magnetization reversal in FGT material. Our simulations reveal that while thin regions exhibit rapid saturation dominated by strong perpendicular magnetic anisotropy, thicker regions support the formation of stable skyrmion lattices that evolve into faceted patch domains. Crucially, we identify that sharp gradients in the demagnetization field at physical thickness step edges create localized potential wells, governing domain wall pinning behaviors. Building upon this understanding of static energetics, we transition to the active, current-driven manipulation of these textures in the room-temperature ferromagnet FGaT. We model the deterministic transformation from a dense skyrmion lattice to a labyrinthine stripe-domain state. This transition is identified as an energy-injection-assisted thermodynamic relaxation, where applied spin-orbit and spin-transfer torques overcome topological protection barriers. By quantifying the continuous decay of the total topological charge, we provide definitive evidence of a massive topological annihilation event. Together, these findings establish a robust mechanistic framework, bridging the fundamental physical confinement of static spin textures to their dynamic, non-volatile implementation in artificial spintronic synapses.

J. Garland, J. Fullerton and P. Cai, Adv. Funct. Mater., Vol. 36, p. e18239 (2026)
S. Jin, Y. Wang and H. Zheng, Nano Lett., Vol. 24, p. 5467 (2024)
H. Zhang, Y.-T. Shao and X. Chen, Nat. Commun., Vol. 15, p. 3828 (2024)



Micromagnetic simulation of thickness-dependent magnetization reversal in Fe_3GeTe_2, illustrating domain evolution and pinning at step edges.



Time evolution of the topological charge during the current driven skyrmion to stripe phase transformation in Fe_3GaTe_2

CC-04. Spin-transport Properties of Chiral Helimagnet $Cr_{1/3}TaS_2$ Nanoflakes

K. Yamada[1], N. Jiang[1, 2, 3], F. Tokuda[1], R. Nakamura[1], H. Shoji[4], Y. Kousaka[4], Y. Togawa[4], Y. Niimi[1, 2, 3]

[1]Department of Physics, The University of Osaka, Toyonaka, Japan, [2]Center for Spintronics Research Network, The University of Osaka, Toyonaka, Japan, [3]Institute for Open and Transdisciplinary Research Initiatives, The University of Osaka, Toyonaka, Japan, [4]Department of Physics and Electronics, Osaka Metropolitan University, Sakai, Japan

Chiral helimagnets exhibit a helical spin texture with nearly zero net magnetization, making them attractive candidates for high density information storage devices. The spin phase — the orientation of the magnetic moment at the surface — has attracted growing interest as a potential information carrier in nanoscale spintronic devices. To detect the spin phase, spin currents offer a promising route because they are sensitive to the local magnetic configuration near the surface. Recent spin transport experiments on chiral helimagnet $Cr_{1/3}NbS_2$ have demonstrated all electrical readout of the spin phase [1]. However, these measurements were limited to samples with thicknesses of up to 1.5 helical periods, owing to the long helical pitch of ~48 nm in $Cr_{1/3}NbS_2$ [2]. To deepen our understanding of the magnetic field response of the helical spin texture, spin transport experiments on helimagnets with a larger number of helical periods are strongly desired.

In this study, we focus on $Cr_{1/3}TaS_2$, a chiral helimagnet with a shorter helical pitch of ~22 nm [3], which enables access to samples encompassing a greater number of helical periods using the lateral spin valve geometry as shown in Fig. 1. We first determine a spin diffusion length of ~2 nm at 50 K in $Cr_{1/3}TaS_2$ — more than an order of magnitude shorter than the helical pitch — confirming that the injected spins are sensitive to the surface magnetic moment. Using the same lateral spin valve geometry, we investigate the nonlocal voltage as a function of magnetic field for $Cr_{1/3}TaS_2$ flakes with thicknesses of up to ~2 helical periods. As shown in Fig. 2, the measured nonlocal signal exhibits a systematic evolution with the number of helical periods, providing deeper insight into the field driven reconfiguration of the helical spin texture beyond the single-period regime. Our results extend the understanding of spin phase detection in chiral helimagnets and pave the way toward all electrical probing of the helical spin structure in spintronic devices.

[1] N. Jiang *et al.*, Phys. Rev. B 112, L180402 (2025).
[2] Y. Togawa *et al.*, Phys. Rev. Lett. 108, 107202 (2012).
[3] C. Zhang *et al.*, Adv. Mater. 33, 2101131 (2021).

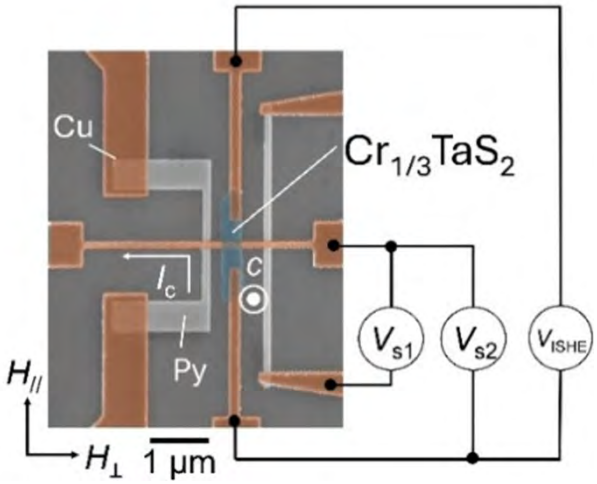


Fig. 1. Scanning electron microscope image of lateral spin valve with a $Cr_{1/3}TaS_2$ nanoflake.

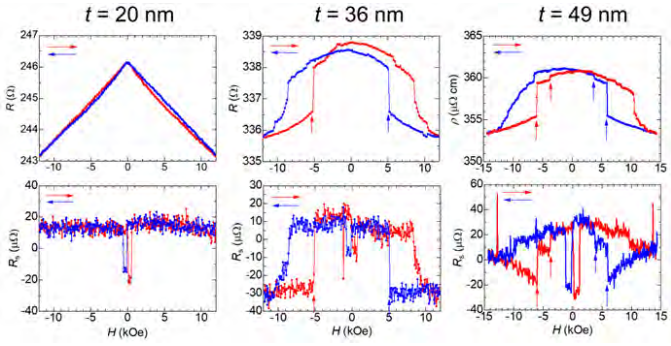


Fig. 2. Thickness *t* dependence of the magnetoresistance (top) and spin signal (bottom) of $Cr_{1/3}TaS_2$ nanoflakes.

CC-05. Evidence of Magnetic Proximity Effect in van der Waals Graphene/Fe_3GeTe_2 Heterostructures

M. Aoki[1, 2], J. E. Medina Dueñas[2, 4], T. Guillet[2], V. Zatko[2], K. Watanabe[3], T. Taniguchi[5], J. H. Garcia[2], J. F. Sierra[2], M. Shiraishi[6, 7], S. Roche[2, 8], S. O. Valenzuela[2, 8]

[1]The Institute for Solid State Physics, The University of Tokyo, Kashiwa, Chiba, Japan, [2]Catalan Institute of Nanoscience and Nanotechnology, Bellaterra, Barcelona, Spain, [3]Research Center for Electronic and Optical Materials, National Institute for Materials Science, Tsukuba, Ibaraki, Japan, [4]Universitat Autònoma de Barcelona, Bellaterra, Barcelona, Spain, [5]International Center for Materials Nanoarchitectonics, National Institute for Materials Science, Tsukuba, Ibaraki, Japan, [6]Department of Electronic Science and Engineering, Kyoto University, Kyoto, Kyoto, Japan, [7]Center for Spintronics Research Network, Kyoto University, Kyoto, Kyoto, Japan, [8]Institució Catalana de Recerca i Estudis Avançats (ICREA), Barcelona, Barcelona, Spain

Van der Waals heterostructures combining graphene with two-dimensional ferromagnets offer a promising platform for exploring the magnetic proximity effect (MPE)[1]. Traditionally, investigating the MPE in graphene-metallic ferromagnet interfaces has been challenging; the high conductivity of bulk metallic layers leads to significant current shunting, which masks the subtle proximity-induced signals in the graphene layer. In this work, we overcome this limitation using the Fe_3GeTe_2(FGT) to provide evidence of the MPE[2].

We fabricated hexagonal boron nitride (h-BN) encapsulated FGT/monolayer graphene (MLG) heterostructures. The devices feature a bare FGT reference and an FGT/MLG heterostructure regions (Fig. 1). The core evidence for the MPE is derived from a comparative analysis of the transverse resistance R_{xy} in the two regions. We observed that the magnitude of the hysteresis induced by the anomalous Hall effect (AHE) is larger in the FGT/MLG compared to the FGT reference (Fig. 2b). Crucially, a standard parallel channel model—where graphene acts as a passive conductor—predicts a decrease in the AHE due to current shunting into the MLG laher. Indeed, based on gate-dependent conductivity analysis, we estimate that over 43% of the total current flows through the MLG. Contrary to this model, our experimental results show an enhancement of AHE in the heterostructure. This discrepancy definitively indicates that the MLG layer acquires a magnetic character via the MPE, contributing its own AHE signal to the total transport.

Our findings demonstrate that MLG/FGT interfaces facilitate a strong MPE that overcomes the conventional shunting limitation, establishing a robust foundation for developing van der Waals spintronic devices.

We acknowledge support from the Spanish Ministry of Science and Innovation and Spanish Research Agency (AEI/10.13039/501100011033) under contracts PID2022-143162OB-I00 and Severo Ochoa CEX2021-001214-S. M.A. acknowledges support from the JSPS.

1. J. F. Sierra, J. Fabian, R. K. Kawakami, S. Roche, and S. O. Valenzuela, Nat. Nanotechnol. Vol. 16, p.856-868 (2021).
2. M. Aoki, J. M. Dueñas, T. Guillet, V. Zatko, K. Watanabe, T. Taniguchi, J. H. García, J. F. Sierra, M. Shiraishi, S. Roche, and S. O. Valenzuela, submitted.

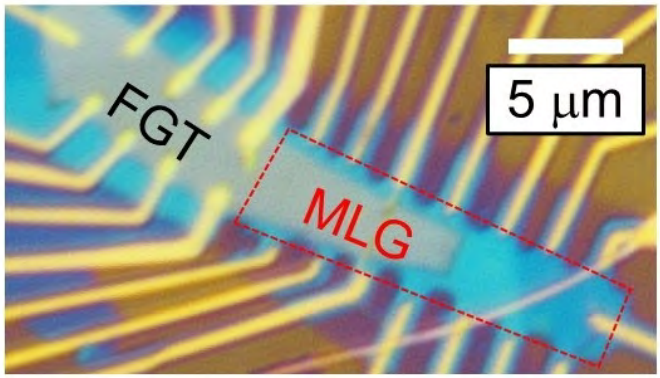


Fig. 1 An optical microscope image of the device.

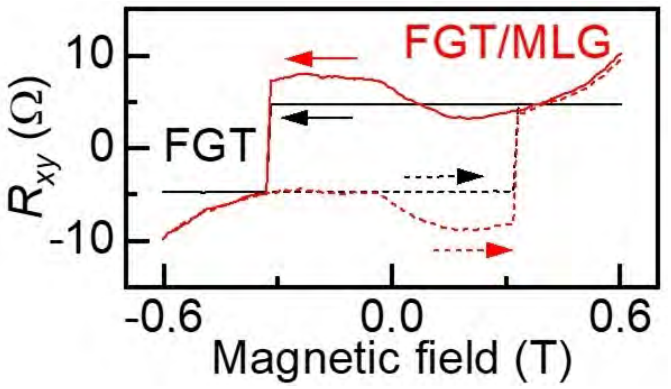


Fig. 2 R_{xy} as a function of magnetic field measured from the FGT reference and FGT/MLG heterostructure regions.

CC-06. Computational and experimental study of metallic interfaces with semiconducting monolayer of MoS_2

A. J. Stollenwerk[1], C. Sadler[1], T. Porter[1], G. Ye[2], C. Nnokwe[2], P. Shand[1], R. He[2], P. Lukashev[1]
[1]Physics, University of Northern Iowa, Cedar Falls, Iowa, United States, [2]Texas Tech University, Lubbock, Texas, United States

Here, we present results of a combined computational and experimental study of metallic interfaces with semiconducting monolayer of MoS_2. In particular, we consider the full coverage of MoS_2 monolayer by the following metals: Au, Cr, Cu, Ni, Fe. It is shown that among the considered systems, MoS_2 / Fe and MoS_2 / Ni retain strong ferromagnetic properties, MoS_2 / Au and MoS_2 / Cu are non-magnetic, while MoS_2 / Cr exhibits ferrimagnetic coupling in the optimized geometry. The electronic and magnetic properties of the considered systems are explained in terms of their binding energies and interlayer distances. In particular, it is shown that the energy gap of MoS_2 monolayer, as well as magnetic properties of the metallic interfaces are very sensitive to the interlayer distance. The calculated binding energies are found to manifest directly in the scanning tunneling microscopy images, with weakly bound metals exhibiting enhanced surface mobility, while more strongly bound metals formed stable interfacial structures. Photoluminescence measurements from heterostructures formed by Ni/Cu/Au/Cr thin films on monolayer MoS_2 are performed to probe the change of electronic band structure of MoS_2 after different metallic overlayer deposition.

A.J.S.'s STM measurements are supported by the US Department of Energy (DOE) under Award Number DE-SC0020334; P.V.L.'s and P.M.S.'s DFT and PPMS research is supported by the National Science Foundation (NSF) (Expanding Capacity in Quantum Information Science and Engineering (ExpandQISE)) under Grant Number 2328889; R.H. acknowledges support by the DOE Office of Science Grant No. DE-SC0020334 subaward S6535A for optical measurements of metal-MoS_2 heterostructures.

CC-07. Emergent topological Hall effect in twisted bilayer Fe_3GeTe_2 moiré system

Y. Li
Nankai University, Tianjin, China

The topological Hall effect is a powerful probe for investigating the topological properties of magnetic materials. This phenomenon typically arises in systems with broken global inversion symmetry, where Dzyaloshinskii-Moriya interactions stabilize such textures. Here, we report the discovery of an emergent giant topological Hall effect in the twisted Fe_3GeTe_2 metallic system, which preserves the general global inversion symmetry. This effect manifests exclusively within a narrow window of "magic" twist angles ranging from 0.35° to 0.75° while it is absent identically outside of that range. Micromagnetic simulations reveal that this topological Hall effect originates from a Skyrmion lattice induced by alternating in-plane and layer-contrasting Dzyaloshinskii-Moriya interactions. Our findings underscore twisted Fe_3GeTe_2 as a versatile platform for engineering and controlling topological magnetic textures in metallic twisted van der Waals magnets, opening brand-new avenues for next-generation spintronic devices.

[1] Hyuncheol Kim†, Kai-Xuan Zhang†, Yu-Hang Li†, *et. al.*, Emergent giant topological Hall effect in twisted Fe_3GeTe_2 metallic system. *Nat. Commun.* 17, 2931(2026).
[2] Yu-Hang Li and Ran Cheng, Moiré magnons in twisted bilayer magnets with collinear order, *Phys. Rev. B* 102, 094404(2020).

CC-08. Carrier-Type-Dependent Valley Polarization Switching in Monolayer WSe_2 via Single-Contact Electrostatic Doping

J. Siao[1], H. Lin[1], T. Lin[1], Y. Chu[1], M. Lin[1, 2, 3]
[1]Physics, National Taiwan University, Taipei, Taiwan, [2]Institute of Atomic and Molecular Sciences, Academia Sinica, Taipei, Taiwan, [3]Research Center for Applied Sciences, Academia Sinica, Taipei, Taiwan

In monolayer transition metal dichalcogenides (ML-TMDCs), strong spin–orbit coupling gives rise to spin–valley locking, enabling valley polarization (VP) as a key degree of freedom

for valleytronic applications, yet remains limited by intrinsic depolarization mechanisms, including long-range electron–hole exchange and phonon-assisted intervalley scattering. Here, we present a single-contact device architecture that enables enhanced electrostatic doping in ML-WSe_2[1]. Compared with conventional back-gate structures, the single-contact configuration exhibits significantly improved photoluminescence modulation and VP tunability, even under large excitation detuning. A high VP on/off ratio of ~7.5 is achieved at 8 K, while distinct polarization states persist up to 225 K, demonstrating strong thermal robustness. The observed polarization switching is attributed to carrier-type-dependent depolarization pathways involving exchange interaction and trion-mediated intervalley scattering. These results establish single-contact electrostatic control as an effective route for achieving high-contrast, reproducible, and thermally robust VP switching, providing a practical non-magnetic strategy for spin–valley state manipulation in two-dimensional materials.

[1] Siao, J.-Y.; Lin, H.-L.; Lin, T.-C.; Chu, Y.-H.; Lin, M.-T. ACS Applied Nano Materials 2025, 8, 7520–7529.

CC-09. Preferential Magnetic Domain Nucleation at Terrace Edges in Fe_3GaTe_2/V-doped WSe_2 heterostructures

J. Lee[1], J. Gu[1], W. Kim[1], J. Lee[3, 5], W. Chao[4], K. Lee[2], Z. Q. Qiu[5], M. Im[4], H. Han[1]

[1]Department of Materials Science and Engineering, Korea National University of Transportation, Chungju, Chungcheongbuk-do, Korea (the Republic of), [2]Department of Materials Science and Engineering, Ulsan National Institute of Science and Technology (UNIST), Ulsan, Ulsan, Korea (the Republic of), [3]Department of Physics, Kyungpook National University, Daegu, Daegu, Korea (the Republic of), [4]Center for X-ray Optics, Lawrence Berkeley National Laboratory (LBNL), Berkeley, California, United States, [5]Department of Physics, University of California, Berkeley, Berkeley, California, United States

Room-temperature van der Waals (vdW) magnets provide atomically clean interfaces without dangling bonds, enabling the formation of high-quality heterostructures with diverse materials and offering a promising platform for efficient spintronic devices such as magnetic magnetic tunnel junctions. [1,2] However, direct correlation between magnetic domain behavior and direct correlation in vdW heterostructures remain unveiled. In this work, when we fabricated a heterostructures composed of the room-temperature Fe_3GaTe_2 and Vanadium (V)-doped WSe_2 with different magnetic origins and anisotropies at room temperature. [3,4] On Si_3N_4 substrate, Fe_3GaTe_2 flakes is partially overlapped by V-doped WSe_2 flake. Through magnetic transmission X-ray microscopy, we directly observe magnetic domains in Fe_3GaTe_2/V-doped WSe_2 at the Fe L_3 absorption edge. We find that the domain width in the bare Fe_3GaTe_2 region is constant with that of the Fe_3GaTe_2/V-doped WSe_2 heterostructure, indicating that V-doped WSe_2 does not affect the magnetic domain of Fe_3GaTe_2 due to weak saturation magnetization. However, when the stripe domain is reduced and expanded with the magnetic field, the domain connected to the overlap boundary,. i.e. terrace-edge, remains stable even in stronger magnetic fields than the surrounding domain. That is, it shows that the terrace-edge plays a crucial role in the formation and annihilation of magnetic domains, offering enhanced stability of stripe domains in Fe_3GaTe_2. By performing micromagnetic simulations, at the terrace-edge, the magnetization is locally tilted and it leads to total magnetic energy, promoting domain nucleation. This work shows a direct correlation between structural boundaries and domain nucleation in vdW heterostructures, and shows that these structural features can be an effective pathway for magnetic domain nucleation. These findings provide a new pathway for a room temperature vdW magnet-based memory architecture.

[1] Z. Zhao, Y. Lin & A. Avsar, *npj 2D Materials and Applications,* 9,30 (2025)
[2] Q. Hao, H. Dai, M. Cai, *Advanced Electronic Materials,* 8,2200164 (2022)
[3] Z. Zhang, R. Sun & Z. Wang, *ACS Nano,* 19,187-228 (2025)
[4] J. Lee, J. Gu, W. Kim, *Advanced Functional Materials,* 36,e16597 (2026)

10:18 AM-10:45 AM
Break

CC-10. Multi-modal spin-orbit torque metrology applied to van der Waals heterostructures

T. Pham[1], S. Fekraoui[2], M. Dehaghani[2], S. Plissard[2], T. Blon[1], T. Guillet[1]

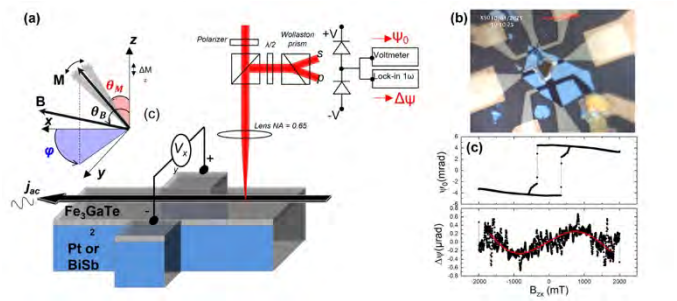
[1]LPCNO, Toulouse, France, [2]LAAS, Toulouse, France

Recent advances in spintronics have revolutionized magnetic random-access memory (MRAM) technologies, transitioning from spin-transfer torque MRAMs to spin-orbit torque (SOT) MRAMs for improved efficiency, scalability, and endurance [1]. SOT mechanisms rely on charge-to-spin conversion via the spin Hall effect in heavy metals or the

Rashba-Edelstein effect at interfaces, with spin-torque efficiency emerging as a critical metric for device optimization [2]. Topological insulators (TIs), with their robust spin-polarized surface states, have become key candidates for efficient SOT generation [3]. However, challenges such as bulk state interference and interfacial intermixing with 3d ferromagnetic layers limit their potential. Recent developments in van der Waals (vdW) heterostructures proposed to interface TIs with 2D ferromagnets [4], this have shown promise in preserving interfacial quality and enhancing spin-charge conversion. The large increase in Curie temperature in recently discovered vdW ferromagnet Fe_3GaTe_2 (T_c > 360K [5]) lifted the last barrier for this concept to be a room temperature application.

In this work, we developed a robust method to mechanically exfoliate and transfer 10- to 20 nm-thick Fe_3GaTe_2 flakes onto sputtered Pt/SiO_2 and MBE-grown $Bi_{1-x}Sb_x$/GaAs (111) TI thin films [6] by using a polymer-assisted pick-up technique in inert atmosphere. We report room temperature ferromagnetism in all measured samples as observed by anomalous Hall effect and Kerr microscopy measurement. In such systems, accurate SOT metrology using conventional techniques faces significant challenges arising from the very strong magnetic anisotropy of Fe_3GaTe_2 and the thermoelectric effects coming from $Bi_{1-x}Sb_x$. We developed a multi-modal technique to overcome those limitations by combining simultaneous harmonic Hall analysis and SOT-modulated Kerr microscopy. The association of both techniques allowed accurate and spurious-free SOT quantification.

[1] S. Bhatti, *et al., Mater. Today* 20, 530 (2017)
[2] A. Manchon *et al.*, *Rev. Mod. Phys.* 91, 035004 (2019)
[3] F. Bonell *et al., Nano Letters* 20, 5893 (2020)
[4] T. Guillet *et al.*, *Nano Lett 24, 822* (2024)
[5] G. Zhang *et al.*, *Nat Commun* 13, 5067 (2022)
[6] M. A. Khaled *et al.*, *ACS Appl. Electron. Mater. 2024,* 6, 5, 3771 (2024)



a) Simultaneous harmonic Hall analysis and SOT-modulated magneto-optical Kerr microscopy technique. b) Optical image of an encapsulated hBN/Fe_3GaTe_3/Pt Hall bar device. c) Characterization of the damping-like torque by SOT-MOKE at room temperature.

CC-11. Epitaxial Growth and Magnetic Ordering of Antiferromagnetic Topological Insulator $MnBi_2Te_4$ Thin Films

S. Choudhury[1], B. Sharif[1], R. E. Baumbach[1, 2], D. Lederman[1, 2]
[1]Department of Physics, University of California, Santa Cruz, Santa Cruz, California, United States, [2]Materials Science and Engineering Program, University of California, Santa Cruz, Santa Cruz, California, United States

$MnBi_2Te_4$ (MBT) is a prototypical antiferromagnetic topological insulator (AFMTI), that offers a platform to study emergent quantum phases where time-reversal symmetry is intrinsically broken. Here we report the molecular beam epitaxy growth of MBT thin films epitaxially grown on insulating Al_2O_3 (0001) substrates with a Bi_2Te_3 buffer layer. Streaky reflection high-energy electron diffraction (RHEED) patterns during deposition and X-ray diffraction measurements confirm smooth surfaces, high crystallinity, and well-defined layered ordering. This talk will present low-temperature magnetization measurements at T=2 K exhibit a primarily linear field dependence with a change in slope consistent with a spin-flop transition reported in bulk MBT single crystals. Low-temperature magnetotransport measurements further reveal clear signatures of antiferromagnetic ordering, spin-flop behavior, and weak anti-localization effects characteristic of topological surface states which disappear near the reported Neel temperature of the material. The dependence of these phenomena on the thickness of the films will also be discussed.

This work was supported by a University of California National Laboratory Fees Research Program grant (L25CR8980).

CC-12. Interfacial Spin–Orbit-Coupling Effects Probed by Spin Hall Magnetoresistance in Graphene/$IrMn_3$/Co Heterostructures

N. Do[1], S. Song[2], S. Park[2], C. Hwang[3], T. Kim[1]
[1]Physics, Ewha Womans University, Seoul, Korea (the Republic of), [2]Department of Physics, Pusan National University, Busan, Korea (the Republic of), [3]Korea Research Institute of Standards and Science, Daejeon, Korea (the Republic of)

Noncollinear antiferromagnets have recently attracted considerable interest due to their potential to host unconventional spin-dependent transport phenomena arising from complex magnetic textures and strong spin–orbit coupling (SOC) [1], [2]. In particular, $IrMn_3$ in the $L1_2$-ordered phase has been proposed as a promising platform for SOC-related effects [3], although experimental studies in the ultrathin limit remain challenging due to difficulties in achieving high crystalline quality and well-defined interfaces.

Here, we investigate interfacial SOC effects in graphene (Gr)/$IrMn_3$/Co heterostructures using spin Hall magnetoresistance (SMR) measurements. An ultrathin (~1.2 nm) $IrMn_3$ layer was grown on wafer-scale chemical vapor deposition (CVD) graphene via ultra-high vacuum molecular beam epitaxy (UHV-MBE), followed by the deposition of a Co overlayer for spin transport detection. Structural characterization confirms high crystalline quality and well-defined interfaces, enabling strong interfacial coupling. Low-temperature magnetotransport measurements reveal a pronounced SMR of approximately 0.5% at 1.5 K, with a clear angular dependence. The signal vanishes for in-plane magnetic fields but emerges when an out-of-plane component is introduced, highlighting the role of symmetry breaking and interfacial SOC. The observed behavior cannot be explained solely by conventional anisotropic magnetoresistance and is instead consistent with SMR arising from spin current reflection and absorption at the interface.

These results suggest that the ultrathin $IrMn_3$ layer enhances SOC-related transport effects in the adjacent Co layer through proximity-induced interfacial coupling. Furthermore, the coexistence of broken time-reversal symmetry, interfacial inversion asymmetry, and enhanced SOC indicates that this system may provide a promising platform for exploring non-reciprocal transport phenomena in future studies.

Overall, our work demonstrates that atomically thin, high-quality $IrMn_3$ can effectively modulate spin-dependent transport in graphene-based heterostructures and highlights the importance of interface engineering in antiferromagnetic spintronic devices.

[1] T. Jungwirth *et al.*, *Nature Nanotechnology*, vol. 11, p231–241 (2016).
[2] V. Baltz *et al.*, *Reviews of Modern Physics*, vol. 90, p015005, (2018).
[3] L. Smejkal *et al.*, *Nature Reviews Materials*, vol. 7, p482–496, (2022).

CC-13. Magnetic properties of epitaxial Fe_3Si/α-$FeGe_2$ multilayer films

M. Rovirola[1], A. Hernández-Mínguez[2], J. Herfort[2]
[1]University of Barcelona, Barcelona, Spain, [2]Paul-Drude-Institue for Solid State Electronics, Berlin, Germany

Recently, we have successfully synthesized at wafer-scale a metastable α-$FeGe_2$ layered phase using a combination of molecular beam epitaxy and solid-phase epitaxy down to only 4 nm in vertical trilayer stacks sandwiched between ferromagnetic Fe_3Si Heusler alloys [1]. Comprehensive X-ray diffraction and transmission electron microscopy (TEM) revealed the formation of the layered α-$FeGe_2$ allotrope (space group P4mm) which does not exist as a bulk [2]. *In situ* TEM experiments revealed the dynamics of the crystallization process, where the amorphous Ge first crystallizes to disordered $FeGe_2$ under the influence of Fe diffusion into the amorphous film and then it transforms into the ordered α-$FeGe_2$ phase [3]. Spin transport investigations have revealed a metallic behavior of α-$FeGe_2$ films [4]. Strikingly, the results also indicate a FM-AFM phase transition where the films are FM at low temperatures [4]. DFT calculations support this experimental result with a ferromagnetic ground state and an antiferromagnetic state with an only slightly different total energy [5].

In order to gain more information on the magnetization behavior, SQUID and ferromagnetic resonance (FMR) measurements on various Fe_3Si/α-$FeGe_2$/Fe_3Si multilayer films, a single layer Fe_3Si as well as on the bilayer system Fe_3Si/α-$FeGe_2$ all on GaAs(001) substrates were performed. The thickness of the α-$FeGe_2$ layer was varied between 4 and 8 nm. The results demonstrate a strong influence of the α-$FeGe_2$ layer on the magnetic properties of subjacent Fe_3Si already in the bilayer case. For the high-symmetry axis [010], the magnetization reversal takes place in two steps with a plateau at zero magnetization. The magnetization curves along the [110] and [-110] directions reveal magnetization reversals without intermediate steps. Low temperature FMR measurements show a splitting of the FMR signal around 5 GHz when the static magnetic field is

applied along the [-110] crystallographic direction, as well as periodic changes in the peak width at higher frequencies. These features are not observed for magnetic fields applied along the [110] direction, thus suggesting an anisotropic coupling between the magnetizations of Fe_3Si and α-$FeGe_2$ films.

(1) S. Gaucher *et al*., Appl. Phys. Lett. 110, 102103 (2017).
(2) B. Jenichen *et al*., Phys. Rev. Mat. 2, 051402(R) (2018).
(3) M. Terker *et al*., J. Phys. Chem. 125, 2779 (2021).
(4) D. Czubak *et al*., Phys. Rev. Mat. 4, 104415 (2020).

CC-14. Strain induced magnetic phase transitions in Fe_3GeTe_2 monolayer

A. Jyothi Bhasu[1], L. Szunyogh[1, 2], L. Rózsa[3, 1], L. Udvardi[1], L. Oroszlány[4], G. Martínez-Carracedo[5], J. Ferrer[5]
[1]Department of Theoretical Physics, Budapest University of Technology and Economics, Budapest, Hungary, [2]HUN-REN-BME Condensed Matter Research Group, Budapest University of Technology and Economics, Budapest, Hungary, [3]Wigner Research Centre of Physics, HUN-REN, Budapest, Hungary, [4]Department of Physics of Complex Systems, Eötvös Loránd University, Budapest, Hungary, [5]Departamento de Física, Universidad de Oviedo, Oviedo, Spain

Room-temperature ferromagnetism that remains robust at the nanoscale is a key requirement for next-generation spintronic and information-storage technologies. Using density-functional methods, we investigate monolayers of the vdW magnet Fe3GeTe2, which exhibits magnetic ordering under ambient conditions. We compute the magnetic interaction parameters using the torque formalism implemented in the GROGU package [1,2]. The magnetic phase diagram is mapped as a function of temperature and geometric distortions by means of Monte Carlo and spin-dynamics simulations. We find that a biaxial strain of ±2% tunes the Curie temperature over a wide range, from 150 K to 500 K. In addition, a conical spin-spiral ordering emerges in the Fe sublattices adjacent to the Te sites, while ferromagnetic ordering remains dominant in the central Fe–Ge layer. The corresponding phase transitions are governed by competing ferromagnetic and antiferromagnetic exchange interactions, as well as by Dzyaloshinskii–Moriya interactions, which stabilize a Néel-type ordering in the Fe sublattices near the Te sites.

[1] Gabriel Martínez-Carracedo *et al*., Pysical Review B 110, 184406 (2024)
https://doi.org/10.1103/PhysRevB.110.184406
[2] https://grogupy.readthedocs.io/en/stable/

CC-15. Controlling magnetism and transports via phase transition in Cr-Te films with intercalated van der Waals structures

S. Mori[1, 2], S. Hatayama[3], K. Hirata[1, 2], T. Hirai[2, 1], S. Takano[1, 2], F. Ando[2], Y. Nakanishi[1, 2], K. Uchida[1, 2]
[1]Department of Advanced Materials Science, Graduate School of Frontier Sciences, The University of Tokyo, Kashiwa, Japan, [2]Research Center for Magnetic and Spintronic Materials, National Institute for Materials Science (NIMS), Tsukuba, Japan, [3]Semiconductor Frontier Research Center, National Institute of Advanced Industrial Science and Technology (AIST), Tsukuba, Japan

Magnetic van der Waals (vdW) crystals have recently attracted considerable attention as a new class of low-dimensional magnet.[1-3] In these systems, the reduced dimensionality and weak interlayer coupling enable exceptional tunability of magnetic properties, highlighting their potential for next-generation spintronic applications. Among a variety of these materials, chromium telluride system ($Cr_{1+\delta}Te_2$), where δ is ranging from 0 to 1, forms a series of self-intercalated structures. Metastable $CrTe_2$ with vdW structures has been synthesized with a relatively high Curie temperature (T_C).[4] With an increase in Cr content, Cr atoms are intercalated in a vdW gap with structural transition, where their magnetic properties are dramatically tuned.[5] Such tunability of $Cr_{1+\delta}Te_2$ films is one of potential interests to design functional layered magnetic films. To address this issue, phase transition observed in chalcogenide materials is promising route to control physical properties.[6] Phase transition in magnetic thin films has been also studied to provide novel device concepts, including reconfigurable junctions in spintronic devices.[7] Here, we studied a change of magnetic properties of $Cr_{1+\delta}Te_2$ films by structural transition as schematically shown in Figure 1.

In this work, we investigate phase transition and physical properties of CrTe thin films via magnetron sputtering as highlighted in Figure 2. Transmission electron microscopy (TEM) images ensure a uniform CrTe film. Moreover, atomic images suggest that structural transition from a monoclinic into hexagonal symmetry occurs via annealing. The magnetic hysteresis curves at 50 K reveal that the as-deposited film exhibits larger magnetization than the post-annealed film, whereas the post-annealed film shows higher coercive field. Temperature dependence of magnetization indicates that T_C of the as-deposited film is much higher than the post-annealed film, ensuring clear contrasts of magnetic properties. These results indicate that structural

transition of CrTe with intercalated vdW structures are promising to develop reconfigurable spintronic applications.
1. C. Gong, L. Li, Z. Li *et al.*, *Nature*, Vol. 546, p.265–269 (2017).
2. B. Huang, G. Clark, E. Navarro-Moratalla *et al.*, *Nature*, Vol. 546, p.279–273 (2017).
3. K. S. Burch, D. Mandrus, J.-G. Park, *Nature*, Vol. 563, p.47–52 (2018).
4. X. Zhang, Q. Lu, W. Liu *et al.*, *Nat. Commun.* Vol. 12, p.2492 (2021).
5. Y. Wang, S. Kajihara, H. Matsuoka *et al.*, *Nano Lett.* Vol. 22, p.9964–9971 (2022).
6. M. Wuttig, N. Yamada, *Nat. Mater.* Vol. 6, p.824–832 (2007).
7. K. Nakagawa, T. Yokouchi, Y. Shiomi, *Sci. Rep.* Vol. 11, p.24216 (2021).

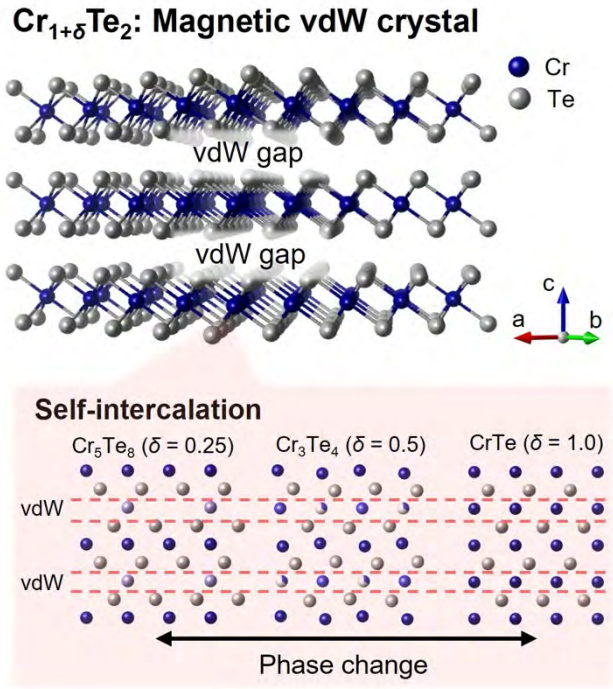


Fig. 1 Crystal structures of $Cr_{1+\delta}Te_2$ series.

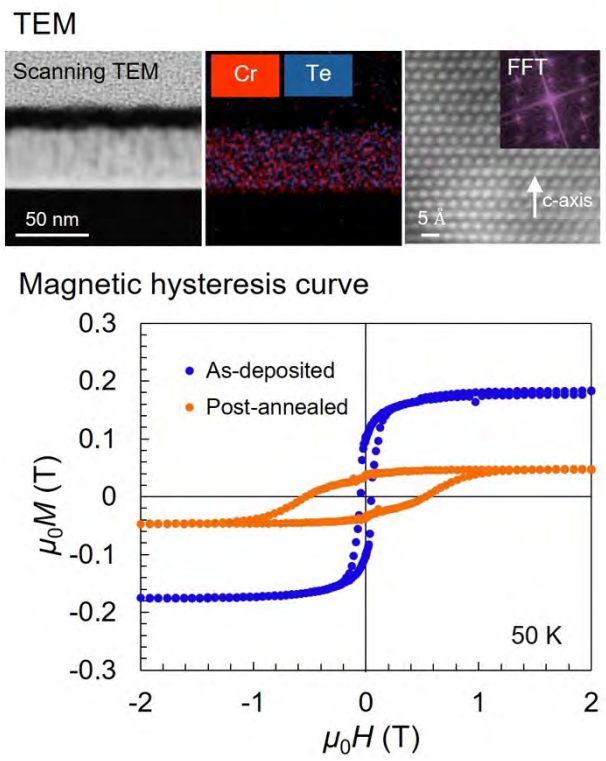


Fig. 2 Highlighted results for TEM observations and magnetic properties.

SESSION CD: BIOMAGNETISM AND BIOMEDICAL APPLICATIONS I

Chair(s): R. L. Hadimani, *Mechanical and Nuclear Engineering, Virginia Commonwealth University, Richmond, Virginia, United States*

Wednesday, November 4, 2026
08:30 AM-12:00 PM
Coral 2

CD-01. Enhanced Magnetic Performance of Anisotropic Iron and Iron Oxide Nanostructures for Advanced Biomedical Applications

F. Fernandez[1], S. Caspani[2], A. Cruz[1], M. Manso[1], D. Navas[3], C. Tavares de Sousa[1]
[1]Fisica Aplicada, Universidad Autonoma de Madrid, Madrid, (Seleccionar), Spain, [2]IFIMUP, Porto University, Porto, Portugal, [3]ICMM-CSIC, Madrid, (Seleccionar), Spain

Magnetic nanostructures have emerged as a highly promising class of materials for biomedical applications, offering unique capabilities in both therapeutics and diagnostics. Their response to external magnetic fields enables remote guidance, targeted drug delivery, and

localized heat generation for minimally invasive therapies, as well as enhanced imaging and sensing functionalities. In this work, we demonstrate that anisotropic iron and iron oxide nanostructures exhibit significantly improved magnetic performance compared to their isotropic counterparts, enabling more efficient control, actuation, and responsiveness in biomedical environments. By precisely tuning their shape, structural features, and surface chemistry, these nanomaterials show enhanced interactions with biological media, improved colloidal stability, and increased functional reliability. These findings highlight the critical role of structural anisotropy in optimizing magnetic behavior and underline the strong potential of engineered iron-based nanostructures to advance next-generation targeted therapies and magnetic-field-assisted biomedical technologies.

1. Magnetoplasmonic nanoparticles synthesized via laser ablation in liquids: photothermal efficiency and contrast agents for optical coherence tomography (OCT). SC Freitas, et. al. Applied Materials Today 48 (2026) 103119.
2. Anisotropic Porous Iron-Based Nanoparticles through Two-Step Hydrothermal and Hydrogen-Based Reduction: Enhanced Magnetic Performance for Potential Biomedical Applications, S Caspani, et. Al. ACS applied materials & interfaces 17 (2025), 16602-16615
3. DFT+ U+ V approach to Fe3O4 (001): Insights into surface chemistry and Cu2+ adsorption. N Naveas, et. Al. Results in Physics 70, (2025) 108158
4. Vortex Nanodiscs Functionalization to Overcome Macrophage Recognition for Efficient Theragnosis Applications. R Magalhães, et. Al. Advanced Engineering Materials 26 (2024), 2400369

CD-02. Bioengineered Magnetic Nanoparticles for Advanced Theranostics

U. Wiedwald
Faculty of Physics, University of Duisburg-Essen, Duisburg, Germany

Magnetic nanoparticles are invaluable for theranostics, integrating multiple diagnostic and therapeutic applications, such as targeted drug delivery, magnetic hyperthermia, and imaging. Mostly prepared ex vivo via wet chemical methods, their biocompatibility and solubility under physiological conditions require critical evaluation. A promising alternative is the use of biological nanocompartments for synthesis via biomineralization, enabling nanoparticles tailored for in vitro and in vivo applications while minimizing adverse effects. Naturally occurring nanocompartments like ferritin (diameter 8 nm) and encapsulin (diameter 30 nm) facilitate biomineralization of Fe and other 3d metal ions, forming Fe oxides, hydroxides, and ferrites with adjustable magnetic properties [1,2]. Their size and anisotropy can be tuned, though some exhibit reduced performance due to polycrystallinity and defects. We investigated ferritin-based and encapsulin-derived nanoparticles offering innovative strategies for precise magnetic remote control in biological systems. Grown in ferritin cages, nanoparticles enable controlled biomineralization. Doping of 7% Co for Fe enhances their magnetic blocking temperature from 35 K to 137 K and thus, improve inductive heating at radiofrequencies. We obtain a temperature rise of $\Delta T = 8$ K suitable for magnetic hyperthermia. Further, reversible spatial manipulation within cellular environments gets possible at high intracellular stability and traceability. We extract an attractive force of 0.5 fN in a droplet assay.
Similarly, encapsulin nanocompartments enable fully genetically controlled biomineralization of 30 nm iron oxide cores (Fig. 1), forming quasicrystalline structures with mixed para- and ferrimagnetic behavior. These nanoparticles generate magnetic moments (10^{-15} Am^2 per cell), comparable to conventional exogenous labels, facilitating magnetic-activated cell sorting (MACS) and precise cell manipulation. Their ability to enable magnetic control without external agents makes them valuable for advanced biomedical applications. The above synthesis strategies for biomineralized nanoparticles may also foster the understanding of endogenous magnetic nanoparticles in mammals, birds, or fish.

[1] A. Neusch, U. Wiedwald, I.P. Novoselova et al., *Nanoscale* 16, 15113 (2024).
[2] M. V. Efremova, U. Wiedwald, F. Sigmund et al., *Adv. Funct. Mater.* 35, 2418013 (2025).

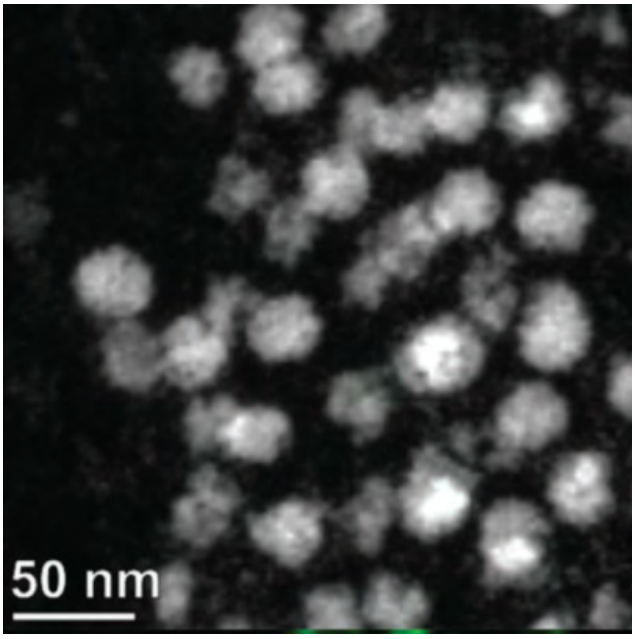


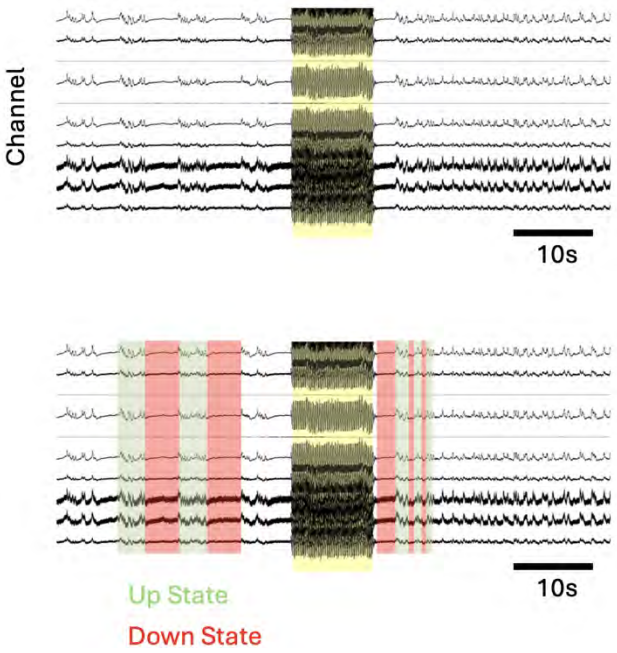
Figure 1. Dark field scanning transmission electron microscopy image of the generated 30 nm Fe oxide nanoparticles in encapsulin nanocompartments [2].

CD-03. Manganese-Substituted Cobalt Ferrite-Barium Titanate Magnetoelectric Core-Shell Nanoparticles Enable Low-Threshold Neural Stimulation In Vivo

A. Vezzoni[1], E. Zhang[1], E. Bondan[1], M. Accursi[1], A. Suarez-Perez[2], J. Merino-Martinez[2], C. Franco[1], S. Pané[1]
[1]MAVT, ETH Zurich, Zürich, Switzerland, [2]Institut d'Investigacions Biomèdiques Pi i Sunyer, Barcelona, Spain

Magnetoelectric nanoparticles (MENPs) have emerged as a promising solution for minimally invasive neural stimulation, enabling wireless neuronal activation through externally applied magnetic fields. While cobalt ferrite-barium titanate (CFO-BTO) core-shell nanoparticles (NPs) are the most widely used combination for this purpose, their activation requires relatively high magnetic field amplitudes to obtain maximum magnetoelectric (ME) response, due to the large coercivity of such composites. Here we introduce manganese substitution into the CFO core, whereby 30% of Co ions are replaced by Mn. This compositional modification alters the crystal structure and consequently the magnetic properties, enhancing the magnetostrictive response at low magnetic fields. We demonstrate that the resulting $Mn_{0.3}Co_{0.7}Fe_2O_4$-BTO (Mn-CFO-BTO) NPs achieve neural activation in vivo at a lower magnetic field threshold than their undoped CFO-BTO counterparts, representing a significant step towards safer and more efficient MENP-based neurostimulation. Both CFO-BTO and Mn-CFO-BTO MENPs were successfully synthesized, showing favorable structural and magnetic properties. Relative to pure CFO, the Mn-CFO core shows higher saturation magnetization and reduced coercivity, with these properties largely retained after BTO shell coating. Both were surface-functionalized with PEG for biocompatibility and evaluated in vivo in a murine model. In vivo experiments show that Mn-CFO-BTO MENPs successfully stimulate neural activity at significantly lower magnetic field amplitudes compared to CFO-BTO. This is consistent with the known shift of the magnetostriction peak to lower magnetic fields upon Mn substitution, enhancing the low-field magnetomechanical response and ME energy conversion efficiency. These findings highlight the potential of compositional tuning of the ferrite core as a strategy to minimize magnetic field exposure in MENP-based neural stimulation, a critical requirement for microrobotic and translational applications where field attenuation through tissue and biological safety limits constrain the amplitude of externally applied fields.

1. K. Yue, R. Guduru, J. Hong, PLoS ONE 7(9) (2012)
2. S. D. Bhame and P. A. Joy, Journal of Physics D: Applied Physics, Vol. 40, Number 11 (2007)
3. W. S. Sarifuddin, Utari, B. Purnama, AIP Conf. Proc. 27 (2019)
4. S. M. Ansari, A. Younis, Y. D. Kolekar, Appl. Phys. Rev. 12 (2) (2025)
5. T. Nguyen, J. Gao, P. Wang, Neurotherapeutics, Vol. 18, p. 2091 (2021)
6. E. Zhang, M. Abdel-Mottaleb, P. Liang, Brain Stimulation, Vol. 15, p. 1451 (2022)
7. E. Zhang, M. Shotbolt, C.Y. Chang, Brain Stimulation, Vol. 17, p. 1005 (2024)
8. T. Jordan, M.A. O'Brien, C.P. Spatarelu, ACS Applied Nano Materials 3 (3) (2020)



Neural recordings during MENP-based stimulation (yellow) in vivo, with up and down states indicated.

CD-04. Magnetophoretic Cell Separation Using Additively Manufactured Magnetic Nanoink Structures

D. M. Phan[1], L. Nguyen T. Tran[1], B. Rezaei[2], R. Vera[1], S. Boswell[1], N. Paul[1], H. Hridoy[1], H. Wang[2], S. Mostufa[2], K. Wu[2], M. Zeng[1], J. Yang[3], Y. Eo[4], J. Gomez-Pastora[1]

[1]Chemical Engineering, Texas Tech University, Lubbock, Texas, United States, [2]Electrical & Computer Engineering, Texas Tech University, Lubbock, Texas, United States, [3]Mechanical Engineering, Texas Tech University, Lubbock, Texas, United States, [4]Physics, Texas Tech University, Lubbock, Texas, United States

Cell fractionation separates cells based on physicochemical differences, and magnetic manipulation enables a non-contact, non-invasive control of particles and cells in microfluidic systems [1]. In this research, label-free magnetophoresis enabled by additive manufactured magnetic nanoink-based devices is employed to fractionate cells into different fractions relying on differences in magnetic susceptibility. This technique allows separation of certain cell populations with distinct magnetic susceptibility without the need for antibody labeling or exogenous magnetic tags. This reduces sample preparation steps, minimizing biological perturbation, and preserving native cellular functionalities.

In this work, Fe_3O_4 magnetic nanoparticles (MNPs) are formulated into printable inks and deposited using direct ink writing (DIW), with a polymer matrix structural binder. During curing, the nanoparticle dipole alignment is locked using magnetic fields, forming a magnetically responsive composite film. The DIW process enables precise control of film geometry, allowing customizable structures to be seamlessly integrated with microfluidic devices [2]. Once cured, the fixed dipole alignment generates strong localized magnetic field gradients when exposed to a constant field from an adjacent permanent magnet. The fabricated devices are characterized using vibrating sample magnetometry (VSM), X-ray diffraction (XRD) for phase identification, and scanning electron microscopy (SEM) to assess post-printing particle alignment. The printed films are further modeled in COMSOL Multiphysics to quantify the resulting magnetic force fields. Following model validation, magnetic field gradients will be systematically analyzed, alongside demonstration of magnetophoretic separation of RBC subpopulations based on intrinsic magnetic susceptibility differences. Alternative magnetic nanoparticle systems, including Fe_4N, will be explored to further enhance magnetic responsiveness and separation efficiency. Integrated within microfluidic channels, these films are expected to generate even higher localized field gradients. Ongoing efforts focus on modeling this platform for RBC separation based on intrinsic magnetic susceptibility and iron content.

[1] Q. A. Pankhurst, J. Connolly, S. K. Jones, and J. Dobson, "Applications of magnetic nanoparticles in biomedicine," *J. Phys. Appl. Phys.*, vol. 36, no. 13, pp. R167–R181, Jul. 2003, doi: 10.1088/0022-3727/36/13/201.

[2] Y. Yin *et al.*, "Nanoscale 3D Printing for Empowering Future Nanodevices," *Adv. Mater. Technol.*, vol. 10, no. 14, p. 2500083, Jul. 2025, doi: 10.1002/admt.202500083.

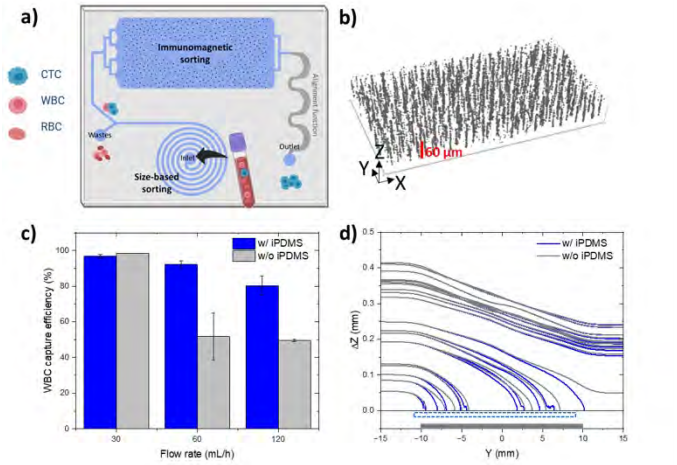
CD-05. Two-stage microfluidic CTC isolation using self-assembled ferromagnetic microstructures

D. Le Roy[1], E. Dupont[1, 2], L. Artinyan[2], C. Brunin[3], M. Piecyk[3], L. Payen[3], A. Deman[2]

[1]Universite Lyon 1, CNRS, Institut Lumière Matière, UMR5306, Villeurbanne, France, [2]Université Lyon 1, CNRS, INSA Lyon, Ecole Centrale de Lyon, CPE Lyon, INL, UMR5270, Villeurbanne, France, [3]Laboratoire de Biochimie Et Biologie Moléculaire, Groupe Hospitalier Sud, Hospices Civils de Lyon, Pierre Bénite, France

The isolation of circulating tumor cells (CTCs) from blood remains challenging due to their extremely low concentration and the strong overlap of physical properties

with white blood cells (WBCs). To address this, we propose a two-stage microfluidic sorting strategy combining size-based pre-enrichment and immunomagnetic separation within a single platform (figure a).
First, a spiral microchannel exploiting Dean vortices enables size-dependent lateral migration. By optimizing channel geometry and flow conditions, efficient pre-enrichment was achieved, allowing separation between WBCs and CTC-like cells at flow rates up to 50 mL/h, compatible with downstream processing. [1]
In the second stage, we introduce a composite PDMS membrane embedding self-organized chains of ferromagnetic particles that generate strong and localized magnetic field gradients (figure b). [2,3] These structured membranes significantly increase the trapping forces exerted on magnetically labeled WBCs, thus enhancing the purification of CTC, over a wide range of flow rates (figure c).
To support and interpret these experimental results, we developed a numerical approach to compute the trajectories of nanoparticle–WBC complexes within the magnetic landscape. The model incorporates magnetic forces, hydrodynamic drag, and flow profiles, enabling prediction of capture efficiency and identification of key parameters governing trapping performance (figure d).
This combined experimental and numerical study demonstrates that this two-stage microfluidic architecture provides a powerful route toward high-throughput, high-purity CTC isolation.
[1] Dupont, E., Artinyan, L., Brunin, C. et al. Effective dean vortex separation at reduced flow rates towards rare cell sorting. Sci Rep 16, 10422 (2026). DOI : 10.1038/s41598-026-40845-4
[2] Descamps, L., Garcia, J., Barthélémy, D., et al, MagPure chip: an immunomagnetic-based microfluidic device for high purification of circulating tumor cells from liquid biopsies. Lab Chip 22, 4151-4166 (2022). DOI : 10.1039/D2LC00443G
[3] Mekkaoui, S., Descamps, L., Audry, M.-C., et al., Nanonewton Magnetophoretic Microtrap Array for Microsystems. Langmuir 6 (48), 14546-14553 (2020). DOI: 10.1021/acs.langmuir.0c02254



(a) Schematic of the two-stage microfluidic sorting device. (b) X-ray tomography of the composite PDMS membrane (iPDMS) with self-assembled ferromagnetic columns (~60 μm). (c) Magnetically labeled WBC capture efficiency versus flow rate, with and without iPDMS. (d) Computed NP–WBC trajectories in the immunomagnetic chamber. Dark grey and blue dashed rectangles indicate the positions of the magnet array and iPDMS membrane, respectively.

CD-06. Viscosity Dependence of Heating Efficiency in High-Efficiency Pulsed-Field Magnetic Hyperthermia

S. Takamatsu, A. Kuwahata, Y. Fukuoka, S. Yabukami
Tohoku University, Sendai, Japan

Pulsed magnetic fields have emerged as an effective approach for enhancing heating efficiency in magnetic hyperthermia (MH)[1,2] using magnetic nanoparticles (MNPs). While their superior performance compared to conventional sinusoidal fields has been reported[3-5], the heating efficiency under viscosity conditions comparable to biological environments remains unclear. Since viscosity significantly affects the dynamic response of MNPs, understanding its role is essential for practical applications. In this study, we investigate the viscosity dependence of heating efficiency under pulsed magnetic fields with pulse widths ranging from 0.7 to 4.0 μs, using samples with controlled nanoparticle concentrations and viscosities. Figure 1 shows various pulse waveforms generated by the developed pulse generator, and measured magnetization, Fourier analysis, and their hysteresis loops. By adjusting the L and C components of the pulse circuit, it is possible to generate magnetic fields with pulse widths ranging from 0.7 to 4.0 μs.（Fig. 1(a)）. The smaller the pulse width, the

greater the harmonic content in the high-frequency range, and the larger the area of the hysteresis loop (Fig. 1(b, c)). These results indicate that heating efficiency improves as the pulse width decreases. Figure 2 shows the viscosity dependence of the hysteresis loop. 1.5 mPa s represents the viscosity of MNPs themselves, while 8 mPa s simulates the biological environment; we also conducted a quantitative evaluation at MNPs concentrations of x1 and x2. At higher frequencies, the difference in viscosity is smaller. Going forward, we will develop a new pulsed magnetic field circuit and proceed with the optimization of the pulsed magnetic field waveform to achieve even higher-efficiency magnetic heating. Our results provide insight into optimizing heating efficiency under biologically relevant conditions.

[1] D. Chang *et al.*, *Frontiers Media S.A.* Aug. 02, 2018.
[2] A. Kuwahata *et al.*, *Sci Rep*, Dec. 2025.
[3] A. Kuwahata *et al.*, *AIP Adv*, Feb. 2023.
[4] Y. Adachi *et al.*, *AIP Adv*, Jan. 2024.
[5] P. Allia *et al.*, *Phys Rev Appl*, Sep. 2019.

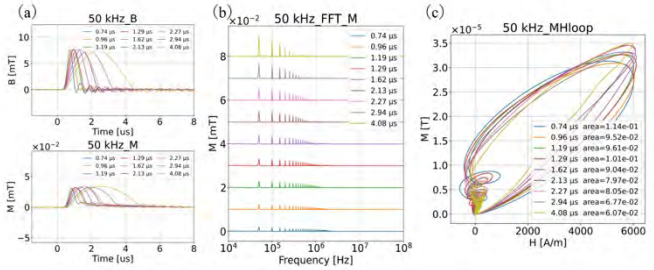
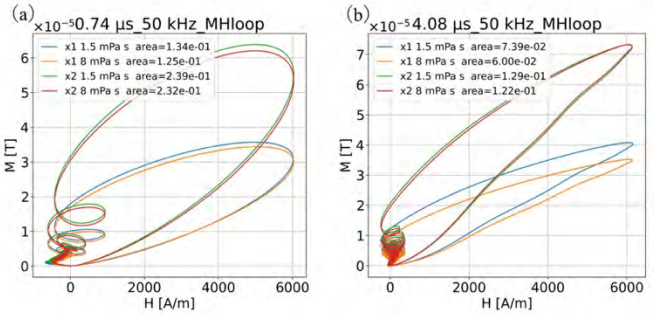


Fig. 1, Measured pulse waveforms: (a) Applied magnetic field B and magnetization M (pulse width: 0.74 µs to 4.08 µs). (b) Fourier analysis of M. (c) Hysteresis loop.



Viscosity dependence of the hysteresis loop: Hysteresis loops of samples with 1.5 and 8 mPa s using x1 and x2 MNPs: pulse width (a) 0.74 µs, (b) 4.08 µs.

CD-07. Magnetic Disk Particles for Hyperthermia, Imaging and directional Biosensing

H. J. Hug[1, 2], E. Mayr[1, 3, 4], J. Ackers[5], H. Wei[5], S. Helbig[6], S. Koraltan[7], M. Krupinski[8], D. Suess[6], M. Graeser[9], I. K. Herrmann[3, 4]

[1]Magnetic and Functional Thin Films, Empa, Duebendorf, Switzerland, [2]Department of Physics, University of Basel, Basel, Switzerland, [3]Department of Mechanical and Process Engineering, ETH Zurich, Zurich, Switzerland, [4]Ingenuity Lab, Balgrist University Hospital and University of Zurich, Zurich, Switzerland, [5]Fraunhofer Research Institution for Individualized and Cell-Based Medical Engineering, Fraunhofer IMTE, Luebeck, Germany, [6]Physics of Functional Materials, University of Vienna, Vienna, Austria, [7]Department of Physics, Technical University Vienna, Vienna, Austria, [8]Institute of Nuclear Physics Polish Academy of Sciences, Krakov, Poland, [9]University Rostock,, Rostock, Germany

Magnetic nanoparticles for biomedical applications are largely limited by the intrinsic constraints of superparamagnetic iron oxide nanoparticles (SPIONs), including low saturation magnetization and restricted tunability. We demonstrate that top-down fabricated magnetic disk particles (MDPs) overcome these limitations by enabling precise control of magnetic architecture, anisotropy, and coupling .

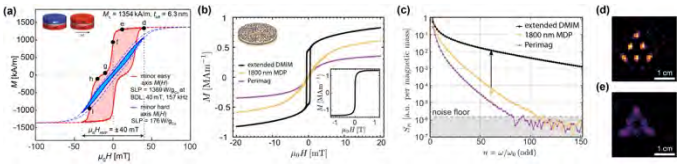
Synthetic antiferromagnetic MDPs (SAF-MDPs) are engineered for sharp field-driven switching and maximize hysteretic losses under clinically relevant alternating fields, achieving heating efficiencies approaching fundamental limits. Superferromagnetic MDPs (SF-MDPs) exhibit steep low-field responses and enhanced higher harmonics, enabling significantly improved sensitivity and spatial resolution in magnetic particle imaging compared to state-of-the-art tracers .

Beyond therapy and imaging, the disk geometry enables a unique directional biosensing concept. MDPs immobilized in an aligned gel show suppressed rotational dynamics and anisotropic magnetic particle spectroscopy (MPS) signals. Upon bacterial or enzymatic degradation of the matrix, rotational freedom is restored, producing an isotropic MPS response independent of excitation direction. This provides a robust, label-free readout of biological activity.

These results establish MDPs as a multifunctional platform combining near-limit hyperthermia, enhanced MPI performance, and sensing capabilities not accessible to conventional nanoparticles.

[1] S. Scheibler, et al, “Approaching the physical limits of specific absorption rate for synthetic antiferromagnetic

nanodisks in hyperthermia applications," Biomaterials Science, vol. 13, no. 22, pp. 6285–6297, 2025.
[2] E. M. Mayr, et al. "Superferromagnetic Disk Particles for Magnetic Particle Imaging," Small Methods, 2025.



(a) M(H) loop of an optimized synthetic antiferromagnetic magnetic disk particle (SAF-MDP) obtained from vibrating-sample magnetometry (VSM) measurements with large hysteretic loss. (c) Hysteresis loops measured for superferromagnetic, discontinuous metal–insulator multilayer (DMIM) extended film (black), 1800nm superferromagnetic disk particles (SF-MDP) patterned from the same multilayer (orange), and Perimag nanoparticles (blue). (c) Corresponding higher-harmonic magnetic particle spectra. (d), (e) Magnetic particle imaging (MPI) images obtained using SF-MDPs (d) and Perimag nanoparticles (e).

CD-08. Latest Strategies in the Synthesis, Characterization, and Deployment of Chiral Magnetic Nanoparticles in Cancer Treatment

A. S. Poulo, M. Khandaker, T. Lamichhane
Engineering & Physics, University of Central Oklahoma, Edmond, Oklahoma, United States

Chiral magnetic nanoparticles (CMNPs) are emerging as multifunctional platforms for cancer theranostics, where structural and surface chirality introduce a tunable degree of freedom in magnetic response, nano–bio interactions, and magneto-optical activity [1,2]. Recent synthesis strategies combine scalable iron-oxide or doped ferrite cores with enantioselective ligands (e.g., amino acids, peptides, and chiral polymers), alongside hierarchical nanoarchitectures such as clusters and core–shell systems. These approaches enhance magnetic anisotropy, specific absorption rate (SAR), and imaging contrast while preserving physiological stability [1,3].
Advances in characterization are shifting from ensemble-averaged measurements to single-particle and multimodal techniques that directly correlate nanoscale magnetization with chiroptical response and heat generation [2,4]. In particular, photothermal magnetic circular dichroism (MCD) enables discrimination of intrinsic chirality from optical artifacts, providing a direct link between magnetization dynamics and heating efficiency [2,4].
In this work, we will also present the synthesis of L-histidine-based chiral magnetic nanoparticles, followed by comprehensive structural, magnetic, and chiroptical characterization. Their magnetic hyperthermia performance will be evaluated to assess heating efficiency and biocompatibility, with the goal of advancing toward in vivo validation using mouse models.
Clinically, CMNPs are enabling imaging-guided precision magnetic hyperthermia, where real-time biodistribution informs spatially controlled thermal dosing to maximize tumor selectivity and minimize off-target effects [3,5]. Collectively, the integration of chirality engineering with advanced magnetic metrology positions CMNPs as a next-generation platform for targeted, image-guided cancer therapy.

1. Batlle X, Moya C, Escoda-Torroella M, Iglesias Ò, Fraile Rodríguez A, Labarta A. *Magnetic nanoparticles: From the nanostructure to the physical properties.* J Magn Magn Mater. 2022;543:168594. doi:10.1016/j.jmmm.2021.168594.

2. Adhikari S, Efremova MV, Spaeth P, Koopmans B, Lavrijsen R, Orrit M. *Single-Particle Photothermal Circular Dichroism and Photothermal Magnetic Circular Dichroism Microscopy.* Nano Lett. 2024;24(17):5093–5103. doi:10.1021/acs.nanolett.4c00448.

3. Patrick PS, Stuckey DJ, Zhu H, Kalber TL, Iftikhar H, Southern P, et al. *Improved tumour delivery of iron oxide nanoparticles for magnetic hyperthermia therapy of melanoma via ultrasound guidance and 111In SPECT quantification.* Nanoscale. 2024;16:19715–19729. doi:10.1039/D4NR00240G.

4. Spaeth P, Adhikari S, Lahabi K, Baaske MD, Wang Y, Orrit M. *Imaging the Magnetization of Single Magnetite Nanoparticle Clusters via Photothermal Circular Dichroism.* Nano Lett. 2022;22(9):3645–3650. doi:10.1021/acs.nanolett.2c00178.

5. Shakeri-Zadeh A, Bulte JWM. *Imaging-guided precision hyperthermia with magnetic nanoparticles.* Nat Rev Bioeng. 2025;3(3):245–260. doi:10.1038/s44222-024-00257-3.

CD-09. Investigating Effects of Magnetostatic Offsets on Hysteresis for Spatially Selective Heating of Magnetite Nanoparticles

X. Smith[1], S. Lee[2], D. Bono[2], J. Beckham[4], M. Christiansen[3], P. Anikeeva[2]
[1]Electrical Engineering and Computer Science, Massachusetts Institute of Technology, Cambridge, Massachusetts, United States, [2]Department of Materials Science, Massachusetts Institute of Technology, Cambridge, Massachusetts, United States, [3]ETH Zurich, Zurich, Switzerland, [4]Research Laboratory of Electronics, Massachusetts Institute of Technology, Cambridge, Massachusetts, United States

The use of single-domain, 10 – 30 nm magnetite nanoparticles as heating agents in the presence of alternating magnetic fields has been previously demonstrated for minimally invasive in vivo control of biological signaling. While engineering magnetic and surface properties of nanoparticles for spatially localized heating is possible, constructing the magnetic instrumentation becomes impractical for many independent targets. It has been previously shown that spatially-varying offset fields (selection field) can localize targeting through suppression of magnetization reversal and hysteretic heating outside a "zero-point", proving to be an attractive alternative strategy. However, the influence of the magnitude and direction of a static offset field on the hysteresis loop area, and spatial distribution of heating in the presence of a selection field has not yet been adequately studied. This work investigates how the coercive field, area of the hysteresis loop, and specific loss power changes as a function of a static offset field. We employ in-plane and out-of-plane magnetostatic fields with respect to an alternating magnetic field, and an accompanying magnetometer to record the hysteresis loops of synthetic, monodisperse, 14-25 nm magnetite nanoparticles. We then define the spatial heating resolution using a selection field for spatially selective targeting. A 3-dimensional Halbach geometry is used to generate a selection field, where the "zero-point" is linearly displaced with offset fields permitting spatially selective heating. Our findings reveal that magnetostatic offset fields can cause asymmetrically distorted hysteresis loops with nonzero area, where the heat suppression depends on their direction. These results are shown to be consistent with a dynamic hysteresis model based on uniaxial anisotropy. We find that the spatial resolution of heat in a selection field depends on anisotropy energy and alternating magnetic field conditions. This work experimentally corroborates the merit of a selection field for localized heating, critical quantitative information guiding the design of apparatuses intended for spatially selective, heat-driven biological signaling.

CD-10. In Vitro Magnetic Hyperthermia of Mn–Zn Ferrite Nanoparticles: Influence of Particle Size and Ultrasound

E. Jaberolansar[1], T. Afsari[2], S. Mohapatra[2, 3], S. Mohapatra[4, 3], H. Srikanth[1]
[1]Physics, University of South Florida, Tampa, Florida, United States, [2]Internal Medicine, Morsani College of Medicine,, University of South Florida, Tampa, Florida, United States, [3]Research Service, James A., Haley Veterans Hospital, Tampa, Florida, United States, [4]Molecular Medicine, Morsani college of Medicine, University of South Florida, Tampa, Florida, United States

Magnetic hyperthermia using superparamagnetic nanoparticles is a promising approach for localized cancer treatment; however, its efficiency is often limited by insufficient cellular internalization and suboptimal heat generation at the target site [1]. In this work, we synthesize superparamagnetic Mn–Zn ferrite nanoparticles with controlled size variations and investigate their magnetic heating performance under an alternating magnetic field (AMF). Particular attention is given to the relationship between particle size and heating efficiency, as well as the potential of low-intensity pulsed ultrasound (LIPUS) as a non-invasive method to enhance nanoparticle uptake [2] and improve overall hyperthermia performance.
The Mn–Zn ferrite nanoparticles were synthesized via a thermal decomposition method, allowing precise control over particle size and uniformity. The nanoparticles were characterized in terms of structural and magnetic properties, and their heating efficiency was evaluated by measuring temperature rise under AMF exposure. In vitro experiments were conducted to assess the effectiveness of nanoparticle-mediated hyperthermia. Cell viability measurements were performed before and after treatment to quantify the therapeutic effect, while the influence of ultrasound was investigated to determine its role in enhancing nanoparticle internalization and heat generation.
Preliminary results indicate a size-dependent heating behavior of Mn–Zn ferrite nanoparticles, with ultrasound-assisted treatment showing potential to further enhance hyperthermia efficiency by increasing intracellular nanoparticle uptake. This study highlights a combined magnetic and acoustic approach for improving nanoparticle-based hyperthermia and provides a framework for optimizing material properties and treatment conditions to

achieve enhanced in vitro performance.
1. Lavorato, G.C., et al., *Hybrid magnetic nanoparticles as efficient nanoheaters in biomedical applications*. Nanoscale Advances, 2021. 3(4): p. 867–888.
2. Georgeous, J., et al., *Review of gold nanoparticles: synthesis, properties, shapes, cellular uptake, targeting, release mechanisms and applications in drug delivery and therapy*. Pharmaceutics, 2024. 16(10): p. 1332.

CD-11. Magneto-Mechanical Driven Nanomagnets for Cancer Therapy: Bypassing Hyperthermia

A. El-Gendy
Physics, University of Texas at El Paso, El Paso, Texas, United States

This presentation offers a comprehensive overview of the extensive body of research accumulated over several decades in the field of magnetic hyperthermia as a modality for cancer treatment. Despite the significant investment of time, resources, and scientific effort, this promising field has yet to produce a single successful clinical trial, a sobering reality that demands serious reflection and a fundamental reassessment of current approaches. The persistent failure to translate laboratory findings into clinically viable therapies can be largely attributed to a critical gap in understanding: the precise mechanisms by which tumor cells are destroyed when magnetic nanoparticles are subjected to an applied alternating magnetic field (AMF). Without a clear and validated mechanistic framework, the optimization of treatment parameters has remained largely empirical, limiting the field's ability to design effective, reproducible, and safe therapeutic protocols.
Against this backdrop, the presentation introduces the speaker's recent and ongoing research efforts, which are specifically aimed at confronting these long-standing challenges head-on. By rigorously investigating the biophysical and biochemical interactions that govern nanoparticle behavior under AMF conditions, the speaker's work seeks to lay the scientific groundwork necessary for AMF-driven magnetic nanoparticles to finally meet the stringent requirements of clinical cancer therapy. This work speaks directly to unresolved questions at the intersection of materials science, biomedical engineering, and oncology. The speaker will present a forward-looking perspective on what the field has overlooked, what foundational knowledge is still lacking, and what experimental and theoretical advances are needed to achieve reliable, non-thermal cancer cell death under AMF, moving beyond hyperthermia toward a broader and more mechanistically grounded therapeutic paradigm.

SESSION CE: MAGNETIC SENSORS AND HIGH-FREQUENCY DEVICES

Chair(s): S. Yabukami, *Tohoku University, Sendai, Miyagi, Japan*
Wednesday, November 4, 2026
08:30 AM-12:00 PM
South Pacific 1/2

CE-01. From Skyrmion Stacks to Ultrasensitive Magnetic Field Sensor

L. Malucelli[1], A. Arredondo-López[1], M. Caseiro[2], E. Yildiz[1], I. Joumard[1], N. Mollard[1], S. Auffret[1], J. Faure-Vincent[1], G. Gaudin[1], B. Dieny[1], C. Baraduc[1], L. Ranno[3], J. Kammerer[4], C. Fermon[2], A. Solignac[2], M. Pannetier-Lecoeur[2], J. Fischer[1], H. Béa[1, 5]
[1]Univ. Grenoble Alpes, CNRS, CEA, SPINTEC, Grenoble, France, [2]Université Paris-Saclay, CEA, CNRS, SPEC, Gif-sur-Yvette, France, [3]Institut Néel, Univ. Grenoble Alpes, CNRS, Grenoble, France, [4]ICube, University of Strasbourg, Strasbourg, France, [5]Institut Universitaire de France (IUF), Paris, France

Magnetic skyrmions are chiral spin textures arising from an antisymmetric exchange interaction, called Dzyaloshinskii-Moriya Interaction (DMI). Skyrmions behave as quasiparticles, they can be manipulated by electrical currents and can be used as data bits. They are usually envisaged for memory, logic, and neuromorphic computing applications [1]. In Ta/FeCoB/TaOx trilayers, we have shown that the skyrmions can be stabilized by fine-tuning material deposition conditions [2] and recently observed a DMI chirality reversal with ferromagnetic thickness that we explained by strain effects [3]. Local and individual manipulation of skyrmions was also managed by applying a gate voltage: their stability was tuned [4] as well as the direction of their motion under a current [5]. This latter effect is due the gate voltage induced reversible chirality change linked to the sign inversion of the interfacial DMI coefficient, driven by oxygen ion migration under gate voltage. This individual control of skyrmions, allowed by the use of a gate voltage, was mainly aimed at developing devices using the quasiparticle nature of skyrmions, i.e. for computing functions.

Furthermore, our optimized skyrmion layers exhibit an ultrasensitive, linear and hysteresis-free magnetic response to out-of-plane fields, making them extremely promising for advanced sensing applications. In fact, combining miniaturization and sensitivity to weak out-of-plane fields remains challenging, e.g. for biomedical and space uses [6], even for spintronics based magnetic sensors that present the advantages of a small size, a low power consumption and a high sensitivity.

Here, we took the opportunity to use this versatile skyrmion platform for sensing purposes. We will present the integration of such linear and highly sensitive skyrmion layers in an out-of-plane sensor as well as its sensing performances. The response of such skyrmion layer to magnetic field is shown in Fig. 1: Magneto-Optical Kerr Effect (MOKE) microscopy allows to image the magnetic texture while measuring the response loop (green curve). From saturation, increasing the field induces skyrmions, then stripes, then skyrmions again before saturation in the opposite direction, with no hysteresis. The ultralow saturation field (± 0.25 mT) implies a high-potential for weak field sensing applications.

The film is patterned into a 100 × 100 μm^2 Hall-bar cross for anomalous Hall effect detection. A linear Hall response is obtained (black curve in Fig. 1) below the saturation field, that superimposes with the MOKE response. Further characterizations show that sensitivity, ie. the variation of output signal per magnetic field, decreases with increasing bias current (Fig. 2a). This is likely due to Joule heating and reduced anisotropy. For sensor development, the noise is also a critical value that should be minimized to be able to measure ultralow fields. Noise has thus been measured (Fig. 2b), and it shows an increase at low bias, as expected [7], but a decrease above 4 mA, which is also likely due to Joule heating and anisotropy changes in the system. Combining both by taking the ratio of the noise over the sensitivity yields to a detectivity - the lower measurable field - as low as ~1 nT/√Hz at 7–10 mA input current (Fig. 2c), comparable to state-of-the-art anomalous Hall effect based devices [8]. These results highlight the potential of skyrmion-hosting Ta/FeCoB/TaOx trilayers as ultrasensitive out-of-plane magnetic field sensors. Ongoing work focuses on improving detectivity and linking it to magnetic texture dynamics and modifications under the biasing current.

[1] A. Fert et al., Nat Rev Mater 2 (2017), 17031
[2] T. Srivastava et al., PRB 100 (2019), 220401
[3] C. Gueneau et al., PRB 113 (2026), 054416
[4] M. Schott et al., Nano Lett.17 (2017), 3006–3012
[5] C.-E. Fillion et al., Nat. Commun. 13 (2022), 5257
[6] P. P. Freitas et al., Proc. IEEE 104 (2016), 1894-1918
[7] K. Wang et al., PRB 108 (2023), 094431-11
[8] X. Liu et a., AIP Advances 14 (2024), 105210

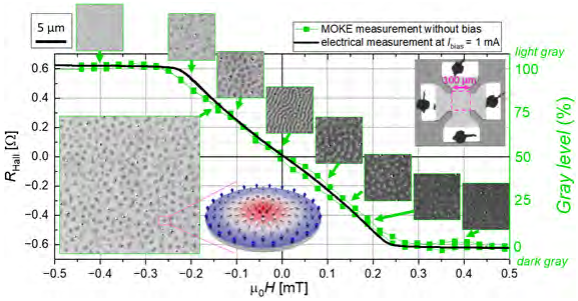


Fig. 1 MOKE loop (green curve) and electrical measurement (black curve) as a function of the applied magnetic field, with representative MOKE images acquired at selected field values.

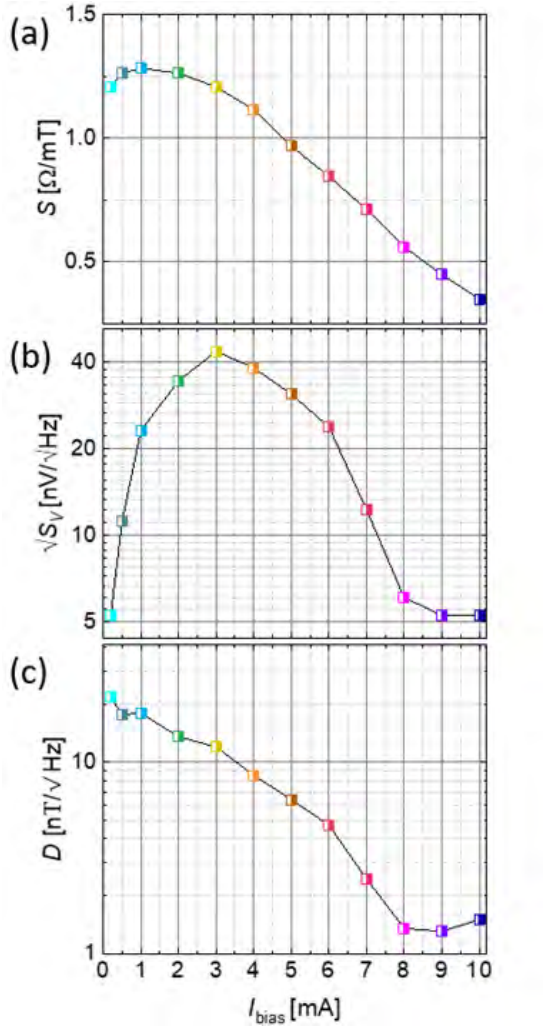
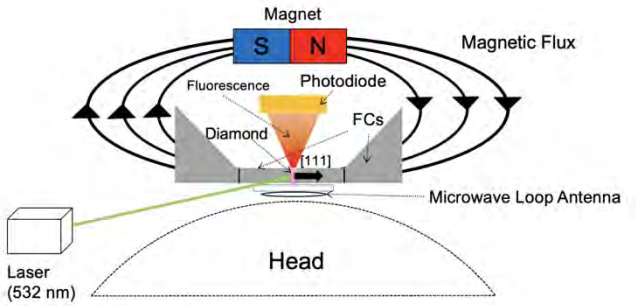


Fig. 2 Sensitivity (a), noise (b) and detectivity (c) measurements as a function of the bias current I_{bias} without external magnetic field for a 100x100 μm^2 Hall sensor.

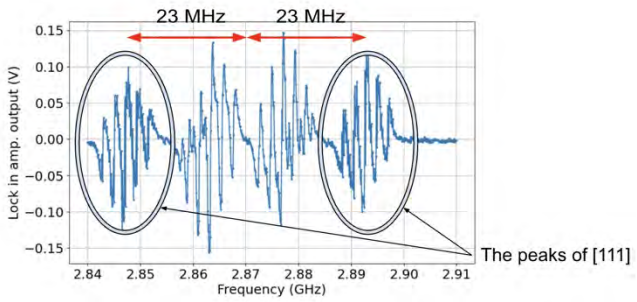
CE-02. Flux Concentrator-Enhanced NV Magnetometry for MEG Applications

Y. Baba[1], T. Zhu[1], n. sekiguchi[2], Y. Kainuma[3], M. Sekino[1]
[1]Graduate School of Engineering, The University of Tokyo, Bunkyo-ku, Tokyo, Japan, [2]Institute of Science Tokyo, Department of Electrical and Electronic Engineering, Meguro-ku, Tokyo, Japan, [3]Global Research and Development Center for Business by Quantum-AI Technology (G-QuAT), National Institute of Advanced Industrial Science and Technology (AIST), Tsukuba, Ibaraki, Japan

Nitrogen-vacancy (NV) center-based magnetic sensors enable room-temperature operation, making them promising for MEG [1]. Using flux concentrators (FCs) is effective for realizing extremely high-sensitivity sensors. However, the FCs specifically designed for MEG applications have not yet been demonstrated in previous studies [2].
In our previous work, we designed the FCs with a cut-trumpet shape, optimized for NV-based MEG measurements to enable measurements close to the scalp, through simulation [3]. In this work, we integrate the constructed FCs with an NV sensor and perform measurements using continuous-wave optically detected magnetic resonance (ODMR).
The system set up scheme is shown in Fig.1. A bias magnetic field was applied using a permanent magnet along the [111] crystallographic direction of the diamond. The fluorescence emitted from the diamond was detected by a photodiode and converted into an electrical signal, which was processed using a lock-in amplifier.
For an incident laser power of 100 mW on the diamond, the photocurrent generated by the fluorescence was 150 μA, and the ODMR spectra were measured. The peak of [111] shifted by approximately 23 MHz from the zero-field splitting frequency (2.87 GHz), as shown in Fig. 2. This shift corresponds to an effective magnetic field of approximately 0.82 mT under an applied bias field of ~10 μT, indicating a magnetic field enhancement factor of about 80. Also, the photon-shot-noise limited sensitivity was approximately 400 pT/Hz$^{0.5}$. According to the FCs enhancement factor of 80, it yields the sensitivity of 5 pT/Hz$^{0.5}$. By increasing the laser power up to 5 W, the sensitivity can be improved by a factor of ~7 to approximately 700 fT/Hz$^{0.5}$.
This work demonstrates that integration of an NV sensor with cut-trumpet-shaped FCs provides both significant sensitivity enhancement and scalp-proximal measurement capability, representing a key step toward practical NV-based MEG.
This study was supported by MEXT Q-LEAP (JPMXS0118067395 and JPMXS0118068379).
[1]Sekiguchi, N., Kainuma, Y. and Fushimi, M. et al. Applied Physics Letters 126.19 (2025)
[2]Fescenko, I., Jarmola, A. and Savukov, I. et al., Physical review research 2.2 : 023394.(2020)
[3]Zhu, T., Sekiguchi, N. and Kainuma, Y. et al., Engineering in Medicine and Biology Society (EMBC). IEEE.p.1-5(2025)



Set up of NV sensor with FCs



Lock-in cw-ODMR with FCs

CE-04. Magnetization Pattern Identification Using Highly Sensitive Tunnel Magnetoresistance Sensors and Deep Learning-Based Classification

T. Hojo[1, 2], T. Kubota[1], H. Fukushima[3], M. Endo[1], K. Fujiwara[3], H. Matsuzaki[3], T. Yoshidome[2], I. Yamane[4], K. Onishi[4], M. Oogane[2, 5], Y. Ando[1, 2, 5]
[1]Advanced Spintronics Medical Engineering, Tohoku University, Sendai, Miyagi, Japan, [2]Department of Applied Physics, Tohoku University, Sendai, Miyagi, Japan, [3]Spin Sensing Factory Corporation, Sendai, Miyagi, Japan, [4]Otsuka Pharmaceutical Co., Ltd., Chiyoda-ku, Tokyo, Japan, [5]Center for Science and Innovation in Spintronics, Sendai, Miyagi, Japan

Medication non-adherence is a critical challenge in treatments requiring precise dosing. Conventional identification approaches require active patient engagement, specialized formulations, or contact-based

operation, limiting their practicality. Magnetic-field-based identification offers a promising alternative, as magnetic signals can be detected passively and noninvasively. In this study, we propose a magnetic-field-based identification method using highly sensitive tunnel magnetoresistance (TMR) sensors [1] combined with deep-learning-based point cloud classification.

Magnetization patterns were fabricated from sputtered magnetic thin films and combined to create 17 distinct patterns, which were embedded into spherical samples to emulate oral tablets. The samples were repeatedly dropped through a vertical pipe, and their stray magnetic fields were measured using a circular array of three-axis TMR sensors. Using an automated system, approximately 60,000 measurements were acquired for each pattern.

The acquired signals were processed using FFT-based filtering and converted into three-dimensional point cloud data, where each point represents a magnetic field vector (Bx, By, Bz).

Up to 50,000 samples per pattern were used to train three types of models: PointNet, PointNet++ (SSG), and PointNet++ (MSG), which extract global and local features from unordered point sets [2,3]. For evaluation, 2,000 samples per pattern were used as test data, and the results are summarized in Table 1. All models successfully distinguished the magnetization patterns, with improved performance observed for the PointNet++ architectures. These results demonstrate that the combination of highly sensitive TMR sensors and deep learning enables accurate classification of magnetization patterns. This method enables passive and noncontact identification without requiring patient involvement or modification of tablet formulation, demonstrating strong potential for practical medical identification systems.

[1] M. Oogane et al., “Sub-pT magnetization field detection by tunnel mag-
neto-resistive sensors”, Applied Physics. Express 14, 123002 (2021)

[2] Qi, Charles R., et al., "Pointnet: Deep learning on point sets for 3d classification and segmentation", *Proceedings of the IEEE conference on computer vision and pattern recognition,* (2017)

[3] Qi, Charles Ruizhongtai, et al., "Pointnet++: Deep hierarchical feature learning on point sets in a metric space.", *Advances in neural information processing systems* 30, (2017)

Model	9 patterns	17 patterns
PointNet	98.6%	88.2%
PointNet++ ssg	99.7%	92.2%
PointNet++ msg	99.8%	92.0%

Table 1 Test data accuracy of 9 and 17 magnetization patterns classification for PointNet, PointNet++ ssg, and PointNet++ msg.

CE-05. Four-Wave Mixing and Tunable Gain in a Hybrid Magnonic–Superconducting Resonator System

P. Pal[1, 2], J. Lim[1], M. Song[2, 3], S. Kruhlov[4], T. W. Cecil[4], U. Welp[2], R. Divan[5], K. Kim[3], V. Novosad[2], A. Hoffmann[1], Y. Li[2]

[1]Department of Materials Science and Engineering and Materials Research Laboratory, University of Illinois Urbana Champaign, Urbana, Illinois, United States, [2]Materials Science Division, Argonne National Laboratory, Lemont, Illinois, United States, [3]Korea Advanced Institute of Science and Technology, Daejeon, Korea (the Republic of), [4]High Energy Physics Division, Argonne National Laboratory, Lemont, Illinois, United States, [5]Center for Nanoscale Materials, Argonne National Laboratory, Lemont, Illinois, United States

Magnon–photon hybrid systems have emerged as a compelling platform for studying coherent interactions between microwave resonators and collective spin excitations, with growing interest in their nonlinear response for signal processing applications. Here, we report four-wave mixing (4WM) and parametric amplification in a 500 nm wide nanowire superconducting coplanar resonator hybridized with a ferromagnetic spin ensemble, the schematic of the device is shown in Figure 1(a). When the resonator is detuned far from the magnon resonance, parametric pumping generates measurable gain, confirming that 4WM is sustained by the intrinsic resonator nonlinearity. Magnon hybridization further enhances this parametric process across both hybrid branches, boosting gain beyond what the bare resonator supports.

The 4WM mechanism for one of the conditions is shown in Figure 1(b). The central finding of this work is that pumping one hybrid mode produces gain in the other — a cross-mode amplification enabled by the hybridization-induced splitting between the two hybrid branches. This carries a critical practical implication: conventionally, driving a spectrally isolated resonator mode requires a pump tone within ~1

MHz of the target, which is technically demanding. By exploiting the ~20 MHz inter-mode separation in the hybrid system, gain in one branch is achieved by pumping the other, dramatically relaxing spectral isolation constraints. This demonstrates that magnonic hybridization actively reconfigures the parametric landscape of the coupled system, rather than acting as a passive spectral perturbation.

These results deepen our understanding of nonlinear magnon–photon interactions and establish that magnon-mediated parametric processes can serve as a practical resource for frequency-selective amplification, signal routing, and coherent microwave control in hybrid quantum and classical devices.

<!--[endif]---->This work was supported by the US DOE BES MSED under contract No. DE-SC0022060. <!--![endif]---->

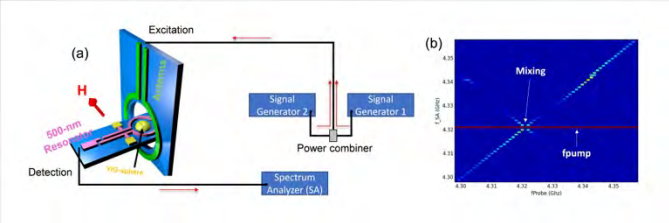


Figure 1: (a) Schematic of the measurement geometry and device structure. (b) The 4-wave mixing for a certain pump and probe frequency.

CE-06.* Magnetically Programmable Multichannel Isolation via Strong Magnon-Phonon Coupling in a Non-Reciprocal Magnetoacoustic Cavity for Advanced RF Routing

B. Luo*[2], J. Yao[1], A. Winkler[3], D. A. Bas[4], H. Schmidt[3], S. Wohlrab[3], J. Dickovick[5], V. Sharma[5], A. Huang[2], T. Zhou[6], M. McConney[4], M. Page[4], M. Sanghadasa[7], V. Lauter[8], M. Wu[5, 2], C. Hu[1], N. X. Sun[2]

[1]Department of Physics and Astronomy, University of Manitoba, Winnipeg, Manitoba, Canada, [2]Department of Electrical and Computer Engineering, Northeastern University, Boston, Massachusetts, United States, [3]SAW Lab Saxony Leibniz IFW, Leibniz Institute for Solid State and Materials Research, Dresden, Germany, [4]Materials and Manufacturing Directorate Institution, Air Force Research Laboratory, Wright-Patterson AFB, Ohio, United States, [5]Department of Physics, Northeastern University, Boston, Massachusetts, United States, [6]Research Laboratory of Electronics, Massachusetts Institute of Technology, Cambridge, Massachusetts, United States, [7]DEVCOM Aviation & Missile Center, U.S. Army Combat Capabilities Development Command, Huntsville, Alabama, United States, [8]Neutron Sciences Directorate, Oak Ridge National Laboratory, Oak Ridge, Tennessee, United States

Integrated non-reciprocal RF components are critical for in-band full-duplex (IBFD) radio systems [1-2]. Ferrite-based isolators preclude CMOS integration, while magnetoacoustic counterparts suffer from high insertion losses (>40 dB) and static, single-channel non-reciprocity [3-5]. Translating programmable non-reciprocity in cavity magnonics [6-7] to on-chip magnetoacoustic platforms is restricted by high magnon loss rates in non-reciprocal stacks (e.g., 525 MHz in CoFeB/Ru/CoFeB [8]), preventing multichannel programmability.

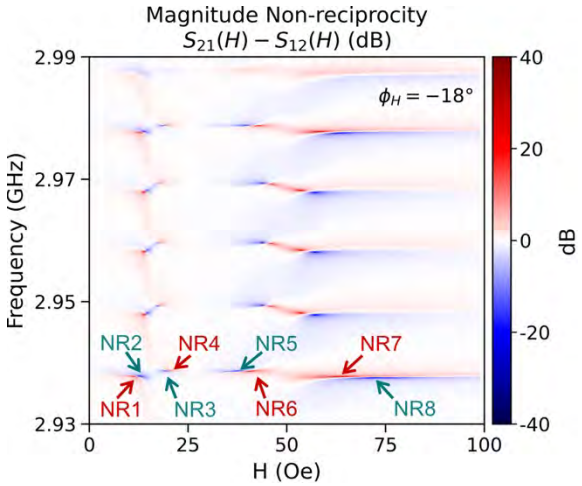
We report the first programmable multichannel magnetoacoustic RF isolation driven by strong magnon-phonon coupling. Integrating a low-damping, non-collinear dipolar FeGaB/SiO_2/FeGaB stack ($\alpha \sim 10^{-3}$) into a high-Q SAW cavity on 128° YX $LiNbO_3$ suppresses magnon loss. This realizes strong coupling between asymmetric out-of-phase dipolar spin-waves and five localized SAW modes, achieving a record cooperativity of 54 alongside a 10 dB insertion loss at the fundamental 2.87 GHz SAW mode. Driven by magnon-phonon hybridization and level repulsion, two staggered anticrossings near 17 and 55 Oe expand conventional single non-reciprocity pair per SAW mode into four distinct hybridized giant non-reciprocity bands per anticrossing, achieving peak isolation of ~250 dB/mm (Fig. 1).

Crucially, varying coupling characteristics across the five SAW modes stagger non-reciprocity fields for each channel. Sweeping bias fields within 11.9–73 Oe sequences these bands, creating 16 distinct magnetoacoustic states that yield five programmable RF transmission channels. This RF routing matrix requires only 0.7 Oe to transit between isolation state vectors (Fig. 2). In-plane field rotation selectively couples SAW modes to in-phase or out-of-phase spin-wave modes, confining giant non-reciprocity (>30 dB) to a 66° window.

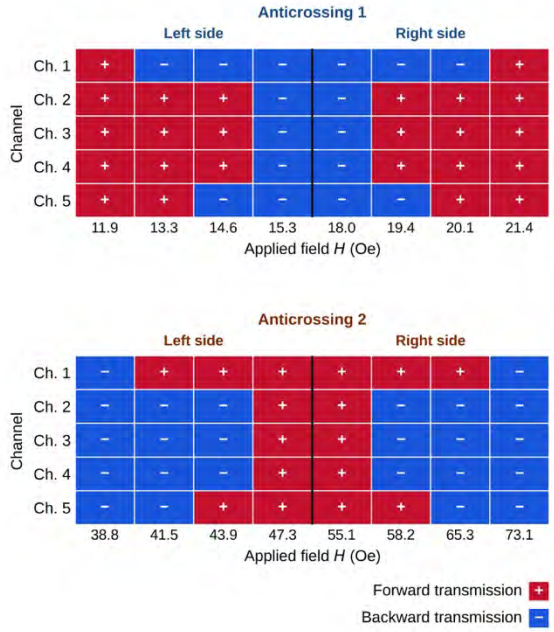
This platform translates quasiparticle hybridization into a scalable field-programmable hardware solution for frequency-multiplexed signal routing in next-generation IBFD transceivers.

[1] A. Nagulu and H. Krishnaswamy, IEEE J. Microwaves, Vol. 1, p. 447 (2021).
[2] N. Reiskarimian and H. Krishnaswamy, Nat. Commun., Vol. 7, p. 11217 (2016).
[3] P. J. Shah, D. A. Bas and M. Page, Science Advances, Vol. 6, p. eabc5648 (2020).

[4] D. A. Bas, R. Verba and P. J. Shah, Phys. Rev. Appl., Vol. 18, p.044003 (2022).
[5] M. Kuß, S. Glamsch and M. Weiler, ACS Appl. Electron. Mater., Vol. 5, p. 5103 (2023).
[6] J. Yao, C. Lu and X. Fan, Phys. Rev. Lett., Vol. 134, p.196904 (2025).
[7] Y.-P. Wang, J. Rao and Y. Yang, Phys. Rev. Lett., Vol. 123, p.127202 (2019).
[8] H. Matsumoto et al., Nano Letters, Vol. 24, p. 5683 (2024).



Magnitude non-reciprocity S_{21}–S_{12} (dB) vs. bias field strength and frequency (bias field angle ϕ_H = −18°).



Magnetically programmable 5-channel transmission/isolation matrix across 16 magnetoacoustic states within 11.9–73 Oe.

CE-07.* Low insertion losses microscale spin-wave RF devices

K. Davídková*[1, 3], F. Bruckner[1], I. K. Douveas[1], C. Dubs[2], K. Levchenko[1], D. Suess[1], A. Chumak[1]
[1]Faculty of Physics, University of Vienna, Vienna, Austria, [2]Technologieentwicklung, INNOVENT e. V., Jena, Germany, [3]Faculty of Physics, Vienna Doctoral School of Physics, Vienna, Austria

The drive toward faster, more efficient 5G communication systems requires radio-frequency (RF) devices to adapt from Frequency Range 1 (FR1, sub-6 GHz) to higher operating frequencies in Frequency Range 2 (FR2, 24.25-71.0 GHz) and the proposed Frequency Range 3 (FR3, 7.125-24.25 GHz). Spin-wave (SW) devices are promising candidates, combining efficient operation in the higher-frequency range (FR3) with multifunctionality, thereby enabling compact, energy-efficient devices [1]; however, practical adoption is constrained by significant insertion losses [2, 3]. We present a systematic study of insertion losses arising during electromagnetic-spin-wave-electromagnetic signal conversion and during SW propagation between a pair of U-shaped transducers in a 1.96 um thick YIG film; see Fig. 1(a, b). Transducer lengths (60-340 um) and widths (1-6 um) are varied to tune impedance matching over a broad frequency range (5-30 GHz). We demonstrate that the insertion loss can be optimized for each operational frequency by selecting the appropriate transducer length; see Fig. 1(c, d). This length defines the spin-wave resistance parameter, which increases as the frequency increases. The lowest measured insertion loss is 6.25 dB at 12 GHz using 200 um-long transducers. Experimental results are compared to micromagnetic simulations [4] to optimize YIG thickness, transducer geometry, and spin-wave mode selection.

[1] K. Levchenko, K. Davídková and J. Mikkelsen, IEEE Trans. Magn. (2026)
[2] K. Davídková, K. Levchenko and F. Bruckner, Phys. Rev. Applied 23, 034026 (2025)
[3] K. Davídková, K. Levchenko and R. Serha, J. Appl. Phys. 138, 14 (2025)
[4] F. Bruckner, K. Davídková and C. Abert, Sci. Rep. 15, 19993 (2025)

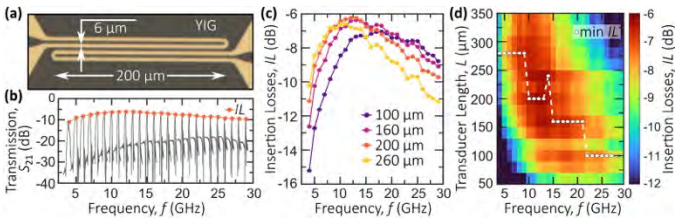


Figure 1. (a) U-shape transducers fabricated on a 1.96 µm thick YIG film. (b) SW transmission measured in the Damon-Eshbach configuration at different applied fields using the transducers from (a); red circles indicate extracted insertion losses (IL). (c) Comparison of extracted insertion losses for different transducer lengths (see legend). (d) Dependence of insertion loss on transducer length and frequency; white circles indicate the smallest insertion losses at each frequency.

CE-09. Optimization of Fe3O4–PDMS Composite Membranes for High-Performance TMR based Gas Sensors

P. Pal, S. Amara, H. Bagci, G. Setti
CEMSE, KAUST, Thuwal, Saudi Arabia

Gas-sensing technologies are crucial for environmental monitoring, industrial safety, and healthcare applications. Conventional sensors have achieved high sensitivity but suffer from limitations. These challenges hinder their application in portable and low-power systems [1]. To address these issues, TMR spintronic-based sensing [2] has emerged as a promising alternative. They offer key advantages making them suitable for next-generation integrated sensing applications. To realize a complete sensing unit, a Fe3O4–PDMS magnetic membrane was integrated with the TMR sensor, where the membrane served as the primary actuation layer. Magnetic membrane deflection alters the distance between the magnetic membrane and TMR sensors, which is transduced into a voltage change. A key aspect of this study was optimizing membrane thickness, as it directly affects response dynamics. The membrane properties were tuned by controlling the PDMS composition, Fe3O4 loading, and spin-coating parameters. Fe3O4-incorporated PDMS membranes were fabricated using the Sylgard 184 elastomer by mixing the base and curing agent in a 20:2 weight ratio, followed by mechanical stirring and vacuum degassing[3]. Fe3O4 nanoparticles were added in varying amounts (5, 7, 10, and 20 g) to tailor the magnetic properties. The mixtures were spin-coated onto PMMA substrates at different speeds (10–400 rpm) to achieve a controlled membrane thickness. Overall, the results shown in Fig. 1 -a), b) demonstrate that the membrane thickness can be effectively tuned by adjusting the spin speed and Fe3O4 content. The membranes were then magnetized by 2T field generated by VSM system coils. We map the different membranes (with varying thicknesses and magnetic powder amounts) using a TMR sensor system, as shown in Fig. 2, to determine the magnetic field magnitude at a fixed distance. This tunability is crucial for optimizing the balance between the magnetic response and gas diffusion, thereby enabling improved performance of TMR-based gas-sensing systems.

1. H. Chai *et al*., "Stability of Metal Oxide Semiconductor Gas Sensors: A Review," in *IEEE Sensors Journal*, vol. 22, no. 6, pp. 5470-5481.
2. Mostufa, Shahriar, et al. "Spintronic devices for biomedical applications." *npj Spintronics* 2.1 (2024): 26.
3. Ali Asghar Paknahad, Mohammad Tahmasebipour,"An electromagnetic micro-actuator with PDMS-Fe3O4 nanocomposite magnetic membrane", Microelectronic Engineering, Volume 216,2019,111031.

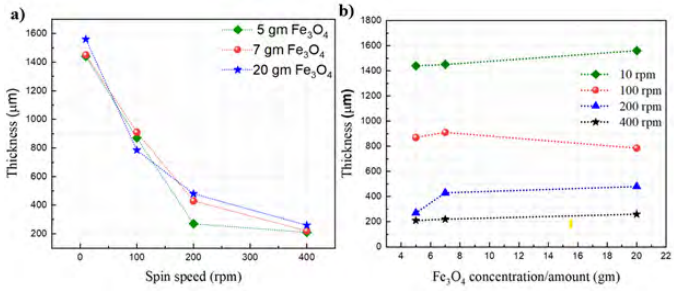


Fig1: a) Thickness vs. spin speed for different Fe3O4 concentrations, b) Thickness vs Fe3O4 concentration at different spin speeds

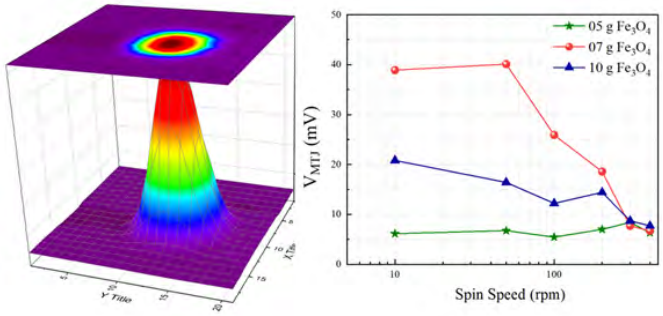


Fig2: Magnetic heatmap of the different magnetic membranes 4 cm^2 scanned by TMR sensors.

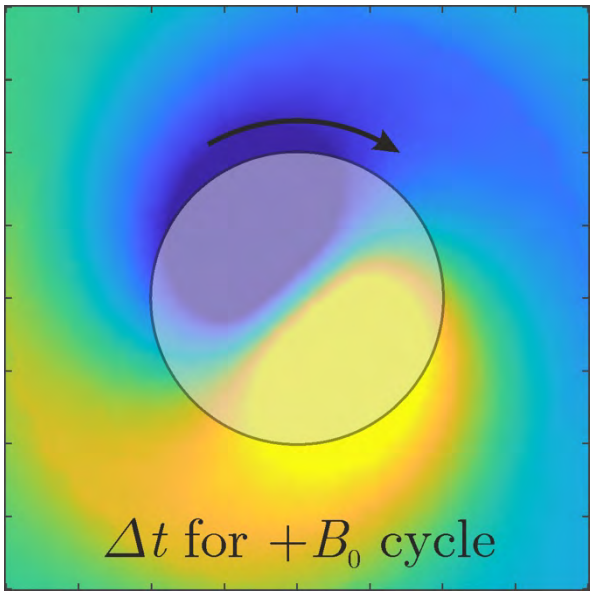
CE-10. Modeling Time-Modulated Magnetoplasmonic Graphene Scatterers Using Quasi-Normal Mode Expansion

S. Amanatiadis[1], T. Ohtani[2], N. V. Kantartzis[1], Y. Kanai[3]
[1]Aristotle University of Thessaloniki, Thessaloniki, Greece, [2]1-17-134 Omachi, Asahikawa, Japan, [3]Niigata Institute of Technology, Kashiwazaki, Japan

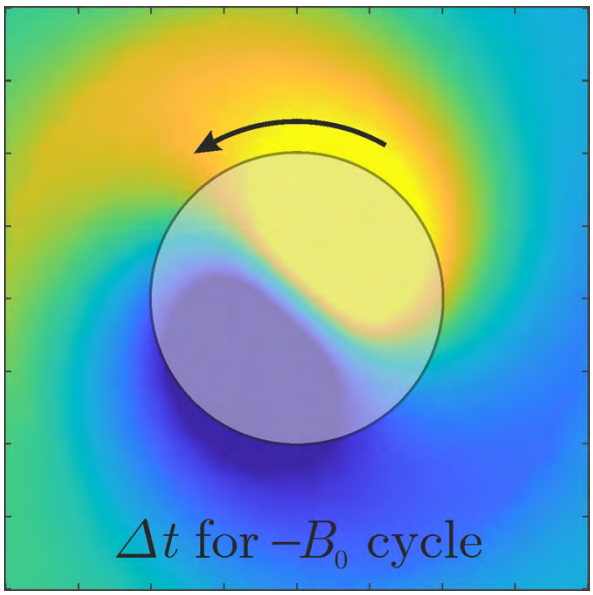
The rapid evolution of modern telecommunications require ultra-high data rates and compact integrated platforms, which pushes the operational frequencies toward the THz regime. However, the development of efficient components for this spectral region remains challenging due to material limitations and the lack of flexible dynamic control of electromagnetic response. In this context, spatiotemporally modulated electromagnetic devices have recently attracted significant attention since they enable functionalities such as frequency up-conversion and dynamic wavefront control [1]. Graphene has emerged as a promising platform for such devices due to its inherent tunable conductivity via external electric and magnetic bias fields leading to a strong plasmonic behavior at low THz frequencies [2]. Nevertheless, the accurate modeling of such systems remains computationally demanding, particularly for the full-wave analysis of broadband responses that support resonant interactions. For this reason, it is imperative to develop efficient theoretical frameworks that are capable of describing the interaction between time modulation and complex resonant structures.

In this work, a semi-analytic framework is proposed based on quasi-normal modes (QNMs) for the investigation of time-modulated magnetically-biased graphene resonators. Initially, the QNMs of the considered scatterer are computed for a discrete set of magnetically-biased graphene states that form a physically meaningful basis for describing the system's electromagnetic response. Then, these modal solutions are employed to evaluate the far-field in a broadband manner for each magnetic bias configuration [3]. Finally, the contribution of the different modal states are combined using the desired time-modulation scheme while accounting for the appropriate phase relationships between propagating wavefronts. As a result, this procedure enables the accurate and efficient representation of the scattered field temporal evolution, avoiding a costly full-wave simulation for any different arrangement.

[1] Ramaccia, D., Alu, A., Toscano, A., & Bilotti, F. (2021). Temporal multilayer structures for designing higher-order transfer functions using time-varying metamaterials. *Applied Physics Letters*, *118*(10).
[2] Salary, M. M., Jafar-Zanjani, S., & Mosallaei, H. (2018). Time-varying metamaterials based on graphene-wrapped microwires: Modeling and potential applications. *Physical Review B*, *97*(11), 115421.
[3] Amanatiadis, S., Ohtani, T., Zygiridis, T., Kanai, Y., & Kantartzis, N. (2025). Far-field Pattern Evaluation for Magnetically-biased Graphene Resonators via Quasi-normal Modes. *IEEE Transactions on Magnetics*.



Scattered field response at a timestep during the positive magnetic bias field cycle.



Scattered field response at a timestep during the negative magnetic bias field cycle.

CE-12. Leveraging Higher Order Mode for Magnetic Field Sensing in AlN-based Single-Port Delay Line Resonator

T. Burman, D. Kaur
Physics, Indian Institute of Technology, Roorkee, Uttarakhand, India

Surface acoustic wave (SAW) resonators hold great potential for the development of sensing applications owing to their less complex structure, higher sensitivities, and wireless capabilities. Herein, we designed and fabricated a single-port delay line magnetic surface acoustic wave (MSAW) sensor working effectively in an externally applied magnetic field range from 0 Oe to 1200 Oe. The fabricated sensor comprises a highly magnetostrictive ferromagnetic shape memory alloy (Ni-Mn-In) delay-line and interdigitated transducers (IDTs) deposited over a piezoelectric aluminium nitride (AlN) thin film on a silicon substrate employing the DC magnetron sputtering technique. The effect of an external magnetic field on the performance of MSAW has been examined. The device exhibits a resonant frequency of 5.511 GHz. A substantial frequency shift of 129 MHz and 419 MHz is observed in the MSAW device at 70 Oe and 750 Oe, demonstrating effective utilization of the ΔE effect. These shifts correspond to magnetic field sensitivities of 1.84 MHz/Oe (18.4 Hz/nT) and 0.558 MHz/Oe (5.58 Hz/nT), respectively. Furthermore, Finite element analysis (FEA) is performed in COMSOL Multiphysics to validate the presence of higher-order modes. The scattering parameters obtained experimentally under varying magnetic fields are fitted using the modified Butterworth-Van Dyke (mBVD) equivalent circuit model. These results highlight the efficacy of combining AlN and ferromagnetic shape memory alloys in MSAW structures, demonstrating promising potential for high-performance CMOS-compatible magnetic sensors in MEMS and IoT applications.

T. Burman, S. Shankhdhar, and D. Kaur, *Sensors and Actuators A: Physical*, vol. 405, p. 117787, Mar. 2026
D. Arora, T. Burman, and D. Kaur, *IEEE Sensors Journal*, vol. 25, no. 15, pp. 28202-28209, 1 Aug.1, 2025

SESSION CF: SUPERCONDUCTING AND ANTIFERROMAGNETIC SPINTRONICS

Chair(s): H. Arava, *Argonne National Laboratory, Lemont, Illinois, United States*
Wednesday, November 4, 2026
08:30 AM-12:00 PM
South Pacific 3/4

CF-01. Non-linear rectification effect in superconducting diode effect

U. Nagata[1], M. Aoki[1], A. Daido[2], R. Ohshima[1], S. Kasahara[3], Y. Kasahara[4], Y. Ando[1], Y. Matsuda[2], Y. Yanase[2], M. Shiraishi[1]
[1]Electronic Science and Engineering, Kyoto University, Kyoto, Japan, [2]Department of Physics, Kyoto University, Kyoto, Japan, [3]RIIS, Okayama University, Okayama, Japan, [4]Department of Physics, Kyushu University, Hukuoka, Japan

Superconducting diode effect (SDE) [1], where nonreciprocal supercurrent flow takes place, has been intensively investigated in spintronics as a novel physical effect. The typical SDE is observed when time-reversal symmetry is broken by a magnetic field with inversion symmetry breaking. Recently, a SDE with new background physics, which is induced by thermoelectric effect, was reported in iron-based superconductors (SCs) with nonmagnetic electrodes [2]. The thermoelectric SDE is fundamentally immune to a magnetic field. Meanwhile, response of the SDE to the magnetic field and ferromagnetic (FM) electrodes has not been surveyed yet, whereas the heterointerface of a FM/SC can create novel interface properties.
In this study, we investigate a field-dependent component of the SDE in iron-based SCs when FM electrodes are equipped. An inset of Fig. 1 shows an optical image of the fabricated device. The $FeTe_{0.6}Se_{0.4}$ (FTS) was exfoliated on a thermally oxidized Si substrate, and the Au/Co electrodes were fabricated. Electric current was flowed between electrodes 1 and 4, and a four-terminal voltage was measured between electrodes 2 and 3 under a magnetic field B perpendicular to the current flow direction shown as the orange arrow. The thermoelectric SDE is dominant even when the FM electrodes are attached as shown in Fig. 1. Meanwhile, we found that a non-linear rectification effect is superimposed on the SDE. To characterize the rectification quantitatively, we define a difference of the four-terminal voltage ΔV as $\Delta V = V(+I) - V(-I)$, where I is an electric current. Finite value of ΔV means the existence of rectification effect. Figure 2 shows the magnetic field dependence of ΔV when I = 1.5 mA at 10 K. Importantly, the polarity of the rectification is field-dependent and non-

linear to the magnetic field. Systematic control experiments proved the rectification effect is certainly due to the interface of SC/electrodes [3]. Interfacial Rashba effect can be an origin of our findings, which will be discussed in the presentation.

[1] F. Ando *et al*., Nature 584, 373 (2020). [2] U. Nagata *et al*., Phys. Rev. Lett. 134, 236703 (2025). [3] U. Nagata *et al*., *J. Magn. Soc. Jpn.,* 50, 34 (2026).

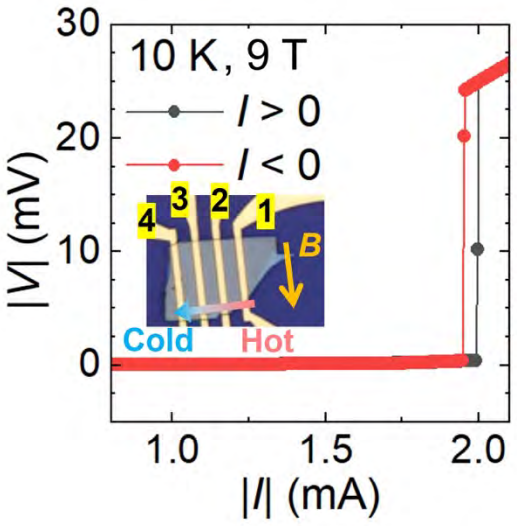


Fig. 1. *I-V* characteristics of the FTS at 10 K and 9 T. Inset is an optical image of the device.

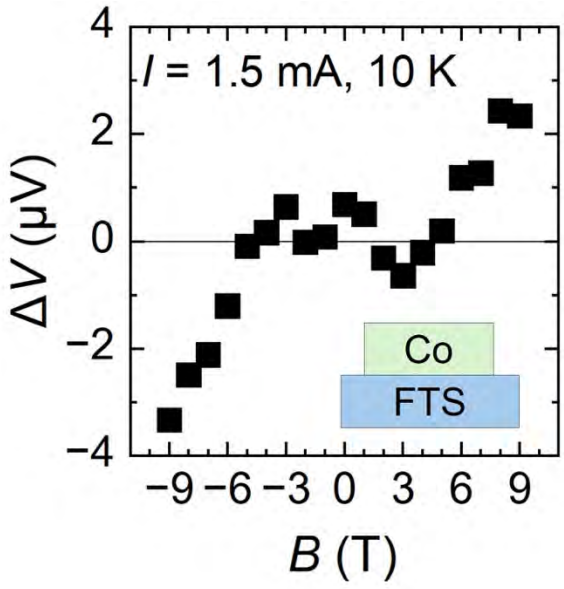


Fig. 2. External magnetic field (*B*) dependence of Δ*V*.

CF-02. Proximity effects in superconductor/magnetic epitaxial heterostructures with magnetic noncollinearity

H. C. TADAHA[1, 2, 3], T. Hauet[1, 2, 3], K. Dumesnil[1, 2, 3]
[1]Institut Jean Lamour, Nancy, France, [2]Université de Lorraine, Nancy, France, [3]CNRS, Nancy, France

The proximity effect (PE) at an interface between a superconductor (S) and a ferromagnet (F) is strongly dependent on the interfacial magnetic configuration. For a collinear F order, the magnetic exchange field suppresses superconductivity (short range PE). Conversely, magnetic noncollinearity (MNC) can restore superconductivity, as in antiparallel F/S/F spin valves [1] and S/F bilayers with magnetic domains [2]. However, MNC can also give rise to the generation of spin-aligned triplet Cooper pairs that would leak into F and lead to a reduced in Tc [3-4] (long-range PE).

To further investigate the role of MNC in these proximity effects, we have undertaken a study based on epitaxial hybrid structures involving rare earth elements. These later present magnetic modulated phases that are a natural source of MNC to promote triplet components [5]. Epitaxial systems are moreover powerful levels to control the magnetic phases via dimension, strains, alloying [6]. We focus here on Nb(30nm)/F(50nm) structures, where F is a pure Ho film, a Ho-based alloy (with Lu or Tb), or a Ho-based superlattice. The Nb critical temperature Tc (Fig. 1 bottom) appears to be significantly modified by changes in the magnetic state (Fig. 1 top). Interestingly, the development of MNC out of the saturated state generates either an increase (with Ho and HoLu) or a decrease (with HoTb and [Ho/Lu]) of Tc. Such a decrease in Tc could be related to the presence of domain walls or a linked to the appearance of long-range triplet components.

We will discuss how the nature and characteristics of the MNC could explain its influence on short and long range PE. Exploring these effects in systems with MNC is vital to aid theory towards improved modelling and to develop superconducting spintronic devices.

[1] S. Oh and D. Youm, Appl. Phys. Lett. 71, 2376 (1997)
[2] A.Y Rusanov, M. Hesselberth, J. Aarts, A.I. Buzdin, Phys. Rev. Lett. 93, 057002 (2004)
[3] F.S. Bergeret, A.F. Volkov, K.B. Efetov, Phys. Rev. Lett. 86, 4096 (2001)
[4] Y.V. Fominov, A.A. Golubov, T.Y. Karminskaia, M.Y. Kupriyanov, R.G. Deminov, L.R. Tagirov, JETP Lett. 90, 308 (2010)

[5] D. Fritsch, F. Annett, J. Phys.:Condens. Matter 26, 274212 (2014)
[6] J.P.P. Swaddling et al., Phys. Rev. B 53, 6488 (1996)

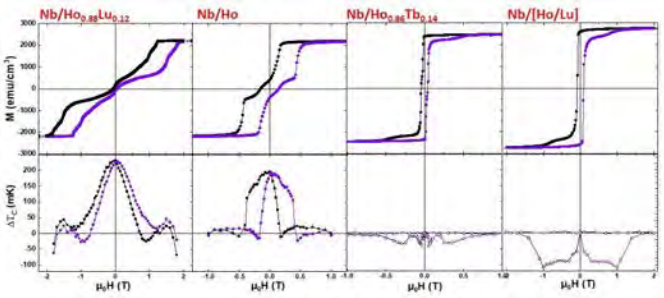


Fig.1: Magnetic and electronic properties for Nb/Ho, $Nb/Ho_{0.88}Lu_{0.12}$, $Nb/Ho_{0.86}Tb_{0.14}$ and Nb/[Ho/Lu] heterostructures. Top curves are magnetization measurements. Bottom curves are the relative variations of the superconducting Tc related to changes in the magnetic state. The black (purple) curve corresponds to the decreasing (increasing) branch.

CF-03. Magnetic and spin-pumping properties of MgB_2-based and NbN-based multilayers

L. Peridon[1, 2, 3], T. Courtois[1, 2, 3], S. Mangin[1, 2, 3], T. Hauet[1, 2, 3], K. Dumesnil[1, 2, 3]
[1]Institut Jean Lamour, Nancy, France, [2]Université de Lorraine, Nancy, France, [3]CNRS, Nancy, France

The interplay of magnetism and superconductivity has been heavily studied over the past 30 years and recently led to the concept of superconducting spintronic. Proximity effects, Cooper pairs-magnons interactions or injection of polarized quasiparticles at superconductor/ferromagnet (S/F) interfaces have been essentially investigated in niobium or aluminium-based heterostructures with critical temperatures (Tc) of the order of few Kelvin. S/F stacks with a higher Tc and carefully tuned interfaces would enable the thorough exploration of new superconducting spintronic features, and would ease the implementation in operating quantum devices. GHz and THz experiments allow to extend the current knowledge to phenomena occurring at short-time scale.
We present the results obtained on epitaxial MgB_2-based and NbN-based stacks. Tc reaches 30 K for MgB_2 films as thin as 15 nm and 15 K for NbN films as thin as 10 nm. The original paramagnetic properties of such thin films are first discussed [1] and extended to a broader range of superconducting materials. Then the temperature dependence of the Gilbert damping of S/F bilayers (FMR) is described as a probe of the spin-transport from F into S. As expected [1,2], the channel of momentum loss in the S layer is partially suppressed by opening of the SC gap below T_c [4]. The role of the interfacial proximity effect on the spin pumping is especially investigated when comparing NbN/X/F stacks where X is either a Pt or Cu interlayer. For T > Tc, the increase of both Cu and Pt thickness leads to a monotonic increase of the damping due to the spin-pumping enhancement. Interestingly, for T<Tc, the damping drop monotonically decreases (in amplitude) with increasing the Cu thickness whereas it peaks around 3 nm for Pt. This intriguing result will be linked to the spin-flip length of the interlayer in the normal phase and its superconductive coherence length in its proximitized state.
These results shed new light on the parameters governing the magnetic hysteresis loop of thin superconductive films and the spin pumping at S/F interfaces.

[1] C. Pfaff *et al.*, Phys. Rev. B 110, 094502 (2024)
[2] C. Bell *et al.*, Phys. Rev. Lett. 100, 047002 (2008)
[3] M. Müller *et al.*, Phys. Rev. Lett. 126, 087201 (2021)
[4] C. Pfaff *et al.*, Appl. Phys. Lett. 125, 102601 (2024)

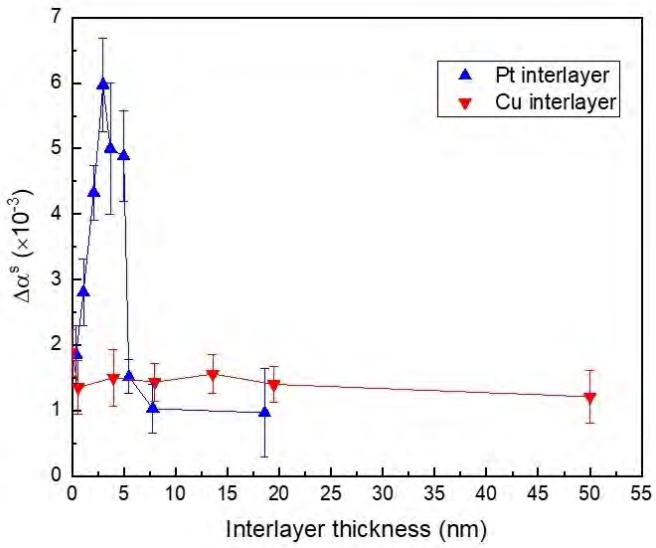


Fig. 1: Temperature dependence of the drop of Gilbert Damping at T_c in NbN/Cu/Py and NbN/Pt/Py stacks

CF-04. Non-reciprocal Properties in Pt/Fe/Pt-inserted Nb/V/Ta Superconducting Superlattices

F. Tokoro[1], H. Matsuki[2, 3], S. Hirata[1], T. Mandokoro[1], R. iijima[1], R. Hisatomi[2, 3], S. Karube[2, 3], Y. Shiota[2, 3], T. Ono[2, 3, 4]
[1]Graduate School of Science, Kyoto University, Uji, Kyoto, Japan, [2]Institute for Chemical Research, Kyoto University, Uji, Kyoto, Japan, [3]Center for Spintronics Research Network, Kyoto University, Uji, Kyoto, Japan, [4]International Center for Synchrotron Radiation Innovation Smart, Tohoku University, Uji, Kyoto, Japan

There has been growing interest in the superconducting diode effect (SDE), which was observed in noncentrosymmetric superconductors [1]. Recently, a zero-field superconducting diode effect has been reported in superconductor/ferromagnet hybrid structures [2]. In this study, we investigate the temperature dependence of the superconducting properties of a Nb/V/Pt/Fe/Pt/V/Ta superlattice, in which strong spin-orbit coupling from Pt and ferromagnetism from Fe are incorporated into a noncentrosymmetric Nb/V/Ta superlattice.
The superlattice thin-film with the structure Pt/Fe/Pt-inserted Nb/V/Ta superlattice was deposited on a MgO(100) substrate by DC sputtering. A Hall-bar device was subsequently fabricated using photolithography and Ar milling. For each measurement, an in-plane magnetic field of 1 T was first applied to saturate the magnetization of the Fe layers and then reduced to zero. An in-plane electrical current, applied perpendicularly to the direction of the remanent magnetization, was used to measure the critical current densities J_c.
Figure 1 shows that the critical current densities in positive directions ($J_{c,+}$) increase below the superconducting transition temperature (3.6 K) and exhibit an inflection point near 3.0 K. Figure 2 shows the non-reciprocal critical current densities $\Delta J_c = J_{c,+} - J_{c,-}$. Notably, ΔJ_c does not increase immediately below the superconducting transition temperature instead emerges below 3.0 K, coinciding with the inflection point observed in J_c. The appearance of this inflection point together with the onset of non-reciprocal critical current suggests a possible connection to novel superconducting phases, such as a Fulde-Ferrell-Larkin-Ovchinnikov (FFLO) state [3] observed in layered superconductors, and its role in generating SDE in the present superlattice structure. We also plan to discuss the results of the critical field measurements during the presentation.

[1] F. Ando , Y. Miyasaka , T. Li *et al.*, Nature, Vol. 584, p.373–376 (2020).
[2] H. Narita , J. ishizuka , D. Kan *et al.*, Adv. Mater., vol. 35, 2304083 (2023).
[3] P. Wan , O. Zheliuk , N . F . Q . Yuan *et al.*, Nature, vol. 619, p.46–51 (2023).

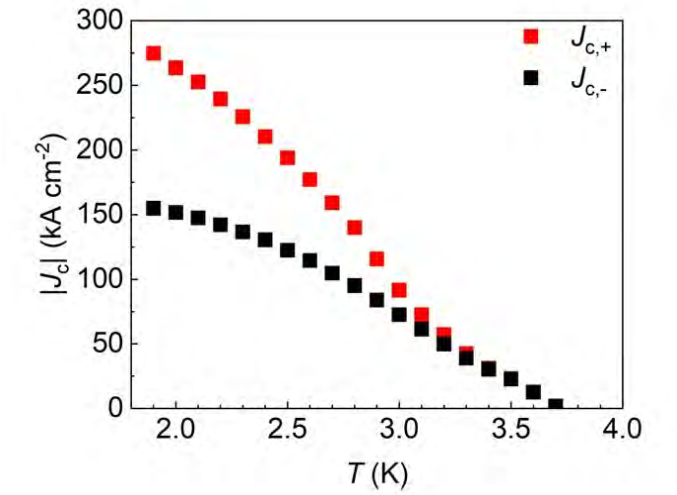


Fig.1: Temperature dependence of J_c.

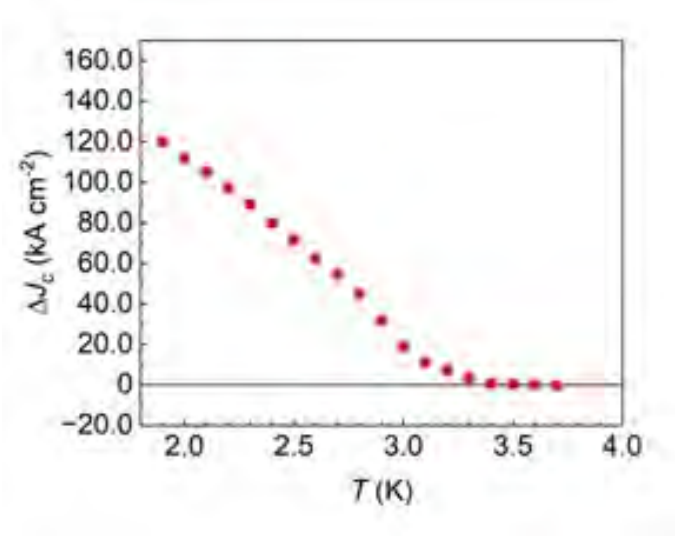


Fig.2: Temperature dependence of ΔJ_c.

CF-05. Charge to Spin Conversion in the Superconducting State

P. Sivakumar, Y. Wu, P. Madhusudan Rao, I. Kindiak, Y. Xie, S. Parkin
NISE, Max Planck Institute of Microstructure Physics, Halle (Saale), Saxony-Anhalt, Germany

The generation, manipulation, and detection of spin-polarized currents underpin spintronic technologies, enabling advanced memory and logic concepts such as magnetic random-access memory (MRAM) [1] and racetrack memory [2,3]. Central to these applications is the efficient generation of spin torques capable of transferring angular momentum and controlling magnetic order [4]. Spin-polarized supercurrents in spin-triplet superconductors have long been predicted to provide a pathway toward dissipationless spin transport [5,6].
Here we show for the first time that spin angular momentum from spin triplet supercurrents created from a conventional superconductor-ferromagnet heterostructure can be transferred to a neighboring magnetic insulator via the creation of magnons and vice versa, thereby, enabling Joule dissipationless spin to charge and charge to spin conversion. By engineering distinct spin configurations of triplet pairs, we observe spin-dependent transverse transport, including Hall-like responses, that persist in the superconducting state analogous to those in the normal ferromagnetic phase.

By generating spin triplet pairs in distinct spin configurations, we show that spin-dependent transverse velocities and Hall currents that generate magnons are present in the superconducting state just as in the normal state of the ferromagnet. The magnons that are generated are detected in a non-local measurement configuration using the inverse spin Hall effect in remote electrodes. These results establish a new class of dissipationless Hall effects in spin-triplet superconducting systems—superconducting analogues of the spin Hall and anomalous spin Hall effects, along with their inverse counterparts. Beyond enabling low-dissipation spin current manipulation, this approach provides a platform for identifying and characterizing spin-triplet superconductivity.
[1] Nguyen, V. D., Rao, S., Wostyn, K. & Couet, S. Recent progress in spin-orbit torque magnetic random-access memory. *npj Spintronics* 2, 48 (2024).
[2] Parkin, S. S. P., Hayashi, M. & Thomas, L. Magnetic Domain-Wall Racetrack Memory. 331 *Science* 320, 190-194 (2008).
[3] Bläsing, R. *et al.* Magnetic Racetrack Memory: From Physics to the Cusp of Applications 333 Within a Decade. *Proceedings of the IEEE* 108, 1303-1321 (2020).
[4] Bader, S. D. & Parkin, S. S. P. Spintronics. *Annu. Rev. Condens. Matter Phys.* 1, 71-88 326 (2010).
[5] Linder, J. & Robinson, J. W. A. Superconducting spintronics. *Nat. Phys.* 11, 307-315 322 (2015).
[6] Eschrig, M. Spin-polarized supercurrents for spintronics: a review of current progress. *Rep. Prog. Phys.* 78, 104501 (2015).

CF-06. Leveraging Magnetic Distortion Symmetry Groups to Elucidate the Multiferroic Origins of Altermagnetism

M. D. Kitcher, G. Beach
Materials Science and Engineering, Massachusetts Institute of Technology, Cambridge, Massachusetts, United States

Altermagnets—materials exhibiting crystal-compensated magnetic order and non-relativistic spin splitting—have gained attention for their unconventional physics and technological promise [1]. In altermagnets, crystallographic rotations connect opposite spin sublattices, distinguishing them from antiferromagnets and ferromagnets under the spin group classification scheme [2]. While their unique symmetry permits non-relativistic piezomagnetism that is odd in the Néel vector (N) [3], many of their properties of interest, such as odd-in-N anomalous Hall conductivity, are mediated by spin–orbit coupling (SOC) [4]. The symmetries of such properties must therefore be predicted by the magnetic symmetry groups, which do not differentiate between altermagnetic and purely relativistic effects [5]. Moreover, given the multipolar nature of altermagnetic order parameters, it is still debated whether altermagnetism is a third phase of collinear magnetism alongside ferromagnetism and antiferromagnetism. In this work, we demonstrate that altermagnets are best described as a primary class of multiferroics analogous to magneto-electrics. To this end, we present a new framework for identifying altermagnetism, leveraging a new formalism for capturing the latent symmetries of structural distortions with respect to a parent crystal [6]. By assigning a magnetic distortion point group (MDPG) to a material, we can determine if it hosts a nonrelativistic coupling between antiferromagnetic order and staggered distortions that break both translation-time (Tt) and parity-time (PT) symmetries. With the same MDPGs, we can also predict the symmetries of SOC-mediated altermagnetic properties and distinguish them from purely relativistic effects based on how they couple to distortions. To demonstrate the power

of our approach, we discuss a case study where we uncover hidden altermagnetic order parameters and reveal the altermagnetic origins of experimentally observed SOC-mediated phenomena. Our work provides valuable insights into the synergetic relationships between multiferroicity, altermagnetism, and spin-orbit coupling—and affirms the MDPG formalism as a powerful tool for identifying and characterizing multiferroics.

1. Šmejkal, L. et al., Phys. Rev. X 12, 040501
2. Šmejkal, L. et al., Phys. Rev. X 12, 031042
3. Bhowal, S. and Spaldin, N., Phys. Rev. X 14, 011019
4. Gonzalez Betancourt, R.D. et al., Phys. Rev. Lett. 130, 036702
5. Šmejkal, L. et al., Sci. Adv. 6, eaaz8809(2020)
6. VanLeeuwen, B., Gopalan, V., Nat. Commun. 6, 8818 (2015)

CF-07. Enhanced field-free spin-orbit torque switching in ferrimagnetic trilayers

S. Ko[1], D. Han[2], N. Kim[2], G. Baek[1], K. Kim[1, 3], B. Park[2]
[1]Physics, Korea Advanced Institute of Science and Technology, Daejeon, Korea (the Republic of), [2]Material Science and Engineering, Korea Advanced Institute of Science and Technology, Daejeon, Korea (the Republic of), [3]Graduate School of Quantum Science and Technology, Korea Advanced Institute of Science and Technology, Daejeon, Korea (the Republic of)

Spin–orbit torque (SOT), originating from the spin Hall current, has been a pivotal mechanism for magnetization manipulation in spintronic devices, enabling low-power and high-speed operation [1,2]. However, conventional SOT-based devices require an external magnetic field for deterministic switching. To overcome this limitation, magnetic trilayer structures have been proposed [3], where unconventional SOT arising from the ferromagnet/non-magnet layers enables field-free SOT switching. Nevertheless, further enhancement of the switching efficiency is required for practical SOT device applications. Here, we study the enhancement of field-free SOT switching efficiency by exploiting spin currents generated from a ferrimagnetic layer [4].

We investigate a ferrimagnetic trilayer Ti (3 nm)/Co_xGd_{100-x} (5 nm)/Ti (3 nm)/CoFeB (1 nm)/MgO (2 nm)/Ti (2 nm), consisting of an in-plane magnetized CoGd layer and a perpendicularly magnetized CoFeB layer. In this structure, the CoGd/Ti bilayer serves as a source of unconventional z-polarized spin current. By systematically varying the CoGd composition, we observe deterministic field-free SOT switching, with the switching polarity reversing between the Co-rich and Gd-rich samples. This suggests that the sign of the z-polarized spin component changes across the magnetic compensation point in the ferrimagnetic layer. In addition, the switching current decreases with increasing Gd content, indicating an enhancement of the z-spin component, which is further supported by loop-shift measurements. These results demonstrate that modulating the magnitude and polarity of the unconventional spin current provides a direct and effective route to lowering the switching current in field-free SOT devices.

[1] I. M. Miron *et al. Nature* 476, 189-193 (2011).
[2] L. Liu *et al. Science* 336, 6081 (2012).
[3] S. C. Baek *et al. Nature Materials* 17, 509-513 (2018).
[4] S.K. Kim *et al. Nature Materials* 21, 24-34 (2022).

CF-10. Nonvolatile optical control of antiferromagnetic domains in $LiNiPO_4$

S. Toyoda[1], V. Kocsis[2], Y. Tokunaga[3], I. Kézsmárki[4], Y. Taguchi[1], T. Arima[1, 3], Y. Tokura[1, 5], N. Ogawa[1]
[1]CEMS, RIKEN, Wako, Japan, [2]Institut für Festkörperforschung, Dresden, Germany, [3]Department of Advanced Materials Science, The University of Tokyo, Kashiwa, Japan, [4]University of Augsburg, Augsburg, Germany, [5]Tokyo College and department of Applied Physics, The University of Tokyo, Tokyo, Japan

All-optical control of magnetism is a key step toward next-generation opto-spintronic devices that integrate the speed of photonics with the memory functionality of magnetic materials. Antiferromagnets are particularly attractive in this respect because of their intrinsically fast spin dynamics and robustness against external perturbations. However, optical detection and control of antiferromagnetic states remain challenging, as conventional opto-magnetic recording and magneto-optical readout techniques rely on net magnetization, which is absent in antiferromagnets.

A promising strategy to overcome this limitation is to exploit magnetic multipoles other than magnetic dipoles. In certain multiferroic antiferromagnets, the magnetic toroidal moment, which arises from vortex-like spin arrangements, acts as a ferroic order parameter that breaks both spatial inversion and time-reversal symmetries. This moment can couple to the linear momentum of light, producing the optical magnetoelectric effect (OME), in which optical properties depend on the direction of light propagation [1]. This coupling further suggests the possibility of the inverse process, namely the inverse optical magnetoelectric effect (IOME), where the propagation direction of light controls the ferrotoroidic moment, as illustrated in Fig. 1.

In this presentation, we experimentally demonstrate all-

optical control of antiferromagnetic domains in ferrotoroidic $LiNiPO_4$ via the IOME. $LiNiPO_4$ crystallizes in a centrosymmetric olivine structure and exhibits antiferromagnetic order below 20.8 K, accompanied by a ferrotoroidic moment along the *b* axis. By irradiating the material with intense femtosecond light pulses at 1700 nm, resonant with the *d*–*d* transition of Ni^{2+} ions, we optically manipulate a ferrotoroidic moment whose sign is reversed by reversing the light propagation direction. We find that this switching process is deterministic, nonvolatile, and sufficiently efficient to switch between single-domain ferrotoroidic states with opposite ferrotoroidic moments, corresponding to the two time-reversed antiferromagnetic domains.

[1] K. Kimura and T. Kimura, Phys. Rev. Lett. 132, 036901 (2024).
[2] S. Toyoda et al., Nature Materials, accepted (arXiv:2506.07051)

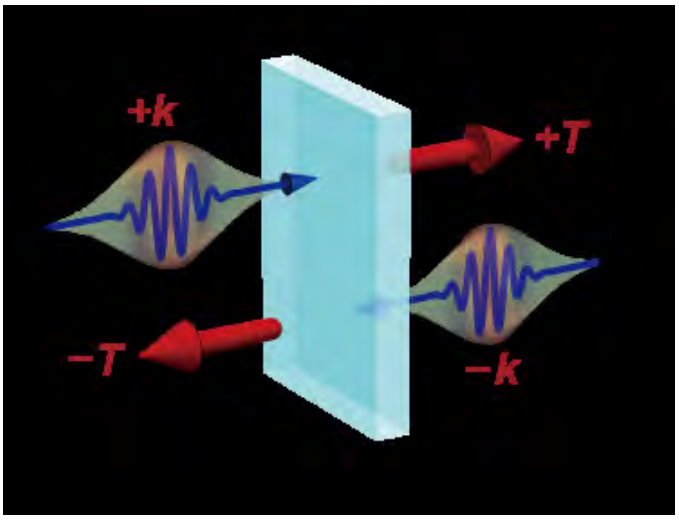


Fig.1. Schematic of the inverse optical magnetoelectric effect

CF-11. A Spin-Orbit Torque Pulley Embedded in an Exchange-Spring-Coupled Antiferromagnet/Ferromagnet Bilayer with Pulse-Dependent Plasticity for Efficient Neuromorphic Computing

M. Yang, C. Yang
Material Science and Engineering, National Yang Ming Chiao Tung University, Hsinchu, Taiwan, Taiwan

Monitoring spin–orbit-torque (SOT) switching of exchange bias (Hex) in FM/AFM bilayers is useful for probing AFMs, whereas Hex mainly reflects interfacial spins and masks depth-dependent order formed under an exchange-spring coupling. In this work, we uncover a nonreported hidden order functioning as a magnetic pulley in sputtered Pt/Co/IrMn trilayers and show how it governs SOT switching [1]. Although Hex is fully reversible, driven by SOT, and features a dynamic interface, reducing the driving stimuli, such as small in-plane fields and short current pulses, it reveals a robust subsurface IrMn order inducing a ratchet-type asymmetry: the analog–digital duality. The polarity of the ratchet can be set and reversed by the initial magnetization–Hex state, consistent with an exchange-spring scenario where progressively stronger bulk IrMn moments act as an embedded pinning backbone, although the interfacial Hex remains mobile. By exploiting pronounced pulse-width-dependent plasticity (10–100 μs), we map the measured SOT switching curves for activation functions with tailorable thresholds and steepness, and deploy them in a convolutional neuronal network architecture. A dynamic-annealing modulation (short→long pulses) attains image-recognition accuracy, approaching that acquired by software ReLU. These results uncover an AFM order beyond Hex and establish a reconfigurable, energy-efficient SOT building block for neuromorphic computing [1].

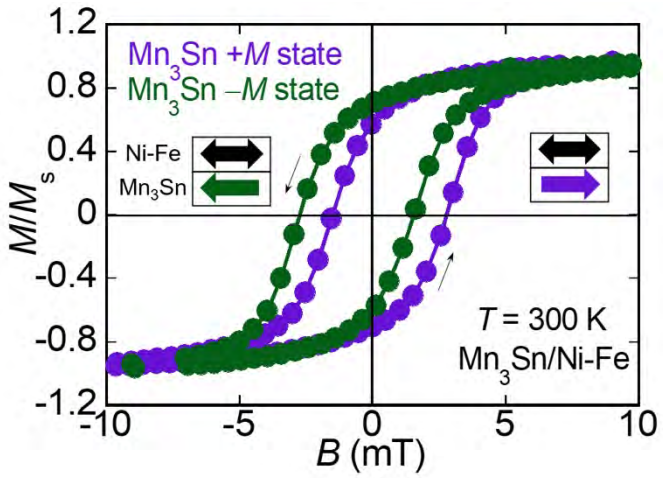
[1] Meng-Chi Yang *et al.*, *ACS Appl. Energy Mater.* 9, 4384–4393 (2026).

CF-12. Isothermal Manipulation of Exchange Bias between the Chiral Antiferromagnet Mn_3Sn and Ferromagnets

M. Asakura[1], T. Higo[2, 1, 3], T. Matsuo[4, 1], Y. Tsushima[1], S. Kurosawa[1], R. Uesugi[5, 1], D. Nishio-Hamane[3], S. Nakatsuji[1, 3, 4]
[1]Department of Physics, The University of Tokyo, Tokyo, Japan, [2]Department of Electronics and Electrical Engineering, Keio University, Yokohama, Japan, [3]Institute for Solid State Physics, The University of Tokyo, Kashiwa, Japan, [4]Institute for Quantum Matter and Department of Physics and Astronomy, Johns Hopkins University, Baltimore, Maryland, United States, [5]Graduate School of Science and Engineering, Ibaraki University, Hitachi, Japan

Exchange bias, observed at interfaces between antiferromagnets and ferromagnets as a shift of the ferromagnetic hysteresis loop, is widely used to stabilize magnetic states in spintronic devices [1]. Conventionally, switching the direction of exchange bias requires heating above the Néel temperature of the antiferromagnet, which limits its controllability. Recently, significant progress has been made in achieving isothermal control of exchange bias in response to growing interest in antiferromagnetic spintronics. Previous approaches have utilized spin–orbit

torque switching, magnetoelectric effects, and resistive switching, in which the macroscopic time-reversal symmetry of the antiferromagnetic layer is preserved [2-4].
In this study, we explored antiferromagnets with broken macroscopic time-reversal symmetry to develop a novel approach for isothermal control of exchange bias [5]. We focused on the chiral antiferromagnet Mn_3Sn [6-8] and fabricated bilayers consisting of Mn_3Sn and various ferromagnets. We observed interfacial magnetic coupling and a finite exchange bias at room temperature. Importantly, the exchange bias was controlled not only by conventional field cooling process but also isothermally through the application of a magnetic field, which switches the magnetic order of the Mn_3Sn layer. This isothermal switching occurred only within the temperature range where Mn_3Sn exhibits its inverse triangular magnetic structure, which breaks macroscopic time-reversal symmetry. Furthermore, both the sign and magnitude of the exchange bias can be tuned by selecting different ferromagnetic layers. These results establish a new route for controlling exchange bias and provide a foundation for next-generation spintronics based on antiferromagnets as active elements.
This work was supported by JST-MIRAI (JPMJMI20A1), JST-ASPIRE (JPMJAP2317), DOE (DE-SC0024469), JST-SPRING (JPMJSP2108), JST-PRESTO (JPMJPR24M8), Murata Science and Education Foundation.
[1] W. H. Meiklejohn and C. P. Bean, Phys. Rev., Vol. 102, p.1413 (1956)
[2] P. H. Lin et al., Nat. Mater., Vol. 18, p.335 (2019)
[3] X. He et al., Nat. Mater., Vol. 9, p.579 (2010)
[4] L. Wei, et al., Adv. Mater., Vol. 30, p.1801885 (2018)
[5] M. Asakura, et al., Nano Lett., Vol. 25, p.10294 (2025)
[6] S. Nakatsuji, N. Kiyohara, and T. Higo, Nature, Vol. 527, p.212 (2015)
[7] H. Tsai, T. Higo, et. al., Nature, Vol. 508, p.608 (2020); T. Higo, K. Kondou, et. al., Nature, Vol. 607, p.474 (2022)
[8] M. Asakura, et. al., Adv. Mater., Vol. 36, p.2400301 (2024)



Exchange bias effect induced in Ni−Fe after the isothermal application of magnetic fields and reversal of the magnetic order of Mn_3Sn ($\pm M$ states) at 300 K.

CF-13. A Metallicity-Screened High-Throughput DFT Workflow for Predicting Magnetic Ground States: Toward the Search for Metallic Altermagnets

S. Pradhan, K. Belashchenko
Department of Physics and Astronomy and Nebraska Center for Materials and Nanoscience, University of Nebraska-Lincoln, Lincoln, Nebraska, United States

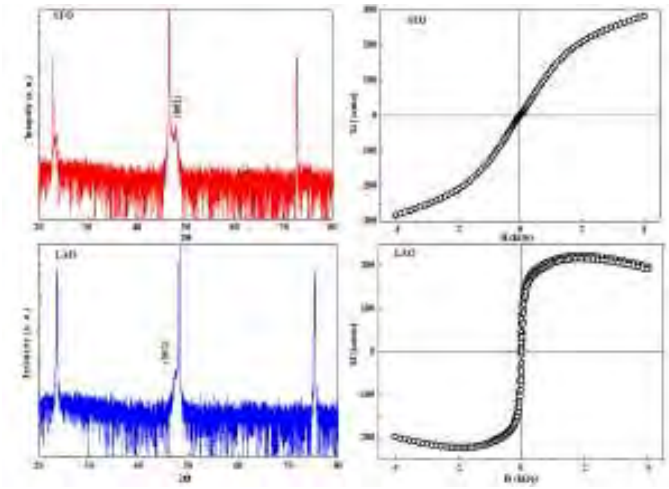
Many applications require screening for magnetic materials with specific magnetic orderings, yet such information remains sparse in existing materials databases. In this work, we develop a computational framework combining machine learning (ML) with high-throughput density functional theory (DFT) for scalable and automated prediction of magnetic ground states. We focus on metallic systems, as their magnetic properties are generally well described within standard DFT without the need for empirical corrections. First, we develop a ML framework for classifying materials as metals or insulators, which is trained entirely on an experimentally verified input sets of metals and insulators. The model employs a tree-based gradient boosting classifier (XGBoost) with descriptors derived from elemental property statistics and features available from Materials Project and the SMACT [1] library. The trained model demonstrates strong separation between metals and insulators with physically meaningful feature importance. Using this ML classifier to preselect metallic compounds, we subsequently employ a high-throughput DFT workflow automated with the Alloy Theoretic Automated Toolkit

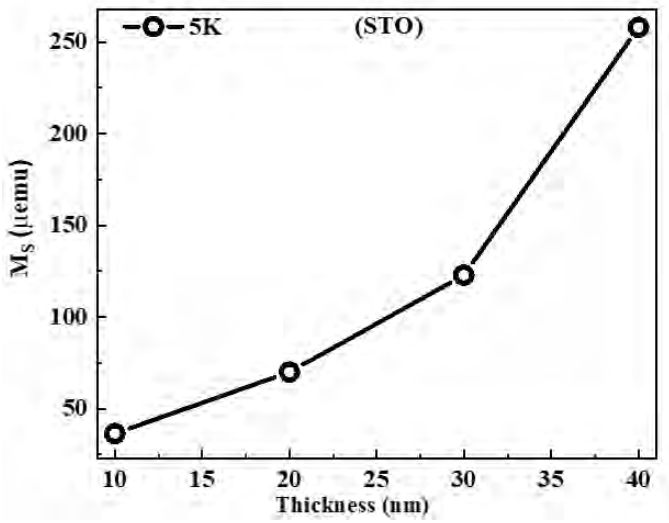
(ATAT) [2] to systematically determine their collinear magnetic ground states. The framework is validated against available experimental data. Utilizing this framework, we conduct a targeted search for metallic altermagnets within the Materials Project database, combining symmetry-based candidate filtering, ML metallicity screening, and high-throughput DFT ground-state determination. This approach provides an efficient route for the systematic computational search of magnetically ordered materials, including rare classes such as metallic altermagnets.

[1] D. W. Davies et al., J. Open Source Softw. 4, 1361 (2019)
[2] A. van de Walle et al., Calphad 26, 539-553 (2002)

CF-15. Thickness-dependent magnetic properties of 25% Mn-doped HoFeO3 thin films: structural comparison on SrTiO3 and LaAlO3 substrates

S. Das, S. Saha, A. Kumar, M. P, P. K. Muduli, S. P. N.
Physics, IIT Madras, Chennai, Tamilnadu, India





Thin films of 25% Mn-doped HoFeO3 were prepared on SrTiO3 (STO) and LaAlO3 (LAO) substrates using pulsed laser deposition in order to study the effect of film thickness and substrate-induced strain on their structural and magnetic properties. X-ray diffraction analysis confirms the growth of well-oriented films on both substrates. The shift in diffraction peak positions for films grown on STO and LAO suggests the presence of different strain states due to lattice mismatch with the substrates.

Magnetic measurements on films grown on STO show a clear dependence of magnetization on film thickness. The observed variation in magnetic moment with thickness may be related to finite size effects, strain relaxation and changes in magnetic interactions with increasing thickness. A comparison of magnetic behavior for films grown on STO and LAO further indicates that substrate induced strain strongly influences the net magnetization, possibly through modification of exchange interactions and spin canting.

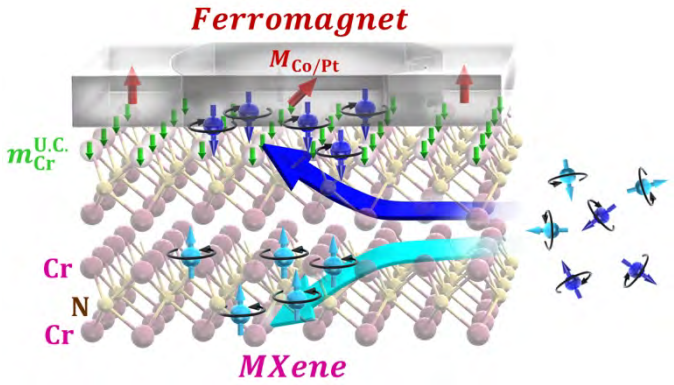
The present results demonstrate that both thickness control and substrate selection are effective ways to tune the magnetic properties of Mn-doped HoFeO3 thin films. Such controllable magnetic behavior makes these materials promising for future spintronic devices, magnetic sensing and multifunctional oxide electronics.

1. F. Tusi et. al., Appl. Phys. Lett., 76, 2421–2423 (2000)
2. B. Paudel et. al., Mater. Res. Lett., 10, 29-35 (2022)
3. y. Li et. al., MMM, 8, 056317 (2018)

SESSION CG: ORBITRONICS
Chair(s): E. A. Montoya, *Physics and Astronomy, University of Utah, South Salt Lake, Utah, United States*
Wednesday, November 4, 2026
08:30 AM-12:00 PM
Sea Pearl

CG-01. Field-free perpendicular magnetization switching in 2D-MXene/FM bilayers without relying on heavy metals
P. Kumar, G. K. Shukla, S. Isogami
NIMS, Tsukuba, Japan

Charge-to-spin interconversion has been widely studied in heavy metals and is central to spintronic applications such as spin–orbit-torque (SOT) and/or orbital-torque (OT) driven nonvolatile magnetic random-access memories (MRAMs). Two-dimensional (2D) materials are promising for scalable, low-power and high-speed devices; however, large-area synthesis and isotropic SOT independent of crystal symmetry remain major challenges [1].
Here, we developed a Cr_2N MXene film, a new class of 2D material, using a conventional reactive nitridation sputtering technique. Field-free perpendicular magnetization switching was demonstrated in Cr_2N/ferromagnet bilayers via isotropic SOTs/OTs, regardless of crystal symmetry [2]. This behavior originates from the generally stabilized nitride phase [3], the orbital Hall mechanisms, and the interfacial uncompensated Cr magnetic moments revealed by X-ray magnetic circular dichroism [4]. Furthermore, electronic states at the Cr_2N/ferromagnet interface was investigated via angle-resolved hard X-ray photoemission spectroscopy, revealing the identical electronic states regardless of the adjacent layers [4]. The representative current density for the field-free magnetization switching of the $Cr_2N/[Co/Pt]_3$ system was comparable to the conventional W/CoFeB systems, and a further challenge to decrease the current density was conducted based on the metastable Cr_2N phase and ultrathin layer insertion between the $Cr_2N/[Co/Pt]_3$ interface. These results and perspects indicate the breakthrough of major challenges, highlighting the potential of 2D-MXene-based SOT/OT devices to accelerate the development of next-generation MRAM technologies [1].
[1] Yang *et al*., Nature 606, 663 (2022); Liu *et al*., ACS Nano, 14, 9389 (2020); Ahn *et al*., npj 2D Materials and Applications 4, 17 (2020); Kajale *et al*., Nano Research, 17, 743 (2024).
[2] Kumar *et al*., Small 21, 2500626 (2025).
[3] Isogami *et al*., Adv. Electron. Mater. 9, 2200515 (2023).
[4] Kumar *et al*., STAM 26, 2551484 (2025).



Schematic illustration showin a spin-orbit torque device with a spin channel of Cr_2N 2D-MXenelayer and possible mechanism for field free switching.

CG-03. Spin angular momentum contributions in the magneto-photogalvanic effect
A. Kamiryo[1], M. Yamamoto[2], T. Nishijima[2], R. Ohshima[2], M. Shiraishi[2], Y. Ando[1]
[1]Physics and Electronics, Osaka Metropolitan Univ., Sakai, Osaka, Japan, [2]Electronic Engineering, Kyoto Univ., Kyoto, Japan

We report a unidirectional photocurrent generated at the edges of a metallic thin-film wire under a DC current and illumination with linearly polarized light [1]. This phenomenon is attributed to the magneto-photogalvanic effect (MPGE), which arises in systems where both spatial inversion and time-reversal symmetries are broken [2]. Conventionally, MPGE occurs in systems with broken spatial inversion symmetry under time-reversal symmetry breaking induced by a magnetic field or magnetization. In contrast, in our study, MPGE is induced by time-reversal symmetry breaking due to spin accumulation generated via the spin Hall effect (SHE), combined with spatial inversion symmetry breaking at the edges of a metallic wire.
In our previous study, we focused on representative spin Hall materials such as Pt and β-W. However, to clarify the correlation between SHE and MPGE, it is necessary to investigate a wider range of materials. In this study, we evaluate MPGE in various materials to elucidate its underlying mechanism and identify the conditions under which it emerges. As a result, we find an additional contribution beyond SHE.
Figure 1 shows photovoltages(V_{photo}) mapping for Pd and β-Ta, which have positive and negative spin Hall angles

(SHAs), respectively. Clear photovoltages appear at the edges, where spin accumulation induces photocurrents in the same direction. exhibits opposite polarities for Pd and β-Ta, consistent with their SHAs.
Figure 2 shows the photocurrent as a function of the spin accumulation for various materials. Although an approximately linear trend is observed, a finite intercept is present. In addition, Al lies above the trend, while Cr and β-W deviate negatively. These results suggest contributions beyond SHE. This behavior can be consistently explained by considering the accumulation of orbital angular momentum induced by the orbital Hall effect.
[1] T. Nishijima *et al*., Phys. Rev. B 111, L140406 (2025)
[2] M. Matsubara *et al*., Nat Commun. 13, 6708 (2022)

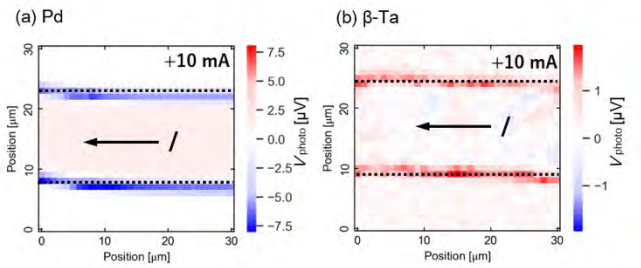


Fig. 1 Spatial two-dimensional maps of V_{photo} for (a) Pd and (b) β-Ta.

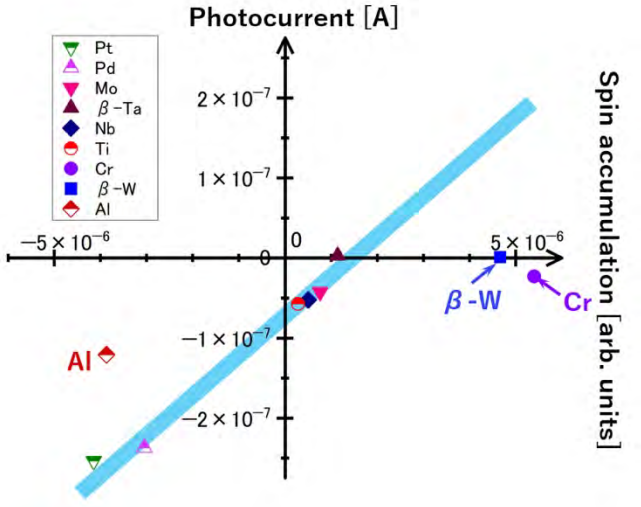


Fig. 2 Correlation between the photocurrent and spin accumulation.

CG-04. Giant orbital Rashba-Edelstein effect in crystalline Cu_2O/Cu heterostructures

S. Ko[2], J. Kang[3], S. Kim[4], H. Jang[1], D. Nam[2], Y. Jung[1], S. Jeong[2,5], K. Kim[2], B. Park[1]
[1]Materials Science and Engineering, KAIST, Daejeon, Korea (the Republic of), [2]Physics, KAIST, Daejeon, Korea (the Republic of), [3]Department of Electrical and Computer Engineering, Northwestern University, Evanston, Illinois, United States, [4]Pusan National University, Busan, Korea (the Republic of), [5]Pusan National University, Busan, Korea (the Republic of)

Orbital current-induced torque (OT) has emerged as a promising alternative to spin-orbit torque owing to the typically larger orbital Hall conductivity. A substantial OT can be generated at metal/oxide interfaces via the orbital Rashba-Edelstein effect (OREE), which has been predominantly reported in surface-oxidized Cu structures. However, the lack of well-defined crystalline and interfacial structures in oxidized Cu has hindered a clear understanding of the underlying mechanism and limited further enhancement of OT. Here, we demonstrate a significantly enhanced OREE in crystalline CuO_x/Cu heterostructures with well-defined interfaces. By employing controlled oxidation of single-crystalline Cu, we fabricate crystalline CuO_x layers with distinct chemical phases and quantify the resulting OT using harmonic Hall measurements. We find that the crystalline Cu_2O/Cu heterostructure exhibits a damping-like OT efficiency approximately seven times larger than that of naturally oxidized Cu, highlighting the crucial role of structural ordering and interface sharpness. Notably, this large OT efficiency, combined with the high electrical conductivity of Cu, yields a spin torque conductivity of 1.9×10^6 $(\hbar/2e)\Omega^{-1}m^{-1}$, exceeding that of Pt. These results establish crystalline Cu_2O/Cu heterostructures as a promising platform for ultralow-power spin-orbitronic devices.

CG-05. Chirality-Induced Spin Selectivity in Conjugated Polymers

U. Lee[1], M. Yoo[1], S. Jeon[2], Y. Chen[2], J. Neu[3], S. Li[1], W. You[3], Y. Diao[2], A. Hoffmann[1]
[1]Materials Science and Engineering, University of Illinois Urbana-Champaign, Urbana, Illinois, United States, [2]Chemical and Biomolecular Engineering, University of Illinois Urbana-Champaign, Urbana, Illinois, United States, [3]Chemistry, University of North Carolina at Chapel Hill, Chapel Hill, North Carolina, United States

Chirality-induced spin selectivity, CISS, has attracted broad interest as a route to generating angular-momentum-dependent charge transport in molecular and soft materials without conventional magnets and heavy metals [1,2]. While CISS has been widely studied in biomolecules and inorganic chiral systems, its manifestation in conjugated polymers remains poorly understood. Structurally chiral conjugated polymers are particularly attractive because their chiral organization, electrical conductivity, and in-plane alignment can be tuned through molecular design and processing.

Here, we investigate chirality-dependent angular-momentum-selective transport in printed films of the conjugated polymer p($g4_2$T-TT) using a lateral device geometry with metallic detectors [3]. We prepare left-handed and right-handed polymer films and measure the transverse voltage generated in the detector under applied longitudinal current in the polymer film. In the devices, the transverse response varies linearly with current and reverses sign with polymer handedness, while racemic control films exhibit strongly suppressed signals. These observations establish a robust chirality-dependent lateral electrical response in chiral conjugated polymer films. To further probe the origin of the response, we compare devices incorporating detector metals with distinct angular-momentum-to-charge conversion characteristics. These results identify chiral conjugated polymers as a versatile platform for studying chirality-driven angular-momentum transport in soft electronic materials and suggest new opportunities for flexible spintronic and orbitronic functionalities.

This work was supported by the Air Force Office of Scientific Research, Multidisciplinary University Research Initiatives (MURI) Program under award number FA9550-23-1-0311.
[1] K. Ray, S. P. Ananthavel and D. H. Waldeck, Science, Vol. 283, p.814 (1999)
[2] B. P. Bloom, Y. Paltiel and R. Naaman, Chem. Rev., Vol. 124, p.1950 (2024)
[3] D. Kiefer, R. Kroon and A. I. Hofmann, Nat. Mater., Vol. 18, p.149 (2019)

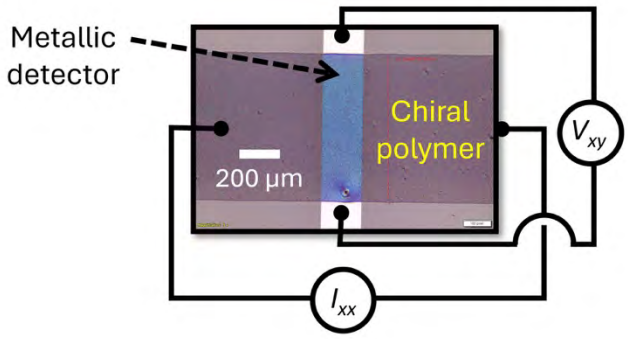


Fig. 1 Schematic of the in-plane device geometry showing the in-plane current I_{xx} and the transverse voltage V_{xy} measured across the metallic detector.

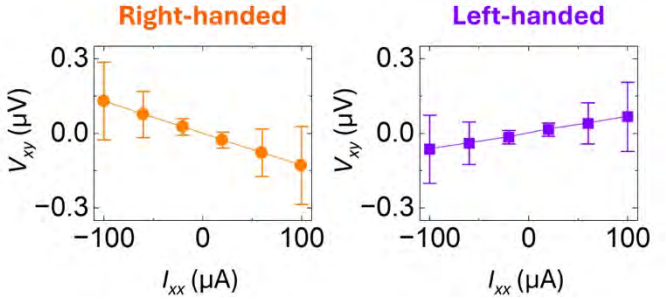


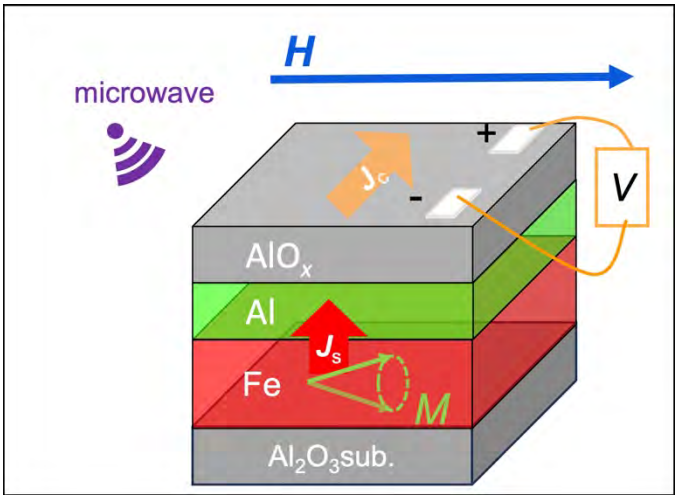
Fig. 2 Transverse voltage V_{xy} across the tungsten detector as a function of applied current I_{xx} for right- and left-handed chiral polymer films.

CG-07. Highly Efficient Spin-to-Charge Conversion in Bylayers of Light Elements

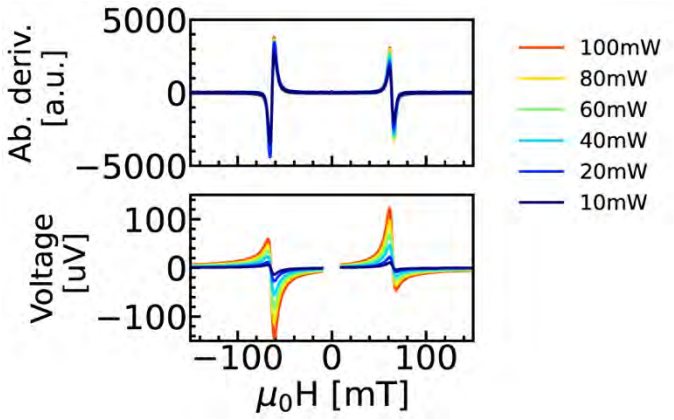
Y. Kabata[1], M. Ishida[1], T. Takeda[3], M. Tanaka[1, 2], L. Anh[1, 2]
[1]Electrical Engineering and Information Systems, The University of Tokyo, Bunkyo-ku, Tokyo, Japan, [2]Spintronics Research Network of Japan, Bunkyo-ku, Tokyo, Japan, [3]Department of Chemical System Engineering, The University of Tokyo, Bunkyo-ku, Tokyo, Japan

Spin-charge interconversion lies at the heart of many spintronics devices, and efficient conversion is essential for energy-effective spintronics. Heavy metals with strong spin-orbit coupling are known to exhibit high conversion efficiency, but these suffer from disadvantages such as high resistivity, which is a major cause of Joule heating, and natural rarity leading to relatively high cost. Therefore,

achieving highly efficient conversion in light elements is important for affordable spintronics. Recently, highly efficient charge-to-spin conversion comparable to that of Pt was observed in Si/Al gradient structures [1] and CuO_x/Cu layers [2,3]. The result of the CuO_x/Cu layer was later proposed to originate from the orbital effect.
In this work, we conducted spin-to-charge conversion (SCC) experiments using spin pumping on Al (thickness d_{Al} nm = 1.5, 2.5, 3.6, 5, and 10)/Fe(4 nm) bilayer heterostructures at room temperature (Fig. 1). The heterostructure was deposited on Al_2O_3 substrates by molecular beam epitaxy, and the Al layer was partially oxidized in air. We observed ferromagnetic resonance on all of the samples around 70-80mT in a cavity-based ESR machine, where a 9.5 GHz microwave and an external in-plane magnetic field were applied. Simultaneously, a voltage signal was detected along the transverse direction of the sample (Fig. 2), which is attributed to SCC within the Al layer. The spin Hall angle ϑ_{SHE}, a figure of merit for SCC efficiency, reaches its maximum of 0.1 at d_{Al} =1.5nm and decreases to approximately 0.01 for thicker Al layers of 5 and 10 nm. Remarkably, 0.1 is comparable to that of the heavy metals. This efficient conversion may occur due to AlO_x/Al gradient composition. Although further investigation is needed to fully elucidate the underlying physical mechanisms, highly efficient SCC with only light elements presents a promising pathway toward developing low-cost spintronic devices.
[1] T. Horaguchi, C. He and Y. Nozaki, Science Advances. Vol. 11, p. eadr9481 (2025).
[2] H. An, Y. Kageyama and K. Ando, Nature Communication, Vol. 7, 13069 (2016).
[3] Go. D, T. Jo and Y. Mokrousov, Physical Review B, Vol. 103, p. L121113 (2021).



Sample structure and spin pumping configuration.



Spin pumping results for the sample with d_{Al} = 1.5 nm. The upper shows FMR spectra in several microwave power values, and the lower represents electromotive force signals observed at the FMR condition (Linear background was subtracted from raw data).

CG-08. Tunneling of orbital angular momentum

A. Du[1], S. Ding[3], M. Leaic[2], S. Krishnia[1], A. Manchon[4], Y. Mokrousov[1, 2], M. Kläui[1]
[1]Institute of Physics, Johannes Gutenberg University Mainz, Mainz, Germany, [2]Peter Grunberg Institute, Forschungszentrum Jülich, Jülich, Germany, [3]Nanyang Technological University, Singapore, Singapore, [4]Aix-Marseille University, Marseille, France

Spin angular momentum transport is the foundation of spintronics, where spin-dependent tunneling in magnetic tunnel junctions (MTJs) enables tunneling magnetoresistance and underpins modern magnetic random-access memory technologies [1,2]. Beyond spin, orbital angular momentum has recently emerged as an efficient carrier of angular momentum in solids, enabling charge-orbital interconversion and magnetization manipulation beyond conventional spin-based mechanisms [3,4]. While orbital currents have been extensively explored in the diffusive transport regime, tunneling transport is crucial for MTJ operation, and it remains an open question whether orbital angular momentum can tunnel across an insulating barrier.
We experimentally demonstrate tunneling of orbital angular momentum through an MgO barrier in MTJ structures, with a schematic illustration of the measurement configuration shown in Figure 1. By employing Cr as the normal metal, which hosts a negative spin Hall effect and a positive orbital Hall effect [5], we disentangle spin and orbital contributions via polarity analysis. Opposite signal polarities in

Cr/MgO/CoFeB and Cr/MgO/Ni devices, together with reciprocal behavior between direct and inverse measurements, provide clear evidence of orbital-current tunneling. First-principles calculations further reveal the microscopic tunneling mechanism and explain the distinct transmission behaviors of orbital and spin angular momentum [6].
These results establish orbital angular momentum tunneling as a new transport phenomenon and extend orbitronics into the tunneling regime, opening a pathway toward orbital-based MTJ devices and all-orbital memory architectures.
[1] S. Yuasa *et al.*, Nat. Mater. 3, 868 (2004).
[2] S. S. P. Parkin *et al.*, Nat. Mater. 3, 862 (2004).
[3] T. Tanaka *et al.*, Phys. Rev. B 77, 165117 (2008).
[4] S. Fukami *et al.*, Nat. Phys. (2025) DOI:10.1038/s41567-025-03143-w
[5] S. Lee *et al.*, Commun. Phys. 4, 234 (2021).
[6] A. Du *et al.,* in preparation.

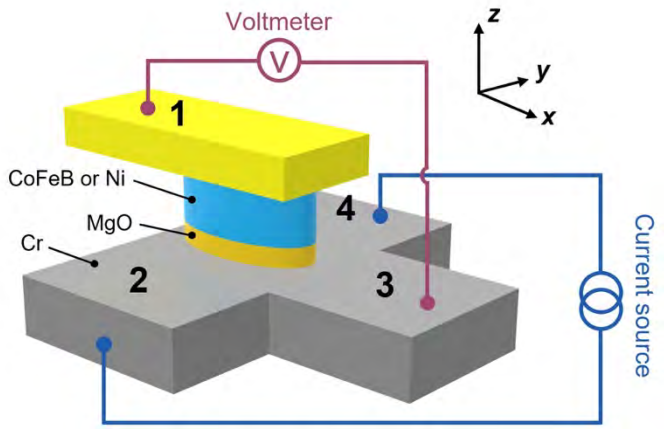


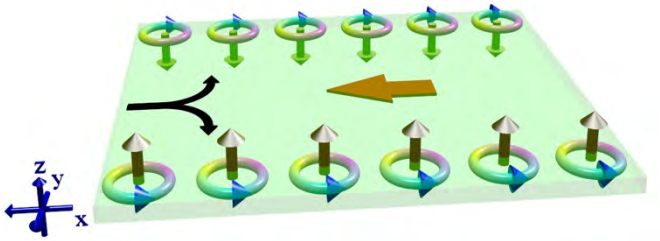
Figure 1. Schematic illustration of the measurement configuration for spin and orbital current tunneling in an MTJ device.

CG-09. Disorder Effects on Orbital Transport in Two-Dimensional Materials

T. G. Rappoport[1, 2, 3]
[1]Brazilian Center of Physical Research, Rio de Janeiro, RJ, Brazil, [2]Physics, Minho University, Braga, Portugal, [3]International Iberian Nanotechnology Laboratory, Braga, Portugal

Recent years have witnessed growing interest in orbitronics, where the orbital degree of freedom of electrons plays an active role in transport and nonequilibrium phenomena. In particular, the orbital Hall effect has emerged as a promising mechanism for generating and manipulating angular momentum in materials with weak or strong spin-orbit coupling, opening new perspectives for spin-orbit torques, magnetic dynamics, and energy-efficient spintronic devices. Understanding the role of disorder in these phenomena is therefore essential, both from a fundamental perspective and for real materials.

In this talk, I will discuss recent theoretical advances on the impact of disorder on orbital transport and orbital dynamics in quantum materials. Using large-scale real-space quantum transport approaches, we investigate how different types of disorder, including vacancies, onsite disorder, and hopping fluctuations, influence orbital Hall responses and related equilibrium and nonequilibrium orbital phenomena. Results will be presented for realistic multiorbital models and materials systems, highlighting the interplay between orbital hybridization, symmetry, localization effects, and disorder-induced scattering. I will also discuss how disorder can modify orbital relaxation and dynamical processes, including regimes where orbital responses remain robust as well as situations where disorder qualitatively changes the behavior of the system. These results contribute to the broader understanding of orbital phenomena in realistic materials and their possible role in future spintronic applications.



SESSION CH: ULTRAFAST I

Chair(s): A. De, *Advanced Institute for Materials Research (AIMR) , Tohoku University, Sendai , Japan*

Wednesday, November 4, 2026

08:30 AM-12:00 PM

Nautilus

CH-01. Picosecond spin pumping from magnetically compensated materials

C. Ciccarelli

University of Cambridge, Cambridge, United Kingdom

Generating ultra-fast spin currents is important in the context of ultra-fast magnetic memories. Antiferromagnets can be efficient spin emitters of sub-picosecond spin current pulses, despite the net-zero magnetisation. I will present our work on the optically induced picosecond spin transfer from magnetically compensated magnets, including antiferromagnets and ferromagnetic alloys, to Pt using time-domain THz emission spectroscopy. We will focus on three studies in antiferromagnetic insulators KCoF3 and KNiF3 [1], in antiferromagnetic metal FeRh [2], and rare earth-transition metal alloy CoGd [3]. Through our studies, we are able to shed light on the microscopy of spin transfer at picosecond timescales and identify key figures of merit for its efficiency.

[1] Nature Communications 14, 538 (2023)
[2] Nature Communications 15, 4958 (2024)
[3] Advanced Optical Materials 2500056 (2025)

CH-02. Tunable Ultrastrong Magnon-Magnon Coupling and Squeezed States in a Triaxial Van der Waals Antiferromagnet

X. Xiao[1], Z. Li[1], Z. Tao[1], L. Chen[2, 3], P. Liu[2], S. Zhang[1], H. Wang[1], Y. Pu[2], R. Liu[1, 4]

[1]School of Physics, Nanjing University, Nanjing, Jiangsu, China, [2]School of Science, Nanjing University of Posts and Telecommunications, Nanjing, Jiangsu, China, [3]Laboratory of Solid State Microstructures, Nanjing, Jiangsu, China, [4]State Key Laboratory of Spintronics, Suzhou, Jiangsu, China

Achieving and quantifying ultrastrong magnon-magnon coupling remains a central challenge in quantum magnonics. Here, we demonstrate tunable ultrastrong coupling between chiral (right- and left-handed) magnon modes and between acoustic and optical magnon modes in the vdW antiferromagnet $CrPS_4$. Using a full quantum model, we resolve the interaction into three microscopic channels: the co-rotating term g_1 for mode hybridization, the counter-rotating term g_2 for two-mode squeezing, and, uniquely in the chiral regime, the self-squared term g_3 for single-mode squeezing. The normalized coupling ratio reaches $g/f_g \sim 0.41$, placing the system in the ultrastrong-coupling regime. We further establish a framework linking these coupling parameters to experimentally accessible signatures of a squeezed magnon vacuum state. Our simulations visualize the chirality and polarization evolution of the hybrid modes and show how magnon squeezing and entanglement connect to spin-dynamic observables, with a squeezing factor up to ~9.7 dB extracted from thermal-noise-driven magnetization dynamics. These results provide a material-specific quantum framework for ultrastrong coupling in low-damping 2D magnets and a practical route to identifying nonclassical magnon states for quantum spintronics and hybrid quantum platforms.

T. Makihara, K. Hayashida and G. T. Noe II, Nat. Commun., Vol. 12, p.3115 (2021)
Y. Wang, Y. Zhang and C. Li, Nat. Commun., Vol. 15, p.2077 (2024)
W. Li, Y. Dai and L. Ni, Adv. Funct. Mater., p.2303781 (2023)
A. Kamra, E. Thingstad and G. Rastelli, Phys. Rev. B, Vol. 100, p.174407 (2019)
H. Y. Yuan, Y. Cao and A. Kamra, Phys. Rep., Vol. 965, p.1 (2022)

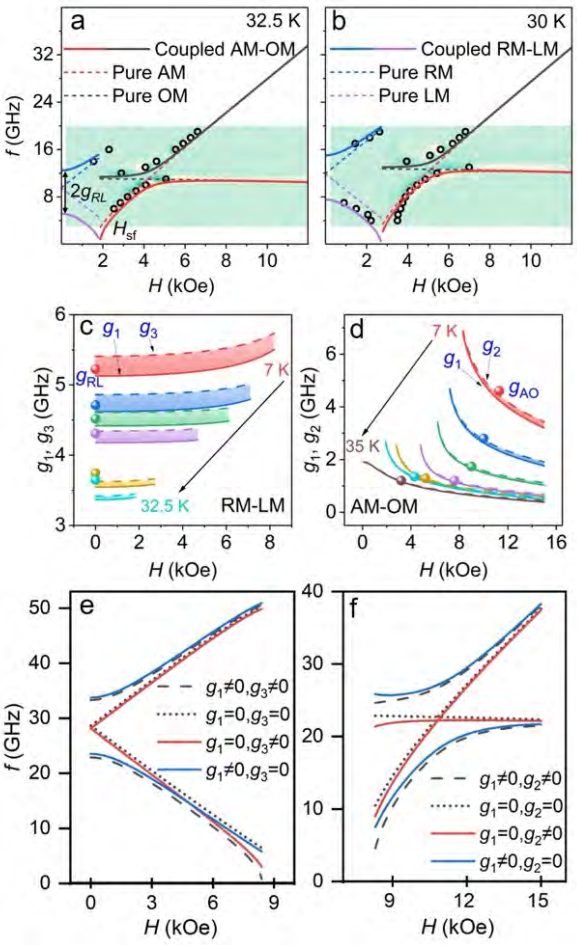


Fig. 1 Experimental AFMR spectra, fitted dispersions, and coupling strengths under an out-of-plane field. (a,b) Spectra at 32.5 and 30 K. Black open circles mark resonance fields. Red/black and blue/purple dashed lines denote pure AM/OM and RM/LM modes; solid lines show the coupled AM-OM and RM-LM dispersions. (c,d) Field-dependent coupling strengths from the quantum model. (e,f) Experimental fits and calculated dispersions at 7 K in the low-field RM-LM and high-field AM-OM regimes.

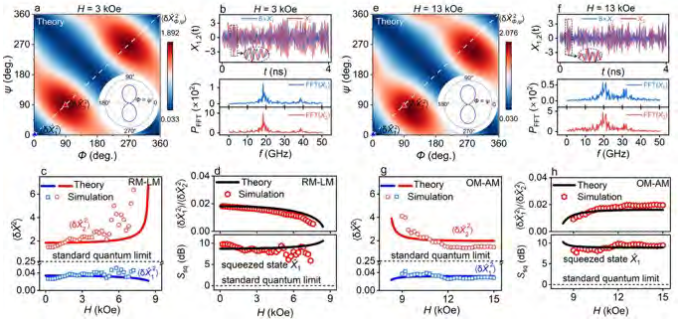


Fig. 2 Theoretical and simulated quadrature fluctuations and squeezing ratios. (a)Fluctuation map versus phase angles Φ and ψ at H = 3 kOe; inset: polar plot along $\Phi = \psi$. (b) Simulated X_1 and X_2 time traces and Fourier spectra at 3 kOe. (c,d) Theory-simulation comparison of quadrature fluctuations, squeezing ratios, and squeezing factors in the low-field RM-LM regime. (e–h) Same analysis at H = 13 kOe for the high-field AM-OM regime.

CH-03. Phonon-Driven Spin Dynamics in Rare-Earth Orthoferrites across Spin Reorientation Temperatures

M. Hales[1], O. Kovalenko[1], D. Afanasiev[2], A. V. Kimel[2], R. V. Mikhaylovskiy[1]

[1]Physics Department, Lancaster University, Lancaster, United Kingdom, [2]Institute for Molecules and Materials, Radboud University, Nijmegen, Netherlands

The pursuit of energy efficient alternatives to conventional electronic devices has become a central focus of scientific research. One promising approach employs spin waves as a means of information transfer to avoid Joule-heating. Additionally, all-optical magnetization switching holds the potential to enhance magnetic data-storage technology, offering high speed operation and improved efficiency.

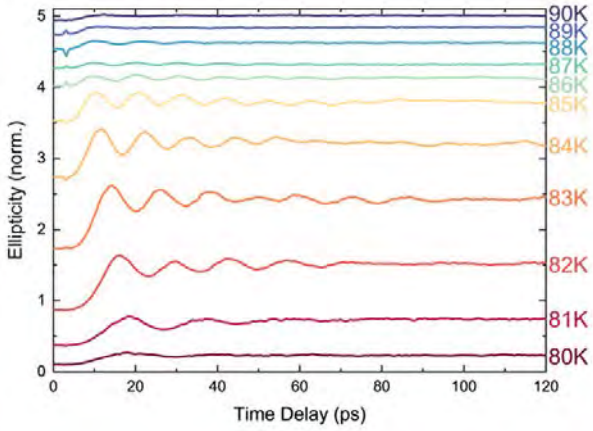
Spin dynamics in rare-earth orthoferrites have been extensively studied due to their canted antiferromagnetic structure, strong spin-lattice coupling and very high magneto-optics. Also of interest is a phase transition during which the antiferromagnetic vector undergoes a spin reorientation. Recently, a phononic pathway to excite spin dynamics has been discovered in rare-earth orthoferrites [1][2], while phonon-driven switching was observed in an iron garnet [3].

To study phonon-driven responses in a single crystal, 60 μm-thick sample of $TmFeO_3$ we performed a time-resolved pump-probe spectroscopy experiment. Mid-infrared pump pulses were tuned at resonance with optical phonons,

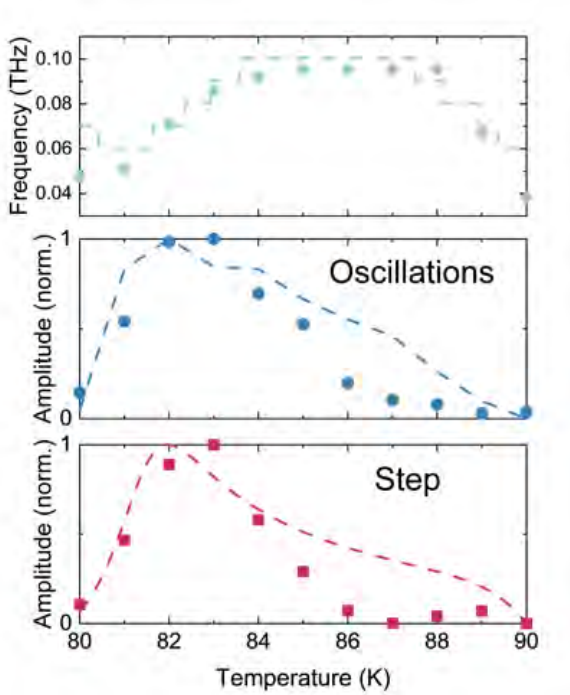
distorting the crystal lattice which induced a torque on the spins, thereby driving them into precessional motion. The spin dynamics were measured by polarization rotation of an 800 nm probe as a function of time-delay with respect to the pump pulse.

Polarization rotation signals reveal the quasi-ferromagnetic magnon mode in $TmFeO_3$ is resonantly excited when pumping at optical phonon frequencies. The frequency dependence over spin reorientation transition temperatures agrees with expected values, and a phenomenological model of spin dynamics induced by ultrafast heating shows a good match with experimental data [4]. A complementary experiment performed on $ErFeO_3$ displays similar behaviour.

[1] J. Nova, A. Cartella, A. Cantaluppi, M. Först, D. Bossini, R. V. Mikhaylovskiy, A. V. Kimel and A. Cavalleri, *Nature Physics*., Vol. 13, p.132 (2017)
[2] D. Afanasiev, J. R. Hortensius, B. A. Ivanov, A. Sasani, E. Bousquet, Y. M. Blanter, R. V. Mikhaylovskiy, A. V. Kimel and A. D. Caviglia, *Nature Materials*., Vol. 20, p.607 (2021)
[3] A. Stupakiewicz, C. S. Davies, K. Szerenos, D. Afanasiev, K. S. Rabinovich, A. V. Boris, A. Caviglia, A. V. Kimel and A. Kirilyuk, *Nature Physics*., Vol. 17, p.489 (2021)
[4] S. Baierl, M. Hohenleutner, T. Kampfrath, A. K. Zvezdin, A. V. Kimel, R. Huber and R. V. Mikhaylovskiy, *Nature Photonics*., Vol. 10, p.715 (2016)



Ellipticity measurements of the optical probe pulse reveal the quasi-ferromagnetic mode within spin reorientation temperatures for $TmFeO_3$ resonantly pumped with a mid-infrared pulse.



Extracted frequency, step and oscillation amplitude of ellipticity measurements (scatter points) across spin reorientation transition for $TmFeO_3$. A phenomenological model modelling transient anisotropy as effective temperature shows good agreement (dotted lines).

CH-04. Magnetization reversal induced by an irradiation of ultrafast pulsed laser

H. Wadati
University of Hyogo, Hyogo, Japan

Ultrafast magnetization switching by pulsed lasers has been actively studied due to its potential for next-generation magnetic recording devices. A phenomenon where magnetization is switched by laser irradiation without applying a magnetic field is called all-optical switching (AOS). We are searching for AOS in oxide thin films to realize future device applications. By performing magneto-optical Kerr effect (MOKE) microscopy measurements of laser-irradiated magnetic domains, we revealed both helicity-dependent and -independent AOS in $NiCo_2O_4$ thin films with a property of perpendicular magnetic anisotropy [1-3]. Here, the sample was irradiated with linearly polarized ultrafast laser pulses generated by the Yb:KGW laser PHAROS (1030 nm, 1 kHz, pulse width ~200 fs). Figure 1 presents the schematics of the laser-pulse-accumulation effect of laser-induced magnetization switching in the $NiCo_2O_4$ thin film. AOS emerged at the perimeter of the laser

spot after irradiating 10^3 - 10^5 pulses. Furthermore, the AOS area increased with the accumulation of laser pulses.
[1] R. Takahashi, H. Wadati *et al*., Appl. Phys. Lett. 119, 102404 (2021).
[2] R. Takahashi, H. Wadati *et al*., ACS Appl. Electron. Mater. 5 (2), 748 (2023).
[3] R. Takahashi, H. Wadati *et al*., Appl. Phys. Lett. 126, 212405 (2025).

CH-05. Interference of Terahertz Antiferromagnetic Magnons via Internal Reflections

G. Baek[1], A. M. Park[1], K. Kim[1, 2]
[1]Physics, KAIST, Daejeon, Korea (the Republic of), [2]Graduate School of Quantum Science and Technology, KAIST, Daejeon, Korea (the Republic of)

A magnon is a quantized quasiparticle representing the collective excitation of spins in a magnetic system. Magnonics, which focuses on the generation, control, and detection of magnons, has attracted significant attention as a platform for spin-based information processing. Since magnons transport angular momentum without charge flow, they enable energy-efficient computing technologies [1]. Moreover, their intrinsic wave nature allows wave-based logic operations through interference and phase manipulation, enabling functionalities such as XOR, AND, and NOT gates [2]. However, most studies have focused on magnons in ferromagnetic or ferrimagnetic systems operating in the gigahertz (GHz) range [3,4]. In contrast, antiferromagnetic magnons, governed by strong exchange interactions, naturally emerge in the terahertz (THz) regime, enabling ultrafast dynamics and quantum functionalities. Here, we experimentally demonstrate that, in the antiferromagnetic insulator NiO, bulk magnons can be selectively enhanced or suppressed via internal reflections of THz pulses. Depending on the Fabry–Pérot cavity condition within the crystal, the magnon amplitude and phase is modulated. While magnons driven by the directly transmitted pulse remain nearly unchanged, those excited by internally reflected pulses exhibit constructive or destructive interference consistent with the cavity condition. Furthermore, by extending the study to MnO, which shares the same type-II antiferromagnetic structure but has a larger damping constant, we investigate the role of dissipation. In MnO, the magnon signal decays more rapidly, reducing the contribution of reflected pulses and leading to distinct modulation behavior. This demonstrates that the interplay between damping and internal reflections determines magnon dynamics. Numerical simulations based on wave interference models reproduce the experimental results. These findings show that intrinsic internal interfaces can control the phase and amplitude of antiferromagnetic magnons, providing a pathway toward wave-based magnonic logic and quantum information platforms.
[1] A. V. Chumak *et al. Nat. Phys.* 11, 453–461 (2015).
[2] A. Khitun *et al. J. Phys. D: Appl. Phys.* 43 264005 (2010).
[3] T. Schneider *et al*., *Appl. Phys. Lett.* 92, 022505 (2008).
[4] V. Vlaminck *et al*., *Science* 322, 410–413 (2008).

This work was supported by the National Research Foundation of Korea (NRF) grant funded by the Korean government (MSIP) (Grant No. RS-2023-00275259).

10:18 AM-10:45 AM
Break

CH-06. Correlating ultrafast demagnetization with THz emission in spintronic heterostructures

S. Shrestha[1], L. Scheuer[1], W. Wu[1], N. Parvez[1], A. Kefayati[1], J. Q. Xiao[1], B. Nikolić[1], B. Jungfleisch[1], L. Gundlach[1, 2]
[1]Physics and Astronomy, University of Delaware, Newark, Delaware, United States, [2]Chemistry and Biochemistry, University of Delaware, Newark, Delaware, United States

Spintronic Terahertz (THz) Emitters (STEs), typically a ferromagnet (FM) and heavy metal (HM) bilayer, have emerged as an economic tabletop THz source and a platform to study ultrafast spin and charge dynamics induced by a femtosecond (fs) laser pulse [1]. THz emission from these heterostructures is described by superdiffusive spin transport [2] arising from ultrafast demagnetization (UDM) [3] in the FM, followed by spin current generation and conversion into a charge current in the HM through the inverse spin Hall effect. Recent theoretical work, including first-principle calculations using time-dependent density functional theory (TDDFT), suggests that charge dynamics within the FM itself play a dominant role in the emitted THz field [4]. Understanding the temporal dynamics of the UDM and THz emission enables decoupling of the microscopic processes involved, but this remains an open experimental question. One approach is to temporally correlate the UDM and THz emission upon a fs laser pulse excitation to understand the chronology of the processes involved.
We present correlated measurements of UDM and THz emission using synchronized time-domain THz spectroscopy (TDTS) and time-resolved magneto-optic Kerr effect (TR-MOKE) in a CoFeB|Pt bilayer in transmission geometry. We also present the effect of introducing a Cu spacer layer

between the CoFeB and Pt layer to delay the spin and charge dynamics [5] measured with this system. We further report the implementation of a TR-MOKE integrated TDTS platform in a reflective geometry, improving signal-to-noise ratio and mitigating substrate-related effects in the measurements. The experimental results are used to reconstruct the transient charge current from the measured THz field, with care to preserve phase information and avoid artifacts introduced by the detection response. This preserves the time dynamics and helps understand the correlated measurement results. The framework enables us to understand the nuanced differences in the temporal dynamics of UDM and THz emission and refine the microscopic models of THz emission from STEs.

This research was supported by NSF through the University of Delaware Materials Research Science and Engineering Center, DMR-2011824.

1. W. Wu, C. Y. Ameyaw, M. F. Doty, Journal of Applied Physics, 130, 091101 (2021)
2. T. Kampfrath, M. Battiato, P. Maldonado, Nature Nanotechnology, 8, 256-260 (2013)
3. E. Beaurepaire, J.-C. Merle, A. Daunois, Physical Review Letters, 76, 4250 (1996)
4. A. Kefayati, Y. Ren, M.B. Jungfleisch, Physical Review B, 111, L140415 (2025)
5. J. Jechumtal, R. Rouzegar, O. Gueckstock, Physical Review Letters, 132, 226703 (2024)

CH-07. Modeling ultrafast spin-current-driven switching in ferromagnetic spin valves

P. Chailloleau[1], V. Raposo[4, 2], Q. Remy[3], C. Henri[1], J. Hohlfeld[1], M. Hehn[1, 5], E. Martinez Vecino[4, 2], H. Jaffrès[6], S. Mangin[1, 5]
[1]IJL, Université de Lorraine, CNRS, Nancy, France, [2]Unidad de Excelencia en Luz y Materia Estructuradas (LUMES), Universidad de Salamanca, Salamanca, Spain, [3]Department of Physics, Freie Universität Berlin, Berlin, Germany, [4]Dpto. Física Aplicada, Universidad de Salamanca, Salamanca, Spain, [5]Center for Science and Innovation in Spintronics, Tohoku University, Sendai, Japan, [6]CNRS, Thales, Université Paris-Saclay, Laboratoire Albert Fert, Palaiseau, France

Single-pulse reversal in fully ferromagnetic [Co/Pt]/Cu/[Co/Pt] spin valves has revealed bipolar optical switching, with both AP-to-P and P-to-AP transitions induced by femtosecond laser excitation [1]. Time-resolved experiments indicate that the final state of the free layer is governed by the ultrafast dynamics of the reference layer: AP-to-P switching is driven by spin current emitted during its demagnetization, whereas P-to-AP switching originates from spin current emitted during its remagnetization [2,3]. This differs from interpretations based mainly on hot-electron superdiffusion and charge reequilibration [4], highlighting the need for models connecting ultrafast spin-current generation, magnetization dynamics and experimental switching maps.

We develop such a multiscale model by combining atomistic magnetization dynamics with an s-d description of ultrafast spin-current generation in metallic spin valves [2,5-7]. A micromagnetic treatment of the laterally excited region under a Gaussian laser fluence profile is added to reproduce spatial switching patterns and fluence thresholds. The model captures the asymmetry between AP-to-P and P-to-AP channels (Fig 1) and the donut shape all optical switching observed in spin valve structure (Fig. 2)

[1] J. Igarashi *et al.*, *Nat. Mater.* 22, 725 (2023).
[2] H. Singh *et al.*, *Phys. Rev. Lett.* 136, 056701 (2026).
[3] J.-X. Lin *et al.*, *Advanced Materials* 0:e22886 (2026).
[4] S. Lepadatu *et al.*, *Phys. Rev. B* 113, 094432 (2026).
[5] M. Beens, R. A. Duine, B. Koopmans, *Phys. Rev. B* 102, 054442 (2020).
[6] Q. Remy, *Ultrafast spin dynamics and transport in magnetic metallic heterostructures*, PhD thesis, Université de Lorraine (2021).
[7] P. Chailloleau *et al.*, in Preparation (2026).

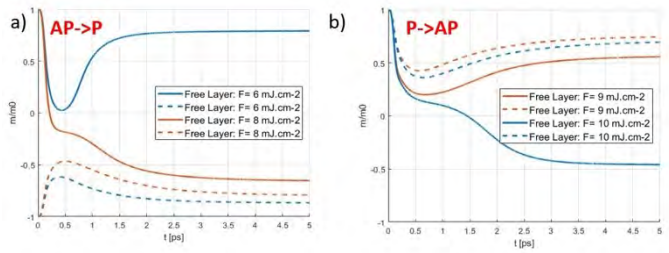


Fig. 1: Simulated m/m0 after a 50 fs laser pulse for the free layer, solid lines, and reference layer, dashed lines, at different fluences. (a) AP-to-P. (b) P-to-AP.

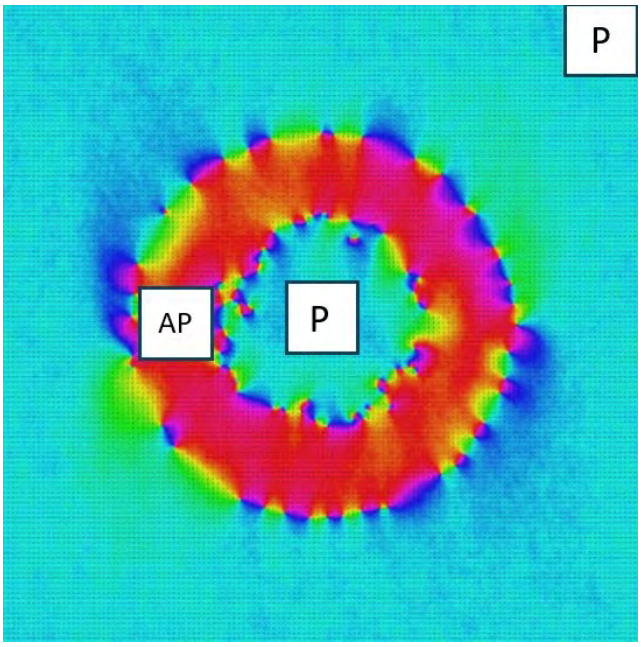


Fig. 2: Final state after Gaussian excitation from AP. Low fluence leaves AP regions unchanged; intermediate fluence switches an annular P region; high central fluence returns to AP, producing a ring-like pattern.

CH-08. Low-Fluence Photo-Induced Magnetization Dynamics in Co/Pd MLs with Perpendicular Anisotropy

V. Yadav[1], G. Lang[1], N. Smith[1, 2], Y. Pleimling[1], A. T. Hanbicki[2], A. Friedman[2], B. Magill[1], H. Munekata[3, 1], G. Khodaparast[1]
[1]Physics, Virginia Tech, Blacksburg, Virginia, United States, [2]Laboratory of Physical Sciences, College Park, Maryland, United States, [3]Institute of Science Tokyo, Tokyo, Japan

Advanced magnetic storage technologies require energy-efficient switching mechanisms, such as current-induced or all-optical switching. In this study, we investigate spin precession in ferromagnetic Co/Pd multilayers (MLs) using Time-Resolved Magneto-Optical Kerr Effect (TR-MOKE) spectroscopy. We report that in the presence of moderate-strength perpendicular magnetic anisotropy (PMA), even at a low-laser-fluence regime (<7 μJ/cm^2), large magnetization precession amplitudes can be detected.

We synthesized two categories of [Co/Pd] MLs via RF/DC magnetron sputtering on Si (110) substrates with a Pd/Ta seed bi-layer. The resulting films exhibited an FCC [111]-oriented polycrystalline texture, facilitating clear PMA (Fig. 1). Previous studies have shown that this [111] axis is responsible for the occurrence of interface anisotropy in these MLs [1, 2]. We employed TR-MOKE measurements, utilizing 100 fs pulses at 790 nm, in a low fluence regime (<7 μJ/cm^2) to reduce thermal effects compared to the conventional high-fluence (mJ/cm^2) regime. Even at these low photoexcitation levels, as shown for a sample with t_{Co}=0.78 nm and t_{Pd}=0.65 nm, we observed a large amplitude of oscillations (Fig. 2).

Our findings demonstrate a direct correlation among the strength of PMA, constituent layer thicknesses, and spin-precession efficiency. By tuning the thicknesses of Co and Pd, we show that heavy-metal interfaces play a critical role in enhancing spin-orbit coupling. This work provides insight into optimizing light-induced switching for all-optical magnetic memory devices, such as waveguide interferometers, where magnetization states modulate light intensity for logic operations, either a node or anti-node (0, or 1 bit) [3]. Our observations suggest that high-amplitude procession, *as well as large spin-precession cone angle* (~ 45°), can be achieved without high thermal loads associated with traditional high-fluence excitations. These large *spin-precession cone angles* offer a pathway toward new and more energy-efficient opto-magnetic devices.

[1] K. Yamamoto, T. Matsuda, *et al.* IEEE Trans. Magn. 49, 3155 (2013).
[2] N. W. Smith, Y. Pleimling *et al.*, Journal of Applied Physics 132, 1 (2022).
[3] H. Munekata, S. Ogawa, *et al.*, Jpn. J. Appl. Phys. 59, SEEA0 (2020).

Acknowledgment: This material is based upon work supported by the Air Force Office of Scientific Research under award number FA9550-24-1-0059.

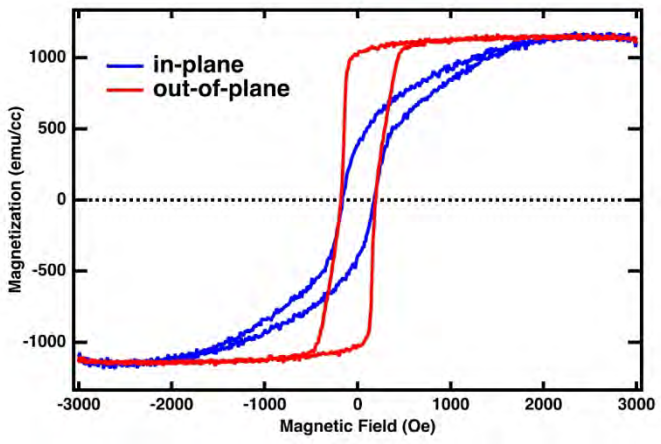


Fig. 1: In-plane and out-of-plane M-H loops

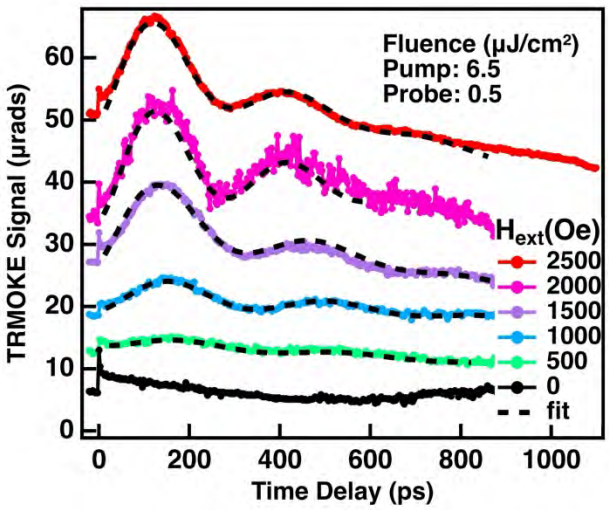


Fig. 2: Magnetic field-dependent TR-MOKE oscillations for one of our Co(0.78nm)/Pd(0.65nm) MLs at low pump/probe fluences (6.5/0.5 μJ/cm^2).

CH-09. Optical control of compact magnetic domains by annular pulsed laser beams in ferro- and ferrimagnetic thin films

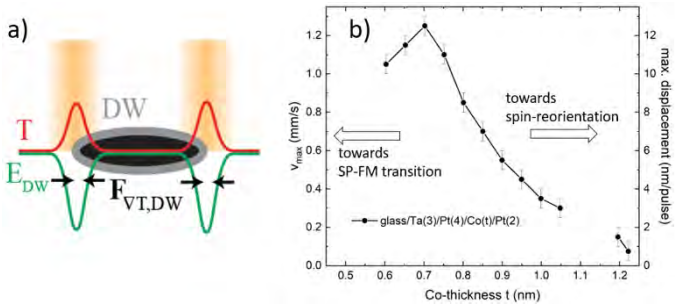
J. Hohlfeld
Universite de Lorraine, CNRS, IJL, Nancy, France

Contactless displacement of magnetic domain walls along arbitrary trajectories is a key objective for magnetic-tweezer and lab-on-chip concepts, yet it usually requires patterned media or complex magnetic-field protocols [1,2]. Here, we demonstrate that annular pulsed laser beams can trap, guide and displace compact magnetic domains, and hence their surrounding walls, in thin ferro- and ferrimagnetic films.

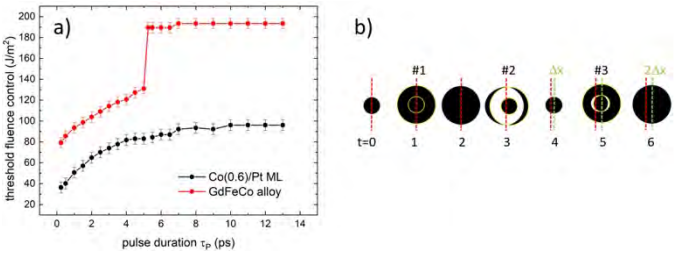
In perpendicularly magnetized Co/Pt multilayers, quasistatic imaging, laser-parameter tuning and micromagnetic simulations show that control is dominated by laser-induced gradients of domain-wall energy [3]. The annular temperature profile reduces the wall energy at the optical ring, producing radial entropic forces that confine the wall to the intensity maximum (Fig. 1a). Varying the Co thickness reveals an optimum transport regime between the superparamagnetic-to-ferromagnetic and spin-reorientation transitions, where the combined evolution of Curie temperature and effective anisotropy maximizes the attainable force (Fig. 1b). Optical control remains possible for pulse durations up to 13 ps. The threshold fluence increases with pulse duration and saturates above about 7 ps, suggesting that similar control may be achievable with continuous illumination if sufficiently large thermal gradients are maintained (Fig. 2a). The effects of DMI and laser helicity support this entropic-force picture [4,5].

Gd-based ferrimagnetic films reveal a different and more efficient mechanism. For pulse durations shorter than the all-optical helicity-independent switching limit, the control fluence drops by nearly 50% and coincides with the toggle-switching fluence (Fig. 2a) [6]. Compact domains then move through single-pulse switching followed by domain-wall-tension-driven erasure of crescent-shaped domains (Fig. 2b) [7]. This process requires no external directional force, reaches higher velocities, and is less sensitive to DMI and light helicity than entropic-force-driven transport.

[1] G. Vieira et al., Phys. Rev. Lett. 103, 128101 (2009).
[2] A. Sarella et al., Adv. Mater. 26, 2384 (2014).
[3] F. Schlickeiser et al., Phys. Rev. Lett. 113, 097201 (2014).
[4] R. E. Camley and K. L. Livesey, Surf. Sci. Rep. 70, 100605 (2023).
[5] C.-H. Lambert et al., Science 345, 1337 (2014).
[6] J. Wei et al., Phys. Rev. Appl. 15, 054065 (2021).
[7] X. Zhang et al., Phys. Rev. Appl. 9, 024032 (2018).



. Entropic trapping and Co-thickness dependence of domain displacement in Co/Pt.



a) Pulse-duration thresholds and b) toggle-switching/tension-driven displacement in GdFeCo.

SESSION CP: RARE-EARTH-FREE PERMANENT MAGNETIC MATERIALS (POSTER SESSION)

Chair(s): A. Hosokawa, *National Institute of Advanced Industrial Science and Technology, Nagoya, Aichi, Japan*

Wednesday, November 4, 2026

09:30 AM-12:30 PM

Coral 4

CP-01. Magnetic Hardening of Fe-Pt and Fe-Pt- M (M=B, Si) Microwires

V. Zhukova[1, 4, 5], M. Ipatov[3], A. Aronin[6], G. Abrosimova[6], A. Zhukov[1, 2, 5]

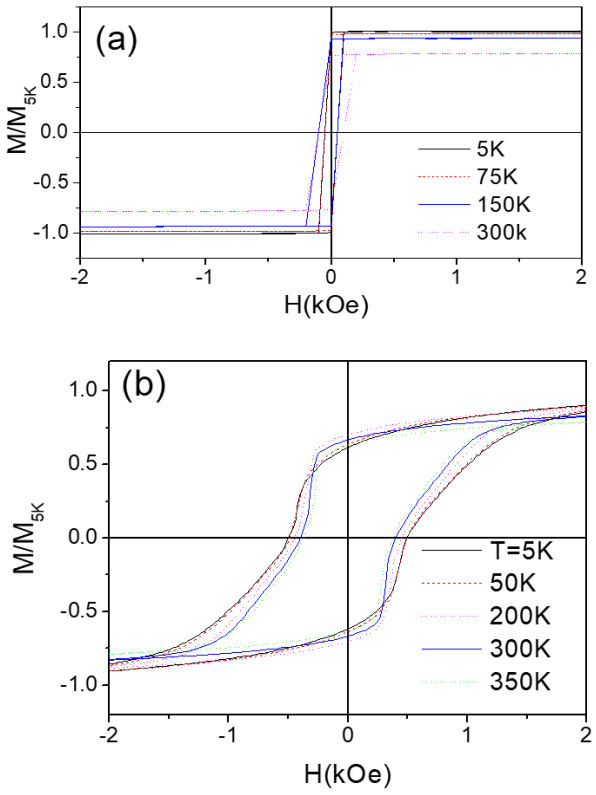
[1]Dept. Appl. Phys.„ University of the Basque Country, San Sebastian, Spain, [2]IKERBASQUE, Basque Foundation for Science, Bilbao, Spain, [3]Magnetic Measurement Service of Advanced Research Facilities (SGIker)„ University of the Basque Country, EHU, San Sebastian, Spain, [4]Dept. Polym. Adv. Mater„ University. of the Basque Country, EHU, San Sebastian, Spain, [5]EHU Quantum Center, University of the Basque Country, EHU„ San Sebastian, Spain, [6]Institute of Solid State Physics, Russian Academy of Science„ Chernogolovka, Russian Federation

Studies of glass-coated amorphous or nanocrystalline microwires prepared by the Taylor-Ulitovsky method have attracted considerable attention due to their soft magnetic properties and giant magnetoimpedance effect (GMI) [1]. Rapid solidification and subsequent processing is also a well-established route to formation of hard magnets [2]. Glass-coating can enhance mechanical and corrosion properties of such microwires, expanding their applications possibilities [1]. Therefore, a few attempts have been made to enhance the coercivity of glass-coated microwires [1,3]. The principal limitation for the preparation of hard magnetic glass-coated microwires using the Taylor-Ulitovsky method is related to the chemical interaction of rare-earth metals with the glass during the melt quenching. Therefore, recently we paid attention on FePt alloys for magnetic microwires preparation [3]. Elevated coercivity of FePt alloys is usually attributed to high magnetocrystalline anisotropy of the L10 FePt phase. Moreover FePt alloys usually present relatively high Curie temperature (*Tc* = 750 K) and spontaneous magnetization $\mu_0 M_s \approx 1.43$ T. Consequently, we have prepared Fe-Pt and Fe-Pt- M (M=B, Si) microwires using Taylor-Ulitovsky technique and studied their magnetic properties. Magnetic properties considerably depend on the metallic core composition and annealing conditions. As-prepared microwires present either amorphous or mixture of amorphous and nanocrystalline phases with a presence of BCC FePt, FCC PtFe and small amount of tetragonal FePt phase. After annealing at 500 °C $Fe_{50}Pt_{40}Si_{10}$ microwires we observed a remarkable magnetic hardening related to crystallization of as-prepared amorphous $Fe_{50}Pt_{40}Si_{10}$ microwires. Coercivity increasing from 5 Oe up to 500 Oe is attributed to the crystallization of amorphous $Fe_{50}Pt_{40}Si_{10}$ microwires. Annealed $Fe_{50}Pt_{50}$ sample present coercivity up to 800 Oe at 5K, but the magnetization of FePt is low and rapidly decreases with temperature. We discussed peculiarity of $Fe_{50}Pt_{50}$ microwires considering the influence of internal stresses on magnetic ordering of Fe-atoms.

[1] A. Zhukov, P. Corte-Leon, L. Gonzalez-Legarreta, M. Ipatov, J. M. Blanco, A. Gonzalez and V. Zhukova, Advanced functional magnetic microwires for technological applications, J. Phys. D: Appl. Phys. 55 (2022) 253003

[2] G. E. Carr, H.A. Davies, and R.A. Buckley, "Crystallite Size Determinations for Melt-spun Fe-Nd-B Permanent Magnet Alloys", Mater.Sci.Eng., 99 (1988) pp147-151

[3] V. Zhukova, A. Talaat, J.J. del Val, M. Ipatov and A. Zhukov, Preparation and Characterization of Fe-Pt and Fe-Pt-(B, Si) Microwires, IEEE Magn. Lett., vol. 7 (2016) 5200704



Hysteresis loops of as-prepared (a) and annealed at 500 °C for 1 h (b) $Fe_{50}Pt_{40}Si_{10}$ microwires

CP-03. Production of $Fe_{16}N_2$ bulk magnets

T. Saito[1], H. Yamamoto[2]
[1]Chiba Institute of Technology, Narashino, Japan, [2]Neoji-consul, Kyoto, Japan

Nd-Fe-B magnets are applied to various advanced electromagnetic devices, including hard disk drives, electric vehicles, and medical equipment [1]. The continuously growing demand for Nd-Fe-B magnets has raised concerns about their prices and the country risk associated with rare earth elements [2]. These severe concerns have led to the study of an alternative magnet that contains no rare-earth elements. Recently, a new production technique for $Fe_{16}N_2$ powder has been developed, and the resulting $Fe_{16}N_2$ powder is available [3]. To realize rare-earth-free magnets, we studied iron nitride (α″-$Fe_{16}N_2$) magnets, which contain no rare-earth elements. $Fe_{16}N_2$ powder exhibits a high saturation magnetization comparable to that of high-performance rare-earth magnets but is unstable at high temperatures. Thus, we consolidated $Fe_{16}N_2$ powder into bulk material at low temperatures using spark plasma sintering (SPS). $Fe_{16}N_2$ bulk magnets were successfully obtained at low temperatures of 373–573 K by the SPS method. Figure 1 shows the hysteresis loops of the $Fe_{16}N_2$ bulk magnets produced at 373–573 K by the SPS method. The $Fe_{16}N_2$ bulk magnets produced at 373 K exhibited a coercivity of 2.6 kOe, which was almost comparable to the original $Fe_{16}N_2$ powder. However, the coercivity of $Fe_{16}N_2$ bulk magnets produced by the SPS method decreased as the consolidation temperature increased.

[1] G. Bailey, N. Mancheri, and K. Van Acker, J. Sustain. Metall. 3, 611 (2017). [2] T. Dutta, K. H. Kim, M. Uchimiya, E. E. Kwon, B. H. Jeon, A. Deep, and S. T. Yun, Environ. Res. 150, 182 (2016). [3] T. Ogawa, Y. Ogata, R. Gallage, N. Kobayashi, N. Hayashi, Y. Kusano, S. Yamamoto, K. Kohara, M. Doi, M. Takano, and M. Takahashi, Appl. Phys. Express, 6, 073007 (2013).

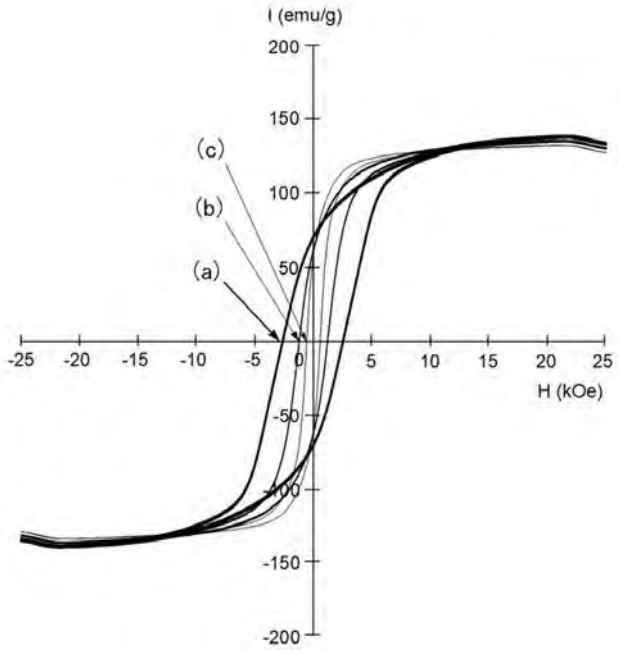


Figure 1 Hysteresis loops of the $Fe_{16}N_2$ bulk magnets produced at (a) 373 K, (b) 473 K, and (c) 573 K by the SPS method.

CP-04. Perpendicular coercivity development in tetragonally distorted FeCoCr films

T. Hasegawa, T. Satou, T. Yamaguchi
Akita University, Akita, Japan

Energy utilized by permanent magnets depends on the magnitudes of the saturation magnetization (Ms) and coercivity (Hc) of magnetic materials. FeCo with bcc structure is a well-known magnetic material characterized by the highest Ms among all transition metal alloys. However, their low magnetic anisotropy (Ku) and Hc make them unsuitable for the permanent magnets. Recent our studies [1] revealed that the epitaxial FeCo thin films with the body-centered tetragonal (bct) structure exhibited high Ku of 10^6 J/m^3 due to the lattice distortion caused by the epitaxial growth on a buffer layer with a lattice constant smaller than that of FeCo. Then, previous studies reported that Cr-doped FeCo undergoes spinodal decomposition, separating into a Cr-poor phase and a Cr-rich phase [2]. Conventional FeCoCr magnets have a granular texture in which acicular bcc FeCo particles are dispersed in a Cr-rich matrix. It is understood that the slight coercivity of $\mu_0 H_c$ = 0.05–0.07 T is obtained due to shape magnetic anisotropy [3]. As mentioned above, magnetic properties of the conventional bcc FeCoCr alloys have been widely reported,

but there have been no reports yet on granularization by adding Cr to the bct FeCo. In this study, FeCoCr is deposited on a Rh buffer layer to achieve the bct structure and high K_u. In addition, Cr is added to form a granular structure.
Fig. 1a shows the magnetization curve of $Fe_{35}Co_{35}Cr_{30}$ (20 nm) film deposited on the Rh buffer layer. The magnetic easy axis is perpendicular, and a high $\mu_0 H_c$ of ~0.5 T is obtained. Figs. 1b and 1c show schematic views of the top and cross-section of the sample, respectively. The crystal structure of the FeCoCr is bct due to the epitaxial stress. The texture of the sample is considered to consist of Cr-poor ferromagnetic particles dispersed in a Cr-rich nonmagnetic matrix.
This work was supported by JSPS KAKENHI (Grant Number JP26K00975).
[1] T. Hasegawa et al., Sci. Rep. 7, 13215 (2017).
[2] S. Sugimoto et al., IEEE Trans. Magn. 23, 3193 (1987).
[3] S. Jin et al., IEEE Trans. Magn. 15, 1748 (1979).

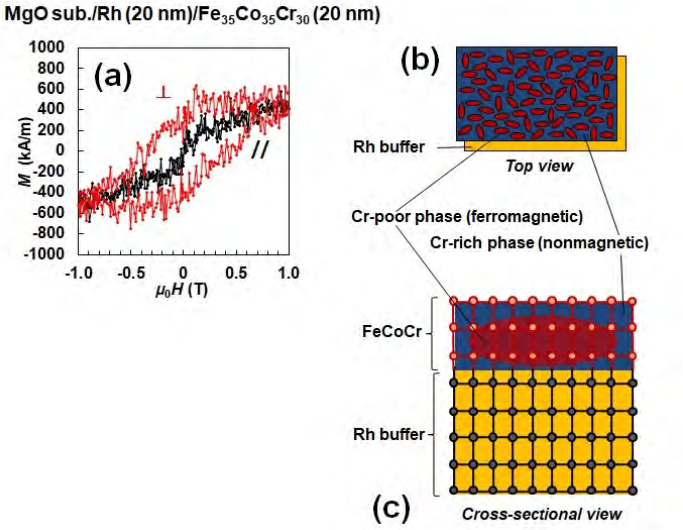


Fig. 1. (a) Magnetization curve of the MgO (100) sub./Rh (20 nm)/$Fe_{35}Co_{35}Cr_{30}$ (20 nm)/SiO_2 (5 nm) films obtained at 298 K. Schematics of (b) top view and (c) cross-sectional view of the sample.

CP-05. Design and optimization of Rare-Earth-Free Co-Zr-Mo-Si-B Permanent Magnets

A. M. Cordero[1], A. Kovacs[2], H. Oezelt[2], D. Böhm[2], T. Schrefl[2], I. Betancourt[1]
[1]Autonomous University of Mexico, México City, Mexico,
[2]University for Continuing Education Krems, Viena, Austria

The development of rare-earth-free permanent magnets is essential to meet current technological demands. In the last decades, there has been significant research on rare earth (RE)-containing alloys to develop advanced permanent magnetic materials. However, the escalating demand for RE magnets has caused scarcity and rising prices of RE elements, driving the need to explore RE-free alternatives. One candidate for such materials is Co-Zr alloys, specifically the $Co_{74}Zr_{16}Mo_4Si_3B_3$ system [1-2]. However, optimizing their microstructure to maximize magnetic properties poses a significant challenge that typically requires extensive empirical methodologies. This work presents a combined computational and experimental approach to accelerate the design and discovery of these nanocomposite alloys. In the first stage, a Machine Learning (ML) model was implemented using data from previous reports to predict the evolution of the hard magnetic phase. The model predicted optimal annealing conditions of 900 K for 150 minutes to maximize the crystallization of the hard magnetic phase ($Co_{11}Zr_2$). Experimental validation, carried out by synthesizing ribbons via melt-spinning and applying the predicted heat treatment, confirmed the accuracy of the model. Rietveld refinement of X-ray diffraction patterns yielded ~93 wt.% of the hard $Co_{11}Zr_2$ phase, while transmission electron microscopy revealed an optimized nanoscale average grain size of 60.9 nm. This microstructural modulation resulted in a enhancement of the magnetic properties, achieving a coercivity of 581 kA/m, a saturation magnetization of 0.2 T, and a Curie temperature of 676 K. To understand the physical origin of this performance, the experimental work was complemented by micromagnetic simulations [3-4]. The models revealed that the refined grain size and the presence of the secondary soft magnetic phase act as pinning sites, proposing a hardening mechanism governed by magnetic domain reversal. This study demonstrates that the synergy among machine learning, guided experimental synthesis, and micromagnetic modeling is a effective methodology for discovering and boosting the properties of advanced permanent magnets.
1. Y. Jin, W. Zhang and P.R. Kharel, AIP Adv., Vol. 6, p.2 (2016)
2. A. Oraon, T. Adhikary and M. Tirugabathina, J. Alloys

Compd., Vol. 965, p.171436 (2023)
3. L. Exl, D. Suess and T. Schrefl, Handbook of Magnetism and Magnetic Materials., Springer (2021)
4. T. Saito and M. Itakura, Crystals., Vol. 15, p.698 (2025)

CP-06. First-principles design of Fe_2Ge-based alloys as rare-earth-free permanent magnets

K. Baatartsogt[1], O. Dorj[2]
[1]Institute of Physics and Technology, Mongolian Academy of Sciences, Ulaanbaatar, Mongolia, [2]Incheon National University, Incheon, Korea (the Republic of)

Fe_2Ge exhibits high saturation magnetization but intrinsically negative magnetocrystalline anisotropy, limiting its applicability as a permanent magnet. Here, we theoretically demonstrate that this limitation can be overcome through Co and B substitution, using a multiscale theoretical framework combining density functional theory, Monte Carlo simulations and micromagnetic modeling. Co substitution at the Fe site drives a transition from biaxial anisotropy to uniaxial anisotropy, yielding a large magnetocrystalline anisotropy energy of ~2 MJ/m^3. This reorientation and enhancement of magnetic anisotropy arise from strong spin-orbit coupling and the associated redistribution of Co 3d electronic states near the Fermi level. However, this gain in anisotropy is accompanied by a reduction in magnetization, reflecting weakened exchange splitting due to modified band filling. Further B substitution at the Ge site enhances magnetization and elevates the Curie temperature from below room temperature in Fe_2Ge to above 400 K. This behaviour is linked to lattice contraction and a reduced c/a ratio, which increase 3d orbital overlap and strengthen exchange interactions, thereby stabilizing ferromagnetic order at elevated temperatures. Together, these results reveal a cooperative mechanism in which Co and B substitutions selectively tune the magnetization, magnetocrystalline anisotropy, and exchange interactions, establishing a pathway for designing Fe_2Ge-based rare-earth-free permanent magnets with enhanced performance.

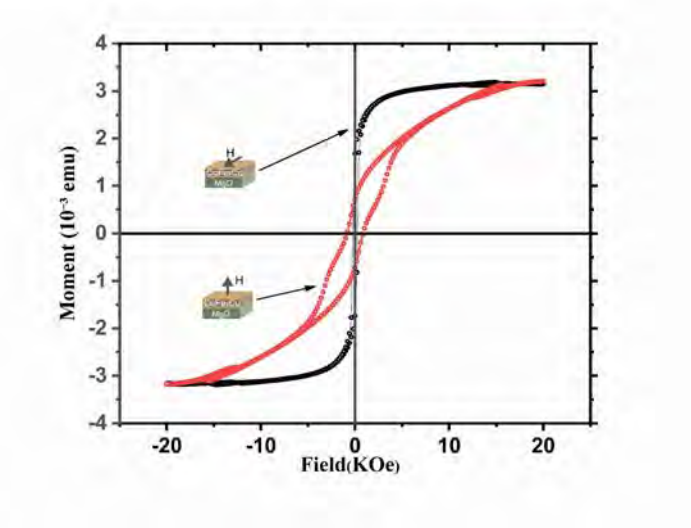
The research is supported by Office of Naval Research (ONR) and Office of Naval Research Global (ONRG) of the US Department of Defense Grant N62909-22-1-2045, and National Research Council of Science & Technology (NST) Grant No. CAP25061-000 and Basic Research Program Grant No. RS-2026-25494250 through the National Research Foundation of Korea.

CP-07. Perpendicular magnetic anisotropy in CoFe2Cu thin films

D. Alharbi[1, 2], F. Efe[1], F. Bakhshizadeh[1], M. Guy[1], A. Lisfi[1]
[1]Physics, Morgan State University, Baltimore, Maryland, United States, [2]The Catholic University of America, DC, District of Columbia, United States

Perpendicular magnetic anisotropy (PMA) is a key property in modern spintronic devices, enabling high-density magnetic recording, spin-transfer torque memory, and field-free switching applications [1,2]. Engineering PMA in transition metal thin films through chemical ordering and epitaxial constraints offers a powerful route to tailor magnetic behavior without relying on heavy metal underlayers [3]. In this work, we investigate CoFe2Cu thin films deposited on (100) MgO substrate at temperatures between room temperature and 600°C using a DC magnetron sputtering. The prepared films were the subject of thorough structural and magnetic characterizations performed with AFM/MFM, XRD and VSM. The XRD measurements reveal that the films are crystalline when deposited at temperatures above 200°C, which is supported by the granular structure observed by AFM analysis. The magnetic measurements performed by VSM illustrate an anisotropic behavior of the films with the existence of a strong out-of-plane anisotropy component as shown in Figure 1. Magnetic force microscopy image further reveals the existence of strong magnetic contrast, which can be attributed to the out-of-plane anisotropy component. The origin of this out-of-plane anisotropy component will be further discussed in the presentation, which will include all the supporting analyses. These findings position CoFe2Cu/MgO as a promising material for PMA-based spintronic applications.

[1] Ikeda et al. 2010 Perpendicular Anisotropy CoFeB MgO, "A perpendicular-anisotropy CoFeB–MgO magnetic tunnel junction," *Nature Materials*, vol. 9, no. 9, pp. 721–724, 2010.
[2] Dieny and Chshiev 2017 Perpendicular Magnetic Anisotropy Review, "Perpendicular magnetic anisotropy at transition metal/oxide interfaces and applications," *Reviews of Modern Physics*, vol. 89, no. 2, 2017.
[3] N. Satchell *et al*., "Thin film epitaxial [111] Co50Pt50: structure, magnetisation, and spin polarisation," *Scientific Reports*, vol. 13, no. 1, p. 12468, 2023



Magnetic hysteresis loops of CoFe2Cu thin film deposited on MgO substrate at 500°C with the applied field parallel (H∥, black) and perpendicular (H⊥, red) to the film plane.

CP-08. Efficient Preparation and Magnetic Characterization of τ -phase Mn-Al

K. N. Ndaru[1], T. F. McKenzie[1], R. Chapai[2], M. Khan[1]
[1]Department of Physics, Miami University, Oxford, Ohio, United States, [2]Department of Physics, Norfolk State University, Norfolk, Virginia, United States

Permanent magnets are at the heart of numerous technologies including miniature speakers, disk drives, motors for hybrid vehicles, and wind generators. The most powerful permanent magnets that are in use today are based on rare earth metals. Due to the criticality of rare-earth elements, there is an immediate need to develop permanent magnetic materials that are free from these critical elements. Mn-Al is a strong candidate in this regard as with proper synthesis, it can be transformed into strong permanent magnets. The primary challenge is the synthesis of the metastable ferromagnetic τ -phase, which is associated with desirable magnetic properties. The formation of this phase occurs through the transformation of the high temperature epsilon-phase during controlled heat treatment that can be challenging. Here, we will present an experimental study on the synthesis and magnetic characterization of a series of Mn-Al compounds with a nominal composition of 56:44. With the goal of facilitating the formation of the τ -phase, the samples are prepared by arc melting the constituent elements followed by drop-casting in zero and applied magnetic fields. Selected samples are annealed at different temperatures. A small percentage of Ti was added to the melt to promote the formation of the τ -phase. The samples are characterized by powder x-ray diffraction, scanning electron microscopy, dc magnetization and electrical resistivity measurements. The experimental results will be presented and discussed in detail.

[1] T. Keller., The phase transformation behavior of Mn–Al rare-earth-free permanent magnets, J. Magn. Magn. Mater. 587, 171331 (2023).

CP-09. Phase Stabilities and Magnetic Properties of Fe-substituted Mn_3Ga with tetragonal structure

H. Okada[1], H. Fujita[1], S. Awaji[2]
[1]Tohoku Gakuin University, Sendai, Japan, [2]Tohoku University, Sendai, Japan

Binary manganese alloys with tetragonal $D0_{22}$ structure are expected to be candidates for novel high performance magnetic materials, because the alloys exhibit high uniaxial magnetocrystalline anisotropy without rare earth elements [1,2]. $D0_{22}$-type Mn_3Ga and Mn_3Ge show small magnetization arising from a ferrimagnetic state. The magnetic moments of crystallographic different two Mn sites are coupled antiferromagnetically, resulting in the ferrimagnetic ordering with the small net magnetization. On the other hand, a theoretical investigation predicted that a tetragonal structure having both high saturation magnetization and perpendicular magnetic anisotropy is realized in Fe-Mn-Ga alloy [3]. It is considered that the introducing of Fe atom for Mn_3Ga strongly affects the structural and magnetic properties of the $D0_{22}$ phase. In this work, we have investigated stractural and magnetic properties of Fe-substituted Mn-Ga alloys with the $D0_{22}$ structure. Polycrystalline samples of $Mn_{73-x}Fe_xGa_{27}$ were synthesized by an arc-melting method. It is confirmed that all the samples are mainly composed of the $D0_{22}$ phase. The Fe substitution leads to a decrease in lattice constant *a* and an increase in lattice constant *c*, resulting in a shrinkage of the unit cell volume *V* and an increase in the axial ratio *c/a*. A structural phase transition temperature from the $D0_{22}$ phase to high temperature phase slightly shifts to higher temperature with increasing the Fe content, indicating that the $D0_{22}$ structure is thermally stabilized by introducing the Fe atoms. Magnetization observed at low temperature increases with increasing the Fe content. However, Hysteresis loop tends to be smaller loop, leading to a decrease of coercivity. These results suggest that site occupation of Fe atom is strongly related to the magnetic properties, and the uniaxial

magnetocrystalline anisotropy is weakened by the substitution of Mn by Fe in the $D0_{22}$ structure.
[1] B. Balke et al., Appl. Phys. Lett. 90, 152504 (2007).
[2] J. Winterlik et al., Phys. Rev. B 77, 054406 (2008).
[3] M. Tshjikawa et al., Jpn J. Appl. Phys. 59, 055506 (2020).

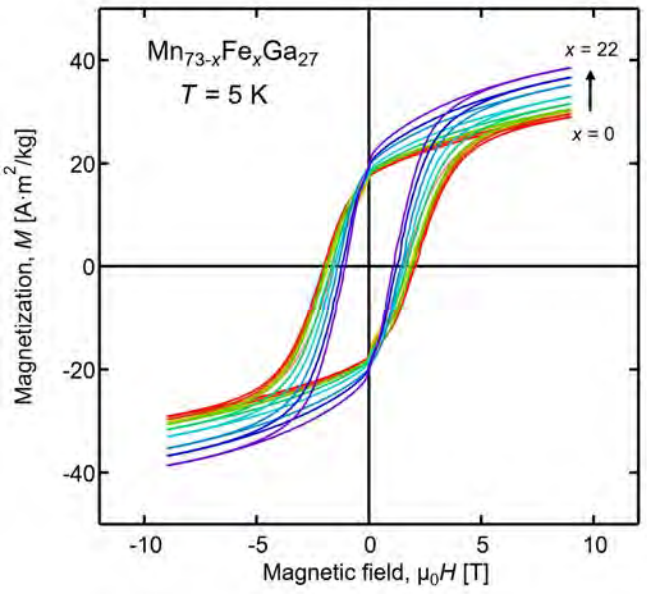


Fig.1 Magnetization curves observed at 5 K of $Mn_{73-x}Fe_xGa_{27}$

CP-10. Tuning Magnetic Anisotropy in Fe_3Sn Nanowire Arrays through Shape Effects and Annealing

A. A. Mendonça[1], V. M. Prida[2], F. Béron[1]
[1]Instituto de Física Gleb Wataghin, Universidade Estadual de Campinas, Campinas, São Paulo, Brazil, [2]Departamento de Física, Universidad de Oviedo, Oviedo, Spain

Permanent magnets are central to energy conversion technologies, driving the search for high-performance rare-earth-free materials. Among Fe-based intermetallics, hexagonal Fe_3Sn stands out due to its Curie temperature above 700 K, high saturation magnetization, and significant magnetocrystalline anisotropy [1]. However, its intrinsic easy-plane anisotropy, with magnetization confined to the basal plane, severely limits its applicability, as permanent magnets require strong uniaxial anisotropy to achieve high coercivity and thermal stability. To overcome this limitation, Fe_3Sn nanowire arrays were electrodeposited into nanoporous alumina templates fabricated by mild anodization, yielding nanowires with diameters of ~50 nm and aspect ratios above 80 (Fig. 1). X-ray diffraction confirms that the nanowires retain the hexagonal crystal structure, while magnetization measurements reveal the emergence of an effective easy axis along the nanowire direction (Fig. 2), evidencing a geometry-driven reorientation of magnetic anisotropy. The magnetic response remains remarkably stable over a wide temperature range: from 2 K to 300 K, the saturation magnetization (M_s), coercive field (H_c), and remanent magnetization (M_R) decrease by around 10-20%, indicating robust ferromagnetic ordering. Thermal processing further reinforces this behavior, as annealing at 500 °C for 12 h significantly enhances H_c, increasing it by more than 110% for out-of-plane and by more than one order of magnitude for in-plane measurements, while M_R increases by 14% and M_R/M_s ratio doubles. A quantitative analysis of anisotropy reveals that, in contrast to bulk Fe_3Sn with easy-plane character, the nanowire array is predominantly governed by shape anisotropy, which accounts for approximately 97% of the effective anisotropy. These findings demonstrate that anisotropic nanoscale confinement combined with thermal processing enables effective tuning of magnetic anisotropy in Fe_3Sn, providing a viable pathway toward rare-earth-free permanent magnets.

Funding: FAPESP (#2017/10581-1; #2022/16839-9; #2024/00998-6) and CNPq (#443930/2023-6; #421070/2023-4; #310084/2025-3).

[1] B. C. Sales *et al.*, Sci. Rep. 4, 7024 (2014).

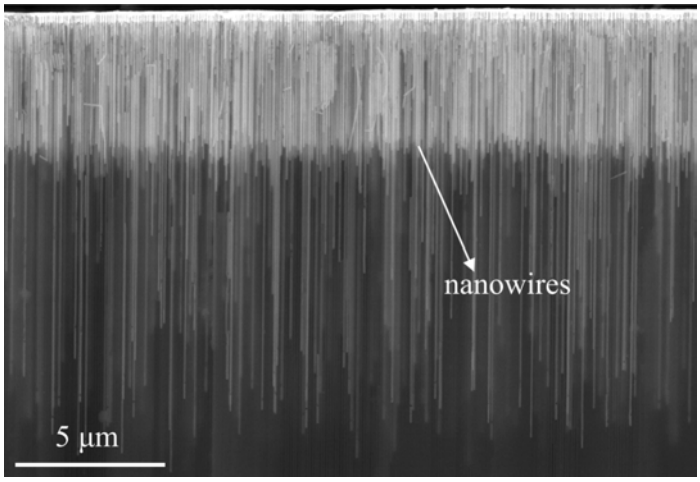


Fig. 1: Fe_3Sn nanowire array microscopy image

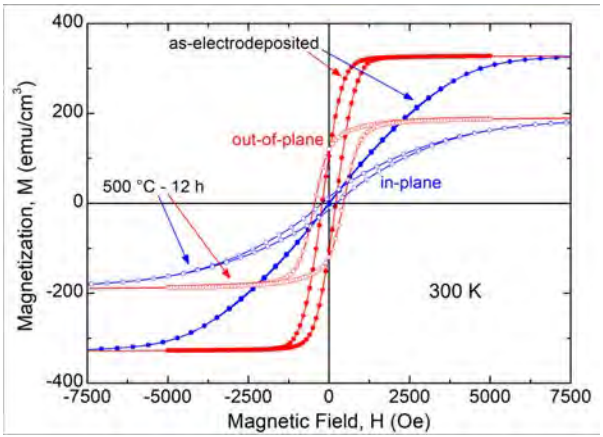


Fig. 2: Room-temperature hysteresis curves

CP-11. Interface-driven exchange decoupling for coercivity enhancement in FeNi magnets

O. Tumentsereg, M. Adiya, B. Narangerel, O. Dorj
Department of Physics, Incheon National University, Incheon, Korea (the Republic of)

The $L1_0$-ordered FeNi phase is a promising rare-earth-free permanent magnet due to its high saturation magnetization and Curie temperature. However, its low long-range crystal ordering and weak coercivity limit its practical applications. Here, we theoretically demonstrate that interfacial exchange decoupling provides an effective pathway to enhance coercivity in FeNi alloys. Here, using first-principles calculations, we show that a nonmagnetic Ni_3P phase, with small lattice mismatch to FeNi, effectively decouples exchange interactions between FeNi layers when its thickness exceeds a critical value. Micromagnetic simulations further reveal that the FeNi/Ni_3P interface acts as an efficient domain wall pinning, leading to a substantial enhancement of coercivity compared to the pure FeNi phase. This enhancement originates from the interplay between exchange decoupling and enhancement of magnetocrystalline anisotropy at the interface. These results identify an interface-driven mechanism for coercivity enhancement and establish phosphide-mediated grain boundary engineering as a viable strategy to improving coercivity in FeNi-based rare-earth-free permanent magnets.

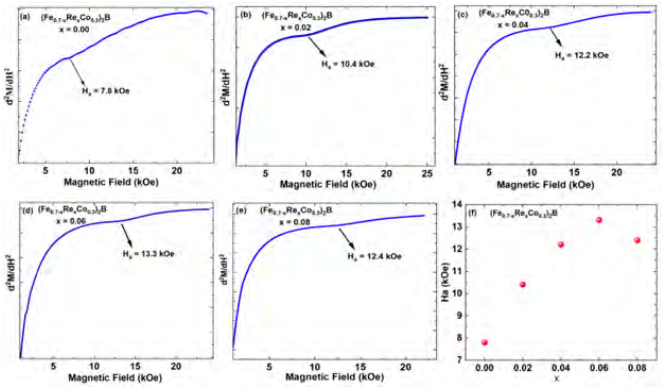
* The research is funded by Office of Naval Research (ONR) and Office of Naval Research Global (ONRG) of the US Department of Defense Grant N62909-22-1-2045, and National Research Council of Science & Technology (NST) Grant No. CAP25061-000 and Basic Research Program Grant No. RS-2026-25494250 through the National Research Foundation of Korea.

CP-12. Tailoring Magnetic Anisotropy in $(Fe_{0.7}Co_{0.3})_2B$ through Rhenium Substitution

T. Karki, H. Abbas, P. Joshi, J. Mohapatra, P. Liu
Physics, The University of Texas at Arlington, Arlington, Texas, United States

Transition metal boride $(Fe_{0.7}Co_{0.3})_2B$ with tetragonal structure has emerged as promising rare-earth-free candidate for permanent magnet applications due to its inherently high saturation magnetization (M_s ~ 1.3 T), moderate magnetocrystalline anisotropy constant (K_1 ~ 0.41 MJ/m$^{3)}$, and high Curie temperature (T_C ~ 933 K) [1]. In this study, we prepared $(Fe_{0.7-x}Re_xCo_{0.3})_2B$ (x = 0, 0.02, 0.04, 0.06, and 0.08) nanocrystallites via arc melting followed by rapid solidification via melt spinning. X-ray diffraction (XRD) confirms the formation of a single phase with the tetragonal structure, with an average crystallite size of 34 nm. Singular point detection (SPD) analysis showed that Rhenium (Re) incorporation enhances the magnetocrystalline anisotropy field (*Ha*) from 7.8 kOe to 13.3 kOe as the Re content increases from x = 0 to x = 0.06 (Figure 1). In addition, the precise variation of Re content leads to the modulation in room-temperature M_s in the range of 125-153 emu/g with an optimum coercivity ~ 0.2 kOe. Bloch's law fitting of magnetization vs. temperature curve suggests a gradual decrease of Bloch's constant, indicating enhanced ferromagnetic exchange interactions with Re doping. This increase in ferromagnetic exchange interactions upon Re doping is attributed to hybridization between the exchange-split *3d* bands of Fe or Co and the *5d* bands of Re [1]. These findings demonstrate that minor Re substitution significantly improves H_a, suggesting $(Fe_{0.7}Co_{0.3})_2B$-based alloys as a promising candidate for next-generation, high-performance permanent magnets.

1. A. Edström, M. Werwinski, D. Iušan, J. Rusz, O. Eriksson, K. P. Skokov, I. A. Radulov, S. Ener, M. D. Kuz'min, J. Hong, M. Fries, D. Yu. Karpenkov, O. Gutfleisch, P. Toson, and J. Fidler, Phys. Rev. B, 2015, 92, 174413.



CP-13. Nanochain-Induced Magnetic Hardening in FeCo Alloys

H. Abbas, P. Joshi, T. Karki, J. Mohapatra, P. Liu
Department of Physics, University of Texas at Arlington, Arlington, Texas, United States

FeCo is a well-known ferromagnetic alloy with high saturation magnetization ($M_s \approx$ 2.4 T) and Curie temperature ($T_c \approx$ 980 K), but its low magnetocrystalline anisotropy (K_u), arising from its body-centered cubic (bcc) structure, limits its suitability for permanent magnet applications. Our recent studies suggest that structural anisotropy at the nanoscale can be exploited to induce coercivity in otherwise magnetically soft systems [1]. In this work, we utilize morphological engineering of FeCo nanocrystals to achieve enhanced magnetic hardness, demonstrating coercivity up to 1.5 kOe at room temperature. Rietveld refinement of the X-ray diffraction pattern (Fig. 1a) confirms the formation of a single-phase bcc FeCo structure without detectable impurities. Electron microscopy (Fig. 1b) shows the formation of extended chain-like nanoarchitectures, which introduce shape anisotropy and promote magnetic hardening. Magnetic measurements (Fig. 1c) show a coercivity of 1.5 kOe and a saturation magnetization of ~150 emu/g. Notably, the system exhibits a maximum energy product $(BH)_{max}$ of ~5 MGOe (Fig. 1d). These results demonstrate that FeCo nanochains provide an effective route to overcome intrinsic limitations associated with low magnetocrystalline anisotropy, enabling the development of high-performance rare-earth-free permanent magnets. This work highlights the critical role of nanoscale structural design in tailoring magnetic properties and offers a promising strategy to reduce reliance on critical rare-earth elements.

<!--[if supportFields]><spanlang=EN-US style='font-family:"Times New Roman",serif'> ADDIN EN.REFLIST <spanstyle='mso-element:field-separator'><![endif]-->

1. Mohapatra, J., et al., *Superstructure magnetic anisotropy in Fe_3O_4 nanoparticle chains*. Nature Communications, 2025. 16(1): p. 5723.

<!--[if supportFields]><span lang=EN-US style='font-size:12.0pt;line-height:115%;font-family:"Times New Roman",serif;mso-fareast-font-family:"Yu Gothic";mso-fareast-theme-font:minor-fareast;mso-ansi-language:EN-US;mso-fareast-language:JA;mso-bidi-language:AR-SA'><![endif]-->

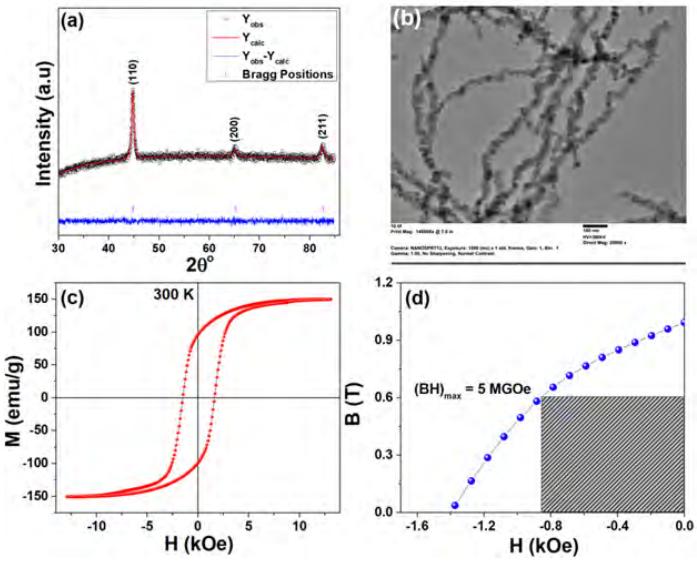


Figure 1: (a) Rietveld refinement of X-ray diffraction pattern, (b) TEM micrograph, (c) M-H loop at 300 K, and (d) Maximum energy product $(BH)_{max}$ for FeCo nanochains.

CP-14. Enhanced Hard Magnetic Properties of FeCo Alloys

B. Narangerel[1], O. Tumentsereg[1], M. Adiya[1], U. Amanjal[2], U. Enkhnaran[2], O. Dorj[1]
[1]Physics, Incheon National University, Yeonsu-Gu, Incheon, Korea (the Republic of), [2]Institute of Physics and Technology, Ulaanbaatar, Mongolia

B2-ordered FeCo alloys exhibit high saturation magnetization (M_s) and Curie temperature (T_c), but their negligible magnetocrystalline anisotropy (K_u) and coercivity (H_c) limit their applicability as permanent magnets. Here, we demonstrate both theoretically and experimentally that magnetic hardness in FeCo can be systematically engineered through a cooperative multiscale strategy

combining substitutional alloying, interstitial doping, and nanoscale size optimization. Using density functional theory, Monte Carlo, micromagnetic simulations, and experimental characterization, we identify Ti substitution as an effective approach to stabilize the structure and enhance magnetic anisotropy, with only a moderate reduction in magnetization. Interstitial B doping in $Fe_{0.875}Ti_{0.125}Co$ further induces a tetragonal distortion that, together with enhanced spin-orbit coupling, increases K_u to 0.7 MJ m^{-3} and H_c to 47 Oe, leading to an improved maximum energy density product $(BH)_{max}$. Micromagnetic simulations reveal an optimal particle size of ~60 nm, where domain wall pinning is maximized. Guided by these predictions, size-dependent coercivity measurements have been carried out, and the results will be discussed. These results establish a unified design framework linking electronic structure, lattice distortion, and nanoscale magnetization processes, providing a viable pathway toward high-performance rare-earth-free FeCo-based permanent magnets.

*The research is funded by Office of Naval Research (ONR) and Office of Naval Research Global (ONRG) of the US Department of Defense Grant N62909-22-1-2045, and National Research Council of Science & Technology (NST) Grant No. CAP25061-000 and Basic Research Program Grant No. RS-2026-25494250 through the National Research Foundation of Korea.

CP-16. Giant-coercivity ε-Fe_2O_3 phase stabilization via lattice incorporation of Si impurities: Insights from a combined DFT and Mössbauer study

D. Kubániová[1, 2], J. Kohout[1], L. Kubickova[2, 1], T. Kmjec[1], V. Chlan[1], P. Brázda[2], M. Klementová[2], P. Bezdička[3]
[1]Faculty of Mathematics and Physics, Charles University, Prague, Czechia, [2]FZU – Institute of Physics of the Czech Academy of Sciences, Prague, Czechia, [3]Institute of Inorganic Chemistry of the Czech Academy of Sciences, Prague, Czechia

Among the five crystalline polymorphs of iron(III) oxide identified under ambient conditions [1], the orthorhombic ε-phase is distinguished by its giant room-temperature coercivity and high-frequency millimeter-wave resonance [2]. Due to its metastability, ε-Fe_2O_3 is synthesized exclusively in nanosized form. While the spatial confinement, required to prevent transformation into thermodynamically stable hematite [3], is essential for synthesis, the potential role of chemical stabilization via Si incorporation into the lattice remains a subject of investigation. This study aims to clarify the stabilization mechanism of ε-Fe_2O_3 by investigating how Si atoms from the silica template incorporated into the crystal lattice during nucleation, thereby altering the electronic state of iron and the resulting hyperfine interactions.

High-purity, ^{57}Fe-enriched ε-Fe_2O_3 nanoparticles were synthetized using a sol-gel method within a mesoporous silica template, followed by thermal treatment at 1050 °C and subsequent leaching of the template [4]. The phase composition and morphology were characterized by X-ray powder diffraction and transmission electron microscopy. The local magnetic structure and electronic environment were probed using ^{57}Fe Mössbauer spectroscopy (MS) from 4.2 to 540 K, complemented by solid-state nuclear magnetic resonance and magnetic measurements. Density functional theory (DFT) calculations were performed to simulate the impact of Si-substitution on the iron valence and structural stability.

The synthesized samples demonstrated an ε-phase content of 91% with a median particle size of 25 nm and a coercivity of 2.1 T. MS spectra revealed a characteristic lineshape asymmetry toward smaller hyperfine magnetic fields, which suggests a distribution of local environments. DFT calculations indicate that the presence of Si within the ε-Fe_2O_3 structure facilitates the partial reduction of Fe^{3+} to Fe^{2+}, suggesting a mechanism for structural stabilization of ε-Fe_2O_3 phase.

[1] L. Machala, J. Tuček and R. Zboril, Chem. Mater., Vol. 23, p. 3255 (2011).
[2] J. Kohout, P. Brázda, K. Závěta, D. Kubániová, T. Kmječ, L. Kubíčková, M. Klementová, E. Šantavá, and A. Lančok, J. Appl. Phys., Vol. 117, p. 17D505 (2015).
[3] D. Kubániová, T. Kmječ and J. Kohout, Phys. Rev. B, Vol. 98, p. 094412 (2018).
[4] L. Kubíčková, J. Kohout, P. Brázda, M. Veverka, T. Kmječ, D. Kubániová, P. Bezdička, M. Klementová, E. Šantavá, and K. Závěta, Hyperfine Interact, Vol. 237, p 159 (2016)

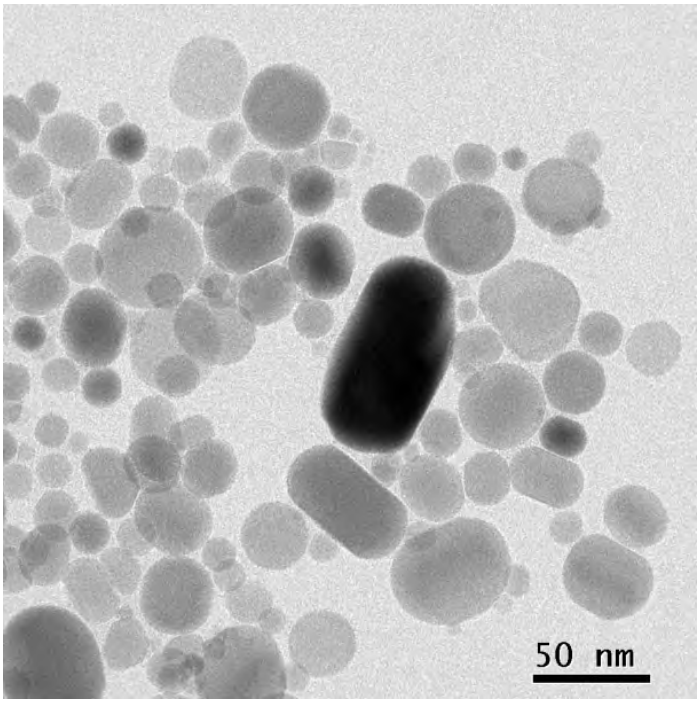


Fig. 1 Brightfield TEM micrograph of ^{57}Fe-enriched ε-Fe_2O_3 nanoparticles collected after silica template dissolution

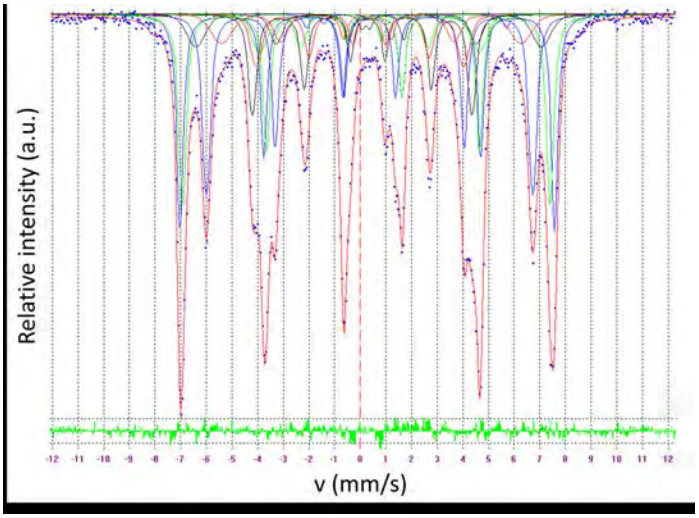


Fig. 2 ^{57}Fe Mössbauer spectrum acquired at 296 K

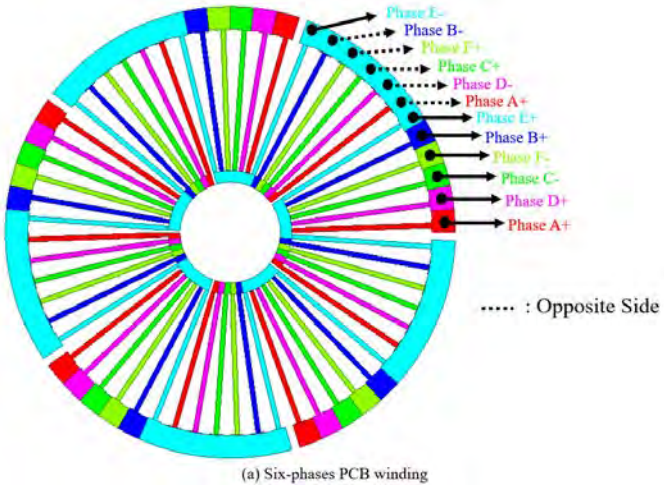
SESSION CQ: PERMANENT MAGNET MACHINES: DESIGN, MODELING AND OPTIMIZATION (POSTER SESSION)
Chair(s): A. Baghel, *Division of Critical Materials , Ames National Laboratory, Ames, Iowa, United States*
Wednesday, November 4, 2026
09:30 AM-12:30 PM
Coral 4

CQ-01. Design of an Asymmetric Six-Phase PCB Winding Motor for Small Drone Applications
C. Lee[1], H. Kim[1], Y. Lim[1], C. Kim[2], W. Kim[3]
[1]Department of Next Generation Smart Energy System Convergence, Gachon University, Seongnam-si, Gyeonggi-do, Korea (the Republic of), [2]Department of Electrical Engineering, Wonkwang University, Iksan-si, Jeonbuk-do, Korea (the Republic of), [3]Department of Electrical Engineering, Gachon University, Seongnam-si, Gyeonggi-do, Korea (the Republic of)

As the use of small drones has expanded into various fields such as logistics, reconnaissance, and facility inspections, demands for both the performance and reliability of their propulsion systems have increased. In particular, since a failure in motor operation during flight can directly affect the stability of the aircraft, ensuring stable motor operation and reliability is considered a critical design factor.
However, in actual operating environments, phase failures can occur due to insulation degradation and reduced mechanical durability resulting from prolonged use. These failures cause current imbalance and torque ripple, which hinder normal operation.
To address this issue, this study proposes a motor for small drones that employs an asymmetric 6-phase PCB winding structure. Due to its multi-phase characteristics, the proposed structure allows operation to be maintained through the remaining phases even if a fault occurs in some phases, making it suitable for drone systems that require continuous operation. Furthermore, the asymmetric winding configuration can mitigate torque ripple by dispersing and reducing specific harmonic components [1].
PCB winding involves directly forming conductor patterns on a substrate, offering high design flexibility that allows for various winding configurations within limited space while ensuring repeatability and consistency in the manufacturing process [2]. Furthermore, the 6-phase structure can be designed with a relatively low number of winding turns under the same output conditions, mitigating increases in winding resistance and offering favorable characteristics in terms of losses and efficiency.
In this study, we aim to analyze the electromagnetic

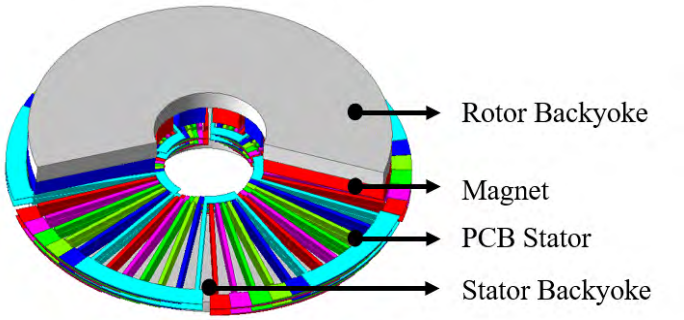
characteristics of the proposed motor based on finite element analysis and evaluate its applicability as a propulsion system for small drones.

[1] E. Levi, "Multiphase electric machines for variable-speed applications," *IEEE Transactions on Industrial Electronics*, vol. 55, no. 5, pp. 1893–1909, May 2008.
[2] O. Taqavi and S. M. Mirimani, "Design aspects, winding arrangements and applications of printed circuit board motors: A comprehensive review," *IET Electric Power Applications*, vol. 14, no. 8, pp. 1505–1518, 2020.



(a) Six-phases PCB winding

Fig.1



(b) Six-phases Winding PCB Structure

Fig.2

CQ-02. Nonlinear Magnetic Equivalent Circuit Based Design of Interior Permanent Magnet Synchronous Motors Considering Magnetic Saturation and Partial Demagnetization

S. Kim[2], K. Yu[2], H. Ban[2], J. Park[2], J. Choi[2], K. Shin[1]
[1]*Changwon National University, Changwon, Korea (the Republic of),* [2]*Chungnam National University, Daejeon, Korea (the Republic of)*

Internal permanent magnet synchronous motors (IPMSMs) require accurate initial design, as magnetic saturation and irreversible demagnetization significantly affect torque performance and reliability [1]. However, the accuracy of conventional linear magnetic equivalent circuit (MEC) models is limited when the iron core exhibits nonlinear behavior and the permanent magnet operating point approaches a knee point [2], [3].

This paper proposes a design and analysis method using a nonlinear magnetic equivalent circuit (MEC) of an interior permanent magnet synchronous motor (IPMSM) considering magnetic saturation and partial demagnetization phenomena. Fig. 1 presents the proposed design procedure. The required specifications and design constraints are defined, and initial sizing is performed. A nonlinear MEC model with B–H iteration is constructed to reflect core permeability variation. Flux linkage and inductance are calculated, and the feasible design region is determined by considering constraints on voltage, torque, current, stack length, stator diameter, and demagnetization, as this procedure is necessary to define the design scope prior to detailed finite element analysis (FEA).

Fig. 2 presents the prototype and validation results. The prototype, test bench, rotor, and stator are presented in Fig. 2(a). In Fig. 2(b), the nonlinear MEC predicts the torque saturation trend and local demagnetization pattern under high current conditions more consistently than the linear model. The demagnetized regions calculated by the MEC also agree with FEM results at different current levels [2], [3]. The measured no-load back-EMF agrees well with the FEM result in Fig. 2(c), confirming the design. These results demonstrate that the proposed method supports reliable and computationally efficient IPMSM initial design by simultaneously considering saturation, parameter calculation, and demagnetization risk.

[1] J.-G. Lee, D.-K. Lim and H.-K. Jung, *IEEE Trans. Magn.* 55 (10), 1-4 (2019).
[2] W. Jeong, S. Paul, P.-W. Han and J. Chang, *IEEE Access* 14, 2637-2646 (2026).

[3] J. Faiz and E. Mazaheri-Tehrani, *IEEE Trans. Ind. Appl.* 53 (3), 2772-2785 (2016).

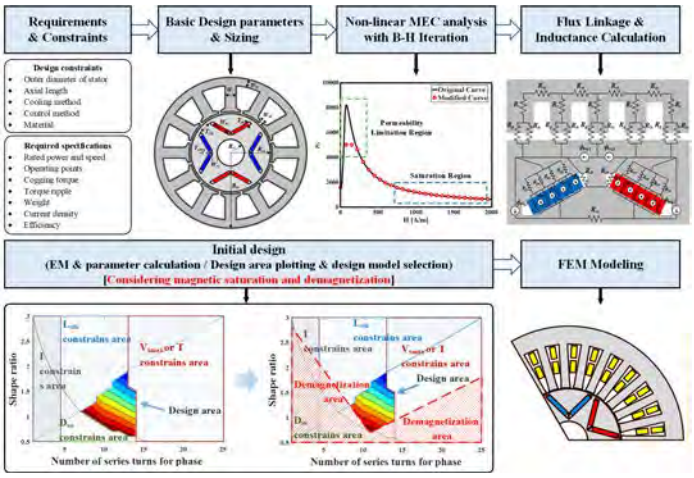


Fig. 1. Nonlinear MEC based IPMSM design procedure considering magnetic saturation and demagnetization constraints.

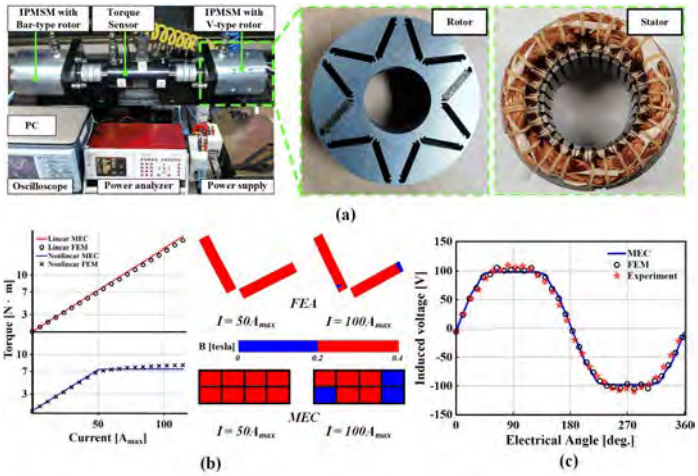


Fig. 2. Prototype and validation results: (a) experimental setup, rotor, and stator, (b) torque saturation and demagnetization comparison between FEM and MEC, (c) comparison of measured FEM and back EMF.

CQ-03. Prediction of Electromagnetic Performance in an Inverter-Coupled Interior Permanent Magnet Synchronous Motor Using an Artificial Neural Network

M. Kim[2], G. Shin[2], G. Lee[2], S. Kim[1], J. Choi[1], K. Shin[2]
[1]Chungnam National University, Daejeon, Korea (the Republic of), [2]Changwon National University, Changwon, Korea (the Republic of)

Interior permanent magnet synchronous motors (IPMSMs) are widely used in household compressor applications because high efficiency and high torque density are required over a wide speed range. In practical drive systems, motors are driven by inverters, and pulse width modulation switching generates harmonic current components that affect loss and efficiency [1]. Therefore, the efficiency prediction of the motor system applies the inverter's harmonic current rather than the sinusoidal current. Since finite element analysis considering the inverter system is performed for all operating regions, it takes a considerable amount of time. [2].

This paper presents an artificial neural network (ANN)-based efficiency map prediction method for an IPMSM considering inverter-induced harmonics, as shown in Fig. 1. The proposed framework consists of a parameterized IPMSM model and a space vector PWM (SVPWM)-based inverter circuit. The inverter current waveforms including harmonic components are applied to the FEA model to calculate torque, loss, and efficiency. Based on these results, an inverter-coupled dataset is used to train the ANN model. The proposed ANN model is verified with FEA results. Fig. 2 shows the parity plots of torque and total loss and the efficiency maps obtained by FEA and ANN prediction. The predicted results agree well with the FEA results, with R2 values of 0.9999 and 0.9998 for torque and total loss, respectively.

The efficiency maps also show similar distributions. The calculation time is reduced from approximately 8 hours using FEA to 7 minutes using ANN prediction. Therefore, the proposed method is effective for performance estimation of IPMSMs under SVPWM inverter-coupled conditions. More specific results and discussions will be presented in the full paper.

[1] L. Chang, M. Alvi, W. Lee, J. Kim, and T. M. Jahns, IEEE Trans. Ind. Appl., Vol. 58, No. 5, pp. 5635–5649, (2022).
[2] S. Zhu, J. Lu, and X. Liang, IEEE Trans. Ind. Electron., Vol. 71, No. 10, pp. 12019–12029, (2024).

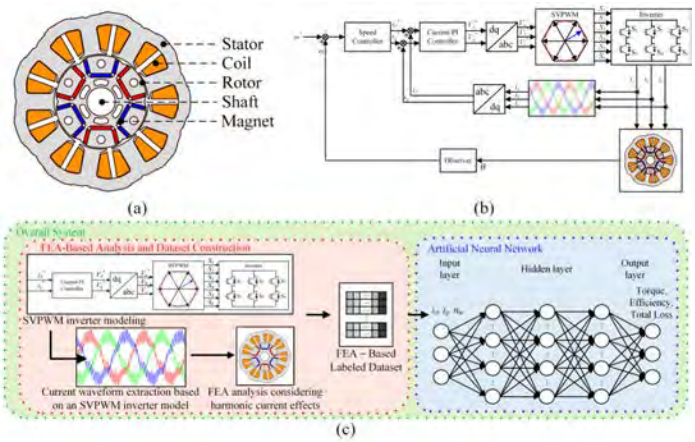


Fig. 1. ANN-based performance prediction framework for the inverter-coupled IPMSM drive system: (a) geometry of IPMSM, (b) inverter circuit and SVPWM switching scheme, and (c) overall prediction process.

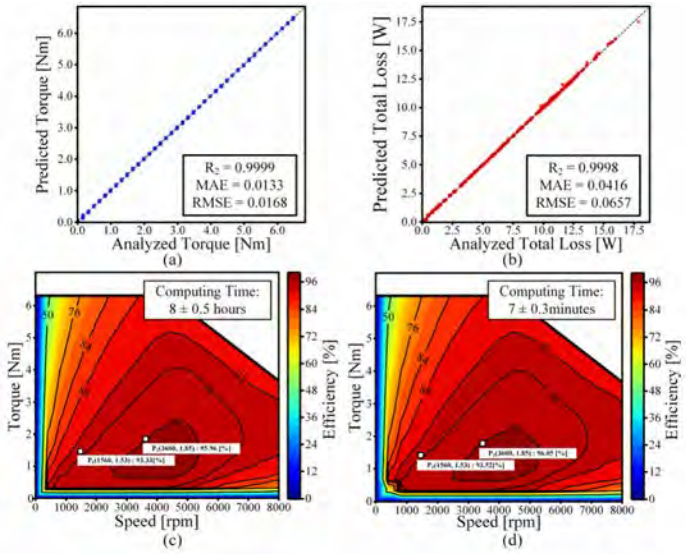


Fig. 2. Validation results of the proposed ANN model: parity plots for (a) torque and (b) total loss, and efficiency maps obtained by (c) FEA and (d) ANN prediction.

CQ-04. A study on industrial DC servo motors employing heavy rare-earth-free anisotropic bonded magnets

J. Lee[1], M. Park[1], Y. Noh[1], K. Lee[1], J. Lee[2]
[1]Korea Electronics Technology Institute, Bucheon, Korea (the Republic of), [2]Hanyang University, Seoul, Korea (the Republic of)

Permanent magnet motors conventionally employ sintered rare-earth magnets composed of light and heavy rare-earth elements to achieve magnetic flux densities exceeding 1.2 T. However, heavy rare-earth elements poses significant supply-chain risks and cost challenges internationally. Although heavy rare-earth-free permanent magnets have been actively developed for large-scale traction motors, their application to small- and medium-capacity motors remains limited due to reduced magnetic performance and thermal stability.

In this study, a heavy rare-earth-free anisotropic bonded permanent magnet is developed and investigated with a focus on magnetic performance, anisotropy, and demagnetization characteristics in a DC servo motor. The proposed magnet exhibits a maximum flux density of approximately 0.95 T, lower than that of conventional sintered magnets; nevertheless, its anisotropic nature and coating-free structure enable improved magnetic utilization in motor applications.

A servo motor platform is used to evaluate the electromagnetic performance of the proposed magnet. By eliminating thin-film surface coatings required in conventional isotropic magnets, the effective air gap is reduced, resulting in enhanced torque density and efficiency. Electromagnetic simulations and experimental measurements are conducted to assess torque characteristics, efficiency, and output performance across multiple power ratings.

Irreversible demagnetization behavior under varying environmental temperatures is further analyzed through numerical simulations and experimental validation to identify optimal operating conditions. The results demonstrate that the heavy rare-earth-free anisotropic bonded magnet is a viable and cost-effective alternative for high-performance servo motor applications, offering comparable output density while significantly reducing material cost and supply-chain dependency.

Acknowledgement
This work was supported by the Technology Innovation Program(RS-2024-00424292, Development of industrial DC servo motor technology of 750W or less using anisotropic

bonded magnets) funded By the Ministry of Trade Industry & Energy(MOTIE, Korea)
Z. Qu, Q. Wu, M. Zhang, Z. Wang, M. Yue and W. Liu, AIP Advances, Vol. 14, p. 025201 (2024).
Y. S. Lee, J. K. Lee, K. D. Lee, W. H. Kim and D. H. Jung, IEEE Trans. Appl. Supercond., Vol. 36, p. 1 (2025)
L. Yin, J. Yan, B. C. Sales and D. S. Parker, Phys. Rev. Applied, Vol. 17, p. 064020 (2022).

CQ-05. Design and Analysis of a Rare-Earth-Free Interior Permanent Magnet Synchronous Motor Using MnBi Magnets with a CFRP Sleeve

K. Kwak[1], S. Kim[1], M. Koo[2], H. Shin[3], J. Choi[1]
[1]Electrical Engineering, Chungnam National University, Daejeon, Korea (the Republic of), [2]Purpose Built Mobility Group, Korea Institute of Industrial Technology, Gwangju, Korea (the Republic of), [3]Specialized Machinery and Robotics Group, Korea Institute of Industrial Technology, Gimje, Korea (the Republic of)

Rare-earth-free permanent magnet machines have attracted attention due to the high cost and unstable supply of rare-earth materials. Among them, manganese–bismuth (MnBi) permanent magnets are promising candidates because of their positive temperature coefficient of coercivity and excellent thermal stability. However, MnBi magnets have relatively low remanent flux density and high material density, which limit electromagnetic performance and increase mechanical stress during high-speed operation. Previous studies on MnBi-based interior permanent magnet synchronous motors (IPMSMs) have relied on increased machine volume to compensate for the low remanence of MnBi magnets. In contrast, this paper proposes a design that maintains the same machine envelope while achieving comparable performance and improved high-speed capability.

To enhance flux concentration, a ribless rotor structure is adopted by removing flux-blocking ribs and bridges. However, the ribless structure cannot satisfy mechanical stress limits, especially when high-density MnBi magnets are employed. To address this issue, a carbon fiber reinforced plastic (CFRP) sleeve is introduced to provide structural reinforcement while preserving the electromagnetic advantages.

This paper investigates the feasibility of a rare-earth-free IPMSM using MnBi magnets and a CFRP sleeve. Comparative analyses of electromagnetic performance and mechanical stress are conducted between conventional and wrapped IPMSM models. The results show that the proposed design can overcome both the electromagnetic and mechanical limitations of MnBi magnets. Further details are provided in the full paper.

[1] K. W. Moon, K. W. Jeon, M. Kang, *IEEE Transactions on Magnetics*, vol. 50, no. 11, pp. 1-4, (2014)
[2] R. M. Brody, P. R. Ohodnicki, M. k. Ghosh, *IEEE Transactions on Industry Applications*, vol. 60, no. 4, pp. 6010-6022, (2024)

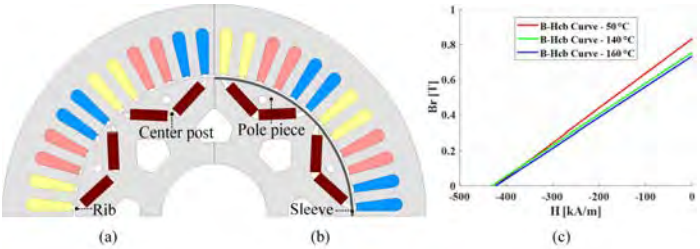


Figure1. (a) Model configurations of conventional and wrapped interior permanent magnet synchronous motors, (b) Comparison of B–H curves of MnBi permanent magnets at different temperatures (–50°C, 140°C, and 160°C).

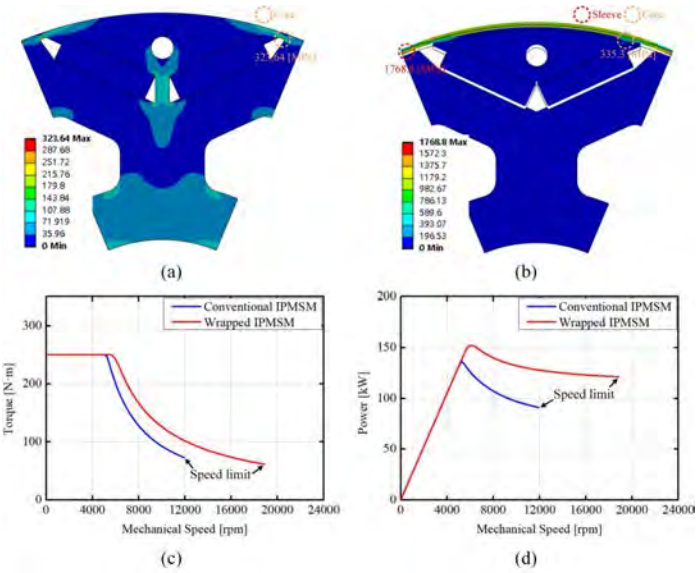


Figure 2. (a) Mechanical stress analysis result of the conventional IPMSM using MnBi magnets at 12,000 rpm, (b) mechanical stress analysis result of the wrapped IPMSM using MnBi magnets at 20,000 rpm, (c) torque–speed characteristics of the conventional IPMSM and the wrapped IPMSM, and (d) power–speed characteristics of the conventional IPMSM and the wrapped IPMSM.

CQ-06. Demagnetization-Constrained Multi-Objective Design Optimization of PMa-SynRM Using Non-Rare-Earth Permanent Magnets

M. Kim[1], M. Seo[1], W. Lee[1], H. Lee[1], K. Yu[2], J. Choi[2], K. Shin[3]
[1]Smart Manufacturing Engineering, Changwon National University, Changwon, Korea (the Republic of), [2]Electrical Engineering, Chungnam National University, Daejeon, Korea (the Republic of), [3]AI Electrical Engineering, Changwon National University, Changwon, Korea (the Republic of)

This paper proposes a demagnetization constrained optimal design methodology for a permanent magnet assisted synchronous reluctance motor (PMa-SynRM) using non-rare-earth permanent magnets. Although PMa-SynRMs with ferrite magnets are alternatives to rare-earth magnet motors, their performance can be degraded by irreversible demagnetization under low temperature and adverse current conditions [1]. Therefore, the proposed framework incorporates demagnetization constraints into a multi-objective optimization process [2]. Fig. 1 summarizes the proposed design process of the PMa-SynRM. The IPMSM and the proposed multi-layer flux barrier PMa-SynRM are compared in Fig. 1(a), and the nonlinear B-H characteristics of neodymium and ferrite magnets at various temperatures are shown in Fig. 1(b). Fig. 1(c) evaluates local demagnetized regions under demagnetizing current conditions. Based on these analyses, Fig. 1(d) shows the proposed optimal design process for deriving a robust design by integrating finite element analysis, sensitivity analysis, Pareto front graph, and demagnetization constraints. Fig. 2 shows the optimization and validation results. The Pareto fronts in Fig. 2(a) present the trade-off between torque density and efficiency considering demagnetization. From these candidates, a robust model is selected to maintain performance while suppressing irreversible demagnetization. To validate the derived model, the experimental setup in Fig. 2(b) is employed, and the measured back-EMF waveform is evaluated against the FEA results in Fig. 2(c). confirming reliability of proposed optimization. The full paper will present detailed demagnetization analysis, optimal design procedure, and performance comparison.

[1] Y. Kong, M. Lin, M. Yin and L. Hao, IEEE Trans. Magn. Vol. 54, Art. no. 8108705, (2018).
[2] T. A. Huynh and M.-F. Hsieh, IEEE Trans. Magn. Vol. 55, pp. 1-9, (2019).

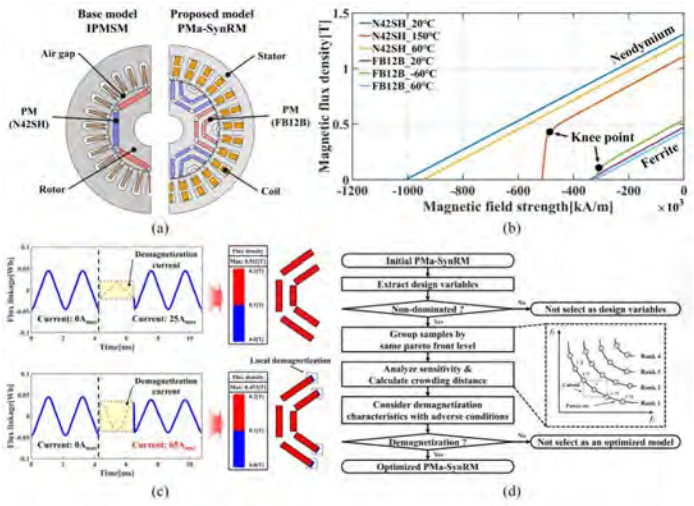


Fig. 1. Proposed design process of PMa-SynRM considering demagnetization: (a) geometries of rare-earth IPMSM and non-rare-earth PMa-SynRM, (b) temperature-dependent B-H curves of neodymium and ferrite magnets, (c) irreversible demagnetization analysis, and (d) proposed optimal design flowchart.

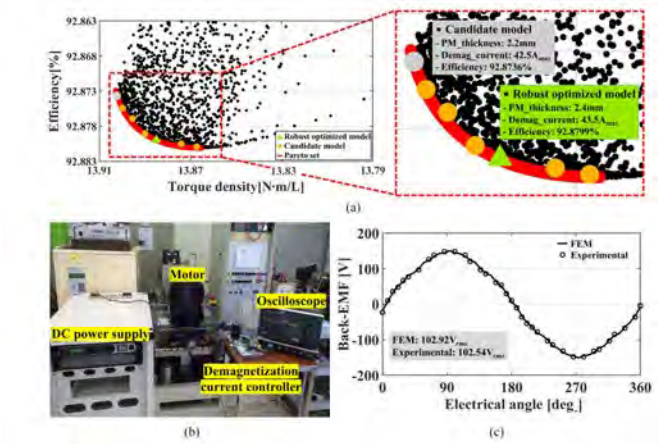


Fig. 2. Optimization and validation results of the optimized PMa-SynRM: (a) demagnetization-constrained Pareto fronts, (b) experimental setup, (c) comparison of FEA and measured back-EMF waveforms.

CQ-07. Analysis of Electromagnetic Characteristics of Surfaced-Mounted Permanent-Magnet Synchronous Machines Using a Physics-Informed Neural Network

S. Eom[1], J. Yang[1], T. Kim[1], K. Yu[1], K. Shin[2], J. Choi[1]
[1]Electrical Engineering, Chungnam National University, Daejeon, Korea (the Republic of), [2]AI Electrical Engineering, Changwon National University, Changwon, Korea (the Republic of)

This paper presents a physics-informed neural network (PINN)-based framework for predicting the electromagnetic characteristics of surface-mounted permanent-magnet synchronous machines (SPMSMs). Accurate evaluation of quantities such as magnetic vector potential, flux density, and harmonic characteristics is essential for SPMSM design and analysis. Although finite element analysis (FEA) provides high accuracy, its computational cost limits repeated simulations. To address this issue, this study investigates a PINN-based model as an alternative framework for electromagnetic analysis of SPMSMs.
The proposed model takes machine geometry and spatial coordinates as inputs and predicts the magnetic vector potential distribution over the computational domain. The flux-density components are then obtained through physics-based post-processing. To ensure physical consistency, the governing electromagnetic equations, boundary conditions, and additional constraint terms are incorporated into the loss function. Fig. 1 illustrates the overall framework of the proposed method.
The effectiveness of the proposed framework is validated through flux-density results. Fig. 2 presents the predicted magnetic-flux-density characteristics, including waveform comparison in Fig. 2(a) and FFT-based harmonic comparison in Fig. 2(b). The results show that the proposed PINN reproduces the overall electromagnetic behavior of the SPMSM with good agreement while preserving the principal waveform characteristics and overall spectral trend of the reference solution. Rather than focusing solely on individual harmonic components, the proposed model captures the machine's global electromagnetic characteristics in a physically consistent manner.
This study demonstrates that the proposed framework captures the representative electromagnetic behavior of the SPMSM and serves as a surrogate framework for rapid electromagnetic characterization in the early design stage. The proposed method can also be extended to broader performance analysis of electric machines.

[1] A. Beltrán-Pulido, D. Aliprantis, I. Bilionis, A. R. Munoz and N. Chase, IEEE Trans. Energy Convers. (2025).
[2] G. E. Karniadakis, I. G. Kevrekidis, L. Lu, P. Perdikaris, S. Wang, and L. Yang, "Physics-informed machine learning," *Nat. Rev. Phys.*, vol. 3, no. 6, pp. 422-440, 2021.
[3] M. Raissi, P. Perdikaris, and G. E. Karniadakis, "Physics-informed neural networks: A deep learning framework for solving forward and inverse problems involving nonlinear partial differential equations," J. Comput. Phys., vol. 378, pp. 686-707, 2019.

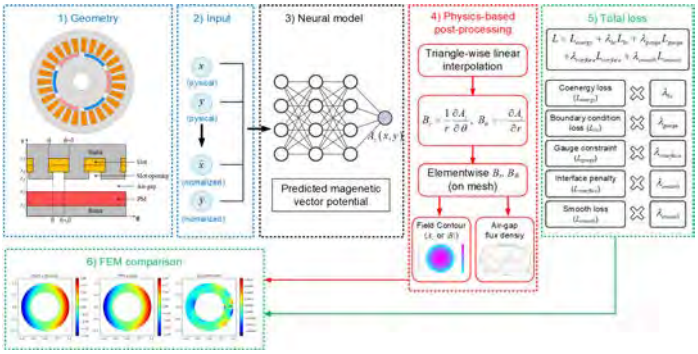
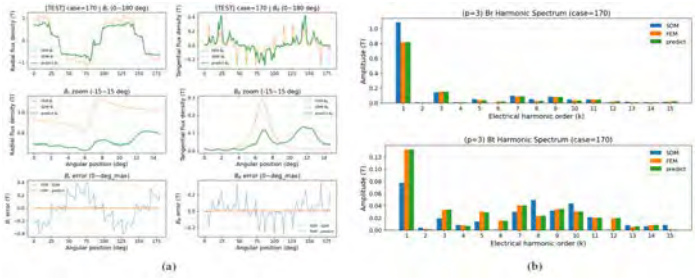


Fig. 1. Overall framework of the proposed PINN framework for electromagnetic field prediction.



Comparison of the air-gap flux density: (a) waveform, (b) FFT results.

CQ-08. Analysis of Magnetic Field Behavior and Core Losses in Permanent Magnet Synchronous Generators for Wave Energy Converter under Load Conditions

W. Jung[1], Y. Yoon[1], S. Kim[1], K. Shin[2], J. Choi[1]
[1]Electrical Engineering, Chungnam National University, Daejeon, Korea (the Republic of), [2]Electrical Engineering, Changwon National University, Changwon, Korea (the Republic of)

Multi-pole permanent magnet synchronous generators (PMSGs) feature a simple magnetic circuit design, fast response, linear torque-current and speed-voltage characteristics, and are suitable for a wide range of speed operations. However, a drawback of renewable energy generation is variability in generation conditions and

output. Therefore, analyzing electromagnetic and loss characteristics of the generator in different regions is essential. This study addresses losses during generator operation. First, the electromagnetic loss characteristics of a 4-pole 24-slot model were analyzed under AC and DC load conditions. The conventional Steinmetz equation was modified to include an ideal eddy current loss coefficient. Loss coefficients were derived through curve fitting of coreloss at different frequencies of electrical steel, and magnetic field behavior in different regions was analyzed to determine coreloss. Coreloss values obtained through FEM were compared with those derived using Steinmetz equation. Fig. 1(a) presents the 2D FEM analysis model. Fig. 1(b) depicts the experimental setup including DC load, AC load, and generator. Fig. 1(c) illustrates the curve fitting process using manufacturer-provided coreloss data to derive hysteresis, eddy current, and modified eddy current loss coefficients. Fig. 1(d) shows the distribution of coreloss for each load condition. Fig. 2(a) and (b) display circuit diagrams and current waveforms for AC and DC load conditions. Fig. 2(c) demonstrates magnetic field behavior during AC load generation, classified into alternating and rotational magnetic fields to derive more accurate coreloss values. Fig. 2(d) compares experimental data, FEM results, and values derived using the modified Steinmetz equation across different load conditions, validating this paper. More detailed data and discussion will be presented in the subsequent full paper.

1. T.-C. Jeong, W.-H. Kim, M.-J. Kim, K.-D. Lee, J.-J. Lee, J.-H. Han, T.-H. Sung, H.-J. Kim and J. Lee, *IEEE Trans. Magn.* 49 (5), 2343-2346 (2013).
2. J.-H. Woo, T.-K. Bang, H.-K. Lee, K.-H. Kim, S.-H. Shin and J.-Y. Choi, *IEEE Trans. Magn.* 57 (2), 1-5 (2020).
3. S.-H. Kim, J.-H. Woo, Y.-J. Kim, J.-Y. Choi and K.-H. Shin, *AIP Advances* 14 (1) (2024).
4. D. Gerada, A. Mebarki, N. L. Brown, C. Gerada, A. Cavagnino and A. Boglietti, *IEEE Trans. Ind. Electron.* 61 (6), 2946-2959 (2013).
5. G. Bramerdorfer, J. A. Tapia, J. J. Pyrhönen and A. Cavagnino, *IEEE Trans. Ind. Electron.* 65 (10), 7672-7684 (2018).

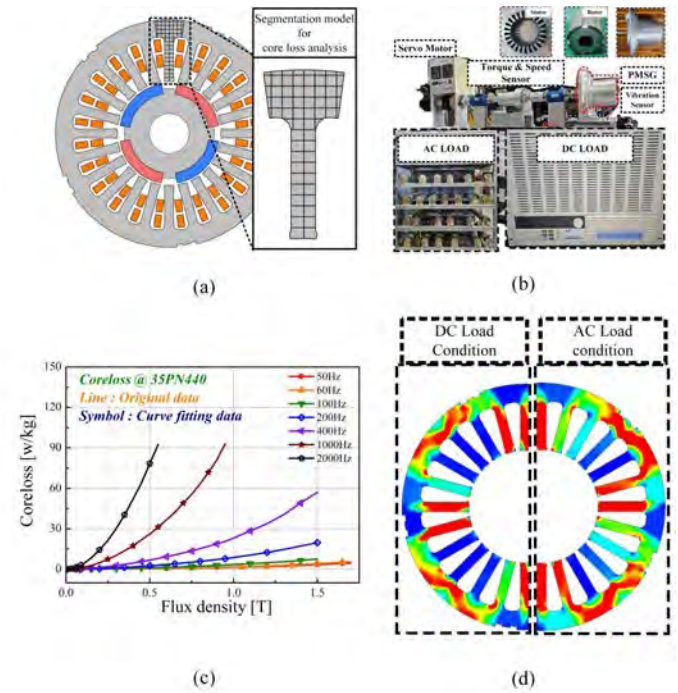


Fig. 1(a) 2D FEM analysis model, (b) experimental setup, (c) coreloss data curve fitting for 35PN250, (d) coreloss distribution of DC and AC load conditions.

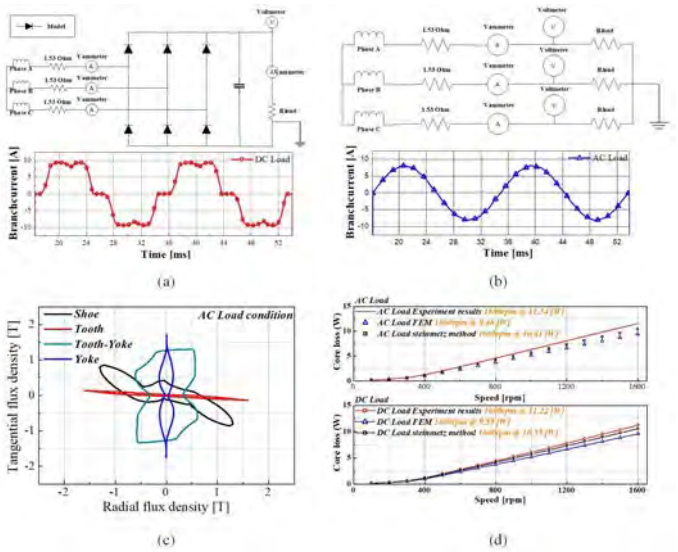


Fig. 2(a) DC load circuit and Branchcurrent, (b) AC load circuit and Branchcurrent, (c) magnetic field behavior of AC load condition ,(d) Comparison of analysis results and experiment results.

CQ-09. Design of a 3D-Printed Hybrid Axial–Radial Flux PM Motor with a Spoke-Type Rotor for Improved Power Density

H. Kim[1], S. Park[1], Y. Lim[1], C. Jin[2], W. Kim[3]
[1]Department of Next Generation Energy System Convergence, Gachon University, Seongnam-Si, Korea (the Republic of), [2]Department of Electrical Engineering, Wonkwang University, Iksan-Si, Korea (the Republic of), [3]Department of Electrical Engineering, Gachon University, Seongnam-Si, Korea (the Republic of)

Electric motors account for a significant portion of global electricity consumption, making improvements in efficiency and power density essential for sustainable energy systems. However, conventional manufacturing processes, such as lamination stacking and stamping, impose geometric constraints that limit the realization of optimized electromagnetic structures, particularly for advanced motor topologies [1].

To overcome these limitations, this paper proposes a hybrid permanent magnet motor that integrates radial flux and axial flux structures, combining the high torque capability of axial flux machines with the structural robustness of radial flux configurations [2]. Additive manufacturing is introduced to enable complex three-dimensional core geometries that are difficult to achieve using conventional fabrication methods, thereby enhancing design flexibility.

Unlike previous hybrid designs employing surface-mounted permanent magnet (SPM) rotors in the radial flux section, this study adopts a spoke-type rotor to achieve flux concentration and improve torque density. While the spoke-type configuration offers superior magnetic utilization, it typically requires rotor barrier structures for magnet retention, which can introduce flux leakage paths and reduce effective air-gap flux.

To address this issue, the proposed design replaces conventional ferromagnetic barrier regions with non-magnetic structures enabled by 3D printing. This approach suppresses flux leakage and improves flux linkage, resulting in enhanced electromagnetic performance. Furthermore, the proposed structure alleviates the constraint of post-assembly magnetization, enabling pre-magnetized assembly.

Three-dimensional finite element analysis is conducted to evaluate electromagnetic characteristics, including flux distribution, torque capability, and power density. The results demonstrate improved flux utilization and higher power density compared to conventional hybrid motor configurations. The proposed approach highlights the potential of additive manufacturing in enabling structurally and electromagnetically optimized motor designs.

[1] A. Tessarolo, "Recent advances in axial flux permanent magnet machines," IEEE Trans. Ind. Appl., vol. 54, no. 3, pp. 1972–1981, May/Jun. 2018.
[2] Y. Du, X. Zhu, and L. Quan, "Design and analysis of a high torque density axial-flux permanent-magnet machine," IEEE Trans. Magn., vol. 55, no. 7, pp. 1–5, Jul. 2019.

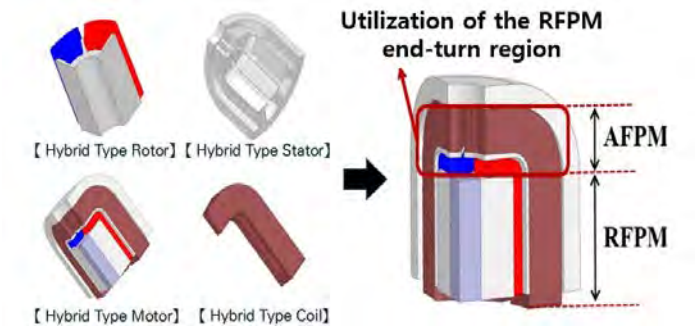


Fig. 1

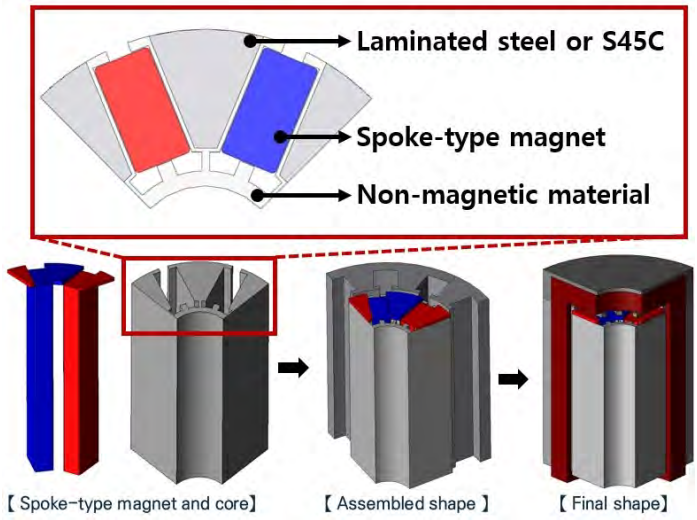


Fig. 2

CQ-10. Improved Rotor Shape Design of Spoke-type Ferrite Motors for Enhanced Magnetization Rate

S. Park[1], H. Kim[1], J. Moon[1], C. Lee[1], W. Kim[2]
[1]Department of Next Generation Energy System Convergence, Gachon University, Seongnam-Si, Gyeonggi-Do, Korea (the Republic of), [2]Department of Electrical Engineering, Gachon University, Seongnam-Si, Gyeonggi-Do, Korea (the Republic of)

With the rapid advancement of the AI and semiconductor industries, the demand for highly integrated manufacturing systems has made the miniaturization and high power density of vacuum pump motors a critical requirement. While conventional high-power motors predominantly use rare-earth magnets, ferrite-based designs have emerged as a sustainable alternative. Specifically, the Spoke-type structure is widely utilized as a reference model to compensate for the low remanent flux density of ferrite magnets through its flux-concentration effect.
In the fabrication of permanent magnet motors, assembling pre-magnetized magnets with the rotor core is challenging due to the strong magnetic attractive forces, which increase the risk of magnet damage and manufacturing difficulty. To mitigate these issues, the "post-assembly magnetization" method—where unmagnetized magnets are inserted into the rotor before being magnetized—is preferred. The existing reference model utilizes magnet holders to ensure assembly precision and mechanical integrity during this process. However, this conventional configuration suffers from a significant drawback: during magnetization, as the magnet reaches saturation and its permeability approaches that of air, a leakage path is formed where the magnetizing flux passes through the magnet holder instead of the magnet interior, thereby degrading the magnetization rate. To address this limitation, this study proposes an improved rotor shape design that replaces conventional magnet holders while maintaining secure mechanical retention and optimizing the magnetization path to minimize flux leakage. Through Finite Element Analysis (FEA), the proposed rotor shape was shown to improve magnetization efficiency and preserve output characteristics compared to the reference model. The results verify that the proposed design is highly effective for the miniaturization and performance preservation of semiconductor vacuum pump systems.

S.-H. Lee, J.-H. Kim and W.-H. Kim, Mathematics., Vol. 13, p.3866 (2025)

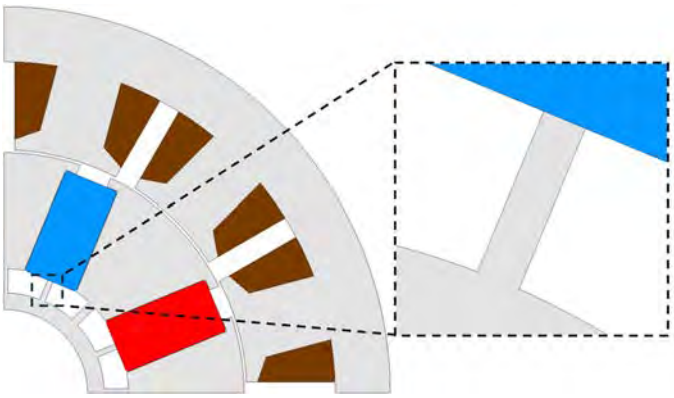


Fig. 1 Configuration of the reference Spoke-type rotor structure with magnet holders

CQ-11. Multi Objective Optimization of an Inverter Fed IPMSM Based on Magnetic Field Behavior and Core Loss Prediction

K. Yu[1], T. Kim[1], S. Eom[1], H. Ban[1], S. Kim[1], J. Park[1], K. Shin[2], J. Choi[1]
[1]Electrical Engineering, Chungnam National University, Daejeon, Korea (the Republic of), [2]Electrical Engineering, Changwon National University, Changwon, Korea (the Republic of)

Accurate core loss prediction is essential for high-efficiency interior permanent magnet synchronous motors (IPMSMs), especially under inverter-fed operation. Pulse width modulation generates current harmonics that distort stator flux density and alter magnetic field behavior. As a result, conventional sinusoidal current-based finite element analysis (FEM) can lead to significant loss errors and reduced design reliability [1].
This paper proposes a core loss prediction-based multi-objective optimization method for an inverter-fed IPMSM. Fig. 1 shows the overall design process. Objectives and constraints are defined to maximize efficiency and torque density while satisfying limits on torque, cost, voltage, and torque ripple. Rotor and stator design variables are selected, and core loss trends are compared between FEM and the proposed method. Sensitivity analysis identifies dominant variables, followed by genetic algorithm-based optimization to obtain the Pareto front [2]. The final design is selected based on the efficiency–torque density trade-off, achieving improvements of 0.1% in efficiency and 1.07% in torque density.

Fig. 2 validates the proposed method. Fig. 2(a) shows the co-simulation model and setup. Fig. 2(b) presents dominant harmonics from fast Fourier transform (FFT) analysis of measured and simulated currents. Fig. 2(c) classifies the stator magnetic field, and core loss is calculated using a modified Steinmetz equation considering normal and tangential flux components [3]. Fig. 2(d) shows that the loss error is reduced from 45.4% to 7.23% with predicted current and 5.86% with measured current. These results confirm improved loss prediction and reliable optimal design.

1. J.-H. Lee, S. Sung, H.-W. Cho, J.-Y. Choi and K.-H. Shin, Energies 15 (23), 9213 (2022).
2. X. Sun, Z. Shi, G. Lei, Y. Guo and J. Zhu, IEEE Trans. Ind. Electron. 68 (1), 139-148 (2020).
3. K.-H. Shin, K. Hong, H.-W. Cho and J.-Y. Choi, IEEE Transactions on Applied Superconductivity 28 (3), 1-5 (2018).

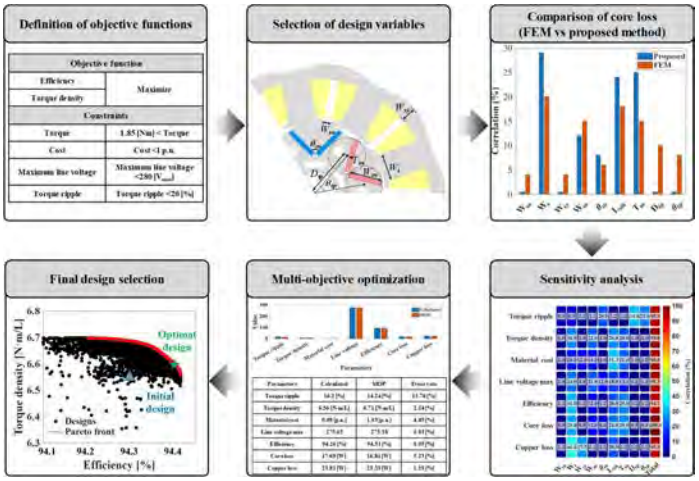


Fig. 1. Optimal design process of the IPMSM: objective definition, selection of design variable, comparison of core loss, sensitivity analysis, multi objective optimization, and final design selection.

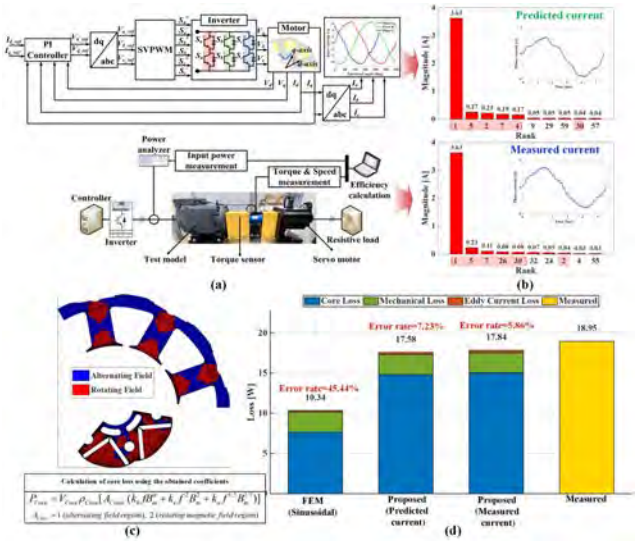


Fig. 2 Validation of core loss prediction: (a) co-simulation and test setup, (b) Current waveform and FFT comparison, (c) magnetic field behavior based loss analysis, and (d) comparison of electromagnetic losses.

CQ-12. Spin Test Validation of a Speed-Dependent Rotordynamic Model for a Superconducting Spoked Rotor

J. Xiao, S. Sirimanna, T. Balachandran, K. S. Haran
Hinetics Inc., Champaign, Illinois, United States

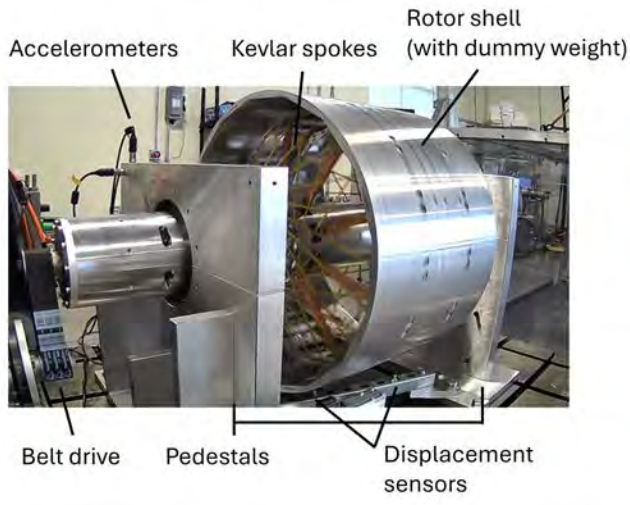
A spoke-supported superconducting rotor transfers high torque while maintaining strong thermal isolation between the warm shaft and the cryogenic rotor shell. However, the flexible spoke system differ from traditional torque tubes from rotordynamics perspective. This work presents an analytical framework for spoke-supported rotors and an experimental spin test that validates the model.

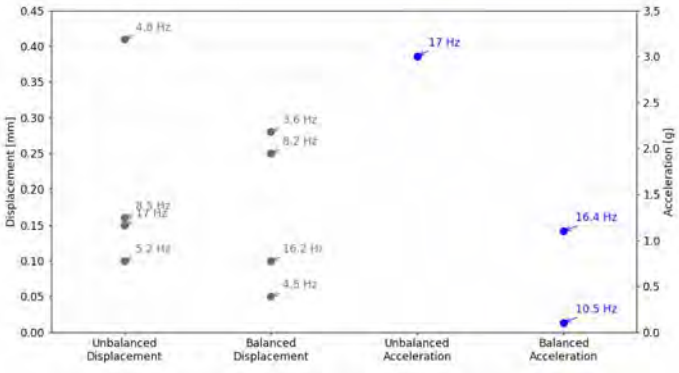
The first part of the study establishes a baseline structural dynamic model by representing the rotor as a spring-mass system and deriving expressions for the system's resonant behavior. The analytical predictions are verified against a 3-D finite element model and impact experiment. The first six mode shapes and their natural frequencies show consistency across analytical, numerical, and experimental approaches. This baseline model forms the foundation for a static Campbell representation of the spoke system.

The second part extends the framework to include speed-dependent phenomena, such as geometric stiffening and spin softening, gyroscopic coupling leading to forward and backward whirl splitting, and support dynamics associated with rolling-element bearings. The model is reformulated as a speed-dependent state-space system and implemented in

Simulink. The rotor support is represented using isotropic stiffness and damping consistent with the installed bearings.
A full-scale spin test is conducted using a rotor with the same mechanical properties and intended operating characteristics as the target machine. The rotor is spun to 1,000 rpm, with three-axis vibration and radial run out recorded. Experimental results demonstrate stable operation and show matching data to the extended model. This work establishes a validated framework to extend the static spoke-suspension models and provides the first experimental evidence supporting the rotordynamic predictability of superconducting spoked rotors.
Figure 1 shows a photo of the physical setup with key components labeled.
Figure 2 summarizes the experimental result, showing the peak vibration amplitudes before and after balancing, with corresponding dominant frequencies annotated.

J. Xiao, H. Rautela and S. Sirimanna, IEEE Transactions on Magnetics., vol. 61, no. 9, pp. 1-5 (2025)
J. Campos, M. Crawford and R. Longoria, IEEE Transactions on Magnetics, vol. 41, no. 1, pp. 274-280 (2025)
J. J. Scheidler, T. F. Tallerico and E. J. Stalcup, IEEE Transactions on Applied Superconductivity, vol. 35, no. 5, pp. 1-5 (2025)
B. T. Murphy, J. R. Kitzmiller and R. Zowarka, IEEE Transactions on Magnetics, vol. 37, no. 1, pp. 310-313 (2001)
B. T. Murphy, S. M. Manifold and J. R. Kitzmiller, IEEE Transactions on Magnetics, vol. 33, no. 1, pp. 474-479 (1997)
J. Xiao, T. Balachandran and A. J. Samarakoon, IEEE Transactions on Magnetics., vol. 58, no. 8, pp. 1–5, Aug (2022)





CQ-13. Improved Quasi-3D Magnetic Equivalent Circuit Model Considering Radial Leakage and Edge Effects for Axial flux Permanent Magnet Machines

S. Kim[1], M. Kim[1], S. Woo[1], J. Park[2], J. Choi[3], K. Shin[4]
[1]Smart Manufacturing Engineering, Changwon National University, Changwon, Korea (the Republic of), [2]Chungnam National University, Daejeon, Korea (the Republic of), [3]Chungnam National University, Daejeon, Korea (the Republic of), [4]Changwon National University, Changwon, Korea (the Republic of)

Axial flux permanent magnet motors (AFPMMs) are used in applications requiring high torque density, but it is difficult to accurately predict electromagnetic performance because the analysis model has a three-dimensional structure. Conventional quasi-three-dimensional (3D) models using radial discretization reduce computational costs but suffer from errors caused by radial leakage flux [1]. Therefore, quasi-3D magnetic equivalent circuit (MEC) approaches have been studied for fast analysis in AFPMMs [2]. To accurately predict the electromagnetic performance of an AFPMM, a

technique that considers leakage between permanent magnets (PM), PM-rotor yoke leakage, edge leakage, and saturation is required [3], [4].

In this paper, an improved quasi-3D MEC model that considers radial leakage flux and edge effects is proposed. As shown in Fig. 1, the 3D geometry is converted into a quasi-3D model, and the main flux paths are combined with leakage between PMs, leakage between PMs and rotor yokes, and edge leakage loops. The effective permeability and equivalent reluctance for each leakage path are derived through analytical permeability equations and integrated into the MEC. Consequently, radial variations and magnetic behavior dependent on nonlinear magnetic field characteristics are reflected in the computationally improved design framework.

As shown in Fig. 2, the proposed MEC is validated by comparison with existing quasi-3D analysis, 3D finite element analysis, and experimental results. The results include back-EMF, torque, and experimental measurement. The proposed model agrees more closely with 3D analysis and measurements than the conventional quasi-3D model, especially for torque and back-EMF. Therefore, the quasi-3D MEC considering leakage is effective for the preliminary design and performance prediction of AFPMM.

[1] Y. Hwang, K.-O. Kim, W.-S. Cha, B.-C. Bae, J.-H. Kim and M.-S. Lim, IEEE Trans. Magn., early access, doi:10.1109/TMAG.2025.3616439(2025).

[2] A. Hemeida, A. Lehikoinen, P. Rasilo, H. Vansompel, A. Belahcen, A. Arkkio and P. Sergeant, IEEE Trans. Ind. Electron. 66(11), 8318–8333 (2019).

[3] J. Zhao, T. Ma, X. Liu, G. Zhao and N. Dong, IEEE Trans. Energy Convers. 36(3), 2120–2130 (2021). [4] Y. Kano, T. Kosaka and N. Matsui, IEEE Trans. Ind. Electron. 57(6), 2124–2133 (2010).

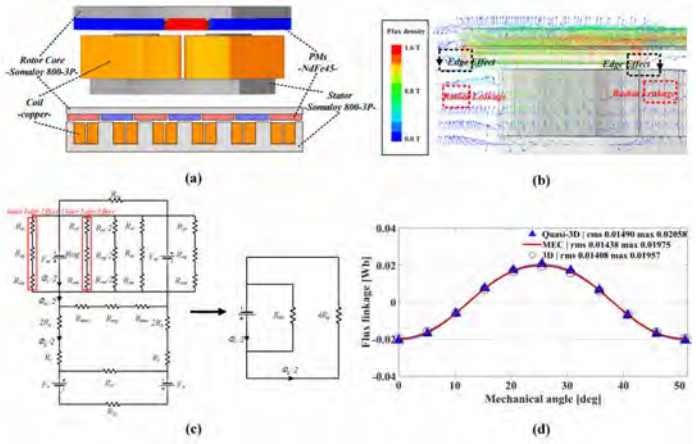


Fig. 1. Proposed quasi-3D MEC framework for AFPM machines: (a) 3D and quasi-3D models, (b) leakage flux loops, (c) MEC formulation with edge effects, and (d) flux linkage under noload condition.

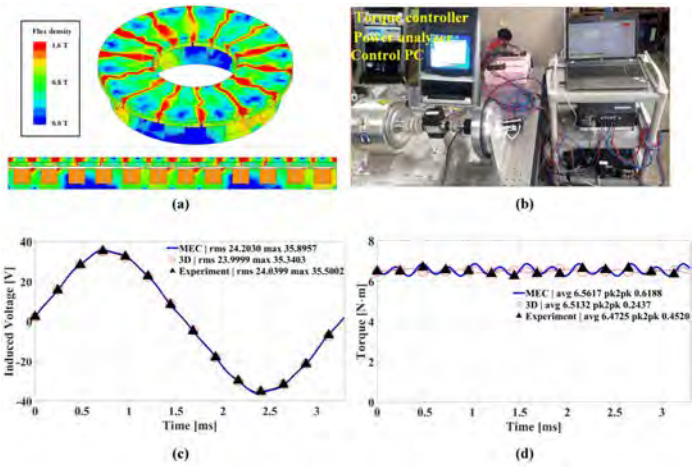


Fig. 2. Validation of the proposed model: (a) magnetic field density distributions, (b) experimental setup, (c) back-EMF comparison, and (d) torque comparison.

CQ-14. Analysis of Electromagnetic Force and NVH Characteristics in Axial Flux Permanent Magnet Motors With Segmented Stator Structures

J. Yang[1], W. Jung[1], K. Shin[2], J. Choi[1]
[1]Department of Electrical Engineering, Chungnam National University, Daejeon, Korea (the Republic of), [2]Department of AI Electrical Engineering, Changwon National University, Changwon, Korea (the Republic of)

Axial flux permanent magnet (AFPM) motors are widely used in applications requiring high torque density within a limited axial length. However, their noise and vibration (NVH) characteristics have become an important design issue due to the complex electromagnetic forces generated by the axial flux structure. In practical designs, segmented stator cores are commonly adopted to improve manufacturability, simplify assembly, and reduce material losses, but their influence on electromagnetic force distribution and NVH behavior has not been clearly identified.

This paper presents an analysis of electromagnetic force and NVH characteristics in AFPM motors with different stator core structures. A 14-pole/12-slot model is selected, and both solid and segmented stator configurations are investigated under identical conditions. Electromagnetic forces acting on the stator tooth surface are calculated using three-dimensional finite element analysis based on the Maxwell stress tensor. The calculated forces are analyzed using fast Fourier transform to identify dominant frequency components and then applied to a structural model to evaluate vibration and noise responses through coupled analysis. Waterfall diagrams are used to examine frequency variations with rotational speed. In addition, order-based analysis is performed to identify the relationship between rotational speed and dominant harmonic components.

Experimental data under no-load conditions are obtained for the segmented stator at discrete rotational speeds. The measured signals are then processed to extract frequency components and used to construct a waterfall representation for comparison with simulation results. The measured data are compared with the simulation results to examine dominant frequency components and their variation trends with rotational speed. More details are provided in the full paper.

[1] F. G. Capponi, G. De Donato, and F. Caricchi, *IEEE Trans. Ind. Appl.*, vol. 48, no. 6, pp. 2190-2205 (2012).
[2] W. Deng and S. Zuo, *IEEE Trans. Ind. Electron.*, vol. 65, no. 3, pp. 2018-2030 (2017).
[3] W. Deng and S. Zuo, *IEEE Trans. Transp. Electrif.*, vol. 5, no. 1, pp. 59-70 (2018).
[4] Y.-K. Lee et al., *AIP Advances*, vol. 13, no. 2 (2023).
[5] M. Wei, C. Zhang, S. Zhao, D. Wang, and Y. Gao, *IEEE Trans. Energy Convers.*, vol. 39, no. 3, pp. 2032-2041 (2024).

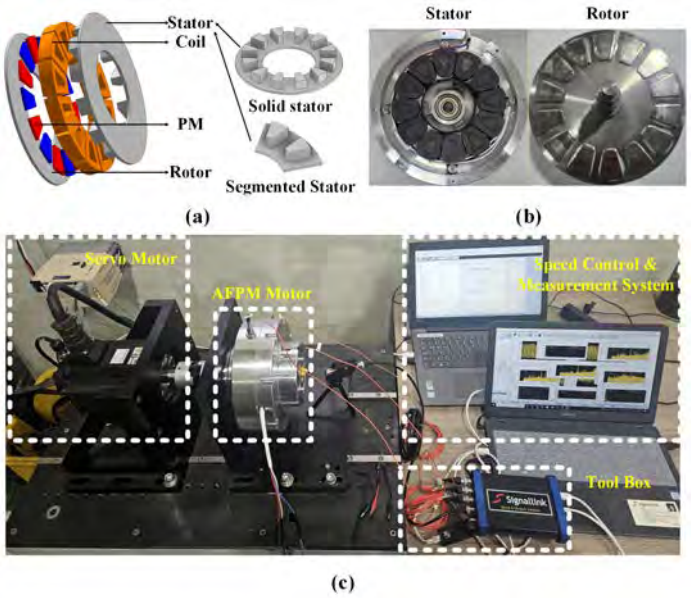


Fig. 1. (a) Geometry of the AFPM motor with solid and segmented stator cores, (b) prototype stator and rotor, (c) experimental set

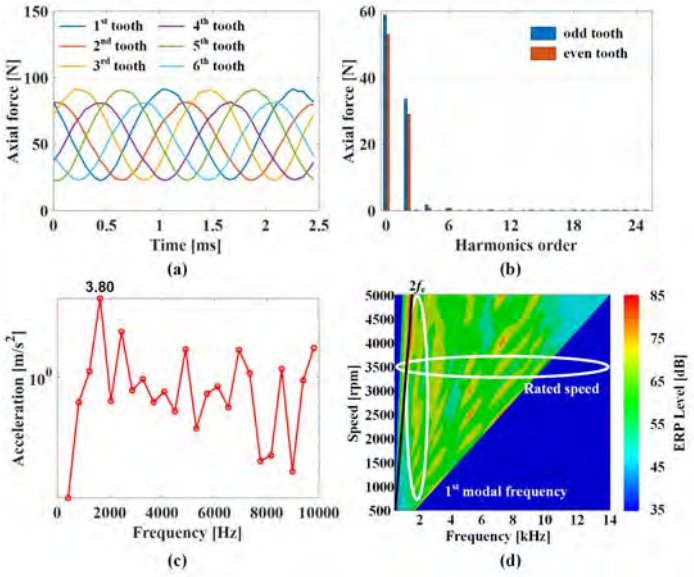


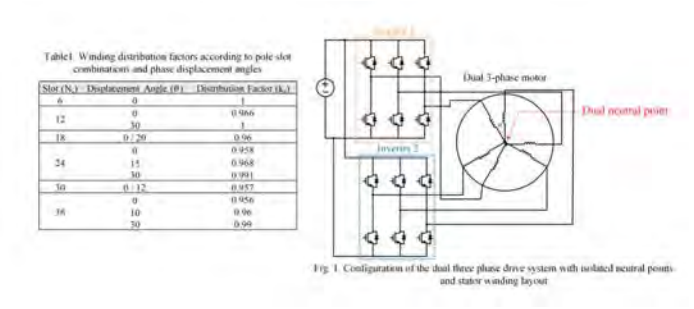
Fig. 2. (a) Axial electromagnetic force waveform, (b) FFT result of axial electromagnetic force, (c) acceleration response at rated speed, and (d) ERP level waterfall diagram

CQ-15. Harmonic Cancellation-Based Mitigation of Permanent-Magnet Eddy-Current Loss in Dual Three-Phase Motors Considering Pole–Slot Combinations

D. Kim, S. Oh, D. Ji, S. Song, H. Lee
Dankook University, Yongin-si, Korea (the Republic of)

The rapid proliferation of next-generation mobility technologies, including electric vehicles (EVs), urban air mobility (UAM), drones, and autonomous systems, has intensified the demand for electric motors capable of delivering high power and torque density within constrained installation spaces. To meet these requirements, dual three-phase (DTP) motor systems have emerged as a key alternative due to their high design flexibility and inherent fault-tolerant capability. This paper investigates the mechanism of magnetomotive-force (MMF) harmonic cancellation and the resulting mitigation of permanent-magnet eddy-current loss in DTP motors through optimization of the phase-displacement angle (θ) between the two winding sets. During high-speed operation, time-varying magnetic flux induces eddy currents in the permanent magnets, and the associated loss can be further aggravated by space-harmonic fields arising from stator MMF harmonics and slotting effects. In this study, the dominant harmonic components are analyzed for different pole–slot combinations, and the corresponding optimal phase-displacement angle is derived to cancel targeted spatial harmonics. Three-dimensional finite element analysis (3D-FEA) results confirm that harmonic cancellation reduces spatiotemporal flux-density variations within the magnets, thereby mitigating local loss concentration and improving thermal robustness. The findings provide a systematic guideline for harmonic-aware phase-displacement selection considering pole–slot combinations, contributing to electromagnetic performance optimization of high-performance DTP electric drives.

[1]E. Fornasiero, N. Bianchi and S. Bolognani, "Slot Harmonic Impact on Rotor Losses in Fractional-Slot Permanent-Magnet Machines," in IEEE Transactions on Industrial Electronics, vol. 59, no. 6, pp. 2557-2564, June 2012, doi: 10.1109/TIE.2011.2168794.
[2]Zhu, Z.; Wang, S.; Shao, B.; Yan, L.; Xu, P.; Ren, Y. Advances in Dual-Three-Phase Permanent Magnet Synchronous Machines and Control Techniques. *Energies* 2021, *14*, 7508. https://doi.org/10.3390/en14227508



CQ-16. Analysis of Electromagnetic Force Distribution and NVH Characteristics in Permanent Magnet Synchronous Machines Under Sinusoidal and Commutation Ripple Current Waveforms

Y. Yoon[1], W. Jung[1], H. Yu[1], C. W. Choi[1], S. Yoon[1], K. Shin[2], J. Choi[1]
[1]Electrical Engineering, Chungnam National University, Dajeon, Dajeon, Korea (the Republic of), [2]AI Electrical Engineering, Changwon National University, Changwon, Korea (the Republic of)

Permanent Magnet Synchronous Machines (PMSMs) are widely used in energy conversion systems due to their high power density and efficiency. However, PMSMs can generate noise, vibration, and harshness (NVH) due to magnetic interactions between the stator and rotor, degrading operational reliability. From an electromagnetic perspective, vibration sources can be divided into two categories: torque pulsations and electromagnetic forces. Accurate NVH prediction requires analysis of these sources and their interaction with mechanical structures.
While previous studies have attempted to mitigate torque pulsations or electromagnetic forces in PMSMs, most have primarily focused on individual characteristics rather than the coupled transfer mechanism. Furthermore, these analyses have limited extension to radiated acoustic noise evaluation. To analyze the NVH transfer mechanism, the electromagnetic sources are compared under two different control strategies: space vector pulse width modulation (SVPWM) and six-step operation. In particular, electromagnetic forces are decomposed into spatial and temporal harmonic components to identify dominant vibration sources. Based on vibration analysis, the radiated acoustic noise is predicted using the finite element method (FEM). The proposed method is validated with measured vibration data.
Fig. 1(a) presents the analysis flow from electromagnetic force to NVH and experimental validation. Fig. 1(b) compares six-step and SVPWM current waveforms, and Fig.

1(c) shows the experimental setup. Fig. 2(a) shows the radial and tangential magnetic pull force, Fig. 2(b) illustrates harmonic components of electromagnetic force density, Fig. 2(c) shows the FEM-predicted radiated noise, and Fig. 2(d) presents experimental validation. This approach improves NVH prediction at the initial design stage. Detailed data will be presented in the full paper.

1. D. Torregrossa, F. Peyraut, B. Fahimi, J. M'Boua and A. Miraoui, IEEE Trans. Energy Convers. 26 (2), 490-500 (2010).
2. J. Zou, H. Lan, Y. Xu and B. Zhao, IEEE Trans. Energy Convers. 32 (4), 1523-1532 (2017).
3. S. Zuo, F. Lin and X. Wu, IEEE Trans. Ind. Electron. 62 (10), 6204-6212 (2015).
4. J. Liang, B. Howey, B. Bilgin and A. Emadi, IEEE Open J. Ind. Appl. 1, 63-73 (2020).
5. W. Liang, J. Wang, P. C.-K. Luk and W. Fei, IEEE Trans. Ind. Electron. 68 (12), 11731-11739 (2020).
6. W. Liang, J. Wang, P. C.-K. Luk and W. Fei, IEEE Trans. Ind. Electron. 68 (12), 11731-11739 (2020).

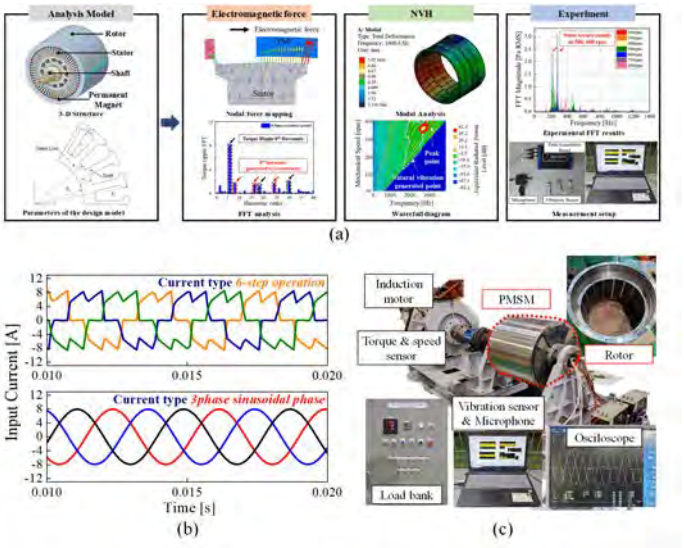


Fig. 1 (a) Overall framework of the NVH analysis, (b) comparative current waveforms, (c) manufactured PMSM and experimental setup.

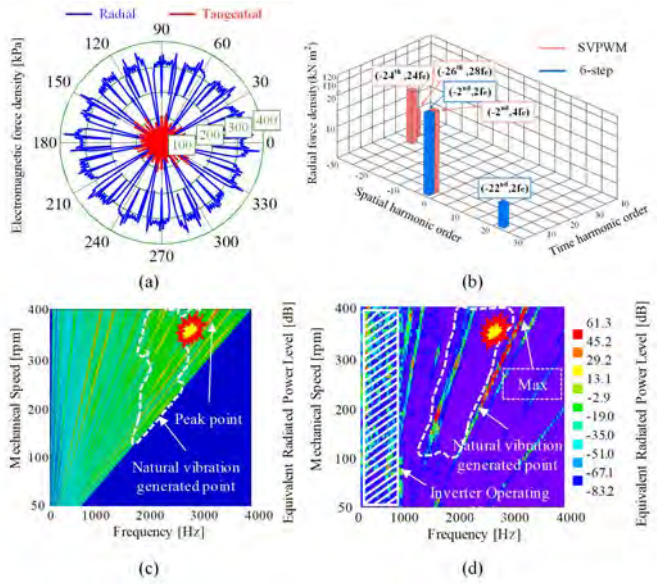


Fig. 2 (a) radial and tangential magnetic pull force, (b) temporal and spatial harmonic decomposition of radial electromagnetic force density, (c) waterfall diagram of equivalent radiated power level, (d) measured NVH results.

SESSION CR: UNCONVENTIONAL COMPUTING AND MAGNETIC MEMORIES I (POSTER SESSION)

Chair(s): P. Wang, *University of Manchester, Manchester, United Kingdom*

Wednesday, November 4, 2026
09:30 AM-12:30 PM
Coral 4

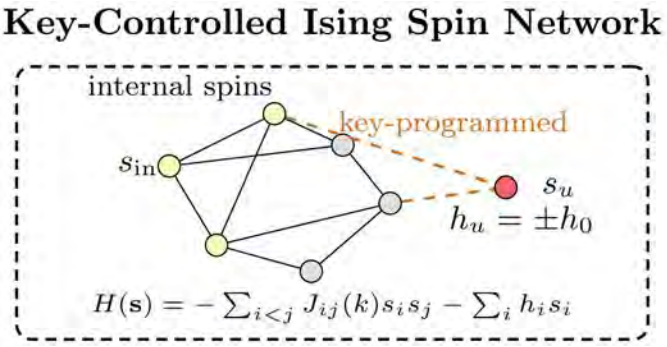
CR-02. Logic Obfuscation in Ising Networks via key-modulated Energy Landscape

D. Divyanshu[1], S. Amara[1], H. Bagci[1], G. Setti[2]
[1]CEMSE, King Abdullah University of Science and Technology, Thuwal, Makkah, Saudi Arabia, [2]Department of Electronics and Telecommunications,, Politecnico di Torino, Turin, Italy

Logic obfuscation protects circuits against reverse engineering by inserting key-controlled gates. But conventional gate-level approaches remain vulnerable to Boolean satisfiability (SAT)-based attacks that eliminate incorrect keys in polynomial time [1]. In this work, we propose a physics-based alternative using a key-controlled Ising spin network, where the secret key is embedded in the spin interaction matrix, reshaping the energy landscape to govern functional behavior in a manner not reducible to

discrete logical queries. An Ising network is a system of interacting binary variables, usually spins, $s_i \in \{-1,1\}$ with energy $E(s) = -\sum_{i<j} J_{ij}s_is_j - \sum_i h_is_i$. The couplings J_{ij} set which nodes prefer to align/anti-align and the field's h_i bias individual spins [2]. Ising models are useful for solving combinatorial optimization problems [3]-[5]. Magnetic systems such as stochastic nanomagnets have been explored to implement Ising networks, where magnetization encodes spins, stochastic switching enables annealing, and current-mediated interactions implement spin coupling [4], [5]. The input is encoded as clamped nanomagnet states, and the system evolves under key-dependent couplings and bias fields, governed by the Ising Hamiltonian. A dedicated control spin (s_u), subject to a key-dependent bias, interacts with the network, and its steady-state magnetization, which is obtained through stochastic dynamics and time-averaged readout, determines whether the circuit is unlocked. The work is evaluated using ISCAS benchmark circuits (I'89), in which the spin network serves as a control layer interfacing with digital logic to ensure correct output. The Ising network (Fig. 1) consists of input spins (s_{in}) clamped to the I'89 input, 24 hidden spins, and key-dependent bias (h_u) on s_u. 5000 samples with 25 repetitions are used. The Ising dynamics employ an inverse temperature schedule with 800 stochastic update steps. The network exhibits high stability and reliable convergence to the correct output. Under incorrect keys, energy landscape distortion reduces stability, confirming physics-based probabilistic obfuscation (see Fig. 2).

[1] K. Shamsi, D. Z. Pan, and Y. Jin, *in 2019 IEEE/ACM International Conference on Computer-Aided Design (ICCAD)*, 2019.
[2] E. Ising, *Z. Phys.*, vol. 31, no. 1, pp. 253–258, 1925.
[3] N. Mohseni, P. L. McMahon, and T. Byrnes, *Nat. Rev. Phys.*, vol. 4, no. 6, pp. 363–379, 2022.
[4] K. Lee, S. Chowdhury, and K. Y. Camsari, *Commun. Phys.*, vol. 8, no. 1, 2025.
[5] Y. Shim, A. Jaiswal, and K. Roy, *J. Appl. Phys.*, vol. 121, no. 19, p. 193902, 2017.



Key-controlled Ising spin network diagram.

Circuit (I'89)	Input	Output	Unlock Probability (Correct Key)	Bit Stability (Correct key)	Bit Stability (Incorrect key)
s27	2	3	85.17%	94.17%	68.24%
s298	4	5	84.60%	94.09%	68.28%
s820	18	19	80.74%	93.08%	70.91%
s832	18	19	82.31%	93.62%	70.37%
s953	4	8	93.17%	97.26%	66.09%
s1238	14	14	80.37%	92.93%	71.06%
s1494	13	14	70.65%	89.43%	74.55%

Performance of the Ising security block on I'89 circuits.

CR-03. Robust Power-Law Computing for Edge Intelligence using Spin-Orbit Torque Magnetic Tunnel Junctions

S. Xiong[1], C. Wan[1, 2], X. Han[1, 3, 2]
[1]Beijing National Laboratory for Condensed Matter Physics, Institute of Physics, University of Chinese Academy of Sciences, Chinese Academy of Sciences, Beijing, Beijing, China, [2]Songshan Lake Materials Laboratory, Dongguan, Guangdong, China, [3]Center of Materials Science and Optoelectronics Engineering, University of Chinese Academy of Sciences, Beijing, Beijing, China

Implementing efficient non-linear power-law operations at the edge is challenging. While Stochastic Computing (SC) based on SOT-MTJs is highly energy-efficient, intrinsic process variations and environmental sensitivities typically necessitate expensive per-device calibration. Here, we report a robust, calibration-free computing architecture enabled by a self-feedback SOT-MTJ sampling mechanism. This closed-loop approach dynamically locks onto target probabilities, transforming physical uncertainties into computational adjustability and enabling arbitrary fractional power operations ($x^{m/n}$) with inherent parallelism. Hardware demonstrations achieve high-quality Gamma correction (PSNR~35dB) and maintain computational accuracy without recalibration, even under magnetic interference or up to 50% device variation. This work establishes a pathway for

resilient, "deploy-and-forget" intelligent hardware.
[1] J. Grollier et al., Nature Electronics., Vol. 3, p.360-370 (2020)
[2] X. H. Li, M. K. Zhao, R. Zhang, et al., Appl. Phys. Lett., Vol. 123, p.142403 (2023)
[3] Y. Q. Xu, X. H. Li, R. Zhang, et al., Appl. Phys. Lett., Vol. 125, p.132403 (2024)
[4] X. H. Li, C. H. Wan, R. Zhang, et al., Nano Letters., Vol. 24, p.5420–5428 (2024)
[5] R. Zhang, X. H. Li, C. H. Wan, et al., Nature Communications., Vol. 17, p.189 (2026)
[6] B. R. Zink, Y. Lv and J. P. Wang, IEEE Journal on Exploratory Solid-State Computational Devices and Circuits., Vol. 8, p.101-114 (2022)

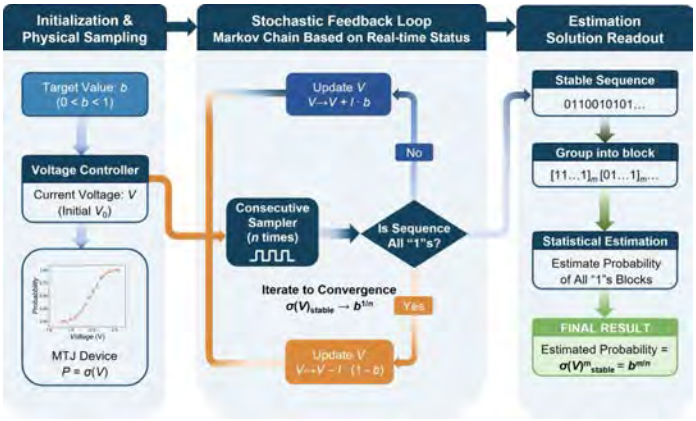


Figure 1. Framework of the calibration-free feedback sampling algorithm. Shows the closed-loop control for stochastic power-law computing. Based on n consecutive Bernoulli trials on the SOT-MTJ, an adaptive voltage controller updates the read voltage V. Using a learning rate l and target constant b, the device's switching probability P converges to $b^{1/n}$ independently of its P-V characteristics. Grouping the stabilized bit-stream enables generalized operations ($b^{m/n}$).

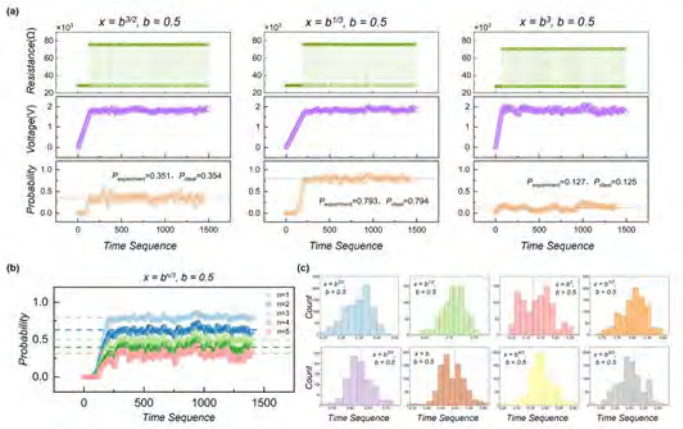


Figure 2. Experimental demonstration of power-law computing. (a) Real-time dynamic tracking of power-law operations ($0.5^{3/2}$, $0.5^{1/3}$, 0.5^{3}), showing rapid convergence of SOT-MTJ resistance, feedback voltage V_k, and estimated probability to theoretical values (V_0 = 0 V, l = 50 mV). (b) Parallel computing of five fractional powers ($0.5^{n/3}$) using a single device's bit-stream. (c) Steady-state probability histograms (e.g., $0.5^{1/2}$, $0.5^{4/3}$) display statistical stability via Gaussian-like distributions centered at theoretical targets.

CR-04. Large spin Hall effect and high thermal tolerance in amorphous Tungsten based spin Hall materials for SOT-MRAM application

Y. Hibino, T. Yamamoto, T. Taniguchi, H. Kubota, K. Yakushiji, S. Yuasa
Research Institute for Hybrid Functional Integration, National Institute of Advanced Industrial Science and Technology, Tsukuba, Ibaraki, Japan

Spin-orbit-torques (SOTs) enable fast and reliable magnetization switching, which can be a new information writing method for magnetoresistive random-access memories (SOT-MRAMs) [1]. Materials with large spin Hall effect (spin Hall materials) is a driving source of SOTs, and material choice is the most important factor for developing SOT-MRAMs [2,3,4,5]. For the integration of SOT-MRAMs in LSI, spin Hall materials need to have not only large spin Hall effect but also high thermal tolerance for the back-end-of-line process. β-phase Tungsten (W) is one of the candidate spin Hall materials due to its large spin Hall angle [2] and compatibility with MRAM architecture [6,7]. However, its low thermal tolerance is a serious challenge for application [5]. In this work, we present amorphous W-based alloys [6] as a new spin Hall material satisfying both large spin Hall effect and high thermal tolerance simultaneously. We prepared W-based spin Hall materials (4–10nm)/Co-Fe-

B(3nm)/MgO/TaO_x by sputtering deposition followed by thermal annealing at 350°C. Here, we used $W_{95.6}B_{4.4}$, $W_{84.2}Ta_{10.6}B_{5.2}$, and $W_{83.9}V_{7.6}B_{8.5}$ (herafer W-B, W-Ta-B, and W-V-B) for W-based spin Hall materials. In Fig.1, we show XRD spectra of 10-nm-thick films after post-annealing at 350°C. W-B show slight XRD peaks owing to b-phase W, while W-Ta-B and W-V-B show no significant XRD peaks but broad hump near 40° showing amorphous feature. Effective spin Hall angle of W-Ta-B and W-V-B reaches up to ~-50% [7], which is larger than the β-W [2] and W-B (Fig.2). Such enhancement may be attributed to enhancement of spin Hall conductivity through Fermi-level tuning by Ta and V doping. These results show that amorphous spin Hall materials provide a key essence for realizing SOT-MRAMs.
This work was partly supported by Grant-in-Aid for JSPS KAKENHI (Nos. 23H01477) and ALCA-Next program (No. JPMJCR18T3) of JST
[1] A. Manchon *et al.*, Rev. Mod. Phys. 91, 035004 (2019). [2] C. F. Pai *et al.*, Appl. Phys. Lett. 101, 122404 (2012). [3] K. Garello *et al.*, IEEE Symposium on VLSI Circuits 81-82, (2018). [4] H. Honjo *et al.*, IEEE Int. Electron. Devices Meet. 28.5.1-28.5.4 (2019). [5] K. Sethu *et al.*, Phys. Rev. Appl. 16, 064009 (2021). [6] Y. Hibino *et al.*, Adv. Elec. Mater. 10, 2300581 (2024). [7] Y. Hibino *et al.*, unpublished.

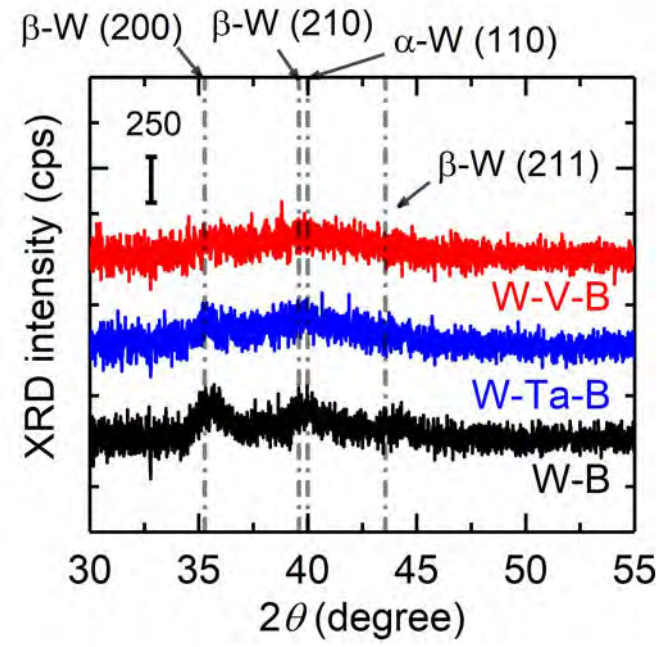
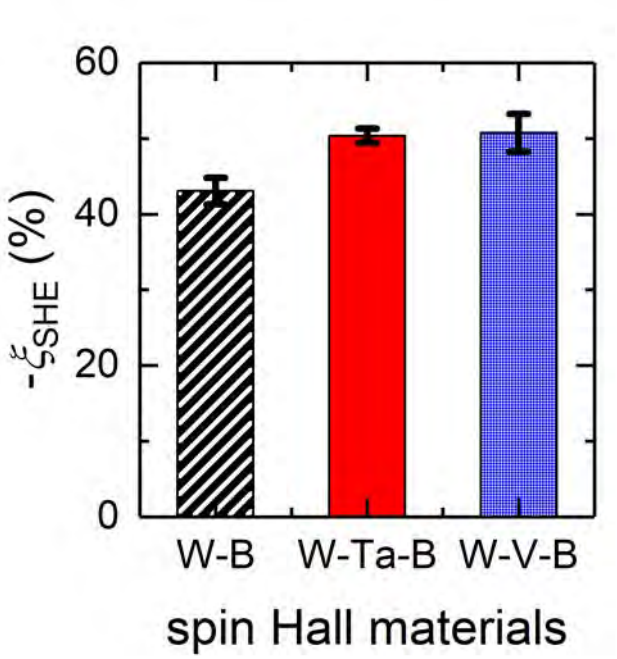


Fig. 1: Grazing-incidence XRD spectra of W-B, W-Ta-B, and W-V-B films. Vertical line corresponds to diffraction peaks of a-phase W and β-phase W.



Effective spin Hall angle ξ_{SHE} of W-B, W-Ta-B, and W-V-B.

CR-05. Scalable In-Memory Computing with *N*-ary Spintronic Crossbar Arrays

A. Moureaux, A. Lopes Temporao, F. Abreu Araujo
IMCN / BSMA, UCLouvain, Louvain-la-Neuve, Brabant Wallon, Belgium

The ever-growing energy and latency demands of AI workloads call for a fundamental shift away from conventional von Neumann architectures [1]. In-memory computing (IMC), which co-locates computation and storage within analog crossbar arrays, is a compelling approach to address the von Neumann bottleneck and the memory wall [2,3]. Among emerging non-volatile memory technologies, multi-state magnetic tunnel junctions (M^2TJs) [4], whose resistance is controlled by the magnetization configuration of crossed ferromagnetic ellipses, stand out for their non-volatility, CMOS compatibility, and intrinsic potential for equidistantly separated resistance levels, making them ideal candidates for *n*-ary neuromorphic IMC [5].

We present a simulation framework for performing multibit neural network inference on *n*-ary crossbar architectures, developed for spintronic M^2TJs but generalizable to any multistate memristive device [6]. The framework retrieves the matrix-vector multiplication (MVM) result from the measured analog output with minimal assumptions,

enabling the crossbar to operate as a standalone AI co-processor. Using simulated 4×4 arrays of 4-state M^2TJs, we demonstrate successful inference on the XOR task and on MNIST handwritten digit classification, achieving 94.48% accuracy against a 97.56% software baseline. This gap is further reduced to 2.79% via PCA dimensionality reduction.

We provide a systematic error analysis identifying weight quantization as the dominant error source. Systematic nonidealities (shared by all cells) and cell-specific random noise are also studied. Critically, cell-specific noise is less detrimental than systematic nonidealities of equal amplitude, owing to beneficial averaging across the array. The RMSE scales as $\sqrt{n}$ with the number of columns while the SNR grows logarithmically, favoring wide crossbar geometries. Finally, we demonstrate the existence of an optimal number of resistance states N_{opt} that minimizes total MVM error by trading off quantization error against state resolution, with N_{opt} decreasing in noisier device environments.

[1] *Big data needs a hardware revolution*, Nature 554 (2018)
[2] Sebastian et al., *Memory devices and applications for in-memory computing*, Nature Nanotechnology 15, 529 (2020)
[3] Jung et al., *A crossbar array of magnetoresistive memory devices for in-memory computing*, Nature 601, 211 (2022)
[4] Das et al., *A four-state magnetic tunnel junction switchable with spin-orbit torques*, APL 117, 072404 (2020)
[5] Soliman et al., *First demonstration of in-memory computing crossbar using multi-level Cell FeFET,* Nature Comms. 14, 6348 (2023)
[6] Moureaux et al., *Multibit neural inference in n-ary crossbar architectures*, under review in Communications Engineering (2026)

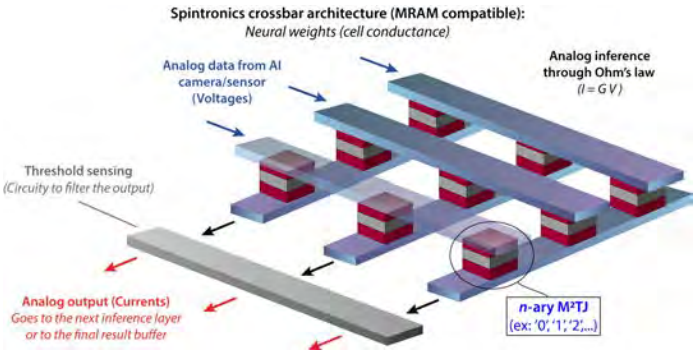


Fig. 1. *Schematic of the n-ary in-memory computing crossbar array based on multi-state magnetic tunnel junctions (M^2TJs).*

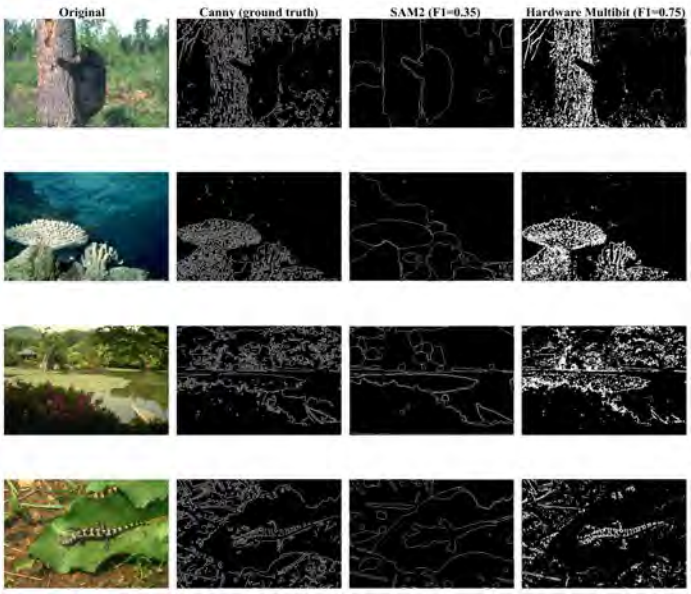
CR-06. Hardware-Efficient Multibit Edge Detection Using Spintronic Power-of-2 Thresholding and Majority Voting

P. Bandgar, K. Singh, D. Das
Department of Electrical & Electronics Engineering, BITS Pilani K K Birla Goa Campus, VASCO DA GAMA, GOA, India

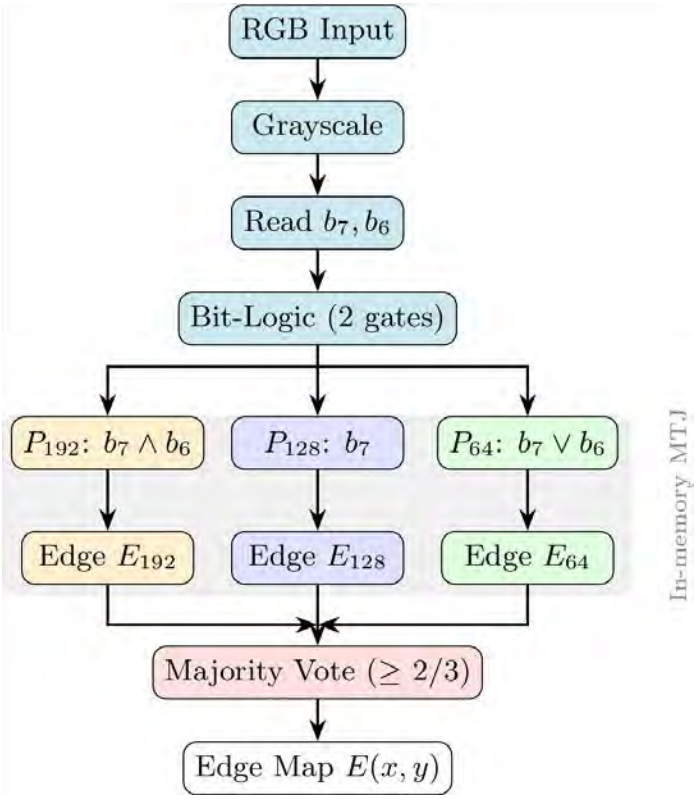
Edge detection is fundamental to computer vision, essential for object recognition, image segmentation, and autonomous navigation. Yet classical methods like Canny[1] require computationally intensive sequential pipelines unsuitable for resource-constrained edge devices. Meanwhile, deep learning approaches such as SAM2 demand GPU-scale energy budgets exceeding 1 J per image. There is a critical need for algorithms that maintain detection quality while enabling deployment on ultra-low-power IoT and battery-powered vision systems. We present a hardware-efficient multibit edge detection method leveraging Spin-Orbit Torque Magnetic Tunnel Junction (SOT-MTJ) devices for in-memory computing. Our key contributions are:
(1) a multibit thresholding scheme using power-of-2 thresholds (192, 128, 64) that map exactly to simple bit-logic operations $P_{192} = b_7$ (AND) b_6, $P_{128} = b_7$, $P_{64} = b_7$ (OR) b_6 - eliminating 8-bit comparators and requiring only two gates per pixel; (2) majority voting across three binary planes for noise-robust detection; and (3) energy modeling via Landau-Lifshitz-Gilbert-Slonczewski simulations demonstrating 78.27 nJ per image. The 3 × 3 neighborhood edge test executes directly in the MTJ crossbar array, exploiting the non-volatile storage and parallel sensing capabilities of spintronic devices. Evaluated on BSDS500 (200 test images) against Canny ground truth with 2-pixel tolerance, our method achieves F1 = 0.750 (precision 0.897, recall 0.662) at 916 µs latency. Under identical conditions, SAM2 achieves F1 score 0f ~0.349, indicating that the proposed spintronic hardware exceeds this large-scale vision model by 2.15× while consuming seven orders of magnitude less energy.

[1] J. Canny, "A computational approach to edge detection," IEEE Transactions on pattern analysis and machine intelligence, no. 6, pp. 679–698,2009.

[2] N. Ravi, V. Gabeur, Y.-T. Hu, R. Hu, C. Ryali, T. Ma, H. Khedr, R. Rädle, C. Rolland, L. Gustafson et al., "Sam 2: Segment anything in images and videos," arXiv preprint arXiv:2408.00714, 2024.



Edge detection comparison on BSDS500: Original, Canny (GT), SAM2, Hardware Multibit.



Algorithm pipeline for the Edge detection method.

CR-07. MEMS-tunable Radio Frequency Spin Diodes for Neuromorphic Computing Applications

M. Cocconcelli[1, 2], A. Angotti[2], A. Begue[1], Y. Wei[1], F. Maspero[2], R. Bertacco[2], D. Sanz Hernandez[1], J. Grollier[1]
[1]Laboratoire Albert Fert, CNRS, Thales, Université Paris-Saclay, Palaiseau, France, [2]Department of Physics, Politecnico di Milano, Milan, Italy

Spin-torque ferromagnetic resonance (STFMR) diodes are promising building blocks for neuromorphic hardware because they rectify RF signals into DC outputs with intrinsically nonlinear and field-tunable responses [1–4]. In RF neuromorphic schemes [2,4], the synaptic weight is defined by the slope of the rectified voltage V_{dc} versus RF input power. Enabling integrated local and reversible control of this slope is a key step toward hardware learning. Here, we implement such control using MEMS-actuated micromagnets in a flip-chip platform combining an RF chip hosting STFMR diode arrays with a MEMS chip integrating soft micromagnets. Voltage-driven cantilevers tune the micromagnet–diode distance and thus the local magnetic field, enabling independent control through a one-to-one cantilever–diode configuration.

Using four STFMR diodes connected in parallel and coupled to four independently actuated MEMS, we demonstrate selective tuning of individual resonances. Voltages up to 30 V induce ~1 GHz shifts toward lower frequencies, corresponding to ~–0.5 mT/V (Fig. 1). The tuning is reversible and limited by mechanical contact between the MEMS and RF chips.

We demonstrate a weighted-sum operation in a two-diode chain under dual RF excitation at f_1=4.29 GHz and f_2=3.87 GHz. Fig. 2a shows that MEMS actuation continuously modifies the slope of V_{dc} versus input power, i.e. the synaptic weight, providing a direct route toward learning through electromechanical control. Fig. 2b shows that the weighted sum is reconfigured by independently actuating the two MEMS. Rectified outputs are obtained at 5 mW input power, highlighting the potential for low-power RF neuromorphic hardware.

These results establish MEMS-controlled local magnetic tuning as a practical route toward programmable and trainable spintronic neuromorphic architectures, where both individual weights and weighted-sum operations can be dynamically adjusted in an integrated platform.

[1] G. Finocchio, M. Carpentieri, E. Martinez and B. Azzerboni, Appl. Phys. Lett., Vol. 118, p.160502 (2021)
[2] N. Leroux, J. Grollier, V. Cros and A. Fert, Neuromorph. Comput. Eng., Vol. 1, p.011001 (2021)

[3] Y. S. Gui, N. Mecking and C.-M. Hu, Phys. Rev. B, Vol. 78, p.134422 (2008)
[4] E. Plouet, N. Leroux, J. Grollier and V. Cros, Proc. IEEE IEDM, p.1 (2024)

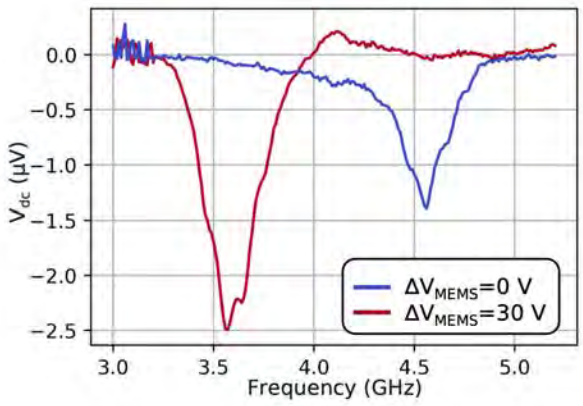


Fig. 1. STFMR response of a four-diode chain at 0 V and 30 V applied to all MEMS.

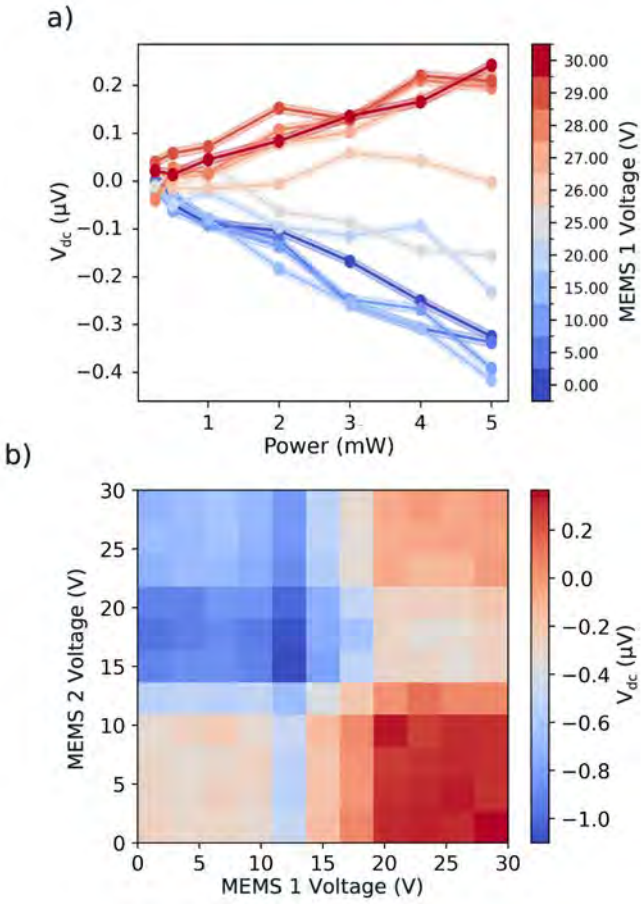


Fig. 2. a) Rectified DC voltage in a two-diode chain under dual RF excitation (f_1=4.29 GHz, f_2=3.87 GHz) vs input power. b) Output at 5 mW vs MEMS A1 and A2 voltages.

CR-08. Spin-regulated Synaptic Plasticity in Memristors Based on HfO_x-Co Granular Films

H. Zhu[1], Z. Yang[1], J. Zhu[1], S. Zheng[1], Z. Yang[1], Y. Ma[1], S. Zhang[1,2], M. Gong[1], T. YU[1]
[1]College of Physics, Sichuan University, Chengdu, Sichuan, China, [2]College of Mechanical Engineering, Guizhou University of Engineering Science, Bijie, Guizhou, China

Memristors, as a cornerstone for neuromorphic computing, have attracted considerable interest for neuromorphic applications [1,2]. Integrating magnetic materials into metal oxide-based memristors provides additional opportunities to enable spin-regulated neuromorphic sensing and computing [3,4]. In this report, HfO_x-Co granular films are utilized as the functional layer in memristors, where the concentration of Co granules were systematically changed by varying sputtering power from 20 W to 100 W. The structural, optical, magnetic and memristive properties were investigated. As expected, a magnetic transition from superparamagnetic to ferromagnetic behavior with increasing Co content is observed, evidenced by enhanced saturation magnetization and coercivity. The pure HfO_x devices exhibit space charge limited current (SCLC) conduction [5], whereas low Co incorporation shifts the transport to an interface-controlled Schottky emission regime [6]. Further increasing the concentration of Co, continuous conductive pathways are formed and the memristor transitions to an Ohmic conduction. Correspondingly, synaptic characterization demonstrates a transition from paired-pulse facilitation (PPF) in pure HfO_x device to paired-pulse depression (PPD) under positive bias [7,8]. This results demonstrate that magnetic nanoparticle incorporation provides an effective route to tune both transport physics and synaptic plasticity in oxide-based memristive systems. A frequency-selective filtering network is further constructed to validate this spin-regulated synaptic plasticity in the HfO_x-Co granular layer memristors.

[1] D. B. Strukov, G. S. Snider, D. R. Stewart, et al., *Nature* 453(7191), 80–83 (2008).
[2] Z. Xia, X. Sun, Z. Wang, et al., *Nano-Micro Lett.* 17, 217 (2025).
[3] Q. Shao, Z. Wang, Y. Zhou, et al., *npj Spintronics* 3, 16 (2025).
[4] J. Grollier, D. Querlioz, K. Y. Camsari, et al., *Nature Electronics* 3, 360–370 (2020).
[5] W. Cheng, X. Liu, L. Zhao, et al., *Solid-State Electron.* 132, 19–23 (2017).
[6] F. Gul, H. Efeoglu, Superlattices Microstruct. 101, 172–179 (2017).

[7] F. Gómez-Casado, J. B. Roldán, F. Jiménez-Molinos, et al., *Microelectron. Eng.* 276, 112445 (2026).
[8] Y. L. Zou, X. Y. Li, N. Ghenzi, et al., *ACS Appl. Mater. Interfaces* 17(33), 47207–47219 (2025).

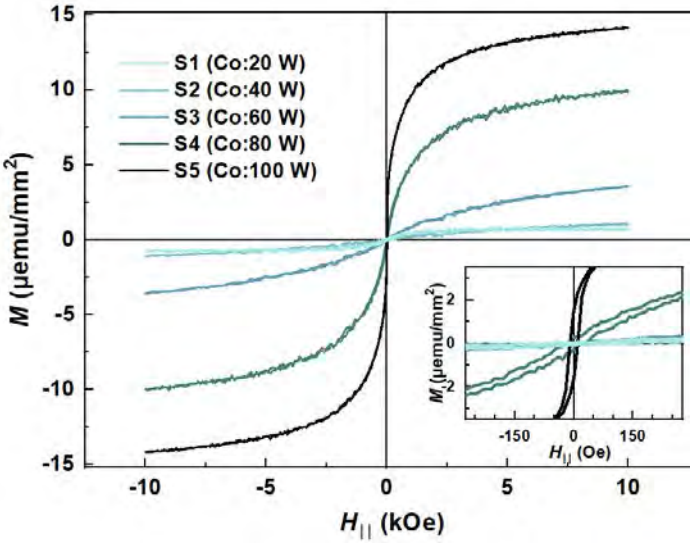


Figure 1 magnetic hysteresis loops for a series of HfO_x-Co granular films.

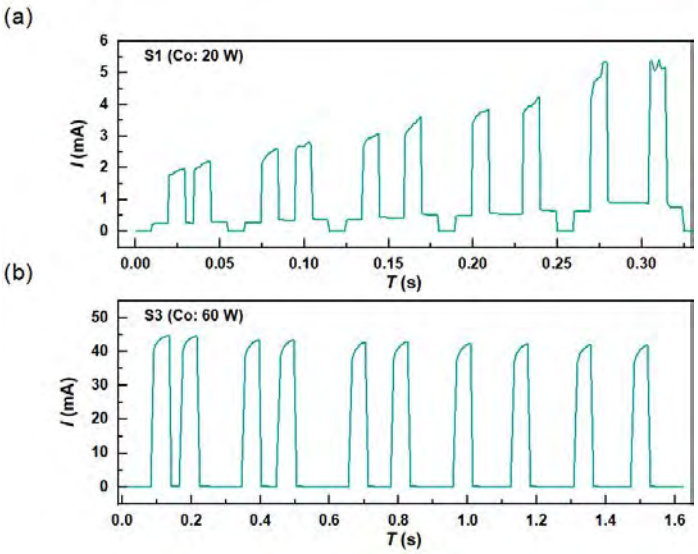


Figure 2 the inversion of the paired-pulse response under positive bias with increasing Co concentration: (a) normal and (b) reversed response.

CR-09. Quantitative analysis of the relationship between physical dynamics and computational capacities in spin-wave-based reservoir computing

R. Nakane[1, 2], Y. Miyasaka[1]
[1]*Department of Electrical Engineering and Information Systems, The University of Tokyo, Tokyo, Japan,* [2]*Systems Design Lab, The University of Tokyo, Tokyo, Japan*

Since our proposal in 2018[1], spin-wave-based reservoir computing (RC) has been studied through simulations and experiments[2-5]. Nevertheless, the specific types and magnitude of nonlinearity required for higher computational performance have yet to be fully elucidated. To tackle this common issue, we experimentally study spin-wave-based RC with computational capabilities of linear (short-term memory STM) and nonlinear (temporal XOR) benchmark tasks while characterizing group velocity v_g and nonlinearity of output spin-wave signals using a unique nonlinear index N_T.
Our device with a 3-μm-thick YIG film has 10 coplanar antennas on the surface(Fig.1), and an in-plane magnetic field was applied to realize the surface wave geometry. To explore various-types of spatiotemporal spin motions, a series random data (0 or 1) was encoded to a time-series input voltage signal with the following parameters: input voltage amplitudes corresponding to 1 and 0 (three conditions), time step length for 1 bit (2, 5, 10, 20, and 50 ns), input carrier wave frequency f_c(= 3, 4, and 5 GHz), and duty ratio of the input in one time step (0-0.5). A time-series output signal at each antenna was transformed into a Discrete Fourier Transform (DFT) spectrum. In addition to the f_c component, the sidelobe corresponding to nonlinear phenomena spreads depending on the input conditions. We define N_T using the correlation between the sidelobe area and the area of the input DFT spectrum. The antenna-dependent linear DFT area in output gives a reasonable v_g =~6 μm/ns.
In RC, the virtual node method was applied to increase the dimension n of the reservoir output vector up to 360, with the weight matrix trained by pseudo-inverse matrix. For all the input conditions, N_T and computational capacities for unknown data were estimated, where both capacities are sufficiently high(Fig.2). Mapping these relationships revealed that while the STM capacity is primarily governed by v_g, peak performance for both tasks is achieved at N_T ~0.5. This clearly indicates a linear and nonlinear trade-off relationship. Our quantitative framework provides fundamental insights into the underlying physics of RC.
[1] R Nakane, G Tanaka, and A Hirose, IEEE access vol. 6, p.

4462 (2018).
[2] R Nakane, A Hirose, and G Tanaka, Phys. Rev. Res. vol. 3, p. 033243 (2021).
[3] R Nakane, A Hirose, and G Tanaka, Phys. Rev. Appl. vol. 19, p. 034047 (2023).
[4] Y Miyasaka, A Hirose, and R Nakane, APL Mach. Learn. vol. 4, p. 016108 (2026).
[5] W. Namiki, et al., Adv. Intell. Syst. vol. 5, p.2300228 (2023).

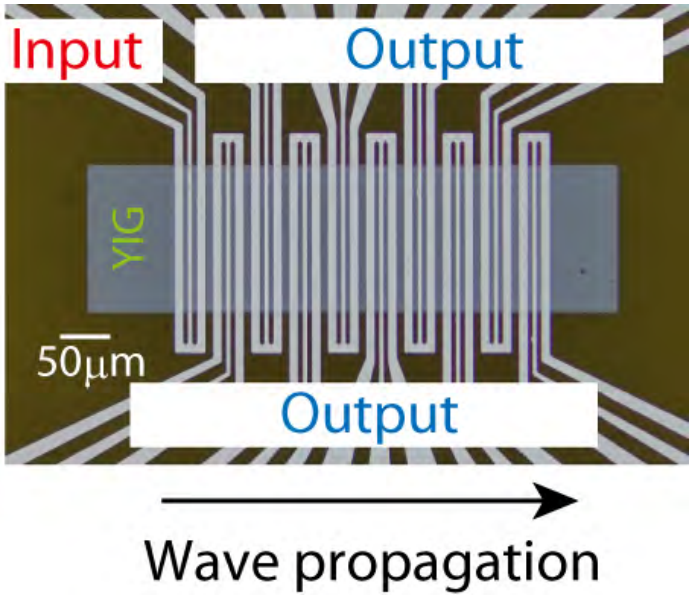


Fig.1 Device structure.

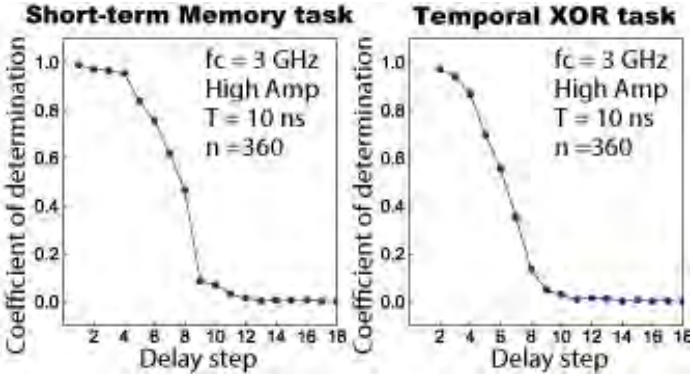


Fig.2 Computational capacities.

CR-10. Chirality-controlled dipolar coupling states in spin-torque vortex oscillator arrays

S. de Wergifosse[1], F. Abreu Araujo[1], J. Gartside[2, 3], T. da Câmara Santa Clara Gomes[4, 1]
[1]Institute of Condensed Matter and Nanosciences, Université catholique de Louvain, Louvain-la-Neuve, Belgium, [2]Blackett Laboratory, Imperial College London, London, United Kingdom, [3]London Centre for Nanotechnology, Imperial College London, London, United Kingdom, [4]Microsistemas e Nanotecnologias (INESC MN), Instituto de Engenharia de Sistemas E Computadores, Lisbon, Portugal

Spin-torque vortex oscillators (STVOs) are promising candidates for unconventional computing and logic operations [1-3], notably due to their ability to synchronize in arrays [4-8]. However, practical schemes to exploit dipolar-coupling-induced synchronization remain poorly defined, while device-to-device resonance frequency variations pose a major challenge for achieving reliable collective dynamics [3,7-8].

Here, we use micromagnetic simulations to investigate coupled STVO systems with different radii reproducing the intrinsic frequency dispersion observed in realistic arrays (Fig. 1). In a triangular three-STVOs system (Fig. 2), we demonstrate a flexible method to control synchronization states by tuning the vortex chirality of each oscillator, which modifies its individual frequency (Fig. 1). This enables multiple distinct coupling configurations within a single geometry, including desynchronized, partially synchronized between specific oscillator pairs, and fully synchronized states, yielding five distinct coupling states. This chirality-encoded control extends to larger systems. In a four-oscillator square system with distinct radii, the same mechanism enables all synchronization regimes, from no synchronization to full collective locking, including partial synchronization of two or three oscillators.

This chirality-encoded control of dipolar interactions provides a robust route to mitigate frequency mismatch and enables programmable synchronization patterns, opening new opportunities for implementing complex logic functions and unconventional computing architectures.

[1] J. Torrejon et al., Nature, vol. 547, p. 428–431 (2017).
[2] H. Junge t al., ACS Nano, vol 6(5), p. 3712–3717 (2012)
[3] J. Grollier et al., Nature Electronics, vol. 3, p. 360–370 (2020)
[4] T. Chen et al., Proceedings of the IEEE, vol. 104(10), pp. 1919-1945 (2016)

[5] D. Li et al., Physical Review B, vol. 86, p. 014418 (2012)
[6] F. Abreu Araujo and J. Grollier, Journal of Applied Physics, vol. 120, p. 103903 (2016)
[7] N. Locatelli et al., Scientific Reports, vol. 5, p. 17039 (2015)
[8] L. Martins et al., Communications physics, vol. 6, p. 72 (2023)

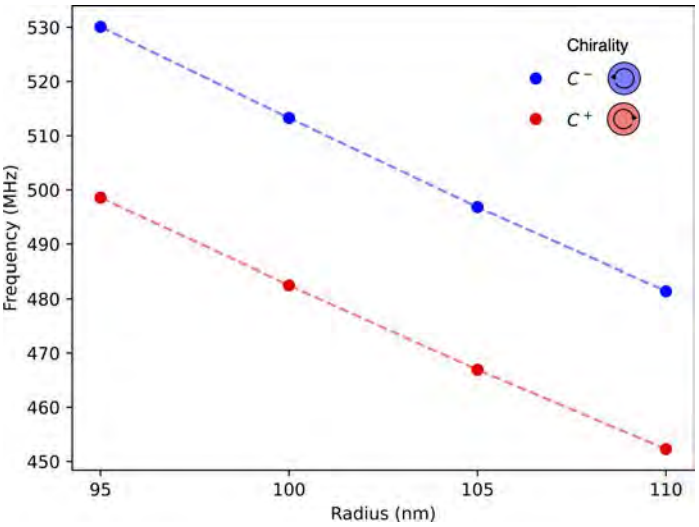


Fig. 1. Steady-state oscillation frequency as a function of the STVOs radius under a DC current density of 7.2 x 10^{10} A/m^2 for positive and negative vortex chiralities.

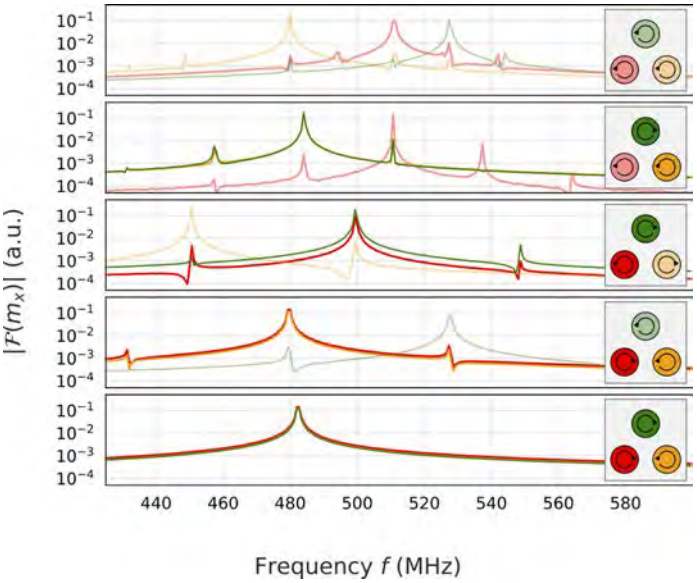


Fig. 2. Synchronization states of a triangular STVO array (top: 95 nm, left: 100 nm, right: 110 nm; edge-to-edge distance 300 nm) as a function of vortex chirality. Depending on the $C^{\pm}$ chirality combination, five regimes are observed: (i) no synchronization (C^-,C^-,C^-), (ii) synchronization between the top and left oscillators (C^+,C^-,C^-), (iii) top-left synchronization (C^+,C^-,C^+), (iv) left-right synchronization (C^-,C^+,C^-), and (v) full synchronization (C^+,C^+,C^-).

CR-11. Reconfigurable Spintronic Diodes for Neuromorphic Computing

A. Begue[1], H. Singh[2], Y. Wei[1], L. Herrera Diez[3], A. Durnez[3], B. Dlubak[1], J. Grollier[1], D. Sanz Hernandez[1]
[1]Laboratoire Albert Fert, CNRS-Thales, Univ. Paris Saclay, Palaiseau, France, [2]VTT Technical Research Center of Finland, Helsinki, Finland, [3]Centre de Nanosciences et de Nanotechnologies, Palaiseau, France

Spintronic devices, including spin-torque ferromagnetic resonance (STFMR) diodes, are promising for neuromorphic computing due to their high-frequency dynamics, nonlinear response, and CMOS compatibility [1], making them ideal for compact, low-power, and large-scale neuromorphic architectures. STFMR diodes rectify RF signals into a DC voltage, with the synaptic weight defined as the ratio of the DC voltage to the RF power. Thus, the synaptic weight can be controlled by tuning the resonance frequency [2]. These diodes serve as building blocks for complex neuromorphic networks [3].

Voltage control of magnetic properties further enhances device functionality by enabling tuning of each diode's resonance frequency. Magnetoionic mechanisms, such as controlled oxygen migration, provide nonvolatile, and reversible modulation of magnetic anisotropy [4-6]. Combining intrinsic spintronic dynamics with magnetoionic control enables reconfigurable, low-power, and nonvolatile neuromorphic hardware.

In this work, STFMR diodes were fabricated using an ultrathin Permalloy layer with a Co/Al bilayer deposited on top, incorporating an HfO2 gate layer as an ionic reservoir [7]. Figure 1 shows that the resonance frequency can be tuned over a wide range up to 7 GHz by applying voltage pulses to the gate, without requiring changes in the applied magnetic field. Figure 2 shows reproducible resonance tuning: negative pulses shift the peak to higher frequencies, positive pulses to lower frequencies. This nonvolatile behavior is attributed to a magnetoionic mechanism that modulates the perpendicular magnetic anisotropy at the interfaces.

These results demonstrate the fabrication of STFMR diodes with electrically controlled, nonvolatile resonance

frequency. This enables reconfigurable diode networks, where voltage pulses efficiently reprogram synaptic weights to implement different low-energy computing tasks.
1. J. Grollier *et al*., "Neuromorphic spintronics" *Nat. Electron.* vol. 3, p. 360 (2020)
2. G. Torrejon *et al*., "Neuromorphic computing with nanoscale spintronic oscillators" *Nature*, vol. 547, p. 428 (2017)
3. G. Finocchio *et al*., "Perspectives on spintronic diodes" *Appl. Phys. Lett.* vol. 118, p. 160502 (2021)
4. G. Bernard *et al*., "Magneto-ionic control of a propagating spin reorientation transition" *Nano Letters*, vol. 25, no. 32, p. 12241 (2025)
5. H. Fulara *et al*., "Giant voltage-controlled modulation of spin Hall nano-oscillator damping" *Nat. Commun.* vol. 11, p. 4006 (2020)
6. Choi, J. et al., "Voltage-driven gigahertz frequency tuning of spin Hall nano-oscillators" *Nat. Commun.* vol. 13, p. 3783 (2022)
7. T. da Câmara Santa Clara Gomes *et al*., "Control of the magnetic anisotropy in multirepeat Pt/Co/Al heterostructures using magnetoionic gating," *Phys. Rev. Applied*, vol. 21, p. 024010 (2024)

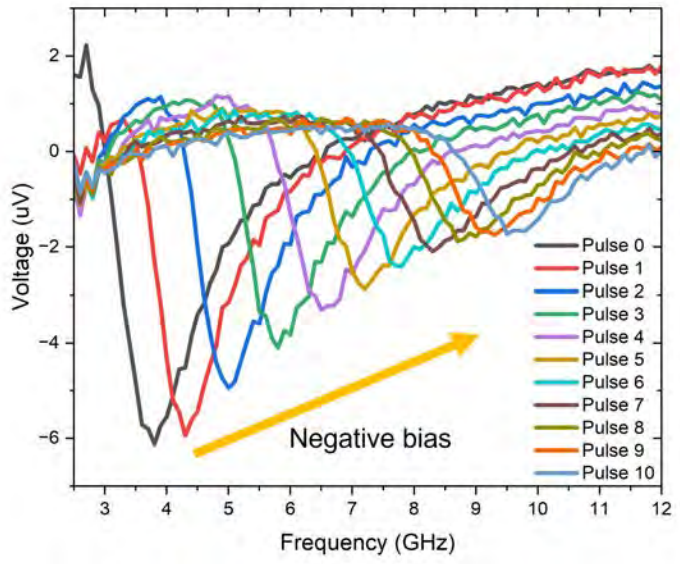


Figure 1. STFMR measurements performed after applying −7 V gate pulses for 1 s.

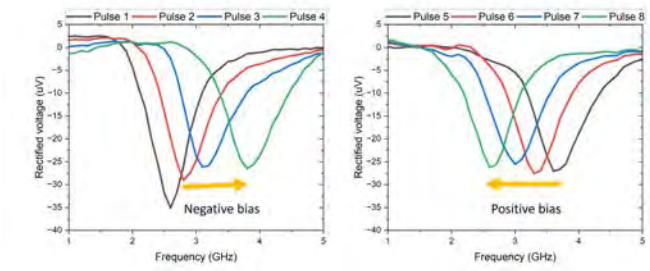


Figure 2. STFMR measurements after applying (a) negative-bias pulses and (b) positive-bias pulses to the gate.

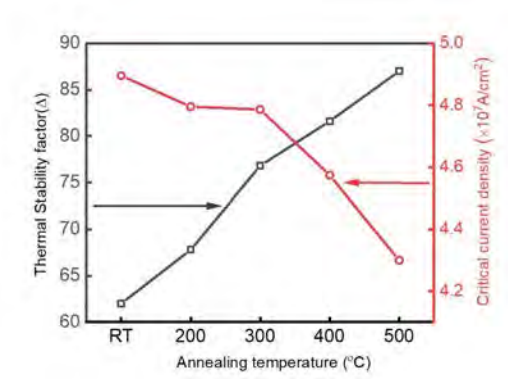
CR-12. Simultaneous Improvement of Thermal Stability and Critical Current Density in Gradient-Pt/Co Heterostructures by Post-Growth Annealing.

V. Yadav, R. S. Yadav, N. Kandwal, A. S. Chauhan, A. Saxena, P. K. Muduli
Physics, IIT Delhi, Delhi, India

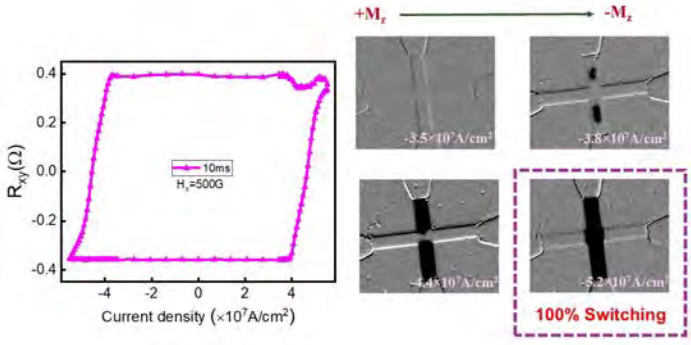
Ferromagnetic metal–heavy metal heterostructures with perpendicular magnetic anisotropy (PMA) enable efficient control of magnetization through spin–orbit torque (SOT) mechanisms[1–3]. This control makes such systems highly suitable for non-volatile memory applications, commonly referred to as SOT magnetic random-access memory(SOT-MRAM). The SOT-MRAM architecture offers several key advantages, including robust data retention, reduced energy consumption, and excellent scalability compatible with CMOS technology. In conventional heterostructures, a trade-off exists between thermal stability and switching current density because SOT mainly originates at the interfaces. This limitation can be overcome by using gradient heavy-metal(HM)/ferromagnet(FM) heterostructures, which maintain a similar order of critical current density while offering greater thermal stability than typical HM/FM/oxide systems[4,5]. As the FM layer thickness increases, thermal stability also increases. However, the critical current also increases, which is a major challenge for energy-efficient devices. In this work, for the gradient Pt/Co heterostructure, thermal stability as well as critical current density(J_c) by post-growth annealing. We measured the thermal stability of the samples annealed at various temperatures using a thermally assisted SOT switching model based on pulse-duration-dependent switching measurements. In Fig1, We observed an improvement in the thermal stability(Δ) with increasing post-annealing temperature, reaching a value of 87 for the 500 °C post-annealed sample, which is higher compared to 62 for the as-grown sample. In addition, the J_c decreased to 4.3×10^7A/cm^2 for the 500°C post-annealed

sample, which is lower than the 4.89×10^7A/cm^2 observed in the as-grown sample. These results demonstrate that post-growth annealing effectively enhances the Δ of gradient-Pt/Co heterostructures, which can lead to higher stability of the mixed states that are essential for non-volatile memory computing.

1. S. Ikeda, K. Miura1, H. Yamamoto, et al., Nature materials ,721-724, 2010.
2. L. Liu, O. J. Lee, T. J. Gudmundsen, et al., Phys. Rev. Lett. 109 (9), 096602, 2012.
3. L. Liu, C.F. Pai, Li, Y., et al., Science 336 (6081), 555, 2012.
4. K. Zhang, L. Chen, Y. Zhang, et al., Appl. Phys. Rev. 9(1), 2022.
5.R.S. Yadav, P. Gupta, V. Yadav, et al., Phys. Rev. Appl., 24(4), 044038, 2025



Variation of thermal stability(Δ) and critical current density(J_c) with post-annealing temperature.



MOKE imaging of SOT switching for a device annealed at 500°C, with images taken at each current pulse, confirming 100% switching.

CR-13. Tuning of properties in Bottom-Pinned Perpendicular Magnetic Tunnel Junctions

M. Syskaki, M. Minhas, J. Wrona, J. Langer, B. Ocker
Singulus Technologies AG, Kahl am Main, Bayern, Germany

Perpendicular magnetic tunnel junctions (pMTJs) with bottom-pinned synthetic antiferromagnetic (SAF) reference layers are key components for advanced magnetic sensors and spintronic devices due to their high tunnelling magnetoresistance (TMR), scalability, and strong perpendicular magnetic anisotropy (PMA). SAF reference layers are essential for minimizing stray fields and stabilizing the magnetic configuration, as their nearly compensated magnetic moment reduces unwanted bias acting on the free layer. However, in bottom-pinned architectures, incomplete compensation or weak interlayer exchange coupling can lead to asymmetric switching and even unintended reference-layer reversal below the free-layer switching field, significantly affecting device reliability [1].

In this work, we investigate switching field control in bottom-pinned CoFeB/MgO pMTJ stacks deposited using high-precision industrial Singulus Rotaris sputtering system. The multilayer stacks incorporate SAF-pinned reference layers with Ru-mediated coupling, enabling systematic tuning of magnetic compensation and interlayer interactions. By varying spacer thickness and reference layer design, we achieve precise control over the effective bias field acting on the free layer.

Magnetometry measurements show that optimized SAF coupling improves the reference layer stability and enables the controlled adjustment of the free-layer switching field while maintaining strong PMA and high TMR, consistent with recent reports on CoFeB/MgO-based pMTJs demonstrating robust switching and high retention at nanoscale dimensions [2]. Furthermore, recent studies indicate that targeted SAF optimisation can significantly reduce stray-field-induced switching irregularities and improve switching efficiency in pMTJ devices.

These results highlight the critical role of precise multilayer deposition and interface engineering in tailoring interlayer coupling and magnetic switching behaviour. The demonstrated approach provides a scalable pathway toward highly stable and tunable bottom-pinned pMTJ devices for next-generation sensing and memory applications.

[1] H. Guchang *et al.*, J. Magn. Magn. Mater., 527, 167789 (2021).
[2] J. Igarashi *et al.*, npj Spintronics, 2, 1 (2024).

CR-14. Nonlinear Encoding Using Exchange-Coupled Spintronic Devices for Edge Intelligence

J. R. Mohan[1, 2], S. Uchiyama[1], R. Feng[1], L. Guofei[1], R. Hamada[1], Y. Ono[1], H. Asada[3], Y. Fukuma[1, 2]

[1]Department of Physics and Information Technology, Faculty of Computer Science and Systems Engineering, Kyushu Institute of Technology, Iizuka, Fukuoka, Japan, [2]Research Center for Neuromorphic AI hardware, Kyushu Institute of Technology, Kitakyushu, Fukuoka, Japan, [3]Graduate School of Sciences and Technology for Innovation, Yamaguchi University, Ube, Japan

Artificial intelligence (AI) is rapidly expanding across applications from autonomous systems to medical diagnostics, placing increasing demands on computational resources, memory, and energy consumption. Specialized hardware such as GPUs, TPUs, and neuromorphic processors aimed to mitigate these challenges at scale, however, they remain inefficient for edge environments where power, latency, and memory are tightly constrained [1]. In such edge-AI systems, raw sensor data are typically transmitted to digital processors or cloud platforms, introducing energy overhead and reliance on communication bandwidth. These limitations motivate alternative approaches such as in-memory computations and in-sensor computational devices [2, 3]. Inspired by biological neural systems, where information processing emerges from the collective dynamics of interacting units. Particularly focussing on cross-frequency coupling phenomena in brain signals, we explore a physical framework for nonlinear encoding using spintronic devices [4, 5]. Here, we demonstrate a radio-frequency (RF)-driven nonlinear encoder based on an exchange-coupled synthetic antiferromagnetic structure based on NiFe(3nm)/Ru(1nm)/NiFe(5nm) multilayer structures. Binary inputs (4-digit) are embedded into amplitude-modulated RF signals, and the coupled magnetization dynamics of asymmetric ferromagnetic layers transform these inputs into a structured physical feature space. Due to the thickness assymetry, different resonace conditions, combined with interlayer coupling, enable modulation-dependent phase and amplitude interactions that produce unique, pattern-dependent responses as shown in Fig. 1. These experimentally extracted features such as voltage amplitudes and resonance field values are applied to image classification tasks as shown in Fig. 2, achieving competitive accuracy of 95.7% with significant reduction of computational complexity. This work establishes a compact and efficient encoding strategy that offers a pathway toward scalable, low-power hardware for edge AI systems.

1. W. Zhang, B. Gao, J. Tang *et al.,* Nature Electronics, Vol. 3, p. 371–382 (2020).
2. J. E. Pedersen, S. Abreu, M. Jobst *et al.,* Nature Communications, Vol. 15, p. 8122 (2024).
3. J.R. Mohan, A.J. Mathew, K. Nishimura *et al,* Scientific Reports, Vol. 13, No. 7909 (2023).
4. C. Yeh, C. Zhang, W. Shi *et al.,* Cyborg and Bionic Systems, Vol. 4, No. 0034, (2023).
5. E.M. Izhikevich, IEEE Transactions on Neural Networks, Vol. 10, no. 3, p. 508-526, (1999).

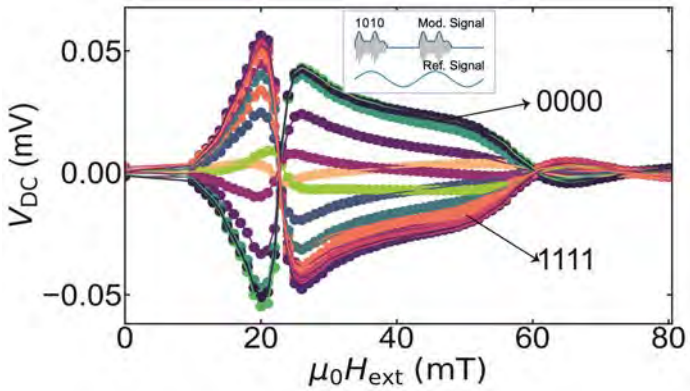


Fig. 1: STFMR spectra of selected input patterns from 0000 to 1111. Inset shows the modulated signal.

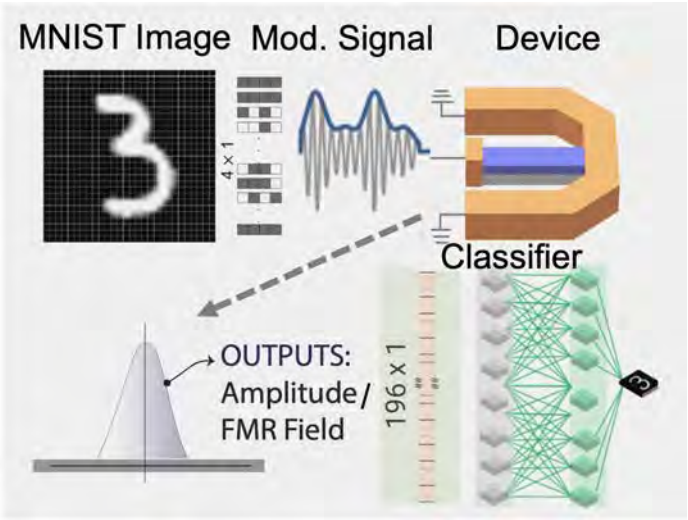


Fig. 2: Feedforward network implementation with encoder.

CR-15. 1.58-bit Reservoir Computing Using Paired Magnetic Tunnel Junctions in a Clustered CIM Architecture

S. Adachi[1], R. Kusunose[1], O. A. Velasco Cardenas[1], A. Schmid[2], K. Ando[1], T. Asai[1], T. Marukame[1]
[1]Hokkaido University, Sapporo, Hokkaido, Japan, [2]EPFL, Lausanne, Switzerland

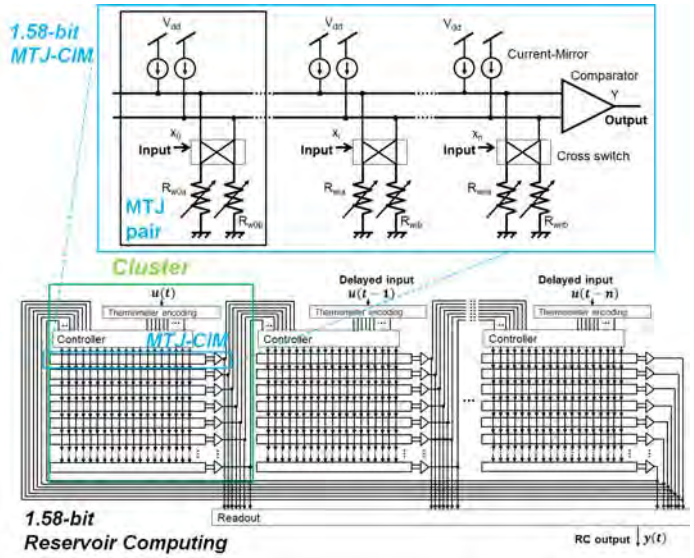
With the rapid growing of AI, especially large language models (LLMs), global concerns are increasing regarding their high energy consumption [1]. To address this issue, attention has turned to Compute-In-Memory (CIM), which enable efficient neural networks and fast vector–matrix operations. Conventional CIM often relies on resistive switching devices with analog values such as ferroelectric tunnel junctions [2]. Although recent studies have explored ternary-weight neural networks (−1, 0, +1; 1.58-bit), CIM using practical non-volatile memory has not yet been realized.

In this study, we focus on magnetic tunnel junctions (MTJs) and propose a CIM architecture highly compatible with digital circuits. MTJs inherently provide two stable states (High/Low), and by pairing two MTJs, three distinct weight states—H/L, L/H, and H/H—can be represented. While ternary signal processing requires large magnetoresistance, we previously demonstrated favorable conductance-voltage characteristics in Co_2MnSi MTJs [3], and confirmed stable CIM operation against variations [4].

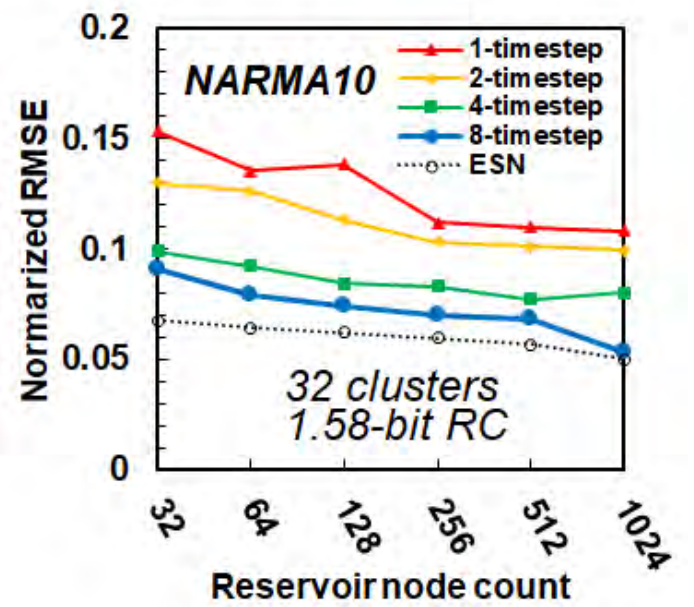
Here, we propose a 1.58-bit reservoir computing (RC) based on this MTJ-CIM and evaluate its performance. RC is attracting attention as a lightweight time-series processing model because it uses fixed recurrent connections in the reservoir layer and trains only the output weights. Our 1.58-bit RC generates dynamic internal states by recursively feeding the CIM output back into the system, while restricting inputs and outputs to binary values and weights to ternary values (Fig. 1).

In this CIM, increasing the number of inputs per node reduces computational resolution, making it necessary to limit fan-in. To address this, we introduce a cluster-based architecture that maintains overall system scale while constraining node input count. Combined with delayed input signals—implemented by shifting inputs in the time domain—the proposed system achieves NARMA10 performance comparable to conventional echo state networks (Fig. 2). Circuit-level analysis further indicates that our CIM can achieve efficient computation of 5 TOPS with 5 mW.

[1] S. Ma, et al., arXiv:2402.17764 (2024)
[2] R. Berdan, T. Marukame, et al., Nature Electronics 3, 259 (2020)
[3] H-x, Liu, et al., Appl. Phys. Lett. 101(13), 132418 (2012)
[4] R. Kusunose, et al., Eng. Res. Express 8 085303 (2026)



1.58-bit Reservoir Computing composed of MTJ-based CIMs.



NARMA10 benchmark results; 1.58-bit Reservoir Computing vs. ESN (software).

CR-16. Probability Processing Unit Based on Nonvolatile Magnetic Tunnel Junctions

D. Kong, C. Wan, X. Li, Y. Xu, S. Xiong, G. Yu, X. Han
Institute of Physics, Chinese Academy of Sciences, Beijing, China

Magnetic Tunnel Junctions (MTJs) have emerged as a competitive nanotechnology for realizing novel probabilistic/stochastic computing paradigms on CMOS-compatible platforms. Leveraging the intrinsic stochasticity of these devices, we propose a ”Probability Processing Unit”(PPU) based on high-barrier spin-orbit torque (SOT) MTJs. By employing a novel ”one-cell, N-write” temporal strategy, the PPU integrates probabilistic bit generation and logical operations directly within a single nonvolatile device. This architecture eliminates the need for discrete logic gates, delivering significant improvements in energy efficiency and area compactness, as well as superior noise robustness validated by application-level image processing benchmarks. Collectively, these results position the PPU as a robust building block for scalable, energy-efficient probabilistic accelerators.

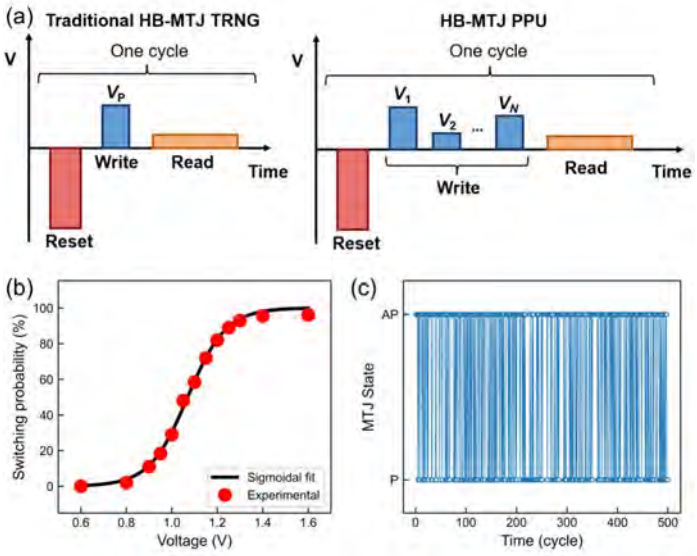


FIG. 1. Implementation principles of the PPU and MTJ-TRNG characterization. (a) Schematics illustrating the pulse application waveforms for the HB-MTJ TRNG and the HB-MTJ PPU. (b) MTJ switching probability as a function of write voltage (V). The solid black line represents a sigmoidal fit described by Pswitch(V) = {1 + exp[A(V + B)]} −1 , with fitting parameters A = −11.8795 and B = −1.0698. Each data point is derived from 500 repeated pulse cycles. (c) Resistance evolution obtained from continuous testing at a fixed voltage of 1.1 V.

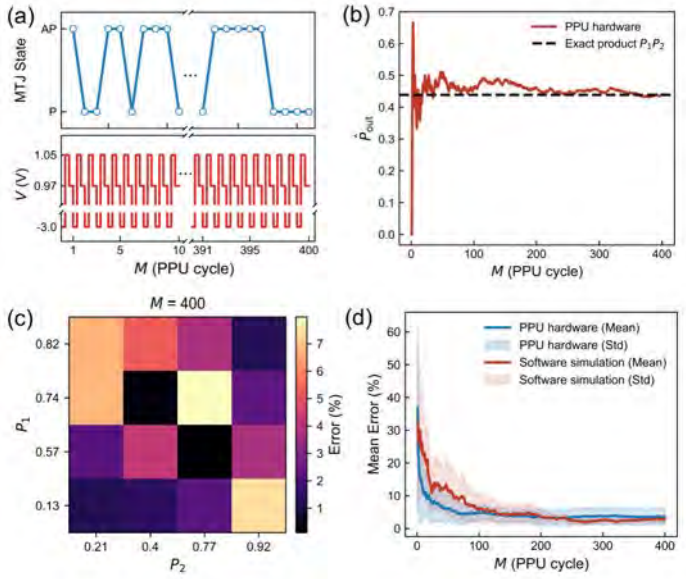
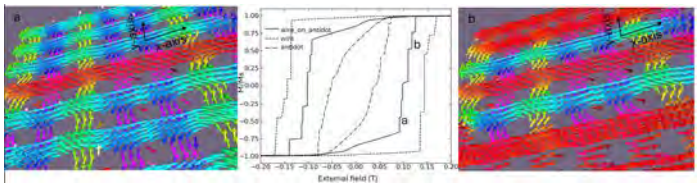


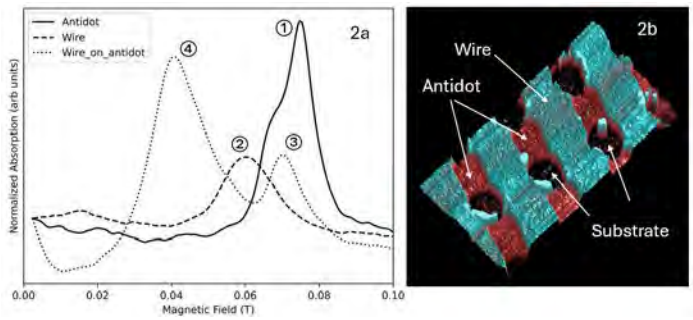
FIG. 2. Experimental demonstration of PPU-based multiplication. (a) Measurement results for the target probability pair (P1, P2) = (0.57, 0.77). The bottom panel displays the applied pulse sequences (with read pulses and inter-pulse intervals omitted for clarity), while the top panel shows the corresponding random-telegraph-like evolution of the MTJ state. (b) Running estimate of the output probability (P_out) as a function of the number of PPU cycles M for the same pair, illustrating convergence. (c) Heatmap visualization of the absolute error |P_out − P1P2| for the tested probability pairs. (d) Mean error plotted as a function of bitstream length M, comparing PPU hardware experimental data with Python simulated RNG results

SESSION CS: MAGNETIC STRUCTURES AND NANOCOMPOSITES (POSTER SESSION)
Chair(s): S. Koraltan, *Zentrum für Quantum Engineering, Technische Universität München, Wien, Austria*
Wednesday, November 4, 2026
09:30 AM-12:30 PM
Coral 4

CS-01. Magnetisation Dynamics of Lithography-Compatible Self-Aligned Nanowires on Antidot Array
N. Suggula, V. Ng
Information Storage and Materials Laboratory, Electrical and Computer Engineering, National University of Singapore, Singapore, Singapore

3D magnetic nanostructures offer enhanced control over magnetisation dynamics compared to conventional 2D magnonic crystals, however, their fabrication remains complex.[1] We successfully fabricated self-aligned Co nanowire on Py antidot arrays (Fig. 2b) and study how vertical structural inhomogeneity influences magnetisation reversal and FMR dynamics.[2]
Mumax3[3] hysteresis studies (Fig. 1) shows distinct reversal mechanisms in the individual structures. Pure antidot lattices form Bloch walls between columns, leading to discrete switching steps, whereas wire arrays reverse quasi-independently with smaller, distributed steps. In contrast, the 3D wire–antidot array exhibits modified behavior: wire-induced anisotropy suppresses Bloch wall formation and promotes stepwise switching.
Fig 2a shows FMR absorption spectra measured at 7Ghz microwave excitation with the magnetic field swept from 0 to 0.10 T. The solid line (antidot) shows a sharp peak 1 near 0.075 T, and the dashed line (wire) produces a broader response at ~0.06 T as peak 2. For the 3D Co nanowire on Py antidot array (dotted line), two new hybrid modes absent in either standalone structure emerge. Peak 3 appears close to mode 2 in the pure wire, retaining partial wire-like character but modified by the underlying antidot. More strikingly, peak 4 emerges at a significantly lower field near 0.04 T, indicating that the antidot's stray dipolar fields strongly bias the wire, lowering its resonance condition.
These two new modes reflect different degrees of antidot–wire coupling. Mode 3 represents a weakly perturbed regime, while mode 4 represents a strongly coupled regime where dipolar interaction dominates, demonstrating that placing the wire on the antidot fundamentally alters the magnetic dynamics beyond a simple superposition of the two individual responses.
We will discuss experimental results with detailed FMR simulations. Our work demonstrates controlled tuning of FMR in a hybrid nanostructure through material contrast, relevant for reconfigurable magnonic and spintronic devices.
1. Gianluca Gubbiotti *et al* . 2025 *J. Phys.: Condens. Matter* 37 143502
2. Myint, B., & Ng, V. (2021. *Physica Status Solidi–Rapid Research Letters,* 15(8), 2100197.
3. Vansteenkiste, A., & Van de Wiele, B. (2011)Journal of Magnetism and Magnetic Materials, 323(21), 2585-2591.


a & b show the evolution of the spin configuration of the 3D nanowire-on-antidot structure

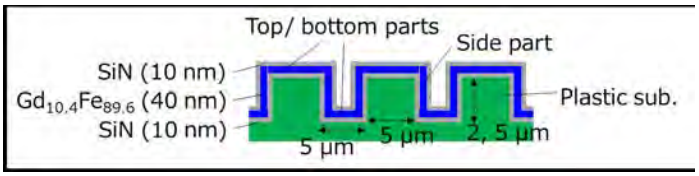


Experimental FMR spectra of antidot, wire and 3D structures with corresponding 3D AFM image.

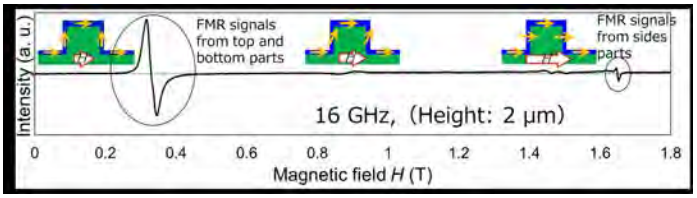
CS-02. Evaluation of magnetic properties of three-dimensional land-groove structure by ferromagnetic resonance
H. Imaeda, T. Takeuchi, H. Awano, K. Tanabe
Toyota Technological Institute, Nagoya, Japan

With the advancement of microfabrication technologies, three-dimensional (3D) spintronics devices incorporating a vertical dimension have attracted significant attention, expanding beyond conventional flat structures [1-3]. We have successfully fabricated fine 3D land-groove microstructure using nanoimprint method [3]. However, evaluating the magnetic properties of such 3D structure using magnetometers, such as a vibrating sample magnetometer, is challenging because they cannot separate

the magnetization of the horizontal and vertical directions of the land-groove structure. To resolve this issue, we investigated the magnetic properties of 3D land-groove structures using ferromagnetic resonance (FMR).
Plastic substrate with a 3D land-groove structure (width: 5 μm, height: 2, 5 μm) were fabricated by nanoimprint method, followed by the deposition of SiN (10 nm)/ amorphous $Gd_{10.4}Fe_{89.6}$ (200 nm)/ SiN (10 nm) using magnetron sputtering (Fig. 1). FMR was measured by placing the sample on a coplanar waveguide and applying microwaves under an external magnetic field. Figure 2 shows the FMR signal intensity as a function of the magnetic field at 16 GHz. Resonances were clearly observed in both low and high magnetic field regions. The resonance in low-field region exhibit behavior similar to that of a flat structure. In the high-field region exceeding 1 T, the magnetization on the side parts of the land-groove overcomes the demagnetization field and aligns in the x-direction. Consequently, the low-field and high-field resonances correspond to the top and bottom horizontal parts, and the vertical side parts, respectively. Thus, we successfully isolated and evaluated the magnetic properties of the horizontal and vertical parts of the 3D structure. Furthermore, our analysis revealed that the in-plane magnetic anisotropy of the side parts is significantly larger than that of the top and bottom parts.
[1] K. Gu *et al*., Nat. Nanotechnol. 17, 1065-1071 (2022).
[2] F. Meng *et al*., ACS Nano 15, 6765-6773 (2021).
[3] H. Imaeda *et al*., APL 125, 044101 (2024).



Schematic diagram for 3D structure sample



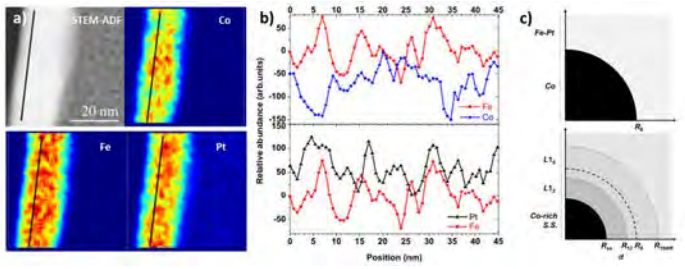
Relationship between magnetic field *H* and FMR intensity. Insets show the direction of magnetization.

CS-03. Microstructure and chemical ordering in Co@FePt nanocomposite magnetic films

D. Le Roy[1], C. Paleo[1], C. Ricolleau[2], O. Boisron[1], V. Dupuis[1]
[1]Universite Lyon 1, CNRS, Institut Lumière Matière, UMR5306, Villeurbanne, France, [2]Université Paris Cité, CNRS, Laboratoire Matériaux et Phénomènes Quantiques, Paris, France

Nanocomposites (NC) combining high-magnetization nanoparticles embedded in a magnetically hard matrix constitute a relevant class of materials from both fundamental and applied perspectives. When the inclusion size approaches the domain wall width of the hard phase, the magnetic response can resemble that of a single-phase system with enhanced energy product. These systems are thus ideal platforms to investigate exchange coupling at the nanoscale and are promising for applications such as data storage and permanent magnets.
We report on tetragonal $L1_0$-FePt films with size-selected Co cluster (fcc, ~8 nm) inclusions, synthesized by gas phase aggregation using LECBD, and focus on the interplay between microstructure, interdiffusion and chemical ordering after annealing.
STEM-ADF and EDX reveal a homogeneous dispersion of Co inclusions in the as-prepared state. The inter-cluster distances avoid coalescence in the chemically disordered A1 matrix. Annealing at ~650 °C induces both A1→$L1_0$ ordering of FePt and progressive intermixing, while preserving Co-rich cluster cores (Fig. a,b).
EXAFS analyses at Fe, Co and Pt edges provide quantitative insight into local environment. While nanofilms (Co thin layers instead of Co clusters) exhibit a full alloying into a chemically disordered $(Co,Fe)_3Pt$ phase upon annealing, NC retain a significant degree of $L1_0$ chemical order. At the Co sites, nearest-neighbor analysis demonstrates partial intermixing, consistent with a core–shell-like structure.
Our results support a thermally-driven evolution toward Co-rich cores surrounded by a $(Co,Fe)_3Pt$ shell embedded into an FePt-$L1_0$ matrix, as illustrated in Fig. c. This heterogeneous chemical ordering explains the conservation of hard and soft magnetic signatures observed by XMCD at Fe and Pt edges and provides a structural basis for exchange coupling in these NC [1,2].
[1] C. Paléo et al., « Impact of Embedded Co Nanoparticles on Local Magnetic Properties of L10-FePt Films », in IEEE Transactions on Magnetics, vol. 59, no. 11, pp. 1-5 (2023), Art no. 2102105, doi: 10.1109/TMAG.2023.3299523.
[2] C. Paléo et al., « Interplay between local structure and magnetic properties of graded exchange-coupled Co@FePt

nanocomposite films », Phys. Rev. B 102, 224409 (2020), DOI: https://doi.org/10.1103/PhysRevB.102.224409



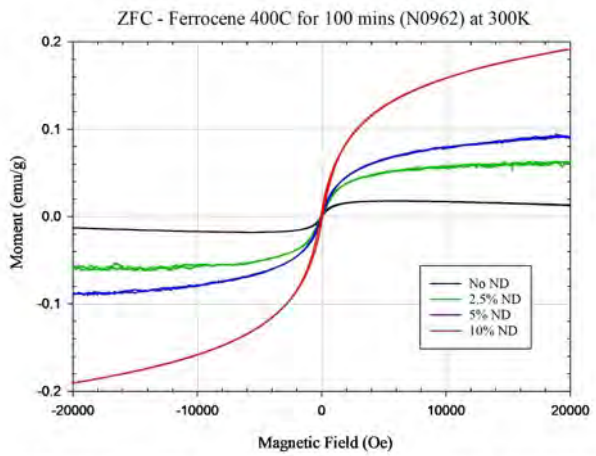
(a) STEM-ADF image and Co, Fe, Pt EDX maps of a lamella from a NC film annealed at 650°C for 20 min. (b) Composition profiles along the line in (a). (c) Schematic of phase distribution before (top) and after annealing (bottom). *d* is the distance from the Co cluster center. « S.S. » = solid solution. R_{SS}, R_{12} , R_{10diff}: maximum radii of the S.S., $L1_2$, and Co-diffusion regions.

CS-04. Induced Magnetism in Polymer Matrix and Enhanced Ferromagnetism in Ferrocene-Derived Systems via Nanodiamond-Assisted Co-Pyrolysis

E. Gutierrez, F. Gonzalez, A. Garcia, A. Prakash, A. Khodagulyan, O. Bernal, A. N. Kocharian
Physics and Astronomy, California State University,, Los Angeles, California, United States

This study investigates the induction of magnetization in high density polyethelene (HDPE) nanostructures as well as the enhancement of ferromagnetism in iron-containing phases formed by ferrocene, through their co-pyrolysis with nanodiamond (ND) powder (1–10 nm). Emphasis is placed on the role of nanodiamond content in controlling the morphological, structural, and magnetic properties of the resulting materials. The work aims to provide deeper insight into how impurities and structural defects within carbon polymer matrices influence magnetic behavior in synthesized nanostructures, as well as the catalytic role of iron in phase formation. Special attention is given to the effect of nanodiamond incorporation on saturation magnetization (M_S) and coercivity (H_C) in hydrogen-rich carbon materials, where the hydrogen-to-carbon (H/C) ratio is ⩾1. Ferrocene is employed as a precursor due to its favorable H/C ratio and intrinsic iron content, enabling the formation of both carbon matrices and embedded iron-based nanoparticles. X-ray diffraction (XRD) is used to analyze the influence of synthesis parameters on the formation of iron carbide (Fe_3C) and iron allotropes (γ Fe, α-Fe), and their correlation with magnetic properties as a function of ND concentration. Other microscopy techniques like SEM/TEM, FTIR, and AFM are also employed to confirm and characterize the presence of nanostructures produced via pyrolysis. Initial magnetization measurements (Fig. 1) indicate that samples without nanodiamond exhibit weak ferromagnetic behavior, whereas the addition of ~10%wt ND results in a significant enhancement of both saturation magnetization and coercivity. The study further examines the effects of ND concentration, pyrolysis temperature, and processing time. In addition, functionalized nanodiamonds, particularly hydrogen-terminated NDs, are explored due to their potential to further enhance magnetic properties through C–H bonding and interfacial effects. The objective is to identify optimal synthesis conditions for integrating nanodiamonds into HDPE nanostructures, thereby advancing their potential applications in biomedicine, radiation detection, spintronics, and quantum information technologies.

This work at Cal State LA was supported by the NSF-Partnerships for Research and Education in Materials under the CATSUS-CREST Grants No. HRD-1547723 and No. HRD-2112554



ZFC Magnetization vs. Magnetic Field of Ferrocene samples with varying concentrations of ND (N0962) from -20 kOe to +20 kOe measured at 300 K.

CS-05. Flow Induced Magnetic Anisotropy of FDM Printed Strontiumferrite/PA12 Composites

A. K. Mandal[1], M. Islam[2], L. Rodriguez[2], M. Rashid[1], J. Tate[3, 2], D. E. Smith[4], W. Geerts[1, 2]
[1]Physics, Texas State University, San Marcos, Texas, United States, [2]MSEC, Texas State University, San Marcos, Texas, United States, [3]Ingram School of Engineering, Texas State University, San Marcos, Texas, United States, [4]Department of Mechanical Engineering, Baylor University, Waco, Texas, United States

As the (BH)max of bonded magnets scales with the squareness, S=Mr/Ms, anisotropic magnetic materials allow for smaller, cheaper, or lighter magnetic circuits. Although these materials can be realized by applying a magnetic field during the 3D printing process, the incorporation of a large field unit that does not negatively affect the print quality will add a lot of mass to the print head slowing it down and increasing its costs. Alternatively, one can use flow during the printing process to induce magnetic anisotropy [1] which we further explore here. 35 wt% Strontiumferrite (SFO)/PA12 filaments were made with a Thermo Fisher co-rotating twin-screw extruder. The SFO particles were 1.4 um non-spherical platelets with a uniaxial magnetic anisotropy. A Rova3D FDM printer with enclosure was used to 3D print samples using a nozzle diameter of 0.5 mm. Samples were printed at two different nozzle temperatures (190, 200 °C) and five different print-layer heights (PLH=01-0.5 mm). The hysteresis curves were measured using a MicroSense VSM along the sample's principal axes. Raw data was corrected for the image effect, the field lag, and the sample-rod's magnetic background. The S-values varies with the field direction and is largest along the print-bed normal (np) and smallest along the print (e) direction, indicating an easy magnetic anisotropy axis along np. For single bead single layer samples, the S-values are maximum for samples printed with a PLH of 0.2 mm and a temperature of 200 oC. Multi-layer samples with a PLH of 0.1 mm show a Smax of up to 0.68 which slightly varies through the sample's thickness. Smaller Smax values and larger variations of Smax through the sample thickness were observed for samples with a PLH of 0.5 mm. The Smax of printed samples were considerably larger than those of freely extruded strands. These results will be discussed in terms of a center gated disk flow model where particles are aligned with shear and stretching, in the nozzle (Poiseuille flow) and in between nozzle and print-bed (Couette flow). Platelet orientation tensors [2] are calculated from Jeffrey's equation [3] and used to estimate the orientation distribution function that directly relates to the measured squareness.

[1] C. Huber, et al., Appl. Phys. Lett. 109 (2016) 162401-1 162401-4.
[2] Suresh G. Advani, Charles L. Tucker, J. Rheology 31, 751 (1987).
[3] G.B. Jeffery, Proc. R. Soc. Lond. 102 (1922)161-179.

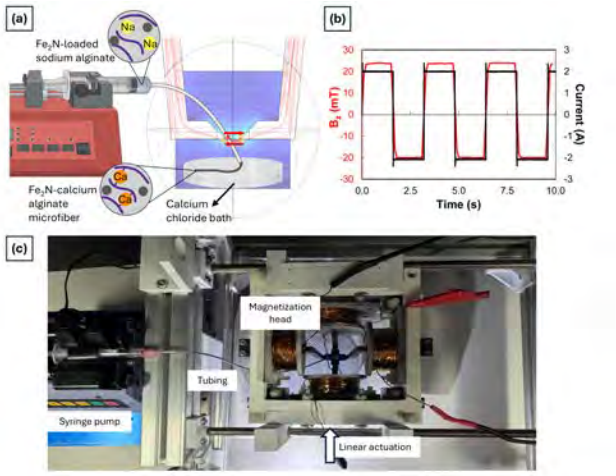
CS-06. 4D-printed Sacrificial Fe_2N–Alginate Microfibers for Perfusable Hydrogel Microchannels

Z. Rajestari[1], N. Tarabay[2], L. Paulsen[1], L. Kulinsky[1], C. Velez[1, 2]
[1]Department of Mechanical and Aerospace Engineering, University of California, Irvine, Irvine, California, United States, [2]Department of Electrical Engineering and Computer Science, University of California, Irvine, Irvine, California, United States

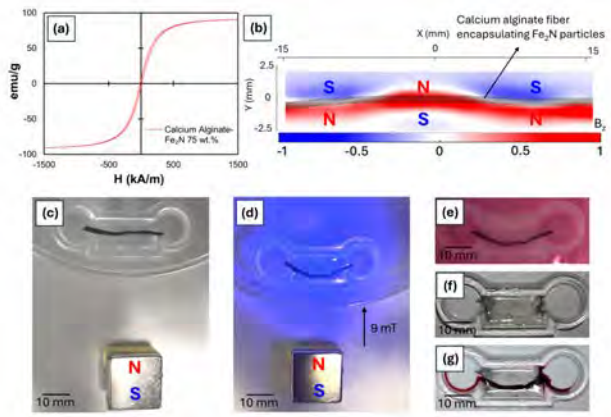
This work presents a 4D printing strategy for generating perfusable microchannels in hydrogels (Fig. 1). Sacrificial calcium alginate microfibers embedded with Fe_2N particles were fabricated by immersed microfluidic spinning [1]. Fe_2N particles were selected due to their biocompatibility and magnetic responsiveness, enabling non-contact manipulation under external magnetic fields [2]. This approach provides a platform for applications requiring microfiber positioning, including vascularized tissue constructs [3], reconfigurable microelectronics [4], and soft microrobotics [5].
Fibers are formed by ionic crosslinking of an 8 wt.% sodium alginate solution, loaded with Fe_2N particles (2–3 μm) at 75 wt.%, and extruded at rate of 0.1 mL/min through a 1.3 mm inner-diameter tube into a 0.1 M calcium chloride bath. The tube passes through a custom magnetization head, which was moved using a linear motor at 6 mm/s, allowing synchronized in-plane magnetic patterning of the fiber during deposition. Polarity was controlled by switching current between -2 and 2 A for a period of 1.6 s, corresponding to -20 to 23 mT magnetic fields (Fig. 1). The resulting microfibers exhibited a coercivity of ~13 kA/m (16 mT), saturation magnetization of 91 emu/g, and viscosity of 0.5 Pa.s. Non-contact positioning of the polarized fiber in the hydrogel was achieved using an external magnetic field, where the fiber aligns according to its magnetic polarity. This was followed by hydrogel crosslinking and fiber dissolution, leaving behind a hollow, perfusable channel (Fig. 2).

[1] Z. Rajestari, J. Kalaus, and L. Kulinsky, *Journal of Micro- and Nano-Manufacturing*, Vol. 11, p. 034502 (2023)
[2] N. Tarabay, M. Shakibmanesh, J. A. López Medina, H. Guan, A. Mitchell, A. R. Balakrishna, and C. Velez, *Advanced Materials Technologies*, p. e01947 (2026)

[3] L. F. Santos, A. S. Silva, and J. F. Mano, *Advanced Healthcare Materials*, Vol. 12 (2023)
[4] Y. Kim and X. Zhao, *Chemical Reviews*, Vol. 122, p. 5317 (2022)
[5] Q. Zhang, G. Yang, L. Xue, G. Dong, W. Su, M. J. Cui, Z. G. Wang, M. Liu, Z. Zhou, and X. Zhang, *ACS Nano*., Vol. 16, p. 21555 (2022)



(a) Schematic of Fe_2N-alginate extrusion from the syringe into calcium chloride bath, including COMSOL-simulated magnetic vector field. (b) Switching current and in-plane magnetic field. (c) Experimental setup including syringe pump, tubing, and custom magnetization head.



(a) M-H curve (b) Gaussmeter scan of in situ magnetized fabricated fiber. (c) Embedded fiber in 5 wt.% GelMA. (d) Fiber reconfiguration under a 9 mT external field, followed by UV crosslinking to lock the aligned fiber in place. (e) Fiber dissolution in chelating solution. (f) Resulting hollow channel with preserved magnetically defined pathways. (g) Red dye perfusion through the hollow microchannel.

CS-07. In-Situ Alignment of Magnetic Particles for Printing of Anisotropic Hard Magnetic Soft Composites Using a Modified SLA-Based 3D Printer

M. Islam[1], L. Rodriguez[1], B. Banjara[2], J. Tate[2, 1], W. Geerts[3, 1]
[1]MSEC, Texas State University, San Marcos, Texas, United States, [2]Ingram School of Engineering, Texas State University, San Marcos, Texas, United States, [3]Physics, Texas State University, San Marcos, Texas, United States

Recent research has attracted increasing attention to magnetic soft composites for artificial muscles and actuators, as they offer flexible design, remote control, and higher magnetostriction compared to traditional magnetic thin films [1, 2]. 3D printing is becoming an effective method for fabricating these materials, as it allows customized shapes and improved performance [3]. In the initial stage of this work, hard-magnetic soft composites were printed using a Photon Mono M7 Pro LCD-based SLA printer with a suspension of strontium ferrite (1–2 wt%) in Elastic 600 resin. A permanent NdFeB magnet (~500 Oe) was placed on top of the build plate to study magnetic particle alignment during printing. The printed samples were characterized by a MicroSense EZ-9 Vibrating Sample Magnetometer (VSM) by measuring the hysteresis curve for various sample orientations. The highest and lowest squareness (S) values were 0.82 and 0.34, respectively, indicating significant magnetic anisotropy (Fig. 1). Magnetic anisotropy and saturation magnetization, however, vary with position relative to the permanent magnet on the build plate. For poorly cured samples, coercivity dropped significantly below 4200 Oe, and high S values indicated gel formation in a less cured state. To improve curing, homogeneity, and packing fraction, a Photon Ultra D2 DLP-based SLA printer was modified (Fig. 2) for magnetic field-assisted additive manufacturing (MFAAM). A magnetic field was applied using a custom-designed Halbach cylinder surrounding a redesigned cylindrical vat and build plate, enabling printing of samples up to 12 mm in diameter. Suitable printing parameters were established for different SF loadings, enabling successful printing of homogeneous anisotropic composites up to 16 wt%, showing an S value of 0.77 along the easy axis and 0.39 along the hard axis. This work demonstrates that the MFAAM SLA printer provides a novel method for preparing anisotropic composites with a helical easy-axis distribution function with unique magneto-elastic properties.

[1] J. Martin, R. Anderson and G. Gulley, Phys. Rev. E 74 (2006) 051507.
[2] L. Lu, P. Guo and Y. Pan, J. Man. Sc. Eng. 139 (2017)

071008-1.
[3] M. Suppan, C. Huber and D. Suess, *SSRN Electronic Journal* (2022).

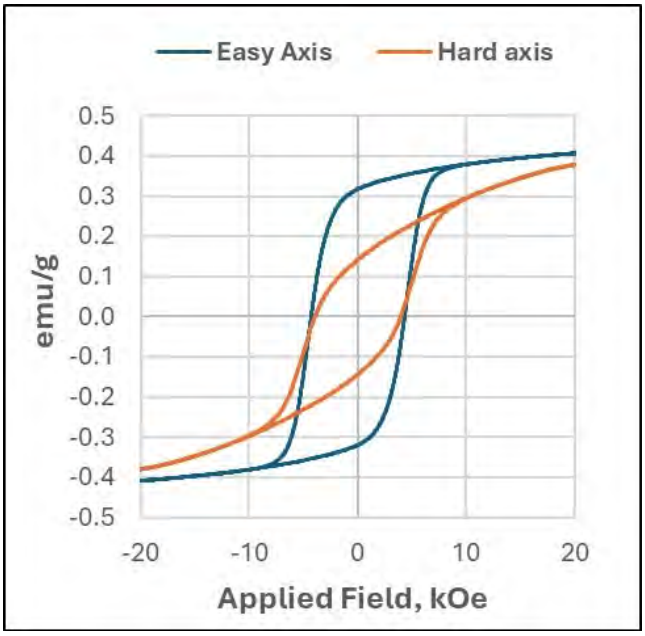


Fig. 1: Hysteresis curves along easy and hard axis of a 1 wt% anisotropic sample printed by LCD-based SLA printer

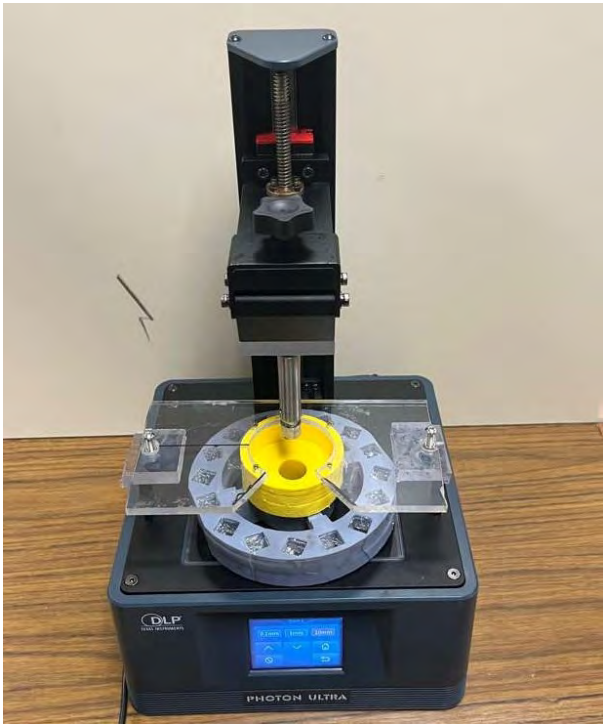


Fig. 2: Modified Photon Ultra D2 DLP-based SLA printer with Halbach cylinder

CS-09. A New Route to Fabricating of Spinel-Ferrite-Based Magnetic Nanocomposites via Eutectoid Decomposition: Application to Cobalt-Ferrite/Fe-Co System

S. Yamamuro, Y. Osumi, S. Koike
Graduate School of Science and Engineering, Ehime University, Matsuyama, Japan

Iron-oxide-based magnetic nanocomposites are currently attracting growing interest for applications such as permanent magnets. When these nanocomposites consist of a nanoscale mixture of soft and hard magnetic phases, the two phases are exchange-coupled through their interfaces, giving rise to superior magnetic properties, such as a high energy product. Here, we present a new approach to fabricating spinel-ferrite-based magnetic nanocomposites. The fabrication process is based on the eutectoid decomposition of wüstite (FeO) phase, which produces a lamellar nanostructure of a ferromagnetic metal (α-Fe) and a ferrimagnetic spinel ferrite (Fe_3O_4). In this work, a portion of Fe^{2+} ions in FeO was substituted by divalent cobalt ions (Co^{2+}) in a composition range of 10~30 at%Co, and subsequently decomposed into cobalt ferrite and Fe-Co alloy phases to achieve further magnetic hardness. Cobalt-substituted FeO powder was formed by heating a mixture of α-Fe, Fe_3O_4 and CoO powders by a solid-state reaction, followed by thermal decomposition in a vacuum-sealed quartz tube to form cobalt ferrite and Fe-Co alloy. X-ray diffraction measurements of the decomposed specimens confirmed the coexistence of spinel ferrite and Fe-Co alloy. The room-temperature magnetization measurements showed an enhanced coercivity exceeding 1 kOe, indicating that cobalt ions were incorporated into the spinel ferrite phase to form cobalt ferrite. The magnetization exceeded the room-temperature saturation magnetization of cobalt ferrite (80 emu/g) at 8kOe, owing to the presence of the Fe-Co phase with its high saturation magnetization. The magnetization curves exhibited smooth, single-phase-like behavior, suggesting that the two magnetic phases could be exchange-coupled. Because the magnetic properties of spinel ferrites can be tuned through substitution of constituent metal ions, the fabrication process described here provides a potential route to producing magnetic nanocomposites composed of various iron oxide and iron-based alloys.

Acknowledgements
This work was supported by JSPS KAKENHI Grant Number 20K05079. The authors are indebted to our department's

Research and Education Center of Materials Engineering for SEM-EDS analysis.

CS-10. Co-Ni Ferrite Nanoparticles as Tracers for Magnetic Particle Imaging – From Magnetic Anisotropy to Magnetic Particle Spectra and Imaging

L. Kubickova[1, 2], T. Voltrova[1, 2], J. Kulickova[1], P. Veverka[1], K. Ahn[1], D. Kubaniova[2, 1], J. Kohout[2], O. Kaman[1]
[1]FZU - Institute of Physics of the Czech Academy of Sciences, Praha, Czechia, [2]Faculty of Mathematics and Physics, Charles University, Praha, Czechia

Magnetic particle imaging (MPI) employs magnetic nanoparticles, typically in the superparamagnetic state, as exogenous tracers for biomedical imaging. It is based on their nonlinear response to a sinusoidally modulated AC magnetic field, which is governed by Néel and Brownian relaxation. The Fourier transform of the time-dependent signal yields a series of higher harmonics – the magnetic particle spectrum (MPS), which is critical for visualization. Using hydrothermal synthesis, we prepared a series of ~8 nm-sized $Co_{1-x}Ni_xFe_2O_4$ particles (CNF-*x*; $x \approx 0$, 0.1, 0.3, 0.5, 0.7, 0.9, 1) as a suitable model system, whose magnetocrystalline anisotropy can be tuned by chemical composition. The increasing Ni content gradually reduced both the magnetization of the bare particles from 72 to 52 $Am^2\ kg^{-1}$ at 300 K in 5 T and their coercivity from 1.45 T to 0.10 T at 5 K. The effective magnetic anisotropy at 5 K, estimated based on the Stoner-Wohlfarth model, was reduced from 6.3×10^5 J m^{-3} to 6.1×10^3 J m^{-3}.

To achieve colloidal stability in water, the ferrite particles were coated with silica. The resulting products (CNF-*x*@SiO_2) consisted of clusters of crystallites with a mean size ~40–50 nm encapsulated in a ~10 nm thick shell. Dynamic light scattering confirmed their colloidal stability (Z-average hydrodynamic size of ~90–110 nm). The ZFC and FC susceptibilities of the coated samples provided a distribution of blocking temperatures and estimates of the Néel relaxation time (Fig. 1).

The MPS study was performed with our custom-built system [1], and illustrative data are shown in Fig. 2. For low Ni content, high magnetocrystalline anisotropy keeps the magnetic moments blocked within the characteristic time window of ~40 μs, meaning the Brownian relaxation is the dominant mechanism. For higher Ni contents, efficient Néel relaxation occurs, and samples with the highest Ni content even surpassed ferumoxytol. The suspensions were also tested with a preclinical Bruker MPI scanner.

[1] O. Kaman, D. Kubániová, L. Kubíčková et al., Journal of Alloys and Compounds, Vol. 978, art. no. 173022 (2024).

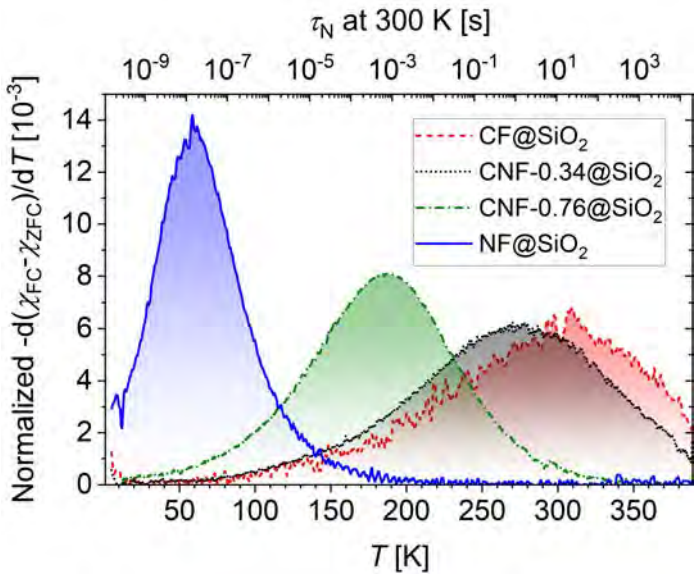


Fig. 1. Temperature derivative of the difference of FC and ZFC susceptibilities in 2 mT.

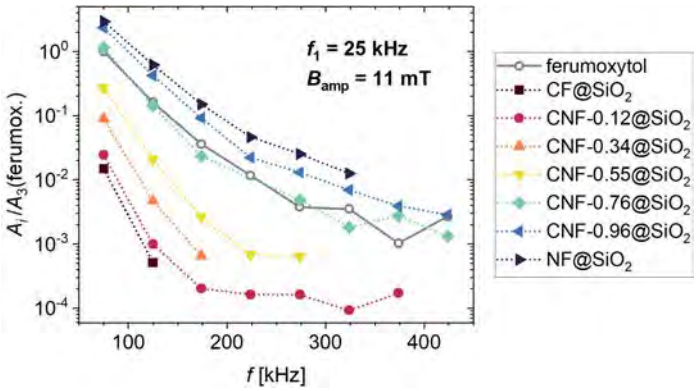


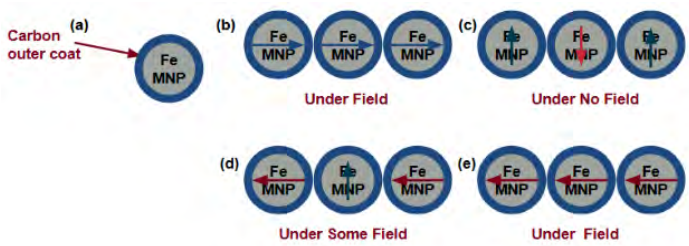
Fig. 2. MPS study of silica-coated particles and ferumoxytol. Sample amount ~120 mg, 30 mg(ferrite)/g, with data normalized to the 3rd harmonics of ferumoxytol.

CS-11. Theoretical Investigation of Magnetic Nanoparticles (MNPs) Based Additively Manufactured Biosensors

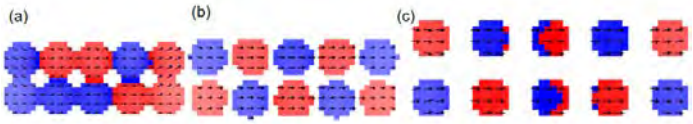
R. Mendonsa[1], S. Liang[2], J. Wang[1, 2]
[1]Electrical and Computer Engineering, University of Minnesota, Minneapolis, Minnesota, United States, [2]Chemical Engineering and Materials Science, University of Minnesota, Minneapolis, Minnesota, United States

Since the discovery of giant magnetoresistance (GMR) [1] Different forms of magnetoresistance have been explored, and magnetic nanoparticles (MNPs) have been shown in a suspension to change resistance in orders of magnitude based on an applied field [2]. Exploring this further, a simple switch based model is able to explain the physical operation of the system, and devices based on this were explored for memory and sensing [3]. Further works began looking at a solid system of MNP's in a polymer matrix, showcasing high GMR ratios without any physical movement detected [4]. Here we further study this phenomenon, and explore GMR based models (Fig. 1) in OOMMF [5] simulations to understand aspects and variables of the operation (Fig. 2). With understanding of the operation of the system, we begin to explore different types of devices possible with such a system and their applications.

Baselt, David R., et al. "A biosensor based on magnetoresistance technology." Biosensors and Bioelectronics 13.7-8 (1998): 731-739.
Meyer, J., Rempel, T., Schäfers, M., Wittbracht, F., Müller, C., Patel, A. V., & Hütten, A. Smart materials and structures, 22(2), (2013) 025032.
Mendonsa, Riyan, Shuang Liang, and Jian-Ping Wang. "Magnetic nanoparticles (MNPs) based additively manufactured memory devices." AIP Advances 14.2 (2024).
Zhou, Benjamin H., and Jeffrey D. Rinehart. "Pseudo spin valve behavior in colloidally prepared nanoparticle films." ACS Applied Electronic Materials 1.7 (2019): 1065-1069.
M. J. Donahue, OOMMF Users Guide, Version 1.0 (1999)



GMR based model used to explain MNP interaction using the MNP carbon coating as the spacer material (a) is a depiction of the MNP (b) showing a group of MNP's under the influence of an external field (c) similar group of MNP's without any application of field in a random orientation, (d) with the application of some field affecting the orientation of some particles, and (e) again the MNP's are under the influence of a strong field in the opposite direction.



OOMMF Simulation results looking at a cross section in the Y plane through the middle. Of 5x5 particle layout. Spacing at 0nm (a), 2nm (b), and 5nm (c).

CS-12LB. Elimination of Nanoparticle Interaction Effects in Magnetic Susceptibility Measurements

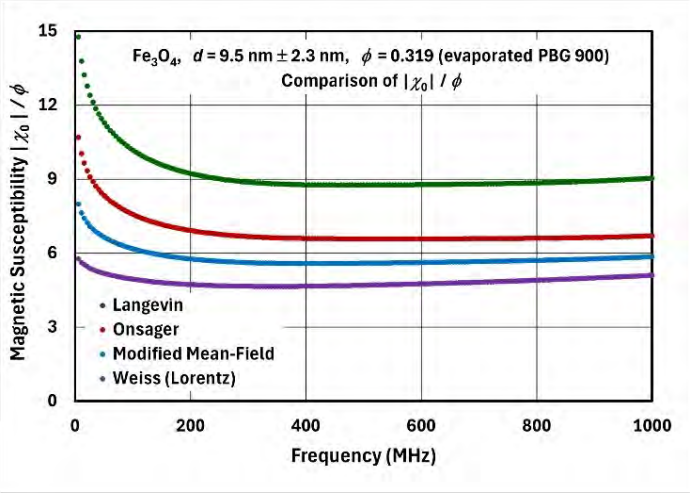
R. Goldfarb
National Institute of Standards and Technology, Boulder, Colorado, United States

A challenge for the measurement of magnetic susceptibility of nanoparticles is accounting for the effect of magnetostatic interactions. Traditional models assume a value for their intrinsic susceptibility and deduce what might be the measured susceptibility as a function of particle concentration and interaction fields. For quality assessment, the inverse approach yields the intrinsic susceptibility from actual measurements.

The magnetic susceptibility of commercial ferrofluids of different concentrations, and therefore different interaction strengths, was measured using the shorted coaxial transmission line technique. At radio frequencies, the susceptibility of nominally superparamagnetic nanoparticles is a complex quantity. Thus, the equations for derived intrinsic susceptibility can be expanded into real (inductive) and imaginary (resistive) parts. Intrinsic susceptibilities

provide a basis for comparison among magnetic nanoparticles for applications such as microelectronic power conversion.

R. B. Goldfarb, "Radio-Frequency Toroid Susceptometry of Magnetic Nanoparticles: What Goes Around Comes Around," *IEEE Access,* vol. 14, pp. 22335-22355, Jan. 2026, doi: 10.1109/ACCESS.2026.3657951.



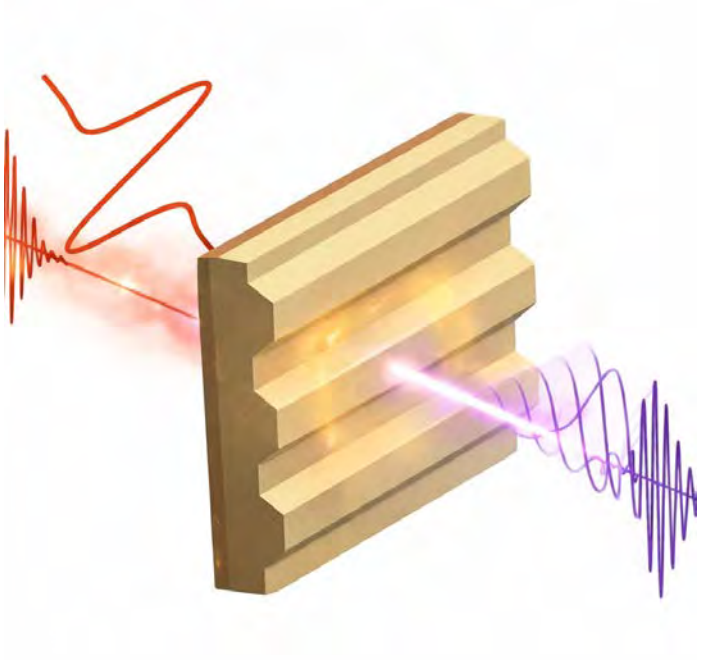
Susceptibility χ_0, scaled by particle concentration φ, of interacting magnetite nanoparticles as a function of frequency. The Langevin model (green data points) ignores particle interactions. Three other models account for particle interactions in different ways. As particles become less concentrated, all models converge to the modified mean-field model (blue data points).

CS-13LB. Enhancing THz light-spin coupling with metasurfaces

L. v. Gerven, V. Bilyk, A. V. Kimel
USCM, Radboud University, Nijmegen, Netherlands

Metasurfaces provide an effective route to enhance the coupling between terahertz (THz) electromagnetic fields and spin dynamics. Here, we present two complementary strategies based on dielectric and metallic metasurface designs. First, we demonstrate an all-dielectric metasurface (Fig. 1) [1] that enables low-loss and versatile spin control by tailoring out-of-plane THz magnetic-field components, allowing three-dimensional torque control in ferrimagnetic iron-garnet films. Second, we introduce a metallic metasurface based on a dragonfly antenna design [2] with wavelength-scale features that, under optical pumping, generates strongly localized out-of-plane THz fields. Together, these approaches illustrate how metasurface engineering can enhance THz–spin coupling, reduce dissipation, and open new pathways for ultrafast and energy-efficient spin manipulation in spintronics, magnonics, and quantum technologies.

[1] van Gerven L, Ignatyeva DO, Konkov DV, Bilyk V, Metzger T, Krichevsky DM, Evstigneeva SA, Vetoshko PM, Belotelov VI, Kimel AV. All-Dielectric Metaphotonics for Advanced THz Control of Spins. Phys Rev Lett. 2026 Mar 20;136(11):116703. doi: 10.1103/h2fr-t1sr. PMID: 41931816.
[2] Pancaldi M, Vavassori P, Bonetti S. Terahertz metamaterials for light-driven magnetism. Nanophotonics. 2024 Feb 2;13(10):1891-1898. doi: 10.1515/nanoph-2023-0801. PMID: 39635617; PMCID: PMC11501536.



Schematic illustration of the THz pump-optical probe metasurface measurement [1]. The pump induces spindynamics in a ferrimagnetic film of iron garnet enabled by the electromagnatic field modulation of the THz all-dielectric metasurface. These spin dynamics cause the polarisation of the probe to rotate.

CS-14LB. Characterizing Magnetic Nanoparticles using Magnetic Force Microscopy

D. Docusen[1], R. Gautam[2], K. Chesnel[2]
[1]Eastern Michigan University, Ypsilanti, Michigan, United States, [2]Brigham Young University, Provo, Utah, United States

Magnetic nanomaterials have previously been characterized through various methods. One method is electron microscopy, such as SEM or TEM, which reveals the physical structure of a sample [1]. Another method is coherent x-ray resonant magnetic scattering (CXRMS), which reveals the magnetic properties of a sample [2]. This latter method, however, requires the use of a synchrotron facility. It is worthwhile to explore the viability of other methods of characterizing magnetic nanomaterials that obtain both physical and magnetic information of a sample directly in the real space. This research explores the use of atomic force microscopy (AFM), magnetic force microscopy (MFM), and vibrating sample magnetometry (VSM) in characterizing Fe3O4 (magnetite) magnetic nanoparticles ranging from 38 nm to 125 nm in average diameter. The physical topography of these particles was obtained through AFM imaging (Fig. 1a, 1c). The resulting MFM images (Fig. 1b, 1d) show that the particles exhibit a nonuniform magnetic domain with dipolar coupling between adjacent particles (Fig. 1d). These preliminary results are promising for revealing the magnetic texture of these particles and understanding how this texture evolves during future in-situ measurements.

[1] K. Chesnel, M. Trevino, Y. Cai, J. M. Hancock, S. J. Smith, and R. G. Harrison. Particle size effects on the magnetic behaviour of 5 to 11 nm Fe3O4 nanoparticles coated with oleic acid. Journal of Physics: Conference Series, 521:012004, 2014.
[2] Karine Chesnel, Alex Safsten, Matthew Rytting, and Eric E. Fullerton. Shaping nanoscale magnetic domain memory in exchange-coupled ferromagnets by field cooling. Nature Communications, 7:11648, 2016.

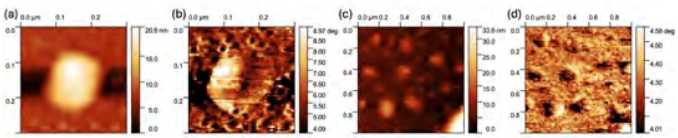


Figure 1: AFM and MFM images of 38 nm nanoparticles: (a) AFM image of a single particle, (b) MFM image of a single particle, (c) AFM image of a particle lattice, and (d) MFM image of a particle lattice.

SESSION DA: **Re-Imagining Spintronic Logic**

Co-Chair(s): S. Rao, *Interuniversitair Micro-Elektronica Centrum, Leuven, Belgium* and J. C. Incorvia, *Electrical and Computer Engineering, The University of Texas at Austin, Austin, Texas, United States*
Wednesday, November 4, 2026
02:00 PM-05:30 PM
Coral 3

DA-01. MRAM-Based Compute-in-Memory Beyond MVMs: From Accelerating Transcendental Functions to Stochastic Computing

M. Mukherjee, A. Holla, K. Roy
Purdue University, West Lafayette, Indiana, United States

Deep neural networks (DNNs) have enabled remarkable advances in applications ranging from computer vision to natural language processing. To accelerate DNN computations, which are dominated by matrix-matrix multiplications, compute-in-memory (CiM) has emerged as a promising approach, effectively reducing data traffic between memory and compute units. However, modern transformer-based workloads also require the evaluation of nonlinear functions such as softmax and GELU, often implemented using lookup tables (LUTs) that incur additional storage overhead and memory traffic. We explore overlaying read-only memory (ROM) containing these LUTs directly onto CiM arrays by duplicating word, bit, or source lines and encoding ROM bits through hard-wired bitcell connections to either the original line or its duplicate. This enables ROM storage in the same array without increasing bitcell area, provided sufficient routing space is available. Spin-transfer-torque magnetic tunnel junctions (STT-MTJs), with their non-volatility and compact one-transistor–one-MTJ bitcell, are particularly attractive for such ROM-overlaid CiM. We review ROM-overlaid CiM approaches with MTJs, analyzing bitcells, array peripherals, and layouts.

We then explore how the switching characteristics of MTJs can enable computation beyond matrix-multiplications through their use in CiM peripherals. For DNNs, we show how MTJs can be used for adaptive digitization of CiM array readouts. The dependence of MTJ switching behavior on input pulse width is used to reduce analog-to-digital conversion overhead. Beyond DNNs, annealing-based combinatorial optimization uses randomness to explore the search space and escape local minima. Finally, we discuss how the stochastic switching of MTJs can be exploited in CiM peripherals to accelerate large-scale annealing.

DA-02. Spin-Orbit-Torque Devices for Database search and Hyperdimensional Computing

A. Naeemi
Georgia Institute of Technology, Atlanta, Georgia, United States

This talk will present a cross-layer modeling and design framework for nanoscale spin-orbit memory devices and their applications in emerging computing paradigms such as database search and HyperDimensional Computing (HDC). For database search, various content addressable memory (CAM) designs will be discussed and benchmarked for nearest neighbor search applications and it will be shown how BEOL compatible transition metal dichalcogenide (TMD) thin-film resistors can be used to significantly improve the resolution of CAMs. For HDC, a novel architecture will be presented that enables in-memory execution of key HDC operations: binding (bitwise multiplication), permutation (bit shifting), and efficient similarity search.

[1] P. Kumar, D. E. Shim, and A. Naeemi, "Comprehensive device to system co-design for SOT-MRAM at the 7nm node," *IEEE Journal on Exploratory Solid-State Computational Devices and Circuits*, vol. 11, pp. 139-147, 2025
[2] S. Narla, P. Kumar, M. Adnaan, A. Naeemi, "Cross-layer modeling and design of content addressable memories in advanced technology nodes for similarity search," *IEEE Trans. Electron Devices, vol. 72, pp. 240-246,* Jan. 2025.
[3] S. Narla, R. Li, S. J. Koester, R. A. Dawley, A. A. Bol, P. Kumar, and Azad Naeemi, "Transition metal dichalcogenide thin-film resistors for content addressable memories with improved search resolution," *IEEE Electron Device Letters,* vol. 47, no. 2, pp. 387-390, Feb. 2026.
[4] M. M. R. Nayan, C.-K. Liu, Z. Wan, A. Raychowdhury, and A. Naeemi, "HyDra: SOT-CAM based vector symbolic macro for hyperdimensional computing," *2025 IEEE/ACM International Conference on Computer Aided Design (ICCAD)*, Munich, Germany, 2025, pp. 1-9.

DA-03. Voltage-controlled ferroelectric spin–orbit devices for beyond-CMOS logic and in-memory computing

G. Gandini, M. Cantoni, C. Rinaldi
Physics, Politecnico di Milano, Milano, Italy

As computing architectures confront the energy cost of data movement and the limits of CMOS scaling, spin-based logic-in-memory concepts have emerged as promising routes toward energy-efficient hardware [1]. A key challenge is the realization of device platforms where memory, signal transduction, and logic operations are co-localized and electrically controlled at the nanoscale.
Here we present ferroelectric spin–orbit devices based on chalcogenide semiconductors as a platform for non-volatile, all-electric spintronic logic. In ferroelectric Rashba semiconductors such as GeTe and related alloys [4,5], ferroelectric polarization encodes the memory state, while spin–orbit-driven spin-to-charge conversion provides a direct electrical readout controlled by polarization. This enables a unified device concept—closely related to FESO [4] and MESO paradigms [1,2]—where write, storage, and read operations are intrinsically coupled within a single layer. In contrast to current-driven spin–orbit torque approaches, this architecture enables voltage-controlled operation, offering reduced energy consumption and simplified integration. Recent extensions toward ferroelectric spin–orbit valves further expand the design space for reconfigurable logic [7].
Building on room-temperature ferroelectric control of spin–charge interconversion [5], we pursue three directions relevant for computing. First, materials-by-design strategies in GeTe-based systems and GeTe-rich layered compounds optimize conductivity, polarization stability, and conversion efficiency [6]. Second, scalable implementations using quasi-two-dimensional ferroelectrics and large-area chiral tellurium target integration with silicon platforms [3]. Third, ongoing scaling studies down to the 50 nm regime address switching voltage, readout signal, and variability, evaluating compatibility with dense integration and circuit-level operation.
These advances are supported by our EFESO startup initiative, aiming to develop ultralow-power spintronic transistors based on ferroelectric spin–orbit coupling. This work positions ferroelectric spintronics as a viable voltage-driven platform for logic-in-memory architectures, beyond-CMOS computing and edge AI systems.

[1] S. Manipatruni et al., *Nature Physics,* Vol. 14, p. 338 (2018)
[2] V. T. Pham et al., *Nature Electronics,* Vol. 3, p. 309 (2020)
[3] D. C. Vaz et al., *Nature Communications,* Vol. 15, p. 1902 (2024)
[4] C. Rinaldi et al., *Nano Letters,* Vol. 18, p. 2751 (2018)
[5] S. Varotto, C. Rinaldi et al., *Nature Electronics,* Vol. 4, p. 740 (2021)
[6] S. Cecchi, C. Rinaldi et al., *Advanced Science,* Vol. 11, p. 2304785 (2024)
[7] L. L. Tao et al., *Physical Review Letters,* Vol. 134, p. 076801 (2025)

DA-04. SuperMag: Superconducting Magnetic Logic

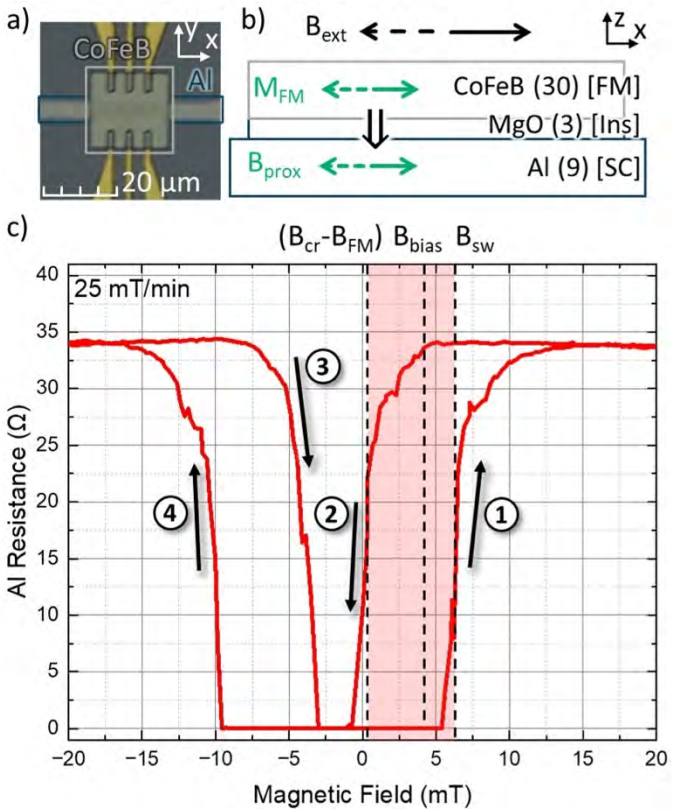
A. Edwards[1, 2], S. Le[1], N. Smith[1], E. C. Usih[3], A. Thomas[1], C. Richardson[1], N. Blumenschein[1], A. T. Hanbicki[1], A. Friedman[1], J. S. Friedman[3]

[1]Laboratory for Physical Sciences, College Park, Maryland, United States, [2]Electrical and Computer Engineering, University of Maryland, College Park, Maryland, United States, [3]Electrical and Computer Engineering, The University of Texas at Dallas, Richardson, Texas, United States

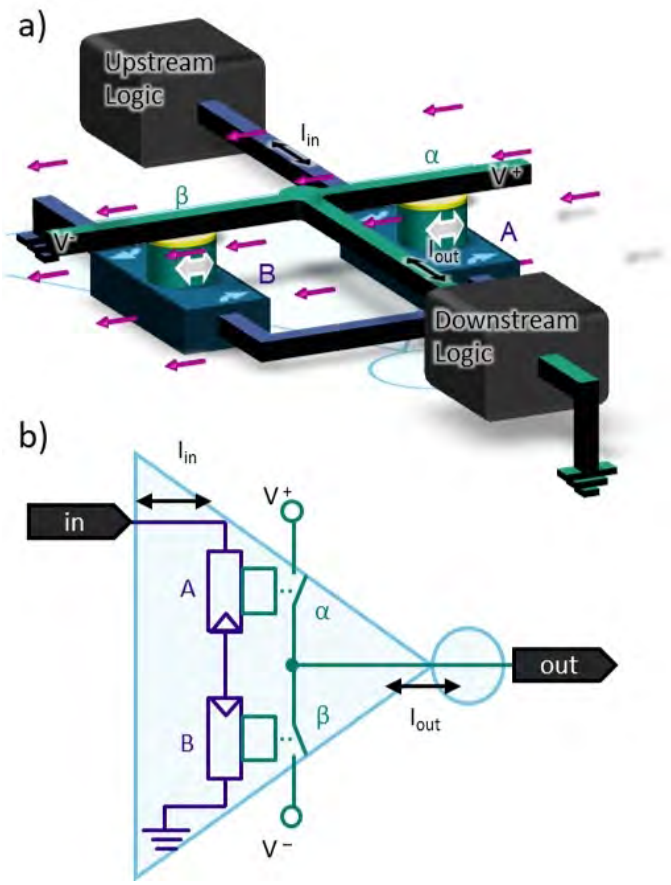
While superconductors are highly attractive for energy-efficient computing, limitations in their logic circuit integration have hindered scaling and led to increased energy consumption. We therefore propose and demonstrate a novel superconducting switching device utilizing the proximity magnetization from a spin-orbit torque (SOT)-switched magnet (FM) to control the resistivity of a superconductor (SC) [1]. As illustrated in Fig. 1 in-plane field (Bext) was swept to switch both the FM and SC of our Al/MgO/CoFeB stack, and crucially, when Bext ≈ 4 mT, the FM magnetization controlled the resistivity of the SC. Therefore, via SOT FM switching, the SC can be entirely controlled electrically.

Based on this mechanism, we propose a SuperMag switch with infinite R_OFF/R_ON ratio and a complete logic family comprising solely SuperMag switches. Fig 2. depicts the working principle of a SuperMag inverter, and similar techniques can be used to create any combinational logic circuit. Additionally, the zero-ohm ON-state channel enables full-swing, lossless transmission gates for highly efficient multiplexers, tri-state buffers, and look-up tables. Finally, SuperMag non-volatility enables native memory and reconfigurable logic. These advantages enable a possible 1,000x improvement in energy efficiency compared with CMOS and single flux quantum (SFQ).

[1] A. J. Edwards, S. T. Le, N. W. G. Smith, E. C. Usih, A. Thomas, C. J. K. Richardson, N. A. Blumenschein, A. T. Hanbicki, A. L. Friedman, J. S. Friedman, Magnetic Field-Mediated Superconducting Logic, arXiv :2602.07146 (2026).



a,b. SuperMag switch. c. Field-swept hysteresis curves indicate proximity field from FM onto SC plus Bext forces SC into normal resistive state. By applying a constant bias field in the red region, SC superconductivity is dictated solely by FM magnetization.



SuperMag inverter. a. FMs (green cylinder) may be switched via SOT from switching wires (blue) according to the blue curved arrows. When FM magnetization is aligned with [opposes] the bias field (purple), the associated SC (green wire) enters the normal resistive [superconducting] state. b. Current in the same [opposite] direction of the triangles close [open] the associated switch. "in"-port current flowing into [out of] the inverter is a logic '1' ['0'] and causes switch A to open [close] and switch B to close [open], resulting in "out"-port current flowing into [out of] the gate through switch beta [alpha], a logic '0' ['1'].

DA-05. Observation of the Magnon Hall Magnetoresistance

S. Mai[1, 2], P. Wu[3, 1], C. Chen[1], S. Huang[1, 4], X. Fan[5], D. Qu[2, 4]
[1]Department of Physics, National Taiwan University, Taipei, Taiwan, [2]Center for Condensed Matter Sciences, National Taiwan University, Taipei, Taiwan, [3]Delta Electronics, Taipei, Taiwan, [4]Center of Atomic Initiatives for New Materials, National Taiwan University, Taipei, Taiwan, [5]Department of Physics and Astronomy, University of Denver, Denver, Colorado, United States

Interconversion between charge and spin currents forms the foundation of spintronics. Magnons, which are the quanta of spin waves, can transport angular momentum with minimal Ohmic losses and couple to conduction electrons via spin-flip scattering. Despite intensive research on magnon spin transport in ferromagnetic insulators, that in ferromagnetic metals has remained largely unexplored due to its entanglement with electron spin currents.

Here, we demonstrate that through the electrical magnon Hall effect, charge currents in ferromagnetic metals can generate transverse magnon spin currents, giving rise to a magnon Hall magnetoresistance [1]. By studying the thickness-dependent magnetoresistance in CoFeB and NiFe up to micrometer thicknesses, we clearly distinguish magnon Hall magnetoresistance from conventional electronic contributions. Significantly, we reveal the conversion efficiency, defined as the product of the spin (magnon) Hall angle and spin (magnon) diffusion length, can be up to four orders of magnitude higher in ferromagnetic metals than in heavy metals. Our results uncover a universal and previously overlooked mechanism for magnon spin current generation in ferromagnetic metals, establishing them as efficient magnon spin current carriers and providing a new pathway for low-loss, long-range spin transport in spintronic devices.

[1] Shuan-Cheng Mai, Po-Hsun Wu, Chao-Wei Chen, Ssu-Yen Huang, Xin Fan and Danru Qu, Observation of the Magnon Hall Magnetoresistance Effect, *Phys. Rev. Lett.* 136, 116704 (2026)

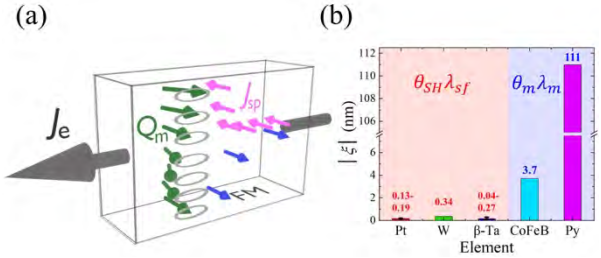


Fig.1 (a) Schematics of the electrical magnon Hall effect. (b) The spin conversion efficiency ξ in different materials.

DA-06. Emerging spintronics-based compute-in-memory systems for low-power edge AI

T. P. Xiao[1], C. H. Bennett[1], S. Liu[2, 3], N. Zogbi[3], I. Velazquez[3], H. Jin[3], Z. A. Landers[3], R. Patel[1], D. Hughart[1], S. Agarwal[1]
[1]Sandia National Laboratories, Albuquerque, New Mexico, United States, [2]National Institute of Standards and Technology, Boulder, Colorado, United States, [3]Electrical and Computer Engineering, University of Texas at Austin, Austin, Texas, United States

The proliferation of intelligent edge systems is driving a growing demand for ubiquitous computation on ultralow-power processing hardware. Compute-in-memory systems, which perform computation using memory devices or within memory arrays, can enable energy-efficient computing by eliminating the enormous data movement costs of traditional processing architectures. This presentation will begin with an overview of analog in-memory computing systems for edge Artificial Intelligence (AI): their advantages, their challenges and opportunities, and the essential trade-offs that inform the co-design of the memory technology, circuits, and system architecture [1,2].

We will then present several emerging compute-in-memory concepts that leverage the unique properties of spintronic devices for edge inference: non-volatility, long-term stability, resilience to radiation, and the presence of unique physical phenomena that enable multiple distinct and tunable functionalities within a device [3]. As an example, domain-wall magnetic tunnel junction (DW-MTJ) devices enable a form of stateful digital logic that can be composed into deeply pipelined, high-throughput matrix multiplication engines. Within analog in-memory computing systems, an MTJ can be engineered for high stochasticity, and moreover, to exhibit a programmable noise strength. This can be leveraged to implement stochastic synapses for Bayesian neural networks that can provide predictions with well-calibrated quantification of uncertainty – an important component of trusted AI [4]. In addition to synapses, magnetic and multiferroic devices can also be used as analog neurons and dendrites to enable energy-efficient spatio-temporal processing.

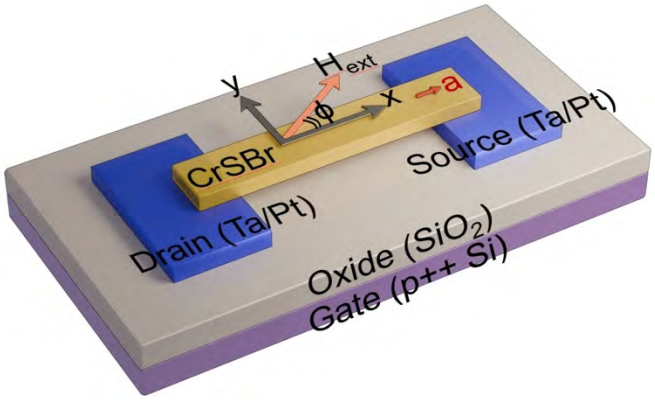
SNL is managed and operated by NTESS under DOE NNSA contract DE-NA0003525.
[1] T. P. Xiao et al, "Analog architectures for neural network acceleration based on non-volatile memory", Applied Physics Reviews vol. 7, p. 031301 (2020).
[2] T. P. Xiao et al, "On the Accuracy of Analog Neural Network Inference Accelerators", IEEE Circuits and Systems Magazine vol. 22. no. 4, pp. 26-48 (2022).
[3] N. Zogbi et al, "Parallel matrix multiplication using voltage-controlled magnetic anisotropy domain wall logic", IEEE Journal on Exploratory Solid-State Computational Devices and Circuits, vol. 9, no. 1, p. 65-73 (2023).
[4] S. Liu et al, "Bayesian neural networks using magnetic tunnel junction-based probabilistic in-memory computing", Frontiers in Nanotechnology, vol. 4 (2022).

DA-07. Magnetic Transistors with Strong Magnetoelectric Coupling and Spin–Orbit–Coupling Induced Nonreciprocity

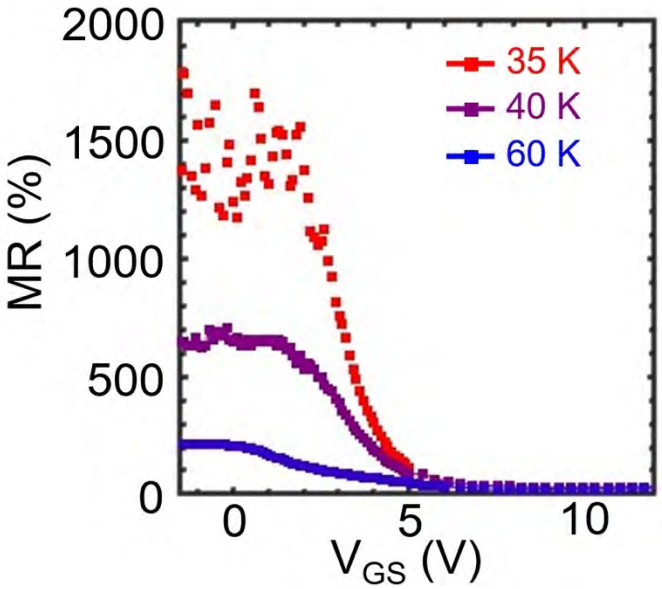
C. Chou[1], E. Park[1], J. Ingla-Aynes[1], J. Klein[1], K. Mosina[2], Y. Onishi[1], Q. Wang[1], J. S. Moodera[1], Z. Sofer[2], F. Ross[1], M. Li[1], L. Fu[1], L. Liu[1]
[1]MIT, Cambridge, Massachusetts, United States, [2]University of Chemistry and Technology Prague, Prague, Czechia

Magnetic transistors represent a new class of spintronic devices where electronic transport is jointly controlled by magnetic order and gate voltage. Here, we experimentally realize such a transistor using the van der Waals antiferromagnetic semiconductor CrSBr [1], which exhibits strong magnetoelectric coupling. By electrostatically tuning the carrier density, we observe a gate-dependent evolution of magnetoresistance that reveals distinct transport regimes governed by magnetically–driven modulation of carrier density and mobility. This strong coupling between magnetic order and electronic conduction enables direct electric control of magnetotransport, enabling intrinsically nonvolatile and energy-efficient operation for spintronic logic applications.
In the magnetic transistor device, we further uncover pronounced nonreciprocal and nonlinear transport arising from gate-induced Rashba spin–orbit coupling [2], which breaks inversion symmetry and introduces asymmetric band dispersion. The resulting nonreciprocity is gate tunable and exceeds that reported in conventional magnetic heterostructures by several orders of magnitude, accounting for up to 5% of the total conductance. We also outline strategies to further enhance the nonlinearity by down-scaling the device dimensions.
Together, these results establish CrSBr-based magnetic transistors as a versatile platform for exploring the interplay among magnetic order, spin–orbit coupling, and electronic transport—paving the way toward energy-efficient spintronic devices that merge transistor logic operation with magnetic memory functionality.

[1] C.-T. Chou, et al., Phys. Rev. Lett. 135, 136702 (2025).
[2] C.-T. Chou, et al., Newton 100331 (2025).



Device structure schematics of the magnetic transistor. The substract is used as back-gate to control Fermi level of CrSBr.



Experimental data of magnetoresistance vs. gate voltage in a CrSBr magnetic transistor. The magnetoresistance is defined as the ratio of the transistor channel resistance in the two CrSBr magnetic states. Large magnetoresistance is observed in the subthreshold regime.

SESSION DB: ALTERMAGNETISM: SUPERCONDUCTIVITY AND P-WAVE MAGNETS

Co-Chair(s): H. Reichlova, *Institute of Physics, CAS, Dresden, Germany* and M. Hirschberger, *Applied Physics, The University of Tokyo, Tokyo, Japan*

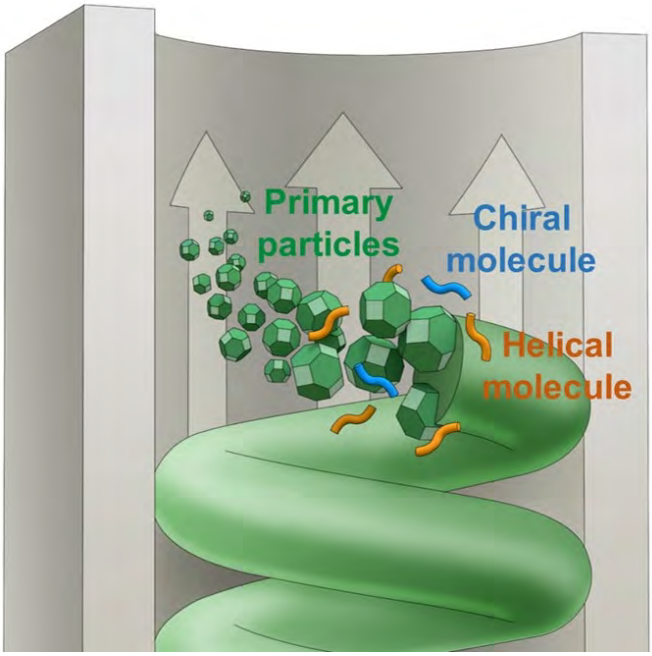
Wednesday, November 4, 2026
02:00 PM-05:30 PM
Coral 5

DB-01. 3D Chiral Spintronics: Spin-Selective Transport through Chiral Magnetic Nanohelices

Y. Jeon[1], E. Jeong[1], K. Nam[2], Y. Kim[1]
[1]Korea University, Seoul, Seoul, Korea (the Republic of), [2]Seoul National University, Seoul, Seoul, Korea (the Republic of)

Chiral crystals with well-defined handedness in atomic arrangements exhibit intriguing properties such as spin selectivity, asymmetric magnetoresistance, and skyrmions. Although similar geometry-induced phenomena have been observed in chiral organic-molecule-based systems, synthesizing uniform inorganic nanostructures with desired chirality using a scalable method remains challenging. We electrochemically synthesized 3D chiral ferromagnetic cobalt-iron nanohelices from nanoparticles in anodized aluminum oxide templates. The spiral directions and the number of strands were regulated by incorporating chiral molecules and applying an appropriate potential. We demonstrate the observation of Faraday's law of induction at the nanoscale and how chiral nanohelices regulate the direction of electron flow. The implications of our findings extend to the technological realm, particularly in the context of charity and ferromagnetism-based spin-tunable devices.

1. Y. S. Jeon and E. Jeong et al., *Science* 389, 1031-1036 (2025)
2. Y. S. Jeon et al., *Nano Today* 42, 101348 (2022)



DB-02. Metallic *p*-wave magnets with commensurate spin helix

M. Hirschberger[1, 2], R. Yamada[1], M. Birch[2], P. Baral[1, 2], S. Okumura[5, 1, 2], M. Ezawa[1], J. Masell[3], T. Nomoto[4], M. M. Hirschmann[2]
[1]Applied Physics, The University of Tokyo, Bunkyo, Tokyo, Japan, [2]Center for Emergent Matter Science, RIKEN, Wako, Saitama, Japan, [3]Karlsruhe Institute of Technology, Karlsruhe, Germany, [4]Physics, Tokyo Metropolitan University, Hachioji, Tokyo, Japan, [5]Quantum-Phase Electronics Center, The University of Tokyo, Bunkyo, Tokyo, Japan

Antiferromagnets with nonrelativistic spin splitting in their electronic structure are drawing significant attention. Among these are *p*-wave magnets as well as *d*- or *g*-wave altermagnets [1]. All of these are thought to be suitable for next-generation applications in spintronics, but the *p*-wave magnet is especially appealing due to a nonrelativistc Edelstein effect, which corresponds to a spin-accumulation driven by an electric current [2,3].

The electronic structure of a *p*-wave magnet features parity-odd spin splitting. In Fig. 1 (right side), the red and blue bars indicate the average spin polarization in a certain sector of momentum space. The region where spin-up and spin-down bands are degenerate is called a nodal plane (dashed line in the image). Ref. [1] points out symmetry conditions for *p*-wave magnetism, stressing the requirement of a lattice-commensurate, noncollinear (but coplanar) magnetic texture.

We have tuned a helimagnetic material to the lattice-commensurate limit by carefully controlling the chemical potential, and observe giant responses in the electronic properties only in the *p*-wave state [4]. In this talk, I will also present our most recent work, where we search new magnetic materials with odd-parity spin splitting.

[1] A.B. Hellenes, J. Sinova, J. Smejkal, *et al.*, arXiv:2309.01607 (2024)
[2] A. Chakraborty *et al.*, Nat. Commun. 16, 7270 (2025)
[3] Q. Song *et al.*, Nature 642, 64–70 (2025)
[4] R. Yamada, M.H. *et al.*, Nature 646, 837–842 (2025).

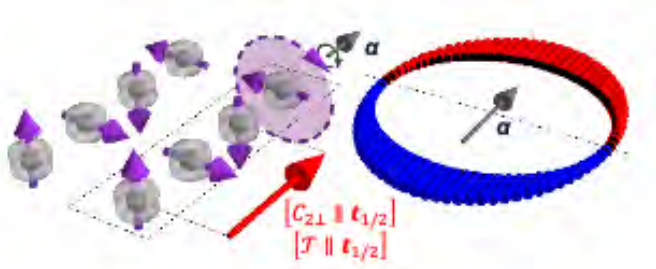


Figure: *p*-wave magnetism (conceptual). Left: commensurate magnetic structures with a coplanar but noncollinear arrangement are required according to Ref. [1]. They must break inversion symmetry but satisfy certain symmetries (red arrow and labels), such as spin rotation + translation. Right: The spin polarization in momentum space is collinear along α, i.e., perpendicular to the spin rotation plane (purple circle) in real space. From Ref. [4].

DB-03. Josephson Diode Effect in Altermagnet and p-wave Magnet Based Junctions

L. Sharma[1], B. Ghimire[2], M. Thakurathi[2]
[1]Physics, Indian Institute of Technology, Delhi, New Delhi, Delhi, India, [2]Physics, Indian Institute of Technology, Hyderabad, Hyderabad, Telengana, India

Unconventional magnets have recently emerged as a new phase of magnetism, classified beyond conventional magnetic group symmetry by invoking spin group symmetry, which decouples spin and real-space transformations. This classification reveals magnetic phases like altermagnets (AM, even-parity spin splitting) and p-wave magnets (PM, odd-parity spin splitting), which break time-reversal symmetry (TRS) with zero net magnetization. The absence of net magnetization makes them naturally attractive for applications requiring broken TRS without the stray fields

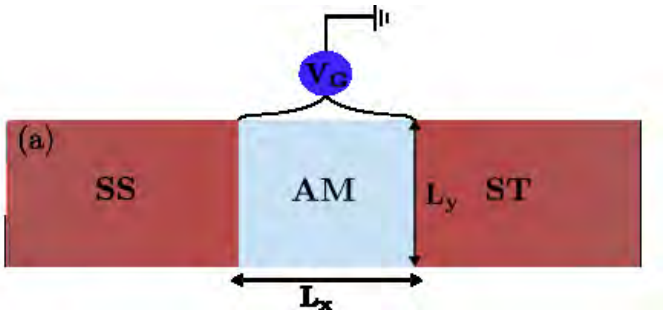
that ferromagnets would generate in superconducting circuits.

In this work, we present two theoretical studies of the Josephson diode effect (JDE), using AM and PM as active elements. In the first study [1], we investigate a spin-singlet superconductor (SC)/AM/spin-triplet SC Josephson junction and demonstrate a field-free JDE (Fig. 1). We identify four requisite conditions for JDE in such junctions: broken TRS, non-identical superconductors across the junction, presence of spin-orbit coupling, pair potential or Fermi surface anisotropy. We show that the diode efficiency is sensitively tunable via lobe angle and gate potential applied in the AM region (Fig. 2), and that the non-reciprocity remains robust against disorder in the AM.

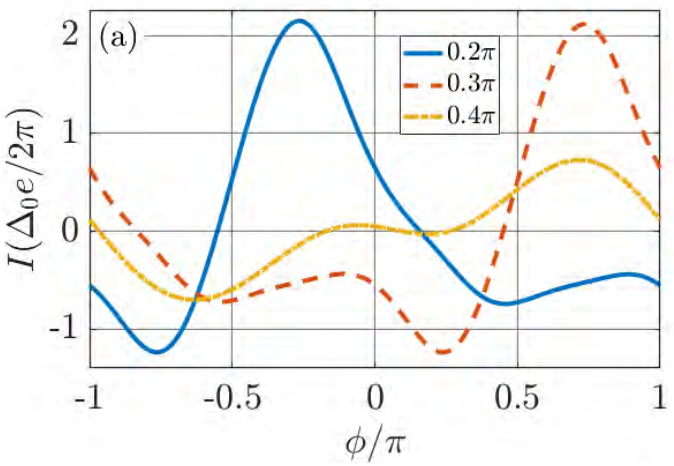
In the second study [2], we construct a Josephson junction using PM with proximity-induced superconductivity as leads and AM as the barrier, and demonstrate JDE in the complete absence of Rashba spin-orbit coupling an ingredient previously previously thought indispensable. Through symmetry analysis, we identify the mirror operation Myz, alongside TRS and inversion breaking, as the key symmetry constraint governing the diode effect in this setup. Together, these results establish that unconventional magnets not only offer a stray field free route to superconducting rectification but also enable richer symmetry driven physics, expanding the design space for field-free superconducting diode devices.

[1] L. Sharma and M. Thakurathi, Tunable Josephson diode effect in singlet superconductor-altermagnet-triplet superconductor junctions, Phys. Rev. B 112 (10), 104506 (2025).

[2] L. Sharma, B. Ghimire, and M. Thakurathi, p-wave magnet driven field-free Josephson diode effect, arXiv:2602.16677 (2026).



Schematic of the SC-singlet/AM/SC-triplet Josephson junction geometry with Gate potential applied at AM.



Non-reciprocal critical currents as function of phase difference Φ and lobe angle of AM

DB-04. Symmetry-Enforced Nodal f-Wave Magnets

M. M. Hirschmann[1], A. Furusaki[1], M. Hirschberger[2]

[1]*Center for Emergent Matter Science, RIKEN, Wako, Japan,* [2]*Department of Applied Physics, The University of Tokyo, Bunkyo, Japan*

The angular dependence of electronic spin splitting can be categorized into even-parity (*s-, d-, g-, i*-wave) [1] and odd-parity (*p-, f-, h*-wave) [2] components. In such magnets, regions in momentum space with opposite spin polarization are separated by nodal lines or nodal surfaces. We analyze the symmetries that enforce an f-wave nodal texture (Fig. 1) [3].

In p-wave magnets, odd-parity spin textures lead to a large anisotropic Edelstein effect [4]. In contrast, *f*-wave magnets exhibit an additional threefold rotation symmetry, which suppresses the Edelstein effect in linear response. Nevertheless, at certain surfaces of f-wave magnets the symmetry is reduced. This enables surface resonances that contribute to an inhomogeneous Edelstein effect. We demonstrate this using a tight-binding model of a nodal f-wave magnet with different surface terminations [3].

[1] L. Šmejkal, J. Sinova, T. Jungwirth, Phys. Rev. X 12, 031042 (2022)

[2] A. B. Hellenes, T. Jungwirth, R. Jaeschke-Ubiergo, et al., arXiv:2309.01607 (2023)

[3] M. M. Hirschmann, A. Furusaki, M. Hirschberger, arXiv:2603.17406 (2026)

[4] A. Chakraborty, A. B. Hellenes, R. Jaeschke-Ubiergo, et al., *Nat Commun* 16, 7270 (2025)

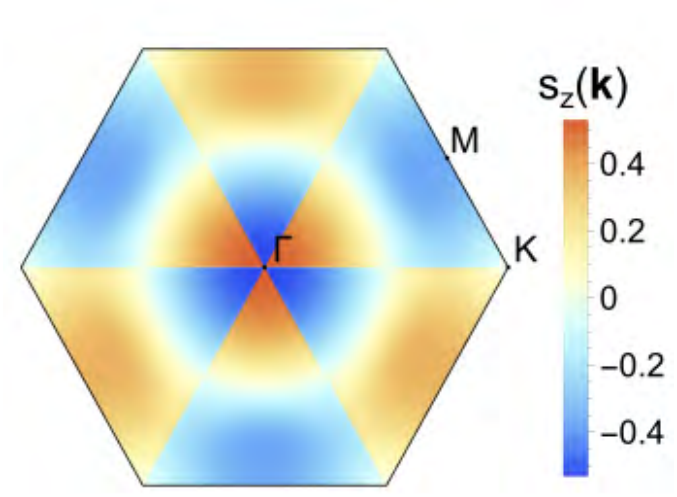


Fig. 1 Spin texture of an f-wave magnet.

DB-05. Magnetic ground state and k-dependent spin splitting in the surface of RuO_2 thin films

T. Kuschel
Johannes Gutenberg University Mainz, Mainz, Germany

Within the new magnetic material class of altermagnets [1], RuO_2 is under huge debate since several studies confirm and others refute the existence of altermagnetism in this material. While the magnetically ordered ground state of RuO_2 is questioned in bulk form [2,3], altermagnetic signatures in RuO_2 thin films can be identified [4,5]. Some transport experiments in RuO_2/ferromagnet bilayers do also not provide a clear evidence for altermagnetism [6]. Besides the magnetically ordered ground state, the k-dependent spin splitting of bands is a prerequisite of altermagnetism. Here, we report on two studies addressing the search for these properties. We investigated RuO_2 thin films by low-energy muon spin rotation/relaxation (μSR) spectrocopy and probed the films depth dependent by variation of the kinetic energy of the muons [7]. We found a magnetic ground state in the first atomic layers of 30nm-thick RuO_2 films indicating different properties at the surface compared to the rest of the layer (Fig. 1).
In addition, we studied time-resolved magneto-optic Kerr effect (TR-MOKE) with circularly polarized pump pulses [8]. The Kerr ellipticity reveals a time delay compared to the Kerr rotation which can be visualized by plotting Kerr ellipticity vs. Kerr rotation obtaining a 'butterfly' shape similarly to observations in topological insulators (Fig. 2).

This time delay is caused by k-dependent spin splitting for transitions in which the electrons have to change spin direction and k position as well. Both experiments support the existence of altermagnetic properties at the surface of RuO_2 thin films.

[1] L. Šmejkal et al., Phys. Rev. X 12, 031042 (2022)
[2] M. Hiraishi et al., Phys. Rev. Lett. 132, 166702 (2024)
[3] P. Keßler et al., npj Spintronics 2, 50 (2024)
[4] Z. Feng et al., Nat. Electron. 5, 735 (2022)
[5] M. Weber et al., arXiv:2408.05187
[6] A. Akashdeep, TK et al., Phys. Rev. Applied 24, 054018 (2025)
[7] A. Akashdeep, TK et al., Appl. Phys. Lett. 128, 022406 (2026)
[8] K. Jäckel, TK et al., arxiv:2603.29641

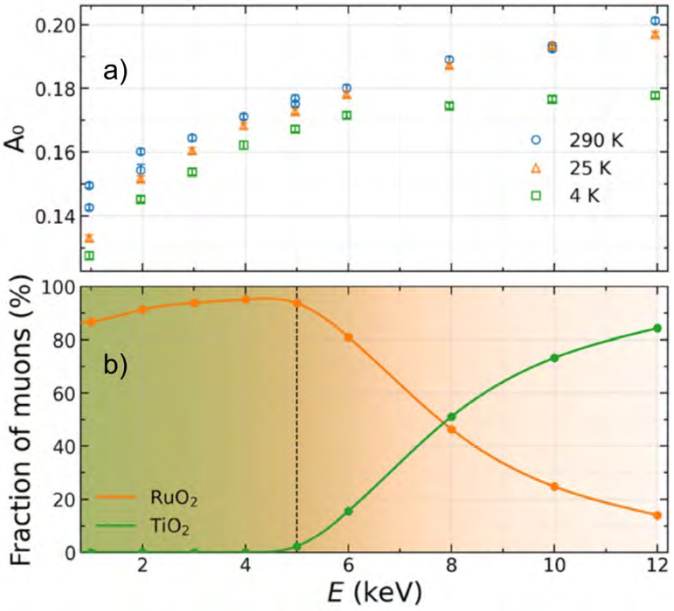


Fig. 1: Magnetic ground state at the RuO_2 surface identified by low energy μSR. a) Asymmetry A_0 decreases with lower kinetic energy which indicates interaction with ordered magnetic moments at the surface. b) Fraction of muons vs. kinetic energy. The muons with only a few keV are probing the surface of the films. Taken from Ref. [7].

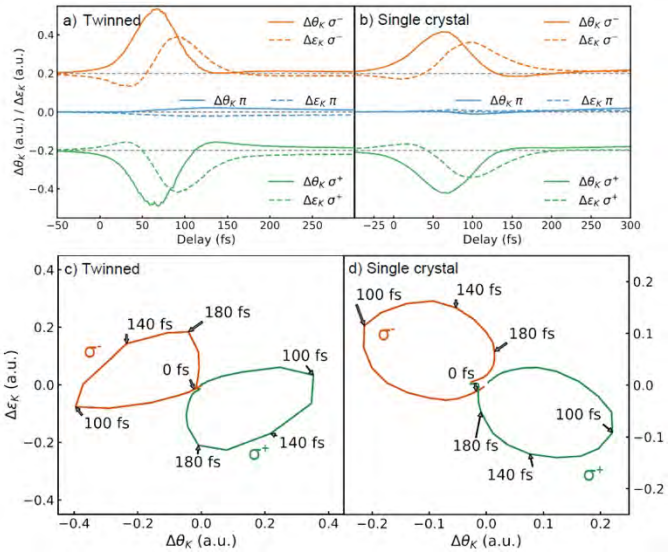


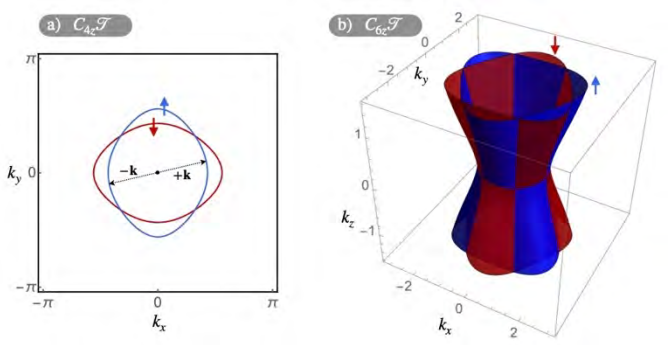
Fig. 2: TR-MOKE after excitation with circularly polarized pump pulses. a),b) Delay between Kerr rotation and ellipticity, c),d) Kerr ellipticity vs. Kerr rotation reveals a 'butterfly' shape indicating k-dependent spin splitting. a),c) twinned and b),d) single-crystal films. Taken from Ref. [8].

DB-06. Topology and persistent spin currents in superconducting altermagnets

M. Franz
University of British Columbia, Vancouver, British Columbia, Canada

At low temperature, altermagnetic metals can naturally support spin-triplet superconducting phases with, effectively, independent condensates for spin-up and spin-down electrons. I will show that such a state generically exhibits non-trivial topology. In addition it can be used to both generate and carry spin-polarized persistent currents that are of interest to spintronic applications. Theses conclusions apply to altermagnets that become intrinsically superconducting at low temperatures, but, remarkably, also to the case when an altermagnet is proximitized with a conventional spin-singlet s-wave superconductor.

1. K. Monkman, J. Weng, N. Heinsdorf, A. Nocera, Y. Barlas, M. Franz, "Persistent spin currents in superconducting altermagnets", Physical Review X 16, 011057 (2026).
2. N. Heinsdorf, M. Franz, "Proximitizing altermagnets with conventional superconductors",Physical Review B 113, L020501 (2025).



DB-07. Altermagnetic Thin Films and Their Interplay with Superconductivity

D. Kriegner
Institute of Physics of the Czech Academy of Sciences, Prague, Czechia

Altermagnets are compensated collinear magnets whose opposite sublattices are related by lattice rotations rather than translations [1]. This symmetry leads to spin-split electronic bands with alternating sign in momentum space despite vanishing net magnetization. We recently demonstrated this band splitting in hexagonal MnTe [2], where it also gives rise to linear response phenomena usually associated with ferromagnets [3].
In this talk I will present our recent progress toward altermagnetic thin films and hybrid structures aimed at superconducting spintronics. First, I will discuss the extension of altermagnetic concepts to sputtered thin films and highlight thin-film materials as a scalable platform for realizing spin-split bands [4], including with a view toward transport signatures such as the anomalous Hall effect. These results establish altermagnetic thin films as a versatile platform beyond bulk model systems. Second, I will show our first steps toward combining altermagnetism with superconductivity. We have recently realized epitaxial superconductor/altermagnet bilayers and are now investigating how superconducting and altermagnetic order interact at the interface [5]. Such heterostructures provide a platform to explore superconducting proximity effects and spin-dependent pairing in spin-split systems without net magnetization.

[1] L. Smejkal, J. Sinova, and T. Jungwirth, Phys. Rev. X 12, 031042 & 040501 (2022).
[2] J. Krempaský et al., Nature 626, 517–522 (2024).
[3] O. J. Amin et al., Nature 636, 348–353 (2024).
[4] S. P. Bommanaboyena et al., Phys. Rev. Materials 9, 064402 (2025).
[5] C. Müller et al., arXiv:2601.06504 [cond-mat.supr-con].

DB-08. Hidden magnetic complexity in a model altermagnet: A neutron and muon study of correlated *d*-wave altermagnet $La_2O_3Mn_2Se_2$

S. Hatt, E. Carlisle, B. Frandsen
Physics and Astronomy, Brigham Young University, Provo, Utah, United States

The altermagnetic compound $La_2O_3Mn_2Se_2$ is a valuable model system for studying altermagnetism, both for its simple geometry as a realization of the Lieb lattice and for its status as a Mott insulator, in contrast to the metallic or semiconducting nature of many other altermagnets. The combination of Mott physics with altermagnetism raises the exciting possibility of emergent orders in $La_2O_3Mn_2Se_2$ and also makes it a candidate for novel applications, such as magneto-optical devices. Here, we use neutron scattering and muon spin spectroscopy to reveal previously unrecognized magnetic complexity in $La_2O_3Mn_2Se_2$, which belies the superficial simplicity of the crystal structure. Magnetic pair distribution function analysis of neutron total scattering data demonstrates the presence of robust, fluctuating, two-dimensional magnetic correlations that persist far into the paramagnetic state at high temperature and coexist with long-range, three-dimensional order below T_N = 165 K, while inelastic neutron scattering data (Fig. 1) show a gapped ground state which transforms into a gapless state with a significantly redistributed spectral weight around 120 K. Separately, the muon asymmetry spectra (Fig. 2) reveal the disappearance of spontaneous oscillations when warming through ~110 K, pointing to a potentially hidden transition not previously understood. We then directly confirm this scenario through temperature-dependent, high-resolution neutron diffraction data. Together, these results paint a much richer picture of the magnetism in $La_2O_3Mn_2Se_2$ than was initially imagined, highlighting the potential for novel physics in this compound and related materials.

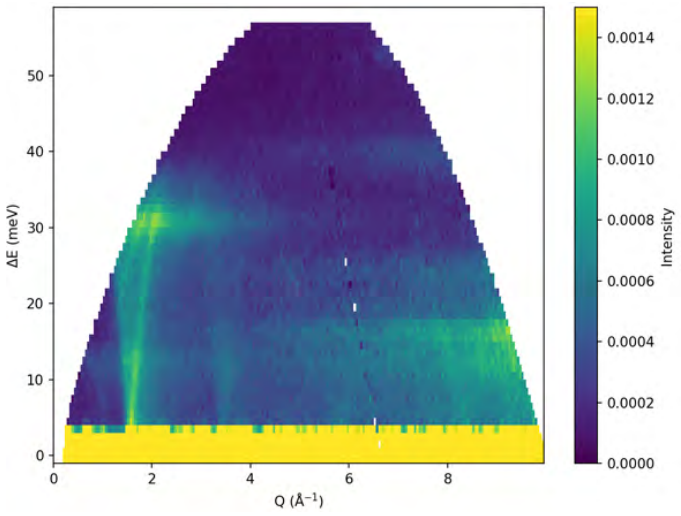


Fig. 1. Inelastic neutron scattering spectrum of $La_2O_3Mn_2Se_2$ at 10 K.

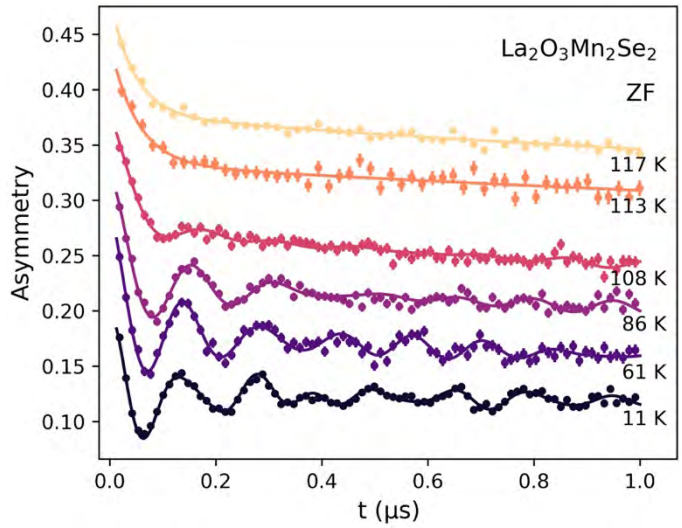


Fig. 2. Muon spin rotation spectra for $La_2O_3Mn_2Se_2$ at various temperatures, offset vertically for clarity.

DB-09. Time-reversal-symmetry-breaking spin injection from an altermagnet

J. Mencos[1], A. Badura[2], E. Dolan[1], S. Beckert[3], I. Kounta[4], W. Campos[5], J. Rial[6], D. Kriegner[2], V. Baltz[6], L. Hueso[1], J. Sinova[5], O. Gomonay[5], T. Jungwirth[2], L. Smejkal[7], L. Michez[4], H. Reichlova[2], F. Casanova[1]

[1]nanogune, San Sebastian, Spain, [2]FZU, Prague, Czechia, [3]TU Dresden, Dresden, Germany, [4]CINaM-CNRS, Marseille, France, [5]JGU, Mainz, Germany, [6]SPINTEC, Grenoble, France, [7]PKS MPG, Dresden, Germany

The emergence of altermagnetism [1, 2] offers a new route for spintronics by combining large non-relativistic spin splitting with zero net magnetization and robustness against external magnetic fields. Here [3] we demonstrate spin-current generation and injection from the compensated magnet Mn5Si3 [4], composed of earth-abundant Mn and Si and exhibiting altermagnetic symmetry. Using lateral spin-valve devices, we show that switching between time-reversed magnetic states modifies the detected spin signal, providing direct evidence of time-reversal symmetry-breaking spin injection. We further observe the spin-splitter effect, a transverse spin-current generation mechanism unique to altermagnets and distinct from the conventional spin Hall effect. The measured spin-injection efficiency is comparable to standard ferromagnets and consistent with first-principles calculations predicting ~10% spin polarization. These results establish Mn5Si3 as an efficient spin-current source and place altermagnets as a promising platform for next-generation spintronic devices based on fully compensated magnets.

[1] L. Šmejkal et al. Physical Review X 12, 040501 (2022)
[2] C. Song, HR et al. Nature Reviews Materials 10, 473–485 (2025)
[3] J. Mencos, HR et al. arXiv:2512.17427 (2025)
[4] H. Reichlova et al. Nature Communications 15, 4961 (2024)

SESSION DC: MULTIFERROIC MATERIALS AND MAGNETO-IONICS

Co-Chair(s): S. Dong, *Physics, Southeast University, Nanjing, Jiangsu, China* and Y. Takamura, *Materials Science and Engineering, University of California, Davis, Davis, California, United States* and B. Prasad, *Materials Engineering , Indian Institute of Science Bengaluru, Bengaluru , KA, India*

Wednesday, November 4, 2026
02:00 PM-05:30 PM
Coral 1

DC-01. Strain and Defect-Tailored Magnetotransport in $NiCo_2O_4$ Thin Films and Free-Standing Membranes

X. Hong

University of Nebraska-Lincoln, Lincoln, Nebraska, United States

The inverse spinel ferrimagnetic $NiCo_2O_4$ possesses high Curie temperature and high spin polarization, making it a promising material candidate for spintronic applications. Epitaxial strain and disorder can significantly modify the electronic and magnetic energy landscapes, which can lead to unconventional magnetotransport phenomena in $NiCo_2O_4$ [1]. We exploit epitaxial $NiCo_2O_4$ films and free-standing $NiCo_2O_4$ membranes as model systems to examine the effects of strain and disorder on the anomalous Hall effect, anisotropic magnetoresistance (AMR), and topological Hall effect (THE). $NiCo_2O_4$ films on (001) $MgAl_2O_4$ substrates exhibit strong perpendicular magnetic anisotropy down to 1.2 nm thickness [2] and two-fold sinusoidal AMR, while (001) $NiCo_2O_4$ on perovskite substrates and $NiCo_2O_4$ membranes exhibit spin canting, with an additional four-fold AMR component emerging due to disorder-induced spin scattering and strain-induced tetragonal magnetocrystalline anisotropy. Electron microscopy studies reveal structural and chemical phase separation in the membranes similar to those in disordered films, explaining the highly consistent magnetotransport properties for $NiCo_2O_4/Sr_3Al_2O_6$ films and $NiCo_2O_4$ membranes [3]. THE has been observed in $NiCo_2O_4$ membranes, which has been correlated with magnetic bubble domain formation, as revealed via magnetic force microscopy. Our study provides effective material strategies for engineering spin transport and magnetic anisotropy in $NiCo_2O_4$ and presents a promising venue for designing flexible magnetic memory, sensor, and spintronic applications.

This work was primarily supported by NSF Award OIA-2044049 and DOE Award DE-SC0026103. Additional support was provided by DOE under Contract DESC0012704, NSF

ECCS: 2025298, and the Nebraska Research Initiative.
[1] Chen *et al.*, *Adv. Mater.* 31, 1805260 (2019).
[2] Chen *et al.*, *APL* 12, 242401 (2022).
[3] Wu *et al.*, *ACS Nano* 20, 11008 (2026).

DC-02. Magnetoelectric Coupling in Freestanding Multiferroic $SrMnO_3$ Membranes

A. Gupta, M. Ahmadi, T. Banerjee
Zernike Institute for Advanced Materials, University of Groningen, Groningen, Netherlands

The increasing demand for novel energy-efficient computing materials and devices has intensified the search for multifunctionality in new material platforms. Multiferroics, exhibiting electric-field control of magnetism are central to designing next generation low power electronics such as in MESO and FESO architectures. The rich material landscape inherent to transition metal oxides allows for a flexibility in designing coexisting magnetic and ferroelectric orders. The perovskite $SrMnO_3$ (SMO) is a demonstrated antiferromagnet [1,2] theoretically predicted [3] to show magnetoelectric coupling with strain. However, the predicted large phase space needed to realize such coupling requires a careful substrate selection, restricting the degree of control in elastic deformation and strain in SMO thin films. Furthermore, electric field manipulation of the magnetic order requires device designs which are incompatible with oxide deposition methods. A way to overcome this challenge is to fabricate freestanding membranes (FS), which enables this by unearthing the hitherto unexplored coupled phases induced by strain in multiferroic SMO.

In this talk, I will discuss the fabrication, characterization and magnetoelectric coupling of FS SMO membranes. Following a rigorous optimization of the water-soluble sacrificial layer stoichiometry, thickness, deposition parameters and transfer protocol, we realize reproducible transfer of large area (>500 μm) SMO membranes. Using a complementary set of structural characterization techniques, we quantified the crystal structure and strain (0.5% OOP compressive) in the FS layer. To investigate the microstructure, HAADF-STEM scans including imaging the oxygen atoms using iDPC-STEM were performed, revealing the perovskite crystal structure in SMO. The magnetic characterization of the FS layer are shown in Figs. 1 and 2, clearly establishing the antiferromagnetic nature of the film. These first demonstrations in FS SMO were further extended to show how the strain state of the FS membrane can be controlled by ex-situ stretching, providing extra flexibility to probe magnetoelectric coupling in such membranes.

[1] JJ.L. van Rijn et al., Phys. Rev. B, Vol. 110, p.144446 (2024)
[2] JJ.L. van Rijn and T. Banerjee, Phys. Status Solidi RRL, Vol. 18, p.2300331 (2024)
[3] A. Edström and C. Ederer, Phys. Rev. Lett., Vol. 124, p.167201 (2020)

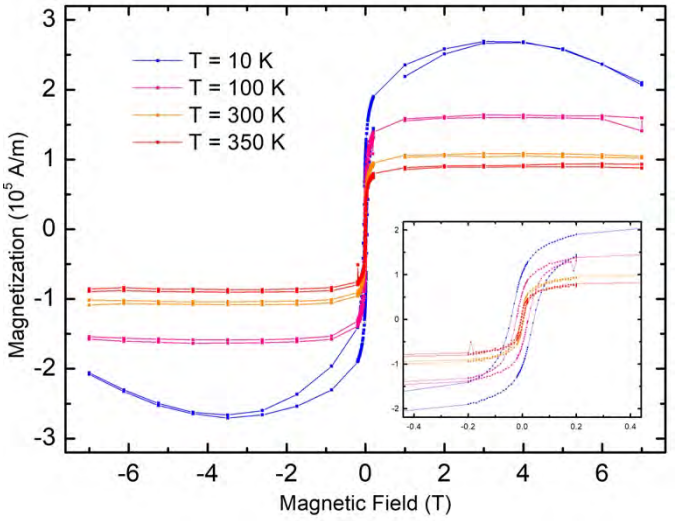


Fig. 1. Field-dependent M in SMO

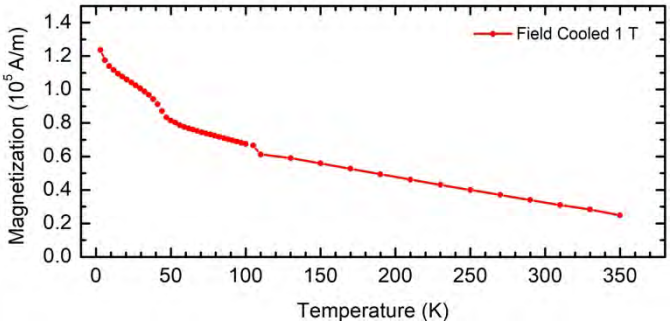


Fig. 2. M-T drop above 110 K, corroborates with Fig. 1.

DC-03. Interplay of Localized Shear Strain and Non-Collinear Easy Axes in Voltage Driven Magnetic Multilayers

S. Lindemann[1], J. E. Shoup[2], T. Hanashima[3], A. J. Grutter[1], P. P. Balakrishnan[1], E. Jeong[1], A. Friedland[1], E. Welp[1], A. Caruana[4], C. Kinane[4], T. Charlton[5], D. B. Gopman[2], P. Gehring[1], J. Borchers[1]

[1]NCNR, National Institute of Standards and Technology, Gaithersburg, Maryland, United States, [2]MSE, National Institute of Standards and Technology, Gaithersburg, Maryland, United States, [3]Neutron Science and Technology Center, CROSS, Tokai, Ibaraki, Japan, [4]ISIS Neutron and Muon Source, STFC Rutherford Appleton Laboratory, Didcot, United Kingdom, [5]Neutron Sciences Division, Oak Ridge National Laboratory, Oak Ridge, Tennessee, United States

Strain mediated magnetoelectric (ME) coupling in ferroelectric (FE) and ferromagnetic (FM) heterostructures provides an exciting path towards the development of low-power memory storage and sensing technologies [1-4]. Recent theoretical work suggests that using a ferroelectric layer to drive non collinear magnetic easy axes in opposite directions can maximize resistance changes in magnetic tunnel junctions via a single voltage step [5], which would enable a simple binary architecture. To translate this concept into scalable device fabrication, we investigated conventional all metallic Co/Ru multilayers sputtered onto the giant piezoelectric (1-x)$Pb(Mg_{1/3}Nb_{2/3})O_3$-(x)$PbTiO_3$ (PMN-xPT) as the FE layer. By utilizing a magnetic field during growth (Figure 1a), we successfully induced the required noncollinear magnetic anisotropy (Figure 1b). However, depth sensitive Polarized Neutron Reflectometry (PNR) measurements show that under voltage induced applied strain, the magnetic moments rotated in the same sense contrary to the anticipated opposite sense predicted by theory (shown in Figure 1c). We identify local shear strains within individual ferroelectric domains as the mechanism inhibiting the predicted divergent rotation of the two Co layers. Rather than a fundamental failure of the model, these results clarify how micro scale shear strains can affect strain mediated coupling between PMN xPT and FM multilayers, laying the necessary groundwork for designing improved prototype geometries capable of fully validating theoretical predictions and realizing low energy ME memory devices.

[1] J.M. Hu, L.Q. Chen, and C.W. Nan, Adv. Mater., Vol. 28, p.15-39 (2016)
[2] Z. Chu, M.J. PourhosseiniAsl, and S. Dong, J. Phys. D. Appl. Phys., Vol. 51, p. 243001 (2018)
[3] S. Lindemann, J. Irwin, et. al., Sci. Adv., Vol. 7, p. eabh2294 (2021)
[4] J.M. Hu, Z. Li, et. al., Nat. Comm., Vol. 2, p. 553 (2011)
[5] J.J. Wang, T.N. Yang, et. al., Adv. Theory, Vol. 4, p. 2000215 (2021)

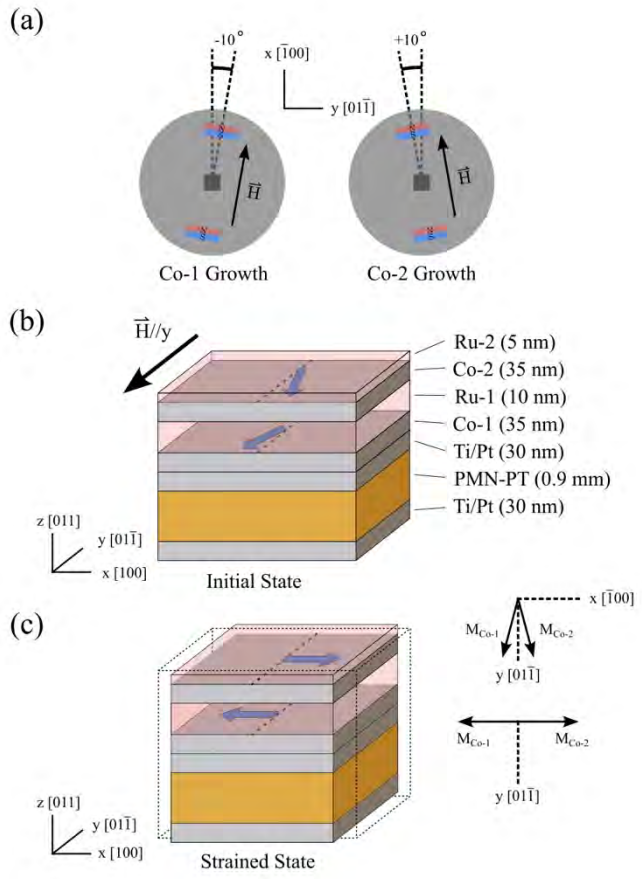


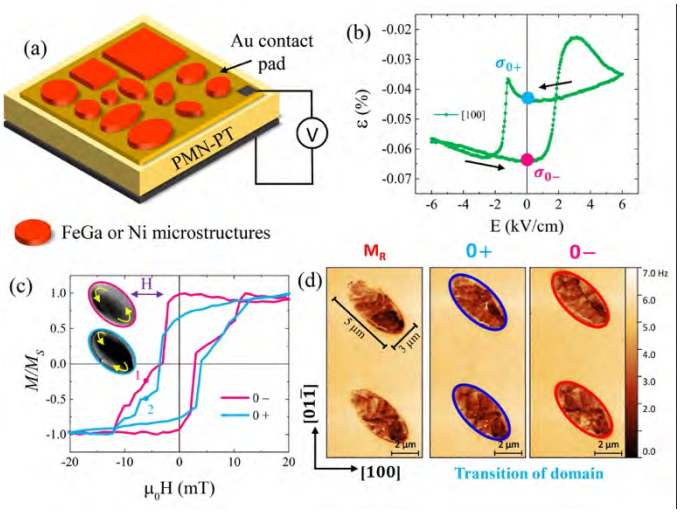
Figure 1: a) Conceptual schematic of magnet arrangement supplying magnetic fields during growth of individual Co layers in the Co/Ru multilayer stack. b) Induced non collinearity between Co layers leads to an initial state magnetic configuration with moments on either side of the y[01-1] principal strain direction of the PMN-PT substrate. c) According to theory, voltage-generated strains should cause opposite-sense rotation of magnetic moments.

DC-04. All-electrical strain-driven control of magnetization in FeGa microstructures on PMN-PT

G. Pradhan[1], F. Celegato[1], A. Magni[1], G. Barrera[1], M. Coisson[1], P. Rizzi[2], P. Tiberto[1]
[1]Advance Materials and Life sciences, INRIM, Torino, Italy,
[2]Department of Chemistry, Università di Torino, Torino, Italy

The recent era of information technology and devices largely focusses on energy saving and cost efficiency. Manipulation of magnetic state of a micro element solely with the use of electric fields has attracted new attention in recent years due to its potential ability to be used in low-power magneto-electronics [1,2]. In the context, artificial magnetoelectric (ME) materials are suitable candidates to be used in these technologies due to its coupling between magnetization and electric-field induced strain, which therefore consumes less power and significantly reduces heat losses [3]. The application of voltage across the piezoelectric layer generates strain at the interface and this strain transfer to a soft magnetic layer from the piezoelectric layer induces change in magnetic anisotropy and domain structures [4,5]. We have investigated the properties of FeGa microstructures fabricated on PMN-PT (Figure 1a) using E-beam lithography under application of electric field across the piezoelectric layer. Due to the [011] crystallographic orientation of PMN-PT, the in-plane strains are anisotropic resulting in a significant difference in remnant strain values, as marked by the blue and pink dots in Fig. 1b. The magnetic hysteresis curves of elliptical disks (5 x 3 μm 2) were recorded using MOKE as represented by the 0− and 0+ states in Fig. 1c (remanent strain states at zero electric field after polarization switching). A difference in the shape of the hysteresis is observed which marks the rotation of magnetic anisotropy in the system (vortex state in 0− state and S-shaped multidomain in 0+ state). Further, electrical pulses were applied to the elliptical disks without any magnetic history where an application of positive and negative pulses modifies the magnetic domains as shown in Fig. 1d.

[1] M. Gajek, et al. Nature materials 6.4 296 (2007)
[2] N. A. Spaldin and R. Rames, Nature materials 18.3 203 (2019)
[3] R. Lo Conte, et al. Nano letters 18.3 1952 (2018)
[4] G. Pradhan, et al. J. Physics: Materials 7.1 015016 (2024)
[5] G. Pradhan, et al. Adv. Electronic Materials (2025): e00558



Schematic of FeGa/PMN-PT heterostructure for voltage application. (b) Effective strain measured in PMN-PT. (c) Magnetic hysteresis and domains structures recorded at remanent strain states. (d) Magnetic states at remanent polarization states.

DC-05. Tuning magnetoelectric effect controlled by magnetic anisotropy in ferromagnetic-piezoelectric heterostructure

P. Finkel, P. Mion, M. Staruch
US Naval Research Laboratory, Washington DC, District of Columbia, United States

The scarcity of single-phase materials with scalable magnetoelectric (ME) coupling necessitates the development of artificial multiferroic heterostructures, where strain-coupling between distinct phases enables giant ME effects. An effective alternative lies in artificial multiferroic heterostructures and composites, where distinct electric and magnetic responses arise from separate phases intricately strain-coupled across an interface. These strain-engineered systems present a promising avenue for achieving giant and tunable ME coupling by leveraging mechanical strain as a mediator between electric polarization and magnetization. In this work, we demonstrate efficient electrical control of magnetism in an FeCo/Ag multilayer thin film deposited on a [011]-poled 001 poled $(Pb(In_{1/2}Nb_{1/2})O_3$-$Pb(Mg_{1/3}Nb_{2/3})O_3$-$PbTiO_3$ (PIN-PMN-PT) relaxor ferroelectric single crystal. By driving the crystal through a ferroelectric-ferroelectric phase transition near the morphotropic phase boundary, we achieve an immense piezoelectric coefficient of ~10,000 pm/V [1]. The highly anisotropic strain, generated by the electrically induced

phase switching from rhombohedral to orthorhombic, is efficiently transferred to the magnetoelastic film. This results in giant magnetoelastic coupling, where the magnetic anisotropy of the film aligns with the substrate's principal strain direction to maximize the converse magnetoelectric effect [2]. Consequently, we report a record-breaking converse magnetoelectric coefficient of ~2.5 x 10^{-5} s/m, the highest value reported for this class of heterostructure. The controllable and repeatable nature of this inter-ferroelectric phase transition makes this approach highly promising for the next generation of energy-efficient spintronics, low-power memory, and high-sensitivity magnetic sensors.

1. Finkel, et al "Phase switching at low field and large sustainable strain output in domain engineered ferroic crystals". *Phys. Status Solidi* 209, 2108–2113 (2012).
2. Garten et al "Enhancing Converse Magnetoelectric Coupling Through Strain Engineering in Artificial Multiferroic Heterostructures". *ACS Appl. Mater. Interfaces* 2022, 14, 25701–2570

DC-06. High-Temperature Anomalous Hall and Magnetoresistance Effects Induced by Spin Fluctuations in the Metallic Delafossite Triangular-Lattice Antiferromagnet $PdCrO_2$

Y. Tao[1], P. Jain[1], Y. Zhang[1], F. Tutt[1], A. Paul[1], D. Phelan[2], C. Balz[3], S. Hatt[4], J. Neuefeind[3], S. Rosenkranz[2], B. Frandsen[4], T. Birol[1], C. Leighton[1]
[1]Chemical Engineering and Materials Science, University of Minnesota, Minneapolis, Minnesota, United States, [2]Materials Science Division, Argonne National Laboratory, Lemont, Illinois, United States, [3]Neutron Scattering Division, Oak Ridge National Laboratory, Oak Ridge, Tennessee, United States, [4]Physics and Astronomy, Brigham Young University, Provo, Utah, United States

Metallic delafossites (*e.g.*, $PdCoO_2$ and $PdCrO_2$) exhibit the highest conductivities among all oxide materials, providing a unique platform to explore the interplay between charge, spin, and lattice degrees of freedom [1, 2]. In the case of $PdCrO_2$, ultraclean metallic transport in the Pd layers coexists with triangular-lattice antiferromagnetism in the Mott-insulating CrO_2 octahedra, with geometric frustration giving rise to a complex, noncollinear spin structure below T_N = 38 K. A particularly striking feature of $PdCrO_2$ is a large anomalous Hall effect (AHE), which has been reported to persist even above T_N, although its microscopic origin remains unresolved. Here, using record-quality single crystals grown by a chemical vapor transport method, we demonstrate that the AHE in $PdCrO_2$ extends far beyond T_N, reaching temperatures up to ~250 K (*i.e.*, seven times T_N), deep in the paramagnetic phase [3]. This behavior is accompanied by a large positive magnetoresistance (MR) exceeding 2000% (Fig. 1) and a pronounced *c*-axis negative thermal expansion (NTE) of up to -5 ppm/K, the largest reported among delafossites [4]. For the first time, we directly probe magnetic order and fluctuations in $PdCrO_2$ using elastic and inelastic neutron scattering, along with magnetic pair distribution function analysis. These measurements reveal a broad temperature regime of strong spin fluctuations that emerge at the same temperature scale (~250 K) as the above-T_N AHE, MR, and NTE, with a correlation length that asymptotes at a single triangular Cr plaquette (Fig. 2). Our results show that spin fluctuations alone stabilize the anomalous magnetotransport and NTE in $PdCrO_2$, while the AHE provides strong evidence for skew scattering arising from short-range chiral spin fluctuations, as predicted theoretically.

*Work supported primarily by the US DOE through the University of Minnesota Center for Quantum Materials.
[1] Y. Zhang, *et al.*, *Phys. Rev. Mater.* 6, 115004 (2022)
[2] Y. Zhang, *et al.*, *Nat. Commun.* 15, 1399 (2024)
[3] Y. Tao, *et al.*, *Proc. Nat. Acad. Sci.* 122, e2524774122 (2025)
[4] Y. Tao, *et al.*, unpublished (2026)

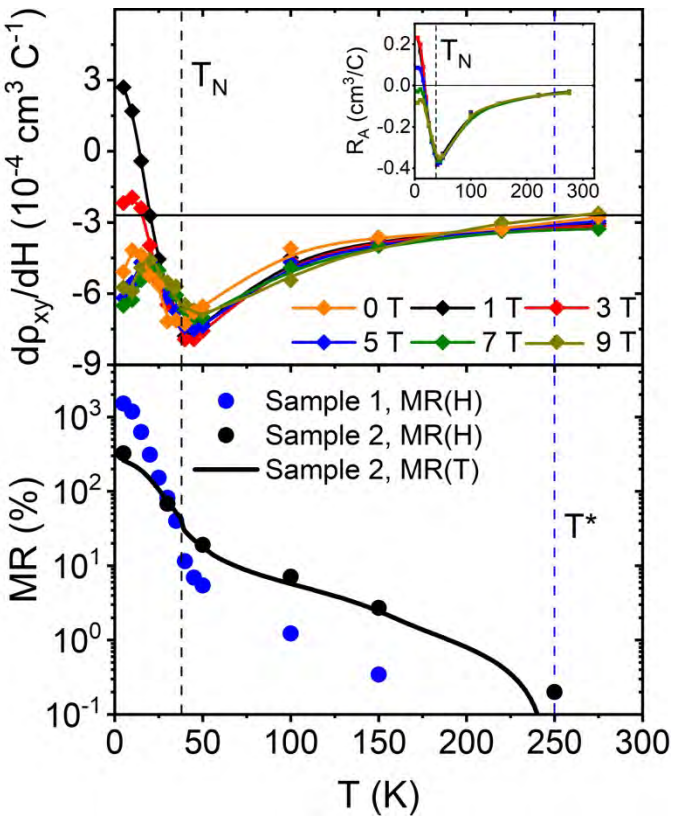


Fig. 1. Temperature (T) dependence of (a) the magnetic field (H) derivative of the Hall resistivity (ρ_{xy}), the anomalous Hall coefficient (R_A, inset) and (b) the 9-T MR of $PdCrO_2$.

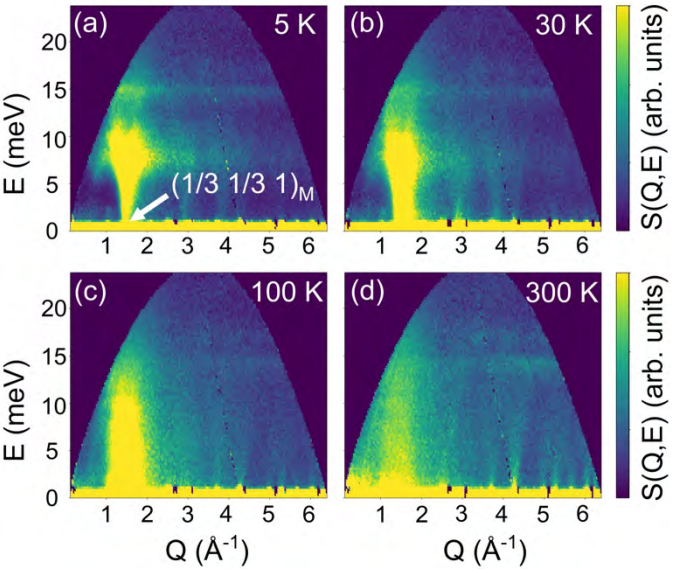


Fig. 2. Neutron dynamic structure factor $S(Q,E)$ *vs.* momentum transfer (Q) and energy transfer (E) at (a) 5 K, (b) 30 K, (c) 100 K, and (d) 300 K for $PdCrO_2$.

DC-07. Unusual metamagnetism studied with ^{57}Fe Mössbauer spectroscopy in $BaRFeO_4$ multiferroics

L. Kubickova[1, 2], T. Kmjec[1], M. Rozprym[1], M. Veverka[1], D. Kubániová[1, 2], V. Chlan[1], C. Kadlec[2], F. Kadlec[2], J. Kohout[1]
[1]Faculty of Mathematics and Physics, Charles University, Prague, Czechia, [2]FZU – Institute of Physics of the Czech Academy of Sciences, Prague, Czechia

The orthorhombic ferrites $BaRFeO_4$ (R = rare-earth ion) provide a model system for studying low-dimensional magnetism, geometric frustration, and anisotropic superexchange interactions. These phenomena arise from the interplay of spin–orbit coupling, crystal electric fields of R^{3+} ions, and competing Fe-3d and R-4f magnetic interactions, leading to rich magnetic phase diagrams and spin-driven ferroelectricity. Employing ^{57}Fe Mössbauer spectroscopy as a sensitive local probe, supported by magnetic measurements, neutron data, and THz spectroscopy, we investigate compounds with R = Y, Er, Ho, Gd, and Yb, including their field-induced metamagnetic behavior. In $BaYFeO_4$, non-magnetic Y^{3+} ions lead to a series of successive magnetic transitions originating from competing interactions between Fe ions, from a spin-density wave (SDW) antiferromagnetic (AFM) order below ~50 K to an AFM cycloid state below ~35 K [1]. In contrast, magnetic R3+ ions provide additional exchange pathways that significantly modify the phase diagram – while magnetic ordering of the Fe sublattice remains at ~50 K, lower-temperature transitions involve the R ions as well (see Fig. 1, 2). Using the different in-field responses of $BaErFeO_4$ and $BaHoFeO_4$ as examples, we highlight the crucial role of magnetic anisotropy of the R ions in governing the magnetic properties of these frustrated antiferromagnets [2], [3]. Moreover, the observed field-induced metamagnetic phase transitions are associated with the R sublattice, being of spin-flip and both spin-flip and spin-flop nature in $BaErFeO_4$ and $BaHoFeO_4$, respectively. Due to strong magnetoelectric coupling and tunable magnetic properties, these materials are promising for multifunctional devices such as energy-efficient memory, sensors, and spintronic components.

[1] D. P. Kozlenko, N.T. Dang, R.P. Madhogaria, et al., Phys. Rev. Mat., vol. 5, art. no. 044407 (2021).
[2] N.T. Dang, D.P. Kozlenko, T.P. Hoang, et al., Phys. Rev. B, vol. 112, no. 5, art. no. 054437 (2025).
[3] N. T. Dang, T. P. Hoang, V. Chlan, T, et al., Phys. Rev. B, under review.

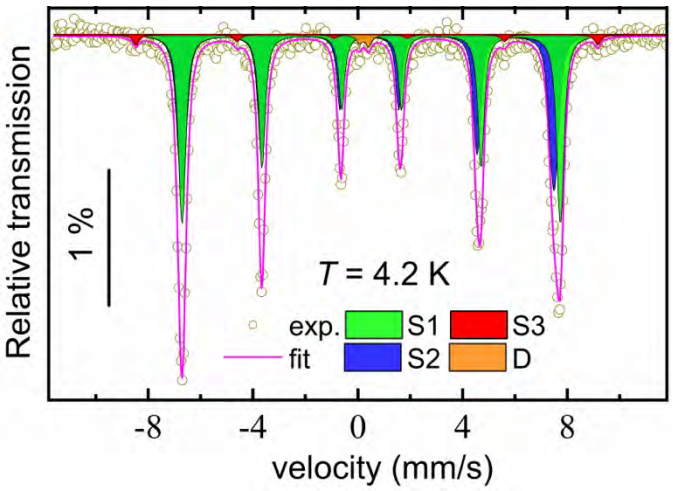


Fig. 1. ^{57}Fe Mössbauer spectrum of $BaErFeO_4$ at 4.2 K, where Fe moments have a collinear AFM configuration, while the Er sublattice adopts a noncollinear arrangement. (S1 – Fe^{3+} ions in octahedra, S2 – Fe^{3+} ions in square pyramidal sites, S3 – $ErFeO_3$ impurity, D4 – Fe in Al foil)

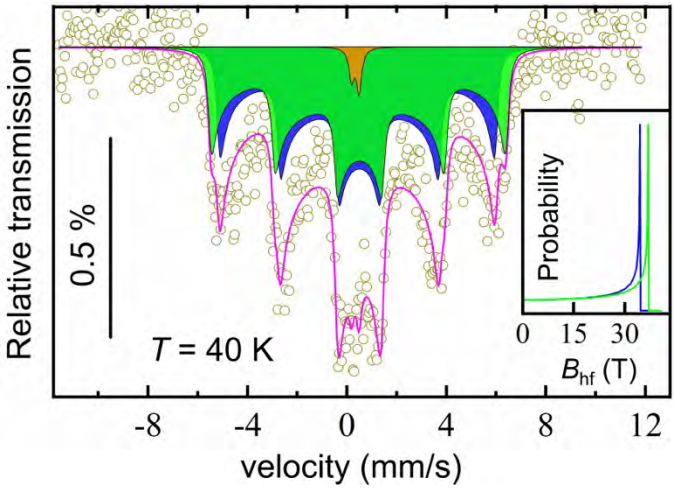


Fig. 2. ^{57}Fe Mössbauer spectrum of $BaErFeO_4$ at 40 K, showing the incommensurate collinear SDW order of the Fe sublattice (hyperfine field distribution in the inset).

DC-08. All-Nitride Magneto-Ionics: From Phase Reconfiguration to Anomalous Hall Transport

Z. Chen[1], C. Jensen[1, 2], Z. Zeng[1], C. Liu[3], Y. Liu[1], N. Naushin[4], G. Leigh[1], C. Kinane[5], A. Caruana[5], J. Herz[1, 6], A. Liu[1], G. Yin[1], Y. Ijiri[7], R. Kukreja[4], A. J. Grutter[2], J. Borchers[2], X. Zhang[3], K. Liu[1]
[1]Physics Department, Georgetown University, Washington, District of Columbia, United States, [2]NIST Center for Neutron Research, National Institute of Standards and Technology, Gaithersburg, Maryland, United States, [3]King Abdullah University of Science & Technology, Thuwal, Saudi Arabia, [4]Department of Materials Science and Engineering, University of California, Davis, Davis, California, United States, [5]STFC Rutherford Appleton Laboratory, ISIS Neutron Facility, Didcot, United Kingdom, [6]Department of Physics, College of William & Mary, Williamsburg, Virginia, United States, [7]Department of Physics and Astronomy, Oberlin College, Oberlin, Ohio, United States

The escalating energy demands of the information technology sector necessitate the development of innovative spintronic materials and control mechanisms. Magneto-ionics, the control of magnetism through ionic motion, has emerged as an energy-efficient pathway for spintronic applications. In particular, nitrogen-based magneto-ionics offer advantages of faster ionic motion and improved reversibility.[1, 2] Here, we introduce an all-nitride magneto-ionic platform composed entirely of manganese nitrides. We demonstrate that the magnetic orders and magneto-transport signals can be effectively modulated through nitrogen ionic motion. This all-nitride system is fabricated via a unique ionically driven synthesis method which utilizes the spontaneous formation of ferrimagnetic Mn_4N where pure Mn is sputtered on top of a Mn_3N_2 seed layer at elevated temperatures.[3] Furthermore, the nitrogen level in this system can be systematically controlled via reactive sputtering pressure, thermal annealing, and voltage-induced nitrogen migration. The variation of nitrogen content can induce a reversible phase transformation between ferrimagnetic Mn_4N and antiferromagnetic Mn_2N, enabling tunable exchange bias and saturation magnetization.[4]

Building on this foundation, we further demonstrate the ionic control of the anomalous Hall effect (AHE) in this all-nitride system. We show that cobalt (Co) incorporation can enable the tuning of the room temperature (RT) magnetic compensation point (MCP) in ferrimagnetic $Mn_{4-x}Co_xN$. Near the MCP, a giant exchange bias of 1.5 T at 5 K is found in this all-ferrimagnetic system. Besides, nitrogen modulation during deposition and post-deposition thermal treatment

enables switching of the AHE signs, allowing post-deposition control of the RT MCP. Furthermore, nickel (Ni) incorporation allowed for the realization of noncollinear antiferromagnetic Mn_3NiN within the same platform. Mn_3NiN exhibits a prominent AHE below the Néel temperature (T_N) despite having negligible net magnetization. The temperature dependence of AHE also reveals the presence and transformation of non-collinear Γ^{4g} and Γ^{5g} spin configurations. Notably, both T_N and the Γ^{4g} / Γ^{5g} transition temperature can be tuned by varying nitrogen content in the all-nitride system. These results establish a versatile all-nitride magneto-ionic system with tunable magnetic orders, exchange bias, magnetic compensation, and noncollinear antiferromagnetism.

This work has been supported in part by the NSF (ECCS-2151809, ECCS-2429995, DMR-2005108, DMR-1828420) and AFOSR (FA9550-23-1-0497).

[1] J. de Rojas et al, Nat. Commun. 11, 5871 (2020)
[2] C. J. Jensen et al, ACS Nano, 17, 6745 (2023)
[3] Z. Chen et al, Appl. Phys. Lett. 123, 082403 (2023)
[4] Z. Chen et al, ACS Nano, 19, 20072 (2025)

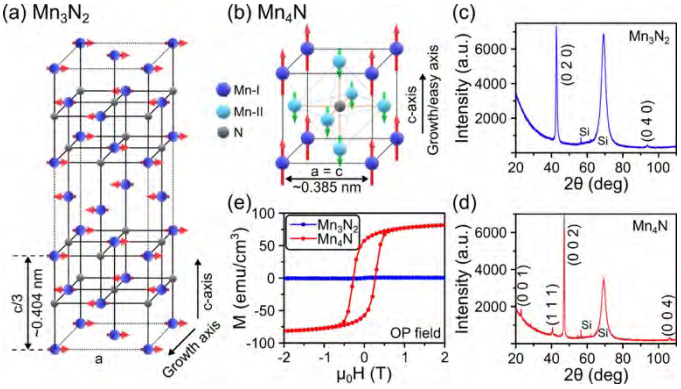


Fig. 1. Crystal structures of (a) Mn_3N_2 and (b) Mn_4N. XRD of the (c) Mn_3N_2 seed layer and (d) Mn_4N film after depositing Mn onto Mn_3N_2. (e) Hysteresis loops for Mn_3N_2 and Mn_4N films.

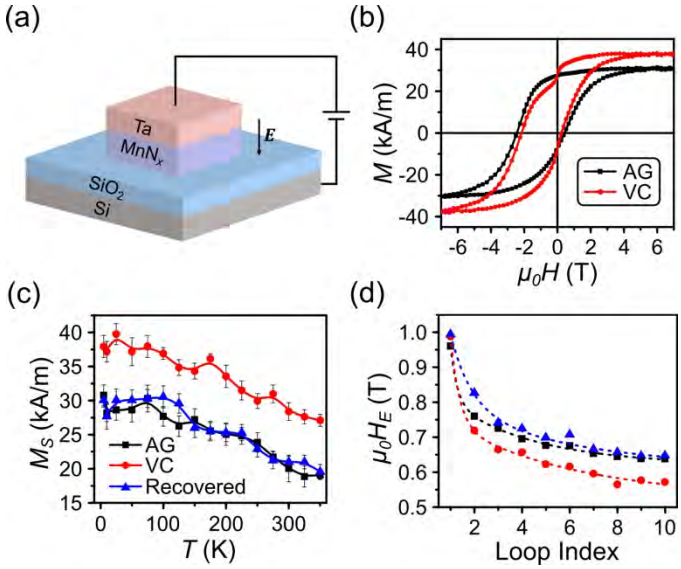


Fig. 2. (a) Schematics showing a voltage bias device with the sample layer structure. (b) Hysteresis of the sample before (AG) and after (VC) voltage bias. (c) Temperature dependence of M_s and training effect of the sample in AG, VC, and recovered states.

DC-10. Interlayer Kondo Effect and Spin Glass Freezing in the Ultraconductive Metallic Delafossite $PdCo_{1-x}Cr_xO_2$

P. Jain[1], F. Tutt[1], Y. Zhang[1], Y. Tao[1], S. Sharma[2], I. Khayr[2], M. Greven[2], C. Leighton[1]
[1]*Chemical Engineering and Materials Science, University of Minnesota Twin Cities, Minneapolis, Minnesota, United States,* [2]*School of Physics and Astronomy, University of Minnesota Twin Cities, Minneapolis, Minnesota, United States*

Metallic delafossites (*e.g.*, $PdCoO_2$, $PdCrO_2$) are under intense study due to their ultraclean metallic transport, involving electronic mean-free-paths >20 μm. Our recent work established chemical vapor transport (CVT) growth of high-quality single-crystal $PdCoO_2$ and $PdCrO_2$, elucidating the sublattice purification mechanism underlying their extraordinary low-temperature (T) conductivity [1], their optical hyperbolicity [2], and the spin-fluctuation-induced high-T anomalous Hall effect in antiferromagnetic $PdCrO_2$ [3]. Here, we study CVT crystals of $PdCo_{1-x}Cr_xO_2$ up to $x \leqslant 0.05$, introducing dilute Cr moments into ultrahigh conductive $PdCoO_2$ host. Structural/chemical characterization supports single-phase, single crystals with uniform Cr substitution. Magnetometry at $T > 2$ K confirms weakly interacting paramagnetism, scaling as expected with T and field (H). Below 2 K, however, clear spin glass freezing

is evidenced in AC susceptibility and specific heat (Fig. 1(a)) measurements down to 50 mK. The spin glass peak in specific heat is suppressed with *H*, as expected (Fig. 1(a)), eventually generating a Schottky anomaly from which the deduced Zeeman splitting gives $g \approx 2.95$ (Fig. 1(b)). Low-*T* transport measurements reveal a weak increase in residual resistivity with Cr substitution, confirming the sublattice purification mechanism [1]. Most interestingly, Kondo effects arise in the low-*T* resistivity, evolving from a simple Kondo minimum to a more complex *T* dependence due to spin glass freezing, the extracted Kondo temperature being ~45 K (Fig. 2). This is the first direct observation of Kondo effects in metallic delafossites, which must arise from indirect, interlayer Kondo interactions between Cr moments in insulating (Co/Cr)-O_6 octahedral layers and itinerant electrons in Pd planes, mediated by O ions.

*Work supported by US DOE through the University of Minnesota Center for Quantum Materials.

[1] Y. Zhang, F. Tutt, *et.al., Nat. Commun.*, 15, 1399 (2024).
[2] S. Macis, A. D'Arco, *et.al., Adv. Funct. Mater.*, 25, 2512820 (2025).
[3] Y. Tao, P. Jain, *et.al., Proc. Nat. Acad. Sci.*, 122, e2524774122 (2025).

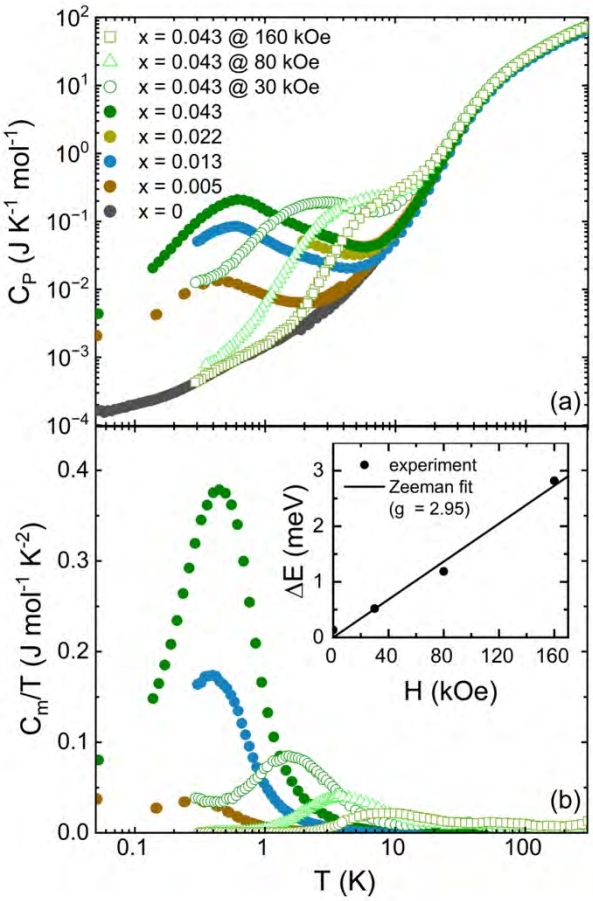


Fig. 1: *T* dependence of specific heat, C_P (a) and magnetic specific heat, C_m/T (b), for $PdCo_{1-x}Cr_xO_2$ single crystals at different *H*. Inset: Zeeman splitting from Schottky anomaly fitting *vs. H*.

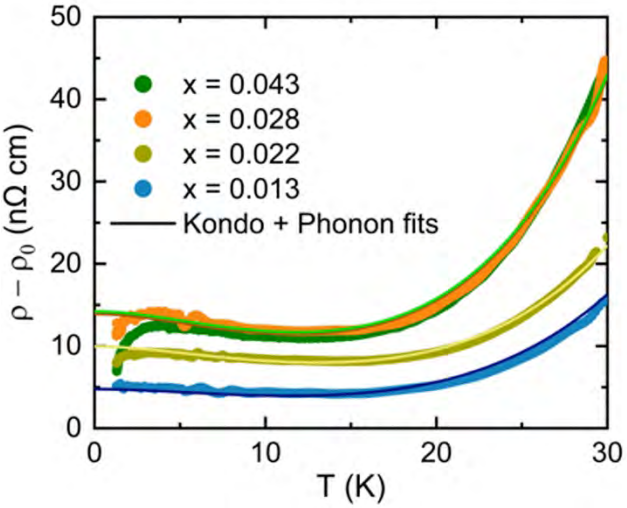


Fig. 2: *T* dependence of ($\rho - \rho_0$), the residual-subtracted resistivity for $PdCo_{1-x}Cr_xO_2$ single crystals, along with Kondo + Phonon fits.

DC-11. Deterministic Control of Nanomagnetic Spiral Trajectories using an Electric Field

S. Moody[1], M. Littlehales[2], D. Mayoh[3], D. Alba Venero[4], G. Balakrishnan[3], P. Hatton[5], J. S. White[1]

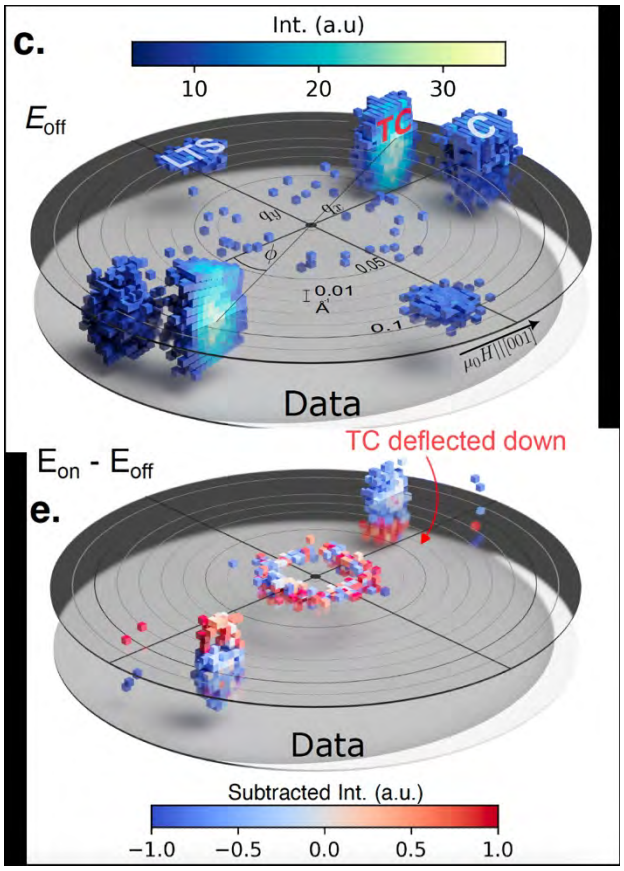
[1]Laboratory for Neutron Scattering, Paul Scherrer Institute, Villigen, Aargau, Switzerland, [2]Physik-Department, Technische Universität München, Garching, Bavaria, Germany, [3]Physics Department, University of Warwick, Coventry, England, United Kingdom, [4]ISIS Neutron and Muon Source, Didcot, United Kingdom, [5]Physics Department, Durham University, Durham, England, United Kingdom

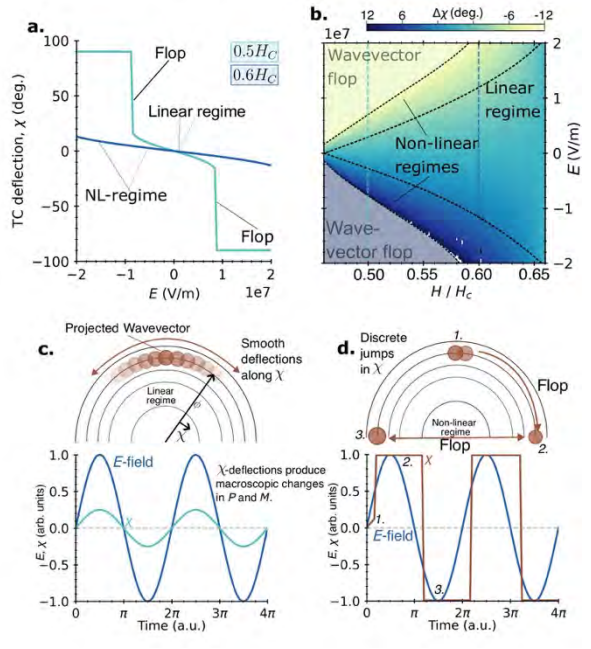
We report a deterministic control of chiral magnetic spiral textures via electric field actuation in the magnetoelectric insulator Cu2OSeO3. Using small-angle neutron scattering, we directly track the evolution of the spiral propagation vector under combined electric and magnetic fields and demonstrate that the spiral direction can be continuously and reversibly steered in a controlled manner. Depending on the magnitude of the applied magnetic field, one can tune the system to exhibit discretized domain switching or a smooth deflection of the spiral wavevector, enabling trajectory-like control of the magnetic structure in reciprocal space.

This behaviour arises from the coupling between the electric polarization and the non-collinear spin texture, which modifies the magnetic free-energy landscape and introduces a directional bias on the spiral orientation. We identify distinct regimes of response, including a linear deflection at low fields and deviations from linearity at higher fields, indicating a customizable magnetoelectric coupling. The observed behaviour suggests an important role of higher-order or anisotropic interactions in stabilising and tuning the spiral state.

Our results demonstrate a pathway toward continuous, low-energy control of magnetic textures without requiring changes in temperature or magnetic field magnitude. This establishes electric-field-driven steering as a viable mechanism for manipulating topological and chiral spin structures, with potential relevance for future spintronic devices based on reconfigurable magnetic states. More broadly, these findings highlight the importance of magnetoelectric coupling in non-centrosymmetric magnets and provide an experimental framework for exploring controlled deformation of long-wavelength magnetic order.

S. H. Moody, M. T. Littlehales, D. A. Mayoh, G. Balakrishnan, D. Alba Venero, P. D. Hatton and J. S. White, *Nature Communications*, Vol. 16, Article No. 5269 (2025).





SESSION DD: SOFT MAGNETIC MATERIALS I

Co-Chair(s): S. Okamoto, *Tohoku University, Sendai, Miyagi, Japan* and J. Jeong, *New-Functionality Powder Materials Research Center, Korea Institute of Materials Science, Changwon, Korea (the Republic of)*

Wednesday, November 4, 2026

02:00 PM-05:30 PM

Coral 2

DD-01. Reduction of high-frequency core loss in nanocrystalline soft magnetic materials by grain boundary engineering

K. Suzuki[1, 2]

[1]Department of Materials Science and Engineering, Monash University, Clayton, Victoria, Australia, [2]Institute of Multidisciplinary Research for Advanced Materials, Tohoku University, Sendai, Miyagi, Japan

Two well-known factors for realizing excellent soft magnetic properties are low magnetocrystalline anisotropy (K_1) and low saturation magnetostriction (λ_s). In nanocrystalline alloys, the former is governed by the mean grain size while the latter reflects the volume-weighted average of the local values in the crystalline and grain-boundary amorphous phases (λ_s^{cr} and λ_s^{am}). Our recent study suggests that λ_s strongly influences dynamic loss and that a low $\lambda_s \sim 10^{-7}$ is ideally required for low core loss at high frequencies [1]. Although community efforts to enhance the saturation polarization (J_s) of nanocrystalline alloys have resulted in high J_s values around 1.8-1.9 T, their λ_s is typically as high as 10^{-5} [2]. Consequently, their high-frequency loss is considerably higher than that of near-zero magnetostrictive alloys such as nc-Fe-Si-B-Nb-Cu (FINEMET) with J_s = 1.2 T [3]. The large λ_s in high-J_s alloys is primarily due to the large λ_s^{am} which scales quadratically with the local J_s of the grain-boundary amorphous phase. Thus, λ_s can be suppressed though a slight sacrificial reduction of the local J_s by modification of grain-boundary chemistry. As a result, $\lambda_s \sim 10^{-7}$ is realized for the grain-boundary engineered Fe-B based nanocrystalline alloys with J_s around 1.6 T and a high initial permeability of 20,000 at 100 kHz. This high-frequency permeability is comparable to that of commercial Co-based amorphous and nc-Fe-Si-B-Nb-Cu alloys [3]. In this talk, the effect of λ_s on core loss is first outlined, followed by the predicted relationship between J_s and λ_s in nanocrystalline alloys. Finally, examples of grain-boundary modification and resulting high-frequency core properties are presented.

[1] H. Huang, H. Tsukahara, A. Kato, K. Ono and K. Suzuki, *Phys. Rev. B* 109, 104408 (2024).
[2] K. Suzuki, *J. Magn. Magn. Mater.* 592, 171677 (2024).
[3] Proterial Ltd., *Nanocrystalline soft magnetic material FINEMET*, Catalogue Number PR-EM07, p. 6 (2023).

DD-02. Powder-sintered Fe-Co-X soft magnetic alloys for high-torque-density motor cores in robotic applications

Y. Cho, K. Jang, J. Jeong

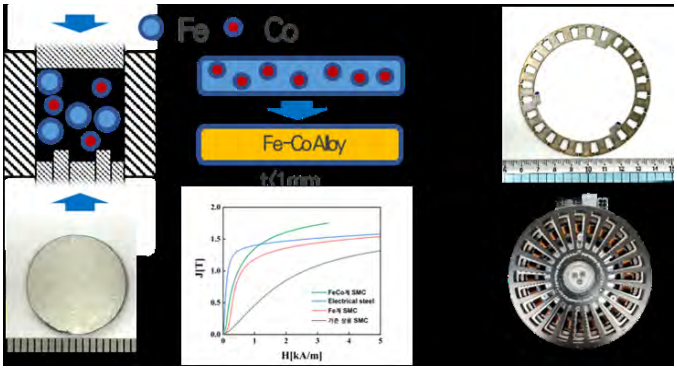
Korea Institute of Materials Science, Changwon, Korea (the Republic of)

The demand for compact and lightweight motors with high torque density is rapidly increasing for advanced robotic systems, including humanoid robots. Conventional Fe–Si electrical steels have been widely used as motor core materials owing to their excellent soft magnetic properties and mature manufacturing processes. However, their saturation magnetization is limited to approximately 2 T, which restricts further improvement in torque density when applied to high-performance motor cores.

Among soft magnetic alloys, Fe–Co alloys exhibit the highest saturation magnetization. In particular, Fe–Co alloys containing approximately 35–50% Co can achieve a high saturation magnetization of up to 2.4 T. Recently, Fe–Co–V electrical steel sheets have been commercialized, and attempts have been made to apply them to high-torque-density motors for robotic applications. Nevertheless, conventional rolled Fe–Co-based sheets require the addition of vanadium to overcome the poor formability of Fe–Co alloys. In addition, the high Co content and complex rolling-based manufacturing process lead to high material and processing costs. Furthermore, when Fe–Co sheets are used for motor core fabrication, significant material loss occurs during the punching process, resulting in a substantial increase in the total material cost for motor production.

In this study, we propose a powder metallurgy-based approach for fabricating Fe–Co alloy motor cores as an alternative to conventional rolled sheet processing. This approach is expected to reduce manufacturing cost, minimize material loss through near-net-shape forming, and enable the design of novel alloy compositions by incorporating various alloying elements followed by sintering. Here, we present a new alloy design and processing strategy for Fe–Co-based soft magnetic materials fabricated by powder metallurgy, together with a case study demonstrating the realization of actual motor core components. The proposed process offers a promising

route toward high-performance motor cores with high saturation magnetization, reduced material waste, and improved manufacturability.



DD-03. Tailoring Permalloy's Complex Permeability Response Through Laser Powder Bed Fusion

N. Ayers[2], H. Baldino[2], D. Hedlund[1], P. Kulik[2, 1], Y. Sohn[2]
[1]Department of Electrical and Computer Engineering, University of Central Florida, Orlando, Florida, United States, [2]Department of Materials Science and Engineering, University of Central Florida, Orlando, Florida, United States

Fabricating complex magnetic shielding components from Permalloy, 79 wt. % Ni- 16 wt. % Fe- 5 wt. % Mo, remains challenging as the material properties are highly sensitive to processing history [1] and conventional manufacturing routes impose constraints on achievable geometries. Laser powder bed fusion (LPBF) offers a pathway to complex macro- and microstructures in materials, including Permalloy [2,3]. This work investigates the printability of Permalloy and how defects influence its complex permeability response. At low scan speeds, <600 mm/s, the samples developed keyhole defects while at high scan speed, >1400 mm/s, lack-of-fusion flaws emerged. Near-fully dense material (99.65%) was achieved at 200 W and 900 mm/s, with minor solidification cracking persisting across all conditions. The complex permeability was measured in the XY plane of the build, which is normal to the fiber texture that develops during LPBF [4]. Among the conditions evaluated, 900 mm/s yielded the highest real permeability (μ'), while 2200 mm/s exhibited the lowest core losses (μ"). Interestingly the keyhole regime did not show the same low loss behavior as the lack of fusion regime, suggesting that defect morphology, not density alone, governs magnetic losses. A transition in fiber texture from (100) to (110) was observed as the scan speed increased above 900 mm/s. The texture change is a result from the formation of two-dimensional defects, rather than retaining energy as microstrain along different crystallographic growth directions. These results demonstrate that the complex permeability of LPBF Permalloy can be modulated through scan parameter selection, with direct correlations to evolving microstructure and crystallographic texture.

[1] C. Li, H. Ruan and D. Chen, *Microscopy Research and Technique*., Vol. 81, p.796 (2018)
[2] H. Li, S. Thomas and C. Hutchinson, *Acta Materialia*., Vol. 226, p.117637 (2022)
[3] B. Li, W. Fu and H. Xu, *Journal of Magnetism and Magnetic Materials*., Vol. 494, p.165754 (2020)
[4] A. E. A. Mohamed, J. Zou and R. S. Sheridan, *Additive Manufacturing*., Vol. 32, p.101079 (2020)

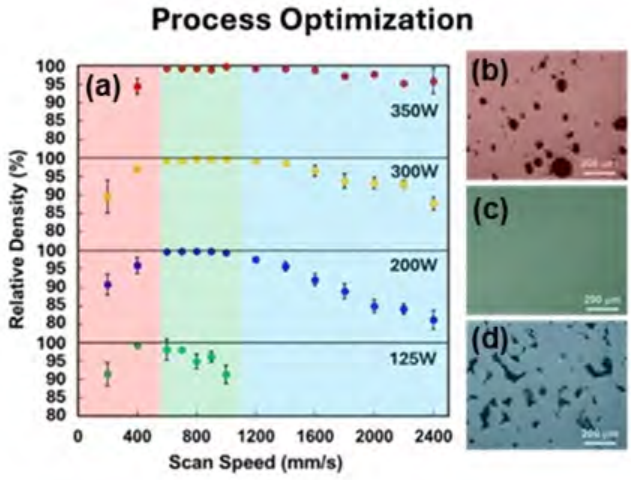


Fig 1. Relative density of AM permalloy as a function of laser power and laser scan speed. Keyhole pores (b) develop at excessively slow scan speeds, solidification cracking (c) was present throughout, and lack-of-fusion flaws (d) were observed at high scan speeds.

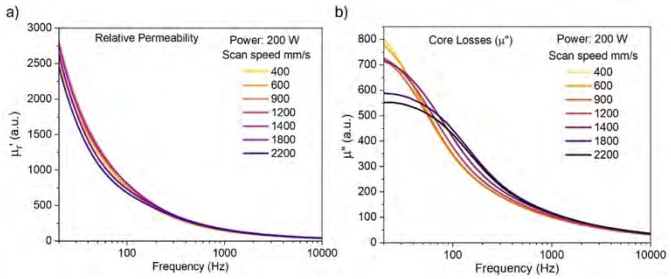


Fig 2. The relative permeability, μ', (a) and core losses, μ", (b) with increasing A/C frequency for as-printed permalloy samples created with a 200W laser power and increasing laser scan speed from 400mm/s to 2200 mm/s.

DD-04. Investigation of the resonance behavior in irreversible permeability spectrum of Fe-based nanocrystalline alloys

Y. Tomita
Corporate R&D Center, Daido Steel Co., Ltd., Nagoya, Aichi, Japan

Along with the increase in the driving frequency of power electronic devices, the development of soft magnetic materials with lower iron loss and higher permeability at high frequencies is becoming increasingly important. Understanding the mechanisms underlying such AC magnetic properties is therefore of great significance for the development of next−generation soft magnetic materials. Although many studies have focused on iron loss from a practical standpoint, research specifically addressing the permeability spectrum remains limited. In this context, the present study investigates the complex permeability spectrum—particularly the irreversible components—and establishes a quantitative formulation.

The complex permeability spectra of a transverse−field−annealed Fe−based nanocrystalline core were measured using an impedance analyzer. The irreversible permeability was calculated using the procedure proposed by Beatrice et al.[1]. The obtained spectra were then analyzed on the complex plane. Fig. 1 shows the irreversible permeability of the TFA nanocrystalline core, which exhibits a resonance−like behavior with a negative real part around 20 kHz. To explore a quantitative description of the irreversible permeability spectrum μ_irr, we applied the mapping f : z →z^(−1/2) to the measured μ_irr. As shown in Fig.2, the locus on the complex plane before the mapping corresponds to a limaçon−type curve, and that the permeability can be expressed by the following formula.

μ_irr = μ_irr, DC / {1+(iωτ)^ε}^2 (1)

The calculated irreversible permeability using Eq. (1) with parameters μ_DC, irr = 120, τ = 10.6 μs, and ε = 0.75 is plotted in Fig. 1 together with the experimental data. The calculated values show good agreement with the experimental results in the frequency range from 5 kHz to 50 kHz.

This quantitative formulation provides a new physical insight into the irreversible magnetic dynamics of nanocrystalline materials at high frequencies.

1) C. Beatrice, et al., J. Magn. Magn. Mater., Vol.429, p.129 (2017)

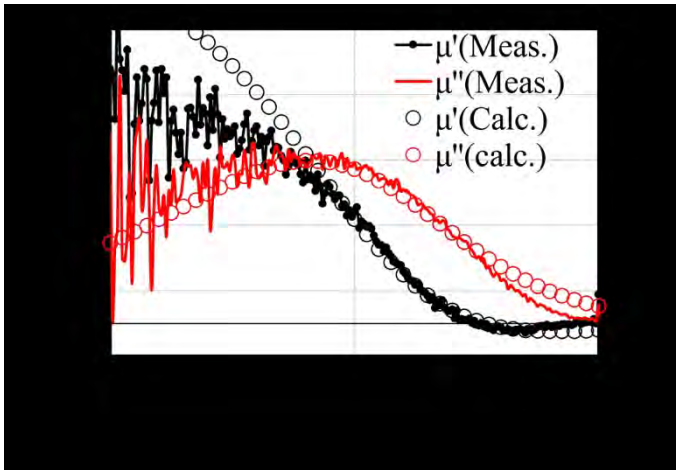


Fig.1 Measured and calculated values of the irreversible permeability spectra

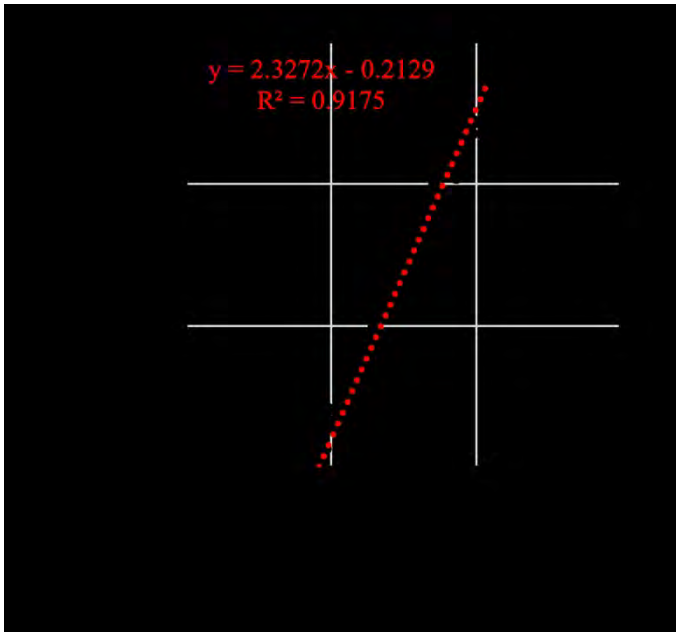


Fig.2 The locus of the irreversible permeability after the mapping f : z → z ^(-1/2)

DD-05. Micromagnetic modelling of quasi-static domain wall pinning and eddy current losses in magnetically soft high frequency metal-ferrite nanocomposites

S. Mullurkara[1], Z. Wang[1], P. Ohodnicki[1], T. Schrefl[2]
[1]University of Pittsburgh, Pittsburgh, Pennsylvania, United States, [2]University for Continuing Education Krems Center for Modelling and Simulation, Neustadt, Viktor Kaplan Straße 2 - Bauteil E, Austria

Increased demand for electrical power necessitates new soft magnetic materials development. Mn-Zn and Ni-Zn ferrites are excellent for frequencies approaching and within the MHz range, but suffer from low saturation flux densities limiting high power applications in small form factors at frequencies <100kHz. Recent investigations show embedding soft magnetic metallic particles in a ferrite matrix can enable flux densities beyond ferrites while retaining high effective resistivities to mitigate eddy current losses. However, nanocomposite losses require elucidation under quasi-static and high frequency switching due to additional loss mechanisms not present in ferrites, including intraparticle eddy currents and domain wall pinning by metallic nanoparticles. The current work explores simulation-based methods to understand and control these additional loss sources.

First, modelling of domain wall pinning is carried out via micromagnetics using OOMMF. Dependence on particle/matrix properties and particle size/morphology are discussed. Potential for attractive or repulsive pinning behavior are identified and correlated to relevant energy contributions of demagnetization, exchange, and magnetocrystalline anisotropy. For eddy current modelling, spatial magnetization is first calculated by mumax and inputted into the COMSOL Maxwell equation solver to derive induced eddy current losses. Unit geometry size is based on achievable metal particle size and volume ratio of metal to ferrite phase. Through micromagnetic modelling calculation and finite element (FE) analysis, exchange coupling between phases and internal fields are considered, leading to eddy current loss estimates of nanocomposites. In both cases, comparisons are made to simplified analytical models to understand degree of quantitative agreement and the additional physics accessible through micromagnetics and FE theoretical methods, and guidance is provided to micro-/nanostructural engineering in metal / ferrite nanocomposites.

[1] Suraj Mullurkara, Susheng Tan, Chris Bracken, Lauren Wewer, Dipika Mandal, Paul Ohodnicki, Novel soft magnetic metal-ferrite nanostructured ceramic matrix composites (NCMCs) with enhanced saturation magnetization, Journal of Alloys and Compounds, Volume 1037, 2025, 182487, 2025.
[2] A. Talaat, M.V. Suraj, K. Byerly, A. Wang, Y. Wang, J.K. Lee, P.R. Ohodnicki, Review on soft magnetic metal and inorganic oxide nanocomposites for power applications, Journal of Alloys and Compounds, Volume 870, 2021.

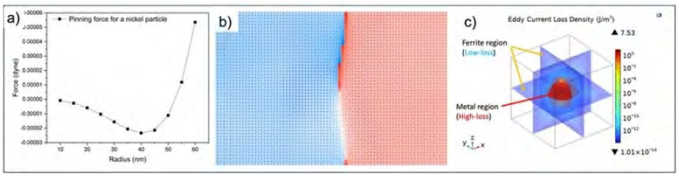


Figure 1: a) Analytical pinning force of metallic nickel particle in NiZn-spinel ferrite. b) OOMMF image of domain wall pinning simulations. c) Spatial eddy current loss distribution of metal-ferrite nanocomposite with mumax and Comsol.

DD-06. Microstructure and Permeability of Fe-deficient Ni-Cu-Zn Ferrites

C. Priese, J. Töpfer
Ernst-Abbe-Hochschule Jena, Jena, Germany

Multilayer inductors use Fe-deficient Ni-Cu-Zn ferrites as soft magnetic materials. The fabrication of multilayer inductors involves cofiring stacked ferrite layers prepared by tape casting, as well as printed Ag/Pd coil patterns, at temperatures ranging from 900°C to 1000°C. The initial permeability of the ferrites depends heavily on the ceramic microstructure. Theoretical concepts based on spin rotation and domain wall motion mechanisms consider grain size to be the most important parameter. However, few experimental studies on the correlation between ferrite grain size and permeability have been reported in the literature, and no consensus has been reached on a theoretical description.
We studied the densification, microstructure evolution, and permeability of Fe-deficient Ni-Cu-Zn ferrite with composition $Ni_{0.30}Cu_{0.20}Zn_{0.52}Fe_{1.98}O_{3.99}$. The samples were sintered at temperatures ranging from 900°C to 1150°C for various hold times. The variation of grain size and density with temperature and dwell time was analyzed. XRD and EDX analysis revealed an increase in the ferrite lattice parameter, a reduction in ferrite phase content, and the formation of a copper oxide secondary phase at grain boundaries as the temperature increased. After sintering at 900°C – 1000°C, the Fe-deficient ferrite decomposes into a

stoichiometric ferrite that coexists with a minority CuO phase. At Ts ⩾ 1050°C, the CuO transforms into Cu_2O and exaggerated grain growth is observed. The permeability of the ferrites increases with sintering temperature up to a maximum permeability of μ = 580 at Ts = 1000°C. At higher sintering temperatures, permeability decreases due to the formation of a microstructure with intra-crystalline porosity in large grains, as well as the presence of a non-magnetic Cu oxide grain boundary phase. We discuss the observed variation in permeability in relation to the ferrites' microstructure. We analyze the dependency of permeability on grain size using the non-magnetic grain boundary model. The formation of intra-crystalline porosity in larger grains and of non-magnetic Cu oxide grain boundary phases with different compositions are key factors that determine the permeability of Ni-Cu-Zn ferrites.

DD-07. High Permittivity Garnet Ferrite for LTCC Circulators

M. Legay[1], R. Lebourgeois[3], R. Mansour[3], D. Caban-Chastas[1], Q. Todoli[1], V. Laur[2]
[1]Thales DMS, Elancourt, France, [2]LAB-STICC, Brest, France, [3]Thales Research and Technology, Palaiseau, France

A circulator is a non-reciprocal passive device housing a ferrite disk magnetized to saturation by a magnet. However, one drawback is its complex manufacturing process because it involves several processes (machining, gluing) which makes the component expensive and difficult to integrate into antenna systems. For this reason, manufacturing the device using the Low Temperature Co-fired Ceramics (LTCC) process is a promising alternative that can significantly reduce manufacturing time and cost.[1]

The objective of this work was to develop a LTCC circulator in the X-band. In this frequency range, the ferrites used are garnets based on $Y_3Fe_5O_{12}$ (YIG : M_s=1800G and permittivity ε=15). Increasing ε could lead to a decrease of the component size. Bismuth, which partially replaces yttrium, is known to increase ε, but it increases lattice parameter so decreases M_s. This reduction was compensated by the incorporation of tin ions in place of iron in octahedral sites. Moreover, copper (with bismuth) has made it possible to lower the sintering temperature from 1500 to 920°C making the ferrite compatible with an LTCC process [2]. Finally, calcium ions were added to improve structural charge balance and stabilize the lattice. The final substituted ferrite ($Y_{2.25-x}Cu_{0.05}Bi_{0.7}Ca_xFe_{5-x}Sn_xO_{12}$) has a permittivity of 21 while retaining magnetic properties similar to those of pure YIG.

To evaluate the new material advantages, we compared microstrip Y-junction circulators fabricated using a high permittivity garnet (ε=21) or a pure YIG ferrite (ε=15). Simulations, performed using Ansys HFSS software, showed that a higher ε reduces the component's surface area by 23%. A demonstrator was manufactured by co-firing at 920°C a ferrite disk, synthesized via a conventional ceramic process, embedded in a high-permittivity dielectric substrate with screen-printed silver conductors. The prototype showed promising results consistent with simulations. The circulator exhibits a 37% bandwidth (isolation >15dB) over which insertion losses with a minimum value of 0.6dB at 8,4GHz (Fig.1). This prototype paves the way for the development of low-cost, compact non-reciprocal devices operating at high frequencies.

[1] T. Jensen, V. Krozer, and C. Kjærgaard, "Realisation of microstrip junction circulator using LTCC technology," *Electron. Lett. (*2011)
[2] R.Lebourgeois, G.Cibien , "Yttrium Iron Garnet , microwave omponent including said ferrite and processes for manufacturing said ferrite and said component" , Patent of Invention, Publication number : EP2622613 (2011)

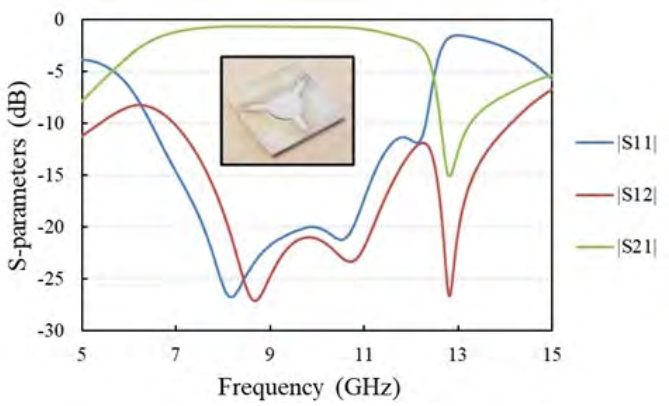


Fig.1 S-parameters of the LTCC circulator

DD-08. High-frequency iron loss and magnetization dynamics of amorphous and nanocrystalline ribbons with various magnetostriction

N. Ono[1], T. Ogasawara[2], S. Hiramoto[1], H. Tsukahara[1], T. Taniguchi[1], K. Suzuki[3], S. Okamoto[1, 4]

[1]Institute of Multidisciplinary Research for Advanced Materials, Tohoku University, Sendai, Miyagi, Japan, [2]National Institute of Advanced Industrial Science and Technology, Tsukuba, Ibaraki, Japan, [3]Department of Materials Science and Engineering, Monash University, Clayton, Victoria, Australia, [4]National Institute for Materials Science, Tsukuba, Japan

In recent years, the development of low iron loss magnetic cores operating in the high-frequency region has become essential for advancing next-generation power electronics. In our previous work, we found that irreversible and reversible magnetization processes were the dominant loss mechanisms for lower and higher frequency regions, respectively [1]. However, the detailed loss mechanisms in each process have not yet been fully clarified. In this study, the effect of dynamic domain structures on iron loss was investigated in ribbon samples with various magnetostriction constants λ_s.

The ring-shaped samples prepared from amorphous ($Fe_{80}Si_9B_{11}$) and nanocrystalline ($Fe_{80}Nb_6B_{14}$, $Fe_{85}Nb_6B_9$ and $(Fe_{0.8}Co_{0.2})_{86}B_{14}$) ribbons were investigated; these alloys were well characterized elsewhere [2].

Figure 1 shows the broadband iron loss W for various λ_s samples. The loss was decomposed into the reversible and irreversible process components (W_{rev} and W_{irr}) following the model in ref. 3. For large λ_s samples, W_{irr} increases significantly in a frequency range of 1-100 kHz. Figure 2 shows dynamic domain structures observed by time-resolved vector MOKE microscopy [4]. For the large λ_s sample, large magnetic domains were generated, and domain wall displacement was the main magnetization process. With increasing frequency, the migratory distance of the domain wall became smaller, indicating that the main process changed to coherent rotation. In contrast, fine domains are seen for the low λ_s sample, and the wall displacement appears limited, indicating that the coherent rotation becomes dominant from a lower frequency region. These results indicate that the increase in W_{irr} associated with λ_s is caused by different dynamics in magnetic domain structures. A detailed discussion, including the effects of eddy currents, will be provided in the presentation.

[1] N. Ono et al., J. Magn. Magn. Mater. Vol. 603, p.172222 (2024)
[2] H. Huang et al., Phys. Rev. B, Vol. 109, p.104408 (2024)
[3] C. Beatrice et al., J. Magn. Magn. Mater. Vol. 429, p.129 (2017)
[4] T. Ogasawara, Jpn. J. Appl. Phys. Vol. 56, p.108002 (2017)

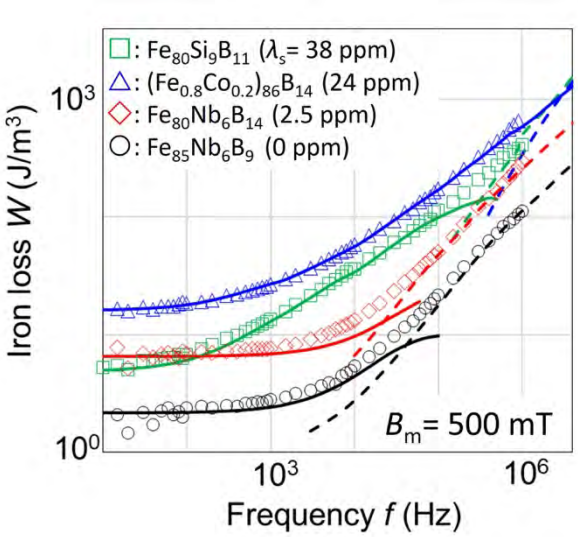


Fig. 1: The broadband iron loss of various λ_s samples. Solid and broken lines are the evaluated W_{irr} and W_{rev}, respectively.

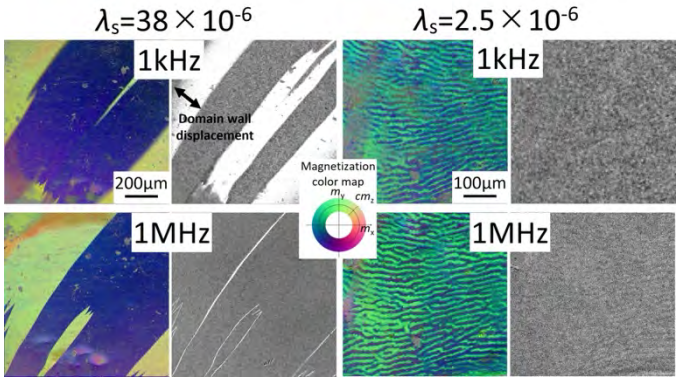
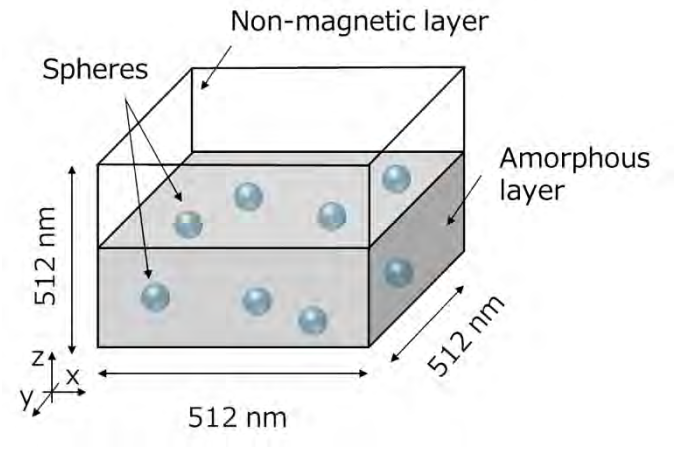


Fig. 2: Dynamic domain structure of different λ_s samples. The white area in grayscale images corresponds to the wall displacement with B_m = ±500 mT.

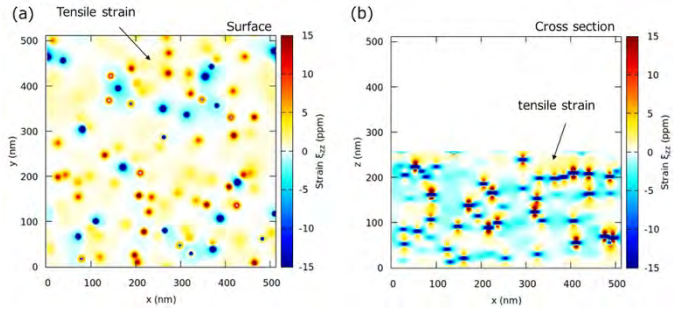
DD-09. Modeling of stress due to crystallization to clarify origin of fin magnetic domain structure in soft magnetic materials

H. Tsukahara[1, 2], N. Ono[1], K. Suzuki[3], A. Kato[4], K. Ono[2], T. Taniguchi[1], S. Okamoto[1, 4]
[1]Tohoku University, Sendai, Japan, [2]Osaka University, Oska, Japan, [3]Monash University, Melbourne, Victoria, Australia, [4]NIMS, Tsukuba, Japan

Soft magnetic materials are essential for various electrical devices, such as power inductors and motors for electric vehicles. The soft magnetic materials generate energy losses which degrade the performance of the devices. In the high-frequency range of around kHz, the energy loss due to the domain wall damping, which is known as excess loss, is dominant. Hence, it is crucial to control the excess loss. More recently, it was reported that fine magnetic domains appear in amorphous alloys in their early stage of crystallization, and the excess loss was found to be suppressed effectively [1]. It is suggested that the origin of the fine magnetic domain structure is perpendicular magnetic anisotropy (PMA). However, the mechanism of PMA remains unclear.
We constructed models of amorphous ribbons at the early stage of crystallization, focusing on local volume contractions due to crystallization, to clarify the strain distribution in these materials. Figure 1 shows the schematic illustration of our model. The model is constructed by the magnetic amorphous and non-magnetic layers, and spherical regions were randomly placed in the magnetic amorphous layer. In spherical regions, we applied the hydrostatic pressure of 100MPa to shrink the volume, considering crystallization. The simulations were performed by the supercomputing system MASAMUME-II, and we used our own code [2].
Figure 2 shows the calculated strain distribution inside the amorphous ribbons at the early stage of crystallization. According to our simulation, the tensile strain tends to appear near the surface, regardless of the random placement of the crystalline regions. Since the amorphous material usually has positive magnetostriction constant, this tensile strain causes PMA. In the presentation, we will introduce the details of the simulation method and the simulation results of the thermal demagnetization state obtained by this model.
[1] R. Gautam, et al., Nature Communication 16, 8022 (2025).
[2] H. Tsukahara, et al., NPG Asia Materials 14, 44 (2022).



The schematic illustration of the model of the low crystallization soft magnetic ribbon. The hydrostatic pressure is applied in the sphere region.



The strain distribution in the low crystallize soft magnetic model. The colour represents the strain along out-of-plane direction.

DD-10. Effect of Hot Rolling Condition on Texture Evolution and Magnetic Properties in 3.4 wt% Si Non-Oriented Electrical Steel

D. Kim
POSCO, Pohang, Korea (the Republic of)

Non-oriented electrical steel containing more than 3 wt.% Si remains in the ferrite single-phase region throughout processing and does not undergo phase transformation-induced recrystallization. As a result, texture evolution is primarily governed by dynamic recrystallization during hot rolling. In this study, the effects of hot-rolling conditions on dynamic recrystallization behavior, texture evolution, and final magnetic properties were systematically investigated. High-temperature compression tests were conducted to evaluate flow-stress behavior as a function of deformation

temperature and strain rate. A higher softening ratio was observed at lnZ > 33, indicating that dynamic recrystallization was promoted under lower-temperature and higher-strain-rate conditions. Based on these findings, hot rolling was performed under different rolling temperatures and thickness reductions to induce variations in dynamic recrystallization behavior. Lower rolling temperatures and higher reductions increased the fraction of dynamically recrystallized grains.
EBSD analysis revealed that the dynamically recrystallized grains exhibited increased fractions of Copper and Brass components. In the hot-rolled sheets, the α-fiber fraction increased whereas the γ-fiber fraction decreased. After identical hot-band annealing, cold rolling, and final annealing, the final grain size remained nearly unchanged regardless of hot-rolling condition. However, the γ-fiber fraction in the final annealed sheets decreased by approximately 3-4% under the lower-temperature and higher-reduction condition.
This reduction in the magnetically unfavorable γ-fiber led to improved magnetic properties. Core loss decreased by 3.4%, and coercivity was also reduced. Loss separation analysis showed that the reduction in hysteresis loss was the primary contributor to the lower total core loss. Although the improvement in B50 was limited, magnetic flux density in the low-field region was clearly enhanced. These results demonstrate that optimization of hot-rolling conditions is an effective strategy for improving the performance of non-oriented electrical steel for high-frequency traction motor applications.

DD-11. Advances in Minnealloy Fabrication, Characterization, and Modeling

A. S. Padgett[1], S. R. Bishop[1], C. R. Riley[1], J. D. Boissiere[1], A. R. Marotta[1], D. Bosomtwi[1], S. Percival[1], P. F. Weck[1], E. Gokce-Polat[2], J. Wang[2], W. Echtenkamp[2]
[1]Sandia National Laboratories, Albuquerque, New Mexico, United States, [2]University of Minnesota, Minneapolis, Minnesota, United States

Soft ferromagnetic materials, necessary for transformers and inductors, are increasingly threatened by supply chain risks to critical materials, with electrical steel, in particular, considered near critical in the medium term [1]. Minnealloy, a body-centered tetragonal iron alloy with nitrogen and carbon alternately located at interstitial sites, α"-Fe_{16}(N,C), is a new, low-coercivity ferromagnet with a saturation magnetization ⩾ 2.47 T [2,3,4,5]. Minnealloy provides a critical materials free alternative to standard and grain oriented electrical steel for distribution transformer cores; with improved engineering of nano-crystalline grain structure, it may be a competitor with amorphous materials for high-power, high-efficiency cores up to 100 MHz [6]. This talk addresses recent progress made in the fabrication and characterization of Minnealloy, including process optimization and scaling of powder fabrication routes, melt-spinning, electrodeposition, nitriding and carburization [7]. We will discuss new results for frequency dependent B-H loops, magnetic permeability, and specific heat. We will compare our experimental results with predictions made via density functional theory. Finally, we will consider possible paths for improving phase purity and reducing magnetic coercivity.
Sandia National Laboratories is a multimission laboratory managed and operated by National Technology & Engineering Solutions of Sandia, LLC, a wholly owned subsidiary of Honeywell International Inc., for the U.S. Department of Energy's National Nuclear Security Administration under contract DE-NA0003525.
[1] D. J. Bauer, R. T. Nguyen, and B.J. Smith, "Critical Materials Assessment," U.S. Department of Energy, DOE/EE-2756 (2023)
[2] M. D. Mehedi, Y. Jiang, P. K. Suri, D. J. Flannigan, *J. Phys. D: Appl. Phys.*, vol. 50, no. 37 (2017)
[3] X. Zhang and J-P Wang, Appl. Phys. Lett., vol. 114, iss. 15 (2019)
[4] G. Guo, J. Liu, and JP Wang, TMS 2020 149th Supplemental Proceedings, p. 1841 (2020)
[5] J. Zhu, and J-P Wang, AIP Adv., vol. 14, iss. 1, pp. 015031 (2024)
[6] E. A. Theisen, IEEE Transactions on Magnetics, vol. 58, no. 8, p. 1-7 (2022)
[7] W. Echtenkamp, A. S. Padgett, S. R. Bishop, *AIP Adv.*, vol. 15, iss. 3, p. 035008 (2025)

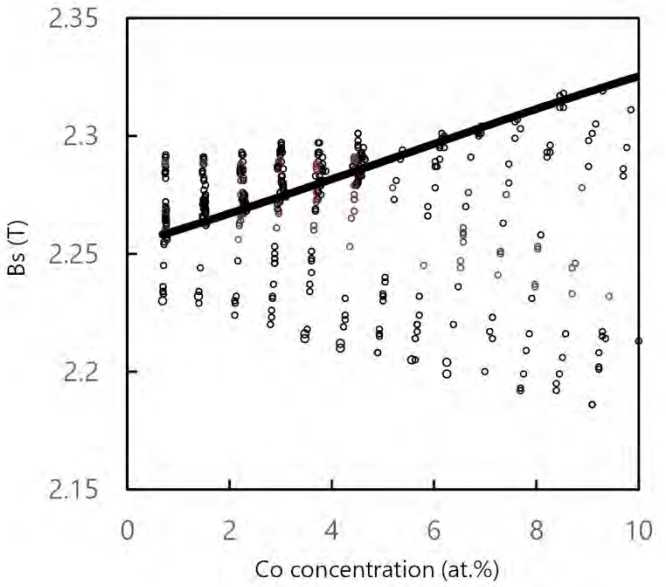
DD-12. Electronic Origin of Enhanced Saturation Magnetic Flux Density in Nitrogen-Deficient $(Fe_{1-y}Co_y)_{16}N_x$

Y. Asari[1], T. Tabata[1], S. Terada[1], M. Enoki[2], T. Ogawa[3]
[1]Hitachi, Hitachi, Ibaraki, Japan, [2]Shimane University, Matsue, Shimane, Japan, [3]Tohoku University, Sendai, Miyagi, Japan

The α" phase of $Fe_{16}N_2$ has attracted considerable attention as a nitride expected to exhibit a high saturation magnetic flux density (Bs)[1]. First-principles calculations based on the GGA predicted that the magnetization of $Fe_{16}N_2$ is higher than that of α-Fe[2], and the that was also demonstrated experimentally in single-phase $Fe_{16}N_2$[3]. However, nitrogen incorporation simultaneously causes lattice expansion, and

consequently, the predicted Bs became comparable to that of α-Fe. We previously discovered that nitrogen vacancies in $Fe_{16}N_2$ enhance Bs[4]. Electronic structure analysis revealed that the enhancement originates from an increase in the number of iron atoms not bonded to nitrogen. Nevertheless, this vacancy-containing structure is not the most stable configuration, and annealing was shown to induce phase separation into α-Fe and fully ordered $Fe_{16}N_2$. In the previous work, we reported that $(Fe_{1-y}Co_y)_{16}N_2$ does not improve Bs[5]. This behavior is attributed to the reduction in magnetization caused by Co-N bonding. Moreover, Co and N are mutually repulsive, rendering the formation of $(Fe_{1-y}Co_y)_{16}N_2$ thermodynamically unfavorable. Consequently, a stable nitride exhibiting enhanced Bs had not been realized. In this study, to enhance the Bs of nitrides, we investigate $(Fe_{1-y}Co_y)_{16}N_x$ with intentionally introduced nitrogen vacancies and theoretically demonstrate that it exhibits a Bs exceeding that of Fe-Co alloys, as shown in Fig. 1. We found that the enhanced magnetization originates from metal atoms that are not bonded to nitrogen. Moreover, the Co concentration is found to be a key parameter, and avoiding direct contact between Co and N contributes significantly to the structural stability. This research is partially based on results obtained from Green Innovation Fund Projects / Next-generation Motor Development (JPNP21026) commissioned by the New Energy and Industrial Technology Development Organization (NEDO).

[1] Y. Sugita, et al., J. Appl. Phys., Vol. 70, p. 5977 (1991).
[2] Y. Asari, et al., 2023 INTERMAG Short Papers, Sendai, Japan, 2023, pp. 1-2.
[3] T. Ogawa, et al., Appl. Phys. Express, Vol. 6, 073007 (2013).
[4] Y. Asari, et al., submitted.
[5] Y. Asari, et al., MMM2025, BD-02 (2025).



Saturation magnetization flux density of nitrogen deficient $(Fe_{1-y}Coy)_{16}N_x$. The values of Fe-Co alloy and nitrides are shown by line and cricles, respectively.

DD-13. Development of Co-Fe-Si-B microwires doped by Ni and Mo with rectangular hysteresis loops and high GMI effect

M. Salaheldeen[1, 2], V. Zhukova[1, 3, 4], P. A. Rodríguez Jiménez[1, 3], A. Zhukov[3, 4, 5]

[1]Department of Polymers and Advanced Materials,, University of the Basque Country, EHU,, San Sebastian, Spain, [2]Physics Department, Faculty of Science,, Sohag University, Sohag, Egypt, [3]Department of Applied Physics , EIG,, University of the Basque Country, EHU, San Sebastian, Spain, [4]EHU Quantum Center, University of the Basque Country, EHU, San Sebastian, Spain, [5]IKERBASQUE, Basque Foundation for Science, Bilbao, Spain

The so-called Taylor-Ulitovsky technique allows the preparation of the magnetic wires with unique combination of soft magnetic properties (giant magnetoimpedance, GMI, effect or magnetic bistability), excellent mechanical properties and corrosion resistance observed with the widest diameters ranging from 0.1 μm to 100 μm g [1-3]. The presence of a thin and flexible glass coating allows for increased corrosion resistance, expanding the potential areas of applications [2-3]. Ni or Mo doping allows more precise tailoring of the magnetostriction coefficient, λs, and improvement of the thermal stability of the amorphous microwires [4].

We studied the influence of annealing on the magnetic properties and GMI effect of $Co_{68.7}Fe_4Si_{11}B_{13}Ni_1Mo_{2.3}$ glass-coated microwires. Upon annealing, a remarkable

transformation in the hysteresis loop shape is observed: from inclined to almost perfectly rectangular (see Fig.1). Simultaneously, a significant enhancement in the GMI ratio, ΔZ/Z, is achieved, increasing from an initial ΔZ/Z ~370% to 470% under optimal annealing conditions (Fig.2a). This enhancement is accompanied by a significant modification in the magnetic field, *H*, dependence of the GMI ratio (ΔZ/Z), characterized by a shift of the GMI peaks to lower magnetic fields. Observed hysteresis loop change is associated to a change in the magnetization reversal mechanism from magnetization rotation towards single DW propagation in the inner axially magnetized single domain. Direct measurements confirm this, revealing fast and uniform DW propagation with velocities, v, up to 850 m/s in samples annealed at 350 °C(Fig.2b). The observed changes in magnetic properties are interpreted considering internal stress relaxation, which promotes a substantial change in the domain structure of studied microwire. Concluding, an appropriate annealing allows obtaining microwires with a unique combination of high GMI effect and fast single DW propagation.

[1] M.H. Phan, H.X. Peng, Progr. Mater. Sci. 53 (2008) 323–420.
[2] H Chiriac, T.A. Óvári, Progr. Mater. Sci. 40 (5) (1996) 333-407.
[3] A. Zhukov, et al.,J. Phys. D: Appl. Phys. 55 (2022) 253003
[4] W.Q. Yu, H.Q. Zeng, Y.M. Sun, Z. Hua, Vacuum 137 (2017) 175–182

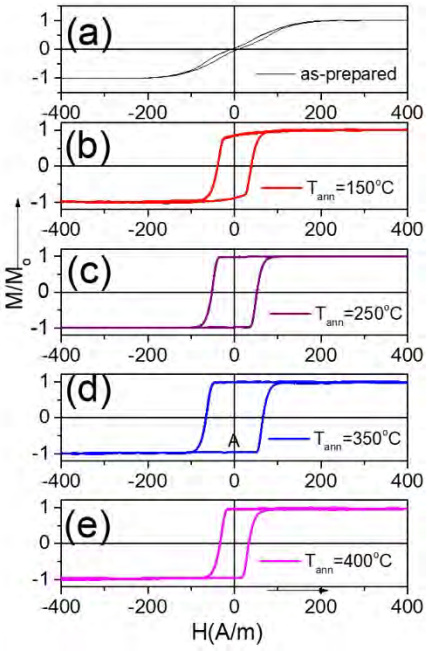


Fig. 1. Hysteresis loops of as-prepared (a) and annealed at °C (b), 250 °C (c), 350 °C (d) and 400 °C (e) sample.

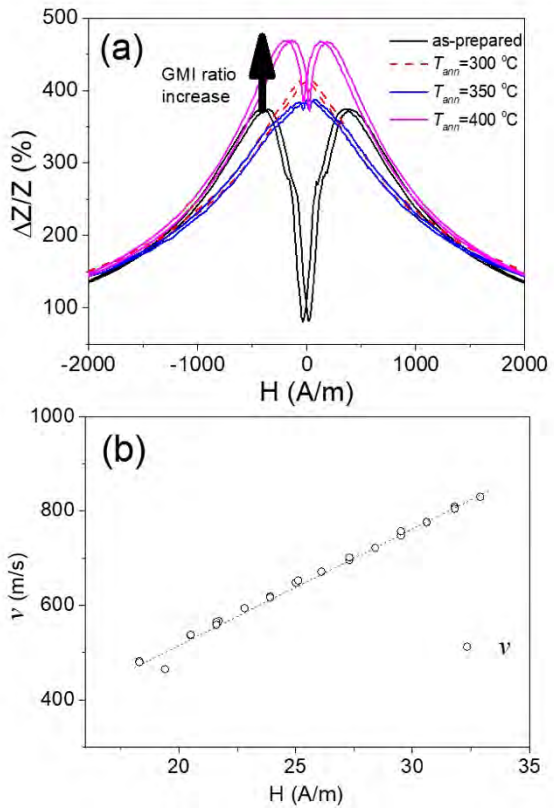


Fig.2. The comparison of Δ*Z/Z(H)* dependencies of as-prepared and annealed microwires measured at 200 MHz (a) and *v(H)* dependence in the sample annealed at 350 °C (b).

SESSION DE: MAGNETIC SENSORS, ENERGY HARVESTERS AND POWER DEVICES

Chair(s): A. Bellini, *DEI, Alma Mater Studiorum, University of Bologna, Cesena, Italy*

Wednesday, November 4, 2026
02:00 PM-05:30 PM
South Pacific 1/2

DE-01. Highly Sensitive Tunnel Magnetoresistance Sensors: Recent Progress and Signal Processing Based on Deep Neural Network

T. Kubota[1], T. Hojo[1, 2], Y. Ando[1, 2, 3]
[1]Advanced Spintronics Medical Engineering, Tohoku University, Sendai, Miyagi, Japan, [2]Department of Applied Physics, Tohoku University, Sendai, Japan, [3]Center for Science and Innovation in Spintronics, Tohoku University, Sendai, Japan

Tunnel magnetoresistance (TMR) sensors offer high sensitivity and a large dynamic range, facilitating unshielded magnetic field measurements in biomagnetic

and industrial applications [1,2]. Recently, TMR sensors have been proposed for medication monitoring, which requires the remote detection of minute magnetic signals from within the body. This presentation provides an overview of recent advancements in TMR sensor performance [3,4] and discusses their implementation in novel medical contexts. First, we explore signal detection from an ingestible event marker (IEM)—a self-powered integrated circuit embedded within a digital pill [5]. We demonstrate successful magnetic field detection from IEMs, enabling remote monitoring from the human stomach [6]. Second, we present a magnetic pattern classification method using high-sensitivity TMR sensors integrated with deep neural networks [7,8]. This system classifies 2 × 2 bit magnetic layouts at distances of several centimeters. Together, these developments expand the practical scope of magnetic sensing and leverage neural network-based classification to extend the effective range of remote magnetic data transmission.

This work was supported in part by Otsuka Pharmaceuticals Co., Ltd., and Spin Sensing Factory Corporation. The author would like to thank Prof. Mikihiko Oogane, and their group members of Tohoku University for the collaboration as well as insightful discussions.

[1] M. Oogane *et al*., Appl. Phys. Express 14, 123002 (2021).
[2] T. Nakano *et al*., Appl. Phys. Lett. 126, 160503 (2025)
[3] S. Takano *et al*., J. Phys. D: Appl. Phys. 59, 025009 (2026).
[4] R. Hirama *et al*., Appl. Phys. Express 18, 103002 (2025).
[5] H. Hafezi *et al*., IEEE Trans. Biomed. Eng. 62, 99 (2015).
[6] T. Kubota *et al*., DG-01, presented in MMM2025.
[7] T. Kubota *et al*., GG-09, presented in INTERMAG2026.
[8] T. Hojo *et al*., GG-10, presented in INTERMAG2026.

DE-02. Micro-patterned $Fe_{65}Co_{35}$ Thin Film for High Frequency Low Loss Integrated RF Inductors

H. Yin, A. El-Ghazaly
Department of Electrical and Computer Engineering, Cornell University, Ithaca, New York, United States

In modern radio frequency front end (RFFE) systems, wideband tunable components are of great interest for their ability to support reconfigurable high-speed communication technologies. To achieve wideband tunability or non-reciprocity for integrated devices, soft magnetic materials were widely explored in previous works to provide field-dependent or voltage-dependent physical properties [1], [2]. Despite the advantage of minimal power consumption and large tunability, soft magnetic materials still face significant challenges in RF systems, including bandwidth limitations set by the ferromagnetic resonance (FMR) frequency and low quality factors [3], [4], [5]. To overcome these obstacles, soft ferrites, such as yttrium iron garnet (YIG), were exploited in previous works for their low conductivity and magnetic damping, and wideband reconfigurable integrated devices were successfully demonstrated [6], [7]. However, due to their ferrimagnetic nature, these soft ferrites have weak magnetizations, with huge insertion loss, large form factors, and require external magnetic field biasing [8], [9]. The difficulty for providing bias fields on chip and depositing YIG films also hinders the implementation of these tunable devices in RF systems.

In this work, we integrate soft ferromagnetic material $Fe_{65}Co_{35}$ with high-frequency high-Q RF inductors. By introducing micro-patterning and taking advantage of the high M_s (1904.93 emu/cc), the FMR of $Fe_{65}Co_{35}$ patterns reaches 15.0 GHz without bias field, showing promise for application in FR3 band. Compared to soft ferrites, $Fe_{65}Co_{35}$ demonstrates a high DC permeability of 67. An inductance enhancement of 9.6% is achieved by our $Fe_{65}Co_{35}$ micro-patterns, and the improvement extends up to 13.6 GHz. The peak quality factor of our $Fe_{65}Co_{35}$ integrated inductor remains high (6.1 at 6.8 GHz). The inductor is purely passive and compact without the need for power consumption or external magnetic field biasing. Therefore, our high frequency high-Q $Fe_{65}Co_{35}$ integrated inductors demonstrate great potential for high-frequency reconfigurable RFFE systems.

[1] A. El-Ghazaly *et al*., "Electrically Tunable Integrated Thin-Film Magnetoelectric Resonators," *Adv. Mater. Technol*., vol. 2, no. 8, p. 1700062, Aug. 2017, doi: https://doi.org/10.1002/admt.201700062.
[2] H. Chen *et al*., "Integrated Tunable Magnetoelectric RF Inductors," *IEEE Trans. Microw. Theory Tech*., vol. 68, no. 3, pp. 951–963, 2020, doi: 10.1109/TMTT.2019.2957472.
[3] A. El-Ghazaly, R. M. White, and S. X. Wang, "Gigahertz-Band Integrated Magnetic Inductors," *IEEE Trans. Microw. Theory Tech*., vol. 65, no. 12, pp. 4893–4900, 2017, doi: 10.1109/TMTT.2017.2728040.
[4] D. S. Gardner, G. Schrom, F. Paillet, B. Jamieson, T. Karnik, and S. Borkar, "Review of On-Chip Inductor Structures With Magnetic Films," *IEEE Trans. Magn*., vol. 45, no. 10, pp. 4760–4766, 2009, doi: 10.1109/TMAG.2009.2030590.
[5] H. Wu, D. S. Gardner, W. Xu, and H. Yu, "Integrated RF On-Chip Inductors With Patterned Co-Zr-Ta-B Films," *IEEE Trans. Magn*., vol. 48, no. 11, pp. 4123–4126, 2012, doi: 10.1109/TMAG.2012.2198448.
[6] C. Devitt, R. Wang, S. Tiwari, and S. A. Bhave, "An edge-coupled magnetostatic bandpass filter," *Nat. Commun*., vol. 15, no. 1, p. 7764, 2024, doi: 10.1038/s41467-024-51735-6.

[7] C. Devitt, S. Tiwari, B. Zivasatienraj, and S. A. Bhave, "Spin-wave band-pass filters for 6G communication," *Nature*, vol. 650, no. 8102, pp. 599–605, 2026, doi: 10.1038/s41586-025-10057-3.
[8] X. Du *et al.*, "A wideband tunable, nonreciprocal bandpass filter using magnetostatic surface waves with zero static power consumption," *Nat. Commun.*, vol. 17, no. 1, p. 1574, 2026, doi: 10.1038/s41467-026-68289-4.
[9] R. Sai, R. D. R. Kahmei, S. A. Shivashankar, and M. Yamaguchi, "High-Q On-Chip C-Band Inductor With a Nanocrystalline MnZn-Ferrite Film Core," *IEEE Trans. Magn.*, vol. 55, no. 7, pp. 1–4, 2019, doi: 10.1109/TMAG.2019.2916699.

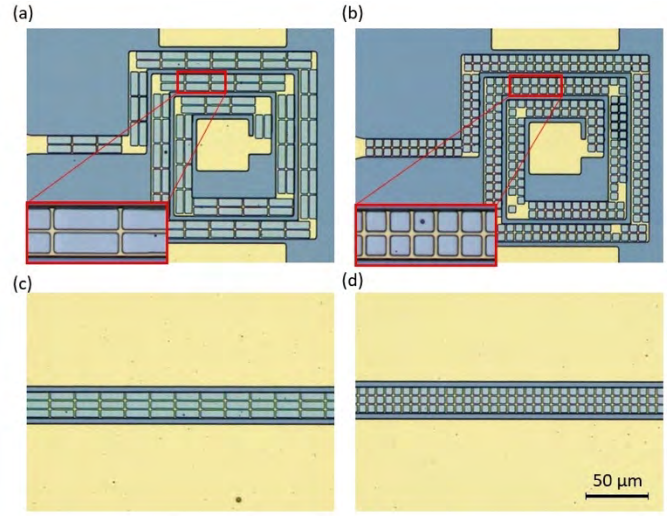


Fig. 1: Photo of $Fe_{65}Co_{35}$ integrated inductors and CPWs.

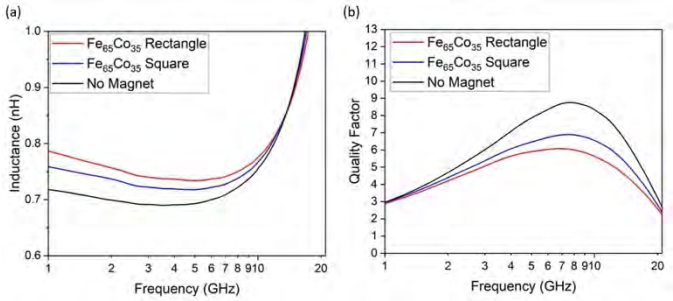


Fig. 2: Measured performance of spiral inductors patterned with $Fe_{65}Co_{35}$.

DE-03. Enhancement of anomalous Hall and Nernst effects in tetragonal distorted FeCo induced by the addition of V and N elements

A. Patel[1], E. Xiao[1], C. Murakami[2], T. Nakatani[1], T. Hasegawa[2], T. Tadano[1], Y. Sakuraba[1]
[1]*Research Center for Magnetic and Spintronic Materials, National Institute for Materials Science, Tsukuba, Ibaraki, Japan,*
[2]*Department of Materials Science, Akita University, Akita, Japan*

FeCo alloys are well known for their high saturation magnetization and Curie temperature. The uniaxial magnetic anisotropy (K_u) of FeCo can be effectively tuned by the addition of VN or VC, as reported in earlier studies[1,2], enabling a large enhancement of K_u from 0.3 × 10^6 J/m^3 to 1.24 and 1.40 × 10^6 J/m^3 with VN and VC additions, respectively. Their detailed analysis revealed that the structural transitions from bcc to bct (stable bct structure) then to fcc upon the N incorporation. The K_u increases during the transition from bcc to bct, reaches its maximum in the bct phase and then decreases as the structure transitions from bct to fcc, which is strongly correlated with a variation in the electronic structure near the Fermi level. Motivated by these findings, we explored the transport properties, such as anomalous Hall effect (AHE) and anomalous Nernst effect (ANE), since the magnitude and sign of AHE and ANE are sensitive to the electronic structure near the Fermi level as well. Therefore, in this study, we investigated AHE and ANE of $((Fe_{0.5}Co_{0.5})_{0.8}V_{0.2})_{100-x}N_x$ (x = 0, 2.4, 4.2, 5.7, 6.7, 7.9, and 8.6) (FCVN) thin films. Fig. 1(a) shows anomalous Hall resistivity (ρ_{yx}^A) at 300 K as a function of c/a. The ρ_{yx}^A for pure bcc-FeCo is found to be very small, approximately 0.09 μΩ cm, while the addition of V (x = 0) increases to 2.96 μΩ cm, which is a 33-fold enhancement while maintaining the bcc phase. With increasing N doping, ρ_{yx}^A increases monotonically with increasing the c/a, reaching 5.20 μΩ cm for x = 8.6, which is a 1.8-fold increase compared to x = 0. The anomalous Nernst conductivity (α_{xy}) at 300 K is shown in Fig. 1(b), increases monotonically with c/a, reaching a maximum of 0.65 A m^{-1} K^{-1} at c/a = 1.15, then decreases to 0.59 A m^{-1} K^{-1} with further increase in c/a. We also performed the first-principles calculation of AHE and ANE of FCVN, which gives a qualitative explanation of the experimental results. This study highlights the effectiveness of structural tuning in controlling transverse transport properties and found FCVN as a good candidate for future magnetic sensors and energy-harvesting applications.

[1]T. Hasegawa, C. Murakami, K. Imamura et al. Sci. Rep. 9, (2019) 5248.

[2] K. Takahashi, M Sakamoto, K Kumagai et al. J. Phys. D: Appl. Phys. 51 (2018) 065005

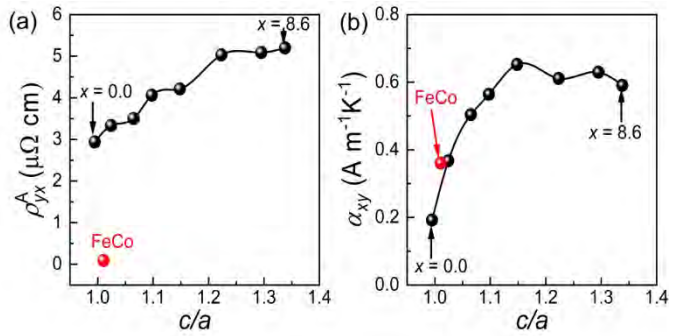


Fig. 1: *c/a* dependence of (a) ρ_{yx}^{A} and (b) α_{xy} at 300 K in FCVN thin films.

DE-04. Ultra-sensitive magnetic field sensor for low frequency applications

L. Malucelli[1], A. Arredondo-López[1], M. Caseiro[2], E. Yildiz[1], I. Joumard[1], N. Mollard[1], S. Auffret[1], J. Faure-Vincent[1], G. Gaudin[1], B. Dieny[1], C. Baraduc[1], L. Ranno[3], J. Kammerer[4], C. Fermon[2], A. Solignac[2], M. Pannetier-Lecoeur[2], H. Béa[1, 5], J. Fischer[1]

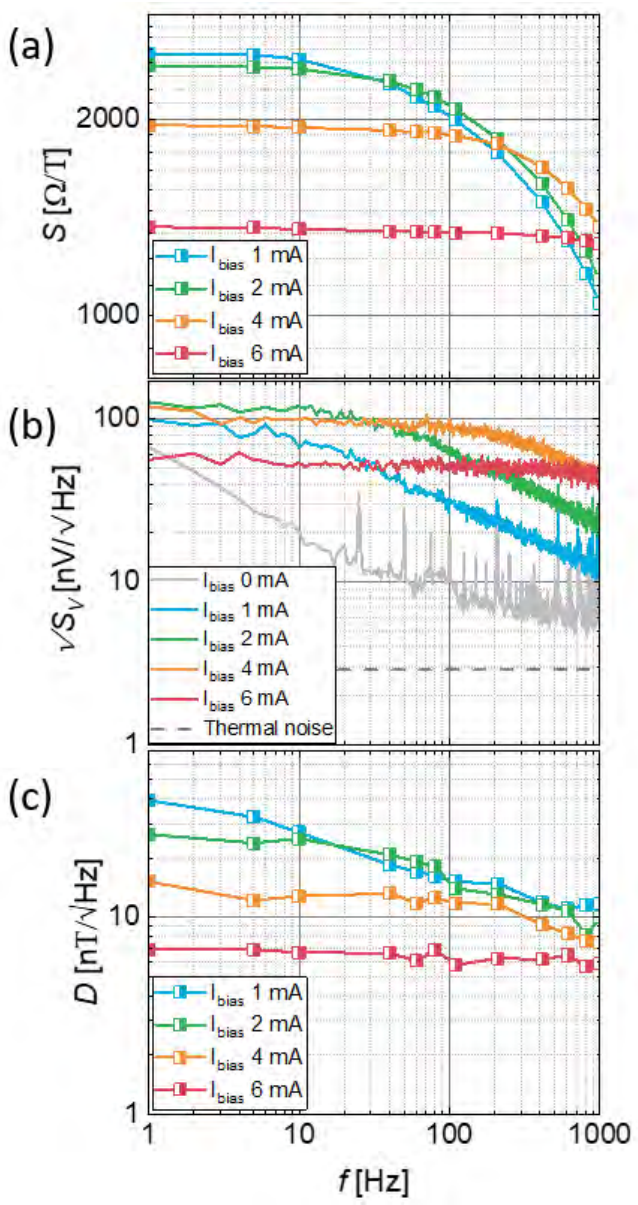
[1]University of Grenoble Alpes, CNRS, CEA, SPINTEC, Grenoble, France, [2]Université Paris-Saclay, CEA, CNRS, SPEC, Gif-sur-Yvette, France, [3]Institut Néel, Univ. Grenoble Alpes, CNRS, Grenoble, France, [4]ICube, University of Strasbourg, Strasbourg, France, [5]Institut Universitaire de France (IUF), Grenoble, France

Spintronic devices such as giant magnetoresistance (GMR), tunnel magnetoresistance (TMR) and Hall effect sensors are widely used for magnetic field detection [1,2]. The possibility to detect weak magnetic fields in miniaturized devices enables reduced size and cost, attractive for space and biomedical applications. In these contexts, relevant frequencies are low: biomagnetic signals span 0.1–100 Hz (brain) and 0.01–100 Hz (heart), while space plasma fluctuations range from 1 mHz to a few Hz [3–5]. Detecting pico to nano Tesla signals requires minimizing detectivity, defined as the noise-to-sensitivity ratio, at low frequencies. In conventional GMR and TMR devices, sensitivity is frequency independent, while noise increases at low frequencies, leading to poor signal-to-noise ratio at low-frequency [6,7].

We report a frequency-dependent study of an out-of-plane magnetic field sensor based on a Ta/FeCoB/TaOx trilayer hosting skyrmions [8]. The device is patterned into a 100 × 100 µm2 Hall cross, where the output signal arises from the anomalous Hall effect. Sensitivity (Fig. 1a) depends on frequency and bias current: at low current it decreases above a characteristic frequency that shifts higher with bias. At 6 mA, the cutoff exceeds 1 kHz. Noise (Fig. 1b) shows mixed 1/f and random telegraph contributions, becoming nearly flat at 6 mA. Detectivity (Fig. 1c) is then constant at very low frequencies under high bias, reaching 7 nT/√Hz below 1 kHz at 6 mA. These effects are attributed to Joule heating and reduced magnetic anisotropy.

These results highlight the potential of Ta/FeCoB/TaOx trilayers hosting skyrmions as highly sensitive out-of-plane magnetic field sensors for <1 kHz applications. This high sensitivity is ascribed to the amorphous Ta buffer and TaOx capping layer, which reduces domain walls and skyrmions pinning, due to the absence of grain boundaries. Further improvements are expected by increasing bias current or sensor size. Ongoing work aims to link the frequency dependence to domain wall and skyrmion dynamics under current and field variations.

[1] H. Fan et al., RSC Adv. 11, 7257 (2021)
[2] P. P. Freitas et al., Proc. IEEE 104, 1894-1918 (2016)
[3] Y. Hu et al., Sensors and Actuators: A. Physical 373, 115404 (2024)
[4] S. Zuo et al., Adv. Mater. Technol. 5, 2000185 (2020)
[5] K. Glassmeier et al., Space Science Reviews 128, 649–670 (2007)
[6] J. E. Davies et al., Appl. Phys. Lett. 118, 062401 (2021)
[7] Y. Zhang et al., Sensors 19, 3537 (2019)
[8] C.-E. Fillion et al., Nat. Commun. 13, 5257 (2022)



Sensitivity (a), noise (b) and detectivity (c) versus frequency without external field for a 100 × 100 μm2 skyrmion Hall sensor at different bias currents.

DE-05. Demonstration of a Bistable Broadband Electromagnetic Vibration Energy Harvester for Low-Frequency Applications

H. Kijima-Aoki[1], K. Nohara[1], K. Kobori[2], H. Katsumura[3], M. Lallart[4, 5], G. Sebald[4, 5], H. Masumoto[6], S. Yabukami[1]
[1]Department of Electrical Engineering, Graduate School of Engineering, Tohoku University, Sendai, Japan, [2]Chuo Spring Co., Ltd., Miyoshi, Aichi, Japan, [3]Kachi Create LLC, Kobe, Hyogo, Japan, [4]Univ. Lyon, INSA-Lyon, Lyon, France, [5]ELyTMaX IRL 3757, CNRS, University Lyon, INSA Lyon, Centrale Lyon, Université Claude Bernard Lyon, Tohoku University, Sendai, Japan, [6]Frontier Research Institute for Interdisciplinary Sciences, Tohoku University, Sendai, Japan

Self-powering onboard sensors is attractive since electric vehicles increasingly embed IoT devices. Vibration energy harvesters for these sensors are desirable to operate under low-frequency, broadband vibrations, rather than relying on conventional narrowband designs tuned to engine vibrations[1]. To harvest energy from low-frequency broadband vibrations, bistable structures based on beam vibration and magnetic interaction have been widely studied [2]. In this study, as shown in Fig. 1(a), a magnetic yoke is attached to the permanent magnets and a flexible non-magnetic beam is introduced to reduce the potential barrier while maintaining the local magnetic field (Fig. 1(b)). A BeCu beam with high flexibility, non-magnetic properties, and excellent fatigue resistance is used. Electrical steel sheets form the core, and the gap between the core and a pair of permanent magnets with a flux-confining back yoke is optimized for low-frequency broadband power generation. Experiments are conducted under both free and forced vibration. Forced vibration tests are performed over 3–10 Hz at 0.5 G. Open-circuit voltage is evaluated under free vibration, while maximum load power is measured under forced vibration with a 365 Ω matched load. Under free vibration(Fig.1(c)), the generated voltage exceeded 1 V over 10 s and decayed with an exponential envelope. Frequency-swept vibration (Fig.1(d)) showed forward–backward asymmetry indicating Duffing-type hardening behavior. Furthermore, a maximum load power of 100 μW was obtained in the low-frequency range of 6–7.5 Hz at 0.5 G. A BLE temperature and humidity sensor powered by the microgenerator is developed. With optimized power management, it operates with as little as 350 μJ per cycle and consumes less than 700 nA in sleep mode. A demonstration in an automotive environment will also be presented.

[1] M. A. Abdelkareem, et al., *Appl. Energy*, *229* (2018) 672-

699.
[2] T. Huguet et al., *Appl. Phys. Lett.*, *111*(17) (2017)

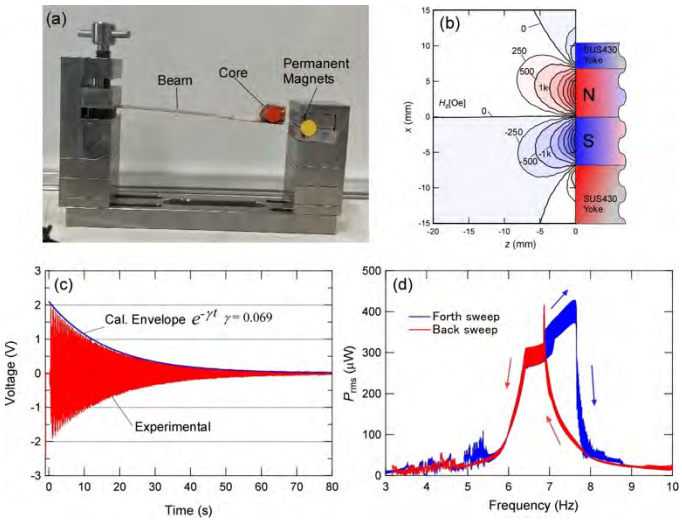


Fig.1 (a) Photograph of the beam-type electromagnetic vibration energy harvester. (b) Magnetic field distribution in front of the permanent magnets with a flux-confining yoke. (c) Open-circuit voltage waveform under free vibration. (d) Frequency dependence of the maximum load power.

DE-06. Fundamental principle of oblique magnetic field assisted vibration power generator and its design for high output power

K. Imamura, Y. Nakamura, M. Ohtake
Yokohama National University, Yokohama, Japan

Electromagnetic vibration power generators with types of movable magnet [1] and inverse magnetostriction [2-4] have attracted much attention as energy harvesters. On the other hand, we reported a new type of electromagnetic generator named perpendicular magnetic field assisted type [5,6]. The generator primarily consists of a soft magnetic cantilever beam, an electromagnetic coil, and a pair of magnets applying magnetic field to the beam. In the present study, we evolve the generator from perpendicular to oblique magnetic field assisted type, which is effective in enhancement of the magnetic flux variation in beam and the output voltage. Fig. 1 shows the schematic diagram of oblique magnetic field assisted generator. A $Fe_{97}Si_3$ (wt. %) alloy sheet of 80 mm length, 20 mm width, and 350 μm thickness is used as the beam material. The magnetic pole surface angle (ϑ) and the distance between beam and magnet (d_{bm}) are varied to optimize the condition of oblique magnetic field. Vibration, whose acceleration is fixed at 19.6 m/s^2 and frequency is varied in a range between 30 and 70 Hz, is applied to the generator. Fig. 2 summarizes the dependences of resonance frequency (f), amplitude ($A_{0\text{-}p}$), magnetic flux density variation (ΔB), and output voltage ($V_{0\text{-}p}$) on the ϑ angle for the different d_{bm} distances. The f and the $A_{0\text{-}p}$ values increase with increasing the ϑ angle, whereas the ΔB value reaches a maximum at a certain ϑ angle. The result suggests that the magnetic force opposing the vibration decreases with increasing the ϑ angle and the strength of magnetic field in beam reaches a maximum at a specific ϑ angle. Furthermore, as the d_{bm} distance increases, the f and the $A_{0\text{-}p}$ values increase, whereas the ΔB value decreases, indicating that the magnetic force and the magnetic field strength decrease. The output property complicatedly varies depending on the magnet placement. A high $V_{0\text{-}p}$ value of 34 V is achieved by optimizing the ϑ and d_{bm} values, that is, by balancing the properties of vibration and magnetic flux variation. The present study has shown that oblique magnetic field assisted-type generator is one of strong candidates for high output energy harvesters.

[1] C. B. Williams and R. B. Yates: *Sens. Actuators A*, 52, 8 (1996).
[2] T. Ueno and S. Yamada: *IEEE Trans. Magn.*, 47, 2407 (2011).
[3] S. Fujieda, S. Suzuki, A. Minato, T. Fukuda, and T. Ueno: *IEEE Trans. Magn.*, 50, 2505204 (2014).
[4] H. Abe, T. Goto, M. Naoe, K. I. Arai, and K. Ishiyama: *T. Magn. Soc. Jpn.*, 8, 73 (2024).
[5] M. Ohtake, T. Kawai, and M. Futamoto: *Japanese Patent*, application no. 2022-086851 / publication no. 2023-174153 (2023).
[6] Y. Nakamura, S. Aketa, S. Kamiya, H. Kamogawa, and M. Ohtake: *IEEE Trans. Magn.*, 61, 8001205 (2025).

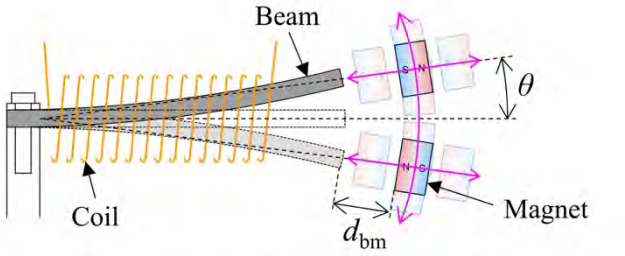


Fig. 1 Schematic diagram showing positional relationship between beam, coil, and a pair of magnets.

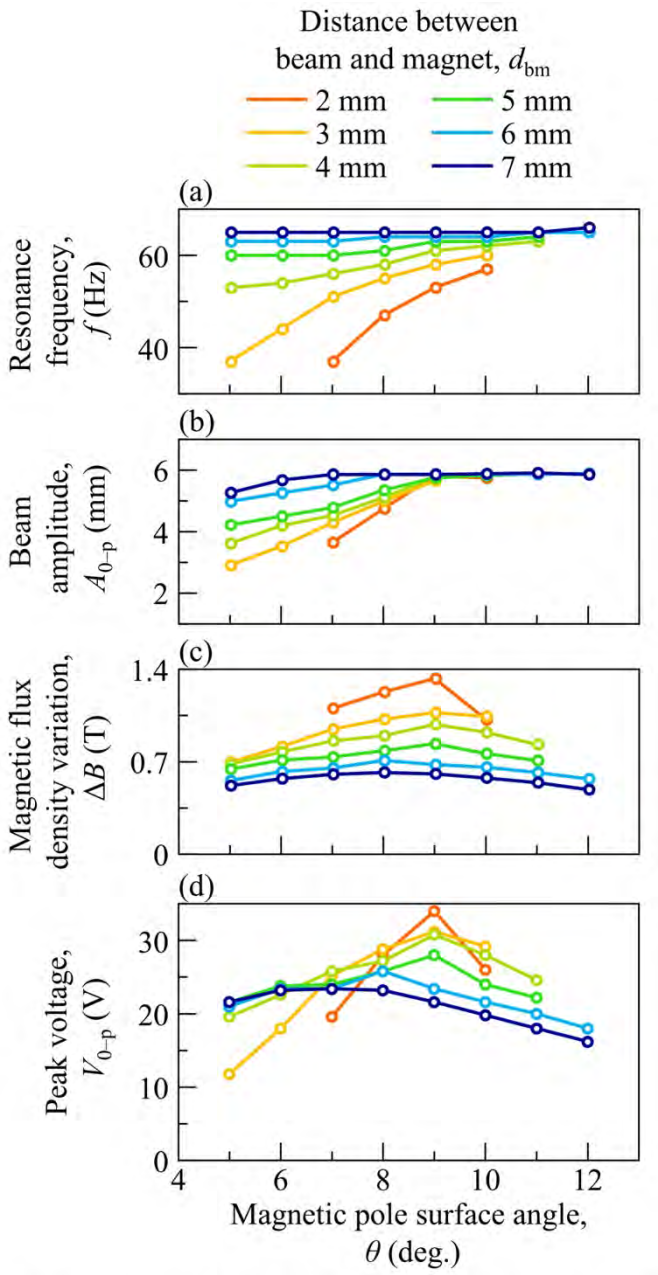


Fig. 2 Dependences on magnet placement of (a) resonance frequency, (b) beam amplitude, (c) magnetic flux density variation, and (d) peak voltage.

DE-07. Magnetically-Modulated Ionization in a MEMS-Based Three Electrode Sensor for Vector Detection of Weak Power Frequency Fields

W. Muhammad[1, 2]

[1]Semiconductor Institute, Guangdong Academy of Science, Guangzhou, Guangdong, China, [2]School of Instrument Science and Technology, Xian Jiaotong University, Xian, Shaanxi, China

Established magnetic sensors rely on solid-state transport or induction and face trade-offs in sensitivity, size, and low frequency response.

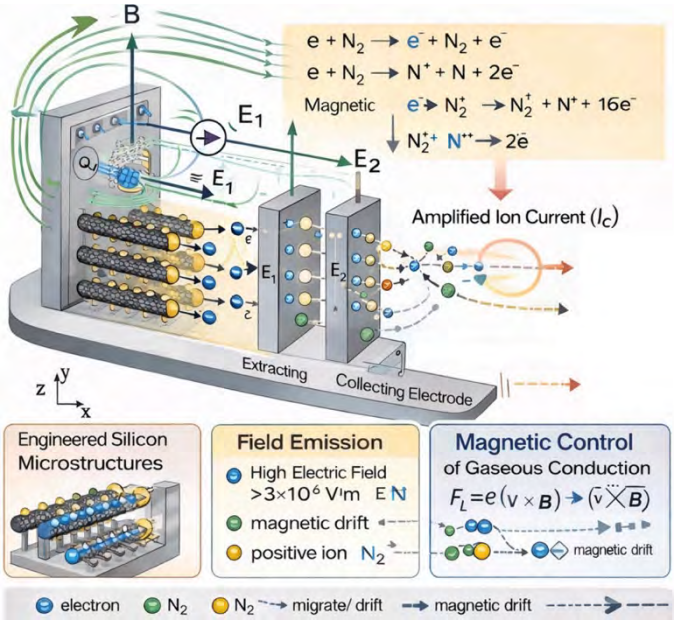
Hall sensors are limited by 1/f noise and μT level resolution at low frequencies [1], magnetoresistive devices require biasing and compensation to mitigate noise and hysteresis [2], fluxgate magnetometers, though highly sensitive, depend on ferromagnetic cores and excitation circuitry that constrain size and power reduction [3], and inductive sensors exhibit frequency dependent output ($V \propto dB/dt$), reducing sensitivity near 50/60 Hz without amplification [4]. Comparative studies consistently document these limitations in weak field detection [5].

We introduce a micro-electromechanical system (MEMS) sensor in which an external magnetic field B modulates a steady state Townsend discharge. The device features a three-electrode structure with engineered silicon column arrays that create localized field enhancements ($E > 3\times10^6$ V/m), initiating field emission by the Fowler-Nordheim equation [6]. Where J_e is the emission current density, Φ the work function, and B_e a material constant. Under applied B-field, orthogonal or parallel to the drift field E, alters electron trajectories via the Lorentz force ($F_L = e(v \times B)$), thereby increasing electron-neutral collision frequencies and enhancing ionization yields. This magnetically amplified ion current provides a direct, linear measure of the AC field magnitude and direction, and thus the ion current I_c collected at the collector electrode.

Experimentally, the sensor shows a sensitivity of 0.152 nA/μT for fields parallel to the electrodes, and 0.08 nA/μT for perpendicular fields. Using an array of sensors with different electrode spacing's and BP neural network processing, directional field detection and zero drift compensation are achieved, improving linearity to 1.60%. This work demonstrates a miniaturized magnetometry approach based on magnetically modulated gas discharge, relevant for environmental and industrial low frequency magnetic field monitoring.

[1] H. Fan *et al.*, "Detection techniques of biological and chemical Hall sensors," *RSC Advances*, vol. 11, pp. 7257–7270, 2021.

[2] S. Tumanski, "Modern magnetic field sensors a review," *Przeglad Elektrotechniczny*, vol. 89, no. 10, pp. 1–12, 2013.
[3] S. Wei, X. Liao, H. Zhang, J. Pang, and Y. Zhou, "Recent progress of fluxgate magnetic sensors: basic research and application," *Sensors*, vol. 21, no. 4, art. 1500, 2021.
[4] N. Hadjigeorgiou, K. Asimakopoulos, K. Papafotis and P. P. Sotiriadis, "Vector Magnetic Field Sensors: Operating Principles, Calibration, and Applications," in *IEEE Sensors Journal*, vol. 21, no. 11, pp. 12531-12544, June. 2021
[5] S. Tumanski, "Magnetic field sensors, a comprehensive assessment," *Sensors and Actuators A: Physical*, vol. 145–146, pp. 271–277, Jul. 2008.
[6] M. Waqas *et al*., "A MEMS Based Three Electrodes Ionization Sensor for Real-Time Detection of Transient Overvoltage in UHV Transmission Systems," *2024 3rd Asia Power and Electrical Technology Conference (APET)*, Fuzhou, China, 2024, pp. 79-84.



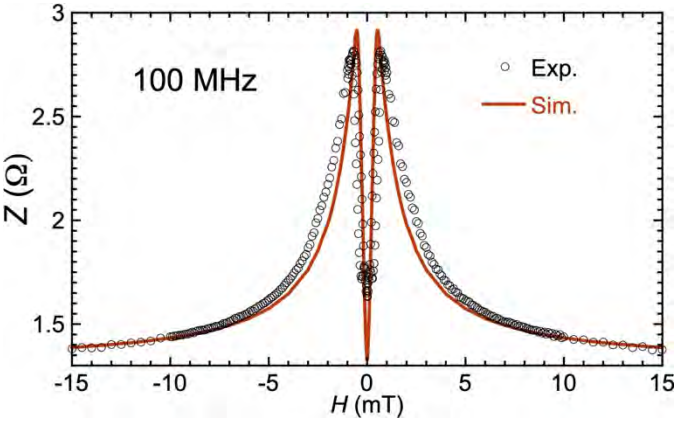
Scheme. 1. Principle of Magnetically-Modulated Ionization in a MEMS-Based Three-Electrode Sensor for Vector Detection of Weak Power-Frequency Fields.

DE-08. Experimentally Validated Multiscale Modeling of Thin-Film MI Sensors

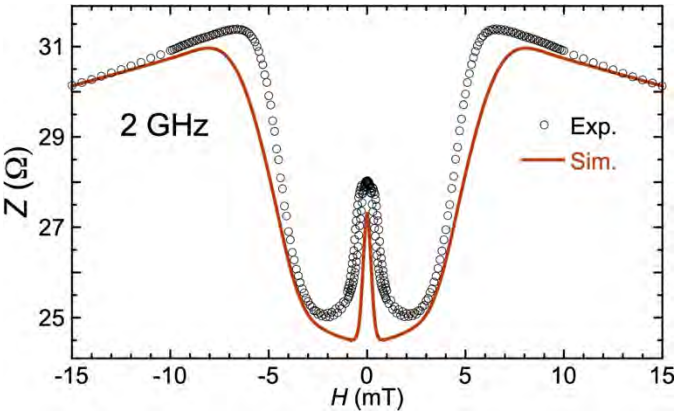
G. Gestoso[1], D. de Cos Elices[3], E. Fernández[2], N. Lete[1], A. García-Arribas[1, 2]
[1]Departamento de Electricidad y Electrónica, Universidad del País Vasco, UPV/EHU, Leioa, Vizcaya, Spain, [2]Basque Center for Materials, Applications and Nanostructures, BCMaterials., Leioa, Vizcaya, Spain, [3]Departamento de Física, Universidad del País Vasco, UPV/EHU, Vitoria, Alava, Spain

We present a multiscale modeling approach to predict the behavior of magneto-impedance (MI) devices by coupling microscopic magnetization dynamics with a macroscopic electromagnetic model. The framework yields a comprehensive description of the MI response that accurately reproduces experimental measurements. The model not only captures low-frequency behavior as a function of both frequency and applied field, but it also naturally accounts for the high-frequency features, including ferromagnetic resonance (FMR) effects [1] and non-resonant low-field absorption features [2].
The method requires only a reduced, unified set of basic material parameters and device geometry as inputs and addresses the intrinsically coupled nature of the MI effect: the permeability depends non-linearly on the amplitude of the AC magnetic field produced by the excitation current, while the field distribution itself is governed by the permeability via the skin effect.
The full permeability tensor is computed from micromagnetic simulations as a function of both DC bias field and AC magnetic field amplitude. This dataset is integrated into the FEM solver, which locally selects the appropriate permeability value based on the instantaneous magnetic field amplitude during the solution process. This approach yields a self-consistent solution without imposing a priori uniform or phenomenological permeability functions.
The modeling procedure is validated through a direct comparison with experimental measurements on a $[Py/Ti]_3/Cu/[Ti/Py]_3$ sandwich multilayer integrated into a microstrip line [3]. Figures 1 and 2 demonstrate the correspondence between measured and calculated impedance as a function of the magnetic field for two selected frequencies. The agreement establishes our modeling approach as a powerful predictive tool for assessing the impact on MI performance of lateral dimensions, layer thicknesses, stack architecture, and induced anisotropies, ultimately enabling the rational design and optimization of MI sensors.

[1] J. M. Barandiarán *et al.* J. Appl. Phys. 99 (2006).
[2] R. Valenzuela *et al.* Phys. Status Solidi (a) 206, 652–655 (2009).
[3] A. García-Arribas *et al.* J. Magn. Magn. Mater. 400, 321–326 (2016).



Comparison of simulated and measured Z(H) curves for a 500μm × 50μm Py-based sandwiched multilayer at 100 MHz.



Same as Fig.1, at 2 GHz. FMR and non-resonant low-field absortion features are observed.

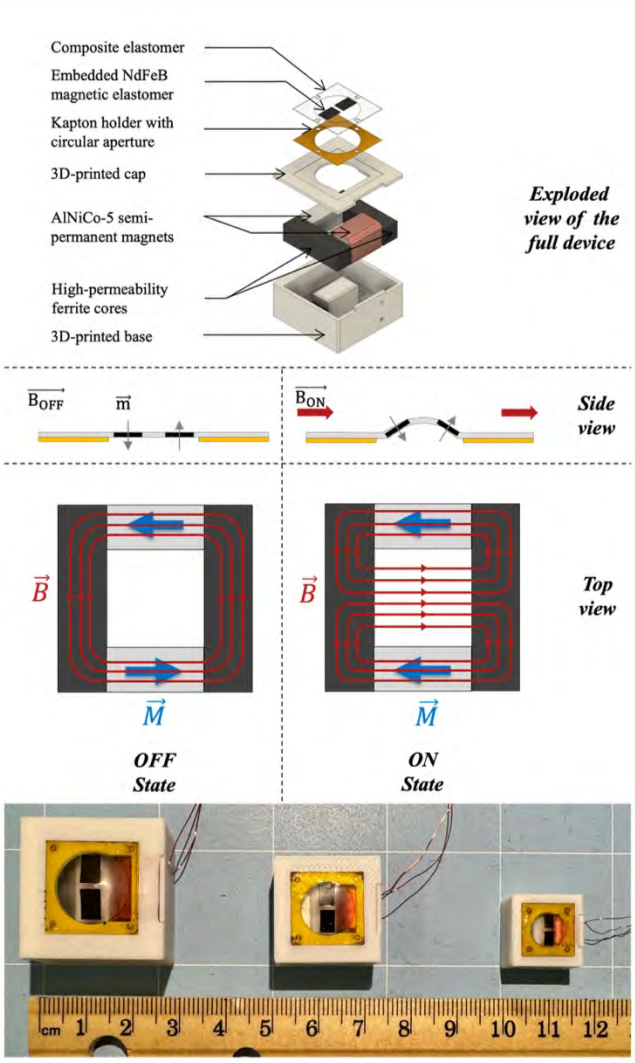
DE-09. Scaling Electropermanent Magnet-Controlled Magnetic Soft Actuators

H. Htet, A. El-Ghazaly
Electrical and Computer Engineering, Cornell University, Ithaca, New York, United States

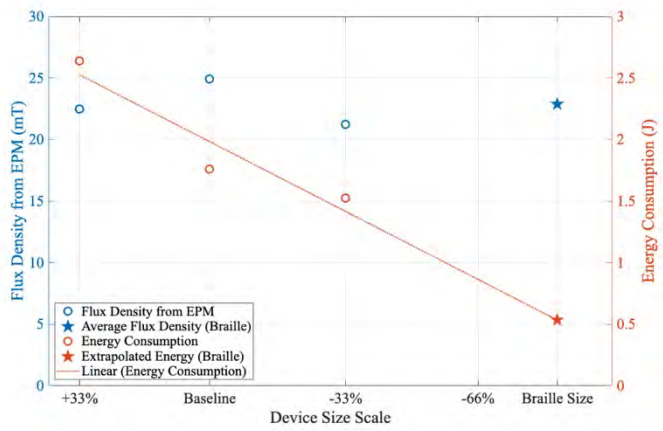
Soft haptic actuators are increasingly vital for applications in virtual reality, robotics, and assistive devices such as refreshable braille displays [1-3]. Yet scaling such systems while preserving functionality remains a key challenge. This work investigates how proportional scaling affects actuator performance in composite elastomer-based torque-mode systems controlled by electropermanent magnets (EPMs). Each tactile unit cell (taxel) consists of a composite elastomer mounted on a holder with a circular aperture and placed atop an EPM frame. The EPM comprises two AlNiCo-5 magnets connected by soft iron cores; one magnet is wound with a coil to enable magnetic state switching. The composite elastomer is embedded with two rectangular out-out-plane anisotropic magnetic elastomers with opposing magnetization directions, which deflect the composite upward due to the torque on the magnetizations when experiencing a uniform magnetic field from the EPM frame in the "ON" state. To study scaling, devices were fabricated at the previous baseline size [4] as well as +33% and -33% sizes.
COMSOL-simulated deflections were 1.26 mm, 0.95 mm, and 0.63 mm for +33%, baseline, and -33% scales, respectively, indicating that the deflection scales proportionally with size. In our design, since the number of turns is kept constant by changing the wire gauge, the current required to flip the AlNiCo magnetization scales proportionally with size. Since current scales linearly with size and resistance scales inversely with size, the result is that power and energy consumption scale down linearly as the dimensions are reduced while flux density (and torque density) remains the same for all sizes. This work illustrates the scaling trends of electropermanent magnet-controlled magnetic soft actuators for use in energy-efficient tactile unit cells.

[1] S. Biswas and Y. Visell, "Emerging Material Technologies for Haptics," Advanced Materials Technologies, vol. 4, no. 4, p. 1900042, 2019.
[2] Ankit, T. Y. K. Ho, A. Nirmal, M. R. Kulkarni, D. Accoto, and N. Mathews, "Soft Actuator Materials for Electrically Driven Haptic Interfaces," Advanced Intelligent Systems, vol. 4, no. 2, p. 2100061, Feb. 2022.
[3] L. Cestarollo, S. Smolenski, and A. El-Ghazaly, "Nanoparticle-Based Magnetorheological Elastomers with

Enhanced Mechanical Deflection for Haptic Displays," ACS Appl. Mater. Interfaces, vol. 14, no. 16, pp. 19002–19011, Apr. 2022.
[4] H. W. Htet and A. S. El-Ghazaly, "Magnetic Soft Actuator Using Composite Elastomer and Electropermanent Magnet for Haptic Displays," 2025 23rd International Conference on Solid-State Sensors, Actuators and Microsystems (Transducers), Orlando, FL, USA, 2025, pp. 1161-1164.



(Top) Exploded view showing components of the device. (Middle top) Side view of the composite elastomer and (Middle bottom) top view of the EPM frame in the ON and OFF states. (Bottom) the size comparison of the fabricated taxels.



Summary of measured EPM flux density and energy consumption values as a function of device size.

DE-10. Magnetic, micromagnetic and magneto-optical characterisation of the degradation of the magnetic properties of electrical steels due to cyclic mechanical loading

M. Smaga, C. Backes, P. Thevaruban
Institute of Materials Science and Engineering (WKK), RPTU, Kaiserslautern, Germany

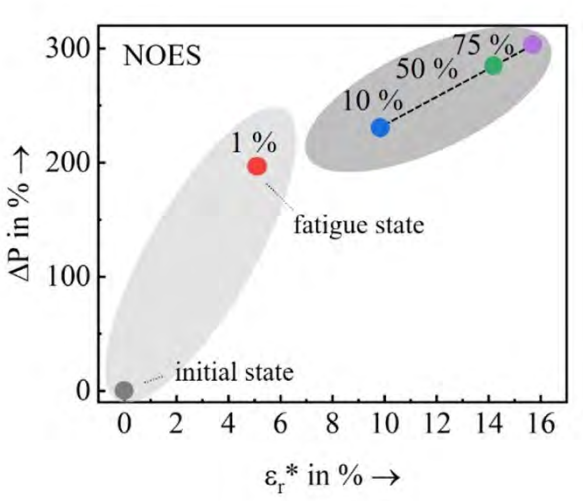
In technical applications such as electrical motors, electrical steels are subjected to cyclic mechanical loading due to centrifugal forces and vibrations. This leads macroscopic to ratcheting strain and to changes in the crystallographic microstructure, resulting in mechanical fatigue. These microstructural changes also influence the magnetic domain structure, altering the magnetisation process [1]. This usually results in a degradation of soft magnetic properties and, consequently, an increase in power losses (Fig. 1). We refer to this phenomenon as 'functional fatigue' [2].

This study investigated both mechanical and functional fatigue. Mechanical fatigue was induced by cyclic loading at room temperature. Functional fatigue was characterised using standardised methods, such as the strip tester (ST). Additionally, micromagnetic measurements were performed using a 3MA sensor and local magneto-optical hysteresis (MOH) was determined using an MOKE microscope (Fig. 2) [3].

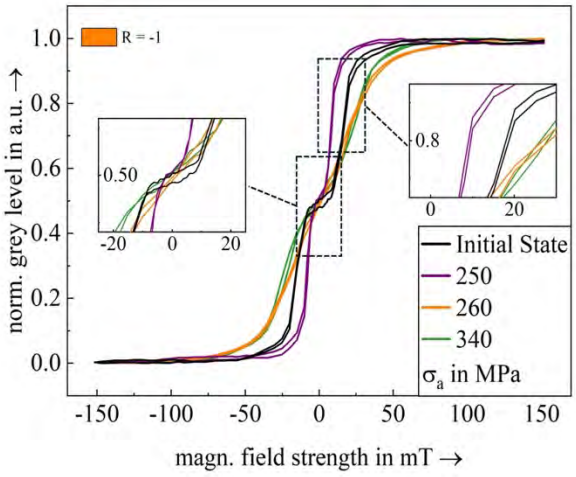
The results demonstrate the influence of mechanical fatigue on functional fatigue. Furthermore, correlations were established between different characterisation methods: standardised strip testing on large specimens (100 mm × 30 mm), 3MA measurements on medium-sized areas (10 mm ×

5 mm) and MOH measurements on a local scale (0.1 mm × 0.1 mm) on flat specimens with a thickness of 0.3 mm. This combined approach enables the characterisation of power losses (ST) and the localised determination of functional fatigue (3MA), as well as achieving a better understanding of magnetic domain behaviour (MOH). Additionally, scanning electron microscopy investigations were conducted to determine fatigue-induced changes in the crystallographic microstructure.

[1] https://doi.org/10.1016/j.jmmm.2026.173950
[2] https://doi.org/10.1016/j.ijfatigue.2024.108410
[3] https://doi.org/10.1016/j.ijfatigue.2025.109251



The change in power losses for different fatigue states as a function of the ratcheting strain for electrical steels cyclically loaded with a maximum stress of 500 MPa



The magneto-optical hysteresis of electrical steel in the initial state and after cyclic loading with different stress amplitudes

DE-11. Optimal Lamination Direction of Magnetic Shields for Tank and Frame in Power Transformer

Y. Takahashi[1], S. Imamori[2], K. Fujiwara[1]
[1]Department of Electrical Engineering, Doshisha University, Kyotanabe, Japan, [2]Advanced Technology Laboratory, Fuji Electric Co., Ltd., Tokyo, Japan

This study aims to minimize stray losses in the tank and frame of a power transformer caused by leakage flux from the primary and secondary windings. To further improve the efficiency of power transformers, it is essential to understand the cause of the stray loss and adopt the appropriate measures [1]-[4]. This study discusses the optimal structure of the tank and frame shields consisting of laminated electrical steel sheets through a stray loss analysis of an oil-immersed transformer using finite-element method.

The rated capacity of the investigated power transformer is 10 MVA. In general, eddy-current loss is the dominant component of stray loss. When structural steels with a sufficient thickness are used for the tank and frame, neglecting the hysteretic properties can result in significant differences in the skin effect due to different incremental permeability. This can lead to an overestimation of iron losses [5]. To improve the accuracy of the 3-dimensional analysis based on a magnetization curve, the conductivity is modified to achieve a skin effect that is almost the same as when hysteretic properties are considered [5]. The laminated structure of the iron core and the magnetic shields are modeled using the homogenization method [6]. Stray loss analysis is performed under short-circuit test conditions because of significant leakage flux. Fig. 1 shows the eddy-current loss density with and without shields. Fig. 2 compares the stray losses when the shield structure varies. In these figures, the maximum values are normalized by P_m and P_{sl}, respectively. The shield structure has a significant impact on stray losses. The shield structure of Case 2 effectively reduces the stray loss in the tank. However, the large losses are generated in the tank shield. In terms of total losses, Case 3 achieves the best performance. Consequently, adopting this shield structure reduces stray losses by around 70 %. The full paper will include the details of the stray loss analysis and discuss the difference in shielding effect due to the structure.

[1] M. Masood, A. Sarwat, and F. Leon, *IEEE Trans. Magn.*, vol. 53, no. 2, Art. no. 8100607 (2017).
[2] K. Park, H. Lee, and S. Hahn, *IEEE Trans. Magn.*, vol. 55, no. 12, Art. no. 7502104 (2019).
[3] Z. Zhu, D. Xie, G. Wang, Y. Zhang, and X. Yan, *IEEE Trans.*

Magn., vol. 48, no. 2, pp. 739-742 (2012).
[4] B. Liu, Y. Takahashi, K. Fujiwara, and S. Imamori, *IEEE Trans. Magn*., vol. 59, no. 11, Art no. 8401606 (2023).
[5] M. Takeda, Y. Takahashi, K. Fujiwara, and S. Imamori, *Electr. Commun. Jpn.,* vol. 41, no. 8, pp. 568-575 (2021).
[6] H. Kaimori, A. Kameari, and K. Fujiwara, *IEEE Trans. Magn*., vol. 43, no. 4, pp. 1405-1408 (2007).

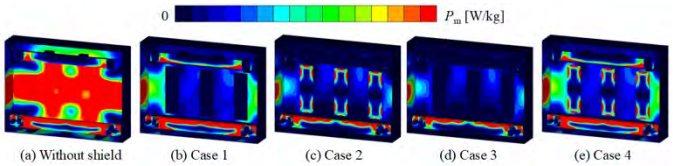


Fig. 1. Distributions of eddy-current loss density in tank, frame, and shields.

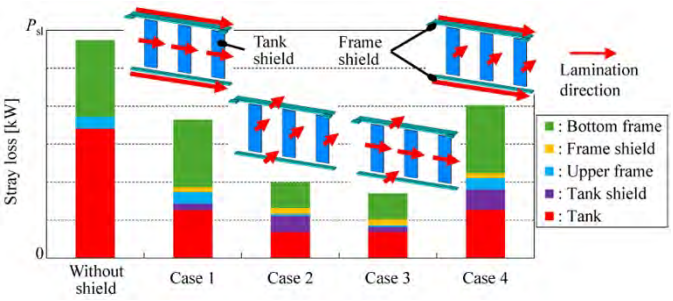


Fig. 2. Comparison of stray losses in a power transformer when applying respective shield structures.

DE-12. An Elevated Temperature Comparison of Magnetic Materials for High-power Wireless Charging of Electric Vehicles

A. K. Bailey, S. Kim, G. Covic
ECSE, University of Auckland, Auckland, Auckland, New Zealand

Inductive power transfer (IPT) for electric vehicles (EVs) has emerged as a promising technology for enabling convenient charging infrastructure[1]. According to SAE J2954, EV charging systems typically operate at 85 kHz and deliver tens of kilowatts of power. In these systems, soft magnetic materials play a crucial role in shaping the magnetic field, improving coupling between the transmitter and receiver coils, and reducing leakage fields.
IPT systems rely heavily on Mn-Zn ferrites due to their high electrical resistivity, low core losses, and good availability. However, ferrites are highly temperature-sensitive, limiting their use in high-temperature environments such as EV charging pads without active cooling. In contrast, Fe-Si-B-Nb-Cu nanocrystalline alloys (NCs) have emerged as promising alternatives due to their high saturation flux density (~1.2 T), lower hysteresis losses, and higher Curie temperatures[2].
However, the conductivity of these materials is very high, which leads to large eddy-current losses at 85 kHz. To reduce the effective conductivity, the ribbon is mechanically fractured into pieces[3]. In addition, the ribbon-based manufacturing process enables laminated structures with thicknesses typically between 14 and 20 µm, which, combined with fracturing, effectively suppresses eddy-current losses despite the relatively high electrical conductivity of the alloy.
This article evaluates six commercial soft magnetic materials for wireless EV charging applications: two Mn-Zn ferrite materials, two non-fractured (NF) NCs, and the same two NCs fractured (F.) to reduce their effective conductivity. These materials include new ferrites and NCs that have not been reported in the literature, with losses <50% of those of the standard N95. With a particular focus on core losses, each material is characterized from room temperature to ~100 °C at 85 kHz, with field amplitudes expected in EV charging (>200 mT). To quantify the trade-offs associated with fractured materials, anisotropic electrical conductivity is also measured.

1. Covic GA, Boys JT. Modern Trends in Inductive Power Transfer for Transportation Applications. IEEE J Emerg Sel Topics Power Electron. 2013 Mar;1(1):28–41.
2. Gaona DE, Jiang C, Long T. Highly Efficient 11.1-kW Wireless Power Transfer Utilizing Nanocrystalline Ribbon Cores. IEEE Trans Power Electron. 2021 Sep;36(9):9955–69.
3. Bailey AK et al. Anisotropic Characterization of Nanocrystalline Alloys for Inductive Power Transfer. IEEE Open Journal of Power Electronics. 2024;5:1830–41.

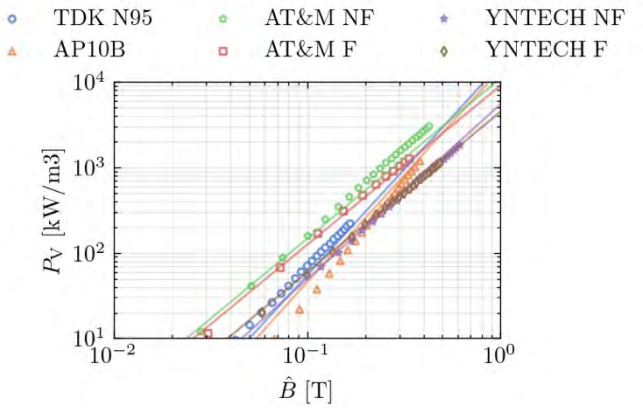


Fig. 1 Measured core loss versus flux density at room temperature for each material.

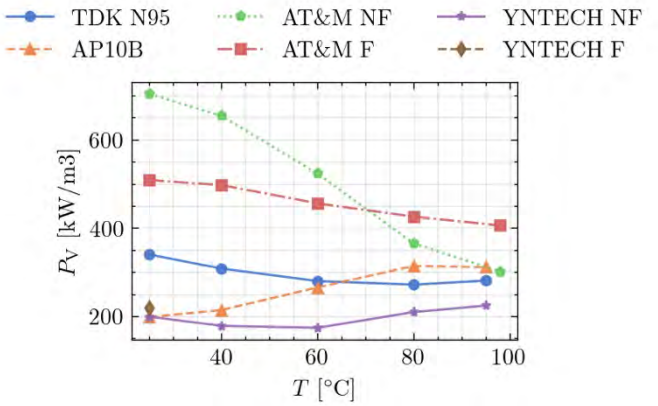


Fig. 2 Measured core loss from room temperature to ~100 °C for each material at 200 mT.

DE-13. Investigation of Output Power Improvement in an Electrothermal Multi-Energy Dual-Stator PMSM Based on an α-Fe/Cr-Rich Dual-Phase Magnetic Composite

J. Yuan[1, 2], Y. Wang[1, 2], H. Wang[1, 2], H. Zhou[1, 2], F. Xiao[1, 2], D. Dong[3]

[1]School of Electrical Engineering and Automation, Wuhan University, Wuhan, Hubei, China, [2]State Key Laboratory of Power Grid Environmental Protection, School of Electrical Engineering and Automation, Wuhan University, Wuhan, Hubei, China, [3]Xiangtan Electric Manufacturing Co., Ltd, Xiangtan, Hunan, China

An electrothermal multi-energy dual-stator permanent magnet synchronous motor (PMSM) can simultaneously deliver electrical and useful thermal power, supporting efficient renewable-energy utilization. In the conventional series-magnetic-circuit topology, the permanent-magnet flux is not fully utilized, leaving room for further improvement of the dual electrothermal outputs. A full-rotor replacement design using an α-Fe/Cr-rich dual-phase magnetic composite (DPC) is therefore proposed with an alternating-pole magnetization pattern matched to the inner and outer PM pole sequence, as shown in Figure 1(a), for output-power improvement in this motor topology. Figure 1(b) shows that the DPC exhibits finite remanence, low coercivity, and adequate flux-carrying capability. Based on these characteristics, it is introduced into the rotor in this work. Compared with the original silicon-steel rotor, the proposed rotor preserves the weak-coupling balance required by the series-magnetic-circuit structure, retains flux conduction, and enhances the air-gap magnetic field through auxiliary magnetization, with the potential to improve output power.

A two-dimensional transient finite-element model was used to compare the original silicon-steel rotor with the proposed DPC rotor. Figures 2(a) and 2(b) show that the proposed rotor reconstructs the flux distribution near the inner and outer air gaps. Figure 2(c) further indicates enhanced air-gap flux density in the generating region. Figure 2(d) shows improved steady-state electrical power, thermal power, and total useful output. Relative to the original rotor, the proposed model improves these three outputs by 13.03%, 1.47%, and 6.96%, respectively. These results indicate that the α-Fe/Cr-rich DPC can enhance the inner and outer air-gap magnetic fields without disturbing the original weak-coupling relationship, thereby improving the output performance of the electrothermal multi-energy dual-stator PMSM and providing a feasible route for applying dual-phase magnetic composites in electrothermal permanent magnet motors.

[1]Jiaxin Yuan, Hao Wang, Bin Peng, Hang Zhou, Qiong Wang, Xiaoguo Chen; Composite dissimilar material based heating power optimization method for electro-thermal multi-energy flexible generator. *AIP Advances* 1 February 2026; 16 (2): 025101.

[2]Jiaxin Yuan, Daixue Zhang, Fuyao Yang, Yang Liu, Cong Wang, Tao Ma, Xinping Guo, Xiaobing Ma, Yijie Zhao, Jiangbo Chen; DFT-based design and magnetic properties optimization of the α-Fe/$Nd_2Fe_{14}B$ dual-phase composite interface. *AIP Advances* 1 April 2026; 16 (4): 045023.

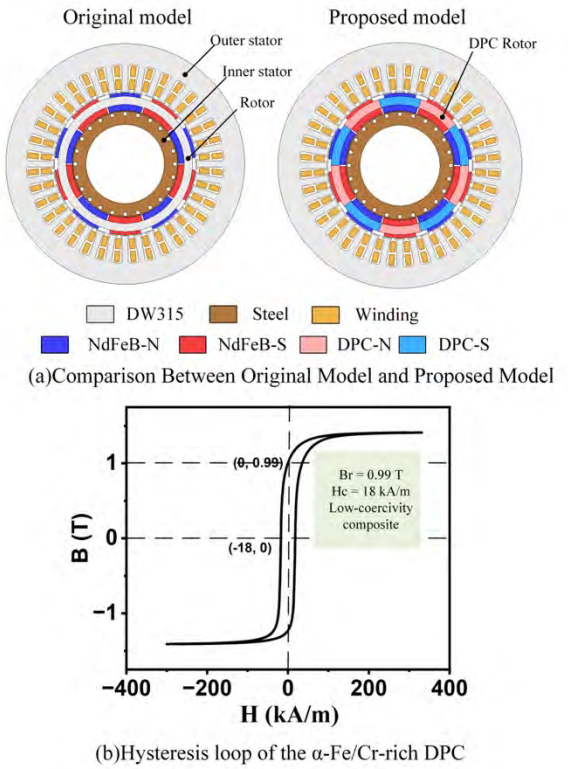


Fig. 1 Proposed rotor design and magnetic property of the DPC.

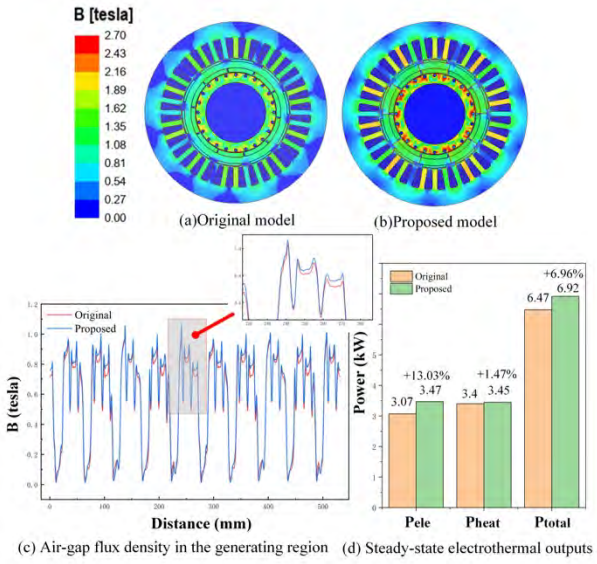


Fig. 2 Magnetic-field redistribution, air-gap flux density, and electrothermal performance.

SESSION DF: MAGNETORESISTANCE I

Chair(s): Y. Li, *Argonne National Laboratory, Lemont, Illinois, United States*

Wednesday, November 4, 2026

02:00 PM-05:30 PM

South Pacific 3/4

DF-01. Large Tunneling Magnetoresistance in All-Oxide Magnetic Tunnel Junctions with Perpendicular Magnetic Anisotropy

T. Banerjee

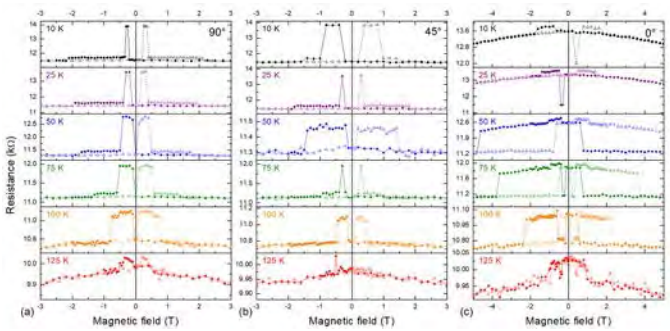
University of Groningen, Groningen, Netherlands

Spintronics has opened many avenues in condensed matter, revolutionized the data storage industry and holds rich prospects for low power computing. Magnetic tunnel junctions (MTJs) based on transition metal ferromagnets are the workhorse of non volatile spintronic devices and has witnessed an evolution, both in the choice of materials and in the physics behind spin-dependent tunneling at their interfaces. The material and design aspects of such MTJs are well explored and today includes antiferromagnets as active elements, expanding computing primitives beyond spin to include orbitals and magnons for new applications. Another material class, that of complex oxides, where the fundamental thrust is on understanding the strong correlations between the electron charge, spin and orbital degrees of freedom has established itself as an equally important material system in Spintronics, with promising applications in unconventional computing schemes. The flexibility in design control of their functional properties realized through strain or doping and modulated through external stimuli such as electric current, heat, or light leads to coexisting and competing ground states, and are unique to these materials.

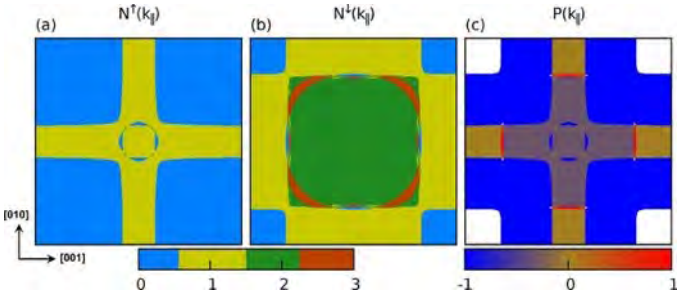
STT-MRAM devices utilizing MTJs of transition metal ferromagnets, typically need a complex stack design to realize the required perpendicular magnetic anisotropy (PMA). In this talk I will discuss an itinerant ferromagnet, SrRuO3 (SRO),which has been extensively investigated for many interesting magnetic phenomena, such as topological Hall effects, Weyl fermions, and topological textures such as skyrmion bubbles. Using SRO in an all-oxide MTJ stack of SRO/SrTiO3 (STO)/SRO, we show how the intrinsic nature of PMA in SRO gives rise to a significantly large TMR value, without the need of complex stack design. For this we tailor the magnetic anisotropy and optimize multilayer stacks with magnetically decoupled SRO layer of varying thickness. The strong spin-orbit coupling of the heavy Ru ions in SRO gives

rise to its magnetocrystalline anisotropy that is exploited to overcome technical challenges related to creating optimized MTJ stack with two ferromagnetic metallic electrodes with PMA. Large TMR values of 25% significantly exceeding previously reported values of TMR in MTJs based on SrRuO3 electrodes were achieved, complemented by density functional theory (DFT) calculations of an expected TMR of 1800%, arising from a significant reduction of transmission in the antiparallel state due to a symmetry mismatch between the propagating Bloch states of the minority and majority spin bands of SRO (001). Uniquely, we also study the angular variation of the TMR which reveals that the electrodes contain multiple magnetic domains with strong perpendicular magnetic anisotropy, allowing the devices to exhibit at least three stable resistance states. Overall, the use of SRO in MTJs provides a facile method for achieving perpendicular magnetic anisotropy and a sizable TMR ratio for potential applications in emerging technologies beyond conventional MRAMs such as in new energy-efficient computing hardware.

[1] Symmetry-driven large tunneling magnetoresistance in SrRuO3 magnetic tunnel junctions with perpendicular magnetic anisotropy; Goossens, A. S., Samanta, K., Jaman, A., Boubaker, W., Van Rijn, J. J. L., Tsymbal, E. Y., & Banerjee, T. Physical Review Materials, 8(9), Article L091401. https://doi.org/(...)vMaterials.8.L091401 (2024)
[2] Anisotropy and Current Control of Magnetization in SrRuO3/SrTiO3 Heterostructures for Spin-Memristors. Goossens, A. S., Leiviskä, M. A. T., & Banerjee, T. Frontiers in Nanotechnology, 3, Article 680468. https://doi.org/(...)89/fnano.2021.680468 (2021).
[3] Robust skyrmion-bubble textures in SrRuO3 thin films stabilized by magnetic anisotropy. Zhang, P., Das, A., Barts, E., Azhar, M., Si, L., Held, K., Mostovoy, M., & Banerjee, T. Physical Review Research, 2(3), Article 032026(R). https://doi.org/(...)RevResearch.2.032026, (2020).



Resistance-area product versus magnetic field of an epitaxial MTJ junction of SRO (28.8 nm)/STO (4.7 nm)/SRO (51.5 nm) with the field applied out-of-plane (left), at 45 degrees and in the plane.



Distribution of the conduction channel, $N(k_{\parallel})$ in the 2D Brillouin zone for (a) majority and (b) minority-spin electrons at the Fermi energy and (c) of the polarization in the 2D Brillouin zone at E_F .

DF-02. Dependence of electrical 1/f noise on annealing conditions in magnetic tunnel junctions with Mg-Al-O barriers

H. He[1], C. Zhang[1, 2], T. Nakano[1, 3], Y. Wang[1], M. Oogane[1, 4]
[1]Tohoku Univ., Sendai, Japan, [2]CIES, Tohoku Univ., Sendai, Japan, [3]Green X-Tech, Tohoku Univ., Sendai, Japan, [4]CSIS, Tohoku Univ., Sendai, Japan

Magnetic tunnel junction (MTJ)-based tunnel magnetoresistance (TMR) sensors are promising for biomedical and weak-field sensing applications [1], where electrical 1/f noise limits performance. This noise mainly originates from charge trapping and detrapping at defects in the tunnel barrier and its interfaces [2]. Compared with conventional MgO-based MTJs, Mg-Al-O (MAO) barriers provide better lattice matching with Fe-based electrodes and have been reported to reduce electrical 1/f noise by nearly one order of magnitude [3]. However, the influence of annealing conditions on electrical 1/f noise remains unclear. MTJ stacks are deposited on Si/SiO2 substrates by magnetron sputtering. The MAO barrier is formed by alternating Mg and Al deposition followed by oxidation. The MAO layer is then annealed at 300 °C (TMAO). After fabrication, samples are post-annealed for 1 h under a 1 T magnetic field, with Ta varied from 250 to 450 °C (Ta). Electrical 1/f noise is measured using a four-probe method and quantified by the Hooge parameter (alpha_ele).
The Hooge parameter alpha_ele exhibits a non-monotonic dependence on Ta, as shown in Fig. 1. It reaches a minimum value of ~1.3 × 10^-9 μm ^2 at Ta ≈ 375 °C and increases at higher annealing temperatures.To clarify the origin of this behavior, selected samples are analyzed using STEM and EDX. Fast Fourier transform (FFT) analysis is performed on

the STEM images. Increasing Ta improves the crystallinity and structural uniformity of the MAO barrier, CoFeB layers, and their interfaces, reaching an optimum at Ta ≈ 375 °C. However, at higher temperatures, Mn diffusion from the IrMn layer into the MAO barrier deteriorates its structural uniformity, which correlates well with the noise behavior. In summary, optimizing annealing conditions to control the crystallinity of the MAO barrier and its interfaces is essential for achieving low-noise MAO-based TMR sensors.
Acknowledge : This work was partially supported by the X-nics project and CSIS, and CIES at Tohoku University, SIP project and BRIDGE project of Cabinet Office, JSPS KAKENHI 24K17316, and research grants of Hirose Foundation.
References: [1] T. Nakano, K. Fujiwara, M. Oogane, Appl. Phys. Lett. 126, 160503 (2025). [2] M. B. Weissman, Rev. Mod. Phys. 60, 537 (1988). [3] S. Nii, C. Zhang, Y. Wang, JSAP conference, 2025.

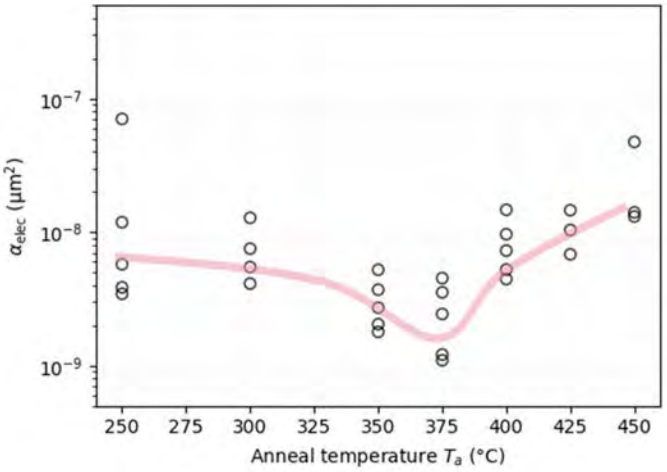


Fig. 1. Hooge parameter (alpha_ele) as a function of post-annealing temperature Ta.

DF-03. Experimental Signatures of Topological Transport in Polycrystalline FeSi Thin Films

R. Mantovan[1], A. Bozhko[2], V. Zhurkin[2], A. Bogach[2], A. Khanas[3], S. Zarubin[3], A. Zenkevich[3], V. Glushkov[2]
[1]Unit of Agrate Brianza, CNR-IMM, Agrate Brianza (MB), Italy, [2]Prokhorov General Physics Institute, Russian Academy of Sciences, Moskow, Russian Federation, [3]Moscow Institute of Physics and Technology, Moskow, Russian Federation

Non-centrosymmetric *M*Si monosilicides (*M*=Fe, Co, Mn, Rh, Ru etc., space group 198, $P2_13$) have renewed keen interest among researchers after *ab initio* calculations predicted exotic massless fermionic excitations with nonzero Berry flux in CoSi [1] and unconventional chiral fermions and large topological Fermi arcs in RhSi [2]. While non-vanishing Berry phase in FeSi was predicted in 2013 [3], its experimental proof is missing so far, and our contribution presents a first convincing step in this direction.
Disorder in any form is considered to be highly detrimental to the experimental exploration of novel phenomena in quantum materials with non-trivial band topology. Here we reliably detect topological features in conductivity of polycrystalline 65-nm-thick ε-^{57}FeSi films grown via solid-state reaction of Fe deposited by pulsed laser deposition (PLD) on a Si(100) substrate [4]. The ^{57}Fe target enrichment allows to conduct conversion electron Mössbauer spectroscopy to confirm the pure ε-FeSi phase [4]. Measuring of the longitudinal and transverse voltages on the hall bars patterned samples under different directions of applied magnetic field B allow to track the anomalous, longitudinal and planar Hall conductivities (σ_{xy}^{AHE}, σ_{xy}^{LHE}, σ_{xy}^{PHE}) at temperatures 1.7K – 300K. Below 200 K, the observed σ_{xy}^{AHE}≈14 μS/sq. ~ const (σ_{xx}), Fig.1(a), firmly proves the AHE in this compound to be intrinsic and originating from a non-trivial Berry phase [4]. The non-trivial topological state of ε-FeSi is also confirmed by a chiral anomaly both in anisotropic magnetoresistance and PHE specific for Weyl semimetals. Relating scaled σ_{xy}^{AHE} to a "quantized" Hall response of a Weyl semimetal the distance between two Weyl points is estimated as $(k_+^W - k_-^W)/(2\pi)$≈0.36, Fig.1(b). Our findings confirm the topological origin of electron transport in the polycrystalline ε-FeSi thin films and discover its potential as a new high temperature and noble metal-free Weyl semimetal [4].
[1] P. Tang et al., Phys. Rev. Lett. 119, 206402 (2017)
[2] G. Chang et al., Phys. Rev. Lett. 119, 206401 (2017)
[3] J. Kübler et al., Europhys. Lett. 104, 30001 (2013).
[4] R. Mantovan et al., arXiv (2026): https://doi.org/10.48550/arXiv.2604.17103

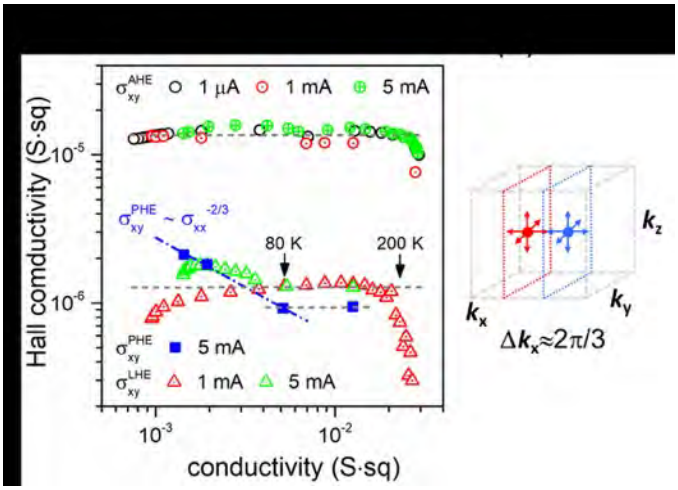


Figure 1. (a) Anomalous, longitudinal and planar Hall conductivities (σ_{xy}^{AHE}, σ_{xy}^{LHE}, σ_{xy}^{PHE}) as a function of σ_{xx}. Horizontal grey dashed lines correspond to intrinsic AHE due to non-zero Berry phase. (b) One pair of Weyl nodes of opposite chirality in 3D momentum space.

DF-04. Large Tunnel Magnetocapacitance of up to 661% at High Frequencies in FeCoB/MgO/FeCoB Magnetic Tunnel Junctions

R. Okazaki[1], Y. Shibata[1], M. Matsuzaka[1], M. Wakamoto[1], J. Uzuhashi[5], T. Ohkubo[5], H. Sukegawa[2], G. Xiao[3], H. Kaiju[1, 4]
[1]Faculty of Science and Technology, Keio University, Yokohama, Kohoku-ku, Kanagawa, Japan, [2]Research Center for Magnetic and Spintronic Materials, National Institute for Materials Science, Tsukuba, Ibaraki, Japan, [3]Department of Physics, Brown University, Providence, Rhode Island, United States, [4]Center for Spintronics Research Network, Keio University, Yokohama, Kanagawa, Japan, [5]National Institute for Materials Science, Tsukuba, Ibaraki, Japan

Magnetic tunnel junctions (MTJs) exhibit a large tunnel magnetocapacitance (TMC) at room temperature (RT) [1]. Recently, a large TMC of 456% has been observed in FeCo/$MgAl_2O_4$/FeCo(001) MTJs [2]. However, the TMC ratios are limited to 22%–100% in the high-frequency (~MHz) region [1–3]. According to the Debye-Fröhlich (DF) model, a large TMC is predicted at higher frequencies in MTJs with a thinner insulator. In this study, we report a giant TMC effect at high frequencies by controlling the interface quality and insulator thickness (d_{MgO}) in FeCoB/MgO/FeCoB MTJs, and we clarify the mechanism of the giant TMC using an extended DF model.
The MTJs were prepared using an ultra-high vacuum magnetron sputtering system, with a base pressure of 5 × 10^{-7} Pa, with the following layer sequence: Si/SiO_2 substrate/[Ta (5)/Ru (20)]$_3$/Ta (5)/FeCoB (4)/FeCo (1)/MgO (d_{MgO} = 1.7–2.5 nm)/annealing/FeCoB (3.5)/FeCo (0.7)/Ru (1.3)/FeCo (3)/IrMn (8)/Ru (8) (unit: nm). Post-heating process after the MgO insulator deposition improves the crystallinity. The TMC effect in MTJs, after patterning into a 10 × 5 μm^2 area, was measured by an AC four-probe method at RT. The bright-field scanning transmission electron microscopy image shows good crystallinity and flatness of the MgO interfaces with highly (001) orientation. We observe a giant TMC ratio of up to 661% in MTJs with d_{MgO} = 1.79 nm at 1 MHz, which is higher than the tunnel magnetoresistance ratio of 350% measured at DC. Futhermore it is the largest value ever reported for MTJs. The TMC ratio increases (decreases) for lower (higher) d_{MgO} at higher frequencies, which is consistent with the extended DF model calculation incorporating the thickness-dependent tunneling term. The MgO thickness dependence of capacitance $C_{P(AP)}$ in the parallel (antiparallel) magnetization state at 1 MHz shows a significant difference between C_P and C_{AP}, resulting in a giant TMC ratio. This study contributes to realizing large TMC at higher frequencies, opening exciting opportunities for novel spintronic applications.
This work was supported by JSPS KAKENHI 24K00948, 24H00408, MEXT Data Creation and Utilization-Type Material Research and Development Project JPMXP1122715503, and Electron Microscopy Unit of NIMS.
[1] H. Kaiju *et al.*, *Appl. Phys. Lett.*, Vol. 107, 132405 (2015).
[2] Y. Shibata, K. Sato, H. Sukegawa, and H. Kaiju, *Appl. Phys. Express*, Vol. 16, 113003 (2023).
[3] P. Padhan *et al.*, *Appl. Phys. Lett.*, Vol. 90, 142105 (2007).

DF-05. Spin–Orbit Torque Memory to In-Memory Computing: Materials, Arrays, and Architectures for Energy-Efficient AI Hardware

Y. Huang
Materials Science and Engineering, National Yang Ming Chiao Tung University, Hsinchu City, Taiwan

The rapid expansion of data-intensive edge computing, autonomous systems, and scientific workloads has exposed the energy and latency limitations of conventional von Neumann architectures, where data movement between memory and logic increasingly dominates power consumption. This challenge motivates the development of memory technologies that are not only dense, fast, and non-volatile, but also capable of performing computation

directly within memory arrays.
Spin–orbit torque magnetic random-access memory (SOT-MRAM) offers a promising platform for this transition because it combines non-volatility, high endurance, ultrafast operation, and decoupled read/write paths. In this talk, I will present our recent progress in advancing SOT-MRAM from materials design to array-level integration and in-memory computing. At the materials level, we use spin-source engineering, including β-tungsten stabilization and symmetry-broken W-based heterostructures, to enhance spin Hall efficiency, reduce switching current, and enable deterministic field-free switching of perpendicular magnetic anisotropy devices.
At the device and circuit levels, we demonstrate a CMOS-compatible 64-kb SOT-MRAM array fabricated on 200-mm wafers, establishing a scalable platform for embedded non-volatile memory. More importantly, the array architecture enables computation to be performed directly where data are stored. By exploiting the conductance states of magnetic tunnel junctions and current summation along bit lines, SOT-MRAM arrays can naturally execute vector–matrix operations, reducing costly data transfer and improving energy efficiency.
Leveraging this hardware foundation, I will further discuss closed-loop analogue in-memory computing based on SOT-MRAM arrays. Unlike conventional open-loop in-memory computing, which primarily performs matrix–vector multiplication, closed-loop operation can directly solve inverse matrix–vector multiplication problems, enabling acceleration of linear-system solvers, optimization tasks, and differential-equation-based workloads. This expands SOT-MRAM from a non-volatile memory technology into a normally-off, instantly-on computing primitive.
Finally, I will place these results in the broader context of low-power functional materials and devices, including ferroelectric and multiferroic systems. Electrode design, polarization engineering, and Landau-Devonshire-guided optimization in $BiFeO_3$- and HfO_2-based heterostructures offer complementary routes to low-voltage switching and improved device stability. Together, these advances show how materials engineering, device physics, array integration, and computing architecture can be co-designed to enable next-generation energy-efficient memory and computational systems.

DF-06. Anisotropic Magneto-transport properties in Te/metal Bilayers

A. Mitsuzuka, Y. Kobayashi, S. Wang, M. Kawaguchi, M. Hayashi
Department of Physics, The University of Tokyo, Tokyo, Japan

Tellurium (Te) is a unique material composed of one-dimensional helical atomic chains[1]. Owing to its chiral crystal structure and anisotropic electronic states, Te has attracted considerable interest for its distinct transport properties, including nonreciprocal magnetoresistance[2] and nonlinear Hall effect[3,4]. Although the transport properties of Te have been actively studied in recent years, most previous works have focused on pristine Te, and the impact of interfacial coupling with dissimilar materials on its magnetotransport remains poorly understood. Understanding transport in Te-based heterostructures is therefore important from both fundamental and device-oriented perspectives.
Here, we study interfacial magnetotransport in Te thin films grown on a metallic seed layer. The samples were fabricated by sputtering and molecular beam epitaxy, and the crystal-axis orientation of Te was controlled by linearly polarized pulsed-laser irradiation, enabling preparation of samples with the Te crystal axis either parallel or perpendicular to the current direction[5]. Longitudinal resistance and Hall signals were measured as functions of magnetic-field and temperature. Despite the fact that the current is expected to flow mainly through the metallic layer, pronounced anisotropic magnetoresistance and planar Hall effect (PHE) signals were observed. These responses show a clear dependence on the Te crystal-axis orientation, indicating the role Te and interfacial coupling play in magnetotransport properties.
In the presentation, we will discuss the dependence of the magnetotransport properties on the choice of metallic seed layer and temperature.
[1] C. Adenis et al., Acta Crystallographica, Section C: Crystal Structure
Communications 45, 941 (1989).
[2] Calavalle, F et al., Nature Materials, 21(5), 526-532 (2022).
[3] Cheng, B et al., Nature Communications, 15(1), 5513 (2024).
[4] Zhang, N et al., Proceedings of the National Academy of Sciences, 117(21), 11337-11343 (2020).
[5] Kobayashi, Y et al., Nano Letters, 26(1), 104-110 (2025).

DF-07. Chirality-Induced Spin Selectivity via Interlayer Exchange Coupling with an Iridium Spacer Layer

S. Miwa[1], S. Yoshioka[1], S. Kamisaka[1], M. Matsuzaka[1], T. Yamamoto[2], T. Nozaki[2]
[1]The Institute for Solid State Physics, The University of Tokyo, Kashiwa, Chiba, Japan, [2]Research Institute for Hybrid Functional Integration, National Institute of Advanced Industrial Science and Technology (AIST), Tsukuba, Ibaraki, Japan

Numerous studies have reported a variety of phenomena related to chirality-induced spin selectivity (CISS) [1]. Among these, one notable phenomenon is the emergence of magnetoconductance (MC) effect in junctions comprising chiral molecules and ferromagnetic electrodes. However, theoretical studies suggest that the chirality-induced MC effect cannot be understood from the perspective of symmetry. Recently, using an electrochemical cell with CoPt/Au, it was proposed that interlayer exchange coupling (IEC) between chiral molecules and ferromagnets provide a physically consistent mechanism for the observed MC effect [2]. Since Ir is known to mediate strong IEC [3], in this study, we further investigated the role of IEC on CISS using an Ir spacer.

We used a custom-made electrochemical cell [2]. The multilayer structure of the electrode was Ta (5 nm)/Pt (10 nm)/[Co (0.25 nm)/Pt (0.15 nm)]$_{20}$/Co (0.25 nm)/Ir (2 nm), as shown in Fig. 1(a). The solution included a chiral electrolyte ((1*S*)-(+)-camphor-10-sulfonic acid ((*S*)-CSA) at a concentration of 4 mM. Figure 1(b) depicts typical current–voltage characteristics. The current exhibited a peak at −1.6 V, indicating electrochemical reduction of CSA. Figure 2(a) shows representative results of the MC measurements at −1.8 V. A magnetic field of ±0.6 T was applied, and the conductance change was monitored for 300 s after switching the polarity of the magnetic field. The MC ratio was defined as $(I_{B=+0.6\ T} - I_{B=-0.6\ T})/(I_{B=+0.6\ T} + I_{B=-0.6\ T})$. Switching the magnetic field polarity caused a gradual change in current, which is the MC effect. Note that the polarity of the MC effect depends on the elapsed time. Figure 2(b) shows the time evolution of the MC ratio, which oscillates, including the sign reversals. This oscillatory MC behavior is attributed to IEC between CoPt and (*S*)-CSA mediated by the Ir layer, as the surface Ir layer dissolves and Ir thickness gradually decreases with time.

We thank T. Ohto for discussion, and Y. Kato for assistance. A part of this work was supported by JSPS-KAKENHI, JST-ASPIRE, Spin-RNJ, and MEXT-Xnics.

[1] R. Naaman *et al*., Nat. Rev. Chem., Vol. 3, 250 (2019).
[2] S. Miwa *et al*., Sci. Adv., Vol. 11, eadv5220 (2025).
[3] K. Yakushiji *et al*., Appl. Phys. Lett., Vol. 110, 092406 (2017).

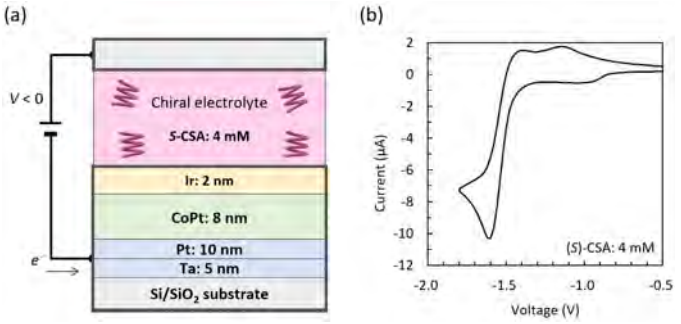


Fig. 1 (a) Sample structure. (b) Current–voltage characteristics.

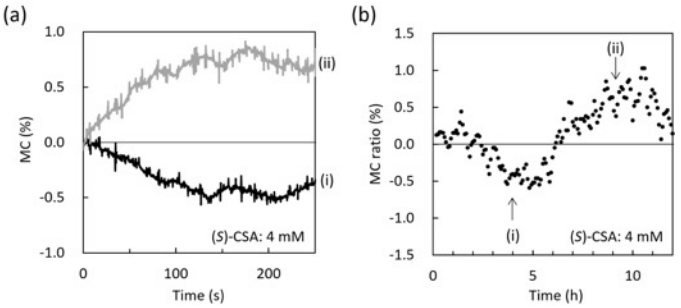


Fig. 2 (a) Typical MC effect. (b) MC ratio as a function of the elapse time.

DF-08. High-entropy oxides tunnel barrier LiTiMgAlGaO for magnetic tunnel junctions

R. R. Sihombing[1, 2], T. Scheike[1], J. Uzuhashi[1], H. Yasufuku[1], T. Ohkubo[1], Z. Wen[1], S. Mitani[1, 2], H. Sukegawa[1, 2]
[1]Spintronics, 1National Institute of Materials Science, Tsukuba, Ibaraki, Japan, [2]Graduate School of Science and Technology, Tsukuba University, Tsukuba, Ibaraki, Japan

High-entropy materials, including high-entropy oxides (HEOs), have emerged as a transformative class of materials due to their unique properties, which differ from those of conventional simple compounds[1]. The peculiar features of HEOs will be promising as a stable barrier of magnetic tunnel junctions (MTJs), which exhibit high tunnel magnetoresistance (TMR) ratios and large interfacial perpendicular magnetic anisotropy (PMA). Especially, an HEO barrier will provide a small band gap[2], which is ideal for reducing the resistance area (*RA*) products of MTJs for use in high-density memories. Here, we developed an HEO ultrathin film, LiTiMgAlGaO (hereafter, L5O), as an MTJ barrier[3]. Epitaxial rock-salt-type L5O(001) films were developed using the atomic lamination of LiTiO and

MgAlGaO oxide layers.
We observed PMA properties at the L5O/$Co_{20}Fe_{60}B_{20}$ (CoFeB) interface. We prepared a stack structure consisting of MgO(001) substrate/$[LiTiO\ (0.3)/MgAlGaO\ (0.4)]_{15}$ (10.5)/CoFeB (1.1)/W (0.3)/Ta (5), (in nm). We found that the L5O layers were epitaxially grown with a high (001) orientation and a homogeneous cation distribution [Fig. 1(a)]. A high interfacial PMA energy of 0.8 erg/cm^2 was obtained at the L5O/CoFeB interface due to the structural stability of L5O and the good interfacial sharpness.
We also observed a high TMR ratio of 84% at room temperature (Fig. 1(b)) using Fe/L5O/Fe(001) MTJs with a stack structure of MgO(001) substrate/Cr (60)/Fe (50)/MgO (0.45)/L5O (1.9)/MgO (0.3)/Fe (5)/IrMn(10)/Ru (10), (in nm). The inserted nano-MgO layers improved the interfacial states. The TMR ratio indicates the occurrence of spin-dependent coherent tunneling through the L5O. Notably, the barrier has a low barrier height of 1 eV, which is half that of MgO, promising to reduce *RA*. Our results demonstrate that HEOs are promising barrier materials for future spintronic devices. This work was partially supported by MEXT Program: Data Creation and Utilization-Type Material Research and Development Project (JPMXP1122715503), MEXT Initiative to Establish Next-generation Novel Integrated Circuits Centers (X-NICS) (JPJ011438), and JSPS KAKENHI (22H04966 and 24H00408).
[1] B. Cantor *et al.*, Mater. Sci. Eng. A 375–377, 213 (2004).
[2] R. R. Katzbaer *et al.* J. Am. Chem. Soc. 145, 6753 (2023)
[3] R. R. Sihombing *et al.*, Mater. Today 88, 12 (2025).

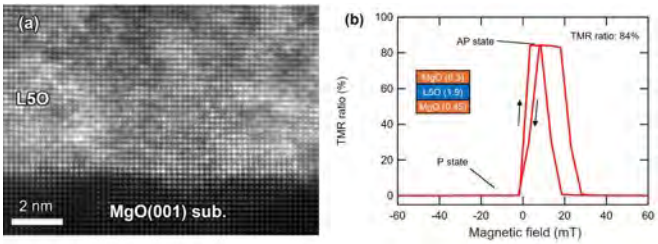


Fig. 1. (a) STEM image of L5O(001) film and (b) TMR curve of L5O-MTJs.

DF-09. Investigation of spin-mediated thermal transport in CoFe/NM multilayers: NM layer thickness and material dependence (NM=Ag, Pt)

F. Makino[1, 2], T. Hirai[2], H. Suto[2], K. Uchida[1, 2, 3], Y. Sakuraba[1, 2]
[1]University of Tsukuba, Tsukuba, Ibaraki, Japan, [2]National Institute for Materials Science (NIMS), Tsukuba, Ibaraki, Japan, [3]The University of Tokyo, Kashiwa, Chiba, Japan

The giant magneto-thermal resistance (GMTR) effect is a phenomenon where the thermal conductivity (κ) changes with the magnetization configuration in alternating stacks of ferromagnetic (FM) and nonmagnetic (NM) materials. Recent studies reported a large MTR ratio in CoFe/bcc-Cu multilayers, which is attributed to additional heat carriers beyond electrons and phonons [1,2]. Ping *et al.* theoretically proposed that the non-equilibrium magnon produces the interfacial thermal resistance in multilayer systems by inducing the spin diffusion in the NM layer [3]. Assuming this mechanism is an origin of additional heat carriers, the spin diffusion length (λ) in the NM layer is expected to affect the magnon-mediated κ. In this study, we investigate the κ in CoFe/NM by varying the NM layer thickness using different NM materials with distinct λ.
$[CoFe/NM]_{20}$/CoFe multilayers were deposited on MgO (001) substrates with varying NM layer thickness (t_{NM}). Ag and Pt were used as the NM layer because λ of Pt (~2 nm) is much shorter than that of Ag (>100 nm). The cross-plane thermal conductivity (κ_{exp}) was measured using the time-domain thermoreflectance method (TDTR) (Fig.1) [4]. We also estimated the electron thermal conductivity (κ_{ele}) using two-current model [5] and Wiedemann-Franz law. Then, we calculated κ_{exp}-κ_{ele} to evaluate the additional thermal conductivity. κ_{exp}-κ_{ele} in the CoFe/Cu (~35 $Wm^{-1}K^{-1}$) [1] is significantly larger than that in CoFe/Ag and CoFe/Pt (Fig.2). Interestingly, κ_{exp}-κ_{ele} in CoFe/Ag is negligibly small although λ of both bcc-Cu and Ag is much longer than 10 nm. This result suggests the interfacial electronic band matching between FM and NM layers [6] is also important to enhance the magnon contribution. In the case of Pt, the exponential decay of κ_{exp}-κ_{ele} was observed, indicating the spin relaxation affects the thermal conductivity in multilayer systems. Our results provide insights into the thermal conduction on the spin transport in magnetic multilayer systems.
[1] F. Makino, T. Hirai, and T. Shiga, Phys. Rev. B, Vol. 112, p.054407 (2025)
[2] H. Nakayama, B. Xu, and S. Iwamoto, Appl. Phys. Lett., Vol. 118, p.042409 (2021)
[3] P. Tang, K. Uchida, and G. E. W. Bauer, Phys. Rev. B, Vol.

111, p.L180407 (2025)
[4] T. Hirai, T. Morita, and S. Biswas, Adv. Funct. Mater., Vol. 35, p.2506554 (2025)
[5] T. Valet and A. Fert, Phys. Rev. B, Vol. 48, p.7099 (1993)
[6] K. B. Fathoni, Y. Sakuraba, and Y. Miura, J. Phys. D: Appl. Phys., Vol. 55 p.125001 (2022)

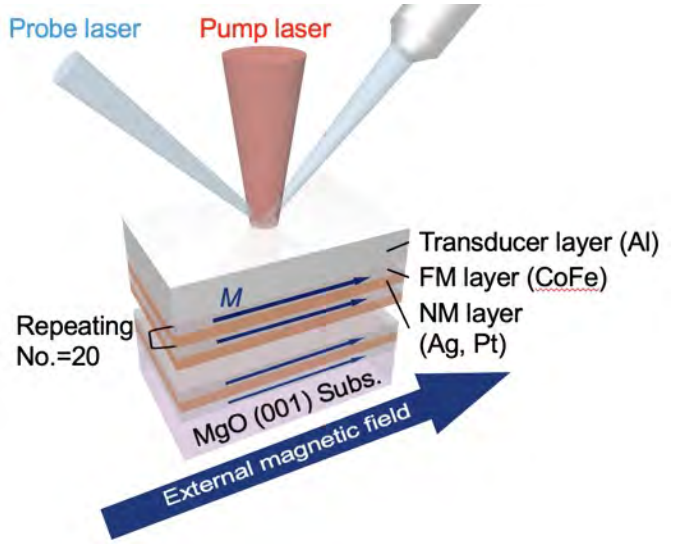


Fig. 1 Schematic of the TDTR method in multilayers consisting of FM and NM layers. Blue arrows represent the magnetization (*M*) direction of the FM layer.

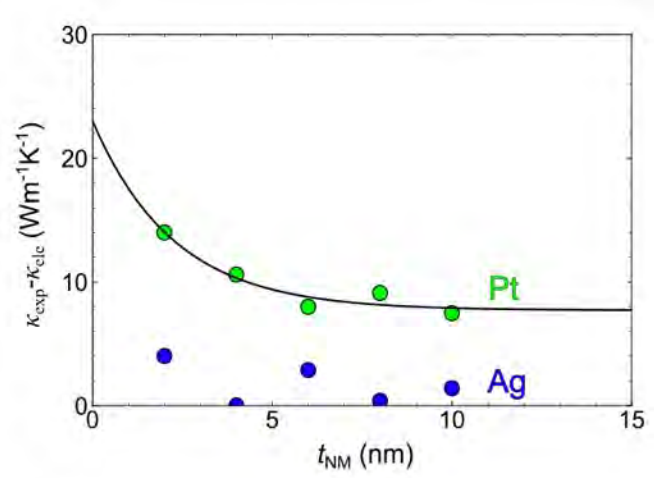


Fig. 2 t_{NM} dependence of deviation between κ_{exp} and κ_{ele}.

SESSION DG: MAGNONICS I

Chair(s): D. R. Hart, *Mathematics and Physics, Southern University and A & M College, Baton Rouge, Louisiana, United States*

Wednesday, November 4, 2026
02:00 PM-05:30 PM
Sea Pearl

DG-01. Magnetic Metamaterials with Time-Varying Permeability

T. Kodama
Institute for Excellence in Higher Education, Tohoku University, Sendai, Japan

Artificial structures called metamaterials exhibit intriguing electromagnetic responses unavailable in natural materials. Very recently, time-varying metamaterials, in which the refractive index is modulated in time, have emerged for a new paradigm of wave generation and manipulation [1]. The temporal modulation of electric permittivity (ε) has been realized so far [2]. While, time modulation of both ε and magnetic permeability (μ) is of great interest in terms of synthetic moving media and quantum electrodynamics [2], experimental demonstration of tempiral μ is lacking.

Ferromagnetic materials show a frequency dispersion of μ in the vicinity of ferromagnetic resonance (FMR) at GHz frequencies. Therefore, μ for microwaves at GHz frequencies can be modulated when the FMR conditions are varied. Previously, we proposed μ modulation using spin-injection in the ferromagnetic/heavy-metal bilayers [3]. Recently, we demonstrate another route to μ time-varying metamaterials using oscillating magnetic fields [4].

Figure 1 show the prepared device for the measurements. In the preparation, a meandering modulation line of Gold (Au) is patterned on an undoped silicon substrate. The Gold thickness is 200 nm. The width of the meandering lines is 5 μm and the line spacing is 10 μm. Next, a silicon oxide (SiO_2) layer of 200 nm thickness is deposited on the portion indicated by blue color. After that, a coplanar waveguide for carrier waves is patterned as indicated by red color. The signal line (S) width is 5 μm and the gap distance between the signal and ground lines (G) is 5 μm. Finally, 5-nm-thick tantalum (Ta) and 250-nm-thick permalloy (Py, $Fe_{20}Ni_{80}$) are deposited at the 5 × 5 μm intersection area of the modulation and carrier lines.

The external dc magnetic field H_{dc} is applied in the x-axis direction. An alternating magnetic field H_{ac}^{m}, generated by the modulation line is parallel to H_{dc}, which causes the modulation of the FMR field. In this way, the carrier waves feel μ variation in time, resulting in the frequency conversions. The time modulation of μ causes the frequency conversions of the carrier microwaves with spacing of modulation frequency f_m.

As shown in Fig. 1, the carrier microwave of 4.0 GHz is injected into the S line from a signal generator and received by a spectrum analyzer. The modulation microwave with f_m = 0.4 - 1.6 GHz is injected to the modulation line by another signal generator. The dc magnetic field $\mu_0 H_{dc}$=24.4 mT is applied using an electromagnet. Figure 2 shows the measured spectrum with various f_m. The first-order sidebands are observed at 4.0±f_m, indicating that the carrier microwaves are up- and down-converted by the temporal μ variation at f_m. Furthermore, the asymmetric frequency conversion, which can be traced back to nonlinear spin dynamics, is unique to μ time-modulating metamaterials.

In summary, we experimentally demonstrate μ time-modulating metamaterials. Since the μ-modulated metamaterials demonstrated here can be integrated with ε-modulated metamaterials, the present study paves a way for simultaneous modulation of ε and μ. The present study paves a way to synthetic moving media and quantum electrodynamics using metamaterials, and accelerate the fusion of spintronics and metamaterial research, such as ultra-strong magnon-polaritons in magnetochiral metamaterials [5].

The authors acknowledge Y. Kanamori for their valuable comments in this work. This work is financially supported by JST-CREST (JPMJCR2102) and JST-FOREST (JPMJFR246R).
[1] Y. Zhou et al., Nat Commun. 11, 2180(2020).
[2] J. Pendry et al., APL Quantum 1, (2024), P. A. Huidobro, et al., Proc. Natl. Acad. Sci. USA 116, 24943 (2019).
[3] T. Kodama et al., Phys. Rev. Appl. 19, 044080 (2023) and Phys. Rev. B. 109, 214419 (2024).
[4] T. Kodama et al., arXiv:2503.04571
[5] K. Mita, T. Kodama et al., Phys. Rev. B. 113, (2026) and Opt. Mat. Expr. 14, 2499 (2024)

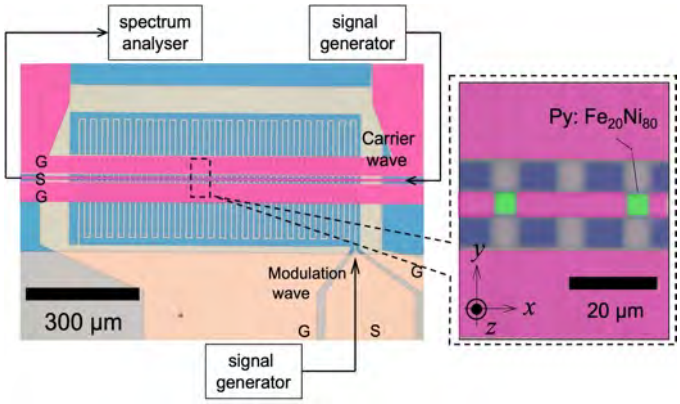


Figure 1 A photograph of the metamaterial device and an enlarged view.

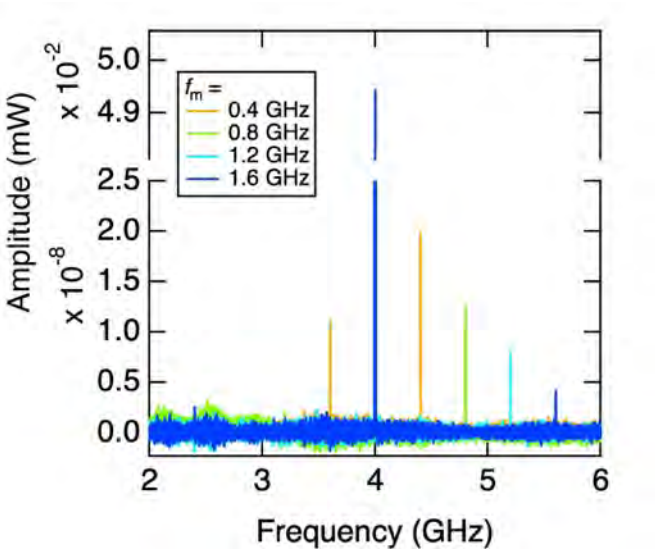


Figure 2 Microwave frequency conversion measurement results at various modulation frequencies f_m.

DG-02. MEMS-magnonic devices for reconfigurable spin-wave interference and inverse design

A. Angotti[1], F. Travagnin[1], M. Cocconcelli[1, 4], B. Heinz[2], A. Papp[3], F. Kohl[2], G. Csaba[3], P. Pirro[2], F. Maspero[1], R. Bertacco[1]
[1]Politecnico di Milano, Milan, Italy, [2]Rheinland-Pfälzische Technische Universität Kaiserslautern-Landau, Kaiserslautern, Germany, [3]Pazmany Peter Catholic University, Budapest, Hungary, [4]Laboratoire Albert Fert, CNRS, Thales, Université Paris-Saclay, Palaiseau, France

The wave-like nature of spin waves (SWs) offers promising perspectives for magnon-based computing. To fully exploit their potential, precise spatial control of the SW amplitude is required. This can be achieved by locally tailoring the magnetic field landscape; similarly to optics, diffraction effects arise depending on the ratio between the SW wavelength and the spatial extent of the field perturbation [1,2].

In this work, we present an integrated and reconfigurable approach to locally tune the effective magnetic field experienced by spin waves, enabling controlled diffraction. A controllable magnetic scatterer is realized by vertically displacing a micromagnet integrated on a micro-electro-mechanical system (MEMS), coupled to a YIG-based magnonic chip via flip-chip bonding. Piezoelectric MEMS technology allows for device operation with very low power consumption (nW range). The magnetic scatterer is used as the basic element of a matrix architecture for inverse design computing, paving the way for ultra-low-power spin-wave computing.

The tunable response of the MEMS-magnonic device (Fig. 1, left panel) has been probed by all-electrical spin-wave spectroscopy. Fig. 1 (right panel) shows a frequency scan of the transmission scattering parameter S12 as a function of the applied MEMS voltage, which controls the out-of-plane displacement (inset Fig. 1, right panel). The modulation of the transmitted RF signal amplitude can be explained by controllable diffraction of spin waves with wavelength comparable to the magnet lateral size (100 μm). This interpretation is confirmed by BLS experiments, showing a strong influence of the micromagnet on spin-wave propagation.

The magnetic scatterer is used as the building block for the spin-wave inverse design architecture shown in Fig. 2. Exploiting this concept, spin-wave power can be redirected toward selected output antennas at a target frequency, enabling simple filtering functionalities.

[1] A. Papp, G. Csaba, "Lens Design for Computing With Anisotropic Spin Waves", IEEE Magn. Lett. 9 (2018)

[2] C. S. Davies, A. Francis, A. V. Sadovnikov et al., "Towards graded-index magnonics: Steering spin waves in magnonic networks", Phys. Rev. B, vol. 95 (2017)

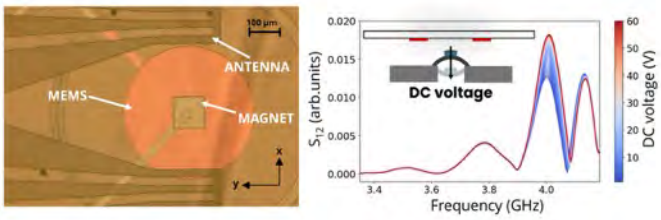


Fig. 1: Optical picture of the single element MEMS-magnonic device (left panel). Absolute value of S_{12}, as a function of the applied voltage to the MEMS. (right panel)

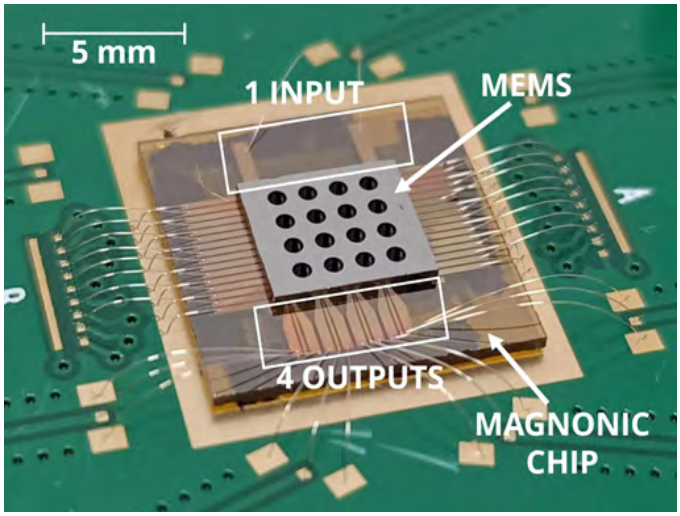


Fig. 2: Overview of the spin wave processor in flip-chip configuration used for magnonic inverse design architecture.

DG-03. Standalone Magnonic Platform with Engineered Micromagnetic Bias and Dual Current- and MEMS-Driven Field Control

M. Cocconcelli[1, 2], A. Angotti[1], F. Maspero[1], A. Cattoni[1], R. Bertacco[1]
[1]*Physics Department, Politecnico di Milano, Milan, Italy,*
[2]*Laboratoire Albert Fert, CNRS, Thales, Université Paris-Saclay, Palaiseau, France*

Engineering magnetic fields at the microscale provides a route to shape spin-wave dynamics in space and drive tunable nonequilibrium behavior in magnonic systems [1,2]. A key challenge is the development of integrated architectures that combine stable on-chip biasing with reconfigurability, eliminating the need for external magnetic fields.

Here, we introduce a hybrid system combining hard and soft magnetic elements to realize an integrated, tunable magnonic device operating at 10 GHz. SmCo permanent micromagnets act as on-chip field sources, generating bias fields up to 50 mT that sustain spin-wave propagation in a CoFeB waveguide positioned above them. This enables standalone operation in the 9.7–12.3 GHz range, as shown by vector network analyser (VNA) measurements (Fig. 1).

We demonstrate two strategies to dynamically reconfigure the magnetic landscape and tune spin-wave propagation. First, current-driven control is achieved via an integrated current line, generating a magnetic field that adds to the micromagnet bias, enabling continuous tuning (Fig. 2a). Second, voltage-driven tunability is achieved using a NiFeMo soft magnet integrated on a piezoelectric MEMS cantilever [3], flip-chipped onto the device (Fig. 2c). Upon actuation, the cantilever brings the NiFeMo element into proximity with the permanent micromagnets, where it captures and redistributes their stray field. The resulting voltage-controlled displacement modulates the coupling between the hard and soft magnetic components, effectively reducing the local bias field. This enables phase control of Damon–Eshbach spin waves (Fig. 2b).

These results establish a platform for current- and voltage-controlled magnonic devices, enabling compact, reconfigurable RF components such as phase shifters and filters, and spatial control of magnonic spectra.

[1] A. V. Chumak, V. I. Vasyuchka, A. A. Serga and B. Hillebrands, Nature Phys., Vol. 11, p.453 (2015)
[2] P. Pirro, V. I. Vasyuchka, A. A. Serga and B. Hillebrands, Nat. Rev. Mater., Vol. 6, p.1114 (2021)
[3] A. Ghisi, N. Boni, R. Carminati and S. Mariani, Eng. Proc., Vol. 4, p.17 (2021)
[4] MandMEMS Project, EU Project 101070536 (2023)

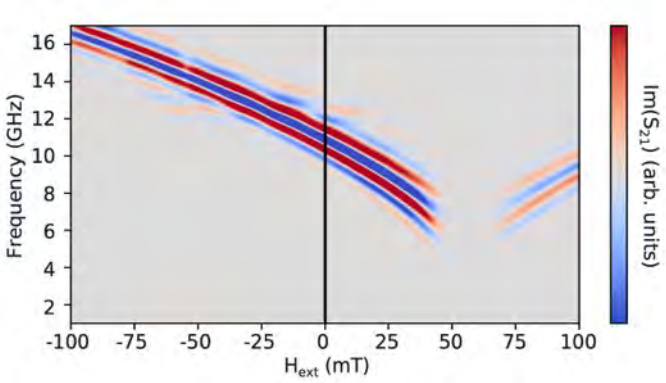


Fig. 1. Color map of the reference-subtracted imaginary part of S_{21} (spin-wave signal) vs frequency and applied magnetic field, measured by VNA.

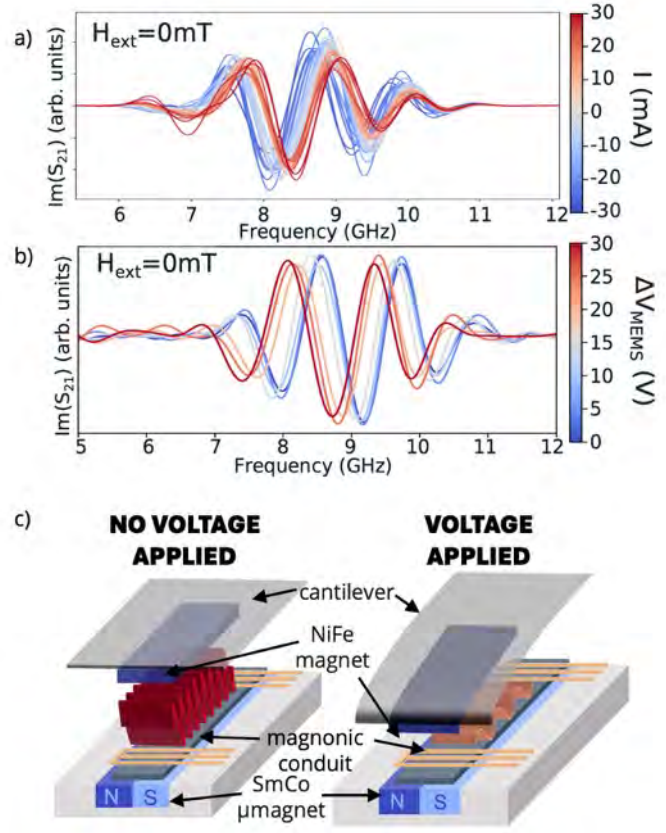


Fig. 2. a) Current- and b) voltage-induced modulation of the spin-wave transmission. c,d) Schematic of the flip-chip device with voltage-actuated MEMS cantilever.

DG-04. Tuning spin wave intensities in a y-shaped magnonic waveguide

L. Compton[1], J. Liu[2], K. Buchanan[1]
[1]Physics, Colorado State University, Fort Collins, Colorado, United States, [2]Georgia Southern University, Statesboro, Georgia, United States

Spin-based devices that use spin waves or magnons to transmit and process information, also known as magnonic devices, offer potential advantages over conventional devices due to their lower energy consumption and because there are many ways to tune the phases and amplitudes of spin waves to encode information. In this work we demonstrate frequency-tunable spin wave amplitudes in a Y-shaped magnonic waveguide and we show how thin film dispersion relations can be used as a framework for estimating spin wave intensities. The Y structure (Fig. 1(a)) is made of 40-nm thick, 2.4-μm wide, Ni_{80} Fe_{20} (Permalloy) strips, and a 10-μm wide gold microstrip antenna is used to excite spin waves in the upper (blue square) and lower (red square) arms of the Y structure. A static magnetic field is applied in-plane such that the upper arm is closer to the surface wave or Dameon Eshbach configuration and the lower arm is closer to the backward volume configuration, as illustrated in Fig. 1(a). This asymmetry leads to a frequency-tunable difference of spin wave intensities in each arm. Fig. 1(b) shows the frequency-dependent spin wave intensities predicted using thin film dispersion relations with imposed width quantization. From the dispersion relations we see when the driving frequency increases, the spin wave intensity in the upper arm (blue squares) decreases while in the lower arm (red triangles) it increases. This trend is also observed experimentally using Micro-focus Brillouin light scattering (MicroBLS) measurements (Fig. 1(c)) and in micromagnetic simulations (Fig. 1(d)), which demonstrates that the calculations based on the thin film dispersion relations can be used as a tool for designing tunable magnonic devices.

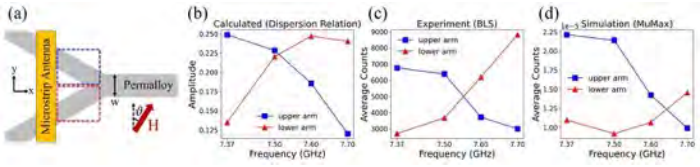


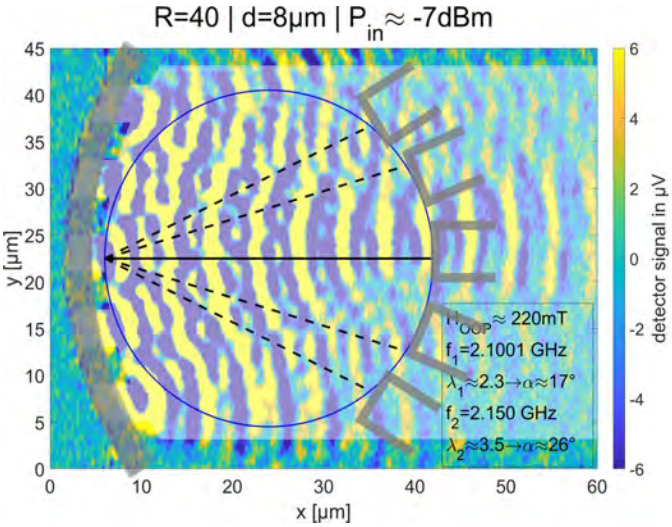
Fig 1: (a) Diagram of the Y structure with an applied magnetic field of $\mu_0 H$=54-mT at θ=5°. The upper arm is boxed in blue and the lower arm in red. Spin wave intensities for the two arms (b) calculated by the dispersion relation, (c) measured using MicroBLS, and (d) micromagnetic simulations.

DG-05. A Spin-Wave-Based Spectrometer with Parallel Electrical Readout

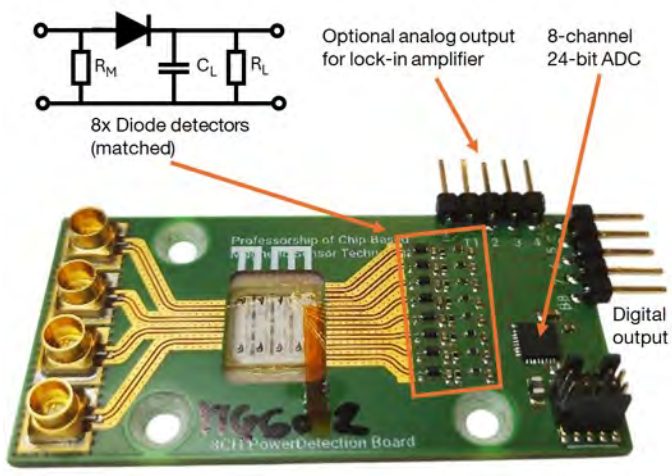
J. Greil[1], M. Hofschen[1], F. Naunheimer[1], V. Ahrens[1], L. Maucha[2], A. Papp[2], G. Csaba[2], M. Becherer[1]
[1]School of Computation, Information, and Technology, Technical University of Munich, Garching bei Muenchen, Bavaria, Germany, [2]Faculty of Information Technology and Bionics, Pázmány Péter Catholic University, Budapest, Hungary

In this work, we present the magneto-optical and electrical characterization of a demonstrator that combines a magnonic spectrometer in a Rowland-circle arrangement with a printed circuit board (PCB) for electrical readout. Our demonstration goes beyond earlier results in [1],[2] by using an integrated electric readout, new fabrication technology, and testing core spectrometric characteristics.
We fabricate the Rowland circles by sputter deposition of Yttrium-Iron-Garnet (YIG) on a Gadolinium-Gallium-Garnet (GGG) substrate, followed by wet-chemical etching of the amorphous YIG film (100nm-500nm) using phosphoric acid at room temperature. In a lithography step, a curved stripline transducer (input) and several u-shaped transducers (outputs) are fabricated (gray lines in Fig. 1).
We have achieved mono-frequency detection with a bandwidth of 45-200MHz around the 2.4GHz center frequency using time-resolved MOKE (trMOKE) measurements. Further, we demonstrate that two-tone excitation and the required spatial wavefront separation in the spectrometer are possible (see Fig. 1).
We performed RF characterizations of the device, contacting the loop-shaped outputs via ground-signal-ground (GSG) probes. While electrical detection is challenging due to low local spin-wave (SW) power levels and electromagnetic crosstalk, we suggest a solution to reduce the latter by about 10dB via engineering the GND planes surrounding the Rowland circle.
Regarding integrated demonstrator devices, we present a powerful method for broadband power detection using RF diodes on the PCB. Therefore, we designed and fabricated a PCB with multiple RF power detectors and wire-bonded the local pickup transducers to them (see Fig.2). While the read-out scheme is capable of detecting propagating SWs in large transducer geometries, it needs further improvement for the local detection in the Rowland arrangement. The detection level can be pushed to -70dBm.

[1] Á. Papp, W. Porod, G. Csaba, et al. Sci Rep 7, 1-9 (2017)
[2] Á. Papp, M. Kiechle, S. Mendisch, et al. Sci Rep 11, 1-8 (2021)



TrMOKE data for a two-tone excitation of a Rowland circle at 2.1GHz and 2.15GHz. The wavefront splitting is indicated in dashed lines. The gray lines indicate the transducers.



The realized parallel 8-channel demonstrator PCB with an embedded magnonic chip. The independent RF power detectors use Schottky diodes.

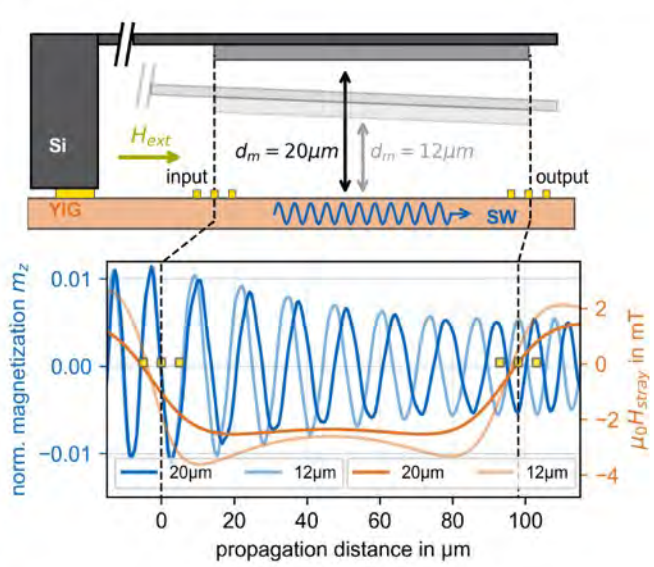
DG-06. A Hybrid Magnonic Phase Shifter Based on the Local Influence on Propagating Spin Waves

J. Greil[1], A. Angotti[2], F. Kohl[3], A. Papp[4], M. Wagner[3], M. Cocconcelli[2], A. Del Giacco[2], F. Maspero[2], B. Heinz[3], G. Csaba[4], R. Bertacco[2], M. Becherer[1], P. Pirro[3]
[1]School of Computation, Information, and Technology, Technical University of Munich, Garching bei Muenchen, Bavaria, Germany, [2]Department of Physics and Polifab, Politecnico di Milano, Milano, Italy, [3]Fachbereich Physik and Landesforschungszentrum OPTIMAS, Rheinland-Pfälzische Technische Universität Kaiserslautern-Landau, Kaiserslautern, Germany, [4]Faculty of Information Technology and Bionics, Pázmány Péter Catholic University, Budapest, Hungary

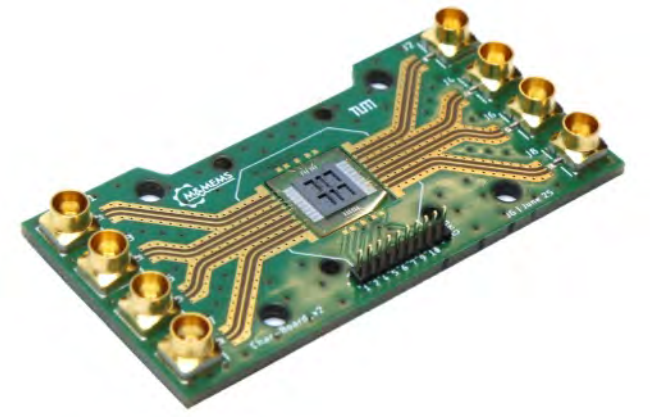
The growing demand for compact, low-power, and frequency-agile radio-frequency (RF) components motivates the exploration of wave-based signal manipulation [1]. This work presents a microscaled, tunable magnonic RF phase shifter that exploits spin-wave propagation in a ferrimagentic film combined with microelectromechanical systems (MEMS) [2]. The device works by locally modifying the effective magnetic field via piezoelectrically actuated cantilevers carrying soft micromagnets, enabling dynamic control of the spin-wave wavelength and, thus, the accumulated phase.
The demonstrated hybrid device achieves phase shifts exceeding 400° at a center frequency of 6.1GHz within an ultra-small core phase-shifting area of <0.02mm^2. Broadband functionality is experimentally validated across 3–8.2GHz by varying the external magnetic bias field, highlighting the intrinsic tunability of spin-wave-based devices. We can verify the functionality above 10GHz using an analytical model. System-level integration is confirmed by embedding the device in a printed circuit board (PCB). Setting the bias field using a permanent magnet demonstrates the system's compatibility with practical RF applications. The experimental findings are based on and compared to detailed micromagnetic simulations and analytical models [3,4].
The phase shifter exhibits a nearly constant maximum phase shift above 4GHz, low phase error, and a voltage-phase sensitivity of 20.3°/V, while maintaining static power consumption in the sub-mW regime. Compared to conventional RF phase shifters, the proposed approach offers significant advantages in footprint and scalability, with potential for multi-channel integration in phased-array systems.

[1] K. Levchenko, K. Davidkova, et al. IEEE Transactions on Magnetics 1-1 (2026)

[2] A. Ghisi, N. Boni, et al. Eng. Proc. 2021, 4(1), 17
[3] F. Kohl, B. Heinz, et al. preprint, arXiv:2050.08656
[4] R. Erdelyi, G. Csaba, et al. Sci Rep 15, 9806 (2025)



Cross-sectional drawing of the hybrid magnonic phase shifter with an actuated piezoelectric cantilever holding a soft magnet at changing distances to the magnonic chip. The propagating SW (blue) is influenced by the local stray field of the soft magnet (orange) between the input and output transducer to achieve the phase shift.



The fabricated 4-channel carrier PCB with the embedded hybrid phase shifter. A convenient RF interface is provided by coaxial connectors, while the DC voltage supply for the MEMS is realized with pin headers.

DG-07. Generation of Ultra-Broadband Frequency Comb in Strongly Bistable Nonlinear Magnonic Resonator

Y. Jiang[3], V. Tyberkevych[1], Y. Huang[3], Z. Yan[3], A. Pishehvar[3], A. N. Slavin[1], X. Zhang[2, 3]
[1]Department of Physics, Oakland University, Rochester, Michigan, United States, [2]Department of Physics, Northeastern University, Boston, Massachusetts, United States, [3]Electrical and Computer Engineering, Northeastern University, Boston, Massachusetts, United States

Frequency combs—spectral structures of evenly spaced lines—play a critical role in precision spectroscopy, communications, and sensing [1,2]. Magnonic frequency combs (MFCs) extend this concept to spin-wave systems, offering compact, tunable platforms for on-chip microwave signal processing [3,4]. Previous MFC demonstrations relied on driving magnonic resonators near resonance, limiting magnon amplitudes due to nonlinear frequency shifts and restricting comb bandwidth to tens of megahertz with fewer than 30 lines [3-5].
Here we introduce a fundamentally different mechanism using a miniaturized YIG thin-film microresonator (0.2×50×50 µm^3, 4–6 orders of magnitude smaller than conventional YIG spheres). The magnon mode is driven with large frequency detuning far above resonance (by more than 100 times the magnon linewidth). By integrating the resonator with a spoof surface plasmon polariton waveguide for slow-wave enhancement [6], we achieve high intra-resonator power density that pushes the system deep into the bistable regime. Parametric spin-wave excitation [7] reduces the threshold for accessing the high-amplitude bistable state, triggering rapid oscillations between bistable branches under two-tone pumping. These sharp transitions generate ultrabroadband frequency combs with spacing set by the pump frequency difference.
Our experiments demonstrate over 350 comb lines spanning 450 MHz—an order-of-magnitude improvement over prior MFCs. The comb exhibits excellent coherence with linewidth below 26 Hz. MFC properties are fully controllable through magnetic bias and pump parameters, with threshold at −7 dBm. The platform operates across 3–10 GHz while its principle applies to broader ranges, opening opportunities for neuromorphic computing, precision metrology, and signal processing.

[1] T. Udem, R. Holzwarth and T. Hänsch, *Nature*, Vol. 416, p.233 (2002)
[2] P. Del'Haye, A. Schliesser, O. Arcizet, et al, *Nature*, Vol. 450, p.1214 (2007)
[3] T. Hula, K. Schultheiss, F. Gonçalves, et al, *Appl. Phys.*

Lett., Vol. 121, p.112404 (2022)
[4] G.-T. Xu, M. Zhang, Y. Wang, et al, *Phys. Rev. Lett.*, Vol. 131, p.243601 (2023)
[5] C. Wang, J. Rao, Z. Chen, et al, *Nature Physics*, Vol. 20, p.1139 (2024)
[6] J. Xu, C. Zhong, S. Zhuang, et al, *Phys. Rev. Lett.*, Vol. 132, p.116701 (2024)
[7] H. Suhl, *J. Phys. Chem. Solids*, Vol. 1, p.209 (1957)

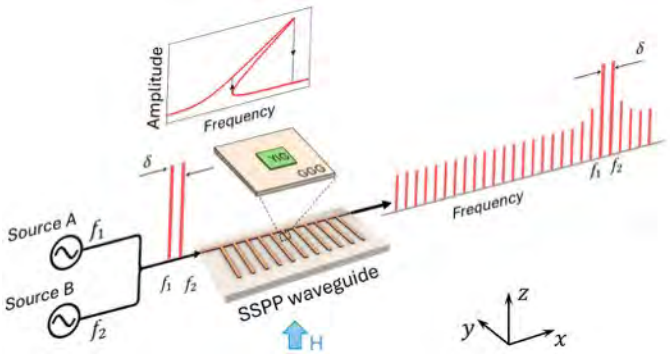


Fig. 1. Device schematic: a normally magnetized YIG microresonator flip-bonded onto a slow-wave waveguide driven by a two-tone pump at fs and fs + δ.

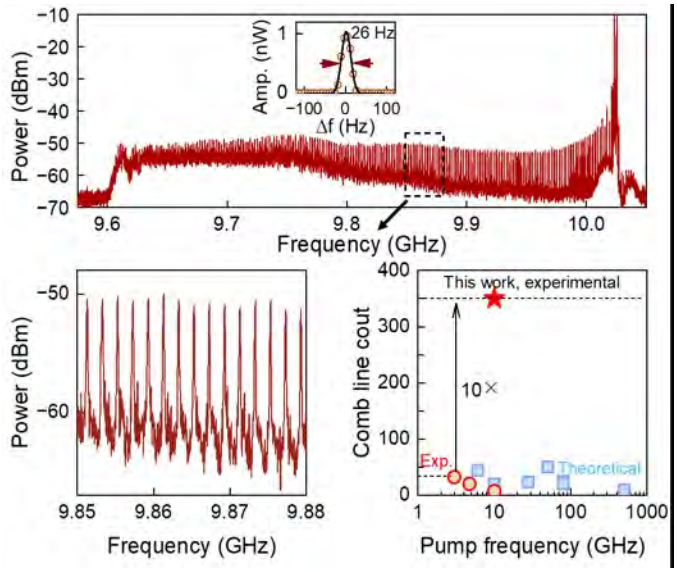


Fig. 2. MFC performance: measured spectrum showing 200 lines at 2 MHz spacing, and comb line count comparison with prior work.

DG-09. State Tomography of Itinerant Magnons

J. Lim[1, 2], M. Kocyigit[1, 2], M. Song[3], K. Kim[4], Y. Li[3], W. Pfaff[1, 5], A. Hoffmann[1, 2, 5]
[1]Materials Research Laboratory, University of Illinois Urbana-Champaign, Urbana, Illinois, United States, [2]Materials Science and Engineering, University of Illinois Urbana-Champaign, Urbana, Illinois, United States, [3]Materials Science Division, Argonne National Laboratory, Lemont, Illinois, United States, [4]Department of Physics, Korea Advanced Institute of Science and Technology, Daejeon, Korea (the Republic of), [5]Department of Physics, University of Illinois Urbana-Champaign, Urbana, Illinois, United States

State tomography is a tool that can fully identify a state, such as the state of a qubit, and has been extensively used as a key technique in quantum information. Magnon state tomography has thus far been demonstrated only for stationary (non-propagating) Kittel magnons in a superconducting qubit–magnon coupled system [1] (quantum regime) and a heavy-metal/ferromagnet heterostructure [2] (classical regime), both via the Wigner functions, which were obtained from displaced parity measurements using a qubit (quantum regime) and homodyne detection of continuous variable (CV) microwave photon fields generated from inverse spin Hall effect induced by spin pumping from parametrically driven magnons (classical regime). Here, we present state tomography of itinerant (propagating) magnons via the Husimi Q-function. We developed a single-shot microwave heterodyne detection system, which is commonly used in circuit quantum electrodynamics (cQED), for the itinerant magnons propagating in a magnonic waveguide made of yttrium iron garnet (YIG). We observe that the distribution of the magnon part exhibits additional phase evolution and elongated phase fluctuations as magnon number increases (Figs. 1 and 2), which might be attributed to a squeezed state or Kerr-type evolution of itinerant magnons. State tomography of itinerant magnons will be an essential tool for advancing both quantum magnonic applications toward quantum information [3] and applications of magnon-based logic devices, such as magnon-based neuromorphic computer or Ising machine.

[1] D. Xu, J.Q. You et al., Phys Rev Lett, 130 (2023) 193603.
[2] T. Hioki, E. Saitoh et al., Phys. Rev. B, 104 (2021).
[3] Z.H. Jiang, J. Lim, A. Hoffmann et al., Appl. Phys. Lett., 123 (2023).

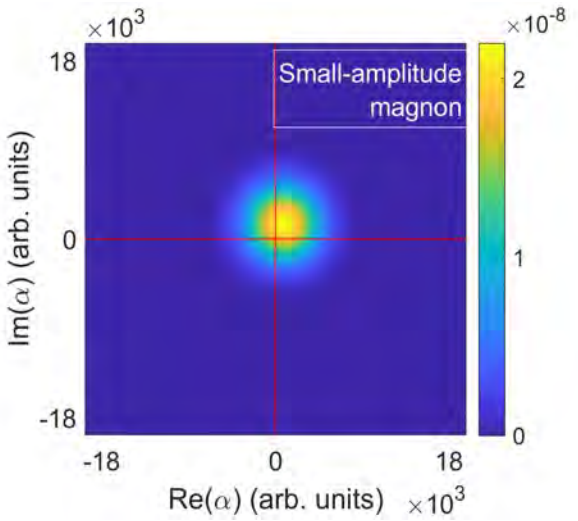


Fig. 1. Husimi Q-function of a small-amplitude itinerant magnon. The state is identified as a coherent state.

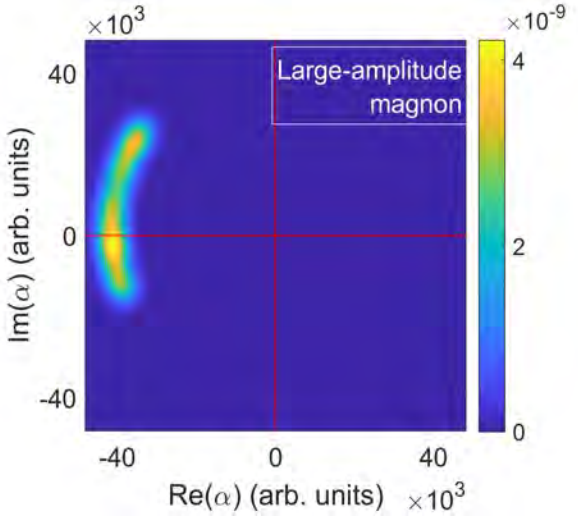


Fig. 2. Husimi Q-function of a large-amplitude itinerant magnon. The state shows an elongated phase fluctuation and is identified as a non-Gaussian state.

DG-11. Nonreciprocal Spin-Wave Propagation in Bi-Substituted Yttrium Iron Garnet Bilayers

J. Marquez Chavez, O. Wojewoda, C. A. Ross
Department of Materials Science and Engineering, Massachusetts Institute of Technology, Cambridge, Massachusetts, United States

The realization of unidirectional magnon transport represents a key advance in controlling spin-wave dynamics for high-frequency microwave technologies, particularly emerging 5G NR applications [1]. This behavior arises when appropriate toroidal moments induce nonreciprocal spin-wave propagation, enabling integrated magnonic components such as diodes or circulators. Although direction-dependent functionality has been demonstrated in systems ranging from ultrathin ferromagnetic films [2] to oppositely magnetized bilayers [3], achieving large-magnitude unidirectional transport with low damping remains challenging, motivating the search for optimized materials. Bi-substituted yttrium iron garnets (BiYIG) are particularly well suited for such applications, as their complex crystal structure enables strong tunability of magnetic anisotropy while maintaining exceptionally low magnetic damping and compatibility with both microwave and optical techniques [4]. In this work, we develop a BiYIG bilayer (70 nm $Bi_{1.5}Y_{1.5}Fe_5O_{12}$ / 70 nm $Bi_{0.8}Y_{2.2}Fe_5O_{12}$) grown on gadolinium scandium gallium garnet (GSGG) (Fig. 1) by pulsed laser deposition, where the Bi concentration in each layer is engineered to produce distinct magnetic anisotropies that differ by 8.8×10^3 J/m^3. The anisotropy difference establishes unequal effective magnetic fields across the bilayer, enabling nonreciprocal spin-wave propagation that can be continuously tuned with an external magnetic field. TetraX and semi-analytical simulations predict a nonreciprocity of 1–3 GHz under Damon–Eshbach (DE) geometry (Fig. 2). We have investigated these properties with the use of intensity-, phase-, and time-resolved μ-BLS measurements. The low magnetic damping of BiYIG, reflected in the linewidth of 0.8 mT at 10 GHz from ferromagnetic resonance measurements, ensures minimal energy loss, making this bilayer a highly efficient platform for directional spin-wave transport.

[1] Levchenko et al., Review on spin-wave RF applications, IEEE Transactions on Magnetics (2026) Bottom of Form
[2] Kuepferling et al., Rev. Mod. Phys., Vol. 95, p.015003 (2023)
[3] F. Gallardo et al., New J. Phys., Vol. 21, p.033026 (2019)
[4] A. C. Kaczmarek et al., Nat. Commun., Vol. 15, p.5083 (2024)

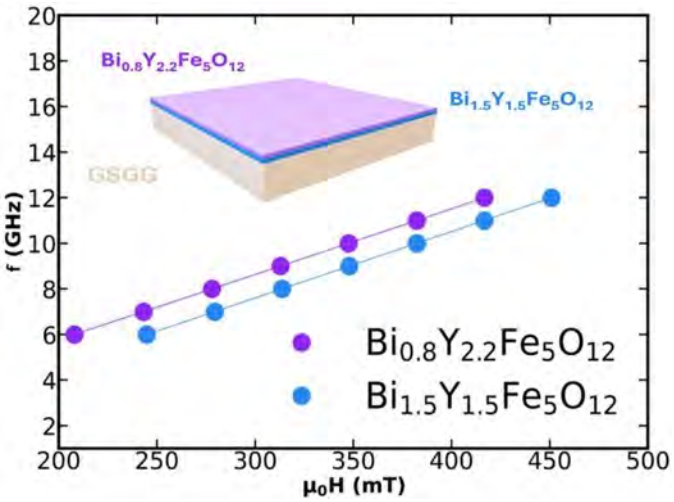


Fig. 1. Resonant spectra as a function of the applied out-of-plane magnetic field

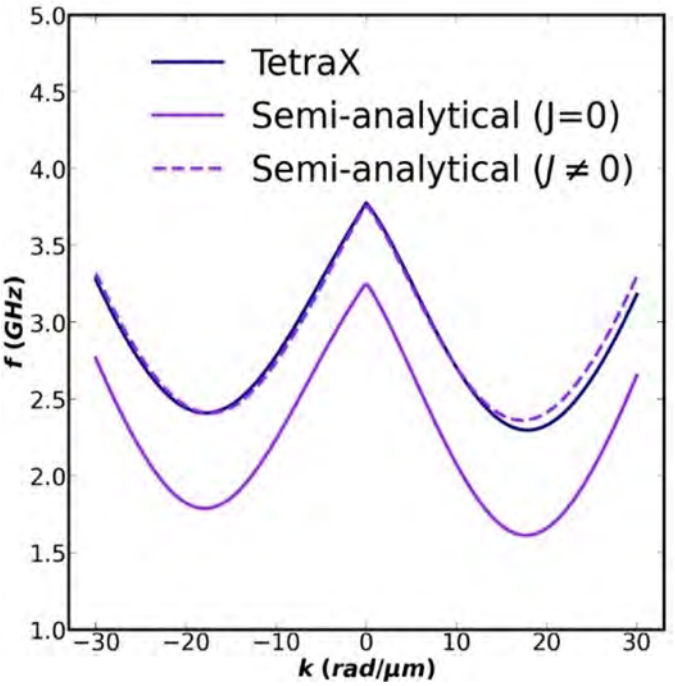


Fig. 2. Spin-wave dispersion relations for the DE modes at 0.2 T, predicted using TetraX and semi-analytical calculations for coupled and uncoupled bilayer configurations

SESSION DH: DOMAINS, SKYRMIONS AND MAGNETIC TEXTURES

Chair(s): P. Upadhyaya, *University of Purdue, W Lafayette, Indiana, United States*

Wednesday, November 4, 2026

02:00 PM-05:30 PM

Nautilus

DH-01. Real Space Imaging of Field Driven Magnetic Domain Wall Motion with Lorentz Transmission Electron Microscopy

H. Arava

Argonne National Laboratory, Lemont, Illinois, United States

I will present on imaging of nanomagnetic domain walls using Lorentz Transmission Electron Microscopy (LTEM). Using lithographically patterned Galton Boards made out of Permalloy ($Ni_{80}Fe_{20}$)[1], we reveal the mechanisms underlying stochastic behavior[2]. Specifically, we find that there are multiple factors affecting domain wall motion in these structures and can be broadly related to Y shaped junctions elsewhere: (1) Domain wall topology dependent path selectivity, (2) structural defects such as pinning and disorder, (3) the role of dissimilarly sized vertices which leads to an uneven energy landscape, and (4) size of the applied field. These experimental observations, captured with sub-50 nm spatial resolution, provide insights into how topological constraints govern domain wall propagation in confined geometries. Our findings have fundamental implications in spintronics for applications in future low power computing devices.

[1] D. Sanz-Hernández *et al.*, Advanced Materials 33, 2008135 (2021).

[2] H. Arava, D. Sanz-Hernandez, J. Grollier, and A. K. Petford-Long, Physical Review Letters 134, 086704 (2025).

DH-02. Time-resolved coherent x-ray scattering measurements on complex oxides

R. Kukreja

Materials Science and Engineering, University of California Davis, Davis, California, United States

Complex oxides such as rare earth nickelates, magnetite etc. exhibit a rich interplay of electronic, magnetic, and structural phase transitions, including a metal-to-insulator transition (MIT). While these transitions have been widely studied, role of nanoscale heterogeneities across the phase transition are mostly unexplored. In this talk, I will discuss our recent ultrafast measurements using coherent x-ray

scattering to investigate magnetic and structural degrees of freedom in complex oxides following laser excitation. These studies will be compared with their equivalent thermally driven phase transition using x-ray photon correlation spectroscopy (XPCS). Using XPCS, our studies have revealed surprisingly strong magneto-structural coupling in rare earth nickelates. On the other hand, for magnetite our measurements clearly show an inherent distinction between dynamical heterogeneities at Fe L-edge vs O K-edge. Our results demonstrate the power of coherent X-ray techniques in capturing nanoscale fluctuation dynamics and provide new insight into the mesoscale behavior of complex oxides.

1. Zhou Hagstroem, N. et al. Critical slowdown of spontaneous fluctuations in the vicinity of metal-insulator transition in rare earth nickelates, in review (2026).
2. Zhang, Y. et al. Fluctuations in magnetic degrees of freedom in rare earth nickelates, in review (2026)

DH-05. Reliable Shifting of 300 nm Magnetic Domains in Nanopatterned W/CoFeB/MgO Devices

M. Quinsat, N. Umetsu, M. Yoshikawa, M. Kado
Frontier Technology R&D Institute, Kioxia, Yokohama, Japan

Domain-wall (DW) magnetic shift registers[1] are strong candidates for future high-density memory. Using a perpendicularly magnetized W/CoFeB/MgO stack with large Dzyaloshinskii-Moriya Interaction[2], we recently demonstrated sub-µs, field-free, digital operation in DW devices integrated on CMOS[3]. Achieving high memory density requires reliable motion of nanometric magnetic domains. While the behavior of µm-long domains in straight 5 µm-wide nanowire devices has been studied[4], here we examine 300 nm-long domains shifted by the spin orbit torque in 200 nm wide nanowire specifically designed for reliable domain shifting control.

We fabricated 2-bit devices (Fig.1) where a modulated wire width enables stable DW positioning and domain formation. A DW set at the first constriction should reach the Hall bar after two shift pulses, and the expected signal change is observed for both up/down or down/up DW polarities under appropriate shift current pulse conditions (Fig.2(a)). When a domain is written, the Hall bar signal returns to its initial state at the third pulse, confirming correct propagation of two closely spaced DWs without mutual interference (Fig.2(b)). We further examined write and shift pulse conditions and found that the domain shifting success rates is explained by the independent DW propagation. We also found a large DW polarity dependence in DW motion characteristics that is well reproduced by micromagnetic simulations with random disorder in the nanowire. These findings provide a foundation for the development of next-generation domain-wall devices targeting domain sizes in the hundreds of nanometers and below.

[1] S.S.P. Parkin, M. Hayashi and L. Thomas, Science, vol. 320, no. 5873, pp. 190-194 (2008).
[2] N. Umetsu et al., Journal of Magnetism and Magnetic Materials, 614, 172738 (2025).
[3] M. Quinsat et al., IEEE Journal of the Electron Devices Society, *in press,* PP(99):1-1 (2025).
[4] M. Ishibashi et al. Science Advance, 10, 43, (2024).

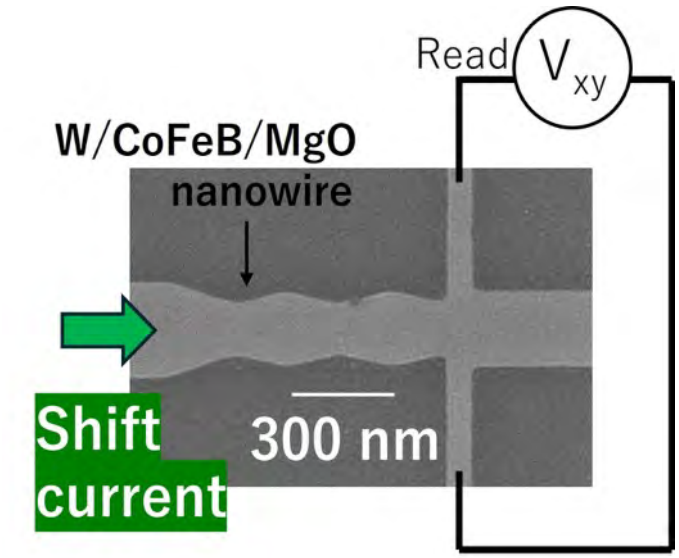


Fig.1: SEM image of studied device and experimental setup.

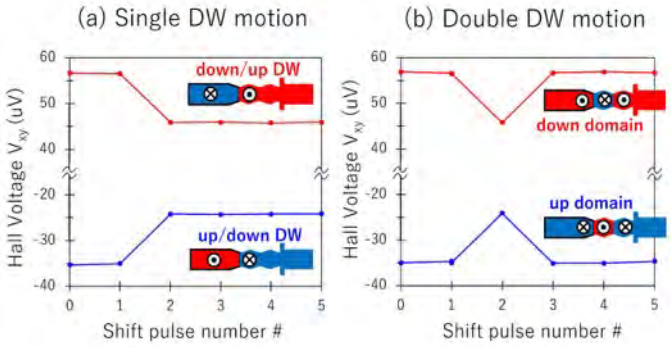


Fig.2: (a) Single DW motion results for up/down or down/up polarity. (b) Double DW motion results, evidencing the 300 nm long up or down domain motion. Pulse width is 40 ns.

DH-06. Domain wall-based spintronic devices beyond binary technologies: from materials to applications

J. Jeon, S. Parkin
Max Planck Institute of Microstructure Physics, Halle, Germany

Recent advances in data-centric computing, including artificial intelligence (AI), have dramatically increased the demand for greater computational power and storage capacity. Spintronic devices, which are non-volatile, low power consumption, high endurance, and high speed, have been proposed as promising logic and memory elements for next generation computing systems. In particular, recent demonstrations of unconventional computing schemes using spintronic devices – such as neuromorphic computing, spiking neural network, and probabilistic bit computing – promise more efficient approaches to solving complex problems [1].

Here, we show that domain-wall-based spintronic devices are highly promising for realizing both conventional and unconventional computing elements in the near future. Over the past two decades, racetrack memory, which is based on current-induced motion of chiral domain walls, has been extensively investigated due to its intriguing physics and features – high speed, high density, and non-volatility [2]. Thus far, racetrack has been primarily considered as a data storage technology with extremely large capacity, since the spacing between domain walls, which define the 'bits', can be tuned very small, with bit information read by integrated magnetic tunnel junctions (MTJs) [2, 3, 4]. Recently, we have demonstrated that the performance of racetrack device, i.e., current-induced domain wall motion, can be maintained down to the 50 nm scale via electrical read [3, 5]. Remarkably, in such nanoscopic racetrack devices, we found that the dynamics of the magnetic domain walls can be actively controlled to exhibit binary, analog, and stochastic outputs within a single device. We will discuss in detail how MTJs or Hall bars can be used to read domain wall dynamics, where the electrical read is proportional to the volume ratio between spin-up and spin-down domains within the detection range. Furthermore, we identify key functional parameters – such as write error rate, shift correctness, and field immunity – that govern device performance. Finally, we will discuss materials, film stacks, interfaces, and device design parameters to realize reliable racetrack devices.

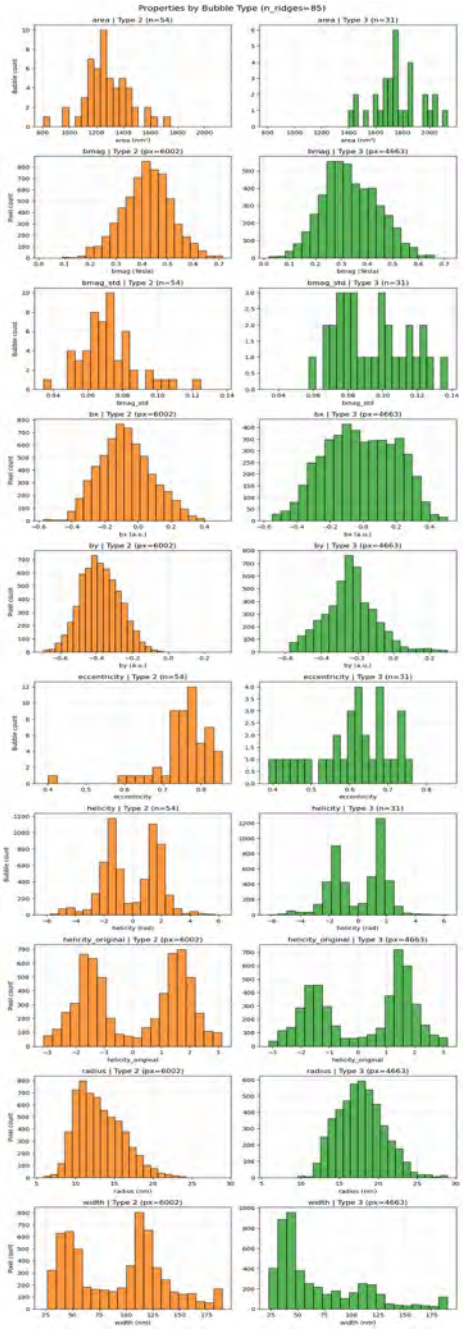
[1] G. Finocchio, *et al. Nano Futures* Vol.8, p.012001 (2024)
[2] S. S. P. Parkin, et al. *Science* Vol.320, p.190 (2008)
[3] J. Jeon, et al. *ACS Nano* Vol.18, p.14507 (2024)
[4] E. Raymenants *et al., Nat. Electron.* Vol.4, p.392 (2021)
[5] J. Jeon, A. Migliorini, J. Yoon, J. Jeong, S. S. P. Parkin, *Science* Vol.386, p.315 (2024)

DH-07. Hybrid topology bubbles in Fe/Gd multilayers

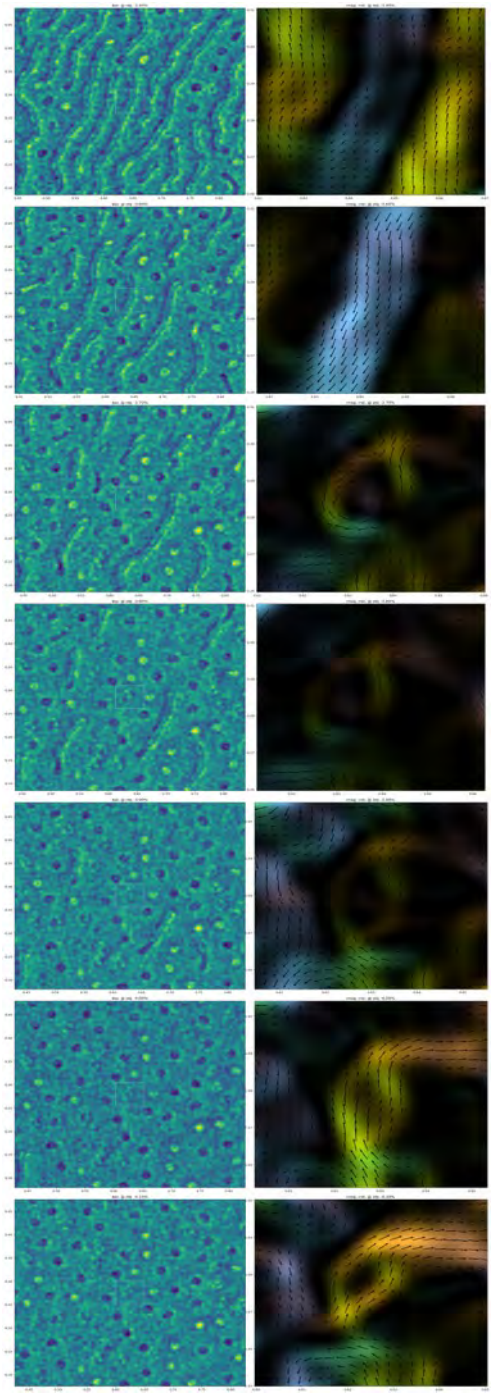
J. A. Reddinger[2], S. Montoya[1], E. Fullerton[1], B. McMorran[2]
[1]*Center for Memory and Recording Research, University of California San Diego, San Diego, California, United States,*
[2]*Physics, University of Oregon, Eugene, Oregon, United States*

Fe/Gd multilayers are known to host populations of topologically trivial (Type-I) and dipole skyrmion (Type-II) bubbles simultaneously [1]. Dipolar skyrmions are named such since they are stabilized by competition between exchange and dipolar energies without significant contribution by the Dzyaloshinskii-Moriya interaction. While both features form during the collapse of stripe domains under external magnetic fields, the process is not as chaotic as it appears. Previous simulation results have shown that, depending on competition between the Zeeman and local demagnetizing fields, the surfaces of nucleated bubbles may collapse into Neel-type skyrmions. This collapse either propagates through the depth of the bubble and results in the formation of a dipole skyrmion or it is halted and results in a novel magnetic bubble with hybrid topology. This talk combines simulation with Lorentz transmission electron microscopy images of Type-III bubble which features a topologically trivial core and Neel type surface domains.

[1] Montoya, S. A., et al. "Tailoring magnetic energies to form dipole skyrmions and skyrmion lattices." *Physical Review B* 95.2 (2017): 024415.



Properties of Type-II (orange) and Type-III (green) bubbles imaged in Lorentz transmission electron microscopy.



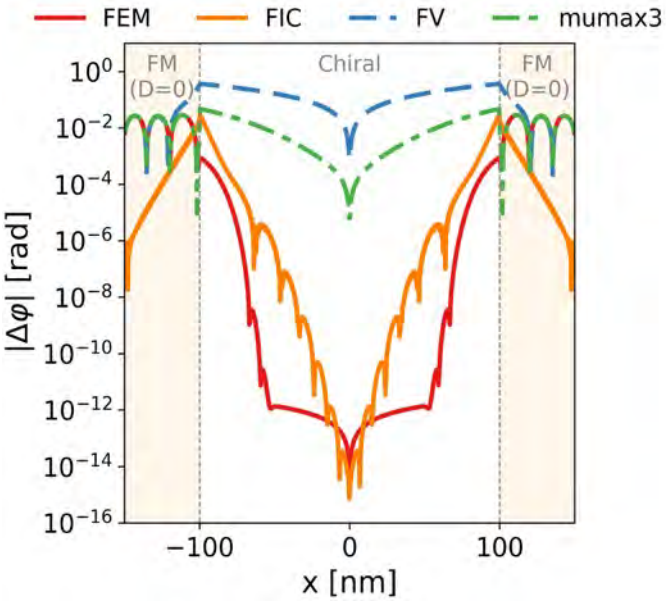
Formation and relaxation of a bubble after stripe collapse. This domain nucleates from a stripe domain and rotates 180 degrees. After rotating, the domain's magnetic induction greatly decreases corresponding to the formation of Neel-type surface domains which do not provide contrast in LTEM. These domains eventually collapse and the bubble's measured magnetic induction increases.

DH-08. Getting chiral heterostructures right: accurate interface treatment in micromagnetic simulations

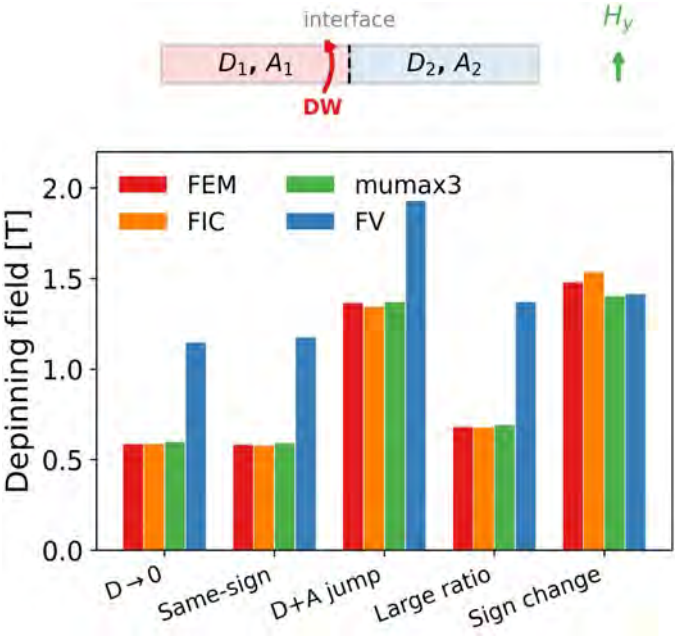
C. Abert, F. Bruckner, D. Suess
University of Vienna, Vienna, Austria

Skyrmion multilayers, synthetic antiferromagnets, and composite chiral magnets derive their functionality from the interplay of the Dzyaloshinskii-Moriya interaction (DMI) with material interfaces where magnetic parameters change abruptly. Predicting interface-sensitive phenomena such as domain-wall pinning, chiral coupling across spacer layers, or helix-to-ferromagnet transitions therefore requires that numerical solvers treat DMI discontinuities accurately. We introduce a FEM-interpolated cell-centred (FIC) scheme that evaluates the effective field via the finite-element weak form while keeping the magnetization on the regular cell-centred grid. FIC inherits the correct interface treatment of nodal FEM - each cell uses its own material parameters without face-averaging compromises - while remaining fully compatible with FFT-based demagnetization and GPU-accelerated solvers. We benchmark FIC against nodal FEM, standard cell-centred finite-volume (FV) discretization, and mumax3 [3] on two test problems: the composite chiral magnet of Laliena et al. [1], whose analytical helix solution allows direct error measurement, and a domain-wall depinning problem extending the phase-boundary benchmark of Heistracher et al. [2] to DMI interfaces. For the helix benchmark, FIC reproduces the nodal FEM solution to within 1e-3 rad, while FV (arithmetic-mean face flux) shifts the helix pitch by 1.7% and the mumax3 harmonic mean shows errors of 4.7e-2 rad at the interface. For depinning, FV overestimates the depinning field by up to 102%. The mumax3 harmonic mean keeps errors below 2% for same-sign DMI but fails when D changes sign across the interface. FIC matches FEM across all five tested configurations with errors below 4%. Both FEM and FIC are implemented in NeuralMag [4], and we discuss the trade-offs of all four approaches for practical heterostructure simulations.

[1] V. Laliena, S. Osorio, S. Bustingorry and J. Campo, Phys. Rev. B, Vol. 109, p.214424 (2024)
[2] P. Heistracher, C. Abert, F. Bruckner et al., J. Magn. Magn. Mater., Vol. 548, p.168875 (2022)
[3] A. Vansteenkiste, J. Leliaert, M. Dvornik et al., AIP Advances, Vol. 4, p.107133 (2014)
[4] C. Abert, F. Bruckner, A. Voronov et al., npj Comput. Mater., Vol. 11, p.193 (2025)



Phase error for the composite chiral magnet benchmark comparing FEM, FIC, FV, and mumax3 against the analytical solution.



Depinning fields for five interface configurations comparing FEM, FIC, mumax3, and FV.

DH-09. The Role of Topology in Magnetic Texture Stability

K. Litzius[1, 2]
[1]University of Augsburg, Augsburg, Germany, [2]Helmholtz-Zentrum Berlin für Materialien und Energie GmbH, Berlin, Germany

Magnetic skyrmions are widely described in terms of non-trivial topology, yet experimentally it remains unclear at which stage of their life cycle topology becomes physically consequential. In this work, we use transmission X-ray microscopy and complementary magnetic Kerr imaging to systematically identify where topological effects emerge in the nucleation-annihilation dynamics of magnetic textures. We first examine skyrmion nucleation under controlled magnetic field protocols. Rather than observing a direct imprint of topological protection at the point of creation, we find that nucleation is governed by a purely dynamical instability: a transient suppression of magnetic anisotropy triggers a spin-reorientation transition, followed by a cascade of modulational instabilities. This sequence of stripe formation, breakup, and bubble fragmentation indicates that skyrmion generation is not initiated by topological constraints, but instead arises from a generic instability-driven pathway that only later selects states with finite topological charge.
We then turn to annihilation dynamics to probe the statistics of skyrmion collapse. In contrast to nucleation, we find a clear signature of topology in the annihilation process: skyrmionic states exhibit broad, thermally activated switching-field distributions, whereas topologically trivial bubble states collapse deterministically with sharply peaked switching fields. This bifurcation in statistics reflects the presence or absence of topological protection, which constrains accessible collapse pathways and modifies the effective energy landscape.
Together, these results establish a separation between topology-insensitive nucleation governed by modulational instability and topology-sensitive annihilation governed by constrained switching dynamics. This provides direct experimental evidence that topology in magnetic textures manifests primarily as a dynamical constraint on decay rather than as a requirement for formation.
[1] R. Battistelli, et al., arXiv:2512.22947 (2025).
[2] S. Zhou et al., Advanced Functional Materials 36, e26052 (2026).

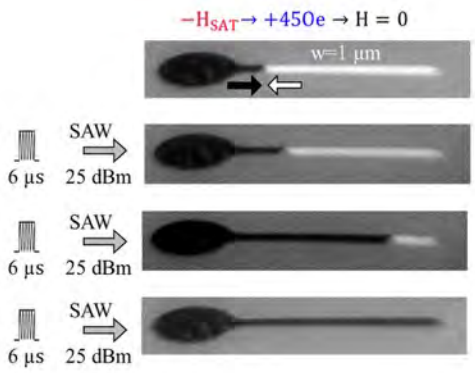
DH-10. Field free magnetic domain wall motion driven by sound

A. Rivelles[1], R. Yanes[2], L. Torres[2], M. Abuin[1], J. Grandal[1], M. Sepehr[1], G. Orero-Gámez[6], R. Guedas[3], L. Frnández-García[4], R. Izquierdo[1], M. C. Maicas[1], M. Sanz[1], J. Pedrós[1], F. Calle[1], S. Ruiz Gómez[5], W. Khaliq[5], M. Angel[5], S. Velez[6], M. Foerster[5], L. Lopez-Diaz[2], J. Prieto[1]
[1]Instituto de Sistemas Optoelectrónicos y Microtecnología (ISOM), Universidad Politécnica de Madrid (UPM), Madrid, Madrid, Spain, [2]Applied Physics Department, Universidad de Salamanca, Salamanca, Castilla y León, Spain, [3]Université Grenoble Alpes, CNRS, CEA, Grenoble INP, SPINTEC, Grenoble, France, [4]Departamento de Física de Materiales, Universidad Complutense de Madrid, Madrid, Madrid, Spain, [5]ALBA Synchrotron Light Facility, Barcelona, Spain, [6]Spintronics and Nanodevices Laboratory, Departamento de Fisica de la Materia Condensada and Condensed Matter Physics Center (IFIMAC), Universidad Autonoma de Madrid, Madrid, Madrid, Spain

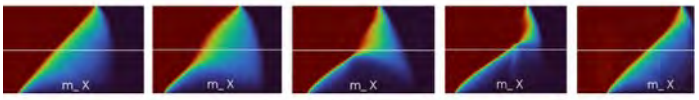
Spintronics seeks efficient strategies to control local magnetization in ferromagnetic materials without relying on external magnetic fields or electric currents. Surface acoustic waves (SAWs) have recently emerged as a promising approach[1], having been used to drive ferromagnetic resonance[2], spin pumping[3], and the manipulation of magnetic textures[4]. Nevertheless, because SAWs are intrinsically harmonic, they were not expected to induce a net unidirectional motion of a magnetic domain wall (DW), as forward and backward displacements over each acoustic cycle should cancel out.
We have recently demonstrated[5] experimentally (Fig1), by means of XMCD-PEEM imaging, that a SAW alone can induce a robust and reproducible displacement of DWs in ferromagnetic nanostrips, always in the direction of acoustic wave propagation and in the absence of any external magnetic field. We observe systematic DW motion under SAW pulses, with velocities reaching up to 12 m/s, even when a small magnetic field is applied in the opposite direction. The DW displacement increases with both the duration and the power of the acoustic pulses, with a power threshold required to trigger motion, while thermal effects are ruled out. By studying nanostrips of varying widths we show the geometrical dependence of the effect, which is essential for identifying its physical origin. Magnetic force microscopy reveals that the stable DW configuration in these structures is an asymmetric transverse domain wall. Micromagnetic simulations reproduce the observed dynamics and unveil the underlying mechanism: during the SAW cycle, magnetoelastic energy accumulates

asymmetrically within the DW, leading to intermittent internal fluctuations that release stress and produce a net forward jump(Fig2).
This process enables the transfer of linear momentum from the acoustic wave to the magnetic texture, establishing a novel mechanism for acoustic manipulation of domain walls and opening new avenues for field-free, energy-efficient spintronic devices.

[1] J. Puebla, et al., "Perspectives on spintronics with surface acoustic waves," *Appl. Phys. Lett.* 30 May 2022; 120 (22): 220502.
[2] Weiler, M. et al., "Elastically driven ferromagnetic resonance in nickel thin films" Phys. Rev. Lett. 106, 117601 (2011).
[3] Weiler, M. et al., "Spin pumping with coherent elastic waves," Phys. Rev. Lett. 108, 176601 (2012).
[4] Yang, Y. et al., "Acoustic-driven magnetic skyrmion motion" *Nat. Commun.* 15, 1018 (2024).
[5] Rivelles, A., Yanes, R, et al., "Moving magnetic domain walls with sound alone." *Nat. Commun.* 16, 9963 (2025).



Sequence of XMCD-PEEM images taken at zero external magnetic field, after the field sequence shown on top of the figure



Micromagnetic simulation sequence of the x component of the magnetization for a DW driven by a SAW

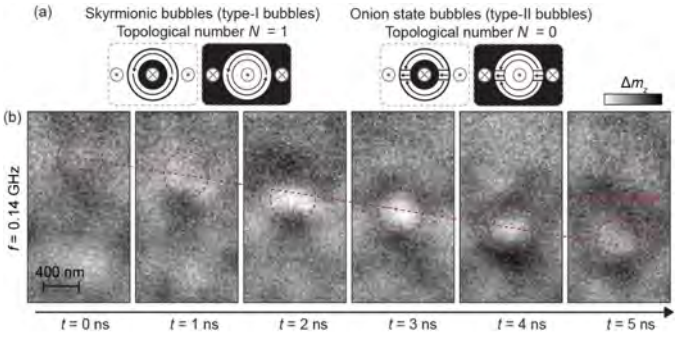
DH-11. Real-space imaging of magnon-driven bubble dynamics in a magnetic insulator

P. Che[1], S. Wintz[2, 3], T. Srivastava[4], N. Reyren[1], D. Gouéré[1], S. Mantion[1], A. El Kanj[1], S. Finizio[5], M. Weigand[2], A. Mucchietto[6], D. Grundler[6, 7], G. Schütz[3], J. Kim[4], V. Cros[1], A. Anane[1]
[1]Laboratoire Albert Fert, CNRS, Thales, Université Paris-Saclay, Palaiseau, France, [2]Helmholtz-Zentrum Berlin für Materialien und Energie GmbH, Berlin, Germany, [3]Max Planck Institute for Intelligent Systems, Stuttgart, Germany, [4]Centre de Nanosciences et de Nanotechnologies, CNRS, Université Paris-Saclay, Palaiseau, France, [5]Swiss Light Source, Paul Scherrer Institute, Villigen, Switzerland, [6]Laboratory of Nanoscale Magnetic Materials and Magnonics, Institute of Materials (IMX), École Polytechnique Fédérale de Lausanne (EPFL), Lausanne, Switzerland, [7]Institute of Electrical and Micro Engineering (IEM), École Polytechnique Fédérale de Lausanne (EPFL), Lausanne, Switzerland

Noncollinear magnetic textures such as skyrmions, bubbles, and domain walls are attracting significant attention in magnonics because they interact with magnons through their internal spin structure and topology. These interactions give rise to nontrivial magnon band topology [1], magnon–skyrmion skew scattering [2], multipole magnon modes [3], and edge-localized magnon transport [4,5], providing new routes to control magnon phase and propagation direction. Moreover, such textures can be stabilized without demanding nanofabrication, making them promising building blocks for nanoscale magnonic devices that enable guided and nonreciprocal signal transmission in magnonic circuits. However, experimental verification and real-space imaging of these magnon-noncollinear magnetic textures interactions remain limited. It is challenging to simultaneously realize both low-damping materials that host rich noncollinear magnetic textures at room-temperature, and a microscopy technique capable of resolving both their static configuration and magnon-driven dynamics at the nanoscale.
Here, we stabilized magnetic skyrmions and bubbles in 20 nm-thick Bi-doped yttrium iron garnet (Bi-YIG) films with perpendicular magnetic anisotropy (PMA) while maintaining low damping down to 10^{-4}. Time-resolved scanning transmission X-ray microscopy (STXM) allows direct visualization of magnon propagation, scattering, and confinement within the textures [5]. We observed that resonantly excited magnons can drive the translational motion of skyrmions and bubbles, reaching a velocity up to 175 m/s (Fig. 1). This provides direct experimental evidence

that magnons transfer momentum to magnetic textures and move them without electrical current. In addition, we image nonreciprocal magnons confined to deep-sub-100 nm-wide domain walls which is the key to construct chiral edge magnons [4,5]. These results show that magnons can manipulate noncollinear textures and use them as information transformation channel, enabling energy-efficient and reconfigurable room-temperature magnonic devices.

[1] T. Weber, D. Fobes and J. Waizner et al., *Science* 375, 1025 (2022).
[2] C. Schütte and M. Garst. *Phys. Rev. B* 90, 094423 (2014).
[3] P. Che, R. Ciola and M. Garst et al., *Commun. Mater.* 6, 139 (2025).
[4] Y. Zhang, L. Qiu and J. Chen et al., *Nat. Mater.* 24, 69–75 (2025).
[5] P. Che, A. J. M. Deenen and A. Mucchietto et al., Adv. Mater. 37, e08181 (2025).



(a) Sketch of skyrmionic and type-II bubbles in magnetic thin films with PMA. (b) Magnon-driven magnetic bubble motion with moving speed of 175 m/s at f = 0.14 GHz.

SESSION DP: SOFT MAGNETIC MATERIALS II (POSTER SESSION)

Chair(s): T. Taniguchi, *Tohoku University, Sendai, Japan*
Wednesday, November 4, 2026
03:00 PM-06:00 PM
Coral 4

DP-01. Evaluation of Domain Wall Width and Magnetic Properties in Low-Anisotropy In-Plane magnetized FeAlSi Nanopillars For Highly Sensitive Magnetic Sensors

R. Hirama[1], T. Kubota[2], S. Ono[3], M. Tsunoda[5, 6], M. Oogane[1, 4]
[1]Department of Applied Physics, Graduate School of Engineering, Tohoku University, Sendai, Miyagi Prefecture, Japan, [2]Department of Advanced Spintronics Medical Engineering, Graduate School of Engineering, Tohoku University, Sendai, Miyagi Prefecture, Japan, [3]International Center for Synchrotron Radiation Innovation Smart, Tohoku University, Sendai, Miyagi Prefecture, Japan, [4]Center for Science and Innovation in Spintronics, Tohoku University, Sendai, Miyagi Prefecture, Japan, [5]Department of Electronic Engineering, Graduate School of Engineering, Tohoku University, Sendai, Miyagi Prefecture, Japan, [6]Research Center for Green X-Tech, Tohoku University, Sendai, Miyagi Prefecture, Japan

Superparamagnetic tunnel junctions (SMTJs) [1–3] are promising candidates for hysteresis-free and highly sensitive two-axis magnetic field sensors, employing Ru/FeAlSi [4] as the free layer. To achieve superior magnetic field resolution, it is necessary not only to increase the volume of the SMTJ but also to maintain a single-domain state. In general, magnetic materials with dimensions smaller than the domain wall width tend to exhibit a single-domain structure; therefore, the domain wall width provides a useful guideline for estimating the upper limit of sensor size and performance.

In this work, the domain wall width of in-plane magnetized FeAlSi thin films with low magnetic anisotropy (K_1 on the order of 100 erg/cm^3) was investigated using X-ray magnetic circular dichroism (XMCD) imaging in total electron yield (TEY) mode at BL14U of NanoTerasu. By imaging flux-closure domain structures in rectangular elements with a thickness of 40 nm and lateral sizes ranging from 7 μm to 3 μm (Fig. 1), the domain wall width was estimated to be in the range of 500–700 nm based on the imaging contrast profile (Fig. 2). This large domain wall width may be attributed to the small K_1 of FeAlSi. Furthermore, a large number of nanopillars with diameters ranging from 1 μm down to 100 nm were fabricated using

electron-beam lithography and Ar ion etching. Their magnetic responses, measured using a SQUID magnetometer, will be presented in the conference. It enables us to evaluate size-dependent domain formation and identify the critical size for maintaining a single-domain state.

[1] R. Hirama *et al*., "Enhancement of magnetic field sensitivity by spin-transfer torque in in-plane magnetized superparamagnetic tunnel junctions," Applied Physics Express, vol. 18, no. 10, 2025.
[2] M. W. Daniels *et al*., "Energy-efficient stochastic computing with superparamagnetic tunnel junctions," Physical Review Applied, vol. 13, no. 3, p. 034016, 2020.
[3] A. Mizrahi *et al*., "Neural-like computing with populations of superpara magnetic basis functions," Nature Communications, vol. 9, no. 1, p. 1533, 2018.
[4] R. Hirama *et al*., "Epitaxial Metallic Buffer Layers for FeAlSi toward High-Sensitivity Magnetic Sensors Using Superparamagnetic Tunnel Junctions," presented at *Intermag 2026*, Manchester, U.K., 2026.

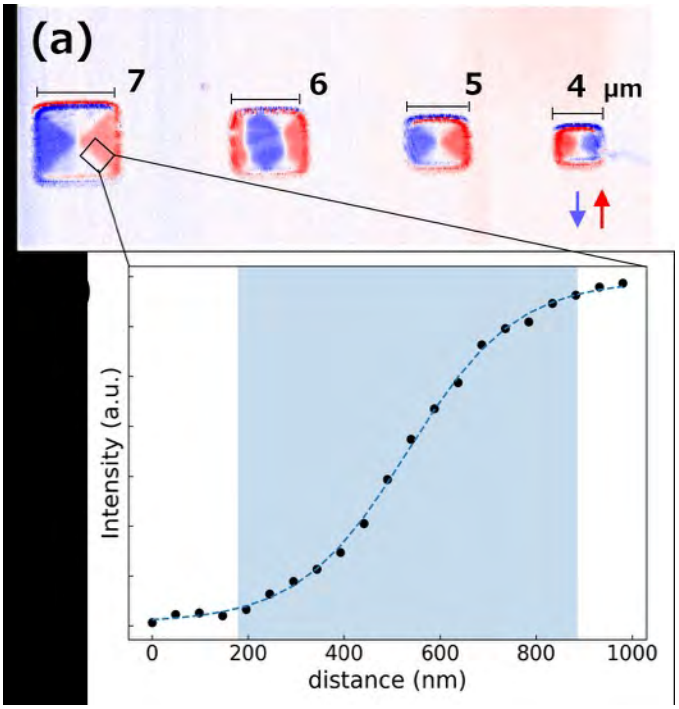


Fig. 1 (a) XMCD images of in-plane magnetized FeAlSi films observed from the top surface of square pillars with side lengths of 7, 6, 5, and 4 μm. Red and blue indicate upward and downward magnetization, respectively. (b) Schematic illustration of the method used to estimate the domain wall width from the imaging contrast profile.

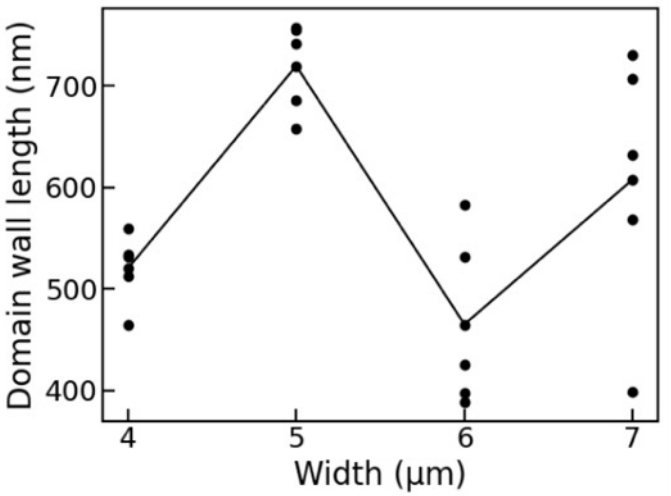


Fig. 2 Dependence of the estimated domain wall length as a function of the pillar width. The solid line represents the average value.

DP-02. Study on magnetic properties of $(Fe_{0.72}Ga_{0.28})_{100-x}Al_x$ films with various Al contents

F. Momota[1], S. Ajia[1], T. Miyazaki[1], S. Muroga[1], Y. Endo[1, 2]
[1]*Tohoku University, Sendai, Japan,* [2]*CSIS, Sendai, Japan*

Fe-Ga films are one of the promising candidates for Micro-Electro-Mechanical-System (MEMS) sensors because of their excellent mechanical properties and large saturation magnetostriction [1]. On the other hand, their relatively high coercivity and large damping constant pose challenges for high-frequency magnetic devices [2].
Until now, our group reported that interstitial dopants (B, C) improved these properties [3, 4], while substitutional elements, specifically rare-earth metals, had limited effect [5, 6]. Herein, we chose Al, as a substitutional third element, and investigated the Al content dependence of magnetic properties for Al doped Fe-Ga films with various thicknesses.
Fig. 1 shows the dependence of on the Al content for various thick Fe-Ga-Al films. In the Al content range below 3.0 at.%, of each film increased to approximately 70-80 ppm, which could be attributed to the change in lattice strain induced by the partial substitution of Ga with Al in the Fe-Ga crystal lattice. In contrast, in the Al content range between 3.0-7.9 at.%, the relationship between and Al content differed by film thickness. Namely, in the case of the 20-nm-thick film, decreased to approximately the same value as that of the Fe-Ga film as the Al content increased. In contrast, in the case of the 30-nm and 50-nm-thick films, each remained almost constant regardless of the Al content.

Fig. 2 shows the change in of various thick Fe-Ga-Al films with the Al content.
Regardless of film thickness, exhibited a decreasing tendency as the Al content increased. It could be attributed to the improvement of magnetic softness such as coercivity, uniaxial magnetic anisotropy, and so on with the increase of Al content.
Therefore, these results demonstrate that the Al addition can improve high-frequency magnetic properties of Fe-Ga films while maintaining their high , and also suggest that Al doped Fe-Ga films are a promising candidate magnetic material for high-frequency magnetic devices.

[1] A. E. Clark et al., *IEEE. Trans. Magn*., 36, 328 (2000).
[2] Y. Endo et al., *IEEE Trans. Magn*., 53, 11, 2502305 (2017).
[3] Y. Endo et al., *The papers of Tech. Meeting "Magnetics", IEEJ, MAG20111* (2020).
[4] S. Muramatsu et al., *AIP Advances*, 11, 025114 (2021).
[5] R. Nishina et al., *T. Magn. Soc. Jpn. (Special Issues)*, 8 (2024).
[6] S. Ajia et al., *AIP Advances*, 15, 3, 035116 (2025).

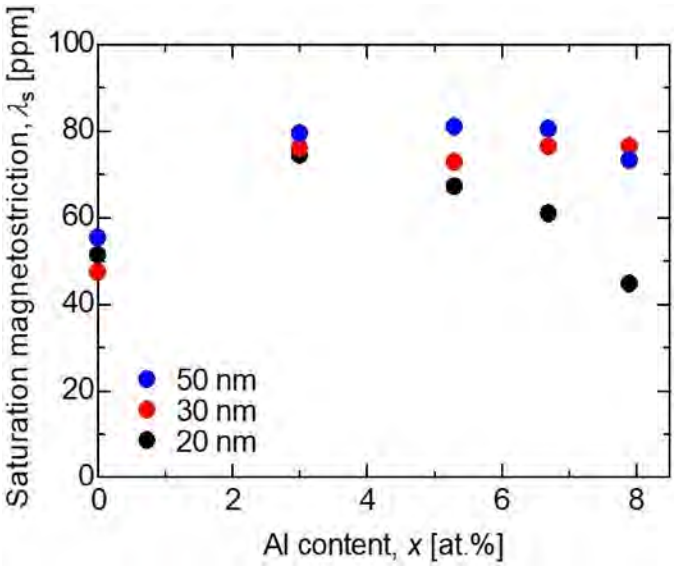


Fig. 1 Dependence of saturation magnetostriction on the Al content for Fe-Ga-Al films with various film thickness.

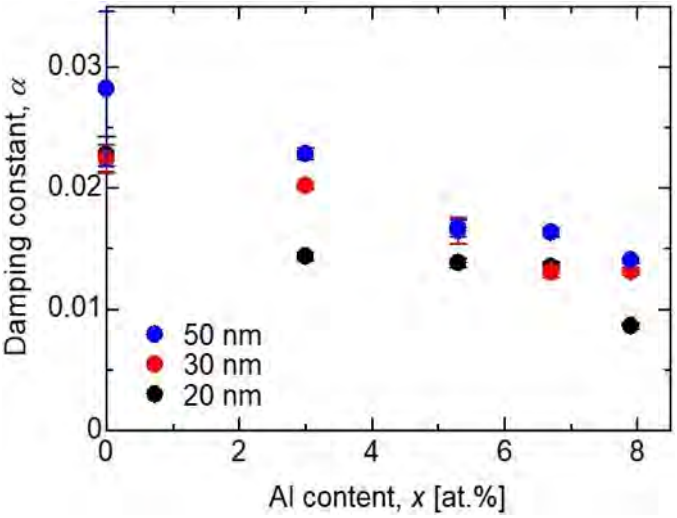


Fig. 2 Dependence of damping constant on the Al content for Fe-Ga-Al films with various film thickness.

DP-03. Magnetic Properties of Fe-6.5Si Soft Magnetic Composites via Micro Fe Based Fillers

J. Seo[1], Y. In[1], D. Lee[1], S. Park[1], D. Kim[2], B. Lee[3]
[1]Physics, Hankuk University of Foreign Studies, Yongin-Si, Gyeonggi-Do, Korea (the Republic of), [2]Kolon industries, Seoul, Korea (the Democratic People's Republic of), [3]Electronic Physics, Hankuk University of Foreign Studies, Yongin-Si, Gyeonggi-Do, Korea (the Republic of)

In this study, the effect of Micro Fe (M-Fe) addition on the magnetic properties of Fe-6.5Si soft magnetic composites was investigated. The crystal structure, microstructure, electrical and magnetic properties of the Fe-6.5Si and M-Fe powders, as well as the electromagnetic properties of the composites with different M-Fe contents, were systematically analyzed. XRD results revealed that both powders possessed an α-Fe (bcc)-based crystal structure. SEM observations confirmed that both powders had spherical morphologies, with average particle sizes of 18.10 μm for Fe-6.5Si and 3.55 μm for M-Fe. Magnetic hysteresis measurements showed that both powders exhibited soft magnetic behavior, while M-Fe had higher saturation magnetization and coercivity than Fe-6.5Si. In the composites, the permeability reached its maximum at 30 wt% M-Fe, which was closely related to the improved packing fraction resulting from the increased core density. In contrast, the Q-factor reached a maximum value of 74 at 1 MHz for the 20 wt% sample, and the total core loss showed a minimum value of 633.67 mW/cm3 at the same composition. These results are attributed to changes in

interparticle contact conditions induced by the addition of fine particles, which affect eddy current paths and contact resistance, thereby governing the core loss behavior. Therefore, M-Fe addition effectively tailors the permeability and loss characteristics of Fe-6.5Si composites, with 20–30 wt% identified as the optimal composition range for soft magnetic core applications.

DP-04. High Anisotropy and Low Damping FeGaB Soft Magnetic Films for C-Band RF Applications

B. Luo[1], J. E. Shoup[2], D. Huang[1], V. Kalappattil[3], M. Wu[3, 1], D. B. Gopman[2], N. X. Sun[1]
[1]Department of Electrical and Computer Engineering, Northeastern University, Boston, Massachusetts, United States, [2]Materials Science & Engineering Division, National Institute of Standards and Technology, Gaithersburg, Maryland, United States, [3]Department of Physics, Northeastern University, Boston, Massachusetts, United States

Metallic soft magnetic films (SMFs) are essential for self-biased RF/microwave components in monolithic microwave integrated circuits (MMICs) [1] and ultracompact magnetoelectric and magnetoacoustic devices [2]. FeGaB is the preferred magnetostrictive SMF due to its low coercive field, high magnetostriction (~70 ppm), CMOS-compatible sputtering, and low Gilbert damping ($\alpha < 0.005$) [3]. However, existing FeGaB thin films exhibit a limited uniaxial anisotropy field (H_k) of 15–30 Oe when induced by an in-situ growth field, constraining the self-biased ferromagnetic resonance (FMR) frequency to ~1.85 GHz (L-band) [3]. While composition-gradient and facing-target sputtering have raised H_k> 500 Oe in FeCoB [4, 5], analogous routes that preserve low damping in amorphous FeGaB remain undemonstrated.
Here, we demonstrate high-anisotropy, low-damping FeGaB soft magnetic films tailored for C-band RF applications. An element gradient and film stress were introduced into a Ru/FeGaB/Ru stack via the co-sputtering of two FeGaB targets in a facing-target configuration. Ru/FeGaB/Ru trilayers with varying thickness combinations (t_{FeGaB} = 30–120 nm, t_{Ru} = 3–20 nm) were characterized using massively parallel broadband VNA-FMR [6] across 16 positions on the deposition chuck. A peak H_k ~ 242 Oe was realized in a 3 nm Ru / 60 nm FeGaB / Ru stack, representing an 8× improvement over conventional FeGaB, while strictly preserving a low Gilbert damping of α=0.0036 (Fig. 1, 2). Consequently, this high-anisotropy FeGaB film exhibits a self-biased FMR of ~5.2 GHz, marking the first successful extension of FeGaB from the L-band into the C-band. Furthermore, H_k exhibits a non-monotonic dependence on t_{FeGaB} (peaking at 60 nm and decreasing at 120 nm), which is consistent with the competing mechanisms of strain accumulation and relaxation. The CMOS-compatible sputtering route to achieve high-H_k, low-loss FeGaB paves the way for advanced C-band inductors, tunable filters, and multiferroic devices [1, 2].

[1] Y. Gao et al., IEEE Trans. Electron Devices, Vol. 61, p. 1470 (2014)
[2] T. Nan et al., Nat. Commun., Vol. 8, p. 296 (2017)
[3] J. Lou, R. Insignares and Z. Cai, Appl. Phys. Lett., Vol. 91, p. 182504 (2007)
[4] S. Li et al., Sci. Rep., Vol. 4, p. 7393 (2014)
[5] K. Hirata, A. Hashimoto and S. Nakagawa, J. Appl. Phys., Vol. 105, p. 07A316 (2009)
[6] D. Gopman and J. Shoup, NIST CHIPS Metrology Report (2025)

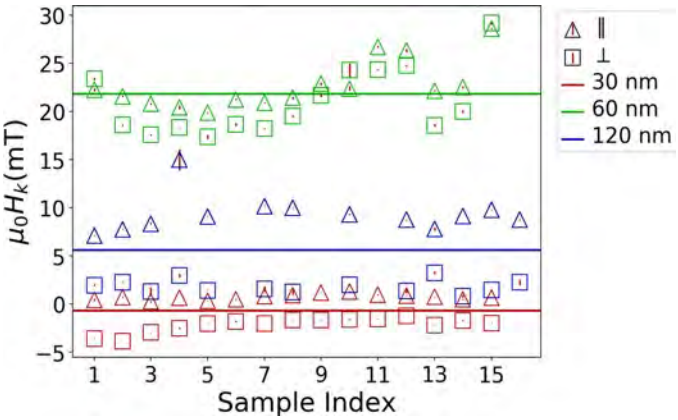


Fig1. Total anisotropy H_k vs sample index from left to the right of the chuck under different thickness of FeGaB films.

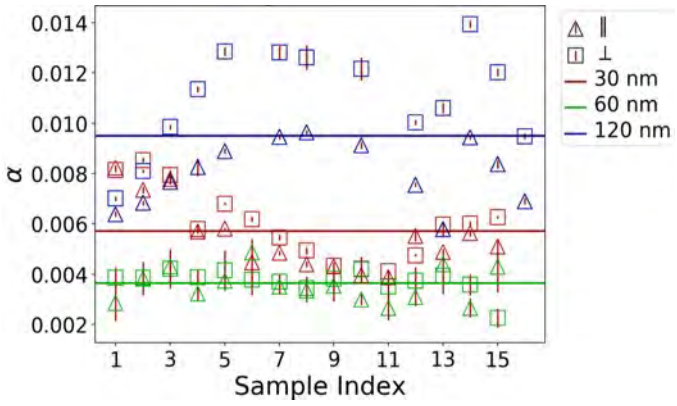


Fig2. Gilber damping constant vs sample index from left to the right of the chuck under different thickness of FeGaB films.

DP-06. High-Frequency Magnetic Characterization of Fe-Based Nanocrystalline Alloys Under Temperature and Rotational Magnetization Effects

M. Yang[1, 4], Y. Li[2], G. Zhou[2], Z. Lin[2], Z. Hu[1, 4], J. Li[1, 4], Q. Yang[3]
[1]School of Vehicle and Mobility, Tsinghua University, Beijing, China, [2]State Key Laboratory of Intelligent Power Distribution Equipment and System, Hebei University of Technology, Tianjin, China, [3]Tianjin University of Technology, Tianjin, China, [4]State Key Laboratory of Intelligent Green Vehicle and Mobility, Tsinghua University, Beijing, China

Driven by the increasing demand for high-speed and compact electric drive systems, Fe-based nanocrystalline alloys have emerged as promising core materials due to their excellent high-frequency magnetic performance. In practical operation, stator cores are typically subjected to high-frequency two-dimensional (2-D) rotational magnetization, under which conventional loss evaluation methods become inadequate. Moreover, high-speed operation often induces significant temperature rises, which modify the intrinsic magnetic properties of the material [1]. Neglecting the effects of rotational magnetization and temperature in the design may lead to parameter mismatch, which can compromise equipment reliability [2].
Existing studies on temperature-dependent magnetic behavior have primarily focused on electrical steels and soft ferrites, whereas investigations of 2-D rotational magnetization are largely limited to electrical steels and amorphous alloys at low frequencies. Systematic studies on Fe-based nanocrystalline alloys that consider temperature dependence and 2-D rotational magnetization, particularly in the high-frequency range, remain relatively scarce, highlighting a critical gap that should be filled to enable their reliable application in next-generation drive motors.
In this paper, a temperature-controlled one-dimensional magnetic property measurement system and a high-frequency 2-D magnetic characterization platform are developed. The alternating magnetic properties of Fe-based nanocrystalline alloy with different annealing processes are experimentally evaluated over frequencies of 1-50 kHz from 20°C to 120°C, with emphasis on temperature-dependent behavior. Furthermore, the rotational magnetic properties of sample are measured within 1-20 kHz. The magnetic anisotropy at different peak flux densities is analyzed. The phase relationship between magnetic flux density *B* and magnetic field strength *H* is examined to characterize anisotropic under circular rotational magnetization. Finally, the distinctions between alternating and rotational magnetic properties are discussed, along with their implications for high-speed motor design.

[1] Y. Wang, L. Mo, C. Q. Jiang, W. Guo, X. Wang, and K. T. Chau, "Temperature-Dependent Magnetic Characteristics and Thermal Runaway Assessment in Passive-Cooled Inductive Power Transfer Systems," *Energy*, vol. 332, Sep, 2025.
[2] Z.-Q. Zhu, S. Xue, W. Chu, J. Feng, S. Guo, Z. Chen, and J. Peng, "Evaluation of Iron Loss Models in Electrical Machines," *IEEE Trans. Ind Appl,* vol. 55, no. 2, pp. 1461–1472, 2019.

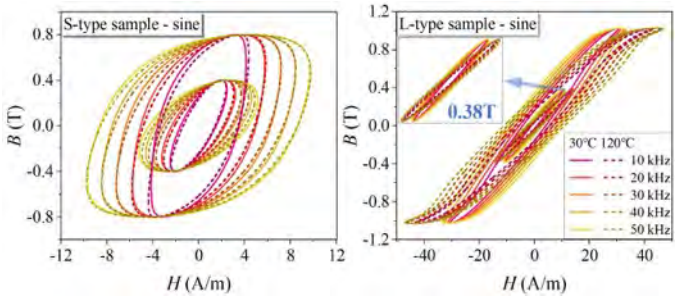


Fig.1 Comparison of B-H loops

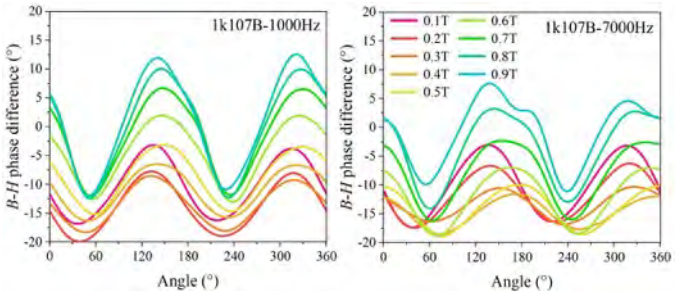


Fig.2 B-H phase difference under rotational excitation

DP-08. A joint theoretical-experimental study of B2 phase $Al_{50}Cr_{25}Co_{25}$ alloy

H. Aihemaiti[1, 2], E. Dastanpour[1, 2], P. Svedlindh[3], L. Vitos[1, 2, 4]
[1]Department of Materials Science and Engineering, KTH Royal Institute of Technology, Stockholm, Sweden, [2]Wallenberg Initiative Materials Science for Sustainability, Department of Materials Science and Engineering, KTH Royal Institute of Technology, Stockholm, Sweden, [3]Department of Materials Science and Engineering, Uppsala University, Uppsala, Sweden, [4]Department of Physics and Astronomy, Uppsala University, Uppsala, Sweden

Density functional theory (DFT) calculations indicate that the ternary $Al_{50}Cr_{25}Co_{25}$ alloy is stable in the ferromagnetic

(FM) state within the ordered B2 structure, whereas the binary AlCr and AlCo alloys show antiferromagnetic (AFM) and nonmagnetic (NM) behavior in the same crystal structure. According to DFT results, ferromagnetism in this ternary alloy mainly originates from the Cr atom with a local magnetic moment of 2.14 μ_B, while the Al and Co moments are negligible. Experimental Scanning Electron Microscope (SEM) results for as-cast samples reveal that the alloy decomposes into a Cr-rich bcc phase and a Co-rich B2 phase. The measured saturation magnetization is 8 Am^2kg^{-1}, which is assumed to be associated with the magnetic B2 phase having a measured Curie temperature (T_C) of 210 K. Indeed, DFT calculations for the measured SEM compositions confirm that the bcc phase is nonmagnetic, while the B2 phase is ferromagnetic with a local magnetic moment of 2.10 μ_B for the Cr atom. The corresponding mean-field T_C estimated from DFT energies is 155 K, in good agreement with the observation.

DP-09. Effect of Nb and W addition on B2 ordering and magnetic properties of Fe-49Co-2V alloy

T. Sato[1], Y. Ikeda[2], M. Enoki[3], T. Iriyama[5], T. Omori[4]
[1]Corporate Research & Development Center, Daido Steel Co., Ltd., Nagoya, Aichi, Japan, [2]Institute for Materials Research, Tohoku University, Sendai, Miyagi, Japan, [3]Faculty of Materials for Energy, Shimane University, Matsue, Shimane, Japan, [4]Graduate School of Engineering, Tohoku University, Sendai, Miyagi, Japan, [5]Corporate Research and Development Laboratory, Daido Steel Co., Ltd., Nagoya, Aichi, Japan

In recent years, increasing attention has been paid to the use of Permendur (Fe-49Co-2V, mass%) for motor cores because of its excellent soft-magnetic properties, including high saturation magnetization, J_s, and low core loss. However, its poor workability, arising from the B2 ordering, has limited its practical application [1]. Although many studies have attempted to suppress ordering through alloying, they employed large amounts of alloying elements, which in turn degraded the soft-magnetic properties [2), 3)]. In this study, the effects of small additions of Nb and W to Fe-49Co-2V on the B2 ordering and the magnetic properties were investigated to improve workability while maintaining favorable soft-magnetic properties.

Four alloys (Fe-49Co-2V, Fe-49Co-2V-0.25Nb, Fe-49Co-2V-0.25W, and Fe-49Co-2V-0.12Nb-0.12W) were produced by melting, casting, forging, and hot rolling. The hot-rolled plates were annealed in air at 1173 K for 3.6 ks and then water-quenched. Specimens for neutron diffraction, Charpy impact, and magnetization measurements were prepared from the quenched alloys. The remaining plates were rolled to a thickness of 0.2 mm, formed into ring cores, and annealed again at 1123 K for 21.6 ks. Core loss was measured on the ring-core samples using a BH tracer.

Fig. 1 shows the degree of B2 ordering in each alloy, obtained from two-phase fitting of the neutron PDF data. A clear suppression of B2 ordering is observed with small additions of alloying elements. In particular, the addition of W appears to suppress B2 ordering more effectively than that of Nb. DFT calculations of the B2 ordering enthalpy also suggest a similar trend, where W addition more effectively destabilizes the ordered phase than Nb. Fig. 2 shows the J_s and core loss of each alloy. Nb- and W-added alloys exhibited good J_s and core loss comparable to those of Fe-49Co-2V. From these results, we developed a new Fe-Co alloy with improved workability while maintaining the excellent soft-magnetic properties of the Fe-49Co-2V.

1) R. S. Sundar and S. C. Deevi, Soft magnetic Fe-Co alloys: Alloy development, processing, and properties, International Materials Reviews 50 (3), pp. 157-192, 2005.
2) C.M. Orrock, The Microstructure and properties of Equiatomic iron-cobalt magnetic alloys with alloying additions, University of London, 1985.
3) Y. Shan, C. Chen, X. Bi, Role of precipitation in strength and ductility of FeCo-2V-Cr alloy with low coercivity, Intermetallics, 54, pp. 164-168, 2014.

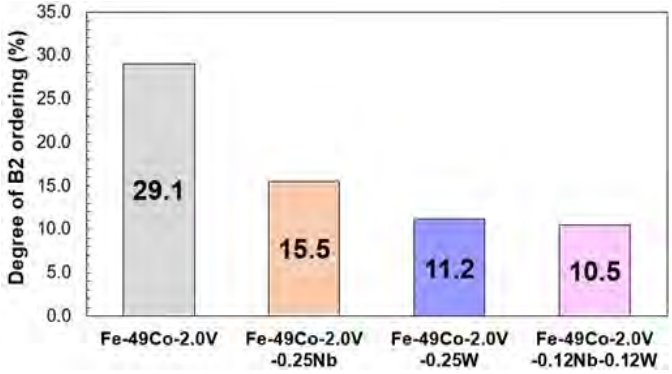


Fig. 1 Effect of Nb and W additions on the degree of B2 ordering in the Fe-49Co-2V alloy.

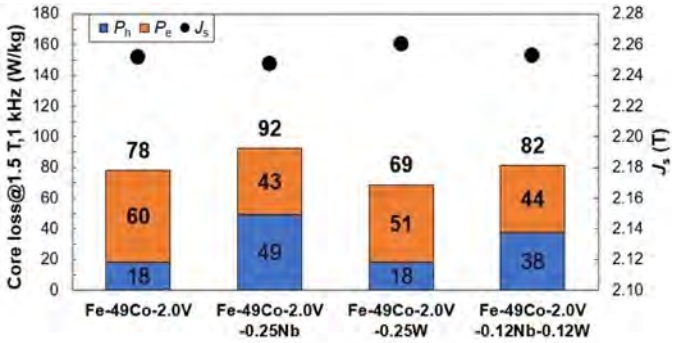


Fig. 2 Effect of Nb and W addition on the core loss, hysteresis loss (P_h), eddy current loss (P_e) and J_s in the Fe-49Co-2V alloy.

DP-10. Exploring the Synthesis, Phase Evolution, and Magnetic Characterization of the Fe9Co7 Phase

S. A. Marini, S. Maness, D. Dunand, G. Snyder
Materials Science and Engineering, Northwestern University, Evanston, Illinois, United States

The integration of iron-cobalt (Fe-Co) phases is critical for next-generation energy and computational technologies, including high-efficiency motors and spintronics, due to their high Curie temperatures and exceptional saturation magnetization. While Fe–Co alloys are well-documented, ordered Fe-Co intermetallic phases are also known. For example, the ordered L10 variants of FeNi, CoPt, and tau-MnAl are known to be good ferromagnets, yet are metastable. In the Fe-Co system, several ordered intermetallic phases have been predicted to be stable, such as FeCo (B2 and L10), Fe11Co5, FeCo3, and Fe9Co7, but not all have been fully characterized. Specifically, the aforementioned phases are expected to be stable at low temperatures, where diffusion is slow; however, the structures are all subtle distortions or superstructures of BCC Fe, making the structural distinguishing features difficult to observe.

This study aims to establish a synthesis protocol to make these Fe-Co phases, starting with Fe9Co7. We explore a non-equilibrium synthesis route to stabilize the compound using high-energy ball milling, while also investigating arc melting synthesis to determine how different methodologies influence phase stability and magnetic properties. By leveraging intense atomic-level mixing in the mechanical alloying process, we aim to access the material phase space necessary to realize the Fe9Co7 stoichiometry. XRD analysis and Rietveld refinement of ball milled samples have the potential to suggest the successful formation of this new target phase, revealing several superstructure 2theta peaks consistent with the predicted Fe9Co7 phase on the Materials Project database.

Additionally, this work aims to explore the optimization of post-synthesis thermal annealing to drive crystallinity and phase purity of Fe9Co7, uncover the processing conditions that result in phase transformations, and characterize with PPMS to determine how it magnetically performs. This research can establish a mechanical framework to experimentally realize other magnetic phases and give rise to discussion on their potential of being engineered to surpass the benchmarks of current Fe-Co magnets.

DP-11. Optimization of Inductance Tuning Range and Core Loss in Orthogonal Controllable Reactors Based on Nanocrystalline Alloys

J. Yuan[1, 2], H. He[1, 2], J. Hou[1, 2], H. Zhou[1, 2], F. Xiao[1, 2]
[1]State Key Laboratory of Power Grid Environmental Protection, School of Electrical Engineering and Automation, Wuhan University, Wuhan, Hubei Province, China, [2]School of Electrical Engineering and Automation, Wuhan University, Wuhan, Hubei Province, China

With large-scale wind and photovoltaic grid integration, power systems face severe voltage fluctuations, urgently requiring controllable reactors with higher reactive power capacity and lower losses. Thus, this paper proposes an orthogonal controllable reactor (OCR) based on a nanocrystalline alloy, featuring a wide inductance adjustment range and low loss. The OCR's basic structure shown in Fig. 1(a) comprises a gapped square AC core and two orthogonally distributed "C-type" DC cores. It smoothly adjusts inductance by regulating the DC control magnetic field to alter the saturation and permeability of the orthogonal core region. Traditional OCRs typically use grain-oriented silicon steel cores, suffering from a narrow inductance adjustment range and high core loss. To optimize these metrics, we compare traditional oriented silicon steel (30Q130), nanocrystalline alloy (NANO), and soft magnetic composite (Somaloy 700HR) applied as the orthogonal region core. B-H and permeability curves are shown in Fig. 1(b) and 1(c). Simulations in Fig. 2 reveal that the 30Q130 OCR's inductance adjustment range is only 27.60%, with an average core loss of 21.86 W due to

material thickness and orthogonal magnetization. Although the Somaloy 700HR OCR reduces average loss to 16.34 W—as its isotropy and high resistivity suppress eddy currents—its adjustment range remains unimproved (26.23%). Conversely, the NANO OCR, leveraging high initial permeability and low saturation flux density, broadens the range to 41.60% while minimizing average core loss to 14.13 W. Results show that the nanocrystalline alloy significantly broadens the inductance adjustment range and reduces energy loss. Compared to 30Q130 and Somaloy 700HR, the NANO OCR relatively expands the adjustment range by 50.78% and 58.55%, respectively, while reducing average loss by 35.37% and 13.50%, demonstrating optimal overall performance.

J. Yuan, X. Zheng and F. Chen, "Analysis and Optimized Design of a Novel Compact Orthogonal Controllable Reactor,", IEEE Transactions on Power Delivery, vol. 37, no. 6, pp. 4527-4538(2022)

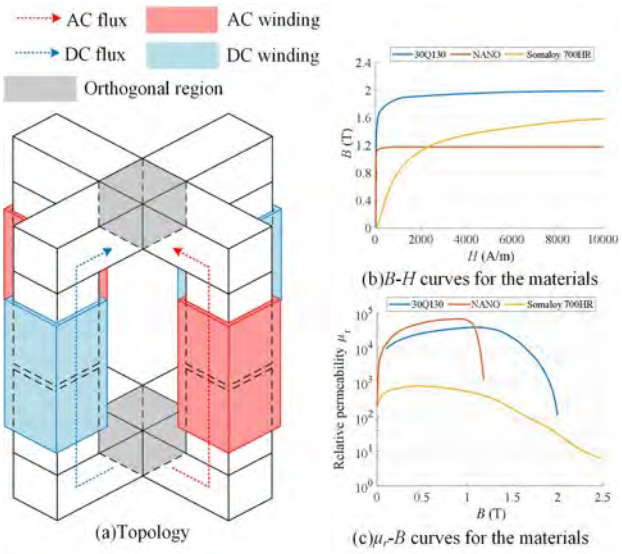


Fig.1 The topology of OCR and the B-H and B-μr curves for the materials

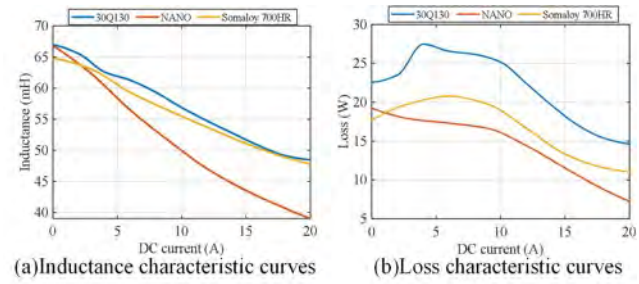


Fig.2 Inductance characteristic curves and loss characteristic curves

DP-12. Deep Magnetic Structural Analyses within Soft Magnetic Materials Using Neutrons

H. Mamiya[2], T. Kumada[1], t. shinohara[3], R. Gautam[2], H. Sepehri-Amin[2]

[1]Japan Atomic Energy Agency, Tokai, Japan, [2]National Institute for Materials Science, Tsukuba, Japan, [3]The High Energy Accelerator Research Organization, Tsukuba, Japan

In soft magnetic materials, surface magnetic structures—affected by surface poles and processing strains—often differ significantly from the interior. However, internal magnetic states cannot be directly observed due to poor penetration of optical, X-ray, and electron beams. Neutrons offer high penetration depth and can directly probe deep magnetic structures. Although neutron techniques are common in basic magnetism, applications to practical soft magnetic materials are still limited. In this study, we explored multi-scale analysis by investigating nanocrystalline ribbons and ferrite sintered cores.

For the millimeter and atomic scales, operando experiments were performed on 13 mm-thick wound ferrite cores using polarized neutron pulses (Fig. 1) [1]. Transmission spectrum mapping enabled direct visualization of magnetization parallel or antiparallel to neutron polarization. Magnetic Bragg-edge analysis confirmed the atomic magnetic structure, indicating the B sublattice spins aligned to the external field.

For the nanometer and micrometer scales, small-angle and ultra-small-angle neutron scattering were conducted on NANOMET nanocrystalline ribbons after aging (Fig. 2) . In the small-angle region, clover-leaf-shaped intensity distribution appeared, showing spin misalignment structures at the nanoscale [2]. In the ultra-small-angle region, the scattering profile hump shifted to higher q with aging, interpreted as direct beam broadening due to increased multiple scattering with domain subdivision.

These findings demonstrate that neutron-based multi-scale methods are powerful for directly elucidating complex, hierarchical deep magnetic structures, which is essential for further progress in soft magnetic materials.

[1] H. Mamiya, N. Terada, K. Hiroi et al., J. Appl. Phys. 138 (2025) 143904.

[2] H. Mamiya, Y. Oba, K. Hiroi et al., IEEE Magn. Lett. 14 (2023) 7100105.

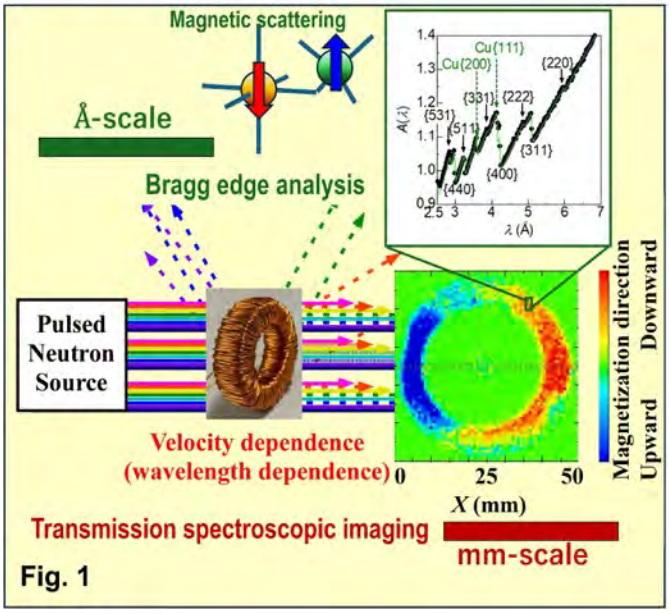


Fig. 1. Magnetic structural analyses at the millimeter and atomic scales in ferrite cores using neutron transmission spectroscopy.

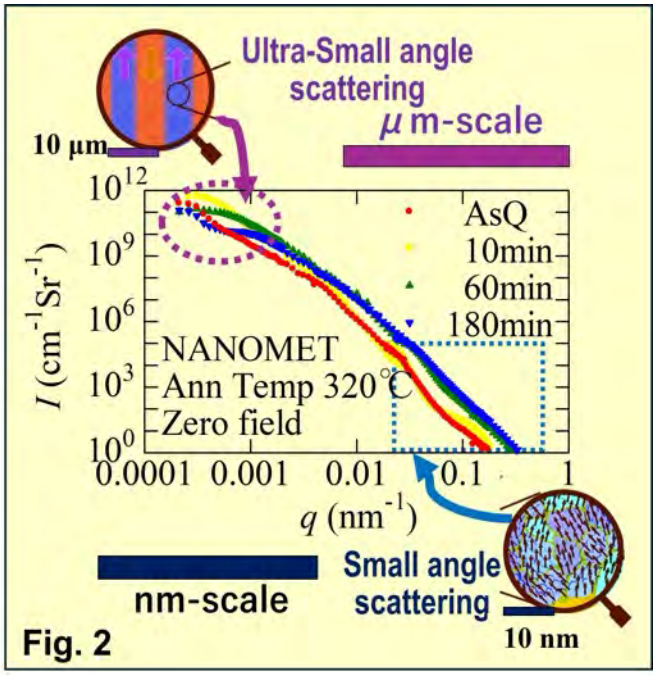


Fig. 2. Magnetic structural analyses at the nanometer and micrometer scales in NANOMET using small-angle and ultra-small-angle neutron scattering.

DP-13. Principal component analysis of first-order reversal curve diagrams for highly neutron-irradiated reactor pressure vessel steels

S. Kobayashi[1], M. Horvath[2], I. Szenthe[2], F. Gillemot[2], L. Almasy[2], A. Horvath[2]

[1]Iwate University, Morioka, Japan, [2]Centre for Energy Research, Budapest, Hungary

Non-destructive evaluation (NDE) of irradiation hardening in reactor pressure vessel (RPV) steels is of crucial important for long-term operation of nuclear plants. Recently, we have focused on a magnetic method using first-order reversal curve (FORC) diagrams, because the diagrams include much information about coercivity distribution and interaction field [1]. In particular, since the FORC diagram is a two-dimensional contour map, magnetic features related to irradiation hardening may be effectively captured by the principal component analysis (PCA). In this study, we performed PCA of FORC diagrams for neutron-irradiated A533B-type RPV steels to seek a possible application of the PCA for the magnetic NDE.

We used block samples with dimensions of 10 x 10 x 30 mm^3, which were neutron-irradiated at 290^{0}C to four levels of fluences: 1.58, 2.29, 9.35, and 11.9×10^{19} n/cm^2. Two samples with different orientations against rolling direction were prepared; the long axis of the sample is parallel (LX) or perpendicular (TX) to rolling direction. FORCs were measured using a homemade fluxmeter and PCA of FORC diagrams was performed using FORCinel [2]. Figures 1(a) and 1(b) show representative FORC diagrams before and after neutron irradiation, respectively. Each FORC diagram has a single peak nearly on the coercivity axis, whose position shifts towards a higher coercivity at high fluence, implying the possible formation of late-blooming nanoscale Mn-Ni-Si-rich clusters [3]. PCA of the FORC diagrams revealed that the approximately 95% of the total data variance was captured by the first three principal components. In particular, the first component shown in Fig. 1(c) exhibits a roughly linear correlation with the position of the FORC peak i.e., the degree of magnetic hardening due to nanoscale precipitates. The results demonstrate that the FORC analysis provides a useful NDE approach for assessing irradiation hardening of RPV steels associated with nanoscale defect formation.

[1] S. Kobayashi, H. Murakami, T. Yamamoto, G.R. Odette, A. Horvath, A. Feoktystov, L. Almasy, Magnetic investigations on irradiation-induced nanoscale precipitation in reactor pressure vessel steels: A first-order reversal curve study, J. Nucl. Mater. vol.552 (2021) 152973.

[2] I. Lascu, R.J. Harrison, Y. Li, J.R. Muraszko, J.E.T. Channell, A.M. Piotrowski, and D.A. Hodell, Magnetic unmixing of first-order reversal curve diagrams using principal component analysis, Geochem. Geophys. Geosyst. vol.16 (2015) 2900-2915.
[3] G. R. Odette, T. Yamamoto, T. J. Williams, R. K. Nanstad, and C. A. English, On the history and status of reactor pressure vessel steel ductile to brittle transition temperature shift prediction model, J. Nucl. Mater. vol.526 (2019) 151863.

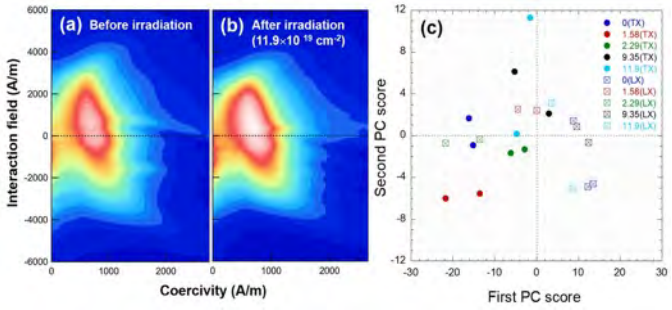


Fig.1. FORC diagrams for samples with LX orientation (a) before and (b) after neutron irradiation to a fluence of 11.9 x 10^{19} n/cm^2. (c) PC score plot between the first and second components for all measured samples.

DP-15. Reduced Core Loss in FeSiB Amorphous Alloy Powder Cores by Controlling TEOS Content

D. Lee[1], J. Seo[1], T. Kim[1], S. Park[1], D. Kim[2], B. Lee[3]
[1]Physics, Hankuk University of Foreign Studies, Yongin-Si, Gyeonggi-Do, Korea (the Republic of), [2]Kolon industries, Seoul, Korea (the Republic of), [3]Electronic physics, Hankuk University of Foreign Studies, Yongin-Si, Gyeonggi-Do, Korea (the Republic of)

In this study, SiO2 insulating coatings using tetraethyl orthosilicate (TEOS) were applied to FeSiB amorphous alloy powder cores for high-frequency inductors, and the effects of TEOS content on their microstructure and electromagnetic properties were analyzed. XRD results showed that the FeSiB powders retained their amorphous structure after TEOS coating, while SEM and EDS analyses confirmed spherical particle morphology and a stable Fe-Si-B composition. In addition, no significant particle agglomeration or morphological deformation was observed after coating. However, as the TEOS content increased, both core density and permeability at 1 MHz decreased, and the deterioration in magnetic properties became more pronounced under high-TEOS conditions because of the increased nonmagnetic SiO2 layer. Core loss measurements showed that the lowest core loss was obtained at 1.0 wt% TEOS coating, indicating the most effective suppression of eddy currents. Therefore, an appropriate TEOS content is essential for improving the electromagnetic performance of FeSiB amorphous powder cores while minimizing reductions in core density and permeability.

DP-16. Transient Magnetic Response of Nanocrystalline Iron Core in Saturated Core Type Fault Current Limiter: How Saturation Flux Density Determines Current-Limiting Dynamics

J. L. Liu, J. Yuan, H. Zhou, Z. Zhang
Wuhan University, Wuhan, China

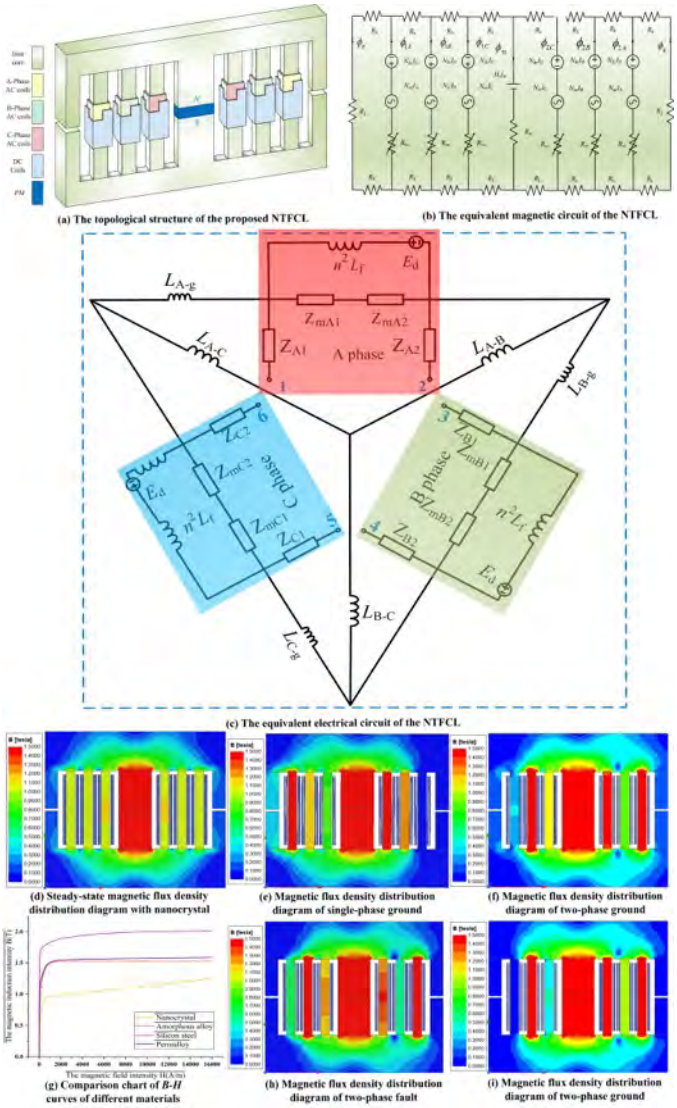
Conventional three-phase saturated-core fault current limiters (TSCFCLs) use silicon steel cores (2.0 T), requiring large DC magnetomotive force to maintain deep saturation and raising system cost. The high saturation point prolongs impedance establishment during faults. Low saturation materials are an alternative, yet how their saturation properties govern transient impedance response remains unaddressed.
Fig. 1 shows the proposed nanocrystalline-core TSCFCL (NTFCL) with an external air-core reactor in parallel with the core (1.25 T). In normal state, DC bias from permanent magnets and windings drives the core into deep saturation, presenting low impedance. In faults, the fault current counteracts the DC bias, causing alternating desaturation. Owing to low saturation flux density, the core exits saturation under smaller opposing magnetomotive force, shortening impedance response time. The core inductance acts as a magnetic switch, rapidly raising impedance while the external reactor is automatically inserted. Fig. 1 displays flux density distributions under steady-state and fault conditions.
Fig. 2a presents di/dt under identical A-phase fault. The nanocrystalline core exhibits the largest instantaneous di/dt (15,027,300 A/s), 3.40% higher than silicon steel, 37.13% higher than amorphous alloy, 2.78% higher than permalloy, and 64.26% higher than the unprotected system. This spike directly evidences shortened impedance response time—low saturation flux density accelerates the transition from deep saturation to high-permeability state. Fig. 2 summarize limiting effectiveness across four fault inception angles (0°–90°). The NTFCL achieves 41.60% transient limiting (current reduced by 37.26 A) and 42.72% steady-state limiting (current reduced by 22.39 A), outperforming silicon steel,

amorphous alloy, and permalloy by 29.98%/28.16%/9.12% in transient limiting and 22.86%/18.91%/5.17% in steady-state limiting, respectively.

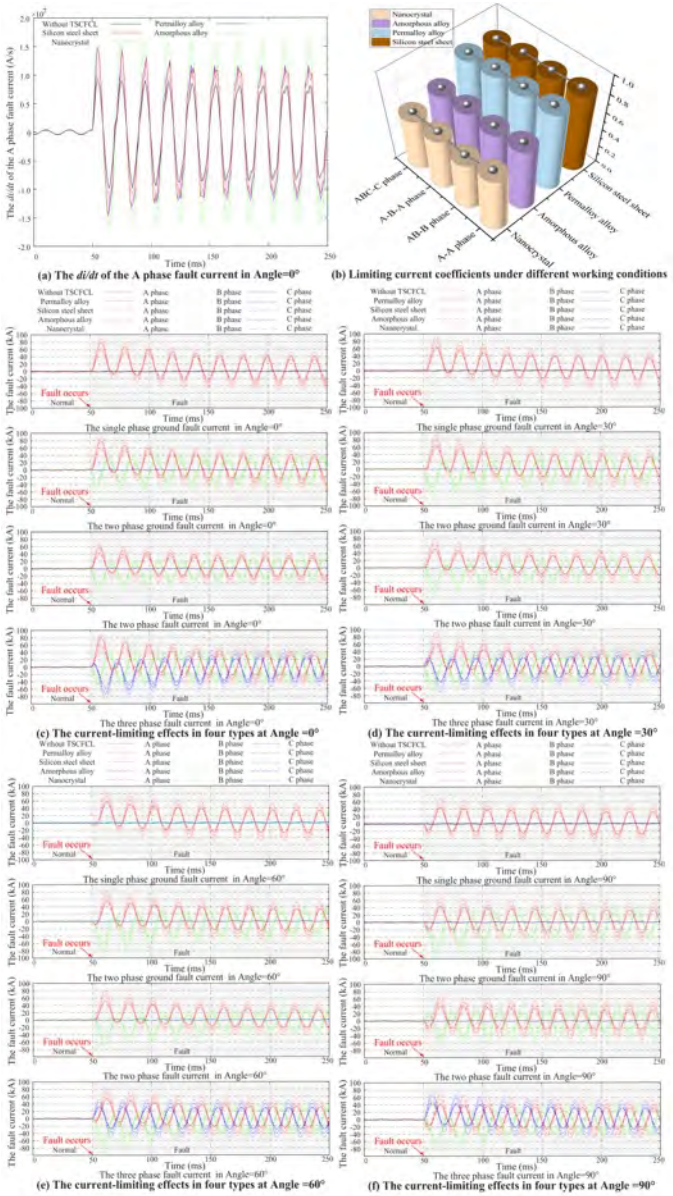
These results confirm that the NTFCL shortens impedance response time, enabling faster and more effective fault suppression for 500kV fault protection.

[1] J. Liu, J. Yuan, Hangzhou and W. Zhang, "The Design and Research Analysis of HVAC System Three-Phase Energy-Draining Fault Current Limiter," *2024 IEEE 21st Biennial Conference on Electromagnetic Field Computation (CEFC)*, Jeju, Korea, Republic of, 2024, pp. 1-2.

[2] J. R. Prigmore, "Comparison of four different types of ferromagnetic materials for fault current limiter applications," IEEE Transactions on Power Delivery 28, 1491–1498 (2021).



Proposed NTFCL's design and magnetic circuit characterization.



Comparative fault current limiting effectiveness at different fault inception angles.

SESSION DQ: ELECTROMAGNETIC MACHINES AND HIGH-FREQUENCY POWER TECHNOLOGIES (POSTER SESSION)
Chair(s): N. A. Natekar, *Western Digital, San Jose, California, United States*
Wednesday, November 4, 2026
03:00 PM-06:00 PM
Coral 4

DQ-01. Two-Stage Optimization of an Induction Motor Considering an Equivalent Circuit Parameter Based Stray Load Loss Model

H. Ban[1], S. Kim[1], K. Yu[1], S. Kim[1], J. Park[1], S. Eom[1], K. Shin[2], J. Choi[1]
[1]*Chungnam National University, Daejeon, Korea (the Republic of),* [2]*Changwon National University, Changwon, Korea (the Republic of)*

Induction motors are generally designed using equivalent circuit models and finite element analysis (FEA). Equivalent circuit models enable fast performance estimation, but their accuracy is limited because magnetic saturation and local flux density variations are simplified by magnetic circuit approximations. Therefore, FEA based verification is required for reliable design [1]. In addition, stray load loss is related to stator and rotor leakage inductances, whereas magnetizing inductance varies with current and slip frequency under saturation. Thus, loss reduction and prediction accuracy should be considered together [2], [3]. This paper proposes a two stage optimization process for an induction motor using a stray load loss model based on equivalent circuit parameters. The stray load loss coefficient, K_{SL}, is defined using leakage and magnetizing inductances and used as an objective function. Fig. 1 shows the proposed process. Design samples are generated by Latin hypercube sampling and rated point FEA, and a surrogate model is trained to estimate efficiency and circuit parameters. In the first stage, global optimization is performed using stator and rotor variables. In the second stage, rotor geometry is refined in the selected design region to improve local prediction accuracy.
Fig. 2 compares the conventional and proposed designs. Fig. 2(a) shows the experimental motor and FE model, and Fig. 2(b) compares flux density in the stator yoke and rotor tooth. The proposed design reduces the stator yoke flux density and the flux density difference between the stator and rotor teeth. Fig. 2(c) presents the Pareto front obtained using K_{SL} as an objective function, and Fig. 2(d) compares loss components and efficiency. The proposed design reduces stray load loss and improves experimental efficiency by 0.45 percentage points. The detailed optimization process and discussion will be presented in the full paper.

[1] W. Li, P. Wang, D. Li, X. Zhang, J. Cao and J. Li, *IEEE Trans. Ind. Electron.* 65 (2), 1704-1710 (2017).
[2] R. Kumar, P. Kumar, T. Kanekawa and K. Oishi, *IEEE Trans. Energy Convers.* 35 (2), 1036-1045 (2020).
[3] D.-H. Park, C.-H. Song, Y.-J. Won, J.-C. Park, H.-S. Kim, H.-R. Park, Y.-D. Yoon and M.-S. Lim, *IEEE Trans. Magn.* 60 (9), 1-5 (2024).

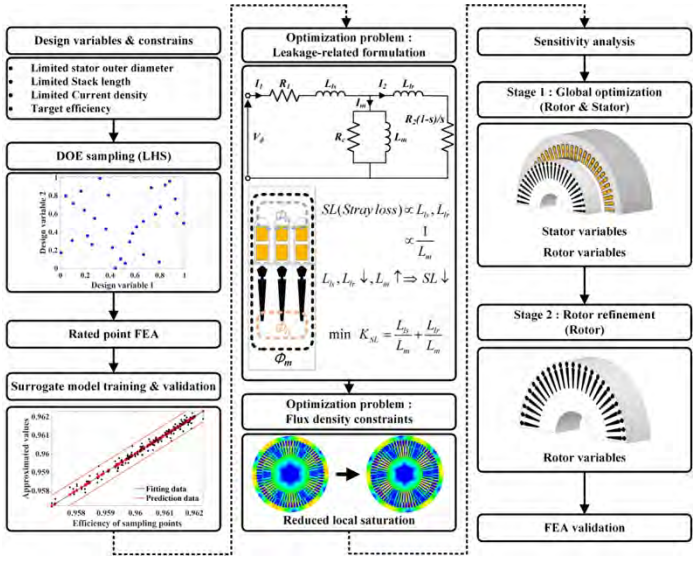


Fig. 1. Two-stage optimization process considering stray load loss.

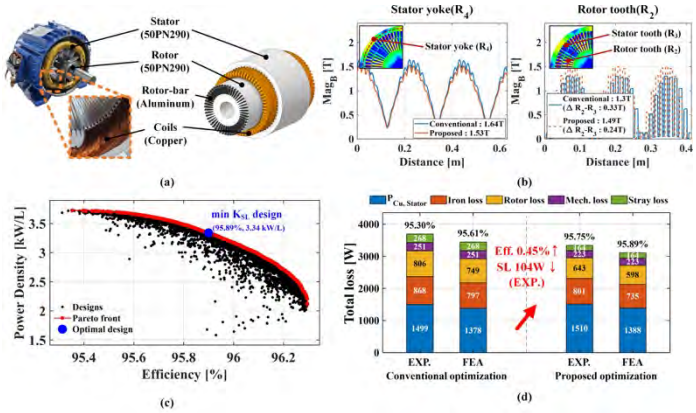


Fig. 2. Comparison of the conventional and proposed optimization results: (a) experimental and FE models, (b) flux density comparison in the stator yoke and rotor tooth, (c) Pareto fronts, and (d) comparison of loss components and efficiency.

DQ-02. Design and Experimental Validation of a Permanent Magnet Synchronous Generator for a Small-Scale Point Absorber Wave Energy Converter under Irregular Waves

J. Park[1], S. Kim[1], H. Ban[1], K. Yu[1], K. Shin[2], J. Choi[1]
[1]Electrical Engineering, Chungnam National University, Daejeon, Korea (the Republic of), [2]AI Electrical Engineering, Changwon National University, Changwon, Korea (the Republic of)

This paper presents experimental verification of a permanent magnet synchronous generator (PMSG) for a small-scale point absorber wave energy converter under irregular wave conditions. The system consists of a point absorber power take off (PTO), a ball screw based linear to rotary converter, a rotational PMSG, and a power conversion system (PCS) [1]. Since irregular waves induce time-varying buoy motion, the generator speed and back-EMF vary continuously. Thus, the PMSG and PCS should be evaluated under transient conditions rather than at a single rated point [2].

Fig. 1 shows the experimental system and input characteristics. The small-scale buoy test, PTO and PMSG structure, rectifier and buck boost converter based PCS, and onshore emulation setup are shown in Fig. 1(a)–(c). The speed and back-EMF in Fig. 1(d) and (e) indicate that the generator operates over a wide and nonperiodic speed range. Therefore, the initial PMSG is designed considering mean and peak operating conditions, and the optimal design point is selected from the Pareto front to improve power density and efficiency.

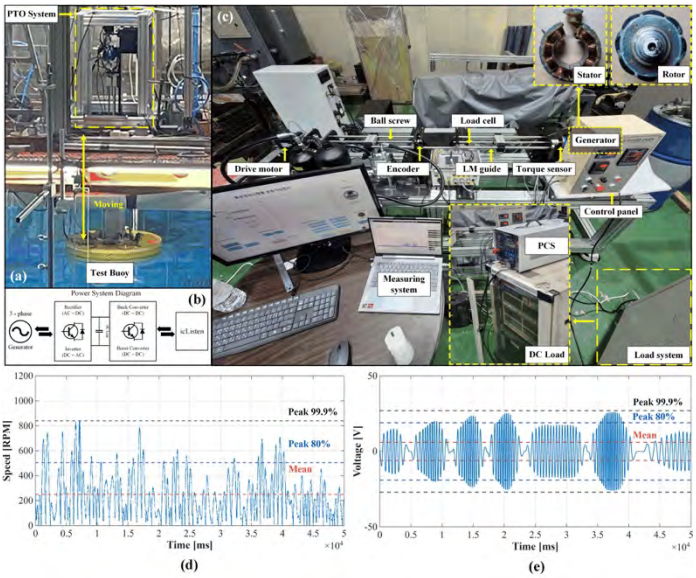


Fig. 1. Experimental system and irregular wave input characteristics: (a) small-scale buoy test, (b) PCS configuration, (c) onshore PTO and PMSG test setup, (d) measured speed profile, and (e) measured back-EMF.

Fig. 2 presents the design and validation results. The no-load back-EMF obtained from 2D finite element method (2D FEM) analysis is compared with the measured result in Fig. 2(b), showing an error within 5%. The simulated output voltage and current are also compared with experimental results under regular and irregular wave conditions in Fig. 2(c) and (d). The discrepancies are within 7–8% for voltage and 6–7% for current, confirming that the model predicts the PCS coupled PMSG performance with reasonable accuracy. These results demonstrate the feasibility of the PMSG for small-scale wave energy conversion. Future work will focus on long-term irregular wave verification and optimal operating region derivation considering the PCS.

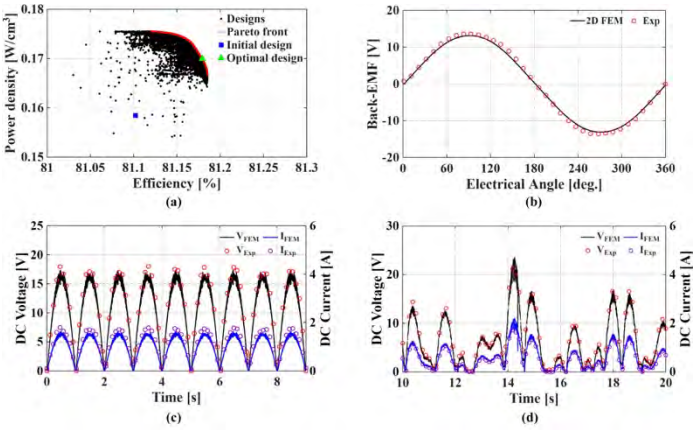


Fig. 2. Design and validation results of the PMSG: (a) Pareto front, (b) no-load back-EMF comparison, (c) voltage and current under regular waves, and (d) voltage and current under irregular waves.

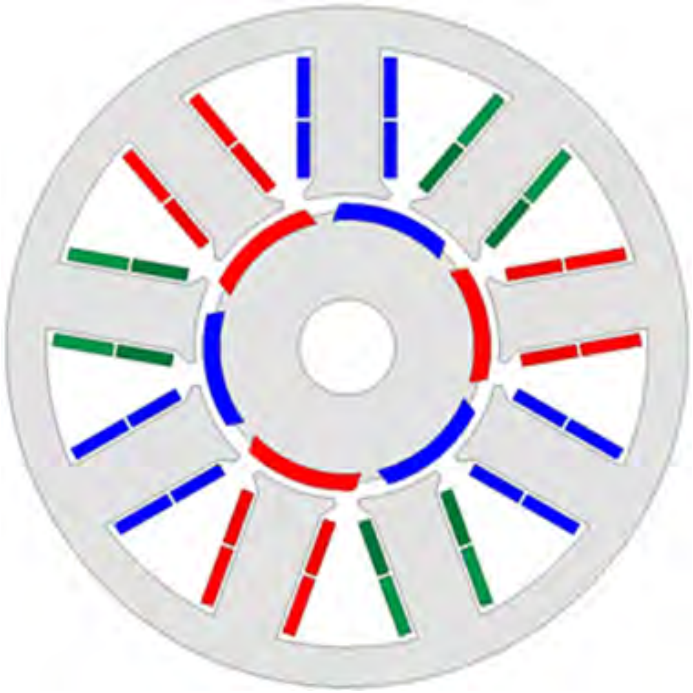
[1] S. Rezaei, A. Rahimi, J. Parvizian and S. Mansoorzadeh, *Energy Conv. Manag.-X* 19, 100385 (2023).
[2] D. Ning and B. Ding, Eds., Modelling and Optimization of Wave Energy Converters. Boca Raton, FL, USA: CRC Press, 2022.

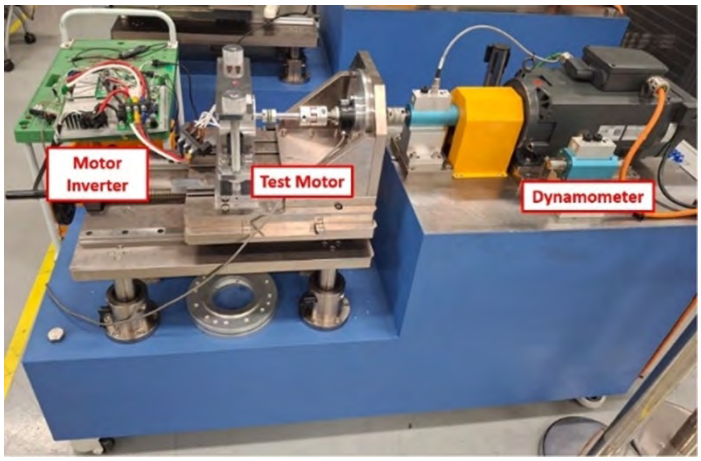
DQ-03. Analysis of Electromagnetic Characteristics of Dual-Winding Motors for High-Reliability Steering Systems

S. Kim[2], S. Jeong[1]
[1]Gwangju University, Gangju Metropolitan City, Korea (the Republic of), [2]Korea Electronics Technology Institute, Gangju Metropolitan City, Korea (the Republic of)

With the rapid advancement of autonomous driving technologies, steering systems have become increasingly critical for vehicle safety, demanding high levels of reliability and fault tolerance. In particular, Electric Power Steering (EPS) systems must ensure continuous operation under component failure conditions.
This paper presents a comprehensive investigation of a dual-winding Permanent Magnet Synchronous Motor (PMSM) designed for EPS applications. Five winding configurations are systematically evaluated under normal, fault, and asymmetric phase operating conditions. Finite Element Analysis (FEA) is employed to analyze electromagnetic, thermal, acoustic, and vibration characteristics in an integrated manner.
The results reveal that the winding configuration significantly influences torque ripple, thermal behavior, and vibration performance, especially under fault and asymmetric conditions. Based on these insights, an optimal winding configuration is proposed to minimize performance degradation while enhancing fault tolerance and system reliability.
Experimental validation using a prototype motor demonstrates the effectiveness of the proposed design, confirming its suitability for safety-critical EPS applications.

[1] Yongchul Kim and Youngwoo Noh, "A Study on the Torque Ripple of Dual Winding Motor According to Winding Arrangement at Fault Case", Journal of the Korean Institute of Illuminating and Electrical Installation Engineers, vol. 38, no. 1, pp. 74-81, 2024.
[2] C. Babetto and N. Bianchi, "Synchronous Reluctance Motor with Dual Three-Phase Winding for Fault- Tolerant Applications," 2018 XIII International Conference on Electrical Machines (ICEM), Alexandroupoli, Greece, 2018, pp. 2297-2303.
[3] Xin. Zhang, Zhang Xin, Shi Guobiao and Lin Yi, "Steering feel study on the performance of EPS," *2008 IEEE Vehicle Power and Propulsion Conference*, Harbin, 2008, pp. 1-5, doi: 10.1109/VPPC.2008.4677441.
[4] B. -K. Song, J. -H. Kim, K. -Y. Hwang and M. -S. Lim, "Electro-Mechanical Characteristics of Dual-Winding Motor According to Winding Arrangement for Brake Systems in Highly Automated Driving Vehicles," in IEEE Transactions on Vehicular Technology, vol. 72, no. 10, pp. 12524-12539, Oct. 2023, doi: 10.1109/TVT.2023.3272729.





DQ-04. Research on Optimization of Core Loss in Phase Shifting Transformers Based on Core Material Selection

J. Yuan, Y. Song, H. Zhou, H. Liu
School of Electrical Engineering and Automation, Wuhan University, Wuhan, China

The integration of renewable energy sources has led to significant fluctuations and uncertainty in power flows, posing new challenges for system. Phase shifting transformer (PST) can effectively regulate power flows and hold broad application prospects. The structure is shown in Figure 1(a). Core loss in PST accounts for a significant proportion of total loss and has a major impact on equipment efficiency and operating costs. Therefore, this paper focuses on dual-core symmetrical PST used in high-voltage power grids. Three representative core materials—conventional grain-oriented silicon steel (B27G120), high-permeability grain-oriented silicon steel (B27P100), and amorphous alloy (2605SA1)—were selected for analysis, and the loss of these three materials was compared. The B-H curves and the core loss curves for the materials are shown in Figures 1(b) and 1(c), respectively.

The simulation results in Figure 2(a) show that the core loss of grain-oriented silicon steel is 48.46 kW. Under the same operating magnetic flux density, amorphous alloy exhibits significantly lower core loss of 7.729 kW. Although high-permeability grain-oriented silicon steel reduces the core volume, the higher operating magnetic flux density causes the core loss to increase to 64.11 kW. The simulation results in Figure 2(b) indicate that replacing the core materials of both the excitation and the series transformers simultaneously results in only a 2.8% greater reduction in core loss compared to replacing only the excitation transformer. The results show that amorphous alloy can significantly reduce core loss, whereas high-permeability silicon steel, although offering greater flexibility in core design, leads to an increase in overall core loss. Furthermore, replacing only the core material of the excitation transformer strikes a balance between loss reduction and cost, whereas replacing both the excitation and series transformers incurs higher costs while offering a limited additional reduction in core loss. The findings of this study provide a reference for the design of PSTs, thereby promoting their adoption.

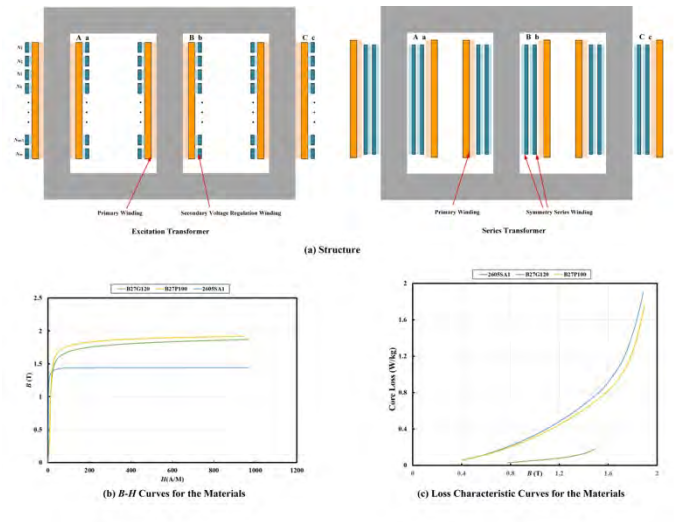


Fig1. Structure, B-H Curves and Core Loss Curves

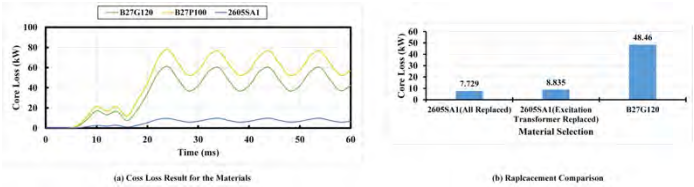


Fig 2. Comparison of Core Loss and Replacement

DQ-05. Influence of Repeater Coil on Transmission Efficiency in Short-Distance for Wireless Power Transfer

T. Takura, Y. Fujimori, Y. Matsuya
Tohoku Institute of Technology, Sendai, Japan

Recently, wireless power transfer technology has been applied to the charging of various devices, attracting significant attention. Among the various methods, we study a method of inductive power transfer. In this method, the power transfer efficiency theoretically depends on the product of the coil quality factor (Q) and the coupling coefficient between the coils. Therefore, in short-range applications where magnetic coupling is strong, it has been reported that high transmission efficiency can be achieved even with an S–N compensation topology that does not employ a resonant capacitor on the secondary side[1]. However, a key challenge lies in the requirement for high-Q coils, whose fabrication is not straightforward. In this study, the method with a repeater coil [2] is adopted for short-range power transfer to improve transmission efficiency. By placing the repeater coil on the primary side, the circuit can be configured without a capacitor on the secondary side,

similar to the circuit configuration of the S-N compensation. Furthermore, the magnetic flux passing through the secondary coil is expected to be the superposition of the fluxes generated by the primary and repeater coils, which may influence the transmission efficiency. The circuit configurations for the S-N compensation method and the method with a repeater coil are shown in Fig. 1. In this study, we measured the load characteristics of the transmission efficiency to clarify the differences in performance between the two circuits. All coils used in the experiment had the same specifications: an outer diameter of 50 mm and 12 turns. Litz wire (0.07 mm, 100 strands) was used for the winding. The transmission frequency was set to 200 kHz and the transmission distance to 2 mm. The measurement results are shown in Fig. 2. As a result, the method with a repeater coil achieves higher efficiency than the S-N compensation method. Therefore, we can improve the transmission efficiency by using repeater coil even if the capacitor is not added on the secondary side.

1. Y. Zhang, et al., IEEE Trans. on Power Electronics, vol. 34, no. 2, pp. 1209-1215 (2019).
2. Y. Ota, T. Takura, et al., IEEE. Trans. Magn., vol.47. no.10, pp.4235-4237 (2011).

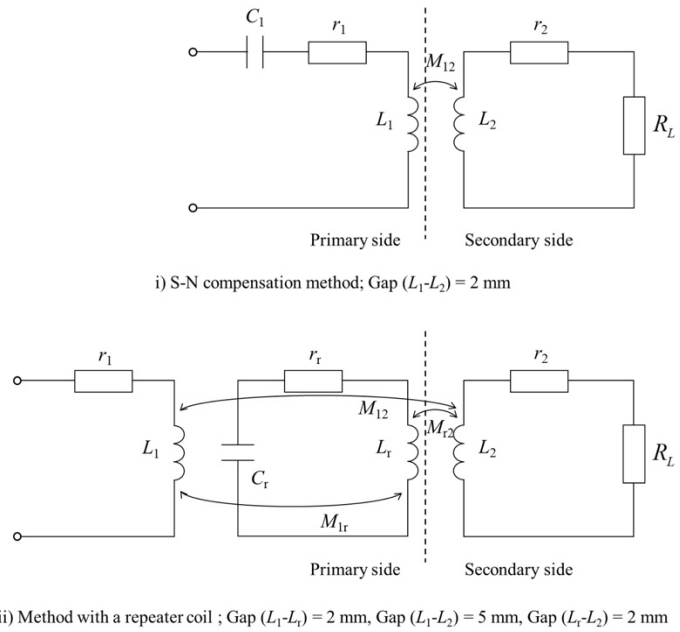


Fig.1 Circuit configurations.

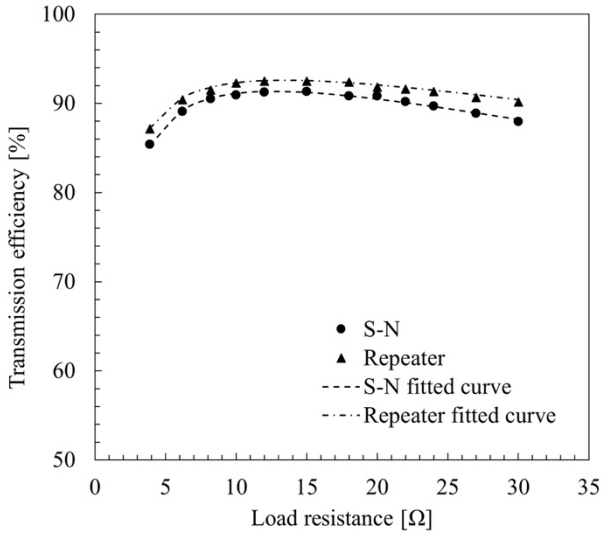


Fig.2 Comparison of efficiency between circuits the S-N compensation method and the method with a repeater coil.

DQ-06. Core Loss Prediction of Induction Machines Considering Rotational Magnetization and Harmonic Loss Separation

J. Kim[1], T. Kim[1], E. Kim[1], M. Lim[1], H. Ban[2], J. Choi[2], K. Shin[3]
[1]Smart Manufacturing Engineering, Changwon National University, Changwon, Korea (the Republic of), [2]Electrical Engineering, Chungnam National University, Daejeon, Korea (the Republic of), [3]AI Electrical Engineering, Changwon National University, Changwon, Korea (the Republic of)

In high-power induction motors, the magnetic fields of the stator and rotor cores consist of not only alternating magnetic fields but also rotating magnetic fields, and the rotor slip frequency changes depending on the load conditions. Therefore, this paper proposes a core loss modeling method for induction machines considering magnetic behavior and slip dependent rotor frequency.
Fig. 1 shows the induction motor and magnetic field behavior used in the proposed model. Fig. 1(a) shows the prototype stator and rotor, and Fig. 1(b) shows the magnetic flux density distribution under no-load and load conditions. The magnetic field behavior according to mesh position in Fig. 1(c) and the magnetic flux density trajectory in Fig. 1(d) show that rotating magnetic field characteristics are dominant in the yoke region, while alternating magnetic field behavior is mainly observed in the tooth region.
Fig. 2 illustrates the loss isolation and analysis results. Figs. 2(a) and 2(b) show the distribution of fundamental and

harmonic core losses, demonstrating that while fundamental losses are concentrated in the stator yoke and tooth regions, harmonic losses are significantly present in specific tooth regions. The experimental set in Fig. 2(c) is used to verify the analysis results. As shown in Fig. 2(d), the measured total core loss is 629.09W, and the existing FEM is 589.29W, which is a difference of 6.33%. By incorporating rotational field weighting, harmonic components, and slip dependent rotor frequency, the proposed model reduces the prediction error to 2.84%. Therefore, it provides an effective basis for core loss separation, accurate prediction, and loss reduction design of induction machines.

[1] J. Yan, C. Di, X. Bao, and Q. Zhu, IEEE Trans. Energy Convers. 38 (2), 971–981 (2023).
[2] S. Abdi, E. Abdi, and R. McMahon, IEEE Trans. Energy Convers. 36 (4), 3221–3230 (2021).

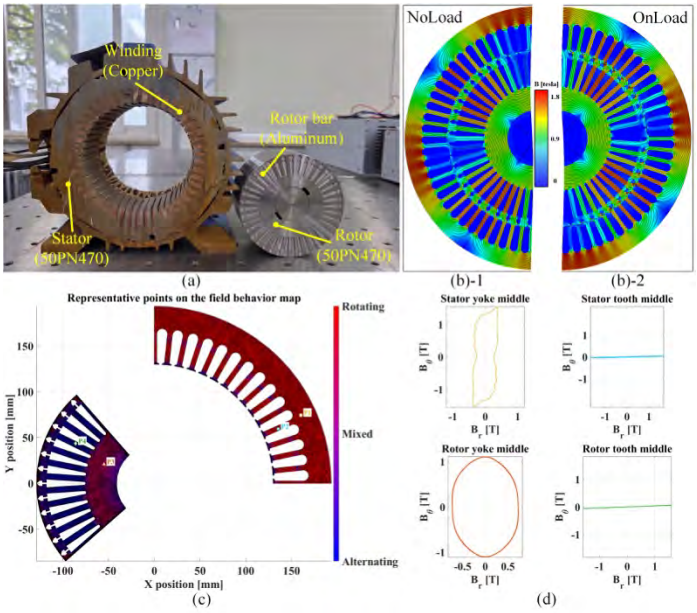


Fig. 1. Target induction motor and field behavior analysis: (a) prototype stator and rotor, (b) no load and on load flux density distributions, (c) representative points in core regions, and (d) flux density loci.

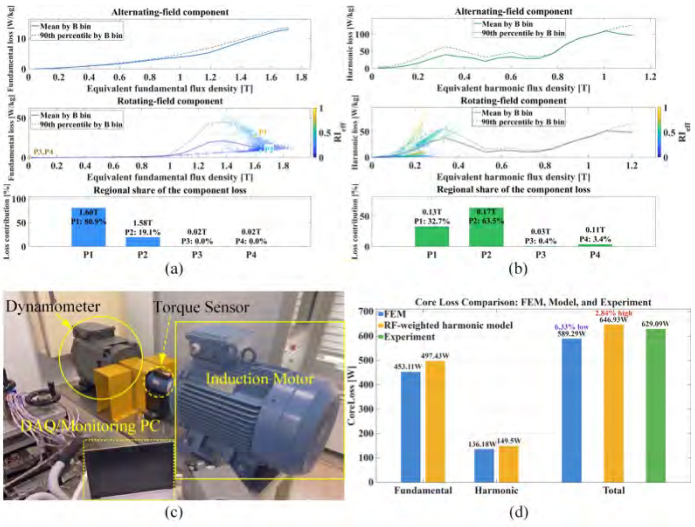


Fig. 2. Core loss separation and validation: (a) fundamental core loss distribution, (b) harmonic core loss distribution, (c) experimental platform, and (d) comparison of FEM, proposed model, and experiment.

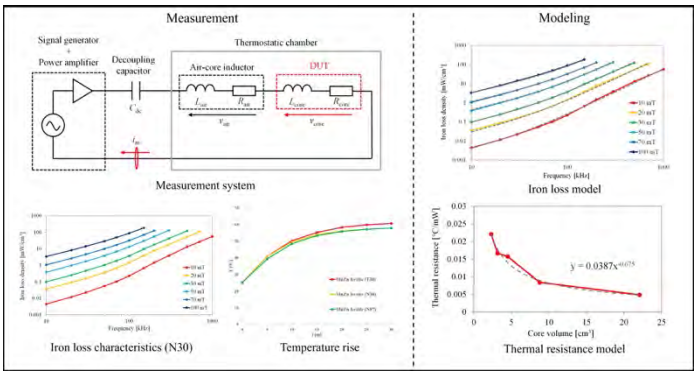
DQ-07. Experimental Evaluation of Thermally Constrained Limiting Flux Density in Magnetic Materials for Common-Mode Transformers

S. Takahashi[1], M. Kato[2]
[1]Nagoya Institute of Technology, Nagoya, Aichi, Japan, [2]Akita University, Akita, Akita, Japan

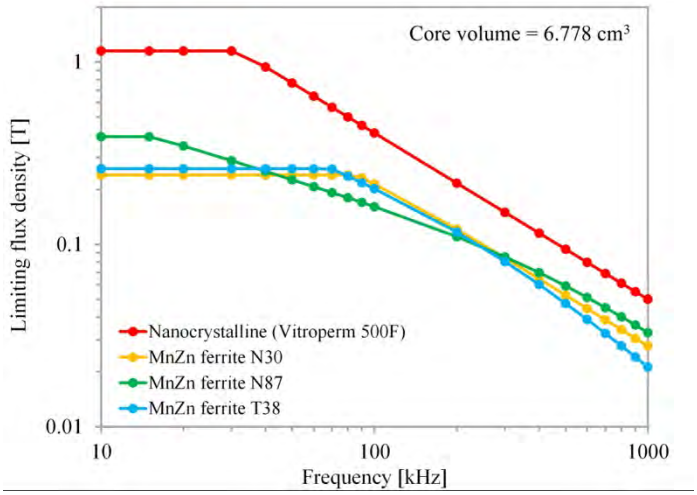
With the widespread adoption of wide-bandgap semiconductor devices, common-mode (CM) noise generated by switching power converters has become a critical source of electromagnetic interference [1-3]. Passive CM noise cancellation using compact CM transformers (CMTs) has attracted significant attention owing to their capability to effectively suppress noise, particularly around the switching frequency, while contributing to the higher power density of power converters [4-6]. However, CMTs are directly subjected to large CM noise voltages, requiring careful consideration of the magnetic material properties under large-signal excitation, including iron loss and thermal behavior.

This study investigates magnetic materials suitable for CMT applications from the perspective of thermal constraints under high-frequency excitation. Four commercially available magnetic materials, including nanocrystalline and manganese-zinc ferrites, were evaluated. First, the iron loss characteristics of toroidal cores were experimentally

measured over a wide range of frequencies and flux densities using a single-winding method (Fig. 1) [7]. The measured data were fitted to empirical loss models to estimate the flux density corresponding to a given loss density.
Next, the temperature rise characteristics were experimentally obtained for cores of various sizes under controlled excitation conditions, clarifying the relationships between the core volume, loss density, and thermal behavior. Based on these results, the limiting flux density, defined as the maximum allowable flux density under a specified temperature increase, was derived as a function of the frequency for each material.
Finally, by comparing the limiting flux density at a given core volume, the suitability of each material for CMT miniaturization was assessed quantitatively. The results demonstrate that nanocrystalline materials exhibit superior performance over a wide frequency range, enabling higher flux operation and reduced core volume compared with ferrite materials (Fig. 2).
Details of the measurement and modeling procedures will be presented in the final manuscript.
[1] D. Han, et al., IEEE Trans. Ind. Electron., vol. 64, no. 10, pp. 8353-8363 (2017)
[2] G. Engelmann, et al., IEEJ J. Ind. Appl., vol. 8, no. 3, pp. 505-511 (2019)
[3] B. Zhang, et al., IEEE J. Emerg. Sel. Top. Power Electron., vol. 8, no. 1, pp. 626-643 (2020)
[4] M. M. Swamy, et al., IEEE Trans. Power Electron., vol. 16, no. 2, pp. 248-255 (2001)
[5] L. Xie, et al., IEEE Trans. Power Electron., vol. 36, no. 8, pp. 9069-9079 (2021)
[6] S. Takahashi, et al., IEEJ J. Ind. Appl., vol. 14, no. 3, pp. 442-449 (2025)
[7] Y. Wang, et al., IEEJ J. Ind. Appl., vol. 15, no. 1, pp. 107-114 (2026)



Overview of the experimental and modeling framework



Calculated limiting flux densities

DQ-08. Magnetic Energy Redistribution Mechanisms in Heterogeneous Resonant Multi-Receiver Wireless Power Transfer Systems

S. Lee
Department of Physical-AI, School of International Engineering and Science, Graduate School of Integrated Energy-A, Jeonbuk National University, Jeonju, Select One, Korea (the Republic of)

Heterogeneous multi-receiver resonant wireless power transfer (WPT) systems inherently exhibit asymmetric magnetic interactions arising from mixed compensation topologies and unequal load requirements. In such configurations, mutual inductance coupling does not simply scale with geometry but dynamically redistributes magnetic energy among receivers, producing nontrivial power allocation patterns.
This study investigates the magnetic energy redistribution mechanisms in a single-transmitter, multi-receiver resonant WPT architecture operating under strong coupling conditions. A three-dimensional electromagnetic model is employed to extract the full mutual inductance matrix of the system, enabling quantitative analysis of coupling asymmetry and reflected impedance interactions. By systematically varying compensation parameters and excitation conditions, the relationship between magnetic flux balance, resonant alignment, and receiver-level power distribution is examined.
Results from a representative 1T–3R system operating at 400 kHz demonstrate that magnetically balanced operation emerges only within a constrained region of the parameter space. Outside this region, energy localization and coupling

competition among receivers lead to unequal power delivery even under nominal resonance conditions. The analysis reveals that maximum system efficiency does not necessarily correspond to magnetically stable energy distribution.
These findings highlight the importance of magnetic coupling topology and inductance matrix structure in determining energy redistribution behavior in heterogeneous resonant WPT systems. The presented study provides physical insight into multi-receiver magnetic interaction phenomena relevant to advanced wireless charging architectures and magnetic energy transfer applications.
[1] S. B. Lee and I. G. Jang, "Precise determination of the optimal coil for wireless power transfer systems through postprocessing in the smooth boundary representation," IEEE Trans. Magn., vol. 53, no. 6, 2017.

[2] S. B. Lee, M. Kim, and I. G. Jang, "Determination of the optimal resonant condition for multireceiver wireless power transfer systems considering the transfer efficiency and different rated powers," IEEE J. Emerg. Sel. Topics Power Electron., vol. 9, no. 2, 2021.

[3] H. Li et al., "An independent dual-coil driving topology for wireless power transfer," IEEE Trans. Power Electron., vol. 38, no. 2, 2023.

[4] Y. Li et al., "A dual-sided LCLC topology for AGV wireless charging system with low leakage EMF," IEEE Trans. Electromagn. Compat., vol. 65, no. 3, 2023.

[5] M. Dong et al., "Enhancing efficiency in multireceiver wireless charging with voltage constraints," IEEE Trans. Power Electron., vol. 39, no. 10, 2024.

[6] A. Triviño et al., "Efficient methodology of the coil design for a dynamic wireless charger," IEEE Access, vol. 10, 2022.

[7] T. Lim and Y. Lee, "Stacked-coil technology for compensation of lateral misalignment," IEEE Trans. Ind. Electron., vol. 68, no. 12, 2021.

[8] J. Cai et al., "Overview of coupling coil design for magnetic coupled resonance wireless charging system of electric vehicles," IEEE Trans. Transp. Electrific., vol. 11, no. 4, 2025.

DQ-09. Analysis of Core Loss of 10MW Direct Drive Permanent Magnet Synchronous Generator considering 3D Magnetic Flux Path and Rotor Overhang

S. Kim[1], K. Kwak[1], H. Shin[2], K. Shin[3], J. Choi[1]
[1]Electrical Engineering, Chungnam National University, Daejeon, Korea (the Republic of), [2]Traction Motor Development Cell, Hyundai Mobis, Uiwang, Korea (the Republic of), [3]Electrical Engineering, Changwon National University, Changwon, Korea (the Republic of)

Accurate prediction of electromagnetic losses is crucial for satisfying the efficiency requirements of generator design. In particular, accurate core loss prediction requires consideration of magnetic field behavior. This study investigates the core loss of a 10 MW direct-drive permanent magnet synchronous generator (PMSG) with an overhang structure, considering the axial magnetic field behavior and leakage flux caused by the overhang.
Figure 1(a) shows the split stator for segmented magnetic field analysis, and Fig. 1(b) illustrates the leakage flux concept induced by the overhang. Figures 1(c) and 1(d) present the magnetic flux density and vector plot, showing significant saturation in the upper region. Figure 1(e) shows the actual model.
For accurate core loss prediction, tangential, radial, and axial magnetic field behaviors were considered. The stator was segmented, and the magnetic field in all three directions was derived for each segment. Core loss was calculated using a modified Steinmetz equation to distinguish alternating and rotating magnetic fields.
The magnetic field behaviors in Regions 15 and 17 are shown in Figs. 2(a) and 2(b). Figure 2(c) shows the core loss of each region obtained by the 2D model considering tangential and radial components, whereas Fig. 2(d) shows the 3D model including the axial component. When the axial direction is included, some regions with alternating magnetic fields change to rotating magnetic fields, increasing core loss.
Figures 2(e) and 2(f) show the single-machine test configuration and experimental results, and the comparison of back EMF between FEM and experiment, respectively. Based on these results, a PMSG with an overhang requires comprehensive 3D core loss analysis to account for axial magnetic field behavior. Detailed comparisons and analysis results are presented in the full paper.
[1] S.-M. Jang, K.-J. Ko, H.-K. Kim, S.-H. Lee, and T.-H. Sung, "An Analysis on Core Loss Characteristics for Permanent Magnet Synchronous Generator considering the Load Conditions", Transaction of the KIEE, vol. 2009, no. 4, pp. 55-

57, Apr. 2009
[2] J.-H. Woo, T.-K. Bang, H.-K. Lee, K.-H. Kim, S.-H. Shin, and J.-Y. Choi, "Electromagnetic characteristic analysis of high-speed motors with rare-earth and ferrite permanent magnets considering current harmonics", IEEE Trans. Magn., vol. 57, no. 2, pp. 1-5, Feb. 2021
[3] C.-W. Kim, J.-M. Kim, S.-W. Seo, J.-H. Ahn, K. Hong, and J.-Y. Choi, "Core loss analysis of permanent magnet linear synchronous generator considering the 3-D flux path", IEEE Trans. Magn., vol. 54, no. 3, pp. 1-4, Mar. 2018

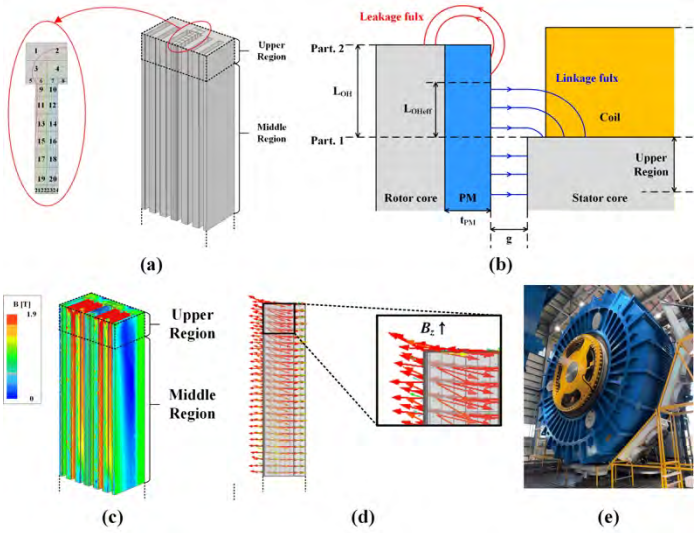


Fig. 1 (a) Split stator, (b) Leakage flux concept, (c) Magnetic flux density, (d) Vector plot, (e) Actual model.

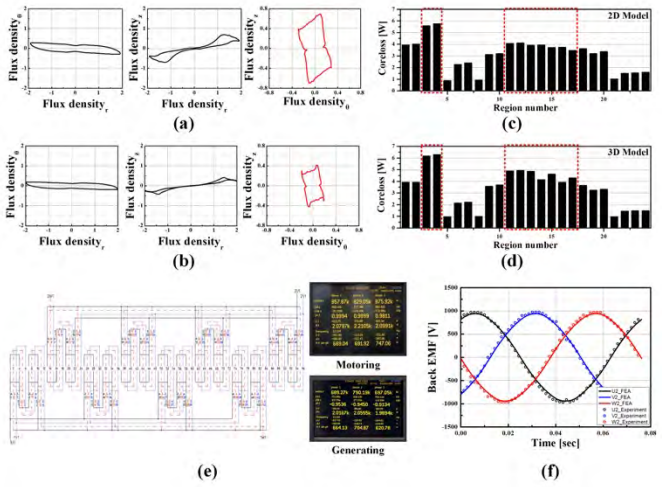


Fig. 2 (a) Magnetic field behavior of region 15, and (b) region 17, (c) Core loss for each region obtained by 2D model, and (d) 3D model, (e) Single-machine test configuration with experimental results, and (f) comparison of back EMF between FEM and experiment.

DQ-10. Design and Validation of a Manufacturable Counter-Torque Reinforcement Structure for Axial-Flux Block-Coil Generators

H. Kim[1], Y. Lim[1], J. Moon[1], C. Lee[1], W. Kim[2]
[1]Department of Next Generation Energy System Convergence, Gachon University, Seongnam-Si, Korea (the Republic of),
[2]Department of Electrical Engineering, Gachon University, Seongnam-Si, Korea (the Republic of)

Slotless axial-flux permanent magnet generators employing block-coil windings have recently attracted attention for urban small wind power systems due to their inherently negligible cogging torque, low acoustic noise, and modular winding architecture[1], [2]. Despite these advantages, the absence of a rigid slot structure makes the stator mechanically vulnerable. In particular, during power generation, electromagnetic torque applied to the rotor produces an equal and opposite counter torque on the stator coils, which is directly transmitted to individual block coils. This can lead to stress concentration, inter-block displacement, and long-term structural degradation, posing a critical challenge for practical implementation.
To address this issue, this paper proposes a stator-plate-integrated counter-torque support structure for a double-rotor single-stator axial-flux block-coil generator. A coupled electromagnetic–structural analysis framework is established, where three-dimensional electromagnetic finite element analysis is used to compute torque distribution, and the resulting counter torque is mapped as equivalent mechanical loading in structural analysis under worst-case contact conditions. Various support topologies, including single-layer, multi-layer, terminal-based, and combined configurations, are evaluated.
From the parametric study, a combined support configuration demonstrates superior structural performance, and a symmetry-preserving four-support design is selected considering both stress reduction and manufacturability. Design refinement incorporates experimentally characterized material properties of injection-molded coil blocks and evaluates assembly tolerance effects using micro-gap modeling.
A 3-kW class prototype incorporating the proposed structure is fabricated and experimentally validated. The results confirm stable operation without mechanical failure or abnormal vibration, while maintaining the inherent advantages of slotless generators, including near-zero cogging torque and high efficiency. The proposed approach provides a practical and robust solution for enhancing the structural reliability of axial-flux block-coil generators in

real-world applications.

[1] A. Tessarolo, "Recent advances in axial flux permanent magnet machines," IEEE Trans. Ind. Appl., vol. 54, no. 3, pp. 1972–1981, May/Jun. 2018.

[2] R. J. Wang and M. J. Kamper, "Analysis and performance of a coreless axial flux permanent-magnet machine," IEEE Trans. Energy Convers., vol. 19, no. 1, pp. 169–175, Mar. 2004.

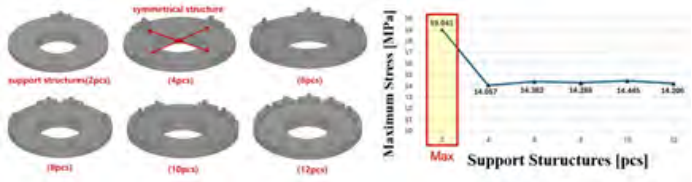


Fig. 1.

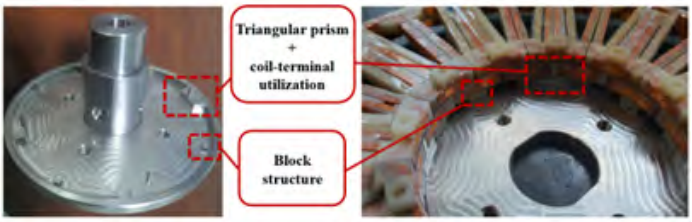


Fig. 2

DQ-11. Design and Thermal Optimization of a High-Frequency Transformer for a Three-Phase LLC-Based EV Charger using SiC Power Semiconductors

Y. Noh, J. Lee, K. Lee, P. Jang, J. Kim
Korea Electronics Technology Institute, Bucheon, Korea (the Republic of)

This paper presents the design of a high-frequency transformer for a 40 kW fast electric vehicle (EV) charger power module based on a three-phase LLC converter. EV fast charging systems require a wide output voltage range of 200V-1000V while achieving high efficiency and high power density. Galvanic isolation between the vehicle battery and the AC grid is provided by a high-frequency transformer in the DC/DC stage.

High-frequency operation up to 250 kHz is achieved using SiC power semiconductors, enabling reduced switching losses and improved efficiency. A three-phase LLC topology is adopted to distribute electrical and thermal stresses, and the transformers in each phase are configured in a series–parallel structure to optimize volume and power capability.

An automotive-grade PL-17 magnetic core material is selected due to its low core loss characteristics at high frequencies. Flat-type Litz wire is employed to reduce copper loss and enhance window utilization, improving both power density and thermal performance.

As EV charging modules are typically cooled by forced air, thermal design is carefully considered. To mitigate localized heating caused by leakage flux near the core air gap, the primary winding is spaced from the core by a defined clearance, improving heat dissipation and reducing proximity losses. Core and copper losses, along with thermal behavior, are analyzed to ensure reliable high-power operation.

Through systematic magnetic and thermal optimization, the proposed charger module achieves a peak efficiency of 98% while maintaining stable operation across the specified voltage and load range, demonstrating its suitability for high-power EV fast charging applications.

Acknowledgement

This work was supported by the Korea Planning & Evaluation Institute of Industrial Technology funded by the Ministry of Trade, Industry & Energy (MOTIE, Korea) [RS-2024-00402727, Development of high power density EV ICCU technology of over 3kW/L based on sub-module for common use by country/capacity]

C. Shen, H. Zhong, and Y. Zhang, IET Electr. Power Appl., vol. 15, no. 1, pp. 114–127 (2021)

J. Shah, S. Rastogi, and S. Bhattacharya, IEEE Trans. Power Electron., vol. 36, no. 6, pp. 6276–6287(2021)

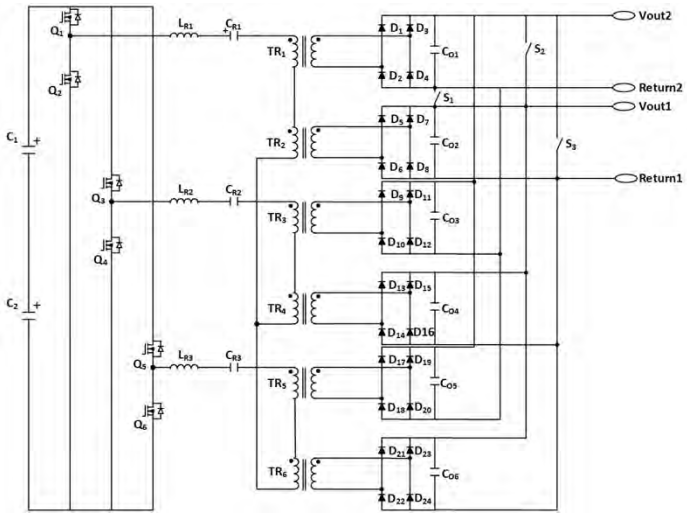


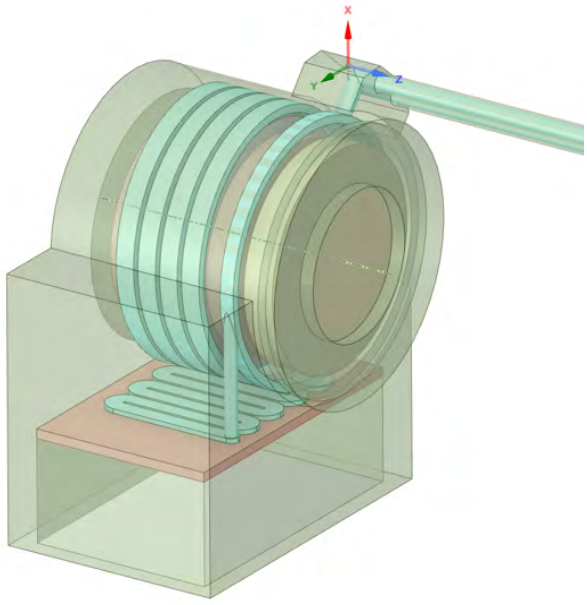
Fig.1 Configuration of a Three-phase LLC Converter

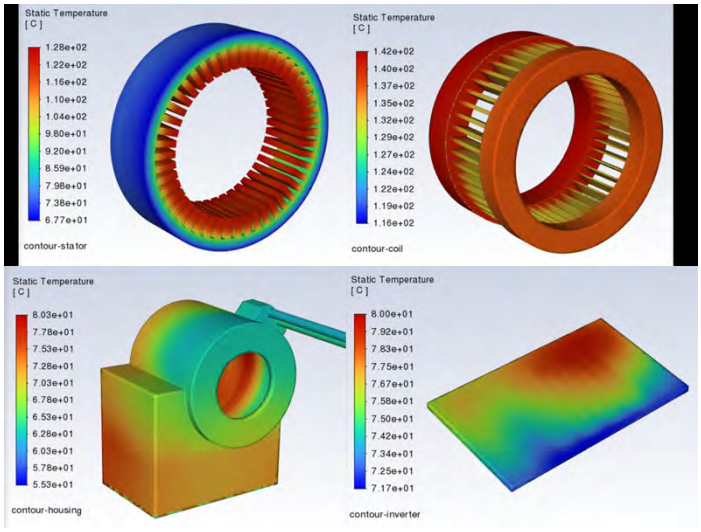
DQ-12. Analysis of Water Jacket Cooling Performance Considering Motor Loss Characteristics

S. Kim, S. Jeong
Gwangju University, Gangju Metropolitan City, Korea (the Republic of)

With the increasing power density and output of electrified systems, thermal management of electric motors has become a critical factor affecting performance and reliability. In particular, motor losses, including copper and iron losses, generate significant heat, leading to temperature rise, insulation degradation, efficiency reduction, and shortened lifetime. To address these challenges, effective cooling structure design is essential, and water jacket cooling has emerged as a promising solution due to its superior heat dissipation capability.
In this paper, a quantitative analysis of the cooling performance of a water jacket considering motor loss characteristics is presented. The thermal distribution is modeled based on major loss components, including copper and iron losses, and Finite Element Analysis (FEA) is conducted for various water jacket structures and flow channel conditions. The effects of coolant channel geometry, flow rate, and heat transfer characteristics on motor temperature distribution and thermal behavior are systematically investigated.
The results indicate that the optimal design of the water jacket varies depending on the spatial distribution of motor losses. In particular, significant differences in cooling performance are observed in regions with concentrated heat generation, such as windings and the stator core. Furthermore, it is confirmed that both temperature reduction and thermal uniformity can be substantially improved through appropriate channel design and flow conditions.
This study highlights the importance of incorporating motor loss characteristics into water jacket design and provides practical design guidelines for enhancing thermal management and reliability in high-power electric motors.

[1] J. R. Hendershot Jr. and T. J. E. Miller, *Design of Brushless Permanent-Magnet Motors*, Oxford, U.K.: Oxford Univ. Press, 2010.
[2] A. Boglietti, A. Cavagnino, and D. Staton, "Thermal analysis of electrical machines," *IEEE Transactions on Industry Applications*, vol. 45, no. 3, pp. 1229–1237, May/Jun. 2009.
[3] D. A. Staton, A. Cavagnino, "Convection heat transfer and flow calculations suitable for electric machines thermal models," *IEEE Transactions on Industrial Electronics*, vol. 55, no. 10, pp. 3509–3516, Oct. 2008.
[4] Y. Zhang, J. Ruan, and Y. Yang, "Thermal analysis of water-cooled permanent magnet synchronous motor," *IEEE Transactions on Magnetics*, vol. 48, no. 11, pp. 2921–2924, Nov. 2012.





DQ-13. Optimal Design of an Active Electromagnetic Damper Based on Eddy Current Damping

M. Shin, M. Jung, T. Jung
Electrical Engineering, Kyungnam University, Changwon, Gyeongsangnam-do, Korea (the Republic of)

This paper proposes an active electromagnetic (EM) damper utilizing eddy currents to reduce vibrations and shocks generated in vehicles and industrial equipment. When a permanent magnet undergoes vertical reciprocating motion relative to a conductive material, eddy currents are induced within the conductor due to the magnetic flux generated by the magnet. The interaction between the induced eddy currents and the magnetic field produces a damping force that opposes the motion of the permanent magnet.

Fig. 1 Current Damping Principe of Permanent Magnet

Conventional eddy current-type dampers suffer from performance degradation due to magnetic flux leakage, as the magnetic flux path is difficult to control. To address this issue, an iron back yoke was applied to the outer region of the conductor to form a defined magnetic flux path, thereby concentrating the magnetic flux toward the conductor and enhancing the effective magnetic flux.

Fig. 2. Eddy Current Type EM Damper Model

In addition, the key design parameters affecting the damping force—namely the thicknesses of the back yoke, copper, and magnet—were selected, and their effects on damping characteristics were analyzed. As the copper thickness increases, the area available for eddy current flow increases, resulting in an increase in damping force; however, beyond a certain thickness, the magnetic reluctance increases, reducing the effective magnetic flux and consequently decreasing the damping force. Similarly, increasing the magnet thickness enlarges the effective flux region, leading to a proportional increase in damping force; however, it also increases the overall volume. Therefore, an optimal design is required to achieve high damping performance while minimizing magnet volume and selecting an appropriate copper thickness. Accordingly, the response surface methodology (RSM) was employed to determine the optimal design parameters that maximize the damping force.

[1] Alista Fow, Mike Duke, "Active electromagnetic damping for lightweight electric vehicles", Proceedings of the 6th International Conference on Automation Robotics and Applications, pp. 1-13, 2015
[2] Min-Sang Seong, Jun-Cheol Jeon, Seung-Bok Choi, "Design and Analysis of Low Friction MR Damper for Washing Machine," Proceedings of the 2011 Spring Conference of the Korean Society of Noise and Vibration Engineering, pp. 568-569, 2011.
[3] Jung-sam Park, Jae-sung Bae, Jai-hyuk Hwang, Kuk-jung Kang, "A study on Dynamic Characteristics of an Eddy Current Damping," Journal of Aerospace System Engineering, vol. 2, no. 2, pp. 24-28, 2008.

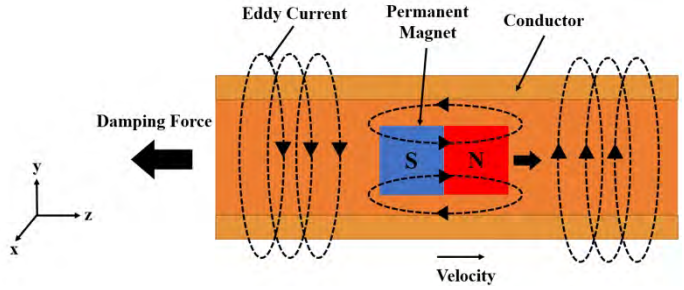


Fig. 1 Current Damping Principe of Permanent Magnet

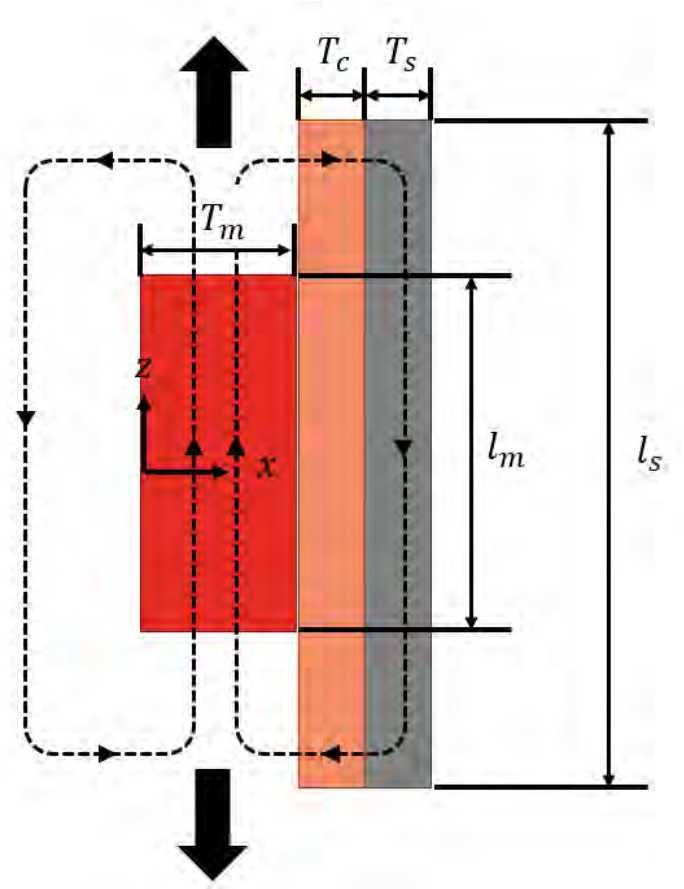


Fig. 2. Eddy Current Type EM Damper Model

DQ-14. Full-Wave Electromagnetic Simulations of Ba–Ni Ferrite Composites for X-Band RCS Control

T. Kim[1], D. Lee[1], S. Park[1], Y. In[1], B. Lee[2]
[1]Physics, Hankuk University of Foreign Studies, Yongin-Si, Gyeonggi-Do, Korea (the Republic of), [2]Electronic physics, Hankuk University of Foreign Studies, Yongin-Si, Gyeonggi-Do, Korea (the Republic of)

We present a simulation analysis of Ba–Ni ferrite (BaNF) composite coatings for radar cross-section (RCS) control in the X-band (8–12 GHz). Frequency-dependent complex permittivity and permeability (ε′, ε″, μ′, μ″) for BaFe12O19:NiFe2O4 composites with ratio of 1:3, 1:6, 1:9 are incorporated into computer simulation technology to realize a materials-informed, full-wave model. The test sample is a 200 mm × 200 mm perfect electric conductor (PEC) plate coated with a BaNF composite, illuminated by a linearly polarized plane wave under open perfectly matched layer boundaries. Far-field quantities are extracted at 10 GHz while sweeping the incidence angle θ from −60° to +60° and resolving elevation/azimuth observation angles. To probe impedance-matching latitude, two coating thicknesses are compared: a thinner coating (2.25 mm on a 2.00 mm PEC) and a thicker coating (3.0 mm on a 3.0 mm PEC). At 10 GHz, all compositions exhibit a clear reduction of the specular lobe relative to the bare PEC reference. The thicker coating maintains stronger attenuation and smoother angular behavior throughout the θ-sweep, consistent with enhanced impedance matching. Composition tuning readjusts magnetic loss (μ″) and dielectric/interfacial loss (ε″), shifting the matching window and dissipation pathways while preserving polarization stability (TE/TM) under oblique incidence. The simulations indicate that BaNF-based coatings achieve low-profile X-band RCS control using materials alone, without metallic resonators or phase codings. They also enable reproducible quantification of composition–thickness trade-offs, providing practical guidance for mixture and thickness selection in coatings and radome-integrated absorbers.

DQ-15. External Magnetic Fields Coupling to Cables Within a Slotted Rectangular Enclosure

H. Park[1, 2], S. Kim[2], G. Covic[2]
[1]The University of Suwon, Hwaseong, Korea (the Republic of), [2]The University of Auckland, Auckland, New Zealand

I. Introduction

Apertures or slots in metallic enclosures act as critical noise paths, allowing external electromagnetic interference (EMI) to couple with internal cables and components. While conventional EMI research has focused on high-frequency coupling, rapid vehicle electrification has intensified challenges regarding low-frequency magnetic interference [1]. Recently, analytical solutions were developed for field penetration into 2-D slotted enclosures [2] and for leakage fields by treating cables as line current sources [3]. Building upon these works, this paper proposes an analytical formulation to calculate currents induced in internal cables by penetrating external magnetic fields.

II. Analytical Formulation

Assuming long cables, the structure is modeled in 2-D (Fig. 1). The domain is divided into three regions where vector magnetic potentials (A_z) are defined to derive magnetic flux density (B_y) and field intensity (H_x). Region (I), an open boundary, uses a Fourier integral for continuous modes, while Regions (II) and (III) employ Fourier series for discrete modes. By enforcing field continuity at the interfaces (y=0, -d) and applying mode orthogonality, a system of equations for the slot mode coefficients is derived [4]. To determine induced currents (I_i), the boundary condition $E_z = 0$ is applied at the cable surfaces. This yields a simultaneous system of equations for both slot coefficients (b_m, c_m) and I_i, enabling precise magnetic field determination across all regions.

III. Results and Discussion

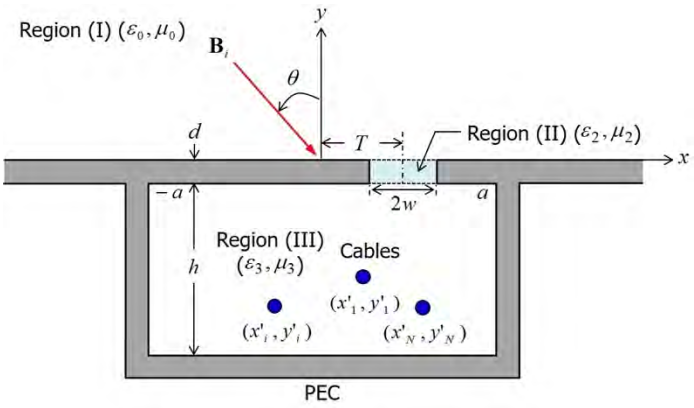
The proposed analytical modal solution was validated by 3-D full-wave simulation [5] across various cable configurations. The results demonstrate high consistency and superior computational efficiency, providing a robust framework for evaluating low-frequency magnetic coupling in complex electronic environments.

Acknowledgment

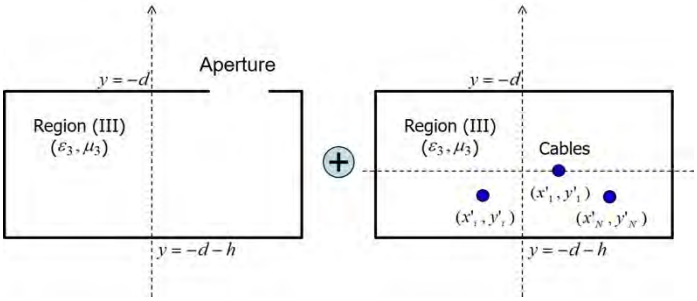
This work was supported by Institute of Information & communications Technology Planning & Evaluation (IITP) grant funded by the Korea government (MSIT) (No.2020-0-00839).

1. S. Matsuzawa, J. Muramatsu, T. Watanabe, and Y. Hattori, "Trench structure to suppress magnetic feld leakage from an aperture in a metallic enclosure," IEEE Trans. Electromagn. Compat., vol. 59, no. 2, pp. 545--548, Apr. 2017.
2. H. H. Park, "Analysis of magnetic field penetration into a slotted rectangular enclosure," Proc. of the 2025 International Symposium on Electromagnetic Compatibility (EMC Europe 2025), Paris, France, September 1–5, pp. 457--460, 2025.

3. J. H. Kwon and H. H. Park, "Magnetic fi eld penetration into a slot on conducting plate and rectangular enclosure by long cables carrying currents," AIP Advances, vol. 16, no. 2, 025205, Feb. 2026.
4. H. J. Eom, "Electromagnetic Wave Theory for Boundary-Value Problems: An Advanced Course on Analytical Methods," Berlin, Germany: Springer, 2004.
5. CST Studio Suite (2023) [Online]. Available: https://www.3ds.com/products/simulia/cst-studio-suite



Geometry of problem: external magnetic fields coupling to cables within a slotted rectangular enclosure.



Vector magnetic potential in region (III) formulated via enclosure mode functions and 2-D cavity Green's functions.

DQ-16. Characteristic Analysis and Air-gap Control of Fixed-Bias Flux Three-phase Magnetic Bearing

Y. Chong[1], J. Kim[1], S. Byun[3], S. Noh[2], H. Cho[1]
[1]Chungnam National University, Daejeon, Korea (the Republic of), [2]Korea Research Institute of Ships & Ocean Engineering, Daejeon, Korea (the Republic of), [3]National Defence Aviation High School, Nonsan, Korea (the Republic of)

FIXED-BIAS FLUX THREE-PHASE MAGNETIC BEARING

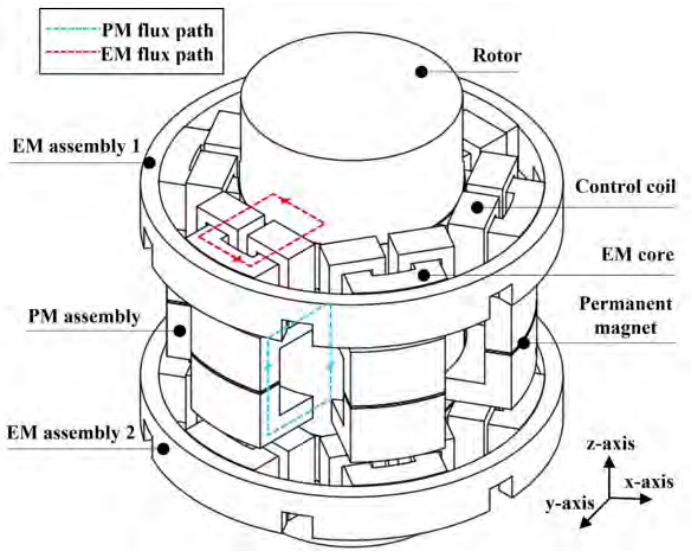
Fig. 1 illustrates the geometry of the fixed-bias flux-type three-phase magnetic bearing proposed in this paper. Radial magnetic bearings on the drive shaft are classified as homopo- lar if their polarity is fixed in the plane, and heteropolar if their polarity varies. Homopolar bearings are typically constructed with permanent magnets, while heteropolar bearings are typically constructed with electromagnets. Based on the z-axis, the 12-pole heteropolar electromagnet part is located at the top, the 6-pole homopolar permanent magnet part is located in the middle, and the 12-pole heteropolar electromagnet part is located at the bottom. Thus, the fixed-bias flux-type three-phase magnetic bearing consists of one permanent magnet part and two electromagnet parts. The permanent magnets are installed at 60 degree intervals, and the electromagnet part consists of four electromagnets connected in a Y-connection, with phases A, B, and C.

ELECTROMAGNETIC CHARACTERSTICS AND CONTROL

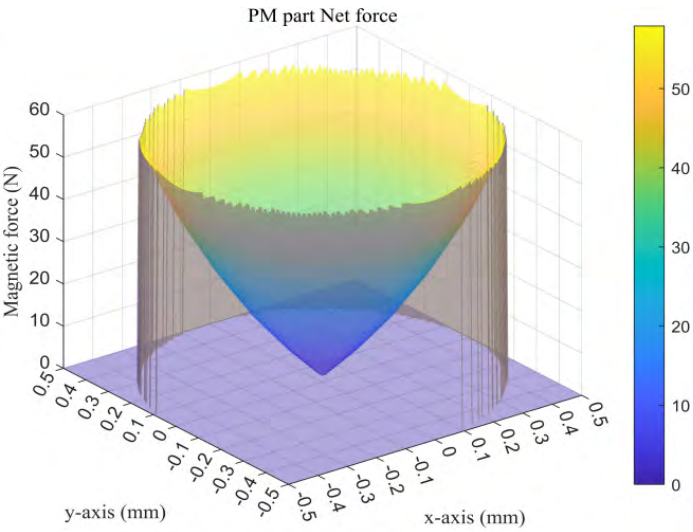
Fig. 2 shows the results of a three-dimensional finite element analysis of the force generated by the permanent magnet part when the rotor position changes from -0.5 mm to 0.5 mm. The force generated when the rotor moves 0.1 mm in the x direction is 9.024 N, and the positional stiffness coefficient of the permanent magnet part is calculated to be 90,240 N/m.

The position controller and current controller are implemented using PID controllers. In the gap control simulation, the disturbance was set to a magnitude of 100 N and the frequency to 300 rad/s. The disturbance was applied 1 second after normal control operation. In the initial transient state, the rotor displaced up to ±25 (2.5 % of the air gap) from the origin, but reached a steady state after a settling time of approximately 0.7 seconds. At this time, the displacement was stably maintained within the ±5 range (0.5 % of the air gap).

[1]H. Bleuler et al., Magnetic Bearings: Theory, Design, and Application to Rotating Machinery, 1st ed. Springer, 2009.



Detailed geometry of fixed-bias flux three-phase magnetic bearing



Force-displacement characteristics of permanent magnet part

SESSION DR: SPINTRONICS AND ORBITRONICS (POSTER SESSION)

Co-Chair(s): B. Park, *KAIST, Daejeon, Korea (the Republic of)* and D. Go, *Department of Physics, Korea University, Seoul , Korea (the Republic of)*

Wednesday, November 4, 2026

03:00 PM-06:00 PM

Coral 4

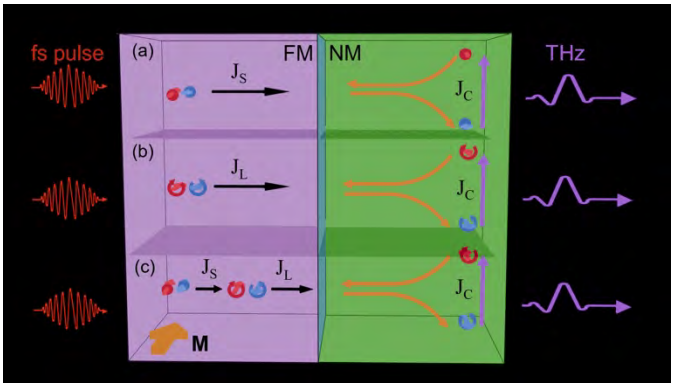
DR-01LB. Spin-orbitronic cascade effects in terahertz emission from magnetic heterostructures

Y. Kim[1], P. Yadav[2], B. Son[1], J. Heo[1], S. Shin[1], D. Ko[3], R. Mishra[2], K. Lee[1]

[1]Pukyong National University, Busan, Korea (the Republic of), [2]India Institute of Technology, Delhi, India, [3]Gwangju Institute of Science and Technology, Gwangju, Korea (the Republic of)

Laser-induced spintronic terahertz (THz) emission from ferromagnet/nonmagnet (FM/NM) heterostructures provides a powerful probe of ultrafast angular-momentum transport on sub-picosecond timescales. Beyond spin, orbital angular momentum has emerged as a promising information carrier owing to its potentially longer transport length and reduced reliance on strong spin-orbit coupling (SOC). Despite recent demonstrations of THz emission mediated by orbital-to-charge conversion, the microscopic origin and evolution of the orbital contribution remain elusive. Here, we investigate THz generation from FM/NM heterostructures to disentangle spin- and orbital-mediated charge conversion. We compare weak-SOC $Ni_{80}Fe_{20}$ and strong-SOC Ni as the FM layers, together with Pt and W as the NM layers, whose opposite spin Hall but identical orbital Hall polarities provide a means to distinguish spin and orbital contributions through the THz polarity. $Ni_{80}Fe_{20}$/W bilayers consistently exhibit negative-polarity THz emission, in agreement with the negative inverse spin Hall response of W. In striking contrast, Ni/W exhibits a pronounced Ni-thickness-dependent polarity reversal near t_{Ni} ~ 4 nm, revealing a crossover from spin-dominated to orbital-dominated emission. Furthermore, increasing the W thickness produces a systematic delay of the THz peak, indicating orbital transport through W followed by orbital-to-charge conversion via the inverse orbital Rashba-Edelstein effect. The emergence of these signatures only for sufficiently thick, strong-SOC Ni points to a sequential spin-to-orbital-to-charge conversion pathway: optical excitation generates a spin current, which is converted into an orbital current within Ni, transported through W, and subsequently converted into a charge current at the W interface. These

results establish a cascading spin-orbital conversion mechanism for THz emission and demonstrate SOC engineering as a route to control ultrafast angular-momentum transport [1].
[1] Younghun Kim, Pinki Yadav, Byungwoo Son, Jooyoung Heo, Sejin Shin, Do-Kyeong Ko, Rahul Mishra, & Kyusup Lee, "Cascading Spin-Orbitronic Terahertz Emission in Ferromagnet/Nonmagnet Bilayers", Adv. Opt. Mater. e71652 (2026).



Schematic illustration of three THz emission mechanisms.

DR-02. Temperature Dependence of Spin–Orbit Torques in Topological Insulator–Magnetic Multilayer Heterostructures

S. Hait[1], B. Brereton[1, 2, 3], A. Yagmur[1], S. Sasaki[1], G. Burnell[1], C. Marrows[1]
[1]School of Physics and Astronomy, University of Leeds, Leeds, West Yorkshire, United Kingdom, [2]ISIS Neutron and Muon Source, Harwell Science and Innovation Campus, Chilton, Oxfordshire, United Kingdom, [3]Diamond Light Source, Harwell Science and Innovation Campus, Chilton, Oxfordshire, United Kingdom

The generation and manipulation of spin–orbit torques (SOTs) is currently a prime research topic related to spintronic memory technologies and unconventional computing [1]. Identifying a combination of material systems that can act as efficient SOT sources and robust memory elements is therefore essential [1]. In multilayer devices, interfacial effects and current shunting can strongly influence both the magnitude and direction of SOTs. Here, we investigate SOTs generated by the topological insulator Bi_2Se_3 acting on magnetic multilayers (MMLs).
The studied samples consisted of Bi_2Se_3 (20 nm) grown by molecular beam epitaxy on Al_2O_3 substrates, followed by Ta spacer layers of varying thickness and a $[Pt/Co_{68}B_{32}/Ru]_6$ multilayer deposited over it by dc magnetron sputtering. Control samples without Bi_2Se_3 were grown on oxidised Si. SOTs were quantified using azimuthal-angle-dependent harmonic Hall analysis on microfabricated Hall bars [2]. For accurate estimation of the SOTs, the proper correction for current shunting using a parallel-resistor model is also carried out. In Bi_2Se_3-containing samples, only ~5% of the current flows through the Bi_2Se_3 due to its higher resistance, with most current shunted through the MML.
The damping like torque scales linearly with the applied current and exhibits opposite signs for different Ta thicknesses, indicating competing contributions from the Ta and Pt layers, each with opposite spin Hall angles. Samples with Bi_2Se_3 exhibit significantly enhanced SOTs compared to the control sample, while increasing Ta thickness slightly reduces the torque magnitude. At room temperature, the Bi_2Se_3/Ta (2 nm)/MML structure demonstrates a DL efficiency of ~0.02 mT per 10^{10} A-m^{-2}, comparable to previous reports using Bi_2Se_3 [3]. These results highlight the importance of multilayer engineering in optimising SOT efficiency for spintronic devices.
[1] V. Nguyen, S. Rao, K. Wostyn, and S. Couet, ," npj Spintronics, vol. 2, p. 48, 2024.
[2] Y. Du, R. Thompson, M. Kohda, and J. Nitta, AIP Adv., vol. 11, p. 025033, 2021.
[3] Q. Lu, P. Li, Z. Guo, G. Dong, B. Peng, X. Zha, T. Min, Z. Zhou, and M. Liu, Nature Commun., vol. 13, p. 1650, 2022.

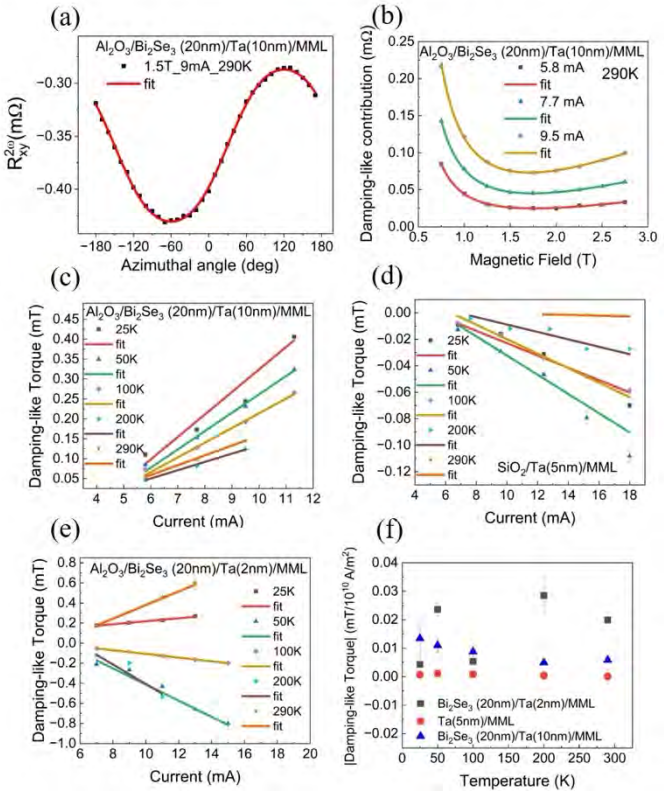


Fig.1: (a) Second-harmonic resistance at 290 K, 1.5 T, and 9 mA and (b) damping like torque (DLT) as a function of applied field for different currents in Al_2O_3/Bi_2Se_3 (20 nm)/Ta (10 nm)/MML. (c–e) DLT vs applied current for all mentioned samples. (f) DLT per current density as a function of temperature for all samples.

DR-03. Spin Accumulation Coefficients in Centrosymmetric Systems

J. Lim, K. Lee
Department of Physics, Korea Advanced Institute of Science and Technology (KAIST), Daejeon, Korea (the Republic of)

The concept of spin current is widely employed to describe and interpret various spintronic phenomena. However, the spin current operator is not uniquely defined due to its non-conservation. Since the physical observable is not spin current but spin accumulation, a direct evaluation of spin accumulation is more appropriate for comparison with experiments. In this respect, the recently proposed spin accumulation coefficient (SAC) [1-3], defined as the response of spin to the gradient of the electric field, has attracted growing attention as an alternative descriptor of the spin Hall effect. In low-symmetry nonmagnetic systems, SAC has been shown to arise purely from extrinsic contributions and to exhibit no correlation with the intrinsic spin Hall conductivity (SHC) [4]. In this study, we compute and compare SAC and SHC in highly symmetric nonmagnetic metals, which have been widely used as spin sources in spin–orbit torque experiments. In contrast to low-symmetry materials, we find that both the sign and magnitude of SAC are strongly correlated with the intrinsic SHC in these materials. This result suggests that, despite the ambiguity in the definition of spin current, the intrinsic SHC provides a practical proxy for estimating spin accumulation in high-symmetric nonmagnetic materials.

[1] Tatara, Phys. Rev. B, 98, 174422 (2018)
[2] Shitade and Tatara, Phys. Rev. B 105, L201202 (2022)
[3] Shitade, Phys. Rev. B 106, 045203 (2022)
[4] Shitade and Minamitani, npj Spintron. 3, 29 (2025)

DR-04. Chirality-Induced Spin Selectivity in Helical Graphene Structures

A. Chugh[1], S. Shin[2], B. Park[2], H. Lee[3]
[1]Applied Physics Program, Rice University, Houston, Texas, United States, [2]Department of Materials Science and Engineering, Korea Advanced Institute of Science and Technology, Daejeon, Daejeon, Korea (the Republic of), [3]Department of Materials Science and NanoEngineering, Rice University, Houston, Texas, United States

Chirality-induced spin selectivity (CISS) has emerged as a promising mechanism for generating spin-polarized currents without ferromagnets, providing a new route toward spintronic functionalities beyond conventional spin injection schemes. [1] While CISS has been extensively studied in molecular and organic systems, its realization in solid-state platforms with controllable chirality remains limited. Artificially engineered chiral structures based on 2D materials provide a controllable platform to explore spin-selective transport. Among them, twisted multilayer graphene offers a unique opportunity to introduce structural chirality through sequential rotational stacking. In such systems, interlayer twist breaks inversion and mirror symmetries, enabling the formation of helical architecture with well-defined out-of-plane chirality, advantageous for spin-selective vertical transport. However, direct observation of CISS in such artificially engineered multilayer 2D chiral systems remains limited.

In this work, we fabricate a helical graphene structure by sequentially stacking individual graphene monolayers with a constant twist angle using a dry transfer method (Fig. 1). To probe CISS, magnetic-conductive atomic force

microscopy (mc-AFM) is employed using a magnetized conductive tip. [2] The tip magnetization, controlled by an external magnetic field, defines the spin polarization of injected carriers, while the helical graphene stack acts as a spin-selective filter. The measured I–V characteristics exhibit a clear dependence on the magnetic field direction used to magnetize the tip, with consistently higher current observed for one magnetization orientation compared to the opposite (Fig. 2). This behavior is reproducible across multiple measurement points. Statistical analysis reveals clear spin-dependent asymmetry, with spin polarization values up to ~46.7% at +2 V and ~69.2% at −2 V. These results provide promising experimental evidence of CISS in multilayer graphene with well-defined helical chirality, highlighting the role of structural chirality in enabling spin-selective transport in 2D materials.

[1] R. Naaman, Y. Paltiel and D. H. Waldeck, Nature Reviews Chemistry., Vol.3, p.250-260 (2019)
[2] J. A. Albro, N. T. Garrett and K. Govindaraj, ACS Nano., Vol.19, p.17941-17949 (2025)

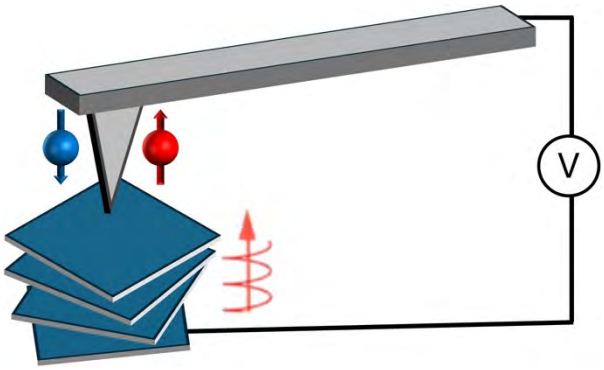


Fig. 1 Schematic of mc-AFM measurement on a helical graphene stack

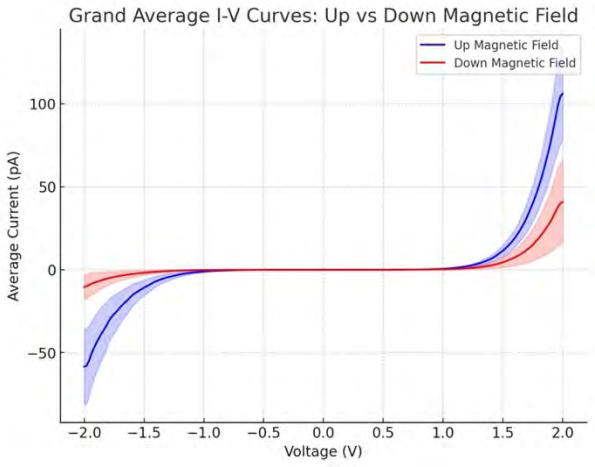


Fig.2 I–V curves under opposite magnetic fields

DR-05. Spin Current Balance for Fully Angular Control of Spin Polarization

X. Qiu, C. Pan, Y. Guan, X. Duan
School of Physics Science and Engineering, Tongji University, Shanghai, Shanghai, China

The operational efficiency, power consumption, and feasibility of achieving all-electrical switching in spintronic devices are fundamentally governed by the spin current polarization direction [1]. However, full angular control of the spin polarization generated from spin-orbital materials has remained a long-standing yet unrealized goal. Here, we introduce the concept of spin current balance to achieve complete angular tunability of the spin polarization. Our architecture comprises a uniform layer and a wedged layer, and by finely adjusting the relative weights of their respective spin currents, a spin current balance is established. As a result, the net spin polarization direction varies sensitively and progressively. This continuous angular tunability is directly evidenced by the phase evolution of the spin Hall magnetoresistance [2] and further corroborated through symmetry evolution of the SOT vector, the associated second-harmonic Hall features, and spin torque switching behaviors. Spin current balance thus constitutes a versatile and important building block for the advanced design of next-generation spintronic devices.

[1] Shuai Hu, Xuepeng Qiu* et al., "Frontiers in all electrical control of magnetization by spin orbit torque", Journal of Physics: Condensed Matter 36, 253001 (2024)
[2] Chang Pan, Shuai Hu,* Fanli Yang, Dongchao Yang, Weijia Fan, Zhong Shi, Liqing Pan,† Shiming Zhou,† Xuepeng Qiu†, "Nonrelativistic Spin Current Generated Unconventional Spin Hall Magnetoresistance in Altermagnetic RuO_2", Advanced Science 2026; 0:e21779

DR-06. Field-Free Switching of Perpendicular Magnetization Driven by Orbital Torque from Ti

H. Seo, S. Shin, B. Park
Material Science and Engineering, KAIST, Daejeon, Daejeon, Korea (the Republic of)

Orbital-current-driven torque (OT) has emerged as a promising mechanism for magnetization switching, offering potentially higher torque efficiency than conventional spin Hall–based approaches [1,2]. However, to date, OT in perpendicular magnetic anisotropy (PMA) systems requires an external magnetic field for deterministic switching. In this study, we demonstrate OT-induced field-free

switching in Ti/ferromagnet (FM)/Ti/CoFeB/MgO structures. Our approach introduces Ti, an efficient orbital current source, as an underlayer to a magnetic trilayer consisting of a FM/Ti/CoFeB structure, which is known to enable field-free switching. In this configuration, orbital currents generated in the bottom Ti are converted into spin currents with out-of-plane spin polarization through the FM layer, thereby enabling deterministic field-free switching. A Ni(2 nm)/Co(2 nm) bilayer was utilized as the FM conversion layer, leveraging the efficient orbital-to-spin conversion of Ni [6].

Fig.1 shows representative switching loops for Ti thicknesses of 15 nm, exhibiting clear field-free switching behavior. Fig.2 presents the switching current density as a function of Ti thickness, demonstrating monotonic decrease with increasing Ti thickness. This trend provides strong evidence that the field-free switching is governed by orbital currents generated in the Ti layer. As the Ti thickness increases, the bulk orbital Hall effect generates larger orbital currents, resulting in proportionally increased out-of-plane spin-polarized currents, thereby reducing the switching current density. These results demonstrate, for the first time, orbital-torque-driven field-free switching of perpendicular magnetization, offering a viable pathway toward low-power PMA spintronic devices.

[1] T. Tanaka, H. Kontani and M. Naito, Physical Review B., Vol. 77, p.165117 (2008)
[2] S. Y. Shin, D. Han and S. Lee, Advanced Functional Materials., Vol. 35, p.2425932 (2025)
[3] S. Baek, V. P. Amin and Y.-W. Oh, Nature Materials., Vol. 17, p.509 (2018)
[4] V. P. Amin, J. Zemen and M. D. Stiles, Physical Review Letters., Vol. 121, p.136805 (2018)
[5] Y.-G. Choi, D. Jo and K.-H. Ko, Nature., Vol. 619, p.52 (2023)
[6] D. Lee, D. Go, H.-J. Park et al., Nature Communications., Vol. 12, p.6710 (2021)

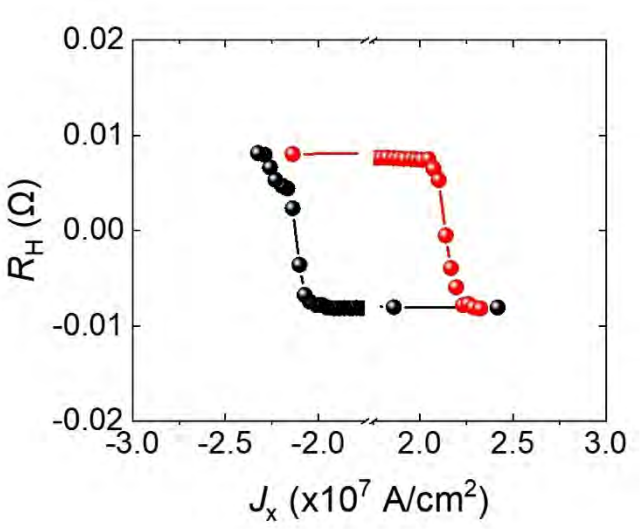


Fig.1 Field-free switching loops of Ti/FM/Ti/CoFeB/MgO devices for Ti thicknesses of 15 nm.

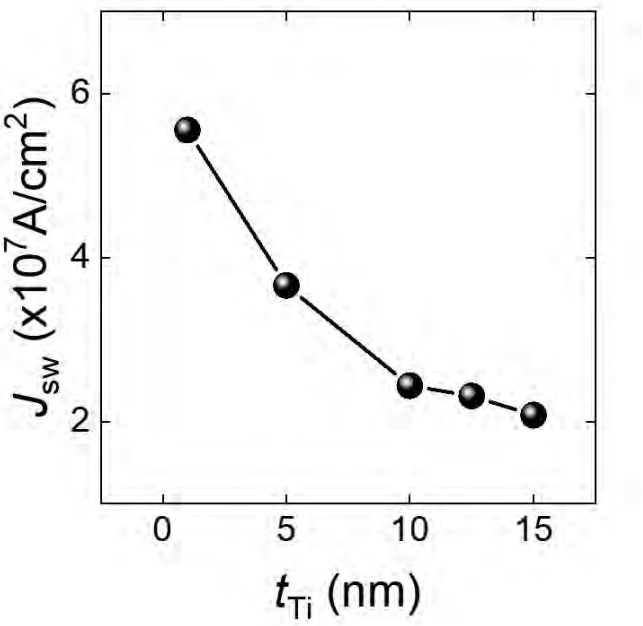


Fig.2. Ti thickness (t_{Ti})-dependent switching current density.

DR-07. Enhanced anomalous Nernst effect in disordered CoPt films compared with ordered CoPt

K. Tanabe, M. Mohammadi, H. Awano
Toyota Technological Institute, Nagoya, Japan

The anomalous Nernst effect (ANE) is of interest for planar thermoelectric devices and microscale heat-flux sensors because it converts a thermal gradient into a transverse electric field in a simple lateral geometry [1]. In CoPt-based alloys, a large intrinsic ANE has previously been reported for ordered CoPt grown on MgO, with maximum S_{ANE}=1.2 μV/K and α_{xy}=2.5 A/mK at Pt-rich composition [2].

Here, we investigate the composition dependence of the ANE and thermal transport in as-deposited $Co_{1-x}Pt_x$ thin films prepared on quartz glass by magnetron co-sputtering without post-annealing. Structural characterization indicates the development of a nanocrystalline disordered A1-type fcc CoPt phase with increasing Pt concentration. The anomalous Nernst coefficient S_{ANE} increases from 0.33 to 3.2 μV/K, while the transverse thermoelectric conductivity α_{xy} reaches nearly 5 A/mK around x=0.5. Analysis of the transverse thermoelectric response suggests that the contribution associated with α_{xy} is dominant near the optimum composition, and the $|\alpha_{xy}|/|\sigma_{xy}|$ scaling is broadly consistent with an intrinsic-like regime. In addition, the thermal conductivity is reduced to about 10 W/mK, yielding a maximum heat-flux sensitivity $E/J_Q \approx 0.30$ μm/A. Our results indicate that disordered or partially crystalline CoPt can outperform ordered CoPt in transverse thermoelectric response, while also offering lower-temperature fabrication and reduced thermal conductivity. This comparison suggests that Pt-induced electronic tuning together with disorder-enabled intrinsic transverse transport provides an effective strategy for high-sensitivity ANE materials for planar thermoelectric and on-chip heat-flux sensing applications.

[1] W. Zhou and Y. Sakuraba, Appl. Phys. Express 13, 043001 (2020).
[2] R. Toyama *et al* ., J. Phys. D: Appl. Phys. 57, 405001 (2024).

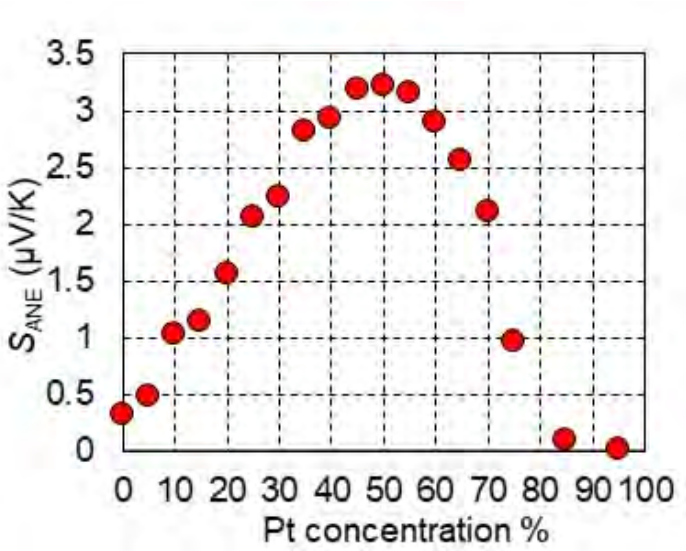


Fig. 1 Anomalous Nernst coefficient as a function of Pt content.

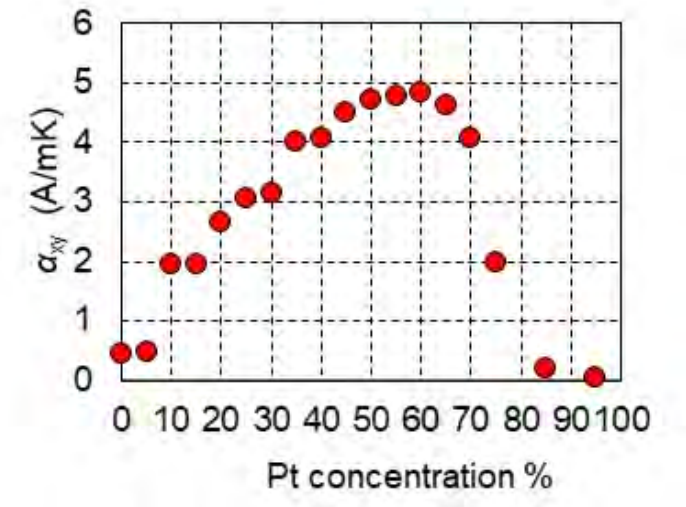


Fig. 2 Transverse thermoelectric conductivity, α_{xy}, as a function of Pt content.

DR-08. Orbital Torque in Oxide Ferromagnet Fe_3O_4/Cr Heterostructures

T. Onuma, H. Koizumi, H. Yanagihara
University of Tsukuba, Tsukuba, Japan

Electrical control of magnetization via spin–orbit torque (SOT) is a key technology for next-generation spintronic devices. While conventional SOT relies on heavy metals with strong spin–orbit coupling, the emerging field of orbitronics exploits orbital angular momentum (OAM) currents originating from orbital textures, such as the orbital Hall effect (OHE), which can arise even in light metals such as Cr or Ti [1]. Previous studies on orbital torque (OT) have mainly focused on nonmagnetic metal/ferromagnetic metal systems [1-5], and its microscopic mechanism in strongly correlated materials—where orbital degrees of freedom play a crucial role—remains largely unexplored. In this work, we report the observation and evaluation of OT in Fe_3O_4, a prototypical correlated oxide ferromagnet.

Fe_3O_4(001)/Cr heterostructures were fabricated on MgO(001) substrates. The orbital torque was quantitatively evaluated using second-harmonic Hall voltage ($V^{2\omega}$) measurements [3,4]. By analyzing the angular and applied field dependence of $V^{2\omega}$, we separated the OT-induced signal from thermally driven contributions, such as the anomalous Nernst effect. As shown in Fig. 1, in Fe_3O_4(30 nm)/Cr (3 nm) samples, a clear damping-like (DL) effective field was observed at 300 K, exhibiting a linear dependence on the current density injected into the Cr layer. The estimated torque efficiency (ξ_{DL}) is approximately 0.09. This value is comparable to reported efficiencies for Ni/Ti (0.03) [2] and Ti/CoTb/Cr (−0.57) [5]. The observation of such a large torque in a system employing Cr—characterized by low spin Hall conductivity but high orbital Hall conductivity [1,4]—indicates that orbital torque can dominate over conventional spin-based mechanisms even in oxide ferromagnets.

In the presentation, we will further discuss the thickness dependence of both Fe_3O_4 and Cr layers, as well as the dependence on current injection direction. These results will be compared with previously reported OT effects in metallic ferromagnets, providing insight into the mechanism of orbital torque in correlated oxides.

[1] Kazuya Ando, J. Phys. Soc. Jpn. 94, 092001 (2025)
[2] H.Hayashi, Daegeun Jo, Dongwook Go, et al., Commun. Phys. 6, 32 (2023)
[3] Siyang Peng, Xuan Zheng, Sheng Li, et al., Nature Materials volume 24, pages1749–1755 (2025)
[4] Soogil Lee, Min-Gu Kan, Dongwook Go, et al., Communications Physics volume 4, Article number: 234 (2021)
[5] Yonghai Guo, Yu Zhang, Wenbo Lv, et al., Appl. Phys. Lett. 123, 022408 (2023)

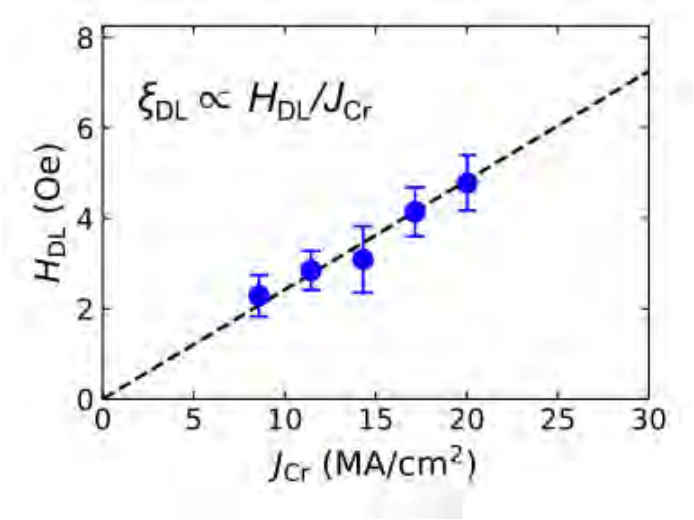


Fig. 1. Current density dependence of the DL effective field in Fe_3O_4(30nm)/Cr(3nm) heterostructures measured at 300 K.

DR-09. Enhanced Spin-torque Generation via Current Distribution Engineering in Si/Al Composition-graded Materials

M. Kawai[1], K. Yamanoi[1], Y. Nozaki[1, 2]
[1]Department of Physics, Keio Univ., Yokohama, Japan, [2]Center for Spintronics Research Network, Keio Univ., Yokohama, Japan

Recent studies have demonstrated that composition-graded materials (CGMs) combing Si and Al, despite their weak spin orbit interaction (SOI), can generate spin-torque comparable to that of Pt, with optimal efficiency observed at specific composition-graded widths.[1] Similar effects have been reported in other gradient systems such as Ti/W,[2] suggesting that nonuniform current density distributions at interfaces between materials with different electrical conductivities play a key role in spin-torque generation. However, the influence of layer thickness on such current distribution effects remains unclear. To elucidate this point, we systematically varied the thickness of the Al layer in Si/Al composition-graded structures, and evaluated damping-like-torque efficiency ξ_{DL}.

The multilayers, consisting of Si(10)/Al(t_i/2)/Si(t_i/2)/Al(t_{Al})/FM(10)/SiO_2(10) (thickness in nm), were deposited on Si substrates. The FM layer was

either $Ni_{95}Cu_5$ or $Ni_{80}Fe_{20}$. The Al layer thickness (t_{Al}) was systematically varied from 3.0 to 15 nm, and composition-graded layer thickness (t_i) was set to 0 or 0.5 nm. ξ_{DL} were evaluated via dc-induced Gilbert damping modulation in spin-torque ferromagnetic resonance measurement. As shown in Figs. 1(a) and 1(b), ξ_{DL} in Si/Al CGMs are comparable to those of Pt, and the samples with t_i=0.5 nm exhibit larger efficiencies than those with t_i=0 nm, consistent with previous studies.[1] Furthermore, as shown in Figs. 1(a)-(c), ξ_{DL} increases with decreasing t_{Al}, irrespective of t_i and the choice of FM layer, (particularly in the range of t_{Al} from 3 to 5 nm). Comparing Fig. 1(a) and 1(c), ξ_{DL} decreases by more than 50% when changing the FM layer from $Ni_{95}Cu_5$ to $Ni_{80}Fe_{20}$. This result suggests a strong FM dependence of the torque generation. However, further studies, such as FM thickness dependence, are needed to clarify the mechanism. These results provide important insight into non-SOI-based spin-current generation mechanisms and offer a design guideline for efficient spin-torque materials based on composition-gradients.

[1] T. Horaguchi, et. Al., Sci. Adv., 11, eadr9481 (2025).
[2] H. Nakayama et Al., Phys. Rev. B, 107, 174416 (2023).

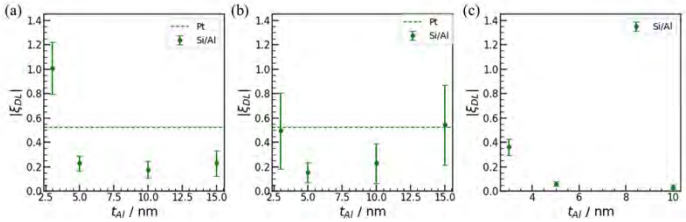


Fig. 1 Dependance of $|\xi_{DL}|$ on t_{Al}. (a) t_i=0.5 nm, FM is $Ni_{95}Cu_5$ (b) t_i=0 nm, $Ni_{95}Cu_5$ (c) t_i=0.5 nm, $Ni_{80}Fe_{20}$. The dashed line indicates for Pt(10)/ $Ni_{95}Cu_5$(10)/SiO_2(10) sample.

DR-10. Chiral-induced Orbital Moment Selectivity in Chiral Semiconductors

I. Baek[1, 2], H. Lee[1, 2], M. Sastges[3, 5, 4], Y. Mokrousov[3, 5], H. Lee[1, 2], D. Go[6, 3, 5]

[1]Department of Physics, Pohang University of Science and Technology, Pohang-si, Korea (the Republic of), [2]Center for Quantum Dynamics of Angular Momentum, Pohang-si, Korea (the Republic of), [3]PGI-1, Forschungszentrum Jülich, Jülich, Germany, [4]Department of Physics, RWTH Aachen University, Aachen, Germany, [5]Institute of Physics, Johannes Gutenberg University Mainz, Mainz, Germany, [6]Department of Physics, Korea University, Seoul, Korea (the Republic of)

Chiral-induced spin selectivity (CISS) has been evaluated in famous chiral metals and semiconductors [1,2]. Considering that orbital angular momentum is a fundamental physical quantity that is converted into spin through spin-orbit coupling [3,4], chiral-induced orbital selectivity (CIOS) can also happen in the same materials [5].

In this presentation, we evaluate CIOS in C40 chiral semiconductors such as $CrSi_2$, $MoSi_2$, and WSi_2. Using modern theory-based analysis, we demonstrate that these materials generate itinerant CIOS that are significantly larger than CISS. The large CIOS comes from the Berry curvature physics, so it cannot be captured using the atomic-centered approximation. The CIOS and CISS can be measured by a nonlinear conductivity measurement. Using first-principles calculation, we show that the Berry-curvature CIOS dominates the nonlinear conductivity compared to CISS in C40 semiconductors.

[1] R. Gupta and A. Droghetti, *Phys. Rev. B* 109, 155141 (2024)
[2] K. Tenzin, A. Roy and Jagoda Slawinska, *Phys. Rev. B* 108, 245203 (2023)
[3] S. R. Park, C. H. Kim, and C. Kim, *Phys. Rev. Lett.* 107, 156803 (2011)
[4] D. Go, D. Jo, and H.-W. Lee, *Phys. Rev. Lett.* 121, 086602 (2018)
[5] K. Hagiwara, D. Go, and C. Tusche, Adv. Mater. 37, 2418040 (2025)

DR-11. Proper Theory of Field-Induced Spin and Orbital Magnetic Moment Transport

H. Lee[1, 2], S. Cheon[1, 2], I. Baek[1, 2], H. Lee[1, 2]

[1]Department of Physics, Pohang University of Science and Technology, Pohang, Korea (the Republic of), [2]Center for Quantum Dynamics of Angular Momentum, Pohang, Korea (the Republic of)

In equilibrium, spin magnetization is determined by the expectation value of the spin operator, whereas orbital magnetization is evaluated through the response of the grand potential to a magnetic field [1,2] or by calculating the expectation value of the orbital angular momentum operator with the Wannier function [3]. On the other hand, determining the transport of spin and orbital angular momentum is challenging due to their non-conserved nature. Early studies using the Kubo formula for conventional spin or orbital current operators [4,5] have pioneered the fields of spintronics and orbitronics. However, subsequent attempts to define a conserved current, including the torque dipole contribution [6,7], have reported results that diverge from the conventional definitions. These approaches derived the conserved spin or orbital Hall

conductivities by applying appropriate spin or orbital current operators to the transport equations of electrons based on semiclassiscal [6] or fully quantum mechanical [7] frameworks.

In this presentation, we propose a proper thermodynamic formalism for field-induced transport of spin and orbital magnetic moments. In our framework, the proper spin and orbital Hall conductivities are obtained by evaluating the response of the free energy current to an external magnetic field. Our results include two distinct contributions: (i) the transport of the electron's intrinsic magnetic moments via anomalous velocity, and (ii) the transport of anomalous magnetic moments, which are induced from the electric field, via group velocity of electrons. While our formalism captures terms similar to those in previous theories, it also reveals critical terms that were previously overlooked. In addition, we also present quantitative comparisons with the previous theories and our formalism using tight-binding models, such as the massive Dirac and Kane-Mele models, as well as first-principles calculations for various d-transition metals. These findings provide a rigorous foundation for understanding angular momentum transport.
[1] D. Xiao, J. Shi and Q. Niu, Phys. Rev. Lett., Vol. 95, p.137204 (2005)
[2] J. Shi, G. Vignale and Q. Niu, Phys. Rev. Lett., Vol. 99, p.197202 (2007)
[3] T. Thonhauser, D. Ceresoli and D. Vanderbilt, Phys. Rev. Lett., Vol. 95, p.137205 (2005)
[4] J. Sinova, D. Culcer and A. MacDonald, Phys. Rev. Lett., Vol. 92, p.126603 (2004)
[5] D. Go, D. Jo and H.-W. Lee, Phys. Rev. Lett., Vol. 121, p.086602 (2018)
[6] C. Xiao and Q. Niu, Phys. Rev. B, Vol. 104, p.L241411 (2021)
[7] T. Valet, H. Jaffres and R. Raimondi, Phys. Rev. Lett., Vol. 135, p.256301 (2025)

DR-12. Origin of Spin-Orbit Torques and Spin Transport in Pt/Co/Cu/NiFe/Cu/Capping Multilayers

Y. Bai, Y. Zhang, T. Wang
Huazhong University of Science and Technology, Wuhan, Hubei, China

Spin-orbit torque (SOT) enables efficient current-driven control of magnetization, offering a promising pathway toward low-power spintronic devices. However, the origin of both damping-like (DL) and field-like (FL) SOTs and the associated spin transport processes in complex multilayers remain unclear. Here, we investigate the NiFe thickness dependence of SOT efficiencies in Ta/Pt/Co/Cu/xNiFe/Cu/Capping multilayers (x = 1-5 nm; Capping = Pt, Al, and SiO_2). By employing a spin rotation geometry, the perpendicularly magnetized Pt/Co/Cu stack serves as a spin source that generates an unconventional spin polarization orthogonal to the Oersted field, thereby eliminating the Oersted-field contribution and enabling unambiguous extraction of SOTs using planar Hall and polar MOKE measurements. To distinguish bulk and interfacial contributions, we introduce a sample-area-normalized magnetic moment, $m = m_{NiFe}/S$, which accounts for thickness-dependent magnetization and reduces uncertainties arising from nominal thickness scaling and magnetic dead layers. We find that DL-SOT follows a nearly linear 1/m scaling, consistent with rapid spin absorption at the Cu/NiFe interface, but exhibits finite intercepts as 1/m approaches zero in both Pt- and Al-capped samples, indicating additional interfacial spin-current contributions at the Cu/Pt and Cu/Al interfaces. In contrast, SiO_2-capped samples show negligible interfacial contributions. Furthermore, FL-SOT deviates markedly from the 1/m scaling, indicating a significantly longer spin dephasing length (~1.7 nm) and more extended propagation of the spin currents responsible for FL-SOT in NiFe compared with those responsible for DL-SOT. Comparative capping-layer studies further corroborate this interface-dependent spin transport behavior. Our findings clarify the origin of DL and FL torques and the associated spin transport processes, providing guidelines for engineering interfacial spin-orbit functionalities in ultrathin metallic heterostructures.
(1) H. Celik, J. Wu and C. Ni, Nat. Commun. 5(1), 3042 (2014)
(2) A.M. Humphries, T. Wang and E.R.J. Edwards, Nat. Commun. 8(1), 911 (2017)
(3) T. Wang, S. Lendinez and M.B. Jungfleisch, Appl. Phys. Lett. 116(1), 012404 (2020)
(4) X. Qiu, W. Legrand and P. He, Phys. Rev. Lett. 117(21), 217206 (2016)

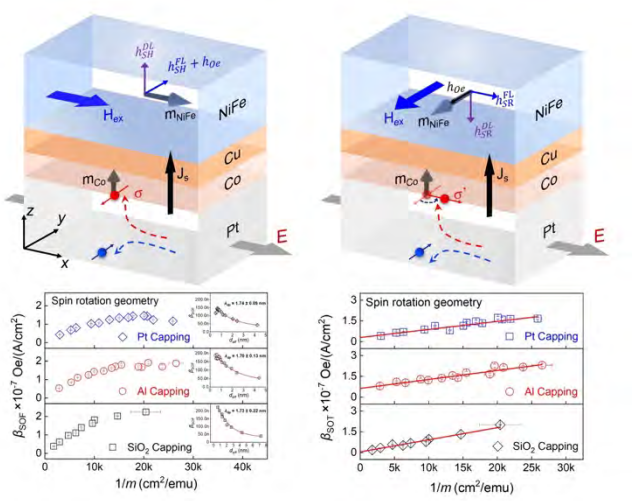


Fig.1 Schematic illustration of SOT measurements under the spin Hall geometry (left) and the spin rotation geometry (right).

DR-13. Spin-orbit torque-based three-dimensional magnetic field sensor using tungsten with modified sputtering conditions

C. Zhang[1, 2], M. Oogane[1, 3]
[1]Graduate School of Engineering, Tohoku Univ., Sendai, Japan, [2]CIES, Tohoku Univ., Sendai, Japan, [3]CSIS, Tohoku Univ., Sendai, Japan

Spin–orbit torque (SOT)-based three-dimensional magnetic field sensors have attracted increasing attention for compact, low-power vector magnetic field detection.[1,2] Tungsten (W), exhibiting a large spin Hall angle, is a promising material for efficient SOT generation and can also serve as a buffer layer in MgO/CoFeB-based magnetic tunnel junctions (MTJs). The crystal structure of W can be tuned by sputtering conditions, strongly affecting both the spin Hall angle and the magnetic anisotropy of the adjacent ferromagnetic layer.[3,4] However, its impact on SOT-driven three-dimensional magnetic field sensing remains unclear. In this work, we investigate the effect of sputtering power on the structural phase of W and its correlation with sensor performance.

W(5 nm)/CoFeB(1.1 nm)/MgO(2 nm)/Ta(2 nm) heterostructures are deposited on Si/SiO_2 substrates by DC/RF sputtering and annealed at 300 °C under a 1 T out-of-plane magnetic field for 1 h. During W deposition, the Ar pressure is fixed at 1.28 kPa while the sputtering power (*P*) is varied from 3 to 12 W. X-ray diffraction measurements on separately prepared W(20 nm) films confirm an increased β-phase fraction at lower *P*. All films are patterned into Hall-bar devices. Magnetotransport measurements show an in-plane easy axis, with the effective anisotropy field increasing from 27 mT to 57 mT as *P* decreases from 12 to 3 W, attributed to the modified interfacial anisotropy associated with the higher β-phase fraction.

Three-dimensional sensing is evaluated via anomalous Hall resistance measurements[2] under a current density of 1.6 MA/cm^2. As *P* decreases from 12 to 3 W, the sensitivities for in-plane fields (H_x, H_y) increase from 5.5 to 22.4 V/A/T, while the out-of-plane sensitivity (H_z) decreases from 77.5 to 15.4 V/A/T. These trends are explained by enhanced SOT efficiency and increased in-plane anisotropy. This work establishes sputtering control of W as an effective strategy to tune SOT and anisotropy, enabling flexible directional sensitivity in three-dimensional magnetic field sensors without additional structural complexity.

This work was partially supported by the X-nics project, CSIS and CIES at Tohoku University, JSPS KAKENHI 24K17316, and the Hirose Foundation.

[1] R. Li *et al.*, Nature Electronics 4, 179 (2021).
[2] R. Li *et al.*, Appl. Phys. Lett. 127, 132408 (2025).
[3] C. Zhang *et al.*, Appl. Phys. Lett. 109, 192405 (2016).
[4] Y. Takeuchi *et al.*, Appl. Phys. Lett. 112, 192408 (2018).

DR-14. Engineering Shape Anisotropy for Field-Free Switching in Perpendicular Nanomagnets

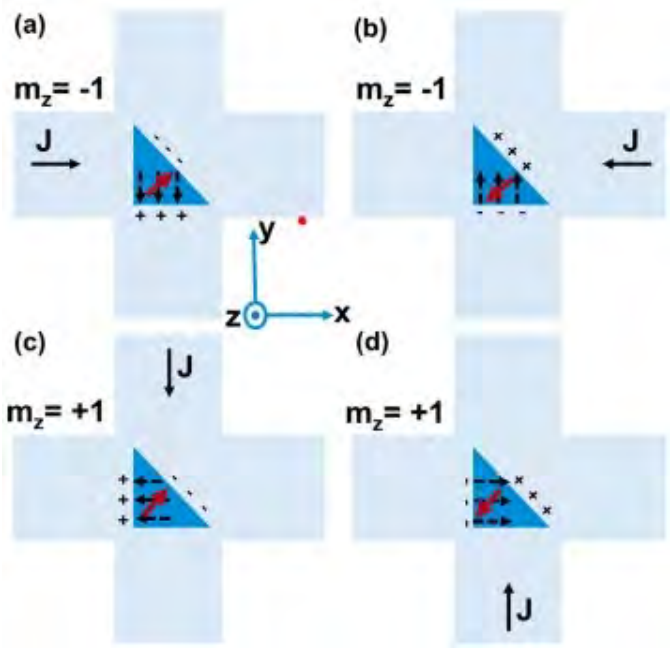
A. Chouhan, H. A. Mendonca, A. Erram, A. A. Tulapurkar
Electrical Engineering, Indian Institute of Technology Bombay, Mumbai, Maharashtra, India

Spintronics-based Spin–Orbit Torque Magnetic Random Access Memory (SOT-MRAM) is emerging as a promising successor to Spin Transfer Torque MRAM (STT-MRAM) due to its enhanced reliability and faster read–write operation. However, deterministic switching of perpendicularly magnetized ferromagnets in heavy metal/ferromagnet bilayers typically requires an external in-plane magnetic field to break symmetry and assist spin–orbit torque (SOT) switching, posing challenges for device scalability and integration.

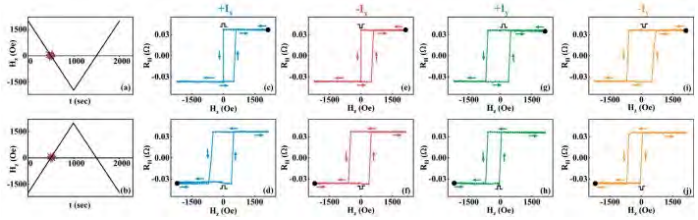
In this work, we experimentally demonstrate a field-free switching approach by engineering the shape anisotropy of the ferromagnetic layer. Triangular nanomagnets of Cobalt were fabricated on Platinum heavy metal underlayers, where the geometric asymmetry induces an effective internal magnetic field that breaks switching symmetry. As a result, deterministic magnetization switching between two

stable perpendicular states is achieved using nanosecond voltage pulses without any external magnetic field. The observed behaviour confirms that shape-induced anisotropy in asymmetric nanostructures can provide a sufficient internal symmetry-breaking field for SOT-driven switching. Compared to alternative approaches—such as thickness gradients, compositional engineering, or unconventional material stacks—this method offers a simpler and more fabrication-compatible route. This proof-of-concept opens pathways toward scalable, field-free SOT-MRAM devices and highlights the potential of such structures for applications in non-volatile memory and magnetic Boolean logic.

[1] C. Safeer, E. Ju'e, A. Lopez, L. Buda-Prejbeanu, S. Auffret, S. Pizzini, O. Boulle, I.M. Miron, G. Gaudin, Spin–orbit torque magnetization switching controlled by geometry, Nature Nanotechnology 11 (2016) 143–146.
[2] Z. Wang, Z. Li, M. Wang, B. Wu, D. Zhu, W. Zhao, Field-free spin–orbit torque switching of perpendicular magnetization aided by uniaxial shape anisotropy, Nanotechnology 30 (2019) 375202.
[3] H. Wu, J. Nance, S.A. Razavi, D. Lujan, B. Dai, Y. Liu, H. He, B. Cui, D. Wu, K. Wong, et al., Chiral symmetry breaking for deterministic switching of perpendicular magnetization by spin–orbit torque, Nano Lett. 21 (2020) 515–521.
[4] A. Chouhan, H. A. Mendonca, A. Erram, and A. A. Tulapurkar, "Shape asymmetry enabled field free switching of perpendicular nanomagnets,"Journal of Magnetism and Magnetic Materials, p. 173537, 2025.



Schematic diagram of the proposed triangular shaped Co PMA nanomagnets over Pt Hall bar. The direction of charge current density (*J*) is indicated in each sub figure. The damping-like torque arising from charge current in Pt aligns the magnetization in-plane as shown by the dotted black arrows. The effective magnetic surface charge density induced on the periphery of triangle is denoted by plus and minus signs. The resultant demagnetization field is shown by red arrow in each sub figure.



Field Free Switching of magnetization of triangular shaped devices, established through AHE measurements.

DR-15. Interfacial Spin–Orbit Coupling Driven Enhanced Spin-to-Charge Conversion in Mn_3Sn/Pt/Py Heterostructures

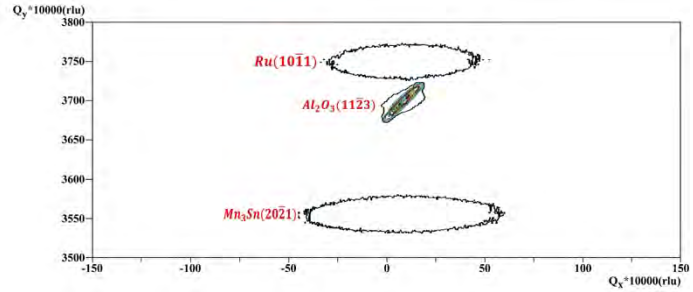
A. Saxena, A. Sahoo, N. Kandwal, P. K. Muduli
Physics, Indian Institute of Technology Delhi, New Delhi, Delhi, India

Interfacial spin orbit coupling (ISOC) has been established to be a key parameter for developing the cost-effective power efficient spintronics devices in recent past. While inverse spin Hall effect (ISHE) has been widely explored in heavy metals like Pt, Ta, W etc. [1,2], there is growing interest in non collinear antiferromagnets due to their large Berry curvature induced spin transport phenomena [3]. Mn_3Sn, a non collinear antiferromagnet with a chiral spin structure, exhibits large anomalous Hall effect and substantial spin Hall conductivity, making it a prime candidate for antiferromagnetic spintronics [3,4]. Despite research into individual heavy metals and non collinear antiferromagnets, the influence of their interfacial properties on spin-to-charge interconversion remains underexplored.

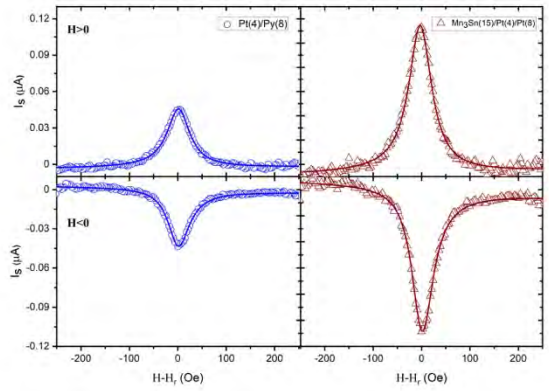
In this work, we investigate the ISHE in epitaxial Mn_3Sn thin films [4] and the role of ISOC at Mn_3Sn/Pt interface. High-quality Mn_3Sn epitaxial thin films growth as well as the crystallinity were confirmed from X-ray diffraction (XRD), reciprocal space mapping (RSM) [Fig.1], and rocking curve measurements. ISHE measurement for Mn_3Sn/Pt/Py heterostructure reveal 150 % enhancement in spin-to-

charge conversion compared to Pt/Py bilayer [Fig.2]. we used the symmetric component of the ISHE current (I_s) as the direct signature to measure this conversion efficiency. This significant enhancement is primarily ascribed to interfacial hybridization at the Mn_3Sn/Pt interface which amplifies the ISOC. These results highlight the critical role of interfacial physics in optimizing spin to charge interconversion for next generation spintronics applications.

1. L. Liu, C.-F. Pai, Y. Li, H. W. Tseng, D. C. Ralph, and R. A. Buhrman, Science 336, 555 (2012).
2. C.-F. Pai, L. Liu, Y. Li, H. W. Tseng, D. C. Ralph, and R. A. Buhrman, Appl. Phys. Lett. 101, 122404 (2012)..
3. S. Nakatsuji, N. Kiyohara, and T. Higo, Nature 527, 212 (2015).
4. H. Bangar, K. I. A. Khan, A. Kumar, N. Chowdhury, and P. K. Muduli, Adv. Quantum Technol. 6, 2200115 (2023).



The map, centered around the Al_2O_3(113) reflection, confirms the epitaxial relationship and high crystalline quality of the film



Comparison of ISHE signals in stacks with and without Mn_3Sn insertion. Open circles and triangles represent experimental data, while solid lines denote the corresponding fits

DR-16. Field-Activated Two-Dimensional Domain Manipulation via Thermally Induced SOT in GdFeCo/Pt Planar Films

H. Awano[1], S. Sumi[1], M. Mohammadi[1], K. Tanabe[1], Y. Nakatani[2]
[1]*Toyota Technological Institute, Nagoya, Aichi, Japan,*
[2]*University of Electro-Communications, Chofu, Tokyo, Japan*

We report reversible domain elongation and contraction driven by laser scanning under an in-plane magnetic field in ferrimagnetic GdFeCo/Pt planar films. The planar geometry enables arbitrary selection of the scanning direction, allowing two-dimensional control of domain propagation. When a focused continuous-wave laser beam is scanned across the film under an in-plane magnetic field Hx, a magnetic domain is continuously elongated along the scanning trajectory, forming a narrow stripe-like domain with a width comparable to the laser spot size (~2 μm) and a length of several tens of micrometers. The domain follows the laser path and can be extended in arbitrary directions. When the laser irradiation is turned off, the elongated domain smoothly contracts along the same trajectory and returns to its original domain-wall position without fragmentation. This path-preserving behavior indicates coherent domain-wall dynamics with low pinning. In contrast, no domain elongation is observed without Hx, demonstrating that the in-plane field is essential. These results suggest that thermal gradients alone are insufficient to drive domain-wall motion unless the domain-wall chirality is stabilized.

We attribute the observed dynamics to a cooperative mechanism between entropic torque and a weak thermally induced spin–orbit torque. The temperature gradient produces a free-energy gradient driving the domain wall toward the hotter region [1], while heat diffusion generates a small charge flow converted into a spin current via spin Hall or spin Nernst effects in the Pt layer [2–4]. Although each contribution is weak, their combined effect enables domain-wall motion. The contraction after laser removal indicates relaxation governed by domain-wall line tension rather than topological stability.

This research was supported in part by the Grant-in-Aid for Scientific Research (25K01273), (25K22102) and the Research Center of Smart Photon and Materials, Totoya Technological Institute.

[1] F. Schlickeiser et al., *Phys. Rev. Lett.* 113, 097201 (2014)
[2] A. Donges et al., *Phys. Rev. Research* 2, 013293 (2020)
[3] K. Uchida et al., *Nature* 455, 778 (2008)
[4] S. Meyer et al., *Nat. Mater.* 16, 977 (2017)

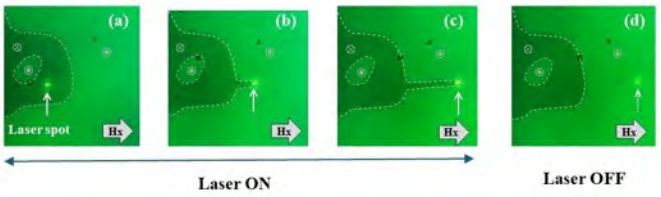


Figure 1. Polar Kerr microscope images of extended magnetic domains by laser scanning with in-plane magnetic field Hx (a)-(c) and return to original state when laser is turned off (d).

SESSION DS: DOMAIN WALL MEMORY AND MAGNETIC COMPONENTS FOR NEXT-GENERATION TECHNOLOGIES (POSTER SESSION)

Co-Chair(s): S. Sayed, *Product Engineering, TDK Headway Technologies, Inc., Fremont, California, United States* and V. Kalappattil, *Physics, Northeastern University, Burlington, Massachusetts, United States*

Wednesday, November 4, 2026
03:00 PM-06:00 PM
Coral 4

DS-01. Enhanced coercivity through geometric interconnects in magnetic nanowire and nanotube networks

A. Pereira[1], S. Guidobeth[4], E. Saavedra[2], J. Escrig[2, 3]
[1]Departamento de Ciencias, Facultad de Artes Liberales, Universidad Adolfo Ibáñez, Santiago, Chile, [2]Departamento de Física, Universidad de Santiago de Chile, Santiago, Chile, [3]CEDENNA, Centro de Nanociencia y Nanotecnología, Santiago, Chile, [4]Departamento de Física, Universidad de Chile, Santiago, Chile

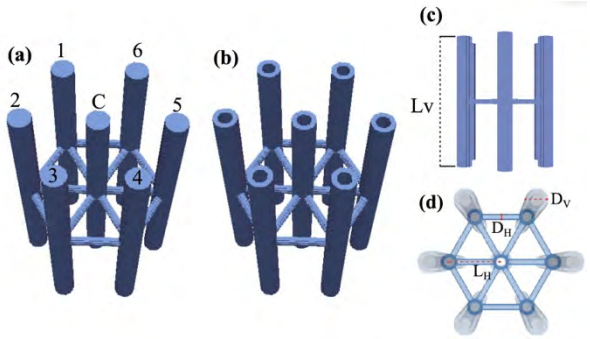
Magnetic nanowire networks provide a versatile platform for tailoring magnetic properties through geometrical design. In this work we investigate the magnetization reversal processes and hysteresis behavior of interconnected cylindrical permalloy nanostructures using micromagnetic simulations. Building upon previous studies of interconnected nanowire networks, we extend the analysis to hybrid architectures composed of vertically aligned nanowires or nanotubes interconnected by horizontal nanowires or nanotubes.

The magnetic response of these systems is studied by solving the Landau–Lifshitz–Gilbert equation using MuMax3. The structures consist of cylindrical elements with dimensions compatible with template-assisted fabrication, with diameters of approximately 50 nm and lengths of about 500 nm. The position of the horizontal interconnects is systematically varied along the vertical elements in order to evaluate its influence on coercivity and normalized remanence.

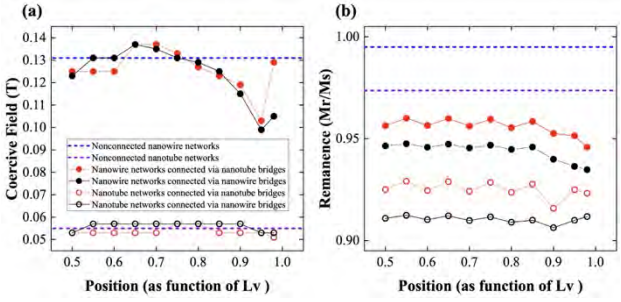
Our results reveal that geometric interconnectivity strongly modifies the magnetization reversal mechanisms and hysteresis behavior. In particular, specific interconnect positions produce a significant increase in coercivity compared to nonconnected arrays, despite the connectors lying in a plane perpendicular to the applied magnetic field. This counterintuitive behavior originates from the modification of dipolar coupling and the redistribution of magnetostatic charges along the vertical elements.

These results demonstrate that architectural design alone can be used to engineer magnetic hardness in nanoscale systems without modifying the material composition, providing new opportunities for tunable nanomagnetic devices and three-dimensional magnetic networks.

A. Pereira, G. Sáez and E. Saavedra, Nanomaterials., Vol. 13, p.1971 (2023)
J. Escrig, D. Altbir and M. Bahiana, J. Appl. Phys., Vol. 117, p.17B305 (2015)
R. Hertel, J. Phys. Condens. Matter., Vol. 28, p.483002 (2016)
M. Yan, R. Hertel and C. Andreas, Phys. Rev. B., Vol. 88, p.220405 (2013)



Schematic representation of interconnected cylindrical nanostructures composed of vertical nanowires or nanotubes linked by horizontal interconnects.



Coercive field as a function of the relative vertical position of horizontal interconnects for different nanowire and nanotube network architectures.

DS-03. Interplay of Static Memory and Dynamic Magnetization Effects in Hysteresis Reversal within Electrical Steels

M. Petrun[1], E. Rahmanovic[1], S. Steentjes[2]
[1]FERI, University of Maribor, Maribor, Slovenia, [2]Institute of Electrical Machines (IEM), RWTH Aachen University, Aachen, Germany

The dynamic magnetization of electrical steels is governed by a complex interplay between intrinsic static memory effects and dynamic phenomena associated with micro- and macroscopic eddy currents [1]. In this study, we systematically model and analyze this interaction, with particular focus on the influence of induced internal fields on hysteresis reversal behavior and the resulting power losses in electrical steels.

The macroscopic static memory is well described by Madelung's rules, encompassing hysteresis symmetry, return-point memory, and wiping-out properties [2]. Under (quasi-)static conditions, the Madelung framework accurately captures history-dependent magnetization paths and reversal points, which are essential for pulse-width-modulated voltage excitations typical of contemporary devices. At higher frequencies, additional temporal and spatial distortions arise due to dynamic field diffusion, further modifying magnetization behavior [1]. To date, no systematic studies addressing the coupled macroscopic behavior have been reported, leaving a gap in theoretical understanding and limiting the applicability of existing modeling approaches. Neglecting these interactions results in substantial underestimation of iron losses and misrepresentation of flux dynamics in modern electromagnetic devices.

We propose a coupled modeling framework in which the G2E model [3] is combined with a physics-based parametric magneto-dynamic model including viscosity effects [1]. The resulting field depends on the instantaneous excitation, its rate of change, and the prior magnetization history. Analysis of reversal points (RPs) and minor loops demonstrates that dynamic effects induce shifts of internal RPs, alter loop curvature, and cause frequency- and waveform-dependent deviations from ideal return-point memory (Fig. 1 and 2).

The final presentation will include a detailed discussion on model implementation, experimental validation and results for various types of distorted excitation waveforms in a wide frequency range.

[1] M. Petrun, and S. Steentjes, "Iron-Loss and Magnetization Dynamics in Non-Oriented Electrical Steel: 1-D Excitations Up to High Frequencies," IEEE Access, vol. 8, pp. 4568-4593, 2020-01-01, 2020.
[2] A. Astorino, M. Swaminathan and G. Antonini, "A New Approach for Magneto-Static Hysteresis Behavioral Modeling," in IEEE Transactions on Magnetics, vol. 52, no. 9, pp. 1-14, Sept. 2016.
[3] E. Rahmanovic, and M. Petrun, "Modelling of unit differential reversal curves in the G2E hysteresis model," Physica B-Condensed Matter, vol. 677, Mar 15, 2024.

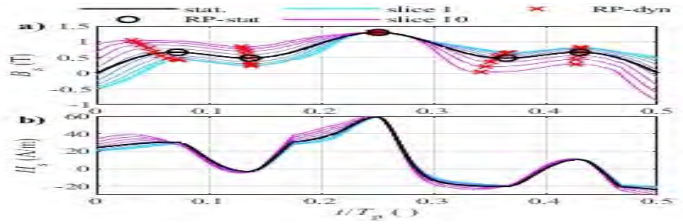


Fig 1. Magnetization waveforms and RPs within NO24 electrical steel comparing static and 100 Hz excitations.

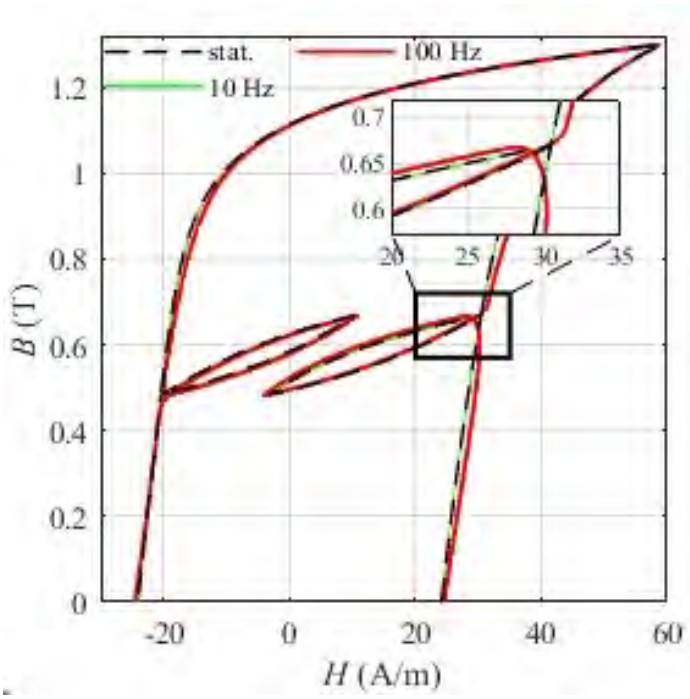


Fig 2. Comparison of corresponding magnetization paths within the hysteresis loop.

DS-04. Demonstration of bit-shifting in vertical domain wall motion memory

D. Jeong[1], F. Ye[1], Y. Shiota[1], R. Hisatomi[1, 2], S. Karube[1], S. Sugimoto[2], S. Kasai[2], T. Ono[1, 3]
[1]Kyoto University, Kyoto, Japan, [2]National Institute for Materials Science, Tsukuba, Japan, [3]Tohoku University, Miyagi, Japan

Domain wall motion memory offers fast and energy-efficient data manipulation, making it a promising candidate for next-generation non-volatile storage. Motivated by these advantages, we propose a vertical multi-bit architecture to realize ultra-high-density memory arrays [1]. In this structure, spin–orbit torque (SOT) is utilized for switching the magnetization of the bottom magnetic layer, while spin–transfer torque (STT) is responsible for shifting the written bits toward the upper magnetic layers. In our previous study, simulations revealed that the vertical structure exhibits both low operating current densities (<10^11 A/m^2) and high thermal stability [2], and the feasibility of data writing and shifting in such a configuration was experimentally demonstrated in a 2-bit memory device [3].
In this presentation, we show the results of controllable data shifting by STT in a 4-bit memory device. Multilayers of Ta (5)/Pt (10)/Co (1.2)/Cu (3)/Co (0.5)/Pt (0.4)/Co (0.5)/Cu (3)/Co (0.5)/Pt (0.4)/Co (0.5)/Cu (3)/Co (0.5)/Pt (0.4)/Co (0.5)/Cu (3)/Pt (3) (unit: nm) on Si-SiO_2 substrate were deposited by magnetron sputtering. Electron-beam lithography was used to pattern pillars device with diameters of 100, 200, and 300 nm and subsequently etched by ion milling system. The magnetization configurations were measured by giant magnetoresistance (GMR) and the anomalous Hall resistance. We observed changes of GMR and anomalous Hall resistance in SOT switching experiments and bit-shift experiments. Our results indicate that current-induced methods enable the implementation of multiple magnetization configurations.
[1] Y. M. Hung et al., Journal of the Magnetics Society of Japan 45, 6 (2021).
[2] Y. M. Hung et al., Applied Physics Express 14, 023001 (2021).
[3] F. Ye et al., IEEE Transactions on Magnetics 61, 3401004 (2025).

DS-05. Gradient Enhanced Physics Informed Neural Networks for Nonlinear Magnetostatic Analysis with Practical Coil Geometries

R. Shahbaz[1], C. Zhang[1], H. Fatima[2], S. Babu[1], A. Rehman[3]
[1]Electrical Engineering, State Key Laboratory of Smart Power Distribution Equipment and System, Hebei University of Technology, Tianjin, Hebei, China, [2]School of Physics, Department of Optical Information Science and Technology, School of Physics, Xidian University, Xia'n, Shaanxi, China, [3]School of Science, Institute of Mathematics, Hebei University of Technology, Tianjin, Hebei, China

Accurate modeling of nonlinear magnetic materials is essential for electrical machines and transformers [1], where magnetic saturation, leakage flux, and practical coil configurations strongly affect performance and efficiency [2]. Although Finite Element Analysis (FEA) provides accurate solutions [3], it often requires high computational cost and limited flexibility for rapid optimization and inverse design [4]. Physics Informed Neural Networks (PINNs) have emerged as promising mesh free alternatives [5], but conventional PINNs often struggle with strongly nonlinear magnetic conditions [6]. This paper presents a Gradient Enhanced Physics Informed Neural Network (gPINN) framework for solving nonlinear magnetostatic problems with practical coil configurations featuring a 60% fill factor. Unlike idealized solid conductor models, the geometry includes insulation thickness, air gaps, and reduced effective current density (J_{eff} = 0.6 A/mm^2), providing a more realistic benchmark. The ferromagnetic cylinder is modeled using a Langevin-type BH characteristic with B_{sat} = 1.8 T, where relative permeability varies from μ_r = 5000 to nearly μ_r = 249 under saturation, producing strong nonlinearity. The reduced peak flux density (B_{max} = 0.982 T versus 1.636 T for the solid conductor case) shifts the operating point deeper into the nonlinear transition region, where convergence becomes more difficult. To address this, gPINN incorporates adaptive loss weighting and residual connections for gradient stability. Validation against high fidelity FEA shows that gPINN achieves a magnetic flux density MAE of 0.0017 T compared to 0.0463 T for vanilla PINN, a 27× improvement, while reducing training epochs from 12,000 to 5,000. These results demonstrate the effectiveness of gPINN for strongly nonlinear electromagnetic problems.
[1] M. Raissi, P. Perdikaris, and G. E. Karniadakis, “Physics-informed neural networks: A deep learning framework for solving forward and inverse problems involving nonlinear partial differential equations,” J. Comput. Phys., vol. 378, pp.

686–707, 2019.
[2] A. Khan and D. A. Lowther, "Physics informed neural networks for electromagnetic analysis," IEEE Trans. Magn., vol. 58, no. 9, pp. 7500404, 2022.
[3] L. Lu, X. Meng, Z. Mao, and G. E. Karniadakis, "DeepXDE: A deep learning library for solving differential equations," SIAM Rev., vol. 63, no. 1, pp. 208–228, 2021.
[4] S. Wang, Y. Teng, and P. Perdikaris, "Understanding and mitigating gradient flow pathologies in physics-informed neural networks," SIAM J. Sci. Comput., vol. 43, no. 5, pp. A3055–A3081, 2021.
[5] O. Noakoasteen, S. Wang, Z. Peng, and C. Christodoulou, "Physics-informed deep neural networks for transient electromagnetic analysis," IEEE Open J. Antennas Propag., vol. 1, pp. 404–412, 2020.
[6] S. Markidis, "The old and the new: Can physics-informed deep-learning replace traditional linear solvers?" Frontiers Big Data, vol. 4, p. 92, 2021.

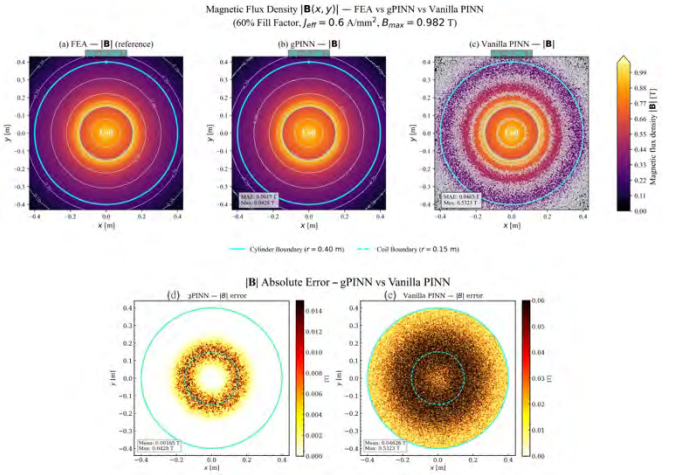


Fig. 1 (a) FEA reference. (b) gPINN: smooth, accurate field (MAE = 0.0017 T). (c) Vanilla PINN: severe gradient noise (MAE = 0.0463 T). (d) gPINN absolute error: concentrated at interface. (e) Vanilla PINN error: 27× larger.

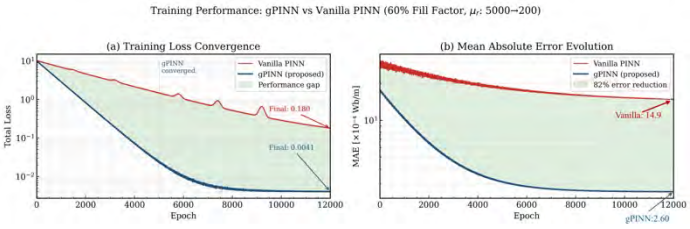


Fig. 2 (a) Total loss: gPINN converges 58% faster with 44× lower final loss. (b) MAE evolution: gPINN maintains 91% lower prediction error. Green shading shows performance gap.

DS-06. A Modified Reversible Field Formulation in Hauser's Energetic Model for Enhanced Hysteresis Modeling of Grain-Oriented Silicon Steel

S. Babu[1, 2], C. Zhang[1, 2], R. Shahbaz[1, 2], R. Saqib Arshad[1, 2], J. Chi[1, 2]
[1]Electrical Engineering, State Key Laboratory of Smart Power Distribution Equipment and System, Hebei University of Technology, Tianjin, Hebei, China, [2]Electrical Engineering, Hebei Key Laboratory of Equipment and Technology Demonstration of Flexible DC Transmission, Hebei University of Technology, Tianjin, Hebei, China

The classical Energetic Hauser model exhibits a fundamental limitation: its constant reversible field scaling factor cannot reproduce field-dependent permeability variations [1], which consequently produces poor hysteresis loop reproducibility across a wide flux density range, as reflected by $R^2 = -0.039$ for initial permeability and an average RMS waveform error of 12.61 mT. Existing extensions of the energetic framework and related variable-parameter hysteresis models improve hysteresis prediction by incorporating dynamic effects, loss mechanisms, and domain-based parameter variations [2], [3], [4], but remain limited in capturing nonlinear magnetic behavior over wide operating conditions. This paper proposes a modification to the reversible field of the Hauser model by introducing a magnetization-dependent scaling term $h_o/(1+\alpha|m|^{\beta})$, where $m = M/M_s$ is the normalized magnetization, which resolves the permeability reproduction issue and significantly improves hysteresis loop reproducibility for Grain-Oriented Silicon Steel (GOSS) under 50 Hz sinusoidal excitation. The modification attenuates the reversible field contribution with increasing magnetization, capturing GOSS saturation-driven permeability reduction. Parameters were identified by two-stage Differential Evolution against experimental B–H loops (50 Hz, 0.1–1.5 T), with numerical state-equation solving ensuring physical consistency. Validation addressed waveform accuracy, core loss prediction, and derived magnetic properties.
The modified model reduces RMS waveform error by 23.1% (12.61 → 9.69 mT) and core loss calculation error by 60.1% (1.62% → 0.65%), with initial permeability correlation improving from $R^2 = -0.039$ to 0.773 and all other metrics at $R^2 > 0.94$. This confirms its effectiveness for hysteresis modeling and core loss prediction.

[1] Hauser, Hans. "Energetic model of ferromagnetic hysteresis: Isotropic magnetization." Journal of applied physics 96, no. 5 (2004): 2753-2767.
[2] Hamimid, Mourad, Souri Mohamed Mimoune, and

Mouloud Feliachi. "Dynamic formulation for energetic model compared with hybrid magnetic formulation of ferromagnetic hysteresis." International Journal of Numerical Modelling: Electronic Networks, Devices and Fields 30, no. 6 (2017): e2225.
[3] Chen, Long, Xin Wen, Tong Ben, Libing Jing, and Qian Liu. "Accurate calculation of global hysteresis properties of grain-oriented silicon steel based on an improved JA model with variable parameters." AIP Advances 13, no. 2 (2023).
[4] Changgeng, Z., Ziran, G., Zhiwei, L., & Yongjian, L. (2025). An improved JA model for iron-based soft magnetic composites considering local demagnetization effect. Journal of Magnetism and Magnetic Materials, 173439.

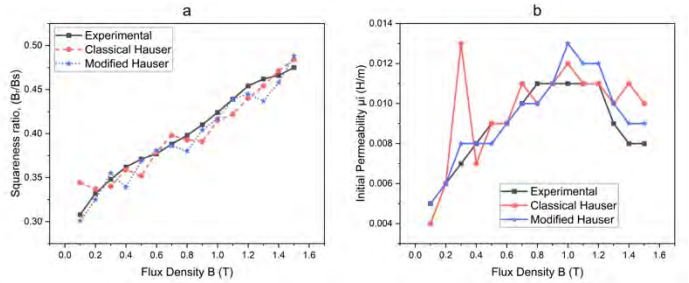


Fig. 1 Modified vs. classical Hauser model for (a) squareness ratio (B_r/B_s, R^2 = 0.9456) and (b) initial permeability (μ_i, R^2 = 0.7733) across 0.1–1.5 T; the classical model yields (R^2= −0.039) for initial permeability.

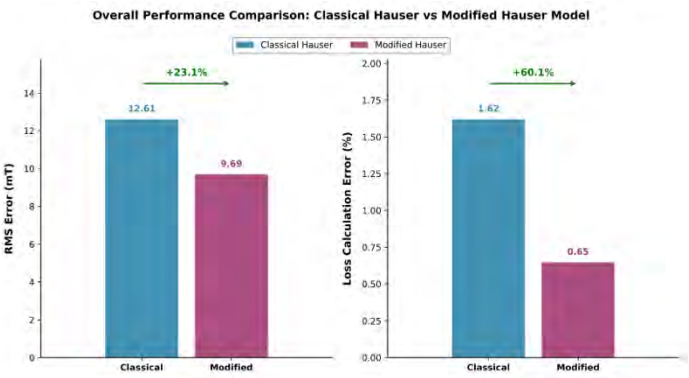


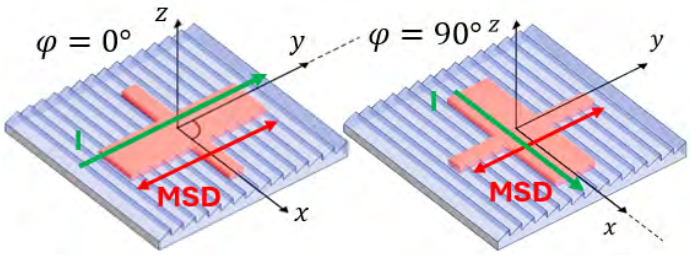
Fig. 2 Model accuracy improvement: RMS waveform error reduced by 23.1% (12.61 → 9.69 mT); core loss calculation error reduced by 60.1% (1.62% → 0.65%).

DS-07. Anisotropic DMI, SOT, and Domain Wall Motion in Pt/Co on Miscut Sapphire Heterostructures

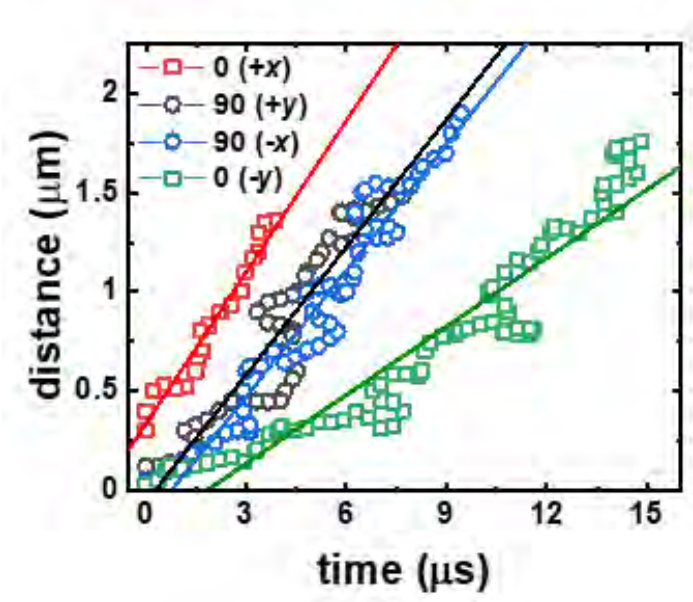
J. Kim[1], S. Kim[1], J. Cho[1], D. Kim[1], J. Cho[2], C. You[1]
[1]Physics and Chemistry, Daegu Gyeongbuk Institute of Science and Technology, Daegu, Gyeongsangbuk-do, Korea (the Republic of), [2]Nanotechnology, Daegu Gyeongbuk Institute of Science and Technology, Daegu, Gyeongsangbuk-do, Korea (the Republic of)

Current-driven domain wall motion is a central phenomenon in spintronics, with its efficiency fundamentally determined by the interplay between spin-orbit torque and interfacial magnetic interactions[1,2]. While substrate-induced symmetry breaking has been shown to modulate interfacial properties, its impact on domain wall dynamics remains largely unexplored. Here, we investigate current-driven domain wall motion in Pt/Co bilayers grown on c-plane sapphire substrates with a controlled 3.25° miscut angle toward the m-plane direction[3].
We first establish through Brillouin light scattering and harmonic Hall measurements that both DMI and SOT efficiency exhibit pronounced azimuthal angle dependence with 180° periodicity[1,4,5].To examine the resulting impact on domain wall dynamics, we define a coordinate system with the x-axis along the miscut direction and employ polar Kerr microscopy[6] to track domain wall displacement under pulsed current injection (J ~ 6.5 × A/m^2, 100 ns pulse width). Experiments are conducted on single bar patterns with currents applied along ±y directions (parallel to MSD, 0° configuration) and ±x directions (perpendicular to MSD, 90° configuration). We observe a striking directional asymmetry: for currents along ±y, domain walls exhibit significantly different velocities depending on current polarity, whereas for currents along ±x, no such asymmetry is observed. This behavior directly reflects the asymmetric step-terrace structure introduced by the substrate miscut. Furthermore, domain walls driven by currents along ±x consistently move faster than those driven along ±y under identical current conditions, correlating with the enhanced SOT efficiency measured along the x-direction. Our distance-time measurements reveal that the substrate miscut not only determines the magnitude of modulated SOT efficiency, iDMI but also controls domain wall velocity response through geometrically asymmetric interfacial structures. These findings establish a direct link between interfacial properties and domain wall dynamics, offering new strategies for optimizing current-driven domain wall devices.
[1] S. S. P. Parkin, M. Hayashi and L. Thomas, *Science*, Vol.

320, p.190 (2008)
[2] T. A. Moore et al., *Appl. Phys. Lett.*, Vol. 93, p.262504 (2008)
[3] S. An et al., *Appl. Phys. Lett.*, Vol. 123, p.062403 (2023)
[4] J. Cho et al., *Nat. Commun.*, Vol. 6, p.7635 (2015)
[5] M. Kuepferling et al., *Rev. Mod. Phys.*, Vol. 95, p.015003 (2023)
[6] I. M. Miron et al., *Nat. Mater.*, Vol. 10, p.419 (2011)



electrical measurement scheme along miscut direction and current.



domain wall time-distance graph.

DS-09. Experimental observation of Walker breakdown of spin-orbit torque driven domain-wall motion in synthetic antiferromagnets

S. Yoon[1], A. Okada[2], S. Choe[1]
[1]Physics and Astronomy, Seoul National University, Seoul, Korea (the Republic of), [2]Samsung Advanced Institute of Technology, Samsung Electronics, Suwon, Korea (the Republic of)

Magnetic domain-wall motion under a constant driving force can be classified into a steady-state regime and a non-steady-state regime. Unlike steady-state domain-wall motion, non-steady-state domain-wall motion is accompanied by time dependent domain-wall velocity and/or the dynamics of the domain-wall internal magnetization. This transition to non-steady-state domain-wall motion is commonly referred to as Walker breakdown (WB). Analytical models of domain-wall motion for a single magnetic layer predict the absence of WB when spin-orbit torque (SOT) is the driving force [1,2]. However, unlike the single magnetic layer case, it has been reported that SOT-driven domain-wall motion in synthetic antiferromagnets (SAFs) exhibits precession of the domain-wall internal magnetization under an applied in-plane magnetic field [3]. In this work, we experimentally demonstrate the occurrence of WB in SOT-driven domain-wall motion in SAFs with perpendicular magnetic anisotropy (PMA), without an applied magnetic field. We counted the cumulative number of current pulses required for a domain wall to travel specified distances using scanning magneto-optical Kerr effect microscopy, and observe a reduction in the average domain-wall velocity under current pulses at higher current densities, consistent with the onset of WB. Our experimental results are consistent with micromagnetic simulations performed using MuMax3.

1. A. Thiaville, S. Rohart and É. Jué, *Europhys. Lett.,* Vol. 100, p.57002 (2012)
2. V. Risinggård and J. Linder, *Phys. Rev. B,* Vol. 95, p.134423 (2017)
3. S.-H. Yang, C. Garg and S. S. P. Parkin, *Nat. Phys.,* Vol. 15, p.543 (2019)

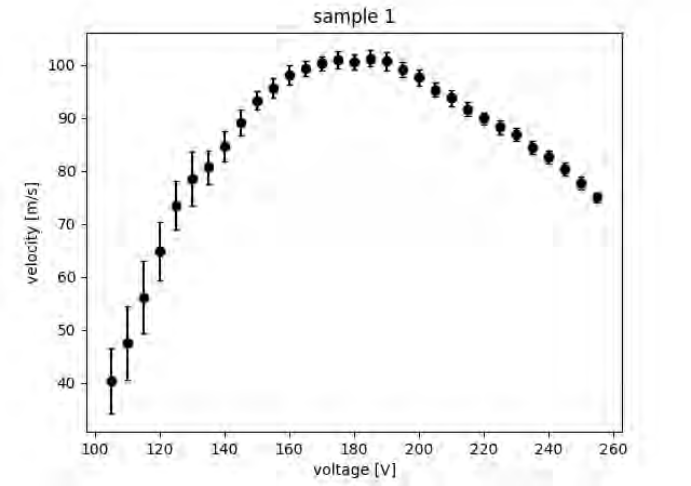


Fig. 1. Domain wall velocity measurement results of SAF sample 1

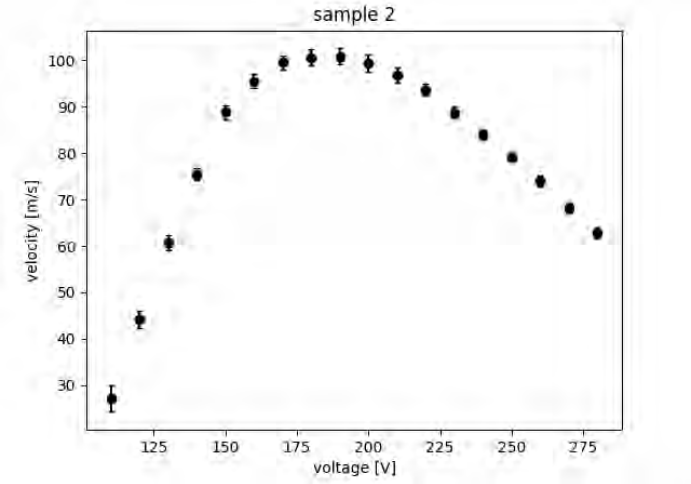


Fig. 2. Domain wall velocity measurement results of SAF sample 2

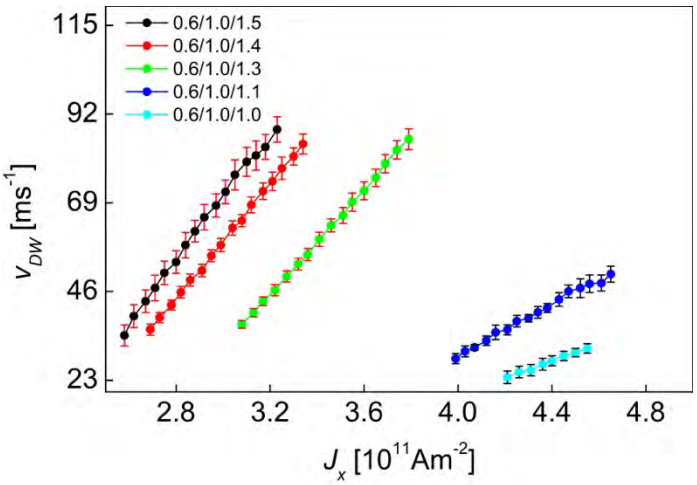
DS-10. Current Density Mapping for Domain Wall Velocity in Pt/Co/Ru/Co/Ta Synthetic Antiferromagnets

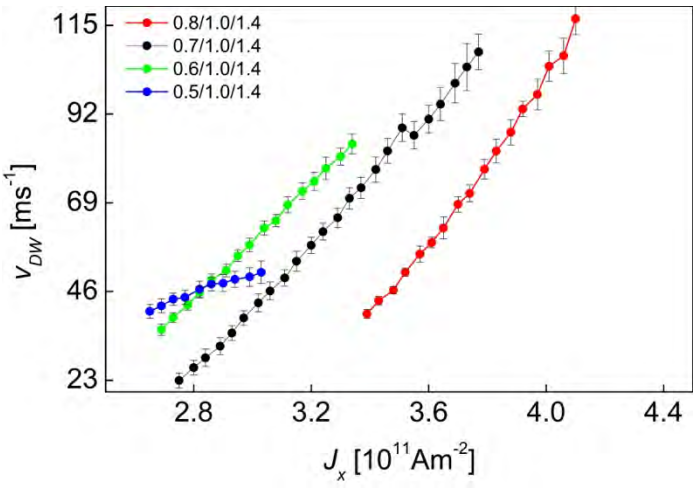
W. Shim, S. Yoon, S. Choe
Department of Physics and Astronomy, Seoul National University, Seoul, Korea (the Republic of)

Current-induced domain wall motion in synthetic antiferromagnets (SAFs) provides a pathway toward high-speed and reliable spintronic devices. SAFs consist of two ferromagnetic layers antiferromagnetically coupled through a nonmagnetic spacer, offering strong resistance to external magnetic fields, enhanced stability, and efficient domain wall dynamics.

In this work, we systematically investigated how the driving efficiency of SAFs can be improved by modulating the thicknesses of the bottom and upper Co layers in Pt/Co/Ru/Co/Ta structures. To clarify the distinct influence of each ferromagnetic layer on the domain wall dynamics, we fabricated a series films on two-dimensional thickness map by independently varying the bottom and upper Co layer thicknesses. We then evaluated the current density required to achieve a fixed domain wall velocity range of 40–80 m/s for each film.

The results show that higher driving efficiency is obtained slightly away from the fully compensated condition between the bottom and upper ferromagnetic layers. This suggests that the two ferromagnetic layers do not contribute equally to the domain wall dynamics. Instead, specific thickness combinations exhibit more efficient driving characteristics by requiring lower current density within the target velocity window. This work provides an effective strategy for optimizing SAF structures for domain-wall-based spintronic applications.





DS-11. Mapping Magnetization Reversal in $Nd_2Fe_{14}B$ Nanoparticles: Coherent-to-Incoherent Transition, Gilbert Damping, and Thermal Effects

J. Lisik[1], A. Terko[1], T. Schrefl[2], E. Girt[1]
[1]Department of Physics, Simon Fraser University, Burnaby, British Columbia, Canada, [2]Center for Modelling and Simulation, University for Continuing Education Krems, Wiener Neustadt, Austria

Predicting nanoparticle performance requires mapping reversal mechanisms and their response to real-world conditions. We present a comprehensive micromagnetic study of single $Nd_2Fe_{14}B$ particles across 13 shapes (5 nm to 1 µm), detailing reversal and isolating the effects of precessional dynamics and thermally-assisted reversal.

We characterize the transition from coherent to incoherent rotation by tracking the standard deviation of magnetic moment angles, σ, during reversal. The critical size where coercivity, H_c, drops below the Stoner-Wohlfarth limit, H_{SW}, does not strictly coincide with the physical onset of incoherent rotation. Particles can exhibit visibly incoherent reversal while maintaining H_c>0.999H_{SW}, provided σ<5° until the average magnetization tilts 25° from the easy axis. As size increases, non-ellipsoids exhibit curling-like reversal before entering a nucleation-and-expansion regime, while ellipsoids develop intricate curling modes, such as unreversed cores pinching off into magnetic “drops” [Fig. 1(a)].

Reducing Gilbert damping from α=1 to 0.1 leaves H_c unchanged but shifts the physical onset of incoherent rotation to smaller sizes [Fig. 1(b)]. Lower damping introduces precessional turbulence, frequently triggering simultaneous reversal of multiple nucleation sites.

Finally, we address thermally-assisted reversal with string-method energy barrier calculations. Without thermal fluctuations, shrinking particles to the coherent limit maximizes H_c. However, this small-size regime is precisely where the energy barrier is low enough for thermal fluctuations to instigate reversal at a reduced coercive field, H_c^{therm} (Fig. 2). Consequently, the maximum achievable H_c^{therm} lies outside the coherent regime for most shapes. While single-particle calculations can approximate weakly-coupled grains, increasing intergranular coupling would raise the energy barrier, potentially allowing a closer approach to H_{SW}.

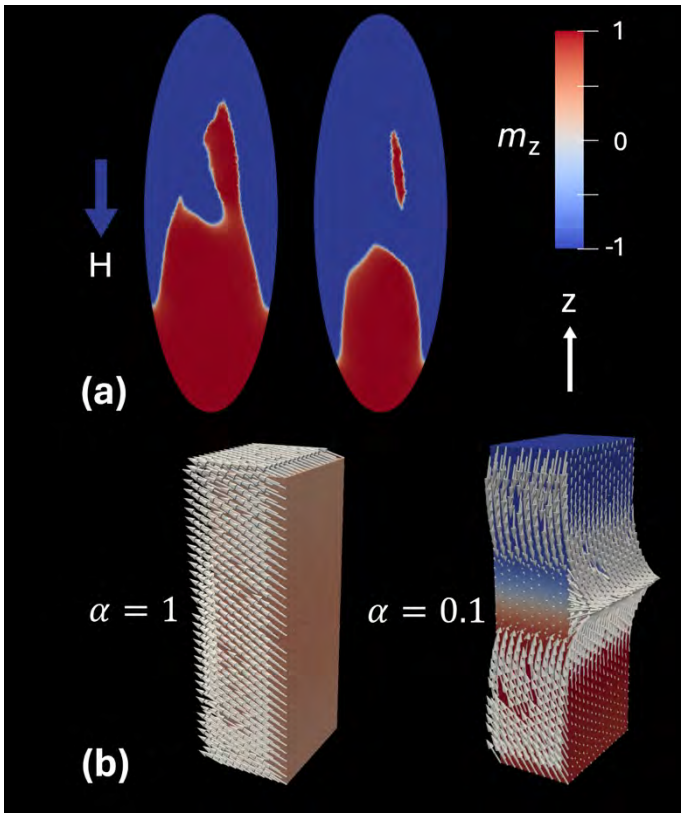


Fig. 1: Reversal snapshots (applied field along -z axis) of (a) 1 µm prolate spheroid cross-section showing a magnetic "drop" and (b) 5 nm rectangular prism at damping 1 (coherent) vs. 0.1 (incoherent).

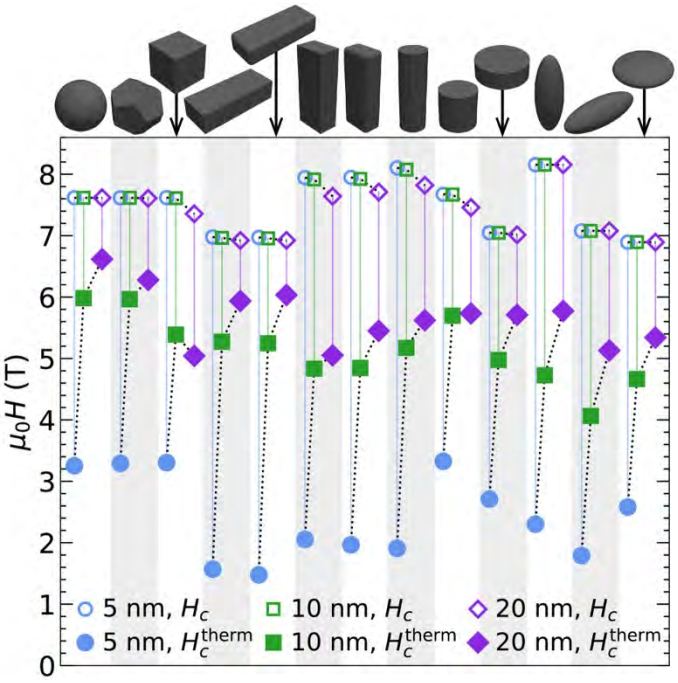


Fig. 2: Coercivity of 13 shapes (5-20 nm) with thermally-assisted reversal (filled) and without (open).

DS-12. Heat Flow Control Model in Isotropic and Anisotropic Nano-Scale Magnetic Systems

C. Westfall, T. Lamichhane
University of Central Oklahoma, Edmond, Oklahoma, United States

Magnetic nanoparticle (MNP) systems enable controllable heat flow at the nanoscale through externally applied fields; however, conventional alternating magnetic fields (AC) produce spatially uniform heating, limiting selectivity. This work develops a heat flow control model for isotropic and anisotropic nanoscale systems by combining AC-driven thermal excitation with a superimposed static magnetic field (DC) that induces nonreciprocal electromagnetic response.

Utilizing systems of particles arranged in linear geometries, near-field radiative heat transfer is modeled through a many-body dipole framework. In the dielectric limit, heat exchange remains reciprocal, yielding symmetric energy transfer between particles. Introducing a DC magnetic bias generates a magneto-optical response with off-diagonal permittivity components, breaking reciprocity, and enabling directional heat flow along the chain.

In isotropic systems, this directional control arises solely from the external magnetic field, producing limited but tunable asymmetry. In contrast, anisotropic nanoparticle configurations enhance field–matter coupling through orientation-dependent polarizability, enabling stronger and more precise localization of heat flow.

This framework demonstrates how the interplay of geometry (rod configuration), magnetic bias, and material anisotropy can be used to engineer spatially selective thermal transport, providing a pathway toward improved control of nanoscale heating in applications such as targeted hyperthermia.

[1] L. Zhu and S. Fan, "Persistent directional current at equilibrium in nonreciprocal many-body near field electromagnetic heat transfer," Physical Review Letters, vol. 117, no. 13, Sep. 2016. doi:10.1103/physrevlett.117.134303

[2] J. S. Googasian, M. P. Perkins, J. Chen, and S. E. Skrabalak, "532- and 52-symmetric au helicoids synthesized through controlled seed twinning and aspect ratio," Nanoscale, vol. 17, no. 8, pp. 4415–4422, 2025. doi:10.1039/d4nr03731f

[3] J. Yang, C. Liu, H. Xie, and W. Yu, "Anisotropic heat transfer properties of two-dimensional materials," Nanotechnology, vol. 32, no. 16, p. 162001, Jan. 2021. doi:10.1088/1361-6528/abdb15

DS-13. Chiral Magnetic Field Generation Using Modified Halbach Arrays for Scalable Functional Materials Design

L. Cosgrove, T. Lamichhane
University of Central Oklahoma, Edmond, Oklahoma, United States

We propose the design and realization of a square chiral magnetic field platform based on a modified Halbach array architecture capable of generating spatially rotating magnetic field vectors with controllable handedness. Inspired by recent demonstrations of quadrupole-field-induced chirality (Yu, Shu-Hong, Natl. Sci. Rev., 2023, 10, nwad221), where spatial variation of magnetic field orientation produces left- and right-handed configurations, this work extends the concept to engineered permanent magnet systems for scalable and robust field generation. The Halbach configuration will be adapted to introduce controlled angular variation in magnetization orientation, enabling continuous rotation of the magnetic field across the

array plane. This approach produces an effective chiral magnetic field characterized by
spatial gradients in both magnitude and direction, analogous to quadrupole-induced
field chirality but realized in a compact, solid-state platform. The magnetic field distribution, vector rotation, and chirality will be quantitatively
designed and optimized using Ansys Maxwell, enabling high-fidelity finite element
simulations of field intensity, directionality, and spatial gradients, consistent with our
prior work (Levi, C. et al., AIP Advances 16, 025146 (2026)). Simulation-guided design
will be used to systematically tailor magnet orientation, array geometry, and boundary
conditions to achieve targeted chiral field profiles while maximizing field uniformity and
strength within the working region.
The resulting system enables deterministic control over magnetic torque, particle
alignment, and field-mediated assembly processes, with potential applications in chiral
materials synthesis, magnetically driven patterning, and advanced functional materials
design. By integrating simulation-driven optimization with experimental validation, the
project establishes a scalable pathway for generating programmable chiral magnetic
environments using permanent magnet architectures.

[1] S.-H. Yu, "Creating chiral superstructures in magnetic quadrupole fields," National Science Review, vol. 10, p. nwad221, 2023.

[2] L. Cosgrove, "Hybrid manufacturing of Halbach arrays using sintered NdFeB magnets and additively manufactured soft magnet frames," AIP Advances, vol. 16, no. 2, p. 025146, 2026, doi: 10.1063/9.0001035.

DS-14LB. Magnetic-Field-Induced Erasure for Magnetoresistive Random Access Memory for Data Sanitization

S. Lindemann[1], J. Parella[1], G. Boyce[1], H. T. Nembach[2], W. K. Peria[2], M. Pufall[2], W. Rippard[2], M. Schneider[2], D. B. Gopman[1]
[1]National Institute of Standards and Technology, Gaithersburg, Maryland, United States, [2]National Institute of Standards and Technology, Boulder, Colorado, United States

Magnetoresistive Random Access Memory (MRAM) is rapidly scaling across wide computing sectors, driven by its unique combination of non-volatility with low access latency, near-zero standby power consumption and high endurance. [1] MRAM adoption now spans radiation-hardened aerospace and thermally-rugged automotive systems [2,3] to enterprise storage architectures [4]. As with many fast-moving emerging technologies, commercial deployment has outpaced technical governance. While early MRAM metrics like MRAM magnetic field immunity are entering standard balloting, hardware security frameworks remain a critical blind spot. The main hardware security standards, NIST 800-88 Rev 2 [5] and IEEE 2883 [6], remain silent on MRAM-specific sanitization requirements.
To bring MRAM into alignment with established hardware security protocols, rigorous data sanitization methods are needed for devices reaching end-of-service or leaving trusted physical boundaries. This work evaluates physical data sanitization via magnetic-field-induced erasure. Magnetic purging (physical sanitization via magnetic field applied to the MRAM package) provides significant benefits over software overwrite: it enables simultaneous batch erasure of multiple devices, functions on physically-damaged or unpowered hardware, and offers a non-destructive pathway for device reuse. We empirically evaluate data erasure effectiveness across commercial MRAM parts as a function of field strength and field angle. This reference data serves as a baseline to inform future revisions of sanitization standards or establishes a standalone documentary standard for MRAM physical purge.

[1] https://www.fortunebusinessinsights.com/magneto-resistive-ram-mram-market-104800
[2] Lee Y.K., et al. Proceedings of the 2018 IEEE Symposium on VLSI Technology. IEEE; New York, NY, USA: 2018. Embedded STT-MRAM in 28-Nm FDSOI Logic Process for Industrial MCU/IoT Application; pp. 181–182.
[3] Montoya, E.A., Chen, JR., Ngelale, R. *et al.* Immunity of nanoscale magnetic tunnel junctions with perpendicular magnetic anisotropy to ionizing radiation. *Sci Rep* 10, 10220 (2020).

[4] https://www.businesswire.com/news/home/20240430370312/en/Next-Generation-IBM-FlashCore-Modules-Feature-Everspins-PERSYST-1-Gigabit-STT-MRAM-Enhancing-Reliability
[5] *Guidelines for Media Sanitization*, NIST SP 800-88 Rev. 2, 2025.
[6] *IEEE Standard for Sanitizing Storage*, 2883, 2022.

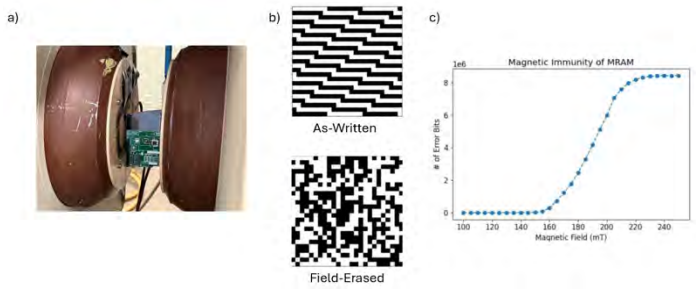


Figure 1: a) Experimental setup for magnetic field erasure of MRAM components. b) Field-induced erasure of byte-wise checkerboard pattern written into MRAM. c) Field-dependence of erased bits showing the onset of magnetic switching of MRAM memory elements.

DS-15LB. Correlation of magnetic materials parameters with degree of atomic ordering in CoFeB MRAM free layers

M. Pufall[1], C. Swindells[2], B. Ravel[3], G. Hu[4], H. T. Nembach[1]
[1]Applied Physics Division, NIST, Boulder, Colorado, United States, [2]Department of Physics, University of Colorado, Boulder, Boulder, Colorado, United States, [3]Materials and Measurement Science Division, NIST, Gaithersburg, Maryland, United States, [4]IBM T.J. Watson Research Center, Yorktown Heights, New York, United States

The free layer in most magnetic random-access memories (MRAM) is based on CoFeB alloys. MRAM performance critically depends on the magnetic properties of the free layer such as magnetic damping, anisotropy, and exchange. Previous work has shown that extended X-Ray absorption fine structure (EXAFS) analysis can estimate the annealing-induced structural order in CoFeB thin films with different capping layers.[1, 2] Using Brillouin Light Scattering (BLS), magnetometry, and ferromagnetic resonance (FMR), we correlate this EXAFS-measured degree of structural order to the change in magnetic parameters including the Heisenberg exchange stiffness, magnetic damping, and magnetic anisotropy. We measured stacks that approximate MRAM free layers, consisting of (thicknesses in nm) TaN(1)/Pt(2)/Co(0.5) /Ta(0.2)/CoFeB(0.3) to mimic the seed layer for MgO growth used in functional stacks, followed by layers of the form MgO(1)/CoFeB(2)/ X(2)/Ru(4)/TaN(4), where the capping layer "X" refers to Nb, W, Ti, MgO.

We show that, as measured by EXAFS, ordering induced by annealing is dependent on capping layer material (see Fig. 1), and correlates with the Boron bond formation enthalpy of the capping material. We then show that exchange stiffness (determined by measuring the spin-wave dispersion manifold using BLS) and saturation magnetization (measured by SQUID-VSM magnetometry) both increase with increasing order (see Fig. 2), consistent with the diffusion of B out of the CoFe lattice. In contrast, the magnetic anisotropy varies in a more complex way with the ordering signature, depending on the capping material, potentially related to the interfacial origin of the anisotropy. In addition, the damping and inhomogeneous broadening show little correlation with ordering, perhaps due to the large roles that spin pumping and interfacial effects, rather than bulk ordering, have on ferromagnetic resonance linewidth in ultrathin films. These results highlight the relationship between the Heisenberg exchange stiffness and the underlying structural order of the ferromagnet and may be of use to guide the materials optimization process in CoFeB-based MRAM.

[1] M. Gottwald, C. Lavoie, J. Jordan-Sweet, S. Brown, G. Hu and B. Ravel, Measurement of CoFeB configurational ordering in magnetic random-access memory stacks using extended x-ray absorption fine structure spectroscopy", J. Vac. Sci & Tech. A, vol. 43, pp 053410-1 - 053410-9, Sept. 2025.
[2] A. K. Rumaiz, J. C. Woicik, W. G. Wang, J. Jordan-Sweet, G. H. Jaffari, C. Ni; J. Q. Xiao and C. L. Chien, "Effects of annealing on the local structure of Fe and Co in CoFeB/MgO/CoFeB tunnel junctions: An extended x-ray-absorption fine structure study", Appl. Phys. Lett., vol. 96, pp. 112502-1 – 112502-3 , March 2010.

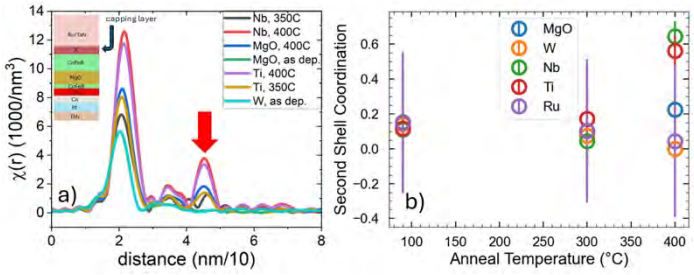


Fig. 1) Fe coordination as probed by EXAFS vs capping layer material. a) Fe-edge coordination response vs. distance. Red

Arrow denotes second shell distance. b) Change in second shell coordination response vs. anneal and capping material.

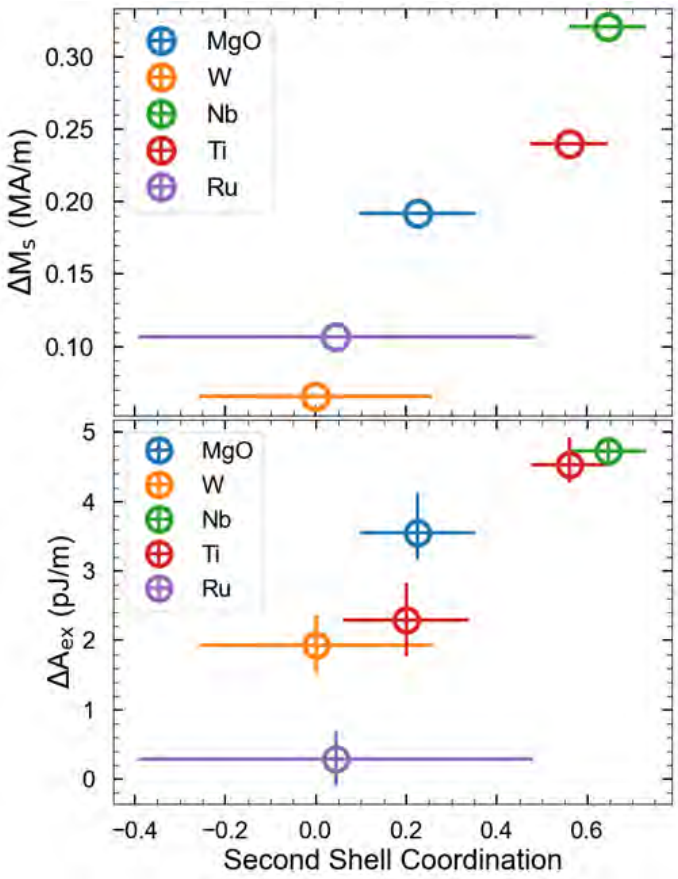


Figure 2: Change in magnetization Ms and exchange Aex vs. Fe second shell coordination signal.

SESSION EA: INTELLIGENT MAGNETIC TECHNOLOGIES: FROM MATERIALS TO SYSTEMS

Co-Chair(s): S. Shreya, *Electrical and Computer Engineering Department, Aarhus University, Aarhus, Denmark* and J. Atulasimha, *Virginia Commonwealth University, Richmond, Virginia, United States*

Thursday, November 5, 2026
08:30 AM-12:00 PM
Coral 3

EA-01. Hybrid Spintronic Neuromorphic Platforms: From Device Physics to brain-inspired Architectures

J. Atulasimha[1, 2]
[1]*Mechanical and Nuclear Engineering, Virginia Commonwealth University, Richmond, Virginia, United States,* [2]*Electrical and Computer Engineering; Physics (courtesy appt.), Virginia Commonwealth University, Richmond, Virginia, United States*

The energy cost of computing is increasing exponentially particularly driven by ever increasing size of neural networks for various complex AI tasks run in data centers. To meet this requirement in a sustainable way, it is imperative that we develop extremely energy efficient computing device technologies and brain inspired computing architectures that can translate device level efficiency into efficiency across the entire computing stack. Such computing technology could also have widespread application IoT devices, where it is important to process data at the edge where both hardware resources and power are extremely limited.

Towards this end, this talk will highlight our work on extremely energy efficient control of nanoscale magnetism, mediated by strain to control domain walls [1], direct voltage control of magnetic anisotropy (VCMA) to create and annihilate skyrmions [2] and magnetoionic control of anisotropy [3]. Leveraging such nanomagnetic devices we will explore two different computing paradigms that are studied in our group: (i) Deep Neural Networks (DNNs), Convolutional Neural Networks (CNNs) and Auto Encoders that can benefit from multiple non-volatile states of nanoscale magnetic devices [4-6] (ii) Reservoir computing that explores the use of nonlinear dynamics and short-term memory in nanomagnet and skyrmion devices to predict or classify time series data [7, 8, 1].

We will then explore experimental realization of such DNNs using domain wall (DW) synapses and the possibility of implementing more complex AI hardware using including

transformers [9]. For reservoir computing, we will discuss futuristic architectures that go beyond simple temporal tasks to classifying spatiotemporal data including from video frames that could make such spintronic reservoirs viable for a range of practical tasks [10]. This will demonstrate the potential of spintronic devices for energy efficient AI hardware in both large scale AI inference such as in data centers as well as in simpler AI inference at the edge.

Acknowledgement: We acknowledge multiple National Science Foundation and Virginia Commonwealth Cybersecurity Initiative grants that funded this work.
[1] Walid Al Misba, et al., ACS Applied Materials & Interfaces, 17, 48, 65946, 2025.
[2] Dhritiman Bhattacharya, et al., Nature Electronics 3, 539, 2020.
[3] Md Mahadi Rajib, et al., Nano Letters, 25, 42, 15369, 2025.
[4] W. Al Misba, et al., IEEE Access, 10, 84946, 2022 [5] S. Dhull, et al. IEEE Transactions on Neural Networks and Learning Systems, 36, 4996, 2025. [6] M. S. Alam, et al., Neuromorph. Comput. Eng. 4 024012, 2024
[7] Md Mahadi Rajib, et al., Neuromorph. Comput. Eng. 2 044011, 2022. [8] Walid Al Misba, et al., IEEE Access, 11, 124725, 2023.
[9] Unpublished. [10] Unpublished.

EA-02. Scaling probabilistic computing for AI and optimization

Q. Shao
ECE, The Hong Kong University of Science and Technology, Hong Kong, Hong Kong

As Moore's Law reaches its limits, CMOS+X (X stands for a CMOS-compatible nanotechnology) architecture emerges as a key direction for future computing. Probabilistic computing is crucial for solving real-world generative AI tasks and combinatorial optimization problems (COPs). The digital CMOS Ising machine is constrained by massive data movement and requirements for pseudo-random number generators (PRNGs) and look-up table (LUT) circuits. The memristor crossbar-based and sMTJ-based Ising machines accelerate deterministic and probabilistic computing, respectively. However, conventional mix-signal CMOS+X schemes introduce additional overheads, such as DACs or ADCs, and the requirement of P-bits sampling. Here, we present our generative AI hardware and fully analog in-memory annealing Ising machine based on CMOS-integrated voltage-controlled magnetic anisotropy magnetic tunnel junction (VCMA-MTJ), developed through a device-circuit-system co-design approach to address bottlenecks in traditional digital CMOS and mixed-signal CMOS+X Ising machines. We leverage the VCMA effect to control the energy barrier of the VCMA-MTJ, enabling it to function as either a C-bit (stable storage for the coupling weight) or a P-bit. For the general AI hardware, we use in-memory computing to perform the multiply-accumulate (MAC) operation and random dropconnect method to emulate stochastic neural equations in situ with external P-bit sampling and transfer. For analog Ising machine (Fig. 1), we directly implement the matrix-vector multiplication between the spin and coupling vector within the array, eliminating the need for P-bit sampling. We fabricated a VCMA-MTJ array chip integrated with 28-nm CMOS technology and developed a fully analog in-memory annealing Ising machine prototype. We validated the functionality and analyzed the performance of the proposed Ising machine using a 32-node Max-Cut problem.
Acknowledgement: This research was supported by ACCESS – AI Chip Center for Emerging Smart Systems, sponsored by the InnoHK initiative of the Innovation and Technology Commission of the Hong Kong Special Administrative Region Government, TRS (T46-705/23R), VP2020S25EG15, and NSFC Cat B (62522410).
References:
[1] Cryogenic in-memory computing using magnetic topological insulators, Nature Materials 24, 559–564 (2025)
[2] In-Memory Neural Stochastic Differential Equations with Probabilistic Differential Pair Achieved by In-Situ P-Bit Using CMOS Integrated Voltage-Controlled Magnetic Tunnel Junctions, 2024 IEEE International Electron Devices Meeting (IEDM)
[3] Spintronic foundation cells for large-scale integration, Nature Reviews Electrical Engineering, 2024
[4] Spintronic memristors for computing, npj Spintronics, 2025.
[5] Fully Analog In-Memory Annealing Ising Machine with Unified Deterministic and Probabilistic Computing Array Using CMOS-integrated VCMA-MTJ, 2025 IEEE International Electron Devices Meeting (IEDM)

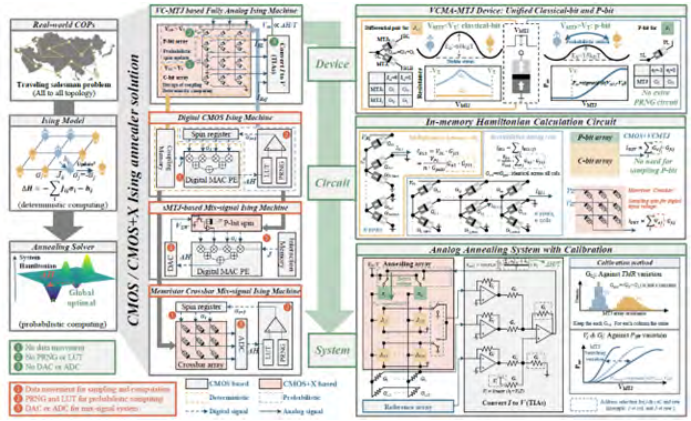


Figure 1: Overall architecture of the proposed fully analog in-memory annealing Ising machine based on CMOS-integrated VCMA-MTJ.

EA-03. Harnessing Magnetization Dynamics for Energy-Efficient Spintronic Intelligent Computing: A Device-to-Circuit Perspective

S. Shreya

Electrical and Computer Engineering Department, Aarhus University, Aarhus, Denmark

Spintronic devices such as magnetic tunnel junctions and spin nano-oscillators exhibit rich magnetization dynamics, including stochastic switching, nonlinear behavior, and phase-coherent oscillations arising from thermal fluctuations and spin-transfer effects. While these phenomena are often treated as limitations, they offer unique opportunities for enabling probabilistic, neuromorphic, and oscillatory computing paradigms [1-2]. However, a key challenge remains: stochasticity, phase noise, and device variability are not yet sufficiently understood or modeled to support reliable circuit- and system-level design.

In this work, I present a physics-informed device-to-circuit framework that systematically links nanoscale magnetization dynamics to functional computing primitives [3]. I first discuss stochastic switching in magnetic tunnel junctions and phase noise in vortex-based oscillators, highlighting critical issues such as temporal correlations, amplitude–phase coupling, and device-to-device variability. Building on this, I introduce compact, EDA-compatible models that incorporate stochastic and nonlinear dynamics beyond conventional white-noise approximations [4, 5]. Finally, I demonstrate how these models enable circuit-level exploration, including probabilistic random number generation, neuron-like dynamics for neuromorphic computing, and synchronization in oscillatory neural networks. The results show how controlled magnetization dynamics can be harnessed as computational resources rather than limitations. This work establishes a scalable pathway toward energy-efficient spintronic hardware for edge intelligence by bridging fundamental magnetic physics with system-level functionality.

1. Sandeep Soni et al 2025 Neuromorph. Comput. Eng. 5 034001
2. B. Sharma, et al., IEEE Open Journal of Nanotechnology, vol. 6, pp. 44-50, 2025.
3. R. K. Raj, S. H. Jony, P. Sengupta and S. Shreya, 2026, *IEEE Magnetics Letters*, doi: 10.1109/LMAG.2026.3685158
4. S. Soni *et al.*, *IEEE Transactions on Magnetics*, vol. 61, no. 9, pp. 1-5, Sept. 2025, Art no. 7001105,
4. R.K. Raj, R. S. Verma, S. H. Jony, S. Saini, and S. Shreya, Journal of Magnetism and Magnetic Materials, Vol. 648, 2026, 174022.

EA-04. Elliptical Voltage-Controlled Magnetic Tunnel Junctions for Probabilistic Computing

J. G. Athas[1], C. Duffee[1], E. Raimondo[2], N. Davila[3], J. Katine[3], G. Finocchio[2], P. Khalili Amiri[1]

[1]Electrical and Computer Engineering, Northwestern University, Evanston, Illinois, United States, [2]Department of Mathematical and Computer Sciences, Physical Sciences and Earth Sciences, University of Messina, Messina, Italy, [3]Western Digital Corporation, San Jose, California, United States

Probabilistic computing paradigms require energy-efficient, high-throughput hardware capable of both deterministic switching and controlled stochastic behavior [1-2]. Voltage-controlled magnetic anisotropy (VCMA) in perpendicular magnetic tunnel junctions (V-MTJs) has been widely explored due to its low-power, voltage-driven operation. However, conventional circular V-MTJs face several limitations. These include rotational in-plane symmetry, resulting in the need for external bias magnetic fields [3-4], and metastable switching pathways, resulting in cycle-to-cycle variations. Here, we present shape engineering as a strategy to overcome these challenges by investigating elliptical V-MTJs, where a preferred in-plane axis modifies the magnetic energy landscape and improves device dynamics.

We experimentally study voltage-driven switching dynamics and observe field-free precessional relaxation into the in-plane state enabled by the modified energy landscape. Compared to circular devices, elliptical V-MTJs exhibit more

well-defined relaxation trajectories. Distinct dynamical regimes are identified as a function of voltage, including direct in-plane relaxation and in-plane precessional motion prior to relaxation (Fig. 1), enabling fast, controllable switching without external fields.
These dynamics are further leveraged to implement a voltage-pulse-driven random number generator (RNG). Operating at the precessional regime edge, elliptical V-MTJs generate high-throughput stochastic bitstreams with reduced bias and improved statistical robustness.
Integration with a p-computing solver shows comparable or improved solution quality with reduced hardware footprints (Fig. 2).
These results establish shape engineering as a powerful design parameter for VCMA-based spintronic devices, enabling improved control over deterministic and stochastic behavior. Elliptical V-MTJs enable field-free operation, reduce bias, and enhance dynamic control, making them strong candidates for probabilistic computing hardware.
[1] C. Duffee, J. Athas, P. Khalili Amiri, Nature Electronics, Vol. 8, pp. 784-793 (2025)
[2] Y. Shao, C. Duffee, P. Khalili Amiri, Nanotechnology, Vol. 34, p. 495203 (2023)
[3] J. Athas, C. Duffee, P. Khalili Amiri, IEEE Electron Device Letters, Vol. 46, no. 9, pp. 1549-1552 (2025)
[4] Y Shao, V. Lopez-Dominguez, P. Khalili Amiri, Advanced Materials Technologies, Vol. 8, p. 2300676 (2023)

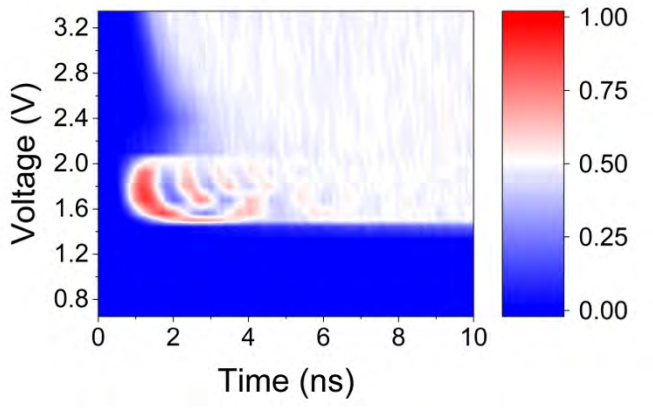


Fig. 1, Simulation results of an elliptical V-MTJ's switching probability under voltage pulses of varying amplitude and duration.

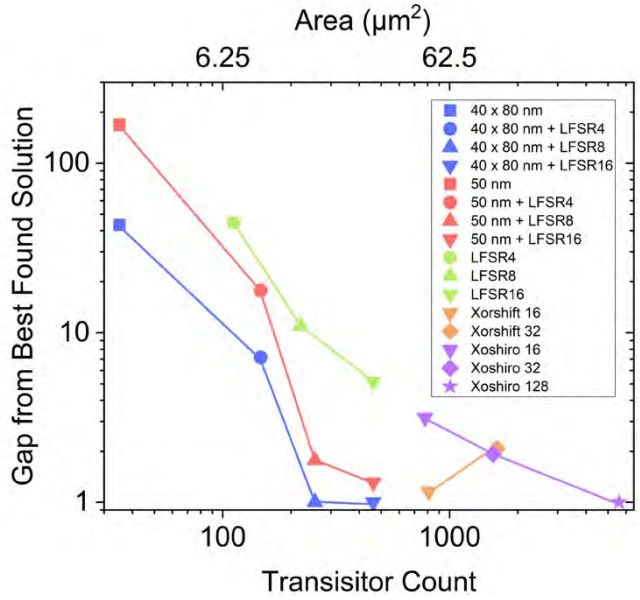


Fig. 2, Probabilistic computing solver results of a MAXCUT problem comparing hardware RNGs.

EA-05. Comparison of Ferrimagnetic and Antiferromagnetic Tunnel Junctions for High-Speed Random Bitstream Generation

A. N. Chin, S. B. Hamid, J. C. Incorvia
Electrical and Computer Engineering, The University of Texas at Austin, Austin, Texas, United States

Magnetic tunnel junctions (MTJs) are entropy sources for true random number generators (TRNGs) due to their intrinsic stochastic magnetization dynamics [1]. However, ferromagnetic MTJs (FMTJs) based implementations are limited to the GHz range because of ferromagnetic resonance [1]. Recent reports of tunnel magnetoresistance (TMR) in both ferrimagnetic (Fi-MTJ) [2] and antiferromagnetic (AFMTJ) tunnel junctions [3] suggest a path to faster devices, but their performance as beyond GHz entropy sources has not yet been evaluated.
Here, we present a comparison of Fi-MTJ and AFMTJ devices with FMTJs as a baseline [4]. The magnetization dynamics of each MTJ is modeled using a macrospin framework based on the Landau-Lifshitz-Gilbert (LLG) equation tailored to the physics of each MTJ [5]. For Fi-MTJs, two opposing sublattices (*A* and *B*) are modeled. AFMTJs are modeled using three exchange-coupled sublattice moments 120° relative to each other.
The resulting coupled LLG equations are then solved numerically. Randomness is evaluated using NIST SP 800-

22 statistical tests [6]. Fi-MTJ and AFMTJ sustain randomness up to 2 and 20 GHz, corresponding to >25× and >100× higher sampling rates, respectively, than FMTJs. The speed advantage of Fi-MTJ and AFMTJ is further utilized for solving an Ising optimization problem where networks of interconnected MTJ-based *p*-bits are used to minimize an Ising Hamiltonian. In both cases, AFMTJ-based implementation exhibits the fastest convergence (~5 ns for 16-spin) followed by Fi-MTJ (~25 ns) and then FMTJ (~900 ns). We benchmark energy per bit and throughput for different technologies, demonstrating a pathway toward high-speed, energy-efficient hardware TRNGs and probabilistic computing.

[1] Z. Fu, Y. Tang and X. Zhao, *Front. Phys.* 9, 638207 (2021). [2] M. Yunokizaki, T. Hibino and H. Idzuchi, *Jpn. J. Appl. Phys.* 64(1), 010904 (2025). [3] J. Shi, S. Arpaci and V. Lopez-Dominguez, *Adv. Mater.* 36(24), 2312008 (2024). [4] S. B. Hamid, A. N. Chin, J. A. C. Incorvia, *IEEE T-ED* (2026, In preparation) [5] Z. Wang, W. Zhao and E. Deng, *J. Phys. D: Appl. Phys.* 48(6), 065001 (2015). [6] A. Rukhin, J. Soto and J. Nechvatal, No. NISTSP80002. (2001).

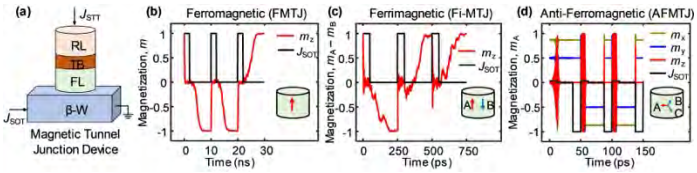


Fig. 1: (a) Schematic of an MTJ device with spin transfer torque (STT) and spin orbit torque (SOT) inputs. (b-d) Modeled free layer (FL) dynamics for (b) FMTJ, (c) Fi-MTJ, and (d) AFMTJ in response to periodic SOT pulses. Insets show sublattice moments of FL in each device.

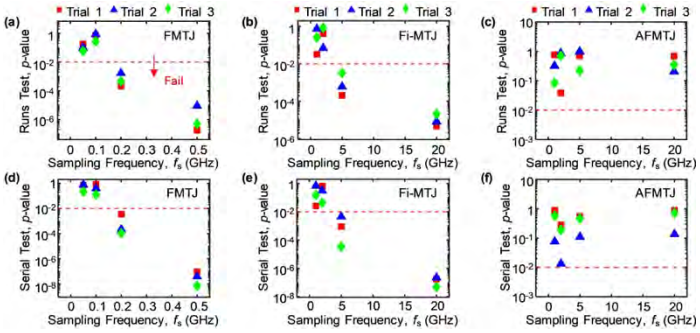


Fig. 2: (a-c) Runs test and (d-f) Serial test metrics from 20,000 bits for (a, d) FMTJ, (b, e) Fi-MTJ, and (c, f) AFMTJ at different sampling frequencies. The dashed red line (p = 0.01) indicates the pass–fail threshold for randomness.

EA-06. Infomorphic Computing Enabled by Spintronic Devices Toward Localized and Interpretable Machine Learning

Z. Teng[1, 2], J. Chen[1, 2], Y. Zhao[1, 2], Y. Zhang[1, 2], H. Li[1], Z. Xiao[3], Q. Shao[3], Y. Yao[1, 2], H. Zhang[4], H. Liu[4], S. Peng[1, 2], S. Li[1, 2], W. Zhao[1, 2]

[1]School of Integrated Circuit Science and Engineering, Beihang University, Beijing, China, [2]National Key Lab of Spintronics, Institute of International Innovation, Beihang University, Hangzhou, China, [3]Department of Electronic and Computer Engineering, The Hong Kong University of Science and Technology, Hong Kong, China, [4]Truth Memory Corporation, Beijing, China

Infomorphic computing, grounded in partial information decomposition, offers a unified and mathematically interpretable framework for neuron-autonomous local learning[1,2]. Its neuronal units operate through dual-input, nonlinear and tunably stochastic dynamics, inherently eliminating the cross-layer error propagation and associated energy overhead of backpropagation[3,4]. However, the lack of hardware primitives that natively embody these dynamics remains a critical bottleneck, preventing its intrinsic algorithmic advantages from translating into practical hardware efficiency.

Here, we demonstrate, to our knowledge, the first physical infomorphic neuron using CMOS-compatible spintronic devices, specifically voltage-gated spin-orbit-torque magnetic tunnel junctions (VGSOT-MTJs). We show that the device physics maps natively onto core information-theoretic operations, establishing what we define as Infomorphic Nonlinear Probabilistic Activation (INPA): the SOT current and gate voltage encode receptive (R) and contextual (C) signals, respectively, jointly modulating the MTJ switching probability to yield a probabilistic binary output. Using this native primitive, we build spintronic infomorphic neural networks (SINN) capable of supervised learning, unsupervised learning, and associative memory tasks with fully local updates, requiring only ~0.5% of the update computation compared to BP in the same task. At the device level, each INPA operates at the picojoule-per-update level (~15.86 pJ, 1.6 ns).

This work establishes a scalable hardware foundation for infomorphic computing, positioning spintronics as a key enabler for next-generation energy-efficient machine intelligence with clear mathematical interpretability and minimal resource overhead.

1. Wibral, M., Priesemann, V. and Kay, J. W. Partial information decomposition as a unified approach to the

specification of neural goal functions. *Brain Cogn.* 112, 25–38 (2017).
2. Gutknecht, A. J., Wibral, M. and Makkeh, A. Bits and pieces: understanding information decomposition from part-whole relationships and formal logic. *Proc. R. Soc. Math. Phys. Eng. Sci.* 477, 20210110 (2021).
3. Lillicrap, T. P., Santoro, A. and Hinton, G. Backpropagation and the brain. *Nat. Rev. Neurosci.* 21, 335–346 (2020).
4. Rudin, C. Stop explaining black box machine learning models for high stakes decisions and use interpretable models instead. *Nat. Mach. Intell.* 1, 206–215 (2019).

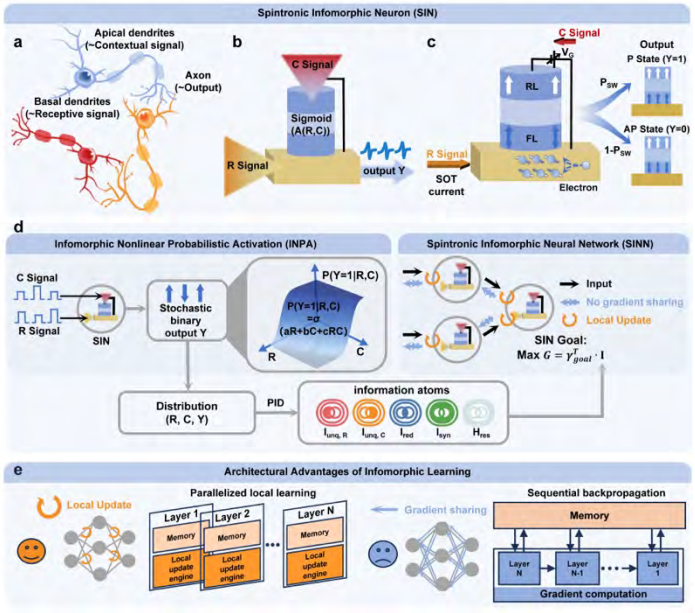
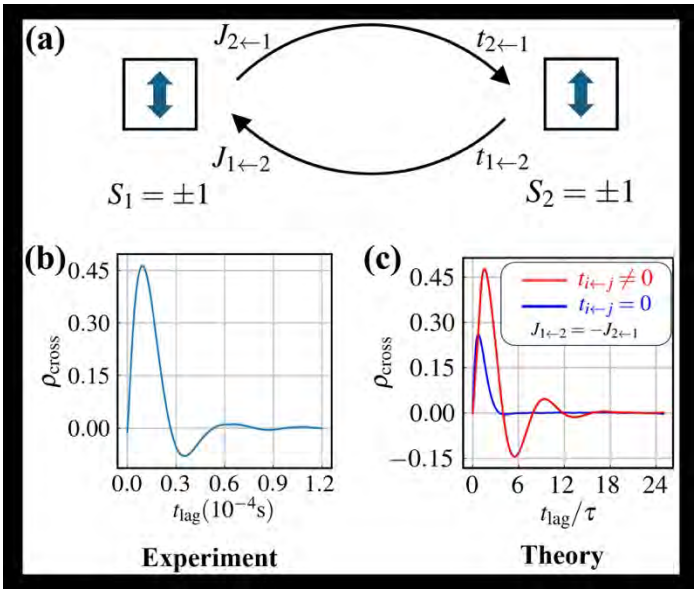


Fig. 1. Spintronic infomorphic neuron and network architecture

EA-07. Physical Ising Machines with Asymmetric and Time-Delayed Interactions

H. Zhang[1, 2], S. Gibeault[3, 2], M. Daniels[4], P. Talatchian[5], U. Ebels[5], A. Madhavan[4], M. Stiles[4]
[1]School of Engineering and Applied Science, The George Washington University, Washington, District of Columbia, United States, [2]Associate, Physical Measurement Laboratory, National Institute of Standards and Technology, Gaithersburg, Maryland, United States, [3]Institute for Research in Electronics and Applied Physics, University of Maryland, College Park, Maryland, United States, [4]Physical Measurement Laboratory, National Institute of Standards and Technology, Gaithersburg, Maryland, United States, [5]Univ. Grenoble Alpes, CEA, CNRS, Grenoble INP, SPINTEC, Grenoble, France

Ising machines based on interacting two-state spins have emerged as powerful hardware platforms for solving NP-hard optimization problems. However, existing Ising machines assume instantaneous and symmetric interactions, although such assumptions may be violated in realistic systems. In many physical implementations, such as those based on superparamagnetic tunnel junctions (SMTJs), signals carrying the information of Ising spins propagate with finite delay, and interactions are naturally asymmetric. How these non-idealities reshape the behavior of Ising machines remains an open and critical question.
With two physical SMTJs, we show that asymmetric and time-delayed interactions qualitatively transform the dynamics of Ising machines, leading to phenomena that cannot be observed in conventional models. We develop a statistical framework based on discrete-time, higher-order Markov processes explicitly capturing memory effects induced by delayed interactions. Our key results are twofold. First, we demonstrate that fully antisymmetric interactions alone can drive oscillatory dynamics, even in the absence of time delay. Second, time delay can enhance these temporal oscillations, in agreement with experimental observations (See Fig. 1). At the same time, we find the counterintuitive result that, despite significant correlations found with long time delays, the probability of each spin state is independent of the coupling strength. These findings establish time delay as a powerful, previously overlooked control parameter in Ising machines rather than a limitation. This enables access to new dynamics and computational behaviors that are inaccessible in conventional, instantaneous models, and connects Ising machines to more general classes of statistical and neural network models.



(a) Two coupled SMTJs representing Ising spins S_i with asymmetric interactions $J_{i\leftarrow j}$ and delay times $t_{i\leftarrow j}$. (b) and (c) are experimental and theoretical cross-correlation functions between two spins with antisymmetric coupling. τ is the intrinsic time of spins. The blue (red) curve in (c) corresponds to instantaneous (time-delayed) interactions.

EA-08. Ultra-fast P-bits for Combinatorial Optimization using Voltage-controlled Magnetic Tunnel Junctions

Y. Zhang[1], S. Li[1], A. Lee[2], Z. Liu[1], Z. Chen[1], Y. Yao[1], H. Zhang[3], H. Liu[3], S. Peng[1], W. Zhao[1]

[1]Beihang University, Beijing, China, [2]InstonTech, Suzhou, China, [3]Truth Memory Corporation, Beijing, China

Physics-inspired Ising machines (IMs) have emerged as promising hardware alternatives to conventional von Neumann architectures for solving computationally intensive combinatorial optimization problems (COPs) [1]. Among various IM paradigms, probabilistic IMs based on spintronic devices—such as magnetic tunnel junctions (MTJs)—have attracted increasing attention due to their demonstrated hardware efficiency, where MTJs naturally serve as probabilistic bits (p-bits) implementing in-situ Ising spins. However, most prior probabilistic IMs rely on spin-torque-driven switching, typically requiring large electric currents, which fundamentally limits scalability and energy efficiency.

To overcome these challenges, we propose a new IM approach that exploits the voltage-controlled magnetic anisotropy (VCMA) effect in MTJs, enabling ultra-fast, energy-efficient, and scalable Ising machine implementations. In an IM, interacting spins dynamically evolve toward the ground state, and spin flipping can be emulated by Glauber-like dynamics exhibiting sigmoidal probabilistic behavior characteristic of p-bits. Leveraging experimental observations that the switching probability of voltage-controlled MTJs (VC-MTJs) follows a sigmoid function of the applied voltage pulse width (0.3-1 ns) or amplitude (1-2.2 V), we employ VC-MTJs as in-situ p-bits. To validate this VC-MTJ-based IM hardware, we fabricated 96-Kb voltage-controlled magnetoresistive random-access memory chips using a 40-nm complementary metal-oxide-semiconductor (CMOS) process. The resulting CMOS-integrated VC-MTJ-based IM (Figure 1) demonstrates sub-nanosecond spin updates with ultra-low energy consumption (< 40 fJ/bit) on-chip [2]. Using routing-type COPs with rugged energy landscapes as benchmarks, we demonstrate solutions to the traveling salesman problem and the Steiner minimum tree problem, achieving up to 100× speedup, 100× reduction in energy consumption, and 3-22× improvement in solution quality compared with state-of-the-art Ising machines.

[1] N. Mohseni, Nat. Rev. Phys. 4, 363 (2022).
[2] Y. Zhang, et al., http://arxiv.org/abs/2505.19106.

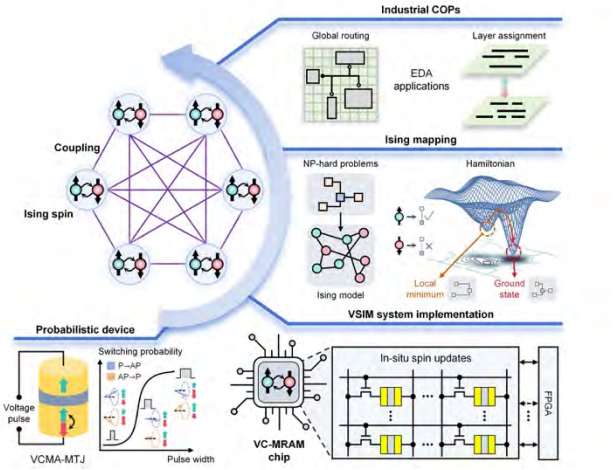


Figure 1: Overview of our voltage-controlled spintronic Ising machine.

EA-09. Wearable Magnetic Sensing for Human Activity Recognition via Deep Learning

S. Rana Muhammad, D. Divyanshu, S. Suhail Mutawakkil, S. Amara, H. Bagci, G. Setti
CEMSE, KAUST, Thuwal, Saudi Arabia

Wearable muscle monitoring has traditionally relied on such as surface electromyography (sEMG), force myography, and mechanomyography, each with limitations related in noise sensitivity, electrode placement, or mechanical coupling [1]–[4]. Magnetic sensing has emerged as a promising non-invasive alternative, though challenges in sensitivity, noise, and system design remain [5].

In this work, we present a wearable magnetic-sensing system for activity recognition, integrated into a flexible belt with a dense array of triaxial Hall-effect sensors positioned along the human backbone. The array captures motion-induced magnetic field variations from the lumbar muscle activity, producing structured spatiotemporal signatures. We segment the acquired signals into temporal windows and apply normalization, magnitude extraction, and temporal difference features to improve class separability. A lightweight Long Short-Term Memory (LSTM) network then models temporal dependencies to classify five activities: standing straight, left twist, right twist, forward bend, and backward bend. We adopt a stratified file-level cross-validation strategy, where splits are made at the recording-file level to prevent data leakage across windows, to ensure robust evaluation. The model achieves a mean validation accuracy of 94.64% ± 6.90% and a macro F1-score of 95.01% ± 6.01%. The normalized confusion matrix confirms strong classification reliability across all five activities, with only notable confusion occurring between the forward bend and right twist due to partially overlapping motion patterns.

The proposed approach demonstrates compact Hall-effect sensor arrays, combined with lightweight temporal deep learning, offer a viable path to accurate wearable activity recognition. It provides a noninvasive, low-power, and privacy-preserving alternative for wearable motion analysis, with potential applications in rehabilitation, healthcare monitoring, and human–machine interaction.

References

M. Al-Ayyad, H. A. Owida, R. De Fazio, B. Al-Naami, and P. Visconti, "Electromyography monitoring systems in rehabilitation: A review of clinical applications, wearable devices and signal acquisition methodologies," *Electronics*, vol. 12, no. 7, p. 1520, 2023.

M. M. Yassin, M. N. Saad, A. M. Khalifa, and A. M. Said, "Advancing clinical understanding of surface electromyography biofeedback: bridging research, teaching, and commercial applications," *Expert Rev. Med. Devices*, vol. 21, no. 8, pp. 709–726, 2024.

N. Schäfer *et al.*, "Wearable ferroelectret sensors for muscle activity measurements," in *2024 IEEE Ultrasonics, Ferroelectrics, and Frequency Control Joint Symposium (UFFC-JS),* 2024, pp. 1–4.

M. A. Islam, K. Sundaraj, R. B. Ahmad, N. U. Ahamed, and M. A. Ali, "Mechanomyography sensor development, related signal processing, and applications: A systematic review," *IEEE Sens. J.,* vol. 13, no. 7, pp. 2499–2516, 2013.

A. Prakash, N. Sharma, A. K. Katiyar, S. K. Dubey, and S. Sharma, "Magnetic-based detection of muscular contraction for controlling hand prosthesis," *Sens. Actuators A Phys.,* vol. 344, no. 113709, p. 113709, 2022.

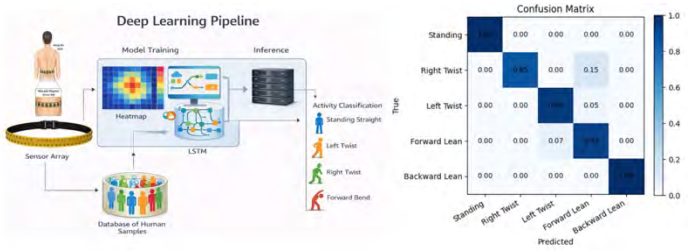


Fig1: a) Overview of the proposed wearable magnetic sensing system.b) Normalized confusion matrix obtained using out-of-fold predictions across five activities.

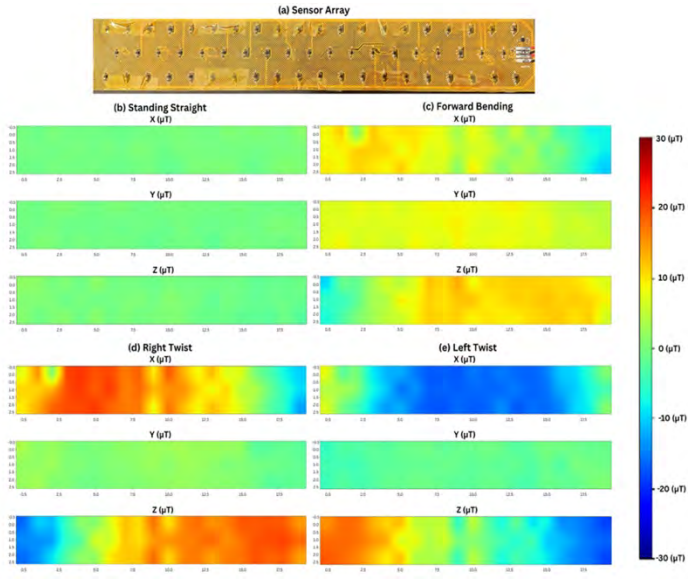


Fig2:a) Flexible sensor array. b–e Heatmaps for different motion classes, showing the 3-axis signals.

SESSION EB: FRONTIERS IN MAGNETIC REFRIGERATION ACROSS SCALES: MATERIALS, MECHANISMS AND DEVICES
Chair(s): S. Säubert, *kiutra GmbH, Munich, Bayern, Germany*
Thursday, November 5, 2026
08:30 AM-12:00 PM
Coral 5

EB-01. Continuous Adiabatic Demagnetization Refrigeration at Scale: Components, Architecture, and Performance Milestones toward Quantum-Ready Millikelvin Cooling
P. Schüßler, A. Kinast, R. A. Chandavar, A. Wendl, J. Rothe, J. Spallek, S. Säubert
kiutra GmbH, Munich, Germany

Millikelvin refrigeration is a foundational enabler of quantum technologies, yet today's dominant approach---helium-3-based dilution refrigeration---faces fundamental scalability constraints as quantum hardware grows in size and complexity. Continuous adiabatic demagnetization refrigeration (cADR) offers a compelling helium-3-free alternative, but realizing its potential at scale demands both a deep understanding of component physics and a rethinking of system architecture.

We present the development of a next-generation cADR platform targeting 20 µW of cooling power at 20 mK, performance on par with state-of-the-art dilution refrigerators and an order-of-magnitude advance over previous cADR demonstrations. Achieving this requires systematic advances across all critical ADR components. We discuss the development and characterization of new magnetocaloric refrigerant packages, improvements to superconducting and mechanical heat switches, and thermal interface engineering, where contact conductance at millikelvin temperatures represents a key bottleneck limiting overall cooling efficiency.

These component developments are guided by and integrated within a comprehensive numerical model of the full cADR cycle and experimentally validated on a dedicated millikelvin test platform. The combined simulation and experimental results yield new insight into cADR component properties, enabling predictive optimization beyond empirical iteration. Building on these results, we outline a modular cADR architecture concept designed to support large-scale quantum infrastructure, where multiple cooling modules can be combined to meet the demands of next-generation quantum devices. Together, the component advances, validated modeling framework, and architectural vision establish a credible and scalable path for magnetic refrigeration from the lab to industry scale.
P. Schüßler, R.A. Chandavar, S.I. Borjeni, et al., *Review of Scientific Instruments*, *97*(2), (2026)

EB-02. Magnetocaloric materials for cryogenic application
X. Tang, H. Sepehri-Amin
National Institute for Materials Science, Tsukuba, Ibaraki, Japan

Magnetic refrigeration (MR) based on the magnetocaloric effect (MCE) can, in principle, surpass conventional gas-compression cooling at cryogenic temperatures, making it especially attractive for hydrogen liquefaction. Yet the scarcity of MR materials that deliver large and reversible magnetocaloric effect, for example in magnetic entropy change, across a broad temperature span remains a central bottleneck for practical deployment (Fig. 1). In the first part of this talk, we will show why second-order transition materials are generally inadequate to cover the full temperature window. We will propose a strategy to achieve giant and reversible MCE across a wide temperature range. This strategy is demonstrated using Er(Ho)Co2-based refrigerants, which exhibit a large magnetic-entropy change ($-\Delta Sm > 0.2$ J $cm^{-3}K^{-1}$) that fully covers 20–77 K, the desired operating temperature for hydrogen liquefaction.
In the second part, we will show how sub-unit-cell covalency control at nanoscale—precise tuning of chemical bonding within the unit cell—tailors the transition and doubles the reversible cooling effect, achieving a giant, reversible MCE at 77 K comparable to that at 20 K. This advance is expected to improve the efficiency of active magnetic regenerator refrigeration system for hydrogen liquefaction.
[1] X. Tang et al. Nature Communications 13 (2022) 1817.
[2] X. Tang *et al.* Adv. Mater. 38 (2026) 7, e14295

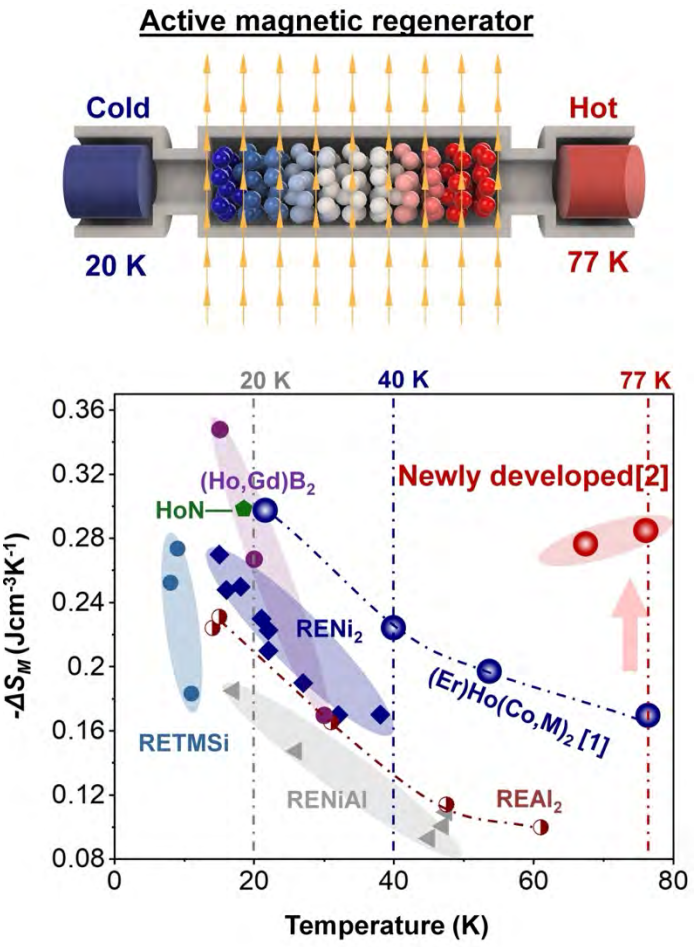


Figure 1. Development of high-performance magnetic refrigerant materials for hydrogen liquefaction.

EB-03. Magnetic Refrigerant for Cryogenic Temperature Magnetic Refrigeration

A. T. Saito[1], H. Takeya[1], X. Tang[1], H. Sepehri-Amin[1], K. Matsumoto[2], H. Kitazawa[1], K. Kamiya[1], K. Natsume[1], T. Numazawa[1]

[1]National Institute for Materials Science, Tsukuba, Ibaraki, Japan, [2]Kanazawa University, Kanazawa, Japan

To realize a hydrogen-based energy society, there is a need to develop highly efficient hydrogen liquefaction technology. Recently, we have demonstrated hydrogen liquefaction by Active Magnetic Regenerative (AMR) refrigeration using $HoAl_2$ magnetic refrigerant, with a relative Carnot efficiency of 60.5 % on the T-S diagram, in JST-Mirai program [1]. Typical indicators of a refrigerant material's contribution to refrigeration performance include the temperature dependence of the magnetocaloric effect and the temperature dependence of specific heat. $HoAl_2$ shows a broad peak of magnetic entropy change (ΔS_M) between 20 K and 40 K (ΔS_{peak} ~0.15 J cm^{-3} K^{-1} at T_C~30 K). Subsequently, HoB_2 and $ErCo_2$-based compounds, which exhibit a giant magnetocaloric effect more than twice that of $HoAl_2$, have been developed as magnetic refrigerants [2, 3]. In the AMR regenerator, absorbing or exhausting heat with temperature drop or rise of such refrigerants accompanied by magnetocaloric effect, and helium heat transfer fluid flows back and forth with heat exchanging to the magnetic refrigerant filled in the regenerator; result in generating large temperature span between both ends of the regenerator. The suitable shape of the refrigerant for the AMR cycle is sphere, and currently we focus on fabrication of spherical particles of these materials. In contrast, the Carnot cycle could achieve significantly higher efficiency than AMR cycle, even temperature span is smaller. Such the Carnot magnetic refrigerator (CMR) can be utilized for hydrogen recondensation, in which the hydrogen gas condenses directly on the surface of the magnetic material. Therefore, we also investigated ceramic refrigerant with chemical stability against hydrogenation. The oxide composite of Eu_2TiO_4 and $Eu_3Ti_2O_7$ exhibits a giant magnetocaloric effect (ΔS_{peak} ~0.3 J cm^{-3} K^{-1} at T~10 K) comparable to that of HoB_2 [4]. In this presentation, we will present the current status of the material research and development in the JST-Mirai Program for hydrogen liquefaction and recondensation.

This work was supported by the JST-Mirai Program under Grant No. JPMJMI18A3, Japan.

[1] K. Kamiya *et al.*, Cryogenics, Vol. 152, 104205 (2025).
[2] P. D. Castro *et al.*, NPG Asia Mater., Vol. 12, 35 (2020).
[3] X. Tang *et al.*, Nature Commun., Vol. 13, 1817 (2022).
[4] K. Matsumoto *et al.*, J. Appl. Phys., Vol. 138, 033901 (2025).

EB-04. Impact of Structural Phase Transitions on the Magnetocaloric Effect

A. Kosogor[1, 2, 3], V. A. L'vov[3]

[1]University of Vienna, Vienna, Austria, [2]University for Continuing Education Krems, Krems, Austria, [3]V.G. Baryakhtar Institute of Magnetism of the NAS of Ukraine, Kyiv, Ukraine

The temperature dependence of magnetization, $M(T)$, measured in an external magnetic field is commonly used to estimate field-induced temperature changes in magnetocaloric materials. It is often assumed that sharp changes in $M(T)$, particularly in systems undergoing coupled magnetostructural phase transitions, correspond to

enhanced magnetocaloric response.

In this work, we apply a theoretical approach that accounts for the influence of structural phase transitions on magnetic interactions to describe experimental magnetization behavior [1]. The model provides a consistent description of the magnetization evolution across the phase transition and enables evaluation of related thermodynamic quantities, including field-induced temperature change and specific heat capacity.

Our analysis reveals that, although structural transitions can lead to abrupt changes in magnetization, this does not necessarily result in an enhanced magnetocaloric effect. Instead, the relationship between magnetization, heat capacity, and temperature change is more complex and depends on the underlying coupling between magnetic and structural degrees of freedom.

These results indicate that a sharp $M(T)$ dependence alone cannot be considered a universal indicator of a large magnetocaloric response.

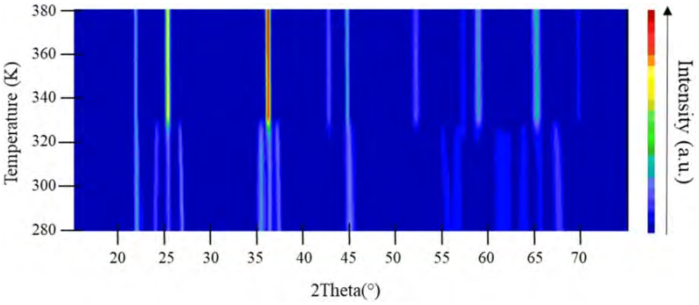
Acknowledgement: Financial support from the Austrian Science Fund (FWF) [10.55776/RIC5537124] is acknowledged.
[1] V. A. L'vov, O. Salyuk, A. Kosogor, Sci. Rep. 15, 31002 (2025). https://doi.org/10.1038/s41598-025-15896-8

EB-05. Decoding the interplay of atomic ordering and magnetism via neutron diffraction to optimize magnetocaloric performance in heusler alloys

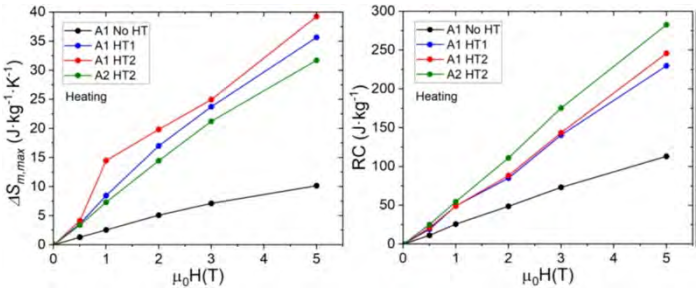
N. Río-López[1], P. Lazpita[1], J. Rodriguez Velamazan[2], V. Chernenko[1, 3], D. Salazar[3], J. Porro[3, 4]
[1]University of the Basque Country, Bilbao, Spain, [2]Institut Laue Langevin, Grenoble, France, [3]BCMaterials, Bilbao, Spain, [4]Ikerbasque, Bilbao, Spain

Heusler type magnetic shape memory alloys (MSMAs) are pivotal for next-generation refrigeration due to their tunable magneto-structural transformations. Our group uses powder neutron diffraction to unravel the relationship between atomic ordering and the multifunctional properties of doped Ni-Mn-Ga and Ni-Mn-Sn systems. The operational temperature range is precisely tuned by dopants such as Cu, Fe, and Co [1]. In Ni-Mn-Ga alloys, Cu and Co additions increase the martensitic transformation temperature (T_M; Fig.1) by enhancing lattice distortion, whereas Fe doping lowers T_M while significantly increasing the Curie temperature (T_C) [2]. Neutron diffraction analysis reveals that these dopants induce specific atomic rearrangements, adjusting Mn-Mn interatomic distances to minimize antiferromagnetic exchange interactions and enhance the total magnetic moment [3]. Furthermore, the magnetocaloric performance is shown to be critically dependent on the structural state and chemical ordering. In Ni-Co-Mn-Sn alloys, as-received melt-spun powders exhibit internal stresses that result in incomplete transformations. We demonstrate that adequate thermal treatments are essential to relieve these stresses and promote $L2_1$ atomic ordering. This leads to a fully completed structural transition, resulting in a large magnetization jump and significantly enhanced refrigeration capacity (Fig.2) [4]. This work establishes neutron diffraction as a fundamental tool for unravelling the atomic mechanisms required to design high-performance magnetocaloric materials.

[1] A. Pérez-Checa *et al.*, Acta Materialia 196, 549-555 (2020)
[2] N.A. Río-López *et al.*, Journal of Alloys and Compounds, 1041, 183639 (2025)
[3] N.A. Río-López *et al.*, Journal of Alloys and Compounds, 1057, 186643 (2026)
[4] B. Rodríguez-Crespo *et al.*, Materials & Design 245, 113279 (2024)



Neutron thermodiffractogram recorded at the D1b instrument of the ILL, evidencing the first order phase transition in one of the MSMAs studied.



Magnetic entropy change (left) and refrigeration capacity (right) of four different NiCoMnSn studied alloys.

EB-06. The Rotating Magnetocaloric Effect – recent advances in experiments and simulations

R. Kiefe[1], H. B. de Souza[1], R. Almeida[2], R. M. Pinto[2], J. O. Silva[2], G. Oliveira[2], J. H. Belo[2], J. Amaral[1]
[1]Department of Physics and CICECO, University of Aveiro, Aveiro, Aveiro, Portugal, [2]IFIMUP – Institute of Physics for Advanced Materials, Nanotechnology and Photonics, Department of Physics and Astronomy, University of Porto, Faculty of Sciences, Porto, Porto, Portugal

The rotating magnetocaloric effect (RMCE) occurs when a magnetic refrigerant undergoes a change in entropy or temperature upon rotation within a homogeneous external magnetic field, offering an alternative route to conventional field-driven magnetocaloric cycles. Unlike the conventional magnetocaloric effect (MCE), which relies on varying the intensity of the applied magnetic field, the RMCE enables cooling through a more compact mechanical rotation process, potentially simplifying device design and improving energy efficiency. The RMCE can be triggered by two distinct mechanisms: magnetocrystalline anisotropy (MCA), due to the dependence of the magnetic moment on the direction of the external field relative to the crystalline lattice axes, and shape anisotropy (SA), arising from demagnetizing fields associated with the sample geometry.

While early studies predominantly focused on MCA-driven RMCE in single crystals and highly anisotropic compounds [1,2,3], recent advances have highlighted the potential of SA-driven RMCE, particularly in refrigerant geometries with large effective shape aspect ratios [4,5]. This shift is especially relevant for practical applications, as SA-driven effects can be realized in polycrystalline compounds without the need for texturing. In this talk, we provide a comprehensive overview of both MCA- and SA-driven RMCE, comparing their merits and drawbacks to those of the conventional MCE. Special attention is given to the role of demagnetizing factors and refrigerant geometry design in maximizing the SA-driven response. We further review recent experimental and computational advances in the study of SA-driven RMCE [6,7,8], focusing on high shape anisotropy refrigerants operating under moderate magnetic fields (below 1 T), which are most compatible with permanent magnet-based cooling technologies.

Finally, we discuss the potential and feasibility of combining both the MCA and SA of a single refrigerant to enhance the overall RMCE response. Strategies for tailoring anisotropy through material selection and texturization approaches are discussed, along with their implications for next-generation solid-state refrigeration devices. The results presented highlight the growing maturity of RMCE research and its potential as a viable pathway toward efficient, compact, and low-field magnetic cooling technologies.

[1] S. A. Nikitin, K. P. Skokov, Yu. S. Koshkid'ko, Yu. G. Pastushenkov, and T. I. Ivanova, Phys. Rev. Lett. 105, 137205 (2010)
[2] Liqun Su, Hu Zhang, He Zhou, Kaili Yan, Daoyong Cong, Rongjin Huang, Yingli Zhang, Yi Long, J. Appl. Phys. 127, 043905 (2020)
[3] M. Balli, S. Jandl, P. Fournier, A. Kedous-Lebouc, Appl. Phys. Rev. 4, 021305 (2017)
[4] R. Almeida, S. C. Freitas, C. R. Fernandes, R. Kiefe, J. P. Araújo, J. S. Amaral, J. O. Ventura, J. H. Belo, D. J. Silva, J. Phys. Energy 6 015020 (2024)
[5] Q. Badosa, L. Mañosa L, E. Vives, A. Planes, B. Weise, L. Beyer and E. Stern-Taulats J. Appl. Phys. 134, 113902 (2023)
[6] R. Almeida, T. Ventura, R. Pinto, J. O. Silva, R. Kiefe, J. S. Amaral, J. P. Araújo, J. H. Belo, arXiv:2601.23056 [cond-mat.mtrl-sci] (2026)
[7] R. Kiefe, J. S. Amaral, Int. J. Refrig. 173 180 - 184 (2025)
[8] H. B. de Souza, R. Kiefe, J. S. Amaral, Appl. Phys. Lett. 127 174104 (2025)

EB-07. Chemical ordering and non-linear magnetic behavior: enhancing the magnetocaloric effect in rare-earth free high-entropy materials

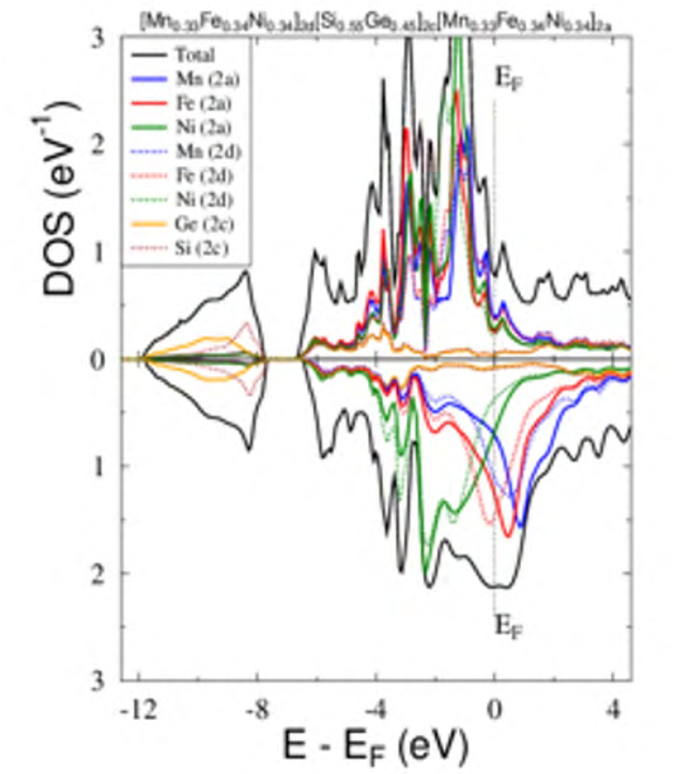
V. Fournee[1], D. Sihom Kwekam[1], G. Lengaigne[1], P. Boulet[1], S. Migot[1], J. Ledieu[1], J. Tobola[2], S. Semsari Parapari[3], S. Raznjevic[3], S. Šturm[3], L. Gallo[4], S. Fabbrici[4], F. Cugini[4, 5], M. Solzi[4, 5], F. Albertini[4]
[1]Institut Jean Lamour, CNRS, Nancy, France, [2]AGH University, Krakow, Poland, [3]Jozef Stefan Institute, Ljubljana, Slovenia, [4]IMEM-CNR, Parma, Italy, [5]University of Parma, Parma, Italy

High-entropy alloys (HEAs) mix five or more elements at near-equal compositions in a single crystalline phase. In principle, they form an ideal solid solution stabilized through a high configurational entropy of mixing [1,2]. This huge compositional space of HEAs offers opportunities to discover new functional materials. However a rational approach is needed to design HEAs with the desired combination of properties [3,4]. Here we present a detailed investigation of the structure, magnetic and magnetocaloric

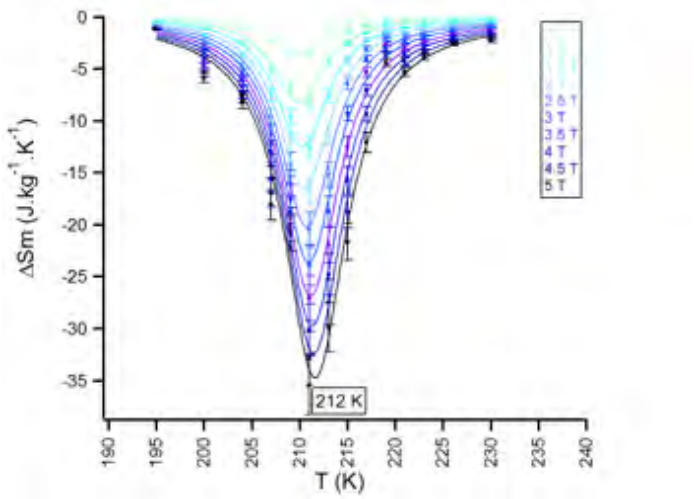
properties of some ultra-pure single phase high entropy materials in quinary FeMnNiGeSi and senary FeMnNiCoGeSi rare-earth free systems.

Our findings indicate the persistence of partial chemical ordering, with transition metal atoms and metalloids preferentially occupying specific crystallographic sites in the FeMnNiGeSi system [5]. This partial ordering is further supported by *ab initio* total energy calculation (Fig. 1). In turn, the magnetic moment - carried out mainly by Fe and Mn - exhibits a strong dependence on the crystallographic sites occupied by these magnetic atoms. By exploring the chemical landscape, we observed highly non-linear magnetic behavior upon Mn doping, resulting in an isothermal entropy change (ΔSm) as high as 35 $Jkg^{-1}K^{-1}$ in 5 T (Fig. 2), while the transition temperature approaches room temperature. Further Co-doping leads to further enhancement of ΔSm ~ 45 $Jkg^{-1}K^{-1}$ in 5 T, and a tuneable transition temperature between 300 to 360 K. These outstanding performances suggest that rare-earth free high entropy materials can rival conventional magnetocaloric materials. Additionally, we find that the first-order magnetostructural transition can evolve into a second-order magnetic transition through chemical tuning. This opens the possibility to discover similar materials near the boundary between first- and second-order transitions, with vanishing hysteresis - potentially addressing their mechanical instability issue.

[1] E.P. George *et al.*, Nat. Review, Vol.4, p.515 (2019)
[2] L. Han *et al.*, Nature Reviews Materials, Vol.9, p.846 (2024)
[3] J.Y. Law *et al.*, J. Alloys. Comp., Vol.855, p.157424 (2021)
[4] Y. Guo *et al.*, APL Mater., Vol.10, p.091107 (2022)
[5] V. Fournée *et al.*, Materials Today Physics, Vol.65, p. 102128 (2026).



KKR-CPA spin-polarized electronic DOS in hexagonal (SG $P6_3/mmc$) FeNiMnGeSi HEAs assuming model partial disorder, where Fe, Ni and Mn are randomly distributed on *2a* and *2d* sites, while Si and Ge randomly occupy *2c* site.



Isothermal entropy change ΔSm in Mn-doped FeMnNiGeSi HEA.

EB-09. AI-Driven Real-Time Adaptive Control of Multi-Stage Active Magnetic Refrigeration with Enhanced Performance

M. Ghahremani
CME Department, Shepherd University, Shepherdstown, West Virginia, United States

Magnetic refrigeration is a promising solid-state cooling technology with potential to surpass vapor-compression systems in efficiency and environmental sustainability [1]. However, practical deployment remains limited by suboptimal system-level control, hysteresis losses, and incomplete integration between magnetocaloric materials and active magnetic regenerative (AMR) cycles [2].
In this work, an AI-driven magnetic refrigeration system is presented by integrating a machine learning–based artificial neural network (ANN) with a multi-stage AMR architecture. The ANN enables real-time adaptive control of key cycle parameters, including magnetic field switching (0.2–1.5 s), fluid flow modulation (0.1–0.5 Hz), and regenerator coordination. Trained on thermo-magnetic response data, the model captures nonlinear system dynamics and continuously optimizes cycle performance beyond conventional rule-based strategies.
The system utilizes advanced magnetocaloric materials, including LaFe11.4Si1.6Hx and MnFe(P,Si)-based alloys, exhibiting entropy changes of 10–20 J/kg.K and adiabatic temperature shifts of 5–8 K [3], [4]. These materials enable refrigerant capacities of 200–500 J/kg and heat exchange across a broad operating window.

Experimental results demonstrate a temperature span of 15–20 K under optimized operating conditions. Cooling power density reaches up to 2–8 W/g under optimized conditions, with maximum performance achieved near 0.8–1.1 s switching delay.
COP improves, reaching values above 4 in optimal regimes near 0.3–0.4 Hz flow modulation. Performance gains of 20–35% are observed compared to non-adaptive control, accompanied by reduced thermal oscillations, improved heat transfer uniformity, and enhanced cycle stability under varying operating conditions.
These results demonstrate that AI-driven control provides a viable pathway toward high-performance, adaptive magnetic refrigeration systems and scalable, low-emission cooling technologies for next-generation applications, particularly in energy-efficient thermal management systems [5].

[1] A. Kitanovski, Adv. Energy Mater., Vol. 10, p.2000675 (2020)
[2] J. Lyubina, J. Phys. D: Appl. Phys., Vol. 50, p.053002 (2017)
[3] J. Liu, T. Gottschall, K. P. Skokov and O. Gutfleisch, Scr. Mater., Vol. 67, p.584 (2012)
[4] V. Franco, J. S. Blázquez, B. Ingale and A. Conde, Annu. Rev. Mater. Res., Vol. 42, p.305 (2012)
[5] A. Kitanovski, U. Plaznik, U. Tomc and A. Poredoš, Int. J. Refrig., Vol. 57, p.288 (2015)

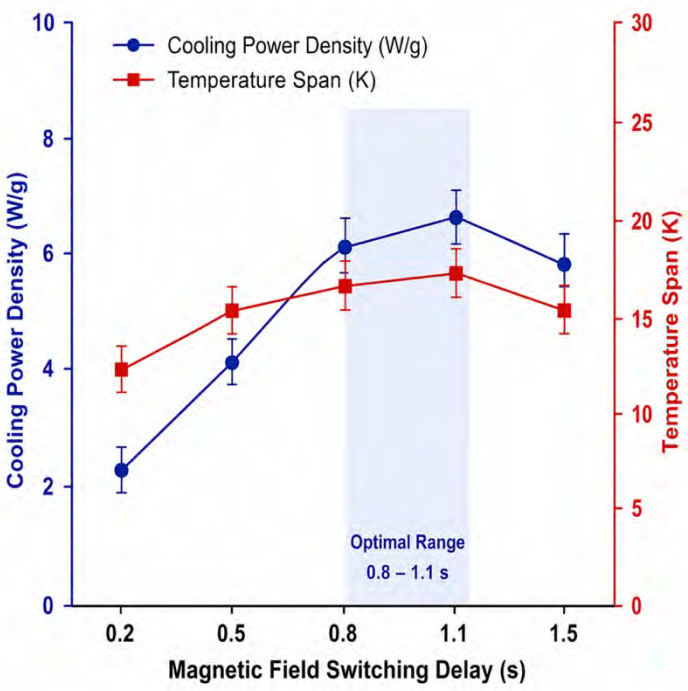


Figure 1: Cooling power density and temperature span versus magnetic field switching delay.

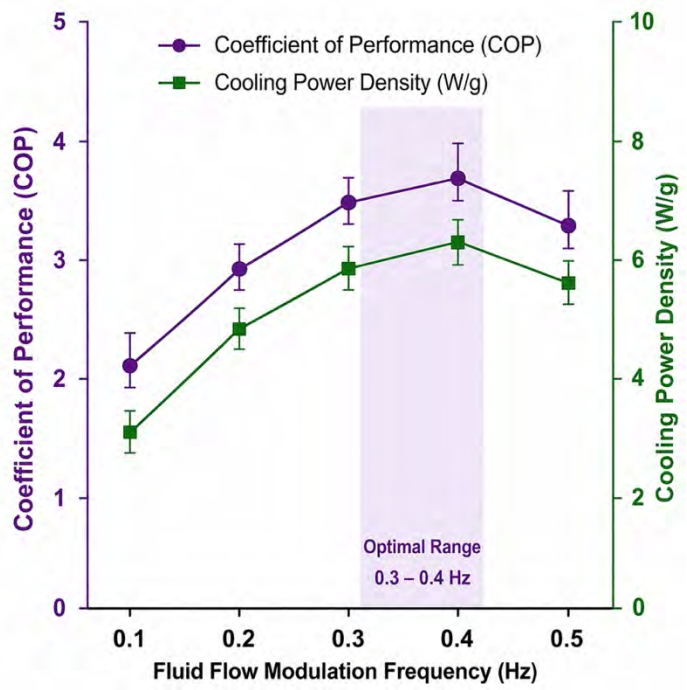


Figure 2: COP and cooling power density versus fluid flow modulation frequency.

SESSION EC: HARD MAGNETIC MATERIALS I: HIGH-COERCIVITY AND RARE-EARTH-EFFICIENT ND-FE-B MAGNETS

Co-Chair(s): W. Tang, *Ames National Laboratory, Ames, Iowa, United States* and S. R. Trout, *Spontaneous Materials, Denver, Colorado, United States*

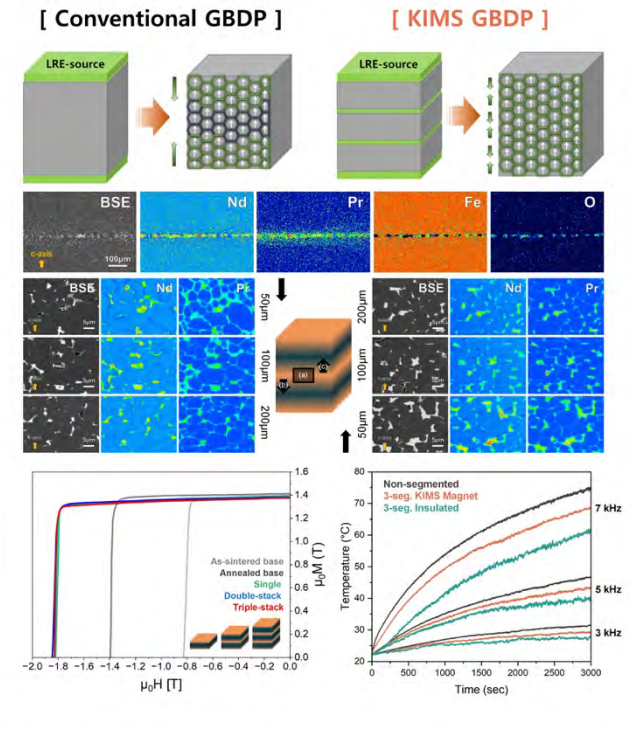
Thursday, November 5, 2026
08:30 AM-12:00 PM
Coral 1

EC-02. A Sandwich-Structured Diffusion-Bonding Strategy for Thick Nd–Fe–B Magnets with Enhanced Coercivity and Resistivity

S. Kim, H. Kim, J. An, T. Kim, J. Lee
Korea Institute of Materials Science, Changwon, Korea (the Republic of)

The grain boundary diffusion process (GBDP) is a key technology that enables Nd–Fe–B permanent magnets to maintain stable performance in high-temperature electric motors, such as those used in hybrid/electric vehicles, by significantly improving the coercivity ($\mu_0 H_c$) while minimizing heavy rare-earth (HRE) consumption. Moreover, conventional HRE-based diffusion alloys possess high melting points, resulting in shallow diffusion depths; consequently, their $\mu_0 H_c$ enhancement is significantly reduced in magnets thicker than approximately 4–5 mm. This limitation restricts the use of GBDP magnets in large-size motors, such as traction motors for electric ships, which require very large magnets with a high $\mu_0 H_c$. [1-4]
To overcome such drawbacks of the HRE-GBDP, low-melting-point diffusion alloys based on light rare-earth Pr elements (*e.g.*, Pr-based eutectic alloys combined with non-ferromagnetic transition metals such as Cu, Al, or Ga) have been extensively investigated. However, the $\mu_0 H_c$-gain achievable with the Pr-GBDP remains limited to 0.4–0.5 T for 10 mm-thick magnets and decreases to nearly zero as the magnet thickness exceeds 10 mm. Therefore, no successful reports exist on achieving a high $\mu_0 H_c$ in Nd–Fe–B magnets thicker than 10 mm, indicating that the current HRE-free Pr-GBDP is not yet suitable for fabricating thick, high-$\mu_0 H_c$ HRE-free magnets for large-size motors. A new strategy is urgently needed for applications requiring large, high-$\mu_0 H_c$ magnets [5,6].
In this study [7], a sandwich-structured GBDP using a low-melting Pr–Cu–Al–Ga (PCAG) alloy is proposed to simultaneously address the challenges of HRE usage and limited diffusion depth of conventional GBDP. The $\mu_0 H_c$ and $\mu_0 H_c$-gain in the 15 mm-thick magnets obtained in this work

are comparable to those obtained of 5 mm-thick magnets after the conventional single-structured PCAG-GBDP. In addition, the sandwich-structured GBDP enhances the electrical resistivity of the magnets, which reduces their eddy-current loss.
[1] K. Hirota, H. Nakamura, T. Minowa, M. Honshima, Coercivity Enhancement by Grain Boundary Diffusion Process to Nd-Fe-B Sintered Magnets, IEEE Trans. Magn. 42 (2006) 2909–2911
[2] S. Kim, D.S. Ko, H.S. Lee, D. Kim, J.W. Roh, W. Lee, Enhancing the coercivity of Nd-Fe-B sintered magnets by consecutive heat treatment–induced formation of Tb-diffused microstructures, J. Alloys Compd. 780 (2019) 574–580
[3] N. Oono, M. Sagawa, R. Kasada, H. Matsui, A. Kimura, Production of thick high-performance sintered neodymium magnets by grain boundary diffusion treatment with dysprosium–nickel–aluminum alloy, J. Magn. Magn. Mater. 323 (2011) 297–300
[4] O. Gutfleisch, M.A. Willard, E. Brück, C.H. Chen, S.G. Sankar, J.P. Liu, Magnetic Materials and Devices for the 21st Century: Stronger, Lighter, and More Energy Efficient, Adv. Mater. 23 (2011) 821–842
[5] H.W. Kwon, M.S. Kang, Prospect of developing Nd–Fe–B-type magnet with high electrical resistivity, Rare Met. 39 (2020) 2–12
[6] J. He, J. Hu, B. Zhou, H. Jia, X. Liu, Z. Zhang, L. Wen, L. Zhao, H. Yu, X. Zhong, X. Zhang, Z. Liu, Simultaneous enhancement of coercivity and electric resistivity of Nd-Fe-B magnets by Pr-Tb-Al-Cu synergistic grain boundary diffusion toward high-temperature motor rotors, J. Mater. Sci. Technol. 154 (2023) 54–64
[7] H. Kim, T. Kim, G. Yoo, D. Lee, J. Kim, K. Bae, S. Lee, D. Kim, J. Lee, S. Kim, J. Lee, Development of thick Nd–Fe–B magnets with high coercivity and resistivity via a sandwich-structured grain boundary diffusion strategy, Scr Mater. 279 (2026) 117-288



EC-03. Microstructure optimization of HREE-free hot-deformed Nd-Fe-B magnets

R. Goto, F. Kihara, Y. Yoshimi, T. Oikawa, H. Miyawaki
Corporate Research and Development Center, Daido Steel Co., Ltd., Nakatsugawa, Japan

Nd-Fe-B permanent magnets are widely used in motors, including those for xEVs. While heavy rare earth elements (HREEs) such as Dy and Tb are typically added to improve the coercivity, recent geopolitical issues have drawn attention to HREE-free magnets. The hot-deformed magnets produced by Daido Steel group exhibit high coercivity even without the addition of HREEs, due to their fine grains[1]. The magnetic properties are significantly influenced by the quality of the melt-spun ribbon used as raw material and the microstructure of the magnets; coarse grains in the ribbon and secondary phases within the magnets adversely affect magnetic properties[2].
In this work, we focused on producing high-quality ribbons with fine and homogeneous grains to obtain high-performance magnets, as well as on reducing the Nd6Fe13Ga phase, which adversely affects the coercivity[3]. Melt spun ribbon was produced by a single wheel melt spinner. Here, nozzle diameter, differential pressure and wheel speed were optimized. The hot-deformed magnets were produced by hot-press followed by hot extrusion. Here, to reduce the Nd6Fe13Ga phase in the hot-deformed

magnet, the TRE was kept constant while varying the amount of Boron.
Based on SEM and VSM analysis, it was confirmed that the ribbon has a nanocrystalline structure. Fig. 1 shows the particle sizes of the conventional and the optimized ribbon. The median grain size of the ribbons produced by optimized conditions was around 37 nm, resulting in finer crystal grains than those of the conventional ribbon (45 nm). Furthermore, the particle size distribution index of the optimized ribbon was 4% smaller than that of the conventional ones, indicating that the particles were more uniform.
As shown in Fig. 2, the microstructure of the optimized magnets consisted of finer and more homogeneous grains. Furthermore, the proportion of coarse grains near the flake boundaries decreased. It was also confirmed that increasing the boron content compared to conventional magnets suppressed the formation of the Nd6Fe13Ga phase during hot deformation. One of the magnetic properties of the HREE-free hot-deformed magnets showed the remanence of 1.416 T at room temperature and coercivity of 580 kA/m at 150dC.
[1] K. Hioki, Sci. Technol. Adv. Mater. 22, 72-84 (2021)
[2] J. Liu et al., Acta Materialia, 82, 336-343 (2015)
[3] X. Xu et. al., *Scripta Materalia.* 160, 9–14 (2019)

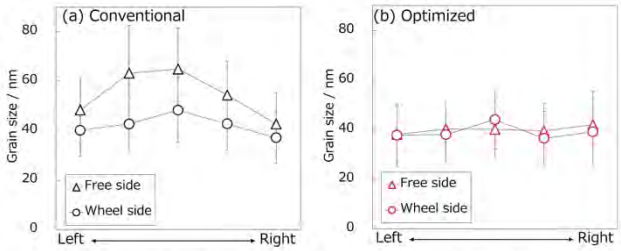


Fig 1. Grain size of melt spun ribbons (a) conventional and (b) optimized ribbon

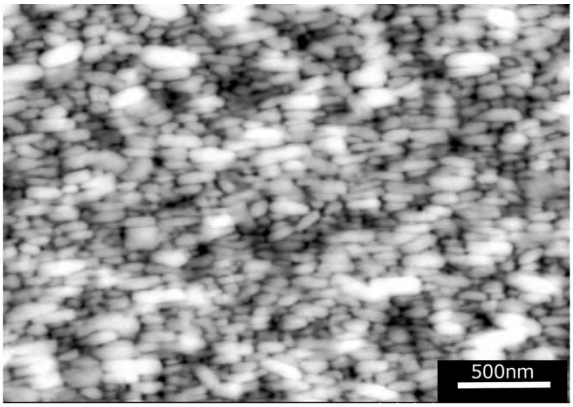


Fig 2. Microstructure of hot-deformed magnets produced by optimized conditions

EC-04. Magnetic domains and microstructures of 2-17 type high Fe-content Sm-Co magnets with high $[BH]_m$ and H_k/H_{cj}
H. Machida, H. Makuta, N. Onishi, A. Urata
Tokin Corporation, Shiroishi, Japan

Permanent magnets with high magnetic properties and heat resistance have been highly demanded along with the progress of electrification and the increase in the number of electric and hybrid electric vehicles. 2-17 type Sm-Co magnets are widely recognized as having the second-highest maximum energy product, $[BH]_m$ and the highest Curie temperature among permanent magnets. To date, we have achieved $[BH]_m$ of 33.6-34.5 MGOe with high squareness, H_k/H_{cj} over 70% by adjusting the composition and heat treatment conditions[1]-[3]. In this study, we prepared a sample with higher Fe content (the developed magnet) than that of the magnets we previously reported to enhance the magnetic properties even more. The developed magnet reached 35.0 MGOe of $[BH]_m$ with H_k/H_{cj} of 82.0% (Fig. 1). To the best of our knowledge, this is the first achievement to realize both such high $[BH]_m$ and H_k/H_{cj} simultaneously. Moreover, since the *B-H* curve was linear even at 150°C, it is applicable to automotive motors.
Magnetic domains and magnetic reversal mechanisms were investigated with XMCD (X-ray Magnetic Circular Dichroism) under applied magnetic fields. The magnetic domains in the demagnetized state had a maze-like shape (Fig. 2), whose size was significantly larger than that of conventional Sm-Co magnets[4]. Regarding the magnetic reversal mechanism, after applying +40 kOe and sweeping the magnetic field toward the negative direction, reverse magnetic domains were generated from the grain interior initially at −5 kOe followed by rapid propagation and expansion throughout the grains at −10 kOe, and the magnetic reversal was almost completed at −15 kOe. The microstructure of the developed magnet was examined with TEM and EDX. The cellular structures were composed of the Fe-enriched 2-17 phase and the Cu-enriched 1-5 phase. Furthermore, the cell size was approximately 200-600 nm, which was almost the same as that of the magnets we reported[3]. The large magnetic domains and cellular structures correlated with high $[BH]_m$ and H_k/H_{cj}.
[1] H. Machida, et al., *IEEE Trans*., Vol. 55(2), p.2868969-1 (2019)
[2] H. Machida, et al., *AIP Advances*., Vol. 9(12), p.120542-1 (2019)
[3] H. Machida, et al., *IEEE Trans*., Vol. 59(11), p.1 (2023)
[4] O. Gutfleisch, et al., *Acta Mater*., Vol. 54(4), p.997 (2006)

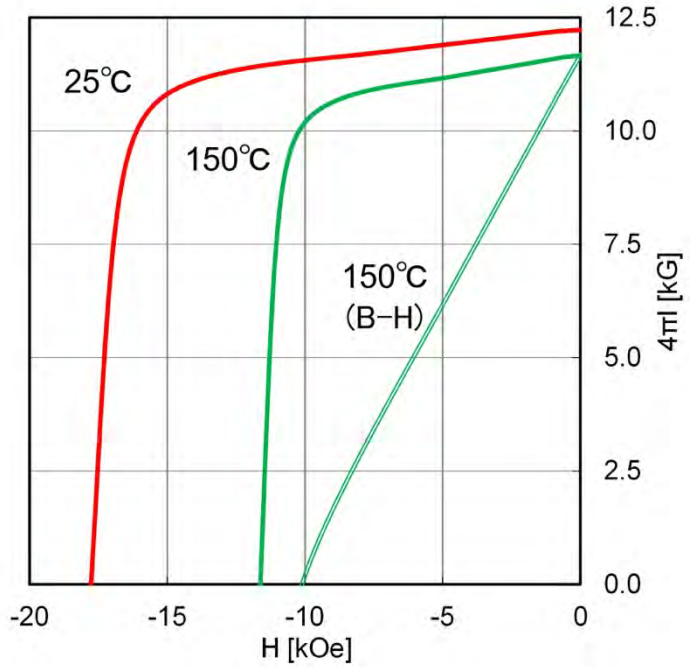


Fig. 1 The demagnetization curves of the developed magnet.

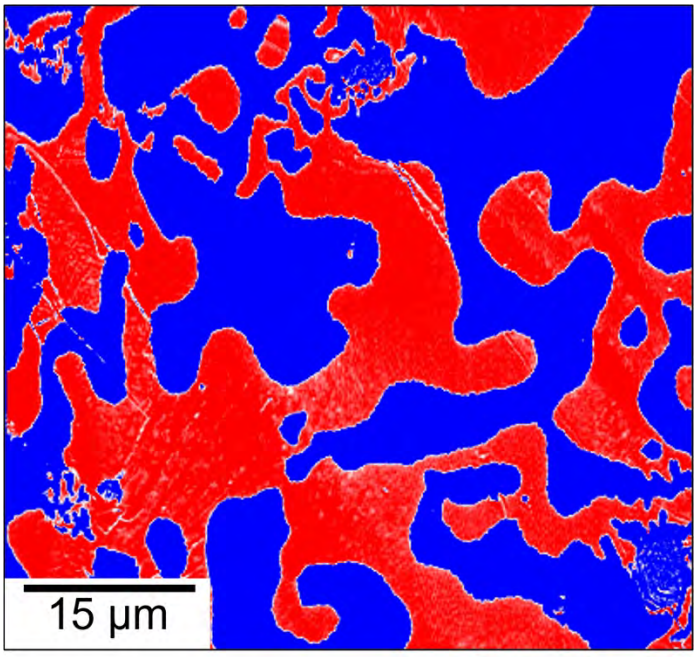


Fig. 2 The magnetic domain structure in the demagnetized state.

EC-05. The Effect of Grain Connectivity on Coercivity Mechanism in Nd-Fe-B Magnets

A. Bolyachkin, N. Kulesh, H. Sepehri-Amin, X. Tang
National Institute for Materials Science, Tsukuba, Japan

High-performance Nd-Fe-B permanent magnets are critically important for high-tech, transportation, and energy applications. Recently, there was remarkable progress in exchange decoupling of the $Nd_2Fe_{14}B$ grains by thick intergranular phases in Ga-doped Nd-Fe-B sintered magnets [1]. However, this insulation is incomplete: FIB-SEM tomography and TEM observations reveal that a thin Fe-rich magnetic intergranular phase (IGP) still provides partial grain connectivity. Consequently, one of the key questions for coercivity engineering in Nd-Fe-B magnets is determining the level of grain connectivity at which the magnetization reversal transforms from the predominant domain wall depinning at IGPs to the nucleation of reversed magnetic domains. In this work, we aim to address this question by means of micromagnetic simulations, focusing on the angular dependence of coercivity and its dependence on crystallographic alignment [2] as practical markers for the coercivity mechanism.

Micromagnetic simulations were performed on a 500×500×500 nm^3 finite element model comprising 192 equiaxed $Nd_2Fe_{14}B$ grains separated by 3-nm-thick IGP and nonmagnetic triple junctions. Following the methodology of Ref. [3], each IGP could be assigned to be either magnetic or nonmagnetic. A defective grain was considered to introduce a region with reversed magnetization exhibiting the domain wall pinning. Then a series of angular dependencies of coercivity and its dependencies on crystallographic alignment were simulated while varying two factors: (i) the strength of exchange coupling through thin magnetic IGPs, (ii) the number of magnetic IGPs and corresponding grain connectivity (Fig. 1). These results provide insight into the prospects for coercivity enhancement in Nd-Fe-B sintered magnets and support the development of new reduced-order models for pinning-type magnets and those with hybrid pinning and nucleation reversal scenarios.

[1] N. Kulesh *et al.*, Adv. Intel. Disc., p.e202500200 (2026).
[2] Y. Matsuura *et al.*, AIP Advances, Vol. 8, p.015226 (2018).
[3] A. Bolyachkin *et al.*, npj Comput. Mater., Vol. 10, p.34 (2024).

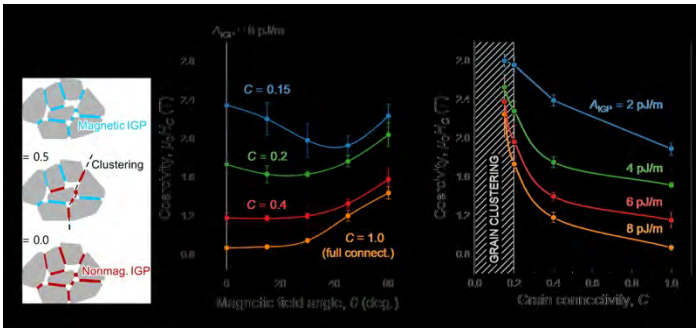


Fig. 1. (a) Schematic illustration of grain connectivity (*C*) through the intergranular phase (IGP). (b) Angular dependence of coercivity for different *C* under strong exchange coupling, A_{IGP} = 8 pJ/m. (c) Coercivity as a function of grain connectivity for various exchange stiffness of the IGP.

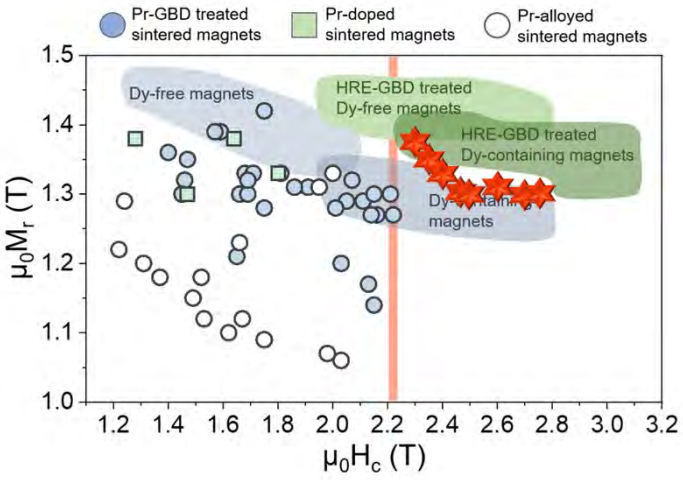
EC-06. Toward achieving high-coercivity in Nd-Fe-B sintered magnets *via* Pr-based grain boundary diffusion process

S. Lee[1], J. An[1], S. Lee[1], G. Kim[2], K. Lee[2], S. Kim[1], T. Kim[1], J. Lee[1]

[1]Korea Institute of Materials Science, Changwon, Korea (the Republic of), [2]Ulsan National Institute of Science and Technology, Ulsan, Korea (the Republic of)

The Pr-based grain boundary diffusion process (GBDP) is the most promising method for obtaining high-coercivity (μ_0H_c) in the magnets without use of heavy rare-earths (HRE)[1]. However, the μ_0H_c gain by the Pr-GBDP is only 0.2-0.3 T[1], which is insufficient to realize a high-coercivity above 2.5 T that can be achieved by the HRE-GBDP[1]. A recent report by Kim *et al.* provides a novel insight into increasing both the GBD-depth of Pr and Pr-concentration of shell[3]. They found that shell formation induces undesirable grain growth during the GBDP because a unique phenomenon, termed chemically induced liquid film migration (CILFM), is dominantly involved in the shell formation[3]. Based on phenomenological feature, the CILFM can be defined as GBD source consuming and grain coarsening phenomenon. Thus, to breakthrough the limit of the μ_0H_c gain by the Pr-GBDP, a CILFM-inhibited GBDP should be developed. Furthermore, according to a recent report[4], the microstructure and chemistry control of GBP to be thicker and non-ferromagnetic is also very important for achieving high-μ_0H_c with Pr-GBDP[4]. In this study, first, we developed HRE-free two-step GBDP consisting of the 1st-step GBDP with refractory metal (RM)-compounds or -alloys for forming the intergranular precipitates to hinder the CILFM, and the 2nd-step GBDP with Pr-based alloys for forming the high-anisotropy Pr-rich shell. Second, we unveiled the key microstructural factor for realizing high-μ_0H_c in Pr-GBDP magnets, and based on this, a guide to design the composition of magnets and GBDP source was established. For the CILFM-inhibited GBDP, the low-melting TaF_5 compound (TF) and eutectic Zr-Cu (ZC) alloy were selected as the RM-containing GBD source for the 1st-GBDP. By the CILFM inhibited two-step GBDP, the μ_0H_c of magnets reached 2.35 T (TF-Pr-GBDP sample) and 2.70 T (ZC-Pr-GBDP sample), respectively, as shown in Fig. 1. In addition, by modifying the composition of initial magnets based on the μ_0H_c -composition relationship established in this work, high-μ_0H_c of 2.6 T was achieved by Pr-based GBDP alone. The μ_0H_c of HRE-free magnets achieved in this work are sufficient to replace the commercial HRE-GBDP magnets.

1. M. Komuro *et al.*, IEEE Trans. Magn., 46 (2010) 3831.
2. T. Oikawa *et al.*, AIP Advan., 6 (2016) 056006.
3. T. H. Kim *et al.*, Scr. Mater., 178 (2020) 433.
4. S. J. Lee *et al.*, Mat. Des., 260 (2025) 115179.



μ_0H_c and μ_0M_r of Pr-GBDP magnets obtained in this work.

EC-07. Recycling of Highly Oxidized End-of-Life Nd–Fe–B Magnets *via* Calciothermic Reduction Process

S. Lee[1, 2], T. Kim[1], K. Bae[3], D. Kim[3], K. Lee[2], J. Lee[1]

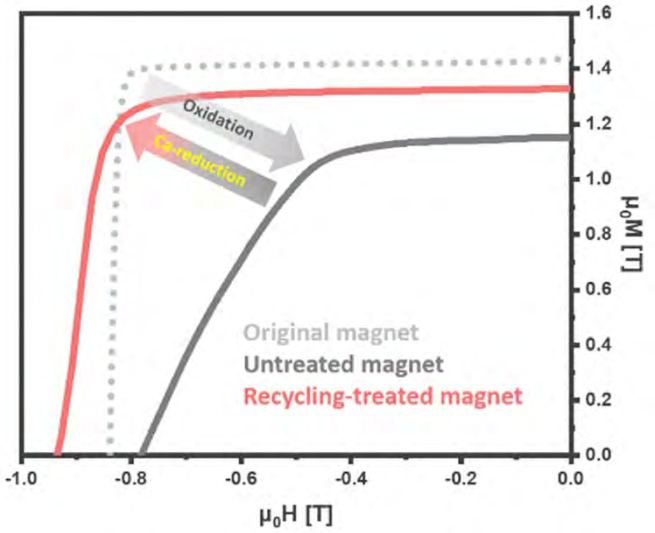
[1]Department of Magnetic Materials, Korea Institute of Materials Science (KIMS), Changwon-si, Korea (the Republic of), [2]Department of Materials Science and Engineering, Ulsan National Institute of Science and Technology (UNIST), Ulsan-si, Korea (the Republic of), [3]R&D Center, Star Group Ind. CO. Ltd., Daegu-si, Korea (the Republic of)

Rising demand for rare-earth elements (REEs) in electric vehicles and renewable energy makes end-of-life (EoL) Nd-Fe-B magnets critical secondary raw materials; however, conventional short-loop recycling remains constrained when processing highly oxidized scrap due to inherent oxygen sensitivity [1, 2]. To resolve this, calciothermic reduction is utilized to synthesize low-oxygen and high-purity $Nd_2Fe_{14}B$ particles from severely oxidized EoL magnets [3, 4]. Although this process reduces the oxygen contents, it necessitates aqueous washing to remove CaO or residual Ca byproducts, a step when preventing re-oxidation is technically challenging [5, 6]. To achieve high-efficiency recycling, we utilized a two-step washing process, specifically designed to suppress secondary oxidation and successfully restore the magnetic properties of the recycled magnets.

The EoL 50M grade Nd-Fe-B magnets (oxygen content 0.62 wt.%) were pulverized to approximately 3.3 μm, increasing oxygen content of 0.80 wt.%. For reduction, the powder was blended with 10 wt.% Ca and heat treated at 900 °C for 30 min under the Ar atmosphere. The two-step washing process established by our group was employed to eliminate the CaO or residual Ca without re-oxidation. First, powders were coated with the ethylenediamine $[C_2H_4(NH)_2)_2]$ to inhibit surface oxidation, then washed with distilled water, methanol, and ammonium nitrate (NH_4NO_3) solution. Second, they were treated with diluted acetic acid to chemically etch the oxide layer.

Consequently, recycled powders with a low oxygen content of 0.26 wt.% were synthesized, enabling the fabrication of highly dense bulk magnets. As shown in Fig. 1, the recycling-treated magnet achieved a $(BH)_{max}$ of 42.01 MGOe, recovering 84% of the original magnet performance. This study demonstrated that combining calciothermic reduction with the two-step washing process provides an effective pathway for high performance functional recycling of severely oxidized EoL magnets.

[1] C. Burkhardt et al., *Journal of Magnetism and Magnetic Materials*., Vol. 588, p.171475 (2023)
[2] M. Schönfeldt et al., *Acta Materialia*., Vol. 283, p.120532 (2025)
[3] K. Bolis et al., *ACS omega*., Vol. 8, p.12246 (2023)
[4] L. Wang and X. Xu, *Molecules*., Vol. 28, p.7918 (2023)
[5] V. Galkin, S. B. Kim and T. H. Kim, *Journal of Magnetics*., Vol. 29, p.1 (2024)
[6] L. Cong, B. Shen and J. Zhang, *Journal of Environmental Chemical Engineering*., Vol. 12, p.112452 (2024)



Demagnetization curves of original, untreated, recycling-treated magnets. The recycling-treated magnet shows significant restoration of magnetic properties after calciothermic reduction and two-step washing, reaching 84% of the original $(BH)_{max}$.

EC-08. Dy-free sintered N40SH grade magnets achieved by combining blend and surface grain boundary diffusion techniques

W. Tang[1], J. Wang[1], Y. Varma[2], C. Pan[1], J. Cui[1, 2]
[1]Ames National Laboratory, Ames, Iowa, United States, [2]Iowa State University, Ames, Iowa, United States

$Nd_2Fe_{14}B$-based magnets are primary candidates for applications such as wind turbines, industrial pumps, and electric vehicles (EVs). Heavy rare earth elements like Dy up to 10 wt% may be required for the magnets capable of operating at 200°C. Unfortunately, Dy is scarce, expensive, and subject to supply chain risks. Consequently, the development of Dy-lean or Dy-free Nd-Fe-B magnets capable of high-temperature operation is of significant interest to the EV industry. Microstructure engineering technique by grain boundary diffusion (GBD) is an effective method to develop Dy-lean or Dy-free HT magnets. GBD methods can be classified into two types: (1) Blending GBD: Grain boundary modifying alloys are blended with primary Nd-Fe-B alloy powder before sintering [1-3]. (2) Surface GBD: The GBD alloy is applied to the surface of sintered magnets in final shape through methods like dip coating, evaporation deposition, etc. [4-6].

In this study, a Pr–Al–Cu alloy was used as the GBD source and diffused into Nd–Fe–B sintered magnets using both

blending and surface GBD methods, aiming to develop Dy-free N40SH grade magnets with target properties of coercivity H_{cj} ⩾ 20 kOe and maximum energy product $(BH)_{max}$ ⩾ 40 MGOe. For the blending GBD approach, adding up to 10 wt% Pr–Al–Cu resulted in a magnet with H_{cj} = 19.2 kOe and $(BH)_{max}$ = 37.2 MGOe. In contrast, the surface GBD method yielded H_{cj} = 21.3 kOe and $(BH)_{max}$ = 33.1 MGOe using only 1.5 wt% Pr–Al–Cu. Considering the respective benefits and trade-offs, an improved hybrid method combining both blending and surface GBD techniques was developed. As shown in Figure 1, the reference (no-GBD) magnet exhibited H_{cj} = 12.0 kOe. After 7.5 wt% Pr–Al–Cu blending GBD, H_{cj} increased to 15.0 kOe, and a subsequent surface GBD (~1.0 wt% Pr–Al–Cu) further enhanced H_{cj} to 19.8 kOe. Although $(BH)_{max}$ slightly decreased at each GBD step, a $(BH)_{max}$ of 40 MGOe was maintained using the combined approach. These results demonstrate that the combined blending–surface GBD technique is a promising route to produce Dy-free, high-performance Nd–Fe–B magnets suitable for high-temperature applications.

1. W. Tang, J. Wang, C. C. Pan, M. C. Kang, L. Zhou, M. J. Kramer, J. Cui, and I. E. Anderson, IEEE Trans. Magn., 2024, 9, 2100505.
2. F. M. Wan, Y. F. Zhang, J. Z. Han, S. Q. Liu, T. Liu, L. Zhou, J. B Fu, D. Zhou, X. D. Zang, J. B. Yang, Y. C. Yang, J. Chen, and Z.W. Deng, J. Appl. Phys.2014, 115,203910.
3. M. Yan, W. Chen, J. Y. Jin, Y. S. Liu, H. S. Chen, S. P. Ringer, J. J. Xu, Y. L. Hou, M. Yue, X. L. Liu, Acta Materialia, 2022, 231, 117873.
4. Z. W. Liu, J. Y. He, R. V. Ramanujan, Materials & Design, 2021, 209, 110004.
5. H. Sepehri-Amin, T. Ohkubo, K. Hono, Acta Mater. 2013, 61, 1982.
6. K. Loewe, C. Brombacher, M. Katter, O. Gutfleisch, Acta Mater. 2015, 83, 248.

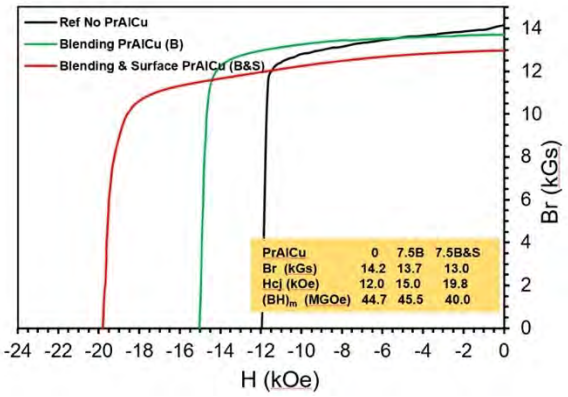


Fig. 1 Demagnetization curves of magnets diffused by Pr-Al-Cu alloy through blending and surface GBD methods

EC-09. Simultaneous improvement in coercivity and remanence of (Nd, Pr)-ultra-saving Ce-substituted RE-Fe-B sintered magnets by grain boundary diffusion process using low-melting Nd-Cu-Al-Ga alloy

S. Lee[1], S. Kim[1], T. Kim[1], K. Bae[2], D. Kim[2], J. Lee[1]
[1]Korea Institute of Materials Science, Changwon, Korea (the Republic of), [2]Star Group Ind. CO., Ltd., Daegu, Korea (the Republic of)

The Nd-Fe-B-based magnets are widely employed in various industries, including wind power generation, intelligent robotics, and electric/hybrid vehicles, due to their superior hard magnetic properties derived from high anisotropy field and saturation magnetization of $Nd_2Fe_{14}B$ (2-14-1) grains[1)]. However, the increasing demand for the Nd-Fe-B magnets has led to depletion of critical rare earth elements (RE), particularly Nd and Pr, raising concerns about cost and supply stability[2)]. Therefore, significant research efforts have been directed toward developing high-performance permanent magnets with reduced Nd and Pr[3)]. Among potential substitutes, Ce has emerged as a promising candidate for partially replacing Nd/Pr due to its abundant availability and cost-effectiveness[4)]. However, the inferior intrinsic properties of $Ce_2Fe_{14}B$ compared to $Nd_2Fe_{14}B$ present a significant challenge in obtaining high-performance (Nd,Pr)-saving magnets. In particular, excessive Ce substitution (>40 % of the total RE) severely degrades hard magnetic properties, creating a significant limit for increasing Nd/Pr-saving rate of the magnets[5)]. In this work, we demonstrate a simultaneous enhancement of coercivity and remanence in ~51 % (Nd, Pr)-saving magnets *via* the grain boundary diffusion process (GBDP) using a low-melting Nd-Cu-Al-Ga (NCAG) alloy as diffusion source. As shown in Fig.1, the coercivity of the as-sintered magnet substantially increased from 0.92 T to 1.52 T after GBD-treatment, and it further increased to 1.62 T after post diffusion annealing. Furthermore, the remanence of the as-sintered magnets also improved to 1.07 T after NCAG-GBDP, exhibiting the remanence gain of 0.03 T. In this presentation, we will discuss the microstructural changes induced by NCAG-GBDP to elucidate the mechanism behind simultaneous enhancement of coercivity and remanence in (Nd,Pr)-saving magnets. In particular, the origin of significant coercivity improvement through NCAG-GBDP was clarified in terms of the compositional changes in the shell and crystal structure of Nd-rich phases. Based on our findings, we will suggest key factors for achieving high-performance high-Ce-content magnets to a level of commercial Nd-Fe-B sintered magnets.

1) M. Sagawa *et al.*, J. Appl. Phys., Vol. 7, p.4094 (1985).
2) K. P. Skokov *et al.*, Scr. Mater., Vol. 154, p.289 (2018).
3) Z. C. Lin *et al.*, Acta Mater., Vol. 200, p.502 (2020).
4) O. Gutfleisch *et al.*, Adv. Mater., Vol. 23, p.821 (2011).
5) X. Song *et al.*, Magn. Magn. Mater., Vol. 606, p.172359 (2024).

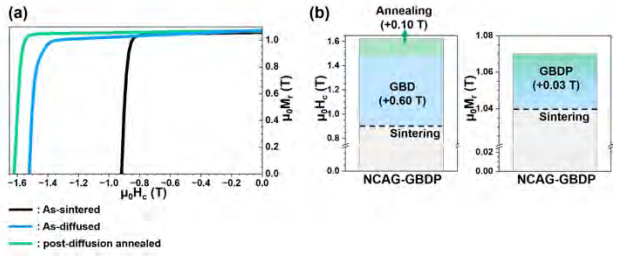


Fig.1

EC-10. Near net shape fabrication of anisotropic Nd-Fe-B magnet using hot roll method

C. Pan, J. Cui, W. Tang
Ames National Laboratory, Ames, Iowa, United States

Nd-Fe-B is the most powerful magnet at room temperature. It plays a dominant role in energy efficiency and renewable energy applications due to its high energy density. However, making Nd-Fe-B magnets, especially into small sizes, can be challenging and costly because of machining failure and low productivity of the conventional batch processing. Moreover, Nd-Fe-B needs critical heavy rare earth elements to be functional at elevated temperature. One approach to bypass this HRE criticality issue is to utilize the grain size effect on coercivity, e.g., nanograin size magnet can perform the same as the micron-grain size magnet with 4-6% of Dy. However, making nanograin magnet requires a two-step process: hot-press for densification and hot-deformation for texture development. It is an inherently expensive process. Here, we report a novel Nd-Fe-B fabrication method that is continuous and near-net-shape. The process starts with loading Nd-Fe-B powders into a metal tube, packing the powder to 60% dense, then hot-rolling the powders into full density. We showed that hot rolling at ~750°C with 70% thickness reduction can result in nearly full density anisotropic magnet with high energy product (44.0 MGOe). This novel method allows cost-effective production of near-net-shape Nd-Fe-B magnetic with good and consistent magnetic properties.

EC-11. Rare-Earth Coating of Nd-Fe-B Powder by a Low-Temperature Reduction-Diffusion Process for Coercivity Enhancement

J. Kim[1], Y. Hirayama[1], S. Sugimoto[1, 2]
[1]National Institute of Advanced Industrial Science and Technology (AIST), Nagoya, Japan, [2]Graduate School of Engineering, Tohoku University, Sendai, Japan

Driven by electrification, demand for permanent magnets for EV drive motors is increasing, and Nd-Fe-B remains the leading commercial system [1]. In sintered Nd-Fe-B magnets, coercivity is governed by magnetic isolation of the $Nd_2Fe_{14}B$ main phase; non-ferromagnetic grain-boundary phases weaken exchange coupling and enhance coercivity [2]. Dy/Tb-based grain boundary diffusion (GBD) has been widely studied, but uniform control remains challenging because diffusion behavior and microstructural evolution are sensitive to the diffusion source, coating method, and heat-treatment conditions [3]. Powder design before sintering can promote core-shell structures and continuous grain-boundary phases after sintering, leading to coercivity enhancement [4]. The low-temperature reduction-diffusion (LTRD) process enables reduction and diffusion at lower temperatures than conventional RD [5] and is favorable for surface reactions and shallow diffusion-layer formation, i.e., coating or core-shell-like powder formation [6]. RD-processed Sm-Fe-N powders with Mn- or Cr-enriched shells have also been reported, demonstrating improved magnetic properties and thermal stability [7,8]. In this study, the feasibility of Dy coating on Nd-Fe-B powder by the LTRD process was investigated.
An annealed cast Nd-Fe-B ingot was coarse-crushed by hydrogen decrepitation, and fine-milled. After vacuum drying and dehydrogenation, the powder (D_{50} = 2.8 μm) was mixed with Dy_2O_3 and treated by LTRD using Ca with LiCl molten salt at 800 °C for 1.5 h. Elemental mapping revealed a Dy-containing region at the outer part of the Nd-Fe-B particles, indicating formation of a Dy-rich surface layer or shell-like surface modification. The coercivity increased from 456 kA/m for the uncoated powder to 1276 kA/m for the Dy-coated sample. These results demonstrate that LTRD is an effective route for Dy surface modification of Nd-Fe-B powders and suggest potential as a precursor process for grain-boundary structure control in bulk magnets.
[1] C. L. Rom, R. W. Smaha, S. O'Donnell, S. Dugu, S. R. Bauers, MRS Bull. Vol. 49, pp. 738-750 (2024).
[2] J. Li, H. Sepehri-Amin, T. Sasaki, T. Ohkubo, K. Hono, Sci. Technol. Adv. Mater. Vol. 22, pp. 386-403 (2021).
[3] J. He, J. Cao, Z. Yu, W. Song, H. Yu, M. Hussain, Z. Liu,

Metals Vol. 11, p. 1434 (2021).
[4] Y. Li, M. Wu, J. Li, J. Mater. Sci.: Mater. Electron. Vol. 31, pp. 7211-7218 (2020).
[5] J. Kim, S. Okada, K. Takagi, AIP Adv. Vol. 12, p. 035306 (2022).
[6] J. Kim, S. Okada, K. Takagi, K. Ozaki, J. Rare Earths Vol. 42, pp. 1889-1894 (2024).
[7] M. Matsuura, K. Yarimizu, Y. Osawa, N. Tezuka, S. Sugimoto, T. Ishikawa, Y. Yoneyama, J. Magn. Magn. Mater. Vol. 471, pp. 310–314 (2019).
[8] R. Matsuda, K. Yarimizu, M. Matsuura, N. Tezuka, S. Sugimoto, T. Ishikawa, Y. Yoneyama, J. Jpn. Soc. Powder Powder Metallurgy Vol. 66, pp. 116–121 (2019).

EC-12. Achieving uniaxial magnetic anisotropy in Ce2Fe17N3 through Co- and Sm-substitution

N. Pokhrel[1], A. Raja[2], B. Sales[1], G. Samolyuk[1], D. Schlagel[2], O. Palasyuk[2], A. Palasyuk[2], D. Parker[1]
[1]Oak Ridge National Laboratory, Oak Ridge, Tennessee, United States, [2]Ames National Laboratory, Ames, Iowa, United States

Th2Zn17-type structure based permanent magnets such as Sm2Fe17N3 offer strong potential as alternatives to neodymium magnets (NdFeB), but their practical use is limited by phase stability and the scarcity of Sm. Ce-based counterparts, particularly Ce2Fe17N3, are attractive low cost candidates, yet their intrinsic planar magnetic anisotropy restricts permanent-magnet performance. Here, we induce uniaxial magnetic anisotropy in Ce2Fe17N3 through two approaches: (i) Co substitution on the Fe sublattice and (ii) partial substitution of Ce with Sm. Combined density functional theory and experimental results show that both strategies modify the 3d–4f interactions and band filling, yielding magnetization values up to ~1.2 T and magnetocrystalline anisotropy energies exceeding 1 MJ/m3 for Co-alloyed compositions, with significantly larger anisotropy achieved upon Sm substitution. In addition, the Sm-substituted Ce2Fe17N3 samples exhibit enhanced high-temperature stability compared to Sm2Fe17N3. These findings demonstrate that Ce2Fe17N3-based alloys can deliver magnetic performance suitable for permanent-magnet applications while reducing cost and reliance on critical rare-earth elements, and they provide practical design guidelines for rare-earth-lean magnets for energy and industrial applications.

EC-13. Enhancing Coercivity of Bulk $ThMn_{12}$-type $SmFe_{10}V_2$ Magnets through Dy-Cu Grain Boundary Diffusion

J. Park[1], X. Zheng[1, 2]
[1]Korea Institute of Materials Science, Changwon-si, Korea (the Republic of), [2]Department of Materials Science and Engineering, Pusan National University, Busan, Korea (the Republic of)

Rare-earth-lean $SmFe_{12}$-based compounds with the $ThMn_{12}$ structure are promising candidates for high-performance permanent magnets. However, stabilization of the $ThMn_{12}$ phase typically requires nonmagnetic elements such as V, which reduces the saturation magnetization (M_s) and creates a trade-off between coercivity (H_c) and M_s. In this work, Dy–Cu grain boundary diffusion processing (GBDP) was applied to bulk V-stabilized $SmFe_{10}V_2$ magnets to enhance H_c without compromising M_s.
As shown in Fig. 1, the $Dy_{70}Cu_{30}$-diffused sample at the optimal temperature of 860 °C exhibits a significantly wider hysteresis loop compared to the original sample, with H_c increasing from 3.8 to 8.5 kOe. Notably, M_s remains nearly unchanged after the process, demonstrating that GBDP effectively alleviates the M_s–H_c trade-off. Microstructural analyses revealed that this enhancement originates from the formation of a continuous Dy- and Cu-rich grain-boundary phase network surrounding the $ThMn_{12}$-type grains.
To directly clarify the coercivity mechanism, in-situ magneto-optical Kerr effect (MOKE) microscopy was performed. Fig. 2 illustrates the digitized magnetization maps during demagnetization, where the propagation of reversed domains is progressively impeded at the Dy-rich intergranular regions. This observation, combined with suppressed low-field response in the initial magnetization curves, confirms a transition from nucleation-dominated behavior to a strong grain-boundary pinning mechanism. These results indicate that Dy–Cu grain-boundary engineering is a practical and effective route for optimizing the magnetic performance of bulk $SmFe_{12}$-type rare-earth-lean permanent magnets.
[1] K. Hono and H. Sepehri-Amin, "Strategy for high-coercivity Nd–Fe–B magnets," Scr. Mater. 67, 530–535 (2012).
[2] Y. Hirayama, et al., "Intrinsic hard magnetic properties of $Sm(Fe_{1-x}Co_x)_{12}$ compound with the $ThMn_{12}$ structure," Scr. Mater. 138, 62–65 (2017).
[3] A.M. Schönhöbel, et al., "Intrinsic magnetic properties of $SmFe_{12-x}V_x$ alloys with reduced V-concentration," J. Alloys Compd. 786, 969–974 (2019).
[4] X. Tang, et al., "Role of V on the coercivity of $SmFe_{12}$-

based melt-spun ribbons revealed by machine learning and microstructure characterizations," Scr. Mater. 200, 113925 (2021).
[5] X. Zheng, J. Park, et al., "Optimizing the microstructure and magnetic properties of $SmFe_{12}$-based bulk magnets by tuning the V-substitution," J. Magn. Magn. Mater. 628, 173177 (2025).

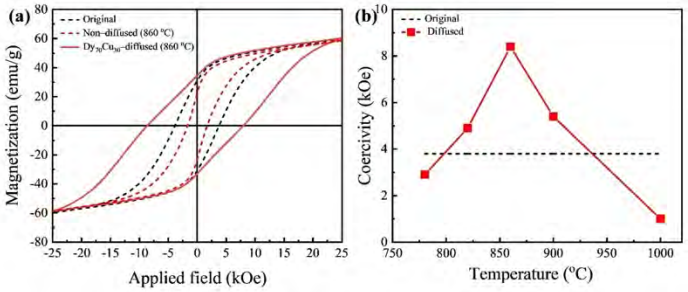


Fig. 1. (a) Magnetic hysteresis loops of the original and $Dy_{70}Cu_{30}$-diffused (860 °C) $SmFe_{10}V_2$ magnets, and (b) variation of H_c as a function of diffusion temperature.

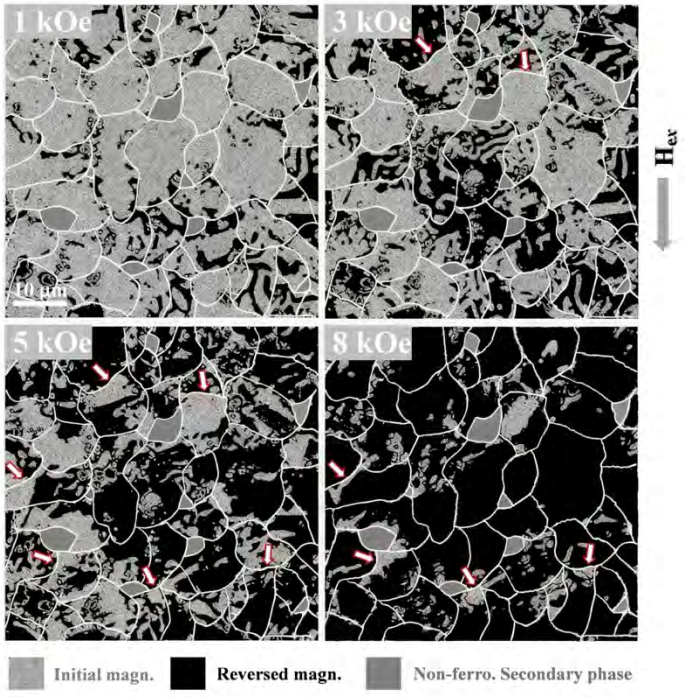


Fig. 2. Digitized magnetization maps reconstructed from in-situ MOKE observations, showing domain-wall pinning at the grain boundaries of the $Dy_{70}Cu_{30}$-diffused magnet.

SESSION ED: AI/MACHINE LEARNING FOR MAGNETISM, HALF-METALS AND MAGNETIC SEMICONDUCTORS

Co-Chair(s): T. Kubota, *Department of Applied Physics, Tohoku University, Sendai, Miyagi, Japan* and J. Nag, *Physics, University of South Florida, Tampa, Florida, United States* and Y. Zhou, *The Chinese University of Hong Kong, Shenzhen, Shenzhen, Guangdong, China*

Thursday, November 5, 2026
08:30 AM-12:00 PM
Coral 2

ED-01. One Model to Rule Them All: From Ultrafast Dynamics to Magnetostatic Modes

E. Iacocca
University of Colorado Colorado Springs, Colorado Springs, Colorado, United States

Numerical simulations have played a pivotal role in predicting and explaining magnetic phenomena. Simulations have become increasingly challenging as atomic-scale phenomena are needed to investigate new materials and effects. On the one hand, atomistic spin dynamics are extremely accurate but cannot simulate a realistically large structure in several cases due to computational limitations. On the other hand, micromagnetic simulations do not have the capability to represent the underlying physics at the atomic scale. This leads to a spatio-temporal region where neither approach is particularly accurate, and multiscale approaches are difficult.

To capture atomic-scale interactions while maintaining the computational advantage of micromagnetic simulations, a pseudospectral Landau-Lifshitz (PS-LL) model was recently introduced [1]. This model uses a convolutional kernel to model atomic interactions within a continuum framework. The PS-LL model has been successfully applied to transient gratings [1,2], multiscale skyrmion dynamics [3], and magnetostatic spin wave modes using a dipole-exchange kernel based on analytical theory [4]. Recently, the model has also been extended to include a new non-equilibrium thermal field to model ultrafast demagnetization [5]. The use of a spectral kernel also allows for the statistical interpretation of the Landau-Lifshitz equation. This is particularly important to integrate machine learning approaches with magnetization dynamics. For example, it has been recently shown that material defect size and density can be predicted based on the dispersion relation and average domain-wall width [6]. The PS-LL model has

the potential to bridge atomic-scale and continuum simulation using multiscale approaches and interface with machine learning to realize a computationally efficient and physics-informed platform aimed at discovering new magnetic materials.

This work was supported by the U.S. Department of Energy, Office of Basic Energy Sciences under Award Number DE-SC0024339.

[1] K. Rockwell, J. Hirst, T. A. Ostler, and E. Iacocca, Phys. Rev. B 109, L180404 (2024)
[2] L. Foglia et al., Nature Communications 15, 10741 (2024)
[3] M. Copus and E. Iacocca, arXiv:2506.21473 (2025)
[4] A. Roxburgh, M. Copus, and E. Iacocca, npj Computational Materials 11, 369 (2025)
[5] E. Iacocca, arXiv:2603:06929 (2026)
[6] C. Eagan, M. Copus, and E. Iacocca, arXiv:2603.10182 (2026)



Figure 1: Illustration of the pseudospectral model describing magnetization dynamics from micromagnetic to atomistic by providing the magnon dispersion relation as a kernel. Image of the one ring from https://en.wikipedia.org/wiki/One_Ring.

ED-02. Fine-Tuned Large Language Models for Multi-Property Prediction and Inverse Design of Magnetic Materials

S. Itani[1], Y. Zhang[1], R. Itani[2], D. Kassym[3], Y. Kao[4, 5], J. Zang[1]
[1]Physics and Astronomy, University of New Hampshire, Durham, New Hampshire, United States, [2]Department of Electrical and Computer Engineering, University of New Hampshire, Durham, New Hampshire, United States, [3]Department of Mathematics, Nazarbayev University, Astana, Kazakhstan, [4]Department of Physics, National Taiwan University, Taipei, Taiwan, [5]Center for Theoretical Physics, National Taiwan University, Taipei, Taiwan

The discovery of high performance magnetic materials is often limited by the need to simultaneously optimize multiple interdependent magnetic properties. Conventional machine learning approaches often focus on single property prediction and struggle to incorporate incomplete or heterogeneous experimental datasets. Here, we present a unified large language model (LLM) based framework for magnetic order classification, multi property prediction, and inverse design of magnetic materials. Using the LLM generated experimental database (NEMAD), we fine-tune foundation models, including Mistral-7B and Qwen-14B, using a two stage training pipeline. In the first stage, models undergo supervised fine-tuning via Low-Rank Adaptation (LoRA); in the second, they are refined through reinforcement learning with Group Relative Policy Optimization (GRPO), guided by a numerically grounded reward function. Our fine-tuned models successfully perform magnetic order classification directly from compositional inputs, distinguishing non magnetic, ferromagnetic, and antiferromagnetic compounds with an overall accuracy of 90.65%. Furthermore, the framework enables the simultaneous forward prediction of multiple properties—including curie temperature, saturation magnetization, coercivity, magnetocrystalline anisotropy constant, and maximum energy product—within a single unified prompt. GRPO refinement with a numerical reward function substantially reduces prediction error for heavy-tailed properties spanning multiple orders of magnitude, raising the coefficient of determination (R2) for maximum energy product from 0.34 to 0.73. Beyond forward prediction, the framework supports inverse design, generating candidate magnetic compositions that satisfy user-specified property constraints. Finally, we apply the framework to screen the GNoME database and identify candidate materials for high-performance permanent magnets, including both rare-earth-free and rare-earth-containing compositions. This work establishes a scalable,

generalizable LLM-based paradigm for data-driven discovery of functional materials.

ED-03. Extracting Material Parameters from Magnetic Domain Patterns with Deep Learning

J. Smith[1, 2], D. Suess[1], F. S. Slanovc[2]
[1]*Faculty of Physics, University of Vienna, Vienna, Austria,*
[2]*Silicon Austria Labs, Villach, Austria*

The accurate measurement of intrinsic material parameters responsible for the formation of complex magnetic domain patterns is of critical importance for the characterisation of magnetic media. Conventionally, such parameters are determined through a combination of experimental and numerical methods. However, these approaches are disjoint, relying either on specialised experimental equipment or computationally intensive simulation techniques [1, 2, 3].

In this work, we present a data-driven framework for the simultaneous extraction of key micromagnetic parameters from magnetic domain patterns using a Convolutional Mixture Density Network. Specifically, we demonstrate the retrieval of Ms, A, Ku, and D from simulated magnetic thin films. An example of such a domain is shown in Fig. 1.

Mixture Density Networks (MDNs) couple a standard neural network with a Gaussian mixture model [4], enabling the output to be expressed as a weighted superposition of Gaussian distributions. This accommodates arbitrary output distributions, including strongly non-Gaussian, multimodal, and truncated cases. Crucially, the MDN framework provides a means of quantifying predictive uncertainty, giving a significant advantage over deterministic regression approaches when considering the interpretability of the results.

Figure 2 presents the parameter extraction results for the sample shown in Fig. 1. The presence of well-defined domain wall structures yields sharply peaked posterior distributions, with predicted mean values in close agreement with the ground truth. Conversely, in cases where the domain pattern contains insufficient information for unambiguous parameter retrieval, the model appropriately reflects this by producing broader, more diffuse distributions, thereby expressing uncertainty in a physically interpretable manner.

We further aim to apply this framework to the extraction of material parameters from magneto-optical Kerr effect (MOKE) microscopy images of sputtered W/CoFeB/MgO thin films.

[1] S. Ikeda, K. Miura, H. Yamamoto et al., Nature Materials, Vol. 9, p.721 (2010)
[2] S. Koraltan et. al., arXiv:2403.16725 (2024)
[3] D. Suess, et. al., Scientific Reports, Vol. 15, p.42867, (2025)
[4] C. Bishop, Neural Computing Research Group Report, Vol. NCRG/94/004, 1994.

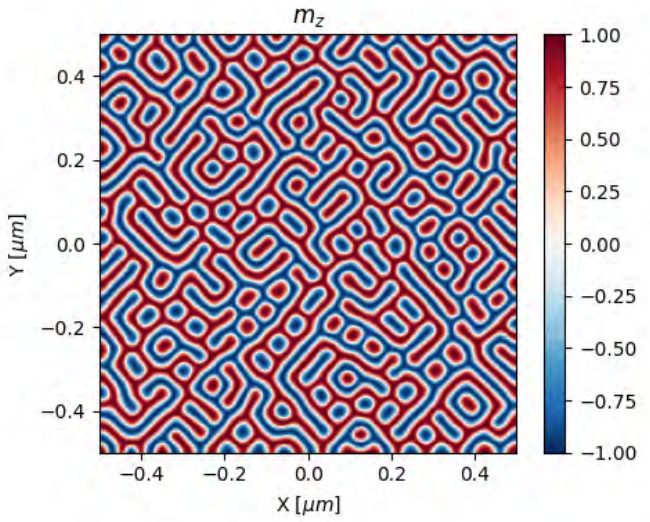


Fig. 1: A representative simulated domain pattern.

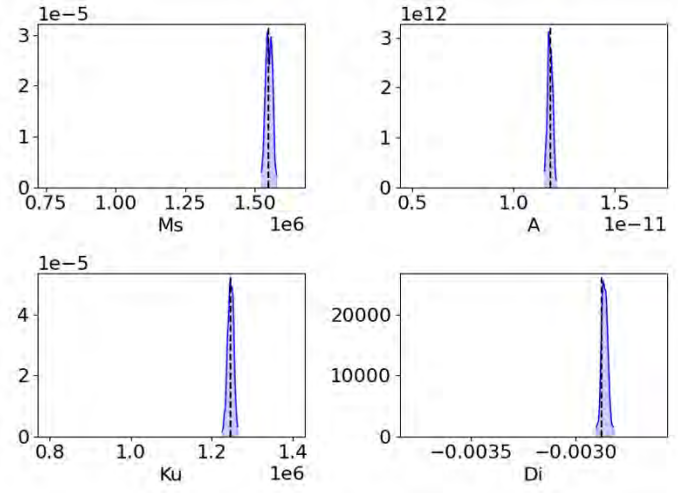


Fig. 2: Probability density functions for parameter extraction of Fig. 1. The distributions are sharply peaked and in close agreement with the ground truth (dotted line).

ED-04. Deep learning statistical defect models on magnetic material dynamic and static properties

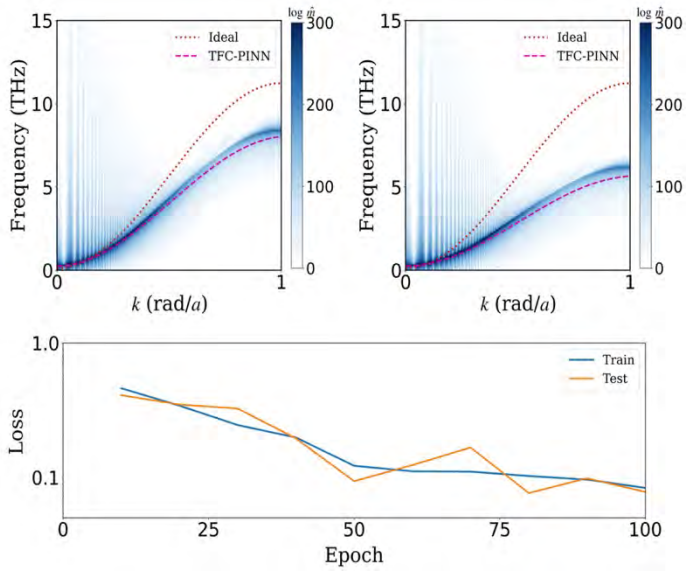
C. Eagan, M. Copus, E. Iacocca
University of Colorado Colorado Springs, Colorado Springs, Colorado, United States

Developments in deep learning techniques show promise in material science to predict new materials and physical properties [1]. Machine learning and artificial intelligence have emerged as complementary approaches to numerical techniques in many areas of science [2], including material discovery. In the field of magnetism, machine learning techniques have been used, e.g., to accelerate computations [3,4]. However, leveraging machine learning to explore the impact of material defects on topological textures has remained virtually unexplored. Deep learning requires training a model on large volumes of data and the process is inherently statistical in nature, lending itself well to statistical training architecture. Here, we present a novel application of deep learning applied to predicting magnetic material responses given specific defect parameter thresholds [4].

Material defects are modeled as random telegraph noise [5] and integrated into a pseudospectral Landau-Lifshitz (PSLL) approach [6] to generate datasets. We leverage a theory of functional connections (TFC) approach inside a physics informed neural network (PINN) to predict dispersion relations specific to corresponding defect density parameters. The results of the TFC-PINN on predicting magnetization behavior in materials based on defect factors are shown in Figure 1. We also leverage a convolutional neural network (CNN) over domain wall profiles to recover the defect parameter thresholds for specific domain wall width and energy. The CNN recovered and predicted the correct relationship between statistical defect parameters and the corresponding domain wall width and energy solutions of the PSLL solver. This work has shown a method for learning and predicting the average effect of defects in the profile of magnetic solitons [7] and will inform novel approaches to predict the material parameters and features required to stabilize higher-dimensional topological states in new materials.

This work was supported by the U.S. Department of Energy, Office of Basic Energy Sciences under Award No. DE-SC0024339.

[1] M. Raissi, P. Perdikaris, and G. E. Karniadakis, J. Comp. Phys. 378, 668-707 (2019)
[2] Y. LeCun, Y. Bengio, and G. Hinton, Nature 521, 436 (2015).
[3] S. Schaffer, N. J. Mauser, T. Schrefl, D. Suess, and L. Exl, IEEE Transactions on Magnetics 58, 7100506 (2022).
[4] L. Exl, N. J. Mauser, S. Schaffer, T. Schrefl, and D. Suess, Journal of Computational Physics 444, 110586 (2021).
[5] S. Machlup, J. Appl. Phys. 25, 341-343 (1954)
[6] K. Rockwell, *et al*., Phys. Rev. B 109, L180404 (2024)
[7] C. Eagan, M. Copus, E. Iacocca, https://arxiv.org/abs/2603.10182



TFC-PINN predicted vs actual modified dispersion with material defect-density. The bottom panel displays the training-loss curve

ED-05. Predicting nonlinear magnetization dynamics with Fourier neural operator

C. Eagan, E. Iacocca
University of Colorado, Colorado Springs, Colorado Springs, Colorado, United States

Machine learning and artificial intelligence (AI) have emerged as complementary approaches to numerical techniques in many areas of science [1]. Neural networks, such as physics-informed neural networks (PINNS), are able to learn and predict specific time-dependent states while adhering to the underlying physics [2], providing a more efficient, accelerated solver solution for complex systems, including magnetism. Machine learning has been used to

solve magnetization dynamics [3], but many methods still must balance accuracy at the expense of computational efficiency. For example, solving ultrafast magnetism dynamics is numerically time consuming due to the compute strain, but such a system is reminiscent of flows [4], and therefore may lend itself to exploration of machine learning techniques suitable to general systems described by flows.

We investigated the suitability and potential applications of the Fourier Neural Operator (FNO) [5] to ferromagnetic magnetization dynamics, with 2D magnetization data generated by the pseudospectral Landau-Lifshitz numerical solver [6]. Our results indicate that the FNO achieves increasingly accurate prediction performance with later timesteps, which correspond to less chaotic dynamics dominated by lower spatial Fourier modes; the FNO is less accurate at earlier timesteps (see figure 1). This result is consistent with the inherent architecture of the FNO, which relies on the cutoff of higher modes for computational efficiency [5]. The degraded early evolution may limit its capacity to resolve the earlier timestep fine-scale features characteristic of nonlinear and far-from-equilibrium dynamics, which is often the regime of greatest physical interest for magnetic materials. Our results suggest that extending the number of retained Fourier modes is a path toward improving early-timestep accuracy for the FNO and balancing computational efficiency with greater predictive capabilities in the interesting regimes for magnetization dynamics in materials.

This work was supported by the U.S. Department of Energy, Office of Basic Energy Sciences under Award No. DE-SC0024339.

[1] Y. LeCun, Y. Bengio, and G. Hinton, Nature 521, 436 (2015).
[2] M. Raissi, P. Perdikaris, and G. E. Karniadakis, Journal of Computational Physics 378, 686 (2019).
[3] L. Exl, N. J. Mauser, S. Schaffer, T. Schrefl, and D. Suess, Journal of Computational Physics 444, 110586 (2021).
[4] Iacocca, E., Liu, TM., Reid, A.H. et al. Nat Commun 10, 1756 (2019). https://doi.org/10.1038/s41467-019-09577-0
[5] Zongyi Li, et al., arXiv:2010.08895
[6] K. Rockwell, et al., Phys. Rev. B 109, L180404 (2024)

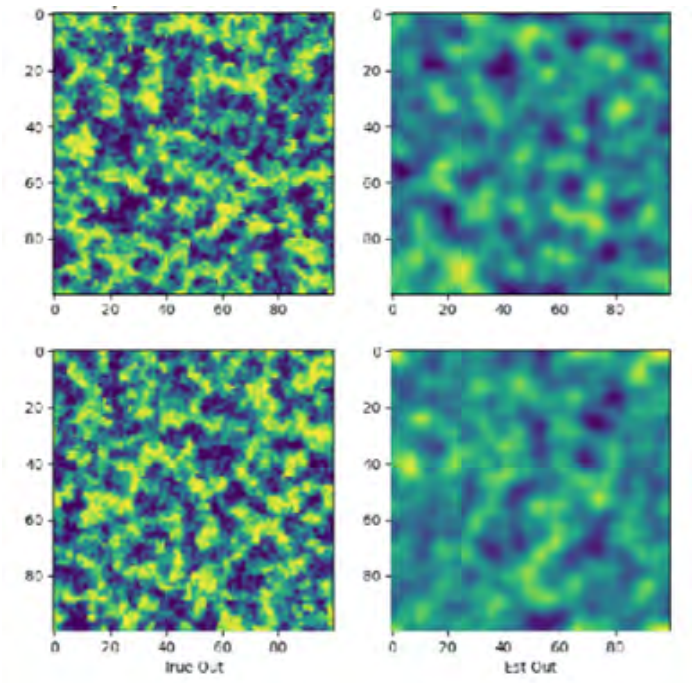


Figure 1. 2D magnetization state: true (left) vs FNO predicted (right)

ED-06. Fourier Neural Operators for full-field Micromagnetic Simulation of Skyrmion breathing dynamics

S. Sabyasachi[1], M. Rajib[1], J. Atulasimha[1, 2]
[1]Mechanical & Nuclear Engineering, Virginia Commonwealth University, Richmond, Virginia, United States, [2]Electrical & Computer Engineering, Virginia Commonwealth University, Richmond, Virginia, United States

Micromagnetic simulations based on the Landau-Lifshitz-Gilbert (LLG) equation are often computationally expensive. Recent approaches incorporate machine learning to reduce computational cost [1, 2]. Chen et al. [1] used Neural ODEs to forecast scalar observables of spintronic experiments, while Cai et al. [2] introduced NeuralMAG, a U-Net that replaces the demagnetizing-field FFT inside the LLG loop and offered generalizable full-field micromagnetic simulation. Resonant dynamical scenarios- such as skyrmion breathing and transfer across spatial discretization remain open.

We have applied a two-dimensional Fourier Neural Operator (FNO) [3] to predict skyrmion breathing dynamics in response to time varying uniaxial anisotropy $K_u(t)$ by learning a global operator in the Fourier space rather than local convolutions. A masked region was identified as region

of interest (ROI) for application of FNO (Fig. 1). The input fields of magnetization components within masked region were elevated to a higher dimensional latent space with 1×1 convolution. Each layer then utilizes a SpectralConv2d block, which performs a truncated Fourier transform and applies learnable complex weights to low frequency modes (separately for positive and negative modes) with a parallel linear combination capturing local channel interactions. With this approach the system captures both long range interactions (dipolar) and shortrange interactions (exchange interactions). Training data comprising magnetization components (m_x, m_y, m_z) and corresponding K_u values was generated using MuMax3 with cell size 2 nm (below the exchange length l_ex ≈ 3.8 nm). A recurrent time-stepping scheme improves long-horizon prediction accuracy. To enforce the |m| = 1 constraint, we combine a soft unit-norm penalty in the loss with hard renormalization at inference. Preliminary results show on 500×500 grid a 5× speedup while reproducing skyrmion breathing mode trajectories (Fig. 2). Ongoing work explores inference at grid resolutions finer than training and characterizes the range of resolution invariance, a capability distinct from fixed-grid U-Net surrogates.

[1] X. Chen, F. A. Araujo, M. Riou, et al., "Forecasting the outcome of spintronic experiments with Neural ODEs," Nat. Commun., vol. 13, p. 1016 (2022)
[2] Y. Cai, J. Li, and D. Wang, "Fast and generalizable micromagnetic simulation with deep neural nets," Nat. Mach. Intell., vol. 6, pp. 1330–1343 (2024)
[3] Z. Li, N. Kovachki, K. Azizzadenesheli, et al., "Fourier neural operator for parametric PDEs," Proc. ICLR (2021).

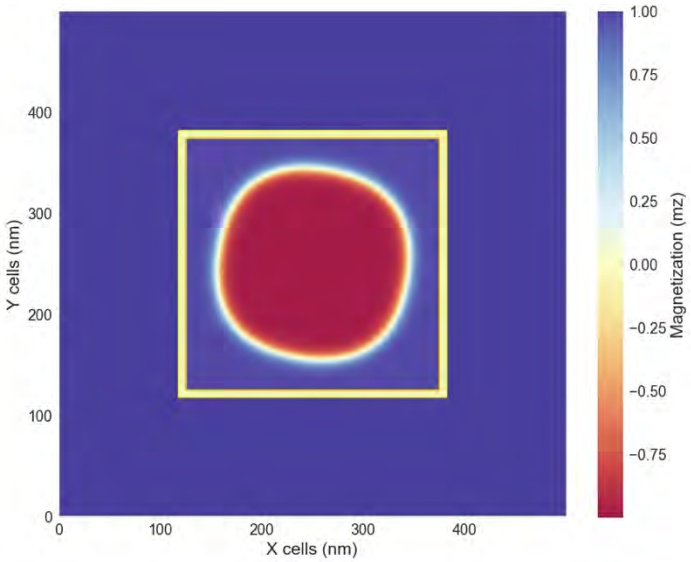


Fig. 1 Masked ROI for application of FNO

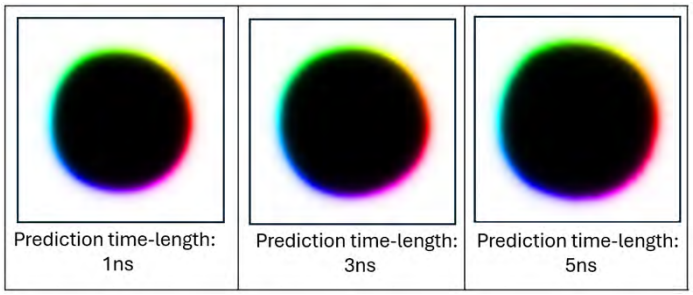


Fig. 2 Skyrmion progressively expands with decreasing uniaxial anisotropy

ED-07. Advanced micromagnetic simulation of several billion magnetic unknowns on multiple GPUs using JAX and AI-assisted programming

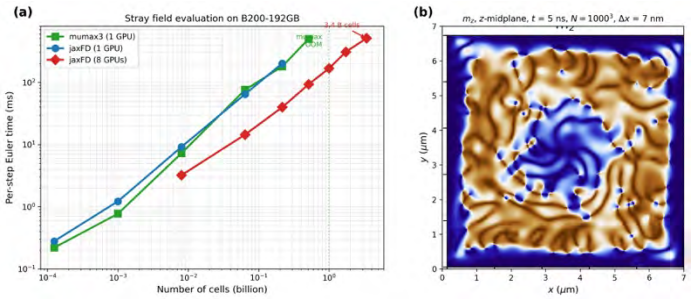
D. Suess, R. Kraft, F. Bruckner, C. Abert
University of Vienna, Vienna, Austria

We review recent developments in our group on GPU-accelerated micromagnetic simulation software built entirely in JAX, covering both finite-difference (jaxFD) and finite-element (jaxFMM [1]) formulations, explicit Dormand-Prince and implicit preconditioned BDF time integrators [2], and multi-GPU parallelization via JAX's shard_map. A key enabler of this rapid development has been agentic engineering, which dramatically accelerates the development of production-grade GPU code.

The finite-difference solver computes the demagnetization field by FFT convolution with the Newell tensor and is validated on muMAG Standard Problem 4. Multi-GPU scaling distributes both the demagnetization kernel and the FFT workspace across devices, enabling simulations with several billion finite-difference cells. On 8 NVIDIA B200-192GB GPUs, we demonstrate stray-field evaluation of a 1504^3 cube (3.4 billion cells) in 492 ms (Fig. 1a). For a direct comparison at N=600 (216 million cells), jaxmag on 8×B200 integrates 1 ns of LLG dynamics in 16.3 s, compared to 327 s for mumax3 on a single B200—a 20× speedup. Fig. 1(b) shows the transient domain state of a 7×7×7 μm^3 Permalloy cube (one billion cells, Δx = 7 nm) after 5 ns of LLG dynamics (integration time 5.6 min, setup time 6 min on 8×B200), corresponding to roughly 1 minute of simulation time per nanosecond of physical time. At these problem sizes, micromagnetic simulations bridge the gap from nanoscale devices to mesoscale structures such as thin films of millimetre lateral extent.

For unstructured meshes, jaxFMM [1] provides a fast multipole method. We compare the implicit preconditioned BDF scheme with explicit Dormand-Prince integration for both stiff and non-stiff problems on finite-difference and finite-element meshes, all running purely on GPU.

[1] R. Kraft et al., arXiv:2511.15269 (2025).
[2] Suess, Dieter, et al. *Journal of Magnetism and Magnetic Materials* 248.2 (2002): 298-311.



10:18 AM-10:45 AM
Break

ED-08. The 4-2 rule: The (Proposed) Answer to Heusler Alloys, Stability, and (Ordering) Everything

P. LeClair, A. Hauser
Physics and Astronomy, The University of Alabama, Tuscaloosa, Alabama, United States

Fabrication of ternary intermetallic alloys with high atomic ordering is a critical step to realizing their predicted functional properties. For example, Heusler alloys have long been predicted with high spin polarization, low spin damping, and high ferromagnetic ordering temperatures. Unfortunately (paraphrasing Douglas Adams), attempts to make highly ordered Heusler alloys have made a lot of people very angry, and has been widely regarded as a bad move. Atomic ordering has typically been lower than predicted, to the detriment of predicted properties. Initial models and rules-of-thumb using, e.g., electron counting, electronegativity, or atomic size fall apart once a wide range of elemental choices are investigated. This result is perhaps not surprising, as Heusler alloys (like modern elevators) are strange and complex entities, but we should not give up and go mad just yet.

In this work, we propose re-imagining the placement of a Heusler alloy system's available Slater-Pauling electrons (the s- and d-orbital electrons available for bonding) in the calculated Full Heusler hybridized molecular orbital structure of Galanakis et al, using the alternating site counts of 4 and 2 spin-down electrons proposed by Butler et al to minimize energy in half-metallic ferromagnets. By applying a system of common sense steps, we posit that one can test the feasibility of formation and site occupations of full ($L2_1$) and inverse (XA) forms of potential Heusler alloys without need for long and computationally expensive calculations, which may still not cover every potential probability that the universe has in store. We reviewed a substantial amount of existing experimental evidence suggesting that alloys that do not follow the electron structure inevitably adopt a different, more energetically favorable structure or exhibit multi-phase structures or phase segregation. We further propose that one can apply the rule set to indicate how one might stabilize an infeasible compositional choice through compensation or elemental substitution. This approach offers a promising solution to the long-standing theoretical-experimental discrepancy problem in this field.

ED-09. Half-Metallicity in Tetragonal Mn_2PtSn with Non-coplanar Spin Structure Revealed by Negative Anisotropic Magnetoresistance

T. Tasaki[2, 1], T. Dohi[2], K. Saijo[2, 1], S. Fukami[2, 1, 3]
[1]Department of Electronic Engineering, Tohoku Univ., Sendai, Japan, [2]Lab. for Nanoelectronics and Spintronics, RIEC, Tohoku Univ., Sendai, Japan, [3]WPI-AIMR, Tohoku Univ., Sendai, Japan

Tetragonal Heusler magnets have attracted great attention as a platform of emergent spin-transport phenomena owing to their rich electronic and magnetic phases. The real-space Berry curvature from scalar spin chirality in noncoplanar spin textures is widely considered to underlie anomalous transport phenomena including the topological Hall effect [1,2]. Recently, it has been suggested that, in addition to real-space spin topology, momentum-space electronic structures such as half-metallicity and Weyl semimetal characteristics play an important role in their transport properties [3,4]. In particular, as the topological Hall effect is weighted by spin polarization, half-metallicity is a key factor for spin transport in these systems. Furthermore, since the density of states is highly sensitive to structural imperfections in Heusler systems [5–7], applying a simple and cost-effective method for probing electronic structure is of particular importance.

I

n this study, we investigate a tetragonal inverse Heusler compound Mn_2PtSn, which hosts a non-coplanar spin structure. We observe a negative anisotropic magnetoresistance (AMR) consistent with the *s*–*d* scattering model [8], indicating a half-metallic band structure.

As shown in Fig. 1, Mn_2PtSn thin films exhibit a negative AMR signal independent of field and temperature. The AMR amplitude (ΔMR) saturates at high fields, consistent with magnetization saturation, indicating its intrinsic magnetic origin. Furthermore, the magnitude of ΔMR increases with decreasing temperature. This suggests that the Fermi level (E_F) is near the half-metallic gap edge or that in-gap states are present [Fig. 2]; in such cases, thermally excited minority-spins reduce ΔMR at higher temperatures, while suppression of thermal excitation at low temperatures enhances the AMR signal. These results reveal a half-metallic electronic structure in Mn_2PtSn, as inferred from AMR, and provide insights that advance understanding of its nontrivial transport properties.

[1] A. K. Nayak, V. Kumar and T. Ma *et al*., Nature, Vol. 548, p. 561 (2017).
[2] Z. H. Liu, A. Burigu and Y. J. Zhang *et al*., Scr. Mater. Vol. 142, p. 122-125 (2018).
[3] A. Bhattacharya, S. PC and A. Ahmed *et al*., Adv. Funct. Mater., Vol. 35, p. 2424841 (2025).
[4] M. Nakamura, D. Morikawa and X. Yu et al., J. Phys. Soc. Jpn., Vol. 87, p. 074704 (2018).
[5] S. V. Faleev, Y. Ferrante and J. Jeong et al., Phys. Rev. Appl., Vol. 7, p. 034022 (2017).
[6] V. K. Kushwaha, S. Kokado and S. Kasai et al., Phys. Rev. Mater., Vol. 6, p. 064411 (2022).
[7] G. Li, Q. Sun and Y. Zheng *et al*., Phys. Rev. B, Vol. 112, p.144439 (2025).
[8] S. Kokado, M. Tsunoda and K. Harigaya *et al*., J. Phys. Soc. Jpn., Vol. 81, p. 024705 (2012).

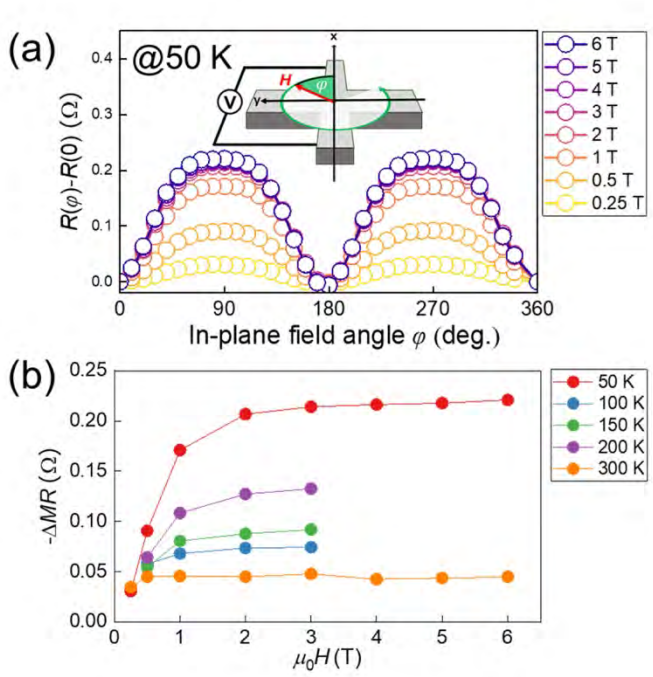


Fig. 1 (a) Angular dependence of the AMR at different field strengths at 50 K. (b) Temperature and field dependence of the AMR amplitude.

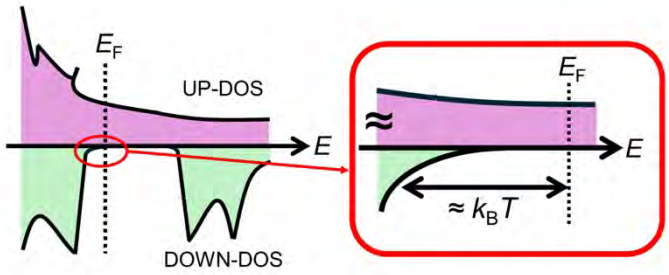


Fig.2 Schematic illustration of a possible half-metallic band in a Mn_2PtSn prepared in this study.

ED-10. Chemical control of electronic structure and emergent transport in quaternary Heusler alloy CoRuCrGe

J. Nag[1, 2], P. Sharma[1], R. Roy Chowdhury[3, 1], S. Jan[1], A. Alam[2], K. G. Suresh[2], M. Phan[1, 4], S. Witanachchi[1], H. Srikanth[1]
[1]Physics, University of South Florida, Tampa, Florida, United States, [2]Physics, Indian Institute of Technology, Mumbai, Maharashtra, India, [3]Physics, Dream Institute of Technology, Maulana Abul Kalam Azad University of Technology, Kolkata, West Bengal, India, [4]Center for Materials Innovation and Technology, VinUniversity, Hanoi, Viet Nam

Engineering the electronic structure of quaternary Heusler alloys through targeted site substitution offers a powerful route to control emergent magnetic and transport phenomena. Here, we investigate the impact of Mn-site substitution by Fe on the structural, magnetic, and magnetotransport properties of the martensitic Heusler system CrRuMnGe. [1] While the parent compound exhibits a low-temperature martensitic transition, the substituted system, CoRuCrGe, stabilizes in a cubic phase (a ~5.90 Å) with ~50% antisite disorder and no structural transformation, providing a clean platform to isolate the role of electronic structure tuning. Magnetic measurements show strong ZFC-FC bifurcation, non-saturating MH behavior (saturation moment of ~1.5 μ_B/f.u.), and field-dependent spin freezing, indicative of a frustrated, glassy magnetic ground state, corroborated by AC susceptibility. Transverse susceptibility measurements further confirm cluster-glass behavior. This alloy shows semiconducting-like longitudinal resistivity, while magnetoresistance and Hall measurements uncover pronounced anomalous transport signatures, pointing to unconventional charge dynamics governed by underlying magnetic correlations. First-principles calculations reveal a semimetallic electronic structure with a ferrimagnetic ground state, where substitution-driven hybridization of transition-metal d-states reshapes the low-energy band structure. Our results demonstrate that Mn-site substitution effectively tunes the electronic structure, suppresses martensitic instability, and stabilizes a frustrated magnetic state that drives unconventional magnetotransport in quaternary Heusler alloy CoRuCrGe.

[1] A. Chanda, J. Nag and N. Schulz, Phys. Rev. B., Vol. 109, p. 224415 (2024)

SESSION EE: COMPLEX MAGNETIC ORDERS AND SPIN TEXTURES

Co-Chair(s): R. Kukreja, *Materials Science and Engineering, University of California, Davis, Davis, California, United States* and Y. Tao, *Chemical Engineering and Materials Science, University of Minnesota, Minneapolis, Minnesota, United States*

Thursday, November 5, 2026

08:30 AM-12:00 PM

South Pacific 1/2

EE-01. Emergent Functionality of Spin Spirals across *p*-Wave and Topological Magnets

S. Okumura[1, 2, 3]

[1]*Quantum-Phase Electronics Center, The University of Tokyo, Tokyo, Japan,* [2]*Center for Emergent Matter Science, RIKEN, Wako, Japan,* [3]*WPI-SKCM2, Hiroshima University, Higashi-Hiroshima, Japan*

Spin spiral states have attracted much attention as a class of antiferromagnets that break spatial inversion symmetry, resulting in odd-parity spin splitting, and have recently been highlighted in the emerging concept of *p*-wave magnetism. These spin spiral states exhibit a variety of emergent phenomena, such as magnetoelectric effects, spin-dependent transport, and optical responses, which are highly controllable through solitonic or conical modulations of spin spirals.

In this talk, we present our recent findings on the emergent electromagnetic functionalities associated with exotic spin textures in itinerant magnets, based on spin–charge-coupled systems. A spin spiral breaks parity due to the chirality and leads to various quantum phenomena. We provide a new insight into the origin of the anomalous Hall effect in a spin spiral (Fig. 1) [1], which arises from the odd-parity spin splitting and is experimentally observed in a metallic p-wave magnet [2]. Reflecting the asymmetric band dispersion, the spin spiral exhibits nonlinear spin transport [3] and an enormous photovoltaic effect [4] depending on the spin chirality (Fig. 2). Furthermore, superpositions of the spin spirals generate various topological spin crystals, such as meron, monopole, and hopfion crystals [5-8]. We suggest the stabilization mechanisms of such complex topological textures, and reveal the characteristic quantum transport, optical responses, and dynamics beyond skyrmion physics.

[1] S. Okumura, M. Hirschmann, and Y. Motome, arXiv:2512.14071 (2025).
[2] R. Yamada, M. Birch, P. Baral *et al.*, Nature 646, 837 (2025).
[3] S. Okumura, H. Ishizuka, Y. Kato *et al.*, Appl. Phys. Lett. 115, 102401 (2019).
[4] S. Okumura, T. Morimoto, Y. Kato *et al.*, Phys. Rev. B 104, L180407 (2021).
[5] K. Shimizu, S. Okumura, Y. Kato *et al.*, Phys. Rev. B 103, 184421 (2021).
[6] A. Kajihara, S. Okumura, and Y. Motome, arXiv:2602.05332 (2026).
[7] S. Okumura, S. Hayami, Y. Kato *et al.*, Phys. Rev. B 101, 144416 (2020).
[8] S. Kasai, K. Shimizu, S. Okumura *et al.*, Phys. Rev. B 112, 184424 (2025).

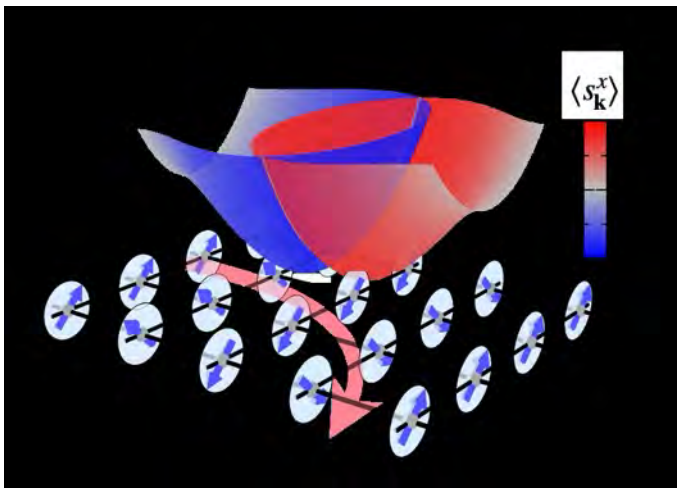


Fig. 1: Odd-parity spin splitting of electronic bands and anomalous Hall effect on a spin spiral.

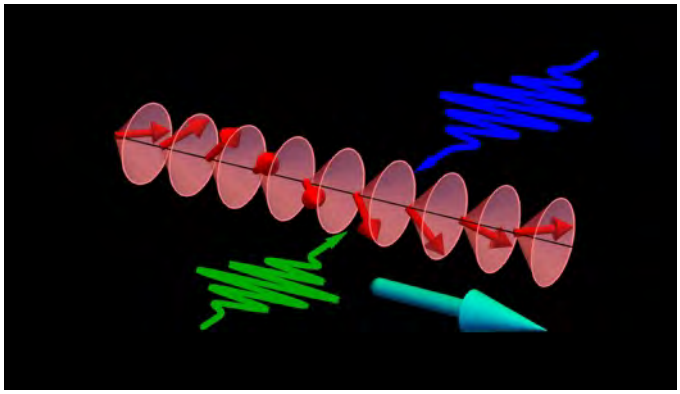


Fig. 2: Schematic of photocurrent in a conical magnetic state.

EE-02. Magnetic Long-range Order In The Purely Organic Triangular Magnet TNN-CH_3CN

M. Pardo-Sainz[1, 2], Y. Kamiya[6], T. Ono[2], K. Kojima[3], K. Ohishi[4], J. Rodriguez Velamazan[5], Y. Hosokoshi[2], J. Campo[1]
[1]Spanish National Research Council (CSIC), Zaragoza, Spain, [2]Osaka Metropolitan University, Sakai, Japan, [3]TRIUMF, Vancouver, British Columbia, Canada, [4]CROSS, Tokai, Japan, [5]Institut Laue Langevin, Grenoble, France, [6]Shanghai Jiao Tong University, Shanghai, China

Equilateral spin triangles have long been a topic of interest in quantum magnetism, offering a fertile ground to explore phenomena such as frustration [1], spin-electric coupling [2], and multiferroic ordering [3]. Despite substantial progress, realizing ideal triangular spin networks remains a challenge, often hindered by structural distortions. The organic compound TNN-CH3CN overcomes these limitations with its isotropic organic radical spins, free from Jahn-Teller effects, allowing uniform exchange interactions. This makes TNN-CH3CN an ideal candidate for exploring novel quantum phases. In fact, the study of its magnetic phase diagram reveals multiferroic behavior, which is the first example for equilateral spin triangles [4].
However, while macroscopic characterization measurements yield valuable insights, they fall short in providing intricate details about the magnetic structure which is developed at atomic or molecular scale within TNN. In this work, we focus on the determination of its magnetic structure at zero-field using single crystal neutron diffraction (SCND) and muon spin relaxation (μSR) experiments. At zero field, the magnetic signal is too weak to be observed in SCND experiments. Nevertheless, by making use of a computational model and DFT calculations, the absence of oscillations in the μSR spectra is shown to be compatible with a high-symmetry magnetic structure at the muon site. The proposed magnetic configuration is consistent with previous studies, as well as with theoretical predictions of its multiferroic nature [5].

[1] J. F. Nossa and C. M. Canali, Phys. Rev. B, 89, 235435 (2014).
[2] S. Nakatsuji *et al.*, Science, 309, 1697-1700 (2005).
[3] Y. Kamiya and C. D. Batista, Phys. Rev. Lett., 108, 097202 (2012).
[4] C. P. Aoyama, PhD thesis, University of Florida (2015).
[5] M. Pardo-Sainz, PhD thesis, University of Zaragoza (2024).

EE-03. Evolution of Competing Magnetic Orders in the Doped Antiferromagnetic Mott Insulator $Ni_{1-x}Co_xS_2$

Y. Tao[1], B. Das[1], M. Maiti[1], K. Heltemes[1], C. Komar[1], G. Rojas[2], J. Garcia-Barriocanal[2], T. Birol[1], C. Leighton[1]
[1]Chemical Engineering and Materials Science, University of Minnesota, Minneapolis, Minnesota, United States, [2]Characterization Facility, University of Minnesota, Minneapolis, Minnesota, United States

For decades, pyrite-structure NiS_2 has been considered a model antiferromagnetic (AF) Mott insulator. Its simple cubic structure, and tunability via electron (Cu) or hole (Co) doping, make it ideal for the study of Mott physics and associated insulator-metal transitions. More recently, NiS_2 has been proposed as a strongly correlated altermagnet, placing it at the forefront of modern materials research [1-4]. Despite extensive prior work, the doping evolution of the electronic and magnetic phases of NiS_2 remains incompletely understood, largely due to overlooked surface (or step-edge) conduction and complex magnetic ordering. Here, we systematically examine $Ni_{1-x}Cu_xS_2$ and $Ni_{1-x}Co_xS_2$ single crystals across their full composition ranges using magnetometry, heat capacity, transport, neutron diffraction, and scanning tunneling microscopy (STM). We show that both electron and hole doping drive the AF/weak ferromagnetic (WF) Mott insulator NiS_2 into an AF metallic phase near $x \approx 0.1$, through a regime of electronic/magnetic phase coexistence (Fig. 1) [3]. In $Ni_{1-x}Co_xS_2$, the system evolves from AF NiS_2 to ferromagnetic (F) CoS_2 but exhibits an unexpected paramagnetic (P) phase at $x \approx 0.6$, with no long-range order or spin-glass freezing down to 0.25 K, likely related to geometric frustration in the FCC lattice. An unusual metamagnetic regime then emerges at $x \approx 0.85$, with field-induced P-to-F transitions. STM further reveals a form of surface-to-bulk crossover at $x \approx 0.5$, coinciding with the onset of the P regime and anomalies in Curie-Weiss behavior (Fig. 2). These results, supported by dynamical mean-field theory, significantly revise the magnetic phase diagram and provide a comprehensive picture of this prototypical Mott insulator [5].

*Work supported primarily by the US DOE through the University of Minnesota Center for Quantum Materials.
[1] S. El-Khatib, *et al.*, *Phys. Rev. Mater.* 5, 115003 (2021)
[2] S. El-Khatib, *et al.*, *Phys. Rev. Mater.* 7, 104401 (2023)
[3] Y. Tao, *et al.*, *Phys. Rev. Mater.* 8, 114420 (2024)
[4] I. Park, *et al.*, *arXiv:2512.17059* (2025)
[5] Y. Tao, *et al.*, unpublished (2026)

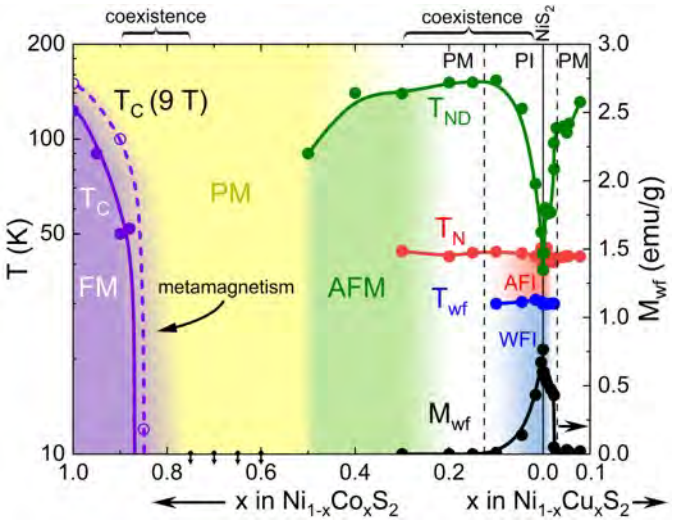


Fig. 1. New magnetic phase diagram of Co- and Cu-doped NiS_2, showing the evolution from AF to P to F phases. Vertical dashed lines mark the Mott insulator (I)-metal (M) transition boundaries.

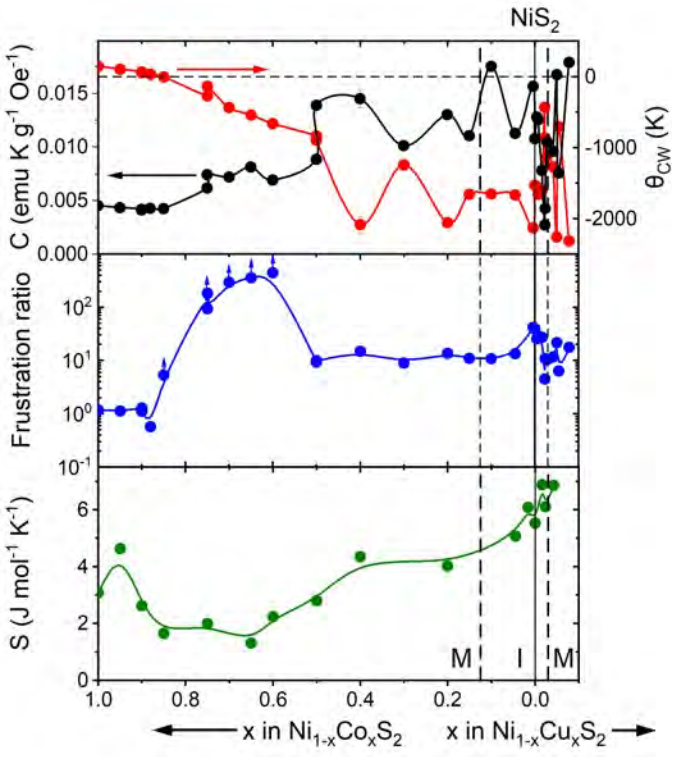


Fig. 2. Doping (x) dependence of magnetic parameters for $Ni_{1-x}Co_xS_2$ and $Ni_{1-x}Cu_xS_2$, showing the Curie constant (C), Curie-Weiss temperature (θ_{CW}), frustration ratio, and magnetic entropy (S).

EE-05. Evolution of Collective Magnetic States in Fe-Doped NiO Nanoparticles: From Antiferromagnetism to Robust Spin Glass

H. Abbas, T. Karki, P. Joshi, J. Mohapatra, P. Liu
Physics, University of Texas at Arlington, Arlington, Texas, United States

In this work, we report the emergence of memory effects and tunable magnetic dynamics in chemically synthesized Fe-doped NiO nanoparticles. While pristine NiO nanoparticles exhibit typical antiferromagnetic behavior, Fe doping induces a transition toward ferromagnetism, accompanied by blocking behavior with blocking temperatures (T_B) of 68 K for 4 % Fe doping and 78 K for 8 % Fe doping. The introduction of Fe enhances the uncompensated magnetic moment and promotes pronounced spin-glass-like behavior, as evidenced by clear memory effects (Fig. 1 (a)), field-cooled relaxation, and a systematic shift in T_B observed in AC susceptibility measurements (Fig. 1 (b)). The frequency dependence of T_B was analyzed using the Néel-Arrhenius, Vogel-Fulcher, and dynamic scaling models (Fig. 1 (c, d)), providing a comprehensive confirmation of the slow magnetic dynamics and cooperative freezing mechanisms underlying the observed memory effects. Additional support is obtained from isothermal remanent magnetization (IRM) and DC demagnetization (DCD) measurements, which indicate the presence of significant dipolar interparticle interactions. Furthermore, field-cooled magnetization loops reveal the emergence of exchange bias, with an exchange bias field of approximately 400 Oe appearing just below the freezing temperature. This behavior suggests the coexistence of surface-spin freezing and core magnetic blocking, consistent with a core-shell-like magnetic structure in the Fe-doped NiO nanoparticles.

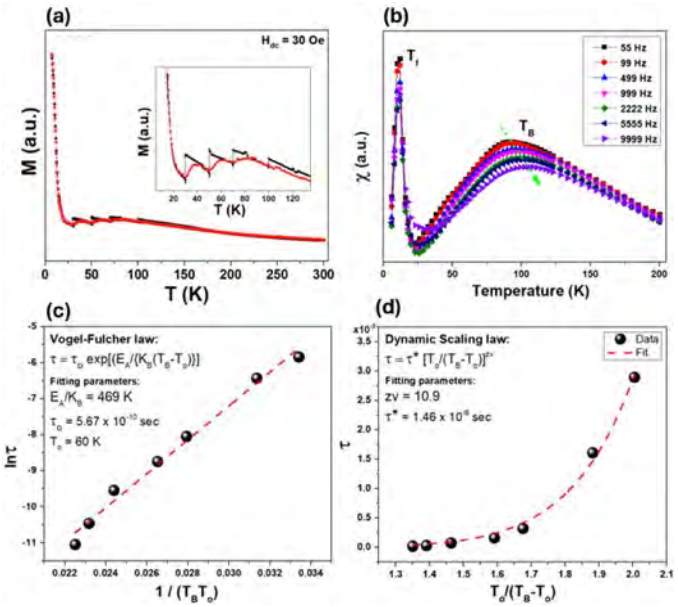


Figure 1: (a) Aging and memory curve, and (b-d) Temperature-dependent ac-susceptibility at different frequencies with Vogel-Fulcher and Dynamic scaling law fitting for Fe-doped NiO nanoparticles.

EE-07. Magnetic and Magnetoelectric Properties of Fluorite-Related Polar Magnets Ln_3RuO_7 (*Ln* = Sm, Eu, Gd)

T. Shirasaki, T. Ishikawa, H. Kuwahara
Department of Engineering and Applied Sciences, Sophia University, Tokyo, Japan

Polar magnets are promising platforms for large magnetoelectric (ME) effects. Here we focus on the antiferromagnetic semiconductors Ln_3RuO_7 (*Ln* = lanthanide), where RuO_6 octahedra form quasi-one-dimensional chains along the *c*-axis [1]. This family adopts a fluorite-related structure and undergoes a transition from a high-temperature non-polar (*Cmcm*) to a low-temperature polar ($P2_1nb$) phase. The transition temperature T_S increases with decreasing *Ln* ionic radius, reaching T_S = 295 K for *Ln* = Eu, thereby stabilizing the polar structure near room temperature [2]. The coexistence of this polar framework with magnetic order makes Ln_3RuO_7 a promising 4*d*-based platform for ME effects, yet detailed investigation of the magnetic and ME properties of this family remains limited. Polycrystalline samples of Ln_3RuO_7 (*Ln* = Sm, Eu, Gd) were synthesized via a solid-state reaction. Fig. 1 shows the temperature dependence of the magnetic susceptibility for Gd_3RuO_7 measured under zero-field-cooled (ZFC) conditions. At μ_0H = 0.1 T, in addition to the Ru^{5+} antiferromagnetic ordering at T_N = 17 K, a distinct anomaly appears at T^* = 8 K. Since Eu^{3+} has a nonmagnetic J = 0 ground state, the absence of a corresponding anomaly in Eu_3RuO_7 supports our assignment of T^* to *Ln* 4*f* ordering. Both anomalies vanish above 5 T. The magnetization curve of Gd_3RuO_7 at 2 K (< T^*) shows a metamagnetic transition around 2.7 T (inset of Fig. 1). Since this transition disappears above T^*, we attribute it to a field-induced reorientation of Gd^{3+} spins. By contrast, the magnetization curve of Sm_3RuO_7 at 2 K exhibits a hysteresis loop with a large coercive field of approximately 4.2 T (not shown). These contrasting behaviors indicate that the magnetic anisotropy of this system is governed by the intrinsic single-ion anisotropy of the respective 4*f* moments. We will discuss the detailed magnetic properties and the possible ME response associated with the polar structure, highlighting the potential for multiferroic behavior in this unique 4*d*-4*f* system.

[1] P. Khalifah, R. W. Erwin, J. W. Lynn, Q. Huang, B. Batlogg and R. J. Cava, Phys. Rev. B, Vol. 60, p.9573 (1999).
[2] M. Wakeshima and Y. Hinatsu, J. Solid State Chem., Vol. 183, p.2681 (2010)

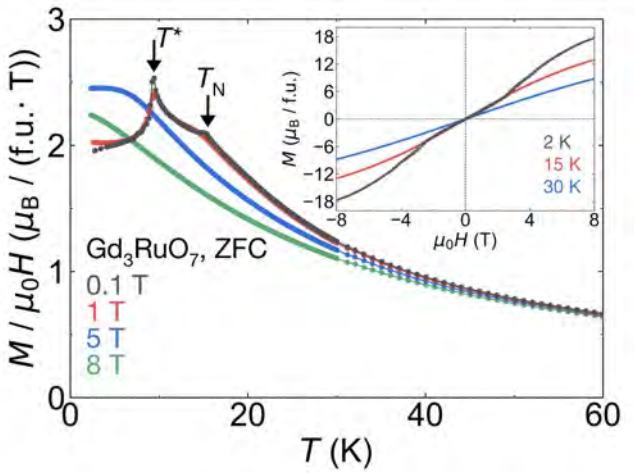


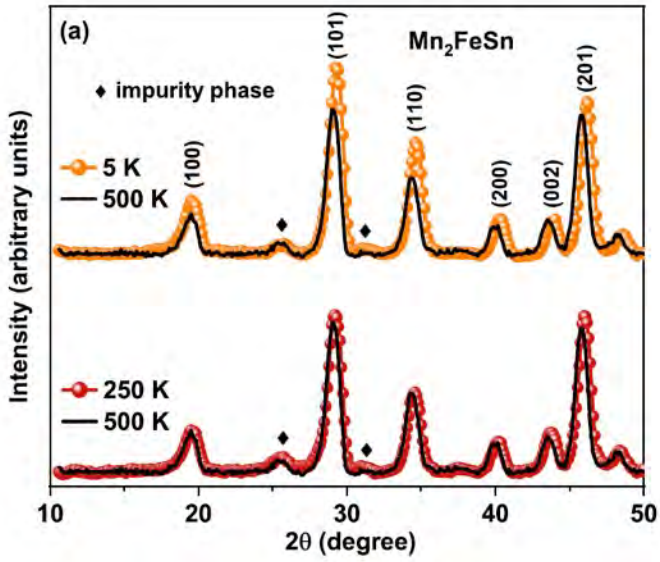
Fig. 1: Temperature dependence of the ZFC magnetic susceptibility of polycrystalline Gd_3RuO_7 at various magnetic fields. The inset shows the magnetic field dependence of magnetization at 2, 15, and 30 K.

EE-08. Complex Spin Structure and Magnetic Properties of Mn3−xFexSn alloys

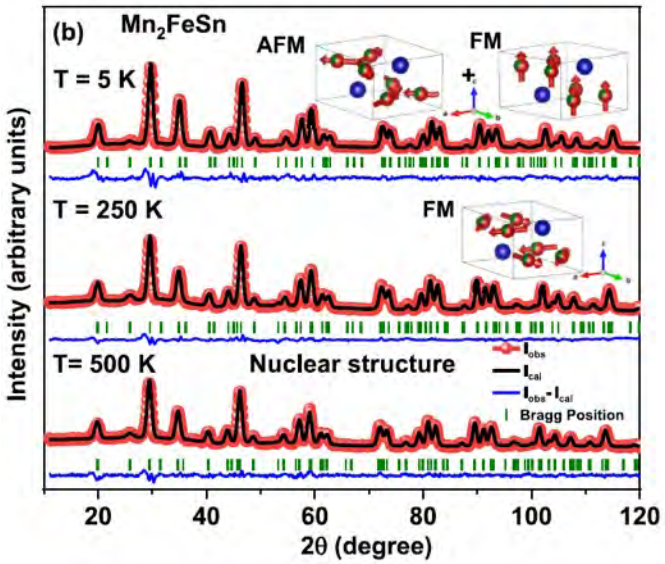
H. Hanggai, N. van Dijk, E. Brück
Delft University of Technology, Delft, Netherlands

The hexagonal Mn3−xFexSn compounds possess several desirable properties that make them suitable magnetocaloric materials, including a ferromagnetic (FM)-to-paramagnetic (PM) transition near room temperature and soft magnetic behavior. In this work, we use the melt-spinning technique to explore the Mn-Fe-Sn ternary system. By combining magnetization measurements, Mössbauer spectroscopy, neutron diffraction (ND), oriented powder x-ray diffraction, and density functional theory (DFT) calculation, the magnetocaloric effect, spin structures, and the intrinsic magnetic properties of polycrystalline Mn3−xFexSn (x = 0.8 − 1.4) compounds are determined. The FM-to-PM transition temperature Tc ranges from 253 K (x = 0.8) to 394 K (x = 1.4). At low temperature, a spin reorientation at Ts is observed, where below Ts a coexistence of FM order with spins along the c axis and antiferromagnetic order with spins within the a − b plane occurs for x = 0.8 and 1.0. However, for compounds with x = 1.2 and 1.4, only FM order with spins along the c axis has been found below Ts. Above Ts, the spin structure corresponds to FM order with spins aligned within the a − b plane for all compositions. The magnetic moments of Mn and Fe were evaluated using DFT, demonstrating good agreement with the ND results.

[1] T. Jungwirth, et al. Nat. Nanotechnol. 11, 231 (2016).
[2] N. H. Sung, et al. Appl. Phys. Lett. 112, 132406 (2018).
[3] J. Liu, et al. Mater. Today Phys. 29, 100871 (2022).



Powder neutron diffraction pattern of the Mn2FeSn compound obtained at 5, 250, and 500 K.



Refinements of the nuclear and magnetic spin structure at different temperature.

EE-09. Analysis of Magnetocrystalline Anisotropy from Atom Pair Statistics in Tetragonally Strained Fe-Si Alloys

W. Shang[1], Y. Gohda[2]

[1]Department of Materials Science and Engineering, Institute of Science Tokyo, Yokohama, Kanagawa, Japan, [2]Department of Materials Science and Engineering, Institute of Science Tokyo, Yokohama, Kanagawa, Japan

Magnetocrystalline anisotropy energy (E_{MCA}) is a quantity underlying magnetoelastic coupling and rooted in spin-orbit coupling (SOC); its strain dependence is central to the design of magnetostrictive actuators, sensors, and strain-engineered spintronic devices. However, the limited availability of reliable E_{MCA}-labeled datasets remains a bottleneck for data-driven exploration and magnetoelastic materials design. Here we present a compact and interpretable atom-pair based linear model for analyzing and predicting E_{MCA} in tetragonally strained alloys, designed to remain effective in small-data regimes. Density functional theory (DFT) calculations incorporating SOC were carried out for approximately 10^3 strained structures, including both 2×2×2 and 3×3×3 Fe–Si supercells, spanning broad ranges of volume V and tetragonality c/a. The descriptors retain explicit pair species, bond lengths, and bond orientations in symmetry-aware Fe-Fe and Fe-Si pair channels up to the third-nearest-neighbor shell. Since the model is linear in these physically motivated pair features, its coefficients can be recast as distance-resolved anisotropy coefficient functions, enabling direct interpretation rather than black-box prediction. The model captures the main E_{MCA} trend for unseen test structures, while first-, second-, and third-neighbor channels all make non-negligible contributions. Bayesian analysis further quantifies the uncertainty of the distance-resolved anisotropy coefficient functions, supporting the robustness of the extracted trends. Methodologically, the same framework can in principle be extended to other lattices and other anisotropic quantities, broader validation remains for future work.

W.C. Shang and Y. Gohda, Comput. Mater. Sci., in press

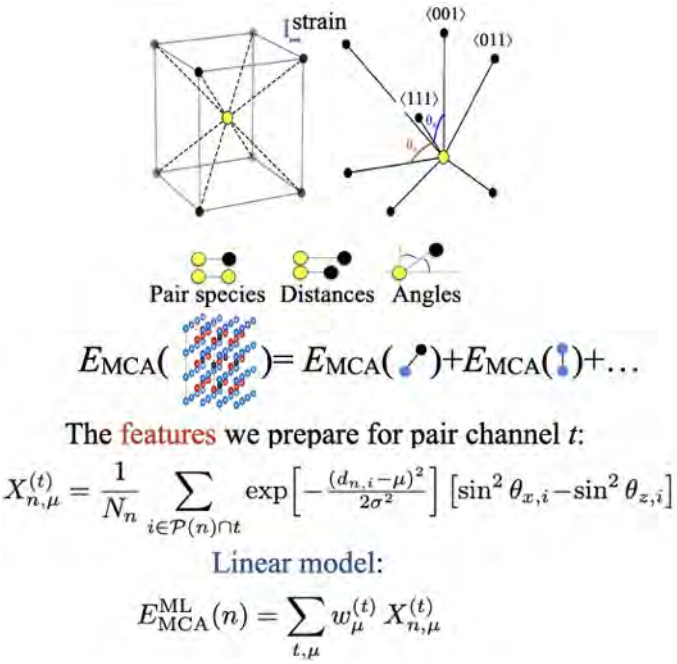


Fig. 1. Physics-guided atom-pair based linear model workflow for tetragonally strained Fe-Si, showing descriptors from pair species, bond distance, and bond orientation and their linear model for E_{MCA}.

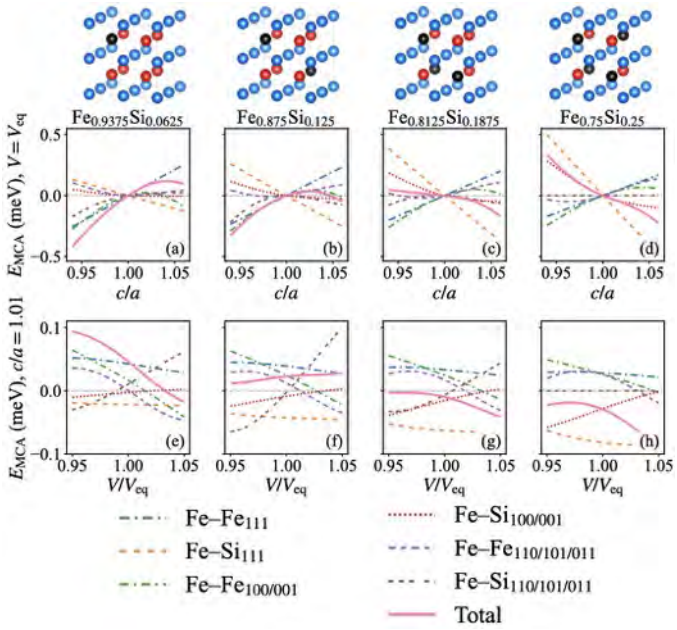


Fig. 2. Pair channel resolved E_{MCA} from the pair-based model for four Fe-Si compositions: (a)-(d), c/a dependence at equilibrium volume V_{eq}; (e)-(h), volume dependence at c/a = 1.01.

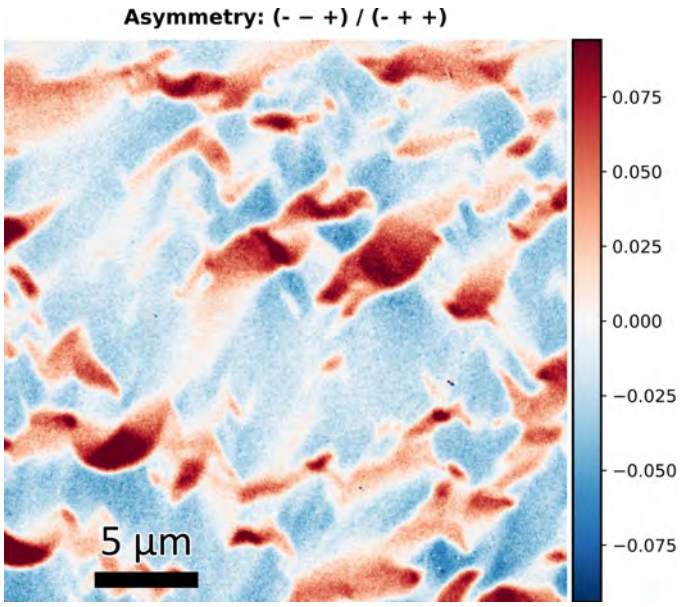
EE-10. Magnetic domain evolution in FeMnCoNi and MnCoNi Multi-Principal Element Alloy Thin Films

N. Naushin[1, 2], C. Li[1], E. Abogado[1], Z. Xie[3], S. Nguyen[1], A. T. N'Diaye[2], N. Tamura[2], C. Klewe[2], B. Achinuq[2], R. Kukreja[1]
[1]Materials Science and Engineering, University of California-Davis, Davis, California, United States, [2]Advanced Light Source, Lawrence Berkeley National Laboratory, Berkeley, California, United States, [3]Physics, University of California-Davis, Davis, California, United States

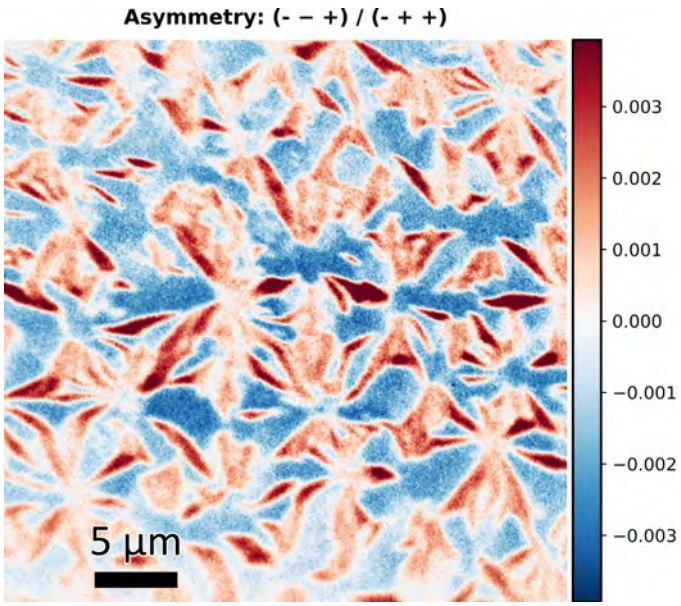
Multi-principal element alloys (MPEAs) exhibit exceptional mechanical performance and complex magnetic behavior. These alloy systems provide a platform to explore complex magnetic behavior arising from competing exchange interactions in chemically disordered systems. In particular, Mn, as an antiferromagnetic element interacting with ferromagnetic Fe, Co, and Ni, can induce frustrated magnetic states that are highly sensitive to composition and local environment.

In this study, we investigate the evolution of element-specific magnetism and magnetic domain structure in FeMnCoNi and MnCoNi thin films. While both films exhibit mixed FCC and HCP phases, MnCoNi shows a pronounced (111) texture. Using X-ray magnetic circular dichroism (XMCD), we find that Fe and Mn moments align antiparallel in FeMnCoNi, whereas Mn moments align parallel to Co and Ni in MnCoNi, indicating a composition-driven modification of Mn-mediated exchange interactions.

To further probe the spatial manifestation of these interactions, we employ XMCD-Photoemission electron microscopy (XMCD-PEEM) to obtain element-resolved magnetic domain images. FeMnCoNi exhibits magnetic domains with an average area of ~3.5 μm^2, where Fe and Mn domains are aligned antiparallel, consistent with strong magnetic frustration at the mesoscale. In contrast, MnCoNi shows smaller domains of ~1.5 μm^2 area with Mn, Co, and Ni moments aligned parallel, along with a sixfold symmetric domain pattern likely associated with the (111) texture. These results demonstrate that Mn acts as a tunable mediator of exchange interactions in MPEAs, where changes in composition lead to significant modifications in both element-specific magnetic alignment and domain structure.



XPEEM image showing magnetic domains of Fe in FeMnCoNi 31 nm thin films at 300 K. The red and blue colorbar indicates magnetic domains aligned along and opposite to the incident x-ray direction.



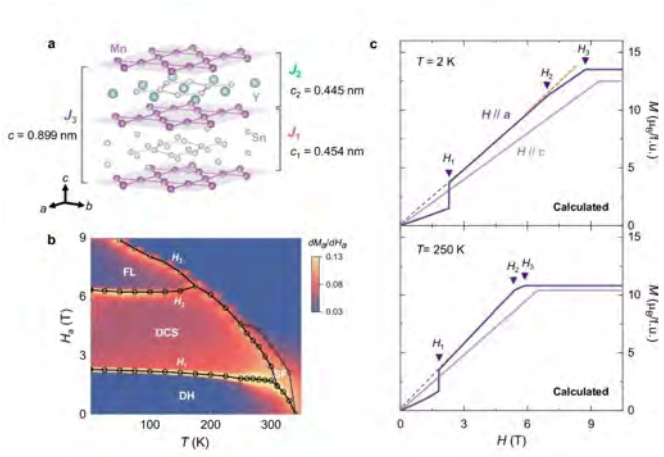
XPEEM image showing magnetic domains of Co in MnCoNi 65 nm thin films at 300 K. The red and blue colorbar indicates magnetic domains aligned along and opposite to the incident x-ray direction.

EE-11. Revealing field-driven distorted conical spiral phase in a weakly anisotropic double helical antiferromagnet

J. Hong, K. Jeong, J. Seo, S. Lim, M. Kim, K. Moon, N. Lee, Y. Choi
Department of Physics, Yonsei University, Seoul, Korea (the Republic of)

A double-helical (DH) order, characterized by alternatingly nested single helices, represents a unique noncollinear spin texture in antiferromagnets, emerging from unevenly frustrated exchange interactions. Leveraging high-sensitivity angle-dependent magnetic torque measurements combined with a frustrated planar-anisotropic spin model, we investigate the intricate magnetic phases of the DH antiferromagnet YMn_6Sn_6, which exhibits a high Néel temperature (T_N = 345 K). Despite a weak magnetocrystalline anisotropy constant (~0.3% of the interlayer exchange interaction), our layer-resolved spin analysis reveals that it significantly influences the evolution of field-driven phases. Visualizations of spin textures demonstrate that an in-plane magnetic field transforms the DH ground state into a distorted conical spiral (DCS) state. This arises because the weak magnetocrystalline anisotropy breaks the uniformity of spin tilting, providing a refined understanding of the spin reorientation process. Furthermore, the rapid suppression of the c-axis spin component within the DCS phase plays a key role in the emergence of a fan-like (FL) intermediate state before complete magnetic saturation. Notably, this newly identified DCS phase coincides with a near-room-temperature (T_N = 345 K) sign-tunable magnetoresistance effect, exhibiting a ~40% variation. This behavior is closely linked to the dynamic modulation of multiple interlayer hopping amplitudes, suggesting a deeper interplay between the evolving spin texture and electronic transport. These findings highlight the critical role of weak anisotropy in DH antiferromagnets and offer comprehensive insights into noncollinear antiferromagnet-based spintronics and magnetotransport phenomena.

Jiang, N., Nii, Y., Arisawa, H., Nat. Commun. 11, 1601 (2020)
Murakawa, H., Onose, Y., Ohgushi, K., *J. Phys. Soc. Jpn.* 77, 043709 (2008)
Ghimire, N. J., *Sci. Adv.* 6, eabe2680 (2020)
Dally, R. L., *Phys. Rev. B* 103, 094413 (2021)



EE-12. Unusual magnetotransport driven by coupled structural and magnetic transitions in the Heusler alloy CrRuMnGe

P. Sharma[1], J. Nag[1, 2], R. Roy Chowdhury[3, 1], S. Jan[1], A. Alam[2], K. G. Suresh[2], M. Phan[1, 4], S. Witanachchi[1], H. Srikanth[1]
[1]Physics, University of South Florida, Tampa, Florida, United States, [2]Physics, Indian Institute of Technology, Mumbai, Maharashtra, India, [3]Physics, Dream Institute of Technology, Maulana Abul Kalam Azad University of Technology, Kolkata, West Bengal, India, [4]Center for Materials Innovation and Technology, VinUniversity, Hanoi, Hanoi, Viet Nam

Equiatomic Heusler alloys provide a versatile platform for emergent functionality arising from the interplay of structure, magnetism, and electronic structure. We report the quaternary Heusler alloy CrRuMnGe, which hosts a complex phase landscape in which structural distortion, magnetic frustration, and disorder are intrinsically coupled. CrRuMnGe crystallizes in the LiMgPdSn-type structure with a lattice parameter of 5.95 Å and ~50% Ru/Mn antisite disorder, as confirmed by Rietveld refinement [1]. Magnetization measurement identifies three distinct magnetic regimes: a low-temperature cluster-glass state below ~50 K, an intermediate martensitic regime between ~150-226 K, and an austenitic phase persisting up to a high Curie temperature of ≈ 575 K. These coupled transitions strongly modulate charge transport. Resistivity exhibits metallic behavior with a crossover from disorder-enhanced electron-electron interactions at low temperatures to phonon- and magnon-mediated scattering above ~55 K. Magnetoresistance shows a clear anomaly near the martensitic transition (~150 K). Hall measurements uncover an emergent topological Hall-like contribution (~0.55 μΩ cm at 2.5 K) at low temperatures, characterized by nonlinear

field dependence and sign reversal, consistent with short-range magnetic correlations and a real-space Berry phase effect [2]. First-principles calculations predict a ferrimagnetic ground state with antiparallel Cr and Mn moments of ~ 1 μ_B/f.u. (Slater-Pauling), in close agreement with the experimentally observed saturation magnetization of ~ 0.9 μ_B/f.u., alongside a nearly semimetallic electronic structure favorable for unconventional transport. These results establish strong coupling among structural disorder, magnetic frustration, and magnetotransport in CrRuMnGe, positioning equiatomic quaternary Heusler alloys as promising platforms for tunable correlated and topological transport functionalities.

[1] A. Chanda, J. Nag and N. Schulz, Phys. Rev. B., Vol. 109, p. 224415 (2024)
[2] J. Nag, B. Bandyopadhyay and S. Goswami, Phys. Rev. B., Vol. 113, p. L020412 (2026)

EE-13. From Spontaneous to Driven: Probing Equilibrium and Non-Equilibrium Fluctuations in Quantum Materials via Coherent X-ray Photons

J. J. Turner
SLAC National Accelerator Laboratory, Menlo Park, California, United States

The transition between competing phases in quantum materials manifests through complex spatiotemporal fluctuations that vary significantly in their origin and energetic scale. This work utilizes advanced coherent X-ray methodologies to quantify these fluctuations in magnetic materials across three distinct, physical regimes: equilibrium, inherent non-equilibrium, and externally-driven. For equilibrium magnetic fluctuations, we use X-ray Photon Fluctuation Spectroscopy (XPFS) to observe novel nanosecond-scale fluctuations in a FeGd skyrmion lattice and near its phase boundary. By leveraging photon-counting statistics to access dynamics near these phase transitions, we map the intrinsic instabilities and contrast variations that emerge as these systems fluctuate between competing magnetic orders. In the unconventional superconductor FeSe, we observe spontaneous, non-diffusive fluctuations within the electronic nematic phase. Here, X-ray Photon Correlation Spectroscopy (XPCS) reveals inherent non-equilibrium dynamics in that structural distortions exhibit "crackling noise" behavior—abrupt, scale-invariant avalanches occurring even in the absence of an external driving force—suggesting a critical lattice instability inherent to the nematic state. Finally, we implement an X-ray pump–X-ray probe scheme to investigate a driven, ultrafast evolution of magnetic order in the Mott insulator Sr_2IrO_4. By tracking the J_{eff} = 1/2 magnetic order as a function of time delay, we directly quantify the characteristic timescales governing the response of the order parameter to an external excitation and its subsequent recovery. Together, these results demonstrate a comprehensive framework for capturing the broad spectrum of magnetic fluctuations, spanning different physical orgins, from spontaneous nanosecond fluctuations to high-energy driven responses.
All three works discussed in this talk are currently unpublished, but some references of related work that may be of interest are as follows:

1. Z. Tumbleson, S. A. Morley, E. Hollingworth, A. Singh, T. Bayaraa, N. G. Burdet, A. U. Saleheen, M. R. McCarter, D. Raftrey, R. J. Pandolfi, V. Esposito, G. L. Dakovski, F.-J. Decker, A. H. Reid, T. A. Assefa, P. Fischer, S. M. Griffin, S. D. Kevan, F. Hellman, J. J. Turner and S. Roy, "Thermodynamic phase transitions of nematic order in magnetic helices", *Sci. Adv.* 11, (2025) doi: 10.1126/sciadv.adt5680

2. H. Yin, C. Heaton, E. G. Blackman, A. E. Gleason, J. J. Turner, G. W. Collins, G. Gregori, J. K. Shang and H. Aluie, "Theory of x-ray photon correlation spectroscopy for multiscale flows", *Phys. Rev. Research* (2025) doi: 10.1103/PhysRevResearch.7.023202

3. A. Mangu, V. A. Stoica, H. Zheng, T. Yang, M. Zhang, H. (. Wang, R. Zu, Q. L. Nguyen, S. Song, S. Das, P. Meisenheimer, E. Donoway, M. Chollet, Y. Sun, J. J. Turner, J. W. Freeland, H. Wen, L. W. Martin, L.-Q. Chen, V. Gopalan, D. Zhu, Y. Cao and A. M. Lindenberg, "Hidden domain boundary dynamics toward crystalline perfection", *Proc. Natl. Acad. Sci. USA* 122, (2025) doi: 10.1073/pnas.2407772122

4. Z. Porter, L. Shen, R. Plumley, N. G. Burdet, A. N. Petsch, J. Wen, N. C. Drucker, C. Peng, X. M. Chen, A. Fluerasu, E. Blackburn, G. Coslovich, D. G. Hawthorn and J. J. Turner, "Understanding the superconductivity and charge density wave interaction through quasi-static lattice fluctuations", *Proc. Natl. Acad. Sci. USA* 121, e2412182121 (2024) doi: 10.1073/pnas.2412182121

5. Z. Chen, C. Peng, A. N. Petsch, S. R. Chitturi, A. Okullo, S. Chowdhury, C. H. Yoon and J. Turner, "Bayesian experimental design and parameter estimation for ultrafast spin dynamics", *Mach. Learn.: Sci. Technol.* 4, 045056 (2023) doi: 10.1088/2632-2153/ad113a

6. M. H. Seaberg, B. Holladay, S. A. Montoya, X. Y. Zheng, J. C. T. Lee, A. H. Reid, J. D. Koralek, L. Shen, V. Esposito, G. Coslovich, P. Walter, S. Zohar, V. Thampy, M. F. Lin, P. Hart, K. Nakahara, R. Streubel, S. D. Kevan, P. Fischer, W. Colocho, A. Lutman, F.-J. Decker, E. E. Fullerton, M. Dunne, S. Roy, S. K. Sinha and J. J. Turner, "Spontaneous fluctuations in a magnetic Fe/Gd skyrmion lattice", *Phys. Rev. Research* 3, 033249 (2021) doi: 10.1103/PhysRevResearch.3.033249

7. L. Shen, M. Seaberg, E. Blackburn and J. J. Turner, "A snapshot review-Fluctuations in quantum materials: from skyrmions to superconductivity", *MRS Adv.* 6, 221 (2021) doi: 10.1557/s43580-021-00051-y

8. V. Esposito, X. Y. Zheng, M. H. Seaberg, S. A. Montoya, B. Holladay, A. H. Reid, R. Streubel, J. C. T. Lee, L. Shen, J. D. Koralek, G. Coslovich, P. Walter, S. Zohar, V. Thampy, M. F. Lin, P. Hart, K. Nakahara, P. Fischer, W. Colocho, A. Lutman, F.-J. Decker, S. K. Sinha, E. E. Fullerton, S. D. Kevan, S. Roy, M. Dunne and J. J. Turner, "Skyrmion fluctuations at a first-order phase transition boundary", *Appl. Phys. Lett.* 116, 181901 (2020) doi: 10.1063/5.0004879

9. M. H. Seaberg, B. Holladay, J. C. T. Lee, M. Sikorski, A. H. Reid, S. A. Montoya, G. L. Dakovski, J. D. Koralek, G. Coslovich, S. Moeller, W. F. Schlotter, R. Streubel, S. D. Kevan, P. Fischer, E. E. Fullerton, J. L. Turner, F.-J. Decker, S. K. Sinha, S. Roy and J. J. Turner, "Nanosecond X-Ray Photon Correlation Spectroscopy on Magnetic Skyrmions", *Phys. Rev. Lett.* 119, 67403 (2017) doi: 10.1103/PhysRevLett.119.067403

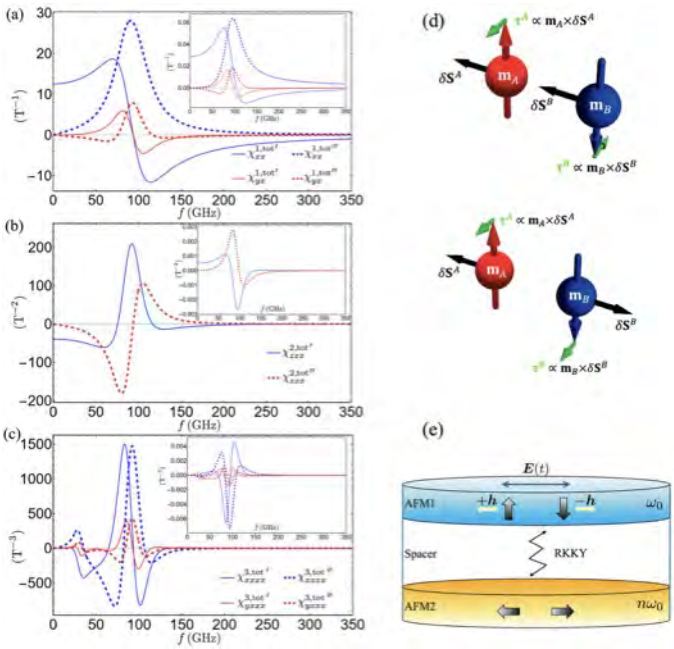
SESSION EF: ALTERMAGNETIC AND ANTIFERROMAGNETIC SPINTRONICS II

Chair(s): S. Kim, *University of Ulsan, Ulsan, Korea (the Republic of)*
Thursday, November 5, 2026
08:30 AM-12:00 PM
South Pacific 3/4

EF-01. Gigantic Harmonic Generation using Néel-Torque Antiferromagnetic Resonance

R. Cheng, K. Deng
University of California, Riverside, California, United States

We theoretically study the resonant and higher-order magnetic responses of a collinear antiferromagnet driven by a harmonic Néel spin-orbit torques (NSOTs). By deriving the dynamical susceptibilities up to the third harmonic, we find remarkable NSOT-induced amplifications of the linear and nonlinear dynamics by orders of magnitude compared to their counterparts using conventional spin torques, enabling highly efficient frequency conversions in the sub-terahertz range. As an illustrative example, we propose a multilayer antiferromagnetic device leveraging the gigantic harmonic generation to achieve unprecedented frequency amplifiers and converters. Our findings uncover a critical but previously overlooked role of the NSOTs in inducing nonlinear dynamics in antiferromagnets.
K. Deng and R. Cheng, Phys. Rev. Lett. 135, 226702 (2025)



NSOT-induced amplification of Néel-vector dynamics. (a)-(c) show the first-, second- and third-order harmonic responses in

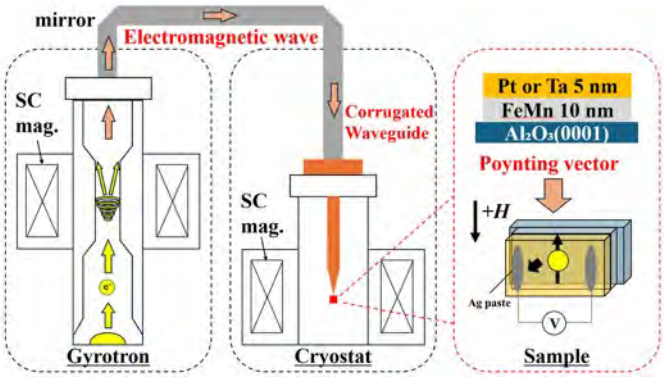
terms of the real (solid curves) and imaginary (dashed curves) parts of the total susceptibilities. (d) Illustration of the ordinary spin torque vs. NSOT, arising from uniform vs. contrasting sublattice spin accumulations, respectively. (e) Schematic of a frequency converter utilizing the NSOT-enabled amplification effect.

EF-02. Electrical detection of magnetic resonance in FeMn/Pt bilayars

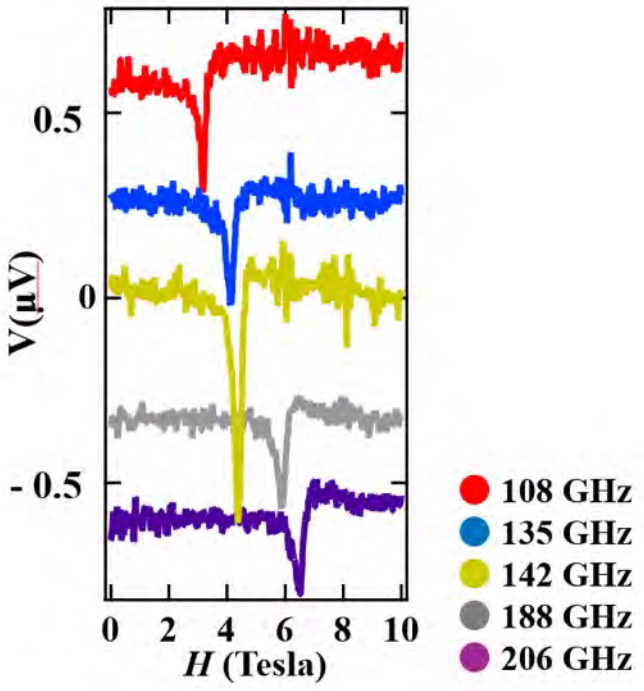
K. Tada[1], T. Hattori[1], T. Shinkai[1], A. Yoshida[1], K. Kawagita[2], K. Yabushita[2], T. Fukamachi[2], K. Hayashi[1], S. Iihama[1], Y. Ishikawa[2], T. Moriyama[1]
[1]Materials Physics, Nagoya University, Nagoya, Aichi, Japan, [2]Research Center for Development of Far-Infrared Region, University of Fukui, Fukui, Japan

Antiferromagnets (AFMs) are attracting considerable attention as key materials for the next generation high speed devices [1] because antiferromagnetic resonance (AFMR) naturally reaches the THz band. Particularly, metallic AFMs are promising candidates for devices since it is possible to access their magnetic properties electrically. However, it is difficult to observe AFMR for metallic AFMs because the presence of free electrons causes them to shield and reflect THz waves. Hence, most of the research on AFMR using the transmission-absorption THz spectroscopy is limited to insulating AFMs [2, 3].
To address this issue, we have developed an AFMR characterization method for metallic AFM films. As shown in Fig. 1, AFMR is measured by sweeping an external magnetic field while irradiating the sample with continuous THz waves. When AFMR occurs in metallic AFM films, an inverse spin Hall effect voltage or a homodyne voltage appears across the sample [4, 5]. In this study, we have investigated the AFMR of FeMn alloy with this experimental setup. To confirm the origin of the observed voltages, we prepared FeMn(10 nm)/Pt (5 nm) and FeMn (10 nm)/Ta (5 nm) bilayers on Al_2O_3 (0001) substrates by magnetron sputtering.
As shown in Fig. 2, we observed clear AFMR signals at various frequencies. The resonance field shifted to higher fields as the frequency increased. The absence of peak polarity reversal between the FeMn/Pt and FeMn/Ta samples indicates that the homodyne effect is the origin of the observed voltage signal. The frequency dependence of the resonance field suggests the peaks are due to one of the FeMn's AFMR modes. In the presentation, we will show the frequency dependence of the observed peaks with the external field applied in different directions and discuss an identification of the different AFMR modes in the FeMn.

[1] V. Baltz *et al.*, *Rev. Mod. Phys.* 90, 015005 (2018).
[2] T. Moriyama *et al.*, *Phys. Rev. Mater.* 3, 51402 (2019).
[3] T. Kampfrath *et al.*, *Nat. Photon.* 5, 31 (2011).
[4] S. Funada *et al.*, *Phys. Rev. Appl.* 19, L031003 (2023).
[5] T. Hattori *et al.*, *Phys. Rev. Lett.* 133, 256701(2024).



(Fig.1) Schematic illustration of the sample and experimental setup.



(Fig.2) The resonant spectra of the FeMn/Pt film for various frequencies.

EF-03. Electron tunneling through altermagnetic RuO_2(110)/MgO/CoFeB junctions

Z. Wen[1], M. Roy Chowdhury[2, 1], J. Okabayashi[3], T. Ma[1], S. Thota[2], J. Uzuhashi[1], T. Ohkubo[1], S. Mitani[1], H. Sukegawa[1]
[1]National Institute for Materials Science (NIMS), Tsukuba, Japan, [2]Department of Physics, Indian Institute of Technology Guwahati, Guwahati, India, [3]Research Center for Spectrochemistry, The University of Tokyo, Tokyo, Japan

Altermagnetic materials, characterized by compensated magnetic order and momentum-dependent spin splitting, provide a promising route toward high-density and highly sensitive spintronic devices [1]. Rutile RuO_2 has emerged as an important candidate due to its high Néel temperature and predicted spin-polarized transport along specific crystallographic directions [2]; however, experimental evidence for spin-polarized electron transport through tunnel junctions remains limited.
In the work, we fabricated asymmetric tunnel junctions composed of RuO_2(110)/MgO(001)/CoFeB stacks grown on TiO_2(110) substrates using ultra-high-vacuum magnetron sputtering. Structural analyses using reflection high-energy electron diffraction, X-ray diffraction, and high-angle annular dark-field scanning transmission electron microscopy confirm the epitaxial growth and well-defined multilayer structure, while revealing partial intermixing and lattice mismatch at the RuO_2/MgO interface. X-ray magnetic linear dichroism measurements demonstrate collinear antiferromagnetic order with the Néel vector aligned along the RuO_2[001]. The stacking structures were patterned into micron-scale four-terminal junctions. Nonlinear *I-V* characteristics and parabolic conductance behavior confirm electron tunneling through the MgO barrier. The resistance-area product exponentially increases with MgO thickness, consistent with quantum tunneling. At 50 K, clear field-dependent resistance modulation is observed when the CoFeB magnetization switches relative to the fixed Néel vector of RuO_2, producing a finite tunneling magnetoresistance (TMR) ratio (~0.12%). Angular-dependent measurements further corroborate spin-polarized tunneling governed by the relative orientation between the magnetization of CoFeB and the Néel order of RuO_2.
The observed finite TMR in the tunnel junctions, despite defects in the MgO barrier and interfacial intermixing, is consistent with the bulk-origin spin polarization arising from momentum-dependent spin-split band structures in altermagnets. These results indicate that the epitaxial RuO_2(110) is a viable altermagnetic electrode and provide direct evidence of spin-splitting electron tunneling toward altermagnetic spintronic devices.

[1] L. Šmejkal, J. Sinova, and T. Jungwirth, Phys. Rev. X 12, 040501 (2022).
[2] C. He, Z. Wen, J. Okabayashi *et al.*, Nat. Commun. 16, 8235 (2025).

EF-04. Quantum Oscillations Reveal Bulk Altermagnetism in CrSb

H. Wang[1, 2], F. Zhou[1, 3], Y. Ma[1], l. song[1, 3], W. Wang[3], G. Li[1], Y. Lau[1, 2]
[1]Institute of Physics, Chinese Academy of Sciences, Beijing, China, [2]University Chinese Academy of Sciences, Beijing, China, [3]Institute of Quantum Materials and Devices, School of Electronics and Information Engineering, Tiangong University, Tianjin, China

Altermagnet is an emerging class of collinear antiferromagnet featuring spin-split bands even in the absence of spin-orbit coupling[1,2]. Among many altermagnet candidates, rutile-type RuO_2 and NiAs-type CrSb with high Néel temperature (>300 K) and large spin splitting (~1 eV) have attracted considerable attention for their potential spintronic applications. While surface-sensitive angle-resolved photoemission spectroscopy (ARPES) clearly identified spin-split altermagnetic band structures in CrSb[3], RbV_2Te_2O[4], and KV_2Se_2O[5], recent quantum oscillation (QO) measurements, however, suggested high-quality RuO_2 is non-magnetic[6]. A convincing experimental proof of bulk altermagnetism is hitherto lacking.
Here, we have grown CrSb single crystals of varying residual resistivity ratios (RRR) via self-flux and chemical vapor transport. The magnetic susceptibility of CrSb along the c-axis is an order of magnitude weaker than that within the ab-plane, consistent with an easy-axis collinear antiferromagnet. CrSb reflects a multi-carrier transport mechanism, exhibiting a quasi-linear unsaturated positive magnetoresistance (MR) of up to 200% at 9 T and 10 K, while the Hall resistance shows a non-linear response to the field. A high carrier mobility of 6600 cm^2/Vs was found for CrSb with a RRR of 21. The MR curves collected from a series of CrSb with varying RRR at various temperatures are found to obey a modified Kohler's scaling, suggesting the transport is governed by the variation of relaxation time.
Next, we studied the QO of CrSb under a 30 T high magnetic field at dilution refrigerator temperatures via torque magnetometry, MR, and capacitive dilatometry. All three independent QO measurements with field along c-axis (ϑ = 0°) consistently reveal a primary oscillation frequency of

~1600 T. Upon rotating the field towards the ab-plane, the QOs shift towards higher frequencies and vanish at $\vartheta \sim 55^{\circ}$. These results are highly consistent with the calculated altermagnetic band structures of CrSb with a small Fermi surface along [001]. In conclusion, this study provides strong experimental evidence for the bulk altermagnetism in CrSb, paving a way towards altermagnetic spintronic devices.

[1] Libor Šmejkal *et al*., *Phys. Rev. X* 12, 031042 (2022).
[2] Cheng Song *et al*., *Nat. Rev. Mater*. 10, 473–485 (2025).
[3] Sonka Reimers *et al*., *Nat. Commun.* 15, 2116 (2024).
[4] Fayuan Zhang *et al*., *Nat. Phys.* 21, 760–767 (2025).
[5] Bei Jiang *et al*., *Nat. Phys.* 21, 754–759 (2025).
[6] Zheyu Wu *et al*., *Phys. Rev. X* 15, 031044 (2025).

EF-05. Hidden and Visible Altermagnetism in Stacked Conventional Antiferromagnetic Layers

Y. Lu
Zhejiang University, Hangzhou, Zhejiang, China

Two-dimensional (2D) altermagnets have been attracting enormous research interest, however the general guidance of global symmetry breaking poses a significant challenge of rather limited material candidates. Here, we propose a simple and widely applicable design strategy for generating both *hidden* and *visible* 2D altermagnetism by local inversion breaking in van der Waals antiferromagnetic multilayers. It is based on a class of conventional antiferromagnets, although not altermagnetic in monolayer form, becoming altermagnetic when stacked into multilayers, by local inversion symmetry breaking. Using a symmetry-guided framework and high-throughput computational screening, we identify diverse *hidden* and *visible* altermagnetic candidates. Notably, the layer-dependent non-relativistic spin splitting exhibits a distinct odd-even effect, differing from that in conventional A-type antiferromagnets. Leveraging *hidden* altermagnetic order, we propose a universal multiferroic scheme for ferroelectric control of spin polarization. This strategy greatly expands the family of 2D altermagnetic materials, circumvents stringent constraints associated with previous methods, and opens new pathways towards altermagnetic spintronics.

EF-06. Observation of hidden altermagnetism in Cs$_{1-\delta}$V$_2$Te$_2$O

Y. Liu
Physics, Zhejiang University, Hangzhou, China

Altermagnets are characterized by anisotropic band/spin splittings in momentum space, dictated by their spin-space group symmetries. However, the real-space modulations of altermagnetism are often neglected and have not been explored experimentally. Here we combine neutron diffraction, angle-resolved photoemission spectroscopy (ARPES), spin-resolved ARPES and density functional theory to demonstrate that Cs$_{1-\delta}$V$_2$Te$_2$O realizes a spatially modulated form of altermagnetism, i.e., hidden altermagnetism. Such a state in Cs$_{1-\delta}$V$_2$Te$_2$O results from its G-type antiferromagnetism and two-dimensional electronic states, allowing for the development of spatially alternating altermagnetic layers, whose local spin polarizations are directly verified by spin-resolved ARPES measurements. Our experimental discovery of hidden altermagnetism broadens the scope of unconventional magnetism and opens routes to exploring emergent phenomena from real-space modulations of altermagnetic order.
arXiv: 2512.00972

EF-07. Deterministic electrical switching in altermagnets via surface antisymmetry groups

K. Belashchenko
Department of Physics and Astronomy, University of Nebraska-Lincoln, Lincoln, Nebraska, United States

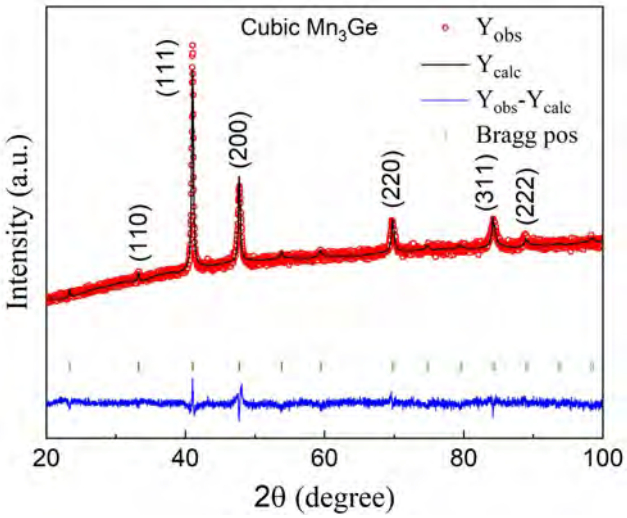
A surface antisymmetry group framework is developed [1] to establish design rules for deterministic electrical switching of the Néel vector in a film of a collinear bipartite antiferromagnet. In centrosymmetric *d*-wave altermagnets, where current-induced torques vanish in the bulk, staggered effective fields can nevertheless exist as an interfacial response, whose allowed tensor form is determined by the surface antisymmetry subgroup for the given surface orientation. Separately, the structure of the spin conductivity tensor determines which surface orientations allow transverse spin current generation via the spin-splitter effect. Taken together, these symmetry-enforced properties establish which surface orientations of *d*-wave altermagnets can serve as deterministically switchable spin current sources in spin-torque heterostructures. Because the design rules are based solely on the surface antisymmetry point group, the required staggered axial response is robust

against averaging over symmetry-equivalent surface facets and equilibrium roughness.
[1] K. D. Belashchenko, arXiv:2603.06537.

EF-08. Chemical Pressure–Induced Stabilization of the Cubic Phase in Mn_3Ge

P. Kharel, M. Pulse, M. Anas
Chemistry, Biochemistry and Physics, South Dakota State University, Brookings, South Dakota, United States

Mn_3Ge is an intriguing material for scientific research because it can be stabilized in multiple crystallographic structures—tetragonal, hexagonal, and cubic—each exhibiting distinct and compelling magnetic properties [1-3]. The tetragonal phase is ferrimagnetic and possesses hard magnetic characteristics [1]. The hexagonal phase hosts an in-plane triangular spin structure, resulting in antiferromagnetic order accompanied by a large anomalous Hall effect [3]. In contrast, the cubic phase is ferromagnetic with a Curie temperature close to 400 K [2]. However, the cubic phase is difficult to synthesize, typically requiring high-pressure and high-temperature conditions, and consequently only limited reports are available. In this work, we demonstrate an alternative approach to stabilizing the cubic phase through chemical pressure. A small amount of carbon doping combined with slightly excess Mn effectively stabilizes the cubic structure. We have prepared Mn_3Ge in both hexagonal and cubic phases using arc melting followed by annealing, and their magnetic properties were systematically compared. The hexagonal phase exhibits a magnetic transition at 365 K, consistent with the reported Curie temperature associated with the residual ferromagnetic component of the triangular antiferromagnetic structure. Upon further heating, a weak transition is observed near 800 K, corresponding to the reported Curie temperature of the tetragonal phase. During cooling, a significant increase in magnetization appears near 700 K, indicating the onset of stabilization of the tetragonal structure. The cubic phase shows ferromagnetic behavior with a Curie temperature of 380 K, in good agreement with the reported value (~400 K). The high-field (3 T) magnetization at room temperature reaches 46 emu/g.
1. A. Kalache et al., APL Mater. 4, 086113 (2016).
2. H. Takizawa et al., J. Phys.: Condens. Matter 14 , 11147 (2002).
3. A. K. Nayak et al., Sci. Adv. 2:e1501870 (2016).



Room-temperature x-ray diffraction pattern of cubic Mn_3Ge.

EF-09. Revealing the origin of XMCD in an altermagnet via three-dimensional control of spins

D. Mallon, P. Radaelli, H. Jani
University of Oxford, Oxford, United Kingdom

Altermagnets are an emerging class of collinear antiferromagnets that exhibit non-relativistic spin-splitting of electronic bands. This has motivated a reclassification of magnets using spin groups, which describe the symmetry-allowed responses in the absence of spin-orbit coupling. Experimental signatures associated with time-reversal asymmetry, such as X-ray magnetic circular dichroism (XMCD), magneto-optical Kerr and anomalous Hall effects, have therefore been recently used as a validation of altermagnetism. However, these responses require spin-orbit coupling and do not remain invariant under spin-space rotations. This brings into question the extent to which they can be considered as direct signatures of altermagnetism. Here, we address this question by exploiting three-dimensional control of spins in the g-type altermagnet α-Fe_2O_3. We demonstrate that XMCD is governed precisely by the spin-direction-induced symmetry breaking that spin groups were designed to ignore. Our vectorial dichroism study shows that XMCD is highly anisotropic, depends on the orientation of the Néel vector, and is specific to the different magnetic point groups contained within the same spin group. Strikingly, the XMCD vector is decoupled from the weak canted moment. Our findings establish that XMCD in altermagnets can emerge from 'effective' magnetic dipoles related to the on-site Faraday tensor, activated

under local magnetic symmetry breaking, which is fundamentally distinct from reciprocal space spin-splitting. We exploit this understanding to reconstruct complete vectorial maps of nanoscale textures in altermagnetic thin films, including domain walls and topological solitons, which are promising for building future spintronics and magnonics devices.

1. D Mallon, Z Wu, J-C Lin, R Xie, B Zhao, C Godfrey, Q He, L Iglesias, P Gargiani, M Valvidares, P Bencok, F Maccherozzi, L Ishibe-Veiga, P Steadman, M Bibes, H Zhang, P G Radaelli, H Jani. *Under Review* (2026)

2. H Jani, J-C Lin, J Chen, J Harrison, F Maccherozzi, J Schad, S Prakash, C-B Eom, Ariando, T Venkatesan, P Radaelli. *Nature* 590, 74 (2021).

EF-10. Quantum Mechanism for Piezomagnetism in $S \geqslant 1$ Altermagnets

D. Yamamoto[1, 2], M. Naka[3]
[1]*Department of Physics, College of Humanities and Sciences, Nihon University, Setagaya, Tokyo, Japan,* [2]*RIKEN Center for Quantum Computing, Wako, Saitama, Japan,* [3]*Department of Science and Engineering, School of Science and Engineering, Tokyo Denki University, Ishizaka, Saitama, Japan*

Altermagnets have recently attracted considerable attention as a new class of collinear magnetic systems exhibiting nonrelativistic spin splitting and unconventional transport responses [1]. Among their cross-correlated phenomena, the piezomagnetic effect [2], namely the induction of a uniform magnetization by lattice distortion, has been actively discussed both from symmetry and microscopic perspectives [3]. While conventional mechanisms often rely on spin–orbit coupling, recent studies have demonstrated that nonrelativistic piezomagnetism can also arise in altermagnets. In particular, theoretical works based on microscopic Hubbard-type and Heisenberg-type models have shown that lattice distortion induces a finite magnetization at finite temperatures through thermally excited spin fluctuations [4]. However, in such scenarios, the effect typically vanishes in the ground state in undoped insulating systems, indicating that it relies on thermally excited spin fluctuations.

We investigate the piezomagnetic response in higher-spin altermagnets, focusing on its intrinsic quantum origin at zero temperature. Considering a localized spin-S ($S \geqslant 1$) model for an altermagnet with sublattice-dependent exchange interactions and easy-plane single-ion anisotropy, we analyze the magnetic response to strain-induced modulation of the model parameters using a flavor-wave approach. We show that the distortion couples linearly to the $k = 0$ excitation, leading to a uniform magnetization even in the absence of spin canting. This mechanism is absent in $S = 1/2$ systems [4] and originates from quadrupolar (Higgs-like) amplitude fluctuations inherent to higher-spin degrees of freedom. Our results demonstrate a purely quantum route to piezomagnetism that does not rely on thermal or carrier-induced excitations, and provide a new perspective on magnetoelastic responses in altermagnetic systems.

[1] K.-H. Ahn, A. Hariki, K.-W. Lee, and J. Kuneš, Phys. Rev. B 99, 184432 (2019); M. Naka *et al.,* Nature Commun. 10, 4305 (2019); L. Šmejkal, R. González-Hernández, T. Jungwirth, and J. Sinova, Sci. Adv. 6, eaaz8809 (2020).
[2] I. E. Dzialoshinski, Sov. Phys. JETP 6, 621 (1958); T. Moriya, J. Phys. Chem. Solids 11, 73 (1959).
[3] S. Hayami, Y. Yanagi, and H. Kusunose, J. Phys. Soc. Jpn. 88, 123702 (2019); H.-Y. Ma *et al*., Nat. Commun. 12, 2846 (2021); T. Aoyama and K. Ohgushi, Phys. Rev. Mater. 8, L041402 (2024).
[4] M. Naka, Y. Motome, T. Miyazaki, and H. Seo, J. Phys. Soc. Jpn. 94, 083702 (2025).

EF-11. Seed Layer Effects on the Anomalous Hall Effect in Polycrystalline Antiferromagnetic FeMn

A. Almahmoud, R. E. Maizel, S. Emori
Department of Physics, Virginia Tech, Blacksburg, Virginia, United States

Noncollinear antiferromagnets (NC-AFMs) may enable ultrafast switching and anomalous Hall readout of the magnetic state [1,2]. However, the requisite high-temperature epitaxial growth hinders integrating NC-AFM films into scalable devices. Recently, we discovered that *room-temperature-grown*, *polycrystalline* NC-AFM films of FeMn can exhibit anomalous Hall conductivities of >10 S/cm [3], rivaling conventional NC-AFMs at 300 K. The anomalous Hall effect emerges in the FCC γ phase of FeMn with a small built-in strain, stabilized with a 1-nm thin FCC Cu seed layer. Without the seed layer, FeMn forms the BCC α phase and shows no anomalous Hall effect. The FCC seed layer is thus essential for engineering NC-AFM FeMn films for scalable memory devices.

Here, we examine the influence of various seed layers on the anomalous Hall effect in polycrystalline NC-AFM $Fe_{60}Mn_{40}$. While the lattice parameter of Cu (0.362 nm) deviates little from FCC FeMn (0.363 nm), we incorporate

nanometer-thin FCC seed layers with significantly different lattice parameters, e.g., Ni (0.352 nm) and Al (0.405 nm). Ni-seeded FeMn displays a negligible anomalous Hall conductivity of < 0.1 S/cm [Fig. 1] due to the dominance of BCC α-FeMn [Fig. 2]. In contrast, Al-seeded FeMn exhibits clear hysteresis [Fig. 1] with a high out-of-plane remanence-to-saturation ratio of ≈ 0.5, coercivity of ≈ 0.05 T, and anomalous Hall conductivity of ≈ 6 S/cm. Yet, the latter still falls below ≈ 13 S/cm of Cu-seeded FeMn. Our structural characterization [Fig. 2] reveals two coexisting phases in Al-seeded FeMn: (i) tensile-strained FCC γ-FeMn that enhances remanence and coercivity (perpendicular anisotropy) and (ii) BCC α-FeMn that dilutes the anomalous Hall response. Our findings indicate that further enhancement of the strained FCC γ phase will enable NC-AFM FeMn films with strong anisotropy and anomalous Hall response for scalable antiferromagnetic memory.

[1] Nakatsuji, S., Kiyohara, N. & Higo, T. Nature 527, 212–215 (2015).
[2] Rimmler, B. H., Pal, B. & Parkin, S. S. Nature Reviews Materials 10, 109–127 (2025).
[3] Maizel, R. E. et al. APS March Meeting 2025, https://meetings-archive.aps.org/smt/2025/mar-q52/11/ (2025).

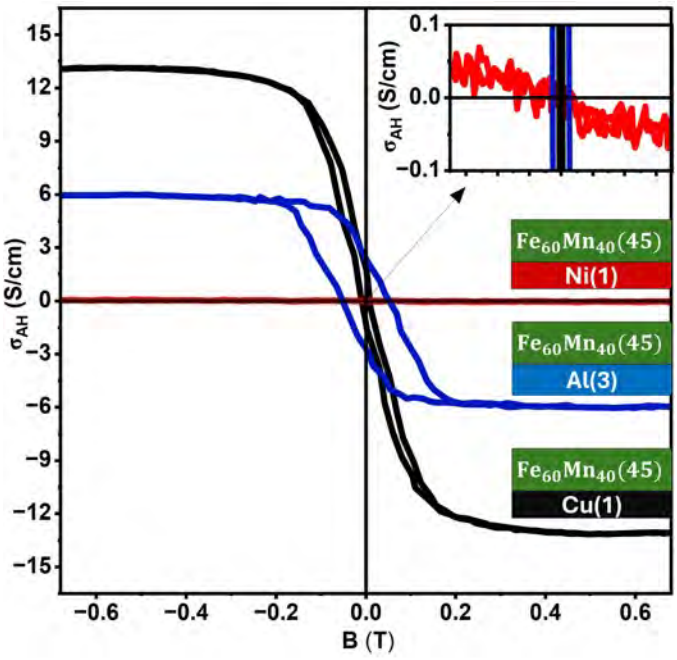


Fig. 1: Anomalous Hall conductivity σ_{AH} vs out-of-plane magnetic field *B* for $Fe_{60}Mn_{40}$ films on different seed layers (1 nm Cu, 1 nm Ni, 3 nm Al).

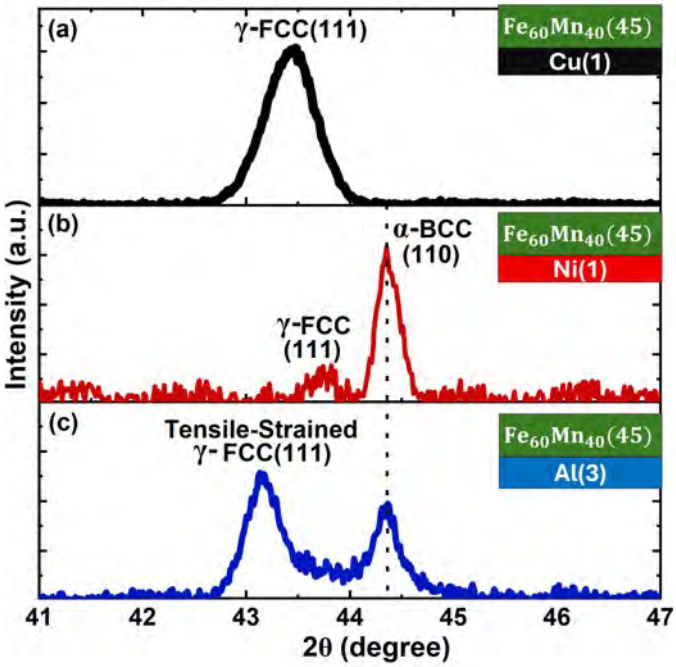


Fig. 2: XRD patterns of $Fe_{60}Mn_{40}$ thin films grown on Cu (1 nm), Ni (1 nm), and Al (3 nm) seed layers.

EF-12. Structural and Magneto-Transport Properties of Sputtered Mn_5Si_3 Thin Films

C. Langton[1], Z. Chen[1], A. Caruana[2], C. Kinane[2], Y. Ijiri[3], A. J. Grutter[4], J. Borchers[4], G. Yin[1], K. Liu[1]
[1]Department of Physics, Georgetown University, Washington, District of Columbia, United States, [2]ISIS Neutron and Muon Source, Didcot, United Kingdom, [3]Department of Physics and Astronomy, Oberlin College, Oberlin, Ohio, United States, [4]NIST Center for Neutron Research, National Institute of Standards and Technology, Gaithersburg, Maryland, United States

Altermagnets are gaining significant interests for spintronic applications by combining ferromagnetic properties with antiferromagnetic traits, such as vanishing net magnetization and ultrafast spin dynamics. A prime candidate is Mn_5Si_3, a predicted d-wave altermagnet with the potential for giant and tunneling magnetoresistance[1, 2]. Experimentally, this altermagnetic behavior is supported by a large anomalous Hall effect observed in its low-temperature, collinear antiferromagnetic phase in thin film samples[3].
Here we report on the structural and magnetic properties of Mn_5Si_3 thin films fabricated via DC magnetron sputtering. We demonstrate two distinct methods for stabilizing the Mn_5Si_3 phase. First, co-sputtering Mn and Si forms a mix of

MnSi, a known low temperature helimagnet[4, 5], along with the desired Mn_5Si_3 phase[6]. Alternatively, this MnSi phase can be suppressed with a 5 nm Pd seed layer, achieving the same Mn_5Si_3 stabilization. X-ray diffraction confirms the growth of a textured Mn_5Si_3 phase oriented in the out-of-plane direction. Polarized neutron reflectometry (PNR) provides depth-resolved magnetic profiling, revealing an Mn_5Si_3 layer with near-zero net magnetization, while identifying localized magnetic contributions arising from mixed-phase regions at the interfaces (Fig. 1). Magnetometry measurements reveal a significant isotropic magnetoresistance in the MnSi-stabilized films, attributed to spin suppression near the MnSi transition temperature ($T_N \approx 40$ K)[5], an effect notably smaller but still present in the Pd-stabilized samples. Additionally, we observe an anomalous Hall effect in both samples, suggesting a complex magnetic landscape in the thin film regime. These two fabrication methods allow us to isolate the effects of MnSi and Pd on the Mn_5Si_3 phase, clarifying how structural stabilization dictates the magnetic symmetry. Ultimately, this comparison provides a framework for understanding the magnetic properties in the candidate altermagnet Mn_5Si_3.

This work has been supported by the NSF (ECCS-2429995 and DMR-1828420).

[1] L. Šmejkal *et al., Phys. Rev. X* 12 040501 (2022)
[2] L. Šmejkal *et al., Phys. Rev. X* 12, 011028 (2022)
[3] H. Reichlova *et al*., *Nat. Commun.*15, 4961 (2024)
[4] E. Magnano *et al., App. Phys. Lett.* 96, 152503 (2010)
[5] S. V. Demishev *et al*., *Phys. Rev. B* 85, 045131 (2012)
[6] I. Kounta *et al*., *Phys. Rev. Mater.* 7 024416 (2023)

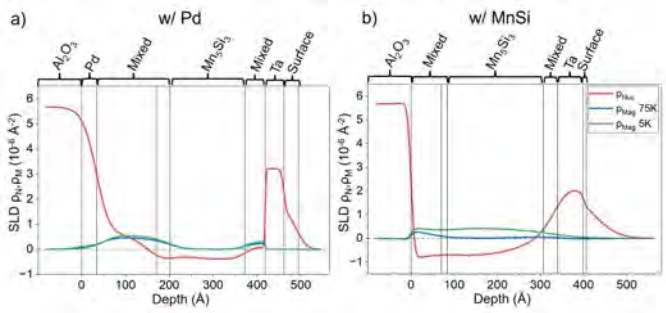


Fig. 1. PNR profiles of nuclear and magnetic SLD versus depth for Mn_5Si_3 samples with (a) Pd and (b) MnSi at 5 K and 75 K.

EF-13. Probing Altermagnetic Order in Canted Antiferromagnetic Epitaxial NiF_2 Thin Film

I. Nihal[1], H. Schiff[2], J. Vinson[3], N. Dale[6], S. A. Morley[1], S. Choudhury[4], B. Sharif[4], E. Sullivan[4], D. Lederman[4], J. Romhanyi[2], C. Klewe[1], S. Roy[1], E. Fullerton[5]
[1]Advanced Light Source, Lawrence Berkeley National Laboratory, Berkeley, California, United States, [2]Department of Physics & Astronomy, University of California, Irvine, Irvine, California, United States, [3]National Institute of Standards and Technology, Gaithersburg, Maryland, United States, [4]Department of Physics, University of California, Santa Cruz, Santa Cruz, California, United States, [5]Department of Electrical and Computer Engineering, University of California, San Diego, San Diego, California, United States, [6]Materials Science, Lawrence Berkeley National Laboratory, Berkeley, California, United States

Altermagnets (AMs) are a reclassified subset of antiferromagnets exhibiting alternating non-relativistic spin splitting along different directions in the Brillouin zone, arising from specific crystal and spin symmetry, despite zero net magnetization. This gives rise to odd Néel vector-dependent effects analogous to those in ferromagnets, such as the anomalous Hall effect, magneto-optical effects, and more. Combined with antiferromagnetic properties like external magnetic field insensitivity and terahertz-frequency spin dynamics, AMs are promising candidates for next-generation spintronic devices [1]. However, experimental detection of AM remains challenging: angle-resolved photoemission spectroscopy requires conductive samples, and inelastic neutron scattering requires large sample volumes. Soft X-ray magnetic circular and linear dichroism (XMCD and XMLD) spectroscopy and domain imaging offer a unique approach to identify AM order in metallic, insulating, and thin film samples, where optimal measurement geometries can be determined by calculating the expectation value of the anisotropic magnetic dipole operator (T operator). Here, we study an epitaxial Pt (3.7 nm) / NiF_2 (29 nm) thin film deposited on (110)-oriented MgF_2 substrate by molecular beam epitaxy. NiF_2 has a rutile structure with four symmetry-equivalent domains with Néel vectors along <010> directions in the *ab*-plane, with a small moment canting yielding net magnetization along corresponding <100> directions [2]. Epitaxial compressive strain results in a predominance of [010]-type domains, suggested by XMCD- and XMLD-photoemission electron microscopy (PEEM) imaging at the Ni L_3 and L_2 edges, respectively. This is supported by XMCD spectra at the Ni $L_{2,3}$ edges measured with and without applied magnetic

fields below the Néel temperature (≈73 K), showing distinct and reversible line shapes (Fig. 1). First-principles calculations isolated the altermagnetic XMCD signal from the canted magnetization contributions. This work establishes soft X-ray magnetic spectroscopy and domain imaging as a critical experimental framework for unambiguously identifying AM order and advancing next-generation spintronic device development.

[1] C. Song, H. Bai, Z. Zhou *et al.*, *Nat. Rev. Mater.*, Vol. 10, p.473 (2025)
[2] A. Hariki, K. Sakurai, T. Okauchi *et al.*, *npj Quantum Mater.*, Vol. 10, p.49 (2025)

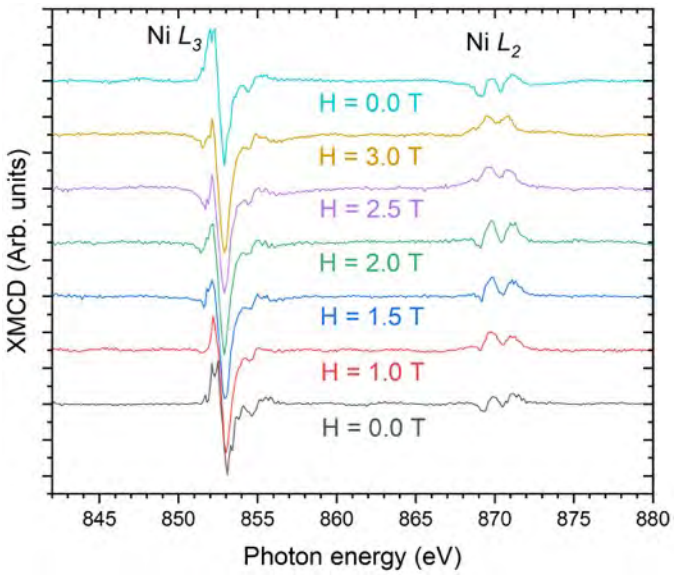


Fig.1: XMCD spectra at Ni $L_{2,3}$ edges

SESSION EG: SPIN DYNAMICS AND MAGNONICS
Chair(s): Y. Shiota, *Institute for Chemical Research, Kyoto University, Uji, Kyoto, Japan*
Thursday, November 5, 2026
08:30 AM-12:00 PM
Sea Pearl

EG-01. Spin Dynamics in the van der Waals Ferromagnet $CrTe_2$ Engineered by Niobium Doping

A. Laraoui[1], D. R. Lawati[1], P. Karki[2], J. Kumar[1], K. Prasad[2], M. A. Elekhtiar[1], K. Huang[1], B. Tiwari[1], S. Lamichhane[1], R. Timalsina[1], Z. Hubble[2], A. E. Aregbesola[2], J. Watt[3], S. Liou[1], E. Y. Tsymbal[1], J. Wang[2], K. Ambal[2]
[1]University of Nebraska-Lincoln, Lincoln, Nebraska, United States, [2]Wichita State University, Wichita, Kansas, United States, [3]Center for Integrated Nanotechnologies, Los Alamos National Laboratory, Los Alamos, New Mexico, United States

Understanding and controlling spin dynamics in van der Waals (vdW) magnets is critical for their application in magnonics and hybrid quantum information platforms. Despite the intense research activity since the initial discovery of 2D magnetism in 2017 [1-2], the spin dynamics of vdW magnets, central to magnonics [3], remain poorly understood or largely unexplored in many newly discovered materials. $CrTe_2$, a member of the transition-metal dichalcogenide (TMD) family, is a particularly promising candidate owing to its robust ferromagnetism and structural versatility. Notably, the 1*T* phase of $CrTe_2$ exhibits ferromagnetism with a Curie temperature (T_C) above room temperature in exfoliated thin flakes and epitaxially grown monolayers [4-5], highlighting $CrTe_2$ as a versatile vdW ferromagnet for spintronic applications. However, despite these advances, the spin dynamics and magnonic properties of $CrTe_2$ have remained largely unexplored.
In this work, we explored and engineered spin dynamics in the vdW ferromagnet 1*T*-$CrTe_2$ by investigating its dynamic magnetic response using ferromagnetic resonance (FMR) spectroscopy at room temperature [6]. To achieve systematic and controllable tunability of these spin-dynamic properties without suppressing robust room-temperature ferromagnetism, we employed niobium (Nb) substitution in $Cr_{1-x}Nb_xTe_2$ (x = 0 – 0.2) crystals grown by indirect synthesis. Nb doping provides a chemically stable and scalable route to modify magnetic interactions, thereby enabling control of spin dynamics. FMR measurements reveal that Nb doping enables wide-band tuning of spin dynamics, yielding a progressive reduction of the resonance frequency and a moderate increase of the Gilbert damping constant α from

~0.066 to ~0.14 [6]. Density functional theory (DFT) calculations attribute these trends to Nb-induced modifications of magnetic anisotropy, spin-orbit coupling, and exchange coupling [6]. Lower (a few GHz) ferromagnetic resonance frequencies of ~100-nm -thick $CrTe_2$ flakes compared to bulk crystals [6] are explained by thickness-dependent magnetic anisotropy [5]. Together, these results establish Nb-doped $CrTe_2$ as a vdW ferromagnet with widely tunable spin dynamics, extending its applicability to magnon spintronics [3].

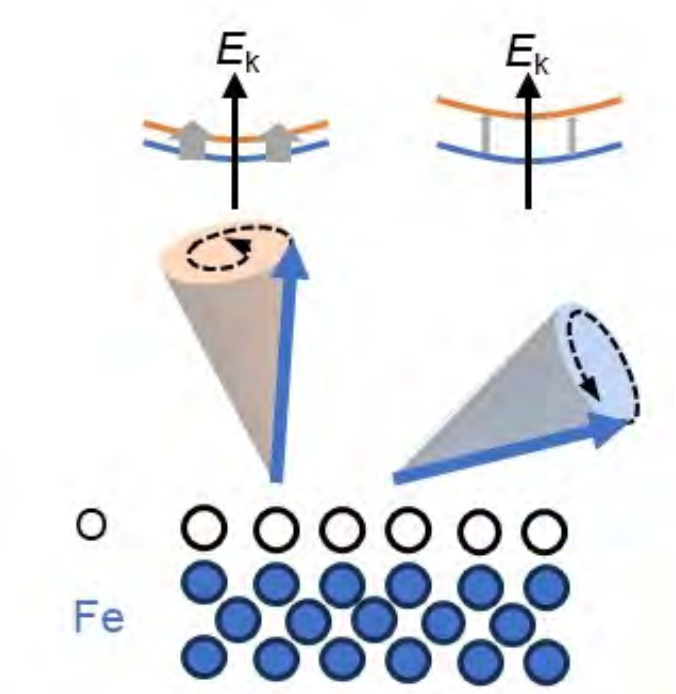
We acknowledge the National Science Foundation (Awards 2328822, 2521415, 2044049, and 2025298); the U.S. Department of Energy (Award DE-SCSC0026103); the University of Nebraska-Lincoln Grand Challenges catalyst award entitled "Quantum Approaches Addressing Global Threats"; and the Center for Integrated Nanotechnologies, an Office of Science User Facility operated for the U.S. Department of Energy, Office of Science. Los Alamos National Laboratory, an affirmative action equal opportunity employer, is managed by Triad National Security, LLC for the U.S. Department of Energy's NNSA, under contract 89233218CNA000001.
[1] B. Huang, et *al*., *Nature* 2017, *546*, 270.
[2] C. Gong, et *al*., *Nature* 2017, *546*, 265.
[3] A. V. Chumak, et *al*., *Nature Phys* 2015, *11*, 453.
[4] X. Zhang, et *al*., *Nat Commun* 2021, *12*, 2492.
[5] L. Meng, et *al*., *Nat Commun* 2021, *12*, 809.
[6] D. R. Lawati, A. Laraoui. et *al*., under review (https://doi.org/10.48550/arXiv.2512.22058).

EG-02. Large Interband-Driven Anisotropic Gilbert Damping in an Ultrathin Fe Layer Interfaced with MgO

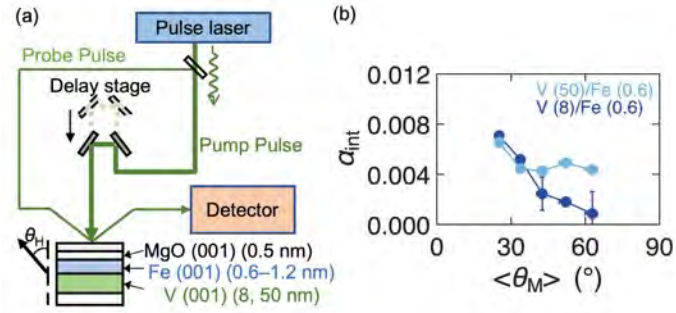
J. Chen[1], I. Kurniawan[2], S. Sakamoto[1, 6], H. Kosaki[1], E. Wei[1], T. Hatajiri[1], K. Ando[3, 4, 5], K. Masuda[2], S. Miwa[1, 7]
[1]The Insititute for Solid State Physics, The University of Tokyo, Chiba, Japan, [2]Research Center for Magnetic and Spintronics Materials, National Institute for Material Science, Tsukuba, Japan, [3]Department of Applied Physics and Physico-Informatics, Keio University, Yokohama, Japan, [4]Keio Institute of Pure and Applied Sciences, Keio University, Yokohama, Japan, [5]Center for Spintronics Research Network, Keio University, Yokohama, Japan, [6]Institute for Materials Research, Tohoku University, Sendai, Japan, [7]Trans-scale Quantum Science Institute, The University of Tokyo, Tokyo, Japan

The Gilbert damping constant is a fundamental parameter representing the magnetization dynamics in magnetic materials. Although it is considered an isotropic parameter in most magnetic materials, theoretical calculations predict that the Gilbert damping can be anisotropic in a single-crystalline system [1]. Recent studies have experimentally discovered in-plane anisotropy in Gilbert damping in epitaxial systems [2–4] and attributed it to intraband electron scattering. However, the contribution of interband scattering to anisotropic Gilbert damping remains elusive, as it is generally considered isotropic at high scattering rates. Here we report anisotropic Gilbert damping in epitaxial V/ultrathin-Fe/MgO multilayers governed by interband scattering [Fig. 1]. We fabricated the epitaxial multilayer by molecular beam epitaxy and characterized the intrinsic Gilbert damping using time-resolved magneto-optic Kerr effect measurements [Fig. 2(a)]. We observe significant anisotropy in the intrinsic Gilbert damping constant, which exhibits a threefold enhancement as the magnetization tilts from the in-plane to the out-of-plane direction [Fig. 2(b)]. The anisotropy is suppressed by strengthening the epitaxial strain through an increase in the thickness of the V underlayer. By comparing the strain-controlled experiments and first-principles calculations, we find that the anisotropic Gilbert damping is consistent with interband scattering, while the intraband contribution exhibits an opposite tendency. Our results identify interband scattering at the Fe/MgO interface as the primary source of the damping anisotropy, challenging the conventional intraband-dominated picture and offering a route for interface- and strain-controlled magnetization dynamics [5].

1. K. Gilmore, M. D. Stiles, J. Seib, Physical Review B, Vol. 81, p.174414 (2010)
2. L. Chen, S. Mankovsky, S. Wimmer, Nature Physics, Vol. 14, p.490–494 (2018)
3. L. Chen, S. Mankovsky, M. Kronseder, Physical Review Letter, Vol. 130, p.046704 (2023)
4. Y. Li, F. Zeng, S. S.-L. Zhang, Physical Review Letter, Vol. 122, p.117203 (2019)
5. J. Chen, I. Kurniawan, S. Sakamoto, under review



Schematic of interband-driven anisotropic Gilbert damping in a few atomic layers of Fe



(a) Setup of the time-resolved magneto-optic Kerr effect measurements. (b) Magnetization-direction dependence of intrinsic Gilbert damping for V (8 and 50)/Fe (0.6 nm)/MgO (0.5 nm) multilayers.

EG-03. Non-equilibrium magnon engineering for thermal transport modulation

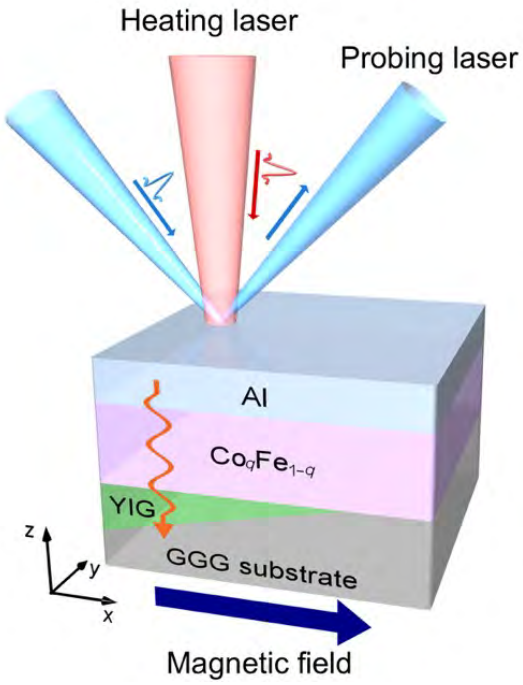
T. Hirai[1, 2], T. Morita[7, 1], S. Biswas[3, 1], J. Uzuhashi[1], T. Yagi[5], Y. Yamashita[5], V. K. Kushwaha[1], F. Makino[6, 1], R. Modak[1, 2], Y. Sakuraba[1, 6], T. Ohkubo[1], R. Guo[2], B. Xu[2], J. Shiomi[2], D. Chiba[7, 4], K. Uchida[1, 2, 6]

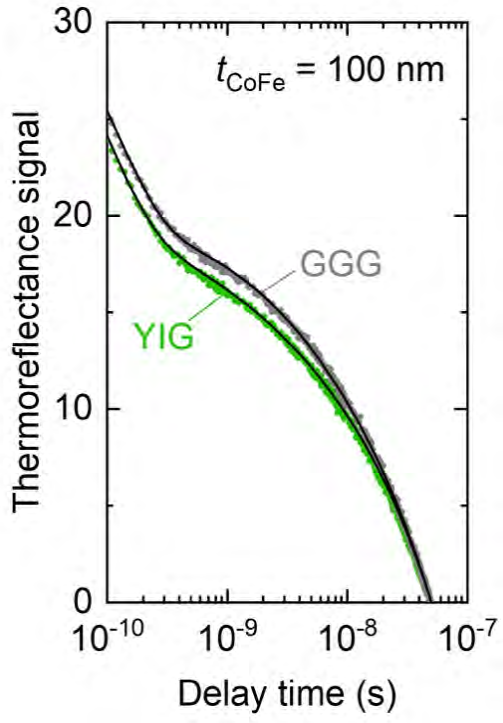
[1]NIMS, Tsukuba, Japan, [2]The University of Tokyo, Kashiwa, Japan, [3]IITG, Guwahati, India, [4]SRIS, Tohoku University, Sendai, Japan, [5]AIST, Tsukuba, Japan, [6]University of Tsukuba, Tsukuba, Japan, [7]SANKEN, The University of Osaka, Ibaraki, Japan

The development of spin caloritronics provides novel concepts and functionalities in thermal management technologies for electronic and spintronic devices. However, most of the spin caloritronics studies focus on the thermal energy conversion, i.e., thermoelectric and thermo-spin effects. To make effective use of spintronic thermal management, various controlling techniques and principles for heat utilizing the spin degree of freedom need to be developed. In this presentation, we show the demonstration of controlling a fundamental thermal transport phenomenon, heat conduction, by utilizing magnon spin currents at room temperature [1].

We fabricated a junction comprising a ferromagnetic metal (FM) film of CoFe or NiFe with a thickness of 100 nm and garnet crystal substrate, where the garnet substrate was composed of a thickness-wedged-$Y_3Fe_5O_{12}$/$Gd_3Ga_5O_{12}$ (YIG/GGG) bilayer and the sample surface was covered by a 50-nm-thick Al layer. The values of cross-plane thermal conductivity of FM (k) and interfacial thermal conductance at FM/garnet (G) were evaluated by use of a time-domain thermoreflectance method (TDTR) (Fig. 1) [2]. We observed the distinct difference in TDTR signals between the FM/GGG and FM/YIG junctions (Fig. 2), resulting the larger k and G values in the FM/YIG junction than those in the FM/GGG junction, which indicates that the nanoscale thermal transport can be controlled by changing boundary condition for spin currents. Furthermore, by inserting a thin nonmagnetic Cu layer between the FM layer and garnet, the observed differences in k and G were significantly reduced, proving that the dominant carrier of spin current for this thermal transport is magnon even at room temperature. The functionality of the magnon-engineered thermal transport provides a new way for thermal engineering and promotes spintronic thermal management.

[1] T. Hirai, T. Morita and S. Biswas, Adv. Funct. Mater., Vol. 35, p.2506554 (2025)
[2] D. G. Cahill, Rev. Sci. Instrum., Vol. 75, p.5119 (2004)





EG-04. Ferromagneto-Elastic Resonance in a Low-Damping Polycrystalline Ferromagnetic Alloy

N. Farhadi, G. T. Street, S. Emori
Physics, Virginia Tech, Blacksburg, Virginia, United States

Interconversion between magnons and phonons is essential for next-generation microwave communications and hybrid quantum information systems. Such interconversion can manifest in *ferromagneto-elastic resonance* (FMER) in magnetic films, where magnon and phonon standing waves interact via magnetoelastic coupling. Although theoretically well established [1], observing FMER in metallic ferromagnets remains challenging because it is often masked by strong spin-electron dissipation, i.e., Gilbert damping [2].

Here, we demonstrate clear signatures of FMER in polycrystalline films of metallic $Fe_{70}V_{30}$ at room temperature. The key enablers are the low Gilbert damping ($\alpha \approx 0.003$) and sizable magnetoelastic coupling ($\lambda_s > 10$ ppm) of FeV [3]. The emergence of FMER is seen in measurements of ferromagnetic resonance linewidth vs frequency [Fig. 1], conducted with the film magnetized out-of-plane. We observe an unusual "peak," superposed on the expected linear trend from Gilbert damping. The central frequency of the peak scales inversely with the FeV thickness, consistent with FMER – i.e., magnons coupling to phonons when the standing-wave condition is met.

The FMER-induced peak is particularly pronounced in FeV on 50-nm-thick thermally grown SiO_2 [Fig. 2]. Due to the acoustic impedance mismatch between the metal and SiO_2, standing-wave phonons remain confined in the FeV film. In contrast, the peak is suppressed in FeV on bare Si [Fig. 2], as phonons are readily pumped out across the better impedance-matched metal/Si interface. Our findings offer a new avenue for magnon-phonon device architecture with scalable polycrystalline ferromagnetic metals and engineered film/substrate interfaces.

[1] T. Kobayashi, R. C. Barker, and A. Yelon, Ferromagnetoelastic Resonance in Thin Films, Phys. Rev. B 7, 3286 (1973).
[2] W. K. Peria, D.-L. Zhang, Y. Fan, J.-P. Wang, and P. A. Crowell, Anomalous temperature dependence of phonon pumping by ferromagnetic resonance in Co/Pd multilayers with perpendicular anisotropy, Phys. Rev. B 106, L060405 (2022).
[3] D. A. Smith, et al., Magnetic damping in epitaxial iron alloyed with vanadium and aluminum, Phys. Rev. Applied 14, 034042 (2020); M. Arora, et al., Magnetic Damping in

Polycrystalline Thin-Film Fe–V Alloys, Phys. Rev. Applied 15, 054031 (2021).

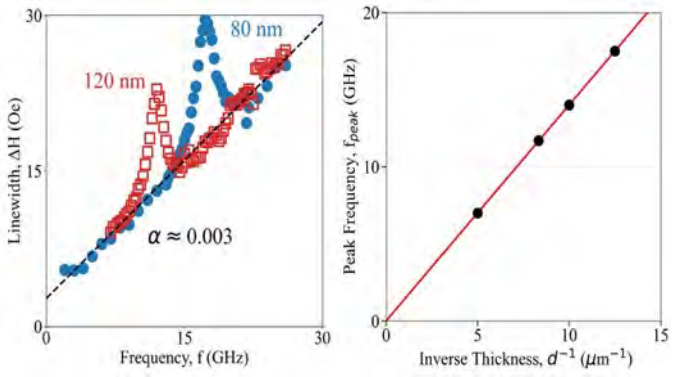


Fig. 1. Left: Ferromagnetic resonance linewidth vs frequency for 80- and 120-nm-thick FeV films. An anomalous "peak" emerges on top of the usual Gilbert-damping-induced linear relation. Right: Central frequency of the peak versus inverse FeV thickness.

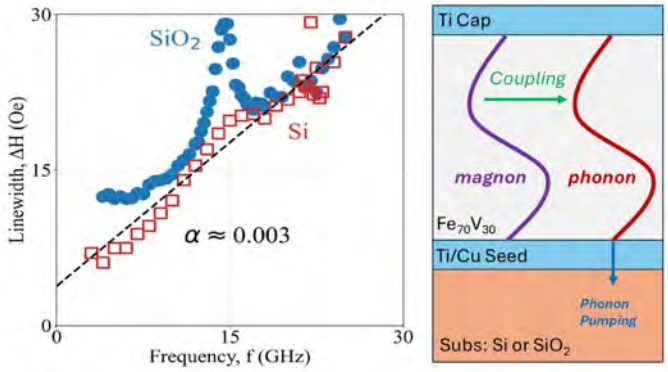


Fig. 2. Left: Ferromagnetic resonance linewidth vs frequency for FeV deposited on SiO_2 (confining phonons) and bare Si (permitting phonon pumping). Right: Schematic of the magnetoelastic coupling and the film-to-substrate phonon pumping.

EG-05. Tuning the Macrospin-to-Vortex Transition Probability in Co-based Artificial Spin Vortex Ice via Perpendicular Magnetic Anisotropy

Y. Maruyama[1], A. Mondal[2], R. Ohshima[1, 3], J. Puebla[1, 3], B. Jungfleisch[2], M. Shiraishi[1, 3]

[1]Kyoto University, Kyoto, Japan, [2]University of Delaware, Newark, Delaware, United States, [3]CSRN Kyoto University, Kyoto, Japan

Artificial spin lattices have attracted significant interest in nanomagnetism and magnonics for its rich microstate space and physical memory [1, 2]. Recently, artificial spin vortex ice (ASVI), which integrates both macrospin (MS) and vortex (V) states, has emerged as a promising platform for physical reservoir computing [2]. Since ASVI utilizes the probabilistic MS-to-V transition as a fading memory property, the control of such transitions has become a new frontier in nanomagnetics.

Previous studies have reported that perpendicular magnetic anisotropy (PMA) tunes the energy landscape of nanomagnets [3,4]. We hypothesize that PMA can also modulate MS-to-V transition probabilities P_{trans}. To test this, stadium-shaped nanomagnets were arranged in a 45-degree tilted square lattice. To vary the PMA, Ti(3)/Co(10)/Ti(3)/Pt(2) (TCT ASVI) and Ti(3)/Co(10)/Pt(2) (TCP ASVI) nanomagnetic arrays were prepared on a coplanar waveguide. The P_{trans} were evaluated via the ferromagnetic resonance (FMR) spectra at 0 mT after N minor field loops between $\pm B_{train}$ where the amplitude of B_{train} was chosen to be larger than the coercive field of MS-state but smaller than the annihilation field of the V-state. The inset of Fig. 1 shows the N dependence of the FMR spectra ΔS_{21} for a 220 nm wide TCT ASVI. The decrease in FMR intensity with increasing N suggests the V formation [2]. Figure 1 presents the symmetric component L_S of the high-frequency FMR mode extracted by fitting the spectra with Lorentzian functions, which showed the most pronounced change during the transition. The P_{trans} was subsequently estimated by fitting the data assuming a constant P_{trans} per minor loop.

Figure 2 shows estimated P_{trans} for both ASVIs. These results are consistent with previous reports [2], where wider nanomagnets are more likely to switch into a V-state. Moreover, P_{trans} for the TCP ASVI was higher than that of the TCT ASVI across all investigated widths. These findings suggest that PMA facilitates vortex formation, identifying PMA as a pivotal design parameter for tuning fading memory characteristics.

[1] R. Sultana *et al.*, J. Appl. Phys., Vol. 138, p. 061101 (2025)

[2] J. C. Gartside *et al*., Nat. Nanotechnol., Vol. 17, p. 460 (2022)
[3] E. R. P. Novais *et al*., J. Appl. Phys., Vol. 110, p. 053917 (2011)
[4] E. R. P. Novais *et al*., J. Appl. Phys., Vol. 114, p. 153905 (2013)

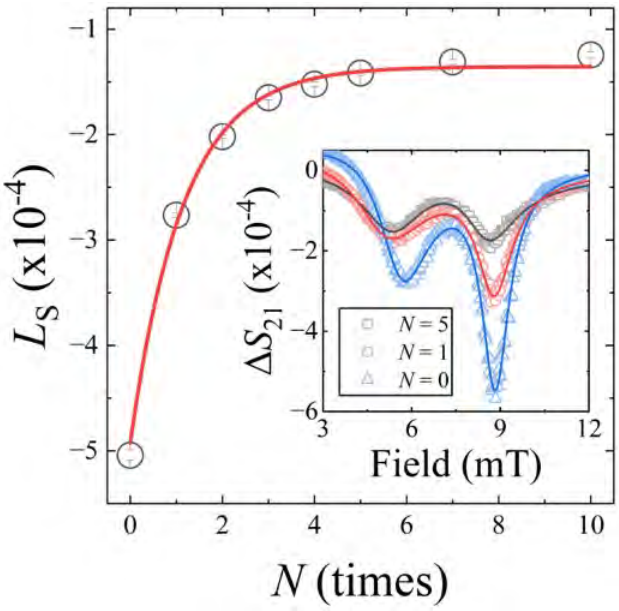


Fig. 1. N dependence of L_S and ΔS_{21} (inset) for 220 nm wide TCT ASVI.

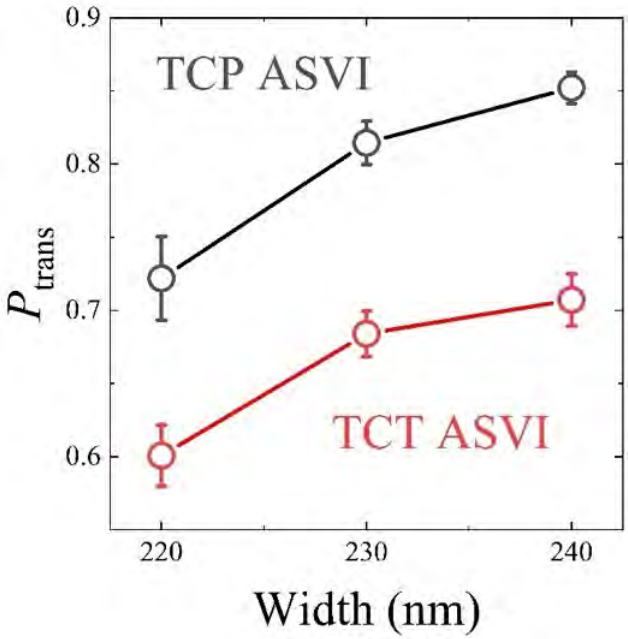


Fig. 2. W dependence of P_{trans} of TCT and TCP ASVIs.

EG-06. Scanning NV Magnetometry for Spin-Wave Demultiplexer Design in YIG Film

T. Zheng, J. Zhu
Electrical and Computer Engineering, Carnegie Mellon University, Pittsburgh, Pennsylvania, United States

Spin-wave propagation can be engineered by facilitating the interplay of spin-wave dispersion, magnetic configuration, and device geometry. In yttrium iron garnet (YIG) thin films, geometric features can shape spin-wave propagation through diffraction, reflection, and interference, while anisotropic spin-wave dispersion can direct the resulting wavefronts into well-defined propagation paths. These effects provide a physical basis for compact magnonic routing and frequency-selective demultiplexing. Scanning nitrogen-vacancy (NV) magnetometry is well suited to probe such behavior by imaging the magnetic stray fields generated by propagating spin waves at room temperature. In this work, we use a scanning NV-center probe to image surface spin waves in a YIG film. The measured real-space beam patterns reveal directional propagation associated with the combined effects of device geometry and spin-wave dispersion (Fig. 1). These results establish an experimental approach for characterizing the propagation pathways underlying frequency-selective spin-wave routing. Building on this imaging capability and inspired by recent inverse-design magnonics, we use micromagnetic simulations to examine a spin-wave demultiplexer design, in which a patterned scattering region directs different excitation frequencies into distinct output channels through engineered wave interference (Fig. 2).
This study demonstrates scanning NV magnetometry as a useful tool for developing and validating frequency-selective magnonic devices with direct observation of spin wave propagation. Its high spatial resolution and sensitivity to spin-wave generated stray fields can help connect simulated demultiplexer designs with experimentally observed propagation patterns.

[1] I. Bertelli, J. J. Carmiggelt and T. Yu, Sci. Adv., Vol. 6, p.eabd3556 (2020).
[2] B. G. Simon, S. Kurdi and J. J. Carmiggelt, Nano Lett., Vol. 22, p.9198 (2022).
[3] Q. Wang, A. V. Chumak and P. Pirro, Nat. Commun., Vol. 12, p.2636 (2021).
[4] A. Voronov, M. Cuervo Santos and F. Bruckner, npj Spintronics., Vol. 3, p.19 (2025).

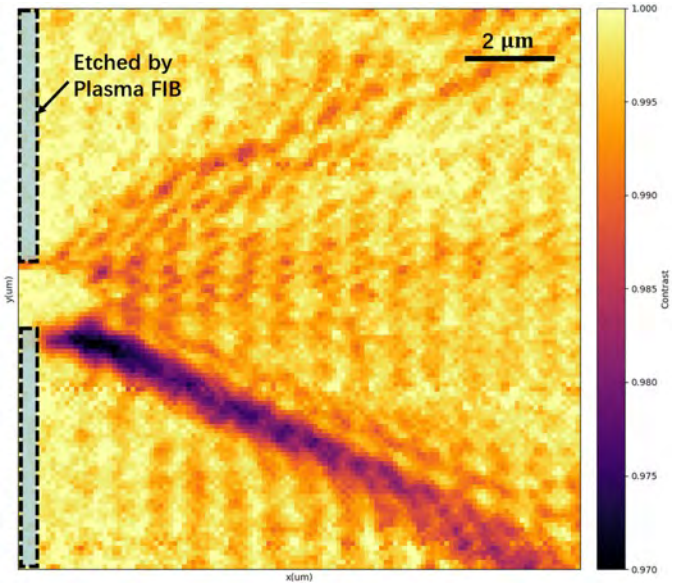


Fig 1. NV image of directional spin-wave propagation through a plasma focused ion beam (FIB) defined single slit in a 109 nm thick YIG film. The spin waves are excited at 2.66 GHz under a 10 mT bias field. The dashed regions indicate fully etched YIG areas, ensuring complete removal of the YIG layer.

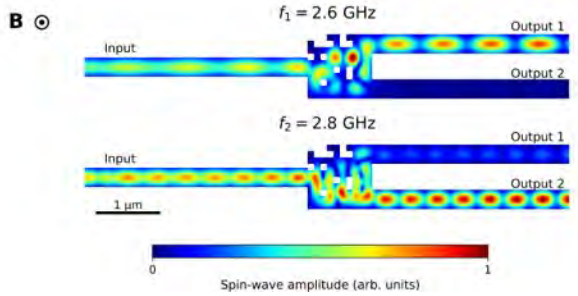


Fig 2. Micromagnetic simulation of a patterned spin-wave demultiplexer in a 100 nm thick YIG film. The design region separates 2.6 GHz and 2.8 GHz spin-wave signals into different output channels.

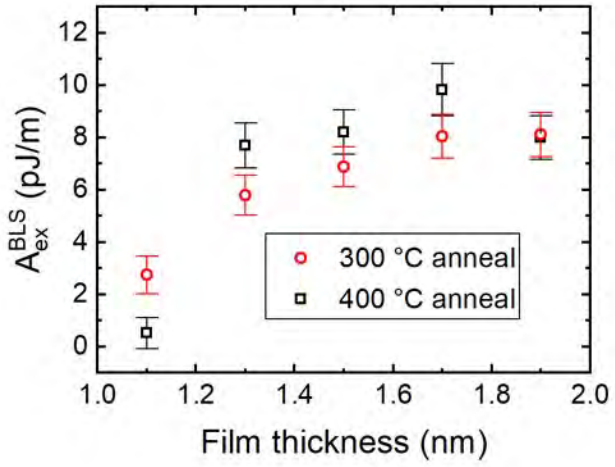
EG-07. Comparison of measurement methods for determining exchange stiffness in ultrathin ferromagnetic films

W. K. Peria[1, 3], C. Swindells[1, 4], J. J. Wisser[5], M. Tanksalvala[5], M. Kiechle[1], G. Hu[2], M. Pufall[5], H. T. Nembach[5]
[1]Associate; Applied Physics Division, National Institute of Standards and Technology, Boulder, Colorado, United States, [2]IBM Research, Yorktown Heights, New York, United States, [3]Department of Physics, University of Colorado Boulder, Boulder, Colorado, United States, [4]Department of Electrical Engineering, University of Colorado Denver, Denver, Colorado, United States, [5]Applied Physics Division, National Institute of Standards and Technology, Boulder, Colorado, United States

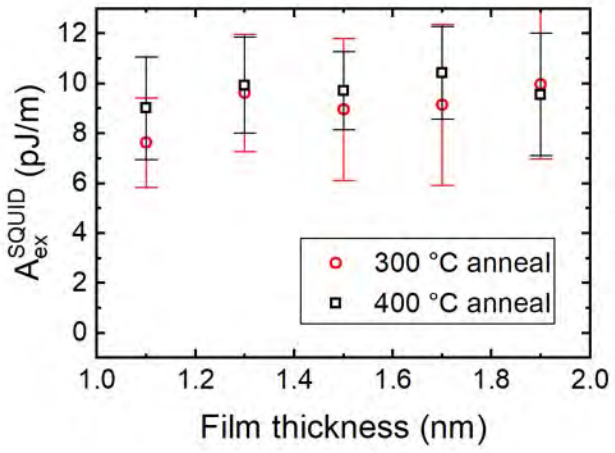
In magnetic memory applications, among the critical material parameters that impact device performance are the magnetic moment, the magnetic anisotropy, the Gilbert damping, and the exchange stiffness. The exchange stiffness is one quantity for which there has been disagreement about how to obtain reliable values in ultrathin films. For instance, the common method of measuring perpendicular standing spin waves (PSSW) in films of thickness ~100 nm is not possible for ultrathin films due to the high frequencies of the PSSW's accompanied by weak signal strength.

In this work, we compare the methods of Brillouin light scattering (BLS) and SQUID magnetometry for determining the exchange stiffness A_{ex} in a series of ultrathin CoFeB films (1.1 nm to 1.9 nm). We introduce methods designed to enhance the accuracy of the analysis of SQUID data, which are necessary for ultrathin films where the exchange stiffness can be quite low. There is a substantially higher uncertainty in the results obtained with SQUID, primarily due to the sensitivity of the fits on the internal field of the films. The uncertainty in the BLS values is mostly due to the uncertainty in film thickness, which is needed when converting the spin-wave stiffness D_e (directly measured with BLS) into A_{ex}. The BLS measurements reveal a decreasing trend with decreasing thickness (see Figure 1), whereas the SQUID values do not show any trend with thickness (see Figure 2). We discuss the challenges associated with determining exchange stiffness from both BLS and SQUID meaurements in ultrathin films, with the BLS measurements ultimately leading to uncertainty approximately 2 to 3 times lower than the values from SQUID measurements.

This work was performed with funding from the CHIPS Metrology Program, part of CHIPS for America, National Institute of Standards and Technology, U.S. Department of Commerce.



Exchange stiffness as a function of film thickness obtained with BLS for 300 °C (red circles) and 400 °C (black squares) annealing temperatures.



Exchange stiffness as a function of film thickness obtained with SQUID for 300 °C (red circles) and 400 °C (black squares) annealing temperatures.

EG-08. Nonlinear Interactions between Surface Acoustic Wave Phonons and Magnons

Y. Todaka, Y. Chen, M. Kawaguchi, M. Hayashi
Department of Physics, The University of Tokyo, Hongo, Tokyo, Japan

Magnon-phonon hybrid systems provide a promising platform for coherent information processing. Surface acoustic waves (SAWs) are commonly employed as a versatile phonon source. Although linear magnetoelastic coupling has been extensively studied, nonlinear SAW–magnon dynamics remain largely unexplored. Here, we experimentally investigate nonlinear SAW–magnon interactions in a hybrid device consisting of interdigital transducers (IDTs) and a magnetic thin film.
The nonlinear acoustic response was evaluated using rf measurements. By systematically varying the input microwave power and external magnetic field, we observed characteristic nonlinear behavior in the transmitted signal. In particular, the transmitted power shows a clear threshold-like dependence on the input power and is strongly modulated at specific magnetic fields, indicating nonlinear coupling between SAW phonons and magnons. To clarify the physical origin of these behaviors, we performed numerical simulations. The calculated magnetic-field and power dependences qualitatively reproduce the experimental trends, supporting nonlinear magnetoelastic coupling as the underlying mechanism. In the presentation, we discuss results from different device designs and implications of their results.

EG-09. Magnetic Resonance of the Chiral TCS Phase in Fe_3Ga_4 Revealed by Broadband FMR

M. P. Whalen[1], S. Nepal[2], F. M. Abel[3, 4], M. E. Jamer[3], J. Q. Xiao[2]
[1]Quantum Science and Engineering Program, University of Delaware, Newark, Delaware, United States, [2]Department of Physics and Astronomy, University of Delaware, Newark, Delaware, United States, [3]The Volgenau Department of Physics, United States Naval Academy, Annapolis, Maryland, United States, [4]Sensor Science Division, NIST, Gaithersburg, Maryland, United States

Helimagnetic materials, first studied extensively in the 1960s [1-2] have regained attention due to interest in systems hosting topological spin textures and emergent quantum phenomena. While most studies focus on non-centrosymmetric systems stabilized by Dzyaloshinskii–Moriya interactions (DMI) [3], centrosymmetric helimagnets

driven by magnetic frustration remain comparatively underexplored, despite exhibiting rich and unconventional magnetic behavior.

Among these, Fe_3Ga_4 is notable for hosting a recently discovered chiral transverse conical spiral (TCS) phase above room temperature [4–6]. This phase gives rise to emergent electromagnetic fields and a topological Hall effect persisting beyond room temperature, highlighting its potential for robust topological transport. Additionally, Fe_3Ga_4 exhibits a complex phase diagram with at least seven highly tunable magnetic phases, as established by neutron scattering [6].

Here, we report the first broadband ferromagnetic resonance (FMR) characterization of the chiral TCS phase in Fe_3Ga_4. With the magnetic field applied along the crystallographic b-axis, we observe a distinct resonance mode below 40 GHz that persists over a wide temperature range, including room temperature. As shown in Fig. 1, FMR maps the full magnetic phase diagram and shows strong sensitivity to magnetic phase transitions, consistent with prior measurements.

The TCS resonance exhibits FM-like behavior unlike other helical magnetic structures, with slight deviations from Kittel-like behavior and relatively high damping, suggesting additional collective dynamics beyond uniform precession. Complementary vibrating sample magnetometry (VSM) measurements identify magnetic phase transitions, in strong agreement with the FMR results. Our work positions Fe_3Ga_4 as a promising platform for exploring beyond room-temperature topological spin dynamics and their integration into microwave and spintronic technologies.

This work is supported by NSF DMR grant No. 2316664.

1. A. Yoshimori Journal of the Physical Society of Japan, Vol. 14, p.807 (1959)
2. T. Nagamiya, Solid State Physics (Academic Press), Vol. 20, p.305 (1968)
3. M. Garst, J. Waizner and D. Grundler, Journal of Physics D: Applied Physics., Vol. 50, p.293002 (2017)
4. B. Wilfong, A. Fedorko and D. R. Baigutlin, Journal of Alloys and Compounds, p.16532 (2022)
5. M. Afshar and I. I. Mazin, Phys. Rev. B., Vol. 104, p.094418 (2021)
6. P. R. Baral, V. Ukleev and I. Zivković, Nature Communications, Vol. 16, p.3898 (2025)

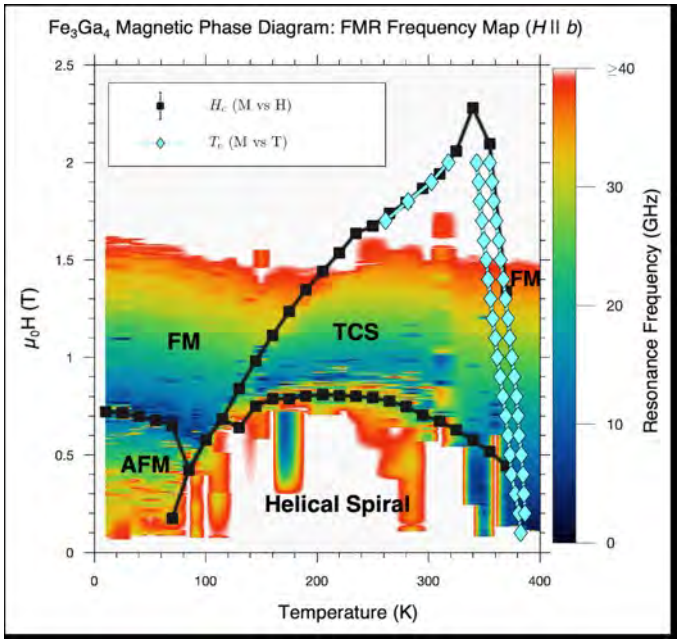


Fig. 1 | Magnetic phase diagram of Fe_3Ga_4 for H ∥ b. Color map shows the FMR as a function of temperature and applied field. Critical fields H_c (from M vs H) and transition temperatures T_c (from M vs T) marking magnetic phase boundaries are overlaid.

EG-10. Voltage control of magnonic Fabry-Pérot resonators

A. Frej, R. Mansell, S. van Dijken
Department of Applied Physics, Aalto University, Espoo, Finland

We demonstrate voltage control of spin-wave transmission in magnonic Fabry-Pérot resonators consisting of a low-damping yttrium iron garnet (YIG) film coupled to a ferromagnetic CoFeB nanostripe. Dynamic dipolar coupling between the two magnetic layers forms a magnonic cavity with a modified spin-wave dispersion. The cavity resonances produce narrow transmission gaps in the spin-wave spectrum while maintaining a low insertion loss, enabling field-tunable control of the spin-wave amplitude [1] and phase [2]. The strong wavelength reduction within the resonator allows long-wavelength spin waves to be manipulated by elements just a few hundred nanometers wide.

Voltage control of the transmission spectrum is achieved by integrating a Pt/$LiCoO_2$/LiPON multilayer onto the CoFeB stripe. This stack functions as a solid-state magneto-ionic battery [3,4], in which LiPON serves as the solid-state electrolyte and $LiCoO_2$ acts as the Li^+ ion reservoir. Applying a voltage to the Pt top electrode drives Li^+ ions into or out

of the CoFeB layer, modulating its magnetization and, through dipolar coupling with the underlying YIG film, shifting the spin-wave transmission spectrum. Device characterization is carried out using propagating spin-wave spectroscopy with two microwave antennas for spin-wave excitation and detection. Figure 1 shows a representative measurement on a voltage-controlled Fabry-Pérot resonator and a reference spectrum from a bare YIG film. Reversible Li^+ migration driven by ±3 V shifts the transmission gaps by 20-30 MHz (Fig.2 a). This allows the transmitted intensity at a given frequency to be controlled (Fig.2 b), creating a solid-state programmable spin-wave filter.

[1] H. Qin et al., Nat. Commun. 12, 2293 (2021)
[2] A. Lutsenko et al., Appl. Phys. Lett. 126, 082406 (2025)
[3] M Ameziane et al., Adv. Funct. Mater. 32, 2113118 (2022)
[4] M. Ameziane et al., Nano Lett. 23, 3167-3173 (2023)

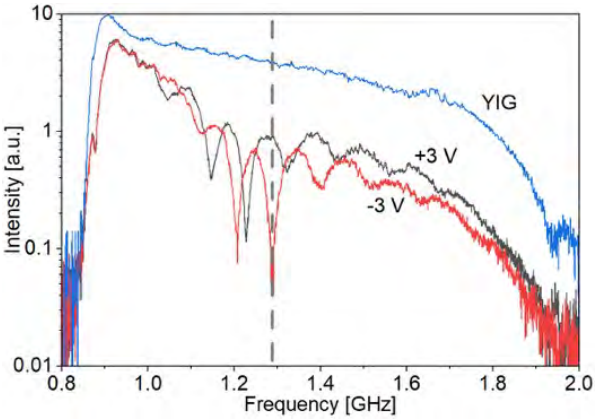


Fig.1 Spin-wave transmission spectra recorded on a 4-µm-wide magnonic Fabry-Pérot resonator biased at +3 V (black) and -3 V (red) under an in-plane applied magnetic field of 7 mT (Damon-Eshbach geometry), with a reference bare YIG film spectrum (blue).

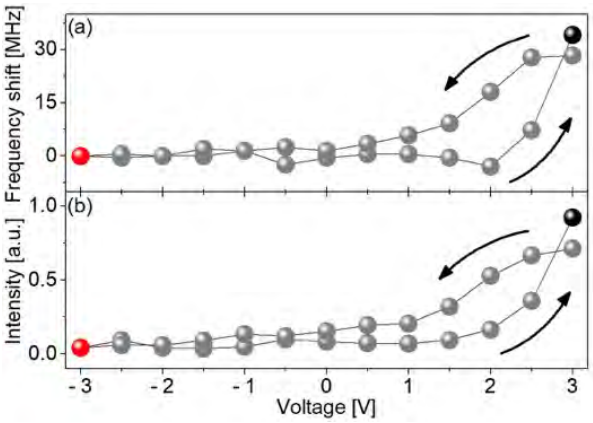


Fig.2 a) Frequency shift of the transmission gap marked with a dashed line in Fig.1 during a +3 V → -3 V → +3 V voltage sweep, demonstrating reversible electrical tuning of the resonance condition. b) Signal intensity change at the selected frequency during the same voltage sweep.

EG-11. Efficient modulation of RF signal in standalone monolithic piezo-magnonic-MEMS

M. Cocconcelli[1, 2], A. Angotti[1], P. Florio[1], N. Pellizzi[1], F. Maspero[1], R. Bertacco[1]
[1]Department of Physics, Politecnico di Milano, Milan, Italy, [2]Laboratoire Albert Fert, CNRS, Thales, Université Paris-Saclay, Palaiseau, France

Advances in tunable magnonic systems offer significant opportunities for next-generation radio-frequency (RF) signal processing, owing to their potential for miniaturization and high energy efficiency [1]. A central challenge, however, is the elimination of external magnetic bias fields required to sustain and control spin-wave propagation.

Here, we present an integrated hybrid approach demonstrating an all-electric, standalone piezo-magnonic microelectromechanical (MEMS) system that enables efficient voltage control of GHz spin-wave signals via magnetoelastic coupling. The device comprises a CoFeB magnonic waveguide integrated onto a piezoelectric MEMS bridge [2], as shown in Fig. 1a. By exploiting growth-induced anisotropy, we achieve field-free spin-wave propagation in the 6–8 GHz range within a fully integrated platform (Fig. 1b).

Furthermore, the large strain generated by the upward bending of the piezoelectric bridge produces magnetoelectric fields of up to 30 mT at 30 V. Modulation of the internal magnetic field alters spin-wave propagation, enabling reversible phase control. Vector network analyzer measurements reveal a phase shift exceeding 700° at 7 GHz for applied voltages below 12 V (Fig. 1c).

At higher voltages (≈20 V), competition between magnetocrystalline anisotropy and magnetoelastic contributions leads to reversible domain nucleation and suppression of spin-wave transmission, enabling switching functionality.

In addition, operation at the first bending resonance of the bridge (~17 kHz) enhances modulation efficiency (Fig. 2), allowing a 2π phase shift with a 2.2 V drive and power consumption of ~6 µW.

These results establish piezo-magnonic MEMS as a promising platform for reconfigurable RF front-end components and analog signal processing.

[1] P. Pirro, V. I. Vasyuchka, A. A. Serga, B. Hillebrands, Nature Reviews Material, vol. *6*, p. 1114–1135 (2021).
[2] A. Ghisi, N. Boni, R. Carminati, S. Mariani, Engineering Proceedings, vol. 4, p. 17 (2021)
[3] https://mandmems.eu/ (EU Project 101070536 — MandMEMS)

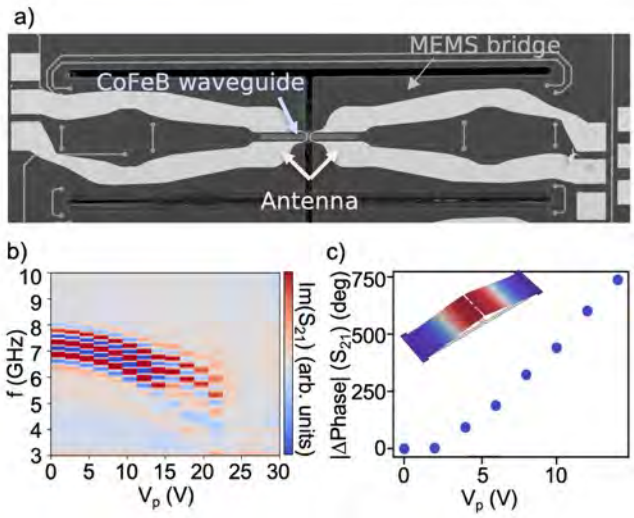


Fig. 1. a) SEM image of the device. b) Color map of the reference-subtracted imaginary part of S21 as a function of frequency and applied bridge voltage (V_p), measured at zero external field. c) Voltage-induced phase shift of the spin-wave signal at 7 GHz; inset: MEMS bridge bending profile.

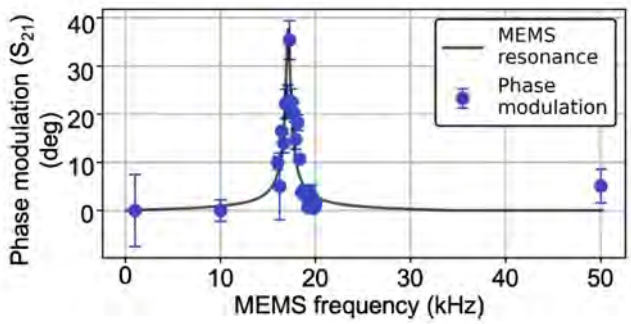


Fig. 2. Phase modulation amplitude (blue dots) vs MEMS AC drive frequency; solid line: fitted resonance curve of the first bending mode.

EG-12. Feedback Control of Exceptional Points and Topological Phases in Cavity Magnonics

R. D. McKenzie, R. L. Stamps
Physics and Astronomy, University of Manitoba, Winnipeg, Manitoba, Canada

Feedback is a ubiquitous control mechanism that has been used to achieve strong magnon-phonon coupling in a hybrid photon-phonon-magnon system [1]. In this study, we explore feedback control of exceptional points and topological phases of a cavity-magnonics system, accounting for the effects of time delay in the feedback loop. A microwave resonator coupled to the Kittel mode of an yttrium-iron-garnet sphere is considered, with feedback of the microwave signal allowing for frequency and linewidth control of the magnon-polariton modes present in the resonator. In recent work, it was shown that the amplitude and phase of input signals in a multi-drive, multi-port, cavity magnonics system can be used to tune a system to antimode exceptional points [2]. Similarly, we show that gain and phase in a feedback loop may be used to tune a system to resonant exceptional points. Time delay in the feedback loop leads to constructive or destructive interference generating a frequency comb.

Control of the magnon-photon coupling strength allows these exceptional points to be tuned to a weakly damped regime which may facilitate topological energy transfer between modes. Gain in the feedback loop may be used to tune the system between topological phases having distinct photonic band structures. Time delay leads to an infinite set of feedback induced modes, and characterization of the topological phases in terms of a winding number is not straightforward. Nevertheless, we demonstrate that an energy eigenvalue surface can be used to characterize different topological phases.

[1] M. Ebrahimi, Y. Huang, V.A.S.V Bittencourt, et al., arXiv:2603.13515v1, (2026)

[2] M. A. Smith, R. D. McKenzie, A. Joseph, et al., Advanced Electronic Materials (2026): 10.1002/aelm.202500738

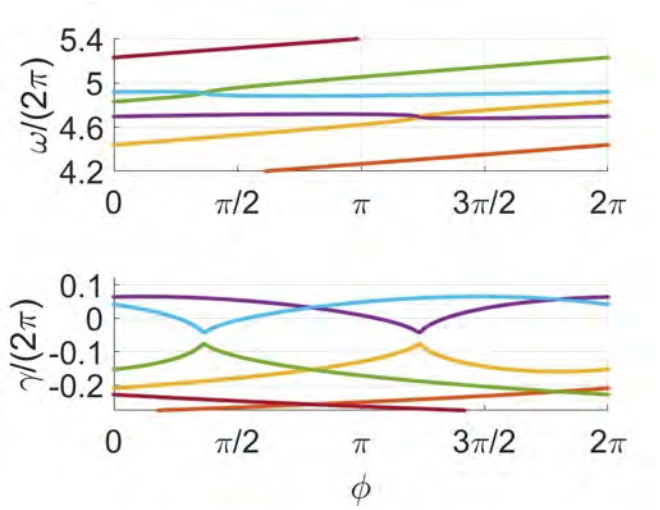


Fig. 1: Resonator spectrum with time delayed feedback. We plot the complex poles, z=ω-iγ/2, of the transmission function with fixed gain as the phase in the feedback loop is tuned. Spectral gaps open or close at exceptional points of the system.

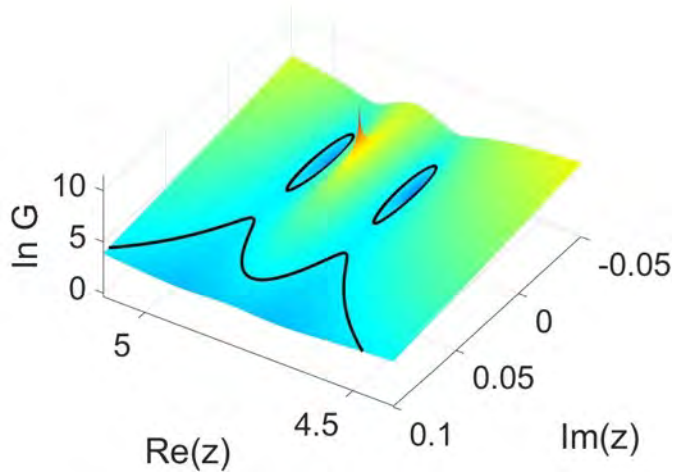


Fig. 2: Magnon-polariton eigenvalue surface with time delayed feedback. For a fixed value of the gain, G, the eigenvalues trace out contours on the surface as ϕ=0 → 2π. Critical points of the surface are exceptional points of the system. The topology of the surface distinguishes phases having distinct band structures.

EG-13. Magnon-Mediated Coupling Between Perpendicular Microwave Resonators via a YIG Sphere

P. Pal[1, 2], M. Song[2, 3], S. Kruhlov[4], T. W. Cecil[4], U. Welp[2], R. Divan[5], K. Kim[3], V. Novosad[2], A. Hoffmann[1], Y. Li[2]

[1]Department of Materials Science and Engineering and Materials Research Laboratory, The Grainger College of Engineering, University of Illinois Urbana-Champaign, Urbana, Illinois, United States, [2]Materials Science Division, Argonne National Laboratory, Lemont, Illinois, United States, [3]Korea Advanced Institute of Science and Technology, Daejeon, Korea (the Republic of), [4]High Energy Physics Division, Argonne National Laboratory, Lemont, Illinois, United States, [5]Center for Nanoscale Materials, Argonne National Laboratory, Lemont, Illinois, United States

Hybrid magnonic systems have emerged as a compelling platform for coherent quantum state transfer, owing to the sufficiently low magnetic damping of spin-wave excitations and their strong, tunable coupling to microwave photons. In this work, we present a purpose-built sample holder architecture in which a planar microwave resonator is physically inserted within the bore of another microwave resonator, enabling a nested, concentric configuration that was designed and fabricated in-house. The mutual perpendicular orientation of the two resonators, which suppresses direct electromagnetic cross-talk between them.

A yttrium iron garnet (YIG) sphere is positioned at the spatial overlap of the microwave field regions of both resonators, simultaneously coupling to each, schematically shown in Fig. 1(a). Acting as a coherent transducer, the magnon mode of the YIG sphere mediates an effective photon-photon interaction between otherwise isolated circuits. We see enhanced transmission due to the interaction. To probe this interaction systematically, we tune the resonant frequency of the in-plane resonator by varying the length, and thereby find the most efficient quantum state transfer between them.

Measurements are performed across both the ports of the circuit using a vector network analyzer, that is, by measuring both S11, S12, and S22 parameters (both reflection and transmission geometry), exploiting the physical isolation between the two resonator circuits to achieve selective readout. The hybridised mode is shown from S12 measurements in Fig. 1(b). This multi-port approach allows us to independently characterize each resonator's response while simultaneously monitoring the magnon-mediated coupling channel, providing a clean spectroscopic signature

of the tripartite interaction.

The demonstrated architecture offers a practical and scalable route toward magnon-based quantum transduction, with direct relevance to hybrid quantum networks.

This work was supported by the US DOE BES MSED under contract No. DE-SC0022060.

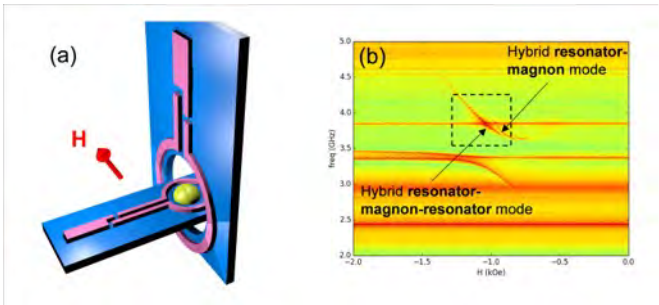


Fig 1: (a) Schematic of the device structure with magnetic field (H) direction. (b) Full power spectrum of the S12 parameter of the hybrid circuit showing microwave photon-magnon-microwave photon anticrossing.

SESSION EP: SOFT MAGNETIC MATERIALS III (POSTER SESSION)

Chair(s): H. Tsukahara, *Tohoku University, Sendai, Japan*
Thursday, November 5, 2026
09:30 AM-12:30 PM
Coral 4

EP-01. High Frequency Magnetic Characteristics on Each Crystal Orientation of Polycrystalline Steel Sheet under Mechanical Stress Supply

K. Fujisaki[1], S. Odawara[2]
[1]Toyota Technological Institute, Nagoya, Japan, [2]Ohtama Co. Ltd., Kawasaki, Japan

Power electronics technology that performs switching operations drives motors and excites transformers (1), and the excitation is not limited to the usual fundamental frequency of 50/60 Hz, but also occurs at high frequencies in the kHz and even MHz ranges (2).
Therefore, in considering ways to improve the efficiency of power electronics, it is important to measure and understand the high-frequency magnetic properties of electrical steel sheets. In this study, the effects of stress application on the basic orientations of electrical steel sheets, namely <100>, <011>, and <111> are measured and analyzed (3).
Because commercially available GO material (20ZHDKH70) has a Goss grain texture within a few degrees (4), the longitudinal direction is considered to be <100>, the perpendicular direction to it is considered to be <011>, and the direction tilted 54.7 degrees from the longitudinal direction is considered to be <111>. The specimen was taken and wound into a toroidal shape, which was considered the stressed state. The wound state was then heat-treated in a vacuum at 780°C for 2 hours, after which the stress was released, which was considered the stress-free state. The results of measuring the relative permeability up to 36 MHz using an impedance analyzer are shown in Figure 1.
In the case of <100>, the magnetic properties deteriorate due to domain wall motion, but in the cases of <011> and <111>, the magnetic properties improve due to the application of stress, possibly due to the rotational excitation of magnetization.

This research is the first to reveal that magnetic properties under stress change depending on the crystal orientation. Compared with a numerical analysis that takes classical eddy currents into account as shown in Figure 2, the difference is significant in the case of <100>, due to the anomalous eddy currents caused by domain wall motion.

(1). K. Fujisaki (eic), "Handbook of magnetic material for motor drive systems", Springer-Nature, 2025.
(2). H. Naitoh, T. Sugimoto, K. Fujisaki, Electrical Engineering in Japan 214(1), June 2021.
(3). S. Odawara, K. Fujisaki, IEEJ, Research report, SA-26-007, RM-26-007, 2026.
(4) K. Honda, and S. Kaya, Sci. Rep. Tohoku, 15, pp.721-752, 1926.

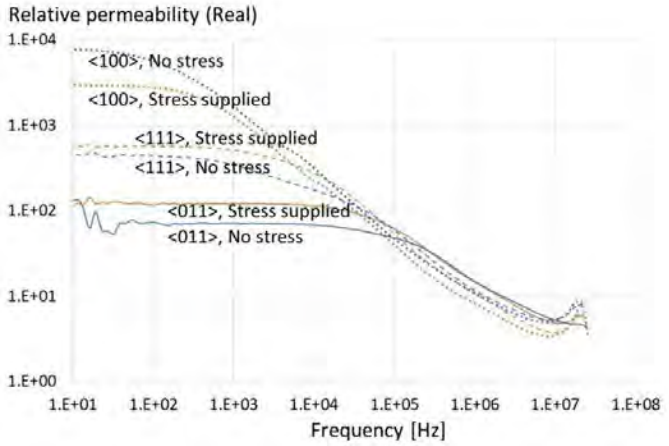


Fig. 1 Frequency characteristics of relative permeability in each direction of electrical steel in stress supplied.

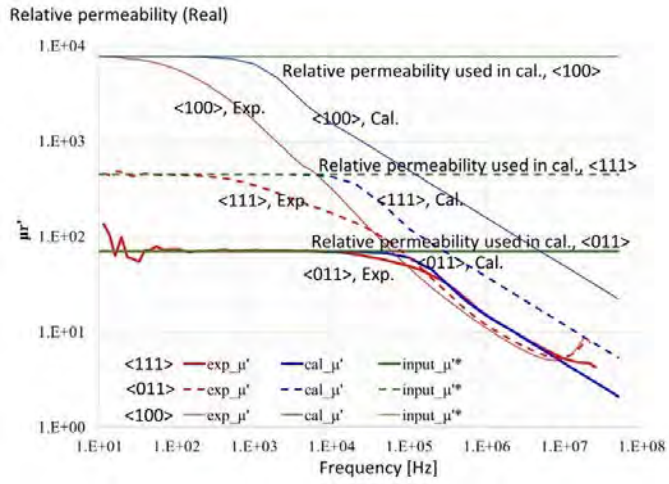


Fig. 2 Relative permeability comparison of experimental and calculation.

EP-02. Improving electromagnetic properties of metal powder through surface modification

S. Park[1], J. Seo[1], D. Lee[1], S. Lee[2], B. Lee[3]
[1]Physics, Hankuk University of Foreign Studies, Yongin-Si, Gyeonggi-Do, Korea (the Republic of), [2]Samsung Electro-mechanics, Suwon, Korea (the Republic of), [3]Electronic physics, Hankuk University of Foreign Studies, Yongin-Si, Gyeonggi-Do, Korea (the Republic of)

This study proposes a surface modification strategy to improve the permeability, oxidation resistance, and mechanical reliability of soft magnetic composites (SMCs) for next-generation high-frequency power inductors. Oxide layer removal, silane coating, and graphene oxide (GO) coating were applied to Fe-Si-B-based amorphous powder (9A4), and their effects were systematically analyzed. Oxide layer removal using ammonium thioglycolate (ATG) improved the permeability from 24.8 to 27.9 and reduced hysteresis loss, although re-oxidation limited high-temperature stability. Methyl trimethoxy silane (MTMS) coating formed a thin protective Si-O-Si layer, improved oxidation resistance at temperatures up to 350°C, reduced the oxygen content to 340 ppm, increased the permeability to 29.4, and significantly enhanced high-temperature mechanical properties. GO coating also improved permeability and enhanced stress and strain, but increased eddy current loss because of reduced electrical insulation. Overall, the integrated surface modification strategy effectively enhanced SMC performance, with MTMS coating showing the most balanced improvement.

EP-03. Impact of Joule heating on the Giant magnetoimpedance effect in Co-rich glass-coated microwires

A. Gonzalez Villegas[1, 2], P. A. Rodríguez Jiménez[1], M. Salaheldeen[1, 2, 3], V. Zhukova[1, 2, 4], A. Zhukov[5, 2, 4]
[1]Dept. Polymers and Advanced Materials: Physics, University of the Basque Country, EHU, San Sebastian, Spain, [2]Dept. Applied Physics, Escuela de Ingeniería de Gipuzkoa EIG, University of Basque Country, EHU, San Sebastian, Spain, [3]Phys. Dept., Faculty of Science, Sohag University, Sohag, Egypt, [4]EHU Quantum Center, University of the Basque Country, EHU,, San Sebastian, Spain, [5]Basque Foundation for Science, IKERBASQUE, Bilbao, Spain

Studies of the Giant Magnetoimpedance, GMI, effect gained special attention owing to the large magnetic field, *H*, sensitivity of the impedance of soft magnetic conductors [1].

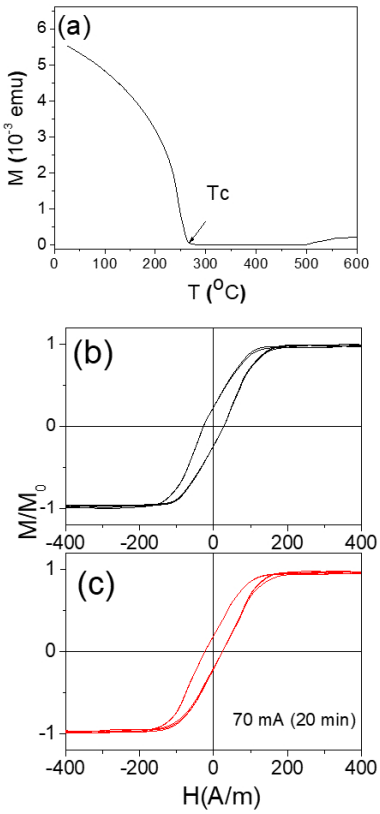
Typically, maximum GMI ratio, $\Delta Z/Z \approx 300\%$ are reported in Co-rich magnetic wires with vanishing magnetostriction coefficient [1]. Recently, $\Delta Z/Z \approx 700\%$ were achieved in carefully processed glass-coated Co-rich amorphous microwires [2]. However, such $\Delta Z/Z$ are still below theoretically predicted $\Delta Z/Z \approx 3000\%$ [3].

IWe provide our latest results on the impact of Joule heating (70 mA for 20 min) on magnetic properties and GMI effect of amorphous $Co_{72}Fe_4B_{13}Si_{11}$ glass-coated microwires (metallic nucleus diameter of 41.1 μm). The crystallization (evidenced as an increase in the magnetization, M) occurs above 500 °C (Fig. 1a). The glass-coating allows better corrosion resistance and biocompatibility, making such microwires suitable for applications in biomedicine, stress monitoring in civil engineering or aircraft industry [2]. Both microwires (as-prepared and Joule heated) present low coercivity, H_c, of about 30 A/m (as-prepared) and 27 A/m (after Joule heating) and magnetic anisotropy fields, H_k, of about 145 A/m and 130 A/m respectively.

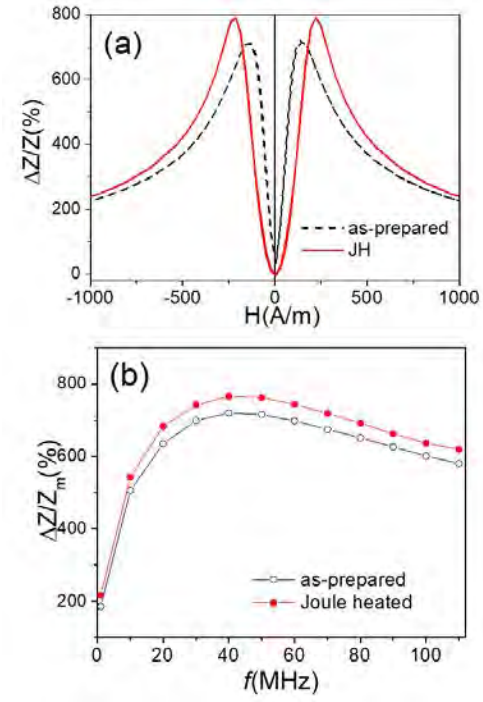
From the $\Delta Z/Z(H)$ dependencies (Fig.2a) measured at frequency, f, of 40 MHz a quite high maximum GMI ratio, $\Delta Z/Z_m$, of about 700 % in as-prepared sample is noticed. After Joule heating maximum GMI ratio, $\Delta Z/Z_m$, was further enhanced up to up to about 800 %. From the $\Delta Z/Z_m$ (f) dependencies (see Fig. 2 b) is evident that the annealed sample presents a consistently higher GMI ratio in all frequency range, being the highest at f = 40 MHz. The $\Delta Z/Z(H)$ dependencies present double –peak character, previously experimentally observed in most of Co-rich microwires and linked to the circumferential character of the magnetic anisotropy of the magnetic wires with low and negative λ_s-values [1-3].

Concluding, by appropriate annealing we were able to enhance the GMI effect of Co –rich microwires up to about 800%.

1. L.V. Panina and K. Mohri, Magneto-impedance effect in amorphous wires, Appl. Phys. Lett. 65 (1994) 1189-1191.
2. P.Corte -León, A.Gonzalez, V.Zhukova, M.Ipatov, J.M.Blanco, A.Zhukov, Optimization of giant magnetoimpedance effect in Co-rich glass-coated microwires by annealing, J. Alloys Compound, 999 (2024) 175023
3. L. Kraus, Theory of giant magneto-impedance in the planar conductor with uniaxial magnetic anisotropy, J. Magn. Magn. Mater. 195 (1999) 764-778.



M(T) dependence (a) and hysteresis loops of as-prepared (b), and annealed (c) samples.



$\Delta Z/Z(H)$ dependences of as-prepared and annealed samples (a), and $\Delta Z/Z_m(f)$ dependence for the same samples (b).

EP-04. Tuning reversible magnetic behavior via exchange length control in nanocrystalline FINEMET wires

T. A. Ovari, M. Lostun, S. Corodeanu, H. Chiriac, N. Lupu
Department of Magnetic Materials and Devices, National Institute of Research and Development for Technical Physics, Iasi, Romania

Reversible magnetic behavior, previously reported in nearly zero-magnetostrictive Co-Fe-based amorphous wires, is associated with stress-induced helical anisotropy that can be reset by thermal relaxation [1]. Extending this concept to Fe-based systems is of interest due to their higher saturation magnetization.
Here, we investigate the emergence of reversible magnetic behavior in nanocrystalline FINEMET wires prepared by in-rotating-water spinning. Annealing, with and without applied tensile stress, was performed between 500°C and 600°C to control nanocrystal size and magnetic anisotropy, and thereby the exchange length. Magnetic properties were measured by inductive and magneto-optical Kerr effect measurements, while differential thermal analysis was used to identify the onset of nanocrystallization.
Reversible magnetic behavior is observed only for samples annealed at 520°C, where relaxation annealing restores the initial hysteresis loop obtained after stress-free annealing, as shown in Fig. 1, for a sample with 120 μm in diameter. This effect disappears at higher annealing temperatures (540 - 550°C), corresponding to more developed nanocrystalline structures. The results indicate that reversibility is linked to reduced nanocrystal size and increased intergrain spacing, allowing reversible modulation of exchange length via anisotropy changes.
These findings demonstrate that magnetic anisotropy in FINEMET wires can be reversibly tuned, offering a pathway toward reconfigurable magnetic responses for sensing applications.

Acknowledgement - work supported by the Romanian Executive Agency for Higher Education, Research, Development and Innovation Funding (UEFISCDI) under project PN-IV-P1-PCE-2023-1896 - Contract no. 12PCE/03.01.2025, and by the Romanian Ministry of Education and Research/National Authority for Research through the NUCLEU Program - Contract 18N/2023, project PN23 11 01 01.
[1] T.-A. Óvári, M. Lostun, S. Corodeanu, G. Ababei, H. Chiriac, and N. Lupu, "Reversible magnetic behavior in amorphous wires for precision sensing applications," Sci. Rep. 16, 9885 (2026).

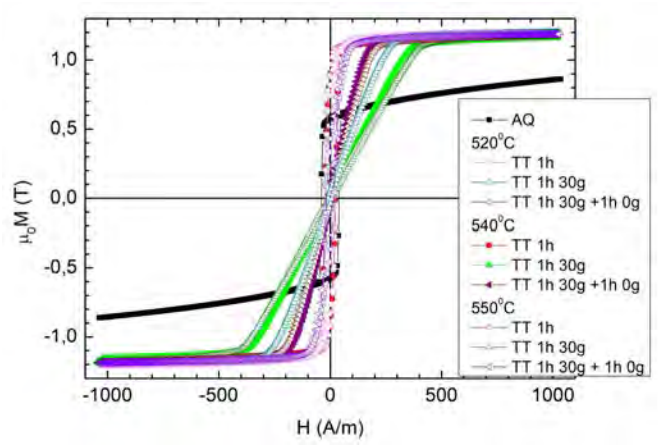


Fig. 1. Inductive hysteresis loops for an as-quenched amorphous FINEMET wire (AQ), for samples annealed (no stress) at 520°C, 540°C, and 550°C, for stress annealed ones, using a 30 g mass, at 520°C, 540°C, and 550°C, and, finally, for the stress annealed samples after stress-free relaxation annealing at 520°C, 540°C, and 550°C.

EP-05. An Investigation of conductive noise suppression performance by magnetic loss in submicron-sized soft magnetic particles composite sheets for Ku band

K. Wakabayashi[1], S. Muroga[1], Y. Endo[1, 2]
[1]Graduate School of Engineering, Tohoku University, Sendai, Japan, [2]Center for Science and Innovation in Spintronics, Tohoku University, Sendai, Japan

With the rapid advancement of miniaturization and enhanced performance in electronic devices, highly integrated electronic components have led to serious electromagnetic interference problems. As a countermeasure for their problems, noise suppression sheets (NSSs) using ferromagnetic resonance (FMR) loss of magnetic materials are widely used in electronic devices [1]. However, eddy currents flowing in the magnetic materials used NSSs affect circuit operation at the high frequency. One effective way to solve this problem is to reduce the submicron-sized particle and make the NSSs high impedance because the effect of eddy current can be suppressed up to the GHz range, thereby confining magnetic loss primarily to FMR. In this study, we synthesized submicron-sized soft magnetic particles with amorphous structure using aqueous solution reduction method and evaluated their magnetic properties and conductive noise suppression performance for Ku band (12 – 18 GHz).
Figure 1 shows a SEM image of Fe-B particles, one of the

synthesized submicron-sized soft magnetic particles. The particles were non-agglomerative and spherical shape with the median size of approximately 450 nm and the size distribution of 300 to 650 nm.

Figure 2 shows the transmission attenuation coefficient (R_{tp}) with composite sheets. R_{tp} of Fe-B composite sheets started to increase from approximately 2 GHz and reached a maximum around 18 GHz, which was attributed to magnetic loss due to FMR of the Fe-B particles. Also, R_{tp} of Fe-B composite sheets and composite sheet composed of epoxy resin which was used as matrix material were approximately matched at the higher frequency than 40 GHz. This result indicate submicron-sized Fe-B particles suppress eddy currents and displacement currents and did not affect circuit operation at the higher frequency than FMR frequency. Therefore, these results suggest that composites with submicron-sized soft magnetic particles have potential for use as a bandstop filter for Ku band because it can suppress a limited frequency component of the properties due to FMR.

[1] M. Sato, S. Yoshida, E. Sugawara et al., J. Magn. Soc. Jpn., Vol. 20, No.2, pp.421-424 (1996)

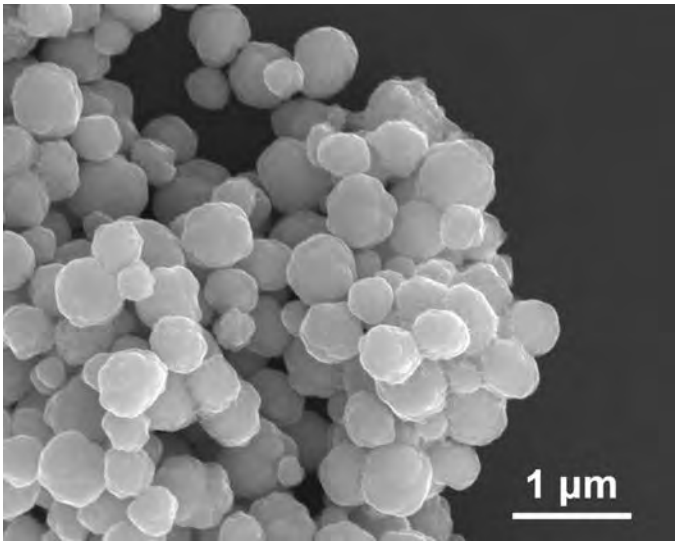


Fig.1. SEM image of Fe-B particles.

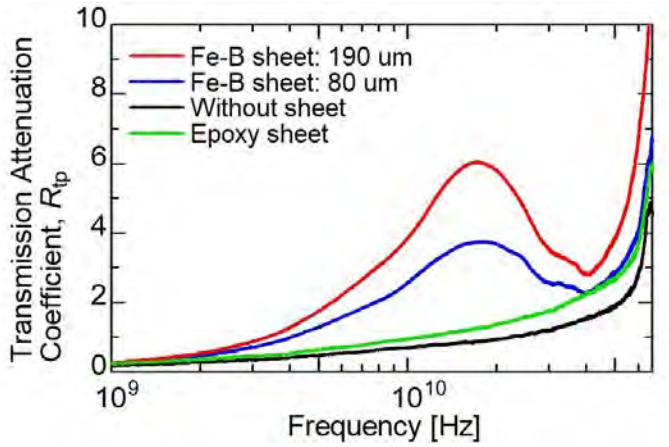


Fig.2. Transmission attenuation coefficient with and without composite sheets.

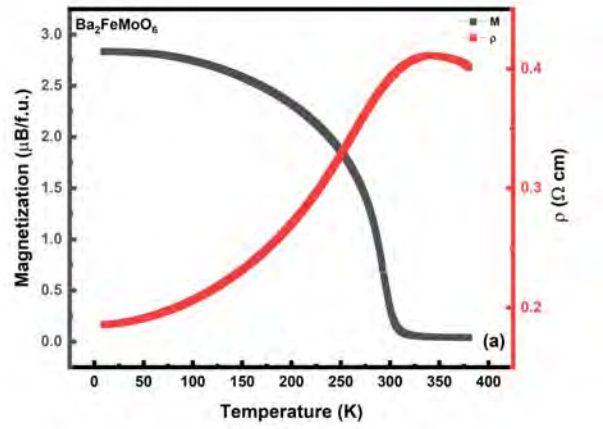
EP-06. RF absorption in Ba_2FeMoO_6 synthesized by microwave irradiation

L. Jiang, M. Marimuthu, M. Ramanathan
Physics, National University of Singapore, Singapore, Singapore

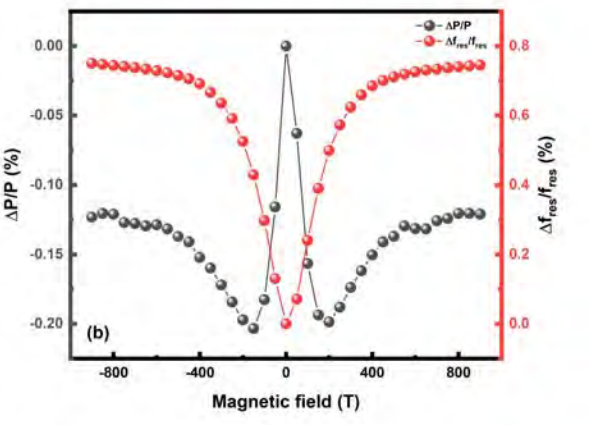
The B-site ordered double perovskite Ba_2FeMoO_6 (BFMO) synthesized through solid-state reaction or soft-chemical methods was studied in the past by researchers in view of tunneling magnetoresistance, high spin polarization, and unconventional ferrimagnetic coupling between Fe and Mo ions [1,2]. In this work, we report synthesis of BFMO by microwave irradiation of oxide precursors, which enables rapid phase formation and improved cation ordering compared with conventional thermal routes. Structural characterization confirms the formation of a well-crystallized double perovskite phase with reduced antistites-disorder. Magnetic measurements reveal robust ferrimagnetic behavior at room temperature (Fig 1(a)) and metallic behavior of resistivity. The sample was synthesized within 40 minutes followed by annealing in 95% Ar+5%H2. There is no earlier report on radio frequency wave absorption or dc resistivity of BMFO synthesized by microwave irradiation. We investigated radio frequency (RF) wave absorption using an inductor-capacitance (LC) resonant circuit reported earlier [3]. The resonance frequency of the LC circuit without a sample is 1 MHz. Field-dependent resonant frequency and oscillator circuit current were monitored to probe the reactive and dissipative components of the RF response. In Fig. 1(b), we show the RF power absorption $\Delta P/P \propto (I_{T,H}-I_{T,H0})/I_{T,H0}$ and resonant frquency shift $\Delta f_{res}/f_{res} \propto (f_{res\ H}-f_{res\ H0})/f_{res\ H0}$ where I is the current drawn by the circuit. The relative power absorption decreases

rapidly below 0.02 T then increases, and exhibits trends to show saturation above ~0.04 T. This power absorption change reveals the dissipation component variation by $\Delta P \propto (\omega\rho|1+\chi|+\chi'')^{1/2}$. In contrast, the resonance frequency shift ($\Delta f_{res}/f_{res}$) increases in low fields and shows a tendency to saturate above 0.04 T. The shift reflects the variation in the reactive component as $\Delta f_{res} \propto (\chi'+\Delta\delta/\delta)$, where χ' is the real part of rf susceptibility and δ is the skin depth. We will discuss the origin of RF power absorption in terms of ac magnetoresistance and domain wall dynamics.

[1] Han, H., et al. *Journal of Applied Physics* 89.11 (2001): 7687-7689.
[2] Chmaissem, O., et al. *Physical Review B—Condensed Matter and Materials Physics* 71.17 (2005): 174421.
[3] Naik, V. B., and R. Mahendiran. *Applied Physics Letters* 94.14 (2009).



Temperature dependent magnetization (black) and DC resistivity (red)



Field dependent power absorption (black) and resonant frequency shift(red)

EP-07. Magnetic order in oxygen-deficient, compositionally-complex $BaIn_{1-x}M_xO_{3-\delta}$ (M = Fe, Co, Sn, Ti) perovskites

A. Stanionyte[1], L. Corredor[2, 3], A. Wolter[4], G. Perversi[5], A. Isaeva[3, 2, 1]
[1]Physics, University of Amsterdam, Amsterdam, Netherlands, [2]Physics, Technical University of Dortmund, Dortmund, Germany, [3]Research Center "Future Energy Materials and Systems", Dortmund, Germany, [4]Leibniz IFW Dresden, Dresden, Germany, [5]Chemistry, University of Maastricht, Maastricht, Netherlands

High-configurational entropy stabilizes single-phase structures in perovskites while introducing strong local disorder that reshapes functional properties.[1] Magnetic behavior of single-ion perovskites ABO_3 is rooted in superexchange or double-exchange mechanisms sensitive to d-metal electronic configurations and B–O bond lengths and angles. The complexity of high-entropy derivatives raises the key question whether long-range magnetic order can develop when many distinct exchange interactions coexist.

We study magnetic properties of the oxygen-deficient $BaIn_{1-x}M_xO_{3-\delta}$ series, obtained as phase-pure samples with on average cubic structure [2]. $Ba(InCo)O_{3-\delta}$, $Ba(InFe)O_{3-\delta}$, $Ba(InCoFe)O_{3-\delta}$, and the high-entropy $Ba(InCoFeSnTi)O_{3-\delta}$ are studied by DC/AC magnetometry and heat capacity measurements. Magnetic behavior in this series is not simply paramagnetic, even in the outmost disordered high-entropy compound. In low-field M(T), an antiferromagnetic-like ZFC/FC splitting develops below ca. 20 K, and M(H) at 2 K shows hysteretic behavior. The characteristic low-temperature feature shifts to lower temperature with increasing compositional complexity, consistent with disorder-driven frustration and a progressive suppression of cooperative ordering. Neutron diffraction confirms that the average cubic perovskite structure remains unchanged down to 2 K.

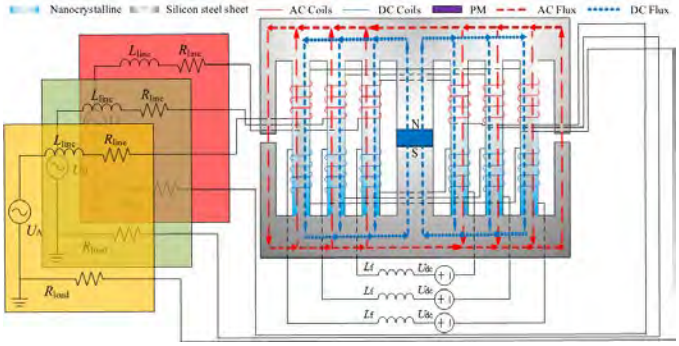
Thermodynamic signatures were assessed by heat-capacity measurements. A field-dependent magnetic entropy release is observed at low temperature. Isolating the magnetic contribution by subtracting the heat capacity of a non-magnetic analogue, $Ba(InTi)O_{3-\delta}$, reveals a more pronounced low-temperature anomaly. The extracted entropy does not match simple theoretical expectations, indicating nontrivial correlations and likely contributions from multiple interacting sublattices. AC susceptibility provides complementary evidence for slow dynamics: transition temperatures shift for frequencies above 100 Hz, and broad features in the imaginary component indicate dissipative,

time-dependent magnetic processes typical of cluster-glass behavior.
Our results combined point to a glassy magnetic ground state comprising interacting clusters.
[1] A.R. Mazza et al., Adv. Sci., Vol. 9, p. 2200391 (2022).
[2] N. Schreiner et al., Solid State Ionics, Vol. 427, p. 116901 (2024).

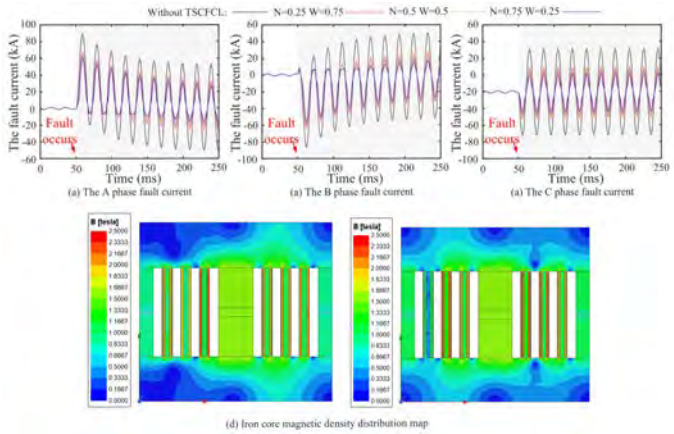
EP-08. How a Dual-Layer Core Reshapes Transient Current-Limiting Characteristics in Saturated-Core Fault Current Limiter ?

J. L. Liu, J. Yuan, H. Zhou
Wuhan University, Wuhan, China

Saturated-core fault current limiters (SCFCLs) face a trade-off: low saturation flux density materials like nanocrystalline (~1.25 T) enable fast desaturation but risk reverse saturation; high saturation flux density materials like silicon steel (~2.0 T) offer larger flux capacity but prolong impedance establishment and demand substantial DC excitation. No single material satisfies all requirements. Fig. 1 presents a composite dual-layer core with an inner nanocrystalline layer and an outer silicon steel layer. This structure provides three key advantages. First, the low saturation flux density of the inner nanocrystalline layer reduces the DC excitation required for deep saturation, lowering system cost. Second, in the fault half-cycle opposing the DC bias, the inner layer desaturates first, rapidly raising impedance for fast current-limiting response. Third, in the opposite half-cycle, the outer silicon steel layer provides reserve flux capacity, preventing excessive reverse saturation and sustaining impedance throughout the full fault cycle.
Fig. 2a–2c show three-phase fault currents under different nanocrystalline-to-silicon-steel area ratios, where N and M denote the proportions of nanocrystalline and silicon steel, respectively. The N=0.25, M=0.75 ratio achieves the best performance: transient limiting 33.17%, steady-state 48.32%. The N=0.75, M=0.25 ratio performs worst: transient 26.08%, steady-state 37.86%. The N=0.50, M=0.50 ratio achieves transient 29.64% and steady-state 37.86%—only moderately lower than the best, while saving substantial nanocrystalline material. Fig. 2d presents the magnetic flux density distribution for N=0.50, M=0.50, confirming the effectiveness of the composite structure in accommodating flux across both fault half-cycles.
Balancing limiting performance, DC excitation reduction, and material economy, N=0.50, M=0.50 represents the optimal design. This passive, structurally simple approach enables effective full-cycle fault current suppression with lower cost.
J. R. Prigmore, “Comparison of four different types of ferromagnetic materials for fault current limiter applications,” IEEE Transactions on Power Delivery 28, 1491–1498 (2021).



Composite dual-layer core structure of the proposed SCFCL.



Three-phase fault current waveforms and iron core magnetic flux density distribution

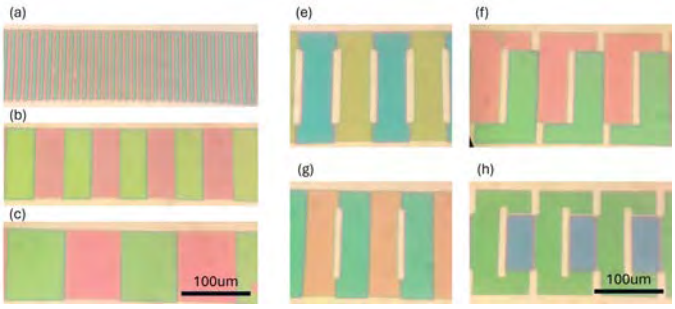
EP-09. Patterned Garnet Configurations with Bipolar Faraday Rotation for Magnet-free Optical Isolators

P. Liu[1], B. Stadler[2, 1]
[1]Chemical Engineering and Materials Science, University of Minnesota, Minneapolis, Minnesota, United States, [2]Electrical and Computer Engineering, University of Minnesota, Minneapolis, Minnesota, United States

High-speed data transmission in modern information systems has made the integration of magneto-optical (MO) garnets onto silicon photonic platforms essential. However, the requirement for external bias magnets to maintain garnet magnetization remains a primary barrier to high-

density integration. While monolithic and heterogeneous integration of garnet thin films has been achieved, external field requirements limit the practical scalability of these on-chip MO devices.[1], [2] Here, we investigate patterned garnet configurations designed to achieve stable, magnet-free operation through garnet's in-plane remanent magnetization. We propose a series of garnet geometries that utilize bipolar Faraday rotation segments to mimic the cumulative MO effect of a single magnetized film. (Figure a-c) Theoretically, these patterned configurations allow neighboring garnet segments to mutually stabilize their magnetic moments along the length direction due to the shape anisotropy.[3] We further consider the stability of these moments by developing various film loop geometries that leverage shape anisotropy to maintain self-biased states. (Figure e-h) The magnetic properties of these patterned films will be characterized using vibrating sample magnetometry (VSM) and magnetic force microscopy (MFM) and then deposited on waveguides to measure the MO effect without external magnets. This study provides a foundational approach for developing sub-millimeter scale, magnet-free MO components by optimizing the geometric configuration of integrated garnet thin films.[4]

[1] L. Bi *et al.*, "On-chip optical isolation in monolithically integrated non-reciprocal optical resonators," *Nature Photon*, vol. 5, no. 12, pp. 758–762, Dec. 2011, doi: 10.1038/nphoton.2011.270.
[2] Y. Shoji and T. Mizumoto, "Magneto-optical non-reciprocal devices in silicon photonics," *Sci. Technol. Adv. Mater.*, vol. 15, no. 1, p. 014602, Jan. 2014, doi: 10.1088/1468-6996/15/1/014602.
[3] K. Srinivasan and B. J. H. Stadler, "Push-pull non-reciprocal phase shifting," US12055756B2, Aug. 06, 2024 Accessed: Mar. 20, 2025.
[4] P.-H. Liu, B. K. Moghal, and B. J. H. Stadler, "Effect of composition and two-step annealing on Ce-doped terbium iron garnets on Si," *Opt. Mater. Express, OME*, vol. 15, no. 7, pp. 1407–1418, Jul. 2025, doi: 10.1364/OME.564014.



photolithographically patterned bipolar garnet films on Si wafer. (a-c) rectangle garnet segments with widths of 5 μm, 40 μm, and 80 μm. The length of segments is 100 μm. (e-h) different shape of garnet segments. The gaps between segments are around 150 nm.

EP-10. Phase Separation and Magnetic Properties of FeCoNiCrAl-Based High-Entropy Alloys

S. Na, J. Yoo, N. J. Jones
Naval Surface Warfare Center Carderock Division, West Bethesda, Maryland, United States

A FeCoNiCrAl-based high-entropy alloy (HEA) system features a transition from a face-centered cubic (FCC) to a body-centered cubic (BCC) phase, offering a unique platform to investigate tunable microstructural features and phase transformations [1,2]. This transformation is also associated with significant changes in magnetic properties, including increased saturation magnetization (M_s) and Curie temperature (T_c) found in $FeCoNiCrAl_X$ alloys [3,4]. This study examines the influence of elemental substitution on phase transformations and magnetic properties within FeCoNiCrAl-type HEAs by systematically varying the Ni/Cr, Ni/Al, and Al/Cr ratios. Disc-shaped specimens, extracted from arc-melted ingots, underwent annealing at various temperatures. Both annealing conditions and alloy composition significantly impacted the resultant phase constitution and magnetic properties. Notably, the valence electron concentration (VEC) emerged as a key parameter governing phase transformation and, consequently, magnetic properties, as evidenced by the substantial changes in M_s accompanying the introduction of the FCC phase into the BCC matrix. Magnetic force microscopy (MFM) directly visualized the ferromagnetic nature of the BCC phase and the paramagnetic or weak ferromagnetic behavior of the FCC phase, the latter characterized by an absence of pronounced magnetic contrast. The VEC dependence of saturation magnetization is illustrated in Figure 1, which shows the results obtained from the as-cast HEAs of $FeCoNiCr_{1-X}Al_{1+X}$, $FeCoNi_{1+X}Cr_{1-X}Al$, and $FeCoNi_{1+X}CrAl_{1-X}$. The MFM image of the as-cast $FeCoNi_{1.5}Cr_{0.5}Al$ HEA is also presented, providing further insight into the magnetic properties of these alloys.

[1] Y. F. Kao, S. K. Chen, T. J. Chen, P. C. Chu, J. W. Yeh, and S. J. Lin, J. Alloys Compd. 509, 1607 (2011).
[2] S. M. Na, P. K. Lambert, H, Kim, J. Paglione, and N. J. Jones, AIP Advances 9, 035010 (2019).

[3] S. Huang, W. Li, X. Li, S. Schönecker, L. Bergqvist, E. Holmström, L. K. Varga, and L. Vitos, Materials and Design 103, 71 (2016).
[4] S. Huang, A. Vida, D. Molnar, K. Kadas, L. K. Varga, E. Holmström, L. Vitos, Applied Physics Letters 66, 107 (2015).

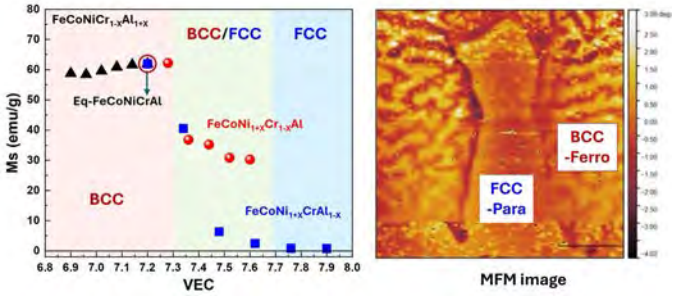
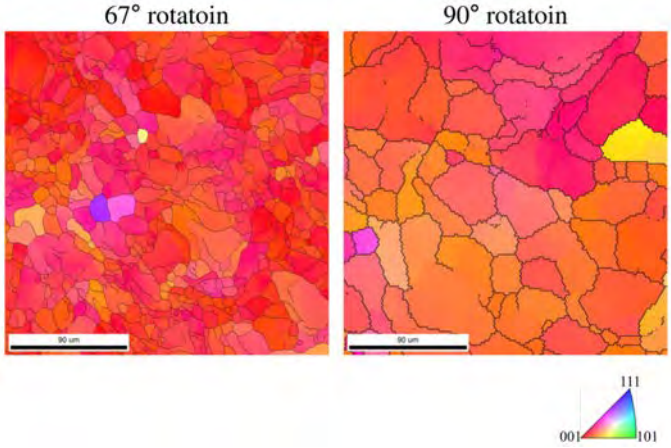


FIG. (left) VEC dependence of saturation magnetization obtained from the as-cast HEAs of $FeCoNiCr_{1-X}Al_{1+X}$, $FeCoNi_{1+X}Cr_{1-X}Al$, and $FeCoNi_{1+X}$ $CrAl_{1-X}$ and (right) MFM image of the as-cast $FeCoNi_{1.5}Cr_{0.5}Al$ HEA.

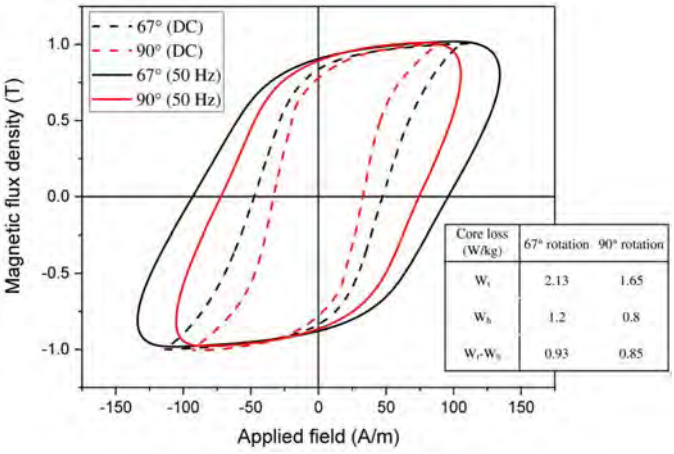
EP-11. Effect of Scan Strategy on Grain Size, Magnetic Properties, and Recrystallization Behavior of Fe-4.5 wt.% Si Cores Fabricated by Laser Powder Bed Fusion

H. Lee, J. Ahn, K. Lee, J. Kim
Hanyang University, Ansan-si, Korea (the Republic of)

Laser powder bed fusion (LPBF) has been studied for the fabrication of Fe–Si motor cores because it enables complex geometries and <100> textures. However, rapid solidification during LPBF produces fine grains, which are not favorable for soft magnetic properties. In this study, Fe–4.5 wt.% Si toroidal cores were fabricated by LPBF. The effect of scan strategy on the as-built microstructure, magnetic properties, and recrystallization behavior was investigated.
Two scan strategies were used. The scan direction was rotated by 67° or 90° between layers, while other parameters were kept constant. Heat treatment was conducted in Ar at 900–1200°C for 2 h. Magnetic properties were measured using a B–H tracer. Microstructure and texture were analyzed by electron backscatter diffraction (EBSD).
EBSD results showed that both samples had a <100> texture (Fig. 1). However, the grain size depended on the scan strategy. The 67° rotation sample had fine grains with an average grain size of 13 μm, whereas the 90° rotation sample had coarser grains with an average grain size of 56 μm. This difference was attributed to dendrite growth behavior and supported by thermal-gradient calculations. The magnetic properties of the samples annealed at 1100 °C showed a clear difference (Fig. 2). The coarse-grained sample showed a lower core loss. From DC B–H measurements, the hysteresis losses at 50 Hz were 1.2 and 0.8 W/kg for the 67° and 90° rotation samples, respectively. This indicates that the decrease in total core loss was mainly caused by reduced hysteresis loss associated with the larger grain size. After heat treatment, both samples showed abnormal grain growth without a distinct primary recrystallization stage. They also developed similar recrystallization textures due to their similar initial textures. However, the 90° rotation sample showed a higher recrystallization temperature due to the lower driving force for grain growth caused by its larger initial grain size. These results show that scan strategy is important for controlling grain size in LPBF-fabricated Fe–Si cores and affects their magnetic properties.



Grain size and crystal orientation of the samples.



BH loops of the samples heat-treated at 1100°C.

EP-12. Magnetocaloric Response and Critical Behavior in Cr-Substituted Spinel Ferrites

M. Islam, A. Hossain
Physics, Bangladesh University of Engineering and Technology, Dhaka, Bangladesh

Chromium substituted cobalt ferrites are promising materials for tunable magnetic and magnetocaloric applications. This work studies magnetic behavior and magnetocaloric properties of Co1-xCrxFe2O4 with 0 <= x <= 0.5 prepared by solid state reaction. Structural analysis confirms formation of single phase cubic spinel ferrites with systematic lattice modification due to chromium substitution. Magnetic measurements show composition dependent changes in magnetization and exchange interactions linked to variation in cation distribution and superexchange pathways. Critical exponent analysis using modified Arrott and Kouvel Fisher methods indicates second order magnetic phase transitions for all compositions. Magnetocaloric evaluation from isothermal magnetization data shows reliable entropy change scaling and improved cooling power for intermediate compositions. These results demonstrate that chromium substitution effectively tunes magnetic properties and magnetocaloric response in cobalt ferrite systems, indicating potential for magnetic refrigeration applications.

Islam MA and Hossain AKMAH, RSC Advances, 2022
Islam MA et al., Heliyon, 2023
Oumezzine M et al., PCCP, 2024

EP-13LB. Cast-Around HV Cable: 36 kV Solid-State Transformers with Ferrite-Nanocrystalline Composite

I. R. Ellithy, M. Esguerra, R. Radhakrishnan
Magment Energy gmbH, Oberhaching, Bayern, Germany

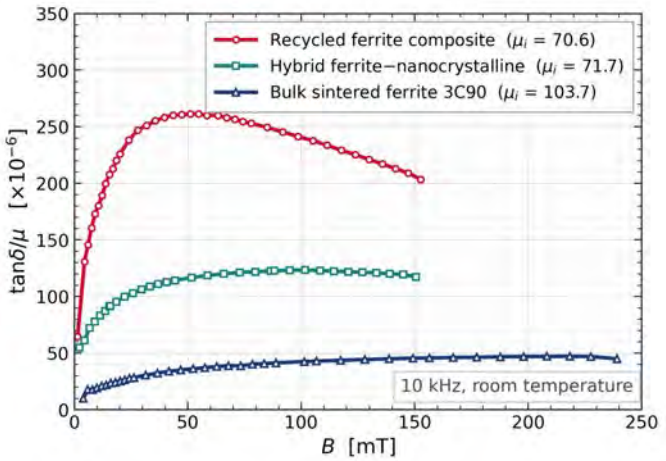
Electrification driven by AI data centers and renewable energy generation is pushing medium voltage toward the load and demanding bidirectional, DC-capable conversion from 36 kV to 800 VDC. The high-frequency transformer (HFT) inside such a solid-state transformer (SST) must be high-voltage, high-power, and compact. Neither bulk ferrite nor nanocrystalline cores, which are size-limited and stress-intolerant, can satisfy these requirements.

A flowable castable magnetic composite changes the build order with respect to conventional wound bulk core magnetics: a rigid winding is placed in a mould and the core cast around it (inside-out). The low-loss magnetic composite is a hybrid blend of recycled nanocrystalline milled ribbons and magnetoelastically compensated MnZn ferrite aggregates (MagFer™) [1].

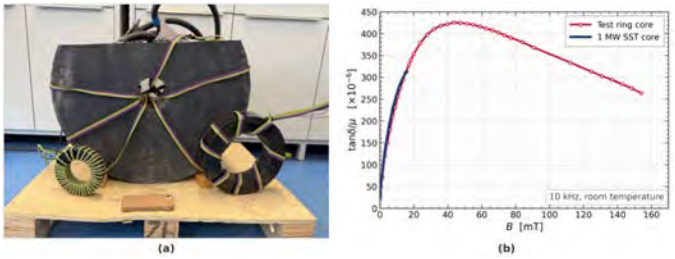
Material development is guided by loss-factor rather than core loss (P_v) with Steinmetz power laws: tanδ/μ vs. flux density displays a maximum that log-log plots hide. According to the Hodgdon-Esguerra hysteresis model, its height scales with the degree of irreversibility ($1/\chi_{eq} = 1/\chi_i - 1/\chi_c$), and its height times its position scales with H_c. The low-coercivity nanocrystalline addition lowers hysteresis losses (Fig. 1)but enhances domain wall damping, increasing losses with frequency. Reversible magnetization is then optimized by controlling this dynamic wall damping, whose behavior is described by fractional differential equations. The HFT core losses are minimized by an optimized blend with respect to trapezoidal voltage at high frequencies and do not depend on core size (Fig. 2).

A further limitation of conventional magnetics is high-voltage insulation at high frequencies: partial discharge at mixed frequencies and thermal stresses limit encapsulated HFT to ~15 kV. Inside-out HFT uses type-tested HV cable as the primary, inheriting proven insulation and PD performance, with aluminium tubes as a secondary that lowers winding-to-core stress. Heat conducts from both windings and dissipates through a high-thermal-conductive composite to air.

[1] I. Ellithy, M. Esguerra, R. Radhakrishnan, "Development of soft magnetic composites cast from ferrites and construction binders with lowest core loss," *AIP Advances* 15, 035205 (2025). doi:10.1063/9.0000925



Relative loss factor tanδ/μ versus peak flux density for a recycled-ferrite composite, the hybrid ferrite-nanocrystalline composite, and a bulk sintered ferrite (3C90, UU Core).



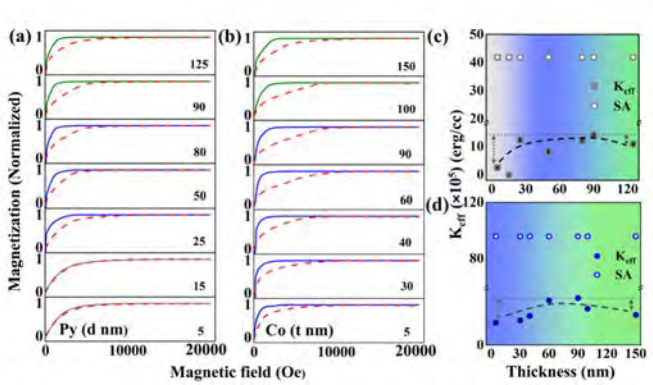
(a) Test ring core, intermediate ring and the 1 MW HFT core cast for the SST, shown to scale. (b) Relative loss factor of the test ring core and of the assembled 1 MW SST core: both follow the same characteristic over the common excitation range.

EP-14LB. Origin of Mixed Anisotropies in Si/fcc-Permalloy and Si/a-Cobalt Thin Films

K. Kirti, B. Ghadai, A. Mishra, R. R, S. Mondal
Department of Physics, Shiv Nadar Institution of Eminence, Delhi NCR, India, Greater Noida, India

Magnetic anisotropy plays a crucial role in deciding the static and dynamic behavior of magnetic thin films.[1] It controls various phenomena, like magnetization reversal, domain formation, domain-wall motion, spin-wave generation, and propagation, etc. [2] We investigate mixed anisotropies in face-centered-cubic Permalloy (fcc-Py) and amorphous Cobalt (a-Co) thin films deposited *via* rf magnetron sputtering on a Si (100) substrate, with thicknesses d = 5-125 nm and t = 5-150 nm, respectively. X-ray diffraction technique, transmission electron microscopy, atomic force microscopy, energy dispersive X-ray spectroscopy, vibrating sample magnetometry, and magnetic force microscopy are employed to study the structural, morphological, and magnetic properties. We adopt a qualitative approach to understand the true nature of the mixed anisotropies for both materials, and the evolution of anisotropies with film thickness is quantified. The role of growth conditions in the emergence of specific anisotropies is discussed in detail. An alteration of the magnetization easy axis from the conventional in-plane orientation is evidenced because of the collective influence of these mixed anisotropies. We categorize our samples into specific regimes. The formation of complex stripe domains is observed.[3] The one-to-one comparison between sputter-deposited crystalline and amorphous magnetic material may provide a stronger foundation for understanding technologically important, tilted anisotropies.

1. Cullity, B.D., and Graham, C.D. (2011) *Introduction to magnetic materials*, John Wiley & Sons.
2. Hämäläinen, S.J., Madami, M., Qin, H., Gubbiotti, G., and van Dijken, S. (2018) Control of spin-wave transmission by a programmable domain wall. *Nat. Commun.*, 9 (1), 1–8.
3. Kim, J. Von, Demand, M., Hehn, M., Ounadjela, K., and Stamps, R.L. (2000) Roughness-induced instability in stripe domain patterns. *Phys. Rev. B.*, 62 (10), 6467–6474.



Normalized in-plane (solid line) and out of plane (dashed line) initial curves for (a) fcc-Py and (b) a-Co. The numbers inside the plot represent thickness in nm. Effective anisotropy values, obtained from area method are plotted together with theoretical shape anisotropy values for both (c) fcc-Py and (d) a-Co thin films. The dashed line provide guide to eye. The colours within the effective anisotropy plot represent evolution of anisotropy components with film thickness.

SESSION EQ: NEW APPLICATIONS AND OTHER EMERGING TOPICS II (POSTER SESSION)

Chair(s): M. Sekino, *The University of Tokyo, Tokyo, Tokyo, Japan*
Thursday, November 5, 2026
09:30 AM-12:30 PM
Coral 4

EQ-01. Effects of Spatial Filtering on MEG Source Localization Accuracy: A Phantom Study

K. Nakagawa, K. Tanaka
Graduate School of Science and Engineering, Tokyo Denki University, Hatoyama-cho, Japan

Magnetoencephalography (MEG) non-invasively measures the weak magnetic fields generated by neuronal currents in the cerebral cortex and provides source localization with high temporal resolution The accuracy of MEG source

estimation is known to depends on the spatial filters applied. during preprocessing to suppress environmental and physiological interference. However, few studies have quantitatively assessed how different spatial filter affect localization accuracy under controlled conditions. The purpose of this study was to compare MEG source localization accuracy with and without the application of representative spatial filters, using phantom data in which the true source locations are known. Phantom MEG data were acquired using an whole-head MEG system installed at the National Institute of Information and Communications Technology (NICT). Source localization was performed on the recorded data, and the localization error relative to the known dipole positions was compared between conditions with and without spatial filtering. First, we examined the effect of Signal Space Projection (SSP), a widely used spatial filter. Application of SSP altered the mean localization error but did not improve localization accuracy. This result is consistent with the fact that SSP is primarily designed to suppress physiological artifacts such as eye blinks and cardiac activity, which are absent from phantom recordings. Next, we evaluated the effect of Signal Space Separation (SSS). Application of SSS likewise did not reduce the localization error. A plausible explanation is that SSS substantially reduces the rank of the data, thereby limiting the spatial degrees of freedom available to the source estimation and consequently increasing the error. Taken together, these findings indicate that the application of spatial filters does not necessarily improve MEG source localization accuracy, and that filter selection should be guided by the characteristics of the noise actually present in the data.

EQ-02. Nonlinear Neural Dynamics under Accelerated rTMS: Effects of Consecutive Sessions on Network Stability

C. Lee[1, 2], H. Chen[4, 1, 2], L. Ye[1, 2], H. Lin[3], C. Chang[4], T. Wu[1, 2]
[1]Graduate School of Materials Science, National Yunlin University of Science and Technology, Douliu, Yunlin, Taiwan, [2]Taiwan SPIN Research Center, National Yunlin University of Science and Technology, Douliu, Yunlin, Taiwan, [3]Department of Neurosurgery, Show Chwan Memorial Hospital, Changhua, Taiwan, [4]Intelligent Recognition Industry Service Research Center, National Yunlin University of Science and Technology, Douliu, Yunlin, Taiwan

Understanding the brain's response to extreme exogenous perturbations requires a dynamical systems perspective. We investigate the nonlinear evolution of neural states under an intensive rTMS protocol, interpreting results through Bienenstock-Cooper-Munro (BCM) and Kuramoto models. We demonstrate that repetitive magnetic stress triggers a systematic collapse of spectral stability and network connectivity.

A single subject underwent four consecutive rTMS sessions (8.7/8.8 Hz, 65% motor threshold) within 3.5 hours at Fz. Each session included 50 trains (5-s stimulation, 10-s interval), totaling 8,600 pulses across the study. Five 32-channel EEG recordings monitored state evolution (Stages 1–5).

The neural system exhibited a two-layered nonlinear trajectory:

Spectral Dysregulation (Micro-scale): The spectral exponent (1/f slope) initially decreased (Stage 2) before surging in Stages 4 and 5, breaching the healthy range (>1.7). Under the BCM model, this "dip-then-surge" suggests a breakdown of homeostatic regulation, where the "sliding threshold" fails to accommodate cumulative excitation, leading to neuro-energetic dissipation.

Topological Collapse (Macro-scale): A critical transition occurred at Stage 5, where the Small-World Coefficient (*s*) dropped from 1.08 to 0.71, signaling a loss of optimal architecture. This was accompanied by a 52% reduction in Global Clustering and a rise in Betweenness Centrality, reflecting stress concentration from reduced topological dimensionality. The system transitioned from a flexible, high-entropy state into a constrained phase , analogous to coupled oscillators reaching global phase-synchronization, limiting information capacity.

Neural fatigue acts as a dynamical phase transition. The decoupling of frequency acceleration from network integrity suggests high-density rTMS pushes the brain into a disordered state , offering biomarkers for monitoring safety limits in neuromodulation.

1 A. Vlachos, “Repetitive magnetic stimulation induces synaptic plasticity through cooperative pre- and postsynaptic activation,” Brain Stimulation 14(6), 1745–1746 (2021).

2 K. Funke, and K. Hoppenrath, “IS 9. Modulation of cortical inhibition by rTMS-a rat model,” Clinical Neurophysiology 124(10), e42 (2013).

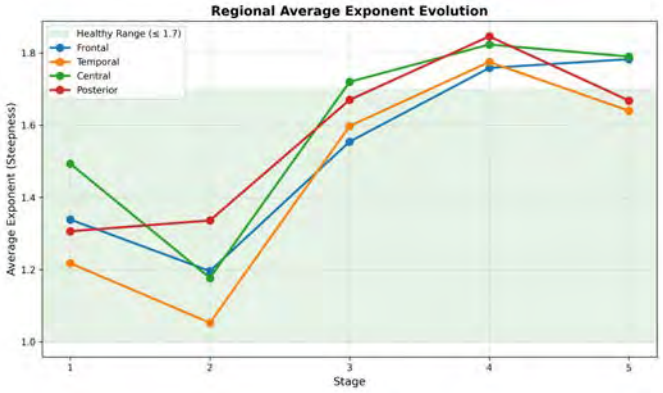


Figure 1. Regional Average Exponent Evolution.

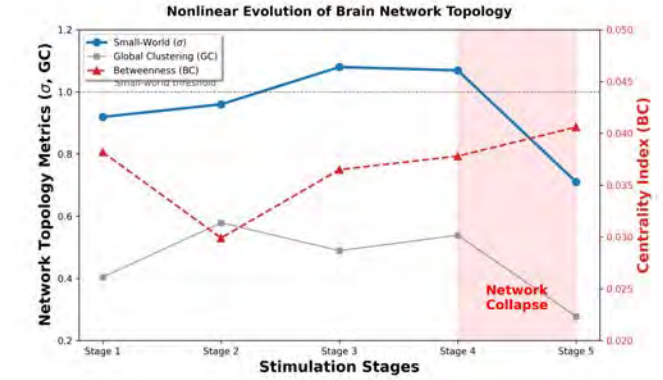


Figure 2. Brain Network Topology Evolution. Primary Y-axis: collapse of small-worldness ($s < 1$) and modularity (GC) at Stage 5. Secondary Y-axis: rising Betweenness Centrality (BC) signaling stress concentration.

EQ-03. Electromagnetic Induction for UXO Detection in Highly Magnetic Backgrounds

A. Alling[1], J. Calimbas[1], J. Fujita[1], M. Matsuo[1], A. Ohta[1], A. Haroon[2]

[1]Electrical and Computer Engineering, University of Hawaii Manoa, Honolulu, Hawaii, United States, [2]Hawaii Institute of Geophysics and Planetology, SOEST, University of Hawaii Manoa, Honolulu, Hawaii, United States

Decades of U.S. military training across the Hawaiian Islands have left hundreds of sites contaminated with metallic unexploded ordnance (UXO), posing persistent risks to public health and land use. Remediation efforts rely on magnetic field induction sensors, which measure the response of an induced eddy-current in the subsurface using induction coil receivers (RX) (Shubitidze et al., 2016). UXO remediation in Hawaii is complicated by the volcanic origin of the soils and bedrock, which contain abundant iron-bearing minerals. These minerals produce elevated magnetic permeability and strong magnetic susceptibility, generating significant magnetic responses that can dominate the transient decay. This leads to the unique problem of trying to detect electrically conductive and magnetically permeable UXOs within electrically conductive and magnetically permeable background environments. This work investigates TX drive circuitry with TX/RX pair coil architectures with the goal of improving UXO detection and classification, with key hardware focus of engineering a prototype tailored to reducing both false positives and false negative detection in highly complex heterogeneous magnetic environments. Full waveform analysis of the induced signal using optimized current step functions enables selective enhancement of early-time target response while suppressing the influence of highly magnetic soils, which dominate at later decay times. We combine technological hardware developments with validation studies using 3D finite element modeling in COMSOL Multiphysics to investigate how spatial variations in magnetic permeability influence measured induced-voltage response. Simulations incorporate realistic subsurface variability in soil magnetic properties and are benchmarked against analytical solutions over the 10^{-4} to 5×10^{-2} second time window, typical of existing systems (Fig.2).

F. Shubitidze, B. E. Barrowes, J. B. Sigman, et al. "UXO Classification Procedures Applied to Advanced EMI Sensors and Models," Thayer School of Engineering at Dartmouth College; White River Technologies, Inc.; ERDC, (2016).

F. Shubitidze, J. P. Fernández, B. E. Barrowes, et al. "The Orthonormalized Volume Magnetic Source Model for Discrimination of Unexploded Ordnance," *IEEE Transactions on Geoscience and Remote Sensing*, (2014).

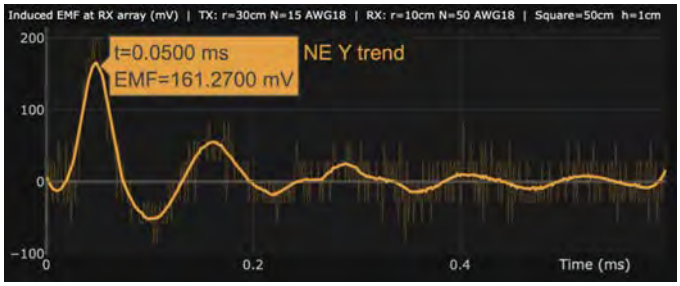


Figure 1. Simulation of voltage induced on the RX coil, based on the measured current (and resulting magnetic field) produced by the TX coil.

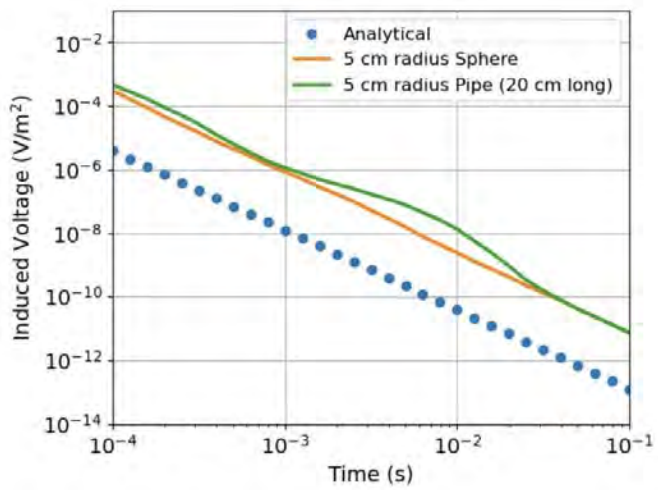


Figure 2. 3D modeling of simple target geometries in magnetic soil effects with TX/RX coil pair, represented through randomized magnetic property distributions across the modeling domain.

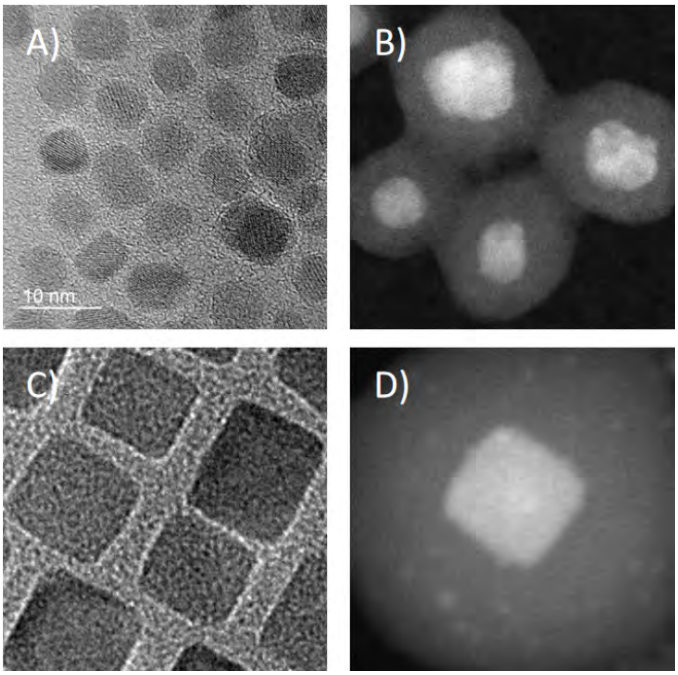
EQ-04. Controlling Dipolar Interactions in Fe_3O_4@SiO_2 Nanohybrids for Magnetic Hyperthermia

M. Brollo, M. V. Guedes, J. R. Menezes, F. d. Ferreira, D. Muraca
Gleb Wataghin Institute of Physics (IFGW), State University of Campinas (UNICAMP), Campinas, Brazil

Magnetic iron-oxide nanoparticles are benchmark systems for magnetic hyperthermia, where energy dissipation under an alternating magnetic field is governed by effective magnetic anisotropy, size distribution and interparticle interactions. In this work, we engineer hybrid Fe_3O_4@SiO_2 nanodevices in which Fe_3O_4 cores, tailored in the 7-25 nm range (Figure 1A,C), are encapsulated in silica shells of tunable thickness, enabling systematic control of interparticle spacing and dipolar coupling within a non-magnetic matrix.

Fe_3O_4 nanoparticles are synthesized by thermal decomposition routes to tune core size and morphology, followed by controlled SiO_2 growth that preserves the crystalline magnetite phase while modulating interparticle interactions via shell thickness. Transmission electron microscopy provides quantitative information on core size distributions, aspect ratio, shell thickness, clustering and interparticle distances, which we correlate with dc magnetization (M-H, ZFC-FC) and magnetic hyperthermia data (specific absorption rate) under alternating fields. High-angle annular dark-field STEM imaging, used for SiO_2-coated samples, enhances Z-contrast between Fe_3O_4 cores and the low-Z silica matrix, allowing reliable measurement of shell thickness and core-shell morphology (Figure 1B,D). X-ray diffraction confirms that the cores crystallize in the magnetite (Fe_3O_4) phase, and room-temperature M-H curves are characteristic of superparamagnetic behavior for cores within the studied size window.

These results show that Fe_3O_4@SiO_2 core-shell architectures allow structural and interaction parameters to be tuned semi-independently, enabling the rational design of hybrid nanoparticles with tailored effective anisotropy and heating performance for future biomedical and environmental applications.



A) TEM image of Fe_3O_4 nanoparticles with an average diameter of 7 nm. B) HAADF-STEM image of the same nanoparticles shown in A, coated with a 5 nm SiO_2 shell. C) TEM image of Fe_3O_4 nanocubes with an edge length of 16 nm. D) HAADF-STEM image of the same nanocubes shown in C, coated with a 15 nm SiO_2 shell. All images are shown at the same magnification; scale bar: 10 nm.

EQ-05. Multimodal Predictors of Resting Motor Threshold and Corticomotor Excitability in Healthy Adults

M. Paslar[1], T. J. Taylor[1], R. Detore[1], C. J. Lewis[6], S. S. Achanta[7], M. Fernandes[5], S. Sabaysachi[2], W. Lohr[1], L. Ma[4], J. Atulasimha[2], R. L. Hadimani[3, 1], C. L. Peterson[1]
[1]Biomedical Engineering, Virginia Commonwealth University, Richmond, Virginia, United States, [2]Computer Engineering, Virginia Commonwealth University, Richmond, Virginia, United States, [3]Mechanical and Nuclear Engineering, Virginia Commonwealth University, Richmond, Virginia, United States, [4]School of Medicine Psychiatry, Virginia Commonwealth University, Richmond, Virginia, United States, [5]School of Medicine, Virginia Commonwealth University, Richmond, Virginia, United States, [6]School of Medicine, UMass Chan Medical School, Worcester, Massachusetts, United States, [7]Computer Science, Virginia Commonwealth University, Richmond, Virginia, United States

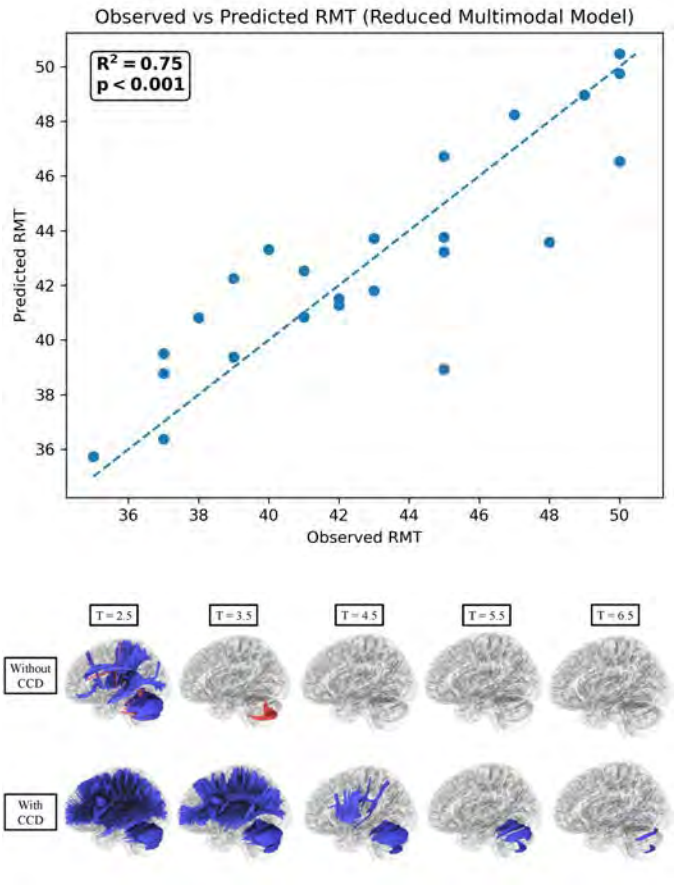
Background: Resting motor threshold (RMT) and corticomotor excitability vary substantially across healthy adults, limiting the precision of transcranial magnetic stimulation (TMS) dosing and interpretation. Prior studies suggest that both network-level anatomy contribute to this variability, but most have focused on single modalities. We investigated whether multimodal resting-state features derived from electroencephalography (EEG), functional MRI (fMRI), and diffusion tensor imaging (DTI) can characterize individual differences in RMT and recruitment-curve measures.

Methods: Thirty healthy adults underwent resting-state EEG, MRI/fMRI, and single-pulse TMS over primary motor cortex. EEG sources were reconstructed into 30 regions of interest using linearly constrained minimum variance beamforming. Functional connectivity was quantified using weighted phase lag index and orthogonalized amplitude envelope correlation, including mean, variability, and graph-based metrics. fMRI analyses estimated effective connectivity among motor-relevant resting-state regions. TMS outcomes included RMT and first dorsal interosseous recruitment-curve measures. Correlational tractography was performed with and without coil-to-cortex distance (CCD) as a covariate to assess associations between fractional anisotropy (FA) and RMT.

Results: Source-level EEG processing generated static and dynamic connectivity matrices for all retained regions and yielded subject-level network features across frequency bands. These measures provided both trait-like and time-varying descriptors of motor-network organization. Integration with fMRI effective connectivity and DTI is being used to test whether directed motor-network interactions improve prediction of RMT and recruitment-curve measures beyond EEG features alone.

Conclusions: A multimodal framework combining EEG, fMRI, and DTI is feasible for studying interindividual differences in corticomotor excitability. White matter connectivity showed a stronger relationship with RMT after accounting for CCD. This approach may help identify biomarkers relevant to personalized TMS dosing and candidate selection for neuromodulation-based rehabilitation.

1. N. Mittal, C. Lewis, Y. Cho, C. L. Peterson, and R. L. Hadimani, “Effect of Fiber Tracts and Depolarized Brain Volume on Resting Motor Thresholds during Transcranial Magnetic Stimulation,” IEEE Trans. Magn.,pp. 1–1, 2022, doi: 10.1109/TMAG.2022.3148214.
2. Christoph Zrenner, Debora Desideri, Paolo Belardinelli, Real-time EEG-defined excitability states determine efficacy of TMS-induced plasticity in human motor cortex, Brain Stimulation, Volume 11, Issue 2, 2018, Pages 374-389, ISSN 1935-861X, https://doi.org/10.1016/j.brs.2017.11.016.
3. V. D. Calhoun, T. Adali, G. D. Pearlson, “A method for making group inferences from functional MRI data using independent component analysis,” Human Brain Mapping, vol. 14, no. 3, pp. 140–151, 2001, doi: https://doi.org/10.1002/hbm.1048
4. K. Wu, B. Jelfs, K. Neville, "fMRI-Based Static and Dynamic Functional Connectivity Analysis for Post-Stroke Motor Dysfunction Patient: A Review," IEEE Access, vol. 12, pp. 133067-133085, 2024, doi: 10.1109/ACCESS.2024.3445580.
5. G. Shou, H. Yuan, C. Li, "Whole-brain electrophysiological functional connectivity dynamics in resting-state EEG," (in eng), J Neural Eng, vol. 17, no. 2, p. 026016, Apr 2 2020, doi: 10.1088/1741-2552/ab7ad3.



EQ-06. Antigen evaluation utilizing the dispersibility of magnetic nanoparticles

S. Yabukami, S. Tohtake, T. Murayama
Tohoku University, Sendai, Japan

This research aims to develop a portable protein sensor that utilizes changes in magnetic phase and dispersibility of aggregates formed by antigen-antibody reactions between magnetic nanoparticles and proteins. A portable sensor capable of simple and highly sensitive measurement of specific proteins would be extremely effective for medical use. Figure 1 shows the system configuration of the proposed protein sensor. We have discovered and elucidated the principle of the phenomenon in which the dispersibility of magnetic nanoparticles and antigens changes sensitively according to the antigen concentration. In this process, magnetic nanoparticles functionalized with antibodies are added to the antigen (GDF15) to induce an antigen-antibody reaction. A static magnetic field is then concentrated, or a large magnetic gradient is applied using a yoke to aggregate the magnetic nanoparticles and the antigen-antibody reactants. After aggregation, an AC magnetic field is applied, and the re-dispersion process of the aggregated magnetic particles is observed with a camera to determine the antigen concentration. Figure 2 demonstrates the evaluation of GDF15 concentration in human urine(nine patients) through dispersibility assessment of the magnetic nanoparticle-antigen aggregates under a large-amplitude magnetic field. The results showed a high correlation of 0.98 ($p < 0.0001$) with ELISA. This method selectively evaluates antigens that aggregate with magnetic nanoparticles via magnetic force; this effectively reduces interference from contaminants in complex biological matrices and enables highly accurate quantification.

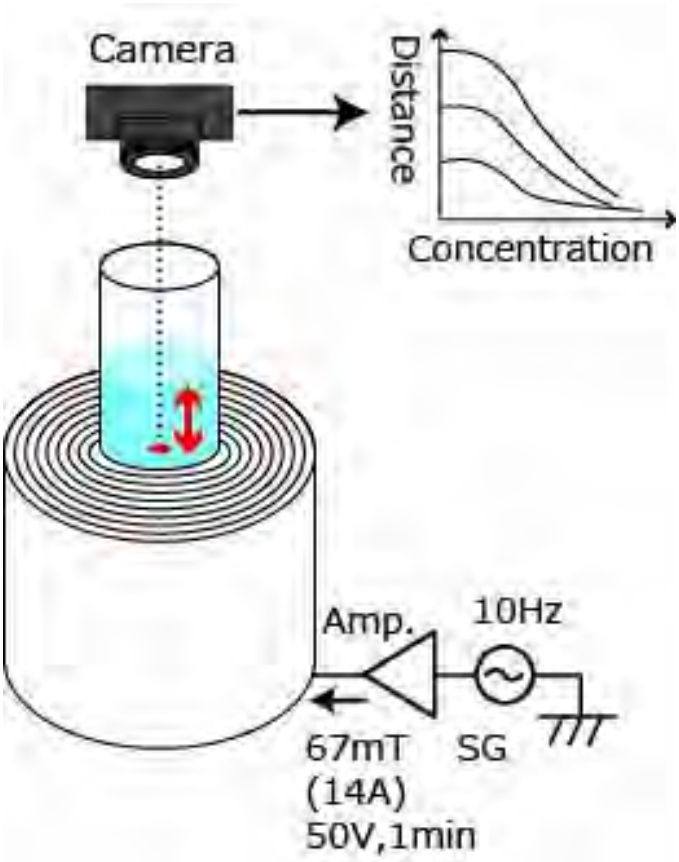


Fig. 1 Evaluation of aggregate dispersibility under alternating magnetic field application using image processing and magnetic signal.

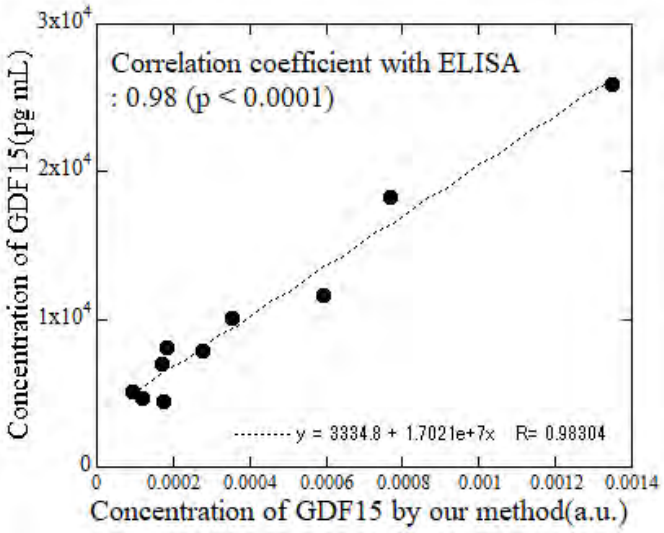


Fig. 2 Evaluation of GDF15 concentration in human urine.

EQ-07. Optimal Design of Inner and Outer Rotor Slotless PMSM for Robotics Based on Outer Diameter to Stack Length Ratio

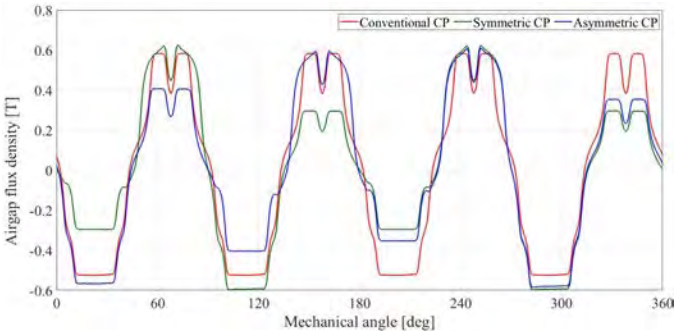
H. Hong, H. Koo, C. Jo, W. Park, J. Lee
Department of Electrical Engineering, Hanyang University, Seoul, Korea (the Republic of)

Permanent Magnet Synchronous Motors (PMSMs) offer high power density compared to induction motors, which have long been used as conventional electric actuators. Due to these advantages, PMSMs are utilized in various application fields, including electric vehicle traction, precision motors, robotic actuators, and servo motors. Permanent Magnet Synchronous Motors are broadly classified into slotted PMSMs and slotless PMSMs. Generally, slotted PMSMs are used in more diverse applications because the presence of iron core slots allows for higher torque density. In contrast, slotless PMSMs do not have slots, which eliminates cogging torque and results in low torque ripple; therefore, they are primarily employed in high precision fields. In this paper, the optimal design of a slotless PMSM for robot joints is conducted. Since robot joint motors are directly linked to the robot's movement, they must exhibit low cogging torque and torque ripple. Therefore, the application of slotless PMSMs which possess no cogging torque and low torque ripple is advantageous. This study analyzes the output characteristics according to the ratio of outer diameter to stack length for various types of slotless PMSMs for robots and proceeds with the optimal design.

EQ-08. Design of Hybrid Consequent Pole PMSM for Low Torque Ripple

C. Jo[1], J. Lee[1], H. Koo[1], W. Park[1], S. Kim[2]
[1]Electrical Engineering, Hanyang university, Seoul, Korea (the Democratic People's Republic of), [2]Korea Testing Certification Institute, Gunpo, Korea (the Democratic People's Republic of)

Hybrid consequent-pole permanent magnet synchronous motors (CP-PMSMs) with symmetric and asymmetric rotor pole arrangements are investigated to reduce torque ripple in electric power steering (EPS) applications. Conventional CP-PMSMs reduce permanent magnet usage by replacing one rotor pole with an iron pole; however, this configuration produces an asymmetric magnetic flux distribution, which introduces additional harmonic components and increases torque ripple.
To address this limitation, a hybrid CP-PMSM is proposed by rearranging permanent magnets and iron poles within a two-dimensional rotor structure. Unlike axial combination approaches that improve flux symmetry by stacking rotors, the proposed method modifies the circumferential pole arrangement without increasing axial length or requiring three-dimensional analysis.
Finite element analysis is conducted under identical conditions to isolate the effect of rotor pole arrangement. A parametric study of the iron pole arc ratio shows that changes in magnetic flux distribution alter the air-gap flux density waveform. The results indicate that torque ripple is influenced not only by the overall waveform distortion but also by the distribution of harmonic components.
The proposed symmetric and asymmetric configurations modify the air-gap magnetic field and reshape the waveform of flux density. As a result, selected harmonic components of the back-EMF and torque are reduced. This leads to a significant reduction in torque ripple compared to the conventional CP, while cogging torque is also decreased. Although a slight reduction in average torque is observed, the overall torque characteristics are improved. The improvement is attributed to the modified rotor pole arrangement, which changes the magnetic flux distribution and alters the harmonic composition of the electromagnetic quantities. Therefore, the proposed hybrid CP-PMSM provides an effective approach for reducing torque ripple without increasing structural complexity.
[1] Zhu, Z.Q.; Howe, D. , Proc. IEEE, Vol. 95, p.746–765 (2007)
[2] Qi, J., IEEE Trans., Ind. Appl. Vol. 58, p.3545–3557 (2022)



Airgap flux density of CP-PMSMs

Contents	Conventional CP	Symmetric CP	Asymmetric CP	Unit
THD of back-EMF	0.08	0.032	0.036	-
Torque	4.32	3.71	3.94	Nm
Torque ripple	45.37	2.76	3.59	%
Cogging torque	192.38	34.66	34.63	mNm

Performance of CP-PMSMs

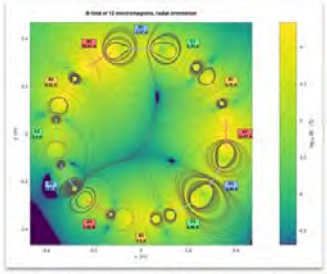
EQ-09. Beyond Conventional Magnetic Hyperthermia: Spatial Control via Superimposed AC/DC Fields in Nanoparticle Superstructures

N. Holt, C. Westfall, A. S. Poulo, M. Khandaker, T. Lamichhane
Engineering & Physics, University of Central Oklahoma, Edmond, Oklahoma, United States

Magnetic nanoparticle (MNP) hyperthermia has emerged as a promising therapeutic strategy for tumor treatment, wherein an alternating magnetic field (AC) induces localized heating in nanoparticles delivered to malignant tissue. However, a fundamental challenge lies in spatially confining the heating effect, as a uniform AC field drives energy dissipation throughout the entire exposed region. In this work, we present the development and implementation of an experimental platform that integrates a superimposed static magnetic field (DC) with the conventional AC excitation to achieve spatially selective hyperthermia. The DC field, generated through a programmable array of electromagnets, is designed to suppress Néel and Brownian relaxation mechanisms of nanoparticles located outside the targeted region, thereby restricting heat generation to the area of interest.

This approach is closely related to prior work demonstrating targeted magnetic fluid hyperthermia using combined AC/DC field configurations (Ho *et al.*, 2012). Building upon this foundation, the present study investigates MNP-based hyperthermia across different nanoparticle superstructures and engineered assemblies, with emphasis on structure–property relationships governing heating efficiency and spatial selectivity. Furthermore, these concepts will be explored using an *in vitro* brain tumor model to evaluate the potential of targeted hyperthermia for deep-tissue therapeutic applications.


Figure - Full design incorporating a Helmholtz coil for AC magnetic field generation


Figure: Simulation of magnetostatic field, indicating regions of low magnitude using a 12-coil configuration

EQ-10. Design and Full-Scale Experimental Verification of Inter-Floor Noise Suppression using Permanent Magnet Repulsion

J. Kim[1], Y. Chong[2], W. Lee[3], J. Han[3], J. Oh[3], H. Cho[1, 2]
[1]Electric., Electron. & Comm. Engineering Education, Chungnam National University, Daejeon, Korea (the Republic of), [2]Department of Convergence System Engineering, Chungnam National University, Daejeon, Korea (the Republic of), [3]Floor Impact Noise Laboratory, SAMSUNG C&T, Yongin city , Gyeonggi-do, Korea (the Republic of)

Inter-floor noise has emerged as a critical social issue in high-rise residential buildings. Analysis of inter-floor noise complaints reveals that children running and adults walking account for 73.1% of cases, with the upper floor identified as the noise source in about 74.5% of incidents [1]. Conventional approaches include increasing slab thickness or applying cushioning materials. however, thicker slabs are limited by structural feasibility, while cushioning layers may deform under sustained loads, degrading damping performance [2]. To overcome these limitations, this study proposes a permanent magnet repulsive force based non-contact floor structure and verifies its noise reduction performance through full-scale experiments.

The proposed structure consists of five permanent magnet blocks. Each block contains two permanent magnets of identical polarity arranged coaxially facing each other to generate a repulsive force, with the upper and lower cases fastened by mounting screws to form a maximum air gap of 6 mm. Finite element analysis and experiments confirmed a repulsive force of 50–150 N per block. Three models with permanent magnet thicknesses of 6, 7, and 8 mm were

fabricated to evaluate the effect of repulsive force. Damping performance was evaluated in a 1 m * 1 m test environment (20 blocks) using a 2.5 kg impact ball dropped from 1 m height. A bare reinforced concrete slab and an EVA foam structure certified as the highest grade by the Korea Conformity Laboratories (KCL) served as control groups. The experimental results demonstrate that all three models exhibit significantly higher damping ratios (15.3%, 12.0%, and 20.7%) than the EVA foam structure (10%). Regarding heavy impact noise, Model 1 and Model 2 achieved mitigation rates of 26.69% and 23.84%, respectively, surpassing the EVA foam structure's 21.89%. These results confirm that the proposed floor structure provides superior damping and noise reduction compared with EVA foam, while ensuring long-term reliability through non-contact energy suppression

[1]Sang-Gon. Cha, "The management system and effect of floor noise at apartment houses," in *Proc. Korean Soc. Noise Vib. Eng. Conf.*, Mokpo, Korea, Oct. 2014, pp. 693–697.
[2]Jung-Min Kim , Yoon-Ki Hong , Jin-Koo Kim, "Evaluation on Expectation of Deflection of Floor Damping Materials Subjected to Long-Term Load," Journal of the Korea institute for structural maintenance and inspection, Vol.20, No.4, 19-26, 2016, .

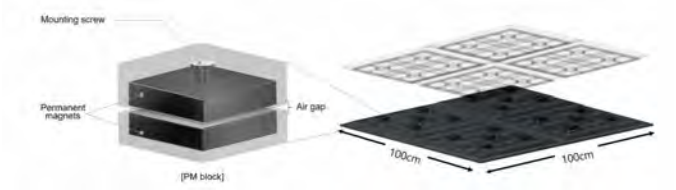


Fig.1. Proposed permanent magnet (PM) block (left) and full-scale test floor assembly (right)

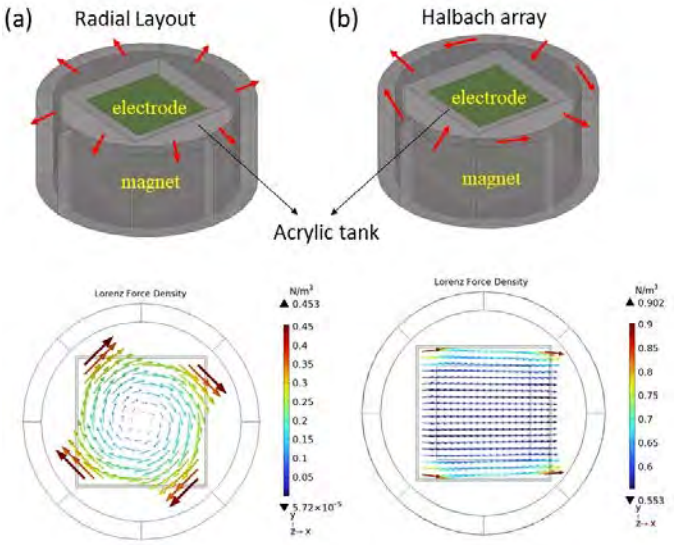
Model types	Damping Ratio (%)	Heavy impact noise (dB)	Mitigate rate (%)
Bare concrete slab	-	56.2	-
EVA foam structur	10	43.9	-21.89
Model 1	15.3	41.2	-26.69
Model 2	12.0	42.8	-23.84
Model 3	20.7	44	-21.71

Table 1. Comparison of noise reduction performance

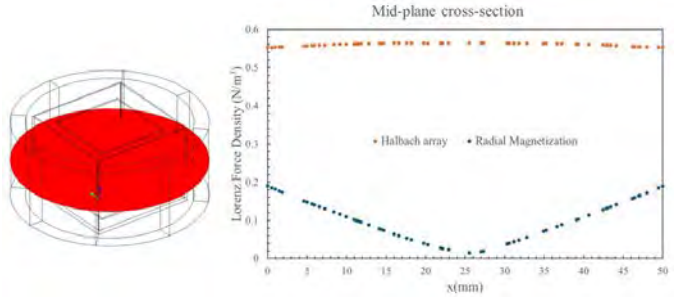
EQ-11. Enhancement of Water Electrolysis Efficiency via Optimized Lorentz Force Distribution using Halbach Array Configurations

Y. Chen[2], Y. Li[1], C. Chen[2]
[1]Department of Mechanical and Aerospace Engineering, National Defense University, Taoyuan, Taiwan, [2]Department of Mechanical Engineering, National Yang Ming Chiao Tung University, Taoyuan, Taiwan

High-efficiency green hydrogen production requires minimizing overpotentials in water electrolysis. A promising method is the magnetohydrodynamics effect, which induces a Lorentz force (F_L=J×B) in the electrolyte. This force drives micro-convection, facilitating rapid gas bubble detachment from electrode surfaces and reducing ohmic and concentration overpotentials. However, effectiveness depends heavily on the spatial distribution and magnitude of the magnetic flux density.
In this study, numerical simulations were performed using COMSOL Multiphysics to evaluate electrolysis enhancement by comparing two permanent magnet arrangements: a standard radial magnetization configuration and a Halbach array (Fig. 1). The model utilizes a pair of platinum (Pt) electrodes (5cm× 5cm) within a controlled electrolytic domain. By coupling the magnetic and electrical field modules, we mapped the Lorentz force density across the active domain.
Results demonstrate that the Halbach array significantly outperforms the radial setup. The Lorentz force density from the Halbach array is three to five times greater—reaching approximately 0.56 N/m^3—and exhibits superior spatial uniformity across the inter-electrode gap (Fig. 2). Comparative analysis shows that radial magnetization produces a "V-shaped" profile with a sharp force drop-off toward the center. In contrast, the Halbach array maintains a near-constant force density across the entire 50 mm span. This uniform profile promotes consistent bubble displacement across the 25 cm^2 electrode surface, preventing localized gas accumulation. These findings suggest that Halbach-induced field enhancement is a superior strategy for industrial-scale electrolyzers to optimize throughput. Experimental validation and comprehensive discussion will be presented in the full paper.



Comparison of Lorentz force density on the x-z plane for the (a)Radial Magnetization and (b)Halbach array. The red arrows within the magnet structure illustrate the specific orientation of the magnetic flux for each array type.



Comparison of the Lorentz force density in the mid-plane cross-section between the two parallel electrodes for Radial Magnetization and Halbach array configurations.

EQ-12. A Stepwise Lightweight Design for a UAV Axial-Flux Permanent-Magnet Motor

C. Li[1], J. Yu[1], S. Liu[2], F. Zhao[1], Y. Luo[3]
[1]Harbin Institute of Technology, Shenzhen, Shenzhen, China, [2]Center for Adaptive System Engineering, ShanghaiTech University, Shanghai, China, [3]School of Electrical and Electronic Engineering, Huazhong University of Science and Technology, Wuhan, China

This paper proposes a lightweight design strategy for a single-stator single-rotor axial-flux permanent magnet (SSSR-AFPM) motor in unmanned aerial vehicle (UAV) propulsion. For UAV applications, considerable research has focused on motor lightweight design using lightweight materials [1], or implementing structural optimizations such as Halbach PM array. While currently, some other advanced lightweight design, such as the low-flux-density-region removal design [2], the end-effect optimization design [3], which have been widely explored in radial-flux motors, are still limited applied in axial-flux motor designs. Therefore, more elaborated lightweight designs are needed for axial-flux motors to better extend their high-torque-density applications.

Hence, a novel stepwise lightweight design is proposed in the paper, aiming at a 12/14 slot-pole AFPM motor shown in Fig. 1. Generally, the lightweight design contains two steps. First, a geometrical optimization baseline is established through weight minimization with torque constraint, using multi-objective genetic algorithm, realizing 5.8% flux density improvement. Second, to leverage motor end effect, an unequal-diameter stator-rotor design is introduced, where the stator and rotor are deliberately designed with unequal inner and outer diameters, to enhance torque output. Response surface methodology (RSM) is employed to effectively construct the response reflection between the torque density and the diameter ratios. Then, a flux-density equalization method is implemented, reallocating magnetic material from low-flux-density regions to high-flux-density regions, whose parameters are annotated in Fig. 1. This step further improves torque density by 11%.

Referring to the torque optimizing process in Fig. 2, the optimized motor achieves a 11.8% weight reduction while delivering higher absolute torque compared to the initial design, resulting in a 17.6% improvement in torque density. Simulation results confirm the effectiveness of the proposed lightweight design method for AFPM motors.

[1] S. Park, H.-W. Kim, T.-H. Ji, et al., Design of axial flux permanent magnet motor for EV traction with SMC core and Nd bonded magnet, *2023 26th Int. Conf. Electr. Mach. Syst. (ICEMS)*, Zhuhai, China, pp. 3360–3363 (2023).
[2] S. Fang, H. Liu, H. Wang, et al., High power density PMSM with lightweight structure and high-performance soft magnetic alloy core, *IEEE Trans. Appl. Supercond.*, vol. 29 (2019).
[3] R. D. Paiva Jr., V. C. Silva, S. I. Nabeta, et al., Magnetic topology with axial flux concentration: A technique to improve permanent-magnet motor performance, J. Microw. *Optoelectron. Electromagn. Appl.*, vol. 16, pp. 881–899 (2017).

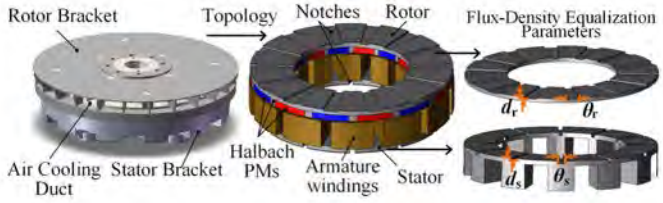


Fig. 1 Topology, assembly and flux-density parameter annotation of the proposed motor.

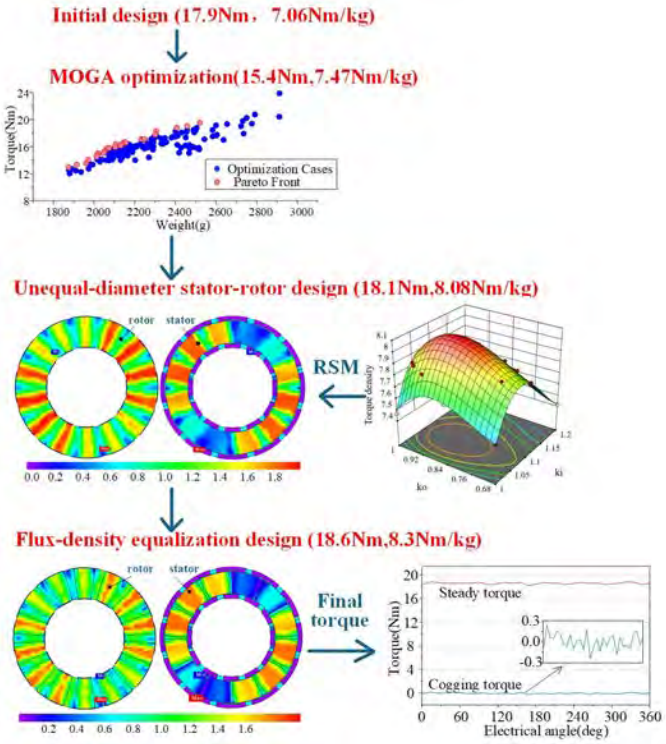


Fig. 2 Torque optimization process of proposed stepwise lightweight design for the AFPM motor.

EQ-13. High-Speed Yield Force Falloff in Magnetorheological Flow-Mode Devices: From Rheometers to Building-Scale Seismic Dampers

S. G. Sherman, Y. T. Choi, N. M. Wereley
Department of Aerospace Engineering, University of Maryland, College Park, Maryland, United States

High-speed yield force falloff — the decrease in controllable yield force as active-gap velocity rises — has been observed in magnetorheological (MR) flow-mode devices ranging from laboratory capillary rheometers to building-scale seismic dampers. Conventional one-dimensional yield force models fail to predict this behavior, leading to speculation that the yield stress itself possesses a fundamental response time that limits the usable design space of MR devices. In previous work [1,2], the authors developed a two-dimensional activation flow computational fluid dynamics (CFD) model that attributes high-speed yield force falloff to momentum-flux changes in the developing plug region, and validated it against double-ended rod impact dampers [3].

The present paper extends that validation to four practical MR devices spanning four orders of magnitude in force capacity and distinct application domains: Goncalves' high-speed capillary slit rheometer [4], Singh's 12 kN single-rod impact damper [5], Choi and Robinson's 8 kN oleo-pneumatic helicopter landing gear damper [6], and Sodeyama's 300 kN Sanwa-Tekki seismic damper [7]. Although these system serve vastly different applications, all operate within the high-speed fluid-dynamic regime on the Reynolds-Hedstrom design map. Figure 1 shows the result for Sodeyama's 300 kN seismic damper: despite a modest piston velocity of 0.4 m/s, the device's large area ratio drives the active-gap velocity to 27 m/s, placing this building-scale damper firmly within the high-speed regime. The activation flow model (solid lines) captures the characteristic rise-then-fall trend in yield force that neither the parabolic (dotted) nor the plug-flow (dash-dot) model can reproduce.

In all four cases, activation flow predicts yield force more accurately than either alternative model. Furthermore, the quasi-static criterion $C_{\tau y} > 0.4$ reliably identifies the onset of inertial effects across all device classes. These findings demonstrate that high-speed yield force falloff is a fluid-dynamic rather than a rheological phenomenon, providing a unified design framework for MR flow-mode devices from rheometer to seismic scale.

[1] S. G. Sherman, M. Mao, Y. T. Choi, and N. M. Wereley, "Experimental validation of a magnetorheological fluid activation flow CFD analysis," Rheologica Acta, 65, pp. 275-285, 2026. https://doi.org/10.1007/s00397-025-01540-9.
[2] S. G. Sherman, Y. T. Choi and N. M. Wereley, "Activation and deactivation flows of magnetorheological fluid," MDPI Actuators, 2026 (in press).
[3] Mao, M., Hu, W., Choi, Y.T., Wereley, N.M., Browne, A.L., Ulicny, J.C.: Experimental validation of a magnetorheological energy absorber design analysis. Journal of Intelligent Material Systems and Structures 25(3), pp. 352–363, 2013. https://doi.org/10.1177/1045389X13494934.

[4] F. D. Goncalves, M. Ahmadian, and J. D. Carlson, "Investigating the magnetorheological effect at high flow velocities," Smart Materials and Structures, vol. 15, no. 1, pp. 75–85, 2006. https://doi.org/10.1088/0964-1726/15/1/036.

[5] H. J. Singh, W. Hu, N. M. Wereley, and W. Glass, "Experimental validation of a magnetorheological energy absorber design optimized for shock and impact loads," Smart Materials and Structures, vol. 23, no. 12, p. 125033, 2014. https://doi.org/10.1088/0964-1726/23/12/125033.

[6] Y.-T. Choi, R. Robinson, W. Hu, et al., "Analysis and Control of a Magnetorheological Landing Gear System for a Helicopter," Journal of the American Helicopter Society, vol. 61, no. 3, pp. 1–8, 2016. https://doi.org/10.4050/JAHS.61.032006.

[7] H. Sodeyama, K. Suzuki, and K. Sunakoda, "Development of Large Capacity Semi-Active Seismic Damper Using Magneto-Rheological Fluid," Journal of Pressure Vessel Technology, vol. 126, no. 1, p. 105, 2004. https://doi.org/10.1115/1.1634587.

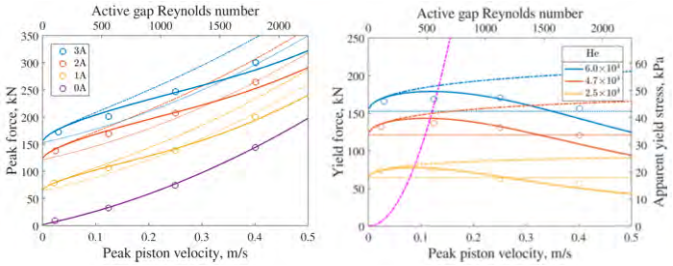


Fig.1: Sodeyama's 300 kN seismic damper [7]

EQ-14. Electronic and Magnetic Interaction Between Pt and Cu Species in ZSM-5 via Ion Exchange and Its Impact on Catalytic Performance

K. Baek
Seoul National University, Hwasungsi, Korea (the Republic of)

Understanding the interplay between electronic structure and magnetic properties in transition metal systems is important for designing functional materials. In this work, we investigate the electronic and magnetic interactions between Pt and Cu species in ZSM-5 prepared via simultaneous ion exchange using ammonium-form precursors. Pt is typically diamagnetic, whereas Cu species can exhibit paramagnetic behavior depending on their oxidation state. When co-exchanged within the zeolite framework, these species can influence each other, leading to modified electronic environments and spin states. Pt–Cu/ZSM-5 catalysts were synthesized through a controlled co-ion exchange process to promote close proximity between Pt and Cu species. Characterization results suggest that the presence of Pt affects the oxidation state distribution of Cu, indicating a shift between Cu2+ and Cu+ species. This change is associated with variations in local magnetic moments and electronic structure. Catalytic testing shows improved activity and reduced N2O formation compared to monometallic systems. These results are attributed to modified electronic interactions and possible spin-dependent adsorption behavior induced by Pt–Cu coupling. The findings suggest that local magnetic interactions at the atomic scale can influence catalytic performance even in systems not traditionally considered magnetic materials.
This work demonstrates that incorporating magnetic and electronic perspectives can provide new insights into the design of transition metal catalysts in confined environments.

EQ-15LB. Analysis of the Relationship Between Muscle Contractions Induced by Electrical and Magnetic Stimulation and Breath VOC Changes in Rats

R. Kaneda, Y. HE, H. Yamahara, G. Ogawa, S. Funatani, I. Mimura, H. Nishi, H. Tabata, M. Nangaku, M. Sekino
The University of Tokyo, Tokyo, Japan

Electrical and magnetic stimulation induce muscle contractions and are explored in rehabilitation and as exercise-mimicking interventions for those unable to exercise [1]. However, these responses often require invasive blood or tissue sampling, motivating less invasive methods. Exhaled volatile organic compounds (VOCs) may reflect exercise-related metabolic and redox changes [2]. We analyzed exhaled VOCs before and after stimulation by gas chromatography-mass spectrometry (GC-MS) to assess whether biological responses could be detected in breath.

Anesthetized rats were intubated and connected to a two-way-valve breath collection system. Artificial air was supplied from one gas bag and breath collected in another. Rats were assigned to electrical, magnetic, or control groups. Electrical stimulation was delivered at 2.5 times the threshold and 1.0 Hz, and magnetic stimulation at 2.5 times the threshold and 10 Hz; both delivered 18,000 pulses over the same duration. Controls underwent the same procedures without stimulation. Breath was collected before and 30

min after stimulation and analyzed by GC-MS.

Compared with controls, 1-heptanol significantly decreased after electrical stimulation, whereas dodecane and hexadecane decreased after magnetic stimulation (Fig. 1, 2). A similar 1-heptanol decrease was reported in volatiles from electrically stimulated postmortem bovine longissimus lumborum [3], suggesting that 1-heptanol may reflect responses to electrical stimulation. Dodecane and hexadecane are reported as exhaled VOC candidates associated with lipid peroxidation [4], and related breath VOCs, including dodecane, decrease after exercise [5]. Thus, these decreases may reflect metabolic changes induced by magnetic stimulation. Different VOC profiles may partly reflect differences in hindlimb electric-field distribution. Overall, these findings suggest that exhaled VOC changes can reflect responses to both stimulation methods, supporting simple, minimally invasive breath monitoring.

References

[1] Beaulieu LD, Schneider C. Neurophysiol Clin. 2015;45:223–237.
[2] Pugliese G, et al. Front Physiol. 2022;13:946401.
[3] Yang J, Dashdorj D, Hwang I. Food Sci Anim Resour. 2019;39:474–493.
[4] Couto M, et al. Pediatr Allergy Immunol. 2017;28:452–457.
[5] Lilien TA, et al. Am J Respir Cell Mol Biol. 2024;70:392–399.

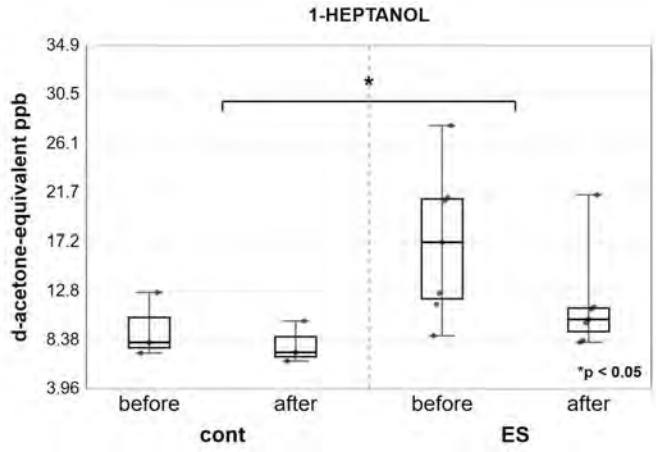


Fig. 1 Change in exhaled 1 – heptanol level before and after electrical stimulation (control, n = 3; stimulation, n = 7)

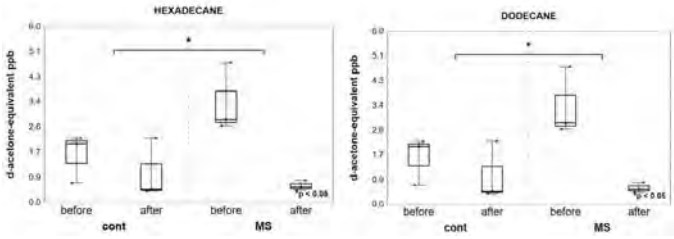


Fig. 2 Change in exhaled HEXADECANE and DODECANE level before and after magnetic stimulation (n = 3)

EQ-16LB. Minor-Loop Programming of Sr-Hexaferrite Remanence for Nonvolatile Multilevel Control of Plasma Streamer Topology

C. V. Vishwesh[1], G. Tenasini[2], Y. Zhang[1]
[1]Unionville High School, Markham, Ontario, Canada, [2]CERN, Geneva, Geneva, Switzerland

Hard ferrites store information in their remanent magnetization; here we show that this stored state can be read out at zero applied field, with multilevel resolution, through the branching topology of a packed-bed CO2 dielectric-barrier discharge under nanosecond pulsing. Vibrating-sample magnetometry of the packing elements gives Ms = 305 kA/m, Mr = 246 kA/m, and Hc = 184 kA/m for hard Sr-hexaferrite (Mr/Ms = 0.806), compared with Mr = 12.6 kA/m and Hc = 3.2 kA/m for soft NiZn ferrite (Mr/Ms = 0.040).

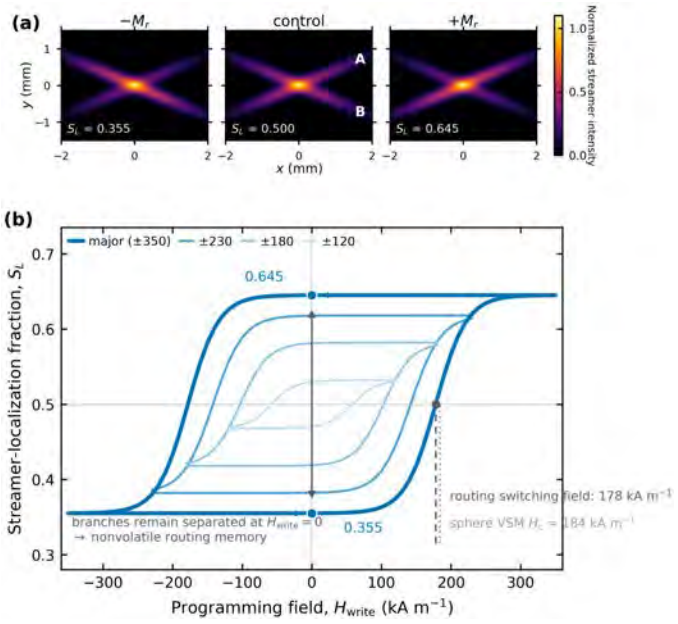
After magnetic writing, the applied field is removed before plasma readout. The streamer-localization fraction SL, defined as the fraction of ionization carried by one of two symmetric branches, reproduces the magnetic memory: its major transfer loop switches at 178 kA/m, closely inheriting the 184 kA/m magnetic coercivity, while retaining zero-field states of SL = 0.355 and 0.645. Three nested minor loops program seven intermediate states between the two saturated remanent states, producing nine resolvable routing levels. Across 500 single-shot discharge images per level, the probability of selecting that branch increases monotonically from 0.088 to 0.918; the two saturated remanent states provide a mean correct-branch routing fidelity of 91.5%.

Magnetic hardness controls retention. After field removal, the low-remanence NiZn packing yields SL = 0.508, whereas Sr-hexaferrite preserves the written routing state and a

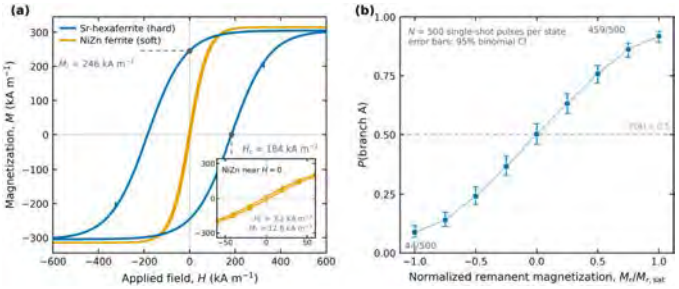
nonmagnetic control of matched permittivity and geometry remains at SL ~ 0.500. Three-dimensional finite-element magnetostatics predicts a saturated interbranch field asymmetry of 0.157 T, approximately 9% below the corresponding two-dimensional approximation, while reproducing all nine programmed localization states to within 0.005 in SL.

Repeated +Mr/-Mr writing shows no systematic loss of routing fidelity over 120 cycles, and repeated zero-field readout drifts by less than 0.6 percentage point during six hours of operation. These results demonstrate direct transfer of coercive and minor-loop magnetic memory into a spatially resolved functional output: Sr-hexaferrite remanence acts as a nonvolatile, multilevel state variable for programmable plasma topology and localized plasma chemistry.

[1] R. C. Pullar, "Hexagonal ferrites: A review of the synthesis, properties and applications of hexaferrite ceramics," Progress in Materials Science, vol. 57, pp. 1191-1334, 2012. doi: 10.1016/j.pmatsci.2012.04.001.
[2] F. Preisach, "Uber die magnetische Nachwirkung," Zeitschrift fur Physik, vol. 94, pp. 277-302, 1935. doi: 10.1007/BF01349418.
[3] K. Van Laer and A. Bogaerts, "Influence of gap size and dielectric constant of the packing material on the plasma behaviour in a packed bed DBD reactor: A fluid modelling study," Plasma Processes and Polymers, vol. 14, 1600129, 2017. doi: 10.1002/ppap.201600129.
[4] K. Van Laer and A. Bogaerts, "How bead size and dielectric constant affect the plasma behaviour in a packed bed plasma reactor: A modelling study," Plasma Sources Science and Technology, vol. 26, 085007, 2017. doi: 10.1088/1361-6595/aa7c59.
[5] S. Nijdam, J. Teunissen, and U. Ebert, "The physics of streamer discharge phenomena," Plasma Sources Science and Technology, vol. 29, 103001, 2020. doi: 10.1088/1361-6595/abaa05.
[6] I. Michielsen, Y. Uytdenhouwen, J. Pype, B. Michielsen, J. Mertens, F. Reniers, V. Meynen, and A. Bogaerts, "CO2 dissociation in a packed bed DBD reactor: First steps towards a better understanding of plasma catalysis," Chemical Engineering Journal, vol. 326, pp. 477-488, 2017. doi: 10.1016/j.cej.2017.05.177.



(a) Streamer maps for -Mr, control, and +Mr states, common scale. (b) Routing hysteresis with minor loops; read at zero field.



(a) VSM loops: hard Sr-hexaferrite vs soft NiZn. (b) P(branch A) vs remanent state; 500 shots each, 95% CIs.

SESSION ER: BIOMAGNETISM AND BIOMEDICAL APPLICATIONS II (POSTER SESSION)

Chair(s): J. Gomez-Pastora, *Texas Tech University, Lubbock, Texas, United States*

Thursday, November 5, 2026

09:30 AM-12:30 PM

Coral 4

ER-01. Quantitative Evaluation of Selective Attention during a Dichotic Listening Test

Y. Yamaguchi, K. Tanaka

Graduate School of Science and Engineering, Tokyo Denki University, Hatoyama-cho, Japan

Humans can perceive their own name or topics of interest even in noisy environments, a phenomenon known as the cocktail party effect. This ability is attributed to selective attention. This study investigates neural response during selective attention to quantitatively evaluate brain activity while participants listened to speech sounds.
A dichotic listening task was employed for the measurements. Different auditory stimuli were simultaneously presented to the left and right ears, and participants were instructed to repeat the words presented to the designated ear. During this task, brain activity was recorded using magnetoencephalography (MEG). The experimental conditions consisted of the right-ear attention condition (repeating the stimulus presented to the right ear) and the left-ear attention condition (repeating the stimulus presented to the left ear). Two-syllable meaningful words were used as auditory stimuli. The stimuli were amplitude-modulated at 35 Hz and 45 Hz to induce auditory steady-state responses (ASSRs) through frequency tagging, enabling discrimination of ASSRs corresponding to each ear. The results revealed significant positive correlation between the word repetition accuracy and the ASSR amplitude in the left auditory cortex during the left-ear attention condition. In contrast, no significant correlation was found during the right-ear attention condition. Previous studies have reported that performance in dichotic listening tasks is significantly better for the right ear than for the left ear (the right-ear advantage). This suggests that greater attentional resources are required for the left ear. Therefore, the accuracy in the left-ear attention condition likely has a wider dynamic range than in the right-ear attention condition, which may explain the observed correlation between repetition accuracy and ASSR amplitude specifically in the left-ear attention condition.

ER-02. Magnetic Resonance-Based Quantification of Iron in Tumor Models Using Non-Contrast MRI

K. Rova[1], S. Rodriguez Caballero[1], K. Paz Gonzalez[1], M. Molinares Ponce[2], B. Rezaei[3], C. Xu[2], K. Wu[3], J. Gomez-Pastora[1]

[1]Chemical Engineering, Texas Tech University, Lubbock, Texas, United States, [2]Industrial, Manufacturing & Systems Engineering, Texas Tech University, Lubbock, Texas, United States, [3]Electrical and Computer Engineering, Texas Tech University, Lubbock, Texas, United States

Iron (Fe) plays a vital role in cellular metabolism, redox regulation, as well as proliferation, and recent research has established that cancer cells particularly acquire Fe for rapid growth, and that tumor Fe content inversely correlates with patient survival rates[1-3]. Since iron and iron-binding species introduce local magnetic susceptibility variations, they can significantly influence transverse relaxation behavior in magnetic resonance imaging (MRI). Therefore, we intend to explore non-contrast MRI as a magnetic characterization tool for probing iron accumulation in three-dimensional (3D) tumor phantom designed to better reproduce tumor-like architecture for establishing a foundation for future cancer prognosis studies. Our preliminary results using two-dimensional (2D) ovarian cancer cell cultures (SKOV3 cells) incubated with Fe-enriched media containing Fe^{2+} and Fe3+ at controlled concentrations revealed that T2-based MRI measurements showed progressive signal attenuation with increasing iron concentration for both ionic states, consistent with enhanced magnetic dephasing caused by iron-associated susceptibility effects. Fe^{2+}-treated samples exhibited slightly stronger signal reduction than Fe^{3+}-treated samples under the same conditions (Fig-1(B)), while untreated controls remained comparatively bright, supporting the interpretation that the observed contrast changes are linked to iron uptake by the cells (Fig-1(A)). Overall, this study provides a proof-of-concept for MRI-based Fe quantification using cultured tumor cells, forming a foundational step toward developing a realistic 3D tumor phantom model which ensures more ethical, reproducible, and controllable preclinical MRI studies of tumor iron metabolism and its correlation to therapy success.

Torti, S. V. & Torti, F. M. Iron and cancer: more ore to be mined. *Nature Reviews Cancer* 13, 342-355 (2013). https://doi.org:10.1038/nrc3495

2 Manz, D. H., Blanchette, N. L., Paul, B. T., Torti, F. M. & Torti, S. V. Iron and cancer: recent insights. *Ann N Y Acad Sci*

1368, 149-161 (2016). https://doi.org:10.1111/nyas.13008
3 El Hout, M., Dos Santos, L., Hamaï, A. & Mehrpour, M. A promising new approach to cancer therapy: Targeting iron metabolism in cancer stem cells. *Seminars in Cancer Biology* 53, 125-138 (2018). https://doi.org:https://doi.org/10.1016/j.semcancer.2018.07.009

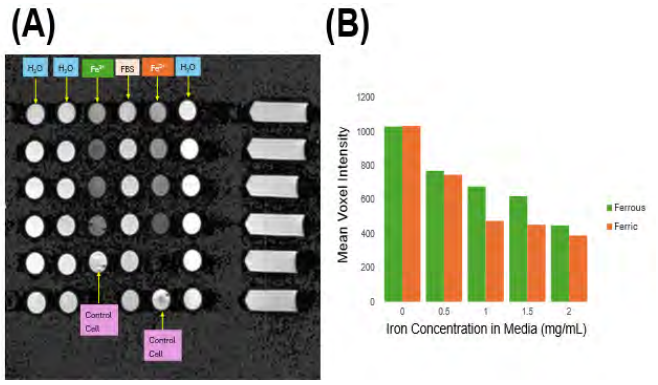


Fig. 1: MRI preliminary results. (A) MRI signal from T2 mapping. (B) Mean Voxel Intensity ± SD (n=5) vs Concentration.

ER-03. Development of a novel Ferromagnetic Suppression Coil to Increase Focality in TMS Procedures on Small Animals

T. V. Atalugama, W. Lohr, R. L. Hadimani
Mechanical and Nuclear Engineering, Virginia Commonwealth University, Richmond, Virginia, United States

Transcranial Magnetic Stimulation is an FDA-approved non-invasive neuromodulation technique that stimulates brain regions via a focalized electric field induced by a time-varying current in wire coils placed above the head. This field is often focalized through a “figure 8” coil design where opposing currents are conducted through two closely placed wire coils, doubling the field strength at their meeting point. A typical approach to TMS focalization is strengthening this central region; however, undesired stimulation still occurs under the rest of the coil. We present a novel approach to TMS focalization that instead inhibits the electric field in the non-central region by placing two half-moon ferromagnetic suppression coils (FSC) with opposing current on the outer quarters of the figure 8 coil and ferromagnetic cores in their centers. The FSC current opposes that of the figure 8, creating a varying magnetic field to destructively interfere with that of non central figure 8 regions, while ferromagnetic cores amplify focality. We test this design on a TMS rat phantom.

In Sim4Life, we designed 2 TMS coils, a standard figure 8 and a figure 8 with two FSCs attached. Cores were made of permendur, a highly magnetically permeable iron-cobalt alloy. An MRI-derived, anatomically accurate rat head model was placed underneath. Magneto Quasi-Static simulations were run at a current amplitude of 1000 A varying at 2.5 kHz, and electric field data was recorded. Results showed significantly less induced electric field in regions directly under the FSCs. The figure 8-FSC coil had a similar maximum V/m to the standard coil on the surface, but was far more focal. This design thus focalizes coils by inhibiting simulation in non-central regions without greatly sacrificing penetration strength of the focal region. The continuity of the coils implies this effect holds at various currents. Future research involves improving FSC coverage for greater focality,physical coil creation for inductance testing, and quantifying focality via sphere testing according to Deng et al.

Z. Deng, S. Lisanby and A. Peterchev, Brain Stimulation., Volume 6, Issue 1, p.1-13 (2013)
L. Hernandez-Garcia, T. Hall T, L. Gomez and E. Michielssen, Brain Stimulation, Vol3(4), p.218-225 (2010)
H. Siebner, K. Funke and A. Aberra, Clinical Neurophysiology., Volume 140, p.59-97(2022)
V. E. Amassian and P.J. Maccabee, Conf Proc IEEE Eng Med Biol Soc. 2006, p.1620–1623(2006)

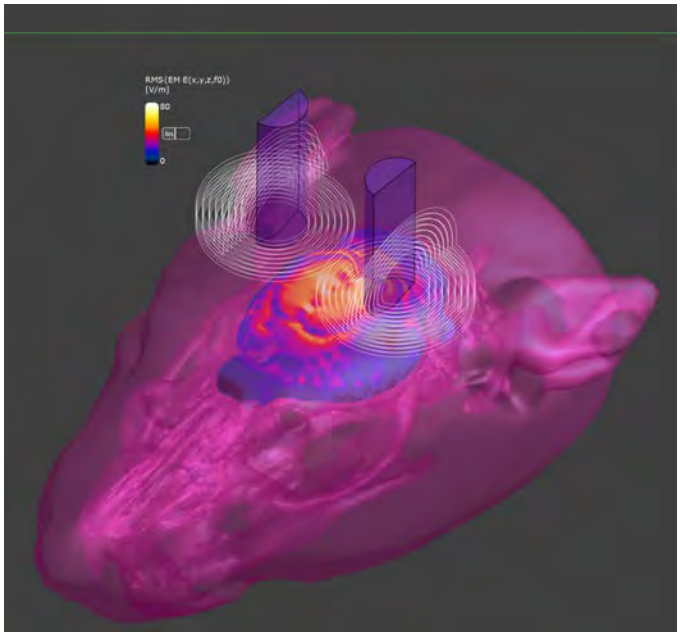


Fig. 2: Figure 8-FSC Coil above Simulation Rat Head.

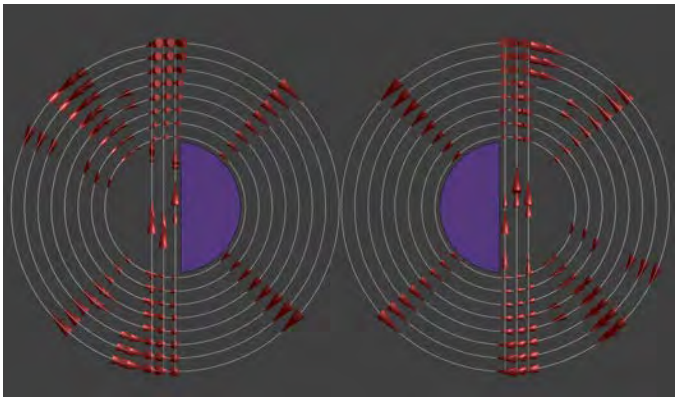


Fig. 1: Coil Design with Direction of Current Flow

ER-04. Enhancement of High-Frequency Output in Electromagnetic Bone Conduction Devices Using Optimized Cantilever and Magnetic Circuits

M. Ezaka[1], W. Kitagawa[1], M. Nakashima[2], R. Masuda[2]
[1]Electrical and Mechanical Engineering, Nagoya Institute of Technology, Nagoya, Aichi, Japan, [2]SANKO MOLD CO., LTD., Nagoya, Aichi, Japan

Electromagnetic bone conduction devices transmit audio information directly to the inner ear by vibrating the cranial bones. These devices are anticipated as next-generation communication tools, particularly for individuals with hearing impairments or for users in noisy environments. Recently, research has expanded into the high-frequency range for medical and welfare applications. However, conventional electromagnetic devices typically utilize circular diaphragms, which struggle to achieve sufficient Vibration Acceleration Level (VAL) at high frequencies due to structural stiffness and mass limitations.

This paper proposes a novel cantilever structure for electromagnetic bone conduction devices to enhance high-frequency output. Unlike circular models, the cantilever device uses a rectangular diaphragm fixed at one end, allowing for larger displacements and flexible resonance mode control. This configuration also enables an independent 2-way driving system for both audible and high-frequency ranges. The design process involved 3D-FEM analysis (JMAG) and a Genetic Algorithm (GA) to optimize performance. The diaphragm contour was mathematically defined using a Fourier series-based function to provide a high degree of freedom for geometric optimization.

The optimization specifically targeted maximizing the VAL at 30 kHz. Comparative analysis among the circular model, original cantilever model, and GA-optimized cantilever model indicates that cantilever designs fundamentally outperform circular models in the high-frequency domain. Specifically, the optimized diaphragm shape achieved a significant 5.2 dB increase in VAL at 30 kHz compared to the initial cantilever shape. These findings confirm that precise geometric modification via GA is highly effective for tailoring the output of bone conduction transducers, demonstrating significant potential for high-performance applications.

S. Ogiso, K. Mizutani and K. Zempo, IEEE 3rd Global Conference on Consumer Electronics (GCCE), pp.573-576 (2014)
S. Nakagawa, Acoustical Science and Technology, Vol. 41, No. 6, pp. 851-856 (2020)

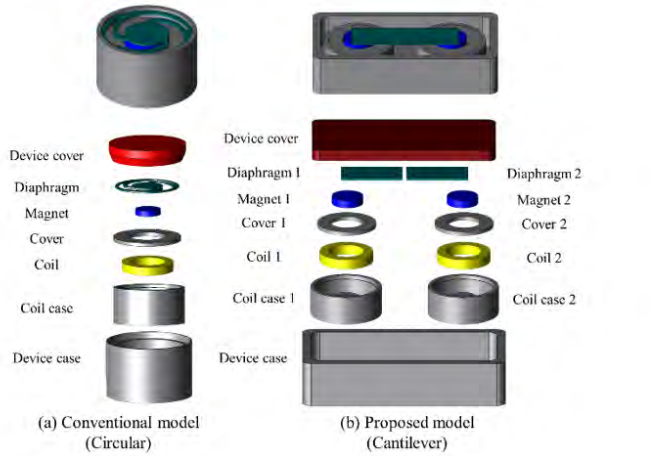


Fig. 1. Comparison of (a) conventional and (b) proposed models.

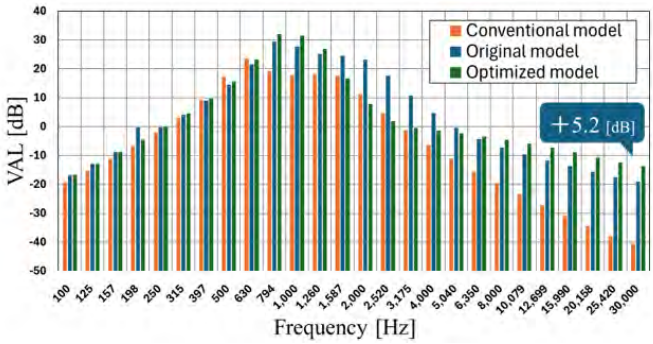


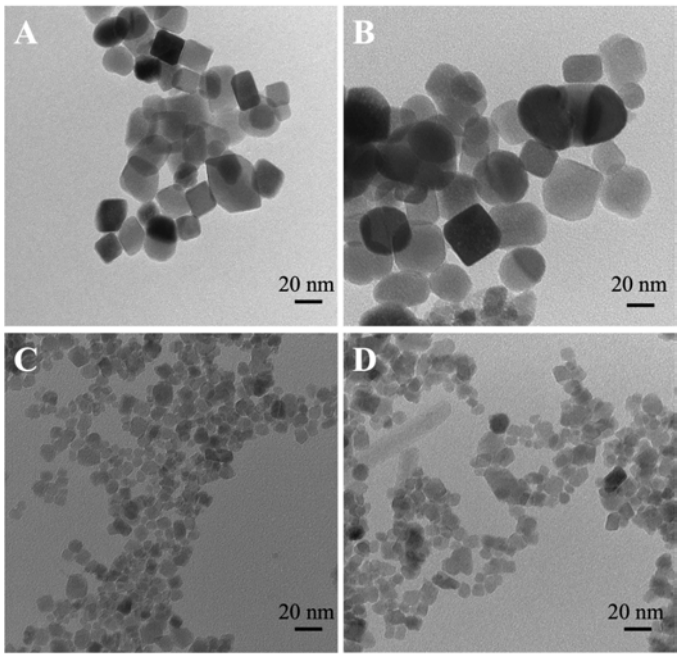
Fig. 2. Analysis results showing the Vibration Acceleration Level (VAL) for each model.

ER-05. Structure-Magnetic Property Relationships in Size-Controlled Cubic Magnetic Nanoparticles for Dual MRI/MPI Applications

B. Rezaei[1], S. Mostufa[1], H. Wang[1], M. Shahriar[2], M. Molinares Ponce[2], C. Xu[2], K. Wu[3]
[1]Department of Electrical and Computer Engineering, Texas Tech University, Lubbock, Texas, United States, [2]Department of Industrial, Manufacturing, and Systems Engineering, Texas Tech University, Lubbock, Texas, United States, [3]University of South Florida, Tampa, Florida, United States

Magnetic nanoparticles (MNPs) have emerged as promising candidates for multimodal imaging because their magnetic properties can be tuned by controlling composition, particle size, and morphology.[1] In this work, we synthesized four types of cubic MNPs with two distinct compositions, Fe_3O_4 and $Zn_{0.4}Fe_{2.6}O_4$, and two different sizes. Representative TEM images of Fe_3O_4 and $Zn_{0.4}Fe_{2.6}O_4$ nanoparticles, shown in Fig. 1, reveal cubic morphologies with average particle sizes of approximately 10 and 30 nm, confirming successful synthesis with controlled composition, size, and shape. We then evaluated their potential for dual-imaging applications in magnetic resonance imaging (MRI) and magnetic particle imaging (MPI).[2] This study was designed to investigate how nanoparticle composition and size influence imaging performance, with particular emphasis on magnetic properties, cellular uptake behavior, and biocompatibility. Magnetic characterization using a physical property measurement system (PPMS) under both low- and high-field conditions demonstrated strong magnetic responses, supporting the potential of these nanoparticles as imaging probes. *In vitro* cell viability studies using SKOV3 ovarian cancer cells showed that all samples maintained high viability after 24 h of incubation, even at a concentration of 500 µg/mL, indicating low cytotoxicity. Overall, these preliminary results highlight the potential of composition- and size-controlled cubic MNPs as biocompatible dual-mode contrast agents for MRI and MPI.

[1] B. Rezaei *et al.*, 'Magnetic Nanoparticles: A Review on Synthesis, Characterization, Functionalization, and Biomedical Applications', *Small*, vol. 20, no. 5, p. 2304848, Feb. 2024, doi: 10.1002/smll.202304848.
[2] T.-H. Shin, Y. Choi, S. Kim, and J. Cheon, 'Recent advances in magnetic nanoparticle-based multi-modal imaging', *Chemical Society Reviews*, vol. 44, pp. 4501–4516, 2015.



TEM images of synthesized cubic MNPs. Representative TEM images show $Zn_{0.4}Fe_{2.6}O_4$ (A&C) and Fe_3O_4 (B&D) nanoparticles with average particle sizes of approximately 10 and 30 nm.

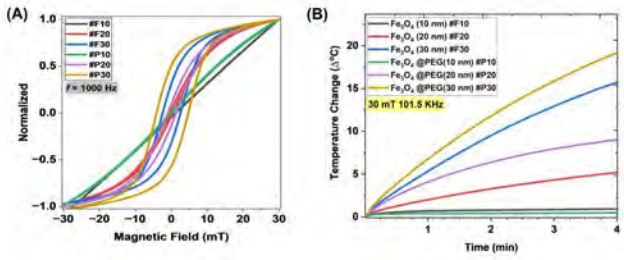
ER-06. Evaluation of Commercial Iron Oxide Nanoparticles for Dual-Functional Magnetic Particle Imaging and Magnetic Hyperthermia

S. Mostufa[1], H. Wang[1], B. Rezaei[1], M. Shahriar[2], C. Xu[2], K. Wu[3]
[1]Department of Electrical and Computer Engineering, Texas Tech University, Lubbock, Texas, United States, [2]Department of Industrial, Manufacturing, and Systems Engineering, Texas Tech University, Lubbock, Texas, United States, [3]University of South Florida, Tampa, Florida, United States

Magnetic nanoparticles (MNPs) have emerged as indispensable materials for biomedical applications, serving both as tracers for magnetic particle imaging (MPI) and as heat mediators for magnetic hyperthermia therapy [1][2]. However, tailoring a single MNP formulation that simultaneously meets the requirements for high-performance MPI and efficient hyperthermia remains a significant challenge. In this work, we report commercial MNPs with various sizes (10 nm (#F10), 20 nm (#F20), 30 nm (#F30)) and coatings (polyethylene glycol (PEG)) with (10 nm (#P10), 20 nm (#P20), 30 nm (#P30)) to evaluate their dual functional behavior. The nanoparticles were then thoroughly characterized to establish correlations between

structural features and magnetic performance. MPI suitability was assessed using magnetic particle spectroscopy (MPS), in which the higher harmonics, signal-to-noise ratio (SNR), and AC magnetic hysteresis (M-H) loops at 30 mT and 1 kHz were analyzed. From these AC M–H loops, we derived the point spread function (PSF) to quantify MPI spatial resolution and tracer suitability for this application. In parallel, for hyperthermia evaluation, specific absorption rate (SAR) and heating efficiency were measured using a calorimetric method under clinically safe field and frequency conditions (101.5 kHz and 20 mT). We have also collected the AC M-H loops of MNPs under hyperthermia excitation field conditions to provide more details on the heat-generation mechanisms. Fig. 1 showcase the TEM images and the hypothermia measurement of these MNPs. The results highlight the feasibility of tailoring MNP properties through controlled synthesis and size optimization to develop multifunctional MNPs suitable for simultaneous imaging and therapeutic use. These dual-functional MNPs are a potential candidate for advancing image-guided cancer treatment and biomedical applications.

[1] Rezaei, B., Yari, P., Sanders, S. M., Wang, H., Chugh, V. K., Liang, S., ... & Wu, K. (2024). Magnetic nanoparticles: a review on synthesis, characterization, functionalization, and biomedical applications. Small, 20(5), 2304848.
[2] Szasz, A. Pulsing Addition to Modulated Electro-Hyperthermia. Bioengineering 2024, 11 (7). https://doi.org/10.3390/bioengineering11070725



(A) MPS AC-MH loop for 1000 KHz and 30 mT excitations (B) Hyperthermia performance is shown under 30 mT and 101.5 KHz excitations, for all samples

ER-07. Electromagnetically Induced Endolymph Flow in the Vestibular System

Y. Lee[2], J. Kim[2], S. Jung[2], H. Song[1], S. Oh[1], I. Na[1], J. Jang[1], K. Noh[1], Y. Park[1], Y. Lee[1], P. Chanwook[1], J. Hong[1]
[1]Control and Instrumentation Engineering, Korea University, Sejong, Korea (the Republic of), [2]BK21 FOUR Smart Mobility Education and Research Team, Korea University, Sejong, Korea (the Republic of)

This study proposes a non-invasive method to induce endolymph flow within the human vestibular system using externally applied low-frequency magnetic fields.

The approach is based on magnetohydrodynamic (MHD) principles, where Lorentz forces act on ionic biofluids under applied magnetic fields. A helical copper coil was designed to generate magnetic fields at a frequency of 250 Hz with field strengths in the millitesla (mT) range.

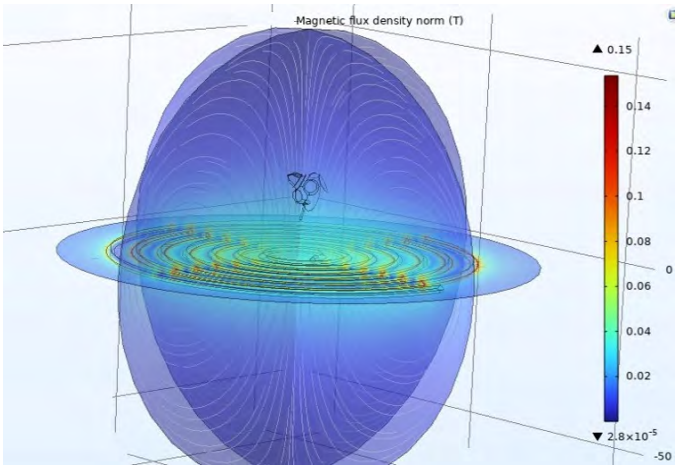
To experimentally validate the approach, an ionic fluid analog was positioned near the coil, and the induced potential was measured. A measurable potential difference of approximately 0.992 mV was observed over a 5 mm electrode spacing, confirming magnetically induced fluid motion. The experimental configuration was designed to approximate geometric constraints relevant to vestibular structures.

In parallel, multiphysics simulations incorporating coupled electromagnetic and laminar flow physics were conducted to predict induced fluid velocity and spatial distribution under varying field strengths and configurations. The simulation results are consistent with the experimental observations and indicate that localized fluid motion can be generated under moderate magnetic field conditions.

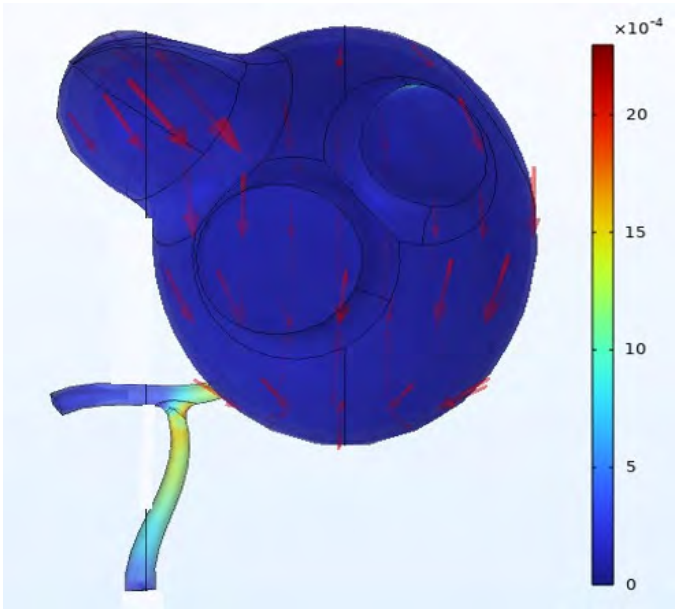
The selection of 250 Hz was guided by safety considerations for electromagnetic exposure in biological tissues. According to ICNIRP 2010 guidelines, exposure limits in this frequency range are defined in terms of induced electric fields within the human body, and the estimated induced electric field in the present study (0.006–0.042 V/m) remains well below the recommended threshold of 0.1 V/m for avoiding neural or retinal stimulation. In addition, the estimated specific absorption rate (SAR) is below 2.0 μW/kg, significantly lower than typical clinical MRI limits (3.2 W/kg), indicating negligible thermal effects.

These findings demonstrate the feasibility of electromagnetically induced fluid motion in confined ionic environments and provide a potential basis for non-invasive vestibular stimulation under physiologically safe conditions.

1. B. K. Ward et al., Front. Neurol., 8, 122 (2017)
2. D. C. Roberts et al., Curr. Opin. Neurol., 26, 74 (2013)
3. J. P. McNabb et al., J. Magn. Reson. Imaging, 49, 1118 (2019)
4. J. Rey-Martinez et al., Front. Neurol., 11, 224 (2020)
5. J. Goyens et al., J. Biomech., 103, 109683 (2020)



Magnetic flux density distribution generated by the coil (250 Hz, mT range)



Simulated velocity distribution and flow direction in the vestibular structure

ER-08. Cell differentiation of mesenchymal stem cells mediated by the presence of core shell $CoFe_2O_4$@$BaTiO_3$ nanoparticles

H. Chiriac, A. Minuti, D. Gherca, N. Lupu
National Institute of Research and Development for Technical Physics, Iasi, Romania

Magnetoelectric nanomaterials have emerged as promising platforms for remotely controlled cellular stimulation in tissue engineering. In this study, cobalt ferrite ($CoFe_2O_4$) nanoparticles with a cubic spinel structure and a median size of approximately 17 nm were synthesized by co-precipitation from aqueous metal chloride solutions. Barium titanate ($BaTiO_3$) nanoparticles were prepared using a sol–gel method involving molecular precursors of titanium and barium ions. These components were subsequently used to fabricate core–shell $CoFe_2O_4$@$BaTiO_3$ (CFO@BTO) nanocomposites with an approximate size of 60 nm (Figure 1), where $CoFe_2O_4$ formed the magnetic core and $BaTiO_3$ constituted the piezoelectric shell.

The design of these composites enables magnetoelectric coupling under magnetic stimulation. The magnetostrictive response of the $CoFe_2O_4$ core induces mechanical strain in the $BaTiO_3$ shell, generating localized electrical signals. This mechanism provides a non-invasive strategy for cellular stimulation without direct electrical contact.

Biocompatibility studies showed that CFO@BTO nanoparticles do not affect viability or proliferation in normal human fibroblast cells and adipose-derived stem cells (ADSCs), with or without magnetic stimulation, confirming their suitability for biomedical use.

Furthermore, the potential of these nanocomposites in directing stem cell fate was investigated. Magnetic stimulation of CFO@BTO nanoparticles showed promising effects in promoting osteogenic and chondrogenic differentiation of ADSCs. The magnetic core contributes to mechanotransductive signaling, while the piezoelectric shell enhances bioelectrical stimulation, creating a synergistic effect that supports lineage-specific differentiation. Notably, the $CoFe_2O_4$ core alone has supported enhanced differentiation under magnetic fields, and the addition of the $BaTiO_3$ shell further amplifies this response through magnetoelectric coupling.

Overall, CFO@BTO core–shell nanoparticles represent a multifunctional and biocompatible platform for magnetically triggered bioelectrical stimulation, with strong potential in bone and cartilage tissue engineering.

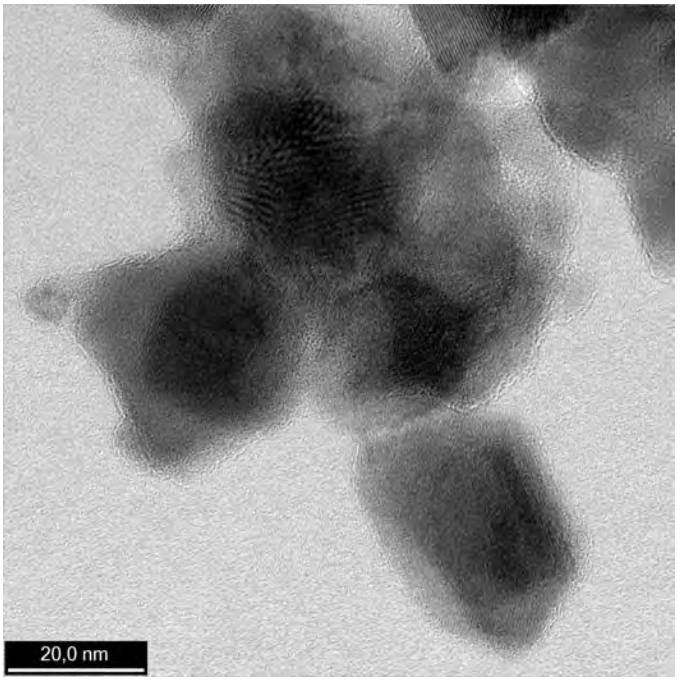


Figure 1. $CoFe_2O_4$@$BaTiO_3$ core shell magnetic particles

ER-09. Magnetic Response of Multiphase Gd/Gd_2O_3 Nanoparticles: Implications for Relaxation Behavior

N. Gunduz Akdogan[1, 2], B. Gungordu[3], C. Bagci[3], O. Akdogan[3, 2]
[1]Piri Reis University, Istanbul, Turkey, [2]NANOTerial Technology, Istanbul, Turkey, [3]Bahcesehir University, Istanbul, Turkey

Gd^{3+} ($4f^7$, S = 7/2) is a typical localized moment system among rare-earth ions [1]. In this work, Gd-based nanoparticles were prepared using a Corylus colurna extract. The synthesis was not carried out under strictly controlled oxygen conditions, so partial reduction during formation is likely.

XRD indicates that the dominant phase is cubic Gd_2O_3 (Ia-3), with weak additional peaks that can be assigned to metallic Gd (hcp, $P6_3/mmc$). The crystallite size estimated from peak broadening is ~20 nm. Thermal analysis shows the expected removal of organic content followed by oxide formation, while SEM points to agglomerated particles rather than well-isolated nanoparticles.

Magnetization at 300 K increases almost linearly with field up to 10 kOe and does not saturate, which is consistent with paramagnetic Gd^{3+} ions in an oxide lattice [1,2]. The high-field slope is in line with weakly interacting moments. At low fields, a small hysteresis is observed. Since Gd_2O_3 is not ferromagnetic, this is most likely due to a minor secondary phase. The presence of metallic Gd in XRD supports this. A rough estimate using the measured moment suggests that the corresponding fraction is well below 1 wt.%, but still enough to affect the low-field response. A contribution from oxygen-deficient regions (Gd_2O_{3-x}) cannot be ruled out [3,4].

MTT measurements indicate reasonable cell viability under the tested conditions. T_1 relaxation measurements are currently ongoing to evaluate whether the paramagnetic contribution can be translated into MRI contrast behavior [5].

Overall, the sample behaves as a paramagnetic Gd_2O_3 matrix with a small ferromagnetic component arising from incomplete oxidation. The balance between these contributions appears quite sensitive to synthesis conditions.

[1] J. Jensen and A. R. Mackintosh, *Rare Earth Magnetism*, Oxford (1991).
[2] S. A. Makhlouf et al., *J. Appl. Phys.*, 81, 5561 (1997).
[3] Q. Xu et al., *Phys. Rev. B*, 77, 134449 (2008).
[4] S. Singhal et al., *J. Phys. Chem. C*, 114, 21590 (2010).
[5] P. Caravan et al., *Chem. Rev.*, 99, 2293 (1999).

ER-10. Fabrication of Luminescent Self-Regulating Magnetic Hyperthermia Core-Shell Nanoparticles of Gadolinium Oxide Shell over Gadolinium Silicide Core

S. Smith[1], S. B. Naranjo[1], J. R. Marin[1], Y. Mudryk[2], A. Kumar[2], R. Kuchi[2], R. L. Hadimani[1]
[1]Virginia Commonwealth University, Richmond, Virginia, United States, [2]Ames National Laboratory, Ames, Iowa, United States

Destroying cancer cells without damaging surrounding healthy cells is a driving force behind research into magnetic hypothermia nanoparticle candidates [1]. Investigation into enhanced applications such as luminescence imaging, opens possibilities to further examine the scope in which gadolinium silicide could be utilized. Given biocompatibility and resilience to x-ray radiation, Gd5Si4 is an attractive option as a core for fabricated nanoparticles [2]. Furthermore, its oxidized state (Gd2O3) has proven luminescence properties [3]. This study explores the construction of luminescent core-shell nanoparticles of gadolinium silicide through oxidation.

Gd5Si4 nanoparticles were prepared using the procedure detailed in previous literature [1]. Samples were set in an oven at an applied heat of 80 C and 100 C for 1 hour then removed. Additional oxidized samples were prepared by heating Gd5Si4, suspended in a DI water solution with sodium hydroxide at 600 C in an autoclave then calcined at 1000 C (sample 1) and 500 C (sample 2) for 1 hour (Fig.1 a-b). Results provide further understanding into the

limitations of oxidized Gd5Si4. A vibrating sample magnetometer was used to measure the magnetization (M) of oxidized Gd5Si4 and commercial Gd2O3 from 4 K-400 K and 200 K-400 K at an applied magnetic field of 100 Oe. Showing a decrease in magnetization from 80 C to 100 C (Fig.2). Results indicate oxidation negatively impacts the magnetization with calcined samples exhibiting near zero magnetization and loss of Gd5Si4 transition (Fig.1). Calcined were emission spectra tested using a FLAME-S-XR1-ES spectrometer. No luminescence was detected. Investigation into doping Gd5Si4 with other rare-earth magnetic materials may serve as a method to boost luminescence and maintain magnetization with minimal oxidation [4]. Expanding the capabilities of Gd5Si4 nanoparticles can utilize the properties that are attractive for magnetic hyperthermia treatment and help develop fabrication methods for core-shell nanoparticles of similar composition and morphology.

[1] Z. Boekelheide, Z. A. Hussein, S. M. Harstad, IEEE Transactions on Magnetics, vol. 53, no. 11, pp. 1-4, Nov. 2017
[2] Smith, S. E., Bermudez, S., Pavan Chaitanya, Nanotechnology, 36(33),(2025)
[3] Raunak Kumar Tamrakar, D.P. Bisen, Upadhyay, K., Superlattices and Microstructures, 88, 382–388. (2015)
[4] Pei S, Ge X, Sun L. Front Chem. (2020) Dec 8;8:610481

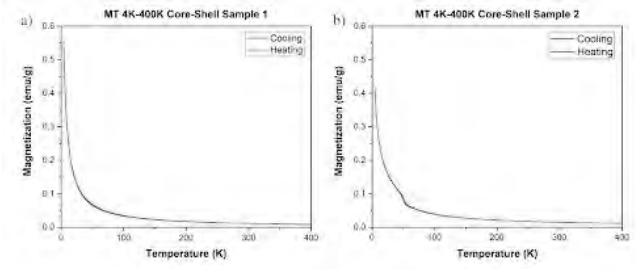


Fig.1 (a) MT data 4 K to 400 K at 100 Oe applied magnetic field for sample 1 (b) and sample 2.

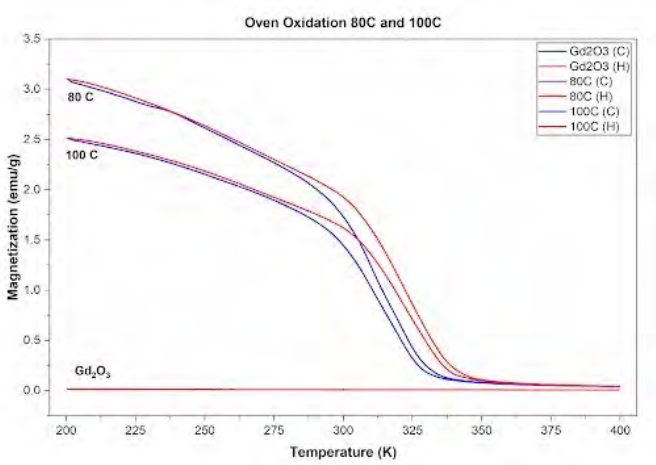


Fig.2 MT data 200 K to 400 K at 100 Oe applied magnetic field for 80 C , 100 C, and Gd2O3.

ER-11. Wireless temperature measurement by mixed-frequency magnetic fields on various viscosity conditions for magnetic hyperthermia

A. Kuwahata, R. Shinohara, S. Yabukami
Tohoku University, Sendai, Japan

In magnetic hyperthermia [1-4], precise wireless temperature measurement is essential for minimally invasive treatment. Techniques utilizing excitation magnetic fields with mixed high- (fH) and low-frequency (fL) components have achieved high-accuracy temperature estimation based on nonlinear magnetization responses [5]. However, the simultaneous execution of magnetic heating and noninvasive temperature monitoring has not yet been demonstrated. In this study, we developed a single platform that integrates temperature sensing and magnetic heating using mixed-frequency excitation magnetic fields.
Figure 1 illustrates the experimental setup for wireless temperature measurement using mixed-frequency magnetic fields under magnetic hyperthermia conditions. Figure 2 presents an evaluation of the measurement sensitivity and linearity at viscosities of 0.86 and 7.7 mPa s (representing biomedical conditions). As the viscosity increases from 0.86 to 7.7 mPa s, the optimal frequency for maximum sensitivity shifts significantly from 2.6 kHz down to 0.7 kHz. Similarly, the peak frequency for maximum linearity decreases from 6.8 kHz to 1.6 kHz. This shift toward the lower frequency range reflects the Brownian relaxation of magnetic nanoparticles (MNPs) in highly viscous environments. Consequently, these results demonstrate that optimizing the

excitation frequency according to the local viscosity of the target biological tissue is crucial for achieving precise and minimally invasive temperature control during magnetic hyperthermia treatments.

[1] H. Fatima *et al.*, *Nanomaterials 11*, 1203 (2021).
[2] X. Liu *et al.*, Theranostics 10, 3793 (2020).
[3] A. Kuwahata *et al.*, Sci. Rep 15, 41933 (2025).
[4] A. Kuwahata *et al.*, AIP Advances 16, 025030 (2026).
[5] S. Guo *et al.*, Rev. Sci. Instrum, 92, 024901 (2021).

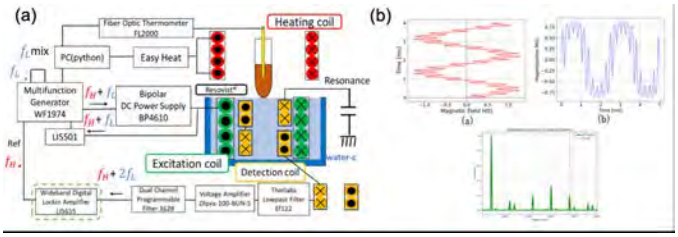


Fig. 1. Wireless temperature measurement using mixed-frequency magnetic fields under magnetic hyperthermia conditions. (a) Experimental setup; (b) Applied mixed-frequency magnetic field, magnetization signal of magnetic nanoparticles, and Fourier analysis of the magnetization signal.

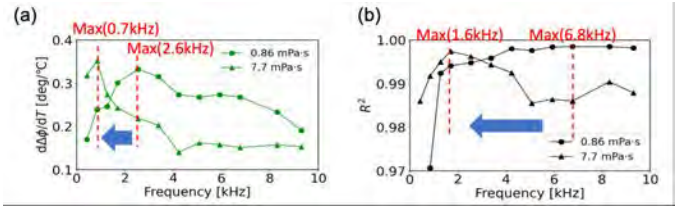


Fig. 2. Wireless temperature measurement based on mixed-frequency excitation under viscosity conditions of 0.86 and 7.7 mPa s. (a) Sensitivity and (b) linearity as functions of frequency of the measurement system, respectively.

ER-12. Induced Magnetic Anisotropy of Magnetic Nanoparticles in Mouse Lymph Nodes

A. Kuwahata, Y. Kamijima, T. Shimano, A. Sukhbaatar, T. Kodama, S. Saito, S. Yabukami
Tohoku University, Sendai, Japan

For the early clinical translation of magnetic hyperthermia (MH) [1-3], maximizing heating efficiency at minimal in vivo nanoparticle doses is imperative. This enhancement is driven by controlling particle orientation, which promotes magnetization reversal along the easy axis. Nevertheless, because prior research has been confined to in vitro models [4], the in vivo induction of shape magnetic anisotropy and its impact on heating properties remain poorly understood.

This study aims to improve heating efficiency by inducing magnetic anisotropy in magnetic nanoparticles injected directly into lymph nodes (biological tissue).
Figure 1 shows the in vivo experimental setup and the heating profiles. Applying a DC magnetic field to a murine right lymph node for 30 minutes induces magnetic anisotropy (Fig. 1(a)). Under a 250 kHz AC magnetic field, this targeted lymph node exhibited significantly enhanced heating efficiency compared to the left lymph node (Fig. 1(b)). To quantitatively validate the magnetic anisotropy, Figure 2 presents the magnetic torque and M-H curves of the biological tissue. Although the formation of anisotropy can be confirmed from the torque measurements of the nanoparticles within the biological tissue (Fig. 2(a)), it cannot be clearly confirmed from the M-H curves (Fig. 2(b)). In contrast, the in vitro epoxy phantom demonstrates pronounced anisotropy formation in both torque measurements and M-H curve observations (Figs. 2(c) and (d)). These results suggest that in vivo magnetic anisotropy behaves similarly to the anisotropy of polycrystalline magnetic materials, owing to the complex structure of the lymph node. This work provides a vital step toward the early clinical implementation of magnetic hyperthermia in practical oncological applications.

[1] H. Fatima *et al.*, *Nanomaterials 11*, 1203 (2021).
[2] A. Kuwahata *et al.*, Sci. Rep 15, 41933 (2025)
[3] Y. Adachi *et al.*, AIP Advances 14, 015144 (2024).
[4] G. Shi *et al.*, *J Magn Magn Mater*, 473, 148 (2019).

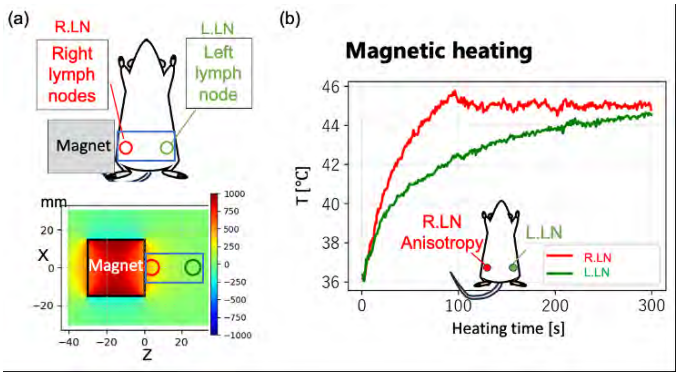


Fig. 1. In vivo induction of magnetic anisotropy. (a) Experimental setup in a murine model, targeting the right lymph node. (b) Magnetic hyperthermia heating profiles, showing significantly enhanced heating efficiency in the targeted lymph node

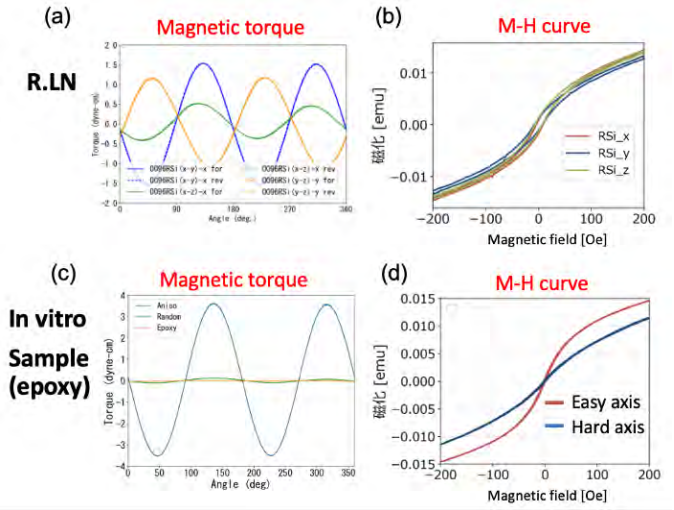


Fig. 2. Quantitative characterization of magnetic anisotropy. (a, b) Magnetic torque and M-H curves of the right lymph node. (c, d) Comparative magnetic torque and M-H curves of an in vitro phantom (epoxy resin)

ER-13. Magnetoencephalographic Correlates of Selective Attention during a Dichotic Listening Task Using Meaningless Words

K. Miyajima, K. Tanaka
Gladuate School of Science and Engineering, Tokyo Denki University, Hotoyama-cho, Japan

Humans can selectively attend to specific sounds of interest even in noisy environments. Although the dichotic listening test is a well-known method for evaluating this selective attention, the detailed relationship between listening performance and the underlying cortical mechanisms of attentional remains unclear. Magnetoencephalography (MEG) offers a non-invasive means to capture the neuromagnetic activity associated with auditory attention at high temporal resolution. In this study, we investigated the magnetic brain responses elicited during selective attention and aimed to quantitatively evaluate attentional function by combining a dichotic listening task using meaningless words with concurrent MEG recording.
Seventeen healthy participants with normal hearing were enrolled. In each trial, two different two-syllable meaningless words were presented simultaneously to the left and right ears, and participants were instructed in advance to attend to either the left ear and or the right ear and to report the word perceived at the attended side. To isolate the cortical magnetic activity driven by each ear, the stimuli were amplitude-modulated to elicit auditory steady-state responses (ASSRs) via frequency tagging. The assignment of modulation frequencies was counterbalanced across sessions: one session used 35 Hz for the left ear and 45 Hz for the right ear, and the other used the reverse assignment. Neuromagnetic responses were recorded with a whole-head MEG system, and ear-specific ASSR amplitudes were extracted in the sensor space.
We then analyzed the correlation between the mean ASSR magnetic amplitude and the response accuracy rate. The accuracy rate for the right ear was significantly higher than that for the left ear, reproducing (the right-ear advantage). Moreover, a significant negative correlation was observed between the mean ASSR amplitude and the accuracy rate in the right-ear attention condition, indicating that higher accuracy was accompanied by lower neuromagnetic ASSR amplitude. These findings suggest that a higher accuracy rate reflects a reduced attentional load, and that MEG-based ASSRs may serve as a quantitative neuromagnetic marker of selective attention.

ER-14. Remote Induction of Lung Cancer Cell Death via Magnetically Responsive Nanocarriers and Targeted Drug Release

A. A. Abdou[1, 2], M. Elabbasi[1, 2], M. A. Garcia[1], S. Dasari[3], A. El-Gendy[1]
[1]Physics, University of Texas at El Paso, El Paso, Texas, United States, [2]Environmental Science and Engineering, University of Texas at El Paso, El Paso, Texas, United States, [3]Metallurgical, Materials and Biomedical Engineering, University of Texas at El Paso, El Paso, Texas, United States

Overcoming cancer resistance to traditional therapies remains a major challenge. The use of magnetic responsive nanoplatforms has emerged as a promising tool for cancer treatment through magnetic hyperthermia and targeted drug delivery. In this study, we developed a new method for synthesizing a multifunctional nanocomposite with superparamagnetic properties, characterized by very low coercivity and very high saturation magnetization. These magnetic features enhance biocompatibility and enable efficient interaction with external magnetic fields, promoting heat generation through Néel and Brownian relaxation mechanisms. The nanocomposite consists of graphene oxide (GO) decorated with zero-valent iron nanoparticles and loaded with doxorubicin as an anticancer drug, providing a dual mechanism of magnetic hyperthermia and targeted drug delivery. Structural and morphological analyses (XRD, SEM) confirmed the successful incorporation

of highly pure, spherical Fe nanoparticles (~85 nm) onto the GO sheets. Vibrating sample magnetometry (VSM) demonstrated superparamagnetic behavior with a high saturation magnetization of 159 emu/g, indicating strong magnetic responsiveness. The nanocomposite also exhibited a high doxorubicin loading efficiency (up to 97%) and capacity (~1 mg DOX per mg Fe/GO), facilitated by π−π stacking interactions, as confirmed by UV−Vis spectroscopy. Under an alternating magnetic field (304 kHz, 100−400 Oe), the Fe/GO nanocomposite generated significant heat, achieving a specific absorption rate (SAR) of 37.2 W/g at 400 Oe, demonstrating its effective magnetic response and potential for combined hyperthermia and drug-delivery applications. In vitro studies on A549 human lung adenocarcinoma cells demonstrated effective internalization of the nanocomposite, biocompatibility of Fe/GO, and enhanced cytotoxicity of Fe/GO and Fe/GO-DOX under low magnetic field exposure achieving ~85% cellular death, confirming synergistic anti-cancer effects. These results highlight Fe/GO as a promising multifunctional nanocomposite for hyperthermia therapy combined with targeted chemotherapy, with potential for future translational cancer applications.

ER-15. Fe_xC_y Nanoparticles and their Potential for NP-mediated AMF Treatment in Liver HEP-G2 Cancerous Cell Line

H. V. Kapetan[1, 3], M. Elabbasi[1, 2], M. A. Garcia[1], R. Morales[1], S. Dasari[4], A. El-Gendy[1, 2]

[1]Physics, University of Texas at El Paso, El Paso, Texas, United States, [2]Environmental Science and Engineering, University of Texas at El Paso, El Paso, Texas, United States, [3]Biological Sciences, University of Texas at El Paso, El Paso, Texas, United States, [4]Metallurgical, Materials and Biomedical Engineering, University of Texas at El Paso, El Paso, Texas, United States

Iron-carbide nanoparticles (ICNPs) hold great promise for diagnostics and theranostics, but despite their promising properties, their medical applications remain significantly understudied. This study focuses on synthesizing Iron Carbide magnetic nanoparticles for targeted alternating magnetic field (AMF) cancer treatment on HEP-G2 liver cancer cells.

Using a solvothermal method, various iron to carbon ratios were used to synthesize ICNPs. Morphological analysis of magnetic nanoparticles was completed using X-Ray Diffraction (XRD), Scanning Electron Microscopy (SEM), Transmission Electron Microscopy (TEM) and Vibrating Sample Magnetometry (VSM). Magnetic saturation (Ms) values were obtained up to 129.72 emu/g, with the average size distribution (SD) ranging from 35-154 nm. Various phases of ICNPs were revealed through XRD analysis, including θ-Fe_3C, h-Fe_5C_7, and o-Fe_7C_3, which correspond to the Fe:C ratios and were validated by TEM. Heating power of magnetic nanoparticles (MNPs) was established using an AC magnetic field to determine the specific absorption rate (SAR). Confocal microscopy and flow cytometry verified NP internalization and measured cell viability. A considerable 48% reduction in cell viability was observed in HEP-G2 cells after implementing an AMF, which demonstrates a viable pathway for ICNPs to be used for biomedical applications, such as AMF-mediated nanoparticle treatments. Collectively, our results establish iron carbide nanoparticles as a viable platform for AMF-mediated nanoparticle cancer therapy and broader biomedical applications.

SESSION FA: INTEGRATED MAGNETICS FOR POWER DISTRIBUTION IN NEXT-GEN CHIPS AND DEVICES

Chair(s): S. Oberdick, *National Institute of Standards and Technology, Boulder, Colorado, United States*

Thursday, November 5, 2026

02:00 PM-05:30 PM

Coral 3

FA-01. The PwrSOC Vision: Performance Needs and Knowledge Gaps for Inductors and Transformers in Power Supplies On Chip

A. Hanson

University of Texas at Austin, Austin, Texas, United States

The power electronics community has long dreamed of achieving the level of integration enjoyed by digital, analog, and rf circuits, namely power supply on chip (PwrSOC) or power supply in package (PwrSIP). This long-running vision has only accelerated over time, with a recent explosion of interest with the rise of AI, ultra-dense computing, and the need for the final stage of power delivery to be placed much closer to the computational and memory elements.

This PwrSOC vision has faced many challenges, perhaps none more acute than the integration of inductive components (inductors and transformers). Small size, extreme aspect ratios, and the need for high-quality and BEOL-compatible materials make for a difficult and interconnected set of constraints. The kinds of inductors dictated by these requirements imply the need for very high converter operating frequencies, which adds to the challenge of developing good core materials.

This talk will introduce the historical and the modern AI-driven need for PwrSOC and integrated inductive components. We will explore (and address misunderstandings) about the needs of yet-to-be-developed core materials and deposition methods. We will further show some recent advancements in material development and long-standing characterization challenges which are opening up a more promising future for PwrSOC.

FA-02. Iron based nanocomposites for superparamagnetic inductor cores

E. F. Scott, R. Delaney, T. Della Cerra, M. Landi, S. Gilbert, T. C. Monson

Sandia National Labs, Albuquerque, New Mexico, United States

Microelectronic power converters require high frequency operation in order to reduce device size. However, these high frequencies then lead to large core losses and low efficiency within the inductor core. At present, most inductors utilize alloys of critical materials such as nickel or cobalt in order to maintain high efficiency. This research presents results on an alternative material, sputtered granular metal iron silicon nitride (Fe-SiN_x). Iron, a more abundant, non-critical material, should present superparamagnetic behavior in a nanoparticle form. In this work, Fe-SiN_x films are fabricated via thin film sputtering to create discrete metallic Fe nanoparticles embedded in an electrically insulating SiN_x matrix. By utilizing this fabrication method, Fe-SiN_x granular metals have the potential to create a superparamagnetic, highly insulating inductor core. Here we present results on the effects of sputtering conditions and annealing on the magnetic, electrical, and structural properties of this material.
Acknowledgment: Supported by the LDRD Program at Sandia National Laboratories. Sandia is managed and operated by NTESS under DOE NNSA contract DE-NA0003525

FA-03. Engineering Low Permeability in Zr-CoFeB Thin Films for High-Frequency Integrated Magnetics

M. Mancias A.[1], N. M. Bruno[2], A. Leary[2], K. Chinnathambi[3], R. D. Noebe[2], K. Srinivasan[1]

[1]Electrical and Computer Engineering, Boise State University, Boise, Idaho, United States, [2]Materials and Structures Division, NASA Glenn Research Center, Cleveland, Ohio, United States, [3]Boise State Center for Materials Characterization, Boise State University, Boise, Idaho, United States

With an increasing demand for emission reduction, electric aircraft and transportation emerge as promising solutions. Thus, there is a need for compact power conversion components (inductors/transformers) that maintain high power density. Low-permeability soft magnetic materials provide a promising pathway, as reduced permeability enables smaller devices while supporting higher drive currents and improved energy storage control [1]. Despite prior efforts to engineer low-permeability materials via

thermo-magnetic (or -mechanical) processing, these approaches are sorted across composition optimization, processing, and performance. Moreover, prior work has predominantly focused on ribbon-based systems, leaving thin film frameworks relatively unexplored.

In this work, we study Zr-CoFeB thin films as a platform for low-permeability soft magnets. CoFeB serves as base soft magnetic alloy with low coercivity and high saturation magnetization, while Zr doping enables increased crystallization temperatures needed for handling higher thermal loads in a smaller form factor [2]. Thin films were sputtered using $Co_{60}Fe_{20}B_{20}$ and high-purity Zr targets. Structural and magnetic properties were measured using X-ray diffraction (XRD), vibrating sample magnetometry (VSM), and magneto-optical Kerr effect (MOKE) imaging. Systematic Zr concentration variation and post-deposition field annealing under inert atmosphere was used to tune effective permeability. VSM results indicate that Zr doping, lower than 5 at.%, does not degrade soft magnetic behavior, seen in Fig.1. Furthermore, field annealing at temperatures as low as 150°C under a 400 Oe field induces an in-plane uniaxial anisotropy with distinct easy and hard axes, see Fig. 2. These results suggest that controlled annealing-driven domain reorientation provides a viable means for tailoring permeability in thin films. Further research using cross-section TEM and MOKE elucidates the relationship between microstructure and induced anisotropy.

[1] A. Leary *et al.*, *J. Mater. Res.*, vol. 31, no. 20, pp. 3089–3107 (2016)

[2] A. Leary, P. R. Ohodnicki, and M. McHenry, *J. Miner.*, vol. 64 (2012)

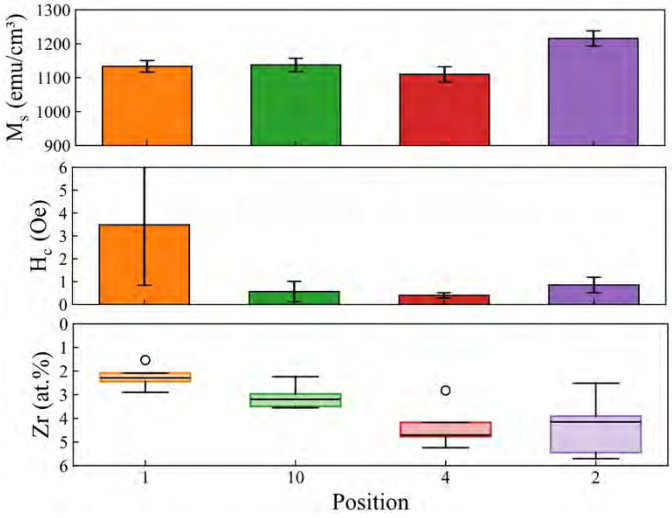


Fig. 1 Saturation mag., coercivity, and Zr concentration across batches. Positions assigned by location in sputtering chamber.

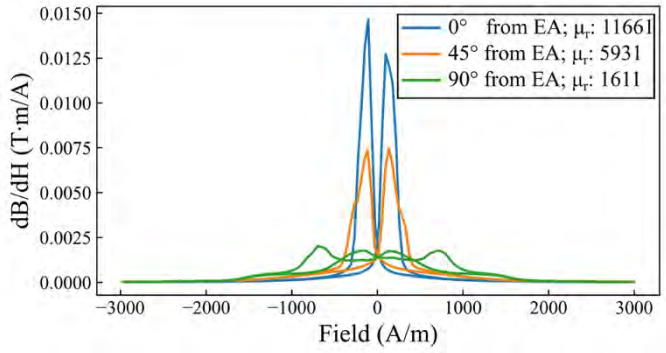


Fig. 2 Differential permeability of field annealed (at 150 °C) Zr-CoFeB sample as a function of angle from easy axis (EA).

FA-04. Heterogeneously Integrated Magnetic Technologies to Power the AI Revolution

C. O'Mathuna[1, 2]

[1]Tyndall National Institute, Cork, Ireland, [2]University College Cork, Cork, Ireland

The next industrial revolution is upon us with AI driving dramatic increases in current density at the processor-level – from today's 2 Amps/mm2 to the expectation of 10 Amps/mm2 over the coming years with processor current expected to reach 10,000 Amps being delivered into a processor with approximate dimensions of 30 x 30 mm2. This dramatic increase in current delivery has driven the move from the traditional, lateral Point-of-Load (POL) dc-dc converter to vertically-integrated power delivery under the processor in order to minimise losses in the power delivery network. This has been enabled by the minimization of converter output inductance, and the associated miniaturisation of bulky wire-wound inductors, through the implementation of integrated voltage regulators operating at frequencies from 25 to 100MHz and higher.

This presentation will introduce the challenges being presented by this AI revolution and will discuss the range of inductor technologies being considered for vertically integrated power converters. These include, among others, thin-film, magnetics-on-silicon (MagIC), electroplated magnetics, soft-magnetic composites embedded in PCB and ultra-thin, discrete chip inductors. These various technologies will be introduced and, where possible, their relative performance will be discussed

The presentation will conclude with a discussion of the considerations in the selection of a suitable inductor technology for vertical power is how the component and its

associated technology can be effectively heterogeneously integrated, initially with other power components such as PMIC and capacitors and then with the processor load and its associated 2.5D or 3D packaging technology. Among other solutions, an example will be presented from the EU Chips Act FAMES Pilot Line, in which Tyndall is collaborating with CEA Leti, Grenoble, France to demonstrate micro transfer printing (MTP) of a PMIC and inductor on silicon on top of a high-density trench capacitor interposer.

FA-05. On–Silicon Coupled–Stripline Micro–Inductors Featuring Laminated CoZrTa/AlN Magnetic Cores and Vias for High-Frequency Power-Supply-on-Chip

A. Tanwar, A. Masood, L. Ye, I. Efimenkov, C. O'Mathuna, R. Sai, S. Khan
Tyndall National Institute, Cork, Cork, Ireland

Meeting transient and density demands due to servers and AI accelerators in on–chip power delivery demand magnetic-core micro-inductors operating efficiently at 10–100 MHz [1, 2]. NiFe-based thin-film cores suffer prohibitive eddy and hysteretic losses above a few MHz [3], and CoNiFe laminates extend this only to ~10 MHz [4]. Amorphous Co–based alloys (CoZrTa, CoZrTaB) uniquely combine high resistivity (ρ∼100 μΩ cm), high permeability (μ'>400), tunable in-plane uniaxial anisotropy, low magnetostriction, and CMOS-BEOL thermal stability – an ideal profile for high-frequency integrated magnetics [5, 6].
We report a CMOS-BEOL-compatible coupled-stripline micro-inductor with an amorphous CoZrTa(250 nm)/AlN(20 nm) laminated core and engineered magnetic vias that vertically stitch the top and bottom laminates, closing the flux path. Two Cu conductors (1500×30 μm^2, 17 μm spacing) are embedded in photosensitive BCB inter-layer-dielectric (ILD) (Figs. 1, 2). A reflowed BCB sidewall (~66–70°) enables conformal sputtering of the top laminate and seamless via formation (Fig. 3), yielding a fully enclosed magnetic circuit. The AlN spacer thickness is kept below the skin depth to break eddy-current loops while preserving μ'≈400 across 10–100 MHz. In-plane anisotropy is induced during reactive sputtering under an in-situ magnetic field, aligning the hard axis with the stripline flux direction to maximize transverse permeability.
VNA measurements (1 MHz–1 GHz) yield L≈9 nH per stripline (within ±10% up to 100 MHz), Q≈3, and coupling coefficient k>0.65 in the low-to-mid MHz range (Fig. 4). Yield exceeds 90% on 100-mm wafers. The closed-flux magnetic-via architecture boosts inductance density and flux linkage; permeability extends to ~1.1 GHz, enabling robust 10–100 MHz operation for next-generation Power-Supply-on-Chip (PwrSoC).

[1] C. R. Sullivan et al., IEEE Trans. Power Electron., 28 (2013), pp. 4342–4353.
[2] N. Sturcken et al., IEEE J. Solid-State Circuits, 48 (2013), pp. 244–254.
[3] W. Xu, et al., IEEE Elec. Dev. Lett., 32 (2011), pp. 69-71
[4] J. Kim et al., J. Phys. D: Appl. Phys., 48 (2015), 462001.
[5] W. J. Lambert et al., IEEE Trans. Power Elec., 35 (2020), pp. 6208–6220.
[6] G. Wei et al., IEEE Trans. Magn., 59 (2023), pp. 1-4.

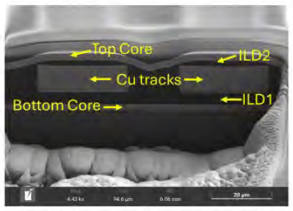


Figure 1: Cross-section of the closed-core coupled-stripline inductor: laminated CoZrTa/AlN cores, Cu conductors, BCB ILDs, and magnetic vias.


Figure 2: Optical micrograph of the fabricated device with exposed pads.

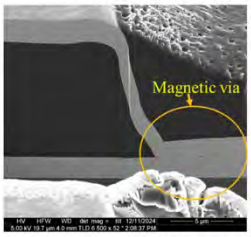


Figure 3: Cross-sectional SEM showing top/bottom laminates, engineered sidewall, and continuous magnetic via.

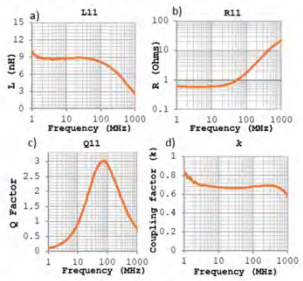


Figure 4: Measured L, R, Q, mutual inductance, and k from 1 MHz–1 GHz.

FA-07. An Electroplating Path to On-Chip MHz Magnetics for Vertical Power Delivery

T. Liakopoulos, M. Khodadadi, K. Ahmadi
Eneira, Hillsborough, New Jersey, United States

As power delivery architectures for AI and high-performance computing move decisively toward vertical integration and MHz-range switching, the magnetic component has emerged as the critical bottleneck. The industry needs inductors and transformers that simultaneously provide low winding resistance for high current capability, low magnetic loss, high saturation flux density, and wafer-compatible integration within a sub-millimeter profile, yet the magnetic materials available today were not designed with these constraints in mind.
The fundamental issue of useful wafer-level magnetics is a materials trade-off that has long been considered unavoidable. On one hand, electrodeposited allo ys offer the

process compatibility and throughput that semiconductor manufacturing demands, but their inherently low electrical resistivity forces reliance on thin, multiply-laminated core structures to control eddy current losses at high frequencies, making this not a viable solution. On the other hand, vacuum-deposited multilayers and nanocomposites can improve resistivity and high-frequency response, but deposition rates and achievable film thickness limit the core cross-section area needed to meet the integrated magnetic device inductance and saturation requirements. Neither path scales well to the current density and frequency requirements that advanced 3D heterogeneous integration now demands.

This talk argues that the way forward lies in re-engineering the electrodeposited alloy itself. By combining high saturation flux density with substantially elevated electrical resistivity through controlled compositional modulation along the film's z-axis, it becomes possible to deposit magnetic cores at practically useful thicknesses with far fewer laminations, using a single-mask electroplating process with no vacuum steps. The winding conductor is an equally important consideration. Conventional interconnect-scale copper imposes hard limits on current carrying capacity and winding density, constraints that grow more severe as die-level current demands increase. Ultra-thick electroplated copper, exceeding 100 µm in thickness, lifts both limits simultaneously, enabling higher per-area current handling and tighter winding pitch, which raises the air-core inductance contribution, increasing the L/R ratio by an order of magnitude, thus reducing the burden placed on the magnetic core material. Together, the re-engineered magnetic alloy and the ultra-thick copper winding yield integrated magnetics with the energy density and current handling that vertical power delivery requires, through a process that is fully compatible with wafer-scale electroplating infrastructure.

Measured device results demonstrate an L/R ratio of 4,000 nH/Ω, a volumetric energy density of 1,200 nJ/mm3, and a current density of 40 A/mm3, across a frequency range of 1 to 30 MHz, all within a 200 µm total device profile compatible with BEOL processes on silicon, GaN, and flexible substrates. The talk will discuss design trade-offs for different device configurations and process capabilities. More broadly, these results point to electrodeposition as an underexplored platform for high-performance magnetic materials, one that merits renewed attention as the demands of integrated power delivery continue to intensify. With the right alloy engineering, electroplating can deliver the combination of high saturation, high resistivity, and manufacturing scalability that the industry needs, and may represent the most practical path toward integrated magnetics becoming a standard element of advanced power delivery platforms.

FA-08. Effect of magnetic viscosity on iron loss under triangular waves via precise iron loss measurements

T. Taniguchi[1], Y. Uehara[2], S. Okamoto[1, 3, 4]
[1]Tohoku University, Sendai, Japan, [2]Magnetic Device Laboratory, Kawasaki, Japan, [3]National Institute for Materials Science, Tsukuba, Japan, [4]Center for Science and Innovation in Spintronics, Sendai, Japan

Soft magnetic materials are used as magnetic passive components in power electronic devices: such as transformers, reactors, and inductors. One of typical technologies used in power electronic devices is pulse width modulation (PWM). PWM utilizes a train of triangular waves of current for the conversion, and therefore, it is essentially important to understand what iron loss is generated under triangular waves. In the present work, we studied mechanism of iron loss under triangular waves, using partial cancellation method [1] with our original improvement.

We used a Sendust toroidal powder core (coreA) and a Ni-Zn ferrite toroidal core (coreB). These cores have a dimension of (inner diameter, outer diameter, height) = (8, 13, 6) and (7.1, 12.7, 4.75) in mm, and their permeability is 33 and 40, respectively. As shown in Fig.1, we obtained well shaped triangular waveforms as designed to the arbitrary waveform generator. As a consequence, we observed that iron loss reduction in coreA by about 10% when the frequency was below 100 kHz. In contrast, coreB showed almost the same iron loss between the sine and triangular waves with frequencies below 10 kHz, and a large reduction occurred when the excitation frequency was 100 kHz. To further discuss the origin of the iron loss reduction, we measured iron loss under trapezoidal waves.

We varied the waiting time of trapezoidal waves, t_1, but held the constant raising and falling speed of the current. As a result, we obtained the relaxation time of each sample: 3 µs for coreA and 10 µs for coreB (Fig. 2). It indicates that the distortion on iron loss can occur when the classical eddy current loss is generated and the frequency is close to the relaxation time, explaining the large distortion at 100 kHz. The relaxation time is so-called magnetic viscosity, and its physical origin was intensively discussed more than decades ago [2-6]. In the presentation, we will discuss possible mechanisms of relaxation time, which strongly affects the

distortion in iron loss.
[1] D. Hou et al., IEEE Trans. Power Electron. 32, 2987 (2017). [2] R. Street and J. C. Woolley, Proc. Phys. Soc. A 62, 562 (1949). [3] R. Street and J. C. Woolley, Proc. Phys. Soc. B 63, 509 (1950). [4] L. Neel, J. de Phys. Rad. 13, 249 (1952). [5] K. Ota, J. Phys. Soc. Jpn. 16 (1961). [6] K. Ohta and T. Yamadaya, J. Phys. Soc. Jpn. 17, 291S BII (1962).

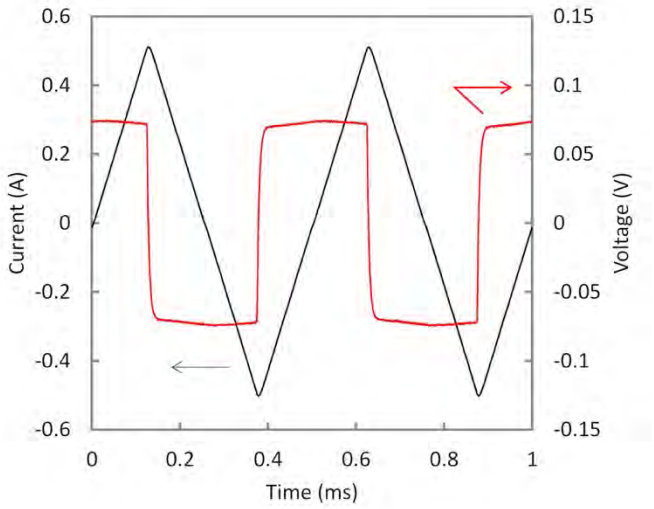


Figure 1. Typical waveform of triangular currents and generated voltages.

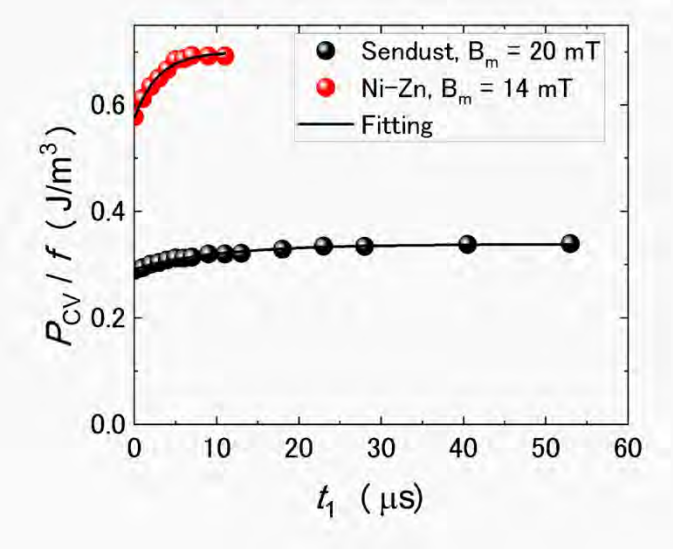


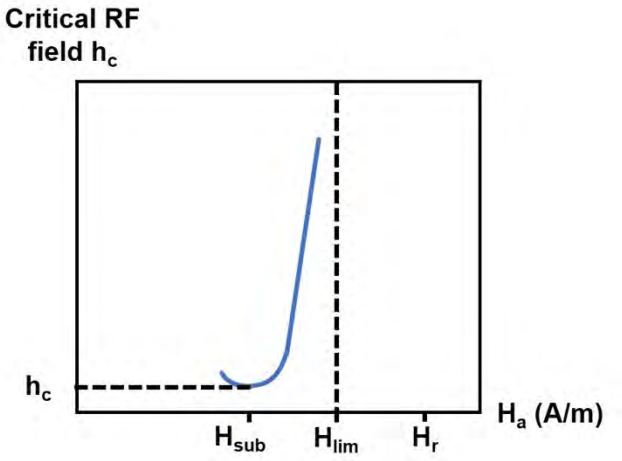
Figure 2. Iron loss as a function of the waiting time t_1.

FA-09. Spinwave linewidth measurement ΔH_k of high-permittivity garnet ferrites

M. Legay[1], R. Lebourgeois[2], R. Mansour[2], D. Caban-Chastas[1], V. Laur[3]
[1]Thales DMS, Elancourt, France, [2]Thales Research and Technology, Palaiseau, France, [3]Lab-Sticc/University of Brest, Brest, France

One promising strategy for miniaturization of microwave components such as circulators, is to increase the dielectric permittivity of the ferrite. This study is focused on garnet ferrites, specifically $Y_3Fe_5O_{12}$ (YIG) with a permittivity ε=15. The substition of yttrium by bismuth, is known to increase ε, but it increases lattice parameter so decreases M_s. This reduction was compensated for by the incorporation of tin ions in place of iron in octahedral sites. In addition, calcium ions were added to balance electrical charges and also to stabilize the structure [1]. The final substituted ferrite $Y_{3-x-y}Bi_xCa_yFe_{4.95-z}Cu_{0.05}Sn_zO_{12}$ has a permittivity of ε=30.
However, the power handling of these synthesized materials, represented by the spinwave linewidth ΔH_k, is unknown and could be a relevant parameter for power applications.
The power threshold of ferrites is reached at a critical RF magnetic field h_c colinear to an applied static magnetic field H_a, where nonlinear spin-wave phenomena arise, leading to additional magnetic losses that rapidly become prohibitive in our devices [2]. These nonlinear effects generally occur at H_a lower than the gyromagnetic field H_r, and at a certain H_a called subsidiary field H_{sub}, a minimum h_c can be observed (Fig. 1) and is directly correlated to the spinwave linewidth ΔH_k with the equation: $\Delta H_k = h_c.\gamma 4\pi M_s/f$ with h_c critical field; γ=2,8 MHz/Oe: gyromanetic ratio
The measurement bench consists of a ferrite ball placed in a sapphire resonator focusing the RF field. This resonator, resonating at 9.7 GHz, is placed in an electromagnet, where a controlled static magnetic field is applied colinearly to a pulsed RF signal. By varying H_a around 0,5 x H_r where subsidiary resonance is expected to occur, the incident and transmitted powers, Pi and Pt, are measured. By plotting the curve P_i(dBm) – P_t(dBm) as a function of P_i(dBm), the onset of a slope change indicates that the minimum critical field has been reached.
These measurements were performed with the synthetized high permittivity garnet material and showed ΔH_k=11Oe much higher than pure YIG ΔHk=1.5Oe showing that these new materials could be used for high power applications.
[1] R.Lebourgeois, G.Cibien , "Yttrium Iron Garnet , microwave omponent including said ferrite and processes

for manufacturing said ferrite and said component" , Patent of Invention, Publication number : EP2622613 (2011)
[2] H. Suhl, "The non linear behaviour of ferrites at high microwave signal levels", proc. Of the IRE, p.1270-1284 (1956)



Critical field as a function of applied static field

SESSION FB: NEW TRENDS IN MAGNONICS: ENGINEERED NONEQUILIBRIUM DYNAMICS IN MAGNETIC SYSTEMS

Chair(s): S. Wintz, *Helmholtz-Zentrum Berlin für Materialien und Energie, Berlin, Germany*

Thursday, November 5, 2026
02:00 PM-05:30 PM
Coral 5

FB-01. Squeezing thermal fluctuation of magnons

T. Hioki[1, 2, 3], K. Tojo[1], M. Elyasi[2], S. Horibe[1], K. Hoshi[2], T. Makiuchi[3], G. Bauer[2, 4, 5], E. Saitoh[1, 3, 2]
[1]Department of Applied Physics, The University of Tokyo, Tokyo, Japan, [2]Advanced Institute for Materials Research, Tohoku University, Tokyo, Japan, [3]Center for Emergent Matter Science, RIKEN, Wako, Japan, [4]Institute for Materials Research, Tohoku University, Sendai, Japan, [5]Kavli Institute for Theoretical Science, University of Chinese Academy of Science, Beijing, Japan

Squeezing is a fundamental concept in modern physics, describing the redistribution of fluctuations between a pair of conjugate variables such that noise is reduced in one quadrature at the expense of enhancement in the other. Quantum squeezing, in which vacuum fluctuations are suppressed, has played a pivotal role in gravitational-wave detection and constitutes a key resource for the generation of quantum entanglement. Thermal squeezing extends this concept into the domain of thermal fluctuations, where it offers not only enhanced sensitivity for metrology but also a route toward engineered nonequilibrium states capable of surpassing classical thermodynamic limitations. Through the redistribution of thermal noise across physical variables, it may become possible to realize fundamentally new modes of energy conversion and information thermodynamics. Achieving squeezing in magnetic systems would therefore mark a major conceptual and technological advance for magnonics. Because magnons can hybridize and exchange energy with other elementary excitations, including photons and phonons, they provide a compelling basis for quantum transducers and engineered nonequilibrium reservoirs. Furthermore, their remarkably short wavelengths relative to microwaves of the same frequency make them well suited to miniaturized architectures, raising the prospect of ultracompact platforms for quantum information processing. To bring squeezing into the realm of magnetic excitations, one must not only invoke parametric excitation as a nonlinear driving mechanism, but also resolve the subthreshold fluctuations from which squeezed dynamics emerge. Although parametric excitation of magnons has long stood as a cornerstone of contemporary magnonics and has been widely studied through microwave and optical probes, thermal squeezing of magnons itself had remained beyond experimental reach. The principal obstacle has been the lack of a measurement framework capable of reading out magnon fluctuations in a genuinely phase-resolved manner.

Motivated by this challenge, we investigated the generation and readout of thermally squeezed magnon states. We developed state-tomography technique that reconstructs the Wigner function, a quasi-probability distribution in phase space that makes visible the fluctuation landscape of driven magnetization dynamics, and applied it to low-loss yttrium iron garnet (YIG), thin films prepared by liquid-phase epitaxy. Through this approach, we found that parametric excitation can generate thermally squeezed states in magnetic films.

We further uncovered correlated fluctuations between magnons localized on the top and bottom of the film with micrometer-scale distances by taking advantage of their nonreciprocal propagation. These correlations arise from a parametric down-conversion process, a central mechanism by which entanglement is generated in many other quantum platforms. Although the present observations do not yet constitute a direct demonstration of magnon entanglement, they identify the essential physical basis upon which

entangled magnon states may ultimately be engineered in magnetic media.

The establishment of thermal squeezing in magnetic systems provides access to a previously unexplored aspect of the fluctuation dynamics of magnetic order and represents a major step toward the observation of quantum effects in magnetic films. At a broader level, these results suggest that magnetic materials, long valued as a core platform of condensed matter physics and spintronics, may also serve as a new frontier for quantum science and technology. By elucidating the principles for the generation, control, and readout of nonclassical magnon dynamics, this work helps define the foundations of an emerging discipline: quantum spintronics.

[1] T. Hioki, H. Shimizu, T. Makiuchi, and E. Saitoh, "State tomography for magnetization dynamics", Phys. Rev. B 104, L100419 (2021).

[2] T. Makiuchi, T. Hioki, H. Shimizu, K. Hoshi, M. Elyasi, K. Yamamoto, N. Yokoi, A. A. Serga, B. Hillebrands, G.E.W. Bauer and E. Saitoh, "Persistent magnetic coherence in magnets", Nature Materials 23, 627–632 (2024).

[3] T. Hioki, K. Tojo, M. Elyasi, S. Horibe, H. Shimizu, K. Hoshi, T. Makiuchi, G.E.W. Bauer and E. Saitoh, "Single- and two-mode magnon thermal squeezing", Nature Physics (Accepted).

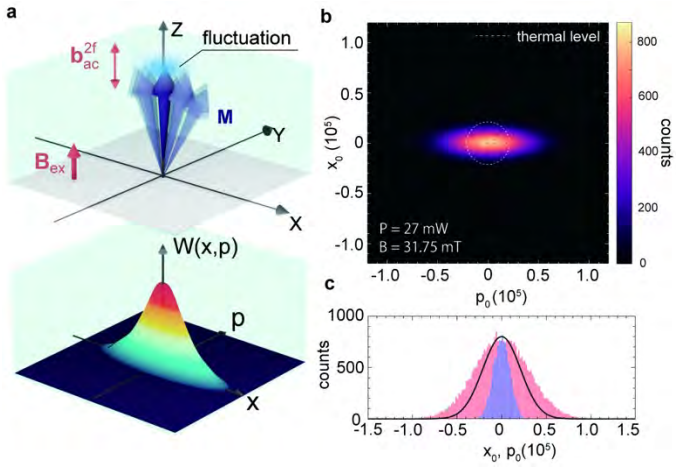


Fig.1 Thermal squeezing of magnons, a. Schematic of thermal squeezing of magnons, b. Wigner function plot of thermally squeezed magnons compared with thermal noise level, c. Bar plot of Wigner function.

FB-02. Magnonic spontaneous oscillation induced by parametric pumping [1]

Y. Li[1], C. Kiehl[2], J. Lim[3], C. Abbott[4], P. K. Pal[1, 3], A. Szymczak[1, 3], J. Li[5], R. Divan[6], C. L. Chang[5], C. Phatak[1], D. A. Bozhko[4], A. Hoffmann[3], V. Novosad[1]

[1]Materials Science Division, Argonne National Laboratory, Lemont, Illinois, United States, [2]Carthage College, Kenosha, Wisconsin, United States, [3]Materials Science Engineering, University of Illinois at Urbana Champaign, Urbana, Illinois, United States, [4]Department of Physics and Energy Science, University of Colorado Colorado Springs, Colorado Spring, Colorado, United States, [5]High Energy Physics, Argonne National Laboratory, Lemont, Illinois, United States, [6]Center for Nanoscale Materials, Argonne National Laboratory, Lemont, Illinois, United States

Spontaneous dynamic systems have attracted significant attention for their rich underlying physics such as phase-locking and synchronization. Particularly, this effect has been cultivated in spintronics through spin torque oscillators, holding great promise in next-generation microelectronics, wireless communication, neuromorphic computing, and unconventional computing. Besides damping compensation, another key mechanism for inducing spontaneous oscillation is parametric excitation. In magnonics, parametric excitation has led to rich nonlinear behaviors primarily via three-wave or four-wave mixing process. Nevertheless, the generated magnons usually span over a broad frequency range similar to thermal magnons, or follow irregular wavenumber-selecting process, leading to lack of controllability and reproducibility for applications.

In this work, we report a new mechanism of generating magnetic spontaneous oscillation via parametric pumping [2]. By applying a pump tone to excite propagating spin waves in a yttrium iron garnet delay line, four-wave mixing converts the pump mode into two phase-autonomous propagating magnon modes, i.e. a spontaneous mode with nearly twice the wavenumber of the pump mode and an idler mode with nearly zero wavenumber. This allows us to reliably generate ultrasharp spin wave dynamics with broad frequency tunability from the pump and magnetic field. We show that the spontaneous mode can be phase-locked to a probe tone, similar to an auto-oscillator. Furthermore, the spontaneous dynamics can be used to implement a high-gain magnonic parametric amplifier with a gain up to 40 dB. Our results open a new avenue for studying nonlinear magnonics and synchronization physics in propagating magnon geometry and for developing new magnonic

devices.
[1] All the experimental works, including sample preparation, microwave characterization, and data analysis, are supported by the U.S. DOE, Office of Science, Basic Energy Sciences, Materials Sciences and Engineering Division under contract No. DE-SC0022060. The lithographic patterning and fabrication of the YIG delay line performed at the Center for Nanoscale Materials, a U.S. Department of Energy Office of Science User Facility, was supported by the U.S. DOE, Office of Basic Energy Sciences, under Contract No. DE-AC02-06CH11357
[2] Y. Li, et al. arxiv:2602.13608

FB-03. Nonlinear Conversion of Coherent Magnonics in Canted Antiferromagnets

R. V. Mikhaylovskiy
Physics, Lancaster University, Lancaster, United Kingdom

Magnonics aims to employ quanta of spin waves, magnons, to carry, transport and process information, avoiding the dissipation of energy inherent to electronics. Experiments on magnons in regular (ferro)magnets have yielded demonstrations of basic logic devices, albeit macroscopic (mm-scale) in size and operating at GHz frequencies. Recently, the spotlight has shifted towards the use of antiferromagnets, in which neighbouring spins are aligned antiparallel to each other. This alternating order leads to significantly higher spin wave propagation velocities and might enable devices operating at terahertz (trillion of hertz) clock-rates. However, the absence of the net magnetisation also makes antiferromagnets magnetically 'invisible': it is very hard to detect and influence the antiferromagnetic order. Yet, in some antiferromagnets strong spin–orbit coupling results in canting of the spins, thereby producing net magnetization. The canted antiferromagnets combine antiferromagnetic order with phenomena typical for ferromagnets and hold a great potential for spintronics and magnonics. In this way they can be identified as closely related to the recently proposed novel class of magnetic materials, called altermagnets. In my talk I will discuss a new functionality of canted antiferromagnets and altermagnets for magnonics and show that these materials facilitate mechanisms allowing to generate, detect and convert propagating magnons at the nanoscale [1-4].
References:
[1] J. Hortensius, et al. Nature Physics 17, 1001 (2021);
[2] R. Leenders and R. Mikhaylovskiy. Phys. Rev. B 107, 094423 (2023);
[3] R. Leenders, D. Afanasiev, A. Kimel, and R. Mikhaylovskiy. Nature 630, 335–339 (2024);
[4] V. Radovskaia, et al. Nature Physics (2026) https://doi.org/10.1038/s41567-026-03230-6 .

FB-04. Self-induced Floquet magnon states

C. Heins[1, 2], L. Körber[1, 3], J. Kim[4], T. Devolder[4], J. Mentink[3], A. Kákay[1], J. Fassbender[1], K. Schultheiss[1], H. Schultheiss[1]
[1]Helmholtz-Zentrum Dresden-Rossendorf, Dresden, Germany, [2]TU Dresden, Dresden, Germany, [3]Radboud University, Nijmegen, Netherlands, [4]Centre de Nanosciences et de Nanotechnologies, Université Paris-Saclay, Paris, France

Magnetic vortices (Fig. 1a) are prominent examples of topology in magnetism, exhibiting a rich set of dynamic properties. They exhibit an intricate magnon spectrum and show an eigen-resonance of the spin texture itself, the gyration of the vortex core. While there have been studies on magnon-assisted reversal of the vortex core polarity [1], the impact of the vortex core gyration on the magnon spectrum has not been addressed so far.
The fundamental modes of both excitation types are clearly separated in their resonance frequencies. While the vortex typically gyrates at a few hundred MHz (Fig. 1b), the magnon modes typically have frequencies in the lower GHz range (Figs. 1c, d). This separation enables experiments to study the temporal evolution of the magnon spectrum when the gyration of the vortex core is driven externally. Under the influence of such a periodic driving field, Floquet states emerge due to a temporal periodicity imposed on the system's ground state, much like the formation of Bloch states in the periodic potential of a crystal lattice. While Bloch states are shifted in momentum space, Floquet states are shifted in energy by multiples of the drive frequency, facilitating the design of novel properties and functionalities in condensed matter systems.
This talk presents experimental results and numerical simulations showing how the regular magnon modes in a magnetic vortex transform into novel Floquet magnon bands (Fig. 1e) when the vortex ground state is modulated in time by simultaneously driving the vortex core gyration [2]. The observed Floquet magnon states are both distinct from the well-known regular magnon modes and from the vortex gyration and represent unique excitations.
The use of an intrinsic dynamic degree of freedom as the periodic modulator, rather than an external drive, opens new avenues for Floquet engineering. Modifying the geometry to a ring structure eliminates the vortex core, suppressing self-induced dynamics, which can subsequently

be recovered through external-field control [3]. Furthermore, the hysteretic nature of the magnon-gyration coupling enables coherent control of the self-induced Floquet states via nanosecond current pulses [4].
Support by the Nanofabrication Facilities Rossendorf (NanoFaRo) at the IBC and funding from the EU Research and Innovation Programme Horizon Europe under grant agreement no. 101070290 (NIMFEIA) is gratefully acknowledged.
[1] M. Kammerer, et al. *Nature Communications*, 2, 279 (2011)
[2] C. Heins, et al. *Science* 391, 6781 (2026)
[3] C. Heins, et al. *APL* 128, 082402 (2026)
[4] C. Heins, et al. *arXiv*:2511.01577 (2025)

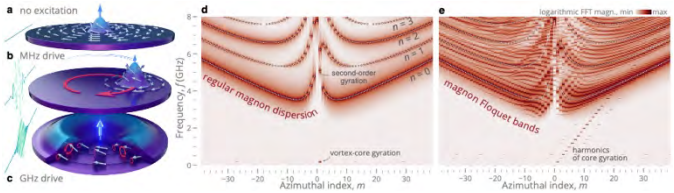


Fig. 1 Schematic illustrations of (a) a static magnetic vortex, (b) a gyrating magnetic vortex driven by a MHz microwave signal, and (c) a magnon mode with lowest radial and azimuthal mode indices (n = 0, m = 0). Dimensions are not drawn to scale. (d) Simulated dispersion of thermally populated magnon modes in the vortex with a static core plotted as a function of azimuthal mode index m for different radial indices n. (f) Micromagnetic simulations of the thermal magnon population in a gyrating vortex show the Floquet magnon bands.

FB-05. Observation of a nonlinear magnetization soliton

O. Wojewoda[1], S. Mayr[2, 3], M. J. Gross[1], J. Klima[4], J. Panda[4], J. Krcma[4], J. Holobradek[4], K. Davidkova[5], A. Chumak[5], R. V. Verba[6], P. Pirro[7], M. Weigand[8], S. Finizio[2], M. Lindner[9], C. Dubs[9], Q. Wang[10], S. Wintz[8], C. A. Ross[1], M. Urbánek[4]
[1]MIT, Cambridge, Massachusetts, United States, [2]Paul Scherrer Institut, Villigen, Switzerland, [3]ETH, Zurich, Switzerland, [4]CEITEC, Brno, Czechia, [5]University of Vienna, Vienna, Austria, [6]Institute of Magnetism, Kyiv, Ukraine, [7]Fachbereich Physik and Landesforschungszentrum OPTIMAS, Kaiserslautern, Germany, [8]Helmholtz-Zentrum-Berlin fur Materialien und Energie, Berlin, Germany, [9]INNOVENT e.V. Technologieentwicklung, Jena, Germany, [10]Huazhong University of Science and Technology, Wuhan, China

Nonlinear response is essential for computational functionality, yet realizing fast and controllable nonlinear elements in physical hardware remains a central challenge. Magnetization dynamics is a particularly attractive platform because it combines intrinsic nonlinearity, electrical accessibility, and direct compatibility with magnetic information storage [1]. Here, we investigate strongly driven magnetization dynamics in low-damping ferrimagnetic garnets with perpendicular magnetic anisotropy and demonstrate the formation of a microwave-driven nonlinear magnetization soliton. Using time-resolved micro-focused Brillouin light scattering in Bi:YIG and time-resolved scanning transmission x-ray microscopy in Ga:YIG, supported by micromagnetic simulations and modeling, we resolve three stages of the dynamics: soliton formation, emission of short-wavelength spin waves, and long-range coherent oscillations. In the in-plane magnetized geometry with perpendicular magnetic anisotropy studied here, the nonlinear frequency of the ferromagnetic resonance has positive shift [2]. Under these conditions, we do not observe direct spin-wave emission beneath the antenna, but instead the nonlinear frequency shift together with the decaying microwave field forms soliton. The soliton is spatially non-decaying and is oscillating in-phase with the driving field. When the local driving field drops below the threshold value required to sustain this state, the soliton collapses and emits short-wavelength spin waves at its boundary. Time-resolved measurements further reveal a time-dependance of the soliton formation, whereas at larger distances coherent oscillations appear without measurable delay. These results uncover a distinct regime of high-amplitude nonlinear magnetization dynamics that combines ultrafast timescales, large precession amplitudes, and nonlocal response, offering opportunities for rapid magnetic-state control and future spin-wave-based computational and signal-processing devices.
[1] P. Pirro, V.I. Vasyuchka, A. A.Serga, B. Hillebrands, Nat. Rev. Mater. 6(12), 1114–1135 (2021)
[2] Q. Wang, Q., R. Verba, O. Wojewoda, et al Sci. Adv. 9(32), 4609 (2023)

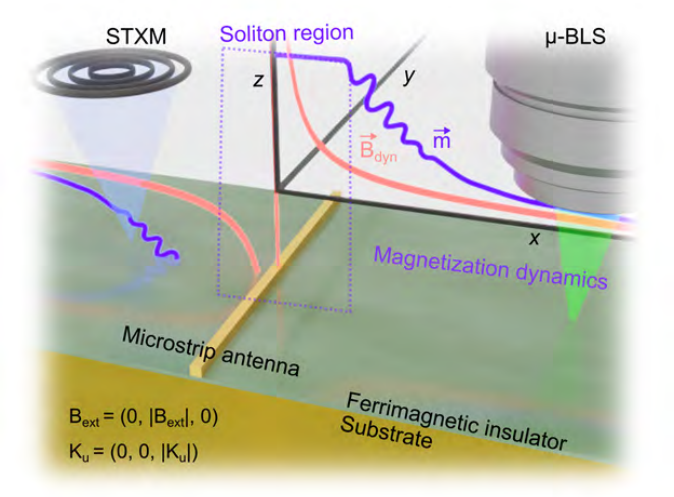


Fig. 1. Schematic picture of the nonlinear soliton formation and spin-wave emission.

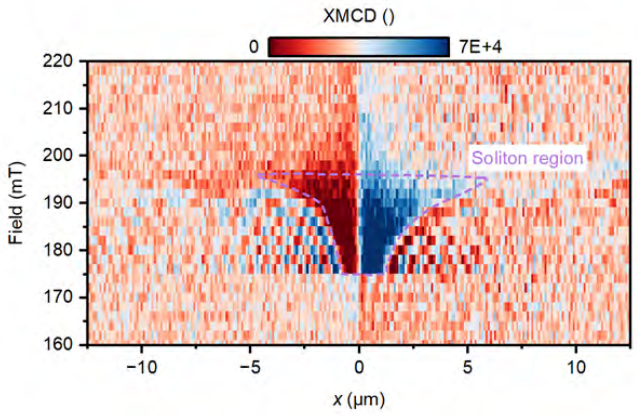


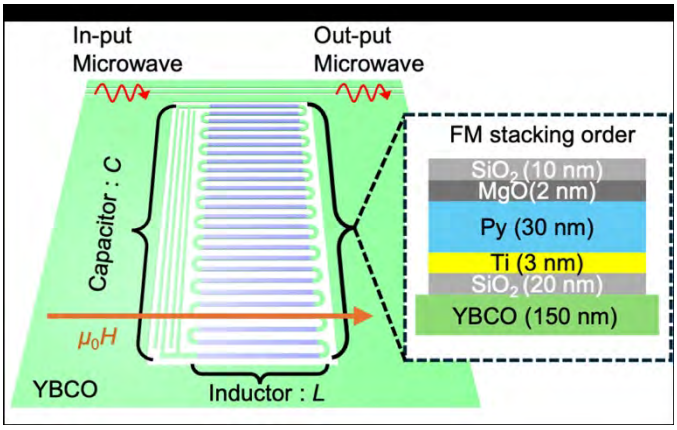
Fig. 2. Scanning transmission x-ray microscopy measurement of the soliton state and excitation of the spin waves at the soliton boundary.

FB-06. On-chip Dicke-type magnon polaritons in the ultrastrong coupling regime via spatially separated nanomagnets

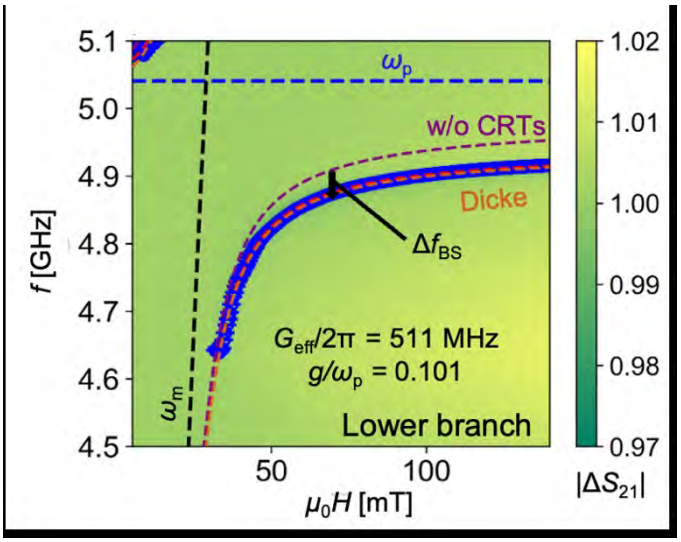
S. Yoshii[1, 2], M. Müller[3], R. Ohshima[1], Y. Ando[4], M. Althammer[3], H. Huebl[3], M. Shiraishi[1]
[1]*Department of Electronic Science and Engineering, Kyoto University, Kyoto, Japan,* [2]*Imperial College London, London, United Kingdom,* [3]*Walther-Meißner-Institute, Munich, Germany,* [4]*Osaka Metropolitan University, Osaka, Japan*

Magnon-photon polaritons – quasiparticles formed by coupling between electromagnetic microwave (photons) and quantized spin waves (magnons) – have been key platforms for exploring quantum electrodynamics in the ultrastrong-coupling regime. Since the coupling strength can be sufficiently large to realize a Dicke-type system, i. e. reach the ultrastrong coupling regime, this hybrid system is prototypical for probing quantum phenomena induced by counter-rotating terms (CRTs) [1]. These terms are key for the generation of entanglement and non-classical states such as two-mode squeezing of the involved quanta.
Despite the existence of multiple reports on the realization of ultrastrong coupling in magnon polaritons[2, 3], the experimental exploration of CRTs has remained sparsely investigated.
Here we present the experimental demonstration of magnon-photon interaction in the ultrastrong coupling regime, involving the collective excitations in a spatially separated ferromagnetic array and a superconducting high-T_C $YBa_2Cu_3O_7$ (YBCO) resonator. In particular, we observe the Bloch-Siegert shift, a key signature of the existence of CRTs [4].
We use ferromagnetic thin films of NiFe (Permalloy) embedded in a layer stack of SiO_2 (10 nm) / MgO (2 nm) / Py (30 nm) / Ti (3 nm) / SiO_2 (20 nm), which has been deposited onto the superconducting resonator made of high-T_C YBCO. We perform our microwave transmission experiment in a cryogenic environment (T=10K, see Fig. 1) and apply the magnetic field in-plane. Figure 2 shows the normalized transmission spectra, . The dispersion of the magnon photon polariton manifests as an absorption signature. A quantitative analysis of the data allows to estimate the coupling strength (g) to be 511 MHz, corresponding to a - ratio exceeding 0.1. Thus the hybrid system enters the ultrastrong coupling regime. The system also shows the expected Bloch-Siegert shift originating from the counter rotating terms of the coupling. In the presentation, we will discuss the experiment, data analysis and the implications of the results regarding the generation of non-classical states.

[1] A. F. Kockum *et al.*, Nat. Rev. Phys., 1, 19-40 (2019). [2] M. Goryachev *et al.*, Phys. Rev. Appl. 2, 054002 (2014).
[3] A. Ghirri *et al.*, Phys. Rev. Appl. 20, 024039 (2023). [4] S. Yoshii *et al.*, arXiv:2507.06065 (2026).



Schematic of measurement set-up.



Transmission spectra of magnon polariton within 30 nm-thick Py film.

FB-07. A Universal Inverse-Design Magnonic Device

A. Chumak, F. Vilsmeier
Faculty of Physics, University of Vienna, Vienna, Austria

Magnonics exploits spin waves and their quanta — magnons — for information transport and processing, offering a compelling path toward power-efficient, beyond-CMOS hardware that operates natively in the GHz–THz regime without the motion of electric charges [1]. Yet each new functionality has so far demanded a re-engineered geometry, material stack, or biasing scheme, leaving magnonic primitives one-of-a-kind [2]. In inverse design, the desired functionality is specified first, and a feedback-loop algorithm then finds a configuration of a complex, reconfigurable magnonic medium that realises it [3,4]. The drawback of these previous approaches is that the inverse problem must first be solved numerically — a step that can become time- and energy-consuming for complex functionalities — and only afterwards can the obtained design be reproduced in experiment, which additionally demands near-perfect calibration between simulation and measurement. Here we report a conceptually different approach that solves the inverse problem experimentally rather than numerically [5,6].

The device consists of a 7×7 array of omega-shaped copper current loops fabricated on an 18 µm-thick single-crystal YIG film of low Gilbert damping; see Fig. 1. Each loop, driven independently by a current between 0 and 110 mA, generates a local Oersted field of up to ±3.46 mT that perturbs a uniform 350 mT out-of-plane bias. Spin waves are excited and detected by two stripline antennas and propagate in the forward-volume magnetostatic configuration at 5.04 GHz. The binary on/off state of every loop defines a programmable landscape of allowed and forbidden paths for the magnons, turning the same chip into an arbitrary RF component selected purely in software.

Using Direct Search and Genetic Algorithm optimization we inverse-designed two representative linear RF components on the same hardware: a notch filter with a transmission dip of more than 20 dB at the target frequency and a two-channel frequency demultiplexer with channel isolation exceeding 15 dB [5]. Extending the concept into the nonlinear regime, the same architecture was recently shown to realise a complete Boolean logic family — NOT, OR, NOR, AND, NAND and a half-adder — with contrast ratios between 9.8 and 53.9 dB [6]. As summarised in Fig. 2, the half-adder simultaneously delivers the sum bit S and the carry bit C with logical-1 outputs reaching 92.3–100% of the input power and parasitic complementary channels staying below 10%. In parallel, level-set topology optimization coupled to an adjoint-state solver of the magnetization dynamics has opened a route toward sub-wavelength, fully passive inverse-designed magnonic elements using numerical simulations [7]. The adjoint method yields the full gradient of the figure of merit with respect to every degree of freedom of the magnetic landscape from only two Landau–Lifshitz–Gilbert simulations — one forward and one backward in time — so that the cost of a gradient-based optimization step becomes essentially independent of the design dimensionality.

These results demonstrate that a reconfigurable Oersted-field landscape, combined with modern optimization algorithms, turns a single YIG-based chip into a universal magnonic processor able to implement arbitrary RF and digital functionalities on demand. Inverse-design magnonics thereby evolves from case-by-case geometry engineering into a software-defined design problem, paving the way toward compact, low-power and reconfigurable beyond-CMOS hardware.

[1] A. V. Chumak, P. Kabos, M. Wu et al., IEEE Trans. Magn., Vol. 58, p. 1 (2022).
[2] X. Ge, R. Verba, P. Pirro et al., Nano Lett., Vol. 25, 13490 (2025).
[3] Q. Wang, A.V. Chumak, and P. Pirro, Nature Commun., Vol. 12, 2636 (2021).
[4] Á. Papp, W. Porod and G. Csaba, Nat. Commun., Vol. 12, p. 6422 (2021).
[5] N. Zenbaa, C. Abert, F. Majcen et al., Nat. Electron., Vol. 8, p. 106 (2025).
[6] N. Zenbaa, F. Majcen, S. Knauer et al., Sci. Adv., Vol. 11, eadu9032 (2025).
[7] A. Voronov, F. Bruckner, C. Abert et al., npj Spintronics, Vol. 3, p. 19 (2025).

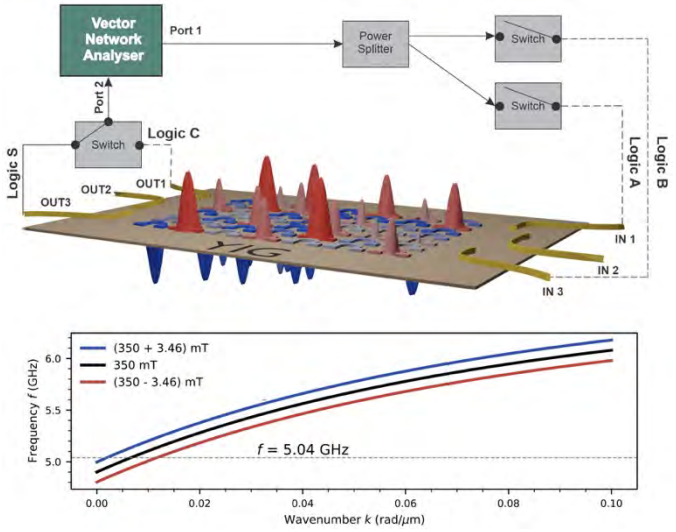


Fig. 1. (a) Schematic of the reconfigurable inverse-design magnonic device. (b) Spin-wave dispersion at the 350 mT bias and under the ±3.46 mT Oersted perturbation generated by an individual loop.

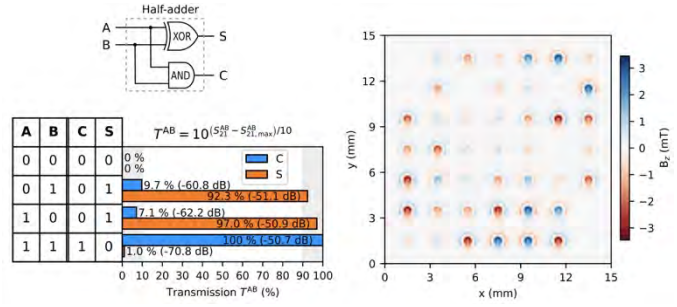


Fig. 2. (a) Circuit-level representation of the half-adder. The truth table reports the measured transmission of the spin-wave signal towards the S (orange) and C (blue) output antennas. (b) Out-of-plane Oersted-field component B_z generated at the YIG surface.

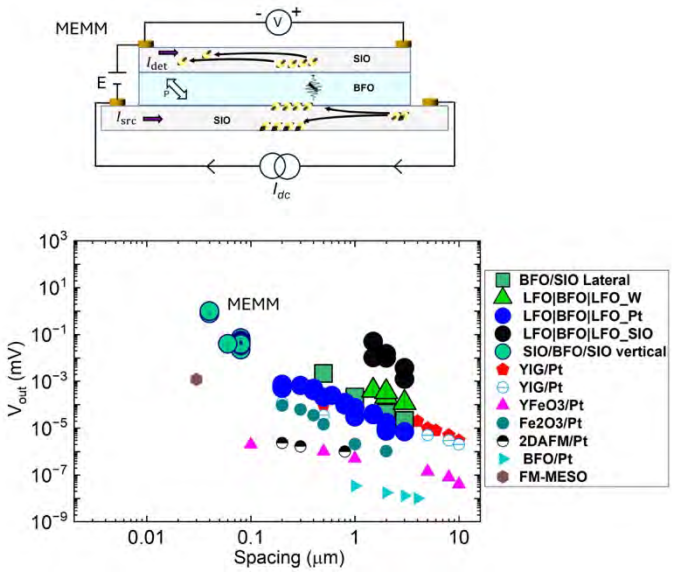
FB-08. Enabling magnetoelectric spin orbit memory with antiferromagnetic magnon current

S. Husain[1, 2], R. Ramesh[1, 2]
[1]*Department of Materials Science and Engineering, University of California Berkeley, Berkeley, California, United States,*
[2]*Department of Physics, University of California Berkeley, Berkeley, California, United States*

Magnon-based memory computing is the most energy-efficient process due to its ability to avoid Joule heating during information transfer. On top of that, magnons in magnetoelectric materials offer an extra degree of freedom by allowing magnetization control through an electric field [1-4]. Magnetoelectric spin-orbit (MESO) logic has been proposed as a low-energy alternative to recent magnetic and static random-access memories [5]. However, the conventional MESO design, which incorporates complex structures and additional ferromagnetic elements, limits its performance. In this talk, I will discuss a non-volatile, non-destructive memory design utilizing a direct magnon-driven sensing capability in an insulating antiferromagnet fully controlled by an electric field. This design leverages strong spin-orbit coupling of spin Hall metal to achieve large output voltages through spin-charge conversion. By employing a simple geometric configuration, we introduce a new non-volatile magnetoelectric magnon memory (MEMM) capacitive element (Figure) as a promising alternative to existing memory technologies functionalized at the attojoule energy per logic operation.

[1] Husain et al Nature Materials, 1-8 (2026)
[2] Husain et al Newton 1 (1), 100026 (2025)
[3] Husain et al Nature communications 15 (1), 5966 (2024)

[4] Harris, Husain et al PRL 134, 016703 (2024)
[5] Manipatruni et al Nature 565, 35 (2019)



Top: Schematic of the vertical spin transport device. Bottom: Inverse spin Hall voltage as a function of the spin orbit metal spacing. This shows the benchmarking of the output voltage measured in non-local spin transport in the range of material systems including the ferrimagnets, antiferromagnets , van der Waals antiferromagnet, MESO with a ferromagnet and multiferroic correlated oxide with spin orbit metals such as Pt, W and $SrIrO_3$.

SESSION FC: NEW APPLICATIONS AND OTHER EMERGING TOPICS I

Co-Chair(s): K. Wu, *Department of Physics, University of South Florida, Tampa, Florida, United States* and A. El-Gendy, *Physics, The University of Texas at El Paso, El Paso, Texas, United States*
Thursday, November 5, 2026
02:00 PM-05:30 PM
Coral 1

FC-01. Shape- and Cation-Engineered Ferrite Nanoparticles for MRI-Guided Magnetic Hyperthermia in Ovarian Cancer Tumor-Mimicking Phantoms

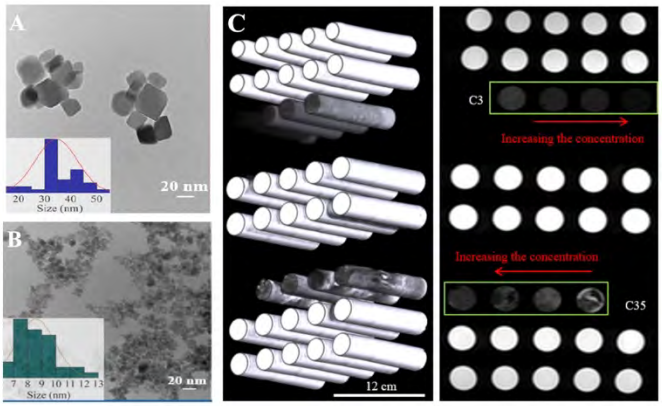
B. Rezaei[1], K. Wu[2]
[1]Department of Electrical and Computer Engineering, Texas Tech University, Lubbock, Texas, United States, [2]University of South Florida, Tampa, Florida, United States

Magnetic hyperthermia integrated with magnetic resonance imaging (MRI), particularly for systemic administration, requires nanoparticles that combine strong heating, T2 contrast, and hemocompatibility.[1] Here, we prepared a citrate-stabilized ferrite nanoparticle library, including Fe_3O_4, $Co_{0.6}Fe_{2.4}O_4$, $Zn_{0.3}Fe_{2.7}O_4$, and $Zn_{0.35}Mn_{0.25}Fe_{2.4}O_4$, in spherical (7.8–10.5 nm) and quasi-cubic (8.5–12 nm) forms, together with highly faceted 35 nm Fe_3O_4 cubes. Shape anisotropy and cation substitution modulated saturation magnetization, coercivity, T2-weighted MRI signal attenuation, and heat dissipation, enabling tunable thermal output and MRI contrast in ovarian tumor-mimicking phantoms under clinically compatible alternating magnetic fields. The 35 nm Fe_3O_4 cubes and quasi-cubic $Zn_{0.35}Mn_{0.25}Fe_{2.4}O_4$ ferrites produced the largest temperature rises, whereas smaller spherical nanoparticles behaved as magnetically softer heaters. All formulations remained biocompatible in SKOV3 ovarian cancer cells (>96% viability at 24 h). However, hemocompatibility analysis revealed that 35 nm Fe_3O_4 cubes induced red blood cell morphology changes despite minimal hemolysis, whereas 9 nm quasi-cubic $Zn_{0.35}Mn_{0.25}Fe_{2.4}O_4$ nanoparticles showed no detectable RBC morphology changes up to 1,000 μg/mL. In perfusable GelMA tumor models, cell viabilities remained 86% and 69% at 500 μg/mL for $Zn_{0.35}Mn_{0.25}Fe_{2.4}O_4$, and Fe_3O_4, respectively. In MRI phantoms, Fe_3O_4 cubes produced susceptibility-induced blooming artifacts that obscured boundary definition, limiting their suitability for systemic MRI applications [2]. Fig. 1 shows the TEM images of quasi-cubic $Zn_{0.35}Mn_{0.25}Fe_{2.4}O_4$ and cubic Fe_3O_4 samples, along with their MRI evaluation in tumor-mimicking phantoms. Overall, 9 nm quasi-cubic $Zn_{0.35}Mn_{0.25}Fe_{2.4}O_4$ nanoparticles are strong

candidates for intravenous theranostic applications, combining robust heating, pronounced T2 MRI contrast, and excellent hemocompatibility, whereas large Fe_3O_4 cubes are better suited for localized intratumoral hyperthermia with limited systemic exposure.

[1] S. Sánchez-Cabezas, R. Montes-Robles, J. Gallo, F. Sancenón, and R. Martínez-Máñez, 'Combining magnetic hyperthermia and dual *T* 1/ *T* 2 MR imaging using highly versatile iron oxide nanoparticles', *Dalton Trans*., vol. 48, no. 12, pp. 3883–3892, 2019, doi: 10.1039/C8DT04685A.

[2] H. B. Na, I. C. Song, and T. Hyeon, 'Inorganic Nanoparticles for MRI Contrast Agents', *Advanced Materials*, vol. 21, no. 21, pp. 2133–2148, Jun. 2009, doi: 10.1002/adma.200802366.



TEM images of (A) 35 nm cubic Fe_3O_4 nanoparticles and (B) 9 nm quasi-cubic $Zn_{0.35}Mn_{0.25}Fe_{2.4}O_4$. (C) MRI phantom evaluation.

FC-02. Magnetic MEMS Devices Based on NdFeB Micromagnets: Micro-Speaker and Micro-Mirror Design

P. Malagò, S. Lumetti, L. G. Enger, M. Ortner, F. S. Slanovc
Silicon Austria Labs GmbH, Villach, Austria

Magnetic microelectromechanical systems (MEMS) are used in many application fields, including automotive, biomedical, space, and IoT technologies [1,2]. Standard magnetic MEMS typically integrate permanent micromagnets and micro-coils, enabling them to function as sensors, actuators, or energy harvesting devices. Their design generally requires high computational power and long calculation times, as it is commonly performed through finite-element simulations.

In this work, a fast semi-analytical method [3] is applied to the design of two MEMS devices: a micro-speaker and a micro-mirror. The micro-speaker consists of arrays of laser-cut NdFeB permanent micro-magnets surrounding micro-coils mounted on a flexible membrane (Fig. 1(a)). When an AC current is supplied to the micro-coils, the membrane is driven into vibration, generating a sound pressure output [4]. This micro-speaker is specifically designed for in-ear applications.

The second device is a MEMS micromirror that includes an array of permanent magnets together with micro-coils fabricated on the suspended micromirror plate around the reflective area (Fig. 1(b)). The actuation mechanism relies on the Lorentz force generated by the interaction between the electrical current flowing through the micro-coils and the magnetic field produced by the permanent magnets. This force enables controlled motion of the suspended reflective region.

The proposed micromirror is intended for applications in satellite and optical communication systems [5].

[1] D. Niarchos, Sensors and Actuators A: Physical, 2003, 109 1–2, 166-173.

[2] O. Cugat, et al, IEEE Transactions on magnetics, 2003, 39.6: 3607-3612.

[3] M. Ortner, et al, SoftwareX, 2020, 100466.

[4] P. Malagò et al, Journal of Physics: Conference Series 2026, 3161 012039.

[5] P. Malagò et al, "On the design of a magnetically driven quasi-static MEMS micromirror", in *AMA Association for Sensors and Measurement* AMA Association for Sensors +measurement. https://doi.org/10.5162/EUROSENSORS2025/TP27

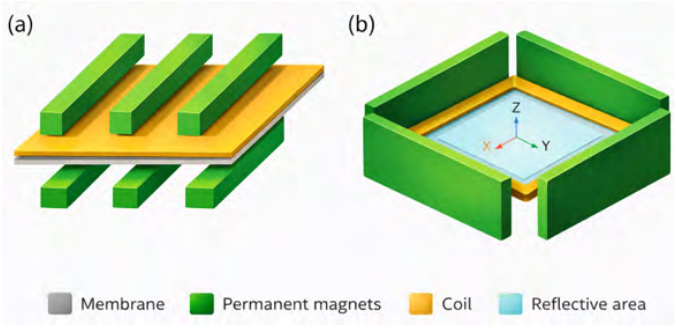


Fig. 1 (a) Sketch of the magnetic MEMS micro-speaker. (b) Sketch of the magnetic MEMS micro-mirror.

FC-03. Development of Magnetic Prussian Blue Composites for Radioactive Material Adsorption and Magnetic Recovery

H. Ok[1, 3], M. Im[2], K. Lee[1, 3]
[1]Materials Science and Engineering, Ulsan National Institute of Science and Technology, Ulsan, Ulju-Gun, Korea (the Republic of), [2]Center for X-ray Optics,, Lawrence Berkeley National Laboratory, Berkeley, California, United States, [3]Blue Magnet Co., Ltd., Ulsan, Ulju-Gun, Korea (the Republic of)

Prussian blue ($Fe_4[Fe(CN)_6]\bullet xH_2O$) is a promising environmental remediation material for cleaning up (or removing) radioactive substances due to its strong affinity for radioactive Cs and its intrinsic magnetic properties. However, the practical use of pure Prussian blue remains limited due to its extremely low Curie temperature of approximately 5 K. Therefore, imparting magnetic properties to Prussian blue at room temperature (RT) and activating its function are essential for efficient post-adsorption recovery, safe handling, and disposal of Cs-loaded radioactive materials. Previous studies have attempted to improve the magnetic performance of Prussian blue at RT through immobilization strategies. Some approaches have employed magnetite@Prussian blue core structures, whereas others have immobilized Prussian blue on non-magnetic polymer supports. However, these methods often incur higher costs and require the addition of bulk materials, which may limit their practical applicability. In this study, we successfully fabricated magnetic reactive Prussian blue with stable magnetic properties at RT by oxidizing the crystal structure of pure Prussian blue in the presence of excess Fe^{3+} ions. The morphology of the resulting powder was confirmed by SEM (Scanning Electron Microscopy), and its crystal structure was analyzed by HR-PXRD (High-Resolution Powder X-Ray Diffractometer). In addition, the magnetic properties were measured using SQUID-VSM at room temperature, low temperature, and around the Curie temperature. As a result, XRD peaks corresponding to Prussian blue and iron oxide phases were observed simultaneously, and our magnetic reactive Prussian blue exhibits distinct (or stronger or superior) magnetic properties at room temperature as well as enhanced magnetic behavior at low temperatures compared to pristine Prussian blue. These results indicate that oxidizing the Prussian blue crystal structures significantly enhances its magnetic functionality at RT.
Moreover, this study demonstrates the potential of fabricated magnetic reactive Prussian blue for effective adsorption of radioactive materials over a wide temperature range, followed by magnetic recovery of the loaded material.

G. Steinhauser, J. Smith and M. A. Buerk, Sci. Total Environ., Vol. 470-471, p.800 (2014)
M. Kaneko, J. Honda and T. Ishii, Front. Energy Res., Vol. 3, p.1 (2015)
H. J. Buser, K. W. K. and A. L. Smith, Inorg. Chem., Vol. 16, p.2704 (1977)
M. A. Busquets, J. Estelrich and A. M. H. M., Drug Discov. Today, Vol. 25, p.1431 (2020)
J. Wang, S. Zhuang and T. Li, Rev. Environ. Sci. Biotechnol., Vol. 18, p.231 (2019)
S.-C. Jang, J.-H. Kim and H.-R. Park, Nanomaterials, Vol. 4, p.894 (2014)
H.-M. Yang, S. Kim and K. Park, J. Alloys Compd., Vol. 657, p.387 (2016)
M. R. Hassan, M. I. Aly and F. A. M., Part. Sci. Technol., Vol. 38, p.236 (2019)

FC-04. Plastic Sorting Using Magnetic Levitation

E. L. Correa, J. Woodcock, A. Davis, C. Dennis, A. Kotula
NIST, Gaithersburg, Maryland, United States

Efficient recycling of plastics requires highly homogeneous streams. However, in most cases, the sorting process is highly inefficient, such as in the common float-sink method. There, plastics are separated solely on whether they float or sink in water and cannot distinguish between the many plastics that float like polypropylene or polyethylene. Here we present a new method based on magnetic levitation to sort plastics. The plastic chips are added to a paramagnetic salt solution (with tunable density and magnetic susceptibility) placed between two permanent (or electro-) magnets. The equilibrium height of the plastic is a balance between gravity, buoyancy, and the force from a magnetic field gradient. As a result, not only will the plastics of different density have different equilibrium heights, but also the plastics with the same density but different magnetic susceptibilities. We therefore measure the magnetic susceptibility, density, and dominant additive element of a range of different commercial plastics composed of polypropylene and low- and high-density polyethylene. We then use this information to quantitatively demonstrate the effectiveness of magnetic levitation as a means for commercial plastic separation, by clearly separating commercial plastics of polypropylene and low- and high-density polyethylene as well as plastics of polypropylene with and without a hematite-containing brown pigment. Magnetic levitation enables separation not only by density but also by magnetic susceptibility, resulting in more

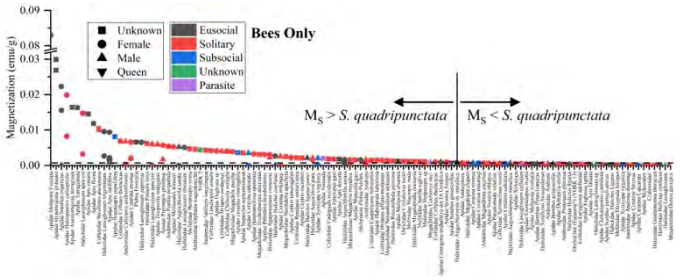
homogeneous recycling streams based on both the polymer and the additive(s).

FC-05. The Secret Life of (Magnetic) Bees

D. A. Gilbert[1], A. Murray[1], L. Russo[1], C. Allen[1], C. S. Jorgensen[1], L. Quigley[1], C. C. Buchanan[1], M. Winklhofer[2], S. G. Brady[3], L. Packer[4]
[1]University of Tennessee, Knoxville, Tennessee, United States, [2]University of Oldenburg, Oldenburg, Germany, [3]Smithsonian, Washington DC, District of Columbia, United States, [4]York University, Toronto, Ontario, Canada

Magnetoreception is typically treated as a specialized capability confined to a small number of migratory organisms.[1] This makes the honeybee a novelty – it is not migratory, but is magnetoreceptive.[2] This was initially associated with the waggle dance. In total, only five bee species have been reported as magnetoreceptive,[3,4] and notably only the honeybee exhibits a waggle dance, immediately raising questions about how magnetoreception is used across the broader clade. From these few species, a wide range of inferences have been made, yet closely related species – which provide a direct test of these ideas – were never examined. Even the basic question of how widespread magnetoreception is in bees remained open.
We addressed this by measuring magnetism across >120 species of bees, extracting magnetic properties and directly comparing them to ecological traits.[4] These measurements show that ferromagnetic signatures consistent with magnetite-based sensing are widespread across bees, with most species exhibiting clear hysteretic responses and many exceeding thresholds associated with known magnetoreceptive taxa . This challenges the conventional view and suggests that magnetically mediated sensing is not exceptional, but broadly distributed. Among the traits examined, body mass shows the strongest correlation with magnetization, while sociality, nesting, and sex are largely uncorrelated.
We extend this work to >300 Hymenoptera species, including ants and wasps, [5] to test persistence across the phylogeny. The result holds: ferromagnetism is common, highly variable, and shows no meaningful phylogenetic signal, indicating that magnetic sensing predates the bee clade and is likely a general feature of Apocrita.
Finally, we incorporate machine learning with environmental metadata, revealing correlations not captured by morphology or life history. These results point to magnetism as a plastic, environmentally coupled property.
Taken together, this reframes insect magnetoreception as a materials-driven phenomenon rooted in nanoscale magnetic particles, broadly distributed and environmentally modulated rather than phylogenetically constrained.

[1] H. Mouritsen. Nature 558, 50-59 (2018)
[2] C.-H. Liang, C.-L. Chuang, J.-A. Jiang et al. Scientific Reports 6, 23657 (2016)
[3] E. Wajnberg, D. Acosta-Avalos, O. C. Alves et al. Journal of The Royal Society Interface 7, S207-S225 (2010)
[4] L. Russo, C. Allen, C. S. Jorgensen et al. Science Advances 12, eaed7391
[5] M. d. G. C. Pereira-Bomfim, W. F. Antonialli-Junior,D. Acosta-Avalos. EntomoBrasilis 9, 01-05 (2016)



Saturation magnetization versus species.

FC-06. Personalized Coil Design for Transcranial Magnetic Stimulation on Subject-Specific Head Models

H. Kim[2], A. Iino[2], M. Fushimi[1], M. Sekino[2]
[1]Faculty of Science and Technology Department of Applied Physics and Physico-Informatics, Keio University, Tokyo, Japan, [2]Department of Bioengineering, The University of Tokyo, Tokyo, Japan

Transcranial magnetic stimulation (TMS) is widely used for treating neurological and psychiatric disorders, yet commercial coils rely on empirical, one-size-fits-all designs that fail to account for individual anatomical variation [1]. While optimizing coil placement for individual patients has been shown to improve stimulation accuracy [2], personalizing the coil geometry itself remains unexplored. Prior coil design methods have also approximated the head as a sphere or simple multilayer structure, neglecting secondary electric fields at tissue boundaries that contribute 20–35% of the total induced field [3].
We propose a subject-specific coil design framework that personalizes both the target electric field and the coil winding surface. Vector Spherical Harmonics (VSH) provide an analytically complete E-field basis inside a sphere [4], and we reconstruct these modes within an individual MRI-derived head model using finite element method, thereby

capturing the secondary fields induced at realistic tissue boundaries. The optimal superposition of VSH modes is determined via a generalized eigenvalue problem that maximizes deep gray matter field strength relative to superficial scalp activation and spatial spread. A coil winding surface is then generated from the same head model by extracting the scalp mesh and expanding scalp normals outward. Finally, surface coil windings that realize the desired E-field on this personalized surface are derived using the target field method.

The framework was validated on the MNI152 population atlas, constructed from 152 healthy young adults. The personalized design achieved an objective function value of 0.0908, a 31.2% improvement over one of the best-performing conventional coil (Double Cone Coil, 0.0692). The reduced coil-to-scalp gap and the use of a subject-matched field target together improve field coupling and realization fidelity. These findings indicate that joint personalization of the desired E-field and the coil winding surface is a critical factor in coil performance, even when applied to a population-averaged brain model.

[1] Somaa FA, et al. Front Neurol., 13, p.793253 (2022)
[2] Liu Y, et al. Front Hum Neurosci., 19, p.1682852 (2025)
[3] M. Wagner, J. Rushmore and U. Eden, Phys. Med. Biol., Vol. 54, p.3907 (2009)
[4] A. Iino, et al. IEEE Trans. Magn., Vol. 60, p.5100205 (2024)

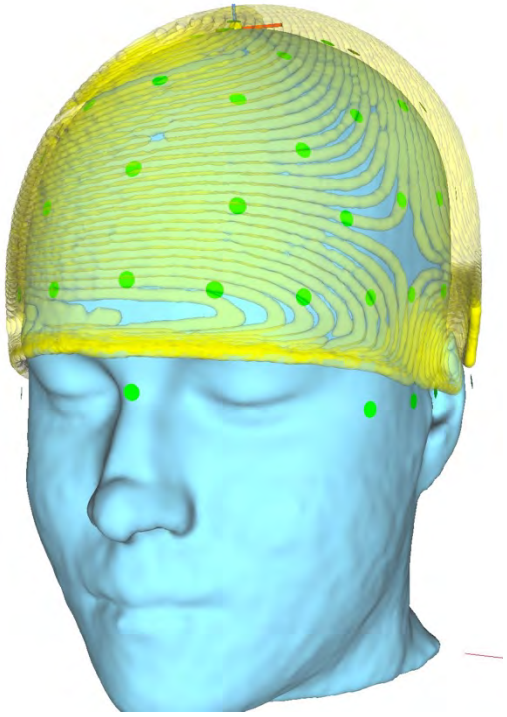


Fig.1 Coil windings derived on a subject-conforming helmet

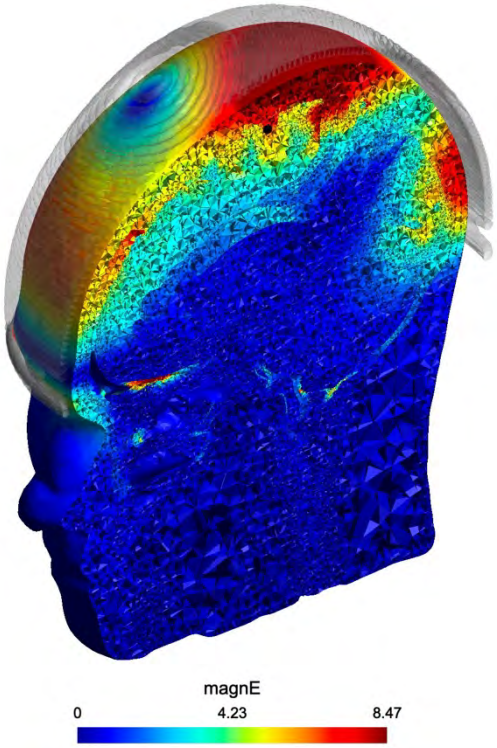


Fig. 2 Cutaway view of induced E-field magnitude (V/m)

FC-07. Magnetic demonstrations to establish a sense of wonder

N. J. Jones[1], S. Wolff[2]
[1]Physical Metallurgy and Fire Performance Branch, Naval Surface Warfare Center, Carderock Division, Bethesda, Maryland, United States, [2]Mechanical Engineering, The Ohio State University, Columbus, Ohio, United States

In the teaching of science and engineering, many concepts are consonant with our daily experiences. However, in establishing a sense of wonder and a lifelong love of learning, it is essential to demonstrate real world examples where the performance is different, and often drastically different, than what is expected. This can provide a magical experience that is nevertheless predictable and describable by the laws of physics. Magnetic materials and magnetic applications provide such an opportunity to surprise students with interactions that don't necessarily make conceptual sense. For students that are not especially excited by science, this also provides an enthralling, physical experience (without equations) to understand the laws they've been learning about. A series of magnetic materials and magnetic applications has been used with

elementary, middle and high school students, with a special focus on magneto-elastic interactions. The demonstrations begin with the simple surprise of the high density of rare earth elements, with a discussion of their benefits and problems in contrast to non-rare earth options. This moves into a discussion of eddy current losses utilizing a moving magnetic through a conductive tube. This demonstration is connected with a bending unimorph, magnetoelastic energy harvester. Three types of magnetic fluids are then discussed, looking at ferrofluids, magnetorheological fluids and magnetic putty, highlighting potential applications. The demonstrations finish with two high impact demonstrations: magnetostrictive speakers and levitating magnets. The first demonstrates a solid-state speaker and how bone-conduction works. The second demonstrates the concept of superconductivity. This specific progression of hands-on demonstrations continually increases the level of surprise, and has been used with 2nd graders up to high school seniors, with minor adjustments to maintain the topics at each group's level of understanding. While the general goal is to engage the students in a fun demonstration, example extensions will be provided that can be linked with equations or concepts which are part of a high school or college physics curriculum.

FC-08. The Attraction of Magnets: Empowering Girls Through Hands-On Magnetism Activities

F. Béron
Instituto de Física Gleb Wataghin, Universidade Estadual de Campinas, Campinas, São Paulo, Brazil

In Brazil, students from the public education system—especially girls—often have limited exposure to STEM, shaped by structural inequalities, scarce resources, and persistent stereotypes that discourage their participation in science. Many develop low confidence in subjects like physics and mathematics early on, which can affect future career choices. To help address this gap, the outreach activity *The Attraction of Magnets* was created in 2019, initially designed for all-girls groups [1] to provide a supportive and engaging introduction to physics.
The workshop is a three-hour, hands-on experience led by a team of six monitors. Its main goal is to demystify magnetic phenomena and highlight their presence in everyday life, without relying on equations or formal calculations. Each participant actively builds and experiments, encouraging autonomy, curiosity, and confidence. At the beginning, participants receive a small magnet to explore basic interactions, which they keep after the session as a tangible link to the experience.
The program centers on two main activities. In the first, participants build a simple loudspeaker using a PET bottle, discovering how electromagnetic induction converts electrical signals into sound (Fig. 1). This activity connects abstract concepts to familiar technology, such as music played on a phone. In the second, participants create magnetic slime using accessible materials like white glue, exploring magnetic forces in a playful and tactile way (Fig. 2). Both activities are designed so that participants construct their own prototypes step by step and take them home.
By removing the barrier of formalism, the workshop allows students who may struggle with mathematics to engage positively with physics, while still offering depth for more curious participants to ask questions and explore further. Feedback collected through post-workshop surveys shows that nearly 90% enjoyed the experience and would recommend it. Most importantly, a large majority reported a shift in their perception of science, recognizing its relevance in everyday life and feeling more confident in engaging with it.
Funding: FAPESP #2024/00998-6; CNPq #310084/2025-3.
[1[G. Castellano *et al*., Revista Internacional de Extensão da Unicamp, Vol. 4, e023002 (2023). [DOI: 10.20396/ijoce.v4i00.18449]



Fig. 1: Loudspeaker testing


Fig. 2: Magnetic slime testing

FC-09. Accelerate the scientific method with agile design of advanced magnetics

T. Costello
CMR Inc, Huntsville, Alabama, United States

This presentation will present a new paradigm in agile/lean design of advanced magnetics. 3D printing has changed the speed at which engineers evaluate iterative physical product designs, speeding research and the discovery process. Now researchers can leverage the same benefits when working with multi-pole magnets. Polymagnet's real time prototyping process enables researchers to design and iterate multiple versions in a single day. No more wasting precious budget dollars on expensive fixtures. No more guessing how good the modeling is. No more compromising on the experimental samples because you can't afford the time and cost of another iteration. No more limitations to the size and proximity of adjacent poles. Free your design envelope and accelerate discovery.

During this presentation we will provide a detailed overview of the design and magnetization process. We will discuss the necessary steps and outputs of each phase, including current operating windows. While the currently available equipment was designed for a specific operating window, the presentation will also cover new frontiers which are being developed to allow the technology to magnetize previously impractical structural geometries. Come and learn how digitally controlled micro magnetization can open the window to magnetic circuit optimization and discovery. polymagnet.com

FC-10. Magnetic Separation of Cathode Materials from Lithium-Ion Batteries

N. Carlstedt, P. Andrei
Department of Electrical and Computer Engineering, FAMU-FSU College of Engineering, Tallahassee, Florida, United States

Lithium-based batteries (LIBs) have become widely used in a variety of applications, from small everyday electronics to large-scale energy storage systems. Although the lifespan of LIBs has improved over the years, it remains limited, as batteries gradually lose capacity after repeated charge-discharge cycles. As a result, LIBs are eventually discarded, sometimes through improper disposal, creating potentially hazardous and flammable waste that can pollute the environment. At present, only a relatively small fraction of LIBs is recycled, in part because manufacturing new cells from raw materials is often less expensive than recovering materials from used cells. One contributing factor is the difficulty of automating the separation of anode and cathode materials, which adds complexity and cost to the recycling process.
In this presentation we introduce a method for the separation of cathode from anode and other nonmagnetic materials which is based on magnetic separation. The batteries are prepared by first being stripped of their casing and the foils of the anode and cathode are uncoiled. The uncoiled anode and cathode are then placed in an office shredder. This produces strips approximately 5x25mm in size. In order to separate the cathode from the anode species, we use a magnetic roller separator composed of alternating steel discs and magnets with the like poles facing one another at the end of a conveyer belt. As the chunks pass over the roller, the cathode material is attracted to the high field gradients at the edges of the iron discs, being pulled to a bin underneath the roller, while the anode material falls off the edge of the roller into a different bin. Using this method, we have been able to effectively separate the two species from one another with relatively little contamination between the two species. Our method provides several major benefits over conventional methods, most importantly that it is environmentally clean and requires relatively little energy. The proposed process is also inherently scalable, making it a promising initial step in the lithium-ion battery recycling process.

FC-11. Magnetically enhanced mass transport for waste-to-resource conversion processes

R. Hernandez[1], L. Bertel Bermejo[1], J. Abarca[2], C. González-Fernández[2], G. Díaz-Sainz[2], J. Gomez-Pastora[1]
[1]Chemical Engineering, Texas Tech University, Lubbock, Texas, United States, [2]Ingenierías Química y Biomolecular, Universidad de Cantabria, Santander, Cantabria, Spain

Industrial waste products are integral components within contemporary industrial frameworks, the transformation of what used to be considered disposal and cost problems to transform into a strategic resource to replace raw materials has become a highly pursued field by the manufacturing industry. Nevertheless, some of the transformation processes used for this end still experience difficulties, such as mass transfer limitations in reactors and separation systems, including poor diffusion and passive mixing. A novel strategy, aiming to overcome said limitations, is introduced by assisting this operation with magnetic fields through the induction of the magnetohydrodynamic effect (MHD), which enhances convection in the fluid solutions, therefore accelerates mixing and increases efficiency. This is achieved by the application of an external magnetic field on an ionic current density. The magnetic field generated interacts with the charged species, resulting in Lorentz forces that modify local hydrodynamics. The resultant forces cause mixing effects on the bulk, enhancing the convective transport of chemical species.
COMSOL Multiphysics is used in this research, to study the effects of permanent magnets in the flow of chemically reactive species. The aim of this study is to examine how the following variables affect the overall mass transport: magnetic field strength/direction, magnet arrays, resulting Lorentz force, ionic solution properties, and species diffusion/reaction, on a laminar flow. Electrocatalytic reduction of carbon dioxide ($ERCO_2$) is strongly constrained by mass transport limitations; therefore, as a proof of concept we will study CO_2 conversion to value-added products within an electrochemical cell. Slow diffusion of CO_2 in aqueous electrolytes and the formation of a thick diffusion boundary layer near the electrode further restrict reactant supply on the electrode surface. MHD effects are being applied on this system to analyze whether the application of a magnetic field will contribute to a significant improvement in the reaction yield. This research aims to provide design guidelines for future experimental and scalable systems in the industry.

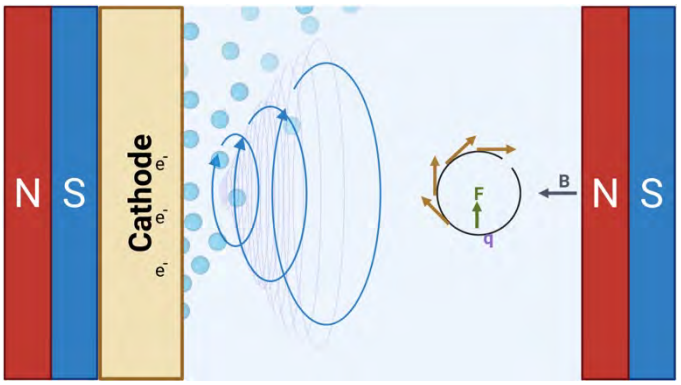


Fig.1 MHD effect on an electrochemical system for $ERCO_2$

FC-12. Selective Enrichment of Phosphors from Crushed Fluorescent Lights Using High Gradient Magnetic Separation

D. Rogers, P. Wang, P. Andrei
Florida State University, Tallahassee, Florida, United States

Yttrium is a critical material with increasing demand in modern technologies. Its supply is limited and concentrated among a small number of exporters, making global supply chains vulnerable. At the same time, significant quantities of yttrium, along with other rare earth and mineral-rich phosphors, are present in discarded fluorescent lights. This bulk supply represents a large, underutilized resource of critical materials.
Our method for selective recovery uses high-gradient magnetic separation (HGMS) to remove glass and contaminants while isolating individual phosphors from crushed fluorescent lightbulb powder. The feed consists primarily of glass and phosphors including YOX, LAP, BAM, CAT, and others. The HGMS system uses a packed column of sub-millimeter magnetic steel spheres placed in a magnetic field generated by an electromagnet. High magnetic field gradients on the spheres' surfaces capture paramagnetic particles based on magnetic susceptibility and particle size. Initial separation is performed at high magnetic fields to remove most glass and non-magnetic contaminants. As the feed passes through the column, paramagnetic particles are attracted to the steel spheres. Afterward, the captured material is flushed from the column to produce a concentrated "mags" sample. This fraction is then passed through the same system at progressively lower magnetic field strengths. As the field is reduced, particles with lower magnetic susceptibilities pass through, isolating particles based on magnetic potential.

HGMS provides a tunable method for recovering phosphors from fluorescent light waste by exploiting differences in magnetic susceptibility. Yttrium-containing phosphors (YOX) are of particular interest due to yttrium's role in LEDs and advanced ceramics; however, HGMS can recover multiple valuable phosphors from discarded lightbulbs. Extracting critical materials from this waste stream
Boelens, P., Lei, Z., Drobot, B., Rudolph, M., Li, Z., Franzreb, M., Eckert, K., & Lederer, F. (2021). High-Gradient Magnetic Separation of Compact Fluorescent Lamp Phosphors: Elucidation of the Removal Dynamics in a Rotary Permanent Magnet Separator. *Minerals*, *11*(10), 1116. https://doi.org/10.3390/min11101116

David Rogers, Peng Wang, Petru Andrei; High gradient magnetic separation for selective recovery of cathode materials from end-of-life lithium ion batteries. *AIP Advances* 1 February 2026; 16 (2): 025144. https://doi.org/10.1063/9.0001044

FC-13. Human-Scale Rotating Magnetic Field Delivery with Permanent Magnets Under Anatomic and Robotic Constraints

T. Le, H. Ceylan
Mayo Clinic, Scottsdale, Arizona, United States

Rotating magnetic fields (RMFs) are widely used to actuate magnetic microrobots, enabling propulsion, orientation control, and programmable deformation in confined biological environments (1–3). While effective at laboratory, translation to human anatomy remains challenging. External magnetic sources must operate at separations of several to tens of centimeters, where rapid field decay severely limits actuation torque. Clinically relevant RMF delivery must also sustain appropriate rotation frequencies, as torque and frequency together govern synchronous actuation and stable propulsion. Electromagnetic coil systems can generate programmable RMFs over large workspaces (4, 5), but maintaining millitesla-level fields at human-scale distances and useful frequencies requires high power, thermal management, and complex infrastructure. Robot-arm-mounted permanent magnets provide a compact alternative without resistive heating, yet their performance is constrained by coupled mechanical and geometric factors, including magnet size, rotational inertia, actuator envelope, and robot payload limits. These constraints directly limit achievable field strength and frequency (3, 6, 7).
This study presents a system-level framework for human-scale RMF delivery using permanent magnets under anatomic and robotic constraints. The framework jointly considers actuator–target separation, magnet geometry, inertia, actuator envelope, and payload limits. It defines a mechanically deliverable RMF envelope of 5–30 mT and 1–30 Hz across representative clinical scenarios. Equal-volume comparisons across canonical magnet geometries reveal how field penetration, inertia, and actuator envelope determine feasible regimes, while payload-constrained design maps clarify trade-offs among magnet size, separation distance, and rotational dynamics. Experimental validation using a robot-arm-mounted rotating magnet actuator demonstrates stable microrobot propulsion in a human-scale vascular phantom under physiologic flow, consistent with predicted field–frequency limits.
In summary, this work establishes quantitative performance limits for permanent-magnet RMF systems and provides a framework for microrobot–actuator co-design toward clinical translation.
1. Abbott JJ, Diller E, Petruska AJ, Annu Rev Contr Robot, Vol. 3, p.57-90, 2020
2. Sitti M, Wiersma DS, Adv Mater, 2020;32(20):e1906766.
3. Le TA, Alabay HH, Singh PG, Austin MG, Urbina PAM, Misra S, et al., Advanced Functional Materials, e31400, 2026.
4. Gervasoni S, Pedrini N, Rifai T, Fischer C, Landers FC, Mattmann M, et al. , Advanced Materials. 2024;36(31):2310701.
5. Li D, Chen B, Huang C, Xu S, Wu X, Xu T., Science China Technological Sciences. Vol. 67, p.3546-58, 2024.
6. Ye B, Fu Y, Zhang S, Wang H, Fang G, Zha W, et al., Journal of Magnetism and Magnetic Materials. 2023;565:170268.
7. Pancaldi L, Özelçi E, Gadiri MA, Raub J, Mosimann PJ, Sakar MS. Flow-driven magnetic microcatheter for superselective arterial embolization. Science Robotics. 2025;10(107):eadu4003.

FC-15. Sub-mm NdFeB Micromagnets Fabricated by Ultrashort Pulsed Laser Micromachining: Enabling Magnetic MEMS and Quantum Applications

S. Lumetti, P. Malagò, P. Smaliukas, L. G. Enger, J. Bardong, M. Montagnese
Silicon Austria Labs GmbH, Villach, Austria

Permanent magnets made of "hard" magnetic materials (e.g., NdFeB, SmCo) feature high energy products and large remanence and coercivity, which makes them critical enabling components for high-performance microscale magnetic machines such as motors, generators, energy harvesters, switches, sensors, actuators, quantum devices

and other microelectromechanical systems (MEMS) that can be utilized in several medical, industrial, research and consumer applications. These microscale devices require the integration of high-quality sub-mm micro-structured magnets with thickness and lateral dimensions ranging from tens to hundreds of μm enabling the generation of strong forces within compact volumes [1]. For this size range, a gap currently exists in magnet manufacturing technologies between bottom-up microfabrication routes (i.e., film deposition techniques, which result in good magnetic properties and precise magnet shapes, but are intrinsically slow, expensive and limited to film thicknesses up to few tens of μm only) and typical top-down approaches like mechanical or electrical-discharge machining of sintered bulk magnets (which enable feature sizes starting from few hundreds of μm but result in a deterioration of the magnetic remanence and coercivity due stress or heat-induced surface degradation) [2].
In this work, we report on the fabrication of permanent magnets with sub-mm thickness and lateral features via ultrashort pulsed laser-micromachining of 300-μm-thick NdFeB sintered foils. The use of ultrashort laser pulses limits the surface damage caused by heat build-up during the machining process, thereby resulting in micromagnets with remanence and coercivity values close to the nominal properties of N50-grade bulk sintered magnets. We illustrate the suitability of these micromagnets to create complex magnetic fields at the sub-mm scale in two use-case applications: (i) a proof-of-concept MEMS device [3] integrating them with planar micro-coils and a flexible polymer membrane for the generation of electromagnetic actuation forces of the order of few mN that could be employed, for instance, as a micro-pump or as a micro-speaker, and (ii) the generation of high-precision magnetic field gradients in ion trap devices.
[1] D. P. Arnold et al, J. Microelectromechanical Syst., 18, 1255-1266 (2009)
[2] G. Villalba-Villanueva et al, Int. J. Adv. Manuf. Technol., 129, 4961-4970 (2023)
[3] P. Malagò et al, J. Phys.: Conf. Ser., 3161, 012039 (2026)

SESSION FD: UNCONVENTIONAL COMPUTING AND MAGNETIC MEMORIES II

Chair(s): N. A. Natekar, *Western Digital, San Jose, California, United States*
Thursday, November 5, 2026
02:00 PM-05:30 PM
Coral 2

FD-01. 3D domain wall motion memory with artificial ferromagnet

T. Ono[1, 2]
[1]*Kyoto University, Uji, Japan,* [2]*Tohoku University, Sendai, Japan*

We proposed a new type of 3D DW motion memory with an artificial ferromagnet and study its feasibility by micromagnetic simulation [1, 2]. 3D DW motion memory proposed in this study consists of an array of cylindrical artificial ferromagnetic wires, which is composed of periodically stacked bilayers of a bit layer with strong magnetic anisotropy and a DW layer with no magnetic anisotropy [1]. The data is written by flipping the magnetization of the bottom bit layer using the spin-orbit torque induced by the current in the word line. The written data can be shifted to the arbitrary position in the artificial magnetic wire by the appropriate current injection through the wire. By repeating the writing and shifting, an arbitrary information sequence can be stored in the magnetic wire. The data can be read out with the topmost magnetic tunnel junction while the data is being shifted by the current through the wire. Micromagnetic simulation shows that the precise DW position controllability, narrow DW width down to 3 nm, and low DW motion current down to 2×10^{10} A/m^2 can be achieved with feasible material parameters [1]. Furthermore, it is found that the high thermal stability and the low DW motion current can be achieved simultaneously [2]. Although the originally proposed method for reading information from this device is destructive, we proposed a novel nondestructive readout method, leveraging the magnetization dynamics induced by the spin transfer torque [3].
Data-writing and shifting processes for 2-bits memory have been demonstrated using devices fabricated from sputtered films [4]. A major challenge is how to fabricate a 3D structure capable of storing many bits. Considering the aspect ratio problem of microfabrication even in the current 2D MRAM, it seems to be an extremely difficult task to fabricate a 3D structure with the currently available microfabrication technology. A possible solution is to first fabricate nanoholes to ensure a columnar structure, and

then electrodeposit artificial ferromagnets inside the nanoholes. Using the latest technology developed for 3D NAND flash memory, it is possible to fabricate high aspect ratio nanohole arrays of tens of nanometers in diameter and several microns in length. Therefore, the remaining challenge is to fabricate nanowires with perpendicular magnetic anisotropy within such nanoholes using electrodeposition. In the presentation, the current status of the fabrication of CoPt nanowires with perpendicular magnetic anisotropy by electrodeposition is also presented [5,6].

This work was partly supported by JST, CREST (Grant Number JP MJCR21C1), Japan.

[1] Y. M. Hung et al., J. Magn. Soc. Jpn. 45, 6 (2021).
[2] Y. M. Hung et al., Appl. Phys. Express 14, 023001 (2021).
[3] H. Jang et al., J. Magn. Soc. Jpn., 49, 9-12 (2025).
[4] F. Ye et al., IEEE Transactions on Magnetics; 10.1109/TMAG.2025.3556016H.
[5] R. Kawana et al., Applied Physics Express 18, 033002 (2025).
[6] D. Araki et al., Electrochemistry Communications, 176 (2025) 107938.

FD-02. Counting magnons: How to measure Heisenberg exchange in ultrathin magnetic systems

C. Swindells[1, 2]
[1]Associate, Applied Physics Division, NIST, Boulder, Colorado, United States, [2]Department of Electrical Engineering, CU Denver, Denver, Colorado, United States

With the recent commercial deployment of MRAM chips for a variety of applications, there is a renewed interest in optimizing and discovering new materials to enhance performance. Despite being several years old, CoFeB / MgO barriers and their variants remain the standard for perpendicular tunnel barriers[1].

Performance of an MRAM cell is typically measured on the device level, hence evaluating new materials requires additional time, effort and resources than simple film level metrology. The thermal stability, switching probability and performance[2,3] of MRAM cells is fundamentally linked to the coupling of a spin to its neighbors, through the Heisenberg exchange. Accurate determination of exchange on the film level would allow for more rapid prototyping of new material platforms.

This is far from a trivial problem. For magnetic systems, the Heisenberg exchange can be experimentally calculated from the exchange stiffness through measurements of the spin wave spectra. Determination of this spectra through neutron scattering is unfeasible on the ultrathin, polycrystalline films used in MRAM.

Brillouin Light Scattering (BLS) provides a feasible alternative to measuring industrially relevant films[4]. By measuring the Stokes and anti-Stokes shift of photons scattering from magnons at a range of wavevectors, one can fit the dispersion to determine the exchange stiffness[5]. Different wavevectors can be accessed by either rotating the sample relative to the applied field (Damon-Eshbach (DE)) or by rotating the plane of the incidence relative to the field (Backward Volume (BV)). As it is far simpler to rotate the sample, this approach is often used to measure a dispersion. However, for very thick films, or higher saturation magnetization samples, the dipolar contribution to the spectra, particularly the DE branch, will dominate over the exchange, making accurate determination of quantities difficult. With an apparatus capable of measuring over both DE and BV geometries, we are able to properly quantify the exchange stiffness in MRAM free layer samples (fig 1).

Though BLS provides a robust method to determine exchange, it is not a technique readily available to most. Another method that uses more common lab equipment, is to infer the response from an emergent property of spin waves, such as the profile of the magnetic moment vs temperature. For a magnetic system at a temperature above 0K, thermal magnons will reduce the total moment. These magnons follow a Bose-Einstein distribution, and in 3D this expression can be integrated to give the well-known Bloch $T^{3/2}$ relation, but the ultrathin films used for MRAM partially quantize the magnon spectrum, requiring that (1) the magnons must be discretely counted, and (2) the spin-wave gap must be given to prevent the distribution from diverging at k=0, both of which add complexity to an already challenging problem.

An alternative to Bloch's law is to use an atomistic model of the system to fit the temperature profile[6]. With this approach I will show the necessity of adding quantum-colored noise[7,8] (fig 2) to properly account for the number of magnons excited, in order to reconcile values of exchange from BLS. I will also highlight how approximating such models with neural networks allows for rapid exploration of parameter landscapes. Finally, I will discuss how values obtained at the film level for typical MRAM materials compare to those from device level measurements.

This work highlights the results of our CHIPS metrology project, exploring and comparing various techniques to quantify the exchange in a robust manner. In all cases, to accurately determine exchange, we cannot escape counting magnons, whether by counting the number excited at a

given temperature to fit Bloch's law, or by counting the number of photons they scatter with BLS.
1. S. Ikeda et al., Nature Materials 9, 721–724 (2010)
2. T. Santos et al., Journal of Applied Physics 128, 113904 (2020)
3. G. Mihajlović et al., Applied Physics Letters, 117 (2020)
4. G. Riley et al., Applied Physics Letters, 120, 112405 (2022)
5. T. Böttcher et al., Physical Review B, 107, 094405 (2023)
6. J. Barker et al., Physical Review B 100, 140401(R) (2019)
7. J. Barker et al., Electronic Structure, 2, 044002 (2020)
8. F.C. Weber et al., Physical Review B, 113, 064423 (2026)

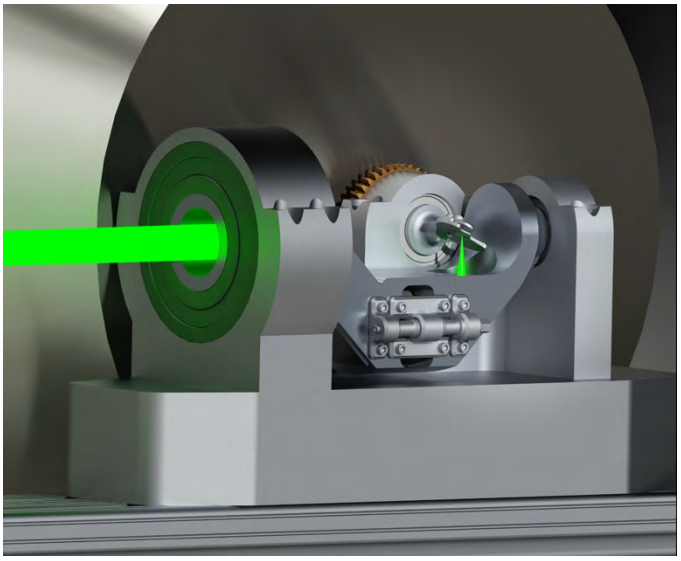


Fig.1 NIST BLS apparatus designed to measure both DE and BV modes

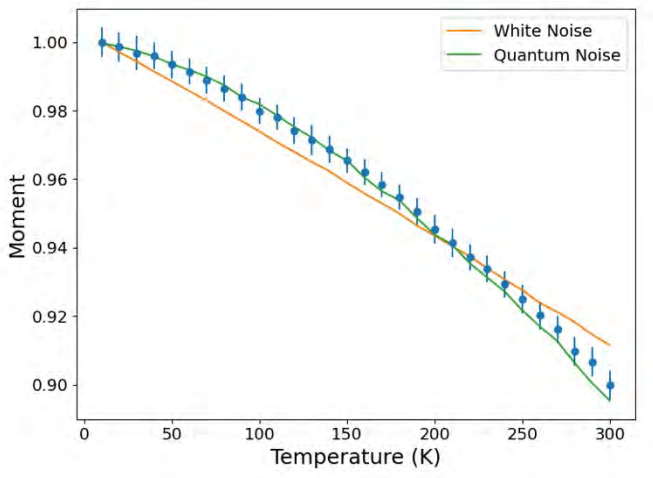


Fig.2 Magnetometry data fitted with atomistic models using classical white noise or quantum colored noise

FD-03. Multi-Weight Wafer-Scale Spin Orbit Torque Magnetic Tunnel Junction Synapses

N. Zogbi[1, 2], D. Giuliano[3], V. Kateel[3], V. Nguyen[3], J. Chatterjee[3], A. Palomino[3], R. Carpenter[3], S. Rao[3], J. Incorvia[1, 2]
[1]Chandra Family Department of Electrical and Computer Engineering, University of Texas at Austin, Austin, Texas, United States, [2]Microelectronics Research Center, University of Texas at Austin, Austin, Texas, United States, [3]imec, Leuven, Belgium

Synaptic devices for neuromorphic hardware directly benefit from a high number of analog weights, as this improves inference accuracy. Iterative programming algorithms can target specific conductance states without requiring deterministic switching, making the number of accessible conductance states the key device-level metric [1]. While magnetic tunnel junctions (MTJs) are intrinsically bistable, multi-bit operation has been achieved using common electrodes across MTJs or via domain wall (DW) pinning at notches to form intermediate states [2-4]. High resistance-area MRAM has also been used to reduce IR drop in crossbar arrays [5]. However, multi-bit operation can also be achieved using spin orbit torque (SOT) to nucleate and propagate a DW underneath a single MTJ, thereby eliminating the need for notches or the integration of multiple MTJs. This approach reduces process complexity while enabling spintronic-based synapses with a tunable analog response.

Here, we demonstrate 300 mm wafer-scale MW artificial synapses using elongated SOT-MTJs engineered to support DW nucleation and pinning [6]. By increasing the MTJ's aspect ratio to ~5:1, Fig. 1, DWs form beneath the MTJ and generate intermediate conductance states. Tuning the IP field modulates SOT symmetry breaking, enabling control over MW behavior at lower fields. Across 128 devices, MTJ artificial synapses exhibit up to eight states, while circular control MTJs remain binary, shown in Fig. 2. We evaluated the devices by implementing them in a neural network performing image classification inference on the MNIST handwritten digit dataset. The results show that increasing the number of conductance states improves inference accuracy, with eight-state synapses achieving an accuracy of 96.1%. These results establish SOT-driven MTJ artificial synapses as a scalable route to MW spintronic synapses.
[1] Esmanhotto, E. et al. Experimental demonstration of multilevel resistive random access memory programming for up to two months stable neural networks inference accuracy. *Advanced Intelligent Systems* 4, 2200145 (2022).
[2] Cai, K. et al. Selective operations of multi-pillar SOT-

MRAM for high density and low power embedded memories. *IEEE Symposium on VLSI Technology and Circuits*, (2022)
[3] Doevenspeck, J. et al. Multi-pillar SOT-MRAM for Accurate Analog in-Memory DNN Inference. *IEEE Symposium on VLSI Technology*, (2021).
[4] Liu, S. et al. A domain wall-magnetic tunnel junction artificial synapse with notched geometry for accuracy and efficient training of deep neural networks. *Applied Physics Letters*, 188 (2021).
[5] Doevenspeck, J. et al. SOT-MRAM based Analog in-Memory Computing for DNN inference. *IEEE Symposium on VLSI Technology*, (2020).
[6] Zogbi, N. et al. Synaptic Multi-Weight Wafer-Scale Domain Wall Magnetic Tunnel Junctions Driven by Spin Orbit Torque. *Under Review*.

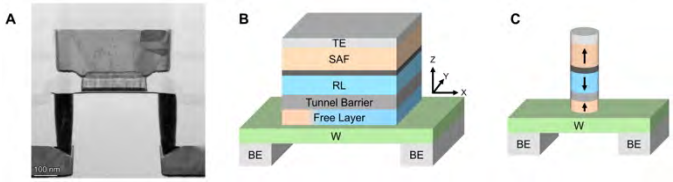


Fig. 1: (A) Cross-sectional TEM of a 350 nm MTJ artificial synapse. (B) Schematic of an MTJ artificial synapse. (C) Schematic of a circular SOT-MTJ.

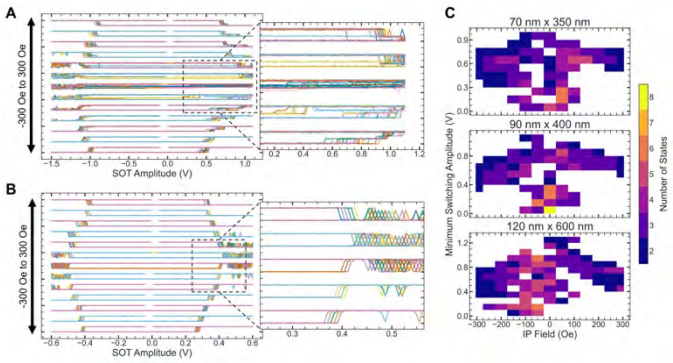


Fig. 2: (A) SOT loops with respect to varying IP fields of the MTJ artificial synapse. (B) SOT loops with respect to varying IP fields of the control. (C) Number of states with different device sizes at varying IP fields.

FD-04. Robotic Navigation Using Spin-Wave-Based Neuromorphic Hardware

J. Zohar[1], D. Pinna[1], G. van der Laan[2], T. Hesjedal[1], C. Safeer[1]
[1]Department of Physics, University of Oxford, Oxford, United Kingdom, [2]Diamond Light Source, Harwell Science Campus, Didcot, United Kingdom

AI workloads demand enormous computational resources, making physics-inspired neuromorphic hardware, including spintronics-based platforms, a promising alternative [1]. Yet, its potential remains largely unexplored in robotics, a major AI application domain. Current robotic systems rely on energy-intensive, cloud-dependent deep neural networks that struggle in dynamic or remote environments, highlighting the need for dedicated neuromorphic hardware for robotics [2].

Here, we present an experimental demonstration of robotic control driven by spin-wave (SW)-based neuromorphic hardware [3]. First, using a water-wave platform that provides direct visual access to wave dynamics, we establish a wave-based reservoir computing framework that achieves near-perfect accuracy in a robotic obstacle recognition task. We further demonstrate real-time robotic navigation controlled entirely by this wave-based computation (Fig. 1a,b). Subsequently, we demonstrate a SW-based hardware implementation for robotic control. Using micromagnetic simulations, we show that nonlinear SW interference in a magnetic material can function as a physical reservoir for robotic pattern recognition tasks. SWs were excited via voltage-controlled magnetic anisotropy in a CoFeB-based device, and the resulting interference patterns, representing the reservoir output states, are read out using magnetic tunnel junctions (Fig. 1c). We achieve accuracies of up to 100% in robotic obstacle recognition and classification tasks (Fig. 1d).

Our results establish wave-based neuromorphic computing as a promising alternative to digital architectures. By demonstrating SW-based robotic hardware, our work opens a new direction for spintronics research in robotic applications.

1. D. Marković, A. Mizrahi and D. Querlioz, and J. Grollier, Nature Reviews Physics., Vol. 2, p.499 (2020)

2. Y. Sandamirskaya, M. Kaboli and J. Conradt, Science Robotics., Vol. 7, p.eabl8419 (2022)

3. J. Zohar, D. Pinna, G. van der Laan, T. Hesjedal, and C.K. Safeer (submitted, under review)

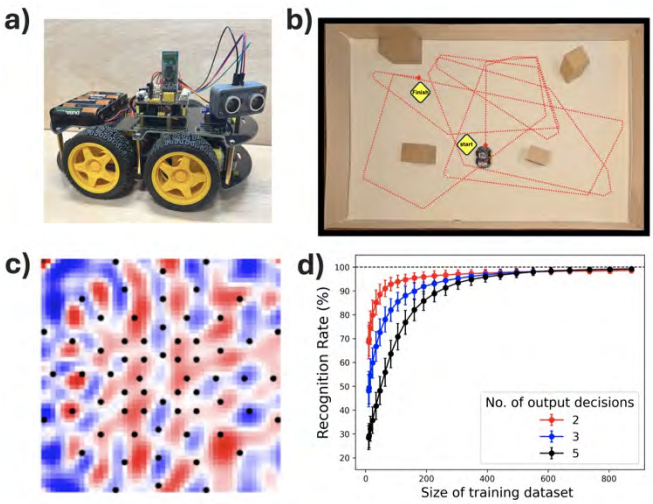


Fig. 1. a) Home-built robotic car. (b) Live robotic navigation demonstrating obstacle avoidance, controlled by wave-based neuromorphic hardware; the dotted line indicates the robot's path. (c) MuMax-simulated nanoscale spin-wave neural network evolving with robot inputs, where the resulting wave-interference patterns are used for classification. (d) Classification accuracy versus training data size for 2-, 3, and 5-maneuver robotic decisions based on obstacle sensing, achieving 100% accuracy.

FD-05. Spin Diodes Neural Chip for Low-Power RF Edge Spectrum Classification

Y. Wei, A. Begue, T. Rageau, F. A. Mizrahi, D. Sanz Hernandez, J. Grollier
CNRS, Thales, Univ. Paris-Saclay, Laboratoire Albert Fert, Palaiseau, France

Modern AI systems require enormous energy for both training and inference, motivating the exploration of alternative computing paradigms. Compute-in-memory (CIM) has emerged as a promising approach, with extensive research based on non-volatile memory technologies such as RRAM, MRAM, and PCM memristors.

For radio-frequency (RF) signal processing, conventional digital architectures require extremely high sampling rates and complex digitization hardware, leading to prohibitive size, weight, power, and cost (SWaP-C) constraints [1]. In contrast, spintronic devices enable direct analog processing of RF signals, offering a pathway toward RF-native neuromorphic computing [2–3].

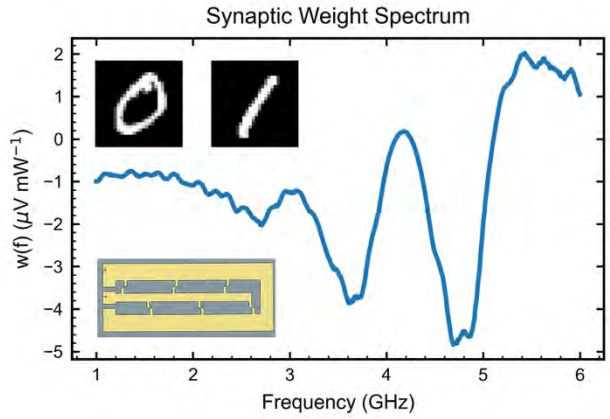
Here we demonstrate the feasibility of using spin diodes to perform large-scale synaptic multiply–accumulate (MAC) operations. Owing to the spin-rectification effect, the rectified DC voltage scales linearly with the injected signal RF power, with a proportionality factor determined by the frequency detuning between the diode resonance frequency and the signal excitation frequency.

The core hardware is a spin-diode chain composed of multiple permalloy microstrips connected in parallel. By placing the device in a magnetic-field gradient, each diode experiences a distinct local field and thus a different resonance frequency, enabling frequency-selective rectification of multiple RF inputs (Fig. 1).

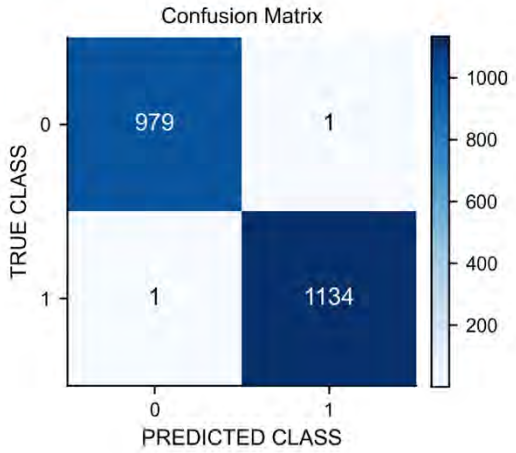
As a first proof of concept, we train a neural network in software to classify MNIST digits (0 vs 1) and transfer the learned weights onto the frequency-dependent responses W(f) of the spin-diode chain. Test images are encoded as distinct RF power spectra, and classification is performed by measuring the DC output voltage of the chain, achieving the same accuracy as the software model (Fig. 2). In this presentation, we will expand this approach towards more complex tasks, including the use of additional diode chains for multi-class classification (e.g., MNIST 0–9).

The architecture and workflows demonstrated by this work open the path to future scaled-up demonstrators in which spin-rectification is employed for efficient AI processing of radio-frequency inputs at a larger scale.

[1] Davis III R A. Combining RF Machine Learning and RF Photonics to Enable New Analog Communications Architectures[D]. Massachusetts Institute of Technology, 2024.
[2] Ross A, Leroux N, De Riz A, et al. Multilayer spintronic neural networks with radiofrequency connections[J]. Nature Nanotechnology, 2023, 18(11): 1273-1280.
[3] Plouet E, Singh H, Sethi P, et al. Convolutions with Radio-Frequency Spin-Diodes[C]//2024 IEEE International Electron Devices Meeting (IEDM). IEEE, 2024: 1-4.



Synaptic weight spectrum W(f).



Confusion matrix of the binary classification.

FD-06. Enriched Coupling Control via Correlated Phase Engineering in $La_{0.67}Sr_{0.33}MnO_3$ Oscillatory Neural Networks

H. Chhabra[1, 2], T. Banerjee[1, 2]
[1]*University of Groningen, Groningen Cognitive System and Materials Centre, Groningen, Groningen, Netherlands,*
[2]*University of Groningen, Zernike Institute for Advanced Materials, Groningen, Groningen, Netherlands*

Unconventional computing approaches exploit material systems that exhibit competing ground states, non-linear transport, and strong coupling between magnetic and electronic degrees of freedom. Examples include spintronic devices such as magnetic tunnel junctions, spin-torque nano-oscillators, and memristive oxides. Precise control of these emergent states is essential for devices beyond von Neumann paradigm.

La0.67Sr0.33MnO3 (LSMO), a strongly correlated mixed-valence manganite, provides a model system where magnetic order and charge transport are intrinsically coupled via the double-exchange mechanism. Under external bias, electro-thermal (Joule heating) effects disrupt Mn3+-Mn4+ eg electron hopping, driving a transition from a ferromagnetic metallic to a paramagnetic insulating phase. This transition manifests as threshold switching and is accompanied by transport instabilities (under non-equilibrium conditions) in the form of negative differential resistance (NDR). This volatile memristor exhibits neuron-like oscillations in a Pearson-Anson circuit [1, Fig.1]. The non-linear current response is temperature dependent [2,3, Fig.2] and is governed by strain-modified orbital hybridization and hopping dynamics [2]. When grown epitaxially on textured LaAlO3 substrates, structural twin boundaries induce spatially varying octahedral distortions, generating an inhomogeneous magnetic and electronic landscape with coexisting metallic and insulating regions. In this work, we engineer epitaxial LSMO films on different substrates and pattern microscale devices. By integrating an active heating channel and varying device dimensions, we control the coexisting magnetic phases responsible for conduction. This approach enhances the coupling between phase competition and transport non-linearity, enabling tunable oscillatory dynamics. Our results demonstrate how controlled manipulation of magnetically driven metal–insulator transition enriches the operational phase space of voltage-tunable oscillators, enabling oscillatory neural networks based on correlated magnetic oxides.

[1] A. Jaman et al., Adv. Funct. Mater., 2419840, 2025
[2] H. Chhabra et al., Adv. Elec. Mater., 12, no. 2 (2026): e00676
[3] P. Salev, et al., *Nat. comm.*, 12(1), 5499 (2021)

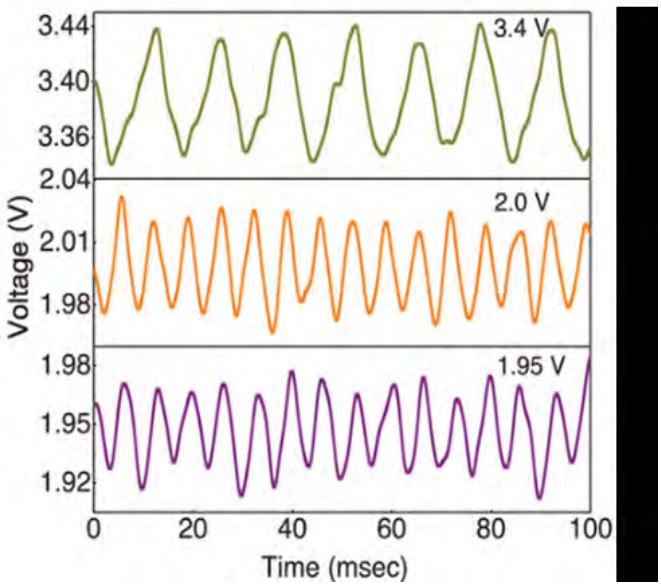


Fig.1 LSMO acting as an oscillatory neuron, recorded as a function of output voltage.

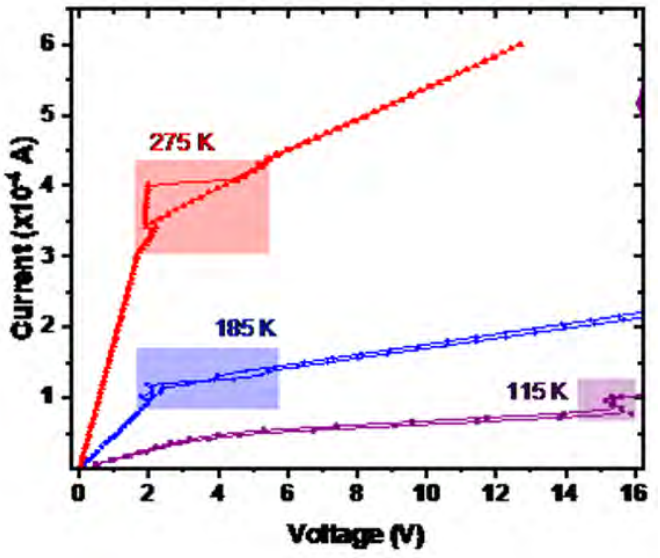


Fig.2 Variations in NDRs with increasing temperature from 115 K to 275 K

FD-07. Effects of Dimensional Scaling on Switching Characteristics of SOT–MRAM

V. Kateel, S. Van Beek, J. Urrestarazu Larranaga, M. Gama Monteiro, A. Das, A. Palomino Lopez, B. Coester, G. Talmelli, V. Nguyen, R. Carpenter, G. Sankar Kar, S. Rao
imec, Leuven, Belgium

Spin-orbit torque-based magneto-resistive random-access memory (SOT–MRAM) with a perpendicular magnetic tunnel junction (MTJ) is a promising solution for memory and in-memory computing applications, owing to its non-volatility, high endurance, and fast writing speeds [1-4]. However, the benefits of SOT–MRAM are counteracted by the high switching current densities. This, in turn, requires larger drive transistors, thereby increasing the bit-cell footprint and limiting SOT–MRAM's competitiveness. Several approaches have been proposed to mitigate this challenge, including the use of novel SOT materials [2], scaling of the SOT channel [3], and channel–less SOT–MRAM [4].

In this work, we investigate the impact of dimension scaling by either scaling the MTJ or by scaling both the SOT channel and the MTJs. The SOT channel width and MTJ CD (Fig. 1a) are scaled by varying the lithography dose during exposure, keeping the design CD constant.

We perform SOT switching at 1 ns and increasing lithography dose on MTJ results in a reduction of the electrical MTJ CD (eCD) to 25 nm and a corresponding reduction in the switching current (Fig. 1b). As illustrated in Fig. 2, deterministic switching with 100% switching probability is observed for devices with eCD > 27 nm. These devices exhibit characteristic SOT–driven behavior, including clockwise loops in the presence of an external magnetic field ($\mu_0 H_x$) = 30 mT. In this talk, we also discuss reliability by showing endurance, bit-error-rate, and field-free switching measurements. For devices with eCD < 25 nm, stochastic switching is observed, as the Delta ~ 21 $k_B T$. Despite the stochastic behavior, switching remains governed by SOT physics. We will explain this regime by correlating the magnetic properties of the MTJs with their chemical and structural characteristics. Overall, the dimensional scaling approach is material–agnostic, offering a practical pathway toward reducing switching current.

[1] L. Liu, et al, Physical Review Letters, vol. 109, no. 9, p. 096602, Aug. 2012.
[2] Q. Shao et al, IEEE Transactions on Magnetics, 57 1-39, (2021).
[3] S. Van Beek *et al.*, "Scaling the SOT track – A path

towards maximizing efficiency in SOT-MRAM," *2023 International Electron Devices Meeting (IEDM)*, pp. 1-4.
[4] E. Liu *et al*., "A Novel Channel-Less SOT-MRAM with 115% TMR, 2 ns Switching, and High Bit Yield (>99.9%)," *2024 IEEE International Electron Devices Meeting (IEDM)* pp. 1-4.

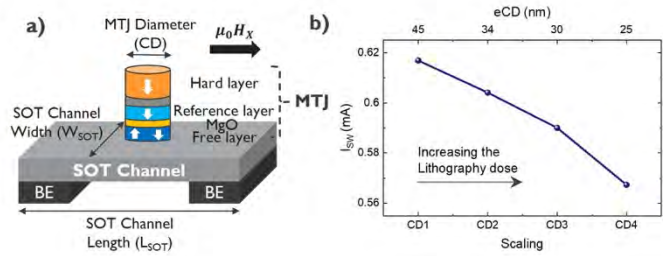


Fig. 1: Schematic of SOT–MRAM. b) Reduction in the eCD and median switching current due to MTJ scaling for over 30 devices per CD.

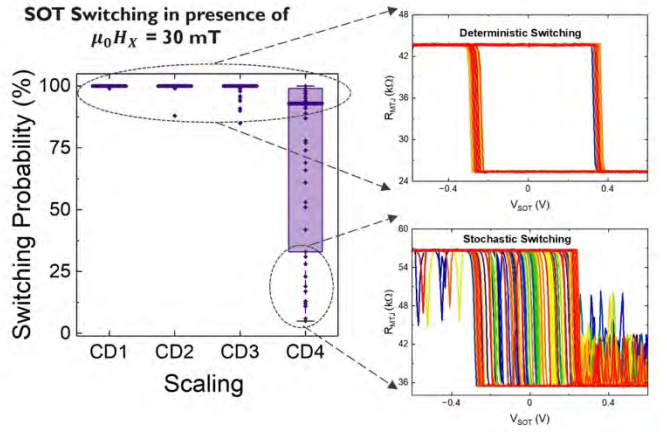


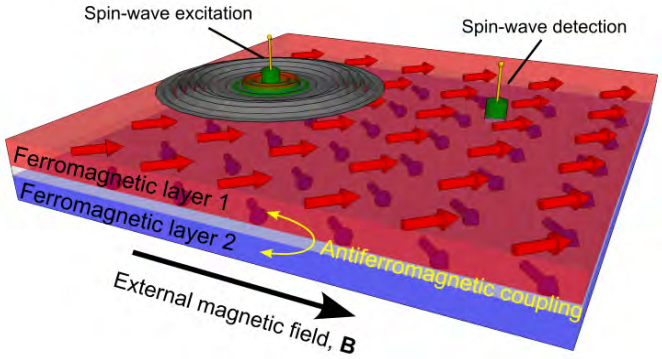
Fig. 2: Switching probability as a function of MTJ scaling. The SOT loop showing deterministic and stochastic switching (colors indicate different switching cycles).

FD-08. Propagating spin waves in synthetic antiferromagnets provide distinct memory properties in spin-wave-based reservoir computing

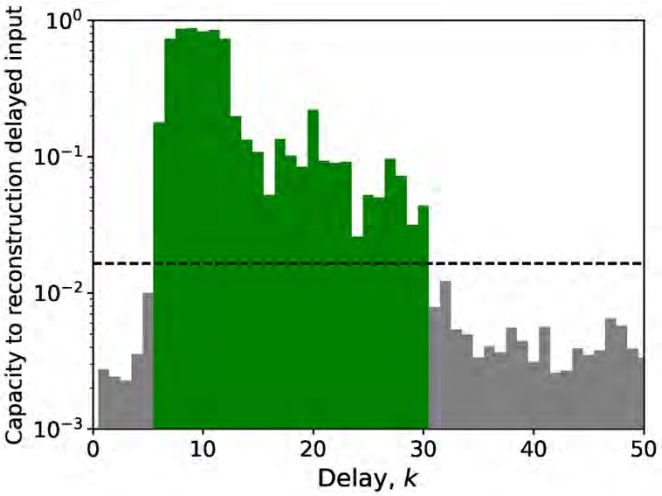
T. Shinkai[1], S. Iihama[1], K. Hayashi[1], S. Mizukami[2, 3], N. Yoshinaga[4], T. Moriyama[1]
[1]Department of Materials Physics, Nagoya University, Nagoya, Aichi, Japan, [2]WPI Advanced Institute for Materials Research (AIMR), Tohoku University, Sendai, Miyagi, Japan, [3]Center for Science and Innovation in Spintronics (CSIS), Tohoku University, Sendai, Miyagi, Japan, [4]Department of Complex and Intelligent Systems, Future University Hakodate, Hakodate, Hokkaido, Japan

Physical reservoir computing (RC) has attracted increasing attention as a promising approach for realizing energy-efficient physical implementations of artificial intelligence. Spin-wave-based RC is particularly attractive due to its high-speed operation and low power consumption. Spin waves can propagate over nanoscale distances at relatively low speeds, leading to larger memory capacities in RC at the nanoscale [1]. However, most of the previous studies have focused on single-layer ferromagnets, where only a single spin-wave mode is available, limiting the degree of freedom in controlling memory properties in RC.
In this work, we investigate spin-wave RC using synthetic antiferromagnets (SAFs) which host two distinct eigenmodes, namely acoustic (AC) and optical (OP) modes (Fig. 1). Micromagnetic simulations were performed using Mumax[3] for a bilayer SAF structure with antiferromagnetic interlayer coupling. Spin waves were locally excited via spin-transfer torque at an input node, and the magnetization dynamics at an output node were detected. The memory property of the spin-wave RC was evaluated by reconstructing delayed input time-series using the spin-wave dynamics. The memory curve was obtained by the capacity to reconstruct delayed time-series with delay *k* as a function of *k* (Fig. 2).
We found that the average delay of the memory curve <*k*> was significantly different between the AC and OP modes in SAFs. This indicates the emergence of two distinct memory properties in the single device of spin-wave-based RC. The average delays <*k*> were quantitatively explained by different spin-wave group velocities in the AC and OP modes [2].
These results demonstrate that SAF-based systems provide additional memory properties, which cannot be realized using single-layer ferromagnets. Our findings suggest that mode-dependent spin-wave propagation in SAFs offers a promising route towards designing distinct memory properties in spin-wave-based RC, which might have potential to be used for prediction of time-series data with diverse timescale dynamics.

[1] S. Iihama *et al*., npj Spintronics 2, 5 (2024)
[2] T. Shinkai *et al.,* arXiv:2603.22696



(Fig. 1) Schematic illustration of spin-wave-based RC using SAF.



(Fig. 2) Typical memory curves obtained by using SAF-based RC

FD-09. Skyrmion-based Spintronic Reservoir Computing for Human Action Classification in Videos

S. Sabyasachi[1], M. Alam[1], M. Rajib[1], J. Atulasimha[1, 2]
[1]Mechanical & Nuclear Engineering, Virginia Commonwealth University, Richmond, Virginia, United States, [2]Electrical & Computer Engineering, Virginia Commonwealth University, Richmond, Virginia, United States

Spatio-temporal data classification is a computationally expensive task. While physical reservoir computing has been widely explored for time series prediction [1], recent approaches expanded it to complex spatio-temporal tasks such as video data classification with photonic implementations [2]. Spintronic reservoirs remain comparatively unexplored in this field despite CMOS compatibility and low energy consumption. Conventional video classification applies CNNs on video frames followed by an LSTM to capture temporal dependencies.. Physical reservoirs can offer energy and latency advantage over LSTM during training and inference. In this work, we replaced the LSTM layer with a spintronic skyrmion based physical reservoir (Fig. 1) preceded by principal component analysis (PCA). UCF11 was selected as the benchmark dataset for video-based human action classification.

The reservoir consists of a thin-film hosting 16×16 skyrmion array (Fig. 2), with each skyrmion occupying 768 nm × 768 nm area. The input data is modulated with uniaxial anisotropy $K_u(t)$ while the out of plane magnetization component $m_z(t)$ is read out as reservoir state. The nonlinear dynamics of skyrmions map input data to a higher dimensional space. The $m_z(t)$ values are passed to the output layer with ridge regression.

The video data is pre-processed prior to transmission to the reservoir. The video frames are sent to a Resnet-50 CNN with the last five layers retrained using transfer learning. The 2048-dimensional output is sent to PCA, reducing dimensionality to 256 to match the 16×16 skyrmion array. Each video is sampled at 20 frames and frame features are streamed to the reservoir at 1 ns intervals. The recorded $m_z(t)$ is passed to ridge regression for classification. The current approach provided 85% classification accuracy on a subset of UCF11, demonstrating the capability of the skyrmion reservoir to capture the temporal dependencies for video data classification. Ongoing work extends the evaluation to the full UCF11 dataset and optimizes the device design for improved latency and energy efficiency

[1] W. A. Misba, H. S. Mavikumbure and M. M. Rajib, IEEE Access., Vol. 11, p.124725 (2023).
[2] E. Picco, P. Antonik and S. Massar, Neural Networks., Vol. 165, p.662 (2023).



Fig. 1: Complete architecture

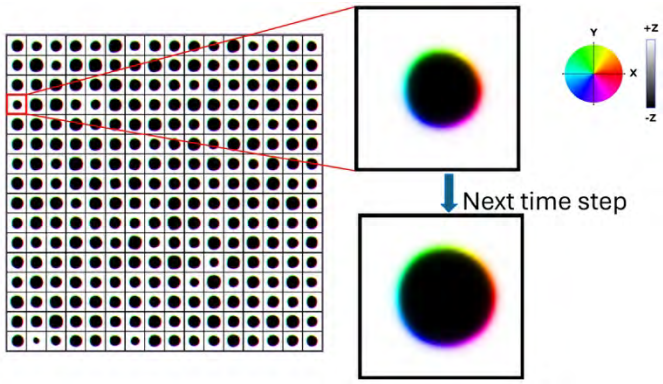
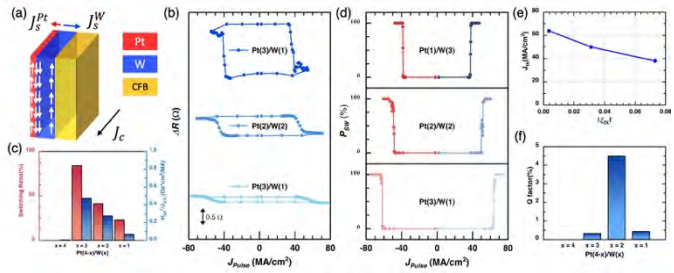


Fig. 2: 16×16 skyrmion array; right: highlighted skyrmion at two consecutive time steps.

FD-10. Competing Spin Hall Effects Enable Field-free Stochastic Switching for True Random Number Generation

J. Hsu[1], C. Hsu[2], Y. Lin[2], W. Chang[3], Y. Tseng[2]
[1]Industry Academia Innovation School, National Yang Ming Chiao Tung University, Hsinchu, None Selected, Taiwan, [2]Materials Science and Engineering, National Yang Ming Chiao Tung University, Hsinchu, None Selected, Taiwan, [3]Powerchips Semiconductor Manufacturing Corporation, Hsinchu, None Selected, Taiwan

Unlike CMOS-based random number generators (RNGs) that require post-processing, MTJ-based RNGs directly exploit thermally driven stochastic magnetization dynamics near the switching threshold. In this regime, randomness naturally emerges from the competition between thermal fluctuations and spin-torque-induced energy modulation, enabling efficient true random number generation (TRNG). We demonstrate field-free switching (FFS) in type-Z spin–orbit torque (SOT) devices with a Pt/W composite channel. The type-Z architecture is key to enabling intrinsic symmetry breaking without external magnetic fields. This arises from the opposite spin Hall angles of Pt and W, which generate competing spin currents and produce an internal net effective field. The effective field and FFS are tunable via the Pt/W thickness combination, with the FFS ratio (defined as $\Delta R_{SOT}/\Delta R_{AHE}$) increasing from 23% to 84%, reflecting controlled modulation of the spin-current balance and energy landscape asymmetry. Increasing W thickness enhances spin Hall efficiency and reduces the threshold current density, consistent with the stronger damping-like torque observed independently. From a stochastic perspective, switching follows a thermally assisted probabilistic process governed by spin torque and thermal noise. The Pt(2 nm)/W(2 nm) stack exhibits the highest Q-factor among all tested configurations, indicating an optimal balance between randomness quality and switching sensitivity. Powerchip Semiconductor Manufacturing Corporation supports this work.



Field-free switching and stochastic dynamics in Pt/W/CoFeB heterostructures.
(a) Schematic of the Pt(4−x)/W(x)/CoFeB stack (total Pt/W thickness = 4 nm), where opposing spin currents arise from Pt and W under charge current.
(b) Field-free (Hx=0) current-induced switching loops for different Pt/W thickness combinations.
(c) Field-free switching ratio (left y-axis & red bars) and effective field efficiency (right y-axis & blue bars) versus Pt/W combination.
(d) Switching probability (P_{SW}) versus pulse current density for different Pt/W thickness combinations.
(e) Correlation between threshold current density (J_{th}) and SOT efficiency ($|\xi_{DL}|$).
(f) Calculated Q-factor comparison across Pt/W combinations.

FD-11. Solving combinatorial optimization problems using Landau-Lifshitz–Gilbert spin dynamics

D. Chen[1], B. H. Chiang[1], D. Sels[2, 3], F. Morone[1], A. D. Kent[1]
[1]Physics, New York University, New York, New York, United States, [2]Physics, Boston University, Boston, Massachusetts, United States, [3]Center for Computational Quantum Physics, Flatiron Institute, New York, New York, United States

Physical dynamics have long inspired new ways of computing. Recent progress in *Ising machines*—physical systems that solve optimization problems by evolving toward minima of Ising-like Hamiltonians—motivates studying how different non-classical computing models derive their computational advantages from underlying physical dynamics. In our previous work, we showed that a bit encoded in a macrospin evolving under Landau–Lifshitz–Gilbert (LLG) dynamics can efficiently find the ground state of the Sherrington–Kirkpatrick (SK) model and

approach the exact solution for the average energy per spin found, the Parisi value, asymptotically as the number of spins approaches infinity[1]. However, the SK model is not hard in the sense that it does not exhibit the overlap gap property (OGP), a topological feature associated with algorithmic hardness[2]. This raises the question of how macrospin-based LLG dynamics perform on problems that do exhibit OGP, and which features of the dynamics may help or hinder traversal between clusters of local minima separated by such gaps.

In this work, we apply the LLG framework to the 3-spin model, which is known to exhibit the OGP. A recent study of the 3-spin model provides the current best results for the 3-spin Hamiltonian and serves as a benchmark for comparison [3]. We also evaluate Glauber dynamics, and will present a comparison to oscillator-based models and p-bits. Our current results for LLG and Glauber dynamics on the 3-spin model, compared with the benchmark, are shown in Fig. 1. We find that LLG dynamics outperform Glauber dynamics, achieving results within 3.4% of the benchmark. To identify the key ingredients underlying this advantage, we further compare zero-temperature LLG dynamics across different anisotropy and damping (α) values. These results provide physical insight into which dynamical properties make certain physical systems advantageous for solving optimization problems, and may help guide the design of future Ising-inspired computing architectures.

[1] D. Chen, A. D. Kent, D. Sels, and F. Morone, Phys. Rev. Res. 7, 013129 (2025)
[2] D. Gamarnik, Proc. Natl. Acad. Sci. U.S.A. 118 (41) (2021).
[3] Boettcher and Lau, Phys. Rev. Lett. 135, 037402 (2025)

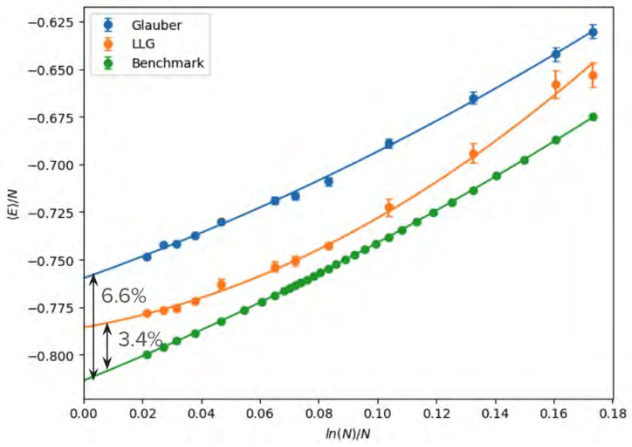


Fig 1. Results for LLG macrospin dynamics, Glauber dynamics on solving the 3-spin model, with benchmark results from Boettcher and Lau [3].

SESSION FE: TOPOLOGICAL MATERIALS, CHIRAL MAGNETS AND CORRELATED SYSTEMS

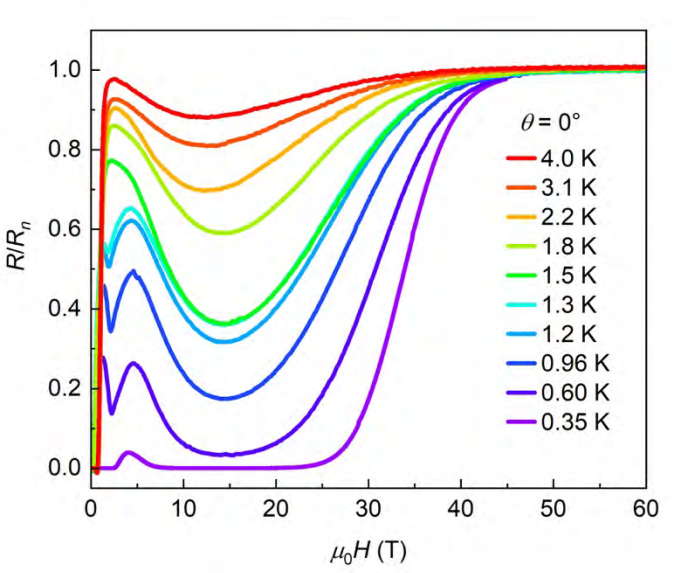
Chair(s): R. He, *The University of Texas at Arlington, Arlington, Texas, United States*
Thursday, November 5, 2026
02:00 PM-05:30 PM
South Pacific 1/2

FE-01. Magnetic field-reentrant superconductivity in infinite-layer nickelates

K. Rubi
National High Magnetic Field Laboratory, Los Alamos National Laboratory, Los Alamos, New Mexico, United States

Magnetic fields typically suppress superconductivity through Pauli and orbital limiting effects. However, there are rare instances of magnetic-field-induced superconductivity, as seen in Chevrel phase compounds [1], organic conductors [2], uranium-based heavy-fermion systems [3, 4], and moire graphene [5] although these materials possess inherently low superconducting transition temperatures (T_c). In this talk, I will present a high field-reentrant superconductivity in a class of materials with a significantly higher T_c: the infinite-layer nickelates [6, 7]. Both low-field and high-field superconducting states (Fig. 1) can be plausibly explained by a compensation mechanism akin to the Jaccarino-Peter effect. These findings highlight the technological potential of nickelates for ultra-high magnetic field applications such as superconducting magnets and quantum magnetometers.

[1] H. W. Meul et al, Phy. Rev. Lett. 53, 497 (1984).
[2] S. Uji et al, Nature 410, 908 (2001).
[3] F. L_evy, I. Sheikin, B. Grenier, and A. D. Huxley, Science 309, 1343 (2005).
[4] S. Ran et al., Science 365, 684 (2019).
[5] Y. Cao et al. , Nature 595, 526 (2021).
[6] S. L. E. Chow, Z. Luo, and A. Ariando, Nature 642, 58 (2025).
[7] K. Rubi et al., arXiv:2508.16290 (2025).



Reentrant superconductivity at high magnetic fields in (Sm-Eu-Ca)NiO_2. Measured renormalized electrical resistivity R/R_n versus magnetic field H of a sample T_c = 9.6 K at different temperatures H applied along the c axis.

FE-02. One-dimensional magnetic soliton layers in a cubic chiral magnet

G. Causer[1, 2], M. Azhar[4], T. Hesjedal[5], M. Garst[3], C. Pfleiderer[2]
[1]European Spallation Source, Lund, Sweden, [2]Technical University of Munich, Munich, Germany, [3]Karlsruhe Institute of Technology, Karlsruhe, Germany, [4]University of Duisburg-Essen, Duisburg, Germany, [5]Oxford University, Oxford, United Kingdom

The discovery of topological protected states in chiral magnets inspired a renaissance in the field of non-collinear magnetism, and led to the identification of several long-wavelength spin objects including skyrmions, merons, solitons, and chiral bobbers. Small angle neutron scattering (SANS) has provided fundamental insights of these magnetic textures in bulk materials, whose associated topological properties are discussed in the context of low-energy information carriers. SANS of such structures in thin films or micro-structured bulk materials is, however, strongly limited by the tiny scattering volume and the prohibitively large background scattering by the substrate and support structures.

In this talk I will discuss near-surface SANS, performed slightly above the critical angle of reflection, as a route to overcome the shortcomings of transmission SANS for extremely small magnetic sample volumes in the thin-film limit [1,2]. Proof-of-concept measurements performed on bulk MnSi establish equivalent scattering patterns of the helical, conical, and skyrmion lattice phases between transmission and near-surface SANS geometries [3]. Near-surface SANS performed on epitaxial MnSi reveals a phase diagram which differs distinctly from bulk, and comprises of a single-domain, out-of-plane propagating helix with λ = 11.5 nm in zero-field. Our experimental findings are supported by micromagnetic simulations which depict a magnetic phase diagram dominated by a field-induced unwinding of soliton layers. Field and temperature history provide specific routes for the nucleation of the distinct soliton phases, comprising namely of four-, three-, two-, and single-soliton layers depending on the field strength. This work showcases the applicability of NS-SANS for the study of nano-confined magnetic materials, which would otherwise possess insufficient scattering volumes to be measured in transmission, and provides insights into the role of anisotropy and dimensionality on the phase diagrams of micro-structured bulk materials.

[1] G. L. Causer, J. Appl. Cryst., 58, 1455-1461 (2025)
[2] G. L. Causer *et al.*, Phys. Status Solidi RRL, 2200421 (2023)
[3] G. L. Causer *et al.*, J. Appl. Cryst., 56, 26-35 (2023)

FE-03. Deciphering the new magnetic state, "B-Phase", found in MnSi at Low Temperatures

M. Pardo-Sainz[1, 3], Y. Kousaka[3], M. Mito[4], K. Ohishi[5], K. Kojima[6], V. Laliena[2], J. Campo[1]
[1]Spanish National Research Council (CSIC), Zaragoza, Spain, [2]University of Zaragoza, Zaragoza, Spain, [3]Osaka Metropolitan University, Sakai, Japan, [4]Kyushu Institute of Technology, Kita-Kyushu, Japan, [5]CROSS, Tokai, Japan, [6]TRIUMF, Vancouver, British Columbia, Canada

In cubic chiral magnets, Dzyaloshinskii-Moriya (DM) interactions within the chiral crystal structure result in diverse magnetic textures, including skyrmion lattices (SkL) and chiral soliton lattices, which hold promise for spintronic and magnonic devices. Among these, MnSi has been extensively studied due to the SkL formation in the so-called "A-phase" just below T_c [1]. Recently, it was suggested theoretically that at low temperatures (T), the conical helimagnetic (CH) and forced-ferromagnetic (FFM) phases in MnSi might not be directly connected but separated by another SkL phase, possibly metastable, or a new phase of unknown nature near the critical magnetic field (B_c) [2]. The theoretical prediction of the new SkL phase at low T is in good agreement with the experiments reported in MnSi and Cu_2OSeO_3 [3,4]. On the other hand, by using careful ac susceptibility measurements at low

temperature, we determined the magnetic phase diagrams of oriented crystals of MnSi [5]. A new anomalous region, termed “B-phase”, was observed when the magnetic field was applied along the main diagonal <111>.
To clarify the nature of the “B-phase”, we performed small-angle neutron scattering (SANS) measurements at TAIKAN in J-PARC and transverse field (TF)-μSR experiments at TRIUMF. At low temperatures and fields near B_c, SANS patterns revealed two peaks along the horizontal axis, corresponding to the magnetic Bragg peaks of the CH state. Notably, no diffraction peaks indicative of a six-fold-symmetric SkL were observed. Meanwhile, μSR results showed a distinct internal magnetic field distribution in the “B-phase”, different from those in the CH or FFM phases, suggesting that the “B-phase” could involve a reorientation of Mn helices within the unit cell.
In the presentation, we will discuss these SANS and μSR findings in detail and their implications for understanding the spin texture in the “B-phase”.
1. S. Mühlbauer *et al.*, Science 323, 915 (2009).
2. V. Laliena and J. Campo, Phys. Rev. B 96, 134420 (2017).
3. T. Nakajima *et al.*, Sci. Adv. 3, e1602562 (2017).
4. A. Chacon *et al.*, Nature Phys 14, 936–941 (2018).
5. M. Ohkuma *et al.*, APL Mater. 10, 041104 (2022).

FE-04. Mn enrichment in candidate magnetic topological insulators Mn-Sb(Ge)-Te: when more becomes less

E. Kochetkova[1], T. Groot[1], M. Tardieux[1], L. Corredor[2, 3], I. Aguilera[1], A. Isaeva[2, 3, 1]
[1]Physics, University of Amsterdam, Amsterdam, Netherlands, [2]Physics, Technical University of Dortmund, Dortmund, Germany, [3]Research Center "Future Energy Materials and Systems", Dortmund, Germany

Magnetic topological insulators enable the quantum anomalous Hall effect and axion electrodynamics,[1] but envisioned applications would require systems that combine net magnetization, high magnetic ordering temperature, and a non-trivial band topology. Van der Waals tellurides MnX_2Te_4 (X = Bi, Sb) is a promising platform because their magnetic order and band inversion can be tuned via Mn/X site intermixing.[2,3]
We find that Mn enrichment in $MnSb_2Te_4$ stabilizes a layered trigonal compound $Mn_{1.90(1)}Sb_{1.39(1)}Te_4$ [4] with ferrimagnetic order up to T_C = 65-73 K (Fig. 1, left). However, simultaneous Mn enrichment and Ge-doping induce a rocksalt-type disordered cubic lattice $Mn_{0.56}Ge_{0.09}Sb_{0.23}Te$, which is a low-temperature antiferromagnet below $T_N \approx 24$ K (Fig. 1, right). Similar order-disorder transitions are well-known in the Ge-Sb-Te phase change materials. Here, we demonstrate for the first time their coupling with the magnetic order.
The trigonal Mn-rich phase [4] has the same lattice as $MnSb_2Te_4$; however, the former hosts three Mn sublattices that strengthen magnetic exchange. DFT+U confirms that coupling between Mn sublattices is antiferromagnetic, but unequal Mn populations generate a net moment. The electronic structure retains a band inversion, suggesting a ferrimagnetic topological material.
The disordered cubic phase is isostructural to a metastable polymorph of MnTe. DFT+U finds several nearly competing antiferromagnetic states, with the lowest-energy configuration consistent with A-type stacking of ferromagnetic (111) planes. The electronic structure is metallic and lacks a topological band inversion near the Fermi level.
“More Mn” is not a sufficient design rule: net magnetization and a topological band structure appear when Mn distribution is inequivalent over magnetic sublattices in a layered lattice. In contrast, statistical disorder in a cubic rocksalt lattice, which is likely entropy-stabilized, suppresses the desired physical properties.
[1] Y. Tokura et al., *Nat. Rev. Phys.*, Vol. 1, p. 126 (2019).
[2] M. Otrokov et al., *Nature*, Vol. 576, p. 416 (2019).
[3] Y. Liu et al., *Phys. Rev. X*, Vol. 11, p. 021033 (2021).
[4] E. Kochetkova et al., *Chem. Mater.*, Vol. 37, p. 1446 (2025).

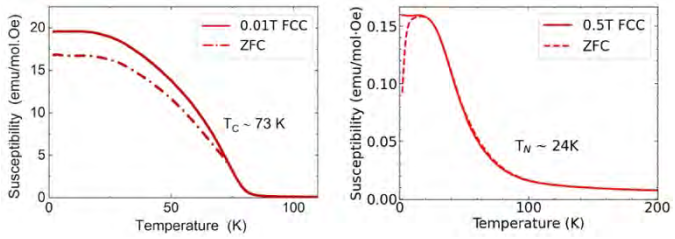


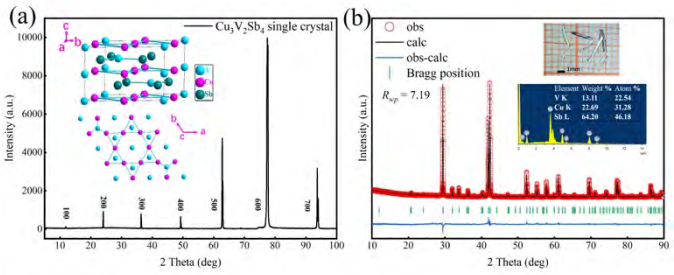
Fig. 1. DC magnetic susceptibility as a function of temperature for layered $Mn_{1.90}Sb_{1.39}Te_4$ (left) and cubic $Mn_{0.56}Ge_{0.09}Sb_{0.23}Te$ (right).

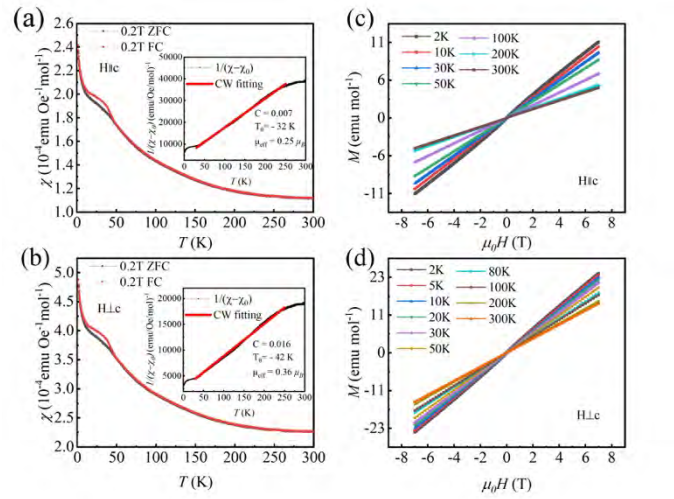
FE-06. Physical properties and correlated electron behavior of Kagome metal $Cu_3V_2Sb_4$

M. Liu[1], C. Liu[1], H. Wu[2, 1], X. Zhou[1], D. Liu[1], S. Li[1], Z. Shi[1]
[1]Southeast University, Nanjing, Jiangsu, China, [2]Jiangsu University of Science and Technology, Zhenjiang, China

Kagome lattice materials have emerged as an ideal platform for exploring topological quantum states and strong correlations due to their unique geometric structures that give rise to Dirac cones, Van Hove singularities, and flat bands[1-5]. We report the successful synthesis and comprehensive characterization of a Kagome metal $Cu_3V_2Sb_4$. This material exhibits a quadratic temperature dependence of resistivity over a broad temperature range, indicative of strong electron-electron interactions, as confirmed by specific heat measurements with the Kadowaki–Woods ratio lies between transition metal and heavy fermion systems. Magnetoresistance measurements reveal a linear magnetic field dependence at low temperatures, while Hall effect measurements display nonlinear behavior describable with a semi-classical two-band model. Angular-dependent magnetoresistance further reveals a twofold symmetry. These results collectively suggest an evolution of the band structure within the temperature range of 50 ~ 80 K. Magnetic susceptibility measurements indicate paramagnetic behavior with evidence of short-range magnetic correlations emerging near 25 K. Our findings broaden the material landscape of Kagome metals and provide a promising platform for exploring correlated electron states and topological quantum phenomena in novel quantum materials.

[1]W. H. Ko, P. A. Lee, X. G. Wen, Doped kagome system as exotic superconductor, *Phys. Rev. B* 79, 214502 (2009).
[2]A. O'Brien, F. Pollmann, P. Fulde, Strongly correlated fermions on a kagome lattice, *Phys. Rev. B* 81, 235115 (2010).
[3]M. L. Kiesel, R. Thomale, Sublattice interference in the kagome Hubbard model, *Phys. Rev. B* 86, 121105(R) (2012).
[4]S. L. Yu, J. X. Li, Chiral superconducting phase and chiral spin-density-wave phase in a Hubbard model on the kagome lattice, *Phys. Rev. B* 85, 144402 (2012).
[5]W. S. Wang, Z.-Z. Li, Y.-Y. Xiang, Q.-H. Wang, Competing electronic orders on kagome lattices at van Hove filling, *Phys. Rev. B* 87, 115135 (2013).





FE-07. Experimental investigation of the third-order nonlinear Hall effect in ferromagnetic Weyl semimetal $Co_3Sn_2S_2$ thin films

S. Kazami[1], J. Han[1], T. Uchimura[1], K. Fujiwara[2], K. Nihei[1], S. Kanai[1], A. Tsukazaki[3, 1], S. Fukami[1]
[1]Tohoku University, Sendai, Japan, [2]Rikkyo University, Tokyo, Japan, [3]The University of Tokyo, Tokyo, Japan

Nonlinear Hall effect, where the Hall voltage is no longer linearly proportional to the applied charge current, effectively probes the topologically non-trivial properties of electronic materials. The nonlinear order is generally determined by the multipole structure of quantum geometry, following symmetry restrictions [1]. In practice, clarifying the quantum-geometric origin of a nonlinear Hall effect is challenging as the nonlinear order goes high, due to the increasing number of competing mechanisms. Here we show a protocol of measuring and interpreting a third-order Hall effect in a ferromagnetic Weyl semimetal $Co_3Sn_2S_2$ (CSS) by taking advantage of its large Berry curvature and simple magnetic order represented by a unit magnetization [2].

The epitaxial CSS films are deposited by magnetron sputtering and patterned to Hall bar devices [3]. The harmonic technique is applied to probe the first- and third-order Hall effects while sweeping an out-of-plane magnetic field at different temperatures. The device exhibits a strong perpendicular magnetic easy axis below its Curie temperature around 180 K. The third-order Hall effect (Fig. 1) flips its sign together with its first-order counterpart, indicating that it is due to magnetization reversal and thus subject to time-reversal symmetry breaking. By varying the device temperature (T), we first evaluate the T-induced variation of the first-order Hall effect and subtract its contribution from the third-order signal, resulting in a finite non-trivial component (Fig. 2). Through a scaling analysis between such non-trivial third-order Hall conductivity and the longitudinal linear conductivity, we disentangle multiple contributions to the third-order signal, by which we find signature that the quantum-geometric contributions become more significant as the longitudinal conductivity decreases (i.e., T increases). This work provides useful insights to understand the trivial and non-trivial contributions to higher-order nonlinear transport in topological magnets.

[1] Q. Ma, *et al.* Nature 565, 337 (2019).
[2] N. Morali, *et al.* Science 365, 1286 (2019).
[3] K. Fujiwara, *et al.* Jpn. J. Appl. Phys. 58, 050912 (2019).

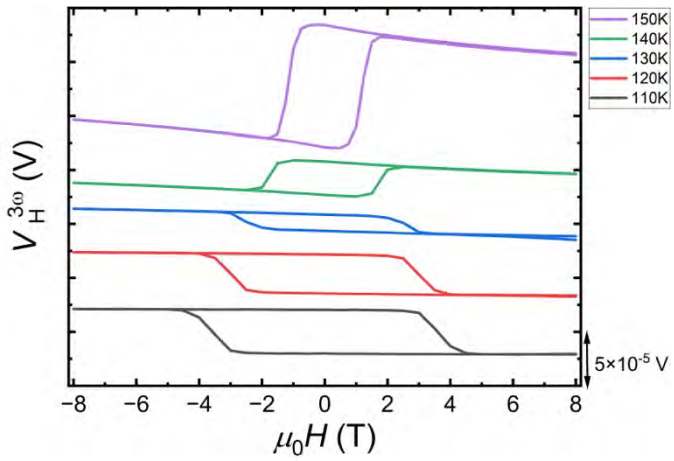


Fig. 1. Third-order Hall voltage *vs* out-of-plane magnetic field, at temperatures from 150 to 110 K.

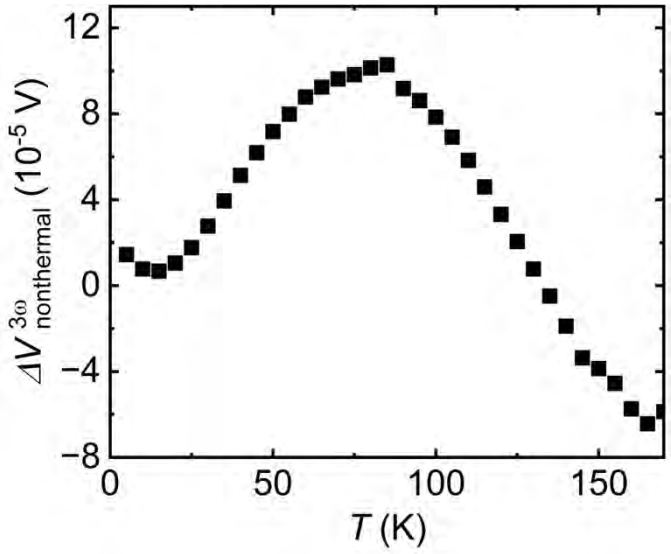


Fig. 2. Magnitude of the third-order Hall voltage *vs* temperature, after subtracting the thermal contribution.

FE-09. Avoiding the Spin Glass: Random Singlet Physics in the Disordered *S* = 1/2 Pyrochlore Antiferromagnet $NaCdCu_2F_7$

A. Kancko[1], H. Sakai[2], C. A. Correa[3], P. Proschek[1], J. Prokleška[1], T. Haidamak[1], M. Uhlarz[4], A. Berlie[5], Y. Tokunaga[2], R. H. Colman[1]

[1]Department of Condensed Matter Physics, Faculty of Mathematics and Physics, Charles University in Prague, Prague, Czechia, [2]Advanced Science Research Center, Japan Atomic Energy Agency, Tokai, Ibaraki, Japan, [3]Institute of Physics, Czech Academy of Sciences, Prague, Czechia, [4]Hochfeld-Magnetlabor Dresden (HLD-EMFL), Helmholtz-Zentrum Dresden-Rossendorf (HZDR), Dresden - Rossendorf, Germany, [5]ISIS Neutron and Muon Source, Rutherford Appleton Laboratory, Science and Technology Facilities Council, Chilton, Oxfordshire, United Kingdom

Weak quenched disorder in geometrically frustrated magnets typically induces spin-glass freezing through disorder-induced randomness in exchange couplings. [1] In contrast, strong $S = ½$ quantum fluctuations can suppress freezing and instead stabilize quantum-disordered states such as the random-singlet (RS) state, characterized by a broad distribution of exchange couplings $P[J] \sim J^{-\alpha}$, leading to a formation of localized singlets over multiple length scales and weakly-coupled "orphan spins". This is noted by a power-law scaling of bulk and local-probe thermodynamic quantities, with data collapse as a function of temperature and field *T*/*H*. [2]

We report conclusive evidence for an RS ground state in the extremely rare instance of a $S = ½$ Heisenberg pyrochlore antiferromagnet – $NaCdCu_2F_7$ [3], where intrinsic cationic Na^+/Cd^{2+} disorder induces random $Cu^{2+}–F^-–Cu^{2+}$superexchange interactions on the frustrated lattice of corner-sharing tetrahedra. No long-range magnetic order or canonical spin freezing is observed down to 58 mK via muon spin relaxation (μSR) and ^{23}Na nuclear magnetic resonance (NMR) measurements, despite strong antiferromagnetic interactions (ϑ_{CW} = -72 K) present in this material. Magnetic susceptibility, isothermal magnetization, and specific heat indicate a disorder-driven network of random singlets and orphan spins. Convincingly, evidence of power-law scaling (with $\alpha = 0.68–0.74$) and data collapse can be found in each of these experimental probes.

Importantly, this behavior contrasts with previously studied isostructural, higher-spin $NaAM_2F_7$ [4–6] (*A* = Ca, Sr, Cd; *M* = Co, Ni, Mn, Fe) pyrochlore fluorides, where comparable magnetic bond disorder leads to the expected spin-glass freezing at $T_f \sim$ 2-4 K. The absence of spin freezing in $NaCdCu_2F_7$ indicates that strong $S = ½$ quantum fluctuations suppress the glassy state and instead stabilize a quantum-disordered RS phase.

These results establish $NaCdCu_2F_7$ as the first realization of an RS state in a three-dimensional frustrated pyrochlore magnet, highlighting the key role of disorder and quantum fluctuations in stabilizing novel quantum phases.

[1] M. B. Sanders *et al.*, J. Phys. Condens. Matter 29, 045801 (2017).
[2] I. Kimchi *et al.*, Nat. Commun. 9, 4367 (2018).
[3] A. Kancko *et al.*, Phys. Rev. Res. 8, 013344 (2026).
[4] A. Kancko, G. Giester, and R. H. Colman, Phys. Scr. 98, 075947 (2023).
[5] A. Kancko, C. A. Corrêa, and R. H. Colman, J. Alloys Compd. 1024, 180142 (2025).
[6] J. W. Krizan and R. J. Cava, Phys. Rev. B 89, 214401 (2014).

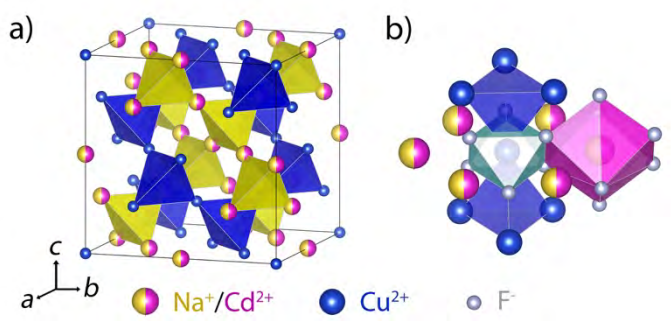


Fig.1: (a) Cubic pyrochlore unit cell of $NaCdCu_2F_7$. (b) Local environment around the Cu^{2+} site.

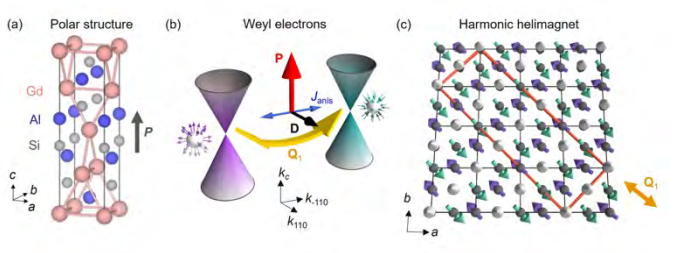
FE-10. Harmonic helimagnetism and competing multi-Q orders in the inversion broken Weyl semimetal GdAlSi

R. Nakano[1], R. Yamada[1], J. Bouaziz[2], M. Colling[3, 4], M. Gen[5, 6], K. Shoriki[1], Y. Okamura[1], A. Kikkawa[5], R. Misawa[1], P. R. Baral[1], S. Kitou[7], Y. Nakamura[8], H. Ohsumi[9], Y. Tanaka[9], H. Sagayama[10], H. Nakao[10], Y. Ishihara[1], K. Gautam[5], O. Fabelo[11], Y. Taguchi[5], Y. Takahashi[1, 5], M. Tokunaga[5, 6], T. Arima[5, 7], Y. Tokura[1, 5, 12], R. Arita[5, 13], J. Masell[4, 5], S. Hayami[14], M. Hirschberger[1, 5]

[1]Department of Applied Physics and Quantum-Phase Electronics Center, The University of Tokyo, Tokyo, Japan, [2]Research Center for Advanced Science and Technology, The University of Tokyo, Tokyo, Japan, [3]Department of Materials Science and Engineering, Norwegian University of Science and Technology (NTNU), Trondheim, Norway, [4]Institute of

Theoretical Solid State Physics, Karlsruhe Institute of Technology (KIT), Karlsruhe, Germany, [5]RIKEN Center for Emergent Matter Science (CEMS), Saitama, Japan, [6]Institute for Solid State Physics, The University of Tokyo, Kashiwa, Japan, [7]Department of Advanced Materials Science, The University of Tokyo, Tokyo, Japan, [8]Japan Synchrotron Radiation Research Institute (JASRI), Hyogo, Japan, [9]RIKEN SPring-8 Center, Hyogo, Japan, [10]Institute of Materials Structure Science, High Energy Accelerator Research Organization, Ibaraki, Japan, [11]Institut Laue-Langevin, Grenoble, France, [12]Tokyo College, The University of Tokyo, Tokyo, Japan, [13]Department of Physics, Tokyo, Japan, [14]Graduate School of Science, Hokkaido University, Sapporo, Japan

The interplay between topological electronic structures and many-body correlations has been a central topic in modern condensed matter physics, and magnetic Weyl semimetals serve as an important platform to explore this issue [1]. However, the variety of magnetic structures realized in these materials remains limited, and in particular, a clear example of an undistorted helimagnetic ground state has not yet been established.
Here, we demonstrate that a Weyl helimagnet can be engineered by introducing weakly anisotropic magnetic ions into a noncentrosymmetric crystal that already hosts Weyl electrons in its paramagnetic state [2,3]. In the compound *R*AlSi (*R* = Gd), we find that an undistorted helimagnetic state emerges as the ground state, and that multi-Q states compete under applied magnetic fields (see Figure) [4]. Our numerical calculations, which incorportate symmetry-allowed Dzyaloshinskii-Moriya and anisotropic exchange interactions, successfully reproduces the complex magnetic textures. Finally, we discuss how the magnetic order is intertwined with the topological Weyl electrons in this material.
[1] N. P. Armitage *et al.*, Rev. of Mod. Phys. 90, 015001 (2018)
[2] G. Chang *et al.*, Phys. Rev. B 97, 041104(R) (2018)
[3] J. Gaudet *et al.*, Nat. Mater. 20, 1650-1656 (2021)
[4] R. Nakano *et al.*, Nat. Commun. 17, 3056 (2026)



(a) Noncentrosymmetric crystal structure of GdAlSi with a polar axis along the c-axis. (b) Illustration of two Weyl cones of opposite charge and the magnetic interactions allowed for the polar (*P*) crystal structure of this material: The Dzyaloshinskii-Moriya interaction $D \perp Q$ and the anisotropic exchange interaction J_{anis}, which plays an important role in magnetism of GdAlSi. (c) Harmonic cycloidal structure realized in GdAlSi.

FE-11. Real-time detection of critical slowing-down in ultrafast quenches of superconductivity

G. Nava Antonio, C. Ciccarelli
University of Cambridge, Cambridge, United Kingdom

We employ optical pump-THz probe spectroscopy to chart the ultrafast superconductivity suppression in NbN over a broad range of excitation fluences. Our measurements uncover a pronounced lengthening of the superconductivity quenching time when the absorbed optical energy is close to the condensation energy of the superconductor, which constitutes a non-equilibrium analog of critical slowing-down on a timescale comparable to that of superconducting fluctuations. Time-dependent Ginzburg-Landau simulations reproduce this behavior and ascribe it to the flattening of the free energy landscape at the dynamical phase transition boundary. Our findings represent a direct observation in real time of slowed-down superconductivity dynamics in proximity to a critical point and open a pathway for investigating out-of-equilibrium critical phenomena with time-resolved THz spectroscopy.

FE-13. Quantitative imaging of magnetic domains in correlated materials by REXS

C. Mazzoli
Brookhaven National Lab, Upton, New York, United States

After introducing the Resonant Elastic X-ray Scattering (REXS), novel results obtained by coherent Fresnel imaging [1] in the soft x-ray regime will be presented. Some relevant examples of magnetic imaging will be compared to other coherent based techniques in similar regimes [2-4], pinpointing the origin of previously debated signals, and offering their full quantitative interpretation. The inclusion of other degrees of freedom and their correlation to magnetism will be considered, together with the effect of external perturbations. The conclusions will focus on the potential impact of this novel approach on a variety of systems with intrinsic heterogeneity and self-organization, as typically realized across this broad class of important materials.

[1] R. Jangid, *et al.*, in preparation.
[2] M.G. Kim, *et al.* Imaging antiferromagnetic antiphase domain boundaries using magnetic Bragg diffraction phase contrast. *Nat Commun* 9, 5013 (2018). https://doi.org/10.1038/s41467-018-07350-3
[3] M.G. Kim, *et al.* Real-space observation of fluctuating antiferromagnetic domains. Sci Adv. 8(21):eabj9493 (2022). doi: 10.1126/sciadv.abj9493
[4] F. Klose, *et al.* Coherent correlation imaging for resolving fluctuating states of matter. *Nature* 614, 256–261 (2023). https://doi.org/10.1038/s41586-022-05537-9

SESSION FF: MAGNETORESISTANCE AND SPIN TRANSPORT

Chair(s): S. Liu, *NIST, Broomfield, Colorado, United States*
Thursday, November 5, 2026
02:00 PM-05:30 PM
South Pacific 3/4

FF-01. Magneto-transport properties of Fe_3GeTe_2 and Fe_3GaTe_2: comparison of current along c-axis and ab-plane

C. Chang[1], N. Hai[1], R. Jain[1], L. Tsai[1], R. Jhang[1], R. Sankar[1], J. Liang[2], S. Lee[1]
[1]*Institute of Physics, Academia Sinica, Taipei, Nangang, Taiwan,* [2]*Department of Physics, Fu Jen Catholic University, Taipei, Taiwan*

Recent discovery of 2D ferromagnets has attracted momentous research attention owing to their potential applications in spintronics, magnonics and skyrmionics. Among all, Fe_3GeTe_2 (FGT), and Fe_3GaTe_2 (FGaT), are particularly interesting due to strong perpendicular anisotropy (PMA) and higher Curie temperature with FGaT being ferromagnet even above room temperature. The magneto-transport studies on FGT and FGaT, reported so far, used the current in ab-plane of the crystal and no investigation is dedicated to the current in c-axis (van der Waals axis), for which the design and device fabrication complex. Here, we report a comparative study of the magneto-transport properties of FGT and FGaT for current in-plane (in ab plane) and current out-of-plane (along c-axis) cases. A specific fabrication procedure using focus ion beam (FIB) was followed which involved cutting out a slab from each crystal (FGT and FGaT) along c-axis and laying it down on Si/SiO_2 substrate in such a way that c-axis of the crystal is now in substrate plane. The dominant charge carriers are found to be holes for both FGT and FGaT. The highest values of charge carrier density (for current along c-axis) observed for FGT and FGaT is 9.6×10^{21} cm^{-3} and 20.1×10^{21} cm^{-3}, respectively. The mobility of the charge carriers, 4.3 $cm^2V^{-1}s^{-1}$ for FGT and 4.9 $cm^2V^{-1}s^{-1}$, is higher for current in ab-plane. We observed only nominal difference in charge carrier concentration and mobility along ab-plane and c-direction which is contrary to the expected large difference. A previous study on FGT reported that it exhibits strong dispersion in k_z, despite the fact that it is vdW layered and this dispersion in k_z might be the reason for comparable in-plane and out-of-plane charge carrier concentration and mobility. In magnetoresistance (MR) measurements, FGT and FGaT show negative MR for all studied temperatures, when both current and external magnetic field are along c-axis. Angular dependence of MR shows two-fold symmetry in all

configurations. The outcomes of this study provide insights on the anisotropic magneto-transport behavior and is a step forward in the developing better understanding of physical properties of these 2D magnets.
X. Xu, Y. W. Li, S. R. Duan et al., Signature for non-Stoner ferromagnetism in the van der Waals ferromagnet Fe_3GeTe_2, Phys. Rev. B 101, 201104(R) (2020).
H. Algaidi, C. Zhang, C. Liu et al., Room-temperature unconventional topological Hall effect in a van der Waals ferromagnet Fe_3GaTe_2, APL Mater. 13, 011108 (2025).
A. M. Ruiz, D. L. Esteras et al., On the Origin of the Above-Room-Temperature Magnetism in the 2D van der Waals Ferromagnet Fe_3GaTe_2, Nano Lett., 24, 7886–7894 (2024).
C. Liu, S. Zhang, H. Hao et al., Magnetic Skyrmions above Room Temperature in a van der Waals Ferromagnet Fe_3GaTe_2, Adv. Mater., 36, 2311022 (2024).
G. Zhang, F. Guo, H. Wu et al., Above-room-temperature strong intrinsic ferromagnetism in 2D van der Waals Fe_3GaTe_2 with large perpendicular magnetic anisotropy, Nature Communications, 13:5067 (2022).

FF-02. Three-order-of-magnitude enhancement in charge/spin conversion efficiency using a Schottky-barrier-free Fe/Mg/SiN/*n*-Si junction with high-resistivity non-degenerate silicon

S. Sato[1, 2], M. Tanaka[1, 2], R. Nakane[1, 3]
[1]Dept. of Electrical Eng. and Information Systems, The University of Tokyo, Bunkyo-ku, Tokyo, Japan, [2]Center for Spintronics Research Network (CSRN), The University of Tokyo, Bunkyo-ku, Tokyo, Japan, [3]Systems Design Lab (d.lab), The University of Tokyo, Bunkyo-ku, Tokyo, Japan

Spin injection into Si using ferromagnetic metal/insulator (I)/Si tunnel junctions has been extensively studied for developing Si-based spintronic devices [1–4]. Our previous work [4] clarified that both low junction resistance R_J and high charge/spin conversion efficiency η_{spin} are both essential for enhancing the spin-dependent device functionality. In conventional studies, however, a heavily-doped degenerate n^+-Si region has been employed for the I/Si interface to reduce the Schottky-barrier contact resistance. Nevertheless, the n^+-Si region drastically decreases η_{spin} due to strong impurity scattering. In other words, there has been a fundamental trade-off between low R_J and high η_{spin} so far.
Here, we overcome this challenge by utilizing a Fe/Mg/SiN/*n*-Si junction having non-degenerate *n*-Si with low donor concentrations N_D. Current-voltage (*I-V*) measurement of the junctions with various Mg thicknesses (t_{Mg} = 0 – 2.0 nm) and $N_D = 5.2 \times 10^{16}$ cm^{-3} demonstrated ohmic-like conduction for $t_{Mg} \geqslant 1$ nm, whereas Schottky-like conduction was obtained for t_{Mg} = 0 nm. These features confirm that a Schottky-barrier-free junction is realized as illustrated in Fig. 1, owing to the Fermi-level depinning effect of the SiN tunnel barrier and the low work function of Mg [2, 5].
We investigated the three-terminal (3T) Hanle signals [1] of the junction with t_{Mg} = 2 nm over a wide range of N_D (= 3.9×10^{15} – 6.9×10^{19} cm^{-3}) and estimated $\eta_{spin} = P_S^2 r_N$, where P_S is the spin polarization of the junction and r_N is the spin resistance of the *n*-Si [4]. Figure 2 shows η_{spin} as a function of N_D. Notably, η_{spin} is enhanced approximately three orders of magnitude compared with that in the degenerate n^+-Si, owing to the high resistivity and suppressed impurity scattering in *n*-Si. Our approach provides a breakthrough technology that enables the implementation of high-performance spin-functional Si devices.

[1] S. Sato et al., Phys. Rev. B 96, 235204 (2017).
[2] R. Nakane et al., Appl. Phys. Lett. 112, 182404 (2018).
[3] T. Tahara et al., Appl. Phys. Express 8, 113004 (2015).
[4] S. Sato et al., Phys. Rev. B 102, 035305 (2020).
[5] D. Connelly et al., IEEE Trans. Nanotechnol. 3, 98 (2004).

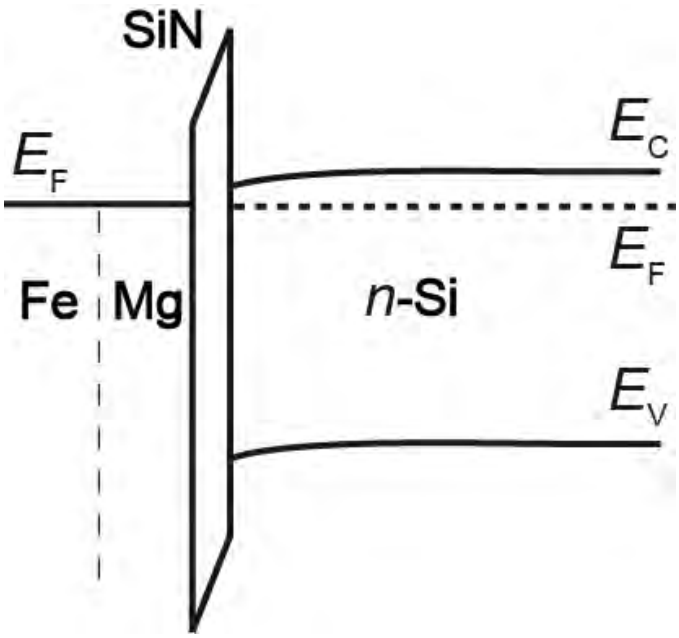


Fig. 1 Schematic energy band diagram of Fe/Mg/SiN/*n*-Si junction. E_C, E_V, and E_F are the conduction band bottom, valence band top, and the Fermi level of *n*-Si, respectively.

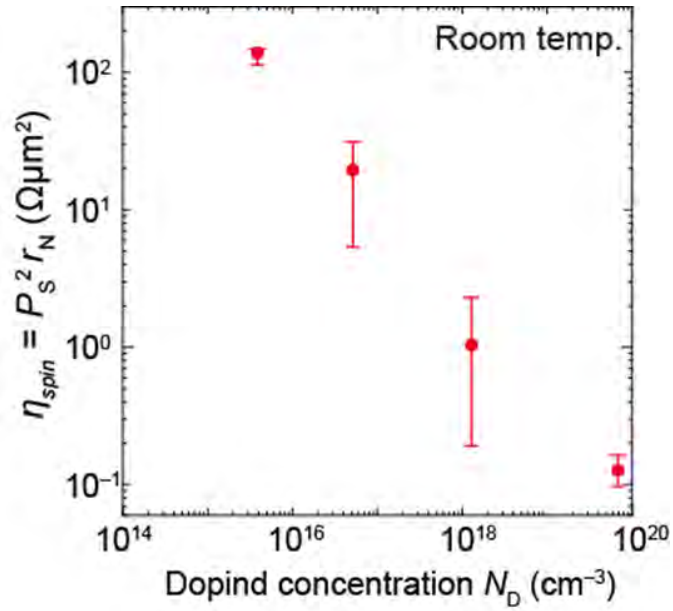


Fig. 2 Charge/spin conversion efficiency $\eta_{spin} = P_S^2 r_N$ for the Fe/Mg/SiN/*n*-Si junctions with various N_D estimated using the 3T Hanle method [1].

FF-03. Magnetic Phase Transition Modulation of Spin–Orbit Torque Efficiency in Epitaxial FeRh/Py Bilayers

J. Lu[1], P. Zhang[1], V. Lomakin[2], J. Hong[3]
[1]HBUT, Wuhan, China, [2]UCSD, La Jolla, California, United States, [3]UC Berkeley, Berkeley, California, United States

Magnetic phase transitions provide an intrinsic route to control spin transport in correlated materials. The B2-ordered alloy FeRh undergoes a first-order antiferromagnetic (AFM)–ferromagnetic (FM) transition near room temperature, accompanied by substantial reconstruction of its electronic and magnetic structure. Although spin pumping and temperature-tunable spin–orbit torque (SOT) phenomena have been reported in FeRh-based heterostructures [1–4], a quantitative determination of intrinsic SOT efficiency across the full AFM–FM transition remains unresolved. Here, we measure temperature-dependent spin–orbit torques in molecular-beam-epitaxy-grown epitaxial FeRh/Py bilayers using spin-torque ferromagnetic resonance. Across the phase transition, the damping-like torque efficiency exhibits a pronounced and reversible modulation, accompanied by correlated variations in Gilbert damping and resistivity. Temperature-dependent x-ray magnetic circular dichroism directly tracks the evolution of the Fe magnetic moment and reveals that the SOT efficiency scales with the magnetic order parameter. These results establish a direct microscopic link between magnetic phase reconstruction and spin–charge conversion efficiency. The demonstrated phase-tunable torque response suggests a pathway toward dynamically reconfigurable spin-torque operation and rapid state control across magnetic phases.

[1] Y. Wang et al., Nat. Commun. 11, 275 (2020).
[2] T. Lee et al., Nature 638, 106–111 (2025).
[3] C. Cao et al., ACS Nano 16, 8, 12727–12737 (2022).
[4] T. Nan et al., Sci. Adv. 6, eabd2613 (2020).

FF-04. Preserving Interfacial Integrity in Fe_3GaTe_2 Structures for All 2D Magnetic Tunnel Junctions

H. R. Stanfield, A. Mehrnejat, I. Vera Marun
Physics and Astronomy, The University of Manchester, Manchester, England, United Kingdom

Room temperature ferromagnets have garnered significant interest in recent years for use in magnetic tunnel junctions (MTJs). Amongst these, Fe_3GaTe_2 (FGaT) has been a promising candidate as a cleavable van der Waals crystal, demonstrating well above room temperature ferromagnetism with large perpendicular magnetic anisotropy [1]. Due to its cleavable nature, FGaT presents an excellent opportunity to explore tunnelling magnetoresistance (TMR) within wholly 2D MTJs, when combined with a 2D insulating barrier, such as ultra-thin hexagonal boron nitride (hBN) [2]. We employ a bottom-up fabrication technique, in which components are manually exfoliated and stacked using a transfer polymer, after which top contacts are fabricated. The constructed contacts are utilised to measure the magnetisation of the individual flakes via the anomalous Hall effect, as well as the junction resistance in a sweeping magnetic field to study the TMR. FGaT suffers from degradation due to oxidation, which leads to an antiferromagnetic phase that couples to the ferromagnetic phase of the bulk FGaT [3]. We have observed that, even when constructed within ideal conditions such as a glovebox, small amounts of this oxide negatively impact the TMR from the resulting heterostructure and form an exchange bias within the individual flakes. To investigate this, we compare the effects on the resulting TMR and AHE of "relaxed" stacking and "fast" stacking procedures to protect FGaT flakes and the junction region from oxidation buildup. Beyond this, we leverage this procedure to fabricate FGaT-based spintronic devices that utilise alternative magnetic contacts, such as 3D cobalt or 2D room temperature ferromagnet $(Co_{0.5}Fe_{0.5})_5GeTe_2$, for a comparative study of TMR across distinct heterostructures

to quantitatively elucidate tunnelling spin polarisation [4]. By mitigating interfacial degradation, our refined fabrication approach provides a framework for integrating oxidation-sensitive van der Waals ferromagnets into room-temperature 2D spintronic heterostructures.

[1] Zhang, G., Guo, F., Wu, H. *et al*. *Nat Commun* 13, 5067. (2022).

[2] Zhang, L., He, M., Wang, X. *et al*. Journal of Physics D: Applied Physics. 58. 10.1088/1361-6463/ada44c. (2025).

[3] Liu, D., Pei, F., Wang S. *et al*. *ACS nano*, *18*(34), 23812–23822. (2024).

[4] Zhang, J., Wang, Z., Xing, Y. *et al. Appl. Phys. Lett.* 124 (10): 103103. (2024).

FF-05. Quantum-well modulated tunnel magnetoresistance in Cr/Fe/MgO multilayers at room temperature with Ir insertion

T. Scheike, T. Nozaki, T. Nozaki, S. Yuasa
AIST, Tsukuba, Japan

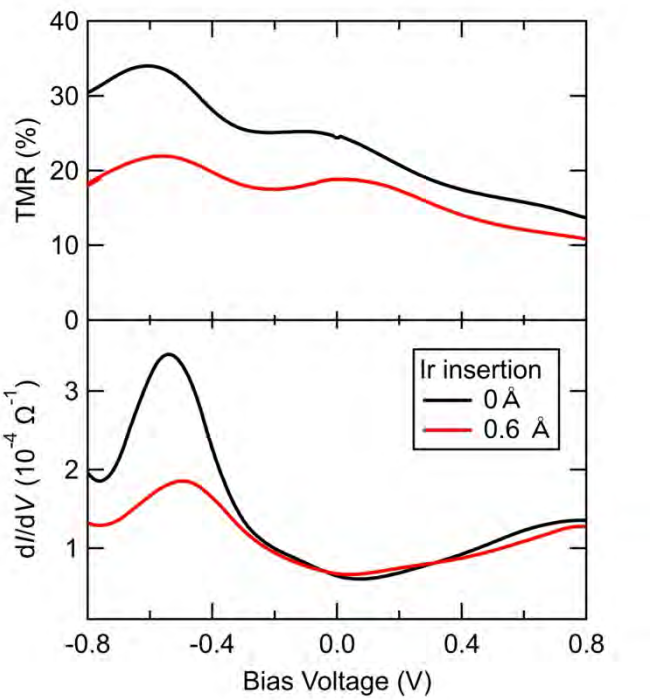
High quality Cr/Fe/MgO magnetic tunnel junctions (MTJs) are known to show quantum well (QW) confinement when the Fe layer is thin. The emergence of QWs in Fe originates from a pseudo band gap of Δ_1 states around the Fermi energy in Cr which can lead to QW resonance in Fe. When highly spin-polarized electrons tunnel through MgO into the Fe, in theory modulation of the tunnel magnetoresistance (TMR) with respect to bias voltage depending on the Fe thickness is expected [1]. However, while experiments could confirm the existence of QW states in Cr/Fe/MgO structures through first order d*I*/d*V* or dTMR/d*V* measurements, a change of TMR-*V* curves was not observed [2]. Here the aim is the fabrication of a Fe QW that can alter the bias voltage dependence of TMR and measure its effect on the voltage-controlled magnetic anisotropy (VCMA) effect.

We fabricated single-crystalline MTJs on a MgO(001) substrate with the following structure: Cr(60)/ Fe(d_{Fe})/ Ir (0 or 0.06)/ Co (0.1)/ MgO(2.4)/ Fe (10)/ Ta(5)/ Ru (7) (in nm). The Fe was deposited in a wedge-shape using a linear motion shutter. The bottom Fe layer has perpendicular magnetic anisotropy (PMA) which allowed us measurements on the VCMA effect. Additionally, we show the effect of an Ir insertion layer on the QW.

Figure 1 shows the TMR (a) and conductance (b) as a function of the bias voltage for a sample without and with Ir insertion and a bottom ferromagnetic layer thickness including Ir of 4.2 Å. A clear shift of the TMR maximum from the commonly observed zero bias to high negative bias can be observed. The TMR maximum coincides with a conduction peak which is a clear indication of QW formation. After inserting Ir, a decrease of the TMR and conductance maximum is observed with unchanged peak positions. The reduction is attributed to increased spin-flip scattering after Ir insertion which leads to a quenching of the electron coherence.

This work was partly based on results obtained from a project, JPNP16007, commissioned by the New Energy and Industrial Technology Development Organization (NEDO) and was supported by Innovative Science and Technology Initiative for Security Grant Number JPJ004596, ATLA, Japan.

[1] X. Zhang *et al*., PRB 56, 5484 (1997).
[2] T. Niizeki *et al*., PRL 100, 047207 (2008).

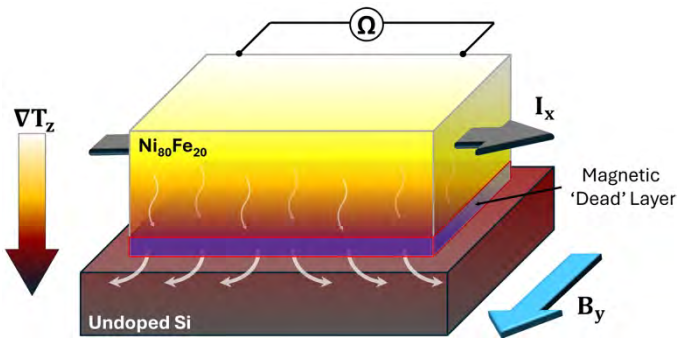


TMR and d*I*/d*V* vs bias of a sample without and with Ir insertion.

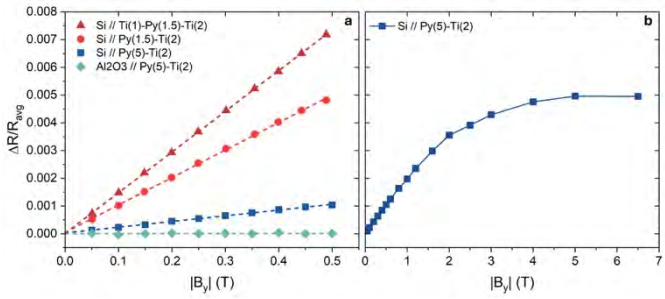
FF-06. Unusual Nernst Effects Originating from Magnetic Film-Substrate Interface

G. T. Street[1], S. Karube[2], Y. Shiota[2], Y. Inaoka[2], T. Ono[2], S. Emori[1]
[1]Physics, Virginia Tech, Blacksburg, Virginia, United States, [2]Institute for Chemical Research, Kyoto University, Uji, Kyoto, Japan

Nernst effects in metallic films can harvest power from waste heat by generating a voltage orthogonal to both a thermal gradient and an effective field (e.g., magnetization). Conventionally, the anomalous Nernst effect (ANE) in a ferromagnetic film originates from its bulk magnetization [1]. Here, we report an unusual Nernst effect in $Ni_{80}Fe_{20}$ thin films grown on undoped Si, which we attribute to disordered magnetism at the film-substrate interface.
A DC current ($J \approx 10^{11}$ A/m^2) along patterned thin film devices generates a vertical thermal gradient via Joule heating (Fig. 1). Meanwhile, we apply an in-plane magnetic field B_y orthogonal to the thermal gradient, resulting in a B_y-polarity dependent resistance shift, $\Delta R = [R(+|B_y|) - R(-|B_y|)]/2$, consistent with a Nernst effect. However, while conventional ANE-driven ΔR in soft $Ni_{80}Fe_{20}$ should saturate at $B_y < 0.01$ T, ΔR continues to increase well beyond the saturation field of the bulk magnetization (Fig. 2a). This unconventional Nernst response emerges exclusively in thin films grown on undoped Si substrates. It is also significantly enhanced upon reducing the magnetic film thickness from 5 nm to 1.5 nm, as well as tuning the ultrathin spacer (e.g., Ti) between the film and substrate. These observations implicate the film-substrate interface as the source of the unusual Nernst effect. Furthermore, the Nernst response exhibits a Brillouin-function-like curve that saturates around 5 T (Fig. 2b), consistent with a disordered superparamagnetic layer (or "dead layer") known to form at the interfaces of ferromagnetic films. Ultimately, our findings demonstrate the untapped potential of ultrathin films – with engineered chemistry and magnetism at the substrate interface – for efficient, scalable thermoelectric power conversion.
[1] M. Mizuguchi and S. Nakatsuji, "Energy-harvesting materials based on the anomalous Nernst effect," *Sci. Technol. Adv. Mater.*, vol. 20, no. 1, pp. 262–275, Mar. 2019, doi: 10.1080/14686996.2019.1585143.



Joule heating in the metal film dissipates into the substrate, establishing a vertical thermal gradient. A magnetic field orthogonal to this gradient drives Nernst-induced resistance shifts, detected via longitudinal resistance measurements.



(a) Field dependence of Nernst-driven resistance shift ΔR, normalized by average resistance, for metal thin films grown on undoped Si and Al_2O_3. (b) High-field ΔR via PPMS, revealing saturation near 5 T.

FF-07. Longitudinal spin pumping and quantum spin transfer

K. Lee
KAIST, Daejeon, Korea (the Republic of)

Spin transfer enables efficient current-driven control of magnetic states, yet it has largely relied on a simplifying assumption: a classical description of localized spins. This talk explores the physics that emerges when this assumption is relaxed.
First, the quantumness of localized spins enables large longitudinal spin pumping, recently observed in FeRh [1], which undergoes a first-order antiferromagnet–ferromagnet phase transition with a time-dependent atomic moment. Current injection into a FeRh/Pt bilayer triggers a nanosecond-scale phase transition, emitting a spin current into Pt and producing an inverse spin Hall signal far larger than expected from conventional transverse spin pumping.

Second, the same quantum nature enables spin transfer from spin-correlated electron pairs to localized spins [2]. Notably, even spin-singlet and triplet (m = 0) pairs, carrying no net spin, can transfer finite angular momentum. This work also clarifies that the independent-electron approximation applies only when injected spin currents are fully incoherent.
Together, these results show that quantum fluctuations and electron correlations can fundamentally govern spin transfer, opening pathways toward coherent spintronics and superconducting triplet technologies.
[1] T. Lee et al., Nature 638, 106 (2025).
[2] S. Hwang et al., arXiv:2601.05100 (2026).

FF-09. Hydrogen-Induced Digital to Analog SOT Switching in CoGd Ferrimagnets for Neuromorphic Computing
R. Yadav, C. Lai
Material Science and Engineering, National Tsing Hua University, Hsinchu, Hsinchu, Taiwan

Biological synapses combine memory and computation, operate across multiple intermediate states, and do so with low energy consumption. Replicating these features in solid-state systems remains challenging. Here, we demonstrate that solid-state ionic control via hydrogenation, combined with spin–orbit torque (SOT), enables tunable magnetic switching between digital and analog regimes in a Ta/Pt/CoGd/Pt device. Hydrogen incorporation at room temperature (0.4 bar) transforms a binary switching device into a multilevel response. Vibrating sample magnetometry reveals the underlying changes in saturation magnetization increases, coercivity decreases, and the squareness ratio approaches unity. Correspondingly, spin-orbit torque (SOT) switching measurements show a transition from abrupt switching between two resistance states to gradual evolution through multiple intermediate states. The underlying chemistry is identified by XPS depth profiling of Gd core-level peaks, which shift to Higher binding energies and broaden after hydrogen exposure, while Co and Pt peaks hold their positions. This indicates selective hydrogen incorporation into the Gd sublattice, leading to the formation of gadolinium hydride without disrupting the overall film structure. However, the domain imaging provides direct insight into the switching mechanism. In the pristine state, sharp one-step domain-wall propagation. After hydrogenation, the process transitions to a nucleation-dominated regime, where isolated magnetic clusters emerge and expand independently. This spatially inhomogeneous switching reflects a modified pinning landscape arising from partial formation of GdH_x and explains the observed multilevel resistance states. These results show that hydrogen incorporation alone without structural redesign can reconfigure magnetic switching dynamics. The resulting analog-like response offers a practical route toward neuromorphic spintronic devices operating at room temperature.

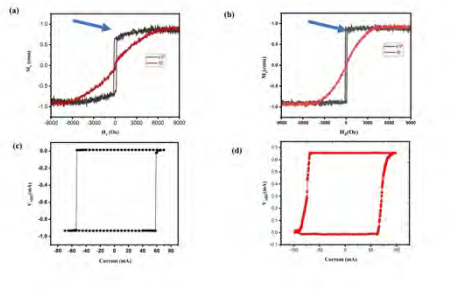


Figure 1. Effect of Hydrogen treatment. (a) M & H loop of VSM data of pristine device. (b) VSM data of the H-treated device. (c) SOT switching behavior of the pristine device. (d) SOT switching behavior of the H-treated device. With H_x = 200 Oe and pulse width 300 μs.

FF-10. Antiferromagnetic domain wall in ferrimagnetic bilayers controlled by magnetic spin Hall effect.
H. Kim[1], S. Ko[1], D. Han[2], J. Kang[2, 3], P. Cao Van[4], W. Choi[5], S. Kim[5], J. Jeong[4], B. Park[2], A. M. Park[1], K. Kim[6], K. Kim[1, 7]
[1]Department of Physics, Korea Advanced Institute of Science and Technology, Daejeon, Korea (the Republic of), [2]Department of Materials Science and Engineering, Korea Advanced Institute of Science and Technology, Daejeon, Korea (the Republic of), [3]Department of Electrical and Computer Engineering, Northwestern University, Evanston, Illinois, United States, [4]Department of Materials Science and Engineering, Chungnam National University, Daejeon, Korea (the Republic of), [5]Department of Physics, University of Ulsan, Ulsan, Korea (the Republic of), [6]Department of Physics, Yonsei University, Seoul, Korea (the Republic of), [7]Graduate School of Quantum Science and Technology, Daejeon, Korea (the Republic of)

Antiferromagnetic (AFM) spintronics promises ultrafast operation speeds and immunity to external magnetic fields, yet the absence of net magnetization makes the electrical control of AFM spin textures a crucial challenge. Here, we demonstrate that compensated ferrimagnets provide a powerful platform for realizing and electrically manipulating AFM domain walls. By constructing a

heterostructure composed of under-compensated and over-compensated ferrimagnets, we show a robust AFM domain wall spontaneously forms at the intermixed interface. This interfacial AFM domain wall arises naturally as Co moment in the upper and lower layer aligns antiparallel to each other and the interface crosses the magnetic compensation point due to the gradual composition transition.
Experimentally, the presence of this domain wall is verified through Hall resistance measurements. A clear anomalous Hall hysteresis is observed during in-plane magnetic field sweep, reflecting a finite out-of-plane (OOP) moment. Temperature-dependent measurement reveals that this signal is only measurable when the Co moments in the upper and lower layer align parallel, indicating the Hall response is linked to the existence of the interfacial domain wall. The observed Hall signal remains nearly unchanged under magnetic fields up to 1.2 T, highlighting the antiferromagnetic character of the domain wall.
We further reveal that this ferrimagnetic bilayer system hosts the magnetic spin Hall effect (MSHE), which generates an unconventional OOP spin-z current under an in-plane charge current. Unlike the conventional spin Hall effect, whose interfacial contribution cancels in the present geometry, the MSHE-induced spin accumulation adds constructively at the interface. Thus, the OOP moment of the interfacial domain wall can be electrically controlled via MSHE. By controlling the amplitude and polarity of applying current, the amplitude of the OOP domain wall moment is linearly modulated and the chirality of the domain wall could also be modulated.
[1] Ko, S., Kim, H., Han, D. *et al.* Antiferromagnetic domain wall in ferrimagnetic bilayers controlled by magnetic spin Hall effect. npj Spintronics 4, 6 (2026).

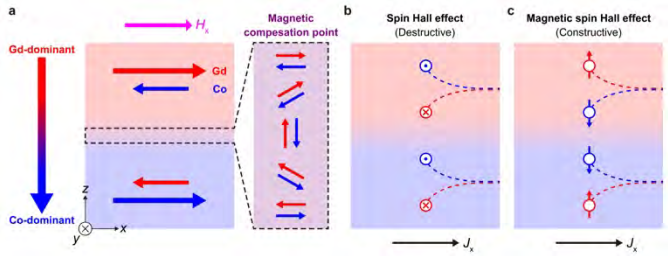


Fig. 1. Interfacial domain wall and magnetic spin Hall effect in ferrimagnetic bilayer.

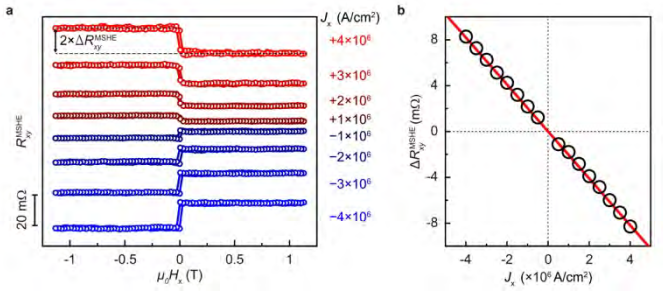


Fig. 2. Current amplitude dependent modulation of out-of-plane domain wall moment via the magnetic spin Hall effect.

FF-11. Room temperature control of axial and basal antiferromagnetic anisotropies using strain

H. Jani
University of Oxford, Oxford, United Kingdom

Antiferromagnetic materials are promising platforms for the development of ultrafast spintronics and magnonics due to their robust magnetism, high-frequency relativistic dynamics, low-loss transport, and the ability to support topological textures. However, achieving deterministic control over antiferromagnetic order in thin films is a major challenge due to the formation of multidomain states stabilized by competing magnetic and destressing interactions. Thus, the successful implementation of antiferromagnetic materials necessitates careful engineering of their anisotropy. Here, we demonstrate strain-based, robust control over multiple antiferromagnetic anisotropies and nanoscale domains in the promising spintronic candidate α-Fe_2O_3 at room temperature. By applying isotropic and anisotropic in-plane strains across a broad temperature–strain phase space, we systematically tune the interplay between magneto-crystalline and magneto-elastic interactions. We observe that strain-driven control steers the system toward an aligned antiferromagnetic state, while preserving topological spin textures, such as merons, antimerons, and bimerons. We directly map the nanoscale antiferromagnetic order using linear dichroic scanning transmission X-ray microscopy integrated with in situ strain and temperature control. A Landau model and micromagnetic simulations reveal how strain reshapes the magnetic energy landscape. These findings suggest that strain could serve as a versatile control mechanism to reconfigure equilibrium or dynamic antiferromagnetic states on demand in α-Fe_2O_3 for implementation in next-generation spintronic and magnonic

devices.
1. J Harrison, J Hu, C Godfrey, JC Lin, TA Butcher, J Raabe, S Finizio, H Jani, P Radaelli. *ACS Nano* 19, 42118 (2025).
2. H Jani, J Harrison, S Hooda, S Prakash, P Nandi, J Hu, Z Zeng, J-C Lin, GJ Omar, J Raabe, S Finizio, A V-Y Thean, A Ariando, P Radaelli. *Nature Materials* 23, 619 (2024).

FF-12. Suppressing Gilbert damping in $L1_0$-FePt thin films by nanostructural control for sub-terahertz spin dynamics

P. D. Bentley[1, 2], Y. Sasaki[1], I. Suzuki[1], S. Isogami[1], Y. K. Takahashi[1], H. Suto[1]
[1]National Institute for Materials Science, Tsukuba, Japan, [2]National Institute for Quantum Science and Technology, Kizugawa, Japan

Terahertz (THz) technologies have recently attracted significant attention from the viewpoint of future high-speed and high-capacity wireless communication, security inspection, and pharmaceutical analysis. In particular, the 100–300 GHz band is expected to be utilized for next-generation communication systems; however, low-cost and scalable emitters and detectors in this frequency range have not yet been established.
THz spintronics, based on spin torque oscillators and related devices[1,2], has emerged as a promising approach to bridge this gap. For ferromagnetic metal-based devices, magnetic materials with both large perpendicular magnetic anisotropy (PMA) and low Gilbert damping constant are essential to achieve high-frequency operation. $L1_0$-ordered FePt is a strong candidate owing to its giant PMA and high spin current efficiency, although its relatively large damping constant has been a major limitation.
In this study, we report the reduction of the damping constant in $L1_0$-ordered FePt thin films by engineering the nanostructure. Continuous FePt films were grown on MgO(001) and $SrTiO_3$(001) substrates, and their magnetization dynamics were characterized using all-optical time-resolved magneto-optical Kerr effect (TRMOKE).[3] By changing the substrate, the lattice mismatch and resulting number of misfit dislocations at the interface were systematically controlled.
Structural analysis revealed improved $L1_0$ ordering and a reduced number of misfit dislocations in FePt grown on $SrTiO_3$ compared to MgO, consistent with the smaller lattice mismatch. Despite only a moderate change in PMA, a significant reduction in the effective damping constant was observed, reaching a minimum value of 0.033 for FePt/$SrTiO_3$, compared to 0.045 for FePt/MgO. This reduction is attributed to suppressed electron scattering due to fewer interfacial defects.[4]
These results demonstrate that nanostructural control, particularly the reduction of misfit dislocations, provides an effective route to tailor damping in FePt without sacrificing PMA.
This work was partially supported by the JST-CREST (Grant No. JPMJC22C3), MEXT-LEADER (Grant No. JPMXS0320230032), and the JSPS-KAKENHI (Grant Nos. 25K17659 and JP18H03787).
[1] S. Miwa, *et al*., Nature Mater. 13, 50-56 (2014).
[2] V. E. Demidov, *et al*., Appl. Phys. Lett. 105, 172410 (2014).
[3] Y. Sasaki, *et al*., ACS Appl. Nano Mater. 6, 5901-5908 (2023).
[4] P. D. Bentley, et al., Appl. Phys. Lett. 126, 022404 (2025).

FF-13. Twisting Light, Steering Spins: Gold Nanoparticle Magnetization via Inverse Faraday Effect and Orbital Angular Momentum

X. Yang[1], C. Hareau[2], M. Mivelle[2]
[1]Dalian University of Technology, Dalian, China, [2]CNRS/Sorbonne University, Paris, France

Controlling magnetic order at ultrafast and nanoscale dimensions is crucial for next-generation data storage and spintronic devices. All-optical methods, particularly the Inverse Faraday Effect (IFE), offer a pathway to near-instantaneous magnetization by driving drift photocurrents in a material. However, current techniques are limited, typically constraining the induced magnetic field to be either parallel or perpendicular to the light's propagation axis, which restricts full spatial control.
Here, we overcome this limitation by introducing a new approach that provides complete three-dimensional control over the induced magnetization [1]. We harness the IFE in a gold nanoparticle, driven by structured Laguerre-Gauss (LG) beams carrying orbital angular momentum (OAM). Our key innovation lies in tailoring the tilt of the beam's isophase planes, which in turn dictates the orientation of the optically-induced drift photocurrents within the nanoparticle. According to the Biot-Savart law, these currents generate a strong, stationary magnetic field.
We demonstrate that the orientation of this field can be tilted by up to 25° relative to the beam axis. Furthermore, we show that this magnetic orientation is fully tunable: the tilt angle is controlled by the radial position of the nanoparticle and the OAM topological charge, while the azimuthal orientation can be swept over 2π steradians by repositioning the particle within the beam. This unprecedented level of all-optical, three-dimensional

magnetic control at the nanoscale, combined with the ultrafast nature of the IFE, opens significant new avenues. Our results pave the way for advanced spin-based applications, from the directional triggering of spin waves in magnetic materials to the design of next-generation magnetic memory and logic devices.

[1] Yang, X.; Hareau, C.; Mivelle, M. Twisting Light, Steering Spins: Gold Nanoparticle Magnetization via Inverse Faraday Effect and Orbital Angular Momentum. Nano Lett. 2025, 25 (30), 11549–11553.

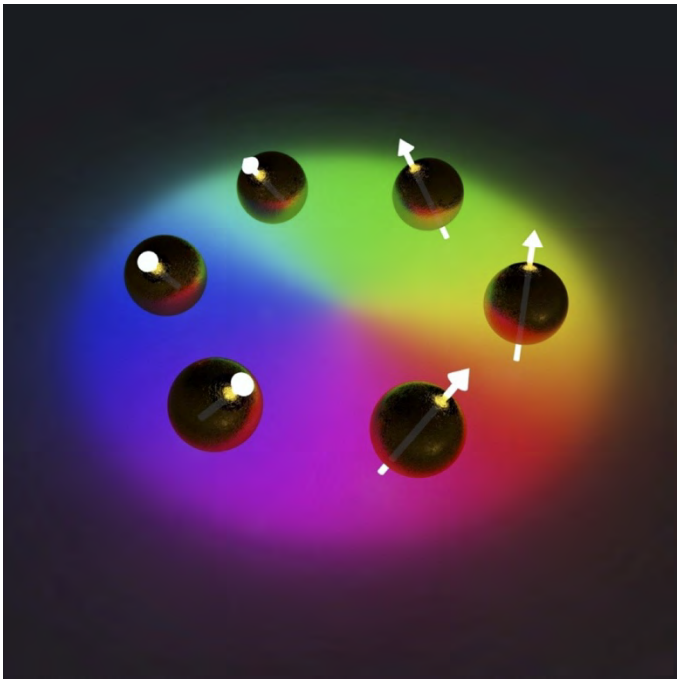


Figure. By placing a gold nanoparticle in a Laguerre-Gauss beam carrying Orbital Angular Momentum, it is possible to control the orientation of the resulting magnetization within the particle via the inverse Faraday effect.

SESSION FG: MAGNETIC INTERACTIONS AND SPIN DYNAMICS

Chair(s): D. Suess, *University Vienna, Wien, Austria*
Thursday, November 5, 2026
02:00 PM-05:30 PM
Sea Pearl

FG-01. Intra-particle volcanos: Identifying the nanoparticle hot spots for magnetic hyperthermia therapy

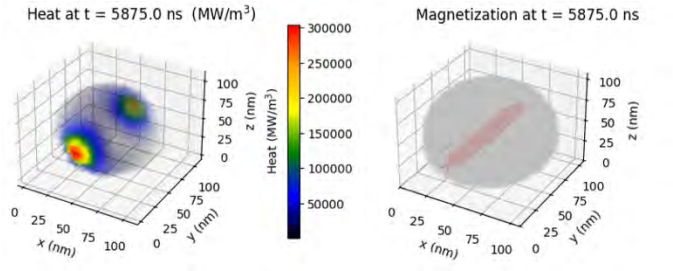
E. M. Jefremovas[1, 2]
[1]Department of Physics and Materials Science, University of Luxembourg, Luxembourg, Luxembourg, [2]Institute for Advanced Studies, University of Luxembourg, Esch-sur-Alzette, Luxembourg

Magnetic nanoparticles (MNPs) are central to nanomedicine, enabling promising applications ranging from targeted drug delivery to magnetic hyperthermia [1]. Despite their progress towards clinical trials [2], there are still several fundamental questions regarding the magnetization dynamics of the MNPs that remain largely unresolved. One example concerns the spatial resolution of the NP heat release, a 3D mapping of the nanoparticle identifying the “hot spots”. This question is not only relevant to fundamental studies, but also to optimally engineer nanoparticle applications: one cannot control what falls beyond understanding.

In this talk, I will show the results of a large-scale micromagnetic study of nanoflowers and chain-arranged nanoparticles reproducing those found in magnetotactic bacteria, two configurations that have experimentally demonstrated enhanced heating performance [3]. By resolving the magnetization dynamics via the Landau-Lifshitz-Gilbert equation, the energy dissipation in response to an alternating magnetic field can be extracted [4], enabling the quantification of heat release with nanometer spatial resolution within the nanostructures. As a result, "heat mappings" can be established for every time step (see Figure), identifying where and when these "hot spots" occur [5].

These results illustrate that there is still “plenty of room at the bottom” beyond the macrospin approximation, which overlooks the rich dynamics associated with non-homogeneous magnetization textures. Micromagnetic simulations equip us with a unique tool to explore new pathways for understanding MNPs at their core, and their applications on the macroscale.

[1] M. Colombo et al. Chem. Soc. Rev. 41.11 (2012): 4306-4334.
[2] Z. V. Díaz-Riascos et al. ACS Appl. Mater. & Interfaces 17.2 (2025): 2924-2939.
[3] E. M. Jefremovas et al. IEEE Access 9 (2021): 99552-99561.
[4] J. Leliaert et al. Nanoscale 13.35 (2021): 14734-14744.
[5] E. M. Jefremovas et al. In prep. (2026).

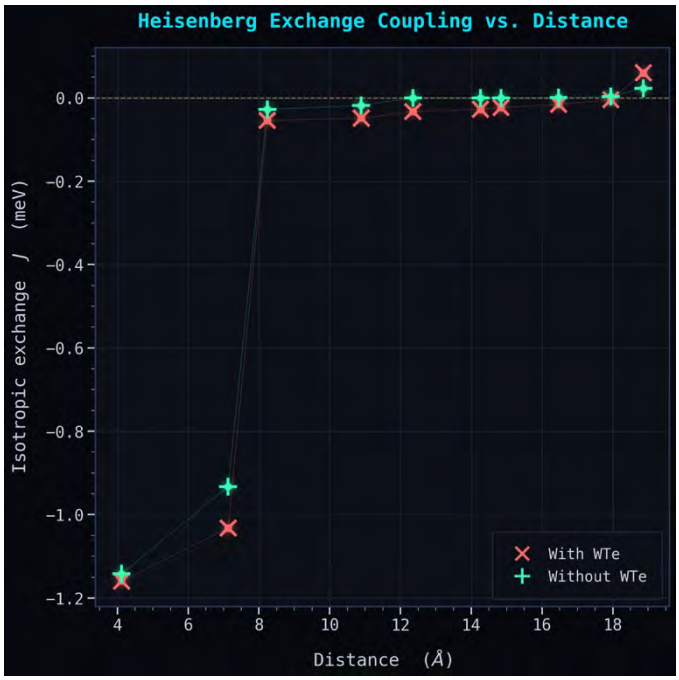


FG-02. Relativistic DFT-to-Spin-Model Mapping for 2D Magnetic van der Waals Heterostructures

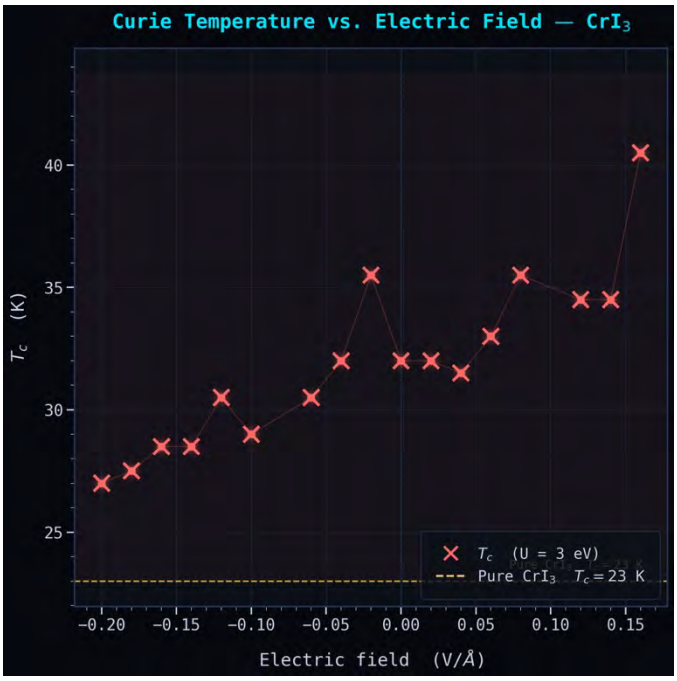
Z. Tajkov[1, 2], D. T. Pozsár[1], A. Garica Fuente[3], J. Ferrer[3], J. Fabian[4], L. Oroszlány[1]
[1]Department of Physics of Complex Systems, Eötvös Loránd University, Budapest, Budapest, Hungary, [2]Nanostructures, HUN-REN Centre for Energy Research, Budapest, Budapest, Hungary, [3]University of Oviedo, Oviedo, Spain, [4]University of Regensburg, Regensburg, Germany

Spin-model descriptions derived from first principles are essential for understanding and engineering magnetism in 2D van der Waals heterostructures, where proximity to high spin-orbit coupling layers can qualitatively reshape the magnetic ground state [1]. Building on the LKAG framework [2], we have developed both the necessary theoretical framework [3,4] and the recently released open-source code grogupy [5] for relativistic DFT-to-spin-model mapping directly from ab initio calculations. A central advance of our approach is the simultaneous and proper treatment of spin-orbit coupling and non-orthogonal LCAO basis sets within one unified workflow. This avoids Wannierization and enables the direct extraction of isotropic exchange, anisotropic exchange, Dzyaloshinskii-Moriya interactions, and on-site anisotropy in a computationally efficient framework. Such a capability is particularly important for realistic 2D hybrid systems, where relativistic effects and the details of the local basis strongly influence the mapped magnetic parameters. As a showcase, we study a CrI3 monolayer coupled to monolayer WTe2. We find that proximity to WTe2 modifies the Cr-Cr exchange landscape (Fig. 1) and enhances relativistic interactions, driving the Cr moments away from the out-of-plane easy axis toward a well-defined in-plane canting direction. The resulting spin model predicts a Curie-temperature increase from 23 K for isolated CrI3 to 32 K in the heterostructure, with additional electric-field control up to about 41 K (Fig. 2). Our results demonstrate a practical route from electronic structure to quantitative magnetic-phase control in 2D hybrid materials, while highlighting the capabilities of a newly available method and code developed within our collaboration [6,7].

[1] K. Zollner, P. E. Faria Junior and J. Fabian, Phys. Rev. B, Vol. 100, p.085128 (2019)
[2] A. I. Liechtenstein, M. I. Katsnelson and V. P. Antropov, J. Magn. Magn. Mater., Vol. 67, p.65 (1987)
[3] L. Oroszlány, J. Ferrer and A. Deák, Phys. Rev. B, Vol. 99, p.224412 (2019)
[4] G. Martínez-Carracedo, L. Oroszlány and A. García-Fuente, Phys. Rev. B, Vol. 108, p.214418 (2023)
[5] grogupy documentation, https://grogupy.readthedocs.io/en/stable/
[6] G. Martínez-Carracedo, A. García-Fuente and L. Oroszlány, Phys. Rev. B, Vol. 110, p.184406 (2024)
[7] G. Martínez-Carracedo, L. Oroszlány and A. García-Fuente, Phys. Rev. B, Vol. 107, p.035432 (2023)



Isotropic Cr-Cr exchange versus distance in CrI3 with and without WTe2, showing proximity-induced changes in Jij.



Curie temperature of the CrI3/WTe2 heterostructure versus external electric field. The dashed line marks the pristine CrI3 reference.

FG-03. Atomically engineering metallic thin films for highly energy efficient non-volatile spintronic memories.

P. Wang, S. Parkin
NISE Department, Max-Planck-Institute of Microstructure Physics, Halle (Saale), Germany

Synthetic antiferromagnetic(SAF) thin film stacks are an essential component for non-volatile spintronic memory devices [1]. The magnetic layers in these devices must display perpendicular magnetic anisotropy (PMA) that is typically derived from interfaces between heavy metal and ferromagnets [2]. Here, we show that 5d transition metal-Al and high entropy alloy (HEA) sputtered thin films that display an $L1_0$ type tetragonal structure form room temperature deposition both show large PMA and giant spin Hall effects that give rise to giant spin orbit torques [3,4]. Using the $L1_0$ type compounds RuAl and RuAlGa as a AF spacer layer we demonstrate novel SAF with an entire [001] crystallographically ordered orientation and yet demonstrate high PMA. We demonstrate state-of-the-art domain wall based spintronic memory devices that exhibit a several-fold increased efficiency for current induced domain wall motion as compared to prior-art materials. These structures are formed on thin Ir_xAl_{100-x} underlayers with an $L1_0$ structure and HEA films containing multi-elements and PMA layers are composed of ultra-thin Co and Ni layers with the $L1_0$ RuAl and RuAlGa as the antiferromagnetic coupling spacer layer. These structures exhibit chiral Néel-type domain walls so that all the domain walls move synchronously along the racetracks at very high speeds under the influence of nano-second long current pulses. Furthermore, we show the formation of Néel-type skyrmions in thin layers of simple ferromagnetic alloys, namely Co-Al and Co-Ni-Al, over a wide range of temperature up to ~773 K, by imposing a strain gradient perpendicular to the sample plane via epitaxy with an Ir-Al underlayer. The Néel skyrmions are directly observed using Lorentz transmission electron microscopy in freestanding membranes at high temperatures and the strain gradient is directly measured from x-ray diffraction asymmetric peak profiles [5]. These novel materials provide a new route for multifunctional usage of spintronic memories that are compatible with complementary metal-oxide semiconductor technologies.

In collaboration with: Hakan Deniz, David Eilmsteiner, Arthur Ernst, Ke Gu, Jae-Chun Jeon, Ilya Kostanovski, Yung-Cheng Li, Andrea Migliorini, Holger Meyerheim, Banabir Pal, Abhay Kant Srivastava, Rana Saha, Eugenia Sebastiani-Tofano, See-Hun Yang, Juan Rubio Zuazo.

[1] S.H. Yang, K.S. Ryu, & S.S.P. Parkin. Nat. Nanotechnol. 10 (2015), 221-226.
[2] K. S. Ryu, L. Thomas, S.H. Yang, & S.S.P. Parkin. Nat. Nanotechnol. 8 (2013), 527-533.
[3] P. Wang, et al. Adv. Mater. 34 (2022), 2109406.
[4] P. Wang⁺, A. Migliorini⁺, et al. Adv. Mater. 37 (2025), 2416820.
[5] P. Wang, R. Saha, H.L. Meyerheim, *et al.* Nat. Commun. 17, 4911 (2026).

FG-04. jaxFMM: Fast and Accurate Stray Field Evaluation for FEM Micromagnetics

R. Kraft[1, 2], F. Bruckner[1], D. Suess[1], C. Abert[1]
[1]Physics of Functional Materials, University of Vienna, Vienna, Austria, [2]Vienna Doctoral School in Physics, University of Vienna, Vienna, Austria

Micromagnetic simulation is an indispensable tool, widely used in the discovery and design of novel magnetic devices and materials. As the complexity and scale of such simulations increases, limits in terms of memory size or simulation runtime are quickly reached. One of the most common bottlenecks is the stray or demagnetizing field: Its computational complexity scales quadratically with the system size due to its long range, whereas most other interactions are short-ranged and hence scale only linearly. Dynamic micromagnetic simulations commonly require tens of thousands of field evaluations - therefore, efficient stray-field evaluation forms the centerpiece of a fast simulation library. We introduce jaxFMM [1], an open-source Fast Multipole Method (FMM) implementation written in JAX [2]. JaxFMM focuses on stray-field evaluation for Finite-Element simulation codes, where the commonly used Fast Fourier Transform (FFT) based approach is no longer applicable. With only linear computational complexity scaling and a highly parallel, memory efficient implementation, jaxFMM enables simulations of very large systems on a single GPU. Timings on an Nvidia A100 (40GB) card show that jaxFMM can even keep up with the FFT on a regular grid, albeit at reduced accuracy (Fig. 1, squares). On more complicated geometries like the sphere shell shown in Fig. 2 or compared to CPU-only routines, jaxFMM's performance and memory efficiency at similar accuracy is unparalleled (Fig. 1, circles and FEMBEM timings). Additionally, using JAX results in extremely concise and flexible code, which can not only run on both CPUs and GPUs but is also ready for machine-learning and inverse-design tasks with automatic differentiation.

[1] R. Kraft et al., arXiv preprint, arXiv:2511.15269 (2025)
[2] J. Bradbury et al., GitHub repository, http://github.com/jax-ml/jax (2018)
[3] C. Abert et al., JMMM, Vol. 345, p. 29 (2013)
[4] C. Abert et al., npj Comput Mater, Vol. 11, p. 193 (2025)

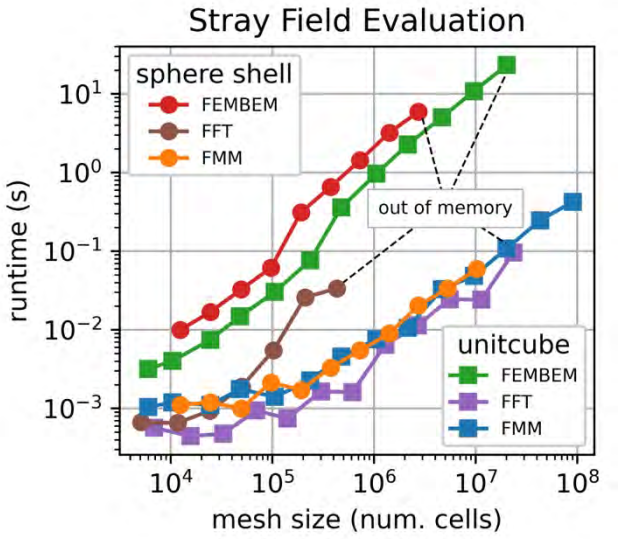


Fig. 1: Stray field evaluation runtimes on a unitcube (squares) / sphere shell (circles) with FEMBEM in magnum.pi [3] (CPU), the FFT in neuralmag [4] (GPU) and jaxFMM (GPU).

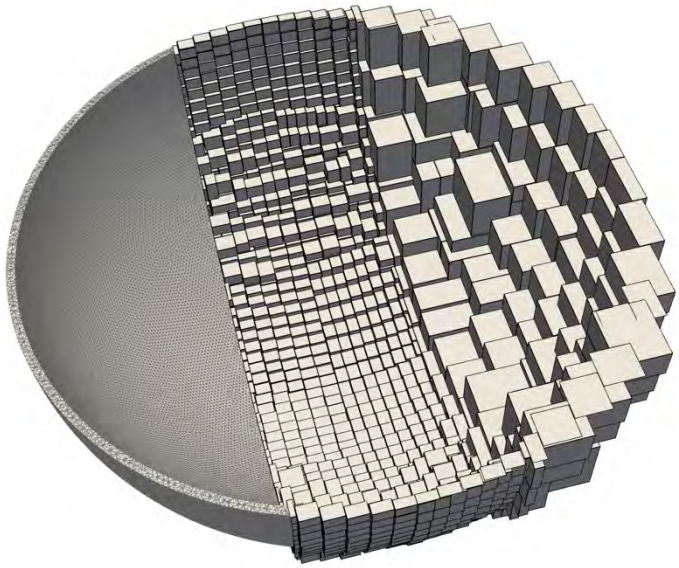


Fig. 2: Sphere shell mesh (N = 7.3e5, cut in half) used in the "sphere shell" timings (Fig. 1, circles) and its representation in the FMM. From left to right: mesh, FMM level 4, FMM level 3.

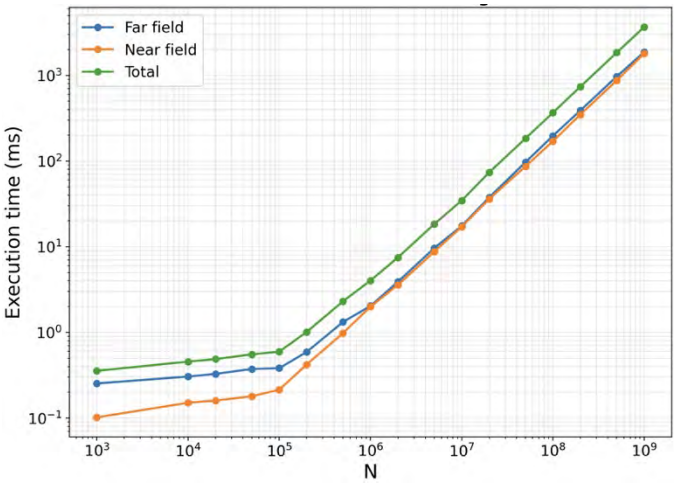
FG-05. Enabling Dynamic Geometries, Evolving Materials, and Extreme-Scale Simulation with On-the-Fly Finite Element Micromagnetic Solver

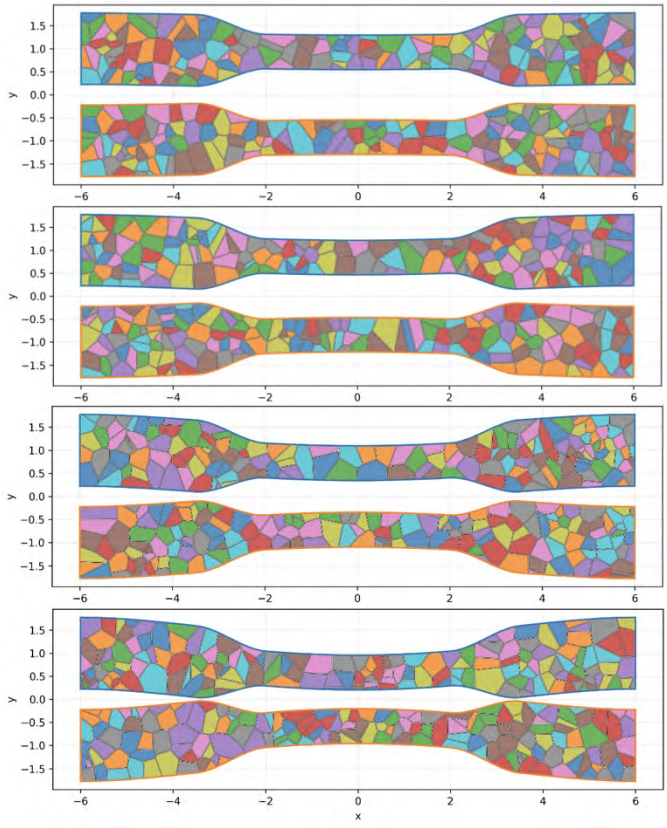
J. Duan, V. Lomakin
ECE, University of California San Diego, San Diego, California, United States

We present a fully on-the-fly finite element method (FEM) solver for high-performance micromagnetic simulation of dynamically evolving magnetic structures. Conventional solvers typically assume static geometries, fixed material parameters, and precomputed field operators. While effective for standard problems, these assumptions become limiting when structures move, deform, or change material state, often requiring repeated preprocessing, remeshing, or operator regeneration, significantly increasing computational cost.

The key contribution is a fully on-the-fly CPU and GPU formulation that eliminates reliance on fixed preprocessing and auxiliary airbox meshes. All effective magnetic field components are evaluated directly at runtime using the current mesh and geometry. This enables simulation of moving and deforming structures without remeshing or rebuilding field data structures, while maintaining low memory usage and supporting highly complex geometries. The solver supports dynamic meshes with strong computational efficiency and scalability, making it suitable for motion, deformation, morphology evolution, and reconfigurable magnetic devices. It also incorporates 1D, 2D, and 3D periodic boundary conditions within a unified GPU framework, allowing isolated, film-like, wire-like, and bulk-periodic systems to be handled consistently. Additionally, it supports mixed FEM meshes, including tetrahedrons, hexahedrons, and pyramids of arbitrary order, enabling high accuracy for complex structures. The approach further allows dynamic material properties during simulation. Local magnetic parameters can evolve with temperature, strain, field, phase, or microstructure. Since no precomputed matrices are used, these parameters can be updated directly at runtime. With these capabilities the solver still achieves high performance, enabling demag-field evaluation of up to 1 billion nodes on a single GPU while exhibiting strong scaling as shown in Fig. 1.

Overall, this solver extends micromagnetic simulation beyond static assumptions, providing a practical framework for studying mechanically active magnetic systems, adaptive materials, and next-generation devices driven by motion, deformation, and evolving material states.





FG-06. Dynamic Atomistic Modelling of Domain Walls in Layered van der Waals Antiferromagnets

R. Rama-Eiroa[1, 2], E. Santos[1, 2, 3]
[1]Institute for Condensed Matter Physics and Complex Systems, The University of Edinburgh, Edinburgh, Midlothian, United Kingdom, [2]Higgs Centre for Theoretical Physics, The University of Edinburgh, Edinburgh, Midlothian, United Kingdom, [3]Donostia International Physics Center, San Sebastián, Spain

Layered van der Waals (vdW) magnets have emerged as a versatile platform for low-dimensional magnetism, enabling long-range magnetic order down to the atomic limit and tunable phases via thickness, stacking, strain, gating, and heterostructure design. In particular, vdW antiferromagnets (AFM) combine the absence of stray fields with ultrafast spin dynamics, robustness against perturbations, and compatibility with nanoscale integration, making them promising for spintronic and magnonic applications. Their layered nature enables stabilization and control of topological spin textures such as domain walls (DW), whose properties can be tuned through interlayer exchange, anisotropy, and twisting. However, AFM are difficult to characterize experimentally due to their vanishing net magnetization, which hinders direct imaging of spin textures. In this context, atomistic spin dynamics simulations are essential for guiding experiments and interpreting observations. They provide an accurate description of exchange interactions, anisotropies, interlayer couplings, and thermal fluctuations at the atomic scale, which is crucial in few-layer systems where continuum micromagnetic models fail.

In CrSBr, an A-type AFM with relatively high Néel temperature and triaxial anisotropy, atomistic simulations complement experimental imaging by revealing Néel-type DW below the resolution of nano-SQUID techniques. They also show that such textures persist in even-layer systems, governed by AFM interlayer exchange (Fig. (a)) [1]. In orthogonally twisted bilayers, simulations reproduce multistep magnetization switching, involving canting of the top layer, nucleation of hybrid DW, and full alignment with the external field. These results highlight the role of Dzyaloshinskii–Moriya interactions and anisotropy mismatch (Fig. (b)) [2]. In $CrPS_4$, simulations explain lateral exchange bias in mixed odd-even systems, showing Bloch DW nucleation near odd-layer corners and field-driven motion governed by magnetization polarity and DW geometry (Fig. (c)) [3].

In summary, atomistic spin dynamics simulations are indispensable for understanding and predicting spin textures in vdW AFM, providing key insight for future antiferromagnetic devices.

[1] Y. Zur et al., "Magnetic imaging and domain nucleation in CrSBr down to the 2D limit," Adv. Mater., vol. 35, no. 47, p. 2307195, 2023.
[2] C. Boix-Constant et al., "Multistep magnetization switching in orthogonally twisted ferromagnetic monolayers," Nat. Mater., vol. 23, no. 2, pp. 212–218, 2024.
[3] Y.-X. Wang et al., "Configurable antiferromagnetic domains and lateral exchange bias in atomically thin $CrPS_4$," Nat. Mater., pp. 1–10, 2025.

FG-07. Micromagnetic Framework for Cluster Magnetic Multipoles

M. Yoo[1], R. Winkler[2, 3], A. Hoffmann[1]
[1]Department of Materials Science and Engineering, University of Illinois Urbana-Champaign, Urbana, Illinois, United States, [2]Department of Physics, Northern Illinois University, DeKalb, Illinois, United States, [3]Materials Science Division, Argonne National Laboratory, Lemont, Illinois, United States

Antiferromagnets have attracted significant interest because of their potential for ultra-dense, ultra-fast spintronic devices for next-generation information technologies [1]. $D0_{19}$-type non-collinear antiferromagnets such as Mn_3Sn are particularly intriguing because of their pronounced transport and optical responses [2]. These responses are closely linked to the electronic band structure and the underlying magnetic octupole order in this materials, which plays a role analogous to that of magnetic dipole order in ferromagnets. The static and dynamic properties of magnetic octupoles have been studied using atomistic simulations [3,4]. However, treating spatially non-uniform octupole textures in submicron and larger systems remains computationally challenging within an atomistic approach.

Here, we introduce a micromagnetic framework for vector-like cluster magnetic multipoles, enabling quantitative and spatially resolved simulations of non-uniform multipolar textures [5]. As a proof of concept, we apply this framework to magnetic-octupole dynamics in the non-collinear antiferromagnet Mn_3Sn. Our simulations capture key collective phenomena, including domain-wall profile deformation and the emergence of an effective inertial mass for the domain wall. This work establishes a practical route for studying mesoscopic dynamics of higher-order cluster multipoles and provides a useful platform for exploring

functional properties of non-collinear antiferromagnets.

This work is supported by the NSF through the Illinois MRSEC (DMR-1720633 and DMR-2309037).
[1] S. A. Siddiqui et al., J. Appl. Phys. Vol. 128, p.040904 (2020)
[2] T. Chen et al., Nat. Commun. Vol. 12, p. 572 (2021)
[3] S. Sugimoto et al., Commun. Phys. Vol. 3, p.111 (2020)
[4] H. Tsai et al., Nature Vol. 580, p. 608 (2020)
[5] M.-W. Yoo et al., arXiv:2501.07513 (2025)

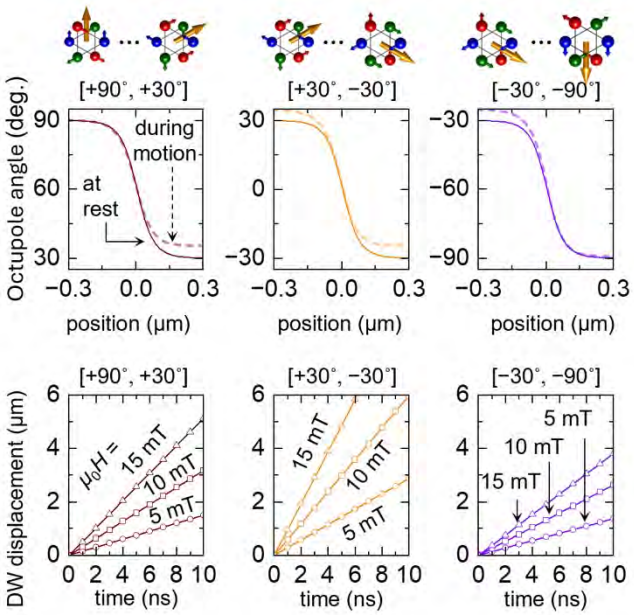


Fig.1 Micromagnetic simulations of magnetic-octupole domain-wall dynamics in the non-collinear antiferromagnet Mn_3Sn. (Top) Domain-wall profiles under applied fields. (Bottom) Field-driven domain-wall displacements.

FG-08. Ferroelectric Control of Chiral Magnetic Interactions in HfO_2-based Ferroelectric/Magnetic Heterostructures

G. Gandini[1], J. Hertel[4], A. Di Pietro[2], A. Magni[2], M. Madami[3], S. Tacchi[3], A. Pezo[5], M. Cantoni[1], C. A. Durner[4], M. Lederer[4], B. Lilienthal-Uhlig[4], M. Kuepferling[2], R. Arras[6], A. Manchon[7], C. Rinaldi[1]
[1]Physics, Politecnico di Milano, Milano, Lombardia, Como, Italy, [2]INRIM, Torino, Piemonte, Italy, [3]Università di Perugia, Perugia, Umbria, Italy, [4]Fraunhofer IPMS, Dresden, Saxony, Germany, [5]Université Paris-Saclay, Palaiseau, Essonne, France, [6]Université de Toulouse, Toulouse, Haute-Garonne, France, [7]Aix-Marseille Université, CNRS, Marseille, Bouches-du-Rhône, France

The efficient control of chiral magnetic textures is a key challenge for next-generation spintronic devices. While current-driven approaches enable the manipulation of domain walls and skyrmions, they suffer from significant energy dissipation, motivating the development of voltage-controlled alternatives [1].

Here we demonstrate non-volatile electric-field control of chiral magnetic interactions in CMOS-compatible ferroelectric/ferromagnetic heterostructures based on $Hf_{0.5}Zr_{0.5}O_2$ (HZO) and Co. The integration of ultrathin Co layers with ferroelectric HZO enables robust magnetoelectric coupling, preserving perpendicular magnetic anisotropy while introducing a strong interfacial tunability of spin–orbit effects [2,3]. Ferroelectric polarization switching induces a sizable modulation of the interfacial Dzyaloshinskii–Moriya interaction (DMI), reaching relative variations up to ~70%, consistent with a polarization-dependent Rashba spin–orbit coupling at the interface [4].

This voltage-driven control of DMI provides a direct handle on chiral spin textures, enabling deterministic tuning of domain wall chirality, domain nucleation processes, and stability of skyrmion-like configurations. The non-volatile nature of the ferroelectric state allows reconfigurable magnetic energy landscapes without the need for sustained current flow, overcoming key limitations of conventional spin–orbit torque approaches.

These results establish HZO/Co heterostructures as a versatile platform for voltage-controlled spintronics and chiral magnetism. In particular, the ability to electrically program interfacial DMI opens new opportunities for reconfigurable domain-wall dynamics and skyrmion-based devices, with strong potential for energy-efficient racetrack memories, magnetic logic, and neuromorphic computing architectures.

[1] A. Fert *et al.*, Rev. Mod. Phys., Vol. 96, p. 015005 (2024).
[2] S. Lancaster *et al.*, ACS Applied Materials and Interfaces, Vol. 15, p. 16963 (2023).
[3] B. Vermeulen *et al.*, ACS Applied Materials and Interfaces, Vol. 11, p. 34385 (2019).
[4] A. Pezo *et al.*, Phys. Rev. B, Vol. 111, p. L140405 (2025).

FG-09. FePt grain switching dynamics under spin-torque effects for storage

S. Chari, A. Venugopal, P. Czoschke
Seagate Technology, Shakopee, Minnesota, United States

Magnetic grain switching under spin-torque effects is important not just from a fundamental physics perspective but also from the perspective of technologies like magnetic hard disk drives. We investigate the influence of external driving mechanisms on the magnetization dynamics of individual grains in magnetic materials using micromagnetic modeling. The non-linear physics necessitates a better understanding of the physical processes at play. By applying effective spin currents on a spin valve structure, we explore how these external excitations can induce controlled switching and/or oscillations within grains, revealing key insights into the interplay between grain size, anisotropy, and excitation strength. We also aim to quantify, through simulations, the critical excitation thresholds required for deterministic switching and assess the switching probability of the grains under such dynamic environments. These findings are expected to inform the design of energy-efficient magnetic recording schemes.

FG-10. Magnetic interactions and their influence on electronic structures in Kagome-lattice magnet Fe_3Sn_2

D. Le[1], J. Kelley[1], G. M. Pantano[1], E. Thareja[1], C. Brennan-Rich[2], M. Phan[1, 3], Y. Mokrousov[4, 5], C. Marrows[2], J. D. Gayles[1]
[1]Department of Physics, University of South Florida, Tampa, Florida, United States, [2]University of Leeds, Leeds, United Kingdom, [3]VinUniversity, Hanoi, Viet Nam, [4]Forschungszentrum Jülich and JARA, Jülich, Germany, [5]Johannes Gutenberg University Mainz, Mainz, Germany

The ability to exhibit topological band features, such as Weyl points or Dirac cones, which give rise to intriguing quantum phenomena, has made Kagome magnets a promising candidate for spintronics. Among the Kagome system, Fe3Sn2 has attracted great attention due to its Massive Dirac fermions [1]. As a result, the intrinsic anomalous Hall effect emerges from a strong source of Berry curvature. This Hall response can be observed in both bulk and thin film [1,2]. On the other hand, in the presence of inversion symmetry, the total of Dzyaloshinskii-Moriya Interaction (DMI) of the whole system should be zero, which would not, in principle, favor the emergence of real-space topological spin textures (i.e., skyrmions). However, multiple experimental studies show that Fe3Sn2 can host skyrmion-like topological spin textures at room temperatures [3]. In addition, the sizable topological thermal transport arising from room-temperature skyrmions could be driven by frustration-stabilized topological spin textures [4]. Yet, there is little theoretical understanding of the magnetic interactions that give rise to nontrivial spin textures and of how different spin configurations can influence electronic structure. In this work, we use first-principles calculations, tight-binding methods, and Wannier tight-binding Hamiltonians to determine the electronic and magnetic properties of Fe3Sn2 in bulk and in two dimensions. Our results show that the exchange stiffness for both scenarios is in good agreement with experimental data. We then calculate the magnetocrystalline anisotropic energy and predict that the magnetic easy axis of this system lies in the in-plane direction. We construct noncollinear, noncoplanar spin textures to further identify the emergence of spin-orbit interactions that can stabilize real-space topological skyrmions and to uncover how they can influence electronic features in k-space. These results suggest several ways to manipulate intrinsic skyrmions via chiral effects.

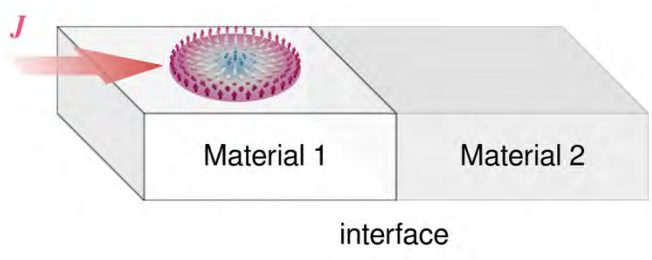
[1] Ye, Linda, et al. (2018). “Massive Dirac fermions in a ferromagnetic kagome metal”. Nature 555.7698: 638-642.
[2] Zhang, Dongyao, et al. (2022). “Anomalous and topological Hall effects of ferromagnetic Fe3Sn2 epitaxial films with kagome lattice.” Applied Physics Letters 120.23.
[3] Altthaler, Markus, et al. (2021). “Magnetic and geometric control of spin textures in the itinerant kagome magnet Fe3Sn2.” Physical Review Research 3.4: 043191.
[4] Du, Qianheng, et al. (2020). “Room Temperature Skyrmion Thermopower in Fe3Sn2.” Advanced Quantum Technologies 3.10: 2000058.

FG-11. Spin Phenomena at Planar (Anti)ferromagnetic and Altermagnetic Interfaces

R. Msiska[1, 2], C. J. Reichhardt[1], C. Reichhardt[1], A. B. Saxena[1]
[1]Theoretical Division, Los Alamos National Laboratory, Los Alamos, New Mexico, United States, [2]Center for Memory and Recording Research, University of California San Diego, San Diego, California, United States

Lateral interfaces between distinct magnetic orders offer a promising route for uncovering new forms of interfacial exchange coupling and spin transport phenomena. While vertical heterostructures combining ferromagnets (FMs) and antiferromagnets (AFMs) have been widely explored in the context of exchange bias, spin-current transfer, and interfacial anisotropy [1–3], comparatively little attention has been given to lateral geometries, where magnetic order varies in-plane and interfacial coupling is mediated by distinct boundary conditions . The recent identification of altermagnets (AMs), collinear compensated magnets that exhibit spin-split band structures despite zero net magnetization [4,5], introduces a new dimension to this problem. In this work, we comparatively examine lateral interfaces formed between FMs, AFMs, and AMs, including representative configurations such as FM/AFM, FM/AM, and AM/AFM, to explore how variations in magnetic properties influence interfacial coupling, spin-wave transmission, and related phenomena. Building on established theoretical frameworks for FM/AFM coupling [6,7] and emerging models of altermagnetic spin polarization [4,5], we analyze how the lateral interface modifies boundary conditions and symmetry constraints relative to conventional layered systems. By positioning this investigation within the broader literature on interfacial magnetism and spin transport, we aim to clarify how combining FM, AFM, and AM orders in planar junctions can yield new coupling regimes and provide symmetry-driven design principles for future spintronic devices.

1. J. Nogués and I. K. Schuller, J. Magn. Magn. Mater. 192, 203 (1999)
2. A. E. Berkowitz and K. Takano, J. Magn. Magn. Mater. 200, 552 (1999)
3. T. Jungwirth, X. Marti, P. Wadley, and J. Wunderlich, Nat. Nanotechnol. 11, 231 (2016)
4. L. Šmejkal, R. González-Hernández, T. Jungwirth, and J. Sinova, Sci. Adv. 6, eaaz8809 (2020)
5. L. Šmejkal, J. Sinova, and T. Jungwirth, Phys. Rev. X 12, 040501 (2022)
6. O. Busel, O. Gorobets, and Y. Gorobets, J. Magn. Magn. Mater. 462, 226 (2018)
7. O. Busel, O. Gorobets, and O. A. Tretiakov, arXiv:2112.14583 (2021)



FG-12. Accurate Computation of the 2D PBC Demagnetization Tensor for Micromagnetics

M. J. Donahue
ACMD, NIST, Gaithersburg, Maryland, United States

Periodic boundary conditions (PBCs) are frequently used to reduce the size of systems that would otherwise be too large to model directly. Implementing PBCs in magnetic systems is complicated by the long range nature of the stray field. Essentially, the interaction tensor $N(\underline{r})$ must be summed across all infinite periodic images to form one composite tensor. Computationally, the infinite sums are truncated at some finite index M and errors arising from the truncation need to be managed. Simple truncation without correction is insufficient because in 2D PBC the truncated tail sum magnitude only decays $\sim O(1/M)$ while the computed number of terms grows $\sim O(M^2)$; e.g. 8 digit accuracy at 1 ns per term requires 100 days of compute time and incurs 8 digits of rounding error. The Euler-Maclaurin formula provides an economical way to control the tail error:

$$\sum f(k) = \int f(x)\,dx + f(M)/2 - \sum^{p} B_{2k}/(2k)!\, f^{(k)}(M) + R_p$$

This replaces the tail sum with an integral and the sum of a small number (p) of weighted derivatives of f; B_{2k} are Bernoulli numbers and R_p is a remainder term. In our case f is the demagnetization tensor N at cell offset $\underline{r}$, and the sums and integral become double sums and a double integral. The main difficulty is that the analytic form of N [1] suffers significant cancellation error at large $\underline{r}$, but far-field asymptotic approximations can rectify this problem (Fig. 1) [2]. The asymptotics and their integrals have the form shown in Fig. 2, which support differentiation algorithmically allowing straightforward implementation of Euler-Maclaurin. The talk will provide implementation details, results, and error analysis of the method.

[1] A.J. Newell, W. Williams, and D.J. Dunlop, *J. Geophysical Research - Solid Earth*, 98, 9551 (1993). doi: 10.1029/93JB00694

[2] K.M. Lebecki, M.J. Donahue, and M.W. Gutowski, J. *Phys. D: Appl. Phys.*, 41, 175005 (2008). doi: 10.1088/0022-3727/41/17/175005

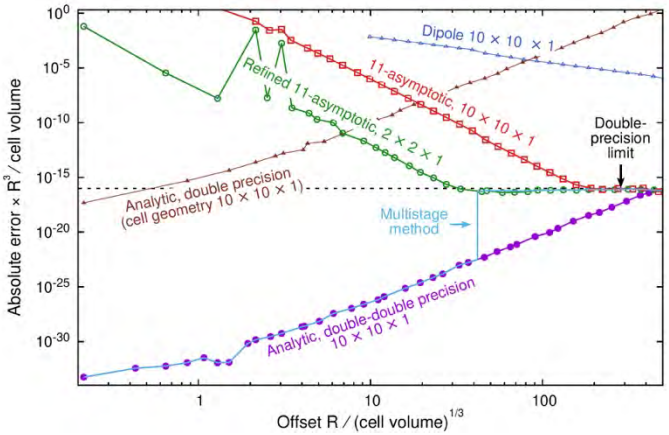


Fig.1 Error in computation of demagnetization tensor component N_{xx} using analytic formulae (filled symbols) and asymptotic approximations (open symbols) vs. normalized offset R. Switching between the two methods at R≈40 provides nearly full double-precision accuracy across all offsets.

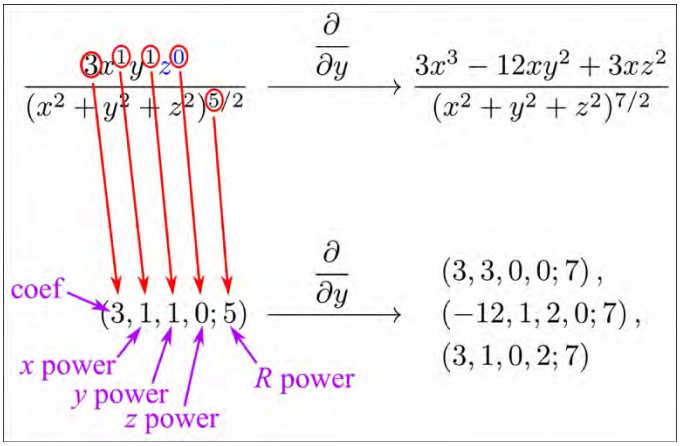


Fig. 2 Asymptotics for N and all derivatives consist of homogenous polynomials divided by powers of R=|r|. Each term can be represented as a list of 5 integers; these can be manipulated algorithmically in code to implement partial differentiation, addition, multiplication, and evaluation at arbitrary offsets r.

FG-13. Reconciling global and local spin models

B. Nyári[1, 3], A. Lászlóffy[2, 4], L. Szunyogh[1, 3]
[1]*Department of Theoretical Physics, Budapest University of Technology and Economics, Budapest, Hungary,* [2]*Wigner Research Centre for Physics, Budapest, Hungary,* [3]*HUN-REN-BME Condensed Matter Research Group, Budapest, Hungary,* [4]*Pázmány Péter Catholic University, Budapest, Hungary*

We present a unified framework that reconciles global and local descriptions of magnetic interactions in itinerant systems, supported with first principles calculations.
Effective spin Hamiltonians derived from density functional theory are commonly formulated either as configuration-independent global models [1,2] or as configuration-dependent local models [2,3]. While both approaches successfully describe complex magnetic states, they often yield apparently inconsistent interaction parameters, including spurious Dzyaloshinskii–Moriya-like terms in non-relativistic systems [5,6].
Within a multiple-scattering Green's function formalism, we derive both global two- and four-spin interactions and local exchange tensors. Using the prototypical Cr trimer on Au(111), we demonstrate that the decomposition of the two-spin variation of the energy to different type of magnetic interactions is depending on the formalism, despite the two-spin variation of the energy is identical. We identify the origin of this ambiguity as longitudinal contributions that do not affect transverse spin fluctuations.
By introducing a projection onto the transverse subspace, we eliminate these unphysical longitudinal terms, with that matching the results of different local formalisms and establish a one-to-one correspondence between local interaction matrices and a global multispin Hamiltonian. The projected local interactions quantitatively reproduce those obtained from the global four-spin model, clarifying the connection between local and higher-order interactions [5]. Our results demonstrate that local spin models represent only the transverse response of global multispin Hamiltonians, providing a consistent interpretation of configuration-dependent effects.

[1] A. I. Liechtenstein, M. I. Katsnelson and V. P. Antropov, J. Magn. Magn. Mater., Vol. 67, p.65 (1987)
[2] L. Udvardi, L. Szunyogh and K. Palotás, Phys. Rev. B, Vol. 68, p.104436 (2003)
[3] A. Szilva, M. Costa and A. Bergman, Phys. Rev. Lett., Vol. 111, p.127204 (2013)
[4] R. Cardias, A. Szilva and A. Bergman, Sci. Rep., Vol. 10, p.20339 (2020)
[5] M. dos Santos Dias, S. Brinker and A. Lászlóffy, Phys. Rev.

B, Vol. 103, p.L140408 (2021)
[6] R. Cardias, J. d. S. Silva and A. Bergman, Phys. Rev. B, Vol. 108, p.224408 (2023)

SESSION FP: INTERFACES AND FUNCTIONAL PROPERTIES IN MAGNETIC NANOSTRUCTURES (POSTER SESSION)

Co-Chair(s): P. Tiberto, *INRIM, Torino, Italy* and F. Albertini, *IMEM-CNR, Parma, Italy*
Thursday, November 5, 2026
03:00 PM-06:00 PM
Coral 4

FP-01. Crystal-orientation-tunable Tellurium Thin Films Grown on Bi_2Te_3 Buffer Layer

Y. Kobayashi, S. Wang, A. Mitsuzuka, M. Kawaguchi, M. Hayashi
Department of Physics, University of Tokyo, Tokyo, Japan

Tellurium (Te) is a unique material composed of helical atomic chains and has recently attracted considerable attention because its chiral crystal structure gives rise to a variety of unusual physical properties, including chirality-dependent magnetoresistance[1], circular photogalvanic effect[2], and possible topological and edge-related electronic states[3]. Controlling the crystal orientation of Te is therefore an important issue not only for understanding its fundamental properties but also for developing functional devices based on its structural chirality and anisotropy. However, in many of the previous reports, such control has been limited to solution-based growth[4] or other restricted fabrication approaches[5], and large-area, uniform control of the crystal orientation in Te thin films remains challenging.
Here, we show that the crystal orientation of Te thin films can be tuned systematically by introducing a Bi_2Te_3 (BT) buffer layer. Owing to its layered structure and interfacial compatibility with Te, the BT buffer influences the nucleation process and the preferred growth orientation of Te. We fabricated Te thin films on BT buffer layers under different growth temperatures conditions and investigated their structural and morphological properties by X-ray diffraction (XRD), Raman spectroscopy, and atomic force microscopy (AFM). We find that crystal orientation of Te can be tuned by varying deposition temperature. This buffer-assisted orientation control may provide a pathway toward Te films with tailored chiral and spin-dependent functionalities.
[1] F. Calavalle et al., Nat. Mater. 21, 526-532 (2022).
[2] C. Niu et al., Nano Lett. 23, 3599 (2023).
[3] K. Nakayama et al., Nature 631, 54-59 (2024).
[4] Y. Wang et al., Nat. Elec. 1, 228-236 (2018).
[5] W. Zheng et al., Small 17, 2007768 (2021).

FP-03. Interfacial Contributions to Electrical Transport in TbFeCo/BiSb Multilayers with Varying Layer Thickness Ratio

M. Ito[1], K. Horiuchi[3], M. Mizuno[1], R. Ando[2], R. Uesugi[1], T. Komine[1]

[1]Ibaraki University, Hitachi, Japan, [2]Ibaraki College, Hitachinaka, Japan, [3]Tohoku University, Sendai, Japan

In recent years, magnetism-related thermoelectric effects, particularly the anomalous Nernst effect (ANE), have attracted attention due to their potential for transverse thermoelectric energy conversion. However, their magnitude is still much smaller than that of the Seebeck effect, requiring further enhancement for practical applications. Previous studies have shown that large ANE-like signals can be achieved in magnetic/nonmagnetic multilayers under a finite external magnetic field [1].

In this study, we fabricated multilayers composed of TbFeCo and BiSb. The TbFeCo layer exhibits spontaneous magnetization at zero field due to perpendicular magnetic anisotropy (PMA), enabling ANE without an external field, while the BiSb layer, as a topological insulator, possesses a relatively large ordinary Nernst effect [2]. The films were prepared by magnetron sputtering on glass substrates with an AlN/TbFeCo/BiSb/AlN structure. The composition of the TbFeCo layer was adjusted to achieve PMA [3].

The longitudinal resistivity (ρ_{xx}) and Hall resistivity (ρ_{yx}) were measured at room temperature under an out-of-plane magnetic field. A parallel conduction model, in which current flows independently in each layer, was used to analyze the transport properties (Fig. 1) [4]. The layer thicknesses were TbFeCo (60 nm) and $Bi_{90}Sb_{10}$ (100 nm), and the model was calculated using parameters from single-layer films.

Figure 1 shows the magnetic field dependence of ρ_{yx}, and Fig. 2 shows the Nernst signal (S_{yx}). In both cases, the measured values are approximately 1.2 times larger than the model predictions, indicating additional contributions beyond the simple bilayer model, likely originating from interfacial effects at the TbFeCo/BiSb interface.

We discuss the dependence on layer thickness ratio and interfacial effects on electrical and thermoelectric transport properties.

[1] W. Zhou, T. Sasaki, K. Uchida, *ADV. Sci*., Vol. 11, 2308543 (2024).

[2] M. Murata, M. Suzuki, K. Aoyama, *Mater. Trans*., Vol. 65, 1162 (2024).

[3] R. Ando and T. Komine, *J. Appl. Phys.*, Vol. 135, 093906 (2024).

[4] H. Matsuura, A. Riss, F. Garmroudi, *Phys. Rev. Res*., Vol. 6, 043071 (2024).

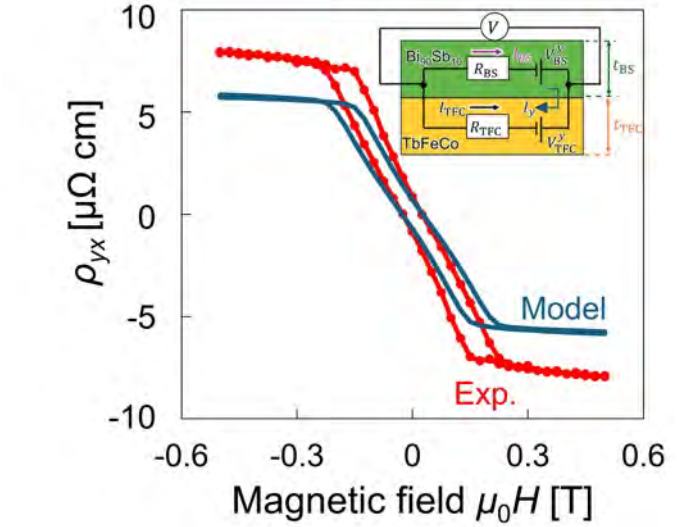


Fig.1 Magnetic field dependence of the Hall resistivity ρ_{yx} (red circle) for the TbFeCo/BiSb multilayers. The blue line indicates the calculated resistivity by parallel conduction model. The Inset shows the schematic illustration of parallel conduction model.

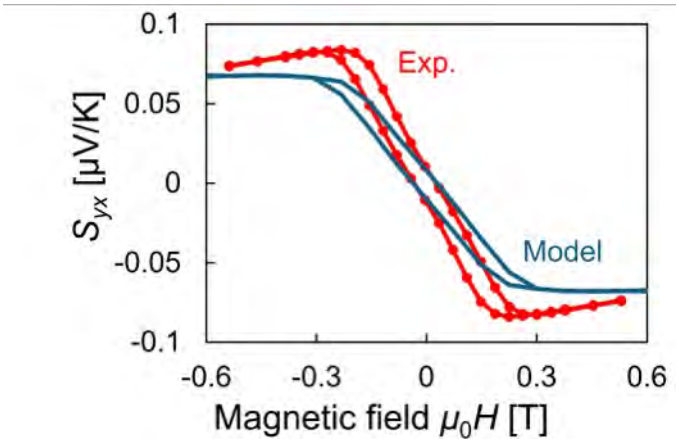


Fig. 2 Magnetic field dependence of the Nernst effect S_{yx} for the TbFeCo/BiSb multilayer.

FP-05. Magnetic Anisotropy and Hyperthermic Efficiency of Polyethylene-grafted Fe_3O_4 Nanocomposites Synthesized via Ring-Opening Metathesis

E. Genfior, E. Gutierrez, A. Garcia, F. Iglesias, A. Khodagulyan, O. Bernal, A. N. Kocharian
Physics and Astronomy, California State University, Los Angeles, California, United States

This study investigates the magnetic anisotropy and hyperthermic efficiency of polyethylene-grafted Fe_3O_4 nanocomposites (PE-g-Fe_3O_4 NPs) synthesized via surface-initiated ring-opening metathesis polymerization (SI-ROMP). Surface-functionalized Fe_3O_4 nanoparticles were employed as initiators for the polymerization of cyclooctene (COE), yielding polycyclooctene-grafted Fe_3O_4 nanoparticles (PCOE-g-Fe_3O_4 NPs) at varying reaction times and Fe_3O_4:COE mass ratios. Subsequent catalytic hydrogenation converted the unsaturated PCOE backbones into polyethylene, enhancing crystallinity, flexibility, and interfacial adhesion between the magnetic cores and polymer matrix. Control over polymerization conditions enabled systematic variation of polymer chain length and Fe_3O_4 loading, facilitating investigation of structure–property relationships. Energy-dispersive X-ray spectroscopy (EDS) confirmed successful surface functionalization, with dominant C and O contributions (39.3 and 35.7 at.%) indicative of polymer encapsulation, and Si (9.6 at.%) and Fe (9.2 at.%) corresponding to silane-linked Fe_3O_4 cores. Elemental mapping revealed a uniform distribution of Fe, Si, and C, supporting effective covalent coupling between inorganic and organic components. Vibrating sample magnetometry (VSM) at ~300 K showed superparamagnetic-like behavior, with saturation magnetization ($M_S \approx 10$ emu $g^{-1)}$, negligible coercivity (Hc ≈ 0 Oe), and near-zero remanence, indicating effective magnetic isolation by the polymer shell. Increasing polymerization time is expected to promote growth of polyethylene chains (up to ~100 nm), which may enhance interparticle interactions and influence magnetic anisotropy and relaxation behavior. The morphology of synthesized nanorod core-shell were characterized also by FTIR, XRD, SEM, TEM and AFM microscopies. These results demonstrate that SI-ROMP-derived PE-g-Fe_3O_4 nanocomposites provide a tunable platform in which polymer architecture governs magnetic response. The combination of controlled grafting, adjustable magnetic properties, and thermal dissipation potential highlights their promise for applications in magnetic hyperthermia, biomedical imaging, and energy-related systems.

This work at Cal State LA was supported by the NSF-Partnerships for Research and Education in Materials under the CATSUS-CREST Grants No. HRD-1547723 and No. HRD-2112554

FP-06. Exploring the Boost in Magnetization of Ni/β-Bi_2Pd Using X-ray Spectroscopies

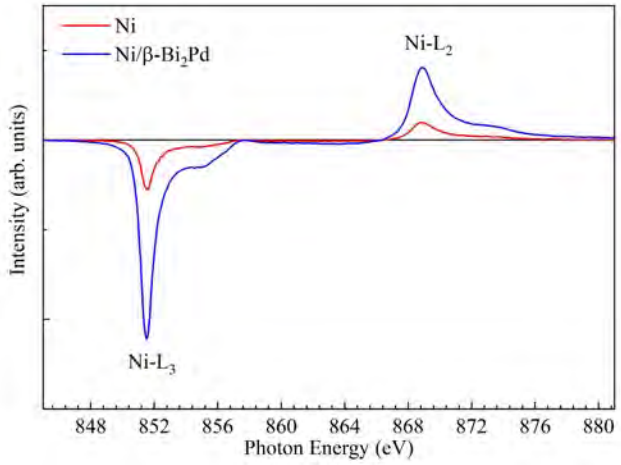
Y. Chin[1], Y. Ku[2], D. Qu[3], S. Huang[2], H. Lin[4], C. Chen[4]
[1]National Chung Cheng University, Chiayi, Taiwan, [2]National Taiwan University, Taipei, Taiwan, [3]Center for Condensed Matter Sciences, National Taiwan University, Taipei, Taiwan, [4]National Synchrotron Radiation Research Center, Hsinchu, Taiwan

The diverse transport properties and associated functionalities of transition metal compounds have attracted considerable interest for decades. Recently, atomic-scale growth has uncovered a wide range of exotic properties absent in the bulk constituents of heterostructures. For instance, charge transfer and orbital reconstruction at interfaces can modify the electronic structures of individual layers, along with their transport and magnetic characteristics [1,2]. β-Bi_2Pd is a tetragonal, low-temperature, centrosymmetric triplet superconductor with a T_C of about 5.3 K, and its strong spin–orbit coupling along with Dirac-like surface states make its thin films a prime candidate for a topological superconductor platform [3-4]. An enhancement in magnetization in Ni/β-Bi_2Pd compared to a Ni thin film was observed [5]. An induced moment in β-Bi_2Pd was anticipated. To elucidate this phenomenon, we conducted X-ray magnetic circular dichroism (XMCD) measurements on Ni/β-Bi_2Pd and Ni thin films.

The Ni $L_{2,3}$-edge XMCD data exhibited a significantly stronger signal for Ni/β-Bi_2Pd than for pure Ni, consistent with the magnetization measurements and indicative of an enhanced Ni moment rather than a proximity effect. Notably, a small loop appeared within the hysteresis loop of the XMCD signals. To investigate this feature and the origin of the magnetization enhancement, X-ray absorption data were examined, revealing that the Ni/β-Bi_2Pd spectrum shifted to lower photon energies relative to Ni. This shift suggests a slightly reduced Ni valence state in Ni/β-Bi_2Pd, likely resulting from charge transfer between Ni and β-Bi_2Pd, potentially enhancing the Ni moment. Hard X-ray photoemission spectroscopy measurements on both Ni/β-Bi_2Pd and β-Bi_2Pd revealed distinct differences in the electronic structures of Bi and Pd within those thin films.

[1] J. Chakhalian, J. W. Freeland, G. Srajer et al., Nature

Physics, Vol. 2, p. 244–248 (2006).
[2] J. Chakhalian, J. W. Freeland, H. U. Habermeier et al., Science, Vol. 318, p. 1114-1117 (2007).
[3] M. Sakano, K. Okawa, M. Kanou et al., Nature Communications, Vol. 6, Article number: 8595 (2015).
[4] C. C. Chiang, H.C. Lee, S.C. Lin et al., Physical Review Letters, Vol. 131, p. 236003 (2023).
[5] Yu-Seng Ku, Chih-Chieh Chiang, Shuan-Cheng Mai et al., Physical Review Applied, Vol. 24, p. 034050 (2025).



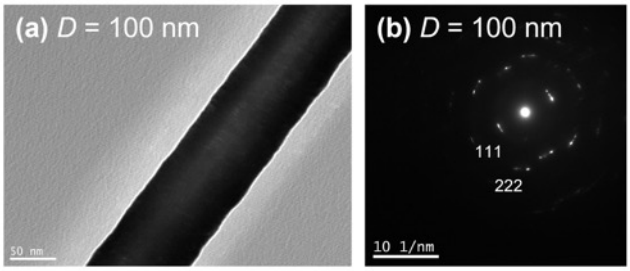
The XMCD curves of Ni/β-Bi_2Pd and Ni.

FP-07. Diameter dependence of magnetic properties and structure in cylindrical CoPt alloy nanowires

R. Kawana[1], D. Oshima[2], M. Saito[3], T. Homma[3], T. Kato[2], T. Ono[4], M. Shima[1], K. Yamada[1]
[1]Gifu University, Gifu, Japan, [2]Nagoya University, Nagoya, Japan, [3]Waseda University, Tokyo, Japan, [4]Kyoto University, Uji, Japan

Three-dimensional domain wall (DW)-based magnetic memory devices have attracted significant attention due to their high-speed operation, high density, and low power consumption. Information is recorded by driving DWs with a current in magnetic multilayer nanowires [1]. To achieve stable current-driven DW motion, materials with high magnetocrystalline anisotropy (K_u) are required [2]. In this study, electrodeposited CoPt nanowires were investigated as a high-K_u material, focusing on their magnetic properties and structure as a function of wire diameter. Cylindrical CoPt nanowires were prepared by electrodeposition under previously reported conditions [3,4] using polycarbonate templates with pore diameters (D) of 30–100 nm. Their structure was characterized by SEM, TEM, and XRD, and magnetic properties were measured using VSM. Figure 1 shows a TEM image and the corresponding SAED pattern of a CoPt nanowire with D = 100 nm. A layered-like structure on the order of a few nanometers is observed, and a strong fcc (111) texture is identified. Figure 2(a) shows magnetic measurement results for nanowires with D = 30, 50, and 100 nm under magnetic fields ($\mu_0 H$) applied along the wire axis at 300 K. As D decreases, both the squareness (M/M_s) and coercivity ($\mu_0 H_c$) increase. This is attributed to the enhanced contribution of shape anisotropy. Temperature-dependent magnetic measurements were performed using VSM in the temperature range of 50–300 K. As shown in Fig. 2(b), M/M_s and $\mu_0 H_c$ increase by approximately 10% and 25%, respectively, with decreasing temperature. These changes are attributed to the suppression of thermal fluctuations, leading to more stable magnetization at lower temperatures. The effective anisotropy constant (K) was estimated from the hysteresis loops. K exhibits only a weak variation within the measured temperature range, likely because the change in the magnitude of magnetization is relatively small.

[1] Y. M. Hung, et. al., J. Magn. Soc. Jpn. vol.45, p.6 (2021)., [2] S. Honda and Y. Sonobe, J. Phys. D: Appl. Phys. vol.55, p.395001 (2022)., [3] N. Oguchi, et. al., J. Magn. Magn. Mater. vol.601, p.172159 (2024)., [4] R. Kawana, et.al., Appl. Phys. Express vol.18, p.033002 (2025).



(a) TEM image and (b) SAED pattern of a CoPt nanowire with D = 100 nm.

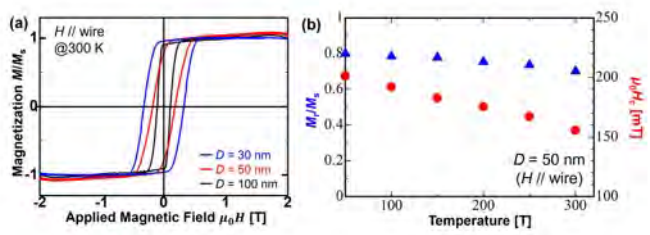


Fig.2 (a) Magnetic hysteresis loops of CoPt nanowires (D = 30, 50, 100 nm) measured at 300 K ($\mu_0 H$ // wire axis) and (b) Temperature dependence of M/M_s and $\mu_0 H_c$ for D = 50 nm measured at 50–300 K ($\mu_0 H$ // wire axis).

FP-08. Engineering of Magnetic Anisotropy in Antiferromagnetic NiO(111) Epitaxial Thin Films

M. Slezak[1], A. Kwiatkowski[1], M. Zajac[2], M. Szpytma[2], A. Koziol Rachwal[1], T. Slezak[1]
[1]AGH University of Krakow, Krakow, Poland, [2]National Synchrotron Radiation Centre SOLARIS, Jagiellonian University, Krakow, Poland

We report on the in-plane magnetic anisotropy of antiferromagnetic NiO(111) films epitaxially grown on Cr(110) buffer layers on W(110) single crystal. Both structural and magnetic characterization of 40 thick NiO films was performed as a function of Cr layer thickness, starting from single pseudomorphic Cr monolayer (ML) up to 75 monolayers. XMLD technique was used to track the Cr thickness dependent magnetic anisotropy of antiferromagnetic NiO. For this reason XAS spectra at the Ni L2 edge were systematically acquired at 80 K with linear polarization of the photon beam. Characteristic two peaks of XAS intensity around the L2 absorption edge of Ni was used to quantify the XMLD effect. The ratio of these two intensity maxima, called R_{L2}, is routinely used as a probe of NiO magnetic moments orientation or spin population distribution. For each particular Cr thickness, the R_{L2} ratio was followed as a function of azimuthal, in-plane angle ϕ between electric field E of incoming beam and chosen NiO[-211] in-plane crystallographic direction. Corresponding polar plots $R_{L2}(\phi)$ are shown in Fig.1. Clearly, Cr thickness induced in-plane SRT in NiO is observed. Results for NiO(111)/Cr(110)/W(110) bilayers are compared to almost isostructural NiO(111)/Fe(110)/W(110) system (red plots in Fig.1) where exactly opposite in-plane SRT in NiO(111) is driven purely by magnetic interaction between Fe and NiO spins [1,2]. In Fig.2 simulated polar plots $R_{L2}(\phi)$ are shown for two orthogonal in-plane spin orientations of NiO(111). Comparison of measured and calculated $R_{L2}(\phi)$ dependencies indicates that with increasing Cr thickness antiferromagnetic spins rotate from parallel to NiO[−211] towards NiO[01−1] direction within (111) sample plane. Analysis of LEED data reveals that such Cr thickness induced AFM SRT originates from evolution of epitaxial strain exerted on NiO layer by Cr buffer.

[1] M. Slezak et al., PHYSICAL REVIEW B 104, 134434 (2021)
[2] E. Swierkosz,et al., M. Slezak, Scientific Reports 15 (2025) 22267

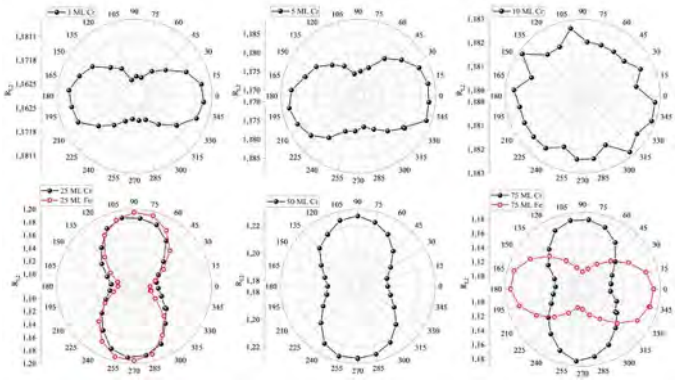


Fig.1. R_{L2} ratio vs ϕ angle, as determined form 80 K XMLD measurements, for increasing Cr buffer layer. Comparison with isostructural NiO/Fe system is also shown (red plots).

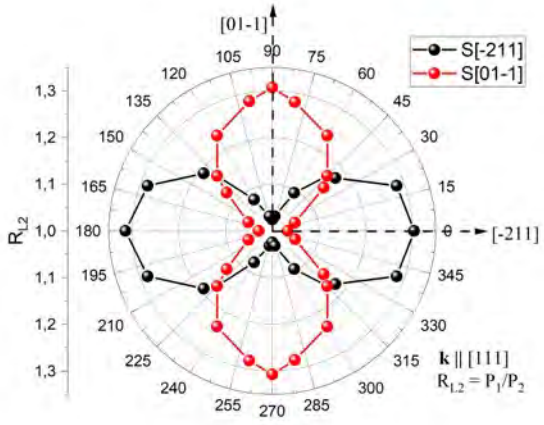


Fig. 2. Simulated polar plots $R_{L2}(\phi)$ for two orthogonal in-plane spin orientations of NiO(111).

FP-09. Engineering of FeB/SiB Multilayers for the Neutron Polarisers

S. K. Jena
Institute of Physics, Chemistry and Biology, Linkoping University, Linkoping, Linkoping, Sweden

Polarized neutrons are vital tools in materials science, magnetism, spintronics, and biology, as they exploit spin-dependent interactions to provide unique contrasts. To maximize the efficiency of neutron scattering experiments, high-performance neutron optics especially Fe/Si multilayers are indispensable. These multilayers are integrated into devices such as monochromators,

waveguides, polarizers, and focusing elements due to their favourable magnetic and structural properties. However, these systems suffer from well-known limitations: reduced reflectivity at high scattering vectors Q, insufficient polarization efficiency, elevated magnetic coercivity, interfacial silicide formation, and enhanced diffuse scattering.

Here, we present a systematic strategy to overcome these limitations through controlled incorporation of Boron into Fe/Si [1-2]. By varying boron concentration in both the magnetic (Fe) and non-magnetic (Si) layers in FeB/SiB heterostructures, we will demonstrate independent tuning of the nuclear scattering length density (nSLD) and magnetic scattering length density (mSLD) by incorporation of Boron [3]. The key design criterion for an ideal polarizer is that in the spin-down neutron channel, the difference between the mSLD and nSLD of the magnetic layer equals the nSLD of the adjacent non-magnetic layer achieving near-zero reflectivity for spin down state while maximizing it for the spin up state [3]. We show how systematic Boron doping allows precise satisfaction of this contrast-matching condition across a wide compositional range. Further, optimal Boron concentration is optimized to achieve both high reflectivity and high polarization efficiency simultaneously by polarized neutron reflectivity, while magnetic coercivity and interfacial intermixing are substantially suppressed.

[1] A. Zubayer, et al., Reflective, polarizing, and magnetically soft amorphous neutron optics with ^{11}B-enriched B_4C. *Sci. Adv.* 10, eadl0402 (2024). DOI:10.1126/sciadv.adl0402.

[2] A. Zubayer et al., et al. Increased neutron reflectivity and polarization of neutron-optical engineered Fe/$^{11}B_4$CTi multilayer optics. *Phys. Rev. B*, 110, 155408 (2024). DOI:10.1103/PhysRevB.110.155408.

[3] S. K. Jena et al., FeB/SiB heterostructures for neutron mirrors (unpublished)

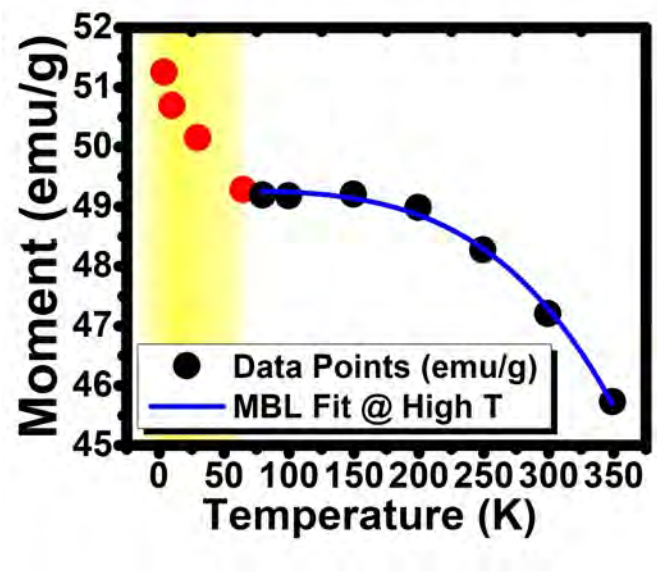
FP-10. Magnetic Surface Spin Disorder and Shape Anisotropy in High-Aspect Ratio Ni Nanorods

S. Jan[1], A. I. Ojo[1], N. Schulz[2], J. Nag[1], P. Sharma[1], E. Jaberolansar[1], R. Yoosuf[3], H. Khurshid[4], D. A. Arena[1], H. Srikanth[1]

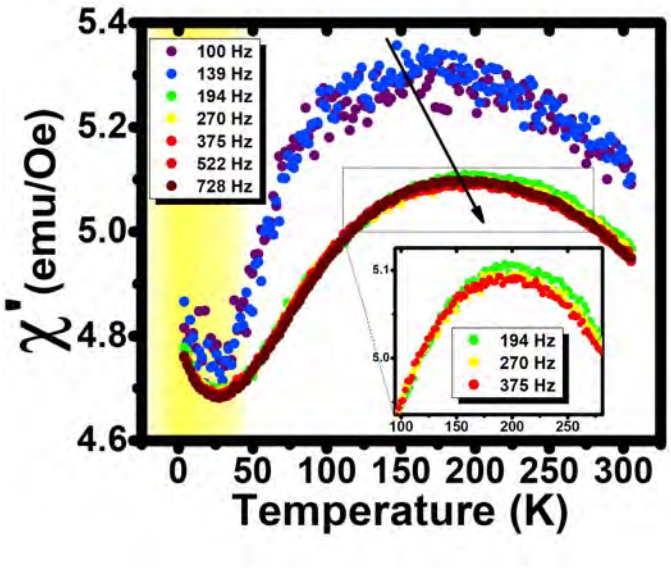
[1]Physics, University of South Florida, Tampa, Florida, United States, [2]Naval Surface Warfare Center, Panama City, Florida, United States, [3]Applied Physics and Astronomy, University of Sharjah, Sharjah, United Arab Emirates, [4]Eberly College of Science, The Pennsylvania State University, University Park, Pennsylvania, United States

High-aspect-ratio Nickel (Ni) nanorod arrays were synthesized and systematically investigated to understand the correlation between their nanostructure and macroscopic magnetic properties. X-ray diffraction confirms the formation of fcc Ni, with a possible minor NiO contribution coming from surface oxidation. Scherrer analysis yields a crystallite size of ~19 nm, indicating a polycrystalline internal structure. Scanning electron microscopy reveals rod-like morphology with diameters in the range of 50–200 nm and lengths extending to several microns. Temperature-dependent magnetization measurements (4–350 K) under zero-field-cooled (ZFC) and field-cooled (FC) protocols exhibit a broad feature around 30–50 K, potentially attributed to spin-freezing or surface spin disorder effects [1]. The absence of a sharp blocking peak and the persistence of magnetic irreversibility suggests a distribution of anisotropy barriers arising from intergranular interactions, domain wall pinning and variations in nanorod dimensions. Saturation magnetization (M_s) follows Bloch-like behavior at higher temperatures; however, an enhanced exponent ($\alpha > 1.5$) with deviation at low temperatures indicate contributions from surface and finite-size effects beyond conventional spin-wave excitations. AC susceptibility measurements reveal relatively modest frequency dispersion consistent with the collective dynamics of interacting magnetic regions governed by domain wall motion and pinning. The system exhibits non-zero coercivity up to 350 K, reflecting shape anisotropy and magnetic stability. These results demonstrate that the magnetic response of Ni nanorods is governed by the combined influence of nanoscale grain structure, geometry-driven (shape) anisotropy, and surface spin dynamics. Future work will focus on probing the dynamic magnetic response via transverse susceptibility (TS) measurements, ferromagnetic resonance (FMR) and evaluating potential applications in high-frequency devices and magnetic hyperthermia.

[1] N. Rinaldi-Montes, P. Gorria and D. Martínez-Blanco, Nanoscale., Vol. 6, p. 457 (2014)



Bloch fitting of the M_s vs. T data.



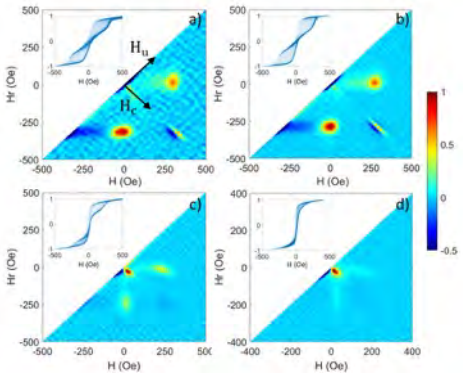
AC susceptibility.

FP-11. Reading the interaction between vortex textures in a FORC diagram

A. Rivelles, A. Parente, J. Prieto, M. Sanz, M. C. Maicas, M. Abuin
Instituto de Sistemas Optoelectrónicos y Microtecnología (ISOM), Universidad Politécnica de Madrid (UPM), Madrid, Madrid, Spain

Large arrays of magnetic nanoelements are central to many emerging spintronic technologies, where interactions between magnetic textures strongly influence collective behavior and device performance [1 to 4]. Experimentally accessing these interactions over macroscopic arrays containing millions of elements remains challenging, as most magnetic imaging techniques lack either sufficient spatial resolution or a wide enough field of view. In this work, we present a comprehensive and citable study demonstrating that First Order Reversal Curve (FORC) diagrams provide a powerful and scalable approach to reveal and quantify interactions between vortex magnetic textures in large arrays of ferromagnetic nanodots.
We perform a systematic FORC analysis on millimeter scale arrays of circular Permalloy nanodots hosting vortex states, with controlled variation of the interdot spacing to tune magnetostatic interactions [5](Fig. 1). Distinct features in the FORC diagram correspond to vortex nucleation and annihilation processes. Beyond their position, we show that the relative intensity and asymmetry of these features encode information about vortex mobility within individual dots. By introducing an asymmetry ratio between nucleation and annihilation features, we establish a quantitative metric sensitive to both intrinsic vortex pinning and the onset of interdot interactions.
As the spacing between nanodots is reduced, FORC diagrams reveal a transition from isolated vortex behavior to a collective regime, where magnetostatic coupling promotes correlated annihilation and multi dot magnetic textures. Micromagnetic simulations reproduce the experimental FORC features and confirm their interpretation[5], linking changes in the diagram to vortex dynamics and interaction strength. Overall, this work provides a single, well defined reference for interpreting FORC diagrams in vortex based systems, enabling the disentanglement of individual and collective magnetization processes relevant to sensing, magnonics, and neuromorphic computing.
1. S. H. Skjærvø, C. H. Marrows, R. L. Stamps and L. J. Heyderman, “Advances in artificial spin ice”, Nature Reviews Physics 2, 13 (2020). . 2. J. C. Gartside, K. D. Stenning, A.

Vanstone, H. H. Holder, D. M. Arroo, T. Dion, F. Caravelli, H. Kurebayashi and W. R. Branford, "Reconfigurable training and reservoir computing in an artificial spin-vortex ice via spin-wave fingerprinting", Nature Nanotechnology 17, 460 (2022).
3. D. Suess, A. Bachleitner-Hofmann, A. Satz, H. Weitensfelder, C. Vogler, F. Bruckner, C. Abert, K. Prüg l, J. Zimmer, C. Huber, S. Luber, W. Raberg, T. Schrefl and H. Brückl, "Topologically protected vortex structures for low-noise magnetic sensors with high linear range", Nature Electronics 1, 362 (2018).
4. S. Wintz, V. Tiberkevich, M. Weigand, J. Raabe, J. Lindner, A. Erbe, A. Slavin and J. Fassbender, "Magnetic vortex cores as tunable spin-wave emitters", Nature Nanotechnology 11, 948 (2016). 9. H. Yu, J. Chen, V. Cros, P. Bortolotti, H. Wang, C. Guo, F. Brandl, F. Heimbach, X. Han, A. Anane and D. Grundler, "Active ferromagnetic metasurface with topologically protected spin texture for spectral filters", Advanced Functional Materials 32, 34 (2022).
5. Alejandro Rivelles, Ana Parente, José L. Prieto, M. Mar Sanz-LLuch, Marco Maicas, Manuel Abuín; Reading the interaction between vortex textures in an FORC diagram. *Appl. Phys. Lett.* 7 July 2025; 127 (1): 012404



FORC diagrams for arrays of Py dots 200 nm in diameter and with 500 nm pitch (a), 400 nm pitch (b), 300 nm pitch (c) and 250 nm pitch (d).

FP-12. Irradiation-Induced Compaction in Amorphous SiO2 Thin Films for Magneto-Optical Systems: Ring-Structure Evolution and Multi-Scale Validation

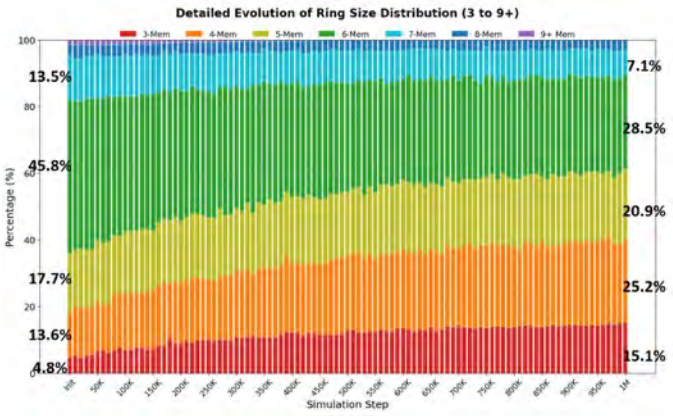
K. Lee[1], K. Lee[2], W. Lee[1]
[1]School of Chemical and Biological Engineering, Seoul National University, Seoul, Korea (the Republic of), [2]Samsung Institute of Technology, Samsung Electronics, Yong-In, Korea (the Republic of)

Amorphous SiO2 thin films are essential optical components in high-precision magneto-optical and spin-photonic devices. Under sustained photon irradiation, these films undergo irreversible structural compaction, causing macroscopic wavefront distortion (Zernike drift) that severely compromises the polarization and focusing fidelity required for magnetic characterization. The atomistic mechanisms driving this degradation and practical mitigation strategies remain incompletely understood.

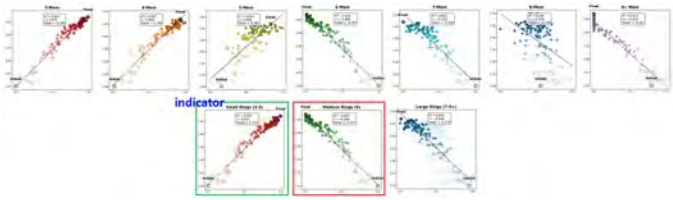
Using a 432-unit Continuous Random Network model, molecular dynamics (MD) simulations of pulsed-laser thermal cycling revealed that irradiation fundamentally alters the Si–O ring-size distribution. Stable 5- and 6-membered rings decrease while high-energy 3- and 4-membered rings accumulate, directly driving macroscopic network densification. To mitigate this, we evaluated hydrogen doping. H-doping effectively passivated undercoordinated Si and dangling-bond O sites, interrupting the bond-distortion cascade. Density Functional Theory (DFT) confirmed this passivation preserves bond order and eliminates localized electronic instability.

Integrating finite element method (FEM) modeling to bridge atomistic and macroscopic timescales, we validated this framework against long-term optical metrology data from commercial high-volume manufacturing (HVM) scanners under equivalent irradiation. Simulated compaction trajectories showed excellent quantitative agreement with the measured linear drift of Zernike aberrations. By linking atomistic ring topology to system-level degradation, this study establishes hydrogen doping as a scalable, field-validated strategy to extend the stability of SiO2 thin films in demanding magneto-optical environments.
[1] Markus Jech, Al-Moatasem El-Sayed, Stanislav Tyaginov, Alexander L. Shluger, and Tibor Grasser, "Ab initio treatment of silicon-hydrogen bond rupture at Si/SiO2 interfaces," Physical Review B, vol. 100, no. 19, 195302, 2019. https://doi.org/10.1103/PhysRevB.100.195302
[2] Katharina Vollmayr, Walter Kob, and Kurt Binder,

"Cooling-rate effects in amorphous silica: A computer-simulation study," Physical Review B, vol. 54, no. 22, pp. 15808-15827, 1996. https://doi.org/10.1103/PhysRevB.54.15808
[3] Philip S. Salmon, Anita Zeidler, Motoki Shiga, Yohei Onodera, and Shinji Kohara, "Ring compaction as a mechanism of densification in amorphous silica," Physical Review B, vol. 107, 144203, 2023. https://doi.org/10.1103/PhysRevB.107.144203
[4] Fenglin Yuan and Liping Huang, "α-β transformation and disorder in β-cristobalite silica," Physical Review B, vol. 85, 134114, 2012. https://doi.org/10.1103/PhysRevB.85.134114



Evolution of the Si-O ring size distribution under prolonged thermal cycling. The topological shift from stable 5- and 6-membered rings to high-energy 3- and 4-membered rings drives progressive macroscopic densification.



Correlation between ring-size category fractions and SiO2 mass density. Small rings (3-5 members) exhibit strong positive linear correlation as high-density indicators, whereas the pristine backbone (6-membered) and voids (7-9+ members) collapse under compression.

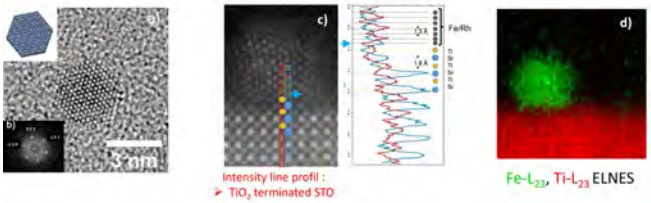
FP-13. Local order and magnetism in chemically ordered FeRh nanocrystals deposited on $SrTiO_3$ (001) substrate.

J. Moreau[1], G. Herrera[1], A. Reyes[1], O. Boisron[1], F. Tournus[1], S. Gonzales[2], I. Canero-Infante[2], M. Bugnet[3], P. Ohresser[4], E. Otero[4], A. Rogalev[5], F. Wilhelm[5], D. Le Roy[1], V. Dupuis[1]
[1]Universite Lyon 1, CNRS, Institut Lumière Matière, UMR5306, Villeurbanne, France, [2]Université Lyon 1, CNRS, INSA Lyon, Ecole Centrale de Lyon, CPE Lyon, INL, UMR5270, Villeurbanne, France, [3]CNRS, INSA Lyon, Université Claude Bernard Lyon 1, MATEIS–UMR 5510, Villeurbanne, France, [4]Synchrotron SOLEIL, Saint-Aubin, France, [5]European Synchrotron Radiation Facility (ESRF), Grenoble, France

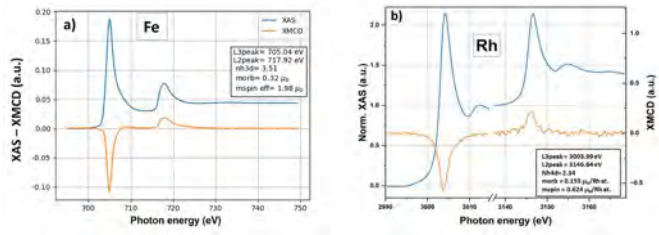
Chemically ordered equiatomic FeRh thin films with the B2-CsCl structure exhibit antiferromagnetic/ferromagnetic (AFM/FM) transition near room temperature accompanied by a 1 % volume expansion that can be electrically driven by only few volts [1]. In our work, we have prepared mass-selected FeRh equiatomic nanocrystallites (NCs) pre-formed in gas phase from LECBD (Low Energy Cluster Beam Deposition) in order to study intrinsic chemical and magnetic order phase transition at nanoscale [2].
We clearly demonstrate a crystallographic phase transition in FeRh NCs embedded in a carbone matrix, from a chemically disordered FCC A1 phase to a chemically ordered B2 phase upon UHV annealing at 700°C. However a FM order persists at low temperature even for equivalent NCs with diameters as large as 20 nm [3], [4].
For B2 FeRh NCs deposited on oxide perovskite substrates, grazing Incidence X-ray scattering experiments reveal epitaxial relationships and atomic coherence, with unusual orientations at the metal/oxide interface [5].
Here, we focus on the chemical nature of the interfacial atomic columns of FeRh NCs deposited on oxide perovskite $SrTiO_3$ (001) substrates (STO), using atomic-scale elemental mapping based on STEM-EELS measurements (Fig. 1). We also explore the coexistence of Fe and Rh local magnetic order contributions by performing element-specific X-ray absorption spectroscopy (XAS) and X-ray magnetic circular magnetic dichroism (XMCD) measurements at the L-edges of both Fe and Rh, at two synchrotron facilities (Fig. 2). These results will be discussed in terms of strong hybridization and strain effects at nanoscale.

1. R. O. Cherifi et al, Nature Materials 13, 345 (2014) M. P. Brown and K. Austin, *Appl. Phys. Letters* 85, 2503-2504 (2004).
2. V. Dupuis et al., *Journal of Nanoparticle Research* 20 (2018)

and *Beilstein Journal of Nanotechnology* 7, 1850 (2016).
3. A. Hillion et al. Physical Review Letters 110 (2013).
4. G. Herrera et al. *European Physical Journal: Applied Physics* 97, 32 (2022) and *Nanoscale* 16, 11679 (2024).
5. A. Reyes et al. *Physical Review B* 109, 245410 (2024).



FeRh NC on carbon grid: HRTEM image with an inset ball model (a) and the corresponding Fourier transform (b); B2 FeRh NC on STO in cross section: STEM-HAADF image (c) and ELNES at L-edges of Fe (green) and Ti (red) (d).



XAS/XMCD of FeRh NCs on STO at L-Fe edge a) and at Rh edge b) from UHV annealing at T = 800°C.

FP-14. Pulsed Laser Deposited $HoCo_2$ Thin Films: Tuning Magnetic Transition and electronic Transport Mechanism

A. Kumar, A. Biswas, Y. Mudryk
Ames National Laboratory, U.S. Department of Energy, Iowa State University, Ames, Iowa, United States

Rare-earth intermetallic compounds are of significant interest due to their wide range of technological applications in permanent magnets, magnetocaloric refrigeration, and quantum transport phenomena arising from strong spin–orbit coupling and large magnetocrystalline anisotropy [1, 2]. The increasing demand for miniaturized devices necessitates their realization in thin-film form. However, the growth of high-quality rare-earth–transition-metal intermetallic thin films is challenging due to differences in vapor pressure and evaporation kinetics, which complicate stoichiometric control. Pulsed laser deposition (PLD) provides a promising route due to its near-stoichiometric material transfer, although the high reflectivity of metallic targets can limit ablation efficiency. The Laves phase RCo2 (R = rare earth) compounds are particularly attractive owing to their first-order magnetic phase transitions and potential for low-temperature magnetocaloric applications [3, 4].
In this work, we investigate the structural, magnetic, and transport properties of HoCo2 thin films grown on Si (100) and MgO (100) substrates using ultra-high vacuum PLD. X-ray reflectivity measurements confirm a film thickness of ~30 nm with low surface and interface roughness (~1 nm), indicative of high-quality growth. Both films exhibit a sharp magnetic transition near 77 K, consistent with the HoCo2 phase, unlike previous studies on Tb- and Dy based thin films, which shows no distinct magnetic transitions [5]. However, magnetization measurements reveal a second-order transition, in contrast to the first-order transition observed in bulk, highlighting the influence of reduced dimensionality and interfacial effects. Electrical transport measurements confirm metallic conduction. These results demonstrate that $HoCo_2$ thin films can be successfully synthesized using PLD and that reduced dimensionality significantly modifies the magnetic phase transition in RCo_2 systems.

Acknowledgments
This work was performed at Ames National Laboratory and was supported by the Division of Materials Science and Engineering of the Office of Basic Energy Sciences, Office of Science of the U.S. Department of Energy (DOE) under Contract No. DE-AC02-07CH11358.

1. O. Gutfleisch, M. A. Willard, E. Brück, C. H. Chen, S. G. Sankar, and J. P. Liu, Magnetic materials and devices for the 21st century: stronger, lighter, and more energy efficient, Advanced Materials 23, 821 (2011).
2. V. K. Pecharsky and K. A. Gschneidner Jr., Giant magnetocaloric effect in $Gd_5(Si_2Ge_2)$, Phys. Rev. Lett. 78, 4494 (1997).
3. E. Gratz and A. S. Markosyan, Physical properties of RCo_2 Laves phases, J. Phys.: Condens. Matter 13, R385 (2001).
4. J. Herrero-Albillos, F. Bartolomé, L. M. García, F. Casanova, A. Labarta, and X. Batlle, Nature and entropy content of the ordering transitions in RCo_2, Phys. Rev. B 73, 134410 (2006).
5. P. Skokowski, M. Matczak, L. Frackowiak, T. Bednarchuk, M. Kowacz, B. Anastaziak, and K. Synoradzki, Magnetocaloric effect in $Tb_{31}Co_{69}$ and $Dy_{31}Co_{69}$ thin films deposited on Si substrates, J. Magn. Magn. Mater. 639, 173781 (2026).

FP-15. Synthesis, Structure, and Size-dependent Superparamagnetism in MnNiSb Nanoparticles: Correlating Nanoscale Order with Magnetocaloric Performance

F. Amoo, S. Brock
Chemistry, Wayne State University, Detroit, Michigan, United States

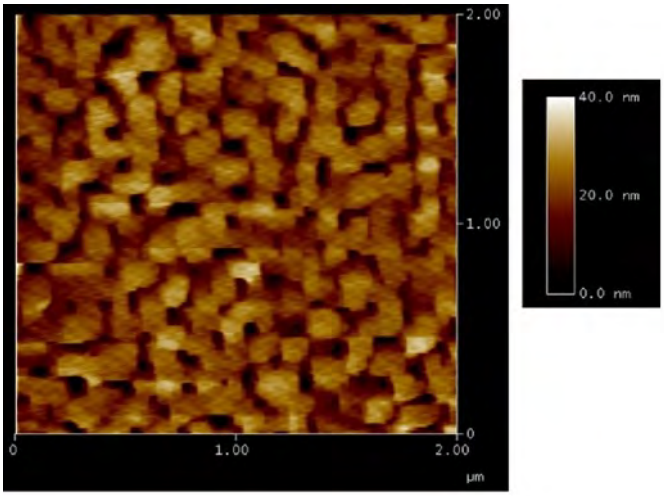
MnNiSb is a ferromagnetic compound with a high Curie temperature (754K), which may be useful in converting low and medium-grade waste heat to electricity through magnetocaloric effect. The unique magnetic properties of nanoparticles arise from their size-dependent coercivity in the critical regime of 1-100nm. A decrease in particle size to that of a single domain results in an increase in coercivity. However, as the size is decreased below the single-domain level, the material is affected by thermal fluctuations, and the system becomes superparamagnetic. In this work, a colloidal synthesis route was developed for the formation of discrete colloidal MnNiSb nanoparticles using dimanganesedecacarbonyl, bis(1,5cyclooctadiene)nickel(0), triphenylantimony, and trioctyl phosphine oxide as solvent, which provides surface capping ligands for the resultant MnNiSb nanoparticles that nucleate at 230 °C and crystallize at 300 °C. Structural characterization using powder X-ray diffraction (PXRD) and transmission electron microscopy (TEM) confirms the formation of well-ordered cubic MnNiSb nanoparticles. These particles are spherical with an average diameter of ~10 nm. While the bulk properties of MnNiSb have been established, the effect of size on factors such as magnetic and thermal hysteresis, Curie temperature, and magnetic entropy, is unknown. Magnetic measurements of MnNiSb nanoparticles reveal distinct size-dependent behavior. At 300 K,it exhibit superparamagnetic behavior, whereas at 50 K they exhibit ferromagnetic behavior with a coercivity of about 100 Oe. High-temperature magnetic measurements up to 900K produce a decrease in magnetization and the absence of the expected T_C at 754 K. Post PXRD and TEM analysis confirm the formation of nanorods that match the crystal structure of monoclinic manganese phosphate phase, presumably formed by reaction of MnNiSb with trioctylphosphine oxide (TOPO) capping groups, with crystalline NiSb formed as a byproduct. Future work is focused on replacing TOPO capping groups with less reactive, non-oxygen-containing phases to stabilize the MnNiSb phase at high temperatures, enable accurate magnetic measurement and enhance their potential for waste heat recovery application.

FP-16. FePt Ferromagnetic Mosaic Structure

A. Lisfi[1], F. Efe[1], F. Bakhshizadeh[1], D. Alharbi[1, 2], M. Guy[1], M. Davis[1]
[1]Physics, Morgan State University, Baltimore, Maryland, United States, [2]The Catholic University, Washington, District of Columbia, United States

Mosaic structures [1] arise during epitaxial growth when multiple lattice-matching configurations exist between a film and its substrate. In this work, we investigate a mosaic structure formed by FePt films epitaxially grown on an STO substrate. FePt is a promising material for heat-assisted magnetic recording [2] due to its exceptionally high magnetic anisotropy in the L10 phase. The minimal lattice mismatch between FePt and STO makes STO a suitable template for epitaxial growth. However, the small tetragonality of L10 FePt (c/a ≈ 0.98) permits more than one epitaxial relationship with the substrate. The films studied (60 nm thick) were deposited via DC magnetron sputtering from an equiatomic FePt target onto (110) STO substrates at 700 °C. Comprehensive characterization was performed, including structural analysis using AFM and XRD, and magnetic measurements and imaging using VSM, a torque magnetometer, and MFM. The surface morphology of the FePt mosaic structure, shown in Figure 1, exhibits a smooth topology composed of uniformly sized (~100 nm) twisted grains that are well interconnected. Magnetic measurements indicate the presence of two in-plane easy axes, oriented along and tilted relative to the film plane, with no evidence of stripe domain structures. Additional studies, including angular-dependent hysteresis loops and remanence measurements, were conducted to identify the magnetization reversal mechanisms in the mosaic structure. The results of this investigation will be presented and discussed.

[1] Adriana Alvídrez-Lechuga, Ricardo López Antón, Luis Fuentes-Cobas, José Holguín-Momaca, Óscar Solís-Canto, et al. “Epitaxial mosaic-like Mn5Ge3 thin films on Ge(001) substrates”. Journal of Alloys and Compounds, 2018, 762, pp.363-369. 10.1016/j.jallcom.2018.05.209
[2] J. U. Thiele, S. Maat, and E. E. Fullerton, “FeRh/FePt exchange spring films for thermally assisted magnetic recording media”, Appl. Phys. Lett. 82, 2859 (2003).



AFM image showing the topography of FePt mosaic structure with twisted crystals.

SESSION FQ: MULTIFERROIC AND HALF-METALLIC MATERIALS (POSTER SESSION)

Co-Chair(s): A. K. Patel, *Research Center for Magnetic and Spintronic Materials, National Institute for Materials Science, Tsukuba, Japan* and T. Hojo, *Advanced Spintronics Medical Engineering, Tohoku University, Sendai, Miyagi, Japan*

Thursday, November 5, 2026
03:00 PM-06:00 PM
Coral 4

FQ-01. Electronic, magnetic and structural properties of Fe 2 XGe (X=Ni, Co, Mo)

G. Buhrow[1], G. Reyes[1], M. Neupane[2], A. Goswami[2], P. Shand[1], P. Kharel[2], P. Lukashev[1]
[1]Physics, University of Northern Iowa, Cedar Falls, Iowa, United States, [2]South Dakota State University, Brookings, South Dakota, United States

Here, we present results of a combined computational and experimental study of
electronic, magnetic, and structural properties of Fe 2 XGe (X=Ni, Co, Mo) Heusler compounds.
Our calculations indicate that the regular cubic phase of this compound may exhibit strong
tetragonal distortion, which may result in large magnetocrystalline anisotropy and non-collinear magnetic alignment. At the same time, the inverted cubic phase of these compounds has lower
energy and does not exhibit tetragonal distortion. In addition, we also studied magnetic and electronic properties of these alloys under uniform and biaxial strain. All three compounds
exhibit large spin-polarization (in certain cases, approaching nearly half-metallic electronic
structure) in a wide range of considered mechanical strain.
We attempted to synthesize bulk
Fe 2 XGe (X = Ni, Co, Mo) samples using arc melting followed by annealing. Single-phase
Fe 2 CoGe and Fe 2 NiGe were successfully synthesized; however, Fe 2 MoGe could not be obtained
as a single-phase material. Both Fe 2 CoGe and Fe 2 NiGe crystallize in an A2-type disordered cubic
structure. The two compounds exhibit ferromagnetic ordering at room temperature (consistent
with our computational results), with high Curie temperatures of approximately 1000 K for
Fe 2 CoGe and 700 K for Fe 2 NiGe. Notably, Fe 2 NiGe shows a sharp magnetic transition near 400
K, characterized by a rapid increase in magnetization, before undergoing a second
ferromagnetic-to-paramagnetic transition at 700 K. The high field (3T) magnetizations are 83
emu/g at 300 K for Fe 2 CoGe (3.6 μ B /f.u) and 100 emu/g (4.4 μ B /f.u) at 350 K for Fe 2 NiGe, in fair
agreement with the calculated magnetization values. As a potential subject of future work, we
hope that the tetragonal phase of these materials may be stabilized, e.g., by atomic substitution
and a subsequent change in the unit cell volume.
This research is supported by the National Science Foundation under grant nos. DMR
2510789 and DMR 2510791 via EPSCoR.

FQ-02. Compositional Tuning of the Structural, Magnetic, and Mechanical Properties of $Co_{2-x}FeV_xAl$ system.

M. Minu[1], T. Grier[2], M. Garrett[2], A. Hauser[1], P. LeClair[1]
[1]Department of Physics and Astronomy, The University of Alabama, Tuscaloosa, Alabama, United States, [2]Department of Metallurgical and Materials Engineering, The University of Alabama, Tuscaloosa, Alabama, United States

Heusler alloys are multifunctional materials widely used in spintronic devices, thermoelectric, and magnetic sensors due to their remarkable structural versatility and functional magnetic and mechanical properties. Their unique functional characteristics of shape memory effects, tunable magnetism, superconductivity etc. make them suitable for advanced applications in memory, energy, and quantum technology. Co_2FeAl is one of the most extensively

investigated full-Heusler alloys owing to its high magnetic moment and Curie temperature (T_c). Doping with low-valent transition metal (e.g., Sc, Ti, V and Cr) has been shown to enhance structural stability in Cobalt based alloys. For instance, Titanium substitution exhibits ordered $L2_1$ or B2 structures. Motivated by these findings, in our study, we explored the effect of Vanadium substitution for Cobalt in Co_2FeAl. Since Vanadium possesses one additional valence electron compared to Titanium, its incorporation is expected to alter the electronic structure differently. Bulk $Co_{2-x}FeV_xAl$ ($0 \leqslant x \leqslant 1$) alloys were made by arc melting and then heat-treated. Initial Energy Dispersive X-ray Spectroscopy results confirm that Vanadium was successfully added and that the samples have nearly correct compositions and single-phase structures. These results show that the synthesis process is reliable and provides a good starting point for future studies on how Vanadium substitution affects the structural, magnetic, and mechanical behavior of $Co_{2-x}FeV_xAl$ alloy series.

FQ-03. Spin polarized singular flat band on the surface pentagonal lattice of a topological ferromagnet

B. Yang
Seoul National University, Seoul, Korea (the Republic of)

Flat bands have been proposed in various geometrically frustrated lattices, yet their experimental realization has been limited only to the two-dimensional (2D) kagome and three-dimensional (3D) pyrochlore lattices. While synthesizing bulk crystals with desired lattice geometry is generally challenging, the surfaces of 3D bulk materials sometimes naturally host 2D lattice structures hardly achievable in 2D bulk crystals. Thus, the electrons localized on such 2D surfaces can be a new platform for exotic flat bands residing on the unexplored lattice geometry. Here,we report the first experimental observation of singular flat bands with band crossings in the 2D pentagonal lattice on the surface of the 3D ferromagnetic topological semimetal CoS2.We demonstrate that the coupling between localized surface flat bands and extended bulk topological bands gives rise to the surface non-Fermi liquid behavior characterized by the quasiparticle scattering rate with linear temperature dependence and pronounced quasiparticle broadening. This study of CoS2 highlights metallic pyrite materials as an ideal platform for exploring the exotic properties of spin-polarized singular flat bands localized on the surface pentagonal lattice, which provides a fresh perspective for investigating correlated electron phenomena in pentagon-based materials.

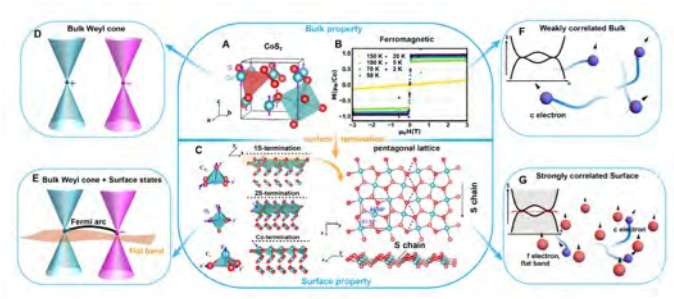


Figure1. Bulk and surface properties of CoS2

FQ-04. Observation of Ferromagnetism in Sputtered Co-doped HfO_2 Thin Films

K. Shilna, A. A. Tulapurkar
Electrical Engineering, Indian Institute of Technology Bombay, Mumbai, Maharashtra, India

Magnetic semiconductors are promising candidates for multifunctional spintronic device applications [1]. The magnetic properties of undoped and Co-doped HfO_2 thin films sputtered on a Si substrate were studied. The room-temperature ferromagnetism has been observed in Co-doped HfO_2. XRD studies confirm that the undoped and Co-doped HfO_2 thin films exhibit a monoclinic structure, and upon doping, an improvement in crystallinity is observed. Moreover, no secondary impurity phases are observed in the Co-doped HfO_2 films. SEM and AFM images confirm that both undoped and Co-doped films show uniform and homogeneous surfaces. Upon doping, the film crystallinity enhances and leads to the formation of smoother and more uniform grain boundaries, thereby reducing the surface roughness, which is obtained from AFM roughness. EDX and XPS analysis confirm the presence of Hf and O in the undoped samples and Hf, Co, and O in the doped samples. Magnetic characterization reveals the diamagnetic nature of HfO_2. On the other hand, the doped samples show M-H hysteresis loops at various temperatures (300, 50, 10, 2 K), suggesting ferromagnetic ordering. It may be due to dopant-induced magnetic exchange interactions, bound magnetic polaron formation, and defect-induced magnetism [2][3]. Additionally, the observed ferromagnetism may be attributed to carrier-mediated exchange interactions, such as RKKY interaction, particularly observed in dilute magnetic semiconducting films. The enhanced crystallinity and dopant-driven magnetic interactions may play a significant role in the observed ferromagnetic nature in the Co-doped HfO_2 thin films.

1. T. Dietl, Nat. Mater. 9 (2010), 965- 974.
2. K. V. Shilna, S. C. Sahoo, and K. J. Thomas, Appl. Mater.

Today 27 (2022), 101427 1-8.
3. M. S. R. Rao, D. C. Kundaliya, S. B. Ogale, L. F. Fu, S. J. Welz, N. D. Browning, V. Zaitsev, B. Varughese, C. A. Cardoso, A. Curtin, S. Dhar, S. R. Shinde, T. Venkatesan, S. E. Lofland, and S. A. Schwarz, Appl. Phys. Lett. 88 (2006), 142505 1-3.

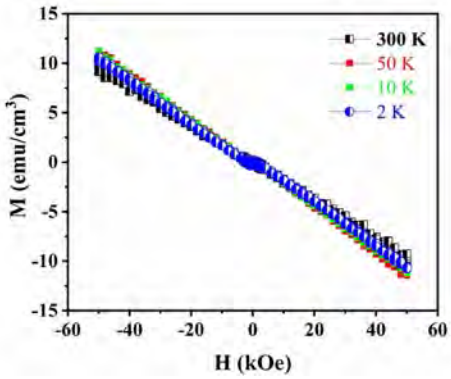


Figure 1: Diamagnetic M–H measurements of an undoped HfO2 thin film at temperatures of 300, 50, 10, and 2 K.

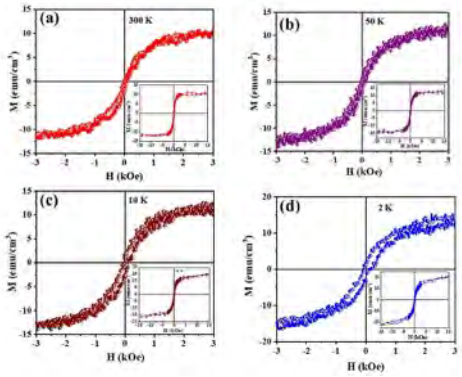


Figure 2: M-H hysteresis loop of Co-doped HfO_2 films at temperatures of (a) 300, (b) 50, (c) 10, and (d) 2 K, after subtracting the diamagnetic contribution. The inset presents the full range loop from −15 to 15 kOe.

FQ-05. An Antiferromagnetic Iron Garnet with Large Kerr Rotation

F. Tutt[1], J. Sýkora[2], M. Hubert[2], J. Marquez Chavez[1], M. Veis[2], C. A. Ross[1]
[1]Department of Materials Science and Engineering, Massachusetts Institute of Technology, Cambridge, Massachusetts, United States, [2]Faculty of Mathematics and Physics, Charles University, Prague, Czechia

Iron garnets ($R_3Fe_5O_{12}$, where R = Y, Bi or rare earth) have attracted considerable attention due to their low Gilbert damping, large magnetooptical response, and tunable magnetic compensation temperatures that make them promising candidates for spintronic, optical, and magnonic device applications [1]. IGs include three cation sublattices in which tetrahedral site cations are antiferromagnetically coupled to octahedral and dodecahedral sites. In this work, we demonstrate the thin film behavior of an antiferromagnetic IG achieved through site selective substitution of Ca and Si into a YIG ($Y_3Fe_5O_{12}$) host, in which the composition $CaY_2SiFe_4O_{12}$ (CaSiYIG) achieves compensated magnetic order at 0 K. CaSiYIG was deposited epitaxially on garnet substrates by pulsed laser deposition. The temperature dependent magnetization (*M(T)*, Fig. 1) of the films shows a Néel temperature (T_N) of ~450 K and a maximum magnetization of ~15 kAm^{-1} across the entire temperature regime. *M(T)* was modeled using molecular field coefficient (MFC) theory, based on the composition of $Ca_{1.00}Y_{2.08}Fe_{3.98}Si_{0.93}O_{12}$ measured through wavelength dispersive spectroscopy. The agreement between the MFC model and measured *M(T)* confirms the tetrahedral site preference of Si and the dilution of the exchange interactions by the non-magnetic substituents. The magnetooptical response of the films was then measured through polar magnetooptic Kerr effect measurements at nearly normal incidence. The spectral dependence of the Kerr rotation angle (Θ_K, Fig. 2) shows a maximum Θ_K of ~0.10 deg with 4 eV incident light, comparable to thin films of YIG [2] despite having less than one tenth of its magnetic moment. When a bilayer of YIG/CaSiYIG is grown and field cooled from above T_N of CaSiYIG, exchange bias is observed with an exchange field of ~1 mT persisting to the highest measured temperature, 395 K, further demonstrating the antiferromagnetic nature of CaSiYIG. This antiferromagnetic garnet, CaSiYIG, therefore offers exceptional properties for garnet-based devices.

[1] S. K. Kim *et al.*, Nat. Mater. 21, 24 (2022).
[2] E. Jakubisova-Liskova *et al.*, J. Appl. Phys. 117, 17B702 (2015).

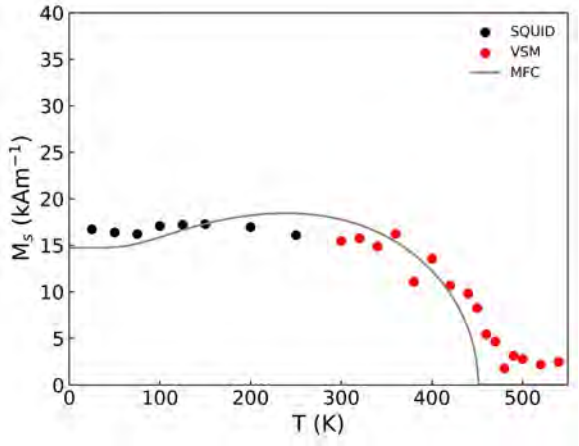


Fig. 1: Temperature dependent magnetization and corresponding MFC fit for CaSiYIG(89 nm)/YSGG.

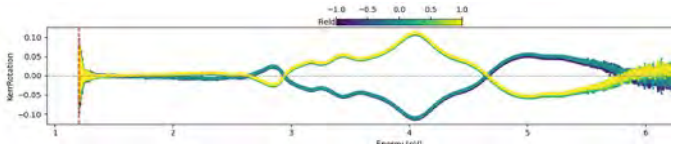


Fig. 2: Spectral dependence of the Kerr rotation angle for CaSiYIG(49 nm)/GGG at various applied fields.

FQ-06. B-Site Fe Substitution–Induced Modification of Structural Phase Transitions in $BaZr_{0.0.5}Ti_{0.95}O_3$: A Neutron Diffraction Study

M. Kumari[2, 1], R. Chatterjee[1]
[1]Physics, IIT Delhi, New Delhi, India, [2]HDD, Western Digital Technologies, San Jose, California, United States

We report a detailed structural investigation of Fe-substituted $BaZr_{0.05}Ti_{0.95}O_3$ (BZT) ceramics with composition $BaZr_{0.05}(Fe_xTi_{(1-3x/4)})_{0.95}O_3$ (x = 0 and 0.015), motivated by previously reported magnetoelectric response in this system [1]. High-resolution synchrotron angle-dispersive X-ray diffraction (ADXRD) confirms the formation of a single-phase perovskite structure with complete solubility of Fe (1.5%) at the B-site and no detectable secondary phases, establishing the high phase purity of the samples.
To probe the effect of Fe substitution on structural stability and phase evolution, temperature-dependent neutron diffraction measurements were carried out over 6–625 K. Rietveld refinement of the diffraction data reveals that Fe ions preferentially occupy the Ti (B-site) position in the perovskite lattice. This selective substitution plays a crucial role in modifying the structural phase behavior compared to undoped BZT.
While pure BZT exhibits multiple successive ferroelectric transitions (rhombohedral–orthorhombic–tetragonal–cubic), the Fe-substituted composition shows a simplified phase sequence [2]. The orthorhombic (Amm2) phase is stabilized over a broad temperature range up to ~350 K, followed by a direct transition to the cubic (Pm–3m) phase at higher temperatures. Intermediate tetragonal and rhombohedral phases are suppressed within the investigated temperature range.
These results demonstrate that dilute Fe substitution at the B-site significantly alters structural phase stability and suppresses intermediate instabilities in BZT. The observed structural evolution provides a basis for understanding previously reported magnetoelectric response in this system and highlights the role of targeted B-site substitution in tuning ferroelectric perovskites.
[1] J. Appl. Phys. 113, 17D918 (2013)
[2] Phys. Rev. B 108, 134117 (2023)

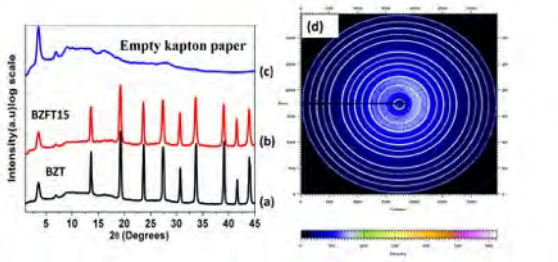


FIG 1: Room temperature ADXRD patterns of (a) empty kapton paper (b) BZT (c) BZFT15; (d) 2D ring pattern taken on the image plate (for BZFT15).

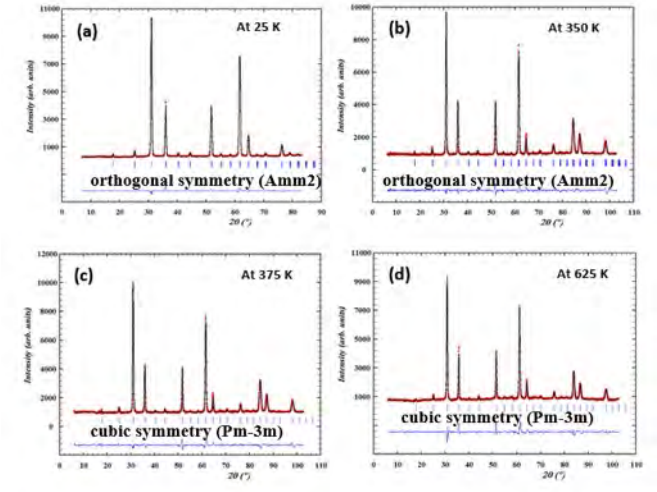


FIG 2: Observed (red dots), calculated (black lines), and difference (bottom of each figure) profiles obtained after Rietveld refinement of neutron powder diffraction data for BZFT15 at (a) 25 K (b) 350 K using orthogonal symmetry of space group Amm2; (c) 375 K (d) 625 K using the cubic symmetry of space group Pm-3m

FQ-07. By passing the Relaxor Transition: Non-Equilibrium Stabilization of Ferroelectric Order and Emergent Magnetism in Fe-Substituted $Bi_{0.5}Na_{0.5}TiO_3$ (BNT)

M. Kumari[1, 2]
[1]HDD, Western Digital Technologies(WD), SAN JOSE, CALIFORNIA, India, [2]Physics, IIT Delhi, Delhi, Delhi, India

$Bi_{0.5}Na_{0.5}TiO_3$ (BNT)-based lead-free ferroelectrics are promising candidates for multiferroic functionality when combined with B-site magnetic substitution [1]; however, their performance is limited by the difficulty of achieving stable polarization due to high coercive fields and an intermediate ergodic relaxor/antiferroelectric-like regime during cooling [2], which suppresses long-range ferroelectric ordering under conventional processing. Here, we show that in Bi0.5Na0.5($Fe_xTi_{1-3x/4}$)O_3 ($0 \leqslant x \leqslant 0.20$), the loss of ferroelectric order is primarily kinetic, arising from traversal through the relaxor/antiferroelectric transition window rather than intrinsic compositional suppression (Fig. 1(a)). To overcome this limitation, we introduce a non-equilibrium field-quenching protocol using a modified corona poling setup [Fig 2), where samples are electrically biased in the paraelectric regime and rapidly quenched to ~77 K, bypassing the ergodic relaxor region[4-5]. This process arrests dipolar dynamics and stabilizes a long-range ferroelectric state inaccessible under conventional field cooling. The quenched state exhibits enhanced ferroelectric switching and electromechanical performance, with a ~38% increase in piezoelectric coefficient (d_{33}) and ~20–25% improvement in unipolar and bipolar strain [Fig 1 (c), (d)). In Fe-substituted compositions, magnetic hysteresis emerges [Fig1(b)), indicating the realization of a multiferroic state within a structurally ordered perovskite framework. The ferroelectric and magnetic order parameters are found to coexist in the same phase, with magnetism arising from Fe substitution and not directly coupled to the polarization state. By bypassing this pathway via non-equilibrium quenching, we establish a general route to stabilize ferroelectric order and realize emergent multiferroic behavior in lead-free perovskite oxides.

1. J. Appl. Phys. 127, 094101 (2020)
2. Appl. Phys. Lett. 106, 092903 (2015)
3. arXiv:2206.02135 (https://doi.org/10.48550/arXiv.2206.02135)
4. Indian patent application 201911019652 (2019).

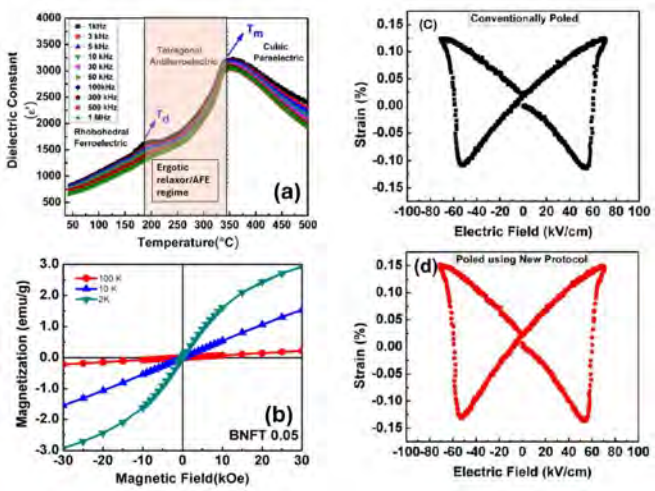


FIG 1: (a) Temperature-dependent dielectric constant highlighting the shaded ergodic relaxor/AFE regime (b) M-H loops at 2–100 K(c) Bipolar strain loop for conventionally poled (d) Bipolar strain loop for quenched BNT

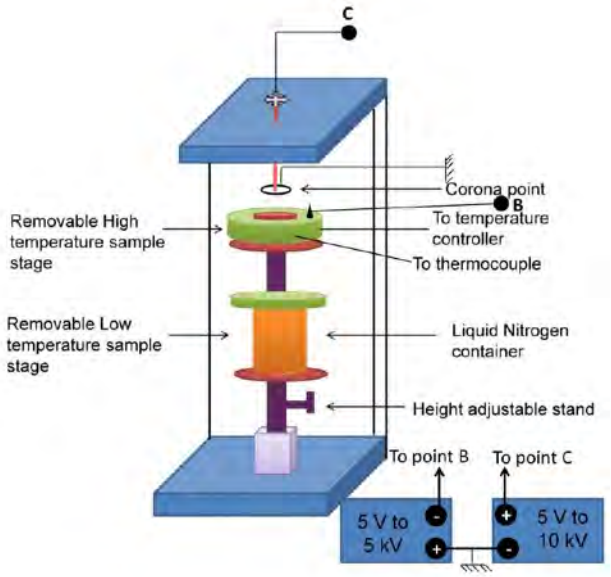


FIG 2: Customized corona poling unit for phase-boundary quenching

FQ-08. Synthesis, Magnetism, and Magnetoelectric Properties of Polar Cluster Cobaltite $Ba_6La_2Co_4O_{15}$

T. Shirasaki, T. Ishikawa, H. Kuwahara
Engineering and Applied Sciences, Sophia University, Tokyo, Japan

$Ba_6Ln_2Fe_4O_{15}$ (*Ln* = lanthanides), which belongs to the polar space group $P6_3mc$ at room temperature, is a new multiferroic material where four Fe^{3+} ions form the Fe_4O_{15} cluster. Due to this cluster structure, the magnetism of this material is naturally described by a cluster total spin S_T, the sum of four Fe^{3+} spins ($|S| = 5/2$). We have successfully synthesized $Ba_6Ln_2Fe_4O_{15}$ (*Ln* = La, Pr, Nd) single crystals and revealed that the magnitude of spontaneous electric polarization can be controlled by a magnetic field even in a paramagnetic phase [1]. On the other hand, although there are reports on the synthesis of polycrystalline $Ba_6La_2Co_4O_{15}$, where the Fe sites are fully substituted with Co, its physical properties remain largely unexplored [2]. Therefore, we investigated the magnetic and magnetoelectric properties of $Ba_6La_2Co_4O_{15}$, with a focus on magnetism arising from the Co_4O_{15} clusters.

Polycrystalline $Ba_6La_2Co_4O_{15}$ was synthesized by a conventional solid-state reaction method. For comparison, the $Ba_6La_2Fe_4O_{15}$ single crystal was grown by the floating zone method under 3 atm of N_2. Fig. 1 shows the temperature dependence of magnetization for the $Ba_6La_2Fe_4O_{15}$ single crystal and $Ba_6La_2Co_4O_{15}$ polycrystal. $Ba_6La_2Fe_4O_{15}$ shows a clear antiferromagnetic phase transition at 13 K, whereas $Ba_6La_2Co_4O_{15}$ shows a magnetization anomaly around 62 K with zero-field-cooled and field-cooled divergence below 40 K. The *M-H* curve measured at 5 K for $Ba_6La_2Co_4O_{15}$ exhibited slight hysteresis (inset of Fig. 1). These results suggest that $Ba_6La_2Co_4O_{15}$ undergoes a magnetic phase transition at a higher temperature than $Ba_6La_2Fe_4O_{15}$ and exhibits spin-glass-like behavior. In this presentation, we will report on the detailed magnetic and magnetoelectric properties of $Ba_6La_2Co_4O_{15}$, as well as the results of our attempts to grow single crystals.

[1] T. Shirasaki *et al*., (unpublished).
[2] H. Mevs and H. Müller-Buschbaum, Z. Anorg. Allg. Chem., Vol. 584, p. 114 (1990).

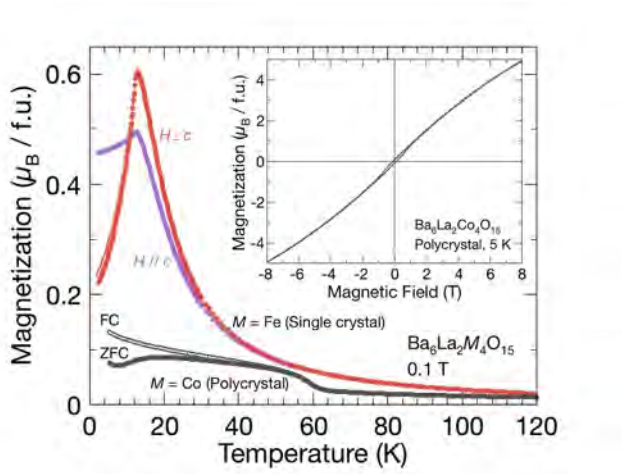


Fig. 1: Temperature dependence of magnetization for polycrystalline $Ba_6La_2Co_4O_{15}$ and single-crystal $Ba_6La_2Fe_4O_{15}$. Solid symbols represent zero-field cooling, and open symbols represent field cooling measurements. The inset shows the magnetic field dependence of magnetization for polycrystalline $Ba_6La_2Co_4O_{15}$ at 5 K.

FQ-09. Comparison of Doping Effects between Cu and Fe Sites for High-Temperature Multiferroic Compound $YBaCuFeO_5$

Y. Yasui, S. Kihara, K. Ikeda, T. Banshodani, R. Mimura
Physics, Meiji University, Kawasaki, Kanagawa, Japan

Multiferroic systems in which ferroelectricity and magnetic ordering coexist, have been actively studied with interest in fields of both basic and applied sciences. If we have multiferroics above room temperature, we may be able to control their ferroelectricity by external magnetic field or their magnetization by external electric field at ambient conditions. We pick up an oxygen-deficiency ordered perovskite $YBaCuFeO_5$ with high temperature multiferroics. $YBaCuFeO_5$ exhibits two magnetic transitions. At a first antiferromagnetic magnetic transition temperature T_{N1} = 426 K, the spin system exhibits ordering with the collinear magnetic structure. At a second magnetic transition temperature T_{N2} = 310K, the magnetic structure changes from the collinear to a spiral one accompanied with a ferroelectricity and multiferroic phenomena [1-2]. It was reported that controlling the heat treatment during sample synthesis increases the chemical disorder of Cu/Fe and thus increases the T_{N2} value [3]. This result is surprising, because the magnetic transition is usually disturbed by disorder of atomic configuration. Then, the stabilizing of the magnetic spiral state and multiferroic state of $YBaCuFeO_5$ is

considered to be induced by novel mechanism.
We have investigated the magnetic properties of $YBaCu_{1-x}M_xFeO_5$ (M= Mn, Ni, and Zn) and $YBaCuFe_{1-y}Ga_yO_5$, because the doping to Cu/Fe site is expected to induce the Cu/Fe chemical disorder. We have synthesized the polycrystalline samples, and carried out measurements of magnetic susceptibility (χ) up to 650K. From anomalies of the $\chi - T$ curves, we evaluated x - dependences of T_{N1} and T_{N2} values. We found that the T_{N2} values raise by Ni-doping up to 370 K at x_c=0.03, by Mn-doping up to 354K at x_c=0.04, and by Zn-doping up to 349 K at x_c=0.09 for $YBaCu_{1-x}M_xFeO_5$ from 319 K for x = 0. However, it was found that x – dependences of T_{N1} and T_{N2} values in the region of $x > x_c$ differs depending on the type of doping ions. For $YBaCuFe_{1-y}Ga_yO_5$ both of T_{N1} and T_{N2} values monotonically decrease by Ga – doping to Fe sites. We discuss the doping effect on magnetic properties of high-temperature multiferroic compound $YBaCuFeO_5$, comparing the Cu and Fe sites.
[1] B. Kundys *et al.*: Appl. Phys. Lett. 94 (2009) 072506.
[2] Y. Kawamura *et al.*: J. Phys. Soc. Jpn. 79 (2010) 073705.
[3] M. Morin *et al.*: Nature Comm. 7 (2016) 1.

FQ-10. Unusual metamagnetism and field-induced phase coexistence in $BaErFeO_4$

T. Dang[4], T. Hoang[4], V. Chlan[3], T. Kmjec[3], M. Rozprym[3], J. Kohout[3], G. Rymski[5], D. Le[1], T. Nguyen[2], M. Phan[2, 1]
[1]University of South Florida, Tampa, Florida, United States, [2]VinUniversity, Hanoi, Viet Nam, [3]Charles University, Prague, Czechia, [4]Duy Tan University, Danang, Viet Nam, [5]Scientific-Practical Materials Research Center of the National Academy of Sciences of Belarus, Minsk, Belarus

The BaRFeO4 family has garnered significant attention due to its rich magnetic behavior arising from competing interactions between Fe-3d and rare-earth 4f moments. In these materials, the Fe sublattice forms robust antiferromagnetic chains, while the choice of rare-earth ion strongly tunes interchain coupling and magnetic anisotropy. Er3+ is unique because it can exhibit either XY-type planar or Ising-like anisotropy depending on the local crystal field. This makes BaErFeO4 an ideal platform to explore anisotropy-driven magnetic ground states and complex phase transitions. Despite this potential, its field-dependent magnetic anisotropic behavior has remained largely unexplored. We present a detailed investigation of the temperature- and magnetic-field-driven magnetic evolution of $BaErFeO_4$ using a suite of complementary techniques, including neutron diffraction, Mössbauer spectroscopy, *dc* magnetization, and transverse susceptibility measurements. Below $T_{N1} \approx 50$ K, the Fe sublattice orders into an incommensurate collinear spin-density-wave state with propagation vector $k_1 = (0, 0, \sim 1/3)$. Enhanced $3d–4f$ exchange coupling drives a transition at $T_{N2} \approx 33$ K to a commensurate noncollinear antiferromagnetic phase characterized by $k_2 = (0.5, 0, 0.5)$ involving both Fe^{3+} and Er^{3+} ions, followed by a further modification of the Er magnetic configuration below $T_{N3} \approx 5.2$ K governed by dominant $4f–4f$ interactions. Field-dependent magnetization reveals a spin-flip-type metamagnetic transition of the Er^{3+} sublattice to field-induced ferromagnetic clusters at $\mu_0 H \approx 0.2$ T. This metamagnetic response remains fully reversible down to 8 K, while a crossover to an irreversible ferromagnetic-like regime occurs at lower temperatures, attributed to kinetic arrest of the field-induced magnetic clusters. A complex field-induced phase separation is established, in which ferromagnetic clusters of distinct populations coexist with the long-range antiferromagnetic order of the Er sublattice. These findings underscore the complex interplay among magnetocrystalline anisotropy, magnetic frustration, and quenched disorder in stabilizing the magnetic ground state of $BaErFeO_4$.

FQ-11. Magnetic field angle dependence of specific heat in multiferroic Ca2CoSi2O7

M. Akaki[1], T. Kihara[2], M. Kimata[3]
[1]Core Facility Center, ARC, Kobe university, Kobe, Japan, [2]Research Institute for Interdisciplinary Science, Okayama university, Okayama, Japan, [3]Japan Atomic Energy Agency, Ibaraki, Japan

Ca2CoSi2O7 is a multiferroic material that exhibits spin-induced electric polarization.
It is known to display rich magnetic behavior due to the strong coupling between its magnetic and dielectric properties, as well as its magnetic anisotropy. In this study, we investigate the anisotropic magnetic properties arising from the magnetoelectric effect using a newly developed angle-resolved specific-heat measurement technique. The compact specific-heat measurement cell developed in this work can be mounted on a two-axis rotation probe, enabling experiments under high magnetic fields up to 25 T and at low temperatures down to 0.5 K. The specific heat is measured using the dual-slope method. In the angle-resolved measurements, a characteristic angular dependence of the specific heat was observed. In this presentation, we will report in detail on the development of the angle-dependent specific-heat measurement and the results for Ca2CoSi2O7.

FQ-12. Magnetocrystalline Anisotropy and Control of Fe^{3+} Spin in Ferroelectric Oxides via Local Structural Distortions: from First-Principles

H. Ahmad[1], B. Barker[2], S. M. Griffin[3], E. Nowadnick[4]
[1]Physics, University of California Merced, Merced, California, United States, [2]Florida Polytechnic University, Lakeland, Florida, United States, [3]Lawrence Berkeley National Laboratory, Berkeley, California, United States, [4]Chemical and Materials Engineering, University of California Merced, Merced, California, United States

Manipulating single spins with electric fields offers a promising route to highly efficient, low-power spintronic devices. Ferroelectric host materials provide an ideal platform for magnetoelectric control by tuning the local structural environment around magnetic dopants. Changing the ferroelectric polarization modifies the local crystal electric field, which, via spin-orbit coupling, directly reorients the magnetic spin. In this work, we employ density functional theory (DFT) to investigate the magnetocrystalline anisotropy energy (MCAE) of Fe^{3+} dopants in the incipient ferroelectric $SrTiO_3$. Specifically, we calculate the MCAE value obtained via non-collinear spin-orbit coupling calculations, extract the zero-field splitting (ZFS) parameter, and compare it with experimentally obtained Electron Paramagnetic Resonance (EPR) data from the literature. While bulk $SrTiO_3$ is non-polar, biaxial strain induces a transition to a ferroelectric state. We map the MCAE surface for Fe^{3+} within these strain-induced polar phases under both compressive and tensile conditions. Furthermore, we examine the non-polar tetragonal bulk phase, explicitly analyzing how anti-ferrodistortive octahedral rotations affect the MCAE. To accurately capture the charge compensation, we systematically evaluate the stability and structural effects of oxygen vacancies, focusing on Fe^{3+}-VO defect complexes at symmetrically distinct coordination sites. The introduction of these vacancies breaks local symmetry, altering the crystal field at the Fe site and, consequently, changing the MCAE. Our findings provide fundamental computational design principles for optimizing the electric-field control of single-spin sites in complex oxide ferroelectrics, advancing the development of novel single-atom magnetoelectric technologies.

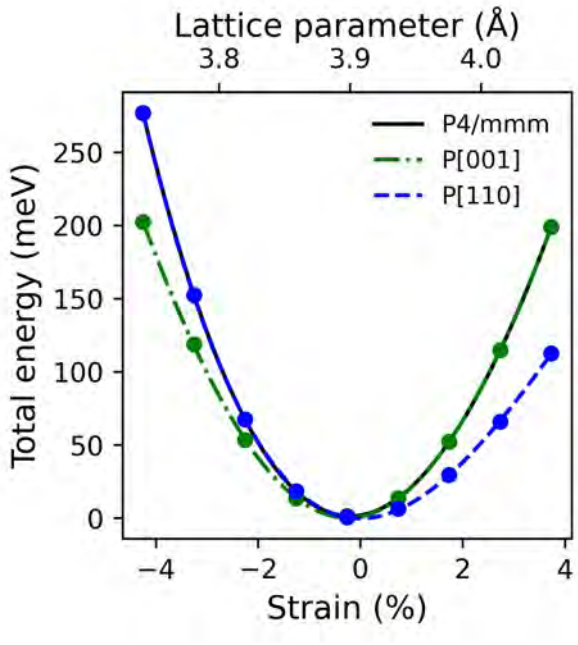


Fig.1 Calculated total energy landscape of $SrTiO_3$ as a function of biaxial strain. Under compressive strain, the tetragonal P4mm having polarization along [001] is the most stable one, and under tensile strain, orthorhombic Amm2 with polarization along [110] is the most stable.

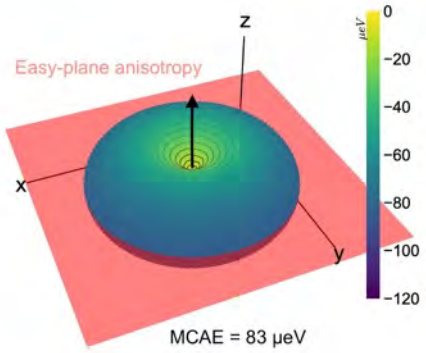


Fig.2 MCAE surface for P4mm with spin-easy plane shown in red, and the black arrow shows the polarization direction.

FQ-13. Ferroelectric-Like behavior at the Surface of Cr_2O_3
J. Keagy, W. Liao, S. Mahesh, N. Mancini, J. Shi
University of California Riverside, Riverside, California, United States

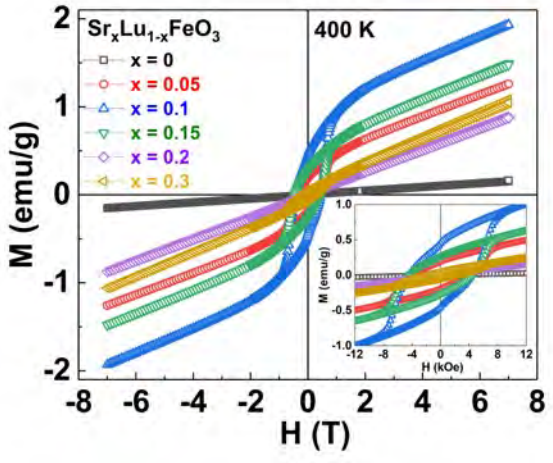
In this work, we systematically investigate bulk Cr_2O_3 (0001) by measuring the magnetoelectric coefficient by applying a time varying magnetic field and measuring the induced voltage across the sample. Single domain selection was observed by magnetoelectric field cooling (MEFC) the crystal through its Néel temperature. The domain selected during field cooling was dependent on the product of the fields used. It was found that magnetic field cooling the crystal through its ordering temperature also resulted in single domain selection. We found that applying an electric field across the crystal above its ordering temperature and measuring its effect on antiferromagnetic domain formation during a magnetic field cool (MFC) had an opposite signed response to the selected domains as compared to MEFC. This opposite-signed response indicates the existence of polarization around the crystal surface that allows for full domain selection during magnetic field cooling. This polarization can be toggled and controlled above the Néel temperature with an applied electric field. Our results demonstrate that even the prototypical magnetoelectric material can have pronounced surface effects that impact the antiferromagnetic domain formation in the crystal.

This work is support by the U.S. Department of Energy (DOE), Office of Science, Office of Basic Energy Sciences under Award Number DE-FG02-07ER46351, and the UC National Laboratory Fees Research Program of the University of California, Grant Number L25CR9003.

FQ-14. Substitution driven room temperature ferromagnetism in hexagonal $Lu_{1-x}Sr_xFeO_3$ ceramics
S. Pittala[1, 2], P. K U[2], P. Anil Kumar[2]
[1]Physics, Dayananda Sagar University, Bengaluru, Karnataka, India, [2]Physics, Indian Institute of Science, Bengaluru, Karnataka, India

$Lu_{1-x}Sr_xFeO_3$ (x = 0 - 0.3) (LSFO) ceramics with $x \leqslant 0.1$ show a metastable hexagonal crystal structure and the mixed phases of hexagonal and orthorhombic for $x \geqslant 0.15$. The co-existence of both Fe^{2+} and Fe^{3+} states in Sr doped, and only Fe^{3+} in undoped samples has been observed. M-T data show a bifurcation between ZFC and FC curves from 400 K in all Sr-substituted samples, indicating a high-temperature magnetic transition. Ferromagnetic M-H loops are observed at 400 K in Sr substituted LFO. Magnetic properties of $LuFeO_3$ enhance remarkably upon Sr substitution, exhibiting $M_{@7T}$ ~ 1.93 emu/g, H_C ~ 4.4 kOe for x = 0.1. The remnant polarization (P_r) of $LuFeO_3$ increases from 0.02 to 0.043 $\mu C/cm^2$ as Sr content changes from x = 0 to x = 0.1. With the exhibition of room temperature ferromagnetism and enhanced polarization, the Sr substituted $LuFeO_3$ could be a promising multiferroic system for device applications.

1. S. M. Disseler, J. A. Borchers, C. M. Brooks, J. A. Mundy, J. A. Moyer, D. A. Hillsberry, E. L. Thies, D. A. Tenne, J. Heron, M. E. Holtz, J. D. Clarkson, G. M. Stiehl, P. Schiffer, D. A. Muller, D. G. Schlom, and W. D. Ratcliff, Phys. Rev. Lett. 114, 217602 (2015).
2. P. Suresh, K. Vijaya Laxmi, A. K. Bera, S. M. Yusuf, Ch. Bheemalingam, J. Jung and P. S. Anil Kumar, Phys. Rev. B. 97, 184419 (2018).
3. P. Suresh, K. Vijaya Laxmi and P. S. Anil Kumar, J. Mag. Mag. Mater. 448, 117 (2018).

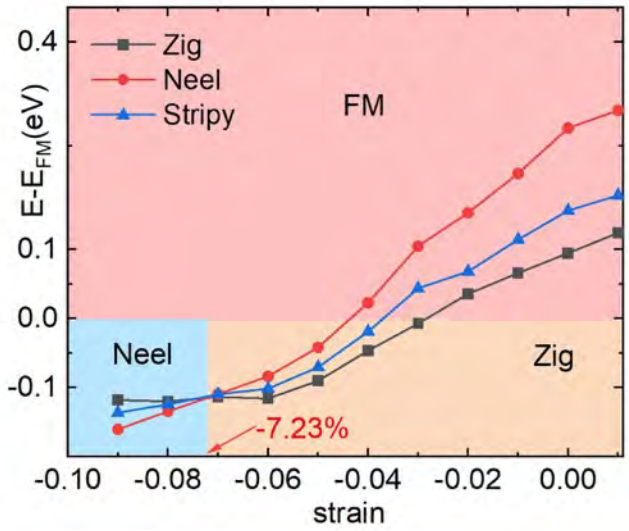


FQ-15. Polarization Reversal and Strain-Driven Magnetic Phase Transitions Enable Reversible Topological Switching in CrGeTe3/In2Se3
W. Li, S. Dong, J. Zhang
Physics, Southeast University, Nanjing, Jiangsu Province, China

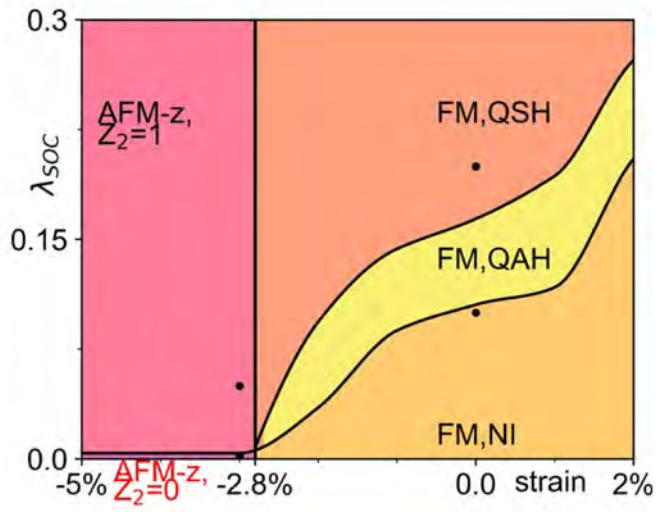
The topologically protected edge states arising from the quantum spin Hall effect enable dissipationless transport. We construct a CrGeTe3/In2Se3 heterostructure and manipulate its magnetic ground state and topological properties via polarization reversal and strain. In the strain-free ferromagnetic (FM) state, when the polarization points outward, band inversion occurs under spin–orbit coupling (SOC), yielding a time-reversal symmetry-broken quantum

spin Hall effect with a spin Chern number of 1. Under 3%–7.25% compressive strain, the system transitions to a zigzag antiferromagnetic (AFM) state, where outward polarization induces a Dirac cone; upon including SOC, a gap opens with Z2 = 1, corresponding to a quantum spin Hall effect protected by MyT symmetry. Further increasing the strain drives the system into the Néel-AFM phase, where altermagnetism and nonrelativistic band splitting emerge, and the anomalous Hall effect can be significantly tuned by the polarization direction. This system enables reversible electric-field control over the trivial and nontrivial topological states of two distinct quantum spin Hall effects within a single material, offering an ideal platform for topological magnetoelectric manipulation.

[1] M.M. Otrokov, I.I. Klimovskikh and H. Bentmann, Nature., Vol. 576, p.416 (2019).
[2] Y. Yang, Z. Xu and L. Sheng, Phys. Rev. Lett., Vol. 107, p.066602 (2011).
[3] J.-J. Zhang, D. Zhu and B.I. Yakobson, Nano Lett., Vol. 21, p.785 (2020).
[4] C. Gong, E.M. Kim and Y. Wang, Nat. Commun., Vol. 10, p.2657 (2019).



Energy of Zigzag, Néel, and Stripy antiferromagnetic configurations relative to the FM state under different strains.



Topological phase diagram of the heterostructure under different strains and spin–orbit coupling strengths λsoc.

FQ-16. Interface Effects on Spin Glass Behavior in Ni/MoS2

A. J. Stollenwerk[1], H. Harms[1], S. Diallo[1], A. Hager[1], E. Ahmetasevic[1], T. Porter[1], C. J. Cunningham[1], C. Hemesath[1], P. Lukashev[1], T. Kidd[1], B. Wei[2], L. Zhou[3], P. Shand[1]
[1]Physics, University of Northern Iowa, Cedar Falls, Iowa, United States, [2]Ames National Laboratory, Ames, Iowa, United States, [3]Materials Science and Engineering, University of Virginia, Charlottesville, Virginia, United States

Incorporating MoS_2 substrates into spintronic devices requires a thorough understanding of the properties of their interface with ferromagnetic metals. To this end, we investigated the magnetic properties of Ni/MoS_2 samples fabricated under several different conditions. Depositing Ni using electron beam evaporation on MoS_2 results in spin glass-like behavior. In samples where Ni was deposited on MoS_2 substrates previously annealed at 300°C under vacuum, the time relaxation of the magnetoresistance was significantly more rapid compared to unannealed samples. Scanning tunneling microscopy images reveal that Ni forms circularly symmetric structures with a diameter of two nanometers in both the annealed and unannealed samples. The only structural difference found between the annealed and unannealed samples was observed in the cross-sectional TEM images. Annealed samples had an abrupt interface, while unannealed samples exhibited Ni intercalation several nanometers into the MoS_2. We hypothesize that the difference in spin glass properties observed in the unannealed samples as compared to the annealed samples is explained by the increased intermixing

at the interface. The increased disorder at the interface may induce stronger and more random anisotropy in the magnetic domains, resulting in a more rugged free energy landscape and hence, slower relaxation.

SESSION FR: LOW DIMENSIONAL MAGNETISM, COMPLEX PHASES, TOPOLOGY AND CHIRALITY (POSTER SESSION)

Chair(s): H. Zeng, *Physics, University of Buffalo, Buffalo, New York, United States*

Thursday, November 5, 2026

03:00 PM-06:00 PM

Coral 4

FR-01. Correlation Between Magnetic Frustration and Spin-Dependent Transport in Fe_2(Mn,Cr)Al Heusler Alloys

A. Ashok[1, 2], N. Bhagat[1]

[1]*Applied Sciences, Symbiosis Institute of Technology, Symbiosis International (Deemed) University, Pune, Maharashtra, India,* [2]*Physics, Savitribai Phule Pune University, Pune, Maharashtra, India*

The influence of Mn/Cr substitution on competing exchange interactions and spin-dependent scattering in Fe_2-based Heusler alloys is systematically investigated through detailed magnetic, transport, and spectroscopic measurements on Fe_2MnAl and Fe_2CrAl. Both alloys exhibit spin-glass behavior at low temperatures, indicating magnetic frustration arising from competing exchange interactions. In the paramagnetic regime, the inverse susceptibility is well described by a modified Curie–Weiss expression,$\chi(T)=C/(T-\theta_{CW})+\chi_0$, where χ_0 accounts for the temperature-independent Pauli paramagnetic contribution. The extracted Curie–Weiss temperatures are −20 K (Fe_2MnAl) and −2 K (Fe_2CrAl), confirming dominant antiferromagnetic correlations, stronger in the Mn-containing compound. Mean-field analysis yields Curie temperatures (T_C) of 370 K and 342 K, respectively, establishing magnetic ordering well above room temperature.

Isothermal magnetization measurements at 5 K reveal soft magnetic behavior with low saturation magnetization (11–15 emu/g). The magnetization curves are accurately fitted using the Langevin function, suggesting cluster-mediated magnetization processes. Electrical resistivity exhibits contrasting conduction mechanisms: Fe_2MnAl displays semiconducting behavior modeled within the Cote–Meisel framework incorporating Debye–Waller and Debye–magnon contributions, whereas Fe_2CrAl shows metallic transport consistent with Bloch–Grüneisen scattering and finite residual resistivity indicative of spin-disorder scattering at low temperatures. Both alloys exhibit negative magnetoresistance of 2–3% over 5–300 K following Kohler scaling. XPS and valence band spectroscopy confirm modifications in near-Fermi electronic states. These results establish a clear correlation between compositional tuning, magnetic frustration, and transport crossover in Fe_2(Mn,Cr)Al alloys.

[1] I. Das, E.V. Sampathkumaran and R. Vijayaraghavan, Phys. Rev. B. 44, 159 (1999).
[2] M. Acet, E. Duman, E.F. Wassermann, et al., J. Appl. Phys. 92, 3867 (2002).
[3] E. Duman, M. Acet, Y. Elerman, et al., J. Magn. Magn. Mater. 238, 11 (2002).
[4] Liu, Z., Ma, X., Meng, F. and Wu, G. J. All. Comp. 509(7), 3219-3222 (2011).
[5] Saha, R., Srinivas, V., and Venimadhav, A. J. Magn. Magn. Mater. *324*(7), 1296-1304 (2014).
[6] M. Belkhouane, S. Amari, A. Yakoubi, et al., J. Magn. Magn. Mater. 377, 211 (2015).
[7] Yadav, K., Sharma, M. K., Singh, S.,and Mukherjee, K., Sci. Rep., 9, 15888 (2019).

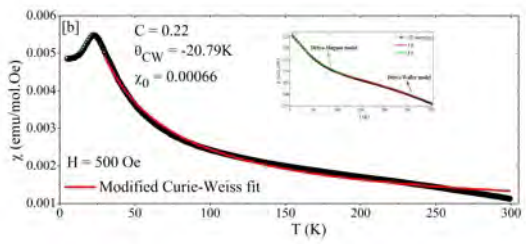


Fig.1: Susceptibility curve fitted using Curie-Weiss model and the inset describing the resistivivty behaviour fitted with Cote–Meisel model on Fe_2MnAl

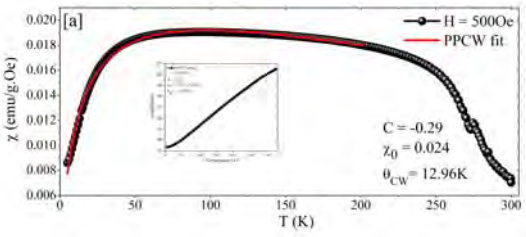


Fig.2: Susceptibility curve fitted using Curie-Weiss model and the inset describing the resistivivty behaviour fitted with Bloch–Grüneisen model on Fe_2CrAl

FR-02. NMR-T_1 study of 1/3-magnetization plateau in equilateral-triangular-lattice antiferromagnet $Ba_2La_2CoTe_2O_{12}$

T. Goto[1], K. Kobayashi[1], S. Daimon[2], T. Ohtsuki[1], H. Tanaka[3], N. Kurita[3], M. Watanabe[3], Y. Kojima[3], T. Sasaki[4]
[1]Physics Division, Sophia University, Chiyodaku, Tokyo, Japan, [2]Quantum Materials and Applications Research Center, National Institutes for Quantum Science and Technology (QST), Tokyo, Japan, [3]Institute of Science Tokyo, Tokyo, Japan, [4]Institute for Material Research, Tohoku University, Sendai, Japan

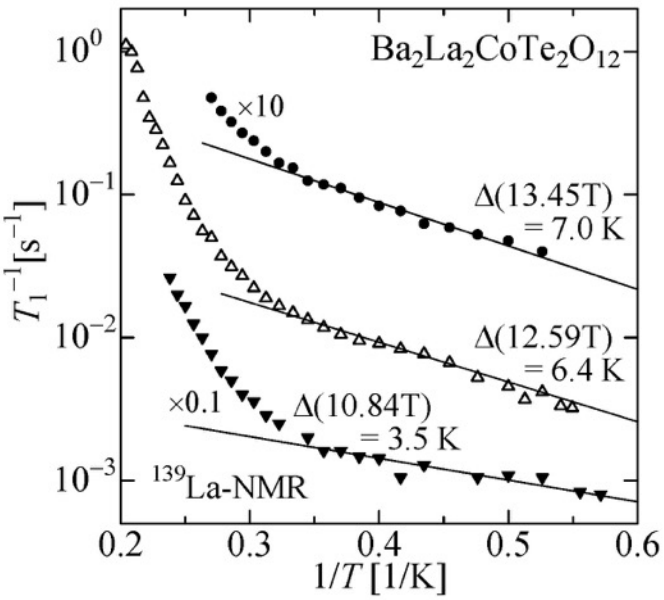
$Ba_2La_2CoTe_2O_{12}$ is a recently reported S=1/2 XXZ quantum spin antiferromagnet (T_N = 3.26 K at zero-field) on an equilateral triangular lattice (TLAF), which exhibits a 1/3 magnetization plateau under high magnetic field between 8.7 and 15.2 T below T_N [1-3]. In this plateau phase, spins are expected to form the up-up-down (uud) structure, accompanied by a finite excitation gap.

We have measured the temperature dependence of ^{139}La-NMR-T_1 in the plateau region and determined the energy gap Δ from its thermally activated behavior (Fig. 1). The obtained gap shows a significant magnetic-field dependence, which is consistent with theoretical predictions [4].

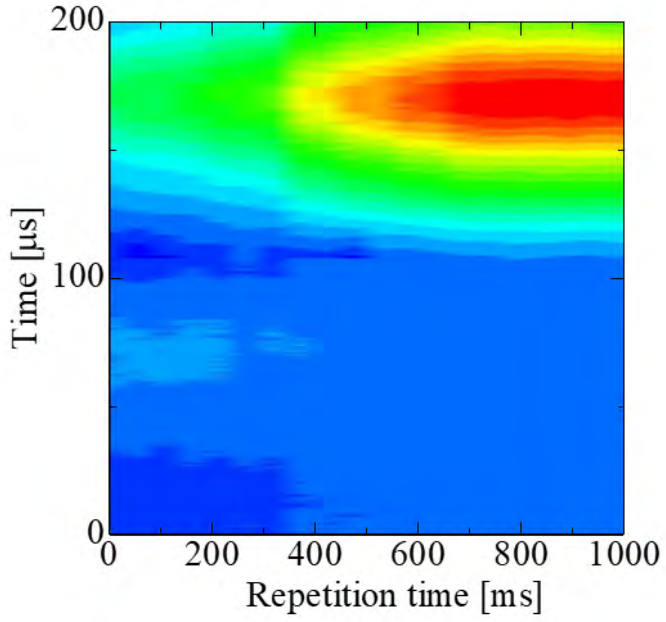
In the course of the T1 measurements, we found that the spin echo shape strongly depends on the repetition time. Conventionally, T_1 is determined only from the recovery of the spin-echo amplitude. In this work, we propose a new method to extract T_1 from the full spin-echo shape using a neural network. Specifically, the time evolution of the echo-shapes at given temperatures are represented as a contour map (Fig. 2) and used as training data for the neural network, which then estimates T_1 at other temperatures. The underlying mechanism of the echo-shape evolution is also analyzed using the simulation based on the Lindblad equation, which successfully reproduces the observed deformation of the echo signal.

This approach will provide a new route for T_1 determination in NMR experiments, especially for cases of operando measurements.

[1] Y. Kojima, M. Watanabe, *et al*., Phys. Rev. B 98, 174406 (2018).
[2] T. Nikuni, H. Shiba, J. Phys. Soc. Jpn. 62(9), 3268 (1993).
[3] Keito Morioka, Takayuki Goto *et al*., J. Low. Temp Phys. 222, 47 (2026).
[4] A. V. Chubukov and D. I. Golosov, J. Phys. Condens. Matter 3, 69 (1991).



Arrhenius plot of $1/T_1$ measured at various magnetic fields in the 1/3-magnetization plateau. Solid lines show the thermal-activation type function with the excitation gap Δ determined by best-fit to the data.



Contour map of the spin-echo shape viewed by the oscilloscope. Abscissa is the NMR measurement repetition interval; the right side limit corresponds to the thermal equilibrium state.

FR-03. Anomalous Hysteresis and Magnetic Phase Transitions in the Heusler Compound $Fe_{1.3}Mn_{1.7}Si$

M. Hiroi, I. Shigeta
Department of Physics and Astronomy, Kagoshima University, Kagoshima, Japan

The Heusler compound $Fe_{1.3}Mn_{1.7}Si$ exhibits three magnetically ordered phases — the ferromagnetic (F), AF, and AF2 phases — as shown in the magnetic field – temperature (B –T) phase diagram in Fig. 1 [1] . The AF phase comprises both ferromagnetic and antiferromagnetic components, whereas the AF2 phase is regarded as a purely antiferromagnetic state. This contrasts with compositions with x <1.65, where only the F and AF phases have been reported [2]. The AF2–AF transition temperature, T_{A2}, decreases with increasing B, consistent with a conventional antiferromagnetic transition. Isothermal magnetization, $M(B)$, shows no hysteresis between increasing and decreasing B above 40 K, whereas the hysteresis width increases markedly at lower temperatures. In particular, below 20 K, the transition field on decreasing B shifts anomalously to lower values.

The temperature dependence of magnetization $M(T)$ at various B, was measured under several protocols: warming in B after zero-field cooling (ZFC), and field-cooled cooling (FCC) and warming (FCW) with the field applied at a high temperature. The $M(T)$ curves for FCC and FCW coincide (hereafter collectively denoted as FC), indicating the absence of supercooling or superheating at T_{A2}. The $M(T)$ curves for ZFC and FC overlap at low fields but bifurcate below T_{A2} at $B \approx 2$T.

Anomalous broadening of hysteresis in $M(B)$ has been reported in other systems [3], where it is often attributed to kinetic arrest associated with first-order transitions. However, the behavior of the AF2–AF transition in $Fe_{1.3}Mn_{1.7}Si$ more closely resembles that of a spin-glass-lile system [4], suggesting that the kinetic-arrest scenario may not be applicable in the present case.

[1] M. Hiroi *et al*., J. Phys: Conf. Ser. 969, 012098 (2018); J. Phys. Soc. Jpn. 90, 103701 (2021).
[2] S. Yoon and J. G. Booth, J. Phys. F: Met. Phys. 7, 1079 (1977).
[3] K. Matsuura *et al*., Sci. Rep. 13, 6876 (2023).
[4] S. Pal, J.Phys.: Condens. Matter. 33, 025801 (2021).

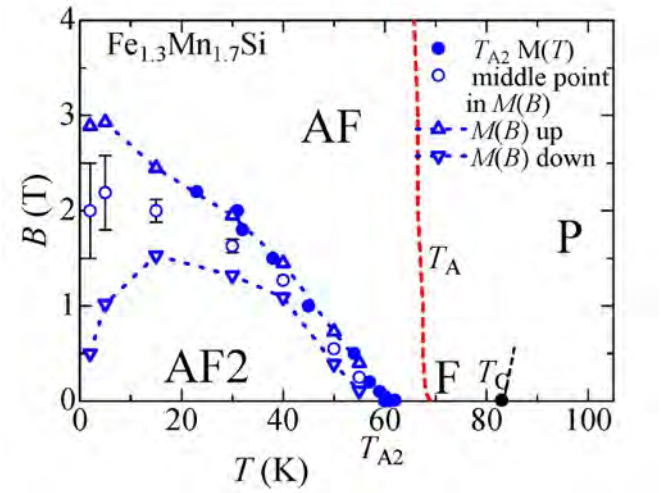


Fig. 1: B - T phase diagram of $Fe_{1.3}Mn_{1.7}Si$. Triangles and inverted triangles indicate the end points of the AF2–AF transition in $M(B)$ for increasing and decreasing magnetic field, respectively.

FR-04. Inverse Magnetocaloric Effect and Magnetic Phase Diagram of $Fe_{3-x}Mn_xSi$ Near x = 1.7

M. Hiroi, T. Takamoto, Y. Koda, I. Shigeta
Department of Physics and Astronomy, Kagoshima University, Kagoshima, Japan

The Heusler compound $Fe_{3-x}Mn_xSi$ exhibits various magnetic phases depending on the Mn concentration, x [1]. These magnetic transitions have been investigated under applied magnetic fields for various values of x [2, 3].

Figure 1 illustrates the magnetic-field–temperature (B–T) phase diagram for x = 1.7 and 1.8. For x = 1.7 at low fields, three distinct magnetic phases are observed, hereafter referred to as the F (ferromagnetic), AF, and AF2 phases [2]. The AF phase, which exists for x > 0.75, comprises both ferromagnetic and antiferromagnetic components. In contrast, the AF2 phase—recently identified near x = 1.7—is considered a purely antiferromagnetic state [2].

Magnetic entropy change was estimated through the analysis of magnetization measurements. Because both ferromagnetic and antiferromagnetic phases exist, magnetocaloric effects of both signs were observed. Notably, a significant inverse magnetocaloric effect was identified in the vicinity of the AF2 phase. For x = 1.7, the estimated magnetic entropy is comparable to that of Mn_5Si_3, which exhibits similar antiferromagnetic transition temperatures and a related magnetic phase diagram [4]. While the absolute maximum entropy values at 5 T are

smaller than those of Mn_5Si_3 for both positive and negative signs, their magnitudes are comparable.
Magnetic transitions in this system are sensitive to composition (x). As x increases, the F phase is suppressed; at low fields, only a transition between the paramagnetic (P) and AF2 phases occurs, as shown in Fig. 1 for x=1.8. Consequently, we investigate the expected modifications to the magnetocaloric effect resulting from these compositional variations.

[1] S. Yoon and J. G. Booth, J. Phys. F: Met. Phys. 7, 1079 (1977).
[2] M. Hiroi *et al*., J. Phys: Conf. Ser. 969, 012098 (2018); J. Phys. Soc. Jpn. 90, 103701 (2021).
[3] T. Nonoyama *et al*., AIP Advances 8, 115018 (2018); R. Kato *et al*., AIP Advances 8, 115019 (2018).
[4] R. F. Luccas et al., J. Magn. Magn. Mater. 489, 165451 (2019).

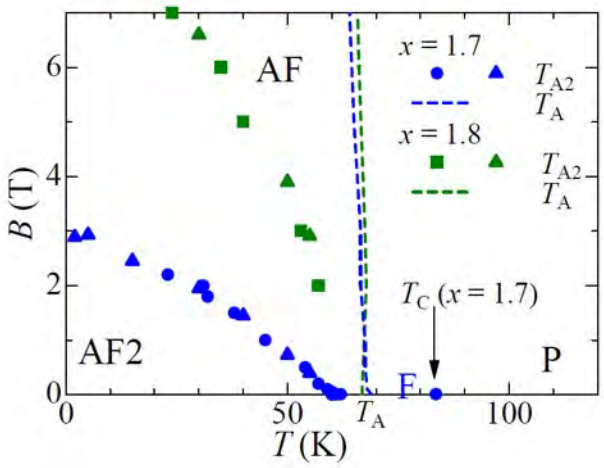


Fig. 1: $B-T$ phase diagram of $Fe_{3-x}Mn_xSi$ for x = 1. 7 and 1.8. For x = 1. 7, the AF2, AF, and F phases are present. Circles and triangles indicate the AF2-AF transition determined from $M(T)$ and $M(B)$, respectively. Broken lines represent the T_A (AF–P) transition. For x = 1.8, the ferromagnetic phase disappears.

FR-05. Magnetic Behavior and Magnetic Ground State of $Ba_3MgRu_2O_9$

U. Iida, T. Tai, D. Sekita, Y. Yasui
Physics, Meiji University, Kawasaki, Kanagawa, Japan

We have investigated the magnetic properties and magnetic ground state of $Ba_3MgRu_2O_9$, which is one of the series compounds represented by chemical formula $Ba_3MRu_2O_9$ (M = Co, Ca, Zn, Mg *etc.*). Various magnetic behavior of the Ru^{5+} spin ($4d^3$, spin S = 3/2) was reported for $Ba_3MRu_2O_9$, which depends on the species of M^{2+} ions. For $Ba_3CoRu_2O_9$, an antiferromagnetic long-range ordering is observed below a transition temperature T_N ~ 100 K [1]. For $Ba_3CaRu_2O_9$, spin system becomes a non-magnetic ground state at low temperatures [2]. $Ba_3ZnRu_2O_9$ was reported to be a candidate quantum spin liquid (QSL) system [3]. Such changes on magnetic properties are considered to arise from slight differences in the spin number of M^{2+} ions and/or in the crystal structure derived from different ionic radii of M^{2+} ions. Although the magnetic ground state of $Ba_3MgRu_2O_9$ attracts much interest, it has not yet been fully elucidated. Previous studies conducted over 40 years ago reported that it is non-magnetic state from magnetic susceptibility (χ) data [2] and antiferromagnetic ordering from Mössbauer measurements [4].
In this study, we have synthesized polycrystalline samples of $Ba_3MgRu_2O_9$ and the non-magnetic Nb^{5+} ions doped systems $Ba_3Mg(Ru_{1-x}Nb_x)_2O_9$ with x = 0.03 and 0.06 using the solid-state reaction method. The X-ray diffraction, magnetization and specific heat (C) measurements have been carried out the obtained samples. The $\chi - T$ curve of $Ba_3MgRu_2O_9$ is found to have kink structure at T_N = 144 K, and the χ values are not approaching zero as $T \rightarrow 0$. Moreover, we observe the jump behavior in the $C/T-T$ curve of $Ba_3MgRu_2O_9$ at T_N=144 K. These results indicate that the magnetic ground state is antiferromagnetic long-range ordering. We have also investigated the magnetic behavior of the Nb-doping system $Ba_3Mg(Ru_{1-x}Nb_x)_2O_9$. From $\chi - T$ curves and the hysteresis loops of the magnetization curves, the Nb^{5+}-substitution for Ru^{5+} is found to suppress the T_N value and to induce the ferromagnetic component in the region of $T < T_N$. It is surprising that the doping of the nonmagnetic Nb^{5+} ion induces the ferromagnetic component. In the presentation, we will discuss the magnetic behavior of $Ba_3Mg(Ru_{1-x}Nb_x)_2O_9$.

[1] P. Lightfoot *et al.*: J. Solid State Chem. 89 (1990) 174.
[2] J. Darriet *et al.*: J. Solid State Chem. 19 (1976) 213.
[3] I. Terasaki *et al.*: J. Phys. Soc. Jpn. 86 (2017) 033702.
[4] I. Fernandez *et al.*: J. Solid State Chem. 34 (1980) 121.

FR-06. Synthesis of Niobium-doped Sodium Cobalt Tellurate ($Na_2Co_2Te_{1-x}Nb_xO_6$) Towards Zero-magnetic Field Stable Quantum Spin Liquids

S. C. Mills[1], N. Hill[2], E. Patterson[1], M. Staruch[1]
[1]Materials Science and Technology Division, US Naval Research Laboratory, Washington, District of Columbia, United States, [2]Howard University, Washington, District of Columbia, United States

Sodium cobalt tellurate ($Na_2Co_2TeO_6$, NCTO), classified as a spin-½ low dimensional honeycomb lattice structure, is considered a potential Kitaev quantum spin liquid (KQSL) that exhibits a field-induced disordered state [1]. This work aims to synthesize niobium doped NCTO (Nb-NCTO) to investigate the effects of doping varied concentrations of Nb into the Te site of NCTO, changing inter-atomic bond lengths and disrupting long range magnetic ordering to potentially achieve a spin-disordered state at low or even zero field [2]. $Na_{2+x}Co_2Te_{1-x}Nb_xO_6$ was synthesized by doping with a non-magnetic atom (Nb) at the Te site at various concentrations using conventional solid-state synthesis. It was determined via X-ray diffraction that Nb > 2.5% leads to sodium niobate and other multi-component oxide impurities, while 2.5% Nb doped NCTO is on the whole of the desired $P6_3/mmc$ space group with a minority impurity phase. Temperature dependent magnetic property measurements will elucidate the effect of doping on the magnetic ordering transitions frustration parameter at zero and applied fields when compared to undoped NCTO. The results here add to a fairly under-explored phase space for KQSLs and provide steps towards phase pure synthesis of the materials, a currently challenging prospect.

[1] Jiao, J., Li, X., Lin, G., et al., *Commun. Mater.* 5, p. 159 (2024)
[2] Pandey, S.K. and Feng, J., *Phys. Rev. B.* 106, p. 174411 (2022)

FR-07. Ancilla-Based Quantum Simulation of Spin Excitation Spectra in One-Dimensional Spin Chains

H. Ryu, J. Byeon, J. Seo, S. Lim, K. Jeong, J. Hong, K. Moon, N. Lee, Y. Choi
Department of Physics, Yonsei University, Seoul, Korea (the Republic of)

We implement an ancilla-based quantum simulation workflow to investigate spin excitation spectra in one-dimensional quantum magnets [1]. The method is applied to the spin-1/2 XXZ chain and extended to spin-1 chain models. By encoding time-dependent spin-spin correlation functions into a single ancillary qubit, the dynamical structure factor S(q, ω) is reconstructed through Fourier transformation. Because this approach does not rely on variational optimization, it enables direct access to dynamical correlation functions.

The quantum simulation results are consistent with theoretical expectations and capture the finite-size effects characteristic of small systems. The simulated spectra clearly resolve distinct dispersion features in both ferromagnetic and antiferromagnetic regimes. In the XXZ model, changes in the exchange anisotropy K and the external magnetic field H_z produce clear shifts in excitation gaps and alter the spectral weight distribution across momentum and frequency. Furthermore, application of this framework to the quasi-one-dimensional material Cs_2CoCl_4 reproduces the field-dependent evolution of the excitation spectrum [2].

For higher-spin systems, each spin-1 site is efficiently mapped onto a two-qubit register while restricting the local dynamics to a three-state subspace. Overall, this study establishes the ancilla-based workflow as an effective tool for extracting the full dynamical structure factors S(q, ω) from quantum many-body systems. Our approach provides a practical route for simulating fundamental magnetic excitations beyond simple ferromagnetic models.

[1] J. S. Pedernales, R. Di Candia and E. Solano, Phys. Rev. Lett., Vol. 113, p.020505 (2014).
[2] P. Laurell, A. Scheie and C. J. Mukherjee, Phys. Rev. Lett., Vol. 127, p.037201 (2021)

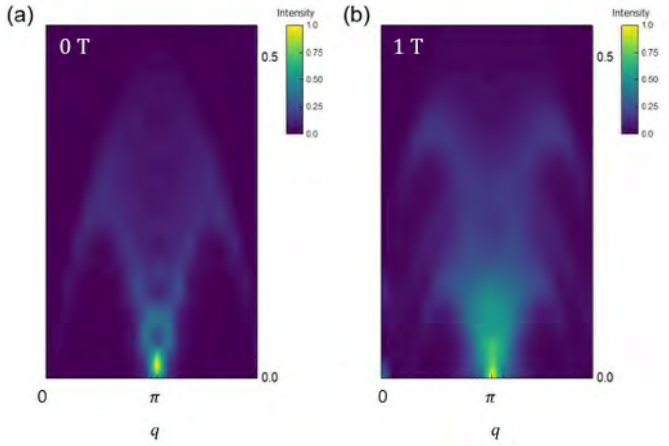


Fig. 1 Simulated dynamical structure factor S(q, ω) of a 20-site spin-1/2 XXZ chain. The intensity maps show the dispersion relation at (a) 0 T and (b) 1 T, highlighting the effect of the external magnetic field on the spectrum

FR-08. Quantum Simulation of Spin-1 Magnetic System Including Magnetocrystallin Anisotropy Using Variational Quantum Eigensolver

J. Byeon, H. Ryu, S. Lim, K. Jeong, J. Seo, J. Hong, H. Kim, K. Moon, N. Lee, Y. Choi
Department of physics, Yonsei University, Seoul, Korea (the Republic of)

We construct the Hamiltonian of a spin-1 system including magnetocrystalline anisotropy (MCA) and perform simulations using the variational quantum eigensolver (VQE) algorithm. To represent the three spin states of a spin-1 particle, we apply Gray encoding with two qubits. Among the four states of the two-qubit system, one acts as a leakage state that can cause computational errors; therefore, it is excluded by employing RY and CRY gates. Total six parameters are required to represent the complex coefficients of the three states, but two of them can be removed through the normalization condition and global phase reduction. In addition, under a strong magnetic field, the magnetic moments are aligned along the field direction, so only the eigenstates of the S_x, S_y, and S_z operators need to be considered. This allows us to further eliminate one parameter, leaving three parameters per spin-1 particle. Using Gray encoding, we expand the S_x, S_y and S_z operators of the spin-1 system in terms of the outer products of Pauli matrices. In conventional spin-1/2 systems, the square of a Pauli matrix becomes the identity, making it impossible to directly include an MCA term of the form $(S \cdot n)^2$. However, since S_i^2 is nontrivial in spin-1 systems, MCA can be explicitly represented. Based on this formulation, we construct the Hamiltonian of a two spin-1 particle system that includes the Heisenberg exchange interaction, Zeeman energy, and MCA energy. Simulations performed using the StatevectorEstimator in IBM Quantum's Qiskit platform reveal that variations in the exchange interaction and MCA coefficients induce both spin-flip and spin-flop transitions.

[1] C. J. Mitchell, Computers & Security, Vol. 93, p.101825 (2020)
[2] Y. Wang, J. Kim and K. Suresh, Journal of Computing and Information Science in Engineering, Vol. 23, p.060817 (2023)
[3] D. Herman, C. Googin, X. Liu, Nature Reviews Physics, Vol. 5, p.450-465 (2023)
[4] J. Getlina, C. Wang, T. Iadecola, Physical Review B, Vol. 109, p.085128 (2024).

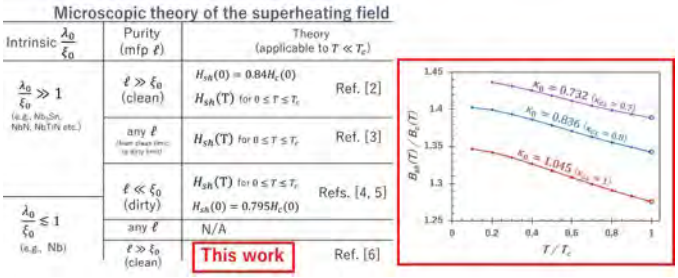
FR-09LB. The Meissner Stability Limit of Clean Niobium at Low Temperatures

T. Kubo
High Energy Accelerator Research Organization, Tsukuba, Japan

The superheating field B_{sh} is the largest applied magnetic field for which a defect-free superconducting surface can retain a metastable, vortex-free Meissner state. Near the critical temperature T_c, its dependence on the Ginzburg-Landau parameter κ_{GL} has been established within Ginzburg-Landau theory [1]. At low temperatures, microscopic calculations have treated clean superconductors in the high-κ local limit [2], impurity effects in high-κ materials [3], and diffusive superconductors within Usadel theory [4,5]. The clean, low-κ regime near the type-I--type-II boundary, directly relevant to high-purity niobium superconducting radio-frequency cavities used in modern particle accelerators, has remained unresolved for decades because the current response is intrinsically nonlocal. This work formulates and solves this missing problem using self-consistent nonlinear nonlocal Eilenberger theory coupled to Maxwell electrodynamics. For a clean semi-infinite superconductor, the spatially varying Meissner state is obtained and its stability is tested against order-parameter and electromagnetic perturbations with arbitrary wave number parallel to the surface. B_{sh} is located from a zero mode of the linearized response operator. The study covers the niobium-relevant range $0.7 < \kappa_{GL} < 1$ and $T/T_c \geq 0.1$. The calculation reproduces the known Ginzburg-Landau result near T_c. At lower temperatures, B_{sh}/B_c exceeds a simple extrapolation of the near-T_c result. For $\kappa_{GL} = 0.7$, consistent with recent measurements of clean niobium near the type-I--type-II boundary, the calculation gives $B_{sh} = 1.44\ B_{c0}$ at $T/T_c = 0.2$. Taking $B_{c0} = 200$ mT gives about 290 mT and an intrinsic accelerating-gradient limit of about 67 MV/m for a TESLA-shaped elliptical niobium cavity used in particle accelerators. The result establishes the intrinsic Meissner-state stability limit of clean niobium and provides a benchmark for the maximum accelerating field of niobium cavities used in modern particle accelerators.

[1] M. K. Transtrum, G. Catelani, and J. P. Sethna, Physical Review B 83, 094505 (2011).
[2] G. Catelani and J. P. Sethna, Physical Review B 78, 224509 (2008).
[3] F. P.-J. Lin and A. Gurevich, Physical Review B 85, 054513 (2012).
[4] T. Kubo, Physical Review Research 2, 033203 (2020).
[5] T. Kubo, Superconductor Science and Technology 34,

045006 (2021).
[6] T. Kubo, arXiv:2606.10420 [cond-mat.supr-con] (2026).



Overview of microscopic theories of the superheating field at low temperatures (left) and the calculated temperature dependence of B_{sh}/B_c for clean low-κ superconductors (right). The present work fills the previously unresolved clean, low-κ regime relevant to Nb. Filled symbols show the nonlocal Eilenberger results, while open symbols at T/T_c=1 indicate the corresponding Ginzburg–Landau limits. For κ_{GL}=0.7, the calculation gives B_{sh}/B_c≈1.44 at T/T_c=0.2, corresponding to B_{sh}≈290 mT for Nb.

FR-10. Magnetic correlations of ferromagnetic domains in plastically strained Pt_3Fe antiferromagnet

S. Kobayashi[1], A. Nakano[1], Y. Ikeda[2], M. Fujita[2], K. hiroi[3], T. Kumada[3], R. Motokawa[3]
[1]Iwate University, Morioka, Japan, [2]Tohoku University, Sendai, Japan, [3]JAEA, Tokai, Japan

$L1_2$-type Pt_3Fe ordered alloy exhibits antiferromagnetic (AFM) ordering below T_N = 170 K, which is characterized by propagation vector q =(1/2, 1/2, 0) [1]. However, after a small plastic strain, Pt_3Fe exhibits ferromagnetic (FM) properties even at room temperature [2]. This strain-induced ferromagnetism can be attributed to the formation of FM domains around antiphase boundaries (APB) on {111} glide planes and may be related to the appearance of various magnetic features such as exchange bias effects at low temperatures [3], large magnetocaloric effects around T_N [4]. However, the morphology of FM domains and their relation with AFM matrix were not understood in detail. In this study, we performed wide-angle and small-angle neutron scattering measurements for Pt_3Fe antifferomagnet with 22% plastic strain to elucidate magnetic correlations within FM domains below and above T_N.
In addition to magnetic reflections characterized by q =(1/2, 1/2, 0), we newly observed broad reflections around (1,0,0) and (0,1,0) reciprocal lattice points at T ~30 K. As the temperature increases, both intensities monotonically decrease and disappear at T ~ 250 K. Interestingly, both intensities exhibit a large drop around T_N and remain even at T = 200 K. This suggests that magnetic correlations of FM domains are present in a wide temperature range below T ~ 250 K, but are enhanced by the aid of AFM ordering in $L1_2$ matrix. Moreover, we found that the effective size of FM domains at T=10K, estimated by Guinier law, was approximately 70-80 nm and FM correlations extend over a wide region with $L1_2$ structure. These findings strongly suggest competing FM and AFM correlations below T_N in plastically strained Pt_3Fe antiferromagnet.
[1] G.E. Bacon and J. Crangle, Proc. R. Soc., vol.A 272, 387 (1963).
[2] S. Takahashi and Y. Umakoshi, J. Phys.: Condens. Matter, vol.2, 2133 (1990).
[3] S. Kobayashi, S. Takahashi, Y. Kamada, and H. Kikuchi, IEEE Trans. Magn., vol.44, 4225 (2008)
[4] S. Kobayashi and Y. Hotta, AIP Advances, vol.13, 095211 (2023).

FR-11. Electronic and Magnetic Properties of Random Fcc Ce_3Al Alloy

R. Wu[1], Y. Li[2], E. Mijit[3], Y. Amakai[1]
[1]Muroran Institute of Technology, Muroran, Japan, [2]Inner Mongolia Normal University, Hohhot, China, [3]Sorbonne Université, Paris, France

Ce-based intermetallic compounds exhibit a variety of strongly correlated electron phenomena, including heavy-fermion behavior and the Kondo effect, originating from the hybridization between Ce 4*f* electrons and conduction electrons. Among them, Ce_3Al has attracted considerable attention because of its unusual electronic and magnetic properties. It is known to crystallize in two structural forms: the *a*-phase with a hexagonal close-packed (hcp) structure and the *b*-phase with a face-centered cubic (fcc) structure [1, 2]. Recently, a random fcc-Ce_3Al phase, suggested to involve disordered site occupation of Ce and Al in an fcc structure, was reported to form under high pressure from amorphous $Ce_{75}Al_{25}$ as the starting material [3], motivating further investigation of its electronic and magnetic properties.
In this work, we used a DC high-rate sputtering method and obtained a random fcc-Ce_3Al alloy. Its electronic and magnetic properties were investigated by X-ray diffraction, magnetic susceptibility, and X-ray photoelectron spectroscopy (XPS). X-ray diffraction confirms that the obtained sample has an fcc structure with the lattice constant of a = 5.64 Å. The temperature dependence of magnetic susceptibility follows a Curie-Weiss law at high

temperatures, and no magnetic ordering is observed down to 2 K. The effective paramagnetic moment per Ce atom is estimated to be μ_{eff} =2.13 m_B/Ce, which is significantly smaller than the value for the free Ce^{3+} ion (2.54 m_B/Ce, J = 5/2). The Ce3*d* spectrum in the XPS measurements exhibits the $4f^1$, $4f^2$, and $4f^0$ peaks. The Ce 4*f*-occupancy n_f is estimated to be 0.95, indicating that Ce remains nearly trivalent in the system. The presence of a pronounced $4f^2$ feature implies hybridization between the Ce 4*f* electron and the conduction electrons. Furthermore, the relative peak intensity ratio [$I(f^2)$/ $I(f^1)$]3*d*5/2 was evaluated and found to be approximately 73%, which is comparable to values reported for correlated Ce compounds [2]. These results indicate that the Ce 4*f* electrons remain nearly localized, while hybridization with conduction electrons persists in this structurally disordered fcc-type phase, which may account for the reduced magnetic moment observed in this system.

[1] W.-H. Li *et al.,* J. Appl. Phys., Vol. 83, p.6426-6428 (1998)
[2] K. Okuda *et al.,* J. Phys. Soc. Jpn., Vol. 58, p.2630-2633 (1989)
[3] *Q. S.* Zeng *et al.,* PNAS, Vol. 106, p.2515-2518 (2009)

FR-12. Magnetic behavior and Phase Diagram of $Ba_3Zn_{1-x}Ni_xRu_2O_9$ ($0 \leqq x \leqq 1$)

J. Sato, Y. Yasui
Physics, Meiji University, Kawasaki, Kanagawa, Japan

Competing magnetic exchange interactions and/or low-dimensional structures often leads to exotic and emergent magnetic phenomena, such as a quantum spin liquid, non-trivial order, dimer state, *etc*. This study picks up the series compounds $Ba_3MRu_2O_9$ (M = Zn, Ni, Ca, *etc.*). The M site can accommodate various divalent ions, and the Ru^{5+} ($4d^3$) ions have a local spin S = 3/2. The magnetic ground state of $Ba_3MRu_2O_9$ depends on the species of M. $Ba_3ZnRu_2O_9$ was reported to be a candidate quantum spin liquid (QSL) system [1]. For $Ba_3CaRu_2O_9$, the paired spins in the Ru_2O_9 dimer form a spin singlet, resulting in the non-magnetic ground state with a spin gap [2]. In contrast, $Ba_3NiRu_2O_9$ exhibits antiferromagnetic ordering at T = 95 K due to enhanced magnetic interactions provided by Ni^{2+} spins (S = 1). The previously reported magnetic structure of $Ba_3NiRu_2O_9$ is debatable [3, 4].

We focus on the solid solution spin system $Ba_3Zn_{1-x}Ni_xRu_2O_9$ ($0 \leqq x \leqq 1$), which provides a unique platform for exploring this relationship. The polycrystalline samples of various Ni-concentration for $Ba_3Zn_{1-x}Ni_xRu_2O_9$ have synthesized using the solid-state reaction method. Magnetic susceptibility (χ) measurements revealed that the χ values in the high temperature region T > 150 K increase with increasing x, reflecting the introduction of the Ni^{2+} spins. At low temperatures, the $\chi - T$ curves of $0.7 < x \leqq 1$ indicate existence in an antiferromagnetic transitions. In contrast, the $\chi - T$ curves of $0.2 < x \leqq 0.7$ exhibit thermal hysteresis below ~ 10 K, indicating characteristics of a spin glass or cluster-glass state of short-range ordering. The results of specific heat measurements further support these findings. We have observed magnetic Bragg peaks by powder neutron diffraction for $Ba_3Zn_{1-x}Ni_xRu_2O_9$ with x = 0.8, and 1. These results allowed the construction of a magnetic phase diagram of $Ba_3Zn_{1-x}Ni_xRu_2O_9$ over the full range of x, showing change from a novel magnetic state (x=0) to long-range antiferromagnetic order (x=1). This study demonstrates how chemical substitution can tune the competing magnetic exchange interaction, contributing to our understanding of the present system.

[1] I. Terasaki *et al.*: J. Phys. Soc. Jpn. 86 (2017) 033702.
[2] J.Darriet et al.:J.Solid State Chem.19(1976)213.
[3] P. Lightfoot *et al.*: J. Solid State Chem. 89 (1990) 174.
[4] J. T. Rijssenbeek *et al.*: J. Solid State Chem. 146 (1999) 65.

FR-13. Field-induced magnetization plateaus in a frustrated spin-1/2 Heisenberg antiferromagnet on a diamond-decorated honeycomb lattice

K. Karlova[1], J. Strecka[1], M. Rouxel[2], A. Honecker[2]
[1]Pavol Jozef Safarik University, Kosice, Slovakia, [2]LPTM, Cergy Paris University, Cergy-Pontoise, France, France

We investigate magnetization plateaus in a frustrated spin-1/2 Heisenberg antiferromagnet on a diamond-decorated honeycomb lattice in an external magnetic field. Using a combination of complementary numerical and analytical approaches, including density-matrix renormalization group, exact diagonalization, and sign-problem-free quantum Monte Carlo simulations, we analyze the magnetization process and its evolution with lattice geometry at zero as well as nonzero temperatures.

We consider both isotropic and distorted realizations of the diamond-decorated honeycomb lattice, extending previous results obtained for different distortion regimes. The interplay of geometric spin frustration, lattice geometry, and magnetic field leads to a rich sequence of fractional magnetization plateaus and field-induced phase transitions. Our results provide a unified picture of the plateau formation in this class of frustrated quantum magnets and highlight the robustness of the underlying mechanisms

across different lattice realizations. The investigated model displays in a presence of the external magnetic field intriguing discontinuous and continuous thermal phase transitions, which imply an enhanced magnetocaloric effect in the respective field regimes.

FR-14. Doping Effect on Paramagnetic-to-Nonmagnetic Phase Transition of $Ba_3BiRu_2O_9$

T. Nakagawa, Y. Yasui
Physics, Meiji University, Kawasaki, Kanagawa, Japan

$Ba_3BiRu_2O_9$ is composed of Ru_2O_9 units (Ru^{4+} spin dimers), which forms a triangular lattice and are stacked alternately with BiO_6 in layers. In this compound, the two Ru^{4+} spins ($4d^4$, spin S=1) form a singlet state as the temperature decreases. A unique behavior was reported for $Ba_3BiRu_2O_9$ at T_c = 175 K, which is a paramagnetic-to-nonmagnetic phase transition accompanied with a change in crystal structure, and singlet formation is strengthened [1,2]. This unique phase transition has only been reported in the case of M=Bi among the series of compounds $Ba_3MRu_2O_9$ (M=Bi, Ti, Zn, Co, *etc.*). The origin of this phase transition at T_c = 175 K remains unclear. Because Bi ions are generally reported to exhibit valency instability, it was proposed that the valency separation of the average valency Bi^{4+} into Bi^{3+} and Bi^{5+} is related to the origin of this phase transition [2,3]. In this study, to clarify whether valency instability for the Bi ions is involved in this phase transition, we performed a $Bi^{4+} \rightarrow Zr^{4+}$ substitution and investigated its effect on the phase transition.
Polycrystalline samples of $Ba_3Bi_{1-x}Zr_xRu_2O_9$ at x = 0, 0.05, and 0.10 were synthesized by solid-phase reaction method. After confirming that each sample is single-phase by X-ray diffraction, the phase transition was investigated by measuring specific heat and magnetic susceptibility. In both the magnetic susceptibility-temperature curves and the specific heat-temperature curves, an anomaly associated with the phase transition is observed at T_c = 175 K for x =0. By the Zr-doping, the anomaly becomes broadened for x = 0.05, and is not observed for x = 0.1. Therefore, it is revealed that substituting Bi with Zr^{4+} destabilizes the phase transition, and that the phase transition disappears with 10% substitution. On the other hand, previous studies reported that the phase transition remains until with $Bi \rightarrow La^{3+}$ substitution [3]. Then, the doping effect for $Bi \rightarrow La^{3+}$ substitution on the phase transition is smaller than in the case of Zr^{4+}, suggesting that the presence of Bi^{3+}/Bi^{5+} due to the valence instability of Bi, is essentially involved in the phase transition in this material.

[1] J. Darriet *et al.*: Eur. J. Solid State Inorg. Chem. 30, 273 (1993).
[2] W. Miiller *et al.*: Phys. Rev. B 84, 220406 (2011).
[3] P. E. R. Blanchard *et al.*: Inorg. Chem. 53, 952 (2014).

FR-15. Dynamics of Emergent Dipole-Moment Conservation in Spin Chains under a Magnetic-Field Gradient

C. Tachibana[1], T. Orito[1], D. Yamamoto[1, 2]
[1]Department of Physics, College of Humanities and Sciences, Nihon University, Setagaya, Tokyo, Japan, [2]RIKEN Center for Quantum Computing, Wako, Saitama, Japan

Spin glasses (SG), characterized by frozen disordered spin configurations, and many-body localization (MBL), marked by suppressed transport and entanglement growth, are representative phenomena in many-body systems with strong randomness. These two perspectives have recently been connected in the context of anomalous relaxation dynamics, as exemplified by the MBL-SG regime [1]. Against this background, randomness has played a central role in discussions of ergodicity breaking, whereas recent studies have reported a disorder-free route to obstructed thermalization in spin models subjected to a magnetic-field gradient. This phenomenon, known as Stark many-body localization (SMBL), can be understood as an interacting extension of Wannier–Stark localization. Conventional MBL is understood in terms of local integrals of motion, which explain its non-ergodic behavior. In contrast, SMBL is often interpreted as a consequence of Hilbert-space fragmentation (HSF) associated with emergent dipole-moment conservation arising from the Stark term [2, 3].
In this work, we consider the non-equilibrium dynamics of localization in one-dimensional spin-1/2 XY and XXZ models in the presence of a linear magnetic-field gradient. In these systems, the interpretation of HSF is supported mainly by spectral signatures that indicate the emergence of a conserved quantity, while the dynamical aspects of its emergence remain not fully understood. To address this issue, we employ a diagnostic tool called entanglement asymmetry, which characterizes how strongly a subsystem state reflects the symmetry-sector structure [4]. Using this tool, we investigate the dynamical relation between the emergence of dipole-moment conservation and its dependence on the initial state. We find that the dynamics retains memory of the initial degree of symmetry breaking via the emergent constraint. This perspective may provide a unified understanding of SMBL dynamics across a range of initial states.

[1] P. Brighi, M. Ljubotina, and M. Serbyn, Phys. Rev. B 111, L220202 (2025).
[2] E. van Nieuwenburg, Y. Baum, and G. Refael, Proc. Natl. Acad. Sci. U.S.A. 116, 9269 (2019).
[3] P. Sala, T. Rakovszky, R. Verresen, M. Knap, and F. Pollmann, Phys. Rev. X 10, 011047 (2020).
[4] S. Liu, H.-K. Zhang, S. Yin, S.-X. Zhang, and H. Yao, Science Bulletin 70, 3991 (2025).

FR-16. Quantum Effects on the Magnetization Curve in the Triangular-Lattice Spin-Chain Compound $CsFeCl_3$

T. Yamane, D. Yamamoto
Department of Physics, College of Humanities and Sciences, Nihon University, Setagaya-Ku, Tokyo, Japan

$CsFeCl_3$ is a frustrated magnet in which Fe^{2+} ions form ferromagnetic one-dimensional chains along the *c* axis and exhibit triangular-lattice antiferromagnetism in the *ab* plane. Its low-energy magnetic properties are described by a pseudospin $S = 1$ model. Due to the strong easy-plane single-ion anisotropy, the ground state is a singlet with $S^z = 0$ [1]. Under an applied magnetic field, the excitation gap closes after a nonmagnetic region, and the magnetization increases almost linearly with the field [2]. The model parameters, namely the intrachain ferromagnetic interaction J_0, the inter-chain antiferromagnetic interaction J_1, and the single-ion anisotropy D, have been estimated by fitting neutron-scattering data [3] and high-field ESR results [4,5] within mean-field and linear spin-wave approximations. However, these parameter sets fail to reproduce the nearly linear increase observed experimentally, instead giving a strongly downward-curved magnetization curve. This discrepancy indicates that the magnetization process cannot be fully captured at this level of approximation and suggests a limitation of the conventional approach.

In this work, we study quantum effects on the magnetization curve of $CsFeCl_3$ to resolve the discrepancy. In general, for gapless systems, classical (mean-field) approaches predict a linear magnetization at zero temperature, while quantum effects introduce a downward curvature due to zero-point fluctuations. In $CsFeCl_3$, however, as mentioned above, the mean-field result already shows a downward curvature, whereas experiments show an almost linear dependence. To address this, we use a cluster mean-field approach that treats intrachain correlations exactly within a finite cluster. As a result, for parameter sets that reproduce the observed excitation gap, quantum effects suppress the curvature of the magnetization curve, leading to a more linear field dependence in agreement with experiment. This finding contrasts with the usual expectation that quantum effects enhance nonlinear behavior and demonstrates that, in gapped systems, they instead enhance the linearity of the magnetization curve, providing an important guideline for interpreting experimental results.

[1] H. Yoshizawa, W. Kozukue, K. Hirakawa, J. Phys. Soc. Jpn. 49, 144 (1980).
[2] M. Chiba et al., Solid State Commun. 63, 5 (1987).
[3] S. Hayashida et al., Sci. Adv. 5, eaaw5639 (2019).
[4] K. Nihongi et al., arXiv:2512.21682.
[5] S. Okubo et al., J. Phys. Soc. Jpn. 38, 011137 (2023).

FR-17LB. Symmetry aspects of Yu-Shiba-Rusinov bands in magnetic atomic chains on a superconductor

B. Nyári[1], A. Lászlóffy[2], L. Szunyogh[1], B. Ujfalussy[2], L. Rózsa[2]
[1]Department of Theoretical Physics, Budapest University of Technology and Economics, Budapest, Hungary, [2]Wigner Research Centre for Physics, Budapest, Hungary

Deploying magnetic atoms on superconducting surfaces leads to the formation of Yu-Shiba-Rusinov (YSR) states. Organizing the magnetic impurities to form a chain leads to band formation of YSR states. In the energy spectrum of finite chains, under given conditions, one can obsereve the formation Majorana zero modes (MZMs), as topologically protected end states. Also have been proposed as a promising basis for Majorana qubits offering great potential for topological quantum computation.
Here, we present the study of Mn chains constructed on a Nb(110) and on a Ta(110) substrate using first-principles calculations. We demonstrate that even and odd YSR states with respect to mirroring on the symmetry plane containing the chain have different dispersions. On the Nb substrate, a wide but topologically trivial minigap is opened in the even states by the spin–orbit coupling, while the odd states display signatures of precursors of MZMs with a smaller minigap. On the Ta substrate, the stronger spin–orbit coupling increases the hybridization between the bands, but no clear minigap can be observed in either of them. These findings highlight the influence of symmetries on interpreting the spectroscopic signatures of candidates for MZMs.
Phys. Rev. B 112, 115414 (https://doi.org/10.1103/cvnq-glw1)

FR-18LB. Annealing-controlled magnetic ordering in $MnSb_2Te_4$

L. Zeni Cunha[1], A. van Dijke[1], N. Hitzelberger[1], L. Corredor[2], A. Isaeva[2]
[1]Institute of Physics, University of Amsterdam, Amsterdam, Netherlands, [2]Physics, TU Dortmund University, Dortmund, Germany

$Mn_{1+x}Sb_{2-x}Te_4$ is a layered ferrimagnet of interest as a candidate magnetic topological material. Mn/Sb site mixing and Mn enrichment can raise its Curie temperature from ca. 25 K to ca. 73 K [1,2]. However, the relative roles of total Mn content and its distribution among crystallographic sites in determining the magnetic structure remain difficult to disentangle. Here, we investigate magnetic tuning through thermal treatment at fixed nominal compositions and its effect on different possible magnetic ordering temperatures. We establish a reproducible solid-state preparation route for polycrystalline $Mn_{1+x}Sb_{2-x}Te_4$ and systematically vary the annealing conditions. For the nominal 1:2:4 stoichiometric composition, increasing the annealing temperature from 550 to 640 °C reproducibly raises T_C from 25 to 34 K across several batches (Figure 1), whereas extending the annealing duration from 20 h to 6 days produces no detectable change.

Combined X-ray and Neutron Powder Diffraction with Rietveld refinement suggests that the enhancement of T_C is associated with increased Mn occupancy of the van der Waals gap, without a comparably substantial change in Mn/Sb mixing within the septuple layers. Whereas interlayer Mn has previously been reported in $Mn_{1.9}Sb_{1.39}Te_4$ [2], our results suggest that this structural degree of freedom may also be relevant in samples with nominal $MnSb_2Te_4$ stoichiometry. Annealing-dependent cation redistribution may therefore provide a means of modifying interlayer magnetic exchange.

As a complementary test, we investigated the effect of increasing Mn content and obtained, for the first time, a polycrystalline $Mn_{1.9}Sb_{1.39}Te_4$ sample by annealing at 640 °C. The sample shows diffraction changes consistent with enhanced interlayer Mn occupancy, $T_C \approx 60$ K, and complex low-temperature magnetization behaviour, possibly arising from distinct magnetic interactions between different Mn^{2+} sublattices. Together, these results highlight thermal history and Mn concentration as tuning knobs for optimizing magnetic ordering in this materials family.

[1] M. Sahoo et al., *Mater. Today Phys.* 38, 101265 (2023), DOI: 10.1016/j.mtphys.2023.101265.
[2] E. Kochetkova et al., *Chem. Mater.* 37, 1446–1456 (2025), DOI: 10.1021/acs.chemmater.4c02729.

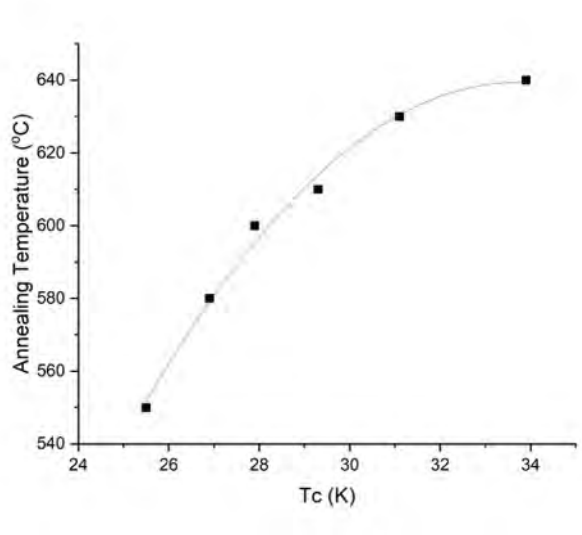


Figure 1. Annealing temperature as a function of Curie temperature (T_C) for $MnSb_2Te_4$ samples annealed for 24 h.

FR-19LB. Room-Temperature Ferromagnetism and Electronic Structure in Cr-Doped $PdTe_2$

S. Cheng[1], H. Shiu[1], T. Chuang[1], Y. Lai[1], W. Chen[1], D. Wei[1], H. Wei[1], C. Lue[2], Y. Hsu[1]
[1]National Synchrotron Radiation Research Center, Hsinchu, Taiwan, [2]Department of Physics, National Cheng Kung University, Tainan, Taiwan

Two-dimensional (2D) transition metal dichalcogenides (TMDs) exhibit diverse electronic and magnetic properties that can be tailored through various approaches, such as defect engineering and chemical doping.[1-4] Here, we investigate Cr-induced magnetism in intrinsically nonmagnetic 1T-palladium ditelluride ($PdTe_2$). Surface vacancies were first introduced into $PdTe_2$ to create active sites for Cr incorporation, following by deposition of a thin chromium layer. The Cr-capped samples were subsequently thermally annealed over a temperature range from room temperature to ~ 503 K. The overall 1T crystal structure is preserved after Cr incorporation, despite local lattice distortion. Synchronized X-ray photoelectron spectroscopy (XPS) was employed *in situ* to monitor the evolution of the Cr, Pd, and Te chemical states during Cr incorporation and thermal annealing (Figure 1). The correlated evolution of the Cr 2p, Pd 3d, and Te 3d core levels, including the emergence of an additional Te 3d component at lower binding energy, supports the formation of Cr-Te bonding

during thermal annealing. Magnetic measurements reveal a pronounced room-temperature ferromagnetic-like response following Cr incorporation (Figure 2). The net magnetic moment exhibits a strong dependence on the surface-vacancy concentration, reaching an optimum at a ~36 % vacancy concentration. These results demonstrate an effective route for engineering room-temperature ferromagnetic-like behaviour in 1T-$PdTe_2$ through the combined control of surface vacancies, Cr incorporation, and thermal annealing. The detail results will be presented in our forthcoming reports.

1. Li Y, Zhou Z, Zhang S, Chen Z. "MoS_2 Nanoribbons: High Stability and Unusual Electronic and Magnetic Properties", J. Amer. Chem. Soc. 130, 16739-16744 (2008).
2. Pan H, Zhang Y-W. "Tuning the Electronic and Magnetic Properties of MoS_2 Nanoribbons by Strain Engineering", J. Phys. Chem. C 116, 11752-11757 (2012).
3. Dolui K, Rungger I, Das Pemmaraju C, Sanvito S. "Possible doping strategies for MoS_2 monolayers: An ab initio study", Phys. Rev. B 88, 075420 (2013).
4. Ramasubramaniam A, Naveh D. "Mn-doped monolayer MoS_2: An atomically thin dilute magnetic semiconductor",. Phys. Rev. B 87, 195201 (2013).

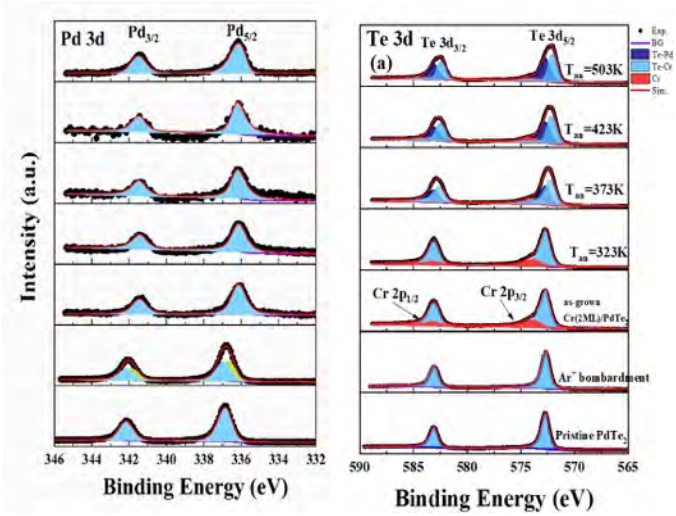


Fig. 1. Chemical characterization of $Pd_{0.71}Cr_{0.29}Te_2$: XPS spectra of the Pd 3d, Te 3d, and Cr 2p core levels measured after Ar^+ bombardment, deposition of a 2 ML Cr layer, and subsequent annealing at different temperatures.

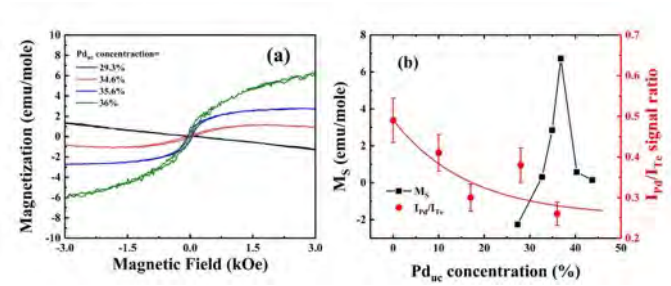


Fig. 2. Emergence and tuning of ferromagnetism in the Cr-incorporated $PdTe_2$: Effect of surface vacancy concentration on the magnetic response. (a) Room-temperature M-H loops measured for samples prepared with different surface vacancy concentrations prior to the deposition of a 2 ML Cr layer. (b) Saturation magnetization (M_S, ■) and the corresponding Pd/Te signal intensity ratio (●) obtained from XPS as a function of surface vacancy concentration.

FR-20LB. High-temperature spin glass behavior at the interface of Ni/MoS_2 heterostructures

T. Kidd[1], P. Shand[2], E. Ahmetasevic[2], P. Nguyen[2], T. Porter[2], C. J. Cunningham[2], H. Harms[2], S. Diallo[2], G. Ye[3], P. Lukashev[2], L. Zhou[4], A. J. Stollenwerk[2], R. He[5]
[1]Ames National Laboratory, Ames, Iowa, United States, [2]Physics, University of Northern Iowa, Cedar Falls, Iowa, United States, [3]Electrical Engineering, Texas Tech University, Lubbock, Texas, United States, [4]Materials Sciences & Engineeing, University of Virginia, Charlottesville, Virginia, United States, [5]Physics, The University of Texas at Arlington, Arlington, Texas, United States

Layered van der Waals (vdW) crystals have emerged as an important class of materials with great potential for next-generation electronic and optoelectronic devices. Their highly anisotropic crystal structure induces a variety of novel electronic and optical properties. Furthermore, their properties are easily tunable, for example by the inclusion of magnetic ions to induce a variety of magnetic phase transitions. In considering potential applications, it is necessary to achieve a fundamental understanding of the metal-vdW crystal interface. Metal contacts play a critical role in determining charge injection, spin transport, and other features important for device performance. Here, we present a comprehensive study of the high temperature spin glass behavior found in Ni/MoS_2 heterostructures, providing new insights into the magnetic interactions that emerge at the interface between magnetic metals and semiconducting vdW crystals. Deposition of Ni onto an MoS_2 substrate forms a granular Ni film with a relatively sharp interface. Measurements of resistance, magnetization, and Raman

spectroscopy all exhibit relaxation with temperature dependent lifetimes in magnetic field strengths up to 9 T and temperatures in excess of 300K. The Raman relaxational response exhibits anisotropy consistent with hybridization of Ni and Mo at the interface, as predicted by DFT calculations. At low temperatures, hysteresis loops show ferromagnetic behavior with a shift due to exchange bias. Combined, these results indicate the spin glass behavior arises at the interface of the Ni/MoS_2 heterostructures. The persistence of spin glass behavior in high fields and relatively high temperatures arises from the strong random anisotropy at the interface generated by disorder and Ni-Mo hybridization.

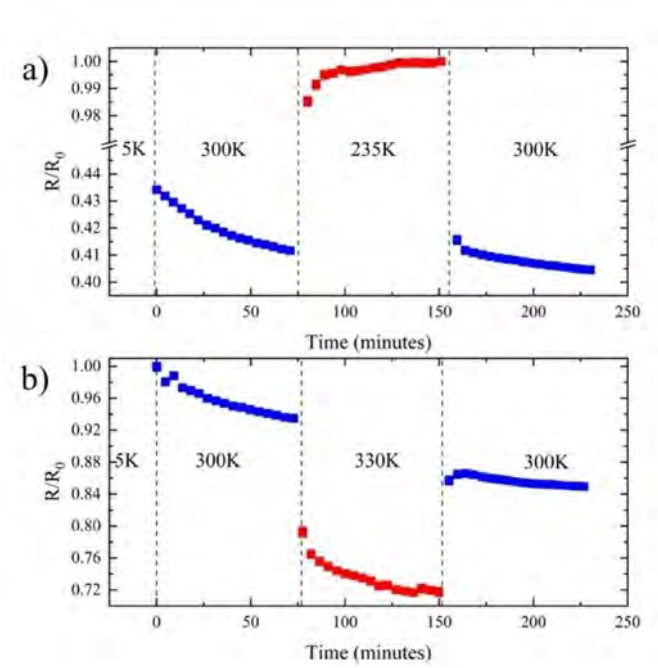
1. Kidd, T. E.; Shand, P. M.; Stollenwerk, A.; Gorgen, C.; Moua, Y.; Stuelke, L.; Lukashev, P. V. Large-Field Magnetoresistance of Nanometer Scale Nickel Films Grown on Molybdenum Disulfide. *AIP Adv.* 2022, *12* (3). https://doi.org/10.1063/9.0000291

2. Agrinskaya, N. V.; Kozub, V. I.; Shumilin, A. V.; Sobko, E. Magnetoresistance in Semiconductor Structures with Hopping Conductivity: Effects of Random Potential and Generalization for the Case of Acceptor States. *Phys. Rev. B* 2010, *82* (7), 075201. https://doi.org/10.1103/PhysRevB.82.075201

3. Stollenwerk, A. J.; Stuelke, L.; Margaryan, L.; Kidd, T. E.; Lukashev, P. V. First Principles Study of Nearly Strain-Free Ni/WSe_2 and Ni/MoS_2 Interfaces. *J. Phys. Condens. Matter* 2021, *33* (42), 425001. https://doi.org/10.1088/1361-648X/ac1881.

4. Kong, L.; Wu, R.; Chen, Y.; Huangfu, Y.; Liu, L.; Li, W.; Lu, D.; Tao, Q.; Song, W.; Li, W. Wafer-Scale and Universal van der Waals Metal Semiconductor Contact. *Nat. Commun.* 2023, *14* (1), 1014. https://doi.org/10.1038/s41467-023-36715-6

5. Boff, M. A. S.; Canto, B.; Baibich, M. N.; Pereira, L. G. A Simple Formulation for Magnetoresistance in Metal-Insulator Granular Films with Increased Current. *J. Appl. Phys.* 2013, *113* (7).



Memory Effects in the Ni/MoS_2 interface
(a) Normalized resistance vs. time done under temperature cycling. The temperature starts at 300 K, is increased to 330 K, and is cooled back to the original temperature. Memory is not quite complete because the resistance does not return to the value it had before the temperature change. (b) Normalized resistance vs. time under temperature cycling. The temperature starts at 300 K, is cooled to 235 K, and is warmed back to the first temperature. Rejuvenation is present at the cooler temperature and memory is present when warmed back to the initial temperature. The applied magnetic field is perpendicular to the plane of the sample.

SESSION GA: SPIN-CHARGE-PHOTON CONVERSION: FROM LEDS TO LASERS

Co-Chair(s): Y. Lu, *Institut Jean Lamour, CNRS, Nancy, France* and H. Lu, *Chemistry, The Hong Kong University of Science and Technology, Hong Kong, Hong Kong*

Friday, November 6, 2026

08:30 AM-12:00 PM

Coral 3

GA-01. Developing spin light emitting diodes toward real optoelectronic applications

Y. Lu

Institut Jean Lamour, CNRS, Nancy, France

Spin light-emitting diodes (spin-LEDs), which can convert carrier spin polarization into photon circular polarization, are essential building block of various spin-optoelectronic concepts and have garnered significant interest over the past two decades [1]. These devices enable high-speed electrical control of light polarization through spin-photon interconversion and hold great potential for various applications such as optical communication, three-dimensional displays, and biomedical analysis. The concept of spin-LED has been proposed for nearly 50 years. While the first spin-LEDs were realized 25 years ago and a significant progress has been made, several key challenges remain before the practical realization: (1) achieving high circular polarization through efficient spin injection, (2) eliminating the need for an external magnetic field, and (3) enabling electrical control of polarization polarity. Recent breakthroughs in spin-LEDs demonstrate that these three challenges can be overcome. In this talk, I will present the state-of-the-art developments in spin-LEDs based on GaAs system, with a focus on the recent advancements in spin injectors that address the above three challenges [2-6].

References:

[1] R. Fiederling, M. Keim, G. Reuscher, W. Ossau, G. Schmidt, A. Waag & L. W. Molenkamp, *Injection and detection of a spin-polarized current in a light-emitting diode*, Nature 402, 787 (1999).

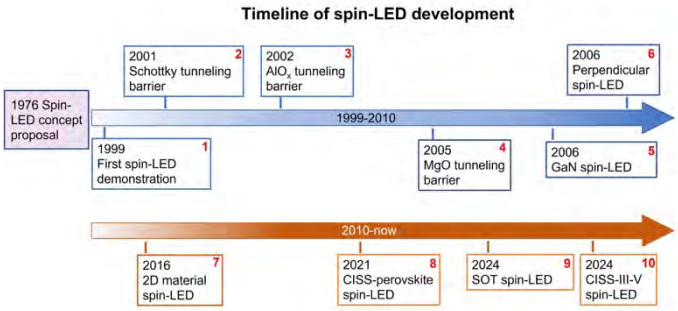
[2] P. Barate, S. H. Liang, T. T. Zhang, J. Frougier, B. Xu, P. Schieffer, M. Vidal, H. Jaffrès, B. Lépine, S. Tricot, F. Cadiz, T. Garandel, J. M. George, T. Amand, X. Devaux, M. Hehn, S. Mangin, B. Tao, X. F. Han, Z. G. Wang, X. Marie, Y. Lu & P. Renucci, *Bias Dependence of the Electrical Spin Injection into GaAs from Co-Fe-B/MgO Injectors with Different MgO Growth Processes*, Phys. Rev. Appl. 8, 054027 (2017).

[3] A. E. Giba, X. Gao, M. Stoffel, X. Devaux, B. Xu, X. Marie, P. Renucci, H. Jaffrès, J.-M. George, G. Cong, Z. Wang, H. Rinnert & Y. Lu. *Spin Injection and Relaxation in p-Doped (In,Ga)As/GaAs Quantum-Dot Spin Light-Emitting Diode at Zero Magnetic Field*, Phys. Rev. Appl. 14, 034017 (2020).

[4] F. Cadiz, A. Djeffal, D. Lagarde, A. Balocchi, B. S. Tao, B. Xu, S.H. Liang, M. Stoffel, X. Deveaux, H. Jaffres, J.M. George, M. Hehn, S. Mangin, H. Carrere, X. Marie, T. Amand, X. F. Han, Z. G. Wang, B. Urbaszek, Y. Lu & P. Renucci, *Electrical initialization of electron and nuclear spins in a single quantum dot at zero magnetic field*, Nano Lett. 18, 2381 (2018).

[5] S. H. Liang, T. T. Zhang, P. Barate, J. Frougier, M. Vidal, P. Renucci, B. Xu, H. Jaffrès, J.-M. George, X. Devaux, M. Hehn, X. Marie, S. Mangin, H. X. Yang, A. Hallal, M. Chshiev, T. Amand, H. F. Liu, D. P. Liu, X. F. Han, Z. G. Wang & Y. Lu, *Large and robust electrical spin injection into GaAs at zero magnetic field using an ultrathin CoFeB/MgO injector*, Phys. Rev. B 90, 085310 (2014).

[6] P. A. Dainone, N. F. Prestes, P. Renucci, A. Bouché, M. Morassi, X. Devaux, M. Lindemann, J.-M. George, H. Jaffrès, A. Lemaitre, B. Xu, M. Stoffel, T. Chen, L. Lombez, D. Lagarde, G. Cong, T. Ma, P. Pigeat, M. Vergnat, H. Rinnert, X. Marie, X. Han, S. Mangin, J.-C. Rojas Sanchez, J.-P. Wang, M. C. Beard, N. C. Gerhardt, I. Zutic & Y. Lu, "Controlling the helicity of light by electrical magnetization switching", Nature 627, 783 (2024).



Timeline of spin light-emitting diode (spin-LED) development with ten milestones. 2D, two dimensional; CISS, chirality induced spin selectivity; SOT, spin-orbit torque.

GA-02. Nanosecond and Field-Free Magnetization Switching using Chromium Orbital Torque for LED Helicity Control

R. T. Victor[1], A. Dainone[2], G. Lan[1], A. Pezo[1], Y. Xu[1], S. Collin[1], F. Godel[1], Y. Lu[2], N. Reyren[1], H. Jaffrès[1], J. George[1]
[1]Laboratoire Albert Fert, Palaiseau, France, [2]Institut Jean Lamour, Université de Lorraine, Nancy, France

Controlling magnetization via spin-orbit torques (SOT) is a promising pathways for spintronic devices. Recent proposals integrate information processing, storage, and transmission through spin light-emitting diodes (spin-LEDs) where the light polarization is defined by the orientation of a magnetic layer controlled via SOTs [1]. However, device implementation requires SOT current below the LED's Schottky barrier. It was recently proposed to use as a supplementary effect the orbital momentum of light element. However, the origin of this orbital polarization is still an open discussion [2-5]. To address these challenges we experimentally investigated the impact of adding a thin layer of Cr.

Using harmonic Hall measurements, we demonstrate that introducing a Cr layer into traditional heavy-metal-based systems (specifically CoFeB/W) enhances damping-like torque (DLT) efficiency by up to 5 times compared to heavy metals that rely solely on the spin Hall effect. This enhancement is attributed to an orbital polarization in Cr, which is efficiently converted into a spin current either in the heavy metal or ferromagnetic layer, exerting a stronger spin-orbit torque. The SOT magnetization switching threshold, evaluated via magneto-transport and Kerr microscopy, is considerably reduced due to the increase of the DL efficiency. Furthermore, as shown in Fig. 1, the DLT and the inverse of the critical electric field follow the same trend, revealing the decisive role of the DLT in magnetization reversal.

It is then possible to electrically control the circular polarization of a spin LED by using SOT. The addition of the Cr layer enable magnetization reversals with nanoseconds pulses and in the absence of an applied magnetic field (Fig. 2), usually required in standard SOT devices. Due to the lower resistivity of Cr compared to traditional heavy metals, a fourfold reduction in power consumption for switching was observed. This low-power operation is essential for preserving the device's integrity and enables nanosecond field-free operation.

[1] P. A. Dainone, N. Figueiredo, Nature, 627, 783-788 (2024).
[2] D. Lee, D. Go, Nature Communications, 12, 6710 (2021).
[3] T. Valet, H. Jaffrès, V. Cros, Phys. Rev. Lett. 135, 256301 (2025).
[4] D. Go, F. Freimuth, Physical review research 2, 033401 (2020).f
[5] S. Lee, M.-G. Kang, D. Go, Communications Physics 4, 234 (2021).

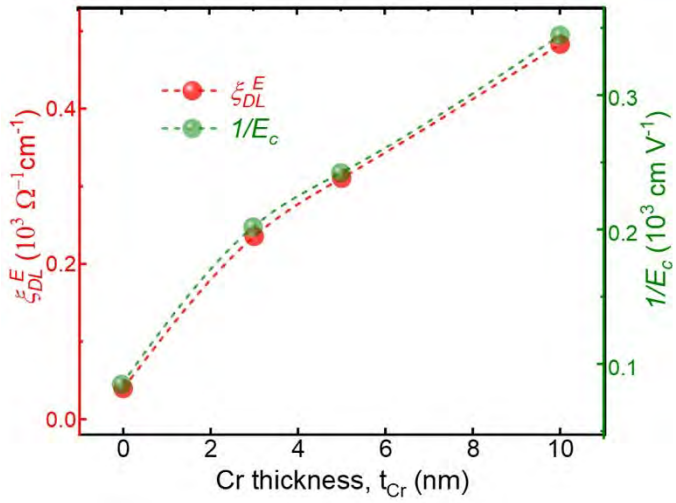


Fig.1 Damping-like torque efficiency (left axis) and the inverse of the critical electrical field (right axis) versus chromium thickness.

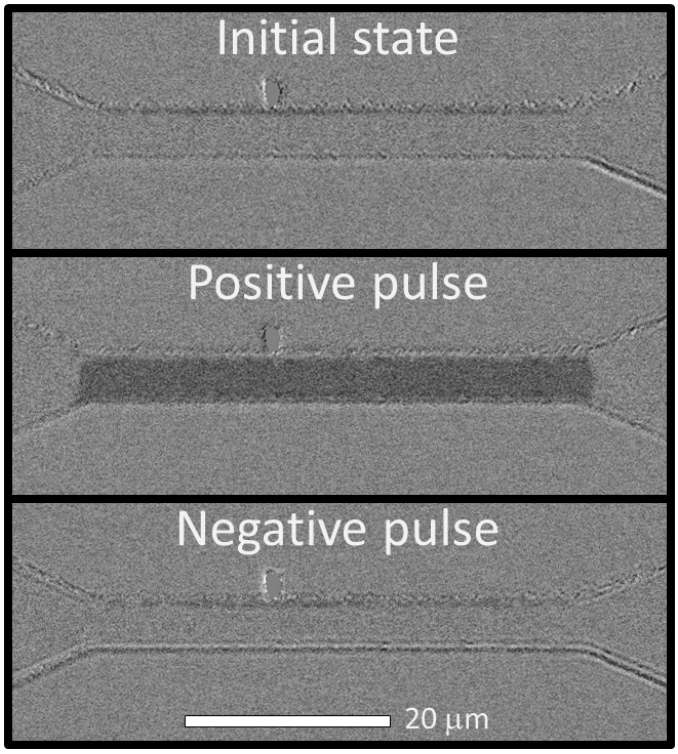


Fig. 2 Kerr microscopy of SOT magnetization switching.

GA-03. Spin-Charge-Photon Conversion and Emission in Electrically Driven Quantum Dots

C. Wijesundara[1], V. Iglesias-Cardinale[1], Y. Lu[2], H. Fotso[1], T. Thomay[1]
[1]Physics, SUNY at Buffalo, Buffalo, New York, United States, [2]Institut Jean Lamour, Nancy, France

Spin-injected, electrically contacted ensembles of InAs/GaAs quantum dots produce circularly polarized single-photon emission, where the helicity is determined by the spin polarization of the injected electrons. A ferromagnetic CoFeB spin-injection layer with perpendicular magnetic anisotropy and an MgO tunnel barrier filters carrier spins prior to injection into the quantum-dot active region, yielding circular polarization degrees up to 35%. These devices realize direct spin-charge-photon conversion in an electrically driven, microelectronics-compatible quantum light source that operates without an external pump laser. Using an extended Hanbury Brown–Twiss interferometer with four detectors and time-tagged readout, we measure time-resolved photon-number statistics that resolve up to |3> Fock states within a single excitation cycle. While single-photon (n=|1>) emission tracks the electrical excitation pulse as expected, the two-photon (n=|2>) statistics exhibit pronounced oscillatory features at multiple temporal positions within the pulse. These oscillations vanish upon demagnetization of the spin-injection layer, establishing a direct link between the multi-photon emission dynamics and the spin polarization of the injected carriers. The observations indicate that spin injection controls not only the helicity of the emitted photons but also higher-order temporal correlations of the emission. Theoretical simulations to identify a consistent microscopic model are underway. The platform thus opens a route to electrically driven, spin-controlled single- and multi-photon Fock-state sources and provides a testbed for spin-conditioned multi-emitter dynamics in solid-state quantum light sources.

S. H. Liang, T. T. Zhang and P. Barate, Phys. Rev. B., Vol. 90, p.085310 (2014)
A. E. Giba, X. Gao and M. Stoffel, Phys. Rev. Applied., Vol. 14, p.034017 (2020)
V. G. Truong, P.-H. Binh and P. Renucci, Appl. Phys. Lett., Vol. 94, p.141109 (2009)
P. A. Dainone, N. Figueiredo Prestes and P. Renucci, Nature., Vol. 627, p.783 (2024)

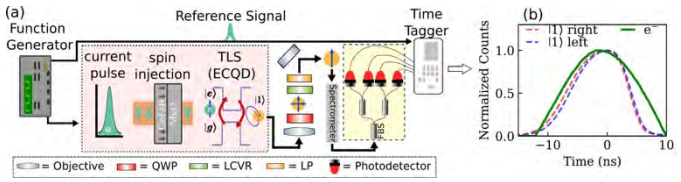


Fig. 1. (a) Experimental setup. Pulsed electrical excitation from a function generator drives carriers through a CoFeB/MgO spin-injection layer into an InAs/GaAs quantum-dot active region; the circularly polarized photoluminescence passes through a QWP/LCVR/LP polarization-analysis stage and is detected by a four-detector extended Hanbury Brown–Twiss interferometer with time-tagged readout. (b) Time-resolved single-photon emission: σ+ (|1> right) and σ- (|1> left) helicities track the electrical excitation pulse (e-).

GA-04. Chirality-driven Spin and Orbital Transfer between Electrons and Light

B. Yan
Physics, Pennsylvania State University, State College, Pennsylvania, United States

Chirality, exemplified by non-superimposable mirror images in systems such as DNA, plays a fundamental role in determining electronic properties [1]. In this talk, I will show that chirality generically gives rise to orbital–momentum locking as a universal feature of electronic states in chiral materials [2]. Under external stimuli, this orbital–momentum locking induces orbital polarization and concomitant spin polarization of charge carriers. These electronic polarizations can be efficiently transferred to the helicity of light in optoelectronic processes. Based on this principle, we have realized unconventional circularly polarized light-emitting diodes, in which the light helicity can be actively switched by the direction of current flow or the emission geometry [3,4].

[1]Yan B, Structural Chirality and Electronic Chirality in Quantum Materials Annu. Rev. Mater. Res. 54:97–115 (2024).
[2] Liu, Y., Xiao, J., Koo, J. & Yan, B. Chirality-driven topological electronic structure of DNA-like materials. Nat. Mater. 20, 638–644 (2021).
[3] Wan, L., Liu, Y., Fuchter, M.J. et al. Anomalous circularly polarized light emission in organic light-emitting diodes caused by orbital–momentum locking. Nat. Photon. 17, 193–199 (2023).
[4] Furlan, F., Šámal, M., Rybáček, J. et al. Electrical control of photon spin angular momentum in organic

electroluminescent materials. Nat. Photon. 19, 1361–1366 (2025).



GA-06. (110)-Oriented III–V Heterostructures for Room-Temperature Spin Lasers

S. Iba[1], Y. Ohno[1, 2]
[1]National Institute of Advanced Industrial Science and Technology (AIST), Tsukuba, Japan, [2]University of Tsukuba, Tsukuba, Japan

Spin lasers, which exploit spin-dependent optical transitions in the active region, have attracted growing interest because they enable static and dynamic control of output polarization for optical communications, computing, and sensing [1,2]. However, compared with spin-LEDs for which high room-temperature performance has already been demonstrated [3], spin lasers with electrical spin injection inevitably require a more complex device architecture, which has so far limited their operation to low temperatures [4], leaving major challenges to be addressed toward room-temperature lasing.
One key challenge is suppressing electron spin relaxation in semiconductors. We have proposed using (110)-oriented III–V quantum wells (QWs) and superlattice structures (SLs), which are expected to provide nanosecond-scale spin relaxation times at room temperature, as the active region and the spin-transport layer of spin lasers, respectively [5–8]. Through systematic crystal growth by molecular beam epitaxy, we have successfully fabricated high-quality (110) (In)GaAs/AlGaAs QWs and SLs. Moreover, for (110) SLs we found that the electron spin relaxation time depends on both the tunnel-barrier thickness and the number of periods, indicating that a target lifetime can be engineered at room temperature. We have also successfully reproduced these trends quantitatively, in good agreement with experiment, using our in-house Monte Carlo simulation method [9].
Another key challenge is electrical spin injection into the active region. While spin injection into (100) GaAs has been extensively studied, investigations for (110) GaAs remain limited and face many unresolved issues. We are therefore exploring both oxide tunnel junctions and Schottky junctions as candidate spin-injection contacts for (110) GaAs. In this talk, we will present our latest progress on these approaches and discuss the outlook toward room-temperature spin lasers.
[1] M. Lindemann *et al*., Nature 568, 212 (2019). [2] I. Zutic *et al*., Solid State Commun. 316, 113949 (2020). [3] P. Dainone *et al*., Nature 627, 783 (2024). [4] D. Basu *et al*., Appl. Phys. Lett. 92, 091119 (2008). [5] Y. Ohno, S. Iba *et al*., Appl. Phys. Express 13, 123003 (2020). [6] S. Iba *et al*., Micromachines 12, 1112 (2021). [7] S. Iba, Y. Ohno, Appl. Phys. Express 17, 033002 (2024). [8] Y. Ohno, S. Iba, R. Okamoto, J. Appl. Phys. 137, 093902 (2025). [9] Y. Ohno, S. Iba, Appl. Phys. Lett. 128, 082401 (2026).

GA-07. Spin-polarised surface plasmon polaritons generated at Ag/oxide interfaces

A. Lee[1], H. Koizumi[1], E. Moedl[1], D. Oue[2], M. Matsuo[4], A. Hirohata[1, 3]
[1]CSIS, Tohoku University, Sendai, Japan, [2]RIKEN, Wako, Japan, [3]Chemical Physics of Solids, Max Planck Institute, Dresden, Germany, [4]Kavli Institute, Beijing, China

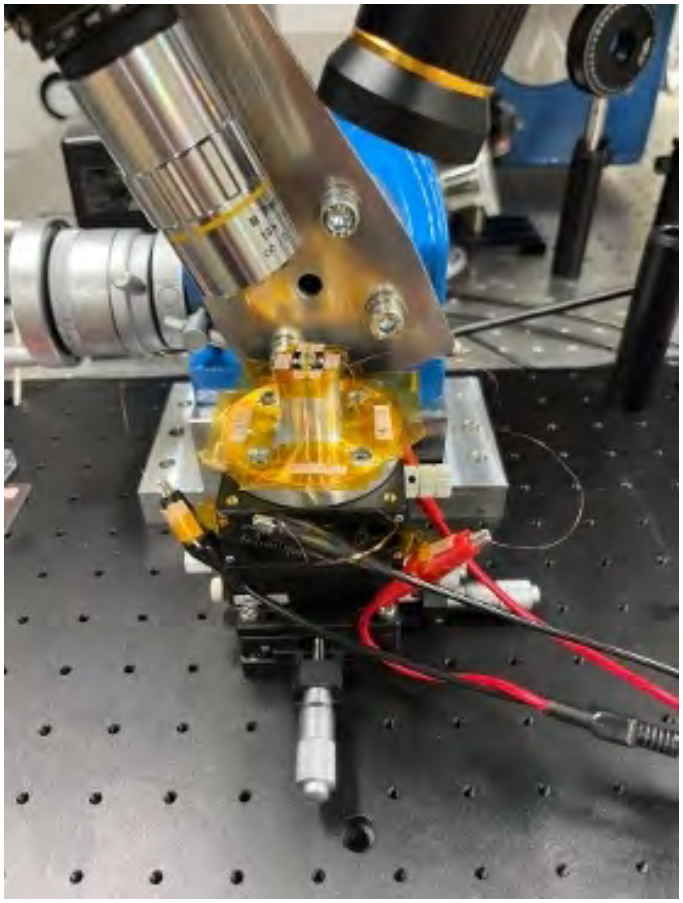
Surface plasmon polaritons (SPPs) have been attracting significant attention as a key platform for data coupling spintronic and opto-spintronic devices [1]. SPPs can be generated by a strong interaction occurred at a non-magnetic metal/oxide insulator interface, allowing an electromagnetic field to be confined beyond the diffraction limit. SPPs are typically within a PHz regime, which can induce a gradient in magnetic moments in a non-magnetic metal and a resulting spin-polarised electrical current.
In this study, SPP-induced spin currents were measured as an inverse spin Hall signal in a Ag/Au bilayer deposited

using ultrahigh vacuum sputtering on a variety of substrates, including SiO_2, γ-Fe_2O_3 and MgO. Among the series of non-magnetic metals investigated, Ag exhibited the strongest SPP signals in our studies. The laser beam contains both *s*- and/or *p*-polarisation by passing through a linear polariser. The laser beam was introduced onto the sample through a half-cylindrical prism at the center of the bilayer and the beam incident angle was controlled from 20 to 70 degrees relative to the film plane with a step of 3 degrees. The inverse spin Hall signals were then measured as a voltage using a source meter (Keithley, 2182) via electrical contacts at the corners of the films. The measurements were carried out up to 150 repetitions with 2 s interval to eliminate the Joule heating by laser introduction at each angle.

For a Ag/SiO_2 sample, a clear Hall voltage signal was observed showing a pronounced dependence on the incident angle. A well defined maximum was measured to be at the incident angle of approximately 52 degrees, which agrees well with the theoretical prediction [1].

This work was supported by the Cooperative Research Project from the Center for Science and Innovation in Spintronics (Core Research Cluster) of Tohoku University, the Japan Science and Technology Agency (JST) Adopting Sustainable Partnerships for Innovative Research Ecosystem (ASPIRE) programme (No. JPMJAP2409) and the Ministry of Education, Culture, Sports, Science and Technology (MEXT) X-nics (No. JPJ011438).

[1] D. Oue and M. Matsuo, *New J. Phys.* 22, 033040 (2020).



Experimental setup of the SPP generation at a metal/oxide interface.

GA-08. Harnessing plasmonic heating for switching in antiferromagnets

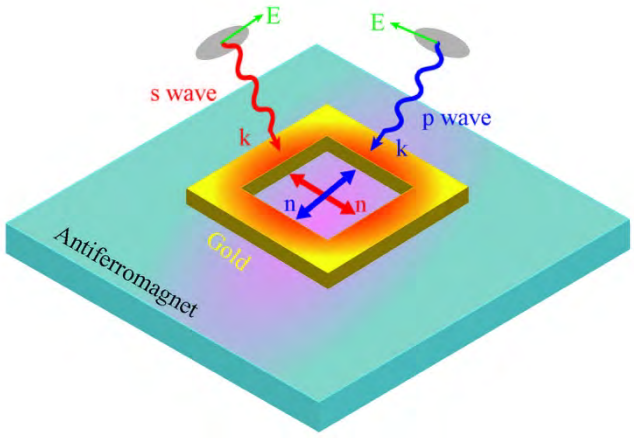
H. Yuan[1], Y. Wu[2], O. Gomonay[3]
[1]Zhejiang University, Hangzhou, Zhejiang, China, [2]Fudan University, Shanghai, Shanghai, China, [3]Johannes-Gutenberg University Mainz, Mainz, Germany

Antiferromagnets (AFMs) are promising candidates for information processing due to their ultrafast dynamics and robustness against stray fields. However, the electric control of AFMs typically requires large current densities, where Joule heating becomes dominant and severely limits device performance. Despite substantial efforts have been made to reduce heat generation, achieving low-energy manipulation of AFM remains a major challenge. Here, we adopt a fundamentally different paradigm: rather than suppress heating, we demonstrate that the engineered nanoscale heating can be adopted as a functional resource for magnetic control.

Here we reveal a previously unrecognized physical mechanism in which plasmon-induced, highly anisotropic thermal fields generate directional strain that enables ultralow-energy switching of AFM domains. Using a simple hybrid nanostructure consisting of a gold nanoframe and AFM thin film, we show that two orthogonal AFM domains can be reversibly switched merely by alternating the polarization of the incident light. The required optical energy is three to six orders of magnitude lower than current-driven switching approaches. The underlying physics arises from the interplay of plasmonic excitations, inhomogeneous heating, and strain effects. Specifically, the optical excitation of the nanoframe produces a strongly anisotropic thermal-strain field, which exerts a torque on the AFM order. By tuning the polarization of the optical waves, the strain field can be selectively controlled to manipulate the AFM orders.

Our findings establish an optical route for controlling antiferromagnets and may and may pave the way for designing energy-efficient spintronic devices.

H. Y. Yuan, Yizheng Wu, and Olena Gomonay, *Harnessing Plasmonic Heating For Switching in Antiferromagnets. Phys. Rev. Lett. (in press).*



Schematic illustration of a gold nanoframe and magnetic thin film hybrid structure. The antiferromagnetic vector within the frame can be reversibly switched by alternating the polarizations of the incident light, enabled by plasmon-induced selective heating and strain effects.

SESSION GB: EXPLORING THE EFFECTS OF REDUCED DIMENSIONALITY ON FRUSTRATED QUANTUM MAGNETS

Chair(s): J. S. Gardner, *Materials Science and Technology, ORNL, Oak Ridge, Tennessee, United States*
Friday, November 6, 2026
08:30 AM-12:00 PM
Coral 5

GB-01. Quantum Criticality and Dimensional Reduction of a Sawtooth-Chain Material

L. Stödter
JCNS at MLZ, Forschungszentrum Jülich GmbH, Garching, Germany

Quantum spin systems with geometrical frustration are characterized by their highly degenerate ground states which make them susceptible to tuning by pressure or an external magnetic field [1]. Such tuning can lead to quantum phase transitions from ordered to disordered states, or vice versa, and the emergent quantum critical points (QCPs) determine the deformed entropy landscapes in the respective phase diagrams. There is a fundamental interest in using the properties arising from such distorted entropy landscapes for applications (e.g. the magnetocaloric effect for low-temperature cooling [2,3]). Here, I will focus on the changes of the dimensionality of the spin system at a quantum phase transition in a real material.

I will discuss in my talk the magnetic properties of the copper mineral atacamite $Cu_2Cl(OH)_3$, a frustrated sawtooth-chain compound where the non-uniform chain units [J ~ 336 K (basal-basal), J' ~ 102 K (basal-apical)] are embedded into a weak network of interchain couplings [4,5]. I will show that the magnetic phase diagram of atacamite contains a field-induced QCP at 21.9(1) T (H || *c* axis) which emerges on a much lower energy scale compared to the leading terms in the spin Hamiltonian derived by means of density-functional theory [4,6]. The QCP separates field regions with and without long-range magnetic order. At the QCP, underpinned by numerical results, an effective dimensional reduction of the spin system from a 3D magnetically ordered state to an effective one-dimensional behavior occurs, but far from full field polarization of the material [6].

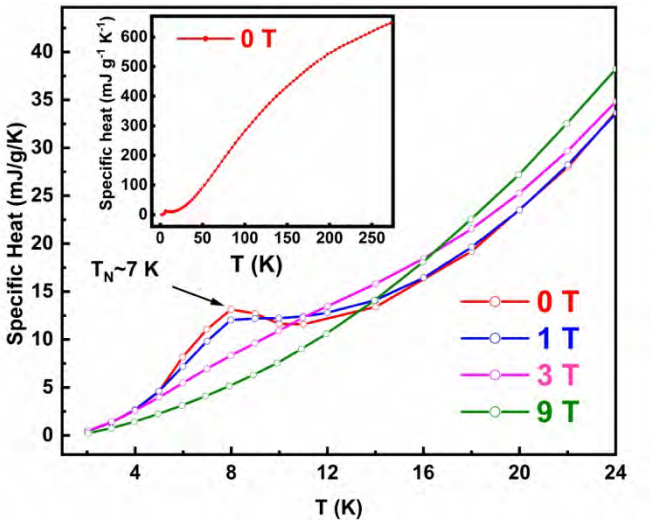
[1] M. Vojta, Rep. Prog. Phys. 81, 064501 (2018).
[2] M. Lang *et al.*, Phys. Status Solidi B 250, 457 (2013).
[3] Y. Tokiwa *et al.*, Commun. Mater. 2, 42 (2021).
[4] L. Heinze *et al.*, Phys. Rev. Lett. 126, 207201 (2021).
[5] J. L. Allen *et al.*, Phys. Rev. B 113, 104410 (2026).
[6] L. Heinze, T. Kotte *et al.*, Phys. Rev. Lett. 134, 216701 (2025).

GB-02. Structure–Property Interplay and Low Field Metamagnetism in Stoichiometric Na_4NiTeO_6

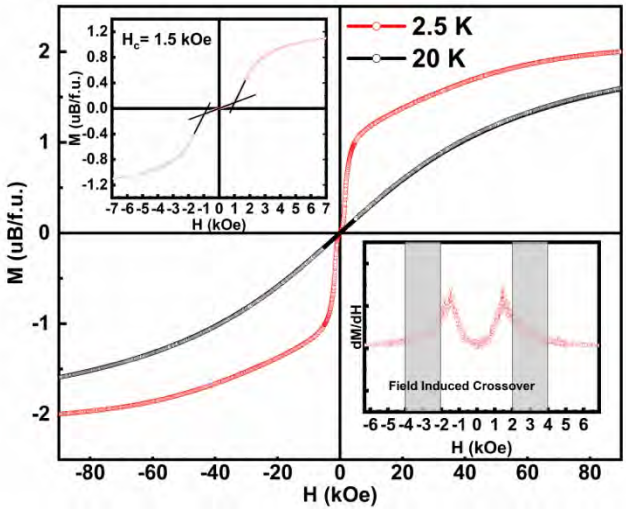
S. Patil[1, 2], A. .[1, 2], S. D. Kaushik[1, 2]
[1]UGC-DAE Consortium for Scientific Research Mumbai Centre, Mumbai, Maharashtra, India, [2]Savitribai Phule Pune University, Pune, Maharashtra, India

Low-dimensional S = 1 quantum magnets with competing interactions provide a fertile setting for field-tunable correlated states that are highly sensitive to disorder. We report the synthesis and comprehensive characterization of stoichiometric Na_4NiTeO_6, synthesized via solid-state reaction method and confirmed by combined X-ray and neutron powder diffraction [1]. Rietveld refinements confirm a triclinic (P-1) lattice comprising quasi-one-dimensional zigzag chains of edge-sharing NiO_6 octahedra, magnetically separated by Na and Te layers, with no evidence of Na deficiency or cation site mixing, thereby clearly distinguishing this compound from previously reported $Na_{4-\delta}NiTeO_6$. DC magnetization, AC susceptibility, and heat capacity reveal a robust second-order antiferromagnetic transition at $T_N \approx 7$ K. Curie–Weiss analysis yields $\theta_{cw} = 8.2$ K and enhanced effective moment $\mu_{eff} = 3.2\ \mu_B/Ni^{2+}$, consistent with dominant ferromagnetic intrachain exchange frustrated by antiferromagnetic interchain coupling. Isothermal M–H at 2.5 K exhibits S-shaped metamagnetic response with $H_c \approx$ 1.5 kOe and two-step spin flips; dM/dH shows a broad enhancement indicative of field-induced crossover. Saturation magnetization reaches 1.9 μ_B/Ni (59.4% of μ_{eff}) at 9 T, substantially below the Curie–Weiss effective moment, pointing to strong low-dimensional fluctuations or spin canting. AC susceptibility and a field-suppressed λ-type anomaly in the heat capacity (above 3 T), without additional low-temperature anomalies, exclude spin-glass freezing and structural transitions in the probed regime. These results establish that this Ni^{2+} (S = 1) tellurate, distinct from its Co/Cu analogs, emerges as a structurally clean quasi-one-dimensional spin-chain compound in which metamagnetism can be tuned by very modest magnetic fields, providing a benchmark platform for structure–property studies of competing exchange and anisotropy in S = 1 chains [2, 3].

[1] C. Su, X.-T. Zeng and Y. Li et al., Sci. China Phys. Mech. Astron., Vol. 65, p.297511 (2022).
[2] Z. He, W. Guo, M. Cui, and Y. Tang, Dalton Trans. 46, 5076 (2017).
[3] Z. He, M. Cui, and C. Qiu, J. Alloys Compd. 748, 794 (2018).



Specific heat capacity as a function of temperature at different magnetic fields. The inset shows zero-field data over the temperature range 2.5–280 K.



Isothermal magnetization curves at 2.5 K and 20 K. The upper inset shows critical field of ~1.5 kOe, while lower inset highlights field-induced crossover.

GB-03. Non Collinear Magnetic Ground State Driven by a Giant Dzyaloshinskii–Moriya Interaction in a Kagome Magnet

D. Tam[1, 3], R. Sibille[1], T. Mazet[2], A. Piovano[3], B. Malaman[2], D. Gawryluk[1], L. Roduit[1], A. Turrini[1], B. Roessli[1], L. Keller[1], Y. Soh[1]

[1]Paul Scherrer Institute, Villigen, Switzerland, [2]University of Lorraine, Nancy, France, [3]Institut Laue-Langevin, Grenoble, France

Previous studies on the kagome ferromagnet $Co_3Sn_2S_2$ have reported many controversial results. By using a variety of experimental techniques, primarily neutron scattering and Mossbauer spectroscopy, we have comprehensively solved the magnetic Hamiltonian, which is dominated by one in-plane nearest-neighbor interaction J, containing a Heisenberg component and a giant antisymmetric Dzyaloshinskii-Moriya Interaction (DMI), which is roughly 1/3 of J, and a small interplanar coupling. The Hamiltonian results in a canted (non collinear) ferromagnetic ground state with the umbrella-type R-3m′ structure, and our experiments provide evidence that this single structure is the true ground state at all temperatures below Tc with constant canting angle. This canted ferromagnetic structure may be the physical origin of the giant anomalous Hall effect previously reported rather than the Weyl nodes lying 60 meV above the Fermi level. Furthermore, this giant DMI may account for the chiral phonons detected in this system.

GB-05. Evidence for a nodal line spin liquid in a Face Centered Cubic Antiferromagnet.

K. Plumb

Physics, Brown University, Providence, Rhode Island, United States

Competing interactions in frustrated magnets act to inhibit static magnetic order at low temperatures. At the same time, the strong interactions impose constraints from which highly correlated but dynamic, liquid like, states of matter can emerge. In the extreme quantum limit, these spin liquids evolve into quantum spin liquids with long-range entanglement. The potential for discovering such exotic phases of matter is one reason that frustrated magnets occupy a major area of quantum materials research. Even when a quantum spin liquid is not realized, new collective physics often arises from frustration. I will discuss neutron scattering measurements on the face centered cubic (FCC) antiferromagnet K_2IrCl_6 that provide evidence for a new type of classical spin liquid state we term a “nodal line spin liquid” [1]. Although the nodal-line spin liquid phase is stable over a finite range of temperatures, it is susceptible to ordering induced by quantum or thermal fluctuations or by long-range exchanges. While each of these selection mechanisms is very weak, they cooperate to stabilize magnetic order at low temperatures. However, proximity to the nodal line spin liquid enhances the effects of quantum fluctuations that dictate the thermodynamics of this material. The results show a new state of fluctuating matter, the nodal-line spin liquid, and show how even when a spin liquid freezes, the physical properties of frustrated systems can be controlled by large quantum fluctuations.

[1] Q. Wang et al. Phys. Rev. X 15, 021021 (2025)

GB-06. Luttinger-Tomonaga liquid in a purely organic spin ladder

M. Pardo-Sainz[1, 2], T. Ono[2], I. Diaz-Ortega[3], T. Kihara[3], H. Nojiri[3], Y. Hosokoshi[2], J. Campo[1]

[1]Spanish National Research Council (CSIC), Zaragoza, Spain, [2]Osaka Metropolitan University, Sakai, Japan, [3]Institute Materials Research, Sendai, Japan

The study of quantum spin systems has attracted much attention for several decades [1]. Recently spin-ladder systems, which are in the crossover region between one and two dimensions, have been at the focus of intensive research towards its understanding, since peculiar phenomena, such as the superconductivity in a hole doped

S=1/2 two-leg spin ladder, are expected to appear [2, 3]. One limitation to the study of these systems is that this spin gap is usually too large to be accessible by the experiments, and only in the case of organometallic or purely organic magnets can be small enough so as to allow a full investigation of the spectrum by applying a magnetic field [1]. However, only very few of such compounds have been synthesized which can be described by the S=1/2 two-leg Heisenberg antiferromagnetic ladder (THAFL) model.
Here we present the compound 4-F-2-NNBIP [= 4-fluoro-2-(1-oxyl-3-oxide-4,4,5,5-tetramethylimidazolin-2-yl) biphenyl], whose magnetic behaviour comes from a spin 1/2 delocalized between the N and O atoms of the nitronyl nitroxide (NN) group. Both powder and single crystal samples have been characterized by means of X-ray diffraction, electron paramagnetic resonance (EPR), specific heat, magnetization and susceptibility measurements at high magnetic fields and very low temperatures. Quantum Monte Carlo (QMC) calculations have also been performed in order to obtain the relevant magnetic parameters of the systems.
The analysis of the crystal structure and the EPR measurements shows that this system can be well described by a THAFL model. A fit to the susceptibility data using QMC calculations allows to estimate the exchange interactions to be J_L/k_B= 2.7(3) K and J_R/k_B= 7.4(1) K, therefore probing this spin ladder to be in the strong coupling limit $\gamma=J_R/J_L$=2.7(4) > 1. The field and temperature dependence of the specific heat is also in agreement with this model, and we can determine the transition to the gapless Luttinger-Tomonaga liquid (LTL) phase, identified by a linear behaviour at very low temperature. From all these data we propose a magnetic phase diagram (Fig. 1 (b)) in which 3 distinct magnetic phases are present: spin liquid phase, a gapless phase and a fully spin polarized phase.
[1] Silva, R. A. L., & Almeida, M. (2021). *Journal of Materials Chemistry C* 9, 10573.
[2] Dagotto, E. & Rice, T. M. (1996). *Science* 271, 618.
[3] Sachdev, S. (2017). *Quantum Phase Transitions*. Cambridge: Cambridge University Press.

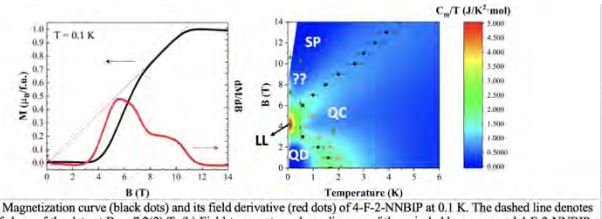


Figure 1. (a) Magnetization curve (black dots) and its field derivative (red dots) of 4-F-2-NNBIP at 0.1 K. The dashed line denotes the change of slope of the data at B_{an} =7.2(2) T. (b) Field-temperature phase diagram of the spin-ladder compound 4-F-2-NNBIP. The contour plot shows the magnetic specific heat as C_m/T. Local maxima are indicated by black circles. Orange squares denote the maximum of dχ/dT, while green triangles mark the critical fields obtained from the magnetization data.

GB-07. The Rare-Earth Hexaaluminates, $REMgAl_{11}O_{19}$, as a playground for Triangular Lattice Magnetism

R. H. Colman[1], S. Kumar[1], G. Bastien[1], A. Kancko[1], C. A. Correa[2], T. Treu[3], P. Gegenwart[3]
[1]Department of Condensed Matter Physics, Charles University, Prague, Czechia, [2]Institute of Physics, Czech Academy of Sciences, Prague, Czechia, [3]Experimental Physics VI, University of Augsburg, Augsburg, Germany

Rare-earth hexaaluminates $LnMgAl_{11}O_{19}$ provide an attractive platform for exploring frustrated magnetism on well-separated triangular lattices (Fig. 1), where crystal-field effects, strong spin-orbit coupling, and structural disorder together generate a wide range of low-temperature magnetic states.
In my presentation, I will summarize our recent studies of single crystals with Ln = Ce, Pr, Nd, Sm, and Gd, together with the related compound $EuAl_{12}O_{19}$. Despite their common structural motif, these materials display a remarkably diverse magnetic landscape. $CeMgAl_{11}O_{19}$ realizes an effective spin-1/2 triangular magnet with strong XXZ anisotropy and no long-range order down to 30 mK [1], placing it close to a field-tuned quantum-disordered regime. $PrMgAl_{11}O_{19}$ hosts non-Kramers quantum Ising magnetism [2], while $NdMgAl_{11}O_{19}$ exhibits pronounced Ising anisotropy, short-range magnetic correlations, and strong adiabatic demagnetization cooling [3]. $SmMgAl_{11}O_{19}$ lies in the extreme weak-exchange limit, with a strongly quenched Kramers doublet and predominantly single-ion behavior. In contrast, $GdMgAl_{11}O_{19}$ behaves as a nearly ideal weakly interacting paramagnet with a large magnetocaloric response, whereas $EuAl_{12}O_{19}$ shows quasi-two-dimensional ferromagnetism [4,5].
Together, these results establish the hexaaluminate family as a versatile playground for triangular-lattice magnetism. In all cases except Ln = Gd, strong single-ion anisotropy plays a central role in shaping the low-temperature magnetic properties. I will discuss how frustration, anisotropy, structural disorder, and magnetocaloric functionality evolve across this family of materials.
[1] G. Bastien, et al., *ArXiv:2506.16207* (2025).
[2] S. Kumar, et al.. *Phys. Rev. B* 111, 174444 (2025).
[3] S. Kumar, et al.. *ArXiv:2505.18898* (2026).
[4] G. Bastien, et al. *Phys. Rev. B* 110, 94436 (2024).
[5] G. Bastien, et al. *Adv. Mater.* 36 (2024).

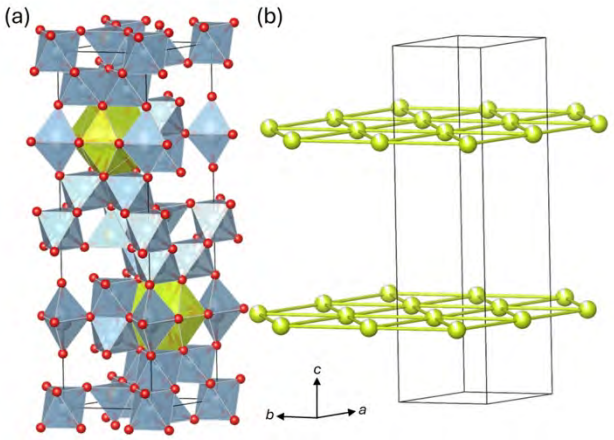


Figure 1. (a) *the hexaaluminate structure, and* **(b)** *the rare-earth triangular lattice.*

GB-08. Observation of Bimeron Crystal and Giant In-plane Topological Hall Effect in a Centrosymmetric Magnet

S. Sun[1], Y. Hao[2], C. Huang[3], S. Chen[2], J. Green[1], H. Roshandel[4], J. He[4], W. Laderer[4], M. Tran[1], P. Diaconescu[4], A. Alexandrova[4], C. D. Batista[2, 3], H. Cao[2], N. Ni[1, 5]

[1]Department of Physics and Astronomy, University of California, Los Angeles, Los Angeles, California, United States, [2]Neutron Scattering Division, Oak Ridge National Laboratory, Oak Ridge, Tennessee, United States, [3]Department of Physics and Astronomy, University of Tennessee, Knoxville, Tennessee, United States, [4]Department of Chemistry and Biochemistry, University of California, Los Angeles, Los Angeles, California, United States, [5]California NanoSystems Institute, University of California, Los Angeles, Los Angeles, California, United States

Topological spin textures offer a unique platform for spintronics due to their emergent electromagnetic responses and nanoscale stability. Unlike skyrmions typically stabilized by out-of-plane fields, bimeron crystals (BmX) are predicted to emerge in easy-plane magnets under purely in-plane magnetic fields [1,2]. In this talk, I will present our experimental realization of an in-plane-field-induced triple-Q BmX in a centrosymmetric magnet. I will show that a giant in-plane topological Hall effect emerges, with a topological Hall angle reaching 10%. Single-crystal neutron diffraction confirms that this THE originates from the formation of a BmX phase. I will further discuss the unique symmetry-governed control of the topological charge of the BmX and show how an effective minimal model captures the stabilization of the triple-Q state and its underlying interactions.

1. S. Hayami, Phys. Rev. B., Vol. 103, p.224418 (2021)
2. S. Hayami, Crystals., Vol. 15, p.834 (2025)

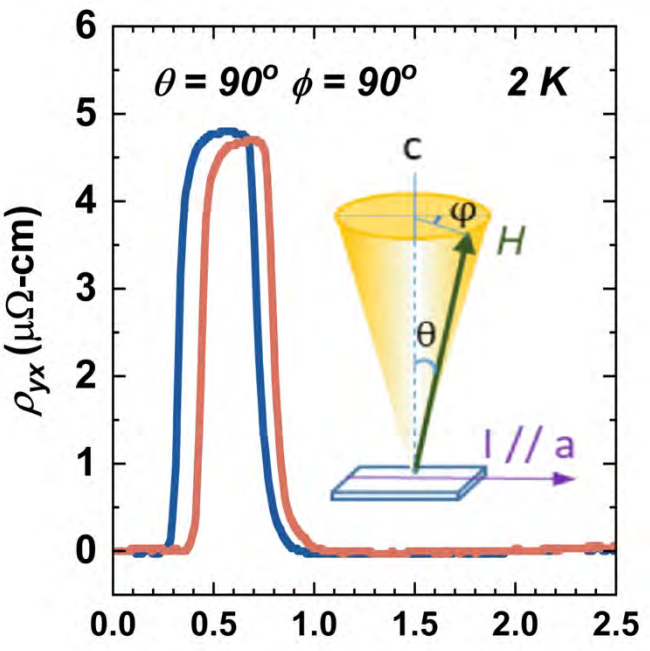


Fig.1 ρ_{yx}(H) measured at 2 K with I || a and H || b*. The measurement geometry is illustrated in the inset.

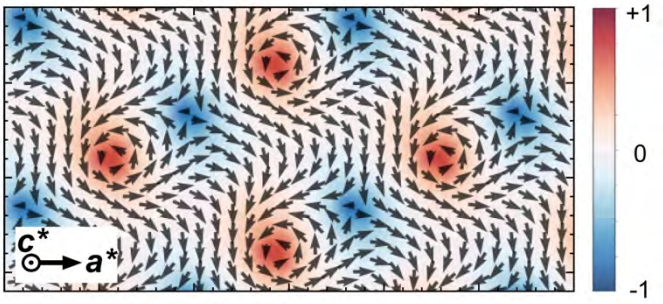


Fig.2 The calculated real-space BmX spin texture for H || (1, −1, 0). Arrows indicate the in-plane spin components, while the colorscale represents Sz (red for up, blue for down).

GB-09. Tailoring Kitaev Quantum Spin Liquid States in Cobalt-Based Honeycomb Oxide Heterostructures

C. Sohn
UNIST, Ulsan, Korea (the Republic of)

Quantum spin liquids, exotic spin states characterized by macroscopic quantum entanglement and fractionalized excitations, represent one of the most elusive phases of matter. While prior investigations have predominantly focused on bulk materials, we employ heterostructure engineering on cobalt-based honeycomb oxides, a promising class of candidates for hosting Kitaev physics. This relatively unexplored research direction allows for the manipulation of the spin Hamiltonian via various degrees of freedom inherent to heterostructures. In this talk, I will present our recent effort to suppress the unwanted long-range order in $Cu_3Co_2SbO_6$. We demonstrate that epitaxial strain effectively destabilizes the magnetic transition, providing a robust route to suppress the long-range ordered phase. Furthermore, we explore the potential of interfacial proximity and optical excitation as additional tuning knobs to further manipulate the spin Hamiltonian. By synergistically employing these heterostructure-based controls, we discuss the possibility of realizing genuine quantum spin liquid states in the absence of an external magnetic field.

SESSION GC: ULTRAFAST II

Chair(s): H. Reichlova, *Institute of Physics of the Czech Academy of Sciences, Prague, Czechia*
Friday, November 6, 2026
08:30 AM-12:00 PM
Coral 1

GC-01. Propagating Antiferromagnetic Magnons in Synthetic Antiferromagnets

Y. Shiota
Institute for Chemical Research, Kyoto University, Uji, Kyoto, Japan

Antiferromagnetic spintronics has advanced rapidly in recent years, and interlayer exchange–coupled synthetic antiferromagnets (SAFs) have emerged as highly versatile platforms for exploring high-frequency spin dynamics[1]. Their magnetic properties can be precisely engineered through careful design of the stacking structure including material selection and layer thicknesses. Owing to their resonance frequencies in the tens of gigahertz, SAFs enable efficient electrical excitation and detection of antiferromagnetic magnons. A particularly intriguing feature of antiferromagnetic magnons is their ability to possess magnon polarization (handedness), a degree of freedom absent in ferromagnetic systems[2-4].
In this work, we demonstrate the generation, manipulation, and electrical detection of propagating antiferromagnetic magnon handedness in perpendicularly magnetized SAFs[5]. The multilayer films were deposited on thermally oxidized Si substrates by DC magnetron sputtering with the following structure (thickness in nm): $Ta(2.0)/Pt(5.0)/[Co(0.3)/Ni(0.6)]_{8.5}/Ru(0.42)/[Co(0.3)/Ni(0.6)]_{8.5}$ /Pt(5.0). The films were patterned into a Hall-bar device, while a spatially separated stripline antenna was used to generate propagating antiferromagnetic magnons. Pulse-modulated microwaves induced magnon propagation toward the Hall bar, where the magnons were electrically detected via the inverse spin Hall effect (ISHE) in the top and bottom Pt layers using lock-in techniques. Under a tilted magnetic field (ϑ_H = 30°), we observed opposite ISHE voltage signs depending on the magnon handedness, demonstrating selective excitation and detection by simply varying the microwave frequency.
Beyond metallic multilayers, we further investigated all-insulating SAFs composed of $Gd_3Fe_5O_{12}/Y_3Fe_5O_{12}$ (GdIG/YIG) bilayers, where antiferromagnetic coupling arises through interlayer exchange across the interface. We performed nonlocal magnon transport measurements [6], and observed characteristic signatures of antiferromagnetic magnon propagation, such as polarity reversal of the detected signal. These studies collectively deepen our understanding of antiferromagnetic magnons in both metallic and insulating SAF platforms and highlight their potential for polarization-multiplexed magnonic devices.
[1] R.A. Duine *et al., Nat. Phys.* 14, 217 (2018).
[2] R. Cheng *et al., Sci. Rep.* 6, 24223 (2016).
[3] J. Lan *et al., Nat. Commun.* 8, 178 (2017).
[4] S.-H. Oh *et al., Phys. Rev. B* 100, 174403 (2019).
[5] Y. Shiota *et al., Nat. Commun.* 5, 9750 (2024).
[6] L.J. Cornelissen *et al., Nat. Phys.* 11, 1022 (2015).

GC-02. Mapping All-Optical Switching Thresholds in Co/Pt Multilayers: A Comparative Study of Tantalum-Buffered and Unbuffered Thin Films

A. Villar[1], Y. L. Guen[2], J. Hohlfeld[2], R. Morales[3, 4], S. Mangin[2], P. Vavassori[4, 5], J. Porro[1, 4]
[1]BCMaterials, Leioa, Spain, [2]Insititut Jean Lamour, Université de Lorraine, Nancy, France, [3]Chemical-Physics, University of the Basque Country, Leioa, Vizcaya, Spain, [4]IKERBASQUE, Bilbao, Spain, [5]nanomagnetism, CIC nanoGUNE, Donosti, Spain

After the discovery of deterministic magnetic switching in Gd-based [1] (and later on Co/Pt multilayer [2,3]) thin films by circularly polarized femtosecond laser pulses began the research of the phenomenon called Helicity-dependent All-Optical Switching (HD-AOS) [Fig.1]. This phenomenon rapidly gained interest due to its potential applications in spintronics, ultrafast magnetisation reversal speed and low energy consumption [4]. The introduction of buffer layers in thin films significantly modifies their magnetic properties [5]. We study the impact of a tantalum (Ta) buffer layer on HD-AOS in Co/Pt multilayers. Two samples with identical Co and Pt layer thicknesses were fabricated via magnetron sputtering, but one of the samples has an extra 5 nm Ta buffer layer with structure: Ta(5nm)/Pt(5nm)/Co(1nm)/Pt(1nm)/Co(1nm)/Pt(2nm). From now on called TaCo1Pt1 and the other sample Co1Pt1. Magnetic characterisation confirmed strong perpendicular magnetic anisotropy (PMA) and square hysteresis loops in both samples. Absorbed fluence thresholds (which are the minimum fluence absorbed by the Co/Pt layers to produce magnetic switching) for AOS, circular multidomain (C-MD), and linear multidomain (L-MD) states were mapped as functions of pulse duration (from 130fs up to 8000 fs), repetition rate (1-10 kHz), and pulse number (100–10,000) [Fig.2]. Results indicate that the Ta buffer layer increases the required fluence thresholds. Furthermore, the proximity of linear multidomain thresholds to AOS or circular multidomain curves varied based on the presence of Ta, suggesting different domain nucleation or reorientation mechanisms. Increasing the number of pulses consistently lowered fluence thresholds and widened the gap between circular multidomain and AOS thresholds. These findings highlight the role of interfacial engineering in controlling AOS for future opto-magnetic applications.

[1] C. D. Stanciu, F. Hansteen, A. V. Kimel *et al.* Phys. Rev. Lett. Vol. 99, p.047601 (2007)
[2] C.-H. Lambert, S, Mangin, B. S. D. Ch. S. Varaprasad *et al.* Science, Vol. 345, p.1337 (2014)
[3] G. Kichin, M. Hehn, J. Gorchon *et al.*, Phys. Rev. Appl., Vol. 12, p.024019 (2019)
[4] A. El-Ghazaly, J. Gorchon, R. B. Wilson *et al.* J. Magn. Magn. Mater.,. Vol. 502, p.166478 (2020)
[5] B. Bersweiler, K. Dumesnil, D. lacour *et al.*, J. Phys.: Condens. Matter., Vol. 28, p.336005 (2016)

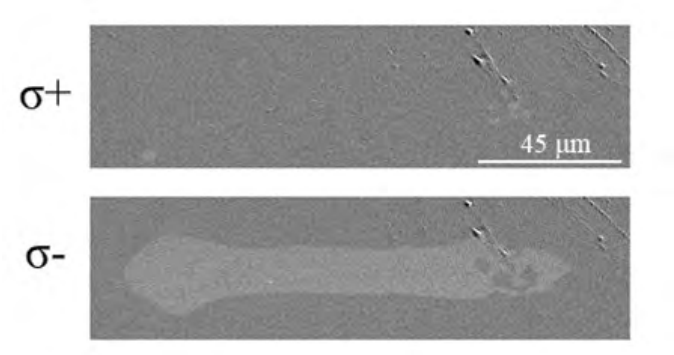


Fig.1:Sweeps with a femtosecond laser beam with (top) dextrogyre and (bottom) levogyre circularly polarized pulses in a sample with positive initial magnetisation state.

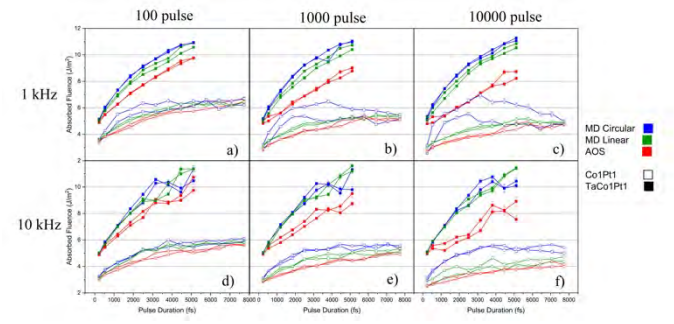


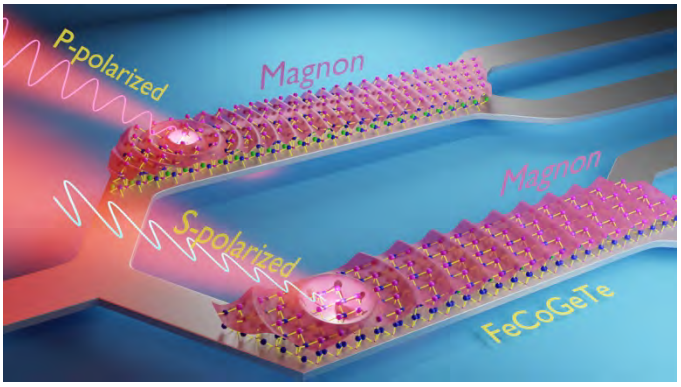
Fig.2: Absorbed fluence thresholds (AOS, C-MD and L-MD) for various number of pulses (100, 1000 and 10000) and laser repetition rates (1-10 kHz) for samples Co1Pt1 and TaCo1Pt1.

GC-03. Strong Optical Control of Magnon and Magnetization Dynamics in van der Waals Ferromagnets

Y. Gong[1], Y. Liang[2], W. Farias[1], A. Bielicki[1], R. Jin[2]
[1]Physics and Astronomy, College of Charleston, Charleston, South Carolina, United States, [2]Physics and Astronomy, University of South Carolina, Columbia, South Carolina, United States

Ultrafast optical control of magnon and magnetization in two-dimensional (2D) materials promises novel functionalities for spintronics and magnonics in atomically thin devices. Here, we report control of optical excited

magnon and magnetization dynamics, using laser polarization, in a ferromagnetic van der Waals (vdW) material, $(Fe_{0.85}Co_{0.15})_5GeTe_2$. The magnetization and magnon excitation amplitudes and lifetime are controlled and monitored by time-resolved pump-probe spectroscopy. We show significant and continuous modulation of magnetization and magnon dynamics as a function of incident laser polarization angle. Our results suggest the modification of the effective demagnetization field and magnetic anisotropy by the pump laser pulses with different polarizations is due to anisotropic optical absorption and superdiffusive spin current generation. This implies that pump laser pulses modify the local spin environment, which enables the launch of magnons with tunable dynamics. Our findings suggest a new route for the development of opto-spintronic or -magnonic devices.



The conceptual image shows the modulation of magnon signal propagating in a magnonic circuit.

GC-04. Spin-torque-driven magnetization dynamics of ferrimagnet $Co_{100-x}Gd_x$ alloy

H. Kim, G. Choi
Sungkyunkwan University, Suwon, Korea (the Republic of)

Electrically induced spin-torque phenomena in rare-earth-transition-metal ferrimagnetic alloys have been extensively studied. However, the key question of which channel absorbs the spin angular momentum has been debated. Magnetization switching follows the same sense in TM-rich and RE-rich samples with respect to the net magnetization, which implies that spin current is absorbed by the net magnetization [1,2]. However, a recent experimental study reveals the asynchronous dynamics of each sublattice during the switching process, which can be attributed to the small antiferromagnetic exchange energy density. They suggest that this phenomenology occurs because the conduction spins predominantly transfer their angular momentum to the TM band, which then indirectly interacts with the RE band through the RE-TM exchange interaction [3]. This discrepancy highlights the need for the direct measurement of the magnetization dynamics, especially under short-pulsed spin injection.

In this work, we investigate the spin-torque-driven magnetization dynamics of ferrimagnet $Co_{100-x}Gd_x$, where Gd composition varies from 0% to 30%, employing optical spin generation in Pt. We observe a sign reversal in the initial tilting direction of magnetization dynamics on the Co sublattice between Co-rich samples and Gd-rich samples (Fig. 1). Additionally, the amplitude of magnetization dynamics exhibits a close correlation with the net magnetization (Fig. 2). Our results present strong evidence that the net magnetization of ferrimagnet primarily absorbs the spin currents.

[1] N. Roschewsky, T. Matsumura, S. Cheema, F. Hellman, T. Kato, S. Iwata, and S. Salahuddin, "Spin-orbit torques in ferrimagnetic GdFeCo alloys," Appl. Phys. Lett. 109, 112403 (2016).
[2] H. Wu, Y. Xu, P. Deng, Q. Pan, S. A. Razavi, K. Wong, L. Huang, B. Dai, Q. Shao, and G. Yu, "Spin-orbit torque switching of a nearly compensated ferrimagnet by topological surface states," Adv. Mater. 31, 1901681 (2019).
[3] G. Sala, C.-H. Lambert, S. Finizio, V. Raposo, V. Krizakova, G. Krishnaswamy, M. Weigand, J. Raabe, M. D. Rossell, E. Martinez, and P. Gambardella, "Asynchronous current-induced switching of rare-earth and transition-metal sublattices in ferrimagnetic alloys," Nat. Mater. 21, 640–646 (2022).

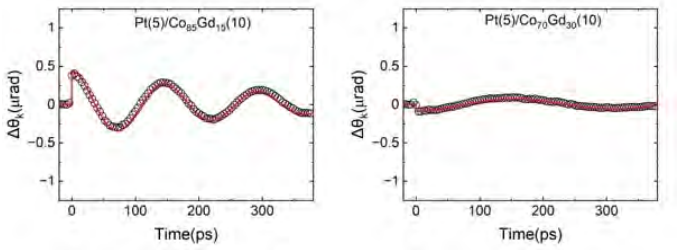


Figure 1. TR-MOKE measurement of the OSOT-driven magnetization dynamics.

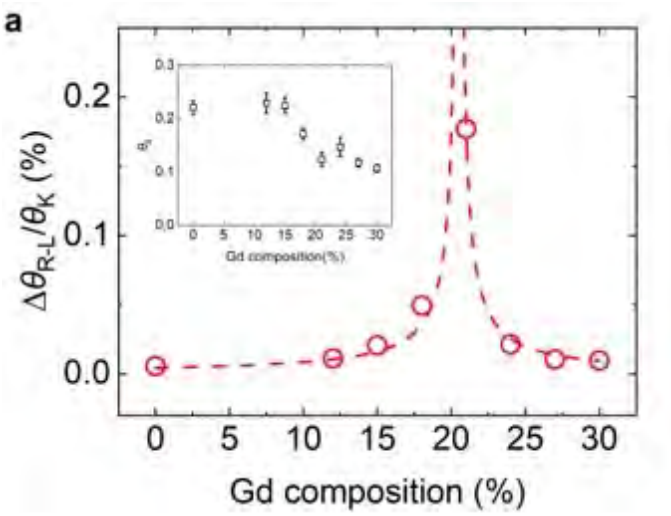


Figure 2. Spin-torque-driven tilting angle as a function of Gd composition. Theta k is the static Kerr rotation at the polar MOKE geometry (inset).

GC-05. Picosecond-scale State-selective All-optical Magnetization Control in Ferromagnetic Nanoislands using the Inverse Faraday Effect

T. Zheng, X. Xiao, R. Oulton, W. R. Branford, J. Gartside
Physics, Imperial College London, London, United Kingdom

All-optical magnetisation switching (AOMS) in ferromagnetic nanoarrays has highlighted the potential for precise, field-free manipulation of magnetic textures. AOMS uses lasers to achieve magnetization control at the nanoscale, offering transformative possibilities for reconfigurable magnetic systems and applications such as energy-efficient data storage and neuromorphic computing. While AOMS has been demonstrated experimentally, the underlying mechanism remains an active area of investigation [1]. Theoretical modelling by Yang et al. (2023) [2] suggests that the inverse Faraday effect (IFE) induced by linearly polarised light in metallic nanostructures could generate plasmonically-enhanced magnetic fields and play a key role in AOMS. Building on these findings, our work explores AOMS-driven mechanisms for controlling magnetization textures in ferromagnetic nanoislands (NiFe). Using Mumax3 micromagnetic simulations, we investigated magnetization dynamics induced by the IFE-generated B-field under varying island geometries, field parameters, and thermal conditions. Key simulation outcomes reveal energy landscapes and magnetization state evolution, highlighting potential benefits for such plasmonically-enhanced IFE effects from linearly-polarised light on AOMS performance. This work paves the way for a deeper understanding and experimental verification of the physics behind AOMS, and it provides a powerful framework for scalable, ultrafast manipulation of magnetic states.

[1] K. D. Stenning et al., "Low-power continuous-wave all-optical magnetic switching in ferromagnetic nanoarrays", *Cell Reports Physical Science*, vol. 4, no. 3, pp. 101291 (2023).
[2] X. Yang et al., "An inverse Faraday effect generated by linearly polarized light through a plasmonic nano-antenna", *Nanophotonics*, vol.12, no. 4, pp. 687–694 (2023).
[3] H. Holder et al., "Magnetic vortex writing and local reversal seeding in artificial spin-vortex ice via all-optical and surface-probe control", arXiv: arXiv:2505.16874 (2025).

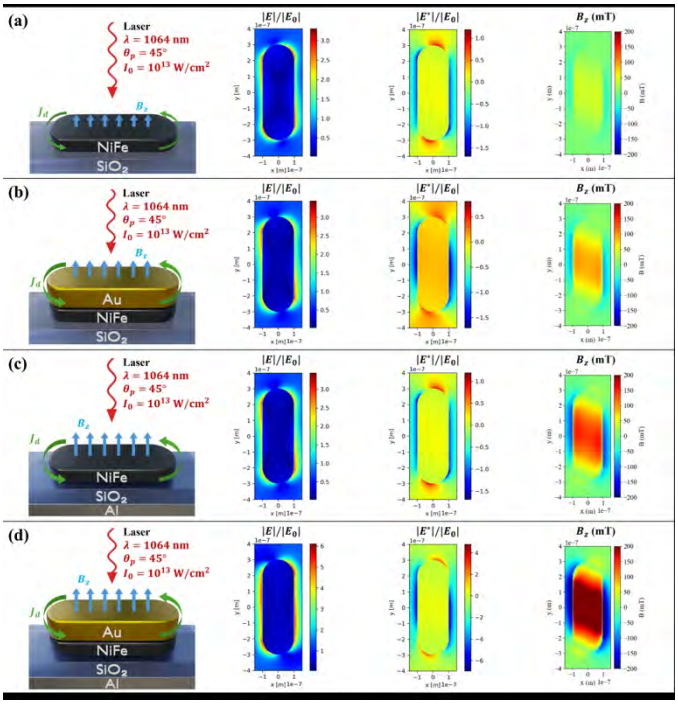


Fig. 1 - Lumerical FDTD simulations of the IFE on a 600 by 200 nm nanoisland. 4 device designs are proposed: (a) NiFe/SiO_2, (b) Au/NiFe/SiO_2, cavity-enhanced (c) NiFe/SiO_2/Al and (d) Au/NiFe/SiO_2/Al. (d–f) Normalised electric-field enhancement in the stacks. (h–j) The out-of-plane component of the IFE-induced magnetic field.

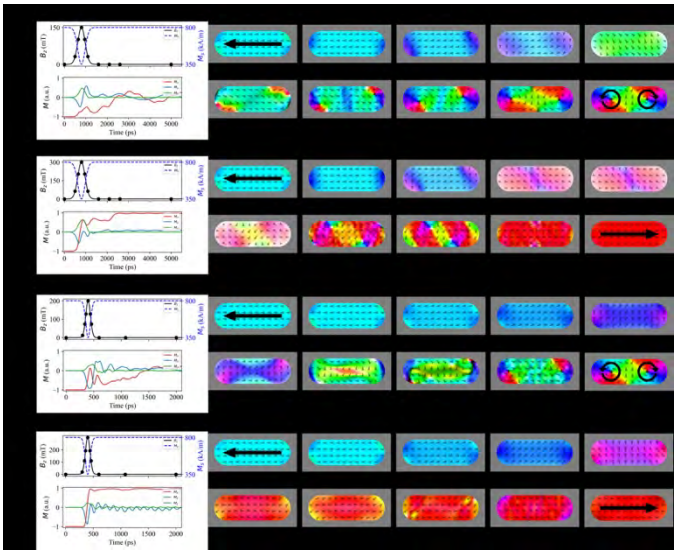


Fig. 2 – Mumax3 simulation with 2 characteristic IFE-induced Bz pulses (400 ps and 100 ps). Thermal effects are approximated by a transient 40% reduction in the saturation magnetisation. Two major types of magnetisation controlling mechanisms are observed: (a)(c) Double vortex formation and (b)(d) macrospin reversal.

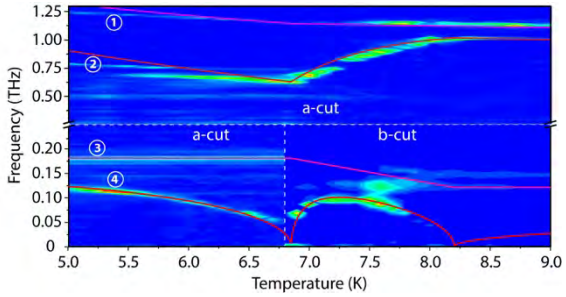
GC-06. Signature of Jahn-Teller-like magnetic instability in $YbFeO_3$ and dynamical strong coupling of Fe spins and Yb orbitals

O. Kovalenko[1], N. Vovk[1], A. Wu[2], R. V. Mikhaylovskiy[1]
[1]Lancaster University, Lancaster, UK, United Kingdom,
[2]Shanghai Institute of Ceramics, Shanghai, China

Magnetic recording is a central technology for long-term data storage. Understanding the physics of ultrafast angular momentum transfer between light and spins is a key problem in magnetism. Antiferromagnetic materials, such as $YbFeO_3$, have emerged as promising candidates for future storage media [1,2]. They offer unique functionalities, such as ultrafast terahertz spin dynamics and low-energy excitation, thanks to the direct interaction of the THz pulse with a spin system [3].
Ultrashort THz pulses were used to excite low-energy orbital transitions in $YbFeO_3$ to reveal angular momentum dynamics at high excitation strengths. The $YbFeO_3$ exhibits a spin reorientation transition (SRT) of the Jahn-Teller type at temperatures below 9K. This SRT originates from the interplay between the Yb-Fe exchange and crystalline anisotropy. These unique properties of $YbFeO_3$, including its energy anti-crossing, make it a vibrant playground for THz applications.

We explored the dynamics in $YbFeO_3$ using a time-resolved pump-probe technique across the SRT. Fig. 1 depicts the Fourier spectral map of the measured polarisation rotation, shown as a function of the sample temperature for the three combinations of sample orientation and detection conditions. Four well-distinguished modes were identified as: 1 – quasi-antiferromagnetic (q-AFM), 2 – quasi-ferromagnetic (q-FM), 3,4 – two orbital rare-earth modes (R1, R2). While the q-AFM and R1 are weakly interacting and show only a small frequency shift, the q-FM and the low-lying R2 are strongly coupled, as reflected in the kink-like behaviour of the q-FM and the softening of the R2 mode. The origin and properties of this interaction will be discussed, along with a theoretical description that yields good agreement with experimental results (red curves in Fig. 1). We believe that our findings represent a major step toward understanding quantum effects and dynamical driving of phase transitions in ultrafast magnetism.

[1] S. Baierl, et al, *Nonlinear spin control by terahertz-driven anisotropy fields*, Nature Photonics 98 (2016).
[2] R. V. Mikhaylovskiy, et al, *Terahertz magnetisation dynamics induced by femtosecond resonant pumping of Dy^{3+}subsystem in the multisublattice antiferromagnet $DyFeO_3$*, Physical Review B 92, 094437 (2015).
[3] S. Schlauderer, et al, *Temporal and spectral fingerprints of ultrafast all-coherent spin switching*, Nature 569, 383 (2019).



The map plot of the Fourier spectra of transient Faraday rotation in $YbFeO_3$ as a function of the sample temperature. The four presented modes were identified as 1: q - AFM, 2: q - FM, 3,4: two rare-earth modes. The solid lines are show the theoretically calculated frequencies.

GC-07. Time-evolution of chiral Néel magnetic domain walls in multilayers probed by soft x-ray resonant magnetic scattering.

Z. Guo[1, 2], C. Léveillé[1, 2], R. Gruber[3], D. Ksenzov[4], E. Pedersoli[5], F. Capotondi[5], C. Gutt[4], M. Kläui[3], V. Cros[2], N. Reyren[2], N. Jaouen[1]

[1]Synchrotron SOLEIL, Gif sur Yvette, France, [2]laboratoire Albert Fert, Palaiseau, France, [3]Institut of Physics, Johannes Gutenberg-Universität Mainz, Mainz, Germany, [4]Department Physik, Universität Siegen, Siegen, Germany, [5]Elettra-Sincrotrone, Trieste, Italy

Non-collinear spin textures in ferromagnetic ultrathin films are attracting a renewed interest fueled by possible fine engineering of several magnetic interactions, notably the interfacial Dzyaloshinskii-Moriya interaction in magnetic multilayers. This allows the stabilization of complex chiral spin textures such as chiral magnetic domain walls (DWs), spin spirals, and magnetic skyrmions among others. We have recently shown that circular dichroism in x-ray resonant magnetic scattering (XRMS) is a powerful tool to determine the domain wall characteristics, i.e., their type (Néel or Bloch) and sense of rotation (chirality) in ferromagnetic or antiferromagnetic multilayers [1,2,3].

In the first part of this presentation, we will report on the ultra-fast (in the first few picoseconds) evolution of the magnetic chirality in multilayers as well as their recovery on longer timescale (few hundreds of picoseconds) using XRMS [4]. Beyond the simple evolution of the magnetic domains' period in magnetic multilayers with large perpendicular anisotropy we have investigated how the chirality of the non-collinear spin texture, and their long-range ordering, evolves in the few picoseconds after a strong optical pulse. The change in the ratio between the chiral and magnetic signals have been related to an ultra-fast distortion of the homochiral Néel shape to transient Bloch-Néel-Bloch domain wall. After a few ps, the DWs return to a homochiral Néel configuration preserving the original sense of rotation (i.e., chirality). At longer timescale, the whole system relaxes towards its original homochiral Néel type equilibrium but the chiral magnetic order in the domain walls recovers faster than the collinear magnetic order in the domains.

In the second part, we will present new results obtained from spin-spiral in synthetic antiferromagnetic multilayers [5]. This recent work has been done thanks to a new mode of operation of FERMI light source allowing to perform time resolved XRMS at Fe L edges (~700eV) [6] following the approach we developed at synchrotron [3].

[1] J.-Y. Chauleau, et al, Phys. Rev. Lett 120, 037202 (2018)
[2] W. Legrand, et al, Science Adv. 4, eaat0415 (2018)
[3] C. Léveillé, et al, Phys. Rev. B., 104(6): art.n° L060402. (2021).
[4] C. Léveillé, et al, Nature Comm., 13: art.n° 1412. (2022).
[5] Z. Guo, et al., Phys. Rev. B 112, L020408 (2025).
[6] C. Spezzani et al., Phys. Rev. B, 110, 174409 (2024).

GC-08. Ultrafast lattice-driven manipulation of ferroic order

A. Kirilyuk

HFML-FELIX, Radboud University, Nijmegen, Netherlands

Vibrations of the crystal lattice have a significant impact on the orbital dynamics of the electrons, and through it, on spins. Ultrafast excitation of phonons resulting in drastic repopulation of phononic system was thus shown to be able to modify the fundamental magnetic interactions [1]. And very recently time-resolved X-ray scattering and electron diffraction experiments demonstrated the angular momentum transfer from magnetization to the phonon system, on a femtosecond time scale, dubbed ultrafast Einstein-de-Haas effect [2,3]. It should therefore be possible to realize the opposite process, by changing the lattice and thus controlling the magnetization, on the same time scale - in femtoseconds!

To confirm this, we have recently shown how the resonant excitation of circularly-polarized optical phonons in paramagnetic substrates can permanently reverse the magnetic state of the overlayer [4]. The helicity-dependence of the switching implies that the lattice vibrations excited in the substrate deliver a directional field that pushes the magnetization towards a switched or non-switched state. The nature of such field is however rather unknown and is a topic of debate.

Moreover, a different behaviour, characterized by displacive modification of crystal potentials, is driven by linearly-polarized excitation. The magnetic switching was shown to create very peculiar quadrupolar spatial domain patterns [5], confirming the mechanism. The mechanism appears to be ultimately universal, as observed in variety of systems, not only magnetic ones [6]. The dynamics of the domain formation was shown to proceed via a strongly inhomogeneous magnetic state resulting in a self-organization of magnon-polarons [7] and formation of magneto-elastic solitons.

1. S. F. Maehrlein et al, Science Adv. 4, eaar5164 (2018).
2. C. Dornes et al, Nature 565, 209 (2019).
3. S. R. Tauchert et al, Nature 602, 73 (2022).
4. C.S. Davies, F. G. N. Fennema, A. Tsukamoto, I. Razdolski, A.V. Kimel & A. Kirilyuk, Nature 628, 540 (2024).

5. A. Stupakiewicz, C.S. Davies, K. Szerenos, D. Afanasiev, K.S. Rabinovich, A. V. Boris, A. Caviglia, A.V. Kimel, & A. Kirilyuk, Nature Phys. 17, 489 (2021).
6. M. Kwaaitaal, D.G. Lourens, C.S. Davies & A. Kirilyuk, Nature Phot. 18, 569 (2024).
7. M. Gidding, T. Janssen, C.S. Davies & A. Kirilyuk, Nature Commun. 14, 2208 (2023).

GC-09. Beyond GdFeCo: single-pulse all-optical switching in heavy rare-earth alloys and multilayers - from thin films to dots

B. Kunyangyuen[1], D. Petty Gweha Nyoma[1], G. Malinowski[1], B. Seng[1], W. Zhang[1], J. Hohlfeld[1], J. Gorchon[1], D. Lacour[1], J. Lin[1], Y. L. Guen[1], L. D. Buda-Prejbeanu[2], E. Fullerton[3], S. Mangin[1], f. montaigne[1], M. Hehn[1]
[1]P2M, Institut Jean Lamour, Nancy, Lorraine, France, [2]Spintec, Grenobled, France, [3]UCLA, San Diego, California, United States

The ability to control magnetization with ultrashort laser pulses has created exciting opportunities for next-generation data storage technologies, allowing sub-picosecond operation time and field-free switching. A key breakthrough was the demonstration of all-optical helicity-independent switching (AO-HIS) in GdFeCo alloys, where a single femtosecond laser pulse can reverse magnetization without any field, achieving switching times on the order of 1 picosecond [1]. Until recently, AO-HIS had been limited to Gd-based ferrimagnetic alloys [2], and multilayers [3]. Here, we report a systematic investigation of single-pulse AO-HIS in heavy rare-earth based thin film alloys and multilayers. Depending on the rare-earth element and its concentration, the reversal process can be tailored from ultrafast angular momentum transfer from rare-earth demagnetization [4] (with typical reversal time of 1ps) towards precessional reversal [5] (with typical reversal time of 100ps) or propagation of domain walls mediated by initial spin-transfer–induced bias [6,7] (with typical reversal time of 1µs, Fig1).
In the latter case, the deterministic reversal resulting from the microscopic stochasticity of domain wall propagation in continuous film is lifted by patterning the thin film into disks with diameter ranging from 1.5 µm down to 400 nm. Our results demonstrate that the lateral confinement induces a fluctuation-dominated regime in which the switching probability exhibits an exponential dependence on disk diameter when excited by a single 35 fs pulse. We complement these results with micromagnetic simulations, revealing a dynamic competition between spin-transfer–torque–induced bias and intrinsic magnetization fluctuations during the relaxation of the strongly demagnetized state.

Fig.1: Single pulse AO-HIS in a Hall cross made of SiO/Ta(5)/Pt(5)/(Co76.5Ho23.5)(3)/Ta(5)/Pt(1) thin film (thicknesses in nm). Normalized Hall voltage as a function of time after laser pulses 1 (full disk), 2 (open disk), 3 (full triangles), and 4 (open triangles). Pulse parameters: fluence of 5mJ/cm2 and duration of 50 fs.

[1] I. Radu et al., Nature, Vol. 472, p. 205 (2011)
[2] R. B. Wilson et al., Phys. Rev. B, Vol. 95, p. 180409(R) (2017)
[3] M. L. Lalieu et al., Phys. Rev. B, Vol. 96, p. 220411 (2017)
[4] B. Kunyangyuen et al., ACS Materials Letters, Vol. 7, p. 3619 (2025)
[5] Y. Peng et al., Nature Comm., Vol. 14, p. 5000 (2023)
[6] Y. Peng et al., Phys. Rev. Appl., Vol. 20, p. 014068 (2023)
[7] B. Kunyangyuen et al., Phys. Rev. B, Vol. 112, p. 094432 (2025)
[8] D. Petty Gweha Nyoma et al., Exponential Size Scaling of Ultrafast All-Optical Switching Reveals Bias–Fluctuation Competition, under review.

GC-10. Emergence of the nontraditional magnetic ordering from RuO2: Importance of nonequilibrium and degeneracy

G. Zhang[1], Y. Liu[2], M. Si[2], J. Wang[3], Y. Bai[1], T. F. George[4]
[1]Indiana State University, Terre Haute, Indiana, United States, [2]Lanzhou University, Lanzhou, China, [3]China University of Mining and Technology, Xuzhou, China, [4]University of Missouri-St Louis, St. Louis, Missouri, United States

It has been argued that RuO_2 is an altermagnet. But there is significant controversy experimentally and theoretically. Most theories add a large Hubbard U term to obtain altermagnetic RuO_2, while experimental results often contradict each other. Here we present a new theory by combining the first-principles density functional theory with the time-dependent Liouville equation of motion. We include the spin-orbit coupling, but not the Hubbard U correction. Our study shows that the excited state configuration and spin-orbit coupling can induce a finite spin moment of larger than 0.2 uB, and can spin-split the energy band by 0.19 eV. When we include the Hubbard U, all these features disappear and RuO2 is just another antiferromagnet. This explains why the Hall measurement and laser excitation can induce a strong magnetic signal, while in some experiments, no magnetic signal is measured. We propose an experimental protocol to test our findings. Our study highlights that adding Hubbard U to a new

material needs extra caution, since it may have uncontrollable consequence. In particular, it may artificially induce an altermagnet which does not exist in the real experiments.

Our study reveals a key insight into antiferromagnets. Different from ferromagnets, antiferromagnets have two spin sublattices which are often made of same types of atoms, so the energy levels are all nearly degenerate, even with the presence of spin-orbit coupling. These highly degenerate energy bands are susceptible to an external perturbation. This happens in high-temperature superconductors, where their parent compounds are insulators, but once they are doped, they become a superconductor. Here in RuO_2 we find that these degenerate bands provide a rare opportunity to induce strong magnetization by a laser pulse or voltage bias. This is probably the reason why the anomalous Hall effect is observed in RuO_2.

G P Zhang, Y H Bai and Thomas F George, Nonlinear optical quantum theory of
demagnetization in L10 FePt and FePd, J. Phys.: Condens. Matter 37 (2025) 495801 (15pp)

SESSION GD: HARD MAGNETIC MATERIALS II: NEXT-GENERATION PERMANENT MAGNETS

Co-Chair(s): I. C. Nlebedim, *Division of Critical Materials, Ames National Laboratory, Ames, Iowa, United States* and X. Tang, *National Institute for Materials Science (NIMS), Tsukuba, Ibaraki, Japan*

Friday, November 6, 2026
08:30 AM-12:00 PM
Coral 2

GD-01. Additive Manufacturing of Permanent Magnets

S. Krishnan[1], A. Paul[1], Q. Guo[1], J. Shield[1, 2]
[1]Mechanical & Materials Engineering, University of Nebraska-Lincoln, Lincoln, Nebraska, United States, [2]Nebraska Center for Materials and Nanoscience, University of Nebraska-Lincoln, Lincoln, Nebraska, United States

Additive manufacturing (AM) has two distinct advantages: (1) it can significantly alter design paradigms, allowing novel shapes not able to be manufactured via other processes, and (2) reduction of waste due to net-shape or near-net-shape manufacturing. The latter is especially important for rare earth permanent magnets due to component material criticality. The magnetic performance is very dependent on the microstructure, and the microstructure evolution depends on the solidification conditions; therefore, the most challenging aspect of AM of Nd-Fe-B materials is to design alloy compositions which produce desired microstructures. Further, the complex solidification and brittle nature of the material further complicates AM of Nd-Fe-B, usually resulting in low densities and defected parts. The UNL team is using low-speed melt spinning as a proxy for AM for high-throughput alloy design, as it has similar cooling rates and heat flow directionality. Early transition metals combined with C successfully broaden the processing window and refine as-solidified microstructures. A number of alloy compositions have been developed with square hysteresis loops with coercivities >15 kOe over a range of low wheel speeds (8-14 m/s), indicating a broad processing window. Several of the alloy compositions have been selected for AM, using comminuted melt spun ribbon as powder feedstock. Despite the irregularity (non-sphericity) of the powder feedstock, we have built fully dense parts free of defects (cracks) [1,2]. The magnetic properties are isotropic (Figure 1) and depend on the scan strategy. Microstructures in the AM part resemble those of the melt spun ribbons, suggesting strong similarities in the solidification conditions (Figure 2).

1. S. Krishnan, B. Balasubramanian, Q. Guo and J.E. Shield, "LPBF-processed high-density Nd-Fe-B Magnets from gas atomized powders," Materials & Design 263, 115610 (2026).
2. S. Krishnan, Q. Guo and J.E. Shield, "Accelerating alloy design for laser powder bed fusion using melt spinning as a cooling rate proxy," Prog. Addit. Manuf. 11, 1989 (2026).

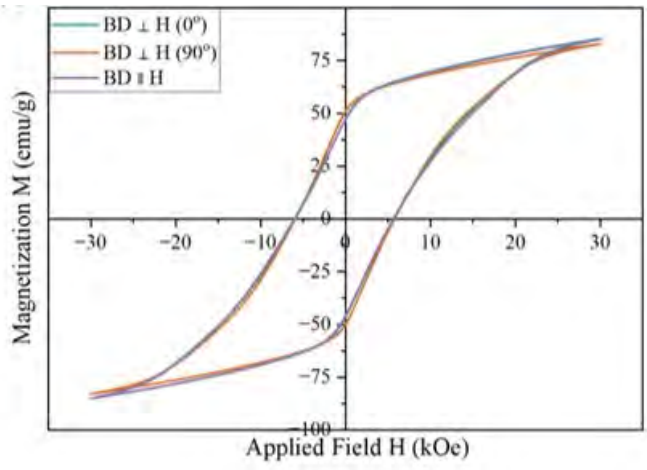


Fig. 1. Hysteresis loop of Nd-Fe-B modified with V and C along 3 directions. The loops overlaying one another indicates isotropic behavior.

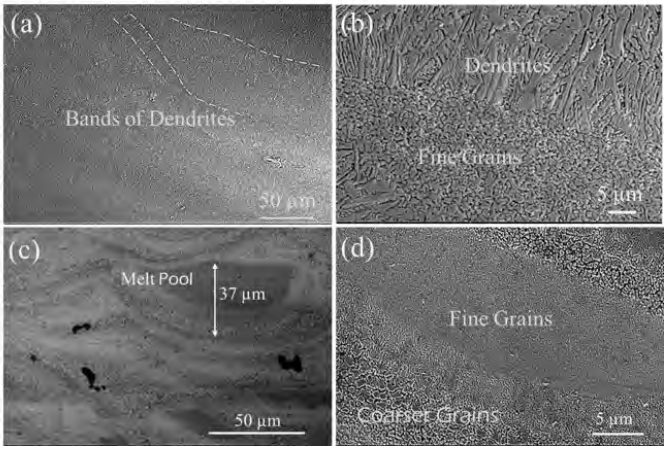


Fig. 2. (a) low-magnification scanning electron microscope (SEM) micrograph of the AM Nd-Fe-B-V-C alloy; (b) higher magnification image of (a) showing bands of equiaxed and columnar grains; (c) Low-magnification SEM micrograph of the AM Nd-Fe-B-Ti-C alloy; (d) higher magnification image of (c) showing heterogeneous but equiaxed microstructure.

GD-03. High Coercivity of 2.8 T in HRE-Free Anisotropic Magnets by Microstructure Engineering

X. Tang[1], Z. Kautsar[1], H. Sepehri-Amin[1], T. Kajiwara[2], H. Miyawaki[2], T. Ohkubo[1], K. Hono[1]

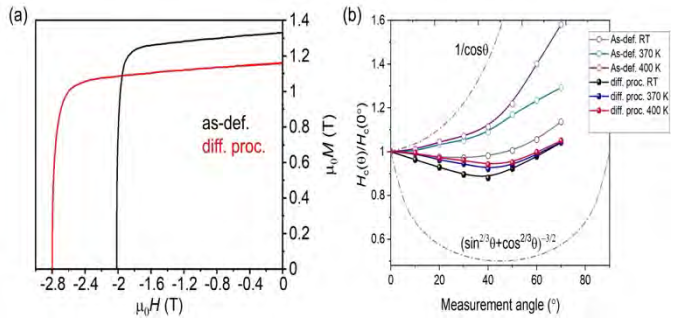
[1]National Institute for Materials Science, Tsukuba, Ibaraki, Japan, [2]Daido Steel Co., Nagoya, Japan

Currently, (Nd,Dy)-Fe-B-based anisotropic magnets used in major applications exhibit coercivity above 2.8 T, typically containing more than 8 wt.% Dy [1]. However, the scarcity of Dy in the earth's crust has driven efforts to develop Dy-free Nd-Fe-B-based magnets with properties comparable to conventional (Nd,Dy)-Fe-B sintered magnets. One approach to enhancing coercivity without reliance on Dy is by reducing grain size [1]. Recent studies on hot-deformed magnets have shown that, despite achieving ultra-fine grain sizes, coercivity remains limited to 2 T due to strong exchange coupling between grains [2]. This suggests that further coercivity enhancement could be achieved by a well-established grain boundary diffusion process [3]. In this study, we applied a heavy rare-earth-free grain boundary diffusion process to ultrafine-grained hot-deformed magnets and demonstrated that an ultra-high coercivity of 2.8 T can be achieved without Dy through microstructure engineering [4].

The starting magnet, with a nominal composition of $Nd_{13.5}Fe_{bal.}Co_{3.5}Ga_{0.57}B_{5.64}$ (at.%), was processed via hot extrusion. Following the diffusion process, the coercivity increased from 2.0 T to 2.8 T (Fig. 1a), which is equivalent to that of commercial sintered magnets containing approximately 8–9 wt.% Dy. The coercivity mechanism was investigated through the angular dependence of coercivity. After diffusion, the mechanism shifts closer to Stoner–Wohlfarth behavior, and this characteristic is retained even at elevated temperatures (Fig. 1b). The microstructural origins underlying this behavior will be discussed.

References

[1] K. Hono et al, Scr. Mater. 67 (2012) 530.
[2] N. Kulesh et al, Acta Mater. 276 (2024) 120159.
[3] H. Sepehri-Amin et al Scr. Mater. 63, 1124-1127 (2010).
[4] X. Tang et al, Scr. Mater. 278, (2026) 117265



GD-04. Direct Recycling of Sm–Co Permanent Magnets: Phase Reconstruction and Coercivity Retention

N. Gunduz Akdogan[1, 2], O. Akdogan[3, 2]

[1]Piri Reis University, Istanbul, Turkey, [2]NANOTerial Technology, Istanbul, Turkey, [3]Bahcesehir University, Istanbul, Turkey

Recycling of Sm–Co permanent magnets is less documented than Nd–Fe–B systems, despite their importance in high-temperature applications. In this work, a direct magnet-to-magnet route is applied to mixed Sm–Co scrap streams (machining residues and end-of-life parts), without prior separation by phase type. The approach focuses on recovering magnetic functionality through phase and microstructural reconstruction rather than elemental extraction. The feedstock was demagnetized, mechanically reduced, and processed under inert atmosphere to limit oxygen uptake. Compaction was followed by vacuum sintering and subsequent aging treatments.

X-ray diffraction after thermal processing indicates the reformation of characteristic Sm–Co phases associated with permanent magnet behavior, while minor $Sm_{<font}$ size="1">2O_3 contributions are observed in the as-milled condition, consistent with the oxidation sensitivity of Sm-

containing compounds [1,2]. Magnetic measurements show that remanence (Br) can be recovered to ~90–95% of reference values. In contrast, intrinsic coercivity (Hcj) is more sensitive to oxygen content and heat-treatment conditions. Samples processed with improved atmosphere control exhibit significantly higher coercivity, in agreement with earlier reports linking rare-earth oxidation and microstructural disruption to coercivity loss [2,3].
The results suggest that the key requirement in Sm–Co recycling is the restoration of phase distribution and microstructural features governing domain wall pinning, rather than strict control of nominal composition alone. Given the variability of incoming scrap (including both 1:5- and 2:17-type materials), the processing window remains narrow, and property recovery is strongly dependent on minimizing oxygen uptake and optimizing post-sintering treatments. Nevertheless, the demonstrated performance recovery supports the viability of direct recycling routes for Sm–Co magnets in applications where thermal stability is critical.
[1] J. F. Herbst, "R–Co permanent magnets," *Rev. Mod. Phys.*, 63 (1991) 819–898.
[2] K. H. J. Buschow, *Permanent Magnet Materials and Their Applications*, Elsevier, 1991.
[3] O. Gutfleisch et al., "Magnetic materials and devices for the 21st century," *Adv. Mater.*, 23 (2011) 821–842.

GD-05. First-Order Reversal Curve Analysis of Bonded and Sintered $SmCo_5$-Based Magnets

T. Suwa[3, 1], K. Park[3], S. Okamoto[1, 2], Y. Hirayama[3]
[1]Tohoku University, Sendai, Japan, [2]National Institute for Materials Science, Tsukuba, Japan, [3]National Institute of Advanced Industrial Science and Technology (AIST), Nagoya, Japan

The magnetization reversal mechanism of permanent magnets depends not only on the intrinsic properties of individual particles but also strongly on interparticle interactions in powder assemblies. However, the overall reversal process involving such interactions has not yet been fully understood. This remains the case even for $SmCo_5$-based magnets, despite their long history of development and practical applications [1].
$SmCo_5$-based magnets can be sintered while suppressing particle growth and largely preserving the morphology of the starting powders. This characteristic enables evaluation of the effects of interparticle interactions without significantly altering particle morphology. Therefore, $SmCo_5$-based magnets provide a suitable model system for investigating the role of interparticle interactions in magnetization reversal behavior and coercivity development. In this study, the statistical features of the magnetization reversal process in $SmCo_5$-based magnets were investigated by first-order reversal curve (FORC) analysis [2].
FORC analysis was performed on isotropic bonded and sintered specimens prepared from the same powder batch. Figure 1 shows the FORC diagrams of the isotropic bonded and sintered specimens. The bonded specimen exhibited higher coercivity and a broader coercivity distribution, whereas the sintered specimen showed lower coercivity with a sharper and more localized distribution. In addition, paired positive and negative features were observed in the FORC distributions of both specimens, suggesting that interparticle dipolar interactions play an important role in their reversal behavior.
[1] W. A. J. J. Velge and K. H. J. Buschow, J. Appl. Phys. 39, 1717–1720 (1968).
[2] A. P. Roberts, C. R. Pike, and K. L. Verosub, J. Geophys. Res. 105(B12), 28461–28475 (2000).

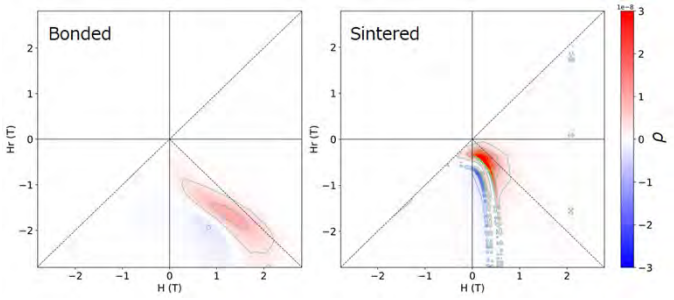


Figure 1. FORC diagrams of isotropic bonded and sintered $SmCo_5$-based magnets prepared from the same powder batch. Here, ρ denotes the FORC distribution.

GD-06. Sm-Co/Fe nanocomposite fine particles prepared by low-oxygen powder metallurgy

K. Park[1], Z. Liu[1], T. Suwa[1, 2], S. Okamoto[2, 3], Y. Hirayama[1]
[1]National Institute of Advanced Industrial Science and Technology (AIST), Nagoya, Japan, [2]Tohoku University, Sendai, Japan, [3]National Institute for Materials Science, Tsukuba, Japan

The accelerating transition to electrification is driving strong demand for next-generation permanent magnets. While Nd–Fe–B remains the highest-performing commercial system, its $(BH)_{max}$ is already near the theoretical ceiling [1], leaving limited room for further gains. Nanocomposite (NC) magnets [2] based on exchange coupling between a high-anisotropy hard phase and a high-

magnetization soft phase offer an alternative route to improved performance. To date, however, clear success has been concentrated in thin films; extending the same concept to bulk materials is difficult because it requires uniform, nanoscale control of multiphase microstructures throughout the entire volume.
Here we develop an anisotropic Sm–Co/Fe NC powder by combining low-oxygen powder processing with surface engineering. Sm–Co nanopowder with high specific surface area was produced by a low-oxygen thermal plasma process, then annealed to increase the $SmCo_5$ fraction and thereby raise coercivity. The powder was subsequently refined by wet-jet milling to obtain anisotropic particles with an average size below ~500 nm. A soft magnetic phase was introduced by depositing Fe onto the Sm–Co particle surfaces by physical vapor deposition (PVD). Transmission electron microscopy confirmed locally formed Fe layers of ~10 nm thickness. Compared with uncoated Sm–Co, the Fe-coated powder exhibited higher saturation magnetization and remanence with little loss of coercivity. These results establish a practical route to nanoscale-integrated Sm–Co/Fe NC powders that maintain coercivity while boosting magnetization, supporting further development toward high-performance bulk NC magnets.
[1] Y. Matsuura, J. Magn. Magn. Mater. 303 (2006) 344-347.
[2] E.F. Kneller, R. Hawig, IEEE Trans. Magn. 27 (1991) 3588-3560.

GD-07. Intrinsic properties of Sm-(Fe-M)-C, N compounds for high-performance permanent magnet

Y. Hirayama[1], Y. Tatetsu[2]
[1]National Institute of Advanced Industrial Science and Technology, Nagoya, Japan, [2]Meio University, Nago, Japan

Rare-earth elements are currently regarded as critical materials due to supply risks and expanding demand. Permanent magnets, which rely on rare-earth elements to achieve high magnetic performance, are indispensable for improving the efficiency of electric motors. Among potential alternatives to Nd–Fe–B magnets, Sm-based compounds have attracted significant attention. These compounds intrinsically exhibit excellent intrinsic magnetic properties; however, converting them into practical permanent magnet forms remains challenging. In particular, their relatively low thermal decomposition temperature critically restricts process windows for magnet fabrication and hinders performance optimization. In this study, we focus on improving the decomposition temperature of Sm-based compounds and report systematic evaluations from both experimental and computational perspectives.
Sm(Fe,Ga) alloys were prepared by high-frequency induction melting, followed by homogenization annealing at 1050 °C for one day to obtain a uniform alloy. Subsequent nitriding and carburizing treatments were carried out at 450 °C using nitrogen and methane gas flow, respectively. Phase identification was performed by X-ray diffraction, and magnetic properties were evaluated by magnetization measurements. Differential thermal analysis (DTA) was employed to estimate the thermal decomposition temperature.
The inductively melted alloys were obtained as nearly single-phase materials, with only a few percent of residual Fe. After nitriding and carburizing, an approximate 6% volume expansion was observed. DTA results revealed that Ga addition increased the decomposition temperature by approximately 30 °C. This enhancement is particularly advantageous, as it allows higher processing temperatures during sintered magnet fabrication, thereby contributing positively to the development of high-performance Sm-based permanent magnets.

GD-08. Cell-like structure of high coercivity $Sm_2(Fe, Mn)_{17}N_x$ coarse powder produced by overnitridation

A. Hosokawa
National Institute of Advanced Industrial Science and Technology, Nagoya, Japan

$Sm_2Fe_{17}N_3$ is a hard magnetic compound with high saturation magnetization, strong anisotropy, and a high Curie temperature. [1] Traditionally, rare earth magnets like Nd-Fe-B and Sm-Fe-N achieve high coercivity by reducing particle size to 1–5 μm through pulverization, followed by sintering to create highly anisotropic magnets. However, $Sm_2Fe_{17}N_3$ presents unique challenges: its decomposition at 620°C prevents the use of hot deformation techniques that work for Nd-Fe-B, limiting process flexibility and resulting in low density and reduced magnetic properties.
A notable exception for $Sm_2Fe_{17}N_x$ magnets is the overnitridation technique, where the nitrogen content x exceeds the stoichiometric value of 3 [2, 3, 4]. This process forms a cell-like microstructure (cell size: 50–300 nm) inside coarse powder particles, significantly enhancing coercivity without reducing particle size. Importantly, the original crystal orientation is preserved after overnitridation, allowing for both high coercivity and strong magnetic anisotropy in large particles—something no other process achieves for $Sm_2Fe_{17}N_x$ magnets [4].

This innovation greatly simplifies powder handling, eliminating the need for inert gas atmospheres and opening the door to scalable production of anisotropic $Sm_2Fe_{17}N_x$ magnets. Additionally, the refined microstructure improves the temperature stability of coercivity, making overnitridation an excellent method for producing heat-resistant, high-performance magnets.

In this study, we produced $Sm_2(Fe,Mn)_{17}N_x$ powder with coercivity up to ~10 kOe using overnitridation. While Mn-free samples reached only ~2 kOe, Mn doping enabled high coercivity without particle size reduction. The detail of experimental procedures was alredy reported elsewhere [4]. A systematic microstructural analysis was newly performed to clarify how these features influence magnetic performance and guide further improvements.

[1] Iriyama et al. (1992) IEEE Trans. Magn. 2326
[2] Imaoka et al. (1995) JALCOM 73
[3] Ohmori et al. (2006) Proceedings of REPM2006 268
[4] Hosokawa and Takagi (2017) Acta Materialia 366

GD-10. Diffusion-Driven Pathways for Development of Rare Earth Free $L1_0$ Ordered FeNi Thin Films for Permanent Magnet Applications

A. Gupta, M. Gupta
Physics, UGC-DAE Consortium for Scientific Research, Indore, Madhya Pradesh, India

The recent rare-earth supply crisis has intensified the quest for developing sustainable permanent magnets based on earth-abundant materials [1]. In this context, $L1_0$-ordered FeNi *aka* tetrataenite, exhibits a large saturation magnetization and a robust uniaxial magnetic anisotropy, making it a valuable gap magnet for permanent magnet applications [2]. However, synthesis of this phase is challenging due to the sluggish interdiffusion of Fe and Ni below the order-disorder temperature of 600 K [3].

We investigated the diffusion-assisted structural and magnetic evolution of equiatomic FeNi thin films using an optimized 5 at. % Cu doping as a diffusion-enhancing element, followed by the exploration of a nitrogen-mediated ordering route [4]. The structural, diffusion, and magnetic properties of the post-annealed films were systematically investigated using x-ray diffraction (XRD), polarized neutron reflectivity (PNR), nuclear resonant scattering (NRS), and SQUID-VSM magnetometry. The results demonstrate that Cu doping significantly accelerates interdiffusion in Fe/Ni by a factor of 50 as shown in fig. 1 (a-d). Building on these results, N insertion and topotactic extraction (NITE) is being explored as a novel approach to tailor diffusion pathways and facilitate atomic ordering. During denitridation, combined analysis of PNR indicates a progressive transition from a nonmagnetic nitrogen-rich FeN/NiN multilayer state to a magnetically ordered FeNi phase as shown in fig. 1 (e) and (f). Also, the increase in perpendicular coercivity provides strong evidence for the formation of the hard $L1_0$-FeNi phase, as shown in fig. 2. These findings establish an effective processing route toward L10-FeNi phase formation, offering a viable pathway for rare-earth-free permanent magnet development.

[1] J.M.D. Coey, IEEE Trans. Magn. 47 (2011) 4671–4681.
[2] Mandal, M. Debata, S. Basu, Crit. Rev. Solid State Mater. Sci. 48 (2023) 703–725.
[3] N. Bordeaux, A.M. Montes-Arango, L.H. Lewis, Acta Mater. 103 (2016) 608–615.
[4] K. Ito, T. Ichimura, M. Hayashida, et al., J. Alloys Compd. 946 (2023) 169450.

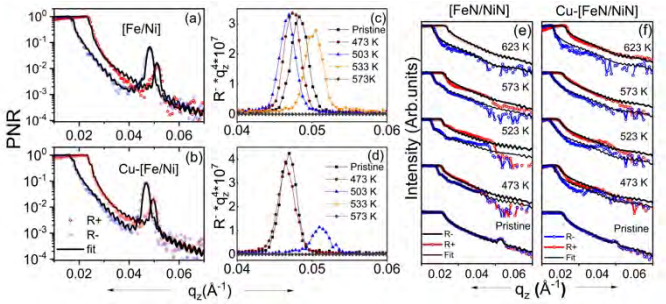


Fig.1 PNR data and Bragg peak comparison of undoped (a,c) and Cu-doped (b,d) Fe/Ni multilayers. PNR data of nitride undoped (e) and Cu-doped (f) samples before and after annealing at different temperatures.

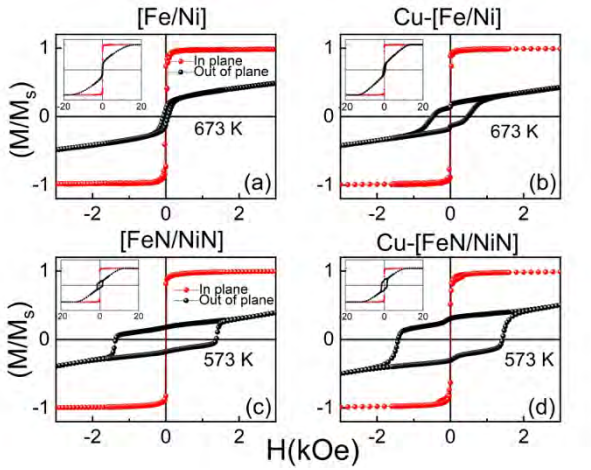


Fig 2. M-H loops for undoped (a) and Cu-doped (b) Fe/Ni multilayers annealed at 673 K. M-H loops of nitride undoped (c) and Cu-doped (d) Fe/Ni multilayers annealed at 573 K. The inset shows the complete M-H loops.

GD-11. Role of orbital magnetic moments in tetragonally distorted FeCo-based alloys studied by X-ray magnetic circular dichroism

J. Okabayashi[1], C. Murakami[2], T. Hasegawa[2]
[1]UTokyo, Tokyo, Tokyo, Japan, [2]Akita Univ., Akita, Akita, Japan

Tetragonally distorted FeCo-based alloys with a body-centered tetragonal (bct) structure exhibit high saturation magnetization and a large magneto-crystalline anisotropy of 1 MJ/m^3 with perpendicular magnetic anisotropy (PMA), making them promising new hard magnetic materials. The formation of bct structures has been reported to be facilitated by adding elements such as V and N [1]. However, the mechanism behind PMA remains unclear. Here, we employ X-ray magnetic circular dichroism (XMCD) to investigate the element-specific anisotropic electronic and magnetic states, enabling analysis of the orbital moment anisotropy responsible for the PMA in FeCo-based alloys.

Samples were prepared by magnetron co-sputtering of Fe-Co-V-N elements with the deposition of a Rh buffer layer on MgO substrates. The amount of N atoms was controlled by adjusting the mixing ratio of Ar and N_2 gases during sputtering. In this study, we used compositions of MgO substrate / Rh (20 nm) / $\{(Fe_{0.5}Co_{0.5})_yV_{100-y}\}_xN_{100-x}$ / Rh capping (2 nm) with variations in x and y. XMCD measurements were performed at the KEK Photon Factory, BL-7A, using a magnet applying ±1 T with a circularly polarized beam. Total electron yield mode was employed. We conducted angular dependence measurements at normal and oblique incidence setups, maintaining parallel alignment of the beam and magnetic field directions.

XMCD for Fe and Co L-edges with angular dependence shows an enhancement of orbital magnetic moments at normal incidence, indicating orbital moment anisotropy for PMA [2]. Not only Fe sites but also Co sites contribute to the anisotropic orbital magnetic moments. Furthermore, the sign of XMCD in V is opposite to those of Fe and Co, explaining the reduction of PMA energy with increasing V concentration. Addition of N dopants expands the c-axis lattice but also reduces the PMA energy, which can also be explained by XMCD. We will discuss detailed concentration dependences for enhancing PMA.

[1] T. Hasegawa et al., Sci. Rep. 15, 28636 (2025).
[2] Y. Miura and J. Okabayashi, J. Phys. Cond. Mat. 34, 473001 (2022).

GD-12. Enhanced Coercivity in C16 phase high-entropy borides through ultrafast high-temperature sintering

B. J. Fugetta[1], T. Li[2], K. Zeng[2], C. Liu[3], W. Beeson[1], X. Zhang[3], G. Yin[1], L. Hu[2], K. Liu[1]
[1]Physics, Georgetown University, Washington, District of Columbia, United States, [2]Materials Science, Yale University, New Haven, Connecticut, United States, [3]Materials Science and Applied Physics Department, King Abdullah University of Science and Technology, Thuwal, Saudi Arabia

Permanent magnets have critical applications in numerous technology sectors, including magnetic recording, robotics, and clean energy generation [1]. Recently, high entropy borides with C16 uniaxial crystal structures have emerged as a promising class of rare-earth-free and precious-metal-free magnets [2]. Here we have investigated the dependence of magnetic anisotropy in high entropy (FeCoNiMn)2B as a function of synthesis conditions. The boride films are synthesized via magnetron sputtering, followed by rapid thermal annealing (RTA). A suitable mixing of the transition metals in their sublattice enables the switching of easy-plane anisotropy in binary borides to easy-axis in high entropy borides, leading to doubling of the coercivity. High-resolution transmission electron microscopy (TEM) confirmed the C16 ordering and tetragonal crystal structure with nanoscale chemical uniformity shown by electron energy loss spectroscopy (EELS). The magnetic anisotropy can be further enhanced using ultrafast high-temperature sintering [3], with a five-fold increase in major loop coercivity to 1.5 kOe at room temperature. First-order reversal curve (FORC) studies reveal the presence of a magnetic hard phase, manifested as a horizontal ridge in the FORC distribution centered around local coercivity of 1.8 kOe (Fig. 1). These results demonstrate a promising avenue to achieve strong magnets using only earth-abundant elements.

This work has been supported in part by the NSF (ECCS-2429995).

[1] O. Gutfleisch, M. A. Willard, E. Brück, C. H. Chen, S. G. Sankar, J. P. Liu, Adv. Mater. 23, 821 (2011).
[2] W. B. Beeson, D. Bhattacharya, D. Bista, B. J. Fugetta, G. Yin, K. Liu, Adv. Mater. 38, e16135 (2026).
[3] C. Wang, W. Ping, Q. Bai, H. Cui, R. Hensleigh, R. Wang, A. H. Brozena, Z. Xu, J. Dai, Y. Pei, C. Zheng, G. Pastel, J. Gao, X. Wang, H. Wang, J. Zhao, B. Yang, X. Zheng, J. Luo, Y. Mo, B. Dunn, L. Hu, Science 368, 521 (2020).

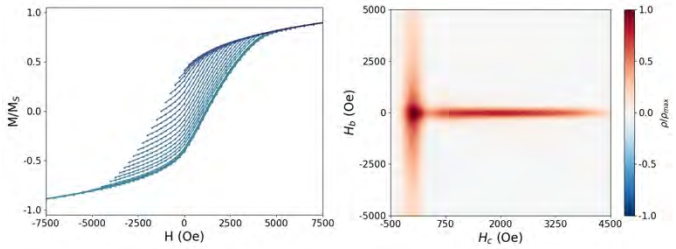


Fig. 1: (Left) Family of FORCs and (Right) the corresponding FORC distribution of an annealed (FeCoNiMn)2B thin film sample.

GD-13. Chemical Bonding Descriptors for Rare-Earth-Free Permanent Magnet Discovery

A. Rauf[1], E. Oliphant[2, 1], W. Sun[1]
[1]Materials Science and Engineering, University of Michigan, Ann Arbor, Michigan, United States, [2]Schwarzman College of Computing, Massachusetts Institute of Technology, Cambridge, Massachusetts, United States

The data-driven discovery of high-performance rare-earth-free permanent magnets has largely relied on descriptors of magnetism derived from the full unit cell such as band structure and density of states. Although useful, these descriptors have not produced general chemical design principles because they do not explicitly encode the local bonding environment around magnetic ions. This local detail is non-trivial to access from DFT due to its delocalized plane wave basis. Here, we apply Crystal Orbital Guided Iteration to atomic Orbitals[1,2] (COGITO), which fits an adaptive local basis to DFT and enables extraction of real-space bonding information. With COGITO, we compute descriptors that capture the interplay of bonding and magnetism, such as bond magnetic moment and local bonding/antibonding energies. Across a dataset of permanent magnetic compounds, we evaluate the predictive value of these descriptors for key performance metrics and identify chemically meaningful correlations, including a link between magnetic ion associated antibonding and saturation magnetization.

1. Oliphant, E., Kioupakis, E. and Sun, W., arXiv:2511.19725 (2026).
2. Oliphant, E., Mantena, V., Brod, M. et al., Mater. Horiz., 12, 3073–3083 (2025).

SESSION GE: COUPLED-FIELD FUNCTIONAL MAGNETICS: MAGNETOELASTIC, MAGNETOCALORIC AND BEYOND

Chair(s): J. Amaral, *Physics, Universidade de Aveiro, Aveiro, Portugal*
Friday, November 6, 2026
08:30 AM-12:00 PM
South Pacific 1/2

GE-01. Magnetoelastic mass sensing: fundamentals, optimization strategies, and applications in harsh environments

A. Lopes[1, 2], A. García-Arribas[1], J. Gutiérrez[1], J. Saiz Garitaonandia[1], A. Lasheras[1]
[1]University of the Basque Country, Leioa, Spain, [2]IKERBASQUE, Basque Foundation for Science, Bilbao, Spain

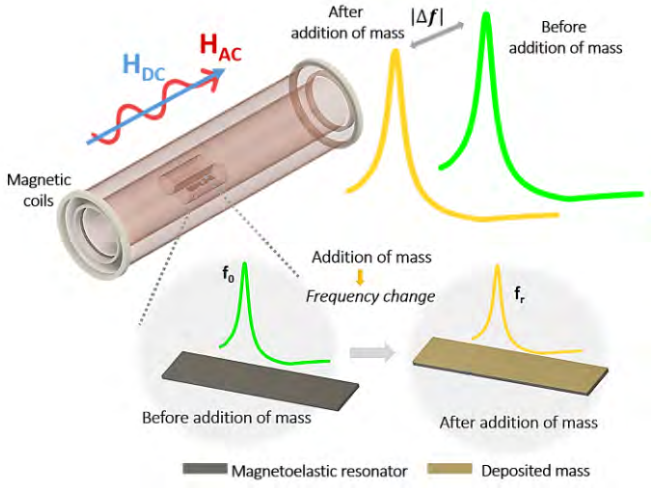
Magnetoelastic sensors constitute a powerful platform for passive and contactless systems, enabling precise monitoring of physical, chemical, and environmental processes. Their operation relies on the magnetoelastic effect, where magnetic and elastic energies are coupled, allowing the excitation of mechanical resonances through an applied magnetic field. As a consequence, variations in resonance frequency produced by changes in mass loading, stiffness, applied stress, temperature, or the viscosity of the medium can be wiressly detected in real time (see Figure 1). This combination of remote readout, fast response, and simple excitation/measurement makes magnetoelastic sensors especially suitable for situations where conventional transducers are difficult or expensive to implement, such as fully remote locations, sealed systems, or harsh and corrosive environments.
Metallic glasses produced by rapid melt spinning offer the optimal combination of soft magnetic behaviour, amorphous structure, and tunable magnetostriction required for efficient magnetoelastic transduction. Their low coercivity and the absence of magnetocrystalline anisotropy allow sharp resonance peaks and high magneto mechanical coupling. In recent years, several strategies have been explored to enhance the performance of these sensors by tuning composition, geometry, and microstructure [1–3]. For instance, geometry engineered resonators, including rhombus shaped structures, have shown sensitivity improvements above 80% when compared with the traditional rectangular geometry commonly used in commercial devices [2]. In parallel, controlled thermal treatments can induce partial nanocrystallization, which is

known to increase resonance frequency, quality factor, and mass sensitivity. Remarkably, crystallized alloys can also exhibit a stable self-bias effect, which eliminates the need for an external magnetic field during operation and greatly simplifies device integration in practical sensing systems [3].
Furthermore, a major limitation of conventional metallic glass sensors is their poor corrosion resistance when operating in demanding or chemically aggressive environments. To overcome this drawback, new Fe–Ni–Cr–Si–B compositions have been specifically developed to provide improved electrochemical stability while preserving favourable magnetoelastic properties. These alloys exhibit significantly reduced corrosion currents and increased polarization resistance compared with standard Metglas, both in the as quenched and crystallized states [4]. After crystallization, the sensors maintain high resonance quality and show robust self biased behaviour, opening opportunities for long term monitoring in applications in aqueous and corrisive media such as ice nucleation detection, sol gel transition studies, environmental monitoringand biological processes involving small mass or viscosity changes. Overall, advances in materials engineering, geometry optimization and controlled crystallization are converging toward a new generation of highly sensitive, robust, and application tailored magnetoelastic sensors capable of operating reliably under increasingly challenging conditions.
[1] P.G.Saiz, D. Gandia, A.Lasheras, A.Sagasti, I.Quintana, M.L. Fez-Gubieda, J. Gutiérrez, M.I.Arriortua, A.C.Lopes, Sens. Actuator B-Chem., 296, 126612 (2019)

[2] P.G.Saiz, J. Gutiérrez, M.I.Arriortua, A.C.Lopes, IEEE Sens. J., 20, 13332 - 13340 (2020)

[3] A. Lasheras, J.S. Garitaonandia, I. Quintana, J.L. Vilas, A.C.Lopes, Sens. Actuators Rep., 8, 100251 (2024)

[4] A. C. Lopes, J. Gutiérrez, A. García-Arribas, A. Aginagalde, A. Ayerdi, I. Quintana, J.L. Vilas, J.S. Garitaonandia, A. Lasheras, J. Alloys Compd., 1043, 184229 (2025)



Schematic representation of the sensing principle based on magnetoelastic resonance

GE-02. Maximizing the Torque Density of Magnetic Elastomer Soft Actuators

H. Htet, A. El-Ghazaly
Electrical and Computer Engineering, Cornell University, Ithaca, New York, United States

Magnetic elastomer soft actuators are promising candidates for deformable tactile displays and soft robots, achieving large deformations (>450% of thickness) [1, 2] under low magnetic fields (25 mT) [3]. Two rectangular magnetic elastomer segments with opposing out-of-plane magnetizations embedded in a larger non-magnetic elastomer matrix (see inset, Fig. 1) are torqued by an in-plane magnetic field to actuate the entire composite upward. In this work, we maximize the remanent magnetization of the magnetic portions of the composites to increase the torque density.
Remanent magnetization depends on both magnetic particle loading and chain-like particle alignment induced by a 350 mT applied field during curing. We first vary the NdFeB volume fraction at a fixed elastomer thickness of 170 μm to measure remanent magnetization, then fabricate composite elastomers using these magnetic elastomer segments to measure deflection under an in-plane field of 25 mT (Fig. 1). Remanent magnetization and, consequently, the deflection of the composite elastomer increase with increasing particle content up to the tested maximum of 25 vol%, which is selected for maximum actuation.
To isolate structural from compositional effects, elastomers with 25 vol% are fabricated at three thicknesses (113, 170, and 225 μm). The remanent-to-saturation magnetization

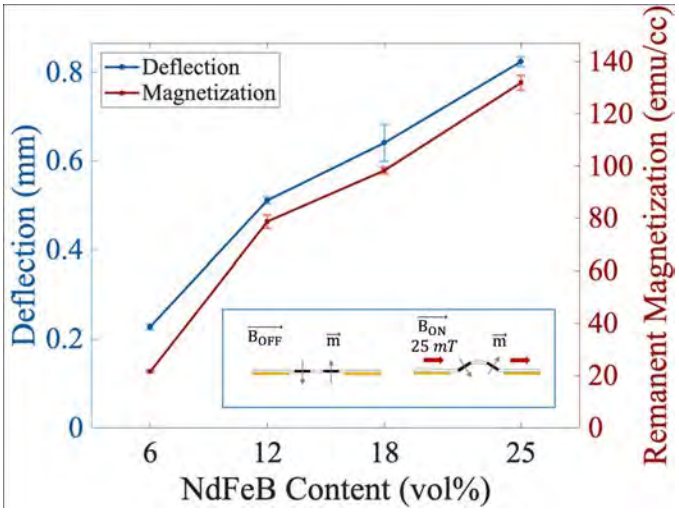
ratio (Mr/Ms) peaks at 170 μm and decreases at 225 μm (Fig. 2), indicating optimal particle chain formation around 170 μm. SEM EDX confirms well-defined chain alignment at this 170 μm intermediate thickness, while 225 μm samples exhibit particle agglomeration, reducing magnetic anisotropy and remanence.

These results demonstrate that both particle loading and geometric constraints during curing critically influence magnetic remanence and, consequently, actuator performance for low-field actuation applications.

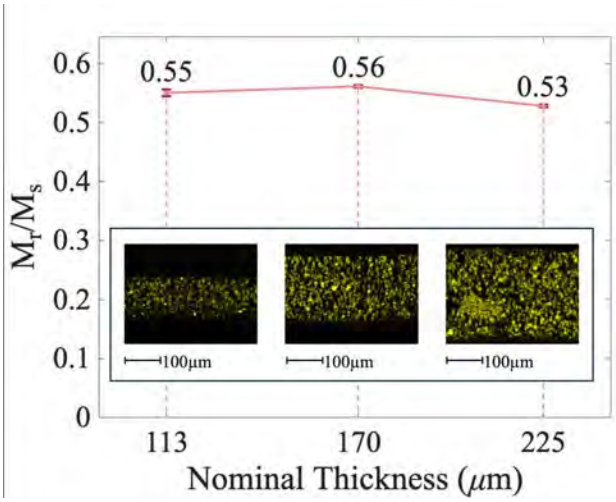
Y. Kim and X. Zhao, *Chem. Rev.*, vol. 122, no. 5, pp. 5317–5364, (2022)

L. Cestarollo, S. Smolenski, and A. El-Ghazaly, *ACS Appl. Mater. Interfaces*, vol. 14, no. 16, pp. 19002–19011, (2022)

H. Htet and A. El-Ghazaly, *Transducers.*, pp. 1161-1164, (2025)



Deflection and remanent magnetization of magnetic elastomer actuators as a function of NdFeB volume fraction, showing increasing remanent magnetization and deflection.



Mr/Ms versus magnetic elastomer thickness for 25% vol NdFeB elastomers, with corresponding cross-sectional SEM EDX images showing particle chain formation and tendency toward agglomeration at larger thicknesses.

GE-03. Stress Tunable Multiferroic Magnetic Circuit : The Magnetic Rheostat

T. R. Mion[1], M. Staruch[1], N. J. Jones[2], J. Yoo[2], R. Olsson[3], M. G. Allen[3], P. Finkel[1]

[1]Material Science & Technology, US Naval Research Laboratory, Washington, District of Columbia, United States, [2]Carderock Division, Naval Surface Warfare Center, Bethesda, Maryland, United States, [3]Department of Electrical and Systems Engineering, University of Pennsylvania, Philadelphia, Pennsylvania, United States

This work presents the development of a magnetic rheostat, a dynamically tunable magnetic circuit element analogous to a variable resistor [1], leveraging the stress-dependent permeability of magnetostrictive materials [2]. Dynamic and precise control of a magnetic field is increasingly critical for diverse applications, yet traditional methods such as electromagnets suffer from power consumption and size limitations. This magnetic rheostat offers a non-volatile, energy-efficient alternative. The device utilizes Galfenol (Fe1-xGax), whose permeability decreases under compressive stress to demonstrate stress-induced modulation of the magnetic flux density within an air gap as shown in Figure 1a. A fabricated prototype, comprising a Galfenol flux conduction element mechanically coupled to a lead-zirconate-titanate (PZT) piezoelectric actuator for stress application (Figure 1b), exhibits a magnetoelectric coupling coefficient of -0.659 mT/V and tuning of the flux density from 176.6 mT to 85.5 mT [3] as shown in Figure 2.

This multiferroic approach, based on stress-mediated permeability changes, demonstrates the feasibility of dynamic, non-current based flux control and opens new avenues for designing tunable magnetic circuits for diverse applications requiring precise magnetic field manipulation. The inherent non-linearity of ferromagnetic materials, while presenting design challenges related to saturation effects, also offers opportunities for performance optimization through tailored geometry and stress application methods.

[1] "Magnetics and Magnetic Equivalent Circuits," in Power Magnetic Devices, (John Wiley & Sons, Ltd, 2021), pp. 43–101
[2] R.M. Bozorth, Ferromagnetism (IEEE Press, 1951)
[3] T. Mion, M. Staruch, P. Finkel et al., *Appl. Phys. Lett.* 127, 252902 (2025)

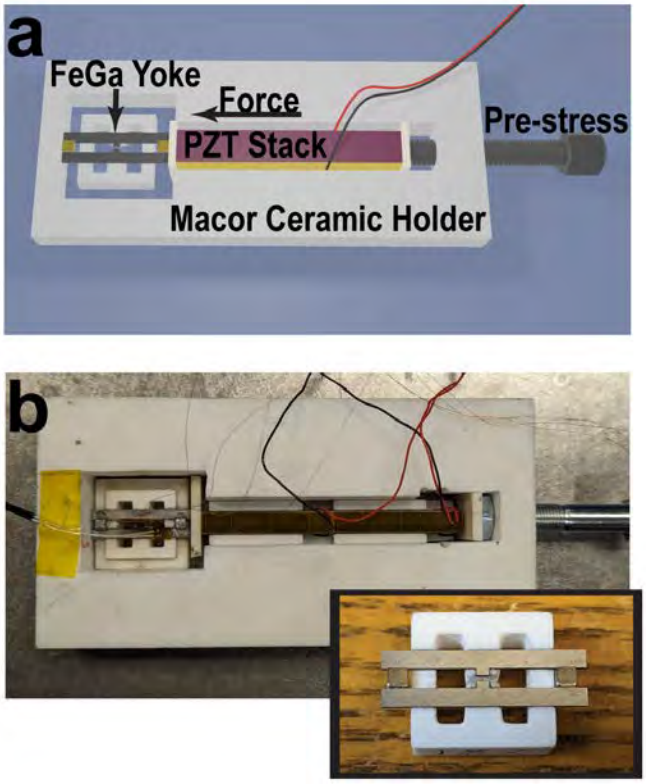


Fig.1 a) Conceptualized design of testing apparatus b) Fabricated testing apparatus during testing of the magnetic rheostat circuit and (inset) a zoomed in picture of the assembled FeGa yoke with NdFeB magnets on a 3D printed fixture

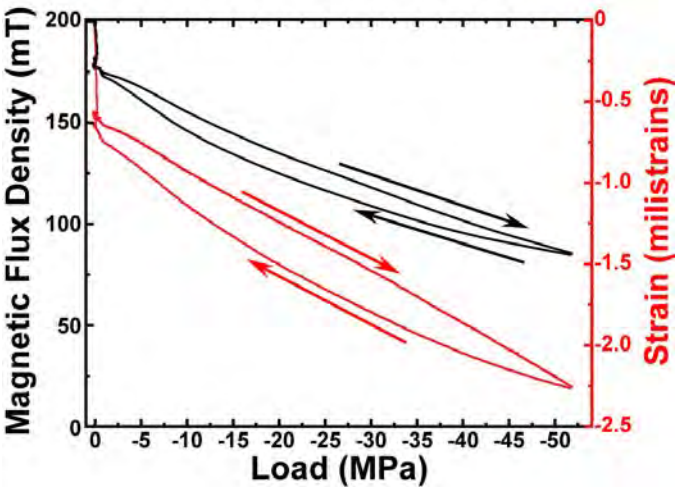


Fig.2 Correlation of applied strain (plotted in millistrains) and magnetic flux across the 1mm gap for yoke alloy Fe0.82Ga0.18

GE-05. Wrong-Way Magnetic Anisotropy in Polycrystalline Alloy Films

O. A. Bakare[1], S. Abdizadeh Kalan[1], G. T. Street[1], A. Almahmoud[1], C. Klewe[2], S. Emori[1]
[1]*Physics, Virginia Tech, Blacksburg, Virginia, United States,* [2]*Advanced Light Source, Lawrence Berkeley National Lab, Berkeley, California, United States*

Engineering uniaxial magnetic anisotropy is essential for various device applications, including sensors, memories, and actuators [1]. A long-established, straightforward method to introduce anisotropy in polycrystalline films is to grow them under an in-plane *in-situ forming field* H_{form} [2]. Conventionally, the magnetic easy axis aligns collinear with H_{form}, due to Néel pair ordering that stabilizes directional short-range order along H_{form} [3]. In this presentation, we demonstrate the surprising emergence of "wrong-way" anisotropy, where the easy axis aligns orthogonal to H_{form} in binary ferromagnetic alloy films.

Our vibrating sample magnetometry (VSM) results in Fig. 1 showcase this unusual anisotropy in polycrystalline FeV. While the easy axis (corresponding to a square hysteresis loop) is along H_{form} in the elemental Fe film, it is orthogonal to H_{form} in the $Fe_{70}V_{30}$ alloy film. Our ferromagnetic resonance (FMR) measurements [Fig. 2] further confirm that the easy axis changes from collinear with H_{form} ($\Delta H_k < 0$) to orthogonal to H_{form} ($\Delta H_k > 0$) as the V content in $Fe_{100-x}V_x$ exceeds $x = 20$. Similar "wrong-way" anisotropy also

emerges in $Ni_{100-x}Fe_x$ alloys [Fig. 2]. We attribute the observed phenomenon to the competition between Néel pair ordering and magnetoelastic coupling, in which a certain sign of magnetostriction can rotate the easy axis away from the H_{form}-induced stress axis. Our findings present fresh fundamental insights into anisotropy in polycrystalline ferromagnetic alloys and may enable high-performance sensors leveraging orthogonal easy axes.

[1] B. Buford, P. Dhagat, and A. Jander *J. Appl. Phys. 115,* 17E309 (2014).
[2] M. Sagawa, S. Fujimura, and N. Togawa, *J. Appl. Phys. 55*(6), 2083-2087 (1984).
[3] A. T. Hindmarch, D. A. Arena, *Phys Rev B 81*, 100407(R) (2010).

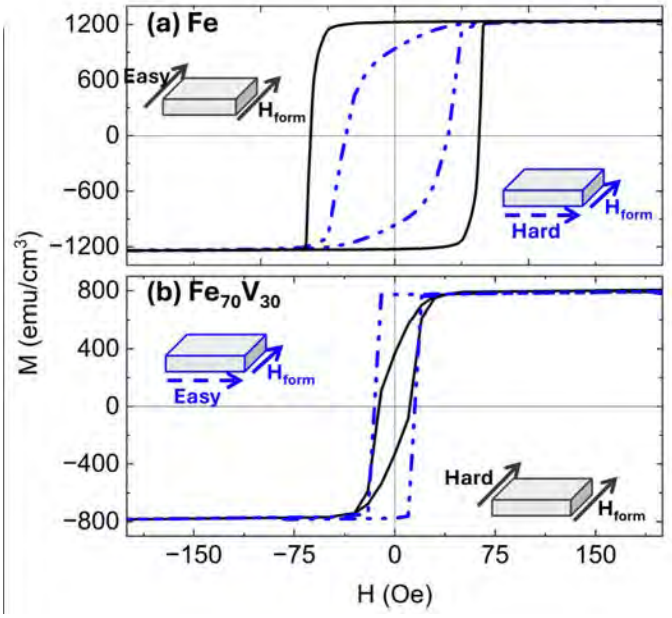


Fig. 1: VSM measurements of 30-nm-thick polycrystalline films grown under an in-situ forming field (H_{form}). (a) Fe: the easy axis is collinear with H_{form}. (b) $Fe_{70}V_{30}$: the easy axis is orthogonal to H_{form}.

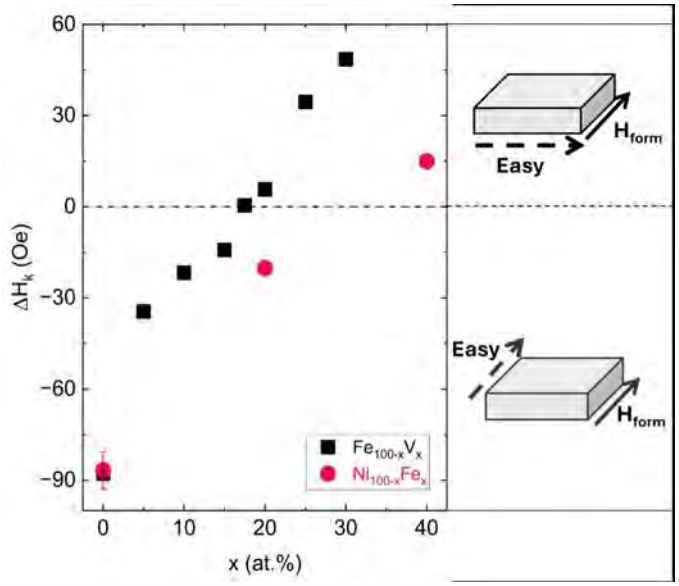


Fig. 2: In-plane uniaxial anisotropy field ΔH_k, obtained from FMR, for 30-nm-thick polycrystalline $Fe_{100-x}V_x$ and $Ni_{100-x}Fe_x$ alloy films. $\Delta H_k < 0$ denotes the easy axis collinear with H_{form}, whereas $\Delta H_k > 0$ denotes the easy axis orthogonal to H_{form}.

GE-07. Magnetic Structure of Antiphase Boundaries in Ni-Mn-Ga Magnetic Shape Memory Alloys

O. Heczko[1], F. Máca[1], V. Drchal[1], L. Straka[1], V. Chlan[2], H. Seiner[4], J. Zemen[1, 3]
[1]Magnetic Materials, FZU – Institute of Physics of the Czech Academy of Sciences, Prague, Czechia, [2]Low Temperature Physics, Faculty of Mathematics and Physics, Charles University, Prague, Czechia, [3]Faculty of Electrical Engineering, Czech Technical University, Prague, Czechia, [4]Institute of Thermomechanics of the Czech Academy of Sciences, Prague, Czechia

Heusler Ni-Mn-Ga alloys are the most promising materials for magnetic shape memory (MSM) applications above room temperature and low magnetic field. Besides of mobile twin boundaries in modulated martensites, critical for MSM effect, the $L2_1$ ordered Heusler alloys contain antiphase boundaries. The antiphase boundaries (APBs) are planar defects that play a critical role in enhancing coercive force and can extend the functionality of the material [1]. However, the structure of APB has been a puzzle due to low resolution of the methods visualizing the APB. In particular, high resolution transmission electron microscopy cannot resolve APBs as there is no atomic contrast due to similarity of atomic species involved.

We combined theoretical, ab initio and micromagnetic calculations to reveal magnetic ordering near the antiphase boundary (APB) in Ni_2MnGa. Electronic structure calculations based on density functional theory were employed to investigate the magnetic ordering in a structure simulating APB's in cubic austenite. It was found that APB region contains two atomically sharp APB with the single atomic layer core. Micromagnetic calculation further demonstrated that even this ultrathin APB region produces sufficient contrast to be detected by magnetic force microscopy (MFM). The comparison of MFM and simulate image is shown in Fig. 1. Further support of suggested structure comes from experimental observations by magnetic Lorenz TEM and nuclear magnetic resonance (NMR) experiment. Moreover, disrupted ferromagnetic coupling may contribute to the formation of 10M modulated martensite exhibiting extreme shear instability [3].

The work was supported by OP JAK project No.CZ.02.01.01/00/22_008/0004591 and Czech Science Foundation Grants No. 24-11361S.

[1] L. Straka et al., Magnetic coercivity control by heat treatment in Heusler Ni-Mn-Ga(-B) single crystals, *Acta Mat.* 169 (2019) 109-121

[2] O. Heczko et al., Antiphase boundaries in Ni-Mn-Ga single crystal— experiment and model, *Appl. Phys. Lett.* 128, 011901 (2026)

[3] K. Repcek et al. Compliant Lattice Modulations Enable Anomalous Elasticity in Ni–Mn–Ga martensite, *Adv. Mater.* 2024, 2406672

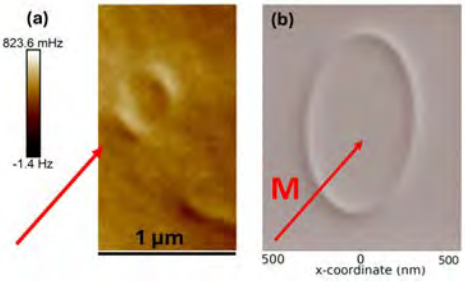


Fig. 1. Comparison of magnetic force microscopy (MFM) image (a) and micromagnetic simulation (b) based on ab initio calculated magnetic structure of single antiphase boundary enclosing antiphase domain in 10M modulated martensite of Ni_2MnGa. The APB magnetic contrast is only visible if the APB line is about perpendicular to magnetization direction (red arrows).

GE-09. Tuning Magnetocaloric Response by Shape Anisotropy in NiCoGa Nanowire Arrays

A. A. Mendonça[1], V. M. Prida[2], V. Vega[2], F. Béron[1]
[1]*Universidade Estadual de Campinas, Campinas, Brazil,*
[2]*Universidad de Oviedo, Oviedo, Oviedo, Spain*

Rising global energy demand motivates the need to recover low-grade thermal energy. Thermomagnetic energy harvesting driven by magnetization changes across phase transitions is a promising route for heat-to-electricity conversion [1]. Ni-rich NiCoGa Heusler alloys remain relatively underexplored and are expected to combine ferromagnetism with first-order martensitic transformations [2]. Here, NiCoGa-based nanowire arrays (180 nm diameter, 6–7 µm long) were synthesized by pulsed electrodeposition into hard-anodized nanoporous alumina templates. Magnetization measurements show a magnetic transition above room temperature and an additional phase transformation near 200 K, observed only for out-of-plane applied magnetic field (parallel to the nanowires), indicating a relevant magnetic anisotropy (Fig. 1). Moreover, both coercivity (H_c) and remanent magnetization (M_R) exhibit pronounced minima at around 200 K - with reduced temperature for in-plane fields - suggesting a magnetostructural origin of the anisotropic phase transformation (Fig. 2). Finally, magnetocaloric analysis reveals an enhanced response around 200 K, with clear anisotropy in both magnitude and temperature dependence. When comparing magnetic field orientations, the parallel configuration (along the nanowire axis) exhibits a 17% higher maximum entropy change (ΔS), while the temperature of this maximum shifts upward by approximately 20 K. This behavior demonstrates that the relative orientation between the nanowire array and the applied magnetic field enables tuning of the temperature range of optimal performance. These findings evidence a strong coupling between magnetic and structural degrees of freedom in NiCoGa nanowire arrays, highlighting their potential for anisotropic thermomagnetic energy conversion at the nanoscale.

[1] D.Dzekan *et al.*, APL Mater. 9, 011105 (2021).
[2] R.V.S. Prasad and G. Phanikumar, Intermetallics 19, 1705 (2011).

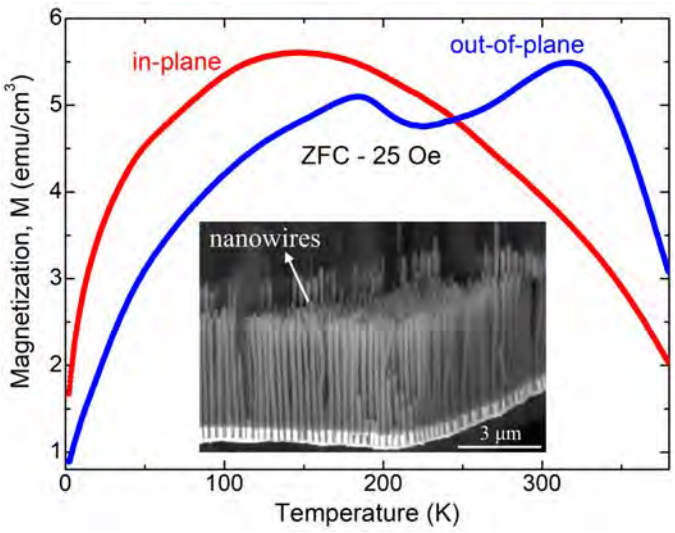


Fig. 1: Temperature dependence of magnetization. Inset showing an SEM nanowire array microscopy image.

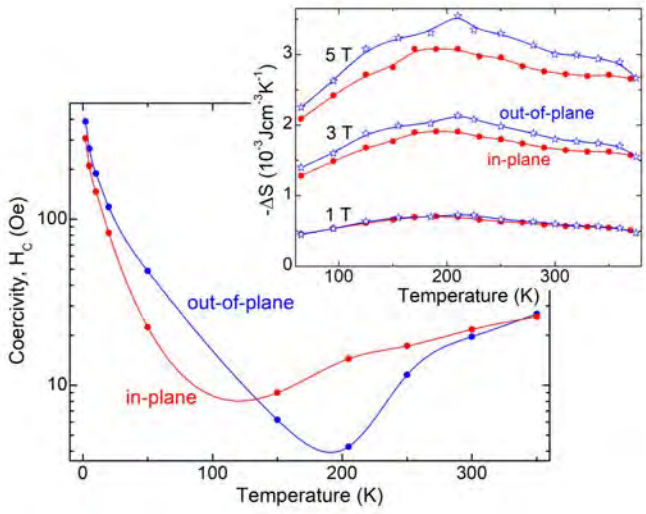


Fig. 2: Temperature dependence of coercivity. Inset: entropy change as a function of temperature.

GE-10. Arc-Melting-Induced Texturing and Its Impact on Magnetic and Magnetocaloric Properties

J. Bae, W. Yang, M. Kim, D. Shin
Korea Institute of Materials Science, Changwon, Gyeongsangnam-do, Korea (the Republic of)

At the laboratory scale, the arc-melting method is widely used to fabricate polycrystalline magnetocaloric effect (MCE) materials. This method generates a high-temperature arc between an arc tip and a hearth, melting the material followed by rapid solidification. While simple and effective, it is often overlooked that grains formed by arc-melting are not fully randomized (see Fig. 1).

In this study, TmGa was synthesized using the arc-melting method to investigate this issue. Bulk XRD and SEM-EBSD analyses reveal strong <100> texturing throughout the sample, indicating that the synthesized TmGa is a textured polycrystal rather than a conventional one. Magnetization measurements using a MPMS show clear anisotropy in both magnetization (m) and magnetic entropy change (ΔS_m) depending on the field direction relative to the texturing direction (TD), demonstrating the significant impact of texturing on magnetic and MCE properties.

Notably, despite being textured along the magnetic easy axis (<100>), the m and ΔS_m values measured parallel to the TD are comparable to those previously reported for nominally polycrystalline TmGa (see Table 1). However, a truly random polycrystal would be expected to exhibit significantly lower values. This suggests that previously reported "polycrystalline" TmGa samples were likely unintentionally textured due to the arc-melting process. Similar indications are also observed in other arc-melted materials. These findings highlight that anisotropy in textured polycrystals can critically affect the accurate evaluation of intrinsic magnetic and MCE properties, emphasizing the need to verify texturing prior to characterization.

Furthermore, strong magnetic anisotropy and anomalous magnetic behavior were identified in textured TmGa. The rotational magnetocaloric effect (RMCE) was also evaluated, indicating that textured TmGa is a promising RMCE material in the hydrogen liquefaction temperature range. These results suggest that arc-melting-induced texturing can be utilized as a new strategy for designing advanced MCE materials.

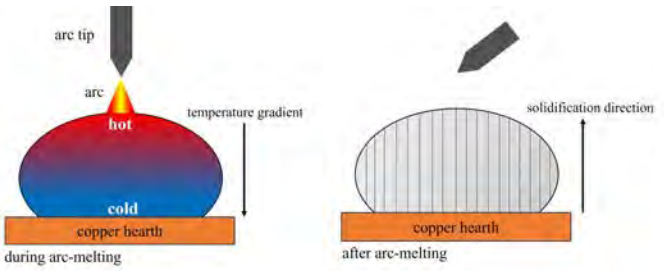


Figure 1. Synthesis of textured polycrystals using the arc-melting method

	TP TmGa $H \parallel$ TD	TP TmGa $H \perp$ TD	PC TmGa (*ref.*)
θ_p (K)	17.4	5.9	15.5
m (50 kOe, 2 K)	$6.6u_B/\mathrm{Tm}^{3+}$	$3.9u_B/\mathrm{Tm}^{3+}$	$6.6u_B/\mathrm{Tm}^{3+}$
$-\Delta S_{m,\max}$ (J/kg K; 50 kOe)	32.3	9.4	34.1

Table 1. Comparison of magnetic and magnetocaloric properties in TmGa

SESSION GF: TOPOLOGICAL MATERIALS AND SPIN TEXTURES

Co-Chair(s): Z. Wen, *National Institute for Materials Science (NIMS), Tsukuba, Ibaraki, Japan* and T. G. Rappoport, *INL Braga, Rio de Janeiro, Brazil*

Friday, November 6, 2026

08:30 AM-12:00 PM

South Pacific 3/4

GF-01. Racetrack Memory – 2D and 3D

S. Parkin

Max Planck Institute for Microstructure Physics, Halle (Saale), Germany

There is a tremendous need for high performance, non-volatile memory that goes beyond today's charge-based devices. Magnetic Racetrack Memory (RTM) is a unique memory-storage device that relies on the current driven motion of multiple domain walls along magnetic conduits. Racetrack Memory has evolved in several distinct stages that we have dubbed versions 1.0-4.0 [1]. In version 4.0 we showed that chiral domain walls can be driven at speeds exceeding 1 km/s in synthetic antiferromagnetic racetracks by spin currents generated via the spin Hall effect in proximal metallic layers [2]. Recently, we have shown that 2D racetracks can be scaled to dimensions of just a few nanometers and that chiral domain walls can be moved via spin-orbit torques at very high speeds (~1 km/s) and positioned with very high accuracy (few nm)[3]. These results establish that Racetrack Memory has the potential to surpass today's leading memory technologies. Racetrack Memory has even greater potential when formed in 3D. We discuss several approaches to building 3D racetracks. One of these uses freestanding membranes composed of atomically engineered thin film heterostructures that comprise the racetrack, that are formed on a sacrificial water-soluble sacrificial release layer. The membranes are then draped over pre-formed 3D hillocks to form 3D racetracks [4]. In a second approach, a novel state-of-the-art multi-photon super-resolution lithography system is used to fabricate 3D racetracks that are twisted in various forms. The geometrical chirality of the physically formed racetrack and the spin chirality of the individual domain walls interact in highly interesting ways e.g. to form a domain wall diode device[5]. In a third approach we discuss the use of atomic layer deposition to deposit the atomically thin magnetic layers that form the racetracks themselves. Such an approach would allow for racetracks to be deposited on vertical walls. These recent developments in 2D and 3D Racetrack Memory show its enormous potential.

1 Parkin, S. S. P. & Yang, S.-H. Memory on the Racetrack. *Nat. Nanotechnol.* 10, 195–198 (2015).

2 Yang, S.-H., Ryu, K.-S. & Parkin, S. S. P. Domain-wall velocities of up to 750 ms^{-1} driven by exchange-coupling torque in synthetic antiferromagnets. *Nat. Nanotechnol.* 10, 221–226 (2015). https://doi.org/10.1038/nnano.2014.324

3 Jeon, J.-C., Migliorini, A., Yoon, J., Jeong, J. & Parkin, S. S. P. Multi-core memristor from electrically readable nanoscopic racetracks. *Science* 386, 315–322 (2024). https://doi.org/10.1126/science.adh3419

4 Gu, K. *et al.* 3D racetrack memory devices designed from freestanding magnetic heterostructures. *Nat. Nanotechnol.* 17, 1065–1071 (2022).

5 Farinha, A. M. A., Yang, S.-H., Yoon, J., Pal, B. & Parkin, S. S. P. Interplay of geometrical and spin chiralities in 3D twisted magnetic ribbons. *Nature* 639, 67–72 (2025). https://doi.org/10.1038/s41586-024-08582-8

GF-03. Differentiating anomalous and topological Hall effects using first-order reversal curve measurements

G. M. Stephen[1], R. Van Haren[1], V. Sharma[1], L. Tai[2, 3], B. Dai[3], H. Chi[4], K. Wang[3], A. T. Hanbicki[1], A. Friedman[1]
[1]Laboratory for Physical Sciences, College Park, Maryland, United States, [2]RIKEN, Wako, Japan, [3]University of California, Los Angeles, Los Angeles, California, United States, [4]University of Ottawa, Ottawa, Ontario, Canada

Next generation magnetic memories rely on novel magnetic phases for information storage. Novel spin textures such as skyrmions provide one possible avenue forward due to their topological protection and controllability via electric fields. However, the common signature of these spin textures, the topological Hall effect (THE), can be mimicked by other trivial effects. Competing anomalous Hall effect (AHE) components can produce a peak in the Hall voltage similar to that of the THE, making clear identification of the THE difficult. By applying the first-order reversal curve (FORC) technique to the Hall effect in candidate topological Hall systems we can clearly distinguish between the THE and AHE. This technique allows for quantitative investigation of the THE and AHE in magnetic materials and heterostructures with topologically non-trivial spin textures. We demonstrate the technique and apply it to several example systems including $Mn_3Sn/Bi_{85}Sb_{15}$ heterostructures, Cr_2Te_3, $MnBi_2Te_4$, and Ta/CoFeB/Ir/MgO/Al_2O_3 stacks.
PHYSICAL REVIEW B 112, 094440 (2025)

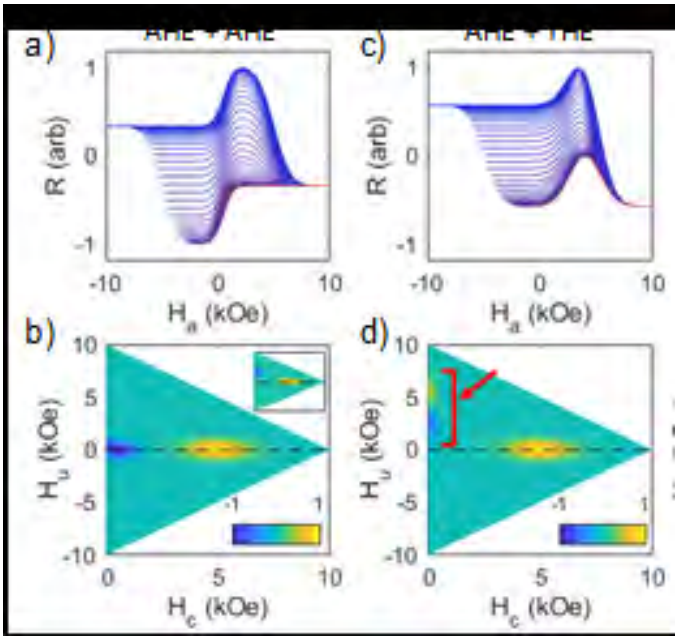


Figure 1(a,c) Simulated reversal curves for (a) dual AHE (c) AHE + THE. (b,d) FORC distributions calculated from the simulated reversal curves. The black dashed line denotes the $H_u = 0$ axis where the AHE component is expected in the absence of exchange bias. The AHE components appear as single peaks. Yellow denotes a positive AHE component, while blue denotes a negative AHE component. THE appears as a grouping of negative and positive peaks as seen in (d), and noted by the red arrow and bracket. The inset to (b) shows the effect of exchange bias in the soft AHE component. The peak is shifted along the H_u axis by the value of the exchange bias. Exchange bias in any AHE component will behave in the same way.

GF-04. Controlling Complex Spin Textures: From Emergent Magnetism to Spintronic Function

L. Kern, G. Beach
Department of Materials Science and Engineering, Massachusetts Institute of Technology, Cambridge, Massachusetts, United States

Understanding and controlling magnetism at the smallest length and fastest time scales is essential for advancing future technologies. Topologically non-trivial magnetic solitons, including skyrmions, are promising building blocks for next-generation spintronic and unconventional computing systems and provide an ideal platform to study nanoscale magnetism [1]. While unit-charge skyrmions have been widely demonstrated and manipulated, controlled formation of higher-order textures such as skyrmion bags remains challenging due to the delicate balance of magnetic interactions required for their stabilization [2,3]. Here, we demonstrate a generalizable pathway to generate, stabilize, and control both conventional skyrmions and higher-order skyrmion bags in ferromagnetic thin films [4,5]. Using focused He^+ ion irradiation, we locally tailor magnetic anisotropy to create deterministic nucleation sites and engineer the energy landscape. These patterned regions enable precise control over skyrmion nucleation, motion, and dynamics, and allow access to controlled skyrmion–skyrmion interactions. Beyond individual skyrmions, we stabilize and manipulate higher-order configurations including skyrmionium, target skyrmions, and reconfigurable skyrmion bags under magnetic fields and ultrafast laser excitation [5]. Skyrmion bags exhibit rich internal degrees of freedom, including shape adaptability and tunable topological charge, which can be reconfigured via spin–orbit torques [6]. Anisotropy engineering locally enhances spin–orbit torque efficiency, enabling low-power electrical control. Their internal dynamics, reconfigurability, and interactions position these textures as promising elements

for energy-efficient neuromorphic systems, adaptive sensing, and dynamic information processing.
High-resolution x-ray microscopy is crucial for resolving these textures and their spatiotemporal behavior, currently providing the only direct access to controlled skyrmion interactions at the nanometer scale. Our results establish a scalable and versatile scheme for on-demand creation of higher-order skyrmion textures, extendable to other material systems.

1. A. Fert, N. Reyren, V. Cros, Nat. Rev. Mat., 2(7), 1-15 (2017).
2. B. Göbel, I. Mertig, O. A. Tretiakov, Physics Reports, 895, 1-28 (2021).
3. F. Rybakov, N. Kiselev, Phys. Rev. B 99, 064437 (2019).
4. L.-M. Kern, B. Pfau, V. Deinhart, et al., Nano Lett., 22(10), 4028-4035 (2022).
5. L.-M. Kern, V. M. Kuchkin, V. Deinhart, et al., Adv. Mater., 2501250 (2025).
6. V. M. Kuchkin, K. Chichay, B. Barton-Singer, et al., Phys. Rev. B, 104(16), 165116 (2021).

GF-05. Investigating topological Hall effect using simultaneous soft x-ray scattering and imaging

A. Us-Saleheen, S. Roy, S. A. Morley
Advanced Light Source, Lawrence Berkeley National Laboratory, Berkeley, California, United States

The Fe/Gd ferrimagnetic system shows non-collinear magnetic structures similar to the widely-studied skyrmion-hosting helimagnetic B20 crystals such as MnSi and FeGe [1,2]. The FeGd thin film multilayer system can be tuned to stabilise non-collinear spin structures at room temperature via careful tuning of the dipolar energy [3]. The nanomagnetic spin phase diagram and its level of ordering can be characterized using soft x-ray magnetic diffraction [4]. In addition, the topological Hall effect has been used as a way to prove the existence of skyrmions in materials. The possible extrinsic factors such as material properties and experimental difficulties can lead to misinterpretation [5]. Here we measure the nanomagentic spin texture and the Hall effect at the same time using soft x-ray diffraction to accurately connect various features in the transport data with the specific nanomagnetic phases [6]. We found that the topological Hall effect (THE) shows peaks with opposite signs, suggesting the presence of different mechanisms. We observe the sign reversal in THE occurs during a transformation between the skyrmion lattice and isolated skyrmion phases, which we interpret as a change from a topology induced mechanism to a skew scattering mechanism.

[1] S. Mühlbauer, B. Binz, F. Jonietz, C. Pfleiderer, A. Rosch, A. Neubauer, R. Georgii, and P. Böni, Science 323, 915 (2009).
[2] X. Z. Yu, N. Kanazawa, Y. Onose, K. Kimoto, W. Z. Zhang, S. Ishiwata, Y. Matsui, and Y. Tokura, Nature Materials 10, 106 (2011).
[3] S. A. Montoya, S. Couture, J. J. Chess, J. C. T. Lee, N. Kent, D. Henze, S. K. Sinha, M.-Y. Im, S. D. Kevan, P. Fischer, B. J. McMorran, V. Lomakin, S. Roy, and E. E. Fullerton, Phys. Rev. B 95, 024415 (2017).
[4] J. C. T. Lee, J. J. Chess, S. A. Montoya, X. Shi, N. Tamura, S. K. Mishra, P. Fischer, B. J. McMorran, S. K. Sinha, E. E. Fullerton, S. D. Kevan, and S. Roy, Applied Physics Letters 109, 022402 (2016).
[5] G. Kimbell, C. Kim, W. Wu, M. Cuoco, and J. W. A. Robinson, Communications Materials 3, 19 (2022).
[6] A. Us Saleheen, A. Singh, D. Raftrey, M. R. McCarter, Z. Tumbleson, M.-Y. Im, S. A. Montoya, E. E. Fullerton, P. Fisccher, S. D. Kevan, S. Roy, S. A. Morley, App. Phys. Lett., 126 (14) (2025)

GF-06. Investigating the 3D Spatial Distribution of Magnetic Correlations in the Chiral Helimagnet $Cr_{1/3}NbS_2$

L. DeBeer-Schmitt[1], M. Henderson[1], A. Aczel[1], M. McGuire[2], N. J. Ghimire[3], S. Kuhn[1], M. Eskildsen[3], D. Mandrus[4]
[1]Neutron Science Division, Oak Ridge National Laboratory, Oak Ridge, Tennessee, United States, [2]MSTD, Oak Ridge National Laboratory, Oak Ridge, Tennessee, United States, [3]Physics Department, University of Notre Dame, Notre Dame, Indiana, United States, [4]Materials Engineering Department, University of Tennessee: Knoxville, Knoxville, Tennessee, United States

The monoaxial chiral helimagnet $Cr_{1/3}NbS_2$ is characterized by a field-tunable chiral soliton lattice (CSL) that is typically modeled as a one-dimensional spin texture. However, small-angle neutron scattering (SANS) measurements conducted at the GP-SANS instrument at Oak Ridge National Laboratory have identified higher-order diffraction harmonics in the zero-field helical state that are not attributable to multiple scattering. These observations indicate that the helimagnet adopts an intrinsically distorted magnetic configuration, while anomalous length-scale evolutions in the conical phase under a H || c field suggest a more complex magnetic landscape than idealized theoretical predictions. In this work, we evaluate the spatial distribution of these magnetic correlations using reconstructive strategies to move beyond traditional planar scattering interpretations. By investigating depth-mediated magnetization of both the helical and field-induced states, we aim to clarify the origin of the observed structural

distortions and the unusual behavior of the conical regime. Resolving these multi-dimensional spin textures is essential for a fundamental understanding of the topological stability of chiral solitons and their potential implementation in nanomagnetism and spintronics applications.

Ghimire, N. J., Ghimire, N. J., D. S. Parker, S. M. Choi, Z. Fisk, and M. D. Lumsden.Magnetic phase diagram and the chiral soliton lattice in $Cr_{1/3}NbS_2$. *Physical Review B*, 87(10), 104403. doi:10.1103/PhysRevB.87.104403.

Togawa, Y., et al. (2012). Chiral Magnetic Soliton Lattice on a $CrNb_3S_6$ Nanoscale Plate. *Physical Review Letters*, 108, 107202.

Kishine, J. and Ovchinnikov, A.S. (2015). Theory of Monoaxial Chiral Helimagnet. *Solid State Physics*, 66, 1-130.

GF-07. Influence of off-stoichiometric composition on the topological surface transport in In-doped SnTe thin films

R. Uesugi[1], R. Ando[2], M. Mizuno[1], T. Aono[1], T. Chiba[3], T. Komine[1]

[1]Ibaraki University, Hitachi, Japan, [2]Ibaraki College, Hitachinaka, Japan, [3]Yamagata University, Yonezawa, Japan

Topological crystalline insulators (TCIs) such as SnTe have attracted significant attention due to their symmetry-protected surface states, which offer a platform for novel quantum transport phenomena. These surface states are particularly promising for spintronic applications, where efficient manipulation of spin degrees of freedom is essential.[1], [2] However, for practical device implementation, it is necessary to establish scalable fabrication methods and to identify compositional conditions that enable reliable surface-dominated transport. In this study, we focus on In-doped SnTe thin films fabricated by RF magnetron sputtering, a technique suitable for large-area and industrial processes. To clarify the conditions under which topological surface transport becomes prominent, we investigate wide range of compositions with $x<0.3$ and $-0.2<\delta<0.2$ of $(In_x Sn_{1-x})_{1+\delta} Te_{1-\delta}$ by controlling the In concentration x and the cation–anion off-stoichiometry δ. This approach allows us to examine the impact of lattice defects and compositional deviation on transport properties.

Magnetoconductance measurements show weak anti-localization (WAL) behavior, indicating contributions from topological surface states of SnTe.[3]–[5] Using the Hikami–Larkin–Nakaoka formula to fit the magnetoconductance yields the channel weight α (Fig. 1) and the phase coherence length l_φ (Fig. 2). By analyzing the composition dependence, we found that near-stoichiometric samples exhibit compensation of Sn vacancies by In doping, leading to reduced carrier density and a crossover in the dominant scattering mechanism from phonon–electron ($l_\varphi \propto T^{-1}$) to electron–electron scattering ($l_\varphi \propto T^{-1/2}$). In contrast, off-stoichiometric films exhibit degraded transport due to precipitated impurities or bulk defects.

These results demonstrate that compositional optimization is crucial for accessing intrinsic topological surface transport in sputtered SnTe films, and provide practical guidelines for composition control and highlight a scalable pathway toward the integration of topological crystalline insulators into spintronic devices.

[1] Y. Ando and L. Fu, *Ann. Rev. Condens. Matter Phys.* 6, 361 (2015).
[2] Q. L. He *et al., Nat. Mater.* 21, 15 (2021).
[3] B. A. Assaf et al., Appl. Phys. Lett. 105, 102108 (2014).
[4] R. Akiyama et al., Nano Res. 9, 490 (2016).
[5] J. Wang et al., Nano Lett. 22, 792 (2022).

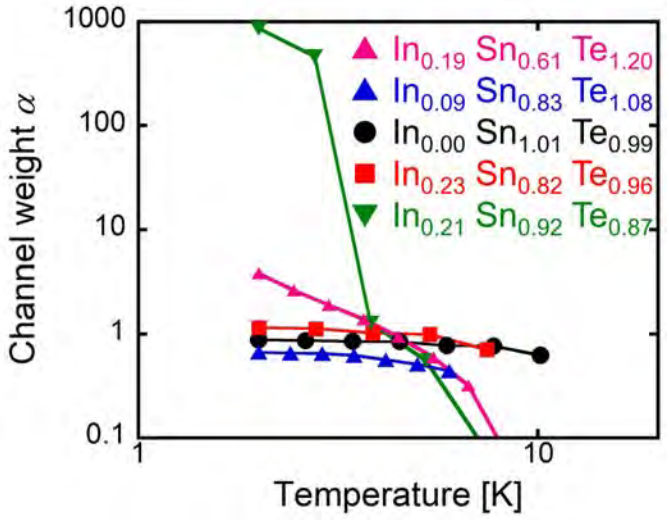


Fig. 1 The temperature dependence of the channel weight α.

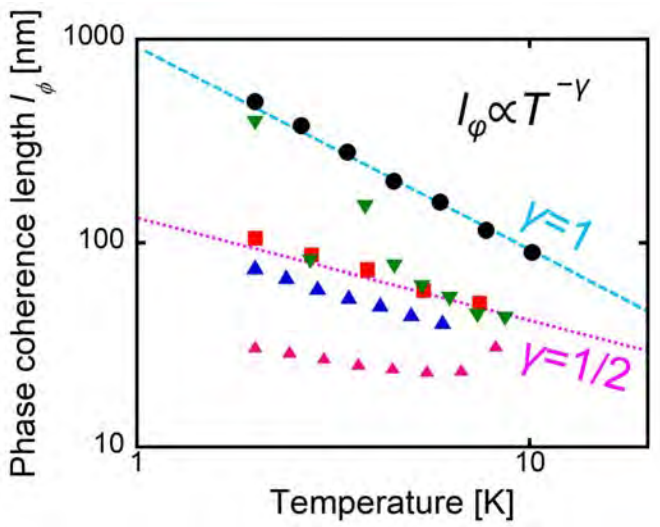


Fig. 2 The temperature dependence of the phase coherence length l_φ.

GF-08. Measurement of Fermi-Surface Geometry and Spin Texture Using Nonlinear-Transport Quantum Oscillations

V. Kalappattil[1], C. Liu[1], Z. Chen[2], V. Sharma[1], K. Liu[2], J. Tang[3], S. Zhang[4], M. Wu[1]

[1]Physics, Northeastern University, Boston, Massachusetts, United States, [2]Physics, Georgetown University, Washington, District of Columbia, United States, [3]Physics, University of Wyoming, Laramie, Wyoming, United States, [4]Physics, Case Western Reserve University, Cleveland, Ohio, United States

Quantum oscillations in electrical transport have long served as a powerful probe of Fermi surface physics, enabling the extraction of quantities such as carrier density, effective mass, Berry phase, and quantum lifetime. However, to date such studies have been largely limited to the linear transport regime, where the electrical response scales directly with the applied electric field [1,2]. As a result, conventional quantum-oscillation measurements primarily probe extremal Fermi-surface area and often remain insensitive to finer details such as Fermi contour geometry and spin texture.

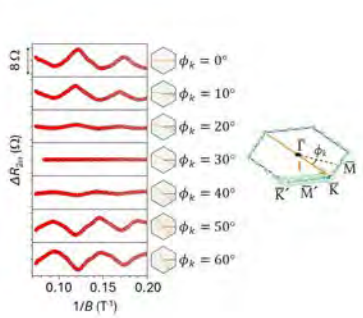
Here, we report the experimental observation of quantum oscillations in nonlinear electrical transport and demonstrate that they provide access to key Fermi surface properties that remain hidden in conventional linear-transport measurements. Using α-Sn, a topological Dirac semimetal that hosts both strong linear and nonlinear transport responses, we resolve clear second-harmonic quantum oscillations arising from nonlinear resistance under perpendicular magnetic field. By comparing first- and second-harmonic responses measured in the same device geometry, we establish that the nonlinear oscillations originate from the topological surface states and probe fundamentally different aspects of the electronic structure. Most importantly, we show that oscillations in the nonlinear resistance are highly sensitive to the geometry and spin texture of the Fermi contour, features to which their linear counterparts are largely insensitive. The angular measurements given in the figure reveal a striking evolution of the nonlinear oscillation amplitude as the current direction is rotated relative to the momentum-space crystal axes. The oscillations gradually weaken, vanish near specific directions, and then reverse phase as the current is further rotated, directly reflecting the hexagonally warped Fermi contour and the corresponding reversal of out-of-plane spin polarization. This angular evolution provides direct experimental access to local spin orientation along the Fermi surface, a capability unavailable in conventional Shubnikov–de Haas measurements.

In addition to this directional selectivity, the nonlinear oscillations display distinct magnetic-field and temperature dependences, revealing fundamentally different underlying physics compared with conventional Shubnikov–de Haas oscillations. Together, these results establish nonlinear-transport quantum oscillations as a powerful new probe of Fermi surface physics, opening a pathway toward uncovering hidden electronic structure in known quantum materials and enabling the discovery of new exotic electronic states and phases [3]. More broadly, this approach can be extended to topological semimetals, Rashba systems, two-dimensional electron gases, and inversion-asymmetric heterostructures where nonlinear transport naturally emerges.

1. L. Chen, A. X. Wu, T. Tulu et al., Nat. Mater., Vol. 23, p. 741 (2024)

2.N. Doiron-Leyraud, C. Proust, D. LeBoeuf et al., Nature, Vol. 447, pp. 565–568 (2007).

3. V. Kalappattil, C. Liu, Z. Chen, V. Sharma, K. Liu, J. Tang, S. S.-L. Zhang and M. Wu, Phys. Rev. Lett., Vol. 136, p.096603 (2026).



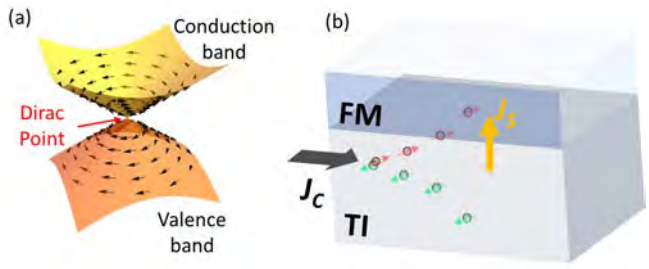
Oscillations of second-harmonic resistance as a function of inverse field measured at current applied along various directions relative to momentum-space orientations.

GF-09. Development of Wafer-Scaled Sb_2Te_3 Topological Insulator for Highly Efficient Spin-Charge Interconversion at Room Temperature

E. M. Longo[2], R. M. Ahmed[1], A. Shafiei[1], M. Belli[3], M. Longo[4], M. Alia[1], C. Wiemer[1], R. Mantovan[1]
[1]Unit of Agrate Brianza, CNR-IMM, Agrate Brianza (MB), Please select one below:, Italy, [2]Laboratory of Multifunctional Oxides and Complex Structures, ICMAB-CSIC, Barcelona, Spain, [3]CNR-IMEM, Parma, Italy, [4]Tor Vergata, Università degli Studi di Roma, Rome, Italy

The second-generation of 3D topological insulators (TIs= Bi_2Se_3, Bi_2Te_3, Sb_2Te_3) have been presented in 2009 [1]. They are characterized by topologically protected surface states (TSS), exhibiting linear Dirac-like energy dispersion and spin-momentum locking, Fig.1(a). 3D-TIs gained interest for their advantageous use in spintronic devices such as spin-orbit torque (SOT)-MRAM or in the MESO, where spin-charge interconversion phenomena are at the core of their functionalities, with Fig. 1(b) depicting SOT basics.
We developed processes based on Metal Organic Chemical Vapour Deposition (MOCVD) to grow epitaxial quality Sb_2Te_3 over 4" areas Si substrates. By conducting a comprehensive campaign of chemical, structural, morphological and (magneto)transport characterization, we show that the developed MOCVD approach allows to obtain high quality Sb_2Te_3 thin films in the 20-40 nm range, which are characterized by TSS-driven transport over the full 4" wafer [2-4]. By making use of spin pumping ferromagnetic resonance (SP-FMR) as conducted on Sb_2Te_3/Au/(Co,Fe)/Au heterostructures, we detect highly efficient spin-charge conversion at room temperature [5-6] that, when interpreted within the inverse Edelstein Effect (IEE), generates a conversion efficiency of λ_{IEE}= 0.14÷0.31 nm as probed along the full 4" wafer. On selected Sb_2Te_3/Au/Co/Au samples we performed harmonic Hall magnetoresistance, which demonstrates highly efficient SOT as indicated by the obtained spin Hall angle of Θ_{SHA}= 63 at room temperature [7].
The reported large spin-charge interconversion as observed at room temperature, validate the MOCVD-produced Sb_2Te_3 as a very good option for boosting the performances of several spintronic devices relying on TIs' functionalities, with the capability to produce them at a 4" scale opening realistic prospective for their future technology transfer. To conclude, the recently observed non-linear quantum metric effects in our MOCVD-produced Sb_2Te_3, may open the route toward the exploitation of unprecedented functionalities [8].

[1] H. Zhang et al., Nat. Phys. 5, 438 (2009)
[2] M. Rimoldi et al., RCS Advances 10, 19936 (2020)
[3] L. Locatelli et al., Scientific Reports 12, 3891 (2022)
[4] A. Shafiei et al., Adv. Mater. Interfaces 2025, 2400961
[5] E. Longo et al., Adv. Funct. Mater. 32, 2109361 (2021)
[6] E. Longo et al., Nano Letters 25, 6888 (2025)
[7] M. Fettizio et al., Adv. Electron. Mater. 11, e00280 (2025)
[8] G. Sala et al., arXiv (2026)
https://arxiv.org/abs/2509.17135v2



(a) Linearly dispersed TSS in a TI. (b) Simplified sketch of charge-spin conversion at TI/Ferromagnet (FM) interface with yellow (black) arrow indicating the spin J_S (charge J_C) current density.

GF-10. Interfacial Transparency and Proximity Effects Governing Spin-to-Charge Conversion in Sputtered $Bi_{85}Sb_{15}$

V. Sharma[1, 2], R. Van Haren[2], V. Kalappattil[3], V. Sharma[3], D. Takhar[4], F. M. Abel[5], G. M. Stephen[2], R. K. Ghosh[4], M. Wu[3], A. T. Hanbicki[2], A. Friedman[2]

[1]University of Maryland College Park, College Park, Maryland, United States, [2]Laboratory for Physical Sciences, College Park, Maryland, United States, [3]Northeastern University, Boston, Massachusetts, United States, [4]IIIT Delhi, Delhi, India, [5]United States Naval Academy, Annapolis, Maryland, United States

Topological insulator $Bi_{85}Sb_{15}$ alloys hold immense potential for next-generation spintronics due to their strong spin-orbit coupling,[1] yet translating this potential into scalable devices remains a critical challenge. In this work, we reveal the interfacial and structural mechanisms governing spin-to-charge conversion in sputtered $Y_3Fe_5O_{12}/Bi_{85}Sb_{15}$ (YIG/$Bi_{85}Sb_{15}$) heterostructures. Through systematic ferromagnetic resonance measurements across a $Bi_{85}Sb_{15}$ thickness range of 3 to 15 nm on a 100 nm YIG film (Fig. 1a), we observe an anomalous, non-monotonic thickness dependence in the spin pumping efficiency. The Gilbert damping enhancement exhibits a sharp, pronounced peak at a critical thickness of 6 nm (Fig. 1b). Furthermore, the effective spin mixing conductance is established to be on the order of 10^{18} m^{-2} (Fig. 1b). While lower than prototypical YIG/Pt interfaces,[2] this magnitude exposes the critical bottleneck of interfacial transparency in sputtered topological spintronic systems. To elucidate the underlying transport physics, we conducted temperature-dependent damping and inverse spin Hall effect (ISHE) measurements, extracting a spin Hall angle on the order of 0.001. To isolate the intrinsic spin-to-charge conversion from the magnetic proximity effect (MPE) induced by the YIG (Fig. 1a), we engineered the interface using an ultra-thin MgO spacer layer. This insertion not only successfully decouples the MPE but also provides a powerful pathway to tune the BiSb crystal orientation for optimized spin transport. Finally, we establish the theoretical upper bound of the spin Hall conductivity in polycrystalline $Bi_{85}Sb_{15}$ using density functional theory (DFT). By directly correlating these first-principles calculations with our experimental findings, we provide a rigorous framework for understanding and engineering interfacial spin transport in scalable topological materials.

1. Chi, Zhendong, et al. "The spin Hall effect of Bi-Sb alloys driven by thermally excited Dirac-like electrons." *Science advances* 6.10 (2020): eaay2324.
2. Wang, H. L., et al. "Scaling of spin Hall angle in 3d, 4d, and 5d metals from Y 3 Fe 5 O 12/metal spin pumping." *Physical review letters* 112.19 (2014): 197201.

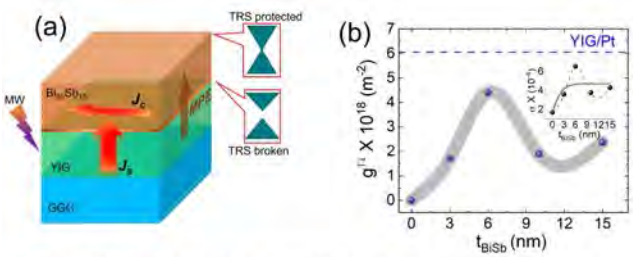


Figure 1: (a) Schematic to show the FMR based spin pumping and effect of magnetic proximity effect at the interface on topological insulator time reversal symmetry (TRS) **(b)** Effective spin mixing conductance ($g^{\uparrow\downarrow}$) as a function of $Bi_{85}Sb_{15}$ thickness, inset shows the variation of Gilbert damping (α), highlighting the role of interfacial transparency in YIG/$Bi_{85}Sb_{15}$ heterostructures.

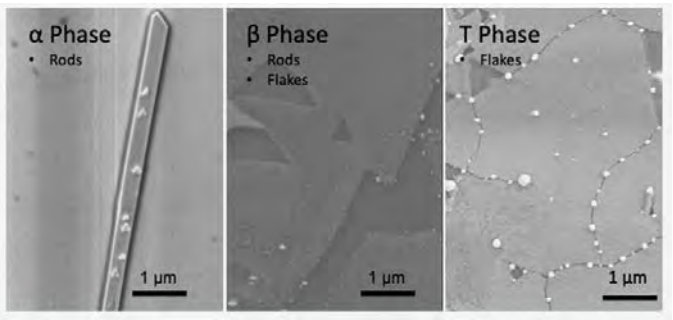
GF-11. Antiferromagnetic Exchange Bias and Magnetic Characterization of T-phase MnSe

J. E. DeMell[1, 2], B. Jordan[2], J. Fleischer[1], J. Kotsakidis[2], K. M. Daniels[2]

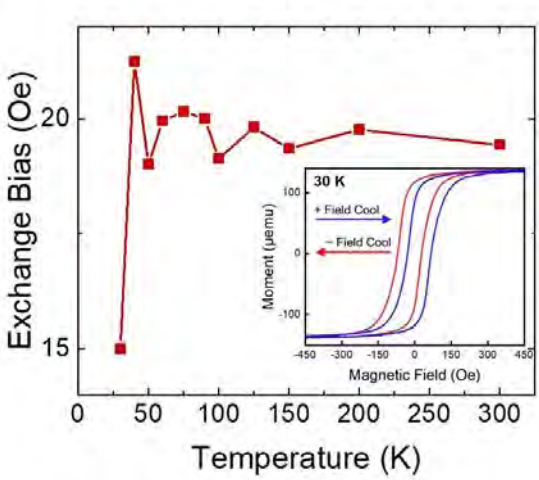
[1]Laboratory for Physical Sciences, College Park, Maryland, United States, [2]IREAP, University of Maryland, College Park, Maryland, United States

Manganese selenide (MnSe) is a promising air-stable two-dimensional magnetic semiconductor, for which theory predicts robust ferromagnetism in monolayers with Curie temperatures approaching 250 K. However, the crystallographic phases and magnetic properties of thin-film MnSe grown by scalable methods remain poorly understood. Here, we demonstrate controllable growth of α-, β-, and T-phase MnSe on C-face sapphire using a three-zone chemical vapor deposition process with elemental Se and $MnCl_2$ precursors in an Ar/H_2 atmosphere. Using Raman spectroscopy, atomic force microscopy, scanning electron microscopy, and X-ray diffraction, we show that our process yields phase-pure α-phase rods and β- and T-phase MnSe triangular flakes with lateral sizes up to 120 μm and thicknesses down to 5 nm. Low-temperature photoluminescence of the T-phase films reveals a band gap of ≈ 2.1 eV. Systematic variation of growth parameters shows that precursor vapor pressure, rather than H_2 partial pressure, is the dominant factor controlling lateral flake size. Contrary to prior reports of ferromagnetism, β-phase MnSe exhibits antiferromagnetic ordering with a Néel temperature of 53 K, while T-phase MnSe demonstrates strong interlayer antiferromagnetic coupling and an exchange bias of 22 Oe persisting up to 300 K. Positive magnetoresistance observed in magnetotransport measurements further indicates strong spin–orbit

interactions and magnetic character. Together, these findings identify T-phase MnSe as a promising, scalable material for incorporation into low-dimensional spintronic devices.



SEM imaging of α-, β-, and T-phase MnSe crystals, grown by chemical vapor deposition.



Antiferromagnetic exchange bias in a permalloy ($Ni_{80}Fe_{20}$)/T-phase MnSe heterostructure exhibiting an exchange bias up to 22 Oe and persisting up to 300 K.

SESSION GG: MAGNONICS II

Chair(s): T. Kuschel, *Institute of Physics, Johannes Gutenberg University Mainz, Mainz, Germany*

Friday, November 6, 2026

08:30 AM-12:00 PM

Sea Pearl

GG-01. Magnons as information carriers in hybrid quantum architectures

S. Viola Kusminskiy

RWTH Aachen University, Aachen, Germany

In this talk I will explore the possibilities and limitations of using magnons as mediators of quantum information in hybrid quantum systems at the nanoscale. In particular, I will discuss our recent theoretical results on implementing magnon-mediated quantum gates for superconducting qubits [1] and steady-state entanglement of spin qubits by leveraging non-reciprocal and chiral magnons [2]. Complementary, I will show the possibility of engineering quantum states of magnons via their coupling to a superconducting qubit [3,4,5]. Further, I will discuss the prospect of harnessing magnon-phonon coherent interaction for transduction and quantum state transfer [6].

[1] Martijn Dols, Sanchar Sharma, Lenos Bechara, Yaroslav M. Blanter, Marios Kounalakis, and Silvia Viola Kusminskiy, Phys. Rev. B 110, 104416 (2024)

[2] Martijn Dols, Mikhail Cherkasskii, Victor Bittencourt, Carlos Gonzalez-Ballestero, Durga Dasari, and Silvia Viola Kusminskiy, arXiv preprint arXiv:2509.13094 (2025)

[3] Marios Kounalakis, Silvia Viola Kusminskiy, and Yaroslav M. Blanter, Phys. Rev. B 108, 224416 (2023)

[4] Sanchar Sharma, Victor Bittencourt, and Silvia Viola Kusminskiy, J. Phys. Mater. 5 034006 (2022)

[5] Sanchar Sharma, Victor Bittencourt, Alexy Karenowska, and Silvia Viola Kusminskiy, Phys. Rev. B 103, L100403 (2021)

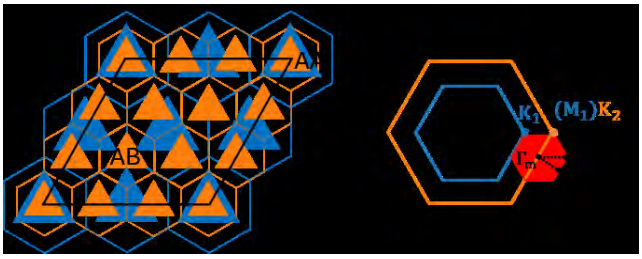
[6] Fabian Engelhardt, Victor Bittencourt, Hans Huebl, Olivier Klein, and Silvia Viola Kusminskiy, Phys. Rev. App. 18, 044059 (2022)

GG-02. Chiral Transport in Hybrid Magnon-Phonon Moiré Superlattice

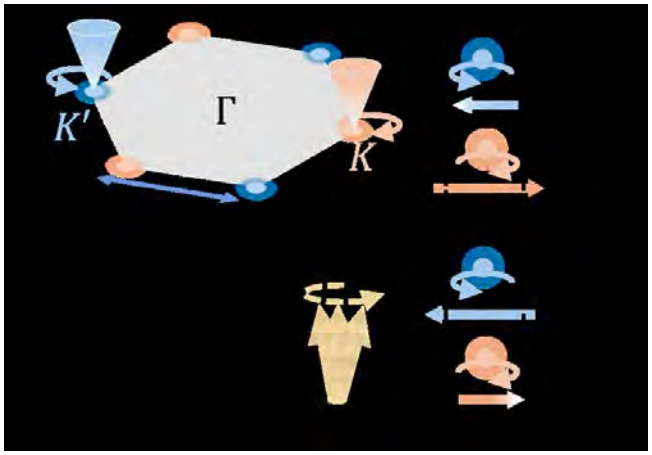
J. Liu[1, 2, 3], L. Liao[2, 4], H. Isshiki[4], Z. Chen[3, 5], J. Puebla[2], Q. Shao[1, 3, 5], Y. Otani[2, 4]

[1]Electronic and Computer Engineering, Hong Kong University of Science and Technology, Hong Kong, Hong Kong, [2]Center for Emergent Matter Science, RIKEN, Wako, Japan, [3]IAS Center for Quantum Technologies, Hong Kong University of Science and Technology, Hong Kong, Hong Kong, [4]Institute for Solid State Physics, University of Tokyo, Tokyo, Japan, [5]Department of Physics, Hong Kong University of Science and Technology, Hong Kong, Hong Kong

Hybridizing collective excitations offers a powerful route to engineer wave transport. While magnon-phonon coupling enables on-chip control of acoustic waves, previous implementations have focused largely on amplitude modulation. Here we integrate a magnetoelastic moiré superlattice into a surface acoustic wave device. Under a tilted magnetic field, magnon-driven chiral channels can be switched between distinct moiré phononic valleys by selecting phonons with opposite out-of-plane angular momentum, deterministically reversing the sign of nonreciprocity. This valley-selective hybridization simultaneously enables tunable phase (group-velocity) control. Our work establishes a moiré-enabled paradigm for hybrid wave control, achieving simultaneous manipulation of transmission amplitude and dispersion.



Geometric properties of real space and reciprocal space



Schematic illustration of chiral transport of phonons at K/K' point in momentum space.

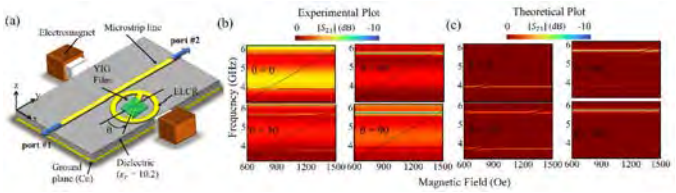
GG-03. Polarization-Driven Level Repulsion and Mode Switching in a Multi-Mode Photon–Magnon Resonator

A. Maurya, S. Verma, R. Singh, B. Bhoi

Department of Physics, Indian Institute of Technology (BHU) Varanasi, Varanasi, Uttar Pradesh, India

Photon–magnon hybrid quantum systems provide a promising platform for quantum information processing [1] through coherent coupling between microwave photons and collective spin excitations, enabling controllable information transfer and reconfigurable light–matter interactions. We report polarization-controlled mode switching and tunable photon–magnon hybridization in a planar microwave resonator–YIG hybrid platform at room temperature [2]. The system consists of a planar electric LC resonator (ELCR) coupled to a ferrimagnetic YIG film, where axial rotation with respect to the incident microwave field selectively excites two orthogonal cavity modes. The radiative coupling strength follows a projection-dependent behavior, enabling continuous geometric control of the magnon–photon interaction. At 0° and 90°, individual cavity modes couple independently to the magnon, while intermediate angles produce simultaneous hybridization, forming a three-mode coupled system. Measured transmission spectra (|S21|) show angle-dependent anti-crossing with tunable coupling strength and transitions between level repulsion and level attraction regimes. The coupling coefficients exhibit systematic angular dependence consistent with projection-squared scaling of radiative damping and intermode coupling. An equivalent circuit model and a non-Hermitian quantum Hamiltonian reproduce the observed hybridization, linewidth evolution,

and mode switching. These results demonstrate a purely geometric approach to engineer light–matter interactions, non-Hermitian dynamics, and multimode magnonic hybridization without modifying material parameters or circuitry, providing a scalable route toward reconfigurable hybrid quantum and spintronic devices.
[1] Y Li, et al 2022 Phys. Rev. Lett. 128 047701.
[2] B Bhoi, et al 2022, J. Appl. Phys. 132 243901.



(a) ELCR–YIG hybrid system schematic showing rotation angle θ control.
(b) Measured |S21| spectra demonstrating angle-dependent photon–magnon coupling.
(c) Calculated spectra showing rotation-controlled mode evolution.

GG-06. Nonlinear and Nonreciprocal Generation of Spin Wave Harmonics and Frequency Combs in Thin Magnetic Films with Interfacial Dzyaloshinskii–Moriya Interactions
L. D. Powell, E. Iacocca, R. E. Camley
Physics, University of Colorado, Colorado Springs, Colorado Springs, Colorado, United States

Nonreciprocity in systems with interfacial DMI is well-known in the linear regime.[1,2] In contrast, we explore how DMI changes nonlinear spin wave harmonics.[3] Multiple surprising and interesting consequences emerge, with measureable results.

We analyze the Landau-Lifshitz (LL) equations, numerically and analytically, for a narrow stripe with interfacial DMI. If the static field is perpendicular to the stripe, spin waves traveling in one direction along the long axis of the stripe can have harmonics that are more than 50 times larger than that for the waves moving oppositely.This results from the nonlinear interfacial DMI torque terms in the LL equations as their amplitude is proportional to the sign and magnitude of the propagation wavevector.

When the external field is parallel to the stripe, and with DMI present, both even and odd harmonics are generated; without DMI only odd harmonics appear- Fig 1. This potentially offers a new way to measure the DMI strength.

Here, and in the work on the perpendicular orientation geometry above, a simple perturbation scheme shows shows the origin of these effects. Wtih larger nonlinearity, frequency combs can appear, centered around each harmonic - Fig 2. Finally, in the standard parallel pumping configuration where both the static and dynamic fields are along the stripe, one can generate two signals which sum to the driving frequency, rather than a single half-frequency signal. This gives another way of measuring the DMI constant.

The parameters used in the calculation are appropriate to create harmonics that can be measured with a network analyzer, a waveguide structure, and a spectrum analyzer or with Brillouin Light Scattering.[

This work was supported by the U.S. Department of Energy, Office of Basic Energy Sciences under Award No. DE-SC0024339 (micromagnetic simulations and pseudospectral Landau-Lifshitz model simulations).
[1] Consequences of Dzyaloshinskii-Moriya Interaction, R. E. Camley and Karen Livesey, Surface Science Reports, 76, 100605, (2023)
[2] Spin wave prpagation in the presence of interfacial Dzyaloshinskii-Moriya interaction, J.-H. Moon et al, Physical Review B, 88, 184404,(2013)
[3] Nonlinear harmonics in thin magnetic films with interfacial Dzyaloshinskii-Moriya interactions, Laurel D. Powell and R. E. Camley, Phys. Rev. B 113, 104421 – (2026)

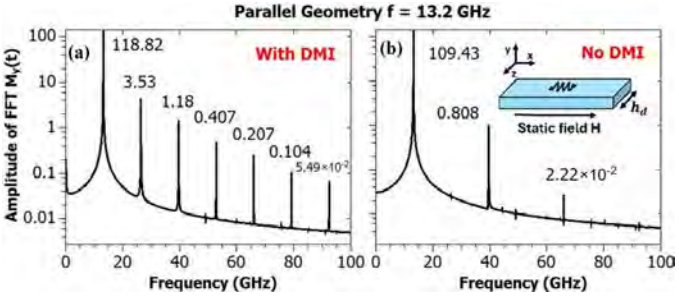


Figure 1. Generated harmonics with and without DMI with the static field perpendicular to the stripe length

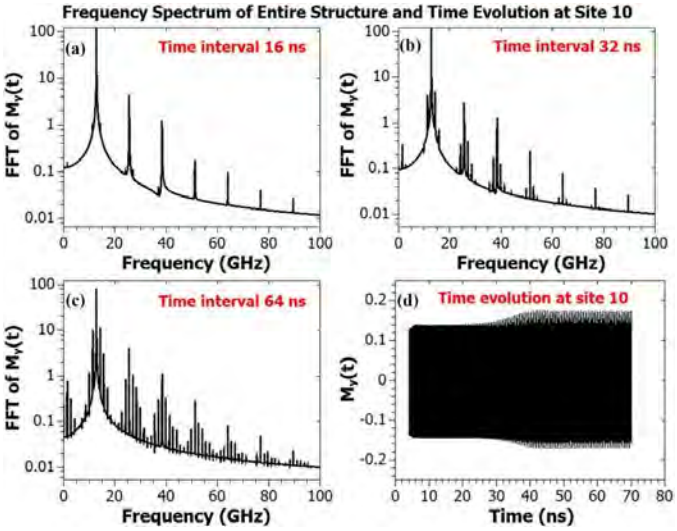


Figure 2. Generation of frequency combs. Over time the system progresses from a quasi-static state just resulting in harmonics to a state with frequency combs centered around each harmonic.

GG-07. Magnonic Frequency Comb in Vertex-Modified Square Artificial Spin Ices

N. Rentzber, E. Iacocca
University of Colorado Colorado Springs, Colorado Springs, Colorado, United States

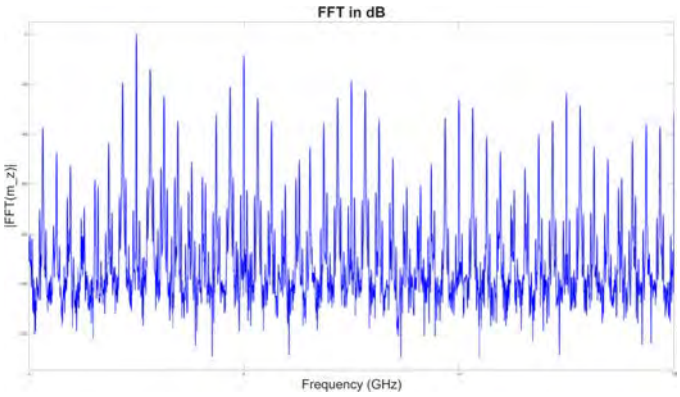
Artificial spin ices provide a platform for engineering spin wave dynamics through geometrical and dipolar coupling [1,2]. We investigate a 2.5D square artificial spin ice system composed of elongated nanomagnets and an elevated cylindrical vertex modifier [3] that overlaps with the nanomagnets in the x-y plane while remaining separated along the z-dimension. This geometry promotes strong dynamic coupling without requiring the modifiers and nanomagnets to occupy the same physical layer in the same x-y plane dimension.

Micromagnetic simulations in MuMax3 reveal a strongly coupled static and dynamic response, with hybridized resonances in addition to the typical bulk and edge modes that are associated with both the nanomagnets and the cylindrical vertex modifiers. The system is then driven with an external in-plane RF magnetic field while varying the excitation magnetic flux amplitude. The simulations identify an optimal excitation amplitude of 5 mT and drive frequency near 5.0 GHz, where the spectral response evolves from isolated resonances into frequency comb-like structures. Additional long-time domain simulations over 200 ns at 5 GHz show a dominant fundamental peak accompanied by multiple equally spaced harmonics in the Fourier frequency-domain spectrum. This frequency comb is shown in Figure 1. The magnetization time trace exhibits both amplitude modulation and frequency modulation, that correspond with the spacing frequency between neighboring harmonic peaks, providing strong evidence of frequency-comb generation.

These results demonstrate that elevated vertex modifiers in square artificial spin ice systems can be used to engineer nonlinear magnon coupling and frequency-comb dynamics. The observed dynamics at the nanoscale are similar to those found in macroscopic spin ices [4], indicating that the vertex provides a strong dynamic coupling. This approach could be used to investigate band structures in ASIs and potential applications in microwave circuits.

This material is based upon work supported by the National Science Foundation under Grant No. 2532497.

[1] S. Gliga, E. Iacocca, and O. Heinonen, APL Materials 8, 040911 (2020)
[2] R. Sultana, et al., J. Appl. Phys. 138, 061101 (2025)
[3] E. Östman, et al., Nature Physics 14, 375 – 379 (2018)
[4] R. R. Peroor, et al., Phys. Rev. Appl. 23, 044010 (2025)



Fast-Fourier Transform (FFT) of the magnetization time-domain transient, depicting a frequency comb with a comb spacing of 318.75 MHz.

GG-08. Tunable spin-wave dynamics in nanoscale bicomponent magnetic fractals

R. Mehta, S. Saha
Physics, Ashoka University, Rai, Haryana, India

Fractals are composed of self-similar structures across different length scales, which look similar under different magnifications. This property is commonly referred to as dilation symmetry. The concept of fractals is introduced in magnetic systems in the form of Sierpinski carpets and gaskets [1]. The magnetization dynamics in the Sierpinski triangle show the appearance of mini frequency gaps and spin-wave localization, owing to the complex demagnetization field profile resulting from the self-similar arrangement of structures [2,3].

In this work, we have investigated the magnetization dynamics of single and bicomponent Sierpinski squares composed of CoFe inclusions within a NiFe matrix with the aid of micromagnetic simulations to show their application in spin-wave transmission [4]. A rich spin-wave spectra is obtained for both cases. The spatial distributions of various spin-wave modes are also examined, and a hierarchical nature in the spin-wave mode patterns and channeling of the spin-waves along the entire length of the structure have been observed, as shown in Fig. 1(a). The channeling can be further tuned by varying the azimuthal angle of the external magnetic field. The inverse participation ratio (IPR) is calculated to quantify the degree of localization of the different spin-wave modes and demonstrate their tunability with respect to the azimuthal angle [See Fig 1 (b)]. The complex distribution of the demagnetization field resulting from the fractal arrangement [Fig.1(c)] as well as the edge effects of structurization, play a key role in modifying the spin-wave spectra of these single and bicomponent fractal structures [Fig.1 (d)]. Finally, the spin-wave propagation through a bicomponent Sierpinski square embedded in a magnetic waveguide and the effect of azimuthal angle on propagation of the spin-wave have also been investigated to demonstrate their application in angular tuned magnonic waveguides and filters.

Acknowledgement :
SS and RM gratefully acknowledge the financial support of SERB, File No. SRG/2022/000191, and the financial aid provided by the Axis Bank to support this research work at Ashoka University. References:

[1] R. Mehta et. Al., J. Phys.: Condens. Matter 36, 443003 (2024).
[2] J. Zhou et. Al. Phys. Rev. B 105, 174415 (2022).
[3] R. Mehta et. Al J. Phys.: Condens. Matter 35, 324002 (2023).
[4] R. Mehta and S. Saha, Phys. Rev. Applied 24, 054034 (2025).

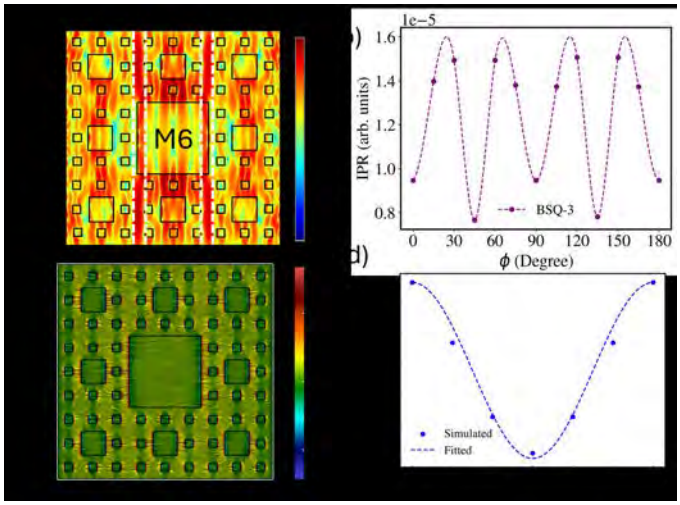


Fig. 1 (a) The Spatial profile of the spin-wave mode(b) the variation of the IPR value with t φ, (c) the distribution of the demagnetization field (d) the variation of the average demagnetization field with φ

GG-09. Spin-wave caustic beam steering and interference in YIG and Permalloy

N. Sahni[1], D. Wagle[1, 2], B. Jungfleisch[1], L. Gundlach[1, 3], Y. Ren[1], J. Q. Xiao[1]
[1]Physics and Astronomy, University of Delaware, Newark, Delaware, United States, [2]Laboratory for Physical Sciences, College Park, Maryland, United States, [3]Department of Chemistry and Biochemistry, University of Delaware, Newark, Delaware, United States

Spin-wave caustics are highly directional, narrow beams that emerge from the anisotropic dispersion of magnetic materials, where energy concentrates along specific group-velocity directions near flat regions of the isofrequency contour. Their intrinsic directionality makes them attractive for spin-wave–based information processing and wave-based computing. Recent studies have demonstrated the excitation of caustic beams in YIG thin films using nano-constricted antennas in both Damon–Eshbach–like and backward-volume–like configurations, supported by micro-focused Brillouin light scattering (μ-BLS) and near-field diffraction (NFD) modeling [1,2]. Here, we extend this framework to arbitrary in-plane magnetic field orientations and demonstrate deterministic steering of caustic beams via the field angle. For a rectangular antenna at 45°, we

observe the emergence of a single, well-defined caustic beam, with reciprocal-space analysis revealing selective excitation of only one of the four caustic points on the isofrequency contour. We further design a two-antenna configuration arranged as mirror images to enable controlled interference of caustic beams. By tuning the phase difference between the RF currents, the interference pattern can be modulated, with destructive interference at zero phase difference and constructive interference at π, achieving a high contrast of up to 96.6%. These results establish field-controlled beam steering, wavevector selectivity, and high-contrast interference, highlighting the potential of caustic spin waves for reconfigurable magnonic circuits and wave-based computing architectures.

This work was supported by the U.S. Department of Energy, Office of Basic Energy Sciences (Award No. DE-SC-0024346), and the NSF Division of Materials Research (Grant No. 2203829).

[1] D. Wagle, D. Stoeffler and L. Temdie, Phys. Rev. B, 113, L060405 (2026)

[2] V. Vlaminck, L. Temdie and V. Castel, J. Appl. Phys., 133, 053903 (2023)

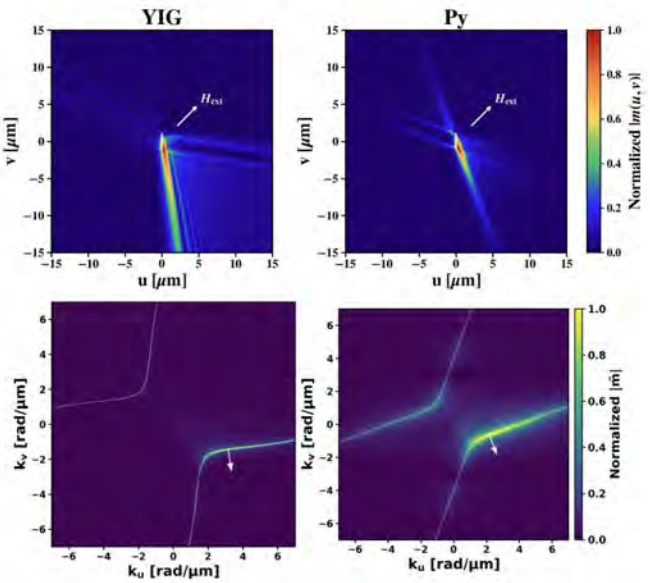


Figure 1: Spin-wave caustics and their reciprocal-space origin in YIG and Py. Top: Real-space maps of the dynamic magnetization amplitude |m| excited by a rectangular antenna at 45° field orientation. Bottom: Corresponding reciprocal-space intensity showing selective excitation along the isofrequency contour (white dotted line). The group velocity, v_g, normal to the contour, determines the caustic beam direction.

GG-10. Magnon-Phonon Coupling and Interfacial Dzyaloshinskii-Moriya Interaction in Heavy-Metal/Ferromagnet Heterostructures

E. Savostin[1, 2, 3], V. Lomakin[1, 2, 3]
[1]*Center for Memory and Recording Research, University of California San Diego, La Jolla, California, United States,*
[2]*Program in Materials Science and Engineering, University of California, San Diego, La Jolla, California, United States,*
[3]*Department of Electrical and Computer Engineering, University of California San Diego, La Jolla, California, United States*

Strain-dependent interfacial Dzyaloshinskii-Moriya interaction (SIDMI) provides a promising mechanism for coupling magnetic chirality and lattice motion in low-symmetry magnetic heterostructures [1,2]. In this work, we investigate the role of SIDMI in hybrid spin-lattice dynamics by combining a continuum magnetoelastic framework with first-principles modeling of representative heavy-metal/ferromagnet interfaces.

Figure 1 illustrates the interfacial atomic geometry considered in this work, where the local heavy-metal/ferromagnet bonding triangle provides the structure that controls the strength of the interfacial DMI and its strain dependence. In this approach, the interfacial DMI is treated as explicitly strain dependent, extending conventional magnetoelastic theory and introducing additional chiral stress terms associated with Lifshitz invariants. This formulation provides a unified description of how strain influences chiral magnetic textures and how nonuniform magnetization, in turn, generates symmetry-selective mechanical response.

Within the continuum picture, SIDMI modifies magnon-phonon coupling in a way that depends on crystal symmetry, wave-vector direction, and magnetic chirality. The resulting interaction opens a route to nonreciprocal and chirality-sensitive hybrid excitations in interfacial magnetic systems, including regimes relevant to anomalous magnon-polaron transport and directional spin-lattice energy flow. Complementary first-principles calculations are used to examine candidate interfaces and to assess how chiral magnetic states, structural relaxation, and interfacial strain are linked at the atomistic level. This work positions SIDMI as a general framework for understanding and engineering chiral spin-lattice coupling in metallic multilayers.

References

[1] N. S. Gusev, A. V. Sadovnikov, S. A. Nikitov, et al., “Manipulation of the Dzyaloshinskii-Moriya interaction in Co/Pt multilayers with strain,” Physical Review B (2020).

[2] E. Savostin and V. Lomakin, "Giant phonon-skyrmion coupling in ferromagnet/heavy metal heterostructures," Physical Review B (2024).
[1] N. S. Gusev, A. V. Sadovnikov, S. A. Nikitov, et al., "Manipulation of the Dzyaloshinskii-Moriya interaction in Co/Pt multilayers with strain," Physical Review B (2020).
[2] E. Savostin and V. Lomakin, "Giant phonon-skyrmion coupling in ferromagnet/heavy metal heterostructures," Physical Review B (2024).

GG-11. Simulation of smooth spin-wave transmission spectra using symmetric two-dimensional magnonic crystals

D. Shabaev[1], Y. Otsuka[1], T. Watanabe[2], E. Negishi[2], K. Ishiyama[1], T. Goto[1]
[1]Research Institute of Electrical Communication, Sendai, Japan, [2]Shin-Etsu Chemical, Gunma, Japan

Manipulation of spin waves (SW) inside magnonic crystals (MCs) is crucial for SW integrated circuits. MCs are periodic structures that create frequency bandgaps essential for SW signal processing and logic. However, miniaturization of SW waveguides remains challenging: in narrow structures, shape-induced demagnetization fields distort the internal field distribution, alter the SW wavelength, and disrupt phase coherence required for interference-based logic. Previously, our research group reported stable SW propagation through a line-defect waveguide in a single-sided Cu hole array/YIG 2DMC. Further improvement of the structure is required to achieve longer propagation distance and more stable SW transmission. Here we propose a symmetric double-sided Cu/YIG/Cu 2DMC. The structure comprises a 12-μm-thick YIG film between 4-μm-thick Cu hole arrays on both surfaces, made of a hexagonal lattice with a lattice constant of 900 μm and a hole diameter of 200 μm. The YIG film remains unpatterned. A line defect in the 2DMC forms a SW waveguide confining propagation to bandgap frequencies. Shape-anisotropy effects are negligible because of the macroscopic size (15 mm × 15 mm) of the YIG film. The simulations show that the proposed structure widens the magnonic bandgap by a factor of 5 compared to the single-sided version. Fig. 1 visualizes the SW propagation along the line-defect waveguide in the double-sided 2DMC. Poynting vector evaluation at the waveguide output indicates that the symmetric configuration delivers at least twice the SW power. As shown in Fig. 2, the transmission spectra of the double-sided structure is cleaner than the single-sided one. The widened bandgap and the stable transmission can be attributed to the symmetric SW confinement provided by the Cu arrays on both surfaces. These results demonstrate that symmetric metallization improves waveguide performance and establishes an inhomogeneous-magnetic-field-free platform for SW integrated circuits with extended propagation distance and improved signal fidelity.

[1] Andrii V. Chumak et al. IEEE Trans. Magn., 58, 0800172 (2022).
[2] Mikhail P. Kostylev et al. Appl. Phys. Lett., 87, 153501 (2005).
[3] Kanta Mori et al. Phys. Rev. Applied, 21, 014061 (2024).

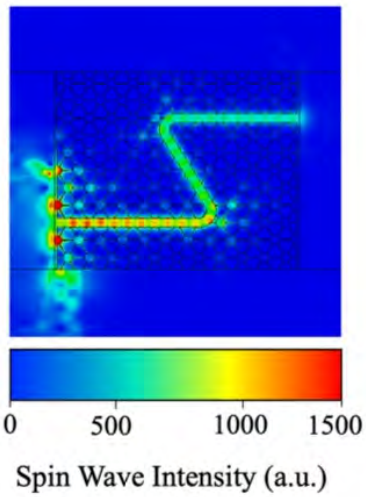


Fig. 1 Numerical simulation of spin-wave propagation along the line-defect waveguide in the double-sided 2DMC.

F

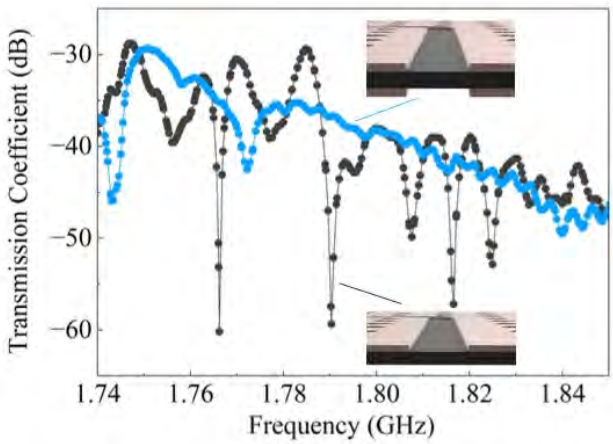


Fig. 2 Comparison of transmission spectra between the single-sided (gray) and double-sided (blue) 2DMCs.

GG-12. Unconventional magnetization states in artificial spin lattices enabled by nanopatterned synthetic ferromagnets.

R. Sultana[1], S. Lendinez[2], S. Josephy[3], B. Jungfleisch[1]
[1]Physics & Astronomy, University of Delaware, Newark, Delaware, United States, [2]Louisiana State University, Baton Rouge, Louisiana, United States, [3]Qzabre LLC, Zurich, Switzerland

Reconfiguring nanoscale magnetic systems is one of the core challenges in the development of low-energy magnetic platforms, where information can be encoded in both collective spin dynamics and static magnetic configurations [1–3]. To this end, engineering interlayer interactions in such structures provides a promising route to control equilibrium magnetic states as well as reconfigure collective magnetization dynamics [4–6].

Here, we investigate multilayer honeycomb artificial spin ice systems with two distinct vertical interlayer coupling regimes: dipolar coupling mediated by a nonmagnetic spacer and exchange coupling enabled by a magnetic interlayer. In the dipolar-coupled multilayer, thickness asymmetry between the ferromagnetic layers induces synthetic ferrimagnetic behavior. Broadband ferromagnetic resonance measurements demonstrate that excitation geometries selectively probe magnon modes that emerge in these structures, identified as optical and acoustic modes through micromagnetic simulations. Beyond emergent dynamic phenomena, we observe multiple stable vortex configurations in exchange-coupled multilayer structures, resulting in checkerboard-like pattern detected by nitrogen-vacancy magnetometry. These results demonstrate interlayer coupling as a control parameter for both emergent non-trivial magnetization textures, such as vortices and reconfigurable dynamic magnon spectra.

This work has been supported by the U.S. Department of Energy, Office of Science, Office of Basic Energy Sciences under Award Number DE-SC-432284.

1. S. Gliga et al., APL Mater. 8, 4 (2020).
2. G. Gubbiotti et al., J. Phys.: Condens. Matter 37, 143502 (2025).
3. R. Sultana et al., J. Appl. Phys. 138, 6 (2025).
4. T. Dion et al., Nat. Commun. 15, 4077 (2024).
5. F. Montoncello et al., J. Appl. Phys. 133, 8 (2023).
6. R. Sultana et al., ACS Appl. Electron. Mater. (2026).

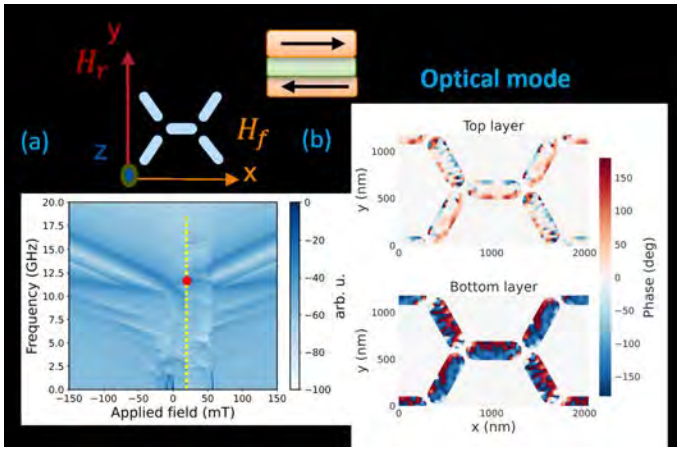


Fig. 1: (a) Frequency–field dispersion. (b) Spatial phase map at 20 mT showing the optical mode.

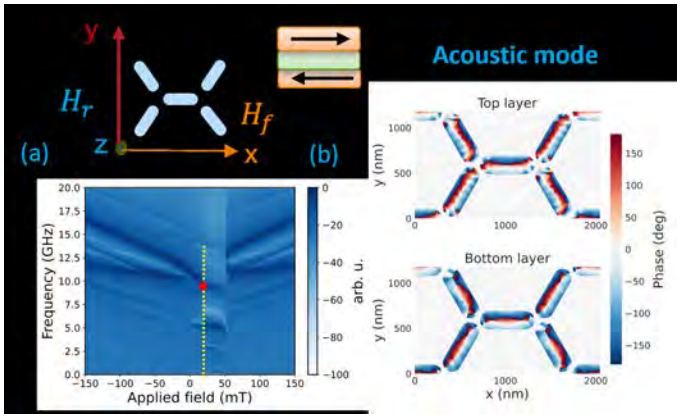


Fig. 2: (a) Frequency–field dispersion. (b) Spatial phase map at 20 mT showing the acoustic mode.

SESSION GP: SKYRMIONS, TOPOLOGY AND CHIRALITY (POSTER SESSION)

Co-Chair(s): C. Murapaka, *Materials Science and Metallurgical Engineering, IIT Hyderabad, Hyderabad, Telangana, India* and H. Arava, *Argonne National Laboratory, Lemont, Illinois, United States*

Friday, November 6, 2026
09:30 AM-12:30 PM
Coral 4

GP-01. Long-range modulation of skyrmion population by local current injection

S. Yadav[1], S. Chatterjee[1], S. Sugimoto[2], S. Kasai[2]
[1]IIT(BHU), Varanasi, India, [2]NIMS, Tsukuba, Japan

The thin-film magnetic skyrmion is designed to interact with each other as nonlinear response, enabling collective magnetic morphology at the nonequilibrium state. We here explore the alternative nonlinear morphology of multiple skyrmions induced by the orthogonal two-current injections for the Pt/Co/Ir multilayer platforms. The global currents induce polarity-dependent driving and accumulation of skyrmions across the whole area of a Hall bar device. Once another local current is injected from a mm width ports, dozens of skyrmions follow their polarity manners of the local injection, resulting in total modulations of skyrmion population governed by a pair of two-current polarities. Such massive morphology tuning at the nonlinear region indicates resemblances with a skyrmion Hall effect, where current-induced accumulation and depletion create the nonequilibrium distributions of skyrmions toward Hall deflections. Our findings propose an alternative controlling method of skyrmion population, threshold-like responses, providing analogies with neuromorphic architectures and other advanced information-processing technologies.

1. A. Fert, N. Reyren, and V. Cros, “Magnetic skyrmions: Advances in physics and potential applications,” Nat. Rev. Mater. 2, 17031 (2017).
2. D. Prychynenko, M. Sitte, K. Litzius, B. Krüger, G. Bourianoff, M. Kläui, J. Sinova, and K. Everschor-Sitte, “Magnetic Skyrmion as a Nonlinear Resistive Element: A Potential Building Block for Reservoir Computing,” Phys. Rev. Appl. 9, 014034 (2018).
3. S. Woo, K. Litzius, B. Krüger, M.Y. Im, L. Caretta, K. Richter, M. Mann, A. Krone, R.M. Reeve, M. Weigand, P. Agrawal, I. Lemesh, M.A. Mawass, P. Fischer, M. Kläui, and G.S.D. Beach, “Observation of room-temperature magnetic skyrmions and their current-driven dynamics in ultrathin metallic ferromagnets,” Nat. Mater. 15, 501 (2016).

GP-02LB. Optimized control protocols for stable skyrmion creation using deep reinforcement learning

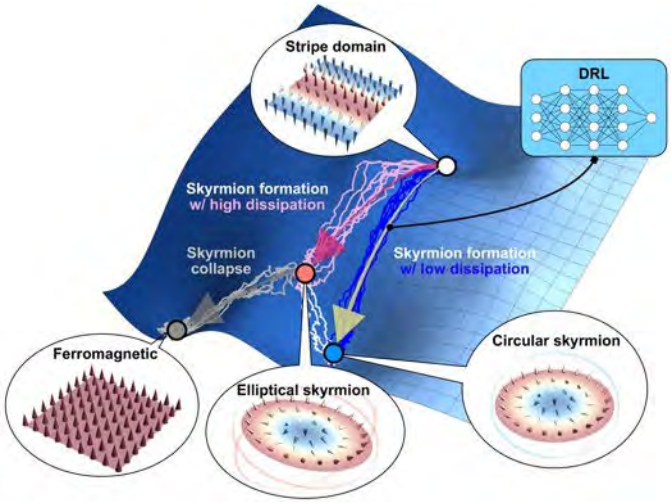
J. Song[1], S. Kim[1], K. Kim[2]
[1]Graduate School of Quantum Science and Technology, Korea Advanced Institute of Science and Technology, Dajeon, Korea (the Republic of), [2]Asia Pacific Center for Theoretical Physics, Pohang, Korea (the Republic of)

Generating stable magnetic skyrmions is essential for the practical application of skyrmion-based spintronic devices in thermally agitating environments. Here, we present a deep reinforcement learning (DRL) approach to identify advanced dynamic magnetic-field-temperature paths that create skyrmions with enhanced thermal stability. The trained DRL agent discovers an optimized field-temperature path that achieves a higher success rate for skyrmion formation in Fe_3GeTe_2 monolayers compared to previous fixed-temperature field sweeps. Additionally, the generated skyrmions exhibit longer lifetimes due to their isotropic shape and equilibrium size, both of which place them near a local energy minimum and thereby hinder annihilation. We demonstrate that these advancements stem from the targeted minimization of the dissipated work, which ensures that the driven skyrmion states remain close to their equilibrium distributions by upper-bounding the Kullback-Leibler divergence. Our findings suggest that a physics-informed DRL framework streamlines the identification of optimized protocols for skyrmion creation.

Song, J.S., Kim, S.K. & Kim, KM. Optimized control protocols for stable skyrmion creation using deep reinforcement learning. *npj Comput Mater* (2026). https://doi.org/10.1038/s41524-026-02270-z

Birch, M.T., Powalla, L., Wintz, S. *et al*. History-dependent domain and skyrmion formation in 2D van der Waals magnet Fe3GeTe2. *Nat Commun* 13, 3035 (2022). https://doi.org/10.1038/s41467-022-30740-7

Whitelam, Stephen. "Demon in the machine: learning to extract work and absorb entropy from fluctuating nanosystems." *Physical Review X* 13.2 (2023): 021005. https://doi.org/10.1103/PhysRevX.13.021005



The trained DRL agent generates a time-dependent protocol for the external magnetic fields and temperature (indicated by the yellow arrow). This control drives the system from an initial stripe domain state to an isolated skyrmion state. By minimizing dissipation, the protocol yields a fully relaxed, circular skyrmion positioned near a local energy minimum. This energetic stability effectively reduces the probability of the skyrmion collapsing into the ferromagnetic ground state during post-protocol relaxation (indicated by the gray arrow), thereby ensuring enhanced longevity. In contrast, the conventional protocol (indicated by the magenta arrow) induces high dissipation, resulting in elliptical skyrmions with higher energy. Such states reside far from the local energy minimum, exhibiting reduced energetic stability and significantly shorter lifetimes.

GP-03. Realization of Maxwell's demon in a two-skyrmion system

S. Miki[1, 2], K. Adachi[2], R. Ishikawa[3, 4, 5], H. Imanishi[2], E. Tamura[2, 6], Y. Shiota[7, 8], T. Nozaki[9], M. Goto[5, 10, 11], H. Nomura[5, 10, 12], Y. Suzuki[2, 5, 13]

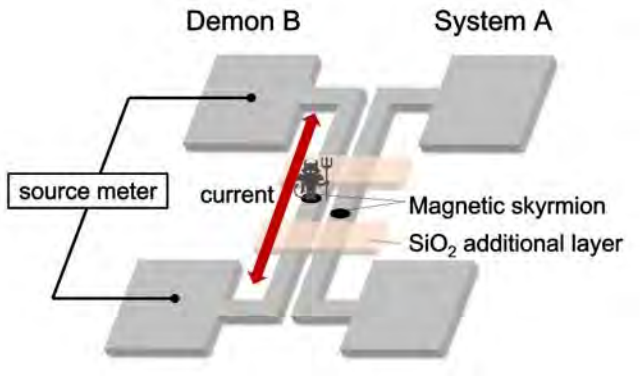
[1]WPI-AIMR, Tohoku University, Sendai, Miyagi, Japan, [2]Graduate School of Engineering Science, The University of Osaka, Toyonaka, Osaka, Japan, [3]Graduate school of Engineering, The University of Osaka, Suita, Osaka, Japan, [4]ULVAC, inc., Suita, Osaka, Japan, [5]OTRI-Osaka, The University of Osaka, Suita, Osaka, Japan, [6]Graduate school of Engineering, Kyoto University, Kyoto, Kyoto, Japan, [7]Institute for Chemical Research, Kyoto University, Uji, Kyoto, Japan, [8]CSRN-Kyoto, Kyoto University, Uji, Kyoto, Japan, [9]AIST, Tsukuba, Ibaraki, Japan, [10]CSRN-Osaka, The University of Osaka, Toyonaka, Osaka, Japan, [11]Tokyo University of Science, Katsushika, Japan, [12]SRIS, Tohoku University, Sendai, Japan, [13]Osaka Institute of Technology, Osaka, Osaka, Japan

To realize ultra-low-power Brownian computing, we have previously proposed and demonstrated Brownian circuits that utilize the Brownian motion of magnetic skyrmions in solids [1,2]. However, the key remaining issue is the realization of a synchronous logic element, the conservative-join (C-join) gate, which requires real-time observation of skyrmions and feedback control. This problem is equivalent to implementing Maxwell's demon, as described by information thermodynamics [3,4], in a solid-state device at room temperature. Therefore, this study aims to demonstrate Maxwell's demon in magnetic skyrmion systems toward designing the C-join circuit.

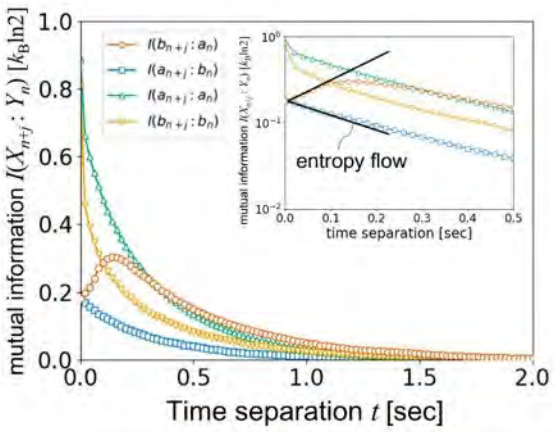
We deposited films with the following stacking structure Si/SiO_2 sub.| Ta(5) | Co-Fe-B(1.2) | Ta(0.22) | MgO(1.5) | SiO_2(3) (described in nm), and fabricated the devices designed for electrical current injection, as shown in Fig. 1. We also deposited additional SiO_2 layers to confine the skyrmions within individual cells. The skyrmion in the left cell (B), acting as Maxwell's demon, observes the position of the skyrmion in the right cell (A) and performs the feedback control. This feedback control induces entropy flow i.e., information flow from skyrmion A to skyrmion B, which is quantified by changes in mutual information. Fig. 2 shows the mutual information between skyrmion A and B $I(X_{n+j}:Y_n)$ ($X, Y = a, b$, representing the binary states of skyrmion A and B) and its semi-log plot in the inset. The slope of $I(X_{n+j}:Y_n)$ at time separation $t = 0$ corresponds to the entropy flow, which is clearly observed. This entropy flow converts to the heat absorption in system A and the conversion efficiency reaches as high as 70%.

This work is supported by KAKENHI (JP20H05666, JP24K22860, JP26K17078), JST CREST (JPMJCR20C1), X-NICS (JPJ011438), and the Asahi Glass Foundation.

[1] YJibiki, S. Miki, *et al.* Appl. Phys. Lett. 117, 082402 (2020).
[2] R. Ishikawa *et al.*, Appl. Phys. Lett. 119, 072402 (2021).
[3] T. Sagawa and M. Ueda, Phys. Rev. Lett 100, 080403 (2008).
[4] J. M. Horowitz *et al.*, Phys. Rev. X. 4, 031015 (2014)



The sample configuration.



Mutual information between skyrmion A and B. inset is a semi-log graph.

GP-04. Stabilization and Angle-dependent Resonant Dynamics of Skyrmions in Re/Co/Pt Multilayers

S. K. Jena
Institute of Physics, Chemistry and Biology, Linkoping University, Linkoping, Sweden

Skyrmions are topologically stable chiral quasi-particles that can be visualized in systems with presence of breaking inversion symmetry arising at the interface of ferromagnetic and heavy metal, i.e. with interfacial Dzyaloshinskii-Morya interaction (iDMI) and high spin orbit coupling [1-4]. Here, I will present the stabilization of skyrmions at remanence in [Re (20 Å) /Co (t_{Co}) /Pt (10 Å)]$_{20}$ multilayers with varying Co thicknesses (6– 24 Å), showcasing a transition from out-of-plane to in-plane magnetic anisotropy [5]. The number of skyrmions stabilization depends upon the iDM strength, effective anisotropy and thickness of the Co. It is found that the iDMI strength is substantially higher compared to the other conventional systems (W/Co/Pt. Pt/Co/Ir, Ta/Co/Pt etc.) and surface iDMI constant approaches to 3pJ/m due to additive nature of iDMI strength at bottom Re/Co and top Co/Pt interfaces [5-8]. Further, ferromagnetic resonance spectroscopy reveals four distinct resonant modes, including low-frequency (2–18 GHz), high-frequency (20–35 GHz) modes, depending on the different chiral domains [5]. The frequency range of these modes narrows with decreasing effective anisotropy and iDMI strength decreases in thicker Co layers in perpendicular configurations [5]. The presentation concludes with a tuning the magnon spectra due to skyrmions and chiral stripes which is very important for the magnonic based spintronic devices.

1. I. Dzyaloshinsky, A thermodynamic theory of "weak" ferromagnetism of antiferromagnetics. Journal of Physics and Chemistry of Solids 4, 241–255 (1958).
2. T. Moriya, New mechanism of anisotropic superexchange interaction. Physical Review Letters 4, 228–230 (1960).
3. T. Moriya, Anisotropic Superexchange Interaction and Weak Ferromagnetism. Physical Review 120, 91–98 (1960).
4. M. Kuepferling, et al., Measuring interfacial Dzyaloshinskii-Moriya interaction in ultrathin magnetic films. Reviews of Modern Physics 95, (2023)
5. S.K. Jena et al., Angle-dependent resonant dynamics of stripes and skyrmions in Re/Co/Pt multilayers, Phy. Rev. B accepted 2026 (https://doi.org/10.1103/78wv-b4np)
6. S.K. Jena et al. Interfacial Dzyaloshinskii–Moriya interaction in the epitaxial W/Co/Pt multilayers, Nanoscale, 13, 7685-7693, 2021
7. S.K. Jena et al. Magnetic Properties of epitaxial Re/$Co_{1-x}Au_x$/Pt heterostructures, under Review Phy. Rev. B (https://arxiv.org/pdf/2501.12961)
8. A. Nomura et al., Additive Dzyaloshinskii–Moriya interaction in Pt/Co/Re films. AIP Advances 12, (2022)

GP-06. Skyrmions in W/CoFeB/MgO/Ta SAFs by Ion Irradiation

M. Wilke, S. Kostadinov, M. Becherer, V. Ahrens
Professorship of Chip-Based Magnetic Sensor Technology, Technical University of Munich, Garching, Bavaria, Germany

Magnetic skyrmions, which are topologically protected magnetic vortices in thin films, are promising for novel spintronic devices and sensors. This requires them to remain stable over a wide range of magnetic fields while being generated by small magnetic fields or electrical currents. These requirements make synthetic antiferromagnets (SAFs) promising candidates as host materials [1].

In this work, we fabricated a $W/Co_{20}Fe_{60}B_{20}/MgO/Ta/W/Co_{20}Fe_{60}B_{20}/MgO/Ta$ multilayer stack using RF magnetron sputtering. In this architecture, CoFeB serves as the ferromagnetic layer and MgO as the insulating tunnel barrier [2], while a Ta/W spacer is utilized to promote both the Dzyaloshinskii-Moriya interaction (DMI) and RKKY coupling.

Figure 1 shows the laser-MOKE hysteresis loops, where the as-deposited sample exhibits no sharp switching (blue). The samples were subsequently annealed to enhance the perpendicular magnetic anisotropy (PMA) [3]. The resulting hysteresis loop (Fig. 1, orange) shows two distinct jumps, which suggest the presence of a SAF.

Wide-field MOKE (WF-MOKE) was employed for further characterization, enabling imaging of magnetic domains and a detailed investigation of switching processes. Reversing the magnetic field after domain formation revealed additional magnetic states, with four distinct contrast levels (Fig. 2a) providing strong evidence of the antiferromagnetic (AF) coupling.

Skyrmion nucleation was successfully induced by local modification of the PMA via irradiation with optimized Ga+ ion doses [4,5]. The resulting phase diagram exhibits a transition from a skyrmion phase to a domain phase (Fig. 2b) and back to a skyrmion phase (Fig. 2c).

These results provide a solid foundation for utilizing stack engineering and ion irradiation to control skyrmion behavior in the investigated SAFs.

[1] W. Legrand, D. Maccariello, F. Ajejas, et al., Nature Materials, Vol. 19, p. 34–42 (2020)
[2] R. Chen, X. Wang, H. Cheng, et al., Cell Reports Physical Science, Vol. 2, p. 11 (2021)
[3] H. Meng, W. H. Lum, R. Sbiaa, et al., Journal of Applied Physics, Vol. 110, p. 3 (2011)
[4] V. Ahrens, C. Kiesselbach, L. Gnoli, et al., Advanced Materials, Vol. 35, p. 2207321 (2023)
[5] S. Mendisch, F. Riente, V. Ahrens, et al., Physical Review Applied, Vol. 16, p. 014039 (2021)

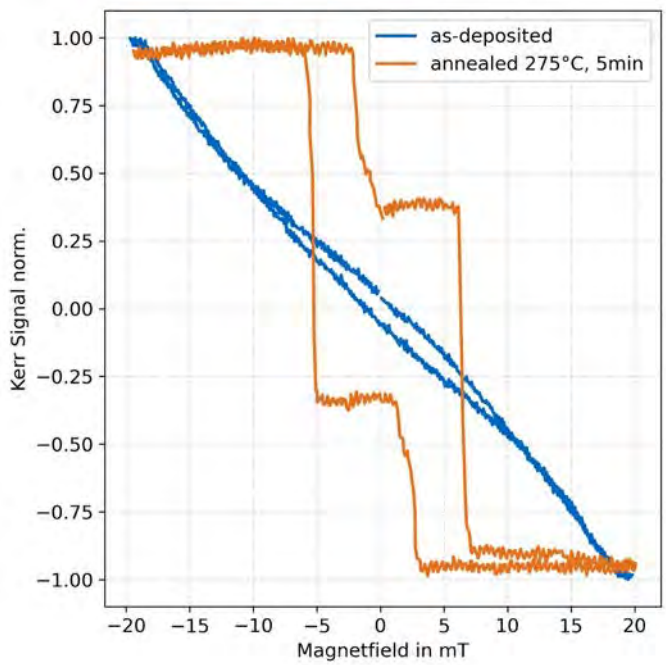


Figure 1: The blue hysteresis loop represents the as-deposited state, while the orange curve shows the sample after annealing, exhibiting two distinct jumps typical for SAFs.

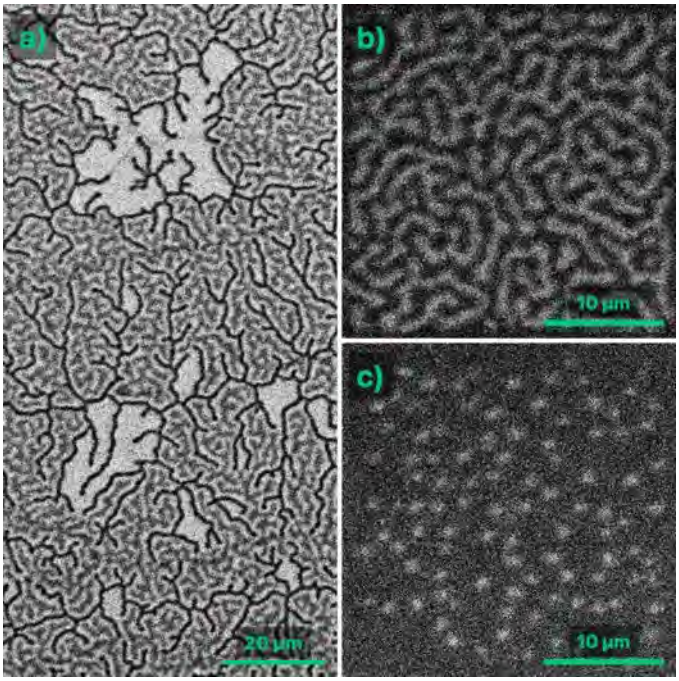


Figure 2: WF-MOKE images showing four contrast levels (a) and the Ga^+ irradiation-induced formation of domains (b) and skyrmion (c) configurations.

GP-07LB. Anomalous Hall Effect in Antiferromagnetic FeMn Doped with Pt

S. Abdizadeh Kalan, S. Emori
Physics, Virginia Tech, Blacksburg, Virginia, United States

Antiferromagnets with anomalous Hall effects (e.g., Mn_3Sn) are actively studied for potential ultrafast memory [1], but they require high-temperature growth that is incompatible with practical device fabrication. We have recently demonstrated *room-temperature-grown*, *polycrystalline* films of γ-FeMn alloy as a highly promising alternative [2]. These antiferromagnetic γ-FeMn films (seeded with Cu that stabilizes the FCC γ phase [3]) exhibit a room-temperature anomalous Hall conductivity of ≈ 15 S/cm, on par with that of Mn_3Sn. The γ-FeMn films also possess a small moment of ≈ 0.05 μ_B/atom from grain-boundary defects and a perpendicular easy axis (due to small residual strain), desirable for memory storage and switching.

Building on our recent discovery [2], this poster will present fresh results revealing the benefits and challenges of alloying γ-FeMn with Pt. We hypothesized that Pt, due to its strong spin-orbit coupling, would enhance the anomalous Hall conductivity and perpendicular anisotropy. Indeed, we find that Pt incorporation into γ-FeMn enhances the anomalous Hall conductivity more than tenfold to ≈ 200 S/cm [Fig. 1], beneficial for reliable electrical read-out of the magnetic order.

However, even Pt concentration < 10 at.% suppresses perpendicular anisotropy [Fig. 1 inset, Fig. 2(a)]. Pt incorporation increases the lattice constant of the film from 3.61 Å (0 at.% Pt) to 3.85 Å (20 at.% Pt), thereby increasing the lattice mismatch with the Cu seed layer [Fig. 2(b)]. The mismatch allows the residual strain to relax, removing the strain-induced perpendicular anisotropy. Our results suggest that strain engineering in γ-FeMn-Pt films could enable scalable antiferromagnetic media with both a large anomalous Hall effect and a robust perpendicular easy axis.

[1] Rimmler, B. H. *et al. Nat. Rev. Mater.* 10, 109–127 (2025).
[2] Maizel, R. E., Abdizadeh, S. *et al.* "Perpendicular Magnetization from Crystallite Boundaries in Polycrystalline Antiferromagnetic *γ*-FeMn" (under preparation).
[3] Abdizadeh, S., Maizel, R. E. *et al. Appl. Phys. Lett.* 128, 132401 (2026).

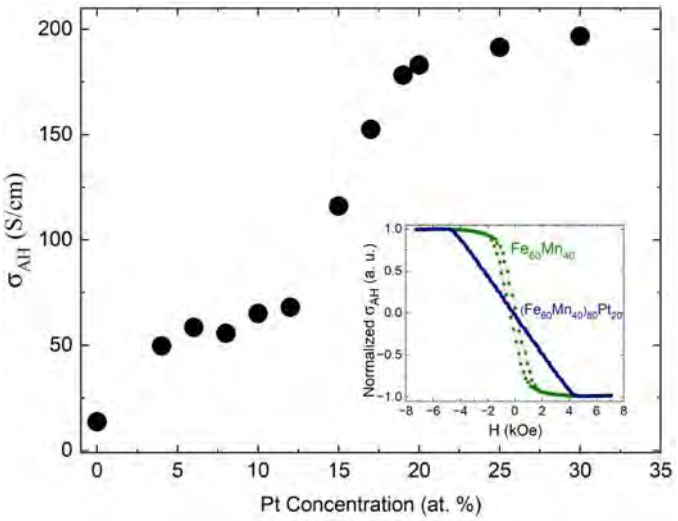


FIG 1. Anomalous Hall conductivity σ_{AH} vs Pt concentration in 50-nm-thick $(Fe_{60}Mn_{40})_{100-x}Pt_x$. Inset: Normalized σ_{AH} vs out-of-plane field for $Fe_{60}Mn_{40}$ and $(Fe_{60}Mn_{40})_{80}Pt_{20}$.

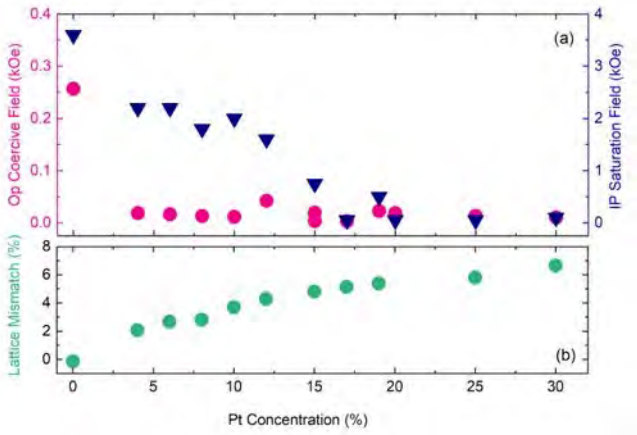


FIG 2. (a) Out-of-plane coercivity, in-plane saturation field, and (b) lattice mismatch of $(Fe_{60}Mn_{40})_{100-x}Pt_x$ with Cu (lattice parameter 3.6 Å) vs Pt concentration.

GP-08. Voltage-Propagated Skyrmion Logic and Memory for Large-Scale Reversible Computing

B. Walker[1, 2], K. Muthukrishnan[1], X. Hu[1], M. Frank[3], F. Garcia-Sanchez[4], A. J. Edwards[1], D. Querlioz[2], J. S. Friedman[1]
[1]Electrical and Computer Engineering, University of Texas at Dallas, Richardson, Texas, United States, [2]Universite Paris-Saclay, Palaiseau, France, [3]Vaire Computing, Sunnyvale, California, United States, [4]Departamento de Fisica Aplicada, Universidad de Salamanca, Salamanca, Spain

Skyrmions have long been of interest for low power computation and memory due to their size, ease of transport, and topological stability [1]. Reversible computing seeks to avoid the entropy created by irreversible logic, allowing for ultra-efficient computation. By exploiting skyrmion-skyrmion interaction, prior works have demonstrated the feasibility of skyrmions as information carriers for reversible computation, using both electronic current [2-3] and voltage-controlled magnetic anisotropy (VCMA) [4] propagation. While VCMA-propagation is highly efficient, no one has calculated its energy consumption at finite temperatures, a necessity for real-world performance estimation and comparison to the Landauer limit. Further, though a plethora of skyrmion memory elements exist, they all interface to the electronic domain, making them useless for reversible systems fully within the spin domain. This work accurately estimates the work done by the VCMA electrodes at temperature in order to obtain a sufficiently small bit-error rate and demonstrates the first-ever skyrmion-to-skyrmion memory element, the missing component necessary for skyrmion-only architectures. This work completes the groundwork for designing large-scale and efficient reversible skyrmion circuits.

[1]: H. Vakili et al., Journal of Applied Physics 130, 070908 (2021)
[1]: M. Chauwin et al., Physical Review Applied 12, 064053 (2019)
[2]: B. W. Walker et al., Applied Physics Letters 118, 192404 (2021)
[3]: B. W. Walker et al., arXiv Preprint, (2023), doi:10.48550/arXiv.2301.10700

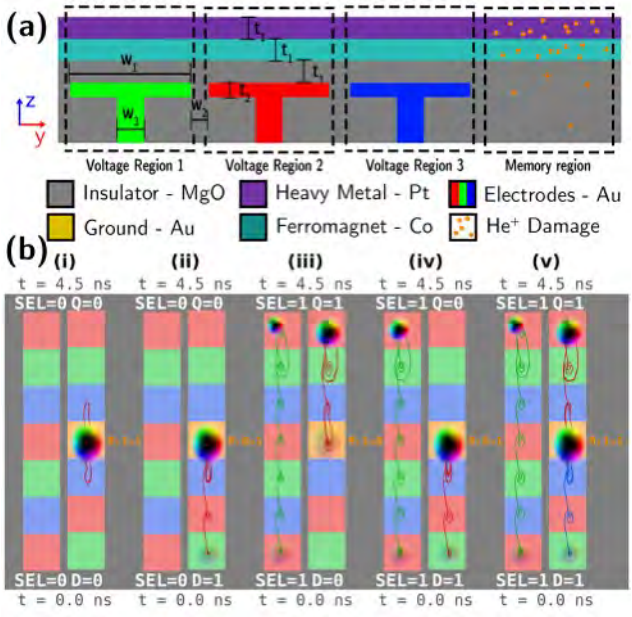


Figure 1. Skyrmion latch element. (a) Device cross section. Electric field applied across the MgO (grey) via Au electrodes (red/green/blue) modifies the perpendicular magnetic anisotropy of the Co/Pt racetrack (teal/purple). He+ irradiation (orange) is used to reduce the anisotropy of the memory region to pin skyrmions. (b) mumax3 results, demonstrating the ability to hold and retrieve data. Skyrmion initial positions are transparent and final positions are opaque. Simulations are run for the following valid and non-trivial state combinations of SEL, D, and M: (i) (0,0,1) (ii) (0,1,0) (iii) (1,0,1) (iv) (1,1,0) (v) (1,1,1).

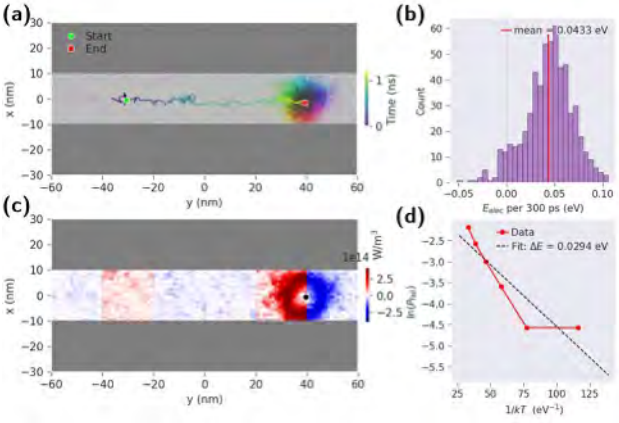


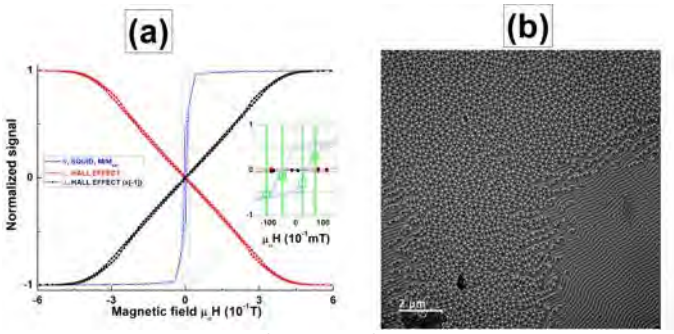
Figure 2. VCMA propagation energy. (a) mumax3 result of a VCMA-propagated skyrmion. (b) Histogram of electrode work to move a skyrmion 20 nm over many thermal seeds at 100 K. (c) Heatmap of work done by the electrodes spatially (d) Log of error rate as a function of inverse temperature, whose linear fit estimates the thermal barrier.

GP-09. Skyrmions lattice in Fe/Gd multilayers with planar magnetic anisotropy driven by wobbling movement

F. Fettar[1], J. Tonnerre[1], E. Mossang[1], A. Masseboeuf[2], A. Bernand-Mantel[3], C. Gatel[3], N. Jaouen[4], H. Popescu[4], A. Wartelle[1], G. Beutier[5], L. Ortega[6], V. P. Nascimento[7], E. C. Passamani[7], N. Rougemaille[1]
[1]Neel Institute, CNRS, Grenoble, France, [2]SPINTEC, CEA, Grenoble, France, [3]CEMES, CNRS, Toulouse, France, [4]Exp Divisio, Synchrotron SOLEIL, Saint-Aubin, France, [5]SIMaP, Université Grenoble Alpes, Université Grenoble Alpes, France, [6]LPS, CNRS, Orsay, France, [7]Physics, Universidade Federal do Espirito santo, Vitoria, Brazil

The appearance of skyrmions in the literature is largely observed for an easy axis of the magnetization perpendicular to layers in multilayered systems [1]. Here, we report the direct observation of a skyrmionic spin network at room temperature by Lorentz Transmission Electron Microscopy (LTEM) [2] for appropriate magnetic fields, (≈5 and ≈10mT as parallel and perpendicular field respectively) in a prototypical [3][Fe(3.4Å)Gd(7.2Å)]$_{x60}$ multilayer behaving a robust planar magnetic anisotropy. The main funding is the control of the relatively well-organized spins structure by a wobbling movement of the multilayer. In Fig1(a) are plotted the normalized (as measured and inverted) magnetization at RT for // and ⊥ magnetic fields. A clear planar magnetic anisotropy is measured with effective anisotropy constant (K_{eff}) and saturation magnetization (M_{sat}), as -6.481110^4 J/m^3 0.4106 MA/m respectively. Here, the out-of-plane magnetic loop is inverted as expected for a rare earth rich rare earth rich film (Gd content τ_{Gd}=43%). An FMR study confirms the magnetic features as well as the damping factor (a=5.8 10^{-3}). The variations of M_{sat} with the operating temperatures in the (5-400)K range permit to deduce the exchange stiffness value (A_{exc}=1.8pJ/m), which is coherent with the FMR results. Finally, the culmination achievement is the obtained LTEM image after the following procedure: (i) A pure perpendicular magnetic field $H_{\perp}$=1T is reduced to 0.1T ; (ii) Then a tilt of the sample is applied in one direction (β=6°) for getting planar alternated magnetic stripes ; (iii) by coming back to β=3° and operating a series of wobbles (x20) between β=-3° and β=3°, the obtained image appears in Fig1(b). A remarkable arrangement of magnetic bubbles is observed, as confirmed by a micro-magnetic approach (Excalibur [4]) with the magnetic parameters (K_{eff},M_{sat},A_{exc}). Our study opens the way for the control of tridimensional textured nanostructures by the movement of the device.

[1] J. Li *et al*, Nature Communications, 5(1), August 2014.
[2] M. He *et al*, Physical Review B, 97(17), 2018.
[3] S. A. Montoya *et al*, Physical Review B, 95(2), 2017.
[4] Rybakov FN, Babaev E (2020). Excalibur software. Available at: http://quantumandclassical.com/excalibur/.



For a sputtered [Fe(3.4Å)/Gd(7.2Å)]$_{N=60}$ multilayer: (a) Magnetic loops at RT [(a)] for ⊥ and // magnetic fields ; (b) : Lorentz Transmission Electron Microscopy (LTEM) image at RT after applying a wobble with ($H_{\perp}$≈100mT and $H_{//}$≈5mT).

GP-10. Magnon Propagation and Topological Phases in Hybrid Breathing-Honeycomb Lattice

P. Andrade[1], M. da SIlva Tavares[1, 2], R. F. Pinto[3]
[1]Department of Physics, State University of Maranhão, São Luís, Maranhão, Brazil, [2]Department of Physics, Federal Institute of Maranhão, São Luís, Maranhão, Brazil, [3]Department of Physics, Federal Institute of Amazonas, Presidente Figueiredo, Maranhão, Brazil

Spin waves are collective excitations in magnetic lattices associated with energy states above the ground state. Originally proposed by Felix Bloch in 1930 and experimentally verified in subsequent decades, these excitations constitute the foundation of spintronics, which has significantly advanced modern computation and its applications. Currently, several studies have sought novel technological platforms by exploring unconventional architectures, including lattice decoration, defect engineering and impurity insertion. The main objective is to reveal emergent topologies or competing interactions within the lattice, which may lead to directional symmetry breaking and induce anisotropies relevant for magnetic stability. In this work, we investigate the effects of a Hybrid Breathing-Honeycomb (HBH) lattice on magnon propagation, focusing on spectral analysis to elucidate the existence of possible topological features, such as robust edge modes. These effects are driven by the contribution of the Dzyaloshinskii–Moriya interaction (DM), in competition with exchange and anisotropic interactions. This competition may lead to the emergence of nontrivial

magnonic bands characterized by topological invariants, such as the Chern number associated with Berry curvature. The system is described by a Heisenberg Hamiltonian including exchange, Zeeman, anisotropic, and DM interactions, the latter being allowed due to the breaking of inversion symmetry between lattice sites. The magnon spectrum is evaluated in reciprocal space using the formalism of second quantization, where bosonic operators yield the spin-wave dispersion relation. From this dispersion, we extract key physical properties, including ground-state stability, magnetic ordering, spin stiffness, group velocity, preferred propagation directions, gap openings, and signatures of possible topological effects.

F. Bloch, Zeitschrift für Physik., Vol. 61, p.206 (1930)
T. Holstein and H. Primakoff, Physical Review., Vol. 58, p.1098 (1940)
A. V. Chumak, V. I. Vasyuchka and A. A. Serga, Nature Physics., Vol. 11, p.453 (2015)
I. Dzyaloshinsky, Journal of Physics and Chemistry of Solids., Vol. 4, p.241 (1958)
T. Moriya, Physical Review., Vol. 120, p.91 (1960)
H. Katsura, N. Nagaosa and P. A. Lee, Physical Review Letters., Vol. 104, p.066403 (2010)
L. Zhang, J. Ren and J.-S. Wang, Physical Review B., Vol. 87, p.144101 (2013)
S. A. Owerre, Journal of Physics: Condensed Matter., Vol. 28, p.386001 (2016)

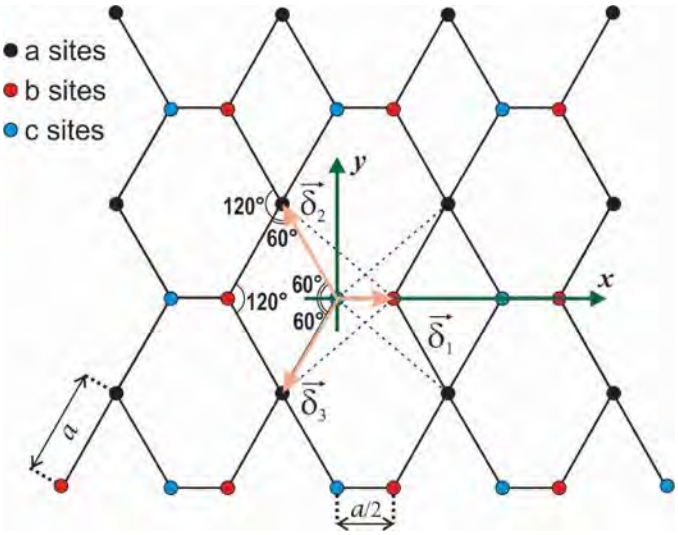


Fig. 1 Hybrid Breathing-Honeycomb ferromagnetic lattice

GP-11. Interplay between long-range magnetic ordering and topological band structure in GdZn

A. Biswas[1], A. Bhattacharya[2, 3], A. Kumar[1], A. Schmidig[1], S. Majee[2, 4], S. DuttaGupta[2], I. Das[2], P. Singh[1], Y. Mudryk[1]
[1]Ames National Laboratory, U.S. Department of Energy, Ames, Iowa, United States, [2]Condensed Matter and Surface Physics Division, Saha Institute of Nuclear Physics, Kolkata, West Bengal, India, [3]Department of Physics, Bar-Ilan University, Ramat-Gan, Israel, [4]Homi Bhabha National Institute, Mumbai, India

Gd intermetallics constitute a versatile platform for investigating correlated magnetism arising from the interplay between localized 4f moments and itinerant electrons. In these systems, RKKY interactions drive magnetic ordering and enable diverse thermomagnetic effects, as well as emergent phenomena associated with nontrivial band topology.[1-6] Here, we present a comprehensive study on GdZn, a magnetic Weyl metal crystallizing in a simple CsCl-type structure. The compound exhibits ferromagnetic ordering with a Curie temperature T_C = 269 K.[3] The magnetocaloric response shows a moderate magnetic entropy change (~ -8 J/ Kg K at 70 kOe) around T_C , consistent with a second-order transition. Critical exponent analysis places the system close to the mean-field universality class, indicating long-range magnetic interactions. First-principles calculations reveal nodal-line features, Weyl points, and flat bands near the Fermi level, indicative of a nontrivial band structure. The flat bands promote Fermi-surface nesting, generating extended parallel regions and enhancing Berry-curvature hot spots. Correspondingly, GdZn exhibits a pronounced anomalous Hall effect dominated by intrinsic mechanisms, with an intrinsic anomalous Hall conductivity of ~549 S/cm. The anomalous Hall angle increases monotonically with temperature and reaches ~8% near T_C, reflecting efficient transverse charge transport governed by the underlying band topology. A sizable positive magnetoresistance (~35% at 5 K) is also observed at low temperatures. These results establish GdZn as a model system for exploring the interplay between magnetism and band topology, and its impact on functional properties such as magnetocaloric, magnetoresistance, and anomalous Hall effect.

The work was supported by the U.S. Department of Energy (DOE), Office of Science, Basic Energy Sciences, Materials Science and Engineering Division. Ames National Laboratory is operated for the U.S.DOE by Iowa State University under contract No. DE-AC02- 07CH11358. I.D, S.D, S.M and A.Bhatt.

acknowledge support from Department of Atomic Energy, India.
1. L. Petit, D. Paudyal, Y. Mudryk, K. A. Gschneidner. Jr., V. K. Pecharsky, M. Luders, Z. Szotek, R. Banerjee, J. B. Staunton, Phys. Rev. Lett., V-115, 207201 (2015).
2. L. Petit, Z. Szotek, D. Paudyal, A. Biswas, Y. Mudryk, V. K. Pecharsky, J. B. Staunton, Phys. Rev. B, V-101, 014409 (2020).
3. A. Biswas, A. Kumar, P. Singh, T. Del Rose, R. K. Chouhan, B. C. Margato, B. P. Alho, E. P. Nobrega, P. J. von Ranke, P. O. Ribeiro, V. S.R. de Sousa, Y. Mudryk, Phys. Rev. Mater., V- 8, 114418 (2024)
4. A. Bhattacharya, A. Ahmed, A. Dutta, A. Kumar, P. Singh, A. Biswas, Y. Mudryk, I. Das, Phys. Rev. B, V-111, 104410 (2025)
5. S. Chakraborty, S. Gupta, S. Pakhira, R. Choydhary, A. Biswas, Y. Mudryk, V. K. Pecharsky, D. D. Johnson, C. Mazumdar, Phys. Rev. B, V-106, 224427 (2022)
6. B. P. Alho, P. O. Ribeiro, V. S. R. de Sousa, B. C. Margato, A. Biswas, T. Del Rose, R. S. de Oliveira, E. P. Nobrega, P. J. von Ranke, Y. Mudryk, V. K. Pecharsky, Phys. Rev. B, V-106, 184403 (2022).

GP-12. Magnetic Properties and Lattice Dynamics study in CVD-Grown Fe-Te Systems: influence of Phase and Composition

B. Jena[1], S. Chandran[2]
[1]*Department of Physics, IIT Madras, Chennai, Tamilnadu, India,*
[2]*Department of Physics, IIT Madras, Chennai, Tamilnadu, India*

The Fe-Te system offers a rich platform for studying the coupling between crystal phase, composition, lattice dynamics, and magnetism, but a unified understanding of these interrelated effects remains limited [1], [2], [3], [4], [5]. Here, we investigate phase and composition-dependent magnetic and vibrational properties in Fe-Te systems synthesized via salt-assisted atmospheric pressure chemical vapor deposition. We achieved tetragonal FeTe, orthorhombic $FeTe_2$, and hexagonal $FeTe_2$ across a wide compositional range ($FeTe_x$: $0.7 \leqslant x \leqslant 2.3$), including both stoichiometric and off-stoichiometric compositions. The grown crystals exhibit lateral sizes of ~150 μm for orthorhombic $FeTe_2$ and ~50 μm for other phases, while maintaining thicknesses down to ~10 nm across all phases. Microstructural analysis of orthorhombic $FeTe_2$ reveals a non-classical crystallization pathway involving oriented attachment and coalescence.
Magnetization measurements show robust room-temperature ferromagnetism across all phases, strongly influenced by non-stoichiometry. The Fe-vacancy dominated regime (x ~ 1.1–1.5) exhibits enhanced saturation magnetization and coercivity, while Fe-rich tetragonal FeTe shows reduced magnetization and Te-rich $FeTe_2$ phases display weaker ferromagnetism. Further, Lattice dynamical properties are probed using temperature dependent Raman and angle-resolved polarized Raman spectroscopy. Distinct phase-dependent vibrational modes are identified. Tetragonal and hexagonal phases exhibit nearly isotropic response, whereas orthorhombic $FeTe_2$ shows pronounced anisotropy and stronger phonon anharmonicity due to reduced symmetry and softer Te-Te bonding. These results establish a direct correlation between phase, non-stoichiometry, and lattice dynamics in tuning magnetic properties in Fe-Te systems.
[1] B. P. Jena and C. Sudakar, "Micron-Sized 2D Marcasite $FeTe_2$ Nanocrystals for Spintronics Applications," *ACS Appl. Nano Mater.*, pp. 1–13, 2024, doi: 10.1021/acsanm.4c05826.
[2] H. D. Lutz and B. Müller, "Lattice vibration spectra. LXVIII. Single-crystal Raman spectra of marcasite-type iron chalcogenides and pnictides, FeX_2 (X=S, Se, Te; P, As, Sb)," *Phys. Chem. Miner.*, vol. 18, no. 4, pp. 265–268, 1991, doi: 10.1007/BF00202579.
[3] L. Kang *et al.*, "Phase-controllable growth of ultrathin 2D magnetic FeTe crystals," *Nat. Commun.*, vol. 11, no. 1, pp. 1–9, 2020, doi: 10.1038/s41467-020-17253-x.
[4] T. L. Xia *et al.*, "Raman phonons of α-FeTe and $Fe_{1.03}Se_{0.3}Te_{0.7}$ single crystals," *Phys. Rev. B - Condens. Matter Mater. Phys.*, vol. 79, no. 14, pp. 1–4, 2009, doi: 10.1103/PhysRevB.79.140510.
[5] S. Chen, H. Liu, F. Chen, K. Zhou, and Y. Xue, "Synthesis, Transfer, and Properties of Layered $FeTe_2$ Nanocrystals," *ACS Nano*, vol. 14, no. 9, pp. 11473–11481, 2020, doi: 10.1021/acsnano.0c03863.

GP-14. Microscopic Magnon–Phonon Coupling in 2D $CrCl_3$: Toward Functional Spin–Lattice Engineering.

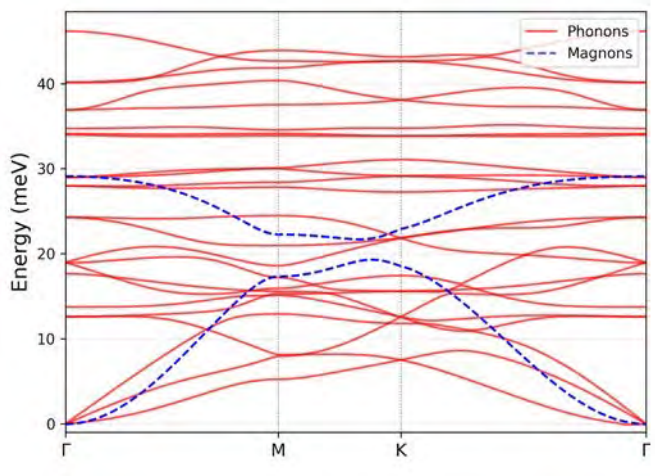
J. Mejia[1, 2], F. Nuñez-Murillo[1, 2]
[1]*Physics, Universidad Católica de Chile, Santiago, Chile,*
[2]*Millenium Institute on Green Ammonia as Energy Vector MIGA-ANID, Santiago, Chile*

Two-dimensional van der Waals magnets provide a unique platform to investigate spin–lattice interactions at the ultimate thickness limit. Among them, $CrCl_3$ stands out as a 2D ferromagnet with a honeycomb lattice and halogen-dependent magnetic anisotropy, making it ideal to explore mode- and momentum-resolved magnon–phonon coupling microscopically. Despite growing experimental evidence of hybrid excitations in layered magnets, a fully reciprocal-

space-resolved theoretical description remains incomplete. Here, we develop a first-principles-based framework combining density functional theory with a displacement-dependent spin Hamiltonian. We compute phonon dispersions and extract effective magnetic parameters, including exchange, anisotropy, and Dzyaloshinskii–Moriya contributions, as functions of atomic displacements. The magnon spectrum is obtained via linear spin-wave theory, enabling quantitative evaluation of spin–lattice coupling across the Brillouin zone (see Fig. 1).

By tracking variations of magnetic interactions under symmetry-resolved lattice distortions, we identify phonon modes and reciprocal-space regions where magnon–phonon hybridization is maximized. Our results reveal microscopic bond-level mechanisms governing spin–lattice coupling in Cr–Cl–Cr linkages and establish clear selection rules for hybrid mode formation.

Beyond elucidating the fundamental origin of magnon–phonon coupling in 2D ferromagnets, this framework provides a platform for functional spin–lattice engineering. The pronounced sensitivity of magnetic interactions to symmetry-resolved lattice distortions suggests hybrid vibro-magnonic modes can modulate bond geometry and spin polarization. We are currently extending this approach to investigate whether phonon-driven spin–lattice distortions influence spin-dependent reaction pathways, focusing on the nitrogen reduction reaction (NRR). Such coupling between collective magnetic excitations and catalytic functionality opens a new avenue for magnetically assisted surface chemistry in two-dimensional materials.



Phonon and magnon dispersion relations of 2D $CrCl_3$ along high-symmetry points in the Brillouin zone. Red lines correspond to phonon modes, while blue dashed lines represent magnon modes.

GP-15. Permutationally Invariant Signatures of Measurement-Induced Phase Transitions

K. Tokue[1], D. Yamamoto[1, 2]

[1]Department of Physics, College of Humanities and Sciences, Nihon University, Setagaya, Tokyo, Japan, [2]RIKEN Center for Quantum Computing, Wako, Saitama, Japan

Magnetic systems, or more generally many-body spin systems, have long served as prototypical platforms for studying phase transitions, ranging from classic examples such as the ferromagnetic–paramagnetic transition to more nontrivial phenomena including topological phase transitions.Recently, a new type of phase transition, the measurement-induced phase transition (MIPT) [1,2], has emerged in the nonequilibrium dynamics of quantum spin systems, or equivalently, qubit systems. It is characterized by a change in the scaling of entanglement with increasing measurement rate, typically from volume law to area law, resulting from the competition between unitary time evolution and local measurements.

In this work, we analyze MIPT from a perspective distinct from conventional entanglement-based approaches, focusing instead on symmetry operations acting on the system. Previous studies have largely relied on entanglement entropy; however, such measures typically require full quantum state tomography, resulting in an exponential measurement cost [3].We introduce a symmetry-based information entropy, termed the permutation-twirled entropy (PTE), constructed from a twirled density matrix obtained via a permutation-twirling operation over spin, or equivalently, qubit labels. The PTE captures labeling-independent information and reflects the spatial complexity of the state.We perform numerical simulations using random quantum circuit models with measurements [1,2], demonstrating that the PTE captures signatures of MIPT. This provides a symmetry-based perspective on MIPT beyond conventional entanglement-based descriptions. The PTE can be efficiently accessed via permutationally invariant quantum state tomography [4], enabling scalable probing of MIPT in larger systems.

[1] B. Skinner, J. Ruhman, and A. Nahum, Phys. Rev. X 9, 031009 (2019).

[2] Y. Li, X. Chen, and M. P. A. Fisher, Phys. Rev. B 100, 134306 (2019).

[3] J. M. Koh, S.-N. Sun, M. Motta, and A. J. Minnich, Nat. Phys. 19, 1314–1319 (2023).
[4] G. Tóth, W. Wieczorek, D. Gross, R. Krischek, C. Schwemmer, and H. Weinfurter, Phys. Rev. Lett. 105, 250403 (2010).

SESSION GQ: ALTERMAGNETIC, ANTIFERROMAGNETIC, TERAHERTZ AND SUPERCONDUCTING SPINTRONICS I (POSTER SESSION)

Chair(s): S. Shreya, *Electrical and Computer Engineering Department, Aarhus University, Aarhus, Denmark*
Friday, November 6, 2026
09:30 AM-12:30 PM
Coral 4

GQ-01. Large Magnetoresistance and Reconfigurable Spin Filtering Efficiency Induced by Nonvolatile Electrical Control of Magnetism in van der Waals Sc_2CO_2/Bilayer-$NiCl_2$/Sc_2CO_2 Multiferroic Heterostructures

H. Wang[1, 2, 3], X. Guo[2], B. Chi[1], Y. Zhu[4], Y. Yan[2], X. Han[1]
[1]Beijing National Laboratory for Condensed Matter Physics, Institute of Physics, Chinese Academy of Sciences, Beijing, China, [2]Key Laboratory of Physics and Technology for Advanced Batteries (Ministry of Education), Department of Physics, Jilin University, Changchun, Jilin, China, [3]Center of Materials Science and Optoelectronics Engineering, University of Chinese Academy of Sciences, Beijing, China, [4]Guangdong Provincial Key Laboratory of Optical Information Materials and Technology and Institute for Advanced Materials, South China Academy of Advanced Optoelectronics, South China Normal University, Guangzhou, Guangdong, China

Nonvolatile electrical control of magnetism in van der Waals (vdW) multiferroic heterostructures with strong magnetoelectric coupling effect holds great significance for designing high-efficiency and low-dissipation spintronic devices beyond Moore's law. Here, we propose a vdW multiferroic heterostructure composed of a bilayer-$NiCl_2$ clamped by two ferroelectric monolayer-Sc_2CO_2 (Sc_2CO_2/bilayer-$NiCl_2$/Sc_2CO_2 vdW heterostructure) and investigate the electronic structure, magnetoelectric coupling properties, and the in-plane spin-dependent transport of the proposed vdW multiferroic heterostructure using first-principles calculations. It is found that the interlayer magnetic coupling of the sandwiched bilayer-$NiCl_2$ can be reversibly switched between antiferromagnetic (AFM) and ferromagnetic couplings by electrically reversing the ferroelectric polarization direction of the top and bottom Sc_2CO_2 layers, respectively. By nonvolatile electrical control of the interlayer magnetic coupling of the sandwiched bilayer-$NiCl_2$, a large magnetoresistance effect of about 470–500%, and the maximum spin filtering efficiency of about 70% can be produced in the vdW heterostructure under zero bias, and the spin filtering efficiency can be effectively tuned by applying an electric field. Intriguingly, the built-in effective electric field along the out-of-plane direction between the two Sc_2CO_2 layers yields a spin filtering efficiency of up to 63–65% under zero bias, even in the interlayer AFM state. Our work presents a promising avenue for developing high-efficiency and low-dissipation spintronic devices.

(1) Zhou, J., Qiao, J. and Duan, C., et al, ACS Appl. Mater. Interfaces, 11, 17647–17653 (2019).
(2) Song, T., Cai, X. and Tu, M., et al, Science, 360, 1214–1218 (2018).
(3) Kim, H. H., Yang, B. and Patel, T., et al, Nano Lett., 18, 4885–4890 (2018).
(4) Zhang, X.; Zhou, Z. and Yu, X., et al, Adv. Funct. Mater., 33, No. 2301353 (2023).
(5) Guo, X., Yang, B. and Zhang, X., et al, Phys. Rev. B, 104, 144423 (2021).
(6) Zhang, X., Liu, B. and Huang, J., et al, Phys. Rev. B, 109, 205105 (2024).
(7) Jiang, S., Li, L. and Wang, Z., et al, Nat. Electron., 2, 159 (2019).
(8) Zhu, Y., Chi, B. and Jiang, L., et al, Phys. Rev. Appl., 20, No. 034010 (2023).

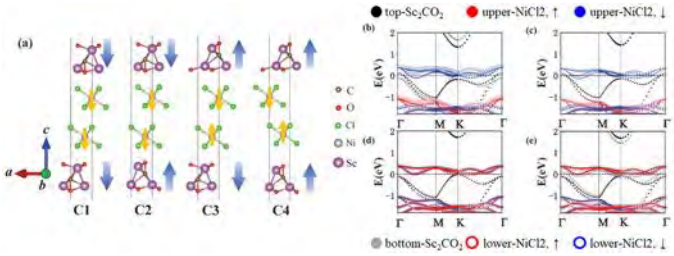
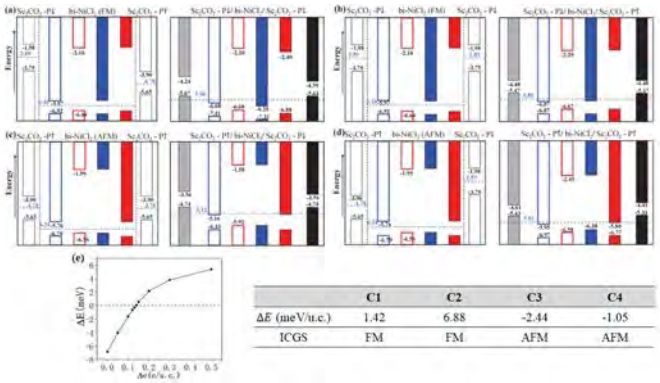


FIG. 1. (a) Side view of the Sc_2CO_2/bilayer-$NiCl_2$/Sc_2CO_2 vdW heterostructure in four polarized configurations. Projected bandstructures of the vdW heterostructure in (b) C1, (c) C2, (d) C3, and (e) C4 configurations.



	C1	C2	C3	C4
ΔE (meV/u.c.)	1.42	6.88	-2.44	-1.05
ICGS	FM	FM	AFM	AFM

FIG. 2. Band alignment diagrams for the system with (a) C1, (b) C2, (c) C3, and (d) C4 configurations, respectively, of freestanding layers (left panels) and that after forming the heterostructure (right panels). (e) ΔE (= $E_{AFM} - E_{FM}$) of the freestanding bilayer-$NiCl_2$ as a function of electron doping concentration (Δe). The Table shows ΔE and the corresponding Interlayer Coupling Ground States (ICGS).

GQ-02. Anomalous magnetic field-dependent spin dynamics in Gd0.3Ho0.7FeO3 single crystal near the ordering temperature of rare-earth ions

A. Wu, Z. Zhang, L. Su
Shanghai Institute of Ceramics, Chinese Academy of Sciences, Shanghai, China

Understanding the magnon dynamics near the rare-earth ion ordering temperature is crucial for revealing the complex exchange interactions between R 3+ and Fe 3+ ions in RFeO3 (where R is a rare-earth element). With Ho 3+ substitution, Gd0.3Ho0.7FeO3 undergoes a Γ4-Γ2 spin reorientation transition in the range 48-34 K which induces complex magnetic competition between the Fe 3+ and R 3+ sublattices. Here, we employ low-temperature terahertz time-domain spectroscopy (THz-TDS) under magnetic field to investigate the magnetic field-dependent spin dynamics of Gd0.3Ho0.7FeO3 single crystals. At 2-6 K, with the magnetic field applied along the c-axis, two magnon resonance peaks are observed, which split between 1-6 T, merge at 7 T, and re-split at 8 T. This anomalous behavior, which contrasts with the simple monotonic splitting in typical canted antiferromagnets, is attributed to the strong Gd 3+ -Fe 3+ antiferromagnetic coupling that drives the reversal of Fe 3+ magnetic moments at a critical field. These results provide in-depth insight into the intricate R 3+ -Fe 3+ coupling in orthoferrite antiferromagnets and offer potential avenues for manipulating magnons excitations.

GQ-03. Engineering magnetic anisotropy and domain evolution in Dy_xCo_{1-x}ferrimagnetic alloy thin films through composition

R. Kaur, Y. V. Shalihotri, C. Murapaka
Materials Science and Metallurgical Engineering, Indian Institute of Technology Hyderabad, Sangareddy, Telangana, India

Magnetic anisotropy plays an important role in influencing the stability, switching behaviour, and domain configurations of magnetic thin films. Specifically, perpendicular magnetic anisotropy (PMA) is preferred for high-density spintronic applications because of its high thermal stability and lower switching current density. Rare-earth transition metals (RE–TM) alloys have garnered considerable interest due to their tunable magnetic properties arising from antiferromagnetically coupled sublattices[1]. The combination of strong spin-orbit coupling of the RE element and high magnetisation of TM enables controllable anisotropy and compensation behaviour. The systematic study of composition-driven magnetic reversal in RE-TM alloys is essential to employ them for spintronic applications. In this work, we have investigated the effect of composition on magnetic anisotropy and domain evolution in co-sputtered Dy–Co ferrimagnetic thin films with constant thickness. By varying the sputtering power, we have tuned the alloy composition to determine magnetic properties. The grazing incidence X-ray diffraction measurements (GIXRD) reveal the amorphous nature of the deposited films, irrespective of the composition. Magnetization reversal measurements are carried out to establish the effect of composition on the magnetic anisotropy. A distinct composition-driven crossover from perpendicular magnetic anisotropy (PMA) to in-plane magnetic anisotropy (IMA) is observed from magneto-optic Kerr effect (MOKE) microscopy measurements. The domain imaging during the reversal has revealed that isolated bubbles are seen in films with low Co content with strong PMA. It is observed that the effective perpendicular anisotropy is reduced with increased Co content, leading to nucleation of labyrinthine domains. At relatively greater Co compositions, the films exhibit no PMA as observed from magnetization reversal. The crossover in magnetic anisotropy can be attributed to the competition between rare-earth–transition-metal exchange interactions, and increasing dipolar anisotropy associated with enhanced magnetization.

S.K. Kim, G.S.D. Beach, K.J. Lee, T. Ono, T. Rasing, and H. Yang, "Ferrimagnetic spintronics," Nat. Mater. 21(1), 24–34 (2022).

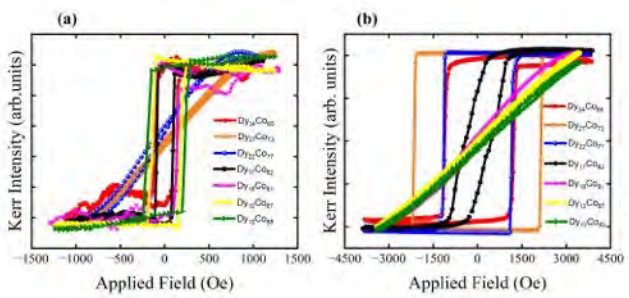


Fig. 1: (a) IP hysteresis loops (b) OOP hysteresis loops for all the compositions deposited.

GQ-04. Spin-splitting-induced anisotropic Hall effect in noncoplanar antiferromagnet

M. Jung[1], H. Yun[1], J. Moon[1], Y. Kim[2], S. Gim[2]
[1]Department of Physics, Sogang University, Seoul, Korea (the Republic of), [2]Department of Physics, KAIST, Daejeon, Korea (the Republic of)

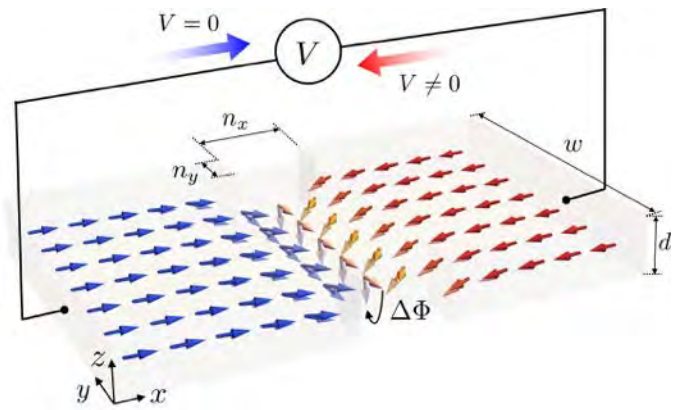
Altermagnetism has recently been emerged as a distinct class of magnetic states, differing from conventional ferromagnetism and antiferromagnetism. It features zero net magnetization with alternating spin polarization, driven by an anisotropic local crystal environment across sublattices, resulting in unconventional spin-polarized band structure in momentum space. Recent reports have highlighted anisotropic spin splitting in $MnTe_2$, dependent on crystal orientation. In this study, we synthesized high-quality $MnTe_2$ single crystals using the chemical vapor transport method and characterized them using X-ray diffraction. Temperature-dependent magnetization and resistivity measurements confirm that $MnTe_2$ is an antiferromagnetic semiconductor with a Néel temperature of $T_N \approx 87$ K. Notably, an anisotropic Hall effect was observed, which depends strongly on the current direction: for I // [100], the Hall resistivity shows a linear dependence with a positive slope, whereas for I // [110], it exhibits a large nonlinear dependence with a negative slope. These anisotropic Hall responses are attributed to direction-dependent spin splitting in the band structure.

GQ-06LB. Superconducting diode effect in magnetic superconductors realized by nonreciprocal domain-wall dynamics

D. Han[1], S. Chung[2], S. Kim[1]
[1]Physics, Korea Advanced Institute of Science and Technology (KAIST), Daejeon, Korea (the Republic of), [2]Physics, University of Seoul, Seoul, Korea (the Republic of)

A superconducting diode effect is shown to arise in ferromagnetic superconductors through the nonreciprocal dynamics of magnetic domain walls. Specifically, we show that current-driven dynamics of a magnetic domain wall under a certain external field can exhibit a nonreciprocal Walker breakdown, possessing two distinct direction-dependent critical currents beyond which the domain wall precesses continuously. In ferromagnetic superconductors, the constant rotation of a domain wall is shown to give rise to phase slips, opening up dissipation channels, whereby the nonreciprocal Walker breakdown is mapped to the superconducting diode effect. For the nonreciprocal Walker breakdown of a magnetic domain wall, we analytically examine its dependence on the magnetic field and the Gilbert damping and verify the theoretical results with micromagnetic simulations. We then extend the analysis to ferromagnetic superconductors by considering additional effects from the superconductivity and identify criteria for experimental conditions to realize the predicted superconducting diode effect. Our work demonstrates that topological defects, such as domain walls, in magnetic superconductors can serve as an intrinsic nanoscale platform for nonlinear nonreciprocal superconducting functionalities within a single homogeneous material, circumventing the need for complicated engineered heterostructures and thereby enabling the miniaturization of superconducting devices down to the nanometer scale that is challenging to achieve with conventional Josephson junctions.

[1] S. K. Kim and S. B. Chung, Current-driven motion of magnetic topological defects in ferromagnetic superconductors, Phys. Rev. B 108, 134509 (2023).
[2] P. A. Volkov *et al.*, Josephson diode effects in twisted nodal superconductors, Phys. Rev. B 109, 094518 (2024).
[3] D. H. Han, S. B. Chung and S. K. Kim, Superconducting diode effect in magnetic superconductors realized by nonreciprocal domain-wall dynamics, arXiv:2606.08999 (2026).



Schematics of the SDE induced by the DW precession ΔΦ in the nonreciprocal WB. In the thin film of width w and thickness d, the DW is pinned at a notch characterized by the geometric parameters n_x and n_y. The measured voltage V originates from the emergent electric fields. For the bias current of the equal magnitude, the voltage V across the DW vanishes for one direction (right in the figure) and is finite for the other direction (left in the figure), thereby giving rise to the diode effect.

GQ-07. Real-Space Imaging of Anomalous Hall Conductivity in Thin Films and Heterointerfaces: A First-Principles Study

F. Ishii[1], Y. Morishima[2], N. Yamaguchi[1]
[1]Nanomaterials Research Institute, Kanazawa University, Kanazawa, Ishikawa, Japan, [2]Graduate School of Natural Science and Technology, Kanazawa University, Kanazawa, Ishikawa, Japan

The anomalous Hall effect (AHE) in magnetic materials originates from Berry curvature and is important for topological transport. In thin films and heterostructures, AHE can vary strongly in real space, but its spatial distribution is not well understood.
In this study, we investigate the real-space distribution of anomalous Hall conductivity (AHC) using first-principles calculations. We combine the Fukui–Hatsugai–Suzuki method [1] extended to metallic systems [2] with hybrid Wannier functions [3], which allows us to decompose AHC along the out-of-plane direction. This method is based on our recent work on layer-resolved AHC [4].
We apply this approach to magnetic thin films (bcc Fe and $SrRuO_3$) and heterostructures (Fe/W and $SrRuO_3$/$SrIrO_3$). In particular, interface-driven AHE has been reported in $SrRuO_3$/$SrIrO_3$ [5]. We find that AHC is not uniform but localized at specific layers and interfaces. Heavy elements such as W and Ir enhance AHC, and sign changes appear near interfaces. We also find that surface layers with large magnetic moments do not always give large AHC.
These results show that AHE in low-dimensional systems is governed by spatially localized Berry curvature. Our method provides a simple way to visualize and understand AHE in real space.

[1] T. Fukui, Y. Hatsugai and H. Suzuki, J. Phys. Soc. Jpn., Vol. 74, p.1674 (2005)
[2] H. Sawahata, N. Yamaguchi, S. Minami and F. Ishii, Phys. Rev. B, Vol. 107, p.024404 (2023)
[3] N. Marzari and D. Vanderbilt, Phys. Rev. B, Vol. 56, p.12847 (1997)
[4] Y. Morishima, F. Ishii and N. Yamaguchi, arXiv:2506.01160 (2025)
[5] J. Matsuno, Y. Ohnuma and M. Ogawa, Sci. Adv., Vol. 2, p.e1600304 (2016)

GQ-08. Deep Learning-Assisted High-Throughput Discovery of Altermagnets for Spintronic Applications

D. Kho[1, 2, 3], V. C. Rogers[2, 3], S. Islam[2, 3], J. C. Incorvia[2, 3]
[1]Department of Electrical and Computer Engineering, Seoul National University, Seoul, Korea (the Republic of), [2]Chandra Family Department of Electrical and Computer Engineering, University of Texas at Austin, Austin, Texas, United States, [3]Microelectronics Research Center, University of Texas at Austin, Austin, Texas, United States

Altermagnetism, with unconventional spin-splitting and zero net magnetization, is promising for both topologically non-trivial phases and ultra-fast, noise-robust magnetic tunnel junctions (MTJs) [1]. However, device realization is hindered by the scarcity of altermagnets that simultaneously exhibit significant spin-splitting near the Fermi level (E_F) and a Néel temperature (T_N) above room temperature [2, 3].
We present a sequential high-throughput screening framework to identify altermagnets meeting these criteria (Fig. 1). From ~150k materials in the Materials Project, we first identified a pool of 16,378 materials possessing at least one altermagnetic state using amcheck [4], a symmetry-based screening tool. To minimize computational overhead before DFT verification, we employed deep learning models, ALIGNN [5] and MaterialsBERT [6], as data-driven filters to exclude candidates with low T_N and small spin-splitting. In this process, the spin-splitting in the ferromagnetic state was utilized as a proxy to estimate the altermagnetic exchange strength. This multi-stage screening reduced the initial pool to 60 high-priority candidates.
To verify the altermagnetic ground states, these 60 candidates were subjected to first-principles calculations.

Our DFT results confirm that 22 materials possess an altermagnetic ground state with a maximum spin-splitting > 0.1 eV within ±3 eV around the E_F. Among these, 11 priority altermagnets, including novel materials such as $CaLa(FeO_3)_2$, Fe_2O_3F, and $FeHO_2$, show spin-splitting > 0.2 eV, with metallic systems exhibiting large spin polarization near E_F and insulators showing large band gap differences along specific k-paths (Fig. 2). These materials exhibit energy differences between the altermagnetic ground state and other magnetic states > 30 meV/magnetic atom, suggesting potential for robust room-temperature altermagnetism. These findings provide a comprehensive library for future altermagnetic spintronic applications.

[1] L. Šmejkal, J. Sinova and T. Jungwirth, Phys. Rev. X., Vol. 12, p.040501 (2022)
[2] A. Sufyan, B. Marfoua and J. A. Larsson, Phys. Rev. Mater., Accepted (2026)
[3] T. Nomoto, S. Minami and Y. Yanagi, Phys. Rev. B., Vol. 109, p.094435 (2024)
[4] A. Smolyanyuk, L. Šmejkal and I. I. Mazin, SciPost Phys. Codebases., Vol. 30, p.30 (2024)
[5] K. Choudhary and B. DeCost, npj Comput. Mater., Vol. 7, p.185 (2021)
[6] P. Shetty, A. C. Rajan and C. Kuenneth, npj Comput. Mater., Vol. 9, p.52 (2023)

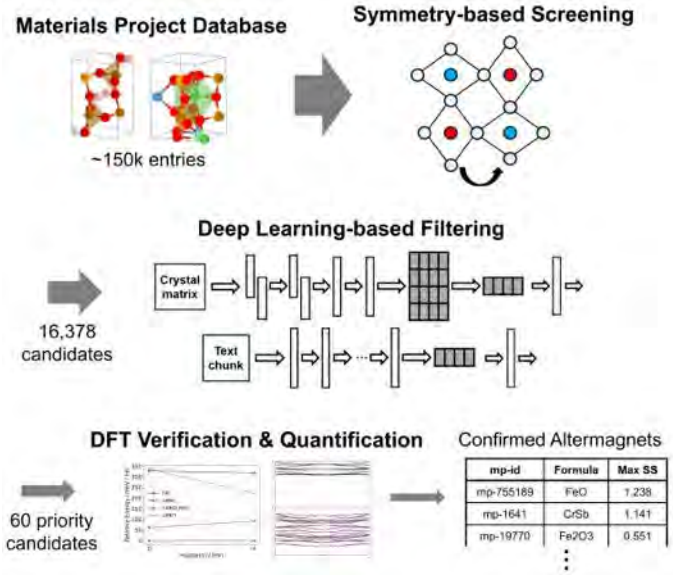


Fig. 1. High-throughput screening workflow combining symmetry analysis, deep learning filters, and DFT.

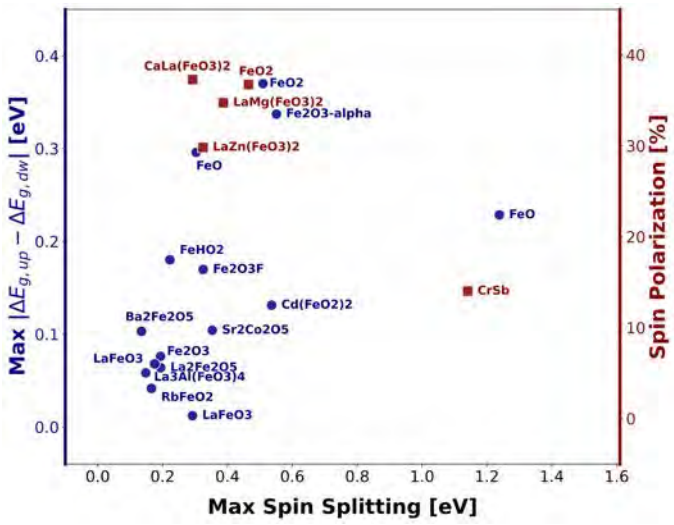


Fig. 2. Property map of identified altermagnets. Left and right axes denote insulator bandgap difference and metallic sublattice spin polarization, respectively.

GQ-09. Unconventional Long-Range Superconducting Proximity Effect in Topological Insulator–Iron-Based Superconductor Heterostructures

T. Wang[1], Z. Xing[2]
[1]School of Mathematics, Nanjing University of Aeronautics and Astronautics, Nanjing, Jiangsu, China, [2]School of Electronic Science and Engineering, Nanjing University, Nanjing, Jiangsu, China

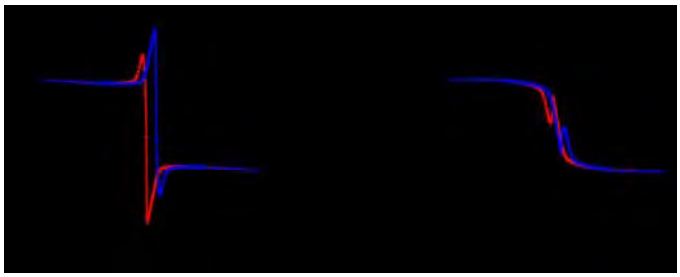
Superconducting proximity effect (SPE) in topological materials offers a promising pathway for exploring topological superconductivity. In this work, we carry out a systematic study of proximity induced superconductivity in heterostructures consisting of three prototypical three-dimensional topological insulators, Sb_2Te_3, Bi_2Se_3, and Bi_2Te_3, epitaxially grown on the iron based superconductor $FeSe_{0.5}Te_{0.5}$. Across all three systems, namely $Sb_2Te_3/FeSe_{0.5}Te_{0.5}$, $Bi_2Se_3/FeSe_{0.5}Te_{0.5}$, and $Bi_2Te_3/FeSe_{0.5}Te_{0.5}$, we consistently observe an anomalous long-range proximity effect.
Transport measurements reveal that superconductivity is induced in the topological insulator layers with thicknesses up to several hundred nanometers. The induced superconducting transition temperatures (T_c) remain robust, typically in the range of ~ 8–12 K depending on thickness and interface conditions, significantly exceeding the expected decay length of conventional proximity effects, which are usually limited to a few atomic layers. This

anomalous behavior is primarily attributed to the topological surface states of the topological insulator forming continuous conductive loops on the surface. To clarify the role of topology, we further investigated $Sb_2Se_3/FeSe_{0.5}Te_{0.5}$ heterostructures, where Sb_2Se_3 possesses a similar crystal structure but lacks nontrivial topology. In this control system, the long-range proximity effect is absent, and no superconducting transition is observed in thick Sb_2Se_3 layers. This contrast indicates that topological surface states do indeed play a key role in long-range SPE. Angle-resolved photoemission spectroscopy (ARPES) measurements further confirm that the topological surface states are preserved in the heterostructures exhibiting long-range SPE. These results highlight an intriguing correlation between topological electronic structure and anomalous superconducting proximity behavior, offering useful guidance for future exploration of topological superconductivity in engineered systems.

GQ-10. Control of d-wave altermagnetic domain by a tilted magnetic field

H. Koizumi[1, 2, 3], M. Kimata[5, 2], H. Yanagihara[1], A. Hirohata[2, 4], Y. Yamasaki[3, 2]
[1]Univ. of Tsukuba, Tsukuba, Japan, [2]Tohoku University, Sendai, Japan, [3]NIMS, Tsukuba, Japan, [4]Max Planck Institute, Dresden, Germany, [5]Japan Atomic Energy Agency, Tokai, Japan

Altermagnets are a novel class of magnetic materials characterized by the coupling of antiferromagnetic spin order and anisotropic crystal symmetry [1]. Owing to their unique electronic and transport properties, they have recently attracted considerable attention. However, because altermagnets belong to the broader class of antiferromagnets, deterministic control of their domains remains highly challenging.
$NiCo_2O_4$ (NCO) is a conductive inverse spinel oxide exhibiting ferrimagnetism with a Néel temperature as high as 400 K. At low temperatures, NCO shows easy-cone magnetic anisotropy, resulting in a conical easy-plane spin state with an in-plane rotational degree of freedom. The in-plane spin components possess the symmetry of a d-wave altermagnet and can induce characteristic transport phenomena such as the quadrupolar anomalous Hall effect (QuadAHE) [2].
In this study, we demonstrate complete control of the altermagnetic domain in NCO by an external magnetic field. Hall measurements at 5 K in the easy-cone state revealed a QuadAHE signal originating from the d-wave altermagnetic component. After applying a tilted magnetic field with an optimized in-plane component, the QuadAHE signal was completely reversed, as shown in Fig. 1, indicating deterministic switching of the d-wave altermagnetic domain. In this presentation, we discuss the experimental results and the underlying switching mechanism.
[1] L. Šmejkal et al., Phys. Rev. X 12, 040501 (2022).
[2] H. Koizumi et al., J. Phys. D: Appl. Phys. 58 253002 (2025).



Hall resistivity of a $NiCo_2O_4$ thin film. The QuadAHE component is switched by a control procedure using a tilted magnetic field.

GQ-11. Evidence of THz Emission from Spin-Charge Conversion in Heavy Metal/Antiferromagnet Insulator

B. Huang, B. Yang, D. Wu
Nanjing University, Nanjing, China

Femtosecond (fs) laser enables magnetic-field-free terahertz (THz) emission via spin-charge conversion (SCC) in heavy metal/antiferromagnet (HM/AFM) heterostructures, offering a critical method to convert ultrafast AFM spin dynamics into charge signals. However, this mechanism has recent been challenged by an experimental observation of dominant nonmagnetic THz emission in Pt/NiO(111). Here, we obverse both SCC and nonmagnetic mechanism dominant THz emission by tuning spin-orbit coupling (SOC) in heavy metal/NiO(111) heterostructures. The THz emission in pure Pt/NiO heterostructure shows a clear signature of SCC mechanism. Upon weakening the SOC in the heavy metal through doping, the THz amplitude is significantly suppressed, and the nonmagnetic THz emission is observed. These findings deepen the fundamental understanding of the ultrafast process in HM/AFM, establishing a robust foundation for controlling and optimizing AFM spintronic devices operating at terahertz frequencies.

GQ-12. Domain Wall-Mediated SOT Switching in Selectively Oxidized $Co_{1-x}Gd_x$ Ferrimagnets Toward Low-Current, High-Stability Spintronic Memory devices

S. Jeong[1], D. Han[2], S. Ko[1], B. Park[2], K. Kim[1]
[1]Physics, Korea Advanced Institute of Science and Technology, Daejeon, Korea (the Republic of), [2]Materials Science and Engineering, Korea Advanced Institute of Science and Technology, Daejeon, Korea (the Republic of)

Practical implementation of spintronic memory devices requires simultaneously achieving low critical switching current density and high thermal stability. [1] Raising the energy barrier enhances data retention but inevitably increases write current. Conversely, lowering the energy barrier reduces write current at the cost of thermal stability. This inherent trade-off has remained a central bottleneck for practical spintronic memory applications.
In this work, we overcome this trade-off by exploiting lateral exchange coupling in a $Co_{1-x}Gd_x$ (x = 0.20, 0.254, 0.30) ferrimagnetic channel. Selective oxidation creates three laterally adjacent regions — Co-dominant, Gd-dominant, and Co-dominant — which enable the formation of Co-submoment domain walls under an applied external field, as shown in Figure 1(a). As the system subsequently relaxes toward a lower-energy state, these Co-sublattice domain walls easily move in order to reduce the exchange and dipolar energies. This relaxation process facilitates magnetization switching, allowing the domain walls to act effectively as switching seeds. As a result, current-induced switching is achieved at 1.33×10^7 A/cm^2 (x = 0.20) while maintaining the coercive field of 1.5 T, suggesting that low critical switching current and high thermal stability can be achievable simultaneously. Therefore, our results suggest that lateral exchange coupling might offer a promising design strategy for simultaneously achieving low switching current and high thermal stability toward the practical realization of spintronic memory devices.
[1] V. D. Nguyen, S. Rao, K. Wostyn and S. Couet, npj Spintronics., Vol. 2, p.48 (2024)

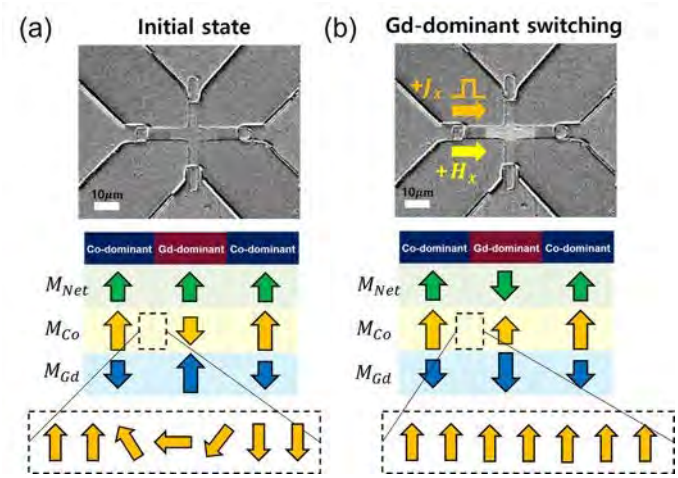


Fig. 1 Polar MOKE images of magnetic domains in $Co_{80}Gd_{20}$ channels. (a) Initial state with three regions : Co-dominant, Gd-dominant, and Co-dominant. (b) Under an applied current pulse ($+J_x$) and in-plane field ($+H_x$), switching occurs in the Gd-dominant region.

GQ-13. Data driven discovery of altermagnetic materials

Y. Khatri, R. Sabirianov
Physics, University of Nebraska at Omaha, Omaha, Nebraska, United States

Altermagnetism is a recently identified class of collinear antiferromagnetism characterized by momentum-dependent spin-split band structures with zero net magnetization, offering promising prospects for next-generation spintronic applications. In this work, we employ a data-driven framework to systematically discover potential altermagnetic materials by combining crystal symmetry analysis with high-throughput density functional theory (DFT) calculations. Using structural data from the Materials Project database, we screened compounds containing even numbers of 3*d* (Ti–Cu) and 4*d* (Mo, Ru) transition-metal elements in primitive or extended antiferromagnetic (AFM) supercells, yielding 51,362 candidate structures. All symmetry-inequivalent collinear AFM configurations were evaluated using Amcheck, revealing that 25,881 materials exhibit at least one altermagnetic configuration—including 9,773 experimentally reported compounds—while 14,121 materials display altermagnetism across all collinear AFM states, of which 4,257 have been experimentally observed. Subsequent high-throughput DFT calculations were performed to determine relative magnetic stability, exchange coupling constants, and local magnetic moments. Representative systems such as $LiMnO_2$ and Cr_2F_5 exhibit clear symmetry-driven spin splitting in their electronic band

structures while maintaining zero net magnetization, highlighting the hallmark features of altermagnetic order. This large-scale screening establishes a comprehensive dataset of candidate altermagnetic materials and provides a robust computational pathway to guide experimental discovery and realization of novel spintronic materials.

GQ-14. Effects of Mo-Site Impurity Doping on Magnetic and Magnetoelectric Properties in $M_2Mo_3O_8$

T. Ishikawa, T. Shirasaki, S. Nakayama, H. Kuwahara
Department of Engineering and Applied Sciences, Sophia University, Tokyo, Japan

$M_2Mo_3O_8$ is a layered polar magnet with space group $P6_3mc$. In this family, the Mo^{4+} ($4d^2$) ions form spin-singlet trimers and are therefore essentially nonmagnetic, so the magnetic properties are governed primarily by the M-site ions. Accordingly, previous studies have mainly focused on tuning the magnetic and magnetoelectric responses by chemical substitution at the M-site [1]. In contrast, we recently reported that impurity substitution at the Mo site in the altermagnetic antiferromagnet $Fe_2Mo_3O_8$ partially breaks the spin-singlet bonds and induces ferromagnetic-like behavior persisting up to room temperature [2]. To clarify how Mo-site impurity doping affects the magnetic and magnetoelectric properties in this class of compounds, we synthesized impurity-doped samples based on M = Fe, Co, and Zn.

As a first step, we optimized the synthesis conditions for high-quality polycrystalline $Zn_2Mo_3O_8$, a nonmagnetic parent compound. $Zn_2Mo_3O_8$ was prepared by mixing $ZnMoO_4$ and Mo in a molar ratio of 2:1−x, followed by sintering at 900 °C for 24 h in an evacuated quartz tube. For x = 0, corresponding to the stoichiometric composition, small amounts of MoO_2 and metallic Mo were detected. In contrast, for x = 0.03, the formation of these impurity phases was significantly suppressed (inset of Fig. 1). Fig. 1 shows the temperature dependence of magnetization for samples prepared with x = 0 and 0.03. Both samples exhibit nearly temperature-independent diamagnetism above 60 K, consistent with the nonmagnetic nature of $Zn_2Mo_3O_8$. Meanwhile, the x = 0 sample shows an upturn in magnetization around 50 K, attributable to impurity phases. This contribution is markedly reduced for x = 0.03, indicating that a slight Mo-deficient starting composition is effective for evaluating the intrinsic magnetic properties of $Zn_2Mo_3O_8$. The effects of Mo-site impurity doping on the magnetic and magnetoelectric properties of the optimized parent compounds will be discussed.

[1] T. Kurumaji, S. Ishiwata, and Y. Tokura, Phys. Rev. X, Vol. 5, p. 031034 (2015).
[2] T. Shirasaki, T. Ishikawa, S. Nakayama, and H. Kuwahara, IEEE Trans. Magn. (in press).

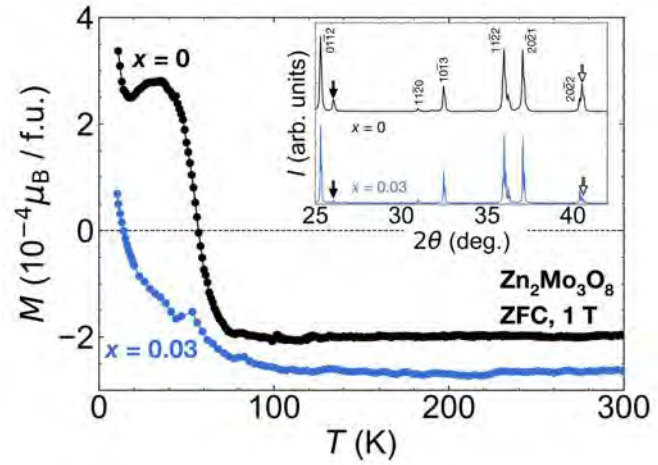


Fig. 1: Temperature dependence of magnetization for polycrystalline $Zn_2Mo_3O_8$ prepared from starting compositions with $ZnMoO_4$:Mo = 2:1−x. The inset shows powder X-ray diffraction profiles at room temperature. Solid and open arrows indicate peaks from MoO_2 and metallic Mo, respectively.

GQ-15. Anomalous Hall Effect in Heavy Metal Layers of Ferrimagnet/Heavy-Metal Bilayers

S. Kim[1], J. Chang[2, 3], Y. Jeong[1, 2], M. Kim[2, 3], A. Lee[4], J. Lee[4], Y. Choi[4], S. Park[4], S. Choe[3], K. Kim[5], D. Kim[2], S. Je[1]
[1]Department of Physics, Chonnam National University, Gwangju, Korea (the Republic of), [2]Center of Spintronics, Korea Institute of Science and Technology (KIST), Seoul, Korea (the Republic of), [3]Department of Physics & Astronomy, Seoul National University, Seoul, Korea (the Republic of), [4]Center for Scientific Instrumentation, Korea Basic Science Institute, Daejeon, Korea (the Republic of), [5]Department of Physics, Yonsei University, Seoul, Korea (the Republic of)

The mechanisms underlying the anomalous Hall effect (AHE) have been experimentally investigated in ferromagnetic systems [1,2], but such studies are largely unexplored for ferrimagnetic materials. While the AHE is known to be proportional to magnetization, the peculiar magnetization-temperature dependence in ferrimagnets significantly complicates these studies. In this work, we investigate the AHE in GdFeCo/Pt, and GdFeCo/Ta amorphous ferrimagnet/heavy metal heterostructures for a wide temperature range including the magnetization

compensation temperature [3]. To account for the peculiar temperature dependence of the magnetization in the ferrimagnet, the FeCo magnetization is extracted and used to normalize the anomalous Hall resistivity. From scaling law analysis, we find that the net AHE in GdFeCo/Pt and GdFeCo/Ta is dominated by the intrinsic spin Hall effect (SHE) occurring in the heavy metal layers [3]. Given that the heavy metal layers play a dominant role in the AHE in such bilayer systems, we also propose a circuit model which allows one to separate the AHE from the ferrimagnet layer and from the heavy metal layer.

[1] Y. Tian et al, Phys. Rev. Lett. 103, 087206 (2009)
[2] D. Maryenko et al, Nat. Commun. 8, 14777 (2017)
[3] S. T. Kim et al, Phys. Rev. B 112, 014426 (2025).
[4] U. Shashank et al, Phys. Rev. B 107, 064402 (2023).
[5] Y. Omori et al, Phys. Rev. B 99, 014403 (2019).

GQ-16. Influence of the Hall-bar geometry and electrodes on the Anomalous Hall voltage

J. Sim[1], Y. Mok[2, 3], M. Kim[2, 3], S. Choe[2], D. Kim[3], S. Je[1]
[1]Department of Physics, Chonnam National University, Gwangju, Korea (the Republic of), [2]Department of Physics & Astronomy, Seoul National University, Seoul, Korea (the Republic of), [3]Center for Spintronics, Korea Institute of Science and Technology, Seoul, Korea (the Republic of)

Although the ordinary Hall effect and the anomalous Hall Effect (AHE) arises completely different physical mechanisms, in the case of ordinary Hall effect, it is well known that the Hall-bar geometry significantly influences the measured Hall voltage. In contrast, such Hall-bar geometry effect in the AHE has not yet been systematically studied, despite its pivotal role in spintronics. This may be because one is primarily interested in the presence of magnetization, despite the fact that AHE contains rich information on spin-dependent scattering and Berry curvature. Therefore, to access such rich physics, it is important to exclude the possible influence arising from the extrinsic factors, such as device geometry including electrode arrangement, from the measured anomalous Hall voltage.

In this study, we investigate the influence of the Hall bar geometry on the anomalous Hall voltage across Hall-bar devices with various dimensions. We find that there exists a universal relation between the Hall voltage and the width-to-length ratio. We also find the coverage of the electrode on the magnetic Hall-bar devices. This effect can be attributed to changes in the boundary conditions used to describe the Hall-bar geometric factors in conventional Hall-bar structures, thereby influencing the anomalous Hall voltage by as much as 30 percent. From our results, we not only extract more accurate experimental data but also propose guidelines for designing the optimal Hall bar device.

SESSION GR: MAGNETIC CHARACTERIZATION (POSTER SESSION)

Co-Chair(s): M. Mivelle, *Physics, CNRS, INSP (INSP - Institut des NanoSciences de Paris - CNRS - Sorbonne Université), Paris, France* and E. Jal, *LCPMR, CNRS, Sorbonne Université, Paris, France*

Friday, November 6, 2026
09:30 AM-12:30 PM
Coral 4

GR-01. Anisotropic Nanoparticle Clusters in Frozen Ferrofluids

A. Nazarov
NIST, Boulder, Colorado, United States

Ferrofluids are colloidal liquid suspensions of magnetic nanoparticles. When subjected to a magnetic field, the magnetic particles form elongated clusters. If the ferrofluid is frozen during application of the magnetic field, the magnetic particles are frozen in clusters with uniaxial anisotropy [1]. Here, a technique is described for the analysis of these clusters using measurements of magnetic susceptibility measured parallel and perpendicular to the anisotropy axes.

Samples were commercial ferrofluids with different concentrations of Fe_3O_4 superparamagnetic nanoparticles, about 10 nm in diameter, measured in liquid and frozen states. Figure 1 shows the measured magnetization curves for a ferrofluid frozen in zero field and in a freezing field H_f of 1.6 MA/m, measured parallel and perpendicular to H_f. Similar curves were obtained for other concentrations. The magnetic susceptibility data were analyzed using a demagnetizing factor model for single-domain particles [2] to deduce structural characteristics of the clusters.

This work was performed with funding from the CHIPS Metrology Program, part of CHIPS for America, National Institute of Standards and Technology, U.S. Department of Commerce.

[1] H. Miyajima et al., *J. Appl. Phys.*, vol. 63, pp. 4267–4269, (1988).
[2] R. Skomski, G. C. Hadjipanayis, and D. J. Sellmyer, *IEEE Transactions on Magnetics,* vol. 43, pp. 2956–2958, (2007).

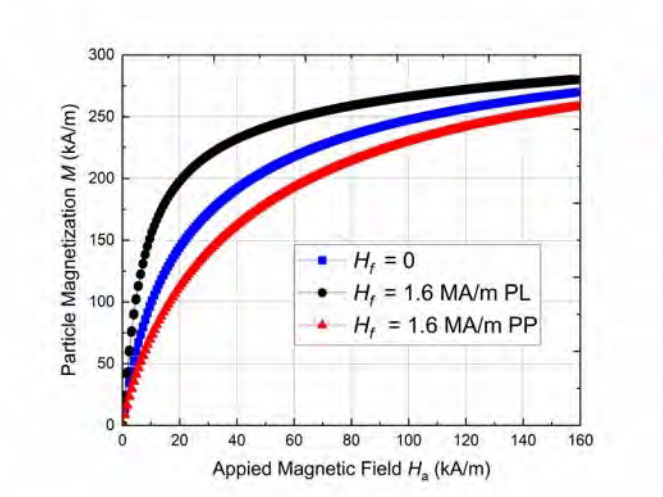


Fig. 1. Particle magnetization M vs. versus applied magnetic field H_a at temperature T = 253 K for a ferrofluid sample frozen in zero field or in H_f = 1.6 MA/m and measured parallel (PL) and perpendicular (PP) to the H_f axis.

GR-02. Estimation of Circumferential Defect Locations in Transported Steel Bars during Conveyance Using the Gradient of Magnetic Flux Density

K. Matsushima[3], K. Shiku[2], T. Nara[2], Y. Gotoh[1]
[1]Faculty of Science and Engineering, Oita University, Oita, Japan, [2]Graduate School of Information Science and Technology, The University of Tokyo, Bunkyo-ku, Tokyo, Japan, [3]Graduate School of Science and Engineering, Oita University, Oita, Japan

C45 steel rods used as spring materials in vehicles are often subjected to high-frequency quenching to enhance surface strength. During this process, surface defects may act as initiation sites for quench cracks. Therefore, surface flaw detection prior to quenching is essential. Currently, a method has been proposed to estimate surface defects and their circumferential positions in steel rods by applying a uniform direct current (DC) magnetic field and the Fourier coefficients of the measuring leakage flux at the defect circumferential positions [1]. On the other, a method has been proposed in which a DC magnetic field with a circumferential flux density gradient is applied to measure the magnetic flux density inside steel rods [2]. In this study, a method is proposed in which a DC magnetic field generated by two rectangular permanent magnets in a repulsive configuration is used to form a circumferential flux density gradient in a steel rod. The vertical component of the leakage flux is then measured using detection coils to detect defects and estimate their circumferential positions. As shown in Fig. 1, the proposed sensor consists of two sets of magnetizers, each comprising two rectangular permanent magnets and four detection coils. The leakage flux signals along the circumference exhibit sinusoidal and cosine spatial variations, referred to as sinusoidal and cosine modes, respectively. The test steel rod has a diameter of 9 mm and a length of 700 mm and contains a surface defect in the form of a round-bottomed hole with a diameter of 0.7 mm. Fig. 2 shows the estimated circumferential positions of defects in the steel rod using the proposed sensor. The maximum error is −20.0° for a defect depth of 0.2 mm and 29.8° for a depth of 0.07 mm. The proposed sensor can detect defect signals down to a depth of 0.07 mm; however, further improvement in estimation accuracy is required through optimization of the permanent magnets, detection coils, and signal processing. This paper presents the results of electromagnetic field analysis conducted to elucidate the underlying phenomena, as well as the results of sensor adjustment.

[1] K. Shiku, N. Shigematsu, Y. Kuwahara, Y. Gotoh and T. Nara, “Noise-robust method using sparsity for locating a crack in a steel rod based on the Fourier coefficients of the leakage magnetic flux,” AIP Advances,16, 025320 (2026)
[2] M. Kuromizu, A. Motoyama, K. Komatsubara, T. Nara and Y. Gotoh,”De tection and Location Estimate of External Surface Dedects Using Velocity Effects from Double-Sided Quadrupole Permanent Magnets,” in IEEE Transactions on Magnetics. , vol. 60, no. 12, pp. 1-4, Dec. 2024.

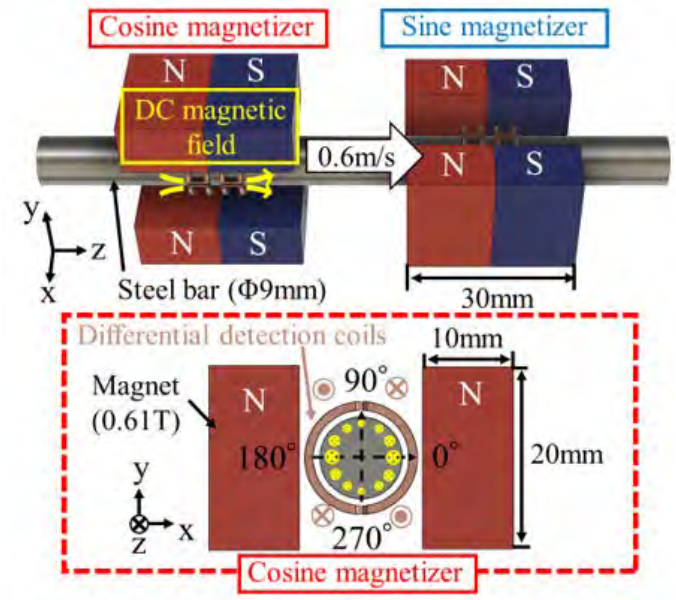


Fig. 1 Sensor and Circumferential Magnetic Flux in Steel Bars

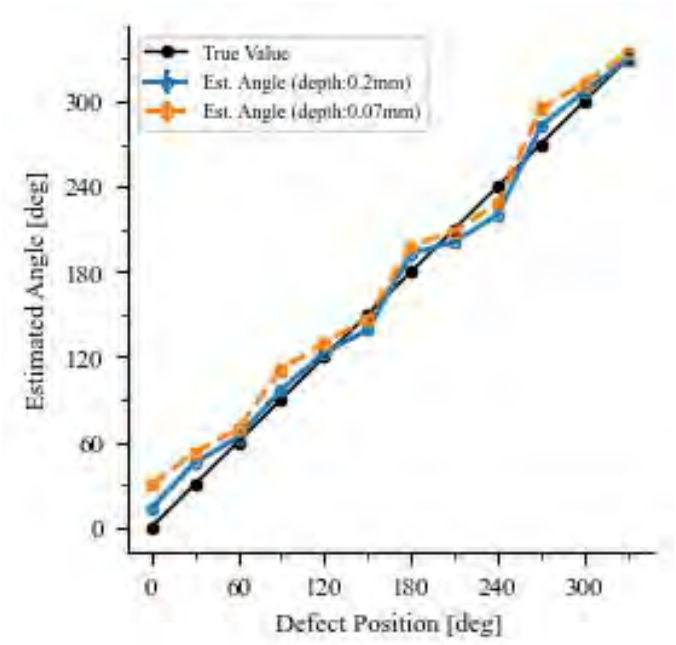


Fig. 2 Estimated Defect Locations

In this work, magnetic characterization is performed using experimental MFB operation data. Three different particle assemblies are analyzed. Each assembly exists out of monodisperse, spherical iron particles with a diameter of either 0.6 mm, 0.8 mm or 1.0 mm. After applying a uniform magnetic field to the particle bed, the gas flow is increased until the ensemble structure breaks due to the high Fd. For each assembly, the magnetic force is derived by coupling the gas velocities to a Fd model. Next, the magnetization of the entire bed as a function of the externally applied magnetic field is derived and compared to the magnetization of a single particle as measured by a SQUID magnetometer. Results show that the slope of the magnetization of the particle bed is almost four times larger than for a single particle (Fig.1). The method is material specific and not influenced by the size of the particles. Based on this derived magnetization and theoretical packing structures of particles, the magnetization of a single particle is reconstructed. It is concluded that this method is adequate in deriving the magnetization of particle assemblies as well as the magnetization of a single particle.

GR-03. Characterization of magnetic particle ensembles in magnetically fluidized beds

C. De Somer[1], R. De Croo[1], H. Poelman[2], V. Galvita[2], G. Heynderickx[2], L. Dupré[1], A. Coene[1]

[1]Department of Electromechanical, Systems and Metal Engineering, Ghent University, Gent, Belgium, [2]Department of Materials, Textiles and Chemical Engineering, Ghent university, Gent, Belgium

Magnetically gas-solid fluidized beds (MFBs) are widely used in a multitude of processes and exist of an assembly of magnetic granular material, held in a container. An upward gas flow, supplied over the particles, exercises a drag force, Fd, directed opposite to the gravitational force, Fg. When Fd equals or exceeds Fg, the particles become suspended and behave like a liquid. Magnetic fields are used to optimize the fluidization properties depending on process requirements. However, optimization requires the magnetic properties of the particle bed to be known. Conventional characterization methods are good to predict the properties of individual particles. However, they are limited to smaller volumes making it more difficult to take the entire particle bed dynamics into account, especially for larger particles. A different method is thus required to derive magnetization curves of MFBs.

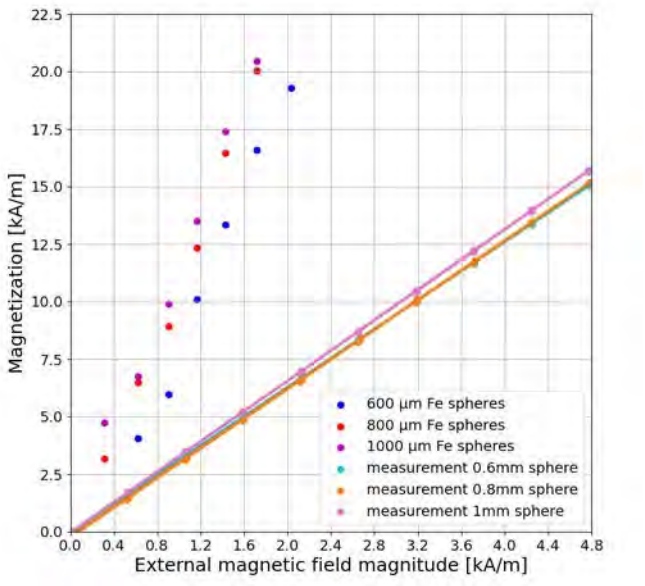


Fig.1: Magnetization of the particle bed as a function of the external magnetic field compared to SQUID measurement data of a single particle

GR-04. Temperature dependent Anomalous Nernst effect in magnetic metallic film by ac higher harmonics technique

J. Wu[1, 3], D. Cahill[2, 3]
[1]Department of Physics, University of Illinois Urbana-Champaign, Urbana, Illinois, United States, [2]Department of Materials Science and Engineering, University of Illinois Urbana-Champaign, Urbana, Illinois, United States, [3]Materials Research Laboratory, University of Illinois Urbana Champaign, Urbana, Illinois, United States

Thermoelectric effects in magnetic materials can generate a transverse electric voltage from a heat flow. The Anomalous Nernst effect (ANE), as a transverse thermoelectric effect, has gained increasing attention because it can probe the topological character of the band structure [1] and leads to the simple construction of thermoelectric devices for measuring heat fluxes [2]. Typical measurements of the ANE require a separate heater element as the source of the temperature gradient. Here we present an ac higher harmonics technique to detect ANE in patterned metal lines with the temperature gradient induced by self-heating. The temperature gradient is determined from dissipated power and thermal conductivity of the metal. The ANE is observed in the second harmonic, and therefore separable from longitudinal magnetoresistance signal, using lock-in detection with a bridge circuit [3]. Using this ac higher detection method, we measured an anomalous Nernst coefficient of 0.3 μV/K in a Ni film at room temperature. Typically, large ANE responses are detected in materials with nonzero Berry curvature. We further investigated the temperature dependence of ANE in disordered Ni_3Pt films prepared by sputter deposition. Ni_3Pt has a moderate ANE coefficient (0.8 μV/K) at room temperature (see Fig. 1). Its ANE coefficient increases linearly below 50 K, reaches a maximum of 1.2 μV/K at 200 K and decreases and subsequently vanishes at the Curie temperature. Finally, we demonstrate that the peak response can be tuned to room temperature by adjusting the stoichiometry of $Ni_{3-x}Fe_xPt$ films. This ac higher harmonics technique gives us a new and simple method to probe the ANE in ferromagnetic and non-collinear antiferromagnetic thin metallic films, facilitating the search for materials with large ANE.

[1] K. Uchida and J. P. Heremans, "Thermoelectrics: From longitudinal to transverse," Joule, vol. 6,no. 10, pp. 2240–2245 (2022).
[2] D. Xiao, Y. Yao, Z. Fang, and Q. Niu, "Berry-phase effect in anomalous thermoelectric transport,"Physical review letters, vol. 97, no. 2, p. 026 603, (2006).
[3] D. G. Cahill, "Thermal conductivity measurement from 30 to 750 K: The 3ω method," Review of scientific instruments, vol. 61, no. 2, pp. 802–808, (1990).

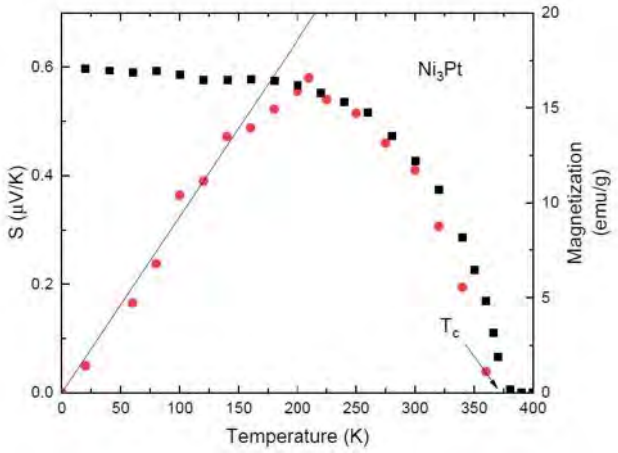


Figure 1: Temperature dependence of anomalous Nernst coefficient S (red dot) and In-plane magnetization at 100 Oe (black square) for Ni_3Pt.

GR-05. Rapid measurement of First Order Reversal Curves (FORCs) for high coercivity rare earth magnets using Pulsed Field Magnetometers (PFMs)

J. Mckenzie, R. Cornelius, J. Wade
Hirst Magnetics, Falmouth, Cornwall, United Kingdom

This paper will review recent progress and results gained from the Hirst generation 8, Pulsed Field Magnetometers from initial curves and First Order Reversal Curves (FORCs) on a PFM.

The initial curve represents the initial magnetization process of a permanent magnet from when it is completely unmagnetized. This curve is important for understanding the composition, metallurgy, and microstructure of a material. We will present results for NdFeB and SmCo magnets.

First order reversal curve (FORC) measurements provide a deeper insight into the magnetic properties of materials, information that is not possible to obtain from a full hysteresis loop alone or initial curves. FORC curves can help in identifying the distribution of switching and interaction fields, and in distinguishing between multiple magnetic phases in composite or hybrid materials containing more than one phase of magnetic materials.

This was a new option on the latest generation 8 PFMs from Hirst in 2025 and takes advantage of the full pulsed field that drives the sample through all four quadrants of the hysteresis loop during a measurement to generate FORCs measurements quickly and full FORCs diagrams in a matter of an hour or so. The combination of the speed of test and the larger sample size possible for PFMs make these FORCs measurements and resulting FORCs diagrams a potentially very valuable analysis tool for the development of new magnetic materials and compositions.

We will present results for NdFeB magnets of various grades and compositions showing how these impact the FORC diagrams.

S. Ruta et al. “First order reversal curves and intrinsic parameter determination for magnetic materials; limitations of hysteron-based approaches in correlated systems” Sci Rep 7, 45218 (2017)

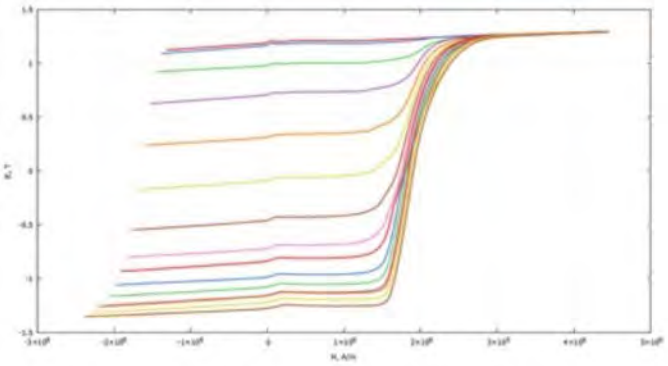


Fig 1 First Order Reversal Curves (FORCs) for NdFeB sample

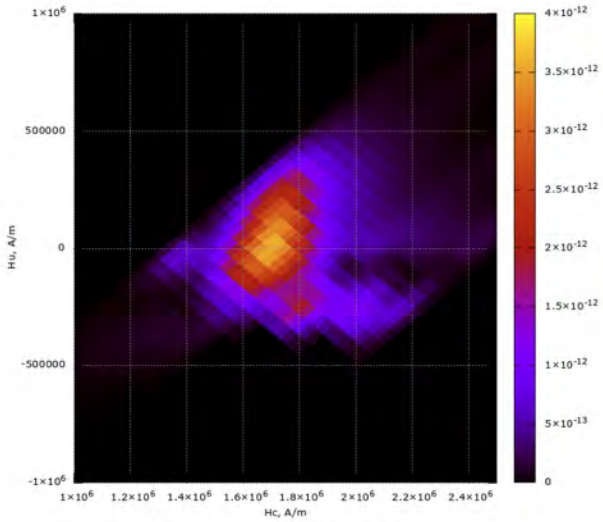


Figure 2 - FORCs diagram in the Hc, Hu plane for a NdFeB sample.

GR-06. Selective Magnetophoretic Separation of Sickle Red Blood Cells Using a Quadrupole Magnetic Sorter

D. M. Phan[1], L. Nguyen T. Tran[1], P. Iyer[2], J. Chalmers[2], J. Gomez-Pastora[1]

[1]Chemical Engineering, Texas Tech University, Lubbock, Texas, United States, [2]William G. Lowrie Department of Chemical and Biomolecular Engineering,, The Ohio State University, Columbus, Ohio, United States

Red blood cell (RBC) exchange transfusion is an effective therapy for managing complications associated with sickle cell disease (SCD), enabling rapid reduction of circulating sickled cells while maintaining oxygen-carrying capacity through remaining healthy RBCs [1]. However, conventional exchange procedures rely on centrifugation-based apheresis systems that require complex instrumentation and large volumes of donor blood, as they do not selectively target pathological cell subpopulations. Magnetic separation offers an alternative approach by exploiting intrinsic differences in magnetic susceptibility associated with hemoglobin oxygenation and oxidation states. Recent single-cell magnetic measurements further indicate substantial heterogeneity in RBC magnetophoretic behavior in SCD, suggesting that only a fraction of cells drive disease pathology [2].

We present a quadrupole magnetic sorter (QMS) as a platform for selective magnetophoretic RBC exchange and quantitatively evaluate its feasibility using COMSOL Multiphysics. The model integrates magnetic field and its gradient distributions, laminar flow transport of a magnetic fluid medium, and particle tracing to predict trajectories of RBC subpopulations with distinct magnetic susceptibility. Simulations show that under strong magnetic energy density gradients, , RBC subpopulations are differentially displaced within the flow channel according to their magnetophoretic response. Highly paramagnetic RBCs migrate toward regions of elevated magnetic field, while less responsive cells remain in bulk flow, enabling continuous spatial segregation of pathological and functional RBCs. Importantly, separation is governed by the distribution of magnetic properties, rather than average susceptibility, providing a physical mechanism for selectively removing disease-relevant subpopulations while preserving a significant fraction of functional cells.

This work establishes a numerical framework for magnetically selective RBC exchange and identifies key physical principles governing separation under flow. It also demonstrates the potential of high-gradient magnetophoresis to enable next-generation blood

processing technologies based on intrinsic cellular properties.
[1] L. R. Wallace and S. R. Thibodeaux, "Transfusion support for patients with sickle cell disease," *Transfus. Apher. Sci.*, vol. 61, no. 5, p. 103556, Oct. 2022, doi: 10.1016/j.transci.2022.103556.
[2] J. Strayer *et al.*, "Sickle Cell Vaso-Occlusive Episodes Correlates with the Magnetic Heterogeneity of Red Blood Cell," *Blood Adv.*, Feb. 2026, doi: 10.1182/bloodadvances.2025018869.

GR-08. Quantitative Analysis of Magnetic Image Effects on Torque Magnetometry for High-Precision Anisotropy Measurements

M. Rashid[1], A. Sapkota[2], L. Rodriguez[2], W. Geerts[2]
[1]Physics, Texas State University, San Marcos, Texas, United States, [2]Texas State University, San Marcos, Texas, United States

Magnetic anisotropy (MA) is a critical parameter for the development of high-performance permanent magnets as well as for magnetic sensors. MA is typically determined from torque curves measured either directly using a true torque magnetometer (TM) [1] or indirectly using a vibrating sample magnetometer. However, when a magnetic sample is positioned between the pole pieces of an electromagnet, it induces magnetic images within the soft ferromagnetic pole pieces [2] which introduce additional torque. This study investigates the quantitative influence of these image effects on observed torque curves. A theoretical model has been developed that suggests the magnetic images exert a torque on a sample centered between pole pieces. The torque increases as the sample moves away from the center. The sample prefers to align itself with its magnetic dipole moment perpendicular to the pole pieces. The effect was demonstrated by a laboratory setup of a 0.5 inch cylindrical magnet mounted on a plastic bearing placed between two mu-metal sheets. Additionally, a MicroSense torque magnetometer with a pole piece gap of 1 inch was used to measure the torque curve of a radially magnetized permanent cylindrical 8emu NdFeB sample in 0 Oe field which showed that the zero field torque curve contains a significant 2θ contribution caused by the image effect (see Fig. below). The data suggest that the magnetic images are similar in strength to the sample. Moving the NdFeB sample away from the center in between the pole pieces increases the observed 2θ component. An 8emu cylindrical NdFeB sample magnetized parallel to its cylindrical axis does not show a 2θ torque component. These results are consistent with the theoretical model. To determine the effect of pole piece images on torque measurements, COMSOL Multiphysics Finite Element Model calculations are being performed. Images are relevant for torque measurements on samples that have a large magnetic dipole moment but a low effective magnetic anisotropy. This ongoing work will establish a calibration framework to correct for instrumental background, ensuring high-fidelity characterization of magnetic materials in standard electromagnet-based TM.
[1] Pierre Weiss, Journal. de Physique. 4 (1906) 469.
[2] S R Hoon, and S N M Willcock, The direct observation of magnetic images in electromagnet vibrating sample magnetometers, J Phys E: Sc. Instrum[1]. 21 (1988) 480-487.

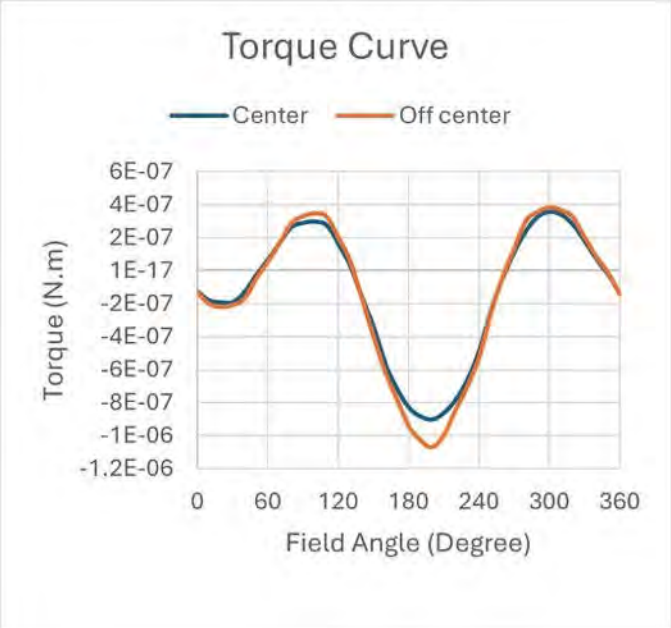


Fig.1: Torque curves measured in 0 Oe

GR-09. Investigation of the Role of Surface Charge in Aggregation Dynamics with Magneto-optical Measurements

M. Syed[1], C. Su[1], T. Ebii[1], H. Petrache[2], D. Maity[2], S. Reza[1]
[1]Physics, Optical Engineering and NanoEngineering, Rose-Hulman Institute of Technology, Terre Haute, Indiana, United States, [2]Physics, Indiana University Indianapolis, Indianapolis, Indiana, United States

Superparamagnetic nanoparticles (SNPs) find many applications in biomedical applications like MRI contrast imaging, magnetic hyperthermia, drug delivery, etc. [1-3]. We have investigated the magneto-optical response of dilute aqueous (ultrahigh purity water) suspensions of single-domain iron oxide nanoparticles under the influence

of applied AC magnetic field [4-5]. We have previously discussed general results from these investigations involving experimental setups (single-pass, double-pass, and interferometer) that capture both even and odd harmonics of the magneto-optic response [6-8]. In this work we focus on the role of surface ligands on particles of fixed size (~ 10 nm diameter) in terms of the spectral composition of the detected optical signal.
All our SNPs have ligands that keep these suspensions stable. By keeping the core size fixed and changing the surface treatment (thereby changing the zeta potential) we are able to gain insights into the role played by the surface chemistry in aggregation dynamics. To study this effect systematically, we investigate samples with different surface treatments, for a range of concentrations. Our results also highlight the role of dipole interactions in the equilibrium cluster configurations that arise due to an applied magnetic field stimulus, and how this results in different effective dipole moment values as well as scattering profiles due to soft aggregate formations. In addition to discussing the role of SNP surface chemistry, the different molecules involved in different surface treatments, also allow us to provide insights into the role of the hydrodynamic radius in scattering and aggregation dynamics. Finally, we provide some early quantitative results based on a model that attempts to accurately capture the competing interplay between attractive (magnetic dipoles, etc.) and repulsive (surface charge) forces in the formation of equilibrium cluster configurations [9].

[1] R. Hergt, S. Dutz, and M. Zeisberger, "Validity limits of the Neel relaxation model of magnetic nanoparticles for hyperthermia," Nanotechnology, vol. 21, (2010).

[2] Y. Xiao and J. Du, "Superparamagnetic nanoparticles for biomedical applications," J. Mater. Chem. B, vol. 8, 3, 354–367, (2020).

[3] K. Ganeshlenin, A. Sudame, P. Bhati, A. Chakrabarty, S.N. Kale, D. Maity*, "Systematic Magnetic Fluid Hyperthermia Studies of Carboxyl Functionalized Hydrophilic SPIONS based Ferrofluids", Journal of Colloid & Interface Science 514 (2018)

[4] S. Vandendriessche, W. Brullot, D. Slavov, V. Valev, and T. Verbiest, "Magneto-optical harmonic susceptometry of superparamagnetic materials," Appl. Phys. Lett., vol. 102, (2013).

[5] C. Patterson, M. Syed, Y. Takemaura, "Harmonic decomposition of magneto-optical signal from suspensions of superparamagnetic nanoparticles," JMMM, 451, 248-253 (2018).

[6] M. Syed, W. Li, N. Fried, and C. Patterson, "Magneto-optical investigation of scattering by superparamagnetic nanoparticles using multi-harmonic analysis," AIP Advances 11, 015328 (2021).

[7] M. Syed, S. A. Reza, P. D. Miller, and B. Roop. "Magneto-optical characterization of TCO films using standard and enhanced configurations." *AIP Advances* 14, no. 2 (2024).

[8] M. Syed, Chong-Yi Su, Baixu Zhu, Xingchen Ye, and Syed Azer Reza. "Multi-harmonic response of superparamagnetic nanoparticles as a function of particle size and concentration across multiple optical configurations." AIP Advances 16, no. 2 (2026).

[9] K. Szymanski and H. I. Petrache, "Composite polarizability and the construction of an invariant function of refraction and mass density for solutions," J. Chem. Phys., vol. 134(14), (2011)

GR-10. Disk Type Magnetizer Design for Post-Assembly Magnetization of Yoke-Less Halbach-Array SPMSM

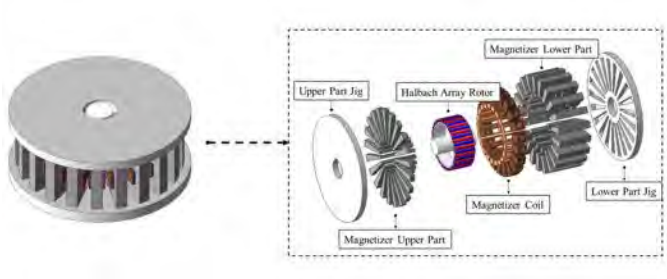
H. Han[1], J. Lee[1], Y. Lee[1], C. Jin[2], W. Kim[3]
[1]Next Generation Smart Energy System Convergence, Gachon University, Seongnam-si, Gyeonggi-do, Korea (the Republic of), [2]Electrical Engineering, Wonkwang University, Iksan-si, Jeonbuk-do, Korea (the Republic of), [3]Electrical Engineering, Gachon University, Seongnam-si, Gyeonggi-do, Korea (the Republic of)

Recent robotic joint applications require electric machines with high power density and lightweight rotor structures. Halbach-array SPMSMs are attractive because the rotor back-yoke can be removed or minimized while maintaining favorable air-gap flux characteristics [1], [2]. However, their segmented magnets with different magnetization directions complicate assembly and make conventional pre-magnetized assembly unfavorable for mass production [1]. In addition, post-assembly magnetization is difficult because the rotor is typically supported by a nonmagnetic guide and lacks an effective magnetic flux path [3]. Although a post-assembly magnetization system for Halbach disk motors has been reported, the previous approach mainly focused on coil design factors such as winding geometry and number of turns, and did not

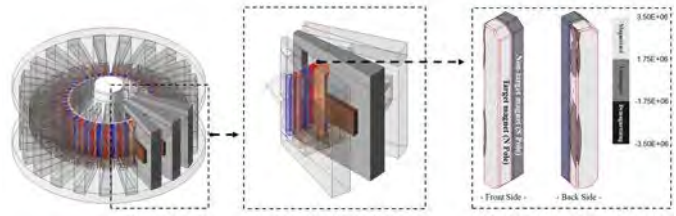
sufficiently address the structural formation of a stable magnetic return path in a yokeless rotor configuration [3].

To address this issue, this paper proposes a Disk Type magnetizer for post-assembly magnetization of Halbach-array SPMSM rotors. The proposed upper and lower magnetizer parts move axially to surround the rotor during magnetization, forming an effective flux path even in a yokeless rotor structure. Auxiliary teeth located behind the rotor guide replace the role of the missing rotor back-yoke, stabilize the magnetizing flux path, and reduce leakage flux between adjacent teeth. Magnetization-demagnetization analysis shows that the magnet center is insufficiently magnetized when only the main winding is applied. Therefore, an auxiliary winding is introduced to reinforce the magnetizing field at the magnet center and improve the magnetization distribution. As a result, the proposed structure reduces the required magnetizing current to approximately one-half of that of the conventional RFM magnetizer. The proposed Disk Type magnetizer provides a new structural solution for post-assembly magnetization of Halbach-array SPMSM rotors and improves manufacturability for mass production.

[1] Y. Ni, X. Jiang and B. Xiao, IEEE Trans. Magn., Vol. 56, Art. 8100811 (2020)
[2] H. Guo, Z. Zhang and C. Zhang, IEEE Trans. Transport. Electrific., Vol. 12, p.3610 (2026)
[3] X. Li, Y. Lv and L. Lv, 2023 IEEE 4th China Int. Youth Conf. Electr. Eng., p.1 (2023)



Structure of the Disk-Type Magnetizer



Electromagnetic Mag–Demag FEA of the Disk-Type Magnetizer

GR-11. Complete Thermodynamic Characterization of Magnetocaloric Materials: Instrumentation Considerations

R. K. Dumas[1], D. Bastos[2], A. Soares[2], L. Andrade[2], J. Amaral[3], K. Dixon-Anderson[4, 5], Y. Mudryk[4, 5], V. Franco[6], J. P. Araújo[2], R. Almeida[2], J. H. Belo[2]
[1]Quantum Design, Inc., San Diego, California, United States, [2]Physics, IFIMUP – Institute of Physics for Advanced Materials, Nanotechnology and Photonics, Porto, Portugal, [3]Physics, University of Aveiro, Aveiro, Portugal, [4]Ames National Laboratory of US Department of Energy, Ames, Iowa, United States, [5]Department of Materials Science and Engineering, Iowa State University, Ames, Iowa, United States, [6]Department for Condensed Matter Physics, University of Seville, Seville, Spain

A comprehensive and accurate characterization of the magnetic entropy change (ΔS_{iso}), adiabatic temperature change (ΔT_{ad}), and heat capacity are necessary to advance the development of magnetocaloric materials for refrigeration devices. Unfortunately, current methods are inconvenient, requiring several instruments to measure each individual property, often in a bespoke setup. Recently, it has been shown by measuring the adiabatic time-varying magnetization in materials exhibiting a non-hysteretic 2nd order phase transition that ΔS_{iso}, ΔT_{ad}, and the heat capacity can be deduced by measurements in a single instrument [1, 2]. More recently this technique has been extended to a hysteretic 1st order phase transition of $Gd_5Si_2Ge_2$ by using equilibrium magnetizations resulting from each magnetic field application at different temperatures as the necessary magnetization to temperature conversion curve [3]. A magnetometer capable of (1) ramping the magnetic field as quickly as possible and (2) performing measurements in a variable pressure environment are necessary requirements. More specifically, an exchange gas at near ambient pressure is first required to ensure the sample is initially in thermal equilibrium, and then as low of a pressure as possible is required to ensure adiabaticity during the field ramps. This presentation will compare the capabilities of several commercial magnetometers that enable such measurements.

Acknowledgements

Univ. do Porto: FCT/MCTES (PIDDAC), UIDB/04968/2020, UIDP/ 04968/2020, UID/4968/2025, PTDC/EME-TED/3099/2020 (IFIMUP), LISBOA-01-0247-FEDER-039985/POCI-01-0247FEDER- 039985. The EU Horizon Europe programme-No. 101161135 — MAGCCINE

R. Almeida: FCT for the PhD grant-ref. 2022.13354.BD Project CICECO Aveiro Inst. of Materials, UID/50011/2025 (DOI 10.54499/UID/50011/2025) \& LA/P/0006/2020 (DOI 10.54499/LA/P/0006/2020), FCT/MCTES (PIDDAC)

Ames National Laboratory is operated for the U.S. DOE by Iowa State University of Science and Technology under Contract No. DE-AC02-07CH11358

V. Franco: PID2023-146047OB-I00 from AEI/10.13039/501100011033, PPIT2024-31833, EU, Ministerio de Hacienda y Funcion Publica, FEDER and Junta de Andalucia, and VII Plan Propio de Investigacion from University of Seville

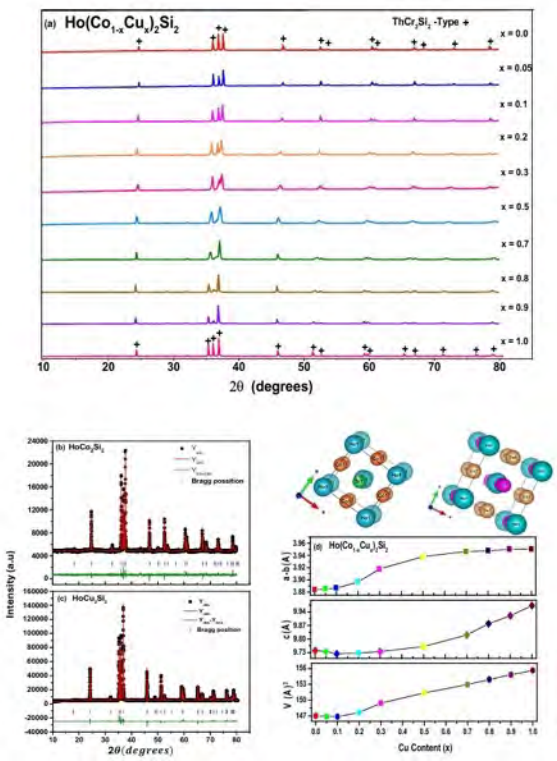
[1] R. Almeida, C. Amorim, J. S. Amaral, J. P. Araujo, and J. H. Belo, "Direct Measurement of the Magnetocaloric Effect through Time-Dependent Magnetometry", Phys. Rev. Appl. 18, 024081 (2022), https://doi.org/10.1103/PhysRevApplied.18.024081.
[2] C. S. Pereira, R. Almeida, R. Kiefe, C. Amorim, D. J. Silva, J. S. Amaral, and J. H. Belo, "Complete thermodynamic characterization of second-order phase transition magnetocaloric materials exclusively through magnetometry", J. Alloy Compd. 976, 173290 (2024), https://doi.org/10.1016/j.jallcom.2023.173290.
[3] D. O. Bastos, A. M. R. Soares, L. Andrade, R. K. Dumas, J. S. Amaral, K. Dixon-Anderson, Y. Mudryk, V. Franco, J. P. Araújo, R. Almeida, J. H. Belo, "Self-thermometry measurements of the adiabatic temperature change in first-order phase transition magnetocaloric materials", https://arxiv.org/abs/2603.25429

GR-12. Tuning Magnetocaloric Response and Metamagnetism in $Ho(Co_{1-x}Cu_x)_2Si_2$ by Cu Substitution

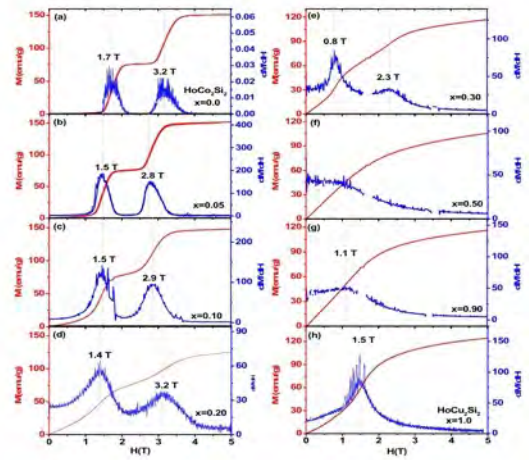
J. D. Peña Serna, D. M. M. A. García, A. Gomes
Institute of Physics, Federal University of Rio de Janeiro, Rio de Janeiro, RJ, Brazil

The magnetic and magnetocaloric properties of the intermetallic series $Ho(Co_{1-x}Cu_x)_2Si_2$ ($0 \leqslant x \leqslant 1$) were systematically investigated to elucidate the impact of Cu substitution on magnetic interactions and field-induced transitions. All compounds crystallize in the tetragonal $ThCr_2Si_2$-type structure and exhibit antiferromagnetic ordering dominated by localized Ho 4f moments, accompanied by low-temperature metamagnetic transitions. These transitions are pronounced at low Cu contents and progressively weaken with increasing Cu concentration due to magnetic dilution and enhanced disorder. The magnetocaloric effect, evaluated from isothermal magnetization data under H = 5 T, shows a conventional response for all compositions. The maximum magnetic entropy change $|\Delta S_M^{max}|$ exhibits a non-monotonic dependence on Cu content, reaching ≈16 $Jkg^{-1}K^{-1}$ at x=0.1, while the relative cooling power is maximized at x =0.05 due to an optimal balance between entropy change magnitude and thermal span. These results demonstrate that Cu substitution effectively tunes magnetic interactions, disorder, and metamagnetic behavior, enabling control of the magnetocaloric performance of Ho-based intermetallics for cryogenic applications.

[1] B. Xu, M. Wu and L. Tian, Materials Today Communications, 38,108458 (2024).
[2] B. Liu, G. Zeng and J. Chen. AIP Advances, 13,2 (2023).
[3] GY Lu, YS Du, XF Wu. Journal of Alloys and Compounds, 906,164343 (2022).
[4] Michael Shatruk. Journal of Solid State Chemistry, 272, 198 (2019).
[5] T. Samanta, I Das, and S Banerjee. Applied Physics Letters, 91,15 (2007).
[6] X. Wang, Z. Ma and Z. Zhang. Applied Physics A, 128,898 (2022).
[7] S. Baran, M Balanda and A Hoser. Journal of alloys and compounds, 507(1):16–20, 2010.



(a) X-ray diffraction (XRD) patterns of the $Ho(Co_{1-x}Cu_x)_2Si_2$ series for different Cu concentrations. (b-c) Experimental data together with the corresponding Rietveld refinements, Bragg reflection positions, and difference curves, confirming the $ThCr_2Si_2$-type tetragonal crystal structure over the entire composition range. (d) Lattice parameters *a* and *c*, and unit-cell volume *V*, as a function of Cu content (*x*).



Magnetization curves *M(H)* (red lines) and their corresponding field derivatives *dM/dH* (blue lines) measured at T = 2 K for $Ho(Co_{1-x}Cu_x)_2Si_2$ samples with different compositions: (a) x = 0.0, (b) x = 0.05, (c) x = 0.10, (d) x = 0.20, (e) x = 0.30, (f) x = 0.50, (g) x = 0.90, and (h) x = 1.0.

GR-13. Energy-Resolved Magnetic Circular Dichroism for Probing Chiral-Induced Spin Selectivity and Spin-Polarized Optical Transitions

H. Hsu[1], W. Liao[1], Y. Shao[2]
[1]Department of Applied Physics, National Pingtung University, Pingtung, Taiwan, [2]National Synchrotron Radiation Research Center, Hsinchu, Taiwan

Chiral-induced spin selectivity (CISS) offers a promising route for controlling magnetic order through molecular chirality, yet its microscopic coupling to spin-polarized electronic states remains difficult to resolve. Here, we present energy-resolved magnetic circular dichroism (ER-MCD) as a spectroscopic probe of CISS-related magnetization switching and spin-polarized optical transitions in ferrimagnetic thulium iron garnet (TmIG).
We demonstrate bidirectional magnetization switching in TmIG induced by adsorption of a single-handed chiral molecule, a Cu(II)–D-leucine coordination complex[1]. Unlike conventional ferromagnetic systems, where opposite molecular chirality is generally required to reverse the switching direction, the same chiral complex drives magnetization reversal from both initial remanent states. This unusual behavior originates from the antiparallel Fe sublattices in TmIG, where octahedral and tetrahedral Fe sites provide distinct spin-selective interaction channels[2]. By combining UV–vis circular dichroism, ER-MCD, and X-ray absorption spectroscopy, we show that CISS-driven switching in ferrimagnets is chirality-dependent, site-selective, and energy-resolved. ER-MCD provides an optical fingerprint of magnetization direction while revealing spin-polarized optical transitions associated with different Fe sublattices. The spectral response is further interpreted using the electronic-structure framework of TmIG, where O 2p → Fe 3d ligand-to-metal charge-transfer transitions and higher-energy Tm 5d-related transitions dominate the magneto-optical response.
These results establish ER-MCD as a bridge between molecular chirality, CISS-induced spin manipulation, and spin-polarized optical transitions, highlighting ferrimagnetic oxides as versatile platforms for site-selective CISS phenomena and chirality-controlled magneto-optical functionalities.

[1] W.-H. Liao, J. Webb, Y.-H. Xue et al., ACS Appl. Electron. Mater., Vol. 8, p.720 (2026)
[2] W.-H. Chang Chien, H.-A. Liu, J.-X. Lin et al., Adv. Electron. Mater., p.2400459 (2024)

GR-14. Effects of Curved Sensing Coils on Triaxial Vibrating Sample Magnetometer (TVSM) Sensitivity and Crosstalk

L. Rodriguez, W. Geerts
Texas State University, San Marcos, Texas, United States

3D printed permanent magnets which leverage magnetic field assisted additive manufacturing (MFAAM) processes introduce(s) complex magnetic anisotropies which require simultaneous measurements of all three magnetic components (M_x, M_y, and M_z) to provide an accurate description of the energy landscape. Current Vibrating sample magnetometers (VSM) are biaxial and can only measure two simultaneous magnetic components. Analytical computational modelling of VSM coils (leveraging Bernards mathematical approximation [1]) was performed to optimize shape, size, location, and orientation to determine the effect each coil configuration has on the sensitivity (S_x, S_y, and S_z) and crosstalk (CT_x, and CT_y) spatial maps for planar coils. Finite element modelling was performed in COMSOL [2] for the same components on coils with cylindrical and spherical axial surface curvature. Coil-sample distance had the largest impact on coil sensitivity (98% increase) when reducing the distance 2.5-fold. Crosstalk spatial distribution was reduced by 30% when doubling coil diameter compared to increasing coil length for horizontally orientated planar coils (h-zcoils). Alternatively, the vertically orientated planar coils (v-zcoils) nearly eliminated CT_y spatial distribution as coil diameter doubled while minimizing coil length. The modelling has shown the sensitivity distribution is altered in a predictable way enabling the control of the size and shape of the sensitivity region(s). S_z for the planar h-zcoils is 2-fold larger compared to the v-zcoils. Introducing curvature to the h-zcoils axial surface reduced coil-sample edge distance by 18% and increased S_z by 30% (with maximum cylindrical curvature) over planar coils. Adding spherical curvature increased S_z by 4% over cylindrically curved h-zcoils. Comparatively, adding maximum cylindrical curvature to the v-zcoils increased S_z 6-fold over planar coils. Peak-to-peak (P2P) and volume root mean square (VRMS) field homogeneity results are also presented. A triaxial coil cylinder housing curved x, y, and z coils for a VSM is proposed in Fig. 1.

Fig. 1 Triaxial VSM coil cylinder with cylindrically curved x and y-coils and spherically curved z-coils

[1] J. P. C. Bernards, "Design of a detection coil system for a biaxial vibrating sample magnetometer and some applications," *Review of Scientific Instruments*, vol. 64, no. 7, pp. 1918–1930, Jul. 1993, doi: 10.1063/1.1143977.
[2] COMSOL Multiphysics® v. 6.4. www.comsol.com. COMSOL AB, Stockholm, Sweden.

GR-15. Effect of La and Ca Substitution on Magnetic and Magnetocaloric Properties of Gd_2NiMnO_6- Based Double Perovskites

J. Sultana[1, 2], S. Mishra[2]
[1]Natural Sciences, Texas A&M University-Texarkana, Texarkana, Texas, United States, [2]Physics and Materials Science, University of Memphis, Memphis, Tennessee, United States

Magnetocaloric materials based on rare-earth double perovskites are promising for energy-efficient magnetic refrigeration. In this study, Gd_2NiMnO_6, $Gd_{1.5}La_{0.5}NiMnO_6$, and $Gd_{1.5}Ca_{0.5}NiMnO_6$ were synthesized via a sol–gel autocombustion method to explore the effect of La^{3+} and Ca^{3+} substitution on their magnetic and magnetocaloric properties. X-ray diffraction confirms single-phase orthorhombic structures (space group *Pnma*) for all compositions.
Magnetization measurements indicate that the combined contribution of Gd^{3+} moments and Ni–O–Mn superexchange interactions governs the magnetic behavior. The Curie temperature (T_N) is tuned from 131 K (Gd_2NiMnO_6) to 160 K with La substitution and to 127 K with Ca substitution, enabling control over the operating temperature range. The maximum magnetic entropy change ($-\Delta S_m$) reaches 24.44 J/kg.K for Gd_2NiMnO_6, while La- and Ca-substituted samples show reduced values of 18.60 and 16.22 J/kg.K respectively. Notably, $Gd_{1.5}La_{0.5}NiMnO_6$ exhibits an enhanced refrigerant capacity of 205.53 J/kg.

These results demonstrate that rare-earth site substitution effectively tailors the balance between entropy change and refrigerant capacity, making these materials promising candidates for cryogenic magnetic refrigeration.

Authors: Jolaikha Sultana, Yenugonda Venkateswara, Arjun K. Pathak, Sanjay R. Mishra

GR-16. Effect of ZrO_2 substitution in nitride grain boundary materials on magnetic properties and nanostructure for FePt granular films

K. Tham[1], D. Miyazaki[1], S. Saito[2]
[1]Tanaka Precious Metal Technologies, Tsukuba, Ibaraki, Japan, [2]Electronic Engineering, Graduate School of Engineering, Tohoku University, Sendai, Japan

The $L1_0$ type FePt phase has been utilized as the heat assisted magnetic recording (HAMR) medium material due to its high uniaxial crystalline magnetic anisotropy energy of 5×10^7 erg/cm^3 at room temperature and moderate Curie temperature of 750 K. To obtain a granular structure, the research of adding grain boundary materials (GBMs), such as carbon[1-2], oxide[3], nitride[4] into FePt thin films have been widely conducted. Especially granular films with nitride GBMs show the possibility to obtain the columnar growth magnetic grains[5]. However, most of the granular films with nitride GBMs show poor magnetic grain separation compared to those of with oxide GBMs. Therefore, we perform experiment of substituting nitrides in FePt granular films with typical oxide, ZrO_2 which has small magnetic grains[6]. In this paper, we will report the evaluation result of magnetic properties and nanostructure and of those granular films.

Fig. 1 shows *M-H* loops of FePt-nitride granular films (5 nm) substituted with ZrO_2. All granular films substituted with ZrO_2 show larger hysteresis with smaller gradient at around coercivity than those of without ZrO_2 substitution.

Fig. 2 shows In-plane TEM images of FePt-nitride granular films (5 nm) substituted with ZrO_2. The images show that the separation of magnetic grains for granular films substituted with ZrO_2 is promoted. Regarding the average magnetic cluster size (*CS*), for typical FePt-BN granular films, *CS* is reduced around 15% from 14.3 to 12.4 nm due to the ZrO_2 substitution.

Based on Fig. 1 and Fig. 2 results, the promotion of grains separation enhances magnetic decoupling between the grains as reflected in the smaller gradient at around coercivity.

1) J. S. Chen et al., *Appl. Phys. Lett.*, 91, 132506 (2007).
2) A. Perumal et al., *J. Appl. Phys.*, 105, 07B732 (2009).
3) Y. F. Ding et al., *Appl. Phys. Lett.*, 93, 032506 (2008).
4) K. K. Tham et al., *AIP Adv.*, 13, 035034 (2023).
5) C. Xu et al., *IEEE Trans. Magn.*, 59, 2690 (2023).
6) K. K. Tham et al., *IEEE Trans. Magn.*, 62, 2300404 (2026).

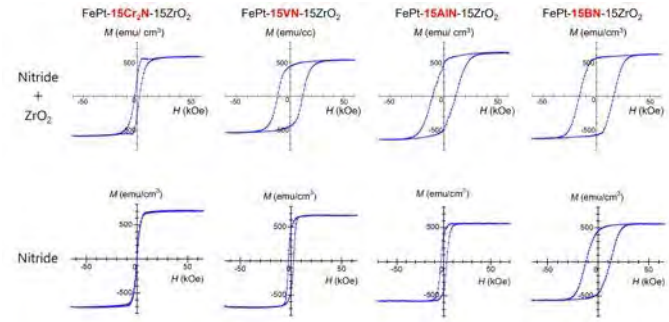


Fig. 2 *M-H* loops of FePt-nitride granular films (5 nm) substituted with ZrO_2.

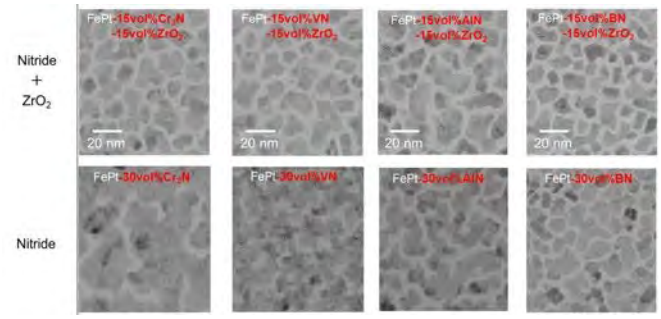


Fig. 2 In-plane TEM images of FePt-nitride granular films (5 nm) substituted with ZrO_2.

GR-17LB. Direct magnetic imaging of magnetite nanoparticles assemblies via resonant x-ray dichroic ptychography

J. Rackham[1], A. Fraile Rodríguez[2], A. I. Figueroa[2], D. Shapiro[3], R. Sandberg[1], K. Chesnel[1]
[1]Physics, Brigham Young University, Provo, California, United States, [2]Institute of Nanoscience and Nanotechnology, University of Barcelona, Barcelona, Barcelona, Spain, [3]Advanced Light Source, LBNL, Berkeley, California, United States

With the rapid development of nanotechnologies and medical applications based on magnetic nanoparticles (MNPs), being able to visualize and manipulate the magnetic state of single particles has become increasingly useful. Most of our current knowledge of the magnetic response of MNPs to external stimuli is based on ensemble-averaged measurements, such as magnetometry, but little has been observed about the behavior of single NPs when in an assembly, such as interparticle magnetic ordering and dynamics of magnetic fluctuations. Also, most imaging tools do not offer magnetic contrast, or if they do, their limited resolution does not allow to distinguish single NPs. Here, we present magnetic images of 20-60 nm Fe3O4

nanoparticles assemblies [1] using the novel technique of resonant x-ray ptychography [2]. To obtain the needed magneto-optical contrast, the x-ray energy is finely tuned to the Fe-L3 resonance [3], and diffraction patterns are collected with circularly polarized light at opposite helicities. The reconstructed image shows the NPs charge distribution (Fig.1a) and the resulting dichroic image shows the magnetic state of single particles with magnetization aligned either up or down out-of-plane (Fig. 1b). Data collected at each of the resonant peaks of the XMCD signal (Fig,1c) show a clear switching in sign (Fig.1d) confirming the pure magnetic nature of the signal. We found that most NPs are magnetically monodomain and their assembly exhibit various amounts of ferromagnetic, antiferromagnetic, and random magnetic alignment, confirming earlier predictions from magnetic scattering (XRMS) data on smaller 5-10 nm NPs [4]. Here, with the superparamagnetic 20 nm NPs, we directly observed changes in the magnetic ordering and in the dynamic magnetic fluctuations when cooling throughout the blocking temperature. [5]

[1] S. Klomp et al., "Size-dependent crystalline and magnetic properties of 5 to 100 nm Fe3O4 nanoparticles: superparamagnetism, Verwey transition…". IEEE Trans. Magn. 56 (11), 2300109 (2020).
[2] F. Pfeiffer "X-ray Ptychography" Nature Photonics 12, 9-17 (2018).
[3] K. Chesnel et al., "Unraveling nanoscale magnetic ordering in Fe3O4 nanoparticle assemblies via x-rays". Magnetochemistry 4 (4), 42 (2018).
[4] J. Rackham et al., "Field-dependent nanospin ordering in monolayers of Fe3O4 nanoparticles throughout the superparamagnetic blocking transition" Phys. Rev. B 108 (10), 104415 (2023).
[5] J.Rackham et al., to be submitted (2026)

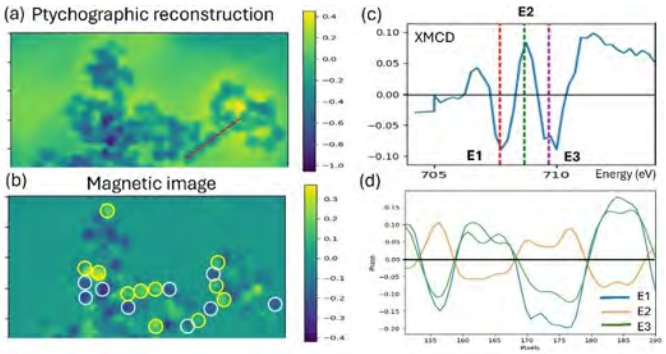


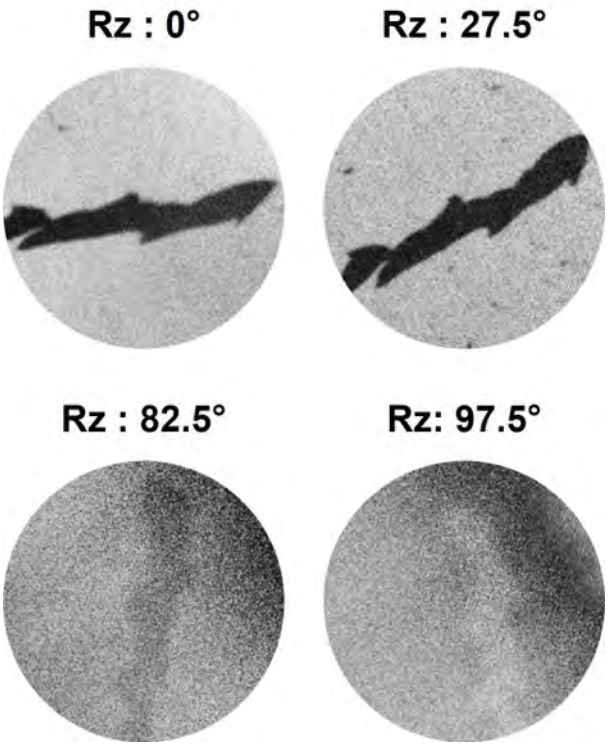
Figure 1: Magnetic imaging of 60 nm Fe_3O_4 nanoparticles via x-ray ptychography. (a) Reconstructed image of a NP assembly; (b) Dichroic image at same location, showing the magnetization orientation of single particles; (c) XMCD signal extracted from the NPs at the Fe-L_3 edge; (d) slices through the red line in (a) collected at the three peaks E2, E2,E3 of the XMCD signal

GR-18LB. Resolving In-Plane Magnetic Domains and Angular Dependence in 8-ML Co/Cu(100) via Soft X-ray Photoelectron Microscopy at the Taiwan Photon Source

J. H. Du[1], H. Wei[2], M. Wu[2], H. Chiu[2], C. Hsu[1], T. Chuang[2], D. Wei[2]
[1]*Physics, Chung Yuan Christian University, Taoyuan, Taiwan,* [2]*National Synchrotron Radiation Research Center, Hsinchu, Taiwan*

An 8-monolayer ultrathin Co film epitaxially grown on Cu(100) serves as a classic model system for surface magnetism, exhibiting room-temperature ferromagnetism with spontaneous in-plane magnetization. We investigated this system utilizing the recently established photoelectron momentum microscope at Taiwan Photon Source (TPS) beamline 27 A2 [1-3].
Position-selective X-ray absorption spectroscopy (XAS) and X-ray magnetic circular dichroism (XMCD) were employed for real-space imaging using circularly polarized soft X-rays. XMCD imaging at the Co L_3 and L_2 edges successfully resolves distinct magnetic domains, while XAS spectra extracted from single domains display opposite dichroism for opposing magnetizations. Furthermore, a series of XMCD images recorded as the sample was rotated about its surface normal demonstrates that the contrast difference accurately traces the cosine relationship of the angle between the photon helicity vector and the magnetization direction. The case demonstrates the capabilities of magnetic imaging at TPS 27A2 with azimuthal-dependent measurements.

[1] Shiu, et al., "When microscopy meets soft X-ray at TLS and TPS", J. Electron Spectrosc. Relat. Phenom. 266, 147363 (2023).
[2] Chuang, et al., "Performance of a photoelectron momentum microscope in direct- and momentum-space imaging with ultraviolet photon source", *J. Synchrotron Rad.* 31, 195 (2024).
[3] Chuang, et al., "Momentum Microscopy Investigation of the Local Band Structure of Monolayer WSe_2 Flakes: Toward Optoelectronic Device in Quantum Size", *ACS Appl. Nano Mater.* 8, 23164 (2025).



XMCD images of the 8-monolayer Co/Cu(100) film at the Co L_3 and L_2 edges, recorded with circularly polarized soft X-rays at four azimuths Rz of the sample about its surface normal.

GR-19LB. Development of the MagXES spectrometer at the APS 4-ID POLAR beamline

F. Frontini, D. Casa, A. Said, Y. Choi, D. Haskel, G. Fabbris
Advanced Photon Source, Argonne National Laboratory, Lemont, Illinois, United States

Hard X-ray XMCD is a well-established technique for probing magnetism, being particularly valuable in complex sample environments [1]. However, the dichroic contrast at the K-edge of 3d elements and $L_{2,3}$-edges of 4f elements is often weak, limiting the exploration of large pressure-temperature-magnetic field phase diagrams. The dichroic signal can be significantly enhanced by measuring the magnetic circular dichroism in resonant X-ray emission spectroscopy (RXES-MCD) [2,3], as illustrated by our proof-of-concept measurements in Fig. 1. Here we present the concept, design and development status of MagXES (Fig. 2), a dedicated RXES-MCD spectrometer at the 4-ID POLAR beamline. MagXES will employ an array of newly developed spherically diced crystal analyzers (SDCAs) whose large dice size captures an entire emission line in a single area-detector exposure, eliminating analyzer scanning and improving the dichroic noise level. Based on our preliminary measurements, we expect that MagXES will enable as much as 100x larger throughput than regular XMCD. Such improved sensitivity will enable measurements in systems with weak dichroic contrast, which includes samples at extreme pressures and dilute magnetic materials.

[1] N. M. Souza-Neto et al., *High Pressure Research* 36, 360 (2016). https://doi.org/10.1080/08957959.2016.1212025
[2] Kirsch et al., *Physical Review Letters* 74, 4931 (1995). https://doi.org/10.1103/PhysRevLett.74.4931
[3] Sikora et al., *Physical Review Letters* 105, 037202 (2010). https://doi.org/10.1103/PhysRevLett.105.037202

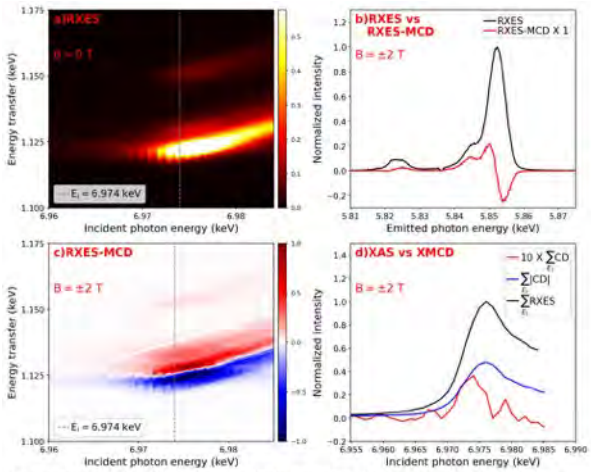


Figure 1: Eu $La_{1,2}$ RXES-MCD measurements of $EuAl_4$, including a) a RXES map at B=0 T, b) the RXES and RXES-MCD spectra at E=6.974 keV, c) the RXES-MCD map at B=+-2 T, and d) the E_i integrated emission (PFY-XAS), dichroism (XMCD), and absolute dichroism spectra.

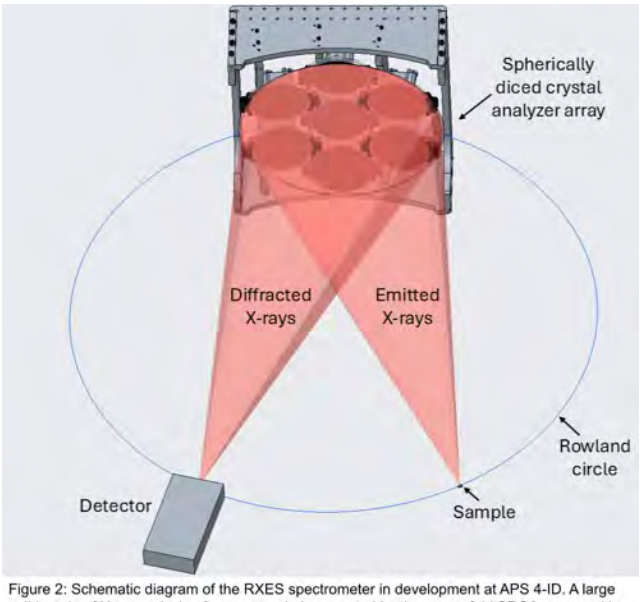


Figure 2: Schematic diagram of the RXES spectrometer in development at APS 4-ID. A large solid angle of X-ray emission from a sample is accepted by the seven-fold SDCA array and is dispersively focused to an area detector.

SESSION HA: MAGNETISM AND THE BRAIN: NEUROMODULATION, NEUROIMAGING AND NOVEL APPLICATIONS

Chair(s): K. Wu, *Department of Physics, University of South Florida, Tampa, Florida, United States*

Friday, November 6, 2026

02:00 PM-05:30 PM

Coral 3

HA-01. Magnetoelectric Nanodiscs for Wireless Neuromodulation

Y. Kim, N. Kent, E. Vargas Paniagua, A. Comite, N. Seethapathi, P. Anikeeva

Massachusetts Institute of Technology, Cambridge, Massachusetts, United States

Wireless neuromodulation technologies offer a promising route toward minimally invasive control of neural activity; however, existing approaches are often limited by poor spatial specificity, reliance on genetic modification, or the need for implanted hardware. Magnetoelectric nanomaterials offer a compelling alternative by enabling remote, transgene-free neuromodulation by converting externally applied magnetic fields into localized electrical stimuli.

A Fe_3O_4–$CoFe_2O_4$–$BaTiO_3$ double core–shell magnetoelectric nanodisc (MEND) architecture has been developed to enhance magnetoelectric coupling efficiency while maintaining stability in physiological environments and biocompatibility. In vitro, neurons decorated with MENDs at a density of 1 μg mm^{-2} exhibit robust responses to applied magnetic fields, despite the electrical polarization generated by individual particles remaining below the threshold for direct neuronal excitation. This apparent discrepancy is explained by a model of repetitive subthreshold depolarization, supported by the steady-state solution of three-dimensional cable theory.

Guided by these experimental and computational insights, stimulation parameters were optimized for in vivo applications. Injection of 1–3 μg of MENDs into deep brain regions, including the ventral tegmental area and subthalamic nucleus (STN), enables modulation of reward-related and motor behaviors, respectively, in genetically intact mice. In a unilateral Parkinsonian mouse model, MEND-mediated stimulation of the STN improves behavioral asymmetry, offering a wireless alternative to conventional electrode-based deep brain stimulation. Quantitative analysis using a computational pipeline further reveals stimulation-dependent changes in gait features, highlighting shifts in movement directionality that are not readily captured by conventional metrics.

Together, these results establish magnetoelectric nanomaterials as a versatile and scalable platform for wireless neuromodulation, bridging nanoscale magnetic materials design with functional control of neural activity and opening new avenues for bioelectronic and therapeutic applications.

HA-02. Magnetic Particle Imaging of the Brain

A. Tonyushkin[1, 2], C. McDonough[1, 2], T. Siddiqua[1, 2]

[1]Physics Department, Oakland University, Rochester, Michigan, United States, [2]Center for Biomedical Research, Oakland University, Rochester, Michigan, United States

Magnetic Particle Imaging (MPI) is a tracer-based imaging modality that directly measures the nonlinear magnetization response of superparamagnetic iron oxide (SPIO) nanoparticles, enabling quantitative, radiation-free imaging of tracer distribution [1]. Similar to PET and SPECT, MPI offers high sensitivity to tracer concentration, along with superior temporal resolution and zero tissue background signal. These characteristics make MPI a strong candidate for functional and molecular brain imaging. However, clinical translation remains challenging due to the difficulty of scaling MPI hardware to human dimensions. Conventional closed-bore MPI systems require high-power electromagnetic coils to generate strong AC and DC magnetic fields, resulting in substantial technical complexity, size, and cost. Existing head-only MPI scanners mitigate some of these challenges but still require bulky coil geometries and high-power operation [2,3].

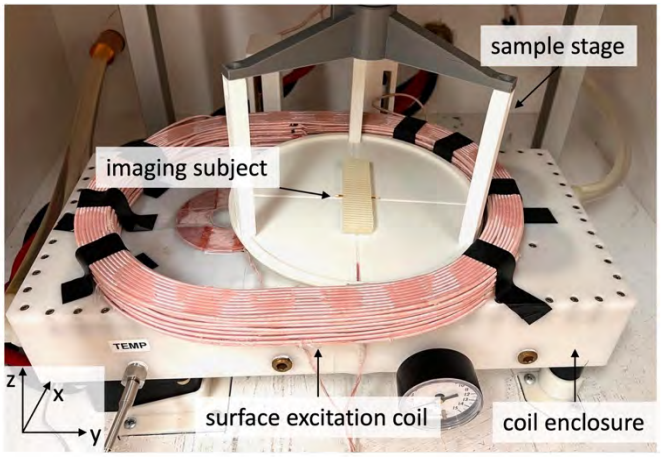
In this talk, I will review the current state of the art in MPI systems for brain imaging, highlighting applications in stroke [4], functional imaging [3], tumor detection, and neurodegenerative diseases such as Alzheimer's. I will then present our approach to overcoming scaling limitations by developing a single-sided MPI architecture, in which all field-generating components are positioned on one side of the imaging volume [5]. This geometry enables substantially lower power consumption and simplified system design while maintaining performance.

Specifically, I will describe our next-generation field-free line (FFL) single-sided MPI system (Fig.1), which achieves significant gains in spatial resolution, sensitivity, and field of view [6]. The system achieves spatial resolution comparable to that of human-head-scale MPI scanners (3–12 mm at gradients of 0.2–1.1 T/m) while expanding the

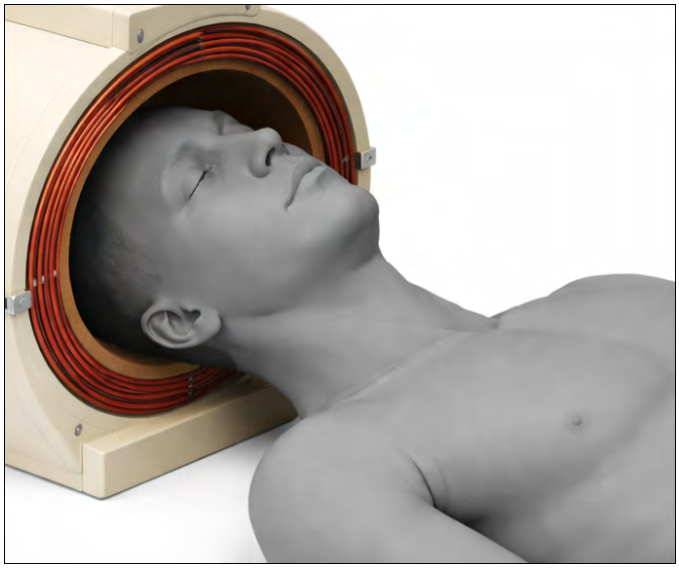
field of view to 8 × 8 × 3.5 cm^3 using fully electronic scanning. These improvements are realized with reduced hardware complexity and power consumption. We validate system performance through imaging of large-volume phantoms with embedded tumor models, as well as in vivo tumor imaging in a mouse model. The platform further supports interchangeable coil configurations, enabling imaging of different anatomical regions, including the brain and breast.

This work demonstrates a scalable and versatile pathway toward clinical MPI, particularly for brain imaging (Fig.2) and other near-surface applications that remain largely underexplored.

1. B. Gleich and J. Weizenecker, *Nature*, Vol. 435, no. 7046, pp. 1214–1217 (2005).
2. M. Graeser, et al., *Nature Commun.*, vol. 10, no. 1, Art. no. 1936 (2019).
3. E. Mattingly, et al., *Physics in Medicine & Biology*, Vol. 70, Art. no. 015019 (2025).
4. P. Ludewig, et al., *ACS Nano*, Vol. 11, pp. 10480–10488 (2017).
5. J. Pagan, et al., *IEEE Trans. Magn.*, Vol. 57, no. 2, Art. no. 5300105 (2021).
6. C. McDonough, et al., *Physics in Medicine & Biology*, Vol. 70, Art. no. 235015 (2025).



A prototype of a single-sided MPI scanner showing the selection-coil enclosure, the organ-specific surface-volume excitation coil, and the subject rotation table.



A concept of a single-sided MPI scanner with head specific surface-volume excitation coil.

HA-03. Novel Transcranial Magnetic Stimulation Coils and Validation Techniques for Human and Animal Studies

R. L. Hadimani
Department of Mechanical Engineering, Virginia Commonwealth University, Richmond, Virginia, United States

Transcranial magnetic stimulation (TMS) is a non-invasive neuromodulation modality whose therapeutic efficacy is fundamentally governed by the spatial distribution, focality, and penetration depth of the induced electric field (E-field). Conventional coil designs, primarily optimized for human cortical stimulation, exhibit limited scalability and inadequate focal targeting when translated to small animal models, thereby constraining mechanistic studies and translational development. This work presents an integrated framework encompassing novel multi-material TMS coil designs and advanced validation methodologies using anatomically and electrically accurate brain phantoms for both human and animal studies.

We introduce a new class of TMS coils incorporating high-permeability ferromagnetic cores, specifically iron–cobalt–vanadium (Permendur) alloys, coupled with diamagnetic shielding elements such as pyrolytic graphite as shown in Fig.1 [1]. The ferromagnetic cores enhance magnetic flux concentration and increase induced E-field intensity, while the diamagnetic shields spatially redistribute magnetic field lines to suppress off-target stimulation. This multi-magnetic material architecture enables improved focality by confining

the induced E-field to targeted neural regions. Finite element modeling (FEM) incorporating nonlinear hysteretic material behavior demonstrates that the parabolic ferromagnetic core (PFC) configuration, augmented with a conformal diamagnetic plate, yields superior field localization compared to conventional figure-of-eight and V-tip coils . The diamagnetic shielding effectively mitigates field spread, enabling precise stimulation of small anatomical targets critical for rodent studies.

To experimentally validate these coil designs, we developed anatomically accurate brain phantoms derived from MRI and CT imaging data, extending prior work on patient-specific phantom fabrication. These phantoms replicate the geometric complexity and heterogeneous conductivity of biological tissues, including skin, skull, cerebrospinal fluid, and gray and white matter compartments. For rodent applications, a 3D-printed rat head phantom was fabricated using polymer composites (PDMS/CNT) with tunable conductivity (~0.5 S/m) to match physiological conditions . Embedded triaxial dipole probes enable direct, spatially resolved measurement of E-field vectors within the phantom, providing a robust platform for quantitative validation of computational models.

Comparative analysis between FEM simulations and experimental measurements demonstrates strong agreement, with reported deviations on the order of ~5% for peak E-field values across multiple coil configurations . These results confirm the reliability of the phantom-based validation framework and highlight its capability to replace or reduce reliance on in vivo animal experimentation [2]. Furthermore, the modular fabrication approach allowed us to extend to human-scale phantoms as shown in Fig. 2, enabling systematic evaluation of coil performance across anatomical scales and supporting translational optimization of neuromodulation protocols.

This framework enables quantitative validation, and optimization of coil geometries and stimulation parameters for preclinical applications. By bridging the gap between computational modeling and experimental validation.

[1] M. Tashli, A. Mhaskar, G. Weistroffer, M. S. Baron, and R. L. Hadimani, “Novel multi-magnetic material transcranial magnetic stimulation coils for small animals application,” *AIP Advances*, vol. 14, no. 1, p. 015324, Jan. 2024

[2] W. Lohr, M. Tashli, C. Dong, P. Sundaram, and R. L. Hadimani, “Measuring transcranial magnetic stimulation-induced electric fields in anatomically and conductively accurate rat head phantoms,” *J. Neural Eng.*, vol. 23, no. 1, p. 016028, Feb. 2026, doi: 10.1088/1741-2552/ae44cf.

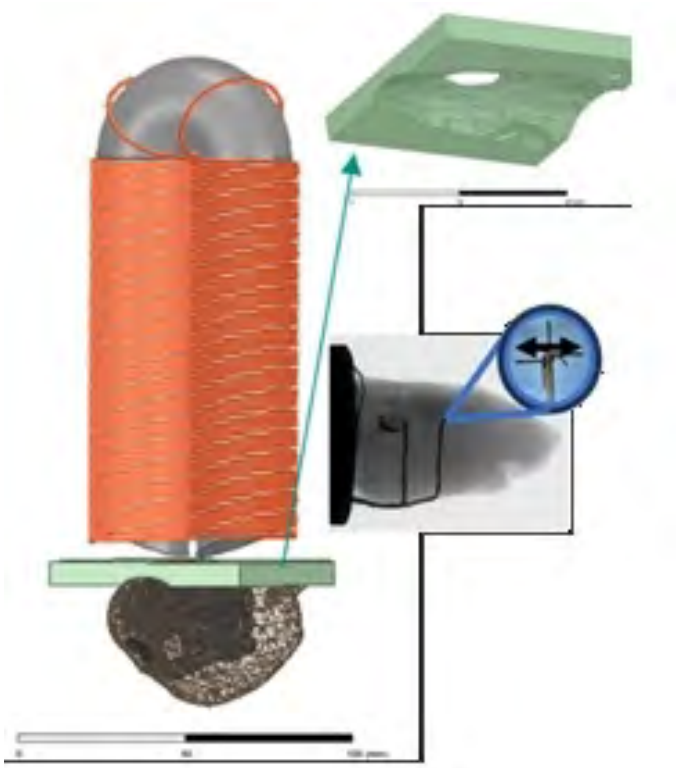
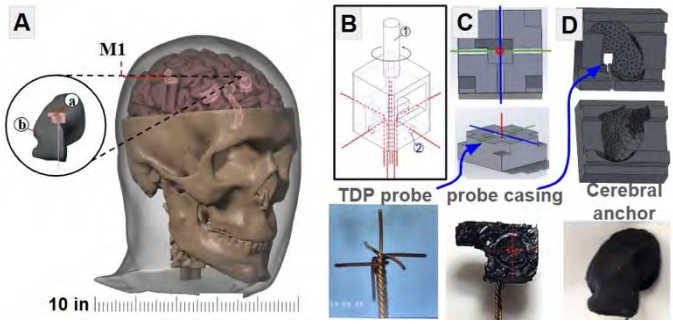


Fig. 2 Novel Parabolic Ferromagnetic Core (PFC) TMS coil with highly diamagnetic pyrolytic graphite shielding plate for a focused stimulation of primary motor cortex (M1) of a rat’s brain.



Cerebral Anchor fabrication. (A) STL head model showing the location of several cerebral anchors (a) TDP placement (b) cerebral anchor STL. B) TDP fabrication. C) TDP is placed in casing mold to trim ends and maintain orthogonality. D) Casing is placed in cube shaped relief of the cerebral anchor mold.

HA-04. From Regeneration to Modulation: Translational Case Studies in Magnetoelectric Neurointerfaces

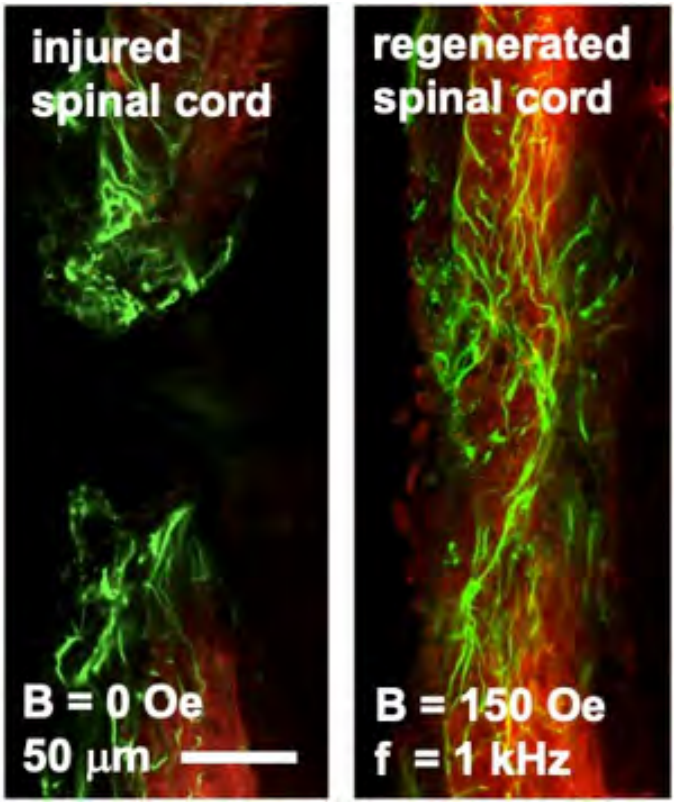
E. Zhang[2], H. Ye[2], N. Cancino[1], A. Suarez[1], A. Vezzoni[2], V. Pustovalov[2], M. Sanchez[1], B. Nelson[2], S. Pané[2]
[1]IDIBAPS, Barcelona, Spain, [2]ETH Zurich, Zurich, Switzerland

Magnetoelectric nanoparticles (MENPs) are emerging as wireless bioelectrical interfaces that convert remotely applied magnetic fields into localized electrical stimuli within tissue. As these materials have decreased in size and improved in functional performance, they have moved from concept-stage neuromodulation tools[1] toward translational biointerfaces[2,3] for neural repair[4] and control[5]. Here, we highlight two in vivo case studies from our group demonstrating this progression.

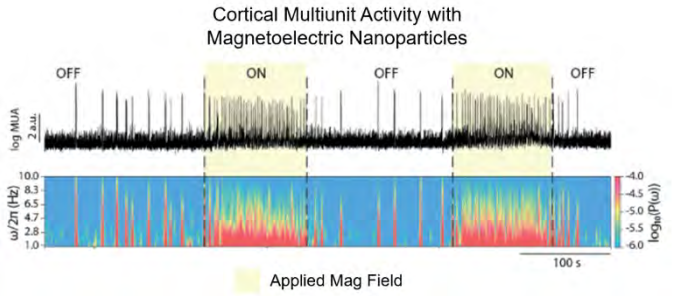
In spinal cord injury models in mice and zebrafish, we incorporated MENPs with neural progenitor cells into magnetically guidable biohybrid microrobots. Using distinct magnetic actuation regimes, we navigated the microrobots against blood flow to the injury site, where a secondary field was applied to drive in situ neuronal differentiation of the progenitor cells, restoring spinal cord integrity and returning motor function to the animals.

In cortical tissue, MENPs deposited in combination with surface recording electrodes enabled closed-loop upregulation and downregulation of brain activity in vivo in rats and in ferret ex vivo preparations, demonstrating dynamic, bidirectional control over distributed brain states. Taken together, these studies position magnetoelectrics as a promising translational platform for wireless neural modulation, regenerative intervention, and future clinical bioelectronic medicine.

1. Zhang, E. *et al.* Magnetic-field-synchronized wireless modulation of neural activity by magnetoelectric nanoparticles. *Brain Stimulation* 15, 1451–1462 (2022).
2. Kozielski, K. L. *et al.* Nonresonant powering of injectable nanoelectrodes enables wireless deep brain stimulation in freely moving mice. *Sci. Adv.* 7, eabc4189 (2021).
3. Kim, Y. J. *et al.* Magnetoelectric nanodiscs enable wireless transgene-free neuromodulation. *Nat. Nanotechnol.* 20, 121–131 (2025).
4. Ye, H. *et al.* Magnetoelectric Microrobots for Spinal Cord Injury Regeneration. *bioRxiv* 2024.08. 06.606378 (2024) doi:10.1101/2024.08.06.606378.
5. Landers, F. C. *et al.* Clinically ready magnetic microrobots for targeted therapies. *Science* 390, 710–715 (2025).



Immunohistochemistry images demonstrating co-labeling of neurites (anti-acetylated tubulin, red) and the glial fibrillary acidic protein (GFAP, green) at the site of injury. Magnetoelectric nanoparticle assisted neural progenitor differentiation lead to the closure of the spinal cord lesion and recovery of motor function.



Ferret cortical multi-unit activity during magnetoelctric neuromodulation. Stimulation with magnetic field and magnetoelectrics produces notable increase in coordinated up-state firing timed to the on-set of magnetic field.

HA-05. Site- and age- dependent variability in TMS-induced cortical E-fields Across Four Clinical Targets: A 40-Subject FEM Study with Cross-Platform Comparison

S. S. Achanta[1], S. A. Neeha[2], R. L. Hadimani[1]
[1]Mechanical and Nuclear Engineering, Virginia Commonwealth University, Richmond, Virginia, United States, [2]Biomedical Engineering, Virginia Commonwealth University, Richmond, Virginia, United States

Transcranial magnetic stimulation (TMS) outcomes remain variable across patients. Finite-element-method (FEM) modeling of induced electric fields enables mechanistic dose control [1]. Age-dependent variability has been shown for transcranial electric stimulation [2], but its TMS analogue, and its interaction with target geometry, is incompletely characterized.

Individualized head models with nine tissue classes were built via SimNIBS CHARM [1] from paired T1w/T2w MRI for 40 subjects, balanced 10/10/10/10 across young-male, young-female, aging-male, aging-female groups. A MagStim 70mm figure-of-eight coil was placed 4 mm above the scalp at four clinically motivated targets: M1 (motor), DLPFC (depression), SMA (OCD), and bilaterally averaged PPC (memory). Stimulator output was normalized at dI/dt=1 A/μs; all reported E-fields are normalized (V/m per A/μs). We computed peak E (99.9th percentile of |E| in gray matter) and V50 (GM volume with |E| ≥ 50% of peak; lower = more focal). Extension to Sim4Life and Ansys Maxwell is underway for cross-platform validation.

Peak E varied systematically with target geometry (M1 1.55 > DLPFC 1.45 > PPC 1.25 > SMA 1.14 V/m per A/μs), consistent with the depth–focality tradeoff for figure-of-eight coils [3]. SMA was a striking focality outlier (V50 ≈ 19.0 cm^3 vs 10.7–12.4 cm^3 at lateral sites; paired t, all $p<10^{-12}$), reflecting its midline sulcal geometry and bilateral current spread. Age effects dissociated across metrics: young subjects exhibited substantially larger V50 than aging subjects at all non-midline targets (M1, DLPFC, PPC; all $p<0.01$; Cohen's $d=-1.51$ averaged across sites), while peak-E differences were smaller and site-dependent. Volumetric contraction in aging brains is consistent with CSF expansion shunting current, paralleling tES findings [2].

These results identify target geometry and age-related anatomy as distinct, focality-dominant sources of TMS dose variability, indicating that fixed-intensity protocols deliver systematically different cortical doses across sites and ages.

[1] O. Puonti, K. Van Leemput and G. B. Saturnino, NeuroImage., Vol. 219, p.117044 (2020)
[2] D. Antonenko, U. Grittner and G. Saturnino, NeuroImage., Vol. 224, p.117413 (2021)
[3] Z.-D. Deng, S. H. Lisanby and A. V. Peterchev, Brain Stimul., Vol. 6, p.1 (2013)

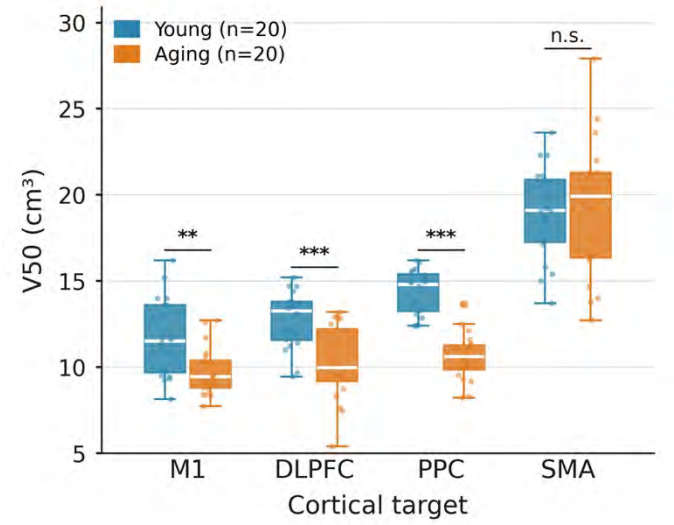


Fig. 1. V50 focality at four cortical targets, by age group. SMA is a midline-driven volumetric outlier; young > aging at all non-midline targets (**p

HA-06. TMS PHANTOMS FOR INVESTIGATING MULTIMODAL NEUROMODULATION PROCEDURES

W. Lohr[2], R. L. Hadimani[1]
[1]Mechanical Engineering, Virginia Commonwealth University, Richmond, Virginia, United States, [2]Biomedical Engineering, Virginia Commonwealth University, Richmond, Virginia, United States

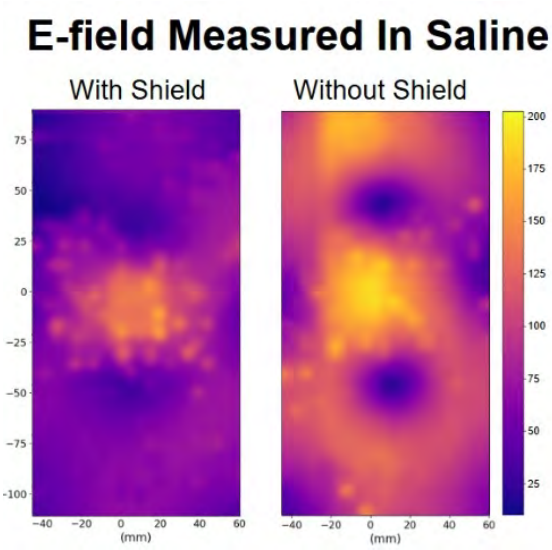
Transcranial magnetic stimulation (TMS) in patients with implanted deep brain stimulation (DBS) systems presents safety challenges due to unintended current induction in conductive leads. This work introduces a magnetic shielding strategy designed to mitigate induced currents while preserving stimulation focality. A high-permeability composite composed of permalloy particles embedded in PDMS was developed and integrated with conductive aluminum layers to enable combined magnetic flux redirection and eddy current attenuation.
A modular shielding system incorporating geometric apertures was designed to control magnetic flux pathways. Simulation studies demonstrated that aperture geometry strongly influences electric field distribution, with smooth,

continuous boundaries improving focality and inner diameter governing peak field magnitude. Experimental validation was performed using a motion-controlled TMS setup, comparing field distributions with and without shielding. Quantitative analysis using Cohen's d demonstrated substantial attenuation, with up to 89% attenuation when conductive layers were incorporated. In anatomical phantoms, the shield reduced peak electric field at the cortical surface by over 50%, decreased the stimulated area above half-maximum, and significantly reduced induced currents in DBS leads, with mean current attenuation exceeding 39%. Notably, focality improved by over 80%, indicating enhanced spatial targeting. These results demonstrate that hybrid magnetic-conductive shielding can effectively reduce unintended coupling while improving stimulation precision. This approach provides a viable pathway toward safer TMS application in patients with implanted neurostimulation devices.

	Without shield	With shield
E max at M1 (V/m)	149.08	81.46
Area above half max (mm^2)	12,450	1,950
Max Current in DBS lead (mA)	6.134	1.741
Mean current in DBS lead (mA)	0.2257	0.0895

p value	3.37E-158
Emax atenuation	54.60%
max current attenuation	28%
mean current attenuation	39.60%
Focality Improvement	84.30%

Statistics showing induced current from TMS in DBS lead is reduced, and focality of Efield is improved



Heatmap of electric field measured in saline, representing a significant increase in focality that decreases Efield magnitude at periphery aiding in protection of DBS implants

HA-07. Effects of repetitive transcranial magnetic stimulation guided by individual alpha frequency versus a 10-Hz control frequency on cortical excitability

H. Lin[1, 2], C. Lee[2, 3], L. Ye[2, 3], S. Chen[4], P. Chiu[5], C. Huang[6], C. Hsieh[7], H. Chen[8], T. Wu[2, 3]

[1]Department of Neurosurgery, Show Chwan Memorial Hospital, Changhua, Taiwan, [2]Graduate School of Materials Science, National Yunlin University of Science and Technology, Douliu, Yunlin, Taiwan, [3]Taiwan SPIN Research Center, National Yunlin University of Science and Technology, Douliu, Yunlin, Taiwan, [4]Department of Mechanical and Mechatronic Engineering, National Taiwan Ocean University, New Taipei City, Taiwan, [5]Department of Neurology, Show Chwan Memorial Hospital, Changhua, Taiwan, [6]Biomechanics Lab., Department of Medical Research, MacKay Memorial Hospital, Taipei, Taiwan, [7]Department of Neurology, Yumin Medical Cooperation, Yumin Hospital, Nantou, Taiwan, [8]Department of Physical Medicine and Rehabilitation, National Taiwan University Hospital Yunlin Branch, Douliu, Yunlin, Taiwan

Individual alpha frequency (IAF) has emerged as a biomarker of neurophysiological functioning. IAF-guided repetitive transcranial magnetic stimulation (rTMS) is increasingly being evaluated for the treatment of neurological conditions. The present study investigated the effects of IAF-guided rTMS on cortical excitability, measured as motor evoked potentials (MEPs), in healthy individuals.

This study included 28 individuals (mean age: 46.6±12.7 years). Each participant received rTMS at 10 Hz (control) and the IAF. Concurrently, MEPs were recorded. MEP amplitudes and power were significantly higher in the IAF group than in the control (both p<0.001). Time-matched MEP amplitudes and power in the IAF group were positively correlated with those in the control group (Pearson correlation coefficients: 0.68 and 0.54, respectively).

IAF-guided rTMS induces higher cortical excitability than dose traditional 10-Hz rTMS. Cortical responses to rTMS may be regulated by intrinsic brain rhythm. IAF-guided rTMS induces higher excitability of motor cortex and its clinical use should be considered.

[1]Ahmed MA, Darwish ES, Khedr EM, El Serogy YM, Ali AM. Effects of low versus high frequencies of repetitive transcranial magnetic stimulation on cognitive function and cortical excitability in Alzheimer's dementia. J Neurol. 2012;259:83-92.

[2]Bhattacharya A, Mrudula K, Sreepada SS, Sathyaprabha TN, Pal PK, Chen R, et al. An Overview of Noninvasive Brain Stimulation: Basic Principles and Clinical Applications. Can J Neurol Sci. 2022;49:479-92.

[3]Cannard C, Wahbeh H, Delorme A. Electroencephalography Correlates of Well-Being Using a Low-Cost Wearable System. Front Hum Neurosci. 2021;15:745135.

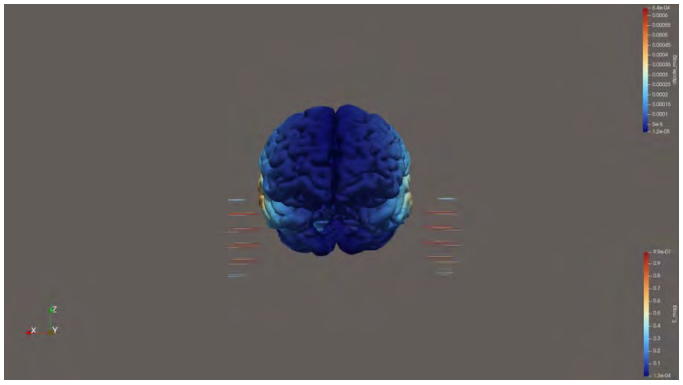
HA-08. A Space-Time Parallel Algorithm for the Electric Field Simulation of Temporal Interference Transcranial Magnetic Stimulation

Y. Zhang[1], X. Yang[2]
[1]Shenzhen Institutes of Advanced Technology, Chinese Academy of Sciences, Shenzhen, China, [2]Hebei University of Technology, Tianjin, China

Temporal interference transcranial magnetic stimulation (TI-TMS) involves the superposition of multiple high-frequency magnetic fields to generate a low-frequency envelope field in deep brain regions. Accurate simulation of the induced electric field is challenging due to the multiscale nature in both time and space, as well as the high computational cost associated with resolving transient electromagnetic fields in realistic head models. Conventional approaches either rely on quasi-static superposition in the frequency domain or full time-stepping finite element analysis, both of which suffer from limitations in accuracy or efficiency.

In this work, a time-domain and region-decomposition parallel solution framework is proposed for efficient and accurate TI-TMS field computation. The method decomposes the computational domain into multiple subregions based on tissue heterogeneity and field intensity distribution, enabling localized refinement and parallel processing. In the time domain, the excitation currents of multiple coils are explicitly modeled, allowing direct reconstruction of the temporal evolution of the electric field without relying on envelope approximations. A coupling strategy between subregions is developed to ensure continuity of electromagnetic quantities across interfaces while minimizing communication overhead in parallel implementation.

To further improve efficiency, a hybrid scheme is introduced in which slowly varying regions are solved with larger time steps, while regions with strong field gradients adopt adaptive fine time stepping. The proposed approach is implemented using a parallel finite element framework and validated against benchmark models. Results demonstrate that the method would achieve significant speedup compared to conventional full-domain transient simulations, while maintaining high accuracy in predicting both primary and secondary electric fields. In particular, the approach captures phase differences and vectorial interactions between fields from different coils, which are critical for precise TI-TMS modulation analysis.



Electric Field Distribution in Cerebral Gray Matter at Zero Second under TI-TMS Stimulation

HA-09. Microwave Guide of Nitrogen-Vacancy Center in Diamond Quantum Magnetometer for Magnetoencephalography

T. Zhu, M. Sekino
The University of Tokyo, Tokyo, Japan

Nitrogen-vacancy (NV) center in diamond quantum magnetometer (DQM) exhibits high magnetic sensitivity and a small stand-off distance at room temperature and offers a wide dynamic range, relaxing the requirements for magnetic shielding for biomagnetic signal measurements [1]. These advantages make DQMs promising candidates for next-generation magnetencephalography (MEG) systems. However, efficient and uniform microwave (MW) delivery remains a key challenge, particularly for continuous-wave optically detected magnetic resonance (CW-ODMR), while MW radiation can also cause undesired electromagnetic exposure in biological tissue, leading to local heating and increased specific absorption rate (SAR) [2].

In this work, a simulation study for the MW guide designed for DQM-based MEG in COMSOL Multiphysics was presented. The MW guide is simulated to operate near the zero-field splitting frequency (~2.87 GHz). The field distribution near the diamond region was investigated for the power and spatial uniformity. In addition, a five-layer head slab model is implemented to assess the electromagnetic field and SAR distribution in tissue. Fig. 1

shows the DQM setup and the MW guide used to measure MEG signals close to the scalp. The electric field distribution shown in Fig. 2 can be used to further calculate the local SAR, yielding a maximum of approximately 0.208 mW/kg. This value is which is significantly below the safety limit suggested in the International Commission on Non-Ionising Radiation Protection (ICNIRP) guideline (10 W/kg) [3]. These results demonstrate that the proposed design provides adequate MW performance while maintaining low tissue exposure.

To the best of our knowledge, no DQM system has yet successfully demonstrated MEG measurements in human subjects, and the MW safety under such conditions has not been systematically studied. This work presents the first investigation of MW safety for DQM-based MEG using a human model and provides a reference for future applications of DQM in human measurements. This work was supported by MEXT Q-LEAP Grant Number JPMXS0118067395.

[1] N. Sekiguchi, M. Fushimi, A. Yoshimura et al., Phys. Rev. Applied 21, 064010 (2024)
[2] D. Le Sage, L. M. Pham, N. Bar-Gill et al., Phys. Rev. B 85, 121202(R) (2012)
[3] International Commission on Non-Ionizing Radiation Protection (ICNIRP), Health Phys. 118(5): 483–524. (2020)

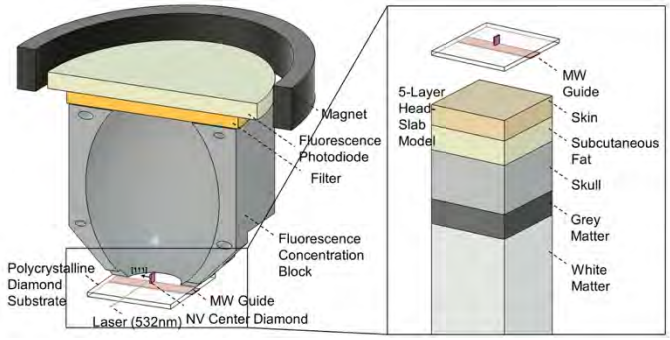


Fig. 1. DQM setup and the head-slab model for MW guide safety assessment

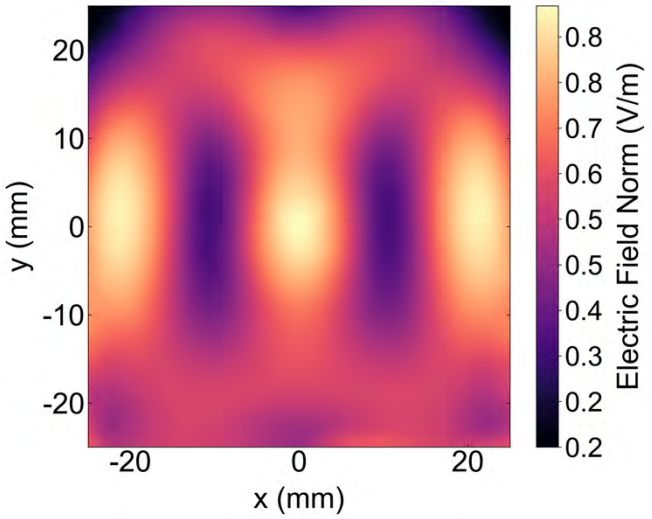


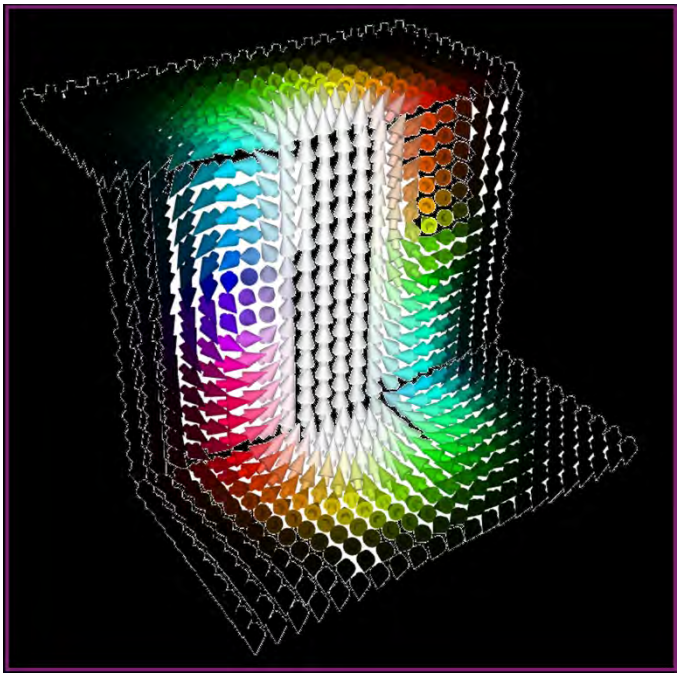
Fig. 2. The electrical field distribution in the head-slab model

SESSION HB: QUANTUM MAGNETISM IN NANOSTRUCTURES
Chair(s): Q. Zhang, *ORNL, Oak Ridge, Tennessee, United States*
Friday, November 6, 2026
02:00 PM-05:30 PM
Coral 5

HB-01. Lorentz Electron Ptychography
K. Nguyen[1], M. Hollis[1], E. Fullerton[2], S. Montoya[2]
[1]Physics, University of Oregon, Eugene, Oregon, United States, [2]Electrical Engineering, University of California, San Diego, San Diego, California, United States

Centrosymmetric skyrmions such as those form from sputtered multilayers of ferromagnet and heavy metal can have both Bloch and Néel domain walls along with two types of helicities, right and left. Indeed, their realization is predicted to be stabilized by interfacial Dzyaloshinkii-Moriya interaction (DMI) from local symmetry breaking and strong spin-orbit coupling, perpendicular magnetic anisotropy, dipole energy, exchange interactions, etc. FeGdPt multilayer thin film skyrmions can exhibit internal Bloch domains and Néel caps for the top and bottom in three-dimensions (3D). Visualizing their 3D structure experimentally would enable a deeper understanding of how these magnetic topological textures form and how their underlying magnetism differ from the conventional DMI-stabilized skyrmions that break inversion symmetry such as B20 FeGe. In our work, we use Lorentz electron ptychography, an iterative computational imaging technique

that recovers the phase of the exit wave function. Here, the phase of the exit wave has structural information encoded and would enable the visualization of this thin-film topological textures in 3D without complex tilts compared to electron tomography or vector holography. Finally, our approach can uncover whether adjacent skyrmions coalesce or pin within the film from their 3D realization.
[1] Montoya, S et al. Physical Review B 95, 024415 (2017).
[2] Hollis, M et al., Microscopy and Microanalysis 31, 7 (2025).



HB-02. Tunable and long-range entanglement of skyrmion qubits
D. R. Candido
University of Iowa, Iowa City, Iowa, United States

Recently, magnetic skyrmions were proposed as a novel qubit based on their well-defined helicity degree of freedom [1,2]. Yet, there are still open problems that need to be addressed to enable their widespread use, including the need for tunable entanglement schemes necessary for fault-tolerant error-correction algorithms. To overcome this, we propose using magnon modes [3,4] to mediate long-range coupling and entanglement between skyrmion qubits. We explore the conditions for realizing both transverse and longitudinal effective coupling between the qubits and discuss corresponding on-resonant and off-resonant entangling protocols for different temperatures and parameter regimes.
[1] C. Psaroudaki and C. Panagopoulos, Phys. Rev. Lett. 127, 067201 (2021).
[2] C. Psaroudaki and C. Panagopoulos, Phys. Rev. B 106, 104422 (2022).
[3] D. R. Candido, G. D. Fuchs, E. Johnston-Halperin, and M. E. Flatte, Mat. Quantum Technol. 1, 011001 (2021).
[4] M. Fukami, D. R. Candido, D. D. Awschalom, and M. E. Flatte, PRX Quantum 2, 040314 (2021).

HB-03. Macroscopic Quantum Tunneling of Magnetic Skyrmions
T. Yokouchi
RIKEN, Wako, Japan

Quantum mechanics typically describes the behaviour of microscopic objects such as electrons, photons, and spins. Remarkably, however, quantum behaviour can also emerge in macroscopic objects that consist of a vast number of microscopic degrees of freedom, notably contributing to the development of modern quantum computing technologies. Recent theoretical studies have proposed the possibility of macroscopic quantum phenomena of topological spin structures called skyrmions and their application as quantum bits[1]. However, macroscopic quantum phenomena involving skyrmions have not yet been experimentally observed, and even candidate conditions or materials required for their emergence have not been established.
In this presentation, we report the experimental observation of creation and annihilation of skyrmions via a quantum tunneling process in the prototypical skyrmion-host material MnSi. In MnSi, the application of hydrostatic pressure stabilizes an ensemble of randomly oriented skyrmion strings, known as the partial-order phase. We find that the transition rate associated with the creation and annihilation of skyrmion strings at the phase boundary of the partial-order phase changes from being temperature-dependent to temperature-independent with decreasing temperature. Systematic experiments and theoretical analysis indicate that the observed temperature-independent transition rate results from the creation and annihilation of skyrmion strings via a quantum tunneling process. Our discovery represents an important step toward constructing a novel platform for quantum devices.
1 Alexander P. Petrovic et al., Rev. Mod. Phys. 97, 031001 (2025).

HB-04. Effective Defect–Carrier Pair Modeling and Electrically Detected Magnetic Resonance of Silicon Vacancy Centers in 4H-SiC for Self-Calibrating Quantum Magnetometry

D. R. Hart
Mathematics and Physics, Southern University and A & M College, Baton Rouge, Louisiana, United States

We combine modeling and experiment to study continuous-wave electrically detected magnetic resonance (cw-EDMR) associated with negatively charged silicon vacancy centers in 4H-SiC diodes. The field-dependent current contrast is simulated using an effective defect–carrier pair model within a steady-state Liouville framework that includes Zeeman, hyperfine, zero-field splitting, dipolar, and exchange interactions, along with singlet-selective recombination and dissociation. Within this reduced phenomenological model, which treats the defect using an effective spin-1/2 representation rather than a full microscopic description of the complete silicon-vacancy spin manifold, the simulations reproduce the dominant resonance positions, current contrast, and overall lineshape observed experimentally in 4H-SiC pn junction devices. The model also predicts weaker spectral features arising from hyperfine-assisted singlet–triplet mixing and dipolar-mediated coupling, including off-resonant sidebands and low-field or half-field responses sensitive to transverse pair-dipolar interactions. Frequency-resolved and power-dependent simulations identify testable signatures for future multi-frequency EDMR measurements and clarify how radio-frequency drive conditions influence resonance amplitude and linewidth. Complementary low-field EDMR and near-zero-field magnetoresistance measurements reveal enhanced singlet–triplet transition rates near zero magnetic field, enabling absolute magnetometry without external calibration. By linking defect-level spin physics to macroscopic device performance, this work supports the development of scalable, radiation-tolerant SiC quantum magnetometers. An effective magnetic-field sensitivity of 13.2 nT/√Hz is demonstrated, highlighting the viability of SiC-based platforms for compact, robust, and self-calibrating space science sensors.

Kraus et al., *Nature Physics*, 2014 — room-temperature SiC spin defects.
Niethammer et al., *Physical Review Applied*, 2016 — SiC silicon-vacancy magnetometry.
Niethammer et al., *Nature Communications*, 2019 — electrical readout of SiC defect spins.
Harmon et al., *Physical Review B*, 2020 — Liouville/spin-dependent recombination theory for EDMR and NZFMR.
Lew et al., *Applied Physics Letters*, 2023 — electrically detected SiC spin-defect magnetometry.
Lew et al., *Physical Review Letters*, 2024 — all-electrical spin readout in SiC.
Gottscholl et al., *Scientific Reports*, 2024 — enhanced electrical readout of spin-dependent recombination in SiC.
Ivády et al., *Physical Review B*, 2017 — microscopic identification of Si-vacancy-related spin centers.

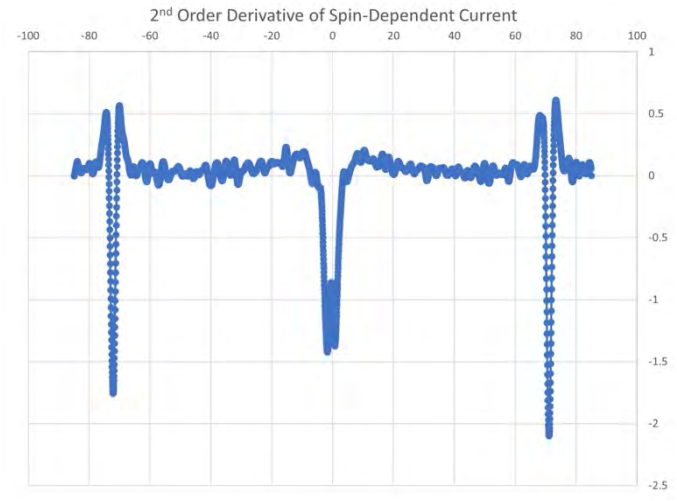


Fig 1. Second order derivative of PN junction spin current. The 2 resonances are at + and - 72 Gauss. . The inflection point at 0 magnetic field hold the quantum reference point for absolute zero magnetic field.

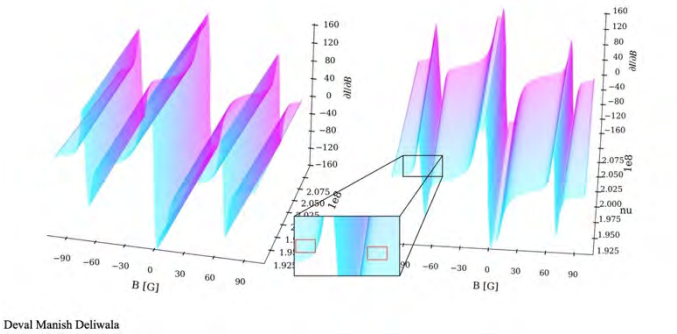


Fig 2. Unidentified transitions. These are transitions were identified as we take the limit of the modulation amplitude toward 0.

HB-05. High-Field EPR Investigation of Metal–Organic Frameworks for Quantum Spin Coherence and Structure–Relaxation Correlations

K. Thangavel
National High Magnetic Field Laboratory, Tallahassee, Florida, United States

Metal–organic frameworks (MOFs) have recently gained increasing attention as a new class of molecular magnetic materials for quantum technologies, following earlier advances in traditional molecular magnets as promising qubit platforms. Their chemically programmable architectures enable precise control over spin spacing, coordination environments, framework rigidity, and nuclear spin density—key factors governing spin–lattice relaxation time (T_1) and phase-memory time (T_m), which are essential parameters for scalable molecular qubits. Despite these advantages, MOF materials remain significantly underexplored using advanced high-field electron paramagnetic resonance techniques, particularly in the context of quantum information science [1-3].
In this project, we investigate Gd-MOFs as tunable platforms for quantum-relevant spin systems because the nearly isotropic spin nature of Gd(III) ions and their well-defined coordination environments make them attractive candidates for probing spin dynamics and coherence behavior. By systematically examining framework structure, linker rigidity, and spin dilution, we aim to establish structure–property relationships that maximize T_1 and T_m and provide design guidelines for MOF-based molecular qubits.
To achieve these goals, we will utilize high-frequency electron paramagnetic resonance (HFEPR) and high-power W-band pulsed electron paramagnetic resonance spectroscopy (HiPER) to probe spin Hamiltonian parameters, relaxation pathways, and inter-spin interactions with high precision. Access to the Electron Magnetic Resonance facility at the National High Magnetic Field Laboratory is therefore essential for enabling these advanced measurements and for establishing quantitative structure–relaxation correlations in MOF-based spin systems relevant to quantum information science.

1. Kobayashi, T.; Salfi, J.; Chua, C.; van der Heijden, J.; House, M. G.; Culcer, D.; Hutchison, W. D.; Johnson, B. C.; McCallum, J. C.; Riemann, H.; Abrosimov, N. V.; Becker, P.; Pohl, H.-J.; Simmons, M. Y.; Rogge, S., Engineering long spin coherence times of spin–orbit qubits in silicon. *Nature Materials* 2021, *20* (1), 38-42.
2. Morton, J. J. L.; Lovett, B. W., Hybrid Solid-State Qubits: The Powerful Role of Electron Spins. *Annual Review of Condensed Matter Physics* 2011, *2* (Volume 2, 2011), 189-212.
3. Atzori, M.; Sessoli, R., The Second Quantum Revolution: Role and Challenges of Molecular Chemistry. *Journal of the American Chemical Society* 2019, *141* (29), 11339-11352.

HB-06. Controlling and Sensing Spin Systems with Free Space Electrons

P. Haslinger[1, 2, 3]
[1]VCQ, Vienna, Austria, [2]USTEM - TU Wien, Wien, Wien, Austria, [3]Atominstitut - TU Wien, Wien, Austria

Coherent control and detection of quantum systems lie at the heart of quantum optics and quantum technologies. While optical and microwave control techniques are well established, the use of *free-space electron beams* as both manipulator and sensors opens an entirely new regime for spatial resolution and spectroscopic access.
In this talk, I will first outline intuitively our theoretical work [1] showing how the non-radiative near-fields of temporally modulated free-space electron beams can coherently drive quantum systems. I show that such manipulation can be performed with only classical control over the electron beam itself and that potential challenges like shot noise and decoherence through back action on the electrons are for certain parameter ranges insignificant for our approach. I will discuss possible implementations and show preliminary data on manipulating spin systems in a sample [2].
I will then present our recent experimental setup on SPINEM (Spin Electron Microscopy) [3], which integrates continuous-wave electron spin resonance (ESR) spectroscopy directly into a transmission electron microscope. By combining a custom microwave resonator with a free space electron beam [4], we achieve in-situ, phase-locked detection of microwave-driven spin precession with *picoradian* deflection sensitivity (~280 prad) and spatial mapping capabilities down to 30 µm. This approach directly senses the magnetic fields generated by precessing spins in the GHz regime, enabling localized spin spectroscopy in a TEM.
I will conclude with perspectives on pushing SPINEM towards atomic resolution and single-spin sensitivity [5]. These advances could open new frontiers in nanoscale spintronics, magnonics, and quantum materials research, and provide an electron-based analogue to magnetic resonance imaging at the level of individual nanostructures.

[1] D. Rätzel, D. Hartley, O. Schwartz, and P. Haslinger, *Controlling Quantum Systems with Modulated Electron Beams*, Phys. Rev. Res. 3, 023247 (2021)

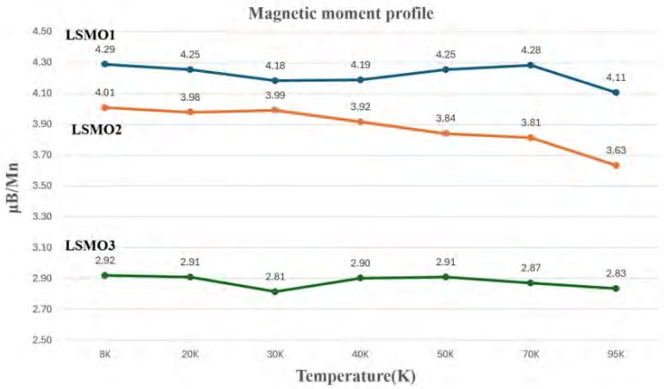
[2] M. Kolb, T. Spielauer, T. Weigner, G. Boero, D. Rätzel, P. Haslinger, *Coherent Driving of a Quantum System with Modulated Free-Space Electrons* arXiv:2509.13904
[3] A. Jaroš, J. Toyfl, A. Pupić, B. Czasch, G. Boero, I. Bicket, P. Haslinger *Electron spin resonance spectroscopy in a transmission electron microscope*, Ultramicroscopy, 278, 114224 (2025)
[4] A. Jaroš, M. Seifner, J. Toyfl, B. Czasch, S. Beltrán-Romero I. Bicket, P. Haslinger, *Sensing Spin Precession with Free Electrons*, ACS Nano 20, 4, 3435 (2026)
[5] P. Haslinger, S. Nimmrichter, D. Rätzel, *Spin Resonance Spectroscopy With an Electron Microscope*, QST, 9, 035051 (2024)

HB-07. Proximity Effect Induced Magnetization Enhancement in the LSMO/YBCO Superlattice System

H. Chou[1, 2], S. Sun[2, 1], Y. Tsai[1], H. Salazar[1], A. J. Grutter[3], D. Cortie[4]
[1]Physics, National Sun Yat-sen University, Kaohsiung City, Taiwan, Taiwan, [2]Applied Physics, National University of Kaohsiung, Kaohsiung City, Taiwan, Taiwan, [3]Center for Neutron Research, National Institute of Standards and Technology, Gaithersburg, Maryland, United States, [4]ANSTO, Lucas Heights, New South Wales, Australia

At ferromagnet/superconductor (FM/SC) interfaces, proximity effects strongly couple the electronic and magnetic degrees of freedom, giving rise to emergent interfacial phenomena such as spin-triplet superconductivity [1-5] and Majorana bound states. [6,7] In this work, $YBa_2Cu_3O_{7-\delta}$ (YBCO)/$(La_{2/3}Sr_{1/3})MnO_3$ (LSMO) superlattices were fabricated by pulsed laser deposition. The individual layer thicknesses were controlled in the range of 5–15 nm by adjusting the growth time.
The magnetic properties of the LSMO layers were systematically investigated as a function of temperature using SQUID magnetometry, X-ray absorption spectroscopy (XAS), X-ray magnetic circular dichroism (XMCD), and polarized neutron reflectometry (PNR). Below 84 K, the diamagnetic response of YBCO dominates the bulk magnetization signal. Previous transport measurements revealed an enhancement of the superconducting critical current under field-cooled conditions, with a pronounced peak at 6000 Oe and 40 K. [8]
XMCD measurements of Cu in total electron yield mode reveal three distinct orientations of the interfacial Cu magnetic moment relative to the external magnetic field (H_ext): antiparallel, perpendicular, and parallel configurations, depending on the field-cooling field. [9] Remarkably, when the system is field cooled at 6000 Oe—where the LSMO layers are fully polarized—the magnetization of the LSMO layers measured by PNR increases dramatically upon cooling from 95 K to 8 K, as shown in Figure 1. This enhancement exceeds that observed in a single LSMO film of comparable thickness, indicating that interfacial proximity effects between YBCO and LSMO induce additional magnetic reconstruction.
Furthermore, XMCD measurements of the top LSMO layer show negligible O-2p magnetic contribution, whereas the Mn-3d orbital moment exhibits a strong enhancement below the superconducting transition temperature, consistent with the PNR results. These findings suggest a superconductivity-induced modification of interfacial ferromagnetism in YBCO/LSMO superlattices, providing insight into emergent proximity-driven magnetic phenomena at oxide FM/SC interfaces.

[1] M. Eschrig, *Spin-polarized supercurrents for spintronics*, Phys. Today 64, 43-49 (2011).
[2] R. S. Keizer, S. T. B. Gönnenwein, T. M. Klapwijk, G. Miao, G. Xiao and A. Gupta A, *spin-triplet supercurrent through the half-metallic ferromagnet CrO_2*, Nature 439, 825-827 (2006).
[3] J. W. A. Robinson, J. D. S. Witt and M. G. Blamire, *Controlled injection of spin-triplet supercurrents into a strong ferromagnet*, Science 329, 59-61 (2010).
[4] D. Sanchez-Manzano, S. Mesoraca, F. A. Cuellar, M. Cabero, V. Rouco and G. Orfila et al., *Extremely long-range, high-temperature Josephson coupling across a half-metallic ferromagnet*, Nat. Mater. 21, 188–194 (2022).
[5] A. Di Bernardo *et al.*, *Intrinsic Paramagnetic Meissner Effect Due to s-Wave Odd-Frequency Superconductivity*, Phys. Rev. X 5, 041021 (2015)
[6] J. Linder and J. W. A. Robinson, *Superconducting spintronics. Nat. Phys.* 11, 307–315 (2015).
[7] D. A. Ivanov, *Non-abelian statistics of half-quantum vortices in p-wave superconductors*, Phys. Rev. Lett. 86, 268 (2001).
[8] S. M. Kumawat, G. D. Dwivedi, P. F. Su, W. S. Shyu, Y. H. Chien, P. W. Su et al., *Magnetic field enhancement in critical current and possible triplet superconductivity in LSMO/YBCO/LSMO heterostructures*, J. Phys. Chem. C 127, 6861-6872 (2023).
[9] H. Chou, S. J. Sun, K. S. Yang, G. D. Dwivedi, C. H. Chen, S. L. Cheng et al., *Controllable spin-triplet superconductivity states and enhanced non-dissipation spin-polarized supercurrents in $YBa_2Cu_3O_7/La_{0.67}Sr_{0.33}MnO_3$ Interfaces*, Appl. Surf. Sci. 644, 158739 (2024).



The mSLD of LSMO layers in a LSMO3/YBCO/LSMO2/YBCO/LSMO1/STO system

HB-08. Large Nonreciprocal Current Induced by Helical Spin States

H. Ishizuka
Physics, Institute of Science Tokyo, Meguro, Tokyo, Japan

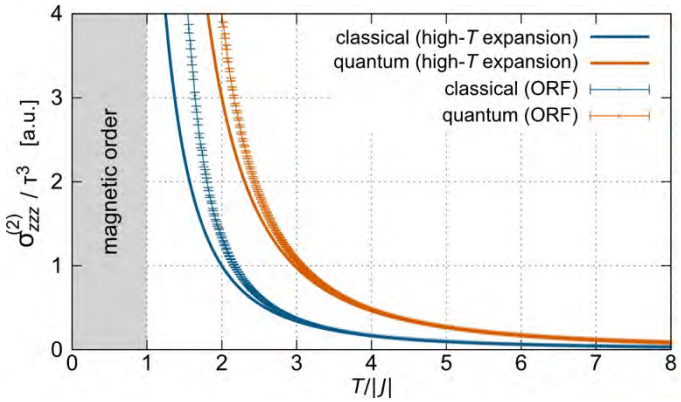
Chiral spin textures have attracted broad interest for their connection to a wide range of material properties, from transport phenomena to multiferroicity. A representative example in transport is the topological Hall effect—an anomalous Hall response (AHE) arising from the scalar spin chirality rather than from a net magnetization. This effect enables electrical detection of chiral and topological magnetic states and provides a route to realizing a large AHE. Beyond linear Hall responses, recent studies have shown that nonlinear transport, such as the nonreciprocal current, is sensitive to helical magnetic states, expanding the toolbox for electrical detection of complex magnetism and opening new avenues for spintronic applications [1-3]. In contrast to the Hall effect, however, the typically small signal of the nonlinear response presents a challenge for practical use.

In this work, we present systematic theoretical studies of the nonreciprocal current induced by helical spin states, focusing on mechanisms that enhance the response. We first address the role of quantum spin fluctuations in the AHE and the nonreciprocal current in the paramagnetic regime. We show that the coexistence of quantum spin fluctuations and vector spin chirality gives rise to a logarithmic temperature enhancement of the electrical magnetochiral effect (eMChE) through a mechanism analogous to the Kondo effect (Fig. 1) [4]. The resulting quantum correction becomes comparable to the classical contribution near the Kondo temperature, highlighting the significant role of quantum fluctuations.

We next turn to the low-temperature limit, where long-range helical magnetic order develops. Near the magnetic transition, the nonreciprocal current is enhanced by orders of magnitude when the Fermi wave vector matches the helical pitch [5]. Such a band-matching condition arises naturally in metallic magnets whose magnetic order is driven by the RKKY interaction.

These results reveal the substantial impact of quantum fluctuations and band reconstruction on chirality-related transport phenomena, providing guidelines for designing magnetic materials with strongly enhanced nonreciprocal response.

[1] T. Yokouchi et al., Nat. Commun. 8, 866 (2017).
[2] R. Aoki et al., Phys. Rev. Lett. 122, 057206 (2019).
[3] H. Ishizuka and N. Nagaosa, Nat. Commun. 11, 2986 (2020).
[4] H. Murata and H. Ishizuka, arXiv:2512.21575 (2025).
[5] H. Murata and H. Ishizuka, in preparation.



Enhanced nonreciprocal response by quantum spin fluctuations.

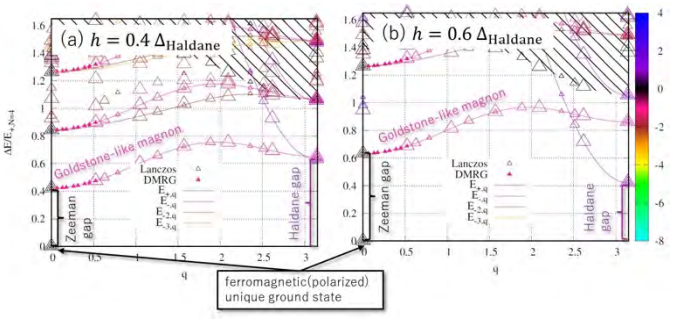
HB-09. Measurement-based Quantum Computing and Quantum Many-body Scars in Quantum Ferromagnets

I. Maruyama[1], S. Miyahara[2]
[1]Department of Information and Systems Engineering, Fukuoka Institute of Technology, Fukuoka, Japan, [2]Department of Applied Physics, Fukuoka University, Fukuoka, Japan

Measurement-based Quantum computing (MBQC) is based on entangled states such as the Affleck-Kennedy-Lieb-Tasaki(AKLT) state [1]. While the original AKLT model [2] is known for its antiferromagnetic and exactly-written ground state under the Haldane gap, it is revealed that some

excited states are also exactly-written, which identified as quantum many-body scars (QMBS) [3]. Recently, the ferromagnetic AKLT ground states as a generalization of the AKLT state have been studied in the context of quantum ferromagnets[4,5]. In this study[6], we investigate the ferromagnetic AKLT chain which is SU(2) symmetric. We demonstrate that its ground states exhibit unique total (macroscopic) spin even in the absence of an external magnetic field, as an important feature of ferromagnets. As for the lowest excitations, we find a coexistence of both a Haldane-type gap (antiferromagnetic character) and a Goldstone-like gapless magnon branch (ferromagnetic character). As shown in the figure, a finite magnetic field stabilizes ferromagnetically AKLT state as a unique ground state with the Zeeman splitting gap and the Haldane gap, suggesting its potential utility for MBQC. Finally, we identify exactly-written excited states in our model, which can be interpreted as a generalizations of QMBS[7].

[1] G. K. Brennen and A. Miyake, Phys. Rev. Lett., Vol. 101, p. 010502 (2008)
[2] I. Affleck, et. al., Phys. Rev. Lett., Vol. 50, p. 1153 (1983)
[3] S. Moudgalya, et. al., Rep. Prog. Phys., Vol. 85, p. 086501 (2022)
[4] I. Maruyama and S. Miyahara, Phys. Rev. B, Vol. 108, p. L140404 (2023)
[5] S. Miyahara and I. Maruyama, Phys. Rev. B, Vol. 110, p. 014433 (2024)
[6] I. Maruyama and S. Miyahara, J. Phys. Soc. Japan, Vol. 95, p. 034704 (2026)
[7] I. Maruyama and S. Miyahara, in preparation



Excitation energy as a function of wave number q for spin S=3 ferromagnetic AKLT chain[6] under a magnetic field h with (a) h=0.4 Delta and (b) h=0.6 Delta, where Delta is the Haldane gap, depicted with total-spin shift from -8 to 4 in the color scale. The total-spin of the ferromagnetic unique ground state in N-site chain is 2 N while that of fully-polalized state is 3 N. The excited states above the Haldane gap has the total-spin shift +1 and will be stabilized with increasing magnetic field. Larger point of open triangles indicates larger system size in 8, 10, and 12 calculated with using the Lanczos method. The small filled triangles are calculated with using the density renormalization group method (DMRG). The solid lined are fitted curves. For further details, see Ref.[6].

SESSION HC: MAGNETOELECTRONIC MATERIALS AND HETEROSTRUCTURES

Chair(s): P. Finkel, *Materials Science Division, Naval Research Laboratory, Washington, District of Columbia, United States*
Friday, November 6, 2026
02:00 PM-05:30 PM
Coral 1

HC-01. Autferroicity: physics & materials

S. Dong, Z. Wang, J. Zhang
School of Physics, Southeast University, Nanjing, Jiangsu, China

Primary ferroicities like ferroelectricity and ferromagnetism are essential physical properties of matter. Multiferroics, with coexisting multiple ferroic orders in a single phase, provide a convenient route to magnetoelectricity. Even so, the general trade off between magnetism and polarity remains inevitable, which prevents practicable magnetoelectric cross-control in the multiferroic framework. In this talk, I will introduce an alternative strategy, i.e., the so-called autferroicity (originally named alterferroicity), to circumvent the magnetoelectric exclusiveness, which exhibits multiple but noncoexisting ferroic orders. The natural exclusion between magnetism and polarity, as an insurmountable weakness of multiferroicity, becomes a distinct advantage in autferroicity, making it an inborn rich ore for intrinsic strong magnetoelectricity. The general design rules for autferroic materials rely on the competition between the instabilities of phononic and electronic structures in covalent systems. Based on primarydensity functional theory calculations, Ti-based trichalcogenides are predicted to be autferroic candidates, which exhibit unique seesaw-type magnetoelectricity. Furthermore, the autferroicity and multiferroicity, can be uniformed within the framework of Laudau theory.

[1] Z.W. Wang, S. Dong. PNAS 120, e2305197120 (2023)
[2] J.J. Zhang, B. Yakobson, S. Dong. Phys. Rev. Lett. 134, 216801 (2025)
[3] J.J. Zhang, Z.W. Wang, S. Dong. Sci. Chin. Mater. DOI:10.1007/s40843-025-3597-2 (2026)

HC-02. Exchange Bias and Magnetoionic Switching in Electrolyte-Gated $LaCoO_3/SrCoO_{3-\delta}$ Bilayers

H. Son, J. Liang, N. Nandakumaran, C. Leighton
Chemical Engineering and Materials Science, University of Minnesota Twin Cities, Minneapolis, Minnesota, United States

Voltage control of magnetism by ionic motion (magnetoionics) offers an energy-efficient route to novel spintronic, neuromorphic, and other forms of devices. Electrolyte gating (Fig. 1) is an attractive approach to magnetoionics, using strong interfacial electric fields in an electric double layer to drive reversible ion migration [1]. Perovskite cobaltites such as $SrCoO_{3-\delta}$ are particularly appealing for such devices as they exhibit low oxygen vacancy formation energy, high oxygen vacancy diffusivity, and voltage-induced reversible topotactic phase transformations between ferromagnetic (FM) perovskite (P) $SrCoO_3$ and antiferromagnetic (AFM) brownmillerite (BM) $SrCoO_{2.5}$ [2,3]. Here, we study ion-gel-gated epitaxial $LSAT/LaCoO_3/SrCoO_{3-\delta}$ heterostructures (Fig. 1) in which tensile-strained $LaCoO_3$ (LCO) serves as an FM layer with $T_C \approx 80$ K [4] and $SrCoO_{3-\delta}$ (SCO) serves as a voltage-tunable layer that can be switched between FM and AFM (with Néel temperature above 300 K [3]), thus controlling exchange bias. In the as-deposited BM-SCO state, clear exchange bias (H_E) of the LCO is observed, which has been studied vs. temperature, cooling field, and both LCO and SCO thickness. A blocking temperature near the LCO Curie temperature is observed, with H_E reaching up to ~600 Oe at 5 K in optimized LCO(10 u.c.)/SCO(35 u.c.) bilayers. 300-K source-drain current vs. gate voltage measurements (Fig. 2) reveal clear, hysteretic BM ↔ P cycling of the ion-gel-gated SCO, inducing resulting changes in magnetic properties that will be discussed in terms of a transition between F/AF exchange bias and F/F exchange spring configurations.

Work supported by NSF through the University of Minnesota MRSEC.

(1) C. Leighton, *Nat. Mater.* 18, 13 (2019)
(2) W. M. Postiglione *et al.*, *ACS Appl. Mater. Interf.* 16, 19184 (2024)
(3) W. M. Postiglione *et al.*, *APL Mater.* 12, 041123 (2024)
(4) V. Chaturvedi *et al.*, *Phys. Rev. Mater.* 4, 034403 (2020)

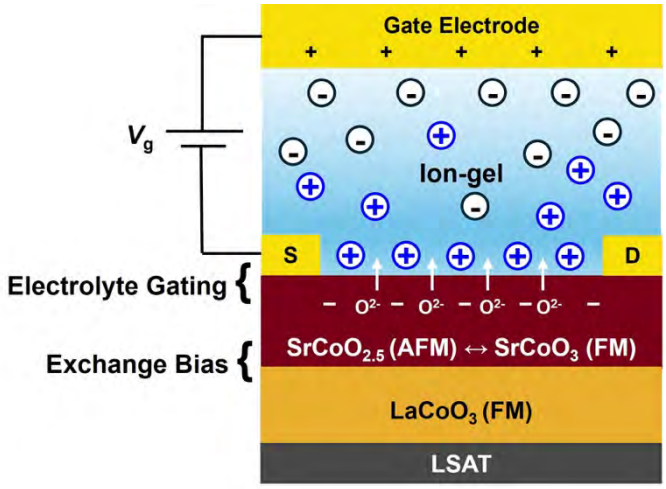


Fig. 1: Schematic of the electrolyte-gate LCO/SCO device.

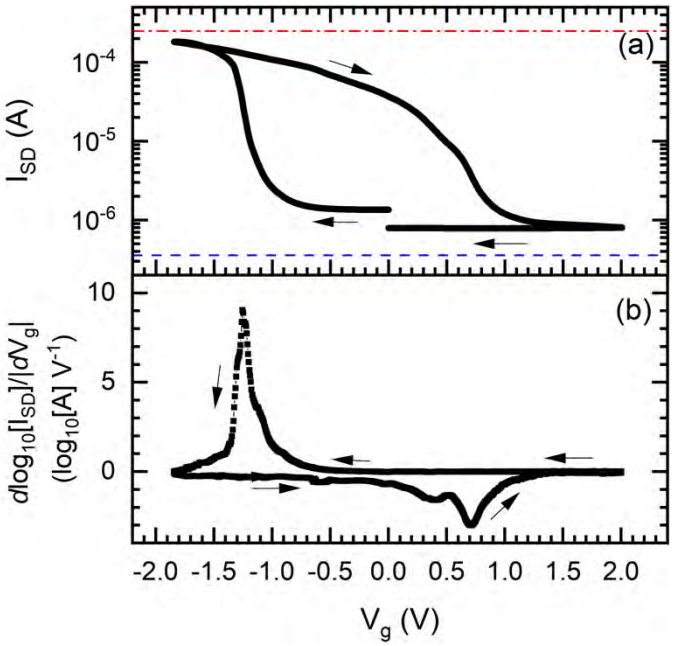


Fig. 2: Gate voltage (V_g) dependence of (a) the source-drain current I_{SD} and (b) $d\ln(I_{SD})/d|V_g|$, for a LCO(10 nm)/SCO(14 nm) film on LSAT(001). Arrows indicate the sweep direction. Red and blue dashed lines represent the calculated I_{SD} based on a parallel resistor model for LCO(10 nm)/P-SCO(14 nm) and LCO(10 nm)/BM-SCO(14 nm), respectively.

HC-04. Strain-mediated Electric-field Control of Perpendicular Magnetic Tunnel Junctions in Multiferroic Heterostructures

X. Li[1], Z. Qu[1], Z. Liu[2], B. Fang[2], Z. Zeng[2], Y. Zhao[1]
[1]Tsinghua University, Beijing, China, [2]Suzhou Institute of Nano-Tech and Nano-Bionics, Chinese Academy of Sciences, Suzhou, China

Magnetic random access memory (MRAM), with the magnetic tunnel junction (MTJ) as the core unit, is regarded as one of the most promising candidates for next-generation memory. Writing information via electric fields instead of charge currents can significantly reduce energy consumption. Multiferroic heterostructures, composed of ferroelectric and ferromagnetic materials, provide a low-energy and less destructive method for electric-field control of MTJs at room temperature[1-3]. So far, most research on the strain-mediated electric-field control of MTJs has concentrated on in-plane magnetic anisotropy MTJs (i-MTJs)[2,3]. By contrast, research on perpendicular magnetic anisotropy MTJs (p-MTJs), which better meet the requirements of high-density storage and have already been industrialized, remains highly desired.
To achieve this goal, we deposited MgO-based MTJ stacks on $Pb(Mg_{1/3}Nb_{2/3})_{0.7}Ti_{0.3}O_3$ (PMN-PT) ferroelectric single crystals. Under external electric fields, PMN-PT generates piezostrain due to the piezoelectric effect, and such strain is transferred to the ferromagnetic layer to change the magnetic anisotropy. Based on the strain-mediated mechanism, we have realized nonvolatile control of p-MTJs with easy-cone magnetic anisotropic free layers[4] and perpendicular magnetic anisotropic free layers[5] at room temperature under zero magnetic field. Although electric-field control of p-MTJs has been realized in our work, the feature size of the fabricated MTJs remains on the micrometer scale. Developing nanoscale MTJs is crucial not only for high-density memory applications, but also for the exploration of distinctive physical phenomena. Through the optimization of MTJ structures and fabrication processes, we have presently realized a giant non-volatile control of up to 160% between high- and low-resistance states in nanoscale p-MTJs[6] and analyzed its mechanism. This work represents a substantial progress over micrometer-scale MTJs, and will promote the development of ultralow energy consumption and high-density spintronic devices.

[1] Jia-Mian Hu, Zheng Li, Long-Qing Chen and Ce-Wen Nan, Nat. Commun. 2, 553 (2011)
[2] Peisen Li, Aitian Chen, Dalai Li, Yonggang Zhao, Sen Zhang, Lifeng Yang, Yan Liu, Meihong Zhu, Huiyun Zhang and Xiufeng Han, Adv. Mater. 26, 4320 (2014)
[3] Aitian Chen, Yan Wen, Bin Fang, Yuelei Zhao, Qiang Zhang, Yuansi Chang, Peisen Li, Hao Wu, Haoliang Huang, Yalin Lu, Zhongming Zeng, Jianwang Cai, Xiufeng Han, Tom Wu, Xi-Xiang Zhang and Yonggang Zhao, Nat. Commun. 10, 243 (2019)
[4] Weideng Sun, Yike Zhang, Kaihua Cao, Shiyang Lu, Ao Du, Haoliang Huang, Sen Zhang, Chaoqun Hu, Ce Feng, Wenhui Liang, Quan Liu, Shu Mi, Jianwang Cai, Yalin Lu, Weisheng Zhao and Yonggang Zhao, Sci. Adv. 10, eadj8379 (2024)
[5] Yike Zhang, Weideng Sun, Kaihua Cao, Xiao-Xue Yang, Yongqiang Yang, Shiyang Lu, Ao Du, Chaoqun Hu, Ce Feng, Yutong Wang, Jianwang Cai, Baoshan Cui, Hong-Guang Piao, Weisheng Zhao and Yonggang Zhao, Sci. Adv. 10, eadl4633 (2024)
6 Xiaoxu Li, Zhiyang Qu, Shiyang Lu, Zhenhao Liu, Daoqian Zhu, Bin Fang, Kaihua Cao, Zhongming Zeng, Weisheng Zhao and Yonggang Zhao, to be submitted

HC-05. Magnetoelectric coupling in LSMO/BTO/Co/Pt multiferroic junctions probed via TMR

J. Pawlak[1, 2], J. Kanak[2], W. Skowronski[2]
[1]Academic Centre for Materials and Nanotechnology, AGH University of Krakow, Krakow, Poland, [2]Institute of Electronics, AGH University of Krakow, Krakow, Poland

The integration of ferroelectric effects into spintronic systems is driven by the prospect of lowering the energy cost of information writing through voltage control, while simultaneously enabling faster switching of device states [1]. Previous work showed coupling of the ferroelectric and ferromagnetic state in the LSMO/BTO/Co structures manifested by the change in the tunneling magnetoresistance (TMR) ratio at low temperatures [2], while room-temperature operation was absent.
In this work, we present fully fabricated nanodevices, using four-step optical lithography process based on multiferroic heterostructure LSMO/BTO/Co/Pt. The structure consists of a ferromagnetic oxide bottom electrode ($La_{0.67}Sr_{0.33}MnO_3$), a ferroelectric $BaTiO_3$ tunnel barrier, and a Co/Pt ferromagnetic/heavy metal top electrode, all grown within a single fabrication process using pulsed laser deposition [3]. The obtained results demonstrate that TMR provides a sensitive probe of magnetoelectric effects in multiferroic systems. We observe TMR at room temperature in LSMO/BTO/Co/Pt junctions, which, has not been previously reported for this type of top electrode, in contrast to Fe-based counterparts [4]. At low temperature (19 K), TMR varies by an order of magnitude with applied bias. In the

low-bias range (−0.1 V to 0.1 V), the TMR changes nearly linearly with voltage, while at higher bias it approaches saturation. Additionally, after applying bias voltage on the order of a few volts, the junction shows a hysteretic TMR response as a function of bias voltage (Fig. 1). This behavior indicates a non-volatile voltage-induced modification of the spin polarization in the ferromagnetic electrodes. Importantly, all observed effects are stable and reproducible over multiple voltage cycles and across different devices and samples.

The Project is partially supported by the National Science Centre, Poland Project no.2021/40/Q/ST5/00209 (Sheng) and the Excellence initiative-research university (IDUB) programme of the AGH University of Krakow

[1] S. Manipatruni et al., Nature Physics 14 (2018) 338
[2] S. Valencia et al. Nature Materials 10 (2011) 753
[3] J. Pawlak et al., Advanced Electronic Materials 9 (2023) 2300122
[4] J. Pawlak et al., Advanced Electronic Materials 8 (2022) 2100574

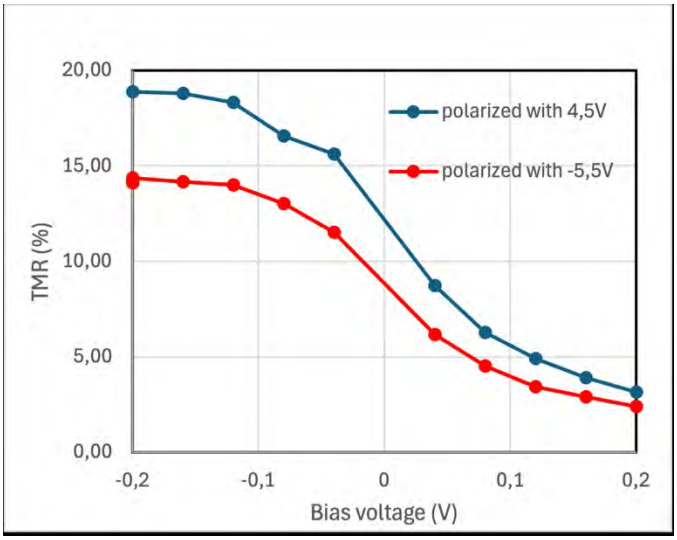


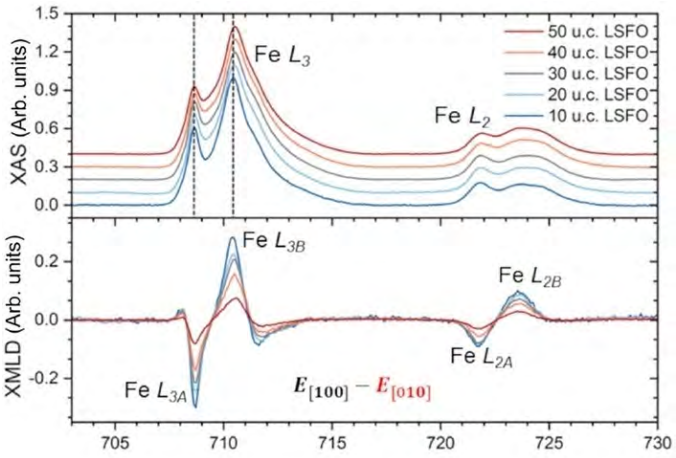
Fig. 1. Hysteresis of the TMR as a function of bias voltage after polarization of the LSMO/BTO/Co/Pt junction with 4,5V and -5,5V bias voltage, measured at 19 K.

HC-07. Manipulating Antiferromagnetic Spin Orientations in $La_{0.5}Sr_{0.5}FeO_3$ / $La_{0.7}Sr_{0.3}MnO_3$ Bilayers

Y. Takamura[1], I. Nihal[1, 2], M. Frame[1], C. Klewe[2]
[1]*Materials Science and Engineering, University of California, Davis, Davis, California, United States,* [2]*Advanced Light Source, Lawrence Berkeley National Laboratory, Berkeley, California, United States*

Antiferromagnetic (AFM) spintronics has gained significant interest for information technology applications due to its potential for lower power consumption, non-volatile memory, and faster data processing speeds compared to their ferromagnetic (FM) counterpart. However, significant challenges remain for manipulating and detecting the orientation of the AFM spins due to their net zero magnetization and strong coupling to the lattice structure. Due to the strong interactions between the charge, spin, lattice, and orbital degrees of freedom present at interfaces between perovskite oxide layers, the manipulation of AFM spin orientations can be realized in the AFM $La_{1-x}Sr_xFeO_3$ (LSFO)/ FM $La_{0.67}Sr_{0.33}MnO_3$ (LSMO) system. [1] We demonstrate that (001)-oriented LSFO/LSMO interfaces are characterized by spin-flop coupling where a perpendicular orientation of the LSFO and LSMO spins is observed and they can be reoriented within the plane of the interface with a modest applied magnetic field < 0.3 T. Detailed soft x-ray magnetic linear dichroism measurements, conducted with and without a magnetic field and with different measurement geometries, were used to examine the extent of the reorientation of the AFM spins and to determine how parameters such as Sr doping level (x), film thickness, and epitaxial strain state impact the strength of the spin-flop coupling. In particular, it was found that the critical LSFO thickness below which spin-flop coupling is preserved can be increased to ~ 60 u.c. in the $La_{0.50}Sr_{0.50}MnO_3$/LSMO system (see Figure 1). At larger LSFO thicknesses, a structural asymmetry develops due to strain relaxation leading to a preferred uniaxial magnetic anisotropy. This comprehensive understanding of the behavior of AFM moments in a spin-flop coupled system under the influence of a magnetic field is crucial for advancing the development of AFM spintronics.

[1] E. Arenholz, Y. Takamura *et al.*, *Appl. Phys. Lett.*, 94, 072503, (2009); Y. Takamura *et al., Phys. Rev. B*, **80**, 180417(R), (2009); I. Nihal, Y. Takamura *et al., Phys. Rev. B*, **110**, 014411 (2024); I. Nihal, Y. Takamura *et al., Phys. Rev. B,* **113,** 174407 (2026)



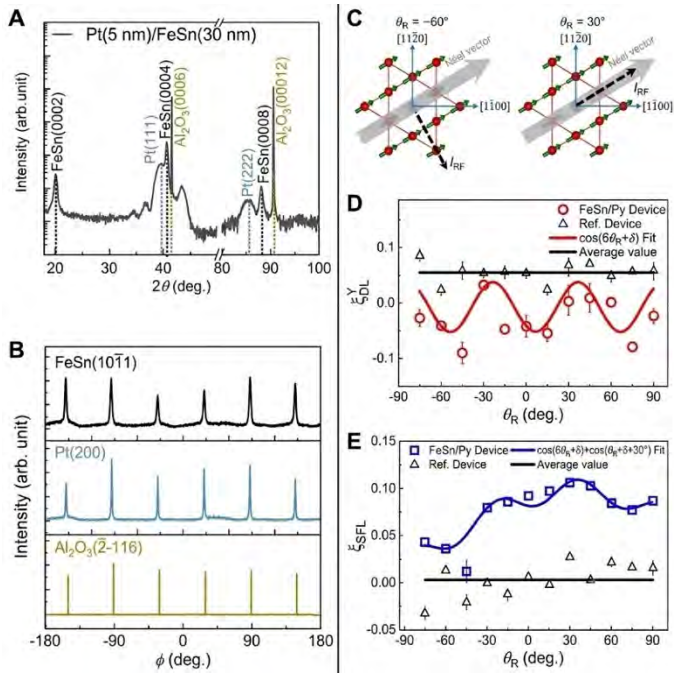
X-ray absorption spectroscopy (XAS) and x-ray magnetic linear dichroism (XMLD) spectra of LSFO/LSMO bilayers as a function of LSFO thickness.

HC-08. Crystalline and Magnetic Symmetry Driven Spin Current Anisotropy in a Collinear Antiferromagnet

P. K. Muduli
Department of Physics, Indian Institute of Technology, Delhi, New Delhi, Delhi, India

Spin-orbit torque (SOT) presents a promising method for energy-efficient spintronics devices, surpassing the limitations of spin-transfer torque. While SOT has been extensively studied in heavy metals, exploring emergent spin torque in antiferromagnetic materials provides a new approach to generate unconventional spin currents.
In this talk, I will present our recent investigation of spin-orbit torque in epitaxial thin films of FeSn, a collinear antiferromagnet hosting a Kagome lattice [1]. FeSn exhibits intriguing topological quantum features, including 2D flat bands and Dirac-like surface states, making it an ideal platform for exploring emergent SOT properties. Epitaxial thin films of FeSn were grown using co-sputtering and with Pt seed layer. Figure 1 (A) shows the XRD measurements performed in θ–2θ mode, confirming the epitaxial growth of the FeSn layer. The epitaxial relation between the FeSn layer, the seed layer, and the substrate was performed using ϕ–scans as shown in Fig. 1 (B) . Using spin-torque ferromagnetic resonance (ST-FMR) measurements, we uncover a pronounced six-fold symmetric damping-like SOT that directly reflects the underlying hexagonal symmetry of the [0001]-oriented FeSn films [Fig. 1 D]. Furthermore, we observe a substantial unconventional field-like torque originating from spin currents with out-of-plane spin polarization. This torque displays a distinctive angular dependence [Fig. 1 (E)] characterized by a superposition of six-fold crystalline symmetry and a uniaxial symmetry associated with the antiferromagnetic spin Hall effect, showing an enhancement when the charge current aligns with the Néel vector [Fig. 1 (C)].
Our density functional theory (DFT) and tight-binding calculations reveal a previously unreported nodal line along the A–L path near the Fermi level. This feature generates a massive Berry curvature, providing a microscopic origin of the six-fold conventional damping-like torque. Our results demonstrate that spin-current anisotropy can be engineered via crystalline and magnetic symmetries in collinear antiferromagnets, offering an exciting pathway toward all-electrical, field-free, deterministic switching for memory and neuromorphic applications.

[1] P. Gupta, K. I. A. Khan, A. Kumar, P. Sahu, R. Agarwal, A. Litvinenko, N. Kandwal, R. S. Yadav, B. R. K. Nanda, J. Åkerman, and *P K Muduli*, "Symmetry Enhanced Unconventional Spin Current Anisotropy in a Collinear Antiferromagnet," *Advanced Functional Materials*, 36, e06816 (2026).



(A) θ-2θ XRD scan and (B) ϕ-scan measurements for Pt(5 nm)/FeSn(30 nm) film on c-Al_2O_3 substrate. The top, middle, and bottom panels of (B) show the ϕ-scans for FeSn(10-10), Pt(200), and Al_2O_3(-2116) reflections, respectively. (C) Kagome structure with Néel vector (grey) and I_{RF} (black dashed) in parallel and perpendicular orientations. (D) DL SOT efficiency due to *y*–spin polarisation and (E) FL SOT efficiency due to *z*–spin polarisation for different values in the FeSn/Py device and Ref. device (without FeSn).

HC-09. Magnetism and Magnetostriction in $La_{1.5}Sr_{0.5}CoMnO_6$

M. Ramanathan, M. Marimuthu, L. Jiang
Physics, National University of Singapore, Singapore, Singapore

The ferromagnetic insulator La_2CoMnO_6 has generated attention in recent years due to observations magnetodielectric effect[1] and giant magnetostriction (λ_{par} ~ -500 to 610 ppm) [2,3] larger than exhibited by $La_{0.5}Sr_{0.5}CoO_3$ possessing mixed valent Co ions (Co^{3+}/Co^{4+})[4]. The giant magnetostriction in La_2CoMnO_6 was attributed to unquenched orbital moment associated with t_{2g} obitals of Co^{2+} (d^7: $t_{2g}^5e_g^2$) and strong spin-orbit coupling, while Mn^{4+} makes a negligible contribution[2,3]. To answer the question whether giant magnetostriction survives if Co^{2+} is partially converted to Co^{3+}, we partially substituted Sr^{2+} for La^{3+}. $La_{1.5}Sr_{0.5}CoMnO_6$ was synthesized using microwave (MW) irradiation as a heating source. Its magnetization (*M*) and magnetostriction λ_{par} parallel to the field direction were measured. *M*(*T, H = 1 kOe*) (see Fig. 1(a)) shows splitting between zero-field and field-cooled curves below the onset of magnetic order T_C = 178 K. As the magnetic field(H) at 10 K is swept from +50 kOe to -50 kOe, *M* undergoes a sudden decrease around the zero field followed a metamagnetic-like behaviour occurs around *H*= -20 kOe (Fig. 1(b)). A similar trend is observed as the field is swept in the reverse direction. λ_{par}(H) isotherm also shows a clear anomaly at the metamagnetic transition and its value (= -30 ppm at 50 kOe) is much smaller than the parent compound. At 100 K, λ_{par} undergoes a sign change from negative at low fields to positive at high fields and exhibits hysteresis over a wider field range whereas *M*(*H*) shows hysteresis only in low fields due to coercivity. We have also measured the magnetostriction transverse to the field direction and calculated the volume and the anisotropic magnetostriction as a function of temperature that will be discussed along with the nature of magnetism.

Acknowledgements: R. M acknowledges the Ministry of Education, Singapore, for supporting this work (Grant numbers: A-8000924-00-00 & A-8001933-00-00)

[1] M. P. Singh *et al*., Appl. Phys. Lett. 91, 042504 (2007); R. X. Silva *et al*., J. Appl. Phys. 117, 214105 (2015).
[2] M. Manikandan, A. Ghosh, and R. Mahendiran, App. Phys. Lett 123, 022403 (2023).
[3] M. Boldrin, A. Bagri, D. Barlettani *et al*., Phys. Rev. Mater. 9,094403 (2025).
[4] M. R.Ibarra, R Mahendiran, C. Marquina *et a*l., Phys. Rev. B. 57, R3217 (1998).

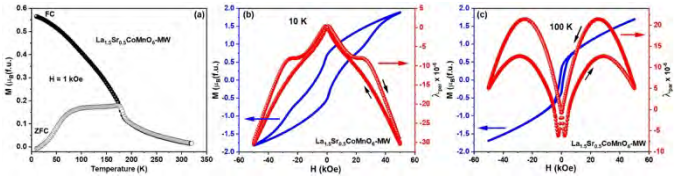


Fig. 1. (a) Temperature dependence of magnetization *M*(*T*) and magnetic field dependence of longitudinal magnetostriction (λ_{par}) on the right y-axis *M* on the left y-axis at 10 K (b) and 100 K (c).

HC-10. Laterally Differentiated Polymorphs: A Route to Magnetoelectric Garnets

P. E. Lauer[1], O. Wojewoda[1], K. Hayashi[2], Y. Kunai[1], C. A. Ross[1]
[1]MIT, Cambridge, Massachusetts, United States, [2]Nagoya University, Nagoya, Japan

The integration of magnetic garnets into magnetoelectric systems has been explored through several methods, such as fabricating Vertically Aligned Nanocomposites (VANs), or direct deposition onto piezoelectric substrates [1] [2]. However, both methods present drawbacks such as unwanted phases and large feature sizes. Here we present a new class of composite thin films dubbed *laterally differentiated polymorphs* in which ferrimagnetic garnet and ferroelectric perovskite are grown simultaneously on a patterned substrate. Electron beam lithography and pulsed laser deposition (PLD) are first used to pattern a 10-20 nm thick $La_{0.67}Sr_{0.33}MnO_3$ (LSMO) seed layer on the surface of a $Gd_3Sc_2Ga_3O_{12}$ (GSGG) substrate, then the LSMO is annealed to form polycrystalline perovskite regions as small as 50 nm wide. We then deposit a film with a composition of $Bi_{2.25}Y_{0.75}Fe5O_{12}$ on the heterogeneous substrate. Guided by epitaxy, the film crystallizes as a garnet (BiYIG) on the exposed GSGG regions, and a perovskite (Fe-rich (Bi,Y)FeO_3 or FBYFO) on the LSMO regions: the two phases have the same composition but dramatically different properties (Figures 1 and 2). The BiYIG displayed bulk-like magnetization, perpendicular magnetic anisotropy, and a low damping of 3.5 x 10^{-4}, whereas the FBYFO exhibited ferroelectricity with a remnant polarization of 11 μC/cm^2. The magnetoelectric properties of the composite resulting from strain transfer at the vertical interfaces were demonstrated with Brillouin light scattering and magneto optic Kerr effect microscopy, in which a 200 MHz shift in the magnon frequency of a 2.5 μm-wide BiYIG waveguide is observed when 10V was applied across the adjacent FBYFO [3]. These magnetoelectric composites enable the excellent magnetic properties of garnets such as ultralow damping to

be integrated into nanoscale, voltage controlled spintronic devices.

[1]: Tingyu Su, Caroline A. Ross, Applied Physics Letters, Vol. 121, Issue 23 (2022)
[2]: Miela J. Gross, Walid A. Misba, Kensuke Hayashi, et al., Applied Physics Letters, Vol. 121, Issue 25 (2022)
[3]: Pete E. Lauer, Kensuke Hayashi, Yuichiro Kunai et al., arXiv:2604.07495 (2026)

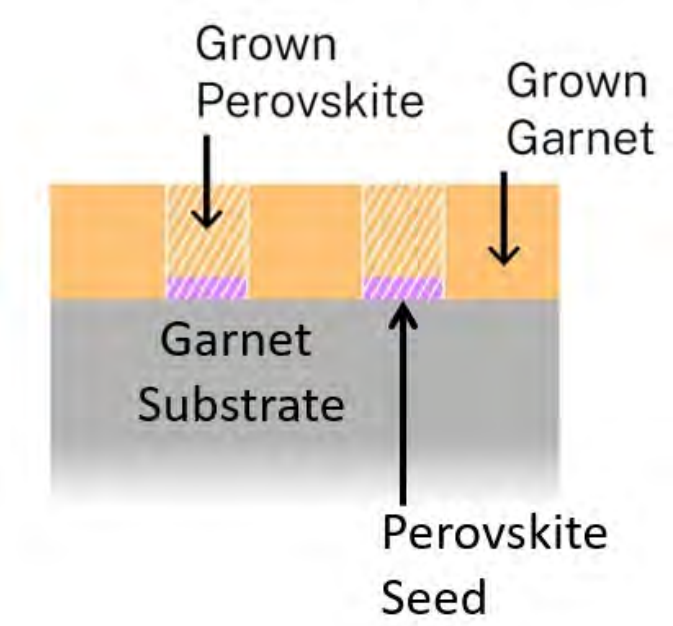


Figure 1: Schematic of garnet-perovskite *laterally differentiated polymorph* cross section.

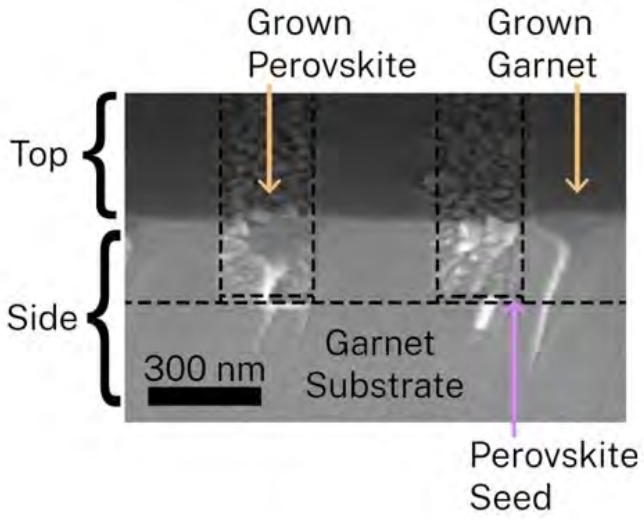


Figure 2: Cross-sectional SEM image of *laterally differentiated polymorph*.

HC-11. Depth-Resolved Profile of the Interfacial Ferromagnetism in $CaMnO3/CaRuO_3$ Superlattices

J. R. Paudel[1, 2], A. Mansouri Tehrani[3], M. Terilli[4], M. Kareev[4], J. Grassi[2], R. K. Sah[2], L. Wu[4], V. N. Strocov[6], C. Klewe[1], P. Shafer[5, 1], J. Chakhalian[4], N. A. Spaldin[3], A. X. Gray[2]
[1]Advanced Light Source, Lawrence Berkeley National Laboratory, Berkeley, California, United States, [2]Physics Department, Temple University, Philadelphia, Pennsylvania, United States, [3]Materials Theory, ETH Zurich, Zurich, Switzerland, [4]Department of Physics and Astronomy, Rutgers University, Piscataway, New Jersey, United States, [5]NSLS II, Brookhaven National Laboratory, Upton, New York, United States, [6]Swiss Light Source, Paul Scherrer Institute, Villigen, Switzerland

Interfacial magnetism in complex oxides presents a rich platform for tuning electronic and magnetic properties, with implications for spintronic and data storage applications. In this study, we investigate the emergence of interfacial ferromagnetism in oxide superlattices containing antiferromagnetic $CaMnO_3$ and paramagnetic $CaRuO_3$ using a combination of synchrotron-based X-ray spectroscopy and X-ray Resonant Magnetic Reflectivity (XRMR) measurements to uncover the depth profile of the interfacial magnetism. Our findings reveal that the emergent interface ferromagnetism exhibits an asymmetric distribution between the top and bottom interfaces and may extend beyond the immediate interface into the nominally antiferromagnetic $CaMnO_3$ layers, suggesting more complex interface interactions than previously assumed.
To understand the microscopic origin of this behavior, we employed density functional theory calculations, which indicate that the observed interfacial ferromagnetism is driven by a double exchange mechanism facilitated by charge transfer from Ru to Mn ions. Furthermore, defect chemistry, such as the presence of oxygen vacancies, may influence the local magnetic moments at the interface and contribute to the asymmetry in the ferromagnetic depth profile.
These results highlight the role of charge transfer and defect engineering in tailoring emergent interfacial properties. By providing a deeper understanding of how interfacial magnetism can be controlled at the atomic level, this work offers new strategies for designing functional oxide heterostructures with tunable magnetic properties [1].

[1] *J. Paudel* et al., Nano Lett. 24 (48), 15195-15201 (2024).

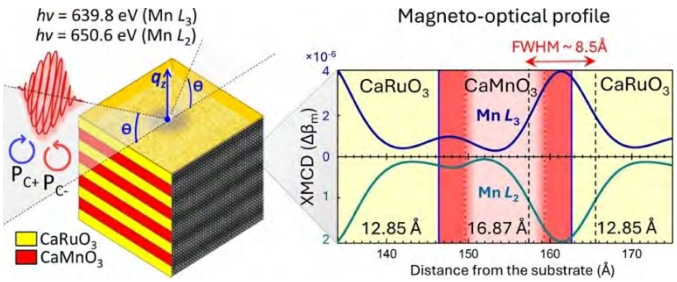


Fig.1.: XRMR measurement geometry of the $CaMnO_3$/$CaRuO_3$ superlattices (left) and the derived magnetic depth profile of a single $CaMnO_3$ layer sandwiched between $CaRuO_3$ (right).

SESSION HD: HARD MAGNETIC MATERIALS III: AI-DRIVEN DESIGN AND ENGINEERING OF PERMANENT MAGNETS

Chair(s): T. Kim, *Korea Institute of Materials Science, Changwon, Korea (the Republic of)*

Friday, November 6, 2026

02:00 PM-05:30 PM

Coral 2

HD-01. AI-accelerated Microstructure Modeling and Design of Permanent Magnets

J. Hu

Materials Science and Engineering, University of Wisconsin-Madison, Madison, Wisconsin, United States

An important topic of materials modeling and design is to predict the process–microstructure–property (PMP) relationships as well as the dynamical evolution of microstructures under complex environmental conditions. The presenter will introduce their recent works on the AI-accelerated forward prediction of the PMP relationships and the inverse process design of permanent magnets. The forward prediction will discuss the application of graph neural network to accelerate the phase-field simulations the effective properties [1,2] (e.g., magnetostriction, coercive field) of polycrystalline permanent magnets, using the giant magnetostrictive alloy $Tb_xDy_{1-x}Fe_2$ as an example [1]. The inverse design will discuss the presenter's collaboration work with Seagate Technology on the inverse microstructure-process design of the FePt-based nanogranular composite thin films for heat-assisted recording media applications, built upon an AI-driven workflow that integrates high-throughput phase-field modeling, automated microstructure classification and quantification, and active learning [3]. The talk will be concluded with a brief outlook and introduction of the presenter's ongoing work of combining physics-informed transformer and heterogeneous multiscale method to accelerate Multiphysics microstructure evolution in large-scale systems.

[1] Dai et al., *npj Comput. Mater.* 7, 103 (2021).
[2] Dai et al., *Comput. Mater. Sci.* 230, 112461 (2023).
[3] Guo et al, *npj Comput. Mater. (In revision).*

HD-02. Landscape of Permanent Magnet Discovery

D. Parker, N. Pokhrel

ORNL, Oak Ridge, Tennessee, United States

Since the 1982 discovery of NdFeB magnets, strenuous efforts worldwide have focused on the development of *new* permanent magnets with desirable properties – efforts that have only increased since the first 'rare earth crisis' in 2010. Much of these efforts have centered on reducing both cost and criticality, with Cerium substitution into NdFeB magnets a good example of this approach, albeit with decreased performance. While there are examples of commercialized magnets, such as Iron nitride ($Fe_{16}N_2$) entirely free of rare earths, most of the community attention has continued to focus on rare earth compositions, such as SmFeN, given the well-known role of localized 4*f* electrons in promoting magnetic anisotropy. The key role of processing techniques, such as grain boundary diffusion, in reducing the usage of scarce, critical and costly heavy rare earths, has also become apparent in recent years.

In all these endeavors one question remains paramount: is it likely that there are new, undiscovered materials which may afford a substantial increase in performance relative to NdFeB magnets? While the current plateauing of the energy product in NdFeB magnets near the theoretical 64 MG-Oe value might appear to argue otherwise, I will take a contrarian view and argue that the latest computational and materials science advances may aid in the discovery of even more promising magnet compositions, provided that one takes advantage of the full potential and variety of the many astonishing elements in the Periodic Table.

HD-03. A Machine Learning Framework for Magnetic Candidate Discovery in Cerium-Based Compounds

T. Lamichhane

Engineering Physics, University of Central Oklahoma, Oklahoma City, Oklahoma, United States

Cerium (Ce), the most abundant and chemically versatile lanthanide [3], offers strong potential for addressing

shortages in high-performance magnetic materials through the discovery of new compounds for gap magnets [1,2]. Predicting ferromagnetic behavior and uniaxial anisotropy in cerium-based compounds remains challenging due to the strong dependence of magnetic properties on crystal structure, exchange geometry, and electronic interactions. In this study, we present a physics-guided computational framework for filtering known cerium-based crystal structures to identify promising magnetic candidates for synthesis. Structural descriptors, including lattice symmetry, valency, bond lengths, and coordination environments [4], guide the screening process and selection of compounds for deeper analysis.

Selected real crystallographic structures are then simulated within an Ising-model-based Monte Carlo framework to probe magnetic phase behavior and critical properties. Phase graphs from these simulations are used to extract tri-critical exponents, enabling quantitative characterization of magnetic regimes, transition behavior, and anisotropy-related effects. To complement this analysis, we apply an unsupervised machine learning approach [5,6] based on autoencoders trained on affinity-based features derived from the simulated configurations. The resulting latent representations capture signatures of phase evolution and transition behavior, providing an interpretable connection between spin configurations and emergent magnetic phenomena.

Together, these methods establish a scalable framework that combines structural screening, statistical-mechanical simulation, critical exponent extraction, and unsupervised learning for magnetic materials discovery. This approach advances the physics-informed filtering of known crystals and provides a pathway for identifying candidates for future synthesis and experimental validation across lanthanide and actinide systems.

1. Lamichhane, T.N., et al., Single-Crystal Permanent Magnets: Extraordinary Magnetic Behavior in the Ta, Cu, Fe-doped CeCo5 Systems. Physical Review Applied, 2019. 11(1): p. 014052.

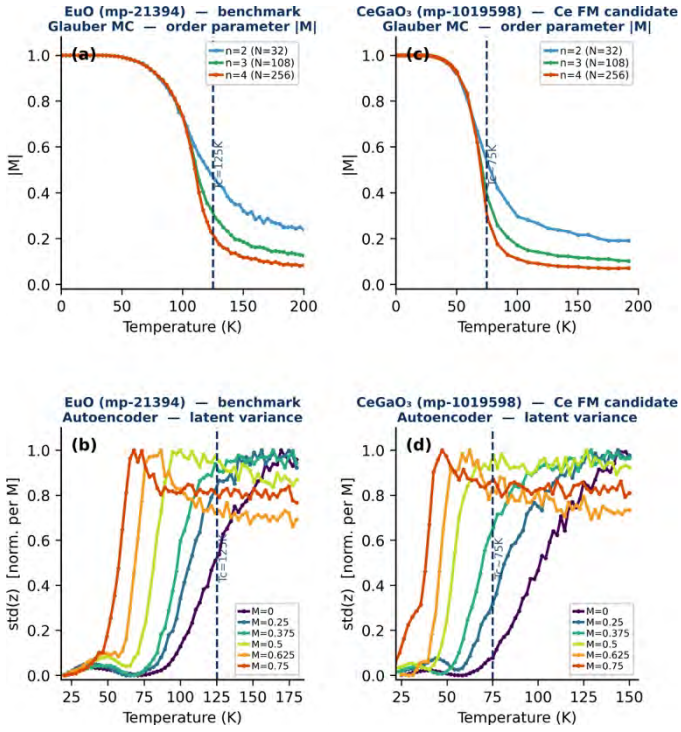
2. Lamichhane, T.N., et al., Ce3-xMgxCo9: Transformation of a Pauli Paramagnet into a Strong Permanent Magnet. Physical Review Applied, 2018. 9(2): p. 024023.

3. Churna Bhandari, G.N.N., Jonathan D.H. Smith, Durga Paudyal, Accurate Machine Learning Predictions of Coercivity in High-Performance Permanent Magnets. 2023.

4. Broyles, C.C., William; Sheng Ran, Structure-Driven Prediction of Magnetic Order in Uranium Compounds. 2024.

5. Jang, Y., & Yethiraj, A. Unsupervised Machine Learning Method for the Phase Behavior of the Constant Magnetization Ising Model. 2024.

6. Jang, Y., Kaur, H., & Yethiraj, A. Importance of Feature Construction in Machine Learning Predictions of Phase Behavior. 2022.



HD-04. Search for rare-earth-free permanent magnets using first-principles calculations and machine learning

M. Werwinski[1], J. Snarski-Adamski[1], J. Rychly-Gruszecka[1], J. Marciniak[2, 1], W. Marciniak[2, 3, 1], P. Palczynski[1]

[1]Department of Theory of Nanostructures and Quantum Materials, Institute of Molecular Physics of the Polish Academy of Sciences, Poznan, Poland, [2]Department of Physics and Astronomy, Uppsala University, Uppsala, Sweden, [3]Faculty of Materials Engineering and Technical Physics, Poznan University of Technology, Poznan, Poland

The best permanent magnets in use today contain neodymium or samarium. These elements belong to the group of rare earth metals, whose availability is limited and prices are variable and relatively high. Therefore, for many

years, new promising hard magnetic materials that do not contain rare earth metals have been sought. The experimental work carried out in this area is supported by density functional theory (DFT) calculations and machine learning.

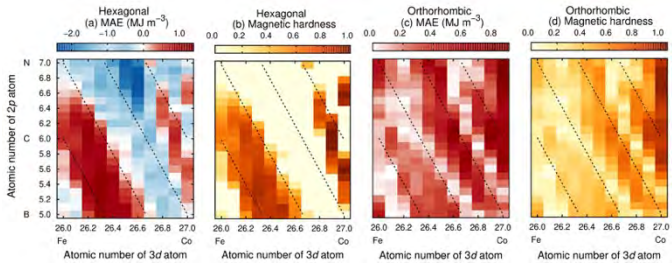
The key parameters we calculate from DFT are formation energy, Curie temperature, magnetic moment, and magnetocrystalline anisotropy energy (MAE) [1-5]. Based on our results for $(Fe–Co)_{16}C$, $(Fe–Co)_3(B,C,N)_1$, and $CeFe_{12}$ alloys, we will discuss two novel issues related to MAE. First is the dependence of the MAE on the choice of the exchange-correlation potential, which we interpret based on fully relativistic fixed spin moment calculation. Second is the isoelectronic nature of the MAE, which indicates that alloying at the 3*d* and 2*p* sites contributing an equal number of electrons to the system can both lead to similar changes in the MAE, see Fig. 1.

Furthermore, we compare the performance of different training approaches for Random Forest models on the magnetic materials datasets, see Fig. 2. A number of feature representations were tested, either using just simple atomic position coordinates, radial density functions, like used in the smooth overlap of atomic positions (SOAP) descriptors [6], or various combinations of those and other simple descriptors. Additionally, the chemical composition representation was tested via different approaches like different simple chemical properties or more comprehensive approaches like the Magpie descriptors [7].

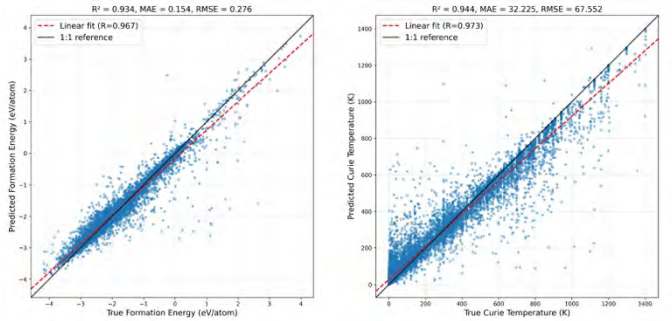
This study provides insight into the electronic origins of MAE and data-driven search for magnetic materials.

We acknowledge the financial support from the National Science Center Poland under grant DEC-2021/41/B/ST5/02894.

[1] J. Snarski-Adamski, M. Werwinski, J. Rychly-Gruszecka, Magnetic hardness of hexagonal and orthorhombic Fe_3C, Co_3C, $(Fe–Co)_3C$, and their alloys with boron, nitrogen, and transition metals: A first-principles study, *APL Materials*, 2025, *13*, 021117.
[2] J. Marciniak, M. Werwinski, $L1_0$ FePt thin films with tilted and in-plane magnetic anisotropy: A first-principles study, *Phys. Rev. B*, 2023, *108*, 214406.
[3] W. Marciniak, M. Werwinski, Structural and magnetic properties of Fe-Co-C alloys with tetragonal deformation: A first-principles study, *Phys. Rev. B*, 2023, *108*, 214433.
[4] J. Marciniak, M. Werwinski, $L1_0$ FePt thin films with tilted and in-plane magnetic anisotropy: A first-principles study, Phys. Rev. B. 2023, 108, 214406.
[5] J. Marciniak, W. Marciniak, M. Werwinski, DFT calculation of intrinsic properties of magnetically hard phase $L1_0$ FePt, J. Magn. Magn. Mat., 2022, 556, 169347.
[6] A. P. Bartók, R. Kondor, and G. Csányi, On representing chemical environments, Phys. Rev. B, 2013, 87, 184115.
[7] L. Ward, A. Agrawal, A. Choudhary, and A. Jain, A general-purpose machine learning framework for predicting properties of inorganic materials, npj Comput. Mater., 2016, 2, 16028.



Magnetocrystalline anisotropy energy and magnetic hardness of $(Fe–Co)_3(B\text{-}C\text{-}N)$ systems calculated with FPLO code using VCA, see Ref. [1].



Predictions vs true values for the formation energy and Curie temperatures obtained with Random Forest model trained on NEMAD and Materials Project databases.

HD-05. Analysis of Site Stability for Substitutional Elements in $Sm_2Fe_{17}M_x$ using Neural Network Potential

Y. Tatetsu[1], Y. Hirayama[2]
[1]University Center for Liberal Arts Education, Meio University, Nago, Okinawa, Japan, [2]National Institute of Advanced Industrial Science and Technology, Moriyama, Nagoya, Japan

Sm_2Fe_{17}-based intermetallic compounds are of significant interest in the field of high-performance permanent magnets due to their exceptionally high saturation

magnetization. However, to realize their full potential in practical applications, it is essential to optimize their magnetic anisotropy and thermal stability, which are often achieved by substituting a small fraction of the iron (Fe) atoms with other elements (*M*). A critical challenge in this process is the complex crystallographic nature of the Sm_2Fe_{17} structure, which contains several distinct Fe sites (such as 6*c*, 9*d*, 18*f*, and 18*h*). The physical and magnetic properties of the resulting alloy are profoundly influenced by which specific site the substituent element occupies. Despite its importance, the comprehensive determination of site preferences for a diverse range of elements is traditionally hindered by the prohibitive computational cost associated with conventional first-principles calculations, as it requires a vast number of structural configurations and electronic relaxations for each single element.

The objective of this study is to clarify the site occupancy preference and the concentration-dependent stability of various substitutional elements in the Sm_2Fe_{17} structure.

We employed the neural network potential provided by Matlantis. This approach enables high-throughput evaluations of multiple crystallographic sites (including 6*c*, 9*d*, 18*f*, and 18*h*) while maintaining accuracy comparable to first-principles calculations. We quantified the stability by evaluating the concentration dependence of the formation energy for each site, focusing on the slope and mean formation energy.

Our results indicate a distinction in the preferred sites depending on the nature of the substitutional element. Specifically, for a group of elements including Ga, the 9*d* site was identified as the most stable. For these elements, the formation energy decreased monotonically as the substitution concentration increased, suggesting a stabilizing effect on the system. In contrast, other elements showed a preference for the 6*c* or 18*f* sites, indicating that site selectivity is strongly governed by the chemical properties of the substituents.
K. H.J. Buschow, Handbook of Magnetic Materials, Vol. 9, p.303 (1995)
S. Takamoto, *et al*., Nat Commun. Vol. 13, p.2991 (2022)

HD-06. High-Throughput Design and Discovery of Novel Magnetic Nitrides
R. W. Smaha
Materials Science Center, National Laboratory of the Rockies, Golden, Colorado, United States

Metal-rich nitrides, such as $Fe_{16}N_2$ and $Sm_2Fe_{17}N_3$, are promising materials for permanent magnetic applications with little or no critical rare earth content. However, developments in nitride magnets have been stymied by the challenge of synthesizing them, given the comparative stability of N_2, and their low thermal stability. As such, the phase space of magnetic nitrides is vastly underexplored, especially compared to those of intermetallics and borides/carbides. Recent advances in experimental methods for synthesizing nitride materials, particularly thin film methods employing radiofrequency co-sputtering to increase the effective synthesis temperature as well as methods to controllably nitride and dinitride, have led to a rapid increase in the number of known ternary nitride phases.
Here, I will discuss the design and discovery of several novel ternary nitrides with interesting magnetism, focusing on nitride antiperovskites. Using high-throughput co-sputtering, we have recently synthesized multiple new Co-based antiperovskite thin films (Co_3XN) that exhibit a range of magnetic behavior from high-temperature ferromagnetism (Co_3PdN) to low-temperature antiferromagnetism (Co_3ZnN).[1,2] Overall, this work allows us to begin to understand the interplay between composition, structure, and properties in a complex phase space, which is crucial for designing and synthesizing novel magnetic materials.
[1] S. Dugu et al. Chem. Mater. 2025, 37, 5, 1906–1913.
[2] S. Dugu et al. arxiv:2512.06516.

HD-07. Developing state-of-the-art machine learning models in search of rare-earth-free permanent magnets
P. J. Palczynski, M. Werwinski
Institute of Molecular Physics Polish Academy of Sciences, Poznan, Wielkopolska, Poland

This work contributes to the ongoing effort of empowering the discoverability of the rare-earth-free hard magnetic materials. There have been many approaches considered in recent years, both on the experimental and the theoretical or computational side. One of the obvious methods that found interest recently is machine learning given the advacements in the field. Those methods have quite a lot of success in many related fields, including those involving prediciting structures and compositions of various compounds. When it comes to the field of magnetic materials however, and discovering new structures and compositions, many of these advancements have not been

transferred and attempted yet, which leaves potentially some easy gains on the table. As it has been shown in many other applications, adding more data, even in a simplistic "brute force" manner, tends to produce improvments in model performance. In the field of magnetic materials however there is a dearth of readily available data, especially for some particular properties. The largest databases include density functional theory (DFT) derived properties and,
due to the method's peculiarities, results in a certain bias towards data that is easier to calculate using it. The alternative, the experimentally derived results, often lack the coverage of the entire range of compositions or structures, or they are obtained via very different experimental methods which complicates their comparison.

We have managed to implement many of those methods, models, and strategies of machine learning, which combined with both the publically available datasets, like Materials Project, NEMAD or NOMAD, as well as our own supplemented data produced interesting results. Namely, we show that even with the limited datasets which are usually one of the largest obstacles, when it comes to the machine learning model training, there are still viable approaches that produce useful predictions of some of the properties like for instance Curie temperature.

We acknowledge the financial support from the National Science Center Poland under grant DEC-2021/41/B/ST5/02894.
James R. Chelikowsky, Cai-Zhuang Wang, Weiyi Xia, et al., Journal of Magnetism and Magnetic Materials, Volume 646, 173978, (2026)
https://next-gen.materialsproject.org/
https://nemad.org/
https://nomad-lab.eu/nomad-lab/

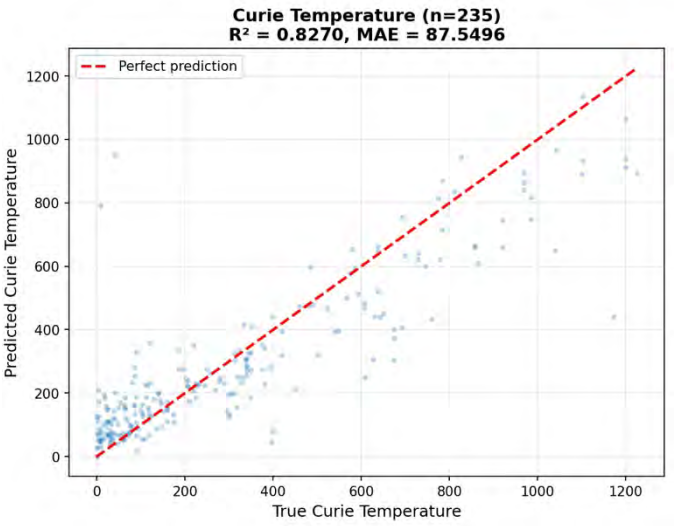


Fig. 1. Decent improvements over the baseline GNN model trained on a very small dataset.

HD-08. Interstitial Boron Driven Magnetic Hardening in FeCo Alloy

B. Narangerel[1], U. Amanjal[2], K. Baatartsogt[2], U. Enkhnaran[2], M. Adiya[1], O. Tumentsereg[1], J. Narmandakh[2], D. Odkhuu[1]
[1]Incheon National University, Incheon, Korea (the Republic of), [2]Mongolian Academy of Sciences, Ulaanbaatar, Mongolia

B2-ordered FeCo is a promising rare-earth-free permanent magnetic material due to its high saturation magnetization and Curie temperature, but its low uniaxial magnetocrystalline anisotropy (K_u) and near-zero coercivity (H_c) limit practical applications. Here, we show that interstitial B atoms break cubic symmetry, inducing tetragonal distortion and lattice expansion, which enhance uniaxial anisotropy and coercivity. First-principles calculations, supported by experiment, identify an optimized FeCoB composition with K_u up to 1.5 MJ/m^3 and H_c up to 85 Oe. These improvements lead to enhanced intrinsic magnetic hardness, approaching ferrite-level performance. Our results demonstrate that interstitial doping provides an effective route to engineer magnetic hardness in FeCo-based alloys.

The research is supported by Office of Naval Research (ONR) and Office of Naval Research Global (ONRG) of the US Department of Defense Grant N62909-22-1-2045, and National Research Council of Science & Technology (NST) Grant No. CAP25061-000 and Basic Research Program Grant No. RS-2026-25494250 through the National Research Foundation of Korea.

HD-09. Orientation-dependent perpendicular magnetic anisotropy in epitaxial Mn_4N thin film on MgO substrate

K. Imamura[1], R. Kuwayama[1], S. Isogami[2], M. Ohtake[1]
[1]Yokohama National University, Yokohama, Japan, [2]National Institute for Materials Science (NIMS), Tsukuba, Japan

Ferrimagnetic Mn_4N thin film has attracted considerable interest in the fields of spintronics [1]–[4] and magneto-ionics [5] owing to its perpendicular magnetic anisotropy. Notable phenomenon such as current-driven magnetization switching [1], [4], high-speed domain wall motion [2], and skyrmion formation [3] have been demonstrated. In previous studies, (001)-oriented films have been employed, and the magnitude of the perpendicular magnetic anisotropy has been correlated with the lattice strain along the *c*-axis [6]. A few studies have also suggested the potential advantage of (111)-oriented films for magnetization switching [4]. Nevertheless, the relationship between three-dimensional crystallographic strain and perpendicular magnetic anisotropy remains insufficiently understood. Studying single-crystalline samples grown with different crystallographic orientations could offer new insights into this fundamental question. In the present study, epitaxial Mn_4N films are grown on single-crystal MgO(001), (011), and (111) substrates. The structure is characterized by RHEED, XRD, and XPS. The perpendicular magnetic anisotropy properties are investigated by anomalous Hall effect (AHE) measurement system. Fig. 1(a) shows the RHEED patterns. Superlattice reflections arising from the ordered crystal structure, indicated by yellow arrows, are clearly observed. Single-phase and single-variant epitaxial films with orientation relationships shown in Fig. 1(b) have been successfully obtained. The deviatoric strains determined from the XRD data in Fig. 1(c) is −1.3%, −1.0%, and −0.7% for the (001), (011), and (111) films, respectively. Although the lattice mismatch with MgO is −8.4% in all cases, the induced strain is largest in the (001) film. Fig. 2 shows the AHE loops. The (001) film shows a well-squared loop, whereas the (011) and (111) films exhibit loops with reduced squareness and smaller anomalous Hall resistivity. These results indicate that the (001) orientation is optimal for achieving strong perpendicular magnetic anisotropy and that the perpendicular magnetic anisotropy can be tuned by controlling the crystallographic orientation.

[1] H.Bai, T.Xu, Y.Dong, H. A.Zhou, and W. Jiang, *Adv. Electron. Mater.*, 8, 2100772 (2022). [2] T. Gushi, M. J. Klug, J. P. Garcia, S. Ghosh, J. P. Attané, H. Okuno, O. Fruchart, J. Vogel, T. Suemasu, S. Pizzini, and L. Vila, *Nano Lett.*, 19, 8716 (2019). [3] C. T. Ma, T. Q. Hartnett, W. Zhou, P.a V. Balachandran, and S. J. Poon, *Appl. Phys. Lett.*, 119, 192406 (2021). [4] S. Isogami, N.Rajamanickam, Y. Kozuka, and Y. K. Takahashi, *AIP. Adv.*, 11, 105314 (2021). [5] S. Damerio, T. Apetrei, and C. O. Avci, *Appl. Phys. Lett.*, 127, 262405 (2025). [6] T. Hirose, T. Komori, T. Gushi, A. Anzai, K. Toko, and T. Suemasu, *AIP Adv.*, 10, 025117 (2020).

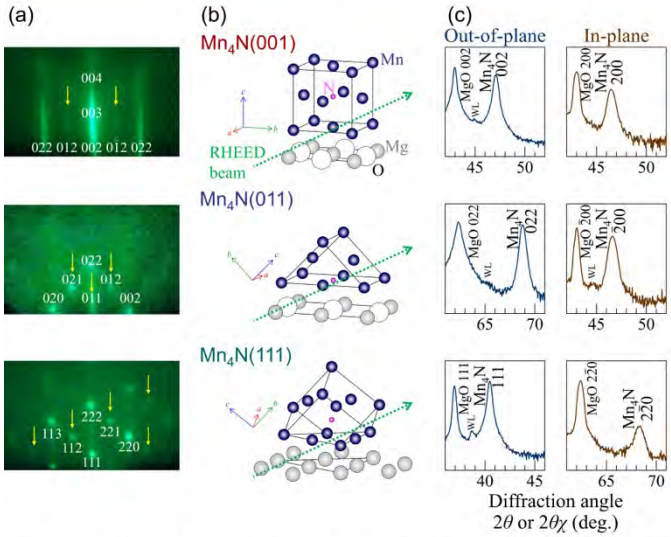


Fig. 1 (a) RHEED patterns observed for Mn_4N films formed on MgO(001), MgO(011), and MgO(111) substrates. (b) Schematic illustrations of crystallographic orientation relationships between Mn_4N and MgO crystals for (001), (011), and (111) planes. (c) Out-of-plane/in-plane XRD patterns measured for Mn_4N films grown on MgO(001), MgO(011), and MgO(111) substrates.

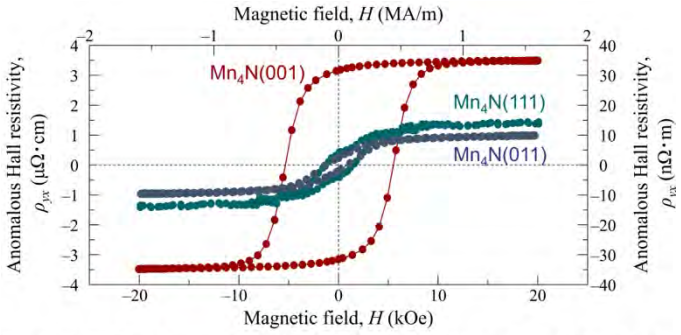


Fig. 2 AHE loops measured for Mn_4N(001), Mn_4N(011), and Mn_4N(111) single-crystal thin films.

HD-11. Thermally Activated Flux Loss of Sintered Nd–Fe–B Magnets under External Opposing Fields

W. Tang[1, 2], J. Wang[1], M. J. Kramer[1], J. Cui[1, 2]
[1]Ames National Laboratory, Ames, Iowa, United States, [2]Iowa State University, Ames, Iowa, United States

Nd–Fe–B magnets are the primary candidates for use in electrical rotating machines. Once installed, it is generally impossible to re-magnetize them in situ if partial demagnetization occurs due to exposure to external opposing magnetic fields or elevated temperatures.
To ensure a guaranteed lifetime of the corresponding electric components, the thermally activated aging behavior of magnets under applied opposing fields must be considered during both machine design and magnet selection. In current industrial practice, higher-coercivity and more expensive magnet grades are often selected to compensate for the gradual magnetic loss expected during service. However, if the magnets can be evaluated under simulated conditions representative of real operating environments in rotating machines, the resulting data would enable designers to make more cost-effective and reliable material choices.
In this work, we investigated the thermally induced flux losses of sintered Nd–Fe–B magnets under various static external opposing magnetic fields. The measurements followed the standard protocol [1] for defining the maximum operating temperature, i.e., the highest temperature at which the open irreversible flux loss remains ⩽ 5 % after the magnet is held at that temperature for 2 hours.
Figure 1 shows the flux loss of different grade magnets as a function of aging temperature for 2 hours under varying external opposing fields. The N42H magnet exhibits less than 5 % flux loss at 120 °C without an external field (Fig. 1a), while N45UH and N35EH magnets maintain flux loss below 5 % up to approximately 220 °C. When external opposing fields of 2 kGs (Fig. 1b) and 6 kGs (Fig. 1c) are applied, these threshold temperatures decrease significantly. For N42H, the thresholds drop to 100 °C and 40 °C, respectively. For N45UH, they decrease to 200 °C and 150 °C, and for N35EH, to 200 °C and 160 °C, respectively. The resulting data provides a valuable foundation for building a database that can assist electrical machine designers in optimizing magnet selection and design parameters.

1. National standard of China, GB/T 13560-2017, “Sintered neodymium iron boron permanent magnets”, May 1, 2018.

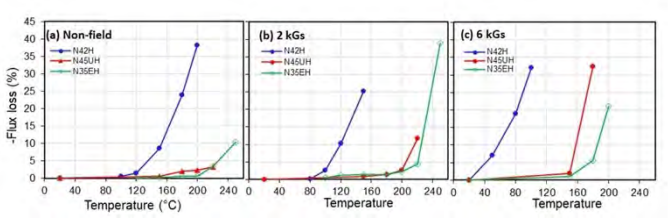


Figure 1. Flux loss of different grade magnets as a function of aging temperature for 2 hours under different external opposing fields, (a) 0 kGs, (b) 2 kGs, (c) 6 kGs

SESSION HE: EMERGENT MAGNETIC FUNCTIONALITIES IN THIN FILMS AND NANOSTRUCTURES

Chair(s): Y. Ichiyanagi, *Engineering Science, The University of Osaka, Yokohama, Japan*
Friday, November 6, 2026
02:00 PM-05:30 PM
South Pacific 1/2

HE-03. Magnetic Nanorod Array Formed Through Bottom-Up Polyol Synthesis and Magnetic-Field Assisted Assembly for Microwave Applications

S. Fultz-Waters[1], W. He[2], S. Alaei[3], J. T. Bryan-Kim[1], J. A. Yang[4], Y. Suzuki[5, 1], Y. Lee[5, 2], W. Tsai[1], E. Pop[4, 1], S. X. Wang[1, 4]
[1]Department of Materials Science and Engineering, Stanford University, Stanford, California, United States, [2]SLAC National Accelerator Laboratory, Stanford University, Stanford, California, United States, [3]Department of Physics, Stanford University, Stanford, California, United States, [4]Department of Electrical Engineering, Stanford University, Stanford, California, United States, [5]Department of Applied Physics, Stanford University, Stanford, California, United States

Arrays of ferromagnetic nanowires have attracted significant attention for microwave applications due to their high ferromagnetic resonance (FMR) frequencies arising from shape anisotropy [1], [2]. Previous studies on magnetic nanowire arrays have largely utilized electrodeposition into nanoporous templates to form vertical arrays that have well-studied FMR properties [1-3]. This study focuses on the magnetic properties of planar cobalt nanorod arrays produced with a bottom-up synthesis that offers higher yield and less complex processing compared to electrodeposition of magnetic nanowires where the process is limited by the template used.
Cobalt nanorods are synthesized using a polyol method from cobalt carboxylate precursors in a weakly basic polyol solution with ruthenium seeding to obtain anisotropic

growth [4]. Transmission electron microscopy (TEM) reveals average dimensions of 25 ± 6 nm in diameter and 150 ± 49 nm in length. Following oleic acid coating, the nanorods are dispersed in chloroform and drop-cast into a micron-scale cavity in silicon under an applied magnetic field to align the nanorods in-plane within the cavity (Figure 1). Magnetic hysteresis measurements yield an effective anisotropic field of 8.5 kOe and saturation magnetization of approximately 125 emu/g (Figure 2). Using these parameters with classical FMR theory, the zero-field FMR frequency is estimated to exceed 23 GHz [3], [5], which is confirmed by experimental measurements. This FMR frequency is believed to be the highest reported for a planar magnetic nanorod array prepared through polyol synthesis and drop-casting.

We thank TSMC for providing support and funding that contributed to this work.

[1] M. Darques, A. Encinas, and L. Piraux, J. Phys.: Condens. Matter., Vol. 16, p.2279-2286, (2004)
[2] L. Piraux, *Appl. Sci*., Vol. 10, p.1832, (2020)
[3] A. Sklyuyev, M. Ciureanu, and A. Yelon, 2006 12th International Symposium on Antenna Technology and Applied Electromagnetics and Canadian Radio Sciences Conference, p.1-4 (2006)
[4] Y. Soumare, C. Garcia, and G. Viau, Adv. Funct. Materials, Vol. 19, p.1971-1977 (2009)
[5] C. Kittel, *Phys. Rev*., Vol. 73, p.155-161 (1948)

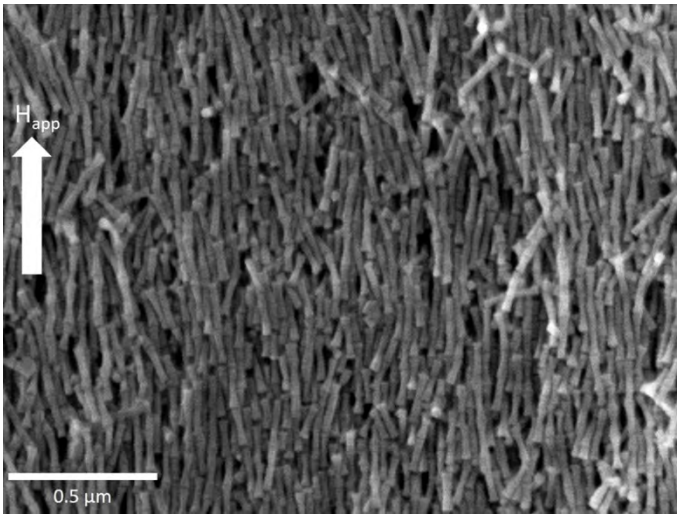


Fig. 1. Scanning electron microscopy (SEM) image of cobalt nanorod array on silicon substrate showing good alignment and relatively tight packing density after solvent evaporation in applied field.

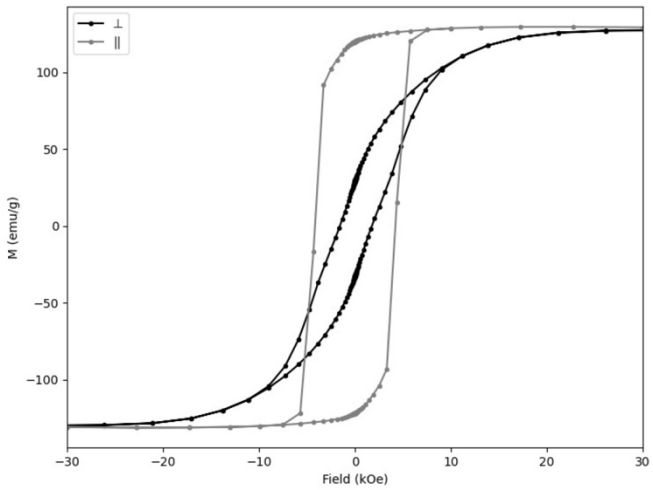


Fig. 2. Easy- and hard-axis magnetization measurements of drop-cast nanorod array taken using a vibrating sample magnetometer (VSM) holder in a physical property measurement system (PPMS). The mass of the sample was determined with inductively-coupled plasma mass spectrometry (ICP-MS) after dissolution in 2% nitric acid.

HE-05. Growth and properties of $NiCo_2O_4$ films on $MgAl_2O_4$/Si(001): Relationship of the magnetic properties with structural strain and defects

S. Sugiyama[1], M. Tanaka[1, 2, 3], R. Nakane[1, 2, 4]
[1]Deptartment of Electrical Engineering and Information Systems, The University of Tokyo, Bunkyo-ku, Tokyo, Japan, [2]Center for Spintronics Research Network (CSRN), The University of Tokyo, Bunkyo-ku, Tokyo, Japan, [3]Institute for Nano Quantum Information Electronics, The University of Tokyo, Bunkyo-ku, Tokyo, Japan, [4]Systems Design Lab (d.lab), The University of Tokyo, Bunkyo-ku, Tokyo, Japan

$NiCo_2O_4$ (NCO) is theoretically a half-metallic ferrimagnet[1] and its heterostructures with Si have a high potential for maximizing the performance of Si-based spin-transport devices. When epitaxially grown on $MgAl_2O_4$ (MAO) substrates, NCO films are under substrate-induced compressive strain[1] that stabilizes their magnetic properties, with high saturation magnetization M_s and spin polarization over 73%[2]. In contrast, NCO films on Si are expected to be polycrystalline and have more defects and lack substrate-induced strain. We study an unclear relationship between M_s and lattice constant in polycrystalline NCO, by varying annealing temperature T_{ANL} to induce changes in defects (e.g. oxygen vacancy) and strain.

After thermal cleaning of a Si(001) substrate at 750°C in our ultra-high vacuum electron-beam evaporation chamber, a 1-nm-thick MAO buffer layer was deposited at a substrate temperature T_{sub} of 650°C. A 36-nm-thick NCO layer was then deposited at T_{sub} = 315°C using RF oxygen plasma (2 ×10^{-3} Pa and 200 W). RHEED confirmed its polycrystalline structure. The samples were annealed at T_{ANL}= 350-500°C for 30 min in 1 atm O_2.

Figure 1 shows T_{ANL} dependence of M_s at 10 K. The maximum M_s is obtained at T_{ANL}= 400°C, reaching ~75% of the theoretical value[3]. This unimodal dependence results from competing effects: (i)reduction of oxygen vacancies at moderate T_{ANL} (≤ 400°C), since oxygen anions mediate ferromagnetic-coupling of Ni cations, and (ii)phase decomposition into anti-ferromagnetic NiO or CoO at higher T_{ANL}. Figure 2 shows the out-of-plane lattice constant and crystallite size estimated from ϑ-2ϑ XRD scans for the T_{ANL} values without the decomposition. It reveals that the increase in M_s with increasing T_{ANL} is accompanied by an increase in the crystallite size and a decrease in the lattice constant toward that of the powder reference[4], indicating decreases in local distortion and oxygen vacancies.

Our NCO film on MAO/Si exhibited fairly high M_s with various preferable structural properties at T_{ANL}= 400°C, highlighting that this new heterostructure is useful for device applications.

[1]X. Xu, C. Mellinger, Z. G. Cheng, et al., Journal of Applied Physics, Vol. 132, p.020901 (2022).
[2]Y. Shen, D. Kan, I.-C. Lin, et al., Applied Physics Letters, Vol. 117, p.042408 (2020).
[3]X. Shi, S. L. Bernasek, and A. Selloni, The Journal of Physical Chemistry C, Vol. 120, p.14892 (2016).
[4]O. Knop, K. I. G. Reid, Sutarno, et al., Canadian Journal of Chemistry, Vol. 46, p.3463 (1968).

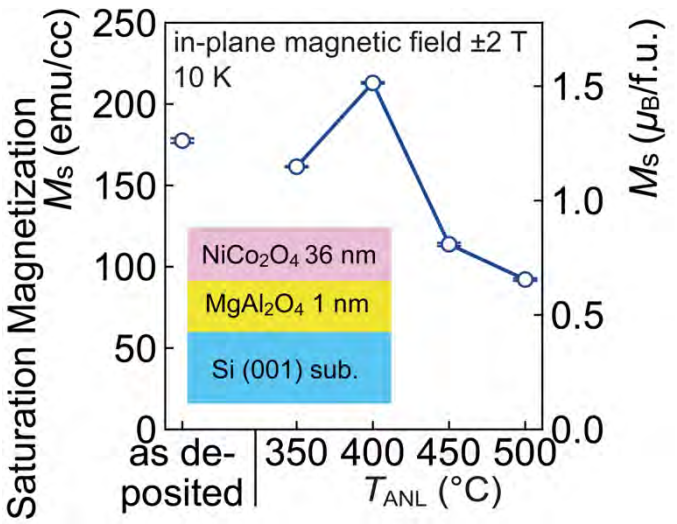


Fig.1 Annealing temperature T_{ANL} dependence of saturation magnetization M_s.

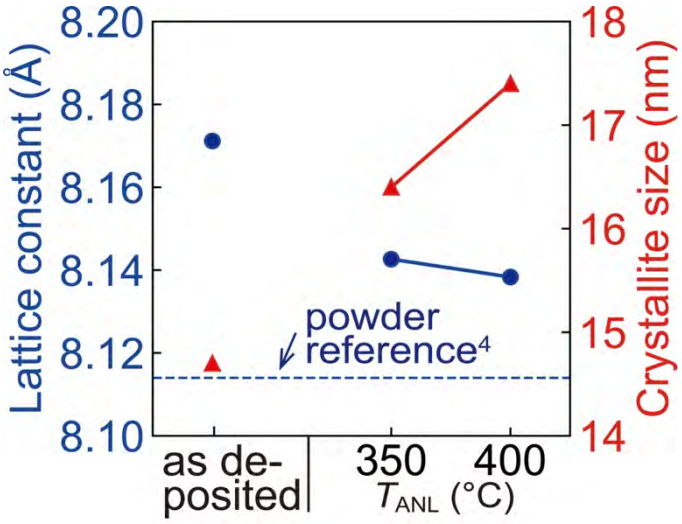


Fig.2 Lattice constant and crystallite size versus T_{ANL}.

HE-06. Epitaxial Growth of Rare Earth High Entropy Alloys

K. Dumesnil[1, 2, 3], J. Ledieu[1, 2, 3], M. Emo[1, 2, 3], S. Migot[1, 2, 3], S. Semsari Parapari[4], S. Sturm[4], P. Kozelj[4], V. Fournee[1, 2, 3]
[1]Institut Jean Lamour, Nancy, France, [2]Université de Lorraine, Nancy, France, [3]CNRS, Nancy, France, [4]Jozef Stefan Institute, Ljubljana, Slovenia

High entropy alloys (HEA) refer to metallic random solid solution made of at least five elements each in an equiatomic concentration [1]. Beyond their exceptional mechanical properties, their surface properties have recently been the focus of interest including their oxidation and corrosion resistance, and their catalytic activity [2]. To get a better understanding of their specific properties, it is now crucial to synthetize model single crystalline HEA. To this end, an extended project is undertaken to grow model HEA films via Molecular Beam Epitaxy.
We present here the results concerning Rare Earth HEA alloys, epitaxially grown on Al_2O_3/Nb by co-evaporation of five RE elements (DyGdHoLuTb) [3]. In-situ RHEED analysis as well as XRD attest for the high crystalline order, the low surface roughness and epitaxial relationships between the bcc Nb(110) and the hcp HEA(0001) growth planes. Cross-sectional TEM analysis and energy dispersive spectroscopy confirm the growth of a random solid solution of hcp structure. STM images confirm a (1 × 1) surface structure with inhomogeneous contrasts across atomic sites. No chemical segregation could be detected.
The magnetic behavior (SQUID) has been explored versus temperature and field to determine a (H,T) phase diagram (Fig. 1) in comparison with polycrystalline systems [4]. The magnetic properties are consistent with an equiatomic combination of the five elements, where individual magnetic features disappear to give rise to characteristics specific to this alloy: a single transition from high temperature PM to a low temperature modulated AFM state that can be driven to an aligned FM order under the application of an external critical field. Both the low temperature M(H) behavior and the comparison between FC and ZFC M(T) curves (with the unusual situation where $M_{ZFC} > M_{FC}$) highlight the strong disorder-induced pinning potential that competes with exchange and Zeeman contributions in such high entropy alloys.
[1] J.W. Yeh *et al*., Adv. Eng. Mat. 6, 299 (2004)
[2] L. Sun *et al*., ACS Mater. Au 4, 547 (2024)
[3] J. Ledieu *et al.* , ACS Nano 19, (2025) 26400
[4] S. Vrtnik *et al*., Intermetallics 105, 163 (2019)

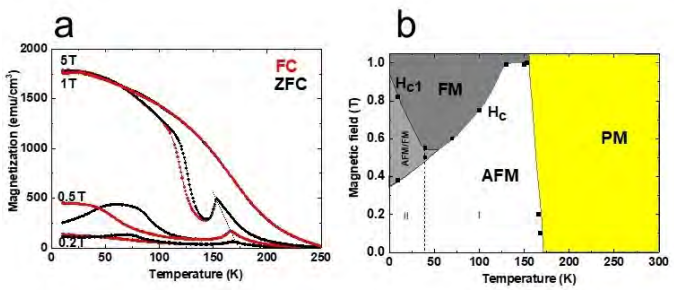


Fig.1: (a) Field-cooled (red) and zero-field-cooled (black) magnetization curves obtained as a function of temperature for external fields applied in the plane of the 100nm thick DGHLT film. (b) Magnetic phase diagram.

HE-07. Comparative study of nitrogen-induced phase formation in Co-N and Fe-N epitaxial thin films on MgO(001)

K. Imamura[1], K. Abe[1], S. Isogami[2], M. Ohtake[1]
[1]Yokohama National University, Yokohama, Japan, [2]National Institute for Materials Science (NIMS), Tsukuba, Japan

3d transition metal nitrides have attracted considerable interest because they form diverse phases with distinctive magnetic properties through the interstitial incorporation of nitrogen atoms into lattice sites. Among these, iron nitride (Fe-N) has been studied extensively and has a large body of literature [1],[2]. Cobalt nitride (Co-N) is equally noteworthy as a compound of nitrogen and a ferromagnetic element, yet reports on this system are few [3], likely due to its lower phase stability [4]. Studying these binary nitride systems from the viewpoint of crystal structure is important for understanding more complex systems such as Fe-Co-N based alloy [5]. Epitaxial thin films are well suited for this purpose, since their structural uniformity allows clear phase identification. In the present study, the phase formation of epitaxial Co-N thin film is investigated as a function of nitrogen content compared to those of Fe-N thin film. $Co_{100-x}N_x$ and $Fe_{100-y}N_y$ films are prepared on MgO(001) substrates by reactive sputtering, with the nitrogen partial pressure ratio varied systematically. The structure is characterized by RHEED and XRD. The magnetic properties are investigated by VSM. Fig. 1 shows the RHEED and XRD patterns. All films grow with a preferential crystallographic orientation relative to the substrate. With increasing the N composition, the phase sequence in Co-N follows *A*3 (α, hcp) + *A*1 (β, fcc) → *A*1 (β, fcc) → *L*'2 (bct) → *B*1/*B*3 (fcc), while that in Fe-N follows *A*2 (α, bcc) →*A*2 (α, bcc) + *L*'1 (γ', sc) → *L*'1 (γ', sc) → *L*'2 (α', bct). Both the *A*1 phase in Co-N and the *L*'1 phase in

Fe-N take an fcc arrangement of the metal sublattice. However, the nitrogen ordering observed in Fe-N is not found in Co-N. Reflections from the *L*'2 phase appear in both systems. Fig. 2(a) shows the XRD pole figures measured for the *L*'2 phase, and the obtained patterns are consistent with the phase transformation of Nishiyama-Wassermann [6] orientation relationship. Fig. 2(b) shows the magnetization curves. Despite the similar crystal structure, Co-N exhibits harder magnetic behavior than Fe-N. Comparing the two systems in a unified framework has thus clarified both the similarities and differences in terms of phase formation.

[1] J. M. D. Coey and P. A. I. Smith, *J. Magn. Magn. Mater.*, 200, 405 (1999). [2] P. Wojciechowski and M. Lewandowski, *Cryst. Growth Des.*, 22, 4618 (2022). [3] N. Pandey, M. Gupta, R. Gupta, Z. Hussain, V. R. Reddy, D. M. Phase, and J. Stahn, *Phys. Rev. B*, 99, 214109 (2019). [4] Y. Imai, M. Sohma, and T. Suemasu, *J. Alloys Compd.*, 611, 440 (2014). [5] T. Hasegawa, C. Murakam, K. Imamura, Y. Nakamura, M. Ohtake, and H. Yamane, *Sci. Rep.*, 15, 28636 (2025). [6] Z. Nishiyama, *Sci. Rep. Tohoku Univ.*, 23, 637 (1934).

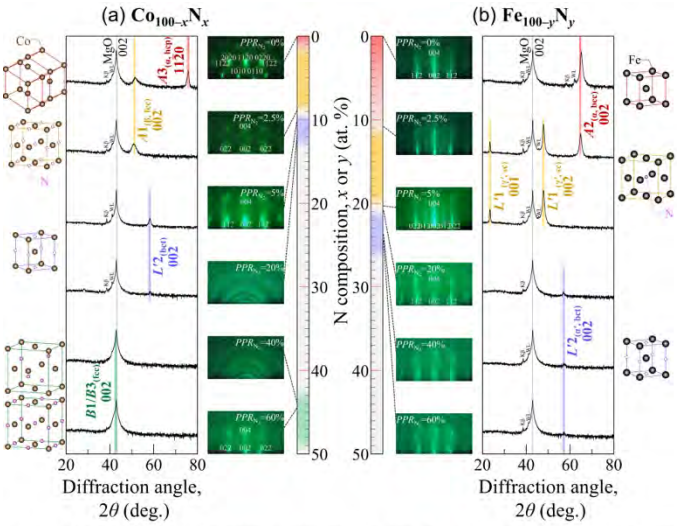


Fig. 1 RHEED and XRD patterns measured for (a) $Co_{100-x}N_x$ and (b) $Fe_{100-y}N_y$ films formed on MgO(001) substrates. Schematic illustrations of the crystal structures are provided alongside the corresponding diffraction patterns.

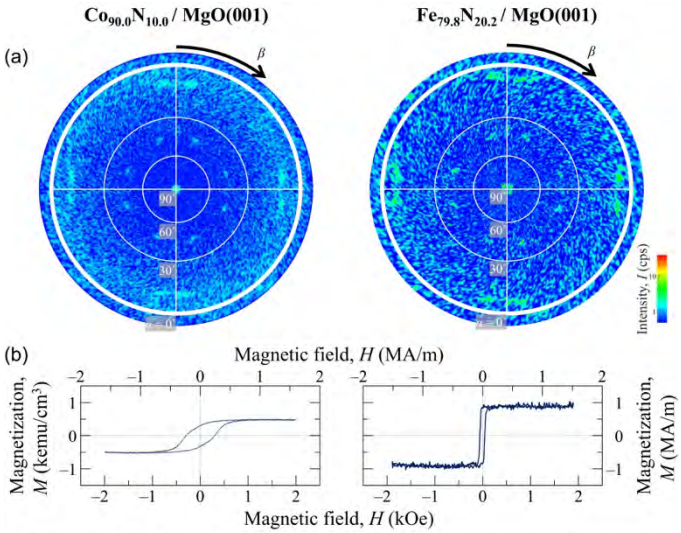


Fig. 2 (a) Pole-figure XRD patterns and (b) magnetization curves measured for $Co_{90.0}N_{10.0}$ and $Fe_{79.8}N_{20.2}$ films formed on MgO(001) substrates. In the XRD measurements, the diffraction angle, $2\theta_B$, is fixed at the angle of *L*'2 002 reflection. Magnetization curves are measured with the magnetic field applied along the in-plane MgO [100] direction.

HE-08. Anisotropy Modulation and Strain Analysis in Yttrium Iron Garnet and Lutetium Iron Garnet Superlattices with Nanometer Scale Layers

T. P. Grossmark, E. Park, C. Chang, F. Ross, C. A. Ross
Materials Science and Engineering, The Massachusetts Institute of Technology, Cambridge, Massachusetts, United States

Rare earth iron garnets (REIGs) are a class of ferrimagnetic oxides demonstrating a wealth of attractive magnetic properties. Despite numerous demonstrations of emergent properties in other oxide interfaces [1], there is little work on magnetic garnet superlattices. We previously synthesized a variety of REIG superlattices using pulsed laser deposition and characterized layering via scanning transmission electron microscopy (STEM) and X-ray diffraction (XRD) [2] but found an increase in interface roughness for films thicker than 25 nm. Here we describe superlattices of yttrium iron garnet (YIG) and lutetium iron garnet (LuIG) with nm layer thickness (Fig. 1). XRD showed satellite peaks indicative of the superlattice period and atomic force microscopy gave RMS roughness values below 0.5 nm. Vibrating sample magnetometry showed an in-plane easy axis with in-plane coercivities below 1 mT and saturation magnetizations (M_s) of 120 kA/m. In a series of multilayers with the same period of ~4 nm but varying YIG/LuIG layer ratios, ferromagnetic resonance (FMR) measurements demonstrate a change in anisotropy field from -0.18 to -0.05 T as the LuIG content increased (Fig. 2). The reduction in

anisotropy is a result of an increasing contribution from the tensile-strained LuIG. The films showed linewidths increasing from 1–4 mT and Gilbert damping increasing from $9x10^{-4}$ to $3.8x10^{-3}$ with increasing LuIG content. High angle annular dark field (HAADF) STEM of a multilayer with LuIG layers only ~0.54 nm thick showed in-plane lattice matching but a modulation in the out-of-plane strain that correlated with composition due to LuIGs higher lattice parameter mismatch with the substrate. These superlattices further the development of anisotropy engineering for low damping garnet thin films used in magnonics and spintronics applications.

References:
[1] H. Hwang, Y. Iwasa, M. Kawasaki *et al. Nature Mater* 11, 103–113 (2012)
[2] B. Khurana, A. Kaczmarek, C. T. Chou *et al. ACS Nano* 18, 52, 35269–35275 (2024)

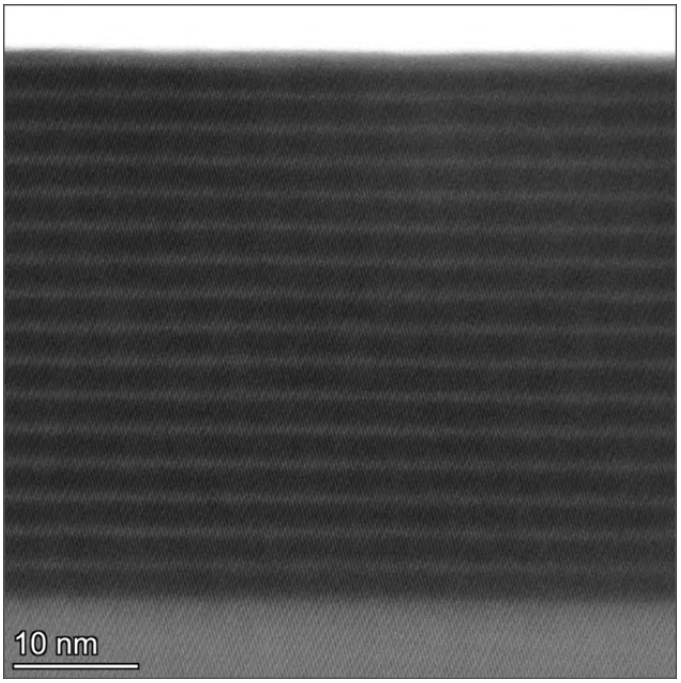


Fig. 1: HAADF-STEM image of YIG/LuIG superlattice. Bottom is gadolinium gallium garnet substrate, dark layers are YIG, and light are LuIG

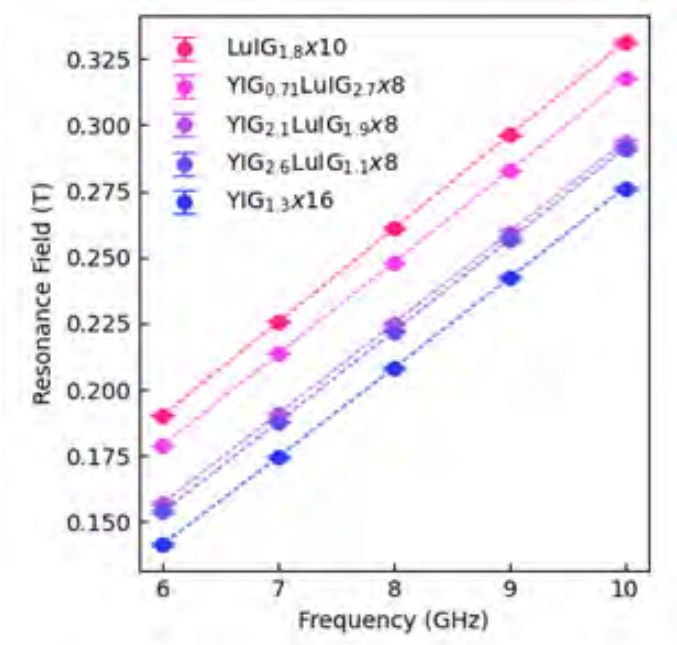


Fig. 2: FMR data for various films with 120 kA/m M_s. The subscript denotes the thickness of the layer in nm and the number after the *x* shows the number of repeats. Data is fit to the in-plane Kittel equation

HE-09. Thermal annealing under oblique magnetic field for controlling interlayer chiral coupling in ferromagnetic multilayers

Y. Hibino, T. Taniguchi, T. Yamamoto, H. Kubota, S. Yuasa, K. Yakushiji
Research Institute for Hybrid Functional Integration, National Institute of Advanced Industrial Science and Technology, Tsukuba, Ibaraki, Japan

Interlayer Dzyaloshinskii-Moriya interaction in ferromagnet/non-manget/ferromagnet (FM/NM/FM) structure promotes interlayer chiral coupling (ICC) between two ferromagnets which result in nontrivial chiral spin structure [1-7]. Such novel interlayer magnetic coupling enables field-free spin-orbit torque switching of perpendicular magnet for MRAM application [6]. While the presence of ICC has been demonstrated in various systems, several works have pointed out that both mangitude and direction of the ICC vary across devices [4,5,7], which is crucial obstcle for application. Therefore, new methods to control the direction and magnitude of ICC are highly demanded. Here, we offer a new method to control the

direction of the ICC by a post-annealing process under an oblique magnetic field.

To show the above concept, we prepared the FM/NM/FM structure consisting of perpendicularlay magnetized layer (PML) and in-plane magnetized layer (IML). The FM/NM/FM structure was annealed at 330 °C under a magnetic field of 1T applied along the polar angle ϑ_H from the out-of-plane direction. The oblique magnetic field can fix the magnetization of PML and IML in certain direction. During the annealing, atomic rearrangement occurs to achieve the stable magnetization configuration, resulting in the induction of ICC. The in-plane magnetization curves of IML annealed under ϑ_H = 60° along the *x*-axis are shown in Fig. 1(b). A shift of bias field (ΔH_s) was observed between the two polarities of the magnetization of PML (+*M* and -*M* states), which originats from the ICC-induced bias field acting on IML. Figure 1(c) shows the dependence of ΔH_s on ϑ_H. The sign of ΔH_s is reversed at ϑ_H =90°, indicating that the sign (or chirality) of the ICC is reversed. The results provide a novel method to design the interlayer magnetic coupling, which could be applied for spintronic devices.

This work was partly supported by Grant-in-Aid for JSPS KAKENHI (Nos. 23H01477 and 24K01336) and ALCA-Next program (No. JPMJCR18T3) of JST.

[1] E. Y. Vedmedenko et.al, Phys. Rev. Lett. 122, 257202 (2019). [2] A. Fernández-Pacheco *et al.*, Nat. Mater. 18, 679-684 (2019). [3] D.-S. Han *et al.*, Nat. Mater. 18, 703-708 (2019). [4] C. O. Avci *et al.*, Phys. Rev. Lett. 127, 167202 (2021). [5] H. Masuda *et al.*, Phys. Rev. Appl. 17, 054036 (2022). [6] W. He *et al.*, Nano Lett. 22, 6857-6865 (2022). [7] Y. Hibino et al., Appl. Phys. Express 19, 031004 (2026).

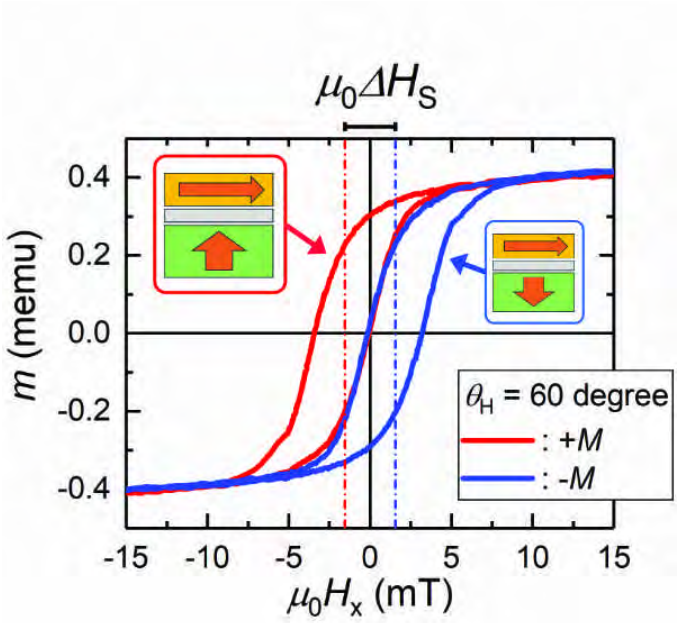


Fig. 1: Magnetization curve of IML under +*M* and -*M* state. The schematic shows the magnetization configuration of the system.

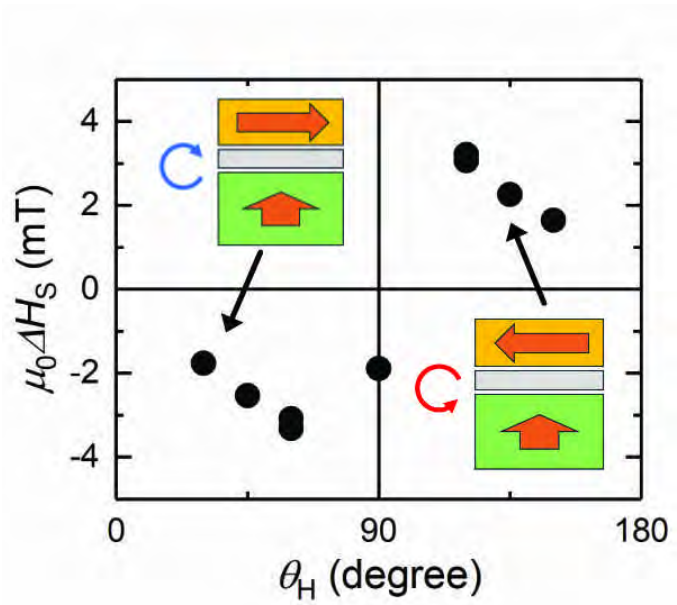


Fig. 2: ϑ_H dependence of the ICC-induced bias field $\mu_0\Delta H_s$. μ_0 is a permeability in vacuum.

HE-10. Spin interactions in hybrid nanostructures composed of chiral molecules adsorbed on a magnetic substrate

L. T. Baczewski[2], S. Yochelis[1], Y. Paltiel[1]
[1]Institute of Applied Physics, Hebrew University, Jerusalem, Israel, [2]Institute of Physics Polish Academy of Sciences, Warsaw, Poland

Enantioselectivity is present in nature and many of the molecules in plants and living organisms have their properties depending on the type of enantiomer. Enantioseparation is an extremely important process in the pharmaceutical and chemical industries. However, despite intensive efforts, obtaining enantiomerically pure synthetic materials remains a challenge, as the cost of separation is relatively high and an extensive effort is required. We have demonstrated a new effect of magnetization switching of ferromagnetic thin film without applying a magnetic or electric field but induced solely by adsorption of chiral molecules. The direction of the magnetization depends on the handedness of the adsorbed chiral molecules. The local magnetization switching is achieved by adsorbing the chiral molecules as a self-assembled monolayer (SAM) on a gold-coated FM layer with perpendicular magnetic anisotropy. The direction of the magnetization depends on the handedness of the adsorbed chiral molecules. It is commonly assumed that recognition and discrimination of chirality, both in nature and in artificial systems, depend solely on spatial effects. However, recent studies have suggested that charge redistribution in chiral molecules manifests an enantiospecific preference in electron spin orientation. Therefore it is possible that the induced spin polarization may affect enantio-recognition through exchange interactions. We have shown experimentally that the interaction of chiral molecules with a perpendicularly magnetized substrate is enantiospecific. Thus, one enantiomer adsorbs preferentially when the magnetic dipole is pointing up, whereas the other adsorbs faster for the opposite orientation of the magnetization. The interaction is not controlled by the magnetic field per se, but rather by the electron spin orientations. The enantioselective interaction of chiral molecules and a magnetic substrate with perpendicular anisotropy provides a potentially generic chromatographic method for enantioseparation which does not require a specific and costly separating column. This new method may also allow the separation of chiral molecules from a mixture of molecules, either chiral or achiral.

[1] O. Ben Dor, S. Yochelis, A. Radko, K. Vankayala, E. Capua, A. Capua, S.-H. Yang, L. T. Baczewski, S. S. P. Parkin, R. Naaman, Y. Paltiel, Magnetization switching in ferromagnets by adsorbed chiral molecules without current or external magnetic field.
Nature Commun. 8, 14567 (2017)
[2] K. Banerjee-Ghosh, O. Ben Dor, F. Tassinari, E. Capua, S. Yochelis, A. Capua, S. H. Yang, S. S. P. Parkin, S. Sarkar, L. Kronik,
L. T. Baczewski, R. Naaman, Y. Paltiel, Separation of enantiomers by their enantiospecific interaction with achiral magnetic substrates
SCIENCE, Vol. 360, Issue 6395, pp. 1331-1334, (2018)
[3] Y. Kapon, D. Merhav, G. Finkelstein-Zuta, O. Blumen, N.i Melamed-Book, Y. Levi-Kalisman, I. Torchinsky, S. Yochelis, D. Sharon,
L.T. Baczewski, E. Gazit, Y. Paltiel, Controlling Amyloid Assembly Dynamics Using Spin Interfaces, ACS Nano, 19, 28326-28334 (2025)

HE-11. Understanding the structural origin of asymmetric interfacial interactions in nominally symmetric Pd/CoFeB/Pd multilayers

M. Singh[1], A. Khadiev[2], I. Carlomagno[3], A. Tiwari[4], s. K. Vayalil[2], D. Novikov[2], C. Meneghini[5], A. Gupta[1]
[1]Department of Physics, University of Petroleum and Energy Studies, Bidholi Campus, Dehradun, India, [2]Deutsches Elektronen-Synchrotron DESY, Hamburg, Germany, [3]Elettra Sincrotrone Trieste, Basovizza, Trieste, Italy, [4]UV Focus Group, Enschede, Netherlands, [5]Department of Science, Roma Tre University, Rome, Italy

Interfacial interactions between ferromagnetic (FM) layers and heavy metals (HM) underpin key spintronic phenomena, including interfacial Dzyaloshinskii–Moriya interaction (iDMI), proximity-induced magnetism (PIM), perpendicular magnetic anisotropy (PMA), and spin–orbit torque (SOT). In nominally symmetric HM/FM/HM multilayers, interfacial iDMI contributions should cancel due to inversion symmetry [1]. However, finite iDMI and asymmetric PIM observed in systems such as Pt/Co/Pt and Pt/CoFeB/Pt, pointing to inequivalence between FM-on-HM and HM-on-FM interfaces [2-4]. While iDMI fundamentally arises from spin–orbit coupling and interfacial electronic structure, atomic-scale variations in composition and local bonding are expected to play a crucial role in modulating these interactions. Here, we investigate such interfacial inequivalence in a Pd/CoFeB/Pd trilayer using depth-resolved X-ray fluorescence (XRF) and X-ray absorption spectroscopy (XAS) under X-ray standing wave (XSW) conditions, enabling sub-nanometer depth selectivity. The sample, grown on a WB4C

multilayer mirror with a Si wedge spacer, allows selective probing of the bottom interface, top interface, or film interior by tuning the standing wave field (Fig 1(a)). The q-dependent Fe and Co fluorescence exhibit distinct modulation profiles across the Bragg peak, indicating different depth distributions. The broader and smoother Fe response compared to Co suggests enhanced interdiffusion and a more spatially distributed interfacial environment for Fe, while Co remains relatively localized (Fig 1 (b)). Depth-selective, polarization-dependent XAS measurements further reveal pronounced structural asymmetry: the bottom interface exhibits a more ordered local environment, whereas the top interface is comparatively disordered, with the film interior showing intermediate behaviour (Fig 1(b)). Quantitative EXAFS analysis confirms systematic variations in coordination number, bond length, and disorder parameters across the layer, along with signatures of interfacial bond distortion. These results demonstrate that significant compositional and structural asymmetry emerges even in nominally symmetric HM/FM/HM stacks.

[1] P. Olleros-Rodríguez et al., ACS Appl. Mater. Interfaces 12 (2020) 25419.
[2] R. Lavrijsen et al., Phys. Rev. B 91 (2015)104414.
[3] A. V. Davydenko et al., Phys. Rev. B 103 (2021) 094435.
[4] B Ravi Kumar et al., J. Phys. D: Appl. Phys. 55 (2022) 445004.

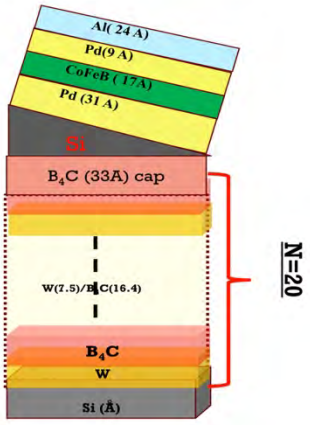


Fig 1(a)

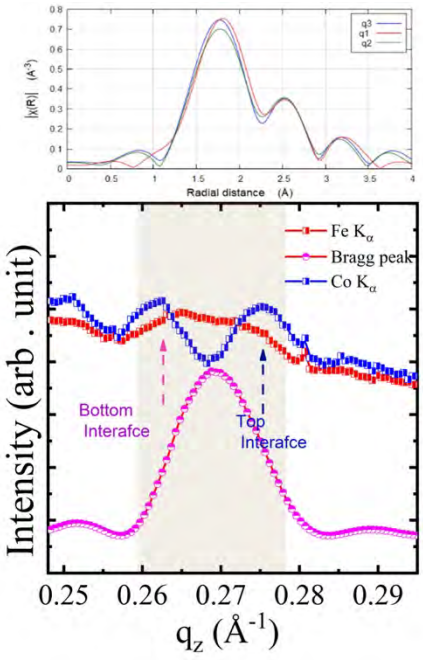


Fig 1(b)

HE-12. Proposal for Ferromagnetic Memtransistor Using Interfacial Proximity Exchange Confinement in a Semiconductor Quantum Well

V. C. Rogers[1, 2], J. Incorvia[1, 2]
[1]*Chandra Dept. of Electrical and Computer Engineering, University of Texas at Austin, Austin, Texas, United States,* [2]*Microelectronics Research Center, The University of Texas at Austin, Austin, Texas, United States*

There is growing demand for performant memories and memristive technologies for use in in-memory computing. Magnetic tunnel junctions (MTJs) have thus far addressed this need from the field of spintronics, though they are limited by their modest on/off ratio at room temperature. Inspired by room temperature exchange splitting in semiconducting EuO/Fe interfaces [2], we propose a memory device [1] that uses two layers of ferromagnetic insulator (FMI) cladding a semiconductor quantum well (QW), as shown in figure 1. A spin-orbit torque line doubling as a gate may allow for ultra-low power logic and memtransistor capabilities. Magnetoresistances in the magnetic quantum well field-effect transistor (MQW-FET) will operate via a bandgap modulation from spin-dependent interfacial electronic confinement.

We analytically derive [1] the energy spectrum, conductivities, and magnetoresistances of the device from a low-energy Hamiltonian model under varying operating conditions, as shown in figure 2. We find that the magnetoresistance (MR) is maximized at charge neutrality and predict that the MR will drop rapidly with gating. We estimate that this device has the potential for very high magnetoresistances possibly exceeding 10^4% at room temperature, supposing a sustained room-temperature interfacial magnetism.

This work motivates experimental demonstration in candidate materials and heterostructures, such as magnetic oxides or TMDs, which may ultimately advance the state of the art in logic, memory, or neuromorphic circuits by leveraging beyond-MTJ spintronic devices.

[1] Vivian Rogers, Jean Anne Incorvia, Arxiv. 2505.11767 (2025)
[2] J. Huang, C. Liu, Y. Ling, et. Al, Sci. Rep. 12 21863 (2022)

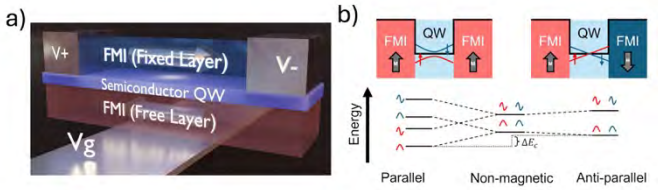


Fig. 1: (a) Diagram of the proposed device, with two FMIs cladding a thin QW. Two electrical contacts probe the resistance of the QW. A gate / spin-orbit write line is noted with Vg. (b) A band diagram and band-edge spectrum of the device is shown for parallel and antiparallel magnetizations.

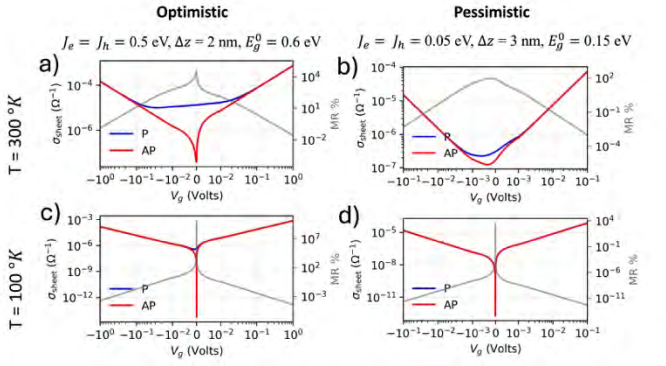


Fig. 2: Sheet conductivities and MRs are shown for a range of parameters [1]. (a,b) Show room temperature operation and (c,d) cryogenic operation respectively. (a,c) Show a highly optimistic case in a thin QW with strong exchange splitting, while (b,d) show poor penetration of the exchange fields in a thicker QW.

SESSION HF: SKYRMIONS

Chair(s): Y. Zhou, *The Chinese University of Hong Kong, Shenzhen, Shenzhen, Guangdong, China*
Friday, November 6, 2026
02:00 PM-05:30 PM
South Pacific 3/4

HF-01. Manipulation of skyrmions by insertion layer

H. Yuasa, Y. Kurokawa, L. Zhang, T. C. Cheng, K. Yamashita
Kyushu University, Fukuoka, Japan

Skyrmion is attracting lots attention for its small size and high transport velocity by low electric power using spin orbit torque (SOT). However, it is difficult to realize these three advantages at the same time, so called a trilemma. To overcome this problem, improving the SOT is paramount. We proposed to insert an ultrathin layer at the interface between heavy metal and PMA layers with skyrmions, based on the previous works increasing the spin mixing conductance [1]. However, as the insertion layer could change the interfacial Dzyaloshinskii-Moriya interaction (DMI) as well as spin mixing conductance, we quantitatively estimated the conditions necessary for skyrmion stabilization, i.e., the DMI coefficient [2]. Next, we moved on the demonstration and material selection for insertion layers. One group consists of rare earth metals, and the other consists of light metals. As rare earth metals, Ga and Tb were tested for two reasons. First, their large atoms would likely have a significant impact. Second, they would mix with Co to form a ferrimagnetic material, reducing the net magnetization and thus increasing the SOT efficiency. When inserting Gd, a clear SOT improvement was not observed and DMI was slightly reduced, increasing the population of Bloch type skyrmions [3]. In the case of Tb insertion, the SOT efficiency is increased by combining the heavy metal W layer. Nanoanalysis revealed that Tb does not decrease in magnetization because it mixes with Pt instead of Co, but when W is inserted, Tb mixes with Co and the magnetization decreases [4]. Compared to such rare-earth insertions, the light metals Ti and Cr showed 2.4 and 3.1 times increase in SOT efficiency [5]. Especially, Ti-insertion exhibited an increase in effective DMI field. In this way, we have been controlling DMI and SOT, and recently we have also succeeded in controlling a skyrmion Hall angle [6]. These results open up the possibility of using skyrmions as data carriers for information devices with high density, fast operation by small power.

[1] T. Niimura, et al., Phys. Rev. B Vol. 102, p.094411 (2020).
[2] T. C. Cheng, et al., Scientific Reports Vol. 15, p.7708 (2025).
[3] K. Tokunaga, et al., J. Phys. D: Appl. Phys. 58, p.135004 (2025).
[4] L. Zhang, et al., APL Materials Vol. 13, p.111112 (2025).
[5] L. Zhang, et al., AIP Advances Vol. 15, p.075304 (2025).
[6] K. Yamashita, et al., Jpn. J. Appl. Phys. Vol. 65 p.04SP16 (2026).

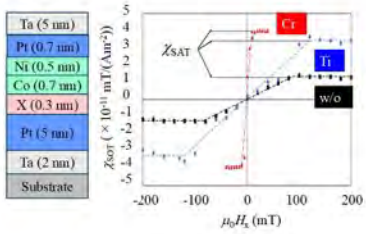


Fig. 1 Damping like torque exhibiting SOT efficiency and the composition depth profile from EDX analysis for [Pt(3.0)/Co(1.6)/Tb(1.0)] system and [Pt(1.5)/Co(*t*Co)/Tb(1.0)/W(1.5)] system.

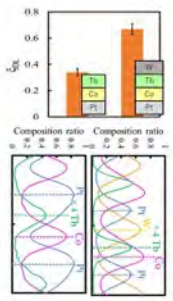


Fig. 2 SOT efficiency for [Pt(5.0)/X(0.3)/Co(0.7)/Ni(0.5)] system where X is Ti or Cr.

HF-03. Domain-Wall-Induced Skyrmion Attraction for Magnetic Memory Applications

M. Kameda[1, 2], Y. Kawaguchi[2, 3]
[1]Institute for Materials Research, Tohoku University, Sendai, Japan, [2]Department of Applied Physics, Nagoya University, Nagoya, Japan, [3]Research Center for Crystalline Materials Engineering, Nagoya University, Nagoya, Japan

Skyrmions are magnetic structures with a topological charge and are promising candidates for magnetic memory applications [1]. For practical use, skyrmion-based magnetic memory requires reliable control of skyrmions. One possible approach is to exploit interactions between skyrmions. However, conventional circular skyrmions interact only repulsively, which constrains trajectory control by requiring a minimum separation [2]. Recently, several systems exhibiting attractive skyrmion-skyrmion interactions have been reported [3,4], although the resulting attractions are typically weak compared to the exchange interaction scale. In the presentation, we propose domain-wall skyrmions (skyrmions with domain walls) as a platform for strong attractive interactions at the exchange-interaction scale [5]. These structures are numerically realized in a model serving as an effective Hamiltonian for Co–Zn–Mn alloys [6], incorporating strong magnetocrystalline anisotropy into a minimal skyrmion-stabilizing Hamiltonian consisting of exchange, Dzyaloshinskii–Moriya, and Zeeman interactions. The background magnetization of excited skyrmions typically aligns with the external field via the Zeeman effect; however, strong anisotropy tilts them to minimize the total energy across multiple easy axes. As a result, skyrmions are embedded in a uniformly tilted background and form domain walls at their boundaries. In this configuration, neighboring skyrmions are connected through magnetic domains, leading to a significant energy gain, i.e., strong attractive interactions. Notably, this attraction can be tuned over two orders of magnitude by applying an in-plane magnetic field, demonstrating potentially high controllability of these skyrmions via external parameters. To assess the effects of lattice discreteness in skyrmion structures, the interactions and other physical properties of small-sized domain-wall skyrmions have recently been investigated [7,8]. As the strong attractions persist for such small skyrmions, they are promising candidates for high-density skyrmion-based magnetic memory. This robustness suggests the potential of domain-wall skyrmions as suitable information carriers not only in stable but also densely integrated devices.

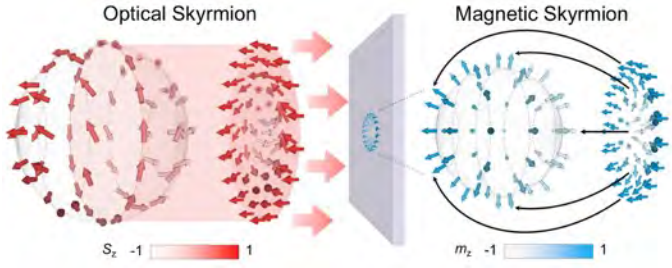
[1] N. Nagaosa and Y. Tokura, Nat. Nanotech. 8, 899 (2013).

[2] X. Zhang, G. P. Zhao, H. Fangohr, *et al*., Sci. Rep. 5, 7643 (2015).
[3] L. Rózsa, A. Deák, E. Simon, *et al*., Phys. Rev. Lett. 117, 157205 (2016).
[4] H. Du, X. Zhao, F. N. Rybakov, *et al*., Phys. Rev. Lett. 120, 197203 (2018).
[5] M. Kameda, R. Koyama, T. Nakajima, *et al*., Phys. Rev. B, 104, 174446 (2021).
[6] T. Nagase, Y. G. So, H. Yasui, *et al*.,Nat. Commun. 12, 3490 (2021).
[7] M. Kameda, K. Kobayashi, and Y. Kawaguchi, Sci. Rep. 16, 12941 (2026).
[8] M. Kameda *et al*., *submitted*.

HF-04. Magnetic Skyrmion Interacting with Optical Skyrmion

L. Bo, M. Mochizuki
Waseda University, Tokyo, Japan

We investigate the dynamics of a single magnetic skyrmion driven by an optical skyrmion beam composed of two orthogonally polarized Laguerre–Gaussian modes. Micromagnetic simulations reveal three nonlinear dynamical modes, namely rotation, skipping, and trochoidal motion. A Thiele-type analysis shows that the optical driving can be decomposed into gradient, orbital angular momentum, and spin angular momentum contributions, which govern radial confinement, azimuthal drift, and precessional modulation, respectively. In particular, the skipping motion is spatially selective and depends on the optical helicity and skyrmion chirality, providing a route to topology-enabled optomagnetic control. Extension to beam propagation further reveals a z-dependent asymmetry associated with the differential Gouy phase.



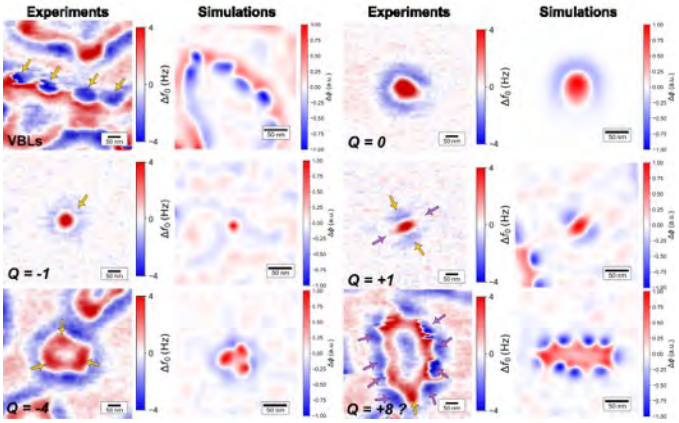
Schematic illustration of a magnetic skyrmion driven by an optical skyrmion beam.

HF-05. Magnetic Force Microscopy Signatures of Higher-Order Skyrmions and Antiskyrmions

S. Koraltan[1], J. Sunny[2], T. Karaman[2], R. Peremadathil-Pradeep[3], E. Darwin[3], F. Buettner[2], D. Suess[4], H. J. Hug[3], M. Albrecht[2]
[1]TU Wien, Vienna, Austria, [2]Uni Augsburg, Augsburg, Germany, [3]EMPA, Zurich, Switzerland, [4]Uni Wien, Vienna, Austria

Higher-order skyrmions and antiskyrmions are topologically protected spin textures carrying integer charges beyond ±1, typically nucleating from vertical Bloch lines (vBLs) within domain walls [1,2]. To date, their observation has been restricted to Lorentz transmission electron microscopy (LTEM) on ferromagnetic multilayers grown on ultrathin SiN membranes, which is challenging for future device integration. Furthermore, the LTEM contrast of different spin textures possesing different topological charges can be similar.
In my talk, I will show that magnetic force microscopy (MFM) operated under vacuum conditions provides a robust and substrate-independent route to identify and distinguish higher-order spin textures in Co/Ni multilayers at room temperature [3]. Guided by large-scale micromagnetic simulations [4], we establish a set of universal MFM fingerprints: higher-order skyrmions ($Q < 0$) exhibit $|Q|-1$ localized attractive lobes within a continuous shadow contrast, whereas higher-order antiskyrmions ($Q > 0$) display $|Q|+1$ repulsive lobes localized at head-to-head Néel segments. After confirming the presence of skyrmionic textures by LTEM, we resolve isolated vBLs as well as spin objects with topological charges up to $Q = +10$ directly by MFM, in excellent agreement with simulations; see Figure 1. Our results establish vacuum MFM as a powerful, device-compatible technique for the qualitative classification of complex spin textures with arbitrary topological charge, opening new opportunities for skyrmionic reservoir and unconventional computing concepts.

[1] M.H, Sabri Koraltan et al. "Dipolar skyrmions and antiskyrmions of arbitrary topological charge at room temperature." *Nature physics* 20.4 (2024): 615-622.
[2] Sabri Koraltan, et al. "The 2026 Skyrmionics Roadmap." *arXiv preprint arXiv:2601.16575* (2026).
[3] Sabri Koraltan, et al. "Magnetic Force Microscopy Signatures of Higher-Order Skyrmions and Antiskyrmions." Advanced Functional Materials (2026): e25716.
[4] F.B., Sabri Koraltan et al. "magnum. np: a PyTorch based GPU enhanced finite difference micromagnetic simulation framework for high level development and inverse design." *Scientific Reports* 13.1 (2023): 12054.



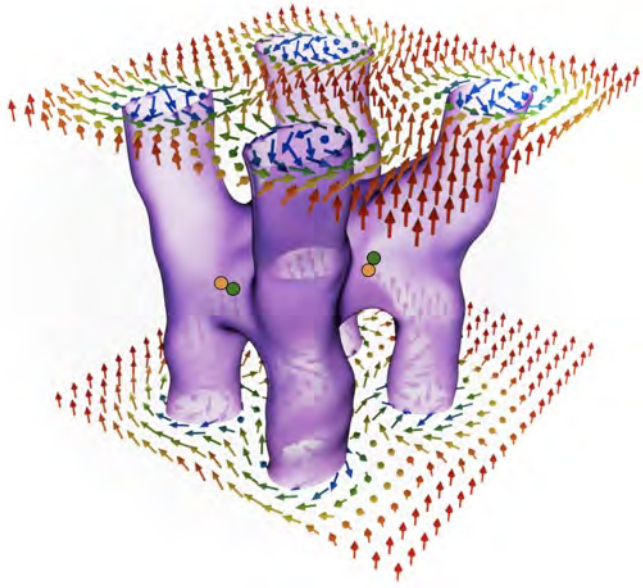
Comparison of experimental and simulated MFM contrasts of different spin-textures.

HF-06. Unwinding Skyrmions in Three Dimensions Through Vortices and Monopoles

M. Henderson[1], D. Kurebayashi[2], B. Heacock[3], W. Chen[3], C. Clark[3], D. Cory[4], D. Sarenac[5], S. Watson[3], J. S. White[6], L. DeBeer-Schmitt[1], O. Tretiakov[2], D. Pushin[7]

[1]Neutron Scattering Division, Oak Ridge National Laboratory, Oak Ridge, Tennessee, United States, [2]Physics, University of New South Wales, Sydney, New South Wales, Australia, [3]Center for Neutron Research, National Institute of Standards and Technology, Gaithersburg, Maryland, United States, [4]Chemistry, University of Waterloo, Waterloo, Ontario, Canada, [5]Physics, University at Buffalo, Buffalo, New York, United States, [6]Center for Neutron and Muon Sciences, Paul Scherrer Institute, Villigen, Aargau, Switzerland, [7]Physics, University of Waterloo, Waterloo, Ontario, Canada

Magnetic skyrmions represent non-collinear topological spin textures which nucleate and annihilate on magnetic singularities. In three dimensions, their stabilization into flexible tubes introduces enhanced dimensionalities and emergent phenomena which endows them with superior functionalities as information carriers in future spintronic devices. Unfortunately, a lack of bulk probes has prevented their complete characterization in three dimensions, inhibiting the development of modern skyrmion device architectures. Here, we present novel experimental visualizations of three-dimensional skyrmion field-induced topological transition pathways across various bulk triangular lattice skyrmion hosts with tunable disorder. Ordered skyrmion states reveal exotic periodic modulations, while disordered states uncover a zoology of exotic metastable Q=0 skyrmion bundles with novel transition pathways via the coupling of merons and monopoles. We explore skyrmion phase energetics as a function of compositional disorder, highlighting topological transitions through vortex and defect-mediated pathways. Our results provide unrivaled access to three-dimensional skyrmion phenomena across diverse compositional systems, unveiling novel methods of nucleation and control to reshape future devices.


Illustration of typical skyrmionium topological transition observed in three-dimensional reconstructions through the merging and separation of 4 individual skyrmion tubes, with coupled monopoles and antimonopoles at transition points.

HF-07. Direct Time-Resolved Imaging of Collective Dynamics in Antiferromagnetic Skyrmion Lattices

T. Dohi[1, 2], M. Bhukta[2], K. Leutner[2], M. Syskaki[2], F. Kammerbauer[2], D. Tran[2], S. Wintz[3, 4], M. Weigand[3, 4], R. Frömter[2], M. Kläui[2]

[1]Research Institute of Electrical Communication (RIEC)), Tohoku University, Sendai, Miyagi, Japan, [2]Institut für Physik, Johannes Gutenberg-Universität Mainz, Mainz, Germany, [3]Max Planck Institute for Intelligent Systems, Stuttgart, Germany, [4]Materialien und Energie GmbH, Helmholtz-Zentrum Berlin, Berlin, Germany

Antiferromagnetic skyrmion lattices in fully compensated synthetic antiferromagnets offer a unique platform for high-density transport of topological spin textures because long-range stray fields and the skyrmion Hall effect are strongly suppressed [1–3]. While fractional antiferromagnetic skyrmion lattices have been reported, their real-space nanosecond dynamics and interaction laws remain largely

unexplored [4]. Here, we use element-selective pump–probe X-ray microscopy to directly image the collective dynamics of a fully compensated antiferromagnetic skyrmion lattice [5]. At low current density, we identify a distinct incoherent-flow regime in which mobile skyrmions are driven toward pinned neighbours, producing transient local compression and a scattering-mediated recoil after the pulse. Inverse analysis of the reproducible post-pulse relaxation trajectories based on the Thiele equation yields an exponentially decaying skyrmion–skyrmion interaction potential with a characteristic range of about 30 nm, in good agreement with micromagnetic simulations. At higher current density, the lattice enters a coherent viscous-flow regime with uniform translation, no measurable skyrmion Hall deflection, no inertial lag within 1 ns resolution, and no dynamical deformation. We further show that in chiral synthetic antiferromagnetic multilayers, the stripe-domain period can be strongly programmed by interlayer exchange across the antiferromagnetic-to-ferromagnetic transition, providing a route to tune the equilibrium lattice spacing that ultimately governs dense antiferromagnetic skyrmion ensembles. These results establish a quantitative framework for collective antiferromagnetic skyrmion dynamics and static length-scale engineering in compensated multilayers.

[1] T. Dohi *et al*., Nat. Commun. 10, 5153 (2019).
[2] W. Legrand *et al*., Nat. Mater. 19, 34 (2020).
[3] V. T. Pham *et al*., Science 384, 307 (2024).
[4] S. Gao *et al*., Nature 586, 37 (2020).
[5] M. Bhukta *et al*., arXiv:2508.17967.

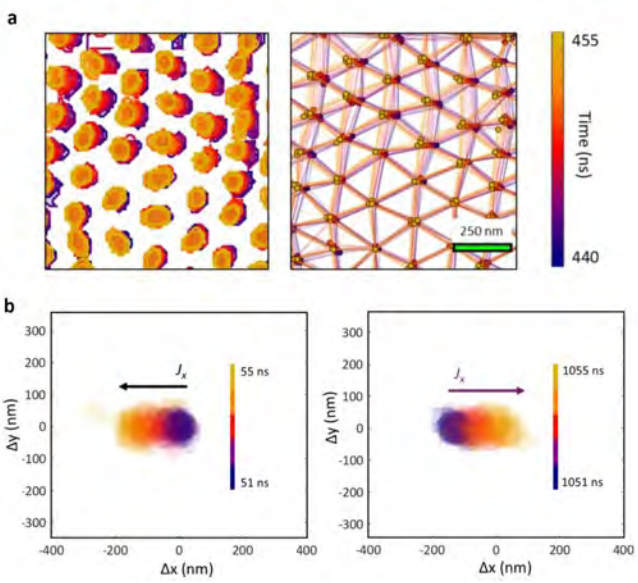


Fig. 1 Nanosecond dynamics of AFM skyrmions (a) in the incoherent-flow regime and (b) in the viscous flow regime.

HF-08. Reliable Switching of Skyrmion Polarity in [Pt (3 nm)/Co (0.8 nm)/Ta (4 nm)]$_{15}$ Multilayered structures

M. Kang[1, 2], H. Han[3], M. Im[1], K. Lee[2]
[1]Center for X-ray Optics, Lawrence Berkeley National Laboratory, Berkeley, California, United States, [2]Ulsan National Institute of Science and Technology, Ulsan, Korea (the Republic of), [3]Korea National University of Transportation, Chungju, Korea (the Republic of)

Magnetic skyrmions, topologically protected quasiparticle-like spin texture, are attracting great interest as a building block for advanced spintronics devices, such energy efficient high dense memory, logic, and computing technologies. The unique topological properties of skyrmions allow them to be stable, densely arranged, and efficiently driven by electric currents [1]. While skymion research has primarily focused on generation, annihilation, and current-driven motion at room temperature [2-4], the switching of skyrmion polarity have rarely been explored [5], despite of its scientific importance and high relevant to technological application. Moreover, a reliable and systematic control of skyrmion polarity switching, particularly at room temperature (RT), has not yet been reported. In our work, we demonstrated that the skyrmion polarity can be reliably switchable at room temperature in perpendicularly magnetized [Pt (3 nm)/Co (0.9 nm)/Ta (4 nm)]$_{15}$ multilayers [6]. Utilizing magnetic transmission soft x ray microscopy (MTXM), we directly observed the switching of skyrmion polarity by injecting current pulses under applied out of plane magnetic fields. Through systematic experiments varying the strength of external magnetic field and the parameters of current pulses, such as the amplitude and the width, we found that switching of skyrmion polarity is highly controllable with specific pulse parameters and magnetic field strength. According to micromagnetic simulations conducted to understand the mechanism of skyrmion polarity switching, thermal effects induced by injected current pulses, combined with other factors such as spin-orbit torque, contribute to the polarity switching, indicating that well-defined manipulation factors are essential for selecting a specific skyrmion polarity in a perpendicularly magnetized multilayer structure at room temperature. This study not only provides insights into the underlying physics of nanospin phenomena, but also contributes to broadening the potential of skyrmions in future electronic technologies by demonstrating the reliable control of skyrmion polarity, which provides an additional binary degrees of freedom.

[1] A. Fert, N. Reyren and V. Cros, Nat. Rev. Mater., Vol. 2,

p.17031 (2017)
[2] K. Litzius, I. Lemesh and B. Krüger, Nature Phys., Vol. 13, p.170 (2017)
[3] S. Je, H. S. Han and S. K. Kim, ACS Nano, Vol. 14, p.3251 (2020)
[4] S. Woo, K. Litzius and B. Krüger, Nature Mater., Vol. 15, p.501 (2016)
[5] X. Zhao, J. Tang and K. Pei, Nano Lett., Vol. 22, p.8793 (2022)
[6] M. Kang et al., to be submitted (2026)

HF-09. Bias-engineered synthetic antiferromagnets hosting sub-20 nm zero-field skyrmions at room temperature

E. Darwin[1], R. Tomasello[2], R. Peremadathil-Pradeep[1, 3], M. Carpentieri[2], G. Finocchio[4], H. J. Hug[1, 3]
[1]Empa, Dübendorf, Switzerland, [2]Politecnico di Bari, Bari, Italy, [3]University of Basel, Basel, Switzerland, [4]University of Messina, Messina, Italy

Magnetic skyrmions are topologically protected nanoscale spin textures with strong potential for high-density, low-power spintronic technologies. However, stabilizing small skyrmions at zero external magnetic field, particularly in synthetic antiferromagnets (SAFs), remains a central challenge [1-2].
We introduce a bias-engineered SAF architecture that enables robust zero-field stabilization of both ferromagnetic (FM) and SAF skyrmions with deterministic polarity control. The approach employs a compensated SAF bias layer that generates a uniform internal exchange field while suppressing domain formation. Ferromagnetic and fully compensated SAF multilayers were fabricated by magnetron sputtering and characterized using high-sensitivity quantitative magnetic force microscopy (MFM) combined with micromagnetic simulations [3].
With zero external field, the SAF bias system stabilizes ferromagnetically coupled skyrmions in the FM multilayer system and antiferromagnetically coupled skyrmions in the SAF multilayer system. This is confirmed by micromagnetic simulations. In both systems, the skyrmions are polarity controllable via a preparatory field application. Quantitative reconstruction of the measured spin textures reveals SAF skyrmions that have diameters as small as 12 nm, representing the smallest experimentally observed SAF skyrmions to date. The bias concept provides a scalable and materials-agnostic pathway toward zero-field operation, size reduction, and polarity control of chiral spin textures, advancing the integration of compensated skyrmions into energy-efficient spintronic devices.

[1] R. Juge, et al., Nat. Comm. 13, 1 (2024).
[2] E. Darwin, et al., Sci. Rep. 14, 95 (2024).
[3] E.Darwin et al. (under review 2026).

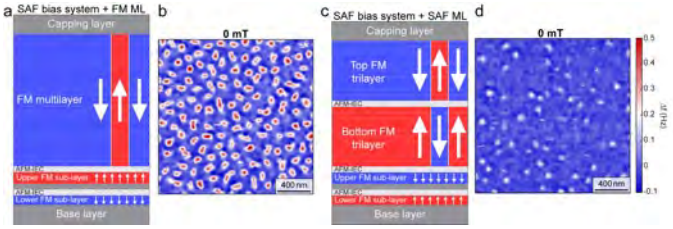


Fig. 1. Schematic of (a) the FM multilayer with the SAF bias system below and (b) the corresponding zero-field MFM data. (c) the SAF multilayer with the SAF bias system belowand (d) the corresponding zero-field MFM data.

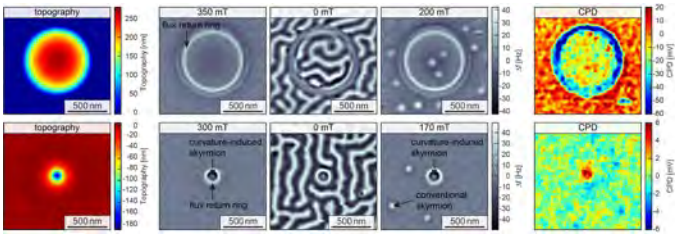
HF-10. Skyrmions induced and suppressed by curvilinear Defects observed by MFM

H. J. Hug[1, 2], E. Darwin[1], D. Rothhardt[1, 2], R. Peremadathil-Pradeep[1, 2], L. Berchialla[3, 4], A. Hrabec[4]
[1]Magnetic and Functional Thin Films, Empa, Duebendorf, Switzerland, [2]Department of Physics, University of Basel, Basel, Switzerland, [3]Empa, Duebendorf, Switzerland, [4]PSI, Villigen, Switzerland

Curvilinear substrates provide a promising route for tailoring the magnetic properties of multilayer systems and may enable the stabilization of topologically non-trivial spin textures such as skyrmions [1]. Here, we deposit Ta(3)/Pt(10)/[Pt(0.7)/Co(1.7)/Ru(1.3)]$_6$/Pt(3) multilayers with perpendicular magnetic anisotropy (PMA) and interfacial Dzyaloshinskii–Moriya interaction (iDMI) onto PMA substrates featuring microfabricated convex and concave curvilinear defects with radii between 100 and 600 nm. We investigate the resulting magnetic configurations using in-vacuum high-sensitivity magnetic force microscopy (MFM) [2] operated with capacitive, frequency-modulated tip–sample distance control [3], enabling simultaneous mapping of topography, contact potential difference (CPD), and magnetic contrast.
For larger defects, stripe domains formed on concave bumps are disconnected from those in the surrounding flat regions. Upon application of sufficiently strong magnetic fields, these stripes evolve into multiple skyrmions both inside and outside the defects, indicating no clear signature of curvature-induced DMI effects. In contrast, for defects with diameters around 200 nm, a pronounced asymmetry between concave bumps and convex dips emerges when reducing the applied field from near saturation. While the magnetization on the bumps remains aligned with the

saturation field direction, a robust, ultra-small skyrmion consistently nucleates inside all convex dips. In agreement with theoretical predictions [1], the radius of these curvature-induced skyrmions is significantly smaller than that of sparse, conventional skyrmions appearing outside the defects at comparable fields. In addition, we observe curvature-dependent variations in CPD, possibly indicating the presence of electric fields associated with non-collinear magnetization textures.

1. V. P. Kravchuk, et al., Phys. Rev. Lett. 120, 067201 (2018).
2. Y. Feng, et al., J Magn Magn Mater 551, 169073 (2022).
3. X. Zhao, et al., New Journal of Physics 20, 013018 (2018).



Topography, magnetic and CPD signals obtained on a 800nm diameter bump (top row) and 200nm diameter dip. A curvature-induced skyrmion appears at the center of the dip.

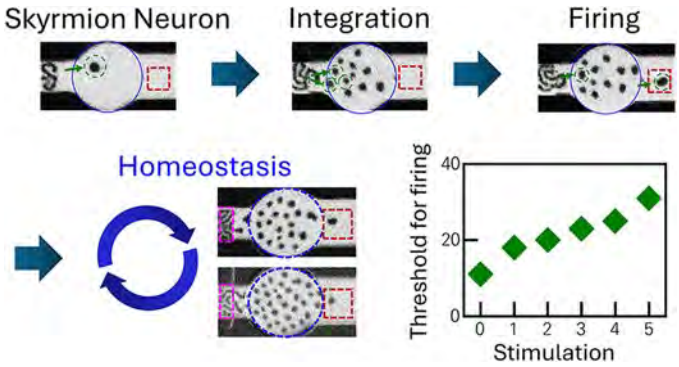
HF-11. Hardware Implementation of Homeostasis in a Magnetic Skyrmion-based Spiking Neuron Unit

S. Yang[1], K. Moon[1], T. Ju[1, 2], J. Son[1], T. Kim[3], Y. Jeong[3], B. Park[4], S. Park[2], C. Hwang[1]

[1]Quantum Technology Institute, Korea Research Institute of Standards and Science, Daejeon, Korea (the Republic of), [2]Department of Physics, Pusan National University, Busan, Korea (the Republic of), [3]Center for Neuromorphic Engineering, Korea Institute of Science and Technology, Seoul, Korea (the Republic of), [4]Department of Physics, Konkuk University, Seoul, Korea (the Republic of)

Breakthroughs in artificial intelligence (AI) are reshaping everyday routines and accelerating developments across various scientific disciplines. Within emerging AI frameworks, spiking neural networks (SNNs) draw significant attention since they mimic the spike-driven data processing of natural brain cells. As AI transitions from cloud-centered data processing to edge computing, hardware realizations of SNNs (H-SNNs) are being extensively investigated for their capabilities in energy-efficient, stimulus-responsive data management. H-SNN architectures demand device-level realizations of essential neuronal and synaptic functions, including leaky-integrate-and-fire (LIF) dynamics or spike-timing-dependent plasticity (STDP) learning. Furthermore, homeostasis, which controls the firing frequency, is equally vital for maintaining stable operation and improving overall network performance. Here, we report an experimental demonstration of a skyrmion-based spiking neuron device and, importantly, the hardware-level implementation of homeostasis [1]. These findings indicate a novel pathway toward power-efficient neuromorphic systems and highlight the potential of skyrmionic devices as fundamental units for upcoming AI edge technologies.

[1] S. Yang, K.-W. Moon, T.-S. Ju, et al., ACS Nano, 20, 1, 240-247 (2026)



HF-12. Light-Driven Skyrmion Crystal Generation in Plasmonic Metasurfaces Through the Inverse Faraday Effect

X. Yang[1], T. da Câmara Santa Clara Gomes[2], N. Reyren[4], J. Gartside[3], M. Mivelle[5]

[1]Dalian University of Technology, Dalian, China, [2]Instituto de Engenharia de Sistemas E Computadores – Microsistemas e Nanotecnologias, Lisbon, Portugal, [3]Imperial College of London, London, United Kingdom, [4]Laboratoire Albert Fert, CNRS, Thales, Université Paris-Saclay, CNRS, Paris, France, [5]CNRS/Sorbonne University, Paris, France

Magnetic skyrmions are topologically robust nanoscale spin textures that hold immense potential for the development of high-density, low-energy spintronic devices. While their optical analogs have opened new frontiers in nanoscale light manipulation, achieving the ultrafast, all-optical generation of magnetic skyrmions remains a major challenge. In this work, we demonstrate the generation of a large-scale magnetic skyrmion lattice by exploiting the Inverse Faraday Effect (IFE) [1-4] on a specifically engineered plasmonic metasurface. Our platform consists of a hexagonal array of gold nanodisks where the transfer of spin angular momentum induces unidirectional drift photocurrents within each disk. Crucially, the interplay between these localized currents and opposite "phantom" currents flowing through the hexagonal interstices creates a stable, periodic arrangement of skyrmionic magnetic

textures. By harnessing plasmonic resonances to enhance local electromagnetic fields, we maximize the IFE-induced magnetization on femtosecond-to-picosecond timescales. This entirely optical and ultrafast mechanism provides a novel pathway to integrate skyrmions into nonmagnetic substrates or thin magnetic films, paving the way for advanced architectures in next-generation spintronics, high-density data storage, and logic applications.

[1] Yang, X.; Mou, Y.; Gallas, B.; Maitre, A.; Coolen, L.; Mivelle, M., Tesla-Range Femtosecond Pulses of Stationary Magnetic Field, Optically Generated at the Nanoscale in a Plasmonic Antenna. ACS Nano 2021.
[2] Mou, Y.; Yang, X.; Gallas, B.; Mivelle, M., A chiral inverse Faraday effect mediated by an inversely designed plasmonic antenna. Nanophotonics 2023, 12 (12), 2115-2120.
[3] Yang, X.; Mou, Y.; Zapata, R.; Reynier, B.; Gallas, B.; Mivelle, M., An inverse Faraday effect generated by linearly polarized light through a plasmonic nano-antenna. Nanophotonics 2023
[4] Yang, X.; Mou, B.; Gallas, B.; Bidault, S.; Mivelle, M., From Dark Modes to Topology: Light-Induced Skyrmion Generation in a Plasmonic Nanostructure Through the Inverse Faraday Effect. Nanophotonics 2025

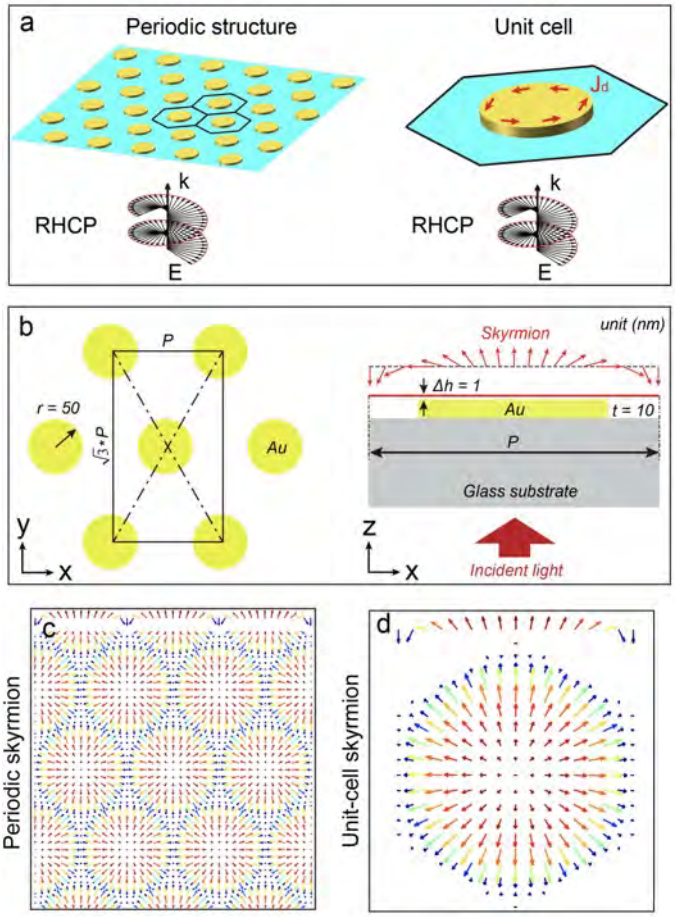


Fig. 1. All-optical generation of a magnetic skyrmion lattice via the Inverse Faraday Effect (IFE). a) Schematic of the plasmonic metasurface composed of gold nanodisks arranged in a hexagonal lattice on a glass substrate, excited by a right-handed circularly polarized plane wave. b) Top view showing the geometric parameters of the unit cell. c) Vector distribution of the IFE-induced magnetic field across the periodic structure, revealing the formation of a large-scale skyrmion lattice. d) Detailed view of the magnetic texture within a single unit cell, highlighting the characteristic topological winding.

HF-13. Magnetic Skyrmions in MnSi and MnSi/(Fe,Co,Mn)Si Thin-Films

C. C. Buchanan[1], N. Liyanage[2], M. A. Maben[1], M. Henderson[3], L. DeBeer-Schmitt[3], D. A. Gilbert[1, 2]
[1]Materials Science and Engineering, University of Tennessee, Knoxville, Knoxville, Tennessee, United States, [2]Physics and Astronomy, University of Tennessee, Knoxville, Knoxville, Tennessee, United States, [3]Neutron Scattering Division, Oak Ridge National Lab, Oak Ridge, Tennessee, United States

As more energy is used in data storage, higher data storage density and lower energy cost becomes increasingly important. Magnetic skyrmions are an attractive choice to address both concerns, as their topological protection shields them from data corruption, and their small size allows for much higher storage density than conventional domain wall storage [1]. One challenge in integrating skyrmions into existing device architecture is that skyrmion materials typically require specific substrates to form the correct crystal structure for hosting skyrmions. For example, MnSi is most commonly grown on the 7x7 reconstructed surface of Si (111) [2,3,4], which only exists at high temperatures on perfectly clean Si [5]. Successfully growing MnSi on this surface requires a precise sequence of cleaning and controlled temperature change under vacuum, which can be lengthy and hard to transfer across different chambers. We have simplified the process by using an in-situ magnetic field normal to the substrate surface during RF magnetron sputtering with room temperature deposition and a separate post-deposition annealing step. Additionally, we have shown that this technique can be used to expand the available substrates for depositing MnSi. This talk will present x-ray diffraction (XRD) data and magnetometry (Fig. 1) for a selection of MnSi films grown with and without an in-situ magnetic field on several substrates. Using this highly scalable method, we were able to prepare large area samples and perform small-angle neutron scattering (SANS) measurements of these MnSi thin-films. The SANS data (Fig. 2) corroborate the presence of skyrmions in MnSi films on Si (100) in the dilute temperature and field range of the stable skyrmion window. XRD and magnetometry indicate improvements in both crystal structure and magnetic properties for films deposited in the presence of a magnetic field. Additionally, we present data showing that doping the MnSi films with Fe and Co results in modified skyrmion stability windows due to the alteration of the exchange and DMI.

[1] X. Zhang et al, *Sci Rep* 5, 7643 (2015).
[2] B. Geisler et al, *Phys Rev B* 86, 115428 (2012).
[3] L. Hu, B. Huang, F. Liu, *Phys Rev Letters* 126, 176101 (2021).
[4] T. Suzuki et al, *Surface Science, 617* (2013).
[5] T. Suzuki et al, *Phys. Chem. Chem. Phys.* 11, 6498-6504 (2009).

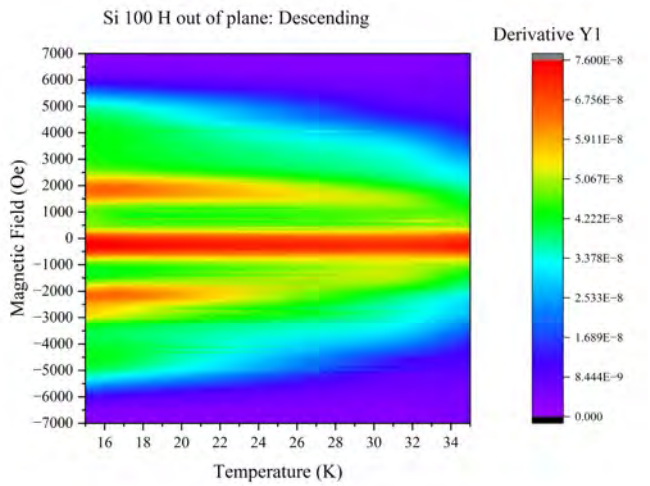


Fig. 1 Magnetometry of MnSi on Si(100).

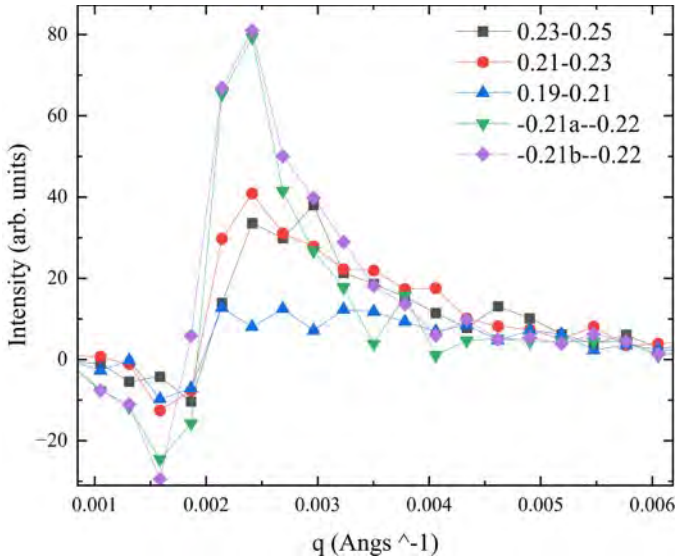


Fig. 2 I vs q of subtracted adjacent field measurements of MnSi on Si (100).

HF-14. Imaging skyrmion phases - from topological phase transitions to flow dynamics phases

R. Gruber, M. Bhukta, J. Rothörl, S. M. Fröhlich, M. A. Brems, K. Leutner, D. Tran, S. Krishnia, R. Frömter, P. Virnau, M. Kläui
Physics, Johannes Gutenberg University Mainz, Mainz, Germany

Novel spintronic devices can play a role in the quest for Green IT if they are stable and can transport and manipulate spin with low power. Devices have been proposed, where switching by energy-efficient approaches is used to manipulate topological spin structures that are stable in multilayers [1] and are manipulated rapidly and with low power using spin-orbit and orbital torques [2-4].

Ensembles of topological spin structures, such as skyrmions exhibit particularly exciting properties as they behave as 2D quasi-particles that form ordered phases. 2D is special because only in 2D, topological phase transitions between the hexatic phase that is unique to 2D exist [5]. Based on thermal dynamics of skyrmions, we can observe by dynamic real-space imaging the stochastic skyrmion dynamics in real-space and real-time [5]. We find that the topological phase transition is mediated by topological defects, such as dislocations and disclinations. The dislocations form as pairs for defects in the hexagonal lattice that then split into disclinations when order becomes lost. As a key observation, the dynamics of the dislocations is found to be orders of magnitude faster than the dynamics of the skyrmions, making topological defects a potential new fast information carrier [5]. By analysis of the defect dynamics using quasi-particle simulations and x-ray based microscopy, we can show how topological defects in these phases can be controlled and manipulated (unpublished).

Finally, we use x-ray microscopy to image the dynamical phases of skyrmion flow. While for single skyrmions, viscous flow dynamics was imaged using dynamic scanning transmission x-ray microscopy [6], ensembles of skyrmions exhibit more complex dynamics. We have recently revealed an incoherent flow regime, where skyrmions exhibit different dynamics within the same lattice at the same time, while showing fully reproducible motion [7]. This dynamical phase allows us to ascertain the interaction potentials dynamically in a regime not previously possible. We also reveal the transition between the different dynamical phases from a pinned via the incoherent flow to the coherent flow phase, which is distinctly different from the dynamics of single skyrmions.

[1] K. Everschor-Sitte et al., J. Appl. Phys., vol. 124, no. 24, 240901, 2018.
[2] S. Woo et al., Nature Mater., vol. 15, no. 5, pp. 501-506, 2016.
[3] K. Litzius et al., Nature Electron., vol. 3, no. 1, pp. 30-36, 2020.
[4] S. Fukami et al., Nature Phys. (2025); DOI:10.1038/s41567-025-03143-w
[5] R. Gruber et al., Nature Nanotechnol. 20, 1045 (2025)
[6] K. Litzius et al., Nature Phys., vol. 13, no. 2, pp. 170-175, 2017
[7] M. Bhukta et al., arxiv:2508.17867

SESSION HG: MAGNONICS III

Chair(s): S. Viola Kusminskiy, *RWTH Aachen University, Aachen, Germany*
Friday, November 6, 2026
02:00 PM-05:30 PM
Sea Pearl

HG-01. Nanosecond Phase Ordering in an Ultra-Large Spin Hall Nano-Oscillator Lattice: Towards Ultra-Fast Ising Machines

N. Behera[1, 4], A. Chaurasiya[1], A. Kumar[1, 2, 3], L. Bainsla[1, 5], A. Litvinenko[1, 6], R. Khymyn[1], A. A. Awad[1, 2, 3], J. Akerman[1, 2, 3]
[1]Department of Physics, University of Gothenburg, Gothenburg, Sweden, [2]Research Institute of Electrical Communication, Tohoku University, Sendai, Japan, [3]Center for Science and Innovation in Spintronics, Tohoku University, Sendai, Japan, [4]School of Basic Sciences, Indian Institute of Technology Bhubaneswar, Jatani, India, [5]Department of Physics, Indian Institute of Technology Ropar, Rupnagar, India, [6]Department of Physics, Oakland University, Rochester Hills, Michigan, United States

While mutually synchronized spin Hall nano-oscillators (SHNOs) [1] can be used for neuromorphic computing [2,3] and Ising machines [4,5], the number of mutually synchronized SHNOs has remained limited to 50 in chains [6] and 64 in 2D arrays [2]. To synchronize larger arrays, one must increase the oscillator coupling strength, for example, by packing them more closely, which requires smaller SHNOs. Using enhanced spin-orbit torque, replacing W with a $W_{88}Ta_{12}$ alloy [7], we demonstrated 10 nm SHNOs operating at threshold currents as low as 26 μA [8]. We then fabricated very large SHNO arrays and found that we can synchronize over 100,000 SHNOs, operating at up to 34 GHz, with quality factors exceeding 10^6. [9] Time-resolved Brillouin Light Scattering microscopy reveals ordering times

ranging from 10 to 50 ns, scaling logarithmically with the number of SHNOs, consistent with the Kuramoto model [10]. We have also demonstrated how we can control the sign and phase of the coupling between SHNOs using a combination of spin-wave-mediated coupling and voltage-controlled magnetic anisotropy [11]. Taken together, these results pave the way towards ultrafast SHNO-based Ising machines [4,5].

[1] A. A. Awad et al., Nature Physics 13, 292 (2017).
[2] M. Zahedinejad et al., Nature Nanotechnology 15, 47 (2020).
[3] M. Zahedinejad et al., Nature Materials 21, 81 (2022).
[4] A. Houshang et al., Phys. Rev. Appl. 17, 014003 (2022).
[5] B. C. McGoldrick et al., Phys. Rev. Appl. 17, 014006 (2022).
[6] A. Kumar et al., Nano Letters 23, 6720 (2023).
[7] N. Behera et al., Phys. Rev. Appl. 18, 024017 (2022)
[8] N. Behera et al., Advanced Materials 36, 2305002 (2024)
[9] N. Behera et al., arXiv:2501.18321 (2025); Nature Nanotechnology, *accepted*.
[10] V. Flovik et al., Scientific Report 6, 32528 (2016).
[11] A. Kumar et al., Nature Physics 21, 245 (2025).

HG-02. Study of Static and Dynamical Properties of Topological Magnetic Vortices with Spin Center in hBN

E. Gomes da Silva[1], H. A. Bukhari[1], C. Patrickson[2], M. Garman[2], P. S. Keatley[2], I. Luxmoore[2], D. R. Candido[1]
[1]Physics and Astronomy, University of Iowa, Iowa City, Iowa, United States, [2]University of Exeter, Exeter, United Kingdom

Spin centers defects in solid-state systems have emerged as a promising platform for different quantum technologies, including qubits and quantum sensors. Their frequency in the GHz range, together with their response to magnetic fields, has promoted magnetic hybrid quantum systems – composed of spin centers and magnets – as a novel platform for coherently controlling spin centers in diamond via magnon modes [1] and for generating magnon-mediated entanglement between spin centers at optically addressable distances [2-4]. Despite recent advances in magnonic hybrid systems, interfacing the spin center with topological magnetic structures and excitations remains largely unexplored. In this talk, we will present recent combined theoretical-experimental development on the study of spin centers coupled to topological soliton-magnetic vortices.

Our system of study consists of hBN hosting spin centers atop a NiFe thin film prepared with a topological-vortex magnetization profile. We first establish the capability of these spin centers to quantitatively reconstruct the static vortex-induced stray-field distribution via optically detected magnetic resonance, and we validate the measurements against theoretical predictions with micromagnetic simulations (MuMax3) and a self-consistent, home-built ODMR simulation of the spin center (See Fig. 1).

Having verified the vortex configuration, we then use spin centers to experimentally study the dynamics of magnetic vortices. Interestingly, we demonstrate that driving the system with ~0.1GHz microwave fields induces a change in the optical contrast, indicating that the gyration mode of the vortex core generates dynamical fringe fields resonant with the spin-center frequency transitions in the GHz regime. Interestingly, this nonlinear excitation of the spin centers occurs only above a threshold microwave power. All of our experimental results are quantitively explained and consistent with theoretical modeling of vortex magnetic dynamics via both micromagnetic simulations and analytical models combined with ODMR simulations.

[1] P. Andrich, F. Charles, X. Liu, H. L. Bretscher, J. R. Berman, F. J. Heremans, P. F. Nealey, and D. D. Awschalom, npj Quantum Inf. 3, 28 (2017).
[2] D. R. Candido, G. D. Fuchs, E. Johnston-Halperin, and M. E. Flatte, Materials for Quantum Technology 1, 011001 (2021).
[3] M. Fukami, D. R. Candido, D. D. Awschalom, and M. E. Flatte, PRX Quantum 2, 040314 (2021).
[4] M. Fukami, J. C. Marcks, D. R. Candido, L. R. Weiss, B. Soloway, S. E. Sullivan, N. Delegan, F. J. Heremans, M. E. Flatté and D. D. Awschalom, PNAS 121 (2024).

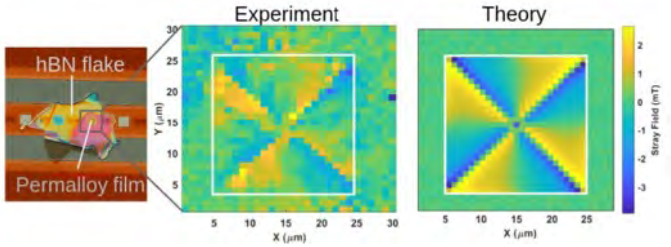


Fig. 1 Experimental and Theoretical Magnanetometry of Permalloy films using hBN flakes. Color indicates static stray field produced by the Py films.

HG-03. Current-Controlled Selection of Synchronization States in Coupled Spin-Torque Oscillators with Modified Free Layers

K. Horizumi[1], T. Chiba[2], T. Komine[1]
[1]Ibaraki University, Hitachi, Ibaraki-ken, Japan, [2]Yamagata University, Yonezawa, Yamagata, Japan

Synchronization in spin-torque oscillators has attracted attention for both fundamental studies of nonlinear dynamics and phase locking and applications such as microwave signal enhancement and oscillator-based information processing [1-3]. We recently proposed a modified vortex spin-torque oscillator (m-VSTO), in which an additional magnetic layer reshapes the confinement potential, enabling self-oscillation below the threshold current of a conventional vortex STO and a nearly linear current dependence of oscillation frequency in the subthreshold regime [4,5]. Here, we investigate current-controlled synchronization states in electrically coupled m-VSTO pairs. Figure 1 shows two electrically coupled m-VSTOs. Because the device resistance depends on both the magnetoresistance ratio and the vortex-core position, the current splitting ratio varies dynamically, so vortex motion in one oscillator modulates the spin torque acting on the other. We numerically solve coupled Thiele equations with self-consistent current redistribution. Figure 2 shows the current dependence of the synchronization states for a conventional-VSTO pair and an identical m-VSTO pair. In the high-current regime, both pairs exhibit anti-phase synchronization, whereas the identical m-VSTO pair exhibits in-phase synchronization in the lower-current regime. In particular, the locked phase of the identical m-VSTO pair changes near the threshold current of the conventional VSTO. Mixed-type pairs, although not shown in Figure 2, do not exhibit robust synchronization and instead display beat-like modulation due to differences in their intrinsic oscillation frequencies. These results show that electrically coupled m-VSTOs constitute a nonlinear synchronization system in which dc current controls both the synchronization state and the locked phase.

[1] N. Locatelli, V. Cros and J. Grollier, Sci. Rep., Vol. 5, p.17039 (2015)
[2] R. Lebrun, S. Tsunegi and P. Bortolotti, Nat. Commun., Vol. 8, p.15825 (2017)
[3] T. Taniguchi, arXiv:1705.04386 (2017)
[4] K. Horizumi, T. Chiba and T. Komine, IEEE Trans. Magn., Vol. 61, p.1400405 (2025)
[5] K. Horizumi, T. Chiba and T. Komine, arXiv:2603.01351 (2026)

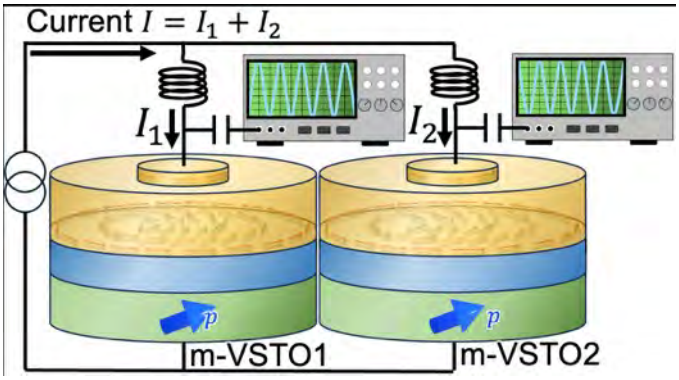


Fig.1 Schematic of two electrically coupled m-VSTOs. The interaction is introduced through current splitting between the two oscillators.

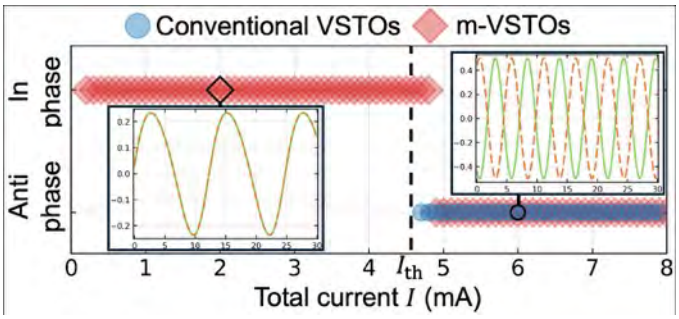


Fig. 2 Synchronization states of a conventional-VSTO pair and an identical m-VSTO pair as a function of total dc current. Insets show time-domain traces for the in-phase and anti-phase synchronized states. I_{th} is the threshold of conventional VSTO.

HG-04. Current-Control of Edge of Chaos in Magnetic Tunnel Junctions under Thermal Fluctuations

R. Tatsumi[1, 2], S. Miwa[3], H. Matsueda[1], T. Chiba[2, 1]
[1]Applied Physics, Tohoku University, Sendai, Japan, [2]Information Science and Technology, Yamagata University, Yonezawa, Japan, [3]The University of Tokyo, Tokyo, Japan

In recent years, physical reservoir computing (PRC) which utilizes nonlinear dynamics in physical systems as neural networks, has attracted significant attention. In PRC, it has been reported that computational performance is enhanced at the "edge of chaos". Magnetization, which exhibit rich nonlinear phenomena, are promising candidates for implementing PRC. Consequently, studies on the generation of chaos in magnetization have been actively pursued [2].

Among these, a model of chaos in magnetic systems with uniaxial magnetic anisotropy, subjected to a perpendicular static and AC magnetic field, has been proposed [3]. Since the emergence of chaos in this model can be flexibly controlled by adjusting the external magnetic field, this model has a practical advantage. Based on this model we investigate chaotic magnetization dynamics in magnetic tunnel junctions under thermal fluctuations and their control via electric current [4].

Figure 1(a) shows a schematic illustration of the magnetic tunnel junction considered in this study. A ferromagnetic layer with an easy axis along the z-direction is placed above another ferromagnetic layer whose magnetization is fixed along the y-direction. An external magnetic field is applied along the x-direction. By injecting a current along the z-direction, DC and AC spin-transfer torques (STTs) are generated.

Using the Landau–Lifshitz–Gilbert equation, we analyzed the phase diagram of chaos. The region where chaos emerges can be controlled by varying the DC current via the STT effect. Furthermore, we found that thermal fluctuations expand the parameter region in which chaos occurs, indicating the emergence of noise-induced magnetic chaos. In this presentation, we will also discuss the details of the model and provide a mathematical analysis of the mechanism underlying the emergence of chaos.

[1] T. Yamaguchi *et al.*, Phys. Rev. B 107, 054406 (2023).
[2] R. Legenstein *et al.*, Neural Networks 20, 323–334 (2007).
[3] R. Tatsumi *et al.*, Phys. Rev. E 111, 064202 (2025).
[4] R. Tatsumi *et al.*, arXiv:2603.03046.

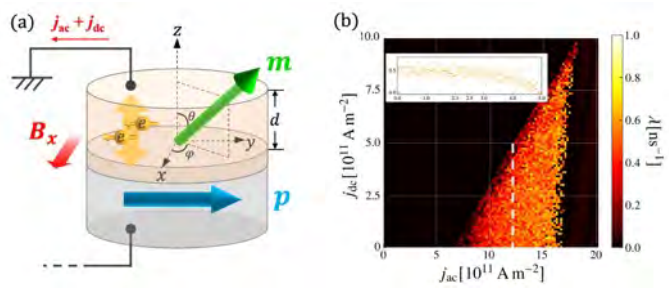


FIG. 1. (a) Schematic illustration of the model. An external magnetic field is applied, with the easy axis along the y-direction, and a current is injected along the z-direction to induce both DC and AC STT.
(b) Dependence of the Lyapunov exponent at room temperature on the strengths of DC and AC spin-transfer torques . A positive Lyapunov exponent (λ) corresponds to chaotic behavior.

HG-05. Spin-Hall Nano-Oscillators Synchronization Mediated by Magnetoelastic Interactions

Y. Lai[2], P. Radhakrishnan[2], E. Savostin[1, 3], Z. Zhang[4], E. Gong[4], A. Hoffmann[4], V. Lomakin[1, 5, 3], A. D. Kent[2]
[1]Center for Memory and Recording Research, University of California, San Diego, La Jolla, California, United States, [2]Center for Quantum Phenomena, Department of Physics, New York University, New York, New York, United States, [3]Program in Materials Science and Engineering, University of California, San Diego, La Jolla, California, United States, [4]Materials Research Laboratory and Department of Materials Science and Engineering, The Grainger College of Engineering, University of Illinois Urbana-Champaign, Champaign, Illinois, United States, [5]Department of Electrical and Computer Engineering, University of California, San Diego, La Jolla, California, United States

Long-range synchronization of nanoscale spintronic oscillators remains a central challenge for improving oscillator characteristics and unconventional computing. In spin-Hall nano-oscillators (SHNO), a direct current in a heavy-metal layer injects spin current into an adjacent ferromagnet, exerting a spin torque that can enables self-sustained auto-oscillations. Coupling SHNOs is essential for synchronization and has been realized through dipolar fields, electrical interactions, and spin waves. Here, we demonstrate a substrate-mediated, long-range synchronization mechanism based on magnetoelastic interactions. SHNO auto-oscillations generate magnetostriction in the ferromagnet that couples to the substrate and launches surface acoustic waves, enabling coupling over micron-scale distances.

We fabricated devices consisting of two Pt(5 nm)/CoFeB(5 nm) nanowires (400 nm width) with separations up to 6 μm on AlN substrates. We measured the spectra of individual nanowires and compared them to spectra obtained under simultaneous excitation (Fig. 1). Simultaneous excitation produces clear signatures of synchronization, including linewidth reduction, frequency locking, and enhanced output power, observed across the full separation range. As a control, Pt/Permalloy (Py) SHNO pairs on AlN show no synchronization under identical conditions, consistent with the weak magnetoelasticity of Py.
Micromagnetic simulations support the experimental behavior and show that synchronization is absent unless magnetoelastic interactions are included. Instantaneous phase analysis further reveals spontaneous phase locking during auto-oscillation, confirming magnetoelastic coupling as the origin of the long-range synchronization.

This work was supported as part of Quantum Materials for Energy Efficient Neuromorphic Computing, an Energy Frontier Research Center supported under Award DE-SC0019273.

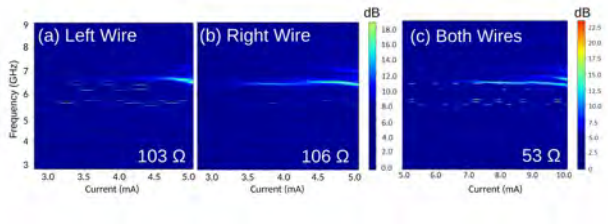


Fig. 1 Auto-oscillation PSD of two Pt/CoFeB SHNOs separated by 2 μm on AlN measured as a function of current. (a)(b) PSD of the left and right nanowires measured individually, with device resistances of 103 Ω and 106 Ω. (c) PSD when both nanowires are driven simultaneously (net resistance 53 Ω), showing an enhanced spectral power and reduced linewidth.

HG-06. Influence of interfacial magnetic pinning on standing spin waves in $La_{1-x}Sr_xMnO_3$ thin films

R. Arakawa[1], S. Komori[2], T. Taniyama[1]
[1]Department of Physics, Nagoya Univeristy, Nagoya, Aichi, Japan, [2]Department of Physics and Electronics, Osaka Metropolitan University, Sakai, Osaka, Japan

The resonance intensity of standing spin waves (SSWs) excited by ferromagnetic resonance (FMR) in ferromagnetic thin films varies between even and odd modes depending on the symmetrical conditions across the film thickness [1]. Although the SSW intensity can potentially be modulated by interfacial magnetic states through symmetry deformation via magnetic pinning, the correlation between SSW intensity and interfacial magnetism remains unexplored. In this study, we investigate the temperature dependence of SSW intensity in $La_{0.5}Sr_{0.5}MnO_3$ ferromagnetic films and find that SSW intensity is reduced due to the emergence of an interfacial antiferromagnetic phase.

Coplanar waveguide-based FMR measurements were performed at temperatures 2–300 K on $La_{0.5}Sr_{0.5}MnO_3$ films, where SSWs were excited normal to the film. To quantify the interfacial magnetic pinning strength, we analyzed the pinning parameter δ, which is estimated from the spin-wave wavelength using Kittel's formula modified by the exchange term Dk^2, where D, $k = (\delta\pi/t_{eff})^2$, and t_{eff} denote the exchange stiffness, the wave number, and the effective ferromagnetic thickness excluding the magnetically dead interfacial layer, respectively [2]. The δ increases with decreasing temperature between 225 and 175 K (Fig. 1), which we attribute to enhanced surface magnetic pinning arising from the transition of the surface superparamagnetic phase to the ferromagnetic phase. Below 50 K, δ further increases concurrently with a reduction in SSW intensity (Fig. 2), indicating that the interfacial paramagnetic phase undergoes phase transition into the antiferromagnetic phase, acting as additional magnetic pinning sites. This combined surface and interfacial magnetic pinning enhances the SSW symmetry by constraining both the top and bottom boundaries. This establishes a correlation between SSW intensity and interfacial magnetism in ferromagnetic films.

This work was supported in part by JSPS KAKENHI Grant Nos. JP24H00380, JP24K21732, JP23KK0086, JSPS International Joint Research Program with the UK (JRP-LEAD with UKRI) JPJSJRP20241705, JST FOREST JPMJFR212V.
[1] S. Klingler, H. Maier-Flaig and R. Gross, J. Phys. D: Appl.

Phys., vol. 48, 015001 (2015).
[2] H. J. Waring, N. A. Porter and C. H. Marrows, J. Appl. Phys., vol. 133, 063901 (2023).

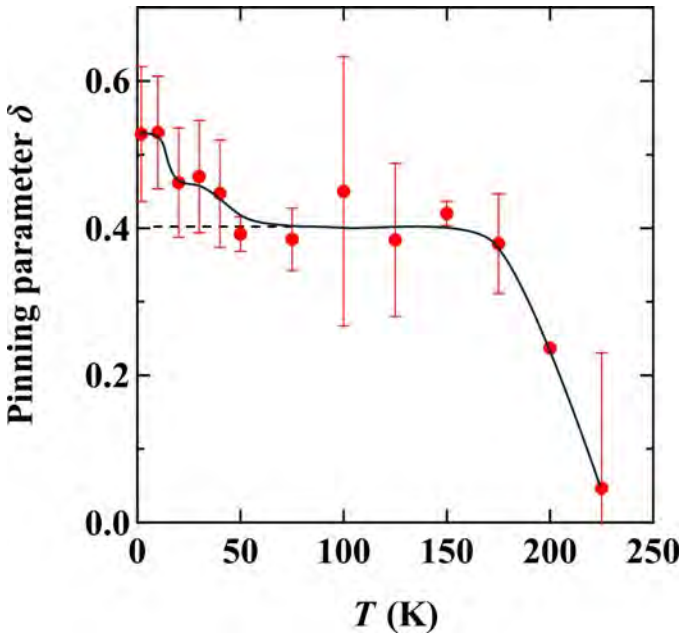


Fig. 1. Temperature dependence of δ in $La_{0.5}Sr_{0.5}MnO_3$.

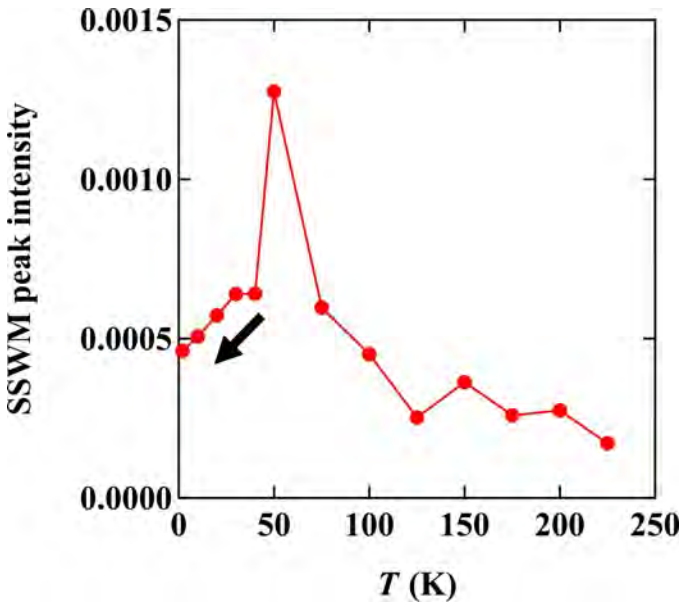


Fig. 2. Temperature dependence of SSW peak intensity for $La_{0.5}Sr_{0.5}MnO_3$.

HG-07. Spin-Photon Interaction: Enhancing and Suppression of Photon-Magnon Hybridisation through Collective Effects

S. Verma, A. Maurya, R. Singh, B. Bhoi
Department of Physics, Indian Institute of Technology (BHU) Varanasi, Varanasi, Uttar Pradesh, India

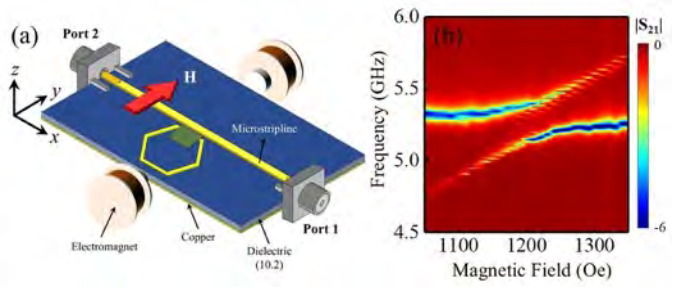
Photon-magnon coupling (PMC) is an emerging interdisciplinary field that combines the microwave, optical, and magnetism communities. It's aim is to leverage the unique advantages of these diverse systems within a single hybrid quantum system, enabling the exploration of new phenomena relevant to quantum information processing [1]. Gaining a profound understanding of PMC and the coupling strength and its manipulation can open doors to uncovering novel phenomena and potential applications [2].

In this paper, by utilizing the numerical simulations with CST Microwave Studio, we investigated photon-magnon coupling generated by hexagonal-ring resonator (HRR) and yttrium iron garnet (YIG) thin film configuration in planar geometry (see Fig. 1(a)). The behaviour of the strength of photon magnon coupling was investigated by varying the YIG film's magnetic Properties and the position of YIG on HRR. This robust hybrid system provides for more reliable control of the net coupling strength variable in the 127 - 62 MHz range at room temperature. To theoretically validate these findings, we developed a quantum model that very accurately reproduced the tuning of coupling strength observed in photon-magnon coupled anti-crossing dispersion spectra as shown in Fig. 1(b).

Using CST Microwave Studio, numerical simulations were performed by varying the YIG damping constant (α) from 1.4 × 10^{-5} to 2.1 × 10^{-2}, revealing an enhanced spontaneous emission rate of microwave photons due to coupling with lossy magnons, i.e., the Purcell effect. A theoretical model was developed that accurately reproduced the simulation results.

These findings demonstrate the Purcell-induced enhancement of decay rates and clarify the relationship between coupling strength, linewidth, and magnon decay in planar hybrid systems. This work provides new insights into photon–magnon interactions and offers a tunable platform for advancing magnonic devices, microwave quantum photonics, and magnetically tunable metamaterials.

[1]. Z.-L. Xiang et al, Rev. Mod. Phys. 85 (2013) 623–653
[2]. Y. Li et al, J. Appl. Phys. 128 (2020) 130902.



(a) Schematic of the hybrid system composed of a YIG film and microstrip-line loaded HRR (yellow). (b) $|S_{21}|$ power as a functions of applied field and microwave frequency

HG-08. Non-Hermitian coherent control and Floquet physics with magnon-polaritons

N. J. Lambert[1, 2], A. Schumer[3], L. Hackner[1, 2], J. Longdell[1, 2], S. Rotter[3], H. Schwefel[1, 2]

[1]University of Otago, Dunedin, Otago, New Zealand, [2]The Dodd–Walls Centre for Photonic and Quantum Technologies, Dunedin, Otago, New Zealand, [3]Institute for Theoretical Physics, TU Wien, Vienna, Austria

Systems of coupled modes are ubiquitous in physics, and are at the heart of many quantum technology platforms. Often these are engineered to have as little energy loss to the environment as possible. However, there has recently been much interest in non-Hermitian systems, for which loss and gain have a significant effect. If the loss/gain imbalance in the coupled modes is sufficiently large, an exceptional point (EP) is reached, at which the eigenvalues and eigenvectors of the system coalesce [1]. EPs have intriguing topological characteristics, and have been used to control systems including lasers based on PT-symmetric waveguides [2] and terahertz pulse generators [3].

In this work we extend the topological control afforded by EPs to a hybrid system of magnon-polaritons, comprising microwave modes supported by tunable resonators strongly coupled to magnons hosted by yttrium iron garnet (YIG) [4]. Our novel microwave resonators consist of a loop of coplanar waveguide with an embedded amplifier to provide gain (Fig. 1). Resonant modes have a $2n\pi$ phase winding around the loop. Control over the amplitude and phase of the propagating wave is provided by an IQ modulator, which in turn gives control over the frequency and loss rate of the modes. By embedding a YIG sphere between the waveguide and ground plane, strong coupling between photons and magnons is achieved. This architecture gives us full control over the frequency and loss/gain of the coupled magnon-polaritons.

We demonstrate Floquet engineering of magnon-polariton states using rapid frequency tuning of the modes supported by the microwave resonator, in contrast to recent works in which the magnon frequency was tuned [5,6]. By applying carefully calibrated voltage waveforms to the embedded modulator, we drive at multiple commensurate frequencies. This qualitatively alters the structure of the quasi-energy levels of the system, and by changing the relative phase between the drive frequencies we change the visibility of the modes.

We also use control over the complex frequencies of the system to carry out coherent fast manipulations on the state of the coupled magnon-polaritons (Fig. 2). First, we take the system along a path on the non-Hermitian manifold which encircles the exceptional point, transferring energy from one eigenstate to another in a topologically robust way. Second, we guide the system along a line that traverses the exceptional point, and demonstrate that this allows us to prepare the system in a balanced superposition of eigenstates. Surprisingly, merely reaching the exceptional point does not erase the history of the system, despite the coalescence of the eigenvectors; this demonstrates that the system must be described in the generalized eigenbasis in this regime. This work extends the toolkit of non-Hermitian manipulation to magnonic systems.

[1] R. El-Ganainy, et al., Nature Physics 14, 11 (2018).
[2] A. Schumer, et al., Science 375, 884 (2022)
[3] M. S. Ergoktas, et al., Science 376, 184 (2022).
[4] N. J. Lambert et al., Nature Physics 21, 1570 (2025).
[5] J. Xu et al., Phys. Rev. Lett. 125, 237201 (2020).
[6] A. Pishehvar et al., Phys. Rev. Appl. 23, 024053 (2025).

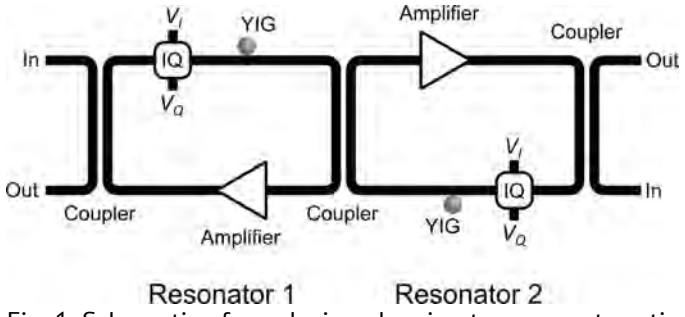


Fig. 1. Schematic of our device, showing two separate active resonators (Resonator 1 and Resonator 2) with YIG spheres embedded. They are coupled to feed lines and each other with directional couplers, and the frequency and loss of supported modes are controlled with an IQ modulator.

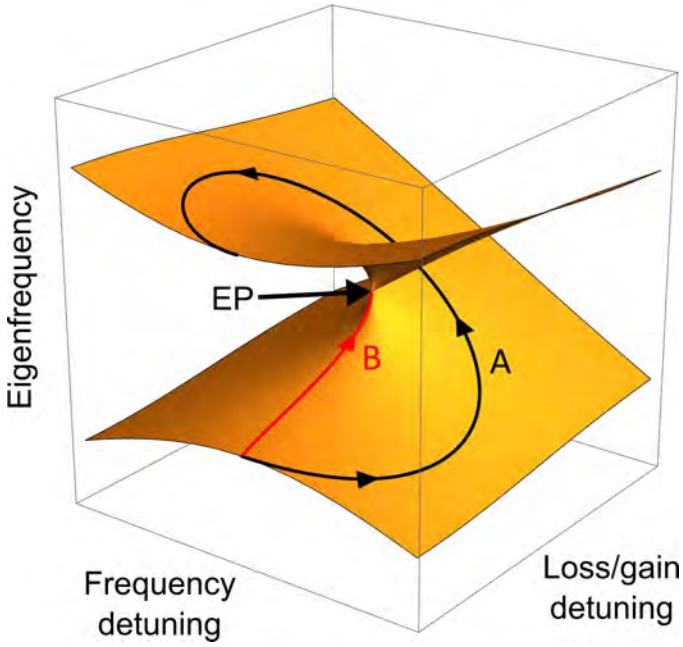


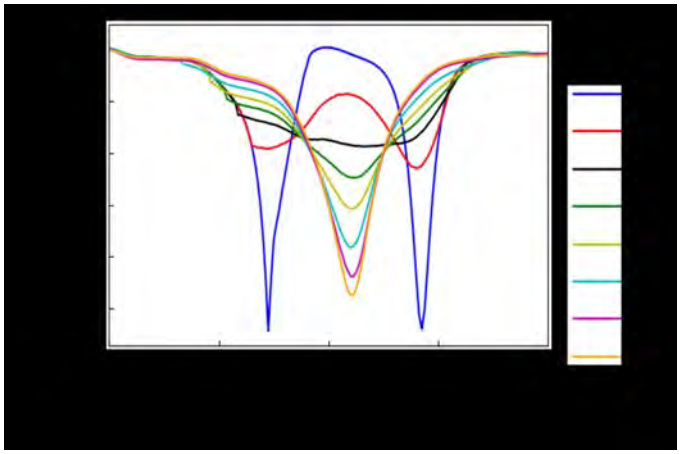
Fig. 2. Control of magnon-polaritons on the non-Hermitian surface. Shown is a cartoon of the non-Hermitian manifold of coupled modes, with (A) a typical EP-encircling trajectory used to switch excitations between modes and (B) a trajectory traversing the EP.

HG-09. Deeply nonlinear magnon-photon hybrid excitation

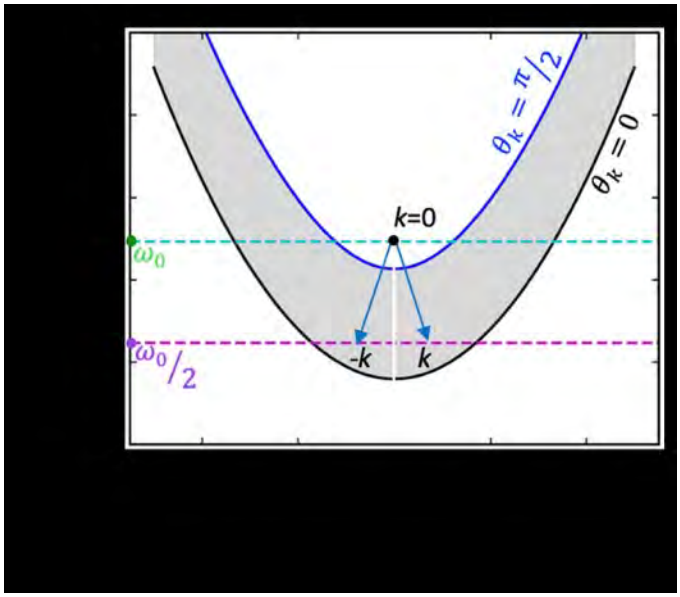
D. Wagle, A. Rai, B. Jungfleisch
University of Delaware, Newark, Delaware, United States

Controlling magnon polaritons—hybrid quasiparticles formed by coupling magnons with microwave photons—is important for their potential applications in coherent information processing. Here, we show that nonlinear spin-wave interactions suppress magnon photon coupling through power-induced dissipation of magnetostatic modes. At low microwave power, strong coupling is observed via pronounced level repulsion. With increasing power, linewidth broadening weakens the coupling and eventually suppresses it below a threshold magnetic field [Fig. 1] due to Suhl's first-order instability, where magnetostatic modes decay into pairs of counter-propagating magnons [Fig. 2]. In contrast, modes above the threshold field remain stable even at high power. These results establish a nonlinear boundary for magnon–photon coupling and identify regimes suitable for applications such as frequency conversion and switching.

Research supported by the U.S. Department of Energy, Office of Basic Energy Sciences, Division of Materials Sciences and Engineering under Award DE-SC0020308.
1. D. Wagle et al, arXiv:2601.21549



Microwave power dependent transmission spectra in the coupling region showing the evolution of resonance features.



Schematic illustrations of three-magnon splitting.

HG-10. Predicting the future with magnons: Forecasting chaotic time series with reservoir computing

Z. Xiong[1, 2], C. Heins[1, 2], T. Devolder[3], F. Kammerbauer[4], M. Kläui[4], J. Fassbender[1, 2], H. Schultheiss[1], K. Schultheiss[1]
[1]Helmholtz-Zentrum Dresden-Rossendorf, Dresden, Germany, [2]Technische Universität Dresden, Dresden, Germany, [3]Centre de Nanosciences et de Nanotechnologies, CNRS, Université Paris-Saclay, Paris, France, [4]Institute of Physics, Johannes Gutenberg University Mainz, Mainz, Germany

The Mackey-Glass time series describes how the density of mature circulating cells changes over time using time delayed differential equations [1]. This is a standard problem to test the performance of physical reservoirs. Here, we use a magnon-scattering reservoir (MSR) to carry out such a chaotic time series prediction task [2]. The memory and nonlinearity of magnons make our MSR a perfect candidate for such tasks [3].

The original data at discrete time steps was converted to frequencies in a range suitable to address magnons in NiFe microstructures. The magnon response was measured using time-resolved Brillouin light scattering micro-spectroscopy. For the analysis, a spectrum was extracted for each time step. Then a simple linear regression was used to predict steps into the future. The general architecture is shown in Fig. 1. We tested the system's performance by predicting up to 300 future time steps. The forecast using our MSR is highly accurate and even follows small changes in the actual data.

Tuning of spectral resolution can be achieved via frequency binning which leads to better forecast. Combining multiple device geometries systematically also boosts performance. The task was carried out using five MSR with different geometries. Results from different MSR were combined to increase the reservoir depth. In general, combination of more reservoirs leads to more accurate forecast.

Based on our recent work on the electrical detection of spin waves [4], the system can be fully integrated with an all-electrical readout. Such an implementation would enable a compact and scalable architecture, making it readily compatible with CMOS technology.

[1] M. C. Mackey and L. Glass, Science 197, 287 (1977).
[2] Z. Xiong *et al.*, Phys. Rev. Applied 25, 044047 (2026).
[3] L. Körber *et al.,* Nature Communications 14, 3954 (2023).
[4] C. Heins, Z. Xiong *et al.,* arXiv:2509.19483 (2025).

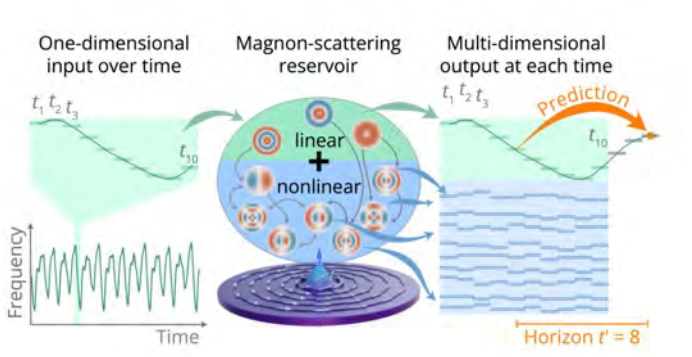


Fig. 1: The 1D temporal input is encoded in a microwave current and applied to a NiFe microdisk in the vortex state (magnon-scattering reservoir). Nonlinear interactions between various magnon modes transform the 1D input into a multi-dimensional spectral output trained to forecast the future trajectory of the chaotic signal.

HG-11. Perspectives on inverse-design magnonics

F. Vilsmeier, F. Bruckner, C. Abert, D. Suess, A. Chumak
University of Vienna, Vienna, Austria

Magnonic devices exploit spin waves — the collective excitations of ordered magnets — for wave-based information processing without charge flow. Their performance hinges on a high-dimensional design space spanning geometry, local material parameters, magnetic field landscape, excitation, and nonlinearity, much of which is inaccessible to manual parameter studies. Inverse design reverses the conventional workflow: the desired functionality is specified as an objective, and an algorithm finds the optimal structure automatically. The field has advanced rapidly since its founding works in 2021 [Wang *et al.*, Nat. Commun. 12, 2636 (2021); Papp *et al.*, Nat. Commun. 12, 6422 (2021)], encompassing topology optimisation of magnonic demultiplexers and filters, ion-irradiation-based gradient-index lenses, experimentally realised reconfigurable radio-frequency devices and Boolean logic gates, and the development of dedicated differentiable micromagnetic solvers that bring the infrastructure of machine learning to the Landau–Lifshitz–Gilbert equation. In this talk, we give an overview of inverse-design magnonics, drawing on recent results from our group and the broader literature, organising the emerging literature along two axes — the design degrees of freedom that can be optimised, and the algorithmic toolbox available to do so — and lay out the principal bottlenecks that currently constrain the field. Building on this, we outline what we view as the most promising open frontiers — such as input

shaping, nonlinear design and integrated amplification — with the long-term vision of a universal, software-defined magnonic device.

SESSION HP: MAGNETICS FOR POWER ELECTRONICS AND CONTROL (POSTER SESSION)

Chair(s): N. Lupu, *National Institute of R&D for Technical Physics, Iasi, Romania*

Friday, November 6, 2026

03:00 PM-06:00 PM

Coral 4

HP-01. Drive Cycle–Aware Optimization of Traction Motors for Less-Critical Magnet Substitutes

A. Baghel, I. C. Nlebedim

Ames National Laboratory, Critical Materials Innovation Hub, Ames, Iowa, United States

The increasing demand for high-performance traction motors [1-2], coupled with supply risks associated with critical rare-earth elements [3-4], necessitates design strategies that reduce material dependency without compromising performance. This work presents an accelerated design optimization framework for traction motors that enables the effective use of less-critical, lower-energy-density magnet materials through integrated system-level modeling and electromagnetic design. The proposed framework combines a recently developed analytical motor modeling approach [5] with multi-objective optimization [6] and drive cycle–based evaluation to rapidly assess material–design interactions. Unlike conventional methods focused on limited operating points, the approach incorporates representative operating states derived from vehicle drive cycles, enabling performance optimization under realistic usage conditions as demonstrated in Fig 1. The analytical model significantly reduces computational cost relative to finite element methods, allowing efficient exploration of the design space. The methodology is demonstrated on a 5 kW, 6000 rpm traction motor platform under consistent performance constraints.

Results show that, when co-optimized with motor geometry and operating conditions, designs using less-critical magnet substitutes can replace conventional Nd–Fe–B magnets while maintaining comparable performance. The findings demonstrate that performance trade-offs associated with alternative materials can be effectively mitigated through integrated design optimization rather than direct substitution. Furthermore, variations in magnet properties are shown to influence motor efficiency maps, which in turn impact energy consumption and battery state-of-charge over the drive cycle. This highlights the capability of the framework to capture the coupled effect of magnet material selection on both motor performance and system-level energy behavior. This work establishes a computationally efficient and scalable pathway for the rapid screening and deployment of sustainable magnet technologies in traction motor applications.

References

W. Cai, X. Wu, M. Zhou, Y. Liang and Y. Wang, *Automot. Innov*., Vol. 4, p.3 (2021)

A. P. S. Baghel and I. C. Nlebedim, *JOM*, Vol. 75, p.557 (2023).

G. Delette, *J. Magn. Magn. Mater*., Vol. 577, p.170768 (2023).

R. Kuchi, D. Schlagel, T. Seymour-Cozzini, J. Zaikina and I. Hlova, *J. Alloys Compd*., Vol. 980, p.173532 (2024).

A. P. S. Baghel, B. Sai Ram and I. C. Nlebedim, *IEEE CEFC*, p.1 (2024).

Y. Cen, H. Shen, X. Wang, W. Yongming and D. Jingjuan, *Energies*, Vol. 17, p.4637 (2024).

HP-02. GCN-Based Finite Difference Model and Electromagnetic Performance Analysis of Motors

H. Wang, Y. Du, X. Zhu

Jiangsu University, Zhenjiang, China

This paper proposes a graph-convolution-assisted finite-difference framework for electromagnetic field computation to improve automation and efficiency. Unlike conventional methods requiring geometry generation and meshing, the proposed approach directly uses image-based representations, where pixels replace mesh discretization and color information encodes material regions.

In the proposed formulation, the electromagnetic governing equation is formulated as a Poisson equation and discretized using finite-difference operators. The second-order Laplacian operator is represented by a fixed stencil, which is equivalently formulated as a convolution kernel acting on the stiffness matrix. The global stiffness matrix is constructed through convolution operations combined with boundary condition. By directly treating pixels as nodes, the need for mesh generation is eliminated. Due to the uniform pixel spacing, the resulting matrix is symmetric and diagonally dominant with positive diagonal entries. In the Poisson equation formulation, the coefficient matrix is symmetric positive definite.This property ensures improved numerical stability and faster convergence in iterative solvers.

For practical validation, a doubly salient permanent magnet machine is used as a case study. A graph convolutional network is designed to analyze a 2D motor image,automatically extracting material regions and interfaces between different materials based on color and spatial relationships. The extracted topology is mapped to the finite-difference grid, where different material properties and source terms are assigned. Interface conditions are incorporated through predefined local units inserted into the global matrix. Furthermore, a GCN-based feature reduction strategy is applied to remove redundant nodes while preserving essential structural information. Compared with the full pixel-based model, the reduced model significantly decreases matrix size and computation time. Finite element comparisons show acceptable error, confirming that the proposed method offers high efficiency with satisfactory accuracy.

[1]Zaman, M.A. Numerical Solution of the Poisson Equation Using Finite Difference Matrix Operators. Electronics 2022, 11, 2365.

[2]Z. Hu, Ed. Analysis and Calculation of Electromagnetic Fields in Electrical Machines. Beijing, China: China Machine Press, 1982.

[3]Y. Du, Y. Mao, F. Xiao, X. Zhu, Y. Sun and L. Quan, "A Pole-Changing Doubly Salient Permanent Magnet Motor," in *IEEE Transactions on Transportation Electrification*, vol. 8, no. 2, pp. 2479-2489, June 2022.

[4]Virtanen, P.; Gommers, R.; Oliphant, T.E.; Haberland, M.; Reddy, T.; Cournapeau, D.; Burovski, E.; Peterson, P.; Weckesser, W.;Bright, J.; et al. SciPy 1.0: fundamental algorithms for scientific computing in Python. Nat. Methods 2020, 17, 261–272.

[5]Nagel, J.R. Numerical Solutions to Poisson Equations Using the Finite-Difference Method [Education Column]. IEEE Antennas Propag. Mag. 2014, 56, 209–224.

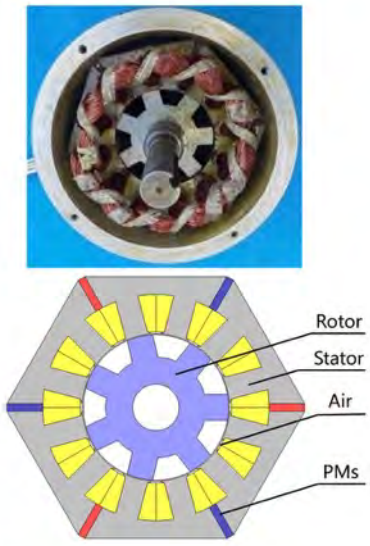


Figure 1 shows the motor topology and prototype.

shows the motor topology and prototype

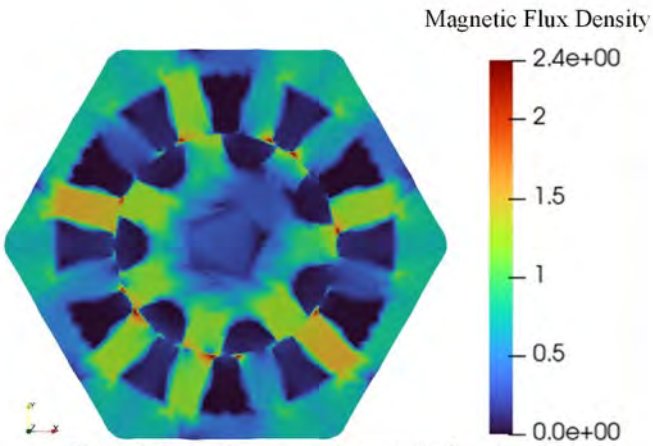


Figure 2 shows the expected magnetic flux density distribution computed by the proposed method.

shows the expected magnetic flux density distribution computed by the proposed method

HP-04. Optimal Design of an Interior Permanent Magnet Synchronous Motor Based on a Nonlinear Magnetic Equivalent Circuit Considering Torque Density

C. W. Choi[1], S. Kim[1], Y. Yoon[1], H. Yu[1], S. Yoon[1], K. Shin[2], J. Choi[1]

[1]Chungnam National University, Daejeon, Korea (the Republic of), [2]Changwon National University, Changwon, Korea (the Republic of)

In recent years, demand for high-performance electric machines has increased, particularly in electric vehicles and renewable energy systems. Interior permanent magnet synchronous motors (IPMSMs), which use rare-earth magnets, are widely adopted due to high power density and efficiency. However, price and supply instability due to political and resource constraints increases production cost and necessitates efficient design methods. Considering torque density in the design enables higher output relative to magnet use, thereby reducing material cost. Achieving this requires accurate performance prediction of IPMSMs considering magnetic saturation and nonlinear material characteristics. Although the finite element method (FEM) provides high accuracy, it is computationally expensive and unsuitable for initial design stages.

To address this limitation, this paper proposes a nonlinear magnetic equivalent circuit (MEC)-based design method for IPMSMs, followed by optimization using a genetic algorithm. The MEC model represents the magnetic system as an equivalent network, enabling efficient analysis of nonlinear magnetic behavior with reduced computational cost. Figure 1(a) presents the model and design specifications, and Fig. 1(b) consists of two plots: the B-H curve and the magnetic equivalent circuit under dq-axis current conditions. A modified μ-H curve is used to reduce the computational load by considering relative permeability. Fig. 1(c) compares electromagnetic characteristics of FEM and MEC during no-load analysis, confirming that the results agree well.

Figure 2(a) shows design parameters, and Fig. 2(b) illustrates the Pareto front of the optimization results. Fig. 2(c)-(d) presents the initial and optimal model, along with a comparison of their electromagnetic analysis results, and Fig. 2(e) depicts the experimental setup. Further details and discussion will be provided in the full paper.

1. X. Liu, H. Chen, J. Zhao and A. Belahcen, IEEE Trans. Ind. Electron.63 (6), 3533–3545 (2016).
2. J.-G. Lee, D.-K. Lim and H.-K. Jung,, IEEE Trans. Magn.55 (10), 1–4 (2019).
3. J.-Y. Song, J. H. Lee, D.-W. Kim, Y.-J. Kim and S.-Y. Jung, IEEE Trans. Magn.53 (11), 1–5 (2017).
4. H. Mirahki, M. Moallem and S. A. Rahimi, IEEE Trans. Magn.50 (3), 114–119 (2013).
5. B. Zang and Y. Chen, IEEE Trans. Energy Convers. 38 (2), 813–824 (2022).

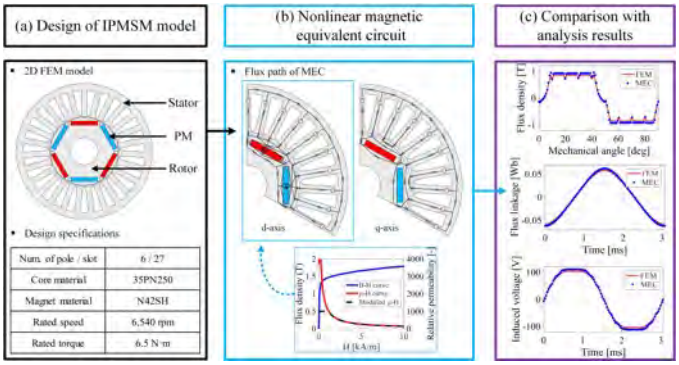


Fig. 1. Overall design structure of the proposed MEC approach.

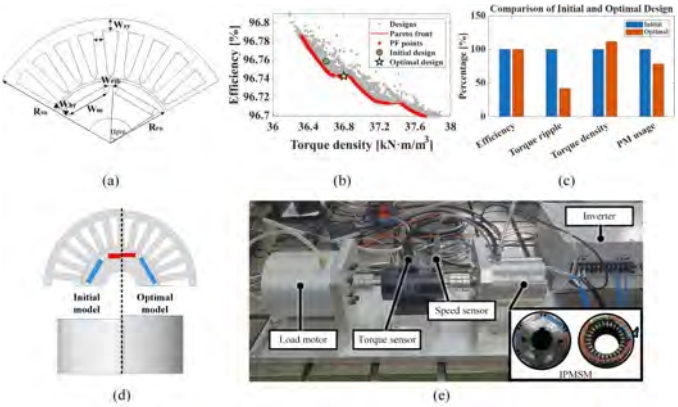


Fig. 2. (a) Design parameters, (b) Pareto front, (c)-(d) Comparison of initial and optimal design electromagnetic analysis results with its electromagnetic analysis comparison results, (e) Experimental setup.

HP-06. Nonlinear Magnetic Equivalent Circuit Modeling and Demagnetization Evaluation of a Ferrite Magnet Axial Flux Permanent Magnet Machine

M. Kim[1], S. Kim[1], S. Woo[1], J. Park[2], J. Choi[2], K. Shin[1]
[1]Changwon National University, Changwon, Korea (the Republic of), [2]Chungnam National University, Daejeon, Korea (the Republic of)

Ferrite permanent magnets are attractive for rare earth reduced electric machines because of their low cost and stable supply. However, their lower remanent flux density and coercivity than NdFeB magnets make it difficult to secure air gap flux and torque density. To compensate for this limitation, ferrite magnet machines require larger magnet volume with overhang structure, increased winding turns, or higher current excitation, which can intensify iron core saturation and irreversible demagnetization under severe conditions [1]. Therefore, electromagnetic analysis considering nonlinearity, overhang, and demagnetization is required for ferrite magnet Axial Flux Permanent Magnet Machines (AFPMMs) [2], [3].

This paper proposes a nonlinear Magnetic Equivalent Circuit (MEC) model for a ferrite magnet AFPMM. As shown in Fig. 1, the analysis model is converted into a quasi 3D MEC with five radial slices, including main flux and overhang leakage paths. The nonlinear B-H curve is assigned to core reluctance elements, and local permeability is iteratively updated from flux density. The air gap flux density and current torque characteristics are compared with 3D finite element method (FEM) results. The nonlinear MEC improves prediction of electromagnetic performance compared with the linear MEC by reflecting saturation.

Fig. 2 presents the nonlinear analysis and demagnetization evaluation. The no load and load flux density distributions show local saturation, and representative values are compared with MEC results. Demagnetization is evaluated under rated current and 2.5 times rated current by dividing the ferrite magnets into segmented regions. The prototype AFPMM and dynamometer test bench are shown for experimental validation. Detailed comparisons among the nonlinear MEC, 3D FEM, and experimental results will be presented in the full paper.

[1] G. Choi and T. M. Jahns, Proc. IEEE Energy Conversion Congress and Exposition (ECCE), pp. 469–475, (2014).
[2] Y. Huang, T. Zhou, J. Dong, H. Lin, H. Yang, and M. Cheng, IEEE Trans. Magn., Vol. 50, Art. no. 8104204, (2014).
[3] Y. Kano, T. Kosaka, and N. Matsui, IEEE Trans. Ind. Electron., Vol. 57, No. 6, pp. 2124–2133, (2010).

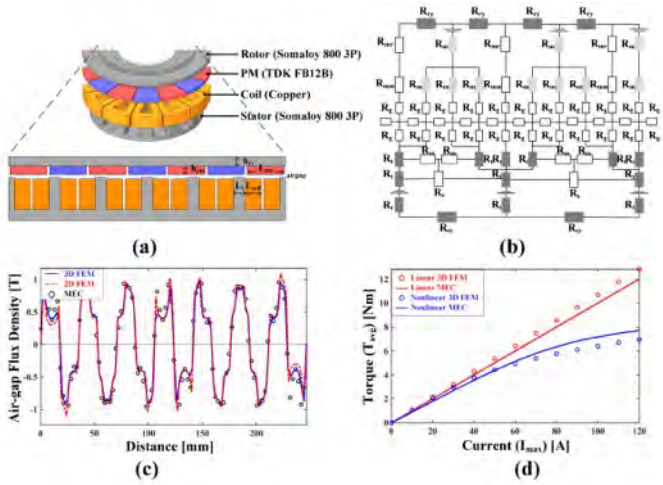


Fig1. Nonlinear MEC model and performance validation: (a) analysis model, (b) MEC network, (c) air gap flux density, and (d) current torque curve.

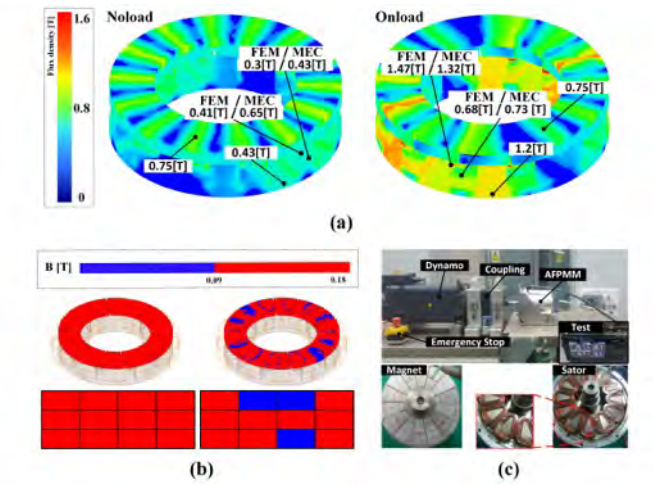


Fig. 2. Nonlinear and demagnetization analysis: (a) flux density distributions, (b) demagnetization results, and (c) prototype test bench.

HP-07. Artificial Neural Network-Based Efficiency Map Prediction of an Inverter-Fed Permanent Magnet-Assisted Synchronous Reluctance Motor Considering the Power Electronics System

W. Lee[1], M. Kim[1], M. Seo[1], H. Lee[1], K. Yu[2], J. Choi[2], K. Shin[3]
[1]Department of Smart Manufacturing Engineering, Changwon National University, Changwon, Korea (the Republic of), [2]Department of Electrical Engineering, Chungnam National University, Daejeon, Korea (the Republic of), [3]Department of AI Electrical Engineering, Changwon National University, Changwon, Korea (the Republic of)

In this paper, a method for predicting the efficiency map of a permanent magnet-assisted synchronous reluctance motor (PMa-SynRM) combined with a power electronic system (PCS) using an artificial neural network (ANN) is proposed. Fig.1(a) and (b) show the geometry of PMa-SynRM and its space vector PWM (SVPWM) drive system. Unlike ideal sinusoidal excitation, this analysis considers harmonic currents from the PCS [1]. Conventional efficiency map generation requires repeated finite element analysis (FEA) at many speed and torque points, causing a large computational burden [2]. To reduce this burden, the proposed procedure integrates inverter simulation, FEA, and data-driven prediction. Fig. 1(c) shows that the combined model accurately reflects actual inverter-fed operation by comparing simulated and measured waveform. The validated harmonic currents are applied to FEA, and the calculated torque, losses, output power, and efficiency are used as training data.

Fig. 2(a) shows the prediction process using an ANN technique, including sampling, training, efficiency map prediction, and accuracy validation. Fig. 2(b) illustrates the experimental setup of the drive system. The predicted efficiency map is compared with the conventional analysis result, as shown in Figs. 2(c) and 2(d). The results show that the ANN model reproduces the high-efficiency region and overall efficiency distribution of the PMa-SynRM drive system. Validation shows an R squared value of 0.953 and an RMSE below 0.634 percent. Therefore, the proposed method provides a practical approach to rapidly predicting the efficiency map of inverter-driven PMa-SynRM drive systems while maintaining reliability and improving computational costs.

[1] D. Jang, S.-W. Jung, H.-W. Yang, I.-S. Song, T.-H. Nam, J. H. Lee and S.-Y. Jung, J. Electr. Eng. Technol. 21, 393-414 (2026).
[2] A. Khan, M. H. Mohammadi, V. Ghorbanian and D. Lowther, IEEE Trans. Magn. 56 (3), 1-4 (2020).

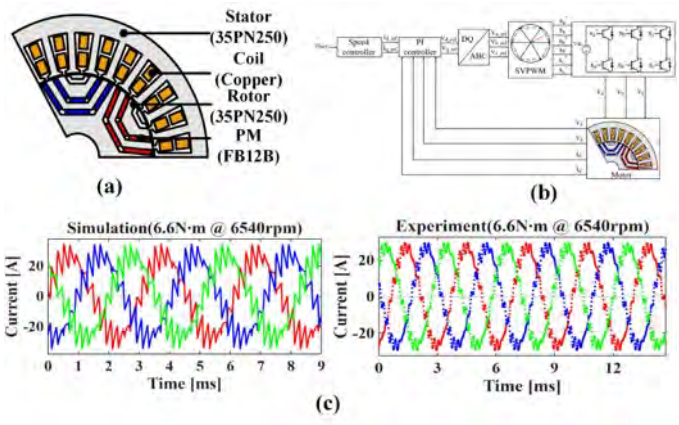


Fig.1. Configuration and current validation of the PMa-SynRM drive system: (a) cross-sectional geometry of the PMa-SynRM, (b) SVPWM-based drive system model, and (c) comparison of simulated and measured current waveforms.

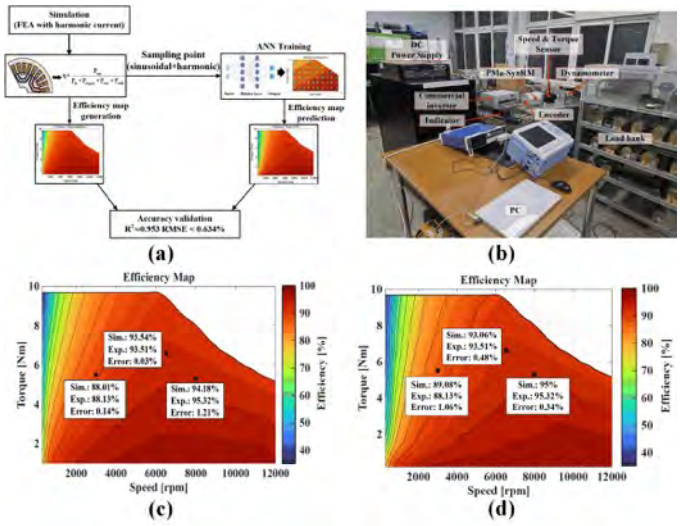


Fig.2. ANN-based efficiency map prediction and validation: (a) proposed prediction procedure based on harmonic-current FEA data and ANN training, (b) experimental setup of the drive system, (c) efficiency map obtained from conventional analysis, and (d) efficiency map predicted by the ANN model.

HP-08. Integrated Electromagnetic and NVH Design Framework for a PMa-SynRM Based on Multi-Variable and Multi-Objective Optimization

M. Seo[1], M. Kim[1], W. Lee[1], H. Lee[1], K. Yu[2], J. Choi[2], K. Shin[3]
[1]Smart Manufacturing Engineering, Changwon National University, Changwon, Korea (the Republic of), [2]Electrical Engineering, Chungnam National University, Daejeon, Korea (the Republic of), [3]AI Electrical Engineering, Changwon National University, Changwon, Korea (the Republic of)

Permanent magnet assisted synchronous reluctance motors (PMa-SynRM) are suitable for high-efficiency drive applications as they can improve torque performance and power factor while reducing reliance on rare-earth materials. However, geometries of flux barrier and permanent magnet affect electromagnetic harmonics, increasing vibration and noise [1]. Therefore, electromagnetic performance and noise, vibration, and harshness (NVH) characteristics should be considered simultaneously in design process of PMa-SynRMs [2]. This paper proposes an integrated design methodology for vibration and noise improvement of a PMa-SynRM according to key design variables. Fig. 1 illustrates the analysis model, design parameters, optimization flow, and Pareto front graph. Finite element analysis is performed on the initial model, and multi-objective optimization is performed to improve torque density and efficiency. Candidate models are selected from a Pareto front including the initial model, the optimal model, and models considering NVH characteristics. The derived models are analyzed for NVH characteristics, including electromagnetic force, vibration response, modal analysis, and equivalent radiated power level (ERPL) evaluation. Experiments are conducted using torque and velocity sensors, encoders, microphones, and accelerometers. ERPL waterfall diagrams from simulation and measurement are compared according to velocity and frequency. The final model is selected by considering electromagnetic performance and ERPL reduction. The simulation and experiment show good agreement, with an ERPL waterfall error below approximately 5%. Detailed optimization results and measurements will be presented in the final paper.

[1] Y. Lu, J. Li, R. Qu, D. Ye, H. Lu, J. Sun, M. Ge and H. Xu, IEEE Trans. Ind. Appl. Vol. 54, pp. 4246-4256, (2018).
[2] S. Das, A. Chowdhury, Y. Sozer, M. B. Kouhshahi, A. Pina Ortega, Z. Wan and J. Klass, IEEE Trans. Ind. Appl. Vol. 58, pp. 3533-3544, (2022).

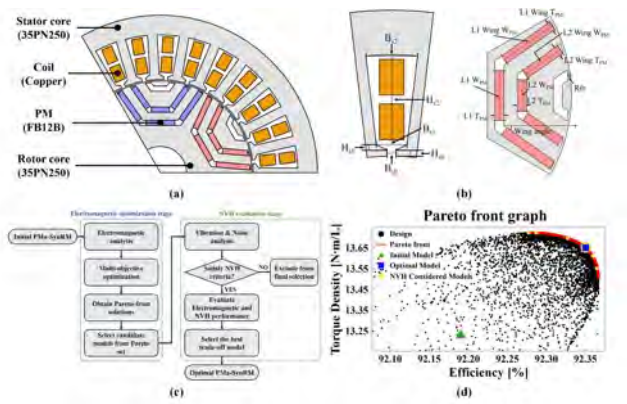


Fig. 1. Integrated electromagnetic and NVH design framework of the PMa-SynRM: (a) analysis model, (b) rotor design variables, (c) optimization procedure, and (d) Pareto front graph.

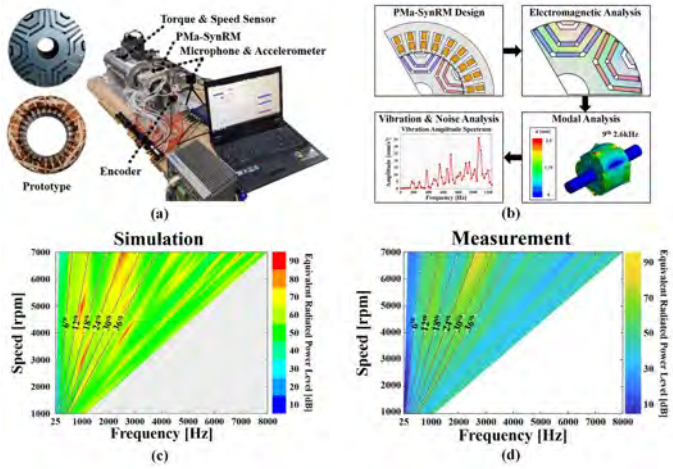


Fig. 2. NVH analysis and validation of the PMa-SynRM: (a) prototype test setup, (b) coupled vibration and electromagnetic analysis procedure, (c) simulated ERPL waterfall diagram, and (d) measured ERPL waterfall diagram.

HP-09. Nonlinear Reluctance Network Model of an Interior Permanent Magnet Synchronous Motor with Magductance for Core Loss Effect

G. Shin[1], G. Lee[1], M. Kim[1], S. Kim[2], J. Choi[2], K. Shin[1]
[1]Changwon National University, Changwon, Korea (the Republic of), [2]Chungnam National University, Daejeon, Korea (the Republic of)

This paper proposes a nonlinear reluctance network model (RNM) with core loss effect for an interior permanent magnet synchronous motor (IPMSM). Finite element method (FEM) is accurate but time consuming for repeated design evaluation, whereas conventional magnetic equivalent circuit models can lose accuracy because leakage flux, saturation, and core loss are simplified. The proposed RNM adopts an anisotropic cross-mesh structure in which radial reluctance represents the main torque producing flux and tangential reluctance reflects leakage flux [1]. The movement of the rotor is implemented in a static network by shifting the node attribute index. Magductance elements are added to the stator yoke, stator teeth, and rotor surface to account for hysteresis and eddy current effects. Based on the complex impedance concept, iron loss caused by time-varying flux is calculated from circuit equations [2]. A nonlinear iterative algorithm updates permeability according to the flux density in the B-H curve.

Fig. 1 shows the RNM construction and FEM validation. The topologies of FEM model and RNM describe the reluctance and magductance paths, while the core loss comparison confirms that magductance improves regional loss prediction. The torque ripple and efficiency results also agree well with FEM. Fig. 2 presents the experimental setup, loss and flux density distributions, and efficiency maps over the operating region. By applying magductance, the efficiency error is reduced from about 10% to below 5% at representative operating points. These results demonstrate that the proposed RNM predicts core loss and efficiency with improved accuracy while maintaining high computational efficiency, making it suitable for cost-effective IPMSM design.

[1] G. Liu, Y. Wang, Q. Chen, G. Xu and D. Cao, IEEE Trans. Magn. 56(6), 8101112 (2020).
[2] X. Zhu, G. Qi, M. Cheng, W. Qin, Y. Liu and J. Huang, IEEE Trans. Transport. Electrific. 11(1), 3538–3548 (2025).

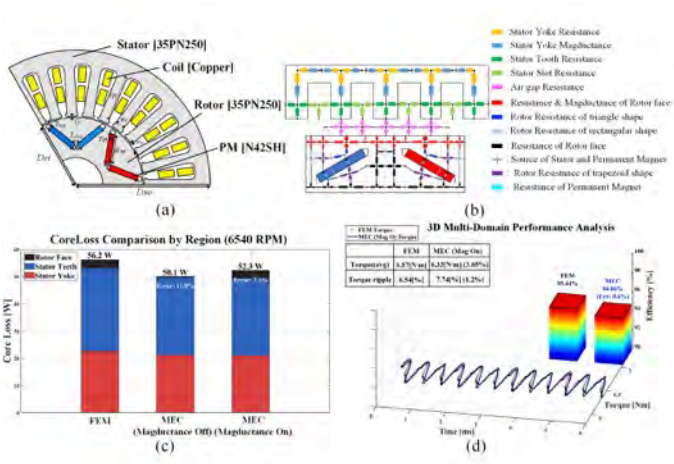


Fig. 1. Proposed RNM construction and FEM validation: (a) structure of IPMSM, (b) RNM topology, (c) core loss comparison, and (d) torque ripple and efficiency comparison.

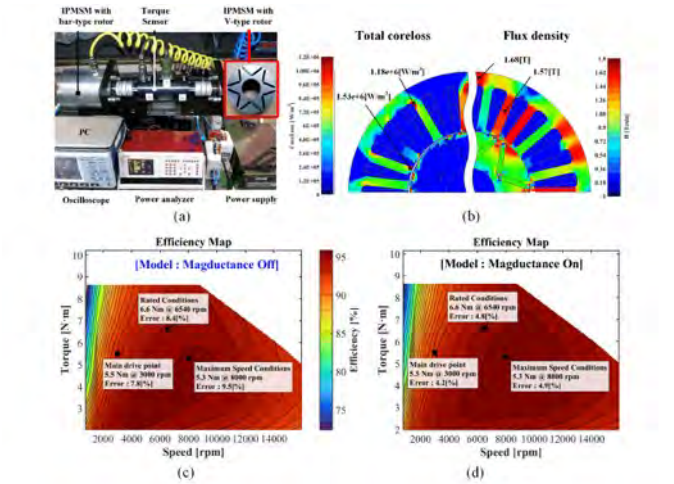


Fig. 2. Experimental validation and operating characteristics in IPMSM: (a) test setup, (b) distribution of core loss and flux density, (c) efficiency map without magductance, and (d) efficiency map with magductance.

HP-10. Temperature Dependent Radial Loss Correction for Quasi-3D Electro-Thermal Analysis of Axial Flux Permanent Magnet Motors

S. Woo[1], S. Kim[1], M. Kim[1], J. Park[3], K. Shin[2], J. Choi[3]
[1]Smart Manufacturing Engineering, Changwon National University, Changwon, Korea (the Republic of), [2]AI Electrical Engineering, Changwon National University, Changwon, Korea (the Republic of), [3]Electrical Engineering, Chungnam National University, Daejeon, Korea (the Republic of)

Axial flux permanent magnet motors (AFPMMs) are attractive for high power density applications, but accurate loss prediction usually requires three-dimensional finite element analysis (3D FEA), with high computational cost [1]. Quasi-3D analysis overcomes this burden by dividing the machine into radial slices. However, its loss prediction accuracy is limited because end effects, leakage flux, and radial loss variation are not fully reflected [2].
Therefore, this paper proposes a temperature-dependent radial loss correction method for quasi-3D electro-thermal analysis of AFPMMs. Fig. 1 shows the procedure of electromagnetic correction. The geometry of AFPMM in Fig. 1(a) is converted into a 2D analysis plane in Fig. 1(b). Magnet and rotor yoke thickness are selected as key variables and normalized by the air-gap length in Fig. 1(c). A design of experiments (DOE) is conducted, and polynomial regression is employed to derive the radial correction factor. As shown in Fig. 1(d), slice-wise core and permanent magnet losses are compared before and after, demonstrating that the proposed factor compensates for radial loss distribution. Fig. 2 presents the validation of the electro-thermal coupled analysis. Corrected losses are applied as heat sources to the thermal equivalent network in Fig. 2(a), and iterative electromagnetic-thermal coupling reflects temperature-dependent properties. The prototype and test system in Fig. 2(b) are used for validation. In Fig. 2(c), measured and calculated back-EMF are compared, while in Fig. 2(d), the proposed quasi-3D model achieves efficiency comparable to 3D FEA and experimental results. The proposed method improves loss prediction accuracy while maintaining high computational efficiency and provides an effective design tool for AFPMMs.

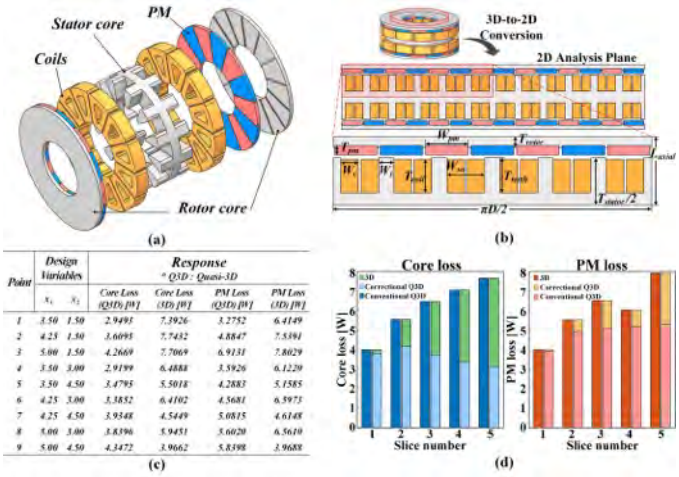


Fig. 1. Quasi-3D radial loss correction process: (a) AFPMM configuration, (b) 2D analysis plane, (c) DOE results for normalized design variables, and (d) loss comparison for each radial slice before and after correction.

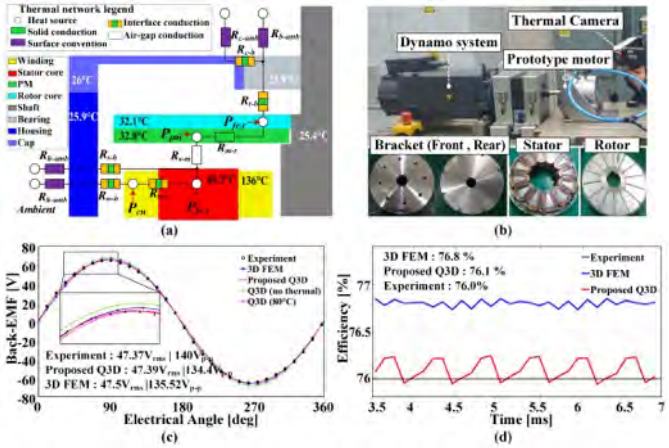


Fig. 2. Electro-thermal analysis and validation: (a) thermal equivalent network, (b) experimental setup and prototype, (c) back-EMF comparison, and (d) efficiency comparison among 3D FEA, experiment, and quasi-3D analysis.

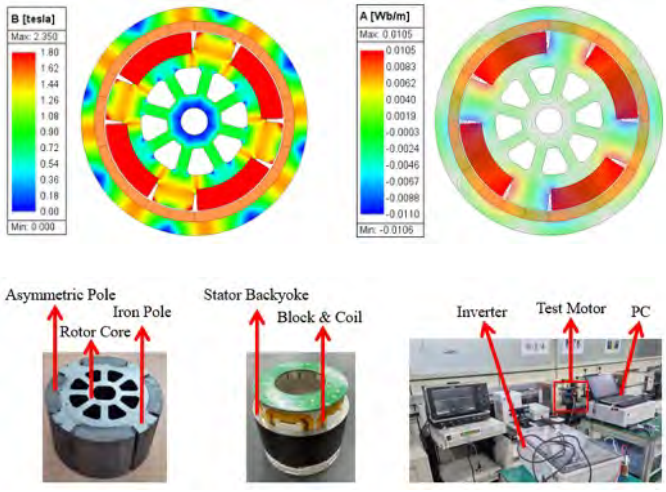
[1] B. Dianati, S. Kahourzade, and A. Mahmoudi, *IEEE Trans. Energy Convers.*, vol. 35, no. 3, pp. 1522–1533, (2020)
[2] H. Zhao, K. T. Chau, T. Yang, Z. Song and C. Liu, *IEEE Trans. Energy Convers.*, vol. 37, no. 2, pp. 1358-1368, (2022)

HP-15. Design of a Consequent Pole Slotless Motor Applying Asymmetric Pole

D. Choi, H. Han, D. Shin, S. Jeon, W. Kim
Gachon University, Seongnam-si, Gyeonggi-do, Korea (the Republic of)

The global electric motor market is currently a crucial industry, with particular significance in the automotive sector. Recently, electric motors, notably the high-efficiency Permanent Magnet Synchronous Motor (PMSM) utilizing permanent magnets, have gained prominence. However, the use of rare earth materials for these permanent magnets poses significant challenges in terms of supply and comes with a high price. The Electric Power Steering (EPS) motor, a crucial component in applications featuring PMSM, such as automotive steering systems, requires careful consideration of important parameters like vibration and noise reduction. In motors with conventional slotted structures, the uneven reluctance during motor operation leads to significant cogging torque and torque ripple, contributing to vibration and noise. Slotless structures, which lack slots by design, offer a solution to mitigate these issues. However, the trade-off is a reduction in output, necessitating an increase in the usage of permanent magnets. Therefore, there is a need for research on applying Consequent Pole (CP) to slotless motors to reduce the usage of permanent magnets. However, in conventional slotted motors, the CP structure leads to an increase in cogging torque and torque ripple due to the asymmetric of the pole configuration. Conversely, when applied to slotless motors, these drawbacks can be mitigated, and iron losses significantly reduced. Additionally, an asymmetrical pole design has been implemented to enhance back electromotive force (back EMF). This paper proposes an Asymmetric Consequent Pole Slotless Motor (ACPSM) design, incorporating an asymmetric pole concept into the consequent-pole structure of slotless motors. The objective is to minimize the reliance on permanent magnets while minimizing output reduction. To systematically determine the design trade-off, weighting factors are introduced based on the reduction ratio of permanent magnet usage and the reduction ratio of the no-load back EMF. By adjusting these coefficients, an optimized ratio is selected to balance magnet reduction and back-EMF degradation, and the final design is determined according to the coefficient-based optimal proportion.

[1] D. -H. Choi, D. -H. Kim, H. -S. Han, D. -H. Jung and W. -H. Kim, "Design of a Slotless Structure for Minimizing Cogging Torque and Torque Ripple in a Column Type EPS Motor for Vehicles," in IEEE Transactions on Magnetics, vol. 60, no. 9, pp. 1-5, Sept. 2024, Art no. 8700305.
[2] H. Dhulipati, S. Mukundan, Z. Li, E. Ghosh, J. Tjong and N. C. Kar, "Torque Performance Enhancement in Consequent Pole PMSM Based on Magnet Pole Shape Optimization for Direct-Drive EV," in IEEE Transactions on Magnetics, vol. 57, no. 2, pp. 1-7, Feb. 2021, Art no. 8103407.
[3] J. Qi et al., "Effect of Pole Shaping on Torque Characteristics of Consequent Pole PM Machines," in IEEE Transactions on Industry Applications, vol. 58, no. 3, pp. 3511-3521, May-June 2022.
[4] J. Li and K. Wang, "Analytical Determination of Optimal PM-Arc Ratio of Consequent-Pole Permanent Magnet Machines," in IEEE/ASME Transactions on Mechatronics, vol. 23, no. 5, pp. 2168-2177, Oct. 2018.
[5] S. Teymoori, A. Rahideh, H. Moayed-Jahromi and M. Mardaneh, "2-D Analytical Magnetic Field Prediction for Consequent-Pole Permanent Magnet Synchronous Machines," in IEEE Transactions on Magnetics, vol. 52, no. 6, pp. 1-14, June 2016, Art no. 8202114.
[6] F. Li, K. Wang, J. Li and H. Y. Sun, "Electromagnetic Performance Analysis of Consequent-Pole PM Machine With Asymmetric Magnetic Pole," in IEEE Transactions on Magnetics, vol. 55, no. 6, pp. 1-5, June 2019, Art no. 8103205.
[7] J. Li and K. Wang, "A Novel Spoke-Type PM Machine Employing Asymmetric Modular Consequent-Pole Rotor," in IEEE/ASME Transactions on Mechatronics, vol. 24, no. 5, pp. 2182-2192, Oct. 2019.
[8] H. Zhou, W. Tao, C. Zhou, Y. Mao, G. -J. Li and G. Liu, "Consequent Pole Permanent Magnet Vernier Machine With Asymmetric Air-Gap Field Distribution," in IEEE Access, vol. 7, pp. 109340-109348, 2019.

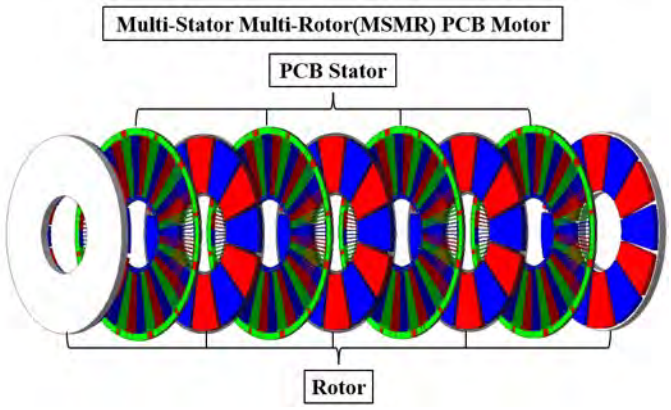


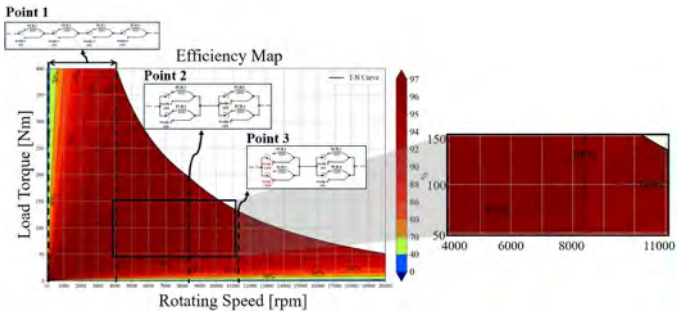
HP-16. EV Traction Motor Design Based on Series-Parallel Switching Control of a Multi-Stator Multi-Rotor Coreless PCB AFPM

D. Choi, Y. Lim, C. Lee, S. Park, W. Kim
Gachon University, Seongnam-si, Gyeonggi-do, Korea (the Republic of)

A series-parallel switching drive concept is developed for electric vehicle (EV) traction using a coreless printed circuit board (PCB) axial-flux permanent-magnet (AFPM) machine with a Multi-Stator Multi-Rotor (MSMR) architecture. Selectively activatable PCB stator modules enable forced flux-weakening, and electrical switching among series/parallel connections extends the feasible high speed operating region under inverter voltage limit. Despite the structural and manufacturing advantages of PCB AFPM machines, the coreless topology generally yields a small separation between L_d and L_q, which can limit speed extension when relying solely on conventional current-angle-based flux-weakening in the voltage-limited region. The current-density inefficiency of a fixed 4-series (4S) configuration is quantified, and staged transitions from 4S to two-parallel–two-series (2P2S) and further to two-parallel–one-series (2P1S) are shown to improve both efficiency and current density utilization. Copper losses in the PCB windings are reduced through trace-pattern optimization and multi-via interconnection, mitigating both AC and DC copper losses. The proposed method enables supports operating point dependent configuration selection to maximize efficiency, achieving a peak efficiency above 97% while reducing current density relative to the conventional fixed 4S operation. Comparative results between fixed 4S operation and reconfigurable series-parallel operation identify a design that simultaneously increases efficiency and lowers current density.

[1] J. de Santiago, H. Bernhoff, B. Ekergård, S. Eriksson, S. Ferhatovic, R. Waters, and M. Leijon, "Electrical Motor Drivelines in Commercial All-Electric Vehicles: A Review," IEEE Transactions on Vehicular Technology, vol. 61, no. 2, pp. 475–484, Feb. 2012.
[2] M. L. de Klerk and A. K. Saha, "A Comprehensive Review of Advanced Traction Motor Control Techniques Suitable for Electric Vehicle Applications," IEEE Access, vol. 9, pp. 125080–125108, 2021.
[3] T. M. Jahns, "Flux-Weakening Regime Operation of an Interior Permanent-Magnet Synchronous Motor Drive," IEEE Transactions on Industry Applications, vol. IA-23, no. 4, pp. 681–689, Jul.-Aug. 1987.
[4] S. Huang, J. Luo, F. Leonardi, and T. A. Lipo, "A Comparison of Power Density for Axial Flux Machines Based on General Purpose Sizing Equations," IEEE Transactions on Energy Conversion, vol. 14, no. 2, pp. 185–192, Jun. 1999.
[5] F. G. Capponi, G. De Donato, and F. Caricchi, "Recent Advances in Axial-Flux Permanent-Magnet Machine Technology," IEEE Transactions on Industry Applications, vol. 48, no. 6, pp. 2190–2205, Nov.-Dec. 2012.
[6] R. Huang, Z. Song, H. Zhao, and C. Liu, "Overview of Axial-Flux Machines and Modeling Methods," IEEE Transactions on Transportation Electrification, vol. 8, no. 2, pp. 2118–2132, Jun. 2022.
[7] F. Marignetti, G. Volpe, S. M. Mirimani, and C. Cecati, "Electromagnetic Design and Modeling of a Two-Phase Axial-Flux Printed Circuit Board Motor," IEEE Transactions on Industrial Electronics, vol. 65, no. 1, pp. 67–76, Jan. 2018.





SESSION HQ: ALTERMAGNETIC, ANTIFERROMAGNETIC, TERAHERTZ AND SUPERCONDUCTING SPINTRONICS II (POSTER SESSION)

Chair(s): J. G. Athas, *Electrical and Computer Engineering, Northwestern University, Chicago, Illinois, United States*

Friday, November 6, 2026

03:00 PM-06:00 PM

Coral 4

HQ-01. Magnetism and Magnetocaloric Effect in GdRhIn

A. A. Maz[1, 2], S. Gupta[2, 1], R. Kumar[2, 1]

[1]*SEAS, Bennett University, Greater Noida, Uttar Pradesh, India,*

[2]*Physics, Bennett University, Greater Noida, Uttar Pradesh, India*

Structural, magnetic and magnetocaloric characteristics of an RTX-type intermetallic GdRhIn are probed with focus on competing exchange interactions. X-ray diffraction reveals a hexagonal Fe_2P-type structure. Magnetic measurements show the presence of two magnetic transitions: antiferromagnetic at T_N 16 K and ferromagnetic at T_C 34 K, suggesting a competition between magnetic exchange interactions, confirmed by heat capacity measurements.

The magnetocaloric effect, obtained from isotherms, displays a maximum entropy change Delta S_m 10.3 J/ kg K for 70 kOe and a refrigerant capacity of about 282 J/kg for 50 kOe. The wide DeltaS_m(T) curve, showing contributions around both T_N and T_C, is related to the two-fold magnetic phase evolution, broadening the cooling cycle.

The irise in magnetocaloric effect is linked to the field-induced antiferromagnetic-ferromagnetic competition. Our findings identify GdRhIn as a new potential material for low-temperature magnetic refrigeration, and suggest magnetic phase competition as a strategy to enhance magnetocaloric properties in RTX compounds.

1. Sachin Gupta, and K. G. Suresh, J. alloys and compounds 618, 562 (2015).
2. V. Pecharsky, and Karl A. Gschneidner Jr., Phys. Rev. Letts. 78, 4494 (1997)).
3. Sachin Gupta, Handbook on the Physics and Chemistry of Rare Earths 63, 99 (2023).
4. R. Kumar, A. A. Maz, S. K. Mishra, and S. Gupta, Sensors, 24, 6326 (2024).

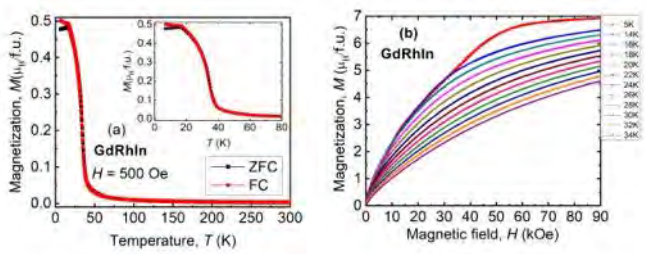


Fig. 1. M(T) at 500 Oe (ZFC/FC) and M(H) at selected temperatures for GdRhIn

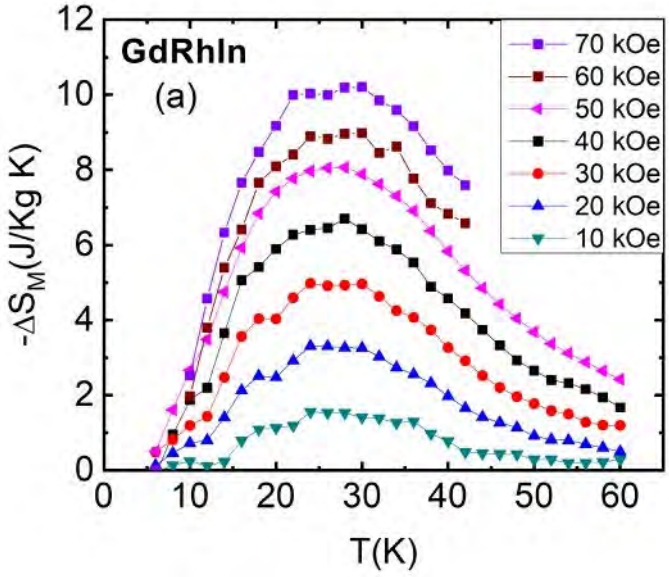


Fig.2. Delta S_m(T) of GdRhIn under different magnetic fields.

HQ-02. Universal Enhancement of Current-Induced Domain Wall Velocity in the Short-Pulse Regime in GdFe/Pt Wires

T. Funae, K. Tanabe, H. Awano
Graduate School of Engineering, Toyota Technological Institute, Nagoya, Aichi, Japan

Racetrack memory has attracted considerable attention as a next-generation nonvolatile memory technology based on current-induced domain wall (DW) motion in magnetic nanowires[1].
For practical applications, it is essential not only achieving fast and efficient DW motion, but also to extend the wire length in order to store more information. Previous studies have reported that DW velocity increases as the pulse width is reduced[2]. In contrast, in the long-pulse regime, DW velocity decreases with increasing pulse duration because Joule heating deforms the DW from an initially flat configuration. Such structural distortion reduces the spin-orbit torque (SOT) transfer efficiency, resulting in slower DW motion[3].

However, the influence of wire length, and thus electrical resistance, on this pulse duration dependent behavior has not been systematically clarified. To address this issue, we fabricated Gd_xFe_{1-x}(20 nm)/Pt(10 nm) wires with different wire lengths *L* , thereby controlling the device resistance *R*. Pulse current with varying pulse widths were then applied to each sample, while the input power *P* was adjusted so that the current density was identical for all devices.

Despite the variation in wire length, a clear enhancement of DW velocity was consistently observed in the short pulse regime in Fig. 1, indicating that the velocity improvement is a universal feature rather than a geometry-specific effect. Magneto-opticalic imaging further revealed that when the injected energy became large, the DW structure changed from a flat shape to a tilted or curved configuration (Fig. 2). Such deformation may reduce the effective transfer of SOT to the DW, thereby suppressing the attainable DW velocity. In addition, the experimental results suggest that wires with lower resistance tend to exhibit faster DW motion, whereas higher-resistance wires may exhibit slower motion.

These findings demonstrate the robustness of short-pulse-induced DW acceleration in ferrimagnetic systems and provide useful design guidelines for high-speed racetrack memory based on GdFe/Pt heterostructures.

[1] S. S. P. Parkin et al., Science 320, 190 (2008).
[2] K. Ogawa et al., Phys. Rev. Research, 5, 033151 (2023).
[3] S. Ranjbar et al., Mater. Adv., 3, 7028-7036 (2022).

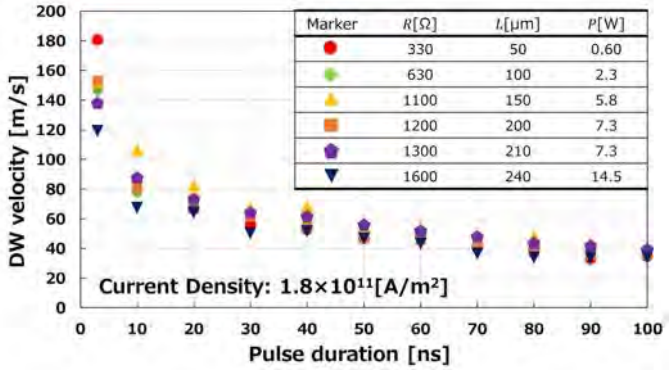


Fig. 1 Relationship between pulse duration and domain wall velocity.

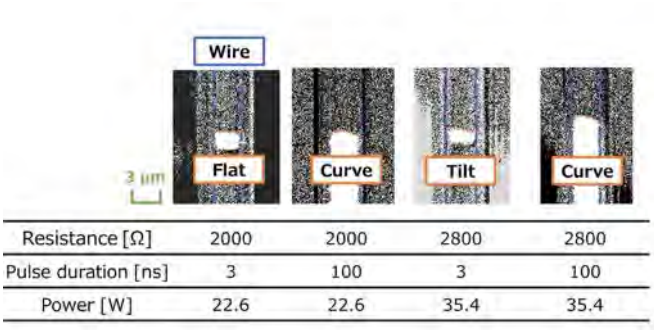


Fig. 2 Difference magnetic domain images before and after current application.

HQ-03. Stacking Order-Dependent Magnetic Behavior in Ta-Seeded TbCo Gradient Ferrimagnetic Structures

L. Ye[1, 2], X. Jiang[1, 2], Y. Yao[1, 2], C. Lee[1, 2], T. Wu[1, 2]
[1]Graduate School of Materials Science, National Yunlin University of Science and Technology, Douliu, Yunlin, Taiwan, [2]Taiwan SPIN Research Center, , National Yunlin University of Science and Technology, Douliu, Yunlin, Taiwan

Here, we study the magnetic properties of ferrimagnetic (FIM) films with Co-rich phase and TM-rich phase for Ta-seeded TbCo Gradient Structures. Under the same magnetic layer structure, different stacking gradient structure produce significantly different hysteresis curves and domain reversal behavior. Our findings indicate that the TM-rich structure has stable hysteresis switch behavior at gradient structures. The magnetic seed layer thickness of a RE-rich structure needs to be at least 2 nm to achieve PMA and a Ku value of 2.7 x 10^{-6} emu/cm^3. However, with the same structure, a TM-rich magnetic seed layer with a thickness of only 1.5 nm can achieve a Ku value as high as 3.5 x 10^{-6} emu/cm^3. The

results revealed that the stacking order has a significant impact on coercivity, magnetic domain reversal behavior, and perpendicular magnetic anisotropy (PMA).
In addition, video images of the domain wall motion were recorded at a rate of 30 frames per second using magneto-optical microscopy. We then calculated the statistical averages of various coercivity values to obtain the coercivity spectrum and distribution from 90,000 micro-hysteresis loops, each with a spatial resolution of 0.34 μm. Micro-hysteresis coercivity spectrum analysis further revealed that the TM-rich structure enables more uniform and faster domain reversal. This study highlights the effectiveness of seed layer and composition engineering for fine-tuning the magnetic properties of ferrimagnetic materials

1) R. C. Bhatt et al., J. Appl. Phys., 125 (2019) 113902.
2) R. C. Bhatt et al., J. Magn. Magn. Mater., 589 (2023) 171575.
3) L.X.Ye et al., IEEE Tran. Magnetics., Vol.41, No.2, (2005) pp.956-pp.958.

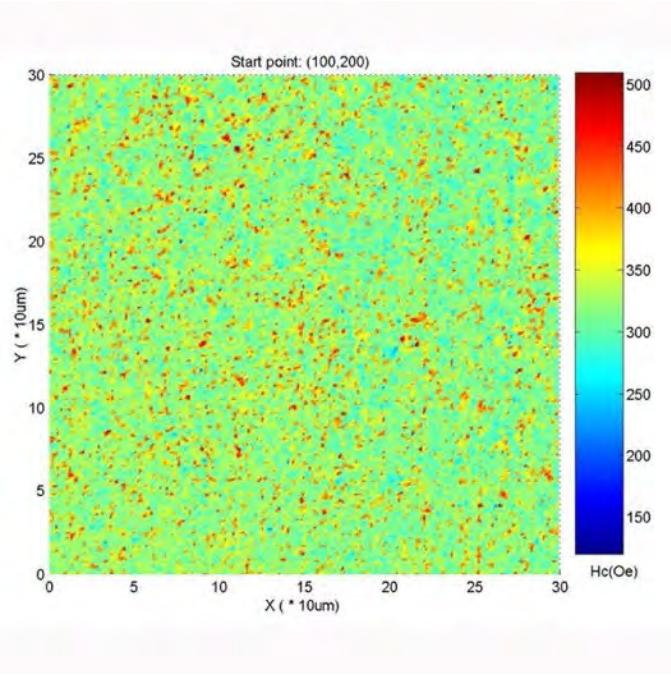


Figure 1. Coercivity spectrum of RE-rich gradient ferrimagnetic structures with 2 nm magnetic seed layer.

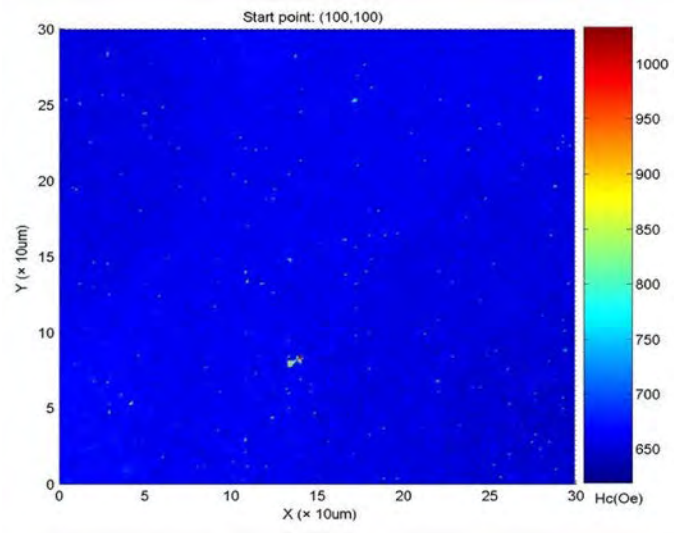


Figure 2. Coercivity spectrum of TM-rich gradient ferrimagnetic structures with 2 nm magnetic seed layer.'

HQ-04. Thickness dependence of self-spin swapping with interfacial Rashba and bulk effects

G. Han, K. Kim, S. Jeon, S. Choe
Seoul National University, Seoul, Korea (the Republic of)

Spin–orbit coupling (SOC) generates various spin current conversion phenomena, such as the spin Hall effect and self-spin swapping (SSS) effects. In this study, we investigated the microscopic origin of the SSS effect by examining its dependence on the thickness of the adjacent nonmagnetic layer. For this study, we prepared thin films with the structure Ta(5 nm)/Pt(3 nm)/Au(3 nm)/Co(0.8 nm)/Au(t_{Au}) by DC sputtering, where t_{Au}—the thickness of the top Au layer—was varied from 2 to 17 nm. The SSS-induced effective magnetic field H_{eff} was measured with respect to the current density J using domain wall depinning measurement based on magneto–optical Kerr effect microscopy [1]. The SSS efficiency ε was then evaluated based on the relation $\varepsilon = H_{eff}/J$, as shown by Fig. 1. Contrary to the expectation that ε would increase with t_{Au} due to the bulk nature of the SSS effect, Fig. 1 shows a decreasing trend with increasing t_{Au}. This behavior indicates that surface effects play a significant role. Quantitative analysis suggests that the surface contribution exceeds the bulk contribution. To further examine this surface-origin scenario, we deposited an ultrathin Pt dusting layer on the top Au surface to systematically modify the interfacial Rashba field. By analyzing the variation of ε with the Pt dusting thickness, we investigate the correlation between

the Rashba field modulation and the SSS efficiency. Based on these observations, we analyze and discuss the microscopic origin of the surface contribution in the SSS effect.

[1] P. P. J. Haazen, E. Murè and J. H. Franken, Nature Materials 12, 299–303 (2013).

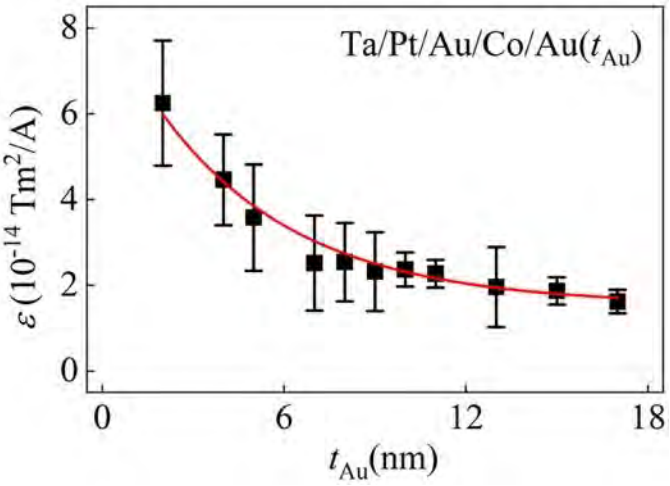


Fig 1. Plot of the SSS efficiency with respect to the thickness of the Au layer

HQ-05. Spin Pumping into [Nb/Ta/V]$_n$ Superconductor Without Inversion Symmetry

S. Hirata[1], R. Kawarazaki[2], R. iijima[1], F. Tokoro[1], T. Mandokoro[1], H. Matsuki[1, 3], R. Hisatomi[1, 3], S. Karube[1, 3], Y. Shiota[1, 3], T. Ono[1, 3, 4]

[1]Institute for Chemical Research, Kyoto University, Uji, Kyoto, Japan, [2]Research Institute of Electrical Communication, Tohoku University, Sendai, Miyagi, Japan, [3]Center for Spintronics Research Network, Kyoto University, Uji, Kyoto, Japan, [4]International Center for Synchrotron Radiation Innovation Smart, Tohoku University, Sendai, Miyagi, Japan

Superconductors without inversion symmetry have long been studied due to various exotic properties such as the superconducting diode effect or FFLO states [1,2]. Some of these phenomena are attributed to the mixing of spin-singlet and spin-triplet pairing states. Probing such mixed pairing states requires experimental techniques that are sensitive to the spin degree of freedom.

Spin pumping provides a powerful probe of superconducting pairing symmetry. By using ferromagnetic resonance (FMR), spin currents can be injected into an adjacent material, and the efficiency of spin injection is quantified through the FMR damping constant. In conventional spin-singlet superconductors, the damping constant decreases upon cooling below the superconducting transition temperature (T_c) [3]. In contrast, spin-triplet superconductors are expected to exhibit a different temperature dependence [4]. Therefore, spin pumping has been used as a probe for unconventional superconductivity.

In this study, a [Nb/Ta/V]$_n$ superlattice (Fig. 1) was deposited on a MgO (001) substrate by DC sputtering at 700 °C. A $Ni_{80}Fe_{20}$ layer was subsequently deposited at room temperature and capped with SiO_2. Spin pumping measurements were carried out using a coplanar waveguide, where a high-frequency current was applied via a vector network analyzer (VNA) while sweeping the magnetic field. The resonance linewidth was identified from the S_{21} parameter, and the damping constant was extracted from the frequency dependence of the resonance linewidth. The temperature dependence of the damping constant does not decrease below T_c, different from the behavior of a conventional superconductor. In this presentation, we discuss possible origins of this anomalous behavior.

[1] F. Ando, Y. Miyasaka, T. Li et al., Nature, Vol. 584, p. 373 (2020)
[2] M. Sigrist, AIP Conf. Proc., Vol. 1162, p. 55 (2009)
[3] C. Bell, S. Milikisyants, M. Huber et al., Phys. Rev. Lett., Vol. 100, p. 047002 (2008)
[4] KR. Jeon, C. Ciccarelli, A. J. Ferguson et al., Nat. Mater., Vol. 17, p. 499 (2018)

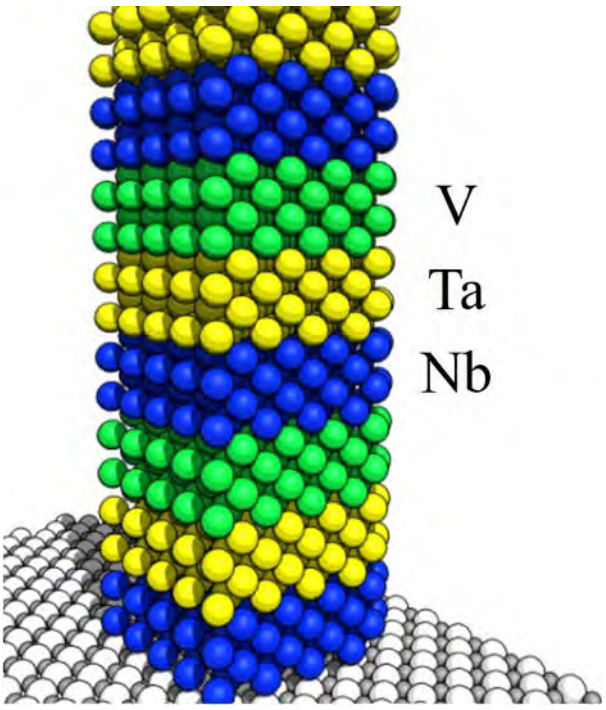


Fig. 1 Schematic image of Nb/Ta/V artificial superlattice

HQ-06. Extrinsic Altermagnetic Spin-Splitting Torque in RuO_2 (101) Thin Film

J. Seo, E. Kim, J. Hur, D. Kim, B. Park
Department of Materials Science and Engineering, KAIST, Daejeon, Korea (the Republic of)

Altermagnetism has emerged as a magnetic phase characterized by spin-split band structure even in the absence of net magnetization. Altermagnet enables the conversion of charge to spin current via a non-relativistic origin, promising a platform for manipulating spin-polarized current [1,2]. Specifically, RuO_2 is a representative altermagnet candidate material with metallic conductivity and high Neel temperature. However, the RuO_2 magnetic phase and spin transport remain controversial. In this work, we demonstrate that the spin-split torque conductivity of RuO_2 follows a linear scaling law with longitudinal conductivity in RuO_2(101)/NiFe bilayer structures. Figure 1 show a cross-sectional TEM image of epitaxial RuO_2(101) with an Ar:O_2 ratio of 4.5:1 on Al_2O_3 (1-102) substrate. By adjusting the Ar and O_2 partial pressures during reactive sputtering, we successfully deposited epitaxial RuO_2 (101) thin film with tunability while maintaining high crystallinity and consistent strain. We quantified the spin torque in RuO_2/NiFe bilayer using harmonic Hall measurements. When current is applied along the [010], the y- polarized and z-polarized spin torque were enhanced by the altermagnetic spin-splitting torque (ASSE) while it remains negligible along the [10-1] direction. Enhanced spin torque in [010] is consistent with the previously reported crystal momentum dependent ASSE in RuO_2. In addition, we observed the linear relationship between longitudinal conductivity and spin-split torque conductivity appears exclusively when current is applied along the [010] in various Ar:O_2 ratios and measurement temperature [Figure 2]. This linear behavior suggests that the ASSE is dominantly governed by extrinsic effects. This finding is consistent with theoretical predictions and highlights an important factor for manipulating ASSE in RuO_2.

[1] L. Šmejkal, J. Sinova, and T. Jungwirth Physical Review X, 12, 040501 (2022)
[2] A. Bose, D. C. Ralph et al. Nature electronics, 5,267-274 (2022)

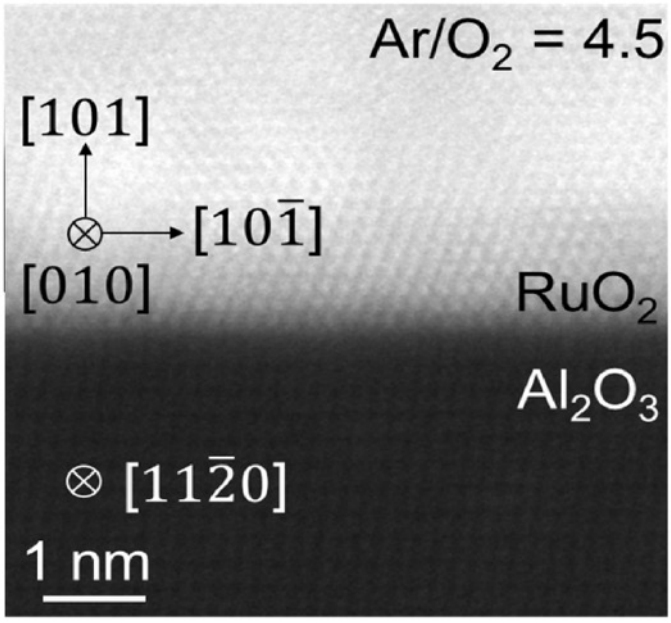


Figure 1.

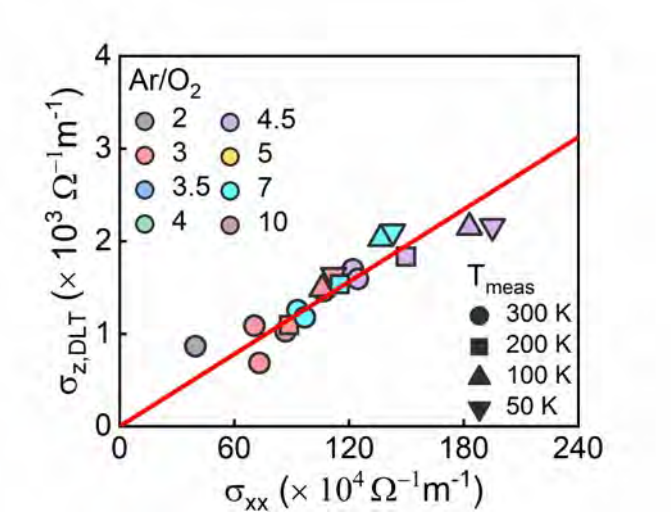


Figure 2.

HQ-07. Investigation of spin-split torque in RuO_2 epitaxial thin film on miscut substrate

S. Kim, C. You
DGIST, Daegu, Korea (the Republic of)

Altermagnetism has recently emerged as a novel magnetic phase in spintronics field. In particular, RuO_2 has been predicted to exhibit altermagnetic properties arising from its unique spin-split band structure, which generates crystal-orientation-dependent spin-split torque (SST) [1]. Previous studies have reported the existence of SST depending on the crystal orientation [2][3]. Especially, RuO_2 grown on flat α-Al_2O_3 c-plane substrate exhibits in-plane 3-fold symmetry due to the hexagonal lattice structure, resulting in triple-domain structure [4]. In such triple-domain systems, the SST generated from 120° relative orientations tends to compensate and reduce the overall efficiency.
In this work, we suggest a new method to modulate the multi-domain system of RuO_2 (100) through interfacial engineering using miscut substrate. RuO_2 thin films is grown on both flat and 3.25° miscut α-Al_2O_3 c-plane substrates using reactive DC magnetron sputtering. The epitaxial quality and crystalline symmetry are measured using XRD (Fig. 1, 2). In contrast to the RuO_2 on flat α-Al_2O_3 c-plane substrate, RuO_2 on miscut α-Al_2O_3 c-plane substrate exhibits a significant difference in symmetry (Fig. 2). This difference is expected to break the balance of SST from triple-domain structure and enhance the SST efficiency by suppressing domain formation. To compare the SST between flat and miscut substrate, RuO_2/FM heterostructure is fabricated and patterned into Hall bar geometry for electronic transport measurements. A more detailed discussion will be provided in the presentation.

[1] L. Šmejkal, J. Sinova and T. Jungwirth, Phys. Rev. X, Vol. 12, 040501 (2022).
[2] T. V. A. Nguyen, H. Naganuma and T. N. H. Vu, Adv. Sci., Vol. 12, 2413165 (2025).
[3] A. Bose, N. J. Schreiber and R. Jain, Nat. Electron, Vol. 5, p.267-274 (2022).
[4] Z. Fatima, D. Oka and T. Fukumura, Cryst. Growth Des., Vol. 21, p.4083-4089 (2021).

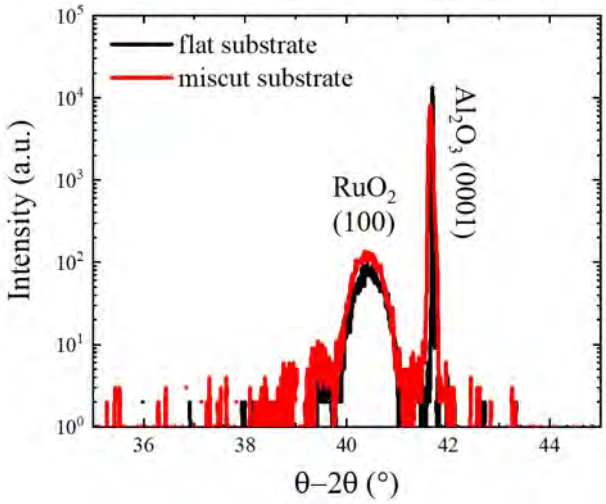


Fig.1 XRD θ-2θ patterns of RuO_2 on flat and miscut Al_2O_3 c-plane substrate.

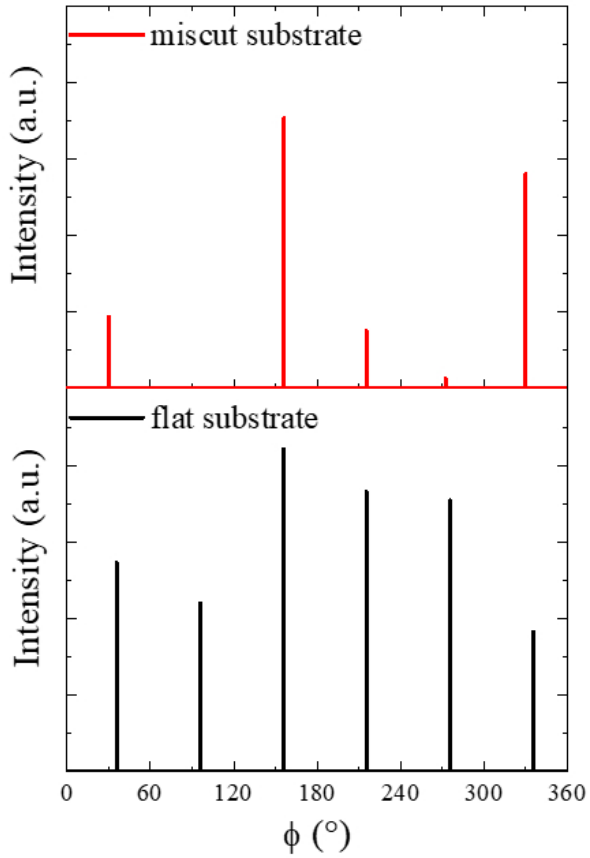


Fig. 2 XRD ϕ-scan of RuO_2 on flat and miscut Al_2O_3 c-plane substrate. RuO_2 on miscut substrate shows two significant domain structure while flat substrate shows triple-domain structure.

HQ-08. Stabilizing Out-of-Plane Magnetization in Thick Co Using Enhanced Exchange Fields

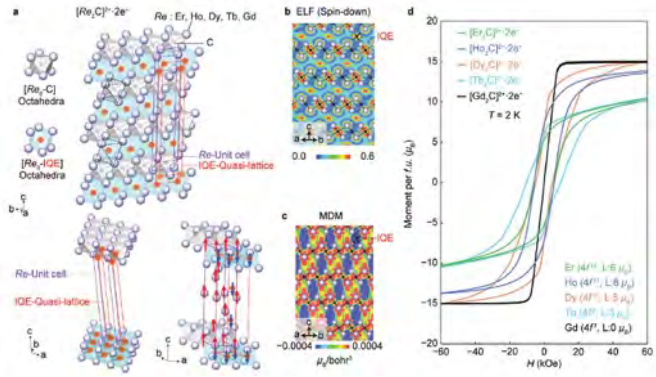
B. Jamshed, S. Das, S. Piramanayagam
School of Physics and Mathematics, Nanyang Technological University, Singapore, Singapore

Efficient control of magnetization orientation in ferromagnetic layers is central to the development of next-generation spintronic devices. Here, we report a pronounced enhancement of the exchange field in spin-reorientation heterostructures, enabling robust stabilization of out-of-plane magnetization in comparatively thick Co layers. Such behavior is unconventional, as increasing ferromagnetic thickness typically favors in-plane anisotropy due to demagnetization effects. Our results reveal that the large Hex, arising from interfacial spin-orbit coupling mechanisms, overcomes this limitation and induces a stable perpendicular magnetic state. This high-Hex regime provides a practical pathway to achieve magnetization pointing upward without the need for external magnetic fields or complex multilayer engineering. Importantly, the ability to sustain perpendicular alignment in thicker magnetic layers enhances thermal stability and signal robustness, making these systems highly suitable for magnetic memory and logic applications. In particular, the observed characteristics are sufficient to meet the requirements for magnetic memory modules (MMM), where deterministic switching and long-term retention are essential. Our findings establish spin-reorientation engineering via enhanced exchange fields as a promising route toward scalable, energy-efficient spintronic technologies.

HQ-09. Permanent Electride Magnets Induced by Quasi-Atomic Non-Nucleus-Bound Electrons

J. Hwang[1], S. Lee[2], K. Lee[1]
[1]Yonsei University, Seoul, Korea (the Republic of), [2]Kongju University, Cheonan, Korea (the Republic of)

Interstitial quasi-atomic electrons (IQEs) in the quantized energy levels of positively charged cavities possess a substantial own magnetic moment and control the magnetism of crystalline electrides depending on the interaction with surrounding cations. However, weak spin-orbit coupling and gentle exchange interaction restricted by the IQEs preclude a large magnetic anisotropic, remaining a challenge for a hard magnetism. It is reported that 2D $[Re_2C]^{2+}$-$2e^-$ electrides (Re = Er, Ho, Dy, and Tb) show the permanent magnetism in a ferrimagnetic ground state, mimicking the ferrites composed of magnetic sublattices with different spin polarizations.Magnetic interaction between Re-spin lattice and IQE-spin lattice in the $[Re_2C]^{2+}$-$2e^-$ electrides results in a large magnetocrystalline anisotropy and high coercivity, giving a maximum energy product of 15 MGOe. It is demonstrated that the spontaneous breaking of magnetic IQE-sublattice through substitution with paramagnetic elements produces a crossover into an antiferromagnetic spin ordering of Re-sublattice, implying that the magnetic sublattice of IQEs drives the permanent magnetism.



HQ-10LB. Ferroelectric switchable altermagnetic-like compensated ferrimagnets with charge ordering

X. Yang
Southeast University, Naniing, JIANGSU , China

Unconventional collinear magnets with almost zero magnetization but prominent nonrelativistic spin splitting, such as altermagnets, can inherit the advantages of both ferromagnets and antiferromagnets. By incorporating more degrees of freedom such as ferroelectricity and charge ordering, these unconventional magnets can be even more interesting and functionalized. With this design principle, the Fe_3O_5 monolayer is predicted to exhibit a hybrid spin-splitting mechanism, with the superposition of the altermagnetic-like *k*-path alternating splitting and ferrimagnet-like Zeeman splitting. Benefiting from the hidden magnetoelectricity based on spin-charge coupling, such spin splitting can be fully switched by an electric field. Its conductivity is highly spin-polarized, with a polarization ratio above 99%, comparable to half-metals but with zero magnetization.

1. Xinyu Yang and Shuai Dong*, J. Am. Chem. Soc. 148, 31352−31358 (2026).
2. Xinyu Yang, Shan-Shan Wang*, and Shuai Dong*, Adv. Funct. Mater. 36, e17921 (2026).

HQ-11. Interface engineering in Co/Tb/Co synthetic ferrimagnets to host room temperature skyrmions

R. Kaur[1], S. Gajarao[1], A. Haldar[2], C. Murapaka[1]
[1]Materials Science and Metallurgical Engineering, Indian Institute of Technology Hyderabad, Hyderabad, Telangana, India, [2]Physics, Indian Institute of Technology Hyderabad, Hyderabad, Telangana, India

Magnetic skyrmions are swirling spin textures with fascinating topological characteristics making them ideal candidates for serving as information carriers in spintronic devices. Dzyaloshinskii-Moriya interactions (DMI) which prefer non-collinear spin orientations with neighbouring moments play a key role in stabilizing skyrmions. Recently, ferrimagnetic alloys and multilayers are attracting great interest to host skyrmions at room temperature. It has been demonstrated that ferrimagnetic skyrmions can be driven with ultra-high speeds with suppressed skyrmion Hall effect (SkHE)[1,2].

In this work, we engineer the interface in rare-earth and transition metal multilayers to tune the anisotropy and Dzyaloshinskii-Moriya interactions (DMI) in Co/Tb/Co heterostructure. We have employed Pt as spacer layer to enhance the interfacial DMI. The effect of Co/Tb/Co stack repetition on the magnetization reversal and evolution of topological spin textures is systematically investigated. The magnetization reversal curves and corresponding magnetic textures (below) obtained from the Kerr microscopy imaging are shown in Figure 1(a-j). We have observed reversal through nucleation of bubble domains in single Co/Tb/Co stack. The evolution of labyrinthine domains in 4 repetitions and transformation to skyrmions with diameters close to 120 nm was observed in 5 repetitions. The stack repetition enhances the perpendicular magnetic anisotropy, DMI, and dipolar interactions promoting robust skyrmion formation at room temperature. Further tuning via Tb thickness reveals a critical threshold for ferrimagnetic ordering. Increasing the Tb thickness enables a transition from negligible magnetic response (0.2 - 0.45 nm) to ferrimagnetic ordering (0.65 nm).

[1] S. Mallick, Y. Sassi, N. Figueiredo Prestes, S. Krishnia, F. Gallego, T. Denneulin, S. Collin, K. Bouzehouane, A. Thiaville, R.E. Dunin-Borkowski, V. Jeudy, A. Fert, N. Reyren, and V. Cros, "*Driving Skyrmions in Flow Regime in Synthetic Ferrimagnets*", Nat. Commun. 15, 8472 (2024).

[2] S. Woo, K.M. Song, X. Zhang, Y. Zhou, M. Ezawa, X. Liu, S. Finizio, J. Raabe, N.J. Lee, S. Il Kim, S.Y. Park, Y. Kim, J.Y. Kim, D. Lee, O. Lee, J.W. Choi, B.C. Min, H.C. Koo, and J. Chang, "*Current-driven dynamics and inhibition of the skyrmion Hall effect of ferrimagnetic skyrmions in GdFeCo films*," Nat. Commun. 9(1), (2018).

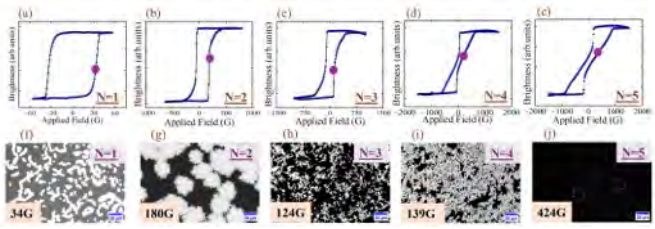


Fig. 1: Magnetization reversal and domain evolution of Co/Tb/Co stack with 1 to 5 repetitions observed from MOKE microscopy imaging.

HQ-12. Observation of double sign changes in temperature dependent anomalous Hall effect of moderately strained thulium iron garnet/ platinum heterostructure

N. Yamashita[3], I. P. Cools[2], L. Yan[1], J. Xu[1], D. P. Dubey[2], S. P. Dash[2]
[1]Graduate School of Information Science and Electrical Engineering, Kyushu Univeristy, Fukuoka, Fukuoka, Japan, [2]Chalmers University of Technology, Gothenberg, Sweden, [3]Faculty of Information Science and Electrical Engineering, Kyushu University, Fukuoka, Japan

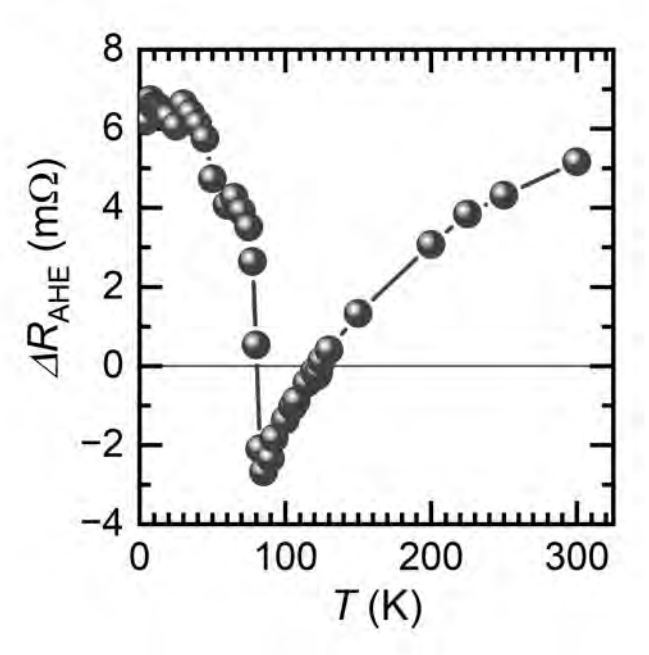
Recently, the magnetic property of strained magnetic garnet gains considerable attention. Compensation-like temperature (T_{CL}) in thulium iron garnet (TmIG, $Tm_3Fe_5O_{12}$) has been observed when grown on a small mismatched GGG substrate[1]. Only Tm sublattice moment flips at T_{CL}, while both Fe and Tm sublattices' moments flip at the magnetic compensation point (T_{MC}). Interestingly, T_{MC} which is absent in bulk TmIG, was also observed in the largely strained TmIG grown on a large mismatch substrate[2]. Although these compensation phenomena is important for realizing ultrahigh speed spin-orbitronic devices, the effects of T_{MC} and T_{CL} on the electrical signal in the Hall voltage is poorly understood, whilst the heterostructure of TmIG and platinum (Pt) is of highly importance for the spin-orbitronics applications[3]. Here, we investigated ultrathin TmIG film grown on GGG substrate and report a signature of T_{MC} in the moderately strained TmIG, by measuring Hall voltage in the proximity magnetized platinum (Pt) film.

A hall cross sample was fabricated by using sputtering grown TmIG/Pt heterostructure. The detail of fabrication method and condition is shown in elsewhere[4,5]. The Hall voltage was recorded while sweeping magnetic field at each temperature. The offset of the ordinary Hall effect proportional to the magnetic field was subtracted. Figure 1

shows the temperature dependence of the anomalous Hall resistance ΔR_{AHE}, the sign changes were observed at 124 K and 81K. We attribute the sign change at 121 K to the switching of the dominant mechanism of AHE in Pt, which has been already published because of the continuous shift of the coercivity. There are two possible mechanisms for the sign change at 81K, T_{MC} or T_{CL} since both mechanisms involves divergence of the coercivity. The detail mechanisms will be discussed in the presentation.

We acknowledge the WISE Knut and Alice Wallenberg Foundation, and Swedish Research Council (VR) (No. 2021–04821), JST ACT-X JPMJAX23KJ, JSPS KAKENHI JP26K17760, The Foundation for The Promotion of Ion Engineering, and R1 TECHNOLOGIES LLC. Device fabrication was supported by Prof. H. Yuasa group at Kyushu University

1. C. C. Soares *et al*, *ACS Appl. Nano. Mater.* 8, 29, 14567-14575 (2025).
2. R. Yui *et al, Adv. Sci.* 12, e06085 (2025).
3. C. O. Avci et al, Nat. Mater. 16, 309-314 (2017).
4. M. Agusutrisno *et al, Thin Solid Films* 788, 14176 (2024).
5. R. Ngaloy, N. Yamashita *et al, npj Spintronics* 3, 40 (2025).



Temperature dependence of anomalous Hall signal in Pt/TmIG/GGG substrate.

HQ-13. Spin transport in a van der Waals triangular lattice antiferromagnet $NiGa_2S_4$ as a candidate for Z_2-vortex ordering

Y. Yamaguchi[1], N. Jiang[1, 6, 7], D. Takafuji[1], K. Ueda[1, 6, 7], J. Matsuno[1, 6, 7], T. Kikkawa[2], Y. Nambu[3], K. Aoyama[5], H. Kawamura[4], Y. Niimi[1, 6, 7]
[1]Department of Physics, The University of Osaka, Toyonaka, Osaka, Japan, [2]Advanced Science Research Center, Japan Atomic Energy Agency, Tokai, Japan, [3]Institute for Integrated Radiation and Nuclear Science, Kyoto University, Kyoto, Japan, [4]Center for Life Photonic Innovation, Kobe University, Kobe, Japan, [5]Graduate School of Advanced Science and Engineering, Hiroshima University, Hiroshima, Japan, [6]Center for Spintronics Research Network, The University of Osaka, Toyonaka, Japan, [7]Institute for Open and Transdisciplinary Research Initiatives, The University of Osaka, Osaka, Japan

In frustrated magnets, the competition between exchange interactions often produces non-collinear magnetic structures. A prominent example is 2D triangular lattice Heisenberg antiferromagnet, which exhibits a 120° structure as a ground state. In such systems, a Kosterlitz-Thouless-type transition exciting vortices formed by local 120° structures is theoretically predicted [1]. Since a vortex can be continuously transformed into an antivortex in the case of isotropic Heisenberg spins as shown in Fig. 1, the vorticity is defined by the presence or absence of the vortex, namely "Z_2 vortex". In the Z_2 vortex state, spin transport is expected to be mediated by the topologically robust vortices, leading to enhanced spin conductance [2].

We investigated spin transport in $NiGa_2S_4$ (NGS), a candidate material for the Z_2 vortex phase. Despite its strong antiferromagnetic interactions (Θw = -80 K), NGS exhibits no long-range order nor quasi-long-range-order. However, it shows anomaly in magnetic susceptibility at $T^* \approx 8.5$ K, which is ascribed to the Z_2 vortex transition [3]. We prepared NGS thin films by the mechanical exfoliation technique and fabricated devices with two Pt wires. Vortices were thermally excited by applying AC currents in the injector, and the magnetic moments carried by free vortices were detected as a non-local second-harmonic voltage in the detector via the inverse spin Hall effect. As demonstrated in the inset of Fig. 2, we obtained a relatively large and atomically flat film of NGS, which is essential for the measurements.

In Fig. 2, we show the second-harmonic voltage measured with the device shown in the inset. With decreasing temperature, the second-harmonic voltage dramatically enhanced below 10 K. This result could be explained by the

theoretical calculation on spin conductance in the Z_2 vortex state [2].

[1] H. Kawamura and S. Miyashita, Journal of the Physical Society of Japan, Vol. 53, p. 4138 (1984)
[2] K. Aoyama and H. Kawamura, Phys. Rev. Lett., Vol. 124, p. 047202 (2020)
[3] S. Nakatsuji, Y. Nambu and Y. Maeno, Science, Vol. 309, p. 1697 (2005)

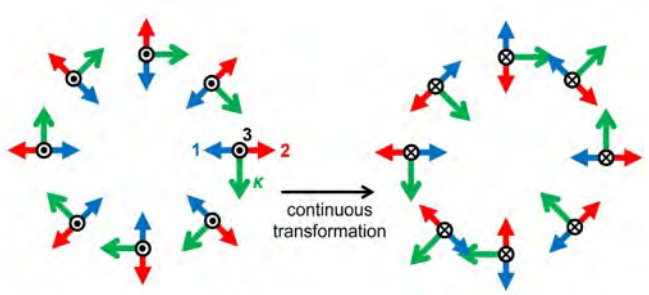


Fig.1: An example of Z_2 vortex (left) and apparent antivortex (right). The blue, red arrow and black circle represent the spins on the sublattices. The green arrows κ indicate the direction of the plane determined by the local 120° structures.

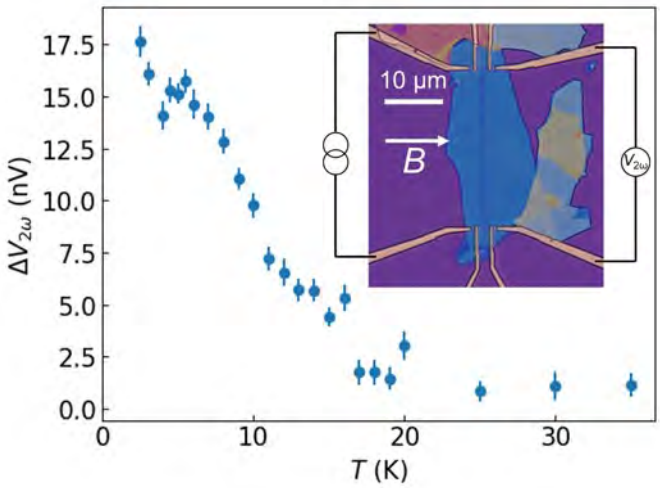


Fig.2: Temperature dependence of the non-local second-harmonic voltage. The inset shows an optical microscope image of the device and the measurement setup.

HQ-14. Evaluation of Magnetic Properties of $Mn_{4-x}Pd_xN$ Epitaxial Thin Films and Demonstration of Magnetization Compensation at Room Temperature

S. Akita[1], T. Yasuda[1], K. Amemiya[2], T. Suemasu[1]
[1]University of Tsukuba, Tsukuba, Japan, [2]High Energy Accelerator Research Organization (KEK), Tsukuba, Japan

We focus on Mn_4N-based thin films for current-driven domain wall (DW) motion. Mn_4N is a ferrimagnet with low saturation magnetization (M_s = 80 kA m^{-1}) and perpendicular magnetic anisotropy (K_u = 0.1 MJ m^{-3}), demonstrating fast DW motion driven by spin-transfer torques at room temperature (RT) [1]. Furthermore, $Mn_{4-x}Ni_xN$ wires exhibited higher DW velocities (3,000 m s^{-1}) at RT due to angular momentum compensation [2]. However, the required current density remains excessively high. To address this, we investigate $Mn_{4-x}Pd_xN$ thin films. While previous studies on $Mn_{4-x}Pd_xN$ exist, they resulted in polycrystalline films, leaving their magnetic compensation (MC) unreported [3]. We therefore fabricated epitaxial $Mn_{4-x}Pd_xN$ thin films and discussed the MC at RT.

In our experiments, thin films were fabricated on $SrTiO_3$(001) substrates using molecular beam epitaxy, and epitaxial growth was confirmed by reflection high-energy electron diffraction and X-ray diffraction. As shown in Figure 1, a minimum in M_s and a sign reversal in the anomalous Hall angle (ϑ_{AHE}) were observed at x = 0.10–0.15. These results suggest that MC occurs at compositions around x = 0.10–0.15. Figure 2 shows the Mn-L_3 edge XAS and XMCD spectra for $Mn_{4-x}Pd_xN$ with x = 0, 0.10, and 0.20. The XMCD spectra showed two characteristic peaks: the α peak, attributed mainly to Mn atoms at corner sites in the anti-perovskite structure, and the β peak, attributed mainly to Mn atoms at face-centered sites [4]. The XMCD spectrum for the x = 0.20 sample exhibited a sign-reversed signal compared to those for x = 0 and x = 0.10, although the signal intensity decreased significantly. This sign reversal is similar to those reported in Mn_4N thin films doped with Ni [5], Co [6], or Cu [7], which are known to exhibit MC. In the presentation, we further discuss the structural evolution based on X-ray absorption fine structure measurements and theoretical calculations, which reveal the preferential substitution sites of Pd atoms.

[1] T. Suemasu *et al.*, J. Phys. Soc. Jpn. 90, 081010 (2021).
[2] S. Ghosh *et al.*, Nano Lett. 21, 2580 (2021).
[3] T. Xu *et al.*, J. Phys. D: Appl. Phys. 51, 055303 (2018).
[4] K. Ito *et al.*, Phys. Rev. B 101, 104401 (2020).
[5] T. Komori *et al.*, J. Appl. Phys. 127, 043903 (2020).

[6] H. Mitarai *et al*., Phys. Rev. Mater. 4, 094401 (2020).
[7] A. Hatate *et al*., Phys. Rev. Mater. 8, L091403 (2024).

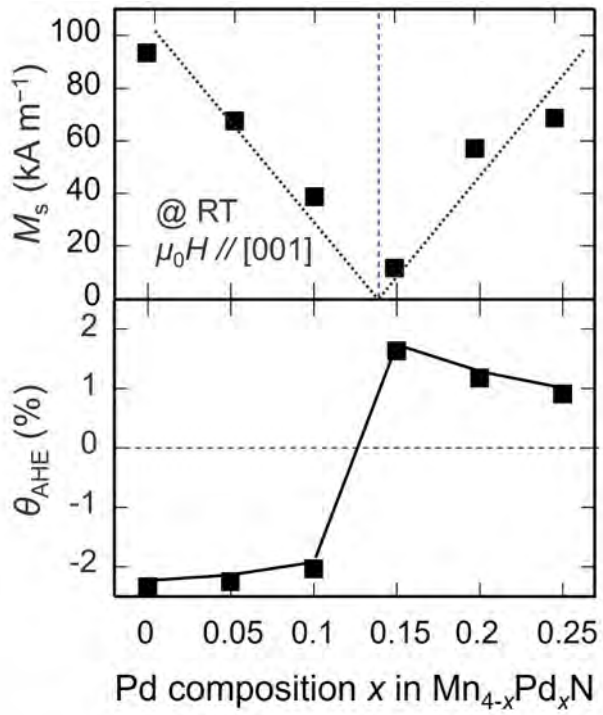


Fig. 1. Composition dependence of saturation magnetization M_s and anomalous Hall angle ϑ_{AHE}.

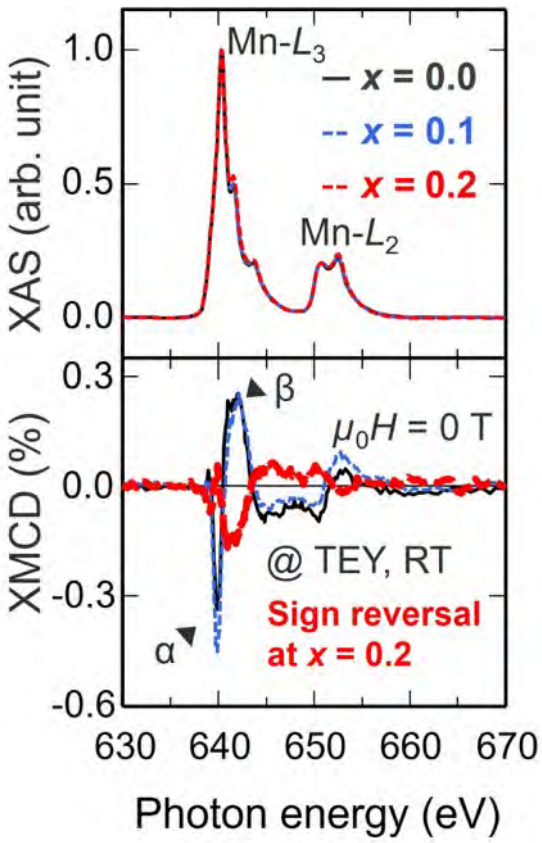


Fig. 2. Composition dependence of XAS and XMCD spectra of $Mn_{4-x}Pd_xN$ films

HQ-15. Three-Dimensional Spin Transport in α-Fe_2O_3 (0001)/$TaIrTe_4$ Heterostructures

J. Chen[1], H. Liu[1], W. Tan[1], T. Qian[2], W. Liao[1], T. Wang[3], I. K. Schuller[3], N. Ni[2], J. Shi[1]
[1]Department of Physics and Astronomy, University of California, Riverside, Riverside, California, United States, [2]Department of Physics and Astronomy, University of California, Los Angeles, Los Angeles, California, United States, [3]Department of Physics, University of California, San Diego, La Jolla, California, United States

Low-symmetry Weyl semimetal $TaIrTe_4$ possesses the unique capability of generating out-of-plane spin polarization, offering a promising route for manipulating magnetic order. Previous studies on magnetic material/Weyl semimetal heterostructures have primarily focused on field-free switching, and spin-torque ferromagnetic resonance in ferromagnets such as permalloy[1,2], Fe_3GaTe_2[3,4], and CoFeB[1,5]. However, spin transport phenomena, particularly

spin Hall magnetoresistance (SMR), in antiferromagnet/Weyl semimetal systems remain largely unexplored. In this work, we observed the spin Hall contribution in the easy-plane phase α-Fe_2O_3 (0001)/$TaIrTe_4$ heterostructure.
A major challenge arises from the dominant crystalline anisotropy magnetoresistance (CAMR), which overwhelms the SMR signal, hindering its experimental identification. In this work, we successfully isolate the SMR contribution from the strong CAMR background and observe a clear negative SMR under in-plane rotation measurements. Furthermore, to probe the out-of-plane spin component, we perform a second harmonic (2ω) measurement in the out-of-plane angular-rotation setup and observe a spin polarization polar angle of approximately 46°. This spin polarization polar angle varied from 46° to 23° when the temperature increased from 2K to 50K.
These results provide direct evidence that low-symmetry Weyl semimetals can generate three-dimensional spin currents capable of exerting torques on antiferromagnets. Our findings establish a viable platform for Néel vector manipulation and open new opportunities for antiferromagnetic spintronics based on topological materials.

This work is support by the U.S. Department of Energy (DOE), Office of Science, Office of Basic Energy Sciences under Award Number DE-FG02-07ER46351, and the UC National Laboratory Fees Research Program of the University of California, Grant Number L25CR9003.
Y. Liu et, al., Nat. Electron., Vol. 6, 732–738 (2023)
L. Bainsla et, al., Nat. Commun., Vol. 15,4649 (2024)
Y. Zhang et, al., Adv. Mater., Vol. 36, 2406464 (2024)
L. Pandey et, al., Nat. Commun., Vol. 16,8722 (2025)
Y. Zhang et, al., Sci. Adv., Vol. 9 (44) (2023)

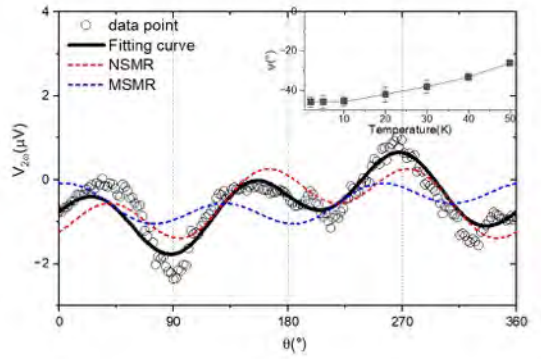


Fig. 1. Polar-angle (θ) dependence of the 2ω longitudinal resistance measured at 2 K under a 14 T magnetic field. The inset shows the temperature dependence of the spin polarization polar angle ψ.

HQ-16LB. Energetics and Octupole-Transfer-Induced Dynamics of Cubic Chiral Antiferromagnets

S. Khare[1], S. Konakanchi[1], J. Kang[2], M. Hamdi[3], P. Khalili Amiri[2], P. Upadhyaya[1]
[1]Electrical and Computer Engineering, Purdue University, West Lafayette, Indiana, United States, [2]Electrical and Computer Engineering, Northwestern University, Evanston, Illinois, United States, [3]Physics & Astronomy, UCLA, Los Angeles, California, United States

Chiral antiferromagnets (c-AFMs) combine the robustness and ultrafast dynamics of antiferromagnets (AFMs) with ferromagnet-like magnetoresistive readout. While hexagonal c-AFMs such as Mn_3Sn (Fig. 1a) have demonstrated tunneling magnetoresistance (TMR) [1], electrical control [2], and sub-ns octupole dynamics [3,7], achieving large room-temperature (RT) TMR remains a key challenge. Very recent demonstrations of RT TMR approaching a few hundred percent and evidence of a novel octupole transfer torque (OTT) in cubic c-AFM Mn_3Pt tunnel junctions [4,5] open a new pathway toward nanoscale all-AFM memory and unconventional computing. Yet, the energy landscape governing the octupoles in cubic c-AFM- and how OTT drives switching between them-remains largely unexplored. Here, using minimum-energy-path (MEP) analysis and a Landau-Lifshitz-Gilbert (LLG) framework, we study the energy landscape and OTT-driven dynamics of cubic Mn_3Pt.
In the strong-exchange limit, cubic symmetry gives rise to eight equivalent energy minima (s_1-s_8) in a three-parameter configuration space (Fig. 1c). First, we find that competition among the three cubic anisotropies suppresses the minimum energy barrier by one order of magnitude relative to the anisotropy scale. Fig. 1d shows a representative MEP between the all-in (s_1) and all-out (s_2) states. In contrast, competing DMI, exchange, and anisotropy in hexagonal Mn_3Sn suppress the barrier by 3 (strained)-6 (unstrained) orders of magnitude [6] (Fig. 1b), suggesting enhanced thermal stability of cubic c-AFMs.
Second, in an all-AFM tunnel junction, the newly discovered current-induced OTT destabilizes seven of the eight equilibrium states, with the selected state determined by the fixed-layer configuration and current polarity (Fig. 2a), enabling electrical selection and writing of a desired octupole state. In Fig. 2b, we show the switching probability between all-in (s_1) and all-out states (s_2) versus pulse amplitude and width as obtained by integrating stochastic LLG with OTT. Similar to spin-transfer torque in ferromagnetic MTJs, OTT produces anti-damping-like

destabilization, with the critical OTT field scaling as αH_{ex}, where α and H_{ex} are the Gilbert damping and exchange field, respectively.

Finally, we show that combining OTT with spin-orbit torque (SOT) substantially reduces the OTT required for state selection while preserving ps switching (Fig. 2c, 2d, 2e, 2f), providing a new pathway toward ps-scale, low-current all-AFM devices.

[1] X. Chen et al., "Octupole-driven magnetoresistance in an antiferromagnetic tunnel junction," Nature, vol. 613, pp. 490–495, 2023, doi: 10.1038/s41586-022-05463-w.

[2] H. Tsai et al., "Electrical manipulation of a topological antiferromagnetic state," Nature, vol. 580, pp. 608–613, 2020, doi: 10.1038/s41586-020-2211-2.

[3] K. Ogawa et al., "Ultrafast time-resolved observation of non-thermal current-induced switching in an antiferromagnetic Weyl semimetal," Nature Materials, vol. 25, pp. 434–439, 2026, doi: 10.1038/s41563-025-02402-8.

[4] J. Shi et al., "Electrically controlled all-antiferromagnetic tunnel junctions on silicon with large room-temperature magnetoresistance," Advanced Materials, vol. 36, Art. no. 2312008, 2024, doi: 10.1002/adma.202312008.

[5] J. Kang et al., "Octupole-driven spin torque switching of antiferromagnetic tunnel junctions," arXiv preprint arXiv:2509.03026v2, 2026, doi: 10.48550/arXiv.2509.03026.

[6] S. T. Konakanchi et al., "Electrically tunable picosecond-scale octupole fluctuations in chiral antiferromagnets," Physical Review Letters, vol. 135, Art. no. 136704, 2025, doi: 10.1103/w2wj-c9jx.

[7] Yutaro Takeuchi *et al*., "Electrical coherent driving of chiral antiferromagnet". *Science*389,830-834(2025).DOI:10.1126/science.ado1611

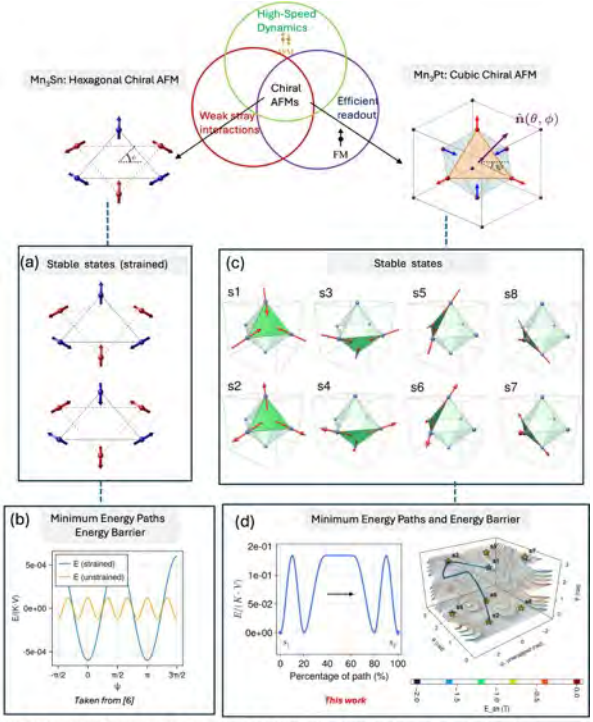


Fig. 1 | Energetics of hexagonal vs. cubic chiral AFMs. (a) Stable states of a strained hexagonal c-AFM. (b) Minimum-energy path (MEP), corresponding to rigid in-plane rotation of spins within the Kagome plane, parameterized by ψ. (c) Eight stable states of a cubic c-AFM. (d) MEP connecting the cubic states, obtained by varying θ, ϕ, ψ in the three-dimensional configuration space.

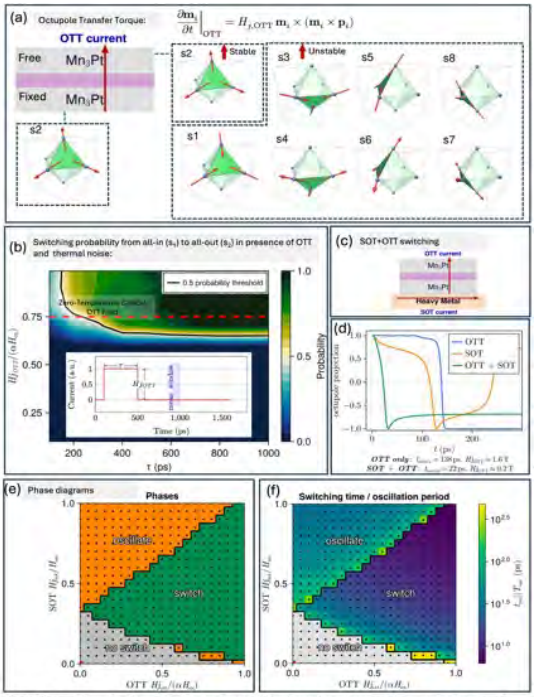


Fig. 2 | Octupole transfer torque (OTT)-induced control of spin configurations and low-current, picosecond-scale deterministic switching of octupole order by combined OTT and SOT. (a) Stability of the eight zero-current equilibrium states under current-induced OTT ($\mathbf{m}_s/\mathbf{p}_l$ label unit vectors along spins in the free/fixed layer) for a given fixed-layer configuration in an all-antiferromagnetic tunnel junction. Insets indicate stable and destabilized states under applied current. (b) OTT-driven switching probability from state s_1 to s_2 as a function of current-pulse amplitude and duration. The dashed horizontal line marks the zero-temperature threshold current calculated analytically. (c) Schematic of an all-antiferromagnetic tunnel junction combining OTT and SOT. (d) Representative deterministic switching trajectory demonstrating reduced threshold current and enhanced switching speed. (e) Switching phase diagram and (f) switching time as functions of current-induced OTT and SOT fields. Here, H_{ani} is the anisotropy field, α is the Gilbert damping parameter, and H_{ex} is the exchange field.

SESSION HR: ADVANCES IN FUNCTIONAL MAGNETISM: MATERIALS AND APPLICATIONS (POSTER SESSION)

Co-Chair(s): A. Lasheras, *Physics, University of the Basque Country, Leioa, Spain* and A. A. Mendonça, *Instituto de Física Gleb Wataghin, Universidade Estadual de Campinas, Campinas, São Paulo, Brazil*

Friday, November 6, 2026
03:00 PM-06:00 PM
Coral 4

HR-01. Magnetic and Magnetocaloric Properties of Ti-Substituted GdMnO3 Single Crystals

M. Ashraf[1], Z. Molčanová[2], M. Mihalik[1], J. Pospíšil[3]
[1]Department of Magnetism, Institute of Experimental Physics SAS, Kosice, Slovakia, [2]Institute of Materials Research, SAS, Kosice, Slovakia, [3]Faculty of Mathematics and Physics, Charles University, Prague, Czechia

$GdMnO_3$ came to the attention of the scientists due to the discovery of multiferroicity in this compound. The compound orders into antiferromagnetic phase below T_N ~ 40 K [1] and then undergoes order-to-order magnetic phase transition into low temperature canted magnetic phase at T_{lock} (~ 20 K). In our previous paper, we reported on Mn-Fe substitution [2], and our present study is focused on Mn-Ti substitution. $GdMn_{1-x}Ti_xO_3$ ($0 \leqslant x \leqslant 0.1$) compounds were synthesized by the floating zone method to understand the role of Ti substitution on structural, magnetic, and magnetocaloric properties. Raman spectroscopy and X-ray diffraction, along with Rietveld refinement, confirm the pure phase of all compositions having an orthorhombic perovskite structure (space group; Pnma). The Neel temperature T_N is not visible on magnetization measurements; however, from the combination of zero-field-cooled; field-cooled magnetization data and hysteresis loops M(B), we concluded the decrease of T_N from 42 K (x = 0) to roughly 30 K (x = 0.1). T_{lock} has been also shifted from ~20 K (x = 0) to ~2 K (x = 0.1). In the temperature interval $T_{lock} < T < T_N$ the M(B) curves show simple antiferromagnetic behavior, however, below T_{lock} the character of M(B) curves changed from complicated butterfly-type (x = 0) to simple ferromagnetic one (x = 0.1). This suggests that Ti destabilizes the magnetic structure or at least prevents the Gd sublattice from ordering. Magnetic entropy change (ΔS_M) is extremely sensitive to the direction of the applied field and can be negative (normal MCE) or positive (inverse MCE). The Gd ordering induces an inverse MC effect along 'c' and 'b' axes, whereas it's not seen along the 'a' axis, revealing complex anisotropic magnetic ordering. The magnetic entropy change displays a broad peak at T1 ~ 13 K with -ΔSM = 11.35, 8.05, and 7.77 J/kg-K and corresponding relative cooling power (RCP) = 197.72, 164.70, and 166.78 J/kg for x = 0.0, 0.05, and 0.1, respectively, under 5 T. A sharp -ΔSM = 0.55 J/kg-K (0.5 T) appears at T_{lock} = 20 K (x = 0.0), which is shifted to higher temperatures with a magnetic field. The large cryogenic MCE suggests these compounds are promising for low-temperature magnetic refrigeration applications.

1. N. Pavan Kumar, G. Lalitha and P. Venugopal Reddy, Phys. Scr., Vol. 83, p.045701 (2011)
2. M. Mihalik Jr., M. Vavra and M. Šestáková, Acta Phys. Pol. A, Vol. 137, p.993 (2020)

HR-02. Growth and Magneto-Optical properties of CeF_3 Crystal for Broadband Applications

Z. Zhang
Shanghai Institute of Ceramics, Chinese Academy of Sciences, Shanghai, China

Magneto-optical crystals, which can induce a directional rotation of the polarization state of laser light under a magnetic field, are essential functional materials for optical isolators. This enables unidirectional transmission of light within laser systems, preventing feedback light from interfering with preceding laser subsystems and thereby ensuring system stability. Currently, mature magneto-optical materials primarily include Tb-containing crystals and YIG crystal, which suffer from the restricted usable wavelength bands and challenges in large-size crystal growth. In this work, we developed a modified temperature gradient technique, to overcome the issues of crystal cracking and coloration and successfully fabricated high-quality CeF_3 crystals with a diameter exceeding 50 mm, which meet the requirements for laser applications. Our research demonstrates that CeF_3 crystal can be utilized across an ultra-broad spectrum ranging from 280 nm to 2500 nm. They exhibit a particularly large magneto-optic coefficient in the ultraviolet region (~650 rad/(T●m) @ 355 nm), holding promising potential for widespread applications in semiconductor manufacturing and metrology.

HR-03. Gilbert Damping Evaluation of 118-Layer Ce:YIG/GGG Multilayer for Magneto-Optical Devices

Y. Otsuka[1, 2], K. Fujiwara[1], T. Watanabe[3], E. Negishi[3], D. Shabaev[1, 2], K. Ishiyama[1], T. Goto[1]
[1]Research Institute of Electrical Communication, Tohoku University, Sendai, Miyagi, Japan, [2]Graduate School of Engineering, Tohoku University, Sendai, Miyagi, Japan, [3]Shin-Etsu Chemical Co., Ltd., Annaka, Gunma, Japan

Magneto-optical (MO) devices based on magnetic garnets are widely used. Recently, we demonstrated single-crystalline cerium-substituted yttrium iron garnet (Ce:YIG) grown on a garnet substrate, exhibiting tiny magnetic domains due to perpendicular magnetic anisotropy (PMA) and a large Faraday rotation (FR) angle [1]. However, the FR angle was 0.51°[1], insufficient for MO applications such as spin-controlled lasers [2]. To enhance the FR while maintaining the tiny PMA domains, a multilayered structure is effective. In this study, we grew such a multilayered garnet and measured its MO response. The Gilbert damping constant α was also evaluated, since the domain-wall velocity in spin-controlled lasers is governed by α in the Landau–Lifshitz–Gilbert equation, with lower α yielding faster domain-wall motion.

The multilayer, comprising 59 Ce:YIG/GGG bilayers, was grown on a 5 × 5 mm^2 SGGG substrate by RF ion-beam sputtering. The total Ce:YIG thickness was 14.142 μm, with an optical transmission bandgap at 1240 nm. The magnetic properties were measured using a vibrating sample magnetometer; the saturation magnetization and out-of-plane saturation field were 70 kA/m and 86.9 mT, respectively. The FR angle was 22° at a wavelength of 633 nm. The damping constant α was evaluated by ferromagnetic resonance (FMR) spectroscopy using a vector network analyzer. FMR measurements were performed in the out-of-plane configuration. Figure 1 shows the sample structure together with the real part of the measured S_{21} spectra, in which clear FMR-derived absorption peaks are observed. From a linear fit of the FMR linewidth versus resonance frequency [3] (Fig. 2), α was determined to be 8.0 × 10^{-2}, of the same order as the value reported for Ce:YIG film (α = 4.8 × 10^{-2}) [1]. These results demonstrate that multilayer growth enables a large total FR while keeping α within the same order as single-layer Ce:YIG, beneficial for the development of MO applications.

[1] T. Goto et al. ACS Appl. Opt. Mater., 3, 2923 (2025).
[2] T. Goto et al. Opt. Express, 24, 17635 (2016).
[3] A. Kehlberger et al. Phys. Rev. Appl., 4, 014008 (2015).

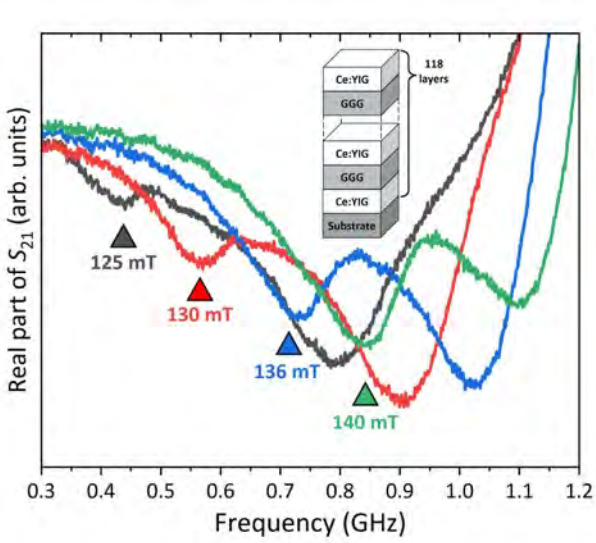


Fig. 1.Real part of the measured S_{21} spectra under various applied fields. Inset shows sample consisting of 59 pairs of Ce:YIG (243 nm) / GGG (50 nm) bilayers.

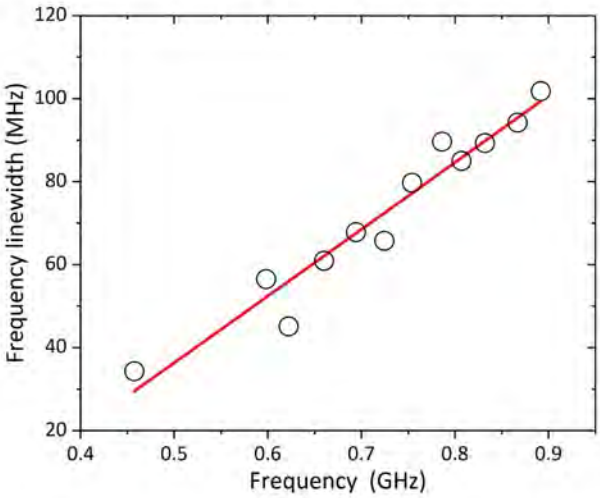


Fig. 2. FMR linewidth as a function of resonance frequency. The slope of the linear fit yields the Gilbert damping constant α.

HR-04. Multiscale theoretical prediction of enhanced magnetocaloric performance in Fe_2P-type alloys

M. Adiya[1], B. Narangerel[1], O. Tumentsereg[1], K. Jong-Woo[2], O. Dorj[1]
[1]Department of Physics, Incheon National University, Incheon, Korea (the Republic of), [2]Korea Institute of Material Science, Changwon, Korea (the Republic of)

Sustainable magnetic refrigeration relies on the development of magnetocaloric materials that offer both a large entropy change (ΔS_m) and low thermal hysteresis (ΔT_{hys}) at room temperature. While Fe_2P-type alloys are promising candidates, their performance is hampered by their large ΔT_{hys} and small reversible magnetic entropy change (ΔS^{rev}) near room temperature, limiting their magnetocaloric performance. Here, we employ a multiscale theoretical framework combining density functional theory, Monte Carlo simulations, the mean-field Bean-Rodbell model, and Landau expansion theory to systematically investigate the structural, magnetic, and magnetocaloric properties of $Mn_xFe_{2-x}P_{1-y}Si_y$ alloys. We find that the orthorhombic FeMnP phase is stable at low temperature and undergoes a transition to the hexagonal structure near y≈0.1. Further increases in Mn and Si stabilize the hexagonal phase, accompanied by a reduction in the c/a ratio, which in turn enhances magnetization and modulates the Curie temperature toward room temperature. More importantly, increasing Si content effectively raises the Curie temperature, while both Mn and Si contents reduce $\Delta T_{hys}$and enhances the ΔS^{rev}. Among the studied compositions, $Mn_{1.2}Fe_{0.8}P_{0.4}Si_{0.6}$ exhibits optimal performance, with an enhanced ΔS^{rev} of 6.3 J $kg^{-1}K^{-1}$, an improved refrigerant capacity (RC) of 26.1 J kg^{-1}, and a low ΔT_{hys} of 0.9 K at 1 T near room temperature, surpassing previously reported compositions. These findings demonstrate a composition-structure-property relationship and provide a pathway to simultaneously enhance entropy change and suppress hysteresis in Fe_2P-based alloys, advancing their potential for practical magnetic refrigeration.

The research is funded by Office of Naval Research (ONR) and Office of Naval Research Global (ONRG) of the US Department of Defense Grant N62909-22-1-2045, and National Research Council of Science & Technology (NST) Grant No. CAP25061-000 and Basic Research Program Grant No. RS-2026-25494250 through the National Research Foundation of Korea.

HR-05. Microscopic Origins of Magnetostriction Enhancement in Boron-Doped $Fe_{80}Ga_{20}$ Thin Films

Z. Zhang[1], H. Ni[1, 2], M. Lim[1], J. Lim[1], J. Zuo[1, 3], A. Schleife[1], A. Hoffmann[1]
[1]Department of Materials Science and Engineering, University of Illinois Urbana-Champaign, Urbana, Illinois, United States, [2]Oak Ridge National Laboratory, Oak Ridge, Tennessee, United States, [3]Monash Centre for Electron Microscopy, Monash University, Clayton, Victoria, Australia

Magnetoelastic materials are critical for enabling phonons to serve as an intermediate medium, bridging the otherwise inefficient direct interactions between microwave photons and magnons. In this work, we systematically investigated boron-doped $Fe_{80}Ga_{20}$ thin films and observed a significant enhancement in magnetostriction with the addition of boron. Maximum magnetostriction is achieved at a boron concentration that induces a mixed-phase region between polycrystalline and amorphous structures. To uncover the microscopic origin of this enhancement, we combined 4-dimensional scanning transmission electron microscopy (4D-STEM) with first-principles calculations. Using 4D-STEM, we statistically quantified the nearest-neighbor (NN) distances and revealed an inverse correlation with magnetostriction as a function of boron concentration. Our computational results elucidate this trend through a three-step mechanism: a decrease in NN distance shifts spin-orbit-active band crossings toward the Fermi level. This proximity increases the strain sensitivity of the magnetocrystalline anisotropy energy (MAE) and causes the k-space distribution of the MAE derivative to transition from destructive cancellation to constructive summation, directly amplifying magnetostriction. These findings demonstrate that boron doping enhances magnetoelastic coupling by locally modifying NN distances to activate this fundamental electronic regime. Finally, we integrated these films into surface acoustic wave (SAW) devices to study magnetoelasticity induced magnon-phonon interactions via acoustically driven ferromagnetic resonance. We observed boron-dependent acoustic absorption consistent with the magnetostriction trend, providing a unified picture of magnetostriction from the atomic scale enhancement to functional microwave applications.

This research was supported by US DOE BES Materials Sciences and Engineering Division under contract No. DE-SC0022060.

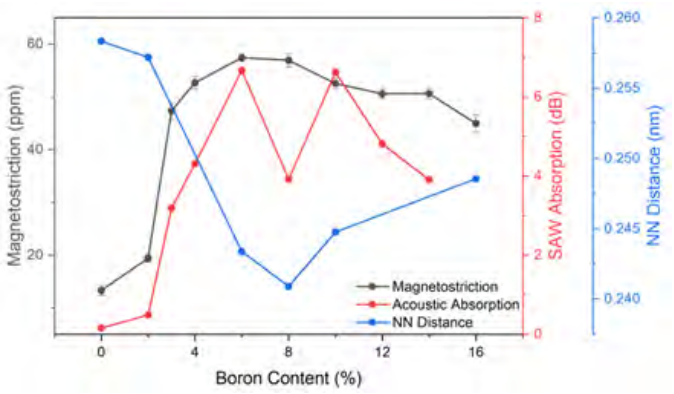


Fig. 1: Boron concentration dependence of magnetostriction, nearest-neighbor distance, and acoustic absorption. The plot shows that the minimum NN distance near 6-8% boron coincides with the maximum values for both magnetostriction and acoustic absorption.

HR-06. Influence of device structure on magnetoelectric coupling in laminate composites of textured Fe-Ga thin sheet and PZT

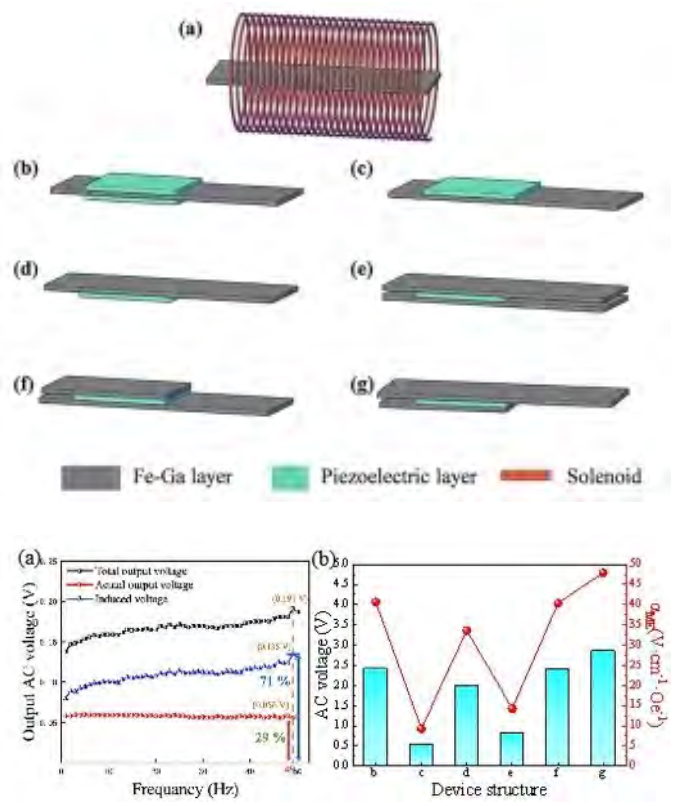
J. Liu[2,1], Z. He[2,1], S. Hu[2,1], Y. Sha[3], L. Chen[2,1], L. Zuo[3]
[1]Shenyang Key Laboratory of Advanced Structural Materials and Applications, Shenyang University of Technology, Shenyang, China, Shenyang, Liaoning Province, China, [2]School of Materials Science and Engineering, Shenyang University of Technology, Shenyang, China, Shenyang, Liaoning Province, China, [3]Key Laboratory for Anisotropy and Texture of Materials (Ministry of Education), Northeastern University, Shenyang, China, Shenyang, Liaoning Province, China

Magnetoelectric (ME) coupling devices using magnetostrictive Fe-Ga alloy sheets and piezoelectric materials have been used in magneto-mechanical-electrical (MME) sensors. The ME response can be tailored by the geometry and phase fractions of the constituent layers. In this paper, seven MME generators with different geometries were prepared using laminated Fe-Ga/PZT sandwich structures. The effect of geometries on the ME responses was investigated by the comparison of the output voltage and the ME coupling coefficients of the ME-coupled device. The ME-coupled device with Fe-Ga/PZT/Fe-Ga structure (the lower layer is a short Fe-Ga thin sheet) exhibits excellent output performance with an output voltage of 2.88 V and the ME coupling coefficient of 47.95 V/cm Oe at a resonant frequency of 42 Hz.

Introduction

Low-frequency and low-amplitude magnetic fields are commonly found around power transmission lines and electrical equipment. A magneto-electric (ME) coupling energy conversion device can be prepared by coupling a magnetostrictive phase and a piezoelectric phase.[1] Fe-Ga alloy combines a giant magnetostrictive coefficient, low saturation magnetic field, and high permeability. Cantilever Fe-Ga/piezoceramic composites exhibit high amplitudes and ME conversion factors upon exposure to magnetic field.[2-8] Although the ME response of laminated Fe-Ga/PZT depends on the phase fraction, dimensions, and geometry of the constituent layers, no attempt has been made to compare the combination of them. To exploit this idea, the laminate ME composites with different geometries were made using a Goss-oriented Fe-Ga thin sheet and commercial PZT piezoelectric. In this paper, seven MME generators with different geometries were prepared using laminated Fe-Ga/PZT sandwich structures. The effect of geometries on the ME responses was investigated by the comparison of the output voltage and the ME coupling coefficients of the ME-coupled device.

[1] G. T. Hwang, V. Annapureddy, J. H. Han, D. J. Joe, C. Baek, D. Y. Park, D. H. Kim, J. H. Park, C. K. Jeong, K. Park, J. J. Choi, D. K. Kim, J. Ryu and K. J. Lee, Adv. Energy Mater. 6, 1600237 (2016).
[2] S. Dong, J. Zhai, N. Wang, F. Bai, J. Li, D. Viehland and T. A. Lograsso, Appl. Phys. Lett. 87, 022504 (2005).
[3] S. Dong, J. Zhai, J. Li and D. Viehland, Appl. Phys. Lett. 89, 252904 (2006).
[4] S. Dong, J. Zhai, F. Bai, J. Li, D. Viehland and T. A. Lograsso, Appl. Phys. Lett. 97, 103902 (2005)
[5] T. Fitchorov, Y. Chen, B. Hu, S. M. Gillette, A. Geiler, C. Vittoria and V. G. Harris, J. Appl. Phys. 110, 1239156 (2011).
[6] H. Song, M. Peddigari, A. Kumar, S. Lee, D. Kim, N. Park, J. Li, D. R. Patil and J. Ryu, J. Alloys Compd. 834, 155124 (2020).
[7] H. Palneedi, S. M. Na, G. T. Hwang, M. Peddigari, K. W. Shin, K. H. Kim, K. H. Kim and J. Ryu, J. Alloys Compd. 765, 764 (2018).
[8] V. Annapureddy, S. M. Na, G. T.Hwang, M. G. Kang, R. Sriramdas, H. Palneedi, W. H. Yoon, B. D. Hahn, J. W. Kim, C. W. Ahn, D. S. Park, J. J. Choi, D. Y. Jeong, A. B. Flatau, M. Peddigari, S. Priya, K. H. Kim and J. Ryu, Energy Environ. Sci. 11, 818 (2018).



HR-07. Reversible Table Like Magnetocaloric Effect over a Broad Temperature Span in Rare-Earth-Ni Compounds Driven by Magnetic Interaction Competition

L. Zhao, A. T. Saito
National Institute for Materials Science, Tsukuba, Japan

Rare earth-based RNi (R = Gd-Er) compounds exhibit well-defined low-temperature magnetic transitions, making them an important family of materials for cryogenic magnetic studies. These compounds crystallize in a low-symmetry orthorhombic structure composed of stacked triangular prisms, with R atoms at the corners and Ni atoms at the centers. Magnetically, all these compounds show ferromagnetic behavior at temperatures ranging from 10-70 K and some compounds display a secondary magnetic transition below T_C[1]. In this series of compounds, the magnetism originates from the rare-earth ions, as Ni is essentially nonmagnetic. Notably, these compounds demonstrate a competitive magnetocaloric effect (MCE) at cryogenic temperatures. They present substantial $-\Delta S_m$ with values between 10-30 J $kg^{-1}K^{-1}$ under an applied field of 5 T prepared by various methods[2-7].
In this work, we investigate the magnetic properties and magnetocaloric effect of (RR')-Ni (R = Er, Ho/ R' = Gd, Tm) compounds. Polycrystalline samples were prepared by arc melting and further heat treatment. XRD results indicate that all compounds maintain a FeB-type crystal structure (*Pnma* space group) with a single phase. In terms of magnetism, R-site substitution with different rare-earth ions has a pronounced influence on the properties of the ErNi/HoNi compounds. The T_C of the double rare-earth compounds increases with the increasing content of the introduced rare-earth ions. Near and above T_C, the ZFC/FC $M(T)$ curves nearly coincide, revealing highly reversible magnetic behavior. Regarding the MCE effect, the $-\Delta S_m$-(T) peak shifted toward the higher temperatures, accompanied by a broadening of the peak by the introduction of rare earth elements. In the zero-field specific heat, the $C(T)$ peaks exhibit the same broadening behavior. We will discuss in detail the table-like behavior related to magnetic interaction competitions and spin frustration.

[1] R. E. Walline and W. E. Wallace, J. Chem. Phys., Vol. 41, p.587 (1964)
[2] S.K. Tripathy *et al.*, Solid State Commun., Vol. 134, p.323 (2005)
[3] P. Kumar *et al.*, J. Phys. D: Appl. Phys., Vol. 41, p.245006 (2008)
[4] R. Rajivgandhi *et al.*, J. Magn. Magn. Mater., Vol. 418, p.9 (2016)
[5] R. Rajivgandhi *et al.*, J. Magn. Magn. Mater., Vol. 433, p.169 (2017)
[6] Aparna Sankar *et al.*, AIP Adv., Vol. 8, p.056208 (2018)
[7] Jinu Kurian *et al.*, J. Magn. Magn. Mater., Vol. 499, p.166302 (2020)

HR-08. Seedlayer-free Ce:TbIG for Si Integrated TM Mode Magneto-Optical Isolator

B. Moghal, B. Stadler
Electrical and Computer Engineering, University of Minnesota, Minneapolis, Minnesota, United States

Waveguide-integrated optical isolators are the connecting part between the laser source and photonic integrated circuits that block the back-reflected light to protect the laser source. In our research, we use rare-earth magneto-optical (MO) garnets, which do not allow light to travel in backward direction due to its unique non-reciprocal behavior. We propose a novel silicon (Si) waveguide-integrated magneto-optical (MO) isolator device that employs cerium-substituted terbium-iron garnet (Ce:TbIG) layer as the non-reciprocal material. The main advantage of using Ce:TbIG is that it does not require a Seedlayer to grow on top of the Si core layer. Moreover, it demonstrates a

moderate Faraday rotation of -830 ± 100 ^{0}/cm which helps to achieve a smaller device footprint. The isolator device is designed based on the Mach–Zehnder interferometer principle, where Ce:TbIG will function as the cladding material to demonstrate the transverse magnetic (TM) mode of light input at 1550 nm wavelength. Here, we have used the Finite-Difference Eigenmode (FDE) solver to design the MO waveguides to find the design parameters for the isolator device. Finally, a unique Si/Ce:TbIG optical isolator device has been designed that shows significant isolation bandwidth at 20 dB.

HR-09. Magnetic-Field Control of Transition Pathways in Eu_2In: A Giant Cryogenic Magnetocaloric Material

A. Kumar[4], A. Biswas[4], T. A. Tyson[1], D. Haskel[2], C. J. Pollock[3], Y. Mudryk[4]

[1]Department of Physics, New Jersey Institute of Technology, Newark, New Jersey, United States, [2]Advanced Photon Source, Argonne National Laboratory, Lemont, Illinois, United States, [3]Cornell High Energy Synchrotron Source, Wilson Laboratory, Cornell University, Ithaca, New York, United States, [4]Ames National Laboratory, U.S. Department of Energy, Iowa State University, Ames, Iowa, United States

Understanding how external magnetic fields modify first-order magnetic phase transitions is crucial for both fundamental physics and the optimization of magnetocaloric responses of materials. While first-order transitions yield large entropy changes desirable for solid-state cooling, the associated thermal hysteresis limits their practical applications. R_2In (R = rare earth) compounds have recently attracted attention due to their large magnetic entropy change (S_M) and negligible hysteresis [1]. Among them, Eu_2In exhibits the largest entropy change of ≈ −28 J/kg-K for H = 20 kOe, with minimal hysteresis (~0.1 K) and negligible volume change across its first-order transition at T_c ≈ 55 K [2]. However, recent theoretical studies predict a magnetic-field-driven crossover from first- to second-order behavior near ~25 kOe, raising key questions about field-tunable transition pathways in this system [3].

Here, we investigate the temperature- and field-dependent magnetization, specific heat, and local structure of Eu_2In [4]. Pronounced anomalies in the magnetocaloric response are observed near ~25 kOe, suggesting a weakening of the first-order character. However, magnetocaloric analysis combined with modified Arrott plots confirms that the transition remains first order at least up to 70 kOe. Specific heat (C_P) measurements reveal a field-induced splitting of the sharp zero-field anomaly into a doublet. However, extended x-ray absorption fine structure measurements show no detectable field-induced changes in the local coordination environment of Eu, ruling out a structural origin of the second peak in the C_P curves. These results indicate a field-induced transformation from a single-step to a two-step transition process rather than a true change in transition order, resolving the discrepancy between theory and experiment and providing insight into field-tunable transition pathways in first-order magnetic systems.

Acknowledgments

This work was performed at Ames National Laboratory and was supported by the Division of Materials Science and Engineering of the Office of Basic Energy Sciences of the U.S. Department of Energy (DOE)under Contract No. DE-AC02-07CH11358.

A. Biswas, A. Kumar, P. Singh, and Y. Mudryk, From Complex Magnetic Ground States to Magnetocaloric Effects: A Review of Rare Earth R_2In Intermetallic Compounds, J. Phys. D: Appl. Phys. 59, 053001 (2026).

F. Guillou, A. K. Pathak, D. Paudyal, Y. Mudryk, F. Wilhelm, A. Rogalev, and V. K. Pecharsky, Non-hysteretic first-order phase transition with large latent heat and giant low-field magnetocaloric effect, Nat. Commun. 9, 2925 (2018).

B. P. Alho, P. O. Ribeiro, P. J. Von Ranke, F. Guillou, Y. Mudryk, and V. K. Pecharsky, Free-energy analysis of the nonhysteretic first-order phase transition of Eu_2In, Phys. Rev. B 102, 134425 (2020).

A. Kumar, A. Biswas, T. A. Tyson, D. Haskel, C. J. Pollock, and Y. Mudryk, Magnetic field induced modification of a first-order ferromagnetic transition in Eu_2In, Accepted in Phys. Rev. B, arXiv:2603.27390.

HR-10. The effect of thickness on the soft magnetic properties and transducers performance of Fe-Ga alloy

S. Hu[1, 2, 3], Z. He[1, 2], H. Hao[3], J. Liu[1, 2], T. Yao[3], X. Zhu[4], L. Chen[1, 2]

[1]School of Materials Science and Engineering, Shenyang University of Technology, Shenyang, Liaoning, China, [2]Shenyang Key Laboratory of Advanced Structural Materials and Applications, Shenyang, Liaoning, China, [3]State Key Laboratory of Baiyunobo Rare Earth Resource Researches and Comprehensive Utilization, Baotou Research Institute of Rare Earths, Baotou, Inner Mongolia, China, [4]Institute of Metal Research, Chinese Academy of Sciences, Shenyang, Liaoning, China

Magnetostrictive transducers can convert electromagnetic energy into mechanical energy and are widely used in industrial fields such as ultra-precision machining, micro-

electromechanical systems (MEMS), and precision polishing. Current transducers prepared by Terfenol-D can not be suitable for high-frequency and harsh environments due to the intrinsic brittleness of Terfenol-D. Galfenol (Fe-Ga) exhibits a combination of excellent magnetostrictive performance, high mechanical strength, and good ductility, allowing it to be used in harsh and shock-prone environments. However, there are still issues with the application of the Fe-Ga alloy thin sheet in the transducer. In this study, the dynamic magnetic performance of Fe-Ga alloy sheets with the thickness ranging from 0.5 mm to 2 mm were investigated under different frequencies. The effect of thickness on the dynamic magnetic performance of Fe-Ga alloy was clarified. The magnetostrictive transducers were fabricated using the Fe-Ga alloy sheet with different thicknesses, and the effect of stress on the performance of the transducers was also studied. An output displacement of 2 μm at 1000 Hz, and an output force of 25 N under a pressure of 600 N at 3000 Hz were obtained in a Fe-Ga alloy transducer fabricated Fe-Ga alloy thin sheet with a thickness of 3.5 mm.

Conclusion

The dynamic magnetic performance of Fe-Ga alloy sheets with the thickness ranging from 0.5 mm to 2 mm were investigated under different frequencies. The effect of thickness on the dynamic magnetic performance of Fe-Ga alloy was clarified. The magnetostrictive transducers were fabricated using the Fe-Ga alloy sheet with different thicknesses, and the effect of stress on the performance of the transducers was also studied. An output displacement of 2 μm at 1000 Hz, and an output force of 25 N under a pressure of 600 N at 3000 Hz were obtained in a Fe-Ga alloy transducer fabricated Fe-Ga alloy thin sheet with a thickness of 3.5 mm.

[1] Cao QH, Qin N, Zhang XX. Research and Analysis on Axial Cutting of Transducer Galfenol Rod for Eddy Current Loss Suppression[J]. Ordnance Material Science and Engineering, 2026, 49(2): 17-25.

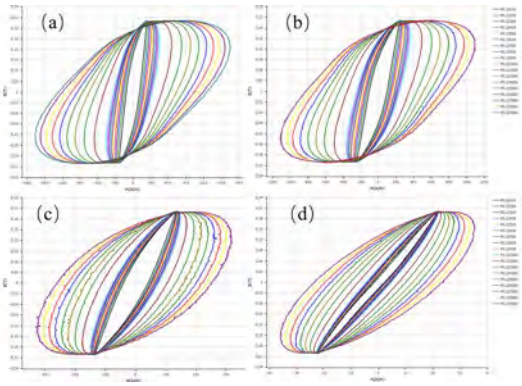
[2] A.M. Balagurov, I.A. Bobrikov, D.Y. Chernyshov , et al. Tetragonal phases in Fe-Ga alloys: A quantitative study[J]. Physical Review Materials, 2024, 8(7): 073604.

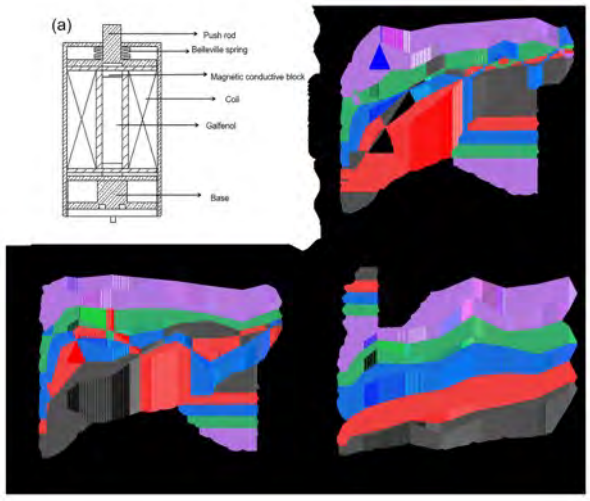
[3] Zhao JH., Mo XP., Chai Y, et al.Fe-Ga single crystal Janus-Helmholtz transducer. Journal of Applied Acoustics, 2023, 48(1): 93-101.

[4] Weng L., Liang SZ, Wang BW et al.Output characteristics of a dual-coil Fe-Ga transducer considering pre-stress.Transactions of China Electrotechnical Society, 2019, 34(23): 4859-4869

[5] Li Y M, Mo X P, Pan Y Z, et al.Design and vibration characteristics of a Fe-Ga driven flexural disk transducer.Journal of Applied Acoustics, 2016, 35(6): 471-479.

[6] Chen Y, Yang T ,Gou J et al. Synergistic effects of magnetic domain re-alignment and precipitation on achieving large magnetostriction in random polycrystalline Fe-Ga alloys[J]. Materials and Design, 2025, 256(3): 114324.





HR-11. Structural and magnetic properties of Ti doped $Ni_{2.3}Mn_{0.7}$ Ga Heusler Alloy

T. F. McKenzie[1], K. N. Ndaru[1], R. Chapai[2], M. Khan[1]
[1]*Physics, Miami University, Oxford, Ohio, United States,* [2]*Physics, Norfolk State University, Norfolk, Virginia, United States*

Solid state materials that exhibit magnetic and structural transitions play a crucial role in enabling technological frontiers like Giant magnetocaloric effects [1], large magnetoresistance [2], and ferromagnetic shape memory effects [3]. Ni-Mn-Z (Z = Ga, In, Sb, Sn) based Heusler alloys have been of longstanding research interest because they exhibit all the above-mentioned functional properties. These materials exhibit coupled first order magnetostructural transitions, are composed of non-critical elements, and their stoichiometry can be manipulated to alter the Curie temperature (T_C) and the martensitic transformation temperature (T_M). Ni_2MnGa is a Heusler alloy that exhibits a first order martensitic phase transition near 200 K in a ferromagnetic state [4]. The martensitic and ferromagnetic phase transition temperatures in this system can be precisely controlled by the partial replacement of Mn with Ni. For x ≈ 0.22, a completely coupled martensitic and ferromagnetic transition occurs at $T_M = T^A_C \approx 325$ K. $Ni_{2.3}Mn_{0.7}Ga$ is an off-stoichiometric derivative of Ni_2MnGa where the martensitic transition occurs in the paramagnetic state. Here, we will present the effect of Ti addition (1 - 4 wt.%) on the ferromagnetic and martensitic phase transition temperatures of $Ni_{2.3}Mn_{0.7}Ga$. The idea is to drive the first order coupled phase transitions by introducing Ti at the interstitial crystalline sites, which would facilitate the structural phase transformation. The results of scanning electron microscopy, energy-dispersive x-ray spectroscopy, x-ray diffraction, dc magnetometry, and electrical resistivity measurements would be presented and discussed in detail.

[1] V. Pecharsky and K. Gschneidner, Jr., Phys. Rev. Lett. Vol. 78, p. 4494 (1997)
[2] A. Pathak, M. Khan, and I. Dubenko et al., J. Appl. Phys., Vol. 103, p. 07F315 (2008)
[3] K. Ullakko, J. Huang, and C. Kantner et al., Appl. Phys. Lett., Vol. 69, p.1966-1968 (1966)
[4] PJ Webster, KRA Ziebeck, and SL Town et al., Philos. Mag. B, Vol 49, p.295–310 (1984)

HR-12. Magnetic Tunnel Junctions Weds Magnetic Molecules: Producing Room Temperature Spin Photovoltaic Effect and Anomalous Magnetoresistance

P. Tyagi
University of the District of Columbia, Washington, District of Columbia, United States

Magnetic tunnel junctions (MTJs) and magnetic molecules (MMs) with tunable spin quantum states represent two of the most powerful advances in modern magnetism. Each has been widely explored for memory, sensing, and quantum information technologies, yet integrating them into a single platform introduces significant materials and device design challenges. This work summarizes two decades of progress in creating hybrid MTJ MM systems that unlock new spin dependent phenomena.
Using conventional lithography and sputtering, we fabricate ferromagnet insulator ferromagnet trilayers whose exposed sidewalls, formed through a simple liftoff process, serve as natural sites for molecular bridging. Thiol functionalized magnetic molecules form robust, air stable bonds with the ferromagnetic electrodes, enabling controlled molecular junctions along the MTJ perimeter. These molecules act far beyond passive spin channels: they induce long range modifications in the electronic, magnetic, and optical properties of the electrodes, extending well outside the immediate junction region. Ferromagnets such as Co, NiFe, and CoFe surrounding MgO based insulators undergo molecule driven transformations into optically active magnetic materials once MM bridges are established. Recent transport and optical studies reveal two striking outcomes of this molecular integration: a room temperature spin photovoltaic effect and anomalous magnetoresistance arising from molecule mediated spin interactions. The union of MTJs with magnetic molecules establishes a new research frontier, offering pathways to enhanced spin polarization, large magnetoresistance, and optically responsive spin transport not achievable in conventional spintronic architectures.

HR-13. Ni-Mn-In Heusler Alloys Ribbon for Magnetocaloric Application

B. Nguyen[1], P. Ari-gur[1], S. Jabran[1], R. D. Noebe[2], I. Felner[3], S. Kaczmarek[1], A. S. Madiligama[4]

[1]Mechanical and Aerospace Engineering, Western Michigan University, Kalamazoo, Michigan, United States, [2]NASA Glenn Research Center, Cleveland, Ohio, United States, [3]Hebrew University, Jerusalem, Israel, [4]Science/Physics, Penn State DuBois, DuBois, Pennsylvania, United States

Solid-state cooling technologies, particularly those based on the magnetocaloric effect (MCE), have gained attention as promising alternatives. Heusler alloys, such as Ni–Mn–In, are well-suited candidates due to their shape memory behavior and giant magnetocaloric effect (GMCE). This effect arises from a first-order magnetostructural martensitic transformation between low-temperature martensite and high-temperature austenite via a diffusionless transition. Manufacturing processes and composition strongly influence the crystal structure and, in turn, the magnetic properties, and thermal efficiency of Ni–Mn–In alloys. In this work, Ni-Mn-In alloys that we have previously identified in their bulk form[1] were prepared by melt spinning (Fig. 1) to achieve a fine microstructure. Their crystallographic and magnetic behavior were studied.

The samples were designated as BMS563 ($Ni_{44.9}Mn_{43}In_{12.1}$) and BMS564 ($Ni_{50}Mn_{34}In_{16}$). They were sealed in argon-filled quartz tubes and heat-treated at 900 °C for either 24 hours or 10 minutes. The 10-minute samples were additionally wrapped in Ta foil to minimize oxidation further.

The X-ray diffraction (XRD) patterns (Fig. 2) show changes in modulation and phase fractions in the as-spun and heat-treated samples. At 900 °C for 24 hrs, undesired decomposition occurs; hence, the presence of MnO_2. BMS563 has 95% austenite ($L2_1$) and 5% monoclinic incommensurate 7M martensite (I2/m). The same sample heat-treated at 900°C for 10 min has 72% austenite ($L2_1$) and 28% martensite (I2/m), with the modulation vector q = 0.0257a* + 0.365c*, indicating ~3/8 incommensurate modulation. The as-spun BMS564 has fractions of austenite ($L2_1$) and non-modulated martensite (I2/m) of 99% and 1%, respectively; for the heat-treated, the fractions are 73% $L2_1$ and 27% non-modulated I2/m. The SQUID results demonstrate behavior that differs from that of the alloys in bulk form and can be characterized as ferromagnetic below the Curie temperature, which in turn affects their magnetocaloric effect.

P. Ari-Gur, A. Madiligama, I. Felner, M. I. Tsindlekht, Y. Ren, D. W. Brown, V. Shavrov, V. Koledov, and A. Mashirov, A. Kayani, The Nature of the Metamagnetic Transition in Heusler Alloy $Ni_{44.9}Mn_{43}In_{12.1}$ Studied for Magnetic Refrigeration Application, *Materials Science and Engineering B* Volume 283, 2022, 115796



Melt-spinning.

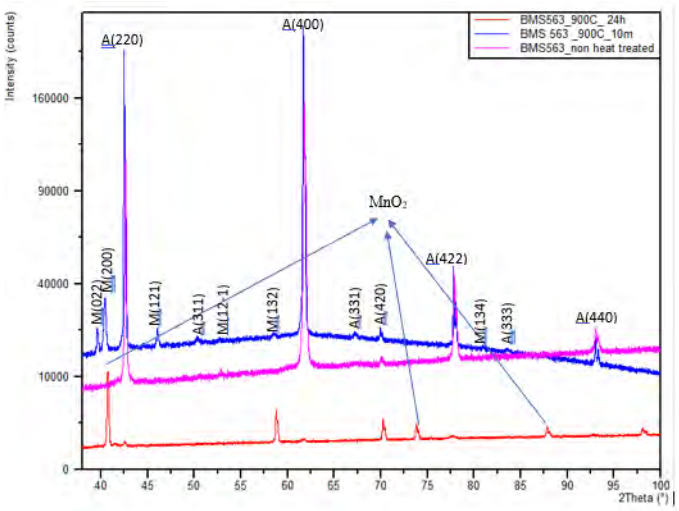


Fig 2: XRD patterns of BMS563 for both heat treatments (free side)

HR-14. Effect of Heat Treatment on Two Melt-Spun Ni-Mn-Ga-Si Heusler Alloys

S. Jabran[2], P. Ari-gur[2], R. D. Noebe[3], A. S. Madiligama[1]
[1]Science/Physics, Pennsylvania State University, DuBois, Pennsylvania, United States, [2]Mechanical and Aerospace Engineering, Western Michigan University, Kalamazoo, Michigan, United States, [3]NASA Glenn Research Center, Cleveland, Ohio, United States

Nickel–Manganese-based Heusler alloys are promising candidates for room-temperature magnetic refrigeration because their cooling effect is magnified by the strong coupling between their magnetocaloric response and crystallographic and magnetic phase transitions. In this work, the influence of melt-spinning parameters and various heat treatments on the structural and magnetocaloric properties of two melt-spun $Ni_{55.4}Mn_{18.9}Ga_{24}Si_{1.7}$ ribbons was investigated. Two ribbon sets with the same composition were fabricated under a helium atmosphere using different melt-spinning conditions (distinct wheel speeds, nozzle widths, and casting temperatures), resulting in different cooling rates.

Ribbons were encapsulated in an inert atmosphere and heat-treated at 900 °C for 18 and 72 h, and at 850 °C for 48 h, followed by quenching in ice water. Room-temperature phase constitution and lattice parameters were determined by X-ray diffraction, refined using GSAS II. Across the investigated conditions, the microstructure consisted of a mixture of cubic $L2_1$ austenite (Fm-3m) and monoclinic martensite (I2/m), with heat treatment reducing wheel-side/free-side differences, altering phase fractions and lattice parameters. Magnetic properties were measured using PPMS-VSM to obtain isothermal M–H curves (0–14 T) in the temperature range 259–335 K.

Curie temperatures were estimated from M–T behavior, showing processing-dependent shifts after heat treatment. The magnetocaloric response was assessed by calculating the magnetic entropy change from magnetization data; the largest was obtained for the lower-cooling-rate ribbon heat-treated at 900 °C for 18 h, reaching (26 J/kg-K) near room temperature. In contrast, the higher-cooling-rate ribbon exhibited a reduced peak magnitude after heat treatment but maintained a broader temperature span of elevated entropy change.

These results demonstrate that different melt-spinning parameters and heat treatments provide practical levers to tune phase stability and magnetocaloric performance in Ni–Mn–Ga–Si Heusler ribbons.

[1] Bhale, P., Ari-Gur, P., Noebe, Materials, 16(19), pp. 6590 (2023).

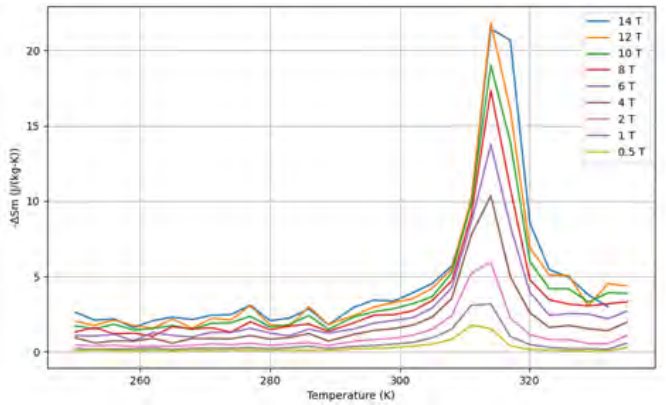


Fig. 1: Change in magnetic entropy, $-\Delta S_m$ (J/kg-K), vs temperature (K) plot for BMS220, heat-treated for 72 hrs. at 900°C

Sample ID	Chemical composition	Cast Temperature (°C)	Nozzle width (mm)	Wheel Speed (m/s)	Avg ribbon thickness (μm)
BMS 220	$Ni_{55.4}Mn_{18.9}Ga_{24}Si_{1.7}$	1300	17	15.7	30
BMS 222		1350	3	19.6	20

Table 1: Sample ID and parameters for melt-spinning [1].

HR-15. Thermal stability of FeCo-Ag multilayer thin films for use in magnetoelectric heterostructures for low SWAP-c magnetic field sensors

T. R. Mion, M. Staruch, K. Bussmann, P. Finkel
Material Science & Technology, US Naval Research Laboratory, Washington, District of Columbia, United States

A growing need for high temperature magnetic field sensing has prompted the search for stable high magnetostrictive materials to be utilized in microelectromechanical systems (MEMS) devices. MEMS base magnetic field sensors function by coupling a piezoelectric and magnetostrictive material in a heterostructure requiring both the piezoelectric and magnetostrictive material to withstand high temperatures for extended time periods and temperature cycling. This investigation studies the thermal and stress properties of FeCo/Ag multilayer thin films prepared by sputter deposition for their potential applications in such magnetoelectric heterostructure devices [1,2,3]. We show rapid thermal annealing of the FeCo/Ag multilayers is robust until annealing temperatures reach 300 – 400 C where a breakdown of the Ag leads to an increased coercive field, and annealing >400 C becomes detrimental to the soft magnetism of the system as the Ag layers deteriorate. X-ray

diffraction and reflectometry measurements yield consistent results showing an increased grain size and breakdown of the Ag layers. Additionally, through application of a negative bias voltage to the substrate during deposition precise control of the as-deposited stress was achieved allowing a tensile to compressive crossover at -95 VDC.

[1] G. Srinivasan, vol. 40, pp. 153–178, Jul. 2010
[2] M. Fiebig, J Phys D Appl Phys, vol. 38, no. 8, p. R123, Apr. 2005
[3] S. Acosta, et al., IEEE Sensors Letters, Vol. 8, Issue: 10, October 2024

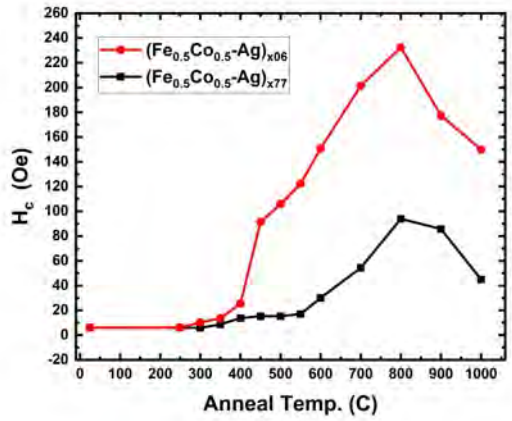


Fig. 1 Intrinsic coercive field of the $Fe_{0.5}Co_{0.5}$-Ag multilayer film with 6 layers (x06) and 77 layers (x77) after rapid thermal annealing and re-measurement at room temperature.

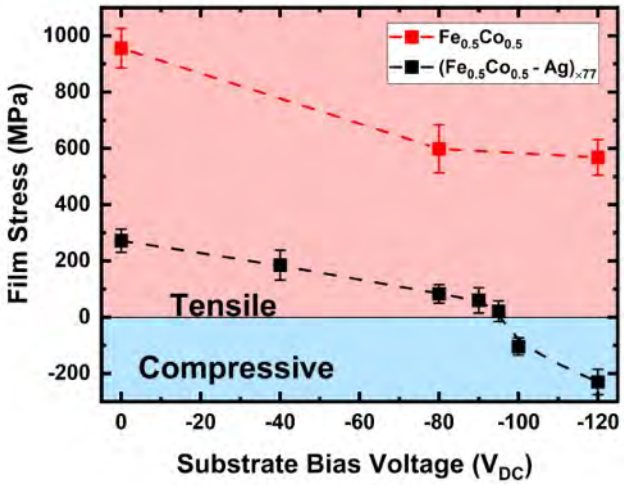


Fig. 2 Control of as-grown $Fe_{0.5}Co_{0.5}$ and $Fe_{0.5}Co_{0.5}$-Ag multilayer film stress through application of a DC bias voltage during deposition

HR-16. Crystal Electric Field Effect on Magnetic and Thermal Properties in Er–Ni Family Compounds

A. T. Saito, L. Zhao
Research Center for Magnetic and Spintronic Materials, National Institute for Materials Science, Tsukuba, Ibaraki, Japan

Rare earth - Nickel intermetallic compounds have been attracting attention as materials for cryogenic applications. In particular, Er_3Ni was developed as a regenerator material for Gifford-McMahon refrigerators [1], and $ErNi_2$ has been considered as a candidate refrigerant of magnetic refrigerators [2, 3]. Here, we focus on the Er–Ni family compounds, specifically Er_3Ni, ErNi and $ErNi_2$, and discuss their physical properties in terms of the similarities in their characteristics. In all these compounds, since Ni is non-magnetic, their magnetism is attributed to the 4f electrons of Er. Both Er_3Ni and ErNi have an orthorhombic crystal structure, with the Er atoms occupying positions that form triangular prisms within the orthorhombic lattice. Therefore, spin frustration exists in the magnetic interaction between Er atoms in Er_3Ni and ErNi. Furthermore, the J=15/2 multiplet of 4f electrons of Er^{3+} ion splits into eight doublets due to the low-symmetry of the crystal electric field in these compounds. Because the energy gap between the ground state and the first excited state is of the same order of the magnitude of the magnetic interaction, the magnetic and thermal properties of these compounds are severely affected by the crystal electric field. On the other hand, $ErNi_2$ possesses a high-symmetry cubic crystal structure, and the energy gap between the four-fold degenerate ground state of the 4f electrons and the first excited state is large compared to the magnitude of the magnetic interaction. The specific heat and magnetic properties of these compounds strongly reflect the differences in the energy states of the 4f electrons arising from structural symmetry.

In this presentation, we will present experimental results concerning the magnetic properties and specific heat of Er–Ni family compounds, as well as the calculated energy levels of 4f electrons derived from the crystal electric field effect, and discuss the origins of these physical properties considering their intrinsic complexity.

This work was supported by the JSPS KAKENHI (24K00826).

[1] A. Takahashi *et al.*, Jpn. J. Appl. Phys., Vol. 33, 1023 (1994).
[2] P. Álvarez *et al.*, Phys. Rev. B, Vol. 84, 024412 (2011).
[3] K. Kamiya, A. T. Saito *et al.*, Appl. Phys. Exp., Vol. 15, 053001 (2022).

HR-17LB. d^0/d^{10} *B′*-Site Doping Enables Magnetic and Magnetocaloric Tuning in Gadolinium Double Perovskites

F. Berardi[1], J. M. Steele[1], H. E. Fischer[2], S. E. Dutton[1]
[1]Department of Physics - Cavendish Laboratory, University of Cambridge, Cambridge, United Kingdom, [2]Institut Laue-Langevin, Grenoble, France

In $A_2BB'O_6$ double perovskites (DPs) with 3d and 5d magnetic ions, the magnetic behavior of the *B* sublattice can be adjusted by selecting nonmagnetic isovalent *B′* cations with d^0 or d^{10} electron configuration. Here we show that d^0/d^{10} *B′*-site doping also enables magnetic tuning in $4f^7$ gadolinium DPs. We substitute Nb^{5+} (d^0) for Sb^{5+} (d^{10}) in the solid solution $Ba_2GdNb_xSb_{1-x}O_6$ ($0 \leqslant x \leqslant 1$) and find tunable local magnetic correlations evolving from weak antiferromagnetic (x=0) to almost suppressed (x=0.75) to minimal ferromagnetic (x=1) interactions, Fig.1.

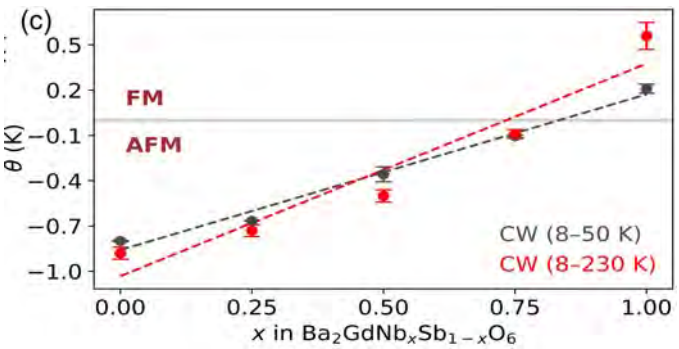
To the best of our knowledge, doping-driven magnetic tuning has not been explored in 4f systems and magnetic crossover from AFM to FM caused by d^0/d^{10} mixing has not been previously observed.

We find that *B′*-site doping tunes the superexchange between nearest neighbor magnetic spins, enabling controlled suppression of the magnetic ordering temperature. In the x=0.75 compound with almost no net magnetic interactions, we calculate a magnetocaloric effect with >99% of the maximum theoretical magnetic entropy for Heisenberg Gd^{3+} spins ($-\Delta S_{max}=R\ln(2J+1)=17.29$ J K^{-1} mol^{-1}) at 1.8 K and 9 T, Fig.2. The $Ba_2GdNb_xSb_{1-x}O_6$ ($0 \leqslant x \leqslant 1$) solid solution provides a platform for tuning the magnetic interactions and, *via* this, controlling the magnetocaloric effect (MCE).

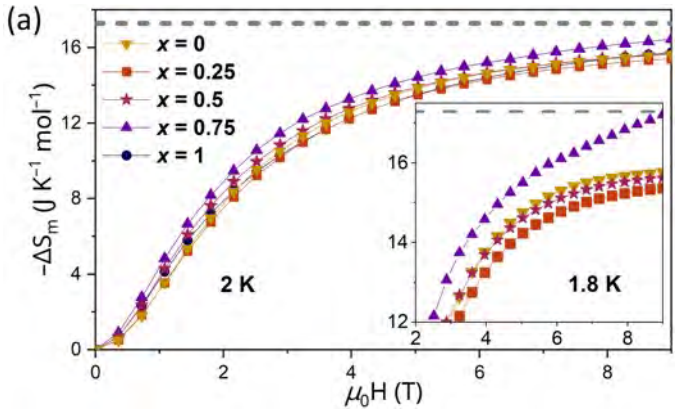
The MCE allows for a change in temperature upon application or removal of an external magnetic field because of a change in entropy associated with the spin configuration in a material. Magnetocaloric candidates are being explored as an energy-efficient and environmentally friendly alternative to cryogenic vapor-compression refrigeration. These materials require suppressed magnetic ordering temperatures; weak magnetic exchange interactions; and a high density of spins with large magnetic moment.

This work demonstrates that *B′*-site doping tunes magnetic interactions in $A_2GdB'O_6$ DPs, highlighting its potential for the rational design of efficient adiabatic demagnetization refrigeration (ADR) materials.

[1] Pecharsky, V. K. & Gschneidner Jr, K. A. Magnetocaloric effect and magnetic refrigeration. Journal of Magnetism and Magnetic Materials 200, 44–56 (1999). doi:10.1016/S0304-8853(99)00397-2.
[2] Koskelo, E. C., Liu, C., Mukherjee, P., Kelly, N. D. & Dutton, S. E. Free-Spin Dominated Magnetocaloric Effect in Dense Gd3+ Double Perovskites. Chemistry of Materials 34, 3440–3450 (2022). doi:10.1021/acs.chemmater.2c00261.
[3] Berardi, F. et al. Structural Phase Transitions and Magnetic Characterization of Ba2GdNbO6 for Low-Temperature Magnetocaloric Refrigeration. Chemistry of Materials 37, 8848–8860 (2025). doi:10.1021/acs.chemmater.5c01937.
[4] Mustonen, O. H. J. et al. Diamagnetic d-Orbitals Drive Magnetic Structure Selection in the Double Perovskite Ba2MnTeO6. Chemistry of Materials 32, 7070–7079 (2020). doi:10.1021/acs.chemmater.0c02971.
[5] Katukuri, V. M. et al. Exchange Interactions Mediated by Nonmagnetic Cations in Double Perovskites. Phys. Rev. Lett. 124, 077202 (2020). doi:10.1103/PhysRevLett.124.077202.
[6] Mustonen, O. et al. Spin-liquid-like state in a spin-1/2 square-lattice antiferromagnet perovskite induced by d10/d0 cation mixing. Nat Commun 9, 1085 (2018). doi:10.1038/s41467-018-03435-1.
[7] Pughe, C. et al. Site-Selective d10/d0 Substitution in an S = 1/2 Spin Ladder Ba2CuTe1−xWxO6 (0 ⩽ x ⩽ 0.3). Inorganic Chemistry 61, 4033–4045 (2022). doi:10.1021/acs.inorgchem.1c03655.
[8] Kanungo, S., Yan, B., Felser, C. & Jansen, M. Active role of nonmagnetic cations in magnetic interactions for double-perovskite Sr2BOsO6(B = Y, In, Sc). Physical Review B 93, 161116 (2016). doi:10.1103/PhysRevB.93.161116.
[9] Feng, H. L., Yamaura, K., Tjeng, L. H. & Jansen, M. The role of nonmagnetic d0 vs. d10 B-type cations on the magnetic exchange interactions in osmium double perovskites. Journal of Solid State Chemistry 243, 119–123 (2016). doi:https://doi.org/10.1016/j.jssc.2016.08.022.
[10] Zhu, M. et al. Tuning the Magnetic Exchange via a Control of Orbital Hybridization in Cr2(Te1−xWx)O6. Phys. Rev. Lett. 113, 076406 (2014). doi:10.1103/PhysRevLett.113.076406.



AFM to FM trend in the $Ba_2GdNb_xSb_{1-x}O_6$ series upon doping. The black and red data points represent the Curie-Weiss temperatures, ϑ, extracted from fits over the ranges T=8–50 K and T=8–230 K, respectively. The dashed lines are guides to the eye.



Magnetic entropy change, $-\Delta S_m$, versus field for $Ba_2GdNb_xSb_{1-x}O_6$ at 2 K. The gray dashed line delimits the maximum change $-\Delta S_{max}$. The inset shows a zoomed-in region of $-\Delta S_m$ at 1.8 K between 2 and 9 T.

HR-18LB. Magnetic and Optical Properties of $[Cu_3(vanox)_2(NO_3)_2]$ Chain Structure- a 2D Supramolecular array

P. Anand, A. Powell
Institute of Inorganic Chemistry, Karlsruhe Institute of Technology, Karlsruhe, Germany

The synthesis of copper-based coordination cluster compounds has attracted considerable attention due to their wide range of potential applications in areas such as magnetism, catalysis, and photophysical processes. In this work, I have successfully synthesised a new three-dimensional copper supramolecular structure utilising the H_2vanox ligand. The reaction was carried out at room temperature and resulted in the formation of greenish-black crystals that remain stable at room temperature.[1,2,3]
The core part of the structure consists of a Cu_3 unit in one plane. The two outer copper atoms are each bonded to five ligands, with a nitrate group occupying the top (axial) position. The central copper atom, on the other hand, is bonded to four ligands. Each of these Cu_3 units is held together and stabilised by two H_2vanox ligands, which help connect the copper atoms and are an integral part of the crystal structure.
The structure $[Cu_3(vanox)_2(NO_3)_2]$ is extended through the bridging nitrate ion, as shown in Figure 1. Moreover, the Cu1–C4 intersheet interactions contribute to the overall stability of the cluster complex. In the direct current (dc) magnetic susceptibility plot, the χT value shows a gradual decrease below 20 K, which can be attributed to zero-field splitting effects. The value stabilises around 0.37 $cm^3K\ mol^{-1}$ up to 150 K. At higher temperatures, the system displays weak antiferromagnetic interactions.

[1] I. A. Kühne, G. E. Kostakis, C. E. Anson, A. K. Powell, *Chem. Commun.* 2015, *51*, 2702.
[2] D. N. Woodruff, R. E. Winpenny, R. A. Layfield, *Chem. Rev.* 2013, *113*, 5110.
[3] Q. Benito, A. Lledós, F. Maseras, J. Benet-Buchholz, *Inorg. Chem.* 2015, *54*, 4483.

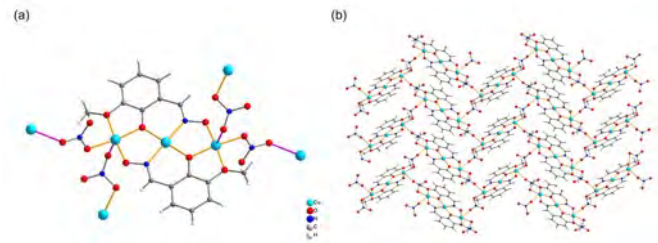


Figure 1. (a) Molecular Structure of $\{Cu_3\}$ crystal. (b) 2D supramolecular arrangement of the crystal.

HR-19LB. Hyperfine field spectroscopy reveals two magnetic subsystems in Fe-Mn-Ga Heusler alloy

O. Heczko[1], D. Kubaniova[1], M. Rames[1], T. Kmjec[2], V. Chlan[2]
[1]FZU - Institute of Physics, Prague, Czechia, [2]Faculty of Mathematics and Physics, Charles University, Prague, Czechia

Near-stoichiometric Heusler alloy $Fe_{44}Mn_{25}Ga_{31}$ is weakly ferromagnetic at room temperature. Similar magnetization curves were measured in [1] but not discussed. Upon cooling the alloys undergoes a structural transformation at about 50 K connected with large and gradual increase of saturation magnetization. The transformation is reversible and exhibits a pronounced thermal hysteresis of about 100 K and magnetization decreases upon heating back to low magnetic state in cubic austenite. To investigate what is behind the strong increase of magnetization we used Mössbauer spectroscopy of ^{57}Fe which probes the magnetic state of Fe via hyperfine field. Surprisingly, the spectroscopy shows that room temperature magnetization does not originate at Fe atoms as these are paramagnetic providing only singlet line in Mossbauer spectrum (Fig.1). The magnetic moments must then originate at Mn atoms common for Mn containing Heusler alloys. Further support comes from nuclear magnetic resonance (NMR) measurement of Mn hyperfine field. However, the volume

magnetization at room temperature is low probably due to strong antiferromagnetic interaction of disordered Mn. The following rise of magnetization during cooling can be fully ascribed to the formation of ferromagnetic order of Fe lattice. Mössbauer spectroscopy reveals that at 4.2 K there is no paramagnetic iron and all Fe atoms are ferromagnetically ordered as there is no detectable singlet and only distributed sextet can be found in Mössbauer spectrum. The rise of ferromagnetism in Fe can be connected with the lattice deformation during strain glass formation [2] and then full martensitic transformation, which is displacive and diffusionless transformation to low symmetry phase. Combined magnetization measurement and hyperfine field spectroscopy indicate that in $Fe_{44}Mn_{25}Ga_{31}$ compound there are two magnetic subsystems which are separated in temperature: the moments on manganese atoms order in cubic phase well above room temperature while the moments on iron only within low symmetry martensite phase [3].

The work was supported by OP JAK project No.CZ.02.01.01/00/22_008/0004591 and Czech Science Foundation Grants No. 23-04806S.

[1] T. Omori,K. Watanabe, R. Y. Umetsu, R. Kainuma, and K. Ishida, Martensitic transformation and magnetic field-induced strain in Fe–Mn–Ga, APL 95, 082508 (2009)
[2] X. Sun et al., Magnetic-field-induced strain-glass-to-martensite transition in a Fe-Mn-Ga alloy, Acta Materialia 183 11-23 (2020)
[3] D. Kubániová, T. Kmječ, M. Rameš and O Heczko, Two magnetic systems in Fe44Mn25Ga31 Heusler alloy revealed by Mössbauer spectroscopy, submitted.

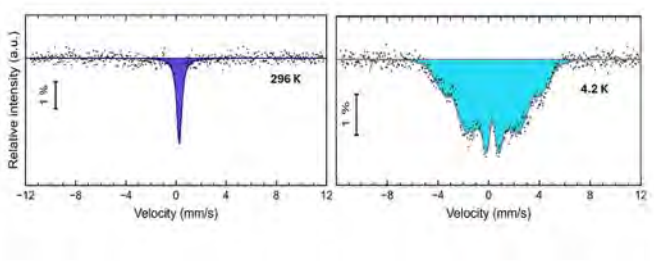


Fig. 1. Mossbauer spectra of Fe-Mn-Ga compound at room temperature (a) and at LHe temperature (b) revealing paramagnetic and ferromagnetic state of Fe, respectively.

SESSION VP: VIRTUAL POSTERS

VP-01. Theoretical analysis of overshoot reduction in power conversion circuits using damping capacitors

D. Kim
Department of Electronic Engineering, Tech University of Korea, Siheung, Korea (the Republic of)

As power conversion modules become more compact while supporting higher power levels, printed circuit boards (PCBs) have become increasingly dense and complex. The presence of high-speed switching components in these systems introduces significant electromagnetic interference (EMI) noise, which has emerged as a critical issue [1]–[2]. In addition, practical PCBs inherently include parasitic elements such as inductance, capacitance, and resistance. These parasitic components contribute to ringing phenomena, leading to voltage overshoot in power conversion systems.
In this study, the effects of parasitic components on a power conversion module are investigated through theoretical analysis. Fig. 1 shows a simplified circuit model of a full-bridge inverter. Depending on the inverter operating mode, Q1 to Q4 are sequentially turned on and off, and in certain modes, the current flows as illustrated in Fig. 1(a). In this case, the equivalent simplified circuit is shown in Fig. 1(b). Since the circuit in Fig. 1(b) can be represented as a series RLC circuit, applying Kirchhoff's Voltage Law (KVL), a second-order differential equation is derived, which its solution can be classified into three cases: underdamped, overdamped, and critically damped conditions. This implies that the voltage waveform depends on the damping coefficient. To achieve an overdamped condition, an additional capacitor is connected across the MOSFETs.
Fig. 2 shows the simulation results illustrating the effect of external capacitors on the MOSFETs. As observed, the voltage overshoot is significantly reduced compared to the case without additional capacitors. As expected, increasing the capacitance leads to an overdamped response, thereby reducing the overshoot.

[1] Z. Zhang, B. Guo, F. Wang, L. M. Tolbert, B. J. Blalock, Z. Liang and P. Ning, IEEE Applied Power Electronics Conference and Exposition, p.2542 (2014).
[2] H. Huang, X. Yang, Y. Wen and Z. Long, IEEE Int. Power Electronics and Motion Control Conf., , p.285 (2016).

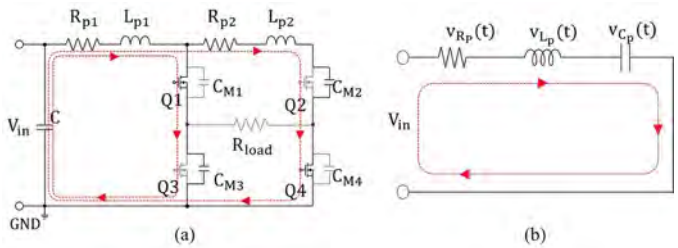


Fig. 1. Circuit diagram of a full-bridge inverter (a) current paths under different switching states; (b) simplified equivalent circuit of a single current loop.

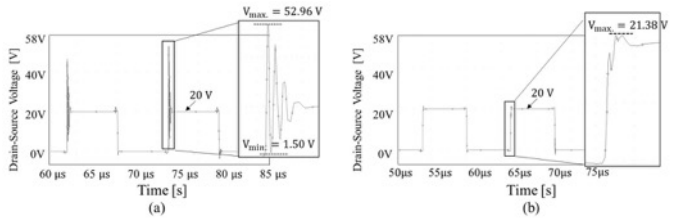


Fig. 2. Drain–source voltage waveforms (a) without the capacitor model; (b) with the capacitor model.

VP-02. Processing Optimization of Sendust Powder Cores for High-Frequency Power Electronics

M. Nguyen[1], T. Kiyota[1], Y. Endo[2], S. Yoshida[2], S. Okamoto[2]
[1]Tamura Corporation, Sendai, Miyagi, Japan, [2]Tohoku University, Sendai, Miyagi, Japan

Sendust alloy (Fe–Si–Al) has been widely used in applications requiring high permeability, high resistivity, and high magnetization, such as inductors, chokes, and filters. In high-frequency applications, the core loss of Sendust cores is approximately 20% of that of conventional iron powder cores. Owing to its near-zero magnetostriction (λs ≈ 0), Sendust is also well suited for applications requiring low audible noise. In general, magnetic properties such as saturation magnetization, permeability, and core loss are influenced by multiple factors, including starting powder characteristics (particle size, morphology, and purity), insulation coating parameters (material and content), and processing conditions. Among these factors, annealing plays a critical role in relieving internal stresses introduced during compaction and processing. Stress relaxation improves magnetic domain mobility, resulting in higher permeability and lower core loss, while also stabilizing the microstructure and insulation layers, thereby enhancing frequency characteristics and thermal stability. In this study, the microstructure and magnetic properties of Sendust powder cores were investigated by varying annealing conditions and starting powder characteristics. The density, saturation magnetization ($4\pi M_s$), and real part of the initial permeability (μ_i') of the cores increased with increasing annealing temperature, which is attributed to improved densification. The permeability showed a significant increase from 43 to 243 as the annealing temperature increased from 600 to 900 °C. However, permeability stability up to 5 MHz was maintained only for samples annealed at 600 and 700 °C, whereas samples annealed at higher temperatures exhibited stability only below approximately 200 kHz, indicating degradation of the insulating layer. Core loss characteristics were further evaluated as functions of magnetic flux density and frequency up to 1 MHz under various processing conditions and starting materials. Based on these results, optimal processing conditions corresponding to different operating frequency ranges are identified and proposed.

References

1. R. Yapp, B.E. Watts and F. Leccabue, J. Magn. Magn. Mater., 215-216, 300 (2000)
2. 4mp.pdf (pacificsowa.co.jp)

Acknowledgement

This work was supported in part by MEXT Program for Creation of Innovative Core Technology for Power Electronics Grant Number JPJ009777 and Data Creation and Utilization-Type Material Research and Development Project (Digital Transformation Initiative Center for Magnetic Materials) Grant Number JPMXP1122715503. This work was supported in part by CSIS, CSRN, and CIES, Tohoku University.

.
., A: GB-02
., N: BR-09

A
Abad, A: BA-01
Abarca, J: FC-11
Abbas, H: BG-10, CP-12, **CP-13**, **EE-05**
Abbassi, L: AE-07
Abbott, C: FB-02
Abdizadeh Kalan, S: GE-05, **GP-07LB**
Abdou, A A.: **ER-14**
Abe, K: HE-07
Abel, F M.: EG-09, GF-10
Abert, C: BE-02, **DH-08**, ED-07, FG-04, HG-11
Abogado, E: EE-10
Abrão, J E.: BB-04
Abreu Araujo, F: AD-01, **CR-05**, CR-10
Abrosimova, G: CP-01
Abuin, M: DH-10, FP-11
Accursi, M: CD-03
Achanta, S S.: EQ-05, **HA-05**
Achinuq, B: **EE-10**
Ackers, J: CD-07
Aczel, A: GF-06
Adachi, K: GP-03
Adachi, S: **CR-15**
Adiya, M: CP-11, CP-14, HD-08, HR-04
Afanasiev, D: AR-13LB
Afanasiev, D: CH-03
Afsari, T: CD-10
Agarwal, S: DA-06
Aguilera, I: BC-02, FE-04
Ahmad, H: **FQ-12**
Ahmad, S: AF-12
Ahmadi, K: FA-07
Ahmadi, M: DC-02
Ahmed, R M.: GF-09
Ahmetasevic, E: FQ-16, FR-20LB
Ahn, J: AP-07, EP-11
Ahn, K: CS-10
Ahrens, V: BR-13, DG-05, GP-06
Aihemaiti, H: **DP-08**
Aislinn, P: AC-11
Ajia, S: DP-02
Akaki, M: **FQ-11**
Akashdeep, A: AF-11
Akdogan, O: ER-09, **GD-04**
Akerman, J: **HG-01**
Akita, S: **HQ-14**
Akiyama, R: **AC-07**
Alaei, S: HE-03
Alam, A: ED-10, EE-12
Alam, M: FD-09
Al Bahri, M: AR-15
Albano, D: BR-13
Alba Venero, D: DC-11
Albertini, F: **BA-03**, EB-07
Albrecht, M: HF-05
Alexandrova, A: GB-08
Alharbi, D: **CP-07**, FP-16
Alia, M: GF-09
Allen, C: FC-05
Allen, M G.: GE-03
Alling, A: **EQ-03**
Almahmoud, A: **EF-11**, GE-05
Almasy, L: DP-13
Almeida, R: EB-06, GR-11
Althammer, M: FB-06
Amakai, Y: FR-11
Amanatiadis, S: CE-10
Amanjal, U: CP-14, HD-08
Amara, S: BE-12, **CE-09**, CR-02, EA-09
Amaral, J: **EB-06**, GR-11
Ambal, K: EG-01
Amemiya, K: CB-02, HQ-14
Amin, O: CB-01
Amiya, K: AQ-16
Amoo, F: **FP-15**
An, J: EC-02, EC-06
Anadón, A: AR-10
Anand, P: **HR-18LB**
Anane, A: DH-11
Anas, M: EF-08
Ando, F: CC-15
Ando, K: EG-02
Ando, K: CR-15
Ando, R: FP-03, GF-07
Ando, Y: CE-04, DE-01
Ando, Y: AQ-06, BP-14, BR-14, CF-01, CG-03, FB-06
Andrade, L: GR-11
Andrade, P: **GP-10**
Andrei, P: FC-10, FC-12
Angayarkanni Ramamurthy, D: BD-02, BD-03
Angel, M: DH-10
Angotti, A: AR-12, CR-07, **DG-02**, DG-03, DG-06, EG-11
Anh, L: CG-07
Anikeeva, P: CD-09, HA-01
Anil Kumar, P: FQ-14
Antl, J: AE-05
Antropov, V: **AB-07**
Aoki, M: **CC-05**, CF-01
Aono, T: GF-07
AOSHIMA, K: AR-08
Aoyama, K: HQ-13
Arakawa, R: **HG-06**
Araújo, J P.: GR-11
Arava, H: **DH-01**
Aregbesola, A E.: EG-01
Arena, D A.: AF-02, AF-09, AR-16, FP-10
Ari-gur, P: HR-13, HR-14
Arima, T: CF-10, FE-10
Arisawa, H: BB-07
Arita, R: FE-10
Aronin, A: CP-01
Arpaci, S: BF-04, CA-07
Arras, R: FG-08
Arredondo-López, A: CE-01, DE-04
Artinyan, L: CD-05
Asada, H: CR-14
Asai, T: CR-15
Asakura, M: BF-06, **CF-12**
Asari, Y: **DD-12**
Ashok, A: **FR-01**
Ashraf, M: **HR-01**
Atalugama, T V.: **ER-03**
Athas, J G.: CA-07, **EA-04**
Atulasimha, J: **EA-01**, ED-06, EQ-05, FD-09
Auffret, S: CA-09, CE-01, DE-04
Awad, A A.: HG-01
Awaji, S: CP-09
Awano, H: CS-02, DR-07, **DR-16**, HQ-02
Ayers, N: **DD-03**
Aykin, A K.: **AG-13**
Azevedo, A: **BB-04**
Azhar, M: FE-02

B
Baatartsogt, K: **CP-06**, HD-08
Baba, Y: **CE-02**
Babu, S: DS-05, DS-06
Back, C H.: AG-09
Backes, C: DE-10
Backes, D: **CB-03**
Baczewski, L T.: **HE-10**
Badie, L: AG-13
Badura, A: DB-09
Bae, J: **GE-10**
Bae, K: AP-04, EC-07, EC-09
Baek, G: AG-05, AR-09, CF-07, **CH-05**
Baek, I: BB-06, **DR-10**, DR-11
Baek, J: BR-05
Baek, K: **EQ-14**
Baek, S: **AR-14**
Bagci, C: ER-09
Bagci, H: BE-12, CE-09, CR-02, EA-09
Baghel, A: **HP-01**
Bai, Y: GC-10

Bai, Y: **DR-12**
Baiao De Albuquerque, G: AA-07
Bailey, A K.: **DE-12**
Bainsla, L: HG-01
Bajpai, A: **AC-06**
Bakare, O A.: **GE-05**
Bakhshizadeh, F: CP-07, FP-16
Balachandran, T: CQ-12
Balakrishnan, G: CB-07, DC-11
Balakrishnan, P P.: DC-03
Baldino, H: **AP-12LB**, BE-04, DD-03
Baltz, V: DB-09
Balz, C: DC-06
Ban, H: BQ-01, BQ-06, BQ-14, CQ-02, CQ-11, **DQ-01**, DQ-02, DQ-06
Bandgar, P: CR-06
Banerjee, A: **AR-06**
Banerjee, T: DC-02, **DF-01**, FD-06
Bangar, H: AG-12, **BF-11**
Banjara, B: CS-07
Banshodani, T: FQ-09
Baraduc, C: CE-01, DE-04
Baral, P: DB-02
Baral, P R.: FE-10
Bardon, M: CA-03
Bardong, J: FC-15
Barker, B: FQ-12
Barman, A: AR-16
Barral, D: AE-07
Barrera, G: AD-12, DC-04
Bas, D A.: CE-06
Basnet, R: CC-03
Bastien, G: GB-07
Bastos, D: GR-11
Batista, C D.: GB-08
Bauer, G: FB-01
Baumann, S: AR-02
Baumbach, R E.: CC-11
Bayaraa, T: **BC-12**, CB-05
Béa, H: CE-01, DE-04
Beach, G: CF-06, GF-04
Becherer, M: AR-12, BR-13, DG-05, DG-06, GP-06
Beckert, S: DB-09
Beckham, J: CD-09
Beeson, W: GD-12
Begue, A: CR-07, **CR-11**, FD-05
Behera, N: HG-01
Belashchenko, K: CF-13, **EF-07**
Belbase, B: AR-06
Belli, M: GF-09
Bellini, A: **BE-08**
Belo, J H.: EB-06, GR-11
Ben Mbarek, S: **BE-12**
Bennett, C H.: DA-06
Bennett, S P.: BD-12
Bentley, P D.: FF-12
Berardi, F: **HR-17LB**
Berchialla, L: HF-10
Berger, F: BA-07
Berlie, A: FE-09
Bernal, O: CS-04, FP-05
Bernand-Mantel, A: GP-09
Béron, F: **CP-10**, **FC-08**, GE-09
Bertacco, R: AR-12, CR-07, DG-02, DG-03, DG-06, EG-11
Bertel Bermejo, L: FC-11
Bertero, G: BD-06
Betancourt, I: CP-05
Betz, N: AR-02
Beutier, G: AE-07, CB-09, GP-09
Bezdička, P: CP-16
Bezsmertna, O: AD-02, CB-05
Bhagat, N: FR-01
Bhattacharya, A: GP-11
Bhattacharya, D: AD-02, AD-03
Bhoi, B: GG-03, HG-07
Bhukta, M: HF-07, HF-14
Bianchini, C: BE-08
Bicket, I C.: AE-05
Bielicki, A: GC-03
Bilyk, V: CS-13LB
Binnie, I: CB-08
Birch, M: DB-02
Birol, T: DC-06, EE-03
Bishop, S R.: DD-11
Biswas, A: **FP-14**, **GP-11**, **HR-09**
Biswas, S: EG-03
Blon, T: CC-10
Blum, V: BD-05
Blumenschein, N: BD-12, DA-04
Bo, L: **HF-04**
Bodnar, S: **BE-03**
Bogach, A: DF-03
Böhm, D: CP-05
Boisron, O: CS-03, FP-13
Boissiere, J D.: DD-11
Bolyachkin, A: AA-06, AB-08, BD-03, **EC-05**
Bonanni, A: BC-01
Bondan, E: CD-03
Bono, D: CD-09
Borchers, J: DC-03, DC-08, EF-12
Borgnic, B: AE-07
Borodavka, F: AC-05
Bosomtwi, D: **DD-11**
Boswell, S: CD-04
Bouaziz, J: FE-10
Boujday, S: AF-07
Boulet, P: EB-07
Bourez, A: BD-06
Boyce, G: DS-14LB
Boyd, N: BP-05LB
Bozhko, A: DF-03
Bozhko, D A.: FB-02
Brady, S G.: FC-05
Braganca, P M.: BA-04
Branford, W R.: GC-05
Braun, H: **AD-07**
Brázda, P: CP-16
Brems, M A.: HF-14
Brennan-Rich, C: FG-10
Brereton, B: DR-02
Brock, S: FP-15
Brockie, R: BD-01, BD-06
Brollo, M: **EQ-04**
Brück, E: EE-08
Bruckner, F: CE-07, DH-08, ED-07, FG-04, HG-11
Brunin, C: CD-05
Bruno, N M.: FA-03
Bryan-Kim, J T.: HE-03
Buchanan, C C.: FC-05, **HF-13**
Buchanan, K: DG-04
Buda-Prejbeanu, L D.: CA-09, GC-09
Buettner, F: HF-05
Bugnet, M: FP-13
Buhrow, G: **FQ-01**
Bukhari, H A.: HG-02
Burman, T: **CE-12**
Burn, D M.: AG-03
Burnell, G: DR-02
Bussmann, K: HR-15
Byeon, J: BC-04, BC-09, BP-10, FR-07, **FR-08**
Byun, S: DQ-16

C

Caban-Chastas, D: DD-07, FA-09
Cabassi, R: BA-03
Caçoilo, N: BP-02
Cahill, D: GR-04
Cai, P: **CC-03**
Cai, Z: BE-09
Calimbas, J: EQ-03
Callahan-Coray, K: BF-02
Calle, F: DH-10
Camley, R E.: GG-06
Campo, J: **EE-02**, **FE-03**, **GB-06**
Campos, W: DB-09
Camsari, K: BF-02
Cancino, N: HA-04
Candido, D R.: **HB-02**, HG-02
Canero-Infante, I: FP-13
Cantoni, M: DA-03, FG-08

Cao, H: GB-08
Cao, S: AF-11
Cao Van, P: BR-05, BR-11, FF-10
Capotondi, F: GC-07
Carlisle, E: DB-08
Carlomagno, I: HE-11
Carlstedt, N: **FC-10**
Carpenter, R: AG-10, CA-03, FD-03, FD-07
Carpentieri, M: CA-07, HF-09
Caruana, A: DC-03, DC-08, EF-12
Casa, D: GR-19LB
Casanova, F: DB-09
Caseiro, M: CE-01, DE-04
Casoli, F: BA-03
Caspani, S: CD-01
Cating-Subramanian, E: CB-08
Cattoni, A: DG-03
Causer, G: AE-11, **FE-02**
Cecil, T W.: CE-05, EG-13
Celegato, F: AD-12, DC-04
Ceylan, H: FC-13
Cha, H: AP-04
Chailloleau, P: AF-04, **CH-07**
Chakhalian, J: HC-11
Chalmers, J: AE-04, BA-02, GR-06
Chan, F: AC-09
Chandavar, R A.: EB-01
Chandran, S: AC-03, AC-04, GP-12
Chang, C: HE-08
Chang, C: FF-01
Chang, C: EQ-02
Chang, C L.: FB-02
Chang, J: **BD-07**, BD-10
Chang, J: GQ-15
Chang, P: BR-16LB
Chang, W: FD-10
Chanwook, P: ER-07
Chao, W: CC-09
Chapai, R: CP-08, HR-11
Chari, S: **FG-09**
Charlton, T: DC-03
Chatratin, I: BD-05
Chatterjee, J: CA-03, FD-03
Chatterjee, R: FQ-06
Chatterjee, S: GP-01
Chauhan, A S.: CR-12
Chaurasiya, A: HG-01
Chavan, A: BE-02
Che, P: **DH-11**
Chelikowsky, J: **AB-01**
Chen, C: DA-05
Chen, C: BF-07, FP-06
Chen, C: EQ-11
Chen, D: **FD-11**
Chen, H: EQ-02
Chen, H: **AC-08**
Chen, H: HA-07
Chen, J: **HQ-15**
Chen, J: EA-06
Chen, J: BF-06, **EG-02**
Chen, J: BB-06
Chen, K: BA-02
Chen, L: HR-06, HR-10
Chen, L: AG-09
Chen, L: CH-02
Chen, R: **BC-07**
Chen, S: GB-08
Chen, S: HA-07
Chen, W: HF-06
Chen, W: BR-16LB, FR-19LB
Chen, X: BC-06
Chen, Y: BP-15
Chen, Y: CG-05
Chen, Y: EQ-11
Chen, Y: BF-07
Chen, Y: EG-08
Chen, Z: GG-02
Chen, Z: EA-08
Chen, Z: **DC-08**, EF-12, GF-08
Cheng, R: AF-09, **EF-01**
Cheng, S: **FR-19LB**
Cheng, T C.: HF-01
Cheon, S: DR-11
Chern, G: **BR-17LB**
Chernenko, V: EB-05
Chesnel, K: CS-14LB, **GR-17LB**
Cheung, S: BF-04, CA-07
Chhabra, H: **FD-06**
Chhetri, S: CC-03
Chi, B: GQ-01
Chi, H: GF-03
Chi, J: DS-06
Chiang, B H.: FD-11
Chiba, D: EG-03
Chiba, T: GF-07, HG-03, HG-04
Chiliquinga-Jacome, J J.: CB-09
Chin, A N.: **EA-05**
Chin, Y: BF-07, **FP-06**
Chinnasamy, C: AP-12LB
Chinnathambi, K: FA-03
Chiriac, H: EP-04, ER-08
Chiu, H: GR-18LB
Chiu, P: HA-07
Chlan, V: DC-07, FQ-10, GE-07, HR-19LB
Chlan, V: CP-16
Cho, H: DQ-16, EQ-10
Cho, J: DS-07
Cho, J: DS-07
Cho, Y: DD-02
Choe, S: BB-08, BR-08, DS-09, DS-10, GQ-15, GQ-16, HQ-04
Choi, C W.: BQ-11, BQ-12, CQ-16, **HP-04**
Choi, D: **HP-15**, **HP-16**
Choi, G: BB-03, GC-04
Choi, H: **TU-01**
Choi, J: BQ-01, BQ-02, BQ-03, BQ-06, BQ-11, BQ-12, BQ-14, CQ-02, CQ-03, CQ-05, CQ-06, CQ-07, CQ-08, CQ-11, CQ-13, CQ-14, CQ-16, DQ-01, DQ-02, DQ-06, DQ-09, HP-04, HP-06, HP-07, HP-08, HP-09, HP-10
Choi, J: AR-06
Choi, J: **AC-02**
Choi, W: FF-10
Choi, Y: GQ-15
Choi, Y: GR-19LB
Choi, Y T.: EQ-13
Choi, Y: BE-05
Choi, Y: AR-07, BC-04, BC-09, BP-10, EE-11, FR-07, FR-08
Chong, Y: **DQ-16**, **EQ-10**
Chou, C: **DA-07**
Chou, H: **HB-07**
Choudhury, S: CC-11, EF-13
Chouhan, A: DR-14
Christiansen, M: CD-09
Chu, Y: CC-08
Chuang, T: FR-19LB, GR-18LB
Chugh, A: DR-04
Chumak, A: CE-07, FB-05, FB-07, HG-11
Chung, S: GQ-06LB
Ciccarelli, C: AF-04, **CH-01**, **FE-11**
Clark, C: HF-06
Clark, T: XA-02
Coates, S: BC-05, **BC-10**
Cobas, E: AF-03
Cocconcelli, M: AR-12, **CR-07**, DG-02, **DG-03**, DG-06, **EG-11**
Coene, A: GR-03
Coester, B: FD-07
Coisson, M: AD-12, DC-04
Collin, S: GA-02
Colling, M: FE-10
Colman, R H.: FE-09, **GB-07**
Combs, N: AF-03
Comite, A: HA-01
Compton, L: **DG-04**
Compton-Stewart, J: **AF-04**
Cools, I P.: HQ-12
Cooper, J: **AE-11**
Copus, M: ED-04

Cordero, A M.: **CP-05**
Cornelius, R: GR-05
Corodeanu, S: EP-04
Correa, C A.: FE-09, GB-07
Correa, E L.: FC-04
Corredor, L: EP-07, FE-04, FR-18LB
Cortie, D: HB-07
Cory, D: HF-06
Cosgrove, L: **DS-13**
Costa, J L.: BB-04
Costello, T: **FC-09**
Couet, S: CA-03
Courtois, H: AD-08
Courtois, T: CF-03
Covic, G: DE-12, DQ-15
Cros, V: CB-09, DH-11, GC-07
Cruz, A: CD-01
Csaba, G: BR-13, DG-02
Csaba, G: AR-12, DG-05, DG-06
Cugini, F: EB-07
Cui, B: **AP-02**, AP-03
Cui, J: AP-02, EC-08, EC-10, HD-11
Cunningham, C J.: FQ-16, FR-20LB
Czoschke, P: BD-09, FG-09

D
da Câmara Santa Clara Gomes, T: **AD-01**, **CR-10**, HF-12
Dai, B: GF-03
Dai, C: BA-04
Daido, A: CF-01
Daimon, S: FR-02
Dainone, A: GA-02
Dal Din, A: CB-01
Dale, N: EF-13
Dang, T: FQ-10
Daniels, K M.: GF-11
Daniels, M: EA-07
Dannegger, T: AF-11
Darling, G: AB-04
Darwin, E: HF-05, HF-09, HF-10
Das, A: AG-10, FD-07
Das, B: EE-03
Das, D: **CR-06**
Das, I: GP-11
Das, S: **CF-15**
Das, S: HQ-08
Dasari, S: ER-14, ER-15
Dash, S P.: AG-12, BF-11, HQ-12
da SIlva Tavares, M: BR-15, GP-10
Dastanpour, E: DP-08
Daughton, D: AP-06
Daurer, B: CB-07
David, P: AE-07
Davidkova, K: FB-05
Davídková, K: **CE-07**
Davila, N: CA-04, EA-04
Davis, A: FC-04
Davis, M: FP-16
De, A: **AF-05**
De, A: AG-11
DeBeer-Schmitt, L: **GF-06**, HF-06, HF-13
de Cos Elices, D: BA-01, DE-08
De Croo, R: GR-03
Dehaghani, M: CC-10
Delaney, R: FA-02
de la Torre Medina, J: AD-01
del Barco, E: AF-02, AF-09
Del Giacco, A: AR-12, DG-06
Della Cerra, T: FA-02
Deman, A: CD-05
Dembski-Villalta, M: AC-13
DeMell, J E.: **GF-11**
Deng, K: EF-01
Dennett, C: XA-02
Denneulin, T: BB-07, BC-01
Dennis, C: **FC-04**
Desai, P C.: AE-04
De Somer, C: **GR-03**
de Souza, H B.: EB-06
Detore, R: EQ-05
Devincenti, A: CA-07
DeVisscher, E D.: **BP-05LB**
Devolder, T: FB-04, HG-10
de Wergifosse, S: CR-10
Dhagat, P: AC-11, BR-01
Dhaliwal, K: **AG-03**
Dhiman, A K.: **BP-03**
Dhuey, S: CB-05
Diaconescu, P: GB-08
Diallo, S: FQ-16, FR-20LB
Diao, Y: CG-05
Diaz-Ortega, I: GB-06
Díaz-Sainz, G: FC-11
Dickovick, J: CE-06
Dieny, B: BA-07, CE-01, DE-04
Dimoulas, A: BF-11
Ding, S: CG-08
Di Pietro, A: FG-08
Di Pietro Martínez, M: CB-07, CB-09
Divan, R: CE-05, EG-13, FB-02
Divyanshu, D: **CR-02**, EA-09
Dixon-Anderson, K: GR-11
Dlubak, B: CR-11
Do, J: AR-05, BP-09
Do, N: CC-12
Docusen, D: **CS-14LB**
Dodrill, B: AP-06
Dohi, T: ED-09, **HF-07**
Dolan, E: DB-09
Dolezal, P: AC-05
Donahue, M J.: **FG-12**
Dong, D: BE-09, DE-13
Dong, S: FQ-15, HC-01
Donnelly, C: BE-02, CB-07
Dorj, O: CP-06, CP-11, CP-14, HR-04
dos Santos, G: XA-01
Douveas, I K.: CE-07
Dravid, V P.: CA-07
Drchal, V: GE-07
Du, A: **BB-07**, **CG-08**
Du, J H.: **GR-18LB**
Du, Y: HP-02
Duan, J: AA-06, **FG-05**
Duan, X: DR-05
Duan, Y: **BC-06**
Dubey, D P.: HQ-12
Dubs, C: CE-07, FB-05
Duffee, C: EA-04
Dumas, R K.: **GR-11**
Dumesnil, K: **CF-02**, **CF-03**, **HE-06**
Dunand, D: DP-10
Dunin-Borkowski, R E.: BB-07, BC-01
Dupont, E: CD-05
Dupré, L: GR-03
Dupuis, V: CS-03, FP-13
Durner, C A.: FG-08
Durnez, A: CR-11
Dutta, D: BC-01
DuttaGupta, S: GP-11
Dutton, S E.: HR-17LB
Dyer, M: AB-04
D'Addario, A: CA-07

E
Eagan, C: **ED-04**, **ED-05**
Ebels, U: EA-07
Ebii, T: GR-09
Echtenkamp, W: DD-11
Edwards, A: BD-12, **DA-04**
Edwards, A J.: GP-08
Efe, F: CP-07, FP-16
Efimenkov, I: FA-05
Eker, C: AD-11
Elabbasi, M: ER-14, ER-15
Elekhtiar, M A.: BE-06, CA-07, EG-01
El-Gendy, A: **CD-11**, ER-14, **ER-15**
El-Ghazaly, A: AD-06, DE-02, **DE-09**, GE-02
El Kanj, A: DH-11
Ellithy, I R.: **EP-13LB**
Elyasi, M: FB-01
Emo, M: HE-06

Emori, S: EF-11, EG-04, FF-06, GE-05, GP-07LB
Endo, M: CE-04
Endo, T: AQ-10
Endo, Y: DP-02, EP-05, VP-02
Endoh, T: AG-02
Enger, L G.: FC-02, FC-15
Enkhnaran, U: CP-14, HD-08
Enoki, M: DD-12, DP-09
Eo, Y: CD-04
Eom, C: BE-06
Eom, J: AC-02
Eom, S: BQ-14, **CQ-07**, CQ-11, DQ-01
Ermoshkina, P: **XA-02**
Erram, A: **DR-14**
Escrig, J: **AR-15**, **DS-01**
Esguerra, M: EP-13LB
Eskildsen, M: GF-06
Evans, E: **TU-02**
Ezaka, M: **ER-04**
Ezawa, M: DB-02

F
Fabbrici, S: BA-03, EB-07
Fabbris, G: GR-19LB
Fabelo, O: FE-10
Fabian, J: FG-02
Fan, R: AG-03
Fan, X: BP-05LB, DA-05
Fan, Y: BA-04
Fan, Y: AA-04, BD-02
Fan, Y: BR-17LB
Fang, B: HC-04
Fang, H: **CB-08**
Farhadi, N: **EG-04**
Farias, W: GC-03
Farinacci, L: AR-02
Farrell, R: BA-02
Fassbender, J: FB-04, HG-10
Fatima, H: DS-05
Faure-Vincent, J: CE-01, DE-04
Feggeler, T: CB-08
Fekraoui, S: CC-10
Fellner, K: AC-13
Felner, I: HR-13
Felser, C: AF-05, CB-07
Feng, R: CR-14
Fermon, C: CE-01, DE-04
Fernandes, M: EQ-05
Fernandez, F: CD-01
Fernández, E: DE-08
Fernandez-Gonzalez, C: AD-02, AD-03, CB-05
Fernandez Gubieda, M: **BA-01**
Ferreira, F d.: EQ-04
Ferrer, J: CC-14, FG-02
Fettar, F: **AE-07**, **GP-09**
Figueroa, A I.: GR-17LB
Finizio, S: DH-11, FB-05
Finkel, P: **DC-05**, GE-03, HR-15
Finocchio, G: CA-07, EA-04, HF-09
Fischer, H E.: HR-17LB
Fischer, J: CE-01, DE-04
Fischer, P: AD-02, AD-03, **CB-05**
Flatau, A: AQ-13
Fleischer, J: GF-11
Fletcher, J: **BR-01**
Florio, P: EG-11
Foerster, M: DH-10
Fotso, H: GA-03
Fournee, V: **EB-07**, HE-06
Fowlie, J: CA-07
Fraile Rodríguez, A: GR-17LB
Frame, M: HC-07
Franco, C: CD-03
Franco, V: GR-11
Frandsen, B: **DB-08**, DC-06
Frank, M: GP-08
Franz, M: **DB-06**
Frej, A: **EG-10**
Friedland, A: DC-03
Friedman, A: BD-12, CH-08, DA-04, GF-03, GF-10
Friedman, J S.: DA-04, GP-08
Frnández-García, L: DH-10
Fröhlich, S M.: HF-14
Frömter, R: HF-07, HF-14
Frontini, F: **GR-19LB**
Fu, L: DA-07
Fu, S: BC-01
Fuchs, G: CA-07
Fugetta, B J.: AD-02, AD-03, **GD-12**
Fuhrmann, F: AF-11
Fujii, Y: BG-02
Fujimori, Y: DQ-05
Fujisaki, K: **EP-01**
Fujita, H: CP-09
Fujita, J: EQ-03
Fujita, M: FR-10
Fujiwara, K: HR-03
Fujiwara, K: FE-07
Fujiwara, K: DE-11
Fujiwara, K: CE-04
Fukamachi, T: EF-02
Fukami, S: BF-03, BP-02, ED-09, FE-07
Fukui, Y: CB-02
Fukuma, Y: AD-08, CR-14
Fukunaga, H: AP-11
Fukuoka, Y: CD-06
Fukushima, H: CE-04
Fullerton, E: CB-08, DH-07, EF-13, GC-09, HB-01
Fullerton, J: CC-03
Fultz-Waters, S: **HE-03**
Funabashi, N: AR-08
Funae, T: **HQ-02**
Funatani, S: EQ-15LB
Furusaki, A: DB-04
Fushimi, M: FC-06
Fushimi, Y: **BF-03**

G
G. Suresh, K: ED-10, EE-12
Gadbois, J: AA-04, BD-02
Gaerner, M: BG-04
Gajarao, S: HQ-11
Galíndez-Ruales, E: AF-11, BB-07
Gallo, L: EB-07
Galvita, V: GR-03
Gama Monteiro, M: CA-03, FD-07
Gandarias, L: BA-01
Gandini, G: DA-03, FG-08
Gao, L: BC-01
Garcia, A: CS-04, FP-05
Garcia, J H.: CC-05
Garcia, M A.: ER-14, ER-15
García-Arribas, A: **DE-08**, GE-01
Garcia-Barriocanal, J: EE-03
García-Prieto, A: BA-01
Garcia Redondo, F: CA-03
Garcia-Sanchez, F: GP-08
Garfias-Dávalos, D: XA-01
Garica Fuente, A: FG-02
Garland, J: CC-03
Garlea, V: AF-01
Garman, M: HG-02
Garrett, M: FQ-02
Garst, M: AC-13, FE-02
Gartside, J: CR-10, GC-05, HF-12
Gashi, A: CB-05
Gatel, C: GP-09
Gaudin, G: CE-01, DE-04
Gautam, K: FE-10
Gautam, R: CS-14LB
Gautam, R: DP-12
Gawryluk, D: GB-03
Gay, F: AE-07
Gayles, J D.: FG-10
Geerts, W: **CS-05**, CS-07, GR-08, **GR-14**
Gegenwart, P: GB-07
Gehring, P: DC-03
Gen, M: FE-10
Genfior, E: **FP-05**
George, J: GA-02

George, T F.: GC-10
Gerven, L v.: **CS-13LB**
Gestoso, G: DE-08
Geuchies, J: BC-01
Ghadai, B: EP-14LB
Ghahremani, M: **EB-09**
Gherca, D: ER-08
Ghimire, B: DB-03
Ghimire, N J.: GF-06
Ghoreyshi, A: **BD-09**
Ghosh, R K.: GF-10
Gibbons, J: BA-04
Gibeault, S: EA-07
Gilbert, D A.: **FC-05**, HF-13
Gilbert, S: FA-02
Gilbert Corder, S: **AC-10**
Gillemot, F: DP-13
Gim, S: GQ-04
Girt, E: BG-07, DS-11
Giuliano, D: FD-03
Glavic, A: AE-11
Gliga, S: **BE-01**
Glushkov, V: DF-03
Go, D: **BB-01**, BB-07, DR-10
Godel, F: GA-02
Gohda, Y: EE-09
Gokce-Polat, E: DD-11
Goldfarb, R: **AE-01**, **CS-12LB**
Gomes, A: GR-12
Gomes da Silva, E: **HG-02**
Gomez-Pastora, J: AE-04, BA-02, CD-04, ER-02, **FC-11**, GR-06
Gomonay, O: BB-07, BC-01, DB-09, GA-08
Gong, E: HG-05
Gong, M: CR-08
Gong, Y: **GC-03**
Gonzales, S: FP-13
Gonzalez, F: CS-04
González-Fernández, C: FC-11
Gonzalez Villegas, A: EP-03
Goodman, M: **AP-09**
Gopman, D B.: DC-03, DP-04, DS-14LB
Gorchon, J: AR-10, GC-09
Goswami, A: FQ-01
Goto, M: AQ-06, GP-03
Goto, R: **EC-03**
Goto, T: **BG-01**, GG-11, HR-03
Goto, T: **FR-02**
Gotoh, Y: AQ-12, AQ-14, AQ-15, GR-02
Gouéré, D: DH-11
Graczyk, P: BP-03
Graeser, M: CD-07
Grandal, J: DH-10
Grassi, J: HC-11
Gray, A X.: HC-11
Greaves, S: **AA-02**, BD-04
Green, J: GB-08
Greening, R W.: BP-05LB
Greil, J: **AR-12**, BR-13, **DG-05**, **DG-06**
Grelier, M: CB-09
Greven, M: DC-10
Grier, T: FQ-02
Griffin, S M.: BC-12, CB-05, FQ-12
Griffiths, J E.: **AB-04**
Grobis, M: CA-04
Groefsema, J: AR-13LB
Grollier, J: CR-07, CR-11, FD-05
Groot, T: FE-04
Gross, M J.: FB-05
Grossmark, T P.: **HE-08**
Gruber, R: GC-07, HF-14
Grundler, D: DH-11
Grutter, A J.: DC-03, DC-08, EF-12, HB-07
Gu, J: CC-09
Guan, Y: DR-05
Gubieda, A G.: BA-01
Guedas, R: DH-10
Guedes, M V.: EQ-04
Guen, Y L.: AF-04, AR-10, GC-02, GC-09
Guidobeth, S: DS-01
Guillet, T: CC-05, **CC-10**
Gundlach, L: CH-06, GG-09
Gunduz Akdogan, N: **ER-09**, GD-04
Gungordu, B: ER-09
Guo, H: **CC-01**
Guo, Q: GD-01
Guo, R: EG-03
Guo, X: GQ-01
Guo, Z: GC-07
Guofei, L: CR-14
Guo-Hua, Z: BC-07
Gupta, A: AD-10, HE-11
Gupta, A K.: AD-08
Gupta, A: **GD-10**
Gupta, A: **DC-02**
Gupta, M: GD-10
Gupta, R: AF-02
Gupta, R: **AD-10**
Gupta, S: HQ-01
Gustafson, J K.: AF-03
Gutierrez, E: CS-04, FP-05
Gutiérrez, J: GE-01
Gutt, C: GC-07
Guy, M: CP-07, FP-16

H
Hackner, L: HG-08
Hadimani, R L.: EQ-05, ER-03, ER-10, **HA-03**, HA-05, HA-06
Hager, A: FQ-16
Hai, N: FF-01
Haidamak, T: AC-05, FE-09
Hait, S: **DR-02**
Haldar, A: HQ-11
Hales, M: **CH-03**
Hamada, R: CR-14
Hamdi, M: BF-04, CA-07, HQ-16LB
Hameed, S: BC-01
Hamid, S B.: BF-04, EA-05
Hammack, A T.: CB-05
Hamrle, J: BG-04
Han, D: **GQ-06LB**
Han, D: CF-07, FF-10, GQ-12
Han, G: **HQ-04**
Han, H: CC-09, HF-08
Han, H: GR-10, HP-15
Han, J: FE-07
Han, J: EQ-10
Han, X: AR-11, CR-03, CR-16, GQ-01
Hanashima, T: DC-03
Hanbicki, A T.: BD-12, CH-08, DA-04, GF-03, GF-10
Hanggai, H: **EE-08**
Hanson, A: **FA-01**
Hanson-Flores, J: AF-02, **AF-09**
Hao, H: HR-10
Hao, R: **AA-05**
Hao, Y: CC-03
Hao, Y: GB-08
Harada, K: BR-03
Haran, K S.: CQ-12
Hareau, C: AF-07, FF-13
Harms, H: FQ-16, FR-20LB
Haroon, A: EQ-03
Hart, D R.: **HB-04**
Hasegawa, S: AC-07
Hasegawa, T: **CP-04**, DE-03, GD-11
Hashimoto, Y: AC-07
Haskel, D: GR-19LB, HR-09
Haslinger, P: AE-05, **HB-06**
Hatajiri, T: EG-02
Hatayama, S: CC-15
Hatt, S: DB-08, DC-06
Hatton, P: DC-11
Hattori, T: EF-02
Hauet, T: AF-04, CF-02, CF-03
Hauser, A: ED-08, FQ-02
Hayami, S: FE-10
Hayashi, K: BD-11, EF-02, FD-08, HC-10

Hayashi, M: DF-06, EG-08, FP-01
Hayden, B: BE-05
Haynes, J A.: AP-12LB
He, H: DP-11
He, H: **DF-02**
He, J: GB-08
He, L: CC-03
He, R: **AC-01**, CC-06, FR-20LB
He, W: HE-03
He, X: BD-05
He, Z: HR-06, HR-10
HE, Y: EQ-15LB
Heacock, B: HF-06
Heczko, O: **GE-07**, **HR-19LB**
Hedlund, D: DD-03
Hehn, M: AE-07, AF-04, AG-13, AR-10, BD-11, CA-09, CH-07, GC-09
Heinonen, O: BD-05
Heins, C: **FB-04**, HG-10
Heinz, B: AR-12, DG-02, DG-06
Helbig, S: CD-07
Hellings, G: CA-03
Hellman, F: CB-05
Heltemes, K: EE-03
Heltman, A: BP-08
Hemesath, C: FQ-16
Henderson, M: GF-06, **HF-06**, HF-13
Henri, C: CH-07
Heo, J: DR-01LB
Heppell, E: CB-03
Herfort, J: **CC-13**
Hernandez, R: FC-11
Hernandez, S: BD-09
Hernández-Mínguez, A: CC-13
Herrera, G: FP-13
Herrera Diez, L: CR-11
Herrmann, I K.: CD-07
Hersam, M C.: CA-07
Hertel, J: FG-08
Herz, J: DC-08
Hesjedal, T: CB-03, FD-04, FE-02
Heynderickx, G: GR-03
Hibino, Y: **CR-04**, **HE-09**
Higashikawa, K: **BP-14**
Higo, T: BF-06, CB-02, CF-12
Hill, N: FR-06
Hindmarch, A: AG-03
Hioki, T: **FB-01**
Hirai, T: CC-15, DF-09, **EG-03**
Hirama, R: **DP-01**
Hiramoto, S: DD-08
Hiraoka, I: AE-09
Hirata, K: CC-15
Hirata, S: BP-01, CF-04, **HQ-05**
Hirayama, Y: EC-11, GD-05, GD-06, **GD-07**, HD-05
Hirobe, D: **BP-07**
Hirohata, A: AF-05, **GA-07**, GQ-10
hiroi, K: FR-10
Hiroi, M: **FR-03**, **FR-04**
Hirschberger, M: **DB-02**, DB-04, FE-10
Hirschmann, M M.: DB-02, **DB-04**
Hisatomi, R: CF-04, DS-04, HQ-05
Hitzelberger, N: FR-18LB
Hlova, I Z.: BG-06
Hoang, T: FQ-10
Hobara, R: AC-07
Hoffmann, A: CE-05, CG-05, DG-09, EG-13, FB-02, FG-07, HG-05, HR-05
Hofschen, M: BR-13, DG-05
Hohlfeld, J: AF-04, AR-10, CH-07, **CH-09**, GC-02, GC-09
Hojo, T: **CE-04**, DE-01
Holla, A: DA-01
Hollis, M: HB-01
Holobradek, J: FB-05
Holt, N: EQ-09
Homma, T: FP-07
Honecker, A: FR-13
Honer, K: BA-04
Hong, H: **EQ-07**
Hong, J: AR-07, BC-04, BC-09, BP-10, **EE-11**, FR-07, FR-08
Hong, J: **BF-05**, FF-03
Hong, J: **ER-07**
Hong, X: **DC-01**
Hono, K: AA-04, GD-03
Horibe, S: FB-01
Horiuchi, K: FP-03
Horizumi, K: **HG-03**
Horvath, A: DP-13
Horvath, M: DP-13
Hosen, K: AA-01
Hoshi, K: FB-01
Hosokawa, A: **GD-08**
Hosokoshi, Y: EE-02, GB-06
Hosono, Y: **AQ-12**, AQ-14
Hossain, A: EP-12
Hou, J: DP-11
Hou, Y: CC-01
Hovančík, D: AC-05
Hrabec, A: CB-07, HF-10
Hridoy, H: CD-04
Hsieh, C: AC-08, AC-09, HA-07
Hsu, C: FD-10
Hsu, C: **BR-16LB**, GR-18LB
Hsu, H: **GR-13**
Hsu, J: **FD-10**
Hsu, W: BF-07
Hsu, Y: FR-19LB
Htet, H: DE-09, **GE-02**
Hu, C: CE-06
Hu, G: DS-15LB, EG-07
Hu, J: **HD-01**
Hu, J: CC-03
Hu, L: GD-12
Hu, S: HR-06, **HR-10**
Hu, X: GP-08
Hu, Z: DP-06
Huai, C: CC-02
Huang, A: CE-06
Huang, B: **GQ-11**
Huang, C: HA-07
Huang, C: GB-08
Huang, D: DP-04
Huang, J: CC-03
Huang, K: EG-01
Huang, S: BF-07, DA-05, FP-06
Huang, Y: **DF-05**
Huang, Y: DG-07
Hubble, Z: EG-01
Hubert, M: FQ-05
Huebl, H: FB-06
Hueso, L: DB-09
Hug, H J.: **CD-07**, HF-05, **HF-09**, **HF-10**
Hughart, D: DA-06
Hughes, S: **BG-05**
Hur, J: HQ-06
Husain, S: **FB-08**
Hwang, C: CC-12, HF-11
Hwang, J: **HQ-09**

I

Iacocca, E: AD-04, AD-07, **ED-01**, ED-04, ED-05, **GG-06**, GG-07
Iba, S: **GA-06**
Ichiyanagi, Y: **BA-05**
Ideta, S: AC-07
Igarashi, J: AR-10
Iglesias, F: FP-05
Iglesias-Cardinale, V: GA-03
Iida, U: **FR-05**
Iihama, S: AR-10, BD-11, EF-02, FD-08
iijima, R: CF-04, HQ-05
Iino, A: FC-06
Ijiri, Y: DC-08, EF-12
Ikeda, A: AE-02
Ikeda, F: **BD-11**
Ikeda, K: FQ-09
Ikeda, S: AG-02
Ikeda, Y: DP-09, FR-10
Im, E: AR-09, **BE-05**, BR-10
Im, M: CC-09, FC-03, HF-08

Imaeda, H: **CS-02**
Imai, Y: AQ-10
Imamori, S: DE-11
Imamura, K: **DE-06**
Imamura, K: **HD-09**, **HE-07**
Imanishi, H: GP-03
In, Y: DP-03, **DQ-14**
Inaoka, Y: FF-06
Incorvia, J C.: CA-07, EA-05, GQ-08
Incorvia, J: BF-04, FD-03, HE-12
Ingla-Aynes, J: DA-07
Inomata, S: **AQ-16**
Inoue, H: BE-11
Inoue, J: AQ-07
Inyang, O: AG-03
Ipatov, M: CP-01
Iriyama, T: DP-09
Isaeva, A: BC-02, EP-07, **FE-04**, FR-18LB
Ishibashi, K: **AR-10**
Ishida, M: CG-07
Ishihara, Y: FE-10
Ishii, F: **GQ-07**
Ishikawa, R: GP-03
Ishikawa, T: EE-07, FQ-08, **GQ-14**
Ishikawa, Y: EF-02
Ishiyama, K: BG-01, GG-11, HR-03
Ishizuka, H: **HB-08**
Islam, M: **EP-12**
Islam, M: AQ-06
Islam, M: CS-05, **CS-07**
Islam, S: GQ-08
Isogami, S: **AA-04**, AF-06, BD-02, CG-01, FF-12, HD-09, HE-07
Isshiki, H: GG-02
Itani, R: ED-02
Itani, S: **ED-02**
Ito, M: **FP-03**
Ivanov, B: AR-13LB
Ivanova, E E.: **AQ-13**
Iwai, H: BF-03
Iwasaki, Y: AB-09
Iyer, P: AE-04, GR-06
Izquierdo, R: DH-10

J
Jaberolansar, E: **CD-10**, FP-10
Jabran, S: HR-13, HR-14
Jaffrès, H: CH-07, GA-02
Jain, P: DC-06, **DC-10**
Jain, R: FF-01
Jakob, G: AF-11, BB-07, BC-01
Jamer, M E.: EG-09
Jamshed, B: **HQ-08**
Jan, S: ED-10, EE-12, **FP-10**
Jander, A: BR-01
Jang, H: CG-04
Jang, J: ER-07
Jang, K: DD-02
Jang, P: DQ-11
Jani, H: **CB-04**, **EF-09**, **FF-11**
Jaouen, N: **CB-09**, **GC-07**, GP-09
Jaros, A: **AE-05**
Je, S: GQ-15, GQ-16
Jefremovas, E M.: **FG-01**
Jena, B P.: **AC-04**
Jena, B: **GP-12**
Jena, S K.: **FP-09**, **GP-04**
Jensen, C: DC-08
Jeon, J: BF-02, **DH-06**
Jeon, S: CG-05
Jeon, S: HQ-04
Jeon, S: HP-15
Jeon, Y: DB-01
Jeong, D: **DS-04**
Jeong, E: DC-03
Jeong, E: DB-01
Jeong, J: **DD-02**
Jeong, J: BR-05, BR-11, FF-10
Jeong, K: AR-07, BC-04, **BC-09**, BP-10, EE-11, FR-07, FR-08
Jeong, S: **GQ-12**
Jeong, S: CG-04
Jeong, S: **DQ-03**, DQ-12
Jeong, Y: HF-11
Jeong, Y: GQ-15
Jhang, R: FF-01
Ji, D: CQ-15
Jia, L: BB-06
Jiang, L: **EP-06**, HC-09
Jiang, N: **AG-01**, AG-04, CC-04, HQ-13
Jiang, W: CC-03
Jiang, X: HQ-03
Jiang, Y: **DG-07**
Jin, C: CQ-09, GR-10
Jin, H: DA-06
Jin, R: GC-03
Jin, Z: AF-05
Jo, C: EQ-07, **EQ-08**
Johnson, T: AE-02
Joisten, H: BA-07
Jones, N J.: EP-10, **FC-07**, GE-03
Jong-Woo, K: HR-04
Jordan, B: GF-11
Jorgensen, C S.: FC-05
Josephy, S: GG-12
Joshi, P: BG-10, CP-12, CP-13, EE-05
Jossart, N: CA-03
Joumard, I: CE-01, DE-04
Ju, T: HF-11
Jubert, P: **BD-01**, BD-06
Jun, E: **AR-09**, BE-05
Jung, J: AC-07
Jung, M: **DQ-13**
Jung, M: **GQ-04**
Jung, S: ER-07
Jung, T: DQ-13
Jung, W: CA-04
Jung, W: **CQ-08**, **CQ-14**, CQ-16
Jung, Y: CG-04
Jungfleisch, B: CH-06, EG-05, GG-09, GG-12, HG-09
Jungwirth, T: DB-09
Jyothi Bhasu, A: CC-14

K
K, A: AG-13
K. Sangwan, V: CA-07
Kabata, Y: **CG-07**
Kaczmarek, S: HR-13
Kadlec, C: DC-07
Kadlec, F: DC-07
Kado, M: DH-05
Kaiju, H: DF-04
Kainuma, Y: CE-02
Kajiwara, T: GD-03
Kákay, A: FB-04
Kalappattil, V: DP-04, GF-08, GF-10
Kaman, O: **CS-10**
Kamba, S: AC-05
Kameda, M: **HF-03**
Kamijima, Y: ER-12
Kamiryo, A: **CG-03**
Kamisaka, S: DF-07
Kamiya, K: EB-03
Kamiya, Y: EE-02
Kammerbauer, F: HF-07, HG-10
Kammerer, J: CE-01, DE-04
Kanai, S: BF-03, BP-02, FE-07
Kanai, Y: AA-02, BD-04, **CE-10**
Kanak, J: HC-05
Kancko, A: **FE-09**, GB-07
Kandwal, N: AG-12, CR-12, DR-15
Kaneda, R: **EQ-15LB**
Kaneko, H: BP-02
Kang, J: BF-04, **CA-07**, CG-04, FF-10, HQ-16LB
Kang, M: **HF-08**
Kano, A: AQ-12, **AQ-14**
Kantartzis, N V.: CE-10
Kao, Y: ED-02
Kapetan, H V.: ER-15
Kapteyn, H C.: CB-08
Karaman, T: HF-05
Karati, A: BG-08

Kareev, M: HC-11
Karki, P: EG-01
Karki, T: **BG-10**, **CP-12**, CP-13, EE-05
Karlova, K: BC-13, **FR-13**
Karube, S: **BF-08**, CF-04, DS-04, FF-06, HQ-05
Kasahara, S: CF-01
Kasahara, Y: CF-01
Kasai, S: DS-04
Kasai, S: BD-03, GP-01
Kassym, D: ED-02
Kataoka, N: BA-05
Kateel, V: **AG-10**, FD-03, **FD-07**
Katine, J: **BA-04**, CA-04, CA-07, EA-04
Kato, A: DD-09
Kato, M: DQ-07
Kato, T: FP-07
Katsumura, H: DE-05
Kaulich, B: CB-07
Kaur, D: CE-12
Kaur, R: **GQ-03**, HQ-11
Kaushik, S D.: GB-02
Kautsar, Z: GD-03
Kawagita, K: EF-02
Kawaguchi, M: DF-06, EG-08, FP-01
Kawaguchi, Y: HF-03
Kawahara, R: AG-01
Kawai, M: **DR-09**
Kawai, T: **AP-10**
Kawamura, H: HQ-13
Kawana, M: **AR-08**
Kawana, R: **FP-07**
Kawarazaki, R: HQ-05
Kawashige, R: CA-05
Kawashima, M: BP-14
Kazami, S: **FE-07**
Kazemian, M: CB-07
Keagy, J: **FQ-13**
Keatley, P S.: HG-02
Kefayati, A: CH-06
Keller, L: GB-03
Kelley, J: FG-10
Kent, A D.: AF-09, AG-13, FD-11, HG-05
Kent, N: HA-01
Kern, L: **GF-04**
Keum, J: AF-09
Kézsmárki, I: CF-10
Khadiev, A: HE-11
Khalili Amiri, P: BF-04, CA-07, EA-04, HQ-16LB
Khaliq, W: DH-10
Khan, M: CP-08, HR-11
Khan, S: **FA-05**
Khanas, A: DF-03
Khandaker, M: CD-08, EQ-09
Khare, S: **HQ-16LB**
Kharel, P: **EF-08**, FQ-01
Khatri, Y: **GQ-13**
Khayr, I: DC-10
Kho, D: GQ-08
Khodadadi, M: FA-07
Khodagulyan, A: CS-04, FP-05
Khodaparast, G: CH-08
Khurshid, H: FP-10
Khymyn, R: HG-01
Kidd, T: FQ-16
Kidd, T: **FR-20LB**
Kiechle, M: EG-07
Kiefe, R: EB-06
Kiehl, C: FB-02
Kihara, F: EC-03
Kihara, S: FQ-09
Kihara, T: FQ-11, GB-06
Kijima-Aoki, H: **DE-05**
Kikkawa, A: FE-10
Kikkawa, T: BB-07, HQ-13
Kim, C: BQ-08, CQ-01
Kim, D: **DD-10**
Kim, D: DP-03, DP-15
Kim, D: AP-04, EC-09
Kim, D: EC-07
Kim, D: BQ-09, **CQ-15**
Kim, D: HQ-06
Kim, D: DS-07
Kim, D: **VP-01**
Kim, D: BB-08, GQ-15, GQ-16
Kim, E: BQ-01, BQ-06, DQ-06
Kim, E: HQ-06
Kim, G: EC-06
Kim, H: BE-05, BR-10
Kim, H: BQ-09
Kim, H: **AR-07**, FR-08
Kim, H: **FC-06**
Kim, H: BQ-07, BQ-08, CQ-01, **CQ-09**, CQ-10, **DQ-10**
Kim, H: EC-02
Kim, H: **FF-10**
Kim, H: **GC-04**
Kim, J: ER-07
Kim, J: DQ-11
Kim, J: DQ-16, EQ-10
Kim, J: AP-07, EP-11
Kim, J: DH-11, FB-04
Kim, J: **EC-11**
Kim, J: **DS-07**
Kim, J: BQ-01, BQ-06, **DQ-06**
Kim, K: AG-05, AR-09, BR-05, BR-11, CE-05, CF-07, CG-04, CH-05, DG-09, EG-13, FF-10, GQ-12
Kim, K: HQ-04
Kim, K: GP-02LB
Kim, K: FF-10, GQ-15
Kim, M: EE-11
Kim, M: **BB-08**, GQ-15, GQ-16
Kim, M: BQ-03, **CQ-06**, HP-07, HP-08
Kim, M: GE-10
Kim, M: BQ-02, **CQ-03**, HP-09
Kim, M: CQ-13, **HP-06**, HP-10
Kim, N: CF-07
Kim, P K.: **AR-13LB**
Kim, S: **CQ-13**, HP-06, HP-10
Kim, S: AR-09, BE-05, BR-10, FF-10
Kim, S: CQ-05, **DQ-09**
Kim, S: DE-12, DQ-15
Kim, S: GP-02LB, GQ-06LB
Kim, S: **GQ-15**
Kim, S: BQ-02, **CQ-02**, CQ-03, CQ-11, DQ-01, DQ-02, HP-09
Kim, S: EQ-08
Kim, S: DS-07, **HQ-07**
Kim, S: CG-04
Kim, S: AP-04, **BB-03**, **EC-02**, EC-06, EC-09
Kim, S: BQ-11, BQ-12, CQ-08, DQ-01, HP-04
Kim, S: DQ-03, **DQ-12**
Kim, T: DP-15, DQ-14
Kim, T: **CC-12**
Kim, T: AP-04, EC-02, **EC-06**, EC-07, EC-09
Kim, T: **BQ-01**, BQ-06, DQ-06
Kim, T: **BQ-14**, CQ-07, CQ-11
Kim, T: HF-11
Kim, W: BQ-05, BQ-07, BQ-08, CQ-01, CQ-09, CQ-10, DQ-10, GR-10, HP-15, HP-16
Kim, W: CC-09
Kim, Y: **HA-01**
Kim, Y: GQ-04
Kim, Y: DR-01LB
Kim, Y: **DB-01**
Kimata, M: FQ-11, GQ-10
Kimel, A V.: AR-13LB, BR-06, CH-03, CS-13LB
Kinane, C: DC-03, DC-08, EF-12
Kinast, A: EB-01
Kindiak, I: CF-05
Kinoshita, T: **BP-02**
Kirilyuk, A: **GC-08**
Kirti, K: **EP-14LB**
Kitagawa, W: ER-04
Kitazawa, H: EB-03
Kitcher, M D.: **CF-06**
Kitou, S: FE-10

Kiyota, T: VP-02
Kizil, R: **BP-08**
Kläui, M: AF-11, BB-07, BC-01, CG-08, GC-07, HF-07, **HF-14**, HG-10
Klein, J: DA-07
Klementová, M: CP-16
Klemmer, T: BD-05
Klewe, C: EE-10, EF-13, GE-05, HC-07, **HC-11**
Klima, J: FB-05
Kmjec, T: CP-16, DC-07, FQ-10, HR-19LB
Ko, D: **DR-01LB**
Ko, S: AG-05, **CF-07**, CG-04, FF-10, GQ-12
Kobayashi, K: FR-02
Kobayashi, S: **DP-13**, **FR-10**
Kobayashi, Y: AQ-16, AQ-16, DF-06, **FP-01**
Kobori, K: DE-05
Kocharian, A N.: **CS-04**, FP-05
Kochetkova, E: FE-04
Kocsis, V: CF-10
Kocyigit, M: DG-09
Koda, Y: FR-04
Kodama, T: ER-12
Kodama, T: **DG-01**
Kohl, F: AR-12, DG-02, DG-06
Köhler, J: **AF-11**, BB-07
Kohout, J: CP-16, CS-10, DC-07, FQ-10
Koike, S: CS-09
Koizumi, H: DR-08, GA-07, **GQ-10**
Kojima, K: EE-02, FE-03
Kojima, Y: FR-02
Komar, C: EE-03
Komine, T: FP-03, GF-07, HG-03
Komori, S: AR-14, HG-06
Konakanchi, S: CA-07, HQ-16LB
Kondou, K: AG-04
Kong, D: **CR-16**
Koo, H: EQ-07, EQ-08
Koo, M: CQ-05
Koopmans, B: AQ-05LB
Koraltan, S: CD-07, **HF-05**
Körber, L: FB-04
Kosaki, H: BF-06, CB-02, EG-02
Kosogor, A: **EB-04**
Kostadinov, S: GP-06
Kotsakidis, J: GF-11
Kotsugi, M: AB-09
Kotula, A: FC-04
Kounta, I: DB-09
Kousaka, Y: AG-01, CC-04, FE-03
Kovacs, A: CP-05
Kovács, A: BB-07, BC-01
Kovalenko, O: CH-03, **GC-06**
Kozelj, P: HE-06
Koziol Rachwal, A: FP-08
Kraft, R: ED-07, **FG-04**
Kramer, M J.: HD-11
Krcma, J: FB-05
Kriegner, D: **BF-10**, **DB-07**, DB-09
Krishnan, S: AP-06, GD-01
Krishnia, S: BB-07, CG-08, HF-14
Kronast, F: BB-07
Kruhlov, S: CE-05, EG-13
Krupinski, M: CD-07
Ksenzov, D: GC-07
Ku, Y: FP-06
K U, P: FQ-14
Kubaniova, D: CS-10, HR-19LB
Kubániová, D: **CP-16**, DC-07
Kubickova, L: CP-16, CS-10, **DC-07**
Kubo, T: **FR-09LB**
Kubota, H: CR-04, HE-09
Kubota, T: CE-04, **DE-01**, DP-01
Kubota, Y: AA-04, BD-02
Kuchi, R: **BG-06**, ER-10
Kudo, K: AG-04
Kuepferling, M: FG-08
Kuhn, S: GF-06
Kukreja, R: DC-08, **DH-02**, EE-10
Kulakarni, S: **AD-06**
Kulesh, N: **AB-08**, EC-05
Kulickova, J: CS-10
Kulik, P: AP-12LB, BE-04, DD-03
Kulinsky, L: CS-06
Kumada, T: DP-12, FR-10
Kumar, A: BC-01
Kumar, A: AC-06
Kumar, A: ER-10, FP-14, GP-11, HR-09
Kumar, A: HG-01
Kumar, A: AC-07
Kumar, A: CF-15
Kumar, D: AE-10
Kumar, J: BE-06, EG-01
Kumar, P: **CG-01**
Kumar, R: HQ-01
Kumar, S: GB-07
Kumar, Y: AC-07
Kumari, G: **AP-01**
Kumari, M: **FQ-06**, **FQ-07**
Kunai, Y: HC-10
Kundu, M: AF-11
Kunyangyuen, B: BD-11, CA-09, GC-09
Kurebayashi, D: HF-06
Kurita, N: FR-02
Kurniawan, I: EG-02
Kurokawa, Y: **AQ-02**, BP-06, BP-15, HF-01
Kurosawa, S: CF-12
Kuschel, T: BB-07, **BG-04**, **DB-05**
Kushwaha, V K.: EG-03
Kusunose, R: CR-15
Kuswik, P: BP-03
Kuwahara, H: **EE-07**, FQ-08, GQ-14
Kuwahata, A: CD-06, **ER-11**, **ER-12**
Kuwayama, R: HD-09
Kwak, K: **CQ-05**, DQ-09
Kwiatkowski, A: FP-08
Kwon, J: **AR-05**

L
L'vov, V A.: EB-04
Lacour, D: AE-07, GC-09
Laderer, W: GB-08
LaGasse, S: BD-12
Lai, C: FF-09
Lai, Y: **HG-05**
Lai, Y: FR-19LB
Laliena, V: FE-03
Lallart, M: DE-05
Lambert, N J.: **HG-08**
Lambertson, E: AC-11
Lamichhane, S: EG-01
Lamichhane, T: AP-09, BG-05, **CD-08**, DS-12, DS-13, **EQ-09**, **HD-03**
Lan, G: GA-02
Landers, Z A.: DA-06
Landi, M: FA-02
Lang, G: CH-08
Langer, J: CR-13
Langridge, S: CB-03
Langton, C: AD-02, **AD-03**, **EF-12**
Laraoui, A: BE-06, **EG-01**
Laroze, D: AR-15
Lasheras, A: **GE-01**
Lászlóffy, A: FG-13, FR-17LB
Lau, Y: **EF-04**
Lauer, P E.: **HC-10**
Laughlin, D E.: BD-07, BD-10
Laur, V: DD-07, FA-09
Lauter, V: CE-06
Lawati, D R.: **BE-06**, EG-01
Lazcano, Z: BR-12
Lazpita, P: EB-05
Le, D: **FG-10**, **FQ-10**
Le, S: DA-04
Le, T: **FC-13**
Le, V: AA-07
Leaic, M: BB-07, CG-08
Leao, L: AR-06
Leary, A: FA-03
Lebourgeois, R: DD-07, FA-09
LeClair, P: **ED-08**, FQ-02

Lederer, M: FG-08
Lederman, D: AF-01, **CC-11**, EF-13
Ledieu, J: EB-07, HE-06
Lee, A: GQ-15
Lee, A: EA-08
Lee, A: GA-07
Lee, B: **DP-03**, DP-15, DQ-14, EP-02
Lee, C: EQ-02, HA-07, HQ-03
Lee, C: BQ-05, BQ-07, **CQ-01**, CQ-10, DQ-10, HP-16
Lee, D: DP-03, **DP-15**, DQ-14, **EP-02**
Lee, G: AR-04LB
Lee, G: **BQ-02**, CQ-03, HP-09
Lee, G: AP-07
Lee, H: DR-04
Lee, H: BC-03
Lee, H: AP-07, **EP-11**
Lee, H: BQ-09, CQ-15
Lee, H: BB-06, DR-10, **DR-11**
Lee, H: **BQ-03**, CQ-06, HP-07, HP-08
Lee, H: BB-06, DR-10, DR-11
Lee, J: **BQ-04**, **CQ-04**, DQ-11
Lee, J: **CC-09**, CC-09
Lee, J: BR-11
Lee, J: AC-02
Lee, J: GQ-15
Lee, J: BQ-04, CQ-04, EQ-07, EQ-08
Lee, J: AP-04, EC-02, EC-06, EC-07, EC-09
Lee, J: BQ-05, GR-10
Lee, K: BQ-04, CQ-04, DQ-11
Lee, K: CC-09, EC-06, EC-07, FC-03, HF-08
Lee, K: **FP-12**, FP-12
Lee, K: **AP-07**, EP-11
Lee, K: HQ-09
Lee, K: AR-04LB, DR-03, **FF-07**
Lee, K: DR-01LB
Lee, N: AR-07, BC-04, BC-09, BP-10, EE-11, FR-07, FR-08
Lee, S: CD-09
Lee, S: EP-02
Lee, S: EC-06, **EC-07**
Lee, S: **DQ-08**
Lee, S: HQ-09
Lee, S: **FF-01**
Lee, S: AR-09, BR-10
Lee, S: **AP-04**, EC-06, **EC-09**
Lee, T: BC-03
Lee, U: **CG-05**
Lee, W: BF-07
Lee, W: FP-12
Lee, W: BQ-03, CQ-06, **HP-07**, HP-08
Lee, W: EQ-10
Lee, Y: ER-07
Lee, Y: HE-03
Lee, Y: ER-07
Lee, Y: **GR-10**
Legay, M: **DD-07**, FA-09
Lei, S: CC-03
Leigh, G: DC-08
Leighton, C: DC-06, DC-10, EE-03, HC-02
Leitao, D: **AQ-05LB**
Lendinez, S: GG-12
Lengaigne, G: EB-07
Le Roy, D: **CD-05**, **CS-03**, **FP-13**
Lesne, E: AF-05
Lete, N: DE-08
Leutner, K: BC-01, HF-07, HF-14
Levchenko, K: CE-07
Léveillé, C: GC-07
Lewis, C J.: EQ-05
Li, C: EQ-12
Li, C: AP-05
Li, C: AF-03
Li, C: EE-10
Li, G: EF-04
Li, H: EA-06
Li, J: DP-06
Li, J: FB-02
Li, M: DA-07
Li, P: CC-03
Li, S: EA-06, **EA-08**
Li, S: FE-06
Li, S: CG-05
Li, T: GD-12
Li, T: CA-05
Li, W: **FQ-15**
Li, X: XA-01
Li, X: CR-16
Li, X: **HC-04**
Li, Y: **EQ-11**
Li, Y: CE-05, DG-09, EG-13, **FB-02**
Li, Y: FR-11
Li, Y: DP-06
Li, Y: CC-03
Li, Y: **CC-07**
Li, Z: **CA-08**
Li, Z: CH-02
Liakopoulos, T: **FA-07**
Liang, J: HC-02
Liang, J: FF-01
Liang, S: AQ-03, CS-11
Liang, W: **BF-06**
Liang, Y: GC-03
Liao, C: CB-08
Liao, L: GG-02
Liao, W: FQ-13, HQ-15
Liao, W: GR-13
Lichtl, H: **AR-02**
Lilienthal-Uhlig, B: FG-08
Lim, J: CE-05, **DG-09**, FB-02, HR-05
Lim, J: **DR-03**
Lim, M: HR-05
Lim, M: BQ-01, **BQ-06**, DQ-06
Lim, P G.: CA-07
Lim, S: AR-07, **BC-04**, BC-09, BP-10, EE-11, FR-07, FR-08
Lim, Y: BQ-05, **BQ-07**, **BQ-08**, CQ-01, CQ-09, DQ-10, HP-16
Lima de Medeiros, J: **BR-15**
Lin, C: BF-07
Lin, H: BC-07
Lin, H: FP-06
Lin, H: CC-08
Lin, H: EQ-02, HA-07
Lin, J: BD-11, CA-09, GC-09
Lin, M: CC-08
Lin, T: CC-08
Lin, W: AG-06
Lin, Y: FD-10
Lin, Z: DP-06
Lin, Z: BC-01, CC-01
Lindemann, S: **DC-03**, **DS-14LB**
Lindero-Hernández, M: XA-01
Lindner, M: FB-05
Liou, S: EG-01
Lisfi, A: CP-07, **FP-16**
Lisik, J: **BG-07**, **DS-11**
Littlehales, M: DC-11
Litvinenko, A: HG-01
Litzius, K: **DH-09**
Liu, A: DC-08
Liu, C: DC-08, GD-12
Liu, C: FE-06
Liu, C: GF-08
Liu, D: FE-06
Liu, H: DQ-04
Liu, H: HQ-15
Liu, H: EA-06, EA-08
Liu, J: DG-04
Liu, J: **GG-02**
Liu, J: **HR-06**, HR-10
Liu, J: **BQ-13**
Liu, J L.: **DP-16**, **EP-08**
Liu, K: **AD-02**, AD-03, DC-08, EF-12, GD-12, GF-08
Liu, L: DA-07
Liu, M: **FE-06**
Liu, P: **EP-09**
Liu, P: BG-10, CH-02, CP-12, CP-13, EE-05
Liu, R: CH-02
Liu, S: **AE-03**, DA-06

Liu, S: EQ-12
Liu, X: AP-02, AP-03, BG-08, BG-09
Liu, Y: **EF-06**
Liu, Y: GC-10
Liu, Y: DC-08
Liu, Y: AB-03
Liu, Z: EA-08
Liu, Z: GD-06
Liu, Z: HC-04
Liyanage, N: HF-13
Lohr, W: EQ-05, ER-03, **HA-06**
Lomakin, V: **AA-06**, BF-05, FF-03, FG-05, GG-10, HG-05
Longdell, J: HG-08
Longo, E M.: GF-09
Longo, M: GF-09
Lopes, A: GE-01
Lopes Temporao, A: CR-05
Lopez-Diaz, L: DH-10
Lostun, M: EP-04
Loth, S: AR-02
Lotsch, B: BC-01
Loyal, M: BB-07
Lu, J: CC-03
Lu, J: BF-05, **FF-03**
Lu, J: BE-10
Lu, X: CA-08
Lu, Y: **GA-01**, GA-02, GA-03
Lu, Y: **EF-05**
Lue, C: FR-19LB
Lukashev, P: **CC-06**, FQ-01, FQ-16, FR-20LB
Lumetti, S: FC-02, **FC-15**
Luo, B: **AQ-09**, **CE-06**, **DP-04**
Luo, Y: BQ-13, **EQ-12**
Luo, Z: CC-01
Lupu, N: EP-04, **ER-08**
Luxmoore, I: HG-02

M
M. A. García, D M.: GR-12
Ma, L: EQ-05
Ma, T: EF-03
Ma, X: AF-11
Ma, X: CC-03
Ma, Y: CR-08
Ma, Y: EF-04
Maben, M A.: HF-13
Máca, F: GE-07
Machida, H: **EC-04**
MACHIDA, K: AR-08
Madami, M: FG-08
Madhavan, A: EA-07
Madhusudan Rao, P: **BF-02**, CF-05
Madiligama, A S.: **HR-13**, **HR-14**
Maeno, Y: AE-02
Magdanz, V: **TU-03**
Magill, B: CH-08
Magni, A: AD-12, DC-04, FG-08
Mahesh, S: FQ-13
Mai, S: **DA-05**
Maicas, M C.: DH-10, FP-11
Maiti, M: EE-03
Maity, D: GR-09
Maity, S: AD-08
Maizel, R E.: EF-11
Majee, S: GP-11
Makarov, D: AD-02, CB-05
Makino, F: **DF-09**, EG-03
Makiuchi, T: FB-01
Makuta, H: EC-04
Malagò, P: **FC-02**, FC-15
Malaman, B: GB-03
Maletinsky, P: BC-01
Malinowski, G: AR-10, BD-11, CA-09, GC-09
Mallon, D: EF-09
Malucelli, L: **CE-01**, **DE-04**
Mamiya, H: **DP-12**
Manchon, A: CG-08, FG-08
Mancias A., M: **FA-03**
Mancini, N: FQ-13
Mandal, A K.: CS-05
Mandokoro, T: CF-04, HQ-05
Mandrus, D: GF-06
Maness, S: DP-10
Mangin, S: AF-04, AG-13, AR-10, BD-11, CA-09, CF-03, CH-07, GC-02, **GC-09**
Mansell, R: EG-10
Manso, M: CD-01
Mansour, R: DD-07, **FA-09**
Mansouri Tehrani, A: HC-11
Mantion, S: DH-11
Mantovan, R: **DF-03**, **GF-09**
Marchal, N: AD-01
Marciniak, J: HD-04
Marciniak, W: HD-04
Marimuthu, M: EP-06, HC-09
Marin, J R.: ER-10
Marini, S A.: **DP-10**
Marotta, A R.: DD-11
Marquez Chavez, J: BR-04, **DG-11**, FQ-05
Marrows, C: DR-02, FG-10
Martella, D: AD-12
Martínez-Carracedo, G: CC-14
Martinez Vecino, E: CH-07
Marukame, T: CR-15
Maruyama, I: **HB-09**
Maruyama, Y: **EG-05**
Maryam, M: **BP-11**
Masell, J: DB-02, FE-10
Masood, A: FA-05
Maspero, F: AR-12, CR-07, DG-02, DG-03, DG-06, EG-11
Masseboeuf, A: GP-09
Masuda, K: EG-02
Masuda, R: ER-04
Masumoto, H: DE-05
Matczak, M: BP-03
Matsuda, Y: CF-01
Matsueda, H: HG-04
Matsuki, H: AE-02, CF-04, HQ-05
Matsumoto, K: EB-03
Matsuno, J: HQ-13
Matsuo, M: GA-07
Matsuo, M: EQ-03
Matsuo, T: CF-12
Matsushima, K: **GR-02**
Matsushita, T: AC-07
Matsuya, Y: DQ-05
Matsuzaka, M: DF-04, **DF-07**
Matsuzaki, H: CE-04
Matt, E: BF-04, CA-07
Mattoni, G: AE-02
Maucha, L: BR-13, DG-05
Maurya, A: **GG-03**, HG-07
Mayoh, D: CB-07, DC-11
Mayr, E: CD-07
Mayr, S: FB-05
Maz, A A.: **HQ-01**
Mazet, T: GB-03
Mazzoli, C: **FE-13**
McConney, M: CE-06
McDonough, C: HA-02
McGuire, M: GF-06
Mckenzie, J: **GR-05**
McKenzie, R D.: **EG-12**
McKenzie, T F.: CP-08, **HR-11**
McMorran, B: **BE-07**, DH-07
Medina Dueñas, J E.: CC-05
Medwal, R: AD-08
Mehrnejat, A: FF-04
Mehta, R: AR-16, BR-09, GG-08
Mehta, S: CA-07
Mejia, J: **GP-14**
Mencos, J: DB-09
Mendes, J B.: BB-04
Mendonca, H A.: DR-14
Mendonça, A A.: CP-10, **GE-09**
Mendonsa, R A.: **AQ-03**
Mendonsa, R: **CS-11**
Meneghini, C: HE-11
Menezes, J R.: EQ-04

Mentink, J: FB-04
Meo, A: CA-07
Merino-Martinez, J: CD-03
Miao, G: CC-02
Miao, J: CB-08
Michal, O: AC-05
Michez, L: DB-09
Micus, L: BB-07
Migot, S: EB-07, HE-06
Mihajlović, G: AE-03, CA-04
Mihalik, M: HR-01
Mijit, E: FR-11
Mikhaylovskiy, R V.: CH-03, **FB-03**, GC-06
Miki, S: AF-05, **GP-03**
Millet, A: BA-07
Mills, S C.: **FR-06**
Milone, M: BE-11
Mimura, I: EQ-15LB
Mimura, R: FQ-09
Minakawa, R: AC-07
Minhas, M: CR-13
Minu, M: **FQ-02**
Minuti, A: ER-08
Mion, P: DC-05
Mion, T R.: **GE-03**, **HR-15**
Mirzakhani, M: AC-12
Misawa, R: FE-10
Mishra, A: EP-14LB
Mishra, R: DR-01LB
Mishra, S: GR-15
Mitani, S: DF-08, EF-03
Mitchell, P: BE-02
Mito, M: FE-03
Mitsumata, C: AB-09, **AE-09**
Mitsuzuka, A: **DF-06**, FP-01
Miura, S: XA-01
Miura, S: AQ-02, **BP-06**
Mivelle, M: **AF-07**, **FF-13**, **HF-12**
Miwa, S: BF-06, CB-02, DF-07, EG-02, HG-04
Miyahara, S: HB-09
Miyai, Y: AC-07
Miyajima, K: **ER-13**
Miyamoto, Y: AR-08
Miyasaka, Y: CR-09
Miyashita, H: BG-01
Miyata, T: AQ-16
Miyawaki, H: EC-03, GD-03
Miyazaki, D: GR-16
Miyazaki, T: DP-02
Mizoguchi, T: **AQ-06**
Mizrahi, F A.: FD-05
Mizukami, S: AF-05, FD-08
Mizuno, M: FP-03, GF-07
Mizuta, S: **AQ-07**
Mochizuki, M: HF-04
Mochizuki, S: **BP-01**
Modak, R: EG-03
Moedl, E: GA-07
Moghal, B: HR-08
Mohammadi, M: DR-07, DR-16
Mohan, J R.: **CR-14**
Mohapatra, J: BG-10, CP-12, CP-13, EE-05
Mohapatra, S: CD-10
Mohapatra, S: CD-10
Mok, Y: GQ-16
Mokkapaty, S: BE-11
Mokrousov, Y: BB-07, CG-08, DR-10, FG-10
Molčanová, Z: HR-01
Molinares Ponce, M: ER-02, ER-05
Mollard, N: CE-01, DE-04
Momota, F: **DP-02**
Mondal, A: EG-05
Mondal, S: EP-14LB
Monson, T C.: FA-02
Montagnese, M: FC-15
montaigne, f: GC-09
Montoya, E A.: **AG-07**
Montoya, S: CB-08, DH-07, HB-01
Montoya-Santiyanes, L: XA-01
Moodera, J S.: DA-07
Moody, S: **DC-11**
Moon, J: GQ-04
Moon, J: **BQ-05**, BQ-08, **CQ-10**, DQ-10
Moon, K: HF-11
Moon, K: **AC-12**, BC-04, BC-09, BP-10, EE-11, FR-07, FR-08
Morales, R: GC-02
Morales, R: ER-15
Moreau, J: FP-13
Moreira, A: BP-08
Morel, R: BA-07
Mori, S: **CC-15**
Moriki, T: AC-07
Morishima, Y: GQ-07
Morishita, H: BP-14
Morita, T: EG-03
Moriyama, T: BD-11, EF-02, FD-08
Morley, S A.: EF-13, **GF-05**
Morone, F: FD-11
Morris, E R.: BP-05LB
Mosina, K: DA-07
Mossang, E: AE-07, GP-09
Mostufa, S: CD-04, ER-05, ER-06
Motokawa, R: FR-10
Moureaux, A: CR-05
Msiska, R: **FG-11**
Mucchietto, A: DH-11
Mudryk, Y: BG-06, ER-10, FP-14, GP-11, GR-11, HR-09
Muduli, P K.: **AG-12**, CR-12, DR-15, **HC-08**
Muduli, P K.: CF-15
Muhammad, W: **DE-07**
Mühlbauer, S: AC-13
Mukherjee, M: DA-01
Müller, M: FB-06
Mullurkara, S: DD-05
Munekata, H: CH-08
Muraca, D: EQ-04
Murakami, C: DE-03, GD-11
Murapaka, C: GQ-03, **HQ-11**
Murayama, T: EQ-06
Murnane, M M.: CB-08
Muroga, S: DP-02, EP-05
Murray, A: FC-05
Muthukrishnan, K: GP-08

N

N'Diaye, A T.: EE-10
Na, I: ER-07
Na, M: AR-13LB
Na, S: **EP-10**
Naeemi, A: **DA-02**
Nag, J: **ED-10**, EE-12, FP-10
Nagahara, Y: **AQ-15**
Nagao, A: **AR-01**
Nagaoka, R: **AB-09**
Nagata, U: **CF-01**
Nair, S: AC-06, **AG-11**
Naka, M: EF-10
Nakagawa, K: **EQ-01**
Nakagawa, T: **FR-14**
Nakamura, R: CC-04
Nakamura, S: BP-14
Nakamura, Y: AA-02, **BD-04**
Nakamura, Y: FE-10
Nakamura, Y: DE-06
Nakane, R: BP-13, **CR-09**, FF-02, HE-05
Nakanishi, Y: CC-15
Nakano, A: FR-10
Nakano, R: **FE-10**
Nakano, T: AQ-04, DF-02
Nakao, H: FE-10
Nakashima, K: AG-04
Nakashima, M: ER-04
Nakatani, O: **BR-14**
Nakatani, T: DE-03
Nakatani, Y: BR-03, DR-16
Nakatsuji, S: BF-06, CB-02, CF-12
Nakayama, H: AQ-16

Nakayama, S: GQ-14
Nakazawa, K: BA-05
Nakazono, T: **AF-06**
Nam, D: **AG-05**, CG-04
Nam, K: DB-01
Nambu, Y: HQ-13
Namikawa, M: BE-11
Nandakumaran, N: HC-02
Nangaku, M: EQ-15LB
Nara, T: GR-02
Narangerel, B: CP-11, CP-14, HD-08, HR-04
Naranjo, S B.: ER-10
Narducci, D: CA-03
Narmandakh, J: HD-08
Narushima, Y: XA-01
Nascimento, V P.: AE-07, GP-09
Nasri, I: BE-12
Natekar, N A.: **AA-07**
Natsume, K: EB-03
Naud, C: BA-07
Naunheimer, F: **BR-13**, DG-05
Naushin, N: DC-08, EE-10
Nava Antonio, G: AF-04, FE-11
Navas, D: CD-01
Nazarov, A: **GR-01**
Ndaru, K N.: **CP-08**, HR-11
Neeha, S A.: HA-05
Neethirajan, J: **CB-07**
Negishi, E: BG-01, GG-11, HR-03
Nelson, B: HA-04
Nembach, H T.: AE-03, DS-14LB, DS-15LB, EG-07
Nepal, S: EG-09
Neu, J: CG-05
Neu, V: BE-03
Neuefeind, J: DC-06
Neupane, M: FQ-01
Neupane, M: AR-06
Ng, V: CS-01
Nguen, T: AG-02
Nguyen, B: HR-13
Nguyen, K: **HB-01**
Nguyen, M: **VP-02**
Nguyen, P: FR-20LB
Nguyen, S: EE-10
Nguyen, T T.: BR-10
Nguyen, T: FQ-10
Nguyen, V: AG-10, FD-03, FD-07
Nguyen T. Tran, L: **AE-04**, BA-02, CD-04, **GR-06**
Ni, H: HR-05
Ni, N: GB-08, HQ-15
Nicolas, A: BA-07
Nihal, I: **EF-13**, HC-07
Nihei, K: FE-07
Niimi, Y: AG-01, AG-04, CC-04, HQ-13
Nikolić, B: CH-06
Nishi, H: EQ-15LB
Nishijima, T: CG-03
Nishio-Hamane, D: CF-12
Niu, W: CC-03
Nlebedim, C I.: BG-09
Nlebedim, I C.: AP-02, **AP-03**, **BG-08**, HP-01
Nnokwe, C: CC-06
Noebe, R D.: FA-03, HR-13, HR-14
Noh, K: ER-07
Noh, S: DQ-16
Noh, Y: BQ-04, CQ-04, **DQ-11**
Nohara, K: DE-05
Nojiri, H: GB-06
Nomoto, T: DB-02
Nomura, H: GP-03
Novikov, D: HE-11
Novosad, V: CE-05, EG-13, FB-02
Nowadnick, E: FQ-12
Nowak, U: AF-11, BC-01
Noyan, M: AF-03
Nozaki, T: DF-07, FF-05, GP-03
Nozaki, T: FF-05
Nozaki, Y: AR-01, BP-16LB, DR-09
Nukui, K: AF-05
Numazawa, T: EB-03
Nuñez-Murillo, F: GP-14
Nyári, B: **FG-13**, **FR-17LB**

O
O'Brien, L: BC-05
Obeid, P: BA-07
Oberdick, S: **AE-08**
Ocker, B: CR-13
Odawara, S: EP-01
Odkhuu, D: **HD-08**
Oezelt, H: CP-05
Ogasawara, T: DD-08
Ogawa, D: BD-03
Ogawa, G: EQ-15LB
Ogawa, N: CF-10
Ogawa, T: DD-12
Oh, H: **BP-09**
Oh, J: EQ-10
Oh, S: **BQ-09**, CQ-15
Oh, S: ER-07
Ohara, K: BA-05
Ohe, J: AG-01
Ohishi, K: EE-02, FE-03
Ohkochi, T: CB-02
Ohkubo, T: AB-08, DF-04, DF-08, EF-03, EG-03, GD-03
Ohno, Y: GA-06
Ohodnicki, P: **DD-05**
Ohresser, P: FP-13
Ohshima, R: CF-01, CG-03, EG-05, FB-06
Ohsumi, H: FE-10
Ohta, A: EQ-03
Ohtake, M: AP-10, DE-06, HD-09, HE-07
Ohtani, M: BP-02
Ohtani, T: CE-10
Ohtsuki, T: FR-02
Oikawa, T: EC-03
Ojo, A I.: FP-10
Ok, H: **FC-03**
Okabayashi, J: **BG-02**, EF-03, **GD-11**
Okada, A: DS-09
Okada, H: **CP-09**
Okada, Y: AQ-07
Okamoto, I: BD-06
Okamoto, S: DD-08, DD-09, FA-08, GD-05, GD-06, VP-02
Okamoto, Y: BD-04
Okamura, Y: FE-10
Okawa, M: AR-14
Okazaki, R: **DF-04**
Okita, K: AQ-10
Okumura, S: DB-02, **EE-01**
Okumura, S: BP-07
Okuyama, Y: AQ-10
Oliphant, E: GD-13
Oliveira, G: EB-06
Olson, T: AA-07
Olsson, R: GE-03
Omori, T: DP-09
Omura, T: BE-11
Onishi, K: CE-04
Onishi, N: EC-04
Onishi, Y: DA-07
Ono, K: DD-09
Ono, N: **DD-08**, DD-09
Ono, S: DP-01
Ono, T: BE-05, BP-01, CF-04, DS-04, **FD-01**, FF-06, FP-07, HQ-05
Ono, T: EE-02, GB-06
Ono, Y: CR-14
Onoda, S: BP-14
Onuma, T: **DR-08**
Oogane, M: AQ-04, CE-04, DF-02, DP-01, DR-13
Ordonez Romero, C L.: **BR-12**
Orero-Gámez, G: DH-10
Orito, T: FR-15

Orlita, M: AC-05
Oroszlány, L: CC-14, FG-02
Ortega, L: AE-07, GP-09
Ortner, M: FC-02
Oshima, D: FP-07
Ostroverkhova, O: AC-11
Osumi, Y: CS-09
Otani, Y: GG-02
Otero, E: FP-13
Otsuka, Y: GG-11, **HR-03**
Oue, D: GA-07
Oulton, R: GC-05
Ovari, T A.: **EP-04**
Overboom, T: BE-11
O'Mathuna, C: **FA-04**, FA-05

P
P, M: CF-15
P. N., S: CF-15
Packer, L: FC-05
Padgett, A S.: DD-11
Page, M: CE-06
Pal, P K.: AR-16, FB-02
Pal, P: BE-06
Pal, P: **CE-05**, **EG-13**
Pal, P: CE-09
Palasyuk, A: BG-06, EC-12
Palasyuk, O: EC-12
Palczynski, P: HD-04
Palczynski, P J.: **HD-07**
Paleo, C: CS-03
Palomino, A: CA-03, FD-03
Palomino Lopez, A: AG-10, FD-07
Paltiel, Y: HE-10
Pan, A V.: **AD-11**
Pan, C: DR-05
Pan, C: EC-08, **EC-10**
Pan, F: AP-05
Panda, J: FB-05
Pandey, L: BF-11
Pané, S: CD-03, HA-04
Pannetier-Lecoeur, M: CE-01, DE-04
Pantano, G M.: FG-10
Papp, A: AR-12, BR-13, DG-02, DG-05, DG-06
Parchinskiy, P: CC-03
Pardo-Sainz, M: EE-02, FE-03, GB-06
Parella, J: DS-14LB
Parente, A: FP-11
Pargon, E: CA-09
Parida, T: BG-08
Park, A M.: AG-05, BR-05, **BR-11**, CH-05, FF-10
Park, B: HF-11
Park, B: AG-05, BR-05, CF-07, **CG-04**, DR-04, DR-06, FF-10, GQ-12, HQ-06
Park, E: DA-07, HE-08
Park, H: **DQ-15**
Park, J: AF-09
Park, J: **EC-13**
Park, J: CQ-02, CQ-11, CQ-13, DQ-01, **DQ-02**, HP-06, HP-10
Park, J: AQ-13
Park, J: BR-10
Park, K: GD-05, **GD-06**
Park, M: BQ-04, CQ-04
Park, S: BQ-07, CQ-09, CQ-10, HP-16
Park, S: DP-03, DP-15, DQ-14, EP-02
Park, S: GQ-15
Park, S: AC-02
Park, S: CC-12, HF-11
Park, T: **BC-03**
Park, W: EQ-07, EQ-08
Park, Y: **AR-04LB**
Park, Y: ER-07
Parker, D: EC-12, **HD-02**
Parkin, S: BF-02, CF-05, DH-06, FG-03, **GF-01**
Parmar, H: AP-03, **BG-09**
Parmeggiani, C: AD-12
Parvez, N: CH-06
Paslar, M: **EQ-05**
Passamani, E C.: AE-07, GP-09
Patel, A: **DE-03**
Patel, R: DA-06
Patil, S: **GB-02**
Patrickson, C: HG-02
Patterson, E: FR-06
Paudel, J R.: HC-11
Paul, A: GD-01
Paul, A: DC-06
Paul, N: AG-10
Paul, N: CD-04
Paul, S: **AE-02**
Paulsen, L: CS-06
Pauriche, B: AF-07
Pawlak, J: **HC-05**
Payen, L: CD-05
Paz Gonzalez, K: AE-04, **BA-02**, **ER-02**
Pedersoli, E: GC-07
Pedrós, J: DH-10
Pellet-Mary, C: BC-01
Pellizzi, N: EG-11
Peña Serna, J D.: **GR-12**
Peng, S: EA-06, EA-08
Percival, S: DD-11
Pereira, A: DS-01
Peremadathil-Pradeep, R: HF-05, HF-09, HF-10
Peria, W K.: DS-14LB, **EG-07**
Peridon, L: CF-03
Pershad, I: AR-16
Perversi, G: EP-07
Pervin, R: AD-08
Peterson, C L.: EQ-05
Peterson, K J.: BP-05LB
Petford-Long, A: CC-03
Petit-Watelot, S: AG-13
Petrache, H: GR-09
Petrelli, G: BE-08
Petrun, M: **DS-03**
Petruzzi, P: BD-12
Petty Gweha Nyoma, D: GC-09
Pezo, A: FG-08, GA-02
Pfaff, W: DG-09
Pfleiderer, C: FE-02
Pham, T: CC-10
Phan, D M.: **CD-04**, GR-06
Phan, M: ED-10, EE-12, FG-10, FQ-10
Phatak, C: CC-03, FB-02
Phelan, D: DC-06
Pi, J: **BR-10**
Piao, X: BF-06, CA-03
Piecyk, M: CD-05
Pinna, D: FD-04
Pinto, R F.: GP-10
Pinto, R M.: EB-06
Piovano, A: GB-03
Piramanayagam, S: HQ-08
Piraux, L: AD-01
Pirro, P: AR-12, DG-02, DG-06, FB-05
Pirruccio, G: BR-12
Pishehvar, A: DG-07
Pittala, S: **FQ-14**
Pleimling, Y: CH-08
Plissard, S: CC-10
Plumb, K: **GB-05**
Poelman, H: GR-03
Pokhrel, N: **EC-12**, HD-02
Pollock, C J.: HR-09
Pop, E: HE-03
Popescu, H: CB-09, GP-09
Porro, J: **EB-05**, GC-02
Porter, T: CC-06, FQ-16, FR-20LB
Pospíšil, J: HR-01
Pospíšil, J: **AC-05**
Poulo, A S.: AP-09, CD-08, EQ-09
Pourovskii, L: BB-07
Powell, A: HR-18LB
Powell, L D.: GG-06
Pozsár, D T.: FG-02
Prabhakaran, D: AG-11
Pradhan, G: DC-04
Pradhan, S: **CF-13**

Prakash, A: CS-04
Prasad, K: EG-01
Prejbeanu, I: CA-09
Prida, V M.: CP-10, GE-09
Priese, C: DD-06
Prieto, J: DH-10, FP-11
Priyadarsini, M: **AE-10**
Prokleška, J: FE-09
Proschek, P: FE-09
Pu, Y: CH-02
Puebla, J: EG-05, GG-02
Pufall, M: AE-03, DS-14LB, **DS-15LB**, EG-07
Pulse, M: EF-08
Pushin, D: HF-06
Pustovalov, V: HA-04
Puthirath Balan, A: **BC-01**

Q
Qi, J: AP-05
Qian, T: HQ-15
Qiu, X: **DR-05**
Qiu, Z Q.: CC-09
Qu, D: BF-07, DA-05, FP-06
Qu, Z: HC-04
Querlioz, D: GP-08
Quessab, Y: **AA-03**
Quigley, L: FC-05
Quinsat, M: CA-05, **DH-05**
Qureshi, N: BR-12

R
R, R: EP-14LB
Raboni Ferreira, M: CB-07
Rackham, J: GR-17LB
Radaelli, P: EF-09
Radhakrishnan, P: HG-05
Radhakrishnan, R: EP-13LB
Radovskaia, V: AR-13LB
Radu, C: **AP-06**
Raftrey, D W.: AD-02
Rageau, T: FD-05
Rahmanovic, E: DS-03
Rai, A: HG-09
Raimondo, E: EA-04
Raiymbekov, Y: XA-01
Raja, A: EC-12
Rajestari, Z: CS-06
Rajib, M: ED-06, FD-09
Rama-Eiroa, R: **FG-06**
Ramanathan, M: EP-06, **HC-09**
Rames, M: HR-19LB
Ramesh, R: FB-08
Ramos, L: AF-02
Rana Muhammad, S: BE-12, **EA-09**
Ranno, L: CE-01, DE-04
Rao, S: AG-10, **CA-03**, FD-03, FD-07
Raposo, V: CH-07
Rappoport, T G.: **CG-09**
Rashid, M: CS-05, **GR-08**
Ratha, S: **BD-02**
Rauf, A: **GD-13**
Ravel, B: DS-15LB
Rayat, A: BR-17LB
Raznjevic, S: EB-07
Reddinger, J A.: **DH-07**
Reese, B L.: BD-07, **BD-10**
Regmi, A: **AF-02**, AF-09
Rego, S E.: **BE-04**
Rehman, A: DS-05
Reichhardt, C: FG-11
Reichhardt, C J.: FG-11
Reichlova, H: **DB-09**
Reiser, P: BC-01
Remy, Q: CH-07
Ren, Y: GG-09
Rentzber, N: **GG-07**
Repcek, D: AC-05
Reyes, A: FP-13
Reyes, G: FQ-01
Reyren, N: CB-09, DH-11, GA-02, GC-07, HF-12
Reza, S: GR-09
Rezaei, B: CD-04, ER-02, ER-05, ER-06, FC-01
Rial, J: DB-09
Richardson, C: DA-04
Richter, H J.: BA-04, CA-04
Ricolleau, C: CS-03
Riley, C R.: DD-11
Rinaldi, C: **DA-03**, **FG-08**
Río-López, N: EB-05
Rippard, W: DS-14LB
Rivelles, A: **DH-10**, **FP-11**
Rizzi, P: DC-04
Roche, S: CC-05
Rodriguez, E: BA-02
Rodriguez, L: CS-05, CS-07, GR-08, GR-14
Rodriguez Caballero, S: AE-04, ER-02
Rodríguez Jiménez, P A.: DD-13, EP-03
Rodriguez Velamazan, J: EB-05, EE-02
Roduit, L: GB-03
Roessli, B: GB-03
Rogalev, A: FP-13
Rogers, D: **FC-12**
Rogers, V C.: BF-04, **GQ-08**, **HE-12**
Rogers, W: CA-07
Rojas, G: EE-03
Rojas-Sanchez, C: AG-13
Romhanyi, J: EF-13
Rondinelli, J M.: CA-07
Rosenkranz, S: DC-06
Roshandel, H: GB-08
Ross, C A.: BR-04, DG-11, FB-05, FQ-05, HC-10, HE-08
Ross, F: DA-07, HE-08
Rosseinsky, M: AB-04
Rothe, J: EB-01
Rothhardt, D: HF-10
Rothörl, J: HF-14
Rotter, S: HG-08
Rougemaille, N: AE-07, GP-09
Rouxel, M: FR-13
Rova, K: AE-04, ER-02
Rovirola, M: CC-13
Roy, K: **DA-01**
Roy, S: EF-13, GF-05
Roy Chowdhury, M: EF-03
Roy Chowdhury, R: ED-10, EE-12
Rozprym, M: DC-07, FQ-10
Rózsa, L: CC-14, FR-17LB
Rubi, K: **FE-01**
Ruiz Gómez, S: DH-10
Russo, L: FC-05
Rychly-Gruszecka, J: HD-04
Rymski, G: FQ-10
Ryu, H: BC-04, BC-09, BP-10, **FR-07**, FR-08
Rzchowski, M: BE-06

S
Saavedra, E: DS-01
Saavedra Díaz, E A.: AR-15
Sabaysachi, S: EQ-05
Sabirianov, R: CC-02, GQ-13
Sabyasachi, S: **ED-06**, **FD-09**
Sadler, C: CC-06
Saenz Rodriguez, A: AC-11
Safeer, C: **FD-04**
Sagayama, H: FE-10
Sah, R K.: HC-11
Saha, S: CF-15
Saha, S: **AR-16**, **BR-09**, **GG-08**
Sahni, N: **GG-09**
Sahoo, A: AG-12, DR-15
Sai, R: FA-05
Said, A: GR-19LB
Saijo, K: ED-09
Saito, A T.: **EB-03**, HR-07, **HR-16**
Saito, M: FP-07
Saito, S: ER-12, GR-16
Saito, T: **AP-08**, **CP-03**
Saito, Y: **AG-02**
Saitoh, E: BB-07, FB-01

Saiz Garitaonandia, J: GE-01
Saji, C: AR-15
Sakai, H: FE-09
Sakamoto, A: **AQ-04**
Sakamoto, K: AQ-14
Sakamoto, S: BF-06, **CB-02**, EG-02
Sakuraba, Y: DE-03, DF-09, EG-03
Salaheldeen, M: DD-13, EP-03
Salazar, D: EB-05
Salazar, H: HB-07
Sales, B: EC-12
Salomoni, D: CA-09
Samanta, V: **AC-03**
Samolyuk, G: EC-12
Samukawa, Y: **AG-04**
Sanchez, M: HA-04
Sandberg, R: GR-17LB
Sands, J: CB-05
Sangeeth, K: AD-10
Sanghadasa, M: CE-06
Sankar, R: FF-01
Sankar Kar, G: CA-03, FD-07
Santos, E: BB-04
Santos, E: CC-03, FG-06
Santos, T: AE-03, **CA-04**
Sanz, M: DH-10, FP-11
Sanz Hernandez, D: CR-07, CR-11, FD-05
Sapkota, A: GR-08
Saqib Arshad, R: DS-06
Sarenac, D: HF-06
Sasaki, I: AG-01
Sasaki, S: DR-02
Sasaki, T: FR-02
Sasaki, Y: AA-04, AF-06, BD-02, BD-03, **FF-12**
Sasayama, T: AQ-01, AQ-15
Sastges, M: DR-10
Satapathy, S: AD-02, CB-05
Sato, J: **FR-12**
Sato, S: **FF-02**
Sato, S: AC-07
Sato, S: **AQ-01**
Sato, T: **DP-09**
Sato, Y: BF-03
Satoh, T: AF-06, BP-01
Satou, T: CP-04
Säubert, S: **EB-01**
Savadkoohi, M: BP-12
Savostin, E: **GG-10**, HG-05
Saxena, A: AG-12, CR-12, **DR-15**
Saxena, A B.: FG-11
Scheike, T: DF-08, **FF-05**
Scheuer, L: CH-06
Schiff, H: EF-13
Schlagel, D: EC-12
Schleife, A: HR-05
Schmalian, J: AE-02
Schmid, A: CR-15
Schmid, M: BE-11
Schmidig, A: GP-11
Schmidt, H: AQ-09, CE-06
Schmitt, C: AF-11, BB-07
Schneider, M: DS-14LB
Schoener, B: **AB-03**
Scholz, T: BC-01
Schrader, C: BC-01
Schrefl, T: BG-07, CP-05, DD-05, DS-11
Schuller, I K.: HQ-15
Schultheiss, H: FB-04, HG-10
Schultheiss, K: FB-04, HG-10
Schulz, N: FP-10
Schumer, A: HG-08
Schüßler, P: EB-01
Schust, J: AR-02
Schütz, G: DH-11
Schwefel, H: HG-08
Scott, E F.: **FA-02**
Sears, J: **AF-01**
Sebald, G: DE-05
Sechovsky, V: AC-05
Seethapathi, N: HA-01
Seifner, M: AE-05
Seiner, H: GE-07
sekiguchi, n: CE-02
Sekino, M: CE-02, EQ-15LB, FC-06, HA-09
Sekita, D: FR-05
Sels, D: FD-11
Semsari Parapari, S: EB-07, HE-06
Seng, B: GC-09
Seo, H: **DR-06**
Seo, J: AR-07, BC-04, BC-09, **BP-10**, EE-11, FR-07, FR-08
Seo, J: **HQ-06**
Seo, J: DP-03, DP-15, EP-02
Seo, M: BQ-03, CQ-06, HP-07, **HP-08**
Sepehr, M: DH-10
Sepehri-Amin, H: AA-06, AB-08, DP-12, EB-02, EB-03, EC-05, GD-03
Sergeev, I: AE-10
Setescak, A J.: **BE-02**
Setti, G: BE-12, CE-09, CR-02, EA-09
Sha, Y: HR-06
Shabaev, D: **GG-11**, HR-03
Shafer, P: HC-11
Shafiei, A: GF-09
Shahbaz, R: DS-05, DS-06
Shahee, A: BC-01
Shahriar, M: ER-05, ER-06
Shalihotri, Y V.: GQ-03
Shand, P: CC-06, FQ-01, FQ-16, FR-20LB
Shang, W: **EE-09**
Shao, Q: **EA-02**, EA-06, GG-02
Shao, Y: GR-13
Shapiro, D: CB-08, GR-17LB
Sharif, B: CC-11, EF-13
Sharma, L: **DB-03**
Sharma, P: ED-10, **EE-12**, FP-10
Sharma, S: DC-10
Sharma, T: AR-16
Sharma, V: GF-03, **GF-10**
Sharma, V: AQ-09, CE-06, GF-08, GF-10
Sharmin, S: AE-09
Shearer, B: CB-08
Shekhar, C: CB-07
Shen, J: **BE-10**
Shen, Z: BF-07
Sherman, S G.: EQ-13
Shi, J: FQ-13, HQ-15
Shi, S: BB-06
Shi, Z: FE-06
Shibata, Y: DF-04
Shield, J: AP-06, **GD-01**
Shigeta, I: FR-03, FR-04
Shiku, K: GR-02
Shilna, K: **FQ-04**
Shim, W: **DS-10**
Shima, M: FP-07
Shimada, K: AC-07
Shimamoto, Y: AG-01
Shimano, T: ER-12
Shimizu, S: AC-07
Shin, D: GE-10
Shin, D: HP-15
Shin, G: BQ-02, CQ-03, **HP-09**
Shin, H: CQ-05
Shin, H: DQ-09
Shin, H: BP-10
Shin, J: **BR-08**
Shin, K: BQ-01, BQ-02, BQ-03, BQ-06, BQ-11, BQ-12, BQ-14, CQ-02, CQ-03, CQ-06, CQ-07, CQ-08, CQ-11, CQ-13, CQ-14, CQ-16, DQ-01, DQ-02, DQ-06, DQ-09, HP-04, HP-06, HP-07, HP-08, HP-09, HP-10
Shin, M: DQ-13
Shin, S: DR-01LB
Shin, S: **DR-04**, DR-06
Shinkai, T: EF-02, **FD-08**
shinohara, t: DP-12
Shinohara, R: ER-11

Shiomi, J: EG-03
Shiota, Y: CF-04, DS-04, FF-06, **GC-01**, GP-03, HQ-05
Shiraishi, M: CC-05, CF-01, CG-03, EG-05, FB-06
Shirasaki, T: EE-07, **FQ-08**, GQ-14
Shiu, H: BR-16LB, FR-19LB
Shoji, H: AG-01, CC-04
Shoriki, K: FE-10
Shoup, J E.: DC-03, DP-04
Shrestha, S: **CH-06**
Shreya, S: **EA-03**
Shukla, G K.: BD-02, CG-01
Si, M: GC-10
Siao, J: **CC-08**
Sibi, H: BD-02, **BD-03**
Sibille, R: GB-03
Siddiqua, T: HA-02
Sierra, J F.: CC-05
Sihombing, R R.: **DF-08**
Sihom Kwekam, D: EB-07
Silber, R: BG-04
Silva, G V.: CC-02
Silva, J O.: EB-06
SIlva Sales, F H.: BR-15
Sim, J: **GQ-16**
Singh, A: BF-07
Singh, H: CR-11
Singh, K: CR-06
Singh, M: **HE-11**
Singh, P: GP-11
Singh, R: GG-03, HG-07
Singh, S: AE-10
Singh, S: AF-09
Sinova, J: BB-07, BC-01, DB-09
Sirica, N S.: AF-03
Sirimanna, S: CQ-12
Sivakumar, P: **CF-05**
Skowronski, W: HC-05
Slanovc, F S.: ED-03, FC-02
Slavin, A N.: DG-07
Slawinska, J: **BB-05**
Slezak, M: **FP-08**
Slezak, T: FP-08
Smaga, M: **DE-10**
Smaha, R W.: **HD-06**
Smaliukas, P: FC-15
Smejkal, L: DB-09
Smith, D E.: CS-05
Smith, J: **ED-03**
Smith, N: CH-08, DA-04
Smith, S: **ER-10**
Smith, X: **CD-09**
Snarski-Adamski, J: HD-04
Snyder, C: XA-02
Snyder, G: DP-10
Soares, A: GR-11
Sofer, Z: AC-11, DA-07
Soh, Y: GB-03
Sohn, C: **GB-09**
Sohn, Y: DD-03
Soldatov, I: BE-03
Solignac, A: CE-01, DE-04
Solzi, M: EB-07
Son, B: DR-01LB
Son, H: **HC-02**
Son, J: HF-11
song, l: EF-04
Song, C: **BF-01**
Song, D: BB-06
Song, H: ER-07
Song, J: **GP-02LB**
Song, M: **CA-02**
Song, M: BR-05, CE-05, DG-09, EG-13
Song, S: CC-12
Song, S: **BQ-10**
Song, S: CQ-15
Song, Y: **DQ-04**
Soon, Y: **BR-05**, BR-11
Sorrentino, A: AD-02, AD-03, CB-05
Sousa, R: CA-09
Sow, C: AE-02
Spaldin, N A.: HC-11
Spallek, J: EB-01
Srikanth, H: CD-10, ED-10, EE-12, FP-10
Srinivasan, K: FA-03
Srivastava, T: DH-11
Stadler, B: **BA-06**, EP-09, **HR-08**
Stamps, R L.: EG-12
Stanfield, H R.: **FF-04**
Stanionyte, A: **EP-07**
Staruch, M: DC-05, FR-06, GE-03, HR-15
Steadman, P: AG-03
Steele, J M.: HR-17LB
Steentjes, S: DS-03
Stefancic, A: CB-07
Stephen, G M.: BD-12, **GF-03**, GF-10
Stiles, M: EA-07
Stödter, L: **GB-01**
Stollenwerk, A J.: CC-06, **FQ-16**, FR-20LB
Straka, L: GE-07
Strecka, J: **BC-13**, FR-13
Street, G T.: EG-04, **FF-06**, GE-05
Strocov, V N.: HC-11
Strugatsky, M: AR-13LB
Sturm, S: HE-06
Su, C: GR-09
Su, L: GQ-02
Su, Y: BR-16LB
Suarez, A: HA-04
Suarez-Perez, A: CD-03
Suemasu, T: HQ-14
Suess, D: CD-07, CE-07, DH-08, ED-03, **ED-07**, FG-04, HF-05, HG-11
Suggula, N: **CS-01**
Sugimoto, S: DS-04, EC-11, GP-01
Sugimoto, T: **BC-08**
Sugiyama, S: **BP-13**, **HE-05**
Suhail Mutawakkil, S: EA-09
Sukegawa, H: DF-04, DF-08, EF-03
Sukhbaatar, A: ER-12
Sullivan, E: EF-13
Sultana, J: **GR-15**
Sultana, R: **GG-12**
Sumi, S: DR-16
Sumida, Y: CB-02
Sun, N X.: AQ-09, CE-06, DP-04
Sun, S: HB-07
Sun, S: **GB-08**
Sun, W: GD-13
Sung, J: BC-03
Sunny, J: HF-05
Suto, H: AA-02, DF-09, FF-12
Suwa, T: **GD-05**, GD-06
Suzuki, I: FF-12
Suzuki, K: **DD-01**, DD-08, DD-09
Suzuki, S: AG-01
Suzuki, Y: GP-03
Suzuki, Y: BD-11
Suzuki, Y: HE-03
Svedlindh, P: DP-08
Swindells, C: AE-03, DS-15LB, EG-07, **FD-02**
Syed, M: **GR-09**
Sýkora, J: FQ-05
Syskaki, M: **CR-13**, HF-07
Szenthe, I: DP-13
Szpytma, M: FP-08
Szunyogh, L: **CC-14**, FG-13, FR-17LB
Szymczak, A: FB-02

Š
Šturm, S: EB-07

T
Tabata, H: EQ-15LB
Tabata, T: DD-12
Tacchi, S: FG-08
Tachibana, C: **FR-15**
Tada, K: **EF-02**
TADAHA, H C.: CF-02
Tadamura, T: AC-07

Tadano, T: DE-03
Taguchi, M: AQ-02, BP-06
Taguchi, T: AQ-15
Taguchi, Y: CF-10, FE-10
Tai, L: GF-03
Tai, T: FR-05
Tajkov, Z: **FG-02**
Takada, S: AG-01
Takafuji, D: HQ-13
Takahashi, S: **DQ-07**
Takahashi, Y: **DE-11**
Takahashi, Y: FE-10
Takahashi, Y K.: AA-04, AF-06, BD-02, BD-03, FF-12
Takamatsu, S: **CD-06**
Takamoto, T: FR-04
Takamura, Y: **HC-07**
Takano, S: AQ-04
Takano, S: CC-15
Takeda, R: **BE-11**
Takeda, T: CG-07
Takeuchi, T: CS-02
Takeya, H: EB-03
Takhar, D: GF-10
Takhsha, M: BA-03
Takura, T: **DQ-05**
Talatchian, P: EA-07
Talmelli, G: AG-10, FD-07
Tam, D: **GB-03**
Tamura, E: GP-03
Tamura, N: EE-10
Tan, W: HQ-15
Tanabe, K: CS-02, **DR-07**, DR-16, HQ-02
Tanahashi, K: AA-07
Tanaka, D: **BP-15**
Tanaka, H: FR-02
Tanaka, H: AQ-16
Tanaka, K: EQ-01, ER-01, ER-13
Tanaka, M: BP-13, CG-07, FF-02, HE-05
Tanaka, R: BP-07
Tanaka, Y: FE-10
Tang, J: GF-08
Tang, J: AF-09
Tang, T: BD-01
Tang, W: AP-02, **EC-08**, EC-10, **HD-11**
Tang, X: **EB-02**, EB-03, EC-05, **GD-03**
Taniguchi, T: CC-05
Taniguchi, T: DD-08, DD-09, **FA-08**
Taniguchi, T: CR-04, HE-09
Taniyama, T: AR-14, HG-06
Tanksalvala, M: EG-07
Tanwar, A: FA-05
Tao, J: CC-03
Tao, Y: **DC-06**, DC-10, **EE-03**
Tao, Z: CH-02
Tarabay, N: **CS-06**
Tardieux, M: **BC-02**, FE-04
Tasaki, T: **ED-09**
Tate, J: CS-05, CS-07
Tatetsu, Y: GD-07, **HD-05**
Tatsumi, R: **HG-04**
Taue, S: AQ-01
Tavares de Sousa, C: **CD-01**
Taylor, T J.: EQ-05
Tenasini, G: EQ-16LB
Teng, Z: **EA-06**
Terada, S: DD-12
Terilli, M: HC-11
Terko, A: BG-07, DS-11
Tey, M N.: CA-07
Thakurathi, M: DB-03
Tham, K: **GR-16**
Thangavel, K: **HB-05**
Thareja, E: FG-10
Thevaruban, P: DE-10
Thomas, A: DA-04
Thomay, T: **GA-03**
Thota, S: EF-03
Thuwal, U C.: **AD-08**
Tiberto, P: **AD-12**, **DC-04**
Tijani, L: AE-04
Timalsina, R: BE-06, EG-01
Tiwari, A: HE-11
Tiwari, B: EG-01
Tobola, J: EB-07
Todaka, Y: **EG-08**
Todoli, Q: DD-07
Togawa, Y: AG-01, CC-04
Tohtake, S: EQ-06
Tojo, K: FB-01
Tokoro, F: **CF-04**, HQ-05
Tokuda, F: CC-04
Tokue, K: **GP-15**
Tokunaga, M: FE-10
Tokunaga, Y: FE-09
Tokunaga, Y: CF-10
Tokura, Y: CF-10, FE-10
Tomasello, R: HF-09
Tomita, H: AC-07
Tomita, Y: **DD-04**
Tonnerre, J: AE-07, GP-09
Tonyushkin, A: **HA-02**
Töpfer, J: **DD-06**
Torres, L: DH-10
Tournus, F: FP-13
Toyoda, S: **CF-10**
Tran, D: AF-11, BB-07, HF-07, HF-14
Tran, M: CA-04, GB-08
Tranquada, J: AF-01
Travagnin, F: DG-02
Tretiakov, O: HF-06
Treu, T: GB-07
Trillaud, F: XA-01
Trinh, Q: **CA-09**
Tsai, L: FF-01
Tsai, W: HE-03
Tsai, Y: HB-07
Tschudin, M: BC-01
Tseng, Y: FD-10
Tsipas, P: BF-11
Tsukahara, H: DD-08, **DD-09**
Tsukamoto, A: BG-02
Tsukazaki, A: FE-07
Tsunoda, M: DP-01
Tsushima, Y: CF-12
Tsymbal, E Y.: BE-06, CA-07, EG-01
Tulapurkar, A A.: FQ-04
Tulapurkar, A A.: DR-14
Tumentsereg, O: **CP-11**, **CP-14**, HD-08, **HR-04**
Turnbull, L: CB-07
Turner, J J.: **EE-13**
Turrini, A: GB-03
Tutt, F: DC-06, DC-10, **FQ-05**
Tyagi, P: **BP-12**, **HR-12**
Tyberkevych, V: DG-07
Tyson, T A.: HR-09

U

Uchida, K: CC-15, DF-09, EG-03
Uchimura, T: FE-07
Uchiyama, S: CR-14
Udvardi, L: CC-14
Ueda, K: HQ-13
Uehara, Y: FA-08
Uesugi, R: CF-12, FP-03, **GF-07**
Uhlarz, M: FE-09
Ujfalussy, B: FR-17LB
Ullerithodi, M: BD-02
Umetsu, N: CA-05, DH-05
Ung, K V.: **BD-12**
Unnikrishnan, A: AR-06
Upadhyay, A: **BE-13**
Upadhyaya, P: CA-07, HQ-16LB
Urata, A: EC-04
Urbánek, M: FB-05
Urrestarazu Larranaga, J: AG-10, FD-07
Usih, E C.: DA-04
Us-Saleheen, A: GF-05
Uzuhashi, J: DF-04, DF-08, EF-03, EG-03

V

Valenzuela, S O.: CC-05
van 't Erve, O M.: **AF-03**
Van Beek, S: FD-07
van der Laan, G: CB-03, FD-04
van Dijk, N: EE-08
van Dijke, A: FR-18LB
van Dijken, S: EG-10
Van Haren, R: GF-03, GF-10
van Kuppevelt, P: **BR-06**
van Riel, F: AQ-05LB
Vargas Paniagua, E: HA-01
Varma, Y: EC-08
Vas, J: AD-08, BC-01
Vavassori, P: GC-02
Vayalil, s K.: HE-11
Vaynzof, Y: BE-03
Vayrynen, J: AR-06
Vega, V: GE-09
Veis, M: AC-05, FQ-05
Velasco Cardenas, O A.: CR-15
Velazquez, I: DA-06
Veldman, L: AR-02
Velez, C: CS-06
Velez, S: DH-10
Venere, M: BA-02
Venugopal, A: **BD-05**, BD-09, FG-09
Vera, R: CD-04
Vera Marun, I: FF-04
Verba, R V.: FB-05
Verma, S: GG-03, **HG-07**
Verschueren, L: CA-03
Veverka, M: DC-07
Veverka, P: CS-10
Vezzoni, A: **CD-03**, HA-04
Victor, R T.: **GA-02**
Victora, R H.: **AA-01**, AA-05
Vigo, H: AR-15
Villanueva, D: BA-01
Villar, A: **GC-02**
Vilsmeier, F: **FB-07**, **HG-11**
Vinson, J: EF-13
Viola Kusminskiy, S: **GG-01**
Vir, P: CB-07
Virasawmy, S: CB-05
Virnau, P: HF-14
Vishwesh, C V.: **EQ-16LB**
Visona, A: **BA-07**
Vitos, L: DP-08
Vodungbo, B: AF-07
Voltrova, T: CS-10
Vool, U: BE-05
Vovk, N: GC-06

W
Wadati, H: **CH-04**
Wade, J: GR-05
Wadley, P: **CB-01**
Wagle, D: GG-09, **HG-09**
Wagner, M: AR-12, DG-06
Wakabayashi, K: **EP-05**
Wakamoto, M: DF-04
Walker, B: **GP-08**
Walsworth, R: BD-12
Walters, A: **AD-04**
Wan, C: AR-11, CR-03, CR-16
Wang, F: **AG-06**
Wang, H: BC-01
Wang, H: CD-04, ER-05, ER-06
Wang, H: BE-09, DE-13
Wang, H: EF-04
Wang, H: **HP-02**
Wang, H: CH-02
Wang, H: **GQ-01**
Wang, J: EG-01
Wang, J: GC-10
Wang, J: AQ-03, CS-11, DD-11
Wang, J: EC-08, HD-11
Wang, K: GF-03
Wang, L: BA-04
Wang, L: CC-03
Wang, P: FC-12, **FG-03**
Wang, Q: FB-05
Wang, Q: DA-07
Wang, S X.: HE-03
Wang, S: AE-06
Wang, S: DF-06, FP-01
Wang, T: DR-12
Wang, T: HQ-15
Wang, T: **GQ-09**
Wang, W: EF-04
Wang, X: BC-01
Wang, Y: **DE-13**
Wang, Y: **BF-07**
Wang, Y: DF-02
Wang, Z: CC-03
Wang, Z: BC-06
Wang, Z: DD-05
Wang, Z: **HC-01**
Wartelle, A: CB-09, GP-09
Watanabe, K: CC-05
Watanabe, M: FR-02
Watanabe, T: BG-01, GG-11, HR-03
Watson, S: HF-06
Watt, J: EG-01
Weck, P F.: DD-11
Wei, B: FQ-16
Wei, D: FR-19LB, GR-18LB
Wei, E: EG-02
Wei, H: FR-19LB, GR-18LB
Wei, H: CD-07
Wei, Y: CR-07, CR-11, **FD-05**
Weidenhiller, F: **AG-09**
Weigand, M: DH-11, FB-05, HF-07
Weightman, E: **BC-05**
Welp, E: DC-03
Welp, U: CE-05, EG-13
Wen, Z: DF-08, **EF-03**
Wendl, A: EB-01
Wereley, N M.: AQ-13, **EQ-13**
Werwinski, M: **HD-04**, HD-07
Westfall, C: **DS-12**, EQ-09
Whalen, M P.: **EG-09**
White, J S.: DC-11, HF-06
Wiedwald, U: **CD-02**
Wiemer, C: GF-09
Wiersma, D: AD-12
Wijesundara, C: GA-03
Wild, P: **AC-13**
Wilhelm, F: FP-13
Wilke, M: **GP-06**
Williams, J: BE-04
Winchell, A J.: **AC-11**
Winkelmann, C B.: AD-08
Winkler, A: AQ-09, CE-06
Winkler, R: FG-07
Winklhofer, M: FC-05
Wintz, S: **AD-05**, DH-11, FB-05, HF-07
Wisser, J J.: EG-07
Witanachchi, S: ED-10, EE-12
Wohlrab, S: AQ-09, CE-06
Wojewoda, O: **BR-04**, DG-11, **FB-05**, HC-10
Wolff, S: FC-07
Wolter, A: EP-07
Wongjom, P: BP-11
Woo, S: CQ-13, HP-06, **HP-10**
Woodcock, J: FC-04
Wostyn, K: CA-03
Wrona, J: CR-13
Wu, A: GC-06, **GQ-02**
Wu, D: GQ-11
Wu, H: FE-06
Wu, J: **GR-04**
Wu, K: CD-04, ER-02, **ER-05**, **ER-06**, **FC-01**
Wu, L: HC-11
Wu, M: GR-18LB
Wu, M: AQ-09, CE-06, DP-04, **GF-08**, GF-10
Wu, P: **AE-06**
Wu, P: DA-05
Wu, R: **FR-11**
Wu, T: **EQ-02**, **HA-07**, HQ-03
Wu, W: CH-06
Wu, X: BA-02

Wu, Y: GA-08
Wu, Y: CF-05

X
Xiao, E: DE-03
Xiao, F: BE-09, DE-13, DP-11
Xiao, G: DF-04
Xiao, J: **CQ-12**
Xiao, J Q.: CH-06, EG-09, GG-09
Xiao, R: **BB-06**
Xiao, T P.: **DA-06**
Xiao, X: **CH-02**
Xiao, X: GC-05
Xiao, Z: EA-06
Xie, Y: CF-05
Xie, Z: EE-10
Xie, Z: BB-06
Xing, Z: GQ-09
Xiong, J: AB-03
Xiong, S: **CR-03**, CR-16
Xiong, Z: **HG-10**
Xu, B: **AB-05**
Xu, B: EG-03
Xu, C: ER-02, ER-05, ER-06
Xu, J: HQ-12
Xu, J: CC-03
Xu, Y: GA-02
Xu, Y: CR-16
Xu, Y: CA-08
Xue, F: **AF-12**

Y
Yabukami, S: **AQ-10**, CD-06, DE-05, **EQ-06**, ER-11, ER-12
Yabushita, K: EF-02
Yactayo, M S.: AG-13
Yadav, P: DR-01LB
Yadav, R S.: AG-12, CR-12
Yadav, R: **FF-09**
Yadav, S: **GP-01**
Yadav, V: AG-12, **CR-12**
Yadav, V: **CH-08**
Yagi, T: EG-03
Yagmur, A: DR-02
Yakushiji, K: CR-04, HE-09
Yamada, K: AG-01, **CC-04**
Yamada, K: AQ-15
Yamada, K: **BR-03**, FP-07
Yamada, K T.: AF-06, BP-01
Yamada, R: DB-02, FE-10
Yamada, T: BC-08
Yamada, Y: AC-07
Yamaguchi, M: AQ-10
Yamaguchi, N: GQ-07
Yamaguchi, T: CP-04
Yamaguchi, Y: **HQ-13**
Yamaguchi, Y: **ER-01**
Yamahara, H: EQ-15LB
Yamamoto, D: **EF-10**, FR-15, FR-16, GP-15
Yamamoto, H: AP-10, **AP-11**, CP-03
Yamamoto, M: CG-03
Yamamoto, R: CB-07
Yamamoto, T: CR-04, DF-07, HE-09
Yamamoto, Y: AC-07
Yamamuro, S: **CS-09**
Yamane, I: CE-04
Yamane, T: **FR-16**
Yamane, Y: BF-03
Yamanoi, K: AR-01, **BP-16LB**, DR-09
Yamasaki, Y: GQ-10
Yamashita, K: HF-01
Yamashita, N: **HQ-12**
Yamashita, Y: EG-03
Yamazaki, T: AB-09
Yan, B: **GA-04**
Yan, L: HQ-12
Yan, Y: GQ-01
Yan, Z: DG-07
Yanagi, N: **XA-01**
Yanagihara, H: DR-08, GQ-10
Yanase, Y: CF-01
Yanes, R: DH-10
Yang, B: GQ-11
Yang, B: **FQ-03**
Yang, C: AC-08, **AC-09**, AE-06, BR-02, CF-11
Yang, J: CD-04
Yang, J A.: HE-03
Yang, J: BC-01, CC-01
Yang, J: BQ-11, CQ-07, CQ-14
Yang, K: BQ-13
Yang, M: **BR-02**, **CF-11**
Yang, M: **DP-06**
Yang, P: BB-06
Yang, Q: DP-06
Yang, S: BR-11
Yang, S: AR-09, **HF-11**
Yang, W: AF-11
Yang, W: GE-10
Yang, X: FF-13, HF-12
Yang, X: HA-08
Yang, X: **HQ-10LB**
Yang, Z: CR-08
Yang, Z: CR-08
Yao, J: CE-06
Yao, T: HR-10
Yao, Y: BE-06
Yao, Y: HQ-03
Yao, Y: EA-06, EA-08
Yasuda, T: HQ-14
Yasufuku, H: DF-08
Yasui, Y: **FQ-09**, FR-05, FR-12, FR-14
Yazdi, S: CB-08
Ye, F: DS-04
Ye, G: CC-06, FR-20LB
Ye, H: HA-04
Ye, L: FA-05
Ye, L: EQ-02, HA-07, **HQ-03**
Yildiz, E: CE-01, DE-04
Yin, G: AD-02, AD-03, DC-08, EF-12, GD-12
Yin, H: **DE-02**
Yitamben, E: **BD-06**
Yochelis, S: HE-10
Yoda, H: **CA-01**
Yokouchi, T: **HB-03**
Yonezawa, S: AE-02
Yoo, J: GE-03
Yoo, J: EP-10
Yoo, M: CG-05, **FG-07**
Yoon, S: **DS-09**, DS-10
Yoon, S: **AQ-11**
Yoon, S: **BQ-11**, BQ-12, CQ-16, HP-04
Yoon, Y: BQ-11, BQ-12, CQ-08, **CQ-16**, HP-04
Yoosuf, R: FP-10
Yoshida, A: BD-11, EF-02
Yoshida, S: VP-02
Yoshidome, T: CE-04
Yoshii, S: BR-14, **FB-06**
Yoshikawa, H: BG-02
Yoshikawa, M: **CA-05**, DH-05
Yoshimi, Y: EC-03
Yoshinaga, N: FD-08
Yoshioka, S: DF-07
You, C: AR-05, BP-09, DS-07, HQ-07
You, W: CG-05
Yousuf, S: BC-03
Yu, C: CC-01
Yu, G: CR-16
Yu, H: BQ-11, **BQ-12**, CQ-16, HP-04
Yu, J: EQ-12
Yu, K: BQ-03, CQ-02, CQ-06, CQ-07, **CQ-11**, DQ-01, DQ-02, HP-07, HP-08
Yu, X: BB-06
YU, T: CR-08
Yuan, H: **GA-08**
Yuan, J: BE-09, DE-13, **DP-11**, DP-16, DQ-04, EP-08
Yuan, L: CA-07
Yuasa, H: AQ-02, BP-06, BP-15, **HF-01**
Yuasa, S: CR-04, FF-05, HE-09
Yun, H: GQ-04

Z
Zaidi, N: AR-06
Zajac, M: FP-08
Zaliznyak, I: AF-01
Zang, J: **AB-02**, ED-02
Zarubin, S: DF-03
Zatko, V: CC-05
Zborowski, M: AE-04
Zeer, M: BB-07
Zelezny, J: **BF-09**
Zemen, J: GE-07
Zeng, H: AB-03, **CC-02**
Zeng, K: GD-12
Zeng, M: CD-04
Zeng, Z: HC-04
Zeng, Z: DC-08
Zeni Cunha, L: **FR-18LB**
Zenkevich, A: DF-03
Zhang, C: **DS-05**, **DS-06**
Zhang, C: DF-02, **DR-13**
Zhang, E: CD-03, **HA-04**
Zhang, G: **GC-10**
Zhang, H: **EA-07**
Zhang, H: EA-06, EA-08
Zhang, J: FQ-15, HC-01
Zhang, L: HF-01
Zhang, M: **BE-09**
Zhang, M: AP-05
Zhang, P: AB-03
Zhang, P: BF-05, FF-03
Zhang, Q: BB-06
Zhang, R: CC-03
Zhang, S: CH-02
Zhang, S: CR-08
Zhang, S: GF-08
Zhang, T: **AR-11**
Zhang, W: GC-09
Zhang, X: CC-03
Zhang, X: DC-08, GD-12
Zhang, X: DG-07
Zhang, Y: DC-06, DC-10
Zhang, Y: ED-02
Zhang, Y: EA-06, EA-08
Zhang, Y: EQ-16LB
Zhang, Y: DR-12
Zhang, Y: CC-03
Zhang, Y: **HA-08**
Zhang, Z: CA-08
Zhang, Z: GQ-02, **HR-02**
Zhang, Z: DP-16
Zhang, Z: HG-05, **HR-05**
Zhao, F: EQ-12
Zhao, L: **HR-07**, HR-16
Zhao, T: BB-06
Zhao, W: EA-06, EA-08
Zhao, Y: EA-06
Zhao, Y: HC-04
Zheng, S: CR-08
Zheng, T: **EG-06**
Zheng, T: **GC-05**
Zheng, X: EC-13
Zheng, Z: BB-06
Zhou, F: EF-04
Zhou, G: DP-06
Zhou, H: DE-13, DP-11, DP-16, DQ-04, EP-08
Zhou, L: FQ-16, FR-20LB
Zhou, T: CE-06
Zhou, X: FE-06
Zhou, Z: BF-01
Zhu, H: **CR-08**
Zhu, J: BD-07, **BD-08**, BD-10, EG-06
Zhu, J: CR-08
Zhu, T: CE-02, **HA-09**
Zhu, T: CC-03
Zhu, X: HR-10
Zhu, X: HP-02
Zhu, Y: GQ-01
Zhukov, A: CP-01, **DD-13**, **EP-03**
Zhukova, V: **CP-01**, DD-13, EP-03
Zhurkin, V: DF-03
Zink, B L.: BP-05LB
Zogbi, N: **BF-04**, CA-07, DA-06, **FD-03**
Zohar, J: FD-04
Zoshki, A: BC-13
Zou, J: CB-08
Zuehlsdorff, T: AC-11
Zuo, J: **AP-05**
Zuo, J: HR-05
Zuo, L: HR-06
Zutic, I: AB-03